supporting partners

The 46th International Congress on Science, Technology and Technology-based Innovation

"POWER OF SCIENCE TO ACHIEVE SDGs"

STT46
Oct 5-7, 2020

~ABSTRACT & PROCEEDING BOOK~

ทรงพระเจริญ

ABSTRACT & PROCEEDING BOOK

The 46th International Congress on Science, Technology and Technology-based Innovation (STT46)

Power of Science to Achieve SDGs

October 5th-7th, 2020
Ramkhamhaeng University,
Bangkok, Thailand

Organized by:
The Science Society of Thailand under the Patronage of His Majesty the King
in Association with
Faculty of Science,
Ramkhamhaeng University

The 46th International Congress on Science, Technology and Technology-based Innovation (STT46)

Published by:
The Science Society of Thailand Under the Patronage of His Majesty the King
Faculty of Science, Ramkhamhaeng University
Published date October 2020 (available in PDF version only)

CONTENT

WELCOME MESSAGE FROM THE PRESIDENT OF THE SCIENCE SOCIETY OF THAILAND UNDER THE PATRONAGE OF HIS MAJESTY THE KING

2020 marks the 72nd Anniversary of the Science Society of Thailand under the Patronage of His Majesty the King. To celebrate this special occasion, on behalf of the Science Society of Thailand, I am proud to announce "The 46th International Congress on Science, Technology and Technology-based Innovation", or STT46, to be held during October 5-7, 2020 in Bangkok, Thailand. It is our annual congress, which originally was the national meeting since 1971, but this year, it is its first time to be held as the international meeting.

In addition, we believe in rewarding undergraduate students for passion and innovation early in their academic career, to encourage them to continue their work through postgraduate study or employment. Accordingly, the Science Society of Thailand is very pleased to initiate the Young Rising Stars of Science award program for the recognition of their excellent senior projects in each science and science-related curricula of all universities in Thailand. These students will present their work in the STT46, where they will meet the experts, learn more about work taking place outside their fields, and consider the path they wish to take in their bright future.

These two main activities are not only a milestone for Science Society of Thailand, but also a testimony to our science community that if we take care of science, science will take care of us.

In this spectacular year, we are honor to have Faculty of Science, Ramkhamhaeng University as our co-host of STT46. The theme of STT46 is, “The Power of Science to Achieve the SDGs”, which is timely and vitally important for a better future of humankinds and nature. That is why we aim to bring together students, academia, researchers and scholars to exchange information and ideas, as well as share experiences and research results about all aspects of specialized and interdisciplinary fields. The event will provide all not only to network regionally and worldwide, but also will lead to further working together to find solutions that are sustainable and beneficial to all life on earth.

The STT46 is designed to explore various applications in science and science-related fields, and so the congress program will be both exciting and ground-breaking in its wide-ranging and multidisciplinary content.

I cordially invite you all, particularly those interested in any aspect of sustainable development to contribute and help shape the STT46 through submissions of your research abstracts and presentations at the congress. Join us for three intensive and interesting days of discussing contemporary scientific and science-related research.

Thank you.

Professor Dr. Supawan Tantayanon

President, the Science Society of Thailand Under the Patronage of His Majesty the King

WELCOME MESSAGE FROM THE CHAIRPERSON OF THE 46TH INTERNATIONAL CONGRESS ON SCIENCE, TECHNOLOGY AND TECHNOLOGY–BASED INNOVATION

The Science Society of Thailand under the Patronage of His Majesty the King is pleased to invite you to join the 46th International Congress on Science, Technology and Technology-based Innovation (STT46), which will be held at Ramkhamhaeng University, during October 5-7, 2020. The opening ceremony will be graciously presided over by Her Royal Highness Princess Maha Chakri Sirindhorn on 5th October, at 9 am.

International Congress on Science, Technology and Technology-based Innovation (STT) is one of the largest annual international scientific meeting with around one thousand local and oversea participants. The aim is to create scientific forum for national and international scientists and technologists as well as young Thai scientists from diversified fields of science and technology and to open an opportunity to share and exchange their experiences. In this year, there are 5 main sessions including

- Biological Sciences “Impact of Biological Science towards SDGs”
- Chemical Sciences “Responsible Chemical Sciences for Future Sustainability”
- Mathematics, Statistical science and Computer science “Math Stat Comp in the Digitally Innovative Era”
- Physics “Challenges in the Frontiers of Physics”
- Technology-based Innovation “Innovations for sustainable future”

There are also 16 symposiums such as 360° COVID-19; Crystallography; Development of Material Science Based on Coordination Compounds; Green and Sustainable Chemistry: Opportunities for Academia and Industry; Green Production Platform for Renewable Biomass Conversion included in this event.

The Congress is highlighted by the Plenary Lecture from the world reputable scientist and the Honorable Lecture from the 2020 Outstanding Scientist(s) of Thailand. And during the Congress, lectures from several renowned invited speakers, and hundreds of contributed papers from various areas of Science and Technology will be presented orally or in the form of posters. Exhibition on advanced scientific and technological knowledge or instruments/appliances from various organizations and several suppliers will be displayed.

Looking forward to welcoming you in this STT46 Congress in October 5-7, 2020.

Professor Dr. Somkiat Ngamprasertsith

Chairperson STT46

WELCOME MESSAGE FROM THE HOST OF THE 46TH INTERNATIONAL CONGRESS ON SCIENCE, TECHNOLOGY AND TECHNOLOGY–BASED INNOVATION

On behalf of the Faculty of Science, Ramkhamhaeng University, it is our great pleasure to welcome you to the 46th International Congress on Science, Technology and Technology – based Innovation (STT46) being held in Bangkok, Thailand during October 5-7, 2020 to celebrate the 46th anniversary of the Faculty of Science, Ramkhamhaeng University. The 46th International Congress on Science, Technology and Technology–based Innovation (STT46) is one of the International Congress on Science and Technology in Thailand with around a thousand participants from local and overseas. With the theme of "Power of Science to Achieve SDGs", the congress aims to build up a platform for sharing and exchange the knowledge and experiences among national and international expertise scientists and technologists, as well as, the young scientists in various fields of Science, Technology and Technology–based Innovation.

On the auspicious occasion for the 46th anniversary of Faculty of Science establishment, we are honored to host the 46th International Congress on Science, Technology and Technology–based Innovation (STT46) together with the Science Society of Thailand under the Patronage of His Majesty the King. In this congress, we are honored to have the world reputable scientist as the keynote speaker. In addition, Thailand Outstanding Scientists, and numerous eminent scientists will present and share their latest research. As for the accomplishment of the congress, we would like to cordially thank our sponsors, advisory boards, invited speakers, reviewers, authors, and all participants. We sincerely hope that the presentations and discussions during the congress will lead to further academic development and fruitful collaboration in this region and worldwide.

Associate Professor Dr.Wanna Musig

Dean of Faculty of Science, Ramkhamhaeng University

HISTORY OF THE CONGRESS ON SCIENCE AND TECHNOLOGY OF THAILAND

International Congress on Science, Technology and Technology- based Innovation (STT) , originally named " The Congress on Science and Technology of Thailand" with the same abbreviation of STT, is one of the most important scientific meetings in Thailand. It was firstly organized in 1974 by the Science Society of Thailand (SST) and Chulalongkorn University. Since then, the alternative Universities in Thailand have gone through the bidding for co-organizing the STT in the following years. It is the annual national congress for 45 years. To mark the 72nd Anniversary of the Science Society of Thailand in 2020, the congress has been changed to the international meeting.

The aim is to create scientific forum for national and international scientists and technologists as well as young Thai scientists from diversified fields of science and technology to meet and to provide them the opportunity to share and exchange their knowledge and experiences. It is our annual congress, which originally was the national meeting since 1971, but this year, it is its first time to be held as the international meeting.

Typically, the Congress Plenary Lecture is given by a Nobel Laureate in Science and Technology, followed by an honorable lecture of the Outstanding Scientist of Thailand in that particular year. During the Congress, lectures by several renowned invited speakers, panel discussions and hundreds of contributed papers from various areas of Science and Technology are presented orally or in the form of posters. In addition, the outstanding teacher awards, the young scientist awards, as well as the innovation awards and the national winners of high school student science projects are awarded in the Congress. An exhibition of advanced scientific and technological instruments and appliances from suppliers and enterprises are also the attractive event of the Congress.

ครั้งที่ ปี / วันที่ เดือน	ชื่อการประชุม	สถาบันเจ้าภาพร่วม	ประธาน (จำนวนผลงานวิจัย)	ประธานในพิธีเปิด
1. พ.ศ. 2514 26-27 พฤศจิกายน	การวิจัยทางวิทยาศาสตร์ กรุงเทพฯ 2514	คณะวิทยาศาสตร์ จุฬาลงกรณ์มหาวิทยาลัย	ศ.ดร.ประชุมสุข อาชวอำรุง (83 เรื่อง)	-
2. พ.ศ. 2516 30 พฤศจิกายน - 2 ธันวาคม	การวิจัยทางวิทยาศาสตร์ กรุงเทพฯ 2516	คณะวิทยาศาสตร์ จุฬาลงกรณ์มหาวิทยาลัย	ศ.ดร.ประชุมสุข อาชวอำรุง (219 เรื่อง)	-
3. พ.ศ. 2518 12-13 ธันวาคม	การวิจัยทางวิทยาศาสตร์ กรุงเทพฯ 2518	คณะวิทยาศาสตร์ คณะแพทยศาสตร์ มหาวิทยาลัยมหิดล	ศ.ดร.กำจร มนูญปิจุ (249 เรื่อง)	-
4. พ.ศ. 2520 16-17 ธันวาคม	การวิจัยทางวิทยาศาสตร์ กรุงเทพฯ 2520	คณะวิทยาศาสตร์ จุฬาลงกรณ์มหาวิทยาลัย	รศ.ดร.กำจัด มงคลกุล (344 เรื่อง)	-
5. พ.ศ. 2521 22-24 ธันวาคม	วิทยาศาสตร์และเทคโนโลยี เพื่อการพัฒนาภาคเหนือ	คณะวิทยาศาสตร์ มหาวิทยาลัยเชียงใหม่	ศ.ดร.พรชัย มาตังคสมบัติ (232 เรื่อง)	-
6. พ.ศ. 2522 21-23 ธันวาคม	วิทยาศาสตร์และเทคโนโลยี เพื่อการพัฒนาประเทศ	คณะวิทยาศาสตร์ มหาวิทยาลัยศรีนครินทรวิโรฒ บางแสน	ศ.ดร.พรชัย มาตังคสมบัติ (232 เรื่อง)	-
7. พ.ศ. 2523 4-6 ธันวาคม	วิทยาศาสตร์และเทคโนโลยี เพื่อการพัฒนาประเทศ	คณะวิทยาศาสตร์ คณะแพทยศาสตร์ มหาวิทยาลัยมหิดล	รศ.ดร.นัยพินิจ คชภักดี (233 เรื่อง)	สมเด็จพระเจ้าลูกเธอเจ้าฟ้าจุฬาภรณวลัยลักษณ์
8. พ.ศ. 2525 28-30 ตุลาคม	วิทยาศาสตร์และเทคโนโลยี เพื่อการพัฒนาประเทศ	คณะวิทยาศาสตร์ จุฬาลงกรณ์มหาวิทยาลัย	รศ.ดร.สัณห์ พณิชยกุล (245 เรื่อง)	-

ครั้งที่ ปี / วันที่ เดือน	ชื่อการประชุม	สถาบันเจ้าภาพร่วม	ประธาน (จำนวนผลงานวิจัย)	ประธานในพิธีเปิด
9. พ.ศ. 2526 27-29 ตุลาคม	วิทยาศาสตร์และเทคโนโลยีเพื่อการพัฒนาภาคตะวันออกเฉียงเหนือ	คณะวิทยาศาสตร์ มหาวิทยาลัยขอนแก่น	รศ.ดร.สัณห์ พณิชยกุล (174 เรื่อง)	รัฐมนตรีว่าการกระทรวงวิทยาศาสตร์เทคโนโลยีและการพลังงาน (ฯพณฯ ดำรง ลัทธพิพัฒน์)
10. พ.ศ. 2527 25-27 ตุลาคม	วิทยาศาสตร์และเทคโนโลยีแห่งประเทศไทย	คณะวิทยาศาสตร์ มหาวิทยาลัยเชียงใหม่	ศ.ดร.มนตรี จุฬาวัฒนทล (280 เรื่อง)	นายกรัฐมนตรี (พลเอก เปรม ติณสูลานนท์)
11. พ.ศ. 2528 24-26 ตุลาคม	วิทยาศาสตร์และเทคโนโลยีแห่งประเทศไทย	คณะวิทยาศาสตร์ มหาวิทยาลัยเกษตรศาสตร์	ศ.ดร.มนตรี จุฬาวัฒนทล (251 เรื่อง)	สมเด็จพระเจ้าลูกเธอเจ้าฟ้าจุฬาภรณวลัยลักษณ์
12. พ.ศ. 2529 20-22 ตุลาคม	วิทยาศาสตร์และเทคโนโลยีแห่งประเทศไทย	คณะวิทยาศาสตร์ มหาวิทยาลัยศรีนครินทรวิโรฒ ประสานมิตร	รศ.ดร.ภิญโญ พานิชพันธ์ (277 เรื่อง)	สมเด็จพระบรมโอรสาธิราชฯ สยามมกุฎราชกุมาร
13. พ.ศ. 2530 20-22 ตุลาคม	วิทยาศาสตร์และเทคโนโลยีแห่งประเทศไทย	คณะวิทยาศาสตร์ มหาวิทยาลัยสงขลานครินทร์ วิทยาเขตหาดใหญ่	รศ.ดร.ภิญโญ พานิชพันธ์ (420 เรื่อง)	สมเด็จพระเจ้าลูกเธอเจ้าฟ้าจุฬาภรณวลัยลักษณ์
14. พ.ศ. 2531 19-21 ตุลาคม	วิทยาศาสตร์และเทคโนโลยีแห่งประเทศไทย	คณะวิทยาศาสตร์ จุฬาลงกรณ์มหาวิทยาลัย	ศ.ดร.จริยา บรอดเคลแมน (259 เรื่อง)	นายกรัฐมนตรี (พลเอกชาติชาย ชุณหะวัณ)
15. พ.ศ. 2532 18-20 ตุลาคม	วิทยาศาสตร์และเทคโนโลยี เพื่อการพัฒนาทรัพยากรภาคเหนือ	คณะวิทยาศาสตร์ มหาวิทยาลัยเชียงใหม่	ศ.ดร.จริยา บรอดเคลแมน (394 เรื่อง)	ผู้แทนสมเด็จพระเจ้าลูกเธอเจ้าฟ้าจุฬาภรณวลัยลักษณ์
16. พ.ศ. 2533 25-27 ตุลาคม	วิทยาศาสตร์และเทคโนโลยีเพื่อการพัฒนาประเทศ	คณะวิทยาศาสตร์ สถาบันเทคโนโลยีพระจอมเกล้า เจ้าคุณทหารลาดกระบัง	ศ.ดร.วิชัย ริ้วตระกูล (369 เรื่อง)	-
17. พ.ศ. 2534 24-26 ตุลาคม	วิทยาศาสตร์และเทคโนโลยีเพื่อการพัฒนาทรัพยากรภาคเหนือ	คณะวิทยาศาสตร์ มหาวิทยาลัยขอนแก่น	ศ.ดร.วิชัย ริ้วตระกูล (349 เรื่อง)	-
18. พ.ศ. 2535 27-29 ตุลาคม	วิทยาศาสตร์และเทคโนโลยีเพื่อการพัฒนาประเทศ	คณะวิทยาศาสตร์ มหาวิทยาลัยเกษตรศาสตร์ ณ ศูนย์การประชุมแห่งชาติสิริกิติ์	ศ.ดร.สุชาติ อุปถัมภ์ (297 เรื่อง)	-
19. พ.ศ. 2536 27-29 ตุลาคม	วิทยาศาสตร์และเทคโนโลยีเพื่อการพัฒนาชายฝั่ง	คณะวิทยาศาสตร์ มหาวิทยาลัยสงขลานครินทร์ ณ โรงแรมดุสิต เจ.บี.หาดใหญ่	ศ.ดร.สุชาติ อุปถัมภ์ (438 เรื่อง)	-
20. พ.ศ. 2537 19-21 ตุลาคม	วิทยาศาสตร์และเทคโนโลยี เพื่อการพัฒนาเศรษฐกิจ สังคม และสิ่งแวดล้อม	คณะวิทยาศาสตร์และเทคโนโลยี มหาวิทยาลัยธรรมศาสตร์ ณ เซ็นทรัลพลาซ่า	ศ.ดร.สมศักดิ์ พันธุวัฒนา (252 เรื่อง)	นายกรัฐมนตรี (นายชวน หลีกภัย)
21. พ.ศ. 2538 25-27 ตุลาคม	วิทยาศาสตร์และเทคโนโลยีเพื่อการพัฒนาอุตสาหกรรม	คณะวิทยาศาสตร์ มหาวิทยาลัยบูรพา ณ โรงแรมแอมบาสซาเอร์ซิตี้ จอมเทียน ชลบุรี	ศ.ดร.สมศักดิ์ พันธุวัฒนา (354 เรื่อง)	นายกสภามหาวิทยาลัยบูรพา (นายเกษม จาติกวณิช)
22. พ.ศ. 2539 16-18 ตุลาคม	วิทยาศาสตร์และเทคโนโลยีเพื่อพัฒนาทรัพยากรมนุษย์	คณะวิทยาศาสตร์ มหาวิทยาลัยรามคำแหง ณ บางกอกคอนเวนชั่นเซ็นเตอร์ เซ็นทรัลพลาซา ลาดพร้าว	รศ.ดร.พิณทิพ รื่นวงษา (333 เรื่อง)	ผู้ว่าราชการกรุงเทพมหานคร (ดร.พิจิตต รัตตกุล)
23. พ.ศ. 2540 20-22 ตุลาคม	วิทยาศาสตร์และเทคโนโลยีเพื่อพัฒนาคุณภาพชีวิตในภูมิภาค	คณะวิทยาศาสตร์ มหาวิทยาลัยเชียงใหม่ ณ โรงแรมโลตัส ปางสวนแก้ว	รศ.ดร.พิณทิพ รื่นวงษา (495 เรื่อง)	รัฐมนตรีว่าการกระทรวงวิทยาศาสตร์เทคโนโลยีและสิ่งแวดล้อม (นายยิ่งพันธ์ มนะสิการ)
24. พ.ศ. 2541 19-21 ตุลาคม	วิทยาศาสตร์และเทคโนโลยีเพื่อการพัฒนาเศรษฐกิจที่มั่นคง	คณะวิทยาศาสตร์ มหาวิทยาลัยมหิดล ณ ศูนย์การประชุมแห่งชาติสิริกิติ์	ผศ.ดร.ทิพาพร ลิมปเสนีย์ (463 เรื่อง)	นายกรัฐมนตรี (นายชวน หลีกภัย)
25. พ.ศ. 2542 20-22 ตุลาคม	วิทยาศาสตร์และเทคโนโลยี เพื่อการพัฒนาทรัพยากรท้องถิ่น	คณะวิทยาศาสตร์ มหาวิทยาลัยนเรศวร ณ โรงแรมอมรินทร์ลากูน พิษณุโลก	ผศ.ดร.ทิพาพร ลิมปเสนีย์ (581 เรื่อง)	รัฐมนตรีว่าการกระทรวงวิทยาศาสตร์เทคโนโลยีและสิ่งแวดล้อม (ดร.อาทิตย์ อุไรรัตน์)
26. พ.ศ. 2543 18-20 ตุลาคม	วิทยาศาสตร์และเทคโนโลยีสู่สหัสวรรษใหม่	คณะวิทยาศาสตร์ จุฬาลงกรณ์มหาวิทยาลัย ณ ศูนย์การประชุมแห่งชาติสิริกิติ์	รศ.ดร.ศุภวรรณ ตันตยานนท์ (739 เรื่อง)	-
27. พ.ศ. 2544 16-18 ตุลาคม	วิทยาศาสตร์และเทคโนโลยีเพื่อการฟื้นฟูเศรษฐกิจไทย	มหาวิทยาลัยสงขลานครินทร์ โรงแรม ลี การ์เดนส์ พลาซ่า	รศ.ดร.ศุภวรรณ ตันตยานนท์ (921 เรื่อง)	ผู้ว่าราชการจังหวัดสงขลา
28. พ.ศ. 2545 24-26 ตุลาคม	วิทยาศาสตร์และเทคโนโลยีเพื่อการพัฒนาเศรษฐกิจที่ยั่งยืน	คณะวิทยาศาสตร์ประยุกต์ สถาบันเทคโนโลยีพระจอมเกล้าพระนครเหนือ ณ ศูนย์การประชุมแห่งชาติสิริกิติ์	รศ.ดร.สุรินทร์ เหล่าสุขสถิตย์ (834 เรื่อง)	สมเด็จพระเจ้าพี่นางเธอเจ้าฟ้ากัลยาณิวัฒนา กรมหลวงนราธิวาสราชนครินทร์
29. พ.ศ. 2546 20-22 ตุลาคม	วิทยาศาสตร์และเทคโนโลยีเพื่อการพัฒนาท้องถิ่น	คณะวิทยาศาสตร์ มหาวิทยาลัยขอนแก่น ณ ศูนย์ประชุมอเนกประสงค์กาญจนาภิเษก	รศ.ดร.สุรินทร์ เหล่าสุขสถิตย์ (1039 เรื่อง)	รองนายกรัฐมนตรี (นายสุวิทย์ คุณกิตติ)

ครั้งที่ ปี / วันที่ เดือน	ชื่อการประชุม	สถาบันเจ้าภาพร่วม	ประธาน (จำนวนผลงานวิจัย)	ประธานในพิธีเปิด
30. พ.ศ. 2547 19-21 ตุลาคม	วิทยาศาสตร์และเทคโนโลยีเพื่อสังคมและเศรษฐกิจฐานความรู้	คณะวิทยาศาสตร์ มหาวิทยาลัยศรีนครินทรวิโรฒ ณ ศูนย์แสดงสินค้าและการประชุมอิมแพ็ค เมืองทองธานี	รศ.ดร.สุรินทร์ เหล่าสุขสถิตย์ (854 เรื่อง)	สมเด็จพระเทพรัตนราชสุดา ฯ สยามบรมราชกุมารี
31. พ.ศ. 2548 18-20 ตุลาคม	วิทยาศาสตร์และเทคโนโลยีเพื่อการพัฒนาที่ยั่งยืน	เทคโนธานี มหาวิทยาลัยเทคโนโลยีสุรนารี	รศ.ดร.สุรินทร์ เหล่าสุขสถิตย์ (1021 เรื่อง)	สมเด็จพระเทพรัตนราชสุดา ฯ สยามบรมราชกุมารี
32. พ.ศ. 2549 10-12 ตุลาคม	วิทยาศาสตร์และเทคโนโลยีเพื่อการเศรษฐกิจพอเพียง เฉลิมฉลองการครองสิริราชสมบัติ ครบ 60 ปี ของพระบาทสมเด็จพระเจ้าอยู่หัว	คณะวิทยาศาสตร์ จุฬาลงกรณ์มหาวิทยาลัย ศูนย์การประชุมแห่งชาติสิริกิติ์	รศ.ดร.นภาวรรณ นพรัตนราภรณ์ (927 เรื่อง)	สมเด็จพระเทพรัตนราชสุดา ฯ สยามบรมราชกุมารี
33. พ.ศ. 2550 18-20 ตุลาคม	วิทยาศาสตร์และเทคโนโลยีเพื่อโลกยั่งยืน เฉลิมฉลองมหามงคลเฉลิมพระชนมพรรษาครบ 80 พรรษาของพระบาทสมเด็จพระเจ้าอยู่หัว	มหาวิทยาลัยวลัยลักษณ์ จังหวัดนครศรีธรรมราช	รศ.ดร.นภาวรรณ นพรัตนราภรณ์ (802 เรื่อง)	สมเด็จพระเทพรัตนราชสุดา ฯ สยามบรมราชกุมารี
34. พ.ศ. 2551 31 ตุลาคม - 2 พฤศจิกายน	วิทยาศาสตร์และเทคโนโลยีสำหรับโลกแห่งความท้าทาย	คณะวิทยาศาสตร์ สถาบันเทคโนโลยีพระจอมเกล้าเจ้าคุณทหารลาดกระบัง	รศ.ดร.นภาวรรณ นพรัตนราภรณ์ (777 เรื่อง)	สมเด็จพระเทพรัตนราชสุดา ฯ สยามบรมราชกุมารี
35. พ.ศ. 2552 15-17 ตุลาคม	วิทยาศาสตร์และเทคโนโลยีเพื่ออนาคตที่ดีขึ้น	คณะวิทยาศาสตร์ มหาวิทยาลัยบูรพา	รศ.ดร.นภาวรรณ นพรัตนราภรณ์ (854 เรื่อง)	ฯพณฯ องคมนตรี นายอำพล เสนาณรงค์
36. พ.ศ. 2553 26-28 ตุลาคม	วิทยาศาสตร์และเทคโนโลยีเพื่อสังคมที่ดีขึ้น	คณะวิทยาศาสตร์และเทคโนโลยี มหาวิทยาลัยธรรมศาสตร์	รศ.ดร.ธารารัตน์ ศุภศิริ (582 เรื่อง)	สมเด็จพระเทพรัตนราชสุดา ฯ สยามบรมราชกุมารี
37. พ.ศ. 2554 10-12 ตุลาคม	วิทยาศาสตร์สร้างสรรค์ เพื่อสรรค์สร้างอนาคต	คณะวิทยาศาสตร์ มหาวิทยาลัยมหิดล	รศ.ดร.ธารารัตน์ ศุภศิริ (699 เรื่อง)	สมเด็จพระเทพรัตนราชสุดา ฯ สยามบรมราชกุมารี
38. พ.ศ. 2555 17-19 ตุลาคม	วิทยาศาสตร์เพื่ออนาคตของมวลมนุษยชาติ	คณะวิทยาศาสตร์ มหาวิทยาลัยเชียงใหม่	รศ.ดร.ธารารัตน์ ศุภศิริ (690 เรื่อง)	สมเด็จพระเทพรัตนราชสุดา ฯ สยามบรมราชกุมารี
39. พ.ศ. 2556 21-23 ตุลาคม	นวัตกรรมวิทยาศาสตร์ เพื่อชีวิตที่ดีขึ้น	คณะวิทยาศาสตร์ มหาวิทยาลัยเทคโนโลยีพระจอมเกล้าธนบุรี	รศ.ดร.ธารารัตน์ ศุภศิริ (495 เรื่อง)	สมเด็จพระเทพรัตนราชสุดา ฯ สยามบรมราชกุมารี
40. พ.ศ. 2557 2-4 ธันวาคม	วิทยาศาสตร์และเทคโนโลยีสู่วิถีพัฒนาอาเซียน	คณะวิทยาศาสตร์ มหาวิทยาลัยขอนแก่น	ศ.ดร. เปี่ยมสุข พงษ์สวัสดิ์ (543 เรื่อง)	สมเด็จพระเทพรัตนราชสุดา ฯ สยามบรมราชกุมารี
41. พ.ศ. 2558 6-8 พฤศจิกายน	ประตูสู่อาเซียนด้วยวิทยาศาสตร์และเทคโนโลยี	มหาวิทยาลัยเทคโนโลยีสุรนารี	ศ.ดร. เปี่ยมสุข พงษ์สวัสดิ์ (384 เรื่อง)	สมเด็จพระเทพรัตนราชสุดา ฯ สยามบรมราชกุมารี
42. พ.ศ. 2559 30 พฤศจิกายน – 2 ธันวาคม	ศาสตร์แห่งแผ่นดิน สู่นวัตกรรมเพื่ออนาคตที่ยั่งยืน	คณะวิทยาศาสตร์ มหาวิทยาลัยเกษตรศาสตร์ ณ เซ็นทาราแกรนด์ แอท เซ็นทรัลพลาซา ลาดพร้าว	ศ.ดร. เปี่ยมสุข พงษ์สวัสดิ์ (290 เรื่อง)	สมเด็จพระเทพรัตนราชสุดา ฯ สยามบรมราชกุมารี
43. พ.ศ. 2560 17-19 ตุลาคม	เข้าใจวิทยาศาสตร์ เข้าถึงเทคโนโลยี สร้างนวัตกรรม นำสังคมยั่งยืน	คณะวิทยาศาสตร์ จุฬาลงกรณ์มหาวิทยาลัย ณ อาคารจามจุรี 10 จุฬาลงกรณ์มหาวิทยาลัย	ศ.ดร. เปี่ยมสุข พงษ์สวัสดิ์ (327 เรื่อง)	สมเด็จพระเทพรัตนราชสุดา ฯ สยามบรมราชกุมารี
44. พ.ศ. 2561 29-31 ตุลาคม	วิทยาศาสตร์ และเทคโนโลยีในยุคพลิกผัน	สมาคมวิทยาศาสตร์แห่งประเทศไทยในพระบรมราชูปถัมภ์ ณ ศูนย์นิทรรศการและการประชุมไบเทค	รศ.ดร.สายวรุพ ชัยวานิชศิริ (270 เรื่อง)	สมเด็จพระเทพรัตนราชสุดา ฯ สยามบรมราชกุมารี
45. พ.ศ. 2562 7-9 ตุลาคม	ต้นกล้านวัตกรรมสู่การพัฒนาที่ยั่งยืน	สำนักวิชาวิทยาศาสตร์ มหาวิทยาลัยแม่ฟ้าหลวง	รศ.ดร.สายวรุพ ชัยวานิชศิริ (338 เรื่อง)	สมเด็จพระกนิษฐาธิราชเจ้า กรมสมเด็จพระเทพรัตนราชสุดา ฯ สยามบรมราชกุมารี

PROGRAM OVERVIEW

Code	Session/Symposium	October 5, 2020				October 6, 2020				October 7, 2020	
		AM		PM		AM		PM		AM	
	Grand Opening Ceremony (Facebook Live /Youtube Live)	King Ramkhamhaeng the Great Auditorium / 501, 5th Fl, SB									
	Plenary Speaker (Facebook Live / Youtube Live): Prof. Dr. John Charles Warner Prof. Dr. Suttichai Assabumrungrat Dr. Wonnop Visessanguan		King Ramkhamhaeng the Great Auditorium / 501, 5th Fl, SB								
	Poster Session		2nd Fl, SB						2nd Fl, SB		
A	Challenges in the Frontiers of Physics						806, 8th Fl, SB				301, 3rd Fl, SB
B	Math Stat Comp in the Digitally Innovative Era										
C	Impact of Biological Science towards SDGs						802, 8th Fl, SB				
D	Responsible Chemical Sciences for Future Sustainability				807, 8th Fl, SB						
E	Innovations for sustainable future				501, 5th Fl, SB						
SP01	Biodiversity of Marine Benthic Fauna										802, 8th Fl, SB
SP02	Climate change in a changing world										803, 8th Fl, SB
SP03	Crystallography					803, 8th Fl, SB					
SP04	Development of Material Science Based on Coordination Compounds							902, 9th Fl, SB			
SP05	Emerging Trends of Quantum Technology							803, 8th Fl, SB			
SP06	Flattening the Curve - Renewable Energy in Times of Climate Change										806, 8th Fl, SB
SP07	From Thailand to Antarctica: the 2020 Thai-Australian Expedition for Space Science										807, 8th Fl, SB
SP08	Green and Sustainable Chemistry: Opportunities for Academia and Industry							501, 5th Fl, SB			
SP09	Green Production Platform for Renewable Biomass Conversion					902, 9th Fl, SB					
SP10	Hydrogen Energy							807, 8th Fl, SB			
SP11	Lichens: Diversity, Ecology and Biomonitoring										501, 5th Fl, SB
SP12	Marine Plastic Abatement							806, 8th Fl, SB			
SP13	Natural Products for Drug Discovery							1201, 12th Fl, SB			
SP14	Promoting Research Integrity (Facebook Live / Youtube Live)		802, 8th Fl, SB								
SP15	Science-based Sustainable Tourism										902, 9th Fl, SB
SP16	360° COVID-19		803, 8th Fl, SB		803, 8th Fl, SB						
	Annual General Meeting of BMB section, STT							301, 3rd Fl, SB			
	Annual Meeting of the SCISDC										
	Meeting of the STT47 Committee							301, 3rd Fl, SB			
	Council of Science Deans of Thailand's Meeting			3rd Fl, Office of the President Building							
	Head of Department Meeting			1002, 1003, 1006, 1007, 10th Fl, SB							
	Science Deans & Department Heads Reception				Sak Phasuk Niran Room, King Ramkhamhaeng the Great Auditorium						
	STT46 Congress Banquet								2nd Fl, King Ramkhamhaeng the Great Auditorium		
	YRSS (Poster Session)		2nd Fl, SB						2nd Fl, SB		1002, 1003, 1006, 1007, 10th Fl, SB
	YRSS (Oral Session)										
	YRSS (Awarding Session)										1201, 12nd Fl, SB
	TYSA										1201, 12nd Fl, SB

301, 3rd Fl, SB - Reserve for YRSS committee discussion

MAP OF RAMKHAMHAENG UNIVERSITY

ACCESS & FLOOR PLAN

Map of the King Ramkhamhaeng the Great Auditorium

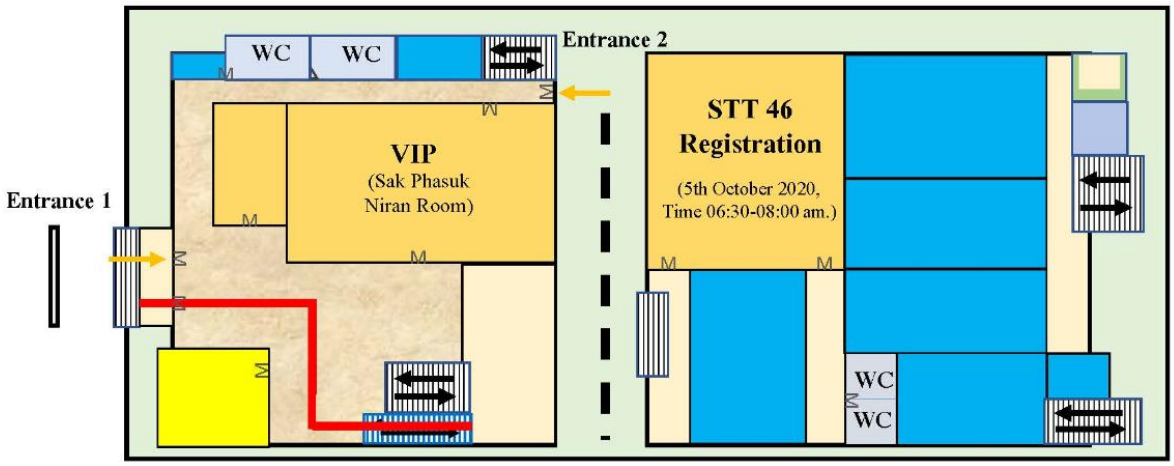

King Ramkhamhaeng the Great Auditorium, 1st Floor

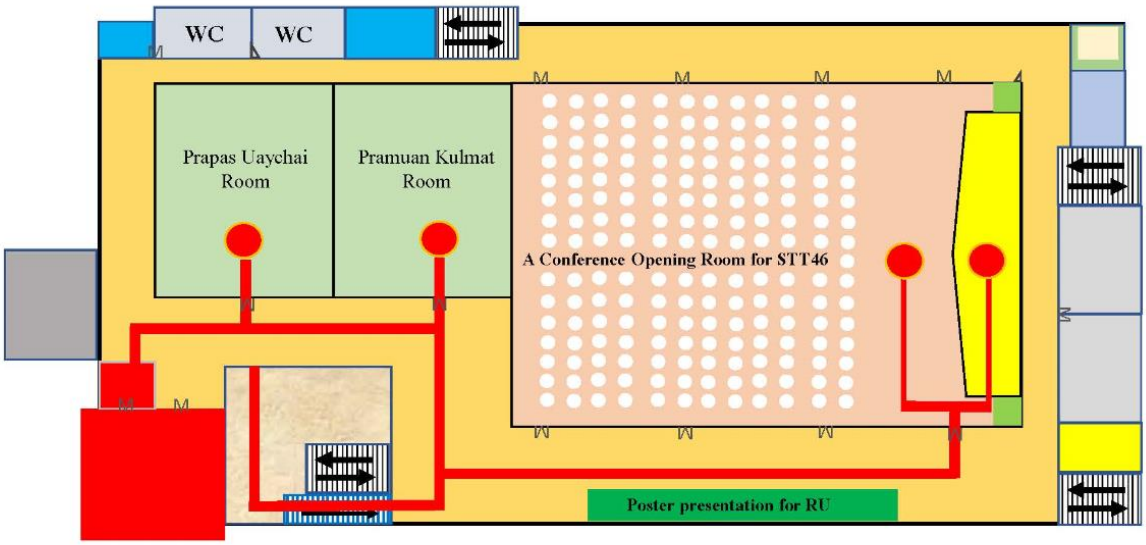

King Ramkhamhaeng the Great Auditorium, 2nd Floor

Map of the Sisattha Building

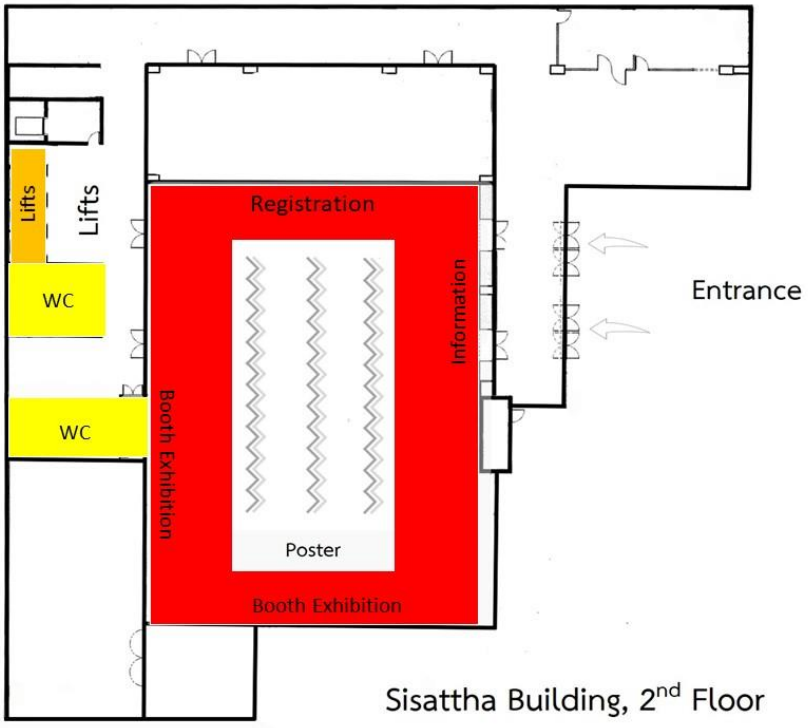

Sisattha Building, 2nd Floor

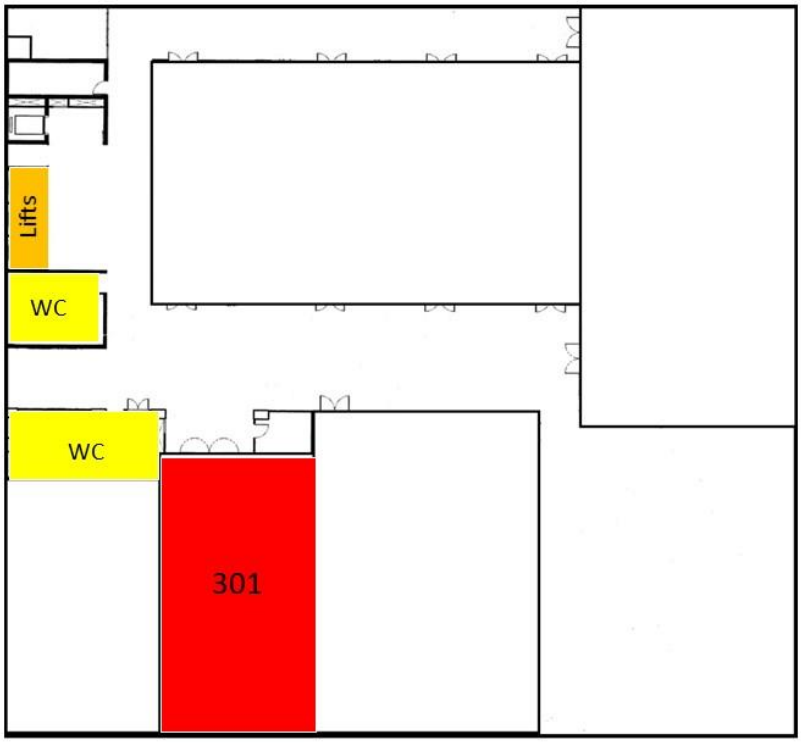

Sisattha Building, 3rd Floor

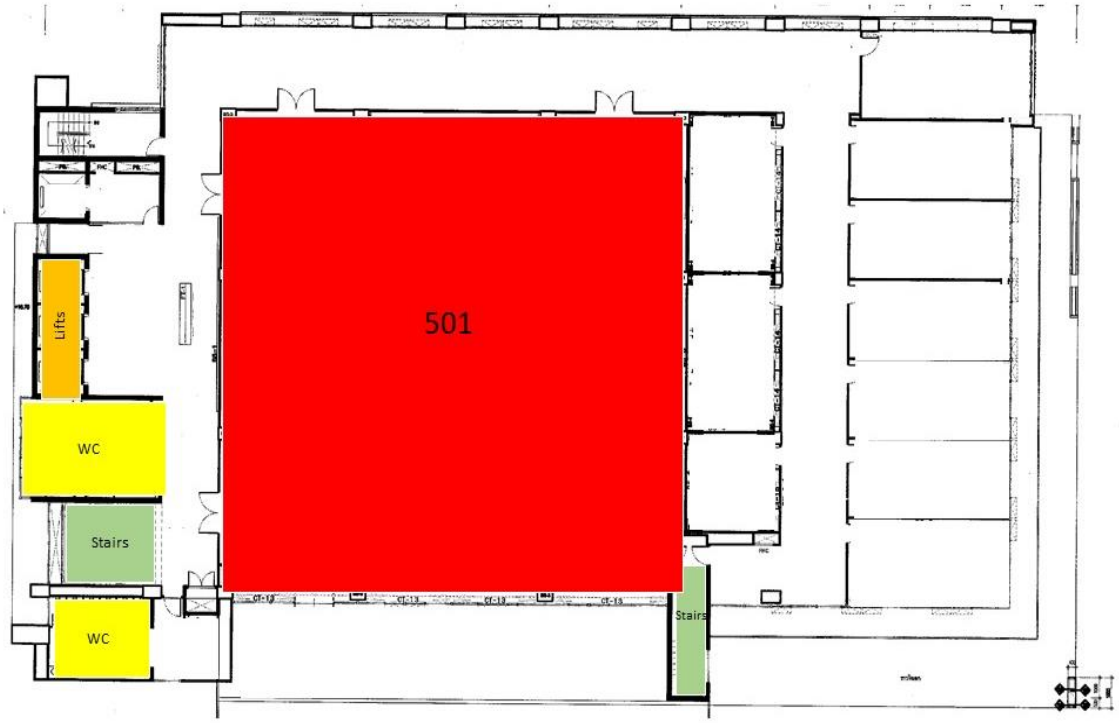

Sisattha Building, 5th Floor

Sisattha Building, 8th Floor

Sisattha Building, 9th Floor

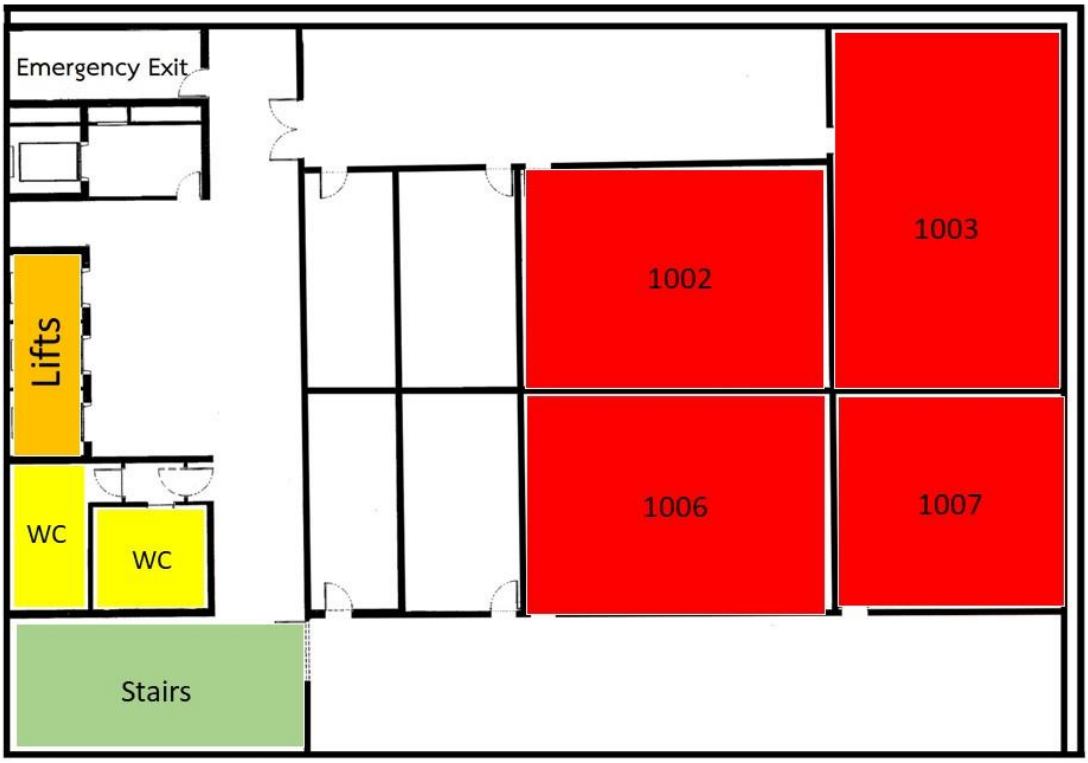

Sisattha Building, 10th Floor

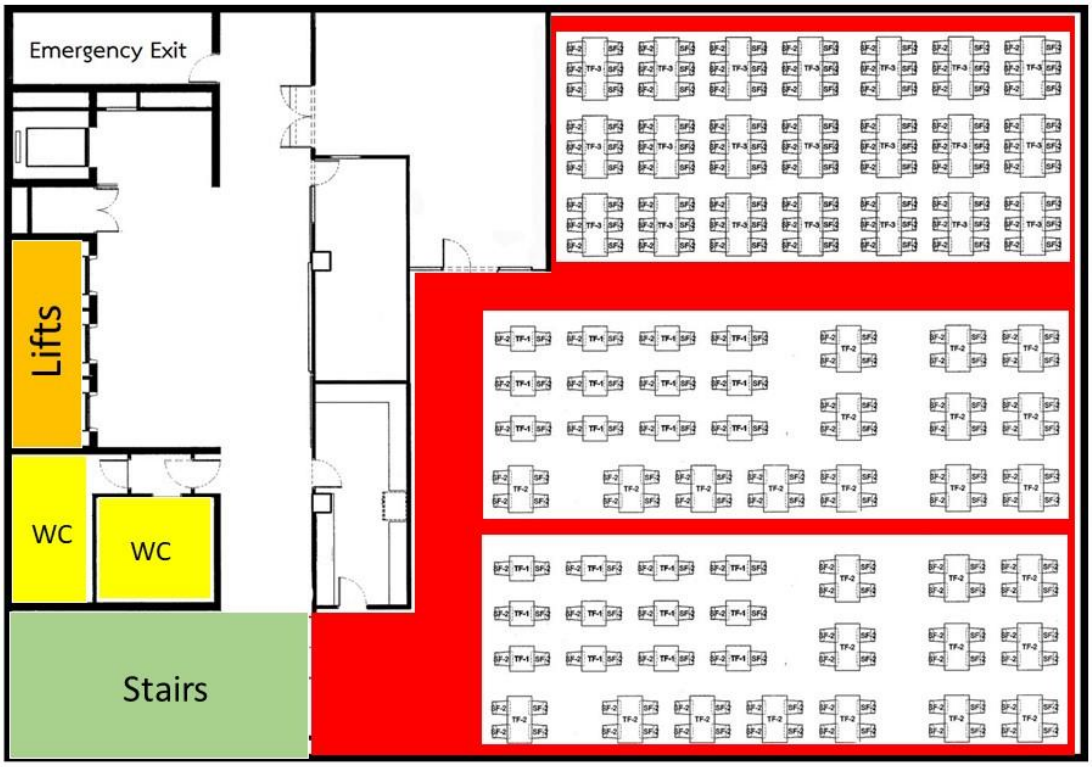

Sisattha Building, 11st Floor

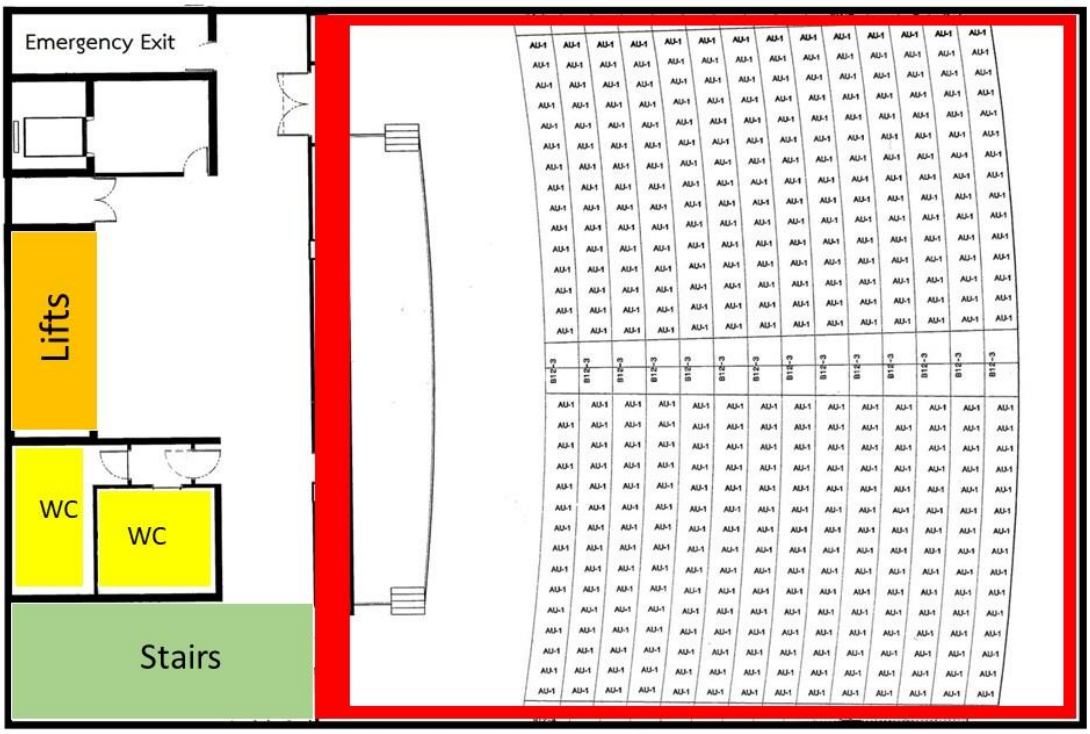

Sisattha Building, 12th Floor

PROGRAM FOR GRAND OPENING CEREMONY OF STT46

OCTOBER 5th, 2020

King Ramkhamhaeng the Great Auditorium
[501, 5th Floor, Sisattha Building (Live)]

Time	Events
8:00	All guests are seated in King Ramkhamhaeng the Great Auditorium, Ramkhamhaeng University
9:00	- Arrival of Her Royal Highness Princess Maha Chakri Sirindhorn
	- The President of SST presents souvenir to HRH - The Rector of Ramkhamhaeng University presents souvenir to HRH - The Chairman of STT46 presents Congress package to HRH - The President of SST presents report on activities of the Science Society of Thailand - Her Royal Highness Princess Maha Chakri Sirindhorn graciously presents awards plaques to 2020 Senior Scientists, 2020 Thailand Outstanding Scientists, 2020 Outstanding Technologist, 2020 Young Scientists, 2020 Young Technologists, 2020 Outstanding Science Teachers, Winners of 2019 National Science Projects Competition, STT46 Premium Sponsors and Rector of Ramkhamhaeng University - The Chairman of STT46 presents report on STT46 - Grand Opening Address by Her Royal Highness Princess Maha Chakri Sirindhorn
9:40	- Dean of Faculty of Science, Ramkhamhaeng University introduces plenary lecturers : Plenary lecturer 1: Professor John Charles Warner, USA (2014 Perkin Medal Award, the highest honor in American Industrial Chemistry) Plenary lecture 2: Professor Dr. Suttichai Assabumrungrat, Thailand (2020 Outstanding Scientist Award) Plenary lecture 3: Dr. Wonnop Visessanguan, Thailand (2020 Outstanding Scientist Award)
9.45-10.15 10.15-10.30 10.30-10.45	- Plenary Lecture 1: “ALL FIELDS OF SCIENCE ADDRESSING THE UN SUSTAINABLE DEVELOPMENT GOALS” (Virtual) - Plenary lecture 2: “PROCESS INTENSIFICATION AND MULTIFUNCTIONAL REACTORS FOR SUPPORTING THAILAND'S TRANSFORMATION TO BIO - CIRCULAR - GREEN (BCG) ECONOMY” - Plenary lecture 3: “FROM FUNDAMENTAL RESEARCH IN FOOD CHEMISTRY TO INNOVATIONS THAT EXPAND NEW HORIZONS FOR THAILAND FOOD AND FEED INDUSTRIES”
10.45-10.55	Her Royal Highness Princess Maha Chakri Sirindhorn visits Ramkhamhaeng University’s Research Exhibition
10.55-11.15	- Her Royal Highness Princess Maha Chakri Sirindhorn presides at photo sessions with - The Council of Science Dean of Thailand - Administrative and Executive Committees of the Science Society of Thailand under the Patronage of His Majesty the King - Administrative and STT46 Organizing Committees of Ramkhamhaeng University - Members of University Head of Department of basic sciences Forum - Her Royal Highness Princess Maha Chakri Sirindhorn presides at Grand Lunch
12.15	Her Royal Highness Princess Maha Chakri Sirindhorn departs from Ramkhamhaeng University

PLENARY SPEAKER: Prof. Dr. John Charles Warner

ALL FIELDS OF SCIENCE ADDRESSING THE UN SUSTAINABLE DEVELOPMENT GOALS

John Charles Warner*

John C. Warner Green Chemistry, LLC, 10 Crystal Road, Wilmington, MA 01887, USA
*e-mail: John.Warner@warnerbabcock.com

Abstract:
When a scientist begins the inventive process; the choice of feedstocks, reagents and reaction condition - all the various decisions that they make will have profound impact on countless people in the future. Industrial profitability, product adoption, worker health and safety, environmental justice, sustainable resource utilization, are just some of the consequences often invisible and unconsidered by the inventor in the lab. The United Nations Sustainable Development Goals are an excellent description of all the various aspects of human civilization and the earth's environment that need to be better understood and cared for. This presentation will describe how the 12 principles of green chemistry can be supportive for ALL scientists to help achieve the 17 UN SDGs using both theory and real world examples.

PLENARY SPEAKER: Prof. Dr. Suttichai Assabumrungrat

PROCESS INTENSIFICATION AND MULTIFUNCTIONAL REACTORS FOR SUPPORTING THAILAND'S TRANSFORMATION TO BIO - CIRCULAR - GREEN (BCG) ECONOMY

Suttichai Assabumrungrat[1,2,*]

[1]Center of Excellence in Catalysis and Catalytic Reaction Engineering, Department of Chemical Engineering, Faculty of Engineering, Chulalongkorn University, Bangkok 10330, Thailand
[2]Bio-Circular-Green-economy Technology & Engineering Center, BCGeTEC, Department of Chemical Engineering, Faculty of Engineering, Chulalongkorn University, Bangkok, Thailand 10330
[*]e-mail: Suttichai.a@chula.ac.th

Abstract:
The concept of Bio – Circular – Green (BCG) economy model according to the Thailand 4.0 policy offers many promising benefits such as being a sustainable growth based on less dependency of fossil-based resources. It provides a new opportunity for industry, research, policy and financing stakeholders to work together to create new values for the country balancing between the economy, society, and environment. However, the transformation of existing chemical and petrochemical industries to those based on the BCG economy model is of great challenge. Generally, a bio-based feedstock is complex in nature and requires additional pretreatment steps or even some major changes of existing process units, and therefore the bio-based process is typically not really competitive compared to the existing one. Process intensification and multifunctional reactors could play an important role to achieve a substantially more efficient technology with cleaner and safer operation, and consequently allow the bio-based process to become more competitive. This presentation will provide some examples of development of process intensification and multifunctional reactors for some applications such as hydrogen production via sorption-enhanced reaction and chemical looping reaction, and biodiesel production using several multifunctional reactors such as tube-in-tube reactor and spinning disc reactor. In addition, an example of transforming an existing pulp and paper process to an integrated bio-based process for combined pulp and biochemicals production will be provided.

PLENARY SPEAKER: Dr. Wonnop Visessanguan

FROM FUNDAMENTAL RESEARCH IN FOOD CHEMISTRY TO INNOVATIONS THAT EXPAND NEW HORIZONS FOR THAILAND FOOD AND FEED INDUSTRIES

Wonnop Visessanguan*

National Center for Genetic Engineering and Biotechnology (BIOTEC), National Science and Technology Development Agency (NSTDA), Pathum Thani 12120, Thailand
*e-mail: wonnop@biotec.or.th

Abstract:
Understanding the changes in physicochemical and biochemical characteristics of the main compositions which contribute greatly to overall product characteristics, of food including color, flavor, texture and safety is the basis of innovations to cope with several long standing challenges of Thai food and feed industries have encountered. Appropriate applications of microbial cells, enzymes and cell metabolites have successfully been demonstrated in research studies which have helped to improve the quality of food products, increase process efficiency and raise the food safety standards, particularly in traditional fermented food products. Throughout the course of extensive research activities, the knowledge has been integrated and synthesized in other areas, serving as a basis for research on utilization of agricultural raw materials and food processing by-products, creating high-value functional food innovation for the country's food and feed industries. This presentation will cover highlights on basic chemistry of Thai traditional fermented products that has motivated further scientific knowledge and industrial development of local or "heritage" foods, quality indication and solution for reduction of product loss, tools and technology for monitoring of starter culture during fermentation, the by-design and systematic developments of starter culture to cover the whole chain of microbial cell production and its industrial application, the development of a simple system for microbial cell production, one-step process for making fruit vinegar by MV-F1, fermented soy products for animal feed, production and utilization of halophilic archaea to degrade histamine in high-salt fermented fishery products, utilization of *Lactobacillus plantarum* as a food-grade protein expression system with a full freedom to operate (FTO), accelerated fermentation process of fish sauce, discovery of novel antimicrobial peptides, development of industrial-scale production of lysozyme peptide under GMP standard, the whole-chain utilization of eggs and egg by-products and new insights in meat quality and its products Through accumulated knowledge, these examples have contributed to a remarkable improvement of food and feed ingredients as well as the processes that expand new horizons for Thailand food and feed industries under the concept of Bio-Circular-Green (BCG) economy model.

PROGRAM FOR SESSIONS, SYMPOSIUMS AND MEETINGS

OCTOBER 5th, 2020

Session:	Poster Presentation		
Room:	2nd Floor		
Building:	Sisattha Building		
Time	ID	Speaker	Title
11:00-13.30	-	-	Poster Presentation (Symposium: SP01-SP16)
11:00-13.30	-	-	Poster Presentation (YRSS)

Symposium:	SP14-Promoting Research Integrity		
Room:	8th Floor, 802		
Building:	Sisattha Building		
Chair person:	Dr. Roderick Bates		
Time	ID	Speaker	Title
13:30-14:00	SP14_INV001	Chien Chou	ESTABLISHING TAIWAN FRAMEWORK OF RESEARCH INTEGRITY PROMOTION: GOVERNMENT POLICY, INSTITUTIONAL MANAGEMENT, RESEARCHERS' TRAINING AND CASE-HANDLING
14:00-14:30	SP14_INV002	Daniel Barr	GUIDING PRINCIPLES FOR RESEARCH INTEGRITY ACROSS ASIA-PACIFIC
14:30-15:00	SP14_INV003	De-Ming Chau	A BOTTOM-UP APPROACH TO FOSTER REARCH INTEGRITY IN MALAYSIA AND ASEAN

Symposium:	SP16-360° COVID-19		
Room:	8th Floor, 803		
Building:	Sisattha Building		
Chair person:	Prof. Dr. Sopit Wongkham		
Time	ID	Speaker	Title
13:30-14:10	SP16_INV001	Kiat Ruxrungtham	COVID-19 VACCINE: GLOBAL AND COUNTRY UPDATE
14:10-14:50	SP16_INV002	Arunee Thitithanyanont	DEVELOPMENT OF PLATFORMS TO MODEL PATHOGENESIS, THERAPEUTIC STRATEGIES AND VACCINE DEVELOPMENT AGAINST SARS-COV-2 INFECTION
14:50-15:30	SP16_INV003	Pilailak (Akkapaiboon) Okada	EARLY TRANSMISSION PATTERNS OF CORONAVIRUS DISEASE 2019 (COVID-19) IN TRAVELLERS FROM WUHAN TO THAILAND, JANUARY 2020

Session:	B1-Math Stat Comp in the Digitally Innovative Era		
Room:	8th Floor, 806		
Building:	Sisattha Building		
Chair person:	Assoc. Prof. Dr. Chartchai Leenawong		
Time	ID	Speaker	Title
13:30-14:00	B_INV001	Antony James Harfield	AI FOR SOCIAL GOOD: AUDIO-BASED THREAT DETECTION FOR PROTECTING FORESTS
14:00-14:15	B_006_OA	Sirirat Singhun	CLOSED (2, 3)-KNIGHT'S TOURS ON THE 1 × *n*, 2 × *n*, 3 × *n* AND 4 × *n* TOROIDAL CHESSBOARDS FOR ALL POSITIVE INTEGER *n*
14:15-14:30	B_024_OA	Jirapha Limbupasiriporn	MINIMUM-WEIGHT BASES FOR CODES FROM COMPLETE MULTIPARTITE GRAPHS
14:30-14:45	B_018_OA	Ponrudee Netisopakul	PREDICTING STOCK PRICE DIRECTION USING TEXT CLASSIFICATION AND SENTIMENT ANALYSIS ON STOCK NEWS
14:45-15:00	B_010_OF	Wittaya Phaengthaisong	AN ADAPTIVE DIFFERENTIAL EVOLUTION ALGORITHM USING PROBABILITY-BASED CONTROL PARAMETERS WITH THE ALTERNATING OF LEARNING AND UTILIZING PERIODS
15:00-15:15	B_012_OF	Watcharida Nararuk	AN ADAPTIVE DIFFERENTIAL EVOLUTION ALGORITHM BY USING MIXED MUTATION AND CROSSOVER STRATEGIES
Break			
15:35-15:50	B_021_OF	Pratchayaporn Doemlim	GRAPH AND NUMBER THEORETIC PROPERTIES OF CERTAIN MAPS OVER FINITE FIELD
15:50-16:05	B_016_OA	Porawat Visutsak	ACTIVITY CLASSIFICATION USING LOW PASS FILTER DEEP CONVOLUTIONAL LSTM
16:05-16:20	B_017_OF	Amarita Ritthipakdee	AN IMPROVED SHARK ALGORITHM FOR OPTIMIZATION PROBLEM

Session:	D1-Responsible Chemical Sciences for Future Sustainability		
Room:	8th Floor, 807		
Building:	Sisattha Building		
Chair person:	Prof. Dr. Orawon Chailapakul		
Time	ID	Speaker	Title
13:30-14:00	D_KEY001	Oliver Reiser	COPPER MAKES THE DIFFERENCE: DEVELOPING SUSTAINABLE PHOTOREDOX CATALYZED TRANSFORMATIONS
14:00-14:30	D_INV001	Taro Toyota	GIANT VESICLE ENGINEERING: BIOSENSOR AND CELL/TISSUE-MARKER
14:30:14:50	D_004_OF	Nitis Meeploy	SYNTHESIS OF DIMETHYL ETHER ON COPPER OXIDE - ZINC OXIDE-ALUMINIUM OXIDE OVER GRAPHENE OXIDE AND (ɣ-Al_2O_3) CATALYSTS
14:50-15:10	D_005_OF	Andaru Dena Prasiwi	SURFACE-ENHANCED RAMAN SCATTERING USING FLUORESCENCE-QUENCHED CARBON QUANTUM DOTS FOR MERCURY ION DETECTION
15:10-15:30	D_007_OF	Trang Pham Thi	SYNTHESIS OF 1,2-NAPHTHOQUINONE DERIVATIVES AS α-GLUCOSIDASE INHIBITORS
Break			
15:40-16:00	D_011_OF	Nattapon Siengdung	HYDROTHERMAL SYNTHESIS OF NITROGEN-DOPED CARBON DOTS FROM AROMATIC AMINO ACIDS UNDER ACIDIC CONDITION
16:00-16:20	D_014_OA	Sunita Chamyuang	COFFEE PECTIN PRODUCTION AN ALTERNATIVE WAY FOR ARGRICULTURAL WASTE MANAGEMENT IN COFFEE FARMS
16:20-16:40	D_016_OF	Watchara Wimonsong	OXIDATIVE COUPLING OF QUINOXALINONE WITH AZOLES AND RELATED COMPOUNDS
16:40-17:00	D_023_OA	Sarunya Promkotra	HYDROGEOCHEMICAL ATTRIBUTES OF GROUNDWATER IN BAN KHAM BON LANDFILL, MUEANG KHON KAEN, THAILAND

Session:	E1-Innovations for Sustainable Future		
Room:	5th Floor, 501		
Building:	Sisattha Building		
Chair person:	Prof. Dr. Tawan Sooknoi		
Time	ID	Speaker	Title
13:30-14:00	E_INV001	Soracha Dechaumphai	MULTIFUNCTIONAL THERANOSTIC RED BLOOD CELL MEMBRANE COATED NANOPARTICLES FOR THE TREATMENT AND DETECTION OF BREAT CANCER
14:00-14:20	E_001_OF	Napat Prompat	STRUCTURE-GUIDED DESIGN OF INTERLEUKIN-18 AS A POTENTIAL CYTOKINE-MEDIATED IMMUNOTHERAPY
14:20-14:40	E_002_OF	Chariya Peeyatu	STRUCTURAL ANALYSIS OF T63 ALTERATION IN HUMAN INTERLEUKIN-18
14:40-15:00	E_008_OA / E_026_OA	Puchiss Phromchang/ Wootinun Ouppapong	STUDY AND DEVELOPMENT OF SOFTWARE FOR MUSIC NOTATION
15:00-15:20	E_009_OA	Kusuma Jaipiam	IMAGE PROCESSING OF CT SCAN IMAGE FOR LIVER LOCALIZATION
Break			
15:30-15:50	E_010_OF / E_028_OF	Kitisak Boonkham / Thanyanan Phuphachong	APPARATUS FOR DETERMINING YOUNG'S MODULUS OF SOLID MATERIALS BASED ON GRAVITATIONAL FORCE ANALYSIS
15:50-16:10	E_016_OF	Amone Phangpyhlavong	APPLICATION OF AIR DECK BLASTING TECHNIQUE AT KHOUNXAY GYPSUM MINE, SAVANNAKHET PROVINCE, LAO PDR
16:10-16:30	E_021_OF	Tanu-udom Maneesing	NUTRITION CARE PROCESS OF MULTIDISCIPLINARY CARE TEAM IN IN-PATIENT DEPARTMENT (IPD) PATIENTS
16:30-16:50	E_031_OF / E_034_OF	Panuphong Northao / Natwara Thongsak	THE PORTABLE DARK FIELD MICROSCOPE

Session:	Council of Science Deans of Thailand's Meeting		
Room:	3rd Floor, 301		
Building:	Office of the President Building		
Time	ID	Speaker	Title
13:30-16:30		-	Meeting

Session:	CEPMART Meeting		
Room:	10th Floor, 1002		
Building:	Sisattha Building		
Time	ID	Speaker	Title
13:30-16:30		-	Meeting

Session:	The 35th Chemistry Department Heads of Thailand Meeting		
Room:	10th Floor, 1003		
Building:	Sisattha Building		
Time	ID	Speaker	Title
13:30-16:30		-	Meeting

Session:	The 3rd Physics Department Heads of Thailand Meeting		
Room:	10th Floor, 1006		
Building:	Sisattha Building		
Time	ID	Speaker	Title
13:30-16:30		-	Meeting

Session:	The 2nd Biology Department Heads of Thailand Meeting		
Room:	10th Floor, 1007		
Building:	Sisattha Building		
Time	ID	Speaker	Title
13:30-16:30		-	Meeting

Session:	Annual General Meeting of BMB section, STT		
Room:	8th Floor, 803		
Building:	Sisattha Building		
Time	ID	Speaker	Title
15:30-16:30		-	Meeting

Session:	Science Deans & Department Heads Reception		
Room:	Sak Phasuk Niran Room		
Building:	King Ramkhamhaeng the Great Auditorium		
Time	ID	Speaker	Title
17:30-20:00		-	Reception

OCTOBER 6th, 2020

Session:	C1-Impact of Biological Science towards SDGs		
Room:	8th Floor, 802		
Building:	Sisattha Building		
Chair person:	Asst. Prof. Dr. Noppadon Kitana		
Co-chair:	Prof. Dr. Supachitra Chadchawan		
Time	ID	Speaker	Title
8:30-9:00	C_INV001	Phiangphak Sukkharak	TOWARDS BRYOPHYTE FLORA OF THAILAND: TAXONOMIC REVISIONS OF THE LIVERWORT GENERA *Frullania*, *Pleurozia*, AND *Metzgeria* IN THAILAND
9:00-9:20	C_036_OA	Kanokorn Rueangsawang	MOLECULAR ANALYSIS OF THE SHRIMP PLANT (*RUNGIA*, ACANTHACEAE) IN THAILAND
9:20-9:40	C_044_OA	Atchaneey Boonprakob	THE MORPHOLOGY AND PHYLOGENY OF THE DIATOM GENERA *Rhizosolenia*, *Proboscia*, *Pseudosolenia* AND *Neocalyptrella* FROM GULF OF THAILAND AND THE ANDAMAN SEA, WITH A DESCRIPTION OF *Proboscia siamensis* sp. nov., AND THE ERECTION OF A NEW ORDER FOR *Proboscia*
9:40-10:00	C_015_OF	Jenjira Asayot	STUDY ON INFLORESCENCE DEVELOPMENT OF LONGAN (*Dimocarpus longan* Lour.) 'PHUANG THONG' GROWN AT SAMUT SAKHON PROVINCE, THAILAND
10:00-10:20	C_033_OA	Kittisak Buddhachat	FEASIBILITY OF CRISPR-cas12a FOR PLANT SPECIES IDENTIFICATION WITHOUT DNA AMPLIFICATION; A CASE OF *Phyllanthus amarus*
Break			
10:30-11:00	C_INV002	Luca Comai	PROGRESS AND OPPORTUNITIES FOR RESHAPING PLANT GENOMES VIA CRISPR
11:00-11:20	C_040_OF	Supakarat Kaewpeng	THE DISRUPTION OF A STRUCTURAL CELL WALL PROTEIN *SED*1 IN *Saccharomyces cerevisiae* FOR YEAST CELL SURFACE DISPLAY
11:20-11:40	C_023_OF	Suthathip Phetlum	PURIFICATION AND BIOCHEMICAL CHARACTERIZATION OF AMYLASE ENZYME FROM *Puntioplites proctozysron*

Symposium:	SP03-Crystallography		
Room:	8th Floor, 803		
Building:	Sisattha Building		
Chair person:	Prof. Dr. Nongnuj Muangsin		
Co-chair:	Asst. Prof. Dr. Kittipong Chainok		
Time	ID	Speaker	Title
8:30-9:00	SP03_INV001	Marie Hoarau	DISCOVERY OF NEW *Plasmodium falciparum* DHFR INHIBITORS USING A FRAGMENT-BASED SCREENING STRATEGY
9:00-9:30	SP03_INV002	Bunyarat Rungtaweevoranit	CHEMISTRY OF METAL-OXIDE NODES IN METAL–ORGANIC FRAMEWORKS AND ITS IMPLICATION IN HETEROGENEOUS CATALYSIS
9:30-9:50	SP03_002_OA	Saruda Yokputtaraksa	SYNTHESIS, STRUCTURAL, ANTIBACTERIAL AND FLUORESCENCE PROPERTIES OF Zn(II) AND Cd(II) IMIDAZOLYMINE COMPLEXES
9:50-10:10	SP03_003_OF	Suwijai Jatupohnkhongchai	PETROGRAPHY AND GEOCHEMISTRY OF QUARTZITES AND METASANDSTONES AS EVIDENCES FOR TECTONIC ENVIRONMENT OF THE SILURIAN-DEVONIAN BO PHLOI FORMATION, KANCHANABURI, WESTERN THAILAND
10:10-10:30	SP03_005_OF	Narongdetch Boothrawong	ENHANCE ELECTRICAL PROPERTIES OF BARIUM CALCIUM ZIRCONIUM TITANATE ($Ba_{0.85}Ca_{0.15}Zr_{0.10}Ti_{0.90}O_3$) LEAD-FREE CERAMICS BY SINTERING TEMPERATURES
10:30-10:50	SP03_006_OF	Lalita Tawee	EFFECTS OF SYNTHESIS ROUTE ON THE PROPERTIES OF 0.99 $Bi_{0.5}(Na_{0.8}K_{0.2})_{0.5}TiO_3$ – 0.01Bi ($Mg_{2/3}Nb_{1/3}$) O_3 LEAD FREE CERAMICS

Session:	B2-Math Stat Comp in the Digitally Innovative Era		
Room:	8th Floor, 806		
Building:	Sisattha Building		
Chair person:	Assoc. Prof. Dr. Chartchai Leenawong		
Time	ID	Speaker	Title
8:30-9:00	B_INV002	Bligetta Servatius	STRESSABILITY OF MULTIDIMENSIONAL FRAMEWORKS
9:00-9:15	B_001_OA	Khwancheewa Wattanatripop	ON nd-K*(n,r)-FULL HYPERSUBSTITUTIONS
9:15-9:30	B_002_OF	Wasin Tranghiranyathorn	IMPROVED MASK FOR ADAPTIVE FRACTIONAL ORDER DIFFERENTIAL METHOD FOR MEDICAL IMAGE ENHANCEMENT
9:30-9:45	B_003_OA	Suriyon Yimnet	MODE-DEPENDENT AVERAGE DWELL TIME APPROACH TO FINITE-TIME BOUNDEDNESS OF LINEAR SWITCHED POSITIVE TIME-DELAY SYSTEMS WITH FINITE-TIME UNBOUNDED SUBSYSTEMS
9:45-10:00	B_004_OF	Siwaphorn Kanchanarat	A MATHEMATICAL STUDY OF DIPHTHREIA MODEL WITH TRANSPORT-RELATED INFECTION AND ASYMPTOMATIC INFECTION
10:00-10:15	B_007_OF	Natdanai Boonsri	MODELING THE IMPACT OF HIV INFECTION ON TB INCIDENCE
Break			
10:30-10:50	B_009_OF	Denpong Pongpipat	THE NORDHAUS-GADDUM INEQUALITIES FOR ACYCLIC NUMBERS ON UNITARY CAYLEY GRAPHS OF FINITE RINGS
10:50-11:10	B_011_OF	Suriyakamol Thongjob	SOME GENERALIZATIONS OF HARDY TYPE INTEGRAL INEQUALITIES FOR (p,q)-INTEGRABLE FUNCTIONS
11:10-11:30	B_014_OA	Thanomsak Laokul	A COMMON ENDPOINT THEOREM FOR A PAIR OF SINGLE-VALUED SUZUKI MAPPING AND MULTIVALUED SUZUKI MAPPING WITHOUT THE COMMUTATIVE CONDITION
11:30-11:50	B_019_OF	Puchong Praekhaow	THE CONDITION AND PROBLEMS ON LEARNING MANAGEMENT IN MATHEMATICS OF UNDERGRADUATE STUDENTS

Session:	D2-Responsible Chemical Sciences for Future Sustainability		
Room:	8th Floor, 807		
Building:	Sisattha Building		
Chair person:	Prof. Dr. Orawon Chailapakul		
Time	ID	Speaker	Title
8:30-9:00	D_INV002	Taweetham Limpanuparb	A VIRTUAL ALTERNATIVE TO MOLECULAR MODEL SETS: CONSTRUCTING AND VISUALIZING MOLECULES IN MOLECULAR GRAPHICS SOFTWARE
9:00-9:30	D_INV003	Pumidech Puthongkham	EXPANDING THE TOOLBOX FOR REAL-TIME ELECTROCHEMICAL DETECTION OF NEUROTRANSMITTERS
9:30-9:50	D_029_OF	Teck Hock Lim	CALCIUM ALGINATE ENCAPSUALTED SULFUR PARTICLES FOR METAL NANOPARTICLES CAPTURE: A CASE STUDY OF SILVER NANOPARTICLES
9:50-10:10	D_030_OA	Saytanar Tun	SYNTHESIS AND CHARACTERIZATION OF MAGNESIUM ALUMINATE NANOPARTICLES BY HYDROTHERMAL METHOD
10:10-10:30	D_031_OA	Rakhi Majumdar	POROUS HYBRID POLYMER COMPOSED OF SILSESQUIOXANE CAGES AND PORPHYRIN MOIETIES: SENSING AND ADSORPTION

Session:	E2-Innovations for Sustainable Future		
Room:	5th Floor, 501		
Building:	Sisattha Building		
Chair person:	Prof. Dr. Tawan Sooknoi		
Co-chair:	Dr. Sasitorn Srisawadi / Dr. Kampanart Silva		
Time	ID	Speaker	Title
8:30-9:00	E_KEY001	Pun-Arj Chairatana	TRILOGY OF CRISIS: REIMAGING INNOVATION FOR SUSTAINABLE FUTURE
9:00-9:30	E_INV002	Sasitorn Srisawadi	NEW 3D PRINTING TECHNOLOGY AND OPPORTUNITIES IN NATURAL RUBBER PRODUCT DESIGN
9:30-9:50	E_022_OA	Onchira Ritbamrung	Detection of *Xanthomonas oryzae* pv. *oryzae* (*Xoo*) CAUSING BACTERIAL LEAF BLIGHT IN RICE USING A pH-SENSITIVE LOOP-MEDIATED ISOTHERMAL AMPLIFICATION (LAMP)
9:50-10:10	E_023_OA	Suphaporn Paenkaew	MOLECULAR DETECTION OF RICKETTSIA, *Ehrlichia canis* and *Anaplasma platys*, IN CANINE BLOOD USING RPA METHOD
10:10-10:30	E_024_OA	Wanrachon Nukool	GENETIC DIVERSITY, GEOGRAPHIC DIFFERENTIATION AND CHEMICAL PROFILE OF ASIATIC PENNYWORT (*Centella asiatica* (L.) URBAN) IN THAILAND
Break			
10:40-11:00	E_025_OA	Tanaporn Kaewcheed	LOGISTICS COST REDUCTION MODEL IN FOOD INDUSTRY, RAYONG
11:00-10:20	E_029_OA	Oranit Kraseasintra	ALTERNATIVE NATURAL HAIR DYE PRODUCT USING THE PIGMENT EXTRACTED FROM CYANOBACTERIA
11:20-11:40	E_032_OF	Siwattra Pruksasri	RAPID AND COST-EFFECTIVE FABRICATION METHOD OF MICROFLUIDIC CELL CULTURE DEVICES USING A STEREOLITHOGRAPHY 3D PRINTING
11:40-12:00	E_035_OA	Nay Mar Soe	STUDY ON FOOD RANCIDITY OF VIGRIN COCONUT OIL IN TANINTHARYI REGIONAL DESSERT (MOHT KALEME)

Symposium:	SP09-Green Production Platform for Renewable Biomass Conversion		
Room:	9th Floor, 902		
Building:	Sisattha Building		
Chair person:	Assoc. Prof. Dr. Nuttha Thongchul		
Time	ID	Speaker	Title
9:30-10:00	SP09_INV001	Nuwong Chollakup	BIODIESEL UPGRADING TECHNOLOGY FOR HIGHER BLEND WITH DIESEL TO REDUCE PM2.5
10:00-10:30	SP09_INV002	Kobkul Laoteng	KEY ELEMENTS AND STRATEGIES FOR FUNCTIONAL LIPIDS PRODUCTION BY FILAMENTOUS FUNGAL PLATFORM
10:30-10:50	SP09_005_OF	Munsuree Kalong	CATALYTIC TRANSFER HYDROGENATION OF FURFURAL INTO FURFURYL ALCOHOL AND 2-METHYLFURAN OVER IRON-PROMOTED COPPER CATALYSTS
10:50-11:10	SP09_008_OA	Myat Hnin Ei	EFFECTIVENESS OF SAPONIN ON PHYTOREMEDIATION OF PETROLEUM - CONTAMINATED SOIL
11:10-12:00	SP09_INV003	Benjamas Chiersilp	BIOCONVERSION OF PALM BIOMASS WASTES TO BIODIESEL FEEDSTOCKS AND CELLULOSE PULPS BY LIGNOCELLULOLYTIC OLEAGINOUS FUNGI

Session:	Annual Meeting of the Science Society of Thailand Under the Patronage of His Majesty the King		
Room:	3rd Floor, 301		
Building:	Sisattha Building		
Time	ID	Speaker	Title
12:00-14:00		-	Meeting

Session:	Meeting of the STT47 Committee		
Room:	3rd Floor, 301		
Building:	Sisattha Building		
Time	ID	Speaker	Title
14:00-15:30		-	Meeting

Session:	C2-Impact of Biological Science towards SDGs		
Room:	8th Floor, 802		
Building:	Sisattha Building		
Chair person:	Asst. Prof. Dr. Noppadon Kitana		
Co-chair:	Prof. Dr. Supachitra Chadchawan		
Time	ID	Speaker	Title
13:30-14:00	C_INV003	Riyoichi Matsuda	JAPANESE JUNIOR AND SENIOR HIGH SCHOOL BIOLOGY EDUCATION ARE FAR FROM “NEW NORMAL”
14:00-14:20	C_002_OF	Kaisone Chanda	MOLECULAR CLONING AND PREDICTION OF ANTIGENIC DETERMINANTS OF 23 KDA INTEGAL MEMBRANE PROTEIN FROM *SCHISTOSOMA MEKONGI*
14:20-14:40	C_032_OF	Hong Do	MOLECULAR CLONING AND B-CELL EPITOPES OF THE GENE ENCODING FATTY ACID BINDING PROTEIN FROM BLOOD FLUKE (*SCHISTOSOMA MEKONGI*)
14:00-15:00	C_039_OF	Sutanya Thanudaksorn	MOLECULAR CHARACTERIZATION OF FLUOROQUINOLONE NON-SUSCEPTIBILITY IN CARBAPENEM-RESISTANT *Klebsiella pneumoniae* ISOLATED FROM SOUTHERN, THAILAND
15:00-15:30	C_INV004	Kesara Margrét Jónsson	IMAGING BIOLOGICAL SAMPLES BY SCANNING ELECTRON MICROSCOPY

Symposium:	SP05-Emerging Trends of Quantum Technology		
Room:	8th Floor, 803		
Building:	Sisattha Building		
Chair person:	Dr. Anucha Watcharapasorn		
Time	ID	Speaker	Title
13:00-13:30	SP05_INV001	Yoshiro Hirayama	HYBRID QUANTUM SYSTEM AND HYPERFINE MEDIATED TRANSPORT PROPERTIES
13:30-14:00	SP05_INV002	Tsutomu Nojima	COMPREHENSIVE VORTEX PHASE DIAGRAM OF ION-GATED TWO DIMENSIONAL SUPERCONDUCTORS
14:00-14:30	SP05_INV003	Shau-Yu Lan	QUANTUM ENGINEERING IN OPTICAL FIBERS
14:30-15:00	SP05_INV004	Areeya Chantasri	ESTIMATING QUANTUM SYSTEM'S STATE DYNAMICS USING CONTINUOUS WEAK MEASUREMENT
15:00-15:30	SP05_INV005	Nithiwadee Thaicharoen	HAMILTONIAN ENGINEERING IN STRONGLY INTERACTING RYDBERG SYSTEMS
15:30-16:00	SP05_INV006	Hai Q. Dinh	NEW QUANTUM CODES FROM CYCLIC AND NEGACYCLIC CODES OF PRIME POWER LENGTHS

Session:	B3-Math Stat Comp in the Digitally Innovative Era		
Room:	8th Floor, 806		
Building:	Sisattha Building		
Chair person:	Assoc. Prof. Dr. Chartchai Leenawong		
Time	ID	Speaker	Title
13:00-13:15	B_008_OA	Adthasit Sinna	A NOTE ON THE CIRCUMFERENCE OF 3-CONNECTED CUBIC PLANE GRAPHS
13:15-13:30	B_015_OA	Thodsaporn kumduang	LEFT VARIABLES TERMS AND APLLICTIONS FOR CLASSIFYING ALGEBRA
13:30-13:45	B_025_OA	Saranya Phongchan	REGULARITY AND FINITENESS CONDITIONS ON TRANSFORMATION SEMIGROUPS WITH INVARIANT SETS
13:45-14:00	B_020_OF	Sainuddeen Nuiphom	BLIND DEBLURING IMAGE VIA L_2 - REGULARIZATION
14:00-14:15	B_022_OF	Areena Hazanee	HYBRID FINITE INTEGRATION METHOD FOR SOLVING ORDINARY DIFFERENTIAL EQUATIONS

Symposium:	SP12-Marine Plastic Abatement		
Room:	8th Floor, 806		
Building:	Sisattha Building		
Chair person:	Prof. Dr. Thammarat Koottatep		
Time	ID	Speaker	Title
14:40-15:10	SP12_INV001	Chongrak Polprasert	PLASTIC WASTE MANAGEMENT AND CURRENT STATUS IN THAILAND: ISSUES OF MARINE PLASTIC WASTE FROM LAND-BASED SOURCES
15:10-15:40	SP12_INV002	Chettiyappan Visvanathan	CO-PROCESSING PLASTIC WASTE FROM DUMPSITES IN CEMENT INDUSTRY A WAY TO CURB MARINE PLASTIC POLLUTION
15:40-16:10	SP12_INV003	Amila Abeynayaka	LIFE CYCLE APPROACH IN MARINE PLASTIC ABATEMENT: PRESENT STATUS AND FUTURE DIRECTIONS
16:10-16:30	SP12_002_OA	Ekbordin Winijkul	EFFECTS OF THE SOURCE SEPARATION ON THE AIRBORNE MICROPLASTICS IN THE AIR NEAR GARBAGE BURNING
16:30-16:50	SP12_003_OA	Tran Thanh Dan	GIS-BASED APPROACH TO MAPPING OF LAND-BASED PLASTIC LEAKAGE
16:50-17:10	SP12_04_OA	Kittipong Phattananuruch	PRELIMINARY STUDY ON TRANSPORTATION AND DISTRIBUTION OF MARINE DEBRIS IN THE GULF OF THAILAND IN 2018 USING HYDRODYNAMIC AND WATER QUALITY SIMULATION MODEL

Symposium:	SP10-Hydrogen Energy		
Room:	8th Floor, 807		
Building:	Sisattha Building		
Chair person:	Prof. Dr. Suttichai Assabumrungrat		
Co-chair:	Asst. Prof. Dr. Pattaraporn Kim-Lohsoontorn		
Time	ID	Speaker	Title
13:30-14:00	SP10_KEY001	Nigel Brandon	INNOVATION IN ELECTROCHEMICAL TECHNOLOGIES FOR THE LOW CARBON ENERGY TRANSITION
14:00-14:30	SP10_KEY002	Arunratt Wuttimongkolchai	OPPORTUNITIES OF HYDROGEN TECHNOLOGIES FOR CLEAN AND SUSTAINABLE GROWTH IN THAILAND
14:30-15:00	SP10_KEY003	Sumittra Charojrochkul	GREY AND GREEN HYDROGEN PRODUCTION
15:00-15:30	SP10_KEY004	Navadol Laosiripojana	CATALYTIC PARTIAL OXIDATION OF METHANE OVER Re-BASED CATALYSTS
Break			
Chair person:	Prof. Dr. Suttichai Assabumrungrat		
Co-chair:	Prof. Dr. Navadol Laosiripojana		
Time	ID	Speaker	Title
15:45-16:10	SP10_INV001	Suwimol Wongsakulphasatch	GREEN TECHNOLOGY FOR CO-PRODUCTION OF HIGH PURITY HYDROGEN AND SYNTHESIS GAS
16:10-16:35	SP10_INV002	Pattaraporn Kim-Lohsoontorn	DEVELOPMENT OF CERIA- AND ZIRCONIA-BASED ELECTROLYZER FOR HYDROGEN PRODUCTION
16:35-17:00	SP10_INV003	Sakhon Ratchahat	POWER-TO-GAS (PTG) TECHNOLOGY AS EFFICIENT ROUTE FOR CO_2 UTILIZATION: DEVELOPMENT OF STRUCTURED CATALYTIC SYSTEM
17:00-17:15	SP10_001_OF	Kritchakorn Aimdate	DEVELOPMENT OF Ni-BASED CATALYST FROM NATURAL KAOLIN VIA MICROWAVE ASSISTED SYNTHESIS FOR CO_2 METHANATION

Symposium:	SP08-Green and Sustainable Chemistry: Opportunities for Academia and Industry		
Room:	5th Floor, 501		
Building:	Sisattha Building		
Chair person:	Prof. Dr. Joseph Samec		
Co-chair:	Dr. Duangamol Tungasmita		
Time	ID	Speaker	Title
13:00-13:30	SP08_INV001	Christian Dahlstrand	PROVIDING A SOLUTION IN THE TRANSITION FROM BLACK TO GREEN FEEDSTOCK IN FUELS AND MATERIALS
13:30-14:00	SP08_INV002	Willem Böttger	DEVELOPMENT OF FACADE ELEMENTS ON BASE OF WASTE MATERIALS OF (WASTE) WATER COMPANIES
14:00-14:20	SP08_006_OF	Yutthanakon Kanaphan	A SIMPLE PRODUCTION METHOD FOR A HIGH PERFORMANCE SiO_2/C NANOCOMPOSITE ANODE MATERIAL DERIVED FROM RICE HUSKS FOR LITHIUM ION BATTERIES
14:20-14:40	SP08_009_OA	Varanya Somaudon	PREPARATION OF Bi_4MoO_9 CATALYST BY PRECIPITATION METHOD FOR PHOTODEGRADATION OF ANIONIC AZO DYES
14:40-15:00	SP08_010_OF	Purumet Pipitworrakul	EFFECTS ON IONIC CONDUCTIVITY OF CO-DOPED LITHIUM LANTHANUM TITANATE SOLID ELECTROLYTES BY Sr^{2+} AND Al^{3+} FOR ALL-SOLID-STATE LITHIUM ION BATTERIES
15:00-15:20	SP08_012_OF	Worranun Wongchompoo	HYDROPHOBIC CELLULOSE FROM CORN HUSK
15:20-15:40	SP08_014_OA	Tammanoon Chankhanittha	SOLVOTHERMAL SYNTHESIS OF ZnO/BI_2MoO_6 CATALYST FOR PHOTODEGRADATION OF FLUOROQUINOLONE ANTIBIOTIC AND CATIONIC DYE

Symposium:	SP04-Development of Material Science Based on Coordination Compounds		
Room:	9th Floor, 902		
Building:	Sisattha Building		
Chair person:	Prof. Dr. Takumi Konno		
Co-chair:	Dr. Mati Horprathum		
Time	ID	Speaker	Title
13:30-14:00	SP04_INV001	Kuang-Lieh Lu	OPTICAL AND ELECTRONIC APPLICATIONS OF METAL–ORGANIC FRAMEWORKS
14:00-14:30	SP04_INV002	Fuk Yee Kwong	PALLADIUM-CATALYZED SITE-SELECTIVE MULTICOMPONENT PROCESSES FOR FACILE ASSEMBLY OF SUBSTITUTION-MANIPULATED POLYCYCLIC ARENES
14:30-15:00	SP04_INV003	Pichaya Pattanasattayavong	SEMICONDUCTORS FROM COORDINATION POLYMERS AND THEIR APPLICATIONS IN ELECTRONIC DEVICES
15:00-15:20	SP04_004_OA	Arnon Kraipok	THE PROPERTIES OF FLUORCANASITE-LITHIUM DISILICATE DENTAL GLASS-CERAMICS WITH DIFFERENT HEAT TREATMENT TEMPERATURES
Break			
15:30-15:50	SP04_005_OA	Manlika Kamnoy	EFFECT OF CaO ON THE HEAT TREATMENT TEMPERATURE, MICROSTRUCTURE AND MECHANICAL PROPERTIES OF LITHIUM DISILICATE-BASED GLASS-CERAMICS FOR DENTAL APPLICATION
15:50-16:10	SP04_010_OA	Chutikan Nakornkhet	RING-OPENING POLYMERIZATION OF MACROLACTONES BY WELL-DEFINED ALUMINUM COMPLEXES
16:10-16:30	SP04_011_OA	Kanokon Upitak	CONTROLLED RING-OPENING POLYMERIZATION OF CYCLIC ESTER MONOMERS BY TITANIUM(IV) COMPLEXES
16:30-16:50	SP04_013_OF	Parinya Thongyindee	SYNTHESIS OF NaA ZEOLITE USING WASTEWATER TREATMENT CHEMICAL SLUDGE FROM GLASS FACTORY AND ALUMINIUM WASTE AS Si AND Al SOURCE
16:50-17:10	SP04_014_OA	Preeyanuch Sangtrirutnugul	SELF-ASSEMBLED COPPER–TRIAZOLE CLUSTERS: SYNTHESIS AND CATALYTIC APPLICATIONS

Symposium:	SP13-Natural Products for Drug Discovery		
Room:	12th Floor, 1201		
Building:	Sisattha Building		
Chair person:	Prof. Dr. Vatcharin Rukachaisirikul		
Time	ID	Speaker	Title
13:00-13:30	SP13_INV001	Apichart Suksamrarn	BIOREDUCTIVE PRODRUG DESIGN OF NATURAL PRODUCTS FOR BREAST CANCER THERAPEUTIC AGENTS
13:30-13:50	SP13_007_OA	Suriphon Singha	POLY-*O*-ACYLATED β-DIHYDROAGAROFURAN SESQUITERPENOIDS FROM *Siphonodon celastrineus* FRUITS
13:50-14:10	SP13_032_OA	Patcharee Arsakhant	DESIGN AND SYNTHESIS OF NEW 12-DITHIOCARBAMATE-14-DEOXY-ANDROGRAPHOLIDES AS ANTICANCER AGENTS
14:10-14:30	SP13_036_OA	Jakkapong Inchai	THE ASSESSMENT OF *Ocimum sanctum L.* AQUEOUS EXTRACT FOR AMELIORATING LIPID CONTENTS IN NON-ALCOHOLIC FATTY LIVER DISEASE
14:30-14:50	SP13_002_OF	Natchapon Kammasit	EFFECT OF *Anoectochilus burmannicus* AQEOUS EXTRACT ON OBESOGENS-INDUCED ADIPOCYTE TRANSFORMATION
14:50-15:20	SP13_INV002	Xiaoguang Lei	TRANSLATIONAL NATURAL PRODUCT RESEARCH
Break			
15:30-16:00	SP13_INV003	Marc Stadler	NEW EVIDENCE ON THE FUNCTIONAL BIODIVERSITY AND SECONDARY METABOLITE PRODUCTION OF THE XYLARIALES (ASCOMYCOTA) BASED ON EXTENSIVE METABOLOMIC STUDIES AND THE EVALUATION OF HIGH QUALITY GENOME SEQUENCES
16:00-16:20	SP13_012_OA	Juthatip Jeenkeawpieam	ANTIFUNGAL ACTIVITY AND MOLECULAR MECHANISMS OF PARTIALLY PURIFIED ANTIFUNGAL PROTEINS FROM *Rhinacanthus nasutus* AGAINST *Talaromyces marneffei*
16:20-16:40	SP13_005_OF	Ratchanon Inpan	NANO-PHYTOSOME ENTRAPPING *Gymnema inodorum* EXTRACT FOR ENHANCING ANTI-INFLAMMATION IN MACROPHAGE

Session:	Poster Presentation		
Room:	2nd Floor		
Building:	Sisattha Building		
Time	ID	Speaker	Title
16:30-18.00		-	Poster Presentation (Session: A-E)
16:30-18.00		-	Poster Presentation (YRSS)

Session:	STT46 Congress Banquet		
Room:	2nd Floor		
Building:	King Ramkhamhaeng the Great Auditorium		
Time	ID	Speaker	Title
18:00-20:00		-	Banquet

OCTOBER 7th, 2020

Session:	YRSS		
Room:	10th Floor, 1002, 1003, 1006, 1007 (YRSS Oral Presentation) / 12th Floor, 1201		
Building:	Sisattha Building		
Time	ID	Speaker	Title
8:30-9:30		-	YRSS Oral Presentation (10th Floor)
Break			
12:00-12:30		-	YRSS Awarding Session (12th Floor)

Session:	TYSA		
Room:	12th Floor, 1201		
Building:	Sisattha Building		
Time	ID	Speaker	Title
10:00-12:00		-	TYSA Workshop “THE FUTURE IS NOW: SCIENCE FOR SDGS”

Session:	A-Challenges in the Frontiers of Physics		
Room:	3rd Floor, 301		
Building:	Sisattha Building		
Chair person:	Dr. Suparerk Aukkaravittayapun		
Time	ID	Speaker	Title
10:00-10:30	A_INV001	Masaru Hori	PLASMA MEDICINE TOWARD A FUTURE MEDICAL CARE
10:30-11:00	A_INV002	Guosheng Xu	NUCLEAR FUSION RESEARCH IN CHINA FOR INEXHAUSTIBLE ENERGY
11:00-11:20	A_006_OA	Wananurat Srijampan	EFFECT OF SILICON CARBIDE CONTENT ON SINTERED STEEL MICROSTUCTURE
11:20-11:40	A_007_OA	Kittikhun Ruangchai	EFFECTS OF Mo AND W ON MICROSTRUCTURE AND HARDNESS IN ANNEALED 28wt.%Cr CAST IRONS
11:40-12:00	A_012_OA	Prasong Kessaratikoon	NATURAL RADIOACTIVITY MEASUREMENT AND EXCESS LIFETIME CANCER RISK EVALUATION IN SURFACE SOIL AND BEACH SAND SAMPLES COLLECTED FROM RAYONG PROVINCE, THAILAND
12:00-12:20	A_008_OA	Nattaphong Nuchsirikulaphong	STUDENT LEARNING TOWARDS DIFFERENT LESSON SEQUENCES IN FORCE AND MOTION

Symposium:	SP01-Biodiversity of Marine Benthic Fauna		
Room:	8th Floor, 802		
Building:	Sisattha Building		
Chair person:	Prof. Supawadee Chullasorn		
Time	ID	Speaker	Title
9:40-10:10	SP01_INV001	Jong Seong Khim	BIODIVERSITY OF MARINE MACROBENTHOS IN KOREA
10:10-10:40	SP01_INV002	Sung Joon Song	BIODIVERSITY OF MARINE MEIOBENTHOS IN KOREA
10:40-11:10	SP01_INV003	Wirulda Pootakham	GENETIC DIVERSITY OF CORALS AND THEIR ASSOCIATED SYMBIONTS
11:10-11:30	SP01_005_OF	Mathinee Yucharoen	DOES COASTAL EROSION INFLUENCE DOMINANT MACROBENTHIC INVERTEBRATES ON SONGKHLA SANDY BEACHES?
11:30-11:50	SP01_006_OA	Suraphol Chunhabundit	STUDY ON THE SURVIVAL RATE OF ASIAN CLAMWORM *Perinereis aibuhitensis Grube*, 1878 REARING IN THE DIFFERENCES DENSITY OF THE SPF CULTURED SYSTEM
11:50-12:10	SP01_008_OA	Anocha Poommouang	DECREASING THE GENETIC DIVERSITY OF DUGONG (*Dugong dugon*) IN THE SEA OF THAILAND

Symposium:	SP02-Climate change in a changing world		
Room:	8th Floor, 803		
Building:	Sisattha Building		
Chair person:	Assoc. Prof. Dr. Suchana Chavanich		
Time	ID	Speaker	Title
9:40-10:10	SP02_INV001	Wenxi Zhu	UN DECADE OF OCEAN SCIENCE FOR SUSTAINABLE DEVELOPMENT (2021-2030)- A DECADE FOR ACCELERATING SOLUTIONS TO CLIMATE CHANGE?
10:10-10:40	SP02_INV002	Kim Holmen	CLIMATE CHANGE IN POLAR REGIONS
10:40-11:10	SP02_INV003	Witiya Pittungnapoo	CLIMATE CHANGE ADAPTATION IN CULTURAL HERITAGE
11:10-11:30	SP02_001_OF	Wachira Suwannarut	EFFECT OF HIGH TEMPERATURE STRESS ON PHOTOSYNTHETIC CAPACITY AND OXIDATIVE DAMAGE IN POTTED YOUNG LONGAN TREE (*Dimocarpus longan* LOUR. 'PHUANG THONG')

Symposium:	SP06-Flattening the Curve - Renewable Energy in Times of Climate Change		
Room:	8th Floor, 806		
Building:	Sisattha Building		
Chair person:	Asst. Prof. Dr. Helmut Duerrast		
Time	ID	Speaker	Title
9:40-10:10	SP06_INV001	Kampanart Silva	ENERGY RESILIENCE: ENHANCING CLIMATE ADAPTATION CAPABILITY OF RENEWABLE ENERGY SYSTEMS
10:10-10:40	SP06_INV002	Pimpa Limthongkul	ENERGY STORAGE AND ITS POTENTIAL IMPACT ON CLIMATE CHANGE MITIGATION
10:40-11:00	SP06_001_OA	Wipada Ngansom	GEOTHERMAL RESOURCES IN SOUTHERN THAILAND – A POSSIBLE CHOICE FOR RENEWABLE ENERGY
11:00-11:20	SP06_002_OA	Waraporn Rattanongphisat	PASSIVE HEAT MITIGATION POSSIBILITY USING METEOROLOGICAL DATA ANALYSIS FOR BUILDING APPLICATION IN THE TROPICS
11:20-11:40	SP06_003_OA	Helmut Duerrast	ACHIEVING 100% RENEWABLE ELECTRICAL ENERGY FOR SOUTHERN THAILAND
11:40-12:00	SP06_004_OF	Fongkul Palichareonpol	OILGAE CULTIVATION IN MUNICIPAL WASTEWATER AND MODIFIED EXTRACTION METHOD

Symposium:	SP07-From Thailand to Antarctica: the 2020 Thai-Australian Expedition for Space Science		
Room:	8th Floor, 807		
Building:	Sisattha Building		
Chair person:	Dr. Alejandro Sáiz		
Time	ID	Speaker	Title
9:40-10:10	SP07_INV001	David Ruffolo	OVERVIEW OF THAI RESEARCH ON COSMIC RAYS
10:10-10:40	SP07_INV002	Waraporn Nuntiyakul	RESPONSE FUNCTIONS OF NEUTRON DETECTORS TO COSMIC RAYS AS MEASURED DURING OCEAN VOYAGES TO ANTARCTICA FROM THE PAST TO THE PRESENT
10:40-11:10	SP07_INV003	Alejandro Sáiz	FROM THAILAND TO ANTARCTICA: THE 2020 THAI-AUSTRALIAN EXPEDITION FOR SPACE SCIENCE
11:10-11:30	SP07_001_OA	Dumrongsak Rodphothong	FLUKA SIMULATIONS FOR EVALUATION OF SPACECRAFT SHIELDING MATERIALS AGAINST SOLAR PARTICLE EVENTS
11:30-11:50	SP07_002_OF	Hannarong Janthaloet	SEARCHING FOR CLUSTERS OF HIGH-ENERGY γ-RAY PHOTONS USING *FERMI* LAT OBSERVATIONS
11:50-12:10	SP07_003_OA	Pradiphat Muangha	NEW GROUND-BASED COSMIC RAY DETECTORS AND UPGRADE OF THE NEUTRON MONITOR AT MAWSON STATION, ANTARCTICA

Symposium:	SP11-Lichens: Diversity, Ecology and Biomonitoring		
Room:	5th Floor, 501		
Building:	Sisattha Building		
Chair person:	Assoc. Prof. Dr. Achariya Rangsiruji		
Time	ID	Speaker	Title
9:40-10:10	SP11_INV001	Ekaphan Kraichak	HOST CHARACTERS INFLUENCING RICHNESS AND ABUNDANCE OF EPIPHYTIC LICHENS
10:10-10:30	SP11_007_OA	Pitakchai Fuangkeaw	ANNUAL LITTERFALL BIOMASS OF EPIPHYTIC MACROLICHENS IN PRIMARY AND SECONDARY FORESTS AT KHAO YAI NATIONAL PARK
10:30-10:50	SP11_008_OA	Vasun Poengsungnoen	SPECIES DIVERSITY OF LICHEN FAMILY GRAPHIDACAEA IN MANGROVE FORESTS: EASTERN AND UPPER SOUTHERN PARTS OF THAILAND

Symposium:	SP15-Science-based Sustainable Tourism		
Room:	9th Floor, 902		
Building:	Sisattha Building		
Chair person:	Dr. Thamasak Yeemin		
Time	ID	Speaker	Title
9:40-10:10	SP15_INV001	Zulfigar Yasin	SCIENCE-BASED SUSTAINABLE TOURISM IN THE TROPICAL MARINE AND COASTAL AREAS
10:10-10:40	SP15_INV002	Si Tuan Vo	RESTORATION AND CONSERVATION OF REEF BENTHIC SPECIES VULNERABLE TO AQUARIUM TRADE FOR SUSTAINABLE TOURISM IN TROPICAL WATERS
10:40-11:10	SP15_INV003	Worajit Setthapun	SMART COMMUNITY CONCEPT FOR RESOURCE AND WASTE MANAGEMENT OF ECO-VILLAGE
11:10-11:40	SP15_INV004	Tadashi Kimura	REPORTS ON THE STATUS OF CORAL REEFS IN EAST ASIAN SEAS REGION: IMPORTANT BASELINE DATA FOR SUSTAINABLE TOURISM MANAGEMENT
11:40-12:00	SP15_001_OA	Felipe M G Mattos	ASSESSMENT OF REEF FISH DIVERSTY IN A TURBID WATER ECOSYSTEM OF MU KO ANG THONG
12:00-12:20	SP15_007_OA	Anirut Klomjit	MACROALGAE DIVERSITY AND COMPOSITION IN CORAL REEF AT SAMUI ISLANDS, THE WESTERN GULF OF THAILAND
12:20-12:40	SP15_016_OA	Thamasak Yeemin	DEVELOPMENT OF MARINE ECOTOURISM SITES ON UNDERWATER PINNACLES IN THE EASTERN AND WESTERN GULF OF THAILAND

SESSION A

Challenges in the Frontiers of Physics
Chair: Dr. Suparerk Aukkaravittayapun

Over many decades, Physics has spilled over its boundaries set by its definition originally quoted, and we now have fields such as econophysics, sociophysics, biological physics, geological physics and medical Physics. Physics is not just Science but also a tool of approaching scientific problems which is different from other sciences. Thailand and the whole world are facing so many crucial problems. What are the frontiers in Physics which may lift-off or relieve those problems; food, energy, environment, disease, human wellbeing, etc.? These are our challenges. This session welcomes presentations from fundamental to applied research related to Physics particularly frontiers in Physics and its interdisciplinary to address possible or potential solutions for present and future of humanity.

Invited Speakers

Prof. Dr. Guosheng Xu

Prof. Dr. Masaru Hori

SESSION B

Math Stat Comp in the Digitally Innovative Era
Chair: Assoc. Prof. Dr. Chartchai Leenawong

In 2016, one of the World's Chinese GO game champions was simply defeated by Google's AlphaGo machine. The more astonishment than the defeat was the algorithms behind the AI. Even more surprisingly, in 2017, another AI machine Libratus also crushed a top Poker player in the world. Due to the game's known nature to be complex and full of psychology use, presumably possessed only in human, it was thus natural to believe that no technological advances could have beaten us! And now AI has proved us all wrong. In this session of Mathematics, Statistics, and Computer Science in the Digitally Innovative Era, the main focus is on the cutting edge of mathematical, statistical, and computational theories, concepts, and algorithms that drive the world of digital innovation. It is aimed to attract diverse groups of all professions including, but not limited to, professors, researchers, graduate students, mathematicians, statisticians, computer scientists, cognitive scientists, policy-makers, software developers, as well as AI practitioners. We hope this session will provide an opportunity for interaction and dissemination of findings among all digital innovators, so as to open up the world of unimaginative possibilities, yet practical and inspirational.

Invited Speakers

Prof. Brigitte Servatius

Dr. Antony James Harfield

SESSION C

Impact of Biological Science towards SDGs
Chair: Asst. Prof. Dr. Noppadon Kitana

1. Active Learning for Biological Science Classes - With this era of learning, 21st century skills are important for this generation. Biological sciences is one of the basic disciplines for SDGs. Previously, biological science classes were full of contents and memorization. Do we still need contents in classes? How can we develop 21st century skills in our students? We would like to invite all instructors to share your experiences in active learning or other learning methodology that can develop the required skills and knowledge in biological sciences in all areas, from molecular biology through ecology.
2. Biological Sciences towards SDGs - In order to reach SDGs, biological sciences research is one of the important pieces. The studies of life sciences in all disciplines and taxa are welcome to share your recent discovery in this congress. These include the researches in microbes, protozoans, plants, animals and human from molecular, cell, whole organism, population through ecological system levels.

Invited Speakers

Prof. Dr. Kesara Anamthawat-Jónsson

Prof. Dr. Luca Comai

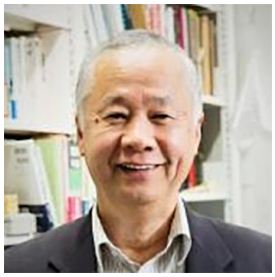

Prof. Dr. Riyoichi Matsuda

Assoc. Prof. Dr. Phiangphak Sukkharak

SESSION D

Responsible Chemical Sciences for Future Sustainability
Chair: Prof. Dr. Orawon Chailapakul

Today, Chemical Sciences face a new challenge: reconciling the technological progress and well-being of people with the preservation of the planet, from a Bioeconomy, Circular economy and Green economy perspectives. The congress has a comprehensive program and includes presentations from a number of eminent scientists. More importantly, the congress aims to bring together scientists from academia and industry to present leading-edge research on the advancements in chemical science, technology and innovation with a particular emphasis on those aiming to preserve and improve the quality of life for future sustainability. The congress will address how to overcome problems such as the economic crisis in a scientific point of view and how to incorporate technology in getting solutions to such problems across the Globe. In addition to the main congress, there are organized several important symposia as showcases of how the chemistry innovation progress under the theme, "Responsible Chemical Sciences for Future Sustainability".

Keynote and Invited Speakers

Prof. Dr. Oliver Reiser

Assoc. Prof. Dr. Taweetham Limpanuparb

Dr. Taro Toyota

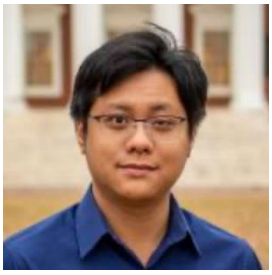

Dr. Pamidech Puthongkham

SESSION E

Innovations for Sustainable Future
Chair: Prof. Dr. Tawan Sooknoi

Innovation has been defined as the process of using knowledge and technology to develop or improve the production or performance of products, services or processes, or to look for solutions to undefined needs that have value in terms of commercial impact, or social benefit. To ensure continued, sustainable growth and development of our future, technology-based innovation is necessarily required. This symposium welcomes contributions from various sectors, actively involving the development of products, services or processes derived from multidisciplinary researches. We are encouraging submission of diverse presentations, both oral and poster presentations, to share and stimulate ideas for the progress of technology-based innovation.

Keynote and Invited Speakers

Dr. Pun-Arj Chairatana

Dr. Sasitorn Srisawadi

Dr. Soracha Dechaumphai

SYMPOSIUM SP01

Biodiversity of Marine Benthic Fauna
Chair: Prof. Supawadee Chullasorn

The purpose of this symposium is to bring researchers from all around the world to share and discuss the taxonomy and ecology of marine benthic fauna. Marine biodiversity includes coastal and marine benthic invertebrates, as well as their genetic variety, habitats and ecosystems. Benthic fauna refers to various organisms and are divided into two groups: Epifauna, which lives on the surface of sandy beaches, mangrove forests, seagrass beds, algal beds, coral reefs, etc., and Infauna, which lives within the sediment of those habitats. This symposium will focus on morphology, evolution, diversity and distribution of sediment-dwelling, e.g. Harpacticoid copepods, Nematodes, Polychaetes, Amphipods, Isopods, etc. Finally, we would like to welcome you to this symposium to share and learn many new aspects of marine benthic fauna.

Invited Speakers

Prof. Dr. Jong Seong Khim

Assoc. Prof. Sung Joon Song

Dr. Wirulda Pootakham

SYMPOSIUM SP02

Climate change in a changing world
Chair: Assoc. Prof. Dr. Suchana Chavanich

Over the last decades, our environment has been threated and impacted globally by the climate change. People are experiencing both partial and severe effects of the climate change. How does the change impact local and global scales? How does the climate change affect the outcome of biological, ecological, and/or socio-economic trajectories in the changing world? What are the key knowledge gaps that must be urgently addressed for a better management? This session welcomes presentations on both basic and advanced research topics related to climate change including but not limited to impact, warning, adaptation, reduction, and solution.

Invited Speakers

Prof. Dr. Kim Holmen

Asst. Prof. Dr. Witiya Pittungnapoo

Wenxi Zhu

SYMPOSIUM SP03

Crystallography
Chair: Prof. Dr. Nongnuj Muangsin

X-ray crystallography is the experimental science and is by far the most powerful method to determine the arrangement of atoms of a crystalline solid in three-dimensional space. This method has been used in structural chemistry and biological macromolecules for over a century. In the biological crystallography, three-dimensional structures of molecules such as proteins and nucleic acids are determined at atomic level. This helps us to understand the basic mechanisms of biomolecules, as well as aid in novel drug discovery. In chemical crystallography, the determination of crystal structures of organic, organometallic and coordination compounds (i.e. coordination polymers and metal-organic frameworks) is of great importance and highly valuable for understanding the structure-property relationship as well as supramolecular interactions (such as hydrogen bonds, halogen bonds, and π–π stacking) of the crystalline solids. Moreover, it also brings about crystal engineering for better structural design and achievement of desired functionalities.

Invited Speakers

Dr. Bunyarat Rungtaweevoranit

Dr. Marie Hoarau

SYMPOSIUM SP04

Development of Material Science Based on Coordination Compounds

Chair: Prof. Dr. Takumi Konno

In the past decades, a large number of coordination compounds have been prepared from a variety of transition metal ions in combination with organic and/or inorganic ligands. In many cases, intra- and intermolecular non-covalent interactions strongly affect the overall structures of the resulting compounds to induce unique functionalities. Thus, the controlled introduction of non-covalent interactions in coordination compounds is greatly desirable for the future innovational development of material science based on coordination chemistry. This symposium will focus on coordination systems, in which intra- and/or intermolecular non-covalent interactions, such as hydrogen-bonding, metallophilic, π-π, and ionic interactions, play an important role to their structures, properties, and functionalities.

Invited Speakers

Prof. Kuang-Lieh Lu

Prof. Fuk Yee Kwong

Dr. Pitchaya Pattanasattayavong

SYMPOSIUM SP05

Emerging Trends of Quantum Technology
Chair: Assoc. Prof. Dr. Anucha Watcharapasorn

Quantum mechanics has entered its second generation where nondestructive individual manipulation and measurement of trapped quantum systems are technologically accessible. Precipitately, disruptive industrial revolution has been realized among scientists and engineers; the result of close collaboration aiming for deep technologies are evidently marvelous. Financially stimulated by numerous parties on a global scale, new breed of scientists who are fluent in quantum mechanics as well as broad engineering skillset uninterruptedly builds up to undertake practical quantum technology. Here, updates on quantum research activities and recent development in accordance with creating a quantum ecosystem are centralized for discussion. All opinions from multi-disciplinary scientists are appreciably invited to participate in this symposium.

Invited Speakers

Prof. Yoshiro Hirayama

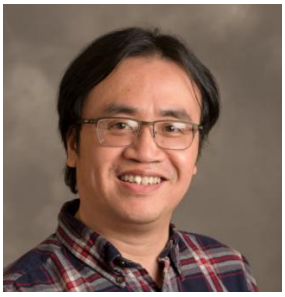

Prof. Hai Q. Dinh

Assoc. Prof. Tsutomu Nojima

Asst. Prof. Shau-Yu Lan

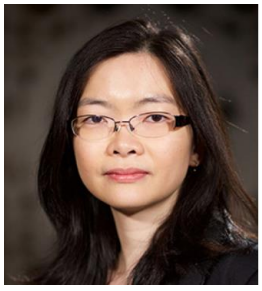

Dr. Areeya Chantasri

Dr. Nithiwadee Thaicharoen

SYMPOSIUM SP06

Flattening the Curve - Renewable Energy in Times of Climate Change
Chair: Asst. Prof. Dr. Helmut Duerrast

Climate change is an ongoing and accelerating threat to mankind, and although developing countries, like Thailand, in the past might not have contributed to the greenhouse gas emissions like others, they will likely experience its impact severely, from droughts, over extreme weather phenomena, to sea level rise. Therefore, the ultimate goal for the next two to three decades has to be a complete decarbonization of the energy, transport, cocking, and cooling/heating sectors through the rise of renewable energy sources, in Thailand mainly solar PV, some wind, hydro, biomass, and geothermal; the latter one has a potential in Thailand, although comparable small, as it is a continuous and time independent source. As the future will be mainly based on electrical energy, it will be supported by a decentralized and intelligent grid structure.

Invited Speakers

Dr. Kampanart Silva

Dr. Pimpa Limthongkul

SYMPOSIUM SP07

From Thailand to Antarctica: the 2020 Thai-Australian Expedition for Space Science

Chair: Dr. Alejandro Sáiz

Between January and March 2020, two scientists from Mahidol University, Thailand, joined the annual expedition to the Australian base of Mawson, Antarctica. Our mission: to perform several upgrades in the Mawson Cosmic Ray Laboratory, the oldest cosmic-ray-science experiment running continuously until the present time in the Southern Continent. After the successful installation of updated software and electronics firmware and some extra neutron detectors, the data obtained from this experiment has been expanded to include, besides the existing measurements of cosmic ray flux, new information about cosmic ray energy. During this long trip onboard the Aurora Australis icebreaker, we also learned about other scientific projects in the Australian Antarctic Program. In this talk, I will present some details about my once-in-a-lifetime experience of visiting Antarctica and the scientific motivation for such an adventurous journey.

Invited Speakers

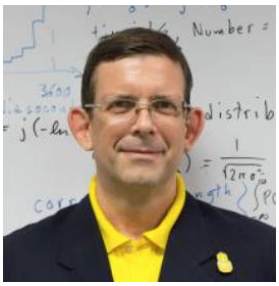

Prof. Dr. David Ruffolo

Asst. Prof. Dr. Waraporn Nuntiyakul

Dr. Alejandro Sáiz

SYMPOSIUM SP08

Green and Sustainable Chemistry: Opportunities for Academia and Industry
Chair: Prof. Dr. Joseph Samec

Even if climate change may not stop us from using fossil fuels, the supply will within 50 years according to BP:s latest report. Thus, we will need to find a new feedstock for our needs for producing chemicals for: food-, material-, transportation-, pharmaceutical production. The non-eatable part of biomass, lignocellulose is such a source that grows widely in both agriculture (stems, husks, etc) and in forestry. In addition to this, chemists will need to build up fundamental understanding and develop new methodologies and processes. This session will discuss how academia and industry can collaborate to smoothen this transition and welcomes papers regarding topics on Green and Sustainable Chemistry: -from fundamental studies to industrial implementations.

Invited Speakers

Christian Dahlstrand

Willem Böttger

SYMPOSIUM SP09

Green Production Platform for Renewable Biomass Conversion

Chair: Assoc. Prof. Dr. Nuttha Thongchul

Recently, bioprocessing and bioproducts have gained commercial interest due to the perceived “GREEN” benefits of using biomass rather than fossil-based feedstocks for the production of chemicals and industrial products. Other key benefits of bioproducts include the sustainability of renewable biomass, replacing depleted fossil energy and reducing greenhouse gas emissions from the petroleum based chemical and energy industries. With the rising crude oil prices and advances in industrial biotechnology, the potential of biomass utilization becomes huge. This symposium will feature the important applications in biotechnology and recent developments in bioprocessing technologies for biomass utilization. All papers from both academia and industry relevant to development of bioprocessing platform development using the tools of molecular biology, genetic as well as metabolic and process engineering are invited.

Invited Speakers

Prof. Dr. Benjamas Chiersilp

Dr. Kobkul Laoteng

Dr. Nuwong Chollacoop

SYMPOSIUM SP10

Hydrogen Energy
Chair: Prof. Dr. Suttichai Assabumrungrat

Hydrogen has become a promising choice of clean and reliable energy carriers for sustainable development of the world. This symposium welcomes researchers, scientists, engineers and professionals from all over the world to present their latest research results, challenges and new ideas in the field of Hydrogen Energy. Topics include, but not are limited to, hydrogen production, hydrogen storage, hydrogen supply chain, hydrogen applications and hydrogen-related technologies.

Keynote and Invited Speakers

Prof. Dr. Nigel Brandon Obe Freng

Prof. Dr. Navadol Laosiripojana

Dr. Sumittra Charojrochkul

Arunratt Wuttimongkolchai

Assoc. Prof. Dr. Suwimol Wongsakulphasatch

Asst. Prof. Dr. Pattaraporn Kim-Lohsoontorn

Dr. Sakhon Ratchahat

SYMPOSIUM SP11

Lichens: Diversity, Ecology and Biomonitoring
Chair: Assoc. Prof. Dr. Achariya Rangsiruji

Lichens consist of fungi that live in a biological relationship with algae or cyanobacteria. Lichens are key players in a variety of environmental processes. Found from cold regions such as polar regions to extremely hot areas like deserts, there are approximately 20,000 species worldwide. There are currently many researches focusing on understanding the nature of lichens. The entire field of research in lichenology, from using genomic approaches to understand the lichen symbiosis to the ecological roles for enhancing our knowledge in diversity and evolution of lichens and applied aspects, such as the use of lichens to monitor air pollution and climate change as well as novel products. This symposium aims to bring together researchers, research scholars, students and those interested to exchange and share their experiences and research results on all aspects of lichen. It also provides a premier interdisciplinary platform for researchers, practitioners and educators to present and discuss the most recent innovations, trends, and concerns as well as practical challenges encountered, and solutions adopted in the fields of lichenology.

Invited Speakers

Asst. Prof. Dr. Ekaphan Kraichak

SYMPOSIUM SP12

Marine Plastic Abatement
Chair: Prof. Dr. Thammarat Koottatep

Plastic waste becomes an issue of global concern as indicated by severe plastic pollution in both terrestrial and marine ecosystems in several countries, mostly lacking of efficient plastic waste policies, management systems, and technologies. This growing concern is about the use of plastics and their effects on the environmental pollution and human health. Innovation is a key solution to address the challenges and bring plastic management towards sustainability. This session focuses on the processes in dealing with growing environmental issues of plastic wastes covering efficient utilization, reuse, recycle, recovery and reduction. The session will contribute to all aspects of plastics waste processing and disposals including technical and non-technical aspects that encompass multidisciplinary researches on how plastics entering the environment, and the risks plastics pose to wildlife, human and aquatic communities.

Invited Speakers

Prof. Chettiyappan Visvanathan

Prof. Chongrak Polprasert

Dr. Amila Abeynayaka

SYMPOSIUM SP13

Natural Products for Drug Discovery
Chair: Prof. Dr. Vatcharin Rukachaisirikul

Natural products (NPs) have played a key role in drug discovery research, as the chemical structure diversity and wide-ranged biological activities of NPs make them the most valuable sources of drugs and drug leads. About 40% of all medicines is either natural products or their semi-synthetic derivatives. NPs research continues to explore a variety of lead structures, which may be used as templates for the development of new drugs by the pharmaceutical industry. Most efforts on NP-based drug discovery have involved a screening of biological samples for desirable bioactivities, the compounds' isolation and characterization followed by drug design and synthesis based on natural compounds. Advances in bioinformatics, structural biology, proteomics, genomics and metagenomics, and analytical technologies, such as high-throughput screening platform, have recently contributed to the rapid identification and characterization of NPs leads. Accordingly, this symposium seeks submissions from scientists, researchers and graduate students to share their latest research findings in the field of natural products. Contributions should be related to isolation and structure elucidation, chemical biology, medicinal chemistry, chemical methods, chemical synthesis and drug design.

Invited Speakers

Prof. Dr. Apichart Suksamrarn

Prof. Dr. Marc Stadler

Prof. Dr. Xiaoguang Lei

SYMPOSIUM SP14

Promoting Research Integrity
Chair: Dr. Roderick Bates

Progress in Science and Technology is based upon trust. We trust that researchers whose work we read or use have been honest, balanced, unbiased and fair. This trust is undermined when we hear of cases of fraudulent or fabricated work, by instances of plagiarism, by disputes over credit and authorship, by the omission of necessary controls and procedures, and by the nefarious activities of predatory publishers. To retain trust, and especially the trust placed in researchers by society, academic institutions have to promote research integrity amongst their faculty, students and staff. How can this best be done, and what are the best practices that can be adopted?

Invited Speakers

Prof. Dr. Chien Chou

Dr. Daniel Barr

Dr. De-Ming Chau

SYMPOSIUM SP15

Science-based Sustainable Tourism
Chair: Dr. Thamasak Yeemin

The tourism industry continues to be a very important sector for the economic development of many countries around the world. Sustainable tourism should make optimal use of environmental resources that can maintain essential ecological processes and conserve biodiversity. A strategy to create integrated planning systems for managing sustainable tourism is using science-based data. Scientific knowledge plays an important role for understanding ecosystems related to tourism and how to sustain their functions. In this symposium, scientists and managers working in Thailand and other countries are gathered to present their experiences from research, management, monitor and conservation aspects, focusing on sustainable tourism. Some lessons learned from terrestrial and coastal tourist destinations will be highlighted, including a capacity enhancement for monitoring and research, community-based management, ecotourism and marine protected areas.

Invited Speakers

Prof. Dr. Zulfigar Yasin

Dr. Si Tuan Vo

Dr. Worajit Setthapun

Tadashi Kimura

SYMPOSIUM SP16

360° COVID-19
Chair: Prof. Sopit Wongkham

Coronavirus disease 2019 (COVID-19) pandemic has ravaged all regions around the world creating serious global health crisis. Coronavirus disease or COVID is caused by coronavirus (CoV) include other well-known diseases such as Severe acute respiratory syndrome (SARS), and Middle East respiratory syndrome (MERS). For COVID-19, it is caused by Severe acute respiratory syndrome coronavirus 2 (SARS-CoV-2), which was first reported last December from Wuhan, China. Until today, more than 25 million confirmed cases of COVID-19 and more than 800 thousand deaths have been reported across the globe. The pandemic has caused great negative social and economic impacts of our generation, which must be extinguished as soon as possible. To accomplish this, knowledge on the molecular mechanisms of the disease, improved methods for screening and diagnosis, and also preventive and therapeutic measures are urgently needed. This symposium brings together leading COVID-19 Thai researchers whose work encompasses everything that will help support the fight against COVID-19 pandemic.

Invited Speakers

Prof. Kiat Ruxrungtham, M.D.

Assoc. Prof. Arunee Thitithanyanont, M.D.

Dr. Pilailak (Akkapaiboon) Okada

ABSTRACTS FOR KEYNOTE AND INVITED SPEAKERS

INVITED SPEAKER: A_INV001

PLASMA MEDICINE TOWARD A FUTURE MEDICAL CARE

Masaru Hori*

Nagoya University, 464-8603, Furo-cho, Chikusa-ku, Nagoya, Japan
*e-mail: hori@nuee.nagoya-u.ac.jp

Abstract:
Applications of plasmas to the medicine is the frontier topics involving many sciences, which have been initiated by the development of non-thermal atmospheric pressure plasmas. In general, these plasmas have directly interacted with cells or with the liquid, where the cells were stimulated through the plasma activated liquid. Their fruits brought a great potential not only for the anti-tumor effects, immunotherapy and the decomposition of infection, but also for the enhancement of the growth of various kinds of cells, which is leading to the hemostasis and wound. Recently, the indirect plasma treatment to cells, where the plasma activated the liquid and the liquid itself is introduced to the cells and animals. It was found out that the plasma activated medium (PAM) and plasma activate lactic acid (PAL) enabled to kill the cancer cells against normal ones in vitro and in vivo. These results are groundbreaking because the plasma activated solution played roles for the therapy as the plasma-synthesized drug. Additionally, these findings have expanded their applications furthermore to the various kinds of medical care.
In this presentation, I will show the characteristics of ultrahigh density atmospheric pressure plasma source of the electron density beyond $10^{16}cm^{-3}$ for the plasma medicine. We investigated the spatial distribution of behaviors of the electron density, the electron temperature and atomic species of H, N, O and OH by using the laser Thomson scattering, the vacuum ultraviolet absorption spectroscopy and the laser induced fluorescence, respectively. Secondary, results of the liquid and/or organism irradiated by these species are discussed. The interactions of reactive species and/or charged particles with such liquid and organism is a key issue to establish the plasma bio science. Particularly, the ROS/RNS species play important roles to stimulate the cells and living tissues. We have investigated the behaviors of ROS/RNS such as short live species of OH and long live species of NO_2^- and NO_3^- together with H_2O_2 by using the Electron Spin Resonance (ESR) and the UV absorption spectroscopy. The kinetics of these chemical element in PAM was much different from those in the PBS and a pure water. Thirdly, I will introduce the great performances of PAM and PAL, which are exhibiting strong antitumor effects on glioblastoma, ovarian, gastric, and pancreatic cancers. Through in vitro and in vivo experiments, we have developed novel and innovative medical uses for the plasma irradiation of culture medium, including selective induction of apoptosis to destroy cancer cells. It is of crucial importance to develop a fundamental theory to explain the control of eukaryotic cellular behaviors by integrating information from the plasma science with the development of the frontier of physics and chemistry, the medical science, the molecular biology, the biochemistry and the cell biology. Understanding of the universal molecular mechanisms underlying the selective cell death induced by plasmas will eventually pioneer the future medical care.

INVITED SPEAKER: A_INV002

NUCLEAR FUSION RESEARCH IN CHINA FOR INEXHAUSTIBLE ENERGY

G.S. Xu*, B.N. Wan

Institute of Plasma Physics, Chinese Academy of Sciences, Hefei 230031, China
*e-mail (speaker): gsxu@ipp.ac.cn

Abstract:
Nuclear fusion that powers the sun potentially offers a clean, environmentally friendly and intrinsically safe energy source with an abundant fuel supply. From nearly seven decades of worldwide effort to develop fusion energy using the hydrogen isotopes deuterium (D) and tritium (T) as fuel, a vast knowledge base has been established of science and technology for creating and controlling high-temperature plasmas. One of the most promising approaches to harnessing fusion energy has been developed by using magnetic fields to confine a plasma inside a doughnut-shaped vessel known as a Tokamak, by heating the plasma to over 100 million degrees Celsius with sufficient density and energy confinement time.
Magnetic confinement fusion research is approaching a new era of fusion power reactor design and construction, as evidenced by a joint international effort to build a power-plant-scale tokamak device, International Thermonuclear Experimental Reactor (ITER, Latin for 'the way'), which will come into operation in 2025, to demonstrate the scientific and technological feasibility of steady-state fusion power production.
As one of key member of the ITER project, China has planned to build a prototype fusion power plants, China Fusion Engineering Test Reactor (CFETR) [1], to bridge the gap between ITER and the first commercial fusion power plant. To develop key technologies of CFETR and build R&D test platforms, a satellite program "Comprehensive Research Facility for Fusion Technology" (CRAFT) has been launched since last year [2].
China now has 3 tokamaks in operation: EAST, HL-2A and J-TEXT. EAST is the world's first fully superconducting tokamak with modern divertor configurations and actively water-cooled plasma facing components. Before EAST, China had serval tokamaks: HT-7, HT-6M, HT-6B, HL-1M, HL-l, CT-6 and KT-5. Besides, a new tokamak HL-2M will come into operation at the end of this year. In recent years, China has made substantial progress in tokamak experiments. It has been demonstrated in the recent EAST experiments that a fully non-inductive high β_p ($\sim$2) H-mode plasma ($H_{98y2} \geq 1.3$) has been obtained for a duration over 100 current diffusion times, which sets another new world record of long-pulse high-performance tokamak plasma operation with the normalized performance approaching the ITER and CFETR regimes [3]. The research conducted in existing devices significantly strengthen the physical basis to achieve high-performance burning plasmas in the next-generation large devices.
A cooperation between China and Thailand has been established in the field of magnetic fusion research. On 15 July 2018, a ceremony for donating HT-6M Tokamak to Thailand was held in ASIPP (Institute of Plasma Physics Chinese Academy of Sciences) with the presence of Princess Sirindhorn, see Figure. Up to now, more than 100 Thai students and young scientists have been trained at ASIPP. This cooperation will strengthen the scientific and technological connection and friendship between China and Thailand.

Reference

[1] Y. X. Wan et al., Nucl. Fusion 57, 185004 *(*2017*).*
[2] J. Li et al., J. Fusion Energy 38, 113 *(*2018*).*
[3] B. N. Wan, Chin. Phys. Lett. 37, 045202 *(*2020*).*

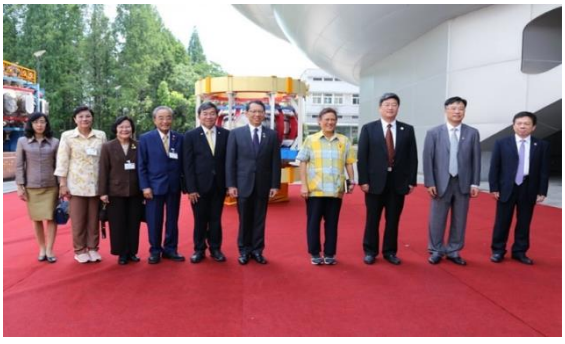

Figure. Ceremony for donating HT-6M Tokamak to Thailand with the presence of Princess Sirindhorn (2018.07.15)

INVITED SPEAKER: B_INV001

AI FOR SOCIAL GOOD: AUDIO-BASED THREAT DETECTION FOR PROTECTING FORESTS

Antony Harfield*

Department of Computer Science & Information Technology Faculty of Science, Naresuan University, Phitsanulok, Thailand
*e-mail: antonyh@nu.ac.th

Abstract:
The last year has seen significant press coverage for the destructive possibilities of artificial intelligence (AI). At the same time, there is a growing area of research into AI for solving humanitarian and environmental challenges, that Google has coined "AI for Social Good". The topic of this talk is using audio-based threat detection models for the environmental challenge of protecting rainforests, national parks and conservation areas. It will explain the components of a system developed by a non-profit organisation, Rainforest Connection, that is successfully catching illegal activity in rainforests in Asia and South America. The critical component is the machine learning model which transforms a raw waveform into a spectrogram and performs image classification using convolutional neural networks (CNNs) to detect vehicles, chainsaws and other human-like activities. Using machine learning models running in real-time on incoming audio streams, the system can alert people on the ground to intervene and it records evidence for the legal authorities to take action.

INVITED SPEAKER: B_INV002

STRESSABILITY OF MULTIDIMENSIONAL FRAMEWORKS

Brigitte Servatius[1,*], Oleg Karpenkov[2], Christian Mueller[3], Gaiane Panina[4], Herman Servatius[1], Dirk Siersma[5]

[1] Worcester Polytechnic Institute (WPI), USA
[2] University of Liverpool, UK
[3] Technical University of Vienna, Austria
[4] St. Petersburg University, Russia
[5] University of Utrecht, Netherlands
*e-mail: bservat@wpi.edu

Abstract:
We prove an equilibrium stressability criterium for trivalent multidimensional tensegrities. The criterium appears in different languages: (1) in terms of stress monodromies, (2) in terms of surgeries, (3) in terms of exact discrete 1-forms, and (4) in Cayley algebra terms.

INVITED SPEAKER: C_INV001

TOWARDS BRYOPHYTE FLORA OF THAILAND: TAXONOMIC REVISIONS OF THE LIVERWORT GENERA *Frullania*, *Pleurozia*, AND *Metzgeria* IN THAILAND

Phiangphak Sukkharak*

Department of Biology, Faculty of Science, Burapha University, Chonburi, Thailand
*e-mail: phiangphak@buu.ac.th

Abstract:
Bryophytes are non-vascular plant group consisting of mosses, liverworts, and hornworts. Few studies of Bryophytes have been conducted in Thailand due to the previous shortage of the expertise on these plants in the country. However, since 2012, Thai bryologists have been actively working together on floristics and taxonomic revisions of bryophytes in Thailand. In 2017, during the 17th Flora of Thailand Conference, the Bryophyte Flora of Thailand project was initiated to accelerate the taxonomic revisions of bryophytes in Thailand through publications and increase awareness of this important group of plants for the future sustainable uses. The progress of the project and the challenges encountered will be discussed. In addition, as part of the project, taxonomic revisions of the liverwort genera *Frullania*, *Pleurozia*, and *Metzgeria* in Thailand will be presented. Of the 39 species of *Frullania* reported in Thailand, three species including *F. hypoleuca*, *F. ramuligera*, and *F. sinuata* are newly recorded for the country. Three species of *Pleurozia* are recognized as well as an appendage on the keel of the dorsal lobule is described in *P. subinflata*. Five species of *Metzgeria* are reported. Of these, *M. kinabaluensis* is newly recorded for Thailand.

Figure. *Frullania sinuata* Sande Lac. (left), *Pleurozia gigantea* (F.Weber) Lindb. (middle), and *Metzgeria consanguinea* Schiffn. (right)

INVITED SPEAKER: C_INV002

PROGRESS AND OPPORTUNITIES FOR RESHAPING PLANT GENOMES VIA CRISPR

Lynagh P, Hungsaprug K, Amundson KR, Ordoñez B, Fossi M, Chadchawan S, Henry IM, Comai L*

Department of Plant Biology and Genome Center, University of California Davis, Davis, CA 95616, USA
*e-mail: lcomai@ucdavis.edu

Abstract:
Plant genome editing is currently practiced for two common purposes: gene knockout and sequence replacement. Both entail a targeted dsDNA cut, while the second requires the additional provision of a homologous DNA template. A third purpose, is the structural remodeling of selected genomic regions. One example is the reshuffling of promoter regions, which we applied to a rice promoter by applying multiple cuts and screening for rearrangements. Another example, is the engineering of chromosomal translocations. We have used induced and natural DNA breaks in arabidopsis and potato to trigger and study these events. We will show the effect of plants' flexible ploidy, meristematic growth, and lack of predetermined germline on the retention of karyotypic novelty. We document both non- homologous and homologous recombination of selected chromosomes including copy- neutral loss of heterozygosity and chromoanagenesis. Our observations provide a framework for understanding the consequences of DNA breaks and strategies for engineering of plant genomes.

INVITED SPEAKER: C_INV003

JAPANESE JUNIOR AND SENIOR HIGH SCHOOL BIOLOGY EDUCATION ARE FAR FROM "NEW NORMAL"

Ryoichi Matsuda[1,2,3*]

[1]Tokyo University of Science, Japan
[2]The University of Tokyo, Japan
[3]The International Biology Olympiad, Germany
*e-mail: cmatsuda@rs.tus.ac.jp

Abstract:
All educational and business facilities were locked down due to the pandemic of COVID-19 from April 7 to the end of May 2020 in Japan. During this period, a 300% increase in unexpected pregnancy in adolescence was reported from pregnancy consultation supporting centers. One of the reasons for the rise was the lack of knowledge of Human Biology in adolescent youth in Japan. Surprisingly, our governmental standard education curriculum for junior high school-biology prescribes to teach the development of non-human animals, such as sea urchins and frogs but not humans. Standard education curriculum physical education clearly defines not to guide human pregnancy. The governmental education curriculum for high school biology also describes the development of non-human animals such as frogs and flies significantly in detail, almost at the college textbook levels, but tends to avoid human cases. The standard education curriculum of high school physical education also mentions to teach a part of human pregnancy but at the minimum level only.
During the International Biology Olympiad week, I had a chance to see a biology textbook for ages 13 to 14 students in the Netherlands, "Your Biology 2a". To my surprise, there are clear descriptions of the mechanism of a human pregnancy and ways for birth control in detail and descriptions of sexually transmitted diseases and the methods to avoid them. "Your Biology 2a" is not the only one to describe Human Biology, but textbooks of other countries also contain Human Biology parts for students. Human Biology should be common knowledge for Japanese teenagers, too. Then, I decided to publish a translated version of "Your Biology2a" in Japanese. The translated version was finally posted on September 10, 2020, making a sensation in Japan.
Human Biology is not limited to reproductive biology, but also other issues such as infection, nutrition, and mental health. For unknown reasons, bacterial and viral diseases, except HIV infection, are also missing in Japanese governmental education standards for junior and high school biology. There is no description for influenza nor hepatitis viruses. There is no description of intoxication caused by microorganisms and toxins. In the 1940s and 50s, Japanese biology textbooks were written by biologists, medical scientists, and agronomists. But for unknown reasons, only biologists wrote biology textbooks after that. I imagine that the cause can be explained by historical discrimination or battle between MDs and PhDs in our country. It is silly and should be fixed if my guess is correct. In my talk, I would like to try to explain these issues in detail. I wonder if this story contains a lesson to be learned from it.

INVITED SPEAKER: C_INV004

IMAGING BIOLOGICAL SAMPLES BY SCANNING ELECTRON MICROSCOPY

Kesara Anamthawat-Jónsson*

Institute of Life and Environmental Sciences, School of Engineering and Natural Sciences, University of Iceland, Askja – Sturlugata 7, Reykjavík, IS-102, Iceland
*e-mail: kesara@hi.is

Abstract:
Scanning electron microscope (SEM) is a type of electron microscope that produces images of a sample by scanning the surface with a focused beam of electrons. The aim of this presentation is to demonstrate the use of the new generation SEM model JEOL-JSM-6610 for imaging various types of biological samples, producing publishable results. This SEM offers an alternative low-vacuum/high-voltage mode (e.g. 20 Pa & 10kV, as opposed to the standard high vacuum mode of 270 Pa & 30 kV). This low-vacuum mode allows observation of uncoated and non-conductive (biological) specimens. This particular SEM is equipped with an additional back-scattered electron detector, which adds topographical resolution. Because there is no need to sputter-coat the sample to make it conductive (which is expensive), our young researchers and students can afford to use it. In this presentation I will show examples of SEM projects conducted so far, from imaging eggshells (Figure, left) and sheep wool in the Viking age archaeological projects, differentiating pollen species in plant genetic researches, seeds and spores in botanical projects, to investigating diatom diversity (Figure, right) in Lake Thingvallavatn, the largest rift valley lake in southwest Iceland, the UNESCO World Heritage Site. SEM is an important tool in scientific research and diagnostic applications.

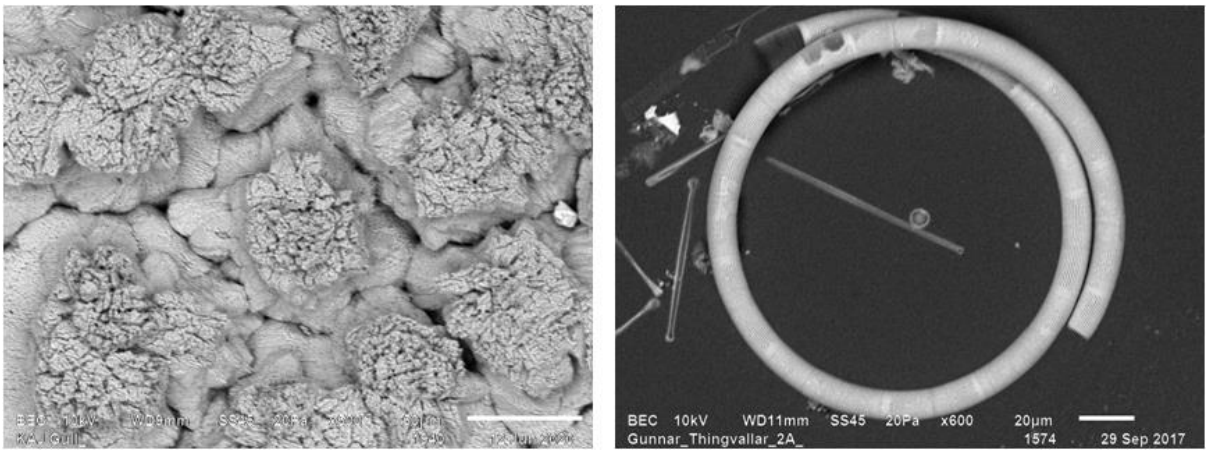

Figure. SEM images of eggshell mammillae from an egg of the black-headed gull (*Chroicocephalus ridibundus*) from Ólafsvík, Snæfellsnes Peninsula, at x500 magnification (left) and of *Aulacoseira islandica*, the largest centric diatom and the most abundant species from Lake Thingvallavatn, at x600 magnification (right).

KEYNOTE SPEAKER: D_KEY001

COPPER MAKES THE DIFFERENCE: DEVELOPING SUSTAINABLE PHOTOREDOX CATALYZED TRANSFORMATIONS

Oliver Reiser*

Institut für Organische Chemie, Universität Regensburg, Universitätsstr. 31, 93053 Regensburg, Germany
*e-mail: oliver.reiser@chemie.uni-regensburg.de

Abstract:
Synthetic organic chemistry undertakes great efforts to develop new catalytic transformations that utilize greener reagents and avoid stoichiometric additives. In this regard, visible-light photoredox catalysis offers a unique activation mode of molecules, which is serving as an alternative to many thermal transition-metals catalyzed reactions. The vast majority of photoredox catalyzed processes capitalizes on heavy metals namely, Ru(II) or Ir(III)-complexes which can serve as single electron oxidant or reductant in their photoexcited states. As a low cost-alternative, organic dyes are also frequently used photocatalysts but suffer in general from lower photostability. Copper based photocatalysts are rapidly emerging, offering not only economic and ecologic advantages, but in addition are able to interact with substrates beyond electron transfer via inner sphere mechanisms, which has been successfully utilized to achieve challenging transformations. Moreover, the combination of conventional photocatalysts with copper(I) or copper(II) salts allows a most efficient merger of photoredox and transition metal based catalysis.
Selected synthetic applications from our laboratory, highlighting the complementary opportunities of copper and iridium based photocatalysts, will be discussed.

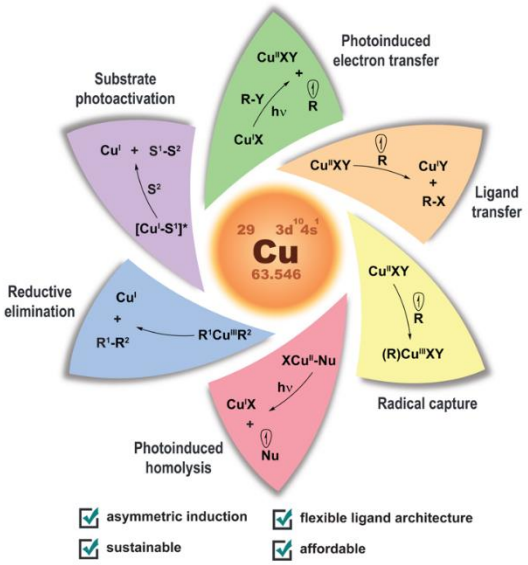

INVITED SPEAKER: D_INV001

GIANT VESICLE ENGINEERING: BIOSENSOR AND CELL/TISSUE-MARKER

Taro Toyota*

Department of Basic Science, Graduate School of Arts and Sciences,
The University of Tokyo, Japan
*e-mail: cttoyota@mail.ecc.u-tokyo.ac.jp

Abstract:
A giant vesicle (GV) is a closed lipid bilayer membrane having a diameter of 1 µm or more in water. GVs can be individually observed in real time under an appropriate optical microscope even though the bilayer membrane has the thickness of 5 – 6 nm. Since their constituent molecules, structure, and size resemble those of cell membranes, GVs have recently attracted interest as cell models not only in chemistry but also in a wide range of research fields including physics, life sciences, and bioengineering.
The preparation and manipulation methods of GVs have been substantially improved for this decade. Among them, we have promoted improvement of two technologies: the water-in-oil (W/O) emulsion template method for GV preparation and the microfluidic device for size-sorting and trapping of individual GVs. The W/O emulsion template method is a process through wrapping W/O emulsion droplets (surrounded by a lipid monolayer) by a lipid monolayer formed at the interface between the emulsion and water phases. As a result, GVs encapsulate water-soluble substances and water-dispersed particles with a high volume ratio. In the manipulation method of GVs, we have developed an integrated microfluidic device with size-sorting mechanics implemented by the deterministic lateral displacement (DLD) and trapping mechanism of GVs. By DLD, large GVs are bumped up when the GV collides to periodically juxtaposed microposts because of its excluded volume, while small GVs swim straightly among the microposts. As a result of a fluidic effect, only GVs of selected diameter are introduced into the trapping microstructure, and secondary GVs cannot enter the microstructure once a GV is trapped. This microfluidic device enables us simultaneous observation of dynamics of multiple GVs upon external stimuli.
GV has drawn much attention as a new sensing device. It provides a micrometer-sized reaction field that is surrounded by soft boundary and composed of biodegradable molecules (i.e. lipids), and membrane proteins anchored in the bilayer membrane become effective for specific molecular sensing at GV. For example, we synthesized an insect hormone receptor which is a complex of two membrane proteins inside of the GV and demonstrated that this receptor functions in GV by the patch clamp technique. The researches on GV-based sensors with high substrate specificity and reaction specificity will continue to leap forward.
In recent years, along with the development of medical technology, the development of minimally invasive medical technology for improving patient's quality of life has been strongly demanded, and laparoscopic surgery is a typical example. In laparoscopic surgery where the lesion cannot be touched directly, careful preoperative simulation and navigation that can accurately indicate the location of the lesion inside the organ to the surgeon during surgery are important. The positioning error of the lesion on the monitor with the navigation system based on the results of X-ray computed tomography (CT) or magnetic resonance imaging (MRI) still remains unsolved. We have proposed a concept of multimodal cell/tissue marker in which contrast agents of each inspection device and near-infrared fluorescent dye (for the near-infrared fluorescence laparoscopy) are densely encapsulated in the same GV or GV aggregate prepared by the W/O emulsion template method. The effective use of multimodality of GVs is expected for medical applications.

INVITED SPEAKER: D_INV002

A VIRTUAL ALTERNATIVE TO MOLECULAR MODEL SETS: CONSTRUCTING AND VISUALIZING MOLECULES IN MOLECULAR GRAPHICS SOFTWARE

Siripreeya Phankingthongkum, Taweetham Limpanuparb*

Science Division, Mahidol University International College, Salaya, 73170, Thailand
*e-mail: taweetham.lim@mahidol.edu

Abstract:
The application of molecular graphics software as a simple and free alternative to conventional molecular modelling media for introductory-level chemistry learners is presented. Based on either Avogadro or IQmol, we proposed four sets of tasks for students, VSEPR theory & Bent's rule, electron density & orbitals, polarity of molecules & vibrational spectroscopy, stereochemistry & bond-line structure. These topics are typically covered in general chemistry for first-year undergraduate students. Details procedures and results from an undergraduate class will be discussed in the session. Instructors and students can adopt one of the two programs in their teaching and learning as a cheaper and long-distance alternative to molecular model sets.

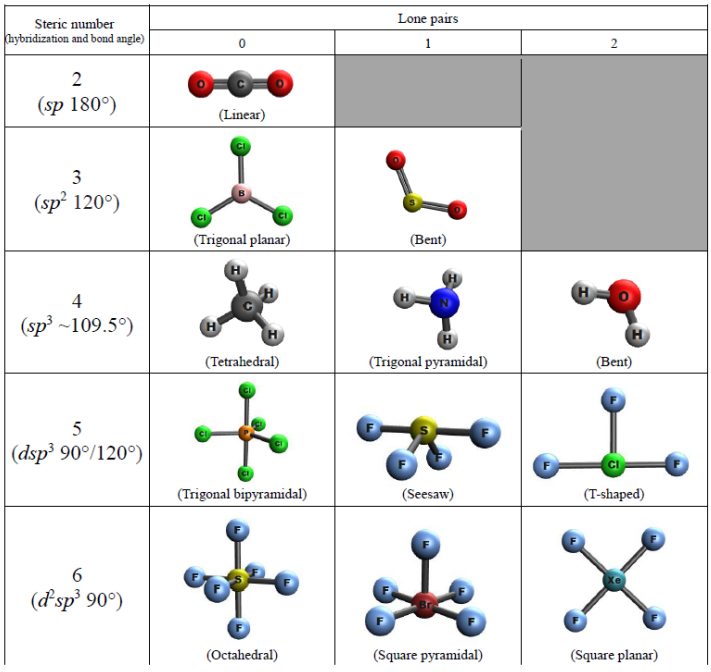

Figure. A sample work for students to build molecules from various templates.

INVITED SPEAKER: D_INV003

EXPANDING THE TOOLBOX FOR REAL-TIME ELECTROCHEMICAL DETECTION OF NEUROTRANSMITTERS

Pumidech Puthongkham*

Department of Chemistry, Faculty of Science, Chulalongkorn University, Bangkok, Thailand
*e-mail: pputhongkham@gmail.com

Abstract:
Chemical neurotransmission in living systems has been mainly investigated by electrochemical techniques. In particular, fast-scan cyclic voltammetry (FSCV) has been developed to study subsecond neurotransmitter dynamics in animal models. Here, we present multiple independent ways to improve the analytical performance of FSCV. First, we explored the redox mechanism of histamine, which is an important neurotransmitter that has not been investigated before. Histamine oxidation required 1.1 V vs Ag/AgCl at carbon electrodes, generated polymer products, and fouled the electrodes. Histamine electrochemical fouling at carbon-fiber microelectrodes was alleviated by Nafion coating. Second, we improved the electrochemical properties of a carbon-fiber microelectrode by nanodiamond coating. Carboxylated nanodiamonds doubled the sensitivity and improved the limit of detection (to 3 nM) toward dopamine detection due to their electrocatalytic properties and surface functional groups. The nanodiamonds also limited electrochemical fouling and biofouling from *in vivo* detection. Third, we developed an image processing-based software to automate the FSCV data analysis for adenosine detection. The software utilized structural similarity index to compare FSCV current-potential-time data to adenosine references, leading to better accuracy and precision (1% false negatives and 5% false positives) for adenosine identification. The algorithm was also generalized to identify adenosine and dopamine co-release simultaneously, demonstrating its potential for multiplex analysis. Overall, mechanism investigation, electrode development, and data analysis are independent ways to improve FSCV and will lead to the powerful tools for the better understanding of our brain chemistry.

INVITED SPEAKER: E_KEY001

TRILOGY OF CRISIS: REIMAGING INNOVATION FOR SUSTAINABLE FUTURE

Pun-Arj Chairatana*

National Innovation Agency (NIA), Thailand
*e-mail: punarj.chairatana@gmail.com

Abstract:
There are three major crisises the world is facing, namely pandemic, climate change, and global economy shrink-down. COVID-19 already accelerate s role of city as an engine of innovation through space and time, marking new life style and new jobs, while existing paradigm of innovation is mainly focuses on competition.
Traditional perception on innovation shows a limitation in responding to contemporary and future demands.
The aforementioned crisises derails mainstream innovation ideology and way we understand process disruption.
Sustainable development and scientific community are required to allign with emerging types of innovation like social, political, and aesthetic innovation.

INVITED SPEAKER: E_INV001

MULTIFUNCTIONAL THERANOSTIC RED BLOOD CELL MEMBRANE COATED NANOPARTICLES FOR THE TREATMENT AND DETECTION OF BREAT CANCER

Suphalak Khamruang Marshall[1,2], Soracha Dechaumphai[2,3*]

[1]Department of Radiology, Faculty of Medicine, Prince of Songkla University, 90110, Thailand
[2]Institute of Biomedical Engineering, Faculty of Medicine, Prince of Songkla University, 90110, Thailand
[3]Department of Biomedical Engineering, Faculty of Engineering, Mahidol University, 73170, Thailand
*e-mail: soracha.dec@mahidol.edu

Abstract:
Worldwide, breast cancer (BC) is the most common women's cancer. With current treatments, it is predicted between 2018 and 2025 deaths will increase by 17.1%. Of these deaths, 90% being caused by metastasis. The therapeutic potential of nanoparticles (NPs) -based drug delivery system for cancer has become greater attention in the past decade. However, the efficacy of NPs depends on how long they travel in the blood circulation and deliver drug safely to the target. Herein, a nature-inspired Targeting Theranostic red blood cell (RBC)-coated nanoparticle (TT-RBC-NP) platform (Figure (a)) was designed and fabricated for the treatment and diagnostic of breast cancer. Chemotherapeutic drug, doxorubicin (DOX), was loaded inside poly (lactic-co-glycolic acid) (PLGA) NP core and achieved a cumulative release over 5 days. The encapsulation efficiency and drug loading of TT-RBC-NPs were 45% and 20 wt.%, respectively. Red blood cell membrane (RBCm) was coated on NPs and used as a stealth shield of NPs to increase half-life of the NPs. TT-RBC-NPs had excellent targeting ability to EpCAM overexpressing BC cells, which resulted in cellular uptake in over 80% of the BC cell population with minimum uptake by the fibroblast cells as shown in Figure (b). Additionally, TT-RBC-NP fluorescence imaging visually indicating the accuracy and specificity of delivery to BC cells, decreasing potential off-target toxicity, functionalized imaging agent enabled real-time monitoring properties and preferentially eliminated cancerous cells. This platform shows promising new treatment for breast cancer.

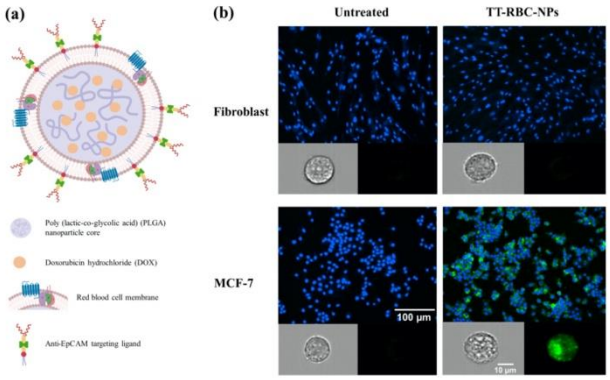

Figure. (a) Schematic representation of the multifunctional theranostic red blood cell membrane coated nanoparticles (TT-RBC-NP) (b) Co- localization of TT- RBC- NPs upon cellular uptake for targeted and non-targeted cells

INVITED SPEAKER: E_INV002

NEW 3D PRINTING TECHNOLOGY AND OPPORTUNITIES IN NATURAL RUBBER PRODUCT DESIGN

Sasitorn Srisawadi*, Panithi Wiroonpochit, Sittikorn Lapapong, Jomkwun Munnae, Kittaporn Utra, Surachai Rodsai

National Metal and Materials Technology Center, 114 Thailand Science Park, Phaholyothin Road, Klong Nueng, Klongluang, Pathumthani 12120, Thailand
*e-mail: sasitors@mtec.or.th

Abstract:
Additive manufacturing (AM; also known as 3D printing) is considered one of the most disruptive technologies because of its unique advantages in geometric design freedom and cost-effectiveness for small production runs. AM techniques for several types of metal and polymer have been thoroughly studied and widely commercialized. However, the technology for natural rubber is still commercially unavailable. This study developed and investigated a 3D fabrication technique of natural rubber products. A stereolithography (SLA) 3D printer, equipped with a UV laser source, was developed specifically for the natural rubber latex. Basically, the natural rubber latex is irradiated with the UV laser to create a layer of the desired shape. The technology was proven to be able to fabricate different types of natural rubber latex formulation upon an appropriate set of process parameters. Those parameters include repetition rate, scan speed, pulse width, hatch space, and layer thickness. The additively manufactured samples have mechanical properties and crosslink density which are comparable to those of the conventionally manufactured ones. In addition, it was found that the technology showed a promising feasibility in fabrication of complex rubber products. Specifically, adjustable internal structure designs enable a customization of product stiffness, while maintaining an exceptional degree of material flexibility. Innovative rubber product designs can be delivered based on the development of this fabrication technology.

INVITED SPEAKER: SP01_INV001

BIODIVERSITY OF MARINE MACROBENTHOS IN KOREA

Jong Seong Khim*, Sung Joon Song

School of Earth and Environmental Sciences & Research Institute of Oceanography, Seoul National University, Seoul, Republic of Korea
*e-mail: jskocean@snu.ac.kr

Abstract:
Here, we present the species assemblages and distributions of macrozoobenthos in Korean coastal waters. A comprehensive review was made by compiling the taxonomic and ecological studies conducted in the past 50 years. A total of 1,915 macrozoobenthic species belonging to 17 phyla has been compiled from 128 references. The phylum Mollusca was found to comprise the most abundant taxa (n=671), followed by Annelida (469), Arthropoda (433), and Cnidaria (103). The faunal distributions greatly varied by geographical regions (or locations) and/or type habitats. For example, the relatively great occurrence of soft bottom invertebrates was featured in the intertidal and subtidal areas of the West Sea and the South Sea. The most diverse taxa inhabit in the South Sea (1,103) followed by the West Sea (858) and the East Sea (621). The higher numbers in the South Sea would reflect its mixed characteristics in oceanographic settings, say combination of soft- and hard-bottom with moderate tidal environment. By habitat, the subtidal area showed the most enriched taxa followed by intertidal and estuarine areas, implying a dynamic underwater diversity. It should be noteworthy that some opportunistic species and/or organic enrichment indicators have long been observed in several specific regions or sites. Anthropogenic impacts such as large-scale reclamation, land-driven pollution, or oil spill accidents during the past decades could have deteriorated certain benthic environments. Overall, the present review confirmed the global marine macrozoobenthos hotspots in Korea. In the future, long-term monitoring efforts looking for the benthic community changes either under natural or altered conditions would be necessary to protect and manage our valuable marine ecosystem in Korea.

INVITED SPEAKER: SP01_INV002

BIODIVERSITY OF MARINE MEIOBENTHOS IN KOREA

Sung Joon Song*, Jong Seong Khim

School of Earth and Environmental Sciences & Research Institute of Oceanography, Seoul National University, Seoul, Republic of Korea
*e-mail: sungjoon@snu.ac.kr

Abstract:
A historical review focusing on marine meiobenthos of Korea is provided here. The studies on marine meiobenthos from Korean coastal waters began in the late 1980s with benthic copepods, and then gradually increased to phyla Tardigrada, Gastrotricha, Kinorhyncha, and Nematoda. To date, all 71 species of tardigrade belonging to 11 families and 27 genera have been described in Korea, of which 11 species in 2 families (6 new to science) were marine animals. Since the first record of gastrotrich in 1998, a total of 29 species of 3 families in order Macrodasyida (marine) were documented, among them 26 species turned out to be a new species (ca. 90%). A kinorhynch species, *Campyloderes macquariae* Johnston, 1938 was described for the first time in 2001. Total 21 species belonging to 8 families in 3 orders were listed as Korean fauna, interestingly, 18 species (ca. 86%) were newly described. Although phylum Nematoda is the most predominant taxon in Korean waters, only 54 species of 3 orders were described from subtidal bottoms (including 45 new species, 83%). Benthic harpacticoid and canuellid copepods, involving relatively many experts, currently comprises 99 genera with 168 species in 32 families, of which 101 species and 6 genera were new to science. We also discussed on the taxonomic status and nomenclature of each taxon.

INVITED SPEAKER: SP01_INV003

GENETIC DIVERSITY OF CORALS AND THEIR ASSOCIATED SYMBIONTS

Wirulda Pootakham[1,*], Wuttichai Mhuantong[2], Thippawan Yoocha[1], Thammasak Yeemin[3], Sittiporn Pengsakun[3], Sithichoke Tangphatsornruang[1]

[1]National Omics Center (NOC), National Science and Technology Development Agency (NSTDA), Pathum Thani, Thailand
[2]National Center for Genetic Engineering and Biotechnology (BIOTEC), National Science and Technology Development Agency (NSTDA), Pathum Thani, Thailand
[3]Marine Biodiversity Research Group, Faculty of Science, Ramkhamhaeng University, Bangkok, Thailand
*e-mail: wirulda@alumni.stanford.edu

Abstract:
Coral reefs are a complex ecosystem consisting of coral animals and a vast array of associated symbionts including the dinoflagellate Symbiodiniaceae, fungi, viruses and bacteria. Several studies have highlighted the importance of coral-associated bacteria and their fundamental roles in fitness and survival of the host animal. Here, we investigate the structure and diversity of algal and bacterial communities associated with five common Indo-Pacific coral species (*Pocillopora* spp., *Pavona decussata*, *Pavona frondifera*, *Porites lutea* and *Platygyra sinensis*) across three reef sites in the Gulf of Thailand, using full-length 16S genes and internal transcribed spacer (ITS) sequences generated from Pacific Biosciences (PacBio) circular consensus sequencing. While the dinoflagellate communities associated with *P. lutea* were dominated with Symbiodiniaceae genus *Cladocopium*, the other four coral hosts were associated mainly with members of *Durusdinium* genus, suggesting that host species was one of the underlying factors influencing the structure and composition of dinoflagellate communities associated with corals in the Gulf of Thailand. Alphaproteobacteria dominated the microbiome of *Pocillopora* spp. while *P. frondifera* and *P. lutea* were associated primarily with Gammaproteobacteria. The degree of influence that host identity had on the algal and bacterial assemblage structure and composition varied among coral species, with *P. lutea* exhibiting a strong influence on both associated Symbioniaceae and bacterial community compositions.

INVITED SPEAKER: SP02_INV001

UN DECADE OF OCEAN SCIENCE FOR SUSTAINABLE DEVELOPMENT (2021-2030)-A DECADE FOR ACCELERATING SOLUTIONS TO CLIMATE CHANGE?

Wenxi Zhu[1]*, Vo Si Tuan[2], Suchana Apple Chavanich[3], Fangli Qiao[4], Ken Ando[5], Yoon-Ho Lee[6], Somkiat Khokiattiwong[7], Thamasak Yeemin[8]

[1]Intergovernmental Oceanographic Commission of UNESCO
[2]Institute of Oceanography, Vietnam
[3]Chulalongkorn University, Thailand
[4]First Institute of Oceanography, Ministry of Natural Resources, China
[5]Japan Agency for Marine-Earth Science and Technology, Japan
[6]Korea Institute of Ocean Science and Technology, Korea
[7]Department of Marine and Coastal Resources, Thailand
[8]Ramkhamhaeng University, Thailand
*e-mail: w.zhu@unesco.org

Abstract:
With a drastic and sudden halt of human activities resulting from the COVID19, ocean ecosystems have been provided with the much-needed breathing time to recover. However, according to the latest United in Science 2020 report, climate change has not stopped for COVID 19, and greenhouse gas concentrations in the atmosphere are at record levels and continue to increase.
The ocean plays a central role in regulating the global climate, as it mediates temperature, drive the weather, and stores the largest portion of carbon on the planet. The increasing impacts of climate change affects oceans, economies and human livelihoods. Our sustainable future cannot be realized without a healthy, resilient and productive ocean. To ensure ocean science can fully support countries in achieving sustainable development of the oceans, seas and marine resources, the UN Decade of Ocean Science for Sustainable Development (2021-2030) offered all ocean stakeholders a unique, and once in a lifetime opportunity to shape a better ocean science agenda and connect ocean science more closely to society. This presentation will brief on the latest development of the Decade and its vision, objectives and Implementation Plan, and further serve as a call for Decade Actions for engagement.

INVITED SPEAKER: SP02_INV002

CLIMATE CHANGE IN POLAR REGIONS

Kim Holmén*

Norwegian Polar Institute, Fram Centre, Post box 6606 Langnes, N-9296 Tromsø, Norway
*e-mail: kim.holmen@npolar.no

Abstract:
Climate change is impacting the entire Earth. Parts of the polar regions are experiencing the largest temperatures changes of the entire globe. There are, however, large differences in how changes are proceeding in the two expanses.
The Arctic is an ocean surrounded by land. The Antarctic is a continent surrounded by ocean. The Northern hemisphere has several significant mountain chains (the Rocky Mountains, the Greenland ice and the Himalaya) creating more efficient exchange in the atmosphere between warmer regions and the high latitudes. In the ocean the currents are guided up the European (Norwegian) coast by the distribution of continents into the Arctic itself transporting heat into the basin. The Antarctic is much more isolated in the atmosphere and is surrounded by the circumpolar current in the ocean. This isolation leads to much lower temperatures in Antarctica than in the Arctic.
One important explanation for Polar amplification of global warming is the so-called albedo effect. The albedo effect is the feedback mechanism created by a surface changing color and thus changing its reflective capacity. When a white surface (ice or snow) is replaced by a darker surface (open water or ground) the surface will absorb more sunlight and consequently warm further.
In Antarctica the area with the most warming to date is on the Antarctic peninsula.
Extensive areas in the Arctic and its surroundings are in the proximity of zero degrees C and thus susceptible to melting also from modest temperature change. The Antarctic areas are much colder and will not be prone to melting even if temperature rises by a few degrees. The albedo effect is thus much more active in the Arctic at the present time.
The Arctic warms, on average, about twice as fast as the rest of the planet. The area in the Arctic that warms the most is the Svalbard archipelago with surrounding seas and the neighboring Franz Josef archipelago.
These warming trends have profound effects for Svalbard. We see decline in sea-ice, snow cover, glacier melting, permafrost thawing, and changes in precipitation. We see many consequences of these physical changes for the biosphere in the deterioration of habitat for the highly specialized high Arctic species. We see entry of lower latitude species in plants, fish, birds, plankton, and mammals. We see consequences for human beings with degenerations in safety, with the need for dramatic (unwanted) adaptation of behavior and life-style as well as economic consequences.
Changes in polar regions are mainly caused by emissions outside the polar regions. The changes in polar regions will impact well beyond the polar regions through changes in weather patterns, sea-level rise, consequences for migrating species, changes in fishing regions, changing shipping opportunities and other influences.
The ongoing climate change is jeopardizing a very special natural heritage on the planet. The polar regions as we know them are at risk, in some areas like Svalbard at severe risk. We must take the forewarning of the severity of climate change that we see in polar regions seriously. Climate changes are already well known elsewhere, but the Polar regions are a shrieking alert signal, for the hardships humanity will face if we fail to reverse the pressures humankind is imposing on the climate system through our emissions of greenhouse gases.

INVITED SPEAKER: SP02_INV003

CLIMATE CHANGE ADAPTATION IN CULTURAL HERITAGE

Witiya Pittungnapoo*

Faculty of Architecture, Naresuan University, Thailand
*e-mail: pwitiya@googlemail.com

Abstract:
A lesson learnt from flooding adaption in water-based archaeology sites in Thailand. Over the last half-decade, flooding is a natural disaster resulting in a wide range of impacts in and around the country; particularly on cultural heritage sites. Climate adaptation planning is a key mechanism to think global and act local which can be applied at local implementation. Flooding adaptation is a case in point which can be successfully applied to protect heritage archaeological sites in Ayutthaya. By integrating cultural heritage into climate change planning is a challenge which multi-disciplinary collaboration is required for achieving a resilient future.

INVITED SPEAKER: SP03_INV001

DISCOVERY OF NEW *Plasmodium falciparum* DHFR INHIBITORS USING A FRAGMENT-BASED SCREENING STRATEGY

Marie Hoarau*, Jarunee Vanichtanankul, Nitipol Srimongkolpithak, Danoo Vitsupakorn, Yongyuth Yuthavong, Sumalee Kamchonwongpaisan*

National Center for Genetic Engineering and Biotechnology (BIOTEC), National Science and Technology Development Agency (NSTDA), Pathumthani 12120, Thailand
*e-mail: marie.hoa@ncr.nstda.or.th; sumaleek@biotec.or.th

Abstract:
In various malaria-endemic regions, the appearance of resistance has precluded the use of antifolate drugs such as Pyrimethamine and Cycloguanil. At the molecular scale, drug resistance is the result of four successive mutations in the *Plasmodium falciparum* Dihydrofolate Reductase (*Pf*DHFR) enzyme active site that prevent drug binding. In order to by-pass this resistance problem, new drugs based on alternative chemotypes are needed.
In this context, we proposed to identify new chemotypes for *Pf*DHFR inhibitors using the fragment-based screening strategy. Starting from a 1163-fragment commercial library, a three-step screening cascade was used to identify eleven fragment hits. All fragments display IC_{50} in the 28-695 µM range and selectivity for *Pf*DHFR. In addition to the known pyrimidine, three new chemotypes were identified that have never been used in antimalarials.
Representative fragments from each chemotype were successfully co-crystallized with *Pf*DHFR, revealing novel modes of binding in the active site, in the vicinity of catalytic residues. Similar binding mode was independently confirmed by molecular docking on all fragment hits. Finally, comparison with similar non-hit fragments provided preliminary input on structure-activity relationship. These data will be used to design new drug candidates that could help forestall parasite resistance.

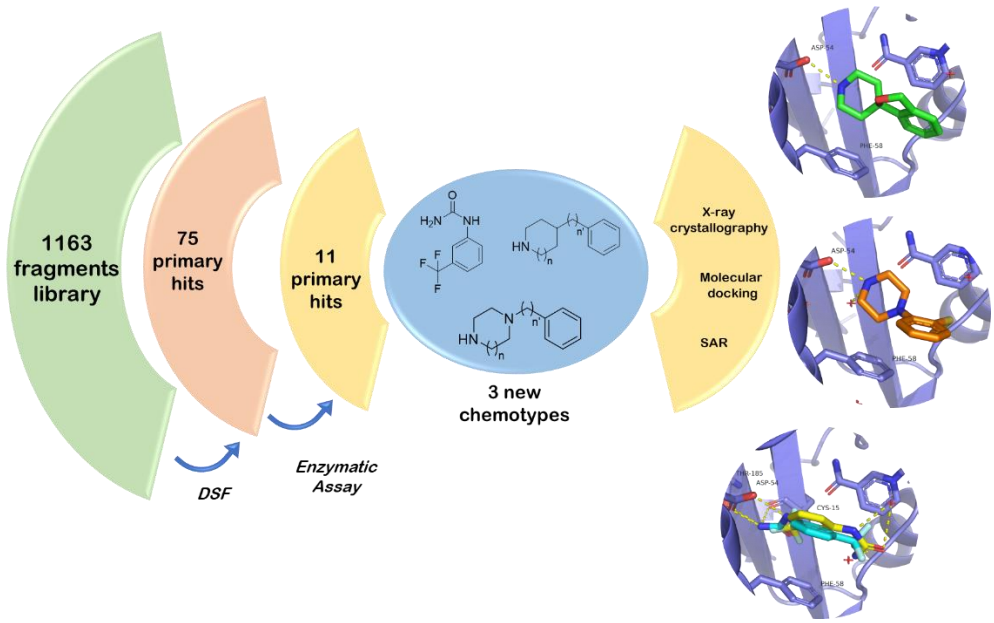

Figure. Graphical summary of the fragment-based screening on *Pf*DHFR.

INVITED SPEAKER: SP03_INV002

CHEMISTRY OF METAL-OXIDE NODES IN METAL–ORGANIC FRAMEWORKS AND ITS IMPLICATION IN HETEROGENEOUS CATALYSIS

Bunyarat Rungtaweevoranit*, Kajornsak Faungnawakij

National Nanotechnology Center (NANOTEC), National Science and Technology Development Agency (NSTDA), Pathum Thani 12120, Thailand
*e-mail: bunyarat.run@nanotec.or.th

Abstract:
Covalent assembly of organic and inorganic components into porous and crystalline materials gives rise to the construction of metal–organic frameworks (MOFs). Atomically-defined structures of this class of materials facilitated by X-ray crystallography provides a path toward rational design, synthesis, and structure-property correlations. These attributes are ideal for a wide variety of applications, one of which is heterogeneous catalysis. The metal-oxide nodes functioning as inorganic components in MOFs possess the chemistry, in some manner, similar to conventional metal oxides that are widely employed as heterogeneous catalysts. The distinctions lie in their i) structural definitiveness where locations of each atom are known; ii) spatial arrangement imposed by the topology of MOFs; and iii) synthetic precision where the size, shape, and composition of the nodes can be controlled. We employed these features to design catalysts for the following reactions. First, acid sites in a Zr-based MOF were used to catalyze the conversion of xylose to lactic acid, a monomer for biodegradable polylactide production. The Zr-oxide nodes were further modified to increase both the number of Lewis acid sites and their acid strength, thereby enhancing lactic acid yield while suppressing the formation of a furfural by-product. Second, the disposition of the metal-oxide nodes in appropriate locations was utilized to precisely place metal-binding ligands in nanospace, approximating a polypeptide backbone of an enzyme. Upon metalation, an active site inspired by particulate monooxygenase (pMMO) was thus created and the catalysts show high selectivity for partial methane oxidation to methanol, one of the holy grails in catalysis. Third, the discrete nature of the metal-oxide nodes in UiO-66 was employed to prepare a single-atom Cu catalyst that exhibits high catalytic activity for CO oxidation. The well-defined structure of the active site prompts us to use this catalyst as a model for a comprehensive mechanistic investigation for CO oxidation. The single-atom nature of the Cu active sites allows us to probe its electronic properties and structure under realistic conditions using element-specific spectroscopies including *in situ* and *operando* diffuse reflectance infrared, X-ray absorption, electron paramagnetic resonance spectroscopies without the need to employ surface-sensitive spectroscopies. Furthermore, the structural definitiveness of the active sites expedites the density functional theory calculation to establish the reaction mechanism where the reactive intermediate is molecular oxygen activated on the oxygen vacancy situated at the interface between Cu and Zr-oxide node of the MOF.

INVITED SPEAKER: SP04_INV001

OPTICAL AND ELECTRONIC APPLICATIONS OF METAL–ORGANIC FRAMEWORKS

Kuang-Lieh Lu[1,2,*]

[1]Institute of Chemistry, Academia Sinica, Taipei 115, Taiwan
[2]Department of Chemistry, Fu Jen Catholic University, New Taipei City 242, Taiwan
*e-mail: kllu@gate.sinica.edu.tw

Abstract:
Expanding the dimensions of metal−organic frameworks (MOFs) applications in the electronics industry has been gaining momentum in recent years. Due to their high porosity, variable functionality and structural tunability, MOFs have many potential applications in areas including gas storage, sensing, chemical separations, catalysis, magnetic and optoelectronics. MOFs with those unique properties promise to make them particularly suitable choices for use as electronic materials in the years to come. Our research has focused on the preparation and physical properties of various MOFs, including the fundamental dielectric, semiconducting and optical properties and we have summarized current state of the theoretical and experimental research. The findings promise to pave the way for further studies of MOFs with interesting potential applications in microelectronics. In this lecture, our journey towards optical and electronic applications of MOFs will be presented.

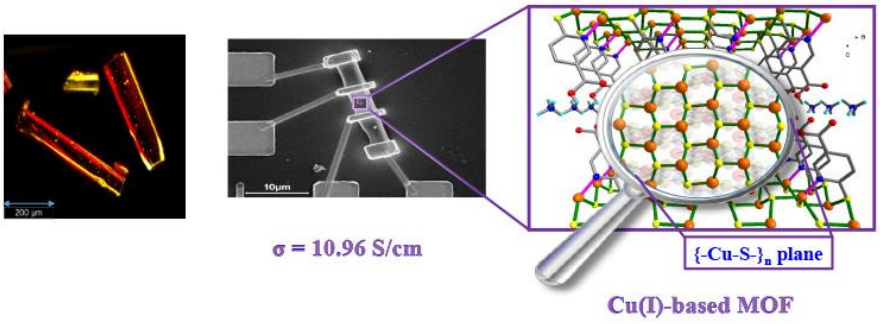

INVITED SPEAKER: SP04_INV002

PALLADIUM-CATALYZED SITE-SELECTIVE MULTICOMPONENT PROCESSES FOR FACILE ASSEMBLY OF SUBSTITUTION-MANIPULATED POLYCYCLIC ARENES

Fuk Yee (Michael) Kwong*

Department of Chemistry, The Chinese University of Hong Kong, Shatin, N.T., Hong Kong, China
*e-mail: fykwong@cuhk.edu.hk

Abstract:
Aromatic π-extension reaction has been versatile for new material assembly. In this presentation, we report the development of the three-component cross-coupling of aryl halides, 2-haloarylcarboxylic acids and norbornadiene. This transformation is driven by the direction and subsequent decarboxylation of the carboxyl group while norbornadiene serves as an ortho-C-H activator and ethylene synthon via a retro-Diels Alder reaction (1st equation). This method also offers a facile regiospecific manipulation of non-planar fused arene structures and also heptagonal-fused scaffolds. With this initial success, we further explored the cascade process of C-H activation/decarboxylation/annulation sequence (2nd equation). Most recently, we employed the arylhydrazone substrate for direct access of unsymmetrical fluorenes via a denitrogenative pathway (3rd equation).

C-H activation - decarboxylation - retro-Diels Alder reaction

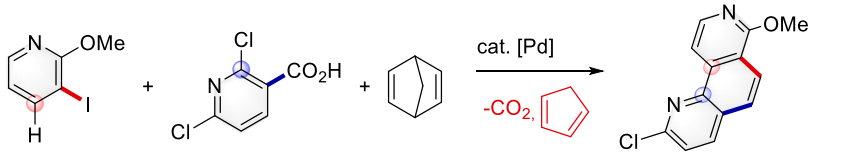

Angew. Chem., Int. Ed. **2017**, *56*, 7166

C-H activation - decarboxylation - annulation

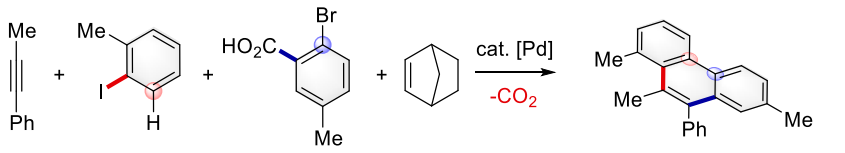

Angew. Chem., Int. Ed. **2018**, *57*, 3381

C-H activation - Heck-type reaction - Wolff-Kishner reduction

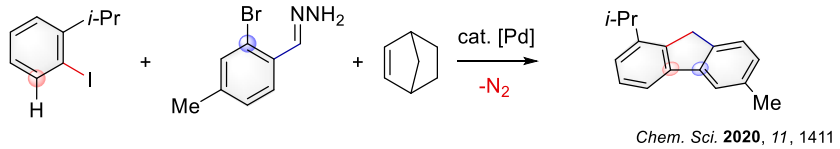

Chem. Sci. **2020**, *11*, 1411

INVITED SPEAKER: SP04_INV003

SEMICONDUCTORS FROM COORDINATION POLYMERS AND THEIR APPLICATIONS IN ELECTRONIC DEVICES

Pichaya Pattanasattayavong[1,2,*]

[1]Department of Materials Science and Engineering, School of Molecular Science and Engineering, Vidyasirimedhi Institute of Science and Technology (VISTEC), Rayong, 21210, Thailand
[2]Research Network of NANOTEC-VISTEC on Nanotechnology for Energy, Vidyasirimedhi Institute of Science and Technology (VISTEC), Rayong, 21210, Thailand
*e-mail: pichaya.p@vistec.ac.th

Abstract:
Beyond silicon and III-V compounds, new semiconductors have emerged from classes of materials previously unexpected of semiconducting properties, such as organic molecules and polymers or metal oxides. Coordination compounds, hybrid materials consisting of metal centers and organic ligands, also contain a large material library with diverse structural variations. However, their electronic properties have been underexplored; some examples include applications that exploit their electronic transitions which give rise to light absorption/emission in dyes/pigments or emissive materials employed in organic light-emitting diodes (OLEDs). Yet, wider applications of their electronic properties have been largely neglected. In recent years, copper(I) thiocyanate (CuSCN), a 3D coordination polymer, has been shown as a promising semiconductor with a wide range of electronic applications successfully demonstrated, such as thin-film transistors (TFTs), OLEDs, organic photovoltaics (OPVs), and perovskite solar cells (PSCs). CuSCN exhibits a unique combination of excellent optical transparency and p-type or hole-transporting characteristics owing to the electronic structures having a large band gap separating the valence band with large band dispersion of dominant Cu 3d character from the high-energy conduction band of CN π* states.
Being a coordination compound, ligands coordination also plays an important role in controlling the physical and electronic properties of CuSCN. We showed in our recent work that diethylsulfide (DES), a common solvent employed for solution-processing of CuSCN, coordinates strongly with Cu(I) centers and significantly affects the film properties. Treating CuSCN films with antisolvents can modify the coordination by DES, change the film morphology on the nanoscale, and subsequently improve the hole-transporting properties. Beyond CuSCN, we are now investigating other coordination polymer semiconductors and starting to glimpse the material design principles for electronic applications. For example, coordinating CuSCN with various types of other ligands (aliphatic sulfides, aliphatic cyclic amines, aromatic imines, and aromatic diimines) can be used to tune the electronic properties of the CuSCN main network, such as shifting light absorption/emission across the whole visible range and generating electron-transporting states and the possibility of ambipolar charge transport. On the other hand, changing the metal from Cu(I) to Sn(II) to realize tin(II) thiocyanate [$Sn(NCS)_2$], the hole-transporting electronic states at the top of the valence band are still dominated by the metal states (Sn 5s instead of Cu 3d), analogous to Cu_2O and SnO systems. $Sn(NCS)_2$ also features a large band gap, characteristic of the π-π* gap of the thiocyanate, but with a deep valence band level; nevertheless, $Sn(NCS)_2$ still yields functional OPVs when employed as an ultrathin hole-transport layer. These examples highlight the potential of developing semiconductors and electronic applications based on coordination polymers or other coordination compounds. Further research may one day lead to the realization of 'coordination electronics'.

INVITED SPEAKER: SP05_INV001

HYBRID QUANTUM SYSTEM AND HYPERFINE MEDIATED TRANSPORT PROPERTIES

Yoshiro Hirayama*

Graduate School of Science, CSRN and CSIS, Tohoku University, Japan
*e-mail: yoshiro.hirayama.d6@tohoku.ac.jp

Abstract:
Quantum systems have received much interests from a view point of not only large scale quantum computation/simulation but also quantum enabled technology (QET), such as a highly-sensitive metrology based on quantum coupling. A variety of QET requests hybridization of charge, spin, nuclear spin, photon, and/or phonon. Such hybridization also provides a way making a quantum coupling across various scales of energy and length. In the first part of my presentation, I will summarize our project "Science of Hybrid Quantum Systems". The "hybrid" also mean hybridization between "classical" quantum system and fully quantum system. The ratio of "classical" varies from 0 to 100%. We have experienced that a trial to hybridization of different physics quantities can sometimes produce high-impact results even with the high "classical" ratio.
In the project, my group in Tohoku University has interested in hybridization between electron and nuclear spins in semiconductor quantum systems. The hyperfine mediated transport enables us dynamic nuclear polarization and RDNMR (resistively-detected nuclearmagnetic-resonance). By using RDNMR, the spin/charge/strain characteristics have been unveiled in the low-dimensional quantum systems. Recently, we have succeeded to extend RDNMR to the low magnetic-field region less than 1 T.
There also exists experimental trials to approach more "coherent" coupling including nuclear spins. When the polarized domains of nuclear spins are exposed to the special electron-spin state (canted spin state) having a long range correlation arising from the Nambu-Goldstone mode, the measured relaxation of nuclear spins exhibits both collective and individual relaxation on very different time scale. The fast decay suggests superadiant like decay, opening up the possibility for the exploration of novel collective behavior in solid state systems.

INVITED SPEAKER: SP05_INV002

COMPREHENSIVE VORTEX PHASE DIAGRAM OF ION-GATED TWO DIMENSIONAL SUPERCONDUCTORS

Tsutomu Nojima[1,*], Yu Saito[2,3], Yuki M. Itahashi[2], Yoshihiro Iwasa[2,4]

[1]Institute for Materials Research, Tohoku University, Japan
[2]Quantum-Phase Electronics Center (QPEC) and Department of Applied Physics, The University of Tokyo, Japan
[3]California NanoSystems Institute, University of California at Santa Barbara, USA
[4]RIKEN Center for Emergent Matter Science (CEMS), Japan
*e-mail: nojima@imr.tohoku.ac.jp

Abstract:
Recently emerging two-dimensional (2D) superconductors with high crystallinity, realized by exfoliation and ionic gating, have uncovered various intrinsic properties of quantum vortices. In this presentation, we report transport properties in zero and finite magnetic fields in ion-gated MoS_2 with the superconducting transition temperature $T_c \sim 8$ K.
In zero magnetic field, we succeeded in observing the Berezinskii-Kosterlitz-Thouless (BKT) transition, clearly evidenced by the universal jump of the power α in the current (I) - voltage (V) characteristics ($V \propto I^{\alpha}$) at low current limit. With increasing I, we found the successive step-like increases in $V(I)$, which can be ascribed to the transformation of the BKT state into the dynamical states with the faster motion of vortices and anti-vortices, one of which is called as the kinematic flow state. In the finite magnetic fields, on the other hand, the BKT state with zero ohmic resistance is easily destroyed into a resistive state called quantum metal, which is explained by the motion of quantum vortices through the quantum tunneling process. Based on all the experimental results in zero and finite magnetic fields, we eventually obtained a comprehensive vortex phase diagram as shown in Figure. We discuss this can be accessed only in the 2D superconductors with less disorder and minimal pinning potential.

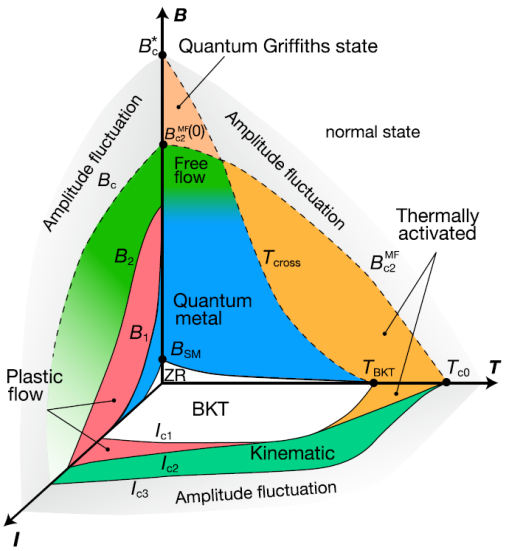

Figure. Comprehensive magnetic field - current - temperature (B-I-T) phase diagram in single-crystal based clean 2D superconductors with weak pinning.

INVITED SPEAKER: SP05_INV003

QUANTUM ENGINEERING IN OPTICAL FIBERS

Shau-Yu Lan*

Division of Physics and Applied Physics, School of Physical and Mathematical Sciences, Nanyang Technological University, Singapore 637371, Singapore
*e-mail: sylan@ntu.edu.sg

Abstract:
Quantum engineering using photonic structures offer new capabilities for atom- photon interactions for quantum optics and atomic physics, which could eventually lead to integrated quantum devices. Coherent manipulation of external and internal degrees of freedom of guided ultra-cold atoms in optical fibres has been attempted, with the aim of enhancing the performance of quantum experiments and to further develop miniaturized quantum devices. In this talk, I will show our recent works on coupling and guiding cold atoms in a hollow-core photonic crystal fiber and present few key cold atom experiments in this hollow-core waveguide environment and discuss their future applications.

INVITED SPEAKER: SP05_INV004

ESTIMATING QUANTUM SYSTEM'S STATE DYNAMICS USING CONTINUOUS WEAK MEASUREMENT

Areeya Chantasri*

Optical and Quantum Physics Laboratory, Department of Physics, Faculty of Science, Mahidol University, Bangkok, 10400, Thailand
*e-mail: areeya.chn@mahidol.ac.th

Abstract:
The advent of atomic- and photonic- scale experiments has led to the implementation of quantum measurements in a regime outside of the idealized strong- projective scheme. Researchers can now probe individual quantum systems by coupling them weakly to another quantum systems and estimate behaviors of the probed ones continuously in time. In this talk, I will review the generalization of quantum measurement theory, the concept of continuous weak measurements, and how one can track quantum system's dynamics in time. The tracking has already been shown in experiments, in particular, for Transmon superconducting qubit experiments, which I will include in this talk research results from my theory- experiment collaboration. I will also present my results on quantum state tomography, utilizing the continuous probe for resource-limited state estimation. The talk includes techniques of quantum state filtering and most-likely path for Transmon qubits. I will also briefly show the quantum state smoothing technique, which uses maximal information from the continuous probe for estimating quantum states in a single run.

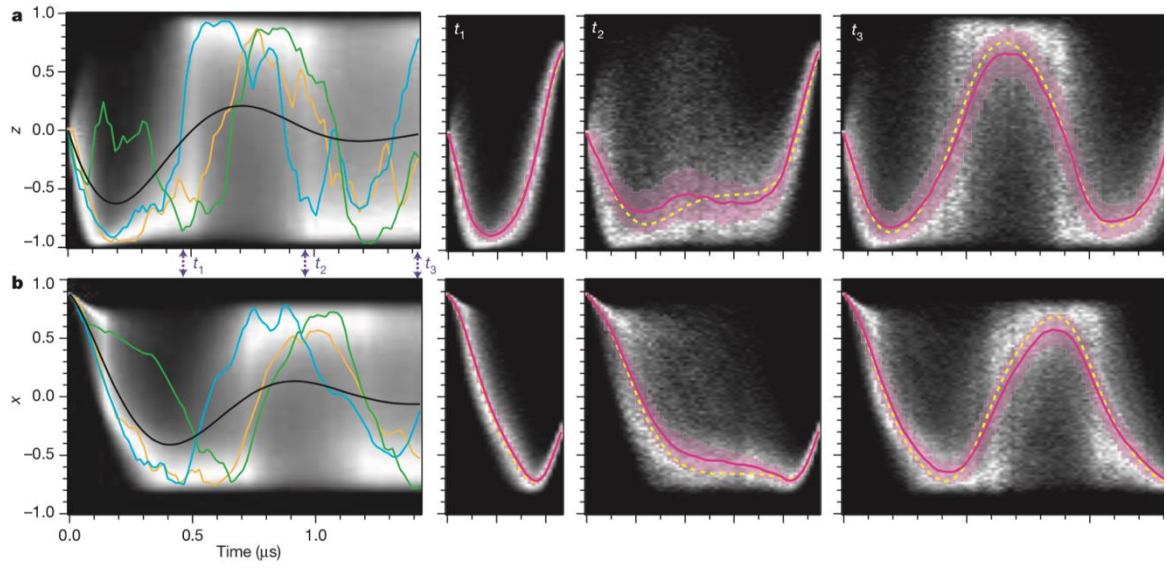

Figure. Quantum trajectories and most-likely paths for Transmon qubits

INVITED SPEAKER: SP05_INV005

HAMILTONIAN ENGINEERING IN STRONGLY INTERACTING RYDBERG SYSTEMS

Sebastian Geier[1], Nithiwadee Thaicharoen[1, 2,*], Clement Hainaut[1],Titus Franz[1], Andre Salzinger[1], Annika Tebben[1], David Grimshandl[1],Gerhard Zuern[1], Matthias Weidemueller[1,*]

[1]Physikalisches Institut, Universitaet Heidelberg, Im Neuenheimer Feld 226, 69120 Heidelberg, Germany
[2]Research Center for Quantum Technology, Faculty of Science, Chiang Mai University, 239 Huay Kaew Road, Muang, Chiang Mai, 50200, Thailand
*e-mail: thaicharoen@physi.uni-heidelberg.de, weidemueller@uni-heidelberg.de

Abstract:
We demonstrate an ability to engineer Hamiltonian of many-body Rydberg spin systems using microwave pulse sequences. In this work, we engineer an arbitrary XYZ Heisenberg Hamiltonian out of an original XX Heisenberg Hamiltonian utilizing Floquet driving. To quantify this new Hamiltonian, we perform time evolution of our spin system under selected choices of initial state and interaction strength. The results are then compared with numerical simulations to extract the efficiency of the pulse sequences and additional effects.

INVITED SPEAKER: SP05_INV006

NEW QUANTUM CODES FROM CYCLIC AND NEGACYCLIC CODES OF PRIME POWER LENGTHS

Hai Q. Dinh*

Department of Mathematical Science, Kent State University, Ohio, USA
*e-mail: hdinh@kent.edu

Abstract:
Classical computers work by manipulating bits that exist in one of two states, namely, 0 or 1. Quantum computers are not just limited to these two states, they are encoded with quantum data in the two conditions of 0 and 1 as quantum bits, or qubits, which can exist in superposition. That means, the qubits are both 0 and 1 and all points in between, which are processed at the same time, giving quantum computers the ability of performing many calculations at once. Qubits represent atoms, ions, photons or electrons and their respective control devices that are working together to act as computer memory and a processor. Since quantum computers can contain these multiple states simultaneously, they have the potential to be millions of times more powerful than the most powerful classical supercomputers. Quantum computers will make use of qubits to encode quantum data and figure complex scientific issues utilizing the resources unique to quantum computers, such as direct access to superposition and entanglement. Using quantum computing, one can harness the magnificent powers superposition and entanglement to tackle complicated issues that classical computer systems cannot practically do.
In this talk, we construct all quantum MDS codes from repeated-root codes of prime power lengths over finite fields using the CSS and Hermitian constructions. We provide all quantum MDS codes constructed from dual codes of repeated-root codes of prime power lengths over finite fields using the Hermitian construction. They are new in the sense that their parameters are different from all the previous constructions. Moreover, some of them have larger Hamming distances than the well-known quantum error-correcting codes in the literature.

INVITED SPEAKER: SP06_INV001

ENERGY RESILIENCE: ENHANCING CLIMATE ADAPTATION CAPABILITY OF RENEWABLE ENERGY SYSTEMS

Kampanart Silva*, Nuwong Chollacoop

Renewable Energy Research Team, National Metals and Materials Technology Center, 114 National Science Park, Phahon Yothin Road, Khlong Luang, Pathum Thani 12120, Thailand
*e-mail: kampanart.sil@mtec.or.th

Abstract:
Renewable energy has been one of the major contributors toward world's greenhouse gas reduction. But at the same time, renewable energy systems, as a part of critical infrastructure, are inevitably affected by climate change. Electricity generating systems have been reportedly attacked by natural disasters. One of the most noteworthy events was the Hurricane Maria which knocked out 80% of the Puerto Rico's electrical grid for almost a year. This talk summarizes our attempt to strengthen resilience of renewable energy systems. Vulnerabilities of four different renewable energy systems toward climate events were explored, and measures to enhance resilience of each system were proposed. Solar systems are basically unguarded at the power distributing system while the most vulnerable part of biomass power plants is the fuel acquisition. Engaging stakeholders at most steps of the resilience assessment resulted in feasible and reasonable resilience measures which will likely be adapted by the power suppliers. Enhancing climate adaptation capability of renewable energy systems through resilience reinforcement will facilitate further introduction of renewable energy to the electrical grid, and consequently flatten the greenhouse gas emission curve.

INVITED SPEAKER: SP06_INV002

ENERGY STORAGE AND ITS POTENTIAL IMPACT ON CLIMATE CHANGE MITIGATION

Pimpa Limthongkul*

National Energy Technology Center (ENTEC), 114 Thailand Science Park, Klong 1, Klong Luang, Pathumthani, 12120, Thailand
*e-mail:pimpal@mtec.or.th

Abstract:
Towards the goal in decelerating global temperature rise to less than 2 degree celcius this century, efforts in technological research, innovation and implementation around the world have been moving towards net zero carbon society with an increase in green energy production and efficiency power and energy management. Energy storage has been one of the key technologies enabling an increase of renewable energy utilization. In this talk, I will discuss on how an advancement in energy storage technology could help alleveate climate change problem, along with recent updated energy storage research and development. A touch on energy storage research at ENTEC, Thailand will also be presented.

INVITED SPEAKER: SP07_INV001

OVERVIEW OF THAI RESEARCH ON COSMIC RAYS

David Ruffolo*

Department of Physics, Faculty of Science, Mahidol University, Bangkok, Thailand
*e-mail: david.ruf@mahidol.ac.th

Abstract:
Cosmic rays, or energetic particles from space, are Earth's natural radiation environment. This presentation provides an overview of Thai research on cosmic rays since 1991. This includes the development of a transport equation to model how energetic particles from solar storms travel to Earth, as well as techniques to fit data from spacecraft or ground-based detectors. From such fitting, we inferred details of the acceleration and transport of the most energetic particles from several major solar storms, as well as the potential radiation dosage for airline passengers. These and other effects of solar storms are collectively known as space weather effects, which also include radiation hazards to astronauts, damage or destruction of satellites and spacecraft, GPS disruption, and power outages.
Regarding Galactic cosmic rays, which continually arrive at Earth due to past supernova explosions in our Galaxy, our team led the establishment of the Princess Sirindhorn Neutron Monitor (PSNM) in 2007 at the summit of Doi Inthanon, Thailand's highest mountain. A neutron monitor is a large ground-based detector to perform precise short- and long-term measurements of the flux of cosmic rays vs. time, to within 0.1%. We use the Earth as a magnetic spectrometer that only admits particles above a minimum threshold (cutoff) in rigidity (momentum per charge). Among the worldwide network of neutron monitor stations, PSNM has the world's highest cutoff rigidity of 16.7 GV, extending precise long-term monitoring to cosmic rays of higher energy. We have examined variations associated with the ~11-year sunspot cycle and the ~22-year solar magnetic cycle, as well as 27-day variations associated with the solar rotation period and daily variations associated with Earth's rotation, which measure the anisotropy in cosmic ray arrival direction. We have also examined the effects of solar storms on Galactic cosmic rays, known as Forbush decreases, and we developed the first theoretical framework to explain precursory anisotropy that could provide advance warning of space weather effects. Using special electronics provided by US collaborators, at PSNM we developed the first capability to track variations in the cosmic ray energy distribution (spectrum) using high-precision single-station measurements, a capability that has been exported to other stations. Finally we describe our 10-year Thai-led multinational research project, supported by the Australian Government, to upgrade and maintain their neutron monitor at Mawson Station, Antarctica. Partially supported by grant RTA6280002 from Thailand Science Research and Innovation.

INVITED SPEAKER: SP07_INV002

RESPONSE FUNCTIONS OF NEUTRON DETECTORS TO COSMIC RAYS AS MEASURED DURING OCEAN VOYAGES TO ANTARCTICA FROM THE PAST TO THE PRESENT

W. Nuntiyakul[*,1,2], P. Yakum[3], S. Khamphakdee[1,2], K. Fongsamut[1,2], P. Jiang[4], P.-S. Mangeard[5], A. Sáiz[6], D. Ruffolo[6,2], P. Evenson[5], K. Munakata[7], J. Madsen[8], P. Chuanraksasat[2], B. Soonthornthum[2], S. Komonjinda[1], and R. Macatangay[2]

[1]Department of Physics and Materials Science, Faculty of Science, Chiang Mai University, Chiang Mai 50200, Thailand
[2]National Astronomical Research Institute of Thailand (NARIT), Chiang Mai 50180, Thailand
[3]Graduate School, Chiang Mai University, Chiang Mai 50200, Thailand
[4]Polar Research Institute of China, Pudong, Shanghai 200136, China
[5]Bartol Research Institute and Department of Physics and Astronomy, University of Delaware, Newark, DE 19716, USA
[6]Department of Physics, Faculty of Science, Mahidol University, Bangkok 10400, Thailand
[7]Department of Physics, Faculty of Science, Shinshu University, Nagano 390-8621, Japan
[8]Wisconsin IceCube Particle Astrophysics Center, University of Wisconsin-Madison, Madison, WI 53703, USA
*e-mail: waraporn.n@cmu.ac.th

Abstract:
Ground- (or sea-) based neutron counters are a standard tool for detecting atmospheric cascade from GeV range primary cosmic rays of either solar or galactic source. The standard neutron monitor (NM64) contains lead, the nuclei of which fragment when struck by a high-energy particle. Some of the fragments are neutrons which are moderated and trapped by polyethylene acting as a reflector and moderator. These neutrons can then be detected by induced nuclear fission of either ^{10}B in a $^{10}BF_3$ or ^{3}He gas proportional counter. Bare neutron counters, a type of lead-free neutron monitor, function much like standard neutron monitors but have different response functions primarily because they are more sensitive to neutrons of lower energy. In 2018, We installed a bare neutron counter in the middle between two NM64s fasten inside an insulated shipping container, which called the "Changvan" neutron detector. When operated together with standard monitors, the different response functions allow estimates to be made of the energy spectrum of galactic or solar particles. At any given location, the magnetic field of the Earth excludes particles below a well-defined rigidity (momentum per unit charge) known as the cutoff rigidity, which can be accurately calculated using detailed models of the geomagnetic field. By carrying a neutron detector to different locations, e.g., on a ship, the Earth itself serves as a magnet spectrometer. In this talk, we will present the response functions to cosmic rays of three NM64s on board a ship from 1994 to 2007, bare neutron counters during 1995 and 2009 survey years, and the Changvan neutron detector during 2019 and 2020 survey years over a wide range of magnetic latitude, that is, a latitude survey. This study is supported in part by the Thailand Science Research and Innovation via Research Team Award 6280002 and Research Grant for New Scholar MRG6280155.

INVITED SPEAKER: SP07_INV003

FROM THAILAND TO ANTARCTICA: THE 2020 THAI-AUSTRALIAN EXPEDITION FOR SPACE SCIENCE

Alejandro Sáiz*

Department of Physics, Faculty of Science, Mahidol University, Bangkok, Thailand
*e-mail: alejandro.sai@mahidol.ac.th

Abstract:
Between January and March 2020, two scientists from Mahidol University, Thailand, joined the annual expedition to the Australian base of Mawson, Antarctica. Our mission: to perform several upgrades in the Mawson Cosmic Ray Laboratory, the oldest cosmic-ray-science experiment running continuously until the present time in the Southern Continent. After the successful installation of updated software and electronics firmware and some extra neutron detectors, the data obtained from this experiment has been expanded to include, besides the existing measurements of cosmic ray flux, new information about cosmic ray energy. During this long trip onboard the Aurora Australis icebreaker, we also learned about other scientific projects in the Australian Antarctic Program. In this talk, I will present some details about my once-in-a-lifetime experience of visiting Antarctica and the scientific motivation for such an adventurous journey. Partially supported by grant RTA6280002 from Thailand Science Research and Innovation.

INVITED SPEAKER: SP08_INV001

PROVIDING A SOLUTION IN THE TRANSITION FROM BLACK TO GREEN FEEDSTOCK IN FUELS AND MATERIALS

Christian Dahlstrand*

RenFuel K2B AB, Box 5845, SE-102 48 Stockholm, Sweden
*e-mail: christian.dahlstrand@renfuel.se

Abstract:
Research and industrial realisation of sustainable biobased fuels and materials is necessary to reach the goals of the EU 2030 climate framework. RenFuel provides a patented catalytical process that utilizes the energy content within the existing waste material lignin, a natural polymer present in wood that is generated in annual amounts of up to 50 million tons globally by the paper and pulp industry. The energy content within lignin can be compared to the one of coal and makes the natural polymer a great substitute for fossil resources. RenFuel's technology converts the residual lignin from mills into liquid hydrocarbon-based catalytic Lignin Oil, LIGNOL™, that can be co-processed in oil-refineries and is compatible with both gasoline and diesel as a drop-in fuel.
Today, RenFuel has 18 pending patent families in over 40 countries covering the process from purification, treatment and refining of lignin as LIGNOL™ and bio-plastics as LIGNISOL™ and LIGNOSET™. RenFuel's strategy of combining academical scientific research with industrial development and commercialization bridges the gap between the forest industry and refinery, with technologies that are applicable in the existing infrastructure. With more than 200MSEK invested in technology development of lignin-based products and with a goal of having the world's first large scale production facility of lignin oil, RenFuel provides realistic solutions for the replacement of finite fossil resources.

INVITED SPEAKER: SP08_INV002

DEVELOPMENT OF FACADE ELEMENTS ON BASE OF WASTE MATERIALS OF (WASTE) WATER COMPANIES

Willem Böttger[1,2,*], Mark Lepelaar[1], Zoya Zarafshani[1], Jasper Sluis[2]

[1]NPSP B.V., Moezelhavenweg 9, NL1043 AM Amsterdam, Netherlands
[2]Center of Expertise Biobased Economy, Lovensdijkstraat 63, NL4818 AJ Breda, Netherlands
*e-mail: willem.bottger@npsp.nl, woj.bottger@avans.nl

Abstract:
As the materials of a building are responsible for more than half of energy use of that building over the whole lifetime, low carbon materials are, in the framework of climate change, a necessity for future building. In 2008 the possibility to use natural fibers like hemp in a composites manufacturing process called Sheet Molding Compound (SMC) were researched. The technical results then were promising, but up to now have not been followed by commercial success, due to the complex processing of natural ingredients into SMC sheets. A process, rather familiar with SMC is called BMC, Bulk Molding Compound, or Dough Molding Compound.
Within this framework the Centre of Expertise in co-operation with bio-composite developer NPSP investigated the feasibility to develop a low carbon façade cladding. A new material based on waste streams has been developed and demonstrated. It consists out of: waste fibers like toilet paper and roadside grass giving strength to the material; Calcium carbonate, a waste material from drinking water companies, Bio-based polyester resin, for 50% produced out of waste glycol of biodiesel production, made from animal waste and frying fat.
These ingredients were replaced in the BMC process that standard uses glass fibers, calcium carbonate filler and a polyester resin. The ingredients are being combined into a dough, which is being pressed under high pressure (10 MPa) and temperature 140°C into a stiff and rigid, thermoset material. The BMC process amongst others used to produce the reflectors of headlights of cars, interior panels in trains and wash basins. It covers 7% of the composite production in Europe.
With above mentioned ingredients and production technique mechanical properties have been determined, a demonstrators has been realized, and first order LCA has been developed.

INVITED SPEAKER: SP09_INV001

BIODIESEL UPGRADING TECHNOLOGY FOR HIGHER BLEND WITH DIESEL TO REDUCE PM2.5

Nuwong Chollacoop[1,*], Peerawat Saisirirat[1], Yuji Yoshimura[1,2]

[1]National Energy Technology Center (ENTEC), National Science and Technology Development Agency (NSTDA), Thailand Science Park, Pathumthani, 12120, Thailand
[2]Emeritus Researcher, National Institute of Advanced Industrial Science and Technology (AIST), Tsukuba, Ibaraki, 305-8560, Japan
*e-mail: nuwongc@mtec.or.th

Abstract:
Fatty Acid Methyl Ester (FAME) or biodiesel has been used as a blend with fossil diesel at various ratios, e.g. B5, B7, B10, B20 and more in future in ASEAN, depending on the diesel engine/exhaust-gas-treatment systems compatibility. In Thailand, current blending ratios as B7, B10 and B20 are commercially available as a result of three-year national projects under Energy Conservation Fund to determine suitable specification of biodiesel for higher blending ratio than B7. When these blending amounts increase, several issues need to be considered, e.g. fuel filter plugging with impurities such as monoglyceride (MG) and acids/sludge/polymers formation via thermo-oxidative degradation of biodiesel during the vehicle use. Impurities such as MG and water can be reduced via operational modification of biodiesel manufacturing process or distillation etc., while oxidation stability of biodiesel can increase via addition of antioxidants. H-FAME (partially Hydrogenated FAME) has been proposed for demonstration along value chain, ranging from near commercial production (continuous process with 1 ton/day production capacity) to 100,000-kilometer on-road test by eight pick-up truck, to confirm upgraded specification for blending as B10 and B20. Increasing biodiesel blending in diesel not only reduce fossil fuel import, but also reduce pollution especially particulate matter with size smaller than 2.5 micron, or PM2.5.

INVITED SPEAKER: SP09_INV002

KEY ELEMENTS AND STRATEGIES FOR FUNCTIONAL LIPIDS PRODUCTION BY FILAMENTOUS FUNGAL PLATFORM

Kobku Laoteng*

Industrial Bioprocess Technology Research Team, Functional Ingredients and Food Innovation Research Group, National Center for Genetic Engineering and Biotechnology (BIOTEC), National Science and Technology Developemnt Agency (NSTDA), Thailand Science Park, Pathum Thani, Thailand
*e-mail: kobkul@biotec.or.th

Abstract:

The trend in functional ingredients towards health and well-being is expected by global consumer's perception. Healthy dietary lipids are of current subjects due to the involvement in an array of metabolic conditions in humans and animals. Particularly, long-chain polyunsaturated fatty acids (LC-PUFAs) play key physiological and structural functions in several biological processes. In addition to the plant and animal-derived origins, the microbial lipids rich in PUFAs are alternatives as non-depleting sources for sustainable production. Key elements are required for the PUFA-rich lipid production by microbial system, and thus knowledge-based strategies are thought to be promising for production development. *Mucor* spp. and *Mortierella* spp., which are promising producers for *n*-6 LC-PUFAs, gamma-linolenic acid (GLA) and arachidonic acid (ARA), respectively, were exploited as oleaginous models for exploring regulatory mechanisms involved in the lipid and PUFA biosynthesis. Through holistic strategies, strain capability and robustness on nutritional and environmental regimes were evaluated by integrating with metabolic phenotypes. By comparative genomic and phenotypic analyses, metabolic significances underlying fungal oleaginicity, including precursor generation, fatty acid biosynthesis, lipid accumulation and turnover processes were uncovered. Further, an oleaginous *Aspergillus oryzae* was also used as a cell chassis for strain improvement through emerging gene editing technology. The fungal production platform was eventually established that would bring to the industrial practice for production of specialty lipids and lipid-based products with diverse applications.

INVITED SPEAKER: SP09_INV003

BIOCONVERSION OF PALM BIOMASS WASTES TO BIODIESEL FEEDSTOCKS AND CELLULOSE PULPS BY LIGNOCELLULOLYTIC OLEAGINOUS FUNGI

Benjamas Cheirsilp*, Rawitsara Intasit

Biotechnology for Bioresource Utilization Laboratory, Department of Industrial Biotechnology, Faculty of Agro-Industry, Prince of Songkla University, Hat Yai, Songkhla, 90112 Thailand
*e-mail: benjamas.che@psu.ac.th

Abstract:
Empty fruit bunch (EFB) is one of abundant lignocellulosic wastes from palm oil industries. They are attractive feedstocks for production of cellulose pulps and subsequent production of fermentable sugars due to their low cost, renewable nature and abundance. This study aimed to produce fungal oil and cellulose pulps from EFB by lignocellulolytic oleaginous fungi. Firstly, oleaginous fungi *A. tubingensis* TSIP9, which originates from palm wastes, was used to pretreat EFB and simultaneously produce fungal oil through non-sterile solid state fermentation (SoSF) using anaerobic digestion (AD) effluent as nutrient source and moisturizing agent. The operating conditions were optimized through response surface methodology. Repeated-SoSF of EFB was performed in order to increase the effectiveness of the process and reduce production costs. The fungal oil obtained was 147-169 mg/g-EFB and the cellulose content in fungal pretreated EFB was increased from 45.76±7.96 % to 57.89±2.14 %. The fungal oil are composed of palmitic acid (60.96±0.27 %), oleic acid (19.69±0.14 %), stearic acid (8.28±0.11 %), and linoleic acid (4.55±0.22 %) which are suitable as biodiesel feedstocks. This study revealed the potential use of in situ lignocellulolytic enzymes producing fungi for bioconversion of lignocellulosic wastes to valuable green products.

INVITED SPEAKER: SP10_KEY001

INNOVATION IN ELECTROCHEMICAL TECHNOLOGIES FOR THE LOW CARBON ENERGY TRANSITION

Nigel Brandon*

Imperial College London, UK
*e-mail: n.brandon@imperial.ac.uk

Abstract:
The paper will discuss the role that electrochemical technologies can play in supporting the cost effective transition to a low carbon energy system, with a particular focus on the role of fuel cells, electrolysers and batteries for applications in transport, heat, and power. Examples will be given of technology innovation in the speakers own group, focusing on fuel cells and flow batteries, discussing the rationale behind innovations, and exploring the process of forming and building companies in this sector, based on academic research.

INVITED SPEAKER: SP10_KEY002

OPPORTUNITIES OF HYDROGEN TECHNOLOGIES FOR CLEAN AND SUSTAINABLE GROWTH IN THAILAND

Arunratt Wuttimongkolchai*

PTT Innovation Institute, PTT Public Company Limited, Ayutthaya, 13170, Thailand
e-mail: arunratt.w@pttplc.com

Abstract:
According to the Paris Agreement entering into force in COP21, it is necessary to reduce carbon emissions by 20- 25% by 2030 together with enhancement energy security from a climate perspective to fulfill the commitment. As the national energy company, PTT is dedicated to creating national energy security to sustain the future position and supporting government policy in Thailand Integrated Energy Blueprint (TIEB). The energy security along with economy and environment must be sustained through a diversity of types and sources of energy. The share of renewable or alternative energy has strong growth recently, but it is still not a primary energy resource comparing to fossil energy. Hydrogen and green hydrogen from the renewable energy source are considered as an alternatively versatile energy carrier, which is being used in numerous applications industrially to mitigate the climate change and to achieve zero- emission. The International Energy Agency expected that green hydrogen could be competitive on an industrial scale leading to a cost reduction of 30% by 2030 ($1-2 USD /kg).
The key impetus of hydrogen technology, which could be the linkage between renewable energy and its applications, is likely to be policy, social awareness, and close cooperation among government, industrial and institution sectors. PTT initiated " Hydrogen Thailand" which was established as a virtual organization in December 2019 with collaboration from seven organizations, including government and industrials sectors. The vision of Hydrogen Thailand is "To drive HYDROGEN as a FUTURE energy platform in decarbonized circular economy in Thailand". Through our activities, we aim to introduce a green hydrogen economy and seek appropriate supports and policies in order to promote and implement hydrogen technologies in Thailand.

INVITED SPEAKER: SP10_KEY003

GREY AND GREEN HYDROGEN PRODUCTION

Sumittra Charojrochkul*, Chaiyuth Saekung, Visarn Lilavivat

National Metal and Materials Technology Center, National Energy Technology Center, National Science and Technology Development Agency, 114 Thailand Science Park, Pathumthani, Thailand
*e-mail: sumittrc@mtec.or.th

Abstract:
A global demand of hydrogen will be increased tremendously if the world is gearing towards 'Hydrogen Economy'. However, the most cost effective way of hydrogen production is not green. This is contradicting with the aim of 'Hydrogen Economy' to be greener than the fossil era nowadays. There have been several attempts to produce a greener hydrogen from renewable sources such as biogas and ethanol but with the conventional reaction. Another alternative is via a chemical cycle which may utilize heat from renewable sources. This talk will elaborate more details of all these methods.

INVITED SPEAKER: SP10_KEY004

CATALYTIC PARTIAL OXIDATION OF METHANE OVER Re-BASED CATALYSTS

Chanittar Cheephat[1], Pornlada Daorattanachai[1], Sakamon Devahastin[2], Navadol Laosiripojana[1,*]

[1] The Joint Graduate School of Energy and Environment, CHE Center for Energy Technology and Environment, King Mongkut's University of Technology Thonburi, 126 Pracha Uthit Rd., Bang Mod, Thung Khru, Bangkok 10140, Thailand

[2] Advanced Food Processing Research Laboratory, Department of Food Engineering, Faculty of Engineering, King Mongkut's University of Technology Thonburi, 126 Pracha Uthit Rd., Bang Mod, Thung Khru, Bangkok 10140, Thailand

*e-mail: navadol.lao@kmutt.ac.th

Abstract:

Partial oxidation reactions of CH_4 over monometallic Ni, Rh, Re and bimetallic Re-Ni catalysts supported by Al_2O_3 were studied. Among monometallic catalysts, Rh/Al_2O_3 exhibited the highest catalytic activity. Lower CH_4 conversion and H_2 yield were observed over Ni/Al_2O_3 catalyst, while Re/Al_2O_3 catalyst did not promote the reaction under the studied condition. Addition of Re over Ni to form a bimetallic catalyst considerably promoted the activity of Ni/Al_2O_3 catalyst, particularly at a higher temperature (600 °C). Re-Ni proportion was then optimized; $Re-Ni/Al_2O_3$ at Re:Ni ratio of 3:7 resulted in a significantly higher CH_4 conversion as well as H2 and CO yields when compared to noble-metal Rh/Al_2O_3 catalyst. Stability testing of $Re-Ni/Al_2O_3$, Ni/Al_2O_3 and Rh/Al_2O_3 catalysts was also conducted. After 18-h operation, $Re-Ni/Al_2O_3$ catalyst still exhibited high stability with slight deactivation in terms of H_2 yield, whereas Ni/Al_2O_3 and Rh/Al_2O_3 catalysts showed higher deactivation rates. Post-reaction temperature programmed oxidation confirmed the better resistance toward carbon deposition of $Re-Ni/Al_2O_3$ catalyst. The effect of steam and CO_2 addition on the $Re-Ni/Al_2O_3$ catalyst performance was also investigated. The presence of a suitable H_2O content could increase H_2 and CO yields and reduce the amount of carbon deposition, whereas the presence of CO_2 showed undesirable influence on the reaction by reducing CH4 conversion and H_2/CO ratio.

INVITED SPEAKER: SP10_INV001

GREEN TECHNOLOGY FOR CO-PRODUCTION OF HIGH PURITY HYDROGEN AND SYNTHESIS GAS

Nichamon Noppakun[1], Rungrote Kokoo[1], Jon Powell[2], M.A.A. Aziz[3], Suttichai Assabumrungrat[4,5], Suwimol Wongsakulphasatch[1,*]

[1] Department of Chemical Engineering, Faculty of Engineering, King Mongkut's University of Technology North Bangkok, Bangkok, 10800, Thailand
[2] International School of Engineering, Chulalongkorn University, Bangkok, 10330, Thailand
[3] School of Chemical and Energy Engineering, Faculty of Engineering, Universiti Teknologi Malaysia, UTM Johor Bahru, Johor, 81310, Malaysia
[4] Center of Excellence in Catalysis and Catalytic Reaction Engineering, Department of Chemical Engineering, Faculty of Engineering, Chulalongkorn University, Bangkok, 10330, Thailand
[5] Bio-Circular-Green-economy Technology & Engineering Center, BCGeTEC, Department of Chemical Engineering, Faculty of Engineering, Chulalongkorn University, Bangkok, 10330, Thailand
*e-mail: suwimol.w@eng.kmutnb.ac.th

Abstract:
Hydrogen is currently considered as an ideal energy carrier and plays a significant role in producing low carbon transportation fuels. In addition, hydrogen is used for different kinds of chemical industry, for refineries, metallurgy, and food, etc. According to high demand of hydrogen together with the awareness of environmental concern worldwide, improvement of hydrogen production in the direction towards the so-called "green production technology" are therefore of interest. Steam methane reforming is a conventional hydrogen production process at present; however, the drawback of this process is high energy consumption due to endothermic reaction and the production of greenhouse gas CO_2 as a by-product**.** Our work aims to design and develop greener hydrogen production technique and evaluate its performance. The application of process intensification concept: a combination of reaction and separation process, named as sorption-enhanced reaction, with the utilization of the produced CO_2 were studied through process simulation via Aspen Plus software. The process was designed for co-production of high purity hydrogen and synthesis gas with the inclusion of chemical looping and calcium looping technologies of which sorption-enhanced steam methane reforming and sorption-enhanced chemical-looping steam-dry methane reforming were combined. The combined process was conducted through the use of multi-functional material, which was composed of metal oxide to act as oxygen transfer and calcium oxide to act as CO_2 sorbent. Process design by Aspen Plus program revealed that the use of mixed-metal NiO:CuO at 0.9:0.1 molar ratio could produce 3.64 kmol H_2/kmol CH_4 feed with hydrogen purity approximately 97% (methane conversion of 91%) and syngas 6.70 kmol for H_2/CO ratio of 1.60. Thermal efficiency of the overall process was 89%, which is greater than the efficiency of conventional steam methane reforming process of 80%.

INVITED SPEAKER: SP10_INV002

DEVELOPMENT OF CERIA- AND ZIRCONIA-BASED ELECTROLYZER FOR HYDROGEN PRODUCTION

Parintorn Temluxme[1], Pattraporn Kim-Lohsoontorn[1,2,*]

[1] Centre of Excellence on Catalysis and Catalytic Reaction Engineering, Department of Chemical Engineering, Facultyof Engineering, Chulalongkorn University, Bangkok, 10330, Thailand
[2] Bio-Circular-Green-economy Technology&Engineering Center, BCGeTEC, Department of Chemical Engineering, Faculty of Engineering, Chulalongkorn University, Bangkok, 10330, Thailand
*e-mail: Pattaraporn.K@chula.ac.th

Abstract:
Steam electrolysis for hydrogen production is investigated in high-temperature electrolyzer. Sc^{3+}, Ce^{4+}, and Gd^{3+} are doped in zirconia (SCGZ) and compared with 8 mol% yttria stabilized zirconia (YSZ) and 10 mol% gadolinium doped ceria (GDC) electrolyte. The activation energy of conduction of the SCGZ electrolyte (Pt/SCGZ/Pt) is the lowest at 65.58 kJ mol^{-1}. Cathode-supported cell having SCGZ electrolyte (Ni-SCGZ/SCGZ/BSCF) shows the highest electrochemical performance. Durability test of the cells in electrolysis mode is carried out over 60 h (-0.3 A cm^{-2}, 800 °C, H_2O to H_2 ratio of 70:30). Significant performance degradation of Ni-GDC/YSZ/GDC/BSCF cell is observed (0.0057 V h^{-1}) whereas the performance of Ni-YSZ/YSZ/BSCF and Ni-SCGZ/SCGZ/BSCF are rather stable under the same operating conditions. Although SCGZ exhibits relatively highest performance, unwanted rhombohedral phase ($Sc_2Zr_7O_{17}$), which is a low conducting phase, occurs during the electrolyte fabrication. Therefore, to achieve even higher performance, stabilization of high conducting cubic phase by adding 1-2 mol% of Bi_2O_3 in SCGZ is investigated. Bi_2O_3 is found to act as both phase stabilizer and sintering aid. In addition, the ionic conductivity of the electrolyte is also improved with adding Bi_2O_3.

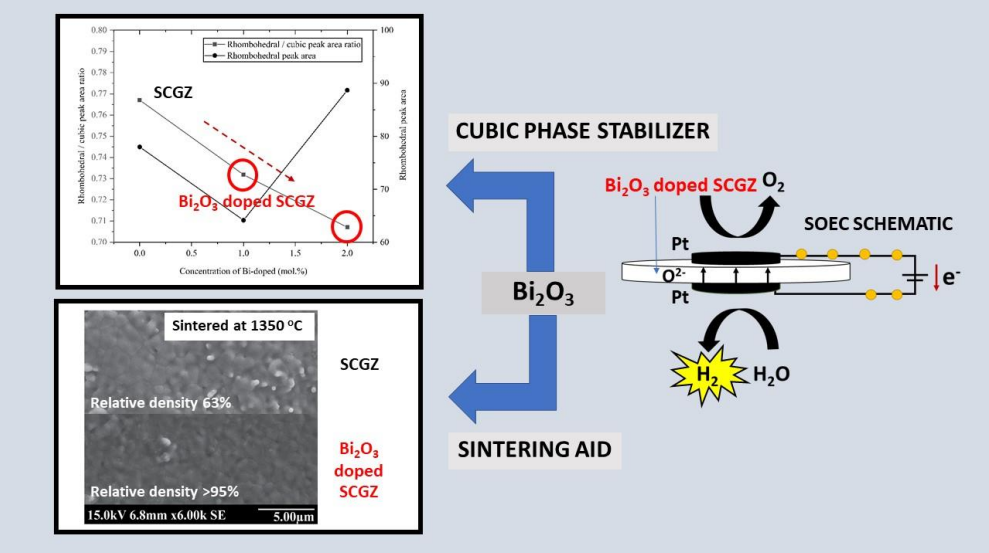

Figure. Effect of Bi_2O_3 on the phase stabilization and densification of SCGZ electrolyte.

INVITED SPEAKER: SP10_INV003

POWER-TO-GAS (PTG) TECHNOLOGY AS EFFICIENT ROUTE FOR CO_2 UTILIZATION: DEVELOPMENT OF STRUCTURED CATALYTIC SYSTEM

Sakhon Ratchahat[1,*], Masao Sudoh[2], Ryo Watanabe[3], and Choji Fukuhara[3]

[1]Department of Chemical Engineering, Faculty of Engineering, Mahidol University, Nakhon Pathom, 73170, Thailand
[2]Amano Institute of Technology, Shizuoka 431-1305, Japan
[3]Department of Applied Chemistry and Biochemical Engineering, Graduate School of Engineering, Shizuoka University, Shizuoka 432-8561, Japan
*e-mail: sakhon.rat@mahidol.edu

Abstract:
Controversial issues of CO_2 emissions on environment are greatly forcing the transformation from fossil fuels to clean/renewable energy. Solar and wind power as renewable energy sources would play an important role in the future energy scenario. Power-to-gas (PtG) technology has gained increased attention as a promising solution for storage of the electricity surplus by CO_2 methanation for methane production from the CO_2 greenhouse gas and the renewable H_2 from water electrolysis. The product methane can be more easily stored and transported than the electricity, while H_2 production by water electrolysis leads to the sustainable process. This promising process will play a substantial role in the future energy storage. It addresses not only the electrical grid stability, but also the reduction of CO_2 greenhouse gas. Recently, there are several approaches to develop the CO_2 methanation processes, especially focusing on the mass and heat transfer enhancement. Structured catalysts like monoliths have been proved for their advantages in the exhaust emission abatement. High-throughput structure of honeycomb monolith could serve the operation at high feed rate with a low pressure drop. High heat conductivity of metallic monolith could further enhance the heat transfer due to the intense heat generation from the exothermic reaction. In our study, various configurations of metallic honeycomb-type catalysts, which are plain, stacked, segment, and multi-stacked have been investigated. The random-flow channels of the stacked type and the gap distance of the segment type demonstrated the increased CO_2 conversion. Under industrial-like condition, the multi-stacked catalyst could maintain the reaction at moderate hotspot condition. The moderate hotspot showed aavantage in re-boosting the CO_2 conversion to a high level. The CO_2 conversion and the CH_4 selectivity were 90% and 99.5% at 300°C, 3L/min and CO_2/H_2 of 0.12/0.88 over 0.3 g of catalyst. The stability showed the dropped conversion less 0.6% over 76 h.

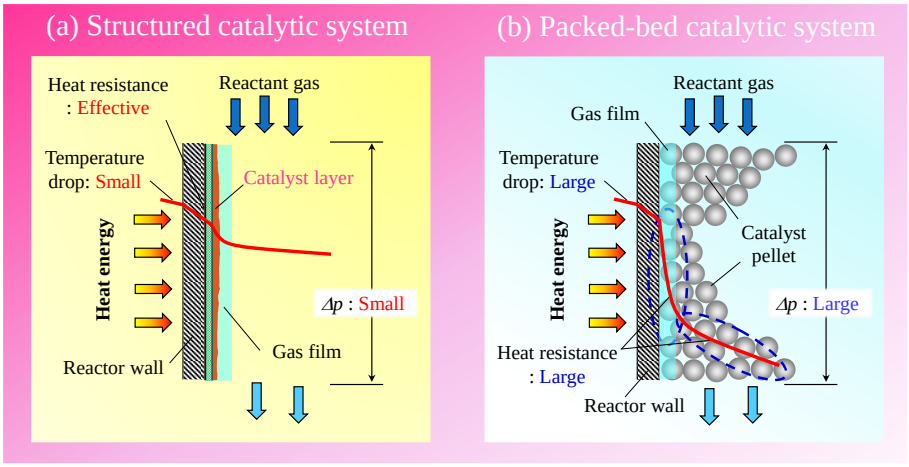

Figure. Comparison of (a) structured catalytic system and (b) packed-bed catalytic system.

INVITED SPEAKER: SP11_INV001

HOST CHARACTERS INFLUENCING RICHNESS AND ABUNDANCE OF EPIPHYTIC LICHENS

Sangsuree Thippawan, Panupong Kongwan, Ekaphan Kraichak*

Department of Botany, Kasetsart University, 50 Ngamwongwan Road, Ladyao, Chatuchak
Bangkok, 10900 Thailand
*e-mail: ekaphan.k@ku.th

Abstract:
Epiphytic lichens are ubiquitous in tropical ecosystems as they exploit vertical spaces of tree bark surfaces. While a number of species of epiphytic lichens have been documented and described, only a handful studied have addressed ecological factors that influence richness and abundances of these lichens. Here in this study, we investigated the effect of host species and host size on occurrences of epiphytic lichens by surveying and estimating the cover of these lichens on 1,326 stems of six common host species in the Khao Chong long-term forest dynamics plot, Trang Province. The survey revealed a total of 33 lichens species. The species richness and abundance of lichens significant differed among the six host species with *Shorea gratissima* hosting the fewest species, while *Barringtonia macrostachya* having the highest number of species. However, the richness and abundance did not change significantly with the size of the tree. Overall, the area for colonization (i.e. bark surface) has a smaller effect on lichen communities than the characters of host species. The results of the study indicate a need to maintain the diversity of tree species with different bark characters to preserve the diversity of the epiphytic lichens.

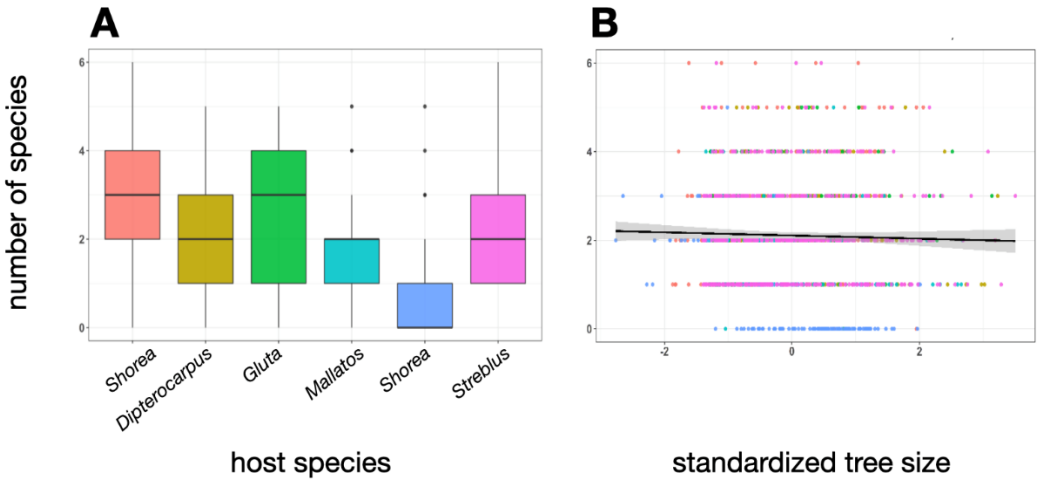

Figure. The number of species of epiphytic lichens in different host species (A) and host's standardized tree sizes in the study area. Colors represent data from different host species.

INVITED SPEAKER: SP12_INV001

PLASTIC WASTE MANAGEMENT AND CURRENT STATUS IN THAILAND: ISSUES OF MARINE PLASTIC WASTE FROM LAND-BASED SOURCES

Chongrak Polprasert[1,*], Sittikorn Kamngam[2], Kesirine Jinda[2], Tatchai Pussayanavin[3], Thammarat Koottatep[2]

[1] Thammasat School of Engineering, Thammasat University, Thailand
[2] School of Environment, Resources and Development, Asian Institute of Technology, Thailand
[3] Faculty of Science, Ramkhamhaeng University, Thailand
*e-mail: pchongrak@gmail.com

Abstract:
The growing populations with changing consumption patterns in developing countries are causing significant challenges with regards to solid waste management. The world generates about 2.01 billion tons of solid waste annually, in which only about 13.5 percent are recycled and more than 50 percent are improperly managed. The solid waste consists about 12% or 241.2 million tons per year of plastic waste generated mainly from household uses, food packaging and water bottles. Plastic waste has become a serious problem when considering the sequential hierarchy of sound solid waste management. At present, a large quantity of single-use plastic is leaking into the environment, including the marine environment, at an unprecedented rate. Approximately 80 percent of ocean plastics come from land-based sources or about 8 million tons of plastic waste are estimated to be dumped into the ocean every year. Thailand has been identified as one of the top 10 countries having mismanaged plastic waste with more than 60,000 tons per year of plastic waste entering the ocean through multiple outlets, including rivers (the 2018 survey data). Marine plastic pollution is one of the most widespread problems affecting the marine environment and ecosystem including fish, dugong, sea turtles; some marine mammals can become tangled in or swallow plastic debris. Moreover, micro-nano plastic particles have been found to contaminate the marine ecosystem and the food chain, including foodstuffs (sea salt, shrimp paste or mackerel) intended for human consumption. Thailand is currently taking actions to minimize these impacts of plastic waste leakage into the environment, including banning single-use plastics; changing petroleum-based plastics to alternative bio-based products such as paper, glass or biodegradable plastics. The role of the manufacturing industries in Thailand in the circular economy, the national policy/regulations associated with plastics waste recycling, and future trend are essential in addressing the plastic waste issues.

INVITED SPEAKER: SP12_INV002

CO-PROCESSING PLASTIC WASTE FROM DUMPSITES IN CEMENT INDUSTRY A WAY TO CURB MARINE PLASTIC POLLUTION

Chettiyappan Visvanathan*

School of Environment, Resources and Development, Asian Institute of Technology,
PO Box 4, Klongluang, Pathumthani, 12120 Thailand
*e-mail: visuvaru@gmail.com

Abstract:

Plastic has emerged as a form of pollution which is affecting water and land equally. The indestructible nature of plastic has turned from a boon to a worrisome complication. The versatility of plastic has led to exponential growth in its use, where we are now surrounded by plastics in different shapes and sizes. This rapid expansion in the use of plastic has to led to an equally rapid expansion in the plastic waste generation.

The dumpsites and landfills are riddled with plastic waste, which is limited to the nation and its efficiency of waste collection system. The leakage in the waste collection systems, especially in the countries with substantial river networks or vast coastlines has led to marine plastic pollution. Numerous efforts are being made around to world to curb the plastic pollution; however, these efforts are inadequate to deal with the large amount of generated waste.

Every year more than 8 million tonnes of plastic waste is dumped in the oceans and more than 80% of the dumped waste is generated from land-based activities. About, 32 million tonnes of plastic waste is mismanaged every year, which is then stored in open dumpsites or insecure landfills. Thus, leading to a leakage in the environment. Majority of the plastic produced till now still exists if not in similar shape, it exists in similar chemical structure. Plastic waste and single use plastics in particular are much more prone to degradation into micro-plastics. Plastic waste in the ocean has brought an onslaught on the marine animals directly. The creatures entangled in the floating debris are facing restricted growth or limited movements. The micro-plastics in the ocean has found its way up the food chain in the food we consume.

The large part of the marine plastic pollution is caused by developing countries. These countries are seeing unprecedented economical and lifestyle growth. 5 Asian countries are known to cause more than 50% of the total pollution. Thailand is one of the top marine plastic polluters in the world. It has observed a meteoric growth in consumerism, where single use packaging plastic has become an active part of day to day life. This sudden growth in plastic usage has led to an increase in plastic waste in raw MSW. In Thailand, raw MSW contains 16% plastic waste which is 4% higher than the world average.

In addition, to the growing plastic usage Thailand also suffers from subpar waste collection and management systems. Only, 23% of the generated waste is managed properly remaining 77% typically finds its way in open dumps or direct marine pollution. Thailand is blessed with a long coastline and vast river networks, but when it comes to waste leakage this boon proves to be a curse for the nation. In a tropical country like Thailand, floods are a common phenomenon. Floods when coupled with river networks and long coastline adds to the severity of indirect waste leakage from dumpsites and landfills.

The analysis of dumpsites and landfills shows that there are about 2380 dumpsites in Thailand which has 97.48 million tonnes of plastic waste, while there are 104 landfills having 90.42 million tonnes of plastic. A substantial number of these dumpsites and landfills are present in the vicinity of rivers or on the coastline. Therefore, such sites are prone to cause marine plastic pollution. On an average dumpsites and landfills are contain 42% of plastic waste, which during the study was seen to be largely made up of single use plastics.

In general, plastic waste can be treated by two ways – Waste to Energy (WTE) and Waste to Material (WTM). However, due to non-recyclable nature of single use plastics, it is impossible to turn them into new materials. Therefore, the only way to reduce the single use plastics is to use them for energy generation. Energy generated from the plastic wastes can be used either to produce electricity or to produce heat in cement kilns.

Previous studies and the analysis of current study suggests that cement kilns are a proven and technologically superior way to utilise plastic waste as fuel. They are typically operating at much higher efficiency over traditional WTE plants. Therefore, boasts better utilisation of energy in the plastic waste. The important aspect where cement kiln outshines WTE plant is waste generation and emissions. A cement kiln is operating at much higher temperature than traditional WTE, therefore the waste and the ash produced from waste combustion fuses with the molten clinker material in the kiln. Hence, there is no solid waste generation from waste co-processing. Another, important aspect is air emissions which are easily controlled in the cement kilns due to pre-existing pollution control devices. Combustion of plastic waste is known to produce dioxins and chlorine emissions. In a cement industry, the raw materials used to produce cement have a much higher concentration of chlorine in it, hence cement factories have existing air pollution control devices in it. Moreover, dioxins are typically produced in a fixed temperature range which is difficult to maintain inside the kiln, where temperatures are much higher than the suitable range of dioxin production. Once, the production process is over the dedusting effect of the kiln reduces the kiln temperature drastically therefore the suitable temperature for dioxin formation is never achieved.

Although, the cement industries and kilns prove to be a better option for waste reduction and can very easily utilised as a way to curb marine plastic pollution, it remains in the hands of authorities to create suitable environment for promotion of waste co-fuelling. As the regulations and policies are inclined towards waste co-fuelling in WTE plants, it is difficult for the cement industries to utilize the waste for the kilns. However, some industries are trying to co-fuel their production process as a part of corporate social responsibility. It will be much more suitable for them as well for the environment if the inclination of the international bodies and governments shift towards the cement industries.

A suitable environment for the growth of waste co-fuelling in cement industry can incubate a steady reduction of waste from final storage units, resulting in reduction of indirect marine plastic pollution. Where no harm is caused to the environment or the quality of the cement products, as cement industry becomes the sink for plastic waste.

INVITED SPEAKER: SP12_INV003

LIFE CYCLE APPROACH IN MARINE PLASTIC ABATEMENT: PRESENT STATUS AND FUTURE DIRECTIONS

Amila Abeynayaka,[1,2,3] Fujio Kojima,[2] Norihiro Itsubo[1]

[1]Graduate School of environment and information studies, Tokyo City University, Yokohama, Japan
[2] Research and development division, Pirika Inc./Pirika association, Ebisu, Shibuya City, Tokyo, Japan
[3]Marine litter and life cycle assessment working group, joint life cycle assessment interest group, the society of environmental toxicology (SETAC) and chemistry and American center for life cycle assessment (ACLCA), Florida, USA
*e-mail: amila@pirika.org

Abstract:
The global production of plastics has increased by about 9% per year since 1950. The revenue of the plastic industry is over 800 billion USD in 2018. The issue of plastics contaminating freshwater resources and oceans is widely discussed in the literature. Research focusing on the impacts associated with the exposure of organisms to aquatic plastics has been ongoing for years. However, studies linking the processes in the plastic value chain to plastics being released to the oceans are only starting to emerge. Lack of solid framework and having plenty of knowledge gaps limit the incorporation of ecosystem damage due to plastics**.** There is substantial work to be done to incorporate the damage due to aquatic plastic pollutants into environmental life cycle assessment **(**LCA**).** This presentation covers a brief description of the present situation of marine plastic incorporation into LCA and future directions**.** Moreover, few ongoing case studies of plastic litter and life cycle impact have been discussed**.** Apart from that, examples are given for the importance of environmental sampling and plastic litter monitoring methods in the life cycle thinking approach to overcome the marine plastic abatement**.**

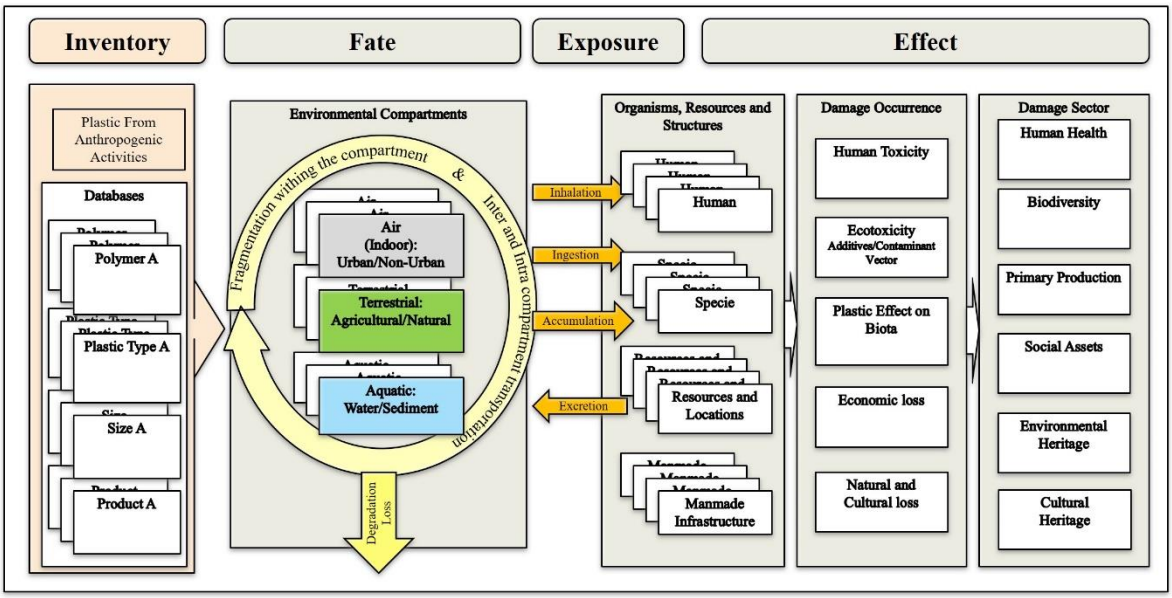

Figure. A conceptual framework to incorporate the end of life plastic into life cycle assessment process.

INVITED SPEAKER: SP13_INV001

BIOREDUCTIVE PRODRUG DESIGN OF NATURAL PRODUCTS FOR BREAST CANCER THERAPEUTIC AGENTS

Apichart Suksamrarn*

Department of Chemistry, Faculty of Science, Ramkhamhaeng University, Bangkok 10240, Thailand
*e-mail: asuksamrarn@yahoo.com

Abstract:
Many anticancer natural products are not target specific and might also quite toxic to normal cells. This disadvantage prevents the possibility of developing these compounds into anticancer drug candidates. To lower the toxicity while keeping the therapeutic property of active natural products, prodrug design is one of the strategies to improve the physicochemical properties of a molecule and overcome unacceptable biopharmaceutical performance. Inclusion of an additional molecular device which is cleavable by a specific enzyme expressed predominantly in tumor cells is a commonly applied strategy in contemporary drug design and development. Bioreductive prodrug can be designed to target specific tumor followed by *in situ* release of the therapeutic drugs with the reductase over-expressed in some tumor cells, for example breast cancer, ovarian cancer, thyroid cancer, adrenal cancer and colon cancer. In this presentation, examples of developing bioreductive prodrugs to reduce toxicity to normal cells while maintaining cytotoxic effect to breast cancer cells will be highlighted. One of the examples is our recent work on the design of bioreductive prodrug of cucurbitacin B, the major triterpenoid constituent of *Trichosanthes cucumerina*. The parent cucurbitacin B was toxic to breast cancer cells and it was also toxic to the normal Vero cells. However, its bioreductive prodrug was found to significantly reduce the toxicity down to 310-fold lower against non-cancerous cells. The prodrug showed satisfactory and comparable effectiveness in controlling tumor growth as that by the reference anti-breast cancer drug, tamoxifen, in the 4T1 xenograft mice model.

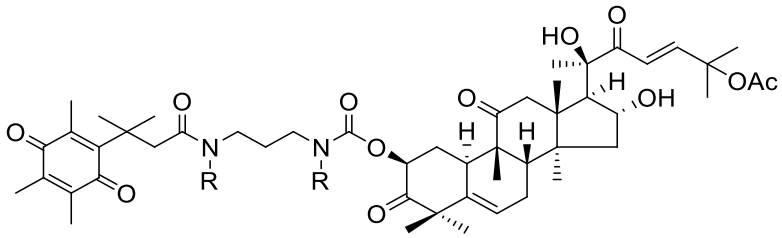

Bioreductive unit Linker Drug (cucurbitacin B)

Bioreductive prodrug of cucurbitacin B

INVITED SPEAKER: SP13_INV002

TRANSLATIONAL NATURAL PRODUCT RESEARCH

Xiaoguang Lei*

College of Chemistry, Peking-Tsinghua Center for Life Science, Peking University, China
*e-mail: xglei@pku.edu.cn

Abstract:
Natural products and their derivatives have long been used as medicinal agents, and they still make up a significant fraction of clinically approved drugs. Natural product synthesis provides a rich and unparalleled opportunity to develop new synthetic transformations, conceive novel and general strategies to access complex structures, and study the mechanism of action of bioactive targets. The combination of the tools and principles of chemistry, together with the tools of modern biology, allows us to create complex synthetic and natural molecules, comprising processes with novel biological, chemical and physical properties. This lecture will illustrate the opportunities that lie at this interface between synthetic organic chemistry and chemical biology by describing a series of examples that we are actively working on in our laboratory at Peking University. We take the inspiration from mother nature to develop new synthetic strategies to achieve the efficient synthesis of complex natural products. In addition, we also study the biosynthesis of plant derived natural product to elucidate new enzymatic mechanisms and apply the chemoenzymatic approach to prepare complex natural products and their derivatives. Moreover, we further use bioactive natural products to explore new biology and develop novel drug candidates for human diseases, such as cancers and autoimmune diseases.

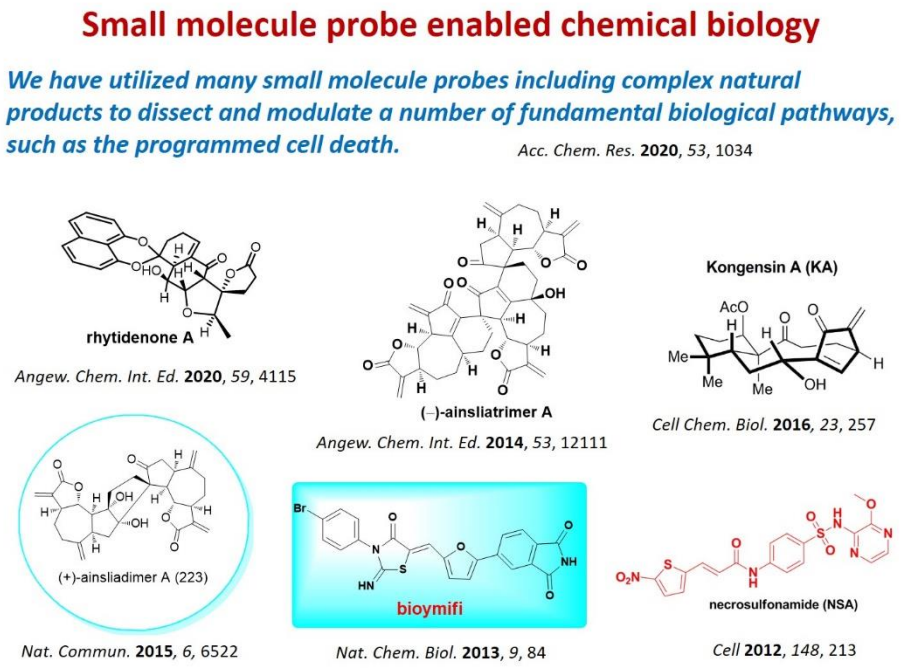

INVITED SPEAKER: SP13_INV003

NEW EVIDENCE ON THE FUNCTIONAL BIODIVERSITY AND SECONDARY METABOLITE PRODUCTION OF THE XYLARIALES (ASCOMYCOTA) BASED ON EXTENSIVE METABOLOMIC STUDIES AND THE EVALUATION OF HIGH QUALITY GENOME SEQUENCES

Marc Stadler*

Department Microbial Drugs, Helmholtz Centre for Infection Research, Inhoffenstr. 7. 38124 Braunschweig, Germany
*e-mail: marc.stadler@helmholtz-hzi.de

Abstract:
The Hypoxylaceae are one of the largest families of Xylariales and have been a main subject of our polyphasic taxonomic studies and bioprospecting approaches over the past decade. In this talk the most important recent findings will be summarized. Several hundreds of strains have been isolated from ascomata collected in the field, subjected to fermentation in submerged liquid culture and the cultures were extracted with organic solvents. The bioactive pigments and other secondary metabolites were purified by preparative HPLC from the aforementioned extracts or directly from the stromata, and their structures were elucidated by spectral methods (NMR, HR-MS). The strains were also studied for morphological and chemotaxonomic features and studied in a multi locus phylogeny. Recently, high quality genome sequences were obtained from a selection of representative species using 3rd generation (PacBio/ Oxford nanopore) technology. All compounds were subjected to an intense biological characterization including e.g. antimicrobial, cytotoxic and nematicidal test systems. Over 100 novel secondary metabolites were discovered, some of which constitute novel natural carbon skeletons. In parallel, the biosynthesis of selected compound classes is now being studied, and their production in heterologous hosts including mutasynthesis has been successfully applied. This strategy led once again to several novel molecules. In parallel the first phylogenomic study using representatives of the major phylogenetic clades of the Hypoxylaceae was carried out based on the HQ genome data, revealing interesting correlations between the genotypes and phenotypes. The most important findings are discussed, exemplified by, but not limited to, recent publications.

INVITED SPEAKER: SP14_INV001

ESTABLISHING TAIWAN FRAMEWORK OF RESEARCH INTEGRITY PROMOTION: GOVERNMENT POLICY, INSTITUTIONAL MANAGEMENT, RESEARCHERS' TRAINING AND CASE-HANDLING

Chien Chou*

National Chiao Tung University, Taiwan
*e-mail: cchou@mail.nctu.edu.tw

Abstract:
Ethics and integrity are the foundation of any research work and thus have become an important topic for global scientific research institutions. To enhance Taiwan's research capacity and achievements, the promotion and practice of research integrity are also crucial topics requiring serious consideration by Taiwan's academic community as well as government. In this speech, a 4-pillar framework was proposed: (1) comprehensive national-level policies (laws and regulations); (2) quality management mechanisms of research institutions (institutional management); (3) adequate education and training of researchers (education and training); (4) rigorous handling of academic ethical violations (misconduct handling). Each of the four pillars is indispensable for achieving the overarch goal that Taiwan remains a trustworthy research partner to the global academic community and contributes to the human knowledge. The presentation will elaborate this conceptual framework and will also cover the experiences gained through the past 10-year implementation.
The presentation will then focus on an e-learning platform, the *Center for Taiwan Academic Ethics Education* (AREE) and the learning materials developed. The AREE demonstrates our endeavor to promote research ethics and integrity education in Taiwan, keeping Taiwan's research quality and ensures that Taiwan is on par with the global scientific community.

INVITED SPEAKER: SP14_INV002

GUIDING PRINCIPLES FOR RESEARCH INTEGRITY ACROSS ASIA-PACIFIC

Daniel Barr*, Paul Taylor

Research and Innovation, RMIT University, Melbourne, Australia
*e-mail: daniel.barr@rmit.edu.au

Abstract:
Principles-based policies and guidelines about research integrity appear important for enabling trustworthy research. The Asia-Pacific Economic Cooperation (APEC) is an economic forum comprised of 21 member economies. Although research is an activity shared across the APEC, there was not shared guidance for research integrity. The absence of guiding principles for research integrity was also seen as a barrier to collaboration and researcher mobility.

To address the deficiency in research integrity guidance, we undertook work to make the *APEC Guiding Principles for Research Integrity.* A desktop review of the research integrity systems across APEC economies was conducted as well as a series of face-to-face consultations with representatives from the research integrity systems of selected APEC economies including Chile, Peru, Viet Nam, Indonesia and Malaysia. A modified Delphi process of iteration with experts from across APEC economies that comprised two online surveys and a face-to-face workshop was undertaken to generate a near to consensus set of guiding principles and responsibilities for research integrity. This process included defining, selecting and ranking the principles and responsibilities that were seen to be the most important for trustworthy and responsible research.

The *APEC Guiding Principles for Research Integrity* we found to be: Honesty, Rigour, Transparency, Responsibility, Fairness, Respect and Diversity. The guiding principles are the shared elements for trustworthy and responsible research. They underpin responsibilities of researchers, institutions, and funders or sponsors of research in APEC economies.

The *APEC Guiding Principles for Research Integrity* were produced with significant contributions made by colleagues and participants from across the APEC economies. There are many challenges in activating and promoting research integrity. The *APEC Guiding Principles for Research Integrity* are intended to support other initiatives that enable trust in research. It is hoped that the guidance will enable greater research collaboration and exchange across Asia-Pacific. How the *APEC Guiding Principles for Research Integrity* can be used during the COVID-19 pandemic will be important to discuss.

INVITED SPEAKER: SP14_INV003

A BOTTOM-UP APPROACH TO FOSTER REARCH INTEGRITY IN MALAYSIA AND ASEAN

Lay-Ching Chai[1], Abhi Veerakumarasivam[2], De-Ming Chau[3]*

[1]Institute of Biological Sciences, Faculty of Science, University of Malaya, 50603 Kuala Lumpur, Malaysia
[2]Department of Biomedical Sciences, Faculty of Medicine and Health Sciences, Universiti Putra Malaysia, 43400 UPM Serdang, Selangor, Malaysia
[3]Department of Biological Sciences, School of Science and Technology, Sunway University, Jalan Universiti, Bandar Sunway, 47500 Subang Jaya, Selangor, Malaysia
Young Scientists Network-Academy of Sciences Malaysia, 20th Floor, West Wing MATRADE Tower, 50480 Kuala Lumpur, Malaysia
*e-mail: deming@upm.edu.my

Abstract:
The research ecosystem in Malaysian has been experiencing rapid growth for more than a decade. The government of Malaysia has invested large amount of resources into developing the research industry in Malaysia. As a result, research in Malaysia has generated significant research output such as technologies, innovations, and ground-breaking knowledge.
In 2015, a national Responsible Conduct of Research (RCR) programme was formally established. Since the Malaysia research enterprise is young and majority of the researchers are early- to mid-career researchers, the Young Scientists Network-Academy of Sciences Malaysia (YSN-ASM) was put in-charge of developing the RCR programme and promoting RCR in Malaysia. This gives YSN-ASM a unique opportunity to build a RCR programme from the bottom-up.
Since the establishment of the YSN-ASM RCR Programme, more than 1000 researchers have attended RCR awareness workshops organised by YSN-ASM and partnering organisations. In addition, YSN-ASM also produced the first *Malaysian Educational Module* on RCR, which was fully developed by young scientists. This module has dual-purpose – it is a reference material on RCR and an instructors guide for RCR instructors.
Building on the success of the YSN-ASM RCR Programme, the ASEAN RCR Project was established in 2019 to promote RCR in ASEAN. This is a three-year project spearheaded by the ASEAN Young Scientists Network to spread the awareness of RCR in ASEAN and to train a pioneer cohort of RCR instructors in ASEAN. These national and regional collaborative efforts aim to elevate RCR to a prominent place in the regional scientific dialogue.

INVITED SPEAKER: SP15_INV001

SCIENCE-BASED SUSTAINABLE TOURISM IN THE TROPICAL MARINE AND COASTAL AREAS

Zulfigar Yasin[1], Aileen Tan Shau Hwai[1,*], Anisah Lee Abdullah[2]

[1]Centre for Marine & Coastal Studies (CEMACS), Universiti Sains Malaysia, 11800 Penang, Malaysia
[2]Geography Section, School of Humanities, Universiti Sains Malaysia, 11800 Penang, Malaysia
*e-mail: aileen@usm.my

Abstract:
The value of tourism in the ASEAN region has surpassed US$ 256 billion (about 11% of total GDP) but with the exception of 2020 (with the restrictions associated with the COVID-19 phenomena) has indicated an increased upward trend. It is projected that international arrivals in Southeast Asia will increase to 152 million visitors by 2025 raising the issue of sustainability. Within this 173,000 km of coastline are natural ecosystems such as coral reefs, mangroves, seagrass beds, coastal forests and estuaries. Uncontrolled and poorly planned coastal development has had a large role in natural habitat destruction – the very reasons that has made these locations an attraction to tourists in the first place. These include the construction of infrastructures such as coastal roads, hotel and support residences, increase in sewage effluents into the coastal seas and non-renewable extractive uses of coastal resources. We also see the elevated pressures of increasing populations that follow these coastal development. Other significant factors are the pressures introduced by the changing climate such as the elevated sea temperatures and ocean acidification and its impact on natural ecosystems exemplified by the degradation on coral reefs, the impacts of sea level rise on costal vegetation and mangroves and the follow-up secondary impacts on fisheries and coastal habitation. The sustainability perspective includes the transdisciplinary approaches into the development of methodologies involving the economic, social and environmental understanding of the system which are unique to the location at hand. The success of these approaches has shown that even the traditional scientific but reductive approaches used have their drawbacks and need to be reassessed. We have taken the example of the Straits of Malacca with its multidimensional issues on sustainability to demonstrate the possibility of a science based sustainable tourism approaches that could be applied here. Such approaches include the use of long-term datasets on multiple scales and underlines the importance of issue based long-term monitoring in the areas of interests. The model includes the understanding of damage to local ecosystems caused by both the anthropogenic and climate factors. Finally, these can be translated to economic denominators involving value judgements over a wide spectrum of issues. Taking into consideration the maritime nature of many ASEAN nations, transboundary issues play an important role in ensuring sustainability but is often absent in national or even regional planning. Finally, the effectiveness of our actions (or inactions) could be mapped out to determine the outcome in future scenarios.

INVITED SPEAKER: SP15_INV002

RESTORATION AND CONSERVATION OF REEF BENTHIC SPECIES VULNERABLE TO AQUARIUM TRADE FOR SUSTAINABLE TOURISM IN TROPICAL WATERS

Xuan Ben Hoang, Si Tuan Vo*, Son Lam Ho and Van Than Doan

Institute of Oceanography, Vietnam Academy of Science and Technology, Vietnam
*e-mail: vosituan@gmail.com

Abstract:
Aquarium trade has developed extensively in the world. A long with exploitation of ornamental fish, collection of reef benthic species for aquarium has occurred in many tropical marine waters. Target species which have been exploited for aquarium purpose belong to different groups, including *inter alia*: hard corals (*Acropora*, *Catalaphyllia*, *Euphyllia*, *Galaxea*, *Goniopora*, *Heliofungia*, *Lobophyllia*, *Plerogyra*, *Trachyphyllia*, *Turbinaria* genera); soft corals (*Sarcophyton*, *Sinularia*, *Xenia*, *Cladiella*, *Clavularia*, *Anthelia*, *Lobophytum*, *Nephthea*, *Dendronephthya* and *Cespitularia* genera); gorgonians (*Ctenocella, Echinogorgia, Ellisella, Euplexaura, Gorgonia, Lophogorgia, Pseudopterogorgia* and *Rumphella* genera); sea anemones (*Stichodactyla haddoni, S. gigantean)*; and giant clams *Tridacna maxima*, *T. crocea* và *T. derasa*). The wild harvest of reef organisms for the aquarium trade has resulted in negative impacts on coral reef ecosystems. It was noted that many benthic reef species exhibited slow growth and uncommon in the wild. They were easy to be collected and become endangered under high pleasure of diving industry. Recently, some efforts in culture of ornamental species have been conducted but main sources for the market have still come from the wild.
The efforts in restoring and preserving reef benthic species which are threaten by aquarium trade are critical for biodiversity conservation. Some proposed activities include (1) Study on appropriate techniques for asexual propagation of selected species in the controlled conditions in order to produce significant amount of colony fragments; (2) Assessment of growth and survival rates of organisms restored in the field using fragment transplantation technique: (3) Monitoring changes, taking into account of natural rehabilitation, of reef communities, a long with restoring and protecting process; and (4) Close integration with private sector in developing sea gardens based on restored sites for long term tourism and conservation. The activities will contribute to address the existing conflicts between conservation and development through provision a chance in uses of research outputs for tourist activities managed by private sector. The further expectation is to preserve and enrich populations of ornamental species in the wild environment to enable sustainable exploitation of living animals for aquarium market.

INVITED SPEAKER: SP15_INV003

SMART COMMUNITY FOR RESOURCE AND WASTE MANAGEMENT OF ECO-VILLAGE

Thananchai Sataklang, Sakollawat Sawetrattanakul, Worajit Setthapun*

Asian Development College for Community Economy and Technology, Chiang Mai Rajabhat University, Chiang Mai, 50300, Thailand
*e-mail: worajit@g.cmru.ac.th

Abstract:
Thailand economy relied heavily on the tourism industry. Community based tourism, cultural tourism and culinary tourism have become very popular especially in the northern region of Thailand. Therefore, the local communities and villages must maintain the natural environment and culture, be eco-friendly and strive toward sustainability. Sustainability is an attractive feature of the tourist destination for attracting the growing environmentally conscious tourists. In this work, the concept of smart community was applied to Mae Ta Man Village, Mae Tang District, Chiang Mai, Thailand. Mae Ta Man Village is famous for the community based tourism and elephant camps and sanctuaries. The smart community concept is based on using data monitoring platform to collect and analyze the community data to efficiently manage the community. The researchers worked with the local village leaders and the municipality to set up a demonstration area where the community resource (energy and water) consumption and waste generation were monitored. The energy, water, and load cell sensors were installed at the selected buildings to monitor energy consumption, water usage, and waste generation, respectively. The sensors installed in the real buildings faced several challenges such as lack of data transmission from blackouts and sensor malfunctions from animals, etc. The data for energy and water usage and the waste generation will be analyzed and presented to the villagers to provide the real context of the community. Then, the researchers will work together with the villagers and the municipality to determine effective measures and guidelines for energy and water conservation and to achieve zero-waste village goal.

INVITED SPEAKER: SP15_INV004

REPORTS ON THE STATUS OF CORAL REEFS IN EAST ASIAN SEAS REGION: IMPORTANT BASELINE DATA FOR SUSTAINABLE TOURISM MANAGEMENT

Tadashi Kimura*

Japan Wildlife Research Center, Sumida, Tokyo 130-8606, Japan
*e-mail: tkimura@jwrc.or.jp

Abstract:
The Global Coral Reef Monitoring Network (GCRMN) was launched in 1996 with the main objective of collecting information on the state of coral reefs and raising awareness concerning coral reef conservation. The GCRMN was in response to the "Call to Action" by the International Coral Reef Initiative (ICRI) in 1995, which encouraged the promotion of linkages between regional and global research and monitoring networks, and the use of regional networks to achieve better coordination and cooperation among national research programs. The GCRMN is also specifically tasked with providing information on the status of coral reefs to assist in their effective conservation and management. A series of reports on "The Status of Coral Reefs of the World", edited by Clive Wilkinson was published in 1998, 2000, 2002, 2004, 2008 and they represented a massive global effort at documenting the condition of the world's reefs based on national monitoring initiatives. Japan's Ministry of Environment and the Japan Wildlife Research Center took the lead for the East Asian Seas region and published the "Status of Coral Reefs in East Asian Seas Region" in 2004, 2010, 2014 and 2018 which was a special issue on the mass coral bleaching event that occurred from 2014 to 2017 and it was recognized as the third global coral bleaching events since 1998. A common pattern of the coral bleaching events during 2014-2017 is the obvious difference in bleaching severity among reef sites. The levels of bleaching susceptibility also varied greatly among coral taxa. Experiments with shading on bleaching recovery and survival of corals in Thailand indicated higher bleaching recovery rates of some coral species that were shaded. Monitoring capacity varies among countries/states. There are logistic and funding constraints especially for those with a large expanse making it challenging to access some of the more remote reefs. One of the important goals of the East Asian Seas regional network is to analyze reef status trends in response to threats and management over the long-term. Continued monitoring and reporting are necessary as they provide the basis for such an analysis and it is expected that national coordinators, all operating voluntarily will maintain their interest and passion for this significant regional collaboration. It is essential to provide more comprehensive data and information for national governments and regional organizations to assist them in their efforts to conserve coral reefs and their ecosystem services, particularly for sustainable tourism.

INVITED SPEAKER: SP16_INV001

COVID-19 VACCINE: GLOBAL AND COUNTRY UPDATE

Kiat Ruxrungtham*

Vaccine Research Center (ChulaVRC), Faculty of Medicine, Chulalongkorn University, Bangkok, Thailand
*e-mail: rkiatchula@gmail.com

Abstract:
Since the end of 2020, Covid-19 has been spreading from Wuhan, China and becoming pandemics in more than 188 countries. Currently there are more than 33 million people confirmed cases and up to a million people died from Covid-19. The new cases report is still on the rise of approximately more than 300,000 a day and more than 6,000 people died each day from Covid-19. Global vaccine development to have safe and effective vaccines is therefore an ultimate goal. There are at least 51 vaccine candidates in human trials, and more than 93 in preclinical studies. Among those candidates, at least 10 are in phase 3 clinical trials, including 4 viral vector-based, 3 viral inactivated, 2 mRNA, and 1 protein vaccines. Based-on the minimal criteria for approval of an effective and safe vaccine by WHO and regulatory authorities to achieve at least 50% efficacy after 6 months post-vaccination, it is likely that we will have a safe and effective vaccine approved no early than in the first quoter of 2021.
One of the global challenges and concern is how to make vaccine(s) accessible worldwide includes people in low-income countries where the Covid-19 also hits very hard. World population is approximately 7.8 billion, the total announced vaccine productive capacity from various vaccine programs by the end of 2021 is likely that will not able to cover >50% of global population. Major in high income countries have made deal for big volume of vaccines for their population, including U.S. (300 million + additional 500 million doses deal), European union (1,100 million doses), Japan (120 million doses), and China (their population is 1,400 million, if aims to cover 50%, they will need >1000 million doses). It is very likely that inequity on Covid-19 vaccine access will be a major issue, COVAX -an international consortium is therefore try to facilitate and support a better global access to vaccine.
Thailand led by the National Vaccine Institute is currently working on 3 strategies to ensure the country can access to at least a safe and effective vaccine as early as possible: 1). To join COVAX consortium to make deal and buy vaccine(s) 2). To make deal with any successful vaccine industries/programs for technology transferring and local manufacturing 3). Own vaccine development and local production. There are 3 vaccine candidates currently have been tested in non-human primates: DNA vaccine (by BionetAsia, has been granted by the Australian Government for conducting phase 1 in Australia), mRNA vaccine (by our Chula Vaccine Research Center), and plant-based protein vaccine (Baiya, a startup company, Pharm Sci, Chulalongkorn University). Chula-Cov-19 mRNA vaccine (ChulaVRC) has shown promising high SARS-Cov2 neutralizing antibody and T-cell responses in both mice and non-human primates; and is currently under cGMP production. We anticipate initiating phase 1 trial by January next year, in parallel with mRNA and lipid nanoparticle technology transfer to a Thai Vaccine Industry, BionetAsia. A plan of large scale 10s of million doses of Chula Cov-19 mRNA vaccine will be manufactured in Thailand by the end of 2021. While an effective vaccine is not yet available, all proven effective means to prevent Covid-19 spreading should remain widely implemented.

INVITED SPEAKER: SP16_INV002

DEVELOPMENT OF PLATFORMS TO MODEL PATHOGENESIS, THERAPEUTIC STRATEGIES AND VACCINE DEVELOPMENT AGAINST SARS-COV-2 INFECTION

Arunee Thitithanyanont[1, 2]*

[1]MU COVID-19 network Thailand
[2]Department of Microbiology Faculty of Science, Mahidol University, Thailand
*e-mail: arunee.thi@mahidol.edu

Abstract:
An outbreak of a novel coronavirus started around mid-December 2019 in Wuhan, China. The global spread of SARS-CoV-2 caused a severe outbreak in more than 215 countries. This disastrous situation emphasized the vital need of the entire population for the effective vaccines for prevention and the effective and inexpensive antiviral therapeutics to fight against the unpleasant disease. Since the end of January 2020, the first 2 isolates of SARS-CoV-2 were cultured from the left over specimens of infected patients in our certified BSL3 at Faculty of Science, Mahidol University. At that point, we urgently used the live virus to set up neutralization assay for diagnosis and vaccine development. In addition, the basic knowledge has been applied to promote innovation of the coronavirus diagnostic test, the RT-LAMP kit in the early development stage, including consulting on technology incubation process with start-up companies. Shortly, we developed a high-content screening for the antiviral candidates using fluorescence-based SARS-CoV-2 nucleoprotein detection in Vero E6 cells coupled with plaque reduction assay. Among 122 Thai natural products, we found that *Boesenbergia rotunda* extract and its phytochemical compounds, panduratin A and pinostrobin exhibited the potent anti-SARS-CoV-2 activities. Treatment with panduratin A or pinostrobin after viral infection radically suppressed SARS-CoV-2 infectivity in Vero E6, Calu-3 cells and human lung organoid. In collaboration with diverse Mahidol experts, development of human primary cell platforms to model pathophysiology, pathogenesis and therapeutic strategies against SARS-CoV-2 infection is ongoing. The implications of the preliminary findings and possible directions for future research will be further discussed.

INVITED SPEAKER: SP16_INV003

EARLY TRANSMISSION PATTERNS OF CORONAVIRUS DISEASE 2019 (COVID-19) IN TRAVELLERS FROM WUHAN TO THAILAND, JANUARY 2020

Pilailuk Okada[1], Rome Buathong[2], Siripaporn Phuygun[1], Thanutsapa Thanadachakul[1], Sittiporn Parnmen[1], Warawan Wongboot[1], Sunthareeya Waicharoen[1], Supaporn Wacharapluesadee[3], Sumonmal Uttayamakul[2], Apichart Vachiraphan[2], Malinee Chittaganpitch[1], Nanthawan Mekha[1], Noppavan Janejai[1], Sopon Iamsirithaworn[2], Raphael TC Lee[4], Sebastian Maurer- Stroh[4,5]

[1] Department of Medical Sciences, Ministry of Public Health, Thailand
[2] Department of Disease Control, Ministry of Public Health, Thailand
[3] Thai Red Cross Emerging Infectious Diseases - Health Science Centre, Chulalongkorn University, Thailand
[4] Bioinformatics Institute, Agency for Science Technology and Research, Singapore
[5] Department of Biological Sciences, National University of Singapore, Singapore
*e-mail: Pilailuk Okada (pilailuk.o@dmsc.mail.go.th)

Abstract:
We report two cases of coronavirus disease 2019 (COVID-19) in travellers from Wuhan, China to Thailand. Both were independent introductions on separate flights, discovered with thermoscanners and confirmed with RT-PCR and genome sequencing. Both cases do not seem directly linked to the Huanan Seafood Market in Hubei but the viral genomes are identical to four other sequences from Wuhan, suggesting early spread within the city already in the first week of January.

POSTER SESSIONS

INFORMATION FOR POSTER PRESENTATION

Time for poster attachment & removal

The location for poster attachment will be specified according to Abstract ID at the congress venue. The abstract ID can be found in this program book. Time for poster attachment and removal are as follows:

Session	Date	Time
Poster Attachment	October 5th, 2020 October 6th, 2020	07:00-08:00 07:00-08:00
Poster Removal	October 6th, 2020	18:00-19:00

SESSION A: Challenges in the Frontiers of Physics

ID	Presenter	Title
A_001_PF	Panapon Savirot	A STUDY OF EFFECTS ON IMAGE QUALITY FROM DIFFERENT SETTINGS OF RADIOGRAPHIC IMAGING SYSTEM USING FLUORESCENCE SCREEN AND DIGITAL CAMERA
A_002_PF	Phatthrawat Janratsamechot	DEVELOPMENT OF SPECTROPHOTOMETRIC TECHNIQUE FOR EFFICIENT COMPONENT ANALYSIS
A_003_PA	Manit Klawtanong	CONTROLLING TRAFFIC JAMS IN A MODIFIED CAR-FOLLOWING MODEL WITH AUTONOMOUS VEHICLES
A_004_PF	Thanakit Klomkliew	INSPECTION AND EVALUATION OF AIR-FILLED VOID INSIDE REINFORCED CONCRETE STRUCTURE BY NON-DESTRUCTIVE TESTING METHODS
A_005_PA	Adisorn Buranawong	THERMAL OXIDATION OF NANOSTRUCTURE TiN THIN FILM DEPOSITED BY REACTIVE DC MAGNETRON SPUTERING TECHNIQUE
A_009_PF	Rakdiaw Muangma	RECTIFICATION OF G-BHN CORRELATION OF FIBROUS COMPOSITES USING POLYNOMIAL REGRESSION WITH AMSE-5-FOLD-CV ANALYSIS
A_010_PF	Suwimon Udphuay	ELECTRICAL RESISTIVITY AND GROUND-PENETRATING RADAR SURVEYS, WIANG THA KAN ARCHAEOLOGICAL SITE, CHIANG MAI PROVINCE, NORTHERN THAILAND
A_011_PA	Kachain Dangudom	THE STUDY OF PHASE TRANSITION TEMPERATURE OF LIQUID MIXTURES BY LIGHT SCATTERING TECHNIQUE
A_013_PA	Thanongsak Nochaiya	THE EFFECT OF SUGARCANE BAGASSE ASH ON ELECTRICAL CAPACITY AND TIME LAG OF PORTLAND CEMENT MORTARS
A_014_PA	Aek Jantayod	CRYSTALLOGRAPHIC ORIENTATION EFFECT ON THE TUNNELING SPECTROSCOPY ACROSS A HALF-METAL/SEMICONDUCTOR WITH DRESSELHAUS SPIN-ORBIT COUPLING JUNCTION
A_015_PF	Thapana Nakprapatsorn	EFFECTS OF UPSTREAM ION SPEED ON THE ION ACCELERATION PROCESS NEAR X-LINE OF COLLISIONLESS MAGNETIC RECONNECTION: A TEST-CHARGE STUDY

SESSION B: Math Stat Comp in the Digitally Innovative Era

ID	Presenter	Title
B_005_PF	Autcha Araveeporn	MODELING OF RANDOM COEFFICIENT AUTOREGRESSIVE MODEL ON TIME SERIES DATA
B_013_PF	Somsri Banditvilai	FORECASTING MODELS OF FOREIGN EXCHANGE RATES U.S. DOLLAR, EURO, YEN AND YUAN AGAINST THE THAI BAHT
B_023_PA	Penpark Sirimark	ON SOME $(C,1)(E,1)$ IDEAL CONVERGENT SEQUENCE SPACES

SESSION C: Impact of Biological Science towards SDGs

ID	Presenter	Title
C_001_PA	Prasan Swatsitang	EFFECTS OF SOLVENTS AND PEANUT SKIN ON ANTIOXIDANT CAPACITY AND PHENOLIC CONTENT OF VIRGIN COCONUT OIL
C_003_PA	Kewalee Jantapo	PROPICONAZOLE APPLICATION ATTENUATES PLANT RESPONSES TO NITROGEN AND PHOSPHORUS DEFICIENCY IN RICE
C_004_PF	Chananwat Kortheerakul	EXPRESSION ANALYSIS OF GENES ENCODING GLUTATHIONE S-TRANSFERASE UNDER STRESS CONDITIONS IN THE EXTREMOPHILE *Halothece* sp. PCC7418
C_005_PA	Thanasin Chalermchat	RE-DESIGNING OF LOW-COST GEL ELECTROPHORESIS AS HIGH SCHOOL INSTRUCTIONAL MEDIA
C_006_PF	Jaruwan Worawittayatada	MOLECULAR CLONING AND EXPRESSION OF INFECTIOUS HYPODERMAL AND HEMATOPOIETIC NECROSIS VIRUS (IHHNV) CAPSID GENE LINKED WITH DOUBLE STRANDED-RNA OF YELLOW HEAD VIRUS
C_007_PA	Tanutcha Patipong	FUNCTIONAL ANALYSIS OF HTRA PROTEASE IN THE HALOTOLERANT CYANOBACTERIUM *Halothece* sp. PCC7418
C_008_PA	Thiri Wai Linn	PRELIMINARY STUDY ON ANTI-HYPERGLYCEMIC EFFECT OF CROCODILE OIL IN SPONTANEOUSLY DIABETIC TORII RATS
C_009_PA	Chutarat Punchkhon	IDENTIFICATION AND VALIDATION OF *MRL1* IN ABIOTIC STRESS IN RICE AND ARABIDOPSIS MODEL
C_010_PF	Pawarit Innachai	EFFECTS OF HISTONE DEACETYLASE INHIBITOR ON FETAL HEMOGLOBIN INDUCTION AND ERYTHROPOIESIS IN β-THALASSEMIA
C_011_PF	Surapong Khuna	SOLUBILIZATION OF INSOLUBLE MINERALS BY SOIL FUNGI COLLECTED FROM NORTHERN THAILAND
C_012_PA	Thammaporn Kojonna	GENOME WIDE ASSOCIATION STUDY FOR GROWTH PARAMETER UNDER DROUGHT STRESS AT SEEDLING STAGE IN LOCAL THAI RICE VARIETIES
C_013_PF	Kritsana Jatuwong	SELECTION OF FILAMETOUS FUNGI AND LIGNOCCELLULOSIC RESIDUES FOR PHYTASE PRODUTION UNDER SOLID-STATE FERMENTATION
C_014_PF	Ingon Inson	INHIBITORY EFFECTS OF ADENOSINE AND ITS COMBINATORIAL EFFECTS WITH CISPLATIN ON CHOLANGIOCARCINOMA
C_016_PA	Patchanee Charoenying	SYNTHESIS OF DIHYDRAZONE STEROID DERIVATIVES DERIVED FROM PREGNENOLONE AND THEIR *IN VITRO* CYTOTOXIC ACTIVITY
C_017_PA	Maneeploy Nualkul	ISOLATION OF ENZYME PRODUCING BACTERIA FROM TERMITE GUTS AND APPLICATION FOR IMPROVING NUTRITIONAL VALUE OF SOYBEAN MEAL
C_018_PF	Ratichon Tiandee	IMPROVEMENT OF NORFLOXACIN DETECTION LIMIT OF LATERAL FLOW IMMUNOASSAYS USING GOLD NANOFLOWERS
C_019_PA	Anumart Buakeaw	ANTIPROLIFERATIVE PROPERTY AGAINST CANCER CELL LINE AND CELLULAR ANTIOXIDANT ACTIVITY OF *Acacia pennata* LEAVES EXTRACT

ID	Presenter	Title
C_020_PA	Songchan Puthong	QUANTIFICATION OF COW CASEIN IN MILK BY AN ENZYME - LINKED IMMUNOSORBENT ASSAY
C_021_PA	Umaporn Pimpitak	DEVELOPMENT OF A PROTOTYPE TEST STRIP FOR THE DETECTION OF NORFLOXACIN RESIDUE IN CHICKEN MUSCLE
C_022_PF	Worawut Chaiyasaeng	NON-TARGETED METABOLIC PROFILING REVEALED THE BIOMARKERS BETWEEM THREE *Aspergillus* SPECIES BY UHPLC-MS COUPLED WITH PRINCIPAL COMPONENT ANALYSIS
C_024_PA	Sajee Noitang	UTILIZATION OF *Ocimum* STRAW TRUNK AS RENEWABLE ENERGY VIA ZERO WASTE MANAGEMENT APPROACH
C_025_PA	Darika Buathong	COMPOSITION AND ABUNDANCE OF ZOOPLANKTON IN THE VICINITY OF PORTS INDUSTRAIL IN THE UPPER AND EASTREN GULF OF THAILAND
C_026_PA	Orathep Muresare	DIVERSITY AND DENSITY OF PHYTOPLANKTON IN THE PORTS OF CHONBURI AND RAYONG PROVINCE
C_027_PA	Nichakorn Phengpol	HIGH FAT DIET INDUCED MATERNAL OBESITY EFFECT TO DYSREGULATION OF AUTOPHAGY PROCESS IN KIDNEY OF MALE OFFSPRING
C_028_PA	Phonphan Watthanarat	ISOLATION OF PROTEOLYTIC *Bacillus* sp. FROM THE GUT OF TERMITE, *Microcerotermes* sp. AND SOLID-STATE FERMENTATION OF SOYBEAN MEAL USING NEWLY ISOLATED BACTERIA
C_029_PA	Saranyu Thaworn	GENOME-WIDE ASSOCIATION STUDY OF ANTIOXIDANT COMPOUNDS AND ACTIVITY IN 159 THAI RICE CULTIVARS
C_030_PA	Klinphaka Phuthaworn	DIVERSITY OF MARINE FUNGI LIVING IN DISEASED CORAL REEFS FROM THE GULF OF THAILAND AND THE ANDAMAN SEA
C_031_PF	Chuttiya Tiva	DNA FINGERPRINT ANALYSIS USING AFLP TECHNIQUE OF *Adenia viridiflora* Craib
C_034_PA	Papon Ganjanasiripong	DIVERSITY OF BACTERIA IN KLONG THOOP MANGROVE FOREST, CHUK SAMET, SATTAHIP, CHONBURI
C_035_PF	Siriporn Riebroy Kim	FERMENTATION AND ANTIOXIDANT PROPERTIES OF LONGAN HONEY INOCULATED WITH *Saccharomyces cerevisiae* var. *burgundy*
C_037_PF	Iyacoob Khunsri	IDENTIFICATION OF GENES INVOLVED IN ANTIMICROBIAL PEPTIDE rALF*Pm*3 RESISTANCE IN *Vibrio parahaemolyticus* AHPND VIA GENOME SEQUENCING
C_038_PF	Pattranit Srisuwanuntanakul	INVESTIGATION OF LONG PRIMER TARGET-ENRICHMENT COMBINING WITH STR TYPING FOR DEGRADED DNA ANALYSIS
C_041_PA	Phiradet Chuabsak	PHYLOGENETIC RELATIONSHIPS OF MICROHYLID FROGS IN RAMKHAMHAENG UNIVERSITY CAMPUSES INFERRED FROM COI GENE
C_042_PA	Natsaran Saichana	ADAPTATION OF THERMOTOLERANT *Acetobacter* sp. FOR VINEGAR PRODUCTION
C_043_PA	Nidsaraporn Petsut	ASSESSMENT ON SEASONAL VARIATION OF FISH IN THE MANGROVE AREA, EASTERN THAILAND

SESSION D: Responsible Chemical Sciences for Future Sustainability

ID	Presenter	Title
D_001_PF	Sirirat Khemasiri	DEVELOPMENT OF A DNA-BASED BIOSENSOR FOR miRNA DETECTION
D_002_PA	Klatnatee Vepulanont	GREEN CORROSION INHIBITOR: *Parkia speciosa* HASSK. EMPTY POD EXTRACTION BY MICROWAVE-ASSISTED EXTRACTION METHOD
D_003_PF	Korakot Navakhun	ANION RECOGNITIONS OF TRICHLOROPHENYL AMIDE-BASED ANION RECEPTORS
D_006_PA	Chawin Srisomwat	ELECTROCHEMICAL PAPER-BASED DNA DEVICE WITH POP-UP ARCHITECTURE FOR HEPATITIS B VIRUS INFECTION DIAGNOSTIC
D_008_PF	Patticha Weerakul	A STUDY OF EXTRUSION AND SPHERONIZATION BEHAVIOUR OF MONTMORILLONITE
D_009_PA	Amnuay Noypha	ANTIBACTERIAL ACTIVITY OF VINEGAR-GRAPHENE QUANTUM DOTS AGAINT *Bacillus Cereus* AND *Escherichia coli*
D_010_PA	Paweena Porrawatkul	MICROWAVE ASSISTED SYNTHESIS OF Ag-ZnO NANOPARTICLES USING EXTRACT OF *Caulerpa sertularioides* AS A NOVEL REDUCING AGENT
D_012_PA	Sudkate Chaiyo	ELECTROCHEMICAL PAPER-BASED SENSORS FOR THE HIGHLY SENSITIVE DETERMINATION OF OXYTETRACYCLINE
D_013_PA	Sirirat Phaisansuthichol	SIMULTANEOUS DETECTION OF LUTEIN AND ZEAXANTHIN IN VEGETABLES BY HPLC
D_015_PF	Weerapat Vichitsangsri	$Ag_2O@TiO_2$ MATERIALS FOR DESULFURIZATION IN MODEL OIL
D_017_PF	Chutima Tangku	PALLADIUM NANOPARTICLES IMMOBILIZED ON TITANOSILICALITE-1 FOR CYCLOADDITION REACTIONS OF CO_2 AND EPOXIDES
D_018_PF	Kanyarat Kwansirikul	GEMOLOGICAL CHARACTERISTICS AND CHEMICAL COMPOSITIONS OF KYANITE CLAIMED TO BE FROM NEPAL
D_019_PA	Kanokwan Sakunrungrit	INVESTIGATION OF USING ELECTROCHEMICAL TECHNIQUE AND SPECTROPHOTOMETRIC TECHNIQUE FOR DETERMINATION OF RETINOIC ACID IN PHARMACEUTICAL PRODUCTS
D_020_PA	Patcharin Kosuwan Jundee	GEOCHEMISTRY OF EXTRUSIVE ROCKS AT KHUN DAN PRAKAN CHON DAM RIDGE, NAKHON NAYOK PROVINCE, THAILAND
D_021_PA	Voranuch Somsongkul	ENHANCED VISIBLE LIGHT RESPONSE OF TiO_2 NANOPARTICLES BY NATURAL DYES
D_022_PF	Wutthikrai Kulsawat	VERTICAL DISTRIBUTION AND RADIOLOGICAL RISKS OF THORIUM-232 IN BURN AND NO-BURN PADDY SOIL
D_024_PA	Saowaluk Madkoksung	FLUORESCENCE SPECTROSCOPY FOR SIMPLE CLASSIFICATION OF SOME COFFEE LEAVES VARIETIESE
D_025_PA	Siripen Modmuang	DETERMINING THE ANTIOXIDANT PROPERTIES, TOTAL PHENOLIC AND TOTAL FLAVONOID CONTENTS OF TRADITIONAL Thai MEDICINAL HERBS, *Anaxagorea luzonensis* A.Gray. AND *Salacia verrucosa* Wight.

ID	Presenter	Title
D_026_PA	Kunlanit Phengphat	SYNTHESIS, CHARACTERIZATIONS AND ITS ENVIRONMENTAL APPLICATION TO REMOVAL OF CATIONIC DYES OF ZEOLITE A
D_027_PA	Sirintip Sangsawang	COMPUTER AIDED MOLECULAR DESIGN OF JAK2 INHIBITORS AS ERYTHROPOIESIS STIMULANT AGENTS FOR THALASSEMIA THERAPY
D_028_PA	Somjintana Taweepanich	SCREENING OF ANTIOXIDANT ACTIVITIES, TOTAL PHENOLIC AND TOTAL FLAVONOID CONTENTS OF *Caesalpinia sappan* L. AND *Bauhinia sirindhorniae* K. Larsen & Larsen FOR THALASSEMIA THERAPY

SESSION E: Innovations for Sustainable Future

ID	Presenter	Title
E_003_PF	Rattikorn Leemahanil	DEVELOPMENT AND EVAUATION OF AN IN-HOUSE COMPETITIVE ELISA FOR DETECTION OF DEHYDROEPIANDROSTERONE SULFATE
E_004_PF	Nattaphorn Natteerapong	DEMONSTRATION OF IN-HOUSE BEAD-BASED IMMUNOASSAY FOR HUMAN SERUM ALBUMIN DETECTION BASED ON MICROFLUIDICS FLOW CYTOMETRY
E_005_PA / E_027_PA / E_030_PA	Punyaphat Surakiatkamjorn / Sirawich Thanawan / Thanat Wongsamut	EXPERIMENTAL DEVICE FOR STUDYING THE MOTION OF MAGNET FALLING THROUGH CONDUCTING PIPES USING ARDUINO AND REAL-TIME DISPLAY
E_006_PA	Chanita Mano	INTEGRATION OF PHASE CHANGE MATERIAL INTO ROOF FOR HEAT ACCUMULATION REDUCTION IN BUILDINGS
E_007_PA	Jantakan Peangkaew	TECHNICAL AND ECONOMIC INVESTIGATION OF ELECTRICAL ENERGY CONSUMPTION PRODUCED FROM SOLAR CELLS INSTALLED ON MOTORCYCLES
E_011_PA	Peeranat Laphom	EXPERIMENTAL STUDY OF MATERIAL TYPES AND INCIDENT ANGLES OF LIGHT SOURCE ON ILLUMINATION PERFORMANCE OF LIGHT PIPES IN BUILDINGS
E_012_PA	Kanyanut Noynun	DESIGN OF JACKET CONTAINING PHASE CHANGE MATERIAL TO REDUCE HEAT THROUGH HUMAN BODIES
E_013_PA	Jittipak Jitsumran	INVESTIGATION OF ILLUMINATION PERFORMANCE OF VERTICAL AND HORIZONTAL LIGHT PIPES FOR ENERGY SAVING IN BUILDINGS
E_014_PA	Pavee Pansritong	INVESTIGATION AND DESIGN OF ENERGY CHARGE SYSTEMS FROM SOLAR CELL ON MOTORCYCLE
E_015_PA	Atthakorn Thongtha	IMPROVEMENT OF THERMAL PERFORMANCE OF LIGHTWEIGHT CONCRETE BUILDING MATERIAL INCORPORATING WASTE POWDER FROM AUTOMOTIVE REFINISHING INDUSTRY
E_018_PF	Chidchanok Meechaisue	ANTIBACTERIAL ACTIVITY AND STABILITY STUDIES OF ELECTROSPUN CELLULOSE ACETATE FIBER MATS CONTAINING INDIAN GOOSEBERRY CRUDE EXTRACT
E_019_PA	Kangsadan Boonprab	BIOGEL BEVERAGE PROCESSING FROM AGAL EXTRACTION

ID	Presenter	Title
E_020_PF	Jiraphorn Mahawan	APPLICATION OF VERTICAL LIGHT TUBE INTEGRATING WITH ROOF FOR ENERGY CONSUMPTION REDUCTION IN BUILDINGS
E_033_PA	Nilobon Thongdorn-Ae	APPLICATION OF CRYOGENIC FREE COMPREHENSIVE HEART-CUT TWO DIMENSIONAL GAS CHROMATOGRAPHY-MASS SPECTROMETRY FOR ANALYSIS OF VOLATILE COMPOUNDS IN PETROCHEMICAL SAMPLE
E_036_PA	Warangkana Sompongse	GEL-FORMING ABILITY OF UNWASHED ROHU AFFECTED BY EGG WHITE
E_037_PF	Krittiya Khuenpet	IMPROVEMENT OF BREAD ENRICHED WITH LARVAL-STAGE MEALWORM (*Tenebrio molitor*) BY USING HYDROCOLLOIDS

SYMPOSIUM 01: Biodiversity of Marine Benthic Fauna

ID	Presenter	Title
SP01_001_PA	Orawan Piyaboon	ANTIMICROBIAL ACTIVITIES OF *Myrothecium indunatum* ISOLATED FROM LEAF BLIGHT DISEASED WATER LETTUCE
SP01_002_PA	Laongdow Jungrak	COMPOSITION AND ABUNDANCE OF MACROFAUNA ON CORAL REEFS COMMUNITIES AT MU KO CHUMPHON, THE WESTERN GULF OF THAILAND
SP01_003_PA	Pronsiri Sriwisait	COMPARING THE MEIOFAUNA COMMUNITIES IN CORAL REEFS AT MU KO CHUMPHON, THE WESTERN GULF OF THAILAND
SP01_004_PA	Suphakarn Phoaduang	ABUNDANCE AND COMPOSITION OF MEIOFAUNA ON A SANDY BEACH AT MU KO ANGTHONG NATIONAL PARK, SURAT THANI PROVINCE
SP01_007_PA	Supawadee Chullasorn	DIVERSITY OF MARINE PHYTAL HARPACTICOID COPEPODS FROM THAILAND
SP01_009_PA	Sitthi Kulabtong	CHANGES IN MACROINVERTEBRATE POPULATIONS IN THE ESTUARY ECOSYSTEM: A CASE STUDY OF MAE KLONG ESTUARY AND THA CHIN ESTUARY, UPPER GULF OF THAILAND
SP01_010_PA	Weerawan Saowakul	DIVERSITY OF HARPACTICOID COPEPODS FROM PAKNAM PRASAE INTERTIDAL SANDY BEACH IN RAYONG, THAILAND
SP01_011_PA	Pawana Kangtia	STUDY ON LIFE CYCLE AND NAUPLIAR DEVELOPMENT OF *Amphiascopsis cintus* COLLECTED FROM *Caulerpa* sp. AT BANPHE, RAYONG PROVINCE, THAILAND

SYMPOSIUM 02: Climate Change in a Changing World

ID	Presenter	Title
SP02_002_PF	Yupa Thasod	DEPOSITIONAL PROCESSES AND CLIMATE CHANGE IN THE CENOZOIC HONGSA COALFIELD, LAO PDR

ID	Presenter	Title
SP02_003_PF	Panutchanat Chinklang	SETTLEMENT AND LIPID CLASS COMPOSITIONS OF PLANULA LARVAE OF CORALS UNDER CHANGES OF TEMPERATURES
SP02_004_PA	Pongthep Suwanwaree	SPATIAL AND SEASONAL VARIATION OF SOIL RESPIRATION IN DRY EVERGREEN FOREST, SAKAERAT BIOSPHERE RESERVE, THAILAND

SYMPOSIUM 03: Crystallography

ID	Presenter	Title
SP03_001_PA	Kamonwan Janwatthana	CRYSTAL STRUCTURE OF COPPER (I) CHLORIDE COMPLEX CONTAINING 4-PHENYLTHIOSEMICARBAZIDE AND TRIPHENYLPHOSPHINE LIGANDS
SP03_004_PF	Apichet Boonsoong	FOURIER TRANSFORM INFRARED SPECTROSCOPY (FTIR) CHARACTERISTICS OF CORUNDUM GEMS IN THE CHANTHABURI-TRAT GEM FIELDS, THAILAND

SYMPOSIUM 04: Development of Material Science Based on Coordination Compounds

ID	Presenter	Title
SP04_001_PF	Chanikan Wongkaew	THE DEVELOPMENT OF PHOTOSWITCHABLE AZOBENZENE DERIVATIVE FOR AMPA RECEPTOR IN RETINAL NEURONS
SP04_002_PF	Suthasinee Somboonsap	THE EFFECT OF SURFACE MORPHOLOGY ON THE MAGNETIC PROPERTIES OF RF-SPUTTERED CO-CU FILM
SP04_003_PA	Kanchanee Niyom	EFFECT OF SURFACE MORPHOLOGY ON TRANSMITTANCE OF AL-DOPED ZINC OXIDE FILMS ON FLEXIBLE SUBSTRATE PREPARED BY SPUTTERING
SP04_006_PA	Tatiya Chokbunpiam	COMPUTER SIMULATIONS OF THE SEPARATION OF CH_4/H_2S IN MATERIAL INSTITUT LAVOISIER- 127 (MIL-127)
SP04_007_PA	Kamonporn Saenkam	ELECTRICAL PROPERTIES OF LEAD-FREE BISMUTH SODIUM TITANATE-STRONTIUM BISMUTH TITANATE PIEZOELECTRIC CERAMICS
SP04_008_PA	Sermsiri Leeporikhon	ZEOLITIC IMIDAZOLATE FRAMEWORK ADSORBENTS FOR SEPARATION IMPURITIES FROM NATURAL GAS
SP04_012_PA	Sirawan Kamavichanurat	SINGLE-SITE ALUMINIUM COMPLEXES IN CATALYSIS OF *rac*-LACTIDE POLYMERIZATION

SYMPOSIUM 08: Green and Sustainable Chemistry: Opportunities for Academia and Industry

ID	Presenter	Title
SP08_001_PF	Sasinun Detsangiamsak	METHOD DEVELOPMENT FOR DETERMINATION OF PHENOLIC ACIDS IN FRUIT USING MICELLAR ELECTROKINETIC CHROMATOGRAPHY AND SOLVENT EXTRACTION
SP08_002_PA	Komgrit Sawangkan	AMPHIPHILIC PULLULAN DERIVATIVES FOR STABILIZING GOLD NANOPARTICLES TRANSDERMAL DELIVERY CARRIERS
SP08_003_PA	Siriluck Pojjanapornpun	MELON SEEDS AS A POTENTIAL SOURCE FOR PREPARATION OF CONJUGATED LINOLEIC ACID
SP08_004_PA	Yuree Wandee	PECTIC OLIGOSACCHARIDE PRODUCTION FROM NaOH-EDTA EXTRACTED POMELO PEEL PECTIN BY ENZYMATIC HYDROLYSIS
SP08_005_PA	Naruthai Hongsa	POLYELECTROLYTE COMPLEX COATED-GOLD NANOPARTICLES AS DRUG CARRIERS FOR ANTICANCER AND INFLAMMATORY ACTIVITY
SP08_007_PF	Chanipron Vadeesirisak	PREPARATION OF LAKE PIGMENT FROM ORCHID USING ADSORPTION METHOD
SP08_008_PA	Satipat Suttayasorranakhom	UTILIZATION OF BRAZILEIN ON TEST STRIP FOR Fe^{2+} DETECTION
SP08_011_PA	Jitnapa Sirirak	LAKE PIGMENT FROM DIN DANG CLAY AND SAPPANWOOD
SP08_013_PA	Weeraya Khummueng	RAPID ANALYSIS OF PALM OIL LOSS FROM SCREW PRESSED PALM FRUIT FIBER

SYMPOSIUM 09: Green Production Platform for Renewable Biomass Conversion

ID	Presenter	Title
SP09_001_PA	Jirabhorn Piluk	ISOLATION AND SCREENING OF THERMOTOLERANT YEAST FOR ETHANOL PRODUCTION FROM CELLULOSIC FEEDSTOCKS
SP09_002_PF	Hataikarn Lekakarn	IDENTIFICATION AND HETEROLOGOUS EXPRESSION OF ENDOGLUCANASE (GH5) FROM *Bacillus amyloliquefaciens* HL25
SP09_003_PF	Manassanum Utapow	PREBIOTIC PROPERTIES DETERMINATION OF RICE BRAN EXTRACTION FROM SOLID STATE FERMENTATION BY LACTIC ACID BACTERIA
SP09_004_PF	Supakorn Boonyuen	THE ASSESSMENT OF PHOTOCATALYTIC ACTIVITY OF CUPROUS AND ZINC OXIDE NANOPARTICLES FROM *Oroxylum indicum* BY ONE POT GREEN SYNTHESIS METHOD
SP09_006_PA	Panaya Kotchaplai	SUSCEPTIBILITY OF THE INDUSTRIALLY-RELEVANT BACTERIAL STRAINS TO 4-VINYLGUAIACOL
SP09_007_PF	Sanya Kudan	ETHANOL PRODUCTION IN MOLASSES MEDIUIM BY *Pichia kudriavzevii* STRAIN RU01

SYMPOSIUM 10: Hydrogen Energy

ID	Presenter	Title
SP10_002_PA	Janenipa Saupsor	NiFe-MgAl BIFUNCTIONAL MATERIAL DERIVED FROM HYDROTALCITE-LIKE PRECURSORS FOR HYDROGEN PRODUCTION FROM CHEMICAL LOOPING REFORMING OF ETHANOL
SP10_003_PA	Talita Nimmas	HYDROGEN PRODUCTION FROM SORPTION-ENHANCED AUTOTHERMAL REFORMING CHEMICAL LOOPING USING NiO-CuO MULTIFUNCTIONAL MATERIAL

SYMPOSIUM 11: Lichens: Diversity, Ecology and Biomonitoring

ID	Presenter	Title
SP11_001_PA	Chaiwat Boonpeng	MORPHOLOGICAL RESPONSE OF LICHEN TRANSPLANTS AS A BIOINDICATOR OF AIR POLLUTION

ID	Presenter	Title
SP11_002_PF	Achariya Rangsiruji	MOLECULAR SYSTEMATICS OF MANGLICOLOUS LICHENS IN THE GENUS *Pyrenula* ON THE WESTERN GULF OF THAILAND
SP11_003_PF	Phimpisa Phraphuchamnong	BIODIVERSITY OF CRUSTOSE DISCOLICHEN IN MANGROVE FOREST AT PRACHUAP KHIRI KHAN PROVINCE, THAILAND
SP11_005_PA	Sutatip Noikrad	OPTIMAL CONDITION FOR MEASURING BARK PH AND CONDUCTIVITY IN LABORATORY
SP11_006_PF	Supattara Phokaeo	THE PYRENOLICHENS AROUND RAMKHAMHAENG UNIVERSITY REGIONAL CAMPUS IN HONOUR OF HIS MAJESTY THE KING, NAKHON PHANOM PROVINCE
SP11_009_PF	Kawinnat Buaruang	*Relicina* (LICHENIZED ASCOMYCOTA) IN THAILAND
SP11_010_PF	Phimpha Nirongbut	LICHEN HERBARIUM DATABASE AND MANAGEMENT AT RAMKHAMHAENG UNIVERSITY I
SP11_011_PF	Udomrak Meethong	DIVERSITY OF FOLIICOLOUS LICHENIZED FUNGI IN MANGROVE FOREST FROM CHUMPHON PROVINCE, THAILAND
SP11_012_PA	Wetchasart Polyiam	A PRELIMINARY SURVEY ON THE OCCRRENCE OF TWO EPIPHYTIC MACROLICHENS IN A POST-FIRE FOREST OF KHAO YAI NATIONAL PARK
SP11_013_PA	Pakarapon Poonsukkho	SECONDARY METABOLITES PRODUCTION IN LICHEN-FROMING FUNGI OF SOME *Arthonia* SPECIES IN THAILAND
SP11_014_PA	Mongkol Phaengphech	SOIL WATERING RETAINS THALLUS WATER CONTENT AND PROLONG ACTIVE PERIOD OF LICHEN *Parmotrema tinctorum* ON TRANSPLANTED FRAMES
SP11_015_PA	Ketkaeo Poonraksa	A PRELIMINARY INVESTIGATION OF TOTAL VOLATILE ORGANIC COMPOUNDS (TVOCs) PRODUCED BY CULTURES OF LICHEN-FORMING FUNGI
SP11_016_PA	Kajonsak Vongshewarat	BIODIVERSITY OF LICHENS FAMILY TRYPETHELIACEAE AROUND RAMKHAMHAENG UNIVERSITY REGIONAL CAMPUS IN HONOUR OF HIS MAJESTY THE KING, KANCHANABURI SURIN AND NAKHON PHANOM PROVINCE

SYMPOSIUM 12: Marine Plastic Abatement

ID	Presenter	Title
SP12_001_PA	Makamas Sutthacheep	ASSESSING MICROPLASTIC CONTAMINANTS IN SHRIMP PASTE FROM THE GULF OF THAILAND AND THE ANDAMAN SEA

SYMPOSIUM 13: Natural Products for Drug Discovery

ID	Presenter	Title
SP13_001_PF	Tanpitcha Yodweerapong	EFFECT OF *Ficus Dubia* EXTRACT ON ADIPOGENESIS
SP13_003_PF	Mia Indria Permatasari	CHEMICAL CONSTITUENTS OF *Dendrobium braianense* AND THEIR α-GLUCOSIDASE INHIBITORY ACTIVITY

ID	Presenter	Title
SP13_004_PF	Manaschanok Lailerd	ANTI-INFLAMMATION AND ANTI-INSULIN RESISTANCE ACTIVITIES OF *Carissa carandas* Linn. FRUIT EXTRACT
SP13_006_PA	Thanesuan Nuanyai	*Cordyceps militaris* EXTRACT USING GLYCERIN AS A SOLVENT
SP13_008_PA	Sudarat Kruakaew	CYTOTOXIC CARDIAC GLYCOSIDES WITH RARE SUGARS AND TRITERPENOID CINNAMATES OF *Vallaris glabra*
SP13_009_PA	Patcharee Pripdeevech	BIOFUMIGATION ACTIVITY OF VOLATILE COMPOUNDS PRODUCED FROM *Pestalotiopsis* ENDOPHYTIC FUNGUS AGAINST *Melissococcus plutonius* IN HONEYCOMB
SP13_010_PF	Radtanaporn Phongvinyan	ANTI-BACTERIAL ACTIVITY OF CRUDE EXTRACTS FROM RED CALYX AND PEEL OF ROSELLE, DRAGON FRUIT, AND PASSION FRUIT
SP13_011_PF	Iyapat Surakkhaka	SCREENING FOR ANTIBACTERIAL ACTIVITY OF CRUDE EXTRACTS FROM DIFFERENT PARTS OF SIAM CARDAMON (*Amomum Krevanh* Pierre)
SP13_013_PF	Sasivimon Promsan	PROTECTIVE EFFECT OF AGOMELATINE ON OXIDATIVE STRESS AND AUTOPHAGY PATHWAY IN OBESITY-INDUCED KIDNEY INJURY
SP13_014_PA	Prempree Sutthasupha	CHITOSAN OLIGOSACCHARIDE PREVENTS KIDNEY INJURY IN PREDIABETIC RATS
SP13_015_PA	Kittima Winyayong	POTENTIAL SYNERGISTIC ANTIMICROBIAL EFFICIENCY OF BINARY COMBINATIONS OF *Amomum testaceum* AND *Zanthoxylum piperitum* ESSENTIAL OILS AGAINST *Staphylococcus aureus* AND *Escherichia coli*
SP13_016_PA	Pamela Weber	SYNERGISTIC ANTIBACTERIAL EFFECTS OF *Zanthoxylum limonella* and *Zingiber cassumunar* ESSENTIAL OILS
SP13_017_PF	Puttachard Hensanghong	INVESTIGATION OF ANTIOXIDANT AND ANTIMICROBIAL ACTIVITIES OF ETHYL ACETATE EXTRACTS FROM FIVE EDIBLE MUSHROOMS
SP13_018_PF	Winyu Wongwiwat	KNOWLEDGE OF THAI TRADITIONAL HEALER ON UTILIZATION OF HERBS IN NAKHON SI THAMMARAT PROVINCE: IN CASE OF MRS. PANEE LUICHAN
SP13_019_PF	Nutkochchatas Jumpeephun	ANTIOXIDANT AND SUN PROTECTION ACTIVITIES OF *Averrhoa bilimbi* L. LEAF EXTRACT AND ITS APPLICATION
SP13_020_PA	Saowanee Petkeereerat	*IN VITRO* SCREENING OF ANTIOXIDANT ACTIVITIES OF FOUR THAI MEDICINAL FLOWERS
SP13_021_PA	Jirapast Sichaem	α-GLUCOSIDASE INHIBITORS FROM THE STEMS AND TWIGS OF *Garcinia schomburgkiana*
SP13_022_PA	Nattharika peedee	INHIBITION OF NITRIC OXIDE AND FREE RADICAL SCAVENGING ACTIVITIES OF SOME SELECTED THAI MEDICINAL FLOWERS
SP13_023_PF	Vachiraporn Ajavakom	SYNTHESIS AND CYTOTOXIC ACTIVITY OF TETRAHYDROCURCUMIN-DIHYDROPYRIMIDINONES AGAINST SMALL CELL LUNG CANCER (NCI-H187) CELL LINES
SP13_024_PA	Teerawut Thothaisong	SESQUITERPENE AND TRITERPENE FROM THE LEAVES OF *Shorea siamensis*
SP13_025_PA	Wachirachai Pabuprapap	TRITERPENOIDS FROM THE FLOWERS OF *Mesua ferrea*
SP13_026_PA	Yuttana Siriwattanasathien	HALOGENATED SESQUITERPENOIDS FROM *Laurencia composita*
SP13_027_PA	Jintana Jantham	CHEMICAL CONSTITUENTS FROM THE AERIAL PARTS OF *Euphorbia lactea* Haw.
SP13_028_PA	Watcharapa Jitkaroon	PHENANTHRENES AND BIBENZYLS FROM *Dendrobrium* 'Suree Classic'

ID	Presenter	Title
SP13_029_PA	Suphaporn Limjirawatthana	CHEMICAL CONSTITUENTS FROM THE STEMS OF *Paederia linearis* HooK.f.
SP13_030_PA	Kiratiya Eiamthaworn	INHIBITORY EFFICACY OF *Cordyceps militaris* EXTRACTS ON SKIN PATHOGENIC BACTERIA AND INFLAMMATION
SP13_031_PA	Engkarat Kingkaew	SCREENING AND IDENTIFICATION OF CHOLESTEROL LOWERING AND BILE SALT HYDROLASE PRODUCING LACTIC ACID BACTERIA FROM THAI PICKLED MUSSELS (*HOI-DONG*)
SP13_033_PA	Suwichada Jaipea	NEW CLASS OF PIPERINE AMIDE ANALOGS AS ACETYLCHOLINE ESTERASE (AChE) INHIBITORS
SP13_034_PA	Jesada Maneewong	TOTAL SYNTHESIS AND STRUCTURE MODIFICATION OF CAERULOMYCIN A, A MARINE NATURAL PRODUCT
SP13_035_PA	Nisachon Tedsree	DIVERSITY AND ANTIMICROBIAL ACTIVITY OF ENDOPHYTIC ACTINOMYCETES ISOLATED FROM THAI ORCHIDS
SP13_037_PF	Nopawit Khamto	STRUCTURAL MODIFICATION OF 2´,4´-DIHYDROXY-6´-METHOXY-3´,5´-DIMETHYLCHALCONE FROM SEEDS OF *Syzygium nervosum* A.Cunn ex DC. AND THEIR ANTICANCER ACTIVITY
SP13_038_PA	Sakchai Hongthong	ALKALOIDS FROM TWIGS OF *Uvaria grandiflora*
SP13_039_PF	Nattasit Akkarawongdacha	SYNTHESIS AND DNA DELIVERY INTO CELLS OF CATIONIC LIPITOIDS
SP13_040_PA	Nichakan Whangchai	POLYPHENOLIC CONTENTS AND ANTIOXIDANT ACTIVITY OF *Phyllanthus emblica* FRUIT EXTRACTS
SP13_041_PF	Patitta Choosub	CYTOTOXIC ACTIVITY SCREENING OF AERIAL PARTS EXTRACTS OF *Boesenbergia violacea* (K.Larsen & Triboun) Mood & L.M.Prince
SP13_042_PF	Jaranwit Srijun	MICROBIAL TRANSFORMATION OF HEXAHYDROCURCUMIN
SP13_043_PF	Nay Thwe Kyi	TAUNGTANGYI AND KARAMET AS NATURAL SKIN BEAUTIFIER THANAKA FROM TANINTHARYI TOWNSHIP
SP13_044_PF	Phyu Phyu Aung	A COMPARATIVE STUDY ON ANTIOXIDANT ACTIVITIES OF PAPAYA LEAVE, SEED AND FLOWER (*Carica Papaya* L.)

SYMPOSIUM 15: Science-based Sustainable Tourism

ID	Presenter	Title
SP15_002_PA	Sittiporn Pengsakun	THE RECOVERY POTENTIAL OF CORALS AT MU KO SICHANG, THE UPPER GULF OF THAILAND
SP15_003_PA	Wanlaya Klinthong	DIVERSITY OF CORAL RECRUITS FROM SETTLEMENT PLATE EXPERIMENTS FROM MU KO ANGTHONG, THE WESTERN GULF OF THAILAND
SP15_004_PA	Ploypailin Rangseethampanya	DISTRIBUTION OF *Chaetodon wiebeli* A COMMON ORNAMENTAL FISH IN MU KO CHUMPHON NATIONAL PARK
SP15_005_PA	Charernmee Chamchoy	COMPOSITION AND ABUNDANCE OF JUVENILE CORALS ON SHALLOW REEF FLATS AND REEF SLOPES IN MU KO ANG THONG NATIONAL PARK
SP15_006_PA	Rattanawadee Neamsiri	ENVIRONMENT FACTORS CONTROLLING CORAL RECRUITMENT IN MU KO SAMET, THE EASTERN GULF OF THAILAND

ID	Presenter	Title
SP15_008_PA	Siriluck Rongprakhon	DISTRIBUTION AND DENSITY OF MACRO-INVERTEBRATES ON SHALLOW REEF FLATS IN KO PHANGAN, SURAT THANI PROVINCE
SP15_009_PA	Wiphawan Aunkhongthong	SCLERACTINIAN CORAL COMMUNITIES ON SHALLOW REEF FLATS AT MU KO CHUMPHON, THE WESTREN GULF OF THAILAND
SP15_010_PA	Napaphach Luangkhamin	THE DISTRIBUTION OF THE FLUTED GIANT CLAM (*Tridacna squamosa*) IN SURAT THANI PROVINCE, THAILAND
SP15_011_PA	Sirirat Jaiharn	ABUNDANCE OF THE MAGNIFICENT SEA ANEMONE (*Heteractis magnifica*) AND ITS TOURISM POTENTIAL IN DIVE SITES AT MU KO CHUMPHON NATIONAL PARK
SP15_012_PA	Bancha Lawang	REEF FISH DIVERSTY IN THE ISLANDS OF CHUMPHON PROVINCE
SP15_013_PA	Pradchek Klangsin	THE ANEMONEFISH *Amphiprion perideraion* IN THE GULF OF THAILAND: IDENTIFYING TOURISM SITES WITH HIGH SIGHTING POTENTIAL
SP15_014_PA	Arirush Wongnutpranont	INCREASING IN DOLPHIN SIGHTINGS AFTER THE PEAK OF COVID-19 PANDEMIC AT HAD KHANOM–MU KO THALE TAI, THAILAND
SP15_015_PF	Vimoltip Singtuen	THE PROTOTYPE OF GEOMORPHOLOGICAL SITES FOR SUSTAINABLE GEOTOURISM IN THAILAND
SP15_017_PA	Makamas Sutthacheep	ACTIVE CORAL RESTORATION USING HIGH STRESS-TOLERANT FRAGMENTS FROM SHALLOW REEF FLATS IN THE WESTERN GULF OF THAILAND

ABSTRACTS AND PROCEEDINGS

A_001_PF: A STUDY OF EFFECTS ON IMAGE QUALITY FROM DIFFERENT SETTINGS OF RADIOGRAPHIC IMAGING SYSTEM USING FLUORESCENCE SCREEN AND DIGITAL CAMERA

Panapon Savirot,[1] Manasavee Lohvithee,[2] Somyot Srisatit[2]

[1]Department of Radiological technology Faculty of Science at Ramkamheang University
[2]Department of Nuclear engineering Faculty of Engineering at Chulalongkorn University
email: panapon8961@gmail.com, manasavee.l@chula.ac.th, somyot.s@chula.ac.th

Abstract:

This research aims to study a quality of an image produced from the X-ray radiographic imaging system using fluorescence screen and digital camera. In the experiments, the X-ray voltages of X-ray generator were varied, as well as the exposure times of the digital camera. Different thicknesses of aluminium sheet were used to imitate different sizes of an object. The data acquisition process of the proposed system starts from X-ray generator, which generates X-ray radiation passing through an object and impinging on fluorescence screen on an opposite side. The fluorescence screen converts X-ray to light that shows an image of shadow on a mirror. This image is a radiographic image that represents details of the object by different levels of image intensity. A digital camera captures the radiographic image and transfers to a computer for recording and further processing. It is promising that the proposed X-ray radiographic imaging system can replace the use of expensive devices such as a digital plate or a digital detector with lower equipment cost. The developed software written in Visual basic 6.0 was used to analyse the radiographic images in terms of noise and contrast level. Experimental results showed that factors such as X-ray voltage, material thickness and exposure time of the digital camera strongly affect the image quality. The shades of radiographic images get darker with increasing thickness of aluminium sheets from 1 to 10 mm. The darker shade means more amount of X-ray attenuated inside the object from thicker size of object, hence, less amount of X-ray impinging on the fluorescence screen and being converted into light. The radiographic images from the lowest voltage have higher levels of contrast than those of the highest voltage. The contrasts at low voltage is high, the noise is higher which leads to lower image quality. It is important to adjust a good balance between all the settings of X-ray generator and digital camera. This depends on the type of materials, the shape and structure of material and the thickness of material. The X-ray radiographic imaging system proposed in this research is an important basis for a development of a low-cost computed tomography imaging system in the future.

Keyword: Radiographic image, Digital camera, Aluminium

Introduction:

Non-destructive testing (NDT) has played a vital role in industrial sector, as well as research and development sector worldwide. NDT is a well-known and commonly used analysis technique in science and technology industry to evaluate the properties of a material or system without causing any damages, as implied by its name. Common NDT methods include visual testing, liquid penetrant testing, magnetic particle testing, ultrasonic testing, eddy current testing and radiographic testing. Among these methods, radiographic testing is the most widely used one due to its capability in detecting minute hidden defects and cracks inside the specimens, which are not visible by inspection. Generally, radiographic image is recorded by film, which requires a development using developing and fixing solutions. The film development is a long and complicated process. As an alternative, a less complicated option is to record the radiographic image using fluorescence screen, which

converts X-ray to light. This type of image is called fluoroscopic image and can be used for NDT. By using the fluoroscopic imaging system, the NDT is, therefore, a highly valuable technique that can save both money and time in material evaluation and researching.

In the system proposed in this research, the fluorescence screen is an important component. The radiographic image captured using the digital camera is the shadow image shown on the fluorescence screen. An amount of X-ray photons attenuated through the object according to the type, internal structure and size of material. In order for the radiographic image to correctly represent an attenuation map of the object, it is important to ensure that a conversion between X-ray photons to light is performed in a linear scale. Moreover, the settings of the X-ray generator and the digital camera should be set properly for each specific material, so that there are adequate amount of X-ray going through the thickness of material and produce a good quality radiographic image.

Methodology:

The main components of the X-ray radiographic imaging system proposed in this research consist of 2 parts, which are X-ray generator and radiation box as shown in figure 1.

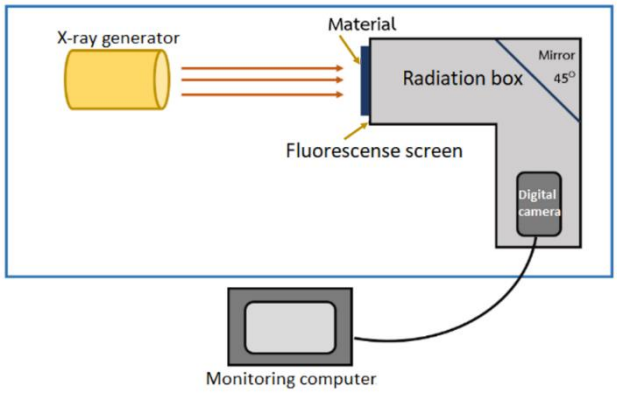

Figure 1
X-ray radiographic imaging system
The details of each component are explained in the following sections.

2.1 *X-ray generator*: The X-ray generator used in this research is Rigaku Radioflex brand, which generates cone-shape X-ray beam with the radiation intensity fixed at 5 mA. The X-ray voltage can be varied in the range of 70-200 kV. The X-ray tube within the X-ray generator is a ceramic X-ray tube with the focal spot size of 2.0 mm x 2.0 mm.

2.2 *Radiation box*: The radiation box is an L-shape box that contains an image acquisition part. It is made of wood and padded with lead sheet inside, to prevent the unwanted radiation penetrating the radiation box from directions other than passing through the object being considered. During the experiments in this research, the radiation box was placed on top of a wood table with the front part aligning in the same level of the centre of X-ray beam. There are three main components inside the L-shape box; *a fluorescence screen* located the front of the radiation box, *a mirror* with 45-degree angle between the fluorescence screen and *a digital camera*. The fluorescence screen used in this research is Gd_2O_2S in GRZ STD of Mitsubishi. The digital camera is Canon EOS1100D with a resolution of 12.2 megapixels and ISO 100-3200. Figure 2. shows the front part of the radiation box with the fluorescence screen opening to reveal the mirror at the end with digital camera reflecting on it.

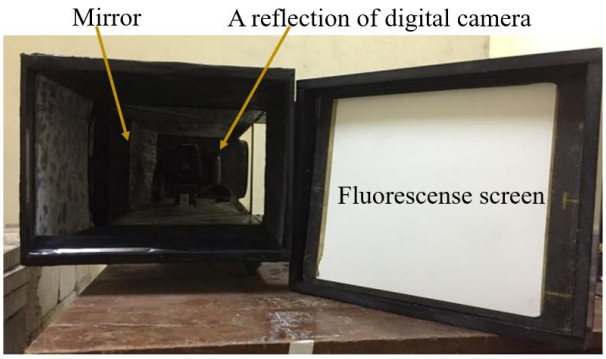

Figure 2
The radiation box.

The experimental protocol to acquire a radiographic image is implemented as following. Firstly, the X-ray generator generates X-ray radiation in a cone-shape beam penetrating through the object in the middle. Some amount of X-ray is attenuated inside the object while some passing through and impinging on the fluorescence screen on the opposite side. Then, the fluorescence screen converts X-ray to light, which produces a radiographic image with different levels of intensities depending on internal structure and thickness of the object. The shadow image reflects on the mirror locating at the corner of the radiation box with 45-degree angle between the fluorescence screen and the digital camera. The Canon EOS Utilities program in the computer was used to control the digital camera via USB cable and capture the image. Then, the image was analysed using the software developed by Visual Basic 6.0. One snapshot of the software is shown in figure 3.

Figure 3
Analysis of radiographic image using the software developed in VB 6.0.

From figure 3., the radiographic image was analysed using the following procedure. First, the image file was opened. Then, the position of the region of interest (ROI) was selected by using the yellow square cursor and the software returned the corresponding X and Y coordinates. The gray scale information of the ROI and the standard deviation (SD) can be obtained by clicking on the calculate button.

An aluminium sheet was used as an object for this research by placing at the centre of the fluorescence screen. The thickness of each aluminium sheet is 1 mm. One sheet was added at a time to increase the object's thickness for the experiments. The X-ray voltage from the X-ray generator was varied from 70 to 200 kV with radiation intensity fixed at 5 mA. For the digital camera, two settings of exposure time were studied; 2 and 4 seconds. The longer the exposure time, the more light is allowed to go through the lens of the camera. Other settings of the digital camera were fixed throughout the experiments of the research i.e. ISO and F were fixed at 400 and 4.0, respectively.

Results and Discussion:

In this research, three experiments were designed to study how different levels of X-ray voltages affect intensities and quality of the radiographic image (in terms of contrast and noise). Different exposure times were also studied and compared. The experiments were done using square Aluminium sheets with different thicknesses by adding one sheet at a time and observe how varying thicknesses of material affects the quality of radiographic image with different settings of X-ray generator and digital camera.

The first experiment aims to study how varying levels of X-ray voltage affects the gray levels of radiographic image from different thicknesses of aluminium sheet. The electrical current of the X-ray generator was fixed at 5 mA and X-ray voltage was varied from 70 to 200 kV with an increment of 10 kV. The thickness of aluminium sheet was varied from 1 mm to 10 mm by adding one aluminium sheet at a time. The digital camera was set at ISO=400 and F=4, while the exposure times were set at 2 and 4 seconds. Figure 4. shows the gray scale of radiographic images from varying thicknesses and X-ray voltages, with exposure time = 2 and 4 seconds shown in figure 4. (left) and (right), respectively. Noted that there are 256 levels of gray scale from 0 to 255, where 0 is the darkest shade and 255 is the brightest shade.

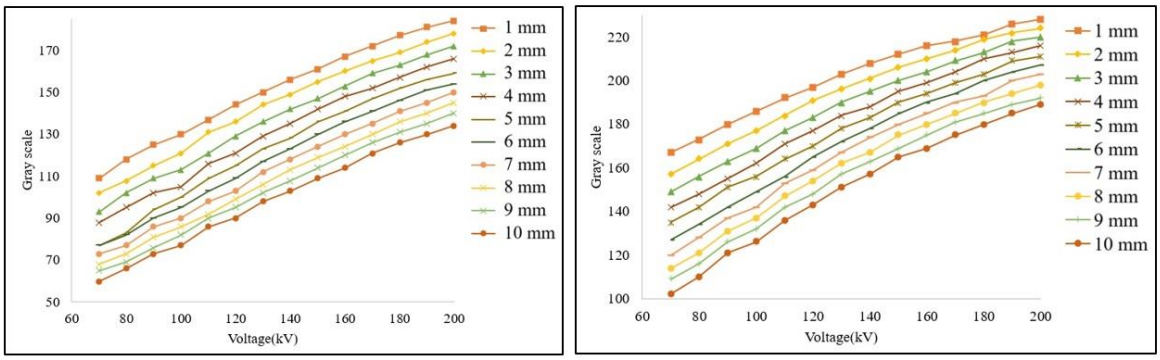

Figure 4
Gray scale levels of radiographic images from varying thicknesses of aluminium sheets and X-ray voltages with exposure times of 2 secs (a) and 4 secs (b).

According to figure 4., at the same X-ray voltage, the shade of radiographic image gets darker (decreasing numbers of gray scale) with increasing thickness of aluminium sheets from 1 to 10 mm. The darker shade means more amount of X-ray attenuated inside the object from thicker size of object, hence, less amount of X-ray impinging on the fluorescence screen and being converted into light. An example of this effect can be seen in figure 5., where the X-ray voltage and exposure time are fixed at 70 kV and 2 seconds, respectively. Increasing thickness from 1 mm in figure 5. (a) to 10 mm in figure 5.(b) results in a much darker shade of radiographic image captured by the digital camera.

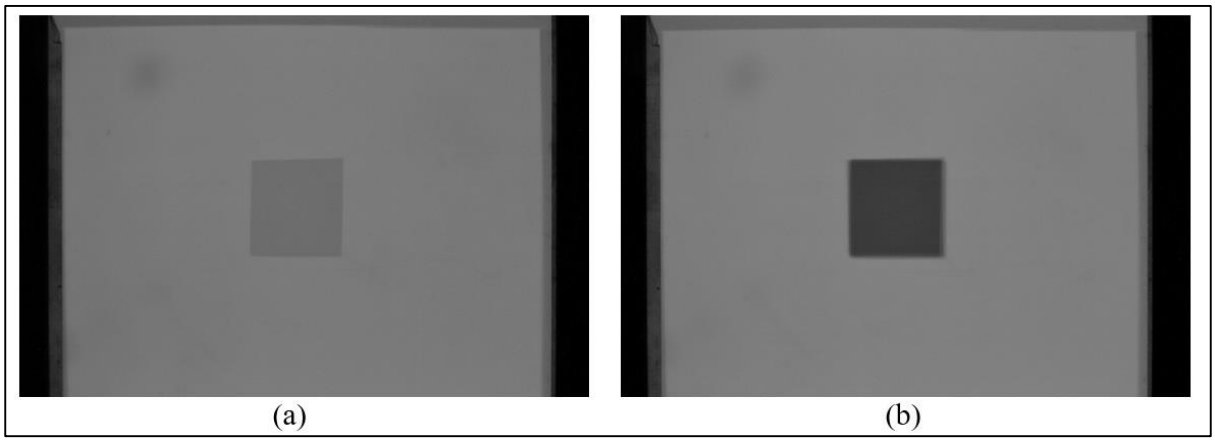

Figure 5
Radiographic images of aluminium sheet with X-ray voltage of 70 kV and exposure time of 2 seconds. (a) Thickness of 1 mm, (b) Thickness of 10 mm.

The next factor to consider is an exposure time. When the exposure time increases from 2 to 4 seconds, the gray scale levels of images shift to higher values as can be seen in figure .4 (a) and (b), corresponding to brighter shade of images. This effect can be seen in figure 6. by comparing between top and bottom rows.

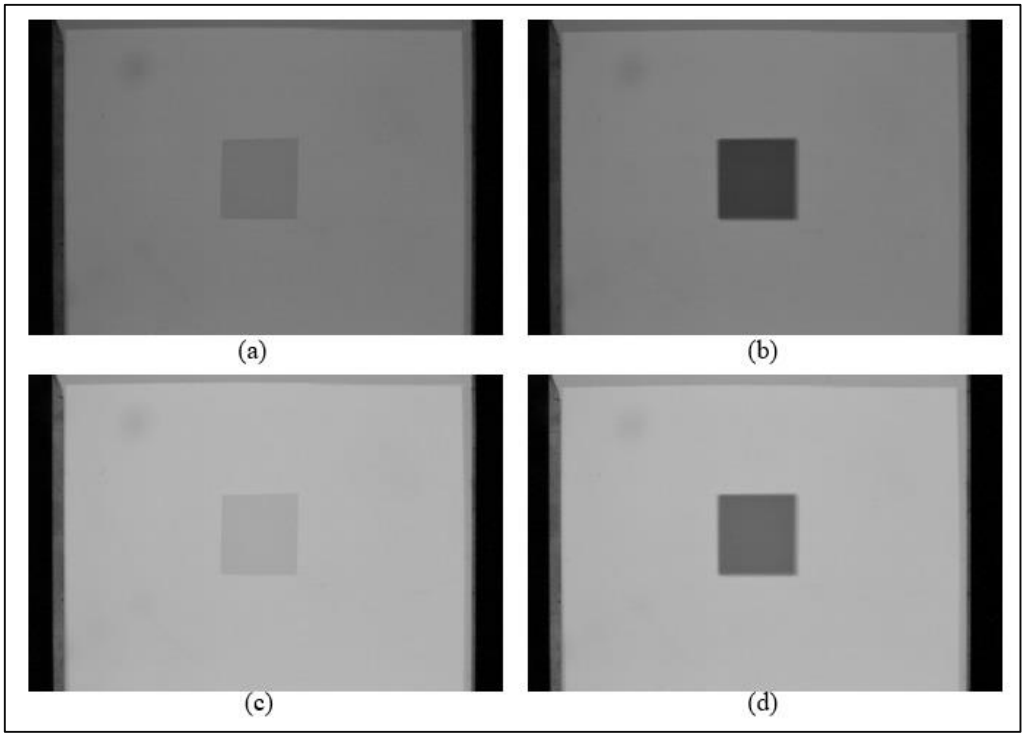

Figure 6
Radiographic images with X-ray voltage of 70 kV: (a) 1 mm thickness with 2-second exposure time, (b) 10 mm thickness with 2-second exposure time, (c) 1 mm thickness with 4-second exposure time and (d) 10 mm thickness with 4-second exposure time.

In case of 10-mm thickness (figure 6. b and d), increasing exposure time allows more X-ray photon passing through the object and impinging on the fluorescence screen. However, when the thickness is only 1 mm as in figures 6.a and c, longer exposure time leads to a very bright image, which makes it difficult to visualise the content of the image.

Next, the contrasts of radiographic images at varying thicknesses using the highest voltage of 200 kV and the lowest voltage of 70 kV are plotted in figure 7. The contrast is one of the factors that determine the quality of an image, which can be calculated from the difference between gray level of the object's ROI and background.

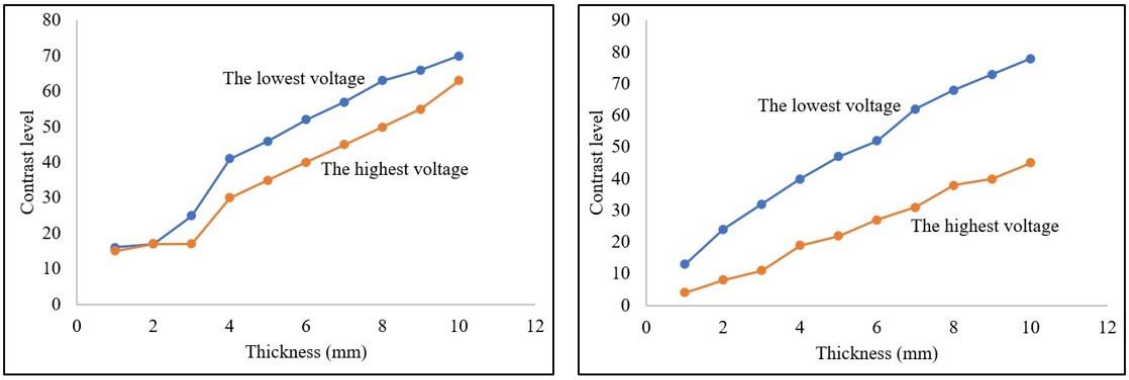

Figure 7

Contrasts of radiographic images at varying thicknesses using the lowest voltage of 70 kV and highest voltage of 200 kV with exposure times of 2 seconds in (a) and 4 seconds in (b).

It can be seen from figure 7. that the radiographic images from the lowest voltage have higher levels of contrast than those of the highest voltage. This can be obviously seen for the entire range of thicknesses and also the case of longer exposure time. However, the contrast is not the only factor being considered in term of image quality. The third experiment is presented to study the levels of noise (using standard deviation, SD) for varying thicknesses and two exposure times. The graphs can be seen in figure 8.

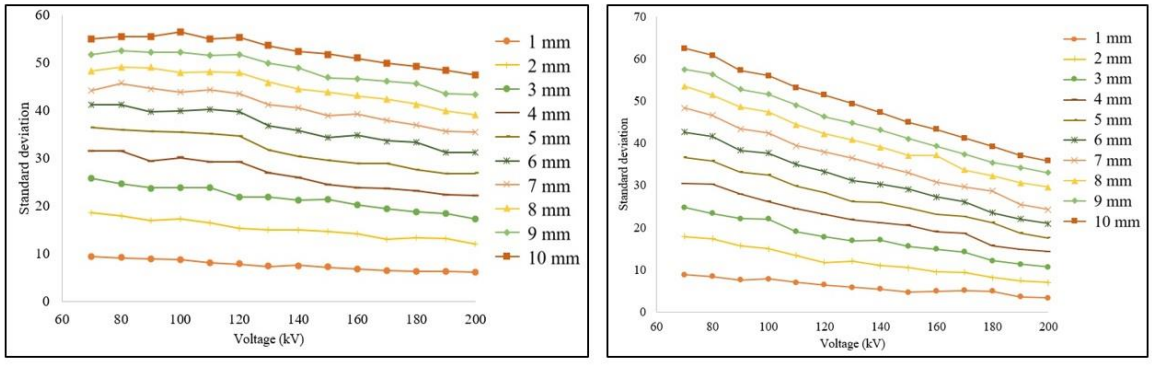

Figure 8

Standard deviation (SD) values for radiographic images of varying thicknesses and voltages with exposure time of 2 seconds in (a) and 4 seconds in (b).

Although the contrasts at low voltage is high, the noise (SD) is higher which leads to lower image quality. Focusing at the graph of 10 mm thick with 4-second exposure time (figure 8.b), it can be seen that, when thickness is higher, adjusting higher X-ray voltage and longer exposure time can help to bring the level of noise down.

Conclusion:

From three experiments in this research, it can be summarised that the factors involved in radiographic image quality are X-ray voltage, material thickness and exposure time of the digital camera.

As the material's thickness increases, the amount of X-ray impinging on the fluorescence screen decreases because more X-ray are attenuated through the object. Thus, an X-ray voltage needs to be increased to produce more amount of X-ray. However, the radiographic image from high X-ray voltage has lower contrast comparing to that of the low X-ray voltage. Although the image from low X-ray voltage has better contrast, the third experiment showed that the level of noise is higher. The exposure time is an important factor to reduce image's noise in case that the high voltage is needed to produce radiographic image.

In order to produce a good quality radiographic image, it is important to adjust a good balance between all the settings of X-ray generator and digital camera. This depends on the type of materials, the shape and structure of material and the thickness of material. The experiments in this research were studied to understand the relationship between all the factors and image quality metrics in terms of contrast and noise. The X-ray radiographic imaging system using fluorescence screen and digital camera proposed in this research can be used to replace expensive devices such as a digital plate or a digital detector. This is an important basis for a development of a low-cost X-ray computed tomography (CT) imaging system in the future.

Acknowledgements:

The experiments in this research were implemented using the equipment at Department of Nuclear engineering, Faculty of Engineering, Chulalongkorn University. The authors would like to express their sincere gratitude to Chulalongkorn University for this opportunity.

References:

1. JT, B., et al., The essential physics of medical imaging, Third edition, Lippincott Williams & Wilkins. 2012, USA: Wolters Kluwers business.
2. Sun W, Brown S B, and Leach R K, An overview of industrial X-ray computed tomography. 2557:1-9.
3. Carmignato, S., W. Dewulf, and R.L. Leach, Industrial X-ray Computed Tomography. Gewerbestrasse. 2018, Switzerland.
4. Visual basic 6 program. 2019 [cited 2019 30 November*]*; Available from*:* http*://*hackdee.biz*/*community*/*index.php?Threads*/*lingkhdaonohld-visual-basic-6-0-enterprise-edition.374*/*.
5. Takahashi , R. Digital camera. 2019 [cited 2019 31 October]; Available from: https://snapshot.canon-asia.com/thailand/article/th/lesson-2-knowing-the-different-parts-of-the-camera.
6. Radiographic film high contrast. 2020 [cited 2020 10 May]; Available from: http://iriheafcq.changeip.com/Long-scale-radiographic-contrast-definition.html.
7. Chalermpong Polee, "Comparative Investigation and Improvement of Film Radiography Speed for Non-Destructive Inspection of Industrial Specimens,"(Doctoral dissertation, Graduate School, Chulalongkorn University, 2015).
8. Parkphum Orachorn, "Development of technique for screening liquids in unopened bottle using low energy x-ray transmission,"(Doctoral dissertation, Graduate School, Chulalongkorn University, 2017).
9. Nopparat Kaewmai, "Development of x-ray imaging technique recorded by digital camera for liquid screening,"(Masteral dissertation, Graduate School, Chulalongkorn University, 2017).

A_002_PF: DEVELOPMENT OF SPECTROPHOTOMETRIC TECHNIQUE FOR EFFICIENT COMPONENT ANALYSIS

Phatthrawat Janratsamechot, Withoon Chunwachirasiri*

Department of Physics, Faculty of Science, Mahidol University, Bangkok, Thailand
*e-mail: withoon.mahidol@gmail.com

Abstract:

The novel generalized net analyte signal standard addition method (GNASSAM) is a multi-component quantitative analysis. The mixture was analyzed with only one standard addition procedure without creating a calibration curve and required less amount of sample. Known amounts of all analyte standard solutions were added into the unknown solution. The response comprises of two parts, an analytical part (also called net analyte signal or NAS) and an interferent part. The interferent part can be removed by the projection method and revealed the mixing ratio quantitatively. The mixture of carmoisine and erythrosine was adopted in this study and the signal of interest is the photoabsorption spectra. The accuracy of the results determined by GNASSAM is discussed. Furthermore, the mixture was allowed to dry to remove the solvent and the photoabsorption measurement of the solid mixture was made. The results from the solid mixture were also analyzed using GNASSAM. The similarity and differences between the mixture solution and solid are discussed along with potential enhancement in measurement methodology currently found in component analysis in mixtures.

Introduction:

In the food dye industry and cosmetics, the component mixture is truly important in order to create accurate planed colors or scents. In the quality control process, High-Performance Liquid Chromatography (HPLC) is normally used as a verification tool. This method is, however, consumes a lot of resources and was particularly complicated in preparations. Other methods are available with different degrees of accuracy and expenses. Most of these methods require a combination of signal data and a mathematical method to quantitatively resolve the ratio of the mixture. The primary method that can be applied is a basic quantitative analysis of multiple components (based on linear combination method). This method uses only a single parameter in acquired signal for its analysis, therefore it is susceptible to data non-uniformity. Recently, the novel generalized net analyte signal standard addition method (GNASSAM), the developed version of the net analyte signal standard addition method (NASSAM), has been proposed. This method allows a mixture to be analyzed with only one standard addition procedure without creating a calibration curve, hence, requires less amount of sample and relatively less complicated sample preparations.

In the present work, we combine the GNASSAM with a spectrophotometric signal for the quantitative component analysis of a binary mixture. The spectrophotometric signal to be used is a widely used photoabsorption measurement. The initial purpose is to verify the validity of the GNASSAM method when being used with simple photoabsorption measurement against more primitive component analysis methods. And the goal of this study is to study how robust this method is when the signal obtained from the samples changes. This is done through the phase change of the samples from solution to solid. The degree of robustness of this method from this work will reveal a decisive factor for determining if this combined technique can be further improved to be applied at the industrial level.

Background:

Absorbance and Beer's Law

The absorbance has a logarithmic relationship to the ratio of the transmitted intensity (I), and the incident intensity (I_0).

$$A = \log_{10} \frac{I_0}{I} \tag{1}$$

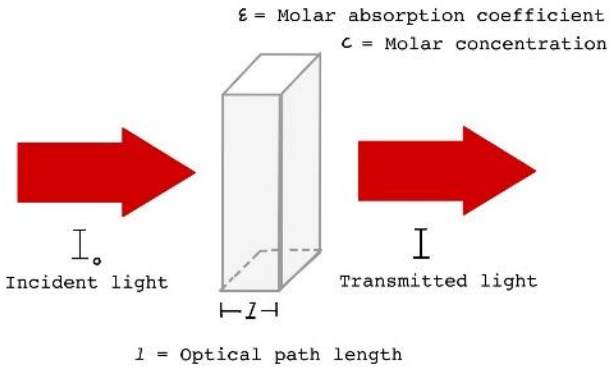

Figure 1. Light intensity before and after pass through substance

The Beer-Lambert law is a linear relationship between the absorbance and the concentration (c), molar absorption coefficient (ε) and optical path length (l) of a solution.[1] This can be written as

$$A = \varepsilon c l \tag{2}$$

Assuming that Beer's Law for a mixture is additive at a given frequency. The total absorbance of a binary mixture of substance *m* and *n* obtained by the basic quantitative analysis is the sum of the absorbance of each component, i.e,

$$A(\lambda) = k_m(\lambda)c_m + k_n(\lambda)c_n \tag{3}$$

$A(\lambda)$ is the absorbance at wavelength λ. $k_m(\lambda)$ and $k_n(\lambda)$ are the constant of substance *m* and *n* at wavelength λ. c_m and c_n are the concentration of substance *m* and *n*, respectively. Two absorbance are measured at wavelength λ_1 and λ_2.

$A(\lambda_1) = k_m(\lambda_1)c_m + k_n(\lambda_1)c_n$ at wavelength λ_1

$A(\lambda_2) = k_m(\lambda_2)c_m + k_n(\lambda_2)c_n$ at wavelength λ_2

The concentration of *m* and *n* in a binary mixture can be calculated by solving linear equations when $k_m(\lambda_1)$, $k_m(\lambda_2)$, $k_n(\lambda_1)$ and $k_n(\lambda_2)$ known.

$$\begin{bmatrix} A(\lambda_1) \\ A(\lambda_2) \end{bmatrix} = \begin{bmatrix} k_m(\lambda_1) & k_n(\lambda_1) \\ k_m(\lambda_2) & k_n(\lambda_2) \end{bmatrix} \begin{bmatrix} c_m \\ c_n \end{bmatrix}$$

So,

$$\begin{bmatrix} c_m \\ c_n \end{bmatrix} = \begin{bmatrix} k_m(\lambda_1) & k_n(\lambda_1) \\ k_m(\lambda_2) & k_n(\lambda_2) \end{bmatrix}^{-1} \begin{bmatrix} A(\lambda_1) \\ A(\lambda_2) \end{bmatrix}$$

For multi-component mixture, this approach can be extended and used to find the unknown initial concentration of each substance.

The standard additional method

The standard additional method (SAM) is a common quantitative analytical technique. This method requires less sample and does not need to make a calibration curve. The assumption of this technique is the instrumental response (*S*) must be directly proportional to analyte concentration (C_a) and have no interference. The equal amount of unknown concentration is added into the flask and added the known concentration to vary the concentration of the sample. After plotting the instrumental response and added concentration, the absolute value of x-intercept is mathematically equal to the initial concentration.

Net analyte signal

Net analyte signal (NAS) is defined as part of the signal that is orthogonal to the spectra of the other components.[2]

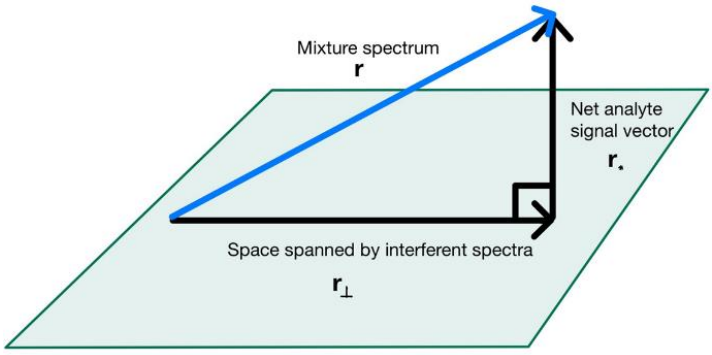

Figure 2. Geometrical representation of NAS vector

Following the definition of the mixture spectrum, the NAS vector ($\boldsymbol{r}_*$) and the spectra of the interferences ($\boldsymbol{r}_\perp$) can be written as[3]

$$\boldsymbol{r} = \boldsymbol{r}_* + \boldsymbol{r}_\perp \tag{4}$$

The NAS vector can be obtained by projecting the mixture spectrum vector.

$$\boldsymbol{r}_* = \boldsymbol{P}\boldsymbol{r},$$

where $\boldsymbol{P}$ is an orthogonal projection matrix. If $\boldsymbol{r}_\perp^+$ is the pseudo-inverse of interferent spectra ($\boldsymbol{r}_\perp$),

$$\boldsymbol{P} = [\boldsymbol{I} - \boldsymbol{r}_\perp(\boldsymbol{r}_\perp^+)].$$

So

$$\boldsymbol{r}_* = [\boldsymbol{I} - \boldsymbol{r}_\perp(\boldsymbol{r}_\perp^+)]\boldsymbol{r} \tag{5}$$

And the norm of $\boldsymbol{r}_*$ is the NAS.

Net analyte signal standard addition method

The net analyte signal standard addition method (NASSAM) is a multi-component quantitative analysis by combining the concept of SAM and NAS. This method does not require to create the calibration curve and also consume fewer samples. For binary mixtures, one of the substances is chosen as the analyte, while the other substance is considered as an interferent.[4] The pure spectrum of each substance was recorded. Then, known amounts of analyte standard solutions were added to the samples, whereas the concentration of the interferent is fixed. The NAS was obtained by projecting the mixture spectrum mentioned previously.

Generalized net analyte signal standard addition method

The generalized net analyte signal standard addition method (GNASSAM) is improving the idea of NASSAM. Instead of selecting one as an analyte and the other as interference in the binary mixture and vary the concentration of solution one at a time, this method treats both mixtures as analytes[5] and vary their concentrations at the same time. Known amounts of both analyte standard solutions are added to the samples.

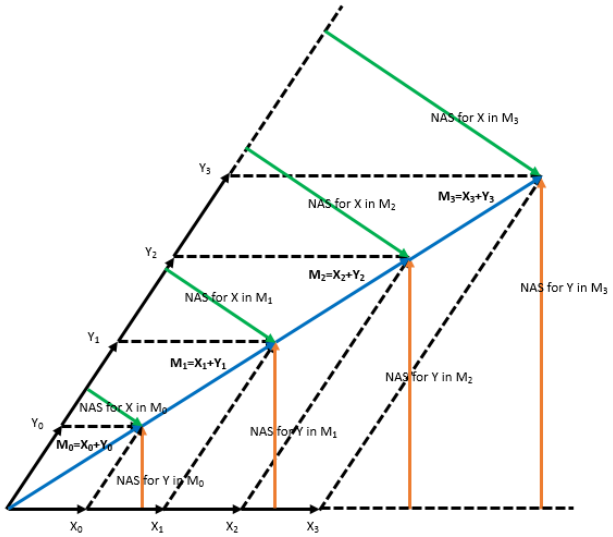

Figure 3. Representation NAS vectors for X and Y in different solutions

The NAS vector of an analyte ($\mathbf{r}_k^*$) for n sensor after m addition is

$$\mathbf{r}_k^* = [\mathbf{I} - \mathbf{S}_{-k}\mathbf{S}_{-k}^{+}]\mathbf{r} \tag{6}$$

Where $\mathbf{r}$ is the $(n \times m)$ data matrix, $\mathbf{I}$ is an $(n \times n)$ identity, $\boldsymbol{S}_{-k}$ is the matrix of component vector except the k^{th} component. The spectrum vector of *X* and *Y* are required. The NAS of the k^{th} component can be determined by the norm of $\mathbf{r}_k^*$. The representation of NAS vector for *X* and *Y* vectors are depicted in Figure 3.

Methodology:

The Carmoisine (CA) and Erythrosine (ER), both are color additives, were chosen as analyte. The concentration of both substances was varied by standard addition procedure. The standard concentration of CA and ER of 200 mg/L was prepared in de-ionized water. The purpose of the proposed procedure is the variation of both mixed substances at the same time. This is done by starting with 20 ml of unknown mixture solution in 4 flasks. Subsequently, the standard concentration of CA and ER were added different into flask number 2 to 4. In the end, the volume of the solution in each flask was adjusted to 250 ml.

To investigate how the change in the amount of solvent will affect the analyses, the solution samples were prepared in the same procedure as above but the standard concentration of CA and ER was increased to 2 g/L. Each of the prepared solutions was then dropped onto a thin cover glass and left to dry for 24 hours before making measurements.

The response used in this work is the photoabsorption spectrum which is the technique that is widely available and inexpensive. To accommodate the ability that the sample can be measured both in solution and solid phase, a customized spectrometer was set up for efficient data acquisition. The setup of the spectroscopic system is shown in Figure 4. A system of convex lenses used to converge light from the light source to the sample and to couple signals transmitted through the sample to the input of optical fiber that connected to the photodetector. The light source is a 3-Watt white LED. The benefit of using LED as a light source is due to its affordable cost while having adequate light intensity beyond 500 nm where the CA and ER have good absorbance. The photodetector is Thorlabs CCS200 having detection range from 200 to 1100 nm with 4 px/nm resolution. The data was acquired via the USB interface and further analyzed using customized codes written on MATLAB R2018b under windows 10.

The photoabsorption spectra of all samples solution were recorded in the range of 450-590 nm. The overall spectrum from the LED light source and standard photoabsorption of CA and ER are shown in Figure 5. From the overlapped spectra, the photoabsorption at the absorption peaks of CA (at 516 nm) and ER (at 526 nm) were selected as the response signals used in the basic quantitative analysis. For the NAS analysis, the absorption data ranging between 540-560 nm where the absorption level is high was used.

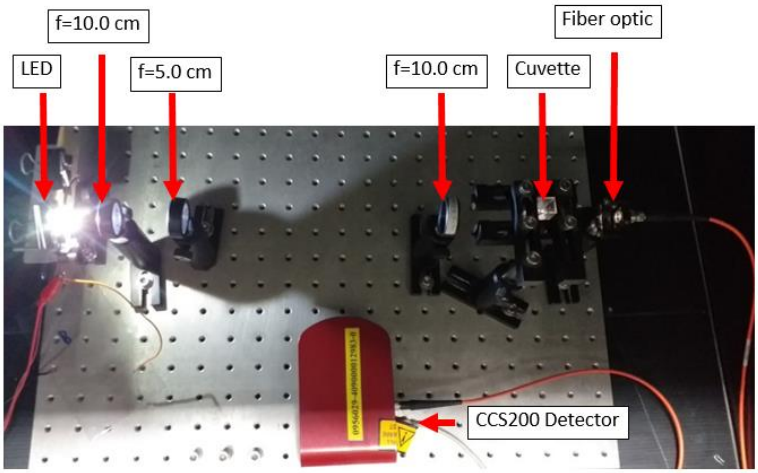

Figure 4. Designed an efficient spectrophotometer

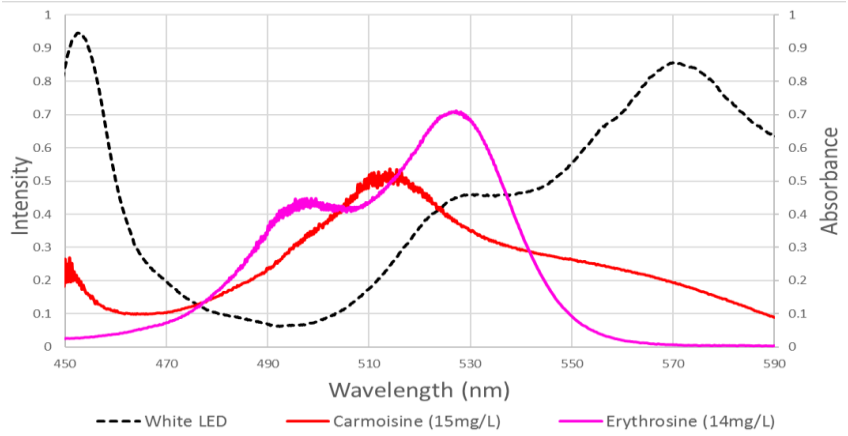

Figure 5. Intensity of 3W white light LED at 400 to 700 nm

Results and Discussion:

GNASSAM in solutions

The amounts of standard concentration added to flask 2 to 4 in this measurement for CA were 19.0, 22.0, and 24.0 ml and ER were 8.0, 10.0, and 12.5 ml respectively. Consequently, after adjusting the solution volume in all flasks to 250 ml, the concentration of all four flasks for CA were 0, 1.6, 4.0, 5.6 mg/L, and ER were 0, 2.4, 4.0, 6.0 mg/L respectively. The correct concentration of CA is 13.60 mg/L and of ER is 4.00 mg/L.

The absorbance of the samples from each flask were measured with 0.2 nm intervals. The NAS from the absorption spectrum between 540 to 560 nm of CA and ER are shown in Figure 6(A) and 6(B) respectively. The norms of NAS are then calculated and plotted versus the amount of standard concentration added. The result shows in Figure 6(C). The x-intercepts calculated by linear regression for CA and ER are listed in Table 1. The calculations give the concentration of CA and ER to be 12.80 (5.9% error) and 3.92 mg/L (2.0% error). The linearity of the curve assures the assumption of the linear relationship between the absorbance and concentration according to Beer's law and also shows the independency of the concentration of the interferent.

Table 1 also shows the concentration calculated by the basic quantitative analysis using the photoabsorption spectra at the peak of CA and ER. The calculations give the concentration of CA and ER to be 15.24 and 3.42 which are 12.1% and 14.5% error respectively. This is as expected that the GNASSAM gives higher accurate results than the results from basic quantitative analysis.

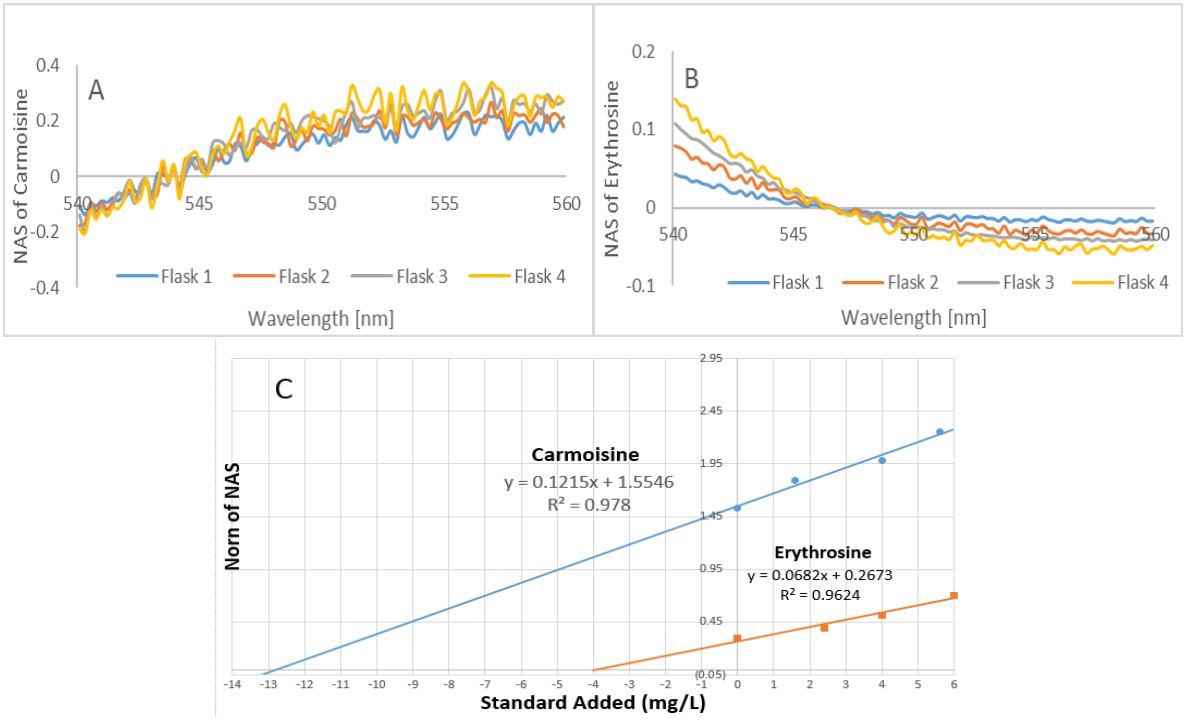

Figure 6. (A) NAS of Carmoisine in the mixture solution. (B) NAS of Erythrosine in the mixture solution. (C) Graph between the norm of NAS and added concentration in the mixture solution: blue solid line for Carmoisine and orange solid line for Erythrosine.

Table 1. Comparison of the results of GNASSAM and the basic quantitative analysis in the mixture solution

	Analyte	Concentration (mg/L)	%Error	R^2
GNASSAM	Carmoisine	12.80	-5.9%	0.978
	Erythrosine	3.92	-2.0%	0.962
Basic quantitative analysis	Carmoisine	15.24	-12.1%	
	Erythrosine	3.42	14.5%	
Correct value	Carmoisine	13.60		
	Erythrosine	4.00		

GNASSAM in solid samples

Similar to the solution case, the 4 varied concentrations of the samples are prepared by adding different amounts of the 2.00 g/L standard concentration in flask 2-4. In this experiment, the prepared concentrations before the drying process of CA were 0.30, 0.55, 0.90 g/L, and of ER were 0.30, 0.55, 1.15 g/L. For the solid case, the photoabsorption spectra were measure from the mixture solution that was left to dry on the thin glass. The absorbance in the wavelengths between 540 to 550 nm was selected to be used in the analysis. The NAS from the absorption spectrum of CA and ER are shown in Figures 7(A) and 7(B) respectively. The initial unknown concentrations obtained by GNASSAM are shown in Table 2. For the CA, the unknown concentration is 0.58 g/L which gives a 10.3% error relative to the correct value initially calculated of 0.65 g/L. In the case of ER, the unknown concentration is 0.72 g/L, a 10.8% error.

The plots between the norm of NAS vs. the amount of standard concentration added show decreased linearity as compared to the case of the solutions. This could be due to the non-uniform thickness from the drying process. Furthermore, this drying process is considered to be uncontrolled so the aggregation of the dye during the drying process can be irregular. This adds another factor of non-uniformity into the mix. Consequently, the location where the collimated light falls on the solid sample for photoabsorption measurement could have been affected and reflects in greater error level as compared to the case of the solution. However, the presence of these non-uniformities can be considered moderate as the level of errors are only around 10% which is still lower than the error level found in the basic quantitative analysis. This opens up an opportunity for improvements.

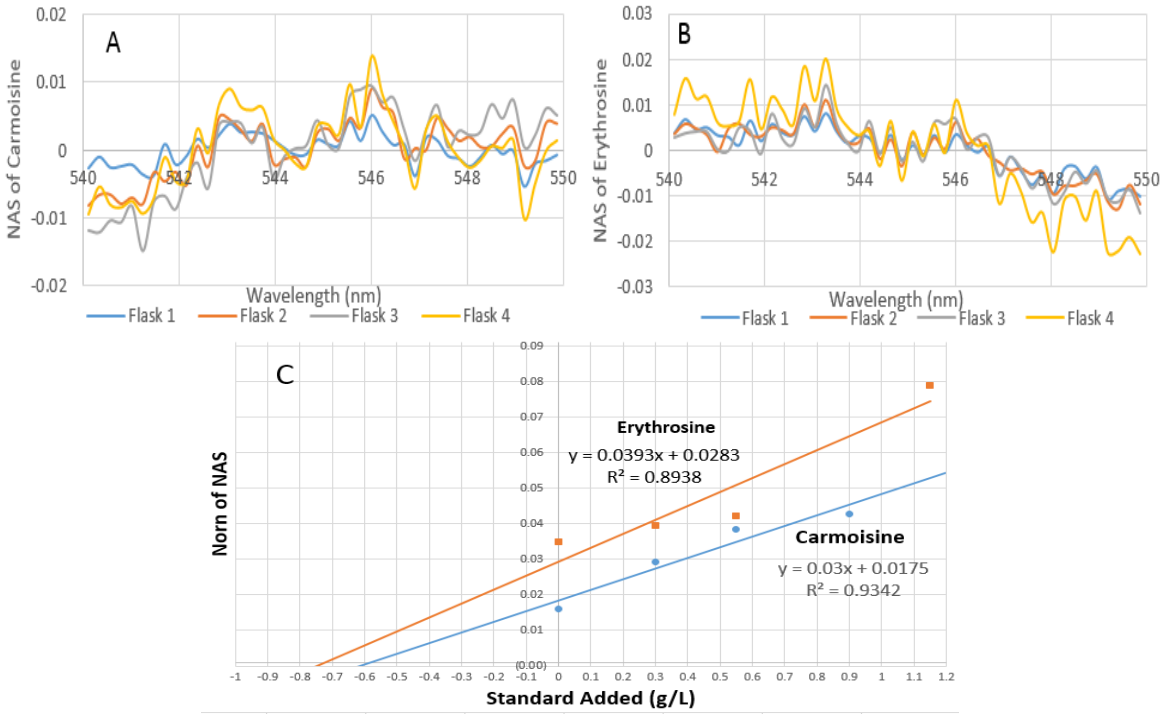

Figure 7. (A) NAS of Carmoisine in the mixture solid. (B) NAS of Erythrosine in the mixture solid. (C) Graph between the norm of NAS and added concentration in the mixture solid: Blue solid line for Carmoisine and orange solid line for Erythrosine.

Table 2. The results of analysis of the binary mixture solid.

	Analyte	Concentration (g/L)	%Error	R^2
GNASSAM	Carmoisine	0.58	-10.3%	0.934
	Erythrosine	0.72	10.8%	0.894
Correct value	Carmoisine	0.65		
	Erythrosine	0.65		

Conclusion:

By applying the generalized net analyte signal standard addition method (GNASSAM) in combination with photoabsorption spectra as response signal for quantitative analysis of multiple components in a binary mixture, the results show greater accuracy as compared to the basic quantitative analysis based on single wavelength response. The reduction of error is due to the use of a range of wavelengths rather than some selected wavelengths. This work takes the measurement of unknown concentration one step further by removing the solvent through the drying process and take the photoabsorption spectra from the samples in the solid phase. The GNASSAM method is then applied to the solid phase spectra to determine the unknown mixture concentration originally in the solvent form. The results are promising. The errors obtained are around 10% and still considered an improvement from the basic quantitative analysis method. The sources of this error are thought to be from the non-uniformity created during the drying process, including uncontrolled spatial variation in thickness and concentration. There are ways to remedy these sources of non-uniformity without too much difficulty and expect a great reduction in error. Once this is done, the possibility to apply this method at the industrial level can be concluded.

References:

1. D. F. Swinehart. Journal of Chemical Education 1962;9(7):333-335.
2. Avraham L. Anal. Chem. 1986;58:1167-1172.
3. Rasmus B, CharlotteA. J. Chemometrics 2003;17:646–652.
4. Asadpour-Zeynali K, Bastami M. Spectrochim Acta A Mol Biomol Spectrosc. 2010;75(2):589-597.
5. Asadpour-Zeynali K, Elhameh S, Javad V, Mehdi B. Journal of AOAC INTERNATIONAL. 2014;91(1):252-258.

A_003_PA: CONTROLLING TRAFFIC JAMS IN A MODIFIED CAR-FOLLOWING MODEL WITH AUTONOMOUS VEHICLES

Manit Klawtanong,[1,*] Surachate Limkumnerd[2,3]

[1]Department of Physics, Faculty of Science, Ramkhamhaeng University, Ramkhamhaeng Road, Bang Kapi, Bangkok 10240, Thailand
[2]Physics of Energy Materials Research Unit, Department of Physics, Faculty of Science, Chulalongkorn University, Phayathai Road, Patumwan, Bangkok 10330, Thailand
[3]Thailand Center of Excellence in Physics, Ministry of Higher Education, Science, Research and Innovation, 328 Si Ayutthaya Road, Bangkok 10400, Thailand
*e-mail: manit.k@ru.ac.th

Abstract:

We consider continuous spatial-temporal evolution of traffic flow on a circular track using a stochastic car-following model with modified optimal velocity. The well-known two-second rule accounting for realistic safety distance is used. To suppress the traffic congestion, self-driving cars obeying simple rules are incorporated into the model. From simulation results, the modification of safety distance enhances the traffic flow in a dense traffic region. The presence of the autonomous cars improves the overall traffic conditions and postpones the traffic congestion. The optimal traffic flow for a particular car density can be achieved by imposing the maximum velocity of the normal cars and autonomous cars.

A_004_PF: INSPECTION AND EVALUATION OF AIR-FILLED VOID INSIDE REINFORCED CONCRETE STRUCTURE BY NON-DESTRUCTIVE TESTING METHODS

Thanakit Klomkliew,[1]* Thanop Thitimakorn [2]

[1]Earth Science Program, Department of Geology, Faculty of Science, Chulalongkorn University, Bangkok 10330, Thailand
[2]Department of Geology, Faculty of Science, Chulalongkorn University, Bangkok 10330, Thailand
*e-mail: Thanakitchula@gmail.com

Abstract:

Nowadays, infrastructures in Thailand are almost reinforced concrete (RC) structure because it can be built many shapes, save time and cost, strong and durable enough against environmental changes. However, the concrete durability will be decreased over time, the proper concrete integrity survey for maintenance works is very important. This research aims to inspect and evaluate flaws in RC structures especially delamination and air-filled void by Non-Destructive Testing (NDT) methods consist of ultrasonic pulse velocity, ultrasonic pule echo, impact echo, and ground-penetrating radar. The research is divided into two sections: Firstly, the NDT methods were performed on RC mock-up with simulate defects that differ in material types, dimensions, and positions along 7, 14, 28, and 56 concrete day life. Secondly, the NDT patterns were performed on the RC structure which selected from visual inspection and hammer sounding methods by using the same principles, methods, and criteria and then randomly verified the precision and accuracy by concrete cores. The results exhibited the accuracy and precision of flaw detection from ground-penetrating radar and ultrasonic pulse-echo is greater than other methods from both RC mock-ups and structure. Besides, the duration of data acquisition and interpretation of both methods were less than the others.

Introduction:

The RC structures in Thailand are the most compromised of a wide range of structure types and too many of them are aging. Thus, inspection, assessment, and maintenance of the existing RC structures have been very important before rehabilitation. The most interested of the inspection and assessment is concrete strength, workability, and some material properties but the integrity has recently considered for decades. The concrete integrity can influence a loading capacity and life-building expectancy. Defected inspection especially air-filled void and delamination in concrete could be caused by three main deterioration. First, physical deterioration can occur in the construction process, an accident from impact, or an unusually high-temperature long time.[1] Second, chemical deterioration can cause corroded rebar occurrence while using the building.[2] Finally, mechanical deterioration is caused by W/C ratio and other admixture designations that always found failure from construction processes. However, the concrete damage can be an effect from a combination of factors that previously described, it will accelerate decrease the concrete durability and cause defects in the RC structures. Besides, if the building has been detected at any significant point which happens to certain large air-filled void or delamination, it could decrease structural stability and environmental durability of concrete materials. Thus, precision and accuracy from the inspection and evaluation of its, such as dimension, position, and shape by the proper NDT methods is a very important and suitable way for remedial work, saving cost and time in the maintenance process.

The purposes of the NDT methods are used to indirectly determine concrete properties and evaluate the condition of the RC structure. ACI committee 228.2 concluded and provided eight of NDT methods. Nevertheless, only two methods composed of radar method and stress-wave method are performed in this paper. The ground-penetrating radar (GPR) uses electromagnetic (EM) pulse waves from antenna transmits short pulses to detect the difference of the dielectric properties in concrete by EM wave reflection. Reflection coefficient (ρ) determines from the ratio of the reflected the incident amplitude of the difference in the dielectric constant of material 1 (ε_{r1}) and 2 (ε_{r2}) as shown in equation 1 below. The EM waves of the GPR method use radar frequency band, 10^4 to 10^9 Hz. Besides, the depth and resolution are depending on the frequency content.[3] At an early age, this method is specifically used for military applications especially bomb detection, and then continuously developed for evaluation of the concrete structure such as, concrete pavement thickness,[4] locating deteriorations and rebars,[5] and locating utility networks.[6,7] However, the EM waves are disturbed by moisture and water content of the concrete,[8] thereby complicates the interpretation for defect detection and identification.

$$\rho = \frac{\sqrt{\varepsilon_{r1}} - \sqrt{\varepsilon_{r2}}}{\sqrt{\varepsilon_{r1}} + \sqrt{\varepsilon_{r2}}} \quad \text{..... (1)}$$

Table 1. Relative dielectric constants and radar wave velocity through the material

Material	Relative dielectric constant of material, ε_r	Radar velocity (m/ns)
Air	1	0.30
Water	81	0.03
Concrete	4 to 10	0.01-0.15
Steel	∞	0
Soil	4 to 6	0.12 to 0.15

On the other hand, the stress-wave method is suddenly pressured and deformed on the surface to generate stress wave propagates through solid with a hemisphere wavefronts. The speed of stress wave propagation is depended on the modulus of elasticity, the density, Poisson's ratio, and the solid geometry. Therefore, the stress-wave method can use for detecting the difference of materials in the layered media as RC structures by the interaction of reflected body waves at the interface between a dissimilar layer. The material has a unique specific acoustic impedance (Z) which is the product of the wave speed and the material density. The reflection (R) of body wave is a ratio of sound pressure of the reflected wave to the sound pressure of the incident wave as shown in equation 2 below. Therefore, the NDT methods based on the stress-wave can detect defects in RC structure due to the reflection coefficient is closely 1.0 when finding an air interface. The following table shows approximate Z-values for general materials.[9]

$$R = \frac{Z_2 - Z_1}{Z_2 + Z_1} \quad \text{..... (2)}$$

Table 2. Approximate impedances for different materials and reflection coefficient at interface for a P-wave traveling through concrete

Material	Specification acoustic impedance (kg/m^2s)	Reflection coefficient at interface
Air	0.4	-1.00
Water	1.5×10^6	-0.65 to -0.75
Concrete	7 to 10×10^6	-
Steel	47×10^6	0.65-0.75
Soil	0.3×10^6	-0.30 to -0.90

The stress wave-based NDT method has three methods in this research compose of ultrasonic pulse velocity (UPV), ultrasonic pulse-echo (UPE), and impact echo (IE). First, the oldest method for determining crack depth[10] by using low-frequency transducers, 40 to 50 kHz, for measuring travel time over a known path length is the UPV method. Moreover, it is possible to determine the concrete integrity[11] because the longitudinal pulse velocity through sound concrete is greater than the concrete with defects. The difference pulse velocity from any points would locate the defect areas of anomalies within the RC structures by classifying the level of concrete quality in table 3 below. However, the limitation of this method requires smooth contact between the probes and the concrete surface for decreasing disturb of signals and reduce the efficiency of measurement.

Table 3. Concrete quality classification by UPV method refer from IAEA, 2002

Longitudinal pulse velocity		Reflection coefficient at interface
(Km/s.10^3)	**(Ft/s)**	
>4.5	>15	Excellent
3.5-4.5	12-15	Good
3.0-3.5	10-12	Doubtful
2.0-3.0	7-10	Poor
<2.0	<7	Very poor

Second, the UPE method is developed from testing metals and then continuously adapted for the RC structure measurement, and the concrete integrity[12] by using high-frequency transducers, 500-kHz. This method is not necessary to assess both sides of the structure surface, due to the pulse is reflected or echoed by interface layers to the same transducers acting like both transmitter and receiver. However, the accuracy of this method for determining the depth of the reflecting interface layers is depended on knowing the wave speed of materials and the configuration of the multiple-static array of transducers.[13]

Third, the old method which generates a stress pulse by the short-duration mechanical impact on the concrete surface and monitors the surface displacement by a transducer is the IE method. At an early age, it is widely used for evaluation of concrete pile and foundation then continuously developed for evaluation of the concrete structure[14] such as concrete thickness[10] and concrete integrity.[15] Due to, data acquisition system records in term of time domain and frequency analysis is recommended for interpretation. Thus, the frequency-domain transforms the time-domain signal by the fast Fourier transform technique and results in an amplitude spectrum. If the frequency (f) and wave speed (C_P) are known, the depth of wave reflection can be determined from equation 3 below. Moreover, a specific vibration mode shape[16] is another criterion in defect detection, especially delamination and honeycomb. Nevertheless, the limitation of this method does not focus on the pulse-like two previous methods and defect dimension (d) should be greater than 0.25 of defect depth (T).

$$D = \frac{C_P}{2f} \quad \text{..... (3)}$$

Therefore, the researcher desires to use the following methods; consist of ground-penetrating radar, impact echo, ultrasonic pulse velocity, and ultrasonic pulse-echo to investigate the difference of dimensions, positions, and shapes of the delamination and air-filled void. After that, any equipment results from the evaluation process be interpreted and then be compared to the precision and accuracy with the actual level of the simulate defect and concrete core sampling method in RC mock-up and on RC building, respectively.

Methodology:

The paper is divided into two sections which tested on the idealized and realistic structure. Thus, the idealized structures were firstly designed and constructed to simulated various sizes, dimensions, and shapes of artificial defects. The specimen configurations were nominally designed 0.30 m thick with lateral dimensions 0.80x1.20 m supported with two parallel beam dimension 0.15x0.50 m. Ready-mixed concrete was designed used 280 ksc or 27.5 MPa. The concrete was made with limestone aggregate as formally used in Thailand. Besides, the RC slabs are reinforced in two dimensions with spacing every 0.20 m and at two layers by deformed bar size 12 mm. The designated concrete covering of the upper and lower-layer rebar is 4.00 and 5.00 mm, respectively. Table 4 and figure 1 provide a summary of the RC mock-ups with simulated defect positions.

Table 4. Summary of the RC mock-ups with simulated defect

Mockup name	Defect number	Material thickness (mm)	Defect type	Defect dimension (mm)	Defect depth (mm)
Delamination & air-filled void	No.01	3.00 mm. Plastic board	Delamination	200x400	60.00
	No.02	3.00 mm. Plastic board	Delamination	200x400	40.00
	No.03	10.00 mm. Foam board	Air-filled void	400x600	120.00
	No.04	3.00 mm. Plastic board	Delamination	200x400	270.00
	No.05	3.00 mm. Plastic board	Delamination	200x400	250.00
Unconsolidated concrete	No.01	50.00 mm. concrete	Honeycomb	200x200	190.00
	No.02	50.00 mm. concrete	Honeycomb	200x200	190.00
	No.03	50.00 mm. concrete	Honeycomb	200x200	190.00
	No.04	50.00 mm. concrete	Honeycomb	200x200	190.00

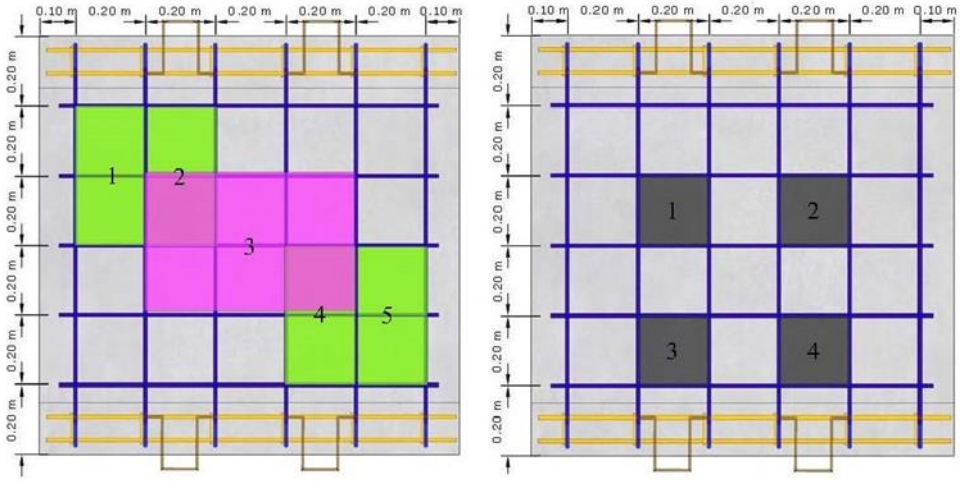

Figure 1
Target simulated defects layout on plan view composed of delamination & air-filled void (left) and unconsolidated concrete (right)

Then, the selected four NDT types of equipment in this paper which difference of detail, data collection, and configuration was following described. First, the GPR surveys refer to ASTM D4748 used PROCEQ GPR Live due to the unique stepped-frequency continuous-wave (SFCW) technology, 0.20 to 4.00 GHz, however, the central frequency value is 2.40 GHz. The GPR data collection was firstly set line spacing at every 0.10 m along with both perpendicular directions and then collected each trace for processing. Second, the UPE surveys used PROCEQ Pundit Live Array because of the operating frequency of 55 kHz with multi-channel with 8 dry point contact channels, a total of 24 dry contacts, for flaw detection. Thus, the results from each trace are higher resolution because the ray paths from all dry point contacts are 56 echoes in a matter of milliseconds. This data collection and interpretation are the same pattern as the GPR method but used different interpreted software. Third, the UPV surveys refer to ASTM C597 used PROCEQ Pundit Lab which composes of 2 transducers with 54 kHz frequency connect with display monitor by power cables before keeping data. Finally, the IE surveys refer to ASTM C1383 used CTG-2. The testing pattern is a grid-point pattern at every 0.10 or 0.20 m as similar to the UPV method but different of interpretation.

After finished performed on all mock-ups over the hardening state, the results were compared in terms of the resolution and precision when they detect the simulated defects in the concrete and setting the appropriate parameters. Moreover, the parameters and results from this step were used to be guidance for detecting real defects in the realistic structure. The realistic structure in the paper was previously selected by visual inspection and hammer sounding refer from ACI 201.1R and ASTM D4580, respectively. The realistic structure in the paper is an old warehouse somewhere in Bangkok, Thailand because a lot of crack lines were found on all researching areas as shown on a plan in figure 2 below. Due to the warehouse is a very large area, approximately 36.78x198.00 m, thus only selected small area, 3.00x3.00 m, was performed. After that, all NDT methods were performed and then randomly rechecked by concrete core sampling methods.

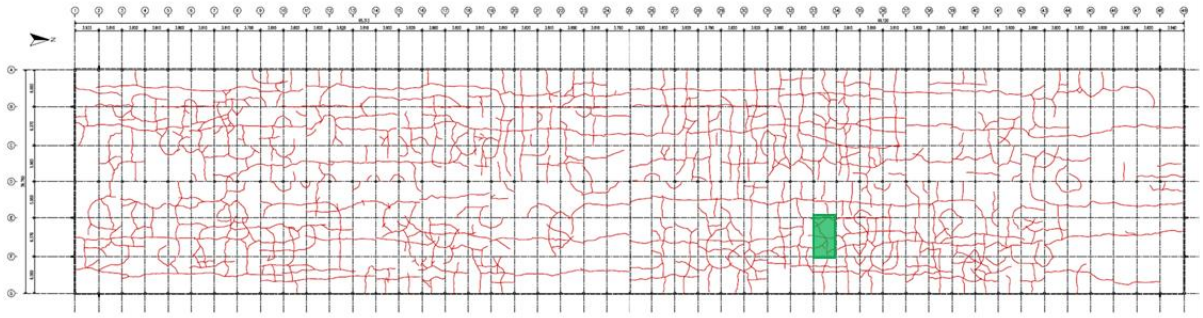

Figure 2
Ground floor plan shows crack (red lines) with testing area (green area)

Results and Discussion:

Due to the paper results from both idealized and realistic structures have both line scan & grid point testing pattern. Thus, the line scan testing patterns of the idealized structures were firstly discussed before one another. The line scan pattern which previously described consists of the GPR & UPE methods. Both methods must be calibrated with known concrete thickness to find suitable parameters before acquiring data along all the traces. The GPR parameter, especially dielectric constant, was setting appropriate values at 8.8, 8.3, 8.2, and 7.5 over the hardening state. The GPR parameter shows that it was significantly decreased over the concrete day-life because the water content is lower from the evaporation process. Thus, all the GPR profiles display higher resolution over the concrete day-life as clearly show the thickness level along with profile scans in figure 3 below. The wave speed values of the UPE method are approximately setting at 2,360, 2,410, 2,486, and 2,453 m/s over the difference of concrete day-life. The UPE parameter shows that it quietly be the same over time moreover, the UPE profiles have still displayed good resolution since the recently hardening state, at 7 days. Figure 3 displays the resolution comparison on selected profiles between the GPR & UPE methods over the hardening state.

The grid point testing patterns consist of the UPV & IE methods. Only the IE must be calibrated the parameter with known concrete thickness for finding suitable the wave speed. The values are setting at 3,476, 3,604, 3,604, and 3,656 m/s over the hardening state, thus the thickness frequency values should be in the range of 5.8 to 6.3 kHz. It was quite as same as the UPE method however, the values were greater due to the difference of pulse wave between P-wave, and S-wave. Owing to the wave speed and thickness frequency from testing are known, the reflection depth was calculated base on equation 3. However, any frequency profiles show the peak amplitude out of thickness range, it means the shallow defects or delamination are found less than approximately 10.00 mm. which call "Flexural frequency mode" as shown in figure 4 below. The UPV method was calibrated itself, thus it did not need to know the concrete thickness. It focuses on the travel time between transducers at any point with known the path ranges for calculating wave velocity. Thus, the concrete quality at any point can be classified as referring from table 3 above. However, the UPV results can not locate the defection level and can not deeply penetrate the signal through the concrete because the indirect method, the same side of transducers, was performed.

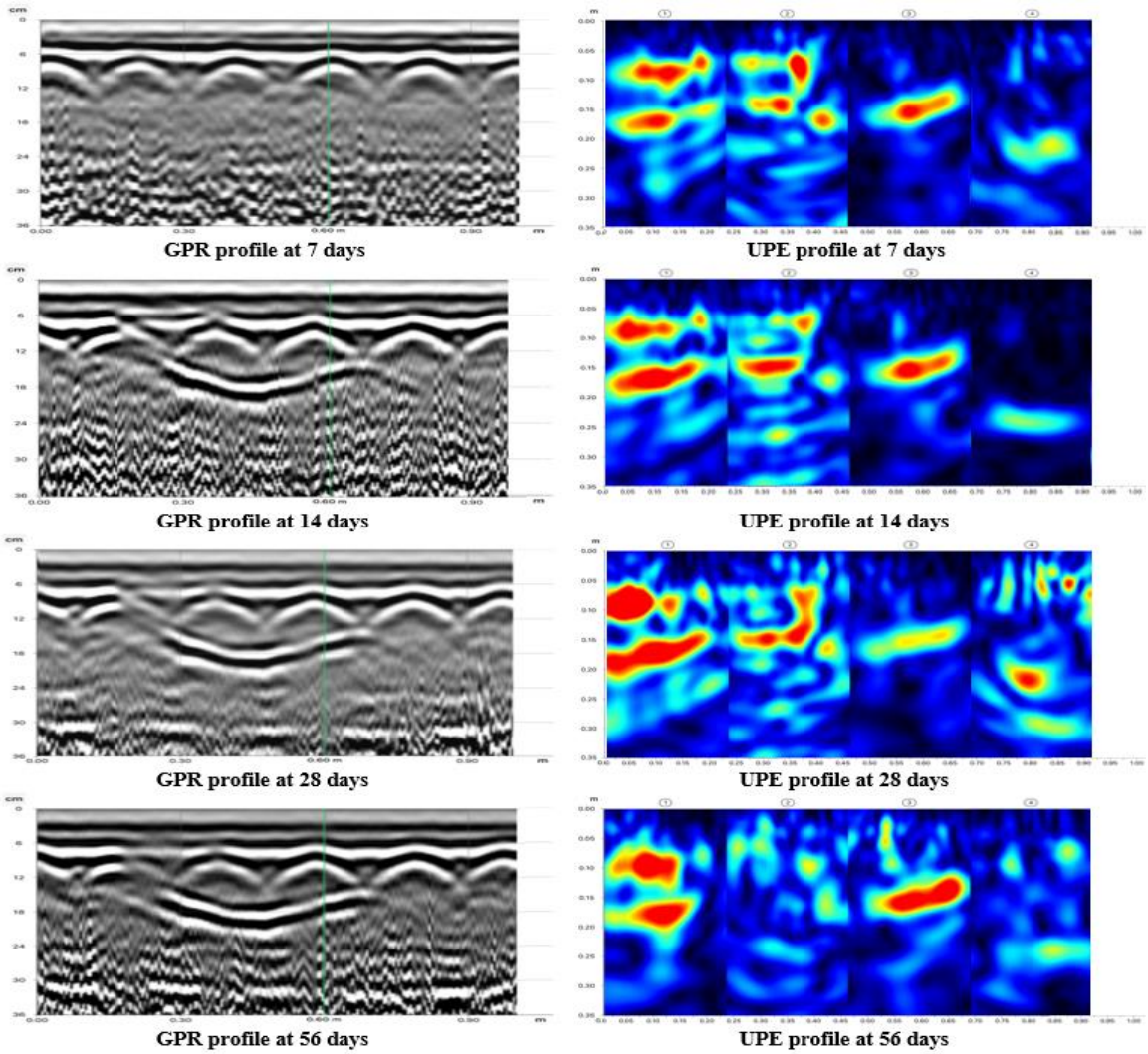

Figure 3
Resolution comparison over hardening state between GPR and UPE methods

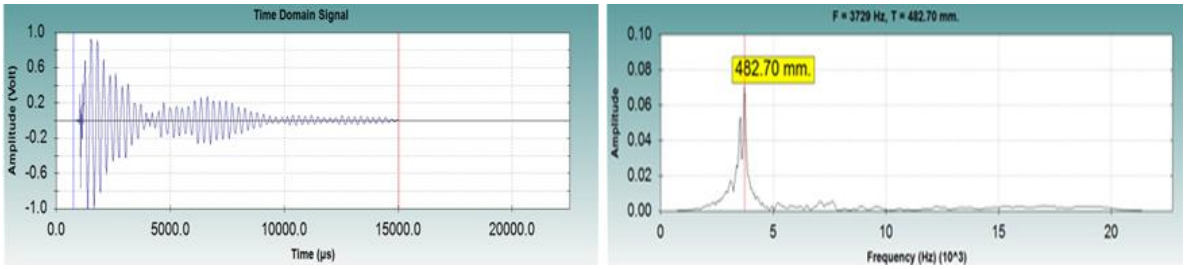

Figure 4
Signal characteristic of Flexural frequency mode of IE method

However, the similar limitation of all methods cannot locate the unconsolidated concrete or honeycombs over the hardening state. The simulated honeycombs were maybe either smaller air-bubble than the realistic or the limitation of the equipment was not sensitive enough to separate it from the sound concrete. Figure 5 display the selected GPR and UPE sectional profiles at 56 concrete days along with the simulated honeycombs, however the pulse of both was pass through it and reflected at thickness level.

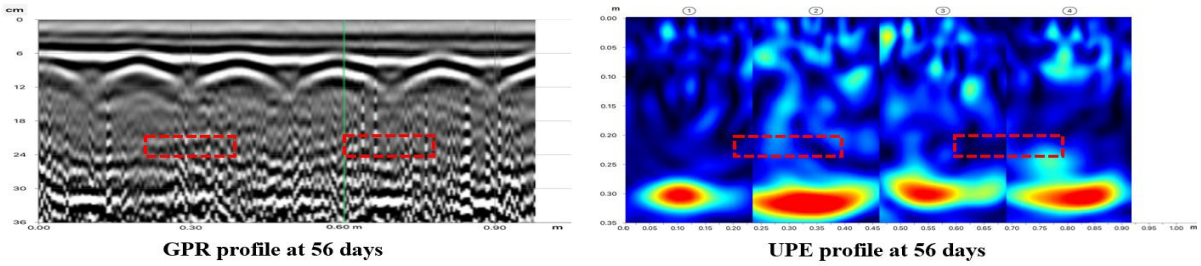

Figure 5
Sectional profiles at 56 days along simulated honeycombs (red rectangular)

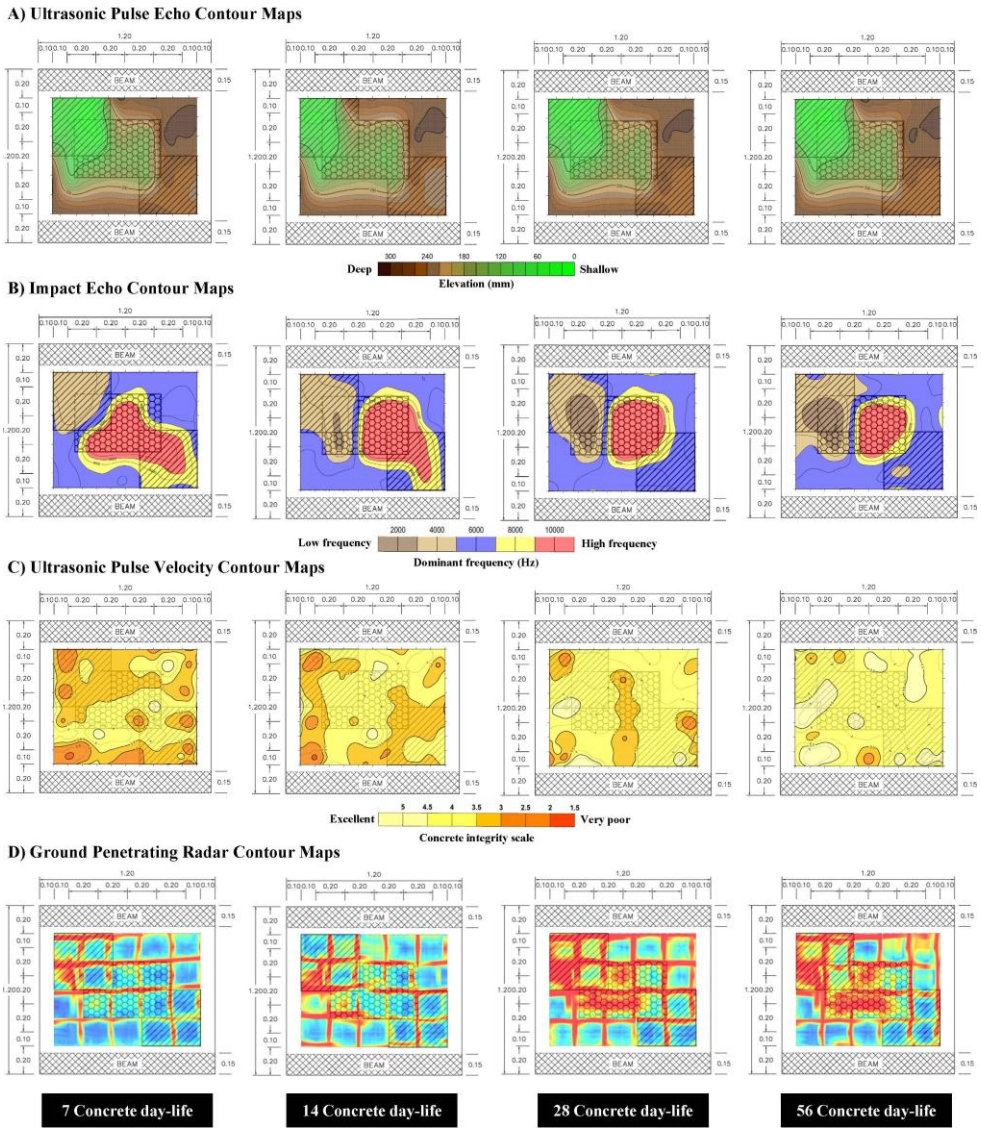

Figure 6
Contour maps represent defect levels of each methods over hardening state

Owing to the previous results were different acquisition, analysis, and interpretation, the probable way for comparing all together was to generate contouring maps that represent the reflection of the dissimilar layer in the RC mock-ups. Only the UPV contour maps over the hardening state were not successful to locate the level and size of the simulated defects because the signal only shallow transmit along the concrete surface. However, the other method can more successfully locate the level and size of the delamination and air-filled void with the difference of indicators as shown in figure 6 below. First, the contour maps of the impact echo method over the hardening state can only separate the level of the simulated defects and preliminary scope the defect dimension by changing of dominant frequency nevertheless, the deep defects, 250 to 270 mm below the surface, cannot be truly detected by this method. Second, the contour maps of the UPE method can separate the level of simulated defects and preliminary scope the defect dimension greater than the IE method due to each sectional profile clearly show the level and size of defects. Finally, the contour maps of the GPR method which were automatically created by software display the level and size of the simulated defects at 28 and 56 days. The contour maps result relates to the W/C ratio over the hardening state which was previously described. Besides, this GPR method showed the rebar position that can separate from the defects. However, the deep defect cannot be successfully located like the UPE method.

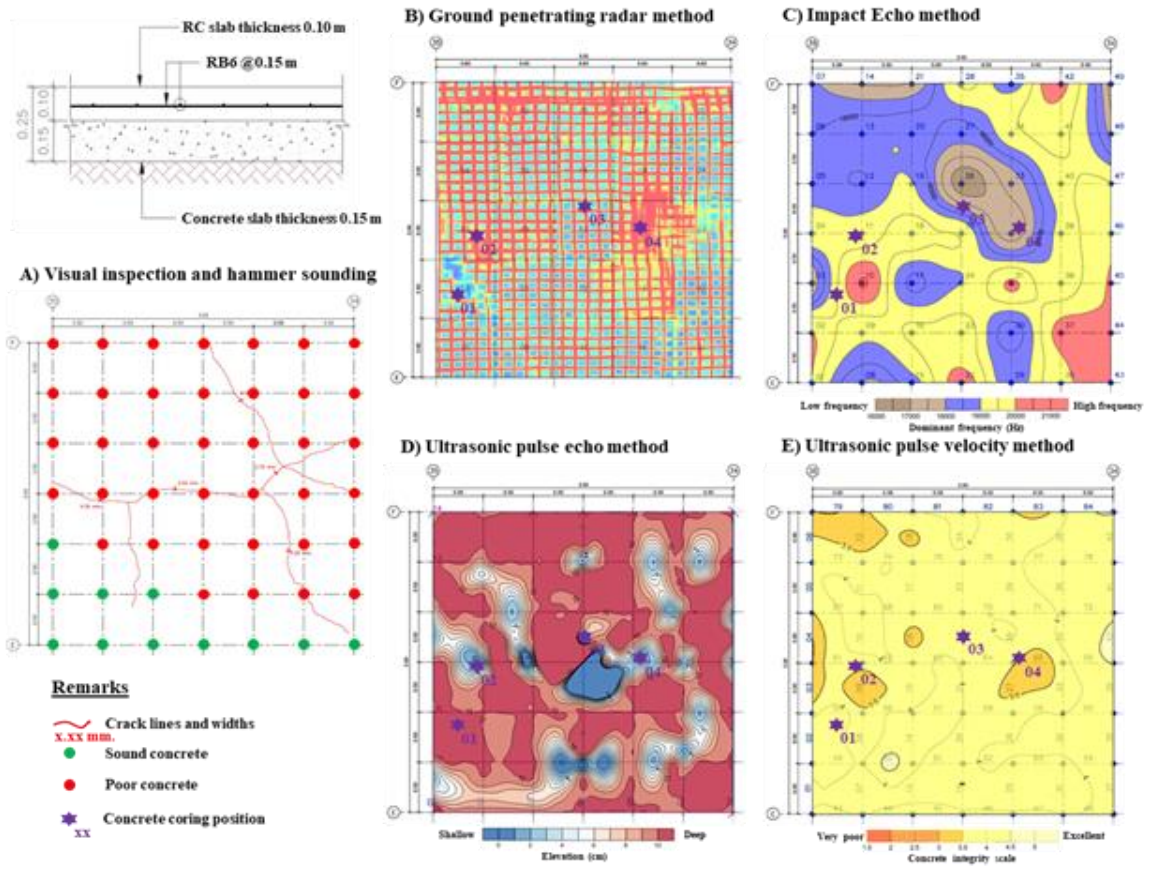

Figure 7

RC slab section detail on left at the corner and all NDT results with randomly four coring positions (Purple stars) on a researching area

After finished performed the idealized structure, the realistic structures were additionally performed to cross-check the results by using the same criteria and techniques. Only selected small area 3.00x3.00 m was performed by all NDT methods due to the realistic structure was a very large warehouse. The background of a researching area was a factory that installed many large machines for production lines, thus the ground slab detail was designed two layers consist of lean concrete thick 0.15 m below and reinforcement concrete slab thick 0.10 m for supporting them. However, the crack lines were too many found by naked eyes with approximately 0.35 to 0.80 mm of crack widths measuring by crack scale ruler. Moreover, the hammer sounding results show ringing sound, red dot, at the almost area, it means two layers of slabs were separate together which could cause the crack lines too. The results beneath the four NDT methods were visual inspection and hammer sounding for previously selected and scoping defect areas as shown in figure 7A above. Owing to the realistic structure was larger than the RC mock-ups, the grid-point testing pattern, especially all stress-wave methods, was changed from 0.20 m to 0.50 m. The results of the testing area and randomly four coring positions for cross-check the results are shown in figure 7 above. Any randomly coring positions were selected for different purposes. The purposes of the first position are to recheck the concrete integrity and the missing of GPR signals due to it maybe causes of moisture or corroded rebar which can lead to delamination occurrence. The purposes of second and fourth positions were an inspection of the significant detection of all the NDT methods which can be defects in this researching area. The purposes of another position are to confirm the thickness and quality of concrete. Table 5 and figure 8 below showed the concrete coring results of any positions are compared with the NDT methods.

Table 5. Descriptive comparison between concrete cores and four NDT methods

Coring No.	Non-destructive testing method				Concrete core results
	GPR	UPV	UPE	IE	
No.01	Found anomaly	Good	Deep	High frequency	- Defect and corroded rebar were found around the bottom slab - Good concrete integrity
No.02	Not found	Good	Shallow	High frequency	- Not found any defect and corroded rebar - Good concrete integrity
No.03	Not found	Good	Deep	Low frequency	- Defect and corroded rebar were found around the bottom slab - Good concrete integrity
No.04	Not found	Doubtful	Shallow	Low frequency	- Not found any defect and corroded rebar - Doubtful concrete integrity due to rust aggregates was found

Figure 8
Four concrete cores represent each of the defects (red rectangle)

Conclusion:

The four selected NDT methods in this research performed very well locating the delamination and air-filled void, over the hardening state except for the UPV method which only detects near-surface defects. The difference of concrete day life only affected the GPR method because the resolution for locating defects and thickness depends on the dielectric constant of material which sensitive to water content in the concrete. Moreover, the limitation of the GPR method was that it cannot detect too deep defects close-up with the opposite side of the structure due to the weak reflection signals that can be merged together. On the other hand, the UPE and IE methods can successfully locate all levels of defects and thickness over the hardening state, but only the UPE results can represent the continuous reflection level and clearly scoping area in a cross-sectional profile. Thus, the most successful method in this research was the UPE method. However, the realistic structure that researcher experiences are often performed on the aging structure longer than 58 days except for the accident from construction process; such as too fast to release concrete mold, concrete explode from release stressing tendon, etc. Thus, the GPR results exhibit the accuracy and precision to detect the delamination and air-filled voids too. Besides, the duration of data acquisition and interpretation of both methods were less than the others. The result of this research suggested that the GPR and UPE methods should be performed together for more accuracy and precision.

Acknowledgments:

The researcher would like to appreciate to my advisor, Assoc.Prof. Thanop Thitimakorn, for advice, guidance, and encouragement throughout my master's degree. Furthermore, this research was supported by Research and Researchers for Industries (RRI) (MSD62I007) and STS Corporation company limited.

References:

1. Landkard D.R, Birkimer D.L, Fondriest F.F, Snyder M.J. American Concrete Institue. 1971;25:59-102.
2. Cusson D, Lounis Z, Daigle L. Computer-Aided Civil and Infrastructure Engineering. 2011;26:524-541.
3. Venkateswarlu B, Tewari V.C. Journal, Indian Geological Congress. 2014;6:35-46.
4. Meyer K, Erdogmus E, Morcous G, Naughtin M. Architectural Engineering Conference (AEI). 2008.
5. Lai W.W, Chang R.K, Sham J.F. Journal of Applied Geophysics. 2018;149:10-17.
6. Jaw S.W, Hashim M. Tunneling and Underground Space Technology. 2013;35:20-29.
7. Metwaly M. Measurement. 2015;60:139-145.
8. Kaplanvural I, Pekşen E, Özkap K. Construction and Building Materials. 2018;166:141-146.
9. Sansalone M, Carino N.J. International Advances in Nondestructive Testing. 1986;12:117-146.
10. Zoidis N, Tatsis E, Christos V, Gotzamanis A, Clausen J.S, Aggelis D.G, Matikas T.E. Construction and Building Materials. 2013;48:1302-1308.
11. Lorenzi A, Caetano L.F, Campagnolo J.L, Lorenzi L.S, Pinto da Silva Filho L.C. e-Journal of Nondestructive Testing. 2015.
12. Stefan M, Salvador V, David S. MATEC Web Conference. 2018;199:1-9.
13. Hoegh K, Khazanovich L, Yu H.T. Transportation Research Record. 2011;2232:85-94.
14. Clausen N.J, Zoidis N, Knudsen A. Emerging Technologies in Non-Destructive Testing. 2012;5:117-122.
15. Andrzej M, Marta M. Procedia Engineering. 2014;91:418-423.
16. Carino N.J. International Symposium Non-Destructive Testing in Civil Engineering. 2015.

A_005_PA: THERMAL OXIDATION OF NANOSTRUCTURE TiN THIN FILM DEPOSITED BY REACTIVE DC MAGNETRON SPUTERING TECHNIQUE

Adisorn Buranawong,[1,2] Nirun Witit-anun[1,2,*]

[1]Department of Physics, Faculty of Science, Burapha University, Thailand
[2]Thailand Center of Excellence in Physics (ThEP), PERDO, MHESI, Bangkok, Thailand
*e-mail: nirun@buu.ac.th

Abstract:

In this study, the influence of the annealing temperature on the thermal oxidation of TiN thin film deposited on Si (100) substrate by reactive DC magnetron sputtering technique was investigated. The films were thermal oxidized in air at temperatures between 400°C and 700°C for 2 h. The as-deposited and the thermal oxidized samples were characterized by X-ray diffraction (XRD) and Field Emission Scanning Electron Microscopy (FE-SEM). The TiO_2 structure was found for oxidation at 450°C and the intensity of the TiO_2 peak was rapidly enhanced through the temperature, which obtained from XRD. A thin oxide layer was formed on the top of the coating at 450°C and significantly increased thickness from 40 nm to 1372 nm indicating the surface oxidation of TiN films governed by temperature, which observed form cross-sectional analysis. The oxidation activation energy, which calculated using Arrhenius plots was 162.37 kJ/mol.

A_006_OA: EFFECT OF SILICON CARBIDE CONTENT ON SINTERED STEEL MICROSTUCTURE

Wananurat Srijampan[1], Amporn Wiengmoon[1], Preeya Nakornkaew[2], Tapany Patcharawit[2], Thanyaporn Yotkaew[3], Nattaya Tosangthum[3], Ruangdaj Tongsri[3,*]

[1]Department of Physics, Faculty of Science, Naresuan University, Phitsanulok, 65000, Thailand
[2]School of Metallurgical Engineering, Institute of Engineering, Suranaree University of Technology 111 University Avenue, Suranaree Sub-District, Muang Nakhon Ratchasima District, Nakhon Ratchasima 30000 Thailand
[3]Powder Metallurgy Research and Development Unit (PM-RDU), Thailand National Metal and Materials Technology Center, Pathum Thani, 12120, Thailand
*e-mail: ruangdt@mtec.or.th

Abstract:

Silicon and carbon are common alloying elements for wrought steel making. Sufficient added silicon content can prevent carbide precipitation so it is commonly used for producing a carbide-free bainitic steel, one of advanced high strength steels. It was found previously that both elements from silicon carbide additive can be alloyed to iron-based powder compacts via solid state sintering. In this work, experimental sintered steels were produced from mixtures of pre-alloyed Fe-0.50Mo-0.15Mn powder with different added silicon carbide contents (1.0, 2.0, 3.0 and 4.0 wt. %) by using 'press and sinter' process. Microstructures of sintered steels changed in accordance to added silicon carbide content. The microstructure consisting of ferrite plate and martensite/austenite constituent in a low silicon carbide-added steel was changed to the microstructure with martensite matrix in a high silicon carbide-added steel (Fig. 1). Surprisingly, diffusional phase transformations resulting in formations of pearlite and inverse bainite were observed to occur prior to diffusionless martensitic transformation in a high silicon carbide-added steel (Fig. 2). Tensile strength increased with increasing martensite volume fraction but dropped with increasing pearlite/inverse bainite volume fraction.

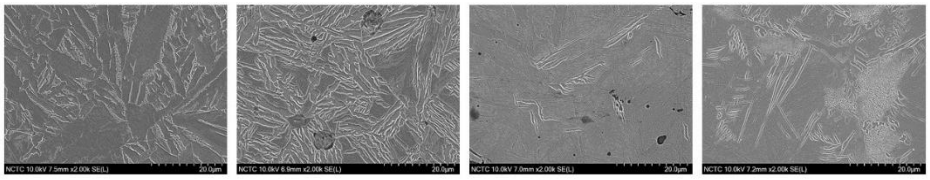

Figure 1
Microstructure of sintered steels with difference SiC contents

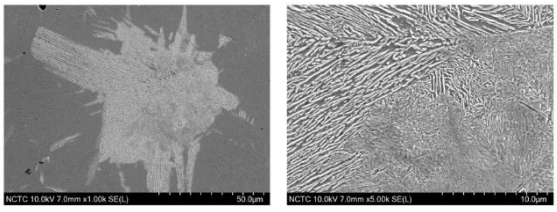

Figure 2
Pearlite and inverse bainite in a high SiC-added steel

A_007_OA: EFFECTS OF Mo AND W ON MICROSTRUCTURE AND HARDNESS IN ANNEALED 28wt.%Cr CAST IRONS

Kittikhun Ruangchai[1], Ruangdaj Tongsri[2], John T.H. Pearce[3], Torranin Chairuangsri[4], Amporn Wiengmoon[1,*]

[1]Department of Physics, Faculty of Science, Naresuan University, Phitsanulok, 65000, Thailand
[2]Powder Metallurgy Research and Development Unit (PM-RDU), Thailand National Metal and Materials Technology Center, Pathum Thani, 12120, Thailand
[3]Panyapiwat Institute of Management, Nonthaburi 11120, Thailand
[4]Department of Industrial Chemistry, Faculty of Science, Chiang Mai University, Chiang Mai 50200, Thailand
*e-mail: ampornw@nu.ac.th

Abstract:

In the present work, the effects of annealing heat treatment on microstructure and hardness in 28wt.%Cr-2.6wt.%C high chromium cast irons with 1wt.%Mo/W addition have been investigated. The as-cast samples were annealed at 800°C for 4 h in an electric furnace and then slow cooled with a cooling rate of 20°/h to temperature of 500°C and held for 4 h, followed by furnace cooled to room temperature. Microstructural investigation was performed by light microscopy, X-ray diffractometry, scanning electron microscopy and energy-dispersive X-ray spectrometry. Vickers macro-hardness was measured on specimens from each condition. The results revealed that the as-cast microstructure of 28wt.%Cr (reference iron) and 28wt.%Cr iron with 1wt.%Mo addition (Mo1) were hypoeutectic containing primary austenite dendrites with an interdendritic eutectic structure of M_7C_3 carbide (M = Fe, Cr, Mo, W) and eutectic austenite which partially transformed to martensite during cooling in the mold. Mo addition promoted the formation of M_6C with brightest contrast, as seen in Figure 1(a). Whereas, the 28wt.%Cr iron with 1wt.%W addition (W1) was hypereutectic containing large primary M_7C_3 with eutectic structure of M_7C_3 carbide and eutectic austenite. After annealing, the ferrite (α) matrix + $M_{23}C_6$ carbide (SC), as seen in Figure 1(b), was observed in all irons, due to decomposition of austenite during annealing. Small areas of pearlite were also present due to microsegregation effects. Mo and W additions led to an increase in as-cast macro-hardness from 506 HV30 in the reference iron up to 529 and 576 HV30 in Mo1 and W1, respectively. The formation of M_6C and primary M_7C_3 were the main reasons for hardness increase. After annealing, the macro-hardness decreased to 390, 463 and 428 HV30 in the reference iron, Mo1 and W1, respectively.

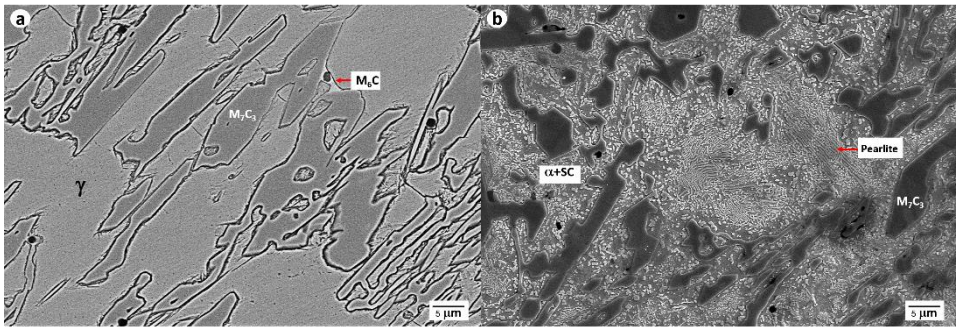

Figure 1
SEM images show the microstructure in the as-cast (a) and after annealing (b):
(a) 1wt.%Mo addition (b) 1wt.%W addition.

A_008_OA: STUDENT LEARNING TOWARDS DIFFERENT LESSON SEQUENCES IN FORCE AND MOTION

Nattaphong Nuchsirikulaphong*, Narumon Emarat, Kwan Arayathanitkul

Department of Physics, Faculty of Science, Mahidol University, Rama 6 Road, Bangkok, Thailand
*e-mail: nattaphong.nuh@student.mahidol.ac.th

Abstract:

Lesson sequence is very important for student learning in many topics. Several physics textbooks arrange contents differently. In the topic of force and motion, some started with Newton's laws of motion first while others started with free-body diagrams. This indicates the importance of the content sequence in such topic. Accordingly, there are two interesting lesson sequences for high-school physics which are teaching free-body diagrams before Newton's laws (sequence A) and teaching Newton's laws before free-body diagrams (sequence B). This study aims to investigate the effect of these lesson sequences on student understanding of force and motion. The sample groups were grade-10 students from two schools. One school used sequence A (n=62) and the other used sequence B (n=134) An assessment test was developed and used to survey student understanding. The test consisted of three parts which were (1) problem-solving part, (2) Newtonian concepts part and (3) free-body diagrams part. The result shows that the same pattern of student answers for both sequences was found in the Newtonian concepts part. However, there were differences in the problem-solving and free-body diagrams parts. In the problem-solving part, many students could not complete the equation of motion. Some forces were missing from the equation, especially and surprisingly the weight of an object. This result was found more in students from sequence B. A misconception was shown in the free-body diagrams part. Students drew extra forces involving Newton's third law; both action and reaction forces were drawn in a diagram of one object. This misconception was found more from the answers of sequence B students. From the results, lesson sequence seems to affect student skills in solving problems and drawing free body diagrams.

A_009_PF: RECTIFICATION OF G-BHN CORRELATION OF FIBROUS COMPOSITES USING POLYNOMIAL REGRESSION WITH AMSE-5-FOLD-CV ANALYSIS

Rakdiaw Muangma,[1,*] Voravit Kosalathip,[2] Taswal Kumpeerapun [2]

[1]Faculty of Education, Chiang Rai Rajabhat University, Chiang Rai, Thailand, 57100
[2]Department of Physics, Faculty of Science, King Mongkut's University of Technology Thonburi, Bangkok, Thailand, 10140
*e-mail: rakdiaw.mua@crru.ac.th

Abstract:

Non-Linear Phenomena (NLP) of wood-free-based (WF-based) fibrous composites was interpreted using the constitutive modelling which is the point of view in this research. The novel clarifying of NLP can be obtained using the numerical-experimental-data of G-BHN correspondence associated with Degree of Polynomial (DP) instead of stress-strain analysis. By this way, these data were collected using prototype of Brinell-macro-hardness tester with 7.68 mm of steel-ball-indenter diameter. The empirical conditions used grammage of WF-based fibrous composites varying as: 150, 180, 210, and 240 grams and imprinted time at 20 seconds. After that, G-BHN relations were computed using theoretical model based on quadratic (DP2) polynomial functions, and then, these simulations were presented. For analytical procedure, the rectified model was occurred by using the varying of DP from 1 to 7 associated with three strategies including: R-squared (R^2), adjusted-R-squared (adj-R^2), and least of Average Mean Square Error (AMSE) of 5-fold-Cross-Validation analysis. After analysis, it was perceived that the cubic (DP3) and the sextic (DP6) polynomial function could be the optimal DP which elucidated the maximum adj-R^2 associated with the least of AMSE of 5-fold-CV analysis. Finally, the comparison between this theoretical and validated model described in this discussion.

Introduction:

In metallurgical research, hardness is the one part of mechanical properties that used as an essential factor in microstructure analysis. For instance, Vickers harness can be related to the mechanical strength of the work-hardened metal that illustrated differ from the Bulk Metallic Glasses (BMGs) [1]. In addition, this hardness assessment could be used as the controlled parameter of ultrasonic power for the aluminum foils (Al3003-H18) which joined using Very High Power Ultrasonic Additive Manufacturing (VHP-UAM). This experimental result exhibited that the hardness decreased when the vibration amplitude of ultrasonic power was increased [2]. Therefore, the explanation of relationship between experimental results and others properties using the optimized model is the crucial point for materials characterizations.

In structural analysis, the theoretical approaches for most materials regularly inaugurated using the linearity approximation, whereas, the natural behaviors of them were mostly presented using the non-linear regimes. These phenomena can be inferred using the Non-Linear Phenomena that caused by the various kinds of persuasion. Regularly, there are four manners that resulted in the materials Non-Linear Phenomena including: First, the material demeanor that interpreted using the linear-elastic conditions but the generally presentation is the non-linear in its nature. Second, the Non-Linear Phenomena attributed to the large rotations that the plate-shaped materials can be changed to the cylinder-shaped during the rolling procedures. Third, the geometric Non-Linear Phenomena is caused by the large displacement combined with the rotation inside of the thin-material components which resulted in the changing of material stiffness. The last one is caused by the changing of load distribution associated with the materials deformation during indentation mechanisms [3,4], consecutively.

Regularly, the model prophecy is investigating in many research areas for interpretation of correlation between the observation variable and the prediction variable. In many explorations, the procedure regularly used the fundamental of statistics to interpreted the data associated with the supervised learning. For example, the prognosis of designed perovskite oxide in term of phase stability, can be calculated by using the Density Function Theory (DFT). For fast and effective resultants, the statistical-based machine learning used the extra tree classifier coupled with DFT for classification of compound examining and resulting that the best regression model was obtained using the kernel ridge models [5].

On the other hand, the Artificial Neural Network (ANN) based on R-squared analysis can be used for modelling of spin-transitions phenomenon of molecular magnet which investigated using the measured data of spin configurations and thermal hysteresis properties. And then, the ultra-thin film of molecular magnet materials can be designed using this ANN modelling [6]. The next implementation revealed that the using of ANN for the experimental designing which was used to interpret the connection between the commanding parameters and the quantity of $NiNb_2O_6$ phase. This literature presented that the rate of heating-cooling and the dwell time were less significant, whereas, the influence of calcined temperature on $NiNb_2O_6$ phase was remarkable factor [7]. For other applications, the performance of the energy forecast model measured by combining the meteorological variables and other parameters concluded that the optimum number of hidden layer nodes could be obtained by using of Root Mean Squared Error (RMSE) associated with using Least Absolute Shrinkage and Selection Operator (LASSO) for the correlation analysis [8]. Next, the curve modelling for wind turbine power was approximated by using the non-linear regression model which based on the Mean Absolute Percentage Error (MAPE) of different function. And then, the conclusion is that the best model analyzed using polynomial and modified hyperbolic tangent functions signified the lowest value of MAPE [9].

Following that, the polynomial-based regression method is the one branch of supervised learning, was used as the main processing for this analytical research [10]. Although the high-degree polynomial model symbolized the side-effect in accuracy that compared using the low-degree polynomial models in the ways of efficiency and simplicity. It was found that when the degree increased, the conditions that expressed the largest value of adj-R^2 [11], then, the identified-model could be obtained in eventually.

In addition, to use the processing by Cross-Validation (CV) that the analytical data were separated into K subgroups where K is an integer number. In this process, the testing data by leaving of the n-th group out and trained by using of the other groups and repeating this procedure until n reached to K. This method called as the K-fold-CV analysis [12]. These procedures were adapted to use in this examination.

This exploration invigorates with the precursory inquisition [10], and then, to focus on the constitutive modelling for elucidation of NLP based on G-BHN correlation which the optimal DP can be analyzed using machine-based learning. In this way, the analytical results illustrated in difference inclination when using higher DP. After that, the value of R^2 [6], the value of adj-R^2 [11], and the least of AMSE-5-fold-CV analysis, were used for this interpretation. These processes used for decision that one can be the constitutive-model and can be used as the predictive model for the next explanation.

Methodology:

In this representation, the experimental-data of the G-BHN relation which were measured by using the Brinell-macro-hardness measuring machine [10] were used for this analysis. These measured data used the conditions including: The grammage of WF-based fibrous composites was varied as: 150, 180, 210, and 240 grams, and then, the indentation time and the diameter of steel-ball-indenter used at 20 seconds and 7.68 mm, consecutively. For instance, the conditions including: 150 grams of grammage with 20 seconds of imprinted time can be referred using WF150T20, respectively. Furthermore, the value of G. d. D^{-1} referred to the shear modulus and the value of BHN^{-1}. d. D^{-1} declared as the ability of plastic deformation. This G-BHN connection described as Eq. (1).

$$G = \frac{\alpha}{2\beta}\left\{\left[\frac{\beta}{BHN}\right] + \left[\frac{\beta}{BHN}\right]^2\right\} \quad (1)$$

$$\alpha = \frac{0.102dD\tau^2}{(d - d_0)\sqrt{D^2 - d^2}} \quad (2)$$

$$\beta = \frac{0.102dD\tau}{\sqrt{D^2 - d^2}\left[D - \sqrt{D^2 - d^2}\right]} \quad (3)$$

From Eq. (1) to Eq. (3) [10], G is the shear modulus (Unit: MPa), BHN is the Brinell hardness number (Unit: MPa), shear stress (Unit: N/mm^2). Following that, d is the indentation diameter (Unit: mm), d_0 is the least diameter of indentation (Unit: mm), and D is the indenter diameter (Unit: mm), respectively.

After that, analytical procedure used the value of BHN^{-1}. d. D^{-1} as the observation variable while the value of G. d. D^{-1} as the prediction variable, consecutively. And then, this analytical process used Eq. (4) for rectification which described the relationship between the value of adj-R^2 [11] and R^2 [6]. Where n is the n^{th} degree of polynomial function, p is the number of predictor variables, respectively.

$$Adj\_R^2 = 1 - \left[\frac{n-1}{n-p}\right](1 - R^2) \quad (4)$$

Eventually, the least of AMSE of 5-fold-CV analysis associated with varying from DP1 to DP7 were used in the finalized process. By the way, these analytical results were posted in the next section.

Results and Discussion:

For interpretation, the Inflection Point (IP) used associated with the sequential fitting by varying of DP1 to DP7, to analyzed these numerical data. In this way, the IP is defined at the point that exhibited the changing rate changed to opposite sign which used for determination of G-BHN alliance. Since, the dynamic curves of interpolated data of G-BHN interconnection were demonstrated by Figure 1 to Figure 4, respectively.'

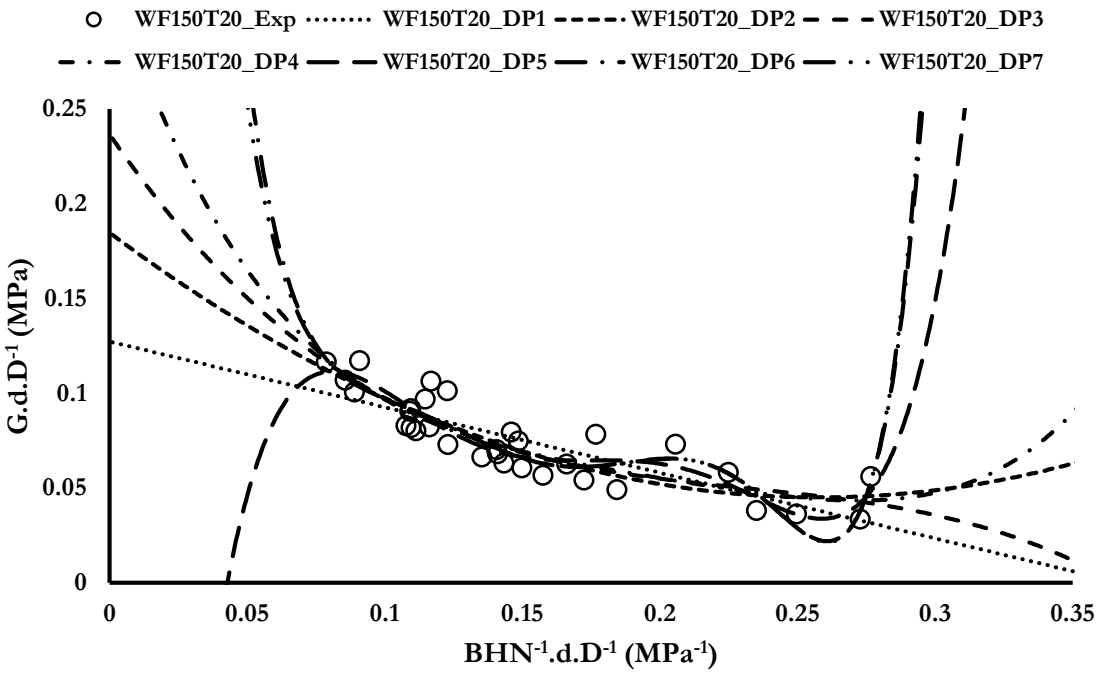

Figure 1

Illustration of the relationship between G. d. D^{-1} and BHN^{-1}. d. D^{-1} for WF150T20 data and fitting curve with conditions that varying from DP1 to DP7, respectively.

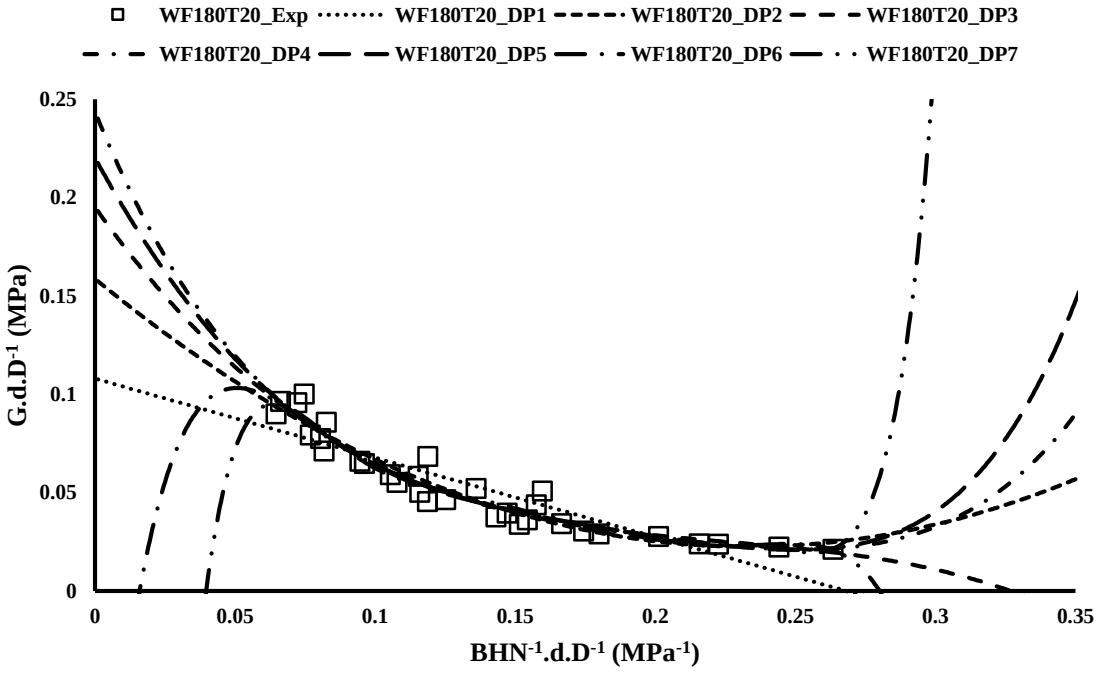

Figure 2

Illustration of the relationship between G. d. D^{-1} and BHN^{-1}. d. D^{-1} for WF180T20 data and fitting curve with conditions that varying from DP1 to DP7, respectively.

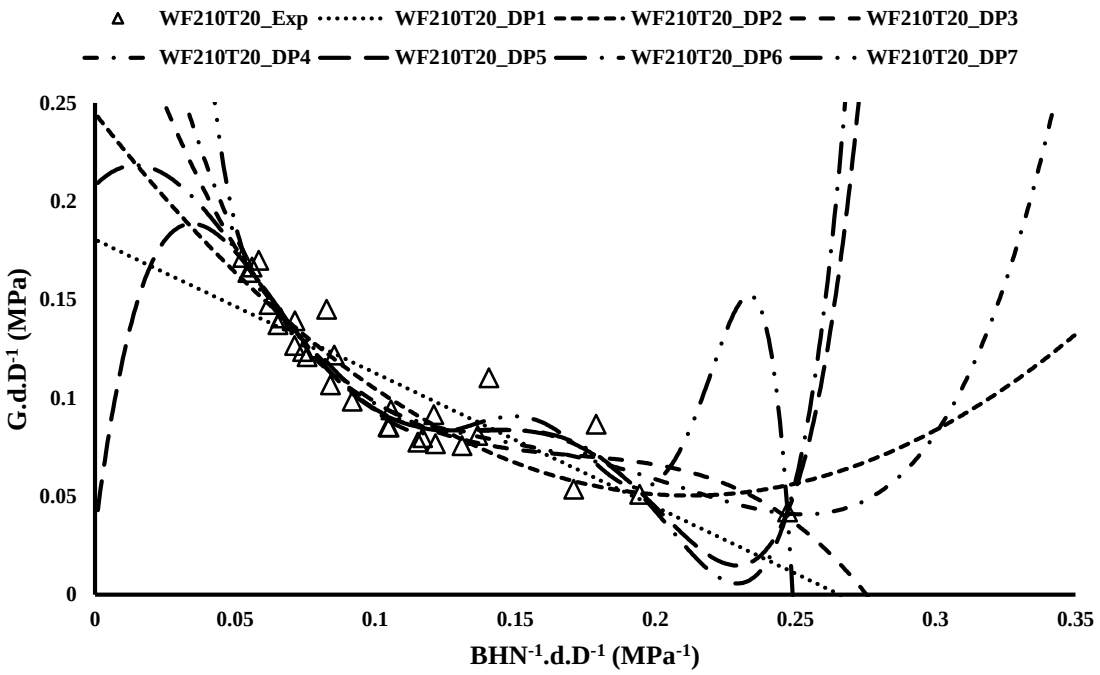

Figure 3

Illustration of the relationship between G. d. D^{-1} and BHN^{-1}. d. D^{-1} for WF210T20 data and fitting curve with conditions that varying from DP1 to DP7, respectively.

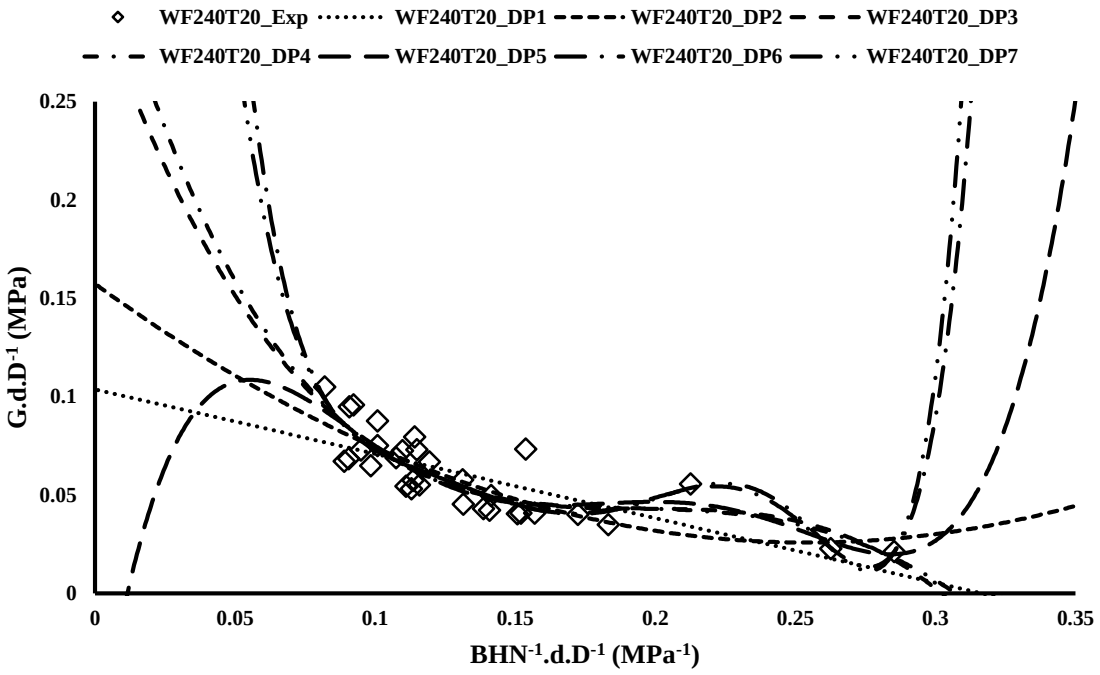

Figure 4

Illustration of the relationship between G. d. D^{-1} and BHN^{-1}. d. D^{-1} for WF240T20 data and fitting curve with conditions that varying from DP1 to DP7, respectively.

Form Figure 1 to Figure 4, this analytical procedure for these dynamic curves used the steepness of DP1 and the amount of IP for determination of G-BHN relation. These were summarized in Table 1.

Table 1.

The analytical results were interpreted using the steepness of DP1 and the amount of IP.

Sample	Steepness of DP1	Amount of IP						
		DP1	DP2	DP3	DP4	DP5	DP6	DP7
WF150T20	-0.35	0	1	0	1	3	3	3
WF180T20	-0.40	0	1	0	1	1	2	2
WF210T20	-0.68	0	1	0	1	2	1	4
WF240T20	-0.33	0	1	0	0	2	3	3

From Table 1, it was found that the steepness of DP1 exhibited the increasing direction when the grammage increased, and then, reached to the maximum value at WF210T20. After that, the decreasing of steepness of DP1 of WF240T20 was observed. In other direction, the non-linear analysis that used the DP as an indicator elucidated that the number of IP of theoretical model based on DP2 presented only one point, while, DP3 of all cases and DP4 for WF240T20 did not have IP. Consequently, the amount of IP increased when the DP increased. Therefore, these resultants demonstrated that the increasing IP can be referred to the changing direction of these regressions. Next procedure, these analytical results were obtained using the value of R^2 and adj-R^2 which were summarized in Table 2 in the next part.

Table 2.

Summarization of the value of R^2 and adj-R^2. These inspections were analyzed by varying from DP1 to DP7 in the sequential fitting.

DP	WF150T20		WF180T20		WF210T20		WF240T20	
	R^2	adj-R^2	R^2	adj-R^2	R^2	adj-R^2	R^2	adj-R^2
1	0.6985	0.6777	0.8185	0.8060	0.7492	0.7299	0.5850	0.5564
2	0.7795	0.7558	0.9263	0.9184	0.8597	0.8429	0.6734	0.6385
3	0.7867	0.7551	0.9327	0.9227	0.9007	0.8841	0.7258	0.6852
4	0.7887	0.7480	0.9341	0.9214	0.9054	0.8848	0.7263	0.6736
5	0.8150	0.7706	0.9342	0.9183	0.9132	0.8895	0.7314	0.6669
6	0.8346	0.7864	0.9357	0.9170	0.9133	0.8844	0.7474	0.6737
7	0.8347	0.7772	0.9379	0.9163	0.9188	0.8863	0.7476	0.6598

Astonishingly, the shearing stress acted on the edge of indentation which considered that the flow stress could be related to the arithmetic mean pressure. It was found that both WF-based and Kraft-based fibrous composites can be used these analytical results for Non-Linear Phenomena explanation when the G-BHN relation determined using the polynomial-based modelling. Furthermore, the correlation of G. d. D^{-1} with respect to BHN^{-1}. d. D^{-1} was used for examination in this report instead of the relation of G. d^2. D^{-2} with respect to BHN^{-1}. d^2. D^{-2} which demonstrated by the earlier report [10]. Because, these two features including: d. D^{-1} and d^2. D^{-2} was declared as the dimensionless-multiplying factors. Therefore, the propagating direction of the G-BHN correlation exhibited the insignificant difference when used with and without these dimensionless parameters.

In other direction, the explanation of WF-based and Kraft-based fibrous composites based on the shear lag model of the earlier review. They presented that the reducing of Young's modulus of composites was caused by the hybrid interaction between different types of fiber [13]. And the next example demonstrated that the non-linear properties can be caused by the hysteresis loop and this report used the time-dependent modelling for explanation. This article interpreted the connection between the tangent shear modulus and the actual strain between loading and unloading using the exponential function [14,15]. While, this presentation used the G-BHN interconnection for explication of NLP of WF-based fibrous composites, consecutively.

However, the interpretation of NLP using the higher DP is the one of most important parameters. This analytical procedure represented the congruence of propensity when compared with the Brinell-macro-hardness measurement. Additionally, not only the initially state of plastic deformation symbolized the non-linear properties that frequently called the lüder elongation, but also indicated in the primary condition for material-hardness measuring. In this way, the transformation between linear to non-linear can be observed in both situations including the lüder elongation [16] and the Brinell-macro-hardness measuring [10], consecutively.

Moreover, the higher DP of NLP can be investigated using previous literatures including: First, the Allen–Cahn equation used the sextic polynomial function for the enhancing of the investigation in topics of the eigenvectors of the discrete Laplacian [17]. Second, the quintic and the septic polynomial function used for explanation of the non-linear dynamics of material stiffness and critical geometrical parameter of three springs system [18]. Similarly, the Non-Linear Phenomena of WF-based fibrous composites in this representation can be investigated using the quantic (DP5), the sextic (DP6), and the septic (DP7) of polynomial function and these analytical results can be cleared in the next explanation.

Following this way, it was perceived that the non-linear property of this interpolated-tendency can be confirmed using the optimal DP as NLP clarification. Furthermore, the optimal DP can be exposed using the least of AMSE-5-fold-CV analysis. These analytical results were elucidated in the next Table.

Table 3.

The analytical results were clarified in term of AMSE for 5-fold-CV analysis.

DP	AMSE of 5-fold-CV			
	WF150T20	**WF180T20**	**WF210T20**	**WF240T20**
1	15.00E-5	10.20E-5	35.34E-5	15.81E-5
2	11.47E-5	4.55E-5	19.57E-5	14.70E-5
3	11.46E-5	4.43E-5	15.59E-5	12.79E-5
4	11.75E-5	4.54E-5	15.70E-5	13.32E-5
5	10.99E-5	4.71E-5	14.89E-5	13.50E-5
6	10.30E-5	4.84E-5	13.56E-5	13.57E-5
7	10.73E-5	4.89E-5	13.36E-5	13.68E-5

In previous review, the 4-fold-CV used 4 subgroups was used to interpret the correlation between the elemental properties and the phase outcome for designing of metal alloy [12], whereas, this presentation used 5-fold-CV to analyze the testing and training data.

From Table 3, the resultants were analyzed using both of the largest value of adj-R^2 and the least of AMSE-5-fold-CV analysis, explicated that the DP3 allocated for WF180T20 and WF240T20, whereas, the DP6 assigned for WF150T20, and, the DP7 described for WF210T20, respectively. On the other hand, the resultant of WF210T20 typified the non-explicit because of the largest value of adj-R^2 could be obtained when using the DP5 whereas the least of AMSE presented as the DP7, consecutively.

Conclusion:

In this research, this constitutive modelling based on generalized polynomial function associated with the optimal DP can be used for affirmation of the Non-Linear Phenomena of WF-based fibrous composites in macroscopic approach. By this way, it was perceived that the Non-Linear Phenomena was caused by the combination of geometry, the changing of load distribution, and the materials deformation. These phenomena were revealed as the G. d. D^{-1} decreased when the BHN^{-1}. d. D^{-1} increased which invigorated that the increasing of the ability of plastic deformation can be resulted in the decreasing of shear modulus. In the same direction, the materials Non-Linear Phenomena which generated by the changing of load distribution and resulted in the strain hardening in the continuum, were reported as the previous articles [13,19].

After analysis, it was perceived that the IP of DP2 presented only one point, while, the IP cannot be observed when using DP3 of all cases and DP4 for WF240T20. And then, the amount of IP increased as the DP increased in all cases. Next, the value of R^2 increased when the DP was increased, whereas, the methodology of using the largest value of adj-R^2 and the least of AMSE-5-fold-CV analysis illustrated the contradiction with respect to the theoretical model, consecutively.

By this way, NLP that obtained using these analytical procedures will be utilized when using the optimal DP of G-BHN connection for correcting of the error. Because of this speculative appearance of NLP acted like an open-ended of scientific comprehension, therefore, the DP2 is an embryonic phase for elucidation of non-linear properties of interpolated results. Ultimately, the least of AMSE of K-fold-CV analysis [12] should be developed for ameliorating of the experimental-numerical analysis in the next future. These analytical procedures and the non-linear properties of composites materials will be scrutinized further.

Acknowledgements:

Authors would like to thanks all technical & service engineers, and all teams of Trinergy Instrument Co., Ltd. (Thailand), for the supreme supporting of Keithley DMM7510 7.5-Digit Graphical Sampling Multimeter. Thanks, **Venus Supply Co., Ltd.**, for supporting of maintenance of RPi 3 model B. Thanks, Prof. Dr. Narongrit Sombatsompop, School of Energy, Environment and Materials, King Mongkut's University of Technology Thonburi, Thailand, Prof. Dr. Paul A. Martin, Department of Applied Mathematics and Statics, Colorado School of Mines, USA, for crucial comments and suggestions. Thanks, Asst. Prof. Dr. Waipot Ngamsaad, Division of Physics, and Asst. Prof. Dr. Kannika Khompurngson, Division of Mathematics, School of Science, University of Phayao, Thailand, for approving of the algorithm based on python and the instrumentation analysis. Thanks, Asst. Prof. Dr. Supattra Wongsaenmai, Dr. Tawat Soitong, Program in Materials Science, Faculty of Science, Maejo University, Thailand, and Assoc. Prof. Dr. Prayoonsak Pluengphon, Faculty of Science and Technology, Huachiew Chalermprakiet University, Thailand, for discussing of Brinell hardness analysis and the mechanical characteristics of fibrous composite materials. Thanks, Mr. Patipol Chaithep, Program in Materials Science, Faculty of Science, Maejo University, Thailand, for discussing of Digital Micro Vickers Hardness Tester operation. Thanks, Faculty of Education and Research and Development Institute, Chiang Rai Rajabhat University, Thailand, for financial support (#B36001002). Finally, thanks, Asst. Prof. Dr. Somboon Kamtaeja, Faculty of Education, Chiang Rai Rajabhat University, Thailand, for supporting of the special segment of lifting device that used for this Brinell-macro-hardness tester.

References:

1. Zhang P, Li SX, Zhang ZF. Mater. Sci. Eng. A. 2011;529:62–73.
2. Sojiphan K, Babu SS, Benatar A, Manonukul A, Norfolk M. Weld. J. 2016;95:185–193.
3. Zhang Q, Yang QS. Mech. Res. Commun. 2017;84:55–59.
4. Stranghöner N, Azizi N, Gorbachov A. J. Constr. Steel. Res. 2019;157:386–396.
5. Li W, Jacobs R, Morgan D. Comput. Mater. Sci. 2018;150:454–463.
6. Laosiritaworn W, Laosiritaworn Y. Polyh. 2013;66:108–115.
7. Laosiritaworn W, Khamman O, Ananta S, Yimnirun R, Laosiritaworn Y. Ceram. Inter. 2008;34:809–812.
8. Guo Y, Wang J, Chen H, Li G, Liu J, Xu C, Huang R, Huang Y. Appl. Energ. 2018;221: 16–27.
9. Marčiukaitis M, Žutautaitė I, Martišauskas L, Jokšas B, Gecevičius G, Sfetsos A. Renew. Energ. 2017;113:732–741.
10. Muangma R, Wongsaenmai S, Soitong T. Key Eng. Mater. 2019;798:370–375.
11. Wu J, Luo Z, Zheng J, Jiang C. Appl. Math. Model. 2016;40:4681–4699.
12. Islam N, Huang W, Zhuang HL. Comput. Mater. Sci. 2018;150:230–235.
13. Henry J, Pimenta S. Compos. Sci. Tech. 2017;152:275–289.
14. Wanga J, Xiaoa Y, Inoueb K, Kawai M, Xue Y. Compos. Struc. 2019;207:894–908.
15. Surrel Y, Vautrin A. Compos. *Sci. Techno.* 1993;49:45–50.
16. Mao B, Liao Y. Mech. Mater. 2019;129:222–229.
17. Lee S, Lee D. Appl. Math. Comput. 2019;51:176–192.
18. Remmi SK, Latha MM. Chin. J. Phys. 2018;56:2085–2094.
19. Sonmez FO, Demir A. J. Mater. Process. Tech. 2007;186:163–173.

A_010_PF: ELECTRICAL RESISTIVITY AND GROUND-PENETRATING RADAR SURVEYS, WIANG THA KAN ARCHAEOLOGICAL SITE, CHIANG MAI PROVINCE, NORTHERN THAILAND

Suwimon Udphuay,[1,*] Tulaya Lhapawong,[2] Benjarong Sinthuya[3]

Department of Geological Sciences, Faculty of Science, Chiang Mai University
*e-mail: suwimon.udphuay@cmu.ac.th

Abstract:

Electrical resistivity and ground-penetrating radar surveys were conducted at Wiang Tha Kan Archaeological Site located in Chiang Mai Province, northern Thailand. The objective of the ER surveys is to detect the existence of missing ancient moat. Archaeologists suspect four sides of Wiang Tha Kan moat according to common Lanna city plan but at present, there are only three sides remaining. Inverted ER profiles show indistinctive ER anomaly at expected locations of the missing moat extending from its present location. Therefore, the ER surveys may not be a suitable tool to support the existence of the missing moat. The GPR surveys were employed to detect an extended ancient wall at Wat Pra Chao Kam area located northeast of Wiang Tha Kan Archaeological Site. Some parts of the ancient wall have been excavated and the extended wall has been presumed to exist. The GPR surveys covered areas connected to the exposed wall. GPR anomaly maps at various depths show a linear anomalous zone connected to the exposed wall at 0.4-0.8 m depth. This zone may be interpreted as a location of the buried ancient wall. The GPR maps are useful for planning of future archaeological excavation.

Introduction:

Geophysical techniques have been effectively used in archaeological prospection. The geophysical methods that are commonly used for archaeological investigations include electrical resistivity (ER) and ground-penetrating radar (GPR) surveys.

ER survey is a geophysical technique to investigate the subsurface resistivity distribution under an area of interest[1]. ER technique utilizes transmitting current into the ground and measurement of the resulting voltage differences. Subsurface resistivity can be estimated from the voltage measurements. The subsurface resistivity is related to various geological parameters such as the mineral and fluid content, porosity and degree of water saturation in the soil and rock. ER survey has been applied not only for geological investigations but also for archaeological prospection[2,3].

GPR survey is a nondestructive high-resolution geophysical technique used to image and map structures in the shallow subsurface that can accurately map the spatial extent of near-surface objects and archaeological features[4,5]. The technique is based on the propagation, reflection and scattering of electromagnetic (EM) waves consistent with changes in subsurface electrical properties. GPR has become an important method in archaeological exploration in the past three decades[6].

In this study, the ER and GPR methods were performed in the northeastern area of Wiang Tha Khan Archaeological Site. The site is located approximately 35 km south of Chiang Mai City in San Pa Thong District, Chiang Mai Province, northern Thailand. Archaeologists presume four sides of Wiang Tha Kan moat according to common ancient Lanna Kingdom city plan but at present, there are only three sides of the moat remaining (Figure 1). Therefore, the ER survey was applied to detect the existence of the north-eastern missing ancient moat.

The GPR surveys were also employed at Wiang Tha Kan archaeological site. The purpose of the GPR surveys is to detect an extended ancient wall at Wat Pra Chao Kam area situated nearby the presumed north-eastern part of the missing moat (Figure 1). Archaeologists have excavated some parts of the ancient wall and they believe that an extended part of the wall may exist (Figure 2).

(a)

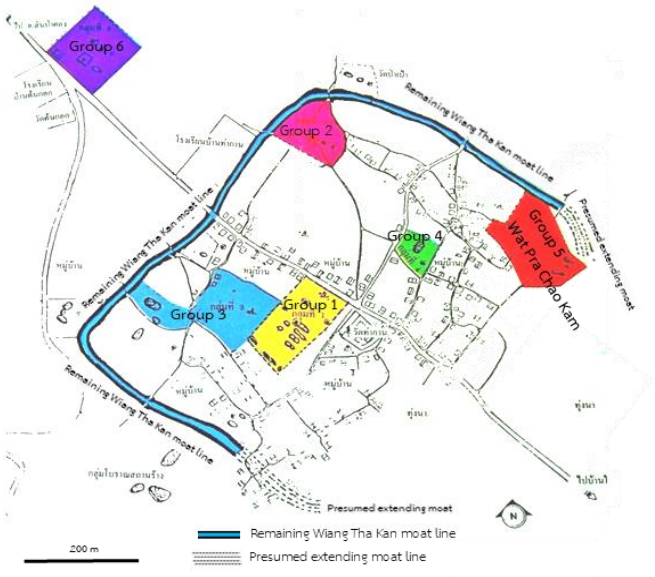

(b)

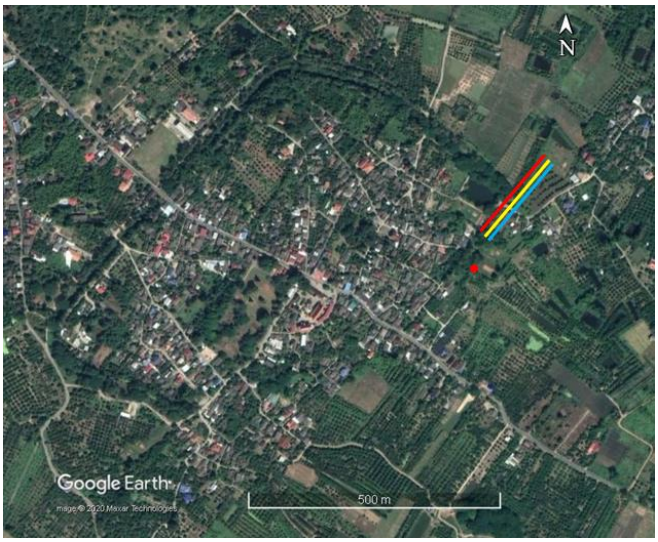

Figure 1

(a) Plan of Wiang Tha Kan archaeological site. (b) Present day Google Earth satellite image of Wiang Tha Kan Archaeological site. Red, yellow, and blue lines are ER profile locations. Red dot is GPR survey area.

Figure 2

Excavated ancient wall at Wat Wat Pra Chao Kam area, Wiang Kum Kam Archaeological Site (Photo looking north).

Methodology:

Three parallel 2D ER profiles were collected across the north-eastern presumed extending moat. All the ER profiles were oriented in the northeast-southwest direction (Figure 1b) with a profile length of 200 m. The separation distance of the red and yellow profiles was 20 m while that of the yellow and the blue profiles were 8 m. The ER data were collected using 4-channel ABEM TERRAMETER SAS4000 with ES10-64C electrode selector. A minimum of 5 m electrode spacing of a dipole-dipole configuration was employed. The ER data were inverted using RES2DINV software[1].

In this study, the GPR surveys were performed using an X-Y perpendicular gridding method, which equally spaced parallel GPR profiles both in X, and Y directions were acquired. The GPR profile spacing was 0.3 m covering an area of approximately 160 m^2 connected to the exposed wall in Wat Pra Chao Kam area (Figure 1a and Figure 2). The GPR data were collected using the pulseEKKO PRO GPR system with 250 MHz and 500 MHz center frequencies. The GPR data were processed using the EKKO_Project software package with standard processing steps including dewow, time-zero correction, background subtraction, frequency filtering, migration, and envelope attribute analysis[5]. Then GPR anomaly maps were generated for data interpretation.

Results and Discussion:

Inverted ER profiles are shown in Figure 3. Locations of the extended moat are presumed to be present on all three ER profiles at the surface distance between 90 and 120 m and at a depth less than 10 m. Note that the moat at the present day is approximately 17 m wide and 8 m deep. A suspect moat location is found on the yellow resistivity profile where a relatively low resistivity anomalous zone is present at the surface distance of 87 to 97 m. However, such an anomalous zone at a similar surface distance is not shown on the red and blue resistivity profiles.

GPR envelope anomaly maps at various depths of 250 MHz and 500 MHz GPR data are shown in Figure 4 and 5, respectively. The depth is converted using an approximate 0.11 m/ns velocity of the soil. A linear GPR anomalous zone at location connected to the excavated ancient wall is present on the 250 MHz maps from the depth of about 0.4 m and below as shown in the black rectangles in Figure 4. This zone may be interpreted as a buried wall, which is possible to extend further to the eastern side. Similar locations of the linear GPR anomaly are also shown on the 500 MHz maps but with comparatively less prominent (Figure 5).

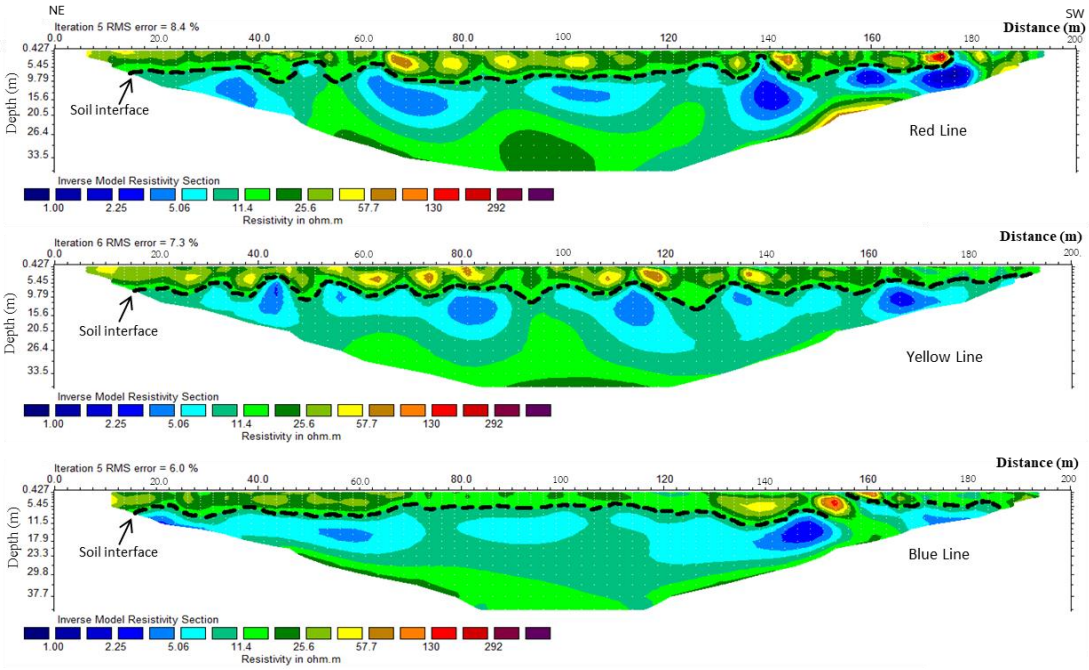

Figure 3

Inverted ER profiles across the north-eastern presumed extending moat of Wiang Tha Kan Archaeological Site.

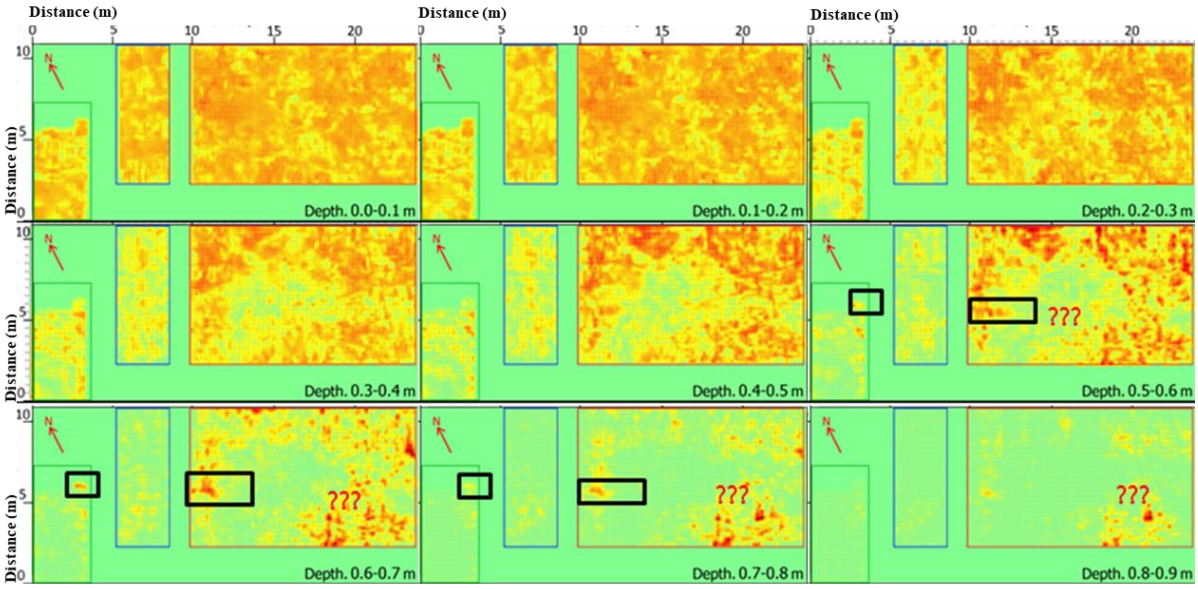

Figure 4

250 MHz GPR anomaly maps at various depths of Wat Pra Chao Kam surveyed area, Wiang Tha Kan Archaeological site.

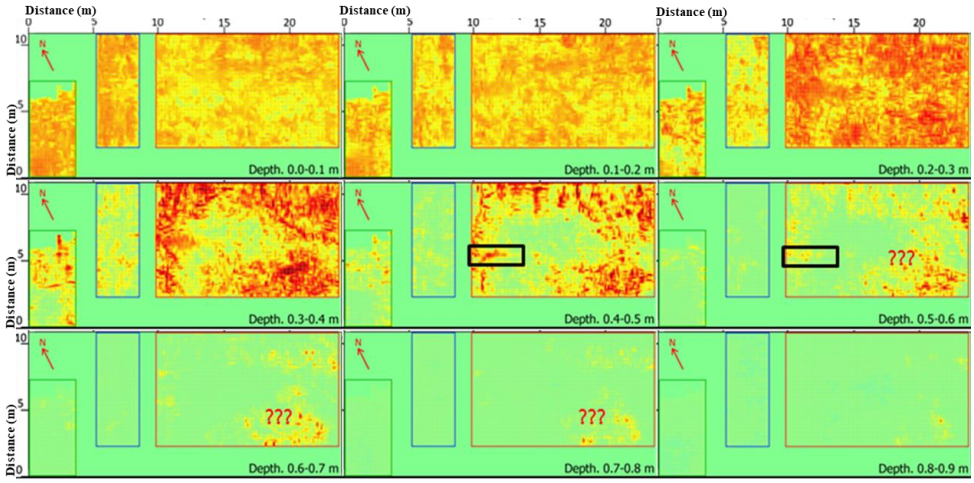

Figure 5

500 MHz GPR anomaly maps at various depths of Wat Pra Chao Kam surveyed area, Wiang Tha Kan Archaeological site.

Conclusions:

The ER profiles show an indistinctive anomaly of ER at expected locations of buried moat extending from their present locations. Therefore, the ER surveys may not be a suitable tool to support the existence of the missing moat. The GPR anomaly maps show a linear anomaly extended from the exposed wall at 0.4-0.8 m depth that may be interpreted as a zone of a buried ancient wall. The GPR results from this study are useful for planning of future archaeological excavations at the site.

Acknowledgements:

This study was sponsored by the Faculty of Science, Chiang Mai University.

References:

1. Loke MH, Rucker D, Dahlin T, Chambers JE. Recent advances in the geoelectrical method and new challenges: A software perspective. FastTimes. 2019; 24: 56-62.
2. Drahor MG. Integrated geophysical studies in the upper part of Sardis Archaeological Site, Turkey. J Appl Geophy. 2006; 59: 205-223.
3. Cardarelli E, Fischanger F, Piro S., Integrated geophysical survey to detect buried structure for archaeological prospecting, a case-history at Sabine Necropolis (Rome, Italy). Near Surf. Geophys. 2008; 6: 15-20.
4. Davis JL, Annan AP. Ground penetrating radar for high-resolution mapping of soil and rock stratigraphy. Geophys. Prospect. 1989; 37: 531–551.
5. Khwanmuang W, Udphuay S. Ground-penetrating radar attribute analysis for visualization of subsurface archaeological structures. Lead. Edge. 2012; 31:946-949.
6. Udphuay S, Paul VL, Everett, ME, Warden RR, Ground-penetrating radar imaging of twelfth century Romanesque foundations beneath the thirteenth century Gothic abbey church of Valmagne, France. Achaeol. Prospect. 2010; 17:199-212.

A_011_PA: THE STUDY OF PHASE TRANSITION TEMPERATURE OF LIQUID MIXTURES BY LIGHT SCATTERING TECHNIQUE

Kachain Dangudom,* Weerapong Kainta

Department of Physics, Faculty of Science, Naresuan University, Phitsanulok, Thailand
*e-mail: kachaind@nu.ac.th

Abstract:

This research was studied phase transition temperature of the liquid mixtures by using the light scattering technique. This is established a system using the laser wavelength 650 nanometers. The laser beam was focused on the center of the sample cell which contained a liquid mixture. Two liquid mixture samples were used in this research are methanol-cyclohexane and methanol-hexane. The experiment was varied temperature during 30.00-60.00 degree Celsius with the resolution of 0.01 degree Celsius and then measured the intensity of light scattering at angle 0 and 90 degree. At the critical temperature, the liquid mixtures are opaque and the intensity of light scattering at angle 90 degree is maximum. This experiment was studied phase transition temperature in two method, first start from the liquid mixture was separated then increase temperature to critical opalescence define as phase combination temperature. The second method start from the liquid mixture was mix well then decrease temperature to critical opalescence define as phase separation temperature. The liquid mixture of methanol and cyclohexane at a ratio of methanol 29%, It was found that the phase combination temperature is 46.90 degree Celsius and phase separation temperature is 47.00 degree Celsius. When changing the ratio of methanol was 26% 28% 30% and 32% the phase combination and phase separation temperatures were increase. The liquid mixture between methanol and hexane at a ratio of methanol 22% would bring the phase combination and phase separation temperature to a minimum. When decrease or increase the ratio of methanol to 20%, 21%, 23% and 24%, the phase separation and phase combination temperatures would be increased. Phase combination and phase separation temperature of liquid mixture methanol-cyclohexane and methanol-hexane are different. The ratio of liquid mixture which has lowest critical temperature be found and can define as critical composition.

A_012_OA: NATURAL RADIOACTIVITY MEASUREMENT AND EXCESS LIFETIME CANCER RISK EVALUATION IN SURFACE SOIL AND BEACH SAND SAMPLES COLLECTED FROM RAYONG PROVINCE, THAILAND

Prasong Kessaratikoon,[1,*], Ruthairat Boonkrongcheep,[2] Sitthipong Polthum[3]

[1]Asst. Prof. Dr., Nuclear and Material Physics Research Unit (NuMPRU), Department of Basic Science and Mathematics, Faculty of Science, Thaksin University, Songkhla Campus, Muang, Songkhla, 90000,Thailand
[2]Research Assistant, Nuclear and Material Physics Research Unit (NuMPRU), Department of Basic Science and Mathematics, Faculty of Science, Thaksin University, Songkhla Campus, Muang, Songkhla, 90000,Thailand
[3]Nuclear Scientist, Thailand Institute of Nuclear Technology (Public Organization) (TINT) 9/9 Moo 7 Saimoon Sub-District, Ongkharak District, Nakhon Nayok, 26120, Thailand
*e-mail: prasong_mi@hotmail.com

Abstract:

Specific activities of natural (^{40}K, ^{226}Ra and ^{232}Th) and anthropogenic (^{137}Cs) radionuclides in 230 surface soil and beach sand samples collected from the areas where have a dense population, invested and have been operated for industrial activities from eight districts (Mueang, Ban Chang, Nikhom Phatthana, Pluak Daeng, Ban Khai, Wang Chan, Khao Chamao and Klaeng) and one beach (Mae Rumphueng beach) in Rayong province, Thailand, have been studied, analyzed and presented. Experimental results were obtained by using a high-purity germanium (HPGe) detector and gamma spectrometry analysis system. The standard reference materials (IAEA/Soil-375) was borrowed from the Office of Atoms for Peace (OAP) to calibrate and evaluate all of the specific activities of required radionuclides. Experimental set-up and all measurement were performed and carried out at Thailand Institute of Nuclear Technology (Public Organization). In addition, the frequency distribution of all measured specific activities of natural (^{40}K, ^{226}Ra and ^{232}Th) and anthropogenic (^{137}Cs) radionuclides were also studied, analyzed and calculated the suitable medium values of all distributions. According to the asymmetrical distribution, the medium values of specific activities of all required radionuclides should be the median values. Furthermore, the median values of natural (^{40}K, ^{226}Ra and ^{232}Th) radionuclides were also used to evaluate the absorbed dose rates in air (D), the radium equivalent (Ra_{eq}), the external hazard index (H_{ex}), the annual effective dose rate (AED_{out}) and Excess Lifetime Cancer Risk (ELCR) for the studied area. Besides, the calculated results were also compared to research data in the southern region of Thailand, the Office of Atoms for Peace (OAP) annual report, global radioactivity measurements and the evaluations and the recommended values which were proposed by United Nations Scientific Committee on the Effects of Atomic Radiation (UNSCEAR, 1988, 1993, 2000). It was found that most of the results were significantly lower than the recommended values as reported by UNSCEAR. Moreover, the radioactive contour map (RCM) for the investigated areas were also constructed and presented.

A_013_PA: THE EFFECT OF SUGARCANE BAGASSE ASH ON ELECTRICAL CAPACITY AND TIME LAG OF PORTLAND CEMENT MORTARS

Thanongsak Nochaiya,[1,2,*] Kritsada Khhaena,[1] Anucha Kaewpoonsuk,[1,2] Pincha Torkittikul,[3] Panisara Disuea[1]

[1]Department of Physics, Faculty of Science, Naresuan University, Phitsanulok 65000, Thailand
[2]Research Center for Academic Excellence in Applied Physics, Naresuan University, Phitsanulok 65000, Thailand
[3]Civil Technology, Faculty of Industrial Technology, Lampang Rajabhat University, Lampang 52000, Thailand
*e-mail: thanongsakno@nu.ac.th

Abstract:

Sugarcane bagasse ash (SCBA) is a by-product from agricultural industry which use as a partial substitution of Portland cement. This research studied flow, electrical capacity and time lag of mortars blended with sugarcane bagasse ash at a percentage ratio of 0-30 by weight of cement. For mortars preparation, a water to binder ratio of 0.5 was conducted for all mixes and then cured in air and in water at 3, 7, 14, 21 and 28 days before test. The results showed that the flow of SCBA-mortars was found to increase when the ratio of SCBA increased. The electric capacity of the mortars was presented to decrease with increasing curing times. Moreover, it was found that the electrical capacity of the mortars after curing in water was higher than that of curing in air. In addition, the mortars blended with SCBA can increase the time lag as well as to reduce the heat from outside to inside of the building.

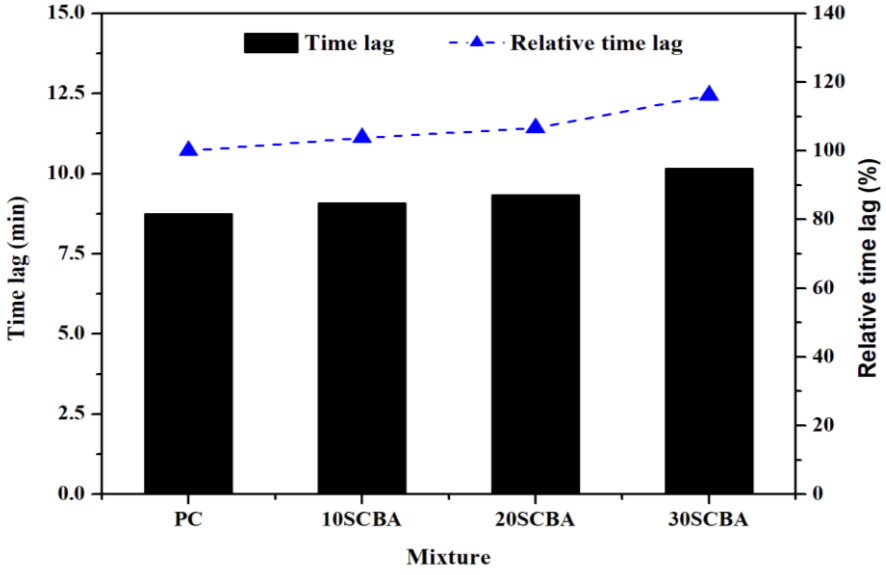

Figure 1

Time lag and relative time lag of mortars containing SCBA 0-30 wt% after curing at 28 days.

A_014_PA: CRYSTALLOGRAPHIC ORIENTATION EFFECT ON THE TUNNELING SPECTROSCOPY ACROSS A HALF-METAL/SEMICONDUCTOR WITH DRESSELHAUS SPIN-ORBIT COUPLING JUNCTION

Achara Siripanadorn,[1] Thanakrit Onsri,[2] Aek Jantayod [2,*]

[1]Department of Physics, Faculty of Science, Udon Thani Rajabhat University, Udon Thani 41000, Thailand
[2] Department of Physics, Faculty of Science, Naresuan University, Phitsanulok 65000, Thailand
*e-mail: aekj@nu.ac.th

Abstract:

Tunneling spectroscopy across a half-metal (HM)/semiconductor with Dresselhaus spin-orbit coupling (DSOC) junction was theoretical studied using the scattering method and the free-electron approximation in a two-dimensional system. With a focus on how the crystallographic orientation of the DSOC affects the charge and spin polarization. It was found that the crystal face (100) makes a negative perpendicular to the normal wave vector of the system, resulting in a maximum value of the conductance spectrum and the spin polarization. In addition, the electron incident angle injection can cause a difference in the transmission probability with up-spin and down-spin, corresponding to the higher charge and spin polarization across the junction.

A_015_PF: EFFECTS OF UPSTREAM ION SPEED ON THE ION ACCELERATION PROCESS NEAR X-LINE OF COLLISIONLESS MAGNETIC RECONNECTION: A TEST-CHARGE STUDY

Thapana Nakprapatsorn,[1] Kittipat Malakit,[1,*] Pakkapawn Prapan[2]

[1]Department of Physics, Faculty of Science and Technology, Thammasat University, Pathum Thani, Thailand
[2]Department of Physics, Faculty of Science, Mahidol University, Bangkok, Thailand
*e-mail: kmalakit@gmail.com

Abstract:

To study the ion energy gain near the X-line of collisionless magnetic reconnection, we obtain the electric and magnetic fields of a reconnection at a steady state from a particle-in-cell simulation. Ions are then released with different speed into the fields upstream of reconnection. Their motions are updated as test charges using Boris algorithm. We found that, for ions that have speed above 0.5 of the Alfven speed based on the upstream density and magnetic field strength, the higher the upstream ion speed, the higher the energy gain. We also found that these ions spend time gaining energy for about the same amount of time on average, independent of their initial speed. We conclude that the reason the higher speed ions gain more energy is because they have larger radius, allowing higher speed ions to travel further along the reconnection electric field before exiting the reconnection region.

Introduction:

It has been known that during magnetic reconnection process, upstream magnetic energy is partially converted to the downstream plasma kinetic energy1. The kinetic energy can be categorized into two types: the kinetic energy of the bulk flow and the kinetic energy of the heating.

To understand the bulk flow and heating, many studies have been done[2,3,4,5,6,7].

However, the understanding of the kinetic energy of the bulk flow and the kinetic energy of heating created during reconnection is still not yet complete.

In this study, we take a different perspective. We aim to understand how much each particle gain their energy. Instead of going with fully kinetic particle-in-cell simulations, we use a test-charge approach. So, we can control the parameters such as the ion initial speed and the direction of the releasing ions easily. We believe the insight obtained from this study can fill some holes in understanding the conversion of magnetic energy into the plasma kinetic energy.

Methodology:

Although our study will eventually be a test-charge approach, we need to get the electric and magnetic fields in the reconnection region to be as realistic as possible. We choose to get the fields from a fully-kinetic particle-in-cell simulation (P3D code[9]) of magnetic reconnection. In the simulation, the magnetic field strengths are normalized to the upstream magnetic field of reconnection B_0. Number densities are normalized to the upstream plasma density of reconnection n_0. Masses are normalized to the ion mass m_i. Times are normalized to the cyclotron time $\omega^{-1}{}_{ci0} = (eB_0/m_i c)^{-1}$. Lengths are normalized to the ion inertial length $d_{i0} = c/\omega_{pi}$ at the reference density. Speeds are normalized to the ion Alfvén speed $c_{A0} = B_0/(4\pi m_i n_0)^{1/2}$. Electric fields are

normalized to $E_0 = c_{A0}B_0/c$. And finally, temperatures (with the Boltzmann constant) are normalized to $kT_0 = m_i c^2{}_{A0}$. A snapshot of the fields is taken after the reconnection have reached a steady state.

After the fields are obtained we release ions into the fields (see Figure 1 for example), the ion motion is updated using Boris algorithm. Ions are released with different initial speeds ranging from $\frac{1}{4}v_{th}$ to $8v_{th}$, where v_{th} = sqrt ($2kT/m_i$) is the thermal speed of ions. Note that the ion mass is 1 and the ion temperature in this simulation is kT=0.25 $m_i c^2{}_{A0}$, making the thermal speed to be 0.71 c_{A0}. All of the ions is released in the upstream where the motion of ions is still $\vec{E} \times \vec{B}$ drift. Furthermore, for each initial speed, the ions are released in 8 different directions: 0, 45, 90, 135, 180, 225, 270, 315 degrees with respect to z in y-z plane.

Results and Discussion:

As seen in Figure 2, once an ion is released into the fields, it will go through different phases of motion. Initially, it undergoes an $\vec{E} \times \vec{B}$ drift motion. The ion is mostly moving in xy-plane without changing its position much in the z-direction. The kinetic energy of the ion oscillates around a value, which is taken to be $E_{k_{in}}$ (Figure 3). After it goes into the diffusion region, it undergoes a meandering motion changing its position in z-direction[8]. Since the electric field has the z-component, it does work on ions that moves in the z-direction leading to a change in ion kinetic energy. The kinetic energy goes up for a period of time before the ion stops gaining energy and leaves the diffusion region with the energy $E_{k_{out}}$ (Figure 3). The time the ion spends gaining the energy is taken to be t_{reconn} (Figure 3). Local peaks in kinetic energy occurs due to the ions goes through the bipolar structure of E_y. Since the meandering of the ion leads to back and forth motion over the E_y structure, net work done by the E_y .is zero. However, whenever an ion goes through the bipolar structure, it gains and loses energy in a short time period leading to the local peaks of energy seen in Figure 3.

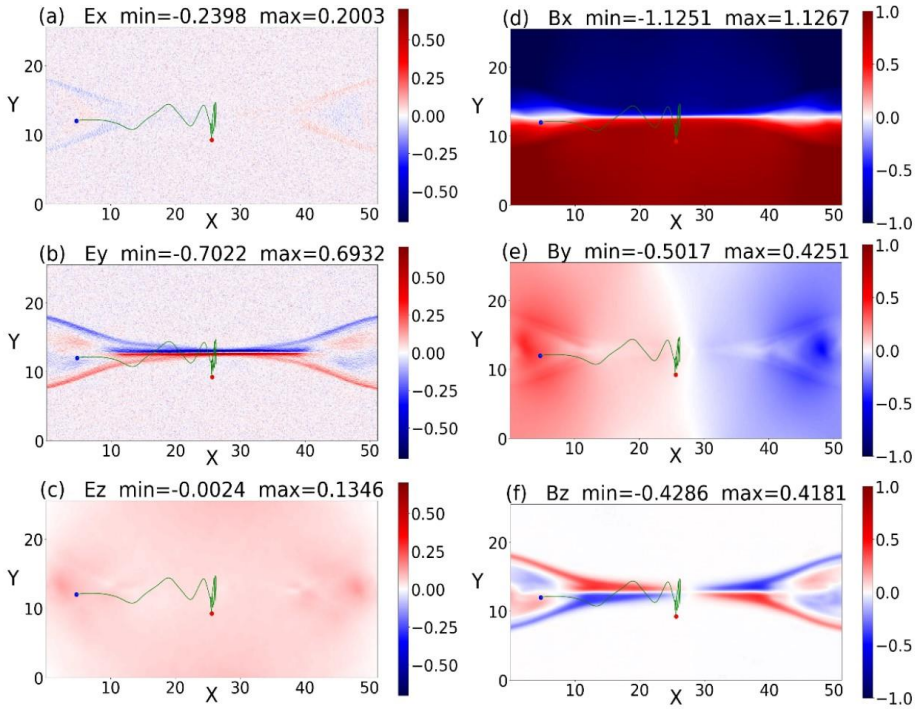

Figure 1

Trajectory of ion overplotted on contours of magnetic field and electric field: (a) electric field in x direction, (b) electric field in y direction, (c) electric field in z direction, (d) magnetic field in x direction, (e) magnetic field in y direction, and (f) magnetic field in z direction. Red point and blue point represent starting point and last point respectively.

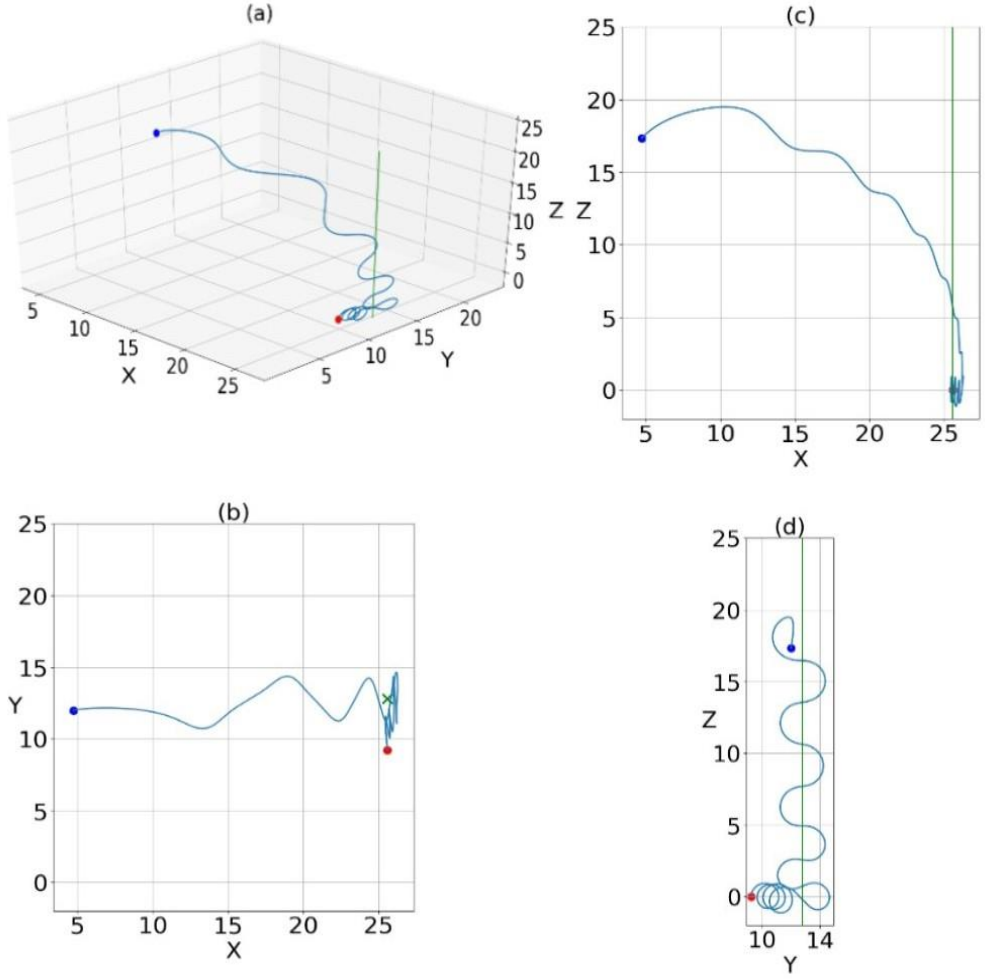

Figure 2

Trajectory of ion in a reconnection region. Red point, Blue point and green line represent starting point, ending point and X-line respectively. (a) 3-dimension of motion. (b) xy-plane, (c) xz-plane and (d) yz-plane.

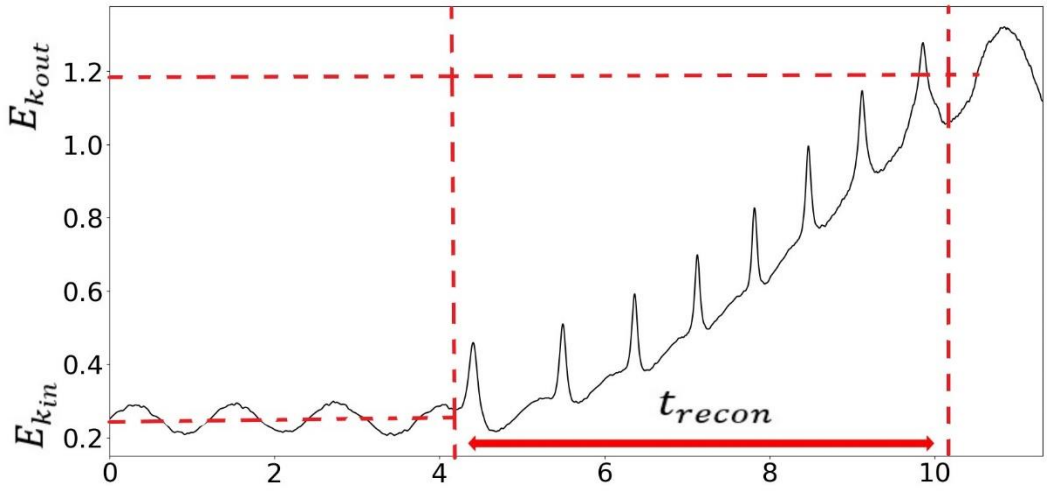

Figure 3

kinetic energy vs. time of the ion seen in Figure 1 and 2

Analyzing ions with different initial upstream speed, we found some interesting behaviors of the energy gain ($E_{k_{out}} - E_{k_{in}}$). We found that there is a local bump in energy gain for ions with initial speed around 0.4-0.5, which is around the outflow speed for this reconnection. Beyond the speed of 0.5, the energy gain increases when the initial upstream speed increases. Then the energy gain seems to level off at very high upstream speeds (See Figure 4a). However, when looking at the energy gain per initial energy ($(E_{k_{out}} - E_{k_{in}})/E_{k_{in}}$) the ratio is high at low initial upstream speed and low at high initial upstream speed (see Figure 4b.). The results here are about the same for all three initial position. So the results here is not that sensitive to ion initial position as long as the ion start moving with $\vec{E} \times \vec{B}$ drift motion.

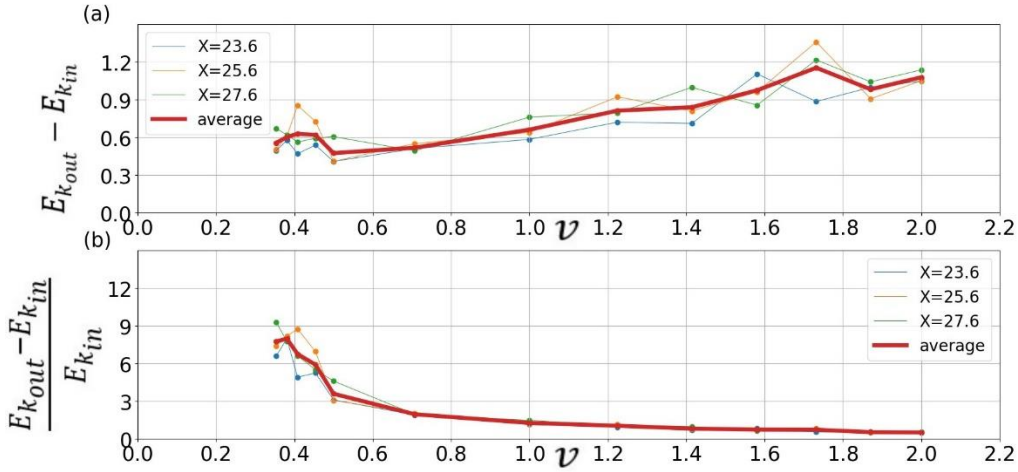

Figure 4

Increasing of kinetic energy during travel through reconnection. (a) show energy gain of ions. (b) show percentage of energy gain.

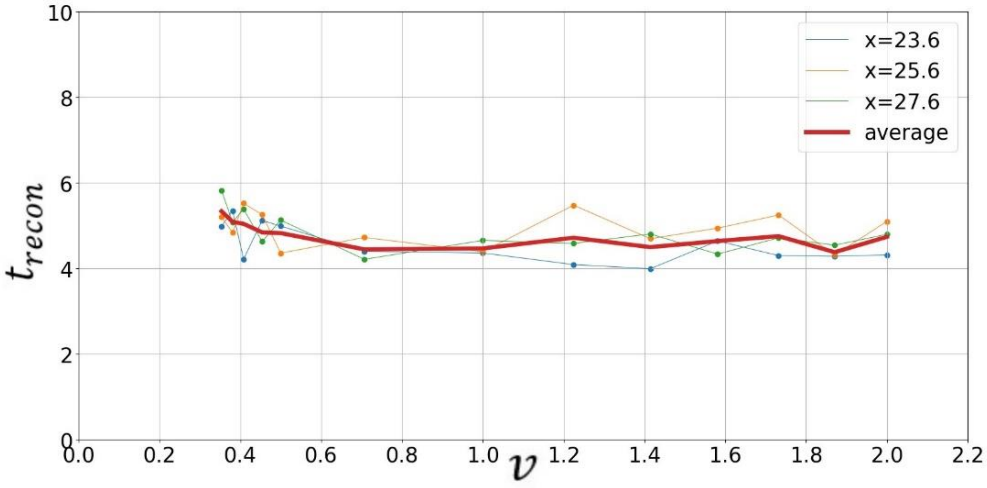

Figure 5.

Time that ions spend on diffusion region gaining their kinetic energy. We use 3 different starting positions but motion is still $\vec{E} \times \vec{B}$ drift.

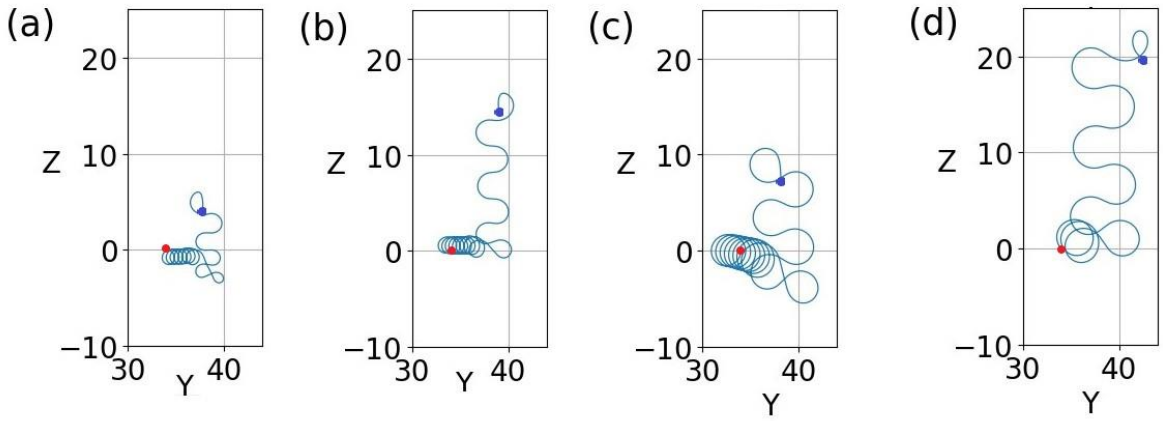

Figure 6.

Ions spend equal time with the other but have different energy gain. (a), (b) and (c), (d) is the same speed. Each of figures have a different distance on z direction. Red point and bule point represent starting point and ending point respectively.

Thinking that time might play a role in controlling the ion energy gain, we study the time each ion spends gaining energy and found that on average ions of different initial speed spends about the same time gaining their energy (Figure 5). This is surprising. So, what makes faster ions gain more energy than slower ions?

Looking at trajectories of ions that spend similar amount of time gaining energy, we found the answer why faster ions gain more energy. Comparing ion with slower speed Figure 6(b) and ion with faster speed Figure 6(d), they spend equal time, but the faster one can gain more energy since the faster ion has larger radius. This is because it can travel longer distances in the z direction.

We also found that diffusion region entering angle matters in dictating how much energy an ion can gain. Figure 6(a) and 6(b) show trajectory of ions with the same initial spped and they spend about the same time gaining energy. However, they gain different energy because in Figure 6(a) the ion enters the diffusion region such that they spend some time decreasing energy first while in Figure 6(b) the ion that enter the diffusion region is ready to move up in the z-direction and gain energy from the beginning.

Conclusion:

From our study, we have found that the higher the ion initial speed, the more the energy gain. However, the time ions spend gaining energy is about the same for all ion speed. The faster ions gain more energy due to their larger radius allowing them to move up in the z-direction more. Finally, we also found that diffusion region entering angle is also an important factor in ion energy gaining.

Acknowledgements:

This work is partially support by Thailand Science Research and Innovation (RTA6280002)

References:

1. Parker EN. J. Geophys. Res. 1957;62;509
2. Drake JF, Swisdak M, Phan TD, Cassak PA, Shay MA, Lepri ST, Lin RP, Quataert E,Zurbuchen TH. J. Geophys Res. 2009;144:A05111.
3. Wygant JR, Keiling A, Cattell CA, Johnson M, Lysak RL, Temerin M, Mozer FS, Kletzing CA, Scudder JD, Peterson W, Russell CT, Parks G, Brittnacher M, Germany G, Spann J. J. Geophys Res. 2000;105:18675-18692.
4. Haggerty CC, Shay MA, Drake JF, Phan TD, McHugh CT. Geophysical Research Letter. 2015;42(22):9657-9665.
5. Haggerty CC, Shay MA, Chasapis A, Phan TD, Drake JF, Malakit K, Cassak PA, Kieokaew R. Physics of Plasmas. 2018;25:102120.
6. Birn J, Drake JF, Shay MA, Rogers BN, Denton RE, Hesse M, Kuznetsova M, Ma ZW, Bhattacharjee A,Otto A, Pritchett PL. Journal of Geophysical Research. 2001;106: 3715-3719.
7. Cassak PA. Shay MA. Physics of Plasmas. 2007;14:102114.
8. Speiser TW. J. Geophys Res. 1965;70:4219.
9. Zeiler A, Zeiler D, Drake JF, Roger BN, Shay MA, Scholer M. J. Geophys Res. 2002;107:1230.

B_001_OA

B_001_OA: ON nd-$K^*(n,r)$-FULL HYPERSUBSTITUTIONS

Khwancheewa Wattanatripop,[1,*] Thawhat Changphas,[2]

Department of Mathematics, Faculty of Science, Khon Kaen University, Khon Kaen, Thailand 40002
Department of Mathematics, Faculty of Science, Khon Kaen University, Khon Kaen, Thailand 40002
*e-mail: khwancheewa12@gmail.com

Abstract:

Term is one of the fundamental concepts of the study in universal algebra, it plays a major role for classifying algebras into subclasses. Sets of terms of type τ are called tree languages. The main aim of this work is to introduce a specific kind of tree language which defined by some classes of full terms. Based on the notion of $K^*(n,r)$-full terms defined by the authors, nd-$K^*(n,r)$-full hypersubstitutions are defined. It turns out that the extension of an nd-$K^*(n,r)$-full hypersubstitution is an endomorphism of algebra of tree languages of nd-$K^*(n,r)$-full terms.

B_002_OF: IMPROVED MASK FOR ADAPTIVE FRACTIONAL ORDER DIFFERENTIAL METHOD FOR MEDICAL IMAGE ENHANCEMENT

Wasin Tranghiranyathorn*, Ratinan Boonklurb

Department of Mathematics and Computer Science, Faculty of Science, Chulalongkorn University, Bangkok, Thailand
e-mail: tr.wasin@gmail.com*, ratinan.b@chula.ac.th

Abstract:

In this paper, we propose a construction of the new 5×5 fractional differential mask that uses sixteen directions of gradient operator and weights each pixel in the mask by the Euclidian distance from the center of the mask to reduce the over-valuation of the gradient from distant pixels. Then, we apply this new mask to the Adaptive Fractional Differential Algorithm (AFDA). The AFDA allows the optimal fractional order of each pixel to be obtained using an adaptive function constructed based on the area feature of image. Experimental results show that, for medical images, the AFDA with the new mask gives better image enhancement than the original AFDA, while also contains more appropriate texture information from its neighborhoods. It makes edges clearer, preserving texture details and improving the contrast of medical images. These improvements can be particularly helpful to doctors' diagnosis using medical imaging techniques.

Introduction:

Medical image quality has become an indispensable part of modern medicine and directly influences the accuracy of doctors' diagnoses and treatments. Low resolution and contrast in medical images have made correct diagnosis difficult; this directly influences the speed and accuracy of doctors' diagnoses. Therefore, it is necessary to improve medical image enhancement to reflect the information of an illness more clearly and accurately[7, 8, 18].

Fractional differential, which is a theory of arbitrary order derivatives, is generalized from integral order differential[4, 10]. Compared with integral order differential approaches, fractional differentials applied to image processing can enhance edges, make texture details clearer and preserve smooth areas[2, 9, 13]. Traditional fractional differentials use the same fractional order to process edges, textures and smooth areas of image; however, while edges would be enhanced by high fractional orders, weak textures and smooth areas would be ignored, and while weaker textures and smoother areas would be preserved by low fractional orders, edges would be weakened. Thus, image enhancement is difficult to attain in practice. To manage these issues, traditional fractional differential algorithms have been developed for digital image processing in[3, 5, 12, 14]. Adaptive fractional derivatives for image denoising problems have also been considered[1, 16, 17]. Especially, in 2015, Li and Xie[6] proposed Adaptive Fractional Differential Algorithm (AFDA) for medical image enhancements that can extract the edges of an image accurately and enhance them while preserving smooth areas and weak textures. It is an evidence that the AFDA gives better results comparing with the existing methods, namely the histogram equalization algorithm, Sobel, Laplacian, traditional fractional differential methods, which are 0.5-order, 0.8-order and 1-order, respectively.

In this work, we present a construction of the new fractional differential mask to improve the AFDA that proposed by Li and Xie[6]. Then, we evaluate the effect of the image enhancement by visual analysis, quality of the edge detection and some metrics, and compare the results with the original AFDA.

Related theories and related works:

The purpose of this section is to recall the necessary theoretical background about the application of fractional differential in signal processing which was presented in[6] and to make this paper self-contained for the readers who are not familiar with such approach.

Fractional Differentiation Definition

There are three classical definitions of fractional calculus, namely, the Grünwald–Letnikov (G-L) definition, the Riemann–Liouville (R-L) definition and the Caputo definition. The G-L definition is deduced from the expression of integer-order differential, whereas the R–L and Caputo definitions are derived from integer-order Cauchy integral formula. Since the G–L definition is less complex than the others and only uses one coefficient, the G–L definition is suitable for signal processing and it is the most popular definitions used in digital image processing.

Let $v \in \mathbb{R}^+$. Considering a function $f(t)$ on an interval $[a,b]$ which has m-order $(m = \lceil v \rceil)$ continuously differentiable. The v-order (G-L) fractional differential of $f(t)$ is defined by:

$$ {}_aD_b^v f(t) = \frac{d^v f(t)}{dt^v} = \lim_{h\to 0} h^{-v} \sum_{j=0}^{[(b-a)/h]} (-1)^j \binom{v}{j} f(t-jh), \quad (1) $$

where [ ] is the integral part and $\binom{v}{j}$ is the binomial coefficient.

When the interval $[a,b]$ of a signal $f(t)$ is divided into equal parts by taking the duration of the signal $h = 1$, then we let $n = \left[\frac{b-a}{h}\right] = [b-a]$ and the v-order fractional differential of $f(t)$ can be approximated by:

$$ \frac{d^v f(t)}{dt^v} \approx f(t) + (-v)f(t-1) + \frac{(-v)(-v+1)}{2} f(t-2) + \cdots + \frac{\Gamma(-v+1)}{n!\,\Gamma(-v-n+1)} f(t-n), \quad (2) $$

where Γ is the gamma function.

Realization of fractional differential masks

For the signal $f(x,y)$ in the region $[a,b] \times [c,d]$, we can extend (2) to obtain the backward difference of the v-order fractional partial differentials on the x- and negative y-coordinates, respectively, as:

$$ \frac{\partial^v f(x,y)}{\partial x^v} \approx f(x,y) + (-v)f(x-1,y) + \frac{(-v)(-v+1)}{2} f(x-2,y) + \cdots + \frac{\Gamma(-v+1)}{n!\,\Gamma(-v-n+1)} f(x-n,y) \quad (3) $$

$$ \frac{\partial^v f(x,y)}{\partial y^v} \approx f(x,y) + (-v)f(x,y-1) + \frac{(-v)(-v+1)}{2} f(x,y-2) + \cdots + \frac{\Gamma(-m+1)}{m!\,\Gamma(-v-m+1)} f(x,y-m), \quad (4) $$

where $n = [b-a]$ and $m = [d-c]$. Figure 1 shows the 3×3 partial fractional differential masks of the x- and y-axes which can be obtained from the first three coefficients of (3) and (4), namely 1, $-v$ and $\frac{v^2-v}{2}$.

				$\frac{v^2-v}{2}$	
$\frac{v^2-v}{2}$	$-v$	1		$-v$	
				1	

Figure 1. 3×3 partial fractional differential masks of the x- and y-axes.

Additionally, Li and Xie[6] can obtained eight masks in each direction (i.e., $0°, 45°, 90°, 135°$, $180°, 225°, 270°$, and $315°$) and the 5×5 mask of eight directions shown in Figure 2 is obtained by rotation and superimposing them. Each pixel of Figure 2 must be divided by $8 \times \left(1 + (-v) + \frac{v^2-v}{2}\right) = 8 - 12v + 4v^2$ to acquire the final 5×5 fractional differential mask. Finally, they used the final 5×5 fractional differential mask to process the medical images by considering airspace filtering of this mask convolution.

$\frac{v^2-v}{2}$	0	$\frac{v^2-v}{2}$	0	$\frac{v^2-v}{2}$
0	$-v$	$-v$	$-v$	0
$\frac{v^2-v}{2}$	$-v$	1×8	$-v$	$\frac{v^2-v}{2}$
0	$-v$	$-v$	$-v$	0
$\frac{v^2-v}{2}$	0	$\frac{v^2-v}{2}$	0	$\frac{v^2-v}{2}$

Figure 2. Superimposing of partial differential mask in 8 directions.

Adaptive fractional differential function

According to Li and Xie[6], they proposed the adaptive order v of fractional differential as

$$v = \begin{cases} \frac{M(i,j)-t}{M(i,j)}, & M(i,j) \geq t \text{ and } \frac{M(i,j)-t}{M(i,j)} \geq v_1 \\ v_1, & M(i,j) \geq t \text{ and } \frac{M(i,j)-t}{M(i,j)} < v_1 \\ v_2, & 2 < M(i,j) < t \text{ and } \frac{M(i,j)}{t} \geq v_2 \\ \frac{M(i,j)}{t}, & 2 < M(i,j) < t \text{ and } \frac{M(i,j)}{t} < v_2 \\ 0, & 0 \leq M(i,j) \leq 2 \end{cases} \quad (5)$$

where $M(i,j)$ is the average gradient of pixel, t is gradient threshold, $v_1$and v_2 are the thresholds of order which are defined by:

$$v_1 = \frac{M_{ed}-Q}{M_{ed}} \text{ and } v_2 = \frac{Q-M_{tex}}{Q}, \quad (6)$$

the parameter Q is the average gradient of the original image, M_{ed} and M_{tex} are the average gradients of edges pixels and texture pixels segmented by Otsu algorithm, respectively. Moreover, they determined threshold t via the improved Otsu algorithm.

An improved fractional differential mask:

In this section, we describe how to construct a new fractional differentiation mask and point out the advantages of the proposed mask. In order to strengthen the anti-rotation performance of AFDA, sixteen directions of the gradient operator are used to construct the new 5×5 fractional differential mask. First, Figure 3(a) shows a $0°$ direction of the gradient. Next, in Figure 3(b), we add a $22.5°$ direction (red dashed line). Here, we notice that the red dashed line passes through two pixels of the level of $-v$. Thus, we divide these $-v$ neighbors into two equal parts. After superimposing the gradient operator in $45°$ direction, the mask becomes Figure 3(c). We repeat this process until we get a full cycle as shown in Figures 3(d-h). Figure 3(i) shows the 5×5 mask of sixteen directions which is obtained by the sum of every value in each pixel of Figure 3(h).

To reduce the over-valuation of the gradient from distant pixels, we weight each pixel in the mask by the Euclidian distance from the center of the mask. Consider Figure 3(j). First, we label the center of the mask with $"0"$. Second, we label the layer of $-2v$ with $"1"$ and $"1'"$. Third, we label the layer of $\frac{v^2-v}{2}$ with $"2"$, $"2'"$ and $"2''"$. In Figure 3(j), the pixels labeled by

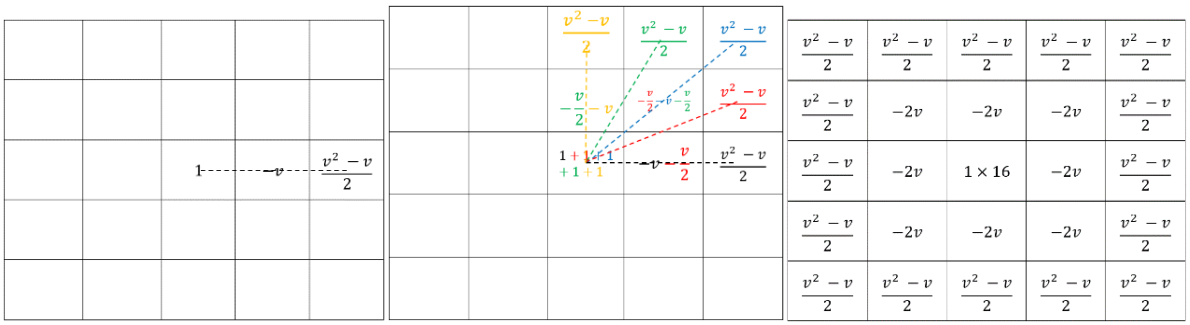

(a) (e) (i)

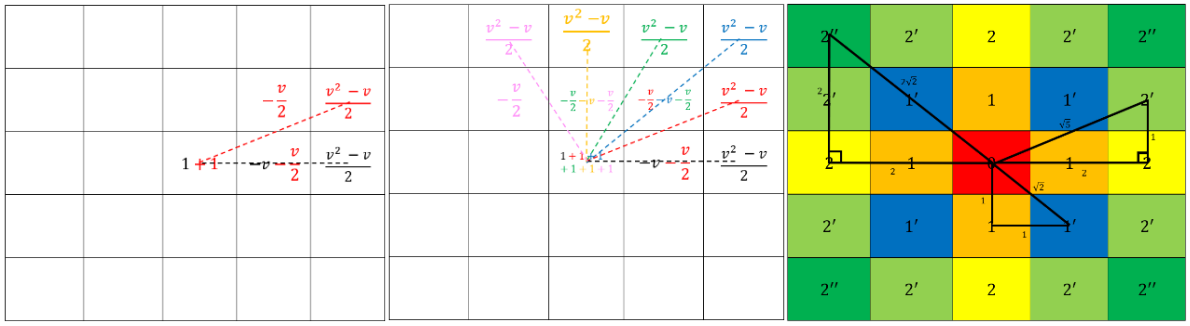

(b) (f) (j)

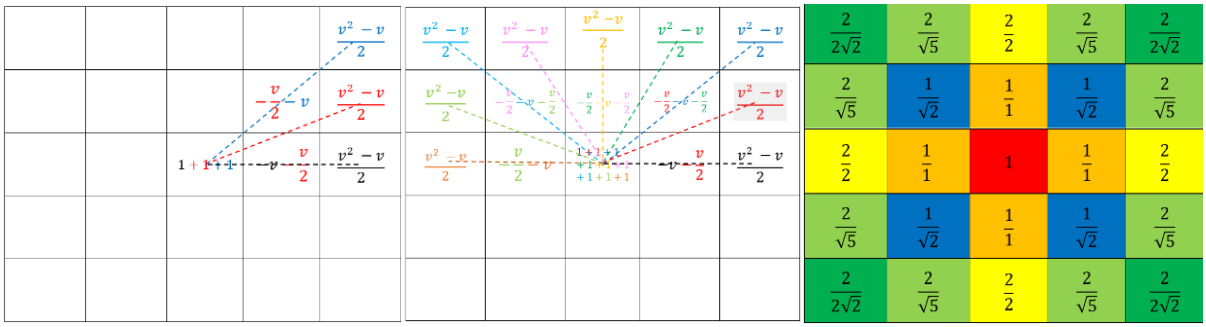

(c) (g) (k)

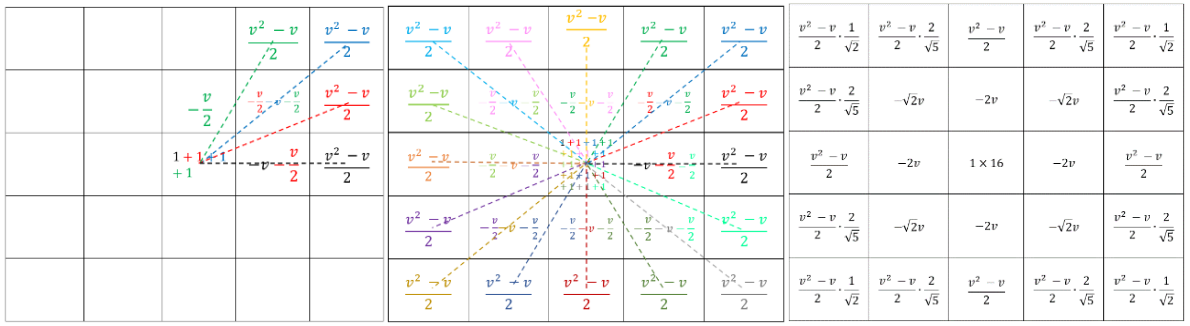

(d) (h) (l)

Figure 3. Construction of new fractional differential mask

"1" and "1′" are 1 and $\sqrt{2}$ unit away from the center, respectively. Therefore, we weight the gradient of 1-pixels and 1′-pixels with $\frac{1}{1}$ and $\frac{1}{\sqrt{2}}$, respectively, to decrease their values as shown in Figure 3(k). In Figure 3(j), the pixels labeled by "2", "2′" and "2′′" are $2, \sqrt{5}$ and $2\sqrt{2}$ unit away from the center, respectively. Therefore, we weight the gradient of 2-pixels, 2′-pixels and 2′′-pixels with $\frac{2}{2}$, $\frac{2}{\sqrt{2}}$ and $\frac{2}{2\sqrt{2}}$, respectively, to decrease their values as shown in Figure 3(k). Next, we multiply each pixel of Figure 3(i) by each pixel of Figure 3(k) componentwise to obtain our new 5×5 weighted fractional differential mask of sixteen directions as shown in Figure 3(l). Finally, we divide each pixel of Figure 3(l) by the sum of all values in the mask, $S = 16 + \left(-10 - 5\sqrt{2} - \frac{8\sqrt{5}}{5}\right)v + \left(2 + \sqrt{2} + \frac{8\sqrt{5}}{5}\right)v^2$. Note that S has no real root which implies that the denominator cannot be zero.

Results and Discussion:

We choose four medical images as shown in Figures 4(a) – 7(a) to represent common medical images. Figure 4(a) shows an image of ultrasound in pregnancy. Figure 5(a) shows a lung sectional CT image, Figure 6(a) shows a knee-joint MRI and Figure 7(a) shows a target of breast molybdenum image, respectively. The resolutions of all images are 256×256 and the gradient threshold t of these four original images can be obtained by using the improved Otsu algorithm[6]. The parameters v_1 and v_2 can be obtained by (6). The effect of image enhancement is evaluated by visual analysis, quality of the edge detection and some metrics.

Table 1 Parameters of these four images

Image	v_1	v_2	t
Ultrasonic image	0.7283	0.2406	5
CT image	0.7070	0.2875	13
MRI image	0.7324	0.2395	6
Target of breast molybdenum image	0.7514	0.2283	4

According to Li and Xie[6], the effect of image enhancement of the original AFDA was better when compared with those of the histogram equalization algorithm, Sobel, Laplacian, traditional fractional differential methods, which are 0.5-order, 0.8-order and 1-order, respectively. The results of the histogram equalization method which improve the brightness of the object. However, the local texture details are disappeared and the grays change unnaturally. The results of the traditional fractional differential methods. The 0.5-order method enhances edges and preserve some local texture details while the 0.8-order method strongly enhances edges but produces significantly more noise. The 1-order method can extract only the edges, it strongly vanishes weak textures and smooth areas in the image. In other words, the 1-order method extracts a large amount of marginal information, but weak textures and smooth areas are severely reduced, making it hard to see the complete structure of the image. Thus, the enhancement effects of the traditional fractional differential methods are not desirable. The original AFDA comprehensively considered global and local information in medical images and yielded better enhancement effects than the existing image processing methods. Thus, in this section, instead of comparing with the existing methods as mentioned above, we only compare the effect of image enhancement of the improved AFDA with the new mask with the original AFDA.

Evaluation by visual analysis

The original images (Figures 4(a) - 7(a)) have a low resolution and significant amounts of noise. Figures 4(b - c) and 7(b - c) show that the original AFDA and the improved AFDA with the new mask have enhanced the original image to some extent. Both of methods can enhance image edges and preserve weak textures and smooth areas concurrently. Considering both global and local information, the images processed by the improved AFDA with the new mask look clearer with weak textures and smooth areas preserved more appropriately. On the other hand, the images processed by the original AFDA sometimes look too sharp with undesirable noises (indicated by circles).

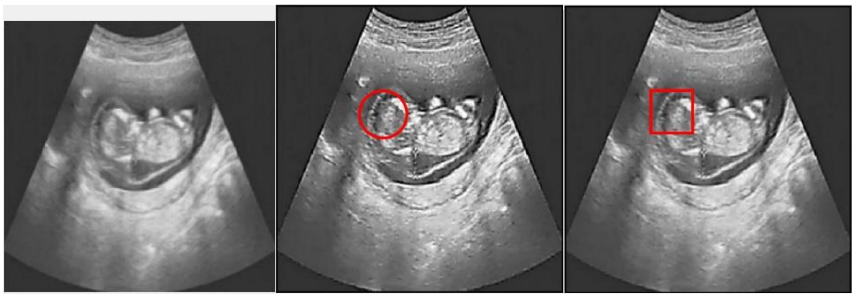

(a) Original image (b) Original AFDA (c) Improved AFDA

Figure 4. Type-B ultrasound image enhancement

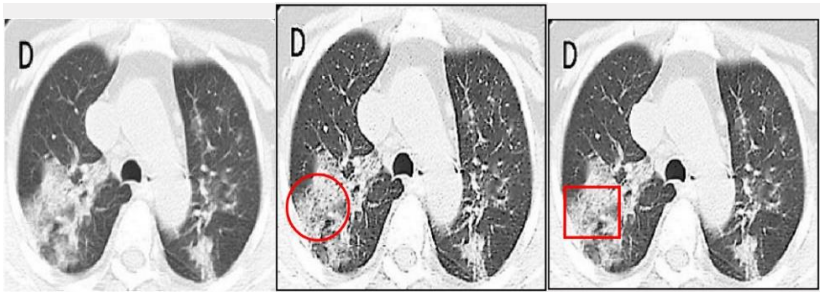

(a) Original image (b) Original AFDA (c) Improved AFDA

Figure 5. CT image enhancement

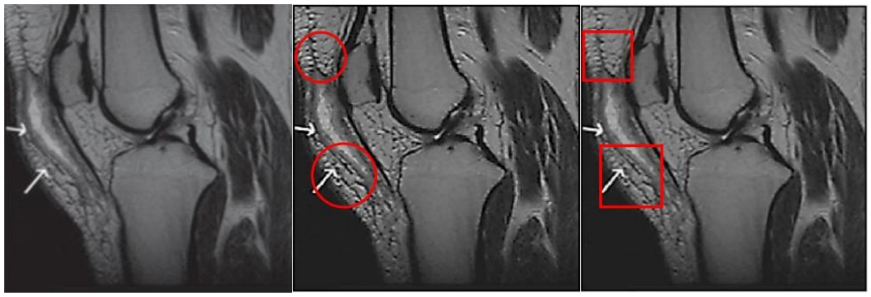

(a) Original image (b) Original AFDA (c) Improved AFDA

Figure 6. MRI enhancement

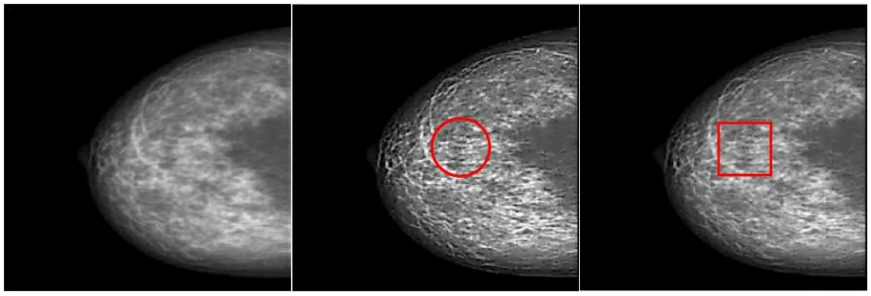

(a) Original image (b) Original AFDA (c) Improved AFDA

Figure 7. Target of breast molybdenum image enhancement

Moreover, we find that there are some black and white spots appear in the images processed by the original AFDA (indicated by boxes) that do not occur on the original image. This effect is improper for medical image enhancement. Therefore, the improved AFDA with the new mask visually produces better medical image enhancement than the original AFDA with higher adaptability and more appropriate.

Evaluation by edge detection

The validation of the improvement can also be assessed by the quality of the edge detection. We use the Sobel and Laplacian operators to create an image emphasizing edges. They are commonly used as edge detection schemes. The Sobel and Laplacian operators are the gradient based edge detector and the Laplacian based edge detector, respectively. In other words, the Sobel and Laplacian operators are first-order and second-order linear differential operators, respectively. They can strongly enhance edges while strongly weaken weak textures and smooth areas of an image[15]. We use the CT and MRI images as examples to compare the quality of the edge detection.

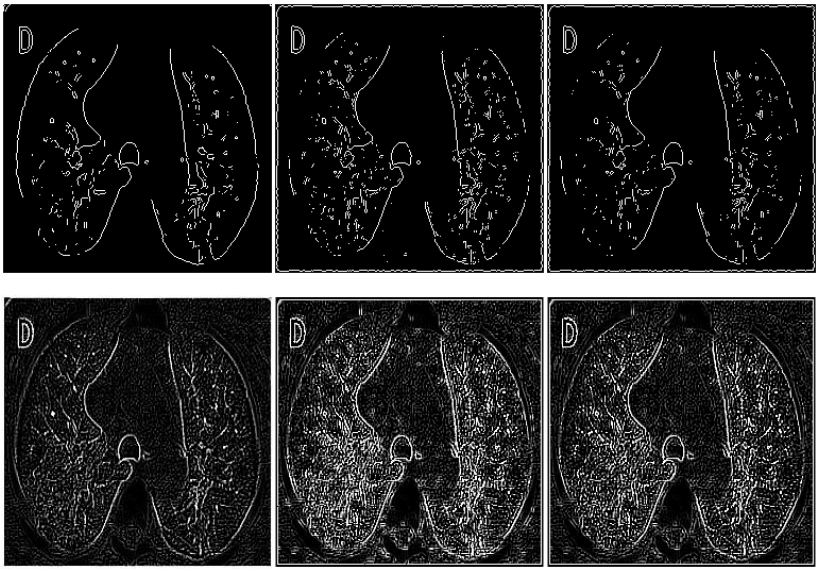

(a) Original image (b) Original AFDA (c) Improved AFDA

Figure 8. Edge detection results of CT images using Sobel (top) and Laplacian (bottom)

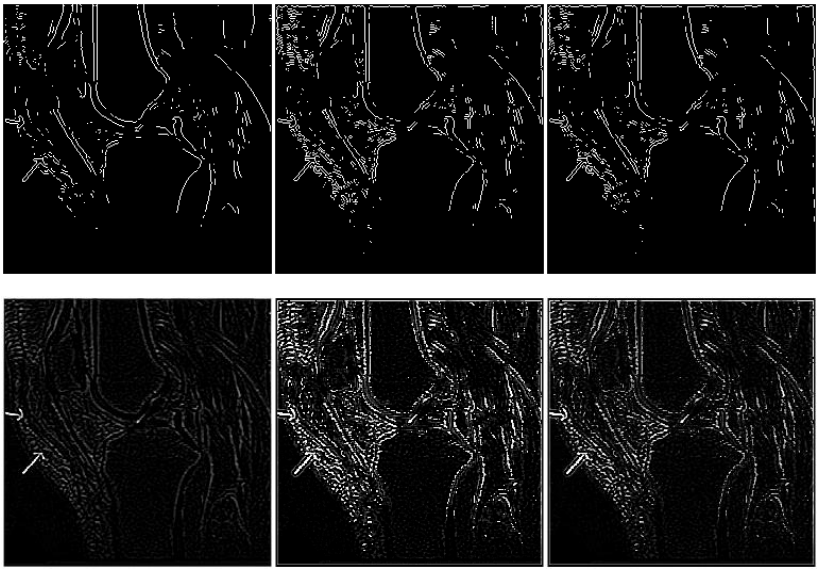

(a) Original image (b) Original AFDA (c) Improved AFDA

Figure 9. Edge detection results of MRI images using Sobel (top) and Laplacian (bottom)

Figures 8 and 9 show the effect of image segmentation. The original AFDA and the improved AFDA with the new mask are shown to be significantly better than that of the original image. However, the edges enhanced by the original AFDA method is too sharp because the gradient has been given over-valuation by the original 8-direction mask. The improved AFDA with the new mask is shown to yield the better edge detection quality.

Evaluation by some metrics

Finally, we use 5 metrics, namely the proportion of edge pixels, the average gradients of edge pixels, the average grays of texture pixels, the information entropy and the contrast ratio to analyze the effect of image enhancement using the improved AFDA with the new mask.

The proportion of edge pixels, the average gradients of edge pixels and the average grays of texture pixels can be obtained from the improved Otsu algorithm[6]. Here, the information entropy is given by $H = -\sum_{k=0}^{255} p(k)\ln p(k)$, where $p(k)$ is the frequency of gray values, i.e., $p(k) = \frac{1}{A\times B}\sum_{f(i,j)=k} 1$ for a digital image $f(i,j)$ with resolution $A \times B$. While, the definition of contrast ratio is $Contrast\ ratio = C_{processed}/C_{original}$, where $C_{original}$ and $C_{processed}$ are the contrast of the image before and after being processed, respectively. We consider 3×3 pixels to be a unit of an image. The parameter C is the average contrast of all 3×3 units. The evaluation parameters are given in Tables 2 - 5.

Table 2 The evaluation parameters of the ultrasonic image

Type/parameter	Proportion of edge pixels	Average gradient of edge pixels	Average gray of texture pixels	Entropy of information	Contrast ratio
Original image	0.1188	9.4547	99.1850	6.4804	1.0000
Original AFDA	0.1410	37.3990	95.9056	6.6147	1.4607
Improved AFDA	0.1663	23.0451	98.0728	6.6195	1.3416

Table 3 The evaluation parameters of the lung sectional CT image

Type/parameter	Proportion of edge pixels	Average gradient of edge pixels	Average gray of texture pixels	Entropy of information	Contrast ratio
Original image	0.1149	22.3739	192.6722	6.9584	1.0000
Original AFDA	0.1365	82.1330	188.4240	6.7774	1.5560
Improved AFDA	0.1329	65.1363	187.7429	6.9197	1.4420

Table 4 The evaluation parameters of the knee-joint MRI

Type/parameter	Proportion of edge pixels	Average gradient of edge pixels	Average gray of texture pixels	Entropy of information	Contrast ratio
Original image	0.0962	10.9120	81.0635	6.6909	1.0000
Original AFDA	0.1238	37.4280	77.9944	6.8983	1.6103
Improved AFDA	0.1250	24.8553	78.4106	6.8430	1.5370

Table 5 The evaluation parameters of the target of breast molybdenum image

Type/parameter	Proportion of edge pixels	Average gradient of edge pixels	Average gray of texture pixels	Entropy of information	Contrast ratio
Original image	0.1357	7.0911	43.6800	4.8078	1.0000
Original AFDA	0.1489	36.1885	42.0671	4.8315	2.3445
Improved AFDA	0.1318	22.5202	43.7205	4.7926	2.2659

From Table 2 - 5, the improved AFDA with the new mask can enhance the proportion of edge pixels significantly better than the original AFDA in the ultrasonic image. However, the proposed mask produces no different the proportion of edge pixels in enhancing the lung sectional CT image and the knee-joint MRI image to the original AFDA. Although, the new mask has less proportion of edge pixels than the original AFDA in the target of breast molybdenum image, the improved AFDA has the average gray of texture pixels higher and has the entropy of information closer to the entropy of the original image than the original AFDA which indicate that the improved AFDA with the new mask can preserve the weak textures more appropriate than the original AFDA. The average gradient of edge pixels of every processed images by the improved AFDA is significantly less than using the original AFDA because of the assigned weight in the proposed mask. The closer entropies of images show that images processed by the improve AFDA with the new mask have a similar information quality to that of the original images more than the original AFDA. In addition, the average gradient of edge pixels and the contrast ratio are considerably increase from the original image but still less than the original AFDA which indicate that the improved AFDA with the new mask can enhance the edges looking not too sharp.

Conclusion:

In this paper, we propose a construction of the new 5×5 fractional differential mask that uses sixteen directions of gradient operator and weights each pixel in the mask by the Euclidian distance from the center of the mask to reduce the over-valuation of the gradient from distant pixels. We performed both quantitative and qualitative comparative analysis with existing edge detectors and some metrics, respectively. From quantitative analysis, it is observed that an improvement of information entropy of image through the improved AFDA with the new mask is more than the original AFDA, thus enhancing more textural information. The proposed mask can improve the visual quality of images while preserving more information in medical images and improving the clarity and contrast of medical images. In addition, we find that there are some black and white spots appear in the images processed by the original AFDA method that do not occur on the original image. This effect is improper for medical image enhancement. Therefore, the improved AFDA with the new mask visually produces better medical image enhancement than other methods with higher adaptability and more appropriate which help doctors to diagnose illness more efficiently and accurately.

Acknowledgements:

I would like to express my sincere gratitude to the Development and Promotion of Science and Technology Talents Project (DPST) for the scholarship and all the opportunities.

References:

1. Chan R, Lanza A, Morigi S, Sgallari F. An adaptive strategy for the restoration of textured images using fractional order regularization. Numer Math Theor Meth Appl 2013;6(1):276–296.
2. Gao CB, Zhou JL, Hu JR, Lang FN. Edge detection of colour image based on quaternion fractional differential. IET Image Process 2011;5(3):261–272.

3. Gao CB, Zhou JL, Zheng XQ, Lang FN. Image enhancement based on improved fractional differentiation. J Comput Inform Syst 2011;7(1):257–264.
4. Kilbas AA, Srivastava HM, Trujillo JJ. Theory and applications of fractional differential equations. Amsterdam, Netherlands: Elsevier Science; 2006.
5. Li B, Xie W. Adaptive fractional differential algorithm based on otsu standard. In: Proc. IEEE 26th Chinese control and decision conference; 2014:2020–2025.
6. Li B, Xie W. Adaptive fractional differential approach and its application to medical image enhancement. Elsevier Sci. 2015;45:324-335.
7. Lu J, Healy DM, Weaver JB. Contrast enhancement of medical images using multi-scale edge representation. Opt Eng 1994;33(7):2151–2161.
8. Michailovich OV, Tannenbaum A. Despeckling of medical ultrasound images. IEEE Trans Ultrason Ferroelectr Frequency Control 2006;5(1):64–78.
9. Nakib A, Schulze Y, Petit E. Image thresholding framework based on two-dimensional digital fractional integration and Legendre moments. IET Image Process 2012;6(6):717–727.
10. Oldham KB. Fractional calculus: theory and applications, differentiation and integration to arbitrary order. New York: Academic; 1974.
11. Otsu N. A threshold selection method from gray level histogram. IEEE Trans Syst 1979;9(1):62–66.
12. Pu YF, Wang WX. Fractional differential masks of digital image and the numerical implementation algorithms. Acta Automatica Sinica 2007;33(11):1128–1135.
13. Pu YF, Zhou JL, Yuan X. Fractional differential mask: a fractional differential-based approach for multiscale texture enhancement. IEEE Trans Image Process 2010;19(2):491–511.
14. Wang WX, Wan J, Yang Z. Fractional algorithms for rock fracture images. Imaging Sci J 2012;60(3):103–111.
15. Woods RE, Eddins SL. Digital image processing. New York: Pearson; 1997.
16. Zhang J, Wei ZH, Xiao L. Adaptive fractional-order multi-scale method for image denoising. J Math Imaging Vision 2012;43(1):39–49.
17. Zhang J, Wei ZH, Xiao L. A fast adaptive reweighted residual-feedback iterative algorithm for fractional-order total variation regularized multiplicative noise removal of partly-textured images. Signal Process 2014;98:381–395.
18. Zong XL, Laine AF, Geiser EA. Speckle reduction and contrast enhancement of echocardiograms via multiscale nonlinear processing. IEEE Trans Med Imag 1998;17(4):532–540.

B_003_OA: MODE-DEPENDENT AVERAGE DWELL TIME APPROACH TO FINITE-TIME BOUNDEDNESS OF LINEAR SWITCHED POSITIVE TIME-DELAY SYSTEMS WITH FINITE-TIME UNBOUNDED SUBSYSTEMS

Suriyon Yimnet,* Piyapong Niamsup

Department of Mathematics, Chiang Mai University, Chiang Mai 50200, Thailand
*e-mail: suriyon_yim@cmu.ac.th

Abstract:

In this paper, the problem of finite-time boundedness for switched positive linear time-delay systems with finite-time unbounded subsystems is addressed. A class of quasi-alternative switching signals is designed to analyze the switching behaviors of the system. Mode-dependent average dwell time (MDADT) switching, consisting of a slow mode-dependent average dwell time (SMDADT) switching and a fast mode-dependent average dwell time (FMDADT) switching, is applied to the system whose subsystems are bounded and unbounded. By establishing a suitable copositive Lyapunov-Krasovskii functional and adopting the MDADT switching strategy, some computable sufficient conditions are formulated to guarantee the underlying system is finite-time bounded. Finally, an illustrative example is provided to verify the effectiveness of the proposed method.

B_004_OF: A MATHEMATICAL STUDY OF DIPHTHREIA MODEL WITH TRANSPORT-RELATED INFECTION AND ASYMPTOMATIC INFECTION

Siwaphorn Kanchanarat, Settapat Chinviriyasit,* Wirawan Chinviriyasit

Department of Mathematics, Faculty of Science, King Mongkut's University of Technology Thonburi (KMUTT)
e-mail: siwaphorn.kan@mail.kmutt.ac.th,
*e-mail: settapat.chi@kmutt.ac.th

Abstract:

Vaccination is the most effective strategy against diphtheria and transport-related infection may cause the effect to vaccination coverage among cities. In this paper, a diphtheria model with transport-related infection, asymptomatic infection, and vaccination is formulated and analyzed to explore the effect of transport-related infection on the vaccination coverage among cities. The epidemiological threshold related transport-related infection, called the basic reproductive number, R_m, is derived. If $R_m \leq 1$, the disease-free equilibrium of the proposed model is globally asymptotically stable and unstable when $R_m > 1$ in the sense that the disease can be eradicated from the community. The study results indicate that the travelling can bring disease among two cities but cannot spread if the population in each city have enough vaccine coverage level.

Introduction:

Nowadays, traveling from one city to another, which cities may be justified by migration and travel within city[1], is a factor in the spread of disease because of the possibility for the individuals to become infected during travel, such as influenza, SARS, and diphtheria, which can be easily transmitted from one region to another[2,3].

Mathematical epidemiology have been developed in the literature to gain insights into the effect of population dispersal on the spread of disease as follows. In 2006, Liu and Takeuchi[4] proposed SIQS model to indicate that entry screening is helpful for disease eradication even when the disease is endemic in both isolated cities. In 2013, Denphedtnong et al. formulated an SEIRS model with transport-related infection and found that the transport-related infection is effected to the number of infected individuals and the duration of SARS outbreak in such the way that the disease becomes more endemic due to the movement between two cities[1].

Diphtheria is an acute infectious disease of the respiratory system. It is easily transmitted through coughing and sneezing or exposure to diphtheria patients. This disease is prevented by vaccination due to it has reduced the mortality and morbidity of diphtheria dramatically[5]. However, diphtheria is still a significant child health problem in countries with poor vaccination coverage. Thus, population dispersal from one region to another region may cause easily diphtheria transmission resulting in the vaccination coverage of each city. For these reasons, the aim of this paper is to formulate a diphtheria model with transport-related infection, asymptomatic infection, and vaccination to explore the effect of transport-related infection on the vaccination coverage among cities.

Model Formulation:

Diphtheria bacteria spreads from person to person, usually through respiratory droplets, or touching infected open sores or ulcers. The incubation period of diphtheria disease is 2-5 days (range 1-10 days) which is the cause that asymptomatic populations are often carriers of diphtheria transmission[6]. Although diphtheria is an acute infectious disease of the respiratory system that can cause death but it is preventable with a vaccine. For this reason, many countries, including Thailand, have provided the diphtheria vaccine schedule for children at 2, 4, 6, 18 months of age and re-booster at the ages of 4 and 12 years, respectively. However, diphtheria is still a significant child health problem in countries with poor vaccination coverage due to the limitations of receiving the vaccination[5,7–11] and the transport-related infection among cities. Therefore, the diphtheria transmission among cities is formulated by modifying the SEIR epidemic model with asymptomatic population, vaccinated population, and transport-related infection. The total population in city $i, i=1,2$ denoted N_i is divided into 6 sub-populations of susceptible individuals (S_i) who have not received the vaccine or have not received full immunity, vaccinated individuals (V_i) who have partial immunity, exposed individuals (E_i) who infected diphtheria in the incubation period but cannot transmit diphtheria, asymptomatic individuals (A_i) who infected diphtheria but can transmit diphtheria without symptom, infected individuals (I_i) who can spread diphtheria with symptom, and recovered individuals (R_i) who recovered from diphtheria and have immunity which need to prevent by booster vaccination as soon as possible, respectively. Thus, the total population of two cities is given by

$$N(t)=N_1(t)+N_2(t),$$

where $N_i(t)=S_i(t)+V_i(t)+E_i(t)+A_i(t)+I_i(t)+R_i(t)$ for $i=1,2.$

Since the epidemiology of diphtheria in both cities is identical, i.e. the demographic parameters are the same for each city, as follows. All sub-populations die at the same natural death rate μ and diphtheria induced mortality at the rate α. Exposed individuals develop symptoms to asymptomatic individuals and infected individuals at the rates $a\sigma$ and $(1-a)\sigma$, respectively. Asymptomatic and infected individuals recover at the rates γ and τ, respectively. Since immunity produced by the diphtheria vaccine need to booster every ten years, recovered individuals will become susceptible after recovering from diphtheria at the rate θ. Due to the limit of vaccine in each city, the susceptible population is generated at the recruitment rate in each city which is defined by logistic growth rate

$$rN_i\left(1-\frac{N_i}{K}\right),\ i=1,2,$$

where r is birth rate and K is the limit of vaccine program for populations. Diphtheria is transmitted with the standard incidence from asymptomatic and infected populations at the rate,

$$\frac{\beta S_i(\delta A_i+I_i)}{N_i},\ i=1,2,$$

where β is transmission rate and δ is ability to cause infection by asymptomatic population within city i, respectively. All sub-populations leave from city i to city j at the movement rate m. When the individuals in city *i* travel to city *j*, disease is transmitted with the incidence rate,

$$\frac{md(\delta A_i+I_i)}{N_i},i=1,2$$

where d is transport-related transmission rate. Therefore, the dynamics of all subpopulation in each city with transport-related infection are shown in Figure 1. The diphtheria model with transport-related infection, from Figure 1, is given by the system of nonlinear differential equations:

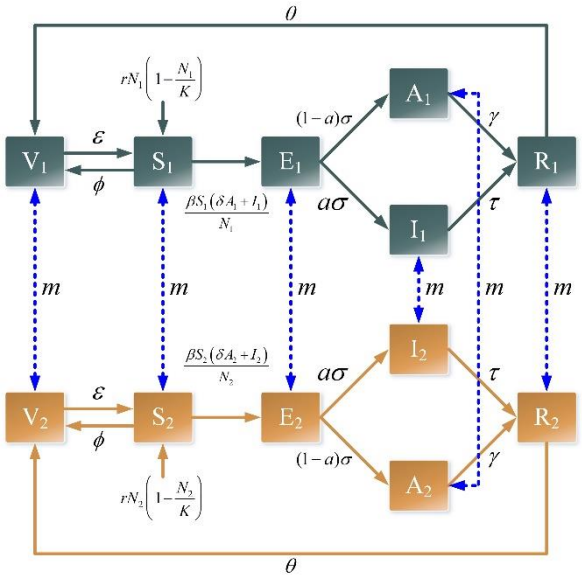

Figure 1.

Transfer diagram of the diphtheria model with transport-related infection.

$$
\left.
\begin{aligned}
\frac{dS_1}{dt} &= rN_1\left(1-\frac{N_1}{K}\right)-\frac{\beta S_1\left(\delta A_1+I_1\right)}{N_1}-\left(\mu+\phi\right)S_1+\varepsilon V_1-mS_1+mS_2-\frac{mdS_2\left(\delta A_2+I_2\right)}{N_2},\\
\frac{dV_1}{dt} &= \phi S_1+\theta R_1-\left(\mu+\varepsilon\right)V_1-mV_1+mV_2,\\
\frac{dE_1}{dt} &= \frac{\beta S_1\left(\delta A_1+I_1\right)}{N_1}-\left(\mu+\sigma\right)E_1-mE_1+mE_2,\\
\frac{dA_1}{dt} &= \left(1-a\right)\sigma E_1-\left(\mu+\gamma\right)A_1-mA_1+mA_2,\\
\frac{dI_1}{dt} &= a\sigma E_1-\left(\mu+\alpha+\tau\right)I_1-mI_1+mI_2,\\
\frac{dR_1}{dt} &= \gamma A_1+\tau I_1-\left(\mu+\theta\right)R_1-mR_1+mR_2,
\end{aligned}
\right\} \quad (1)
$$

$$
\left.
\begin{aligned}
\frac{dS_2}{dt} &= rN_2\left(1-\frac{N_2}{K}\right)-\frac{\beta S_2\left(\delta A_2+I_2\right)}{N_2}-\left(\mu+\phi\right)S_2+\varepsilon V_2-mS_2+mS_1-\frac{mdS_1\left(\delta A_1+I_1\right)}{N_1},\\
\frac{dV_2}{dt} &= \phi S_2+\theta R_2-\left(\mu+\varepsilon\right)V_2-mV_2+mV_1,\\
\frac{dE_2}{dt} &= \frac{\beta S_2\left(\delta A_2+I_2\right)}{N_2}-\left(\mu+\sigma\right)E_2-mE_2+mE_1,\\
\frac{dA_2}{dt} &= \left(1-a\right)\sigma E_2-\left(\mu+\gamma\right)A_2-mA_2+mA_1,\\
\frac{dI_2}{dt} &= a\sigma E_2-\left(\mu+\alpha+\tau\right)I_2-mI_2+mI_1,\\
\frac{dR_2}{dt} &= \gamma A_2+\tau I_2-\left(\mu+\theta\right)R_2-mR_2+mR_1.
\end{aligned}
\right\} \quad (2)
$$

where all parameters and their values are described and given in Table 1. From the biological point of view, the number of the susceptible during travelling should be nonnegative, that is, for all $S_i, A_i, I_i \geq 0$, $mS_i-\frac{mdS_i\left(\delta A_i+I_i\right)}{N_i}\geq 0, i=1,2.$ Further, it can be shown that the biological region

$$
\Omega=\left\{\left\{\left(S_1,V_1,E_1,A_1,I_1,R_1,S_2,V_2,E_2,A_2,I_2,R_2\right)\mathbb{R}\in R_+^{12}\ \middle|\ N(t)\leq\frac{2K(r-\mu)}{r}\right\}\right. \quad (3)
$$

is positively invariant and attracting with respect to the system (1)-(2) where R_+^{12} denotes the non-negative cone of R^{12} including its lower dimension faces. Thus in $\Omega,$ the diphtheria model with transport-related infection (1)-(2) is well-posed epidemiologically and mathematically[12]. Hence, it is sufficient to study the dynamics of the basic model (1)-(2) in Ω.

Disease-free equilibrium and reproductive number:

The disease-free equilibrium (DFE) for the system (1)-(2) is given by

$$
P_m^0(S_1^0,V_1^0,0,0,0,0,S_2^0,V_2^0,0,0,0,0)
$$

where $$S_1^0=S_2^0=\frac{K(r-\mu)\left(\mu+\varepsilon\right)}{r\left(\mu+\phi+\varepsilon\right)},\ V_1^0=V_2^0=\frac{K\phi(r-\mu)}{r\left(\mu+\phi+\varepsilon\right)}.\mathbb{R} \quad (4)$$

Using the concept of next generation matrix[13] and the reproductive number method presented in[14], we define

$$F=\begin{pmatrix} 0 & \frac{\beta\delta(\mu+\varepsilon)}{\mu+\phi+\varepsilon} & \frac{\beta(\mu+\varepsilon)}{\mu+\phi+\varepsilon} & 0 & \frac{md\delta(\mu+\varepsilon)}{\mu+\phi+\varepsilon} & \frac{md(\mu+\varepsilon)}{\mu+\phi+\varepsilon} \\ 0 & 0 & 0 & 0 & 0 & 0 \\ 0 & 0 & 0 & 0 & 0 & 0 \\ 0 & \frac{md\delta(\mu+\varepsilon)}{\mu+\phi+\varepsilon} & \frac{md(\mu+\varepsilon)}{\mu+\phi+\varepsilon} & 0 & \frac{\beta\delta(\mu+\varepsilon)}{\mu+\phi+\varepsilon} & \frac{\beta(\mu+\varepsilon)}{\mu+\phi+\varepsilon} \\ 0 & 0 & 0 & 0 & 0 & 0 \\ 0 & 0 & 0 & 0 & 0 & 0 \end{pmatrix},$$

$$V=\begin{pmatrix} \mu+\sigma+m & 0 & 0 & -m & 0 & 0 \\ -(1-a)\sigma & \mu+\gamma+m & 0 & 0 & -m & 0 \\ -a\sigma & 0 & \mu+\alpha+\tau+m & 0 & 0 & -m \\ -m & 0 & 0 & \mu+\sigma+m & 0 & 0 \\ 0 & -m & 0 & -(1-a)\sigma & \mu+\gamma+m & 0 \\ 0 & 0 & -m & -a\sigma & 0 & \mu+\alpha+\tau+m \end{pmatrix}.$$

Let $R_m=\rho(FV^{-1})$ is the spectral radius of the matrix FV^{-1}. Hence, the reproductive number for (1) is

$$R_m=\rho(FV^{-1})=R_0(1-p)\left(1+\frac{md}{\beta}\right). \quad (5)$$

Where $R_0=\frac{\beta\sigma\left(a(\mu+\gamma)+\delta(1-a)(\mu+\alpha+\tau)\right)}{(\mu+\sigma)(\mu+\gamma)(\mu+\alpha+\tau)}$ is the reproductive number of diphtheria model (1) without vaccination and transport-related infection $(\phi=\varepsilon=m=d=0)$ and $p=\frac{V_i^0}{S_i^0+V_i^0}, i=1,2$ is the vaccine coverage in each city.

According to Theorem 2 in Van den Driessche[15] the following result is established

Theorem 1. The disease-free equilibrium (DFE), P_m^0, of the system (1) is locally asymptotically stable (LAS) if $R_m<1$ and unstable when $R_m>1$.

This theorem verifies that the threshold value is the reproductive number of diphtheria model with transport-related infection (1)-(2) in the sense that the disease will be eradicated from the community when $R_m<1$ and the initial sizes of six state variables which is given in the following theorem.

Theorem 2. The disease-free equilibrium, P_m^0, is globally asymptotically stable whenever $R_m\le 1.$

Proof. let consider the Lyapunov function:

$$L(t)=\frac{\sigma(ak_4+\tilde{a}\delta k_5)}{k_3}(E_1+E_2)+\delta k_5(A_1+A_2)+k_4(I_1+I_2)$$

and the time derivative of $L(t)$ along the solution of the system (1)-(2) becomes

$$
\begin{aligned}
L'(t) &= \frac{\sigma\left(ak_4+\delta\tilde{a}k_5\right)}{k_3}\left(E_1'+E_2'\right)+\delta k_5\left(A_1'+A_2'\right)+k_4\left(I_1'+I_2'\right),\\
&= \frac{\sigma\left(ak_4+\delta\tilde{a}k_5\right)}{k_3}\left(\frac{S_1(\beta+md)(\delta A_1+I_1)}{N_1}+\frac{S_2(\beta+md)(\delta A_2+I_2)}{N_2}+k_3\left(E_1+E_2\right)\right)\\
&\quad+\delta k_5\left(\tilde{a}\sigma\left(E_1+E_2\right)-k_4\left(A_1+A_2\right)\right)+k_3\left(a\sigma\left(E_1+E_2\right)+k_5\left(I_1+I_2\right)\right),\\
&\le \left(\delta\left(A_1+A_2\right)+\left(I_1+I_2\right)\right)\left(\frac{\sigma k_2(\beta+md)\left(ak_4+\delta\tilde{a}k_5\right)}{k_3k_7}-k_4k_5\right) \quad \text{since } \frac{S_i}{N_i}\le\frac{k_2}{k_7}, i=1,2,\\
&= k_4k_5\left(\delta\left(A_1+A_2\right)+\left(I_1+I_2\right)\right)\left[R_m-1\right].
\end{aligned}
$$

Clearly, that $L'(t)\le 0$ when $R_m\le 1$ and $L'(t)=0$ if and only if $A_1=A_2=I_1=I_2=0.$

By Lyapunov-Lasalle theorem[16], the disease-free equilibrium, P_m^0 is global asymptotically stable when $R_m\le 1$. This completes the proof of this theorem.

The epidemiological implication of this theorem is that if the model parameters can be selected that $R_m\le 1$, then the disease will be eradicated from the community.

Endemic equilibrium:

In the Occurrence of infection, let $P_m^*(S^*,V^*,E^*,A^*,I^*,R^*,\ S^*,V^*,E^*,A^*,I^*,R^*)$ be endemic equilibrium at steady state and let

$$\lambda^*=\frac{\beta\left(\delta A_1^*+I_1^*\right)}{N_1^*}=\frac{\beta\left(\delta A_2^*+I_2^*\right)}{N_2^*}. \tag{6}$$

Be the force of infection at steady state. By solving the system (1)-(2), we get

$$
\left.\begin{aligned}
&S^*=\frac{K}{r\tilde{R}_m}\left(k_1\left(\frac{r\tilde{R}_m}{k_1}-1\right)+\frac{\varepsilon\phi}{k_2}+\left(\frac{\varepsilon\theta Q_1}{\beta k_2k_3k_4k_5k_6}-\frac{md}{\beta}-1\right)\lambda^*\right),\ V^*=\left(\phi+\frac{Q_1\theta\lambda^*}{\beta k_3k_4k_5k_6}\right)\frac{S^*}{k_2},\\
&E^*=\frac{(\beta+md)\lambda^*S^*}{\beta k_3},\ A^*=\frac{\tilde{a}\sigma(\beta+md)\lambda^*S^*}{\beta k_3k_4},\ I^*=\frac{a\sigma(\beta+md)\lambda^*S^*}{\beta k_3k_5},\ R^*=\frac{Q_1\lambda^*S^*}{\beta k_3k_4k_5k_6}
\end{aligned}\right\} \tag{7}
$$

where $k_1=\mu+\phi,\ k_2=\mu+\varepsilon,\ k_3=\mu+\sigma,\ k_4=\mu+\gamma,\ k_5=\mu+\alpha+\tau,\ k_6=\mu+\theta,\ k_7=\mu+\phi+\varepsilon,$

$\tilde{a}=1-a,\ Q_1=(\beta+md)\left(ak_4\tau+\tilde{a}k_5\gamma\right)\sigma,\ \tilde{R}_m=\frac{\sigma(\beta+md)\left(ak_4+\tilde{a}\delta k_5\right)}{k_3k_4k_5}$. Substituting (7) into (6), and simplifying, we have

$$\lambda^*\left(a_1\lambda^*-a_0\right) \tag{8}$$

where $a_0 = \beta k_3 k_4 k_5 k_6 k_7 (R_m - 1)$, $a_1 = Q_1(\theta + k_2) + k_2 k_6 (\beta + md)(a\sigma k_4 + \tilde{a}\sigma k_5 + k_4 k_5)$. In the case $\lambda^* \neq 0$, it follows from (7) that $\lambda^* = \frac{a_0}{a_1}$. Obviously, $\lambda^* > 0$ if and only if $R_m > 1$ and clearly that, when $R_m \leq 1$, Eq (8) has no positive solutions of endemic equilibrium point (7). Hence, the following theorem is established.

Theorem 3. The system (1)-(2) has a unique endemic equilibrium, P_m^*, when $R_m > 1$, and no P_m^* if $R_m \leq 1$, .

Numerical results

In this section, the diphtheria model with transport-related infection (1)-(2) is simulated with $m = 0.01$, $d = 1500$, $\phi = 0.1473$ and the other parameter values tabulated in Table 1. The initial sizes of sub-population use simulation are

$$E_1(0) = E_2(0) = A_1(0) = A_2(0), R_1(0) = R_2(0) = 0, \quad I_1(0) = I_2(0) = 0.1,$$

respectively. Figure 2 shows that the numbers of susceptible, vaccinated and infected individuals in each city *i* approach to the disease-free equilibrium for all different initial conditions. This means that the disease will be eradicated from the population irrespective of the initial sizes of the six state variables as guaranteed by Theorem 2.

When $m = 0.01$, $d = 1500$, the other parameters given in Table 1 and the rate of vaccination ϕ is vary to be $\phi = 0.0376, 0.0532, 0.0846, 0.0950, 0.1249$ which correspond to $p = 0.8, 0.85, 0.9, 0.91$ and 0.93, respectively. These values give the reproductive number $R_m = 2.6648, 1.9986, 1.3324, 1.1992 > 1$ which verifies that the endemic equilibrium exists and the disease becomes endemic as guarantee by Theorem 3. The study results in Table 2 show that increasing the rate of vaccination ϕ would increase the vaccination coverage, which lead to decrease R_m < 1. The results in Table 2 also show that the number of infected individual decrease as ϕ increased.

Table 1. Definition and parameter values of model diphtheria model with transport-related infection (1)-(2)

Parameter	Definition	Value
β	Transmission rate	18.5
a	Proportion of infected population	0.55[17]
δ	Ability to cause infected by asymptomatic individual	0.7[17]
ϕ	Rate of vaccination	0.1473[18]
r	Recruitment rate	0.0101[19]
σ	Rate that exposed individual become asymptomatic and infected individuals	6[6]
γ	Recovered rate of asymptomatic and infected individuals	2.1429[6]
μ	Natural death rate	0.0011[20]
α	Diphtheria mortality rate	0.05[6]
ε	Rate of vaccine waning	0.0083[6]
θ	Rate of recovered individual becoming vaccinated individual	0.6667[6]
τ	Recovered rated of infected individual	2.1429[6]
K	Carrying capacity of community	10,000
m	Rate of movement	0.01[21]
d	Transport-related infection	1,500

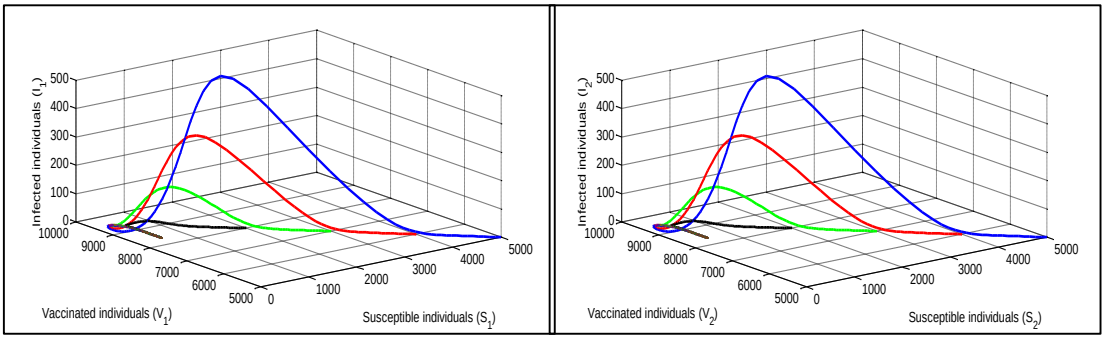

Figure 2.

Trajectories of diphtheria model with transport-related infection and asymptomatic infection (1)-(2) for different initial conditions with $R_m = 0.7990 < 0.$

Table 2. Effect of rate of vaccination (ϕ)

ϕ	p	$S_1^* = S_2^*$	$V_1^* = V_2^*$	$E_1^* = E_2^*$	$A_1^* = A_2^*$	$I_1^* = I_2^*$	$R_1^* = R_2^*$	R_m
0.0376	0.8	663	8066	9	11	13	76	2.6648
0.0532	0.85	664	8101	7	9	10	61	1.9986
0.0846	0.9	667	8172	3	4	5	31	1.3324
0.0950	0.91	667	8195	2	3	3	20	1.192
0.1249	0.93	623	8287	0	0	0	0	0.9327

The combined effect of the rate of movement m and transport-related infection d on the value of R_m is investigated by plotting the contour plot of R_m as the function of the rate of movement m and rate of vaccination p as shown in Figure 3. It is found that if the rate of movement, m increases, the vaccine coverage p must increase to make the value R_m less than unity. This result suggests that if there is travelling among cities and transport-related infection, the rate of vaccination must be increased, which leads to increasing the vaccination coverage in community for each city, and then diphtheria will eradicate from the community.

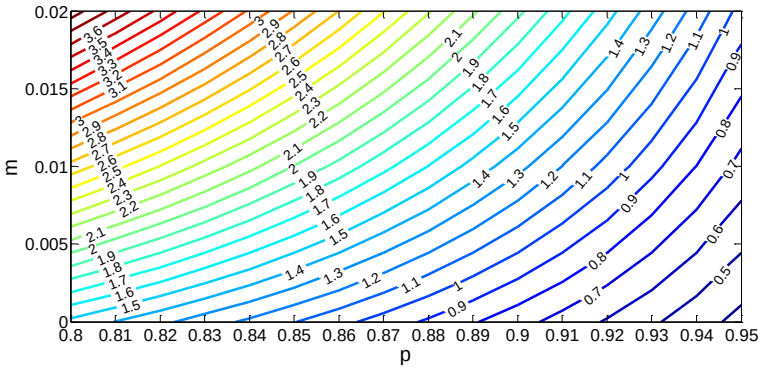

Figure 3. The reproductive number (R_m) changes over vaccine coverage (p) and rate of movement (m).

Results and Discussion:

In this paper, we presented a diphtheria model with transport-related infection in order to investigate the impact of movement among cities on the vaccination coverage in the community. It is found that the disease-free equilibrium is globally asymptotically stable when $R_m \leq 1$ where R_m is the reproductive number of the proposed model (1)-(2). This means that the disease will be eradicated from the population irrespective of the initial sizes of the six state variables as shown in Figure 2. The impact of movement among cities on the vaccination coverage in the community is investigated by plotting the contour plot of R_m as the rate of movement and the vaccination coverage. It is found that the movement among cities is the cause of increasing the number of infected populations because it is impact to reduce the vaccination coverage in each city. Therefore, when the rate of movement $m = 0.01$, increasing the vaccination coverage to 93% in both cities would be able to prevent the diphtheria epidemic, see Table 2. To this end, although tourism has caused an outbreak of the city but from the result show that diphtheria can be eradicated, if the population in each city have immunity by getting enough vaccination that will help to prevent diphtheria as well.

References:

1. Denphedtnong A, Chinviriyasit S, Chinviriyasit W. On the dynamics of SEIRS epidemic model with transport-related infection. *Math Biosci*. 2013;245(2):188-205. doi:10.1016/j.mbs.2013.07.001
2. Wang W, Ruan S. Simulating the SARS outbreak in Beijing with limited data. 2004;227:369-379. doi:10.1016/j.jtbi.2003.11.014
3. Berge T, Bowong S, Lubuma JM. ScienceDirect Global stability of a two-patch cholera model with fast and slow transmissions. *Math Comput Simul*. 2015. doi:10.1016/j.matcom.2015.10.013
4. Liu X, Takeuchi Y. Spread of disease with transport-related infection and entry screening. *J Theor Biol*. 2006;242(2):517-528. doi:10.1016/j.jtbi.2006.03.018
5. Wanlapakorn N, Yoocharoen P, Tharmaphornpilas P, Theamboonlers A, Poovorawan Y. Diphtheria outbreak in Thailand, 2012; seroprevalence of diphtheria antibodies among Thai adults and its implications for immunization programs. *Southeast Asian J Trop Med Public Health*. 2014;45(5):1132-1141.
6. CDC. *Diphtheria*.; 2015. https://www.cdc.gov/vaccines/pubs/pinkbook/downloads/dip.pdf.
7. Finger F, Funk S, White K, Siddiqui MR, Edmunds WJ, Kucharski AJ. Real-time analysis of the diphtheria outbreak in forcibly displaced Myanmar nationals in Bangladesh. *BMC Med*. 2019.
8. Sein C, Tiwari T, Macneil A, et al. Diphtheria outbreak in Lao People's Democratic Republic, 2012–2013. *Vaccine*. 2016;34(36):4321-4326. doi:10.1016/j.vaccine.2016.06.074
9. Tosepu R, Gunawan J, Effendy DS, Ahmad LOAI, Farzan A. The outbreak of diphtheria in Indonesia. *Pan Afr Med J*. 2018;31:1-5. doi:10.11604/pamj.2018.31.249.16629
10. Matsuyama R, Akhmetzhanov AR, Endo A, et al. Uncertainty and sensitivity analysis of the basic reproduction number of diphtheria: A case study of a Rohingya refugee camp in Bangladesh, November-December 2017. *PeerJ*. 2018;2018(4). doi:10.7717/peerj.4583
11. Sornbundit K, Triampo W, Modchang C. Mathematical modeling of diphtheria transmission in Thailand. *Comput Biol Med*. 2017;87(January):162-168. doi:10.1016/j.compbiomed.2017.05.031
12. Hethcote HW. The Mathematics of Infectious Diseases. *Soc Ind Appl Math*. 2000;42(4):599-653.
13. Diekmann O, Heesterbeek JAP, Metz JAJ. On the definition and the computation of the basic reproduction ratio R0 in models for infectious diseases in heterogeneous populations. *J Math Biol*. 1990;28(4):365-382. doi:10.1007/BF00178324
14. Van Den Driessche P, Watmough J. Reproduction numbers and sub-threshold endemic equilibria for compartmental models of disease transmission. *Math Biosci*. 2002;180(1-2):29-48. doi:10.1016/S0025-5564(02)00108-6
15. P. van den Driessche JW. Reproduction numbers and sub-threshold endemic equilibria for compartmental models of disease transmission. *Math Biosci*. 2002;180(1-2):29-48. doi:10.1016/S0025-5564(02)00108-6
16. LaSalle J. *The Stability of Dynamical Systems*. New Jersey: Hamilton Press; 1976.
17. Bureau TTM. Diphtheria Information. https://www.tmb.ie/vaccinations/diphtheria.
18. *Annual Epidemiological Surveillance Report 2017*.; 2017. https://apps.doe.moph.go.th/boeeng/download/AESR-6112-24.pdf.
19. Fertility rate, total (births per woman) - Thailand. The World Bank. https://data.worldbank.org/indicator/SP.DYN.TFRT.IN?locations=TH.
20. Death rate, crude (per 1,000 people). The World Bank. https://data.worldbank.org/indicator/SP.DYN.CDRT.IN.
21. *Population Migration Survey*.; 2019. http://www.nso.go.th/sites/2014/DocLib13/ด้านสังคม/สาขาประชากร/การย้ายถิ่น/2562/Pocketbook_2562.pdf.

B_005_PF: MODELING OF RANDOM COEFFICIENT AUTOREGRESSIVE MODEL ON TIME SERIES DATA

Autcha Araveeporn*

Department of Statistics, Faculty of Science, King Mongkut's Institute of Technology Ladkrabang, Bangkok, 10520.
*e-mail: autcha.ar@kmitl.ac.th

Abstract:

This paper compares the least-squares method and the Bayesian analysis for estimating an unknown parameter in the Random Coefficient Autoregressive (RCA) model. We concentrated on only the first-order models of the RCA model. The least-squares method is a widely used method by minimizing the sum of squared residuals and differential concerning unknown parameters. The Bayesian analysis carries out Markov Chain Monte Carlo (MCMC) method to generate samples from a posterior distribution, which, after being averaged, gave the estimated value of the unknown parameter. We used a Gibbs sampling algorithm in our MCMC calculation. The efficiency of two methods was considered by mean square error for real data. They were used to estimate a series of monthly averages of the Stock Exchange of Thailand (SET) index. The result shows that the least-squares method still worked better than the Bayesian analysis.

Introduction:

The modeling of time series data has applied in a field of finance, business, and economics. Usually, the time series data exhibits changing data as a trend, volatility, stationary, nonstationary, and random walk, especially when the time-series data are systematically collected over a long period. Several time series models can help to estimate and forecast the values in future time.

A model widely uses to fit the stationary data such as the Autoregressive (AR) model, Moving Average (MA) model, and Autoregressive Moving Average (ARMA) model. For nonstationary time series data, the Autoregressive Integrated Moving Average (ARIMA) model can use. These models have some problems to over-specify the model and estimate the integration parameter. An alternative way to model by volatility is to use the Conditional Heteroscedastic Autoregressive Moving average (CHARMA) model ([1]). Nicholls and Quinn [2] proposed the Random Coefficient Autoregressive (RCA) model based on volatility that employed the least-square and maximum likelihood methods to estimate parameters. Wang and Ghosh [3] used the Bayesian approach to obtain the first-order estimate of an RCA model.

The least-squares method is a well-known method used to determine a parameter of best fit by minimizing the sum of squares. Furthermore, the Bayes analysis considers a hierarchical model that related to the prior distribution. So the Bayesian estimator is computed the parameter on the RCA model from the mean of posterior distribution by Markov Chain Monte Carlo (MCMC) method ([4]). We also carry out the Gibbs sampling algorithm ([5]) from the MCMC method by rjags package of R program to estimate an unknown parameter.

This study is interested in estimating the RCA model's parameter based on the least-squares method and Bayesian analysis, the performance of the least-squares method, and Bayesian analysis with that of the Mean Square Error (MSE) method using both simulated and real data.

The RCA Model:

The general class of Random Coefficient Autoregressive (RCA) model of order p ,that is given by

$$x_t = \alpha + \sum_{i=1}^{p} \beta_{ti} x_{t-i} + \varepsilon_t, t = 2,3,...,n. \quad (1)$$

Wang and Ghosh [3] suggested

$$\underline{\beta}_{ti} = \underline{\mu}_{\beta} + \Omega_{\beta} \underline{u}_t,$$

where α is the scalar of constant, $\underline{\beta}_{ti} = (\beta_{t1}, \beta_{t2}, ..., \beta_{tp})'$, is a sequence of independent random vectors with mean $\underline{\mu}_{\beta} = (\mu_{t1}, \mu_{t2}, ..., \mu_{tp})'$ and covariance matrix Ω_{β}. It is assumed that ε_t's are the sequence of iid (independent and identically distributed random variables) from distribution mean zero and unit variance.

In this paper, we focus on the simplicity case study of the first order on RCA(1) following

$$x_t = \alpha + \beta_{t1} x_{t-1} + \varepsilon_t, \ t = 2,3,...,n \quad (2)$$

$$\beta_{t1} = \mu_{\beta} + \sigma_{\beta} v_t,$$

where x_t's are iid random variables with mean μ_{β}, and variance σ_{β}^2, ε_t's are iid random variables with mean zero and variance σ_{ε}^2. The RCA(1) model can be rewritten as

$$x_t = \alpha + \beta_t x_{t-1} + \varepsilon_t = \alpha + \mu_{\beta} x_{t-1} + u_t, \quad (3)$$

where $u_t = \sigma_{\beta} v_t x_{t-1} + \varepsilon_t$, where v_t is a random variable with mean zero and variance one and independent of ε_t.

Method of Parameter Estimation:

To estimate the parameter of the RCA(1) model, we propose the concept of least squares criterion and Bayesian analysis based on the MCMC method.

Least-Squares Method

The first estimated method, we propose the least-squares criterion to estimate parameter $\theta = (\alpha, \mu_{\beta})$ by minimizing sum of squared residuals. Let γ_t be the information set up to time t, and $u_t = x_t - \mu_{\beta} x_{t-1}$, then it can see that

$E(u_t | \gamma_{t-1}) = 0$, $E(u_t^2 | \gamma_{t-1}) = \sigma_{\varepsilon}^2 + \sigma_{\beta}^2 x_{t-1}^2$, and $Var(u_t | \gamma_{t-1}) = \sigma_{\varepsilon}^2 + \sigma_{\beta}^2 x_{t-1}^2$.

Given a sample $x_1, x_2, ..., x_n$, the parameter $\theta = (\alpha, \mu_\beta)$ is to estimate by minimizing $\sum_{t=1}^{n} u_t^2$ with respect to $\theta = (\alpha, \mu_\beta)$, thus the least-square estimator $\hat{\theta}_{LS} = (\hat{\alpha}_{LS}, \hat{\mu}_{\beta,LS})$ is given by

$$\sum_{t=1}^{n} (u_t)^2 = \sum_{t=1}^{n} \left(x_t - \alpha - \mu_\beta x_{t-1} \right)^2. \tag{4}$$

Differential concerning parameter $\hat{\alpha}_{LS}$,

$$\frac{\partial}{\partial \alpha} \sum_{t=1}^{n} (u_t)^2 = \frac{\partial}{\partial \alpha} \sum_{t=1}^{n} \left(x_t - \alpha - \mu_\beta x_{t-1} \right)^2$$
$$= 0.$$

Then we get

$$\hat{\alpha}_{LS} = \frac{\sum_{t=1}^{n} x_t}{n} - \mu_\beta \frac{\sum_{t=2}^{n} x_{t-1}}{n}. \tag{5}$$

The least square estimate $\hat{\mu}_{\beta,LS}$ is obtained by,

$$\frac{\partial}{\partial \mu_\beta} \sum_{t=1}^{n} (u_t)^2 = \frac{\partial}{\partial \mu_\beta} \sum_{t=1}^{n} \left(x_t - \alpha - \mu_\beta x_{t-1} \right)^2 = 2 \sum_{t=1}^{n} \left(x_t - \alpha - \mu_\beta x_{t-1} \right) x_{t-1}$$
$$= 2 \sum_{t=2}^{n} x_t x_{t-1} - 2\alpha \sum_{t=2}^{n} x_{t-1} - 2\mu_\beta \sum_{t=2}^{n} x_{t-1}^2$$
$$= 0$$

, and

$$\hat{\mu}_{\beta,LS} = \frac{\sum_{t=2}^{n} x_t x_{t-1} - \hat{\alpha}_{LS} \sum_{t=2}^{n} x_{t-1}}{\sum_{t=2}^{n} x_{t-1}^2}. \tag{6}$$

From (6), let us replace in (5) and the solution of $\hat{\alpha}_{LS}$ is

$$\hat{\alpha}_{LS} = \frac{\sum_{t=2}^{n} x_{t-1}^2 \sum_{t=1}^{n} x_t - \sum_{t=2}^{n} x_t x_{t-1} \sum_{t=2}^{n} x_{t-1}}{\left(n \sum_{t=2}^{n} x_{t-1}^2 - \left(\sum_{t=2}^{n} x_{t-1} \right)^2 \right)},$$

or $\hat{\mu}_{\beta,LS}$ can rewrite as

$$\hat{\mu}_{\beta,LS} = \frac{n \sum_{t=2}^{n} x_t x_{t-1} - \sum_{t=1}^{n} x_t \sum_{t=2}^{n} x_{t-1}}{\left(n \sum_{t=2}^{n} x_{t-1}^2 - \left(\sum_{t=2}^{n} x_{t-1} \right)^2 \right)}.$$

For RCA(1) model, it can be fitted model as

$$\hat{x}_t = \hat{\alpha}_{LS} + \hat{\mu}_{\beta,LS} x_{t-1} \quad , t = 2,3,...n.$$

Bayesian Analysis

In Bayesian estimation for RCA(1) model, we proposed a three-level hierarchical model. At the first level is the conditional distribution of the data x_t's given the observed random variables x_{t-1}, coefficient α, β_t, and σ_ε^2. The second level consists of the conditional distribution β_t given the parameter μ_β and σ_β^2. Finally the last level shows the prior distribution of $\theta = (\alpha, \mu_\beta)^\top$. Consequently, given the sample variables $x_1, x_2, \ldots, x_n$, we are able to express the RCA(1) model in the following hierarchical structure,

$$\begin{aligned} x_t \mid x_{t-1}, \alpha, \beta_t, \sigma_\varepsilon^2 &\sim N(\alpha + \beta_t x_{t-1}, \sigma_\varepsilon^2), \\ \beta_t \mid \mu_\beta, \sigma_\beta^2 &\sim N(\mu_\beta, \sigma_\beta^2), \\ (\alpha, \mu_\beta) &\sim p(\alpha, \mu_\beta), \end{aligned} \tag{7}$$

where $p(\cdot)$ is the prior density of θ which reflects our prior about the unknown parameters. Following (7), we can express the likelihood function of θ as,

$$L(\alpha, \mu_\beta \mid x_1, x_2, \ldots, x_n, \varepsilon_1, \ldots, \varepsilon_n) = \phi(x_1; \alpha, \sigma_\varepsilon) \prod_{i=2}^{n} \phi\left(x_t; \alpha + \mu_\beta x_{t-1}, \sqrt{\sigma_\varepsilon^2 + \sigma_\beta^2 x_{t-1}^2}\right), \tag{8}$$

where $\phi(x; \mu, \sigma)$ denotes the density function of a normal distribution with mean μ and standard deviation σ. Therefore, the joint posterior density of the parameters is given by,

$$f(\theta \mid x_1, x_2, \ldots, x_n) \quad \propto \quad L(\theta \mid x_1, x_2, \ldots, x_n) p(\theta)$$

where $p(\theta)$ is a prior density of θ. From the hierarchical structure in (8), the joint posterior density can be written as

$$f(\alpha \mid x_1, x_2, \ldots, x_n) \propto \int f(\alpha, \mu_\beta, \sigma_\beta^2, \sigma_\varepsilon^2 \mid x_1, x_2, \ldots, x_n) d\mu_\beta \, d\sigma_\beta^2 \, d\sigma_\varepsilon^2,$$

and

$$f(\mu_\beta \mid x_1, x_2, \ldots, x_n) \propto \int f(\alpha, \mu_\beta, \sigma_\beta^2, \sigma_\varepsilon^2 \mid x_1, x_2, \ldots, x_n) d\alpha \, d\sigma_\beta^2 \, d\sigma_\varepsilon^2.$$

To deal with the complicated likelihood function, we used the so-called Markov Chain Monte Carlo (MCMC) method to generate samples from the posterior distribution of $\theta = (\alpha, \mu_\beta)^\top$. We will carry out the Gibbs sampler ([6]), a widely used MCMC method, to obtain the parameter from the posterior distribution using the software R on package rjags.

***Prior Distributions*.**

The Bayesian analysis combines prior information about model parameters with data from observed data, thereby generating a posterior distribution. Bayesian analysis requires prior distribution, which is challenging to specify analytically for the model considered.

For the parameter estimation of RCA(1) model, the prior distribution of $\theta = \left(\alpha, \mu_\beta\right)^\top$ are considered to be a continuous random variable in the set of real numbers following normal distribution.

***Posterior Distribution*.**

To manage Bayesian analysis for RCA(1), we interested in the properties of the density of $\theta = \left(\alpha, \mu_\beta\right)^\top$ Deriving the joint posterior density for θ amounts to integrating out the unobserved coefficients α and μ_β. We can perform the likelihood function to obtain posterior estimator.

MCMC methods consist of algorithms to construct a Markov Chain of the parameters such that its stationary distribution is our distribution of interest. That means, under some regularity conditions, the realization of this Markov Chain can though of as points sample from the posterior distribution.

We use the Gibbs sampler ([7]), the most popular MCMC method, to obtain dependent samples from the posterior distribution. Specifically, we derive the condition densities each parameter θ.

The condition densities of parameter in RCA(1) model is $f\left(\alpha \mid \mu_\beta, \sigma_\beta^2, \sigma_\varepsilon^2, \underline{x}\right)$, and $f\left(\mu_\beta \mid \alpha, \sigma_\beta^2, \sigma_\varepsilon^2, \underline{x}\right)$ as the full conditional densities of α and μ_β respectively, based on Model (2).

The Gibbs sampling algorithm is:

1. Initialize $\alpha^{(0)}$ and $\mu_\beta^{(0)}$, for $k = 1, 2, \ldots, m+M$

2. Draw $\alpha^{(k)}$ from $f\left(\alpha \mid \mu_\beta^{(k-1)}, \sigma_\beta^{2(k-1)}, \sigma_\varepsilon^{2(k-1)}, \underline{x}\right)$

   Draw $\mu_\beta^{(k)}$ from $f\left(\mu_\beta \mid \alpha^{(k)}, \sigma_\beta^{2(k-1)}, \sigma_\varepsilon^{2(k-1)}, \underline{x}\right)$

where m is burn-in and M is the number of samples generated after burn-in. Repeating the above sampling steps, we obtain a discrete-time Markov chain $\left\{\left(\alpha^{(k)}, \mu_\beta^{(k)}\right); k = 1, 2, \ldots\right\}$ whose stationary distribution is the joint posterior density of the parameters.

Gibbs sampling algorithm is proposed above a software R and package rjags. A Markov chain of parameters of α and μ_β, are constructed by computing the mean sampling from the joint posterior density as standard distribution following:

$$\hat{\alpha}_{Bayes} = \frac{\sum_{k=1}^{M} \alpha^{(k)}}{M} \quad \text{and} \quad \hat{\mu}_{\beta,Bayes} = \frac{\sum_{k=1}^{M} \mu_\beta^{(k)}}{M}.$$

For observed fitting values of RCA(1) model, it can be written as

$$\hat{x}_t = \hat{\alpha}_{Bayes} + \hat{\mu}_{\beta,Bayes} x_{t-1} \quad , t = 2, 3, \ldots n.$$

Application of Real Data:

In this section, we consider applying the RCA(1) model using the least squares criterion and Bayesian analysis developed in the previous section. The monthly average of Stock Exchange of Thailand (SET) index applies for RCA(1) model in terms of real-time series data. The SET index started for trading on April 30, 1975, and we are fitted data from 1976 to 2017 for estimating the parameter of RCA(1), then we forecast data from 2018-2019. This data collected from http://www.set.or.th/th/market/market/statistics.html, which shown in Figure 1.

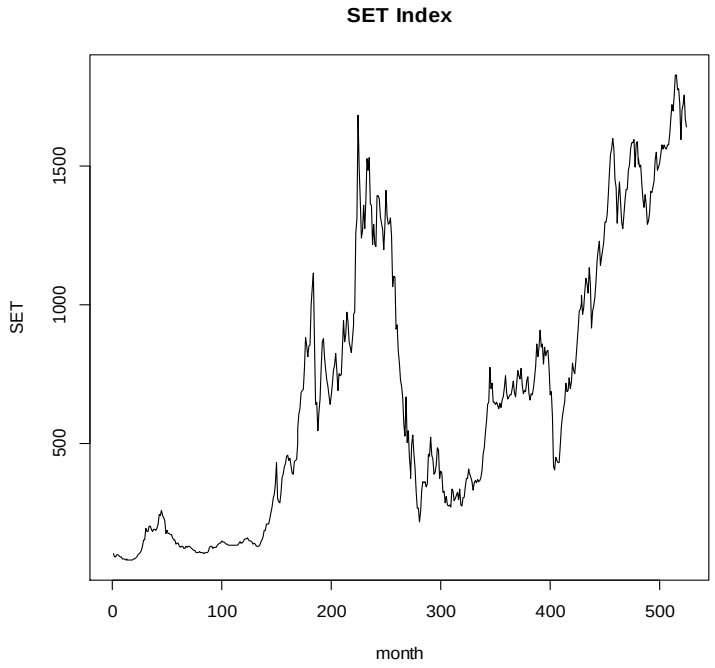

Figure 1. The time series plot for SET index

Based on fitting an RCA(1) model to the fitted SET index volume data, we calculated the point forecasts and the forecasting values. Figure 2 gives the plot of the SET index and the dashed line of the least-squares method and the dotted line of Bayesian analysis. The Mean Square Error (MSE) evaluates the difference between the real values and forecasting values. We also compute the MSE as the criterion defined following:

$$MSE = \frac{\sum_{t=1}^{24}(x_t - \hat{x}_t)^2}{24},$$

where x_t denotes the real values, and $\hat{x}_t$ denotes the forecasting values.

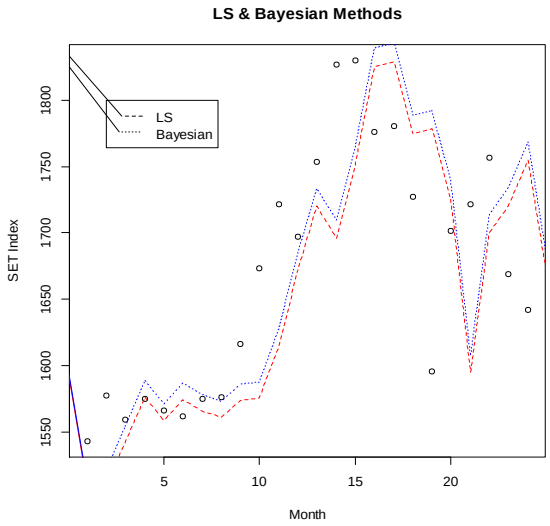

Figure 2. The plot for SET index and forecasting of least squares method (LS) and Bayesian Analysis (Bayesian)

Compare with Figure 2, and it can see that the forecasting values of the least-squares method are relatively close to the observed series. Therefore, we should more convince by the MSE of the least-squares method given 2649.224, but the MSE of Bayes analysis is shown by 2677.601.

Conclusion:

In this paper, we studied the least-squares method and Bayesian analysis for estimating the first order in RCA or called RCA(1) model. We are also interested in the power of estimating by the mean square error for application in real data. We can see that the least-squares method outperforms the Bayesian analysis similar to the results of the simulation study. We would recommend fitting RCA(1) model on time series data by the least-squares method where stationary and non-stationary data are expected. It is indicated that the RCA(1) model is affected on past observed data more than the informative prior to Bayesian Analysis.

References:

1. Tsay C, Conditional heteroscedastic time series models, Journal of the American Statistical Association. 1987;82: 590-604.
2. Nicholls D F, Quinn B G, Random coefficient autoregressive models: An introduction, Springer- Verlag Inc, New York. 1982.
3. Wang D, Ghosh S K, Bayesian estimation and unit root tests for random coefficient autoregressive models, Model Assisted Statistics and Applications. 2008;3: 281-295.
4. Gilks W, Richardson S, Speigelhalter D, Markov Chain Monte Carlo in Practice, Interdisciplinary Statistics, Chapman & Hall, Suffolk. 1996.
5. Gelfand A, Hills S, Racine-Poon A, Smith A, Illustration of Bayesian inference in normal data models using Gibbs sampling, Journal of the American Statistical Association. 1990;85: 972-985.
6. Gelfand A, Smith A F M, Sampling-based approaches to calculating marginal densities, Journal of American Statistical Association. 1990;85:398-409.
7. Geman S, Geman D, Stochastic relaxation, Gibbs distributions and the Bayesian restoration of images, IEEE Transactions on Pattern Analysis and Machine Intelligence. 1984;6:721-741.

B_006_OA: CLOSED (2, 3)-KNIGHT'S TOURS ON THE 1 × *n*, 2 × *n*, 3 × *n* AND 4 × *n* TOROIDAL CHESSBOARDS FOR ALL POSITIVE INTEGER *n*

Adthasit Sinna, Peranat Chuchard, Natkamon Khemngoen, Sirirat Singhun*

Department of Mathematics, Faculty of Science, Ramkhamhaeng University, Bangkok, Thailand
*e-mail: sin_sirirat@ru.ac.th

Abstract:

Chia and Ong introduced an *(a, b)-knight's move*, the knight moves *a* squares vertically or *a* squares horizontally and then *b* squares at 90 degrees angle. A *closed (a, b)-knight's tour* is a sequence of (*a*, *b*)-knight's moves such that the knight lands on every square once and returns to its starting square. They obtained sufficient and necessary conditions for the 5*k* × *n* chessboard where (5*k*, *n*) ≠ (5, 18) to have a closed (2, 3)-knight's tour. Singhun et al. obtained closed (2, 3)-knight's tours of the 5*k* × *n* cylindrical chessboard, and the 9*k* × *n* cylindrical chessboard for $n \in \{4, 5, 7, 8, 9, 10, 11, 12, 13\}$. Moreover, they showed that there is no closed (2, 3)-knight's tours on the *m* × *n* cylindrical chessboard where (i) $m \in \{1, 2, 3, 4, 6, 7, 8\}$ and (ii) $m = 9$ and $n \in \{1, 2, 3, 6\}$. Then these raise the question about which *m* × *n* toroidal chessboards, for $m \in \{1, 2, 3, 4, 6, 7, 8\}$, have any closed (2, 3)-knight's tours. In this talk, we give a positive answer to this question when $m \in \{1, 2, 3, 4\}$ by constructing closed (2, 3)-knight's tours in each *m* × *n* toroidal chessboard.

B_007_OF: MODELING THE IMPACT OF HIV INFECTION ON TB INCIDENCE

Natdanai Boonsri,[1,2] Kornkanok Bunwong,[1,2] *

[1] Department of Mathematics, Faculty of Science, Mahidol University, Bangkok 10400, Thailand
[2] Centre of Excellence in Mathematics, CHE, Bangkok 10400 Thailand
*Corresponding author e-mail: kornkanok.bun@mahidol.ac.th

Abstract:

Since the 20th Century, drugs and treatments of tuberculosis (TB) and human immunodeficiency virus (HIV) have been available. We, therefore, introduce the compartmental model consisting of three states for HIV (HIV susceptible individuals, HIV infected individuals, and HIV-infected individuals under ART) with three states for TB (TB susceptible individuals, latent TB individuals, and TB infected individuals). For various circumstances of HIV dynamics, the basic reproduction numbers (R_0) for the spread of TB are derived using the next-generation method (NGM). The useful information from the Department of Disease Control, Ministry of Public Health, Thailand and relevant disease control agencies leading to parameter estimation. The numerical results finally reveal the relationship between R_0 and TB successful treatment rate in each group of HIV infection.

Keywords: basic reproduction number, epidemic model, tuberculosis (TB) and human immunodeficiency virus (HIV) co-infection, transmission dynamics, antiretroviral therapy

Introduction:

The world has continuously faced new disease. The development and strengthening of the existing health system are required and the supply of equipment and medicines are needed. TB is currently one of the top 10 causes of death worldwide and causes serious health problems.[1] TB is an airborne infection that is caused by a specific type of bacterium called Mycobacterium tuberculosis. The bacteria typically attack the lungs, but it also attacks any part of the body such as the brain, kidneys, spine, or another organ system.[2] TB infection occurs when droplet nuclei containing TB germs are inhaled into the lungs. It is spread when people with lung TB cough, sneeze, speak or sing. TB germs are passed through the air. These germs can float in the air for several hours. Persons who inhale only a few of these germs can become infected. We can group TB infection as latent and active TB. In 2018, World Health Organization (WHO) reported that 10 million people fell ill with TB worldwide. Fortunately, TB is curable and preventable so the number of new cases decreases.

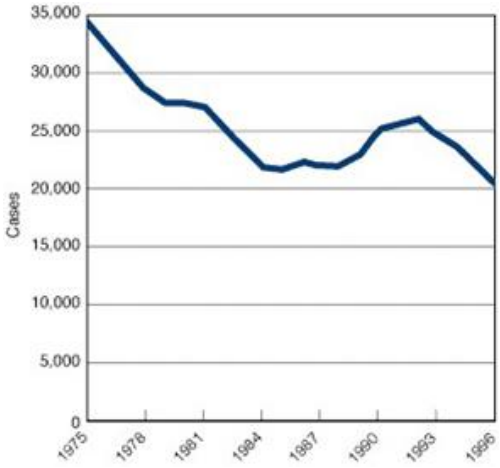

Figure 1. Evolution of incidence of tuberculosis cases in U.S.A. between 1975 and 1996.[3]

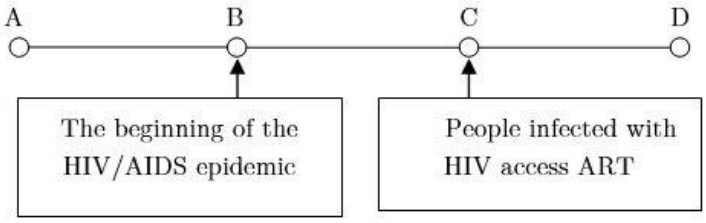

Figure 2. An outline of Figure 1 representing TB historical timeline in three circumstances of HIV dynamics. A=1975, B=1981, C=1990, D=1995

States for HIV are divided into three intervals according to TB historical timeline as shown in Figure 2. During the interval between A and B, TB incidence drop because the guidelines on preventing TB transmission in health care facilities are issued. During the interval between B and C, equivalently to 1980s, the beginning of the HIV epidemic has played important roles in the re-emerged of TB. People with HIV are at high risk for accelerating the course of the disease. In addition, people with HIV can also face health from opportunistic infections and TB is the most common opportunistic infection. Due to medical advances, antiretroviral therapy (ART) is the use of HIV medicines to maximally suppress the HIV virus and stop the progression of HIV disease. Although HIV cannot be cured, HIV medicines help people infected with HIV to live longer and healthier. It leads to increased chances of successfully treating TB as shown in the last interval and the spread of TB can be controlled if the HIV-infected patient accepts and is under medical care. Therefore, understanding HIV model with treatment is increasingly important. Huo H et al.[4] presented a simple HIV/AIDS epidemic model with treatment and estimated parameter values from the demographic and HIV/AIDS data of South Africa. Their results showed that after treatment, the probability of HIV-infected individuals becoming AIDS patients decrease and the risk of passing disease to future generations is reduced.

This paper is an extended version of Bunwong K et al.[5] by adding HIV-infected individuals under ART. The main objective of this study is to compute R_0 for the spread of TB through three HIV groups by using NGM[6, 7] and investigate the relationship between the basic reproduction number and TB successful treatment rate for people in HIV submodels.

Methodology:

1. Model Formulation

We present a mathematical model with nine compartments for interaction between TB and HIV/ART epidemics. The compartmental structure of our model combines three states for HIV with three states for TB. The notation for all variables and all parameters are shown in Table 1 and Table 2, respectively. The diagram of the model is shown in Figure 3. According to the three states of HIV infection, the model can be grouped as follows.

Table 1. The Notation for the populations in the co-infection model

Variable	Description
S_N	HIV susceptible individuals with TB susceptible
E_N	HIV susceptible individuals with latent TB infection
I_N	HIV susceptible individuals with active TB infection
S_H	HIV-infected individuals with TB susceptible
E_H	HIV-infected individuals with latent TB infection
I_H	HIV-infected individuals with active TB infection
S_T	HIV-infected individuals under ART with TB susceptible
E_T	HIV-infected individuals under ART with latent TB infection
I_T	HIV-infected individuals under ART with active TB infection

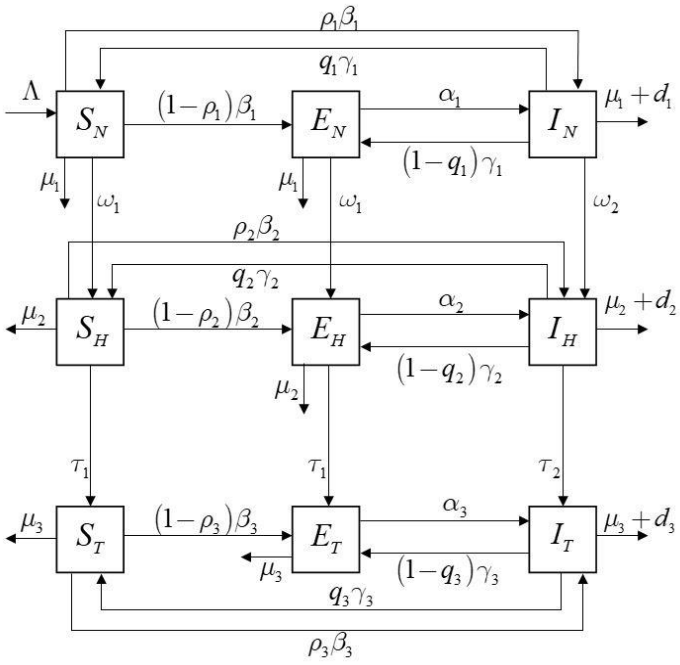

Figure 3. A transition diagram between epidemiological classes for the transmission dynamics of TB-HIV/ART.

Table 2. Description of parameters for TB-HIV/ART co-infection model

Parameter	Description
Λ	Birth rate
μ_1	Mortality rate without HIV
μ_2	Mortality rate with HIV
μ_3	Mortality rate with ART
d_1	Death rate caused by TB without HIV
d_2	Death rate caused by TB with HIV
d_3	Death rate caused by TB with ART
ρ_1, ρ_2, ρ_3	Proportion of active TB in HIV susceptible, HIV and ART groups
$\beta_1, \beta_2, \beta_3$	TB detection rate in HIV susceptible, HIV and ART groups
$\alpha_1, \alpha_2, \alpha_3$	TB activation rate in HIV susceptible, HIV and ART groups
q_1, q_2, q_3	TB successful treatment for people in HIV susceptible, HIV and ART groups
$\gamma_1, \gamma_2, \gamma_3$	TB recovery rate in HIV susceptible, HIV and ART groups
ω_1, ω_2	HIV detection rate without and with infectious TB
τ_1, τ_2	Treatment rate of HIV without and with infectious TB

The following group of equations is assumed to describe the rate of change of the HIV susceptible individuals group.

$$\frac{dS_N}{dt} = \Lambda + q_1\gamma_1 I_N - \beta_1 S_N I_N - \mu_1 S_N - \omega_1 S_N. \tag{1.1}$$

$$\frac{dE_N}{dt} = (1-\rho_1)\beta_1 S_N I_N + (1-q_1)\gamma_1 I_N - (\alpha_1 + \mu_1 + \omega_1) E_N. \tag{1.2}$$

$$\frac{dI_N}{dt} = \rho_1\beta_1 S_N I_N + \alpha_1 E_N - (\gamma_1 + \mu_1 + d_1 + \omega_2) I_N. \tag{1.3}$$

The following group of equations is assumed to describe the rate of change of the HIV-infected individuals group.

$$\frac{dS_H}{dt} = \omega_1 S_N + q_2\gamma_2 I_H - \beta_2 S_H I_H - (\mu_2 + \tau_1) S_H. \tag{1.4}$$

$$\frac{dE_H}{dt} = (1-\rho_2)\beta_2 S_H I_H + (1-q_2)\gamma_2 I_H + \omega_1 E_N - (\alpha_2 + \mu_2 + \tau_1) E_H. \tag{1.5}$$

$$\frac{dI_H}{dt} = \rho_2\beta_2 S_H I_H + \alpha_2 E_H + \omega_2 I_N - (\gamma_2 + \mu_2 + d_2 + \tau_2) I_H. \quad (1.6)$$

The following group of equations is assumed to describe the rate of change of HIV-infected individuals under ART group.

$$\frac{dS_T}{dt} = \tau_1 S_H + q_3\gamma_3 I_T - \beta_3 S_T I_T - \mu_3 S_T. \quad (1.7)$$

$$\frac{dE_T}{dt} = (1-\rho_3)\beta_3 S_T I_T + (1-q_3)\gamma_3 I_T + \tau_1 E_H - (\alpha_3 + \mu_3) E_T. \quad (1.8)$$

$$\frac{dI_T}{dt} = \rho_3\beta_3 S_T I_T + \alpha_3 E_T + \tau_2 I_H - (\gamma_3 + \mu_3 + d_3) I_T. \quad (1.9)$$

2. The basic reproduction numbers

2.1 TB only submodel

The TB only submodel is composed of equations (1.1)-(1.3) describing the rates of changes of two TB infected states (E_N, I_N) and one TB uninfected state (S_N). At the TB-infection free equilibrium point $E_N = I_N = 0$, the equilibrium population for S_N is $S_{N,1}^* = \Lambda/\mu_1$. The appearance of S_N in equation (1.1)-(1.3) can now replace by Λ/μ_1. For small (E_N, I_N), we obtain the following linearized system about the TB infection-free equilibrium point:

$$\frac{dE_N}{dt} = (1-\rho_1)\beta_1\left(\frac{\Lambda}{\mu_1}\right) I_N + (1-q_1)\gamma_1 I_N - (\alpha_1 + \mu_1) E_N, \quad (2.1)$$

$$\frac{dI_N}{dt} = \rho_1\beta_1\left(\frac{\Lambda}{\mu_1}\right) I_N + \alpha_1 E_N - (\gamma_1 + \mu_1 + d_1) I_N. \quad (2.2)$$

Let $X = (E_N, I_N)'$ where the prime denotes transpose. We rewritten the linearized subsystem in the form

$$\dot{X} = (T + \Sigma) X$$

where the matrix T corresponds to transmissions:

$$T_{TB} = \begin{bmatrix} 0 & (1-\rho_1)\beta_1\left(\frac{\Lambda}{\mu_1}\right) \\ 0 & \rho_1\beta_1\left(\frac{\Lambda}{\mu_1}\right) \end{bmatrix}$$

and the matrix Σ corresponds to transitions:

$$\Sigma_{TB} = \begin{bmatrix} -(\alpha_1 + \mu_1) & (1-q_1)\gamma_1 \\ \alpha_1 & -(\gamma_1 + \mu_1 + d_1) \end{bmatrix}.$$

Hence, the next generation matrix (NGM) with large domain is two-dimensional and given by $K_L^{TB} = -T_{TB}\sum_{TB}^{-1}$.

$$K_L^{TB} = -\frac{1}{A}\begin{bmatrix} 0 & (1-\rho_1)\beta_1\left(\frac{\Lambda}{\mu_1}\right) \\ 0 & \rho_1\beta_1\left(\frac{\Lambda}{\mu_1}\right) \end{bmatrix}\begin{bmatrix} -(\gamma_1+\mu_1+d_1) & -(1-q_1)\gamma_1 \\ -\alpha_1 & -(\alpha_1+\mu_1) \end{bmatrix},$$

$$= \frac{1}{A}\begin{bmatrix} (1-\rho_1)\beta_1\left(\frac{\Lambda}{\mu_1}\right)(\alpha_1) & (1-\rho_1)\beta_1\left(\frac{\Lambda}{\mu_1}\right)(\alpha_1+\mu_1) \\ \rho_1\beta_1\left(\frac{\Lambda}{\mu_1}\right)(\alpha_1) & \rho_1\beta_1\left(\frac{\Lambda}{\mu_1}\right)(\alpha_1+\mu_1) \end{bmatrix},$$

where $A = (\alpha_1+\mu_1)(\gamma_1+\mu_1+d_1) - \alpha_1(1-q_1)\gamma_1$.

The spectral radius of a matrix A is defined by $\rho(A) := \sup\{|\lambda| : \lambda \in \rho(A)\}$ where $\sigma(A)$ denotes the spectrum of A. By definition, the basic reproduction number is the largest eigenvalues of the NGM. Thus, $R_0 = \rho(K)$. Consequently,

$$R_0^{TB} = \rho\left(K_L^{TB}\right) = \frac{1}{2}\left(tr\left(K_L^{TB}\right) + \sqrt{tr\left(K_L^{TB}\right)^2 - 4\det\left(K_L^{TB}\right)}\right). \tag{2.3}$$

Since $\det\left(K_L^{TB}\right) = 0$, we can conclude right away that $R_0 = tr\left(K_L^{TB}\right)$.

Finally, the basic reproduction number for the TB only submodel is

$$R_0^{TB} = \frac{\beta_1 S_{N,1}^*}{A}(\alpha_1 + \rho_1\mu_1). \tag{2.4}$$

Here some parameters have superscripts or subscripts to indicate the model they belong to. For example, R_0^{TB} is the basic reproduction number for TB only submodel.

2.2 TB and HIV co-epidemic model

The TB-HIV co-epidemic model is composed of equations (1.1)-(1.6) describing the rates of changes of four TB infected states (E_N, E_H, I_N, I_H) and two uninfected states (S_N, S_H). At the TN infection free equilibrium point $E_N = E_H = I_N = I_H = 0$. Hence,

$$S_{N,2}^* = \frac{\Lambda}{\mu_1+\omega_1} \text{ and } S_{H,2}^* = \left(\frac{\omega_1}{\mu_2}\right)\left(\frac{\Lambda}{\mu_1+\omega_1}\right)$$

For small (E_N, E_H, I_N, I_H), we obtain the following linearized system:

$$\frac{dE_N}{dt} = (1-\rho_1)\beta_1\left(\frac{\Lambda}{\mu_1+\omega_1}\right)I_N + (1-q_1)\gamma_1 I_N - (\alpha_1+\mu_1+\omega_1)E_N. \tag{2.5}$$

$$\frac{dE_H}{dt}=(1-\rho_2)\beta_2\left(\frac{\omega_1}{\mu_2}\right)\left(\frac{\Lambda}{\mu_1+\omega_1}\right)I_H+(1-q_2)\gamma_2 I_H+\omega_1 E_N-(\alpha_2+\mu_2)E_H. \tag{2.6}$$

$$\frac{dI_N}{dt}=\rho_1\beta_1\left(\frac{\Lambda}{\mu_1+\omega_1}\right)I_N+\alpha_1 E_N-(\gamma_1+\mu_1+d_1+\omega_2)I_N. \tag{2.7}$$

$$\frac{dI_H}{dt}=\rho_2\beta_2\left(\frac{\omega_1}{\mu_2}\right)\left(\frac{\Lambda}{\mu_1+\omega_1}\right)I_H+\alpha_2 E_H+\omega_2 I_N-(\gamma_2+\mu_2+d_2)I_H. \tag{2.8}$$

We will calculate R_0 from these equations by using the next generation method as described by Diekmann et al.[7] Let $X=(E_N,E_H,I_N,I_H)'$. Then we obtain the following results $K_L^{TB-HIV}=-T_{TB-HIV}\sum_{TB-HIV}^{-1}$. Since $\det K_L^{TB-HIV}=0,$ we can reduce the high dimensional matrix to the NGM with small domain which is given by $K_S=-R\sum^{-1}C$ where

$$R=\begin{bmatrix}0&0&1&0\\0&0&0&1\end{bmatrix}$$

$$C=\begin{bmatrix}(1-\rho_1)\beta_1\left(\frac{\Lambda}{\mu_1+\omega_1}\right)&0\\0&(1-\rho_2)\beta_2\left(\frac{\omega_1}{\mu_2}\right)\left(\frac{\Lambda}{\mu_1+\omega_1}\right)\\\rho_1\beta_1\left(\frac{\Lambda}{\mu_1+\omega_1}\right)&0\\0&\rho_2\beta_2\left(\frac{\omega_1}{\mu_2}\right)\left(\frac{\Lambda}{\mu_1+\omega_1}\right)\end{bmatrix}$$

Therefore, the basic reproduction number for TB-HIV co-epidemic model $\left(R_0^{TB-HIV}\right)$ can be obtained easily from the trance and the determinant of the corresponding two-dimensional matrix.

$$R_0=\rho(K_S)=\frac{1}{2}\left(trace(K_S)+\sqrt{trace(K_S)^2-4\det(K_S)}\right). \tag{2.9}$$

2.3 TB and HIV/ART co-epidemic model

The TB-HIV/ART co-epidemic model is composed of equations (1.1)-(1.9) describing the rates of changes of six TB infected states $(E_N,E_H,E_T,I_N,I_H,I_T)$ and three TB uninfected states (S_N,S_H,S_T). At the TB infection free equilibrium point $E_N=E_H=E_T=I_N=I_H=I_T=0,$

$$S_{N,4}^*=\frac{\Lambda}{\mu_1+\omega_1},\ S_{H,4}^*=\left(\frac{\omega_1}{\mu_2+\tau_1}\right)\left(\frac{\Lambda}{\mu_1+\omega_1}\right)\text{ and }S_{T,4}^*=\left(\frac{\tau_1}{\mu_3}\right)\left(\frac{\omega_1}{\mu_2+\tau_1}\right)\left(\frac{\Lambda}{\mu_1+\omega_1}\right).$$

For small $(E_N,E_H,E_T,I_N,I_H,I_T),$ we obtain the following linearized system:

$$\frac{dE_N}{dt} = (1-\rho_1)\beta_1\left(\frac{\Lambda}{\mu_1+\omega_1}\right)I_N + (1-q_1)\gamma_1 I_N - (\alpha_1+\mu_1+\omega_1)E_N, \tag{2.10}$$

$$\frac{dE_H}{dt} = (1-\rho_2)\beta_2\left(\frac{\omega_1}{\mu_2+\tau_1}\right)\left(\frac{\Lambda}{\mu_1+\omega_1}\right)I_H + (1-q_2)\gamma_2 I_H + \omega_1 E_N - (\alpha_2+\mu_2+\tau_1)E_H, \tag{2.11}$$

$$\frac{dE_T}{dt} = (1-\rho_3)\beta_3\left(\frac{\tau_1}{\mu_3}\right)\left(\frac{\omega_1}{\mu_2+\tau_1}\right)\left(\frac{\Lambda}{\mu_1+\omega_1}\right)I_T + (1-q_3)\gamma_3 I_T + \tau_1 E_H - (\alpha_3+\mu_3)E_T, \tag{2.12}$$

$$\frac{dI_N}{dt} = \rho_1\beta_1\left(\frac{\Lambda}{\mu_1+\omega_1}\right)I_N + \alpha_1 E_N - (\gamma_1+\mu_1+d_1+\omega_2)I_N, \tag{2.13}$$

$$\frac{dI_H}{dt} = \rho_2\beta_2\left(\frac{\omega_1}{\mu_2+\tau_1}\right)\left(\frac{\Lambda}{\mu_1+\omega_1}\right)I_H + \alpha_2 E_H + \omega_2 I_N - (\gamma_2+\mu_2+d_2+\tau_2)I_H, \tag{2.14}$$

$$\frac{dI_T}{dt} = \rho_3\beta_3\left(\frac{\tau_1}{\mu_3}\right)\left(\frac{\omega_1}{\mu_2+\tau_1}\right)\left(\frac{\Lambda}{\mu_1+\omega_1}\right)I_T + \alpha_3 E_T + \tau_2 I_H - (\gamma_3+\mu_3+d_3)I_T. \tag{2.15}$$

R_0 can be calculated from these equations by using the next generation method as described by Diekmann et al.[7] Let $X = (E_N, E_H, E_T, I_N, I_H, I_T)'$. Following Diekmann's recipe, we obtain the following results $K_L^{TB-HIV/ART} = -T_{TB-HIV/ART}\sum_{TB-HIV/ART}^{-1}$. Since $\det K_L^{TB-HIV/ART} = 0,$ we can reduce the high dimensional matrix to the NGM with small domain which is given by $K_S = -R\sum^{-1} C$ where

$$R = \begin{bmatrix} 0 & 0 & 0 & 1 & 0 & 0 \\ 0 & 0 & 0 & 0 & 1 & 0 \\ 0 & 0 & 0 & 0 & 0 & 1 \end{bmatrix}$$

$$C = \begin{bmatrix} (1-\rho_1)\beta_1 S_{N,4}^* & 0 & 0 \\ 0 & (1-\rho_2)\beta_2 S_{H,4}^* & 0 \\ 0 & 0 & (1-\rho_3)\beta_3 S_{T,4}^* \\ \rho_1\beta_1 S_{N,4}^* & 0 & 0 \\ 0 & \rho_2\beta_2 S_{H,4}^* & 0 \\ 0 & 0 & \rho_3\beta_3 S_{T,4}^* \end{bmatrix}$$

Therefore, the basic reproduction number for TB-HIV/ART co-epidemic model $\left(R_0^{TB-HIV/ART}\right)$ can be obtained from the trace and the determinant of the corresponding two-dimensional matrix according to equation (2.9).

Results and Discussion:

Most parameter values are obtained using information from the Epidemiological Information Section, Bureau of Epidemiology, Department of Disease Control, Ministry of Public Health, Thailand (Epidemiological Information Section, 2015). The useful information from related disease control departments led to parameter estimation shown in Table 3.

Table 3. Description of the parameters, their values (per year) and references with regard to HIV/ART and TB.

Model Description	**Without HIV Parameter value**		**With HIV Parameter value**		**With HIV under ART Parameter value**	
Mortality rate	μ_1	$0.64\%^{f}$	μ_2	$0.88\%^{f}$	μ_3	$0.70\%^{f}$
TB mortality rate	d_1	$5.95\%^{f}$	d_2	$14.00\%^{d}$	d_3	$10\%^{f}$
TB detection rate	β_1	$1.20\%^{f}$	β_2	$67.40\%^{f}$	β_3	$10\%^{f}$
Proportion of active TB	ρ_1	0.1^{b}	ρ_2	0.1^{b}	ρ_3	0.1^{b}
TB recovery rate	γ_1	$89.00\%^{a}$	γ_2	$89.00\%^{a}$	γ_3	$89.00\%^{a}$
TB successful treatment rate	q_1	0.97^{a}	q_2	0.97^{a}	q_3	0.97^{a}
TB activation rate	α_1	$10.00\%^{b}$	α_2	$30.00\%^{b}$	α_3	$20.00\%^{b}$
Model Description	**Without infectious TB Parameter value**				**With Infectious TB Parameter value**	
HIV detection rate	ω_1	$0.16\%^{f}$			ω_2	$16.00\%^{a}$
Treatment rate of HIV	τ_1	$90\%^{e}$			τ_2	$90\%^{e}$
Birth rate			$12\%^{a,c}$			

[a]Bureau of Tuberculosis, Department of Disease Control, Ministry of Public Health, Thailand (2014)

[b]Nateniyom S (2013)

[c]Official Statistics Registration Systems (2015)

[d]Tuberculosis Center Region 12 (2015)

[e]UNAIDS (2019)

[f]calculated from data of a, b, c and Official Statistics Registration Systems 2015

Using parameter values in Table 3, the basic reproduction number R_0^{TB} is calculated to indicate the spread of TB. Figure 4 shows the trends of the basic reproduction number R_0^{TB} when TB successful treatment rate for people in HIV varies. In the case of TB successful treatment rate for people in HIV susceptible class (q_1), the value of R_0^{TB} clearly decreases as q_1 increases. The thresholds of $R_0^{TB}=1$ for a HIV susceptible group occur at $q_1=0.112.$ It implies that the numbers of people with TB in a HIV susceptible group decline and the infections tend to disappear from the system.

In Figure 2, there was a turnaround of rising in new TB cases in the interval between B and C because of the onset of the HIV/AIDS epidemic. Obviously, in Figure 4, curve of R_0^{TB-HIV} with TB successful treatment rate for people in HIV group (q_2) is above 1. This implies that the TB-HIV co-infection will remain in the system.

ART stop the progression of HIV disease resulting in a reduced incidence of TB cases in the last interval between C and D in Figure 2. Figure 4 illustrates trend of the basic reproduction number $R_0^{TB-HIV/ART}$ with TB successful treatment rate for people in ART group (q_3). Clearly, the value of $R_0^{TB-HIV/ART}$ decreases as q_3 increases. The thresholds of $R_0^{TB-HIV/ART}=1$ for a HIV-infected under ART group occur at $q_3=0.32$ causing the trend of new TB cases decreasing.

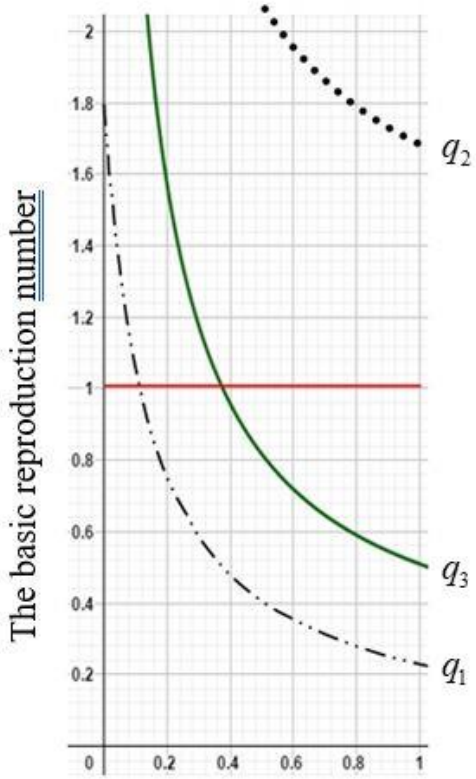

Figure 4. The relationship between the basic reproduction number and TB successful treatment rate for people in HIV susceptible q_1 , HIV infected q_2 and HIV-infected under ART q_3 submodels.

Conclusion:

A mathematical model for the transmission dynamics of TB and HIV/ART co-infection is proposed and analyzed. In this study, the basic reproduction numbers predicting the invasion of TB through three HIV groups, namely HIV susceptible individuals, HIV infected individuals, and HIV-infected individuals under ART are obtained by Diekmann's recipe. Using information from the Epidemiological Information Section, Bureau of Epidemiology, Department of Disease Control, Ministry of Public Health, Thailand and related disease control departments, our numerical results imply that the TB disease will eventually fade out from the population when TB successful treatment rate in HIV susceptible individuals is greater than 0.112. However, after HIV epidemic occurs, TB successful treatment is no more effective in HIV-infected individuals. Thus TB disease persist in a population. Once ART is available, TB successful treatment rate in HIV-infected under ART individuals is higher than 0.32. Therefore, it implies that TB disease will eventually disappear from the system if TB successful treatment rate is high enough. Finally, the more data, the better numerical result.

Acknowledgements:

This research was supported by 1) the Department of Mathematics, Faculty of Science, Mahidol University, 2) the Centre of Excellence in Mathematics, Commission on Higher Education, Ministry of Education

References:

1. Hickson R, Mercer G, and Lokuge K. MODSIM. 2011; 926-932.
2. Bowong S, Tewa J. J. Elsevier. 2010; 15:3621-3631.
3. https://archives.drugabuse.gov/news-events/nida-notes/1998/07/rise-fall-tuberculosis-in-united-states
4. Huo H, Chen R, and Wang X. Appl. Math. Model. 2016; 000:1-10.
5. Bunwong K, Sae-jie W, and Boonsri N. Kasetsart J. (Nat. Sci.). 2015; 49:990-1000.
6. Heffernan J M, Smith R J, and Wahl L M. J. R. Soc. 2005; 2: 281-293.
7. Diekmann O, Heesterbeek J A P, and Metz J A J.J Math Biol. 1990; 28(4): 365-382.

B_008_OA: A NOTE ON THE CIRCUMFERENCE OF 3-CONNECTED CUBIC PLANE GRAPHS

Adthasit Sinna*

Department of Mathematics, Faculty of Science, Ramkhamhaeng University, Bangkok, Thailand
*e-mail: adthasit@rumail.ru.ac.th

Abstract:

A graph G is *cubic* if all vertices of G have degree exactly three. A graph G is *3-connected* if $G - \{u, v\}$ is a connected graph for all vertices u, v of G. The *circumference* of a graph G as the length of longest cycle in G, denoted by $cir(G)$. For any even integers n, let $c(n) = min\{cir(G) \mid G$ is a 3-connected cubic plane graph with n vertices$\}$.

Tait conjectured that $c(n) = n$ for all integers n. Tutte disproved this by constructing the 46-vertex graph with circumference 45. This graph contains three disjoint 15-vertex graphs, which is called *Tutte fragment*. Later, Holton and Mckay showed that $c(n) = n$ if $n \leq 36$, and $c(38) = 37$. Otherwise, the exact value of $c(n)$ is still unknown for $n \geq 40$. For a lower bound of $c(n)$, Liu, Yu and Zhang showed that $c(n) \geq \Omega(n^{0.8})$ for all integers n. For an upper bound of $c(n)$, Lu constructed a family of graph with circumference $n - \sqrt{n + \frac{49}{4}} + \frac{5}{2}$ so this value is an upper bound of $c(n)$ for infinitely many integers n. To find the exact value of $c(n)$, both upper and lower bounds of $c(n)$ must be improved.

In this talk, we tighten an upper bound of $c(n)$ to $\frac{133n}{136} + 1$ for infinitely many integers n. This can be done by constructing a family of graphs using Tutte fragments.

B_009_OF: THE NORDHAUS-GADDUM INEQUALITIES FOR ACYCLIC NUMBERS ON UNITARY CAYLEY GRAPHS OF FINITE RINGS

Denpong Pongpipat,[1] Nuttawoot Nupo[2,*]

[1,2]Department of Mathematics, Faculty of Science, Khon Kaen University, Khon Kaen, 40002, Thailand
*e-mail: nuttanu@kku.ac.th

Abstract:

The unitary Cayley graph Γ_n of a finite ring $\mathbb{Z}_n$ is the graph with vertex set $\mathbb{Z}_n$ and two vertices x and y are adjacent if and only if $x-y$ is a unit in $\mathbb{Z}_n$. A nonempty subset A of $\mathbb{Z}_n$ is said to be acyclic if the subgraph $< A >$ induced by A contains no cycles. The maximum cardinality of an acyclic set in Γ_n is called an acyclic number and denoted by $\alpha(\Gamma_n)$. In this paper, the Nordhaus-Gaddum inequalities for acyclic number of Γ_n are investigated in the sense of Γ_n and its complement.

Introduction:

Throughout the paper, all sets and graphs are assumed to be finite. For each $n \geq 2$, let Γ_n denote the unitary Cayley graph of a ring $\mathbb{Z}_n$, the ring of integers modulo n with vertex set is $\mathbb{Z}_n$ itself and two vertices x and y are joined by edge if $x-y$ is a unit in the ring $\mathbb{Z}_n$. Let us denote all elements in $\mathbb{Z}_n$ by integers $0,1,2,\ldots,n-1$. It is well known that all units in the ring $\mathbb{Z}_n$ are the integer a in which $\gcd(a,n)=1$. Therefore, the edge set of Γ_n can be expressed as $\mathrm{E}(\Gamma_n)=\{\{x,y\} : x,y \in \mathbb{Z}_n, \gcd(x-y,n)=1\}$. Some prominent results of unitary Cayley graphs were studied by several researchers. In 1995, Dejter [4] showed that unitary Cayley graphs are unions of disjoint Hamilton cycles and presented the sufficient condition for being bipartite graphs. In 2007, Klotz and Sander [9] determined some invariant properties of unitary Cayley graphs and studied their perfectness. In 2008, Boggess et.al. [2] explored structural properties of unitary Cayley graphs. In 2009, Akhtar et.al [1] computed an automorphism group of a unitary Cayley graph of a finite ring. In 2012, Kiani and Aghaei [8] provided isomorphism theorems for unitary Cayley graphs of rings associated with Jacobson radicals. In 2014, Naghipour [14] considered some properties of induced subgraphs of unitary Cayley graphs of commutative rings.

One of interesting parameters of graphs is an acyclic number which is the maximum number of vertices that the subgraph induced by such vertices contains no cycles. Many results about this parameter were presented. For instance, in 2009, Samodivkin [16] investigated an acyclic number of graphs having cut-vertices. Later in 2017, Petrusevski and Skrekovski [15] proposed a conjecture on this parameter. Moreover, they provided some conditions that make such the conjecture weaker for planar graphs.

For studying invariant properties of graphs, Nordhaus-Gaddum type inequalities are remarkable. They are concerned with some properties of graphs and their complements. Many researchers presented such inequalities for several parameters of graphs. In 2005, Furedi et.al [3] studied Nordhaus-Gaddum type theorems for decompositions of graphs. In 2011, Jiang and Kang [7] considered these inequalities for total outer-connected domination in graphs. In the same year, Henning et.al [6] presented more results of Nordhaus-Gaddum type inequalities for total domination numbers. Other results of these inequalities for several parameters of graphs can be found in [3], [10], [11], [12] and [13]. For this paper, we introduce Nordhaus-Gaddum inequalities for acyclic numbers of unitary Cayley graphs of rings $\mathbb{Z}_n$, where $n \geq 2$.

Methodology:

In this section, we will mention about definitions and some related theorems used in this research.

Definition 4.1 Let $\phi(n) = \{k \in \mathbb{Z}^+ : 1 \leq k \leq n, \gcd(k.n) = 1\}$. The cardinality $|\phi(n)| = \varphi(n)$ is called Euler's phi function.

Definition 4.2 Let G be a nonempty set. A Group is an ordered pair $(G,*)$ where $*$ is a binary operation on G such that the following axioms are satisfied:

(i) $a * (b * c) = (a * b) * c$ for all $a, b, c \in G$;

(ii) there exists $e \in G$ such that $a * e = a = e * a$ for all $a \in G$; and

(iii) for each $a \in G$, there exists $a' \in G$ such that $a * a' = e = a' * a$.

Definition 4.3 A Ring is a triple $(R, +, *)$, where $R \neq \emptyset$, " $+$ " and " $*$ " are binary operations such that the following axioms are satisfied:

(i) $(R, +)$ is an abelian group;

(ii) $(R, *)$ is a semigroup; and

(iii) for all $x, y \in R$,

$x * (y + z) = (x * y) + (x * z)$ and $(y + z) * x = (y * x) + (z * x)$.

Definition 4.4 A graph G is a subgraph of a graph H if $V(G) \subseteq V(H)$, $E(G) \subseteq E(H)$.

Definition 4.5 A graph $G(V, E)$ is an induced subgraph of $H(V', E')$ If G is a subgraph of H with an additional condition that E consists of all edges that their endpoints belong to V.

Definition 4.6 An independent set is a set of vertices that induces no edges.

Definition 4.8 A graph G is a bipartite graph if $V(G)$ can be partitioned into two independent sets and partite set are those two partitioned set.

Theorem 4.9 Let G be a graph of order at least 2. A graph G is bipartite if and only if it has no odd cycles.

Definition 4.10 [(9)]. For $n \in \mathbb{N} \setminus \{1\}$. The Unitary Cayley graph $\Gamma_n = Cay(\mathbb{Z}_n, U_n)$ is defined by the additive group of the ring $\mathbb{Z}_n$ and the multiplicative group U_n of its units such that $V(\Gamma_n) = \mathbb{Z}_n$ and $E(\Gamma_n) = \{\{a, b\} : a, b \in \mathbb{Z}_n, \gcd(a - b, n) = 1\}$.

Definition 4.11 [(9)]. Let Γ_n be a unitary Cayley graph of $\mathbb{Z}_n$. The complement $\overline{\Gamma_n}$ of Γ_n is the graph in which $V(\overline{\Gamma_n}) = \mathbb{Z}_n$ and $E(\overline{\Gamma_n}) = \{\{a, b\} : a, b \in \mathbb{Z}_n, \gcd(a - b, n) \neq 1\}$.

Definition 4.12 A nonempty subset A of a vertex set $V(G)$ of a graph G is called an acyclic set if a subgraph of G induced by A contains no cycles. An acyclic number of a graph G, denoted by $\alpha(G)$, is the maximum order of G that induces no cycles.

Lemma 4.13 [(2)]. If n is an even positive integer, then Γ_n is bipartite.

Theorem 4.14 [(2)]. If n is an even positive integer, then Γ_n has no odd cycles. In particular, Γ_n has no triangles.

Results and Discussion:

In this section, we mention about the construction of cycles of lengths 3 and 4 which is useful for studying the results of acyclic numbers of the unitary Cayley graphs and their complements.

Lemma 5.1 For each positive integer $n \geq 3$, $\varphi(n)$ is an even number.

Lemma 5.2 For each even positive integer $n \geq 8, \varphi(n) \geq 4$.

Proof Let $n \geq 8$ be an even positive integer. Assume that $n = 2^k t$ for some $n, t \in \mathbb{N}$ such that $\gcd(2^k, t) = 1$.

Case 1 : $t = 1$. Then $k \geq 3$. Consider

$$\varphi(n) = \varphi(2^k t) = \varphi(2^k)\varphi(t) = \varphi(2^k)(1) = 2^{k-1} \geq 2^{3-1} = 4.$$

Case 2 : $t = 3$. Then $k \geq 2$. Consider

$$\varphi(n) = \varphi(2^k t) = \varphi(2^k)\varphi(t) = \varphi(2^k)\varphi(3) = 2^{k-1}(2) = 2^k \geq 4.$$

Case 3 : $t \geq 3$. Then : $k \geq 1$. Suppose that : $t = p^m q$ where p is a prime number greater than 2 and $m, q \in \mathbb{N}$ such that $\gcd(p^m, q) = 1$ and $\gcd(2, q) = 1$.

Subcase 3.1 : $m = 1$. Then $t = pq$.

Subcase 3.1.1 : $q = 1$. Thus $p = t \geq 5$ and

$$\varphi(n) = \varphi(2^k t) = \varphi(2^k)\varphi(t) = \varphi(2^k)\varphi(pq) = 2^{k-1}(p-1)\varphi(1) \geq 2^{1-1}(5-1)(1) = 4.$$

Subcase 3.1.2 : $q \geq 3$. By Lemma 5.1, we get that

$$\varphi(n) = \varphi(2^k t) = \varphi(2^k)\varphi(t) = \varphi(2^k)\varphi(pq) = \varphi(2^k)\varphi(p)\varphi(q) = 2^{k-1}(p-1)\varphi(q) \geq 2^{1-1}(3-1)(2) = 4.$$

Subcase 3.2 : $m \geq 2$. Then $t = p^m q$ and so

$$\varphi(n) = \varphi(2^k t) = \varphi(2^k)\varphi(p^m q) = \varphi(2^k)\varphi(p^m)\varphi(q) = 2^{k-1}(p^{m-1})(p-1)\varphi(q) \geq 2^{1-1}(3^{2-1})(3-1)(1) = 6 > 4.$$

Consequently, for each even positive integer $n \geq 8, \varphi(n) \geq 4$. as desired. ∎

Theorem 5.3 For each even positive integer $n \geq 8$, The Unitary Cayley Graphs Γ_n contains a cycle C_4 of length 4 as a subgraph.

Proof Let $\phi(n) = \{k \in \mathbb{Z}^+ : 1 \leq k \leq n, \gcd(k.n) = 1\}$ be such that $|\phi(n)| = \varphi(n)$. For convenience we write $\phi(n) = \{1, a_1, a_2, \ldots, a_{\phi(n)-1}\}, a_i < a_j$ and $1 \leq i < j \leq \phi(n) - 1$.

Let $n \geq 8$ be an even positive integer. We claim that C_4 is contained in Γ_n.

Firstly, since $\gcd(1 - 0, n) = \gcd(1, n) = 1$, there exists an edge between vertices 0 and 1 in Γ_n.

Secondly, we consider $a_1 \in \phi(n)$, we have $\gcd(a_1 - 0, n) = \gcd(a_1, n) = 1$. Then there exists an edge between vertices 0 and a_1 in Γ_n. Next, by Lemma 5.2, we get that $a_1 + 1 < n$. Then $a_1 + 1 \in \mathbb{Z}_n$ and $\gcd((a_1 + 1) - a_1, n) = 1$. Then there exits an edge between vertices a_1 and $a_1 + 1$ in Γ_n.

Finally, we have $\gcd((a_1 + 1) - 1, n) = \gcd(a_1, n) = 1$. It follows that there exists an edge between vertices $a_1 + 1$ and 1 in Γ_n. Hence $0, 1, a_1$ and $a_1 + 1$ form a cycle of length 4 in Γ_n.

Consequently, our claim is completely proved. ∎

To illustrate more clearly, we provide the results of $\alpha(\Gamma_4)$ and $\alpha(\Gamma_6)$ as follows.

Remark 5.4 The Unitary Cayley Graph Γ_4 and Γ_6 are shown as follows:

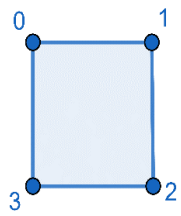

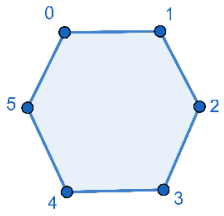

Therefore, $\alpha(\Gamma_4) = 3$ and $\alpha(\Gamma_6) = 5$.

In order to complete our results of the part of acyclic numbers of Γ_n, we present such the numbers as follows

Theorem 5.5 If $n > 1$ is an odd integer, then $\alpha(\Gamma_n) = 2$.

Proof Let $n > 1$ be an odd integer. Since $0,1$ and 2 form a cycle C_3 and Γ_n contains C_3 as a subgraph, so $\alpha(\Gamma_n) = 2$. ∎

Theorem 5.6 If $n > 6$ is an even integer, then $\alpha(\Gamma_n) = 3$.

Proof Let $n > 6$ be an even integer. By Corollary 4.14, Γ_n does not contain a triangle. It follows that $\alpha(\Gamma_n) \geq 3$. By Theorem 5.3, we can construct C_4 which is contained in Γ_n. Then $\alpha(\Gamma_n) \leq 3$. Therefore, $\alpha(\Gamma_n) = 3$. ∎

As the fact that Nordhaus-Gaddum inequalities concern with the results of graphs and their complements, we then investigated the results of the complements of Γ_n. We start with the illustration of $\alpha(\overline{\Gamma_4})$ and $\alpha(\overline{\Gamma_6})$.

Remark 5.7 The Complement Unitary Cayley Graph $\overline{\Gamma_4}$ and $\overline{\Gamma_6}$ are shown as follows

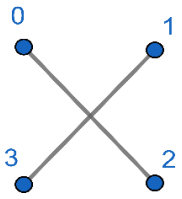

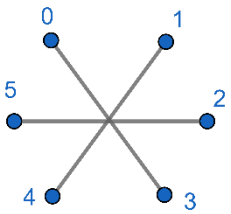

Therefore, $\alpha(\overline{\Gamma_4}) = 4$ and $\alpha(\overline{\Gamma_6}) = 6$.

Theorem 5.8 Let $n \geq 8$ be a positive integer. Then $\alpha(\overline{\Gamma_n}) = \begin{cases} 2 \ ; \ n \ is \ not \ prime. \\ n \ ; \ n \ is \ prime. \end{cases}$.

Proof Let $n \geq 8$ be a positive integer.

Case 1 : n is not prime.

Case 1.1 : n is an even integer. Since $\overline{2}, \overline{4}$ and $\overline{6}$ form a cycle C_3 and $\overline{\Gamma_n}$ contains C_3 as a subgraph, so $\alpha(\overline{\Gamma_n}) = 2$.

Case 1.2 : n is an odd integer and $n = p_1^{m_1} \cdot p_2^{m_2} \cdots p_t^{m_t}$ where p_i, m_i are prime and positive respectively such that $i = 1,2, \ldots, t$, $p_i < p_j$ for $i < j$. Since $0, p_1$ and $2p_1$ form a cycle C_3 and $\overline{\Gamma_n}$ contains C_3 as a subgraph, so $\alpha(\overline{\Gamma_n}) = 2$.

Case 2 : n is prime. Then Γ_n is a complete graph which implies that $\overline{\Gamma_n}$ is an empty graph. Then $\alpha(\overline{\Gamma_n}) = n$, immediately.

Consequently, the statement is proved. ∎

Remark 5.9 In case $n = 3,5,7$ we have that Γ_n is a complete graph. Hence $\overline{\Gamma_n}$ is an empty graph and then $\alpha(\Gamma_n) + \alpha(\overline{\Gamma_n}) = 2 + n$ and $\alpha(\Gamma_n)\alpha(\overline{\Gamma_n}) = 2n$.

Remark 5.10 If $n = 4$, then $\alpha(\Gamma_4) + \alpha(\overline{\Gamma_4}) = 7$ and $\alpha(\Gamma_4)\alpha(\overline{\Gamma_4}) = 12$.

Remark 5.11 If $n = 6$, then $\alpha(\Gamma_6) + \alpha(\overline{\Gamma_6}) = 11$ and $\alpha(\Gamma_6)\alpha(\overline{\Gamma_6}) = 30$.

Theorem 5.12 If $n > 8$ is an odd integer and not prime, then $\alpha(\Gamma_n) + \alpha(\overline{\Gamma_n}) = 4$ and $\alpha(\Gamma_n)\alpha(\overline{\Gamma_n}) = 4$.

Proof Let $n > 8$ be an odd integer and not prime. Then by Theorem 5.5 and Theorem 5.8, the results hold. ∎

Theorem 5.13 If $n > 8$ be an odd integer and prime then $\alpha(\Gamma_n) + \alpha(\overline{\Gamma_n}) = 2 + n$ and $\alpha(\Gamma_n)\alpha(\overline{\Gamma_n}) = 2n$.

Proof Let $n > 8$ be an odd integer and not prime. Then by Theorem 5.5 and Theorem 5.8, the results hold. ∎

Theorem 5.14 If $n \geq 8$ is an even integer and not prime, then $\alpha(\Gamma_n) + \alpha(\overline{\Gamma_n}) = 5$ and $\alpha(\Gamma_n)\alpha(\overline{\Gamma_n}) = 6$.

Proof Let $n \geq 8$ be an even integer and not prime. Then by Theorem 5.6 and Theorem 5.8, the results hold. ∎

Conclusion:

The objectives of this research are to investigate an acyclic number of the unitary Cayley graphs and their complements such that the results of the study are as follows:

Theorem If $n > 8$ is an odd integer and not prime, then $\alpha(\Gamma_n) + \alpha(\overline{\Gamma_n}) = 4$ and $\alpha(\Gamma_n)\alpha(\overline{\Gamma_n}) = 4.$

Theorem If $n \geq 8$ is an even integer and not prime, then $\alpha(\Gamma_n) + \alpha(\overline{\Gamma_n}) = 5$ and $\alpha(\Gamma_n)\alpha(\overline{\Gamma_n}) = 6.$

Remark If $n > 8$ is an odd integer and prime then $\alpha(\Gamma_n) + \alpha(\overline{\Gamma_n}) = 2 + n$ and $\alpha(\Gamma_n)\alpha(\overline{\Gamma_n}) = 2n.$

Remark If $n = 4$, then $\alpha(\Gamma_4) + \alpha(\overline{\Gamma_4}) = 7$ and $\alpha(\Gamma_4)\alpha(\overline{\Gamma_4}) = 12.$

Remark If $n = 6$, then $\alpha(\Gamma_6) + \alpha(\overline{\Gamma_6}) = 11$ and $\alpha(\Gamma_6)\alpha(\overline{\Gamma_6}) = 30.$

Remark In case $n = 3,5,7$ we have that Γ_n is a complete graph. Hence $\overline{\Gamma_n}$ is an empty graph and then $\alpha(\Gamma_n) + \alpha(\overline{\Gamma_n}) = 2 + n$ and $\alpha(\Gamma_n)\alpha(\overline{\Gamma_n}) = 2n.$

Acknowledgements:

The authors would like to thank to the referees for their helpful comments and suggestions on the manuscript. This research was supported by Khon Kaen University.

References:

1. Akhtar R, Boggess M, Henderson T.J, Jimenez I, Karpman R, Kinzel, Pritikin D. Electron. J. Combin. 2009; 16: https://doi.org/10.37236/206.
2. Boggess M, Henderson T.J, Jimenez I. Karpman, R. SUMSRI. 2008.
3. Chen L, Li X, Lian H. Graphs Combin. 2013; 29: 1235-1247
4. Dejter, I. and Giudici, R.E. J. Combin. Math. Combin. Comput. 1995; 18: 121-124.
5. Furedi Z, Kostochka A.V, Skrekovski R, Stiebitz M, West D.B. Nordhaus-Gaddum type theorems for decomposition into many parts. J. Graph Theory. 2005; 50: 273-292.
6. Henning M.A, Joubert E.J, Southey J. Discrete Math. Theoret. Comput. Sci. 2011; 13: 87-96.
7. Jiang H.X, Kang L.Y. Acta Math Sin. (Engl. Ser.). 2011; 27: 607-616.
8. Kiani D, Aghaei M.M.H. Electron. J. Combin. 2012; 19: https://doi.org/10.37236/2214.
9. Klotz W, Sander T. (2007). Electron J. Combin. 2007; 14: https://doi.org/10.37236/963.
10. Li W, Li X, Magnant C, Zhang J. Results Math. 2017; 72: 2079-2100.
11. Li X, Mao Y. Discrete Appl. Math. 2014;185: 102-112.
12. Lin H, Shu J, Wu B, J. Combin. Optim. 2017; 34: 916-930.
13. Lu D, Du J, Lin N, Zhang K, and Yi, D. (2015). J. Comb. Optim. 2015; 29: 502-510.
14. Naghipour A. Miskolc Math. Notes. 2014; 17: 965-977.
15. Petrusevski M, Skrekovski R. Ars Math. Contemp. 2017; 13: 317-322.
16. Samodivkin, V. (2009). Acta Mathematica Academiae Paedagogicae Nyiregyhaziensis. 2009; 25: 1-7.

B_010_OF: AN ADAPTIVE DIFFERENTIAL EVOLUTION ALGORITHM USING PROBABILITY-BASED CONTROL PARAMETERS WITH THE ALTERNATING OF LEARNING AND UTILIZING PERIODS

Wittaya Phaengthaisong*, Jeerayut Wetweerapong, Pikul Puphasuk

Department of Mathematics, Faculty of Science, Khon Kaen University, Khon Kaen, 40002, Thailand
*e-mail: wittaya_paengthaisong@kkumail.com

Abstract:

In this research, we propose an adaptive differential evolution algorithm using probability-based control parameters with the alternating of learning and utilizing periods (ADEPC) for solving continuous optimization problems. The proposed method uses 3 values of scaling factor and 3 values of crossover rate with the adaptive and competitive probabilities based on the success of trial vectors in selection process. The probabilities are also controlled by the alternating of learning and utilizing periods. The ADEPC with the suitable learning and utilizing periods is tested and compared with some well-known adaptive differential evolution algorithms on several benchmark functions of different types and difficulties. The experimental results show that the ADEPC is effective and overall outperforms the compared methods.

Introduction:

Optimization whose objective is to find the optimal solutions is an important technique applied in many fields such as science, engineering, and economics. Various optimization methods are used to solve problems in Pattern recognition[1], Feed-Forward Neural Networks[2], Logistic processes[3], Horizontal directional drilling[4], and constrained portfolio optimization[5]. Since the problems are difficult to solve when the objective functions are discontinuous, non-differentiable or inconvenient to calculate derivatives, the methods using derivatives such as gradient descent and Newton-Raphson methods have limitations to solve them. In addition, the problems are much more difficult when the functions are in high dimensions or have many local minima. Thus, the global search methods have been studied and proposed.

The differential evolution (DE) algorithm proposed by Storn and Price[1,6], is a simple and efficient population-based method for solving global continuous optimization problems. However, the performance of DE depends on its three control parameters: scaling factor F, crossover rate CR, and population size NP. The scaling factor is known to relate to the convergence speed while the crossover rate is sensitive to the problem's property and complexity such as the non-separability and multimodality[7]. Many recommended rules for control parameter selection from literature are general suggestions which may not be able to solve some types of problems[8]. Thus, several researchers have proposed adaptive control parameters to improve the performance of DE[9-20]. In 2006, Brest et al.[9] presented self-adaptive control parameters in DE, which is called jDE. The control parameters F and CR are adjusted by means of evolution and are applied at the individual level. The better parameter values are propagated by the selection operation. The results show that jDE is better than the basic DE algorithm with $F = 0.5$ and $CR = 0.9$. In 2009, Qin et al.[10] proposed a self-adaptive DE (SaDE) algorithm, in which both trial vector generation strategies and their associated control parameter values are gradually self-

adapted. The mutant vector strategies are used with the probabilities which are calculated from the number of previous success trial vectors. The *F* and *CR* values are generated by normal distributions for each individual in the population. They showed that SaDE is more effective than jDE and the basic DE algorithm using the control parameters (*F, CR*) = (0.9, 0.1), (0.9, 0.9), (0.5, 0.3). In 2009, Zhang and Sanderson[11] introduced an adaptive differential evolution with optional external archive, called JADE. It implements a new mutation strategy "DE/current-to-pbest" with optional external archive operation that utilizes historical data, and adaptive control parameters *F* and *CR*. The result shows that JADE outperform the jDE, SaDE and basic DE with *F* = 0.5 and *CR* = 0.9.

In this research, we propose an adaptive differential evolution algorithm using probability-based control parameters with the alternating of learning and utilizing periods (ADEPC). The algorithm aims to use some values of scaling factor and crossover rate with the adaptive and competitive probabilities which are also controlled by the alternating of learning and utilizing periods.

Methodology:

The ADEPC is an adaptive differential evolution algorithm in which the scaling factor *F* and crossover rate *CR* values are randomly selected from the predefined sets to generate the trial vectors. Their values are associated with the corresponding probabilities which depend on the success counters of trial vectors in selection operation. The alternating of learning and utilizing periods consist of fixed numbers of generations and are used alternatively by ADEPC. At the beginning of the learning period (*LP*), all the probabilities are set to the same value for each *F* and each *CR* and are used for the whole *LP* generations. During this period, the success counters are updated accordingly. At the end, the probabilities are adjusted using the final counters. Then the algorithm enters the utilizing period (*UP*) with these probabilities without updating the counters for the whole *UP* period.

The algorithm of ADEPC*:* The procedure of ADEPC consists of the following steps.

Step 1. Setting parameters

Population size: *NP*

Dimension: *D*

Lower and upper bounds of population vectors: $x_{\min}$ and $x_{\max}$

Value to reach: *VTR*

Maximum number of function evaluations: *MAXFEs*

Scaling factors: F_1, F_2, F_3

Crossover rates: CR_1, CR_2, CR_3

Number of generations for learning and utilizing periods: *LP* and *UP*

Step 2. Initialization

Generate the initial population $P = [x_i]$ of random vectors $x_i = [x_{i1}, x_{i2}, \ldots, x_{iD}]$, for $i = 1, 2, \ldots NP$. Calculate their fitness values and find the best vector x_{best} and its value f_{best}. Set the probability variables

pF_k and pCR_k for the scaling factor F_k and the crossover rate CR_k, respectively. And set the corresponding counters $nsF_k = 0, nsCR_k = 0$ where $k = 1, 2, 3$.

Step 3. Updating the probabilities

Step 3.1 Learning period

Before entering the learning period, the probabilities pF_k, pCR_k are initialized or reset to $\frac{1}{3}$ for $k = 1, 2, 3$. Then, their values are fixed for the whole period while the counters are updated in the selection operation.

Step 3.2 Utilizing period

Before starting the utilizing period, adjust the probabilities pF_k, pCR_k by

$$pF_k = \frac{nsF_k}{\sum_{i=1}^{3} nsF_k}, k = 1, 2, 3,$$

$$pCR_k = \frac{nsCR_k}{\sum_{i=1}^{3} nsCR_k}, k = 1, 2, 3.$$

Their values are also fixed for the whole period while all counters are reset to 0 and not updated.

Step 4. Choosing the control parameters F and CR

The scaling factor *F* and the crossover rate *CR* for each target vector are chosen as follows:

$$F = \begin{cases} F_1, \ if \quad 0 \le a < pF_1 \\ F_2, \ if \quad pF_1 \le a < pF_1 + pF_2 \\ F_3, \ if \quad pF_1 + pF_2 \le a \le 1 \end{cases},$$

$$CR = \begin{cases} CR_1, \ if \quad 0 \le b < pCR_1 \\ CR_2, \ if \quad pCR_1 \le b < pCR_1 + pCR_2 \\ CR_3, \ if \quad pCR_1 + pCR_2 \le b \le 1 \end{cases},$$

where *a, b* are uniformly random numbers in [0, 1] generated before each mutation and crossover, respectively.

Step 5. Mutation operation

For each target vector x_i, generate the mutant vector v_i by using the following equation:

$$v_i = x_{r1} + F \cdot (x_{r2} - x_{r3}),$$

where *F* is obtained from step 3 , and the different indices *r1, r2, r3* are generated randomly in the range of {1,2,3,…,*NP*} and are also different from *i*.

Step 6. Crossover operation

Generate a trial vector u_i by exchanging some components between the mutant vector v_i and the target vector x_i as follows:

$$u_{ij} = \begin{cases} v_{ij}, \ if \quad rand() \le CR \ or \ j = I_{rand} \\ x_{ij}, \ otherwise \end{cases},$$

where *j*=1,2,3,…,*D*, the *CR* is obtained from step 3 , and I_{rand} is a randomly fixed integer in the range {1,2,3,…,*D*}.

Step 7. Selection operation

Compare the fitness value of the trial vector with that of the target vector to select the vector for the next generation. The selection operation is expressed as follows:

$$x_i = \begin{cases} u_i, \ if \quad f(u_i) < f(x_i) \\ x_i, \ otherwise \end{cases}.$$

If the fitness of a trial vector corresponding to F_k, CR_k is better than that of target vector in the learning period, then increase the counters $nsF_k, nsCR_k$ as follows:

$$nsF_k := nsF_k + 1,$$

$$nsCR_k := nsCR_k + 1$$

Step 8. Repeat the steps 3-7 until the stopping condition is satisfied and report the best vector x_{best} and its value f_{best}.

Experimental design: In this section, three experiments are conducted. Suitable learning and utilizing periods (*LP* and *UP*), and *NP* for the ADEPC algorithms are investigated in first and second experiments, respectively. The third experiment compares the performance of ADEPC with those of other methods. All experiments use eight benchmark functions. Table 1 shows their names, formulations, types (US: unimodal separable function, UN: unimodal non-separable function, MS: multimodal separable function, MN: multimodal non-separable function), global optimums and search ranges.

Experiment 1: Finding suitable learning and utilizing periods (LP and UP) for the ADEPC algorithm

The aim of this experiment is to find the suitable learning and utilizing periods (LP and UP) of the ADEPC for solving several benchmark functions. The $LP = 25, 50$ and $UP = 50, 100, 200, 300$ are varied using 3 values of scaling factor *F* = 0.5,0.7,0.9 and 3 values of crossover rate *CR* = 0.1,0.5,0.9 with adaptive and competitive probabilities based on the success of trial vectors in selection process. The population size *NP* = 50, the dimension *D* = 30 and the maximum number of function evaluations *MAXFEs* = 1,500,000 are set. The value to reach *VTR* = 10^{-10} is set and each configuration is performed 30 independent runs. The number of successful runs (NS), the mean of number of function evaluations (*Mean*), and the percentage of standard deviations of the number of function evaluations (%*SD*) are reported.

Experiment 2: Finding suitable population size for the ADEPC algorithm

This experiment aims to find smaller sizes of population for the ADEPC algorithm. The population sizes *NP* = 20,30,40,50 are varied and the suitable learning and utilizing periods are obtained from experiment 1. The other settings are the same as experiment 1. The *NS, Mean,* and *%SD* are reported.

Experiment 3: Comparing the performance of ADEPC with those of other DE variants

The aim of this experiment is to compare the ADEPC with other adaptive DE algorithms for solving several benchmark functions. The ADEPC with the suitable learning and utilizing periods obtained from experiment 1 is compared with JADE, jDE, and SaDE algorithms. We set the population size *NP* = 30, the dimension *D* = 30, the learning period *LP = 25* and the utilizing period *UP = 200*. The maximum number of function evaluations MAXFEs are set as in the reference[11]. Each algorithm is performed 50 independent runs for each test function. The mean of the best function values (*Meanfb*) and the standard deviations (*SD*) are reported.

Table 1. Test functions.

Test function	Formulations	Type	Global optimum X*	Search range
$f_1(x)$: Sphere	$f_1(x)=\sum_{i=1}^{D} x_i^2$	US	$\overline{0}$	$[-100,100]^D$
$f_2(x)$: Schwefel 1.2	$f_2(x)=\sum_{i=1}^{D}(\sum_{j=1}^{i} x_j)^2$	UN	$\overline{0}$	$[-100,100]^D$
$f_3(x)$: Rosenbrock	$f_3(x)=\sum_{i=1}^{D-1}[100(x_{i+1}-x_i^2)^2+(x_i-1)^2]$	MN	$\overline{1}$	$[-100,100]^D$
$f_4(x)$: Schwefel 2.22	$f_4(x)=\sum_{i=1}^{D}\lvert x_i\rvert+\prod_{i=1}^{D}\lvert x_i\rvert$	UN	$\overline{0}$	$[-10,10]^D$
$f_5(x)$: Rastrigin	$f_5(x)=\sum_{i=1}^{D}[x_i^2-10\cos(2\pi x_i)+10]$	MS	$\overline{0}$	$[-5,5]^D$
$f_6(x)$: Schwefel	$f_6(x)=418.9828872724D-\sum_{i=1}^{D} x_i\sin(\sqrt{\lvert x_i\rvert})$	MS	$\overline{420.96}$	$[-500,500]^D$
$f_7(x)$: Ackley	$f_7(x)=-20\exp\left(-0.2\sqrt{\frac{1}{D}\sum_{i=1}^{D}x_i^2}\right)+\left(-\exp\left(\frac{1}{D}\sum_{i=1}^{D}\cos(2\pi x_i)\right)+20+e\right)$	MN	$\overline{0}$	$[-32,32]^D$
$f_8(x)$: Griewank	$f_8(x)=\frac{1}{4000}\sum_{i=1}^{D}x_i^2-\prod_{i=1}^{D}\cos\left(\frac{x_i}{\sqrt{i}}\right)+1$	MN	$\overline{0}$	$[-600,600]^D$

Results and Discussion:

In this section, we present experimental results and discussion of suitable learning period utilizing period and population size for ADEPC algorithm and comparison of the ADEPC with other adaptive DE algorithms.

Suitable learning and utilizing periods (LP and UP) of the ADEPC algorithm

The performances of the ADEPC algorithm with the different learning and utilizing periods are shown in Tables 2. For each function, the number of successful runs *NS* = 30 is considered first. Then, the least *Mean* value is examined. The best values are indicated in bold.

Table 2. The performance comparison of the ADEPC algorithm with different learning and utilizing periods.

LP	25				50			
UP	**50**	**100**	**200**	**300**	**50**	**100**	**200**	**300**
Sphere (*NS/Mean/%SD*)	30/76900/ 1.53	30/74065/ 1.33	**30/73038/ 1.21**	30/76900/ 1.52	30/80925/ 2.07	30/77274/ 1.53	30/74500/ 1.65	30/74661/ 1.64
Schwefel 1.2 (*NS/Mean/%SD*)	30/82006/ 1.33	30/78922/ 1.32	**30/77899/ 1.48**	30/82006/ 1.32	30/86970/ 1.50	30/81895/ 1.29	30/80274/ 1.18	30/79048/ 1.56
Rosenbrock (*NS/Mean/%SD*)	30/433823 /3.94	30/429217 /3.35	**30/42470 5/3.96**	30/433823 /3.91	30/448488 /3.01	30/436802 /2.87	30/426408 /3.14	30/428534 /3.37
Schwefel 2.22 (*NS/Mean/%SD*)	30/111684 /0.94	30/107502 /1.20	**30/10566 7/1.00**	30/111753 /0.86	30/118775 /1.23	30/112324 /1.09	30/107712 /1.23	30/107070 /1.54
Rastigin (*NS/Mean/%SD*)	30/124203 /1.77	30/115381 /2.12	**30/11329 1/2.48**	30/124591 /1.77	30/138834 /2.27	30/124750 /2.04	30/117187 /2.30	30/116632 /2.47
Schwefel (*NS/Mean/%SD*)	30/93589/ 1.58	30/89067/ 1.72	**30/87788/ 1.94**	30/93922/ 1.98	30/101432 /1.69	30/94831/ 1.79	30/91043/ 1.71	30/91109/ 1.53
Ackley (*NS/Mean/%SD*)	30/122884 /1.45	30/117815 /1.42	**30/11584 7/1.07**	30/122900 /1.09	30/129884 /1.14	30/123045 /0.97	30/118913 /1.22	30/116666 /1.25
Griwank (*NS/Mean/%SD*)	30/81837/ 3.32	30/78444/ 3.13	**30/77434/ 4.16**	30/81166/ 3.23	30/86599/ 3.52	30/81699/ 2.63	30/79104/ 2.52	30/78608/ 3.45

Table 2 shows that the ADEPC using *LP = 25* and *LP = 50* with all cases of *UP* give NS=30 for all test functions. Among all 8 combinations, *LP = 25* and *UP = 200* provides the least mean of number of function evaluations. These suitable leaning and utilizing periods are used for the ADEPC algorithm to compare its performance with other algorithms.

Suitable population size of the ADEPC algorithm

The performances of the ADEPC algorithms using *LP = 25* and *UP = 200* with different population sizes are shown in Tables 3. For each function, the number of successful runs *NP* = 30 is considered first. Then, the least *Mean* value is examined. The best values are indicated in bold.

Table 3. The performance comparison of the ADEPC algorithm with different population sizes.

Function	***NP* = 20** **(NS/Mean/%SD)**	***NP* = 30** **(NS/Mean/%SD)**	***NP* = 40** **(NS/Mean/%SD)**	***NP* = 50** **(NS/Mean/%SD)**
$f_1(x)$	**30/27211/2.51**	30/42443/2.16	30/57679/1.82	30/73038/1.21
$f_2(x)$	**30/29022/2.26**	30/45388/2.28	30/62057/1.83	30/77899/1.48
$f_3(x)$	28/609742/24.36	**30/295455/9.20**	30/348623/4.78	30/424705/3.96
$f_4(x)$	**30/39540/2.06**	30/61143/1.69	30/83866/0.94	30/105667/1.00
$f_5(x)$	25/42859/3.46	**30/65964/3.42**	30/90041/2.52	30/113291/2.48
$f_6(x)$	29/33554/3.21	**30/51990/2.18**	30/69671/1.68	30/87788/1.94
$f_7(x)$	30/42937/2.56	30/67401/2.14	30/91453/1.45	30/115847/1.07
$f_8(x)$	28/29382/4.71	**30/45356/4.17**	30/62025/3.16	30/77434/4.16

Table 3 shows that the ADEPC algorithms with $NP = 30, 40, 50$ give all successful runs *NS* = 30 for all test functions while the ADEPC with *NP* = 20 succeeds only 4 out of 8 functions. The ADEPC with *NP* = 30 ranks the first for 4 out of 8 cases and the second for the remaining cases. Therefore, *NP* = 30 is considered the suitable population size for ADEPC algorithm.

Performance comparison of ADEPC with other DE variants

The performances of the ADEPC algorithm with the suitable learning and utilizing periods *LP* = 25, *UP* = 200, and *NP* = 30 are compared with those of JADE w/o archive, jDE, and SaDE. Table 4 shows *Meanfb* and *SD* for different *MAXFEs*. The best function values for each test function are indicate in bold. The best values of the compared methods are taken from the reference[11].

Table 4 shows that the ADEPC outperforms jDE and SaDE for 10 and 11 out of 13 cases, respectively and gives the same results for the remaining cases. When compared with JADE, the ADEPC gives the best results for 9 out of 13 cases and the same results for 3 cases while JADE gives the best result only 1 case. It is clear that the ADEPC overall outperforms the compared methods.

Table 4. The performance comparison of JADE, jDE, SaDE and ADEPC for 30- dimensional functions, corresponding to its *MAXFEs* over 50 independent runs.

Function	*MAXFes*	ADEPC *Meanfb (SD)*	JADE *Meanfb (SD)*	jDE *Meanfb (SD)*	SaDE *Meanfb (SD)*
$f_1(x)$	150,000	6.3E-27 (5.5E-27)	**1.8E–60 (8.4E–60)**	2.5E–28 (3.5E–28)	4.5E–20 (6.9E–20)
$f_2(x)$	500,000	**1.13E-98 (1.78E-98)**	5.7E–61 (2.7E–60)	5.2E–14 (1.1E–13)	9.0E–37 (5.43E–36)
$f_3(x)$	300,000	**1.1E-02 (1.5E-02)**	8.0E–02 (5.6E–01)	1.3E+01 (1.4E+01)	2.1E+01 (7.8E+00)
	2,000,000	**0 (0)**	8.0E–02 (5.6E–01)	8.0E–02 (5.6E–01)	1.8E+01 (6.7E+00)
$f_4(x)$	200,000	5.9E-22 (2.8E-22)	**1.8E–25 (8.8E–25)**	1.5E–23 (1.0E–23)	1.9E–14 (1.05E–14)
$f_5(x)$	100,000	**6.1E-07 (6.2E-07)**	1.0E–04 (6.0E–05)	1.5E–04 (2.0E–04)	1.2E–03 (6.5E–04)
	500,000	**0 (0)**	**0 (0)**	**0 (0)**	**0 (0)**
$f_6(x)$	100,000	**0 (0)**	3.3E–05 (2.3E–05)	7.9E–11 (1.3E–10)	4.7E+00 (3.3E+01)
	900,000	**0 (0)**	**0 (0)**	**0 (0)**	4.7E+00 (3.3E+01)
$f_7(x)$	50,000	4.8E-04 (1.1E-04)	**8.2E–10 (6.9E–10)**	3.5E–04 (1.0E–04)	2.7E–03 (5.1E–04)
	200,000	**3.9E-15 (1.1E-15)**	4.4E–15 (0.0E+00)	4.7E–15 (9.6E–16)	4.3E–14 (2.6E–14)
$f_8(x)$	50,000	4.5E-05 (6.6E-05)	**9.9E–08 (6.0E–07)**	1.9E–05 (5.8E–05)	7.8E–04 (1.2E–03)
	300,000	**0 (0)**	**0 (0)**	**0 (0)**	**0 (0)**

Conclusion:

In this paper, the adaptive differential evolution algorithm using probability-based control parameters with the alternating of learning and utilizing periods (ADEPC) is designed to enhance the performance the basic DE algorithm. The experimental results recommend the ADEPC using learning period *LP* = 25, utilizing period *UP* = 200, and population size *NP* = 30. The ADEPC algorithm is tested and compared with JADE, jDE and SaDE. The performance comparison shows that the ADEPC overall outperforms the compared methods.

Acknowledgements:

Wittaya Phaengthaisong would like to thank the Science Achievement Scholarship of Thailand (SAST) for the financial support.

References:

1. Storn R, Price K. J. Global Optim. 1997;11:341–359.
2. Ilonen J, Kamarainen J K, and Lampinen J. Neural Processing Letters. 2003;17:93–105.
3. Silva C.A, Sousa J.M.C, Runkler T, Palm R. International Journal of Approximate Reasoning. 2005;40:280–301.
4. Patino-Ramirez F, Layheeb C, Arsona C. Tunneling and Underground Space Technology. 2020;103:103450.
5. Zhu H, Wang Y, Wanga K, Chen Y. Expert Systems with Applications. 2011;38:10161–10169.
6. Storn R, Price K. J. Global Optim. 1995; 95:012.
7. Storn R. Studies in Computational Intelligence. 2008;143:1-31.
8. Gämperle R, Müller S D, Koumoutsakos P. WSEAS Press. 2002;293–298.
9. Brest J, Zumer V, Maucec M S. Proc. IEEE Congr. Evol. Comput. 2006;215–222.
10. Qin K, Huang V L, and Suganthan P N. IEEE Trans. Evol. Comput. 2009;13:398–417.
11. Zhang J, Sanderson A C. IEEE Tran. Evol. Comput. 2009;13:945–958.
12. Liu J, Lampinen J. Soft Comput. 2005;9:448–462.
13. Ghosh A, Das S, Chowdhury A, Giri R. Inf. Sci. 2011;181:3749–3765.
14. Leon M, Xiong N, J. Artif. Intell. Soft Comput. Res. 2016:6:103–118.
15. Teo J, Soft Comput. 2006;10:673–686.
16. Das S, Abraham A, Chakraborty U K, Konar A. IEEE Trans. Evol. Comput. 2009;13:526–553.
17. Islam S.M, Das S, Ghosh S, Roy S, Suganthan P N. IEEE Trans. Syst. Man Cybern. B Cybern. 2012;42:482–500.
18. Tanabe R, Fukunaga A. Paper Presented at the IEEE Congress on Evolutionary Computation (CEC 2013). 2013;20–23.
19. Zhao S Z, Suganthan P.N, Das S. Soft Comput. 2011;15: 2175–2185.
20. Gong W, Cai Z, Ling C X, Li H. IEEE Trans. Syst. Man Cybern. B Cybern. 2011;41:397–413.

B_011_OF: SOME GENERALIZATIONS OF HARDY TYPE INTEGRAL INEQUALITIES FOR (p,q)-INTEGRABLE FUNCTIONS

Suriyakamol Thongjob*, Kamsing Nonlaopon

Department of Mathematics, Khon Kaen University, Khon Kaen, 40002, Thailand
*e-mail: suriyakamol_t@kkumail.com

Abstract:

In this paper, we establish some generalizations of (p,q)-Hardy type integral inequalities for (p,q)-integrable functions. By taking q tends to 1 and $p = 1$, our results reduce to classical results on some generalizations of Hardy type integral inequalities.

Introduction:

In recent years, quantum calculus or q-calculus has been actively developed and many researchers have been increasingly interested in the topic of q-calculus due to applications of the q-calculus in mathematics and physics. The history of q-calculus can be tracked back to Euler, who first introduced q-calculus in the track of Newton's work on infinite series. In 1910, F. H. Jackson[1] defined q-derivative and definite q-integral, which is known as the q-Jackson integral. It was the starting point of q-calculus in a systematic way. Today the interest in q-calculus been arising due to high demand of mathematics in this field. The q-calculus numerous applications in various fields of mathematics and other areas such as combinatorics, dynamical systems, fractals, number theory, orthogonal polynomials, special functions, mechanics and also for scientific problems in some applied areas, see[2,3,4,5,6,7,8,9,10] for more details.

Recently, M. Tunc, and E. Gov[11] studied the generalization of q-calculus called (p,q)-calculus. They defined the (p,q)-derivative and (p,q)-integral on finite interval. Furthermore, they studied some properties of (p,q)-calculus and (p,q)-analogue of some important integral inequalities. The (p,q)-integral inequalities have been studied and rapidly developed in during this period by many authors, see[12,13,14,15,16,17] and the references therein.

Mathematical inequalities were applied in various branches of mathematics as analysis, differential equations, geometry, etcetera. One typical such example is Hardy inequalities. Let us just mention that in 1920, G. H. Hardy[18] presented the following famous inequality for f is a non-negative integrable function and $s>1$, then

$$\int_0^\infty \left(\frac{1}{x}\int_0^x f(t)dt\right)^s dx \le \left(\frac{s}{s-1}\right)^s \int_0^\infty f^s(x)dx, \qquad (1)$$

which is now known as Hardy inequality.

Hardy inequality have been studied by a large number of authors during the twentieth century. Over the last twenty years a large number of papers have been appeared in the literature which deals with the simple proofs, various generalizations and discrete analogue of Hardy inequality, see[19,20,21,22,23] for more details.

In 2014, L. Maligranda et al.[24] studied a *q*-analogue of Hardy inequality (1) and some related inequalities. It seems to be a huge new research area to study which of these so called q-Hardy type inequalities. They obtained more general results on q-Hardy type inequalities. By taking *q* tends to 1 and obtained classical results on Hardy inequality (1). Next, L.-E. Persson and S. Shaimardan[25] studied some *q*-analogue of Hardy type inequalities for the Riemann-Liouville fractional integral operator, see[26,27] for more details.

The purpose of this paper is to establish some generalizations of (*p,q*)-Hardy type integral inequalities for (*p,q*)-integrable functions by using (*p,q*)-derivative and (*p,q*)-integral. By taking *q* tends to 1 and *p* = 1, our results reduce to classical results on some generalizations of Hardy type integral inequalities.

Methodology:

In this section, we recall some known concepts and basic results of (*p,q*)-calculus. Throughout this paper, we let *p,q* be constants with $0 < q < p \leq 1$ and $[a,b] \subseteq \mathbb{R}$. We give some definitions and theorems for *(p,q)*-calculus, which will be used in the sequel.[11,12,13,14,15,16,17]

First, we give some *(p,q)*-notation, which would appear in this study quite frequently. For any real number *n*, the *(p,q)*-analogue of *n* is defined by

$$[n]_{p,q} = \frac{p^n - q^n}{p - q} \tag{2}$$

and

$$[-n]_{p,q} = \frac{1}{(pq)^n}[n]_{p,q}.$$

If *p* = 1, then (2) reduce to

$$[n]_q = \frac{1-q^n}{1-q},$$

which is *q*-analogue of *n*.

Definition 1 [11]: The *(p,q)*-derivative of the function *f* on [*a,b*] at *x* is defined by

$${}_aD_{p,q}f(x) = \frac{f(px+(1-p)a) - f(qx+(1-q)a)}{(p-q)(x-a)}, \quad x \neq a, \tag{3}$$

The function *f* is said to be (*p,q*)-differentiable function on [*a,b*] if ${}_aD_{p,q}f(x)$ exist for all $x \in [a,b].$

Since $f:[a,b] \to \mathbb{R}$ be a continuous function, then we have ${}_aD_{p,q}f(a) = \lim_{x \to a} D_{p,q}f(x).$ In Definition 1, if *a* = 0, then ${}_0D_{p,q}f = D_{p,q}f$ is defined

$$D_{p,q}f(x) = \frac{f(px) - f(qx)}{(p-q)x}, \quad x \neq 0. \tag{4}$$

And, if $p = 1$, then $D_{p,q}f(x) = D_q f(x)$ which is the *q*-derivative of the function *f*, and also if $q \to 1$ in (4), then it reduces to classical derivative.

Definition 2 [11]: Let $f:[a,b]\to\mathbb{R}$ is a continuous function and $0<a<b,$ then the (*p,q*)-integral is defined by

$$\int_a^b f(x)\ {}_ad_{p,q}x=(p-q)(b-a)\sum_{k=0}^{\infty}\frac{q^k}{p^{k+1}}\ f\left(\frac{q^k}{p^{k+1}}b+\left(1-\frac{q^k}{p^{k+1}}\right)a\right), \tag{5}$$

And, *f* is said to be (*p,q*)-integrable function on [*a,b*] if $\int_a^b f(x)\ {}_ad_{p,q}x$ exists for all $x\in[a,b]$. If *a* = 0 in (5), then one can get the classical (*p, q*)-integral defined

$$\int_0^b f(x)d_{p,q}x=(p-q)b\sum_{k=0}^{\infty}\frac{q^k}{p^{k+1}}\ f\left(\frac{q^k}{p^{k+1}}b\right), \tag{6}$$

and

$$\int_a^b f(x)d_{p,q}x=\int_0^b f(x)d_{p,q}x-\int_0^a f(x)d_{p,q}x.$$

If *p* = 1 in (6), then we have the classical *q*-integral [4].

The proof of the following Theorems are given by [10].

Theorem 1: Let $f,g:[a,b]\to\mathbb{R}$ be continuous functions, $t\in[a,b]$ and α be constants, then the following formulas are hold:

1. ${}_aD_{p,q}\int_a^t f(x)\ {}_ad_{p,q}x=f(t);$
2. $\int_c^t\ {}_aD_{p,q}f(x)\ {}_ad_{p,q}x=f(t)-f(c)$ *for* $c\in(a,t);$
3. $\int_a^b[f(x)+g(x)]\ {}_ad_{p,q}x=\int_a^b f(x)\ {}_ad_{p,q}x+\int_a^b g(x)\ {}_ad_{p,q}x;$
4. $\int_a^b\alpha f(x)\ {}_ad_{p,q}x=\alpha\int_a^b f(x)\ {}_ad_{p,q}x;$
5. $\int_a^b(x-a)^{\alpha}\ {}_ad_{p,q}x=\frac{(b-a)^{\alpha+1}}{[\alpha+1]_{p,q}};$
6. $\int_c^t f(px+(1-p)a)\ {}_aD_{p,q}g(x)\ {}_ad_{p,q}x=(fg)(x)\Big|_c^t-\int_c^t g(qx+(1-q)a)\ {}_aD_{p,q}f(x)\ {}_ad_{p,q}x.$

Theorem 2: Let $f,g:[a,b]\to\mathbb{R}$ be continuous functions and $r>1$ with 1/r+1/s=1, then

$$\int_a^b|f(t)g(t)|\ {}_ad_{p,q}t\le\left(\int_a^b|f(t)|^r\ {}_ad_{p,q}t\right)^{1/r}\left(\int_a^b|g(t)|^s\ {}_ad_{p,q}t\right)^{1/s}. \tag{7}$$

Theorem 3: Let $f,g:[a,b]\to\mathbb{R}$ be continuous functions and $0<r<1$ with 1/r+1/s=1, then

$$\int_a^b|f(t)g(t)|\ {}_ad_{p,q}t\ge\left(\int_a^b|f(t)|^r\ {}_ad_{p,q}t\right)^{1/r}\left(\int_a^b|g(t)|^s\ {}_ad_{p,q}t\right)^{1/s}. \tag{8}$$

The proof is similar to the proof of Lemma 2.2 in [20].

Results and Discussion:

The following results gives a generalization of Hardy type integral inequalities. Throughout this section, we let $a = 0$.

Theorem 4: Let f be non-negative (p,q)-integrable function on $[0,x]$, g is positive function, $r>1$ and $m>r-1+1/r$. If $x/g(x)$ is non-increasing. Then

$$\int_0^\infty \frac{1}{g^m(x)}\left(\int_0^x f(t)d_{p,q}t\right)^r d_{p,q}x \le \frac{1}{[1-1/r]_{p,q}^{r-1}[-1/r-r+1+m]_{p,q}}\int_0^\infty \frac{(xf(x))^r}{g^m(x)}d_{p,q}x. \quad (7)$$

Proof.: From Theorem 2, we get

$$\int_0^\infty \frac{1}{g^m(x)}\left(\int_0^x f(t)d_{p,q}t\right)^r d_{p,q}x \le \int_0^\infty g^{-m}(x)\int_0^x t^{1-1/r} f^r(t)d_{p,q}t\left(\int_0^x t^{-1/r}d_{p,q}t\right)^{r-1} d_{p,q}x. \quad (8)$$

And by Theorem 1(5), we obtain

$$\left(\int_0^x t^{-1/r}d_{p,q}t\right)^{r-1} = \frac{x^{(1-1/r)(r-1)}}{[1-1/r]_{p,q}^{r-1}}.$$

Since the assumption of the function $x/g(x)$, we have

$$\int_0^\infty \frac{1}{g^m x)}\left(\int_0^x f(t)d_{p,q}t\right)^r d_{p,q}x$$

$$\le \frac{1}{[1-1/r]_{p,q}^{r-1}}\int_0^\infty g^{-m}(x)\int_0^x x^{(1-1/r)(r-1)}t^{1-1/r} f^r(t)d_{p,q}t\,d_{p,q}x$$

$$= \frac{1}{[1-1/r]_{p,q}^{r-1}}\int_0^\infty t^{1-1/r} f^r(t)\int_t^\infty x^{(1-1/r)(r-1)}g^{-m}(x)d_{p,q}x\,d_{p,q}t$$

$$\le \frac{1}{[1-1/r]_{p,q}^{r-1}}\int_0^\infty t^{1-1/r} f^r(t)\left(\frac{t}{g(t)}\right)^m \int_t^\infty x^{r+1/r-2-m}d_{p,q}x\,d_{p,q}t$$

$$= \frac{1}{[1-1/r]_{p,q}^{r-1}[-1/r-r+1+m]_{p,q}}\int_0^\infty \frac{(tf(t))^r}{g^m(t)}d_{p,q}t.$$

This proof is completed.

Remark 1: If $p = 1$, then (7) reduces to generalization of q-Hardy inequality as

$$\int_0^\infty \frac{1}{g^m(x)}\left(\int_0^x f(t)d_qt\right)^r d_qx \le \frac{1}{[1-1/r]_q^{r-1}[-1/r-r+1+m]_q}\int_0^\infty \frac{(xf(x))^r}{g^m(x)}d_qx. \quad (9)$$

Also if $q\to 1$, then (9) reduces to the well known generalization of Hardy inequality as

$$\int_0^\infty \frac{1}{g^m(x)}\left(\int_0^x f(t)dt\right)^r dx \le \frac{1}{(1-1/r)^{r-1}(-1/r-r+1+m)}\int_0^\infty \frac{(xf(x))^r}{g^m(x)}dx.$$

which rapidly appeared in [19].

In particular, if we put $m = r$ and $g(x) = x$ we obtain [23].

The following results concern the converse inequalities.

Theorem 5: Let f be non-negative (p,q)-integrable function on $[0,x]$, g is positive function, $0 < r < 1$ and $m > r+1-1/r.$ If $x/g(x)$ is non-decreasing. Then

$$\int_0^\infty \frac{1}{g^m(x)}\left(\int_0^x f(t)d_{p,q}t\right)^r d_{p,q}x \ge \frac{1}{[1+1/r]_{p,q}^{r-1}[1/r-r+m-1]_{p,q}}\int_0^\infty \frac{(xf(x))^r}{g^m(x)}d_{p,q}x. \qquad (10)$$

Proof.: From Theorem 3, we get

$$\int_0^\infty \frac{1}{g^m(x)}\left(\int_0^x f(t)d_{p,q}t\right)^r d_{p,q}x \ge \int_0^\infty g^{-m}(x)\int_0^x t^{1/r-1}f^r(t)d_{p,q}t\left(\int_0^x t^{1/r}d_{p,q}t\right)^{r-1} d_{p,q}x.$$

And by Theorem 1(5), we obtain

$$\left(\int_0^x t^{1/r}d_{p,q}t\right)^{r-1} = \frac{x^{(1+1/r)(r-1)}}{[1+1/r]_{p,q}^{r-1}}.$$

Since the assumption of the function $x/g(x)$, we have

$$\int_0^\infty \frac{1}{g^m(x)}\left(\int_0^x f(t)d_{p,q}t\right)^r d_{p,q}x$$

$$\ge \frac{1}{[1+1/r]_{p,q}^{r-1}}\int_0^\infty g^{-m}(x)\int_0^x x^{(1+1/r)(r-1)}t^{1/r-1}f^r(t)d_{p,q}t\,d_{p,q}x$$

$$= \frac{1}{[1+1/r]_{p,q}^{r-1}}\int_0^\infty t^{1/r-1}f^r(t)\int_t^\infty x^{(1+1/r)(r-1)}g^{-m}(x)d_{p,q}x\,d_{p,q}t$$

$$\ge \frac{1}{[1+1/r]_{p,q}^{r-1}}\int_0^\infty t^{1/r-1}f^r(t)\left(\frac{t}{g(t)}\right)^m\int_t^\infty x^{r-1/r-m}d_{p,q}x\,d_{p,q}t$$

$$= \frac{1}{[1+1/r]_{p,q}^{r-1}[1/r-r+m-1]_{p,q}}\int_0^\infty \frac{(tf(t))^r}{g^m(t)}d_{p,q}t.$$

This proof is completed.

Remark 2**:** If $p = 1$, then (10) reduces to generalization of q-Hardy inequality as

$$\int_0^\infty \frac{1}{g^m(x)}\left(\int_0^x f(t)d_q t\right)^r d_q x \geq \frac{1}{[1+1/r]_{p,q}^{r-1}[1/r-r+m-1]_q}\int_0^\infty \frac{(xf(x))^r}{g^m(x)}d_q x. \quad (11)$$

Also if $q \to 1$, then (11) reduces to the well known generalization of Hardy inequality as

$$\int_0^\infty \frac{1}{g^m(x)}\left(\int_0^x f(t)dt\right)^r dx \geq \frac{1}{(1+1/r)^{r-1}(1/r-r+m-1)}\int_0^\infty \frac{(xf(x))^r}{g^m(x)}dx.$$

which rapidly appeared in [19].

In particular, if we put *m* = *r* and *g(x)* = *x* we obtain [23].

Next, we generalize the latest integral inequality and the reverse integral inequality by given the value *m.*

Theorem 6: Let f be non-negative (*p,q*)-integrable function on [0,*x*], *g(x)* is positive function, $r>1$ and $m > \frac{r-1+1/r}{2}$. If $x^2/G(x)$ is non-increasing and

$$G(x) = \int_0^x g(t)d_{p,q}t,$$

then

$$\int_0^\infty \frac{1}{G^m(x)}\left(\int_0^x f(t)d_{p,q}t\right)^r d_{p,q}x \leq \frac{1}{[1-1/r]_{p,q}^{r-1}[-1/r-r+1+2m]_{p,q}}\int_0^\infty \frac{(xf(x))^r}{G^m(x)}d_{p,q}x. \quad (12)$$

Proof.: From Theorem 2, we get

$$\int_0^\infty \frac{1}{G^m(x)}\left(\int_0^x f(t)d_{p,q}t\right)^r d_{p,q}x \leq \int_0^\infty G^{-m}(x)\int_0^x t^{1-1/r} f^r(t)d_{p,q}t\left(\int_0^x t^{-1/r}d_{p,q}t\right)^{r-1} d_{p,q}x.$$

And by Theorem 1(5), we obtain

$$\left(\int_0^x t^{-1/r}d_{p,q}t\right)^{r-1} = \frac{x^{(1-1/r)(r-1)}}{[1-1/r]_{p,q}^{r-1}}.$$

Since the assumption of the function $x^2/G(x)$ is non-increasing, we have

$$\int_0^\infty \frac{1}{G^m(x)}\left(\int_0^x f(t)d_{p,q}t\right)^r d_{p,q}x$$

$$\leq \frac{1}{[1-1/r]_{p,q}^{r-1}}\int_0^\infty G^{-m}(x)\int_0^x x^{(1-1/r)(r-1)}t^{1-1/r} f^r(t)d_{p,q}t\,d_{p,q}x$$

$$= \frac{1}{[1-1/r]_{p,q}^{r-1}}\int_0^\infty t^{1-1/r} f^r(t)\int_t^\infty x^{(1-1/r)(r-1)}G^{-m}(x)d_{p,q}x\,d_{p,q}t$$

$$\leq \frac{1}{[1-1/r]_{p,q}^{r-1}} \int_0^{\infty} t^{1-1/r} f^r(t) \left(\frac{t^2}{G(t)} \right)^m \int_t^{\infty} x^{r+1/r-2-2m} d_{p,q}x d_{p,q}t$$

$$= \frac{1}{[1-1/r]_{p,q}^{r-1}[-1/r-r+1+2m]_{p,q}} \int_0^{\infty} \frac{(tf(t))^r}{G^m(t)} d_{p,q}t.$$

This proof is completed.

Remark 3: If $p=1$, then (12) reduces to generalization of *q*-Hardy inequality by given the value *m* as

$$\int_0^{\infty} \frac{1}{G^m(x)} \left(\int_0^x f(t) d_q t \right)^r d_q x \leq \frac{1}{[1-1/r]_q^{r-1}[-1/r-r+1+2m]_q} \int_0^{\infty} \frac{(xf(x))^r}{G^m(x)} d_q x. \quad (13)$$

Also if $q \to 1$, then (13) reduces to the well known generalization of Hardy inequality by given the value *m* as

$$\int_0^{\infty} \frac{1}{G^m(x)} \left(\int_0^x f(t) dt \right)^r dx \leq \frac{1}{(1-1/r)^{r-1}(-1/r-r+1+2m)} \int_0^{\infty} \frac{(xf(x))^r}{G^m(x)} dx,$$

which rapidly appeared in [20].

In particular, if we put $m = r/2$ and $G(x) = x^2$ we obtain [23].

Theorem 7: Let f be non-negative (*p,q*)-integrable function on [0,*x*], *g(x)* is positive function, $0 < r < 1$ and $m > \frac{r+1-1/r}{2}$. If $x^2 / G(x)$ is non-decreasing and

$$G(x) = \int_0^x g(t) d_{p,q}t,$$

then

$$\int_0^{\infty} \frac{1}{G^m(x)} \left(\int_0^x f(t) d_{p,q}t \right)^r d_{p,q}x \geq \frac{1}{[1+1/r]_{p,q}^{r-1}[1/r-r+2m-1]_{p,q}} \int_0^{\infty} \frac{(xf(x))^r}{G^m(x)} d_{p,q}x. \quad (14)$$

Proof.: From Theorem 3, we get

$$\int_0^{\infty} \frac{1}{G^m(x)} \left(\int_0^x f(t) d_{p,q}t \right)^r d_{p,q}x \geq \int_0^{\infty} G^{-m}(x) \int_0^x t^{1/r-1} f^r(t) d_{p,q}t \left(\int_0^x t^{1/r} d_{p,q}t \right)^{r-1} d_{p,q}x.$$

And by Theorem 1(5), we obtain

$$\left(\int_0^x t^{1/r} d_{p,q}t \right)^{r-1} = \frac{x^{(1+1/r)(r-1)}}{[1+1/r]_{p,q}^{r-1}}.$$

Since the assumption of the function $x^2 / G(x)$ is non-decreasing, we have

$$\int_0^\infty \frac{1}{G^m(x)}\left(\int_0^x f(t)d_{p,q}t\right)^r d_{p,q}x$$

$$\geq \frac{1}{[1+1/r]_{p,q}^{r-1}}\int_0^\infty G^{-m}(x)\int_0^x x^{(1+1/r)(r-1)}t^{1/r-1}f^r(t)d_{p,q}t\,d_{p,q}x$$

$$= \frac{1}{[1+1/r]_{p,q}^{r-1}}\int_0^\infty t^{1/r-1}f^r(t)\int_t^\infty x^{(1+1/r)(r-1)}G^{-m}(x)d_{p,q}x\,d_{p,q}t$$

$$\geq \frac{1}{[1+1/r]_{p,q}^{r-1}}\int_0^\infty t^{1/r-1}f^r(t)\left(\frac{t^2}{G(t)}\right)^m \int_t^\infty x^{r-1/r-2m}d_{p,q}x\,d_{p,q}t$$

$$= \frac{1}{[1+1/r]_{p,q}^{r-1}[1/r-r+2m-1]_{p,q}}\int_0^\infty \frac{(tf(t))^r}{G^m(t)}d_{p,q}t.$$

This proof is completed.

Remark 4: If $p=1$, then (14) reduces to generalization of *q*-Hardy inequality by given the value *m* as

$$\int_0^\infty \frac{1}{G^m(x)}\left(\int_0^x f(t)d_qt\right)^r d_qx \geq \frac{1}{[1+1/r]_q^{r-1}[1/r-r+2m-1]_q}\int_0^\infty \frac{(xf(x))^r}{G^m(x)}d_qx. \qquad (15)$$

Also if $q\to 1$, then (15) reduces to the well known generalization of Hardy inequality by given the value *m* as

$$\int_0^\infty \frac{1}{G^m(x)}\left(\int_0^x f(t)dt\right)^r dx \geq \frac{1}{(1+1/r)^{r-1}(1/r-r+2m-1)}\int_0^\infty \frac{(xf(x))^r}{G^m(x)}dx.$$

which rapidly appeared in [20].

In particular, if we put $m=r/2$ and $G(x)=x^2$ we obtain [23].

Conclusion:

In this paper, we established (*p,q*)-Hardy type integral inequalities for (*p,q*)-integral functions. We also obtained more general results on (*p,q*)-Hardy integral inequalities. Our work has improved the results of [19], [20] and can be reduced to [23]. By taking $q\to 1$ and $p=1$, our results gave classical inequality formulas.

Acknowledgements:

This work is supported by Science Achievement Scholarship of Thailand, SAST and National Research Council of Thailand.

References:

1. Jackson FH. Quart. J. Pure Appl. Math. 1910;41:193-203.
2. Jackson FH. Amer. J. Math. 1910;32:305-314.
3. Asawasamrit S, Sudprasert C, Ntouyas, S, Tariboon J. Inequal. Appl. 2019;2019:154.
4. Kac, V, Cheung P. 2002. p. 1-75.
5. Bangerezako G. J. Math. Anal. Appl. 2005;306:161-179.
6. Tariboon J, Ntouyas SK. Adv. Difference Equ. 2013;2013:282.
7. Tariboon J, Ntouyas SK. J. Inequal Appl. 2014;2014:121.
8. Ernst T. UUDM Report 2000:16, 2000.
9. Aslam M, Awan MU, Noor KI. J. Math. Inequal. 2016;10:1013-1018.
10. Gauchman H. Comput. Math. Appl. 2002;47:281-300.
11. Tunc M, Gov E. RGMIA Res. Rep. Coll. 2016;95:1-12.
12. Tunc, M, Gov E. RGMIA Res. Rep. Coll. 2016;97:1-13.
13. Tunc M, Gov E. RGMIA Res. Rep. Coll. 2016;98:1-12.
14. Prabseang J, Nonlaopon K, Tariboon J. Axioms. 2019;8:68.
15. Kunt M, Iscan I, Alp N. Rev. Real Acad. Cienc. Exactas Fis. Nat. Ser. A Mat. 2018;112:969-992.
16. Sadjang PN. Results. Math. 2013;73:1-21.
17. Kalsoom H, Amer M, Junjua MD, Hassain S, Shahzadi G. Mathematics. 2019;7:683
18. Hardy GH. 1967. p. 239-243.
19. Sroysang B. J. Math. Inequal. 2014;8:497-501.
20. Khaled M. Afr. Mat. 2017;28:451-457.
21. Wu S, Sroysang B, Li S. J. Nonlinear. Sci Appl. 2018;9:1093-1102.
22. Bougoffa L. J. Inequal. Pure Appl. Math. 2006;7:60.
23. Sulaiman WT. Appl. Math. Lett. 2012;25:520-525.
24. Maligranda L, Oinarov R, Persson LE. Czech. Math. J. 2014;64:659-682.
25. Persson LE, Shaimardan S. J. Inequal. Appl. 2015;1:296.
26. Shaimardan S. Eurasian Math. J. 2016;7:84-99.
27. Baiarystanov AO, Persson LE, Shaimardan S, Termirkhanova A. J. Math. Inequal. 2016;3:761-781.

B_012_OF: AN ADAPTIVE DIFFERENTIAL EVOLUTION ALGORITHM BY USING MIXED MUTATION AND CROSSOVER STRATEGIES

Watcharida Nararuk*, Jeerayut Wetweerapong, Pikul Puphasuk

Department of Mathematics, Faculty of Science, Khon Kaen University, Khon Kaen, 40002, Thailand
*e-mail: watcharida.n@kkumail.com

Abstract:

In this research, an adaptive differential evolution algorithm by using mixed mutation and crossover strategies (ADEMIX) is proposed for solving continuous optimization problems. The proposed method mixes the basic and x_{best} mutations and also mixes the crossover rates by using the adaptive control process. The ADEMIX algorithm is tested on several benchmark functions and compared the performance with those of some well-known adaptive differential evolution methods. The experimental results show that the proposed method can solve all test functions and overall outperforms the basic DE and the compared methods.

Introduction:

Optimization methods are used to find the best solutions of optimization problems and are applied for solving complex problems in science, engineering and economics. There are various metaheuristic methods developed for solving the problems, which include Particle swarm optimization algorithm (PSO) [1,2], Artificial bee colony algorithm (ABC) [2,3], Cuckoo Search algorithm (CK) [2] and Differential evolution algorithm (DE) [4,5].

In this research, we focus on the differential evolution algorithm (DE) which was proposed by Storn and Price in 1997. DE is one of the most popular population-based methods for solving continuous optimization problems. Although the DE algorithm is simple and efficient, its performance depends on the test functions and the choice of control parameters: scaling factor (*F*), crossover rates (*CR*), and population size (*NP*). Some rules for choosing parameters *F, CR* and *NP* are recommended [6], but they cannot be used for general problems. Therefore, many researchers have proposed adaptive control processes to improve the performance of DE.

In 2006, Brest et al. [7] proposed self-adaptive DE called jDE in which the control parameters F and CR are adjusted by means of evolution and are applied at the individual level. They showed that jDE overall outperforms basic DE on 25 benchmark functions with $F = 0.5$ and $CR = 0.9$. In 2009 Qin et al. [8,9] presented a self-adaptive DE called SaDE in which the trail vector generation strategies and their correlative control parameters are gradually self-adapted. Four mutant vector generation strategies are used and the probabilities to choose each strategies are initialized to equal probability. For each individual population vector, its *F* and *CR* values are initialized by normal distributions. The result show that SaDE overalls outperforms jDE and basic DE on several test functions with various static values of *F* and *CR*. Also in 2009, Zhang and Sanderson[10] introduced an adaptive differential evolution with optional external archive called JADE. To diversify the population and improve the convergence performance, the method implements a new mutation strategy that utilizes some top best individuals and the optional archive operation that utilizes historical data. Their simulation results show that JADE performs better than the classic DE with $F = 0.5$ and $CR = 0.9$.

We propose an adaptive differential evolution algorithm by using mixed mutation and crossover strategies (ADEMIX). The algorithm aims to mix the basic and x_{best} mutations and also mixes the crossover rates with the adaptive control process.

Methodology:

The ADEMIX algorithm uses the mixed mutation and crossover strategies. The mutation strategy consists of basic and x_{best} mutations. The basic mutation diversifies the search but gives a slow convergence while the x_{best} mutation intensifies the search but may give a convergence to a non-solution or a local solution. Therefore, the adaptive mutation strategy is aimed to balance diversification and intensification. And from the fact that the low crossover rate is suitable for separable and multimodal functions while the high crossover rate is suitable for non-separable functions[11], two crossover rates 0.1 and 0.9 are used in the ADEMIX algorithm.

The proposed algorithm is described as follows:

Step 1. Initialization

Generate the initial population $P=[x_i]$ of random vectors $x_i=(x_{i1},x_{i2},...,x_{iD})$ for all *i=1,2,3…,NP* where *NP* is population size, *D* is dimension. Find the fitness values $f(x_i)$ for all *i* and find the best vector and the best fitness value, denoted by x_{best} and f_{best}, respectively. Set the initial probabilities pm_1 = 0.9 for the basic mutation and pm_2 = 0.1 for the x_{best} mutation and the corresponding counters $nm_1=nm_2=0$ for mutation. Set the initial probabilities $pc_1=pc_2=0.5$ and the corresponding counters $nc_1=nc_2=0$ for crossover.

Step 2. Mutation

For each target vector x_i*, choose four distinct random vectors* $x_{r1},x_{r2},x_{r3},x_{r4}\in P$ *different from* x_i*. Create the mutant vector* v_i *by*

$$v_i=\begin{cases}x_{r1}+F(x_{r2}-x_{r3}),\ if\ \ rand()\le pm_1\\ x_{best}+F(x_{r1}-x_{r2})+\mathrm{F}(x_{r3}-x_{r4}),\ otherwise\end{cases}$$

where the scaling factor F is 0.5.

Step 3. Crossover

Select CR values by

$$CR=\begin{cases}0.1,\ if\ \ rand()\le pc_1\\ 0.9,\ otherwise\end{cases}.$$

Create the trial vector u_i *by*

$$u_{ij}=\begin{cases}v_{ij},\ if\ \ rand()\le CR\ or\ \ j=I_{rand}\\ x_{ij},\ otherwise\end{cases}$$

where I_{rand} *is a fixed random numbers in {1,2,3,…D} which guarantees a change at least one position,* $rand()$ *are random numbers in [0,1].*

Step 4. Selection

Compare the fitness values of the trial vector u_i *and the target vector* x_i *. If the fitness value of* u_i *is better than* x_i *then replace* x_i *, with* u_i *. If the value is also better than* f_{best} *then update* x_{best} *and* f_{best} *.*

Step 5. Updating control parameters

Update pm_1, pm_2, pc_1 and pc_2 as follows.

If a better solution found in the selection is generated by using basic mutation then increase $nm_1 := nm_1 + 1$; otherwise, increase $nm_2 := nm_2 + 1$. Similarly, if the solution is generated by

using *CR* = 0.1 then increase $nc_1 := nc_1 + 1$; otherwise, increase $nc_2 := nc_2 + 1$.
If $(nm_1 + nm_2) \geq 100$ then adjust $nm_1 := nm_1 + 10$ and $nm_2 := nm_2 + 10$ (to prevent both of them from 0) . Update $pm_1 = (w)\,pm_1 + (1-w)cpm_1 / (cpm_1 + cpm_2)$ and $pm_2 = 1 - pm_1$, and update $pc_1 = (w)\,pc_1 + (1-w)cpc_1 / (cpc_1 + cpc_2)$ and $pc_2 = 1 - pc_1$ where *w* = 0. 9. Reset the associate counters to 0 when the probabilities are updated.
Step 6. Repeat 2-5 until the stopping condition is reached.

Experimental design: To assess the performance of ADEMIX algorithm, three experiments are conducted using different settings and performance measurements. Eight benchmark functions consisting of four different types (US, UN, MS, MN) as presented in Table 1 are selected to test the performance of ADEMIX and the compared methods. Type of functions US, UN, MS and MN are unimodal separable, unimodal non-separable, multimodal separable, multimodal non-separable functions, respectively. Their 2D surface plots are shown in Figure 1.

Table 1. Test functions.

Functions	***Type***	***Range***	***Formulation***
$f_1(x)$: *Sphere*	*US*	$[-100,100]^D$	$f_1(\mathrm{x}) = \sum_{i=1}^{D} x_i^2$
$f_2(x)$: *Schwefel 1.2*	*US*	$[-100,100]^D$	$f_2(\mathrm{x}) = \sum_{i=1}^{D} (\sum_{j=1}^{i} x_j)^2$
$f_3(x)$: *Rosenbrock*	*UN*	$[-100,100]^D$	$f_3(\mathrm{x}) = \sum_{i=1}^{D-1} 100(\mathrm{x}_{i+1} - x_i^2)^2 + (\mathrm{x}_i - 1)^2$
$f_4(x)$: *Schwefel 2.22*	*UN*	$[-100,100]^D$	$f_4(\mathrm{x}) = \sum_{i=1}^{D} \lvert x_i \rvert + \prod_{i=1}^{D} \lvert x_i \rvert$
$f_5(x)$: *Rastrigin*	*MS*	$[-5,5]^D$	$f_5(\mathrm{x}) = 10D + \sum_{i=1}^{D} x_i^2 - 10\cos(2\pi x_i)$
$f_6(x)$: *Schwefel*	*MS*	$[-500,500]^D$	$f_6(\mathrm{x}) = 418.98288727243369\,\mathrm{D} - \sum_{i=1}^{D} x_i \sin(\sqrt{\lvert \mathrm{x}_i \rvert})$
$f_7(x)$: *Ackley*	*MN*	$[-32,32]^D$	$f_7(\mathrm{x}) = -20 \cdot \exp(-0.2\sqrt{\frac{1}{D}\sum_{i=1}^{D} x_i^2})$ $-\exp \cdot (\frac{1}{D} \cdot \sum_{i=1}^{D} \cos(2\pi \cdot x_i)) + 20 + \exp(1)$
$f_8(x)$: *Griewank*	*MN*	$[-600,600]^D$	$f_8(\mathrm{x}) = \frac{1}{4000}\sum_{i=1}^{D} x_i^2 - \prod_{i=1}^{D} \cos(\frac{x_i}{\sqrt{i}}) + 1$

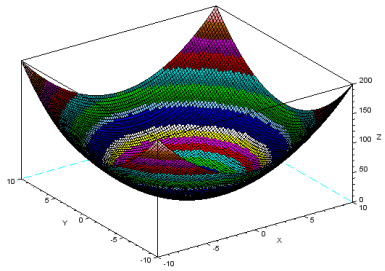

$f_1(x)$: Sphere function

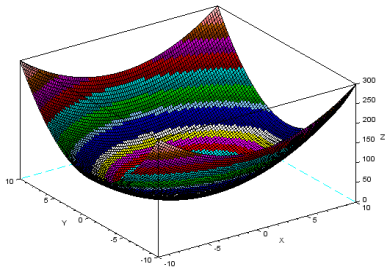

$f_2(x)$: Schwefel 1.2 function

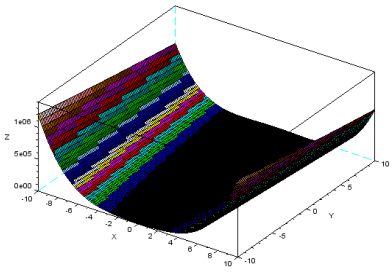

$f_3(x)$: Rosenbrock function

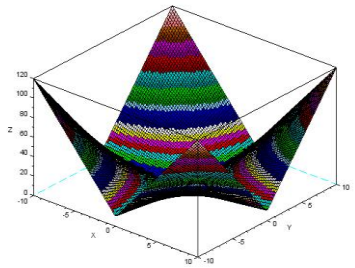

$f_4(x)$: Schwefel 2.22 function

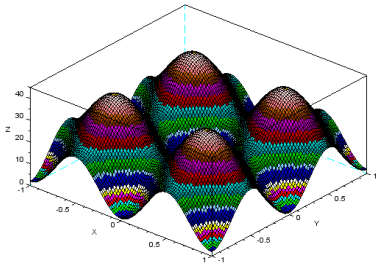

$f_5(x)$: Rastrigin function

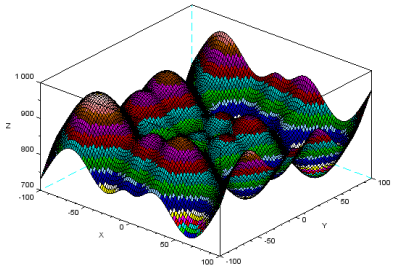

$f_6(x)$: Schwefel function

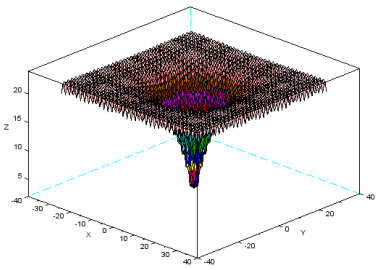

$f_7(x)$: Ackley function

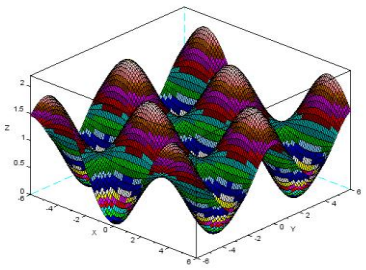

$f_8(x)$: Griewank function

Figure 1. 2D surface plots of test functions

Experiment I: Comparing the performance of the ADEMIX algorithm with those of DE algorithms

In this experiment, the performances of the ADEMIX algorithms are compared with those of the DE algorithms. We set the parameters *NP* = 50 for ADEMIX algorithm and *NP* = 50,100 for DE algorithms and *D* = 5,10,30,50. Each configuration is performed 30 independent runs at the value to reach $VTR = 10^{-10}$. The maximum number of function evaluations *Maxnf* = 20,000D is set. The number of successful runs (*NS*), mean of number of function evaluations (*Mean*), and percentage of standard deviation of the function evaluations *(%SD*) are reported.

Experiment II: Comparing the performance of the ADEMIX algorithm with those of PSO, DE, ABC, and CK algorithms

In this experiment, the performances of ADEMIX algorithm are compared with those of PSO, DE, ABC, CK algorithms for 30-dimensional functions. For ADEMIX, the parameters *NP* are set the same as in experiment I. The maximum number of function evaluations *Maxnf* = 2,000,000 and the value to reach $VTR = 10^{-16}$ are set as in the original paper [3]. Each configuration is performed 20 independent runs. The mean of best function values (*Mean fb*) and the standard deviation (*SD*) are reported.

Experiment III: Comparing the performance of the ADEMIX algorithm with those of JADE, jDE, and SaDE algorithms

In this experiment, the performances of ADEMIX algorithm are compared with those of JADE, jDE, and SaDE algorithms. For ADEMIX, the parameters *NP* are set the same as in experiment I. Each configuration is performed 50 independent runs. The maximum number of function evaluations *Maxnf* are set as in the original paper [10]. The mean of the best function values (*Mean fb*) and the standard deviations (*SD*) are reported.

Results and Discussion:

In this section, we present comparison results and discussion of the ADEMIX algorithm and other algorithms.

The performances of DE algorithms and ADEMIX algorithm

The performance comparison of ADEMIX algorithm and DE algorithms on test functions are presented in Table 2. For each function and dimension, we consider the numbers of successful runs *NS* = 30 first. Then, the least mean of number of function evaluations is highlighted. From Table 2, ADEMIX algorithm can solve all cases with good convergence performances. It gives the best results for 19 out of 32 cases whereas the basic DE with *NP* = 50 gives the best results for the remaining 13 cases. The basic DE with *NP* = 100 provides more successful runs than DE with *NP* = 50, but it requires a larger number of function evaluations. It is clear that the mixed mutation and crossover strategies greatly enhance the performance of basic DE.

The performance comparison of ADEMIX, PSO, DE, ABC, and CK algorithms

The performance comparison of ADEMIX algorithm and PSO, DE, ABC, CK algorithms on several benchmark functions are presented in Table 3. The best values of the compared methods are taken from the reference [3]. If the best function values of the compared methods are not reported in the reference, the notation "N/A" is used. The table shows that ADEMIX algorithm outperforms CK, DE, ABC and PSO for all cases and gives the same results for the remaining 4, 3, 2, and 1 cases, respectively. This indicates that the ADEMIX outperforms all compared methods.

Table 2. The performance comparison of DE algorithm and ADEMIX algorithm.

Functions	D	DE						ADEMIX		
		NP 50			NP 100			NP 50		
		NS	Mean	%SD	NS	Mean	%SD	NS	Mean	%SD
Sphere	5	**30**	**6144**	**3.82**	30	12460	3.41	30	6522	3.02
	10	**30**	**13190**	**2.60**	30	29245	2.47	30	14095	2.86
	30	**30**	**39266**	**2.90**	30	106818	2.60	30	48945	1.56
	50	**30**	**68588**	**3.76**	30	169446	2.12	30	85175	1.43
Schwefel 1.2	5	**30**	**6279**	**3.33**	30	12810	3.32	30	6745	2.95
	10	**30**	**13640**	**3.52**	30	30527	2.42	30	14784	2.74
	30	**30**	**42032**	**2.90**	30	114997	1.66	30	52249	1.29
	50	**30**	**76312**	**5.94**	30	182751	1.73	30	92654	1.41
Rosenbrock	5	20	15029	29.05	30	25518	10.56	**30**	**14513**	**5.87**
	10	16	138207	29.02	30	75194	4.04	**30**	**33768**	**5.35**
	30	0	-	-	30	406157	3.97	**30**	**179142**	**4.63**
	50	0	-	-	10	945149	4.32	**30**	**456618**	**2.63**
Schwefel 2.22	5	30	11788	3.67	30	24374	1.89	**30**	**11465**	**3.20**
	10	30	26533	3.71	30	61567	2.48	**30**	**24981**	**2.39**
	30	**30**	**74550**	**3.30**	30	234491	2.99	30	83124	1.09
	50	**30**	**112458**	**4.07**	30	344964	3.12	30	141995	0.73
Rastrigin	5	30	20853	11.80	30	47827	6.94	**30**	**10171**	**3.75**
	10	15	82248	15.63	1	172650	-	**30**	**23297**	**3.07**
	30	0	-	-	0	-	-	**30**	**104247**	**2.47**
	50	0	-	-	0	-	-	**30**	**299369**	**3.95**
Schwefel	5	30	11094	9.91	30	23296	8.20	**30**	**8843**	**4.89**
	10	30	39341	12.81	30	102797	12.16	**30**	**19676**	**3.04**
	30	0	-	-	0	-	-	**30**	**69108**	**1.83**
	50	0	-	-	0	-	-	**30**	**130755**	**1.71**
Ackley	5	**30**	**10574**	**3.16**	30	21745	1.71	30	11228	2.60
	10	**30**	**21978**	**2.14**	30	49210	1.75	30	23450	2.15
	30	**30**	**63271**	**2.80**	30	173446	1.41	30	78458	1.37
	50	23	112612	3.43	30	269857	1.71	**30**	**134997**	**0.92**
Griewank	5	23	37473	15.12	20	92794	6.90	**30**	**23042**	**8.05**
	10	2	43756	9.97	15	163510	15.42	**30**	**34996**	**8.41**
	30	21	40209	3.79	29	109871	2.46	**30**	**52381**	**3.53**
	50	23	70551	3.79	30	170345	2.07	**30**	**86779**	**1.46**

The performance comparison of ADEMIX, JADE, jDE, and SaDE algorithms

The performance comparison of the ADEMIX algorithm with those of JADE, jDE, and SaDE on several benchmark functions are presented in Table 4. The best values of the compared methods are taken from the reference [10]. The table shows that the ADEMIX outperforms JADE and jDE for 10 and 12 out of 13 cases, respectively and gives the same results for the remaining 3 cases. When compared with SaDE, the ADEMIX outperforms SaDE for all cases and gives the same results for the remaining 2 cases. It is clear that the ADEMIX overall outperforms the compared methods.

Table 3. The performance comparison of ADEMIX, PSO, DE, ABC, and CK algorithms.

Functions	**Statistics**	**PSO**	**DE**	**ABC**	**CK**	**ADEMIX**
Sphere	Mean fb	N/A	N/A	N/A	N/A	**0.00E+00**
	SD	N/A	N/A	N/A	N/A	**0.00E+00**
Schwefel 1.2	Mean fb	7.39E-10	**0.00E+00**	4.75E+01	**0.00E+00**	**0.00E+00**
	SD	2.43E-09	**0.00E+00**	2.32E+01	**0.00E+00**	**0.00E+00**
Rosenbrock	Mean fb	2.36E+00	**0.00E+00**	6.09E-02	**0.00E+00**	**0.00E+00**
	SD	3.33E+00	**0.00E+00**	9.94E-02	**0.00E+00**	**0.00E+00**
Schwefel 2.22	Mean fb	**0.00E+00**	**0.00E+00**	4.00E-16	**0.00E+00**	**0.00E+00**
	SD	**0.00E+00**	**0.00E+00**	0.00E+00	**0.00E+00**	**0.00E+00**
Rastrigin	Mean fb	2.80E+01	1.54E+01	**0.00E+00**	1.28E+00	**0.00E+00**
	SD	7.87E+00	4.96E+00	**0.00E+00**	1.04E+00	**0.00E+00**
Schwefel	Mean fb	3.64E+03	6.30E+02	2.00E-07	6.40E+01	**0.00E+00**
	SD	9.12E+02	2.04E+02	1.87E-12	7.64E+01	**0.00E+00**
Ackley	Mean fb	8.00E-15	4.40E-15	3.00E-14	4.40E-15	**4.17E-15**
	SD	0.00E+00	0.00E+00	2.50E-15	0.00E+00	**7.94E-16**
Griewank	Mean fb	9.23E-03	1.11E-03	**0.00E+00**	**0.00E+00**	**0.00E+00**
	SD	1.05E-02	3.44E-03	**0.00E+00**	**0.00E+00**	**0.00E+00**

Table 4. The performance comparison of ADEMIX, JADE, jDE, and SaDE algorithms.

Functions	Maxnf	Statistics	JADE	jDE	SaDE	ADEMIX
Sphere	150,000	Mean fb	**1.8E-60**	2.5E-28	4.5E-20	6.3E-41
		SD	**8.6E-60**	3.5E-28	6.9E-20	1.2E-41
Schwefel 1.2	500,000	Mean fb	5.7E-61	5.2E-14	9.0E-37	**2.6E-144**
		SD	2.7E-60	1.1E-13	5.4E-36	**8.3E-144**
Rosenbrock	300,000	Mean fb	8.0E-02	1.3E+01	2.1E+01	**5.4E-26**
		SD	5.6E-01	1.4E+01	7.8E+00	**2.2E-25**
	2,000,000	Mean fb	8.0E-02	8.0E-02	1.8E+01	**7.5E-30**
		SD	5.6E-01	5.6E-01	6.7E+00	**1.8E-29**
Schwefel 2.22	200,000	Mean fb	1.8E-25	1.5E-23	1.9E-14	**1.4E-29**
		SD	8.8E-25	1.0E-23	1.1E-14	**7.4E-30**
Rastrigin	100,000	Mean fb	1.0E-04	1.5E-04	1.2E-03	**3.1E-08**
		SD	6.0E-05	2.0E-04	6.5E-04	**9.6E-08**
	500,000	Mean fb	**0.0E+00**	**0.0E+00**	**0.0E+00**	**0.0E+00**
		SD	**0.0E+00**	**0.0E+00**	**0.0E+00**	**0.0E+00**
Schwefel	100,000	Mean fb	3.3E-05	7.9E-11	4.7E+00	**0.0E+00**
		SD	2.3E-05	1.3E-10	3.3E+01	**0.0E+00**
	900,000	Mean fb	**0.0E+00**	**0.0E+00**	4.7+00	**0.0E+00**
		SD	**0.0E+00**	**0.0E+00**	3.3E+00	**0.0E+00**
Ackley	50,000	Mean fb	**8.2E-10**	3.5E-04	2.7E-03	1.9E-06
		SD	**6.9E-10**	1.0E-04	5.1E-04	6.4E-07
	200,000	Mean fb	**4.4E-15**	4.7E-15	4.3E-14	5.8E-15
		SD	**0.0E+00**	9.6E-16	2.6E-14	1.8E-15
Griewank	50,000	Mean fb	9.9E-08	1.9E-05	7.8E-04	**7.3E-10**
		SD	6.0E-07	5.8E-05	1.2E-03	**1.0E-09**
	300,000	Mean fb	**0.0E+00**	**0.0E+00**	**0.0E+00**	**0.0E+00**
		SD	**0.0E+00**	**0.0E+00**	**0.0E+00**	**0.0E+00**

Conclusion:

We have presented an adaptive differential evolution algorithm by using mixed mutation and crossover strategies (ADEMIX). The ADEMIX algorithm mixes the basic and x_{best} mutations and also mixes the crossover rates by using the adaptive control process. The performance comparisons on several testes functions show that it enhances the performance of the basic DE and overall outperforms PSO, ABC, CK, JADE, jDE, and SaDE algorithms.

Acknowledgements:

The authors would like to thank Department of Mathematics, Faculty of Science, Khon Kaen University for simulation equipment support.

References:

1. Kameyama. K., IEICE Tran Inf Syst, 2009; E92-D:1354-1361.
2. Civicioglu P., Besdok E., Artiflntell Rev. 2013;39:315-346.
3. Sharma S., Bhambu P. IJCA, 2016;149:pp11-19.
4. Storn R., Price K., Technical Report. 1995;95:012.
5. Storn R., Price K., J Glob Optim. 1997;11:341-359.
6. Storn R., Studies in Computational Intelligence, 2008;143:1-31.
7. Brest J., Greiner S., Boskovic B., Mernik M., and Zumer V., IEEE Tran Evol Comput. 2006;10:646-657.
8. Qin A. K., Suganthan P. N., IEEE Congr Evol Comput. 2005;2:1785-1791.
9. Qin A. K., Huang V. L., Suganthan P. N., IEEE Tran Evol Comput. 2009;13:398-417.
10. Zhang J. Q., Sanderson A. C., IEEE Trans Evol Comput., 2009;13:945-958.
11. Poontong T., Master Thesis, Khon Kaen university, 2018.

B_013_PF: FORECASTING MODELS OF FOREIGN EXCHANGE RATES U.S. DOLLAR, EURO, YEN AND YUAN AGAINST THE THAI BAHT

Somsri Banditvilai,[1,]*Siriluck Anansatitzin[2]

[1]Department of Statistics, Faculty of Science, King Mongkut's Institute of Technology Ladkrabang, Bangkok 10520 Thailand
[2]Department of Computer Science, Faculty of Science, King Mongkut's Institute of Technology Ladkrabang, Bangkok 10520 Thailand
*e-mail: somsri_b2000@yahoo.com

Abstract:

This research presents a comparative study of three different forecasting methods based on monthly exchange rates of the U.S. Dollar, Euro, Yen and Yuan against the Thai baht. The Triple Exponential Smoothing method, the Box-Jenkins method and the Artificial Neural Networks are compared. The data are taken from the Bank of Thailand starting from January, 2010 to December, 2019. The data are divided into 2 sets. The first set from January, 2010 to December, 2018, is used for constructing and selection the forecasting models. The second set from January, 2019 to December, 2019, is used for computing the accuracy of the forecasting model. The forecasting models are chosen by considering the smallest root mean square error (RMSE). The mean absolute percentage error (MAPE) is used to measure the accuracy of the model. The results show that Artificial Neural Networks is the most appropriate method for forecasting the exchange rates of U.S. dollar/ Thai baht, the Box-Jenkins method is the most suitable method for predicting the exchange rates of Yen /Thai baht and the Triple Exponential Smoothing method is the most preferable method for forecasting both exchange rates, the Euro/Thai baht and the Yuan/Thai baht. Forecast errors measure by MAPE for the exchange rates of U.S.Dollar, Euro, Yen and Yuan against the Thai baht are 2.17%, 1.52%, 2.29% and 1.48% respectively.

Introduction:

All countries have different currency systems .Therefore, the foreign exchange rates system was developed .If we don't know about foreign exchange rates, it will be impossible to compare international product prices .In addition, the appreciation and depreciation of the exchange rates will affect competition in international trade .When the Thai baht depreciates, it will cause the export prices of Thai products to be cheaper compared to the world market .The export sector gain a benefit from more product sales, but the import price of raw materials and machinery from foreign countries will be increased resulting in higher production costs .On the other hand, when the Thai baht appreciates, it will cause the export prices of Thai products to be higher in the world market and the price of raw materials and machinery imported from foreign countries to become cheaper resulting in lower production costs .

Fluctuations in exchange rates are difficult to predict. There are various factors that affects the movement of exchange rates such as economic fundamentals in the country, monetary and fiscal policy, global economic conditions, predictions and speculation, as well as political stability in the country and abroad. To reduce the effects of foreign exchange fluctuations, businesses in the import-export sector need to know the accurate forecast of foreign exchange rates for planning production and distribution. This research aims to forecast the foreign exchange rates of the U.S. Dollar, Euro, Yen and Yuan against the Thai baht as they are the main currency used to trade with Thailand.

Forecasting the exchange rate can be done with regression analysis and time series analysis. But time series is more popular since there is no need to collect independent variables that may have affected to the exchange rate.

There are two methods that are commonly used in time series forecasting. First, the Exponential Smoothing method which is widely used and is proven to provide good predictions. Second, the Box-Jenkins method is reputed to have high accurary in short-term forecasting. Fat, Codruta Maria and Dezsi, Eva[1] employed the Exponential Smoothing method and the Box-Jenkins method in forecasting the exchange rate of the Romanian Leu against other currencies. The result showed that the Exponential Smoothing method in some cases outperformed the Box-Jenkins method. Ahmed Emam[2] used the Artificial Neural Networks to predict the exchange rate USD/JPY. The results showed that Artificial Neural Network model learns well and is most likely to give the best result. Latife Ghalayini[3] investigated the ARIMA model to forecast the exchange rate time series and the ARIMA including two macroeconomic variables. The results showed that a simple ARIMA model can provide an evolution equation with a simple interpretation. Artificial Neural Networks is a popular method that produces very accurate results and is widely used in forecasting. Gregorius A. et al.[4] compared the Single Exponential Smoothing, the Double Exponential Smoothing, the Triple Exponential Smoothing and the Artificial Neural Networks to forecast rice production in Indonesia. The result confirmed that the Artificial Neural Networks provided the best prediction result. Therefore, this research employs the Exponential Smoothing method, the Box-Jenkins method, and the Artificial Neural Networks to model the currency exchange rates.

Data Collection and Methodology:

The exchange rates U.S. Dollar (USD), Euro (EUR), Japanese Yen (JPY) and Chinese Yuan (CNY) against the Thai baht are collected from the Bank of Thailand starting from January, 2010 to December, 2019. The data are divided into 2 sets. The first set from January, 2010 to December, 2018 is used for constructing and selection the forecasting models. The second set from January, 2019 to December, 2019 is used for computing the accuracy of the forecasting model. This research employs three forecasting methods which are the Triple exponential smoothing method, the Box-Jenkins method, and the Artificial Neural Networks.

The Triple Exponential Smoothing method involves quadratic trend and three smoothed statistics. It begins with taking partial or the whole time series to estimate the parameter $\beta_0, \beta_1, \beta_2$ for the quadratic trend and estimate $a_0(0), a_1(0), a_2(0)$ then compute $A_0(0), A_1(0), A_2(0)$ from equations (1)-(3) and recursively apply equations (4)-(6)[5]

$$A_0 = a_0(0) - \left(\frac{(1-\alpha)}{\alpha}\right)a_1(0) + \left(\frac{(1-\alpha)(2-\alpha)}{2\alpha^2}\right)a_2(0) \qquad (1)$$

$$A_0' = a_0(0) - \left(\frac{2(1-\alpha)}{\alpha}\right)a_1(0) + \left(\frac{2(1-\alpha)(3-2\alpha)}{2\alpha^2}\right)a_2(0) \qquad (2)$$

$$A_0'' = a_0(0) - \left(\frac{3(1-\alpha)}{\alpha}\right)a_1(0) + \left(\frac{3(1-\alpha)(4-3\alpha)}{2\alpha^2}\right)a_2(0) \qquad (3)$$

$$A_t = (1-\alpha)A_{t-1} + \alpha Y_t \qquad (4)$$

$$A_t' = (1-\alpha)A_{t-1}' + \alpha A_t \qquad (5)$$

$$A_t'' = (1-\alpha)A_{t-1}'' + \alpha A_t' \qquad (6)$$

A_t, A_t', A_t'' are the single, double and triple smoothed statistics and Y_t is the observed data at time t. and p is the p[th] steps ahead of time t. Finally, we obtain the forecasting equation as follows:

$$\hat{Y}_{t+p}(t) = \left(6(1-\alpha)^2 + (6-5\alpha)\alpha p + \alpha^2 p^2\right)\left(\frac{A_t}{2(1-\alpha)^2}\right) - \left(6(1-\alpha)^2 + 2(5-4\alpha)\alpha p + 2\alpha^2 p^2\right)\left(\frac{A_t'}{2(1-\alpha)^2}\right) + \left(2(1-\alpha)^2 + (4-3\alpha)\alpha p + \alpha^2 p^2\right)\left(\frac{A_t''}{2(1-\alpha)^2}\right) \quad (7)$$

The Box-Jenkins method was developed in 1974 and is widely used in modelling and forecasting exchange rate. Box-Jenkins method uses Autocorrelation Function (ACF) and Partial Autocorrelation Function (PACF) to identify the model under the stationary condition. Box-Jenkins method is a four-step process

Step 1: Tentative identification: Historical data are used to tentatively identify an appropriate Box-Jenkins model.

Step 2: Estimation: Historical data are used to estimate the parameters of the tentatively identified model.

Step 3: Diagnostic checking: Various diagnostics are used to check the adequacy of the tentatively identified model. In some cases may need to suggest an improved model, which is then regarded as a new tentatively identified model.

Step 4: Forecasting: Once a final model is obtained, it is used to forecast future time series values.

It is possible that several models may be identified, and the selection of an optimum model is necessary. Such selection of models is usually based on the Akaike Information Criterion (AIC)[6] defined as follows:

$$AIC = -2\ln L + 2k$$

Where L represents the likelihood function, k is the number of parameters that estimated. The optimum model gives the minimum AIC.

The Box-Jenkins model of $ARIMA(p,d,q)\times SARIMA(P,D,Q)_L$ is defined as follows:[7]

$$\phi_p(B)\phi_P(B^L)Z_t = \theta_0 + \theta_q(B)\theta_Q(B^L)\varepsilon_t \quad (8)$$

when

$$\phi_p(B) = (1-\phi_1 B - \phi_2 B^2 - \phi_3 B^3 - \cdots - \phi_p B^p)$$
$$\phi_P(B^L) = (1-\phi_{1L} B^L - \phi_{2L} B^{2L} - \phi_{3L} B^{3L} - \cdots - \phi_{PL} B^{PL})$$
$$\theta_q(B) = (1-\theta_1 B - \theta_2 B^2 - \theta_3 B^3 - \cdots - \theta_q B^q)$$
$$\theta_Q(B^L) = (1-\theta_{1L} B^L - \theta_{2L} B^{2L} - \theta_{3L} B^{3L} - \cdots - \theta_{QL} B^{QL})$$
$$Z_t = (1-B^L)^D (1-B)^d Y_t$$

where

Y_t is the observed data at time t

B is backward shift operator

θ_0 is a constant

ϕ_p is the non-seasonal autoregressive model of order p

θ_q is the non-seasonal moving average model of order q

$\phi_P(B^L)$ is the seasonal autoregressive model of order P

$\theta_Q(B^L)$ is the seasonal moving average model of order Q

ε_t is the error at time t and have normal distribution which mean is equal to zero and constant variance and statistical independent

d is the number of regular difference

D is the number of seasonal difference

This research employed Minitab 18.0 in analyzing the Box-Jenkins model.

The Artificial neural networks was designed to mimic the characteristics of the biological neurons in the human brain and nervous system[8]. In the case of modelling the exchange rates time series, the historical exchange rates are sent into the input neurons, and corresponding forecasting exchange rate is generated from the output neurons after the network is adequately trained. The network learns the information contained in the exchange rate time series by adjusting the interconnections between layers. The structure and neural networks can only be viewed in terms of the input, output and transfer characteristics. The specific interconnections cannot be seen even after the training process. There is no easy way to interpret the specific meaning of the parameters and interconnections within networks trained using the exchange rate time series data. There are two advantages of employing neural networks for forecasting time series data. First, they can fully extract the complex nonlinear relationships hidden in the time series. Second, they have no assumption of the underlining distribution for the collected data[9].

Backpropagation Neural Networks are a type of feed forward artificial neural networks. In feed-forward neural networks, the data flow is in one direction and the answer is obtained solely based on the current set of inputs. Backpropagation Neural Networks consist of an input layer, a hidden layer, and an output layer. Each layer is formed by a number of nodes, and each node represents a neuron. The upper-layer and lower-layer nodes are connected by the weights. The common structure of a Backpropagation Neural Networks model is illustrated in Fig. 1

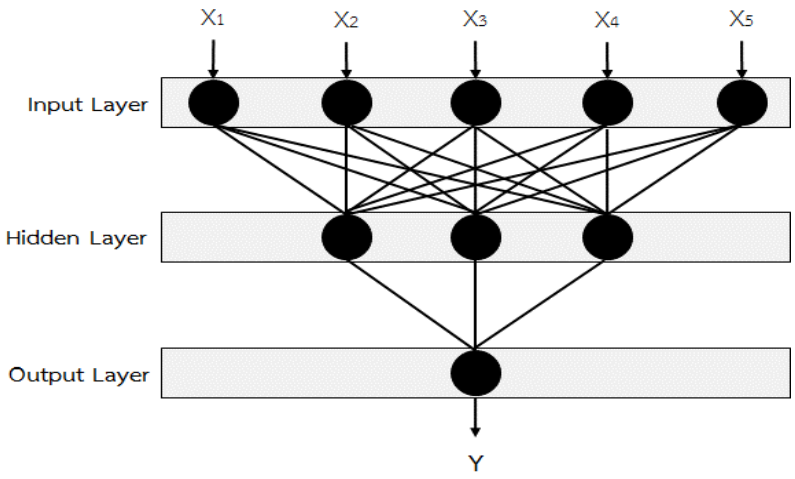

Fig. 1. Schematic of Back Propagation Neural Networks

Backpropagation Neural Networks training includes three steps: (1) the forward feeding of the input training pattern, (2) the calculation and back-propagation of the associated error, and (3) the adjustment of the weights. With n input neurons, m hidden neurons, and one output neuron, the outputs of all hidden layer nodes are calculated as follows:

$$net_j = \sum_{i=0}^{n} \omega_{ij} x_i (i = 0,1,2,...,n;\ j = 1,2,...,m) \qquad (9)$$

$$y_j = f(net_j)(j = 1,2,...,m) \qquad (10)$$

Where net_j is the activation value of the *jth* node, the connection weight from input node *i* to hidden node *j*, x_i the *ith* input, y_j the corresponding output of the *jth* node in the hidden layer, and f the activation function of a node, which is usually a sigmoid function.

$$f(x) = \frac{1}{1+\exp(-x)} \qquad (11)$$

The outputs of all output layer neurons are expressed as

$$O = f_0(\sum_{j=0}^{m} \omega_j, y_j)(j = 0,1,2,..,m) \qquad (12)$$

Where f_0 is the activation function, which is usually a line function; ω_j is the connection weight from the hidden node *j* to the output node, and y_j is the corresponding output of the node *jth* in the hidden layer. All the connection weights are initialized randomly, and then modified according to the results of the Backpropagation Neural Networks training process. Several methods have been proposed for the adjustment of the connection weights, such as the steepest descent algorithm, Newton's method, Gauss-Newton's algorithm and Levenberg-Marquardt algorithm[10].

The time series of exchange rates U.S. Dollar, Euro, Yen and Yuan against Thai baht were divided into three subsets. The exchange rates from January, 2010 to December, 2016 were employed as the training set used for training the network. The exchange rates from January, 2017 to December, 2018 were employed as the validation set. The remaining set of the series were used as the test set.

This research employed Weka 3.8.1 in modelling Back propagation Neural Networks. The number of inputs of the neural networks was determined by the characteristic of time series mixed with randomly selected. Therefore, eight, sixteen, twenty four, thirty two, forty were selected as the number of input layer for the USD/THB exchange rate. Five, eleven, seventeen, twenty three, twenty nine were selected as the number of input layer for the EUR/THB exchange rate. Six, twelve, eighteen, twenty four, thirty were selected as the number of input layer for the JPY/THB exchange rate. Eight, thirteen, eighteen, twenty three, twenty eight were selected as the number of input layer for the CNY/THB exchange rate. The output layer of artificial neural networks contains only one neuron representing the forecast value of the exchange rate of next month. This research employed Weka 3.8.1 in running artificial neural networks. The different learning rate were examined from 0.01 to 0.3 with 0.01 increments. The different momentum were examined from 0.4 to 0.8 with 0.05 increments. The different iteration were examined from 500, 1000 and 1500. The number of hidden neurons were varied from 2 to 20 at an increment of 1.

MODEL SELECTION CRITERION

The forecasting models are chosen by considering the smallest root mean square error (RMSE). Mean absolute percentage error (MAPE) is used to measure the accuracy of the model.

$$RMSE = \sqrt{\frac{1}{n}\sum_{t=1}^{n} e_t^2} \qquad (13)$$

$$MAPE = \sum_{t=1}^{n} \left| \frac{e_t}{Y_t} \right| \times 100 \qquad (14)$$

Results and Discussion:

The first set of data from January, 2010 to December 2018 is employed to build the Triple Exponential Smoothing model and Box-Jenkins model. Fig. 2-4 show time series plots of exchange rates U.S. Dollar, Euro, Yen and Yuan against the Thai baht. From Fig. 2-4 show non-stationary and none of them show linear trend or exponential trend. Since the EUR/THB and CNY/THB exchange rates show quadratic trend, this research employs Triple exponential smoothing method to model the currency exchange rates.

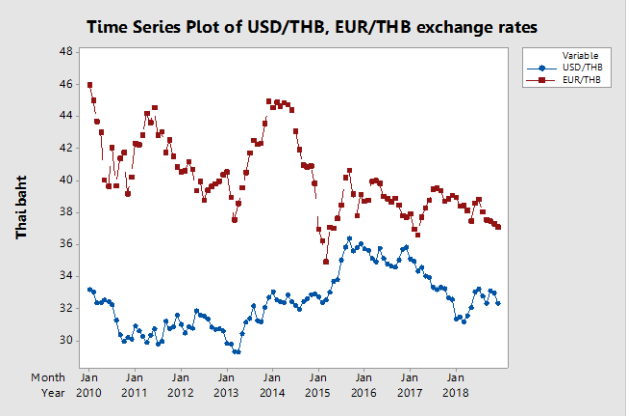

Fig. 2. Monthly USD/THB and EUR/THB exchange rates.

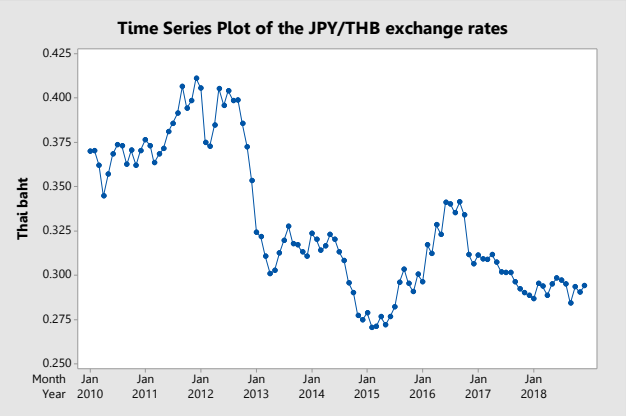

Fig. 3. Monthly JPY/THB exchange rates.

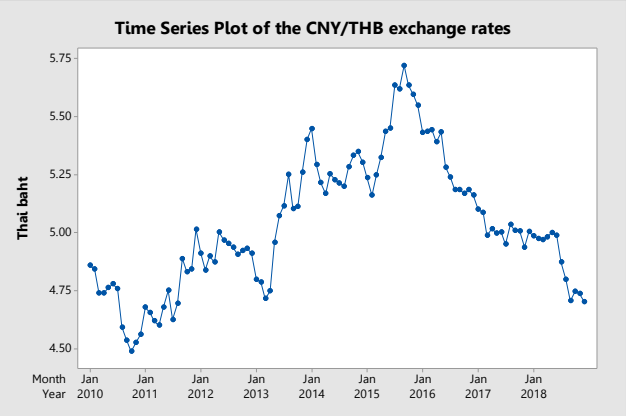

Fig. 4. Monthly CNY/THB exchange rates.

Table 1: The estimating parameter and RMSE from triple exponential smoothing method

Exchange Rate Model	α	RMSE
USD/THB	0.329774	0.151617
EUR/THB	0.335530	0.464701
JPY/THB	0.332592	0.000073
CNY/THB	0.323738	0.003312

Table 2: Box-Jenkins models with RMSE and AIC

USD/THB exchange rate model	RMSE	AIC
$ARIMA(0,1,0)\times SARIMA(1,0,1)_{32}$	0.137455	-
EUR/THB exchange rate model	RMSE	AIC
$ARIMA(4,1,4)$	0.973262	16.0542
$ARIMA(0,2,1)$	1.010119	1.9798
JPY/THB exchange rate model	RMSE	AIC
$ARIMA(4,1,4)$	0.000071	-
CNY/THB exchange rate model	RMSE	AIC
$ARIMA(0,1,1)\times SARIMA(0,0,1)_{23}$	0.005310	14.47633
$ARIMA(0,2,1)\times SARIMA(0,0,1)_{23}$	0.005495	14.40783

Table 3: The model from artificial neural networks

	Model	Learning rate	Momentum	Iterations
USD/THB	32-4-1	0.10	0.50	500
EUR/THB	11-4-1	0.05	0.75	1000
JPY/THB	12-5-1	0.03	0.85	1500
CNY/THB	23-5-1	0.04	0.80	1500

Table 4: The RMSE of training and validation set from artificial neural networks

Exchange rate against Thai baht	RMSE	
	Training set	Validation set
U.S. Dollar	0.1118	0.1357
Euro	0.5867	1.0591
Yen	0.0074	0.0138
Yuan	0.0088	0.0096

Table 5: Minitab output of Box-Jenkins model of the exchange rate Yen/Thai baht.

The exchange rate Yen/Thai baht model $ARIMA(4,1,4)$				
Type	**Coef**	**SE Coef**	**t-value**	**p-value**
$\hat{\phi}_1$	0.656	0.101	6.51	0.000
$\hat{\phi}_2$	-0.612	0.128	-4.78	0.000
$\hat{\phi}_3$	0.473	0.122	3,88	0.000
$\hat{\phi}_4$	-0.6721	0.0935	-7.19	0.000
$\hat{\theta}_1$	0.5332	0.0632	8.44	0.000
$\hat{\theta}_2$	-0.6504	0.0829	-7.44	0.000
$\hat{\theta}_3$	0.5183	0.0729	7.11	0.000
$\hat{\theta}_4$	-0.9581	0.0510	-18.77	0.000

Table 1 shows the optimal α and RMSE from Triple exponential smoothing method. Table 2 shows Box-Jenkins models with RMSE. Table 3 shows the models from Artificial Neural Networks with learning rate, momentum and Iteration. Table 4 shows the RMSE of training set and validation set of the model from Artificial Neural Networks. From Table 2, based on the minimum of AIC value, the model $ARIMA(0,2,1)$ and $ARIMA(0,2,1)\times SARIMA(0,0,1)_{23}$ are the Box-Jenkins optimal models for the EUR/THB and CNY/THB exchange rates. $ARIMA(0,1,0)\times SARIMA(1,0,1)_{32}$ is the Box-Jenkins optimal model for the USD/THB exchange rate and $ARIMA(4,1,4)$ is the Box-Jenkins optimal model for the JPY/THB exchange rate.

Table 6: Minitab output of the exchange rate Yen/Thai baht model $ARIMA(4,1,4)$

Modified Box-Pierce (Box-Ljung) Chi-Square statistic				
Lag	12	24	36	48
Chi-Square	3.14	9.71	20.84	32.01
DF	4	16	28	40
p-value	0.535	0.881	0.832	0.812

Table 7: The RMSE of three forecasting methods

Exchange rate against Thai baht	Triple Exponential Smoothing	Box-Jenkins	Artificial Neural Networks
U.S. Dollar	0.151617	0.137455	0.1118
Euro	0.464701	1.010119	0.5867
Yen	0.000073	0.000071	0.0074
Yuan	0.003312	0.005495	0.0088

Table 5, 6 show that all parameters from the JPY/THB exchange rates model $(\phi_1,\phi_2,\phi_3,\phi_4,\theta_1,\theta_2,\theta_3,\theta_4)$ are statistically significant from zero, since all p-values are less than 0.05. From Box-Ljung test, residuals from the model are independent since p-values are greater than 0.05 for all lags. Therefore, the model $ARIMA(4,1,4)$ fits with the JPY/THB exchange rates.

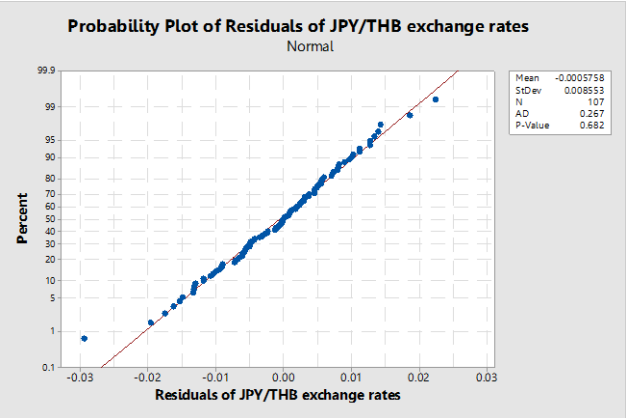

Fig. 5. Anderson-Darling Normality Test for Residuals of JPY/THB exchange rates.

Since the residuals of Box-Jenkins models need to have normal distribution. Fig. 5 shows Anderson-Daring Normality test for residuals of the JPY/THB exchange rates. The results show that residuals of the JPY/THB exchange rates has normal distribution since p-value is greater than 0.05. (p-value = 0.682) Fig 6-7 show Anderson-Daring Normality test for residuals of EUR/THB and CNY/THB exchange rates. The results show that residuals of EUR/THB and CNY/THB exchange rates have normal distribution since p-value are greater than 0.05. (p-value = 0.067, 0.059 respectively.) In case of the residuals of Triple Exponential Smoothing method have normal distribution, these confirms that the models best fit with EUR/THB and CNY/THB exchange rates

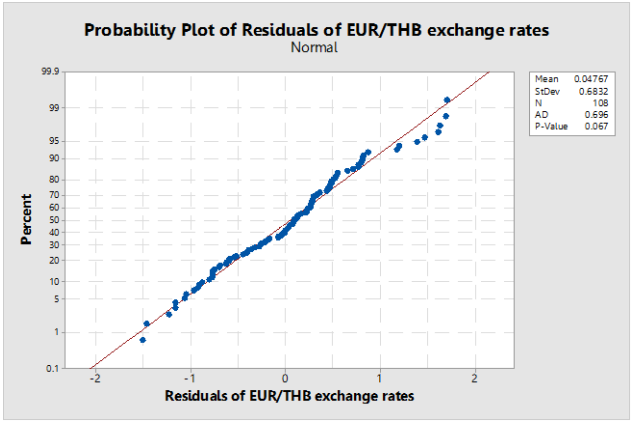

Fig. 6. Anderson-Darling Normality Test for Residuals of EUR/THB exchange rates.

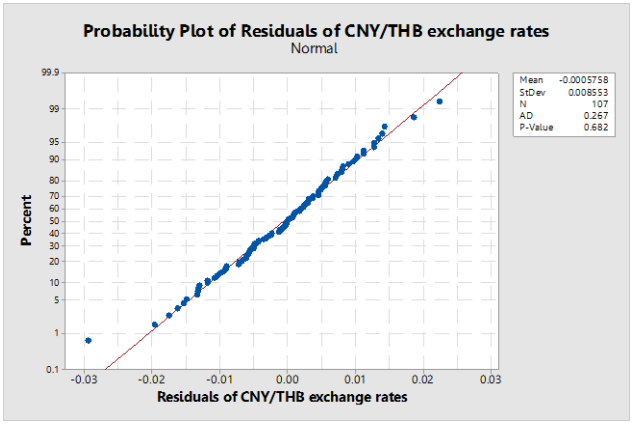

Fig. 7. Anderson-Darling Normality Test for Residuals of CNY/THB exchange rates.

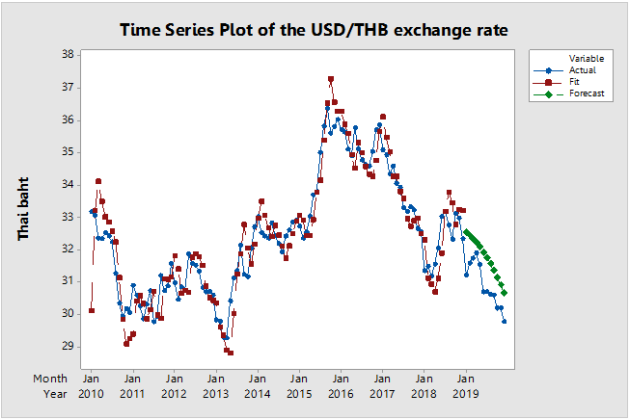

Fig. 8. USD/THB exchange rates and forecast values by Artificial Neural Networks.

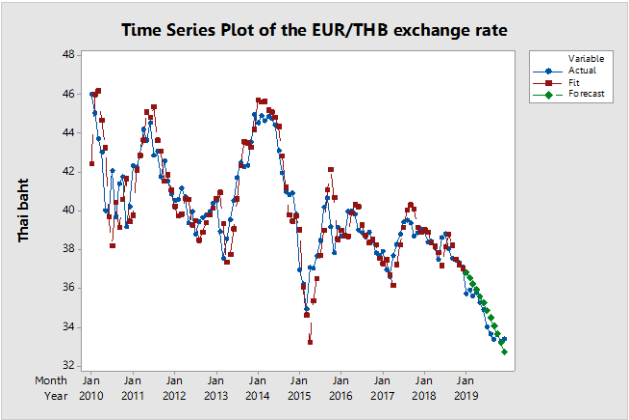

Fig. 9. EUR/THD exchange rates and forecast values by Triple Exponential Smoothing method.

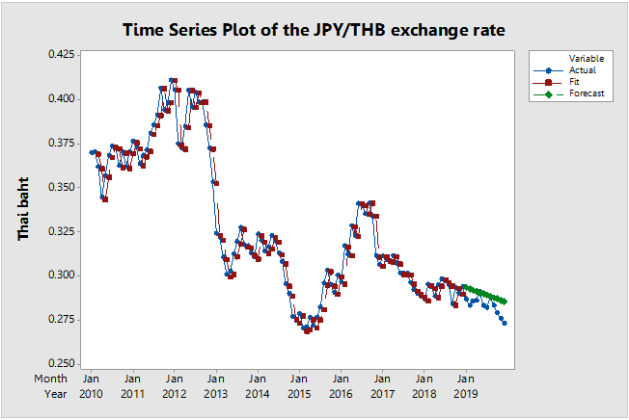

Fig. 10. JPY/THB exchange rates and forecast values by Box-Jenkins method.

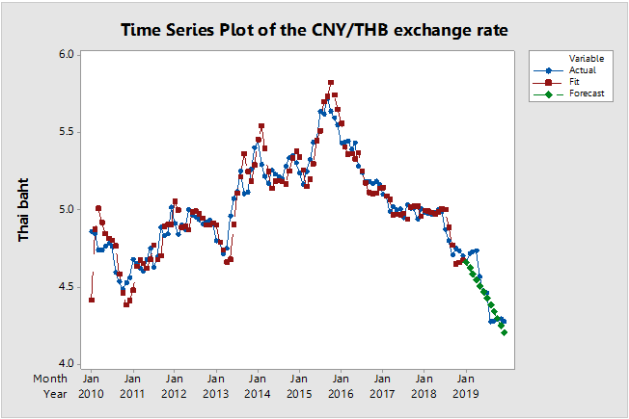

Fig. 11. CNY/THB exchange rates and forecast values by Triple Exponential Smoothing method.

From Table 7, It is found that Artificial Neural Networks obtains the minimum RMSE for the USD/THB exchange rate. Therefore, the Artificial Neural Networks are preferable method for modeling USD/THB exchange rate. Since Box-Jenkins method gains the smallest RMSE for the JPY/THB exchange rate, Box-Jenkins method is the appropriate method for modeling JPY/THB exchange rate. Triple exponential smoothing method achieves the minimum RMSE for both EUR/THB and CNY/THB exchange rates. Thus Triple exponential smoothing method is the suitable method for modeling EUR/THB and CNY/THB exchange rates.

Fig 8-11 show USD/THB, EUR/THB, JPY/THB and CNY/THB exchange rates and forecast values of 12 months ahead.

Conclusion:

This research presents three different forecasting methods which are Triple Exponential Smoothing method and Box-Jenkins method and Artificial Neural Network to model the exchange rates U.S. Dollar, Euro, Yen, and Yuan against Thai baht. The results show that Artificial Neural Networks is the suitable model for the exchange rate of U.S. Dollar/Thai baht and Box-Jenkins method give the appropriate model for the exchange Yen/Thai baht. Triple Exponential Smoothing method are the most suitable models for the exchange rates Euro, Yuan against Thai baht. MAPE in the forecasting process for the exchange rates U.S. Dollar, Euro, Yen and Yuan against the Thai baht are 2.17%, 1.52%, 2.29% and 1.48% respectively.

This study indicates that Triple Exponential Smoothing method which is simpler method and require less data to estimate can outperform more complex methods such as Box-Jenkins method and Artificial Neural Network in case of the time series shows the quadratic trend. Artificial Neural Network requires more time and effort and it is not guaranteed to get the most accurate forecasting result.

References:

1. Fat Codruta Maria and Dezsi Eva, “Exchange-Rate Forecasting: Exponential Smoothing Techniques and ARIMA Models” Annals of the University of Oradea: Economic Science, 2011; (1): pp. 499-508.
2. Ahmed Emam, “Optimal Artificial Neural Network Topology for Foreign Exchange Forecasting” ACM-SE’08, March 28-29, 2008, USA. 63-68.
3. Ghalayimi, Latife. “Modeling and Forecasting the US Dollar/Euro Exchange Rate”, International Journal of Economics and Finance, 2014, Vol. 6 No. 1: 194-207.

4. Gregorius Airlangga, Agatha Rachmat, Dodisutarma Lapihu,"Comparison of Exponential Smoothing and Neural Network to Forecast Rice Production in Indonesia", TELKOMNIKA, Vol. 17, No. 3, June 2019, pp 1367-1375
5. Bowerman, O'Connell and Koehler, Forecasting, Time Series, and Regression: an Applied Approach. 4th ed. Thomson. USA, 2005.
6. Koehler, AB, Murphree ES., "A Comparison of the Akike and Schwarz Criteria for Selection Model Order", Journal of the Royal Statistical Society Series C (Applied Statistics) Vol. 37,1988, pp. 187-195.
7. Box, G. E. P., Jenkins G. M., Reinsel G. C., Time Seried Analysis Forecasting and Control. Prentice Hall, 1994.
8. Jiang L-H, Wang A-G, Tian N-Y, Zhang W-c, Fan Q-L, "BP Neural Network of Continuous Casting Technological Parameters and Secondary Dendrite Arm Spacing of Spring Steel", Journal of Iron and Steel Research. 2011, Vol 18, pp 25-29.
9. Zhang G., Eddy Patuwo B., Y. Hu M.,"The State of the Art", International Journal of Forecasting. 1998, Vol 14, pp. 35-62.
10. Wilamowski Bm., Iplikci S., Kaynak O., Ele Mo., "An Algorithm for Fast Convergence in Training Neural Networks. IEEE 3, 2001, pp. 1778-1782.

Acknowledgements:

This work was supported by King Mongkut's Institute of Technology Ladkrabang Research Fund.

B_014_OA: A COMMON ENDPOINT THEOREM FOR A PAIR OF SINGLE-VALUED SUZUKI MAPPING AND MULTIVALUED SUZUKI MAPPING WITHOUT THE COMMUTATIVE CONDITION

Thanomsak Laokul,[1]* Bancha Panyanak,[2]

[1] PhD's Degree Program in Mathematics, Department of Mathematics, Faculty of Science, Chiang Mai University, Chiang Mai 50200, Thailand
[2] Research Center in Mathematics and Applied Mathematics, Department of Mathematics, Faculty of Science, Chiang Mai University, Chiang Mai 50200, Thailand
*e-mail: Thanomsak_l@cmu.ac.th

Abstract:

Endpoint theory has many applications in mathematical science, especially in 1986, Corley proved that a maximization with respect to a cone is equivalent to the problem of finding an endpoint of a certain multivalued mapping. In this work, we prove an endpoint theorem for multivalued Suzuki mappings in uniformly convex hyperbolic spaces. As a result, we obtain a common endpoint theorem for a pair of single-valued and multivalued Suzuki mappings by relaxing the commutative condition.

Keywords: endpoint, fixed point, Suzuki mapping, uniformly convex hyperbolic space.

References:

1. Corley H.W., Some hybrid fixed point theorems related to optimization, J. Math. Anal. Appl. 120 (1986) 528-532.
2. Espinola, R., Hosseini, M., Nourouzi, K., On stationary points of nonexpansive set-valued mappings. Fixed Point Theory Appl. 2015:236.
3. Saejung, S., Remarks on endpoints of multivalued mappings in geodesic spaces. Fixed Point Theory Appl. 2016:52 (2016).
4. Panyanak, B.: Approximating endpoints of multi-valued nonexpansive mappings in Banach spaces. J. Fixed Point Theory Appl. 20:77 (2018).
5. Kudtha, A., Panyanak, B.: Common endpoints for Suzuki mappings in uniformly convex hyperbolic spaces. Thai J. Math. Special issue, 159-168 (2018).
6. Leustean, L.: Nonexpansive iterations in uniformly convex W-hyperbolic spaces, in Nonlinear Analysis and Optimization I. Nonlinear Analysis, vol. 513 of Contemporary Mathematics, pp.193-210, American Mathematical Society, Providence, RI, USA, (2010).

Acknowledgments:

This work was supported by Department of Mathematics, Faculty of Science, Chiang Mai University, Chiang Mai 50200, Thailand.

B_015_OA

B_015_OA: LEFT VARIABLE TERMS AND APPLICATIONS FOR CLASSIFYING ALGEBRA

Nuthawud Sungtong,[1] Thodsaporn Kumduang,[2] Sarawut Phuapong [3,*]

[1,3] Department of Mathematics, Faculty of Science and Agricultural Technology, Rajamangala University of Technology Lanna, Chiang Mai 50200, Thailand
[2] Department of Mathematics, Faculty of Science, Chiang Mai University, Chiang Mai 50200, Thailand
*e-mail: phuapong.sa@gmail.com

Abstract:

In this talk, we present the concept of a specific class of terms in which the first position of terms is an arbitrary variable. In this situation, we call a left variable terms. Some concrete examples of such terms are provided. Particulary, we define the partial many-sorted superposition operation on the set of such terms and the partial many sorted algebra, called the partial clone of left variable terms, satisfying the superassotive law. Based on the idea of hyperidentity theory, a hypersubstitution is said to be left variable if it takes any operation symbol to a left variable term of same arity. We give several properties of its and prove that the collection of them form a partial monoid under a suitable partial binary associative operation.

B_016_OA: ACTIVITY CLASSIFICATION USING LOW PASS FILTER DEEP CONVOLUTIONAL LSTM

Porawat Visutsak[1,*] and Pavarit Vanijkachorn[2]

[1,2]Affiliation Department of Computer and Information Science, Faculty of Applied Science, KMUTNB, Bangkok, Thailand
*e-mail: porawatv@kmutnb.ac.th

Abstract:

Activity analysis systems or activity recognition systems for the elderly is recently a part of the smart home systems design. This assisted system normally helps the senior people to live alone in a house, safely and improve a quality of life. Therefore, learning to recognize which activities are safe is necessary for classifying the activities of the elderly. Furthermore, this information will give us some insights to understand the basic daily lives of the elderly and it also helps us to monitor activities of the senior people. In this paper, we collected activities data using the multi-sensor motion sensors embedded inside the smartwatch. We also present the novel method for detecting and recognizing the activity using Low Pass Filter Deep Convolutional LSTM (Long Short-Term Memory). This paper shows that the proposed method yields 98.268% of accuracy for activity classification. The paper also compares the results with Deep Convolution LSTM (88.425% of accuracy) and Radial Basis Function Neural Network (47.402% of accuracy). In addition, the proposed method can reduced the number of layers up to 50% compared with the original Deep Convolution LSTM.

Figure 1. The elderly wears the wearable device and the screen captured of the application.

B_017_OF: AN IMPROVED SHARK ALGORITHM FOR OPTIMIZATION PROBLEM

Amarita Ritthipakdee[1], Somkid Soottitantawat[2], OrawanChaowalit[3], Fuangfar Pensiri[4]

[1]Department of Information Technology, [2]Department of Computer Science
[1,2]Faculty of Science and Technology, Phranakorn Rajabhat University, Bangkok, Thailand.
[3]Department of Computing, Faculty of science, Slipakorn University, Nakhon Pathom, Thailand
[4]Faculty of Science and Technology, Suan Dusit University, Bangkok, Thailand.
amarita@pnru.ac.th, somkid@pnru.ac.th, chaowalit_o@su.ac.th, fuangfar_pen@dusit.ac.th

Abstract:

This research proposes a method for improving the shark algorithm for solving nonlinear optimization problems. The inspired by the swarm behavior of predatory sharks, they use their noses to smell the blood released by injured victims. In shark society, large and strong predators are the leader of the herd. The algorithm based on the consensus, the researcher has improved two parts of the shark algorithm. 1) Recognition of the smell of the injured victim's blood and assign to calculate the perception of prey from calculating prey, the intensity of the prey of all sharks. 2) Improve the movement based on $GSpeed_i^{NP}$ best group speed. The experimental results by testing with 4 standard functions, which are GOLDSTEIN- PRICE, SUM SQUARE FUNCTION, LEVY FUNCTION and SCHFFER 1 FUNCTION. The algorithm improvements can find optimal positions when measuring success rate performance.

Introduction:

[1] This research has solved the problem of drought and water shortage to consider the importance of water reservoir such as multiple reservoir systems to increase the additional efficiency of water management utilization, an optimization algorithm for different situation study cases. Comparison of 4 water reservoirs in China is engineered to measure the water level of reservoirs using statistical approach, RMSE and MAE. The results reveal using the proposed algorithm increase the water management utilization is success. [2] This research has used Shark Algorithm to solve an increment water reservoir and dam operations. The proposed Shark Algorithm have been measured the performance with other optimization algorithms, Genetic Algorithm (GA) and Particle Swarm Optimization (PSO). The results show that the proposed Shark Algorithm performance is better than other algorithms and obtained a higher Reliability Index and less Vulnerability Index. Furthermore, the standard deviation and coefficient of change in Shark Algorithm are less than the other two algorithms. [3] This research proposes fish electrolocation optimization (FEO) inspired from food finding of an elephant nose fish. The elephant nose fish uses electric discharge at the tail to detect the object by analyzing shape, body and defined as it is prey of food. The proposed algorithm compares with Differential Evolution (DE) and Simulated Annealing (SA), the result reveals better than those DE and SA. [4] This research proposes medical imaging enhance based on modified Shark Smell Optimization Algorithm, to enhance the medical image processing for final diagnostic with main idea of using the improvement of Shark Algorithm, considered both Global and Local enhancement. The results measured with 5 different measure indexes with 5 popular methods and reveal superiority.

Methodology:

Nature Inspiration

The optimization problem is finding the best solution. A problem in engineer and science need to apply for solving complicated problems. In this research, we improved a shark algorithm that is well known in search local optima and popular method for solving continuous optimization problem. The predatory shark has hunting prey by smell of bold and evaluate position of prey with 2 assumptions,

1) Every fish or sharks that live in the water are considered hunters
2) Blood scattered in the water, with nearby predators be able to pick up intense of blood from farther away

Initial population

Randomize generation of predatory vector and prey populations vector in the water to initialize under search space of objective function by equation (1)

$$X = \left[X_1^1, X_2^1, \dots X_{NP}^i\right] \quad (1)$$

Where X is vector of shark population and position

NP is population size

The population of shark initial position by equation (2)

$$\text{population of shark} \quad = X_i^1 = [X_{\mathrm{i}}^1, X_{\mathrm{i},2}^1, \dots X_{i,ND}^1], i = 1, \dots NP \quad (2)$$

Where $X_{i,j}^1$ is j^{th} position of shark

ND is number of decision variables

Shark speed

In the water, shark has speed for movement to prey. We randomly generate shark speed vector is as follow by equation (3),

$$V_1^1, V_2^1, \dots, V_{i,ND}^1 \quad (3)$$

Where V is the velocity vectors of shark movement in water containing with the following parameters by equation (4),

$$\left[V_1^1, V_2^1, \dots, V_{i,ND}^1\right] \quad (4)$$

Evaluate Smell of Blood

The prey's blood scattered in water and shark can detect by nose. The intense of blood relates by fitness function. In this step, we calculate speed movement of shark, can be calculated by equation (5)

$$V_i^k = \rho_k \cdot R_1 \cdot \nabla(OF)|x_i^k \quad (5)$$

Where V_i^k is speed of shark

ρ_k is coefficient between 0 and 1

R_1 is random coefficient 0 and 1

k is number of phase in the shark

OF is objective function

Evaluate of move forward

The shark can move speed when meet prey, can be calculated by equation (6),

$$Y_i^{k+1} = X_i^k + V_i^k \Delta_k^t \quad (6)$$

Where Y_i^{k+1} is the current position of shark

X_i^k is the previous location of the shark

V_i^k is speed of shark

Δ_k^t คือ is the temporal step

Proposed Algorithm

This research has proposed the improvement of shark algorithm using recognition of the smell of the injured victim's blood to assign the perception calculation of prey from calculating prey, the intensity of the prey of all sharks and improve the movement based on $GSpeed_{\mathrm{i}}^{NP}$, called best group speed.

Initial population

First step, initialization the hunter shark with random population which means location of shark swarm to defines a solution. And Sk denoted shark swarm population in position, NP is dimension.

$$Sk = \left[Sk_1^1, Sk_2^1, \ldots Sk_{NP}^i\right] \quad (7)$$

Evaluate function

1. Calculate fitness function
2. Define hunter shark to calculate the position intense blood of prey, scattered in water from the equation (8),

$$Prey_{Sk_{ij}} = \mu \cdot e^{-0.03} + \nabla(OF) \quad (8)$$

Where $Prey$ is intense of blood, calculate from equation (9) and μ is distant between hunter and prey

$\nabla(OF)$ is fitness function

$$\mu_{i,j} = \left|S_i - S_j\right| = \sqrt{\sum_{i=1}^{d}(S_i - S_j)^2} \quad (9)$$

3. Define hunter shark's speed, to determine opportunity of the neighbor shark to find the prey by randomly shark vector from equation (10),

$$\left[Sp_1^1, Sp_2^1, \ldots, Sp_{i,ND}^1\right] \quad (10)$$

Calculate Shark's velocity from equation (11),

$$Speed_{\mathrm{i}}^{NP} = \rho_k \cdot prey_{Sk} \quad (11)$$

Where ρ_k is random Coefficient between 0 and 1

Movement

Calculate shark's movement from equation (12)

$$Sk_i^{k+1} = Sk_i^k \times Speed_i^k + rand(0,1) \quad (12)$$

Shark's movement for next cycle,

$$\varphi_i^{k+1} = (Sk_i^k - Sk_c^k) + GSpeed_i^{NP} \quad (13)$$

Where φ_i^{k+1} is new shark's position,

Sk_i^k is previous position,

Sk_c^k is current shark's position,

$GSpeed_i^{NP}$ is Global best of group speed

Results and Discussion:

The experiments are tested with 4 well-known minimal benchmark functions. We set parameter for test 5000 iterations and 10 rounds for Success Rate.

1) GOLDSTEIN-PRICE is function minimum Where search space is between −2 ≤ xi ≤ 2, i = 1, 2, optimum value is $f(x*) = 3$

$$\boldsymbol{f(x) = (1 + (x_1 + x_2 + 1)^2 \times (19 - 14x_1 + 3x_1^2 - 14x_2^2 + 6x_1x_2 + 3x_2^2)) \times (30 + (2x_1 - 3x_2)^2 \times (18 - 32x_1 + 12x_1^2 + 48x_2 - 36x_1x_2 + 27x_2^2))}$$

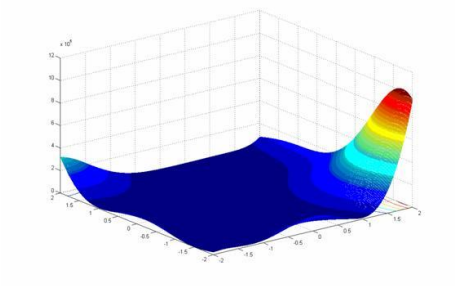

Figure 1. GOLDSTEIN-PRICE

2) SUM SQUARE FUNCTION Where search space is between −5.12 ≤ xi ≤ 5.12, i = 1, 2, optimum value is $f(x*) = 0$

$$f(x) = \sum_{i=1}^{d} ix_i^2$$

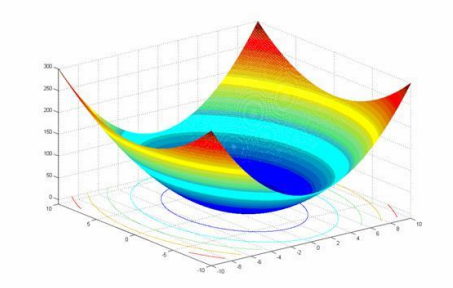

Figure 2. SUM SQUARE FUNCTION

3) LEVY FUNCTION Where search space is between −10 ≤ xi ≤ 10, i = 1, 2, optimum value is $f(x*) = 0$

$$f(x) = sin^2(\pi w_i) + \sum_{i=1}^{d-1}\{(w_i - 1)^2[1 + 10\,sin(\pi w_i + 1)^2]\} + (w_n - 1)^2[1 + sin(2\pi w_d)]$$

$$w_i = 1 + \frac{x_i - 1}{4}$$

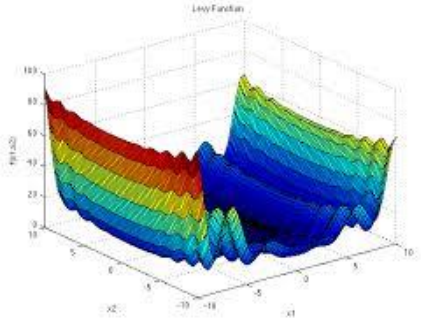

Figure 3. LEVY FUNCTION

4) SCHFFER 1 FUNCTION Where search space is between −100 ≤ xi ≤ 100, i = 1, 2., optimum value is $f(x*) = 0$

$$f(x) = 0.5 + \frac{sin^2\sqrt{x_1^2 + x_2^2} - 0.5}{(1.0 + 0.001 \times (x_1^2 + x_2^2))^2}$$

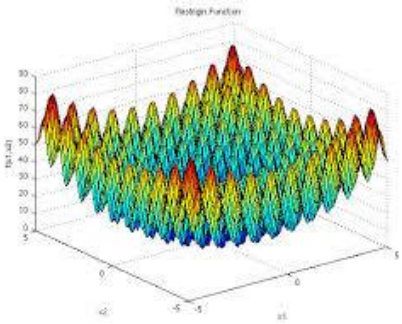

Figure 4. SCHFFER 1 FUNCTION

The results show in table 1 are number of global optima values. F2 thru F4, global optima is 0 and only F1, global optima is 3, All proposed algorithms convergence.

Table 1. proposed algorithms

Function	Optimum	Proposed Algorithm
F1 GOLDSTEIN-PRICE	3	**3**
F2 SUM SQUARE FUNCTION	0	**0**
F3 LEVY FUNCTION	0	**0**
F4 SCHFFER 1 FUNCTION	0	**0**

In the table 2, shows performance of success rate percentage and average iteration.

Table 2. Performance

Function	Success Rate (%)	Average iteration
F1 GOLDSTEIN-PRICE	95	122.5
F2 SUM SQUARE FUNCTION	100	44.5
F3 LEVY FUNCTION	100	96.5
F4 SCHFFER 1 FUNCTION	100	112.5

Conclusion:

The proposed algorithm, an approvement of shark algorithm is developed to solve the local optima using movement and $GSpeed_{\mathrm{i}}^{NP}$ best group speed approaches. The proposed algorithm is tested with 4 well-known minimal benchmark functions, the results reveal all convergence. Performance is measured with accuracy with success rate, F1 is equal to 95 percentage and F2 thru F4 are equal to 100 percentage. Average iteration, F2 and F4 convergence at minimum iterations. The average iteration of F1 is equal to 122.5 and F4 is equal to 112.5 respectively.

References:

1. Dojgan Dianatikhah, Hojat Karami, Khosrow Hosseini, Generation of Crean Hydropower Energy in multi-Reservoir system baesd on new Evolutionary algorithm,2020,34,1247-1264
2. Mohammed Ehteram, Hojat Karami, Sayed-Farhad Mousavi, Ahmed El-Shafie , Zahra Amini, Optimizing dam and reservoirs operation based model utilizing shark algorithm approach,2017;122,26-38
3. Vivekananda Haldar, Niladri Chakraboty, A novel evolutionary technique based on electrolocation principle of elephant nose fish and shark: fish electrolocation optimization, 2016;21,3827-3848
4. Yuebin Zhou, Jianmin Ye, Yujin Du & Fatima Rashid Sheykhahmad, New Improved Optimized Method for Medical Image Enhancement Based on Modified Shark Smell Optimization Algorithm,2020,

B_018_OA: PREDICTING STOCK PRICE DIRECTION USING TEXT CLASSIFICATION AND SENTIMENT ANALYSIS ON STOCK NEWS

Ponrudee Netisopakul,[1,*] Woranun Saewong[1]

[1] Knowledge Management and Knowledge Engineering Laboratory
Faculty of Information Technology, King Mongkut's Institute of Technology
Ladkrabang, Bangkok, Thailand
*e-mail: ponrudee@it.kmitl.ac.th

Abstract:

The Stock Exchange of Thailand (SET) has been growing, both in terms of the number of common stocks and the number of investors. The number of common stocks has increased from 3,680 in 2016 to 4,785 stocks in 2019, or about 30 percent increased; while the number of investors has increased from 0.6 million internet trading accounts in 2013 to 2.4 million accounts in 2019, or more than 300 percent increased. Most investors rely on the company's financial information and news to make trading decisions. This article investigates the influences of news issued daily toward the company's stock price direction. The research aims to answer the following questions. First, whether the company's stock news impacts on the company's stock price changes or not? Second, can machine learning techniques such as text classification be used to predict the stock price direction? Third, whether the sentiment of stock news helps to predict the stock price direction. Lastly, are there any 'word clues' the machine can learn to predict the stock price direction more accurately? Data collection of stock news from January to December 2018 contains 11,489 news. After filtering out general news, expert opinion news, news without matching stock names, news without matching previous day prices, there remains 1,911 news. This dataset is then used to train 6 machine learning text classification algorithms, namely, naïve Bayes, decision tree, random forest, SVM, and three-layer and five-layer backpropagation neural networks. The testing dataset is collected from January to March, 2019 stock news. The highest accuracies obtained from the training dataset are 85.6 percent without sentiment and 'word clues' attributes, and 92.3 percent with both attributes, both of which are from five-layer NN.

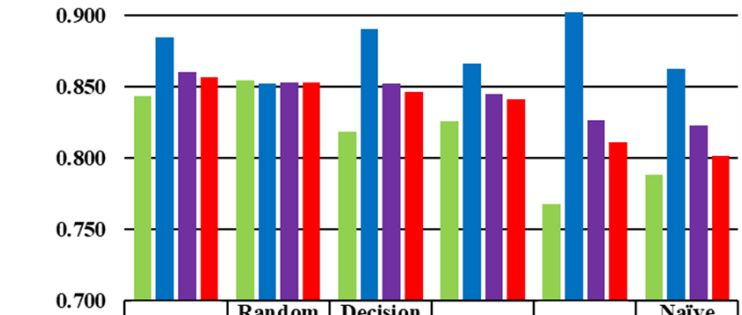

	5L-NN	Random Forest	Decision Tree	SVM	3L-NN	Naïve Bayes
Precision	0.843	0.855	0.818	0.825	0.768	0.788
Recall	0.884	0.852	0.890	0.866	0.902	0.862
F1	0.860	0.852	0.852	0.845	0.827	0.822
Accuracy	85.6%	85.3%	84.6%	84.1%	81.1%	80.2%

Figure 1. Precisions, recalls, F1 and accuracies of six text classifiers for predicting stock price changes from stock news

B_019_OF: THE CONDITION AND PROBLEMS ON LEARNING MANAGEMENT IN MATHEMATICS OF UNDERGRADUATE STUDENTS

Puchong Praekhaow,[1]*Tweesak Chidanurak ,[2]

[1]Faculty of science, King Mongkut's University of Technology Thonburi, Thailand
[2] School of Education, Sukhothai Thammathirat Open University, Thailand
*e-mail: puchong.pra@kmutt.ac.th

Abstract:

The objective of this research is to study the condition and problems on learning management in Mathematics of undergraduate students. Results of this research are used to develop the learning management model in Mathematics. The research was conducted over one year in two groups, 1) the first sample group was collected with 376 students studying Mathematics in academic year 2020, and 2) the second sample group was collected with 116 professors of public universities in Thailand. Questionnaires were used as a tool of research. The results shown that, the opinions of students and professors on condition and problems of learning management can be summarized as follows: 1) The students' opinions for corrections in aspects sorted in descending order are group learning and teamwork, steps of solving problems, learning model that is real situations, and the problems-based learning. 2) The professors' opinions for corrections in aspects sorted in descending order are student interaction, academic achievement, the problems-based learning, and learning management model that is current situations. 3) The factors of learning management model that professors and students need to solve this problem. It is the new learning management model that should contain the components as follows; group learning, problem-based learning, and active learning.

Introduction:

Nowadays, our world is at the beginning of the 21st century. The condition and problems on learning management in higher education of Thailand need to be adjusted to solve the problems that arise. For example, Research report on Graduate Employment in the Academic Year 2015 of King Mongkut's University of Technology Thonburi found the five problems of graduates as follows, working together with colleagues, socializing, problem solving, applications in work, ethics, and human relations [1] . The results of the mathematical ability test of students when they first entered King Mongkut's University of Technology Thonburi at the bachelor's degree level for the academic year 2017 showed that students had problems with low mathematical achievement. They have an average score of 15.72 points out of 54, and there are 21.11 percent of students who have to study general mathematics [2], corresponds to the Mathematics exam results in the past three years. The students failed examinations in the Mathematics since 2014-2016, 10.12%, 13.05%, and 14.59%, respectively. In one academic year, approximately 2000 students are required to enroll in general mathematics [3].

Based on the above information, the student's problem is mathematical achievement and ability to solve mathematical problems, which is a national student's problem. This issue is presented as the main topic of research in the Thailand Educational Development Plan 2017-2032 [4]. The above issues are the problem that should be developed in the 21st century of students and higher education graduates, in order to solve new

problems that have not been encountered by myself [5]. King, R. wrote in the Student Handbook for 21st Century Learning that problem solving involves solving mathematical problems [6]. Problem solving consists of critical thinking, creative thinking, collaboration, and communication. These things can be achieved through working together as a brainstorming group to define a problem, analyze the problem, then plan to find the answer, bring relevant knowledge to develop problem solving and evaluation as shown in Figure 1.

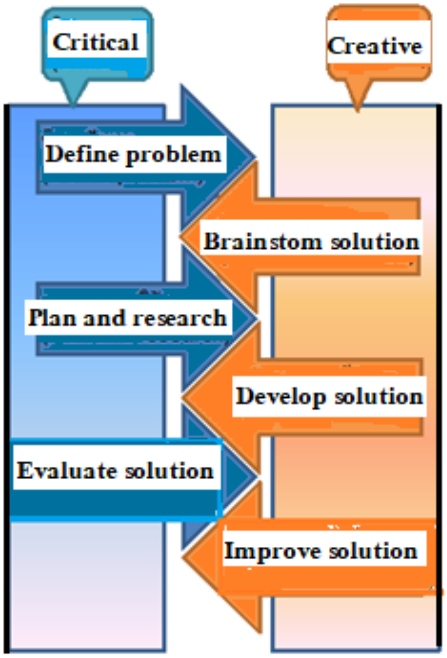

Figure 1

Steps of troubleshooting [6]

From Figure 1, in line with the National Education Association and Partnership for 21st Century Skills, 3R × 4C is defined the core elements of the 21st century learning framework, where mathematics is one of the 3R subjects [7]. Because of creative thinking, logical thinking, and problem analysis, this can be made in humans to help solve problems, forecast, plan, make decisions and apply them in daily life. It is also a tool on improving the quality of life [8].

The problems of higher education in Thailand and abroad were presented to higher education institutions. To find on new learning management model that can solve the problems for current conditions, researchers agree that we should develop learning management model in mathematics. The condition and problems of learning management in Mathematics should be studied on the first thing, in accordance with the concepts and principles of the systematic model development (ADDIE Model) that consisting of 1) Analysis, 2) Design, 3) Develop, 4) Implement, and 5) Evaluate [9,10,11]. Therefore, the first thing that researchers should be interested in is developing a learning management model. Study the condition and problems of mathematics learning management of the undergraduate level. The research question is what the students and professors want to solve in learning management of mathematics. The objectives of research can be defined as follows.

Research Objectives

To study the condition and problems of mathematics learning management of undergraduate students as well as to propose guidelines for the development of learning management models in mathematics courses in the university.

Research hypothesis

1. The condition and problems of mathematics learning management of undergraduate students and professors were at a high level.

2. The components of a mathematics learning management model that should be developed include group learning, problem- based learning to stimulate interest in research, and presentations to increase interaction with peers and professors.

Methodology:

This research study was based on the methodology of survey research. Those composed of the details were as follow:

1. Population and sample: The population used in this research consisted of 2 parts. 1) 6,178 undergraduate students of Engineering Faculty who studied mathematics in public universities, Thailand [12]. 2) 164 professors of mathematics department in public universities, Thailand, including Chulalongkorn University, King Mongkut's University of Technology Thonburi, King Mongkut's University of Technology Ladkrabang, King Mongkut's University of Technology North Bangkok, Khon Kaen University, Burapha University, Naresuan University, Chiang Mai University, Songkhla University, Thaksin University, and Silpakorn University. The samples of students and professors were selected by stratified sampling that the stratums are Bangkok and the region. The sample size was calculated by Taro Yamane formula, with the sampling error can occur not more than 5% and then divided in equal proportions as follows. 1) 379 undergraduate students were selected by sampling from Engineering Faculty. 2) 116 professors were selected by sampling from mathematics department in public universities.

2. Research variables and study duration: For the independent variables in this research provided as condition and problems of mathematics learning management in University, and for the dependent variables consisted of the problem level of mathematics learning management in each area, which took during the 2020 academic year for the study.

3. The research instruments: The student and professors' questionnaire of learning management in Mathematics was constructed by using problem situations with rubric scoring for assessing. The 15 questions of questionnaire were in the format of Likert rating scale 5 levels, where the quality of the questionnaire had been evaluated by relevant experts and tryout in the 30 students. It was found that the IOC index of questionnaires, each question was in the range of 0.8 -1.0, and the value of Cronbach's alpha coefficient was 0.821 for students' questionnaires and 0.812 for professors' questionnaires. It was show that quality of all tools was more than the required criteria.

4. Data Collection: The researcher has requested permission to the mathematics department of the target university. The questionnaire was distributed to samples in the university. Students and professors voluntarily responded to the questionnaires according to the volunteer's consent document of Human Research Ethics Committee of King Mongkut's University of Technology Thonburi, which has conducted the research project evaluation of the researcher and agreed. To pass the human research ethics assessment by certificate number KMUTT-IRB-COA-2020-025.

5. Data analysis: 1) Calculate the mean of each question of the condition and problems in the questionnaire. The mean is interpreted by the Likert criteria [13]. 2) The condition and problems of learning management in questionnaires were used to calculate the factor components by factor analysis. To summarize the problems and needs of students and professors in the development of learning management model.

Results and Discussion:

The research results are presented as follows:

1. The analysis is shown on the Table 1 of the 15 questions from professors. It is found that the relevant study of the learning management problems to be solved of professors in mathematics, the results showed that the vast majority of professors thought the current learning management problems at a high level.(Mean = 3.51, SD. = 0.39) The problems that should be developed in the following order: helping each other in learning, low academic achievement, the unsuitable learning management style for the current situation, interaction with peers and professors, and problem-based learning.

Table 1.

The interpretation of the professor's effects on the condition and problems

Questions	Mean	SD	Interpretation
1.Teaching assessments have clear criteria.	4.41	0.79	High
2.Questions are used to stimulate interest in teaching.	3.94	3.08	High
3.The learning outcome is clearly defined in the learning objective	3.88	1.05	High
4.Teaching and learning are self-learning from the exercises.			
5.Your teaching approach is a lecture style.	3.82	0.63	High
6. Teaching mathematics should be solving problems from real situations.	3.76	0.56	High
7. The learning style of the students lacked the search for knowledge.	3.65	0.70	High
8. The professor's learning management model is suitable for the current situation.	3.53	0.62	High
9. Your learning management style opens up opportunities for interaction between learners	3.47	0.80	Moderate
10.Your learning management model is problem-based learning.	3.47	0.71	Moderate
11.Your students do not have a step-by-step solution to math problems.	3.29	0.84	Moderate
12.Your learning management style does not offer group learning in classroom.	3.24	0.83	Moderate
13. My students have low academic achievement.			
14. Your teaching does not offer solutions by students in the classroom.	3.18	1.01	Moderate
15. Your students lack mutual assistance in learning.	3.12	0.85	Moderate
	3.12	1.16	Moderate
	2.82	0.80	Moderate
Total	3.51	0.39	high

2. The analysis show on the Table 2 of the 15 questions from students. It is found that the relevant study of the learning management problems to be solved of students in mathematics, the results showed that the vast majority of students thought the current learning management problems at moderate level.(Mean = 3.30, SD. = 0.34) The problems that should be developed in the following order: team collaboration, experience in the presentation, steps of solving math problems, the unsuitable learning management style for the current situation, interaction with peers and professors, and problem-based learning.

Table 2.

The interpretation of the student's effects on the condition and problems

Questions	Mean	SD	Interpretation
1.Mathematics creates a curiosity and interest in problem solving.	3.77	0.86	High
2.The students are trained to have a problem-solving process in Mathematics.	3.70	0.84	High
3.Mathematics focuses on solving mathematical problems.			
4.Mathematics is a subject that taught me a lot of methodology for solving problems	3.66	0.80	High
5. Mathematics is taught mostly by lectures.	3.58	0.94	High
6. Mathematics is taught to build knowledge by students.	3.55	0.91	High
7. Mathematics should provide to learn by solving problems.			
8. Teaching mathematics should be interactive with peers and professors.	3.49	1.04	Moderate
9.Mathematics is a subject that I can apply to in my daily life.	3.43	0.95	Moderate
10. Mathematics gives students the opportunity to present their work.	3.34	0.91	Moderate
11.Problem-based learning is used in mathematics teaching.			
12. I still lack the ability to solve math problems in mathematics	3.30	1.04	Moderate
13. I still lack to do a well-structured in math subjective test.			
14. Mathematics is a subject that trains learners to have experience in presentations.	3.26	1.05	Moderate
15. Mathematics is a subject that trains learners who know how to work together in groups	3.19	0.92	Moderate
	2.83	0.97	Moderate
	2.83	0.99	Moderate
	2.75	1.07	Moderate
	2.75	1.10	Moderate
Total	3.30	0.34	Moderate

3. The main ideas to create a learning management model of professors were shown by analysis results in Table 3

Table 3.

The results of factor analysis of professors

Factors	number of variables	variance	% Variance
1.Group learning and problem-based learning 2.Stimulating interest and research	5	4.47	29.81
3.Solving problems in mathematics	4	3.08	20.55
4.Presentation and interaction with peers and professors	4	1.82	12.14
	2	1.21	8.04
Total	15		70.55

KMO = 0.50, Bartlett's Test has p-value < 0.01

From Table 3: Fifteen questions relating to reasons for learning management model were factor analyzed using principal component analysis with Varimax(orthogonal) rotation. The analysis yielded four factors explaining a total of 70.55% of the variance for the entre set of variables. Factor 1 was group learning and problem-based learning. This first factor explained 29.812% of the variance. The second factor was stimulating interest and research. This second factor explained 20.558% of the variance. The third factor was solving problems in mathematics. This third factor explained 12.141% of the variance. And the fourth factor was presentation and interaction with peers and professors. The variance explained by this factor was 8.041%. The KMO (Kaisser-Meyer-Olkin Measure of Sampling Adequacy) was 0.50 and Bartlett's Test of Sphericity (p-value < 0.01) both indicate that the set of variables are at least adequately related for factor analysis

4. The main ideas to create a learning management model of students were shown by analysis results in Table 4

Table 4.

The results of factor analysis of students

Factors	number of variables	variance	% Variance
1.Group learning and problem-based learning 2.Solving problems in mathematics	5	5.41	36.08
3.Solving problems in real situations 4. Learn from problem solving	4	2.21	14.75
	4	1.43	9.54
	2	1.30	8.69
Total	15		69.06

KMO = 0.72, Bartlett's Test has p-value < 0.01

From Table 4: Fifteen questions relating to reasons for learning management model were factor analyzed using principal component analysis with Varimax(orthogonal) rotation. The analysis yielded four factors explaining a total of 69.06% of the variance for the entre set of variables. Factor 1 was group learning and problem-based learning. This first factor explained 36.08% of the variance. The second factor was solving problems in mathematics. This second factor explained 14.75% of the variance. The third factor was solving problems in real situations. This third factor explained 9.54% of the variance. And the fourth factor was learn from problem solving. The variance explained by this factor was 8.69%. The KMO (Kaisser-Meyer-Olkin Measure of Sampling Adequacy) was 0.72 and Bartlett's Test of Sphericity (p-value < 0.01) both indicate that the set of variables are at least adequately related for factor analysis.

5. The main ideas relationship between professors and students to develop mathematics learning management model from factor analysis. There is consistency in the learning management problem that should be addressed by the new learning management model. The model should consist of the first elements being group learning and problem-based learning, the next is steps of problem solving. Those will be stimulated by questions, search, actions, presentation, and interaction with peers and professors. The results of multiple regression analysis support the ideas of students and professors, it was shown in Tables 5 and 6.

Table 5.

The ANOVA of professors

Model	Sum of squares	df	Mean square	F	Sig
Regression	6.729	4	1.682	117.378	< 0.001
Residual	1.591	111	0.014		
Total	8.320	115			

Adjusted R square = 0.802, Durbin Watson = 1.31

From Table 4: A multiple linear regression was calculated to predict Y (problem level of learning math) based on independent factors (group learning and problem-based learning, stimulating interest and research, solving problems in real situations, and learn from problem solving). A significant regression equation was found ($F(4,111) = 117.378$, $p < 0.001$), with an R^2 of 0.802.

Table 5.

The ANOVA of students

Model	Sum of squares	df	Mean square	F	Sig
Regression	100.191	4	25.048	14338.79	< 0.001
Residual	0.646	370	0.002		
Total	100.838	374			

Adjusted R square = 0.894, Durbin Watson = 1.882

From Table 5: A multiple linear regression was calculated to predict Y (problem level of learning math) based on independent factors (group learning and problem-based learning, solving problems in mathematics, solving problems in real situations, and learn from problem solving). A significant regression equation was found ($F(4,370) = 14338.79$, $p < 0.001$), with an R^2 of 0.894.

Conclusion:

From the study results, condition and problems of mathematics learning management of undergraduate students, there are some interesting points to discuss:

1.Levels of learning management problems for professors and undergraduate students. It appears that overall mathematics students had a moderate level of satisfaction in mathematics learning management problems. While the professors were at a high level. That was, students need to adjust to condition and problems more than professors. This was consistent with the students' academic achievement and math problem solving ability, which was the problems. It is also consistent with the research hypothesis that the conditions and problems of mathematics learning management of students are at the high level and greater than the professors.

2.When considering the condition and problems of mathematics learning management in various fields from the factor analysis found that there were interesting observations as follows: The professors and students would like to revise their learning management in the following areas of (1) Group learning and problem-based learning, (2) Steps of Problem-solving, (3) Learning in in real situations, and (4) Presentation and interaction with peers and professors

3. This research results are consistent with the concepts and principles of 21st century learning management, where mathematics is in the 3R × 4C of core components [7]. The reason that mathematics makes students creative think logically, work systematically, able to analyze problems, help to solve problems. It helps to predict events, plan, make decisions and apply them in daily life. It was also a tool for studying other sciences, improving the quality of life [8]. It was consistent on issues that we should developed in the 21st century [5]. Those were essential for students and higher education graduates to solve new problems that have not been encountered by myself. Which the problem-solving ability in mathematics problem related to solving real-life problems [6].

4. The components of the learning management model were presented by professors and students based on the analysis results. There are several learning theories that support the concept of a new learning management model: Constructivism Theory [14], Students can learn through social and environmental interactions in different ways. Sociocultural Theory [15], Human learning is the result of exchanging knowledge and comparing one's thoughts with others. Pragmatism Theory [16], Students can learn from real experiences and activities. Theory of Cooperative or Collaborative Learning [17], Group processes in subgroups with different members provide mutual assistance in learning.

Acknowledgements:

The authors would like to thank very much the human research ethics committee of King Mongkut's University of Technology Thonburi, which has conducted the research project evaluation of the researcher and agreed. To pass the human research ethics assessment by certificate number KMUTT-IRB-COA-2020-025.

References:

1. Institute Research and Information. Report on the monitoring of work and continuing education of graduates KMUTT. 2015: 6.
2. Educational work for the talented people. Report of mathematical proficiency test of first students enter the bachelor's degree KMUTT.2017: 1-3.
3. Registration office KMUTT. Retrieved August 25, 2017 from https://studentacademic.kmutt.ac.th/NewAcis/login.jsf.
4. Office of the Education Council Secretariat. National Education Plan 2017-2036: Bangkok, Prikwan Graphic Co., Ltd. 2017:15-16.
5. Schwartz S., The Guardian. Retrieved May 2, 2018 from https://www.theguardian.com/higher-education-network/blog/wisdom-as-an-employability-skill
6. King R., What are 21st century skills? Retrieved May 17, 2018, from https://k12.thoughtfullearning.com/FAQ/what-are-21st-century-skills.
7. Phanich V., Methods for creating learning for students in the 21st century; Bangkok, Sodsri-Sarit Wongkis Foundation.2012:16-21.
8. Ministry of Education. Basic Education Core Curriculum, B.E.2560. Bangkok. Teachersapa Publishing House.2017:56.
9. Dick & Garey., Dick and Carey Model. Retrieved from InstructionalDesign.org. Retrieved July 23, 2019 from http://www.instructionaldesign.org/models/dick_carey_model/
10. Khaemmanee T., Pedagogy. Knowledge for effective learning process. Bangkok: Chulalongkorn University.2014: 199-201.
11. Richey R., Klein J., & Tracey, M., The instructional design knowledge base. New York: Taylor & Francis.2011:19.
12. Office of the Permanent Secretary, Ministry of Education. Education statistics for the year 2016. Bangkok. The Agricultural Cooperative Association of Thailand Publishing Co., Ltd. 2017:26.
13. Wongratana C., Techniques for building research tools. Bangkok: Amon Publication. 2017:137.
14. Piaget J., Judgment and reasoning of child. London: Poutledge and Kagen Paul.1965:7.
15. Eggen P., & Kauch, D., Strategies and models for teachers content and thinking skills. Boston: Pearson. 2006: 251-252.
16. Eggen P., & Kauchak D., Strategies and models for teachers. Teaching content abd thinking skills. Pearson Higher Ed. 2011: 6.
17. Johnson D. W., & Johnson R. T., An educational psychology success story: Social interdependence theory and cooperative learning. Educational Researcher. 2009:38(5): 365-379.

B_020_OF: BLIND DEBLURRING IMAGE VIA L_2 - REGULARIZATION

Sainuddeen Nuiphom,[1,2,*] Aniruth Phon-on,[1] Kittiya Khongkraphan[1]

[1]Department of Mathematics and Computer Science, Faculty of Science and Technology, Prince of Songkla University, Pattani 94000, Thailand
[2]Center of Excellence in Mathematics, CHE, Bangkok 10400, Thailand
*e-mail: sainuddeen_sai@hotmail.com

Abstract:

This paper presents a novel and efficient approach for deblurring the generic image. The proposed method based on the iterative concept and blind deconvolution which is an ill-posed problem. The clear image and blur kernel that generated the blurred image, have many pairs. It requires regularization to get an accurate answer. Our work proposes new L_2 – regularization prior based on the sum of gradient with a suitable bound for solution of a deblurring problem. The method will adjust the values of pixels in the blurred image according to the suitable bound in each iteration. Furthermore, our work used an optimization algorithm based on a quadratic splitting technique that guarantees that each sub-problem approach to solution and fast convergence. The experiments on synthesized images present that our approach outperforms non-regularization method. In addition, we compare for finest weigh parameter for regularization term.

Introduction:

Motion blur in image is the exciting topic in image processing. The blur caused by camera shake always degradation the quality of image. As captured moment are ephemeral and some type of image difficult to retake, it is interesting to restore the image to high quality. Blind image deblurring is a method used to recover a sharp image from blurred image, which is ill-posed problem. The pair of sharp image and blur kernel be able to find by energy minimization problem based on the general conditioning, the image construction can be modeled by the linear convolution

$$y = x * k + n \tag{1}$$

where y, x, and n denote the vector forms of blurred image, sharp image, and noise, respectively. The matrix k denotes the blur kernel with a row vector corresponding to the pixel location of blur kernel. In addition, $*$ is the convolution operator. As we only known y, we need to find both of x and k concurrently.

Regularization is help to find the most accurate pair of x and k, many researcher purposed a statistical priors of blur kernels, sharp images, or both[1,2,3,4,5]. Fergus et al.[6] purposed a mixture-of-Guassian model on gradients magnitudes. The blur kernel is estimated from input image, it used to the values of sharp image. They alternately compute both from coarse-to-fine level. Levin et al.[7] presented a regularization on gradient sparsity. While estimate of both blur kernel and sharp image are difficult, only kernel optimization is easily to computation. Pan et al.[8] introduced a new regularization based on intensity and gradient to deblurring text image. The optimization algorithm based on the half-quadratic splitting that guarantees each sub-problem has a closed-form solution.

Our work has motivation from the observation on the sum of gradient value. The sum of gradient of the blurred image is greater than the sharp image when considering on the small gradient values. We propose a new regularization priors based on sum of gradient. The algorithm is to seek on the group of pixels that have blur.

Methodology:

From observation on the sum of a gradient, when considering on a low gradient, the sum of gradient of the blurred image tend to greater than a sharp image (Figure 1)[9]. The idea used to adjust the blurred image into a sharp image is adjusting the sum of the gradient to a small value, so we will get a clearer image.

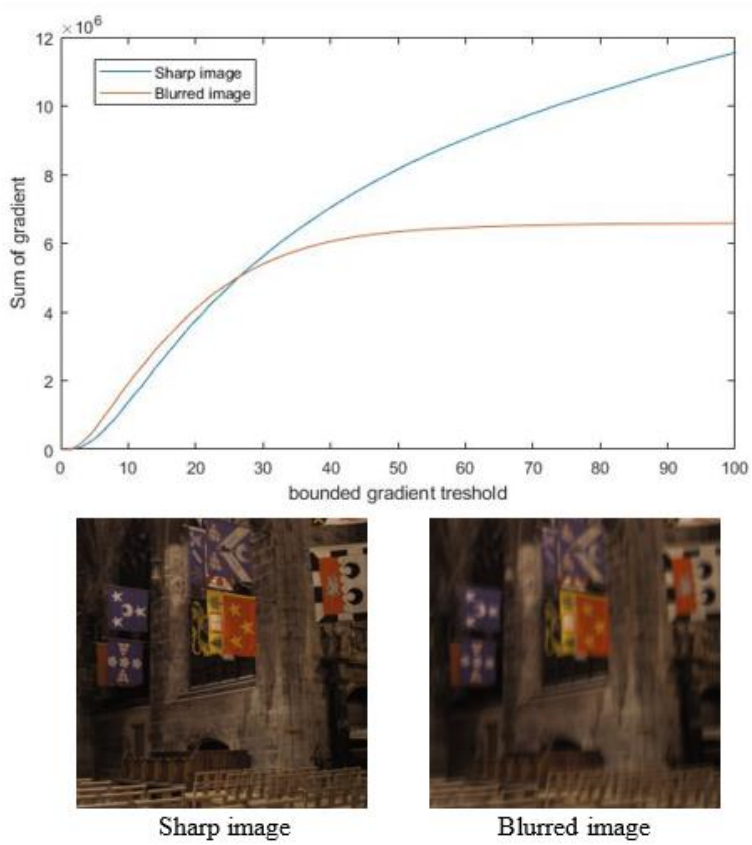

Figure 1.

Comparison of the sum of gradient of sharp image with blurred image.

We first describe the sum of gradient with condition term and it role in image deblurring. For an image X, the x_b is defined by

$$x_b = \begin{cases} \nabla x, & |\nabla x| \le b, \\ 0, & |\nabla x| > b, \end{cases}$$

where ∇ denotes a gradient symbol and b is the bounded threshold value. From (1) blind deconvolution is the determination of two variables which are clear image x and blur kernel k. Since the solutions of (1) will be multiple sets, the different value of clear image convoluted with a blur kernel that has the smallest

difference with the blur is the most accurate result. The difference is the distance, which is an euclidean norm defined by $\left\|\vec{a}\right\|_2 = \sqrt{a_1^2 + a_2^2 + a_3^2 + \cdots + a_n^2}$ where $\vec{a} = \left(a_1, a_2, a_3, ..., a_n\right) \in \mathbb{R}$ the minimization function used to find the smallest difference can be written as

$$\min_{x,k}\left(\left\|x * k - y\right\|_2^2 + \lambda\left\|k\right\|_2^2 + \delta\left\|x_b\right\|_2^2\right), \tag{2}$$

where the first term imposes that the convolution output of the recovered image and the blur kernel; the second and the third are used to regularize the solution of the blur kernel and sharp image, respectively. λ and δ are weigh parameters. The deblurring process is modeled as the optimization problem by alternately computing the sharp image x

$$\min_{x}\left(\left\|x * k - y\right\|_2^2 + \delta\left\|x_b\right\|_2^2\right), \tag{3}$$

and the blur kernel k ,

$$\min_{k}\left(\left\|x * k - y\right\|_2^2 + \lambda\left\|k\right\|_2^2\right). \tag{4}$$

The details of two sub-problem are shown as follow:

Estimating the sharp image: From (3), to update the value of x in each iteration, we add a new term for (3) and introduce variables u and g with conforming to x and x_b respectively, the objective function can rewrite as

$$\min_{x,u,g}\left(\left\|x * k - y\right\|_2^2 + \beta\left\|x - u\right\|_2^2 + \mu\left\|\nabla x - g\right\|_2^2 + \gamma\left\|g\right\|_2^2\right), \tag{5}$$

where β and μ are penalty parameters. When β and μ are close to infinity, the solution of (5) approaches that of (3). Similarly, (5) will be effectively when alternately compute x , u , and g separately by fixing the other variables. The solution of x is obtained by solving

$$\min_{x}\left(\left\|x * k - y\right\|_2^2 + \beta\left\|x - u\right\|_2^2 + \mu\left\|\nabla x - g\right\|_2^2\right), \tag{6}$$

the closed-form of x for this least squares minimization problem is

$$x = \mathcal{F}^{-1}\left[\frac{\overline{\mathcal{F}\left(k\right)}\mathcal{F}\left(y\right) + \beta\mathcal{F}\left(u\right) + \mu \mathrm{F}_G}{\overline{\mathcal{F}\left(k\right)}\mathcal{F}\left(k\right) + \beta + \mu\overline{\mathcal{F}\left(\nabla\right)}\mathcal{F}\left(\nabla\right)}\right], \tag{7}$$

where $\mathcal{F}\left(\cdot\right)$ and $\mathcal{F}^{-1}\left(\cdot\right)$ denote the Fourier transform and inverse Fourier transform, respectively; the $\overline{\mathcal{F}\left(\cdot\right)}$ is the complex conjugate operator; and $\mathrm{F}_G = \overline{\mathcal{F}\left(\nabla_h\right)}\mathcal{F}\left(g_h\right) + \overline{\mathcal{F}\left(\nabla_v\right)}\mathcal{F}\left(g_v\right)$ where ∇_h and ∇_v denote the horizontal and vertical differential operators. Given x , we compute u and g independently by

$$\min_{u}\left(\beta\left\|x - u\right\|_2^2\right),$$

$$\min_{g}\left(\mu\left\|\nabla x - g\right\|_2^2 + \gamma\left\|g\right\|_2^2\right),$$

the closed-form of u and g are

$$u = x,$$

$$g = \mathcal{F}^{-1}\left[\frac{\mu\mathcal{F}(\nabla)\mathcal{F}(x)}{\mu+\gamma}\right]. \quad (8)$$

Estimating the blue kernel: As the solution directly from (4) based on intensity value is not accurate[8,10], we use gradients instead of the intensity to calculate (4). Given x, the closed-form solution for least squares minimization problem of k is

$$k = \mathcal{F}^{-1}\left[\frac{\overline{\mathcal{F}(x)}\overline{\mathcal{F}(\nabla)}\mathcal{F}(y)}{\overline{\mathcal{F}(x)}\overline{\mathcal{F}(\nabla)}\mathcal{F}(\nabla)\mathcal{F}(x)+\lambda}\right]. \quad (9)$$

The process to find sharp image and blur kernel are shown in Algorithm 1.

Algorithm 1 Sharp image and blur kernel estimation algorithm

Input: Blur image y

initialize k with the result from the coarser lelvel.

for $i=1\rightarrow 5$ **do**

solve the sharp image

$x \leftarrow y,\ \beta = 4\gamma b.$

repeat

$u \leftarrow x.$

$\mu \leftarrow 3\delta.$

repeat

solve for g using (8).

solve for x using (7).

$\mu \leftarrow 2\mu\,.$

until $\mu > \mu_{\max}$

$\beta \leftarrow 2\beta$

until $\beta > \beta_{\max}$

solve the blur kernel using (9).

end for

Output: Blur kernel k and intermediate sharp image x.

Results and Discussion: In this section, we present result of the proposed algorithm on synthesized images. In all experiment, we set $\delta = 8e^{-3}, \lambda = 3,$ and $b = 5$, respectively. We also set $\beta_{\max} = 2^3$ and $\mu_{\max} = 1e^5$ in Algorithm 1.

(a) (b) (c)

Figure 2.

Example result on synthesis images (a) blurred image. (b) deblurred images with non-regularization term ($\delta = 0$). (c) our results.

Table 1. Peak Signal to Noise Ratio (PSNR) comparison.

Image	PSNR of non-regularization result	PSNR of our result
Camera man	19.6587	23.9091
Lighthouse	20.9173	25.7259

From Figure 2 our proposed method gives a more good result on deblurring than non-regularization term. The result also shows that our method has less artifact. The higher of PSNR Indicate the good quality of the image, Table 1 show our result has PSNR greater than non-regularization that means our regularization term has more efficiency.

In addition, we compare value of gamma (γ) of each image by looking on the PNSR. The example of result on three image (Figure 3) show that the best gamma value of each image is different.

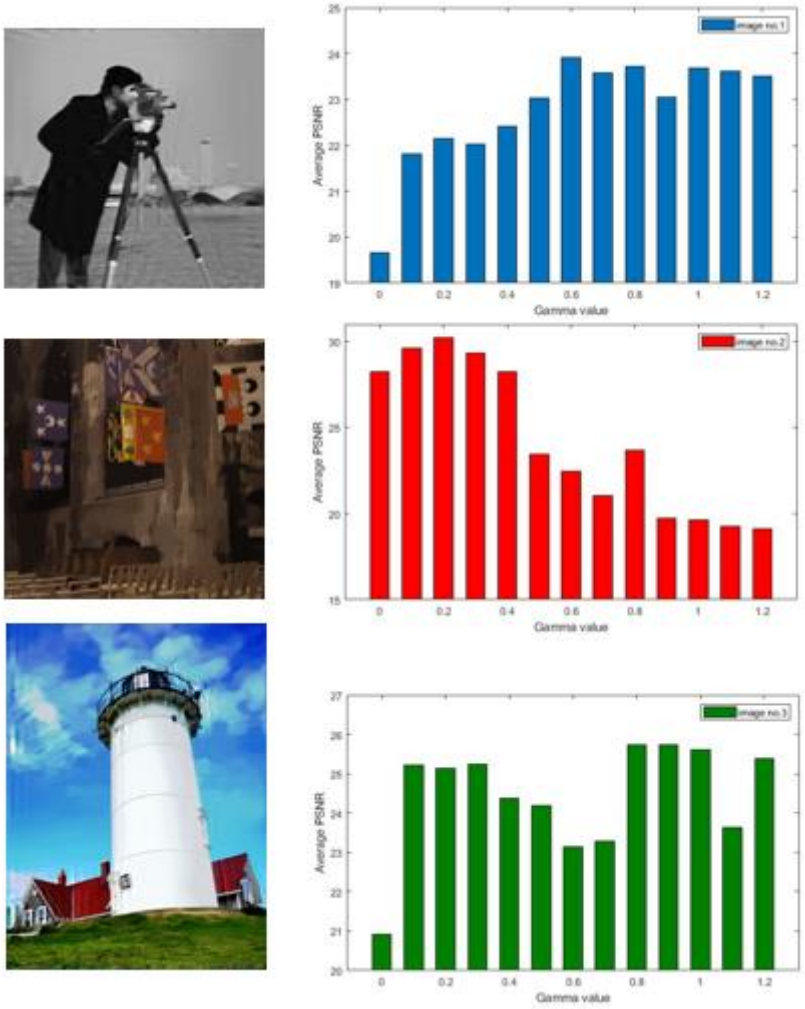

Figure 3.

Comparison of gamma value 0 - 1.2 of three images

Conclusion:

In this paper, we propose a new regularization prior for image deblurring. The proposed method based on the gradient properties of image. The result on synthetic expresses that the least-square minimization require regularization term for a good result. Other side, the regularization parameter of each image is different. Our future work will focus on improving the method for deblurring on natural image deblurring and compare the result with previous methods.

Acknowledgements:

This research is (partially) supported by the Centre of Excellence in Mathematics, The commission on Higher Education, Thailand

References:

1. Agrawala A, Raskar R. CVPR. 2007;1-8.
2. Chan T F, Wong C K. IEEE. 1998;7:370-375
3. Dey N, Blanc-Fraud L, Zimmer C, Kam Z, Roux P, Olivo-Marin J, Zerubia J. Proc. IEEE. 2004;1223-1226.
4. Jia J. CVPR. 2007;1-8.
5. Shan Q, Jia J, Agarwala A. ACM Trans. Graphics. 2008;27.
6. Fergus R, Singh B, Hertzmann A, Roweis S T, Freeman W T. ACM Trans. Graph. 2006;25:787-794.
7. Levin A, Weiss Y, Durand F, Freeman W T. CVPR. 2011;2657-2664.
8. Pan J, Hu Z, Su Z, Yang M H. IEEE. 2017;39:342-355.
9. Köhler R, Hirsch M, Mohler B J, Scholkopf B, Harmeling S. ECCV. 2012;27-40.
10. Cho S, Lee S. ICCV. 2011;495-502.

B_021_OF: GRAPH AND NUMBER THEORETIC PROPERTIES OF CERTAIN MAPS OVER FINITE FIELD

Pratchayaporn Doemlim,[1,] * Vichian Laohakosol,[2] Tuangrat Chaichana[3]

[1]Department of Mathematics and Computer Science, Faculty of Science, Chulalongkorn University, Bangkok 10330, Thailand
[2]Department of Mathematics, Faculty of Science, Kasetsart University, Bangkok 10900, Thailand
[3]Department of Mathematics and Computer Science, Faculty of Science, Chulalongkorn University, Bangkok 10330, Thailand
*e-mail: pratchayaporn2539@gmail.com

Abstract:

We consider the graph over a finite field $\mathbb{F}_q$, q prime number, obtained by iterations of the map $x \to x^p$, where p is a prime number. Some properties of the graphs such that characterization of their vertices and the number of cycles with specific length are determined.

Introduction:

Let q be a prime number and $\mathbb{F}_q$ the finite field of q elements. Let $g: \mathbb{F}_q^* \to \mathbb{F}_q^*$ be a function. The iterates of g are defined by $g^i(x) = g(g^{i-1}(x))$ for all $i \in \mathbb{N}$ where $g^0(x) = x$. The graph from the iteration of g is defined to be $G_g = (V, E)$ a directed graph whose vertex set is $V \subseteq \mathbb{F}_q$ and whose directed edges in E are given by $(x, g(x))$ for all $x \in \mathbb{F}_q^*$. The **reverse graph** of the graph G_g, denoted by $(G_g)_R$, is the graph (V, E_R) where $E_R := \{(x, y): (y, x) \in E\}$. Let $x \in \mathbb{F}_q^*$. An **orbit** of x is the directed path in a graph G_g of the map g starting at x. Since $\mathbb{F}_q$ is finite, there exists a least positive integer $s := s(x)$ such that $g^s(x) \in \{g^0(x), g^1(x), \dots, g^{s-1}(x)\}$. Let $t := t(x) \in \{0, 1, \dots, s-1\}$ be the least non-negative integer such that $g^s(x) = g^t(x)$ and let $c := c(x) = s(x) - t(x)$. We then have c is the smallest positive integer such that $g^t(x) = g^{t+c}(x)$. The **tail** for x is the list of elements $x, g(x), g^2(x), \dots, g^{t-1}(x)$ in the orbit of x and the **cycle** for x is the list of elements $g^t(x), g^{t+1}(x), \dots, g^{t+c-1}(x)$ in the orbit of x. Note that the tail length of x is $t(x)$ and the cycle length of x is $c(x)$. See Figure 1.

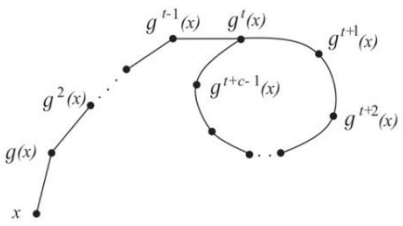

Figure 1.
The tail and cycle of an iteration.

For each x in the group of invertible elements modulo n, by $ord_n(x)$ we mean the least positive integer i such that $x^i \equiv 1 \pmod{n}$. We denote the exponent of the largest power of a prime p which divides an integer n by $v_p(n)$.

In 1996, T.D. Rogers[1] studied properties of graphs obtained from iterating the quadratic map $g(x) = x^2$ over $\mathbb{F}_q$, where q is a prime number. The formula of the number of cycles relative to g was derived. In 2004, T. Vasiga and J. Shallit[2] studied properties of the graph obtained from iterates of the map $g(x) = x^2$ over a finite field $\mathbb{F}_q$, where q is an odd prime. They characterized vertices of the directed graph $G_{x\to x^2}$ in terms of primitive elements. They gave formulars for the length of tail and cycle for particular x in V. The number of cycles with specific length and the number of elements in all cycles were also determined.

In this paper, we extend the ideas of T.D. Rogers[1] and T. Vasiga et. al.[2] by considering the graph over $\mathbb{F}_q$ obtained by the map $g: x \to x^p$ where p is a prime.

Results and Discussion:

We consider the graph over a finite field $\mathbb{F}_q$, q prime number, obtained by iterations of the map $x \to x^p$, where p is a prime number.

Theorem 1. Let $\alpha \in \mathbb{F}_q^*$ and $ord_q\alpha = p^e l$ where $e \in \mathbb{N} \cup \{0\}$ and $l \in \mathbb{N}$ with $gcd(p, l) = 1$. If $t := t(\alpha)$ is the tail length for α and $c := c(\alpha)$ is the cycle length for α, then $t = v_p(ord_q\alpha)$ and $c = ord_l p$.

Proof. We have $g^t(\alpha) = g^{t+c}(\alpha)$. Then $\alpha^{p^t} = \alpha^{p^{t+c}}$ and so

$$\alpha^{p^t(p^c-1)} = \alpha^{p^{t+c}-p^t} = 1.$$

Therefore $p^e l | p^t(p^c - 1)$. Since $gcd(p^e, p^c - 1) = 1 = gcd(l, p^t)$, $p^e | p^t$ and $l|(p^c - 1)$. We first show that $t = e = v_p(ord_q\alpha)$. Obviously, $e \le t$. If $e < t$, then $p^e < p^t$. Since t is the smallest such that $g^t(\alpha) = g^{t+c}(\alpha)$, we have $g^e(\alpha) = g^{e+c}(\alpha)$ and so

$$\alpha^{p^e(p^c-1)} = \alpha^{p^{e+c}-p^t} \neq 1$$

which contradicts with the fact that $p^e l | p^e(p^c - 1)$. Hence the first part of theorem is done.

Next, we will show that $ord_l p = c$. Since $l|(p^c - 1)$,

$$p^c \equiv 1 \pmod{l}.$$

Then $ord_l p \le c$. Suppose that there exist $d \in \mathbb{N}$ such that $1 \le d < c$ and

$$p^d \equiv 1 \pmod{l}.$$

Then $l|(p^d - 1)$ and so $p^e l | p^t(p^d - 1)$. This implies that

$$\alpha^{p^{t+c}-p^t} = \alpha^{p^t(p^c-1)} = 1.$$

Consequently, $g^{t+d}(\alpha) = g^t(\alpha)$ which contradicts the minimal of c. □

As an example, the graph of $g(x) = x^3$ over $\mathbb{F}_{109}^*$ is shown in Figure 2.

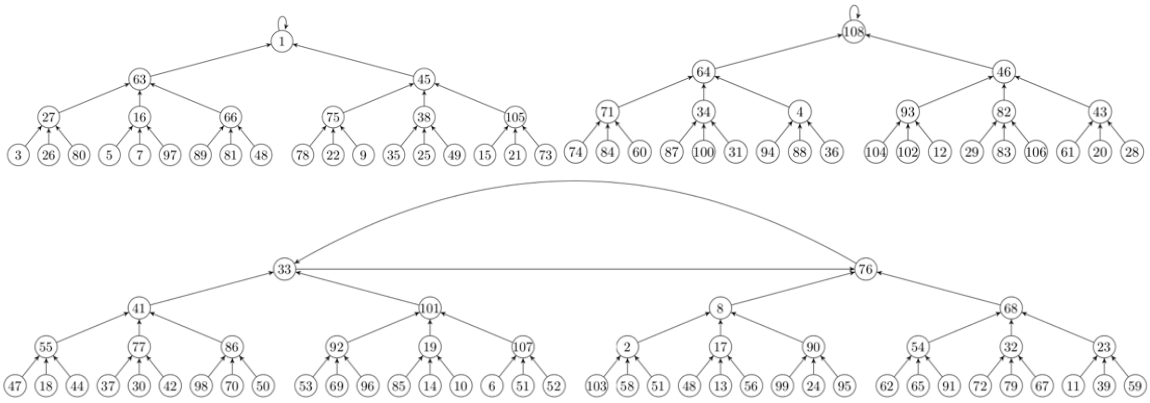

Figure 2.
The graph of $g(x) = x^3$ over $\mathbb{F}_{109}^*$

We can compute the tail length and the cycle length of each element in $\mathbb{F}_{109}^*$ as shown in Table 1.

Table 1.

The length of tails and cycles of elements in of $G_{x \to x^3}$ for $p = 109$

α	$t(\alpha)$	$c(\alpha)$
1,108	0	1
33,76	0	2
8,41,68,101	1	1
45,46,63,64	1	2
4,14,27,34,38,43,66,71,75,82,93,105	2	1
2,17,19,23,32,54,55,77,86,90,92,107	2	2
3,5,7,9,12,15,20,21,22,25,26,28,29,31, 35,36,48,49,60,61,73,74,78,80,81,83, 84,87,88,89,94,97,100,102,104,106	3	1
6,10,11,13,14,18,24,30,37,39,42,44, 47,48,50,51,52,53,56,57,58,59,62,65, 67,69,70,72,79,85,91,95,96,98,99,103	3	2

Theorem 2. Let γ be primitive element of $\mathbb{F}_q^*$. Then

(a) $\{a \in \mathbb{F}_q^* : t(a) = 0\} = \{\gamma^i : 1 \le i \le q-1 \text{ and } v_p(i) \ge v_p(q-1)\}$;

(b) For $1 \le k \le v_p(q-1)$, we have

$$\{a \in \mathbb{F}_q^* : t(a) = k\} = \{\gamma^i : 1 \le i \le q-1 \text{ and } v_p(i) = v_p(q-1) - k\}.$$

Proof. Let $q - 1 = p^\tau \rho$ where $gcd(p, \rho) = 1$. First, we claim that there exists $l \ge 1$ such that $\rho | (p^l - 1)$. To prove claim, choose $l = ord_\rho p$. Then $p^l \equiv 1 \pmod{\rho}$ which implies that $\rho | (p^l - 1)$.

(a) Let $a \in \mathbb{F}_q^*$ with $t(a) = 0$. Then $a = \gamma^i$ for some $1 \le i \le q-1$ and there is $l \ge 1$ such that

$$a = g^0(a) = g^{l+0}(a) = a^{p^l}.$$

Then we have $a^{p^l - 1} = 1$ and so $(\gamma^i)^{p^l - 1} = 1$. Therefore $p^\tau \rho | i(p^l - 1)$. Since $\gcd(p^\tau, p^l - 1) = 1$, $p^\tau | i$. Hence

$$v_p(i) \ge \tau = v_p(q-1).$$

Conversely, consider $\gamma^i \in \mathbb{F}_q^*$ where $1 \le i \le q-1$ and $v_p(i) \ge v_p(q-1) = \tau$. We get $p^\tau | i$. By claim there exists $l \ge 1$ such that $\rho | (p^l - 1)$. Therefore, $p^\tau \rho | i(p^l - 1)$. Thus $(\gamma^i)^{p^l - 1} = 1$. Now we have $(\gamma^i)^{p^l} = \gamma^i$. It follows that $g^l(\gamma^i) = g^0(\gamma^i)$. By the definition of the length of tail, $t(\gamma^i) = 0$.

(b) Let $k \in \mathbb{N}$ be such that $1 \le k \le v_p(q-1)$. Let $a \in \mathbb{F}_q^*$ with $t(a) = k$.
Then $a = \gamma^i$ for some $1 \le i \le q-1$ and there exists $l \ge 1$ such that

$$g^k(a) = g^{k+l}(a) \text{ and } g^{k-1}(a) \ne g^{k-1+l}(a).$$

Then we have

$$(\gamma^i)^{p^k} = (\gamma^i)^{p^{k+l}} \text{ and } (\gamma^i)^{p^{k-1}} \ne (\gamma^i)^{p^{k-1+l}}.$$

Consequently, we get

$$(\gamma^i)^{p^{k+l} - p^k} = 1 \text{ and } (\gamma^i)^{p^{k-1+l} - p^{k-1}} \ne 1.$$

Then $(q-1) | ip^k(p^l - 1)$ and $(q-1) \nmid ip^{k-1}(p^l - 1)$.
We claim that $p^\tau \nmid ip^{k-1}$. To prove claim, write $i = p^r w$ where $gcd(p, w) = 1$. Suppose that $p^\tau | ip^{k-1}$. Then $p^\tau | p^r w p^{k-1}$. Since $gcd(p, w) = 1$, $p^\tau | p^r p^{k-1}$. From $p^\tau \rho | p^r w p^k (p^l - 1)$ and $gcd(\rho, p) = 1$, we have $\rho | w(p^l - 1)$.
Therefore $p^\tau \rho | p^r w p^{k-1}(p^l - 1)$, that is, $(q-1) | ip^{k-1}(p^l - 1)$ which is a contradiction. Note that $p^\tau | ip^k$. By claim, we get $v_p(p^\tau) = v_p(ip^k)$.
Now we obtain $\tau = v_p(i) + k$ and so

$$v_p(i) = \tau - k = v_p(q-1) - k.$$

Conversely, consider $\gamma^i \in \mathbb{F}_q^*$ where $1 \le i \le q-1$ and $v_p(i) = v_p(q-1) - k$. Then we have

$$v_p(ip^k) = v_p(q-1) = v_p(p^\tau \rho).$$

Then $p^\tau | ip^k$ but $p^\tau \nmid ip^{k-j}$ for all $1 \le j \le k$. By the first claim, there exist $l \ge 1$ such that $\rho | (p^l - 1)$. Then $(q-1) | ip^k(p^l - 1)$ and $(q-1) \nmid ip^{k-j}(p^l - 1)$ for all $1 \le j \le k$. So $(\gamma^i)^{p^k(p^l - 1)} = 1$ and $(\gamma^i)^{p^{k-j}(p^l - 1)} \ne 1$ for all $1 \le j \le k$. We then have $g^k(\gamma^i) = g^{k+l}(\gamma^i)$ and $g^{k-1}(\gamma^i) \ne g^{k-1+l}(\gamma^i)$. Hence k is the smallest such that $g^k(\gamma^i) = g^{k+l}(\gamma^i)$. By the definition of the tail length $t(\gamma^i) = k$. □

For example the graph of $g(x) = x^3$ over $\mathbb{F}_{109}^*$, we know that 6 is primitive root modulo 109.

So we have $v_3(108) = 3$, by Theorem 2. (a) and $t(1) = 0$, can write $1 = 6^{108}$ (mod 109).

By Theorem 2. (b)

$t(2) = 2$, we obtain $v_3(i) = v_3(108) - 2 = 1$, so we can write $2 = 6^{57}$ (mod 109) and

$t(3) = 3$, we obtain $v_3(i) = v_3(108) - 3 = 0$, so we can write $3 = 6^{52}$ (mod 109).

Theorem 3. Let $q - 1 = p^\tau\rho$ where $\tau \in \mathbb{N} \cup \{0\}$ and $\rho \in \mathbb{N}$ with $gcd(p, \rho) = 1$.

(a) The total number of element in all cycle is ρ.

(b) For each positive integer divisor d of ρ, $G_{x\to x^p}$ contain $\frac{\varphi(d)}{ord_d p}$ cycles of length $ord_d p$.

(c) Off each element in these cycles there hang reversed complete p-tree of height $\tau - 1$ containing $\frac{p^\tau - 1}{p-1}$ elements.

Proof. Let γ be primitive elements over $\mathbb{F}_q^*$. Let $x \in \mathbb{F}_q^*$ and $q - 1 = p^\tau\rho$ with $gcd(p, \rho) = 1$.

(a) If x is in a cycle, we have $t(x) = 0$. By Theorem 2 (a), $x = \gamma^i$ where $1 \le i \le q - 1$ and $v_p(i) \ge v_p(q - 1) = \tau$. So x must be of the form γ^{jp^τ} where $1 \le j \le \rho$. Hence the total number of elements in all cycles is ρ.

(b) From (a), we have the set of elements in cycles form a cyclic group order ρ, i.e.,

$$\{\gamma^i : 1 \le i \le q - 1 \; and \; v_p(i) \ge v_p(q - 1)\} = < \gamma^{p^\tau} >.$$

We know that if $d|\rho$, there are $\varphi(d)$ elements of order d. Note that $ord_p(\gamma^{p^\tau\frac{\rho}{d}}) = d$. Therefore, the element of order d are given by $\gamma^{jp^\tau\frac{\rho}{d}}$ for $0 \le j < d$ and $gcd(j, d) = 1$. Since $ord_p\left(\gamma^{jp^\tau\frac{\rho}{d}}\right) = p^0 d = d$, by Theorem 1, $c(x) = ord_d p$. Hence for all $d|\rho$, $G_{x\to x^p}$ contain $\frac{\varphi(d)}{ord_d p}$ cycles of length $ord_d p$.

(c) An element $x \in \mathbb{F}_q^*$ with $t(x) = 1$ whose $x^p = \gamma^{p^\tau j}$ in a cycle is one of those of the form $\gamma^{jp^{\tau-1}}$ where $0 \le j \le p - 1$.
In general, if γ^i is an element with tail size t $(1 \le t \le \tau)$, the element with tail size $t + 1$ are

$$\gamma^{\frac{i+j(q-1)}{p}} \text{ for } 0 \le j \le p - 1.$$

Since the longest tail length is τ, we have the reversed complete p−tree of height $\tau - 1$ containing $1 + p + p^2 + \cdots + p^{\tau-1} = \frac{p^\tau - 1}{p-1}$ elements. □

Again, we consider the graph of $g(x) = x^3$ over $\mathbb{F}_{109}^*$. We have $108 = 3^3 4$ with $\rho = 4$. Moreover, it is easily seen from Figure 1. that the total number of elements in all cycles is $4 = \rho$. Table 2 shows the number of cycles of length $ord_d 3$ for each $d|\rho$.

Table 2.

The structure of $G_{x\to x^3}$ for $p = 109$

d	$\varphi(d)$	$c = ord_d 3$	#cycle
1	1	1	1
2	1	1	1
4	2	2	1

From Figure 2., off each element in the cycles there hang reversed complete 3-tree of height 2 containing $\frac{3^3-1}{3-1} = 13$ elements. See Figure 3.

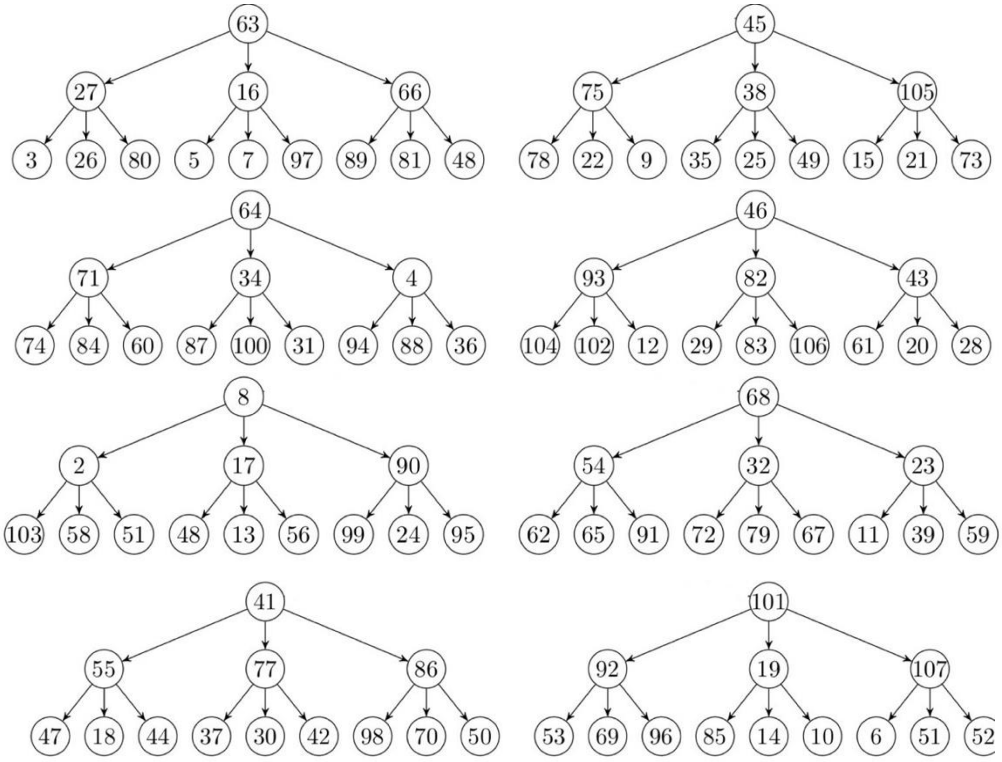

Figure 3.

The reversed complete 3-tree graph.

References:

1. Rogers T.D, The Graph of the Square Mapping on the Prime Fields. Discrete Math. 1996;148:317-324
2. Vasiga T, Shallit J. On the iteration of certain quadratic maps over GF(p). Discrete Math. 2004;277:219-240

B_022_OF: HYBRID FINITE INTEGRATION METHOD FOR SOLVING ORDINARY DIFFERENTIAL EQUATIONS

Nifatamah Makaje, Areena Hazanee,* Aniruth Phon-on

Department of Mathematics and Computer Science, Faculty of Science and Technology,
Prince of Songkla University, Pattani Campus, 94000, Thailand
*e-mail: areena.h@psu.ac.th

Abstract:

This research study aims to modify a finite integration method (FIM) which is a numerical method for solving ordinary differential equations (ODE). This modified FIM is studied based on the research of P.H. Wen *et al*.[1] which was a research for establishing a re-new numerical method for solving linear differential equations with the use of numerical integration techniques. The trapezoidal rule combined with the Simpson's rule is applied in this study in order to establish the first order integral matrix and use to solve the *n*-th order ODE. Here, the integral matrix is formed as the lower triangular matrix which can reduce computational cost and saves on memory requirements. In order to test the accuracy of the approximations, numerical examples are presented and discussed in comparison with the finite difference method and the traditional FIM (FIM based on the trapezoidal rule).

Introduction:

Ordinary and partial differential equations are commonly occurred as mathematical models in many branches of science, engineering and economy. Many differential equations cannot be solved using analytically, this leads that numeric approximation techniques are unavoidable for seeking approximate solutions to simulate the dynamics and characteristics of the models. As the advance of computational methods, the numerical approximation can usually meet the reliable agreement between the analytical solution and its numerical approximation with high accuracy. There are many numerical techniques to deal with differential equations such as the Finite Difference Method (FDM), Finite Element Method (FEM) and Boundary Element method (BEM).

In 2013, Wen *et al*. [1] have introduced a re-brought up numerical method for solving the *n*-th order ordinary and partial differential equations by using either Ordinary Linear Approach (OLA) or Radial Basis Function (RBF) interpolation to construct an (one layer) integral matrix to obtain the integration matrix with *n* layers, namely the Finite Integration Method (FIM). Using FIM starts at considering the integral matrix to be applied to solve the *n*-th order differential equation by employing the *n*-th power of one (first order) integral matrix, this is an advantage of the use of FIM, i.e. using only an (one layer) integral matrix to solve any *n*-th order differential equation. There are many developments of FIM study in order to improve the accuracy of the solution by applying various numerical methods/techniques to establish the first order integral matrix such as the trapezoidal rule[1,2], radial basis interpolating function[1,2], Simpson's rule, Cotes integral formula, Lagrange formula[3], Chebyshev Polynomial interpolation[4], or Legendre Polynomial interpolation[5] which solve differential equations in 1D and extended to multi-dimensional partial differential equation in cases of time-dependent and

independent. Moreover, traditional- and modified-FIM have been researched to solve in both cases of direct and indirect problems[6-10].

Along many modifying FIMs, the first order integral matrix seems to be the main point of development as any *n*-th layer finite integration matrix, formed from the *n*-th order differential equation, can be obtained directly by using a matrix of the first order integration. The structure of the first order integral matrix of various FIM is normally formed as full matrix, however, there is a form of lower triangular integral matrix which can make the FIM procedure to be more simply and save the computational core memory. The lower triangular form, obtaining based on using the trapezoidal rule considered as the integration approximation, i.e. FIM(OLA), brings our curiosity to whether the FIM(OLA) is capable enough to be the most simple FIM to be employed or there is more simple and accurate FIM than the traditional one. Therefore, this study is aimed to propose the FIM with successive and simply numerical integrations to form the triangular integral matrix of the first order for solving differential equations and more accuracy than the use of the traditional one; FIM(OLA).

Methodology:

In this study, we propose to construct the hybrid FIM based on the trapezoidal rule together with Simpson's rule for solving differential equations. Two methods of numerical integration and the FIM are reviewed in order to understand the idea for establishing this hybrid FIM as follows:

***Trapezoidal Rule*:**

The basic concept of the trapezoidal rule is that approximating the definite integral $\int_a^b f(x)dx$ via the first-order interpolating polynomial $P_1(x)$ to connect two points equally spaced between $(x_i, f(x_i))$ and $(x_{i+1}, f(x_{i+1}))$ for N intervals of $x \in \{a = x_0, x_1, x_2, ..., x_N = b\}$, $x_i = a + ih$ and $h = \frac{b-a}{N} = x_{i+1} - x_i$. Here, the first-order polynomial is given as

$$P_1(x) = \frac{(x - x_{i+1})}{(x_i - x_{i+1})} f(x_i) + \frac{(x - x_i)}{(x_{i+1} - x_i)} f(x_{i+1}).$$

Then the integral approximation becomes

$$\int_{x_i}^{x_{i+1}} P_1(x)dx = \frac{h}{2}\left[f(x_i) + f(x_{i+1}) \right]. \quad (1)$$

Therefore the definite integral approximation can be approximated as a numerical integration formula namely the trapezoidal rule as

$$\int_a^b f(x)dx = \frac{h}{2}\left[f(x_0) + 2\sum_{i=1}^{N-1} f(x_i) + f(x_N) \right]. \quad (2)$$

***Simpson's Rule*:**

In the use of higher order polynomial interpolation for estimating the definite integral $\int_a^b f(x)dx$, one is the Simpson's rule which uses the second-order interpolating polynomial $P_2(x)$ to connect three points equally spaced between $(x_i, f(x_i))$ and $(x_{i+2}, f(x_{i+2}))$ as the following polynomial,

$$P_2(x)=\frac{(x-x_{i+1})(x-x_{i+2})}{(x_i-x_{i+1})(x_i-x_{i+2})}f(x_i)+\frac{(x-x_i)(x-x_{i+2})}{(x_{i+1}-x_i)(x_{i+1}-x_{i+2})}f(x_{i+1})$$

$$+\frac{(x-x_i)(x-x_{i+1})}{(x_{i+2}-x_i)(x_{i+2}-x_{i+1})}f(x_{i+2}).$$

Therefore, the definite integral can be approximated as

$$\int_{x_i}^{x_{i+2}}P_2(x)dx=\frac{h}{3}\left[f(x_i)+4f(x_{i+1})+f(x_{i+2})\right]. \tag{3}$$

Hence, the Simpson's rule is formulated as

$$\int_a^b f(x)dx=\frac{h}{3}\left[f(x_0)+4\sum_{i=1}^{\frac{N}{2}}f(x_{2i-1})+2\sum_{i=1}^{\frac{N}{2}-1}f(x_{2i})+f(x_N)\right]. \tag{4}$$

Note that the subinterval N to be imposed for the Simpson's rule has to be even number since the index of formula has to be divided by 2.

***Traditional finite integration method*:**

In order to establishing the hybrid FIM, we firstly introduce the traditional FIM (FIM based on the trapezoidal rule) which has first re-brought up for solving the partial differential equations[1]. The procedure of FIM starts with considering the finite integral from 0 to the region $x\in[0,L]$, i.e. $F^{(1)}(x)=\int_0^x f(y)dy$, and then approximate the integral with the ordinary linear approximation namely the trapezoidal rule over the discrete space domain $x_i\in[0=x_0,x_1,...,x_N=L]$ for $x_i=ih$ and $h=\frac{L}{N}=x_{i+1}-x_i$ as

$$F^{(1)}(x_k)=\int_0^{x_k}f(y)dy=h\left(\frac{f(x_0)}{2}+f(x_1)+...+f(x_{N-1})+\frac{f(x_N)}{2}\right)=\sum_{i=0}^{k}a_{ki}f(x_i),$$

where $a_{0i}=0$ and $a_{ki}=\begin{cases}\frac{1}{2}h & ;i=0,k,\\ h & ;i=1,2,...,k-1,\\ 0 & ;i>k.\end{cases}$

This can be rewritten in a matrix form as

$$\underline{\mathbf{F}}^{(1)}=\mathbf{A}\underline{\mathbf{f}},$$

where $\underline{\mathbf{F}}^{(1)}=\left[\int_0^{x_0}f(y)dy,\int_0^{x_1}f(y)dy,...,\int_0^{x_N}f(y)dy\right]^T$, $\underline{\mathbf{f}}=\left[f(x_0),f(x_1),...,f(x_N)\right]^T$

and $\mathbf{A} = h\begin{bmatrix} 0 & 0 & 0 & 0 & \dots & 0 & 0 \\ \frac{1}{2} & \frac{1}{2} & 0 & 0 & \dots & 0 & 0 \\ \frac{1}{2} & 1 & \frac{1}{2} & 0 & \dots & 0 & 0 \\ \frac{1}{2} & 1 & 1 & \frac{1}{2} & \dots & 0 & 0 \\ \dots & \dots & \dots & \dots & \dots & \dots & \dots \\ \frac{1}{2} & 1 & 1 & 1 & \dots & \frac{1}{2} & 0 \\ \frac{1}{2} & 1 & 1 & 1 & \dots & 1 & \frac{1}{2} \end{bmatrix}_{(N+1)\times(N+1)}$.

As it has shown in the research of Wen *et al.*[1] that, by the use of the trapezoidal rule for the higher order integration, the n layers integral becomes $F^{(n)}(x) = \underbrace{\int_0^x \dots \int_0^{y^{(2)}} \int_0^{y^{(1)}} f(y)dy\, dy^{(1)} \dots dy^{(n-1)}}_{n \text{ layers}}$, for $x \in [0, L]$ and this gives the discrete n layers integration which can be expressed as

$$F^{(n)}(x_k) = \int_0^{x_k} \dots \int_0^{y^{(2)}} \int_0^{y^{(1)}} f(y)dy\, dy^{(1)} \dots dy^{(n-1)}$$

$$= \sum_{i=0}^{k} \dots \sum_{j=0}^{i} \sum_{p=0}^{j} a_{ki} \dots a_{ij} a_{jp} f(x_i) = \sum_{i=0}^{k} a_{ki}^{(n)} f(x_i).$$

This can see that the n layers integration function can also be rewritten in a matrix form[1] as,

$\underline{\mathbf{F}}^{(n)} = \mathbf{A}^n \underline{\mathbf{f}}$, for $n \in \mathbb{N}$.

Note that the integral matrix $\mathbf{A}$ is a lower triangular whose its first row are all zeros. However the left boundary node at $x = x_0 = 0$ needs to be known or eliminated in order to avoid the singular matrix.

***Hybrid finite integration method*:**

As mentioned above that the hybrid FIM is proposed to establish from the combination of two numerical integration techniques which are the trapezoidal rule and the Simpson's rule. Here the first order definite integral $F^{(1)}(x_k) = \int_0^{x_k} f(y)dy$ over the discrete space domain $x_i \in \{0 = x_0, x_1, \dots, x_N = L\}$ for $x_i = ih$ and $h = \frac{L}{N} = x_{i+1} - x_i$ is approximated as follows.

- When $k = 1$, the definite integral is approximated via the trapezoidal rule (1),
$$\int_{x_0}^{x_1} f(y)dy = \frac{h}{2}\left[f(x_0) + f(x_1) \right].$$
- When $k = 2$, the definite integral is approximated via the Simpson's rule *(3)*,
$$\int_{x_0}^{x_2} f(y)dy = \frac{h}{3}\left[f(x_0) + 4f(x_1) + f(x_2) \right].$$

- When k and $N = N_{odd}$ are odd numbers, $k = 3,5,\ldots,N_{odd}$, the definite integral is approximated via the combination of the trapezoidal rule (2) and the Simpson's rule *(4)* as,

$$\int_{x_0}^{x_k} f(y)dy = \int_{x_0}^{x_{k-1}} f(y)dy + \int_{x_{k-1}}^{x_k} f(y)dy, \quad k-1 \text{ is even,}$$

$$= \frac{h}{3}\left[f(x_0) + 4\sum_{i=1}^{\frac{k-1}{2}} f(x_{2i-1}) + 2\sum_{i=1}^{\frac{k-3}{2}} f(x_{2i}) + f(x_{k-1}) \right] + \frac{h}{2}\left[f(x_{k-1}) + f(x_k) \right]$$

$$= \frac{h}{6}\left[2f(x_0) + 8\sum_{i=1}^{\frac{k-1}{2}} f(x_{2i-1}) + 4\sum_{i=1}^{\frac{k-3}{2}} f(x_{2i}) + 5f(x_{k-1}) + 3f(x_k) \right].$$

- When k and $N = N_{even}$ are even numbers, $k = 4,6,\ldots,N_{even}$, the definite integral is approximated via the Simpson's rule *(4)* as,

$$\int_{x_0}^{x_k} f(x)dx = \frac{h}{3}\left[f(x_0) + 4\sum_{i=1}^{\frac{k}{2}} f(x_{2i-1}) + 2\sum_{i=1}^{\frac{k}{2}-1} f(x_{2i}) + f(x_n) \right].$$

Therefore the first order definite integral $F^{(1)}(x_k) = \int_0^{x_k} f(y)dy$ can be rewritten in a matrix form as

$$\underline{\mathbf{F}}^{(1)} = \mathbf{A}^{(1)}\underline{\mathbf{f}}, \tag{5}$$

where $\underline{\mathbf{F}}^{(1)} = \left[\int_0^{x_0} f(y)dy, \int_0^{x_1} f(y)dy, \ldots, \int_0^{x_N} f(y)dy \right]^T$, $\underline{\mathbf{f}} = \left[f(x_0), f(x_1), \ldots, f(x_N) \right]^T$

and $\mathbf{A}^{(1)}$ is a coefficient matrix of the first order definite integral and we denote $\mathbf{A}^{(1)} = \mathbf{A}$ which can be expressed in matrix form as

$$\mathbf{A} = \frac{h}{6}\begin{bmatrix} 0 & 0 & 0 & 0 & 0 & \ldots & 0 & 0 \\ 3 & 3 & 0 & 0 & 0 & \ldots & 0 & 0 \\ 2 & 8 & 2 & 0 & 0 & \ldots & 0 & 0 \\ 2 & 8 & 5 & 3 & 0 & \ldots & 0 & 0 \\ 2 & 8 & 4 & 8 & 2 & \ldots & 0 & 0 \\ \ldots & \ldots & \ldots & \ldots & \ldots & \ldots & \ldots & \ldots \\ \ldots & \ldots & \ldots & \ldots & \ldots & \ldots & \ldots & \ldots \\ 2 & 8 & 4 & 8 & 4 & 8 & 5 & 3 \end{bmatrix}_{N_{odd}+1} \quad \text{for } N \text{ is odd,}$$

$$\mathbf{A}=\frac{h}{6}\begin{bmatrix} 0 & 0 & 0 & 0 & 0 & \dots & 0 & 0 & 0 \\ 3 & 3 & 0 & 0 & 0 & \dots & 0 & 0 & 0 \\ 2 & 8 & 2 & 0 & 0 & \dots & 0 & 0 & 0 \\ 2 & 8 & 5 & 3 & 0 & \dots & 0 & 0 & 0 \\ 2 & 8 & 4 & 8 & 2 & \dots & 0 & 0 & 0 \\ \dots & \dots & \dots & \dots & \dots & \dots & \dots & \dots & \dots \\ \dots & \dots & \dots & \dots & \dots & \dots & \dots & \dots & \dots \\ 2 & 8 & 4 & 8 & 4 & \dots & 5 & 3 & 0 \\ 2 & 8 & 4 & 8 & 4 & \dots & 4 & 8 & 2 \end{bmatrix}_{N_{even}+1} \quad \text{for } N \text{ is even.}$$

By approximating the first order definite integral in (5), it is obvious to see that the first order definite integral $\int_0^{x_k} f(y)dy$ can be written as

$$\int_0^{x_k} f(y)dy = \sum_{j=0}^{k} a_{kj} f(x_j), \tag{6}$$

where a_{kj} is the element of matrix $\mathbf{A}^{(1)}$ corresponding to (5) for $k, j = 0,1,2,...,N$.

Next, we consider the second order definite integral $F^{(2)}(x_k) = \int_0^{x_k}\int_0^{y^*} f(y)dy\,dy^*$ by using the approximation in (6) as $\int_0^{x_k}\int_0^{y^*} f(y)dy\,dy^* = \sum_{i=0}^{k}\sum_{j=0}^{i} a_{ki}a_{ij} f(x_j)$ which can be expressed as,

$$\int_0^{x_1}\int_0^{y^*} f(y)dy\,dy^* = (a_{10}a_{00}+a_{11}a_{10}) f(x_0)+(a_{11}a_{11}) f(x_1),$$

$$\int_0^{x_2}\int_0^{y^*} f(y)dy\,dy^* = (a_{20}a_{00}+a_{21}a_{10}+a_{22}a_{20}) f(x_0)+(a_{21}a_{11}+a_{22}a_{21}) f(x_1) + (a_{22}a_{22}) f(x_2),$$

$$\int_0^{x_3}\int_0^{y^*} f(y)dy\,dy^* = \sum_{k=0}^{3} a_{3k}a_{k0} f(x_0)+\sum_{k=1}^{3} a_{3k}a_{k1} f(x_1)+\sum_{k=2}^{3} a_{3k}a_{k2} f(x_2)+a_{33}a_{33} f(x_3),$$

...

$$\int_0^{x_N}\int_0^{y^*} f(y)dy\,dy^* = \sum_{k=0}^{N} a_{Nk}a_{k0} f(x_0)+\sum_{k=1}^{N} a_{Nk}a_{k1} f(x_1)+...+\sum_{k=N}^{N} a_{Nk}a_{kN} f(x_N).$$

Therefore the second order definite integral $F^{(2)}(x_k) = \int_0^{x_k}\int_0^{y^*} f(y)dy\,dy^*$ can be rewritten in a matrix form as

$$\underline{\mathbf{F}}^{(2)} = \mathbf{A}^{(2)}\underline{\mathbf{f}},$$

where $\mathbf{A}^{(2)}$ is a coefficient matrix of the second order definite integral. It can be observed that $\mathbf{A}^{(2)}$ is a multiplication matrix of $\mathbf{A}$, i.e. $\mathbf{A}^{(2)} = \left[a_{ij}^{(2)} \right]$, which can be expressed as

$$\mathbf{A}^{(2)} = \left[a_{ij}^{(2)} \right] = \left[\sum_{k=0}^{N} a_{ik} a_{kj} f(x_j) \right] = \mathbf{A} \cdot \mathbf{A} = \mathbf{A}^2 .$$

Considering in the same way for the higher order definite integral, we have the matrix form of $F^{(n)}(x_k) = \underbrace{\int_0^{x_k} \ldots \int_0^{y^{(2)}} \int_0^{y^{(1)}} f(y) dy \, dy^{(1)} \ldots dy^{(n-1)}}_{n \text{ layers}}$ as

$$\underline{\mathbf{F}}^{(n)} = \mathbf{A}^{(n)} \underline{\mathbf{f}} = \mathbf{A}^n \underline{\mathbf{f}} .$$

One thing to note that the coefficient matrix $\mathbf{A}$ is a lower triangular matrix, then $\mathbf{A}^n$ is also a lower triangular matrix.

***Hybrid FIM for solving ODE*:**

As we proposed that the hybrid FIM introduced earlier can solve ODE as the traditional FIM can solve the *n*-th order ODE. In order to test the proposal, the following second order ODE is investigated,

$$\frac{d^2 u}{dx^2} + p(x)u = q(x), \quad x \in [0, L], \tag{7}$$

where $u = u(x)$ is an unknown function and $p(x)$, $q(x)$ are given functions. By applying integration operation twice on both sides of the equation yields,

$$u(x) + \int\int p(x)u(x)dxdx = \int\int q(x)dxdx + c_0 x + c_1 .$$

This gives the matrix equation,

$$\underline{\mathbf{u}} + \mathbf{A}^2 \mathbf{P} \underline{\mathbf{u}} = \mathbf{A}^2 \underline{\mathbf{q}} + c_0 \underline{\mathbf{x}} + c_1 \underline{\mathbf{i}}, \tag{8}$$

where $\underline{\mathbf{u}} = \left[u(x_0), u(x_1), \ldots, u(x_N) \right]^T$, $\underline{\mathbf{q}} = \left[q(x_0), q(x_1), \ldots, q(x_N) \right]^T$, $\underline{\mathbf{x}} = [x_0, x_1, x_2, \ldots, x_N]^T$, $\underline{\mathbf{i}} = [1,1,1,\ldots,1]^T$ are $N+1$ column vectors, $\mathbf{P} = diag(p(x_0), p(x_1), \ldots, p(x_N))$ is $N+1$ diagonal matrix and c_0, c_1 are integral constants corresponding to the above equation.

There are various types of conditions commonly encountered in the solution of the differential equations. In this sample study, the use of hybrid FIM to solve the boundary value problem is reviewed, we consider the second order differential equation (7) with initial conditions

$$u(0) = \alpha \text{ and } \frac{du}{dx}(0) = \beta . \tag{9}$$

Looking more closely for the derivative condition $\frac{du}{dx}(0)=\beta$ by applying integration operation on both sides of the equation (7), this gives

$$\frac{du}{dx}+\int p(x)udx=\int q(x)dx+c_0\,. \tag{10}$$

Therefore, the discrete form of equation (10) at $x=0$ yields

$$\beta+\sum_{i=0}^{N}a_{0i}^{(1)}p(x_i)u(x_i)=\sum_{i=0}^{N}a_{0i}^{(1)}q(x_i)+c_0\,.$$

Since $a_{0i}^{(1)}=0$ for all $i=0,1,2,...,N$, the initial conditions (9) become

$$u(x_0)=\alpha\,,\ c_0=\beta\,. \tag{11}$$

Here, the second order ODE (6) with boundary conditions (9) can be solved by considering $N+1$ linear algebraic equations (8) and two extra conditions (11) which can be formed as a system of linear equations with $N+3$ unknowns including $\underline{\mathbf{u}}$, c_0 and c_1 as

$$\left[\begin{array}{cccc:cc} & & & & -x_0 & -1 \\ & I+\mathbf{A}^2\mathbf{P} & & & -x_1 & -1 \\ & & & & \cdots & \cdots \\ & & & & -x_N & -1 \\ \hdashline 1 & 0 & \cdots & 0 & 0 & 0 \\ 0 & 0 & \cdots & 0 & 1 & 0 \end{array}\right]\left[\begin{array}{c} u_0 \\ u_1 \\ \cdots \\ u_N \\ \hdashline c_0 \\ c_1 \end{array}\right]=\left[\begin{array}{c} \\ \mathbf{A}^2\underline{\mathbf{q}} \\ \\ \hdashline \alpha \\ \beta \end{array}\right], \tag{12}$$

where $u_i=u(x_i)$.

Another problem to be considered is the differential equation (7) with boundary conditions

$$u(0)=\alpha \text{ and } \frac{du}{dx}(1)=\beta\,. \tag{13}$$

This problem is similar to the above problem, i.e. the DE (7) together with the initial conditions (9). Only one thing different is the flux condition $\frac{du}{dx}(1)=\beta$ where one consider at $x=0$ and another one consider at $x=1$. This gives the discrete form of conditions (13) to be

$$u_0=\alpha\,,\ \sum_{i=0}^{N}a_{Ni}^{(1)}p(x_i)u_i-c_0=\sum_{i=0}^{N}a_{Ni}^{(1)}q(x_i)-\beta\,,$$

where $p_i=p(x_i)$ and $q_i=q(x_i)$. Therefore, the system of linear equations with $N+3$ unknowns becomes,

$$\left[\begin{array}{c|cc} I+\mathbf{A}^2\mathbf{P} & \begin{matrix}-x_0 & -1\\ -x_1 & -1\\ \cdots & \cdots\\ -x_N & -1\end{matrix} \\ \hline \begin{matrix}1 & 0 & \cdots & 0\\ a_{N0}^{(1)}p_0 & a_{N1}^{(1)}p_1 & \cdots & a_{NN}^{(1)}p_N\end{matrix} & \begin{matrix}0 & 0\\ -1 & 0\end{matrix}\end{array}\right]\left[\begin{array}{c} u_0\\ u_1\\ \cdots\\ u_N\\ \hline c_0\\ c_1\end{array}\right]=\left[\begin{array}{c} \mathbf{A}^2\underline{\mathbf{q}}\\ \hline \alpha\\ \sum_{i=0}^{N}a_{Ni}^{(1)}q_i-\beta\end{array}\right]. \tag{14}$$

By above consideration, it can be seen that the use of the hybrid FIM can solve any *n*-th order differential equation with the system of linear equations with $N+n$ unknowns

Results and Discussion:

In this section, we propose to apply the hybrid FIM to solve a benchmark test example[1,3,5-6],

$$\frac{d^2u}{dx}-2(1+2x^2)u=0, \qquad x\in[0,1], \tag{15}$$

with the initial conditions $u(0)=1$ and $\frac{du}{dx}(0)=0$. The analytical solution is given by

$$u(x)=\exp(x^2). \tag{16}$$

The average relative error (ARE) introduced below is used for this example in order to analyze the accuracy of the results.

$$E_{ARE}=\frac{1}{N+1}\sum_{i=0}^{N}\frac{|Exact(x_i)-Appox(x_i)|}{|Exact(x_i)|}. \tag{17}$$

where $Exact(x_i)$ and $Appox(x_i)$ represent the analytical and numerical solutions of $u(x_i)$, respectively.

To solve the initial value problem (15), the system of linear equations (12) with $p(x)=-2(1+2x^2)$, $q(x)=0$, $\alpha=1$ and $\beta=0$ becomes

$$\left[\begin{array}{c|cc} I+\mathbf{A}^2\mathbf{P} & \begin{matrix}-x_0 & -1\\ -x_1 & -1\\ \cdots & \cdots\\ -x_N & -1\end{matrix} \\ \hline \begin{matrix}1 & 0 & \cdots & 0\\ 0 & 0 & \cdots & 0\end{matrix} & \begin{matrix}0 & 0\\ 1 & 0\end{matrix}\end{array}\right]\left[\begin{array}{c} u_0\\ u_1\\ \cdots\\ u_N\\ \hline c_0\\ c_1\end{array}\right]=\left[\begin{array}{c} 0\\ 0\\ \cdots\\ 0\\ \hline 1\\ 0\end{array}\right]. \tag{18}$$

Table 1. The average relative errors of the numerical solutions obtained by using the hybrid FIM compared with the traditional FIM, FDM, FIM(Simpson I) and FIM(Simpson II) for $N \in \{6,7,8,9,10\}$.

N	Hybrid FIM	Traditional FIM[a]	FDM[a]	Simpson I FIM[a]	Simpson II FIM[a]
6	3.2797×10^{-3}	1.2283×10^{-2}	8.3822×10^{-3}	3.1693×10^{-3}	2.3005×10^{-3}
7	2.3917×10^{-3}	8.7043×10^{-3}	6.9142×10^{-3}	2.0935×10^{-3}	1.6259×10^{-3}
8	1.4599×10^{-3}	6.4860×10^{-3}	5.8770×10^{-3}	1.4538×10^{-3}	1.1809×10^{-3}
9	1.1456×10^{-3}	5.0177×10^{-3}	5.1070×10^{-3}	1.0498×10^{-3}	8.8015×10^{-4}
10	7.7381×10^{-4}	3.9962×10^{-3}	4.5134×10^{-3}	7.8247×10^{-4}	6.7157×10^{-4}

[a]The average relative errors presented by Li *et al*.[3].

Table 1 shows the ARE of the numerical results obtained by solving the linear system (18) based on the use of the hybrid FIM. It can be seen that the numerical results with small number of grid points $N \in \{6,7,8,9,10\}$ are found to be accurate with the accuracy degree of 10^{-3} to 10^{-4}. Additionally, the numerical results obtained by using various methods presented by Li *et al*.[6], i.e. FDM, FIM(Simpson I), and FIM(Simpson II), are shown to be compared in **Table 1**. We choose the FDM to be compared as it is a standard numerical method for solving ODE, whereas FIM(Simpson I) and FIM(Simpson I) are the FIMs based on the alternative extended Simpson's rule together with the Cotes and Lagrange formulas introduced by Li *et al*.[3] One thing to note that Li *et al*.[3] discretized the space domain by $x_i \in \{0 = x_1, x_2, ..., x_N = L\}$ for $x_i = ih$ and $h = L/(N+1)$, then the numerical results obtained by using FDM, FIM(Simpson I) and FIM(Simpson II) with $N \in \{6,7,8,9,10\}$ in **Table 1** represent the numerical results with $N \in \{7,8,9,10,11\}$ from Li *et al*.[3], respectively. Looking at the comparison test results, it found that the numerical results obtained by using the hybrid FIM is more accurate than the traditional FIM and the FDM, while the average relative errors when $N = 10$ are at the accuracy degree 10^{-4} with the results obtained by the hybrid FIM, FIM(Simpson I) and FIM(Simpson II).

Furthermore, we consider the extension of the number of grid points to be $N \in \{15,20,25,30\}$ and displayed the average relative errors in **Table 2**. We found that the numerical results obtained by using the hybrid FIM are significantly more accurate than the traditional FIM with around one decimal different.

Table 2. The average relative errors of the numerical solutions obtained by using the hybrid FIM compared with the traditional FIM for $N \in \{15,20,25,30\}$.

N	Hybrid FIM	Traditional FIM
15	2.5497×10^{-4}	1.5872×10^{-3}
20	1.0430×10^{-4}	8.8293×10^{-4}
25	5.6203×10^{-5}	5.6148×10^{-4}
30	3.1751×10^{-5}	3.8830×10^{-4}

Conclusion:

In this paper, the finite integration method based on the hybrid of using the trapezoidal rule and the Simpson's rule was formulated to solve the one-dimension initial value problem and boundary value problem. Only first order integral matrix was used to solve the *n*-th order differential equation with the *n*-th power of one (first order) integral matrix. In comparison of the numerical results with the standard method, FDM, and the traditional FIM, the numerical results obtained by using the hybrid FIM were more accurate than the FDM and the traditional one, and improved the accuracy with increasing the number of grid points.

Acknowledgements:

Authors would like to acknowledge the financial support received from the Office of Research Affairs of the Faculty of Science and Technology, Prince of Songkla University, Pattani campus, Thailand, under the Research Career Development Grant 2020.

References:

1. Wen PH, Hon YC, Li M, Korakianitis T. 'Finite integration method for partial differential equations, Applied Mathematical Modelling'. Appl Math Model. 2013;37:10092-10106.
2. Li M, Chen CS, Hon YC, Wen PH. 'Finite integration method for solving multi-dimensional partial differential equations'. Appl Math Model. 2015;39:4979-4994.
3. Li M, Tian ZL, Hon YC, Chen CS, Wen PH. 'Improved finite integration method for partial differential equations'. Eng Anal Bound Elem. 2016;64:230-236.
4. Boonklurb R, Duangpan A, Treeyaprasert T. 'Modified finite integration method by using Chebyshev polynomial for solving linear differential equations'. J Numer Anal Ind Appl Math. 2018;12:1-19.
5. Sahakitchatchawan T, Boonklurb R, Singhum S. 'Modified finite integration method by using Legendre polynomials for solving linear ordinary differential equations'. Chamchuri J Math. 2018;10:14-27.
6. Li M, Hon YC, Korakianitis T, Wen PH. 'Finite integration method for nonlocal elastic bar under static and dynamic loads'. Eng Anal Bound Elem. 2013;37:842-849.
7. Yu Y, Xu D, Hon YC. 'Reconstruction of inaccessible boundary value in a side ways parabolic problem with variable coefficients-Forward collocation with finite integration method'. Eng Anal Bound Elem. 2015;61:78-90.
8. Lesmana R, Hazanee A, Phon-On A, Saelee J. 'A finite integration method for a time-dependent heat source identification of inverse problem'. Proc 5th AASIC. 2017:444-451.
9. Hazanee A. 'Finite integration method for the time-dependent heat source determination of inverse problem'. Proc 6th BUU Conf. 2017:391-401.
10. Hazanee A. 'Finite integration method based on a trapezoid rule for solving inverse source problem for the heat equation with a non-local boundary condition'. Burapha Sci J. 2018;23:1345-1358.

B_023_PA: ON SOME $(C,1)(E,1)$ IDEAL CONVERGENT SEQUENCE SPACES

Penpark Sirimark,[1*] Ekrem Aljimi (Alimi)[2]

[1] Department of Science and Mathematics, Rajamangala University of Technology Isan Surin Campus, 145 Surin-Prasart 32000 Surin Thailand
[2] Faculty of Computer Science, University "Kadri Zeka", St.Zija Shemsiu nn 60000 Gjilan Kosovo
*e-mail: penpark.si@rmuti.ac.th

Abstract:

In this paper, we introduced a new type of statistical convergence called (C,1)(E,1) Ideal Convergent and some new ideal convergent sequence spaces $C^I_{(C,1)(E,1)}$, $(C_0)^I_{(C,1)(E,1)}$ and $(l_\infty)^I_{(C,1)(E,1)}$ that are related to the (C,1)(E,1) - summability. Also, we investigated some properties of these spaces and prove some inclusion results.

B_024_OA: MINIMUM-WEIGHT BASES FOR CODES FROM COMPLETE MULTIPARTITE GRAPHS

Jirapha Limbupasiriporn,[1,*] Prasit Limbupasiriporn[2]

Department of Mathematics, Faculty of Science, Silpakorn University,
Nakorn Pathom 73000 Thailand
*e-mail: Limbupasiriporn_j@su.ac.th

Abstract:

The complete multipartite graphs $K_{n_1,n_2,\ldots,n_r}$ where $n_1 \le n_2 \le \cdots \le n_r$ are disconnected graphs with vertex sets partitioned into r parts of cardinalities $n_1, n_2, \ldots, n_r$ and with adjacency defined by two vertices being adjacent if they belong to different parts. The binary codes obtained from the row spans of adjacency matrices of those graphs are $[n, r, n_1]_2$ if r is even and $[n, r-1, n_1+n_2]$ if r is odd, where $n = n_1 + n_2 + \cdots + n_r$, due to Seneviratne [P. Seneviratne, Codes from multipartite graphs and minimal permutation decoding sets, Discrete Math., Alg. and Appl., 7(4): 1550060:1-1550060:7 (2015).]

In this talk we examine bases of minimum-weight vectors for such codes and their duals including those for the case where $n_1 = n_2 = \cdots = n_r$. We show that the number of minimum-weigh codewords in the codes is equal to the number of components of the complements of the graphs of order n_1 if r is even and n_2 if r is odd. Further these codes has no bases of minimum-weight vectors provided that $n_r > n_1$ if r is even and that $n_r > n_2$ if r is odd.

B_025_OA: REGULARITY AND FINITENESS CONDITIONS ON TRANSFORMATION SEMIGROUPS WITH INVARIANT SETS

Saranya Phongchan,[1,*] Preeyanuch Honyam[2]

[1]PhD Degree Program in Mathematics, Faculty of Science, Chiang Mai University, Thailand
[2]Department of Mathematics, Faculty of Science, Chiang Mai University, Thailand
*e-mail: saranya_ph@cmu.ac.th

Abstract:

Let X be a nonempty set and $T(X)$ denote the semigroup (under composition) of transformations from X to itself. For a fixed nonempty subset Y of X, let $S(X,Y)=\{\alpha\in T(X):Y\alpha\subseteq Y\}$. Then $S(X,Y)$ is a semigroup of total transformations of X which leave a subset Y of X invariant. In this study, we consider the semigroup $S(X,Y)$ when X is finite or infinite. We characterize coregular elements of $S(X,Y)$ and find necessary and sufficient conditions for $S(X,Y)$ to be coregular. Moreover, we give necessary and sufficient conditions for $S(X,Y)$ to be unit regular and directly finite.

C_001_PA: EFFECTS OF SOLVENTS AND PEANUT SKIN ON ANTIOXIDANT CAPACITY AND PHENOLIC CONTENT OF VIRGIN COCONUT OIL

Phanuphong Wannapong, Prasan Swatsitang*

Department of Biochemistry, Faculty of Science, Khon Kaen University, Thailand
*e-mail: prasan@kku.ac.th

Abstract:

Virgin coconut oil (VCO) from *Cocos nucifera* L. is emerging as functional food oil. It gains popularity among people who are aware of health. Peanut skin is a by-produtct of peanut processing, and also known for greater value of phenolic compounds. Adding peanut skin to VCO might increase its antioxidant capacity. This study aimed to investigate the effect the solvents and peanut skin on antioxidant capacity and total phenolic content of VCO and VCO+peanut skin. VCO and VCO+peanut skin were extracted by 4 different solvents including hexane+ ethanol, ethanol, hexane+ methanol, and methanol. The phenolic content of the extracts was determined by Folin Ciocalteu assay. The antioxidant capacity of the extracts was analyzed by DPPH, ABTS and FRAP assays. The ethanol extract of VCO+peanut skin exhibited the greatest antioxidant capacity by giving the value of 12.07 ± 0.01 mg TE (trolox equivalent)/g oil determined by DPPH assay, the hexane+methanol extract of VCO+peanut skin showed the greatest antioxidant capacity by giving the value of 10.95 ± 0.01 mg TE/g oil determined by ABTS assay, and the methanol extract of VCO+peanut skin revealed the greatest antioxidant capacity by giving the value of 6,030.55 ± 16.69 µg TE/g oil determined by FRAP assay whereas the values of antioxidant capacity of VCO were 0.36 ± 0.002, 0.22 ± 0.002 and 319.96 ± 0.60 mg TE/g oil determined by DPPH, ABTS and FRAP assays, respectively. The methanol extract of VCO+peanut skin exhibited the greatest value of total phenolic content by giving the value of 7,402.57 ± 34.43 µg GAE (gallic acid equivalent)/g oil whereas that of VCO showed the value of 622.96 ± 38.27 µg GAE/g oil. All extracts of VCO+peanut skin exhibited greater values of antioxidant capacity and total phenolic content. Peanut skin could increase phenolic content and antioxidant capacity of VCO.

Keywords: Virgin coconut oil, Peanut skin, Antioxidant capacity, Phenolic content

C_002_OF: MOLECULAR CLONING AND PREDICTION OF ANTIGENIC DETERMINANTS OF 23 KDA INTEGAL MEMBRANE PROTEIN FROM *SCHISTOSOMA MEKONGI*

Kaisone Chanda[1,2], Wanwisa Peonsamut[1], Manaw Sangfuang[1], Yanin Limpanont[3], Charoonroj Chotwiwatthanakun[4], Present Sobhon[5], Narin Preyavichypudee[1,*]

[1]Faculty of Animal Sciences and Agricultural Technology, Silpakorn University, Phetchaburi IT Campus, Phetchaburi, Thailand
[2]Department of Veterinary Medicine, Faculty of Agriculture, National University of Laos, Vientiane Capital, Lao PDR
[3]Applied Malacology Unit, Department of Social and Environmental Medicine, Faculty of Tropical Medicine, Mahidol University, Bangkok, Thailand
[4]Mahidol University, Nakhonsawan Campus, Nakhonsawan, Thailand
[5]Department of Anatomy, Faculty of Science, Mahidol University, Ratchathewi, Bangkok, Thailand
*e-mail: jnnarin@hotmail.com

Abstract:

Schistosoma mekongi is one of the important human parasitic worms causing liver damage in South-east Asia. 23 kDa protein is an integral membrane protein of the blood fluke genus *Schistosoma* and its expressed in all parasite stages. In this study, we cloned the 23 kDa protein-encoding gene *(*Smek23*)* from *S. mekongi,* characterized and predicted immunogenic epitope of the protein. The partial cDNA encoding Smek23 was 686 bp. in size, and encoded a polypeptide containing 218 amino acid residues with the predicted molecular weight at 23.62 kDa. The alignment of the deduced Smek23 amino acid sequences showed the highest degree of identity with *S. turkestanicum* at 91.2*%* and its resembled epitope regions 111-KIDA-114, 125-DHP-127 and 150-PNDYKGSVPDSCKEGQVPYT-169 of Smek23 from *S. mekongi* based on hydrophilicity scale and recognized by B-cells. These regions could be the focused target for future diagnosis or vaccine development.

Introduction:

Schistosomiasis is a chronic debilitating disease caused by trematode flatworm of the genus *Schistosoma*, which affects more than 230 million people worldwide (1). In Asia, *Schistosoma mekongi* is endemic in Lao People's Democratic Republic (Lao PDR) and Cambodia, approximately 140,000 people are at risk of infection (2, 3). Praziquantel (PZQ) is the single drug for treatment against schistosomiasis. Due to its intensive large scale and repeated use of the same chemotherapeutic agent in the field, there is serious concern for the emerging of drug-resistant mutants of the parasite (4-6). Vaccine is an alternative strategy to combat against schistosomiasis, which may use alone or in combination with chemotherapeutic drugs could provide effective and sustainable strategy for long term controlling the transmission of the disease (7-9).

A 23 kDa transmembrane membrane protein is one of tetraspanin protein family (10). Its expressed in all stages of schistosome, including cercariae, lung-stage schistosomula, and adult worms (11-15). The 23-kDa membrane protein from *S. mansoni* (Sm23) and *S. japonicum* (Sj23) were shown to be promising immunogenic antigen for prophylaxis and immune-diagnosis. Sm23 is one of five major tegumental membrane proteins which elicits strong antibody response to schistosomiasis infection in mice, rats and human (16). The protein has been detected by all stages of human infected serum, especially the lung stage, and therefore this protein could be one of vaccine candidates (17). Besides, so the large hydrophilic domain (LHD) of recombinant Sj23 could induce protection against *S. japonicum* infection in various host including mice, sheep, cattle and buffalo (18, 19).

Prediction methods that define epitope which induce an effective immune response could provide a new strategy for elimination the pathogen (20). Therefore, this study focuses on predicting Smek23 B cell epitope which may provide a promising vaccine or immunodiagnostic target for future solution to eliminate schistosomiasis in endemic areas.

Methodology:

1. Cloning of Smek23 cDNA sequence

cDNA of the adult *S. mekongi* from research project "Development of Serodiagnosis for *Schistosoma mekongi* in Mice by Sandwich ELISA and Localization of Cathepsin B on the Worm" which was approved by Animal Care and Use Committee of Faculty of Tropical Medicine, Mahidol University (FTM-ACUC 023/2017) was amplified by PCR using the following set of primers: forward primer (5'-ATGGCGACTTTGGGTACTGGGATGA-3') and reverse primer (5'-GAGTAGTCCACACACACTACACTC-3'). The primer was designed from 23 kDa protein of *S. japonicum* mRNA (Genbank: M63706.1). The PCR was performed in 35 cycles at 94 ◦C for 30 s, 55 ◦C for 30 s and 72 ◦C for 90 s. The PCR product was ligated into the pGEM-T easy vector (Promega, USA) and the sequence confirmed by using the Capillary Electrophoresis Sequencing (CES) method (Macrogen, South Korea), the sequence reads from the forward reactions by used universal primer. The sequence was verified homology by using the basic local alignment search tool (BLAST).

2. Bioinformatics identification and characterization of Smek23

Smek23 DNA sequences generated from cDNA clones and the deduced protein sequences were subjected to search the nucleic acid and protein databases using BLASTN, BLASTP and BLASTX program (http://ww.ncbi.nih.gov/BLAST/). The multiple alignment of homologous sequences from closely related *Schistosoma* species were carried out by Clustal Omega program (https://www.ebi.ac.uk/Tools/msa/clustalo/). Neighbor-joining analysis (21) was performed by MEGA version X program (22) with bootstrap resampling 1000 repetitions (23). The Smek23 protein structural analysis was done by using TMpred, a program to predict transmembrane regions and their orientation (24).

3. Prediction of antigenic sites

In this research work, the potential hydrophilic antigenic epitopes of Smek23 were found out in order to identify the antigenic determinants. Antigenic epitopes are determined using several prediction methods, including Hopp and Woods (25); Welling et al. (26); HPLC/Parker et al. (27); Kolaskar & Tongaonkar antigenicity (28) and BepiPred Server (29).

Results and Discussion:

1. Cloning and sequencing of Smek23

The cDNA encoding Smek23 of adult *S. mekongi* was cloned by PCR. The nucleotide sequence of Smek23 was 686 bp in length. The nucleotide sequence of Smek23 showed an open reading frame encoding 23 kDa integral membrane protein containing 218 amino acids. The molecular weight of Smek23 which predicted from its constituent amino acids is 23.62 kDa (Figure 1). The primary amino acid sequence of Smek23 was determined for the presence of functional sites, the motifs were including: GAGAYVEVK, tyrosine kinase phosphorylation; ATLGTGMRC, threonine kinase phosphorylation; and EVKFSQYGA, DYKGSVPDS, and SVPDSCKEG, Serine kinase phosphorylation (Figure 1).

Figure 1.

Nucleotide and the deduced amino acid sequence of Smek23. The predicted start ATG and stop TAA codons are shown in underlined and bold face. Nucleotide residues are numbered in the left and amino acid residues in the right. Putative functional sites are threonine kinase phosphorylation (underlined); tyrosine kinase phosphorylation (boxed) and Serine kinase phosphorylation (dash line).

2. Bioinformatics identification and characterization of Smek23

The multiple alignment of deduced amino acid sequences of Smek23 with 23 kDa protein from related schistosome species *(*Genbank*:* P19331.1, AAA29900*.*1, AGA82198.1 from *S. mansoni*; AAC46959.1, AGA82213.1 from *S. haematobium*; P27591.1, AAA29920.1 from *S. japonicum;* AIA24557.1 from *S. turkestanicum:* AGA82218.1 from *S. bovis:* AGA82206.1 from *S. curassoni*; AGA82202.1 from *S. guineensis*; AGA82204.1 from *S. intercalatum*; AGA82201.1 from *S. margrebowiei* and AGA82199.1 from *S. rodhaini)*, showed in Figure 2*.* The Smek23 amino acid sequences showed the highest degree of identity with *S. turkestanicum* 23 kDa *(*GenBank*:* AIA24557*.*1*)* at 91*.*2*%.* The identity of Smek23 amino acid sequences with 23 kDa amino acid sequences from *S. mansoni (*Genbank*:* AAA29900*.*1*)*, *S. japonicum (*Genbank*:* AAA29920*.*1*)* and *S. haematobium (*Genbank*:* AAC46959*.*1*)* showed at 89*.*4, 88*.*0 and 87*.*6*%*, respectively*.* Phylogenetic analysis through the MAGA version X program *(*Neighbor Joining with 1,000 replicates*)* showed that Smek23 was closely related to *S. japonicum* 23 kDa *(*Figure 3*).* The transmembrane topology of Smek23 was predicted by using TMpred program *(*Figure 2*).* The putative domains of Smek23 fall within the transmembrane 4 superfamily *(*TM4SF*)* as follows*:* cytoplasmic domains, CYT 1 *(*position 1-16*)* 16 amino acids, CYT 2 *(*position 73-80*)* 8 residues, CYT 3 *(*position 206-218*)* 13 residues; extracellular domains, EXT 1 *(*position 37-55*)* 19 residues, EXT 2 *(*position 109-183*)* 75 residues; transmembrane domains, TM 1 *(*position 17-36*)* 20 residues, TM 2 *(*position 56-72*)* 17 residues, TM 3 *(*position 81-108*)* 20 residues, and TM 4 *(*position 184-205*)* 22 residues. The conservation of this domain structure with other 23 kDa proteins showed in *(*Figure 2*).*

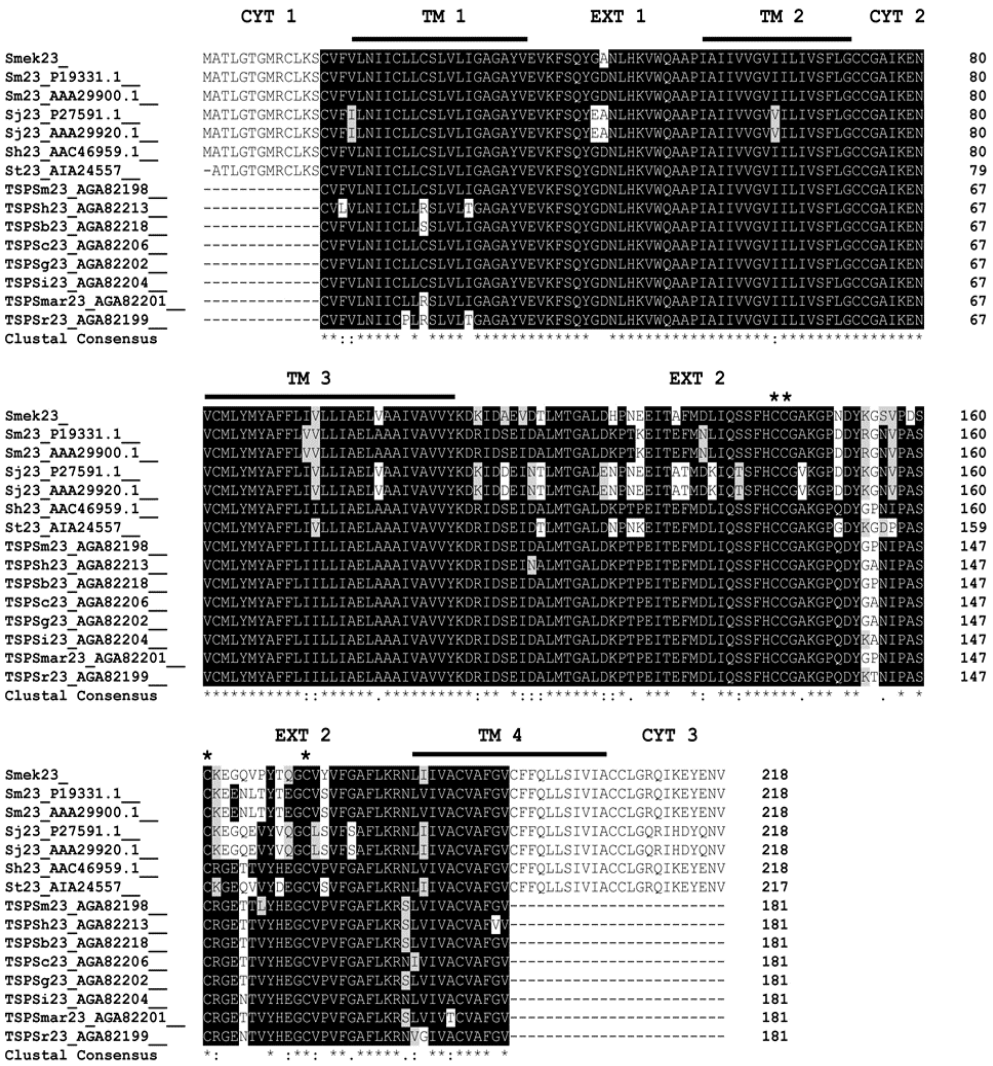

Figure 2.

Multiple sequences alignment of the deduced amino acid sequences of Smek23 with other Schistosome 23 kDa protein. The amino acid sequences of Smek23 with other 23 kDa protein sequences showing highly conserved amino acids by grey and black outlines. The asterisk *(*)* indicates identical amino acids, two dots *(:)* indicates conserved amino acid substitutions and dot *(.)* indicate semi-conserved amino acid substitutions. The cysteine residues involved in disulfide bonding is indicated by *(*)*. The TM4SF-like domains of Smek23 are indicated as follows*:* CYT 1 to 3, cytoplasmic domains; TM 1 to 4, transmembrane domains; EXT I and 2, extracellular domains. Smek*: Schistosoma mekongi*; Sm*: S. mansoni*; Sj*: S. japonicum*; Sh*: S. haematobium*; St*: S. turkestanicum*; Sb*: S. bovis*; Sc*: S. curassoni*; Sg*: S. guineensis*; Si*: S. intercalatum*; Smar*: S. margrebowiei*; Sr*: S. rodhaini.* Database accession numbers for the proteins aligned here: Sm23*:* P19331.1, AAA29900.1, AGA82198.1; Sh23*:* AAC46959.1, AGA82213.1; Sj23*:* P27591.1, AAA29920.1; St23*:* AIA24557.1*:* Sb23*:* AGA82218.1; Sc23*:* AGA82206.1; Sg23*:* AGA82202.1; Si23*:* AGA82204.1; Smar23*:* AGA82201.1; Sr23*:* AGA82199.1

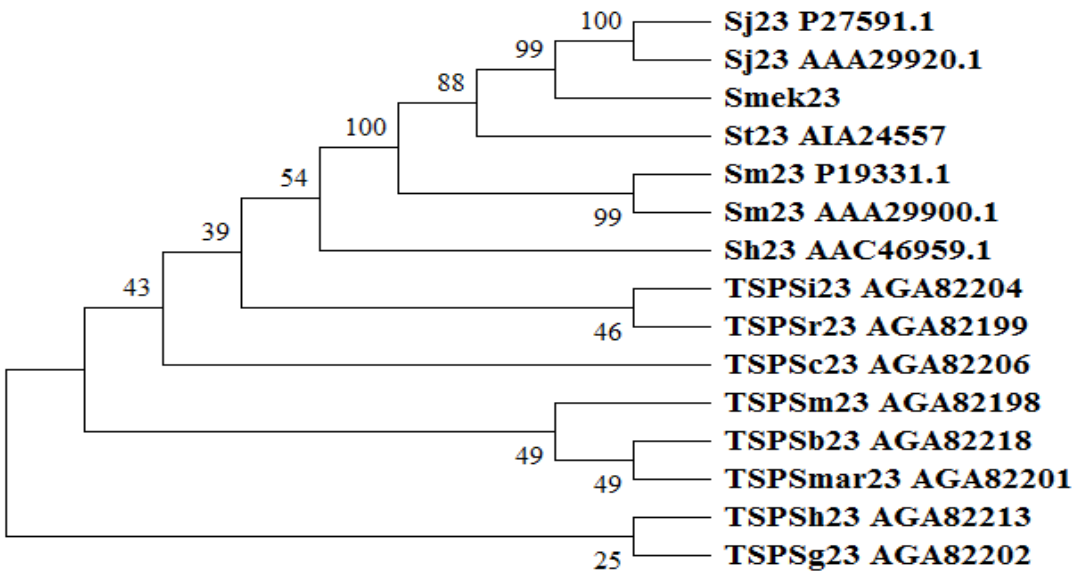

Figure 3.

The phylogenetic analysis of Smek23 was constructed by neighbor-joining method in MEGA X program**.** The percentage of replicate trees in which the associated taxa clustered together in the bootstrap test **(**1000 replicates**)** are shown next to the branches**.** The numbers at the branching point indicate percent bootstrap value**.** Branches corresponding to partitions reproduced in less than 50**%** bootstrap replicates are collapsed**.** Smek*: Schistosoma mekongi*; Sm*: S. mansoni*; Sj*: S. japonicum*; Sh*: S. haematobium*; St*: S. turkestanicum*; Sb*: S. bovis*; Sc*: S. curassoni*; Sg*: S. guineensis*; Si*: S. intercalatum*; Smar*: S. margrebowiei*; Sr*: S. rodhaini.* Database accession numbers for the phylogenetic analysis here*:* Sm23*:* P19331.1, AAA29900.1, AGA82198.1; Sh23*:* AAC46959.1, AGA82213.1; Sj23*:* P27591.1, AAA29920.1; St23*:* AIA24557.1*:* Sb23*:* AGA82218.1; Sc23*:* AGA82206.1; Sg23*:* AGA82202.1; Si23*:* AGA82204.1; Smar23*:* AGA82201.1; Sr23*:* AGA82199.1

3. Determination of antigenic peptides

In the present study, we use five methods including, Hopp and Woods, Welling, Parker, Kolaskar and Tongaonkar and BepiPred Server, to predict the possible antigenic epitope region in 23 kDa protein of the human blood fluke *S. mekongi*. By analyzing graphical and numerical data, it was found that according to Hopp and Woods scale the regions 9-10, 76-79, 109-119, 125-130, 132-133, 147-166, 209-214 contained the potential hydrophilic regions (Hydrophilicity: score > 0). The analysis found high in position between 109-119 (Maximum Score 1.578) in a protein, which present in extracellular domain 2 (EXT 2), assuming that this antigenic region would be presented on the protein surface and thus would be placed in hydrophilic regions (Figure 4A).

In the Welling et al. antigenicity plot gives value as the log of the quotient between percentage in average proteins and percentage in a sample of known antigenic regions, the predicted hydrophilic regions were 36, 38, 44-53, 97-98, 101-108, 109-115, 125-127,150-151, 156, 158. The data found high in extracellular domain 1 (EXT 1) in position 44-53 (Maximum Score 0.702) (Figure 4B).

We also study the hydrophobicity plot of HPLC/Parker and the predicted hydrophilic regions were 5-11, 33-36, 37-46, 48-50, 72, 75-79, 107-108, 109-119, 120-133, 137, 139-140, 142-171, 173-174, 209-214. The highest peak is found high in extracellular domain 2 (EXT 2) in position between 143-171 (Maximum Score 5.157) (Figure 4C).

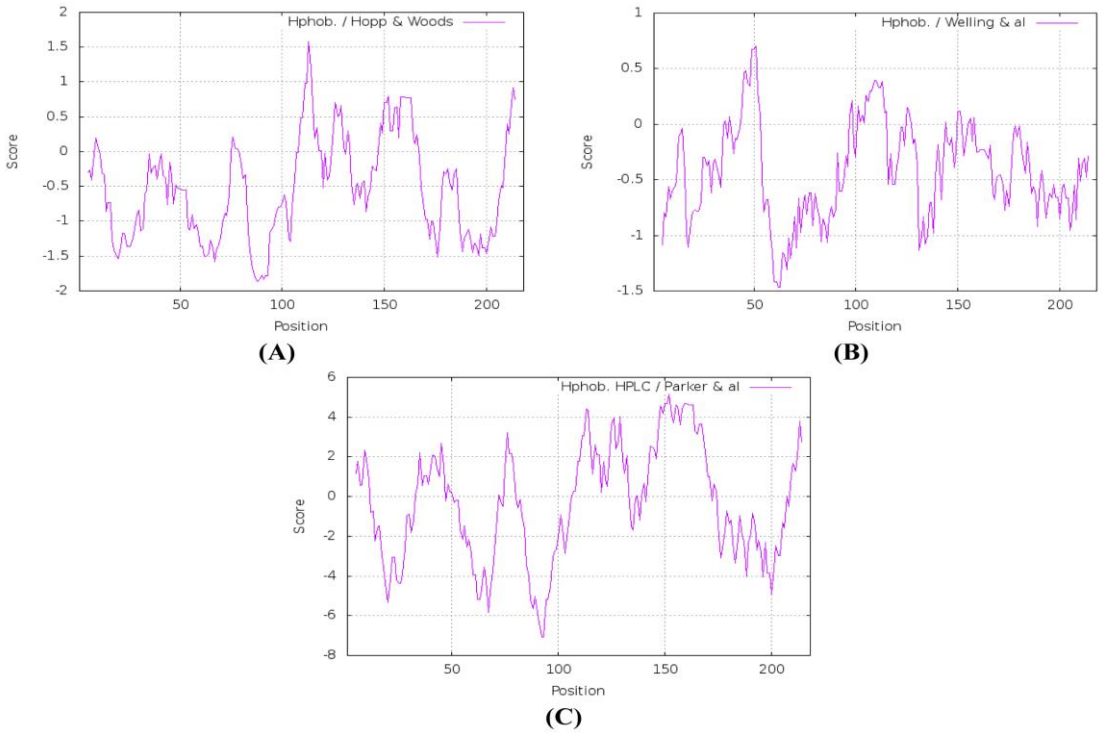

Figure 4.

Graphical representation of antigenic peptide evaluation by Hopp and Woods **(**A**)** Welling et al**.** ***(***B***)*** and HPLC**/**Paker et al**. (**C**)**

According to Kolaskar and Tangaonkar antigenicity scale, at 1**.** 1 as the threshold level, the most likely antigenic determinants were at 11- LKSCVFVLNIICLLCSLVLI- 30, 56- IAIIVVGVIILIVSFLGCCGA- 76, 90- FLIVLLIAELVAAIVAVVYK- 109, 169- TQGCVYVF G- 177, 186- IVACVAFGVCFFQLLSIVIACCLG- 209 ***(*** Figure 5A***) .*** BepiPred predicts the location of linear B-cell epitopes result found that between 147-169 is 147-AKGPNDYKGS VPDSCKEGQVPYT-169 and the maximum score ***(***1.999***)*** is found at the position 152 ***(***Figure 5B***).***

Prediction of immunogenic region which exposed on the surface of the protein is a necessary step for epitope-based vaccine design**.** In this study, the hydrophilic regions of Smek23 proteins which are supposed to be antigenic and exposed to the surface of the protein were identified for antigenic determinants**.** The overlapping sequences of prediction epitopes have been summarized in Table 1**.** There were three major overlapping regions which were hit by all programs ***(***Hopp & Woods; Welling, Parker and BepiPred***).*** These regions were 111-KIDA-114, 125-DHP-127 150-PNDYKGSVPDSCKEGQVPYT-169**.** All of these three regions were located in extracellular domain 2 ***(***EXT 2***)***, which is a large hydrophilic domain ***(***LHD***)*** of Smek23 molecule**.** The large hydrophilic domain from *S. japonicum* has been reported to be one of potential candidate vaccine antigens**.** Zhu, Fu ***(***30***)*** demonstrated that large hydrophilic domain of Sj23 induced 54**.**3-58**.**8**%** protection against the infection in mice ***(***30***).*** Similar results have been reported by Shi, Zhang ***(***18***)*** and Shi, Zhang ***(***19***)*** they showed that the recombinant protein of *S. japonicum* 23 kDa and its large hydrophilic domain ***(***LHD***)*** could produce protection against *S. japonicum* infection in mice, sheep, cattle and buffalo**.** Furthermore, Wang, Krai ***(***31***)*** demonstrated that antibody responses to the Sj23HD antigen could be monitored for early detection of schistosome infection in mice by immunoblotting and ELISA ***(***31***).*** Li, Wang ***(***32***)*** also demonstrated that large hydrophilic domain ***(***LHD***)*** of Sj23 molecule could use as antigen for immunodiagnosis by ELISA for *S. japonicum* infection in cattle**.**

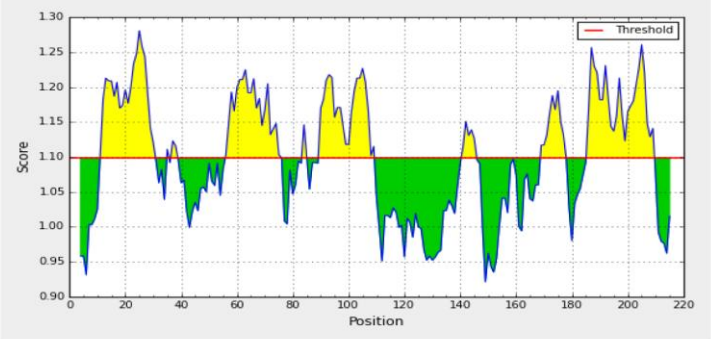

(A) Kolaskar and Tongaonkar antigenicity

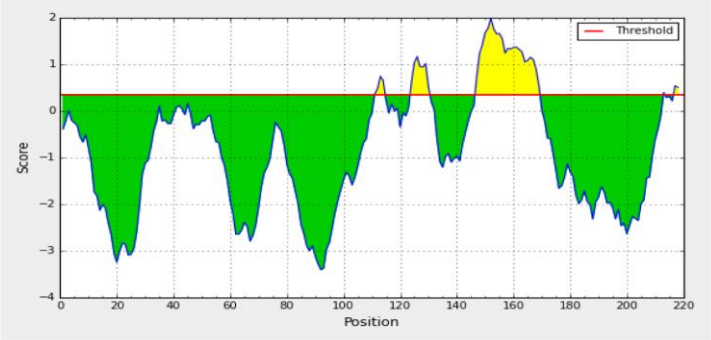

(B) Bepipred Linear Epitope Prediction

Figure 5.

Graphical representation of antigenic peptide evaluation by *(A)* Kolaskar and Tongaonkar Antigenicity for Smek23 *(B)* Bepipred Linear Epitope Prediction for Smek23

Table 1

The potential hydrophilic regions and epitope prediction sites from Hopp & Woods, Welling et al., Parker et al., Kolaskar & Tongaonkar and BepiPred programs.

TM4SP	Hopp & Woods	Welling et al.	Parker et al.	Kolaskar & Tongaonkar	Bepipred
CYT 1 (1-16)	9-10		5-11	11-30	
TM 1 (17-36)		36	33-36		
EXT 1 (37-55)		38, 44-53	37-46, 48-50		
TM 2 (56-72)			72	56-76	
CYT 2 (73-80)	76-79		75-79		
TM 3 (81-108)		97-98, 101-108	107-108	90-109	
EXT 2 (109-183)	109-119,	109-115	109-119		111-114
	125-130, 132-133	125-127	120-133		124-130
			137, 139-140		
	147-166	150-151, 156, 158	142-171, 173-174	169-177	147-169
TM 4 (184-205)				186-209	
CYT 3 (206-218)	209-214		209-214		213

Conclusion:

We characterized and predicted immunogenic epitope of transmembrane protein Smek23. The partial of cDNA encoding Smek23 was 686 bp and its encoded for 218 amino acid with the predicted molecular weight at 23.62 kDa. The alignment of the deduced Smek23 amino acid sequences showed a highest degree of identity with *S. turkestanicum* at 91.2% and its resembled *S. mansoni*, *S. haematobium*, and *S. japonicum* with similarity at 87.6-89.4%. We predicted three immunogenic epitopes based on hydrophilicity scale and recognized by B-cells: 111- KIDA- 114, 125- DHP- 127 and 150- PNDYKGSVPDSCKEGQVP YT-169. They were located in a part of extracellular domains. Fragment identified through this approach tend to be high immunogenic and was a promising antigen for diagnosis and immuno-prophylaxis.

Acknowledgements:

This research work was financially supported by the under The Thailand International Postgraduate Program under Thailand international development cooperation agency (TICA). Similarly, it was supported by grants and laboratories of the Faculty of Animal science and Agriculture technology, Silpakorn University, Phetchaburi IT Campus.

References:

1. Colley DG, Bustinduy AL, Secor WE, King CH. Lancet. 2014;383(9936):2253-2264.
2. Phongluxa K, van Eeuwijk P, Soukhathammavong PA, Akkhavong K, Odermatt P. Acta Trop. 2015;141:281-288.
3. Urbani C, Sinoun M, Socheat D, Pholsena K, Strandgaard H, Odermatt P, et al. Acta Trop. 2002;82(2):157-168.
4. Coles GC. Acta Trop. 1989;5(7):214.
5. Coles GC, Kinoti GK. Acta Trop. 1997;13(4):157-158.
6. Geerts S, Coles G, Gryseels B. Acta Trop. 1997;13(4):149-151.
7. Botros S, Sayed H, Amer N, El-Ghannam M, Bennett JL, Day TAJIJfP. Int J Parasitol. 2005;35(7):787-791.
8. Doenhoff MJ, Pica-Mattoccia LJEroa-it. 2006;4(2):199-210.
9. Fonseca CT, Braz Figueiredo Carvalho G, Carvalho Alves C, de Melo TT. J Parasitol Res. 2012;3:541268.
10. Gaugitsch HW, Hofer E, Huber NE, Schnabl E, Baumruker TJEjoi. 1991;21(2):377-383.
11. Harn DA, Mitsuyama M, Huguenel ED, David JR. J Immunol. 1985;135(3):2115-2120.
12. Oligino LD, Percy AJ, Harn DA. Molecular and biochemical parasitology. 1988;28(2):95-103.
13. Jiang N, Cai P, Yin J, Hao L, Lu H, Wang X, et al. Acta Trop. 2010;116(1):9-14.
14. Tran MH, Pearson MS, Bethony JM, Smyth DJ, Jones MK, Duke M, et al. Nat Med. 2006;12(7):835-840.
15. Cai P, Bu L, Wang J, Wang Z, Zhong X, Wang H. Biochem Biophys Res Commun 2008;372(1):197-202.
16. Krautz-Peterson G, Debatis M, Tremblay JM, Oliveira SC, Da'dara AA, Skelly PJ, et al. PLoS Negl Trop Dis. 2017;11(1):e0005306.
17. Reynolds S, Shoemaker C, Harn D. Res J Immunol. 1992;149(12):3995-4001.
18. Shi F, Zhang Y, Ye P, Lin J, Cai Y, Shen W, et al. Vaccine. 2001;20(3-4):462-467.
19. Shi F, Zhang Y, Lin J, Zuo X, Shen W, Cai Y, et al. Vaccine. 2002;20(31-32):3629-3631.
20. Shah K, Chaubey P, Mishra N. Indian J Biotechnol. 2010;9(4):351-359.
21. Saitou N, Nei M. Mol Biol Evol. 1987;4(4):406-425.
22. Kumar S, Stecher G, Li M, Knyaz C, Tamura K. Mol Biol Evol. 2018;35(6):1547-1549.
23. Felsenstein J. Mol Biol Evol. 1985;39(4):783-791.
24. Hofmann K. Biol Chem Hoppe-Seyler. 1993;374:166.
25. Hopp TP, Woods KR. Proc Natl Acad Sci USA. 1981;78(6):3824-3828.
26. Welling G, Weijer W, van der Zee R. FEBS Lett.188:215-218.
27. Parker J, Guo D, Hodges R. Biochemistry. 1986;25(19):5425-5432.

28. Kolaskar A, Tongaonkar PC. FEBS letters. 1990;276(1-2):172-174.
29. Larsen JEP, Lund O, Nielsen M. Immunome research. 2006;2(1):2.
30. Zhu Z, Fu Z, Zhang M, Han Y, Hong Y, Li D, et al. Parasite Immunol. 2012;34(6):341-344.
31. Wang F, Krai P, Deu E, Bibb B, Lauritzen C, Pedersen J, et al. Mol Biochem Parasitol. 2011;175(1):10-20.
32. Li Y, Wang L, Fang R, Nie H, Zhou Y, Zhao J, et al. Vet Parasitol. 2012;188(3-4):247-254.

C_003_PA: PROPICONAZOLE APPLICATION ATTENUATES PLANT RESPONSES TO NITROGEN AND PHOSPHORUS DEFICIENCY IN RICE

Kewalee Jantapo [1,2], Sompop Pinit [1,2], Lili Zhou [3], Wenfei Wang [3], Juthamas Chaiwanon [2,*]

[1]Program in Biotechnology, Faculty of Science, Chulalongkorn University, Bangkok, 10330, Thailand
[2]Center of Excellence in Environment and Plant Physiology, Department of Botany, Faculty of Science, Chulalongkorn University, Bangkok, 10330, Thailand
[3]Fujian Provincial Key Laboratory of Agroecological Processing and Safety Monitoring, College of Life Sciences, Fujian Agriculture and Forestry University (FAFU), Fuzhou 350002, China
*e-mail: juthamas.c@chula.ac.th

Abstract:

Propiconazole (PPZ) is one of the most widely used systemic fungicides in many crop plants. The increased and repeated use of the fungicides in agricultural fields potentially leads to the increased contamination in the environments. Plants have evolved diverse mechanisms to sense the availability of nutrients in the soil and undergo adaptation at morphological, physiological and transcriptional levels. Here, the interaction of PPZ and nitrogen (N) and phosphorus (P) deficiency was investigated in rice seedlings grown under laboratory conditions. PPZ-treated plants showed retarded growth and biomass reduction. Moreover, N and P contents were lower under deficient conditions. N and Pi transporter genes were also suppressed by PPZ treatments under N- and P- deficient conditions. These results suggested that PPZ contamination in the environment could restrain plant growth and adaptation responding to both N and P deficiency, which could reduce foraging capacity of plants to find available nutrients in the soil.

C_004_PF: EXPRESSION ANALYSIS OF GENES ENCODING GLUTATHIONE S-TRANSFERASE UNDER STRESS CONDITIONS IN THE EXTREMOPHILE *Halothece* sp. PCC7418

Chananwat Kortheerakul[1], Hakuto Kageyama[2,3] and Rungaroon Waditee-Sirisattha[1,*]

[1] Department of Microbiology, Faculty of Science, Chulalongkorn University, Pathumwan, Bangkok, Thailand
[2] Graduate School of Environmental and Human Sciences, Meijo University, Nagoya, Aichi 468-8502, Japan
[3] Department of Chemistry, Faculty of Science and Technology, Meijo University, Nagoya, Aichi 468-8502, Japan
*e-mail: rungaroon.w@chula.ac.th

Abstract:

Glutathione s-transferase (GST) superfamily is a set of enzymes that involved in multicellular processes. They are essential for cellular detoxification and adaptation against drugs, xenobiotic substrates, pollutants or even harsh environments. Nowadays, GSTs have been identified and extensively studied in many aspects, such as molecular structures, physiological roles and biotechnological applications. Among GST superfamilies, cytosolic GST is the most diverse group and plays various physiological roles in cells, such as stress tolerance, cellular apoptosis, secondary metabolite transportation and antibiotic resistance. Discovery of novel GST is therefore challengeable. In this study, we analyzed GSTs from the extremophile *Halothece* sp. PCC7418 as well as GST orthologs from extremophilic cyanobacteria whose genomic sequences are available in KEGG database. Phylogenetic analysis revealed that four putative *Halothece* GSTs (PCC7418_0647, PCC7418_0729, PCC7418_1478, and PCC7418_3557) were in the different clades**.** Furthermore, gene expression analysis of four putative GST encoding genes in *Halothece* sp. PCC7418 was performed under salt-, oxidative-, and combined stresses. PCC7418_3557 was found to be the most robustly induced gene under our tested conditions. This GST has homology with the Zeta class GST which typically exerts glutathione-dependent peroxidase activity.

Introduction:

Glutathione s-transferase (GST) superfamily is a set of enzymes that involved in multicellular processes. They involved in cellular detoxification and adaptation against drugs, xenobiotic substrates, pollutants or even harsh environments. Based on subcellular localization, GST can be divided into four superfamilies. These are cytosolic GST, mitochondrial GST, microsomic membrane-associated proteins in eicosanoid and glutathione metabolism (MAPEG) and fosfomycin resistance protein[15]. Among these superfamilies, cytosolic GST is the most diverse group. To date, 19 subclasses of cytosolic GSTs were reported. These include Alpha-, Beta-, Delta-, Epsilon-, Zeta-, Eta-, Theta-, Iota-, Lambda-, Mu-, Nu-, Xi-, Pi-, Rho, Sigma-, Tau-, Phi-, Chi- and Omega-class GSTs. Considerable evidence has shown that cytosolic GST plays various physiological roles, such as stress tolerance, cellular apoptosis, secondary metabolite transportation and antibiotic resistance[12].

Enzymatic mechanism of GST is known by catalyzing the conjugation reaction between glutathione and xenobiotic substrates to form the conjugated products. Consequently, these products become less reactivity, more soluble and more stable[14]. Additionally, GST is associated with other detoxification enzymes, such as glutathione peroxidase (GPX), superoxide dismutase (SOD) and catalase (CAT), to eliminate different types of toxicants step-by-step from cells. Finally, these responsive mechanisms induce morphological and physiological adaptations against biotic- and abiotic stress conditions[14].

Cyanobacteria, an enormously diverse group of prokaryotes, are oxygenic phototrophs that ubiquitously inhabit our planet. Some of them are known as extremophiles which can thrive under extreme environments encompassing vastly diverse terrains, such as hypersaline lakes, hot springs, deserts, and polar regions [1,4,7]. Based on KEGG database (https://www.genome.jp/kegg/kegg2.html), there are at least 10 extremophilic cyanobacteria whose genomic sequences are available. These include thermophilic cyanobacteria (*Thermosynechococcus elongatus* and *Gloeobacter kilaueensis*), halophilic cyanobacteria (*Dactylococcopsis salina, Halothece* sp. PCC7418, and *Euhalothece natronophila*), xerophilic cyanobacteria (*Gloeocapsa* sp. PCC7428, *Gloeothece verrucosa* and *Gloeobacter violaceus* PCC7421), a psychrophilic cyanobacterium (*Geitlerinema* sp. PCC7407) and an alkaliphilic cyanobacterium (*Arthrospira platensis*). In this study, we analyzed GSTs from *Halothece* sp. PCC7418 in comparison with ten strains of extremophilic cyanobacteria. *Escherichia coli* K12 was used as a representative member of mesophilic bacteria. Furthermore, gene expression analysis of four putative GST encoding genes in *Halothece* sp. PCC7418 was performed under salt stress (2M NaCl), and under oxidative stress (H_2O_2) as well as the combined stresses (2M NaCl+H_2O_2). Results obtained from this study would be the key to understand cellular detoxification and adaptation under stress condition of extremophilic cyanobacteria, and might be applied in biotechnology approaches in the future.

Methodology:

Phylogenetic analysis

The amino acid sequences of four putative GST encoding genes in *Halothece* sp. PCC7418 and 67 orthologs from extremophilic cyanobacteria were obtained from KEGG database (https://www.kegg.jp). In this analysis, extremophilic cyanobacteria include *Dactylococcopsis salina, Euhalothece natronophila, Thermosynechococcus elongatus, Rivularia* sp. PCC7116*, Acaryochloris marina, Halomicronema hongdechloris, Prochlorococcus marinus, Gloeocapsa* sp. PCC7428, *Stanieria* sp. NIES-3757 and *Pleurocapsa* sp. PCC7327. *Escherichia coli* K12 GST was used as the representative member of mesophilic bacteria. The alignment and phylogenetic tree reconstructions were conducted using MEGA7 program[5]. The alignment was performed with MUSCLE method[3]. The tree was constructed using neighbor-joining method[13].

Strain, culture condition and stress treatments

Halothece sp. PCC7418 was cultured in blue-green medium (BG-11) supplemented with Turk Island salt solution containing 0.5 M NaCl[16], under continuous white fluorescent light (950-1,000 lux) with shake at room temperature (28.0±2°C). The cell growth was measured via the absorbance at 730 nm (OD_{730}) using a UV-240 spectrophotometer (Shimadzu, Japan). For salt-stress treatment, *Halothece* sp. PCC7418 cells were cultured in BG-11 medium supplemented with Turk Island solution (0.5M NaCl) until the cells reached the exponential phase ($OD_{730} \approx$ 0.7-0.9). The cells were then harvested and transferred into fresh media containing 2.0 M NaCl. Cells were harvested at the indicated times for RNA extraction. For oxidative-stress treatment, cells were cultured as same as salt stress treatment. When the cells reached exponential phase, they were harvested and transferred into fresh media containing 0.5 M NaCl supplemented with indicated H_2O_2 concentrations. The control cells were cultured in BG-11 medium (0.5 M NaCl) without addition of H_2O_2. The cells were subjected to oxidative stress for 6 hours. Stressed cells were harvested for RNA extraction. For combined-stress treatment, cells were cultured in normal condition (0.5 M NaCl) until exponential phase, as same as previous treatments. Then, they were harvested and cultured to new media containing 2.0 M NaCl together with indicated H_2O_2 concentrations. The cells were subjected to this combined stresses for 6 hours before RNA extraction. The control cells were cultured in BG-11 medium (2M NaCl) without addition of H_2O_2.

RNA extraction and cDNA conversion

Total RNA was extracted from control and the stressed cells, using TRIzol® reagent (Invitrogen, USA) according to the manufacturer's instructions. RNA concentration and quality were determined using a Nanodrop 2000 (Thermo Scientific, USA) and gel electrophoresis, respectively. For cDNA synthesis, 2000 ng of total RNA was reverse transcribed using a SuperScript®III First-Stranded synthesis kit (Invitrogen, USA) according to the manufacturer's instructions.

Gene expression analysis

Specific primer pairs for four putative *Halothece* GSTs were designed with PerlPrimer software, version 1.1.21 (https://perlprimer.sourceforge.net/). A specific primer pair that amplified the *AprnpB* gene was used as an internal control[11]. Semi-quantitative RT-PCR analysis was conducted to examine transcriptional levels of genes encoding GST in *Halothece* sp. PCC7418 after treating with stresses. The PCR products were electrophoresed on a 1.2% (w/v) agarose gel. Relative intensity was quantified using Image Lab™ 3.0 software (https://www.bio-rad.com/en-ch/product/image-lab-software). The statistical difference was assessed with a Student's t-test or one-way ANOVA using SPSS software (https://www.ibm.com/analytics/spss-statistics-software).

Results and Discussion:

Phylogenetic analysis

A phylogenetic tree of four putative GST from *Halothece* sp. PCC7418 and 67 orthologs was constructed (Figure 1). Additionally, the GST from *E. coli* K12 was also employed as a representative member of mesophilic bacteria. The tree revealed the diversity of four *Halothece* GSTs. They were distributed in different clades of the tree. For instance, PCC7418_0647 had the highest homology with GST from *Dactylococcopsis salina* (Dacsa_2391), with 18% amino acid sequence identity. Moreover, it is also closed to GST from *Thermosynechococcus elongatus* (tlr0207), which was classified as a novel Chi-class GST[17]. However, it had only 17% amino acid identity between these two GSTs. PCC7418_0729 had the highest homology with *D. salina* GST (Dacsa_2853), with approximately 77% sequence identity. PCC7418_1478 shares the highest homology with GST from *Euhalothece natronophila* (FRE64_15440), with 65% sequence identity. Lastly, PCC7418_3557 shares the highest homology with *D. salina* GST (Dacsa_1405), with 87% amino acid identity. In addition, it also shares high homology to GST from *Prochlorococcus marinus* (Pro_0130), which was classified as Zeta-class GST[2], with 37% amino acid identity. From the database search suggests that both *D. salina* and *Euhalothece* sp. are regarded as halophilic cyanobacteria. To classify GST, cytosolic GSTs within the same class should share more than 40% identity at amino acid level[8]. Thus, these results only implicate that PCC7418_0647 whose closest Chi-class GST homolog. For PCC7418_3557, this protein is closest Zeta-class GST homolog. In contrary, PCC7418_0729 and PCC7418_1478 are not related to any known GST classes. It should be noted that phylogenetic tree is one of informative tools. For further classification, the specific enzyme activity, xenobiotic substrate and protein-protein interaction should be considered[10].

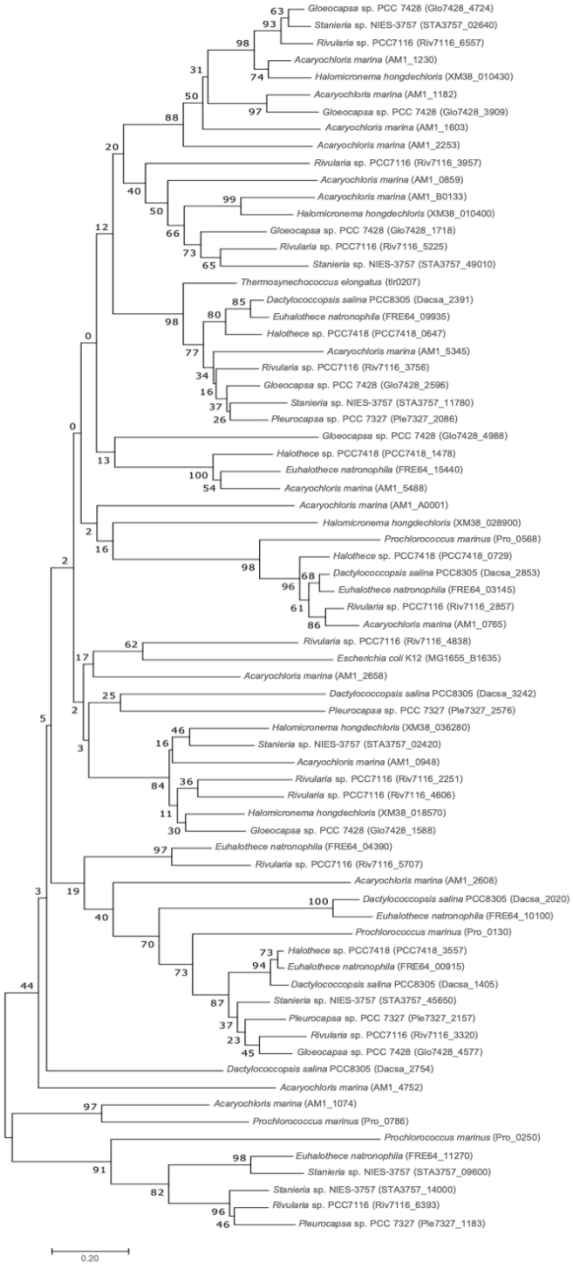

Figure 1

Phylogenetic tree of *Halothece* GSTs and cyanobacterial orthologs. The amino acid sequences of *Halothece* GST and all orthologs were retrieved from the KEGG database. The tree was generated with the neighbor joining method, with the 300 replicates bootstrap. The tree was presented with the microorganism name followed by the accession number of each sequence. The bars represent evolutionary distance. The scale bar comprises 0.2 expected changes per amino acid site (0.2 substitutions/site). Bootstrap probabilities are shown at the nodes.

Reversed Transcription-Polymerase Chain Reaction (RT-PCR)

Total RNA extracted from all treatments were analyzed for RNA integrity and concentrations. We obtained high quality of RNA (data not shown). Total RNA was further converted into cDNA. Thereafter, gene expression was performed by using semiquantitative RT-PCR with specific primers for each GST encoding gene. Under salt-stress condition, PCC7418_3557 was significantly up-regulated (Figure 2a). The highest level was observed after treating with 2M NaCl for 6 hours (11.19±3.2 folds). PCC7418_0647 was slightly up-regulated at 6 hours, however; it turned to be significantly down-regulated at 12 and 24 hours. Lastly, PCC7418_0729 was

drastically up-regulated from 6 to 24 hours. For oxidative-stress condition, there are four H_2O_2 concentration used to induce stress: 0, 0.9, 1.8 and 2,7 mM, (control, half of IC_{50}, IC_{50} and over IC_{50}, respectively). PCC7418_0647 exhibited significantly up-regulated when treating with 0.9mM H_2O_2. The highest transcriptional level obtained from the treated concentration of 1.8mM H_2O_2 (4.34±0.5 folds) (Figure 2b). PCC7418_0729 was up-regulated at the treated concentration of 1.8mM H_2O_2 whereas PCC7418_3557 was significantly up-regulated at two treated concentrations (1.8 and 2.7 mM H_2O_2). Lastly, for the combined stresses, all genes except for PCC7418_1478 were up-regulated in different manners (Figure 2c). These results revealed the different gene expression profiles of *Halothece* GSTs under salt and oxidative stresses. Under salt stress, the genes involved in cellular detoxification might be expressed in various kinds, some genes were up-regulated and some genes were down-regulated, but all together resulted in cellular adaptation and homeostasis[6]. In contrast, the effects of oxidative stress were more severe than salt stress. Absorption of hydroperoxide directly cause the accumulation of ROS. Some GST classes possess glutathione-dependent peroxidase activity, the detoxification mechanism against hydroperoxide compound using glutathione conjugation. PCC7418_0647 and PCC7418_3557 both behaved the up-regulated expression patterns under oxidative stress induced by H_2O_2. As shown from phylogenetic tree (Figure 1), these two gene were close to the representative members of Chi- and Zeta-class GSTs in which possess peroxidase activity[9]. It should be noted that PCC7418_1478 did not express under our conditions tested (Figure 2). The plausible reasons are as follows (1) transcriptional level of PCC7418_1478 is extremely low even under non-stressed condition; (2) this gene is a silent gene that may requires special stimulus to induce this gene expression[8].

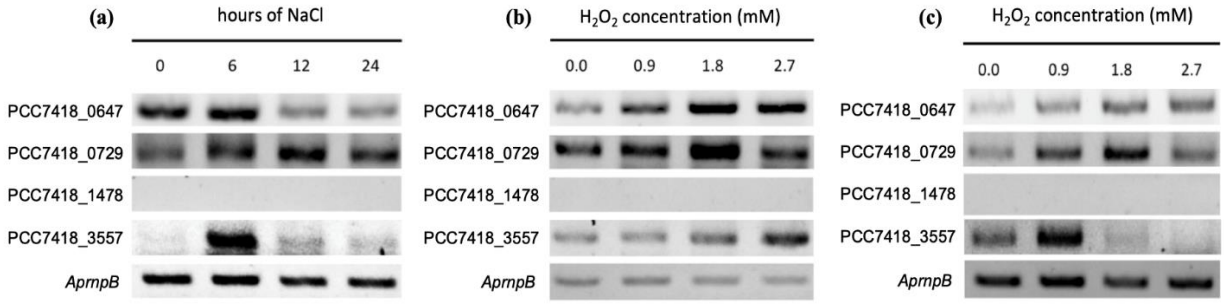

Figure 2

Expression level of *Halothece* GSTs which analyzed by RT-PCR and electrophoresed onto 1.2% (w/v) agarose gel: (a) under salt stress condition, (b) under H_2O_2 induced oxidative stress, and (c) under combined stress (2M NaCl+varied H_2O_2 concentration). Specific primer pair that amplified the *AprnpB* gene was used as an internal control.

Conclusion:

GST is one of essential enzymes for cellular detoxification and adaptation under stress. The phylogenetic analysis indicated that four *Halothece* GSTs are diversed. PCC7418_0647 and PCC7418_3557 are closed to Chi-class and Zeta-class GST, respectively. These two GST were up-regulated under oxidative stress. Thus, they possibly exert glutathione-dependent peroxidase activity. Moreover, PCC7418_3557 in which up-regulated under both salt- and oxidative stresses might be the most crucial gene for survival under stress environment.

Acknowledgements:

This work was gratefully supported by the Scholarship from the Graduate School, Chulalongkorn University to commemorate the 72nd anniversary of his Majesty King Bhumibol Adulyadej.

References:

1. Amarouche-Yala S, Benouadah A, El Ouahab Bentabet A, López-García P. Extremophiles. 2014;18(6):1035-1047.
2. Dufresne A, Salanoubat M, Partensky F, Artiguenave F, Axmann IM, Barbe V, Duprat S, Galperin MY, Koonin EV, Le Gall F, Makarova KS, Ostrowski M, Oztas S, Robert C, Rogozin IB, Scanlan DJ, Tandeau de Marsac N, Weissenbach J, Wincker P, Wolf YI, Hess WR. Proc Natl Acad Sci USA. 2003;100(17):10020-5.
3. Edgar RC. Nucleic Acids Res. 2004;32(5):1792–1797.
4. Hagemann M. FEMS Microbiol Rev. 2011;35(1):87-123.
5. Kumar S, Stecher G, Tamura K. Mol. Biol. Evol. 2015;33:1870-1874.
6. Laloknam, S. J Res Unit Sci Technol Environ Learning. 2011;2(1):82-88.
7. Nadeau T, Castenholz RW. J Phycol. 2000;36:914-923.
8. Ochi K. J antibiont. 2017;70:25–40.
9. Pandey T, Chhetri G, Chinta R, Kumar B, Singh DB, Tripathi T, Singh AK. FEBS Open Bio. 2015;5:1-7.
10. Pandey T, Shukla R, Shukla H, Sonkar A, Tripathi T, Singh AK. Int J Biol Macromol. 2017;94:378-385.
11. Patipong T, Hibino T, Kageyama H, Waditee-Sirisattha R. Extremophiles. 2020;24:377-389.
12. Perperopoulou F, Pouliou F, Labrou NE. Crit Rev Biotechnol. 2018;38(4):511- 528.
13. Saitou N, Nei M. Mol. Biol. Evol. 1987;4:406-425.
14. Singh PK, Wang W, Shrivastavae AK. Aquat Toxicol. 2018;202:36-45.
15. Theoharaki C, Chronopoulou E, Vlachakis D, Ataya FS, Giannopoulos P, Maurikou S, Skopelitou K, Papageorgiou AC, Labrou NE. Funct Integr Genomic. 2019;19(1):112.
16. Waditee-Sirisattha R, Kageyama H, Sopun W, Tanaka Y, Takabe T. Appl Environ Microbiol. 2014;80(5):1763-1769.
17. Wiktelius E, Stenberg G. Biochem J. 2007;406(1):115–123.

C_005_PA

C_005_PA: RE-DESIGNING OF LOW-COST GEL ELECTROPHORESIS AS HIGH SCHOOL INSTRUCTIONAL MEDIA

Thanasin Chalermchat,[1] Peeradon Tumstan, Punnapat Ashariyapakorn[1], Jatuporn Puntree,[1] Orawan Piyaboon,[1]*

[1]Department of Biology and Health Science, Mahidol Wittayanusorn School, Nakhon Pathom, Thailand
*email: orawan.piy@mwit.ac.th

Abstract:

Gel electrophoresis is a standard method to separate and analyze biomolecules. This method is widely used in many ways including as a high school biomolecular instructional media but its price is expensive. As the price comparison in 2019, from the standard model that this study was based on, the price of normal gel electrophoresis including its gel plate were around 30,000 Baht. While our planned gel electrophoresis will have the theoretical cost celling of around 5,000 Baht. The objective of this study was to design and build a low-cost gel electrophoresis system as a high school instructional media. An electrophoresis system was composed of gel electrophoresis components and a power supply. The gel electrophoresis was designed in separated components, gel electrophoresis chamber with the size 60 x 60 x 5 millimeters, and a tray and comb with a size of 5.5 x 6 millimeters were built. Furthermore, the power supply was designed and assembled composing of electric gadgets and its covering. Then, the efficiency of both power supplies from standard gel electrophoresis and the prototype were compared. Statistically, voltages from both of them had no significant difference. And the distances of DNA bands from both standard gel electrophoresis and the prototype were compared. Statistically, the distances from both of them had no significant difference.

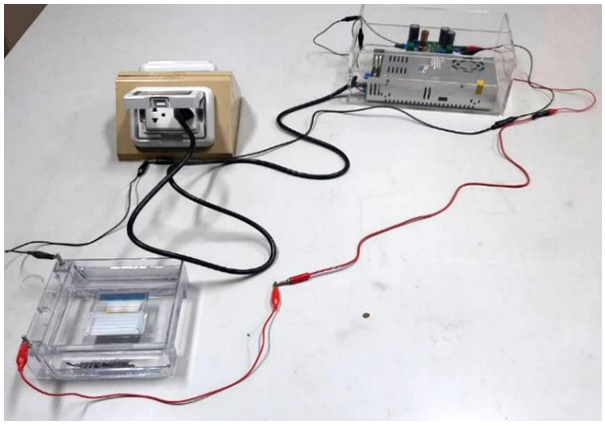

Figure 1.

Demonstration of prototype Gel Electrophoresis (without main control system)

C_006_PF: MOLECULAR CLONING AND EXPRESSION OF INFECTIOUS HYPODERMAL AND HEMATOPOIETIC NECROSIS VIRUS (IHHNV) CAPSID GENE LINKED WITH DOUBLE STRANDED-RNA OF YELLOW HEAD VIRUS

Jaruwan Worawittayatada,[1] Pongsopee Attasart[2], Wanchai Assavalapsakul[1]*

[1]Department of Microbiology, Faculty of Science, Chulalongkorn University, Bangkok, 10330, Thailand
[2]Institute of Molecular Biosciences, Mahidol University, Nakorn Pathom, 73170, Thailand.
*e-mail: wanchai.a@chula.ac.th

Abstract:

Yellow head virus (YHV) is a pathogen which causes extensive mortality in many shrimp species, resulting in the massive production loss to the shrimp farming industry in Thailand. Nowadays, double-stranded RNA (dsRNA)-associated RNAi pathway is applied to control and prevent viral infection in many organisms including shrimps. However, the limitation of dsRNA delivery is still a problem. Therefore, the objective of this work is to clone infectious hypodermal and hematopoetic necrosis virus capsid gene (cpIHHNV) linked with dsRNA of YHV Protease (dsRNA-YHV-*pro*) into the expression vector. The recombinant protein was successfully expressed in *E. coli* Rosetta-gami after induction with 0.4 mM IPTG. The result showed approximately 37 kDa of recombinant cpIHHNV protein, which was detected by the anti-histidine tag monoclonal antibody. However, the presence of dsRNA-YHV-pro will be further clarified.

Introduction:

Thailand has been among the top exporter of shrimps since early 1990s till present[1]. However, the outbreak of viral diseases has become a major problem in shrimp culture causing a fluctuation of income yearly. Yellow head virus (YHV) is the causative agent yellow head disease (YHD) that affect a variety of shrimp species. Up to 100% mortality is possibly witnessed after the outbreak of the disease within in 3 to 10 days[2].

To date, the RNA interference (RNAi) is one of the immune mechanisms which can be applied to reduce specific protein synthesis by mRNA-specific dsRNA. Briefly, long or short dsRNA in cell will be cleaved by RNase III Dicer into small interfering RNAs (siRNAs) of about ~22 nucleotides. Subsequently, one stand of siRNA becomes part of multicomponent RNA-induced silencing complex (RISC) which unwinds the ds-siRNA. Next, the anti-sense RNA is retained in RISC and used as a guide to target viral mRNA. Finally, the mRNA target is degraded[3,4] leading to viral suppression and decrease infected shrimp mortality. Therefore, it is becoming powerful strategy to suppress replication of both DNA and RNA viruses in shrimp[5]. Previous studies have shown YHV Protease (*pro*) gene can be a target for YHV inhibition[6,7,8,9,10]. However, the effective dsRNA delivery system is still required.

Viral like particle (VLP) is one of the nucleic delivery systems into the cell[11]. Infectious hypodermal and hematopoietic necrosis virus (IHHNV) is one of pathogenic shrimp viruses has been studied and show that the its capsid gene could express in the bacterial system and self-assemble to form the viral-like particle[12,13]. Therefore, the objective of this study was to construct the recombinant plasmid which contains capsid protein gene of the Infectious hypodermal and hematopoetic necrosis virus (cpIHHNV) linked with dsRNA of YHV *pro* gene and to express recombinant protein in *Escherichia coli* Rosetta-gami expression system.

Methodology:

1. Bacterial stain, plasmid and culture condition

Escherichia coli DH5α either carried pET17b plasmid contains two double-stranded RNA, (pET17b-ds*rr2*-ds*pro*_two stems11) which encoded Ribonucleotide reductase small subunit (*rr2*) gene of white spot syndrome virus and Protease (*pro*) gene of yellow head virus or pET28a plasmid which encoded IHHNV capsid gene (pET28a-cpIHHNV12) was cultured into Luria-Bertani (LB) broth medium containing 100 µg/ml ampicillin or 50 µg/ml kanamycin, respectively, and incubated at 37 °C with shaking.

2. Plasmid DNA extraction

The bacterial cells were harvested by centrifugation at 8,000 rpm for 1 min at room temperature and resuspended in STET buffer. (8% (w/v) sucrose, 0.1% (v/v) Triton X-100, 50 mM EDTA and 50 mM Tris, pH 8.0). The lysozyme was added into the solution, incubated at 37 °C for 10 min, and boiled at 100 °C for 45 sec. Then, the supernatant was collected following centrifugation at 13,000 rpm for 15 min at 4 °C. 5% (w/v) Cetyltrimethylammonium bromide (CTAB) was added after the cell debris was removed. Next, the mixture was centrifuged at 13,000 rpm for 20 min at 4 °C and discarded the supernatant. The pellet was dissolved in 1.2 M NaCl containing 10 µg/ml RNase A following incubation at 37 °C for 30 min. An equal volume of chloroform was added, mixed and the solution was centrifuged at 13,000 rpm for 15 min at 4 °C. The aqueous phase was transferred into the new microcentrifuge tube and precipitated with equal volume of isopropanol at -20 °C for 1 hour. Then, the solution was centrifuged at 13,000 rpm for 15 min at 4 °C. The pellet was washed with 75% ethanol and centrifuged at 13,000 rpm for 10 min at 4 °C. Finally, the pellet was dried, dissolved in distilled water and analyzed by gel electrophoresis.

3. Cloning of recombinant plasmid

The pET17b-ds*rr2*-ds*pro* plasmid was digested with *Xho* I to obtain the short stem dsRNA of *pro* gene for subcloning into the pET28a-cpIHHNV expression plasmid. The recombinant plasmids were transformed into *E. coli* DH5α. The recombinant clones were selected on LB agar containing 50 µg/ml kanamycin. The plasmid DNA was subsequently extracted and verified by DNA sequencing (Bioneer, Korea). The nucleotide sequences of cpIHHNV-ds*pro* were compared with the reference sequences by Align X program.

4. Expression of recombinant protein in E. coli Rosetta-gami

The corrected recombinant plasmid (pET28a-cpIHHNV-ds*pro*) was transformed into *E. coli* Rosetta-gami for expression. The recombinant clones were cultured in LB medium containing 34 and 50 µg/ml of chloramphenicol and kanamycin, respectively, at 30 °C with vigorously shaking until the OD at 600 nm reached 0.4. The expression was performed with isopropyl-β-D-thiogalactopyranoside (IPTG) induction at a final concentration of 0.4 mM. After that, the bacterial cells were further incubated at 30 °C for 3 hours and harvested by centrifugation at 12,000 rpm for 10 min at 4 °C. The recombinant protein was analyzed by 12% SDS-PAGE and western blotting analysis with anti-His tag monoclonal antibody (R&D system Inc., USA) and anti-mouse IgG conjugated with HRP (Sigma, USA).

Results and Discussion:

In this study, the short stem dsRNA of *pro* gene (~1,100 bp) was successfully cloned into the pET28a-cpIHHNV expression vector (**Figure 1**). For short stem dsRNA of *pro* gene, it was constructed the sense fragment of *pro* gene with loop and an anti-sense fragment of the same region (**Figure 2**). The recombinant plasmid was sequenced using T7 promotor and T7 terminator primers. Sequencing results showed 1,050 nucleotides of cpIHHNV and 1,092 nucleotides of short stem dsRNA of *pro* gene. The nucleotide sequences of cpIHHNV-ds*pro* were shown 100% identity with the reference sequences of cpIHHNV (GenBank Accession No. HQ699073) and dsRNA of *pro* gene (GenBank Accession No. FJ848675.1) (**Figure 3**).

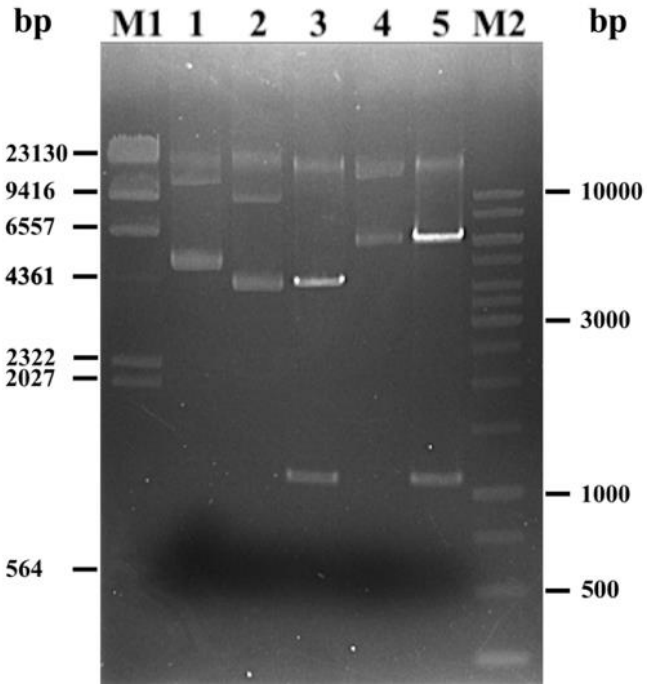

Figure 1. Recombinant plasmid extraction on agarose gel electrophoresis.
Lane M1 and M2: Lambda DNA/*Hind* III marker and 1 kb DNA ladder, respectively.
Lane 1: pET28a-cpIHHNV plasmid.
Lane 2: pET17b-ds*rr2*-ds*pro*_two stems plasmid.
Lane 3: pET17b-ds*rr2*-ds*pro*_two stems plasmid treated with *Xho* I.
Lane 4: pET28a-cpIHHNV-ds*pro* plasmid.
Lane 5: pET28a-cpIHHNV-ds*pro* plasmid treated with *Xho* I.

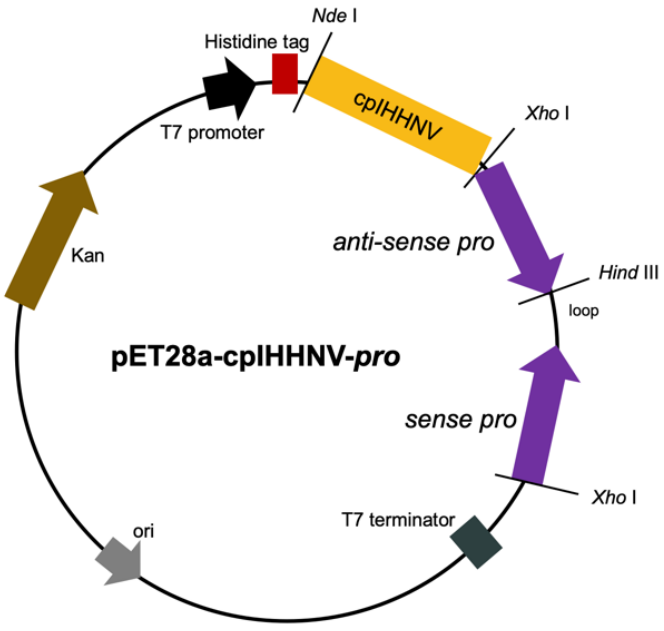

Figure 2. The construction of pET28a-cpIHHNV- ds*pro* plasmid.

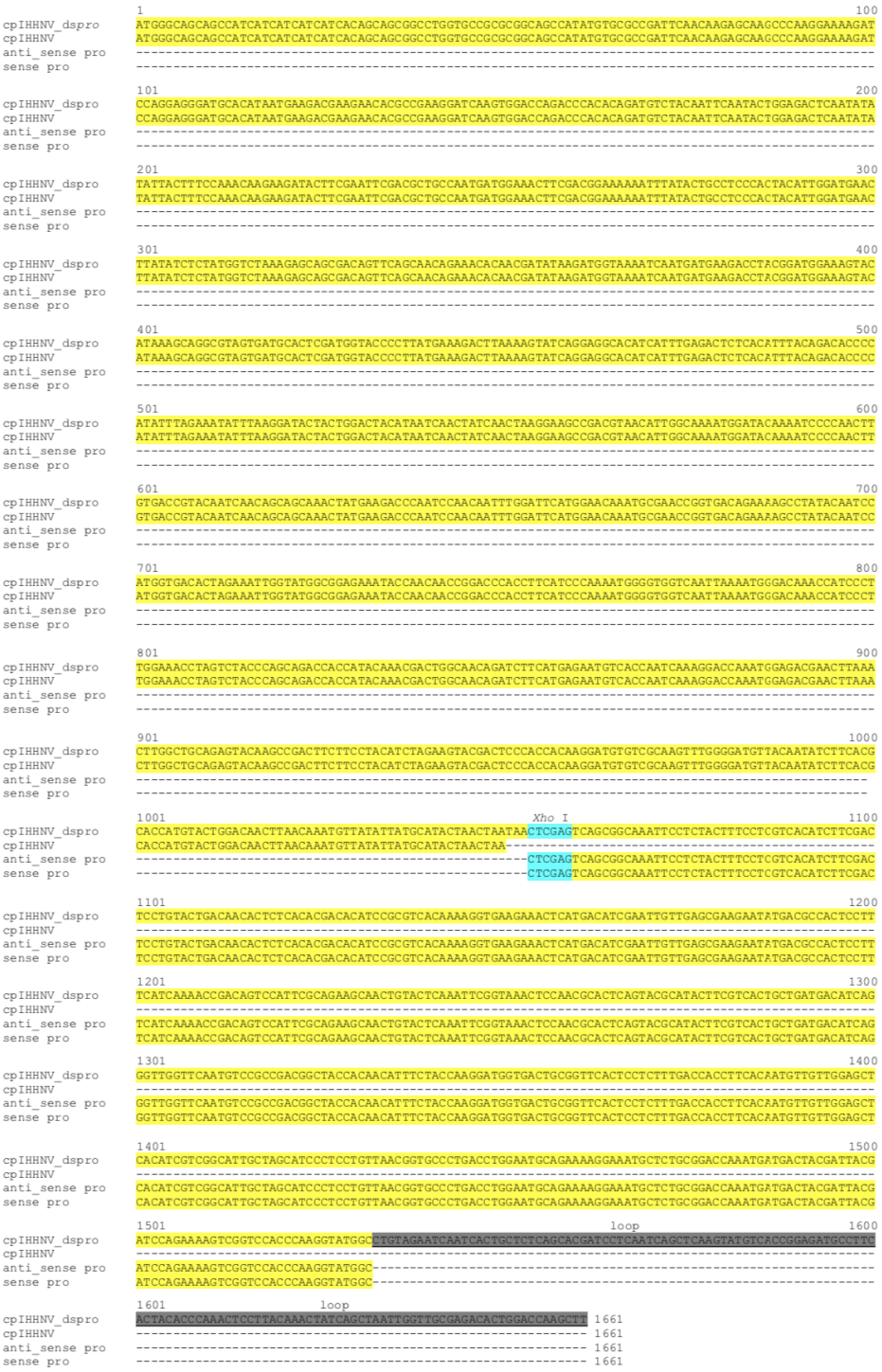

Figure 3. Nucleotide sequences alignment of recombinant plasmids.

The blue highlight indicates restrictor enzyme site (*Xho* I) and gray highlight indicates loop.

The recombinant protein was expressed in *E. coli* Rosetta-gami after induction with final concentration of 0.4 mM IPTG at 30 °C for 3 h. The total cell lysates were analyzed by SDS-PAGE and western blotting (**Figure 4**). The results showed the recombinant protein has approximate 37 kDa (lane I). This size of the recombinant protein was corresponded to the molecular weight of IHHNV capsid protein in previous studies[11,12]. This expressed protein will be further purified by using specific affinity column.

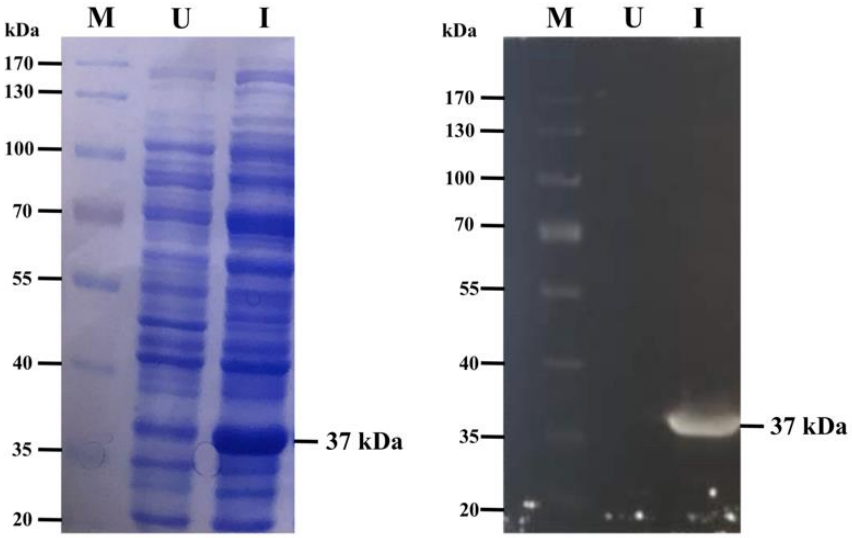

Figure 4. Expression of recombinant protein in *E. coli* Rosetta-gami.

All samples were analyzed by 12% SDS-PAGE and visualized with Coomassie blue stain (left) and western blotting analysis with the anti His-tag monoclonal antibody (right).

Lane M: pre-stained protein marker.

Lane U and I: Uninduced and Induced *E. coli* Rosetta-gami recombinant clone, respectively.

Conclusion:

The recombinant plasmid containing IHHNV capsid coding gene and short stem dsRNA of YHV *pro* was successfully constructed. The recombinant cpIHHNV protein, approximately 37 kDa, could be expressed in *E. coli* Rosetta-gami after induction with 0.4 mM final concentration of IPTG at 30 °C for 3 h. However, the presence of dsRNA-YHV-*pro* will be proved in the future.

Acknowledgements:

This research was supported by the 90th Anniversary of Chulalongkorn University, Rachadapisek Sompote Fund.

References:

1. Tanticharoen M, Flegel TW, Meerod W, Grudloyma U, Pisamai N. Int J Biotechnology. 2008;10:588–603.
2. Flegel TW. J Invertebr Pathol. 2012;110:166–173.
3. Shan G. Int J Biochem Cell Biol. 2010;42:1243–1251.
4. Shekhar MS, Lu Y. Mar Biotechnol. 2009;11:1–9.
5. Itsathitphaisarn O, Thitamadee S, Weerachatyanukul W, Sritunyalucksana K. J Invertebr Pathol. 2017;147:76–85.
6. Yodmuang S, Tirasaphon W, Roshorm Y, Cinnirunvong W, Panyim S. Biochem Biophys Res Commun. 2006;341:351–356.
7. Tirasophon W, Roshorm Y, Panyim S. Biochem Biophys Res Commun. 2005;334:102–107.

8. Tirasophon W, Yodmuang S, Chinnirunvong W, Plongthongkum N, Panyim S. Antiviral Res. 2007;74:150–155.
9. Assavalapsakul W, Chinnirunvong W, Panyim S. Dis Aquat Org. 2009;84:167–171.
10. Chaimongkon D, Assavalapsakul W, Panyim S, Attasart P. J Biotechnol. 2020;321:48–56.
11. Fuenmayora J, Gòdiaa F, Cerverab L. N Biotechnol. 2017;39:147–180.
12. Hou L, Wu H, Xu L, Yang F. Arch Virol. 2009;154:547–553.
13. Sinnuengnong R, Attasart P, Duncan RS, Panyim S, Assavalapsakul W. J. Biotechnol. 2018;267:63–70.

C_007_PA: FUNCTIONAL ANALYSIS OF HTRA PROTEASE IN THE HALOTOLERANT CYANOBACTERIUM *Halothece* sp. PCC7418

Tanutcha Patipong,[1,2] Masaki Honda,[2] Takashi Hibino,[2,3] Rungaroon Waditee-Sirisattha,[1] Hakuto Kageyama[2,3,*]

[1]Department of Microbiology, Faculty of Science, Chulalongkorn University, Pathumwan, Bangkok 10330, Thailand
[2]Department of Chemistry, Faculty of Science and Technology, Meijo University, Nagoya, Aichi 468-8502, Japan
[3]Graduate School of Environmental and Human Sciences, Meijo University, Nagoya, Aichi 468-8502, Japan
*e-mail: kageyama@meijo-u.ac.jp

Abstract:

The HtrA protein belongs to an evolutionarily conserved family of serine proteases that are widely distributed across taxa. These proteins exert proteolytic activity towards multiple target substrates. They are crucial for survival under stress conditions and involved in various cellular pathways including function as monitors of protein synthesis. The physiological roles of HtrA proteases have been reported in a number of organisms; however, the information is still limited in halotolerant species. In this study, gene expression analysis of all putative serine protease in the halotolerant cyanobacterium *Halothece* sp. PCC7418 was conducted under salt-stress conditions. Among 30 genes examined, the *PCC7418_3553* gene encoding for HtrA2 was up-regulated significantly. The localization of HtrA2 was highly indicated as a soluble protein in cytoplasm as well as in thylakoid and plasma membranes. Interestingly, HtrA2 was distinctively accumulated in plasma membrane under salt- and heat stresses. Thus, HtrA2 is a multi-subcellular localization protein which is induced both at transcription and translation levels in respond to stresses. Taken together, these results suggest that HtrA2 is involved in the response to salinity and heat stresses in halotolerant cyanobacterium *Halothece* sp. PCC7418.

C_008_PA: PRELIMINARY STUDY ON ANTI-HYPERGLYCEMIC EFFECT OF CROCODILE OIL IN SPONTANEOUSLY DIABETIC TORII RATS

Thiri Wai Linn,[1] Metas Ngernjan,[2] Parichart Toejing,[1] Anongporn Kobroob,[3] Doungporn Amornlerdpison,[2] Orawan Wongmekiat,[1] Narissara Lailerd.[1]*

[1]Department of Physiology, Faculty of Medicine, Chiang Mai University, Chiang Mai 50200, Thailand
[2]Faculty of Fisheries Technology and Aquatic Recourses, Maejo University, Chiang Mai 50290, Thailand
[3]Division of Physiology, School of Medical Science, University of Phayao, Phayao 56000, Thailand
*e-mail address: narissara.lailerd@cmu.ac.th

Abstract:

Type 2 diabetes is a chronic metabolic disorder with increasing worldwide prevalence. Consumption of monounsaturated fatty acid (MUFA) has a beneficial role in treating diabetes according to its stimulating effect on insulin secretion. MUFA-enriched crocodile oil, a waste product from crocodile industry, has been showed to improve *in vitro* hemi-diaphragm glucose uptake in our preliminary study. This study examined possible beneficial effects of crocodile oil (CO) on glycemia in Spontaneously Diabetic Torii (SDT) rats, non-obese type 2 diabetic rat model. After diabetic verification at 12 weeks of age, SDT rats were randomly assigned to receive vehicle or CO at the dose of 1000 mg/kg BW for 28 weeks. Age-matched non-diabetic Sprague-Dawley rats were given vehicle or CO. Non-fasting plasma glucose, oral glucose tolerance test and plasma insulin levels were evaluated at the end of experiment. Interestingly, the results revealed that supplementation of CO significantly improved glucose tolerance, non-fasting plasma glucose, plasma insulin and pancreatic insulin secretion as indicated by insulinogenic index. Whereas, no significant metabolic alterations were found in CO-treated non-diabetic rats. These findings firstly demonstrate that long-term supplementation of CO has a positive therapeutic potential on type 2 diabetic rats due to its anti-hyperglycemic and insulinogenic actions.

C_009_PA: IDENTIFICATION AND VALIDATION OF *MRL1* IN ABIOTIC STRESS IN RICE AND ARABIDOPSIS MODEL

Chutarat Punchkhon,[1,2] Jonaliza L. Saingliw,[3] Theerayut Toojinda,[3] Nuria De Diego,[4] Lukáš Spíchal,[4] Supachitra Chadchawan,[1,*]

[1]Center of Excellence in Environment and Plant Physiology, Department of Botany, Faculty of Science, Chulalongkorn University, Bangkok 10300, Thailand
[2]Program in Biotechnology, Faculty of Science, Chulalongkorn University, Bangkok 10300, Thailand
[3]Rice Gene Discovery Unit, National Center for Genetic Engineering and Biotechnology, Kasetsart University, Kamphangsaen Campus, Nakhonpathom 73140, Thailand
[4]Centre of the Region Haná for Biotechnological and Agricultural Research, Palacký University, Olomouc, Czech Republic
*e-mail: Supachitra.C@chula.ac.th

Abstract:

Drought stress and salt stress can affect plant growth and productivity. Kao Dawk Mali 105 ('KDML105') is one of the crops which has to face both drought and salt stresses as it is grown in rain-fed saline soil in the northeastern region of Thailand, where the irrigation is limited. CSSL8-104, a chromosome substitution line with 'KDML105' genetic background, was developed in order to improve drought tolerant ability of 'KDML105' rice by transferring the drought tolerant QTL region from double haploid line, DH103. Photosynthesis parameters of CSSL8-104 and its parental lines, 'KDML105' and DH103, were investigated, when they were grown in normal, drought stress and salt stress conditions. Net photosynthesis rates of all lines were similar in normal condition. In drought and salt stress conditions, net photosynthesis rate of all lines were declined, but CSSL8-104 and DH103 rice had the significant higher photosynthetic rate than 'KDML105' rice under drought-stressed condition, but not salt-stressed condition, suggesting the positive effects of drought tolerant QTL from DH103. Based on the SNPs comparison between CSSL8-104 and 'KDML105' rice, one of genes involved in photosynthesis, *MRL1*of CSSL8-104 contains a SNP that results in the stop codon in coding sequence. MRL1 (Os10g0181200) is pentatricopeptide repeat (PPR) protein involve in stabilization of *rbcL* mRNA. The *MRL1* knocked-out Arabidopsis mutant line was used to validate the role of MRL1 under drought stress condition using PlantScreen™ XYZ system. It was revealed that *MRL1* knocked-out mutant had the higher total leaf area and green leaf area under drought-stressed condition, which was consistent with the response in rice. These data support the role of MRL1 protein in drought tolerance.

C_010_PF: EFFECTS OF HISTONE DEACETYLASE INHIBITOR ON FETAL HEMOGLOBIN INDUCTION AND ERYTHROPOIESIS IN β-THALASSEMIA

Pawarit Innachai,[1] Orapan Sripichai,[2] Sukanya Chumchuen,[3] Chokdee Wongborisuth,[3] Duantida Songdej,[3] Usanarat Anurathapan,[3] Suradej Hongeng,[3] Amornrat Tangprasittipap,[3,*] Chalermchai Mitrpant,[1,*]

[1]Department of Medical Biochemistry and Molecular Biology, Faculty of Medicine Siriraj Hospital, Mahidol University, Bangkok, Thailand
[2]National Institute of Health, Department of Medical Sciences, Ministry of Public Health, Nonthaburi, Thailand
[3]Faculty of Medicine Ramathibodi Hospital, Mahidol University, Bangkok, Thailand
*e-mail: amornrat.tar@mahidol.ac.th; chalermchai.mit@mahidol.edu

Abstract:

Fetal hemoglobin (HbF; α2γ2) induction can ameliorate clinical severity of patient with β-hemoglobinopathy, including β-thalassemia. Epigenetic modifications partly regulate gene expression. Inhibition of histone deacetylase (HDAC) 1 and HDAC2 can induce HbF expression in erythroleukemic cell lines and hematopoietic progenitor cells. Entinostat, an HDAC inhibitor, was shown to induce γ-globin expression in normal adult erythroid progenitor cell cultures. However, the effects of entinostat in β-thalassemia erythroid cells has not been evaluated. Here, we report the HbF-inducing activity of entinostat in erythroid progenitor cells derived from healthy donors and β-thalassemia/HbE patients. Treatment with entinostat at 500 nM led to 1.5-fold increase in levels of γ-globin mRNA and approximately 10% increase of HbF level without significant alteration in cell differentiation. Higher expression of γ-globin mRNA and HbF levels were observed in cell treated with entinostat at 1000 nM, but inhibition of cell proliferation was also noted. Slight increase of HbF level exhibited in erythroid cells treated with entinostat at 100 nM. Similar effects on HbF production and erythropoiesis were found in normal individual derived erythroid cells treated with entinostat. These findings indicate that entinostat has potential as a HbF-induction agent for β-thalassemias and could be of interest in developing treatment for patients with β-thalassemia. However, appropriate dose titration and time-course of this compound must be further investigated for HbF induction and cell proliferation.

Introduction:

β-Thalassemia is a common genetic blood disorder that is caused by the mutation in the β-globin gene. This mutation results in a reduction or absence of the β-globin chain synthesis, which in turn, reduced adult hemoglobin (HbA; α2β2) production in erythrocytes.[1] Imbalance between α- and β-globin chains leads to precipitation of unmatched α-globin chains in erythroid cells, causing anemia, hemolysis, and ineffective erythropoiesis.[2,3] Patients with β-thalassemia show disease heterogeneity, ranging from nearly asymptomatic to severe, transfusion-dependent thalassemia.[4] It is known that reactivation of fetal γ-globin gene expression and induction of HbF (α2γ2) production can ameliorate the β-thalassemia disease severity due to reduced degree of globin chain imbalance.[4,5] The γ-globin gene expression in adult is suppressed by various repressors including epigenetic factors.[6]

Histone deacetylases (HDACs) are the epigenetic modifying enzymes, which have been investigated as potential therapeutic targets for HbF induction in β-hemoglobinopathies.[7] HDACs existed in several repressor complexes. HDAC1 and HDAC2 are the core components of the nucleosome remodeling and deacetylase (NuRD) complex and CoREST complex, while HDAC3 interacts with SMRT/NCoR complex associated with γ-globin gene silencing factors such as BCL11A, GATA-1 and FOG-1.[8,9] It has been demonstrated that γ-globin gene induction in human hematopoietic progenitor cells is associated with inhibition of HDAC1 and HDAC2 activity by either HDAC inhibitor or genetic ablation of HDAC1 or HDAC2.[10,11] Selective inhibition of HDAC1/2/3 by the pharmacological agent entinostat has been shown to induce γ-globin mRNA expression in K562 erythroleukemic cell line[12,13] and erythroid progenitor cells from normal individuals.[14] In this study, the HbF-inducing activity of entinostat was evaluated in erythroid progenitor cells derived from β-thalassemia/HbE patients. These data demonstrate that entinostat potently elevates levels of HbF, suggesting therapeutic potential of HDAC inhibitor for β-thalassemia treatment.

Methodology:

In vitro human erythroid progenitor cell culture: Participants were recruited underwritten informed consent in accordance with the Declaration of Helsinki. The study protocols were approved by the Institutional Review Board of Mahidol University, Thailand (COA. No. MURA2018/654). Mononuclear cells were separated from peripheral blood of healthy donors and β-thalassemia/HbE patients by density separation (Lymphoprep, density 1.077; Axis-Shield, Oslo, Norway). $CD34^+$ progenitor cells were selected using the CD34 microbead kit with cell separation columns following the manufacturer's instructions (Miltenyi Biotec, Gladbach, Germany). Cells were cultured in a three-phase culture system for 14 days at 37 ^oC, 5% CO_2. Three different erythroid differentiation culture media were used; phase I (days 0-4), phase II (days 5-8) and phase III (days 9-14). The basal medium composed of Iscove's modified Dulbecco medium (Biochrom GmbH, Berlin, Germany), 20% fetal bovine serum (Merck, Temecula, CA, USA), 300 µg/mL holo-transferrin (ProSpec, Rehovot, Israel), 1x glutamax (Gibco, Grand Island, NY, USA) and 100 U/mL penicillin-streptomycin (Gibco). $CD34^+$ cells were cultured in the basal medium supplemented with 10 ng/mL human interleukin-3 (Miltenyi Biotec), 50 ng/mL human stem cell factor (SCF; Miltenyi Biotec), and 2 U/mL erythropoietin (EPO; Janssen-Cilag, Bangkok, Thailand) in phase I, then transfer to phase II medium of the basal medium containing 10 ng/mL SCF and 2 U/mL EPO and phase III medium of the basal medium containing 4 U/mL EPO.

Chemical compounds treatment of erythroid progenitor cells: Entinostat was purchased from MedChemExpress, Monmouth Junction, NJ, USA. Entinostat was dissolved in dimethylsulfoxide (DMSO; Sigma-Aldrich, St. Louis, MO, USA) and was freshly diluted in culture media to the designated concentrations. Culture medium containing 0.1% v/v of DMSO served as a vehicle control.

Cell viability, proliferation, and differentiation: Cell viability and proliferation were stained by trypan blue staining and determined using a hemocytometer under the light microscope. Flow cytometry analysis was used to investigate erythroid cell differentiation. Cells were collected after treated with compounds for 96 hours and monitored by using antibodies against erythroid surface markers; an allophycocyanin (APC)-conjugated anti-human glycophorin A (CD235a; BD Biosciences, San Jose, CA, USA), and a phycoerythrin (PE)-conjugated anti-human transferrin receptor (CD71; Biolegend, San Diego, CA, USA). The stained cells were analyzed on the BD FACSCalibur flow cytometer (BD Biosciences) and the data analysis was performed using FlowJo version 10.3.0 software (FlowJo LLC, Ashland, OR, USA).

RNA isolation and quantitative RT-PCR: Total RNA was isolated from cells at day 10 of culture using TriZol reagent (Ambion, Carlsbad, CA, USA) and subjected to cDNA synthesis using RevertAid First-Strand cDNA Synthesis Kit (ThermoFisher Scientific, Carlsbad, CA, USA) according to the manufacturer's instruction. The expression level of γ-globin mRNA was analyzed by quantitative real-time RT-PCR in the LightCycler® 96 Instrument (Roche, Mannheim, Germany) using FastStart Essential DNA Green Master (Roche) according to the manufacturer's instruction. PCR primers used in this study were HBG-F (5'-TCACAGAGGAGGACAAGGCTA-3') and HBG-R (5'-

GCTTTATGGCATCTCCCAAG-3'). Relative expression was calculated using the $2^{-\Delta\Delta Ct}$ method. GAPDH was used as a reference gene for normalization of targeted gene expression.

High performance liquid chromatography (*HPLC*) *analysis*: At least one million cells at day 14 of culture was used for hemoglobin analysis by HPLC. The proportion of HbF was determined by the Shimadzu HPLC LC-20A (Shimadzu, Japan) following the β-thalassemia short program protocol (Bio-Rad Laboratories, Hercules, CA, USA). The relative percentage of hemoglobin was analyzed by the area under individual hemoglobin peak from HPLC chromatogram.

Statistical analysis: Data are presented as mean ± standard deviation (SD). All statistical analyzes were performed using Student's t-test on GraphPad Prism version 8.2.0 (GraphPad Software, San Diego, CA, USA). Statistical significance was assumed at a *p*-value less than 0.05.

Results and Discussion:

In this study, the three-phase culture system was performed to determine the therapeutic potential of entinostat as a HbF inducer. This culture system promotes erythroid differentiation on $CD34^+$ hematopoietic progenitor cells isolated from peripheral blood. $CD34^+$ cells differentiate into erythroid lineage progenitors during phase I (days 0–4) and phase II (days 5–8) of culture. Cells underwent terminal erythroid maturation during phase III (days 9–14) of culture. We initially determined the effect of varying the concentrations of entinostat on HbF induction in normal erythroid progenitor cells. Entinostat at a concentration of 100, 500, or 1000 nM was added to cells during phase III of culture. We found that addition of entinostat at 500 and 1000 nM increased HbF percentage (%HbF = 13.5±2.1 and 14.7±2.1, respectively) compared with low dose of entinostat and DMSO control (%HbF = 11.9±2.2 and 0.6±1.8, respectively) (n=3; Figure 1A). The dose-dependent effect of entinostat on the induction of HbF was also observed in β-thalassemia/HbE cells (Figure 1B). Of note, the increased HbF achieved by entinostat treatments in β-thalassemia/HbE erythroid cells was higher than that in normal cells. Due to the high HbF baseline levels in β-thalassemia/HbE cells, Δ%HbF; the increase in percentage of HbF from the baseline levels of DMSO-treated cells from the same donor, was also calculated. The Δ%HbF in β-thalassemia/HbE cells increased from 2.6% and 4.1% in entinostat at 100 nM to 7.4% and 10.4% in 500 nM entinostat, and 8.1% and 13.9% in 1000 nM entinostat (n=2; Figure 1C). This result indicated that although the %HbF baseline levels in β-thalassemia/HbE individual cases varied between 22% and 33%, both of them responded to the same extent upon entinostat addition. Similarly, the average Δ%HbF was elevated from 2.4 ± 1.3% in 100 nM entinostat-treated cells to 3.6 ± 0.7% and 4.0 ± 1.1% in 500 nM and 100 nM entinostat-treated cells derived from healthy donors, respectively. These findings showed that entinostat increased HbF reproducibly in normal and β-thalassemia/HbE erythroid progenitor cells in a dose-dependent manner. Additionally, the levels of γ-globin mRNA were examined in β-thalassemia/HbE cells at day 10 of culture in order to demonstrate whether the increase in HbF levels were correlated well with the increase in γ-globin mRNA levels. The results revealed that entinostat induced γ-globin mRNA expression to 1.8 ± 0.4-fold increase in 500 nM entinostat and 2.3 ± 0.3-fold increase in 1000 nM entinostat compared with DMSO-treated cells. However, upregulation of γ-globin mRNA was only 1.5 ± 0.2-fold increase in cell treated with entinostat at 100 nM.

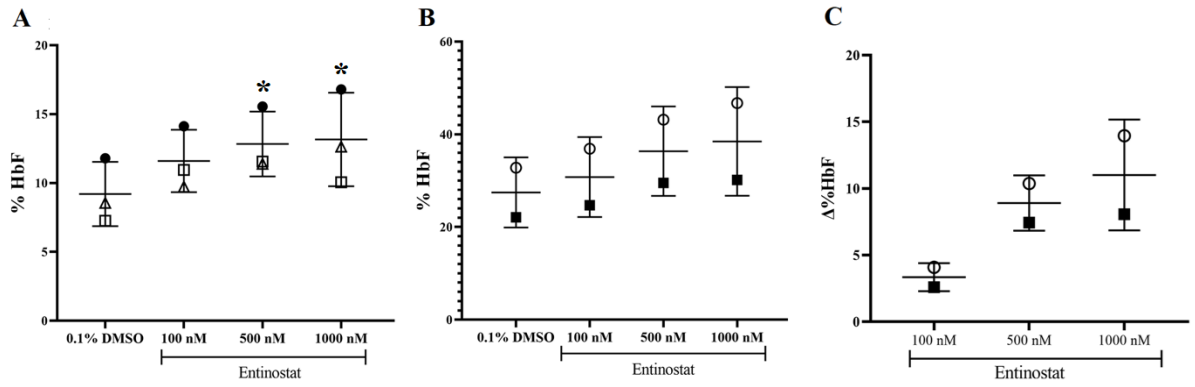

Figure 1. Entinostat-mediated induction of HbF in erythroid cell culture.
Erythroid progenitor cells recovered from the peripheral blood of normal donors (n = 3) and β-thalassemia/HbE patients (n = 2) were cultured in the presence of entinostat at the indicated concentrations during days 9-14 of culture. The percentage of HbF in (A) normal and (B) β-thalassemia/HbE erythroid cells analyzed by HPLC at day 14 of culture. (C) The increase in HbF percentage in β-thalassemia/HbE erythroid cells (n = 2) was expressed as Δ%HbF (%HbF [entinostat treatment] − %HbF [DMSO control]). The asterisk represents *p*-value less than 0.05 as compared to 1% DMSO control.

The erythroid proliferation and viability in the absence or presence of entinostat was analyzed at days 8, 10, 12, and 14 of culture. The addition of 100 nM entinostat to cells during days 9–14 did not affect cell proliferation and viability (Figure 2). However, a significant reduction in cell proliferation and viability during erythroid differentiation was evident at 500 and 1000 nM of entinostat in both normal and β-thalassemia/HbE cells.

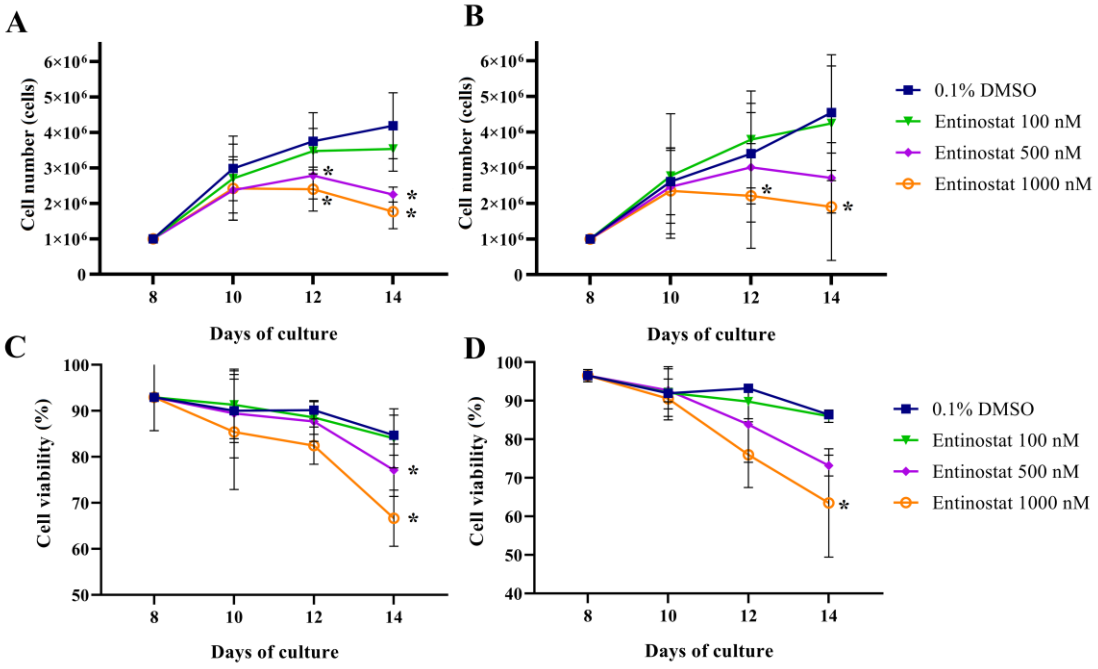

Figure 2. Effect of entinostat on erythroid cell proliferation and viability.
Erythroid progenitor cells recovered from the peripheral blood of normal donors (n = 3) and β-thalassemia/HbE patients (n = 2) were cultured in the presence of entinostat at the indicated concentrations during days 9-14 of culture. The cell proliferation in (A) normal and (B) β-thalassemia/HbE erythroid cells was expressed as a cell number. Percentage of cell viability of (C) normal and (D) β-thalassemia/HbE erythroid cells during erythroid differentiation assessed by trypan blue staining. The asterisk represents *p*-value less than 0.05 as compared to 1% DMSO control of each days of culture.

We next determined erythroid differentiation pattern after 12 days of culture by flow cytometry. As expected, delayed terminal maturation was observed in β-thalassemia/HbE erythroid cells compared to normal cells as evidenced by a higher number of cells with high levels of CD71 (Figure 3). The results showed the comparable differentiation pattern of erythroid cells in the presence or absence of entinostat. Altogether, erythroid cell viability, proliferation, and differentiation were not significantly altered after entinostat treatment at 100 nM, suggesting that there are no significant cytotoxic effects of entinostat under these conditions. Although treatment with high concentration of entinostat at 500 and 1000 nM were not affected erythroid cell differentiation; but associated with a significant reduction in cell proliferation and viability.

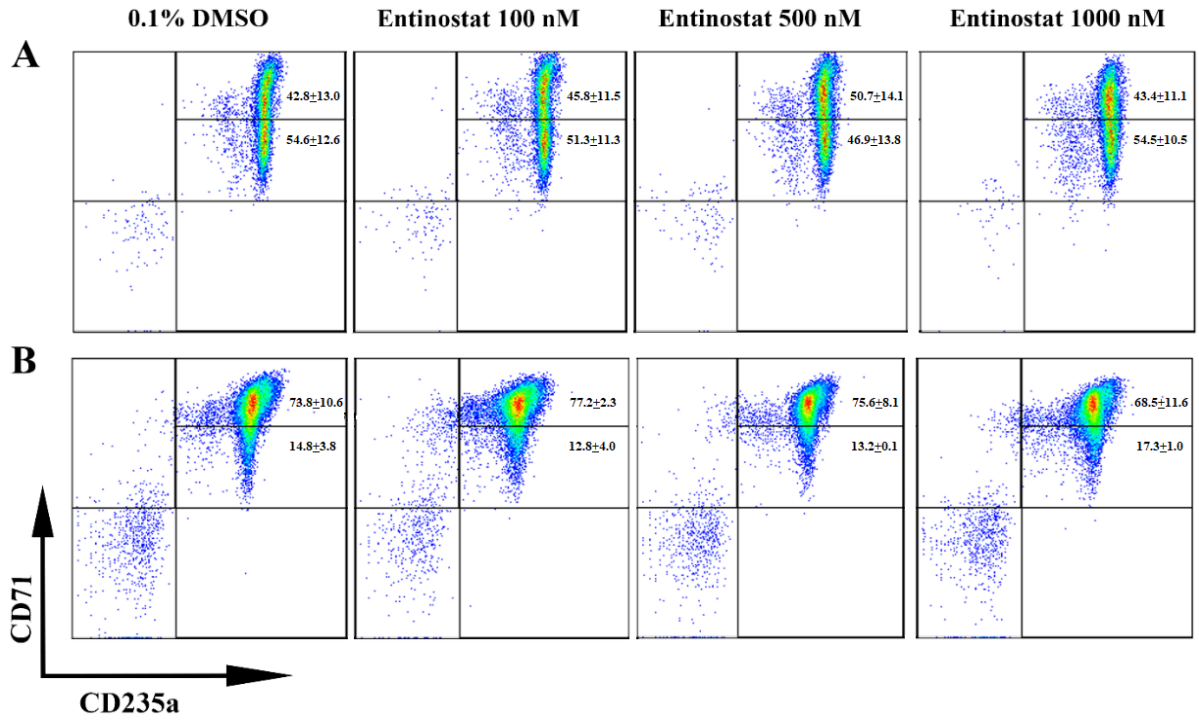

Figure 3. Effect of entinostat on erythroid cell differentiation.
Representative flow cytometry dot plots of day 12 of erythroid cells derived from (A) normal donor and (B) β-thalassemia/HbE patient cultured in the presence of entinostat at the indicated concentrations. Erythrocyte populations were gated into 5 groups; $CD71^{neg}/GPA^{neg}$, $CD71^{pos}/GPA^{neg}$, $CD71^{high}/GPA^{pos}$, $CD71^{low}/GPA^{pos}$, $CD71^{neg}/GPA^{pos}$. The numbers indicated in $CD71^{high}/GPA^{pos}$ and $CD71^{low}/GPA^{pos}$ gates were the mean ± SD of normal donors (n = 3) and β-thalassemia/HbE patients (n = 2) stained erythrocytes.

Taken together, these results suggest that the histone deacetylase inhibitor entinostat is a potent HbF inducer without cytotoxicity under low dose tested conditions. However, we found that treatment with entinostat at 100 nM slightly increased levels of HbF and γ-globin mRNA expression compared with DMSO-treated cells. Combinatorial therapy by multiple HbF-inducing agents is one of a promising therapeutic strategy for high-level HbF induction to achieve a significant clinical improvement of β-thalassemia patients. Since using low amount of each combinatorial agents to achieve greater HbF induction and avoid its toxicity could reduce adverse effects from using high amount of single-agent treatment, hence combining low amount of entinostat with other HbF inducers may further increase in HbF and γ-globin expression. Previous study showed that the combination of entinostat and UNC0638, an EHMT1/2 inhibitor, had additive effects on the induction of γ-globin gene expression in primary human adult erythroid cells derived from normal individuals.[15] In addition, some study has experienced that the level of HbF induction was more pronounced when added compounds at an early erythroid differentiation stage than added in a late stage of erythroid differentiation,[16] which may due to the

highly regulated and reversible of globin gene expression during early stage. This study was investigated the effect of entinostat only in the late stage of erythroid differentiation (days 9-14). Thus, the time of addition of entinostat in erythroid cell culture should further evaluate aiming to find the most effective period to achieve the maximal effect on HbF induction. Furthermore, a dose titration of the compound to reduce the negative effect on cell proliferation and viability while maintaining the high level of HbF induction and not altered erythroid differentiation could further examined.

Increase in γ-globin and induction of HbF expression has been shown to ameliorate the pathophysiology and severity of β-thalassemia patients. The γ-globin repression and silencing of HbF in adults is mediated by epigenetic changes, including DNA methylation and histone modifications, and several chromatin-modifying enzymes. The epigenetic-modifying enzymes, including DNA methyltransferase, histone methyltransferase, and histone deacetylase are of interest as therapeutic targets for induction of HbF.[17] Entinostat has demonstrated a HbF-inducing activity in *in vitro* erythroid cell culture systems of both normal and β-thalassemia cells (evident herein) We found a dose-dependent fashion of entinostat in induction of HbF, but a significant reduction in cell proliferation and viability during erythroid differentiation at high dose was exhibited. The combination of compounds that have different mechanisms of action was proposed for the potential to additively increase HbF expression. Further analyzes of entinostat alone or in combination with other epigenetic-modifying compounds may lead to improved treatments for β-thalassemia.

Conclusion: Inhibition of histone deacetylase by entinostat induces the HbF production in β-thalassemia/HbE erythroid progenitor cells, supporting further evaluation to clinical application of entinostat in the treatment of β-thalassemia.

Acknowledgements: This work was supported by Mahidol University research grant. P.I. was supported by the Siriraj Graduate Scholarship, Faculty of Medicine Siriraj Hospital, Mahidol University.

References:

1. De Sanctis V, Kattamis C, Canatan D, Soliman AT, Elsedfy H, Karimi M, et al. Mediterr J Hematol Infect Dis. 2017; 9(1):e2017018.
2. Fard AD, Hosseini SA, Shahjahani M, Salari F, Jaseb K. Int J Hematol Oncol Stem Cell Res. 2013;7(3):47-54.
3. Fibach E, Rachmilewitz EA. P. F1000Res. 2017;6:2156.
4. Sripichai O, Fucharoen S. Expert Rev Hematol. 2016;9(12):1129-37.
5. Winichagoon P, Fucharoen S, Chen P, Wasi P. J Pediatr Hematol Oncol. 2000;22:573-80.
6. Diepstraten ST, Hart AH. Blood Reviews. 2019;33:11-23.
7. Lavelle D, Engel JD, Saunthararajah Y. Semin Hematol. 2018;55(2):60-7.
8. Seto E, Yoshida M. Cold Spring Harb Perspect Biol. 2014;6(4): a018713.
9. Ginder GD. Transl Res. 2015;165(1):115-25.
10. Bradner JE, Mak R, Tanguturi SK, Mazitschek R, Haggarty SJ, Ross K, et al. Proc Natl Acad Sci U S A. 2010;107(28):12617-22.
11. Shearstone JR, Golonzhka O, Chonkar A, Tamang D, van Duzer JH, Jones SS, et al. PLoS One. 2016;11(4):e0153767.
12. Witt O, Monkemeyer S, Ronndahl G, Erdlenbruch B, Reinhardt D, Kanbach K, et al. Blood. 2003;101(5):2001-7.
13. Durlak M, Fugazza C, Elangovan S, Marini MG, Marongiu MF, Moi P, et al. PLoS One. 2015;10(10):e0141083.
14. Esrick EB, McConkey M, Lin K, Frisbee A, Ebert BL. Am J Hematol. 2015;90(7):624-8.
15. Renneville A, Galen PV, Canver MC, McConkey M, Krill-Burger JM, Dorfman DM, et al. Blood. 2015;126(16):1930-9.
16. Krivega I, Byrnes C, de Vasconcellos JF, Lee YT, Kaushal M, Dean A, et al. Blood. 2015;126(5):665-72.
17. Adelvand P, Hamid M, Sardari S. Expert Rev Hematol. 2018;11(1):71-81.

C_011_PF: SOLUBILIZATION OF INSOLUBLE MINERALS BY SOIL FUNGI COLLECTED FROM NORTHERN THAILAND

Surapong Khuna[1,2], Nakarin Suwannarach[1,3], Jaturong Kumla[1,3], Saisamorn Lumyong[1,3,*]

[1]Department of Biology, Faculty of Science, Chiang Mai University, Chiang Mai 50200, Thailand
[2]PhD's Degree Program in Applied Microbiology, Department of Biology, Faculty of Science, Chiang Mai University, Chiang Mai 50200, Thailand
[3]Research Center of Microbial Diversity and Sustainable Utilization, Chiang Mai University, Chiang Mai 50200, Thailand
*e-mail: saisamorn.l@cmu.ac.th

Abstract:

Mineral nutrients are important for plant growth and crop production. Only 1 to 5% of mineral nutrients in the soil are in a soluble and plant-available forms. In nature, the mineral solubilizing fungi play an important role in supplying soluble mineral to plants by the solubilizing of insoluble minerals in the soil. The objective of this study was to isolate and screen the mineral solubilizing fungi from rhizosphere soil in some agricultural areas in northern Thailand. Among three sampling sites in this study, the highest positive colonies were found from the soil sample collected from site 1 as 55.00 CFU/g following by site 2 and 3 as 17.00 and 15.00 CFU/g, respectively. The most effective three fungal strains, SDBR-CMUI1, SDBR-CMUI4, and SDBR-CMUO2 were selected and evaluated their solubilizing abilities of insoluble minerals. The result showed that all three fungal strains could solubilize $Ca_3(PO_4)_2$, $CoCO_3$, CuO, $FePO_4$, $MgCO_3$, MnO, and $ZnCO_3$. The molecular analysis identified them into the genera *Aspergillus*.

Introduction:

Mineral nutrients in soil are essential for plant growth and development.[1] The mineral nutrients for plant growth are divided into main two groups including macrominerals (calcium, magnesium, nitrogen, phosphorus, potassium, sodium, and sulfur) and microminerals (boron, chloride, copper, iron, manganese, molybdenum, nickel, and zinc).[2] Approximately 95–99% of mineral nutrients in soil are dissolved and found in insoluble form of carbonate form [$CaCO_3$, $MgCO_3$, $Mg_5(CO_3)_4(OH)_2{\cdot}4H_2O$, $SrCO_3$, $FeCO_3$, $MnCO_3$ and $Na_2CO_3{\cdot}10H_2O$], phosphates form [$Ca_3(PO_4)_2$, $Fe_3(PO_4)_2{\cdot}8H_2O$, $FePO_4{\cdot}2H_2O$, $Zn_3(PO_4)_2{\cdot}2H_2O$, $Co_3(PO_4)_2{\cdot}8H_2O$, Cu_2OHPO_4 and $AlPO_4{\cdot}2H_2O$], oxides form [Fe_2O_3, MnO, ZnO and CuO) and complex form (feldspar ($KAlSi_3O_8$), leucite ($KAlSi_2O_6$) and trachyte].[3,4] Therefore, they have low availability in many agricultural soils and slowly available to plants.[5,6] The application of chemical fertilizers was used to increase the available nutrient in soil and crop yield.[7] However, chemical fertilizers have led to reduction in soil fertility by disturbing microbial diversity, environmental degradation, consequently reduced yield of corps, and also increasing costs of crop production.[8,9] Soil fungi and other microorganisms are having potentiality to solubilize insoluble form of minerals and make that soluble for plants uptake.[10] Previous studies reported that mineral solubilizing fungi in soil were constituted about 0.1–0.5% of the total fungal populations.[11] The ability of soil fungi to solubilize the insoluble minerals has been attributed to their capacity to reduce pH by the production of organic acids, chelation and mineralization.[9] Soil fungi can enhance plant growth through the production of phytohormones, antibiotics, siderophore and control plant diseases.[12,13] The objective of this study was to isolate the mineral solubilizing fungi from agricultural soil in Chiang Mai province, northern Thailand. The most effective fungal strains were

selected for evaluation of the insoluble metal minerals solubilization. In addition, the selected fungal strains were identified by molecular analysis of the internal transcribed spacers (ITS) of the ribosomal DNA (rDNA).

Methodology:

Sampling and fungal isolation

Three soil samples were collected from agricultural areas of Chiang Mai province, Thailand in August 2017. The samples were air-dried at room temperature for 3 days, sieved and mixed through a 2 mm mesh prior to isolation of fungi by serial dilution. The dilution spread plate method was used with three serial dilutions in 0.5% NaCl solution. After dilution, 0.1 ml of suspension was spread on modified Aleksandrov agar for detection of the solubilization of insoluble phosphate.[14] The plates were incubated at 30ºC in darkness for 5 days. Colonies which produced clear zones were considered phosphate solubilizing strains and were selected for further experiment. Soil texture was determined by the hydrometer method[15] and the pH was measured by a pH meter equipped with a glass electrode with a soil: distilled water ratio of 1:2. The organic matter was determined by dosage of organic carbon using the potassium dichromate oxidation method.[16]

Evaluation of the insoluble minerals solubilization ability

The most effective fungal strains from the previous experiment were selected and used. This experiment was carried out using basal medium with the addition of different insoluble metal minerals such as $Al_3(PO_4)_2$, $Ca_3(PO_4)_2$, $CoCO_3$, CuO, $FePO_4$, $MgCO_3$, MnO, and $ZnCO_3$ to the desired final concentration 0.5%.[17] The medium was autoclaved at 121ºC for 15 min. After autoclaving, 25 ml of test media was poured into Petri dishes. Mycelial inocula were prepared by growing fungal strain on potato dextrose agar (PDA) at 30ºC in darkness for 3 days. Mycelial plug (5 mm diameter) was inoculated into the center of the tested media. All plates were incubated at 30ºC in darkness for 5 days. Colony diameter and solubilization zone (halo zone) were measured. The solubilization index (SI) was calculated as a halo zone diameter divided by a fungal colony diameter.[18,19] SI values of less than 1.0, between 1.0 and 2.0, and more than 2.0 were regarded as low, medium and high solubilization activities, respectively. Each treatment was carried out in three replications.

Identification of selected fungi by molecular analysis

The identification of selected fungal strains was based on molecular analysis. Fungal DNA were extracted from each pure culture using genomic extraction DNA kit (FAVOGEN, Taiwan). The ITS of rDNA was amplified by ITS4 and ITS5 primers[20] under the following thermal conditions: 95ºC for 3 min, 35 cycles of 95ºC for 30 s, 52ºC for 30 s, and 72ºC for 1 min. NucleoSpin Gel and PCR Clean-up Kit (Macherey-Nagel, Germany was used during PCR purification. The sequences were determined in a genetic analyzer at 1st Base Company (Kembangan, Malaysia). Sequences were compared with other sequences found in GenBank database via BLAST analysis (http://blast.ncbi.nlm.nih.gov).

Statistical analysis

The data was analyzed by one-way analysis of variance (ANOVA) by SPSS program version 16.0 for Windows, and Tukey's range test was used for significant differences (P <0.05) between treatments.

Results and Discussion:

Sampling and fungal isolation

The pH, characteristics and organic matter content of soil samples are shown in Table 1. A total of 87 fungal strains showed solubilization zone on the modified Aleksandrov agar. The highest number of recovered fungal strains and organic matter content were found in site 2. This result was supported by the previous studies reported that the soil with higher organic matter content had a greater microbial biomass.[21,22] Soil type is a major determinant of the structure of microbial communities such as soil texture and structure, organic matter, microaggregate stability, pH, and nutrients.[23] The highest number of the positive strains was found in soil sample collected from site 1 (Table 1). It was found that three fungal strains (SDBR-CMUI1, SDBR-CMUI4 and SDBR-CMUO2) were the most effective strain and selected for their ability to solubilize insoluble minerals.

Table 1. Rhizosphere microbial density and characteristics of soil samples

Collection site	Total (CFU/g)	Positive colony (CFU/g)	Soil texture	pH	Organic matter (%)
Site 1	198 b	55 a	loamy sand	4.75±0.01^{b}	4.74±0.09^{b}
Site 2	306 a	17 b	loamy sand	6.85±0.01^{a}	5.22±0.18^{a}
Site 3	141 c	15 b	sandy clay loam	6.86±0.06^{a}	3.49±0.06^{c}
Total number	645	87			

Value with the different letters within the same column indicated the significant difference at P <0.05 according to Tukey's range test.

Evaluation of the insoluble minerals solubilization ability

Three fungal strains (SDBR-CMUI1, SDBR-CMUI4 and SDBR-CMUO2) were used in this experiment. Their ability to solubilize metal minerals depended on type of minerals and strain. In some solubilization cases, fungal strains produced a solubilization zone in agar that was larger than the fungal colonies (Figure 1A–G, I–L), while in other cases the solubilization zones were found beneath the fungal colonies (Figure 1H). The solubilization activities were expressed in terms of a SI value and are shown in Figure 2. The solubilization activity of all fungal strains in presence of $Ca_3(PO_4)_2$, $CoCO_3$, CuO, $FePO_4$, $MgCO_3$, and $ZnCO_3$ was characterized as medium (1.0<SI<2.0) activity. All fungal strains showed a low solubilization activity (SI<1.0) for MnO. However, all fungal strains could not solubilize $Al_3(PO_4)_2$.

In the terrestrial environment, fungi play important roles in the biogeochemical cycling of elements.[24,25] Soil fungi can mobilize and solubilize insoluble mineral into forms available for cellular uptake and leaching from the system, e.g. complexation with organic acid, other metabolites and siderophore.[4,26] In this study, pure cultures of fungi were able to solubilize different insoluble minerals (P, Co, Cu, Fe, Mg, Mn, and Zn-containing minerals) and the solubilization demonstrated very different activities for the different minerals. This result is similar to previous studies that reported fungi isolated from soils are able to solubilize insoluble minerals.[27–37] The solubilization indices on agar plate of three fugal strains, SDBR-CMUI1, SDBR-CMUI4 and SDBR-CMUO2 in this study were compared with other *Aspergillus* strains. Mahamuni et al.[38] reported that the SI for $Ca_3(PO_4)_2$ solubilization of *A. niger* NFCCI 1991, *A. awamori* NFCCI 1992 and *A. fumigatus* NFCCI 1993 were 1.37, 1.48 and 1.13, respectively. While, Bakri[39] reported that the SI for $Ca_3(PO_4)_2$ and $Zn_3(PO_4)_2$ were in the ranging of 2.10 to 3.50 and 2.06 to 2.26, respectively.

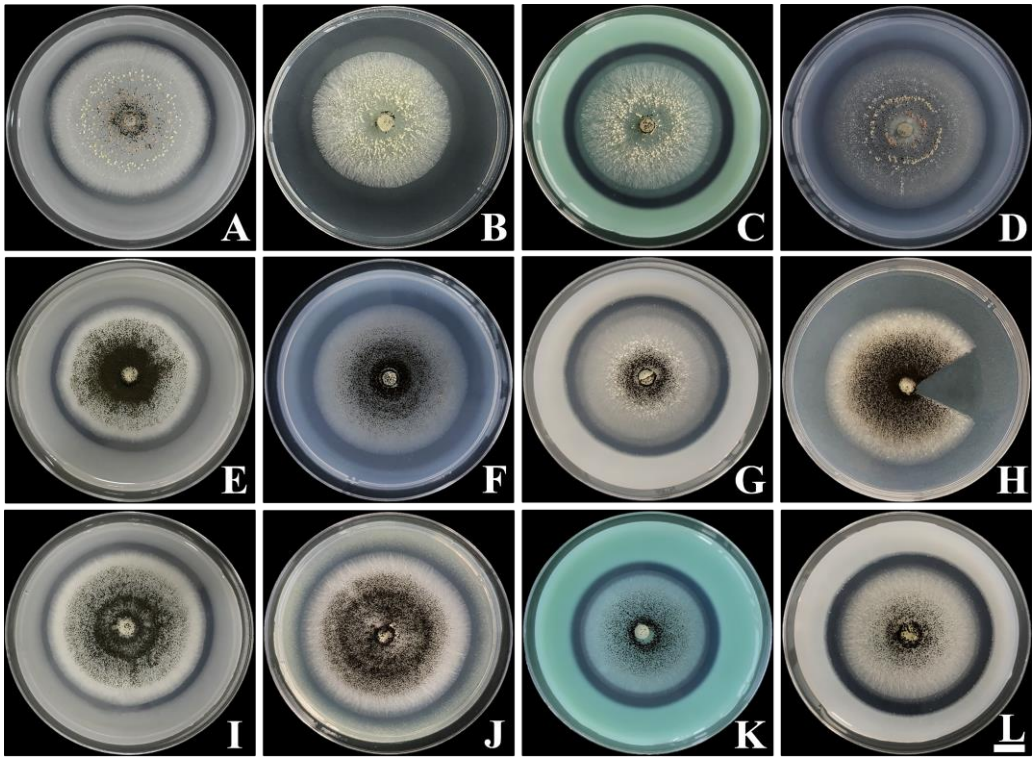

Figure 1. Solubilization of insoluble minerals in agar media by the selected fungal strains. **SDBR-CMUI1**: A) $Ca_3(PO_4)_2$, B) $CoCO_3$, C) CuO, D) $MgCO_3$. **SDBR-CMUI4**: E) $Ca_3(PO_4)_2$, F) $MgCO_3$, G) $ZnCO_3$, H) MnO. **SDBR-CMUO2**: I) $Ca_3(PO_4)_2$, J) $FePO_4$, K) CuO, L) $ZnCO_3$. Scale bars = 10 mm. Fungal colonies in H was cut for the solubilization area (halo zone) observation.

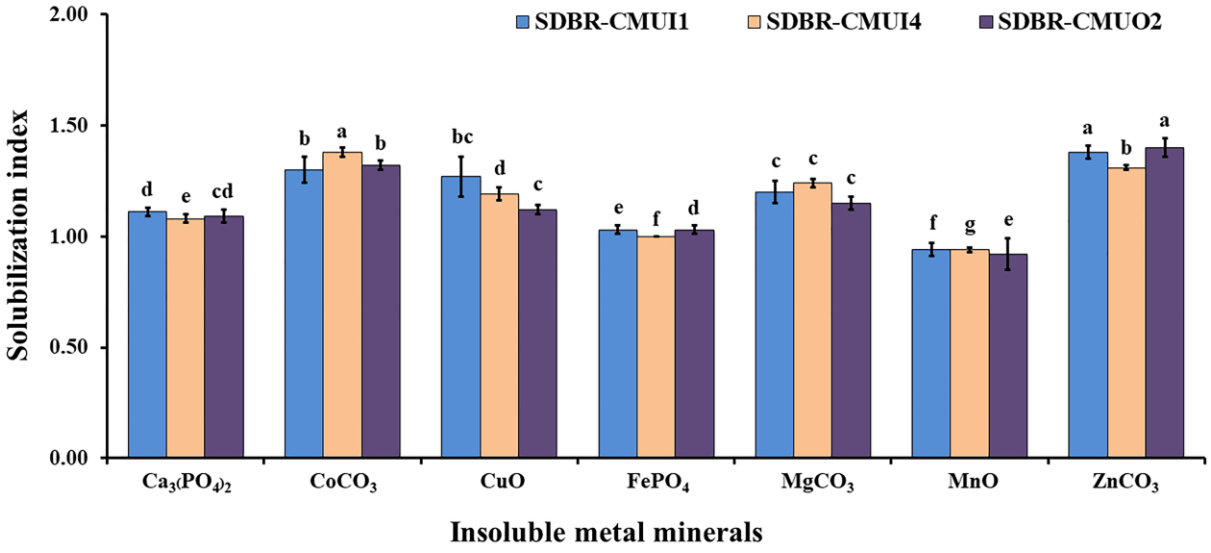

Figure 2. Solubilization index of the ability to solve insoluble mineral by selected fungal strains. Data are means of three replicates. Error bar at each point indicates ± SD. Different letters above each graph indicate that the means are significantly different by Tukey's range test (P <0.05).

Previous studies have been demonstrated that these soil fungi could solubilization inorganic minerals through mechanisms that involve the mainly production of organic acids (acetic, ascorbic, citric, formic, fumaric, gluconic, malic, succinic, tartaric, lactic, and oxalic acids) and hydrolytic enzymes (phytase and phosphatases).[29,32,33,40,41] However, insoluble minerals solubilization by fungi is not a simple phenomenon and may be determined by many factors, such as nutritional, physiological, and the growth conditions of the fungi.[41] Therefore, we need further studies on the mechanisms of three selected fungal strains and evaluated in terms of its effectiveness to plant growth promoting under pot and field experiments.

Identification of selected fungi by molecular analysis

The ITS sequences analysis showed that three fungal strains SDBR-CMUI1, SDBR-CMUI4 and SDBR-CMUO2 were belonged to a genus *Aspergillus* (Table 2). Strains SDBR-CMUI1, SDBR-CMUI4 and SDBR-CMUO2 were closely related to *A. piperis*, *A. welwitschiae* and *A. tubingensis*, respectively. However, the current species identification in a genus *Aspergillus* requires the multigene analysis and extrolite analysis.[42–44] This result was similar to the previous studies that fungi in the genus *Aspergillus* was commonly isolated from rhizosphere soils and has ability to solubilize the insoluble minerals.[45–47] Our result is agreed with the several previous studies have found that the fungi in genera *Aspergillus*, *Apophysomyces*, *Arthroderma*, *Alternaria*, *Fomitopsis*, *Fusarium*, *Geotrichum*, *Mucor*, *Ovularopsis*, *Penicillium*, *Rhizopus*, *Talaromyces*, and *Trichoderma* isolated from soils could solubilize the insoluble minerals.[27–37]

Table 2. BLAST result of ITS sequence of the selected fungal strains in this study

Strain	Sequence length (bp)	BLAST result		
		Closely organism	Accession	Similarity (%)
SDBR-CMUI1	598	*Aspergillus piperis*	MT529169	100
SDBR-CMUI4	597	*Aspergillus welwitschiae*	MT318166	100
SDBR-CMUO2	594	*Aspergillus tubingensis*	MK450659	100

Conclusion:

A total 87 fungal strains in the positive phosphate solubilization were recovered from agriculture soil in northern Thailand. Three fungal strains, SDBR-CMUI1, SDBR-CMUI4 and SDBR-CMUO2 showed the most effective phosphate solubilization ability. Moreover, three selected fungal strains have ability to solubilize the insoluble minerals including $Ca_3(PO_4)_2$, $CoCO_3$, CuO, $FePO_4$, $MgCO_3$, MnO, and $ZnCO_3$. All selected fungal strains were belonged to a genus *Aspergillus* based on the ITS sequences analysis. Therefore, the future study requires the multigene analysis and extrolite analysis for species identification of selected fungal strains. The mechanism for their solubilize the insoluble mineral will be investigated.

Acknowledgements:

This work was supported by grants from Center of Excellence on Biodiversity (BDC), Office of Higher Education Commission (BDC-PG4-161008) and Graduate School Chiang Mai University, Chiang Mai, Thailand.

References:

1. Fernández LA, Zalba P, Gómez MA, Sagardoy MA. Biol Fertil Soils. 2017;43:805–809.
2. Soetan KO, Olaiya CO, Oyewole OE. Afr. J. Food Sci. 2010;4:200–222.
3. Lian B, Chen Y, Zhu L, Yang R. Earth Sci. Front. 2008;15:90–99.
4. Gadd GM. Microbiology. 2010;156:609–643.
5. Martínez-Viveros O, Jorquera MA, Crowley DE, Gajardo G, Mora ML. J. Soil Sci. Plant Nutr. 2010;10:293–319.
6. Haro R, Benito B. Int. J. Mol. Sci. 2019;20:3169.
7. Khan MS, Zaidi A, Ahemad M, Ahemad M, Wani PA. Arch. Agron. Soil Sci. 2010;56: 73–98.
8. Gyaneshwar P, Kumar GN, Parekh LJ, Poole PS. Plant Soil. 2002;245:83–93.
9. Etesami H, Emami S, Alikhani HA. J. Soil Sci. Plant Nutr. 2017;17:897–911.
10. Sattar A, Naveed M, Ali M, Zahir ZA, Nadeem SM, Yaseen M, Meena VS, Farooq M, Singh R, Rahman M, Meena HN. Appl. Soil Ecol. 2019;133:146–159.
11. Kucey RMN. Can. J. Soil Sci. 1983;63:671–678.
12. Mittal V, Singh O, Nayyar H, Kaur J, Tewari R. Soil Biol Biochem. 2008;40:718–727.
13. Sharma SB, Sayyed RZ, Trivedi MH, Gobi TA. SpringerPlus. 2013;2:1–14.
14. Parmar P, Sindhu SS. J Microbiol Res. 2013;3:25–31.
15. Bouyoucos GJ. Agron. J. 1962;54:464–465.
16. Walkley A, Black IA. Soil Sci. 1934;37:29–38.
17. Fomina MA, Alexander IJ, Colpaert JV, Gadd GM. Soil Biol Biochem. 2005;37:851–866.
18. Vitorino LC, Silva FG, Soares MA, Souchie EL, Costa AC, Lima WC. Int. Res. J. Biotechnol. 2012;3:47–54.
19. Kumla J, Suwannarach N, Bussaban B, Matsui K, Lumyong S. Ann. Microbiol. 2014; 64:707–720.
20. White TJ, Bruns T, Lee S, Taylor J. PCR protocol, a guide to methods and applications. Academic Press, San Diego. 315–322.
21. Buyer JS, Roberts DP, Russek-Cohen E. Can. J. Microbiol. 1999;45:138–144.
22. Fan Z, Lu S, Liu S, Guo H, Wang T, Zhou J, Peng X. Sci. Rep. 2019;9:8761.
23. Garbeva P, van Veen JA, van Elsas JD. Annu. Rev. Phytopathol. 2004;42:243–270.
24. Gadd GM. Microbiol. Spectr. 2017;5:1–6.
25. Frąc M, Hannula SE, Bełka M, Jędryczka M. Front. Microbiol. 2018;9:707.
26. Mapelli F, Marasco R, Balloi A, Rolli E, Cappitelli F, Daffonchio D, Borin S. J. Biotechnol. 2012;157:473–481.
27. Akintokun AK, Akande GA, Akintokun PO, Popoola TOS, Babalola AO. Int. J. Soil Sci. 2007;2:301–307.
28. Mahamuni SV, Wani PV, Patil SA. AJBPR. 2012;2:237–244.
29. Acevedo E, Galindo-Castañeda T, Prada F, Navia M, Romero HM. Appl. Soil Ecol. 2014;80:26–33.
30. Kanse OS, Whitelaw-Weckert M, Kadam TA, Bhosale H. Ann. Microbiol. 2014;65:85–93.
31. Patel S, Panchal B, Karmakar N, Katagi RB, Jha S. Ecol. Environ. Conserv. 2015;21: 223–231.
32. Yin Z, Shi F, Jiang H, Roberts DP, Chen S, Fan B. Can. J. Microbiol. 2015;61:913–923.
33. Zhao L, Zhang Y. J. Integr. Agric. 2015;14:1588–1597.
34. Gaind S. Microbiol. Res. 2016;193:94–102.
35. Kasana RC, Panwar NR, Burman U, Pandey CB, Kumar P. nt J Curr Microbiol Appl Sci. 2017;6:1752–1762.
36. Karmakar P, Sharma D, Das P, Saha AK. RJLBPCS. 2018;4:330–336.
37. Khuna S, Suwannarach K, Kumla J, Meerak J, Nuangmek W, Kiatsiriroat T, Lumyong S. MycoKeys. 2019;45:75–92.
38. Mahamuni SV, Wani PV, Patil AS. AJBPR. 2012;2:237–244.
39. Bakri MM. BioNanoSci. 2019;9:238–244.
40. Jain R, Saxena J, Sharma V. Ann. Microbiol. 2012;62:725–735.
41. Xiao C, Fang Y, Chi R. Res Chem Intermed. 2015;41:2867–2878.
42. Vesth TC, Nybo JL, Theobald S, Frisvad JC, Larsen TO. Nat. Genet. 2018;50:1688–1695.
43. Matsuzawa T, Abliz P, Yaguchi T, Gonoi T, Horie Y. Mycoscience. 2019;60:354–360.
44. Cai W, Huang P, Yan Y, Sun B, Jiang X, Chen AJ. Mycoscience. 2020;61:71–75.
45. Li X, Luo L, Yang J, Li B, Yuan H. Appl Biochem Biotechnol. 2015;175:2755–2768.
46. Elias F, Muleta D, Woyessa D. J. Agric. Sci. 2016;8:204–218.
47. Amrutha G, Savalgi VP, Jagadeesh KS, Hebsur NS. Int.J.Curr.Microbiol.App.Sci. 2018;7:988–998.

C_012_PA: GENOME WIDE ASSOCIATION STUDY FOR GROWTH PARAMETER UNDER DROUGHT STRESS AT SEEDLING STAGE IN LOCAL THAI RICE VARIETIES

Thammaporn Kojonna,[1,2] Teerapong Buaboocha,[3] Monnat Pongpanich,[4] Supachitra Chadchawan[1]

[1]Center of Excellence in Environment and Plant Physiology, Department of Botany, Faculty of Science, Chulalongkorn University, Bangkok 10300, Thailand
[2]Program in Biotechnology, Faculty of Science, Chulalongkorn University, Bangkok 10300, Thailand
[3]Molecular Crop Research Unit, Department of Biochemistry, Faculty of Science, Chulalongkorn University, Bangkok 10300, Thailand
[4]Department of Mathematics and Computer Science, Faculty of Science, Chulalongkorn University, Bangkok 10300, Thailand
*e-mail: Supachitra.C@chula.ac.th

Abstract:

Drought is one of abiotic stress factors that affect the rice growth and productivity. In this study, the parameters of physiological responses, shoot fresh weight, shoot dry weight, root fresh weight, root dry weight, and root/shoot ratio under normal and drought stress conditions of 119 local Thai rice cultivars were used to perform genome-wide association study (GWAS) to predict the putative genes that play a crucial role in drought tolerance. Total of 27 potent candidate genes were predicted. Eleven of them were located in the previously reported drought tolerant QTLs in rice. Furthermore, one of the predicted drought tolerant genes, *Os11g0683700* is homolog to Arabidopsis *pectinesterase gene (AT5G19730)*, which was reported as drought resistant gene (patent: WO2013122473A1). These suggested that *Os11g0683700* might play the similar role under drought stress. Based on these data, GWAS can be a potential tool to predict drought tolerant genes in local Thai rice population and validation of the putative drought tolerant genes should be performed in order to use for drought tolerant breeding program in the future.

C_013_PF: SELECTION OF FILAMETOUS FUNGI AND LIGNOCCELLULOSIC RESIDUES FOR PHYTASE PRODUTION UNDER SOLID-STATE FERMENTATION

Kritsana Jatuwong,[1,2,3] Jaturong Kumla,[1,2] Nakarin Suwannarach,[1,2] Saisamorn Lumyong[1,2*]

[1]Department of Biology, Faculty of Science, Chiang Mai University, Chiang Mai, Thailand
[2]Research Center of Microbial Diversity and Sustainable Utilization, Chiang Mai University, Chiang Mai, Thailand
[3]Ph.D. Degree Program in Applied Microbiology, Department of Biology, Faculty of Science, Chiang Mai University, Chiang Mai, Thailand
*e-mail: scboi009@gmail.com

Abstract:

Phytase is an enzyme that hydrolyzes phytic acid to myo-inositol and inorganic phosphate. It is the most common enzyme used in the feeding monogastric animals (poultry, pigs, and fishes) to enhance the digestibility of phosphorus. Phytase has a wide distribution in plants, animal tissues, and microorganisms (bacteria, yeast, and filamentous fungi). Microorganisms are the most important source for phytase production. Several microorganisms considered as potential phytase producers when they grew on lignocellulosic materials. This work aims to study the phytase production from filamentous fungi under SSF. The twenty-seven fungi were used for phytase activity screening by agar assay. It was found that five fungi (*Pholiota adiposa*, *Ganoderma mastoporum*, *Piptoporus* sp., *Amauroderma rugosum*, and *Marasmius* sp.) showed the positive phytase production. They were selected for the phytase production under the SSF process with lignocellulosic residues (sawdust, coffee parchment, oil palm empty fruit bunch, rice bran, and water hyacinth). The results indicated that *Pholiota adiposa* showed the most effective fungus and water hyacinth showed the most suitable substrate for phytase production.

Introduction:

Phytic acid ($C_6H_{18}O_{24}P_6$) (myo-inositol hexakisphosphate (IP6), or myo-inositol polyphosphate), also known as phytate when is in the salt form. It is the primary storage form of phosphorus in most plant tissues such as cereal grains, legumes, and oilseeds, which are a major ingredient in animal feeds.[1,2] Monogastric animals and humans are unable to digest phytate completely and do not benefit from the phosphate of phytate because they lack the gastrointestinal phytase enzyme.[3] Phytase has a wide distribution in living tissues.[4] Several microorganisms including bacteria, yeast, protozoa, actinomycetes, and filamentous fungi have the phytase-production ability.[5] Generally, the phytase produced from fungi is extracellular belonging to fungal genera *Aspergillus, Mucor, Penicillium*, and *Rhizopus*. *Aspergillus ficuum* NRRL 3135 was defined as the most active fungal phytase producer.[6,7] Other known fungi that produce phytase such as *A. carbonarius*, *A. fumigatus*, *A. niger*, *A. oryzae*, *Cladosporium* species, *Mucor piriformis* and *Rhizopus oligosporus*.[8,9,10] Moreover, some mushrooms species have also been examined such as *Agaricus bisporus*, *Grifola frondosa*, *Lentinula edodes*, *Pleurotus ostreatus*, *P. cornucopiae*, and *Schizophyllum commune*.[11,12] Moreover, some species of yeast, bacteria and actinomycete have been reported for their phytase production ability.[13,14] However, *Aspergillus* has been most commonly employed for phytase production. Haefner et al. (2005)[15] have been reported that the first commercial phytase product obtained from *A. niger* was launched into market in 1991. Now a day, phytase products from several microorganisms such as *A. oryzae*, *Schizosaccharomyces pombe*, and *Trichoderma reesei* are available in the market.[16] The production of

phytase has been performed using different fermentation methods; namely solid-state (SSF), semi-solid, and submerged fermentation (SmF).[17,18] Among the different fermentation methods, phytase produced by filamentous fungi has been mostly performed under solid-state fermentation (SSF) using different types of lignocellulosic residues as a substrate. Several studies of SSF using filamentous fungi have been reported for phytase production. For examples, *A. ficuum*, *A. niger*, *A. tubingensis*, *Ganoderma stipitatum*, *Grifola frondosa*, *Penicillium purpurogenum*, *Schizophyllum commune*, and *Trametes versicolor* have been performed under fermentation using different types of lignocellulosic residues such as wheat bran, soybean meal, brown rice, corn cob and corn bran.[11,18,19,20,21,22,23] In this study, the phytase production under SSF from the selection of filamentous fungi and substrates were investigated.

Methodology:

Microorganisms

Twenty-seven filamentous fungi were obtained from the Sustainable Development of Biological Resources Laboratory (SDBR), Department of Biology, Faculty of Science, Chiang Mai University, Chiang Mai, Thailand. The cultures were maintained in 15% glycerol at -20°C. The isolates were reactivated on potato on potato dextrose agar (PDA) and incubated at 30°C for 7 days.

Lignocellulosic residues

Five types of natural substrates including, sawdust, coffee parchment, oil palm empty fruit bunch and water hyacinth were collected from a local place in Chiang Mai province.

Screening of the effective phytate-producing fungi

The selection of fungal phytase producer was carried out in modified phytase screening medium (PSM).[11,24] containing (gram per liter) glucose 20, Na-phytate 4, $CaCl_2 \cdot 2H_2O$ 2, NH_4NO_3 5, KCl 0.5, $MgSO_4 \cdot 7H_2O$ 0.5, $FeSO_4 \cdot 7H_2O$ 0.01, $MnSO_4.7H_2O$ 0.01, agar 15. Mycelial plug (0.5 cm in diameter) was inoculated onto the agar medium. The clearance zone and colony diameter were measured after 3 days of incubation at 30°C. The strains that degraded sodium phytase were selected to evaluate the production of phytase under SSF.

Screening of lignocellulosic residues for phytase production under SSF of selected fungi

Different five types of lignocellulosic substrates including, sawdust, coffee parchment, oil palm empty fruit bunch, rice bran and water hyacinth were used as substrates for SSF of the phytase production. Each substrate was transferred to glass tube and moistened with the modified PSM solution. The initial moisture content in the substrate was adjusted to approximately 80% (w/v). The tubes were sterilized at 121°C for 15 minutes, cooled to room temperature, and inoculated with selected fungal strains and incubated at 30°C for 7 days. After fermentation, the fermented material was harvested and assayed for phytase activity. All experiments were performed in triplicate.

Effect of different carbon and nitrogen sources on phytase production of selected fungi

Fermentation of P. adiposa with water hyacinth was optimized on the effect of nutrients for phytase production in modified PSM. Fermentation was carried out with different carbon source (sucrose, fructose, maltose, and corn starch) at a concentration of 2.0 %, by replacing the glucose in the modified PSM. Fermentation was optimized using different organic and inorganic nitrogen source (urea, peptone, tryptone, malt extract, yeast extract and ammonium sulfate) at concentrations of 0.5% was replaced the ammonium nitrate. Fermentation was performed using deionized water as a control.

Phytase activity assay

The SSF samples were extracted with 0.2 M sodium acetate buffer, pH 5.5 under cool temperature for 60 min. The suspension was centrifuged at 5000 rpm at 4°C for 10 min and the clear supernatant was used as crude enzyme. Phytase activity was determined by measuring the amount of inorganic phosphorus liberated from sodium phytate solution during the enzymatic. Phytic acid sodium salt hydrate was used as substrate. The reaction was determined by the colorimetric method (Harland and Harland, 1980) and measured at 660 nm. One unit (U) of phytase activity was defined as the amount of enzyme that liberates one µmol of inorganic phosphate per minute under assay conditions. The activity of the enzyme is expressed as units per gram dry substrate (U/g ds).

Statistical analyses

Experimental values were given as mean ± standard deviation (SD). The experiment data was analyzed using one-way analysis of variance (ANOVA) in SPSS version 17.0 program for windows and treatments mean compared using Turkey' test with a significance level $p \leq 0.05$ followed by post-hoc tests.

Results and Discussion:

Screening of the effective phytate-producing fungi

The phytase production of filamentous fungi were screened on a medium containing 0.4% sodium phytate as a selective agent. Among, the twenty-seven fungal isolates only five fungal strains were shown the clearing zones around the colonies that positive the phytase production (**Figure 1**). Accordingly, those isolates were chosen for further investigations.

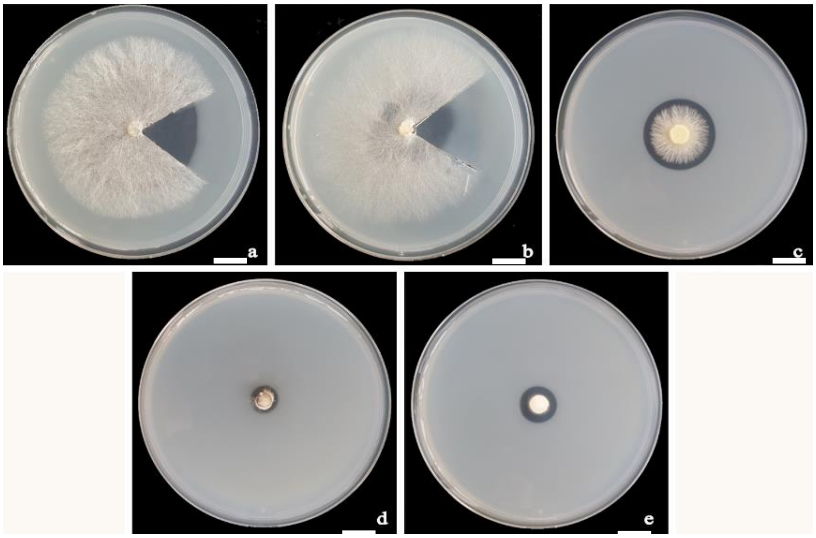

Figure 1. Growth and clear zones of filamentous fungi on agar for phytase production a) *Pholiota adiposa*, b) *Ganoderma mastoporum*, c) *Piptoporus* sp., d) *Amauroderma rugosum*, e) *Marasmius* sp. Scale bar: 10 mm.

Screening of lignocellulosic residues for phytase production under SSF of selected fungi

This work was started by evaluating the production of phytase by using different lignocellulosic residues. The results showed that the maximum phytase productivity of 17.02 U/g ds was achieved with water hyacinth by *P. adiposa* followed by oil palm empty fruit bunch by *Amauroderma rugosum* (8.28 U/g ds) while rice bran and sawdust had not supported phytase production for all fungal strains selected (**Figure 2**). Therefore, *P. adiposa* was selected as the most strains and water hyacinth was selected as the most suitable substrate for investigation of the optimum condition for increasing the phytase activity. There are several substrates such as citric pulp, wheat bran, corn cobs, corn bran, and rice bran are commonly reported to use for phytase production in SSF process.[20,25,26,27] However, wheat bran is one of the most substrates that were used for fungal phytase production. For instance, Salmon et al. (2012)[11] who reported *Schizophyllum commune* to produce phytase through SSF using wheat bran as a substrate. They reported that after the optimization of phytase production, a maximal level of phytase was 113.7 U/g ds. The phytase production by *A. flavus*, *A. ficuum*, *A. niger*, *Ganoderma stipitatum*, *Thermomyces lanuginosus* and *Trametes versicolor* using wheat bran was also reported ranging from 16–200 U/g ds.[3,18,19,27,28] Furthermore, Awad et al. (2012)[20] reported that corn cob mixed corn bran was the suitable substrate for phytase production by *P. purpurogenum* GE1. While, Huang et al. (2018)[23] reported a

phytase production from *Grifola frondosa* under SSF using brown rice. However, water hyacinth and *P. adiposa* have not been reported before.

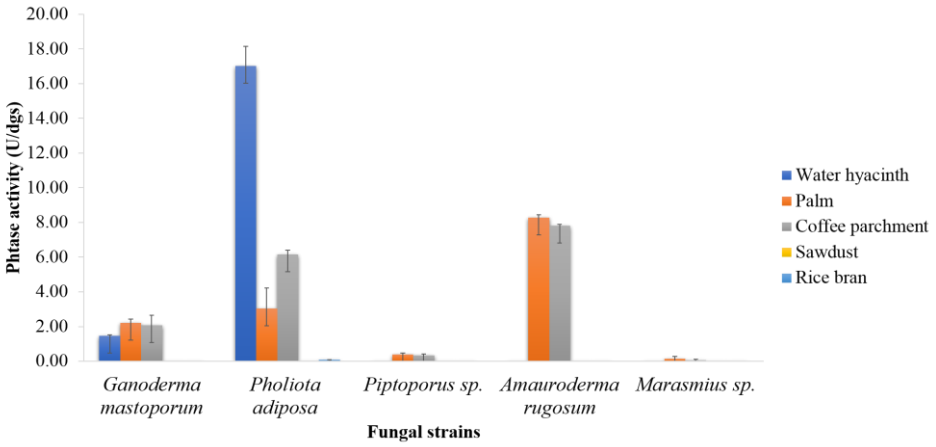

Figure 2 Phytase production during SSF using different natural substrates by the fungal isolates.

Effect of different carbon and nitrogen sources on phytase production of selected fungi

The experiments were performed to examine the suitable nutrient sources for the phytase production from *P. adiposa* under SSF. Water hyacinth was selected as a substrate for phytase production. The effect of carbon and nitrogen sources was studied on the phytase production. The results indicated that glucose was showed the highest phytase with average of 23.24 U/g ds followed by fructose, maltose, and starch with an average of 22.68, 20.07, and 19.83 U/g ds, respectively (**Figure 3a**). However, glucose is one of the most important as simple and easy carbon sources consumed by microorganisms.[20,29] The result consistent with the previous study that glucose supported phytase production by *A. adeninivorans*, *A. niger* NCIM, *A. tubingensis*, *Candida krusei* and *P. purpurogenum* GE1.[20,22,30,31,32] While, Gunashree and Venkateswaran (2008)[33] and Suleimenova et al (2016)[34] reported sucrose was selected as a suitable carbon source for *A. niger*. Salmon et al (2016)[35] who studied the effect of different carbon sources on phytase production by *Ganoderma* sp. MR-56 and found that the maximal phytase activity was obtained when used soybean molasses as a carbon source.

The medium was supplemented with different nitrogen sources included both organic and inorganic nitrogenous sources. The results indicated that the phytase production was significantly ($P < 0.05$) increased when use ammonium nitrate (**Figure 3b**). Ammonium nitrate was shown the great enhancement of enzyme production with 24.48 U/g ds. However, other nitrogen sources could support on phytase production. Therefore, this study indicated that ammonium nitrate is the most efficient source for phytase production by *P. adiposa* in SSF using water hyacinth. This result is similar to the previous report by Suleimenova et al (2016).[34] They reported that ammonium nitrate supported phytase production in *A. niger*. On the contrary, Gunashree and Venkateswaran (2008)[33] and Awad et al (2014)[20] reported that peptone was found to be the most favorable nitrogen source for *A. niger* CFR 335 and *P. purpurogenum* GE1 phytase production. On the other side, Salmon et al. (2016)[35] reported that yeast extract significantly increased the phytase production by *Ganoderma* sp. MR-56.

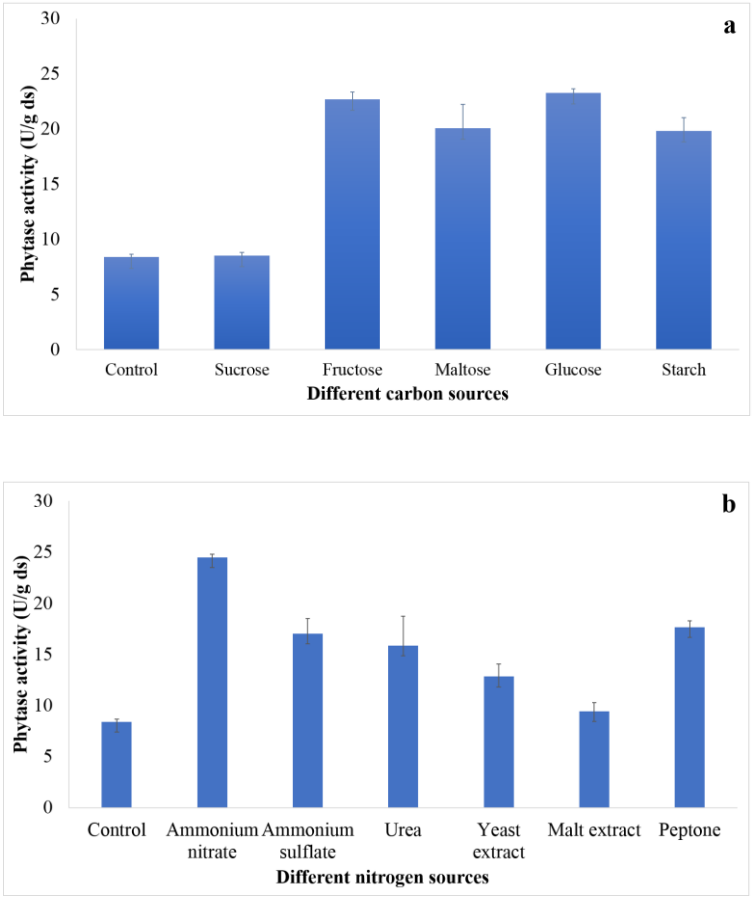

Figure 3 Effect of different carbon and nitrogen sources on phytase production by *Pholiota adiposa* using water hyacinth in solid-state fermentation.

Conclusion:

In conclusion, among the twenty-seven different filamentous fungi are evaluated and selected for the efficient phytate-producing under agar plate assay. Only five fungi were showed clearing zone around colonies on the agar medium. They were selected and grown with five different types of lignocellulosic substrates including, sawdust, coffee parchment, oil palm empty fruit bunch, rice bran, and water hyacinth. The result indicated that the highest enzyme productivity of 17.02 U/g ds was achieved with water hyacinth by *P. adiposa*. Carbon and nitrogen sources were investigated for the increasing phytase production. Our investigation revealed that optimal productively of phytase was achieved using water hyacinth supplemented with glucose as a carbon source and ammonium nitrate as a nitrogen source. The future experiment will find the optimum condition such as temperature for incubation, pH, and incubation period for increasing the enzyme activity including characterization and stability.

Acknowledgements:

The authors would like to acknowledge the TA&RA Scholarship, graduate school, Chiang Mai University, Chiang Mai for support in this research.

References:

1. Hidvegi M, Lasztity R. Chem Eng. 2002;46:59–64.
2. Vats P, Banerjee UC. Enzyme Microb Technol. 2004;35:3–14.
3. Berikten D, Kivanc M. Prep Biochem Biotechnol. 2014;44:834–848.
4. Vohra A, Satyanarayana T. Crit Rev Biotechnol. 2003;23:29–60.
5. Mukhametzyanova AD, Akhmetova AI, Sharipova MR. Microbiology. 2012;81:267–275.
6. Ullah AH, Gibson DM. Prep Biochem. 1987;17:63–91.
7. Chelius MK, Wodzinski RJ. Appl Microbiol Biotechnol. 1994;41:79–83
8. Howson SJ, Davis RP. Enzyme Microb Technol. 1983;5:377–382.
9. Casey A, Walsh G. J Biotechnol. 2004;110:313–322.
10. Quan S, Wang N. Tour Manag. 2004;25:297–305.
11. Salmon DNX, Piva LC, Binati RL, Rodrigues C, de Souza Vandenberghe LP, Soccol CR,
12. Spier MR. Bioproc Biosyst Eng. 2012;35:1067–1079.
13. da Luz JMR, Paes SA, Torres DP, Nunes MD, da Silva JS, Mantovani HC, Kasuya MCM.
14. LWT Food Sci Technol. 2013;50: 575–580.
15. Aly MM, Tork S, Al-Garni SM, Kabli SA. Int J Agric Biol. 2015;17:515–522.
16. Jorquera MA, Gabler S, Inostroza NG, Acuña JJ, Campos MA, Menezes-Blackburn D, Greiner R. Microb Ecol. 2018;75:387–399.
17. Haefner S, Knietsch A, Scholten E, Braun, J, Lohscheidt M, Zelder O. Appl Microbiol Biotechnol. 2005;68:588–597.
18. Menezes-Blackburn D. Gabler S, Greiner R. J. Agric. Food Chem. 2015;63:6142–6149.
19. Han YW, Gallagher DJ, Wilfred AG. J Ind Microbiol. 1987;2:195–200.
20. Shivanna GB, Venkateswaran G. Sci World J. 2014;2014:1–6.
21. Spier MR, Salmon DN, Binati RL, Piva LC, Medeiros AB, Soccol CR. World Acad Sci Eng Technol. 2012;6:427–431.
22. Awad GEA, Helal MMI, Danial EN, Esawy MA. Saudi J Biol Sci. 2014;21:81–88.
23. Saithi S, Tongta A. Agric Agric Sci Procedia. 2016;11:25–30.
24. Qasim SS, Shakir KA, Al-Shaibani AB, Walsh MK. Food Sci Nutr. 2017;8:733–745.
25. Huang SJ, Chen CH, Tsai SY. Int. J. Food Eng. 2018;4:263–267.
26. Demirkan E, Baygın, E, Usta, A. Turk. J. Biochem. 2014;39:206–214.
27. Spier MR, Rodrigues M, Paludo L, Cerutti ML. Enzymes in Human and Animal Nutrition. 2018:89–104.
28. Das S, Ghosh U. J. Sci. Ind. Res. 2014;73:593–597.
29. Shahryari Z, Fazaelipoor MH, Setoodeh P, Nair RB, Taherzadeh MJ, Ghasemi Y. Int. j. recycl. org. waste agric. 2018;7:345–355.
30. Karthik N, Binod P, Pandey A. Biocatal. Biotransformation. 2018;36:296–306.
31. Hassouni H, Alaoui MI, Perraud IG, Augur C. Roussos S. Micol. Aplicada. Int. 2006;18:29–36.
32. Sano K, Fukuhara H, Nakamura Y. Biotechnol. Lett. 1999;21:33–38.
33. Quan CS, Zhang, Wang Y, Ohta Y. J. Biosci. Bioeng. 2001;92:54–160.
34. Soni SK, Khire JM. World J. Microbiol. Biotechnol. 2007;23: 1585–1593.
35. Gunashree BS, Venkateswaran G. J. Ind. Microbiol. Biotechnol. 2008;35:1587–1596.
36. Suleimenova Z, Akhmetsadykov N, Kalieva A, Mustafin K, Saduyeva Z. Adv. Enzyme Res. 2016;4:62–67.
37. Salmon DNX, Fendrich RC, Cruz MA, Montibeller VW, Vandenberghe LPS, Soccol CR, Spier MR. Biochem. Eng. J. 2016;114:288–297.

C_014_PF: INHIBITORY EFFECTS OF ADENOSINE AND ITS COMBINATORIAL EFFECTS WITH CISPLATIN ON CHOLANGIOCARCINOMA

Ingon Inson,[1] Rutaiwan Tohtong,[1] Kanlaya Katewongsa,[1,2] and Kornkamon Lertsuwan[1,3*]

[1] Department of Biochemistry, Faculty of Science, Mahidol University, Thailand
[2] School of Materials Science and Innovation, Faculty of Science, Mahidol University, Thailand
[3] Center of Calcium and Bone Research (COCAB), Faculty of Science, Mahidol University, Thailand
*e-mail: kornkamon.ler@mahidol.edu

Abstract:

Cholangiocarcinoma (CCA) is commonly known as bile duct cancer. The epidemiological study indicated that the northeastern region of Thailand had the highest incidence of CCA worldwide. However, most CCA patients were diagnosed at the aggressive stage, and current radiotherapy and chemotherapy showed unsatisfactory results with severe deleterious side effects. Thus, therapeutic strategies for CCA need to be improved. Many studies indicated that a high concentration of adenosine had inhibitory effects on various types of cancer. In this study, KKU-213 was used to represent CCA cell line, and our results showed that adenosine also had the ability to suppress CCA cell growth. Interestingly, a synergistic effect of adenosine with cisplatin was reported in ovarian cancer. However, the effects of adenosine on cisplatin sensitivity of CCA have not been studied. Our results showed that the combination of adenosine and cisplatin showed synergistic effect and could also induce higher apoptosis in KKU-213 as compared to adenosine or cisplatin treatment alone. As adenosine could be phosphorylated by adenosine kinase into AMP led to an increased ratio of AMP/ATP resulting in AMPK activation. The level of AMPK phosphorylation in KKU-213 treated with adenosine was investigated. However, our results showed that adenosine did not induce AMPK phosphorylation in KKU-213. In addition, the sensitivity of KKU-213 on 5-FU, the common nucleoside-based drug for CCA was determined and compared to adenosine. Our results showed that KKU-213 is more sensitive to 5-FU than adenosine. However, with its previous report of lower side effects and its ability to improve cisplatin sensitivity, adenosine is still a good candidate for novel therapeutic for CCA. These findings may open new treatment options to overcome limited chemotherapy in CCA.

Introduction:

Cholangiocarcinoma (CCA) is commonly known as bile duct cancer[1]. Epidemiological study indicates that the incidence and mortality rate of CCA have been increasing worldwide in recent decades[2]. In Thailand, CCA shows the highest incidence in the world and becomes a major public health issue in the Northeastern region[3]. Currently, the treatments for CCA includes surgical resection, radiotherapy and chemotherapy. Unfortunately, these current treatments possess some limitation. Surgery is only effective at an early stage of the disease; however, most CCA patients are diagnosed at the aggressive stage because CCA symptom remains silent at an early stage. Moreover, more than 50% of patients relapse after surgery within a few years[4]. This makes radiotherapy and chemotherapy are the only options for unresectable CCA patients. Unfortunately, radiotherapy and chemotherapy show severe deleterious side effects and provide unsatisfactory results[5]. Thus, the therapeutic strategies for CCA need to be improved. Since CCA is not responsive to several current chemotherapeutic drugs including cisplatin. There are many studies indicating that adenosine at high concentration has negative effects on various types of cancer, including hepatoma, prostate cancer and colon

cancer[6-9]. Interestingly, previous study shows that CCA was more sensitive to adenosine than other types of cancer[7-9], and CCA cell lines are more sensitive to adenosine than the immortalized cholangiocyte (imCho) cell lines[10]. Therefore, adenosine may be a good candidate as a novel therapeutic compound for CCA. Interestingly, a synergistic effect of adenosine with cisplatin was reported in ovarian cancer. Adenosine could sensitize cisplatin-resistant ovarian cancer cells to cisplatin and induce apoptosis in ovarian cancer[11]. However, the effects of adenosine on cisplatin sensitivity of CCA have not been studied. Herein, we propose to investigate the role of adenosine in improving the sensitivity of CCA cells to cisplatin, the current chemotherapeutics for CCA. We proposed that a combination of adenosine and cisplatin may have synergistic effect and induce apoptosis in CCA. As adenosine could be phosphorylated by adenosine kinase into AMP led to increase ratio of AMP/ATP and AMPK activation[12]. Level of AMPK phosphorylation in KKU-213 treated with adenosine was investigated in this study. These findings may open new treatment options for CCA.

Methodology:

Cell culture and reagents

MMNK-1 was used to represent immortalized cholangiocyte cell line, and KKU-213 was used to represent CCA cell line. Both cell lines were a kind gift of Associate Professor Dr. Rutaiwan Tohtong (Department of Biochemistry, Faculty of Science, Mahidol University). All cell lines were cultured in Dulbecco's modified Eagle's medium (DMEM) (Gibco, catalog no.12800017) supplemented with 10% fetal bovine serum (FBS) (Gibco, catalog no.10270098), 1% MEM non-essential amino acid (Gibco, catalog no.11140050) and 1% penicillin-streptomycin (Gibco, catalog no.15140122). These cell lines were incubated at 37°C with 5% CO_2.

MTT cell viability assay

MMNK-1 was used to represent immortalized cholangiocyte cell line and KKU-213 was used to represent CCA cell line. These cells were plated at 3,000 cells/well in 96-well plate. Twenty four hours after plating, the cells were treated with adenosine (Sigma Aldrich, catalog no.A4036), cisplatin (Tokyo Chemical Industry, catalog no.D3371) or 5-FU (Sigma Aldrich, catalog no.F6627,) at 1 to 1000 µM. For combination treatment, adenosine was combined with 10 µM cisplatin. After 48 hours, cell viability was measured by using MTT (3-(4,5-dimethylthiazol-2-yl)-2,5-diphenyltetrazolium bromide) assay. MTT reagent (Invitrogen, catalog no.1808898) was added to the final concentration of 1 mg/mL and incubated for 3 hours at 37°C. After that, formazan dissolving solution containing 10% SDS (Sigma, catalog no. L4390) in 50% N, N-dimethyl-formamide (Sigma, catalog no.227056) was added to dissolve formazan. The absorbance of each well representing cell viability was determined at 595 nm by a microplate reader (Thermo, Multiskan EX).

Protein extraction and western blot analysis

The CCA cell line used is KKU-213. These CCA cells were plated at 3 x 10^5 cells/well in 6-well tissue culture plate. CCA cells were treated with 500 µM and 1000 µM of adenosine (A4036, Sigma Aldrich) for 48 hours before collecting cell pellets by scraping. CCA cell pellets were washed twice with cold PBS, and proteins were extracted by modified radioimmunoassay precipitation (RIPA) buffer containing 10% protease inhibitor for 60 minutes on ice. Cell lysates were centrifuged at 7,500 rpm for 30 minutes and supernatants were collected. Protein concentration of samples were measured by using BCA protein assay kit (Thermo scientific, catalog no.23225). Twenty-five micrograms of proteins were separated in 8-15% acrylamide gel at 100 volts for 100 minutes and transferred to nitrocellulose membrane at 12 volts for 120 minutes. Membranes were blocked for 2 hours at room temperature in blocking buffer containing 4% bovine serum albumin (BSA) in 0.1% Tween 20 in Tris buffer saline (TBST). After that, membranes were washed 3 times with TBST and incubated with specific antibody for AMPKα (5832, Cell Signaling Technology) and phosphorylatedAMPKα T172 (2535, Cell Signaling Technology) for overnight at 4°C. Then, membranes were washed 3 times with TBST and incubated with 1:5000 anti-rabbit IgG secondary antibody (7074s, Cell Signaling Technology). Signal was visualized by enhanced chemiluminescence (ECL) and exposed to X-ray film. Band intensity was analyzed by using ImageJ software.

Annexin V apoptosis assay

These CCA cells were plated at 4 x 10^5 cells/ well in 6- well tissue culture plate. CCA cells were treated with 10 µM of cisplatin (Tokyo Chemical Industry, catalog no. D3371), 350 µM of adenosine (A4036, Sigma Aldrich) or the combination of 10 µM of cisplatin and 350 µM of adenosine for 48 hours before collecting cell pellets by centrifuge. After centrifugation, the supernatant was removed, and the cells were resuspended with ice- cold 1X binding buffer. One hundred microliters of the cell suspension was mixed gently with 5 µL of propidium iodide dye solution (Thermo scientific, catalog no. P1304MP) and 5 µL annexin V- FITC solution (Thermo scientific, catalog no. A13199) and incubated in the dark for 15 minutes. Apoptotic CCA cells were analyzed by flow cytometry.

Results and Discussion:

Adenosine suppressed CCA cell growth.

After 48 hours of treatment, high concentration of adenosine could inhibit KKU-213 CCA cell viability (Figure 1). As shown in Figure 1, even though low concentration of adenosine could stimulate KKU-213 cell growth, CCA cell viability was suppressed in high concentration of adenosine. The IC_{50} of adenosine on KKU-213 was 873 µM (Figure 1). KKU-213 was more resistant to adenosine than other subtypes of CCA cell lines, HuCCA-1 and RMCCA-1 reported in previous study[10]. In addition, 5-FU, the common nucleoside-based drug for CCA was determined and compared to adenosine. Our results showed that IC_{50} of 5-FU on KKU-213 was 30 µM (Figure 1) indicating that KKU-213 was more sensitive to 5-FU than adenosine. However, with its previously report of lower side effects and its ability to improve cisplatin sensitivity[11], adenosine is still a good candidate for novel therapeutic for CCA.

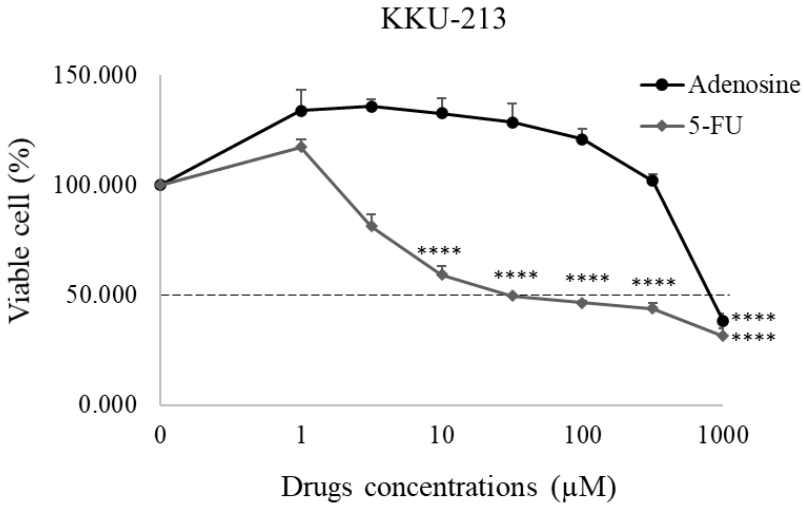

Figure 1. 5-FU and adenosine inhibited KKU-213 cell viability after 48 hours of treatments.

****p<0.0001 as compared to control.

The combination of adenosine and cisplatin showed synergistic effect in CCA cells viability suppression.

Adenosine cytotoxicity was determined and compared to cisplatin and its combination. As observed in Figure 1 and Figure 2, lower concentration of adenosine stimulated cell viability in KKU-213. Not surprisingly, 350 µM adenosine increased CCA cell viability under cisplatin treatment. However, when CCA cells were treated with the combination of cisplatin and 500 µM adenosine, this resulted in the further reduction of CCA cell viability (Figure 2.). After treated for 48 hours, IC_{50} of adenosine for CCA cells was 873 µM; while, CCA had the IC_{50} for cisplatin at 10 µM in KKU-213 cells. When cisplatin was combined with 350 µM and 500 µM adenosine, IC_{50} of the combination were 23 and 9 µM respectively (Figure 2.). In addition, the mode of interaction (additive effect or synergism) between adenosine and cisplatin combination was determined by combination index (CI). The CI were calculated by CompuSyn software. The result showed that combination of cisplatin and 500 µM adenosine had the CI value at 0.83 (Table 1.) which below 1.0 indicating synergism between cisplatin and 500 µM adenosine[13]. Our results corresponded with the results from previous study showing the synergistic effect of adenosine and cisplatin in ovarian cancer.[7] These findings would be beneficial in therapeutic development for CCA.

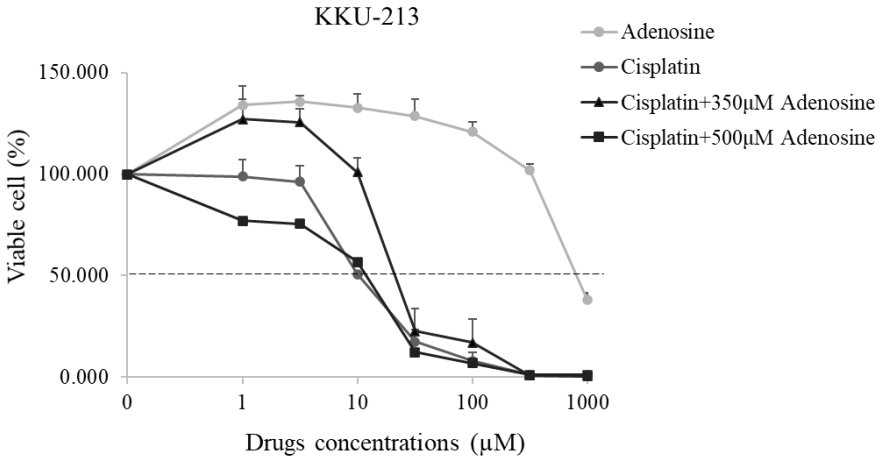

Figure 2. Effects of adenosine, cisplatin and its combination on KKU-213 CCA cell viability.
The combination of adenosine and cisplatin showed synergistic effect on CCA cell viability suppression.

Table 1. Summary of IC50, Combination indices (CI) from the combination of adenosine and cisplatin. CI values was calculated by CompuSyn.

Cell line	*Conditions*	*IC_{50} (µM)*	*Combination index (CI)*
KKU-213	*-1000 µM Adenosine*	*873*	
	-1000 µM Cisplatin	*10*	
	1-1000 µM Cisplatin + 350 µM adenosine	*23*	*2.21*
	1-1000 µM Cisplatin + 500 µM adenosine	*9*	*0.83*

Adenosine did not induce AMPK phosphorylation in CCA cell.

As previous study reported that adenosine could activate AMPK phosphorylation lead to cancer cell death[12], effects of adenosine on level of AMPK and phosphorylated AMPK were determined by western blot (Figure 3A). As shown in Figure 3, adenosine at 300 µM did not induce AMPK expression and phosphorylation in KKU-213 and immortalized cholangiocyte cell line (MMNK-1). However, our group had recently found that adenosine at 500 µM could increase phosphorylated AMPK in other subtype of CCA cell lines, HuCCA-1, RMCCA-1, and CCLP-1 (Unpublished). Therefore, 500 µM adenosine treated KKU-213 should be investigated in future study.

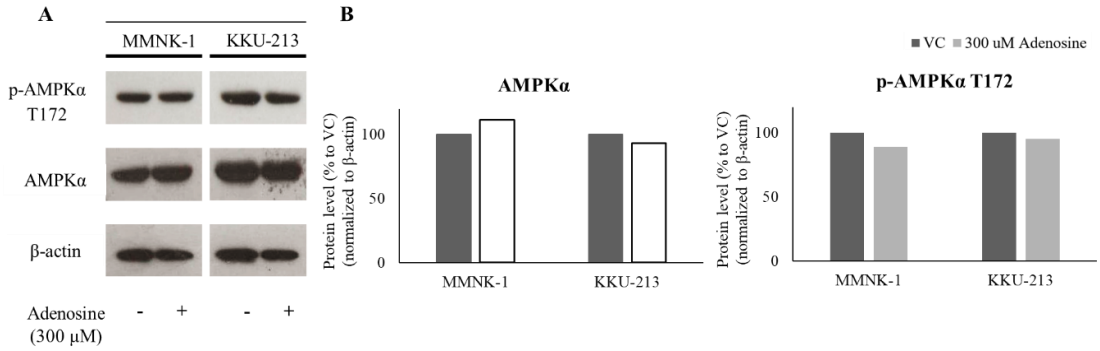

Figure 3. Levels of AMPK and phosphorylated AMPK in adenosine-treated KKU-213 cells were investigated. Adenosine did not induce AMPK phosphorylation in either CCA cells or immortalized cholangiocytes.

The combination of adenosine and cisplatin induced apoptosis in CCA cells.

As shown in Figure 4, adenosine at 350 µM did not increase apoptosis when compared to vehicle control treated cells. Ten micro molars of cisplatin increased KKU-213 apoptosis by approximately 2 folds. However, the combination of 350 µM adenosine and 10 µM cisplatin could induce higher apoptosis in KKU-213 as compared to adenosine or cisplatin alone (Figure 4). This finding may open the new strategy for CCA cell apoptosis induction.

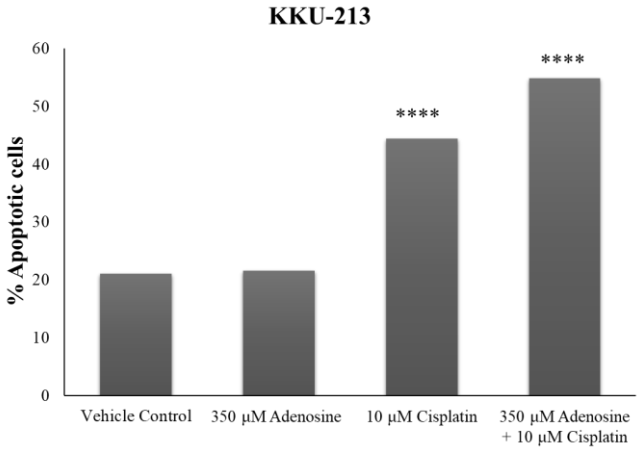

Figure 4. CCA cell apoptosis was determined in KKU-213 cells exposed to adenosine, cisplatin or the combination of adenosine and cisplatin for 48 hours. The combination of adenosine and cisplatin induced higher apoptosis in CCA cells as compared to individual treatment alone.

Conclusion:

Adenosine had ability to suppress CCA cell growth but did not induce AMPK expression and its phosphorylation. The combination of adenosine and cisplatin showed synergistic effect and could also induce apoptosis in CCA cells. Even though CCA cells were also sensitive to 5-FU, the common nucleoside-based drug for CCA, serious side effects of 5-FU on cancer patients were reported[14]. However, with its lower side effects and its ability to improve cisplatin sensitivity previously reported[11], adenosine is still a good candidate for novel therapeutic for CCA. These findings could provide the invaluable data for therapeutic improvement for CCA in the future.

Acknowledgements:

This study was supported by Science Achievement Scholarship of Thailand (SAST) awarded to Ingon Inson and the CIF grant, Faculty of Science, Mahidol University, Thailand awarded to Associate Professor Dr. Kornkamon Lertsuwan.

References:

1. *Blechacz B, Gores GJ. Hepatology. 2008;48:308-321.*
2. *Saha SK, Zhu AX, Fuchs CS, Brooks GA. The oncologist. 2016;21:594–599*
3. *Imsamran W, Chaiwerawattana A, Wiangnon S, Pongnikorn D, Suwanrungrung K, Sangrajrang S, Buasom R. Cancer in Thailand. 2015;8:5-69.*
4. *Rizvi S, Khan SA, Hallemeier CL, Kelley RK, Gores GJ. Nature reviews Clinical oncology. 2018;15:95.*
5. *Sirica AE. Hepatology. 2005;41:5–15.*
6. *Yu S, Hou D, Chen P, Zhang Q, Lv B, Ma Y, Liu F, Liu H, Song EJ, Yang D, Liu J. Biochemical and biophysical research communications. 2015;460:759–765.*
7. *Zhou XT, Pu ZJ, Liu LX, Li GP, Feng JL, Zhu HC, Wu LF. Oncology reports. 2019;41:829–838.*
8. *Nogi Y, Kanno T, Nakano T, Fujita Y, Tabata C, Fukuoka K, Gotoh A, Nishizaki T. Cellular Physiology and Biochemistry. 2012;30:61–74.*
9. *Lertsuwan K, Peters W, Johnson L, Lertsuwan J, Marwa I, Sikes RA. Anticancer research. 2017;37:529–537.*
10. *Lertsuwan J, Ruchirawat M. Anticancer research. 2017;37:3553-3561.*
11. *Sureechatchaiyan P, Hamacher A, Brockmann N, Stork B, Kassack MU. Purinergic signalling. 2018;14:395-408.*
12. *Aymerich I, Foufelle F, Ferré P, Casado FJ, Pastor-Anglada M. Journal of cell science. 2006;116:1612-1621.*
13. *Chou TC. Cancer research. 2010;70:440-446.*
14. *Katona C, Kralovánszky J, Rosta A, Pandi E, Fónyad G, Tóth K, Jeney A. Oncology. 1998;55:468-474.*

C_015_OF: STUDY ON INFLORESCENCE DEVELOPMENT OF LONGAN (*Dimocarpus longan* Lour.) 'PHUANG THONG' GROWN AT SAMUT SAKHON PROVINCE, THAILAND

Jenjira Asayot[1], Panida Kongsawadworakul[1], Watcharra Chintakovid[2], and Aussanee Pichakum[1]*

[1]Department of Plant Science, Faculty of Science, Mahidol University, Rama 6th Road, Phayathai, Bangkok, 10400 Thailand
[2]Division of Agricultural Science, Mahidol University Kanchanaburi Campus, Sai Yok District, Kanchanaburi 71150, Thailand;
*e-mail: aussanee.pic@mahidol.ac.th

Abstract:

Off-season longan (*Dimocarpus longan* Lour.) at Ban Phaeo district, Samut Sakhon province usually encounters with climate change as hot wind. Successful annual growth in the inflorescence and flowering were needed for good productivity, however the perfection in growth and development process was altered depending upon environmental circumstances. Recently, longan growers at Ban Phaeo district have self-studied on the floral growth of 'Phuang Thong' to eliminate an obstruction. In order to clarify communication, this study aimed to observe inflorescence developmental profile using the criteria by local longan growers and the standardization phenological growth stages of longan (BBCH scale). The results showed that the different appearance of inflorescence by the longan glower's scale was classified into 8 stages (stage#0 - stage#7). The inflorescence elongation occurred on the first stage and has completed its length at stage#4, however the visually flower organ was still unclear. On the other hand, the inflorescence length unchanged during later period of stage#4 - stage#7, but the floral organ developed instead. The male or female flowers began opening at stage#5 and the fertilized flowers happened at stage#6, later the initial fruit set was at stage#7. The growth stage by longan grower's scale as 0, 1, 2, 3, 4, 5, 6, and 7 on 'Phuang Thong' inflorescence sequence correlated with the BBCH scale of 510, 511, 513, 515, 610, 613, 611-615, and 617, respectively.

Introduction:

Longan (*Dimocarpus longan* Lour.); a fruit tree in tropical and subtropical zones belonging to Sapindaceae family, is a major economic crop in Southeast Asia[1]. Many commercial cultivars such as 'E-daw', 'Si Chomphoo', 'Biaokhiao', 'Heao' and 'Phuang Thong' were produced in various regions of Thailand[2]. Presently, cultivated area has grown up to 62 provinces (Online information on agricultural production in 2017 from Department of Agricultural Extension). In northern region, major longan orchards perform in-season cultivation whereas in central and eastern ones, i.e., Chantaburi or Samut Sakhon provinces, usually produce off-season[3]. The off-season production shows a trend to increase because of an over production and low selling price of in-season longan[3]. In addition, department of intellectual property has registered Ban Phaeo 'Phuang Thong' as a Geographical Indication (GI) product of Samut Sakhon province.

Annual growth stage of longan can be divided into vegetative and reproductive phases[4]. The first phase starts as bud development, leaf development and shoot development, respectively, following by reproductive phase with inflorescence emergence, flowering, fruit development, and ending with fruit maturity[4]. Flowering process starts with the initiation of inflorescence primordia, then inflorescence emergence, and later flower development. The first visually step as inflorescence emergence and flower development need for the perfection of reproductive growth prior fruit producing[5]. Nevertheless, some characterized inflorescences or flowers, flower percentage, and the periods in flowering process are different depending on the environmental circumstance and the genetic background or cultivar. Early period of growth stage such as the flower initiation or inflorescence primordial is indistinctly to visual sign. Especially local researchers as longan growers are unable to define accuracy growth pattern. Therefore, this study aimed to observe inflorescence developmental profile in off-season longan 'Phuang Thong' grown at Ban Phaeo district, Samut Sakhon province and draw a parallel

between the criteria of the longan growers with the BBCH (Biologische Bundesanstalt, Bundessortenamt und Chemische Industrie) scale which is the standardization phenological growth stages of longan.

Methodology:

Study site

The study operating in commercial longan plot located in Ban Phaeo district, Samut Sakhon province, Thailand (E13.592768, N100.069948). Nineteen year olds trees cv. Phuang Thong were applied potassium chlorate to induce flowering on late June, 2018. Soil drenched in the rate of 100 g/m of canopy diameter and foliar sprayed at 1,500 ppm on 7 days later. The flowers next occurred on August, 2018. Annual pruning, fertilizer application, irrigation and crop protection were normal cultural practiced.

Data collection

All stages of longan inflorescences were randomly collected on August 4-18, 2018. Ten uniform inflorescences on each stage were carefully selected. Firstly, the different characters of each stage were identified following the criteria of longan growers. Secondly, inflorescence lengths were measured, and the flower characters were identified as bloom, male, female, hermaphrodite, and fertilized flower, then flower position on each panicle were recorded. Lastly, all information was analyzed as BBCH scale following Pham et.al. (2015)[4] and (2016)[6].

Results and Discussion:

A detail description of inflorescences on longan 'Phuang Thong' was classified into 8 developmental stages using the criteria by the longan growers as follows (Figure 1).

Stage#0; a whole apical shoot was brown with the undefined development sign which becoming an inflorescence or leaf. Average shoot length was 2.9 cm (minimum-maximum of 2.3-4.2 cm).

Stage#1; the flower buds were initiated at lateral portion of shoot axis with average length of 6.0 cm (minimum-maximum of 4.5-8.0 cm). The color became dark green.

Stage#2; the developed inflorescence was green with average length of 10.4 cm (minimum-maximum of 7.5-14.5 cm), the beginning of primary panicle development clearly found and initial immature flowers happened.

Stage#3; the advanced inflorescence was green and becoming 50% full length with the average in 13.6 cm (minimum-maximum of 11.0-16.0 cm). The secondary panicle was noticeable. Also, the number of immature and closed flower progressively increased.

Stage#4; the fully length with the average of 23.1 cm (minimum-maximum of 18.0-27.7 cm) obviously happened in green inflorescence and mature flowers at just before anthesis stage occurred.

Stage#5; the developed inflorescences were green with average length of 24.6 cm (minimum-maximum of 17.0-29.5 cm). The first bloom completely happened whether it was be male or female flower.

Stage#6; the progressive green inflorescence was average length of 23.8 cm (minimum-maximum of 19.4-27.0 cm). The initial fertilized flowers occurred, while the senescing step happened such as the fallen petal down, the dried stamens and stigmas. Such character was similar to the pollinated flowers on 2 weeks after the anthesis as Pham et al. (2016)[6].

Stage#7; the fully developed inflorescence was average length of 21.7 cm (minimum-maximum of 15.5-28.0 cm). Initial fruits were visible clearly indicating to the fertilized flower. The ovary enlargement showed the characteristic in progressive fruiting step. Also the senescing became increasingly. It was the same appearance to the pollinated flowers on 3 weeks after the anthesis as Pham et al. (2016)[6].

Length of inflorescence on longan 'Phuang Thong' (Figure 1B) represented that the inflorescences elongated during the first phase (stage#0 - stage#4) becoming completely length at stage#4. The inflorescence on stage#0 and stage#1 unclear found any visible flower parts. Then the beginning of immature flowers happened in stage#2 (Figure 1C). However, during stage#2 - stage#4 visualized flower development was uncertain. Thus, the inflorescence on stage#0 - stage#4 by longan scale belonged to inflorescence emergence (PGS5) stage according to BBCH scale as Pham et al. (2015)[4].

An increase in inflorescence length (21.3-24.6 cm) was not observed during stage#4 - stage#7 (Figure 1B). On the other hand, the flower development visually found in stage#5 - stage#7 and the beginning of the opened flowers found at stage#5, next the fertilized flowers found at stage#6, lastly the initial fruit setting occurred at stage#7 (Figure 1C). Consequently, the inflorescence during stage#5 - stage#7 belonged to flowering (PGS6) stage according to the BBCH scale as Pham et al. (2015)[4].

Longan inflorescence characters displayed continuously growth, thus the differential flower types simultaneously found in each inflorescence stage as shown in Figure 1C.

The closed flowers began in stage#2 and the opened one started later in stage#5. Then in stage#6 the fertilized flowers occurred, and the appeared fruit setting initiated in stage#7 (Figure 1C). Additionally, the amount of each flower types differed depending on inflorescence stages (Figure 1D). The inflorescence in stage#2, #3 and #4 showed 100% of closed flowers. The inflorescence in stage#5 gave 97.1% closed flowers and 2.9% opened ones, respectively. The inflorescence in stage#6 showed 82.5%, 11.8%, and 5.7% in closed, opened, and fertilized flowers, respectively. Lastly, the inflorescence in stage#7 gave 49.6%, 39.6%, and 7.0%, in closed, opened, and fertilized flowers, respectively and 3.8% initial fruit. The development in inflorescence length, primary panicle length, and flower number per primary panicle were showed in Figure 2.

The collected information of longan inflorescence compared with the BBCH scale (Pham et al., 2015)[4]. The inflorescence in stage#0 closely resembled with the BBCH scale 510 as reproductive buds dormant, while the stage#1 imitated to the BBCH scale 511 of brownish scales separating and flower buds visible. The inflorescence in stage#2 and the BBCH scale 513 were similar that primary branches visible found. In addition, at 50% inflorescence length as the stage#3 and completely developed length as the stage#4 matched with the BBCH scale 515 and 519, respectively. The inflorescence in the stage#5 with firstly flowers opening was identical the BBCH scale 610. But the stage#6 which starting to find the fertilized flower had 17.5% accumulated opened and fertilized flowers was unclear to identify to BBCH code in flowering stage (PGS6). However, the stage#6 might be roughly stated in the BBCH scale 611-615 which being 10-50% accumulated opened flowers. Finally, the stage#7 meant likewise the BBCH scale 617 with some initial fruit set.

Conclusion:

The different characters of inflorescences on longan 'Phuang Thong' grown at Ban Phaeo district, Samut Sakhon province classifying by the criteria of longan growers as the growth stage of 0, 1, 2, 3, 4, 5, 6, and 7 which consequently correlated with the BBCH scale of 510, 511, 513, 515, 610, 613, 611-615, and 617, respectively. The result might use to correspondingly understand on flowering process and next to provide information for developing proper cultural practice.

Acknowledgements:

The authors thank for field supporting of longan orchardist; Mr. Phairat Teantong at Ban Phaeo district, Samut Sakhon province. Also our teams thank Thailand Science Research and Innovation (TSRI) via research project no. RDG612003, Mahidol University and Development and Promotion of Science and Technology Talents Project (DPST).

References:

1. Jia T., Wei D., Meng S., Allan A.C. and Zeng L., PLoS ONE. 2014;9(12):e114568.
2. Thitiprasert, W. and et al. Agricultural Cooperative Federation of Thailand Ltd. 2002.
3. Sukhvibul, N., Department of Agricultural Extension. 2015.
4. Pham, V., Herrero, M. and Hormaza, Sci Hortic. 2015;189:201-207.
5. Swamy, S., JTBSRR. 2012;1:122-137.
6. Pham, V., Herrero, M. and Hormaza, J., Ann Appl Biol. 2016;169: 357-368.

(A)

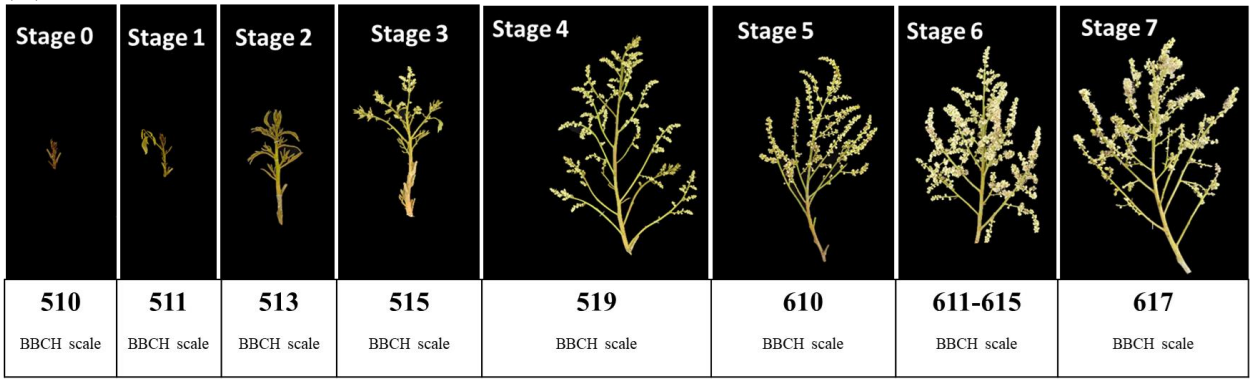

(B)

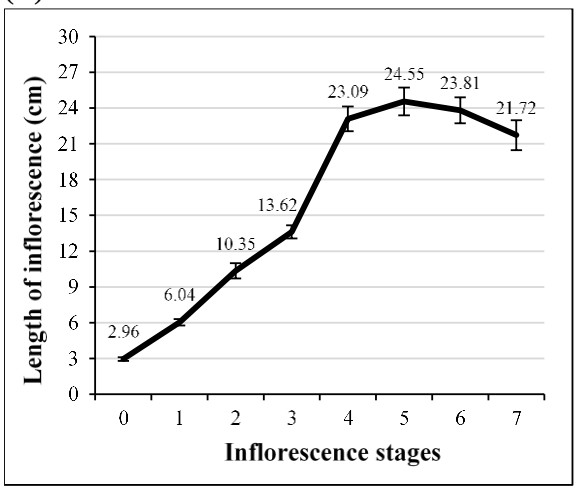

(C)

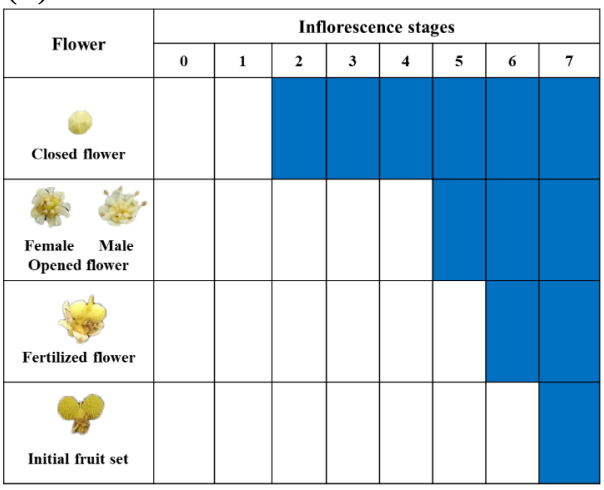

(D)

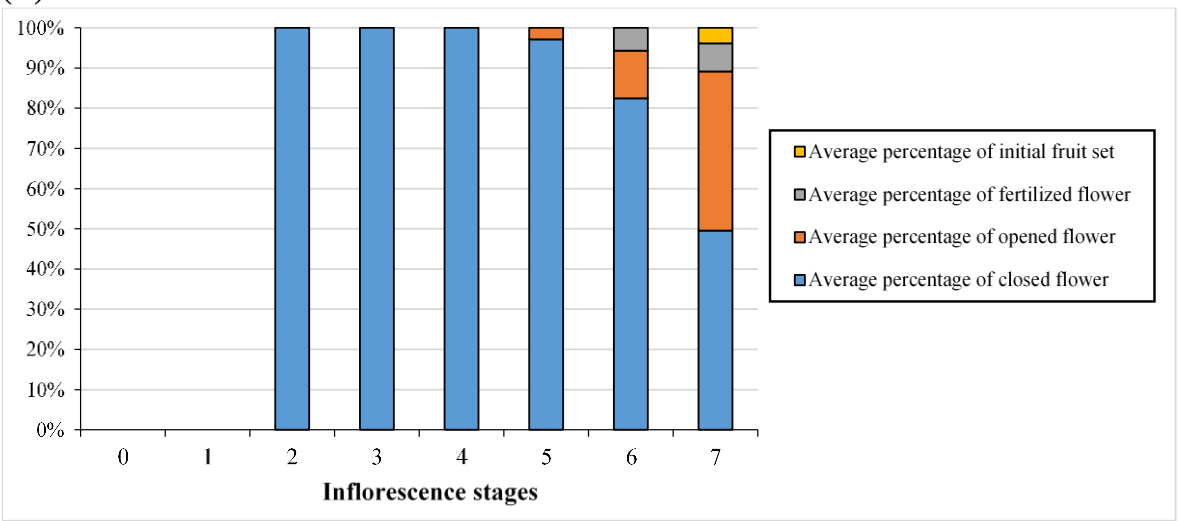

Figure 1. Developmental stage of inflorescence in longan 'Phuang Thong'. (A) Comparing of growth stages between longan growers scale and BBCH scale (Pham et al., 2015 and 2016). (B) Inflorescence length in each longan growers scale. (C) Flower types occurring in each longan growers scale. (D) The average percentage of flower types in each longan growers scale.

Inflorescence Development of Longan ‘Phuang Thong’

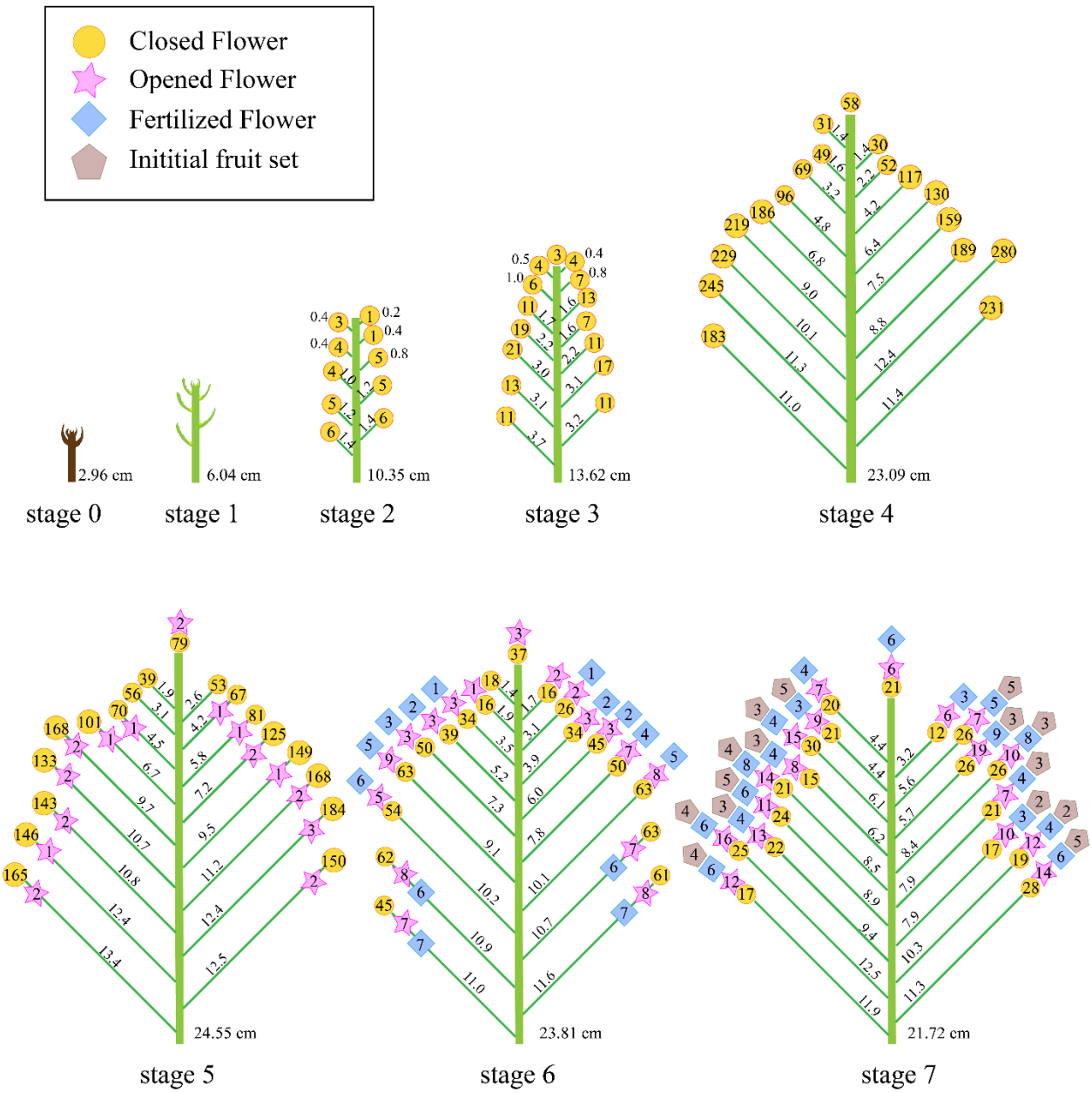

Figure 2. Diagram of inflorescence performance in longan ‘Phuang Thong’. Value in circle or square or pentagon or star represents flower number. Value at the base of inflorescence represents length unit as centimeter.

C_016_PA: SYNTHESIS OF DIHYDRAZONE STEROID DERIVATIVES DERIVED FROM PREGNENOLONE AND THEIR *IN VITRO* CYTOTOXIC ACTIVITY

Patchanee Charoenying[1*], Nawasit Chotsaeng[1]

[1]Department of Chemistry, Faculty of Science, King Mongkut's Institute of Technology Ladkrabang, Bangkok 10520, Thailand

[*]e-mail: patchanee.ch@kmitl.ac.th

Abstract:

A series of pregnenolone derivatives containing dihydrazone unit was synthesized *via* a convenient condensation procedure, and which evaluated for their potential cytotoxic activity. The scheme illustrates the transformation of the starting pregnenolone **(1)** into pregnenolone-20-hydrazone **(2)**, then **(2)** was treated with various aromatic aldehydes to obtain the target compounds **(3a-j)**. The structures of the compounds were confirmed by spectral (^{1}H NMR, ^{13}C NMR and FT-IR) analyses and mass spectrometry. Using MTT method, the cytotoxicity of the synthesized compounds against four human cancer cell lines; HT29 (human colon adenocarcinoma cell line), MCF7 (human breast carcinoma cell line), KB (human oral epidermal carcinoma cell line) and P388 (murine leukemia cell line) was investigated. The results of the *in vitro* study showed that the compounds **(3a)** (IC_{50} = 1.36 μmol/mL against KB), **(3b)** (IC_{50} = 1.62 μmol/mL against P388) and **(3e)** (IC_{50} = 1.90 μmol/mL against HT29) were identified as the most active compounds in all hydrazone derivatives of pregnenolone.

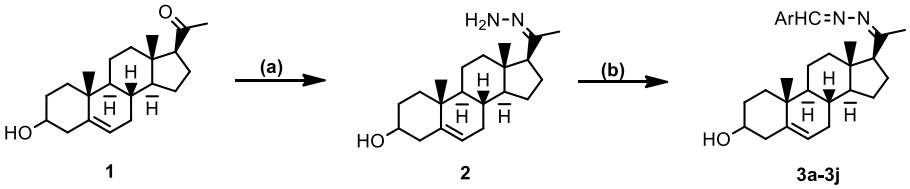

1 2 3a-3j

Scheme 1. Synthesis of dihydrazone pregnenolone derivatives. Reagents and conditions: (a) $NH_2NH_2.H_2O$, EtOH, 60°C, (b) ArCHO, EtOH, 60°C

3a; Ar = C_6H_5—
3b; Ar = 4-$OMeC_6H_4$—
3c; Ar = 2,4,6-$(OMe)_3C_6H_2$—
3d; Ar = 2-OH-3-$OMeC_6H_3$—
3e; Ar = 2-$CH_3C_6H_4$—
3f: Ar = 3-$NO_2C_6H_4$—
3g; Ar = 2,4-$(NO_2)_2C_6H_3$—
3h; Ar = 4-ClC_6H_4—
3i; Ar = 2,4-$(Cl)_2C_6H_3$—
3j; Ar = 4-$COOHC_6H_4$—

C_017_PA: ISOLATION OF ENZYME PRODUCING BACTERIA FROM TERMITE GUTS AND APPLICATION FOR IMPROVING NUTRITIONAL VALUE OF SOYBEAN MEAL

Maneeploy Nualkul,[1] Bundit Yuangsoi,[2] Pinsurang Deevong [1,*]

[1] Department of Microbiology, Faculty of Science, Kasetsart University, Bangkok 10900, Thailand
[2] Department of Fisheries, Faculty of Agriculture, Khon Kaen University, Khon Kaen 40002, Thailand
[*]e-mail: fsciprd@ku.ac.th

Abstract:

This study isolated the endospore forming bacteria from the guts of termite, *Termes propinquus* for soybean meal (SBM) fermentation. Among all different morphology representatives, 10 isolates showed positive results of crude soymilk degradation. These isolates were tested for their ability to produce various plant-based ingredient degrading enzymes (cellulase, xylanase, pectinase, amylase, protease, lipase and phytase). The isolates Tp-5 and Tp-7 presented all enzyme activities tested. Based on 16S rRNA gene sequencing, both isolates were closely related to non-pathogenic *Bacillus* species (*B. amyloliquefaciens*, *B. velezensis* and *B. siamensis*, with 100% similarity). Because of their high efficacy and safety, they were selected for solid-state fermentation of SBM for 24 and 48 h, and their growth were determined. Comparing to unfermented SBM, 48 h-fermented SBM (FSBM) with Tp-5 and Tp-7 revealed an increasing of crude protein (16.35% and 17.49%, respectively) while decreasing of crude fiber (26.30% and 22.79%), nitrogen free extract (10.52% and 13.05%), neutral detergent fiber (31.65% and 38.15%), acid detergent fiber (32.16% and 27.21%) and acid detergent lignin (37.37% and 50.10%). Moreover, analysis of antioxidant activity founded that 2,2-diphenyl-1-picryl-hydrazyl-hydrate (DPPH) scavenging ability of FSBM were stronger than unfermented SBM. The results indicated that fermentation by the potential strains from termite guts cloud improve nutritional value and bioactivity of SBM.

C_018_PF: IMPROVEMENT OF NORFLOXACIN DETECTION LIMIT OF LATERAL FLOW IMMUNOASSAYS USING GOLD NANOFLOWERS

Ratichon Tiandee,[1] Anumart Buakeaw,[2] Songchan Puthong,[2] Sudkate Chaiyo,[2] Umaporn Pimpitak,[2] Kittinan Komolpis,[2,3,*]

[1]Program in Biotechnology, Faculty of Science Chulalongkorn University, Bangkok 10330, Thailand
[2]Institute of Biotechnology and Genetic Engineering, Chulalongkorn University, Bangkok 10330, Thailand
[3]Food Risk Hub, Research Unit of Chulalongkorn University, Bangkok 10330, Thailand
*e-mail : kittinan.k@chula.ac.th

Abstract:

Lateral flow immunoassay (LFIA) or strip test is an immunological method which has been widely used for screening detection of various types of antigen such as biomolecules, chemicals and antibiotics due to its easy to use, inexpensive and portable. However, its use is limited by low sensitivity of the test. There are many factors such as antibody capability and numbers of gold nanoparticle conjugated to the antibody which affect sensitivity or limit of detection (LOD) of the LFIA. Many methods have been studied to improve the sensitivity of the LFIA. One interesting method is the use of larger multi-branched gold nanoflowers (AuNFs) as the reporting molecule instead of conventional gold nanospheres (AuNSs). In this study, LFIAs using AuNFs and AuNSs were developed to detect residual of norfloxacin (NOR), a synthetic fluoroquinolone antibacterial agent. It was found that LFIA with AuNFs (LOD = 10 ng/ml) was more sensitive than LFIA with AuNSs (LOD = 50 ng/ml). In summary, AuNFs could be used to improve sensitivity of the LFIA.

Keywords: Lateral flow immunoassay, Gold nanospheres, Gold nanoflowers, Norfloxacin, Detection

1. Introduction

Nor is a synthetic antibacterial agent that belongs to the fluoroquinolone group (FQ). Nor has been widely used to treat infection in human but it has been banned to be used in animals destined for human consumption due to possibly drug resistant problem of bacteria. In addition, NOR residue can cause medication problems, gastrointestinal symptoms, vomiting, diarrhea, abdominal pain in the nervous system which may lead to confusion, seizures or hallucinations (Hua et al.,2020). Therefore, surveillance detection of NOR residue in food products is required to ensure safety of the consumers. Lateral flow immunoassay (LFIA) is one of the most popular express methods for the detection of different important substances. It is widely used in pharmaceutical and food industry, veterinary medicine, environmental protection, etc. because of their unique advantages of simplicity, rapidity, portable and low cost (Petrakova et al., 2019; Zhang et al., 2019). This detection method is based on the combination of the separation of the target substance from the mixture and the specific capture between antibody and the target substance on the same membrane. Main components of the test strip consist of sample pad, conjugate pad, analytical membrane and absorbent pad (Bahadir et al., 2016) as shown in figure 1.

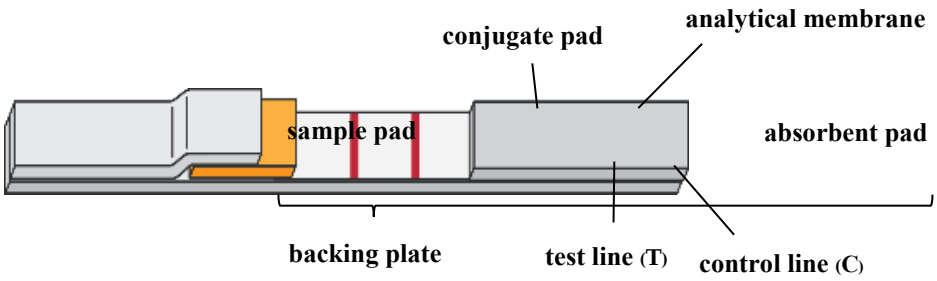

Figure 1. Conventional component of a test strip.

The traditional LFIA using gold nanospheres (AuNSs) with the diameter of 20-30 nm as signal intensity reporters, usually has relatively low sensitivity (Ji et al., 2015). Gold nanospheres with diameter larger than 30 nm are unstable for the assay. Compared with conventional AuNSs, gold nanoflowers (AuNFs) have better colloidal stability and larger total surface area than the AuNSs of the same size due to their complex three-dimensional structure, thus resulting in high yield of immobilized antibodies (Kseniya et al.,2016).

In this study, detection limits of the LFIA developed by using AuNSs and AuNFs as the signal reporting molecule were compared in the norfloxacin detection. Information obtained from this study could be used in the development of LFIA for detecting other target substances.

2. Materials and Methods

2.1 Chemicals and materials

Chloroauric acid (HAuCl4), trisodium citrate and hydroquinone were purchased from Sigma-Aldrich (St. Louis, MO, USA), bovine serum albumin (BSA) was purchased from Capricorn Scientific GmbH (Ebsdorfergrund, Germany), Goat anti-mouse antibody (GAM) was purchased from Jackson ImmunoResearch Laboratories Inc. (West Grove, PA, USA), anti-NOR mAbs, NOR-BSA conjugates, NOR-OVA conjugates, 0.01 M phosphate buffer (PB) pH 7.4, 0.1% tween 20 in 0.01 M phosphate buffer (PB) pH 7.4 (PBT), Sodium borate buffer (BB) pH 8.2, 0.2 M Sodium carbonate (Na_2CO_3) and 10% Sodium chloride (NaCl) were prepared and used in this study. Sample pad, conjugate pad and absorbent pad were purchased from GE Healthcare Life Sciences Whatman (Buckinghamshire HP7 9NA, UK), nitrocellulose membrane was purchased from Sartorius (New York, USA), plastic backing card (MIBA-080; DCN, CA, USA) and BioJet HR™ Non-Contact Solenoid Dispenser coupled with a XYZ3210 Dispense Platform (Biodot, CA, USA)

2.2 Synthesis of gold nanoparticles

2.2.1 Gold nanospheres (AuNSs)

Boil 0.01% 100 ml of chloroauric acid (HAuCl4) solution until boiling, then add 1% trisodium citrate of 1 ml under constant stirring. Then boil the solution for 10-15 minutes under stirring and set it at room temperature.

2.2.2 Gold nanoflowers (AuNFs)

Gold seeds were obtained by adding 3 ml of 1% trisodium citrate solution to 100 mL 0.01% chloroauric acid (HAuCl4) solution with constant stirring under boiling conditions. Then add 1% of 0.75 ml of chloroauric acid solution to 100 ml of double deionized water (DDI) under strong stirring conditions, Subsequently, mix 0.5 ml of gold seed solution, 220 ml of 1% sodium citrate and 1.0 ml of 0.03 M of hydroquinone at room temperature for 30 minutes.

2.3 Optimization of monoclonal antibody concentration for conjugation

Twenty-five microliter monoclonal antibody (mAb) at different concentrations (0 – 800 µg/ml) in sodium borate buffer (BB), pH 8.2 were mixed with 250 µl of colloidal gold nanoparticles solution (pH 8.2) in the wells of 96 well plate. The plate was incubated at room temperature for 15 minutes under shaking. Then, 250 µl of 10% NaCl was added into

each well. Absorbance at the maximum wavelength of each gold particle sizes was measured. The optimum concentration of the MAb was justified at the least mAb concentration that yielded the highest absorbance value.

2.4 Preparation of mAb-gold conjugate

Add 1 ml of mAb at the optimum concentration to 10 ml of colloidal gold solution and shake the mixture at room temperature for 30 minutes. Then, add 1 ml of 3% (w/v) BSA into the solution and shake for 30 minutes. Subsequently, centrifuge at 25,000 x g, 4 °C for 30 minutes. The mAb-gold conjugate pellet was re-dissolved in 1 ml of DDI water and stored at 4 °C for further uses.

2.5 Preparation of lateral flow immunoassay

The test strip was composed of a 4 × 17 mm sample pad, a 4 × 10 mm conjugate pad, a 4 × 25 mm analytical membrane, and a 4 × 17 mm adsorption pad. The NOR-protein conjugate and goat anti-mouse immunoglobulin (IgG (GAM) were applied to the reaction pad at the test line (T-line) and control line (C-line) using a BioJet HR™ Non-Contact Solenoid Dispenser coupled with a XYZ3210 Dispense Platform at the flow rate of 1 µl/cm. The mAb-gold conjugate was applied onto the conjugate pad by soaking the pad in 2 µl and 4 µl of the mAb-AuNSs and mAb-AuNFs solution, respectively. All pads were dried at 42°C for 30 min and then attached to a 4 × 60 mm plastic backing card in a conventional layout and placed in a cartridge. The test strips were placed in sealed aluminum foil bags containing silica gel and kept in a humidity-controlled chamber (≤20% relative humidity) at room temperature until use. The concentrations of NOR-protein conjugate and GAM were varied to obtained the optimized concentration that yielded the noticeably purple T and C lines. Ovalbumin (OVA) and bovine serum albumin (BSA) were comparatively conjugated to NOR and used in the LFIA.

2.6 Detection of norfloxacin

The test was conducted by dropping 100 µl of the standard NOR into the sample well of the test strip. The concentrations of standard NOR were varied in a range of 0 - 100 ng/ml. The strip was left standing at room temperature for 15 min. The appearance and intensity of a purple color at the test line and control line were observed using the naked eye. The lowest NOR concentration that gave the colorless T line was defined as the limit of detection (LOD).

3. Results and Discussion

3.1 Conjugation of antibody with gold nanoparticles

3.1.1 Optimization of antibody concentration

In the mAb-gold conjugation, the concentration of mAb must be first optimized to obtain the least mAb concentration that can prevent the aggregation of the gold nanoparticles. In this experiment, different concentrations of mAb were separately mixed with AuNSs and AuNFs. Then NaCl was added to activate the aggregation of the gold nanoparticles. If the surface of the gold nanoparticles was fully covered with the mAb, the aggregation could not occur, thus resulting in a cherry red solution. On the contrary, if the mAb molecules were not enough and the aggregation occurred, the solution turned greyish. The least concentration of mAb could be justified by the measurement of the solution absorbance at the maximum wavelength of AuNSs (532 nm) and AuNFs (236 nm), respectively. The absorbances of the solution mixtures at different concentration of the MAb were shown in Figure.2. The result showed that the minimal concentrations of the MAb to stabilize both types of gold nanoparticles were at 200 µg/ml.

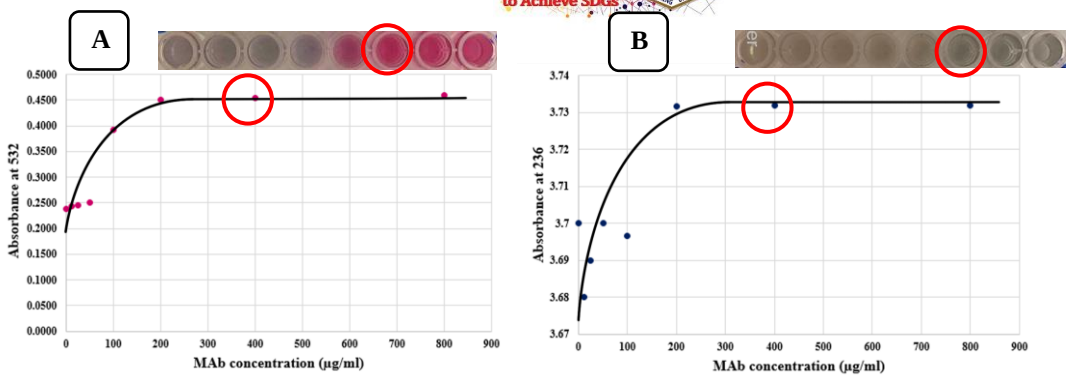

Figure.2 Absorbance of mAb-gold solutions measured at 532 nm for AuNSs *(A)* and 236 nm for AuNFs *(B)* after the addition of NaCl

3.2 Optimization of NOR-protein conjugates and mAb-gold conjugates

The LFIA used in this study was based on the competitive format. Norfloxacin in the sample or standard will bind with the mAb-gold conjugate. Therefore, a lower amount of mAb-gold conjugate is freely left to bind with the NOR-protein conjugate immobilized at the T line. So, the important parameters needed to be studied in order to improve the sensitivity of the strip test is the concentration of NOR immobilized at the test line of the analytical membrane and the amount of mAb-gold conjugate loaded at the conjugate pad because they could affect the degree of competition between NOR in the sample and NOR immobilized at the T line in the binding of mAb-gold conjugate, thus affecting the color intensity at the T line. In this experiment, two types of NOR-protein conjugate such as NOR-ovalbumin *(*NOR-OVA*)* and NOR-bovine serum albumin *(*NOR-BSA*)* were compared. In addition, two types of gold nanoparticles such as gold nanosphere and gold nanoflower were conjugated with mAb and used in the strip preparation. After testing with 0.1% PBT as the sample, the test results were shown in Figure.3. When AuNSs were used, the suitable concentration of the NOR-OVA for immobilization was 0.5 µg/ml because the color intensity at the test line was too weak when the NOR-OVA concentration was lower than 0.5 µg/ml. In case of AuNFs, the suitable concentration of NOR-BSA was 0.7 µg/ml. Therefore, these conditions were used in the preparation of the test strip in further study.

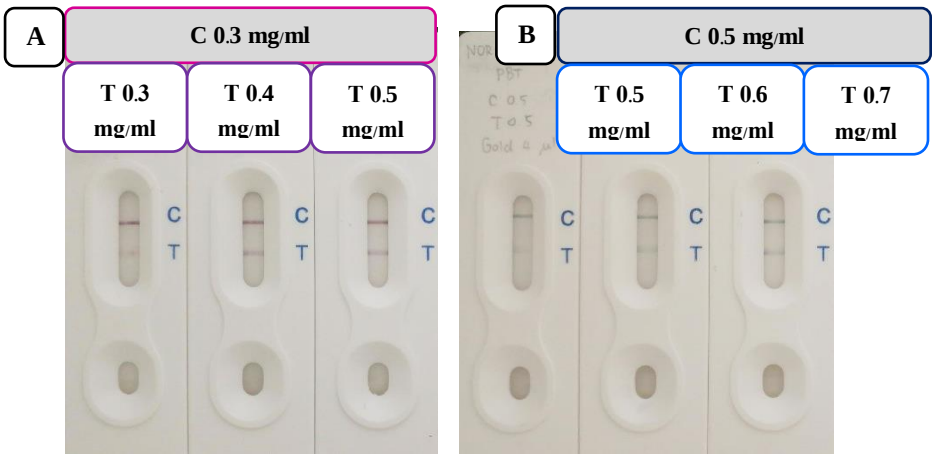

Figure.3 Test strips were prepared at different conditions; *(A)* goat anti-mouse IgG *(*0.3 mg/ml; flow rate, 1 µl/cm*)* and NOR-OVA conjugate *(*0.3-0.5 mg/ml; flow rate, 1 µL/cm*)* for AuNSs, *(B)* goat anti-mouse IgG *(*0.5 mg/ml; flow rate, 1 µl/cm*)* and NOR-BSA conjugate *(*0.5-0.7 mg/ml; flow rate, 1 µL/cm*)* for AuNFs. The tests were performed by dropping 100 µL of 0.1% PBT. The test results were observed after 15 min.

3.3 Sensitivity of the LFIA

The sensitivity of the strip test was quantified in term of limit of detection *(*LOD*)* indicating the lowest concentration of norfloxacin standard solution that yields about 80% reduction in color intensity at the test line when compared to the color intensity of the blank sample. Figure 4 and 5 shows the color intensity of the test line after testing with standard NOR at different concentrations *(*0, 5, 10, 20, 30, 50, 80 and 100 ng/ml in 0.1% PBT*)* when AuNSs and AuNFs, respectively, were used as the reporting molecules. The results showed that the LOD of the assay when AuNSs were used was 50 ng/ml while the LOD of the assay when AuNFs were used was 10 ng/ml. These results indicated that the use of AuNFs could improve the LOD of the LFIA.

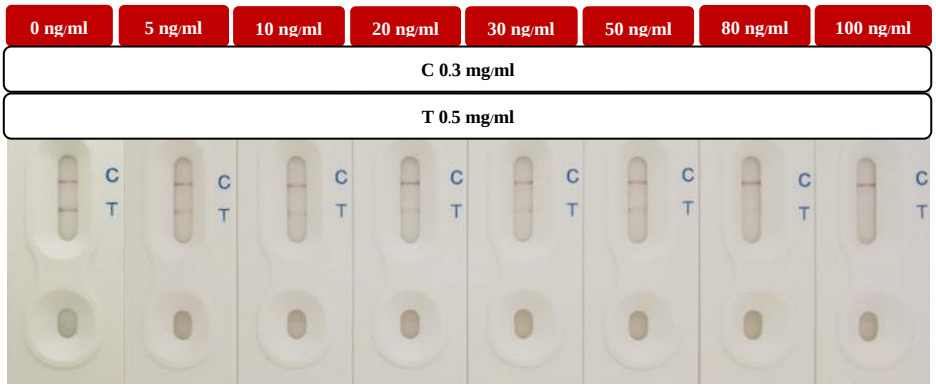

Figure.4 Detection of NOR at 0, 5, 10, 20, 30, 50, 80 and 100 ng/ml in 0.1% PBT by the test strips prepared at the optimal condition of goat anti-mouse IgG *(*0.3 mg/ml; flow rate, 1 µl/cm*)* and NOR-OVA conjugate *(*0.5 mg/ml; flow rate, 1 µl/cm*)*

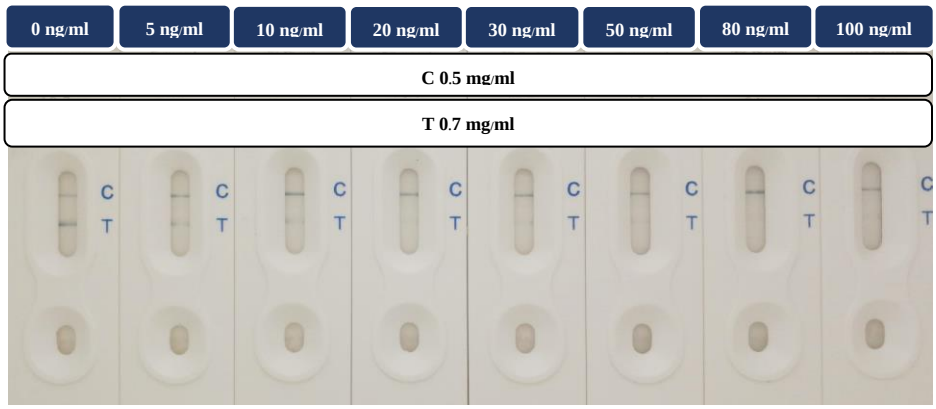

Figure.5 Detection of NOR at 0, 5, 10, 20, 30, 50, 80 and 100 ng/ml in 0.1% PBT by the test strips prepared at the optimal condition of goat anti-mouse IgG *(*0.5 mg/ml; flow rate, 1 µl/cm*)* and NOR-OVA conjugate *(*0.7 mg/ml; flow rate, 1 µl/cm*)*

4. Conclusion

Limit of detection of the LFIA prepared with gold nanoflower as the reporting molecule was lower than that of the LFIA prepared with gold nanosphere about 5 times. Gold nanoflower could replace gold nanosphere in the strip preparation to improve the sensitivity of the LFIA.

Acknowledgements*:*

The authors would like to thank Thailand Science Research and Innovation *(*TSRI*)* for financially support and Electrochemistry and Optical Spectroscopy Center of Excellence *(*EOSCE*)*, Chulalongkorn University for helping in gold nanoparticle preparation.

References

1. Bahadır EB, Sezgintürk MK. Trends in Analytical Chemistry. 2016;82:286-306.
2. Hua S, Liua J, Zhanga G, Wanga Z, Xiaoa X, Lib D, Pengb J, Laia W. Talanta. 2020;219:121245.
3. Zhang W, Duana H, Chena R, Maa T, Zengb L, Lenga Y, Xiong Y. Talanta. 2019;194:604-610.
4. Petrakova A, Urusov A, Zherdev A, Dzantiev B. Analytical Biochemistry. 2019;568:7-13.
5. Ji Y, Ren M, Li Y, Huang Z, Shu M, Yang H, Xiong Y, Xu Y. Talanta. 2015;142:206-212.
6. Kseniya V, Jeanne V, Alexander P, Dulal S, Denis V. Nano Hybrids and Composites. 2016;13:47-53.

C_019_PA: ANTIPROLIFERATIVE PROPERTY AGAINST CANCER CELL LINE AND CELLULAR ANTIOXIDANT ACTIVITY OF *Acacia pennata* LEAVES EXTRACT

Songchan Puthong[1], Umaporn Pimpitak[1], Kittinan Komolpis[1,2] and Anumart Buakeaw[1,*]

[1]Institute of Biotechnology and Genetic Engineering, Chulalongkorn University, Bangkok, Thailand.
[2]Food Risk Hub, Research Unit of Chulalongkorn University, Bangkok 10330, Thailand
*e-mail: anumart.b@chula.ac.th

Abstract:

Cha-om (*Acacia pennata*) is a vegetable which has long been used in many dishes of Thai food. Cha-om is in the family *Leguminosae*, subfamily Mimosoideae It has been reported that plants in this species are used in folk medicines because they contain secondary substances such as alkaloids, saponins, polysaccharides, terpenoids, concentrated tannins and flavonoids which have anti-inflammation properties. In this research, antiproliferative property against cancer cell lines and cellular antioxidant activity of crudes extracted from both fresh (F) and dried (D) leaves of *A. pennata* were investigated. Leave crude extracts were obtained by either water (H) or 95% ethanol (E) extraction. Cytotoxicity activity based on MTT colorimetric assay of the extracts was performed on fourteen cell lines (cancer cell lines = A375, BT474, CaCo-2, Chago-K1, Hep-G2, HT-29, KATO-III, KB, MCF-7, MDA-MB-231, NUGC-4 and SW620 ; normal cell lines = CCD-986SK, MCF-10A and WI-38). The results showed that both FH and DH extracts had low toxicity to all fourteen cell lines with the 50% inhibition concentration (IC_{50}) values higher than 500 µg/ml (survival percentage = 63 – 124%) while the FE extract was toxic to both cancer and normal cell lines (IC_{50} = 13.4 – 113.2 µg/ml). Interestingly, the DE extract was highly toxic to only cancer cell lines (IC_{50} 24.8 – 483.3 µg/ml) but less toxic to normal cell line of epithelial cell (MCF-10A), lung cell (WI-38) and skin cell (CCD-986SK). Because of its low toxicity to normal cell lines, study of antioxidant activity of the DE extract (2000 µg/ml) was tested on human colon cancer cell line CaCo-2 and HT-29 cells and was found to be 76.8% and 34.5%, respectively. In addition, anti-inflammatory effect of the DE extract at the concentration of 100 µg/ml was found to be 28%. Information obtained from these studies suggested that cha-om could be a promising source of anti-cancer agents.

C_020_PA: QUANTIFICATION OF COW CASEIN IN MILK BY AN ENZYME - LINKED IMMUNOSORBENT ASSAY

Anumart Buakeaw[2], Kanokporn Patipatsinlapakij[1], Umaporn Pimpitak[2], Nanthika Kongchareonporn[2,3], Kittinan Komolpis[2,3] and Songchan Puthong[2,*]

[1]Program of Biotechnology, Science, Chulalongkorn University, Bangkok 10330, Thailand.
[2]Institute of Biotechnology and Genetic Engineering, Chulalongkorn University, Bangkok 10330, Thailand.
[3]Food Risk Hub, Research Unit of Chulalongkorn University, Bangkok 10330, Thailand.
*e-mail: songchan.p@chula.ac.th

Abstract:

Cow milk is an important source of protein for human. However, for some consumers, especially children, they could not consume cow milk due to allergy of a certain substance in cow milk. The allergic symptoms could vary from mild such as vomiting to deadly severe. It has been reported the major substance which causes cow milk allergy is casein, 80% of total proteins in cow milk. Therefore, these consumers must rely on milks from other animal sources such as goat and buffalo. However, these milks are expensive. Consequently, illegal mixing of these milks with cow milk to reduce cost of the products could be harmful to the consumers. Therefore, several methods have been developed to detect casein. Chemical methods such as high performance liquid chromatography are accurate and precise but they are complex and require expensive instrument. Alternatively, immunological methods have been developed and applied to detect casein. In this study, anti-casein monoclonal antibody (mAb) CN1F4 produced by the Institute of Biotechnology and Genetic Engineering was selected for the preparation of an indirect competitive enzyme-linked immunosorbent assay (ELISA). At the optimized condition of coating antigen concentration, mAb concentration and 2nd antibody-horse radish peroxidase concentration, the prepared ELISA was sensitive to detect standard casein at the limit of detection of 2.46 ± 0.01 µg/ml and the 50% inhibition concentration (IC_{50}) of 17.01 ± 4.29 µg/ml. In addition, the prepared ELISA was used in the detection of standard casein (1.25, 2.5, 5, 10 and 20 µg/ml) spiked in casein-free soybean milk. The percentages of recovery were found to be 144.8, 164.5, 149.8, 113.5 and 77.7%, respectively while the percentages of coefficient of variation were found to be 9.26, 4.80, 1.88, 0.67 and 0.20%, respectively. Subsequently, the developed ELISA was used in the quantification of casein in 7 cow milk samples. It was found that the casein concentrations were in a range of 15 - 50 mg/ml which were in an agreement with values reported in other studies. These results indicated that the prototype of the developed indirect competitive ELISA could be used in the measurement of cow casein.

C_021_PA: DEVELOPMENT OF A PROTOTYPE TEST STRIP FOR THE DETECTION OF NORFLOXACIN RESIDUE IN CHICKEN MUSCLE

Umaporn Pimpitak[1,*] Songchan Puthong,[1] Anumart Buakeaw,[1] Nanthika Khongchareonporn,[1] and Kittinan Komolpis[1]

[1]Institute of Biotechnology and Genetic Engineering, Chulalongkorn University, Bangkok, Thailand
*e-mail: Umaporn.P@chula.ac.th

Abstract:

Norfloxacin (NOR) is a fluoroquinolone antibiotic which has long been used in the treatment and prevention of both Gram positive and Gram negative bacteria in human and food producing animals. Widely uses and misuses of NOR leads to drug resistance of *Pseudomonas spp.*, *Escherichia coli* and *Streptococcus spp*. In addition, drug residue in food products could adversely affect to consumers' health, such as diarrhea, vomiting, headache and hallucination. For food safety concern, maximum residue limit (MRL) of NOR has been set in many countries. In Thailand this MRL value was set at 20 µg/kg (20 ppb) for chicken muscle. Detection of NOR could be performed by using several methods. Lateral flow immunoassay or strip test is the most convenient and suitable for screening detection of a large group of sample. Any suspicious samples would then be tested by a standard method for confirmation of the residual concentration. In this research, test strip for detection of NOR residual in chicken muscle was developed. The prototype test strip was based on the competition between NOR residue in the sample and the NOR standard immobilized on the test strip. The amount of NOR immobilized at the test line of the strip, the concentration of gold-antibody conjugate and the concentration of secondary antibody at the control line of the strip were simultaneously optimized. After sample loading for 5-15 min, test result was observed with unaided sight. If color was clearly noticed at the test line of the strip, the NOR concentration in the sample was < 10 µg/kg. If color was absent at the test line, the NOR concentration in the sample was ≥20 µg/kg. If color was noticeable but at low color intensity, the NOR concentration in the sample was between 10 µg/kg and 20 µg/kg. In all cases, the color at the control line must be clearly observed, otherwise the test was invalid. The developed prototype will then be validated to acquire accuracy, sensitivity and specificity of the test in the future.

C_022_PF: NON-TARGETED METABOLIC PROFILING REVEALED THE BIOMARKERS ON THREE *Aspergillus* SPECIES BY UHPLC-MS COUPLED WITH PRINCIPAL COMPONENT ANALYSIS

Worawut Chaiyasaeng,[1] Boon-ek Yingyongnarongkul,[1] Klinphaka Phuthaworn,[2]
Kanokkorn Longmatcha,[2] Malik Alimuhammad,[2] Jamrearn Buaruang[2,*]

[1]Department of Chemistry and Center of Excellence for Innovation in Chemistry, Faculty of Science, Ramkhamhaeng University, Bangkapi, Bangkok, 10240, Thailand
[2]Marine Microbe Environment Research Unit, Division of Environmental Science, Faculty of Science, Ramkhamhaeng University, Bangkapi, Bangkok, 10240, Thailand
*E-mail: jbuaruang@gmail.com

Abstract:

A. micronesiensis and *A. awamori* are common species of a genus *Aspergillus* from Surat Thani (Thong Tanote), Phuket (Koh He) and Trad (Koh Chang) provinces, respectively. *A. micronesiensis* and *A. awamori* are important commercially and clinically due to they contain potent bioactive compounds. However, the metabolic profiling of the different *Aspergillus* species have not been documented. The species identification usually was considered via the basic morphological features. However, some species give the same features which could not be identified under microscopic technique. Therefore, the present study aimed to evaluate the differences between *Aspergillus* species based on non-targeted metabolic profiling by Ultrahigh Performance Liquid Chromatography-Mass Spectrometry (UHPLC-MS). Three species including *A. micronesiensis, A. awamori* and unknown *Aspergillus* sp were used in this study. Based on Principal Component Analysis (PCA) scores plots and loading plots based on the UHPLC-MS non-targeted metabolic profiling, thirty eight ions mass were identified as marker compounds for species differentiation. The most significant biomarkers of each sample were revealed. Thus, an unknown *Aspergillus* sp. was differed from known species. In the future, the unknown *Aspergillus* sp. will be submitted for DNA sequencing for species identification, the structure and biological activity of biomarkers will be studied.

Introduction:

In Thailand, of the country's 77 provinces, 23 including Bangkok are coastal provinces, 17 of these are in the Gulf and 6 provinces border the Andaman Sea, that is an enormously valuable marine and coastal resource because there is a variety of organisms.[1] One of them are filamentous fungi such as *Aspergillus* which is a genus of fungi consisted of more than 300 species including both pathogenic and beneficial species.[2] Several bioactive compounds are produced such as norsolorinic acid (e.g., from *A. parasiticus and A. nidulans*), p'-coumaric acid, cinnamic acid, gallic acid, ascorbic acid (e.g., *from A. awamori*), amichalasines A-C (e.g., from *A. micronesiensis PG-1*). Therefore, species of *Aspergillus* are important commercially and clinically.[3-5]

In surveying and utilization, the classification and identification of *Aspergillus* species have been made which base on morphology, which does not receive their chemical information. However, over the last decade classification of fungus specie was strongly influenced by molecular and chemotaxonomic characterization. The metabolomics term is defined as both quantitative and qualitative analyses of all metabolites, (including metabolic

intermediates, hormones and other signaling molecules, and secondary metabolites) present in a specific cell or organism. They are the end products or the final downstream result of its gene and environmental expression. These are the low molecular weight compounds in an organism that participate in the network of chemical reactions supporting cell growth and function.[6] Focusing on non-targeted metabolic profiling comprehensively analyzes all measurable analytes in a sample including chemical unknowns is opened a new window for biomarker and new compound discovery.[7] Biomarkers are compounds or a set of compounds those are objectively measured and evaluated as an indicator of the living organism. They must be quantitatively, sensitively, specifically, and easily measurable.[8] Recently, metabolomics was studied in various fields of plant research, such as plant biochemistry, food chemistry, environmental and taxonomy-based metabolomics. Metabolomics has also been applied for marine organisms.[9] *A. micronesiensis*, *A. awamori* and *Unknown sp.* are common species of a genus *Aspergillus* from Surat Thani (Thong Tanote), Phuket (Koh He) and Trad (Koh Chang) provinces, respectively. *A. micronesiensis* and *A. awamori* are important commercially and clinically due to their potent bioactivities.[3-5] However, the metabolic profiling of the different *Aspergillus* species have not been documented; on the species identification usually was considered via the basic morphological features. However, some species give the same features and their chemical information has not been not revealed.

In this work, we provide morphological characteristics and information on HPLC-MS-based non-targeted metabolic profiling studies coupled with PCA for biomarkers discovery on three *Aspergillus* species (*A. micronesiensis* (AM), *A. awamori* (AA), and an unknown *Aspergillus* sp. (UN)). Overview of this work is shown in Scheme 1.

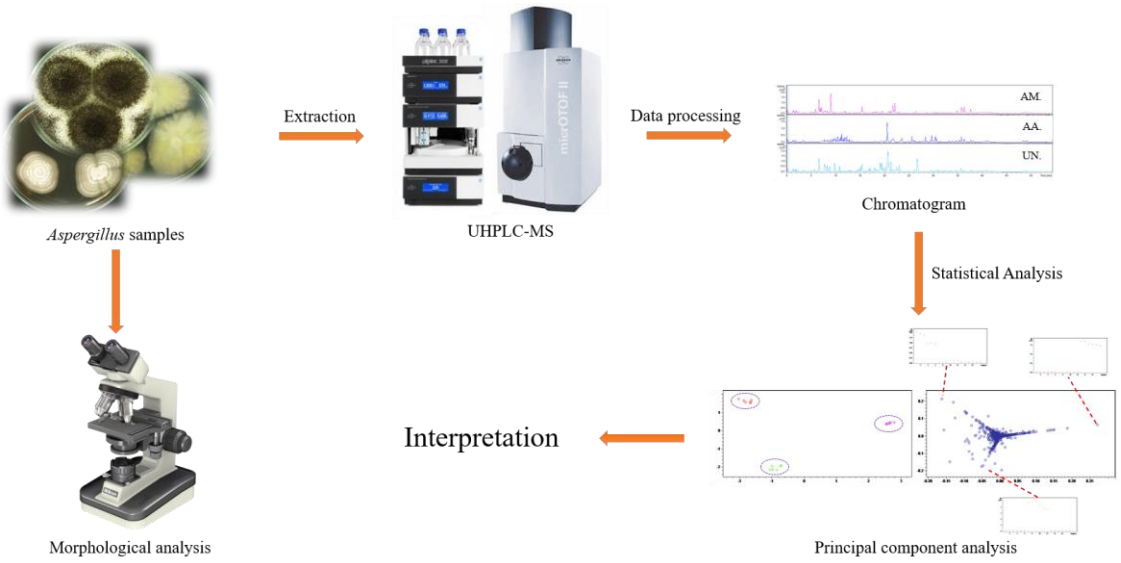

Scheme 1. Overview of this work.

Methodology:

Chemicals and reagents: Methanol (CH_3OH, HPLC grades), acetonitrile (C_2H_3N, HPLC grades), formic acid (CH_2O_2, MS grade) were purchased from Fisher Scientific. Agar powder, peptone, Czapek Dox agar (CZA), and malt extract powder were purchased from HiMedia (Mumbai, Maharashtra 400086, India). Glucose anhydrous was purchased from Kemaus (Cherrybrook NSW 2126, Australia), Sodium hypochlorite (NaClO, 0.06%) was prepared by diluted 10% of sodium hypochlorite 6 mL to 1000 mL with distilled water prior to sterilization. Ethyl acetate ($C_4H_8O_2$, commercial grade) was purchased from Scientific Equipment (Wattana Bangkok 10110, Thailand). Natural seawater was collected from the Bangsaen Sea at Chonburi, Thailand. Ultra-high purity deionized water (DI-water; 18MΩ-cm) was prepared by filtration using a Milli-Q system from Millipore (Bedford, MA, USA). Sodium formate (10 mM) was

prepared with DI-water (12.5 mL), acetonitrile (12.5 mL), Conc. formic acid (50 µL) and 1M of sodium hydroxide (250 µL) for MS calibration reagent.

Isolation of fungal strains: Marine organisms (*Hypnea pannosa*, *Acanthogorgia* sp., *Acropora* sp.) were collected at three different sites, Trad (Koh Chang), Phuket (Koh He), and Surat Thani (Thong Tanote) provinces which are shown in Table1. They were cleaned and disinfected with 0.06% sodium hypochlorite (NaClO) prior to wash three times with sterile seawater and cultures on sterile CZA media for seven days at room temperature. Three fungi samples (*A. micronesiensis* (AM), *A. awamori* (AA), and an unknown sp. (UN) were identified base on morphology by compound light microscope and stereo microscope at Marine Microbe Environment Research Unit, Ramkhamhaeng University, Thailand. Some the part of a single species was kept as stock pure cultures in the fridge at -20°C.

Table 1. The source, Host, Species of *Aspergillus* samples used in this analysis.

Accession	Species	Host	Source	Collected mouth, year
AM	*A. micronesiensis*	*Hypnea pannosa*	Surat Thani (Thong Tanote)	May, 2017
AA	*A. awamori*	*Acanthogorgia* sp.	Phuket (Koh He)	May, 2017
UN	Unknown sp.	*Acropora* sp.	Trad (KohChang)	April, 2017

Culture of fungi for morphology: Three *Aspergillus* samples were left to grow for seven days at room temperature on CZA media prepared with 49g/L of Czapek Dox agar, natural seawater 700 mL, distilled water 300 mL. These components were heated to dissolve before sterilization at 121°C for 1 hour by Autoclave (RAU-530D operating instructions). After growth in culture, fungi are identified based on visual characteristics such as colony morphology and color using compound light and stereo microscopy.

Culture of fungi for metabolic profiling analysis: Three *Aspergillus* species were left to grow in duplicates using Erlenmeyer flasks containing 200 mL of liquid medium (liquid medium, ME) prepared with natural seawater 1000 mL, peptone 1g/L, glucose 20g/L, malt extract powder 20g/L. They were incubated at room temperature for 20 days under natural light.

Extract preparation: Fungi were separated from their medium and ground before extracted with ethyl acetate (100 mL) by shaking for 2 h. Extraction was repeated for three times. Then, the organic layer was filtered with Whatman filter paper and evaporated to dryness. The residues were stored at 4°C for further UHPLC-MS analysis.

UHPLC-MS analysis: 4 mg of the crude *Aspergillus* samples were dissolved in HPLC grade MeOH and filtered through a syringe filter membrane 0.45µm to the removal of particulate impurities from liquid samples. 2 µL of samples solution was injected into a C-18 column (2.1x150 mm, 3 µm; Thermo Scientific, Waltham, MA, USA) in triplicate (n=3) of a UHPLC to separated metabolites, which was performed using a Thermo Scientific Dionex UltiMate 3000 UHPLC system and Bruker micrOTOF II was used as a mass analyzer. Analytical parameters were set as follows our previous work.[10]

Data Processing of Principal Component Analysis: Principal Component Analysis were calculated by Bruker Compass Profile Analysis 2.1 (Billerica, MA, USA). Find molecular features were applied to UHPLC-MS data under these parameters: S/N threshold, 5; correlation coefficient threshold, 0.7; minimum compound length, 10; smoothing

width, 1. The UHPLC-MS datasets were evaluated in a time range from 0.5 to 55 min and in a mass range from m/z 50 to 1000. A sum of bucket values was used for normalization, and Pareto scaling was applied.

Results and Discussion:

Morphological characteristic: Aspergillus samples were cultured on sterilize CZA media at room temperature for seven days and determined under camera digital, Stereo microscope and Compound light microscope.

A. micronesiensis, GenBank accession No. (ITS); KP987080: Characteristics were identified following the research done in previous reports.[11] Description see Figure 1: Colony diameter, at 25°C for seven days on CZA was 5.8 cm. Colonies and Sporulation yellowish white (A), Reverse brownish orange (B). Conidiophore smooth-walled, Light brown (D). Conidial heads radiating, Vesicles globose, Metulae is covering of head, Phialides (biseriate Aspergilla) (C-E). Conidia globose to subglobose, Smooth to finely roughened (F).

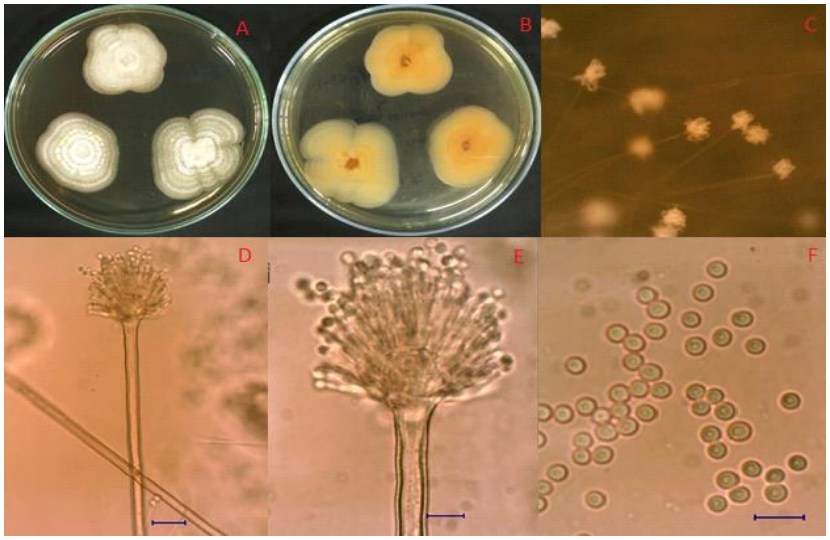

Figure 1. *A. micronesiensis* was incubated for seven days, at room temperature. Colonies (A, Yellowish white) obverse view on CZA, Reverse view (B). Conidial head (C-E). Conidiophore, Vesicles, Metulae, Phialides (E). Conidia (F). Scale bars: D = 10 µm, E= 5µm, F = 5 µm.

A. awamori, GenBank accession No. (ITS); MH011355: Characteristics were identified following the research done in previous reports.[12] Description see Figure 2: Colony diameter, at 25°C for seven days on CZA was 5.7 cm. Colonies were being black in color with white margins with floccose mycelia and sporulation were dark brown to black color in central area centers (A), Reverse creamy color and showed dark brown centers (B). Conidiophore smooth-walled, Light brown (D). Conidial heads radiating, Vesicles globose 30-40 µm in diameter, Metulae is covering of head, Phialides (C-E). Conidia spherical, Predominantly smooth to roughened 3-4 µm in diameter (F).

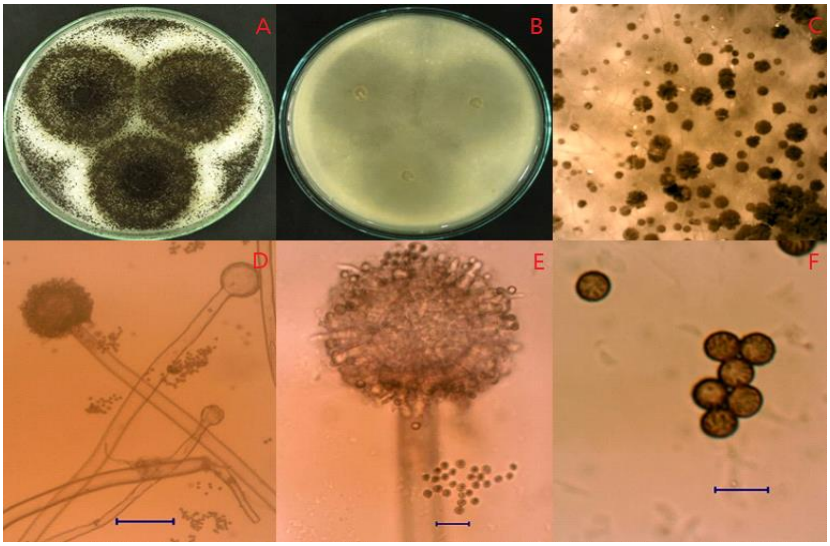

Figure 2. *A. awamori* was incubated for seven days, at room temperature. Colonies (A, dark to dark brown) obverse view on CZA, Reverse view (B). Conidial head (C-D). Conidiophore (D). Vesicles, Metulae, Phialides (E). Conidia (F). Scale bars: D =50 µm, E=10µm, F =5µm.

Unknown *Aspergillus* sp.: Characteristics showed on Figure 3. Description: Colony diameter, at 25°C for seven days on CZA was 5.8 cm. Colonies were yellowish white with floccose mycelia (A). Reverse showed yellow color (B). Conidiophore smooth-walled, Light brown (D). Conidial heads radiating, Globose vesicles, Metulae is covering of head, Phialides (biseriate Aspergilla) (C-E). Conidia spherical, Predominantly smooth to roughened (F).

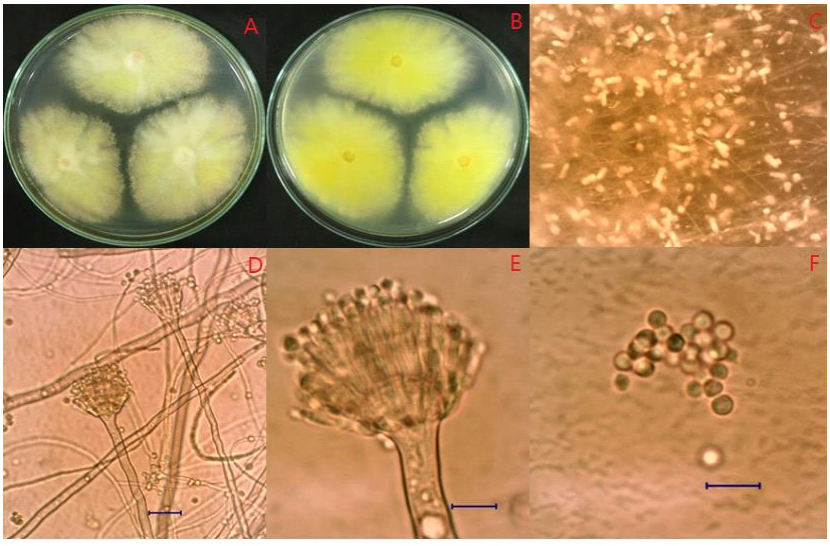

Figure 3. Unknown *Aspergillus* sp. was incubated for seven days, at room temperature. Colonies (A, Yellowish white) obverse on CZA. Reverse view (B). Conidial head (C-D). Conidiophore (D). Vesicles, Metulae, Phialides (E). Conidia (F). Scale bars: D = 10 µm, E=5µm, C = 5µm.

UHPLC-MS peak identification: The metabolites content of crude ethyl acetate extract of *Aspergillus* species was analyzed by UHPLC–MS, ionized in the electrospray ionization (ESI) source, eluting of all analytes within 55 min. Metabolites were separated on a C18 column and analyzed by MS in the negative mode. UHPLC-MS base peak chromatogram (BPC) of *A. awamori, A. micronesiensis*, and unknown *Aspergillus* sp. is shown in Figure 4. Their chromatogram below demonstrated the different metabolites from each *Aspergillus* species under the same growth and extraction conditions. Most interestingly, the signals detected at m/z 129.0553, 574.2372, and 335.0752 are the most significant biomarkers of *A. micronesiensis, A. awamori,* and unknown *Aspergillus* sp., respectively, which were selected with the ProfileAnalysis software.

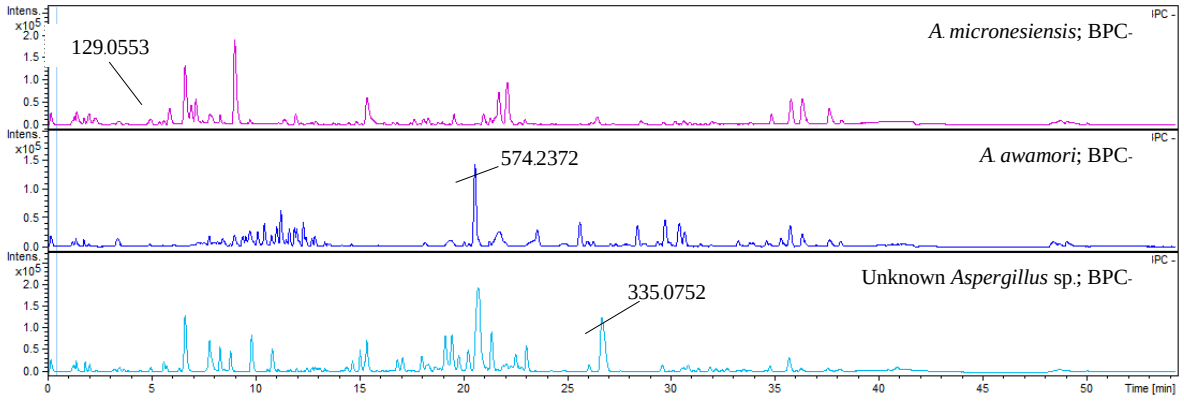

Figure 4. Shows the base peak chromatogram (BPC) of *A. micronesiensis*, *A. awamori,* and Unknown *Aspergillus* sp. samples separated on UHPLC and Time-of-flight mass spectrometry in negative ion mode as a detector.

Multivariate PCA analysis of UHPLC-MS data: Initially, to understand the relationship between the extract of the same species and between *Aspergillus* species, all the six extracts of three *Aspergillus* species in triplicate (n=3) were subjected for analysis. The first and second principal components (PC1 and PC2) accounted for 32.6% and 21.1%, respectively, all of the total variability in the amounts of the data matrix. Principal Component Analysis (PCA) scores plots and loading plots based on the UHPLC-MS data were calculated by Bruker Compass ProfileAnalysis 2.1 (Billerica, MA, USA) to reveal the difference of the crude ethyl acetate extract based on their chemical profiles. In the scores plot, three *Aspergillus* species were clearly classified into three distinct groups, replicates of cultures and reproducibility of the triplicate *Aspergillus* samples were good under the same conditions as shown in Figure 6a. Simultaneously, the loadings plot revealed three groups of ions mass differentially accumulated and extracted the most significant biomarkers of the three *Aspergillus* species with 95% confidence as shown in Figure 6b.

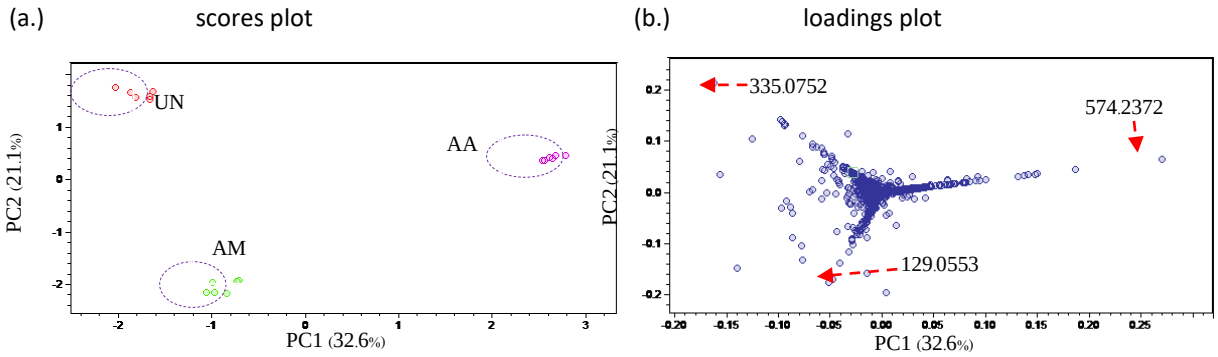

Figure 6. PCA scores and loadings plot for three *Aspergillus* species in six samples derived with three replicates from negative ionization mode UHPLC-MS data (m/z 50 – 1000). (a), The scores plot is constructed by plotting PC1 versus PC2 (PC1, First principal component;PC2, Second principal component: *A. micronesiensis* (●), *A. awamori* (●), Unknown *Aspergillus* sp. (●). (b), For molecules that were unique to that strain were color-coded in the same dark blue in the loadings plot.

The signals detected for m/z 129.0553 at 6.07 min showed high intensity in *A. micronesiensis* (●) only, which was low intensity signals in any other species (see Figure 5a). Intensity signals for m/z 574.2372 of *A. awamori* (●) at 20.67 min and m/z 335.0752 of unknown *Aspergillus* sp. (●) at 27.19 min show in Figure 5b, 5c. From the mentioned above confirming that the UHPLC–MS technology coupled with multivariate statistics can provide much more information than chromatography and morphological characteristic. Besides, the PCA process is also given to the significant biomarkers of each *Aspergillus* sp., shown in Table 2. This study demonstrated that the chemotaxonomic application of three common *Aspergillus* species could be achieved using our analytical platform coupled with appropriate multivariate statistical analysis. These abilities will help prevent possible side effects and unexpected biological activity resulting from incorrect species identification.

(a.) (b.)

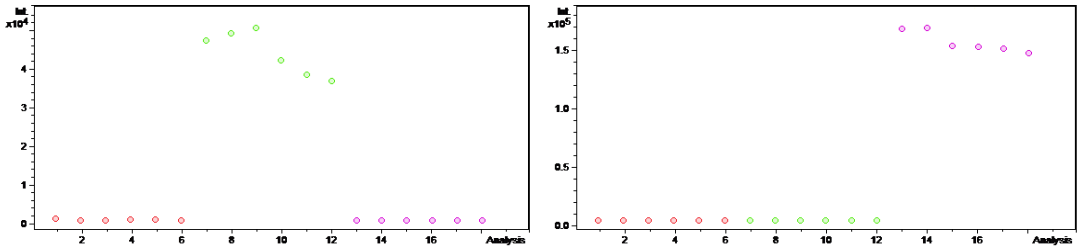

(c.)

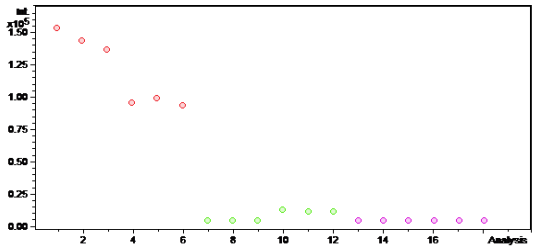

Figure 5. Intensity of the most significant biomarkers versus six samples of three *Apergillus* in triplicate(n=3): a.) 129.0553 m/z of *A. micronesiensis* (●) at 6.07min b.) 574.2372 m/z of *A. awamori* (●) at 20.67 min c.) 335.0752 m/z of Unknown *Aspergillus* sp. (●) at 27.19 min.

Table 2. List of significant biomarkers for the performance of classifiers between species.

Species	m/z of discriminant features	RT (min)	Ion type	Elemental composition	Error (ppm)
A. micronesiensis	129.0553	6.07	$[M-H]^-$	$C_6H_9O_3$	+3.1
	223.0825	1.79	$[M-H]^-$	$C_8H_{15}O_7$	-0.9
	238.0712	5.46	$[M-H]^-$	$C_{11}H_{12}NO_5$	+3.7
	151.0401	5.62	$[M-H]^-$	$C_8H_7O_3$	0.0
	195.0297	7.35	$[M-H]^-$	$C_9H_7O_5$	+0.9
	233.1031	8.07	$[M-H]^-$	$C_{10}H_{17}O_6$	-0.1
	167.0353	9.61	$[M-H]^-$	$C_8H_7O_4$	-1.8
	175.0981	11.27	$[M-H]^-$	$C_8H_{15}O_4$	+3.0
	275.1142	11.90	$[M-H]^-$	$C_{12}H_{19}O_7$	+0.6
	375.0735	14.43	$[M-H]^-$	$C_{19}H_{11}N_4O_5$	0.0
	523.3989	32.05	$[M-H]^-$	$C_{28}H_{47}N_{10}$	+0.4
	599.5265	37.50	$[M-H]^-$	$C_{37}H_{67}N_4O_2$	-0.8
A. awamori	528.3398	8.34	$[M-H]^-$	$C_{22}H_{38}N_{15}O$	+1.7
	627.4460	8.38	$[M-H]^-$	$C_{32}H_{55}N_{10}O_3$	+0.6
	740.5298	9.32	$[M-H]^-$	$C_{22}H_{66}N_{19}O_9$	-1.1

Table2. (continud)

Species	m/z of discriminant features	RT (min)	Ion type	Elemental composition	Error (ppm)
A. awamori	483.3171	9.38	$[M-H]^-$	$C_{23}H_{47}O_{10}$	+0.8
	454.2917	10.39	$[M-H]^-$	$C_{23}H_{40}N_3O_6$	-1.1
	596.4014	10.43	$[M-H]^-$	$C_{27}H_{46}N_{15}O$	+0.2
	610.4172	11.05	$[M-H]^-$	$C_{28}H_{48}N_{15}O$	0.0
	867.5899	11.17	$[M-H]^-$	$C_{39}H_{75}N_{14}O_8$	-0.2
	709.4866	11.49	$[M-H]^-$	$C_{39}H_{65}N_6O_8$	-0.5
	597.3870	11.61	$[M-H]^-$	$C_{23}H_{41}N_{20}$	-1.9
	822.5685	11.85	$[M-H]^-$	$C_{38}H_{72}N_{13}O_7$	+0.2
	485.3330	12.00	$[M-H]^-$	$C_{21}H_{37}N_{14}$	+0.3
	680.4582	12.06	$[M-H]^-$	$C_{31}H_{58}N_{11}O_6$	-0.7
	710.4681	12.31	$[M-H]^-$	$C_{32}H_{60}N_{11}O_7$	-0.2
	936.6384	13.31	$[M-H]^-$	$C_{45}H_{78}N_{17}O_5$	-0.7
	574.2372	20.67	$[M-H]^-$	$C_{21}H_{24}N_{19}O_2$	+1.1
	564.2126	20.70	$[M-H]^-$	$C_{15}H_{18}N_{25}O$	+1.0
	399.2772	33.17	$[M-H]^-$	$C_{23}H_{35}N_4O_2$	+1.7
Unknown	172.0977	8.84	$[M-H]^-$	$C_8H_{14}NO_3$	-1.2
	165.0556	9.38	$[M-H]^-$	$C_9H_9O_3$	-1.0
	206.0826	9.80	$[M-H]^-$	$C_{11}H_{12}NO_3$	+1.6
	245.0931	10.61	$[M-H]^-$	$C_{13}H_{13}N_2O_3$	-0.2
	335.0752	27.19	$[M-H]^-$	$C_{13}H_7N_{10}O_2$	-2.2
	455.2783	31.50	$[M-H]^-$	$C_{24}H_{35}N_6O_3$	-1.6
	481.2939	32.50	$[M-H]^-$	$C_{26}H_{37}N_6O_3$	-1.2
	366.0939	1.80	$[M-H]^-$	$C_{15}H_{16}N_3O_8$	+1.1

Conclusion: In this work, we demonstrated the difference between *A. micronesiensis, A. awamori*, and unknown *Aspergillus* sp. by ions mass differentially accumulated of each species on PCA scores plot and loadings plot. The structure of biomarkers from each *Aspergillus* sp. will be elucidated in the future.

Acknowledgements: This work was supported by the Center of Excellence for Innovation in Chemistry (PERCH-CIC) and the research promotion award granted by the Thai Government to Ramkhamhaeng University for the fiscal year B.E. 2563.

References:

1. Kheawwongjan A, Kim DS. Ocean & Coastal Management. 2012;57:21-33.
2. John IP, John WT, The Mycological Society of America, Lawrenc. 2014;5:1051–1062.
3. Tanja TB, Jens F, Peter BK, Thomas OL. Molecules. 2013;18:11338-11376.
4. Raj KS, Sukhvinder SP, Kawaljit SS. Biotech. 2017;7:164-172.
5. Zhaodi W, Qingyi T, Xiaotian Z, Peng Z, Chong D, Jianping W, Chunmei C, Hucheng Z, Yonghui Z. Org. Lett. 2019;21:1026-1030.
6. Bree, B.A.; Kyu, Y.R. Curr. Opin. Microbiol. 2014;19:90-96.
7. Xiaoling Z, María EM, Facundo MF. TrAC Trends in Anal Chem. 2019;118:158-169.
8. Roux A, Lison D, Junot C, Heilier JF. Clin. Biochem. 2011;44:119-135.
9. Margit D, Laura PF, Paul RW, Paul DF. J. Microb Methods. 2014;106:23-32.
10. Chaiyasaeng W, Buaruang J, Yingyongnarongkul BE. PACCON. 2020;-:201-206.
11. Visagie CM, Hirooka Y, Tanney JB, Whitfield E, Mwange K, Meijer M, Amend AS, Seifert KA, Samson RA. Studies in Mycology. 2014;78:63-139.
12. Bruno AQS, Seteno KON, James HD. Environ Biotech. 2013;-:123-146.

C_023_OF: PURIFICATION AND BIOCHEMICAL CHARACTERIZATION OF AMYLASE ENZYME FROM *Puntioplites proctozysron*

Suthathip Phetlum*, Chamaiporn Champasri**

Department of Biochemistry, Faculty of Science, Khon Kaen University, 40002 Khon Kaen, Thailand
*e-mail: suthathip.por@gmail.com
**e-mail: chamai@kku.ac.th

Abstract:

Amylase enzyme from *Puntioplites proctozysron* was purified and characterized. The enzyme was extracted from whole digestive tract. Purification was performed with the combination step of ammonium sulfate precipitation, anion exchange chromatography, and size exclusion chromatography, respectively. The partially purified amylases were collected in three fractions including unbound fraction (UB), P1, and P2, which were then subjected for biochemical characterization. SDS-PAGE and zymogram showed the partially purified enzymes. All fractions exhibited the same optimum pH at 8.0 and different optimum temperatures at 60 ºC for UB and at 45 ºC for P1 and P2. The enzymes revealed stable at pH of 7.0-9.0 with residual activities more than 80% after both incubation of 1 h and 6 h. Upon incubation for 1 h, all three fractions exhibited high thermal stability at 29 ºC with increasing residual activity of 126.0% to 160.0%. Once increasing of incubation time to 6 h, the residual activities of enzymes reduced. However, P1 and P2 were still displayed high residual activities 94% and 95%, respectively. In addition, effects of metal ions and chemical reagents on enzyme activity showed that the amylase activities of all fractions were slightly enhanced in the presence of 2 mM Ca^{2+} ion and were strongly inhibited by Zn^{2+}, SDS and EDTA, while monovalent cations of K^{+} and Na^{+} did not make any change of their activities.

Introduction:

Puntioplites proctozysron is an omnivorous fish in cyprinid species that widely distributes in several freshwater habitats such as a swamp, dam and aquaculture industry in Thailand. The digestive system is an important process that relates to growth and development of small fish[1]. Digestive enzymes found in the gut of fish compose of pepsin, trypsin, chymotrypsin, cellulase, and amylase [1,2]. Amylases are glycoside hydrolases (GHs), appear to digest starch molecules into glucose unit producing a small fragment of maltose, glucose, and dextrin. Amylases produced from several organisms have different characteristics and action patterns, as well as huge variations in thermostability, temperature and pH optimal. Study of amylase enzymes is an essential step towards understanding the mechanism of carbohydrate digestion. Currently, the study of digestive enzymes in fish has a wide range of interesting. Characterization of the digestive enzyme has been reported in three cyprinid species[3], *Salmo salar L*[2]., and scaleless carp[4]. Different fish species reveal different activities of digestive enzymes. Moreover, the previous study on isoenzymes analysis of amylase and alkaline proteases in seven cyprinid by using Native-PAGE and zymography revealed different isoform patterns and different molecular weight of enzyme isoforms[5].

Isoenzyme or isozyme is a group of enzymes that catalyze similar reactions, but they are different from each other slightly in chemical structure, kinetic properties, and regulatory properties. All living systems apparently require multiple molecular forms of certain enzymes in order to maximize biological capacity. Along with *Puntioplites proctozysron* was not reported about isoform patterns and biochemical characteristics of amylase digestive enzyme. The objectives of this research aimed to purify and characterize the biochemical properties of amylase enzyme extracted from *Puntioplites proctozysron*. The pH stability, thermostability, and the effects of metal ions on the enzyme activity were also determined.

Methodologies:

Reagents: Acrylamide, *N, N'*-methylene-bis-acrylamide, Coomassie Brilliant Blue R-250, ammonium persulfate, and Tetramethyl ethylenediamine (TEMED) were purchased from GE healthcare. Tris, sodium dodecyl sulfate (SDS), soluble starch were purchased from Bio Basic Inc. Magnesium chloride, potassium iodide, potassium chloride, sodium chloride, sodium hydroxide, and zinc chloride were purchased from CARLO ERBA Reagents. Starch was purchased from SIGMA and ethylenediaminetetraacetic acid (EDTA) was purchased from USB Corporation. 3, 5-Dinitrosalicylic acid and manganese chloride was purchased from Honeywell Fluka™.

Sample collection and extraction: Fish sample was randomly collected from Nong Kong Kaew swamp, Khon Kaen, Thailand, only the digestive tract was dissected and weighted. Crude enzyme was extracted by grinding the whole of digestive tracts on ice-colded extraction buffer (0.05 M Tris-HCl buffer, pH 7.5) with the wet weight per buffer volume of 1: 3 ratio. The homogenate was centrifuged at 22,000 x g for 20 min in order to separate protein sample from cell debris and subsequently kept at 4 ºC until use.

Protein determination and amylase activity assay: Protein content of sample was measured according to Bradford's method[6] with bovine serum albumin as standard protein. Absorbance at 595 nm of the protein sample was monitored after 7 min incubation of sample and dye. The dinitrosalicylic acid (DNS) method[7] was used to analyze amylase activity with maltose as standard sugar. The reaction mixture was composed of 500 µl of 0.5% starch in 0.05 M Tris-HCl buffer, pH 8.0, 480 µl of 0.2 M Tris-HCl buffer, pH 8.0, and 20 µl of enzyme sample. The reaction was incubated at room temperature (29 ºC) for 15 min and subsequently stopped by 500 µl of DNS solution, after that boiled the reaction for 10 min prior to centrifuge at 16,000 x g for 10 min and measured the absorbance at 540 nm. The amount of produced sugar was calculated from the maltose standard curve. One unit (U) of enzyme activity was defined as the amount of enzyme releasing 1 mmol ml^{-1} of maltose per minute, under the assay condition.

Amylase purification: Initially, the crude extract was precipitated by ammonium sulfate (80% saturation) with gentle stirring at 4 ºC for 3 h. After centrifugation at 22,000 x g for 20 min, the precipitant proteins were dissolved in extraction buffer followed by dialyzing in dialysis buffer (0.02 M Tris-HCl buffer, pH 7.5 containing 0.02 M NaCl, 0.5% glycerol) for 3 h. The enzyme solution was loaded onto a Q Sepharose Fast Flow column (GE Healthcare, 1.5 x 15 cm) which pre-equilibrated with dialysis buffer. Binding proteins were eluted with stepwise gradient of elution buffer (0.02 M Tris-HCl buffer, pH 7.5, 0.5% glycerol containing 0.1-2.0 M NaCl) at a flow rate of 2.5 ml/ min. Flow-through from the first column containing 0.02 M NaCl was dialyzed to dilute salt concentration and reloaded on the Q-Sepharose Fast Flow. Fractions containing amylase activity were pooled and concentrated by using concentrator (Amicon® Ultra-15 Centrifugal Filter Unit, MWCO 10 kDa). The concentrated samples were loaded onto a Sephacryl S-200 High Resolution column (GE Healthcare, 1 x 100 cm) pre-equilibrated with dialysis buffer and eluted with the same buffer at flow rate of 1 ml/3 min. The active fractions were separately pooled, protein concentration, and enzyme activity were determined followed by SDS-PAGE and zymogram analysis.

SDS-PAGE and zymography analysis: The purity of enzyme was analyzed by sodium dodecyl sulphate polyacrylamide gel electrophoresis (SDS-PAGE) and zymogram analysis, which were carried out according to the method of Champasri[5] with slight modifications. The gel was performed with 5% stacking and 10% separating gels by using Mini-PROTEAN Tetra cell. The enzyme was mixed with 1x SDS sample buffer (62.5 mM Tris-HCl buffer, pH 6.8 containing 25% glycerol, 0.02% bromophenol blue dye, 2% SDS) before loading onto the gel. The electrophoresis was run with 150 volts at 4 ºC about 90 min. The gel was stained in 0.15% Coomassie Brilliant Blue R-250 for 1 h and destained with destaining solution with a mixture of acetic acid-ethyl alcohol-water (1:3:6 v/v) until the blue band of protein is observed against a clear background.

Zymogram analysis was performed after electrophoresis, the gel was incubated in 0.05 M Tris-HCl buffer, pH 8.0 containing 2% Triton X-100 for 15 min followed by incubation in the same buffer without Triton X-100 with gentle shaking for 15 min. Gel was immediately incubated in 2% (w/v) soluble starch in 0.05 M Tris-HCl buffer, pH 8.0 at 4 ºC for 30 min prior to transfer to incubate at 45 ºC for 1 h with gentle shaking. The location of amylase on gel was detected by staining with iodine solution for 10 min until the appearance of the clear bands with amylolytic activity against a dark brown background.

Effects of pH and temperature on enzyme activity and stability: The amylase was assayed in 0.02 M of various pH buffer range from 5.0-11.0 under standard condition. The tested buffers include sodium acetate buffer (pH 5.0), sodium phosphate buffer (pH 6.0-7.0), Tris-HCl buffer (pH 8.0-9.0), and glycine-NaOH buffer (pH 10.0-11.0). Relative activities at the different pH were calculated and the maximum activity was considered to be 100%. The pH stability

was determined by preincubating the enzyme in buffers pH 6.0-10.0 for 1 h and 6 h and then the activity of amylase was assayed. The activity at pH 8.0 was defined as 100% of residual activity.

The amylase was assayed at various temperatures between room temperature (29 ºC) to 70 ºC. The temperature displaying the maximum activity was taken as 100% and the relative activities at different temperatures were calculated. Thermostability was performed by pre- incubating the enzyme in optimal buffer at different temperature from room temperature (29 ºC) to 60 ºC for 1 and 6 h. After that, the incubated enzymes were assayed at incubated temperatures for 15 min. The 100% relative activity was calculated from the enzyme activity without preincubating.

Effects of metal ions and additive reagents on enzyme activity: The amylase enzyme was incubated with metal ions at the final concentrations of 2 mM, 5 mM, and 10 mM ($CaCl_2$, $MnCl_2$ $MgCl_2$, $ZnCl_2$, KCl, and NaCl) and some additive reagents (EDTA and SDS) for 30 min. The residual activities were measured under standard condition and amylase activity without metal ions and additive reagents was defined as 100% of relative activity.

Results and Discussion:

Purification of amylase*:* The amylase is one of digestive enzymes from digestive tract of P. proctozysron. It was partially purified by ammonium sulfate precipitation. Q-Sepharose FF column displayed seven peaks of proteins upon elution with buffers containing 0.1-2.0 M of NaCl. Only P1 and P2 peak showed significantly higher amylase activity than the other as shown in Figure 1A. Many unwanted proteins were removed by Q-Sepharose FF column. Moreover, unbound *(*UB*)* fraction exhibited highest activity after detected the absorbance at 280 nm. SDS-PAGE revealed several protein bands in each fraction and high enzymatic activity, as shown in Figure 1B. Therefore, three amylase fractions including UB, P1, and P2 were separately collected and concentrated before loading on Sephacryl S-200 HR column.

Figure 2 showed the chromatograms, SDS gel and zymogram of three fractions of amylases *(*UB, P1, and P2*)* after Sephacryl S-200 HR chromatography. Fractions containing amylase activity were pooled and concentrated. SDS-PAGE of all amylases exhibited four or five protein bands after Sephacryl S-200 HR and zymogram analysis showed the different isoform patterns of amylases and different levels of enzyme activities *(*Figure 2B*).*

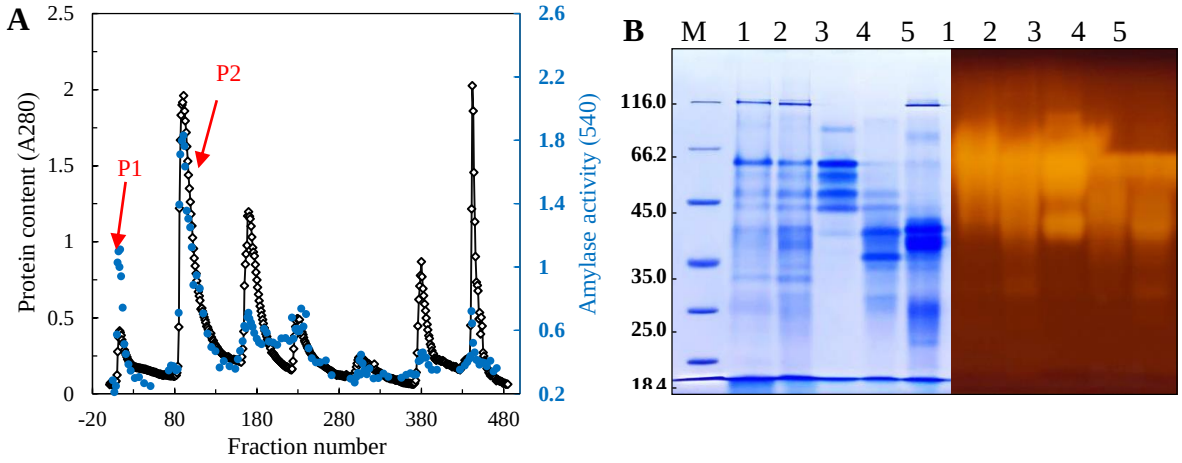

Figure 1.

Chromatogram (A), SDS-PAGE staining with Coomassie Brilliant Blue R-250 and zymogram (B) of *P. proctozysron* amylase after purification with Q-Sepharose FF column Lane M; protein markers, lane 1; crude enzyme extract, lane 2; 80% ammonium sulfate precipitation, lanes 3-5; UB, P1, and P2, respectively.

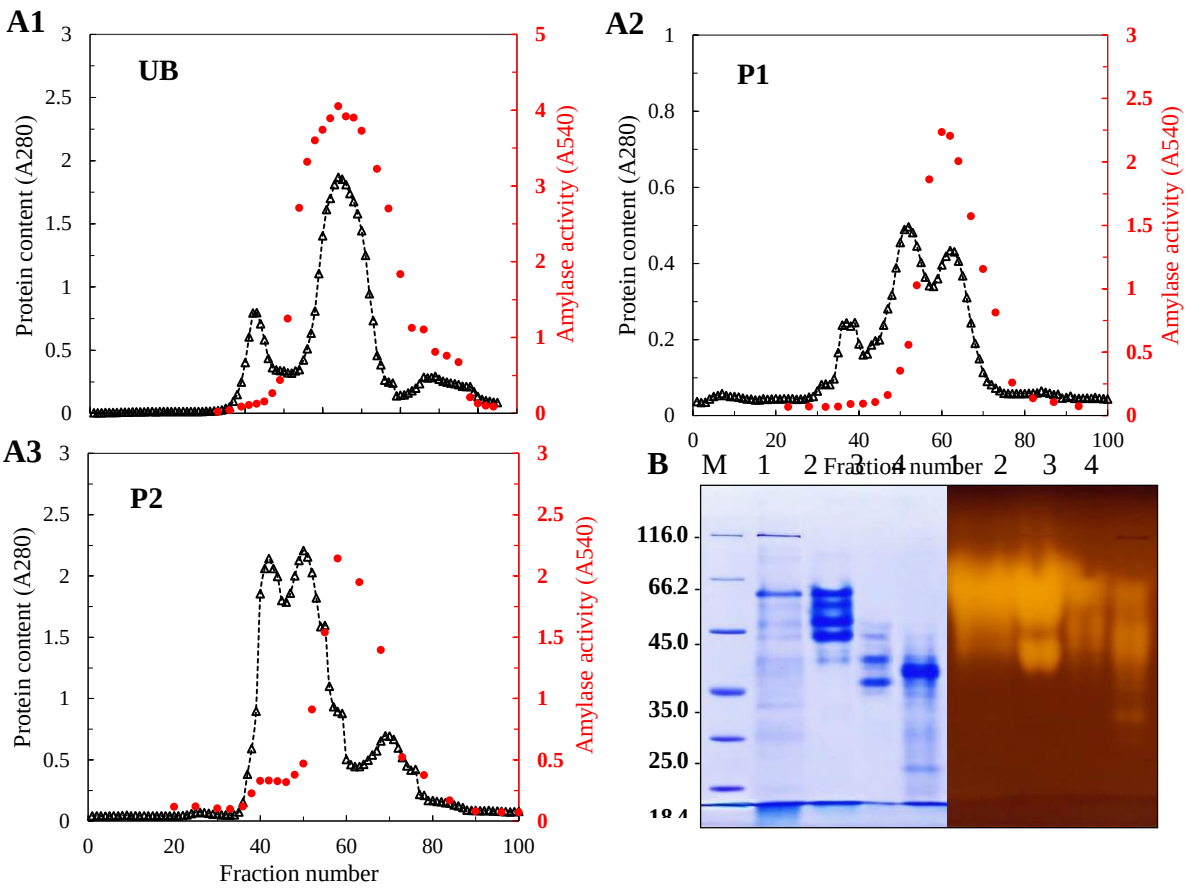

Figure 2.
Chromatograms (A), SDS-PAGE staining with Coomassie Brilliant Blue R-250 and zymogram (B) of *P. proctozysron* amylase after purification with Sephacryl S-200 HR column. Lane M; protein markers, lane 1; crude enzyme extract, lanes 2-4; UB, P1, and P2, respectively.

The purifications folds of partially purified amylases UB, P1, and P2 were increased to 1.49, 3.02, and 1.23-fold purification with specific activity of 11.49, 23.36, and 9.50 units/mg protein, respectively. Partial purification procedure in this study was purified by sequential purification of three steps as summarized in Table 1. The purification yields of amylase UB, P1, P2 (1.75%, 1.23%, and 1.56%) were lower than those reported in *Bacillus* sp. YX-1[8] (6.6%) and *T. pseudokoningii*[9] (18.0%). However, the purification yield obtained in this study was higher than those reported in *E. coli*[8] (0.093%).

Table 1.
Summary of purification of the amylase from *P. proctozysron*.

Procedure	Total activity (U)	Total protein (mg protein)	[a]S.A.	Yield (%)	Purification (Fold)
Crude enzyme extract	2403.7	310.52	7.74	100	1
$(NH_4)_2SO_4$ precipitation	617.96	185.16	3.34	25.71	0.43
Q-Sepharose FF					
Unbound (UB)	49.44	6.01	8.24	2.06	1.06
0.1 M NaCl (P1)	35.01	6.85	1.58	1.60	0.73
0.2 M NaCl (P2)	42.09	24.87	1.69	1.75	0.22
Sephacryl S-200 HR					
UB	42.10	3.66	11.49	1.75	1.49
P1	29.60	1.27	23.36	1.23	3.02
P2	37.53	3.95	9.50	1.56	1.23

[a]S.A.; Specific activity (total units/ mg protein)

Effects of pH values on activity and stability: The influence of pH on activity and stability of the amylases are shown in Figure 3. The maximum activities of all amylases UB, P1, and P2 were displayed at the same values at pH 8.0 corresponded to amylases from previous study in seven cyprinid fishes[5],thermophilic amylase from *Thermus sp*[9] and *amy*175 from Antarctic sea ice bacterium[10]. The partially purified amylases UB, P1, and P2 was stable in a wide range of pH 7.0-9.0 with residual activities more than 80 % after 6 h incubation similar to wtAmy175[11]. The result indicated that these amylases had a broad pH range. Interestingly, amylase UB revealed most stable in pH 6.0 with 146% and 113% relative activity after 1 h and 6 h incubation, respectively.

Effects of temperatures on activity and stability: The effects of temperature on the activities of amylases were measured in range of 29-70 ºC as shown in Figure 4. The optimal temperature of amylase UB exhibited highest activity at 60 ºC, whereas these of amylases P1 and P2 were processed at 45 ºC. The activity of amylase P1 and P2 decreased sharply when assayed above 55 °C. All three amylases exhibited the most stable at 29 ºC upon incubation for 1 h with the remaining activities more than 120% particularly P3 amylase whose remaining activity were up to 160%. After incubation for 6 h, the residual activities of all amylases reduced. However, P1 and P2 were still displayed high activities with remaining activities 94% and 95%, respectively. This results showed that the amylase UB had higher stability than α-amylase A4 from *T. pseudokoningii*[12] and those of *A. flavus* NSH9[13] after 1 h incubation.

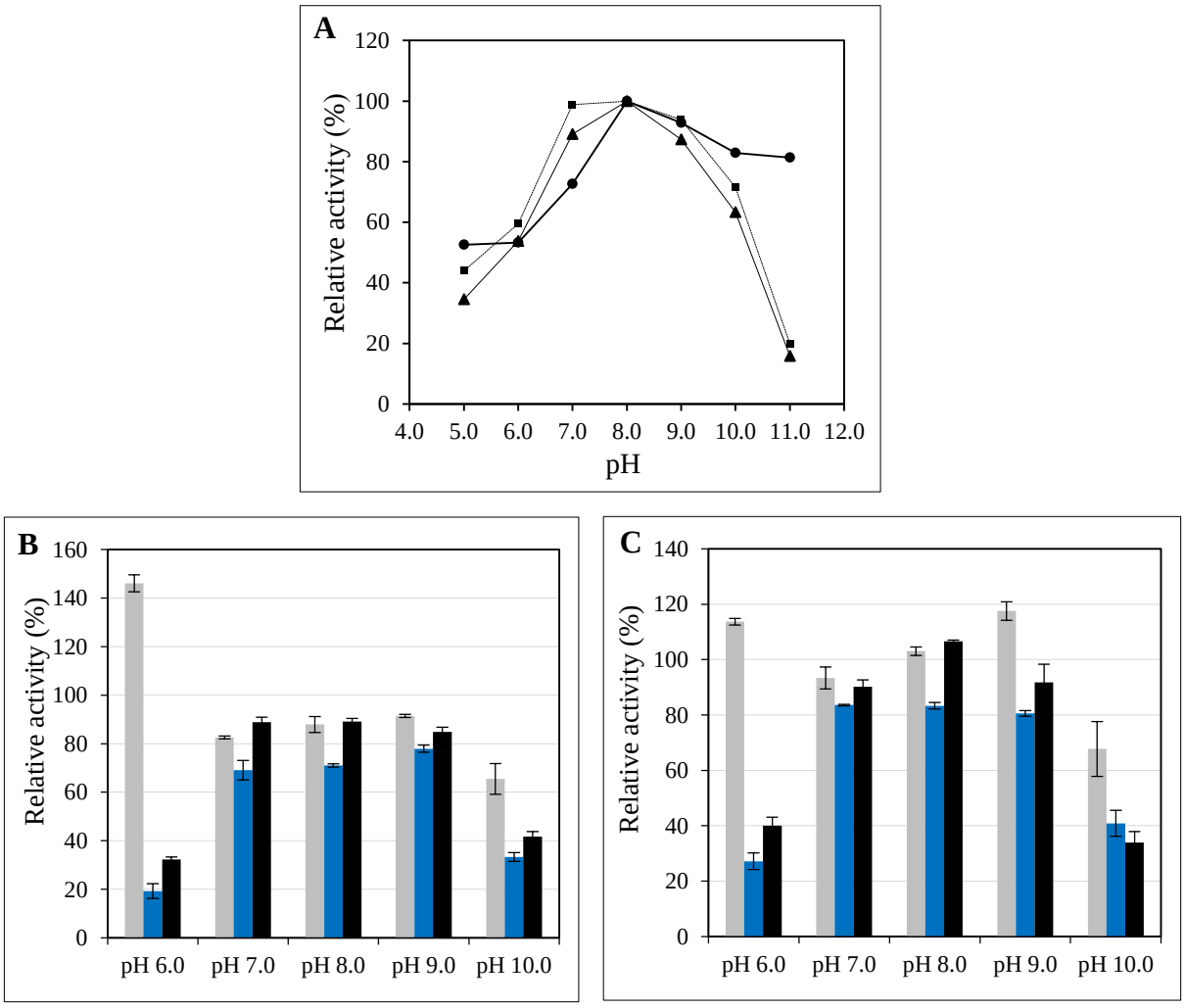

Figure 3.

Effect of pH on activities of the partially purified amylases; UB (-●-), P1 (-▲-), and P2 (-■-) (A). The effects of pH on enzyme activity were determined in the pH ranges of 5.0-11.0 under standard condition. Reactions were performed in duplicate and mean values were presented. The maximum activity was defined as 100% relative activity. The stability was determined by preincubating the enzyme in various pH buffers for 1 h (B) and 6 h (C) of UB (■), P1 (■), and P2 (■). Reactions were assayed in triplicate. Enzyme activities without preincubation at certain pH were defined as 100%. The relative activity (%) were expressed as mean ± SD.

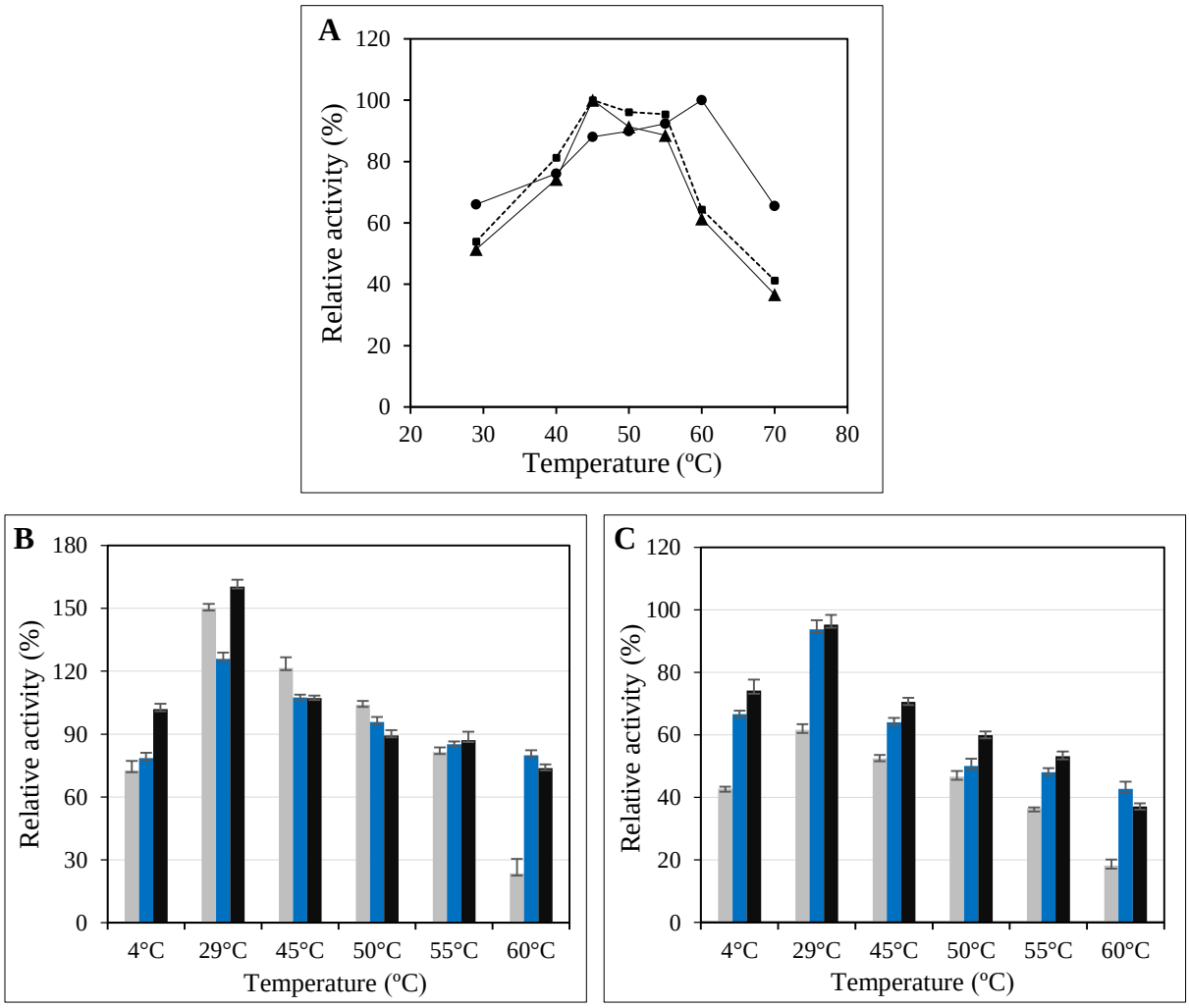

Figure 4.

Effects of temperatures on activities of the partially purified amylases; UB (-●-), P1 (-▲-), and P2 (-■-) (A). The effects of temperature on enzyme activities (A) were analyzed in the temperatures range from 29ºC to 70ºC. Activities without preincubation at certain temperatures were defined as 100%. Reactions were determined in duplicate and mean values were indicated. The stabilities of UB (▒), P1 (■), and P2 (■) were determined by preincubating enzyme in various temperatures from 4 ºC to 60 ºC for 1 h (B) and 6 h (C) followed by determining enzyme activity under certain incubated temperatures. The amylase activity without preincubation was defined as 100%. Reactions were performed in triplicate. The relative activity (%) were expressed as mean ± SD.

Effects of metal ions and additive reagents on enzymatic activity: As shown in Figure 5, all amylase activities were slightly enhanced by 2 mM Ca^{2+}, whereas Na^{+} and K^{+} ions had no significant effects on their activities. The significantly increased enzyme activities in the presence of Ca^{2+} ion have been reported[12,15,16]. The stimulating effect revealed dose-independent activation[12,14]. Our result suggested that these all three amylases might be the metalloenzymes. The assumption was supported by the strong inhibition by Zn^{2+} and EDTA corresponded to the previous reports[13,14].

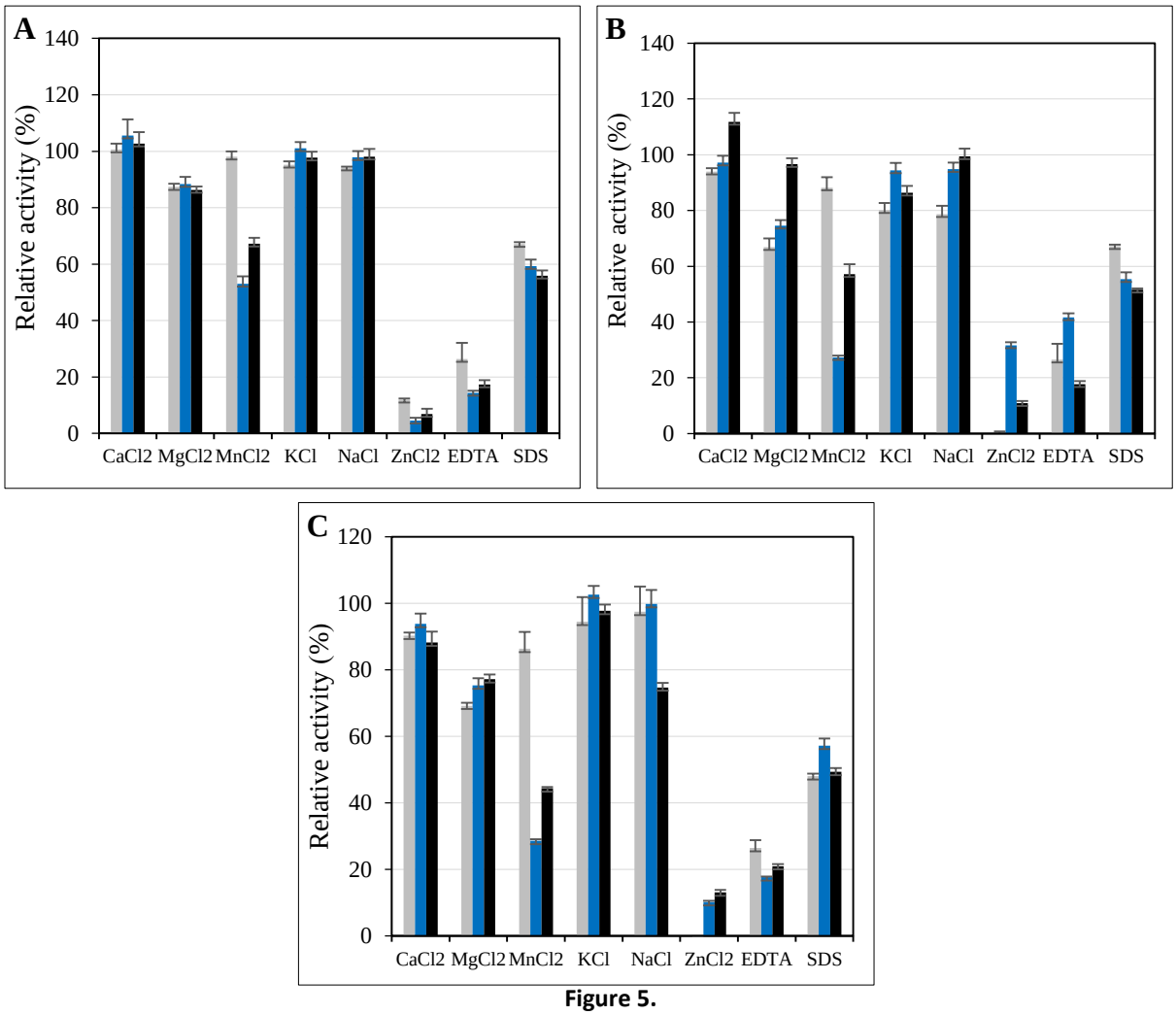

Figure 5.

Effects of metal ions and some additive reagents on the amylase activities. The relative activities of UB (■), P1 (■), and P2 (■) were determined by preincubating enzyme with 2 mM (A), 5 mM (B), and 10 mM (C) in various metal ions and some additive reagents for 30 min before assaying. The amylase activity without metal ions and additive reagents was defined as 100%. Reactions were tested in triplicate. The relative activity (%) was expressed as mean ± SD.

Conclusion:

In summary, this work was aimed to purify the amylase enzyme from *Puntioplites proctozysron* by three steps of ammonium sulfate precipitation followed by anion-exchange and size exclusion chromatography. Three peaks amylases UB, P1 and P2 were partially purified, which were confirmed by SDS-PAGE analysis. The biochemical characterization of these amylases was analyzed. The enzymes were processed the optimal activity and stability at pH 8.0 and pH 7.0-9.0, respectively. The optimal temperatures were varied at 45 ºC and 60 ºC. All three fractions revealed maximum activities with high thermal stability at 29 ºC after incubation for 1 h and demonstrated extreme decrease at 60 ºC for UB amylase. The partially purified amylases displayed higher activity in the presence of 2 mM $CaCl_2$ and were strongly inhibited by $ZnCl_2$ and EDTA suggesting that these enzymes were metalloenzymes.

Acknowledgments:

The research capability enhancement program through graduate student scholarship, Faculty of Science, Khon Kaen University, is gratefully acknowledged.

References:

1. Krogdahl A, Hemre GI, Mommsen TP. Aquac Nutr. 2005;11(2):103-122.
2. Sunde J, Taranger GL, Rungruangsak-Torrissen K. Fish Physiol Biochem. 2001;25(4):335-345.
3. Al-Tameemi R, Aldubaikul A, Salman NA. Turkish J Fish Aquat Sci. 2010;10(3):411-414.
4. Tian H, Meng Y, Li C, et al. Aquac Reports. 2019;13(September 2018):100174.
5. Champasri C, Champasri T. J Fish Aquat Sci. 2017;12(6):264-272.
6. Bradford MM. A Anal Biochem. 1976;72:248-254.
7. Miller GL. Anal Chem. 1959;31(3):426-428.
8. Hassan BA, Alsalami NY, Jebor MA. J Pharm Sci Res. 2018;10(7):1691-1696.
9. Fatoni A, Zusfahair. Songklanakarin J Sci Technol. 2012;34(5):525-531.
10. Wang X, Kan G, Ren X, et al. Biomed Res Int. 2018;2018:16.
11. Wang X, Kan G, Shi C, et al. Protein Expr Purif. 2019;164(June):105444.
12. Abdulaal WH. BMC Biochem. 2018;19(1):4-9.
13. Karim KMR, Husaini A, Sing NN, Sinang FM, Roslan HA, Hussain H. 3 Biotech. 2018;8(204):1-14.
14. Galabova D, Velcheva P. Acta Microbiol Bulg. 1983;Vol. 19(2):56-62.
15. Sethi BK, Nanda PK, Sahoo S, Sena S. Cogent Food Agric. 2016;2(1).
16. Irfan M, Nadeem M, Syed Q, Shakir HA, Qazi JI. Chem Biochem Eng Q. 2016;30(4):429-437.

C_024_PA: UTILIZATION OF *OCIMUM* STRAW TRUNK AS RENEWABLE ENERGY VIA ZERO WASTE MANAGEMENT APPROACH

Sajee Noitang, Thanaporn Wichai, Weradej Sukaead, Ruengwit Sawangkeaw, Sarintip Sooksai*

The Institute of Biotechnology and Genetic Engineering, Chulalongkorn University, Bangkok, THAILAND
*e-mail: sarintip.so@chula.ac.th

Abstract:

This is an approach to develop a zero-waste management of the aflatoxin-free Hairy basil (*Ocimum* spp.) production by dry-scattering of *Ocimum* seeds for biochar production. Hairy basil straw is concerned as agricultural waste, when the straw is left in the field after harvest. The fermentation of the waste causes methane, one of the most potent greenhouse gasses (GHGs). The fully-gasification or combustion also generates large amounts of CO_2 as GHGs. Therefore, farmers are encouraged to re-use the *Ocimum* straw by using as an ingredient in mushroom baglog by replacing high-priced sawdust or producing biochar in a partial pyrolysis process resulting in a by-product of household energy. The biochar made of *Ocimum* trunk is 39-43% of the original weight and the pH of 7.72 was detected in its suspension in water. When scanned with SEM at 1000x magnification, it shows the porous layers like a stacked rectangular (Figure 1). Adsorption isotherm of methylene blue is consistent with the Langmuir model; in other words, it is complying with monolayer absorption phenomenon. A maximum adsorption capacity of synthesized biochar is 38.3 g/g at 30□C. Addition of biochar in planting materials can increase water holding capacity by more than 5%. Moreover, when biochar was added to acidic soil, plant productivity was increased. Therefore, converting the agricultural waste to energy and biochar is simultaneously reducing in household energy costs, strengthening the community, and reducing the environmental impact, especially by reducing GHGs from the burning of agricultural waste materials.

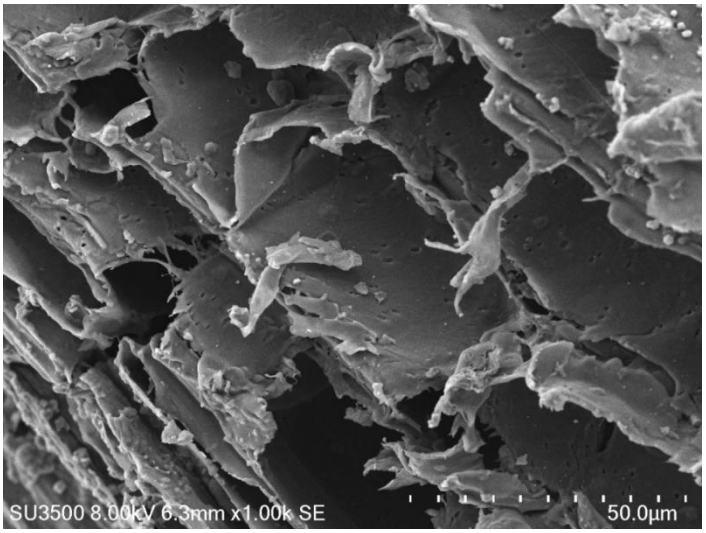

Figure 1.

Biochar prepared from *Ocimum* straw trunk by SEM at 1000x

C_025_PA: COMPOSITION AND ABUNDANCE OF ZOOPLANKTON IN THE VICINITY OF PORTS INDUSTRAIL IN THE UPPER AND EASTREN GULF OF THAILAND

Darika Buathong,*, Pronsiri Sriwisait, Orathep Muresare, Makamas Sutthacheep, Thamasak Yeemin

Marine Biodiversity Research Group, Department of Biology, Faculty of Science, Ramkhamhaeng University, Huamark, Bangkok, Thailand
*e-mail: darikabeathong@gmail.com

Abstract:

Zooplankton play a substantial role in marine ecosystems as they serve as a link for energy transfer from primary producers to higher trophic levels. Zooplankton can also be applied as bioindicator for detecting marine ecosystem fertility and water pollution. This study aimed to investigate the composition and abundance of zooplankton in the vicinity of port industrial in the Upper and Eastern Gulf of Thailand. Zooplankton were collected from 3 sites in Rayong Province, i.e., Hin Khong, Hat Nong Fab and Ko Saket, the Eastern Gulf of Thailand, and 3 sites from Chonburi Province, including Ao Bang Lamung, Ao Laem Chabang and Ao Udom, the Upper Gulf of Thailand. The zooplankton were collected by standard 120 µm mesh plankton net hauled horizontally. It revealed that the highest density of phytoplankton was recorded at Ao Bang Lamung accounting for 8,039 ind./m^3 and the lowest one was found at Hin Khong with the density of 4,059 ind./m^3. The dominant groups of zooplankton that found in Rayong Province included *Sagitta* sp., *Lucifer* sp., *Creseis acicula*, Gastropod larva And *Calanus* sp. while the zooplankton community in Chonburi Province was dominated by bivalve larvae, *Oikopleura* sp., *Calanus* sp. and *Mitella mitella*. These results suggest that zooplankton abundance might be shaped by ecological condition of water in such marine ecosystem and may potentially be used as bioindicators of marine water quality.

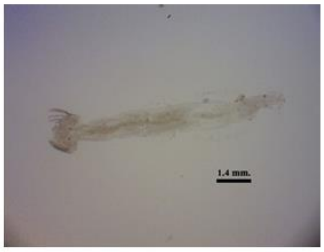

Sagitta sp.

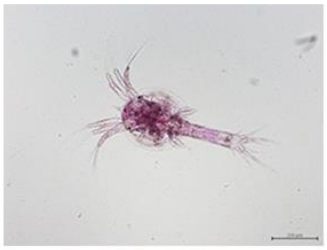

Lucifer sp.

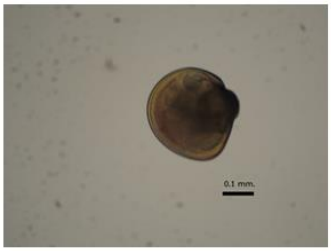

Bivalve larvae

Oikopleura sp.

Dominant of zooplankton in study site

C_026_PA: DIVERSITY AND DENSITY OF PHYTOPLANKTON IN THE PORTS OF CHONBURI AND RAYONG PROVINCE

Orathep Muresare,*Thamasak Yeemin, Makamas Sutthacheep

Marine Biodiversity Research Group, Department of Biology, Faculty of Science, Ramkhamhaeng University, Huamark, Bangkok, Thailand
*e-mail: sfxlr@hotmail.com

Abstract:

Phytoplankton is the main component of food webs in marine and coastal ecosystems and can be used as a bioindicator to investigate water quality, ecosystem fertility, and ocean circulation which are also important for the fisheries in Thailand. Phytoplankton communities reflect climate variability and changes that occur in coastal and marine ecosystems. Here, we aimed to study the diversity and density of phytoplankton in the Chonburi and Rayong ports. Phytoplankton were collected by using a 20-micron mesh size plankton net with horizontal hauling from the Ao Udom, Laem Chabang Port and Ao Bang La Mung in Chonburi Province and the Hin Khong, Hat Nong Fab and Ko Saket in Rayong Province. A total of fourteen groups of phytoplankton were found in Chonburi Province and twelve groups of Rayong Province. The highest density of phytoplankton was recorded at Laem Chabang Port accounting for 5,172± 278ind./m^3 and the lowest one was found at Hin Khong with the density of 2,576± 248ind./m^3. The density of phytoplankton found at Laem Chabang Port was significantly higher than those found at other study sites ($P<0.05$). The dominant groups found in Chonburi Province included *Guinardia flaccida*, *Chaetoceros curvisetus* and *Streptotheca tamesis* while the phytoplankton community in Rayong Province were dominated by *Proboscia alata*, *Guinardia flaccida*, and *Ceratium trichoceros*. The spatial variation of phytoplankton densities across the study sites may be influenced by currents, availability of nutrients, and coastal human activities.

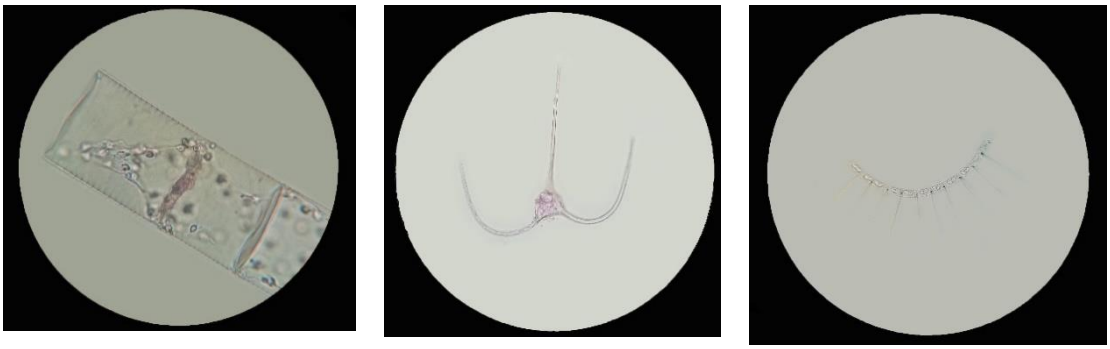

Dominant of Phytoplankton at the study sites.

C_027_PA: HIGH FAT DIET INDUCED MATERNAL OBESITY EFFECT TO DYSREGULATION OF AUTOPHAGY PROCESS IN KIDNEY OF MALE OFFSPRING

Nichakorn Phengpol[1], Anusorn Lungkaphin[1]*

[1]Department of Physiology, Faculty of Medicine, Chiang Mai University,
Chiang Mai, Thailand
*Correspondence: Anusorn Lungkaphin, Department of Physiology, Faculty of Medicine, Chiang Mai University, Chiang Mai, 50200, Thailand
(Email: onanusorn@yahoo.com; anusorn.lungka@cmu.ac.th, Tel: +66 53-945362-4, Fax: +66.53-945365)

Abstract:

As the prevalence of obesity has increased worldwide and more women are entering pregnancy overweight or obesity. Consequently, these women could impact their babies to increase risk of obesity and insulin resistance in later life. Moreover, obesity is associated with type 2 diabetes mellitus (T2DM), hypertension, and dyslipidemia. All of these are the important factors influencing the development and progression of chronic kidney disease (CKD). It is possible that maternal overweight and obesity could affect to offspring's kidney. Therefore, this study considerable interest in understanding mechanism of maternal overweight or obesity, which may lead to kidney injury in the offspring. Autophagy is an essential cellular process that maintains homeostasis by recycling damaged organelles and nutrients. The defects in autophagy has been associated with kidney disease. Therefore, in this study hypothesized that maternal obesity induced by high fat diet consumption effect to dysregulation of autophagy process in male offspring's kidney.

Male offspring of maternal obesity had significantly increased blood glucose and insulin level which represented insulin resistance. The kidney of male offspring born to obese mother showed significantly higher mTOR protein expression which affected to inhibit autophagy process. The initiation protein of autophagy including beclin-1 significantly decreased along with reduced LC3-II protein expression, that represented to decreased autophagosome formation, in the kidney of male offspring born to obese mother.

Maternal obesity has significant adverse effects on male offspring kidney via inhibition of the autophagy process by decreasing autophagosome formation.

C_028_PA: ISOLATION OF PROTEOLYTIC *Bacillus* sp. FROM THE GUT OF TERMITE, *Microcerotermes* sp. AND SOLID-STATE FERMENTATION OF SOYBEAN MEAL USING NEWLY ISOLATED BACTERIA

Noppawan Suttisak, Phonphan Watthanarat, Pinsurang Deevong*

Department of Microbiology, Faculty of Science, Kasetsart University, Bangkok 10900, Thailand
*e-mail: fsciprd@ku.ac.th

Abstract:

Soybean meal (SBM) is an excellent protein source and widely used as ingredient in feeds for many animals. However, fermentation could nutritionally improve SBM with using proteolytic and cellulolytic enzymes obtained from symbiotic bacteria in xylophagous insects, such as wood-feeding higher termite, *Microcerotermes* sp. This study aimed to isolate endospore forming bacteria and improve the nutritional value of fermented soybean meal by proteolytic enzyme production of *Bacillus* sp. newly isolated from the guts of termites using heat treatment and morphological characterization. Forty-eight isolates of endospore forming Gram positive rod were isolated. They were tested for the abilities to produce proteolytic enzymes on nutrient agar (NA) added with 1% soymilk, 1% skimmed milk, 1% gelatin. Moreover, their cellulolytic activity to degrade 0.5% carboxymethyl cellulose (CMC) was investigated. The results showed that, 41 isolates could produce at least one enzyme and 36 isolates could degraded soymilk. From the total isolates, 12 high ability isolates were selected to test soymilk degrading capability on Berg's agar. Overall, the isolates Mc-H-29, Mc-H-36 and Mc-H-39 were used to test growth potential in fermented soybean meal. Based on 16S rRNA gene sequencing, these three isolates were related to the species of *Bacillus.* This study suggested that, the newly isolates produced high active proteolytic and cellulolytic enzymes potentially useful for solid-state fermentation of soybean meal.

C_029_PA: GENOME-WIDE ASSOCIATION STUDY OF ANTIOXIDANT COMPOUNDS AND ACTIVITY IN 159 THAI RICE CULTIVARS

Saranyu Thaworn[1], Teerapong Buaboocha[2,5], Supachitra Chadchawan[3,5], Chanita Paliyavuth[4] and Waraluk Kasettranan[4,*]

[1] Program in Biotechnology, Faculty of Science, Chulalongkorn University, Bangkok 10330, Thailand
[2] Molecular Crop Research Unit, Department of Biochemistry, Faculty of Science, Chulalongkorn University, Bangkok 10330, Thailand
[3] Center of Excellence in Environment and Plant Physiology, Department of Botany, Faculty of Science, Chulalongkorn University, Bangkok 10330, Thailand
[4] Department of Botany, Faculty of Science, Chulalongkorn University, Bangkok 10330, Thailand
[5] Omics Science and Bioinformatics Center, Faculty of Science, Chulalongkorn University, Bangkok 10300, Thailand
*E-mail address: waraluk.k@chula.ac.th

Abstract:

The antioxidant traits in rice are controlled by polygenes. These traits are complex and difficult to evaluate the genetic mechanisms. Understanding the genetic basis of antioxidant traits is necessary for the improvement of nutritional quality by breeding. In this research, 159 local Thai rice cultivars were used to identify the single nucleotide polymorphisms (SNPs) significantly associated with antioxidant compounds and activity in the rice grains. GWAS were performed by GEMMA software and the mixed linear model (MLM) using 209594 SNPs and total phenolic content (TPC), total flavonoid content (TFC) and antioxidant capacity (AC) by ABTS (2,2'-azino-bis-3-ethylbenzthiazoline-6-sulphonic acid). A total of 158 significant SNPs was detected. They are located on promotors and exomes of almost all chromosomes, except chromosome 10 and 11. One hundred and eight significant SNPs associated with two or three antioxidant traits were identified in 40 loci on chromosome 1, 2, 3, 4, 5, 6, 7 and 8. Some significant SNPs on these chromosomes showed R^2 in the range of 0.10 - 0.37. Interestingly, the significant SNPs on *Rc* gene, encoding bHLH transcription factor regulating proanthocyanidin production in rice seeds, were detected. Moreover, SNPs found on chromosome 4 was potentially linked with the genes encoding anthocyanin regulatory Lc protein. Therefore, these data suggest that this study can provide new candidate molecular markers for antioxidant trait in rice seeds, which can be applied antioxidant quality improvement by marker-assisted selection approach.

C_030_PA: DIVERSITY OF MARINE FUNGI LIVING IN DISEASED CORAL REEFS FROM THE GULF OF THAILAND AND THE ANDAMAN SEA

Klinphaka Phuthaworn[1], Kanokkorn Longmatcha[1], Malik Alimuhammad[1], Worawut Chaiyasaeng[1], Onuma Piasai[2], Makamas Sutthacheep[3], Thamasak Yeemin[3] and Jamrearn Buaruang[1,*]

[1]Marine Microbe Environment Research Unit, Division of Environmental Science, Faculty of Science Ramkhamhaeng University Bangkapi, Bangkok 10240, Thailand
[2]Department of Plant Pathology, Faculty of Agriculture, Kasetsart University, Bangkok 10900, Thailand
[3]Marine Biodiversity Research Group, Department of Biology Faculty of Science, Ramkhamhaeng University, Bangkapi, Bangkok 10240, Thailand
*e-mail: jbuaruang@ru.ac.th

Abstract:

Diseased organisms including sponge (*Xestospongia* sp.), seafan (*Melithaea* sp.) and coral (*Acropora* sp., *Montipora* sp., *Pavona decussate*, *Porites lutea*, *Turbinaria frondens* and *Turbinaria* sp.) were collected from the Gulf of Thailand and the Andaman Sea between May 2013 and May 2017. All 23 samples, marine fungi from infected sea fan and coral tissue were isolated using the tissue transplanting method on malt extract agar (MEA) with 70 percent sea water and incubated at 28˚C for five to seven days. Marine fungi were identified based on morphological characteristics such as colony growth rate and growth pattern on standard culture media, namely malt extract agar (MEA).

A total of 102 fungal samples were isolated in this study. The number of 72 isolates from The Gulf of Thailand was found including *Acremonium* spp., *Aspergillus flavus*, *Aspergillus japonicas*, *Aspergillus parasiticus*, *Aspergillus wentii*, *Aspergillus* spp., *Cladosporium* spp., *Curvularia* spp., *Emericella* sp., *Nigrospora* sp., *Penicillium citrinum*, *Penicillium* spp., *Syncephalastrum* sp., *Trichoderma* sp., *Zygosporium* sp. and *sterile mycelium*. *Cladosporium* spp. was found with the highest number of 15 isolates. The organisms that isolated the most fungi were the sea fan (*Melithaea* sp.). The total of 30 isolates from the Andaman Sea included *Acremonium* sp., *Cladosporium halotolerans*, *Cladosporium* sp., *Penicillium citrinum*, and *Penicillium* sp. and *sterile mycelium*. *Penicillium* spp. was found at the most 6 isolates. The organisms that isolated the most fungus were sponge (*Xestospongia* sp.).

Storage cultures of marine fungi in grains at the temperature of -20ºC for about one year exhibited the survival of marine fungi from the Gulf of Thailand and the Andaman Sea at 59.72 percent and 36.66 percent.

References:

1. Amy SG, Timothy YJ, Anthony SA. Curr. Bio. 2019;19: R191-R195.
2. Taboonpong K, Manoch L, Chamswarng C, and Piasai O. Thai J. Agric. Sci. 2014;44:81-91.
3. Noor AZ, Latiffah Z. Hayati J. Biosciences. 2017;24: 26-34.
4. Chi-Ching T, James YMT, Susanna KPL, Patrick CYW. Comput. Struct. Biotechnol. J. 2018;16: 197-210.

C_031_PF

C_031_PF: DNA FINGERPRINT ANALYSIS USING AFLP TECHNIQUE OF *Adenia viridiflora* Craib

Chuttiya Tiva[1]*, Sophon Boonmewisate[1], Piyarat Parinyapong Chareonsap[2], Patcharawadee Wattanawikkit[1], Prasit Boonthai[1] and Orachorn Chotiyarnwong[2]

[1] Department of Biology, Faculty of Science, Ramkhamhaeng University, Bangkok 10240, Thailand
[2] Plant Genetic Conservation Project under The Royal Initiative of Her Royal Highness Princess Maha Chakri Sirindhorn (RSPG), Chitralada Palace, Dusit, Bangkok 10303, Thailand
*e-mail: Chuttiya2531@hotmail.com

Abstract:

Genetic diversity and relationships among thirty-five genotypes of *Adenia viridiflora* Craib that collected from various sources in Thailand was investigated using AFLP (Amplified Fragment Length Polymorphism) markers. Fifteen AFLP primers gave 289 amplified reproducible polymorphic fragment products, and cluster analysis was then conducted using UPGMA method by Jaccard similarity coefficients. The results demonstrated that these collections were clearly separated into four groups which are (1) samples from the northeastern provinces of Nakhon Ratchasima, Sisaket, Buriram, Khon Kaen and Nakhon Phanom (2) samples source from northern and western provinces: Kanchanaburi, Uthai Thani, Nakhon Sawan, Phetchabun, Chiang Mai and Uttaradit (3) samples from Nakhon Sawan and Sa Kaeo provinces, at similarity level of 0.48. The cophenetic correlation of r = 0.77 indicated that these samples were fairly well grouped.

Key words: Phak I-nun, *Adenia viridiflora* Craib, AFLP, DNA fingerprint

Introduction:

Adenia viridiflora Craib (Phak I-nun) is classified into the family Passifloraceae (Passion fruit) contains 100 species, mostly in Africa and Madagascar, India, Myanmar, southern China, southern Vietnam, Cambodia, Laos, the Malay Peninsula and Sumatra. In Thailand, it can be found in almost every region. There are different names according to each local name: Pak I-nun (Nakhon Ratchasima), Anoon, I-nun (Central region), Nang Nun, Phak Roach (North). Phak I-nun is local vegetables in Thailand. I-nun plant is a favorite native vegetable, preferable to young tips, flowers and immature fruits. It is useful as edible products and for some medical purposes with fairly height price. It was found that the plant were scattered in most of the thin forest areas. When the drought season, I-nun will shed leaves and produce fruit, which is an important period for the villagers to collect and sell.

Adenia viridiflora Craib is used for medicinal properties. Their important activities were effective in cure diarrhea, nourish the liver, nourish the blood, purulent urine pills. There is a phytochemical analysis report. Two groups of important phenolic groups were found, ferulic acid and sinapic acid, in young leaves (Khumlert *et al*, 2018).

AFLP technique is therefore a suitable technique for exploring the genome of plants or animals that have not been studied before. It is a fast way to locate genes, or DNA markers, that are closely related to economic importance. It is helped to create a saturated linkage map in a short time. This increases the chances of getting markers that are linked with the key traits.

The objective of this study was to assess genetic diversity of thirty-five *A. viridiflora* Craib that collected from various sources in Thailand using AFLP markers.

Methodology:

Plant material

Thirty-five *A. viridiflora* Craib were collected from various sources in Thailand and growing at the Plant Genetic Conservation Center, Plant Genetic Conservation Project under the Royal Initiative of Her Royal Highness Princess Maha Chakri Sirindhorn, Nakhon Ratchasima Province (Table 1)

Genomic DNA extraction and AFLPs procedure

Approximately 10 g of young leaf was ground in liquid nitrogen using mortar and pestle. Isolation of total DNA was done following the protocol described by Doyle and Doyle (1990).

The AFLP procedure was carried out as reported by Vos *et al*. (1995) with a few modification. Approximately 100 ng/µl of DNA was digested by two restriction enzymes, i.e. *Eco*RI and *Tru*9I in 10x buffer A (Promega) and incubated for 1 h at 37°C. The restricted DNA fragment was ligated to *Eco*RI-adapter and *Mse*I-adapter for at least 3 h at 37 °C to generate template DNA for amplification. Five microliters of the 1:10 diluted DNA template generated was first pre-amplified using *Eco*RI+A and *Mse*I+C primers. Then the pre-amplified DNA was diluted to 1:9 with sterilized distilled water and 3 µl of the product was used for selective amplification in a reaction tube containing 20 µl of selective amplification mixtures. AFLP adapters and 15 primers pairs (E+CAG/M+TAC, E+CAG/M+TGA, E+ACC/M+CAT, E+ACC/M+CCA, E+ACC/M+CGA, E+ACC/M+CTT, E+ACT/M+CAT, E+ACC/M+CGA, E+CGT/M+TAC, E+CGT/M+TGA, E+ACA/M+CGG, ACA/M+CGC, E+AAG/M+CCC, E+AAG/M+CAT and E+ACA/M+CCC) were used for the selective amplification. The final PCR products were run on a 4.5% denaturing polyacrylamide gel electrophoresis in 1x TBE buffer in a Sequi-Gen GT Sequencing Cell (Bio-Rad, USA). DNA fragments on gels were visualized using silver nitrate staining protocol (Bassam *et al*., 1991). The gel was rinsed with distilled water and air-dried on mirror plates.

Data analysis

For the genetic similarity analysis, AFLP fragments were visually scored as present (1) or absent (0) to create a binary data set. The data was entered into a binary data matrix as discrete variables. Jaccard's coefficient of similarity (Sneath and Sokal, 1973) was calculated for all pair-wise comparisons among the Citrus cultivars as follows: Jaccard=N_{AB}/ (N_{AB}+N_A+N_B), where N_{AB} is the number of fragments shared by two cultivars (A and B), N_A represents amplified fragments in cultivar A and N_B represents fragments in cultivar B. A dendrogram was constructed using NTSYS version 2.1 (Exeter Software, Setauket, NY, USA) (Rohlf, 2000) based on the Unweighted Pair Group Method of the Arithmetic Average (UPGMA).

Results and Discussion:

An example of AFLP profiles of thirty-five 'I-nun' *A. viridiflora* Craib, using primer E+ACT/M+CAT is shown in Figure 1.

The number of AFLP fragments generated per primer set ranged from 15 to 46, suggesting that each primer generated an average of 26.67 fragments and 19.27 of them were polymorphic. A total of 400 AFLP fragments were detected, of which 289 were polymorphic (72.25%) (Table 2).

The genetic similarity coefficient was 0.42-0.82 with cophenetic correlation of r=0.77 indicated that these samples were moderately well grouped. Thirty-five *A. viridiflora* Craib were grouped into four clusters at similarity level of 0.48 (Figure 2). The use of AFLP markers can identify the genetic relationship of *A. viridiflora* Craib collected from various sources: Group 1 is samples from the northeastern provinces of Nakhon Ratchasima, Sisaket, Buriram, Khon Kaen and Nakhon Phanom. Group 2 is samples source from northern and western provinces: Kanchanaburi, Uthai Thani, Nakhon Sawan, Phetchabun, Chiang Mai and Uttaradit. Group 3 is an example from Nakhon Sawan and Sa Kaeo provinces. It shows that the 15 AFLP primers used in this study can distinguish the genetic relationship of I-nun into areas. This means that I-nun is genetically diverse, although not very high, but can use molecular markers to differentiate. In this regard, the interestingly, the samples collected from Nakhon Sawan (AC21 and AC22) were

not classified in the same group, and AC9 samples from Nakhon Ratchasima province. If there is a more in-depth study or additional amorphous examination, it is likely to be more important to these samples.

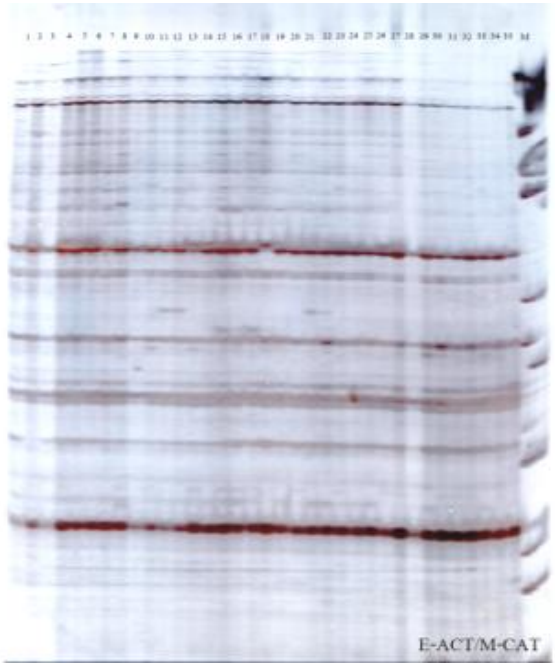

Figure 1.

AFLP profiles of 35 *A. viridiflora* Craib, using primer E+ACT/M+CAT. The samples are arranged from left to the right in the order of 1-35 as list in the table 1 and M (DNA Ladder)

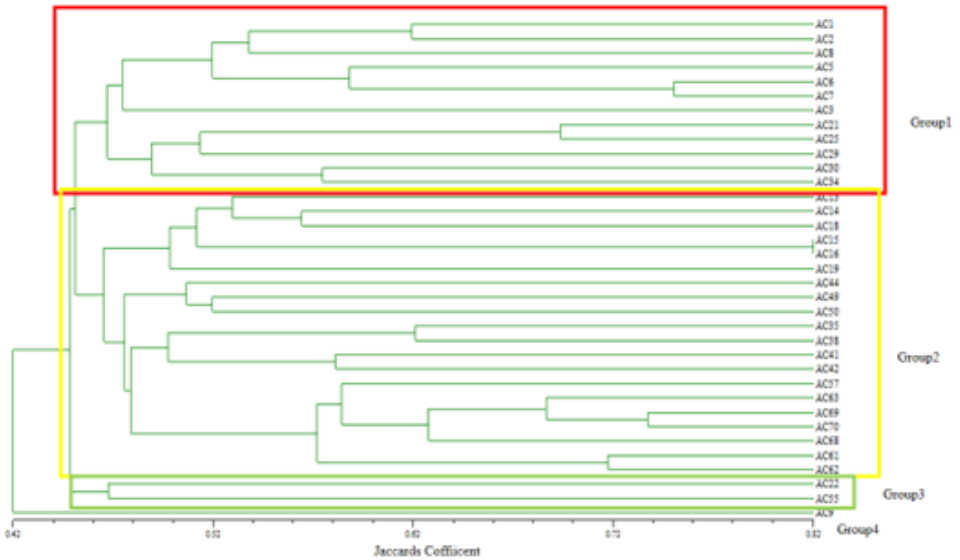

Figure 2.

Dendrogram of thirty-five *A. viridiflora* Craib resulting from a UPGMA cluster analysis based on Jaccard estimates of similarity obtained from 289 polymorphic AFLP bands.

Table 1.

List of 35 *A. viridiflora* Craib used in this study.

	Accession Number	Thai name	Source Location
1	AC1	I-nun	Chokchai, Nakhon Ratchasima Province
2	AC2	I-nun	Chokchai, Nakhon Ratchasima Province
3	AC3	I-nun	Chokchai, Nakhon Ratchasima Province
4	AC5	I-nun	Kham Thale So, Nakhon Ratchasima Province
5	AC6	I-nun	Chokchai, Nakhon Ratchasima Province
6	AC7	I-nun	Chokchai, Nakhon Ratchasima Province
7	AC8	I-nun	Chokchai, Nakhon Ratchasima Province
8	AC9	I-nun	Chokchai, Nakhon Ratchasima Province
9	AC13	I-nun/Nang Nun	Phanom Thuan, Kanchanaburi Province
10	AC14	I-nun	Ban Rai, Uthai Thani Province
11	AC15	I-nun	Ban Rai, Uthai Thani Province
12	AC16	I-nun	Ban Rai, Uthai Thani Province
13	AC18	I-nun	Ban Rai, Uthai Thani Province
14	AC19	I-nun	Ban Rai, Uthai Thani Province
15	AC21	I-nun/Nang Nun	Mueang, Nakhon Sawan Province
16	AC23	I-nun/Nang Nun	Mueang, Nakhon Sawan Province
17	AC25	Pak sab	Pho Si Suwan, Sisaket Province
18	AC29	Pak sab	Nong Hong, Buriram Province
19	AC30	Pak sab	Nam Phong, Khon Kaen Province
20	AC34	Pak sab	Wang Yang, Nakhon Phanom Province
21	AC35	Pak sab	Wang Yang, Nakhon Phanom Province
22	AC38	I-nun	Si Thep, Phetchabun Province
23	AC41	I-nun	Si Thep, Phetchabun Province
24	AC42	I-nun	Si Thep, Phetchabun Province
25	AC44	I-nun	Chom Thong, Chiang Mai Province
26	AC49	I-nun	Tron, Uttaradit Province
27	AC50	I-nun	Tron, Uttaradit Province
28	AC55	Pak sab	Watthana Nakhon, Sa Kaeo Province
29	AC57	Pak sab	Kamphaeng Phet
30	AC61	Pak sab	Pak Chong
31	AC62	Pak sab	SUT
32	AC63	Pak sab	Uthai Thani
33	AC68	Pak sab	Kamphaeng Phet
34	AC69	Pak sab	Ban Rai, Uthai Thani Province
35	AC70	Pak sab	Phaisali, Nakhon Sawan Province

Table 2.

AFLP primer combinations, total number of bands generated by each primer set, number of polymorphic bands detected, and percentage of polymorphic bands used in the study in 35 *A. viridiflora* Craib

Primer pairs	Total number of fragments	Number of polymorphic bands	Percentage of polymorphic bands (%)
E+CAG/M+TAC	30	26	86.66
E+CAG/M+TGA	35	32	91.42
E+ACC/M+CAT	27	20	74.07
E+ACC/M+CCA	24	17	70.83
E+ACC/M+CGA	16	11	68.75
E+ACC/M+CTT	17	9	52.94
E+ACT/M+CAT	43	32	74.41
E+CGT/M+TAC	16	9	56.25
E+CGT/M+TGA	20	14	60.00
E+AAG/M+CAG	37	30	81.08
E+ACA/M+CGG	17	13	76.47
E+ACA/M+CGC	15	13	86.66
E+AAG/M+CCC	34	18	52.94
E+AAG/M+CAT	46	30	65.21
E+ACA/M+CCC	23	15	65.21
Total	400	289	72.25
Average	26.67	19.27	72.25

Conclusion:

The AFLP marker was able to distinguish all 35 samples of *A. viridiflora* Craib by using 15 pairs of primers into four groups at similarity level of 0.48. The cophenetic correlation of r=0.77 indicated that these samples were fairly well grouped. Although the use of molecular markers in species classification is more reliable than the morphological classification, but the use of morphology is still important in the identification of species traits. Or, for clarity, other molecular markers may need to be further classified in the future.

Acknowledgements:

We would like to show our gratitude to Plant Genetic Conservation Project under The Royal Initiative of Her Royal Highness Princess Maha Chakri Sirindhorn (RSPG) Chitralada Palace for staffs, laboratory facility, and all field collaborators.

References:

1. Bassam, B. J., Caetano Anolles, G., Gresshoff, P. M. Fast and sensitive silver staining of DNA in polyacrylamide gels. Anal. Biochem. 1991; 196: 80-83.
2. Blears M.J, De Grandis S, Lee H, Trevors J, 1998. Amplified fragment length polymorphism (AFLP): a review of the procedure and its applications. J. Ind. Microbiol. Biotechnol. 2, 99-114.
3. Doyle, J.J., Doyle J.L, 1990. Isolation of plant DNA from fresh tissue. Focus 12, 13-15.
4. Khumlert R, Sukthumrong A, Thepnarong P, Chareonsap P and Chuthamas P, 2018 Conservation and utilization of I nun plant **(***Adenia viridiflora* Craib**).** KHON KAEN AGR**.** J**.** 46 SUPPL1 332-338**.**
5. Rohlf, F. J. NTSYS+pc: Numerical Taxonomy and Multivariate Analysis System. Version 2.11T. Exter Software, New York: Setauket; 2000.
6. Sneath, P. H. A. and Sokal, R. R. Numerical Taxonomy. USA: Freeman, San Francisco; 1973.
7. Vos, P., Hogers, R., Bleeker, M., Reijans, M., van de Lee, T., Hornes, M., Frijters, A., Pot, J., Peleman, J., Kuiper, M., and Zabeau, M. AFLP: a new technique for DNA fingerprinting. Nucleic Acids Res. 1995; 23: 4407-4414.

C_032_OF: MOLECULAR CLONING AND B-CELL EPITOPES OF THE GENE ENCODING FATTY ACID BINDING PROTEIN FROM BLOOD FLUKE (*SCHISTOSOMA MEKONGI*)

Hong Thi Cam Do[1], Wanwisa Peonsamut[1], Manaw Sangfuang[1], Yanin Limpanont[2], Charoonroj Chotwiwatthanakun[3], Prasert Sobhon[4], Narin Preyavichyapugdee[1,*]

[1]Faculty of Animal Science and Agricultural Technology, Silpakorn University, Phetchaburi IT Campus, Phetchaburi, Thailand
[2]Applied Malacology Unit, Department of Social and Environmental Medicine, Faculty of Tropical Medicine, Mahidol University, Bangkok 10400, Thailand
[3]Mahidol University, Nakhonsawan Campus, Nakhonsawan 60130, Thailand.
[4]Department of Anatomy, Faculty of Science, Mahidol University, Rama VI Rd, Ratchathewi, Bangkok 10400, Thailand
*e-mail: jnnarin@hotmail.com

Abstract:

Schistosomiasis is one of zoonotic disease that affected people in Lao PDR and Cambodia in Mekong river basin. World Health Organization (WHO) has recognized the Fatty acid binding protein is one of vaccine candidates against human schistosomiasis. In the present study, we cloned, characterized and predicted immunogenic epitope of Fatty acid binding protein from *Schistosoma mekongi*, a novel gene namely SmekFABP from *S. mekongi*. Our results showed that the partial of SmekFABP contains 582 bp nucleotides and, and its open reading frame encoded for 132 amino acid with the predicted molecular weight 14.82 kDa. The protein alignment was performed by using Clustal Omega and BioEdit indicated that the FABP sequence of *S. mekongi* showed a highest degree of identify with *S. japonicum* at 95.4% and its resembled epitope regions 87-DSESKITQTQKDAKN-101 of SmekFABP from *S. mekongi* based on hydrophilicity scale and recognized by B-cell. This immunogenic epitope could be target for vaccine development against *S. mekongi* in the future.

Introduction:

Schistosomes cause chronic disease in more than 230 million people worldwide living in poor countries (1, 2). In Asia, approximately 140,000 people are at risk for *Schistosoma mekongi* infection: 80,000 people in Cambodia and 60,000 in Lao PDR (3). Even though, praziquantel (PZQ) is a drug of choice against *S. mekongi*, the large extension of endemic areas and the constant reinfections still be reported. Chemotherapy is not an solely strategy approach to eliminate this disease effectively (4). Therefore, much effort has been devoted to research for vaccine development, which may use alone or in combination with chemotherapy to provide sustainable strategy for long-term controlling the transmission of the disease.

Currently, fatty acid binding proteins (FABPs) are one of six candidate vaccine antigens selected by the WHO to study against schistosomiasis (5). There are various degrees of therapeutic effects (5, 6). FABP belongs to large family of intracellular lipid-binding proteins which have the low molecular weight (14 -15 kDa). FABPs have the functional role as molecule transportation (7, 8). In schistosomes case, lipids play an important role for the synthesis

of the unique outer membrane that is continually shed and renewed. Although their requirement for fatty acids is particularly high, they cannot synthesize this *de-novo* condition. In addition, lipids taken from the host play an immune-protective role (9). In 2003, Valiar et al., selecting epitope from *Fasciola hepatica* FABP could induce protection against at least two species of trematode including *F. hepatica* and *S. mansoni*; the percentage of protection 42-50% (10). Furthermore, the latest researching from Rahmani et al., FABP is one of immunogenic epitope that has been chosen to construct a multi-epitope vaccine against *S. mansoni.* Based on immunoinformatic analysis, this multi-epitope molecule could stimulate T- and B-cell mediated immune responses (11).

This study focuses on prediction of SmekFABP immunogenic B-cell epitope which could provide a promising vaccine against *S. mekongi* for future solution to eliminate schistosomiasis in endemic area.

Methodology:

1. Cloning of SmekFABP cDNA sequence

cDNA of the adult *S. mekongi* from the project "Development of Serodiagnosis for *S. mekongi* in Mice by Sandwich ELISA and Localization of Cathepsin B on the Worm" which was approved by Animal Care and Use Committee of Faculty of Tropical Medicine, Mahidol University (FTM-ACUC 023/2017). The method of cDNA libraries described by Sangfuang et al. (12) Briefly, total RNA was isolated from the whole adult *S. mekongi* worms by TRIzol reagent (Molecular Research Center, Inc.) using the protocol provided by the manufacturer. The cDNA libraries from adult of *S. mekongi* were constructed using the SuperScript™ III Reverse Transcriptase (Invitrogen), according to the manufacturer's protocol. The partial cDNA sequence of the SmekFABP was amplified by PCR using the following set of primers: forward primer (5'-ACTTTAGGCGTTCAGTCAATCGGAA-3') and reverse primer (5'-GCAATGTTTATTGAACAAAAGTGAAGCTG-3'). These primers were designed by based on GenBank: FN315763.1 of *S. japonicum*. Briefly, the final concentrations for a typical 50 µl PCR reaction are as follows: add 1 µl of cDNA libraries from adult *S. mekongi* was used as templates to obtain amplified DNA fragments of the FABP gene by a standard PCR with *Taq* DNA polymerase (5 units/1 µl) and add 5 µl of 10X standard *Taq* reaction buffer it contains 15 mM $MgCl_2$, add 1 µl of 10 mM dNTPs, add 1 µl of 10 µM forward primer and 1 µl of 10 µM reverse primer and add sterile distilled water to obtain a 50 µl final volume per reaction. The PCR was performed in 35 cycles at 94 ◦C for 30 s, 50 ◦C for 30 s, and 72 ◦C for 90 s. The PCR product was visualized on 1.5% agarose gel and stained with ethidium bromide. The gel was exposed to UV light and the picture taken with a gel documentation system. The PCR product was ligated into the pGEM-T easy vector (Promega, USA) and the sequence confirmed by DNA sequence analysis (Macrogen, South Korea).

2. Bioinformatics identification and characterization of SmekFABP

SmekFABP DNA sequences generated from cDNA clones and the deduced protein sequences were subjected to search the nucleic acid and protein databases using the basic local alignment search tool (BLAST) (http://www.ncbi.nih.gov/BLAST/). The multiple alignment of homologous sequences from closely related Schistosoma species were carried out by Clustal Omega Program (https://www.ebi.ac.uk/Tools/msa/clustalo/). Neighbor-joining analysis (13) as performed by MEGA version X program (14) with bootstrap resampling 1000 repetitions (15). The prediction of 3D model was visualized the I-TASSER program (16-18).

3. Prediction of antigenic sites

In this study work, the potential hydrophilic antigenic epitopes of SmekFABP were found out in order to identify the antigenic determinants. Antigenic epitopes are determined using several prediction methods, for example, Hopp and Woods (19); Welling & al (20); HPLC/Parker & al (21); Kolaskar & Tongaonkar antigenicity (22); B-EpiPred Server (23) and ABCpred Prediction Server (24).

Results and Discussion:

1. Cloning and sequence of S. mekongi FABP (SmekFABP)

The partial sequence of adult SmekFABP was identified by using PCR. The fragment of nucleotide sequence of SmekFABP with length of 582 bp was obtained. The deduced amino acid sequence containing 132 amino acid with the predicted molecular weight 14.82 kDa (Figure 1). The structure of SmekFABP was predicted by I-TESSER program (18), and this protein shared a common tertiary structure as present in other FABPs, consisting of 10 anti-parallel β-strands forming a clam shell-like β-barrel structure, which together with two α-helices, enclose an internal cavity which form the ligand binding site for hydrophobic molecule (25). These molecules adopt the same basic three-dimentional structure which are strong evolutionary conservation and present in a spectrum of species including Drosophila melanogaster, Caenorhabditis elegans, mouse and human (26).

2. Bioinformatics identification and characterization of SmekFABP

The multiple alignment of deduced amino acid sequences of SmekFABP with FABPs from related schistosome species (GenBank: AAA64426 from *S. japonicum*; 2POA_A from *S. mansoni*; BAF62288 from *S. haematobium*; AAT39384 from *S. bovis*; CAB65015 from *Fasciola hepatica*; AAB06722 from *F. gigantica*; 3STN_A from human liver; and 2JU3_A form Rat liver, showed in the Figure 2. The SmekFABP amino acid sequences showed the highest degree of identity with *S. japonicum* (GenBank: AAA64426) at 95.4%. The identity of SmekFABP amino acid sequences with FABPs amino acid sequences from *S. mansoni* (GenBank: 2POA_A), *S. haematobium* (GenBank: BAF62288) and *S. bovis* (GenBank: AAT39384) showed 91.7%, 90% and 89.4% respectively. (Figure 2).

```
55   ACTTTAGGCGTTCAGTCAATCGGAAATAATGTCTTCTTTTTTGGGAAAGTGGAAA
                                   M  S  S  F  L  G  K  W  K    9
109  CTGAACGAATCACACAACTTCGATGCTGTTATGTCAAAGCTCGGTGTTTCGTGG
     L  N  E  S  H  H  N  F  D  A  V  M  S  K  L  G  V  S  W   27
163  GCGACCCGACAGATTGGGAACACAGTGACGCCAACTGTCACTTTTACAATGGAT
     A  T  R  Q  I  G  N  T  V  T  P  T  V  T  F  T  M  D   45
217  GGGGATACGATGACCATGCTGACAGAGTCAACTTTCAAGAACCTCTCAGTCACG
     G  D  T  M  T  M  L  T  E  S  T  F  K  N  L  S  V  T   63
271  TTCAAATTCGGTGAGGAATTCGATGAGAAAACCAGTGATGGTAGGAACGTTAAG
     F  K  F  G  E  E  F  D  E  K  T  S  D  G  R  N  V  K   81
325  TCAGTCGTTATCAAAGATTCAGAGTCAAAGATAACTCAAACTCAGAAGGATGCT
     S  V  V  I  K  D  S  E  S  K  I  T  Q  T  Q  K  D  A   99
379  AAGAACACAACTGTAATCGTTCGTGAAATAATAGGTGATACTATGAAAACTACT
     K  N  T  T  V  I  V  R  E  I  I  G  D  T  M  K  T  T  117
433  GTAACTGTTGATGATGTTACGGCTATTCGGAATTACAAACGATTATAACCCCTG
     V  T  V  D  D  V  T  A  I  R  N  Y  K  R  L  *        132
487  CAAGCTGACAGACTGGTCAAATGTTTCTTGAAAGCGCTTGTATTTCAACTGACA
541  TTATCACAAAAATGACCACCGGTGGACGCATTTTGTCACGCATGTGTCATTCCA
582  TATTTAATTAATCAGCTTCACTTTTGTTCAATAAACATTGC
```

Figure 1.

Diagram showing the full DNA sequence and the deduced amino acid sequence of *S. mekongi* FABP. The start (ATG) and stop (TAA) codon are bold and underlined. The 2D-structure was predicted by I-TESSER program, and it contained two α-helix (highlight in gray) and ten β-sheet chain (underlined).

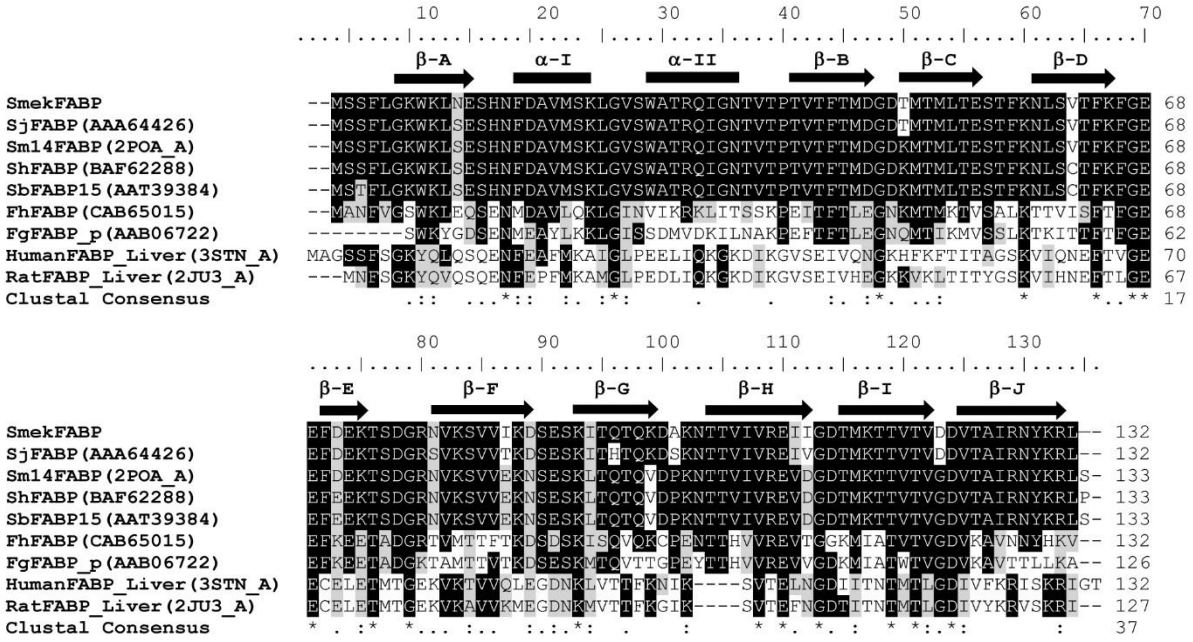

Figure 2.

Multiple sequences alignment of the deduced amino acid sequences of SmekFABP with FABPs from related schistosome species and host. The amino acid sequences of SmekFABP with other FABPs showing highly conserved amino acids by grey and black outlines. The asterisk (*) indicates identical amino acids, two dots (:) indicates conserved amino acid substitutions and dot (.) indicate semi-conserved amino acid substitutions. Arrows and rectangle indicate β-strands and α-helices in SmekFABP. Smek: *S. mekongi*; Sm: *S. mansoni*; Sj: *S. japonicum*; Sh: *S. haematobium*; St: Sb: *S. bovis*; Fh: *F. hepatica*; Fg: *F. gigantica*.

A phylogenetic tree was constructed based on FABP sequences**.** The evolutionary history was inferred using the Neighbor**-**Joining method**.** The percentage of replicate trees in which the associated taxa clustered together in the bootstrap test **(**1000 replicates**)** is show next to the branches**.** This analysis involved 16 amino acid sequences**.** All ambiguous position positions were removed for each sequence pair **(**pair-wise deletion option**).** The result revealed that *S. mekongi* FABP was closely similar to group of *S. japonicum* FABP **(**GenBank**:** AAA64426**).** Whereas, *S. mekongi* FABP was distant relative to group of dog FABP **(**GenBank**:** NP001273980**)** and pig FABP Liver **(**GenBank**:** P49924**.**1**) (**Figure 3**).** A high degree of similarity and identity of *S. mekongi* and S. *japonicum* FABP indicates that they share a common ancestor. The immunogenic property of FABP molecule from *S. japonicum* FABP have been previously reported, and conferred the protection against challenge infection **(**27, 28**).** So it is possible that the molecule of *S. mekongi* FABP could be one of candidate vaccine molecules against the *S. mekongi* infection**.**

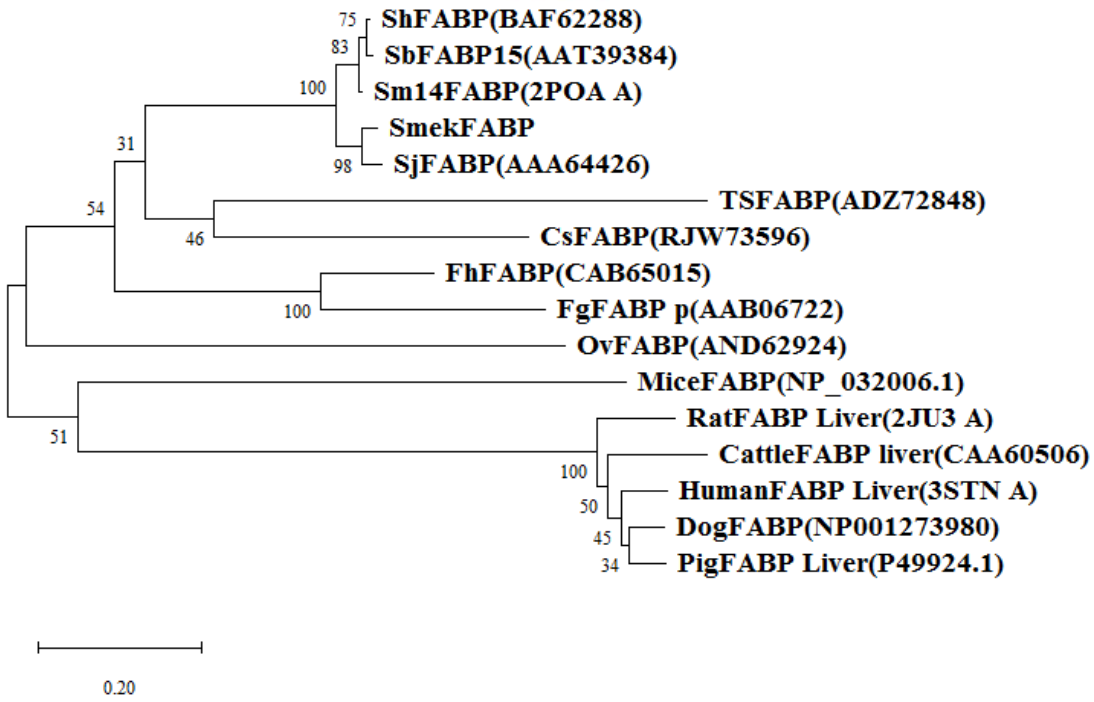

Figure 3.

Phylogenetic tree of FABP for *S.mekongi* was constructed by amino acid sequence analysis. Numbers at the branching point indicate percent bootstrap value. Branches corresponding to partitions reproduced in less than 50% bootstrap replicates are collapsed. Smek: *Schistosoma mekongi*; Sh: *S. haematobium*; Sb: *S.bovis* ;Sm: *S. mansoni*; Sj: *S. japonicum*; Ts: *Taenia solium* ; Cs: *Clonorchis sinensis*, Fh: *F. hepatica*; Fg: *F. gigantica*; Ov: *Opisthorchis viverrini*. Database accession numbers for the phylogenetic analysis here: BAF62288; AAT39384; 2POA_A; AAA64426; ADZ72848; RJW73596; CAB65015.

3. Determination of antigenic peptides

S. mekongi causes chronic effect, highly debilitating diseases involving extensive liver damage. Although using praziquantel as mass drug treatment is effective, the reinfection still be found in an endemic area. However, advances in bioinformatic analysis and database access to the DNA and protein sequences of *Schistosoma* species, are becoming an important tool in prediction of candidate immunogenic epitope for diagnosis and vaccine development.

By analyzing graphical and numerical data, it was found that according to Hopp and Woods scale the regions 9-11, 13-16, 49-51, 57-58, 67-104, 108-112, 114-119, 123-128 contained the potential hydrophilic regions **(**Hydrophilicity**:** score > 0**).** The analysis found high in position between 67-104 **(**Maximum Score 1**.**711**)** in a protein **(**Figure 4A**).**

In the Welling et al**.**, 1985 antigenicity plot gives value as the log of the quotient between percentage in average proteins and percentage in a sample of known antigenic regions, the predicted hydrophilic regions were 6-7, 9-15, 61-62, 82-85, 94-101, 126-128**.** The high score show in position 9-15 **(**Maximum Score 0**.**482**) (**Figure 4B**).**

We also study the hydrophobicity plot of HPLC**/**Parker and the predicted hydrophilic regions were 9-22, 25-59, 65-105, 109-128**.** The highest peak is found in position between 65-105 **(**Maximum Score 6**.**900**) (**Figure 4C**).**

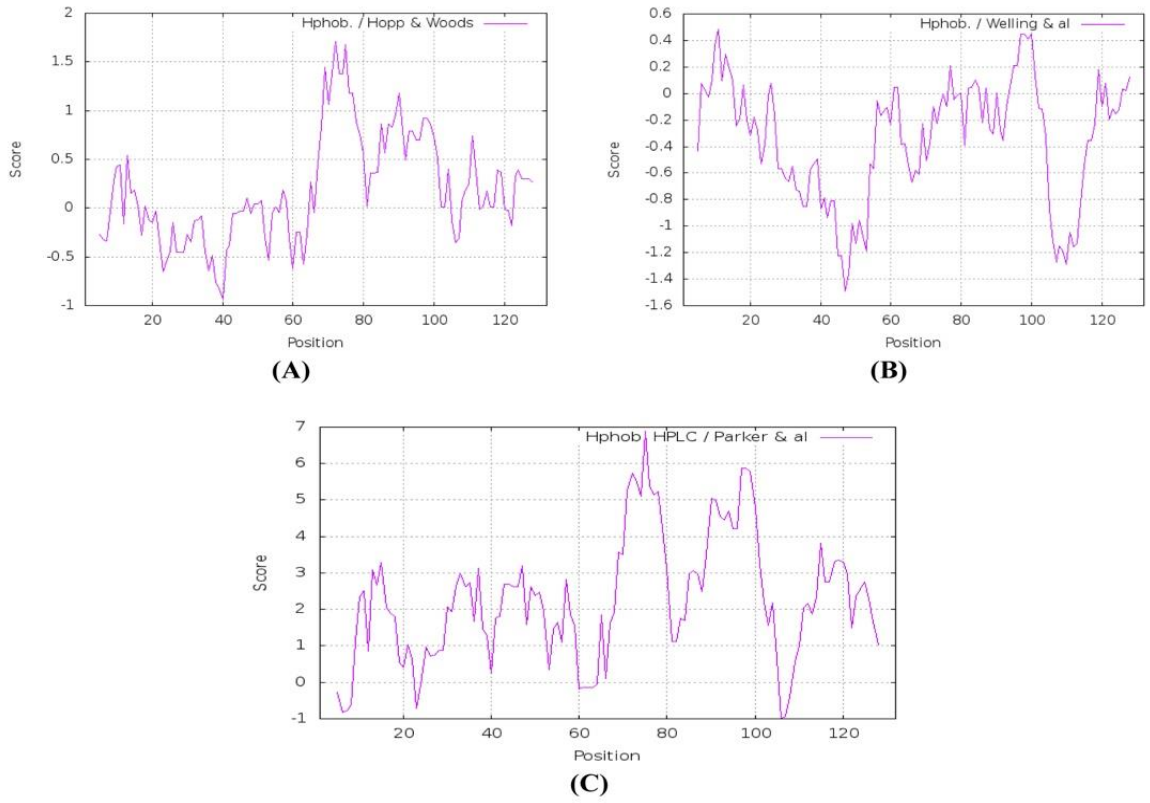

Figure 4.

Graphical representation of antigenic peptide evaluation by Hopp and Woods (A) Welling & al (B) and HPLC/Paker & al (C)

According to Kolaskar and Tangaonkar scale, at 0.995 as the threshold level, the most likely antigenic determinants were at 16-FDAVMSKLGVSWA-28, 58-KNLSVTFK-65, 80-VKSVVIKD-87, 102-TTVIVREI-109, and 117-VTVDDVTAI-126 **(**Figure 5A**).** B-BepiPred predicts the location of linear B-cell epitopes result found that between 30-RQIGNTVTPT-39, 41-TFTMD-45, 69-EFDEKTSDGRN-79, 87-DSESKITQTQKDAKN-101 and 115- KTTVTV -120**.** The maximum score **(**1.754**)** is found at the position 75 **(**Figure 5B**).** The ABCpred server was used to predict the B-cell epitopes **(**16 amino acid**)** and a total of 10 epitopes for the three proteins **(**23-38, 61-76 and 88-103**)** that showed the highest score was selected for designing the subunit vaccine design along with suitable linkers and an adjuvant**.**

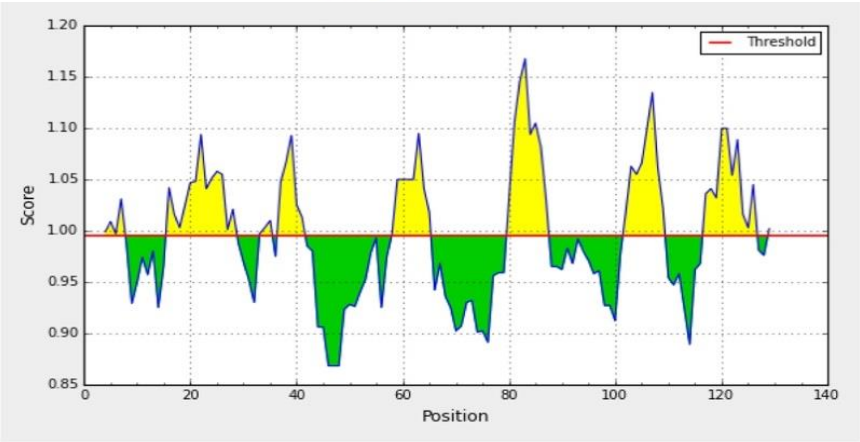

(A) Kolaskar & Tongaonkar Antigenicity

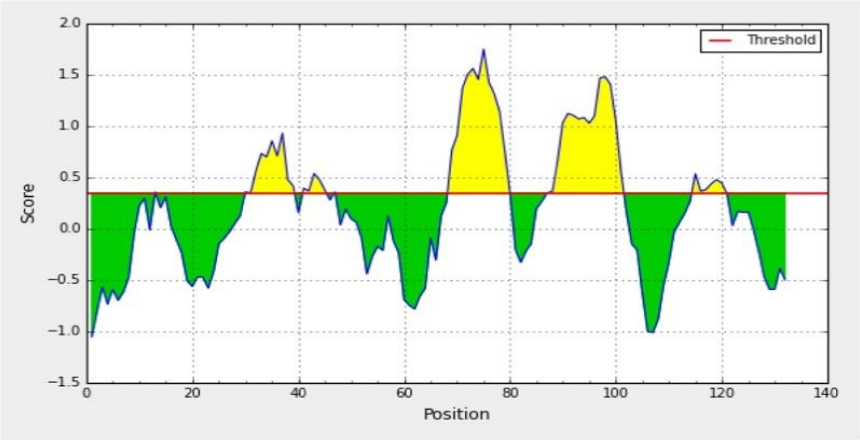

(B) Bepipred Linear Epitope Prediction

Figure 5.

Graphical representation of antigenic peptide evaluation by (A) Kolaskar and Tongaonkar Antigenicity for SmekFABP (B) Bepipred Linear Epitope Prediction for SmekFABP

Prediction of immunogenic region which exposed on the surface of the protein is a necessary step for epitope-based vaccine design**.** In this study, the hydrophilic regions of SmekFABP proteins which are supposed to be antigenic and exposed to the surface of the protein were identified for antigenic determinants**.** The sequences of predict epitopes have been summarized in Table 1**.** One major overlapping region which were hit by 5 programs from all 6 programs **(**Hopp & Woods; Welling, Parker, B-EpiPred and ABCpred**)**, is region 87-DSESKITQTQKDAKN-101**.** The region is located on β-strands (Figure2: βE and βF) which forming a clam shell-like β-barrel structure of the ligand binding site for hydrophobic molecule. This epitope is present on ***β*-**sheets regions, which have high antigenic response than helical region as previously reported by **(**29**) .** Besides, Vilar et al**. (**10**)** have demonstrated that the immunogenic epitope conferred protection against at least 2 species of trematode: *S. mansoni* and *F. hepatica*. The protection is between 42-50%.

Table 1.

The potential hydrophilic regions and epitope prediction sites from Hopp & Woods, Welling & al, Parker & al, Kolaskar & Tongaonkar. B-EpiPred and ABCpred program

Hopp & Woods	Welling & al	Parker & al	Kolaskar & Tangaonkar	B-Epipred	ABCpred
9-11,13-16, 18	6-7, 9-15, 18	9-22		13	
	26	25-59	16-28	30-39, 41-45	23-38
47, 49-51, 55, 57-58			58-65	47	
65, 67-104	61-62, 77	65-105		69-79	61-76
	80, 82-85, 87, 90, 94-101		80-87	87-101	88-103
108-112, 114-119	119	109-128	102-109, 117-126	115-120	
	121, 126-128				

Conclusion:

Fatty acid-binding proteins (FABPs) are cytosolic proteins, distributed both in invertebrates and vertebrates. It involved in the uptake and transport of fatty acid which play multiple crucial roles in cellular functions from the plasma membrane to intracellular sites (30-32). Here, we have cloned, characterized and defined antigenic epitope of novel FABP from *S. mekongi*. The partial SmekFABP cDNA was 582 bp long encoded for 132 amino acid with the predicted molecule weight at 14.82 kDa. The alignment of the deduced SmekFABP amino acid sequences showed a highest degree of identity with *S. japonicum* at 95.4%. We predicted one immunogenic epitope based on hydrophilicity scale and recognized by B-cells at regions 87-DSESKITQTQKDAKN-101. The predicted immunogenic determinant identified through this approach is possible to be high immunogenic and was a promising antigen for immuno-prophylaxis.

Acknowledgements:

I wish to express my acknowledgement for the financial supports of Thailand International Cooperation Agency (TICA). My thanks are extended to all staffs in faculty of Animal Sciences and Agriculture Technology, Silpakorn University for the courses of master program. Many my thanks wish to send to the entire staff in faculty of Animal Sciences and my lab-mates for their suggestion and help in my experimental works.

References:

1. Bergquist NR. Trends Parasitol. 2002;18(7):309-14.
2. Colley DG, Bustinduy AL, Secor WE, King CH. Lancet. 2014;383(9936):2253-64.
3. Urbani C, Sinoun M, Socheat D, Pholsena K, Strandgaard H, Odermatt P, et al. Acta Trop. 2002;82(2):157-68.
4. Pearce EJ. Schistosomiasis. Proselytizing with immunity. 1993.
5. Bergquist N. Mem Inst Oswaldo Cruz. 1995:221-7.
6. Bergquist N, Colley D. Parasitology Today. 1998;14(3):99-104.
7. Meyer F, Meyer H, Bueding E. Biochim Biophys Acta, Lipids Lipid Metab. 1970;210(2):257-66.
8. Ockner RK. Mol Cell Biochem. 1990;98(1-2):3-9.
9. Bennett M, Caulfield J. Am J Clin Pathol. 1991;138(5):1173.
10. Vilar MM, Barrientos F, Almeida Ml, Thaumaturgo N, Simpson A, Garratt R, et al. Vaccine. 2003;22(1):137-44.
11. Rahmani A, Baee M, Rostamtabar M, Karkhah A, Alizadeh S, Tourani M, et al. Int J Biol Macromol. 2019;141:125-36.
12. Sangfuang M, Chusongsang Y, Limpanont Y, Vanichviriyakit R, Chotwiwatthanakun C, Sobhon P, et al. Acta tropica. 2016;155:11-9.
13. Saitou N, Nei M. Mol Biol Evol. 1987;4(4):406-25.
14. Kumar S, Stecher G, Li M, Knyaz C, Tamura K. Mol Biol Evol. 2018;35(6):1547-9.
15. Felsenstein J. Evolution. 1985;39(4):783-91.
16. Roy A, Kucukural A, Zhang Y. Nat Protoc. 2010;5(4):725-38.
17. Yang J, Zhang Y. Nucleic Acids Res. 2015;43(W1):W174-W81.
18. Zhang Y. BMC Bioinform. 2008;9(1):40.
19. Hopp TP, Woods KR. Proc Natl Acad Sci USA. 1981;78(6):3824-8.
20. Welling GW, Weijer WJ, van der Zee R, Welling-Wester S. FEBS lett. 1985;188(2):215-8.
21. Parker J, Guo D, Hodges R. Biochemistry. 1986;25(19):5425-32.
22. Kolaskar A, Tongaonkar PC. FEBS Lett. 1990;276(1-2):172-4.
23. Larsen JEP, Lund O, Nielsen M. Immunome Res. 2006;2(1):1-7.
24. Saha S, Raghava GPS. Proteins. 2006;65(1):40-8.
25. Zimmerman A, Veerkamp J. Cell Mol Life Sci. 2002;59(7):1096-116.
26. Smathers RL, Petersen DR. Human genomics. 2011;5(3):1-22.
27. Tu Y, Hu Y, Fan G, Chen Z, Liu L, Man D, et al. PLoS One. 2014;9(1):e86575.
28. Wei F, Liu Q, Zhai Y, Fu Z, Liu W, Shang L, et al. Acta tropica. 2009;111(3):284-8.
29. Waghmare S, Chavan R. Metabolomics. 2012;2(113):2153-0769.1000113.
30. Li J, Henry E, Wang L, Delelis O, Wang H, Simon F, et al. PLoS One. 2012;7(12):e51079.
31. Storch J, McDermott L. J Lipid Res. 2009;50(Supplement):S126-S31.
32. Storch J, Thumser AE. Biochim Biophys Acta Mol Cell Biol Lipids. 2000;1486(1):28-44.

C_033_OA: FEASIBILITY OF CRISPR-cas12a FOR PLANT SPECIES IDENTIFICATION WITHOUT DNA AMPLIFICATION; A CASE OF *Phyllanthus amarus*

Kittisak Buddhachat[a,*], Nattaporn Sripairoj[a]

[a]Department of Biology, Faculty of Science, Naresuan University

*corresponding author: kittisakbu@nu.ac.th

Abstract

Species identification is one of the most important tasks for several areas such as plant biology, taxonomy, systematics, evolution, conservation, forensics and even in medicinal plant industry. To shorten the processes of species identification, molecular tools e.g. DNA barcodes DNA fingerprint and high resolution melting analysis (HRM) have been allowed to facilitate species confirmation especially in case of incomplete specimens or insufficient necessary organ to species delimitation. However, DNA amplifications (PCR and isothermal amplifications) are still required. In this study, the feasible exploitation of CRISPR-cas12a (cpf1) was preliminarily assessed using *Phyllanthus amarus* (PA) as a model. The different species of herbaceous species of *Phyllanthus* were included for determining the specificity. We designed two guided RNA (gRNA) based on *trnL* region. The preliminary results demonstrated that the suitable ratio to form binary complex (cpf1:gRNA) was at 100 nM : 100 nM. The performance of gRNA was tested using PCR products obtained from different species as result of the presence of positive with only PA. The limit of detection of this method can be observed at 0.2 pg of DNA template. In addition, CRISPR-cas12a for aiding PA identification without PCR enable to be successfully detected when amount of DNA was higher than 10 ng. Our findings demonstrated the feasibility for exploitation of CRISPR-cas12a system for plant species identification.

Keywords; Phyllanthus; trnL; fluorescence; species identification

C_034_PA: DIVERSITY OF BACTERIA IN KLONG THOOP MANGROVE FOREST, CHUK SAMET, SATTAHIP, CHONBURI

Papon Ganjanasiripong , Thanaporn Chuen-Im*

Department of Microbiology, Faculty of Science, Silpakorn University
*corresponding author, Email: suy85@hotmail.co.uk

Abstract

Mangrove forests are an important natural treasure because it is a diverse source of life and microorganisms. This research was aimed to quantitatively and qualitatively determine bacteria in water and sediments from Klong Thoop mangrove forest, Chuk Samet , Sattahip , Chonburi. This mangrove forest is located in the Eastern Economic Corridor (EEC) zone where all resources are used to support industrial environmentally friendly. In the study, bacteria quantity was investigated using spread plate technique and then identified by biochemical test. Samples, sediments and water, were collected between August 2019 and February 2020. It was found that the pH, temperature, salinity of samples were between 7.34-9.55, 26-29°C, and 0.2-21 g / l, respectively. The total plate count of heterotrophic bacteria in water on Nutrient agar+ 1%NaCl (NA+1%NaCl) was ranging from $8.0x10^1$ to $5.3x10^2$ CFU/ml, and in sediments was $1.49x10^2$ to $2.75x10^4$ CFU/g. Identification of 68 bacterial isolates revealed bacteria taxonomical belonging to 23 genus, including *Paenibacillus* spp., *Lactobacillus* spp., *Aliivibrio* spp., *Aeromonas* spp., *Vibrio* spp., *Kluyvera* spp., *Shigella* spp., *Serratia* spp., *Aneurinibacillus* spp., *Pasteurella* spp., *Brecibacillus* spp., *Viridibacillus* spp., *Lysinibacillus* spp., *Staphylococcus* spp., *Citrobacter* spp., *Pantoea* spp., *Edwardsiella* spp., *Pragia* spp., *Rahnicella* spp., *Salinicoccus* spp., *Streptococcus* spp. and *Bacillus* spp. The highest number of isolates was identified as *Paenibacillius* spp. (17 isolates, 25%), followed by *Bacillus* spp. (11 isolates, 16.18%), *Lactobacillus* spp. (6 isolates, 8.82%), *Aliivibrio* spp. (4 isolates, 5.88%), *Aeromonas* spp. (4 isolates, 5.88%), and *Aneurinibacillus* spp. (4 isolates, 5.88%). Future plan is to study enzyme activity of these bacterial isolates; particular lipase, amylase, protease, and gelatinase.

C_035_PF: FERMENTATION AND ANTIOXIDANT PROPERTIES OF LONGAN HONEY INOCULATED WITH *Saccharomyces cerevisiae* var. *burgundy*

Siriporn Riebroy Kim,[1]* Yada Thamniam,[1] Maneenuch Jaidee, [1]Atsalek Rattanawannee,[2] Amporn Jamphon,[1] Tipakorn Muangtuk, [1] Tiwaporn Maneerattanasuporn[1]

[1]Food and Nutrition Program, Department of Home Economics, Faculty of Agriculture, Kasetsart University, Bangkok, Thailand
[2]Department of Entomology, Faculty of Agriculture, Kasetsart University, Bangkok, Thailand
*e-mail: siriporn.r@ku.th

Abstract:

Honey wine or "mead" has become a more interesting alcoholic beverage. This study was aimed to monitor the fermentation and antioxidant activity of longan honey inoculated with commercial *Saccharomyces cerevisiae* var. *burgundy* at 10^5 cfu/ml (SB105) and 10^6cfu/ml (SB106). Longan honey was diluted with mineral water to make the honey-must with total soluble solid of 18 °Brix. After inoculation, samples were fermented at room temperature (30-32°C) for 15 days. During fermentation, the decrease in pH with the concomitant increase in total acidity was observed. At the end of fermentation, the pH of SB105 and SB106 samples were 3.19 and 3.37, respectively. Reducing sugar content decreased dramatically, whereas alcohol content increased throughout the fermentation (p<0.05). SB106 sample had higher alcohol production than that in SB105 (p<0.05). SB105 and SB106 samples exhibited 10% and 12% alcohol by volume after 15-day fermentation. After fermentation, reducing sugar content remained about 30%. From the results, the formation of alcohol that indicates yeast consumed sugar as a carbon source. Changes in total phenolic content and 2,2-diphenyl-1-picrylhydrazyl (DPPH) radical scavenging activity in mead samples during fermentation were also investigated. As the fermentation proceeded, total phenolic content in SB106 sample slightly increased (p<0.05). After 3 days of fermentation, $DPPH^{\cdot}$ radical scavenging activity of both samples were not different and stable throughout fermentation (p>0.05). This indicated that alcoholic fermentation might not be possible not effect on antioxidative activity. As the results, *S. cerevisiae* var. *burgundy* can be used a potential starter for mead fermentation. From a practical point of view, the inoculum level of commercial *S. cerevisiae* var. *burgundy* is an important factor for honey fermentation to obtain an alternative alcoholic drink product.

Introduction:

Honey is a complex natural product, mainly containing various sugars and to a lesser extent, other compounds such as minerals, proteins, vitamins, organic acids, flavonoids, phenolic acids, and enzymes.[1] This composition accounts for the widespread use of honey to sweeten food and improve the palatability of medicines. Nowadays, honey is not only used as a concentrated sugar for food, but its benefits are recognized in nutrition researches. The components in honey reported to be responsible for its antioxidant effects are flavonoids, phenolic acids, ascorbic acid, catalase, peroxidase, carotenoids, and the products of Maillard reaction products.[2] Honey consumption can improve the lipid profile (total cholesterol, triglycerides and low-density lipoproteins and increase high-density lipoproteins when compared to sucrose.[3] It is well established that due to its antiviral effects, with

potential in both traditional and official medicines, and also as a natural food antioxidant.[4] Honey antioxidant capacity can be attributed to a combined effect of its constituents as therapeutic potential of phenolic antioxidant.[5]

Mead or honey wine is an indigenous fermented beverage for thousands of year. Honey is generally fermented by the yeast *S. cerevisiae*, the most important microorganism in alcohol fermentation because its high capacity for fermentation, its high tolerance to ethanol and other inhibitors, and its capacity for rapid growth under anaerobic conditions.[6] Mead is a traditional honey-derived alcoholic beverages resulting from the alcoholic fermentation of diluted honey by yeasts. To making dilution of honey, an adequate amount of water or fruit juice or spices could be added. Mead fermentation is a time-consuming process, often taking several months to complete, depending on the type of honey, yeast strain and honey-must composition.[7] Chen et al. reported that longan mead produced from diluted honey with multiple *S. cerevisiae* inoculations were accomplished without undesirable flavors.[8] Generally, alcoholic beverage obtained by fermenting honey-must that contains 8-18% (v/v) ethanol.[9] The yeasts used in the production of mead are usually strains of *S. cerevisiae*, similar to that used in wine, beer, and champagne productions. These yeasts metabolize sugars, such as glucose and fructose, resulting in the formation of ethanol and carbon dioxide. Pereira et al. verified that significant differences did not exist between the strains. *S. cerevisiae* strains isolated from honey were similar to commercial and reference strains which are suitable for mead production.[10] Traditional mead is made using either honey from a particular flower source or multifloral honey.[11] According to the Sustainable Development Golds (SDG), microorganisms are used judicially and they can contribute significantly to the sustainable development. The fermentation is one of green technology as well as the preservation of natural resources. Ross et al. suggested that microorganisms play a fundamental role in achieving the SDG.[12] By employing microbes like *Lactobacillus*, *Saccharomyces* and *Acetobacter*, some primary and secondary metabolites with wide applications in food preservation are produced.[12]

Longan honey is commercially produced in Northern of Thailand, particularly Chiang Mai and Lumphun.[13] The largely popularity of honey is due to it being natural sweetener with bioactive compounds for health benefits. In addition, honey is generally used as a sweetener and other functions such as thickener, binder and colorant. So far, the study on the honey fermentation for making mead could be used as basic information to assist local honey producers. Mead seems to be a good option for increasing the income of honey producers, allowing the development of a beverage in Thailand with a great commercial potential. The starter culture, *S. cerevisiae* var. *burgundy*, is usually used for fruit wine fermentation and it is safe and available. The process of mead production can be handled by honey producers with uncomplicated. The inoculum level of yeast starter was investigated for the feasibility of mead fermentation. Therefore, this study was aimed to study the preliminary experiment for honey fermentation by commercial *S. cerevisiae* var. *burgundy* at different inoculum levels.

Methodology:

Preparation of yeast starter culture

Pure culture of *Saccharomyces cerevisiae* var. *burgundy* was purchased from Institute of Food Research and Product Development (IFRPD), Kasetsart University, Thailand. The yeast culture was generally maintained at 4°C on slants of Yeast Peptone Dextrose agar. Before use, the growth curve of the yeast starter cultured in honey-water (37:100 w/w) was determined by incubating at 30°C in an orbital shaker (125 rpm) for 24 h. Before use, the starter culture was prepared by pre-growing the yeast in Yeast Malt broth.

Preparation of honey-must for fermentation

Longan honey from European honey bee (*Apis mellifera*) was obtained from San Pa Tong, Chiang Mai. It was stored at room temperature (30-33°C) in the dark. Honey-must was prepared according to the method of Mendes-Ferreira et al. with slight modifications.[14] Honey (37 g) was diluted with 100 ml mineral water (Minéré,

Nestlé, Thailand) and mixed to homogeneity. The total soluble solid of honey-must was 18°Brix. The pre-growing of starter culture was inoculated to the honey-must with initial population of 10^5 (SB105) and 10^6 CFU/ml (SB106). The fermentations were conducted in 250-ml flask sealed with silicone stopper. Samples were incubated at ambient temperature (30-33°C) without shaking for 15 days. Samples were taken at day 0, 3, 6, 9, 12 and 15 of fermentation for analyses.

Determination of pH and total acidity

The pH value was measured directly by using a pH meter (SevenCompact, Medtler Teledo, Switzerland). Total acidity was determined by titration with NaOH until a pH of 8.2 was reached.[15] The total acidity was calculated and expressed as percentage of tartaric acid.

Determination of total soluble solid and reducing sugar content

The total soluble solid content was measured using a hand refractometer (Hand-Held Refract Meter, N-1E, Atago, Tokyo, Japan). The reducing sugar content was determined according to the method of James with a slight modification.[16] Sample (1 ml) was mixed with 50 ml distilled water and mixed well. The mixture was incubated with water bath at 70°C for 10 min. Then the mixture was filtered with Whatman No. 4 filter paper. The filtrate (500 □l) was pipetted into a test-tube and 500 □l of 3,5-dinitrosalicylic acid (DNS) solution was added and then mixed well. Distilled water (1 ml) was added and transferred to incubate at 100°C for 20 min then cooled with ice and water for 5 min. The reducing sugar content was measured absorbance at 540 nm by spectrophotometer. A D-glucose solution (0-1.5 mg/ml) was used as a standard for reducing sugar and expressed as g glucose/L of sample.

Determination of alcohol content

The alcohol content was measured using vinometer. Samples were measured in five replications.

Determination of total phenolic content (TPC) and antioxidant activity

The TPC was determined by Folin-Ciocalteu spectrophotometric method.[17] In brief, 100 □l of sample was mixed with 2 ml distilled water and 0.5 ml Folin-Ciocalteu reagent in a 10 ml volumetric flask. After 2 min, 1.5 ml sodium carbonate (20% w/v) was added, the solution was stirred and the volume measured with distilled water, after homogenization. The solution was centrifuged and kept at room temperature for 1 h in the dark. The absorbance was measured at 765 nm. TPC was calculated and reported as mg gallic acid equivalent (GAE)/ml.

The free radical ($DPPH^*$) scavenging activity of sample was measured by the method as described by Aljadi and Kamaruddinwith a slight modification.[18] In the presence of an antioxidant activity, the purple color of DPPH decays, and the change in absorbance at 517 nm can freshly prepared DPPH methanol solution (0.1 mM). A methanol solution of DPPH (0.1M) was utilized as a control. After incubation at room temperature for 30 min in the dark, the absorbance was measured at 517 nm and DPPH radical scavenging activity (%) was calculated;

$$DPPH\ (\%) = [(Ac-As)/Ac] \times 100$$

Where Ac is the absorbance of the control and As is the absorbance of the sample.

Determination of color

The color of sample was measured in L*, a* and b* of CIE (angle 10°, illuminant D65) using a HunterLab (ColorFlex, Hunter Associates Laboratory, Reston, VA, USA).

Statistical analysis

The data are presented as mean values with standard deviation. Data were analyzed statistically by ANOVA and t-tests using the SPSS software program (SPSS Inc., Chicago, IL, USA). A *p*-value <0.05 was considered significant.

Results and Discussion:

Changes in pH and total acidity during mead fermentation

Changes in pH (A) and total acidity (B) during fermentation of mead inoculated with *S. cerevisiae* var. *burgundy* at 10^5 cfu/ml (SB105) and 10^6 cfu/ml (SB106) are depicted in Figure 1. The initial pH of both samples was 5.9. The pH sharply decreased to 3.6 during 3 days of fermentation, thereafter the pH of both samples was stable (Figure 1A). The total acidity of mead inoculated with *S. cerevisiae* var. *burgundy* at 10^5 CFU/g (SB105) and 10^6 CFU/g (SB106) increased continuously as fermentation proceeded (Figure 1B). Generally, the pH of honey ranges between 3.4 and 6.1 with an average of 3.9. The initial pH of honey-must was different from Chen et al. who reported longan honey-must pH was 3.96.[8] This might be due to the pH of honey and diluent in this experiment. In addition, the pH is not directly related to acidity, due to the buffering action of acids and minerals found in honey. Its acidity is due to the presence of organic acids, particularly gluconic acid, pyruvic acid, malic acid, and citric acid. Furthermore, the low pH has been pointed out as one cause of sluggish or premature fermentation arrest in alcoholic beverages.[19] Considering the low pH and low buffering capacity of honey-musts the monitoring of pH during alcoholic fermentation was performed in both experiments to assess whether or not incomplete sugar break down could be accounted for low pH in this type of beverage.[20] Mendes-Ferreira et al. reported that pH of mead inoculated with *S. cerevisiae* UCD522 at 10^5 CFU/ml was 3.6.[14] Generally, most *S. cerevsiae* strains grow at pH-values between 2.50 and 8.50, but they are acidophilic organisms and grow better under acidic condition.[21] The optimal pH range for yeast growth can vary from pH 4.00 to 6.00, depending on temperature, the presence of oxygen, culture, and the strain of yeast.[22] Total acidity increased after alcoholic fermentation which indicates production of acids by yeast.[23] Zamora reported that organic acids are produced throughout alcoholic fermentation such as acetic acid, succinic acid and lactic acid.[24] Generally, the dominant acids responsible for increase in total acidity are reported to be succinic and acetic acid.[20] In addition, the volatile acidity, acetic acid, was possibly observed in mead but it was below the legal limits specified for alcoholic beverages. The total acidity represents the acidic taste owing to organic acid produced during the fermentation process.[8] Chen et al.[8] suggested that volatile acidity, mainly acetic acid, should be as low as possible to avoid the vinegar off-character. Mendes-Ferreira et al. reported that total acidity of mead was 3 g/L tartaric acid after 25 day of fermentation.[14] Chen et al. found that the main acids to form are the acetic and succinic acids which reduce the pH during early days of fermentation.[8] Sroka and Tuszynski reported that the acetic and succinic acids formed during diluted honey fermentation reduced the mead's pH and led to an increased non-dissociated fatty acid content, which, in addition to the presence of relative large amounts of medium-chain fatty acids, can cause the fermentation to slow down or stop.[20] From the result, the pH of honey-must was a suitable environment for fermentation by *S. cerevisiae* var. *burgundy*. When total acidity tended to increase with the increase in fermentation time, the pH tended to decrease. Both samples displayed a similar decline in pH value during 6 days of fermentation and tended to become stable throughout fermentation.

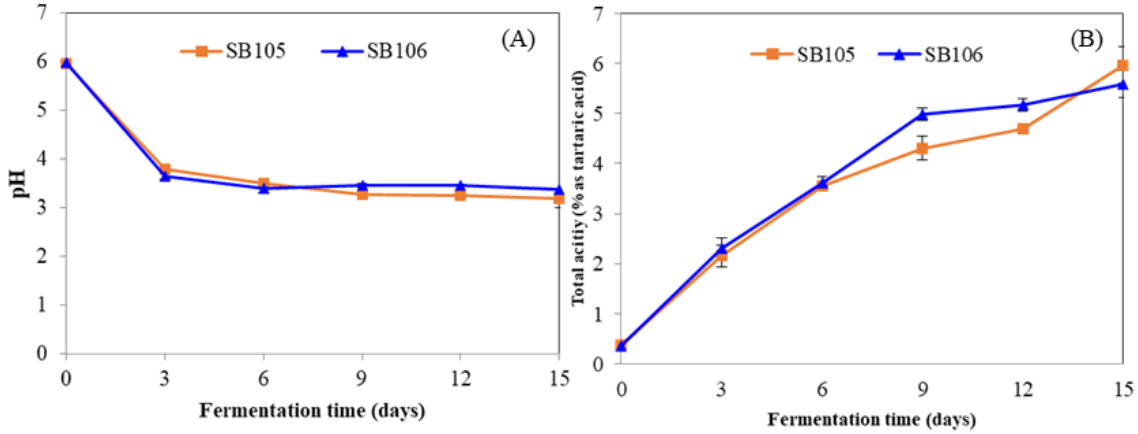

Figure 1.
Changes in pH (A) and total acidity (B) during fermentation of mead inoculated with *S. cerevisiae* var. *burgundy* at 10^5 CFU/ml (SB105) and 10^6 CFU/ml (SB106).

Changes in total soluble solid and reducing sugar content

Decrease in total soluble solid and reducing sugar contents were observed during mead fermentation (Figure 2). The initial total soluble solid content of honey-must was 18 °Brix. The total sugar measured as the total soluble solids.[8] In this study, the reducing sugar content in initial honey-must was 15 g/100 ml. This was lower than initial total soluble solid content because of other components such as proteins, organic acids, non-reducing sugars, and vitamins.[25] Reducing sugar (mainly fructose and glucose) constituent the main components of honey.[26] This indicates that reducing sugars are major carbohydrate in honey. During fermentation, the decreasing rate of total soluble solids in SB106 was faster than that of SB105 ($p<0.05$) (Figure 2A). In addition, the reducing sugar content also decreased as the fermentation time increased ($p<0.05$) (Figure 2B). At higher inoculation of yeast (SB106), the lower total soluble solids and reducing sugars remained after 15 days of fermentation. At the end of fermentation (day 15), the total soluble solids and reducing sugars of SB105 and SB10 samples were 12% and 10% and 5% and 4%, respectively. Alcoholic fermentation is the anaerobic transformation of sugars (mainly glucose and fructose) into ethanol and carbon dioxide. Sugar was substrate of alcoholic fermentation. Among sugars, yeast tend to utilize glucose first.[27] Chen et al. reported that mead contain 10.4% total soluble solid and 1.8% reducing sugar after 20 days of fermentation.[8] The total soluble solid and reducing sugar in mead varied, depending on honey dilution and starter culture inoculation. From the results, the decrease in total soluble solid and reducing sugar contents caused by fermentation honey-must by *S. cerevisiae* var. *burgundy*.

Changes in ethanol content

After 15 days fermentation, the amount of ethanol produced by yeast in mead inoculated with SB105 and SB106 were 10% and 12% (v/v), respectively (Figure 2C). The increase in ethanol indicates fermentation rate. From the result, the higher inoculation of *S. cerevisiae* var. *burgundy* (SB106) showed the higher fermentation rate. Generally, yeast metabolizes sugars in honey, producing alcohol, acids, gas, and other products. Chen et al. reported that fermented mead had 11-13% ethanol content.[8] Vidrih and Hribar reported that mead contained 14.2% ethanol after 24-day fermentation.[28] The result was concomitant with the increase in acidity of the mead during fermentation (Figure 1B). This indicates that there was an increase in acidity during the progression of alcoholic fermentation of honey by yeast. Many of the distinctive flavor compounds in mead owe their origin to the botanical and geographic origin of the honey. During fermentation, some of these compounds may act as carbon and nitrogen

sources for yeast metabolism, or be chemically transformed. As a result, the alcohol content of both samples was satisfied by the specification of fruit wine (less than 15% alcohol by volume).[29]

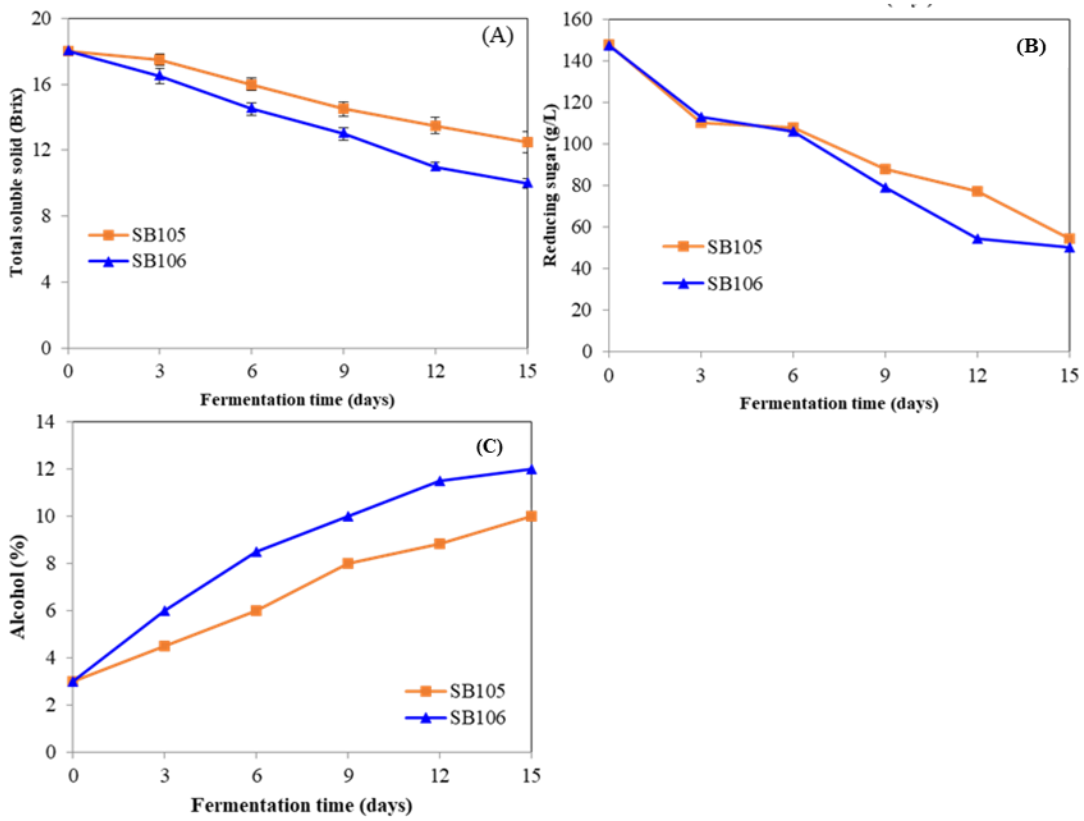

Figure 2.

Changes in total soluble solid (A), reducing sugar (B), and alcohol (C) during fermentation of longan honey inoculated with *S. cerevisiae* var. *burgundy* at 10^5 cfu/ml (SB105) and 10^6 cfu/ml (SB106).

Changes in total phenolic content and DPPH radical scavenging activity

Figure 3 shows total phenolic content (A) and DPPH radical scavenging activity (B) of honey-must inoculated with SB105 and SB106 during fermentation. No change in total phenolic content in SB106 during 6 days of fermentation was observed (p<0.05). During day 6 to 15 of fermentation, the total phenolic content of SB106 slightly increased (p<0.05), while those of SB105 sample tend to be decreased during 9 days (p<0.05). The total phenolic content depends on the different geographical and botanical sources of honey. Generally, total phenolic content of diluted honey varied, depending on type of pollen. The concentration and type of phenolic substances depend on the floral origin of the honey and are mainly responsible for its biological activities. The antioxidant activity of both samples slightly decreased during first three days of fermentation (p<0.05), thereafter no change in antioxidant activity throughout the fermentation. From the results, the phenolic content in honey, indicating its antioxidant potential. It has been recorded that the antioxidant potential as a DPPH radical scavenging activity is stable throughout after 3 days of fermentation. Honey contains an extensive diversity of phenolic compounds as secondary constituents, notably flavonoids and phenolic acids.[9] The flavonoid in honey consists of mainly flavanones and flavones. The main flavonoids are myricetin, tricetin, quercetin, hesperidin, luteolin, kaempferol, pinocembrin,

chrysin, pinobanksin, genkwanin, naringenin, and galangin. Additionally, the dominant acids in phenolic acids are gallic acid and *p*-coumaric acid, followed by the caffeic, ferulic, ellagic, chlorogic, syringic, vanillic, cinnamic, and *p*-hydroxybenzoic acids.[30] From the results, total phenolic content and antioxidant activity of samples were slightly changed during fermentation. SB106 had higher total phenolic content than that of SB105. The honey-must was possibly fermented by *S. cerevisiae* var. *burgundy* at 10^6 cfu/g.

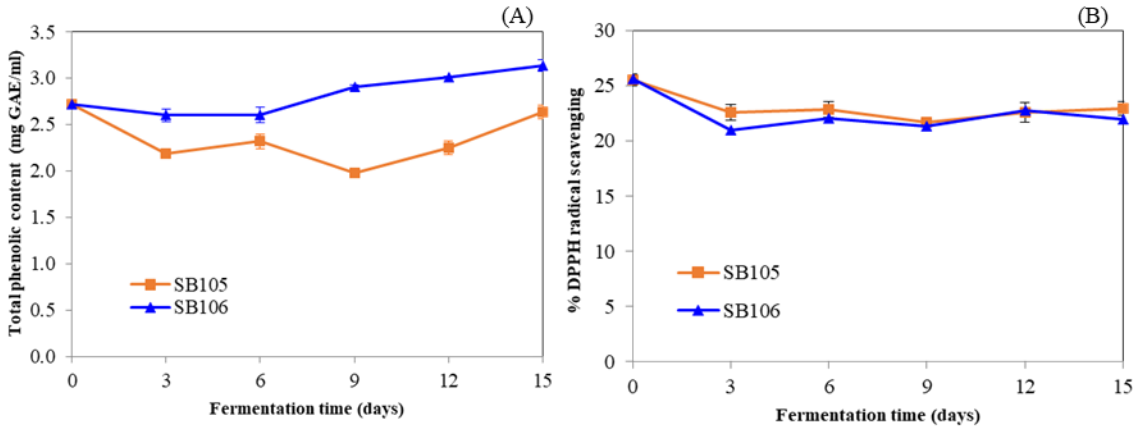

Figure 3.

Changes in total phenolic content (A) and DPPH radical scavenging activity (B) during fermentation of longan honey inoculated with *S. cerevisiae* var. *burgundy* at 10^5 cfu/ml (SB105) and 10^6 cfu/ml (SB106).

Conclusion:

The fermentation of longan honey-must could be accomplished by inoculation of commercial *S. cerevisiae* var. *burgundy*. The different inoculum levels of starter might contribute on reducing sugar consumption and ethanol production. Mead with a higher inoculation level exhibited higher ethanol content. During fermentation, total phenolic content of both samples was different; their DPPH radical scavenging activity, however, was not different after 3 days of fermentation. Therefore, this work will aid local honey producers in Thailand for mead production. However, the considerable research is still needed to characterize both honey and mead constituents that are responsible for its organoleptic properties.

Acknowledgements:

Authors would like to acknowledge Prof. Dr. Chanpen Chanchao from Department of Biology, Faculty of Science, Chulalongkorn University, Thailand for encouraging inspiration about a preliminary experiment for honey wine/mead fermentation.

References:

1. Bertoncelj J, Dobersek U, Jamnik M. Golob T. Food Chem. 2007; 105 (2): 822-828.
2. Gheldof N, Wang XH, Engeseth NJ. J. Agric. Food Chem. 2002; 50 (21): 5870-5877.

3. Rasad H, Entezari MH, Ghadiri E, Mahaki B. Clinical Nutrition ESPEN. 2018; 26:8-12.
4. Alvarez-Suarez JM, Giampieri F, Battino M. 2013. Curr. Med. Chem. 2013; 20: 621-638.
5. Al-Mamary M, Al-Meen A, Al-Habori M. Nutr. Res. 2002; 22 (9): 1041-1047.
6. Knauf M, Kraus K. Sugar Ind. 2006; 131:753-758.
7. Navrátil M, Šturdik E, Gemeiner P. Biotechnol. Lett. 2001; 23:977-982.
8. Chen C-H, Wu Y-L, Lo D, Wu M-C. J. Inst. Brew. 2013; 119:303-308.
9. Ramalhosa E, Gomes T, Pereira P, Dias T, Estevinho LM. Advances in food and nutrition research. 2011; 63:101-118.
10. Pereira AP. Dias T, Andrade J, Ramakhosa E, Estevinho LM. Food Chem. Toxicol. 2009; 47: 2057-2063.
11. Pereira AP, Oliveira JM, Mendes-Ferreira A, Estevinho LM, Mendes-Faia A. Current Developments in Biotechnology and Bioengineering: Food and Beverage Industry. 2017; 407-434.
12. Ross R, Morgan S, Hill C. Int. J. Food Microbiol. 2002; 3-16.
13. Chaikham P, Prangthip P. Food Bioscience. 2015; 10: 1-7.
14. Mendes-Ferreira A, Cosme F, Barbosa C, Falco V, Ines A, Mesdes-Faia A. Int. J. Food Microbiol. 2010; 144: 193-198.
15. Zoecklein BW, Fugelsang KC, Gump BH, Nury FS. Wine analysis and production. 1995; Chapman & Hall: New York.
16. James CS, Analytical Chemistry of Foods. 1999; 124-125.
17. Velioglu YS, Mazza G, Gao L, Oomah BD. J. Agric. Food Chem. 1998; 46: 4113-4117.
18. Aljadi AM, Kamaruddin MY. Food Chem. 2004;85:513-518.
19. Bisson LF. Am. J. Enol. Viticult.1999; 50:107-119.
20. Sroka P, Tuszyński T. Food Chem. 2007; 104 (3):1250-1257.
21. Carmelo V, Bogaerts P, SaCorreia I. Arch. Microbiol. 1996; 166(5):315-320.
22. Narendranath NV, Power R. Appl. Environ. Microbiol. 2005; 71 (5): 2239-2243.
23. Boulto RB, Singleton VL, Bisson LF, Kunkee RE. Principle and practices in winemaking. 1996. Chapman & Hall.
24. Zamora F. Wine chemistry and biochemistry. 2009; 3-26.
25. de Silva PM, Gauche C, Gonzaga V, Costa ACO, Fett R. Food Chem. 2016; 196:309-323.
26. Moniruzzaman M, An CY, Rao PV, Hawlader MNI, Azlan SABM, Sulaiman SA, Gan SH. BMRI. 2014; 2014:1-11.
27. Lui X, Jia B, Sun X, Ai J, Wang L, Wang C, Zhao F, Zhan J, Huang W. J. Food Sci. 2015; 80 (4):M800-M808.
28. Vidrih R, Hribar J. Acta Alimentaria. 2007; 36:151-162.
29. Thai Community Product Standard 2/2003. Fruit wine. 2003; Ministry of Industry. Thailand.
30. Anklam E. Food Chem. 1998; 63(4): 549-562.

C_036_OA: PHYLOGENETIC ANALYSIS OF THE SHRIMP PLANT (*RUNGIA*, ACANTHACEAE) IN THAILAND

Kanokorn Rueangsawang[1*], Somran Suddee[2], David A. Simpson[3], Pranom Chantaranothai[4]

[1] Department of Biology, Faculty of Science, Ramkhamhaeng University, Bangkok 10240, Thailand.
[2] The Forest Herbarium, Department of National Parks, Wildlife and Plant Conservation, Chatuchak, Bangkok 10900, Thailand.
[3] Royal Botanic Gardens, Kew, Richmond, Surrey TW9 3AB, UK.
[4] Department of Biology & Centre of Excellence on Biodiversity (BDC), Faculty of Science, Khon Kaen University, Khon Kaen 40002, Thailand.
[*]e-mail: rukanok@yahoo.com

Abstract:

Rungia is a complex genus of Acanthus family. The genus comprises ca. 50 species and is distributed throughout tropical and subtropical Africa and Asia. Fourteen species are presented in Thailand, of which eight are endemic. The objective of this study is to investigate the systematic position of the genus. We used molecular and morphological data to estimate the phylogenetic relationship of genus *Rungia* and its closely related genera. Maximum parsimony, maximum likelihood, and Bayesian analyses using chloroplast *accD- psal* and *trnL- trnF* intergenic spacer resolved a monophyletic clade of *Rungia*, which was sister to *Justicia.* The result shows that bract with or without hyaline margins and a capsule with the placentas tearing from the capsule wall at dehiscence are congruent with the resolved tree topology.

C_037_PF: IDENTIFICATION OF GENES INVOLVED IN ANTIMICROBIAL PEPTIDE rALF*Pm*3 RESISTANCE IN *Vibrio parahaemolyticus* AHPND VIA GENOME SEQUENCING

Iyacoob Khunsri,[1] Supitcha Wanvimonsuk,[2] Htut Htut Htoo,[1] Pinidphon Prombutara,[3] Kunlaya Somboonwiwat,[2] Poochit Nonejuie[1,*]

[1] Institute of Molecular Biosciences, Mahidol University, Nakhon Pathom 73170, Thailand
[2] Center of Excellence for Molecular Biology and Genomics of Shrimp, Department of Biochemistry, Faculty of Science, Chulalongkorn University, 254 Phayathai Road, Bangkok 10330, Thailand
[3] Omics Science and Bioinformatics Center, Faculty of Science, Chulalongkorn University, Bangkok, 10330, Thailand
*e-mail: poochit.non@mahidol.edu

Abstract:

Acute Hepatopancreatic Necrosis Disease (AHPND) is a disease found in post larva shrimp caused by *Vibrio parahaemolyticus*. Normally, farmers would use antibiotics to control the infection, however, the misuse of antibiotics can lead to antibiotic resistance in bacteria. Previous studies on the innate immunity of shrimps revealed that anti-lipopolysaccharide factors3 (ALF*Pm*3), a subtype of antimicrobial peptides (AMPs) found in *Penaeus monodon,* has board antimicrobial activities, and plays an important role in inhibiting the growth of bacteria. Albeit the potential of ALF*Pm*3 as an antibiotic alternative for disease control, to date, the information on the mechanism by which ALF*Pm*3 induces resistance in bacteria still lacking. Thus, this study aims to elucidate the mechanism of resistance of *V. parahaemolyticus* AHPND to ALF*Pm*3. Our results showed that the growth of *V. parahaemolyticus* was inhibited by ALF*Pm*3 at 2.5 µM. We, then, succeeded in inducing the resistance of *V. parahaemolyticus* AHPND to ALF*Pm*3, by subjecting the bacteria to a series of passages for approximately 120 generations, giving a total of three resistant strains that exhibited two to eight times higher minimum inhibitory concentration (MIC) of ALF*Pm*3 than the control strain. Lastly, whole genome sequencing and bioinformatics analysis revealed a total of four gene candidates that might be involved in ALF*Pm*3 resistance in bacteria. These include hypothetical protein, LysR family transcriptional regulator, AcrB/AcrD/AcrF family protein and Hemolysin–type calcium–binding repeat family protein, some of which have previously been reported to be responsible for bacterial resistance to other AMPs.

Introduction:

Acute Hepatopancreatic Necrosis Disease (AHPND) or Early Mortality Syndrome (EMS) is a disease that is found in post larva shrimp within 20 to 30 days after culturing them in a pond that causes the liver and pancreas to fail eventually resulting in death within 2 to 3 days (1-4). In Asia, the first outbreak of the disease was reported in 2009 resulting in 80% loss of shrimp production. In Thailand, the disease was first reported in 2012 causing a 25% reduction of shrimp products (5, 6). Previous studies on the cause of the disease revealed that *Vibrio* spp. were responsible for the outbreak including *V. parahaemolyticus* AHPND which was first isolated in Vietnam (7).

V. parahaemolyticus AHPND is a halophilic gram negative bacterium in the marine environment and considered as one of the important aquatic zoonotic pathogens that cause disease in penaeid shrimp (2, 3, 5). *V. parahaemolyticus* AHPND infects shrimp's gastrointestinal track and produces a toxin named Photorhabdus insect related (Pir) toxin which includes Pir-A and Pir-B toxins (1, 5, 7). The infection leads to tissue destruction, cell

dysfunction and cell death resulting in visible characteristics such as pale and atrophied hepatopancreas followed by the rapid death of the infected shrimp (1, 5).

Commonly, farmers used antibiotics to control the infection but, to date, there is no supporting evidence that antibiotics are effective in controlling disease in shrimp farming environment. Moreover, long-term misuse of antibiotics has been well-documented to induce antibiotic resistance in bacteria (8-10). Apart from the higher risk of inducing antibiotic-resistant bacteria in shrimp farm, one of the major concerns is the transfer of antibiotic resistant genes across different species of bacteria, especially to other animal or human related pathogens (11-13). Therefore, the reduction of antibiotic use in shrimp farming is encouraged while simultaneously finding other methods that are suitable and effective in controlling the disease. One of the methods that can be used is employing biomolecules identified in shrimp immunity to inhibit the growth of the pathogen.

Many studies on the innate immune system of higher organisms revealed that antimicrobial peptides (AMPs), which commonly are cationic antimicrobial agents, play an important role in defense against bacterial infection of the host organism (14-16). The growth inhibition mechanism of AMPs against bacterial pathogens include blocking the passage of solute across the outer membrane of gram negative bacteria and interacting with teichoic acid in the cell wall of gram positive bacteria (17-20). Currently, the study of AMPs showed that there are four main groups of AMPs including penaedin, clustin, anti-liposaccharide factors (ALFs) and stylicin whereof each group play different roles against the growth of bacteria (18, 21, 22).

Anti-lipopolysaccharide factor 3 isolated from *Peneus monodon* (ALF*Pm*3), a sub-type of Anti-lipopolysaccharide factors (ALFs) family, have been previously reported on its broad antibacterial activity against the growth of various gram negative bacteria including *Vibrio harveyi* (21-23). So far, many studies on the mechanism of ALF*Pm*3 showed that the peptide binds to lipopolysaccharides on the outer membrane of gram negative bacteria with electrostatic force and introduces pores on the cell membrane causing the cell to leak and eventually die (16, 20, 23-25) highlighting its potency to be used as an antibiotic alternative in disease control.

However, the use of ALF*Pm*3 against bacteria for a long term also raises concerns about the induction of resistant characteristics. It is possible that the ALF*Pm*3 resistant mechanisms overlap with those of other antibiotics including antibiotics that are used in other animals and humans (26). Therefore, the study of ALF*Pm*3 induced-resistant mechanism in bacteria will provide crucial pieces of information for safe and responsible use of ALF*Pm*3 as an antibiotic alternative in the future. Here, we first investigated the antibacterial activity of ALF*Pm*3 against *V. parahaemolyticus* AHPND using microdilution method. Then, ALF*Pm*3 resistant *V. parahaemolyticus* AHPND were successfully induced with serial passage method. Lastly, whole genome sequencing was performed on all ALF*Pm*3 resistant and wild type control strains, and mutated genes were analyzed to identify which genes might be involved in bacteria resistant against ALF*Pm*3.

Methodology:

1. Bacterial strains and media

Bacterial strains used in this study *V. parahaemolyticus* AHPND (Table 1). Tryptic soy broth (TSB) supplemented with 1.5% NaCl was used to grow *V. parahaemolyticus* AHPND in all experiments performed in this study.

2. Recombinant ALF*Pm*3 (rALF*Pm*3) preparation and purification via cation exchange chromatography by FPLC (fast performance liquid chromatography)

The recombinant ALF*Pm*3 (rALF*Pm*3) has been produced from other experiment. Briefly, *Pichia pastoris* (*P. pastoris*) were grown in BMGY at 30°C overnight then overnight *P. pastoris* was transferred into fermentation tank of basal salt medium and PTM for fed batch culture. Later, methanol (100%) was added into fermentation tank to induce *P. pastoris* to produce rALF*Pm*3 (30°C, pH 5.5, 30% oxygen) and rALF*Pm*3 were harvested by centrifuge at 5000 x g for 15 minutes. rALF*Pm*3 were analyzed by SDS-PAGE. Bradford was then used to measure the concentration (27). rALF*Pm*3 were purified via cation exchange chromatography by FPLC (5 mm. Hitrap SP HP; GE healthcare) and monitored with 15% SDS-PAGE.

3. Minimum inhibitory concentration (MIC) test of *V. parahaemolyticus* AHPND using microdilution method

Microdilution method was used to determine the lowest concentration of antimicrobial agents that can inhibit growth of bacteria (28, 29). Briefly, overnight culture of *V. parahaemolyticus* AHPND was diluted 1:100 into the new media for day culture. Then, the day culture was grown at 30°C to early log phase of bacteria (OD600 =0.2). The early log phase culture was then diluted to OD600 =0.1. Lastly, the diluted bacteria were added into the media containing various concentration of ALF*Pm*3 (32µM-0.0625µM) in 96 well plate and incubate at 30°C with shaking overnight. The results were interpreted by analyzing the turbidity of cells in all wells – the well that is the least turbid can be interpreted as having the lowest concentration of ALF*Pm*3 that can kill the bacteria.

4. Bacteria resistance induction by Serial passage method

Serial passage method was used to induce the resistance of *V. parahaemolyticus* AHPND resistance to ALF*Pm*3 (30, 31). By growing *V. parahaemolyticus* AHPND in media with sub-MIC level of ALF*Pm*3 and repeatedly sub-cultured the growing culture into slightly higher concentration of drug or active compounds until bacteria can grow into higher concentration than original MIC (25, 32). Briefly, day culture of *V. parahaemolyticus* AHPND were prepared from overnight culture in fresh media to early log phase (OD600 =0.2) and diluted to OD600 =0.1. The diluted day culture was grown in half MIC of ALF*Pm*3 in the 96-well plate overnight at 30°C. Then, the bacteria that were grown in half of MIC were subsequently sub-cultured to the new media containing a slightly higher concentration of ALF*Pm*3. This was repeated until the bacteria consistently grow in the desired concentration of ALF*Pm*3. A control was grown in only media in parallel with the resistant selection, to use as media adaptation controls to determine the rate of spontaneous mutation that are caused by culturing bacteria in the same media for a long time (33).

5. Genome extraction and 16s rRNA analysis

The fresh bacterial cell of *V. parahaemolyticus* AHPND (wild type, media adaptation control and resistance strains) were grown in media for 18-20 hours at 30°C and genomic DNA was extracted from cell pellet with FavorPrep™ Tissue Genomic DNA Extraction Mini Kit. The 16s rRNA amplification was performed with primers named as BSF8/20 (5'-AGAGTTTGATCCTGGCTCAG-3') and REVB ('-GGTTACCTTGTTACGACTT) (34, 35). The PCR condition was as follows: Denaturation at 94°C for 4 minutes, 35 cycles of 94°C for 30 seconds, 50°C for 30 seconds and 72°C for 105 seconds, and final elongation at 72°C for 7 minutes. PCR products (product size ~1.5 kb) was monitored by gel electrophoresis. PCR products were purified by GenepHlow™ Gel/PCR Kit according to the manufacturer's instructions. The 16s rRNA sequence data from sequencing were analyzed by comparing with the National Center for Biotechnology Information (https://blast.ncbi.nlm.nih.gov/Blast.cgi) database.

6. Whole Genome sequencing and mutated gene analysis

Whole genome sequencing (WGS) was performed in all strains of *V. parahaemolyticus* AHPND including the wild type, media adaption control and resistance strains via Omics Science & Bioinformatics Center at

Chulalongkorn university (Illumina MiSeq platform). Quality check of the raw data from WGS was performed via FASTQC (v0.11.9). Then, the irrelevant data from WGS were eliminated with Trim Galore (v0.6.2). After that, the fragments of trimmed DNA were subjected to de novo assembly via SPAdes (v3.14.1). After DNA were assembled, the SNIPPY software (v4.3.6) was used to investigate mutations in genome of media adaptation control strain and ALF*Pm*3 resistant *V. parahaemolyticus* strains and compared with the reference strain *V. parahaemolyticus* RIMD 2210633 (NCBI txid 223926). At the end, the genome of all strains was annotated with Prokka (v1.13.4) software to identify any mutated genes in their genomes. Reported mutation position shown in Table 2 are the result of subtracting spontaneous mutations found in the media adaptation control strain.

Results and Discussion:

Minimum inhibitory concentration (MIC) test of *V. parahaemolyticus* AHPND

A previous study showed that ALF*Pm*3 exhibits antibacterial activity against various bacteria including *V. harvayi* (23). However, the antibacterial activity of ALF*Pm*3 against *V. parahaemolyticus* AHPND have never been tested before. Moreover, each batch of lab-made purified ALF*Pm*3 can result in slightly different levels of antibacterial activity. Thus, we first tested whether ALF*Pm*3 used for this study can inhibit the growth of *V. parahaemolyticus* AHPND using microdilution method. The minimum inhibitory concentration (MIC) of ALF*Pm*3 against the *V. parahaemolyticus* AHPND is 2.5 µM (Table 1) which were similar to previously reported data from other *Vibrio* species suggesting that ALF*Pm*3 also exhibits antibacterial activity against *V. parahaemolyticus* AHPND.

Isolation of bacteria resistant strain in *V. parahaemolyticus* AHPND.

After the MIC of ALF*Pm*3 against the *V. parahaemolyticus* AHPND was confirmed, isolation of ALF*Pm*3 resistant strains was performed in *V. parahaemolyticus* AHPND. Since AMPs resistance are usually a result of accumulation of various mutations in the genome of the bacteria, the serial passage method was recommended for isolating resistant mutants for such antibacterial molecules (25, 30, 31). Performing in 96-well plates, seven out of eight different cultures of *V. parahaemolyticus* AHPND were first inoculated in half MIC of ALF*Pm*3 for commencing resistant selection while the remaining one culture was used as a media adaptation control by inoculating into media without ALF*Pm*3. After incubation for a few days, the cultures that successfully adapted to grow in the specific concentration of ALF*Pm*3, were repeatedly sub-cultured into the media containing higher concentration of ALF*Pm*3. After four weeks of serial passage isolation step, we were able to isolate the total of three resistant strains namely PN1028, PN1030 and PN1032 with media adaptation control PN1026. At the end of the selection, 16s rRNA sequencing was performed on all isolated strains including media adaptation control PN1026, PN1028, PN1030 and PN1032 to confirm that the isolated strains were not contaminated with other microorganism during selection. Then, the sequence data were compared with sequence database in National Center for Biotechnology Information (https://blast.ncbi.nlm.nih.gov/Blast.cgi). The result indicated that all isolated strains are *V. parahaemolyticus* AHPND and not contaminated by any microorganism.

After obtaining purified resistant isolates, MIC test for ALF*Pm*3 was performed on all resistant strains. MIC results showed that *V. parahaemolyticus* resistant strains gave MIC levels two to eight times higher than that of wild type *V. parahaemolyticus* AHPND (Table 1) this suggests that resistance in these strains has been maintained over many generations and that they are indeed resistant to ALF*Pm*3

Whole genome sequencing and mutated gene candidate analysis of ALF*Pm*3 resistant *V. parahaemolyticus*

In order to investigate which genes in the resistant strains might be responsible for ALF*Pm*3 resistance phenotype, whole genome sequence analysis was performed. Genomic DNA of the isolated strains PN1028, PN1030 and PN1032 and the media adaptation control PN1026 were extracted and subjected to genomic DNA sequencing.

The media adaptation control strain was used as a random mutation background during the long-term isolation to rule out any spontaneous mutations that might occur during resistance selection. After obtaining the raw sequence data, data quality control was performed prior to de novo assembly and data analysis via bioinformatics software to find mutations in the bacterial genome. The result indicated that there are total of four possible mutated genes on the genome of ALF*Pm*3 resistant *V. parahaemolyticus* strains, PN1030 and PN1032, while no mutation was detected in PN1028 strain. Zero mutation found in PN1028 is unexpected since the strain showed highest level of ALF*Pm*3 resistance (Table 1). It is possible that the genome data obtained from the sequencing analysis of the strain is not adequate to reveal the possible mutations in the genome. Moreover, the fact that, unlike the *E. coli* genome, the standard genome reference of *V. parahaemolyticus* AHPND is still lacking which, in turn, resulted in genome analysis difficulties. In order to investigate if PN1028 contains any mutations on the genome, another batch of whole genome sequencing of the strain is strongly needed.

For the strain PN1030, the mutated genes found include hypothetical protein, AcrB/AcrD/AcrF family protein and LysR family transcriptional regulator. Full list of mutations can be found in Table 2. Interestingly, there are 2 mutated genes that have been reported to be involved in bacteria resistance to antibiotics including AcrB/AcrD/AcrF family protein and LysR family transcriptional regulator. AcrB/AcrD/AcrF family protein is a member of the resistance nodulation division (RND) located in outer membrane channel and a periplasmic fusion protein that is known to infer antibiotic resistance in bacteria by acting as an efflux pump in bacteria to pump out toxic compounds including antibiotics from bacterial cells (36). Thus, the presence of AcrB/AcrD/AcrF family protein among the mutations in ALF*Pm*3-resistant *V. parahaemolyticus* might be responsible for the ALF*Pm*3 resistant phenotype. Apart from the possible role of efflux pump in ALF*Pm*3 resistance, two component signaling components are also known to be involved in the AMPs resistance (36). One of the promising mutations found in our ALF*Pm*3 resistant strains is LysR family transcriptional regulator. Previous studies showed that LysR family transcriptional regulator is involved in regulating quorum sensing systems in gram negative bacteria including QseC/QseB which in turn regulate expression of *phoPQ* and *pmrB* genes (37, 38). The *phoPQ* and *pmrB* genes have been reported to be involved in bacteria resistance to colistin, a cationic lipopeptide antibiotic (39, 40). The fact that ALF*Pm*3 is also a cationic AMP similar to colistin suggests that the LysR family transcriptional regulator mutation found in our ALF*Pm*3 resistant strains might be responsible for the ALF*Pm*3 resistant phenotype. However, since the mutations found in AcrB/AcrD/AcrF family protein and LysR family transcriptional regulator were predicted to be synonymous by bioinformatics, further studies are needed in order to confirm whether the amino acid sequence of protein products were altered due to the DNA mutation or not. It is also possible that the actual codon usage in the *V. parahaemolyticus* AHPND is different from the predicted codon usage used in the bioinformatics analysis (41, 42). Whether or not hypothetical protein, AcrB/AcrD/AcrF and LysR mutations found in the ALF*Pm*3 resistant *V. parahaemolyticus* PN1030 have direct roles in ALF*Pm*3 resistance, renders the need for further studies.

Lastly, for the strain PN1032, there are five mutation positions found in hemolysin-type calcium-binding repeat family protein. However, this protein family has never been reported to be involved in any antibiotic resistance. This finding corresponds to the fact that the MIC of the strain PN1032 against ALF*Pm*3 was only two times higher than that of wild type control. Thus, it is possible that hemolysin-type calcium-binding repeat family protein has little or no effect on ALF*Pm*3 resistant phenotype.

Table 1. Minimum inhibitory concentration (MIC) of ALF*Pm*3 against *V. parahaemolyticus*

Strains	SIR[a]	MIC (μM)	Reference
V. parahaemolyticus AHPND[b]	S	2.5	(43)
V. parahaemolyticus PN1026[c]	S	2.5	This study
V. parahaemolyticus PN1028[d]	R	20	This study
V. parahaemolyticus PN1030[d]	R	10	This study
V. parahaemolyticus PN1032[d]	R	5	This study

[a] Interpretation key for the antibiogram S = sensitive; normal concentration of ALF*Pm*3 can kill bacteria sensitive strain, I = intermediate; ALF*Pm*3 may be effective against microorganism at higher concentration, R = resistant; bacteria can survive in normal concentration of ALF*Pm*3

[b] *V. parahaemolyticus* wild type strain

[c] Media adaptation control for *V. parahaemolyticus* resistant strains

[d] *V. parahaemolyticus* resistant strains that isolate in this study by using Serial passage method

Table 2. The mutation of gene products found in ALF*Pm*3 resistant *V. parahaemolyticus* strains

Strains	**Gene product**	**Nucleotide change**	**Amino acid change**
V. parahaemolyticus PN1030	Hypothetical protein	c.3165T>C	p.Asp1055Gly
	AcrB/AcrD/Acr family protein	c.1207G>A	p.Val402Val
	LysR family transcriptional regulator	c.388G>A	p.Thr129Thr
V. parahaemolyticus PN1032	Hemolysin-type calcium binding repeat family protein	c.36C>T	p.Pro12Leu
		c.69C>T	p.Pro23Leu
		c.74_77delAGTGinsGATT	p.GlnTer25ArgLeuext*?
		c.131_137delTTACGCGinsGTATGCC	p.PheThrArg44CysMetPro
		c.407A>G	p.His136Arg

Conclusion:

In conclusion, our study of the activity of ALF*Pm*3 activity against *V. parahaemolyticus* AHPND by microdilution method found that the minimum inhibitory concentration (MIC) of ALF*Pm*3 in *V. parahaemolyticus* AHPND was 2.5 µM. After four weeks of serial passage of *V. parahaemolyticus* AHPND into escalating concentrations of ALF*Pm*3, we successfully isolated a total of three resistant *V. parahaemolyticus* AHPND strains; PN1028, PN1030 and PN1032, which exhibited two to eight times higher MIC than wild type *V. parahaemolyticus* AHPND. Lastly, the result from whole genome sequencing and bioinformatics analysis revealed that four mutated genes might be associated with resistant characteristics of the bacteria. In particular, two possible mutated genes found in this study; AcrB/AcrD/AcrF family protein and LysR family transcriptional regulator, have been previously reported to be involved in multidrug resistance phenotype and in colistin resistance in other bacteria, respectively. As a future perspective, conventional targeted sequencing of mutated genes and the study of individual resistant genes, in a wild type genetic background of *V. parahaemolyticus* AHPND, would be highly essential to confirm the relationship between the mutated genes and phenotype of ALF*Pm*3 resistance found in *V. parahaemolyticus* AHPND.

Acknowledgements:

This study was supported by Agricultural Research Development Agency (ARDA) (ID: CRP6105021050). We thank Melanie Lim Boon Jin from Institute of Molecular Biosciences, Mahidol University for other related work performed during bioinformatic analysis.

References:

1. Zorriehzahra J, Banaederakhshan R. Early Mortality Syndrome (EMS) as new Emerging threat in shrimp industry. Advances in Animal and Veterinary Sciences. 2015;3:64-72.
2. Theethakaew C, Nakamura S, Motooka D, Matsuda S, Kodama T, Chonsin K, et al. Plasmid dynamics in *Vibrio parahaemolyticus* strains related to shrimp Acute Hepatopancreatic Necrosis Syndrome (AHPNS). Infection, Genetics and Evolution. 2017;51:211-8.
3. Zhang Q, Ding A, Yue Q, Li W, Zu Y, Zhang Q. Dynamic interaction of neutrophils and RFP-labelled *Vibrio parahaemolyticus* in zebrafish (*Danio rerio*). Aquaculture and Fisheries. 2017;2(6):269-77.
4. De Schryver P, Defoirdt T, Sorgeloos P. Early Mortality Syndrome outbreaks: A microbial management issue in shrimp farming? PLOS Pathogens. 2014;10(4):e1003919.
5. Ahmmed S, Khan MA-A-K, Eshik MME, Punom NJ, Islam ABMMK, Rahman MS. Genomic and evolutionary features of two AHPND positive *Vibrio parahaemolyticus* strains isolated from shrimp (*Penaeus monodon*) of south-west Bangladesh. BMC Microbiology. 2019;19(1):270.
6. Soonthornchai W, Chaiyapechara S, Klinbunga S, Thongda W, Tangphatsornruang S, Yoocha T, et al. Differentially expressed transcripts in stomach of *Penaeus monodon* in response to AHPND infection. Developmental & Comparative Immunology. 2016;65:53-63.
7. Sirikharin R, Taengchaiyaphum S, Sanguanrut P, Chi TD, Mavichak R, Proespraiwong P, et al. Characterization and PCR detection of binary, Pir-like toxins from *vibrio parahaemolyticus* isolates that cause Acute Hepatopancreatic Necrosis Disease (AHPND) in shrimp. PLOS ONE. 2015;10(5):e0126987.
8. Okeke IN, Lamikanra A, Edelman R. Socioeconomic and behavioral factors leading to acquired bacterial resistance to antibiotics in developing countries. Emerging infectious diseases. 1999;5(1):18-27.
9. LIEBERMAN JM. Appropriate antibiotic use and why it is important: the challenges of bacterial resistance. 2003;22(12):1143-51.
10. Wolff MJ. Use and Misuse of Antibiotics in Latin America. Clinical Infectious Diseases. 1993;17(Supplement_2):S346-S51.

11. Bérdy J. Thoughts and facts about antibiotics: Where we are now and where we are heading. The Journal of Antibiotics. 2012;65(8):385-95.
12. Phillips I, Casewell M, Cox T, De Groot B, Friis C, Jones R, et al. Does the use of antibiotics in food animals pose a risk to human health? A critical review of published data. Journal of Antimicrobial Chemotherapy. 2004;53(1):28-52.
13. Holmström K, Gräslund S, Wahlström A, Poungshompoo S, Bengtsson B-E, Kautsky N. Antibiotic use in shrimp farming and implications for environmental impacts and human health. International Journal of Food Science & Technology. 2003;38(3):255-66.
14. Ganz T. Defensins: antimicrobial peptides of innate immunity. Nature Reviews Immunology. 2003;3(9):710-20.
15. Epand RM, Vogel HJ. Diversity of antimicrobial peptides and their mechanisms of action. Biochimica et Biophysica Acta (BBA) - Biomembranes. 1999;1462(1):11-28.
16. Tassanakajon A, Somboonwiwat K, editors. Antimicrobial peptides from the black tiger shrimp *Penaeus monodon* a review2012.
17. Tassanakajon A, Amparyup P, Somboonwiwat K, Supungul P. Cationic antimicrobial peptides in Penaeid shrimp. Marine Biotechnology. 2011;13(4):639-57.
18. Rolland J-L, Abdelouahab M, Dupont J, Lefèvre F, Bachere E, Romestand B. Stylicins, a new family of antimicrobial peptides from the Pacific blue shrimp Litopenaeus stylirostris. Molecular immunology. 2010;47:1269-77.
19. da Cunha NB, Cobacho NB, Viana JFC, Lima LA, Sampaio KBO, Dohms SSM, et al. The next generation of antimicrobial peptides (AMPs) as molecular therapeutic tools for the treatment of diseases with social and economic impacts. Drug Discovery Today. 2017;22(2):234-48.
20. Epand R, Walker C, Epand R, Magarvey N. Molecular mechanisms of membrane targeting antibiotics. Biochimica et biophysica acta. 2015;1858.
21. Destoumieux D, Bulet P, Loew D, Van Dorsselaer A, Rodriguez J, Bachère E. Penaeidins, a new family of antimicrobial peptides isolated from the shrimp *Penaeus vannamei* (Decapoda). The Journal of biological chemistry. 1997;272(45):28398-406.
22. Destoumieux D, Bulet P, Strub JM, Van Dorsselaer A, Bachère E. Recombinant expression and range of activity of penaeidins, antimicrobial peptides from penaeid shrimp. European journal of biochemistry. 1999;266(2):335-46.
23. Jaree P, Tassanakajon A, Somboonwiwat K. Effect of the anti-lipopolysaccharide factor isoform 3 (ALF*Pm*3) from *Penaeus monodon* on *Vibrio harveyi* cells. Developmental and comparative immunology. 2012;38(4):554-60.
24. Nicolas P. Multifunctional host defense peptides: intracellular-targeting antimicrobial peptides. The FEBS journal. 2009;276(22):6483-96.
25. Andersson DI, Hughes D, Kubicek-Sutherland JZ. Mechanisms and consequences of bacterial resistance to antimicrobial peptides. Drug resistance updates : reviews and commentaries in antimicrobial and anticancer chemotherapy. 2016;26:43-57.
26. Fleitas O, Franco OL. Induced Bacterial Cross-Resistance toward Host Antimicrobial Peptides: A Worrying Phenomenon. Front Microbiol. 2016;7:381-.
27. Somboonwiwat K, Marcos M, Tassanakajon A, Klinbunga S, Aumelas A, Romestand B, et al. Recombinant expression and anti-microbial activity of anti-lipopolysaccharide factor (ALF) from the black tiger shrimp *Penaeus monodon*. Developmental & Comparative Immunology. 2005;29(10):841-51.
28. Carson CF, Hammer KA, Riley TV. Broth micro-dilution method for determining the susceptibility of *Escherichia coli* and *Staphylococcus aureus* to the essential oil of *Melaleuca alternifolia* (tea tree oil). Microbios. 1995;82(332):181-5.
29. Wiegand I, Hilpert K, Hancock REW. Agar and broth dilution methods to determine the minimal inhibitory concentration (MIC) of antimicrobial substances. Nature Protocols. 2008;3(2):163-75.
30. Privett BJ, Broadnax AD, Bauman SJ, Riccio DA, Schoenfisch MH. Examination of bacterial resistance to exogenous nitric oxide. Nitric Oxide. 2012;26(3):169-73.

31. Morrissey I, Salman H, Bakker S, Farrell D, Bébéar CM, Ridgway G. Serial passage of *Chlamydia* spp. in sub-inhibitory fluoroquinolone concentrations. Journal of Antimicrobial Chemotherapy. 2002;49(5):757-61.
32. Lewis K. Platforms for antibiotic discovery. Nature Reviews Drug Discovery. 2013;12(5):371-87.
33. Lofton H, Pränting M, Thulin E, Andersson DI. Mechanisms and fitness costs of resistance to antimicrobial peptides LL-37, CNY100HL and wheat germ histones. PLOS ONE. 2013;8(7):e68875.
34. Greenwood SJ, Keith IR, Després BM, Cawthorn RJ. Genetic characterization of the lobster pathogen Aerococcus viridans var. homari by 16S rRNA gene sequence and RAPD. Diseases of aquatic organisms. 2005;63(2-3):237-46.
35. Yeates C, Gillings MR, Davison AD, Altavilla N, Veal DA. Methods for microbial DNA extraction from soil for PCR amplification. Biol Proced Online. 1998;1:40-7.
36. Horiyama T, Nishino K. AcrB, AcrD, and MdtABC multidrug efflux systems are involved in enterobactin export in *Escherichia coli*. PLOS ONE. 2014;9(9):e108642.
37. Kostakioti M, Hadjifrangiskou M, Pinkner JS, Hultgren SJ. QseC-mediated dephosphorylation of QseB is required for expression of genes associated with virulence in uropathogenic *Escherichia coli*. Molecular microbiology. 2009;73(6):1020-31.
38. Weigel WA, Demuth DR. QseBC, a two-component bacterial adrenergic receptor and global regulator of virulence in Enterobacteriaceae and Pasteurellaceae. Mol Oral Microbiol. 2016;31(5):379-97.
39. Maddocks SE, Oyston PCF. Structure and function of the LysR-type transcriptional regulator (LTTR) family proteins. 2008;154(12):3609-23.
40. Jochumsen N, Marvig RL, Damkiær S, Jensen RL, Paulander W, Molin S, et al. The evolution of antimicrobial peptide resistance in *Pseudomonas aeruginosa* is shaped by strong epistatic interactions. Nature Communications. 2016;7(1):13002.
41. Gouy M, Gautier C. Codon usage in bacteria: correlation with gene expressivity. Nucleic acids research. 1982;10(22):7055-74.
42. Sharp PM, Bailes E, Grocock RJ, Peden JF, Sockett RE. Variation in the strength of selected codon usage bias among bacteria. Nucleic acids research. 2005;33(4):1141-53.
43. Junprung W, Supungul P, Tassanakajon A. HSP70 and HSP90 are involved in shrimp *Penaeus vannamei* tolerance to AHPND-causing strain of *Vibrio parahaemolyticus* after non-lethal heat shock. Fish & Shellfish Immunology. 2017;60:237-46.

C_038_PF: INVESTIGATION OF LONG PRIMER TARGET-ENRICHMENT COMBINING WITH STR TYPING FOR DEGRADED DNA ANALYSIS

Pattranit Srisuwanuntanakul,[1,*] Nathinee Panvisavas,[2] Punchapat Sojikul[3]

[1]Forensic Science Unit, Faculty of Science, Mahidol University.
[2]Department of Plant Science, Faculty of Science, Mahidol University.
[3]Department of Biotechnology, Faculty of Science, Mahidol University.
*e-mail: pattranit.sri@student.mahidol.ac.th

Abstract:

This study aimed to develop an alternative for the analysis of degraded DNA samples by long primer target-enrichment combining with short tandem repeat (STR) typing. The CSF1PO locus was selected for the investigation. This locus is one of the large STR locus and often being the first locus to be drop out from the STR profiles of degraded DNA. Analysis results by agarose gel electrophoresis showed that the 344-bp PCR product of was amplified from the artificially degraded DNA samples that were amplified by CSF1PO long primers prior to the single-locus CSF1PO-STR typing, but not those without the long primer amplification step. These suggested the promising application of long primers in the target-enrichment step prior to STR typing. Further investigation was conducted by using the automated capillary electrophoresis, the routinely used instrument in forensic DNA typing. Optimizations were carried out by reducing concentration of long primers to eliminate the non-target peaks from being excessive. Results also showed the expected CSF1PO peak was detected from the artificially degraded DNA sample that was pre-amplified using the long primers prior to STR typing, but not from the artificially degraded sample that was directly typed. Although, non-target peaks of smaller sizes were reduced, they were still present in the electropherogram. In summary, experiments demonstrated that CSF1PO long primer amplification could help to restore the dropped-out locus in STR profiles of degraded DNA samples by enriching the target locus prior to STR typing. Further optimizations in the long primer amplification step and its application to STR typing is suggested.

Introduction:

Forensic analysis of degraded DNA samples remains challenging nowadays. Forensic scientists often deal with human remains and biological specimens that undergone extreme conditions from criminal activities, natural disasters, terrorist attacks, etc. In these cases, biological specimens are directly exposed to factors such as heat, moisture, UV, DNase, etc., which accelerate degradation of the samples and their DNA unpredictably. As a result, either incomplete or null DNA profiles would be generated, causing difficulties or failure in the human identification process. Although, there are many techniques for human identification, DNA-based human identification still plays the key role [1].

Currently, DNA profiles from degraded DNA can be generated by mini-Short tandem repeat (STR) typing and analysis of single nucleotide polymorphisms (SNPs) [2]. Mini-STR typing can be used to type DNA template with smaller fragment size. Due to the smaller number of loci being analyzed, the power of discrimination would be lower

when compare with the 16-loci STR typing kit [3]. This technique improved the DNA typing results of degraded samples by reducing the length of PCR target, therefore the PCR product decreased. However, DNA typing of highly degraded biological samples with fragmented DNA sizes less than 200-bp long is still a limitation for mini-STR analysis. For SNPs analysis, the technique allows the analysis of single nucleotide polymorphisms present in shorter DNA fragments. However, it is suggested that analysis of 40-60 SNPS is recommended to equivalent the same power of discrimination for human identity testing using 16 STR-loci that is routinely used [4, 5].

Muatner, Santangelo and Corti (2017), reported the development of long primer pairs or 'superprimers' for degraded DNA analysis. These long ssDNA polynucleotides are designed to anneal closer to the target repeat sequences which would reduce the requirement of the actual length of intact DNA. Thus, allowing the analysis of smaller amplicon size variations being analyze in a similar way with mini-STRs. However, the size of the amplified product would also be large enough for the routine DNA fragment analysis by automated capillary electrophoresis [6, 7].

Because the nature of forensic biological evidence is often present in very small amount and being degraded (or low quality), the use of long primer to enrich the DNA target in degraded samples prior to the routine STR-typing protocol is proposed. In this study, the CSF1PO locus, which is categorized as a large STR fragment in the STR profile and often drop-out in the analysis of degraded DNA samples, was investigated. It is expected that the success of target enrichment by long primer amplification could restore the locus from being drop-out from the STR-profile generated by the validated STR typing kit used routinely.

Methodology:

DNA preparation

Whole blood was centrifuged at 2,500 g for 10 min to separate 3 layers of blood components; plasma, buffy coat (white blood cells and platelets) and red blood cells. The buffy coat which the source of DNA materials was extracted using QIAamp® DNA mini kit (QIAGEN, 2016). DNA concentration was estimated by spectrophotometry (Nanodrop™, USA). The DNA extract was then stored at -20 °C.

To prepare artificially degraded DNA, an aliquot of 100 µL of 5 ng/µL DNA extract was put into an ultrasonic bath. The sonication time was varied to 30, 45, 60, 75, 90, 105, and 120 min to generate different ranges of DNA fragment size (or different degree of degradation).

DNA amplification

For standard STR-typing, the DNA profile was generated by using AmpFLSTR® Identifiler® Plus PCR Amplification kit (Applied Biosystem, USA), which composed of multiplex primers for 15-STR loci and a sex determination locus (AMEL). Amplification was carried out in a total volume of 12.5 µL, containing 5 µL of the AmpFLSTR® Identifiler® Plus master mix, 2.5 µL of AmpFLSTR® Identifiler® Plus primer set, DNA template and sterile double distilled water. Amplification was performed in GeneAmp 9700 thermocycler (Applied Biosystem, USA) using the following condition; initial denaturation at 95 ºC for 11 min following with 28 cycles of denaturation at 94 ºC for 20 seconds, annealing and extension at 59 ºC for 3 min, then the final extension at 60 ºC for 30 min. (Applied Biosystem, 2015). The size of detected fragments was used for grouping the different levels of degraded sample with the manner of sonicated time and fragment sizes.

For CSF1PO single-locus typing, amplification was carried out in a total reaction volume of 25 µL, the reaction consists of 1X PCR buffer, 1.5 mM of $MgCl_2$, 200 µM of dNTPs, 1 unit of AmpliTaq gold® DNA polymerase, 10 pmole of each forward and reverse CSF1PO-STR primers and DNA template. Primer sequences [forward primer: 5'- CCG GAG GTA AAG GTG TCT TAA AGT -3'; reversed primer: 5'- ATT TCC TGT GTC AGA CCC TGT T -3'] were obtained

from PowerPlex® 16 Primer Pairs [8]. Amplification was performed in Gene Amp 9700 thermocycler (Applied Biosystem, USA) using the following condition; initial denaturation at 95 ºC for 5 min following with 28-34 cycles of denaturation at 94 ºC for 1 min, annealing at 64 ºC for 1 min and extension at 72 ºC for 1 min, then the final extension at 60 ºC for 30 min. [9]

Amplification using the CSF1PO long primers prior to the STR-typing was carried out in a total reaction volume of 20 µL, the reaction consists of 1X PCR buffer, 1.5 mM of MgCl2, 200 µM of dNTPs, 1 unit of GoTaq® DNA polymerase, 0.5 pmole of each forward and reverse primer and 5 ng of DNA template. CSF1PO long forward primer sequence was 5'- CGG AGG TAA AGG TGT CTT AAA GTG AGA AAG AAT AAC TGC ATC TTA ACC TAT TGG GAG GTC ATT GTA AAG AGG AGA GTG ATG GGG TCA GAT TGT ACA GAG GAG GCA CTT CGT GGT GGT CAG GAG CAC ACA CTC CAG GGC AGT GTT CCA ACC TGA GTC TGC CAA GGA CTA GCA GGT TGC TAA CCA CCC TGT GTC TCA GTT T-3' and CSF1PO long reverse primer sequence was 5'- ATC TCC TGG TGC ACA CTT GGA CAG CAT TTC CTG TGT CAG ACC CTG TTC TAA GTA CTT CCT-3' [6]. Amplification was performed in Gene Amp 9700 thermocycler (Applied Biosystem, USA) using the following condition; initial denaturation at 94 ºC for 5 min following with 35 cycles of denaturation at 94 ºC for 10 seconds, annealing and extension at 72 ºC for 1 min, unless otherwise stated. Then, long primer amplified mixture was used for STR-typing according to previously described protocols.

DNA separation and detection

For DNA separation and detection by agarose gel electrophoresis, PCR products were separated in 2%(w/v) agarose/Tris-borate-EDTA (TBE) buffer. Agarose gel was prepared by weighing 1.4 g of agarose powder, then dissolved in 70 mL of 1X of TBE buffer and stained with 10 mg/mL of ethidium bromide. An aliquot of 10 µL of PCR product was mixed with 2 µL of gel-loading dye and loaded into the well. The 100-bp DNA ladder was used as DNA marker of. Separation was carried out 75 voltages for 90 min. After that, the separated DNA bands were visualized under UV light and photographed using a gel documentation system (BIORAD CO., USA). [10]

For DNA separation and detection by automated capillary electrophoresis, an aliquot of 1 µL of PCR product was mix together with 10.7 µL of hi-di formamide (Applied Biosystem, USA) and 0.3 µL of LIZ internal size standard (Applied Biosystem, USA) in an Eppendorf tube. The tube was heated at 95 °C for 5 min to separate double-stranded DNA into single-stranded. The tube was then immediately chilled on ice for 2 min before loading the samples into the sample tray of the ABI PRISM 310® Genetic Analyzer (Applied Biosystem, USA). Samples were injected into capillary by electrokinetic injection. Electrophoresis was carried out using the POP-4™ polymer (Applied Biosystem, USA), which is recommended for electrophoresing DNA under denaturing conditions. Injection time was allowed for 5 sec, and the run time for data collection was 24 min for each sample. the module and matrix files were set according to the ABI PRISM 310® Genetic Analyzer User's Manual. At the end of the run, the samples were automatically analyzed by the GeneMapper® Analysis Software. The electropherograms could then be viewed in the result control window. (Applied Biosystem, USA)

Results and Discussion:

STR typing of artificially degraded DNA

Artificially degraded DNA samples, generated by using different sonication time, were typed by AmpFLSTR® Identifiler® Plus PCR Amplification kit. STR loci and their allele size ranges of the AmpFLSTR® Identifiler® Plus PCR Amplification kit are showed in Table 1. Results in table 2 showed that full STR profile was only obtained from the 30-min sonicated DNA sample. Other sonicated samples gave partial STR profiles. Results also showed that larger STR loci dropped out before smaller ones. Allele and loci with amplified product sizes larger than approximately 300 bases were absent (or drop-out) when sonication time was 45, 60, and 75 min. Less than approximately 150 bases fragments were present when sonication time was 90 and 120 min. Thus, longer sonication time resulted in an

increase of loci drop-outs. It is also noted that the smallest fragment, which is the 106-bp AMEL locus, was amplified in all samples, implying that approximately DNA fragments of 100 bp-long were present when 120-min sonication time was applied.

When DNA samples are sonicated, the ultrasound breaks the H-bond and C-O bond in the DNA molecule in random positions, resulting in fragmented DNA of different sizes [11]. In addition, these random fragmentations of the DNA molecule could result in the loss of primer binding sites [12]. Longer sonication time would then increase the number of fragmentation event, as well as the loss of primer binding sites. Hence, no PCR product would be amplified. Table 3 summarized the sonication time and fragment size ranges of the artificially degraded DNA generated. These suggested that 3 different levels of degraded DNA were generated in this study.

Table 1. STR loci present in AmpFLSTR® Identifiler® Plus PCR Amplification kit (Applied Biosystem, USA) and their fragment size ranges.

STR locus name	Size ranges of STR fragment (bases)
AMEL	106-112
D19	92-150
D3	97-145
D8	123-175
D5	130-178
vWA	152-212
TH01	160-204
D21	138-256
D13	193-241
TPOX	209-257
FGA	196-352
D7	253-293
D16	248-296
D18	264-351
CSF1PO	301-345
D2	291-359

Table 2. The STR profiles generated from different time of sonication samples by size.

Sonicated time (min)	AMEL	D19	D3	D8	D5	vWA	TH01	D21	D13	TPOX	*FGA*	D7	D16	D18	CSF1PO	D2
0	√	√	√	√	√	√	√	√	√	√	√	√	√	√	√	√
30	√	√	√	√	√	√	√	√	√	√	√	√	√	√	√	√
45	√	√	√	√	√	–	√	×	√	–	×	×	–	×	×	×
60	√	√	√	√	–	×	√	×	×	×	×	×	×	×	×	×
75	√	√	√	–	√	–	√	×	√	–	×	×	×	×	×	×
90	√	–	×	×	×	×	×	×	×	×	×	×	×	×	×	×
105	√	×	–	×	×	×	×	×	×	×	×	×	×	×	×	×
120	√	–	–	×	×	×	×	×	×	×	×	×	×	×	×	×

√ complete locus

× locus dropout

– allele dropout

Table 3. Different time of sonication generated ranges of fragment sizes.

Sonicated time (min)	Fragment size[a] (bp)
≤ 30	> 300
45-75	150-300
≥90	< 150

[a] Fragment sizes of target product which generated the STR profile using AmpFLSTR® Identifiler® Plus PCR Amplification kit (Applied Biosystem, USA).

Investigation of CSF1PO long primers-coupled with single-locus CSF1PO locus typing

The human c-fms proto-oncogene for CSF-1 receptor gene (CSF!PO) locus is one of the core STR loci in the Combined DNA Index System (CODIS) database. Allele for this locus contain 5-16 repeat units of tetranucleotide AGAT, giving amplification product size 317-361 bp [13]. So, CSF1PO locus was selected for the investigation because the size of its amplification product is a large and reported to be drop out in the analysis of degraded DNA samples [14]. Firstly, primers were tested. Amplification using 10 pmole of CSF1PO-STR primers for single-locus analysis [9] and 5 pmole of CSF1PO long primers [6] gave a 344- and 370-bp product, respectively. However, amplification using

CSF1PO long primers according to [6] showed a smaller-size band at the lower part of the agarose gel, which may have been excess primers or shorter oligonucleotides. Further optimizations were made to eliminate this band by reducing the primer concentration from 5 to 2.5 pmole, and the thermocycling condition was changed to 2-steps amplification at 72°C. Then, these primers were used to amplify different levels of artificially degraded DNA samples. Results showed that the 344-bp PCR product of the CSF1PO-STR primers (figure 1a) was detected only form the 30-min-sonicated DNA sample (lane 3). No PCR products were detected in other lanes. For the amplification by the CSF1PO long primers, the 370-bp product was detected from 30- and 45-min sonicated DNA samples (lane 3 and 4 in figure 1b). Results suggested that long primer showed the advantage of detecting the target CSF1PO locus from a higher-level of artificially degraded DNA sample. The CSF1PO long primers was previously developed by extending the primer length from the standard primers of 20-25 bp to 60-200 bp. Binding site of the CSF1PO long primers was shifted closer to the STR region than the CSF1PO-STR primers but still generate the same large fragment size as STR typing kit [6]. These features increased the chance of target annealing and amplification.

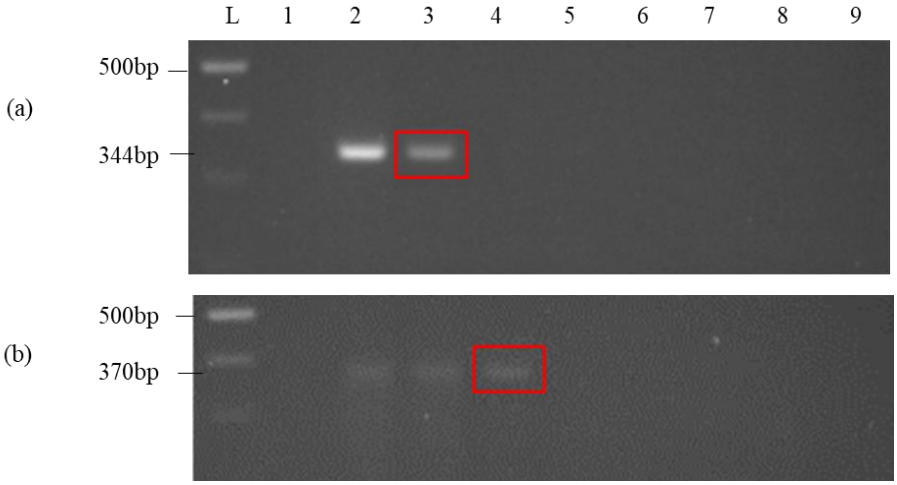

Figure 1. Amplification of artificially degraded DNA samples using (a) CSF1PO primers for single-locus analysis, and (b) CSF1PO long primers (2.5 pmole). Lane L: 100-bp DNA ladder. Lane 1: negative PCR control, lane 2: positive PCR control (non-degraded DNA sample), lane 3-9: artificially degraded DNA samples (sonication time was 30, 45, 60, 75, 90, 105, and 120 min, respectively)

Then, the CSF1PO long primer was applied for target enrichment prior to STR amplification. After artificially degraded DNA was amplified by long CSF1PO long primers, 1 µL of the amplification mix was used as template for the single-locus CSF1PO-STR amplification. Amplification results were showed in figure 2, the 344-bp PCR products were clearly detected from all artificially degraded DNA samples. The CSF1PO long primer amplification served as a target-enrichment step prior to the single-locus CSF1PO-STR typing. Intensities of the 344-bp DNA band became fainter when the DNA template was sonicated for a longer time. This may be due to a smaller number of target molecules were present in those samples being longer sonicated. The presence of an unexpected 200-bp DNA band was clearly noted throughout all lanes in figure 2. Intensities of these 200-bp DNA bands increased according to the level of DNA degradation, suggesting that these may be due to excess amount of the CSF1PO long primer in the target-enrichment step. Although the correct PCR product size could be detected from all artificially degraded DNA samples, further optimization of target-enrichment step by long primer amplification is needed to eliminate the unexpected 200-bp DNA band. Further optimization was then carried out for DNA separation and detection by

automated capillary electrophoresis (CE), which is the routine method used for STR-typing. This separation and detection platform are more sensitive than agarose gel electrophoresis.

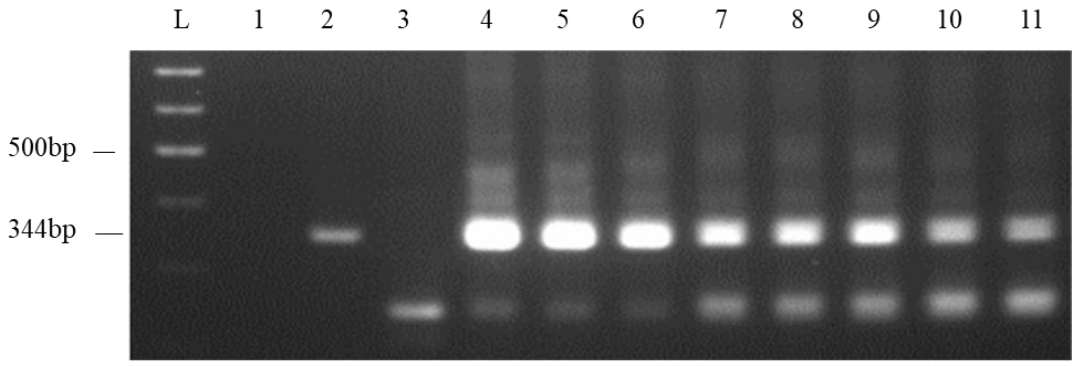

Figure 2. Amplification of artificially degraded DNA sample using CSF1PO long primers-coupled with CSF1PO-STR primers. L: 100-bp ladder. Lane 1 and 2: negative and positive PCR controls for CSF1PO-STR primers; Lane 3 and 4: negative and positive controls for CSF1PO long primer amplification followed with CSF1PO-STR primers using artificially degraded DNA samples as templates (sonication time was 30, 45, 60, 75, 90, 105, and 120 min, respectively).

Detection of amplification product CSF1PO long primers-coupled with CSF1PO single-locus typing by automated capillary electrophoresis

DNA fragment analysis by automated capillary electrophoresis is the routinely used technique in forensic laboratories for casework. Though in the previous section target enrichment by using 2.5 pmole of CSF1PO long primers and followed by the single CSF1PO-single locus STR typing using 28 cycles showed satisfying amplification results for degraded DNA samples in the agarose gel, but it still needs further optimization to eliminate those non-target DNA bands which might interfere the STR profiles if this approach is applied to enrich target locus prior the routine 16-loci STR typing.

To reduce or eliminate the non-target peaks, concentration of CSF1PO long primers for target-enrichment step was reduced from 2.5 to 1, 0.5 and 0.25 pmole. No DNA amplification using the 3 different long primer concentrations were carried out prior to CSF1PO single-locus typing. In figure 3, non-target peaks were detected in these no DNA controls electropherograms. Height of these non-target peaks reduced as the concentration of the CSF1PO long primers reduced to 1 and 0.5 pmole (Figure 3a and 3b), and no non-target peak was observed when the CSF1PO long primer concentration was 0.25 pmole (Figure 3c). Therefore, the long primer concentration of 0.25 pmole was applied for target enrichment.

Next, 0.25 pmole of CSF1PO long primers were applied for target-enrichment and followed by CSF1PO single-locus typing. As showed in figure 4, amplification products were detected from the non-degraded DNA sample, and allele 12 of the CSF1PO locus was correctly typed from the non-degraded DNA sample (figure 4a). In contrast, no amplification product was detected when tested with the 30-min-sonicated DNA sample (figure 4b). This may be due caused by too less DNA template was present for CSF1PO single-locus typing.

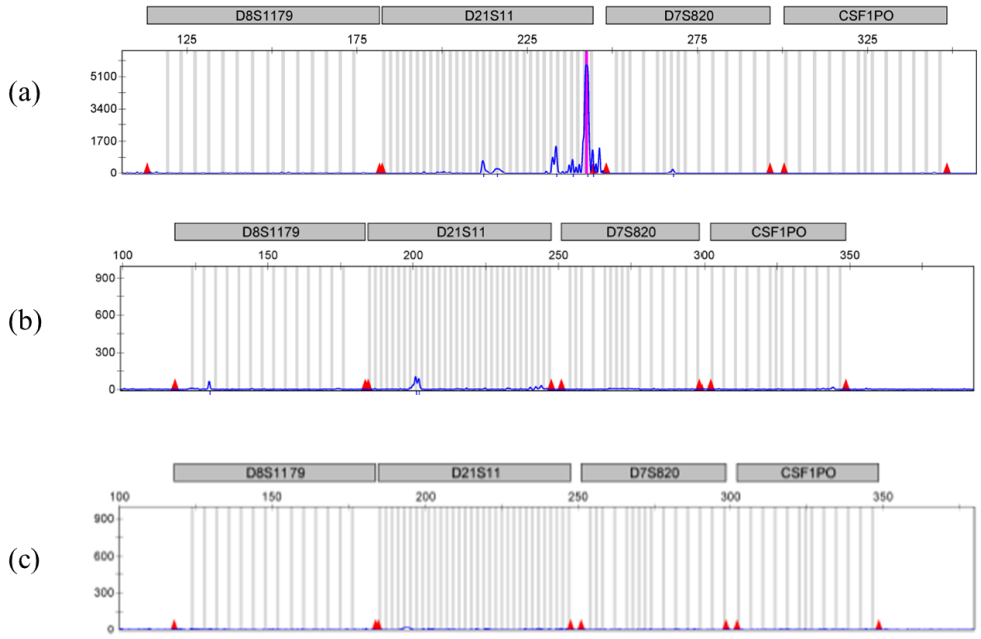

Figure 3. Electropherograms obtained from CSF1PO single-locus typing of 'no DNA' CSF1PO long primer amplification (negative controls) using 3 different long primer concentrations for target-enrichment, i.e., 1 pmole (figure a), 0.5 pmole (figure b), and 0.25 pmole (figure c). Heights of the primer-dimers (non-target peaks) reduced when primer concentrations were lower. Using 0.25 pmole CSF1PO long primer gave a flat base-line.

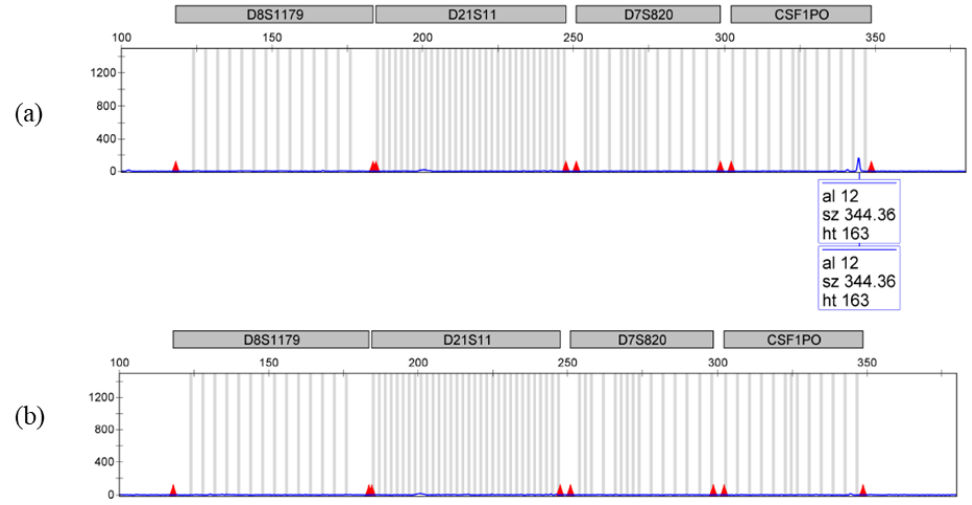

Figure 4. Electropherograms obtained from 28-cycle CSF1PO single-locus typing of target-enriched samples; non-degraded DNA sample (figure a) and 30-min sonicated DNA sample (figure b). Target-enrichment was carried out using 0.25 pmole of CSF1PO long primer prior to single-locus typing.

Then, the amplification condition for single-locus typing was increased from 28 to 34 cycles. Increase of thermocycling cycle from 28 to 34 is an alternative for low template DNA amplification [17], as the amplification product would be increased. Non-degraded and 30-min sonicated (degraded) DNA samples were typed, using 34 cycles. Results showed that the target CSF1PO product (or peak) was present in both target-enriched samples (Figure 5a and b) and without target enrichment amplification for non-degraded sample (Figure 5c). No peak was present in the electropherogram of the degraded DNA sample without the long primer target enrichment step (figure 5d). Results demonstrated that the application of CSF1PO long primer for target enrichment prior to single-locus CSF1PO-STR typing could restore the locus from drop-out.

In addition, peak heights of the amplified target product obtained from single-locus typing of long primer target-enriched DNA samples (Figure 5a and b) are higher than those obtained from single-locus typing without long primer target-enrichment step (Figure 5c and d), and higher than peaks obtained from 28-cycle amplifications. However, non-target peaks were also present in the electropherograms obtained from long primer target-enriched samples. The presence of these non-target peaks in the electropherogram can interfere the interpretation of the 16-loci STR profiles or DNA profiles from any multiplex typing.

There are alternative techniques for degraded DNA analysis such as mini-STR typing kit, SNPs, and long primer typing panel. However, laboratories additionally implementing these techniques would require more investments in chemicals (kits) and facilities. Whereas the amplification of degraded sample using long primers-coupled with STR typing in this study demonstrated the potential that this could simply generate the target product from highly degraded samples, and there's no requirement for special facilities. Although the correct amplification product could be obtained from degraded DNA analysis by using long primers-coupled with STR typing the further optimizations of the long primer amplification for target-enrichment and optimization for STR typing application is suggested.

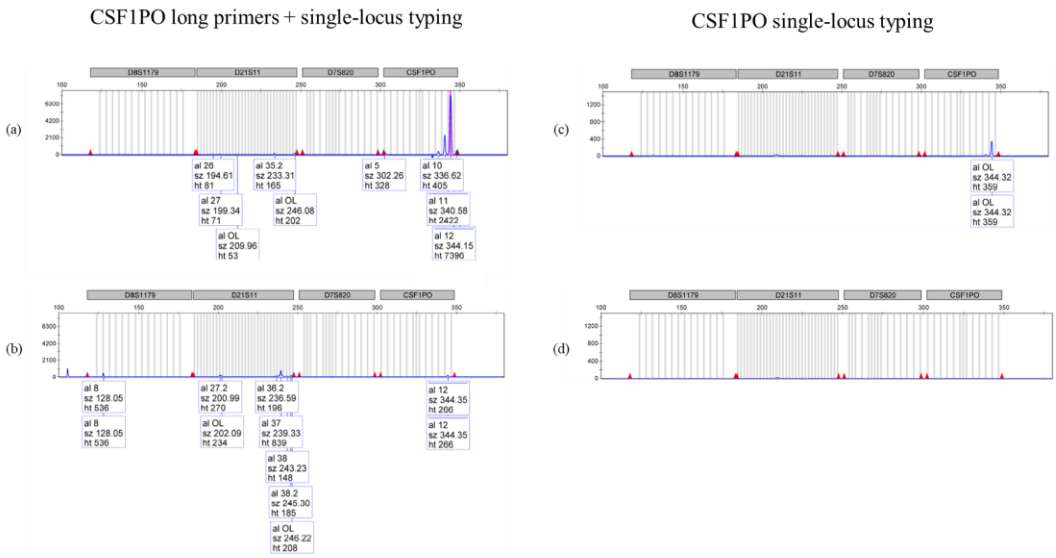

Figure 5. Electropherograms obtained from 35-cycle CSF1PO single-locus typing of target-enriched samples, i.e., non-degraded DNA sample (figure a) and 30-minute sonicated DNA sample (figure b); compared with 35-cycle CSF1PO single-locus typing (without target-enrichment) i.e., non-degraded DNA sample (figure c) and 30-minute sonicated DNA sample (figure d). Results showed that the target CSF1PO peak was present in the CSF1PO target-enriched degraded sample (figure b), but no peak was obtained from the single-locus typing without target-enrichment by long primers. However, non-target peaks were also present in the electropherogram.

Conclusion:

In this study, it has been demonstrated that target-enrichment by long primer amplification could restore the locus in degraded DNA that was drop-out from STR profile generated by a standard protocol. This provided an alternative strategy to generate DNA profiles from degraded DNA samples. However, further optimization of the long primer target-enrichment step and its application in STR typing is suggested.

Acknowledgements:

This work was partially supported by the Faculty of Graduate Studies and Graduate studies of Mahidol University Alumni Association and Grant to Support Graduate Student in Academic Presentations in Thailand.

References:

1. Hughes-Stamm S, Ashton K, Daal A. Int J Leg Med. 2011;125:341–348.
2. Senge T, Madea B, Junge A. Leg Med. 2011;13:68–74.
3. Coble M, Butler J. Forensic Sci. 2005;50:43-53.
4. Butler J, Coble M, Vallone P. Forensic Sci Med Pathol. 2007;3:200-205.
5. Senge T, Madea B, Junge A. Leg Med. 2011;13:68-74.
6. Muatner M, Santangelo A, Corti Bielsa A. PLOS ONE. 2017:1-20.
7. Muatner M, Caputo M, Corach D. Forensic Sci Int Genet. 2017;6:448–450.
8. Elsner H, Lindblad E. DNA. 1989;697-701.
9. Thamnurak C, Bunakkharasawat W, Riengrojpitak S, Panvisavas N. Forensic Sci Int Genet. 2011:524-525.
10. Sambrook J, Russell DW. Molecular Cloning. 2001.
11. Krenke B, Tereba A, Anderson S. Forensic Sci. 2002;47:773-785.
12. Butler J, Shen Y, McCord B. Forensic Sci. 2003;48:1055-1064.
13. Butler J. Forensic Sci. 2006;51:253-265.
14. Vernarecci S, Ottaviani E, Agostino A. Forensic Sci Int Genet. 2015;16:77-85.
15. Balding D, Buckleton J. Forensic Sci. Int. Genet. 2009;4:1–10.

C_039_OF: MOLECULAR CHARACTERIZATION OF FLUOROQUINOLONE NON-SUSCEPTIBILITY IN CARBAPENEM-RESISTANT *Klebsiella pneumoniae* ISOLATED FROM SOUTHERN, THAILAND

Sutanya Thanudaksorn,[1] Sarunyou Chusri,[2] Arnon Chukamnerd,[1] Rattanaruji Pomwised[3,] *

[1]Department of Biomedical Sciences, Faculty of Medicine, Prince of Songkla University, Hat Yai Campus, Songkhla, Thailand
[2]Division of Internal Medicine, Faculty of Medicine, Prince of Songkla University, Hat Yai Campus, Songkhla, Thailand
[3]Department of Microbiology, Faculty of Science, Prince of Songkla University, Hat Yai Campus, Songkhla, Thailand
*e-mail: rattanaruji.p@psu.ac.th

Abstract:

Plasmid-mediated quinolone resistance (PMQR) genes are an emerging problem worldwide. This study aimed to investigate the PMQR genes among fluoroquinolone non-susceptible and carbapenem-resistant *Klebsiella pneumoniae* isolates. All 459 carbapenem-resistant Gram-negative bacteria (CR-GNB) isolates were received from the Microbiology Laboratory in 7 hospitals in Southern, Thailand. Among 459 CR-GNB isolates, 21 isolates were classified as carbapenem-resistant *Klebsiella pneumoniae* (CRKP). Ciprofloxacin susceptibility was evaluated by broth microdilution. The result showed that all isolates were non-susceptible to ciprofloxacin with the MIC ranged from 2 to >128 µg/ml. Moreover, the MIC_{50} and MIC_{90} among CRKP isolates were 64 µg/ml and >128 µg/ml, respectively. The presence of PMQR determinants (*qnrA, qnrB, qnrS, qepA,* and *aac(6')-Ib-cr* genes) were investigated in fluoroquinolone non-susceptible CRKP isolates using PCR. The *qnrS* gene was high prevalent PMQR gene (76.19 %), followed by *aac(6')-Ib* (57.14%), *aac(6')-Ib-cr* (23.81%), and *qnrB* (23.81%) genes. Interestingly, 10 isolates (47.62%) co-carried both *aac(6')-Ib* and *qnrS* genes. This study revealed a high prevalence of PMQR genes among fluoroquinolone non-susceptible CRKP clinical isolates. It is necessary to concern about the spread of this pathogen and the appropriate treatment for this infection.

Introduction:

Klebsiella pneumoniae, a Gram- negative pathogen, frequently causes of nosocomial infection and community- acquired infection, which involves in many diseases, such as respiratory tract infection, pneumonia, urinary tract infection, wound infection, and bacteremia.[1]

Carbapenems are generally used as a treatment for multidrug- resistant *K. pneumoniae*. However, resistance to carbapenems has increased worldwide, especially in *K. pneumoniae* (carbapenem-resistant *Klebsiella pneumoniae*; CRKP). The carbapenem resistance is mainly caused by carbapenemase production.[2] Carbapenemase is typically associated with multidrug resistance since multiple genes are located on the same plasmid. The co-existence of carbapenemase genes and other antimicrobial resistance genes (e.g. aminoglycoside, fluoroquinolone, and β-lactams resistance genes) has been reported in many countries, particularly in China.[3] Fluoroquinolones are a member of the quinolone group, which contains a fluorine atom in their structure. They are a broad- spectrum bactericidal that act on Gram-positive and Gram-negative bacteria. Fluoroquinolones are classified base on the basis

of their spectrum of activity and their pharmacokinetic profile. They are divided into four generations, including first-generation (e.g. nalidixic acid and oxolinic acid), second-generation (e.g. ciprofloxacin, norfloxacin, and ofloxacin), third-generation (e.g. levofloxacin), and fourth-generation (e.g. sitafloxacin and moxifloxacin).[4] Fluoroquinolones act by inhibiting two enzymes involved with bacterial DNA synthesis (DNA gyrase and topoisomerase IV). These enzymes control DNA supercoiling. They are extensively used for the treatment of infection in both human and veterinary medicine. However, the most frequent use of these drugs is associated with an increased level of quinolone resistance.[5] Moreover, in many decades, the emergence of ciprofloxacin-resistant *K. pneumoniae* isolates has been widely reported in Europe, North America, and Asia.[6] The mechanism of fluoroquinolone resistance is occurred by two main mechanisms. First, mutations in chromosomal genes encoding the quinolone targets, which are DNA gyrase (*gyrA* and g*yrB*) and topoisomerase IV (*parC* and *parE*), lead to amino acid substitutions in the structure of target protein. Then, it decreases the binding affinity of fluoroquinolone to the enzyme. These mutations are usually conferred higher-level resistance to fluoroquinolones.[7] Second, plasmid-mediated quinolone resistance (PMQR), in the last few decades, PMQR has been found all over the world.[8,9] The PMQR determinants have been described, including Qnr determinants (QnrA, QnrB, QnrC, QnrD, and QnrS), which protect DNA gyrase and topoisomerase IV from inhibition by quinolones[5], and a variant of aminoglycoside acetyltransferase (AAC(6')-Ib-cr), which can reduce the activity of norfloxacin and ciprofloxacin by adding an acetyl group to this agent.[10] In addition, a plasmid-mediated fluoroquinolone efflux pump, QepA (a proton-dependent transporter) involves pumping fluoroquinolones out of bacterial cells.[11] The PMQR confers low-level resistance to fluoroquinolones.

Currently, there are few studies focusing on the prevalence of PMQR determinants in *K. pneumoniae* clinical isolates in southern, Thailand. Thus, we aimed to investigate the prevalence of PMQR genes (*qnrA*, *qnrB*, *qnrS*, *qepA*, and *aac(6')-Ib-cr* genes) among fluoroquinolone non-susceptible CRKP isolates from 7 hospitals in southern, Thailand.

Methodology:

Bacterial collection and identification

A total of 459 carbapenem-resistant Gram-negative bacteria (CR-GNB) isolates were collected during March-August 2019 from the Microbiology Laboratory in 7 hospitals in southern, Thailand. The bacterial isolates were selected on the result of antimicrobial susceptibility, which showed resistance to carbapenem and they were classified as CR-GNB by the routine Microbiology Laboratory. Then, the *K. pneumoniae* was identified by Matrix-Assisted Laser Desorption/Ionization-Time of Flight (MALDI-TOF). To clarify the carbapenem-resistant *K. pneumoniae* (CRKP), MICs of imipenem and meropenem were evaluated by broth microdilution.

MIC evaluation of ciprofloxacin

The minimal inhibitory concentration (MIC) of ciprofloxacin was measured by broth microdilution in CRKP isolates. Briefly, the turbidity of the bacterial culture was adjusted to 0.5 McFarland standard and was diluted 1:100. One hundred microliters of bacterial culture were added into 96 well-plates, which contained a 2-fold serial dilution of ciprofloxacin (Sigma, Steinheim, Germany). Then, they were incubated at 37 °C for 18 hours. *K. pneumoniae* ATCC 700603 and *E. coli* ATCC 25922 were used as quality control, according to the Clinical Laboratory Standard Institute (CLSI) guideline, 2018.[12] The results were interpreted as susceptible, intermediate, and resistant, if the MIC values are ≤1, 2, and ≥4, respectively.

DNA extraction

DNA was prepared by a rapid boiling method.[13] A single colony was picked into 3 ml of TSB (Becton, Dickinson, Sparks, MD) and incubated at 37°C for 6 hours in a shaking incubator. One milliliter of the bacterial culture was aliquoted to a 1.5 ml microcentrifuge tube. Then, they were washed with 0.1 M phosphate buffer saline (PBS),

pH 7.4. After that, they were boiled at 95 °C for 10 minutes, immediately kept on ice for 5 minutes, and centrifuged at 11,000 ×*g* for 10 minutes. The supernatant containing DNA was transferred to a new 1.5 ml microcentrifuge tube and diluted 1:10 with sterile deionized water to use it as a DNA template for PCR.

Genotypic detection of plasmid-mediated quinolone resistance (PMQR)

The presence of PMQR genes (*qnrA*, *qnrB*, *qnrS*, *qepA*, and *aac(6')-Ib-cr*) was investigated by PCR.[14,15] All PCR primers used in this study are described in Table 1. The PCR condition for *qnrA*, *qnrB*, and *qnrS* genes was initial denaturation step at 95°C for 10 minutes; 35 cycles of denaturation step at 95°C for 1 minute, annealing at 55°C for 1 minute, and extension at 72°C for 1 minute; final extension 72°C for 10 minutes. Meanwhile, the PCR condition for *qepA* gene was performed with initial denaturation step at 95°C for 10 minutes; 35 cycles of denaturation step at 94°C for 45 seconds, annealing at 52°C for 45 seconds, and extension at 72°C for 45 seconds; final extension 72°C for 10 minutes. The PCR products were visualized using 1% agarose gels electrophoresis at 80 voltage for 50 minutes and stained with ethidium bromide. The gel was imaged with the Gel Doc™ XR+ with Image Lab software (Bio-Rad).

To investigate the presence of *aac(6')-Ib* gene, it was performed by PCR. The amplification was carried out in 50 µl volumes composed of 31.6 µl of deionized water, 10 µl of 5X reaction buffer (5 mM dNTPs, 15 mM $MgCl_2$, stabilizers, and enhancers) (Bioline, UK), 0.4 µl of 5U My *Taq* DNA polymerase (Bioline, UK), 2 µl of each 10 µM primer (Table 1), and 4 µl of DNA template. Afterward, the *cr* variant was detected by using the restriction enzyme. PCR product of *aac(6')-Ib* gene was digested by *BseGI* restriction endonuclease (Thermo Fisher Scientific). Briefly, reaction mixtures (125 µl) contained 89 µl of deionized water, 10 µl of 10X FastDigest buffer, 1 µl of *BseGI* (Fast Digest), and 25 µl of PCR product. Afterwards, the master mix was incubated at 37°C for 30 to 60 minutes and kept on ice for stopping the reaction. For the interpretation, if the PCR product was cut by *BseGI*, it was interpreted as a wild-type gene (which had a *BseGI* restriction site). While, if the PCR product was not claves by this restriction enzyme, it was interpreted as a mutant gene and was classified as *aac(6')-Ib-cr* gene. The positive controls for all of the PMQR genes were kindly provided by PR516 Laboratory, Department of Microbiology in Faculty of Science, Prince of Songkla University. *K. pneumoniae* ATCC 700603 and *E. coli* ATCC 25922 were used as a negative control.

Table 1. **Primers used in this study**

Gene	Primer[a]	Primer sequence	Product size (bp)	Reference
qnrA	QnrAm-F	AGAGGATTTCTCACGCCAGG	580	[14]
	QnrAm-R	TGCCAGGCACAGATCTTGAC		
qnrB	QnrBm-F	GGMATHGAAATTCGCCACTG	264	[14]
	QnrBm-R	TTTGCYGYYCGCCAGTCGAA		
qnrS	QnrSm-F	GCAAGTTCATTGAACAGGGT	428	[14]
	QnrSm-R	TCTAAACCGTCGAGTTCGGCG		
qepA	qepAF	AACTGCTTGAGCCCGTAGAT	596	[15]
	qepAR	GTCTACGCCATGGACCTCAC		
aac(6')-Ib	aacIbF	TTGCGATGCTCTATGAGTGGCTA	482	[15]
	aacIbR	CTCGAATGCCTGGCGTGTTT		

[a] F: forward primer, R: reward primer

Results and Discussion:

Bacterial collection and identification

Among, 21 out of 459 CR-GNB isolates were identified as carbapenem-resistant *K. pneumoniae* (CRKP). The MICs values of imipenem and meropenem of these isolates were ranged from 0.5 to >128 µg/ml and 1 to >128 µg/ml, respectively. Most of the isolates were obtained from sputum (38.1%), followed by urine (28.57%), stool (14.29%), catheters (9.52%), wound, and blood (4.76% each).

MIC evaluation of ciprofloxacin

In the MICs evaluation of ciprofloxacin, the results demonstrated that among 21 CRKP isolates, 1 isolate (4.76%) was intermediate to ciprofloxacin, while 20 isolates (95.24%) were resistant to ciprofloxacin. Besides, the MICs of ciprofloxacin were ranged from 4 to >128 µg/ml (Table1.). Moreover, the MIC_{50} and MIC_{90} among CRKP isolates were 64 µg/ml and >128 µg/ml, respectively. This finding was indicated that due to the isolates resisted to the ciprofloxacin with high MIC values, it is not considered to use in patients who are infected with this pathogen.

Detection of plasmid-mediated quinolone resistance (PMQR) genes

The presence of PMQR genes was investigated in 21 fluoroquinolone non-susceptible CRKP isolates. We found that all isolates (100%) carried at least one of the PMQR genes, which is similar to the other report from Singapore. Deepak et al. (2009) found that many PMQR genes are frequently found in 45.9% of the *K. pneumoniae* isolates, while a few PMQR genes are also found in 1.8% of the *E. coli* isolates.[16] The PMQR genes usually reduce sensitivity to ciprofloxacin.[17]

In the *aac(6')-Ib-cr* detection, we found that 20 isolates carried *aac(6')-Ib* gene. After digestion of *aac(6')-Ib* gene by *BseGI* restriction enzyme, the result exhibited that 12 isolates (57.14%) were the *aac(6')-Ib* wide-type gene, which showed the fragments of 272 bp and 210 bp on agarose gel electrophoresis. In the previous study, the *aac(6')-Ib*-carrying isolates resulted in the resistance to aminoglycoside (tobramycin, kanamycin, and amikacin).[10] Meanwhile, 5 isolates (23.81%) were the mutant *aac(6')-Ib* gene, named *aac(6')-Ib-cr* (482 bp). Due to the lack of the recognition site on the *aac(6')-Ib-cr* gene, the *BseGI* cannot cut the *aac(6')-Ib* gene. Like the previous study, the cr variant isolates reduce susceptibility to ciprofloxacin by N-acetylation of its piperazinyl amine, leading to resistance to both aminoglycosides and fluoroquinolones.[18] Hence, it is very important to determine the antibiotic susceptibility among these strains, which harbored *aac(6')-Ib* or *aac(6')-Ib-cr* variant to find the appropriate antibiotic treatment. Moreover, 3 isolates (14.29%) harbored both *aac(6')-Ib* and *aac(6')-Ib-cr* variant, which exhibited 3 DNA fragments (482 bp, 272 bp, and 210 bp) on gel-electrophoresis after cutting by *BseGI*. Kim et al. (2011) hypothesized that this phenomenon can be explained by the theory of genetic heterozygote. The different mutations within a single gene locus cause the same phenotypic expression. This co-existence of *aac(6')-Ib*-wide type and *aac(6')-Ib-cr* variant was an interesting phenomenon that describes in many studies.[19, 20]

The *qnrS* gene is mostly found in 16 isolates (76.19 %). The results of this study were similar to reports from many countries.[21,22] They found that *qnrS* was predominant in *K. pneumoniae* isolates.[21,22] In addition, the quinolone has been used in agriculture as shown in a previous report. Thus, this may involve the spread of *qnr*-mediated resistance in Enterobacteriaceae.[6] The *qnrS* gene was also detected in *K. pneumoniae* ATCC 700603, whereas it was not detected in *E. coli* ATCC 25922. Furthermore, 5 isolates (23.81%) were positive for *qnrB* gene, while *qnrA* and *qepA* genes were not found in any isolates. This result was concordant with other studies that did not found *qnrA* and *qepA* gene in *E. coli* and *K. pneumoniae* isolates from Morocco.[23] Interestingly, 10 isolates (47.62%) harbored both *aac(6')-Ib* and *qnrS* genes, 2 isolates (9.52%) harbored *qnrB*, *qnrS*, and *aac(6)-Ib-cr*. In the study of Yang et al. (2008), they supported that the different PMQR genes in clinical isolates of *K. pneumoniae*, *Enterobactor cloacae,* and *Citrobacter freundii* could transfer to other bacteria by conjugation experiments. Thus, the presence of transferable PMQR genes are associated with different PMQR spread among Enterobacteriaceae isolates.[22] Also, our

result demonstrated that one *qnrB*-positive isolate also carried *aac(6')-Ib-cr*. It was concordant to another report from Srinagarind hospital, Khon kaen University, Thailand.[21] The result of other co-existence of *qnr* genes is shown in Table 2. According to the MIC result of ciprofloxacin in this study, we found that the presence of PMQR genes is not associated with the MIC values of ciprofloxacin. Thus, we hypothesized that some isolates probably have many resistance mechanisms, including chromosomal mutations in the quinolone resistance determinant region (QRDR). The QRDR is the main mechanism of quinolone and fluoroquinolone resistance. This result was concordant with the study of Redgrave et al. (2014). They found that this resistance phenomenon might be because of a multiple expression of PMQR genes only or PMQR combined with chromosomal mutations, especially *gyrA* and *parC* genes.[24]

Table 2. Prevalence of PMQR genes and MIC of ciprofloxacin

No. of isolates	Ciprofloxacin MIC (µg/ml)	Plasmid-mediated quinolone resistance genes						
		qnrA	***qnrB***	***qnrS***	***qepA***	***aac(6')-Ib***	***aac(6')-Ib-cr***	***aac(6')-Ib + aac(6')-Ib-cr***
CRKP9	2	-	✓	✓	-	-	✓	-
CRKP4	4	-	-	✓	-	✓	-	-
CRKP8	8	-	✓	-	-	-	✓	-
CRKP1	16	-	-	✓	-	✓	-	-
CRKP3	16	-	-	✓	-	✓	-	-
CRKP21	16	-	✓	✓	-	-	-	-
CRKP2	32	-	-	✓	-	✓	-	-
CRKP5	64	-	-	-	-	-	✓	-
CRKP6	64	-	-	✓	-	✓	-	-
CRKP15	64	-	✓	✓	-	-	✓	-
CRKP16	64	-	-	✓	-	✓	-	-
CRKP17	64	-	-	-	-	✓	-	-
CRKP18	64	-	-	✓	-	✓	-	-
CRKP19	64	-	-	✓	-	✓	-	-
CRKP20	64	-	-	✓	-	✓	-	-
CRKP7	128	-	-	✓	-	✓	-	-
CRKP11	128	-	-	✓	-	-	✓	-
CRKP10	≥128	-	-	-	-	✓	-	-
CRKP12	≥128	-	✓	-	-	-	-	✓
CRKP13	≥128	-	-	✓	-	-	-	✓
CRKP14	≥128	-	-	✓	-	-	-	✓

Conclusion:

Most CRKP clinical isolates were resistant to ciprofloxacin with a high MIC value. In addition, this finding demonstrated that all of the fluoroquinolone non-susceptible CRKP isolates harbored PMQR genes. Thus, it was indicated that these resistance genes might have the ability to transfer the PMQR genes to other bacteria, resulting in the dissemination of fluoroquinolone non-susceptible CRKP. The use of appropriate antibiotics for treating CRKP infection in hospital settings is necessary.

Acknowledgments:

We are grateful to thank the Microbiology Laboratory in the 7 hospitals, including Trang hospital, Satun hospital, Songkhla hospital, Phatthalung hospital, Yala hospital, Narathiwat hospital, and Pattani hospital for the bacterial isolates used in this research. In addition, we would like to thank the Department of Biomedical Science in Faculty of Medicine, and the Department of Microbiology in Faculty of Science, Prince of Songkla University for kindly providing control strains and skillful technical assistance. Finally, this research was supported by the Graduate Scholarship from the Faculty of Medicine, Prince of Songkla University.

References:

1. Livermore DM. Korean J Intern Med. 2012;27(2):128.
2. Nordmann P, Dortet L, Poirel L. Trends. Mol. Med. 2012;18(5):263-272.
3. Hou XH, Song XY, Ma XB, Zhang SY, Zhang JQ. Braz. J. Microbiol. 2015;46(3):00-00.
4. Ezelarab HA, Abbas SH, Hassan HA, Abuo-Rahma GE. ARCH PHARM. 2018;351(9):1800141.
5. Robicsek A, Jacoby GA, Hooper DC. Lancet Infect Dis. 2006;6(10):629-640.
6. Strahilevitz J, Jacoby GA, Hooper DC, Robicsek A. Clin. Microbiol. Rev. 2009;22(4):664-689.
7. Majlesi A, Kakhki RK, Nejad AS, Mashouf RY, Roointan A, Abazari M, Alikhani MY. Saudi J Biol Sci. 2018;25(3):426-430.
8. Briales A, Rodríguez-Martínez JM, Velasco C, de Alba PD, Rodriguez-Bano J, Martinez-Martinez L, Pascual A. Int. J. Antimicrob. Agents. 2012;39(5):431-434.
9. Hooper DC. mBio. 2003:41-67.
10. Robicsek A, Strahilevitz J, Jacoby G A, Macielag M, Abbanat D, Park C H, Bush K, Hooper D C. Nat. Med. 2006;12(1):83-88.
11. Yamane K, Wachino JI, Suzuki S, Kimura K, Shibata N, Kato H, Shibayama K, Konda T, Arakawa Y. Antimicrob. Agents Chemother. 2007;51(9):3354-60.
12. Wayne, PA. CLSI. 28th ed. 2018.
13. Sukkua K, Patungkaro W, Sukhumungoon P. Southeast Asian J. Trop. Med. Public Health. 2015;46(5):901.
14. Cattoir V, Poirel L, Rotimi V, Soussy C-J, Nordmann P. J. Antimicrob. Chemother. 2007;60(2):394-397.
15. Kim H B, Park C H, Kim C J, Kim E-C, Jacoby G A, Hooper D C. Antimicrob. Chemother. 2009;53(2):639-645.
16. Deepak RN, Koh TH, Chan KS. Ann Acad Med Singap. 2009;38(12):1070.
17. Tran JH, Jacoby GA.PNAS USA. 2002;99(8):5638-5642.
18. Hidalgo-Grass C, Strahilevitz J. Antimicrob. Agents Chemother. 2010;54(8):3509-3511.
19. Kim YT, Jang JH, Kim HC, Kim H, Lee KR, Park KS, Lee HJ, Kim YJ. BMB Rep. 2011;44(4):262-266.
20. Guillard T, Duval V, Moret H, Brasme L, Vernet-Garnier V, de Champs C. J Clin Microbiol. 2010;48(1):286-289.
21. Pasom W, Chanawong A, Lulitanond A, Wilailuckana C, Kenprom S, Puang-Ngern P. Jpn. J. Infect. Dis. 2013;66(5):428-432.
22. Yang H, Chen H, Yang Q, Chen M, Wang H. J. Antimicrob. Chemother. 2008;52(12):4268-4273.
23. Benaicha H, Barrijal S, Ezzakkioui F, Elmalki F. J GLOB ANTIMICROB RE. 2017;10:321-325.
24. Redgrave LS, Sutton SB, Webber MA, Piddock LJ. TRENDS MICROBIOL. 2014;22(8):438-45.

C_040_OF: THE DISRUPTION OF A STRUCTURAL CELL WALL PROTEIN *SED*1 IN *Saccharomyces cerevisiae* FOR YEAST CELL SURFACE DISPLAY

Supakarat Kaewpeng,[1] Choowong Auesukaree,[1] Kallaya Sritunyalucksana-Dangtip,[2] and Chuenchit Boonchird[1,*]

[1]Department of Biotechnology, Faculty of Science, Mahidol University, Bangkok 10400
[2] Center of Excellence for Shrimp Molecular Biology and Biotechnology, Faculty of Science, Mahidol University, Bangkok 10400
*e-mail: chuenchit.boo@mahidol.ac.th

Abstract:

Yeast surface display (YSD) is a powerful technology that allows a heterologous protein to localize on cell surface for special function by attaching with glycosylphosphatidylinositol (GPI) anchoring domain of native cell wall proteins. However, the efficiency of protein display is depending on availability of area on cell wall. To promote the incorporation of target protein on yeast cell wall, we focused on the construction of suitable host strain by removal of the most abundant cell wall protein Sed1p that expresses in stationary phase. The *SED*1 gene disruption (*sed*1Δ) was performed in *Saccharomyces cerevisiae* CEN.PK113-7B strain (*leu2*) which has high growth rate in complex and defined media. The *SED*1 gene was disrupted by *LEU*2 selectable marker using two-step PCR method. The growth rate and growth characteristic of *sed*1Δ strain in various stresses (ethanol, oxidative and Calcoflour white) were investigated. The results shown that *sed*1Δ did not affect the growth profile and growth under stresses. However, the resistance to cell wall lytic enzyme of stationary-phase cells as examined by Zymolyase sensitivity was decreased. The result suggested that the elimination of Sed1p perturbed the cell wall organization. The surface display of target proteins in *sed*1Δ strain will be further investigated.

Keywords: *Saccharomyces cerevisiae*, Yeast Surface Display, *SED*1

Introduction:

Yeast cell surface display (YSD) has been developed for various biotechnology and biomedical applications such as biocatalyst, bioconversion, biosensor, vaccine, antibody development, *etc*[1]. Yeast *Saccharomyces cerevisiae* has been frequently used as a host to display proteins of interest because it is a "generally regarded as safe" microorganism that can be simply and rapidly cultivated to a high cell density in low cost media. Moreover, its rigid cell wall structure makes this yeast suitable for various applications. About half of yeast cell wall mass is made from mannoproteins which liked to β-1,6-glucan layer by glycosylphosphatidylinositol (GPI)[2, 3]. These cell wall proteins have GPI anchoring domain so-called GPI-CWPs. Some of GPI anchoring domains such as agglutinin (Agα1, Agal-Aga2), Cwp2, Flo1, Sed1, *etc* have been applied to display heterologous proteins by fusion with target protein either at N or C-terminus[1]. There are approximately 60 native GPI proteins[2]. Thus, the display proteins have to compete with abundant GPI-CWPs which limited the incorporation capacity into the cell wall[4]. Previous investigation by engineering of host cell wall enhanced the displayed protein productivity. The *SED*1 (Suppression of Exponential Defect) gene encodes a structural GPI-CWP in stationary phase which is heavily glycosylated and exhibits lytic enzyme resistance[1, 5]. Attractively, *SED*1 disruption strain increased the incorporation of β-glucosidase on yeast cell surface[6, 7].

In this study, we are interested in the construction of cell wall mutant *S. cerevisiae* CEN.PK113-7B host strain by disrupting *SED*1 gene with the aim to increase shrimp *Penaeus monodon* (*Pm*Rab7) protein displayed on yeast cell surface. This protein could bind to an envelope protein VP28 of white spot syndrome virus (WSSV) causing a severe infection in shrimps[8, 9]. Yeast CEN.PK family was previously reported as a platform for cell-factory research and product formation[10]. *SED*1 gene disruption (*sed*1Δ) was performed by PCR-based method and its effect on growth profile and growth characteristic under various conditions were investigated. The cell wall perturbation by *sed*1Δ was demonstrated by sensitivity to cell wall stress chemical, Calcoflour white, and glucan degrading enzyme, Zymolyase, of stationary-phase cells.

Methodology:

Strains and culture condition

S. cerevisiae CEN.PK113-7B (MATα *leu*2-1 *trp*1 *ura*3) (Gift from Dr P. Kotter, Institute of Microbiology, J.W. Goethe Universität Frankfurt, Germany) was used as a wild type strain in this experiment. Moreover, *S. cerevisiae* BY4742 (Gift from Assoc. Prof. Choowong Auesukaree, Department of Biotechnology, Faculty of Science, Mahidol University) was used as source of genomic DNA. All yeast strains were routinely cultured in Yeast Extract Peptone Dextrose medium (YPD; 1% yeast extract, 2% peptone and 2% dextrose; 2% agar if required) at 30 °C. The *SED*1 gene-disrupted transformants were selected in Synthetic Complete medium drop-out leucine (SC-leu; 0.67% YNB, 2% dextrose and 0.2% drop-out leucine mixture; 2% agar if required). The YPD agar consisted of 6-12% ethanol, 6-10 mM H_2O_2 and 20-60 mg/ml Calcofluor white were applied to examine the growth under stress conditions. Yeast growth profile was examined in YPD broth.

*Construction of S. cerevisiae CEN.PK113-7B sed*1Δ *strain*

The *SED*1::*LEU*2 deletion cassette was constructed by using two-step PCR. In the first step, the upstream and downstream regions of *SED*1 gene and *LEU*2 gene were amplified using genomic DNA[11] of yeast *S. cerevisiae* BY4742 strain and pGAD424 plasmid (Clontech), respectively. These *SED*1 gene fragments were amplified by pairs of primer Up-*SED*1_FW and Up-*SED*1_RW, and Dw-*SED*1_FW and Dw-*SED*1_RW. While *LEU*2 gene fragment was generated by primers Up *SED*1-*LEU*2_FW and Dw *SED*1-*LEU*2_RW tagged with 21-22 bp of *SED*1 gene. In the second step, the amplified upstream and downstream regions of *SED*1 gene were applied as primers to create *SED*1::*LEU*2 deletion cassette using the generated *LEU*2 gene fragment as template (**Figure 1**). The *SED*1::*LEU*2 deletion cassette was finally transformed in to yeast *S. cerevisiae* CEN.PK113-7B by lithium acetate method[12] and transformants were selected as Leu^+ colonies. The primers details were described in **Table 1**. The PCR conditions for all steps were as follows: initial denaturation, denaturation/annealing/extension (35 cycles) and final extension at 95 °C for 5 min, 95 °C/53 °C/72 °C for 30 sec/30 sec/15-30 sec per Kb and 72 °C for 7 min, respectively.

*Verification of S. cerevisiae CEN.PK113-7B sed*1Δ *strain by colony PCR*

The *sed*1Δ in Leu^+ transformants was confirmed by colony PCR using 2 pairs of specific primer Cf-UpΔ*SED*1_FW and Cf-UpΔ*SED*1_RW, and Cf-DwΔ*SED*1_FW and Cf-DwΔ*SED*1_RW (**Table 1)** which amplified further upstream and downstream region of *SED*1 locus **(Figure 1)**. The PCR conditions for verification were the same as above except annealing step was at 50 °C

Investigation of growth profile

Growth profile was performed to investigate growth characteristic of *sed*1Δ strain comparing with wild type strain. Yeast strains were precultured in YPD broth at 30 °C, 200 rpm shaking for 16-18 h. Afterward, the cultures were transferred into fresh YPD broth with initial OD_{660} = 0.1 and continuously grown in the same condition. OD_{660} was measured at in 3 h intervals for 48 h.

Table 1. Primers used in this study

Primers	Sequence (5' to 3')
Up-*SED*1_FW	ACGGTCATTGATTACTTTATTTGG
Up-*SED*1_RW	TGCTTGTCTTTGTAGTTACGACTA
Dw-*SED*1_FW	ACGGTGGTGTTTGACACATCC G
Dw-*SED*1_RW	GCTTTTAGAAAACCCTGTCTTGAA
Up *SED*1-*LEU*2_FW	TAGTCGTAACTACAAAGACAAAACTGTGGGAATACT
Dw *SED*1-*LEU*2_FW	CGGATGTGTCAAACACCACCGTTTAAGCAAGGATTTT
Cf-UpΔ*SED*1_FW	TTTTCATTACGAAAGAGGAGAGGG[a]
Cf-UpΔ*SED*1_RW	AATTTGATTCTGTGCGATAGCGCC[b]
Cf-DwΔ*SED*1_FW	TTGGATGCAGGTATCAGAACTG[b]
Cf-DwΔ*SED*1_RW	GATTAAGAGATCAATGGAGAGCAC[a]

[a]Homologous sequence with further upstream (Up) and further downstream (Dw) of *SED*1 locus in *S. cerevisiae*.
[b]Homologous sequence with promoter (Up) and terminator regions (Dw) of *LEU*2 locus in *S. cerevisiae.*

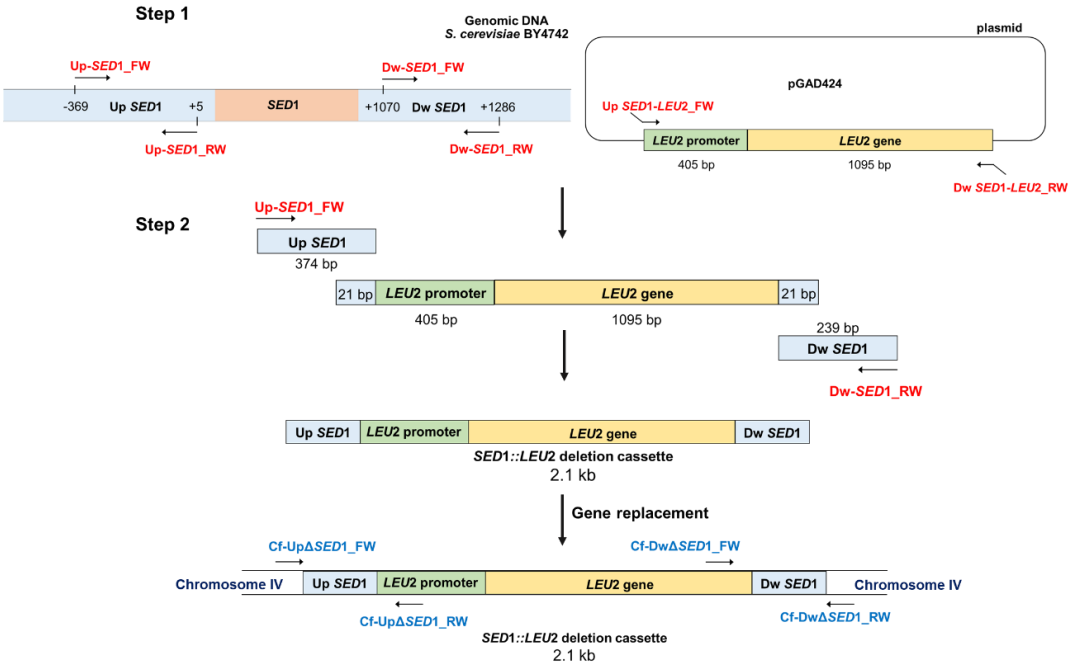

Figure 1.

Schematic diagram of *SED*1::*LEU*2 deletion cassette construction by two-step PCR and gene replacement at *SED*1 locus. In the first step, PCR products of upstream (Up *SED*1), downstream (Dw *SED*1) and *LEU*2 gene were generated. In the second step, *LEU*2 gene with Up *SED*1 and Dw *SED*1 flanked at 5' and 3' ends was created. The *SED*1::*LEU*2 deletion cassette was replaced at *SED*1 locus by homologous recombination.

Spot dilution growth assay

The *S. cerevisiae* CEN.PK113-7B *sed*1Δ and control strains (CEN.PK113-7B wild type, BY4742 wild type and *sed*1Δ) were cultured in YPD broth at 30 °C with 200 rpm shaking condition for 16-18 h. Yeast cells were harvested and washed twice with PBS buffer. Cells were resuspended in PBS buffer to obtain OD_{660} = 1. A 10-fold serial dilution was spotted by microplate replicators on YPD agar supplemented with ethanol, H_2O_2 and Calcofluor white. Cells were incubated at 30 °C for 1-4 days and visually analyzed.

Zymolyase sensitivity test

Yeast strains were cultivated in YPD media with shaking condition at 30 °C for 24 h until stationary phase. Cells were harvested and washed twice with TE buffer. The initial OD_{660} of 0.5 cells in TE buffer (10 mM Tris-HCl and 1 mM EDTA) with 1 U of Zymolyase 100T was prepared and incubated at 37 °C. The cell density at OD_{660} was measured every 1 h intervals for 4 h.

Results and Discussion:

In this study, the *SED*1 gene was disrupted by *LEU*2 auxotrophic marker using gene replacement of *SED1* locus with *SED*1::*LEU*2 deletion cassette which created by two-step PCR **(Figure 1**). Firstly, the PCR products of upstream, downstream *SED*1 gene and *LEU*2 gene size around 370, 240 bp and 1.5 kb were generated (**Figure 2A).** Secondly, *LEU*2 ORF flanked with upstream and downstream of *SED*1 gene at 5' and 3' was created using PCR products in the first step as primers in order to accomplish *SED*1::*LEU*2 deletion cassette size around 2.1 kb (**Figure 2B**). The CEN.PK113-7B *sed*1Δ strain was successfully constructed by transformation of yeast strain CEN.PK113-7B with the deletion cassette mentioned above which transformants were selected as Leu^+ colonies on SC-Ura selective plate. To confirm the successful of knock out strain, three Leu^+ candidate colonies were verified by colony PCR using specific primers which homologous to outside *SED*1 locus and internal sequence of *LEU*2 gene replacing at *SED*1 locus (**Table 1**). The gene replacement was confirmed by primers Cf-UpΔ*SED*1_FW and Cf-Up Δ*SED*1_RW which had homolog sequence with further upstream of *SED*1 locus in yeast genome and inside *LEU*2 gene, respectively. The results in **Figure 3** clearly showed that upstream region of disrupted *SED*1 locus size around 530 bp was generated (Lane 3, 5, 7) while the downstream region gave size around 440 bp (Lane 4, 6, 8) using Cf-DwΔ*SED*1_FW and Cf-DwΔ*SED*1_RW which also had homologous sequence with *LEU*2 gene and further downstream of *SED*1 locus, respectively. The negative result of wild type strain supported the success of strain construction. Thus, the results suggested that the *SED*1 gene was completely knockout in *S. cerevisiae* CEN.PK113-7B strain.

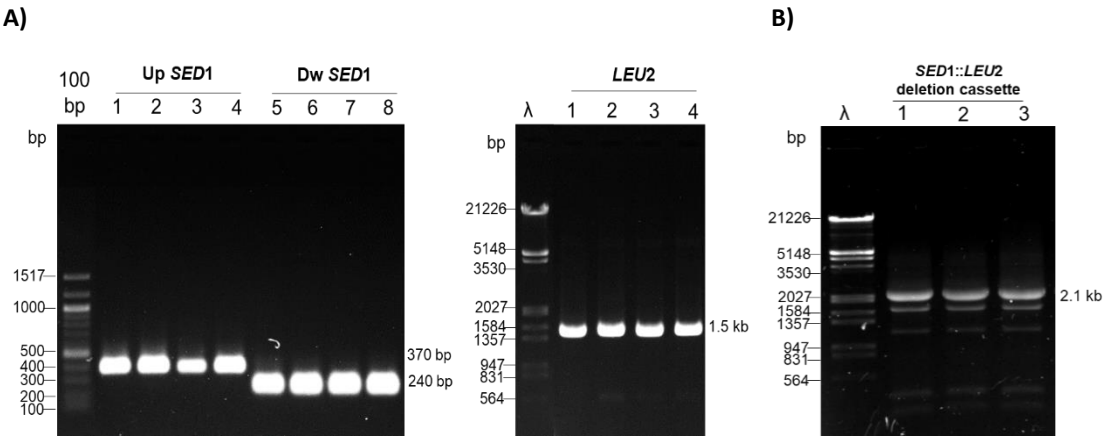

Figure 2.

Construction of S*ED*1::*LEU*2 deletion cassette by two-step PCR. The PCR product size of (A) upstream (Up *SED*1), downstream (Dw *SED*1) of *SED*1 gene, and *LEU*2 gene in the first step around 370, 240 bp and 1.5 kb, respectively; (B) *SED*1::*LEU*2 deletion cassette in the second step around 2.1 kb were created.

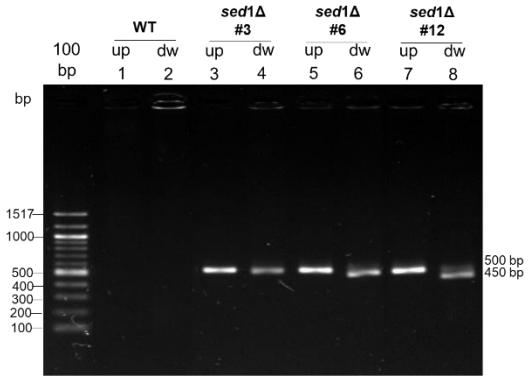

Figure 3.

Confirmation of CEN.PK113-7B *sed*1Δ strain by colony PCR. Further upstream (up) and downstream (dw) regions of disrupted *SED*1 in three Leu$^+$ candidate transformants (#3, #6, #12) were examined which generated PCR product size 500 (up) and 450 (dw) bp, respectively.

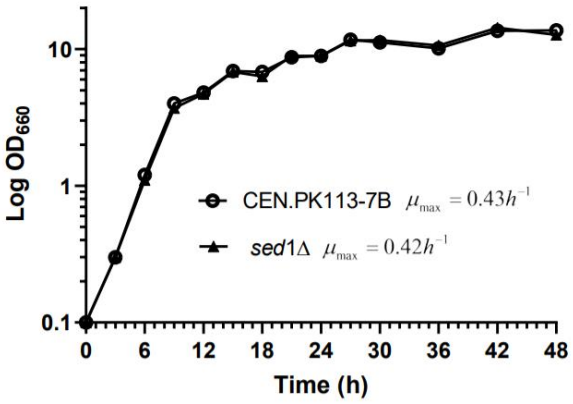

Figure 4.

The representative growth profile of CEN.PK113-7B *sed*1Δ and wild type strains. Yeasts were cultured in YPD broth with initial OD_{660} = 0.1 shaking at 30 °C, 180 rpm. The experiment was performed in three independents, duplicate each.

The growth characteristic of *SED*1 gene disruption was investigated under various stress conditions which presented during fermentation such as ethanol and oxidative stresses[13]. The ethanol is known to inhibit yeast growth and change lipid membrane fluidity. The oxidative stress is generated during yeast respiration which cause a DNA and protein denaturation. The growth on agar plate of 3 candidate mutant *sed*1Δ strains was comparing with CEN.PK113-7B wild type. Both strains were spotted on YPD agar plate without any supplements as a positive control to compare with all treatments during incubation period. The *sed*1Δ strains were suppressed by ethanol higher than 10%, and H_2O_2 more than 10 mM (**Figure 5B and C compared to Figure 5A**). From the results mentioned above, the sensitivity of *sed*1Δ in various stresses were not different from its wild type strain. The results provided that disruption of cell wall protein *SED*1 did not affect growth under stress conditions tested.

As *SED*1 is one of major GPI-CWP gene which linked to chitin through β-1,6-glucan layer, the effect of *sed*1Δ on cell wall organization was examined. Yeast cells were spot on YPD agar supplemented with Calcofluor white (CFW) which perturbs cell wall formation by alteration the assembly of chitin fibril[14]. The result shown that the CFW sensitivity of CEN.PK113-7B *sed*1Δ strain was slightly increase (**Figure 5 D**) at higher concentration of CWF, 60 µg mL^{-1} as compared to 20 and 40 µg mL^{-1}. Study on the other GPI-CWP gene namely covalently linked cell wall (*CCW12*), demonstrated that the growth of *CCW*12 mutant was highly sensitive to Calcofluor white [15] at 10 µg mL^{-1} and chitin content was increased. The difference of sensitivity to Calcofluor white seems to depend on cell wall organization with chitin.

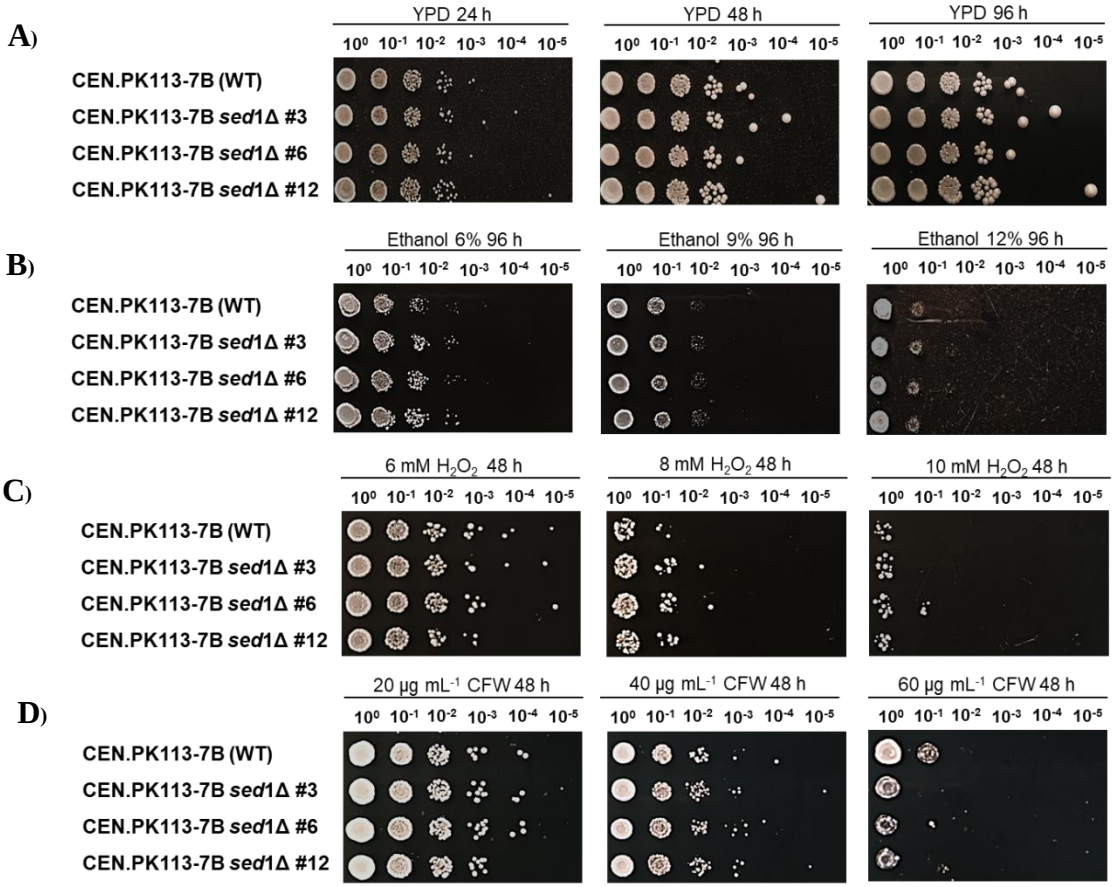

Figure 5.

Growth characteristic of CEN.PK113-7B *sed*1Δ strain under stress conditions examined by 10-fold dilutions spot assay with initial OD_{660} = 1. Yeasts grown in YPD broth were spotted on (A) YPD (control), (B) YPD supplement with 6-12% ethanol, (C) 6-10 mM H_2O_2 and (D) 20-60 µg mL^{-1} Calcofluor white and incubated at 30 °C with different time. The experiment was performed in three independents, triplicate each.

The stationary phase yeast cell wall is known to be more resisted to many stresses than exponential phase cells due to the thicker cell wall structure. As Sed1p is a major cell wall protein expressed in stationary phase and is likely to play role in cell wall integrity. In this work, the Zymolyase sensitivity of *sed*1Δ cells in stationary phase at 24 h of growth referenced from growth profile (**Figure 4**) was examined. The 24 cultured cells were treated with zymolyase incubated at 37°C for 4 h. From the result, the cell density of *sed*1Δ strains were slightly decreased during the treatment period. The disruption strain was more sensitive to Zymolyase than its wild type (**Figure 6**). The observation was consistent to the previous study[5]. It could be suggested that the loss of Sed1p affected cell wall organization that easily allowed accessibility of glucan degrading enzyme. However, there are other genes that related to the Zymolyase resistance expressed in stationary phase[5] that might be affected to the sensitivity of lytic enzyme in *sed*1Δ strain.

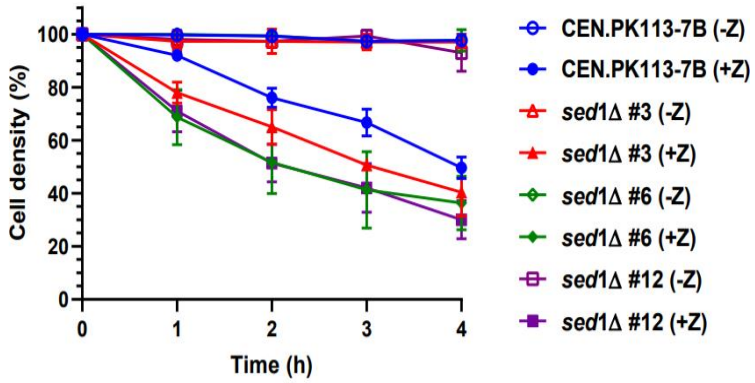

Figure 6.

Zymolyase sensitivity test of CEN.PK113-7B *sed*1Δ strain. Yeast grown in YPD broth for 24 h were harvested and diluted in TE buffer (10mM Tris-HCl and 1mM EDTA) with initial OD_{660} of 0.5. The cell density at OD_{660} was measured periodically after 1U Zymolyase 100T addition (+Z) compared with without addition (-Z). The experiment was performed in three independents, triplicate each.

Conclusion:

The construction of *sed*1Δ in *S. cerevisiae* CEN.PK113-B strain was achieved by two-step PCR method. The growth profile of disruption strain was not changed from wild type strain with the same specific growth rate around 0.4 h^{-1}. In addition, the growth characteristics of *sed*1Δ in various stress conditions were similar to wild type strain. The effect of *sed*1Δ on cell wall organization was indirectly demonstrated by the increase in Calcofluor white sensitivity and Zymolyase sensitivity of 24 h stationary phase cells which related to chitin and glucan composition.

References:

1. Andreu C, Del Olmo ML. Yeast arming systems: pros and cons of different protein anchors and other elements required for display. Appl Microbiol Biotechnol. 2018;102:2543-2561.
2. Pittet M, Conzelmann A. Biosynthesis and function of GPI proteins in the yeast *Saccahromyces cerevisiae*. Biochim Biophys Acta. 2007; 1771: 405-420.
3. Lesage G, Bussey H. Cell wall assembly in *Saccharomyces cerevisiae*. Microbiol Mol Biol Rev. 2006; 70:317-343.
4. Van der Vaart JM, te Biesebeke R, Chapman JW, Toschka HY, Klis FM, Verrips CT. Comparison of cell wall proteins of *Saccharomyces cerevisiae* as anchors for cell surface expression of heterologous proteins. Appl Environ Microbiol. 1997; 63: 615-620.
5. Shimoi H, Kitagaki H, Ohmori H, Iimura Y, Ito K. Sed1p is a major cell wall protein of *Saccharomyces cerevisiae* in the stationary phase and is involved in lytic enzyme resistance. J Bacteriol. 1998; 180:3381-3387.
6. Kotaka A, Sahara H, Kuroda K, Kondo A, Ueda M, Hata Y. Enhancement of beta-glucosidase activity on the cell-surface of sake yeast by disruption of *SED*1. J Biosci Bioeng. 2010; 109:442-446.
7. Bamba T, Inokuma K, Hasunuma T, Kondo A. Enhanced cell-surface display of a heterologous protein using *SED*1 anchoring system in *SED*1-disrupted *Saccharomyces cerevisiae* strain. J Biosci Bioeng. 2018; 125:306-310.

8. Ananphongmanee V, Srisala J, Sritunyalucksana K, Boonchird C. Yeast surface display of two proteins previously shown to be protective against white spot syndrome virus (WSSV) in shrimp. PLoS One. 2015; 10:e0128764.
9. Sritunyalucksana K, Wannapapho W, Lo CF, Flegel TW. *Pm*Rab7 is a VP28-binding protein involved in white spot syndrome virus infection in shrimp. J Virol. 2006; 80:10734-10742.
10. Van Dijken JP, Bauer J, Brambilla L, Duboc P, Francois JM, Gancedo C, et al. An interlaboratory comparison of physiological and genetic properties of four *Saccharomyces cerevisiae* strains. Enzyme Microb Technol. 2000;26:706-714.
11. Lõoke M, Kristjuhan K, Kristjuhan A. Extraction of genomic DNA from yeasts for PCR- based applications. Biotechniques. 2011;50:325-328.
12. Gietz R, Woods R. Transformation of yeast by lithium acetate/single-stranded carrier DNA/polyethylene glycol method. Methods Enzymol. 2002;350:87-96.
13. Gibson BR, Lawrence SJ, Leclaire JP, Powell CD, Smart KA. Yeast responses to stresses associated with industrial brewery handling. FEMS Microbiol Rev. 2016;31:535–569.
14. Elorza V, Rico H, Sentandreu, Calcofluor white alters the assembly of chitin fibrils *in Saccharomyces cerevisiae* and *Candida albicans* cells. J Gen Microbioly. 1983;129:1577-1582.
15. Hagen I, Ecker M, Lagorce A, Francois JM, Sestak S, Rachel R, et al. Sed1p and Srl1p are required to compensate for cell wall instability in *Saccharomyces cerevisiae* mutants defective in multiple GPI-anchored mannoproteins. Mol Microbiol. 2004;52:1413-1425.
16. R Enrico, Sipiczki M, Strahl S. Characterization of Ccw12p, a major key player in cell wall stability of *Saccharomyces cerevisiae.* Yeast. 2007;24:309-319.

Acknowledgements:

We would like to thank Department of Biotechnology, Faculty of Science, Mahidol University for the facility support and also CIF Grants, Faculty of Science, Mahidol University.

C_041_PA: PHYLOGENETIC RELATIONSHIPS OF MICROHYLID FROGS IN RAMKHAMHAENG UNIVERSITY CAMPUSES INFERRED FROM COI GENE

Phiradet Chuabsak[1], Kowit Noikotr[1,*]

[1]Department of Biology, Faculty of Science, Ramkhamhaeng University, Bangkapi Bangkok, 10240 Thailand.
*e-mail: kowit@ru.ac.th

Abstract:

Ramkhamhaeng University campuses located throughout Thailand are suitable habitats for sanctuary of animals from around agricultural area. Microhylid frog is the one of amphibian families, adapting to survive from agriculture invasion of their habitats. To investigate a genetic relation among microhylid frogs distributed in the campus of Ramkhamhaeng University, 40 samples and 2 out-group samples were collected from 5 campuses: Surin, Nongbualamphu, Nakhonphanom, Sukhothai and Phrae campuses. COI gene of the collected samples was amplified, and the sequence data were analyzed using Neighbor-Joining and Minimum Evolution methods to construct a phylogenetic tree. All samples were grouped by species, but each single species was separated by geography. Relationships among genera were separated into 2 clades, *Microhyla* with *Glyphoglossus* and *Micryletta* with *Kaloula*. There was widely separated between *Micryletta inornata* form Phrae and Surin campuses while the separation degree was the same between *Microhyla berdmorei* and *Microhyla pulchra* from Nongbualamphu campus. It is suggesting that they might be membered in difference species and needs further investigation.

C_042_PA: ADAPTATION OF THERMOTOLERANT *Acetobacter* sp. FOR VINEGAR PRODUCTION

Nattida Pankaew,[1] Pornnatcha Titchob,[1] Pattana Kakumyan,[1] Natsaran Saichana[1,2,*]

[1]School of Science, Mae Fah Luang University, Chiang Rai, Thailand, 57100
[2]Microbial Products and Innovation Research Group, Mae Fah Luang University, Chiang Rai, Thailand, 57100
*email: natsaran.sai@mfu.ac.th

Abstract:

A thermotolerant acetic acid bacterium, designated as *Acetobacter* sp. 2-16, was isolated from fruit in Thailand for its ability to grow and produce acetic acid at 38ºC, at which growth of most mesophilic strains of acetic acid bacteria are inhibited. Thermotolerant acetic acid bacteria are required in process for vinegar fermentation in hot countries to eliminate cost of cooling during the fermentation. Moreover, strains with higher tolerant to ethanol concentration are also of interest for vinegar fermentation. In this study, *Acetobacter* sp. 2-16 was used for adaptation to grow and produce acetic acid at higher temperatures or higher ethanol concentrations. For thermo-adaptation, the original strain was repeatedly grown in a medium containing ethanol at temperature starting from 38ºC for several generations until no lag phase was observed. The growth temperature was shifted up for 0.5ºC in the next generation if the growth delay was not observed. The adaptation experiment was conducted to achieve healthy growth at higher temperature. The adaptation for higher ethanol concentration was carried out at 38ºC in the medium having ethanol concentration shifted from 4%v/v to higher ethanol concentration for next generation when no growth delay was observed. The results showed that the thermo-adapted *Acetobacter* sp. 2-16 strain could grow up to 40°C in the medium with 4%v/v ethanol while the ethanol-adapted *Acetobacter* sp. 2-16 strain could grow at 38°C with ethanol concentration up to 6%v/v. The two adapted strains showed the higher growth and acid production compared to the original strain. The adapted strains generated by mean of adaptation to force the bacteria to survive in stress condition can be used for vinegar fermentation at higher temperature or higher ethanol concentration.

C_043_PA: ASSESSMENT ON SEASONAL VARIATION OF FISH IN THE MANGROVE AREA, EASTERN THAILAND

Nidsaraporn Petsut,[1*] Sitthi Kulabtong[2] and Jirawaeth Petsut[1]

[1]Department of Agricultural Technology, Faculty of Science, Ramkhamhaeng University, Bangkok, Thailand

[2]Faculty of Agro-Industrial Technology, Rajamangala University of Technology Tawan-ok Chantaburi Campus, Chantaburi, Thailand

[*]e-mail: nidsaraporn@rumail.ru.ac.th

Abstract

The fish biodiversity and distribution pattern of freshwater, blackish water and sea water in the mangrove area, eastern Thailand was studied at Chonburi Province, Rayong Province Junthaburi Province and Trat Province from April to December 2017. The fish samples and environmental factors were collected very 4 months; covering, hot-dry (April), rainy (August) and cool-dry (December) seasons at eight sampling stations followed longitudinal gradient. Fish specimens were collected using the pull net, mesh size 1X1 millimeter, 10 meters width and 1.2 meter depth. A total of 1,655 individuals fish representing 33 families and 53 species were found. The family Gobiidae is dominant with 6 species (11%) followed by Ambassidae, Blenniidae, Engraulidae, Leiognathidae and Siganidae with 3 species (6%) and other families with one or two species each. One blackish water fishes, *Neostethus lankesteri* was newly recorded in Rayong River and Trat mangrove area. In terms of water quality that related to the fish species, the distribution of fishes in the study areas can be separated into 2 main groups: 1) mangrove area of mainstream or canal ecosystem, was influenced by salinity and 2) mangrove area of coastal ecosystem was influenced by the sea directly. Additionally, found that many species of fishes had potential for commercial culture such as *Terapon jarbua*, *Abudefduf vaiqiensis*, *Siganus fuscescens, Neostethus lankesteri*, *Ambassis kopsii* and *Moolgarda cunnesius*.

C_044_OA: THE MORPHOLOGY AND PHYLOGENY OF THE DIATOM GENERA *Rhizosolenia*, *Proboscia*, *Pseudosolenia* AND *Neocalyptrella* FROM GULF OF THAILAND AND THE ANDAMAN SEA, WITH A DESCRIPTION OF *Proboscia siamensis* sp. nov., AND THE ERECTION OF A NEW ORDER FOR *Proboscia*

Atchaneey Boonprakob[1,2,3], Nina Lundholm[2], Linda Medlin[4] & Øsvind Moestrup[3]

[1]Department of Biology, Faculty of Science, Ramkhamhaeng University, Bangkok 10240, Thailand
[2]Natural History Museum of Denmark, University of Copenhagen, Sølvgade 83S, DK–1307 Copenhagen K, Denmark
[3]Section of Marine Biology, Institute of Biology, University of Copenhagen, Universitetsparken 4, DK–2100 Copenhagen Ø, Denmark
[4]Marine Biological Association of the UK, The Citadel, Plymouth, PL1 2PB, UK
*e-mail: kungocean8888@yahoo.com

Abstract:

The marine planktonic diatom genera *Rhizosolenia*, *Proboscia, Pseudosolenia* and *Neocalyptrella* have been studied with emphasis on morphology and phylogeny. Material was collected October 2008 – January 2011 at seven localities in the four provinces of the marine coastal waters of Thailand: Rayong, Chonburi, Chumphon and Phuket. Fifty strains were established in culture and used for morphological and phylogenetic analyses, complemented with morphological studies of field material. Morphological studies were done using light microscopy, scanning and transmission electron microscopy. Ten species and two varieties of *Rhizosolenia* were identified and described in detail: *R. styliformis*, *R. acuminata*, *R. bergonii*, *R. clevei* var. *clevei*, *R. clevei* var. *communis*, *R. formosa*, *R. hyalina*, *R. imbricata*, *R. fallax*, *R. ostenfeldii*, *R. setigera*. and *R. pungens*. *Pseudosolenia calcaravis* was also found, and detailed studies indicated that this taxon formed a species complex. *Proboscia* was represented by *P. indica* and *P. siamensis* sp. nov., but more species probably occur. *Neocalyptrella* was represented by *N. robusta*. The molecular studies supported *Pseudosolenia*, *Proboscia* and *Neocalyptrella* as separate genera. Culturing and molecular analyses were often difficult or unsuccessful. The data show that *Rhizosolenia* can be a monophyletic genus if *R. pungens* and *R. setigera,* who are distantly related to the remaining *Rhizosolenia* species, are described as a new genus. This will be done in a companion study of the type material of *R. setigera (*Medlin et al., in press*).*

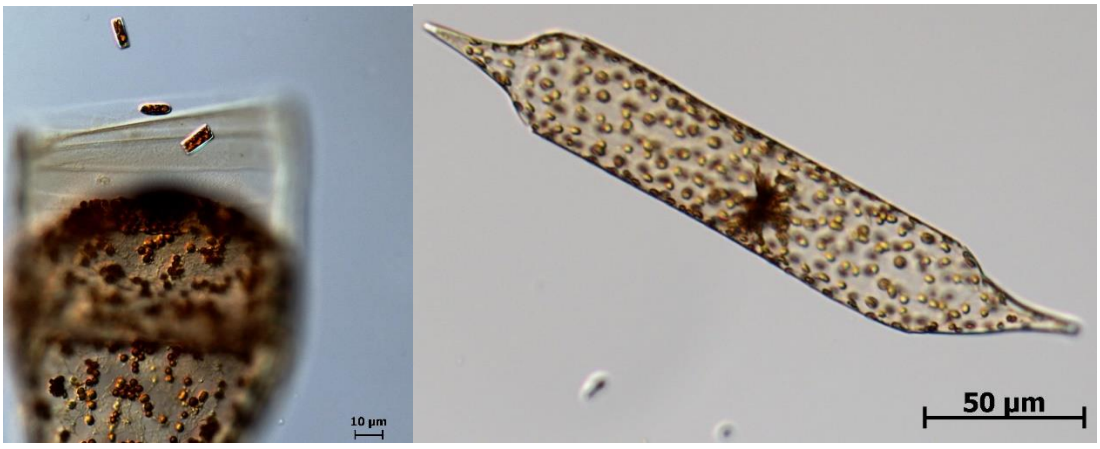

Figure 1. *Neocalyptrella robusta* (G.Norman ex Ralfs) Hernández-Becerril & Meave del Castillo (left) and *Rhizosolenia bergonii* H.Peragallo (right)

D_001_PF: DEVELOPMENT OF A DNA BASED BIOSENSOR FOR miRNA DETECTION

Sirirat Khemasiri,[1] Chittanon Buranachai,[2] Panote Thavarungkul,[2] Proespichaya Kanatharana,[1] Chongdee Thammakhet-Buranachai,[1]*

[1]Department of Chemistry, Faculty of Science, Prince of Songkla University, Thailand
[2]Department of Physics, Faculty of Science, Prince of Songkla University, Thailand
Center of Excellence for Trace Analysis and Biosensor, Prince of Songkla University, Thailand
*e-mail: chongdee.t@psu.ac.th

Abstract:

In this work, a DNA-based biosensor for microRNA detection was developed. MicroRNA is a short single-stranded and noncoding RNA that plays a role in many cellular and physiological processes by regulating specific genes expression. It was demonstrated that microRNA could be a biomarker for some potential diseases. For instance, miR-29 and miR-24 are biomarkers for diabetes, miR-144-5p, miR-374 and miR-221 for Alzheimer's disease, and miR-122 for hepatocellular carcinoma in human. According to a trace level of microRNA in real biological samples and its limited length about 20-24 nucleotides, the amplification using polymerase chain reaction (PCR) technique before detection is problematic. Hence, this work aims to develop a DNA-based biosensor that eventually can detect microRNA at low concentration. The catalyzed hairpin assembly (CHA) technique for non-enzymatic amplification was utilized, in conjunction with the Förster resonance energy transfer (FRET) technique, to detect a 22-nucleotide DNA analog of miR-122. The current limit of detection of the sensor is at 3.23 nM with only 30 minutes incubation time. It is expected that with additional optimization, the developed biosensor could be applicable to detecting miR-122 in real biological samples.

Introduction:

In recent years, hepatocellular carcinoma (HCC) has been a major cause of cancer-related death worldwide1 HCC frequently develops from cirrhosis associated with viral hepatitis and the symptoms might not show up until most liver cells are destroyed.[1-2] Even though it can be cured if detected at an early stage, there is still no effective treatment for late-stage HCC.[1] Therefore, early diagnosis is very important. MicroRNAs are a type of short non-coding RNAs, approximately 20 – 24 nucleotides, that could be found in human tissues and fluids.[3,4] They play major roles in posttranscriptional regulation of protein expression and affect various biological processes. For instance, cell proliferation, differentiation and apoptosis.[5-6] Interestingly, according to previous reports, microRNAs express in aberrant levels in patients with tumors.[7-8] It indicates that they could function as tumor suppressors (as in cases of miR-15a and miR-16-1) or associate with oncogenes (as in case of miR-155).[9-10] Therefore, released microRNAs are now considered as potential biomarkers for early diagnosis of some cancers.

Polymerase chain reaction (PCR), microarray and next-generation sequencing (NGS) are common techniques for quantifying miRNAs although none of them are rapid and simple.[11] Therefore, alternative techniques for miRNA detection are highly desired. Interesting candidates are biosensors and chemical sensors (or "sensors" in short) because of their simplicity and sensitivity.[12] Sensors based on various platforms, for instance,

electrochemical[13], colorimetry[14], surface-enhanced Raman spectroscopy[15] and fluorescence spectroscopy[16], have been developed for miRNA detection. However, using these methods to detect microRNAs are still problematic due to the short length and trace amount of microRNAs in real biological samples. Thus, signal amplification is necessary for the detection. Among the non-enzymatic amplification, the catalyzed hairpin assembly (CHA) is an interesting technique due to design simplicity[17] making it suitable for the detection of short oligonucleotides, such as miRNA. As appeared in previous works[18,19], CHA was used in developing sensors to detect miRNA-163, miRNA-21 and miRNA-141. Even though both of them provided quite low limit of detection, the methods still require at least an hour for incubation. Hence, we propose the detection method with two CHA loops in expectation that it will reduce the incubation time as well as increase sensitivity. Briefly, the target oligonucleotide acts as a catalyst for the hybridization of two metastable DNA hairpins, named H1 and H2. Initially the target binds to hairpin H1's toehold, causing H1 to unfold and open hairpin H2. Finally, catalyst is released after the hybridization of H1-H2 and continue catalyzing H1-H2 hybridization until the DNA hairpins are exhausted. Therefore, a presence of short oligonucleotide target even at low concentration yields a large amount of H1-H2 duplex, which can be measured more easily. Herein, catalytic hairpin assembly (CHA) technique was adopted in conjunction with Förster resonance energy transfer (FRET) for the miR-122 detection as shown in Figure 1. Fluorescein and TMR were used as a FRET donor and acceptor fluorophores, respectively. A presence of miRNA will lead to the catalyzed hybridization of H1-H2, resulting in high FRET signal. To ensure high sensitivity and short incubation time, a second CHA loop was incorporated into the amplification circuit. Duplex H1-H2 acts as the second loop's catalyst producing another H3-H4 duplex, which in return, catalyzes H1-H2 hybridization. It is hypothesized that this cross reactivity could enhance the sensor sensitivity and reduce the incubation time even further compared with that from using just a single loop CHA.

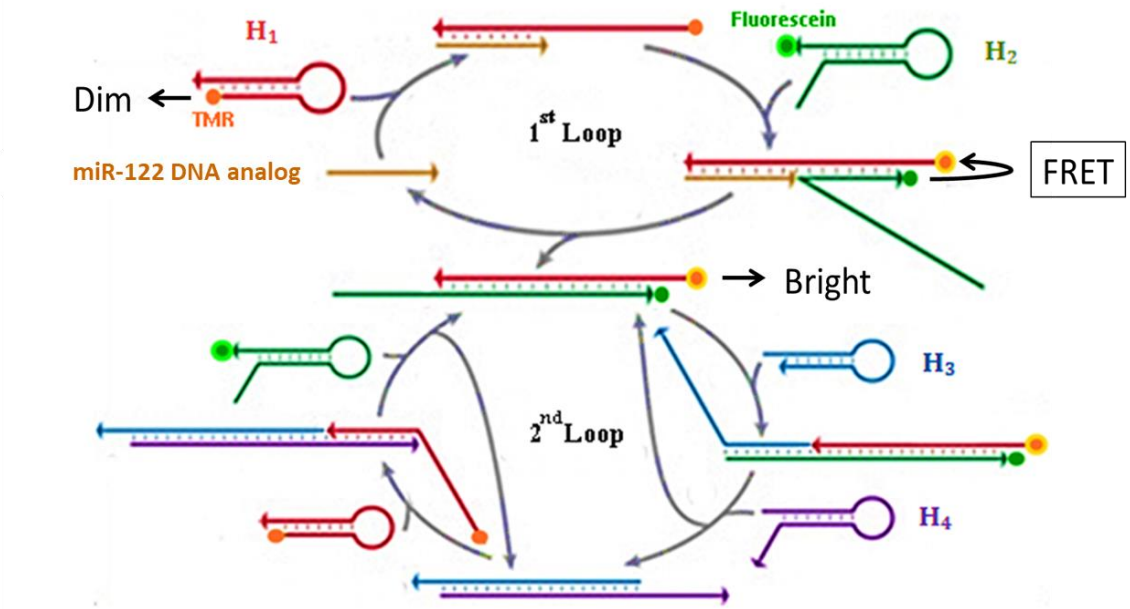

Figure 1.

The sensing mechanism of the sensor based on dual catalyzed hairpin assembly (CHA) reactions. The miR-122 DNA analog acts as the CHA catalyst.

Methodology:

A. Materials and chemicals

In this initial stage of development, the DNA analog of miR-122 was used as analyte to avoid complication due to RNA degradation[20]. All oligonucleotides were purified by HPLC and shipped from Integrated DNA Technology (IDTDNA, Coralville, IA, USA). The concentrations of the unlabeled oligonucleotides were calculated from OD260 under a UV-Vis Spectrophotometer (U-2900, Hitachi High Technologies America Inc., Schaumburg, IL, USA) using extinction coefficients from the manufacturer. For H1 and H2, the concentrations were calculated from OD_{495} and OD_{558} using ε_{495} = 46,000 M^{-1} and ε_{558} = 75,200 M^{-1} [21] for fluorescein and TMR respectively. NaCl and $MgCl_2$ were purchased from Univar (Bangkok, Thailand), while Tris was purchased from Sigma-Aldrich (St.Louis, MO, USA).

Table 1.

DNA sequences used in developing the sensor

DNA	Sequence
H1	/56-TAMN/ CAA TGG TGT TGC TTT AGA TGT GAC ACA ACA CCA TTG TCA
H2	ATT GCA GTG CTT TAG ATG TGA CAA TGG TGT TGT GTC ACA TCT AAA GCA ACA CC /36-FAM/
H3	TCT AAA GCA CTG CAA TCT TTA GAT GTG ACA ATT GCA GTG CT
H4	CTG CAA TTG TCA CAT CTA AAG ATT GCA GTG CTT TAG ATG TGA CAA TGG TGT TG
miR-122 DNA analog	TGG AGT GTG ACA ATG GTG TTG

B. FRET measurement and analysis

Hairpin H1, H2, H3 and H4 were added into 10 mM Tris buffer pH 8.0 containing 500 mM NaCl and 2 mM $MgCl_2$. The solution was mixed before adding DNA target at desired concentration. Then the solution was mixed thoroughly and incubated at room temperature for 30 minutes. All fluorescence emission spectra were measured by a spectrofluorometer (LS55, Perkin Elmer Inc., Waltham, MA, USA) using a quartz microcuvette (Starna Scientific Ltd., Essex, UK). Emission spectra were collected between 500 – 710 nm with the fluorescein excitation at 485 nm and TMR excitation at 558 nm. The FRET efficiency (E) was presented as the (ratio)A value21, which is the fluorescence intensity of TMR excited via FRET divided by that via direct excitation.

C. Optimizations

Hairpin H1, H2, H3 and H4 were added into 10 mM Tris buffer pH 8.0 containing 500 mM NaCl and 2 mM $MgCl_2$. The solution was mixed before adding DNA target at desired concentration. Then the solution was mixed thoroughly and incubated at room temperature for 30 minutes. All fluorescence emission spectra were measured by a spectrofluorometer (LS55, Perkin Elmer Inc., Waltham, MA, USA) using a quartz microcuvette (Starna Scientific Ltd., Essex, UK). Emission spectra were collected between 500 – 710 nm with the fluorescein excitation at 485 nm and TMR excitation at 558 nm. The FRET efficiency (E) was presented as the (ratio)A value[21], which is the fluorescence intensity of TMR excited via FRET divided by that via direct excitation.

Results and Discussion:

A. Materials and chemicals

The sensor responses toward various concentrations of miR-122 DNA analog were tested first. Figure 2A shows the change in fluorescein and TMR emission spectra when excited at 485 nm. As target oligonucleotide concentration increases, the emission peak at 520 nm that corresponding to fluorescein decreases while the emission peak of TMR at 578 nm (Figure 2A) increases due to increasing FRET as expected.

B. Optimizations

Next, the optimal DNA hairpin concentrations in each CHA loop were investigated separately, starting with H1 and H2 (Figure 2B) followed with H3 and H4 (Figure 2C). The strand ratio in each CHA loop were fixed at 1:1 following the optimal ratio in a previous work[22]. In Figure2A, up until 175 nM, the sensitivity tends to increase with H1 and H2 concentrations, possibly due to faster H1-H2 duplex formation. Afterwards, it is hypothesized that the H1-H2 duplex formation rate was high even at the low target oligonucleotide concentration making the sensitivity drop. Therefore, 175 nM is the optimal concentration of H1 and H2. In the case of H3 and H4 (Figure 2C), we observed no initial increase in the sensitivity at early concentrations of H3 and H4 possibly because the sensor was already operating near its optimal condition even at very low concentration of H3 and H4. Increasing the hairpin concentrations beyond 50 nM causes the sensitivity to drop likely because the rate of H1-H2 duplex formation was very high even at the low concentrations of target oligonucleotide. Therefore 50 nM is the optimal concentration of H3 and H4.

Afterwards, the effect of incubation time was studied using the optimal DNA concentrations. Figure 2D shows that the sensitivity increases with longer incubation time until 30 minutes. This is possibly because a longer incubation time allows more duplex H1-H2 formation. However, after 30 minutes the sensitivity decreases and it is likely because excessive incubation time causes the spontaneous hybridization even in blank or at low concentration of target oligonucleotide.

Optimizations of NaCl and $MgCl_2$ concentrations were done next. The results in Figure 2E and 2F show initial increases in the sensor sensitivity as salts' concentrations increase. This is possibly due to the fact that Na^+ and Mg^{2+} could reduce the electrostatic repulsion between phosphate groups on the DNA backbone, facilitating the duplex formation resulting in the higher sensitivity. However, when NaCl and $MgCl_2$ concentrations were beyond their optimal values, the sensitivity decreases. We hypothesize that this is because the H1-target duplex stability was too high causing the reduction in H1-H2 formation rate. Although NaCl and $MgCl_2$ play the same role, differences in their atom size and ionic strength cause a difference in ability which leading to the use of two salts in this work. Therefore, 500 mM and 2 mM were chosen to be the optimal concentrations of NaCl and $MgCl_2$, respectively.

C. Sensor Performance

As shown in Figure 3, under the optimal conditions, the sensor's sensitivity is at 0.0797 ± 0.0050 nM^{-1} over the linear range of 0-10 nM. The limit of detection is 3.23 nM for a standard microRNA.

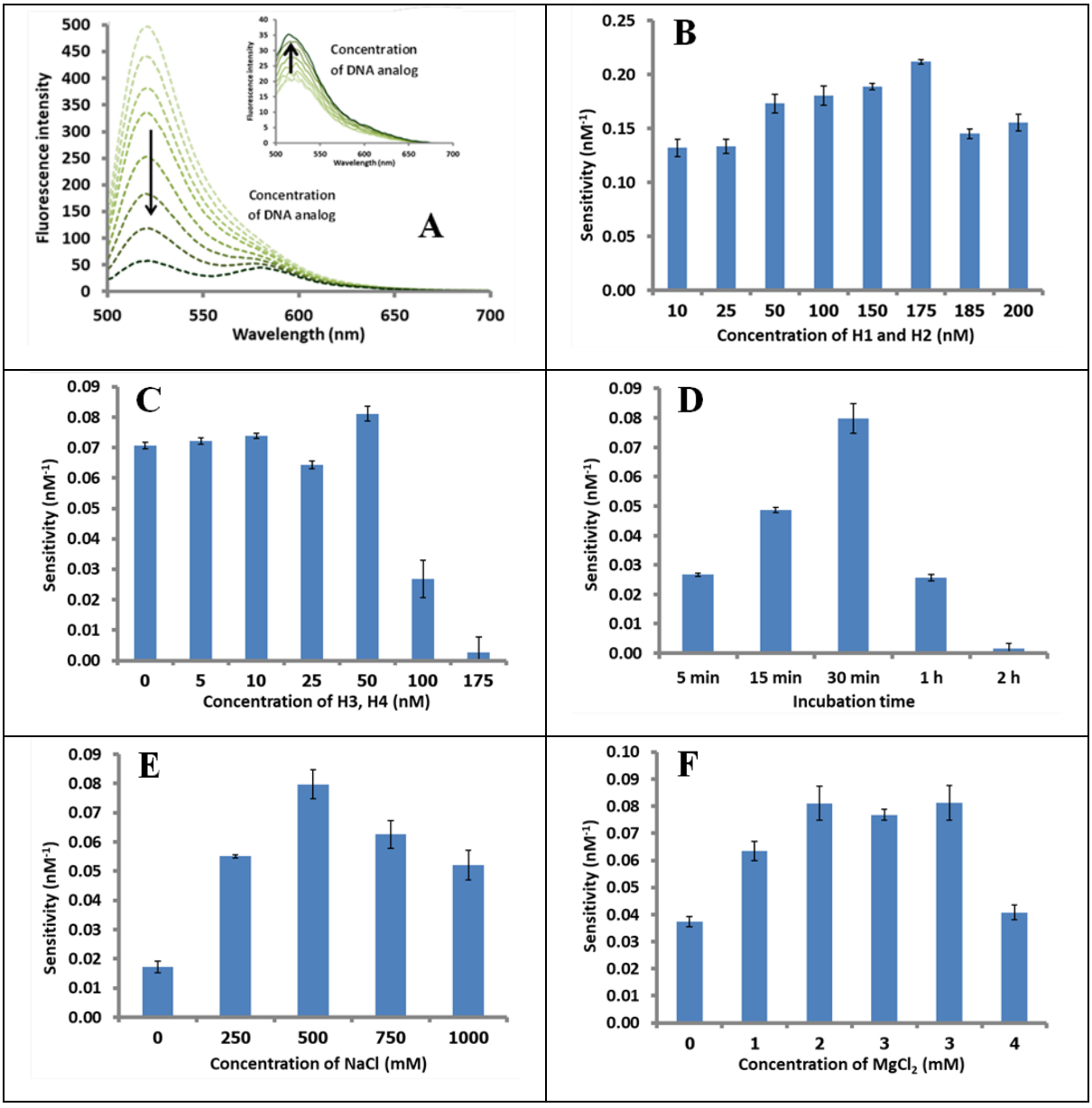

Figure 2.

(A) The change in fluorescence emission spectra of fluorescein (emission peak at 520 nm) and TMR (emission peak at 578 nm) after being excited at 520 nm at various concentrations of miR-122 DNA analog. The sensor sensitivities at various concentrations of H1 and H2 (B) and H3 and H4 (C), incubation times (C), NaCl concentrations (E) and $MgCl_2$ concentrations (F)

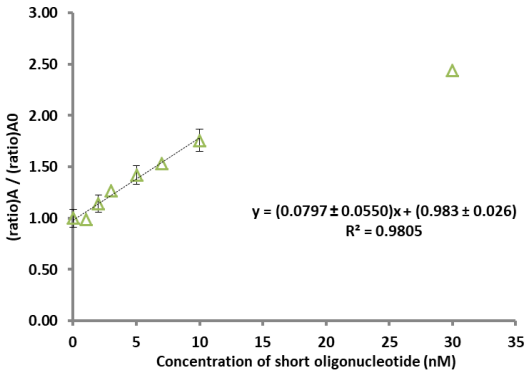

Figure 3.

The linearity under the optimal conditions

Conclusion:

A DNA-based biosensor with a potential to detect miR-122 based on was successfully developed. Even though the limit of detection is still high, further optimization of affecting parameters will likely improve the sensor efficiency. In addition, the sensing mechanism can be applied to detect other oligonucleotides by simply adjusting the sequences on the H1-H4 DNA hairpins to suit the target.

Acknowledgements:

This work was financially supported by Development and Promotion of Science and Technology Talents Project (DPST) and The Thailand Research Fund (TRF) grant no. MRG5680027. The Center of Excellence for Trace Analysis and Biosensor Research Center (TAB-CoE), Department of Physics, Department of Chemistry, Faculty of Science, Prince of Songkla University, Hat Yai, Songkhla, Thailand are all gratefully acknowledged.

References:

1. Aydin Y, Kurt R, Song K, Lin D, Osman H, Youngquist B, Scott J W, Shores N J, Thevenot P, Cohen A, Dash S. Cancers. 2019;11:1407.
2. Musaddaq G, Shahzad N, Ashraf M A, Arshad M I. Biomarkers. 2019; 24:103-109.
3. Vecerova A, Hudcova K, Pilarova I, Masarik M, Trnkova L. Monatsh. Chem. 2016;147: 105–110.
4. Jansson M D, Lund A H. Mol. Oncol. 2012;6:590-610.
5. Bartel D P. Cell J. 2004;116:281-297
6. Harfe B D. Curr. Opin. Genet. Dev. 2005;15:410-415.
7. Esquela-Kerscher A, Slack F J. Nat. Rev. Cancer. 2006;6:259-269.
8. Giovannetti E, Erozenci A, Smit J, Danesi R, Peters G J. Crit Rev Oncol Hemat. 2012;81:103-122.
9. Aqeilan R I, Calin G A, Croce C M. Cell Death Differ. 2010;17:215-220.
10. Witten L W, Cheng C J, Slack F J. Oncogene. 2019;38:2151-2161.
11. Moody L, He H, Pan Y X, Chen H. Clin Epigenetics. 2017;9:119-119.
12. Mohammadinejad A, Oskuee R, Eivazzadeh R, Rezayi M, Baradaran B, Maleki A, Hashemzaei M, Mokhtarzadeh A, Guardia M. Trends Analyt Chem. 2020;
13. Zhao L-L, Pan H-Y, Zhang X-X, Zhou Y-L. Anal. Chim. Acta. 2020;1116:62-69.
14. Niazi A, Jorjani O N, Nikbakht H, Gill P. Mol Diagn Ther. 2013;17:363-370.
15. Pang Y, Wang C, Lu L, Wang C, Sun Z, Xiao R. Biosens. Bioelectron. 2019;130:204-213.

16. Lavaee P, Taghdisi S M, Abnous K, Danesh N M, Khayyat L H, Jalalian S H. Talanta. 2019;202:349-353.
17. Yin P, Choi H M T, Calvert C R, Pierce N A. Nature. 2008;451:318-322.
18. Li Y, Yu C, Zhao C, Ren C, Zhang X. Anal. Chim. Acta. 2019;1084:93-98.
19. Kim H, Kang S, Park K, Park H. Sens. Actuators B Chem. 2018;260:140-145.
20. Ivica J, Williamson P T F, de Planque M R R. Anal. Chem. 2017;89:8822-8829.
21. Clegg R M, Murchie A I H, Zechel A, Carlberg C, Diekmann S, Lilley D M J. Biochemistry. 1992;31:4846-4856.
22. Chu-Mong K, Thammakhet C, Thavarungkul P, Kanatharana P, Buranachai C. Talanta. 2016;155:305-313.

D_002_PA: GREEN CORROSION INHIBITOR: *Parkia speciosa* HASSK. EMPTY POD EXTRACTION BY MICROWAVE-ASSISTED EXTRACTION METHOD

Chuleeporn Prateep Na Talang,[1] Kanyanat Leelawathanaroch,[2] Klatnatee Vepulanont,[3]*

[1] Journal of International Studies (JIS) and Research, Faculty of International Studies, Prince of Songkla University, Phuket Campus
[2,3] Department of Chemistry, Faculty of Science, Prince of Songkla University, Hatyai Campus
*e-mail: klatnatee.v@psu.ac.th

Abstract:

In this research, microwave-assisted extraction (MAE) had been used to extract *Parkia speciosa* Hassk. empty pod. Microwave and maceration extraction had been compared. Heat energy form microwaves had been absorbed by solvent and *Parkia speciosa* Hassk. empty pod tissues, which increase the kinetic of extraction. The results from the experiments show that MAE is faster than maceration extraction 112- 672 times depending on experimental conditions. The crude oil had been investigated by ^{1}H-NMR, FT-IR, UV-Vis and MS-MS for its structure before using as a green corrosion inhibitor. Immersed and non-immersed specimens in crude extracts had also been studied using E_{corr} vs Time and linear polarization for corrosion behaviour. The electrochemical results consistently identify the extract as an efficient corrosion inhibitor. The results from weight loss technique showed a maximum inhibition efficiency of 77.94% obtained at the concentration of 2.0 g/L crude extract.

D_003_PF: ANION RECOGNITIONS OF TRICHLOROPHENYL AMIDE-BASED ANION RECEPTORS

Korakot Navakhun,* Pantipa chungla

Department of Chemistry and Center of Excellence for Innovation in Chemistry, Faculty of Science, Ramkhamhaeng University, Huamark, Bangkapi, Bangkok 10240, Thailand
*e-mail: n_korakot@ru.ac.th

Abstract:

Trichlorophenyl amide-based anion receptors, *N*,*N*'-bis(2,4,6-trichlorophenyl)isophthalamide, **1**, *N*,*N*'-bis(2,4,5-trichlorophenyl)isophthalamide, **2**, *N*,*N*'-bis(2,4,6-trichlorophenyl) pyridine-2,6-dicarboxamide, **3**, *N*,*N*'-bis(2,4,5-trichlorophenyl)pyridine-2,6-dicarboxamide, **4**, 2,6-bis**(**2,4,6-trichlorophenylcarbamoyl**)**pyridinium, **5**, and 2,6-bis**(**2,4,5-trichlorophenyl carbamoyl**)**pyridinium, **6**, have been synthesized. Their structures and binding properties with F^-, Cl^-, Br^-, $H_2PO_4^-$, HSO_4^-, NO_3^- and CH_3COO^- have been studied using chemical calculation methods with DFT at the B3LYP/6-31G+(d) level of theory in gas phase. In experimental methods, NMR titration techniques in DMSO-d_6 solution have been used in order to evaluate K_{assoc} of the complexation of compounds **1**–**6** with TBA·F, TBA·Cl, TBA·Br, TBA·H_2PO_4, TBA·HSO_4, TBA·NO_3 and TBA·CH_3COO. The experimental results reveal that trichlorophenyl amide-based anion receptor **2** has potential to be used as CH_3COO^- ion receptor.

Introduction:

Anions play an importance role in agricultural, environmental and medicinal applications due to their variety of functions.[1,2] To study their properties, it is necessary to design the anion receptor host structures suitable for the target ion guest species. It has to consider that what is the nature of these anions and in which environment they are in. Moreover, the functional groups including in the receptor molecule are also important.[3,4] Isophthalamide scaffold has been studied most extensively to use as anion receptor molecules. Addition of substitutes which is the electron withdrawing groups in isophthalamide structure causes the increasing of anion receptor efficiency.[5-8] In addition, the use of molecular orbital calculation method could help the researches in this field understand the properties of the anion receptors and their complexes.[9-13] Therefore, the research in this area would be a guidance to obtain the effective new synthetic anion receptors, optimize factors of the binding, and finally to be the nano tools in advance. Herein, we report the synthesis of novel trisubstituted electron withdrawing group isophtalamide-base anion receptors, the optimized structures, thermodynamic properties and their F^-, Cl^-, Br^-, $H_2PO_4^-$, HSO_4^-, NO_3^- and CH_3COO^- ions recognition properties.

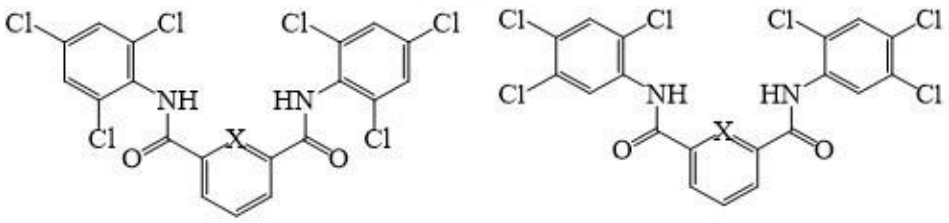

1, X = CH
3, X = N
5, X = NH^+

2, X = CH
4, X = N
6, X = NH^+

Methodology:

Experimental

The ^1H and ^{13}C nuclear magnetic resonance (NMR) spectra were recorded on a AVANCE 400 MHz NMR spectrometer. All studied ligands were dissolved in deuterated dimethylsulfoxide (DMSO-d_6). The electrospray mass spectra (ESMS) were measured using a Finnigan LC-Q mass spectrometer. The high resolution mass spectra were obtained using a Bruker microTOF-II mass spectrometer.

Synthesis of Isophthalamide Amide-Based Anion Receptor

N,*N*'-Bis(2,4,6-trichlorophenyl)isophthalamide, **1**

To a solution mixture of isophthaloyl dichloride (110.0 mg, 0.54 mmol) and 2,4,6- trichloroaniline (245.3 mg, 1.36 mmol) in acetonitrile (CH_3CN) (2.0 mL) was added triethylamine **(**TEA**) (**0.20 mL, 1.43 mmol**)** and 4-*N*, *N*-dimethylaminopyridine **(**DMAP**) (**12.0 mg, 0.11 mmol**)** used as base and catalyst**.** The reaction mixture was stirred at 60-80 °C for 24 hours before being quenched with water and extracted with EtOAc**.** After removal of the solvent, purification was accomplished by column chromatography eluting with (0.5%) CH_3OH-CH_2Cl_2 to give product **1** as a white solid **(**145.8 mg, 0.28 mmol, 51 **%** yield**).**

M.p. >270 °C**.** **^{1}H NMR (DMSO-d_6, 400 MHz)** δ 7.82 **(**4H, *s*, ArH**),** 7.74 **(**1H, *t*, *J* **=** 7.6 Hz, ArH meta to CONH**),** 8.23 **(**2H, *d*, *J* **=** 7.6 Hz, ArH ortho to CONH**),** 8.59 **(**1H, *s*, ArH ortho to CONH**),** 10.57 **(**2H, *s*, CONH**). ^{13}C NMR (DMSO-d_6, 100 MHz)** δ 127.47 **(**CH_{Ar}**),** 128.48 **(**4xCH_{Ar}**),** 129.19 **(**CH_{Ar}**),** 131.19 **(**2x C_{Ar}-NH**),** 132.56 **(**CH_{Ar}**),** 132.89 **(**2x C_{Ar}-Cl**),** 133.67 **(**2x C_{Ar}-CONH**),** 134.95 **(**4x C_{Ar}-Cl**),** 164.80 **(**2xCONH**). HR-TOFMS (ES$^+$):** *m/z* 544.8723 $[M+Na]^+$; calcd for $C_{20}H_{10}Cl_6N_2O_2$+Na, 542.8765.

N,*N*'-Bis(2,4,5-trichlorophenyl)isophthalamide, **2**

To a solution mixture of isophthaloyl dichloride (101.9 mg, 0.50 mmol) and 2,4,5- trichloroaniline (242.5 mg, 1.25 mmol) in CH_3CN (2.0 mL) was added TEA **(**0.20 mL, 1.43 mmol**)** and DMAP **(**12.0 mg, 0.11 mmol**)** were used as base and catalyst**.** The reaction mixture was stirred at 60-80 °C for 24 hours before being quenched with water and extracted with EtOAc**.** After removal of the solvent, purification was accomplished by column chromatography eluting with (25%) EtOAc-Hexane gives product **2** as a white solid **(**127.2 mg, 0.24 mmol, 48 **%** yield**).**

M.p. >270 °C**.** **^{1}H NMR** (**DMSO-d_6, 400 MHz**) δ 8.00 **(**2H, *s*, ArH ortho to NHCO**),** 7.96 **(**2H, *s*, ArH para to NHCO**),** 7.74 **(**1H, *t*, *J* **=** 8.0 Hz, ArH meta to CONH**),** 8.20 **(**2H, *d*, *J* **=** 8.0 Hz, ArH ortho to CONH**),** 8.55 **(**1H, *s*, ArH ortho to CONH**),** 10.46 **(**2H, *s*, CONH**). ^{13}C NMR (DMSO-d_6, 100 MHz)** δ 127.55 **(**CH_{Ar}**),** 128.97 **(**2xCH_{Ar}**),** 129.15 **(**2x CH_{Ar}**),** 129.88 **(**2x C_{Ar}-NH**),** 129.15 **(**2x C_{Ar}-NH**),** 129.75 **(**CH_{Ar}**),** 131.25 **(**2x C_{Ar}-Cl**),** 130.77 **(**2x C_{Ar}-Cl**),** 133.90 **(**2x C_{Ar}-CONH**),** 135.22 **(**2x C_{Ar}-Cl**),** 165.06 **(**2xCONH**). HR-TOFMS (ES$^+$):** *m/z* 544.8730 $[M+Na]^+$; calcd for $C_{20}H_{10}Cl_6N_2O_2$+Na, 542.8765.

Synthesis of Pyridine-Base Anion Receptor

N,*N*'-Bis(2,4,6-trichlorophenyl)pyridine-2,6-dicarboxamide, **3**

To a solution mixture of 2,6-pyridine dicarbonyl dichloride (100.9 mg, 0.49 mmol) and 2,4,6-trichloroaniline (245.9 mg, 1.24 mmol) in CH_3CN (2.0 mL) was added tri-*n*-buthylamine **(**TBA**) (**0.35 mL, 0.15 mmol**)** and DMAP **(**12.0 mg, 0.1085 mmol**)** were used as base and catalyst**.** The reaction mixture was stirred at 60-80 °C for 24 hours and extract before being quenched with water and extracted with EtOAc**.** After removal of the solvent, purification was accomplished by column chromatography eluting with (100%) CH_2Cl_2 to give product **3** as a white solid **(**122.0 mg, 0.23 mmol, 47 **%** yield**).**

M.p. >270 °C**.** **^{1}H NMR** (**DMSO-d_6, 400 MHz**) δ 7.90 **(**4H, *s*, ArH ortho to NHCO**),** 8.33 **(**1H, *t*, *J* **=** 7.6 Hz, ArH meta to CONH**),** 8.39 **(**2H, *d*, *J* **=** 7.6 Hz, ArH ortho to CONH**),** 11.12 **(**2H, *s*, CONH**). ^{13}C NMR (DMSO-d_6, 100 MHz)** δ 125.85 **(**2xCH_{Ar}**),** 128.62 **(**4xCH_{Ar}**),** 132.01 **(**2xC_{Ar}-NH**),** 133.26 **(**2xC_{Ar}-Cl**),** 135.00 **(**4xC_{Ar}-Cl**),** 140.62 **(**CH_{Ar}**),** 147.60 **(**2x$C_{Pyridine}$-CONH**),** 162.00 **(**2xCONH**). HR-TOFMS (ES$^+$):** *m/z* 545.8676 $[M+Na]^+$; calcd for $C_{19}H_9Cl_6N_3O_2$+Na, 543.8718.

N,*N*'-Bis(2,4,5-trichlorophenyl)pyridine-2,6-dicarboxamide, **4**

To a solution mixture of 2,6-pyridine dicarbonyl dichloride (101.7 mg, 0.50 mmol) and 2,4,5-trichloroaniline (246.8 mg, 1.25 mmol) in CH_3CN (2.0 mL) was added TBA **(**0.35 mL, 0.15 mmol**)** and DMAP **(**13.20 mg, 0.11 mmol**)** were used as base and catalyst**.** The reaction mixture was stirred at 60-80 °C for 24 hours and extract before being quenched with water and extracted with EtOAc**.** After removal of the solvent, purification was accomplished by column chromatography eluting with (100%) CH_2Cl_2 to give product **4** as a white solid **(**98.6 mg, 0.19 mmol, 38 **%** yield**).**

M.p. >270 °C**.** **^{1}H NMR** (**DMSO-d_6, 400 MHz**) δ 8.06 **(**2H, *s*, ArH meta to NHCO**),** 8.67 **(**2H, *s*, ArH ortho to NHCO**),** 8.25 **(**1H, *t*, *J* **=** 8.0 Hz, ArH meta to CONH**),** 7.82 **(**2H, *d*, *J* **=** 6.4 Hz, ArH ortho to CONH**),** 7.83 **(**2H, *d*, *J* **=** 6.0 Hz, ArH ortho to CONH**),** 10.51 **(**2H, *s*, CONH**). ^{13}C NMR (DMSO-d_6, 100 MHz)** δ 129.15 **(**2xCH_{Ar}**),** 129.35 **(**2xCH_{Ar}**),** 130.01 **(**2x C_{Ar}-NH**),** 131.24 **(**2x C_{Ar}-NH**),** 140.43 **(**CH_{Ar}**),** 134.32 **(**2x C_{Ar}-Cl**),** 132.26 **(**2x C_{Ar}-Cl**),** 148.83 **(**2x $C_{Pyridine}$-CONH**),** 135.67 **(**2x C_{Ar}-Cl**),** 165.78 **(**2xCONH**). HR-TOFMS (ES$^+$):** *m/z* 545.8572 $[M+Na]^+$; calcd for $C_{19}H_9Cl_6N_3O_2$+Na, 543.8625.

Synthesis of hexafluorophosphate salts

1 Equivalent of the synthesized compounds **3** and **4** were dissolved in dichloromethane **(**DCM**)** and 1 equivalent of hexafluorophosphoric acid **(**60**%** wt in water**).** The solution was stirred for 15 minutes and the solvent was removed and dried in rotary evaporator to give 2,6-bis**(**2,4,6-trichlorophenylcarbamoyl**)**pyridinium, **5** and 2,6-bis**(**2,4,5-ttrichlorophenyl carbamoyl**)**pyridinium, **6** respectively.

Computational method

The optimized structures of compounds **1**-**6** and their complexes with F^-, Cl^-, Br^-, $H_2PO_4^-$, HSO_4^-, NO_3^- and CH_3COO^-, their thermodynamic properties and have been computed with the density functional theory (DFT) at the B3LYP/6-31G+(d) level of theory in gas phase using the GAUSSIAN09 program.[14]

Nuclear magnetic resonance titration techniques

The anion binding properties of compounds **1**-**6** have been studied in DMSO-d_6 by the NMR titration techniques. The anions have been used as tetrabutylammonium salts which are TBA·F, TBA·Cl, TBA·Br, TBA·H_2PO_4, TBA·HSO_4, TBA·NO_3 and TBA·CH_3COO. The EQNMR program has been used to calculate the binding constants (K_{assoc}) of receptors **1**-**6** with these anions by monitoring the proton chemical shifts of the receptors.[15]

Results and Discussion:

Trichlorophenyl amide-based anion receptors were synthesized by the coupling reaction of isophthaloyl chloride, 2,6-pyridine dicarbonyl dichloride, 2,4,6-trichloroaniline and 2,4,5-trichloroaniline to obtain compounds **1**-**4** in 51, 48, 48 and 38 % yield respectively. Their structures were elucidated based on ^{1}H-NMR, ^{13}C-NMR and high resolution mass spectrometry. The protonation reactions were used to synthesize compounds **5** and **6** from the compounds **3** and **4** respectively.

The optimized structures of compounds **1**-**6** obtained by the computational methods in gas phase are shown in Fig .1 .The optimized complexes structures of these compounds with F^-, Cl^-, Br^-, $H_2PO_4^-$, HSO_4^-, NO_3^- and CH_3COO^- have been shown in Figure 2 - Figure 8 respectively .These results show that the receptors transformed their geometries from *syn-anti*, for compounds **1**-**6**, to *syn-syn* forms for all of the complexes with F^-, Cl^-, Br^-, $H_2PO_4^-$, HSO_4^-, NO_3^- and CH_3COO^-. Their NH-amide and CH-phenyl protons have been used to bind these anions.

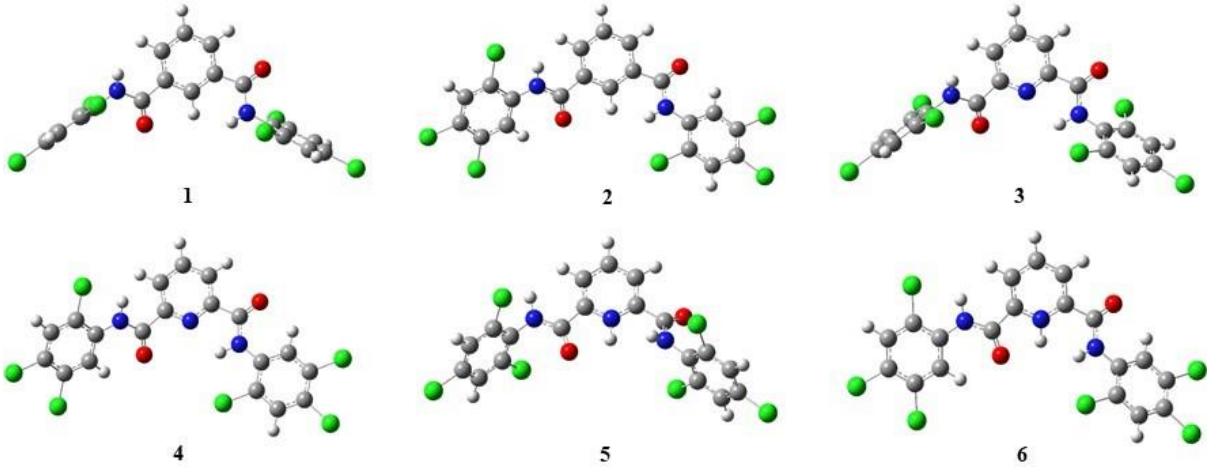

Figure 1.

The optimized structures of compounds **1**-**6**.

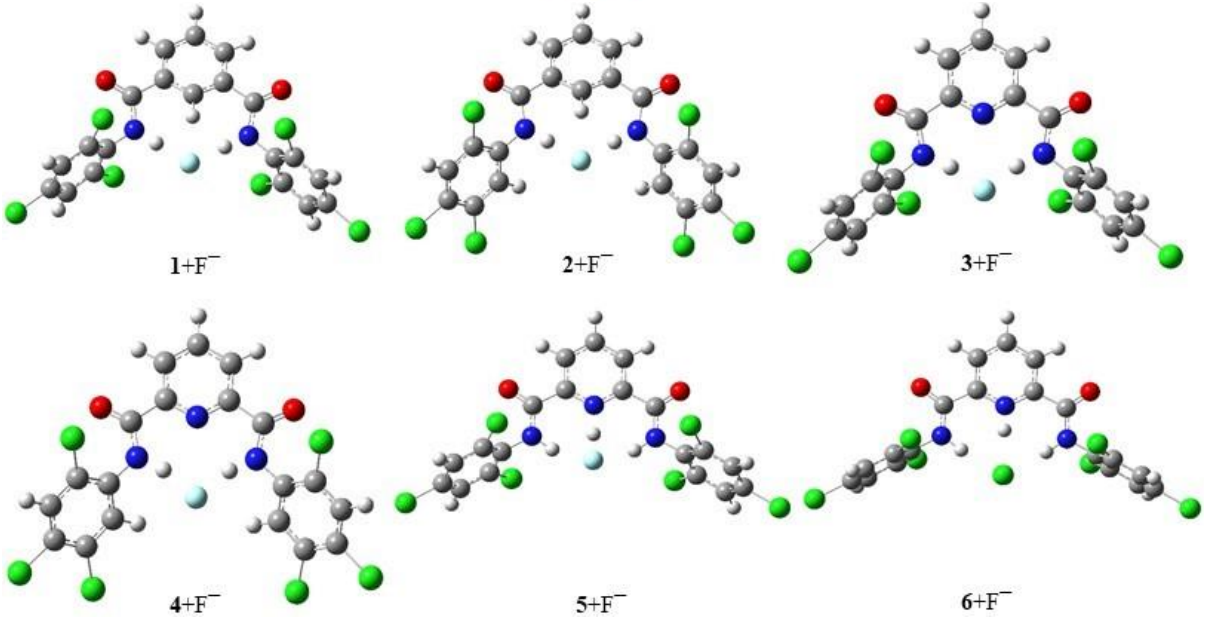

Figure 2.

The optimized complexes structures of compounds **1**-**6** with F^-.

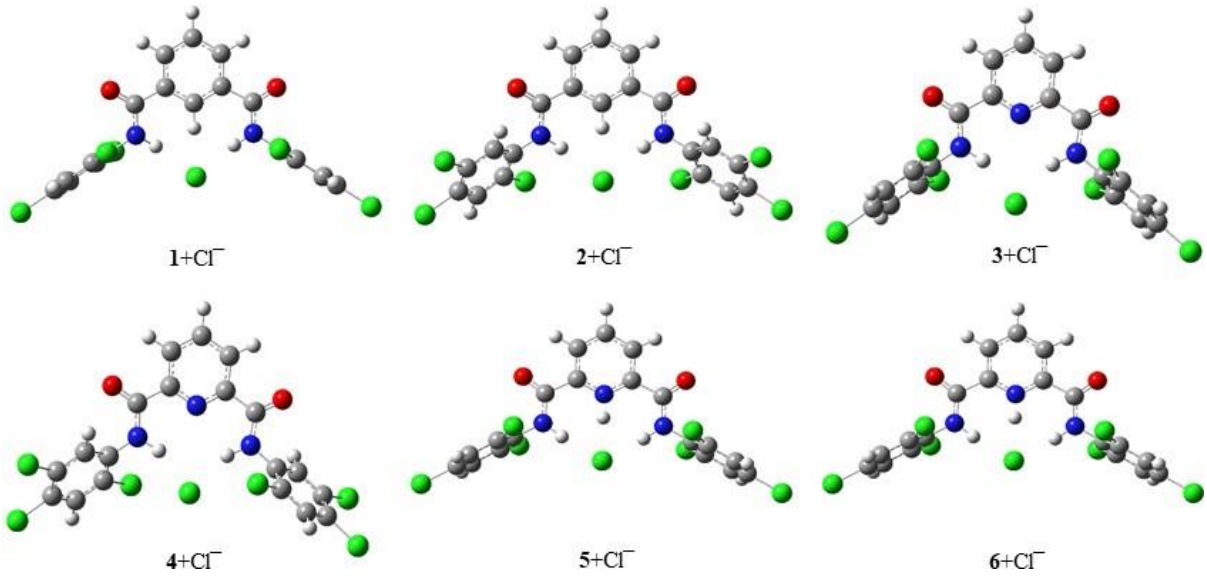

Figure 3.

The optimized complexes structures of compounds **1**-**6** with Cl^-.

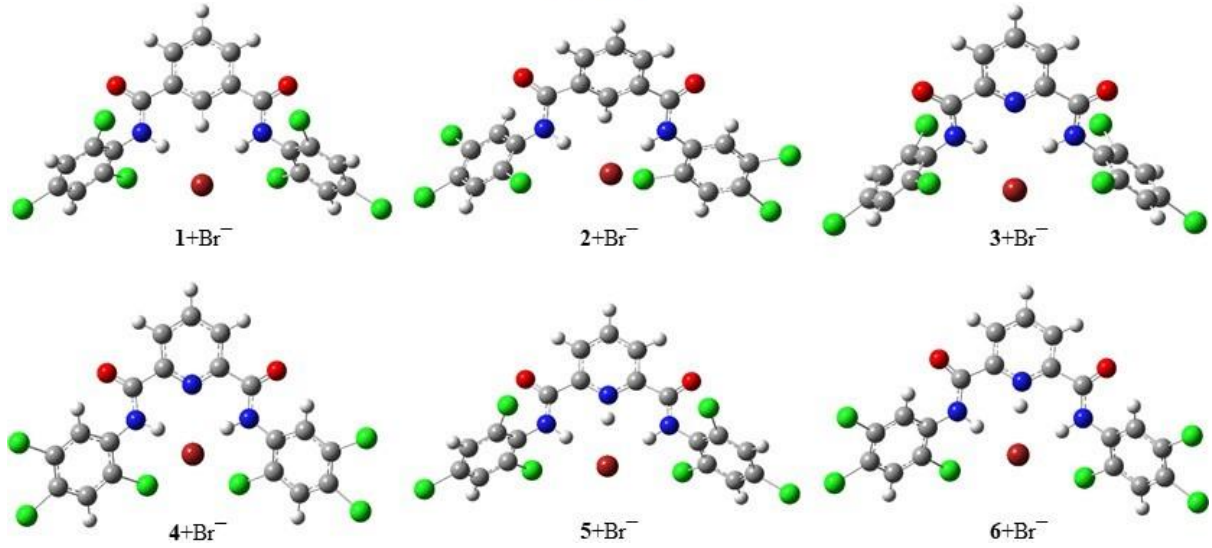

Figure 4.

The optimized complexes structures of compounds **1**-**6** with Br^-.

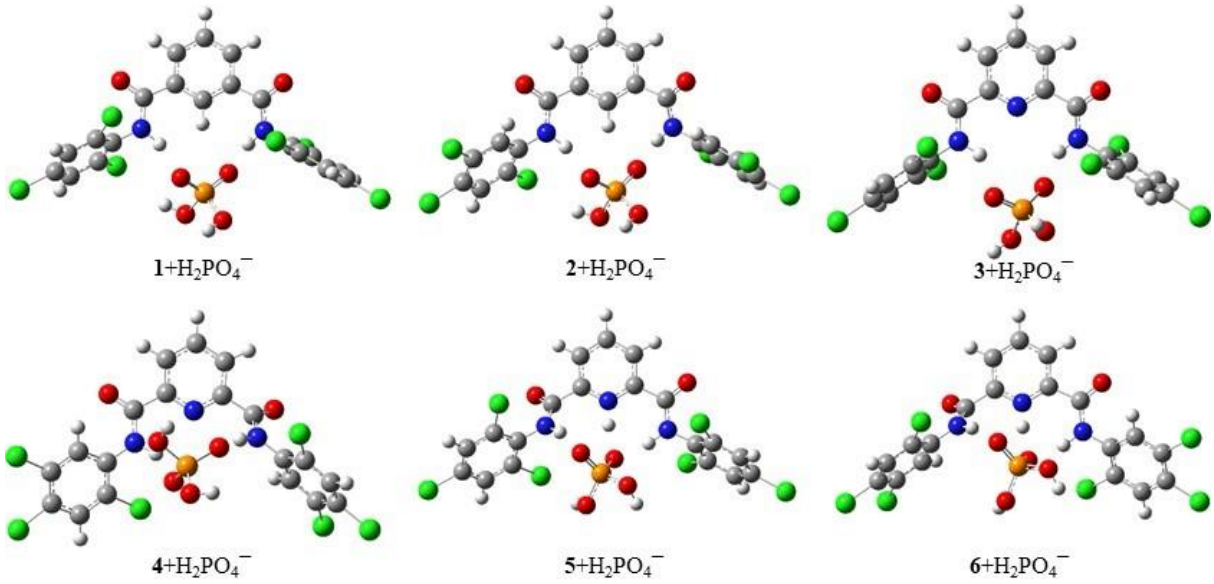

Figure 5.

The optimized complexes structures of compounds **1**-**6** with $H_2PO_4^-$.

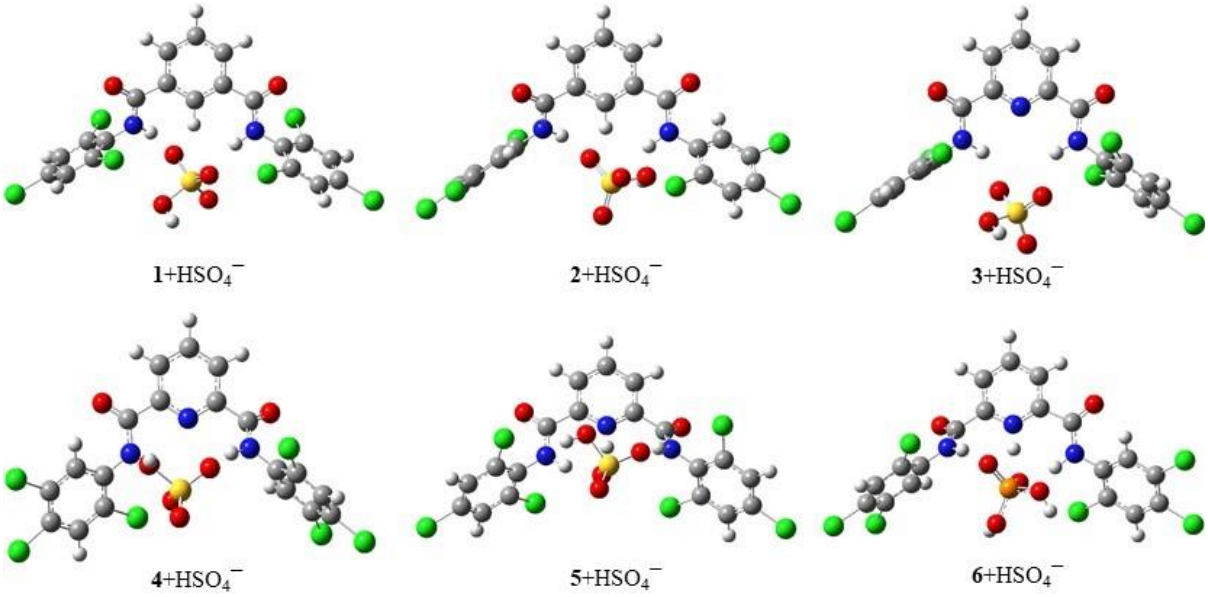

Figure 6.

The optimized complexes structures of compounds **1**-**6** with HSO_4^-.

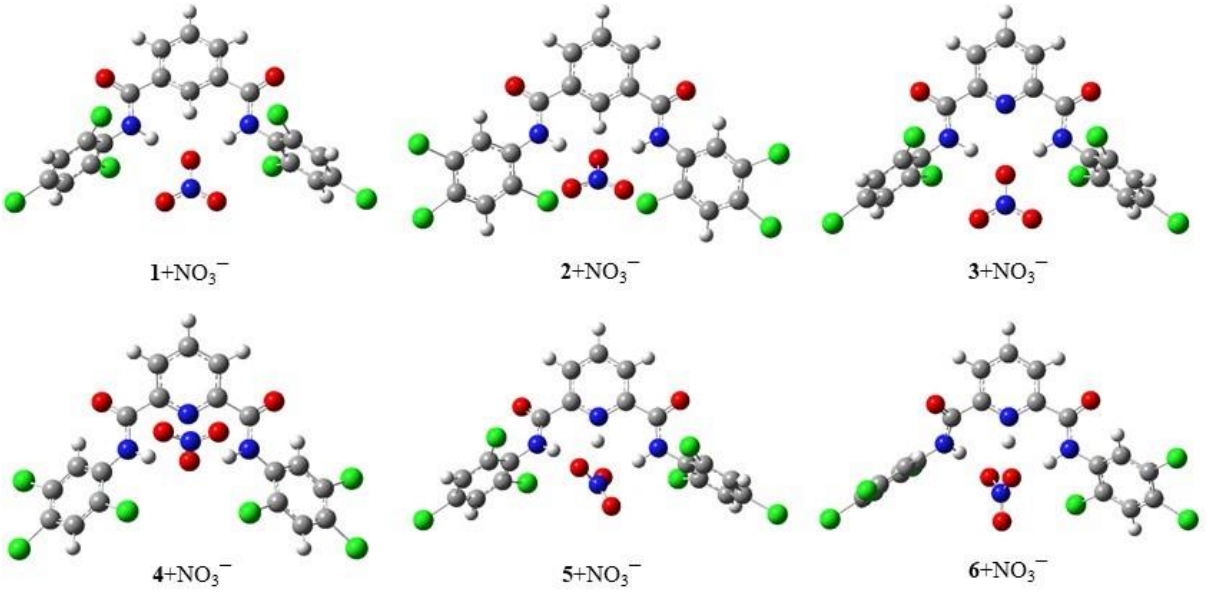

Figure 7.

The optimized complexes structures of compounds **1**-**6** with NO_3^-.

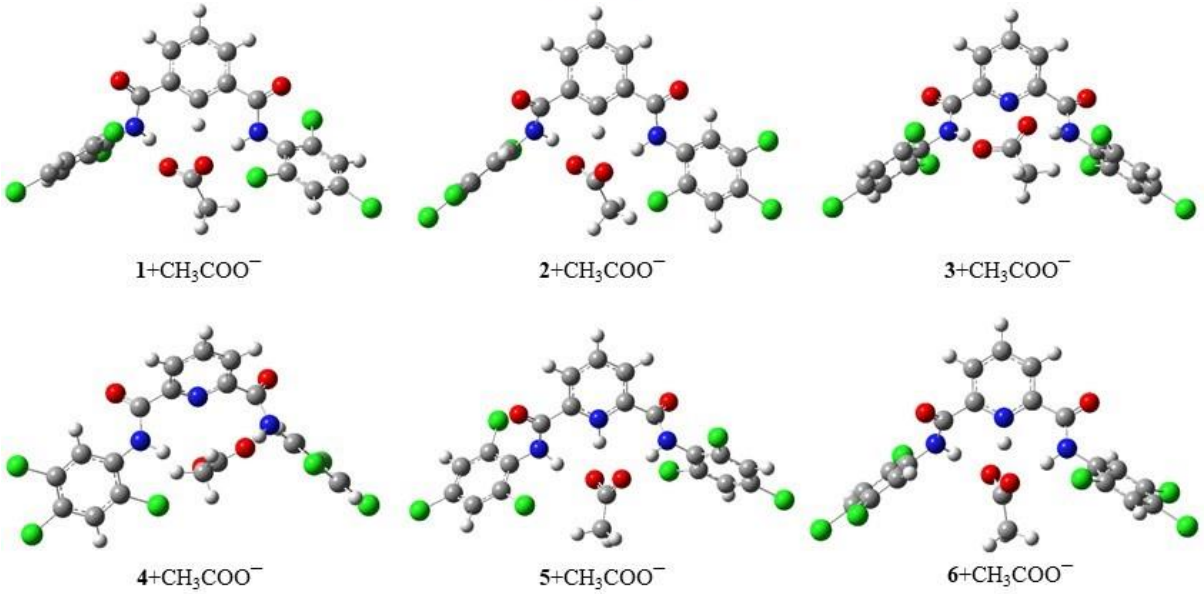

Figure 8.

The optimized complexes structures of compounds **1**-**6** with CH_3COO^-.

Changes of enthalpy (ΔH^0_{298}) and standard Gibbs free energy (ΔG^0_{298}) of compounds **1**-**6** with F^-, Cl^-, Br^-, $H_2PO_4^-$, HSO_4^-, NO_3^- and CH_3COO^- computed at B3LYP/6-31G+(d) in gas phase have been shown in Table 1. The calculated results show that most of these trisubstituted isophthalamide-base anion receptors **1**–**6** prefer to bind fluoride ion due to their highest ΔH^0_{298} and standard ΔG^0_{298} comparing with the others complexes. Since the basicity property of fluoride ion is harder than other anions in this study.

Table 1.

Change of Enthalpy (ΔH^0_{298}) and standard Gibbs Free energies change (ΔG^0_{298}) of compounds **1**-**6** complexes with F^-, Cl^-, Br^-, $H_2PO_4^-$, HSO_4^-, NO_3^- and CH_3COO^- computed at the. B3LYP/6-31+G(d) level of theory.

Complexes	F^-	Cl^-	Br^-	$H_2PO_4^-$	HSO_4^-	NO_3^-	CH_3COO^-
ΔH^0_{298} (kcal.mol^{-1})							
1	-65.67	-38.65	-44.12	-38.59	-31.05	-33.94	-44.01
2	-63.17	-34.58	-39.30	-33.99	-27.08	-30.08	-39.96
3	-67.34	-37.74	-44.28	-34.72	-29.41	-35.04	-40.83
4	-64.57	-32.35	-38.77	-29.58	-24.13	-25.45	-35.60
5	-158.07	-114.90	-117.58	-114.26	-100.75	-105.27	-131.57
6	-153.88	-111.92	-115.31	-111.75	-99.79	-102.93	-132.71
ΔG^0_{298} (kcal.mol^{-1})							
1	-56.07	-30.79	-35.92	-25.95	-19.36	-22.41	-32.81
2	-53.59	-26.60	-31.17	-21.31	-15.44	-18.23	-27.68
3	-58.85	-31.03	-36.12	-24.76	-19.03	-24.62	-31.31
4	-55.24	-24.62	-30.47	-18.59	-13.08	-12.26	-24.25
5	-149.93	-107.34	-109.54	-100.42	-87.48	-93.11	-119.29
6	-146.07	-104.14	-106.96	-99.16	-87.52	-91.21	-122.01

The associate constants (K_{assoc}) of compounds **1**-**6** with TBA·F, TBA·Cl, TBA·Br, TBA·H_2PO_4, TBA·HSO_4, TBA·NO_3 and TBA·CH_3COO in DMSO-d_6 have been investigated via the EQNMR program using the NH-amide proton chemical shifts data, shown in Table 2.

Table 2.

The associate constants (K_{assoc}) of compounds **1**-**6** with TBA·F, TBA·Cl, TBA·Br, TBA·H_2PO_4, TBA·HSO_4, TBA·NO_3 and TBA·CH_3COO obtained from the NMR titration techniques in DMSO-d_6.

Cpds	K_{assoc} **(kcal.mol^{-1})**						
	TBA·F	TBA·Cl	TBA·Br	TBA·H_2PO_4	TBA·HSO_4	TBA·NO_3	TBA·CH_3COO
1	N.D.	243±27	34±1	594±59	421±71	201±2	147±55
2	N.D.	102±17	33±1	336±35	305±11	192±21	$2.22x10^5$±$2.92x10^3$
3	N.D.	118±4	59±2	153±7	350±16	101±2	194±31
4	N.D.	97±1	165±4	219±20	101±2	88±6	65±18
5	N.D.	164±11	157±2	96±3	64±2	157±2	323±18
6	N.D.	104±1	200±23	139±10	100±8	199±2	39±3

N.D. = cannot detected

The ^{1}H NMR chemical shift of NH-amide protons of compounds **1**-**6** shifted to downfield shift when amounts of TBA·F, TBA·Cl, TBA·Br, TBA·H_2PO_4, TBA·HSO_4, TBA·NO_3 and TBA·CH_3COO were increased during the titrations. However, the change could not be monitored in the TBAF titrations as the proton signals of the NH-amide of the receptors were disappeared at high concentration of fluoride due to the hydrogen atom at NH-amide could be deprotonated by fluoride at high concentrations.[16] Whereas hydrogen bonding to fluoride occurred at low concentration of fluoride. This protonation was not observed with others less basic anion in this work. These downfield shifts occurred because of the compounds interacted with the anions. The binding data of anions fitted a 1:1 receptor:anion binding model well according to the calculated results. These results show that receptors **2** bind CH_3COO^- with the highest K_{assoc} values. These results indicate that receptor **2** can provide suitable binding sites for the acetate ion.

Conclusion:

Trichlorophenyl amide-based anion receptors, *N*,*N*'-bis(2,4,6-trichlorophenyl)isophthalamide, **1**, *N*,*N*'-bis(2,4,5-trichlorophenyl)isophthalamide, **2**, *N*,*N*'-bis(2,4,6-trichlorophenyl) pyridine-2,6-dicarboxamide, **3**, *N*,*N*'-bis(2,4,5-trichlorophenyl)pyridine-2,6-dicarboxamide, **4**, 2,6-bis**(**2,4,6-trichlorophenylcarbamoyl**)**pyridinium, **5**, and 2,6-bis**(**2,4,5-trichlorophenyl carbamoyl**)**pyridinium, **6**, have been synthesized. Their fluoride, chloride, bromide, dihydrogenphosphate, hydrogensulfate, nitrate and acetate ions recognition properties have also been investigated using the DFT calculations and nuclear magnetic resonance spectroscopy techniques. The results show that receptor **2** can be used as acetate receptor.

Acknowledgements:

We would like to thank the Center of Excellence for Innovation in Chemistry (PERCH-CIC) for financial supported for PC. The Research and Development Institute and Department of Chemistry, Faculty of Science, Ramkhamhaeng University are gratefully acknowledged.

References:

1. Gale P. A., Howe E. N. W., Wu X., Spooner M. J. Coord. Chem. Rev. 2018;375:333-372.
2. Gale P. A., Davis J. T., Quesada R. Chem. Soc. Rev. 2017;46(9):2497-2519.
3. Camiolo S., Gale P. A., Hursthouse M. B., Light M. E., Shi A. J. Chem. Commun. 2002:758-759.
4. Gale P. A., Navakhun K., Camiolo S., Light M. E., Hursthouse M. B. J. Am. Chem. Soc. 2002;124:11228-11229.
5. Kavallieratos K., de Gala S. R., Austin D. J., Crabtree R. H. A. J. Am. Chem. Soc. 1997;119:2325-2326.
6. Kim Y. H., Calabrese J., McEwen C. J. Am. Chem. Soc. 1996;118:1545-1546.
7. Coles S. J., Frey J. G., Gale P. A., Hursthouse M. B., Light M. E., Navakhun K., Thomas G. L. Chem. Commun. 2003;568-569.
8. Light M. E., Gale, P. A.; Navakhun, K. Acta Cryst. 2006;E62:o1097-o1098.
9. K. Navakhun, Sawangsri R., Ruangpornvisuti V. Mol. Struct. 2014;1061:32-40.
10. Navakhun K., Ruangpornvisuti V. J. Mol. Struct.(Theochem). 2006;772:23-30.
11. Navakhun K., Ruangpornvisuti V. J. Mol. Struct.(Theochem). 2007;806:145-153.
12. Navakhun K., Ruangpornvisuti V. J. Mol. Struct.(Theochem). 2008;864:26-30.
13. Navakhun K., Ruangpornvisuti V. J. Mol. Struct.(Theochem). 2009;907:131-134.
14. Frisch M. J., et al. Gaussian 09, Revision B.01, Gaussian, Inc., Wallingford CT. 2009.
15. Hynes M. J. J. Chem. Soc., Dalton Trans. 1993;311-312.
16. Elmes R. B. P., Turner P., Jolliffe K. A. Org. Lett. 2013;15:5638-5641.

D_004_OF: SYNTHESIS OF DIMETHYL ETHER ON COPPER OXIDE - ZINC OXIDE-ALUMINIUM OXIDE OVER GRAPHENE OXIDE AND (ɣ-Al_2O_3) CATALYSTS

Nitis Meeploy[1], Pootanet Chaiyaphat[1], Anusorn Whangphuklang[1], Nanchapak Piyabunditgul[1], Montree Thongkum[1,2*]

[1]Department of Chemistry, Faculty of Science, King Mongkut's Institute of Technology Ladkrabang, Bangkok 10520, Thailand
[2]Center of Excellence on Automotive Performance Testing and Super Clean Fuels Research Unit
King Mongkut's Institute of Technology Ladkrabang, Bangkok 10520, Thailand
*e-mail: montree.th@kmitl.ac.th

Abstract:

The catalyst for dimethyl ether synthesis from syngas by using $CuZnOAl_2O_3$/ɣ-Al_2O_3 and $CuZnOAl_2O_3$/graphene oxide with different catalyst preparation methods. As $CuZnOAl_2O_3$ catalyst was prepared by co-precipitation method of CuO, ZnO and Al_2O_3 in molar ratio of 6:3:1. After $CuZnOAl_2O_3$ /ɣ-Al_2O_3 catalysts were prepared by physical mixing and $CuZnOAl_2O_3$ on graphene oxide catalysts in weight ratio of 2:1 were prepared by co-precipitation impregnation methods, the catalysts were then used as a bifunctional catalyst for direct dimethyl ether synthesis from synthesis gas. It was found that the $CuZnOAl_2O_3$ /ɣ-Al_2O_3 catalyst prepared by physical mixing dominated CO conversion percentage, DME selectivity percentage and DME yield percentage of 49.17, 42.39 and 23.95 mol%, respectively.

1. Introduction

Energies are a fundamental factor for every country and people. We use much nonrenewable energy as coal, oil shales, tar sands, crude oil, fuel and natural gas. Petroleum can produce toxic gas and waste, there are negative effect for environment. Recently, the most using alternative fuel for instead the nonrenewable energy, it can be produced without the toxic is Dimethyl Ether (DME). DME have a property as Liquefied Petroleum Gas (LPG) and diesel engine because it has cetane number like diesel, is very clean. Process to produce DME has 2 methods. First, the indirect method, methanol is synthesized on a Copper-based catalyst and then methanol will be dehydrating to dimethyl ether on solid acid catalyst. Second the direct method, DME is synthesized from synthesis gas co-using the bifunctional catalyst, copper-based catalyst incorporated ɣ-Al_2O_3. In this study, the synthesis of DME from syngas (H_2:CO = 1:1) on Cu-based catalyst over different supporter between ɣ-Al_2O_3 and graphene oxide, First the catalyst, $CuZnOAl_2O_3$ prepared by co-precipitation in mole ratio 6:3:1. After that, was mixed with ɣ-Al_2O_3 by physical mixing. Second catalyst, $CuZnOAl_2O_3$ (molar ratio 6:3:1) was mixed with graphene oxide (GO) by co-precipitation impregnation with a weight ratio 2:1. The catalyst activity was studied the reaction with fixed-bed reactor by the bifunctional catalyst. The product was analyzed by Gas Chromatography (GC). The catalyst was characterized by characteristic technique X-ray diffraction (XRD), scanning electron microscope (SEM) and Bruneur-Emmet-Teller Surface Area Analysis (BET).

2. Materials and Methods

2.1. Synthesis of Cu-based catalyst with ɣ-Alumina.

The precursor of the catalyst was prepared with co-precipitation method by adding of a mixed aqueous solution of copper, zinc and aluminium nitrates with the mole ratio 6:3:1 and the aqueous solution of sodium carbonate 0.05 mol/L into a beaker containing a small amount of deionization water. The solution was continuously stirred and controlled pH at 7±0.1 and warmed 70ºC. After precipitation, the solution was stirred at the same

temperature for 1 h and aging for 24 h. The sediment was washed by 80ºC of deionization water and then dried at 80ºC for 12 h. Finally, the sediment was calcined at 350ºC for 3 h. This was $CuZnOAl_2O_3$ (CZA). After that, the catalyst was mixed with solid acid catalyst or supporter, which ɣ-Alumina (ɣ-Al_2O_3) commercial grade by physical mixing in weight ratio 2:1. ɣ-Al_2O_3 was calcined at 550ºC for 3h.

2.2 Synthesis of Cu-based catalyst with graphene oxide.

The graphene oxide was prepared with graphite powder mixed with sodium nitrate into the round bottom flask and aged on cold water bath, then added concentration of sulfuric acid and continuously stirred, added the potassium permanganate into solution at the same time and continuously stirred 15 min. The solution was heated with water at 40ºC and continuously stirred until the suspension moved to dark green color, and then added distilled water while cooling and stirred at 90ºC, that moved to brown color, then added hydrogen-peroxide and 10%V/V hydrochloric acid**.** The sediment was washed by distilled water and then was sonicated at current 50A vibrate 25 sec for 2 hr. Finally, the sediment was centrifuged at 7000 rpm for 5 min, which a suspension of graphene oxide. The Cu-based catalyst over graphene oxide was prepared with co-precipitation method by adding of a mixture between aqueous solution of copper, zinc and aluminium nitrates in mole ratio 6:3:1 with aqueous solution of graphene oxide in weight ratio 2:1 and the aqueous solution of sodium carbonate 0.05 mol/L containing graphene oxide with a small amount of deionization water. The solution was continuously stirred and controlled pH at 7±0.1 and 70ºC. After precipitation, the solution was stirred at the same temperature for 1 h and aging for 24 h. The sediment was washed by 80ºC of deionization water and then dried at 80ºC for 12 h. Finally, the sediment was calcined at 350ºC for 3 h, which copper oxide zinc oxide aluminium oxide over graphene oxide catalyst.

2.3 Catalyst characterization

All of the catalysts were characterized by characterization technique. X-ray diffraction (XRD) studied about the type of solids with crystalline or amorphous structure and can be investigate a kind of composition within the compound. The microstructure was studied by Scanning Electron Microscope (SEM). and the catalyst surface area, pore size and pore volume were determined by Bruneur-Emmet-Teller Surface Area Analysis (BET).

2.4 Catalytic activity test

The bifunctional catalysts were mixed with quartz sand in weight ratio 1:1 and added it into the fixed-bed reactor. The catalysts were eliminated oxygen gas or the other gas by N_2 at 150ºC for 30 minutes and the catalysts were reduced by 5% H_2 at 250ºC for 2 hours under atmospheric pressure. Before reaction, the synthetic gas (syn gas) was collected for detected with gas chromatography (GC). In the reaction, the syngas, the mole CO:H_2 ratio 1:1, was fed into the reactor with flow rate 20 ml/min at 250ºC and 40 bars, temperature and pressure were controlled by back pressure valve. The weight of catalyst to flow rate of syngas ratio 10.20 g.h.mol^{-1}. The product was collected every hour until 6 hours and analyzed by gas chromatography (GC). The synthetic gas and gas product were detected by a flame ionization detector (FID) and thermal conductivity detector (TCD). The FID was used for separate DME, MeOH, CO_2 and hydrocarbons. The TCD was used for separate CO, Ar, O_2, N_2 and H_2. Argon (Ar) was used as a carrier gas.

3. Results & Discussion

3.1 Catalyst Characterization

3.1.1 XRD Analysis

The XRD patterns of the CZA, prepared by co-precipitation method were shown in Fig.1. The CuO pattern was shown at 2θ 35.50º and 38.60º. The ZnO pattern was shown at 2θ 31.60º, 34.50º and 36.10º. The Al_2O_3 pattern was shown at 2θ 35.10º and 37.37º. Fig.2 showed the catalyst CZA over ɣ-Al_2O_3 prepared by physical mixing in pattern at 2θ 37.70º, 45.90º and 66.90º. Fig.3 shown the catalyst CZA over graphene oxide prepared by co-precipitation impregnation method in pattern at 2θ 11.61º, 13.52º.

3.1.2 SEM Analysis

Fig. 4(a)-4(b) represented the morphology of CZA was prepared by co-precipitation method. The CZA particles were small crystals with unregulated dispersion and agglomerate. Fig. 5(a)-5(b) showed the morphology of CZA/ɣ-Al_2O_3. The ɣ-Al_2O_3 particles were small flaky, which porosity and high surface area. Fig. 6(a)-6(b) showed the morphology of CZA/GO. The graphene oxide particles were large flaky. Table 1 indicated a figure of crystalline size and dispersion of different catalyst.

3.1.3 BET Analysis

Surface area and porosity of catalysts, prepared by different method, were shown in Table 2. CZA/ɣ-Al_2O_3 had a highest surface area, pore volume and pore size are 109.80 m^2/g, 0.58 cm^2/g and 2.11 nm. That results indicated better than CZA/GO, which had a surface area, pore volume and pore size are 96.35 m^2/g, 0.52 cm^2/g and 2.16 nm. The characterization by XRD, SEM, BET represented the different results because the catalyst was prepared by difference of solid acid or supporter.

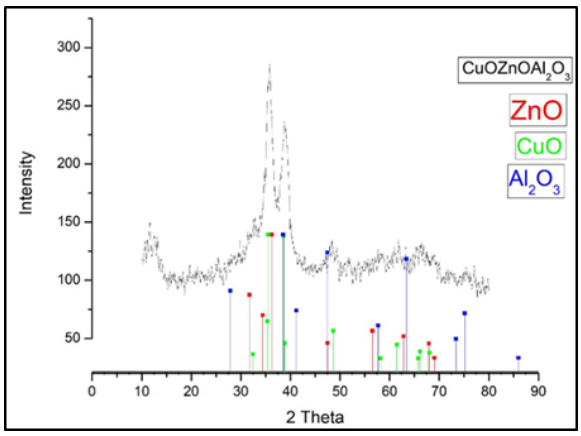

Figure 1. XRD pattern standard of CZA was prepared by co-precipitation method.

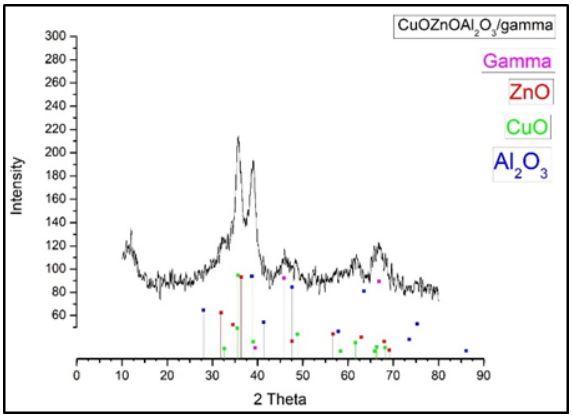

Figure 2. XRD pattern of CZA/ɣ-Al_2O_3 was prepared by physical mixing process. That results be according with standard pattern of Al_2O_3 in fig.1.

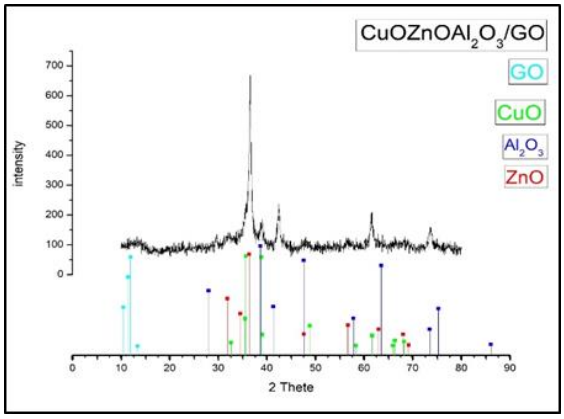

Figure 3. XRD pattern of CZA/GO was prepared by co-precipitation impregnation method.

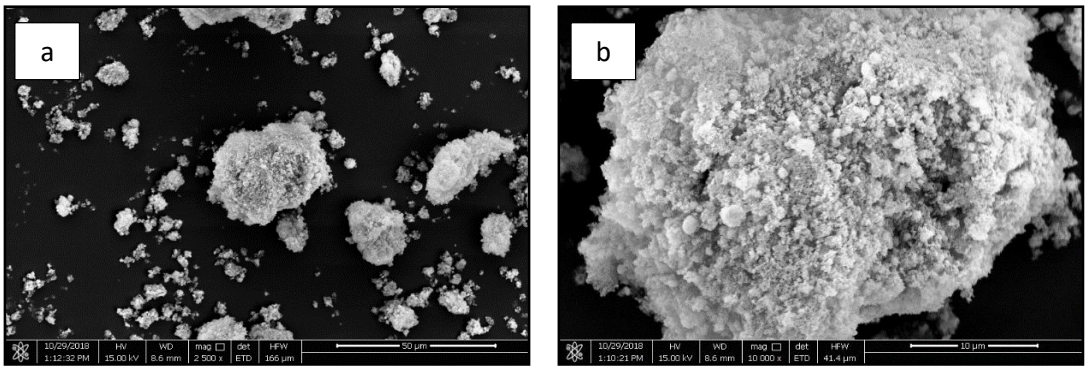

Figure 4(a)-4(b). SEM image of CZA was prepared by co-precipitation, which represented the morphology and dispersion. (a) 5000X (b) 10000X

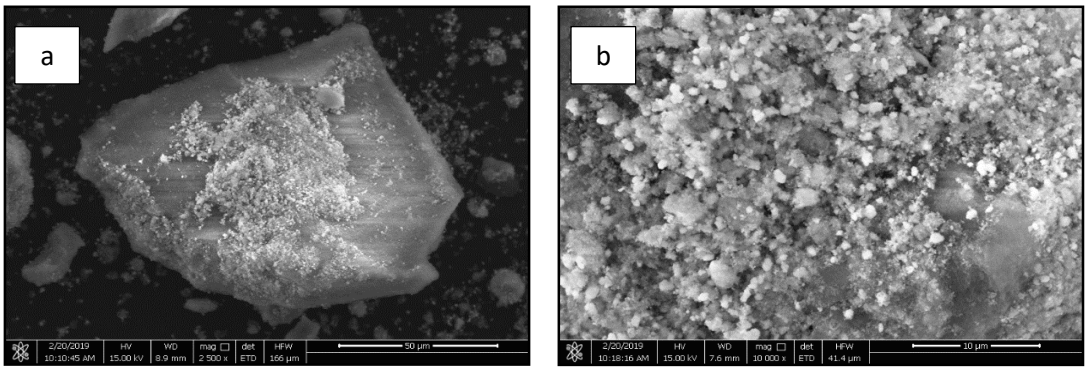

Figure 5(a)-5(b). SEM image of CZA/ɣ-Al_2O_3 was prepared by physical mixing, which represented the morphology and dispersion. (a) 5000X (b) 10000X

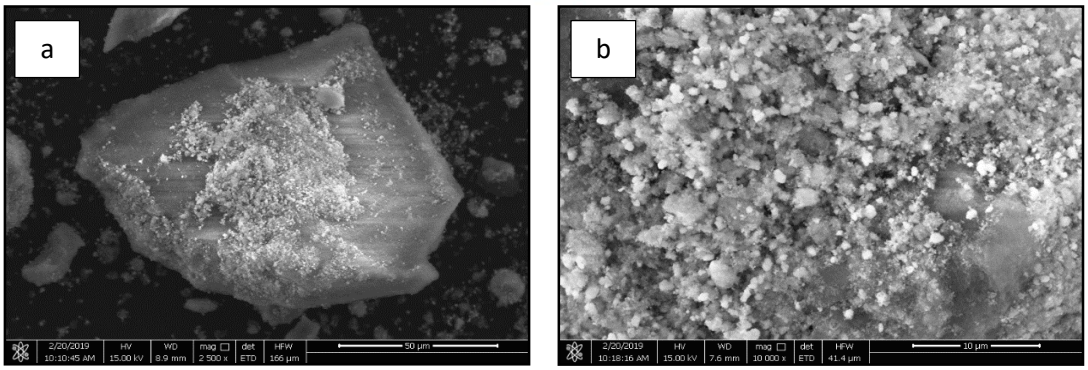

Figure 6(a)-6(b). SEM image of CZA/GO was prepared by co-precipitation impregnation, which represented the morphology and dispersion. (a) 5000X (b) 10000X

Table 1. represented to crystalline size and dispersion of different supporter.

Sample	Cu:Zn:Al ratio	Crystal size	Dispersion (%)
CZA	6:3:1	20.9	4.9
CZA/ɣ-Al_2O_3	6:3:1	19.5	5.6
CZA/GO	6:3:1	42.6	2.5

Table 2. represented the surface area, pore volume and pore size of different supporter.

Sample	Surface area	Pore volume	Pore size
CZA	81.22	0.45	2.21
CZA/ɣ-Al_2O_3	109.80	0.58	2.11
CZA/GO	96.35	0.52	2.16

Table 3. showed %CO conversion, DME selectivity and DME yield by catalysts prepared in different supporter.

Catalyst	%CO conversion	% Selectivity			%Yield of DME
		DME	Methanol	By product	
CZA/ɣ-Al_2O_3	49.71	42.39	0.52	52.33	23.95
CZA/GO	50.50	2.02	3.63	93.71	7.78

3.2 Catalytic Performance

Table 3 shows the catalytic performance of different catalyst. CZA/ɣ-Al_2O_3 was prepared by physical mixing and CZA/GO was prepared coprecipitation impregnation. The catalyst was tested the performance by fixed-bed reactor. First catalyst, CZA/ɣ-Al_2O_3 gave the average CO conversion 49.71 mol%, DME selectivity 42.39 mol%, by product 52.33 mol% and DME yield 23.95%. CZA/GO gave the average CO conversion 50.50 mol%, DME selectivity is 2.02 mol%, by product 93.71 mol% and DME yield 7.78%. That results indicated CZA/ɣ-Al_2O_3 can be catalyze the reaction because it had the highest of %CO conversion, DME selectivity-main product and DME yield also had the least of by product selectivity-unnecessary product. Due to CZA/ɣ-Al_2O_3 had the highest surface area impact to better reaction. The CO conversion, selectivity and yield depend on two factors. First, the surface area of Cu metal for CO hydrogenation reaction. Second, the solid acid or supporter of catalyst, it an important factor.

4. Conclusion

The Cu-based catalysts mixed with ɣ-Al_2O_3 was prepared by different method of solid acid or supporter. The XRD pattern showed the crystallinity and composition of catalyst. The microstructure and morphology were studied by SEM. The catalyst surface area and porosity volume were determined by BET. That can indicate the highest surface area and dispersion more than Cu-based over graphene oxide prepared by co-precipitation impregnation method. The result of catalytic performance showed CZA/ɣ-Al_2O_3, prepared by physical mixing method, used in fixed-bed reactor to synthesize DME from syngas, is the best method that had given highest the percentage of CO conversion, DME selectivity and DME yield, that depend on the surface area of Cu metal and solid acid.

Acknowledgments

This work is supported by King Mongkut's Institute of Technology Ladkrabang, Department Chemistry, Faculty of Science, KRIS and APT-SCFRU research unit.

References

1. Troy A. S., Rodney L. B., Howard L. G. Dimethyl Ether as an Alternative Fuel. Journal of Power Sources. 156 : 497-511. (2006)
2. J. Abu-Dahrieh, D. Rooney, A. Goguet, Y. Saih. Activity and Deactivation Studies for Direct Dimethyl Ether Synthesis using CuO-ZnO-Al_2O_3 with NH_4ZSM-5, HZSM-5 or ɣ - Al_2O_3. Chemical Engineering Journal. 203 : 201-211. (2012)
3. M. Stiefel, R. Ahmad, U. Arnold, M. Doring. 2011. Direct Synthesis of Dimethyl Ether from Carbon-Monoxide-Rich Synthesis Gas: Influence of Dehydration Catalyst and Operating Conditions. Fuel Processing Technology. 92 : 1466-1474. (2011)
4. S.C. Lee, K. Schneider, J. Schumann, A.K. Mogakicherla. Effect of Metal Precursor on Cu/ZnO/Al_2O_3 Synthesized by Flame Spray Pyrolysis for Direct DME Production. Chemical Engineering Science. 138 : 194-202. (2015)
5. G.R. Moradi, S. Nosrati, F. Yaripor. Effect of the Hybrid Catalyst Preparation Method upon Direct Synthesis of Dimethyl Ether from Synthesis Gas. Catalysis Communications. 8 : 598-606. (2007)

D_005_OF: SURFACE–ENHANCED RAMAN SCATTERING USING FLUORESCENCE–QUENCHED CARBON QUANTUM DOTS FOR MERCURY ION DETECTION

Andaru Dena Prasiwi,[1,2] Sanong Ekgasit,[1,2] Prompong Pienpinijtham,[1,2]*

[1]Sensor Research Unit, Department of Chemistry, Faculty of Science, Chulalongkorn University, 254 Phayathai Road, Wangmai, Pathumwan, 10330, Bangkok, Thailand
[2]National Nanotechnology Center of Advanced Structural and Functional Nanomaterials, Department of Chemistry, Faculty of Science, Chulalongkorn University, 254 Phayathai Road, Wangmai, Pathumwan, 10330, Bangkok, Thailand
*e–mail: prompong.p@chula.ac.th

Abstract:

Mercury ion (Hg^{2+}) is one of the most challenging problems due to its high toxicity at low concentration as well as bioaccumulative effects affecting human health. Herein, we propose a strategy to exploit the fluorescence quenching of carbon quantum dots (CQDs) combined with surface-enhanced Raman scattering (SERS) technique to detect Hg^{2+}. CQDs exhibit strong fluorescence emission interfering SERS measurement. However, with the presence of Hg^{2+}, fluorescence from CQDs can be quenched, and SERS spectrum can be collected. In this work, SERS spectra of Rhodamine 6G (R6G) incorporated with CQDs and Hg^{2+} (0.1–100 ng/L) were studied. The SERS spectra of R6G was used as an indicator for Hg^{2+} concentration**.** Upon the addition of Hg^{2+}, SERS spectra showed changes in the ratio between the intensity of CQDs fluorescence at 2000 cm^{-1} and the intensity of R6G at 615 cm^{-1} **(**I_{615}**/**I_{2000}**).** The lowest concentration of Hg^{2+} that can be determined was found to be at 0.5 ng/L Hg^{2+} by using our protocol.

Introduction:

Mercury **(**Hg^{2+}**)** is a heavy metal that is extremely dangerous for all biological organisms **(**animals, plants, *etc***.)**, and human because of its bioaccumulation and toxicity**.**[1,2] Even minor quantity of bioccumulated mercury can cause health problems related to vital body and organs like the spinal cord, kidney, *etc***.**[3] The world health organisation **(**WHO**)** suggested 6 µg**/**L of inorganic mercury as the guideline tolerable value for mercury in drinking water**.** Mercury is a global pollutant that contaminates the environment and affects human health**.** In recent years, traditional detection methods such as atomic absorption spectroscopy **(**AAS**)**, atomic fluorescence spectrometry **(**AFS**)**, gas or liquid chromatography**–**mass spectrometry **(**GC/LC-MS**)**, and colorimetric methods have been used to detect mercury ion Hg^{2+}. However, current analytical methods are often limited by sensitivity (colorimetric detection), high cost, and complex procedures, including pretreatment of samples (AAS, AFS, GC/LC-MS).[4,5] Therefore, there is a strong need for the design of highly sensitive, selective, low-cost, and convenient analytical procedures to detect Hg^{2+}.

Surface-enhanced Raman scattering (SERS) has received wide recognition in various fields because of its high sensitivity, noninvasiveness, high resolution, and fingerprint information about chemical structures.[6] SERS as a powerful sensing technology, provides high sensitivity by using metal nanoparticles (MNPs), such as silver nanoparticles (AgNPs) as a substrate to enhance signal of analytes**.**[7]

Carbon quantum dots (CQDs) are fluorescent carbon nanoparticles with the size less than 10 nm comprising graphitic cores surrounded by various surface functional units.[8,9] CQDs have been applied as a sensing platform for Hg^{2+} due to their broad color range, fluorescence brightness, biocompatibility, and simple synthesis procedures.

Fluorescence of CQDs can interfere SERS measurement. Fortunately, fluorescence of CQDs can be quenched by Hg^{2+} effectively. Therefore, we aim to quench the fluorescence of CQDs by Hg^{2+} to observe SERS signal of Raman dye (rhodamine 6G), as shown in **Figure 1.** Finally, we can determine Hg^{2+} concentration from SERS signal.

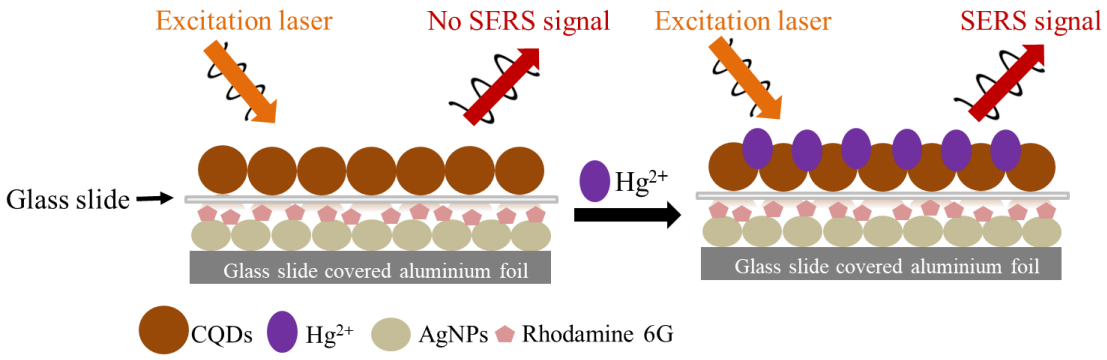

Figure 1. A SERS strategy using fluorescene-quenched CQDs to detect Hg^{2+}.

Methodology:

Chemicals

Citric acid monohydrate, ethylenediamine, and mercury (II) chloride ($HgCl_2$) were purchased from Merck. Silver nitrate ($AgNO_3$), trisodium citrate dihydrate, and rhodamine 6G (R6G) were purchased from Aencore Chemical Co., Ltd., Carlo Erba Reagents S.A.S., and Sigma Aldrich, respectively. All chemicals were used without any further purification. Milli-Q water from Milli-Q-system (Millipore, Bedford, MA, USA), and deionized water were employed as a solvent.

Synthesis of CQDs

CQDs were prepared by a bottom-up hydrothermal method.[10] Typically, 5.0 g citric acid and 1.5 mL ethylenediamine were dissolved in 10 mL milli-Q water. Then, the solution was heated in a Teflon-lined stainless autoclave at 165 ^{o}C for 150 min. After that, the mixture was cooled to room temperature. The mixture turned from colorless to clear brown. The obtained clear brownish liquid was stored at 4 ^{o}C for further characterization and use.

Synthesis of AgNPs

Silver nanoparticle colloid was synthesized by the reduction of $AgNO_3$ with $Na_3C_6H_5O_7$.[11] Briefly, 90 mg of silver nitrate was dissolved in 500 mL milli-Q water and heated until it boiled. A solution of 1% trisodium citrate (10 mL) was added dropwise into a boiling silver nitrate solution under a vigorous stir. The mixture was kept boiling and constantly stirring for 1 hour. The mixture color changed from colorless to milky grey, indicating the formation of silver nanoparticles. The mixture was cooled down to room temperature, and then stored in the flask wrapped by aluminum foil to prevent light degradation of the colloid.

Characterizations

UV–visible spectra and fluorescence spectra were obtained using GENESYS 10S Vis spectrometer (ThermoScientific) and Cary Eclipse fluorescence spectrophotometer (agilent), respectively.

SERS measurement

The prepared AgNPs were mixed with a solution of R6G (1.0 x 10^{-7} M) in the volume ratio of 1:1. The mixture was dropped and dried on a glass slide covered with aluminum foil. After that, the clear glass slide (without aluminum foil) was placed upon the previous glass slide. Then, the synthesized CQDs were separately mixed with Hg^{2+} solutions of different concentrations (0.1, 0.5, 1, 5, 10, 50, and 100 ng/L) in the volume ratio of 1:1 and dropped on the clear glass slide above the dried droplet of AgNPs and R6G mixture. Each sample was measured by focusing on the dried droplet of AgNPs and R6G with 9 repeats (3 drops × 3 different areas). SERS spectra were recorded using DXR Raman microscope (Thermo scientific) with a 532-nm excitation lasers at a laser power of 10 mW using a 25-µm pinhole aperture, and an exposure time of 2 seconds.

Results and Discussion:

UV–visible spectroscopy was carried out to obtain the absorbance spectra of aqueous compounds. The UV–visible spectra of Hg^{2+}, CQDs, AgNPs, and R6G, are shown in **Figure 2.** Since Hg^{2+} is colorless, it does not absorb in the visible region of the spectrum. However, there is a weak absorption in UV region with a maximum at ~200 nm, which is characteristics of Hg^{2+} with nearly zero absorbance intensity.[12] CQDs show a shoulder peak at 242 nm and an absorption band centered at 346 nm. The shoulder peak at 242 nm attributes to π–π* transition of aromatic C=C bond while the absorption band at 346 nm attributes to n–π* transition of C=O bond.[13] AgNPs are known to exhibit a UV–visible absorption maximum in the range of 400–500 nm because of surface plasmon resonance. The broad peak at 413 nm implies a broad distribution of particle size. A shoulder peak at 323 indicates the formation of large particles.[14,15] Furthermore, R6G, which is a cationic dye, has a strong UV–visible absorption at 530 nm in water. This band is responsible for color originated from the aromatic rings connected by amino groups.[16]

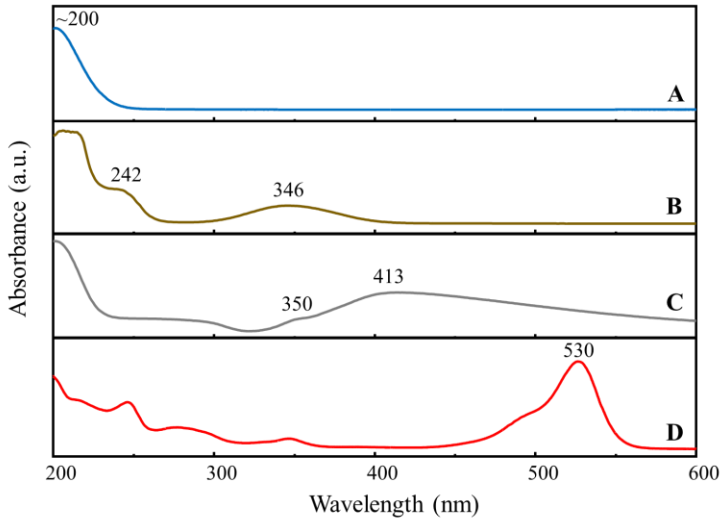

Figure 2. UV–visible spectra of (A) Hg^{2+}, (B) CQDs, (C) AgNPs, and (D) R6G.

The fluorescence spectra of CQDs are shown in **Figure 3.** The maximum excitation and emission wavelengths of CQDs are 346 and 450 nm, respectively. As shown in **Figure 3**, the as-prepared CQDs exhibit strong fluorescence emission, which can be decreased by the addition of Hg^{2+}**.** The sensing principle for fluorescence quenching of CQDs by Hg^{2+} is due to the electron or energy transfer process**.**[17,18] This may be ascribed to the fact that Hg^{2+} has a stronger affinity towards the rich carboxylic group on the surface of CQDs**.**[19]

This study investigated the viability of SERS as a method for the detection of Hg^{2+}**.** Raman spectra of AgNPs, CQDs, and CQDs in the presence of Hg^{2+} are shown in **Figure 4.** As shown in **Figure 4**, the spectrum of only AgNPs is inactive**.** For CQDs with and without Hg^{2+}, there is no peak observed**.** Only baseline shift due to the fluorescence can be detected**.** This measurement proves that the coupling between Hg^{2+}, CQDs, AgNPs, and R6G in producing the SERS active spectrum for Hg^{2+} detection is necessary**.**

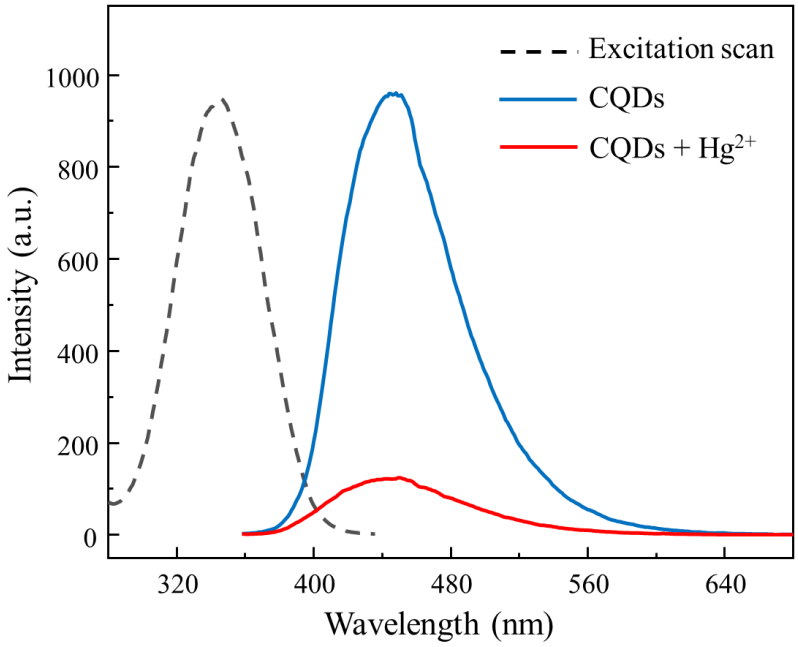

Figure 3. Fluorescene spectra of CQDs in the prescence and absence of Hg^{2+}**.**

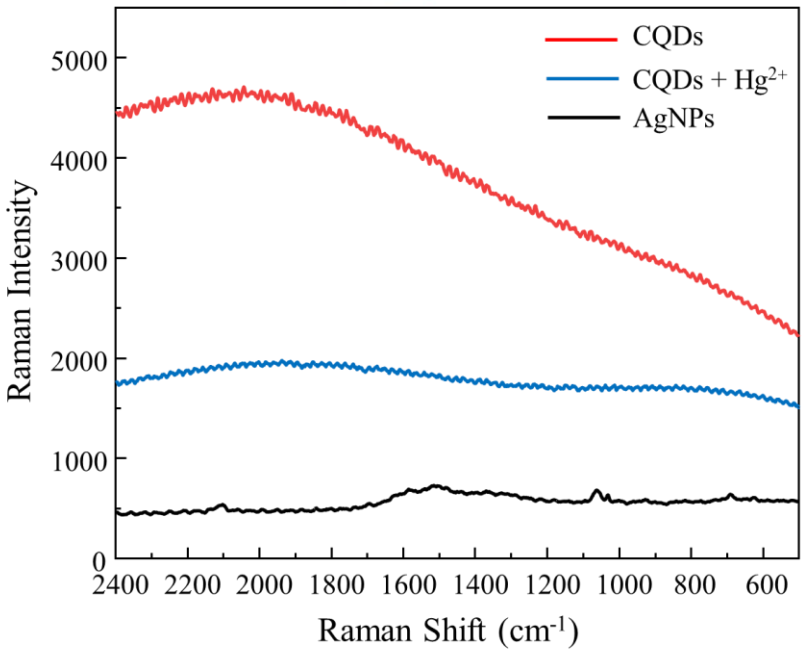

Figure 4. Raman spectra of AgNPs, CQDs, and CQDs in the presence of Hg^{2+}**.**

The SERS active spectra conducted by the coupling between Hg^{2+}, CQDs, AgNPs, and R6G are shown in **Figure 5.** AgNPs attract R6G molecules to assemble on their surface structures, resulting in SERS signal enhancement.[20] The existence of CQDs in the system of AgNPs and R6G generates strong fluorescence leading to a decrease in SERS signal. However, the addition of Hg^{2+} can quench the fluorescence of CQDs in the system, producing an increase in SERS signal.

Figure 5 clearly shows that the coupling of AgNPs-R6G-CQDs-Hg^{2+} enabled SERS detection**.** The band assignments of R6G are shown in **Table 1.** The spectra in **Figure 5** shows the coupling of AgNPs-R6G-CQDs with different concentrations of Hg^{2+} ranging from 0.1, 0.5, 1, 5, 10, 50, and 100 ng**/**L Hg^{2+}**.** SERS spectra demonstrate a clear correlation between the intensity of SERS and Hg^{2+} concentration**.** A decrease in the concentration of Hg^{2+} leads to a decrease in the intensity of SERS signal**.**

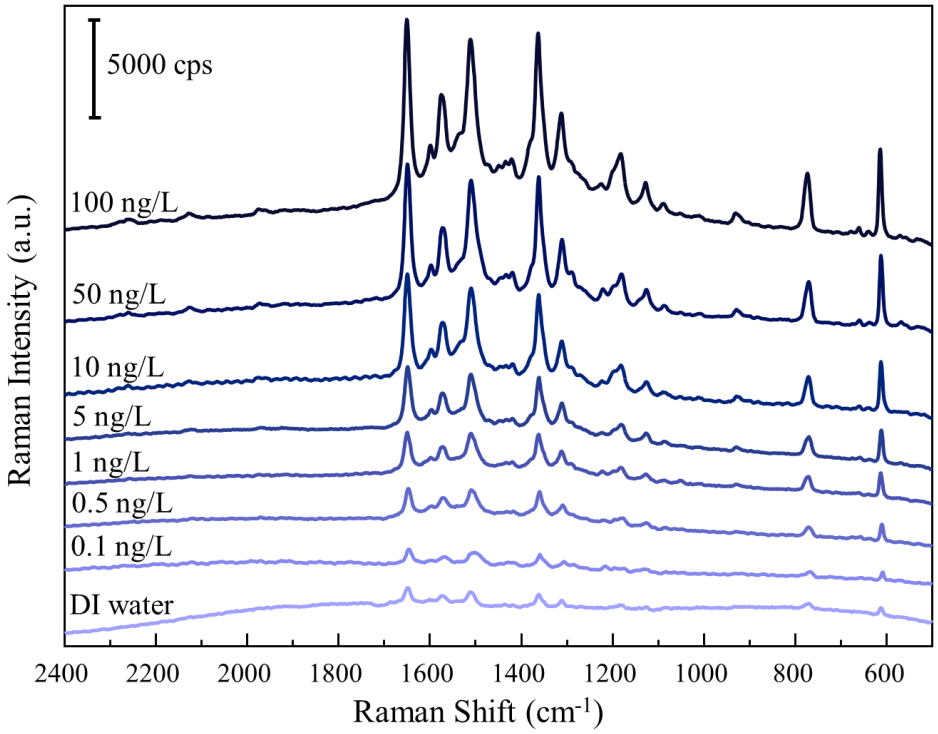

Figure 5. SERS spectra of R6G incorporated with CQDs and different Hg^{2+} concentrations.

Table 1.

Band assignments of R6G spectra

Band assignment	Peak position (cm^{-1})	
	Reference[21]	This work
Aromatic C–C stretching	1652	1651
Aromatic C–C stretching	1575	1577
Aromatic C–C stretching	1509	1510
Aromatic C–C stretching	1365	1367
C–O–C stretching	1312	1316
Aromatic C-H bending	1187	1187
C–H out of plane bending	776	773
C–C–C ring in plane bending	614	615

The intensity ratio plot in **Figure 6** is used to determine the effect of Hg^{2+} concentration on CQDs fluorescence quantitatively. CQDs fluorescence gives a baseline shift in Raman spectrum. Hence, the intensity of the highest fluorescent baseline at 2000 cm^{-1} was chosen to calculate the intensity ratio. On the other hand, R6G peaks can be overwhelmed by strong fluorescence of CQDs, which the addition of Hg^{2+} can generate strong SERS signal due to the quenching of CQDs fluorescence. Accordingly, the peak at 615 cm^{-1} is chosen as the characteristic peak of R6G and can be used as an indicator of Hg^{2+} concentration. As a result, the intensity ratio is determined by dividing a peak height of R6G at 615 cm^{-1} with the intensity of CQDs fluorescence at 2000 cm^{-1}. **Figure 6** displays the intensity ratio between 615 cm^{-1} and 2000 cm^{-1} **(I_{615}/I_{2000})** with different Hg^{2+} concentrations. As the concentration of Hg^{2+} is increased, the intensity ratio increases. The R6G peak is not overwhelmed by CQDs fluorescence and more visible. It can be concluded that the fluorescence of CQDs is effectively quenched by Hg^{2+}. The lowest concentration of Hg^{2+} that can be determined was found to be at 0.5 ng/L Hg^{2+}.

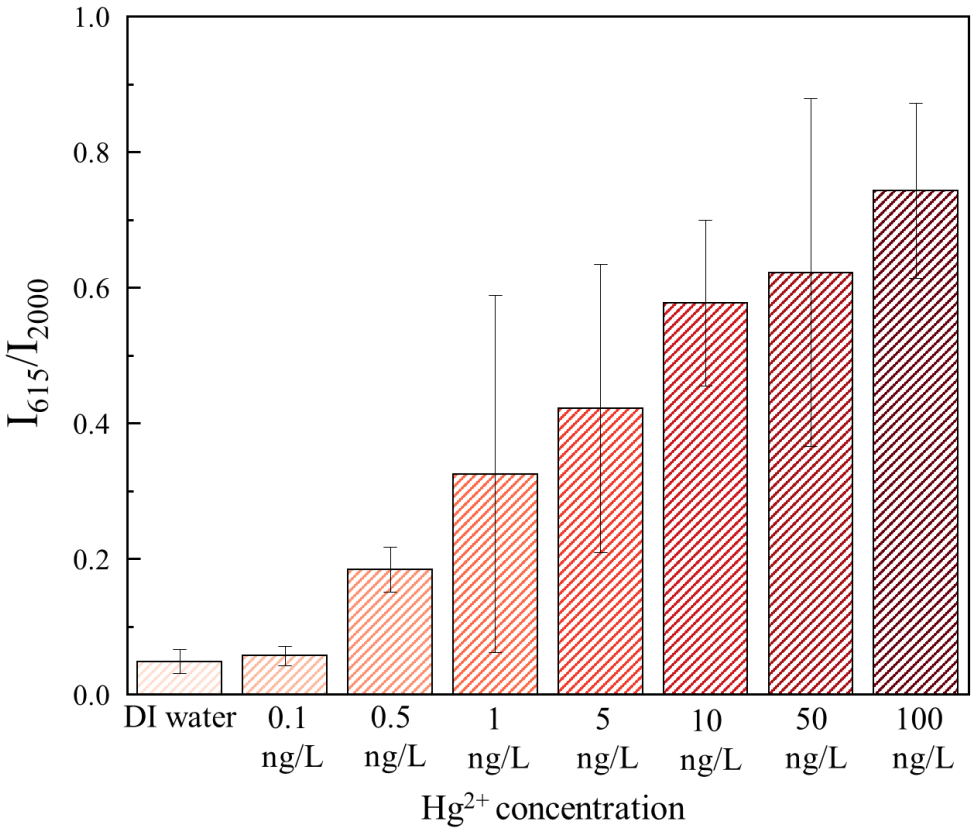

Figure 6. Plot of I_{615}/I_{2000} against Hg^{2+} concentration.

Conclusions:

In summary, a new SERS method for Hg^{2+} detection is proposed based on the coupling between AgNPs, CQDs, Hg^{2+}, and R6G. The proposed method was performed at room temperature and time economical. The addition of Hg^{2+} quenches CQDs fluorescence, generating SERS signal of R6G. The lowest concentration of Hg^{2+} that can be determined was found to be at 0.5 ng/L Hg^{2+}. The probe exhibits good sensitivity for Hg^{2+}, suggesting its promising application. This method will be implemented in tap water and artificial seawater samples in the future study.

Acknowledgements:

This work has been partially supported by the National Nanotechnology Center (NANOTEC), National Science and Technology (NSTDA), Ministry of Science and Technology, Thailand, through its Research Network NANOTEC (RNN) program. Andaru Dena Prasiwi is a scholarship student under ASEAN Scholarship, Department of Chemistry, Faculty of Science, Chulalongkorn University, Thailand.

References:

1. Clarkson TW, Magos, L. Crit. Rev. Toxicol. 2006;36(8):609-662.
2. Castoldi AF, Coccini T, Manzo L. Rev. Environ. Health 2003;18(1):19-32.
3. Onyido I, Norris AR, Buncel E. Chem. Rev. 2004;104(12):5911-5930.
4. Chen L, Zhao Y, Wang Y, Zhang Y, Liu Y, Han XX, Zhao B, Yang J. Analyst 2016;141:4782–4788.
5. Wang Y, Wen G, Ye L, Liang A, Jiang Z. Sci. Rep. 2016;6:19650.
6. Cerf A, Molnar G, Vieu C. ACS Appl. Mater. Interfaces 2009;1:2544-2550.
7. Nie SM, Emory SR. Science 1997;275:1102–1106.
8. Bhunia SK, Nandi S, Shikler R, Jelinek R. Nanoscale 2016;8:3400-3406.
9. Bhunia SK, Pradhan N, Jana NK. ACS Appl. Mater. Inter. 2014;6:7672–7679.
10. Walters, CM, Pao C, Gagnon BP, Zamecnik CR, Walker GC. Adv. Mater. Interfaces 2018;30:1705381.
11. Lee P, Meisel DJT. J. Phys. Chem. A. 1982;86:3391-3395.
12. Nain A, Barman SR, Jain S, Mukherjee A, Satija. Appl. Nanosci. 2017;7(6): 299-307.
13. Zhu S, Song Y, Zhao X, Shao J, Zhang J, Yang BJNR. Nano Res. 2015;8(2): 355-381.
14. Amendola V, Bakr OM, Stellacci F. Plasmonics 2010;5(1),85-97.
15. Panda, SK, Chakraborti S, Basu RN. B. Mater. Sci. 2018;41(4):90.
16. Lasio B, Malfatti L, Innocenzi P. J. Photoch. Photobio A. 2013;271:93-98.
17. Sastry M, Mayya K, Bandyopadhyay K. J. Colloid Surface A. 1997;127(1-3):221-228.
18. Gong YJ, Zhang XB, Chen Z, Yuan Y, Jin Z, Mei L, Zhang J, Tan W, Shen GL, Yu RQ. Analyst 2012;137(4):932-938.
19. Xia YS, Zhu CQ. Talanta 2008;75(1):215-221.
20. Chai F, Wang C, Wang T, Ma Z, Su Z. Nanotechnology 2009;21(2):025501.
21. Deng H, Yu H. Chem. Phys. Lett. 2018;692:75-80.
22. Li H, Liu P, Liang Y, Xiao J, Yang GJN. Nanoscale 2012;4(16),5082-5091.

D_006_PA: ELECTROCHEMICAL PAPER-BASED DNA DEVICE WITH POP-UP ARCHITECTURE FOR HEPATITIS B VIRUS INFECTION DIAGNOSTIC

Chawin Srisomwat,[1] Nattaya Chuaypen,[2] Pisit Tangkijvanich,[2] Tirayut Vilaivan,[3] Orawon Chailapakul[1,*]

[1]Electrochemistry and Optical Spectroscopy Center of Excellence (EOSCE), Department of Chemistry, Chulalongkorn University, Pathumwan, Bangkok, 10330, Thailand
[2]Center of Excellence in Hepatitis and Liver Cancer, Department of Biochemistry, Faculty of Medicine, Chulalongkorn University, Pathumwan, Bangkok, 10330, Thailand
[3]Organic Synthesis Research Unit, Department of Chemistry, Chulalongkorn University, Pathumwan, Bangkok, 10330, Thailand
*e-mail: corawon@chula.ac.th

Abstract:

In this work, a pop-up DNA device combining pop-up structure and DNA sensing for label-free electrochemical detection was first proposed. Inspired by a pop-up greeting card, a pop-up structure with reagent, sample, and electrode zones were designed and fabricated. The sample and reagent zones were used for the hybridization of target DNA and the electrochemical detection, respectively. The paper sensing device was fabricated by the wax-printed method onto the filter paper. Utilizing this structure, time control, and the multistep procedure is enabled within a single device. Herein, the pyrrolidinyl polypeptide nucleic acid (acpcPNA), was used as a probe and immobilized onto sample zone while a working electrode was constructed at the back of this area. After the target DNA was hybridized, the device was folded to perform the differential pulse voltammetry (DPV). The presence of the target DNA exhibited the decrease of current signals from hexacyanoferrate (III)/(II). Of this idea, we reported the proposed device for screening Hepatitis B virus (HBV). Under optimal conditions, a linearity in a range of 50 pM to 100 nM was constructed with the LOD of 1 pM. Furthermore, this DNA pop-up device is capable to differentiate the signal obtained from the target sequences, partially mismatch, and non-complementary sequences. Interestingly, the LOD in a picomolar level was achieved without the labeling and modification steps. The proposed device also showed great potential for applying in samples from patients. Benefiting from this sensing architecture such as its simple operational step and time controlling features, this proposed sensor can open up new possibilities and further extend to a range of point-of-care testing devices.

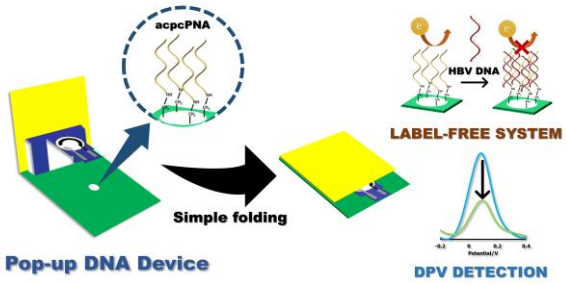

Figure 1. The conceptual idea of the pop-up DNA sensor for infectious disease diagnostic

References

[1] Srisomwat, C., Teengam, P., Chuaypen, N., Tangkijvanich, P., Vilaivan, T., & Chailapakul, O. (2020). Pop-up paper electrochemical device for label-free hepatitis B virus DNA detection. *Sensors and Actuators B: Chemical*, 128077.

D_007_OF: SYNTHESIS OF 1,2-NAPHTHOQUINONE DERIVATIVES AS α-GLUCOSIDASE INHIBITORS

Trang Pham Thi, Ade Danova, Warinthorn Chavasiri*

Center of Excellence in Natural Products Chemistry, Department of Chemistry, Faculty of Science, Chulalongkorn University, Bangkok 10330, Thailand.
*e-mail: warinthorn.c@chula.ac.th

Abstract:

Naphthoquinones are one of the most active natural products found in plants and microorganisms. They represented a variety of pharmacological effects including anti-diabetic, anti-inflammatory and MALT1 inhibition, as well as exhibited significant activity against *Trypanosoma cruzi* and hepatitis C virus. In this research, phenylamino and alkylamino derivatives of 1,2-naphthoquinone were synthesized and evaluated for their anti α-glucosidase activity. The results showed that substituted-aniline component played an important role to in inhibit α-glucosidase. The most active compound was phenylamino derivative **2f** with IC_{50} value of 18.02 μM.

Introduction:

In 2016, WHO evaluated that diabetes mellitus was the seventh most leading cause of mortality for human beings. Diabetes is the main cause of many kinds of chronic diseases such as blindness, kidney failure, heart attacks, stroke and lower limb amputation. With rapid enhancing in diabetic patients, there is an urgent need to develop a new therapy for diabetes.

Diabetes can be classified into two major varieties, types 1 and 2, and several minor variants. Type 1 diabete (5-10%) is due to the loss of insulin-secreting beta cells.[1] Type 2 diabetes (90-95%) involves the host organisms which cannot produce enough insulin.

There are two structural distinct naphthoquinones: 1,4-naphthoquinones (1,4-NQs) and 1,2-naphthoquinones (1,2-NQs) due to the position of carbonyl groups.[2] In recent years, researches on structural modifications and potential therapeutic effects of naphthoquinones for anti-diabetic have received a great deal of attention[3]. Naphthoquinones present their anti-diabetic activity through a variety of mechanisms such as the inhibition of α-glucosidase and protein tyrosine phosphatase 1B[1].

Natural 1,4-NQs are ubiquitous in plants such as plumbagin (**1a**) and menadione (**1b**), both of which exert anti-diabetic effects.[4, 5] In 2002, Ahn *et al*.[3] synthesized a series of 4-aryl-1,2-naphthoquinones with substituents at R^4 position as a PTP1B inhibitor. The results suggested that that the introduction of alkyl or aryl groups at R^4 position increased inhibitory activity.

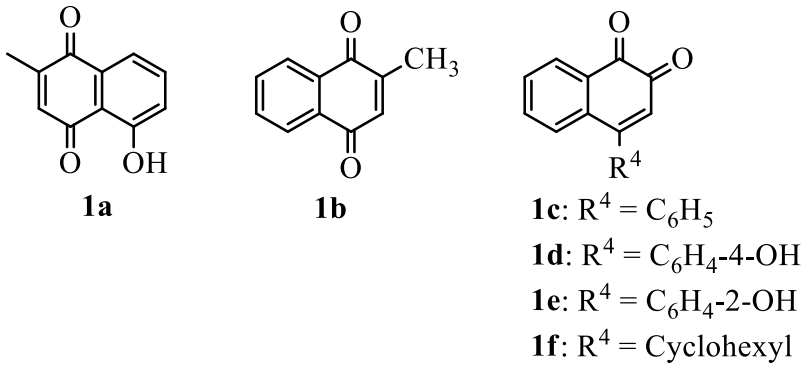

Firgure 1. Plumbagin (**1a**), menadione (**1b**) and some reported 1,2-NQs (**1c**-**1f**)

Methodology:

General: ^{1}H and ^{13}C spectra were performed in $CDCl_3$ or DMSO-d_6 or pyridine-d_5 were recorded by using a Bruker Ultrashield 400 Plus NMR spectrometer with an Oxford YH400 magnet operating at 400 MHz for ^{1}H and 100 MHz for ^{13}C or a Jeol NMR spectrometer. High-resolution mass spectra (HRMS) were recorded on a Bruker Daltonics microTOF using electron spray ionization (ESI). All solvents were distilled prior to use except those which were reagent grades. Thin-layer chromatography (TLC) was performed on aluminum sheets precoated with silica gel (Merck Kieselgel 60 PF254). Silica gel (No. 7734 and 9385, Merck) was used as stationary phase on open column chromatography.

General procedure for the synthesis of phenylamino 1,2-naphthoquinone derivatives: The naphthoquinone derivatives were prepared as previously reported with some modification.[6] Diverse anilines (1.1 equiv) were reacted with sodium 1,2-naphthoquinone-4-sulfonate (1 equiv) in water (150 mL) at room temperature for 2-24 hours (TLC monitoring). In the situation that naphthoquinones precipitated, they were collected by filtration and crystallization from MeOH. In other situations, the mixture was then partitioned with EtOAc. The organic layer was combined, washed with brine, and dried over anhydrous Na_2SO_4 and purified by utilizing silica gel chromatography to give the target compounds **2a**-**2h**.

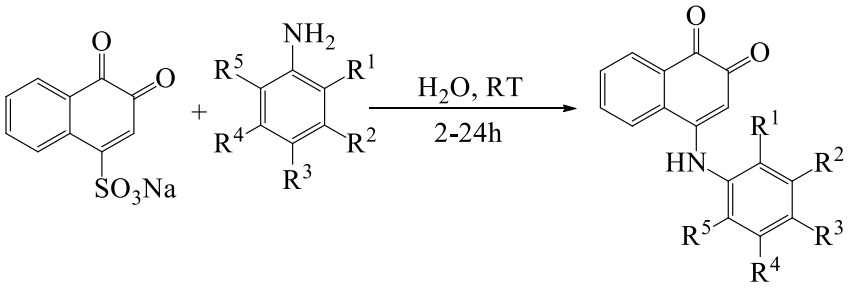

2a $R^1 = R^2 = R^3 = R^4 = R^5 = H$
2b $R^2 = R^3 = R^4 = R^5 = H$, $R^1 = COOH$
2c $R^1 = R^2 = R^4 = R^5 = H$, $R^3 = OMe$
2d $R^1 = R^2 = R^4 = R^5 = H$, $R^3 = Me$
2e $R^1 = R^2 = R^4 = R^5 = H$, $R^3 = F$
2f $R^1 = R^2 = R^4 = R^5 = H$, $R^3 = NO_2$
2g $R^1 = R^2 = R^4 = R^5 = H$, $R^3 = OPh$
2h $R^1 = R^2 = R^4 = R^5 = H$, $R^3 = CH_2CH_2OH$

Scheme 1. Synthesis of phenylamino 1,2-NQ derivatives

General procedure for the synthesis of alkylphenylamino 1,2-naphthoquinone derivatives: The naphthoquinone derivatives were prepared as previously reported with some modification.[7] The corresponding alkylamino (2 equiv), $CeCl_3.7H_2O$ (5% mmol in respect to sodium 1,2-naphthoquinone-4-sulfonate), and sodium 1,2-naphthoquinone 4-sulfonate (1 equiv) in water (20 mL for 1 mmol of sodium 1,2-naphthoquinone-4-sulfonate) were stirred at room temperature for 24-48 hours (TLC monitoring). The mixture was then partitioned with EtOAc. The organic layer was combined, washed with brine, and dried over anhydrous Na_2SO_4 and purified by utilizing silica gel chromatography to give the target compound **3a** and **3b**.

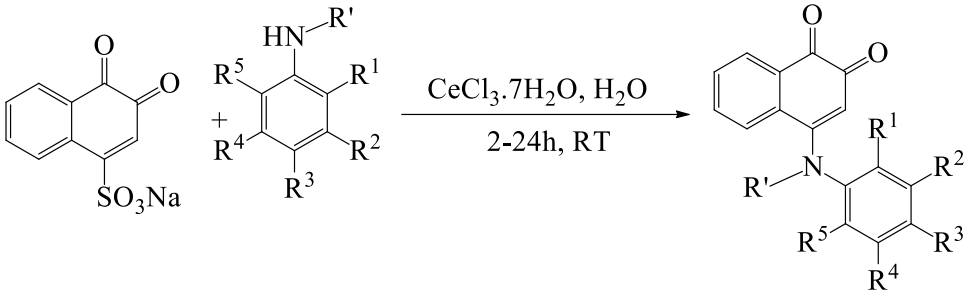

3a $R^1 = R^2 = R^3 = R^4 = H = R^5 = H$, R' = Me

3b $R^1 = R^2 = R^3 = R^4 = H = R^5 = H$, R' = Et

Scheme 2. Synthesis of alkylphenylamino 1,2-NQ derivatives

The synthesis of 4-amino-1,2-naphthoquinone: Compound **4a** was prepared as previously reported.[2] To a solution of 1,2-naphthoquinone (1 equiv) in acetic acid (15 mL) at 40°C, a solution of NaN_3 (1.7 equiv) in water (5 mL) was added. The mixture was stirred at 40°C in 2 hours (TLC monitoring). The precipitate was collected by filtration, washed with brine, and dried over anhydrous Na_2SO_4 and purified by utilizing silica gel chromatography to give the target product.

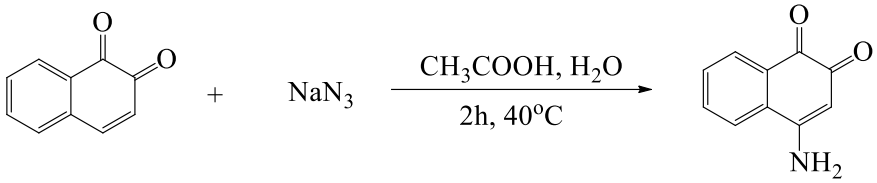

4a

Scheme 3. Synthesis of 4-amino-1,2-NQ (**4a**)

The naphthoquinone derivatives **4b**-**4h** were prepared as previously reported with some modification.[8] The corresponding aliphatic amine (1.11 equiv), K_2CO_3 (2.02 equiv) and sodium 1,2-naphthoquinone-4-sulfonate (1 equiv) in water (10 mL for 1 mmol of sodium 1,2-naphthoquinone-4-sulfonate) were stirred at room temperature for 24-48 hours (TLC monitoring). The mixture was then partitioned with EtOAc. The organic layer was combined, washed with brine, and dried over anhydrous Na_2SO_4 and purified by utilizing silica gel chromatography to give the target product.

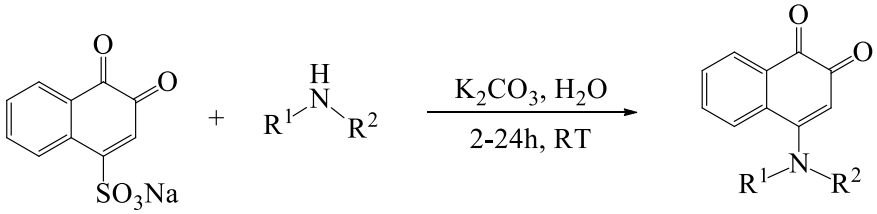

4b R^1 = H, R^2 = Et
4c R^1 = H, R^2 = Propyl
4d R^1 = H, R^2 = Butyl
4e R^1 = H, R^2 = Isobutyl
4f R^1 = H, R^2 = Cyclohexyl
4g R^1 = H, R^2 = Benzyl
4h R^1 = R^2 = Et

Scheme 4. Synthesis of alkylamino 1,2-NQ derivatives

(4-(phenylamino)naphthalene-1,2-dione) (**2a**) (224 mg, 90%): ^{1}H NMR (DMSO-d_6, 400 MHz): δ (ppm) 8.32 (d, *J* = 8 Hz, 1H), 8.04 (d, *J* = 7.6 Hz, 1H), 7.86 (t, *J* = 8 Hz, 1H), 7.74 (t, *J* = 7.6 Hz, 1H), 7.49 (t, *J* = 7.6 Hz, 2H), 7.31 (t, *J* = 7.6 Hz, 1H), 7.24 (brs, 2H), 5.85 (s, 1H). ^{13}C NMR (DMSO-d_6, 400 MHz): δ (ppm) 189.1, 181.3, 155.0, 134.2, 131.6, 129.4, 127.5, 126.1, 124.2, 101.4.

(2-((3,4-dioxo-3,4-dihydronaphthalen-1-yl)amino)benzoic acid) (**2b**) (19.9 mg, 6.8%): ^{1}H NMR (DMSO-d_6, 500 MHz): δ (ppm) 8.04 (d, *J* = 7.5 Hz, 1H), 8.00 (d, *J* = 7.5 Hz, 1H), 7.94 (d, *J* = 7.5 Hz, 1H), 7.84 (t, *J* = 7.5 Hz, 1H), 7.77 (t, *J* = 7.5 Hz, 1H), 7.63 (t, *J* = t Hz, 2H), 7.17 (t, *J* = 7.5Hz, 1H), 6.52 (s, 1H). ^{13}C NMR (DMSO-d_6, 500 MHz): δ (ppm) 183.8, 182.0, 144.3, 140.6, 135.6, 134.2, 133.5, 132.9, 132.5, 130.8, 126.9, 125.9, 123.7, 120.9, 105.2. HRMS (ESI): calcd for $C_{17}H_{11}NO_4$ $[M+Na]^+$: 316.0586, found 316.0578.

(4-((4-methoxyphenyl)amino)naphthalene-1,2-dione) (**2c**) (256.7 mg, 92%): ^{1}H NMR (DMSO-d_6, 400 MHz): δ (ppm) 9.82 (s, 1H), 8.29 (d, *J* = 6.8 Hz, 1H), 8.03 (d, *J* = 7.2 Hz, 1H), 7.86 (t, *J* = 8.4 Hz, 1H), 7.73 (t, *J* = 7.6 Hz, 1H), 7.31 (d, *J* = 7.6 Hz, 1H), 7.07 (d, *J* = 8.0 Hz, 2H), 5.56 (s, 1H), 3.80 (s, 3H). ^{13}C NMR (DMSO-d_6, 400 MHz): δ (ppm) 181.4, 175.7, 158.1, 155.1, 134.4, 132.8, 131.6, 131.4, 130.9, 130.3, 128.2, 127.6, 123.8, 114.7, 100.1.

(4-(*p*-tolylamino)naphthalene-1,2-dione) (**2d**) (164.4 mg, 62.5%): ^{1}H NMR (Pyridine-d_5, 400 MHz): δ (ppm) 8.63 (d, *J* = 8.0 Hz, 1H), 8.34 (d, *J* = 7.6 Hz, 1H), 7.69 (t, *J* = 7.6 Hz, 1H), 7.6 (s, 1H), 7.22 (s, 2H), 7.16 (s, 2H), 6.66 (s, 1H), 2.30 (s, 3H), ^{13}C NMR (Pyridine-d_5, 400 MHz): δ (ppm) 182.9, 156.7, 134.1, 132.4, 131.7, 130.7, 125.7, 21.4.

(4-((4-fluorophenyl)amino)naphthalene-1,2-dione) (**2e**) (130.8 mg, 49%): ^{1}H NMR (Pyridine-d_5, 400 MHz): δ (ppm) 8.61 (d, *J* = 8.0 Hz, 1H), 8.34 (d, *J* = 7.6 Hz, 1H), 7.71 (t, *J* = 7.2 Hz, 1H), 7.65 (t, *J* = 8.8 Hz, 1H), 7.21 (brs, 2H), 7.19 (brs, 2H), 6.61 (s, 1H). ^{13}C NMR (Pyridine-d_5, 400 MHz): δ (ppm) 182.8, 162.1, 160.2, 156.5, 134.1, 132.3, 131.8, 127.4, 125.8, 123.6, 116.9, 116.7, 104.5.

(4-((4-nitrophenyl)amino)naphthalene-1,2-dione) (**2f**) (40.3 mg, 13.7%): ^{1}H NMR (Pyridine-d_5, 400 MHz): δ (ppm) 8.56 (d, *J* = 7.6, 1H), 8.34 (m, 2H), 8.31 (m, 1H), 7.77 (t, *J* = 7.6, 1H), 7.70 (d, *J* = 7.6, 1H), 7.19 (d, *J* = 8.4, 2H), 6.48 (s, 1H). ^{13}C NMR (Pyridine-d_5, 400 MHz): δ (ppm) 182.8, 157.9, 145.0, 135.4, 134.3, 132.3, 132.2, 127.5, 127.2, 126.5, 125.9, 121.8, 113.7, 105.0. HRMS (ESI): calcd for $C_{16}H_{10}N_2O_4$ $[M+Na]^+$: 317.0538, found 317.0555.

(4-((4-phenoxyphenyl)amino)naphthalene-1,2-dione) (**2g**) (76 mg, 22.3%): ^{1}H NMR (DMSO-d_6, 500 MHz): δ (ppm) 8.28 (d, *J* = 8 Hz, 1H), 8.01 (d, *J* = 7.5 Hz, 1H), 7.82 (t, *J* = 7.5 Hz, 1H), 7.70 (t, *J* = 8 Hz, 1H), 7.39 (t, *J* = 8 Hz, 2H), 7.25 (brs, 1H), 7.13 (t, *J* = 7.5 Hz, 1H), 7.09 (d, *J* = 8.5 Hz, 2H), 7.04 (d, *J* = 8 Hz, 2H), 5.81 (s, 1H). ^{13}C NMR (DMSO-d_6, 500 MHz): δ (ppm) 172.6, 156.8, 140.1, 134.7, 132.0, 130.6, 124.2, 119.7, 119.1. HRMS (ESI): calcd for $C_{22}H_{15}NO_3$ $[M+Na]^+$: 364.0950, found 364.0958.

(4-((4-(2-hydroxyethyl)phenyl)amino)naphthalene-1,2-dione) (**2h**) (80 mg, 27.3%): ^{1}H NMR (DMSO-d_6, 500 MHz): δ (ppm) 8.26 (d, *J* = 8 Hz, 1H), 7.98 (d, *J* = 7.5 Hz, 1H), 7.80 (t, *J* = 8 Hz, 1H), 7.68 (t, *J* = 7.5 Hz, 1H), 7.30 (d, *J* = 7.5 Hz, 2H), 7.15 (brs, 2H), 5.76 (s, 1H), 4.71 (s, 1H), 3.61 (t, *J* = 7 Hz, 2H), 2.73 (t, *J* = 7 Hz, 2H). ^{13}C NMR (DMSO-d_6, 500 MHz): δ (ppm) 181.7, 155.4, 134.7, 132.0, 131.6, 130.3, 128.6, 124.6, 62.6, 39.0. HRMS (ESI): calcd for $C_{18}H_{15}NO_3$ $[M+Na]^+$: 316.0950, found 316.0966.

(4-(methyl(phenyl)amino)naphthalene-1,2-dione) (**3a**) (19.9 mg, 6.8%): ^{1}H NMR ($CDCl_3$, 400 MHz): δ (ppm) 8.05 (d, *J* = 7.6 Hz, 1H), 7.33 (t, *J* = 7.2 Hz, 3H), 7.21 (t, *J* = 7.2 Hz, 2H), 7.11 (d, *J* = 7.6 Hz, 2H), 7.02 (d, *J* = 8 Hz, 1H), 6.27 (s, 1H), 3.49 (s, 3H). ^{13}C NMR ($CDCl_3$, 400 MHz): δ (ppm) 180.9, 178.7, 159.7, 148.0, 133.4, 132.8, 132.3, 130.1, 130.0, 129.2, 129.0, 126.5, 125.5, 111.1, 44.3.

(4-(ethyl(phenyl)amino)naphthalene-1,2-dione) (**3b**) (19.9 mg, 6.8%): ^{1}H NMR ($CDCl_3$, 400 MHz): δ (ppm) 8.08 (d, *J* = 7.6 Hz, 1H), 7.37 (t, *J* = 7.6 Hz, 3H), 7.28 (brs, 1H), 7.22 (d, *J* = 8 Hz, 1H), 7.13 (d, *J* = 8 Hz, 1H), 6.47 (s, 1H), 4.05 (q, *J* = 7.2 Hz, 3H), 1.34 (t, *J* = 7.2 Hz, 2H). ^{13}C NMR ($CDCl_3$, 400 MHz): δ (ppm) 181.0, 146.2, 133.3, 132.6, 130.3, 130.1, 129.2, 129.1, 126.7, 126.0, 110.6, 51.0, 12.3.

(4-aminonaphthalene-1,2-dione) (**4a**) (20 mg, 59%): ^{1}H NMR (DMSO-*d*$_6$, 400 MHz): δ (ppm) 8.04 (d, *J* = 7.6 Hz, 1H), 7.96 (d, *J* = 6.8 Hz, 1H), 7.80 (t, *J* = 7.6 Hz, 1H), 7.68 (d, *J* = 7.6 Hz, 1H), 5.74 (s, 1H). ^{13}C NMR (DMSO-*d*$_6$, 400 MHz): δ (ppm) 182.2, 174.7, 158.1, 134.2, 131.7, 131.6, 130.5, 127.8, 124.0, 101.0.

(4-ethylamino)naphthalene-1,2-dione) (**4b**) (13.9 mg, 6.9%): ^{1}H NMR (DMSO-*d*$_6$, 500 MHz): δ (ppm) 7.97 (dd, *J* = 8, 1.5 Hz, 1H), 7.94 (dd, *J* = 7.5, 1.5 Hz, 1H), 7.82 (td, *J* = 7, 1 Hz, 1H), 7.72 (td, *J* = 7.5, 1.5 Hz, 1H), 7.54 (t, *J* = 6 Hz, 1H), 5.66 (s, 1H), 3.21 (quint, *J* = 7 Hz, 2H), 1.16 (t, *J* = 7.5 Hz, 3H).

(4-propylamino)naphthalene-1,2-dione) (**4c**) (18 mg, 8.4%): ^{1}H NMR (DMSO-*d*$_6$, 400 MHz): δ (ppm) 8.45 (s, 1H), 8.13 (d, *J* = 8 Hz, 1H), 7.98 (dd, *J* = 7.6, 1.6 Hz, 1H), 7.80 (td, *J* = 8, 1.6 Hz, 1H), 7.67 (t, *J* = 7.6 Hz, 1H), 5.69 (s, 1H), 3.34 (d, *J* = 6.8 Hz, 2H), 1.68 (m, 2H), 0.95 (t, *J* = 7.6 Hz, 3H), ^{13}C NMR (DMSO-*d*$_6$, 400 MHz): δ (ppm) 182.1, 174.8, 155.1, 134.2, 131.3, 130.9, 127.9, 123.4, 98.1, 44.9, 21.1, 11.5. HRMS (ESI): calcd for $C_{13}H_{13}NO_2$ $[M+Na]^+$: 238.0844, found 238.0858.

(4-butylamino)naphthalene-1,2-dione) (**4d**) (20 mg, 11.6%): ^{1}H NMR (DMSO-*d*$_6$, 400 MHz): δ (ppm) 8.42 (s, 1H), 8.11 (d, *J* = 8 Hz, 1H), 7.98 (d, *J* = 7.6 Hz, 1H), 7.81 (t, *J* = 7.6 Hz, 1H), 7.68 (t, *J* = 7.6 Hz, 1H), 5.69 (s, 1H), 1.65 (quint, *J* = 7.2 Hz, 2H), 1.38 (m, 2H), 0.92 (t, *J* = 7.2 Hz, 3H). ^{13}C NMR (DMSO-*d*$_6$, 400 MHz): δ (ppm) 174.8, 155.0, 134.3, 131.4, 130.9, 127.9, 123.4, 98.1, 43.0, 29.8, 19.8, 13.7.

(4-isobutylamino)naphthalene-1,2-dione) (**4e**) (39 mg, 17.2%): ^{1}H NMR (DMSO-*d*$_6$, 400 MHz): δ (ppm) 8.47 (s, 1H), 8.15 (d, *J* = 8 Hz, 1H), 7.98 (d, *J* = 7.6 Hz, 1H), 7.81 (d, *J* = 7.6 Hz, 1H), 7.68 (d, *J* = 7.6 Hz, 1H), 5.70 (s, 1H), 3.20 (t, *J* = 7.2 Hz, 2H), 2.05 (m, 1H), 0.95 (d, *J* = 6.4 Hz, 6H), ^{13}C NMR (DMSO-*d*$_6$, 400 MHz): δ (ppm) 182.1, 174.8, 155.3, 134.3, 131.4, 131.3, 130.9, 127.9, 123.4, 98.3, 50.6, 27.2, 20.3. HRMS (ESI): calcd for $C_{14}H_{15}NO_2$ $[M+Na]^+$: 252.1000, found 252.0995.

(4-cyclohexylamino)naphthalene-1,2-dione) (**4f**) (51 mg, 20%): ^{1}H NMR (DMSO-*d*$_6$, 400 MHz): δ (ppm) 8.22 (d, *J* = 8 Hz, 1H), 7.97 (d, *J* = 6.8 Hz, 1H), 7.91 (d, *J* = 7.6 Hz, 1H), 7.80 (t, *J* = 7.6 Hz, 1H), 7.67 (t, *J* = 7.6 Hz, 1H), 5.76 (s, 1H), 3.61 (m, 1H), 1.95 (d, *J* = 11.6 Hz, 2H), 1.76 (d, *J* = 12.4 Hz, 2H), 1.64 (d, *J* = 13.2 Hz, 2H), 1.43 (m, 4H). ^{13}C NMR (DMSO-*d*$_6$, 400 MHz): δ (ppm) 182.1, 174.9, 153.8, 134.0, 131.3, 131.2, 130.9, 127.8, 123.6, 98.2, 52.4, 31.5, 25.1, 24.5. HRMS (ESI): calcd for $C_{16}H_{17}NO_2$ $[M+Na]^+$: 278.1157, found 278.1161.

(4-benzylamino)naphthalene-1,2-dione) (**4g**) (12.4 mg, 4.7%): ^{1}H NMR (DMSO-*d*$_6$, 400 MHz): δ (ppm) 9.06 (t, *J* = 6 Hz, 1H),) 8.18 (d, *J* = 7.6 Hz, 1H),) 7.99 (dd, *J* = 7.6, 1.2 Hz, 1H), 7.85 (td, *J* = 7.6, 1.6 Hz, 1H), 7.70 (t, *J* = 7.6 Hz, 1H), 7.37 (m, 4H), 7.29 (m, 1H), 5.60 (s, 1H), 4.64 (d, *J* = 6 Hz, 2H). ^{13}C NMR (DMSO-*d*$_6$, 400 MHz): δ (ppm) 182.2, 175.4, 155.5, 137.9, 134.8, 131.8, 131.7, 131.3, 129.1, 128.4, 127.7, 127.5, 123.8, 99.5, 46.7.

(4-diethylamino)naphthalene-1,2-dione) (**4h**) (41.4 mg, 18.1%): ^{1}H NMR (DMSO-*d*$_6$, 400 MHz): δ (ppm) 8.09 (d, *J* = 7.6 Hz, 1H), 7.61 (d, *J* = 7.6 Hz, 1H), 7.57 (brs, 1H), 7.55 (brs, 1H), 6.00 (s, 1H), 3.51 (q, *J* = 7.2 Hz, 2H), 1.31 (t, *J* = 6.8, 3H). ^{13}C NMR (DMSO-*d*$_6$, 400 MHz): δ (ppm) 133.8, 130.8, 129.6, 126.9, 124.8, 124.2, 108.4, 46.3, 12.7.

Results and Discussion: Eighteen naphthoquinones were synthesized in low to high yield including seven new compounds. The series of these 1,2-NQ derivatives were firstly evaluated for their α-glucosidase inhibition.

Table 1. Inhibitory activity of phenylamino-1,2-NQs against α-glucosidase

Compounds	IC_{50} (μM)
2a	105.63±2.14
2b	35.95±2.99
2c	NA
2d	36.55±0.69
2e	86.06±8.96
2f	18.03±2.61
2g	34.62±3.22
2h	56.04±3.39
Acarbose	93.63±0.49

According to the IC_{50} values shown in Table 1, the introduction of substituents on phenyl ring enhanced potency and also showed better activity than acarbose. Whereas, 4-methoxy substituted phenyl analogue (**2c**) was weaker than unsubstituted phenylamino-1,2-NQ (**2a**).

Table 2. Inhibitory activity of alkylphenylamino-1,2-NQs against α-glucosidase

Compounds	IC_{50} (μM)
3a	32.20±3.30
3b	109.33±1.40
Acarbose	93.63±0.49

According to the IC_{50} values shown in Table 2, the introduction of methyl group on nitrogen linker enhanced potency compared with phenylamino-1,2-NQ (**2a**) and also showed better activity than acarbose. Whereas the introduction of ethyl group on nitrogen linker decreased the activity.

Table 3. Inhibitory activity of alkylamino-1,2-NQs against α-glucosidase

Compounds	IC_{50} (μM)
4a	39.91±2.72
4b	61.08±1.71
4c	156.93±3.50
4d	>200
4e	187.62±14.20
4f	122.15±6.36
4g	>200
4h	62.68±2.62
Acarbose	93.63±0.49

According to the IC_{50} values shown in Table 3, the introduction of alkylamino groups impaired potency. The activity decreased when increased the chain length. Among them, 4-amino-1,2-NQ (**4a**) showed the best potency. Ethylamino-1,2-NQ (**4b**) exhibited comparable activity with diethylamino-1,2-NQ (**4h**).

Overall, the presence of phenyl ring improved the potency, while the alkylamino groups resulted in loss of activity.

Acknowledgements:

I would like to thank Chulalongkorn University's Graduate Scholarship Program for ASEAN or Non-ASEAN Countries for help during my MSc study.

References:

1. Shah, M. A.; Keach, J. E.; Panichayupakaranant, P. Chem. Pharm. Bull. 2018;*66* (5):483-492.
2. Shukla, S.; Srivastava, R.; Shrivastava, S.; Sodhi, A.; Kumar, P. J. Appl. Biochem. Biotechnol. 2012;*167* (5):1430-1445.
3. Ahn, J. H.; Cho, S. Y.; Du Ha, J.; Chu, S. Y.; Jung, S. H.; Jung, Y. S.; Baek, J. Y.; Choi, I. K.; Shin, E. Y.; Kang, S. K. J. Bioorg. Med. Chem. Lett. 2002;*12* (15):1941-1946.
4. Sunil, C.; Duraipandiyan, V.; Agastian, P.; Ignacimuthu, S. J. Food. Chem. Toxicol. 2012;*50* (12):4356-4363.
5. Demir, Y.; Özaslan, M. S.; Duran, H. E.; Küfrevioğlu, Ö. İ.; Beydemir, Ş. J. Environ. Toxicol. Pharmacol. 2019;*70*:103195.
6. Tseng, C.-H.; Cheng, C.-M.; Tzeng, C.-C.; Peng, S.-I.; Yang, C.-L.; Chen, Y.-L. J. Bioorg. Med. Chem. 2013;*21* (2):523-531.
7. Benites, J.; Valderrama, J. A.; Bettega, K.; Pedrosa, R. C.; Calderon, P. B.; Verrax, J. J. Eur. J. Med. Chem. 2010;*45* (12):6052-6057.
8. Lim, S. M.; Jeong, Y.; Lee, S.; Im, H.; Tae, H. S.; Kim, B. G.; Park, H. D.; Park, J.; Hong, S. J. J. Med. Chem. 2015;*58* (21):8491-8502.

D_008_PF: A STUDY OF EXTRUSION AND SPHERONIZATION BEHAVIOUR OF MONTMORILLONITE

Patticha Weerakul, Narueporn Sutanthavibul, Jittima Chatchawalsaisin*

Department of Pharmaceutics and Industrial Pharmacy, Faculty of Pharmaceutical Sciences, Chulalongkorn University, Bangkok 10330, Thailand
*e-mail: jittima.c@chula.ac.th

Abstract:

Clays and clay minerals are considered as a candidate excipient for pelletization by extrusion/ spheronization. In this study, extrusion and spheronization behaviour of montmorillonite (MMT) was investigated. The mixtures of isopropyl alcohol (IPA)/water mixtures were used as binding liquid. The wet mass was ram extruded and then spheronized. Extrudability was evaluated by force displacement profile; and ability to be spheronized was demonstrated by product's quality, e.g. appearance and the amount of pellets in the desired size fraction. The results showed that the MMT wet mass prepared with 50-100% IPA could be extruded with steady state flow and provide round pellets. With the appropriate IPA concentration, more than 90% of pellets in the size range of 0.71-1.40 mm could be obtained. The pellets prepared with 100% IPA were prone to abrasion. However, their mechanical strength could be significantly improved at the IPA concentrations of 50-75%. This finding demonstrates potential use of MMT as excipient in the pellet formulation when organic solvent is required.

Introduction:

Extrusion/ spheronization is one of the most widely used techniques for manufacturing pellets in pharmaceutical industry. The process can produce round pellets with uniform size, smooth surface and low friability, which are desirable for modified release coating.[1] In formulation, microcrystalline cellulose (MCC) is the most common excipient. The main function of this material when mixed with binding liquid is to provide plasticity to the wet mass and allow deformation to occur. The structure of MCC can also help to retain the binding liquid in the wet mass when subjected to forces during extrusion/spheronization.[2, 3] MCC is more suitable for pellet formulation in which water is used as binding liquid. With the relatively high proportion of organic solvent such as ethanol and isopropyl alcohol (IPA) in the binding liquid, the MCC pellets tend to have poor mechanical strength.[4-6] This hinders the use of MCC for producing pellets of water sensitive drugs. Non-MCC pellets have been reported but very few studies focused on the use of organic solvent as binding liquid.[7] Among these studies, cellulosic materials, i.e. hydroxypropyl methylcellulose and hydroxyethyl cellulose could form pellets with acceptable properties by using hydroxypropyl cellulose solution in IPA as binding liquid.[8] Alternatively, clay materials have been proposed to substitute for MCC in non-aqueous formulation of pellets.[9] However, how they perform in extrusion/spheronization is unclear.

Montmorillonite (MMT), a main component of bentonite, is a clay mineral in dioctahedral smectite group. The structure is composed of an alumina octahedral sheet sandwiched with two silica tetrahedral sheets, giving tetrahedral-octahedral-tetrahedral (TOT) layer, as a basic unit layer. The individual unit layers are held together to form stacks, representing clay particles, by charge compensating interlayer cations.[10, 11] MMT has been used in

pharmaceutical products and useful for treatment of diarrheoa.[12, 13] It has colloidal nature and high surface area as well as adsorptive property. MMT imparts plasticity to the clay when wet.[14] It can adsorb water in interlayer space, resulting in swelling of the clay mineral and modifying rheology of dispersion.[10, 11] The unique properties of MMT may find application in extrusion/spheronization. In this study, extrusion and spheronization behaviour of MMT was evaluated using IPA/water mixtures as binding liquid.

Methodology:

Materials: MMT (Batch No.180330001, Life Pharmaceuticals, Nanyang, Henan, China), MCC (Avicel® PH101, Lot No. P116830164, FMC Corporation, Philadelphia, Pennsylvania, USA) and IPA (T.S. Inter Lab Limited Partnership, Bangkok, Thailand) and deionized water were used as received.

Experimental:

Extrusion and spheronization: The face-centered central composite experimental design (Minitab® 17, USA) was used to study the effect of concentrations of IPA in IPA/water mixtures which were used as binding liquid and binding liquid levels on extrusion and spheronization of MMT wet mass (**Table 1**). Initially, MMT was mixed with the IPA/water mixture in a planetary mixer (Model 5K5SS, KitchenAid, USA) for 5 min. Then, the wet mass was manually packed into a 25.4 mm diameter and 200 mm height barrel, fitted with a 1 mm diameter and 4 mm length die. The wet mass was ram extruded at a speed of 200 mm/min through the crosshead of universal testing machine with a 50 kN load cell (LR50K plus, Lloyd Instrument, Bognor Regis, West Sussex, UK) connected to Nexygen Plus software version 3.0 (Lloyd Instrument, Bognor Regis, West Sussex, UK). Force-displacement profiles were recorded. Then, extrudates were spheronized on a 25 cm diameter, cross-hatched plate operated at 600±5 rpm for 5 min. Resultant pellets were dried in hot air oven at 60°C for 3 h. The dried pellets were weighed and yields were calculated based on solid weight in the formulation. The MCC wet mass was used as reference and prepared with 100% IPA and water for comparison.

Table 1.

Matrix of central composite experimental design, showing studied variables

Experiment No.	Formulation code	A: % IPA in water (% v/v)	B: % Binding liquid in wet mass (%w/w based on solid content)
1	DS-50/45	50	45
2	DS-100/45	100	45
3	DS-50/65	50	65
4	DS-100/65	100	65
5	DS-50/55	50	55
6	DS-100/55	100	55
7	DS-75/45	75	45
8	DS-75/65	75	65
9	DS-75/55	75	55
10	DS-75/55	75	55
11	DS-75/55	75	55
12	DS-75/55	75	55
13	DS-75/55	75	55

Characterization of products:

Morphology of extrudates and pellets: Surface morphology of dried extrudates and pellets was examined using scanning electron microscope (Model JSM-IT300, JEOL, Tokyo, Japan) at magnification of 45 and 80, respectively.

Size distribution of pellets: Pellet size distribution was determined by sieve analysis. The dried pellets were placed on a set of sieves with 2.0, 1.4, 1.0, 0.71, 0.5, 0.355 mm aperture size (Model O: FT-200M, Filtra, Barcelona, Spain). The sieves were shaken for 10 min. The percentage of pellets retained on the desired size range (0.71-1.40 mm) was determined.

Shape of pellets: The aspect ratio, i.e. the ratio of the maximum Feret's diameter to the Feret's diameter at 90 degree, of 50 pellets in the 0.71-1.40 mm sieve size was determined using a stereo microscope connected to NIS element basic research software (Nikon Corporation, Tokyo, Japan).

Mechanical strength of pellets: The ability of pellets to withstand abrasion was measured by modified tablet friability testing method. Accurately weighed of 6.5 g pellets in the main size range of 0.71-1.00 mm or 1.00-1.40 mm, depending on pellets' size distribution, were mixed with 5 mm glass beads (6.472 g or 39 beads) and placed in the tablet friability tester (Type TAP, Nr 27635, Western Germany). Then, the friability tester was operated at 25 rpm for 4 min. At the end of the test, the fraction of fine particles defined as the particles that passing through the initial sieve size was calculated.

Results and Discussion:

Extrusion behaviour: The MMT wet mass prepared with the IPA/water mixture could be extruded with steady state flow over the range of the IPA concentrations studied (**Figure 1A**). The MCC wet mass could achieve steady state flow only when water was the binding liquid (**Figure 1B**). The presence of steady state flow indicates the production of uniform extrudates and the ability to retain the binding liquid in the wet mass under pressure. For the MCC wet mass, water can be absorbed in a "molecular sponge" [2] or form crystallite gel.[3] In the case of MMT, water and other polar liquid can possibly retain in the interlayer space after uptake.[10] The different proportions of IPA in water may induce varied degrees of swelling and modify the plasticity of the wet mass. The length of compression stage, similarly to the MCC wet mass prepared with water, was dependent on the binding liquid level.[15] At the relatively low level of binding liquid (45%), the compression stage was longer, indicating less compressibility.

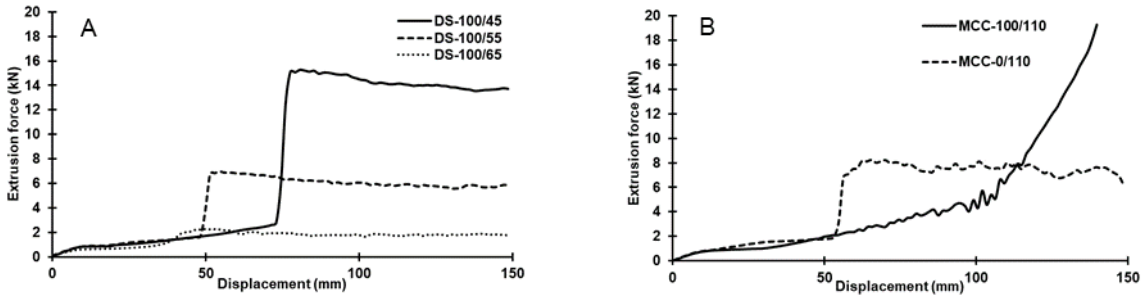

Figure 1.

Examples of force displacement profile from extrusion of A) MMT wet mass prepared with 100% IPA at three levels: 45% w/w (DS-100/45), 55% w/w (DS-100/55) and 65% w/w (DS-100/65); B) MCC wet mass prepared with 100% IPA at 110% w/w (MCC-100/110) or with water at 110% w/w (MCC-0/110).

The extrusion force required at steady state flow (SSF) was dependent on both the IPA concentration and the binding liquid level as described by the quadratic equation:

SSF (kN): $55.7 + 0.040A - 1.514B + 0.002011A^2 + 0.01357B^2 - 0.00560AB$

Where A and B are coded for % IPA in water and % binding liquid in the wet mass, respectively.

Although the extrudates were produced under steady state condition, the extrudates with smooth surface were observed only when the MMT wet mass prepared with 50% IPA or with the relatively high proportion of water in the binding liquid.

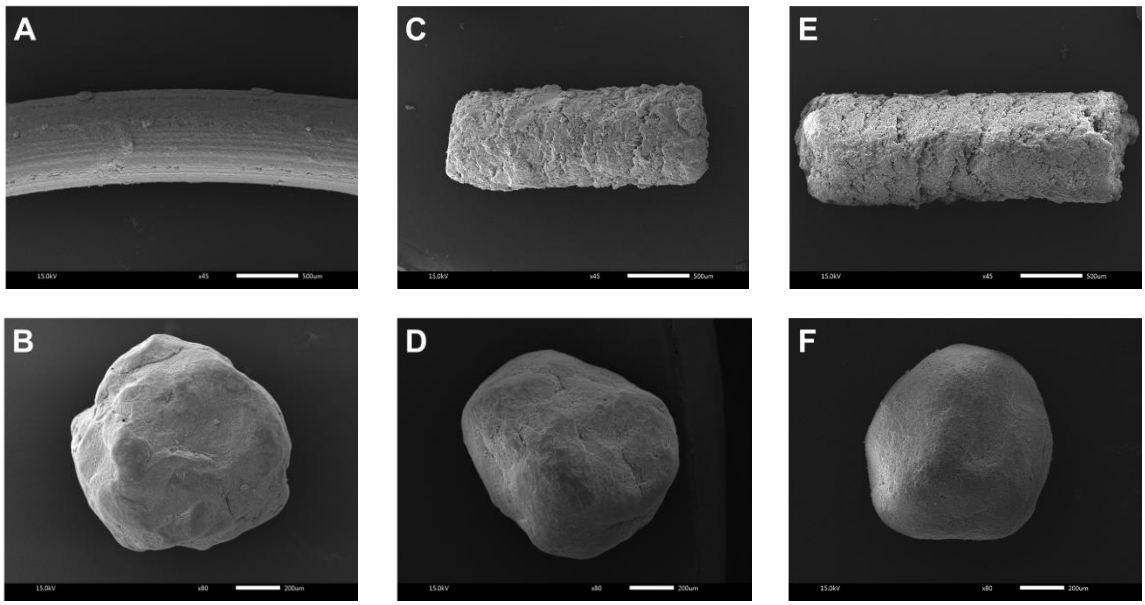

Figure 2.

Scanning electron micrographs of MMT extrudates (x45) and pellets (x80) using varied concentrations of IPA: A, B) 50% IPA; C, D) 75% IPA and E, F) 100% IPA at the binding liquid level of 55% w/w.

Spheronization behaviour: The plasticity and brittleness of the MMT extrudates allowed formation of round pellets in spheronization step (**Figure 2**). At 50% IPA concentration, the contraction of dried pellets was observed. This resulted from higher degree of hydration and more swelling of the MMT wet mass prepared with the relatively high content of water. At 100% IPA, the pellets were not markedly contracted but they were easily broken under the friability test. The effects of studied variables on the quality of pellets are expressed by the following equations:

%Yield: $35.19 + 0.447B$

%Pellets in the size range of 0.71-1.40 mm: $-330 + 11.77A - 0.0811A^2$

%Fines: $109.2 - 3.592A + 0.02887A^2$

Aspect ratio: $0.8017 + 0.006333B$

Where A and B are coded for % IPA in water and % binding liquid in the wet mass, respectively.

It can be summarized that yield and aspect ratio of pellets depended on the binding liquid level. The higher binding liquid level provided higher yield and resulted in a decrease in roundness of pellets. In addition, the amount of pellets in the desired size range and the fraction of fines after testing were affected by the concentration of IPA. The use of 100% IPA as binding liquid gave a small amount of 0.71-1.40 mm pellets and the pellets having poor mechanical strength (**Figure 3**).

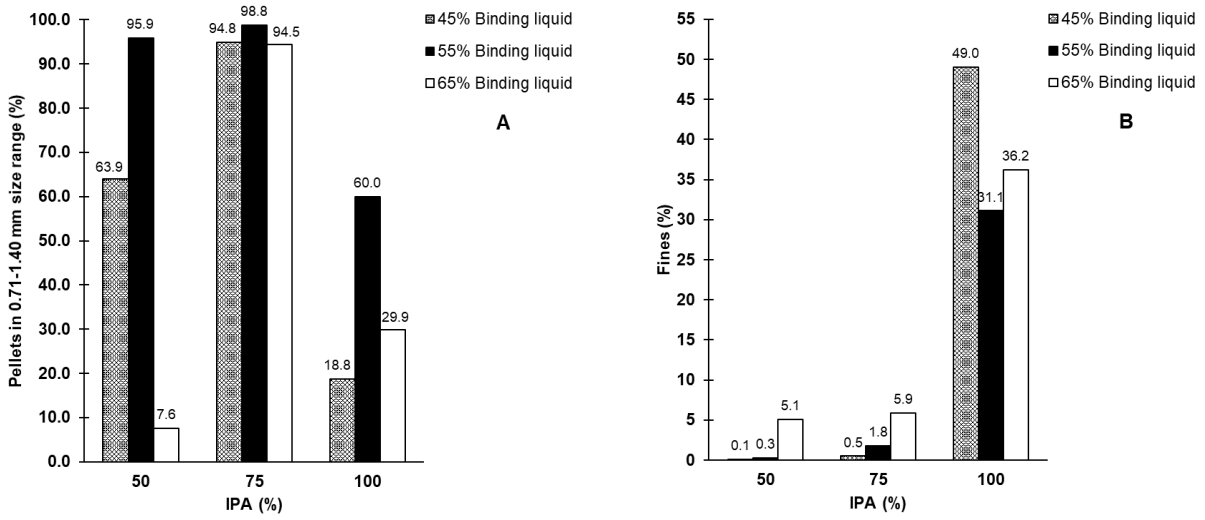

Figure 3.

The effect of IPA concentration and binding liquid level on: A) the amount of 0.71-1.40 mm pellets and B) the fraction of fines after testing.

Conclusion:

MMT is proved to be a potential extrusion/spheronization aid in the formulation where organic solvent such as IPA is used as binding liquid. The extrusion and spheronization behaviors as well as properties of pellets can be modified by varying the proportion of IPA/water in the binding liquid.

Acknowledgements:

This work was supported by the grant for joint funding, Ratchadaphiseksomphot endowment fund.

References:

1. Ghebre-Sellassie I, Knoch A. Pelletization techniques. In: Swarbrick J, Boylan JC, editors. Encyclopedia of Pharmaceutical Technology. New York and Basel: Marcel Dekker, Inc.;2002:2067-2080.

2. Fielden KE, Newton JM, O'Brien P, Rowe RC. Thermal studies on the interaction of water and microcrystalline cellulose. Journal of Pharmacy and Pharmacology. 1988;40(10):674-678.

3. Kleinebudde P. The crystallite-gel-model for microcrystalline cellulose in wet-granulation, extrusion, and spheronization. Pharmaceutical Research. 1997;14(6):804-809.

4. Millili GP, Schwartz JB. The strength of microcrystalline cellulose pellets: The effect of granulating with water/ethanol mixtures. Drug Development and Industrial Pharmacy. 1990;16(8):1411-1426.

5. Schröder M, Kleinebudde P. Structure of disintegrating pellets with regard to fractal geometry. Pharmaceutical Research. 1995;12(11):1694-1700.

6. Dreu R, Širca J, Pintye-Hodi K, Burjan T, Planinšek O, Srčič S. Physicochemical properties of granulating liquids and their influence on microcrystalline cellulose pellets obtained by extrusion-spheronisation technology. International Journal of Pharmaceutics. 2005;291(1):99-111.

7. Dukić-Ott A, Thommes M, Remon JP, Kleinebudde P, Vervaet C. Production of pellets via extrusion–spheronisation without the incorporation of microcrystalline cellulose: A critical review. European Journal of Pharmaceutics and Biopharmaceutics. 2009;71(1):38-46.

8. Chatlapalli R, Rohera BD. Physical characterization of HPMC and HEC and investigation of their use as pelletization aids. International Journal of Pharmaceutics. 1998;161(2):179-193.

9. Newton JM. Extrusion and extruders. In: Swarbrick J, Boylan JC, editors. Encyclopedia of Pharmaceutical Technology. New York and Basel: Marcel Dekker, Inc.; 2002:1220-1236.

10. Pusch R. Bentonite clay: Environmental Properties and Applications. Boca Raton: CRC Press; 2015.

11. Eisenhour D, Reisch F. Bentonite. In: Kogel JE, Trivedi NC, Barker JM, Krukowski ST, editors. Industrial Minerals & Rocks: Commodities, Markets, and Uses. 7th ed. Colorado: Society for Mining, Metallurgy, and Exploration, Inc.; 2009:357-368.

12. Khediri F, Mrad AI, Azzouz M, Doughi H, Najjar T, Mathiex-Fortunet H, et al. Efficacy of diosmectite (smecta) in the treatment of acute watery diarrhoea in adults: a multicentre, randomized, double-blind, placebo-controlled, parallel group study. Gastroenterology Research and Practice. 2011;2011:783196.

13. García-Villén F, Carazo E, Borrego-Sánchez A, Sánchez-Espejo R, Cerezo P, Viseras C, et al. Chapter 6 - Clay minerals in drug delivery systems. In: Mercurio M, Sarkar B, Langella A, editors. Modified Clay and Zeolite Nanocomposite Materials: Elsevier; 2019:129-166.

14. Ghosh B. Clays and their constituents - Definitions and a brief overview. In: Mukherjee S, editor. The Science of Clays: Applications in Industry, Engineering and Environment. New Delhi: Capital Publishing Company; 2013.

15. Harrison PJ, Newton JM, Rowe RC. The characterization of wet powder masses suitable for extrusion/spheronization. Journal of Pharmacy and Pharmacology. 1985;37(10):686-691.

D_009_PA

D_009_PA: ANTIBACTERIAL ACTIVITY OF VINEGAR-GRAPHENE QUANTUM DOTS AGAINT *Bacillus Cereus* AND *Escherichia coli*

Amnuay Noypha[1], Prawit Nuengmatcha[1,2]*

[1]Creative Innovation in Science and Technology, [2]Nanomaterials Chemistry Research Unit,
Department of Chemistry, Faculty of Science and Technology, Nakhon Si Thammarat Rajabhat University, 80280, Thailand.
*e-mail: prawit_nue@nstru.ac.th

Abstract:

Vinegar–graphene quantum dots (Vg-GQDs) were successfully synthesized hydrothermal and co-pyrolysis method using acetic acid as the precursor. All samples were characterized using ultraviolet- visible spectrophotometry (UV-vis), scanning electron microscopy (SEM) and energy-dispersive X-ray spectroscopy (EDX). The antibacterial activity of Vg-GQDs against strains of *Bacillus cereus* and *Escherichia coli* was determined by using the disc diffusion method for preliminary screening. Their minimum inhibitory concentration (MIC) and minimum bactericidal concentration (MBC) were determined by broth macro dilution method. Their inhibition zones were compared with those of acetic acid. It was found that the synthesized Vg-GQDs demonstrated excellent antibacterial activity against *Bacillus cereus* at 99.2 % and *Escherichia coli* at 97.3 %. In addition, the MIC of Vg-GQDs against *Bacillus cereus* was 1.56 mg/ml, while MBC was not exhibited at 50 mg/ml. Whereas MIC and MBC of Vg-GQDs against *Escherichia coli* were 3.125 mg/ml and 6.25 mg/ml.

D_010_PA: MICROWAVE ASSISTED SYNTHESIS OF Ag-ZnO NANOPARTICLES USING EXTRACT OF *Caulerpa sertularioides* AS A NOVEL REDUCING AGENT

Paweena Porrawatkul[1], Prawit Nuengmatcha[1,2]*

[1]Creative Innovation in Science and Technology, [2]Nanomaterials Chemistry Research Unit,
Department of Chemistry, Faculty of Science and Technology, Nakhon Si Thammarat Rajabhat University, 80280, Thailand
*e-mail: prawit_nue@nstru.ac.th

Abstract:

In this research, the Ag doping ZnO nanoparticles (Ag-ZnO) are successfully prepared via green synthesis using the ethanolic extract of *Caulerpa sertularioides* as a novel reducing agent under microwave irradiation from a domestic microwave oven. The Ag-ZnO nanoparticles were prepared in a different not only molar concentration of silver nitrate solutions but also the volume of extract solution. The formations of green synthesized Ag-ZnO nanoparticles were confirmed using UV– Vis spectroscopy and powder X-ray diffraction. Scanning electron microscopy and energy dispersive X-ray analysis exhibited the morphology and elemental analysis of the green synthesized Ag-ZnO nanoparticle. The obtained Ag-ZnO materials (20-40 nm) showed a spherical form with a smaller size than ZnO (80-100 nm). The antibacterial behavior against pathogenic gram-negative (*E. coli*) and gram-positive (*S. aureus*) bacteria of Ag-ZnO and undoped ZnO were investigated. The Ag-ZnO nanoparticles exhibited higher antibacterial activity against both *E. coli* and *S. aureus* than that of undoped ZnO. The Ag-ZnO showed good antibacterial activity for *E. coli* and *S. aureus* with a clear zone of inhibition 17 ± 0.4 mm and 23.25 ± 0.6 mm, respectively.

D_011_OF: HYDROTHERMAL SYNTHESIS OF NITROGEN-DOPED CARBON DOTS FROM AROMATIC AMINO ACIDS UNDER ACIDIC CONDITION

Nattapon Siengdung,[1,2] Sanong Ekgasit,[1,2] Prompong Pienpinijtham[1,2,*]

[1]Sensor Research Unit, Department of Chemistry, Faculty of Science, Chulalongkorn University, 254 Phayathai Road, Wangmai, Pathumwan, 10330, Bangkok, Thailand
[2]National Nanotechnology Center of Advanced Structural and Functional Nanomaterials, Department of Chemistry, Faculty of Science, Chulalongkorn University, 254 Phayathai Road, Wangmai, Pathumwan, 10330, Bangkok, Thailand
*e-mail: prompong.p@chula.ac.th

Abstract:

In this research, nitrogen-doped carbon dots (NCDs) are hydrothermally synthesized from aromatic amino acids, *i.e.*, L-histidine (His), L-phenylalanine (Phe), L-tyrosine (Tyr), and L-tryptophan (Trp), under an acidic condition. The results show that molecular structure and (O+N)/C ratio of precursors affect the optical properties and morphology of NCDs. Particle sizes of NCDs synthesized from His, Phe, Tyr, and Trp are 0.83±0.04, 0.76±0.01, 0.89±0.02, and 8.91± 0.40 nm, respectively. Excitation-dependent fluorescence emission can be observed from all synthesized products. Phe-NCDs show the highest difference between λ_{ex} and λ_{em} value due to the widest additional interband induced by heteroatoms.

Introduction:

Carbon dots (CDs) is accidentally discovered during the electrophoretic purification of single-walled carbon nanotubes.[1] Most of the CDs are quasi-spherical with a diameter of less than 10 nm.[2-4] Carbons with sp^2 hybridization are formed as a graphitic carbon framework at the core of particles surrounded by sp^3 carbon on a surface. Heteroatoms such as nitrogen (N), oxygen (O), and sulfur (S) may be included in the structure in the form of defects in graphitic carbon core or functional groups on the surface. The unique properties of CDs are photoluminescence emission and biocompatibility. Thus, CDs are widely used in various applications such as bioimaging, biosensors, chemosensors, and catalysts.

There are two types of the synthetic paths: top-down and bottom-up syntheses.[2] Top-down synthesis can be operated by dividing bulk carbon materials or large materials whose main component is carbon into smaller CDs. In contrast, bottom-up is the way that CDs are produced by combining small carbon building blocks.[5] There are many synthesis methods such as hydrothermal,[6-8] microwave-assisted,[9-10] laser ablation[11], electrochemical,[12] and chemical oxidation.[13]

Doping heteroatoms, such as nitrogen or sulfur, in CDs is another facile method to adjust the optical properties of CDs.[6-7] Nitrogen-doped carbon dots (NCDs) can be synthesized in several ways, including bottom-up synthesis using molecular precursors that contain nitrogen atoms.[10] Amino acids are interesting precursor for nitrogen-doped carbon dots (NCDs) because of their high natural abundance and low toxicity.[4, 6-7, 9-10, 14-15] In this work, four aromatics amino acids, *i.e.*, L-histidine, L-phenylalanine, L-tyrosine, and L-tryptophan; are used as NCDs precursors (**Figure 1**). Synthesized NCDs are characterized by various techniques to observe optical properties and morphologies.

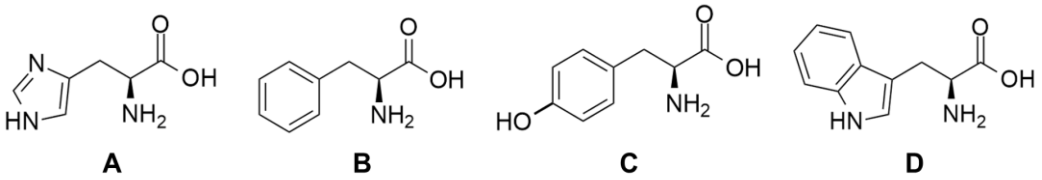

Figure 1.

Molecular structure of (A) His, (B) Phe, (C) Tyr, and (D) Trp

Methodology:

Chemicals

L-histidine (His), L-phenylalanine (Phe), L-tyrosine (Tyr), L-tryptophan (Trp), and hydrochloric acid (HCl) were purchased from Sigma-Aldrich. All chemicals were analytical reagent grade and were used as a received without further purification. Milli-Q water obtained from Milli-Q-system (Millipore, Bedford, MA, USA), and deionized water were used as a solvent.

Synthesis of NCDs

Amino acid (6.25 mmol) was dissolved in 25 mL of 1 M HCl, and then stirred until the solution was clear. The amino acid solution was transferred to Teflon liner and was sealed in a hydrothermal reactor. The hydrothermal reactor was heated at 200 ºC for 12 hours. Then, the liquid was centrifuged at 15,000 rpm for 30 minutes. The supernatant was collected for further characterizations. NCDs obtained from L-histidine, L-phenylalanine, L-tyrosine, and L-tryptophan were labeled as His-NCDs, Phe-NCDs, Tyr-NCDs, and Trp-NCDs, respectively.

Characterizations of NCDs

UV-visible spectroscopy, fluorescence spectroscopy, and dynamic light scattering (DLS) were done by GENESYS 10S Vis spectrometer (Thermo Scientific), Cary Eclipse fluorescence spectrophotometer (Agilent) and Zetasizer Nano S90 (Malvern), respectively, using colloidal NCDs. FT-IR spectroscopy was done by Nicolet iS5 FT-IR spectrometer (Thermo Scientific) using powder samples.

Results and Discussion:

After amino acid solutions were heated and centrifuged, solutions with different colors were obtained, as shown in **Figure 2**. UV-visible spectra of His-NCDs, Phe-NCDs, Tyr-NCDs, and Trp-NCDs are shown in **Figure 3**. There are two absorption regions: around 200–230 nm and 250–300 nm. The absorption band around 210–240 nm attributes to π–π* electron excitation in C=C bond and that around 270–300 attributes to n–π* excitation in C=O or C–N bond.[16-17]

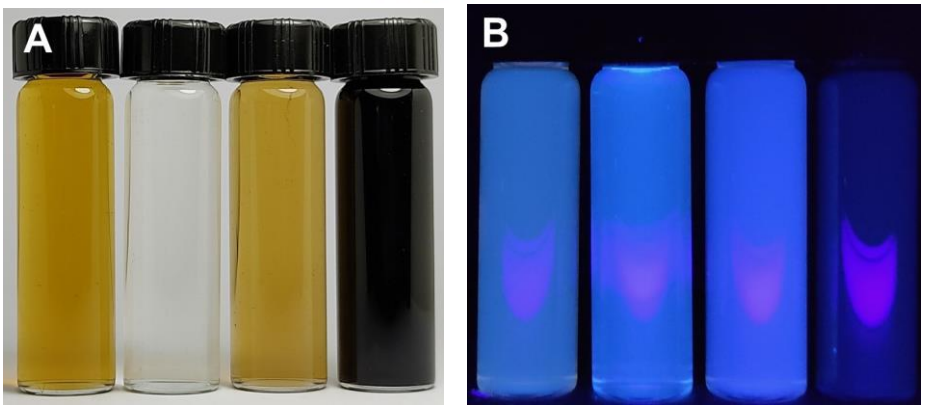

Figure 2.

His-NCDs, Phe-NCDs, Tyr-NCDs, and Trp-NCDs under (A) white light and (B) UV light

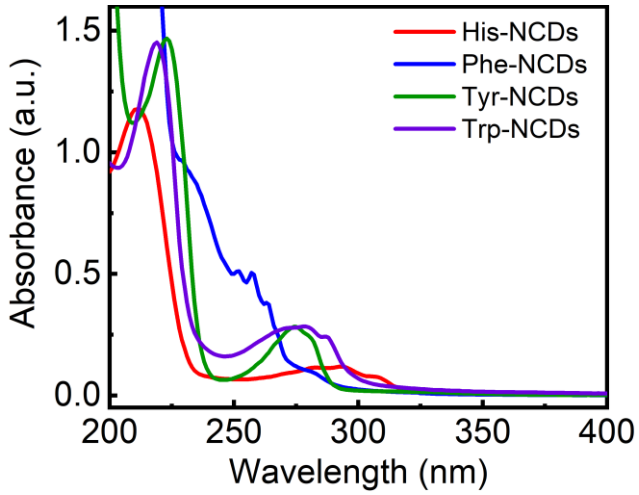

Figure 3.

UV-visible spectra of His-NCDs, Phe-NCDs, Tyr-NCDs, and Trp-NCDs

The unique characteristic of NCDs is an excitation-dependent fluorescence emission. The fluorescence emission spectra of His-NCDs, Phe-NCDs, Tyr-NCDs, and Trp-NCDs are shown in **Figure 4**. The excitation wavelength varies from 300–480 nm with 20 nm increments. The results show that all of NCDs show the excitation-dependent fluorescent emission.

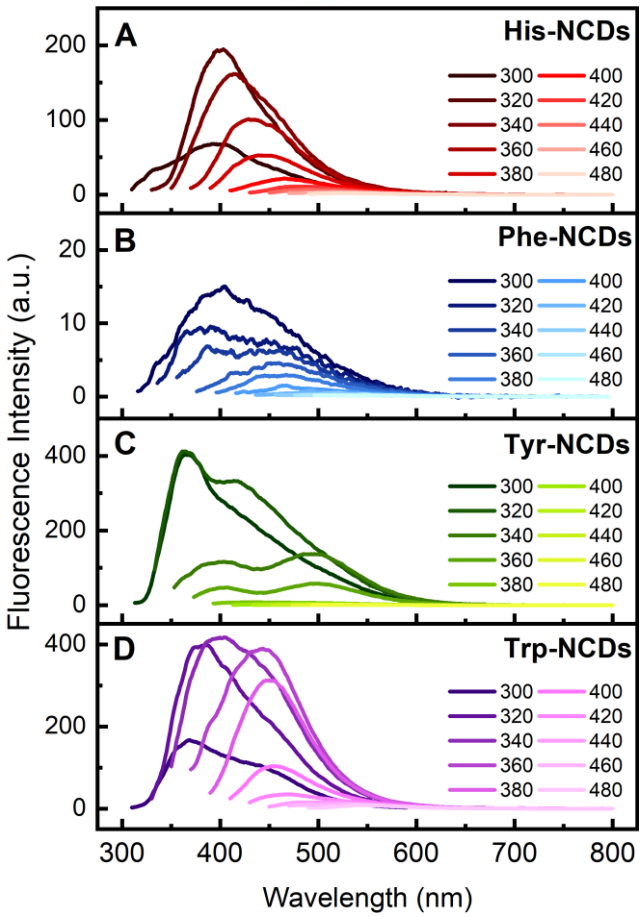

Figure 4.

Fluorescence emission (A) His-NCDs, (B) Phe-NCDs, (C) Tyr-NCDs, and (D) Trp-NCDs. The excitation wavelength was varied from 300–480 nm with increments of 20 nm.

Table 1.

Maximum excitation (λ_{ex}) and emission (λ_{em}) wavelength, the difference between λ_{ex} and λ_{em} and (O+N)/C ratio of precursors.

NCDs	λ_{ex} (nm)	λ_{em} (nm)	Δλ(nm)	(O+N)/C ratio[a] of precursors
His-NCDs	320	403	83	0.83
Phe-NCDs	270	401	131	0.33
Tyr-NCDs	310	370	60	0.44
Trp-NCDs	330	386	56	0.36

[a]Ratio between the sum of number of oxygen and nitrogen atoms and number of carbon atoms.

The excitation-dependent fluorescence emission mechanism can be illustrated in **Figure 5**. Electrons in the highest occupied molecular orbitals (HOMO) move to the lowest unoccupied molecular orbitals (LUMO) when they are excited with discrete energy. Then, they return back to HOMO again by emitting photons to reduce their energy. However, the energy of emission photons always less than excitation because of additional interband which is induced by heteroatoms on the surface of NCDs.[15] From **Table 1**, the width of additional interband can be indicated by Δλ value. These results show that Δλ and (O+N)/C ratio of precursors are varied in the same trend in the case of His-NCDs, Tyr-NCDs, and Trp-NCDs. Higher (O+N)/C ratio shows wider additional interband. While in the case of Phe-NCDs, there is the highest value of Δλ, which indicates that there is the widest additional interband, but they have the lowest value of (O+N)/C ratio of precursor because Phe is polymerized and carbonized through a different mechanism.

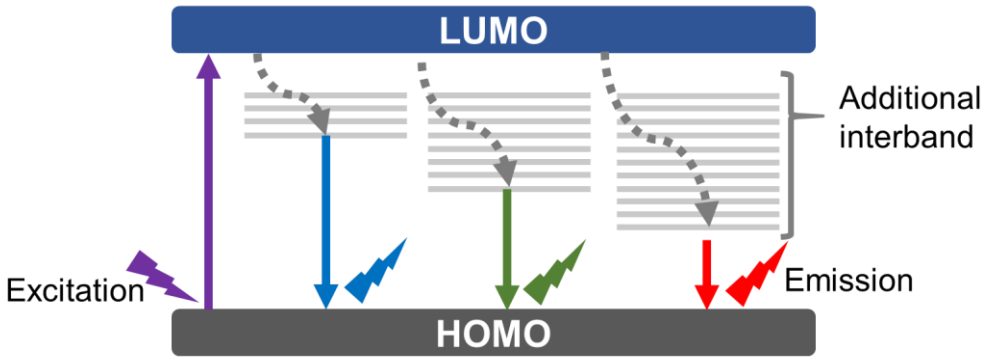

Figure 5.

HOMO, LUMO, and additional interband induced by heteroatoms on the surface.

In the typical formation mechanism of NCDs, molecular precursors are polymerized at the first step. Then, the core of particles is formed by carbonization when time is prolonged. Surface passivation is the final step if there are proper passivating molecules in the system. In this research, the formation mechanism is proposed, as shown in **Figure 6**. As shown in **Figure 1**, His, Phe, Tyr, and Trp have the same backbone and terminals, including amino and carboxyl groups, but different substituents. His and Trp have nitrogen atoms in aromatic rings, and Tyr has a hydroxyl group attached to the aromatic ring. Both nitrogen atoms and a hydroxyl group can promote the reactivity of sidechain, which makes polymerization can be operated on both carboxyl terminals and sidechain. In other words, whole molecules of His, Tyr, and Trp can be polymerized and carbonized. However, sidechain of Phe is only phenyl group, remarkably inert, so that polymerization can be done only on the backbone and carboxyl terminals which (O+N)/C ratio of this part is 1. Thus, Phe-NCDs has the highest (O+N)/C ratio in the particles and has the widest additional interband.

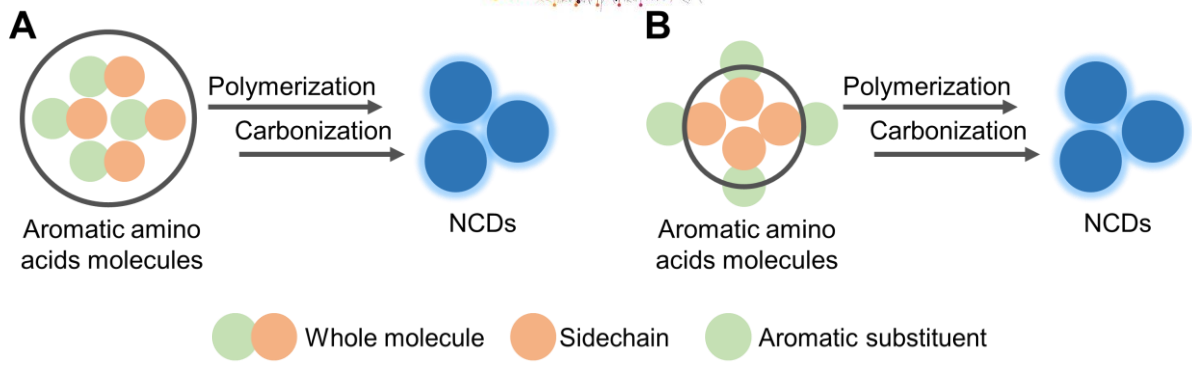

Figure 6.

The formation mechanism of (A) His-NCDs, Tyr-NCDs, and Trp-NCDs, and (B) Phe-NCDs.

Size distribution of NCDs are shown in **Figure 7**. The results show that the average diameter of His-NCDs, Phe-NCDs, Tyr-NCDs, and Trp-NCDs are 0.83±0.04, 0.76±0.01, 0.89±0.02, and 8.91±0.40 nm, respectively. These results indicate that differences in the structure of precursor and formation mechanism can be lead to different sizes of NCDs. Trp has two aromatic rings, while others have only one. Hence, the particle size of Trp-NCDs is larger than others because two aromatic rings in each molecule are combined to generate a large carbon core.

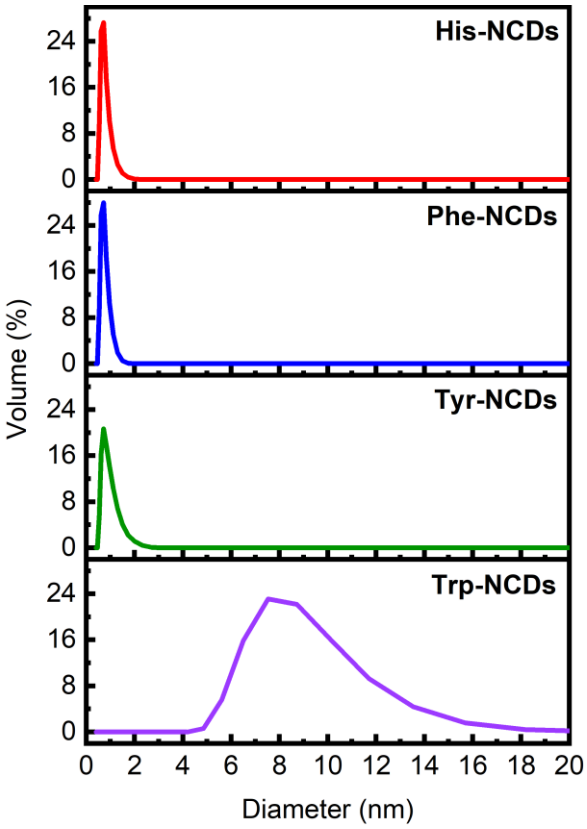

Figure 7.

The size distribution of His-NCDs, Phe-NCDs, Tyr-NCDs, and Trp-NCDs.

Conclusions:

L-His, L-Phe, L-Tyr, and L-Trp are hydrothermally treated under the acidic condition to form NCDs. All of them are aromatic amino acids with different structures and (O+N)/C ratios. The results in this research show that Phe-NCDs has the highest difference between λ_{ex} and λ_{em} due to the widest additional interbands, and Trp can produce NCDs with the largest diameter at 8.91±0.40 due to their two aromatic rings in its molecular structure.

Acknowledgements:

This work has been partially supported by the National Nanotechnology Center (NANOTEC), NSTDA, Ministry of Science and Technology, Thailand, through its Research Network NANOTEC (RNN) program. N. Siengdung is a scholarship student under the Development and Promotion of Science and Technology Talents (DPST) project.

References:

1. Xu X, Ray R, Gu Y, Ploehn H J, Gearheart L, Raker K, Scrivens W A. J Am Chem Soc. 2004;126:12736-12737.
2. Du F, Jin X, Chen J, Hua Y, Cao M, Zhang L, Li J, Zhang L, Jin, J, Wu C, Gong A, Xu W, Shao Q, Zhang M. J Nanopart Res. 2014:16.
3. He J, Zhang H, Zou J, Liu Y, Zhuang J, Xiao Y, Lei B. Biosens Bioelectron. 2016;79: 531-535.
4. Sinduja B, Abraham John S, Spectrochim Acta A. 2018;193:486-491.
5. Huang D, Zhou H, Wu Y, Wang T, Sun L, Gao P, Sun Y, Huang H, Zhou G, Hu J. Carbon. 2019;142:673-684.
6. Pei S, Zhang J, Gao M, Wu D, Yang Y, Liu R. J Colloid Interface Sci. 2015;439:129-33.
7. Zeng Y W, Ma D K, Wang W, Chen J J, Zhou L, Zheng Y Z, Yu K, Huang S M. Appl Surf Sci. 2015;342:136-143.
8. Fang Q, Dong Y, Chen Y, Lu C H, Chi Y, Yang H H, Yu T. Carbon. 2017;118:319-326.
9. Jiang J, He Y, Li S, Cui H. ChemComm. 2012;48:9634-9636.
10. Huang H, Li C, Zhu S, Wang H, Chen C, Wang Z, Bai T, Shi Z, Feng S. Langmuir. 2014;30:13542-13548.
11. Sun Y P, Zhou B, Lin Y, Wang W, Fernando K A S, Pathak P, Meziani M J, Harruff B A, Wang X, Wang H, Luo P G, Yang H, Kose M E, Chen B, Veca L M, Xie S Y, J Am Chem Soc. 2006;128:7756-7757.
12. Lu J, Yang J x, Wang J, Lim A, Wang S, Loh K P. ACS Nano. 2009;3:2367-2375.
13. Qia, Z A, Wang Y, Gao Y, Li H, Dai T, Liu Y, Huo Q. ChemComm. 2010;46;8812-8814.
14. Wang Z, Xu C, Lu Y, Chen X, Yuan H, Wei G, Ye G, Chen J. Sens Actuators B Chem. 2017;241:1324-1330.
15. Yang J, Chen W, Liu X, Zhang Y, Bai Y. Mater Res Bull. 2017;89:26-32.
16. Zhi B, Gallagher M J, Frank B P, Lyons T Y, Qiu T A, Da J, Mensch A C, Hamers R J, Rosenzweig Z, Fairbrother D H, Haynes C L. Carbon. 2018;129:438-449.
17. Yoshinaga T, Iso Y, Isobe T. J Lumin. 2019;213:6-14

D_012_PA: ELECTROCHEMICAL PAPER-BASED SENSORS FOR THE HIGHLY SENSITIVE DETERMINATION OF OXYTETRACYCLINE

Sakda Jampasa[1], Nanthika Khongchareonporn[1,2], Orawon Chailapakul[3], Sudkate Chaiyo[1, 2, 3,*]

[1] Institute of Biotechnology and Genetic Engineering, Chulalongkorn University, Bangkok 10330, Thailand
[2] Food Risk Hub, Research Unit of Chulalongkorn University, Bangkok 10330, Thailand
[3] Electrochemistry and Optical Spectroscopy Center of Excellence (EOSCE), Chulalongkorn University, Bangkok 10330, Thailand
*email: Sudkate.c@chula.ac.th

Abstract:

Oxytetracycline (OTC) has been administered in numerous essential health implications; nonetheless, long-term exposure to excessive amounts of OTC can lead to an untreatable human and livestock disease. Therefore, a method that can be used to accurately determine OTC is tremendously required. In this work, we describe a new "signal-on" electrochemical biosensor based on a competitive immunoassay with a label-free format for sensitive and cost-effective determination of OTC. The device pattern was custom-designed and constructed onto a disposable paper-based analytical device (PAD) using a wax printing technique. A specific anti-OTC antibody was first anchored onto the PAD surface, followed by the competitive binding of OTC-BSA and OTC target. In the presence of OTC, a remarkable increase in the current response of the redox employed was observed, whereas it was negligible in the absence thereof. The detected OTC concentration was linear over a range of 1-200 ng·mL^{-1}, and the LOD and LOQ were found to be 0.33 and 1.1 ng·mL^{-1}, respectively. This developed biosensor successfully quantified the amount of residual OTC in agricultural products with the satisfactory results. Thus, it can be stated that this fabricated biosensor may be employed as an alternative tool for OTC quantification and other broader applications.

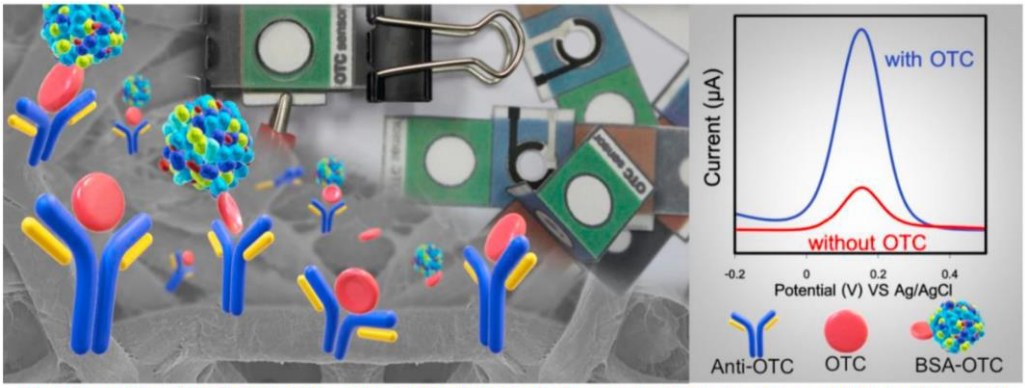

Figure 1.

Electrochemical paper-based sensors for the highly sensitive determination of oxytetracycline(OTC)

D_013_PA: SIMULTANEOUS DETECTION OF LUTEIN AND ZEAXANTHIN IN VEGETABLES BY HPLC

Sirirat Phaisansuthichol[1]*, Nicharat Akephaisanpong[1], Manoch Thanomwat[1], Saengtong Pongjareankit[2]

[1]Program in Chemistry, Faculty of Science, Maejo University, Chiang Mai 50290, Thailand
[2]Program in Genetics, Faculty of Science, Maejo University, Chiang Mai 50290, Thailand
*Corresponding author e-mail: phaisansuthichol@gmail.com

Abstract:

Lutein and zeaxanthin are two types of carotenoids, which are pigment including red, yellow and orange hues and generally found in vegetables, fruits and other plants. The direct determination of lutein and zeaxanthin in basal leaf sheath by reversed phase HPLC was proposed. The HPLC system was equipped with hypersil ODS C18. The isocratic mobile phase consisting of solvent A (acetonitrile: methanol, 9:1 v/v) and solvent B (ethyl acetate) at ratio 70:30 (v/v) as at flow rate of 1.00 mL min^{-1}. The concentrations of lutein and zeaxanthin were calculated based on the absorbance at 540 nm using photodiode array detector. The linearity ranges were in range of 0.050-100 mg L^{-1} for lutein and zeaxanthin. The limit of detection of the method was 0.010 mg L^{-1} and limit of quantification was 0.033 mg L^{-1}. The recoveries of lutein and zeaxanthin by this method showed satisfactory results ranging between 89.2-105.7%. While the relative standard deviations (%RSD) were observed at 4.0-6.3%. This method was simple, sensitive, and specific for determination of lutein and zeaxanthin in vegetables. The result obtained suggests that the ethanolic extracts from vegetables with high lutein and zeaxanthin for drug or natural product.

Keywords: Lutein, Zeaxanthin, HPLC

D_014_OA: COFFEE PECTIN PRODUCTION AN ALTERNATIVE WAY FOR ARGRICULTURAL WASTE MANAGEMENT IN COFFEE FARMS

Sunita Chamyuang,[1,2,*] Amorn Owatworakit,[1,2] Uraiwan Intatha,[1,3] Sitthi Duangphet[1,2]

[1]School of Science, Mae Fah Luang University, Chiang Rai, Thailand 57100
[2]Microbial Products and Innovation Research Group, Mae Fah Luang University, Chiang Rai, Thailand 57100
[3] Center of Innovative Materials for Sustainability, Mae Fah Luang University, Chiang Rai, Thailand 57100
*e-mail: sunita@mfu.ac.th

Abstract:

Chiang Rai Province is home to the largest Arabica coffee plantation in Thailand. The annual coffee bean production is 8,451 tons comprising around 50% of the overall coffee production in the Upper North area of Thailand. During the process of separating green beans from coffee cherries, 45% of the coffee pulp is treated as agricultural waste. This study aimed to increase the value of the coffee cherry pulp by using it as an alternative source of pectin. A double extraction process was used to extract pectin: in the first extraction, acid was used to extract the coffee pulp, which was then used for the second extraction with base. Both acid and base solutions yielded from the extractions were combined prior to the pectin precipitation step. The pectin yield from this double extraction method was 2-fold higher than that yielded from previous methods. Furthermore, during the extraction method we replaced the use of hydrochloric and nitric acid with citric acid, which is less toxic than the other two acids. Three heating conditions were used in the extraction: boiling, autoclave and microwave. The boiling method yielded the highest pectin yield at 15.68%. Unlike the pectin yield from citrus, which is the high methoxy pectin (HMP) type, the coffee pectin from the boiling and microwaved methods was categorized as the low methoxy pectin (LMP), while autoclave method yields the high methoxy pectin (HMP). The LMP from coffee cherry can be used as prebiotic fiber supplement or in wound dressing film production. Importantly, producing LMP has the potential to reduce post-harvest agricultural waste by 3,800 tons per year in Chiang Rai Province alone. Thus, producing coffee pectin provides value to agricultural waste and additional income to coffee growers.

D_015_PF: $Ag_2O@TiO_2$ MATERIALS FOR DESULFURIZATION IN MODEL OIL

Weerapat Vichitsangsri, Wipark Anutrasakda*

Department of Chemistry, Faculty of Science, Chulalongkorn University, Bangkok 10330, Thailand
*e-mail: wipark.a@chula.ac.th

Abstract:

Nowadays, the study on ultra-deep desulfurization gains high attention due to the requirement for low-sulfur diesel fuel. In this work, a series of $Ag_2O@TiO_2$ materials with different Ag_2O loading amounts including pure TiO_2, 5% $Ag_2O@TiO_2$, 15% $Ag_2O@TiO_2$, and 25% $Ag_2O@TiO_2$ were synthesized by an incipient wetness impregnation method and were investigated for their desulfurization efficiency at mild conditions. The materials were characterized by XRD, N_2 adsorption-desorption, and SEM techniques. For the desulfurization testing, dibenzothiophene (DBT) in dodecane was used as the refractory sulfur-containing model oil in this experiment. The results show that $Ag_2O@TiO_2$ exhibited high efficiency for the removal of refractory sulfur in the model oil at room temperature, especially when air was flowed into the system. In addition, the 15% loading amount of Ag_2O on TiO_2 (15%$Ag_2O@TiO_2$) was found to be the optimum value by giving the highest sulfur removal efficiency of 91.4%.

Introduction:

Diesel fuel is one of the most important energy sources in the world. Therefore, development of diesel fuel refinery process has been received high attention from researchers in various fields including the removal of small-scale sulfur compounds or ultra-deep desulfurization. Due to the environment concerns, the sulfur content in diesel fuel was controlled by responsible organization in each country. Otherwise, those compounds are combusted in vehicle engines and turn into sulfur oxide that causes air pollution[1]. For example, sulfur content for nonroad engines and onroad vehicles in the United States has been controlled to not exceed 15 ppm since 2014. Also, in Thailand, sulfur content has been set under 50 ppm, and tends to decrease to lower limit in the near future.

In general, most of sulfur compounds in diesel fuel are excluded by a traditional method called hydrodesulfurization[2]. Extremely high hydrogen pressure and temperature are required to turn sulfur compounds into hydrogen sulfide in this process. However, this method has some disadvantages. First, the reaction condition is harmful and causes expensive cost. Second, hydrodesulfurization cannot remove refractory sulfur compounds such as dibenzothiophene (DBT) and its derivatives due to their heat-stable property[3].

In this work, a series of $Ag_2O@TiO_2$ materials were synthesized by an incipient wetness method and used as materials for sulfur removal in model oil. The materials were tested for their desulfurization effectiveness using dibenzothiophene in dodecane as the model diesel fuel. Factors affecting the desulfurization effectiveness including air feeding, and Ag_2O loading amount were also studied to search for optimum conditions for desulfurization.

Methodology:

15% $Ag_2O@TiO_2$ preparation: Incipient wetness impregnation method was used to prepare the material[4]. Briefly, anatase TiO_2 was ground to fine powder and dried at 110 ^{0}C for 2 h. Then, 0.65 g of $AgNO_3$ was dissolved in 1.4 mL of deionized water. After that the $AgNO_3$ solution was added dropwise onto 2.5 g of dried TiO_2 powder under sonication for 30 min. The substance was dried in the oven at 110 ^{0}C for 2h and was then calcined at 350 ^{0}C. Grey powder of 15%$Ag_2O@TiO_2$ was obtained. 5%$Ag_2O@TiO_2$ and 25%$Ag_2O@TiO_2$ materials were also synthesized using the same procedure except that different amounts of $AgNO_3$ were used.

Characterization: The crystalline phases of the synthesized materials were examined using X-ray powder diffraction technique. The XRD patterns were collected by Rigaku smartlab diffractometer with Cu Kα radiation source. The surface properties were investigated by BEL Japan BELSORP- mini 28SP instrument. The morphology of representative materials was studied using JSM-6480LV (JEOL) scanning electron microscope.

Model oil preparation: 200 ppmS of dibenzothiophene in dodecane was prepared as model oil for the desulfurization test. Briefly, 0.1034 g of dibenzothiophene was dissolved in dodecane. Dodecane was gradually added until the total weight of the solution was equal to 90 g.

Desulfurization test: 0.25 g of 15%$Ag_2O@TiO_2$ was weighed in a glass vial with 5.0 g of model oil. The mixture was stirred at room temperature for 3 h. After that the solid component was removed from the solution using 0.45 µm syringe filters. The sulfur concentration in desulfurized oil was measured by ultraviolet-visible spectrophotometer.

In order to investigate the effect of air feeding on desulfurization efficiency, air was bubbled into the reaction with the flow rate of 7 cm^3/min.

Results and Discussion:

Characterization: According to XRD patterns shown in Fig. 1, all synthesized $Ag_2O@TiO_2$ materials exhibited only diffraction peaks of anatase TiO_2 at 25.50^0, 37.90^0, 48.30^0 and 62.90^0, corresponding to (101), (004), (200) and (204) reflection planes of anatase TiO_2 respectively[5]. It should be noted that the diffraction peaks of Ag_2O were not observed, suggesting that Ag_2O nanoparticles were well-dispersed on the TiO_2 surface.

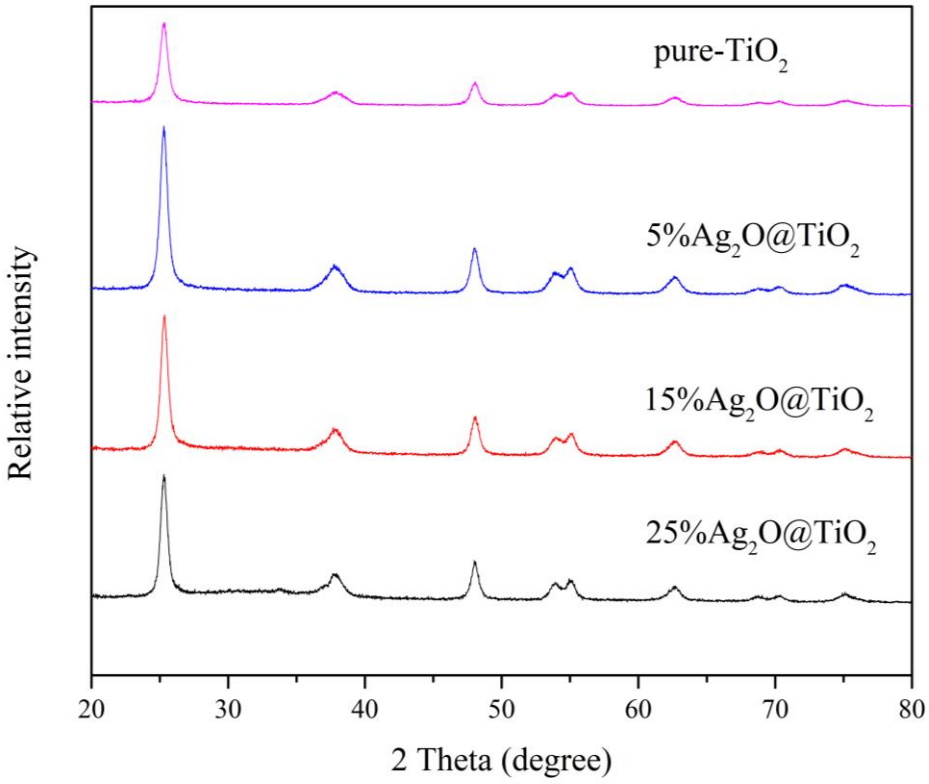

Figure 1.

XRD patterns of pure-TiO_2 and Ag_2O@TiO_2 materials.

Table 1.

Textural properties of pure-TiO_2 and Ag_2O@TiO_2 materials.

Sample	Surface area (m^2/g)	Total pore volume (cm^3/g)
Pure-TiO_2	131.4	0.36
5%Ag_2O@TiO_2	95.8	0.29
15%Ag_2O@TiO_2	67.1	0.27
25%Ag_2O@TiO_2	43.8	0.23

The N_2 adsorption/desorption isotherms of pure TiO_2 and Ag_2O@TiO_2 materials exhibited type IV-mesoporous materials according to the IUPAC classification[6] (Fig. 2), suggesting that the incorporation of Ag_2O did not significantly affect the mesoporousity of TiO_2. The textural properties of the synthesized materials (Table 1) show that the surface area and the total pore volume were decreased with increasing of the Ag_2O loading amount, indicating that the synthesis process led to the formation of new species decorating on TiO_2 pores and surface.

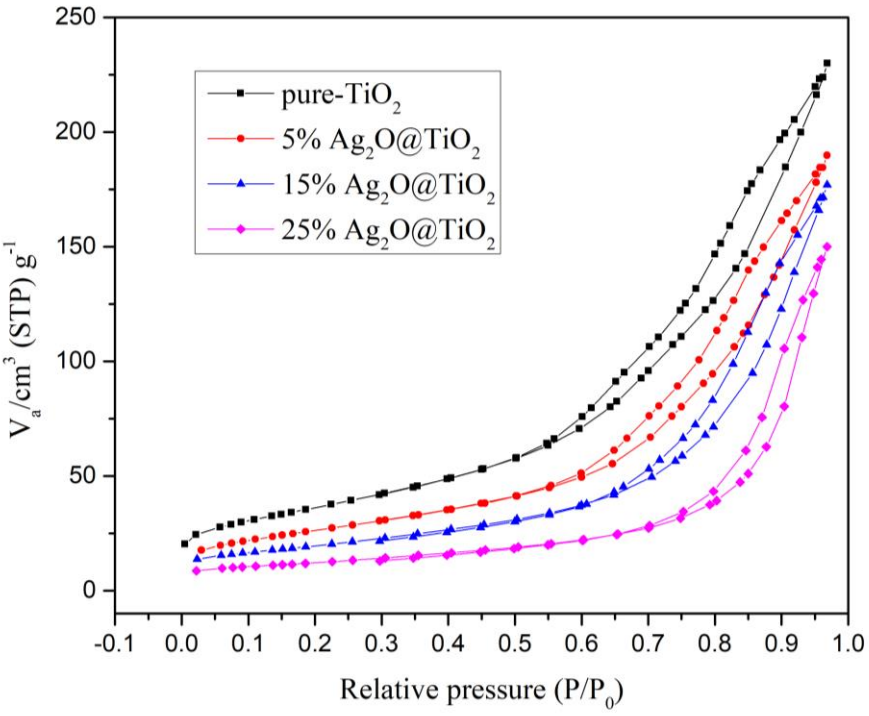

Figure 2.

N_2 adsorption/desorption isotherms of pure TiO_2 and $Ag_2O@TiO_2$ materials.

SEM-EDX was used to observe changes after doping Ag_2O on TiO_2. In this case, pure TiO_2 and 15% $Ag_2O@TiO_2$ were used to be representative materials from all synthesized products. The spectra in Fig. 3 and EDX mapping analysis in Fig. 4 show the appearance of silver element dispersion on 15% $Ag_2O@TiO_2$ while pure TiO_2 result shows only composition of titanium and oxygen. These results confirm the successful synthesis of silver species on the surface of TiO_2 via the incipient wetness impregnation method.

Desulfurization testing: From the desulfurization test as shown in Fig. 5, the synthesized Ag_2O onto TiO_2 surface materials resulted in high efficiency for the removal of sulfur in model oil when compared to pure TiO_2 (17.4% of sulfur removal). Moreover, the absence/presence of air during desulfurization could make significant impact on the reaction. Specifically, the desulfurization performance of the synthesized materials increased in the range of 5% to 60% after bubbling air into the reaction. The Ag_2O loading amount was also another factor that affected the desulfurization performance. The results show that the desulfurization efficiency was increased with the increase of the Ag_2O content from 0% to 15% and suddenly dropped when the Ag_2O content reached 25%.

Based on the obtained results, the mechanism of oxidative-adsorptive desulfurization was proposed as described in Fig. 6[7]. First, the chain reaction was initiated by converting dibenzothiophene (DBT) and oxygen molecule (O_2) to their radical ions, $\cdot DBT^+$ and $\cdot O_2^+$. After that $\cdot DBT^+$ reacted with O_2 to generate $\cdot DBT\text{-}O_2^+$. $\cdot DBT\text{-}O_2^+$ can abstract electrons from DBT to produce DBT-sulfone (DBT-O_2) and $\cdot DBT^+$. Polar DBT-O_2 can be adsorbed on TiO_2, whereas $\cdot DBT^+$ further reacted with other oxygen molecules in the reaction.

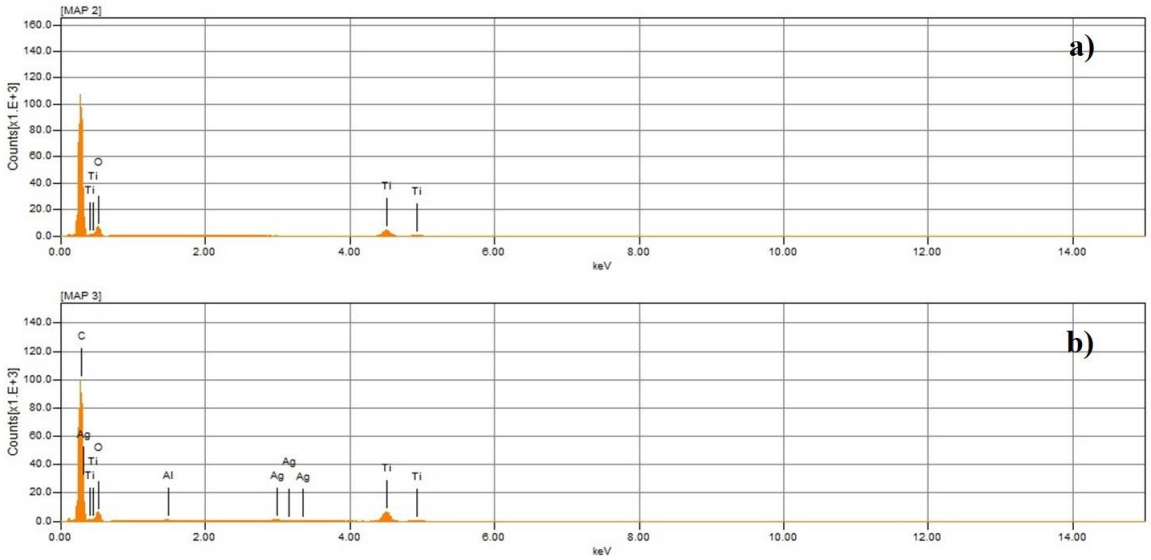

Figure 3.

EDX spectra of a) pure-TiO_2 and b) 15% Ag_2O@TiO_2

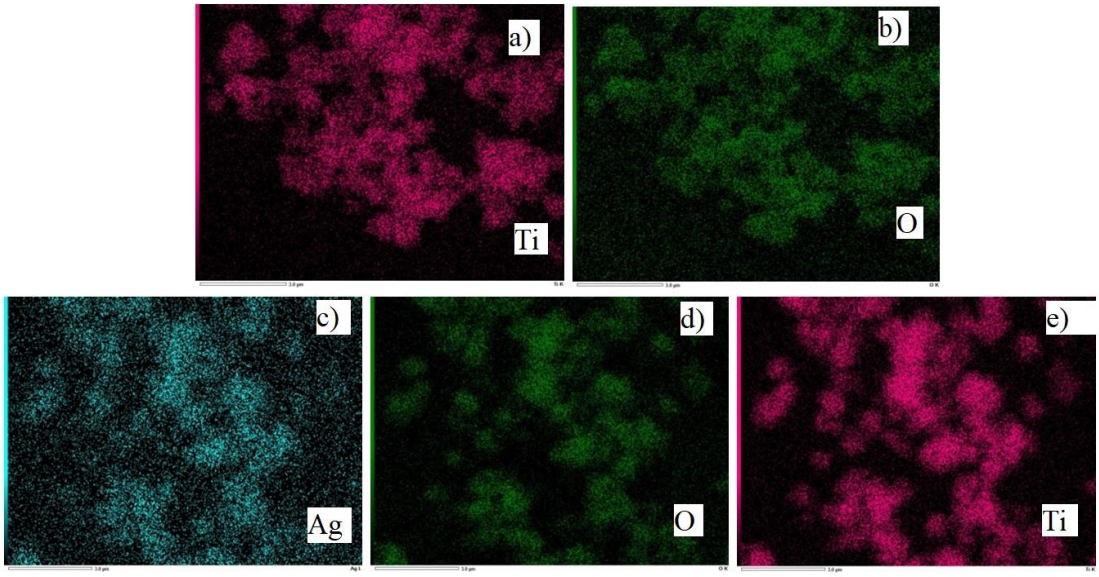

Figure 4.

SEM-EDX mapping analysis of a) titanium and b) oxygen from pure-TiO_2 and c) silver, d) oxygen and e) titanium from 15% Ag_2O@TiO_2

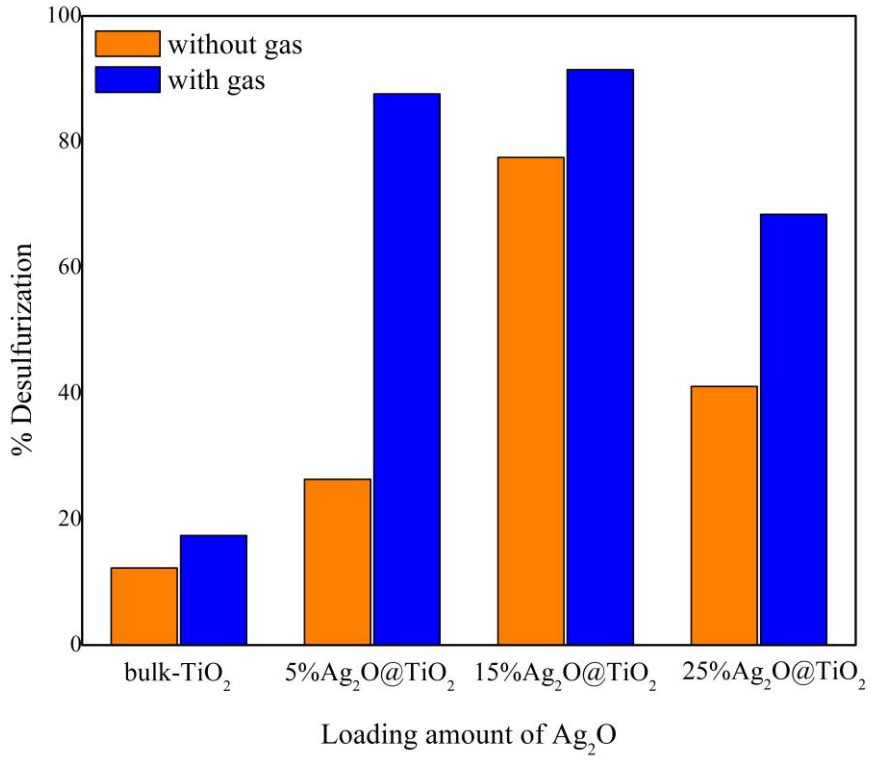

Figure 5.

Desulfurization efficiency of $Ag_2O@TiO_2$ with different loading amounts of Ag_2O (Conditions: 200 ppmS of dibenzothiophene in dodecane, weight ratio of $Ag_2O@TiO_2$:model oil = 1:20, 3 h, room temperature)

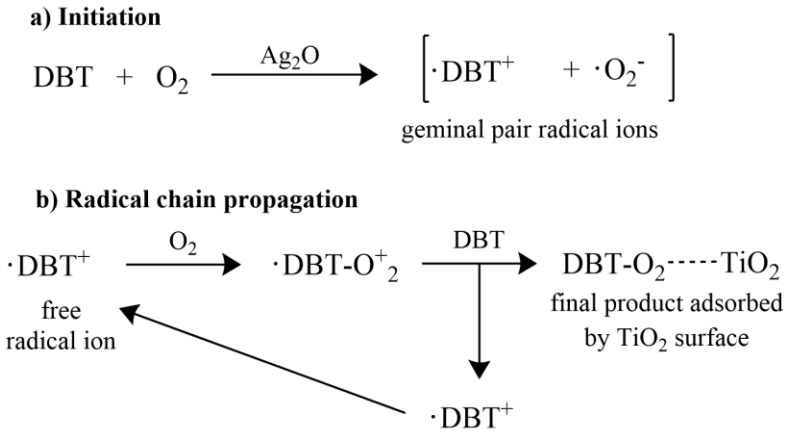

Figure 6.

Proposed mechanism of oxidative desulfurization by oxidizing DBT to DBT-O_2[7]

Conclusion:

The series of $Ag_2O@TiO_2$ materials were synthesized by incipient wetness impregnation method and exhibited the high potential for desulfurization in model oil at mild condition. Feeding air during the reaction gave positive results because the ability of O_2 in air to work as the oxidizing agent. Moreover, the effect of Ag_2O loading amount showed that 15% $Ag_2O@TiO_2$ exhibited the highest desulfurization efficiency of 91.4%. However, the reusability test will be further studied for examining the practical use in fuel refinery industry.

Acknowledgements:

This work received financial support from Development and Promotion of Science and Technology Talents Project (DPST).

References:

1. Wu P, Zhu W, Wei A, Dai B, Chao Y, Li C, Li H, Dai S. Chem. 2015;21:15421-15427.
2. Li X, Zhu W, Lu X, Zuo S, Yao C, Ni C. Chem Eng. 2017;326:87-98.
3. Satterfield CN. Heterogeneous catalysis in industrial practice, 2nd ed; McGraw Hill: New York, NY. 1991.
4. Ye F, Miao G, Wu L, Wu Y, Li Z, Song C, Xiao J. Chem Eng Sci. 2017;168:225-234
5. Gannoruwa A, Ariyasinghe B, Bandara J. Catal Sci Technol. 2016;6:479-487
6. Sing KSW, Everett DH, Haul RAW, Moscou L, Pierotti RA, Rouquerol J, Siemieniewska T. Pure & Appl Chem. 1985;57:603-619.
7. Bhadra BN, Jhung SH. Appl Catal. 2019;259:118021-118045.

D_016_OF: OXIDATIVE COUPLING OF QUINOXALINONE WITH AZOLES AND RELATED COMPOUNDS

Watchara Wimonsong, Sirilata Yotphan*

Department of Chemistry, Faculty of Science, Mahidol University, Bangkok 10400, Thailand
*e-mail: sirilata.yot@mahidol.ac.th

Abstract:

A facile and effective oxidative cross-coupling reaction of quinoxalin-2(1*H*)-ones with azoles under metal-free condition has been disclosed. This method provides a powerful and convenient approach to provide 3-((1*H*)-azo-1-yl)quinoxalin-2(1*H*)-one in moderate to excellent yields by using PIDA as an oxidant to give potential biological active molecules containing 3-((1*H*)-azo-1-yl)quinoxalin-2(1*H*)-one core.

Introduction:

2-Hydroxyqunoxalines, quinoxalin-2(1*H*)-ones or quinoxalinones are versatile classes of nitrogen-containing heterocycles. They have received significant attention in the fields of organic synthesis, pharmaceutical industries and agricultural science because they play a diverse range of biological activities for example, herbicide, insecticide, and usable drugs. Some quinoxalinone derivatives have been reported to show antimicrobial[1], anti-inflammatory[2], antibacterial[3], antifungal[4], antiviral[5] and anticancer[6] activities. Furthermore, they have recently been assayed as anticancer agents[7]. Examples of biologically active agents of these structural motifs are 3-hydrazinyl quinoxalinone, an antimicrobial agent[7], 3-amino quinoxalinone, a glycogen phosphorylase inhibitor[8], 3-piperazinyl quinoxalinone, a 5-HT3 activator[9], and 3-phenoxy quinoxalinone, a type-II VEGFR-2 inhibitor[10] (Figure 1).

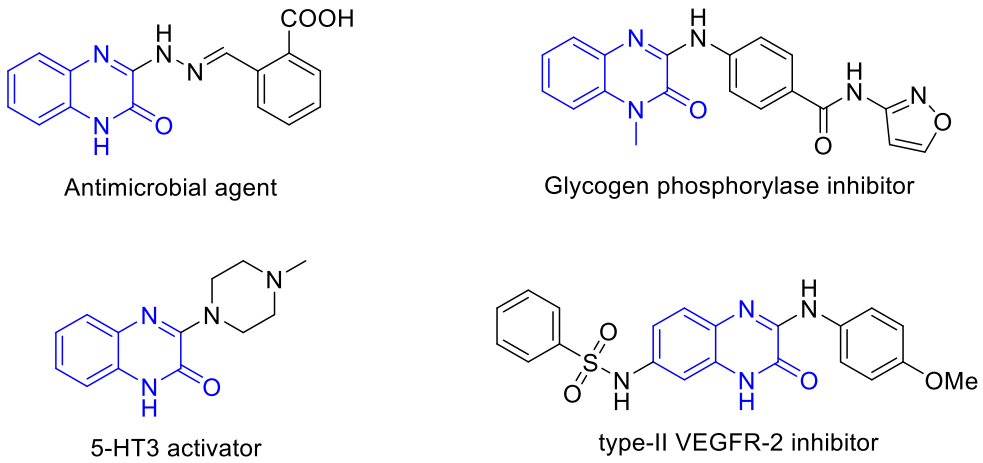

Figure 1.

Biologically active 3-substituted quinoxalinones

Although they have been used in many applications, only few synthetic approaches to these compounds were found in literature. Traditionally, nucleophilic aromatic substitution (S_NAr) of 3-halo quinoxalinone with an amine can connect the heterocyclic ring of quinoxalinone[8] (Scheme 1).

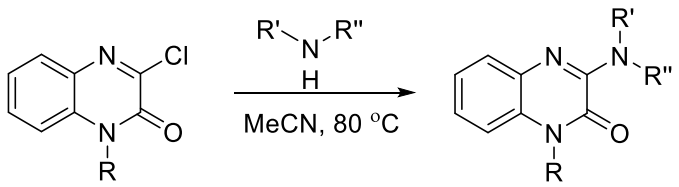

Scheme 1. Synthesis of 3-*N*-substituted quinoxalinones by S_NAr

In 2017, iodine-catalyzed selective functionalization of the C–H bond to build the C–N bond was reported. The advantages of this method as followings; (a) high versatility, (b) metal-free, (c) generate non-hazardous by-products such as tert-butyl alcohol and water. However, the limitation of this synthetic route is it can be applied only to nucleophilic aliphatic amine[11] (Scheme 2).

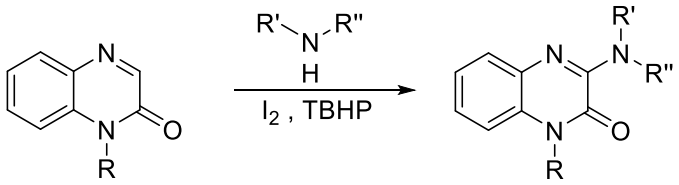

Scheme 2. Synthesis of 3-*N*-substituted quinoxalinones under iodine-catalyzed condition

Methodology:

Unless otherwise specified, all experiments were carried out under air atmosphere. All reagents were obtained from commercial suppliers and used without further purification. Oven-dried glassware was used in all cases. Column chromatography was performed over silica gel (SiO_2; 60 Å silica gel, 70−230 Mesh). GC experiments were carried out with a GC-FID/TCD (7890B) on a chromatograph equipped with an HP-1 polysiloxane column (30 m × 0.25 mm × 0.25 µm). ^1H and ^{13}C NMR spectra were recorded at 400 and 100 MHz in $CDCl_3$ or DMSO-d_6 solution. NMR chemical shifts are reported in ppm and were measured relative to $CHCl_3$ (7.26 ppm for ^1H and 77.16 ppm for ^{13}C) or DMSO (2.54 ppm for ^1H and 39.52 ppm for ^{13}C). High resolution mass spectroscopy (HRMS) data were analyzed by a high-resolution microTOF instrument with electrospray ionization (ESI).

Results and Discussion:

To investigate the direct oxidative azolation reaction of quinoxaline-2-one (quinoxalinone) and azole, we chose 1-ethylqunoxaline-2(1*H*)-one (**1a**) and 1*H*-1,2,4-triazole (**2a**) as a model substrate. We primarily used the previous reported condition[12] to test the reactions under metal-free condition using iodine (I_2) as a catalyst, and various types of oxidants. However, the combination of iodine and oxidants such as *tert*-butyl hydroperoxide (TBHP), potassium peroxymonosulfate (oxone), *m*-chloroperbenzoic acid (*m*CPBA), and potassium persulfate ($K_2S_2O_8$) at 60 °C only provided the cross-coupling product in low to moderate yields (Table 1, entry 1-4). On the other hand, we tried to use others oxidized iodine as an oxidant such as iodine pentoxide (I_2O_5), potassium iodate (KIO_3), and hypervalent iodine (e.g. phenyliodine(III)diacetate (PIDA)). Surprisingly, when we used PIDA as an oxidant, the cross-coupling product was obtained in excellent isolated yield (Table 1, entry 7; 87%).

Having established the optimal condition for this azolation reaction of quinoxalinone (Table 1, entry 7; 1 equiv of qunoxaline-2-one, 2 equiv of azole, 1.5 equiv of PIDA, DCE, 60 °C, 16 h), we explored the substrate scope of this transformation under the established conditions. As shown in Table 2, various types of azoles were coupled with quinoxalinones to provide the corresponding products (**3a-3f**) in moderate to excellent yields. From the transformation of the product (**3a-3f**), we can conclude that this reaction took place specifically at the C3 position of quinoxalinones.

Table 1.

Selected Reaction Conditions Optimization

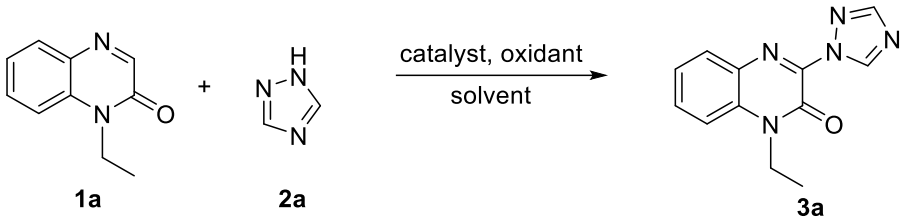

1a **2a** **3a**

Entry	Catalyst	Oxidant	Solvent	Yield (%)[a]
1[c]	I_2	TBHP	DCE	7
2[c]	I_2	oxone	DCE	42
3[c]	I_2	*m*CPBA	DCE	19
4	I_2	$K_2S_2O_8$	DCE	15
5	-	I_2O_5	DCE	0
6	-	KIO_3	DCE	0
7	-	PIDA	DCE	89 (87)[b]

The reaction conditions are 1a (0.25 mmol), 2a (0.5 mmol), oxidant (0.38 mmol), solvent (1 mL) stirred at 60 °C for about 16 h. [a]GC yields. [b]Yield of isolated product. [c]Catalyst (0.38 mmol) and oxidant (0.5 mmol) were used.

1-Ethyl-3-(1*H*-1,2,4-triazol-1-yl)quinoxalin-2(1*H*)-one (3a)

^{1}H NMR (400 MHz, $CDCl_3$): δ 9.83 (s, 1H), 8.22 (s, 1H) 8.08 (d, J = 7.9 Hz, 1H), 7.67 (t, J = 7.9 Hz, 1H), 7.48–7.44 (m, 2H), 4.48 (q, J = 7.2 Hz, 2H), 1.47 (t, J = 7.2 Hz, 3H) ppm; ^{13}C NMR (100 MHz, $CDCl_3$): δ 152.6, 149.7, 146.7, 141.1, 131.6, 131.3, 131.2. 130.9, 124.9, 113.8, 38.6, 12.4 ppm; HRMS (ESI): m/z $[M+H]^+$ calcd for $C1_2H_{12}N_5O$: 242.1036; found: 242.1034.

3-(1*H*-Benzo[d][1,2,3]triazol-1-yl)-1-ethylquinoxalin-2(1*H*)-one (**3b**)

^{1}H NMR ($CDCl_3$, 400 MHz,): δ 8.13 (d, J = 8.4 Hz, 1H), 8.00 (d, J = 8.4 Hz, 1H), 7.95 (d, J = 7.8 Hz, 1H), 7.64 (t, J = 7.4 Hz, 1H), 7.57 (t, J = 7.7 Hz, 1H), 7.45–7.39 (m, 3H), 4.46 (q, J = 7.2 Hz, 2H), 1.45 (t, J = 7.2 Hz, 3H) ppm; ^{13}C NMR ($CDCl_3$, 100 MHz): δ 132.9, 132.7, 131.7, 131.4, 130.8, 128.9, 125.0, 124.6, 120.3, 114.0, 113.4, 38.7, 12.6 ppm; HRMS (ESI): m/z $[M+Na]^+$ calcd for $C_{16}H_{13}N_5ONa$: 314.1012; found: 314.1016.

3-(1*H*-Benzo[d]imidazol-1-yl)-1-ethylquinoxalin-2(1*H*)-one (**3c**)

^{1}H NMR ($CDCl_3$, 400 MHz): δ 9.60 (s, 1H), 8.62 (d, J = 7.5 Hz, 1H), 7.97 (d, J = 8.0 Hz, 1H), 7.87 (d, J = 8.4 Hz, 1H), 7.62 (t, J = 7.8 Hz, 1H), 7.47–7.38 (m, 4H), 4.48 (q, J = 7.2 Hz, 2H), 1.48 (t, J = 7.2 Hz, 3H) ppm; ^{13}C NMR ($CDCl_3$, 100 MHz): δ 132.8, 131.6, 131.2, 130.2, 129.8, 124.7, 124.6, 124.4, 120.5, 116.0, 113.9, 38.6, 12.6 ppm; HRMS (ESI): m/z $[M+H]^+$ calcd for $C_{17}H_{15}N_4O$: 291.1240; found: 291.1243.

3-(1*H*-1,2,4-Triazol-1-yl)quinoxalin-2(1*H*)-one (**3d**)

^{1}H NMR (DMSO-*d6*, 400 MHz): δ 13.67 (s, 1H), 9.59 (s, 1H), 8.32 (s ,1H), 7,82 (dd, J = 8.0, 0.8 Hz, 1H), 7.61–7.57 (m, 1H), 7.42–7.36 (m, 2H) ppm; ^{13}C NMR (DMSO-*d6*, 100 MHz): δ 152.1, 150.7, 146.4, 142.7, 131.9, 130.7, 130.1, 128.5, 124.1, 115.6 ppm; HRMS (ESI): m/z $[M+Na]^+$ calcd for $C_{10}H_7N_5ONa$: 236.0543; found: 236.0544.

6-Chloro-3-(1*H*-1,2,4-triazol-1-yl)quinoxalin-2(1*H*)-one (**3e**)

^{1}H NMR (DMSO-d_6, 400 MHz) δ 14.03 (s, 1H), 9.62 (s, 1H), 8.34 (s, 1H), 7.46 (d, J = 2.2 Hz, 1H), 7.65 (dd, J = 8.8, 2.3 Hz, 1H), 7.41 (d, J = 8.8 Hz, 1H) ppm; ^{13}C NMR (DMSO-d_6, 100 MHz): δ 152.2, 150.7, 146.6, 143.6, 131.2, 130.9, 130.5, 127.6, 127.3, 117.4 ppm; HRMS (ESI): m/z $[M+Na]^+$ calcd for $C_{10}H_6ClN_5ONa$: 270.0153; found: 270.0152.

Methyl-2-(2-oxo-3-(1*H*-1,2,4-triazol-1-yl)quinoxalin-1(2*H*)-yl)acetate (**3f**)

^{1}H ($CDCl_3$, 400 MHz): δ 9.74 (s, 1H), 8.21 (s, 1H), 8.08 (dd, J = 8.1, 1.1 Hz, 1H), 7.65–7.61 (m, 1H), 7.47 (t, J = 7.7 Hz, 1H), 7.19 (d, J = 8.4 Hz, 1H), 5.17 (s, 2H), 3.81 (s, 3H) ppm; ^{13}C NMR ($CDCl_3$, 100 MHz,): δ 166.9, 152.9, 150.1, 146.8, 141.0, 131.9, 131.7, 131.1, 123.5, 113.4, 53.3, 44.3 ppm; HRMS (ESI): m/z $[M+Na]^+$ calcd for $C_{13}H_{11}N_5O_3Na$, 308.0754; found: 308.0753.

Table 2.

Substrate Scope with Azoles[a,b]

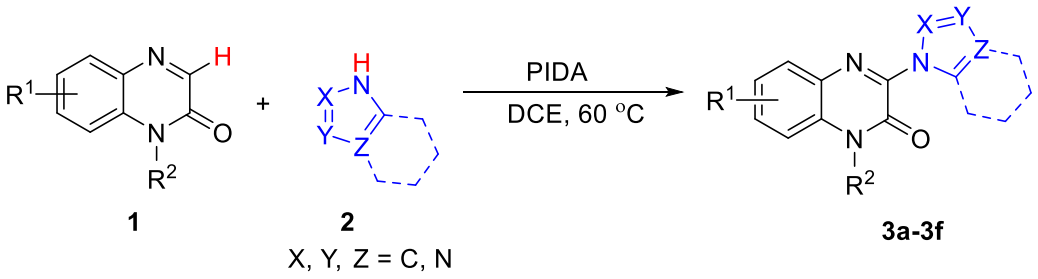

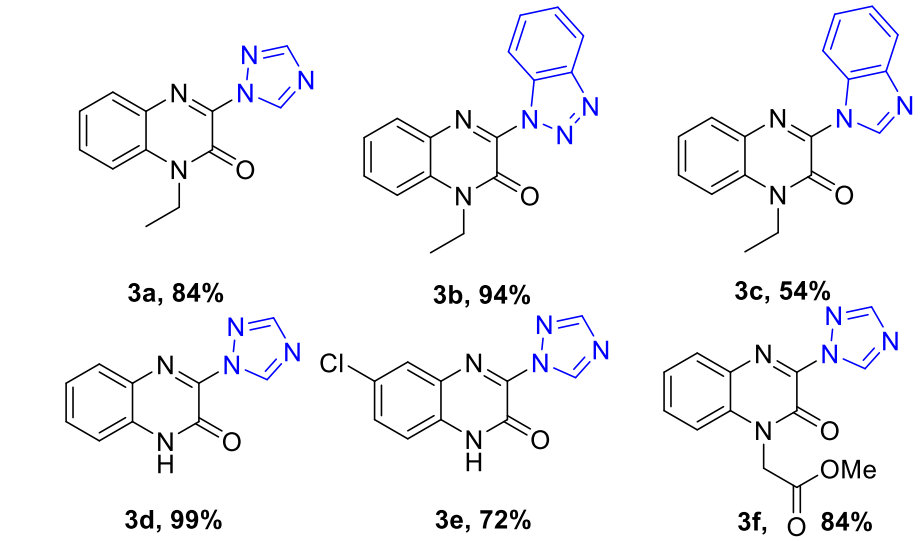

[a]The reaction condition is **1** (0.25 mmol), **2** (0.5 mmol), PIDA (0.38 mmol), 1,2-dichloroethane (DCE) (1 mL) stirred at 60 °C. [b]Yields of isolated product.

Conclusion:

In summary, we have developed a useful and effective synthetic approach for regio- and chemoselective oxidative C−N bond coupling of quinoxalinones with azoles. This oxidative coupling reaction provides a convenient synthetic route to a wild range of 3-((1*H*)-azo-1-yl)quinoxalin-2(1*H*)-one for further use in medicinal chemistry.

Acknowledgements:

The authors gratefully acknowledge financial support from Thailand Research Fund (TRF) Grant (RSA5980008 and DBG6080007), Center of Excellence for Innovation in Chemistry (PERCH-CIC), Faculty of Science, Mahidol University, the Ministry of the Higher Education Commission and Mahidol University under the National Research Universities Initiative. In addition, the authors would like to thank the Department of Chemistry and the Central Instrument Facility (CIF) at the Faculty of Science, Mahidol University for providing research facilities, and the Development and Promotion of Science and Technology Talent Project (DPST), the Institute for Promotion of Teaching Science and Technology for financial support through student scholarship (to W. W.)

References:

1. Ali MM, Ismail MMF, El-Gaby MSA, Zahran MA, Ammar YA molecules 2000;5:864.
2. Sridevi Ch, Balaji K, Naidu A, Kavimani S, Vankappayya D, Suthakaran R, Parimara S Int. J. Pharmatech. Res. 2009;1:816.
3. Badran MM, Abouzid KAM, Hussein MHM Arch. Pharm. Res. 2003;26:107
4. Carta A, Sanna P, Gherardini UD, Zannetti S Farmaco 2001;56:933.
5. Hamida MAH Carbohydr Res. 2003;338:2301
6. Sanna P, Carta A, Loriga M, Zanetti S, Sechi, L. Farmaco 1999;54:161.
7. Bayoumi AH, Ghiaty AH, El-Gilil SMA, Husseiny EM, Ebrahim MA J. Heterocyclic Chem. 2019;56:3220.
8. Dudash J, Zhang Y, Moore JB, Look R, Liang Y, Beavers MP, Conway BR, Rybczynski PJ, Demarest KT Bioorg. Med. Chem. Lett. 2005;15:4792.
9. Thompson AJ, Verhij AHP, van Muijlwijk-Koezen JE, Lummis SCR, Leurs R, de Esch IJP ChemMedChem 2013;8:948.
10. Shahin AI, El Ella DAA, Ismail NSM, Abouzid KAM Bioorg. Chem. 2014;56:20.
11. Gupta A, Deshmukh MS, Jain N J. Org. Chem. 2017;82:4784.
12. Beukeaw D, Udomsasporn K, Yotphan S J. Org. Chem. 2015;80:3448.

D_017_PF: PALLADIUM NANOPARTICLES IMMOBILIZED ON TITANOSILICALITE-1 FOR CYCLOADDITION REACTIONS OF CO_2 AND EPOXIDES

Chutima Tangku[1,2], Wipark Anutrasakda[1,2]*

[1] Department of Chemistry, Faculty of Science, Chulalongkorn University, Bangkok 10330, Thailand
[2] Center of Excellence on Petrochemical and Materials Technology, Chulalongkorn University, Bangkok 10330, Thailand
*e-mail: wipark.a@chula.ac.th

Abstract:

This work reports the synthesis of palladium nanoparticles immobilized on titanosilicalite-1 (Pd/TS-1) and its use as heterogeneous catalyst for the cycloaddition reactions of CO_2 and epoxides to cyclic carbonates. The Pd/TS-1 material was synthesized by immobilizing Pd (II) ions on the surface of TS-1 via an incipient wetness impregnation method, followed by the reduction of Pd (II) ions to Pd nanoparticles using H_2 gas. The synthesized material was characterized by X-ray diffraction (XRD), scanning electron microscopy (SEM), and N_2 adsorption-desorption. The results indicated that the MFI structure of TS-1 was retained and the surface area was still high after the immobilization of Pd nanoparticles on TS-1. For the catalytic tests, the use of Pd/TS-1 as heterogeneous catalyst and tetrapropylammonium bromide as co-catalyst was found to be an efficient catalytic system for cyclic carbonate synthesis from CO_2 and epoxide. Besides, a possible catalytic mechanism involving cooperative metal-bonding activation of epoxide which exhibited a synergistic effect with the halide anions was proposed.

Introduction:

Over the past century, human activities have required a tremendous amount of energy mostly produced from the fossil fuel combustion. This has caused pollution, greenhouse gases (GHG) and eventually a climate change over a period of time. Hence, attempts to reduce CO_2 concentration in the atmosphere has been of worldwide interest. In order to control the CO_2 concentration in the atmosphere, CO_2 capture and storage or CCS technologies have been used to reduce CO_2 concentration [1-3]. However, CO_2 can be chemically used as the starting material to synthesize several chemical products. Therefore, there are many researches that report the conversion of carbon dioxide into value-added chemicals [4, 5]. One of the most feasible strategies is the cycloaddition of CO_2 with epoxides to produce cyclic carbonates which can be used in the field of chemical processes such as precursors for synthesizing polycarbonates, solvents, electrolytes in battery and additives in pharmaceuticals [6, 7]. At present, various catalysts for cycloaddition of CO_2 have been developed including transition metal complexes [8], metal salen complexes [9], alkali metal salts [10], ionic liquids [11] and organic ammonium salts [12]. However, heterogeneous catalysts have been becoming focused because the use of heterogeneous catalysts does not only give high catalytic efficiency, but also reduce toxicity, equipment corrosion and make the regeneration process easier.

One type of interesting supporting materials is porous solid materials including activated carbon, metal organic frameworks, polymers, porous silicas and zeolites. Titanosilicalite-1 (TS-1), which is a type of zeolite, has

played an important role in a variety of catalytic processes including hydroxylation [13], ammoximation [14], epoxidation [15] and oxidative desulfurization [16].

In the present study, palladium nanoparticles immobilized on titanosilicalite-1 material (Pd/TS-1) were synthesized. The obtained material was employed as heterogeneous catalyst for cycloaddition reactions of CO_2 and epoxides to produce cyclic carbonate.

Methodology:

Chemicals and reagents: The chemicals including tetraethyl orthosilicate (TEOS, 98%), titanium (IV) butoxide (TBOT, 97%), palladium chloride ($PdCl_2$), tetrapropylammonium bromide (*t*-Pr_4NBr), epichlorohydrin (ECH) and styrene oxide (SO) were purchased from Sigma-Aldrich. Tetra-n-propylammonium hydroxide (TPAOH, 20-25 wt. % in water) was obtained from Tokyo Chemical Industry (TCI). Biphenyl was purchased from Fluka. Ethanol and acetone were acquired from Merck. All commercial chemicals were used without further purification.

Catalyst preparation: The TS-1 material was hydrothermally prepared according to a previously published procedure [17]. Briefly, 8.5 g of TPAOH aqueous solution and 19.4 g of deionized water were first mixed. The mixture of 5.0 g of tetraethyl orthosilicate (TEOS) and 0.2 g of titanium (IV) butoxide (TBOT) was then added dropwise to the mixed solution under stirring. The mixture precursor was hydrolyzed for 18 h at room temperature. The obtained clear gel was transferred into a Teflon-lined steel autoclave and heated to 180 °C for 72 h. The molar composition of the gel was: $1SiO_2$: $0.025\ TiO_2$: 0.4 TPAOH: 60 H_2O. After the crystallization process, the solid product was separated by centrifugation, washed thoroughly with deionized water and dried at 100 °C overnight. Finally, the treated material was calcined at 550 °C for 6 h. Then, the metal nanoparticles immobilized on titanosilicalite-1 were prepared by an incipient-wetness impregnation method reported by Gong and coworkers [18]. An aqueous solution of $PdCl_2$ was used in the impregnation method. The samples were dried at 110 °C for 24 h and then calcination in air at 300 °C for 2 h. Subsequently, the samples were reduced in H_2 atmosphere at 300 °C for 1 h to obtain metallic Pd nanoparticles. The final material was designated as Pd/TS-1.

Material characterizations: The crystalline phase of the materials was examined by X-Ray diffraction (XRD) using Rigaku, Smartlab with Cu Kα radiation source worked at 40 kV and 30 mA. The textural properties were estimated at 77 K using the BELSORP, mini-II nitrogen adsorptometer. The morphology and particle sizes of samples were observed by a scanning electron microscope (SEM-Jeol-JSM-7610F).

Cycloaddition of CO_2 with epoxides: All the experiments were performed in a 50 mL stainless steel autoclave equipped with a magnetic stirrer. In a typical reaction, epoxide (20 mmol), *t*-Pr_4NBr (30 mg) and the catalyst (100 mg) were charged into the reactor with no solvent. The reaction was carried out under a 5 bar pressure of CO_2. The autoclave was heated to 70 °C for 1 h. After the completion of the reaction time, the reactor was cooled in an ice bath to the ambient temperature. The catalyst was separated through centrifugation, and finally, the reaction mixture was analyzed by a Varian CP-3800 gas chromatograph equipped with a flame ionization detector (FID) using biphenyl as the internal standard.

Results and Discussion:

Characterization of materials: Fig. 1 shows the X-ray diffraction patterns of TS-1 and Pd/TS-1, all the diffraction peaks were identified as the zeolitic TS-1 according to ICSD no.09-3539, which was assigned to MFI topology structure [19]. It can be seen that the XRD pattern of Pd/TS-1 sample was similar to that of the pure TS-1, indicating that the immobilization of Pd nanoparticles on TS-1 did not destroy the MFI framework structure. Moreover, the peak intensities of Pd/TS-1 material were decreased, compared to those of TS-1, resulting from the

fact that the immobilization of Pd nanoparticles on the surface of TS-1 affecting the crystallinity of the MFI structure. It should be noted that no palladium crystalline phase was observed for Pd/TS-1, suggesting that Pd nanoparticles were highly dispersed on the surface of TS-1.

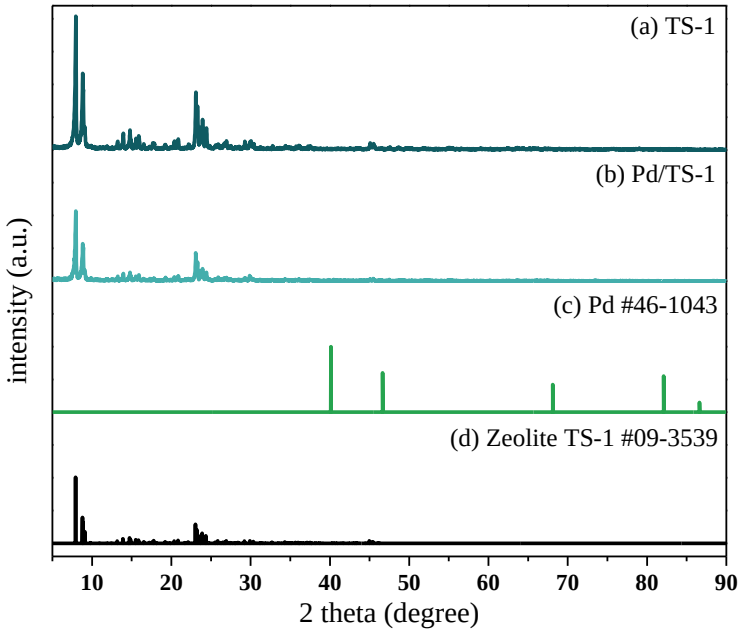

Fig. 1 XRD patterns of TS-1 (a), Pd/TS-1 (b),

JCPDS no. 46-1043 (c), ICSD no.09-3539 (d).

The microstructure and elemental constituent of the synthesized materials were observed from FE-SEM images and EDX mapping. Both TS-1 and Pd/TS-1 materials exhibited well crystal edges of regular hexagonal morphology with sizes of about 250 nm (Fig. 2a and e). The EDX mapping results show that TS-1 and Pd/TS-1 were composed of Si, O and Ti (Fig. 2b,c,d,f,g,h). In case of Pd/TS-1, it can be observed that Pd species were well-dispersed on the TS-1 surface, indicating that Pd/TS-1 was successfully synthesized.

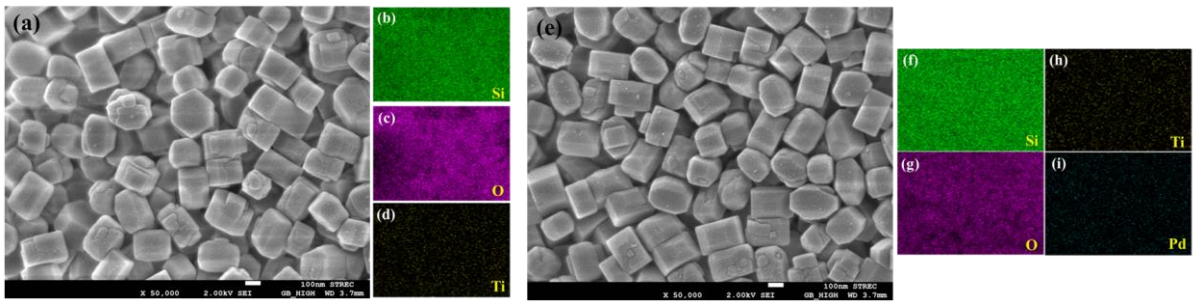

Fig. 2 FE-SEM images of TS-1 (a)and Pd/TS-1 (e). EDX mappings of silicon (b) and oxygen (c) and titanium (d) for TS-1. EDX mappings of silicon (f) and oxygen (g) titanium (h) and palladium (i) for Pd/TS-1.

N_2 adsorption/desorption isotherms of TS-1 and Pd/TS-1 are illustrated in Fig. 3. The isotherms of TS-1 and Pd/TS-1 exhibited Type II, a typical characteristic of microporous materials based on IUPAC classification [20]. This observation indicated that microporous structure was preserved after the modification, implying that the immobilization with Pd particles did not destroy the structure of TS-1 structure. Table 1 reports textural properties of the synthesized materials. The pure TS-1 had a surface area of 438 m^2/g with a high internal surface area of 423 m^2/g and a micropore volume of 0.21 cm^3/g. In case of Pd/TS-1, the pore characteristics of the material were found to be decreased. This result suggests the successful immobilization of Pd particles inside the microporous channels of TS-1.

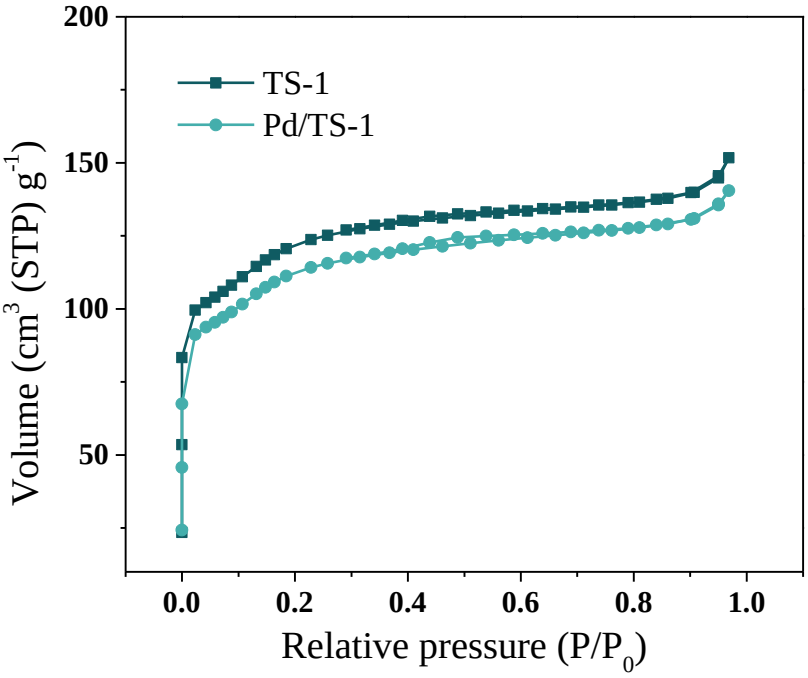

Fig. 3 N_2 sorption isotherms of TS-1 and Pd/TS-1

Table 1 Texural properties of TS-1 and Pd/TS-1 materials.

Sample	S_{BET}[a] (m^2/g)	S_{int} (m^2/g)	S_{ext}[b] (m^2/g)	V_{tot}[b] (cm^3/g)
TS-1	438	423	15	0.21
Pd/TS-1	399	382	13	0.19

[a] S_{BET} (total surface area) calculated using the BET equation.

[b] S_{ext} (external surface area) and V_{total} (total volume) determined by the *t*-plot method.

Catalytic performance in cycloaddition of CO_2: The catalytic activities of the synthesized materials as heterogeneous catalyst with *t*-Pr_4NBr as co-catalyst were tested for the cycloaddition of CO_2 with epichlorohydrin at

70 °C under 5 bar pressure of CO_2 and the reaction time of 1 h. The results are reported in Table 2. In the absence of any catalyst, epichlorohydrin hardly reacted with CO_2 (Table 2, Entry 1). Cycloaddition with Pr_4NBr alone gave an epichlorohydrin conversion of 42% with 99% selectivity for epichlorohydrin carbonate (Table 2, Entry 2). The epichlorohtdrin conversion was higher (51%) for the reaction containing TS-1 catalyst with Pr_4NBr (Table 2, Entry 3). When both Pd/TS-1 and Pr_4NBr were used, the conversion of epichlorohydrin was increased to 62% (Table 2, Entry 4), which was resulted from the synergistic effect of the acidic Pd site on the TS-1 surface and Pr_4NBr. Interestingly, the TS-1 material could also act as catalyst for this reaction probably because the Ti sites in TS-1 structure could bond to the oxygen atom of the epoxide ring, facilitating the ring opening. Under the same reaction conditions, the cycloaddition of CO_2 with styrene oxide was also investigated. The results showed the same trend as in the case of cycloaddition of CO_2 with epichlorohydrin, except that the reactivity of styrene oxide was slightly lower than that of epichlorohydrin, probably due to the steric effect of the bulky phenyl ring of styrene oxide.

Table 2 Catalytic testing for the cycloaddition of CO_2 with epichlorohydrin [a]

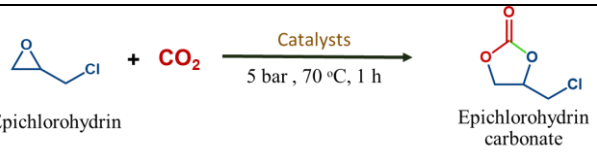

Epichlorohydrin — Epichlorohydrin carbonate

Entry	Catalyst	Co-catalyst	Reaction results[b]	
			Conversion (%)	Selectivity (%)
1	-	-	0	0
2	-	Pr_4NBr	42	99
3	TS-1	Pr_4NBr	51	99
4	Pd/TS-1	Pr_4NBr	62	99

[a]Reaction conditions: Epichlorohydrin 20 mmol, catalyst 100 mg, *t*-Pr_4NBr (30 mg), CO_2 pressure 5 bar, temperature 70 °C, reaction time 1 h.
[b]Conversion and selectivity refer to GC analysis.

Table 3 Catalytic testing for the cycloaddition of CO_2 with styrene oxide [a]

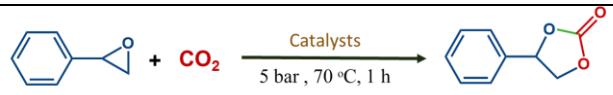

Styrene oxide — Styrene carbonate

Entry	Catalyst	Co-catalyst	Reaction results[b]	
			Conversion (%)	Selectivity (%)
1	-	-	0	0
2	-	Pr_4NBr	25	99
3	TS-1	Pr_4NBr	36	99
4	Pd/TS-1	Pr_4NBr	43	99

[a]Reaction conditions: Epichlorohydrin 20 mmol, catalyst 100 mg, *t*-Pr_4NBr (30 mg), CO_2 pressure 5 bar, temperature 70 °C, reaction time 1 h.
[b]Conversion and selectivity refer to GC analysis.

Possible mechanism: A possible reaction mechanism was proposed as shown in Scheme 1. Firstly, Lewis acid metal sites on TS-1 surface work as electron donors to activate the epoxide molecules, facilitating the ring opening. Subsequently, Br^- ions attack at the less steric carbon atom of the epoxide ring to form a C-Br bond and the ring opening occurs. Then, the alkoxide anion, which acts as a nucleophile, attacks the electrophilic carbon atom of CO_2, producing a new intermediate. Finally, the cyclic carbonate product is generated via the ring closing of the intermediate and the catalyst is regenerated.

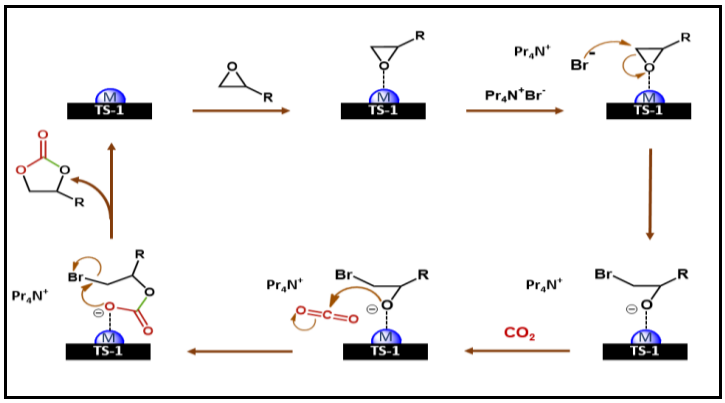

Scheme 1 A possible reaction mechanism of CO_2 and epoxide over the Pd/TS-1 and Pr_4NBr catalytic system

Conclusion:

Pd nanoparticles immobilized on titanosilicalite-1 was successfully synthesized and could be efficiently used as heterogeneous catalyst for the synthesis of cyclic carbonates from epoxides and CO_2 without the addition of an organic solvent. The catalytic results showed good conversion of epichlorohydrin (62%), conversion of styrene oxide (43%), and high selectivity of cyclic carbonates (99%) within a short period of time (1 h).

Acknowledgements:

This work received financial support from the Center of Excellence on Petrochemical and Materials Technology, Chulalongkorn University.

References:

[1] R. Sanz, G. Calleja, A. Arencibia, E.S. Sanz-Pérez, Applied Surface Science, 256 (2010) 5323-5328.

[2] R. Kishor, A.K. Ghoshal, Chemical Engineering Journal, 300 (2016) 236-244.

[3] J. Yuan, M. Fan, F. Zhang, Y. Xu, H. Tang, C. Huang, H. Zhang, Chemical Engineering Journal, 316 (2017) 903-910.

[4] M. Mikkelsen, M. Jørgensen, F.C. Krebs, Energy & Environmental Science, 3 (2010) 43-81.

[5] A.J. Hunt, E.H.K. Sin, R. Marriott, J.H. Clark, ChemSusChem, 3 (2010) 306-322.

[6] B. Schäffner, F. Schäffner, S.P. Verevkin, A. Börner, Chemical Reviews, 110 (2010) 4554-4581.

[7] H. Zhang, H.-B. Liu, J.-M. Yue, Chemical Reviews, 114 (2014) 883-898.

[8] S. Kumar, S.L. Jain, B. Sain, Catalysis Letters, 142 (2012) 615-618.

[9] M.Y. Wani, S. Kumar, C.T. Arranja, C.M.F. Dias, A.J.F.N. Sobral, New Journal of Chemistry, 40 (2016) 4974-4980.

[10] K.R. Roshan, A.C. Kathalikkattil, J. Tharun, D.W. Kim, Y.S. Won, D.W. Park, Dalton Transactions, 43 (2014) 2023-2031.

[11] W. Dai, Y. Zhang, Y. Tan, X. Luo, X. Tu, Applied Catalysis A: General, 514 (2016) 43-50.

[12] Y. Tsutsumi, K. Yamakawa, M. Yoshida, T. Ema, T. Sakai, Organic Letters, 12 (2010) 5728-5731.

[13] Y. Luo, J. Xiong, C. Pang, G. Li, C. Hu, Catalysts, 8 (2018) 49.

[14] H. Xin, J. Zhao, S. Xu, J. Li, W. Zhang, X. Guo, E.J.M. Hensen, Q. Yang, C. Li, The Journal of Physical Chemistry C, 114 (2010) 6553-6559.

[15] W. Jiao, Y. He, J. Li, J. Wang, T. Tatsumi, W. Fan, Applied Catalysis A: General, 491 (2015) 78-85.

[16] T. Napanang, T. Sooknoi, Catalysis Communications, 11 (2009) 1-6.

[17] S. Du, Q. Sun, N. Wang, X. Chen, M. Jia, J. Yu, Journal of Materials Chemistry A, 5 (2017) 7992-7998.

[18] T. Gong, Y. Huang, L. Qin, W. Zhang, J. Li, L. Hui, H. Feng, Applied Surface Science, 495 (2019) 143495.

[19] Y.S. Ko, W.S. Ahn, Korean Journal of Chemical Engineering, 15 (1998) 182-191.

[20] M. Thommes, K. Kaneko, A.V. Neimark, J.P. Olivier, F. Rodriguez-Reinoso, J. Rouquerol, K.S.W. Sing, Pure and Applied Chemistry, 87 (2015) 1051-1069.

D_018_PF: GEMOLOGICAL CHARACTERISTICS AND CHEMICAL COMPOSITIONS OF KYANITE CLAIMED TO BE FROM NEPAL

Keerawich Charoensrisan,[1] Kanyarat Kwansirikul,[1,*] Phisit Limtrakun,[1]

[1]Department of Geological Sciences, Faculty of Science, Chiang Mai University, Chiang Mai, Thailand 50200
*e-mail: kanyarat.k@cmu.ac.th

Abstract:

Nine pieces of oval cabochon greenish blue kyanite (a variety of Al_2SiO_5 mineral) claimed to be from Nepal were studied on gemological characteristics and chemical compositions including the cause of color. Their specific gravity (SG) ranged from 3.57 to 3.66. Their refractive indices (RI) of n_α ranged from 1.715 to 1.717 and n_γ ranged from 1.729 to 1.731. Birefringence was in the range from 0.012 to 0.015. All samples were inert under both-short wave (SWUV) and long-wave ultraviolet radiations (LWUV). The specimens exhibited pleochroism from moderate greenish blue or blue to light blue, and dark blue. Internal features included cleavage, fracture, negative crystal, reddish brown crystal, needle-like inclusion or hollow tube, ilmenite, feldspar, and/or zircon. Ultraviolet-Visible-Near Infrared (UV-Vis-NIR) spectra of the specimens displayed absorption peaks at approximately 370, 380, 417, 432, and 446 nm. due to Fe^{3+}. The absorption band between 500 and 700 nm. was caused by Fe^{2+} - Ti^{4+} charge transfer. The twin absorption peaks at approximately 690 and 708 nm. were associated with Cr^{3+}. Chemical analyses revealed Al_2O_3, SiO_2, Fe_2O_3, TiO_2, and Cr_2O_3. According to the absorption spectra and chemical results, iron, titanium, and chromium are the elements responsible for blue and green colors in the studied samples.

Introduction:

Kyanite is a mineral in aluminium silicate group. Its name derives from the Greek word "kyanos" which means blue, the common color of the species. Its chemical formula is Al_2SiO_5 and it crystalizes in triclinic system. Crystal habit of kyanite is commonly blade shape. It shows perfect cleavage on one direction. The hardness scale of this mineral is between 4 to 5 along axes and 6 to 7.5 across axes on the Mohs' hardness scale[1-4]. Kyanite together with andalusite and sillimanite belongs to the same polymorphic family. Those three minerals can be used as rare gemstone or collector gemstone. They are isolated tetrahedral silicates with the same chemical formula but have distinctly different structures. The crystal structure of kyanite considered as a distorted cubic close-packed arrangement of O atoms, with 10% of the tetrahedral sites filled with Si and 40% of the octahedral sites filled with Al[5]. There are four crystallographically distinct Al sites (Al1, Al2, Al3, and Al4) and two Si sites (Si1 and Si2). The Al1 and Al2 sites are in the zigzag edge-sharing octahedral chains. The chains are cross-linked by alternating SiO_4 tetrahedra and AlO_6 octahedra with Si1 and Al4 on one side and Si2 and Al3 on the other. The Al1 and Al3 octahedra share five edges with neighboring octahedra, whereas Al2 and Al4 share four edges with adjacent octahedra[5].

Kyanite occurs in metamorphic rocks of moderately high-pressure low-temperature regional metamorphism such as schists, gneisses and granite pegmatites[5]. Associated minerals are quartz, feldspar, mica, garnet, zircon, ilmenite, rutile, and other opaque minerals[1-4].

Kyanite has a wide range of colors such as blue, white, brown, gray, orange, and green. However, only the blue variety is popular in gems and jewelry market nowadays because it is similar to blue sapphire which is one of the well-known and expensive gemstones. The color of kyanite is caused by impurity replacement of some major elements in the mineral structure. Blue coloration in kyanite is similar to blue coloration in sapphire. It is due to Fe^{2+} - Ti^{4+} charge transfer and/or Fe^{2+} - Fe^{3+} charge transfer which replace Al^{3+} in the structure. Some kyanites also show greenish blue color which is caused by Fe^{2+} - Ti^{4+} charge transfer (cause of blue color) and Cr^{3+} which replace Al^{3+} in structure[1-3].

Nowadays, gem-quality kyanite has been known only from Nepal, Brazil, Kenya, Tanzania, Madagascar, and India. Although blue kyanite is more popular than other colors, attractive greenish blue to bluish green kyanite is also desirable for jewelry mounting because of its unique and uniform color. Therefore, this study aims to investigate gemological characteristics, chemical compositions and cause of color of the greenish blue kyanite samples claimed to be from Nepal for better understanding of their properties and cause of color when comparing with kyanite from other deposits.

Methodology:

Nine oval cabochon transparent greenish blue kyanite samples ranging from 2.77 to 4.16 ct. claimed to be from Nepal were studied (Figure 1). The size of samples were approximately 0.8 x 1 x 0.35 cm. The GIA GemSet. the Gemological Institute of America's (GIA) grading system, was used to describe color of the studied samples. This color grading system can describe hue (the main body color), tone and saturation. Standard gemological instruments were used to investigate gemological properties including specific gravity, refractive indices, optic sign, pleochroism, fluorescence, and inclusions. Chemical compositions of the samples were analyzed by Philips PW 2440 wavelength dispersive X-ray fluorescence spectrometer (WDXRF). Cause of color of the samples were investigated by Hitachi U-4100 ultraviolet-visible-near infrared spectrophotometer (UV-Vis-NIR) covering wavelengths between 300 to 800 nm. in two directions, parallel and perpendicular to b-axis. All experiments and analyses were done at Faculty of Science, Chiang Mai University, Chiang Mai, Thailand.

Results and Discussion:

The colors of the samples according to The GIA GemSet showed very strongly greenish Blue (vstgB) hue, dark to very dark tone, and slightly grayish to very slightly grayish saturation. The specific gravity of all samples ranged from 3.57 to 3.66 (average 3.63). Optic sign of all samples showed that they were anisotropic mineral. Their refractive indices (RI) of n_α ranged from 1.715 to 1.717 and n_γ ranged from 1.729 to 1.731. Birefringence was in the range from 0.012 to 0.015. These values are typical for kyanite. All samples were inert under both short-wave (SWUV) and long-wave ultraviolet radiations (LWUV). Pleochroism of the specimens exhibited from moderate greenish blue or blue to light blue, and dark blue. The samples revealed inclusions including negative crystal and ilmenite which were found in every samples. Cleavage, fracture, needle-like inclusion or hollow tube, feldspar, and/or zircon were also found in some samples, and reddish brown crystal was found in only 2 samples (Figure 2). The obtained gemological data of the kyanite samples claimed to be from Nepal are similar to those of kyanite from other localities around the world[1-4].

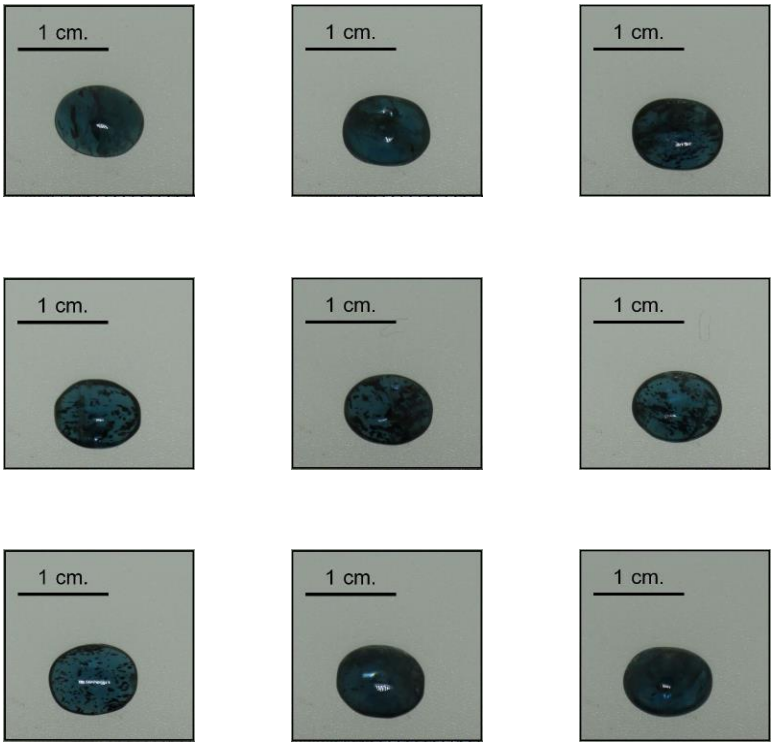

Figure 1. 9 oval cabochon kyanite samples with greenish blue color claimed to be from Nepal.

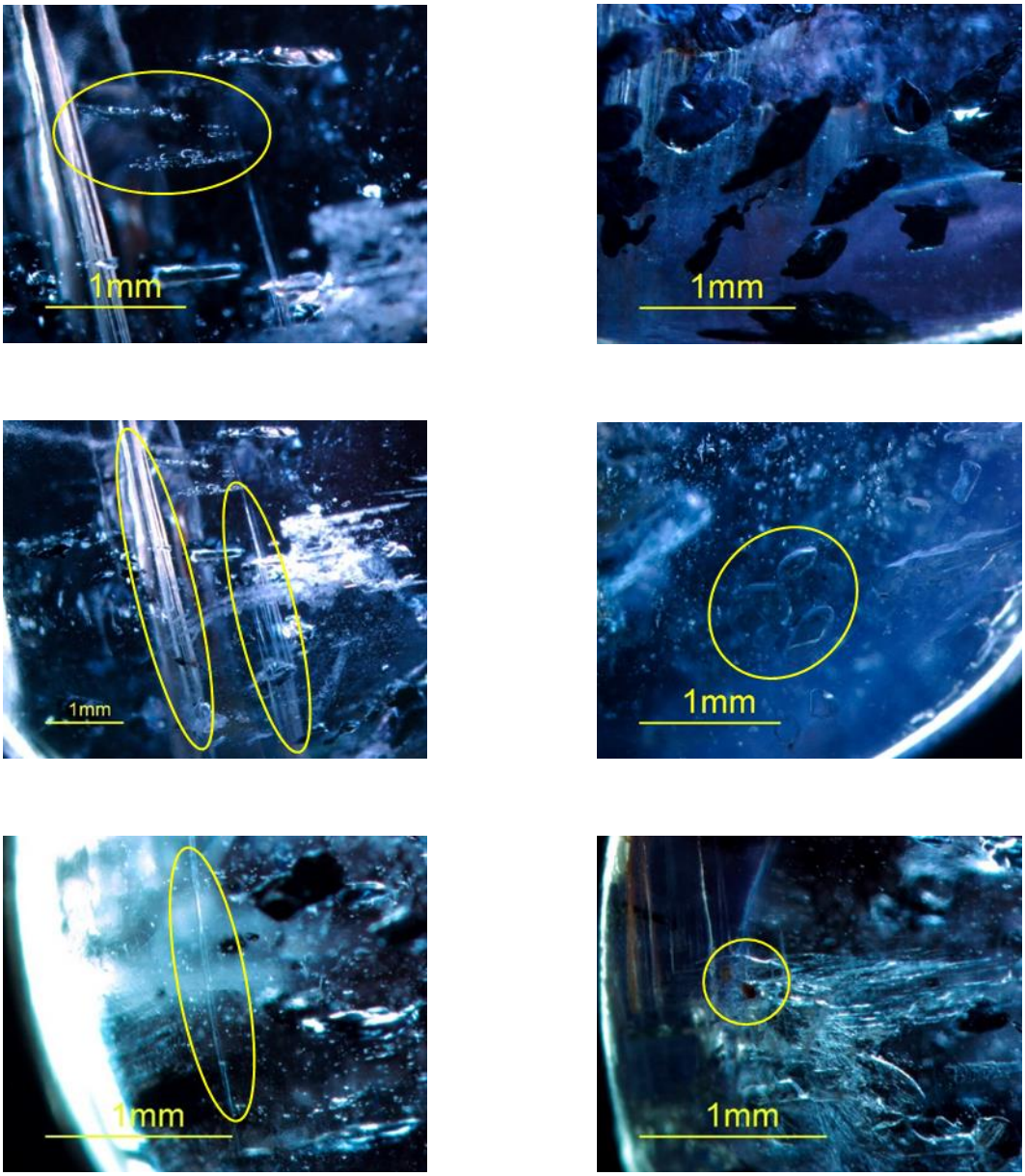

Figure 2. Example of inclusions in kyanite claimed to be from Nepal showing negative crystal (top left), ilmenite (top right), cleavage (middle left), feldspar (middle right), hollow tube (bottom left), and reddish brown crystal (bottom right).

Ultraviolet-visible-near infrared (UV-Vis-NIR) spectra of the samples displayed absorption peaks at approximately 370, 380, 417, 432, and 446 nm. due to Fe^{3+} [1]. The absorption band between 500 and 700 nm. was caused by Fe^{2+} - Ti^{4+} charge transfer[1]. The twin absorption peaks at approximately 690 and 708 nm. were due to Cr^{3+} [1] (Figure 3 and 4).

Chemical compositions analyzed by wavelength dispersive X-ray fluorescence spectrometer (WDXRF) showed major elements of Al_2O_3 (41.58 - 60.58 wt%) and SiO_2 (37.56 - 55.20 wt%). Minor and trace elements detected composed of TiO_2 (1.46 - 2.45 wt%), Fe_2O_3 (0.20 - 2.08 wt%), and Cr_2O_3 (0.08 - 0.26 wt%) (Table 1).

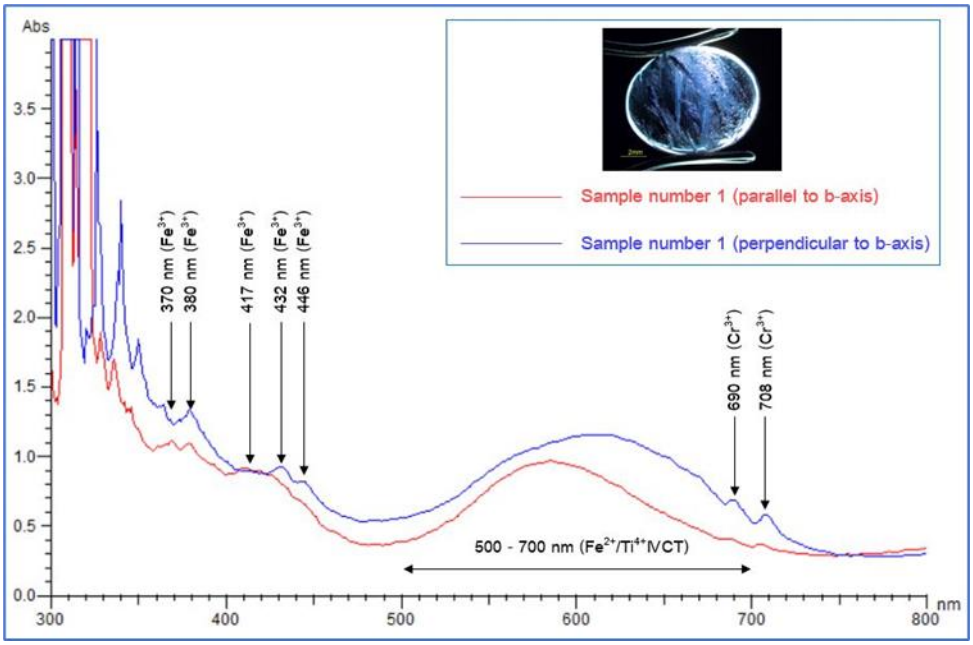

Figure 3. The UV-Vis-NIR absorption spectra of the kyanite sample, parallel and perpendicular to b-axis, showing color grading of vstgB 7/2.

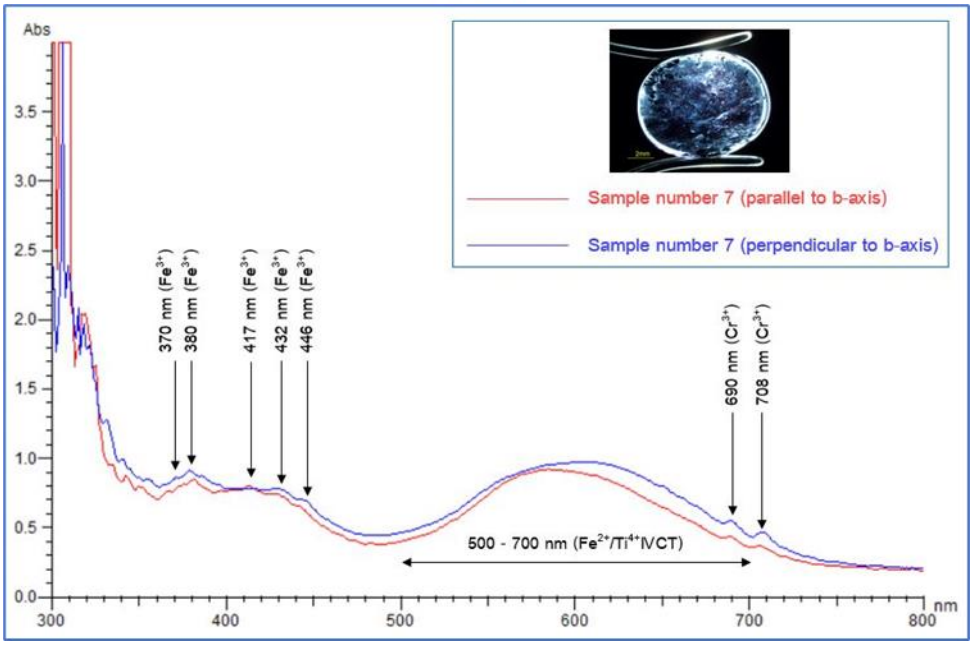

Figure 4. The UV-Vis-NIR absorption spectra of the kyanite sample, parallel and perpendicular to b-axis, showing color grading of vstgB 8/3.

Table 1. Chemical compositions of the studied kyanite claimed to be from Nepal by WDXRF.

Sample number	Oxide concentration (wt.%)					
	Al_2O_3	SiO_2	TiO_2	Cr_2O_3	Fe_2O_3	Total
1	60.580	38.339	-	-	1.081	100
2	41.583	55.198	2.178	-	1.041	100
3	60.039	39.762	-	-	0.199	100
4	57.975	39.154	1.459	-	1.412	100
5	58.826	39.964	-	-	1.209	100
6	57.832	37.557	2.446	0.080	2.084	100
7	58.442	40.742	-	-	0.816	100
8	47.396	51.877	-	0.261	0.466	100
9	58.702	40.486	-	-	0.812	100

The UV-Vis-NIR absorption spectra obtained from the greenish blue kyanite samples were consistent with their chemical compositions and similar to those spectra of Cr-rich kyanite from India[1]. Titanium, iron, and chromium which were important trace elements responsible for the blue and green colors in kyanite, as mentioned in the introduction section, iron could be detected in all samples while titanium and chromium were detected in some samples. The Fe^{2+} - Ti^{4+} charge transfer band between 500 and 700 nm. and Cr^{3+} peaks at approximately 690 and 708 nm. were likely to cause blue color and green color, respectively, in these studied samples. However, the absorption band with a maximum at 590 nm. of slightly greenish blue kyanites from Tanzania was interpreted differently[6]. Since no iron content was detected from those kyanites from Tanzania by EDXRF analysis, the absorption band with a maximum at 590 nm. was assigned to Cr^{3+} and V^{3+}, not Fe^{2+} - Ti^{4+} charge transfer, and suggested to be cause of blue color in the Tanzanian kyanites[6].

Conclusion:

From this study, it can be concluded that the gemological properties of the kyanite samples claimed to be from Nepal are typical for kyanite. The obtained absorption spectra together with trace elements detected in these samples suggest that Fe^{2+} - Ti^{4+} charge transfer are the main blue color-causing elements. Cr^{3+} is probably responsible to green hue in the samples. Saturation and variation of blue to green color in the kyanite should vary with iron, titanium, and chromium contents.

Acknowledgements:

The authors would like to thank 50th Geological Anniversary Chiang Mai University and Faculty of Science, Chiang Mai University for providing the financial support of this research. Thanks are extended to Mr. Siwakon Chimnakphant, Ms. Opor Saidum, and staffs at the Department of Geological Sciences, Faculty of Science, Chiang Mai University for providing the facilities.

References:

1. Pradat T, Choudhary G. Gems. Gemol. 2014;50(1):87-88.
2. Burns RG. Gems. Gemol. 2002;38(1):96-97.
3. Renfro N, Andy S. Gems. Gemol. 2013;49(2):122-123.
4. Quinn EP, Laurs BM. Gems. Gemol. 2004;40(4):341-342.
5. Yang H, Downs RT, Finger LW, Hazen RM, Prewitt CT. Am. Mineral. 1997;82:467-474.
6. Zwaan JC. J. Gemm. 2014;34(3):198-200.

D_019_PA: INVESTIGATION OF USING ELECTROCHEMICAL TECHNIQUE AND SPECTROPHOTOMETRIC TECHNIQUE FOR DETERMINATION OF RETINOIC ACID IN PHARMACEUTICAL PRODUCTS

Kanokwan Sakunrungrit[1], Jutamas Jaewjaroenwattana[1], Jidapa Juanjankarn[1], Jutima Siriboon[1], Petcharat Sirisakwisut[1], Yosita Yensamran[1], Chanpen Karuwan[2] and Sumonmarn Chaneam[1,3,*]

[1]Department of Chemistry, Faculty of Science, Silpakorn University, Nakhon Pathom, 73000, Thailand
[2]Graphene and Printed Electronics for Dual-Use Applications Research Division (GPERD), National Science and Technology Development Agency (NSTDA), Pathum Thani, 12120, Thailand
[3]Flow Innovation Research for Science and Technology Laboratories (FIRST Labs), Bangkok, Thailand
*e-mail: schaneam@gmail.com

Abstract:

Retinoic acid is one of the active forms of vitamin A that has been used in the cosmetic and treatment of skin disorders products. Whereas, it can irritate skin, when used in large quantities in a long period of time. Therefore, many countries, including Thailand, have prohibited the use of retinoic acid. In this work, two methods were developed for analysis of retinoic acid which are electrochemistry and spectrophotometry. Firstly, retinoic acid behaves as an electroactive species at the glassy carbon electrode. According to the cyclic voltammograms, retinoic acid is irreversibly oxidized at approximately 0.87 V vs SCE in MeOH:Acetate buffer pH 5.0. Effect of scan rate and supporting electrolyte was investigated. At the optimum condition, the linear response was obtained in the range of 20 to 280 µM with sensitivity of 0.0055 µA/µM (R^2 = 0.995). Secondly, absorption spectrophotometry was also developed using the formation of the colored compound of retinoic acid and trifluoroacetic acid. The absorbance at 564 nm was used to construct a calibration curve. Preliminary study showed linear range between 10 to 60 µM with R^2 of 0.990. Our results indicated that the proposed methods could be applied for determination of retinoic acid in pharmaceutical products such as anti-acne cream. Sample analysis results obtained from the two methods were described and discussed.

D_020_PA: GEOCHEMISTRY OF EXTRUSIVE ROCKS AT KHUN DAN PRAKAN CHON DAM RIDGE, NAKHON NAYOK PROVINCE, THAILAND

Patcharin Kosuwan Jundee,[1]* Warisa Hansakulcharoenchai,[2] Burapha Phajuy,[1] and Piyathida Sangtong,[2]

[1]Department of Geological Sciences, Faculty of Science, Chiang Mai University, Chiang Mai, Thailand
[2]Geoscience program, Mahidol University, Kanchanaburi campus, Kanchanaburi, Thailand
*e-mail: patcharinkosuwanp.j@cmu.ac.th

Abstract:

The extrusive rock samples were collected from Khun Dan Prakarn Chon Dam ridge, Nakhon Nayok Province. They are a part of the pre-Cretaceous Khao Yai Volcanics that are located at the southern end of the western Loei – Petchabun – Nakhon Nayok volcanic subbelt. Based on the petrological study, the extrusive rock samples can be classified into four groups as felsic pyroclastic rocks, felsic volcanic lava flows, mafic pyroclastic rocks, and mafic to intermediate volcanic/hypabyssal rocks (dikes and plugs). Whereas geochemical characteristics of the extrusive rock samples can be divided into two groups that are mafic to intermediate extrusive rocks (subalkalic andesite and andesite/basalt) and felsic extrusive rocks (subalkalic rhyodacite and rhyolite). Although the major and some trace element signatures of these extrusive rocks are identical to those of typical calc-alkalic magmas, the tectonic discrimination diagram for least-altered rocks shows that they are different in the magmatic suit and erupting episode. These discriminant diagrams can be successfully used to identify the tectonic environments of extrusive rocks, and to evaluate the tectonic history of a region. The incompatible trace element plot on the tectonic discrimination diagram for the mafic to intermediate extrusive rock samples are indicated high affinity with a within plate tectonic setting, while the felsic extrusive rock samples are high affinity with continental volcanic arc tectonic setting. Furthermore, the tectonic setting of these mafic to intermediate extrusive rock samples can be correlated with the Khao Kwang mafic and intermediate dykes that located north of Khun Dan Prakarn Chon Dam, which could be associated with a range of stages in the development of the Indosinian Orogeny from the early tectonic stages in the Mid-Permian to the post-collisional stages in the Late Triassic.

D_021_PA: ENHANCED VISIBLE LIGHT RESPONSE OF TiO_2 NANOPARTICLES BY NATURAL DYES

Voranuch Somsongkul[1,*], Nutnicha Ountuloa[1], Hatcha Nakpaoa[1], Prae Chirawatkul[2], Chanapa Kongmark[3,*]

[1]Department of Industrial Chemistry, Faculty of Applied Science, King Mongkut's University of Technology North Bangkok 10800, Thailand
[2]Synchrotron Light Research Institute (Public Organization), Suranaree University of Technology, Nakhon Ratchasima 30000, Thailand
[3]Specialized center of Rubber and Polymer Materials in agriculture and industry (RPM), Department of Materials Science, Faculty of Science, Kasetsart University, Bangkok 10900, Thailand
*e-mail: voranuch.s@sci.kmutnb.ac.th, chanapa.k@ku.th

Abstract:

This research aims to develop visible light responding TiO_2 nanoparticles from various natural dyes by applying green synthesis method. The natural dyes are abundant in nature, locally accessible, cheap, and environment friendly. In this experiment, three types of natural dyes such as Turmeric extract, Bergamot fruit extract and Siamese neem leave extract were used as reducing agent. TiO_2 nanoparticles were synthesized by solution-based one-step (TiO_2-natural dye) and two-step (TiO_2 / natural dye) methods. X-ray diffraction (XRD) and Ti K-edge X-ray absorption near edge structure **(**XANES**)** spectroscopy results affirmed that single-phase anatase TiO_2 nanoparticles were obtained for all samples with the average crystallite sizes of 5-8 nm. Moreover, UV-Visible absorption spectra revealed that the natural dyes played an important role in improving the visible light absorption ability of TiO_2 and decreasing the band gap energy of TiO_2 from 3.1 eV to 2.3 eV. The absorption edge energies of two-step samples were found to be lower than those of the one-step sample. The infrared spectra of the two-step TiO_2 displayed complex vibration features which were related to the bond formation between natural dye and the oxygen site of TiO_2 with the aid of carbonyl (C=O) and hydroxyl (O-H) groups. The presence of these functional groups could be responsible for the optical response of TiO_2 nanoparticles in visible wavelength region.

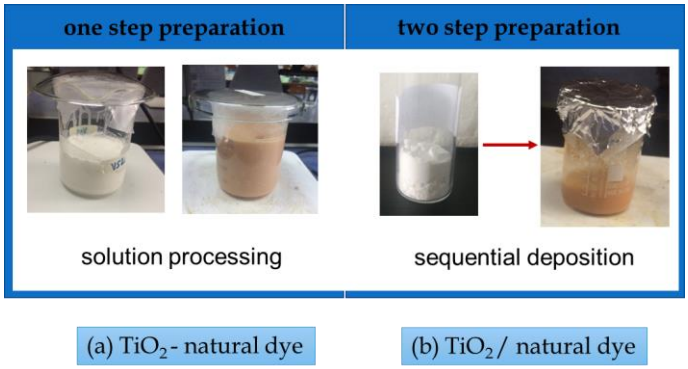

Figure 1. Experiment images of, (a) one step preparation for TiO_2 - natural, and (b) two step preparation for TiO_2 / natural

D_022_PF: VERTICAL DISTRIBUTION AND RADIOLOGICAL RISKS OF THORIUM-232 IN BURN AND NO-BURN PADDY SOIL

Wutthikrai Kulsawat[1] Netnapit Kaewchuay[2,*]

[1]Thailand Institute of Nuclear Technology (Public Organization) 9/9 Moo7, Ongkharak, Nakhon-Nayok 26120 Thailand
[2] Rajamangala University of Technology Thanyaburi, 39 Moo1 Klong 6, Khlong Luang, Phathum Thani 12110 Thailand
*e-mail: jnetnapit@gmail.com

Abstract:

The present study was to investigate the vertical distributions of ^{232}Th in paddy soils of rice straw in-situ burning and no burning in Chiang Khwan district, Roi-et province. Samples were randomly collected at depth levels from 0 to 30 cm. ^{232}Th was determined by using radiochemical analysis and alpha spectrometry. Risk assessment of the radiological hazard has also been estimated. Results of ^{232}Th activities in the straw burning plot ranged from 5.255 ± 0.353 to 13.438 ± 0.566 Bq.kg^{-1} and in no-burning plot from 4.325 ± 0.341 to 11.541 ± 0.562 Bq.kg^{-1}, respectively, which were within the reported world mean. The values of ^{232}Th dramatically decreased along the depth of soil profiles in both plots. The studied results revealed that the ^{232}Th concentrations in burn soils were higher than those in no-burn soils. It was suggested that levels of ^{232}Th concentrations in the soil were affected by the application rates of phosphate fertilizer. The range values of external air-absorbed dose rate and annual effective dose were 3.174 to 8.117 nGy.h^{-1} and 3.648 to 9.954 μSv, respectively, in the straw burning plot and 2.522 to 6.971 nGy.h^{-1} and 3.093 to 8.549 μSv, respectively, in no-burning plot. These values were far below the minimum recommended safety values of 1 mSv. Therefore, these areas were safe use as far as radiological health hazards of the living populations are concerned.

Introduction:

Rice *(Oryza sativa L.)* is the primary food staple for Thais with per capita consumption ranging from 80 kilograms (kg) for city households to around 155 kg for rural households. Thailand is not only one of the world's largest rice producers; it also remains the world's largest rice exporter. [1] Therefore, the sustainability of rice cropping systems is important to the food security and economy in Thailand. Changes in soil properties caused by cultivation and management and their consequences to soil productivity have generated significant concerns. Evidence indicates that the degradation of soil quality is a key factor for the observed declining yield [1, 2]. The challenge is to find a paddy field management system that is economically and environmentally sustainable. Burning rice straw and stubble is a common method used to facilitate soil preparation. This practice decreases soil organic carbon levels compared to soil in its natural condition which increases the risks of soil degradation. Removal of rice-straw from the field limits the return of soil N, P and K element in soils. Meanwhile, retaining rice straw on the surface (no burn management) is one possibility for improving soil quality and cutting the risks of soil degradation. However, straw burning practice is to prevent effect of plant pathogens or deleterious rhizosphere microorganisms and to destroy a specific rotation on pest species proliferation such as stem borers, stalk rot, and leaf blight which negatively affect plant growth and yield [2, 3].

Maintaining an adequate supply of nutrients for high rice yields on paddy soils is fertilizer applications. Chemical fertilizers are important in modern agriculture of both plant bio-mass retention and in situ burning practices. Rice is highly variable in its response to fertilizer application, depending on soil type. The best use of fertilizer for particular soil types at the appropriate rates are formulated from local knowledge and experience and from the results of fertilizer trials conducted by the farmers. However, farmers want to ensure good crop yield by using more than the recommended rates, and apply so much such that it has a residual effect on both the soil and the crop. Fertilizers that are not taken up by plants during the growing season would accumulate in the soil. This is what is referred to as fertilizer residues and it is the effects of such residues on soil and human health as a consequence. [4, 5]

Phosphate rocks, raw material of phosphate fertilizer are source of ^{232}Th decay products. It has been reported that an annual crop rarely takes up more than about 25% of the phosphate applied to it as fertilizer. Thus, the long-continued application of phosphate fertilizers can redistribute and elevate thorium in soil profiles and consequently its external exposure to the outdoor occupation [6-9]. Thorium is considered as one of the highly radiotoxic elements, due to its radioactivity as the daughter products decay of other alpha (α), beta (β), and gamma (γ) ray. The external radiological implication of this radionuclide is due to the γ ray exposure of the body. [8-10]

Therefore, the aim of the study was to evaluate if the vertical distribution and health hazards of ^{232}Th are affected by rice management systems with burn and no burn postharvest. This study was focused on determining the activity concentrations of ^{232}Th in soil samples collected from two plots of paddy field locates in Chiang-Khwan district, Roi-et province and to assess the air-absorbed dose rate and annual effective dose. The ^{232}Th activity concentrations in studied soil samples were determined by using the developed radiochemical analysis method.

Methodology:

A. Study Area

The study area (Figure 1) is situated in Thung Kula sub district, Chiang-Khwan district, Roi-et province (16^0 5’ 49.2” N, 103^0 42’ 39.6” E), Thailand and covers 12,720 ha. Roi-et soils are derived from washed deposits of sand stone and occur on the lower parts of pen plains. The elevation ranges from 100 to 200 m above sea level. This area has a tropical monsoon climate (Köppen 'Aw'). The average annual precipitation in 2019 was 1,225 mm, and the mean annual air temperature ranged from 26 to 28 ◦C [11].

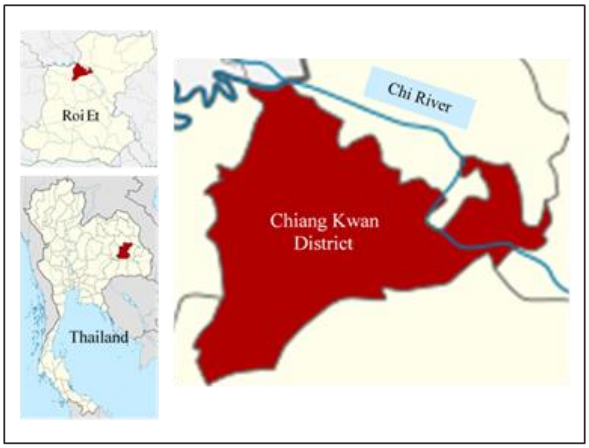

Figure 1

Location of the study area

The major soil type in Roi-Et Province is Ultisol with more than 60% sand content; low soil organic content SOC, ranging from 0.40% to 1.29%; and medium acid surface soil of pH 5.0–6.0. In general, the soils are deep, and are characterized by different colors ;however, the dominant colors are a grayish-brown or light browns and loam A horizon overlying a light brown grading to pinkish-gray sandy clay loam or loam kandic B horizon, which, in turn, overlies a light gray or whitish clay loam or clay C horizon. The soils are mottled throughout the profile, with strong brown or yellowish brown or dark brown and some yellowish red or red mottles being common in the subsoil. The reaction is medium acidic over strong to very strongly acidic [12].

B. Soil Sampling and Preparation

^{232}Th in paddy soils of different rice straw management practices with burn and no burn postharvest was analyzed. The study was conducted in two plots area each of 1.0 hectare. The soil samples were collected from both plots at depth level of 0-30 cm using soil corer (Eijkelkamp, Netherland) from different sampling stations covering each plot of the paddy fields. Each sampling plot was considered as being overlaid by a 20 x 20 m grid, subdivided in 24 cells of 4 x 4 m. Twenty soil cores of 50 cm^2 x 30 cm were sampled in 20 cells selected by a random process. The soil cores were sliced 2-3 cm interval and transported back to the laboratory.

In the laboratory, samples were air-dried as well as ground in a mixer mill (Mixer Mill mm200, Retsh) and sieved through a 125 micron mesh sieve and stored in sealed plastic bag prior to analysis.

C. Radiochemical Analysis

The radiochemical analysis was based on the developed method. Briefly, five grams of dried finely grounded soil sample of each soil depth was processed. Sample was acid digested on hot plate with HNO_3 to near dryness. The residue was treated with $HClO_4$ to remove any remaining organics. Residue was further digested with 3 times HF to near dryness and digested repeatedly with 3 times concentrated HCl. Thorium-232 present in the sample was purified by ion exchange using AG1-X8, 100-200 mesh, Chloride form resin. ^{232}Th was eluted with 50 cm^3 of warm 0.2 M HCl, collected into 50 cm^3 beaker and evaporated to dryness.

The dry residue was dissolved in 0.1 M HNO_3, saturated ammonium oxalate and $(NH_4)_2SO_4$ buffer with pH 2. The solution was transferred to an electrodeposition cell containing a platinum electrode. ^{232}Th was electrodeposited on a stainless steel disc (dia. 1.8 cm^2) for 2 h at 0.95 A. At 1 min prior to the end of this stage, 1 cm^3 of concentrated ammonia solution was added to the cell before switching off the current. The cell was disassembled and the disc was then rinsed and allowed to dry. The electrodeposited uranium was measured using implant ultra-pure silicon detector (450 mm^2 active area ORTEC EG&G) equipped with high resolution alpha spectrometry (ORTEC Model Octete Plus).

The accuracy and precision of the radiochemical method were evaluated using IAEA reference material.

D. Calculation of Air-Absorbed Dose Rate

The absorbed dose rate indicates the received dose outdoors and to assess any radiological hazard and radiation emitted by radionuclides in the soil and other environmental resources. Determination of this rate is the main step for evaluating health risk, and this parameter is expressed in gray. D (nGy.h^{-1}) in air was determined at 1 m above the ground surface to ensure uniform distribution of radionuclides which was calculated according to Eq.1 [13]

$$D\ (\text{nGyh}^{-1}) = 0.604\ A_{Th} \quad (1)$$

where A_{Th} is the activity concentrations of ^{232}Th in Becquerel per kilogram (Bq.kg^{-1}).

E. Calculation of Annual Effective Dose

The annual effective dose (AED) in the paddy soil samples was express in Sievert and calculated from Eq. (2) [13]

$$\text{AED}\ (\mu\text{Sv y}^{-1}) = D\ (\text{nGy.h}^{-1}) \times 8760\ (\text{h.y}^{-1}) \times 0.7 \times (10^{3}\ \text{mSv}/10^{-9}) \times 0.25\ (\text{nGy}^{-1})$$

$$= D \times 1.2264 \quad (2)$$

where D (nGh^{-1}) is the total air absorbed dose rate in the outdoors; 8760 h is the number of hours in one year; 0.20 is the outdoor occupancy factor or Thai people spent ~20% or 5 hours per day of their time outdoors; 0.7 $Sv.Gy^{-1}$ is the conversion coefficient from absorbed dose in air to effective dose received by adults.

Results and Discussion:

A. ^{232}Th concentraions in the soil

The results for the activity concentrations of natural radionuclides ^{232}Th in paddy soil samples of different rice residues practices are reported. The ± values are because of the 1σ variation due to counting errors. The activity concentrations of ^{232}Th in straw burning site ranged from 5.255 ± 0.353 to 13.438 ± 0.566 $Bq.kg^{-1}$, and in straw amendment site or no-burn site ranged from 4.325 ± 0.341 to 11.541 ± 0.562 $Bq.kg^{-1}$. Results of ^{232}Th in this study were lower when compared with worldwide average values. In addition, these values are less than 370 $Bq.kg^{-1}$ which are acceptable for soil safe use [13]. Therefore, these areas were safe use as far as radiological health hazards of the living populations are concerned.

It was revealed that the concentrations of ^{232}Th in both plots were decreased dramatically from surface soil down the soil profile to the bottom depth of 30 cm (Figure 2). The most plausible reasons are the right amount of phosphate fertilizers were applied to the soils and crops have significant effects on ^{232}Th uptake from soil. The observations in this study are agreed with the distribution pattern in Algeria, Qatar and Kuwait [8, 14, 15].

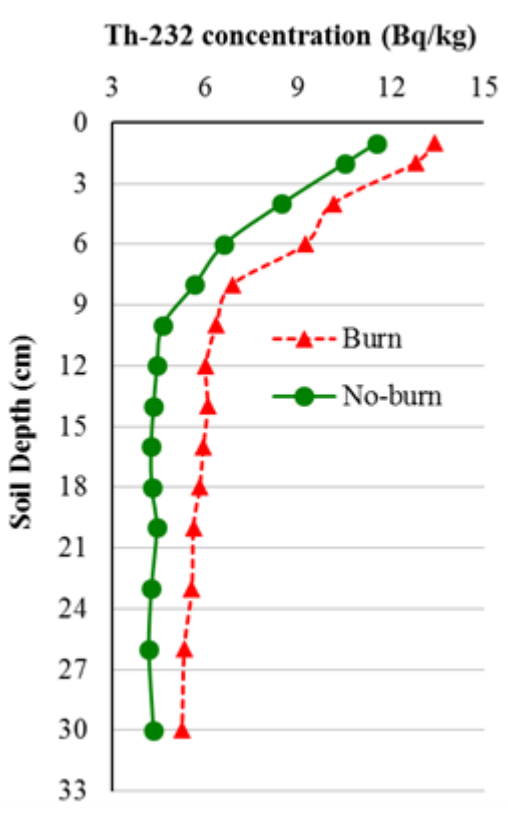

Figure 2

Relationship between ^{232}Th concentrations and soil depth

The obtained results for ^{232}Th have higher values of activity concentrations in burning plot than no-burn, these may be due to the more presence phosphate fertilizer residue in the soil resulting from the higher application rates. The content of natural radionuclides ^{232}Th in the soils depend on many factors: the type and mechanical composition of soil, capacity of absorption, acidity, concentration of exchange forms of carbonates, quantity of phosphate fertilizers application and soil organic substances [2-3]. Although this study met all the basic principles of experimentation: repetition and randomization; areas under rice were homogeneous; with the same soil type; cultivar of rice; the same weather conditions; including the same amount of fertilizers and pesticides. It was revealed that the straw burning site has been usually applied for the higher amount of phosphate fertilizer than in the sampling year. As in the studied year, fertilizer application rate was based on the amount used for the no burn site. Burning rice straw residues resulted in a higher extractable phosphate content in the surface 0-2.5 cm soil layer. Unlike removal or burning, incorporation of straw has been found to increase soil organic matter and available soil N, P and K contents. [3] Therefore, burning site might need excess quantity of phosphate fertilizer resulting in ^{232}Th residue in the soil.

B. Air-Absorbed Dose Rate

The air-absorbed dose rates in air at a height of about 1 m above the ground level due to terrestrial gamma radiation was calculated from the concentration of ^{232}Th. Compared to the average worldwide and the previous reports values, absorbed dose rate in this study was much lower as shown in Table 1.

Table 1

Comparison of ^{232}Th activity and absorbed dose rates of this study with other countries

Country	^{232}Th (Bq.kg^{-1})	D^* (nGy.h^{-1})
Algeria [8]	27	16
Nigeria [9]	30	18
Jordan [16]	18	11
Spain [17]	41	25
Kuwait [15]	5 – 21	7.7
Japan [13]	2 - 88	1.2 - 53
China [13]	1 - 360	0.6 - 217
India [18]	35 - 125	21 - 76
Malaysia [19]	83	50
Egypt (farm soil) [20]	12	7
Worldwide average [13]	30	18
Present study	7	5

Note: The values of D^* (nGy.h^{-1}) were calculated from ^{232}Th activity only.

C. Annual Effective Dose

The studied results for average annual effective dose are less than the world wide average value. The AED calculated from the air-absorbed dose rate of ^{232}Th in straw burning and straw retention soil samples.

The concentrations of ^{232}Th, absorbed dose rate and AED from this study are summarized in Table 2.

Table 2

Range and mean value of ^{232}Th activity (in Bq.kg^{-1}), absorbed dose rates *D* (nGy.h^{-1}) and annual effective dose, AED (μSv) in soil samples of burn and no-burn paddy soil.

	Sample	Maximum	Minimum	Mean
^{232}Th (Bq.kg^{-1})	Burn	13.438 ± 0.566	5.255 ± 0.353	7.477
	No-burn	11.541 ± 0.562	4.325 ± 0.341	5.925
D (nGy.h^{-1})	Burn	8.117	3.174	4.516
	No-burn	6.971	2.522	3.578
AED (μSv)	Burn	9.954	3.648	5.538
	No-burn	8.549	3.093	4.389

Conclusion:

- The measured activity concentrations of ^{232}Th in both study sites; burn and no-burn were lower when compared with the world average values.
- The higher values of ^{232}Th in soil samples of straw burning site may be due to the more presence of phosphate fertilizer residue in the area.
- The ^{232}Th levels revealed the distribution on vertical profile as dramatically decreased along the depth in both plots.
- It is noteworthy that even use of the phosphate fertilizer in the study sites, the ^{232}Th in agricultural soil did not exceed the levels that reported in the world mean.
- The overall outdoor terrestrial gamma dose rate in the straw burning plot and no-burning plot ranged from 3.174 to 8.117 nGy.h^{-1} and 2.522 to 6.971 nGy.h^{-1}, respectively. While the corresponding outdoor annual effective dose in the straw burning plot and no-burning plot were 3.648 to 9.954 μSv and 3.093 to 8.549 μSv, respectively. These values were comparatively lower than the worldwide average and the safety values of 1 mSv. [13]
- Therefore, these areas were safe use as far as radiological health hazards of the living populations are concerned.
- At the present, there were no causes for environmental alarm concerning the ^{232}Th contents detected in the soils studied in this work.
- This study established a baseline information on levels and paddy soil distribution of ^{232}Th in the environment of Chiang Khwan district, Roi-et province. The results of the study serve as a reference for future assessment.
- The application of organic fertilizers, including green manure, farmyard manure, crop residues or straws, and compost manure, is also an effective measure of improving soil fertility and maintaining land productivity. However, at the present status of maintaining soil quality at a desirable level is a very complicated and difficult task. The combined application of organic and inorganic fertilizers, have been proposed to overcome these problems. However, extensive investigation and research on potential adverse effects, long term impacts, and farmer acceptance are still needed.

Acknowledgements:

This research was financially supported by the National Research Council of Thailand. The authors extend further appreciation to Mrs. Prachit Chompooviset for her generously sharing her experiences and allowing access to her land. The anonymous reviewers are thanked for their insightful contributions.

References:

1. *Thailand Grain and Feed Annual 2019. GAIN Report Number*: *TH9031. USDA Foreign and Agricultural Service. 17 pages*
2. Hunke P, Roller R, Zeilhofer P, Schroder B, Mueller EN. Geoderma Reg. 2015:4: 31-43.
3. Rossi CQ, Pereira MG, Loss A, Gazolla PR, Perin A, Dos Anjos LHC. Agr Ecosyst Environ. 2013: 170: 36-44.
4. Jin Z, Shah T, Zhang L, Liu H, Peng S, Nie L. Food Energy Secur. 2020: 9 (2) : 1-13 https ://doi.org/10.1002/ fes3.200
5. Timsina J, Connor DJ. Field Crops Res. 2001: 69:93-132.
6. Sahu SK, Ajmal PY, Bhangare RC, Tiwari M, Pandit GG. J Radiat Res Appl Sc 2014:7: 123-128.
7. Chauhan RP and Kumar A. J Environ Health Sci Eng. 2015: 13: 45-53.
8. Bramki A, Ramdhane M, Benrachi F. J. Radiat Res App Sci. 2018: 11: 49-55.
9. Aghalagha Eo, Avwirib GO, Chad-Umorehb YE. J Envir Radioact 2012: 109: 64-70.
10. Leiterer A, Berard P, Menetrier F. 2010: Rapport CEA-R-6251, 1-48.
11. Wikipedia 2020. Roi-Et: Information on: https://en.wikipedia.org/wiki/Roi_Et_Province.
12. LDD (Land Development Department). Characterization of Established Soil Series in the Northeast Region of Thailand Reclassified According to Soil Taxonomy 2003; Land Development Department, Ministry of Agriculture and Cooperatives: Bangkok, Thailand.
13. United Nations Scientific Comm11ittee on the Effects of Atomic Radiation (UNSCEAR), UNSCEAR 2000 Report Vol.1 United Nations Sales Publication, United Nations, USA.
14. Ahmad AY, Al-Ghouti MA, Al-Sadig I, Abu-Dieyeh M. Sci Rep. 2019: 9:12196 - 12210 https://doi.org/10.1038/s41598-019-48500
15. Bajoga AD, Al-Dabbous AN, Abadullahi AS, Alazemi NA, Bachama YD, Nucl Eng Technol. 2019:51:1638-1649
16. Saleh H, Abu Shayeb M. Annal Nuc Eng. 2014:65: 184-189.
17. Quindos LS, Fernandez PL, Soto J, Rodenas C, Gomez O. Health Physics 2014: 7: 29-39.
18. Singha S, Rania A, Mahajan RK. Radiat Meas 39: 2005: 431–439.
19. Alzubaidi G, Hamid FBS, Abdul-Rahman I. Sci World J. 2016: 1-9 ID 6178103 http://dx.doi.org/10.1155/2016/6178103
20. Ahmed N, El-Arabi A. J. Envir Radioact. 2005: 84: 51-64.

D_023_OA: HYDROGEOCHEMICAL ATTRIBUTES OF GROUNDWATER IN BAN KHAM BON LANDFILL, MUEANG KHON KAEN, THAILAND

Sukanlayanee Saengsri[1], Thidarat Cotanont[1], Sarunya Promkotra[1]*, Tawiwan Kangsadan[2]

[1] Geotechnology, Faculty of Technology, Khon Kaen University, Khon Kaen 40002 Thailand
[2] Chemical and Process Engineering Program, The Sirindhorn International Thai-German Graduate School of Engineering (TGGS), King Mongkut's University of Technology North Bangkok (KMUTNB), Bangsue, Bangkok, Thailand
*e-mail: sarunya@kku.ac.th

Abstract:

Hydrogeochemical attributes of groundwater are considered in Ban Kham Bon Landfill, Mueang District, Khon Kaen Province, Thailand. The Phong River and local streams are bounded by the dividing edge between highlands and lowlands in this region as the SS sub-basin. Major ions and heavy metals in groundwater are compared to both wet and dry seasons. Chemical species of groundwater specify mainly the Na-Ca-(or Ca-Na)-Cl-HCO_3 in wet season and also the Na-Ca-Cl-HCO_3 and Na-Cl in dry season, which typically exposes the mixing of groundwater, except Na-Cl type. Besides, heavy metals of iron, manganese, cadmium, lead, and chromium are analyzed and attained the results in the average of 0.73, 0.64, 4.32, 0.146, and 0.145 mg/L, respectively. Distribution of heavy metals in the study area is associated to flow direction of groundwater in mainly radius of 500 – 1,000 meters from the center at Ban Kham Bon landfill. Saturation index of quartz as a function of total dissolved solids between 100 to 1,000 mg/L is essentially revealed the super saturation that quartz is strongly dominant in groundwater system and imply to sandstone aquifer in this area. Hydrogeochemical attributes of groundwater are applied for the MODFLOW model to enhance the understanding of heavy metal transport. The west area of Ban Kham Bon landfill shows the distribution of heavy metals (lead and chromium) affected to the north and east areas. These heavy metals are dispersed to the west and the east of this SS sub-basin.

D_024_PA: FLUORESCENCE SPECTROSCOPY FOR SIMPLE CLASSIFICATION OF SOME COFFEE LEAVES VARIETIESE

Saowaluk Madkoksung,[1] Jakkarach Sa-udon,[3] Plaipol Dedvisitsakul,[1] Kanchana Watla-iad,[1,2,*]

[1]School of Science, Mae Fah Luang University, Chiang Rai, 57100, Thailand
[2]Center of Chemical Innovation for Sustainability, School of Science, Mae Fah Luang University, Muang, Chiang Rai 57100, Thailand
[3]Mae Lod Royal Agricultural Research Station, Royal Project Foundation, Chiang Mai 50150, Thailand
*e-mail: kanchana.wat@mfu.ac.th

Abstract:

There are many coffee varieties in the world such as Arabica and Robusta Coffee. Each variety contains specific chemical compounds that present different absorption and fluorescence spectroscopic signals. Fluorescence signals of 14 coffee leaves obtained from various varieties planted in the same area (Mae Lod Royal Agricultural Research Station) were investigated for classification. The leaves were extracted using methanol before study. Then, the spectra signals obtained from setting the excitation wavelength at 300, 330, 390, 420, and 450 nm and emission wavelength in the range of 600-760 nm were analyzed based on principal component analysis (PCA) by the Metaboanalyst online program. It was found that the application of PCA analysis to the fluorescence spectra at 300 nm excitation could categorize separately some varieties such as Liberlica, Hibrido de timor (H.D.T), Typica, Geisha, Congensis, and Cattura Vermelho. Therefore, the PCA analysis of fluorescence signals could be used to classify the varieties of coffee.

D_025_PA: DETERMINING THE ANTIOXIDANT PROPERTIES, TOTAL PHENOLIC AND TOTAL FLAVONOID CONTENTS OF TRADITIONAL Thai MEDICINAL HERBS, *Anaxagorea luzonensis* A.Gray. AND *Salacia verrucosa* Wight.

Siripen Modmuang[1], Sirintip Sangsawang[1], Chattiya Pootiya [1], Jutarat Thamyota[1], Ratchanida Charoensomprasong[1], Paptawan Thongdee[1], Issaraporn Seanglam[1], Darunee Sukchit[1], Prajakkit Rawee[1], Duangdao Sattayakul[1], Somjintana Taweepanich[1], Saisamorm Lumlong[1], Kanjana Pangjit[2], Pharit Kamsri[3], Warayuth Sajomsang[4], Pornpan Pungpo[1,*]

[1] Department of Chemistry, Faculty of Science, Ubon Ratchathani University, Ubon Ratchathani, 34190, Thailand
[2] College of Medicine and Public Health, Ubon Ratchathani University, Warin Chamrap, Ubon Ratchathani, 34190, Thailand
[3] Division of Chemistry, Faculty of Science, Nakhon Phanom University, Nakhon Phanom 48000, Thailand
[4] National Nanotechnology Center, NSTDA, 111 Thailand Science Park, Klong Luang, Pathum Thani, Thailand
*e-mail: pornpan_ubu@yahoo.com

Abstract:

The antibacterial activity of some of traditional Thai medicinal herbs such as *Garcinia mangostana*, *Acalypha hispida Burm. F*. and *Hibiscus sabdariffa* were reported. The aim of this study is screening of some biological activities of medicinal herbs for antioxidant. The antioxidant properties, total phenolic and total flavonoid contents of two traditional Thai medicinal herbs, *Anaxagorea luzonensis* A. Gray. and *Salacia verrucosa* Wight. were investigated. Based on DPPH and FRAP assay, the antioxidant activities of methanol crude extracted for both plants were higher than ethyl acetate and hexane crude extracted, respectively. The DPPH inhibition of *Anaxagorea luzonensis* A.Gray. and *Salacia verrucosa* Wight. is obtained with 94.41±0.32 % and 94.94±0.30%, respectively. In the FRAP assay, both methanol extracted of both herbs were higher than ethyl acetate and hexane with 168±17 and 150±9 mg/g ascorbic acid equivalence for *Anaxagorea luzonensis* A.Gray. and *Salacia verrucosa* Wight., respectively. The phenolics of both ethyl acetate and methanol crude extracted of *Anaxagorea luzonensis* A. Gray. were higher than hexane crude extracted with 3,208±131 and 3,087±2.51 mg/g tannic acid equivalence, respectively. Whereas the methanol crude extracted of *Salacia verrucosa* Wight. is higher than 2,500 mg/g tannic acid equivalence (2,746±266). In contrast, the total flavonoid content of hexane crude extracted is higher than ethyl acetate and methanol. These obtained results aided to collect the potential crude of *Anaxagorea luzonensis* A.Gray. and *Salacia verrucosa* Wight. extracted crude for application of antioxidant productions. Based on the good antioxidant activity of both herbs, the antibacterial activity of these herbs will be future investigation.

D_026_PA: SYNTHESIS, CHARACTERIZATIONS AND ITS ENVIRONMENTAL APPLICATION TO REMOVAL OF CATIONIC DYES OF ZEOLITE A

Kunlanit Phengphat[1], Darunee Sukchit[1], Thitinan Jantasee[1], Patthama Srikham[1], Patitta Wannalee [1], Saisamorn Lumlong[1], Malee Prajuabsuk[1], Duangdao Sattayakul[1], Prajakkit Rawee[1], Jitlada Deshativong[1], Pharit Kamsri[2], Pajaree Thavorniti[3] and Pornpan Pungpo [1,*]

[1]Department of Chemistry, Faculty of Science, Ubon Ratchathani University, Ubon Ratchathani,34190, Thailand
[2]Division of Chemistry, Faculty of Science, Nakhon Phanom University, Nakhon Phanom, 48000, Thailand
[3]National Metal and Materials Technology Center, NSTDA, 111 Thailand Science Park, Klong Luang, Pathum Thani, Thailand 12120
*E-mail: pornpan_ubu@yahoo.com

Abstract:

Synthesis of Zeolite A using silica from the extraction of fly ash derived from the Mae Moh power plant, Lumpang province, as the precursor was performed. XRD, SEM, BET and ATR-FTIR were applied to characterize the zeolite A. The obtained zeolites were then used to adsorb cationic dyes, brilliant green (BG) and malachite green (MG) from aqueous solution. Based on preliminary screening at 100 ppm of dyes solution with 20g/L of Zeolite A and 60 min. of adsorption time, the adsorption efficiency of BG and MG dyes on Zeolite A by batch experiment using UV-visible spectroscopy for dye concentration determination are 73.69 and 67.67 %, respectively. The optimum parameters including optimum dosage and optimum adsorption time, were investigated. Moreover, adsorption isotherm, adsorption kinetics, and thermodynamic properties were studied. Based on the obtained results, zeolite A could be used as highly effective adsorbents for industrial dye removal because of its low cost and environmentally friendly.

D_027_PA: COMPUTER AIDED MOLECULAR DESIGN OF JAK2 INHIBITORS AS ERYTHROPOIESIS STIMULANT AGENTS FOR THALASSEMIA THERAPY

Sirintip Sangsawang[1], Bandit Khamsri[1], Somjintana Taweepanich[1], Pharit Kamsri[2], Auradee Punkvang[2], Khomson Suttisintong[3], Kanjana Pangjit[4], Pornpan Pungpo[1]*

[1]Department of Chemistry, Faculty of Science, Ubon Ratchathani University, Ubon Ratchathani 34190, Thailand
[2]Division of Chemistry, Faculty of Science, Nakhon Phanom University, Nakhon Phanom 48000, Thailand
[3] National Nanotechnology Center, NSTDA, 111 Thailand Science Park, Klong Luang, Pathum Thani, Thailand
[4] College of Medicine and Public Health, Ubon Ratchathani University, Warin Chamrap, Ubon Ratchathani, 34190, Thailand
*e-mail: pornpan_ubu@yahoo.com

Abstract:

The targeting of ineffective erythropoiesis pathway is new therapeutic option of thalassemia. JAK2 inhibitors have been investigated as erythropoiesis stimulating agent (ESA). Herein, we applied the computer aided molecular design to identify novel JAK2 inhibitors for ESA. Based on PASS prediction on known JAK2 inhibitors reported in Chembl database, thiophene amide derivatives (CHEMBL3234891 and CHEMBL3234885) showed the erythropoiesis stimulant activity with probability "to be active" values of 0.252 and 0.265, respectively. To get more structural diversity, sub- structure search and similarity search were performed on Zinc database followed by erythropoiesis stimulant activity prediction. The obtained results revealed that nine compounds were obtained with erythropoiesis stimulant activity values in the range of 0.252 to 0.445 and JAK2 inhibitor in the range of 0.136 to 0.236. Based on docking calculations, it was confirmed that finding compounds were favorable for binding in JAK2 binding site. The crucial interaction is hydrogen bond interaction of amide functional with amino acid residue surrounding the active site. Therefore, the finding compounds were proposed as novel and potential JAK2 inhibitors as ESA for thalassemia therapy.

D_028_PA: SCREENING OF ANTIOXIDANT ACTIVITIES, TOTAL PHENOLIC AND TOTAL FLAVONOID CONTENTS OF *Caesalpinia sappan* L. AND *Bauhinia sirindhorniae* K. Larsen & Larsen FOR THALASSEMIA THERAPY

Somjintana Taweepanich[1], Siripen Modmuang[1], Chattiya Pootiya [1], Jutarat Thamyota [1], Ratchanida Charoensomprasong[1], Darunee Sukchit[1], Sirintip Sangsawang[1], Paptawan Thongdee[1], Issaraporn Seanglam[1], Duangdao Sattayakul[1], Prajakkit Rawee[1], Pornpan Pungpo[1], Pharit Kamsri[2], Warayuth Sajomsang[3], Kanjana Pangjit[4,*]

[1] Department of Chemistry, Faculty of Science, Ubon Ratchathani University, Ubon Ratchathani, 34190, Thailand
[2] Division of Chemistry, Faculty of Science, Nakhon Phanom University, Nakhon Phanom 48000, Thailand
[3] National Nanotechnology Center, NSTDA, 111 Thailand Science Park, Klong Luang, Pathum Thani, Thailand
[4] College of Medicine and Public Health, Ubon Ratchathani University, Warin Chamrap, Ubon Ratchathani, 34190, Thailand
*e-mail: kanjana.pa@ubu.ac.th

Abstract:

Iron chelating drug is one alternative way for thalassemia therapy by reducing the level of iron overload in the patients. The aim of this study is to screen the medicinal plants for thalassemia therapy by using natural compounds as iron chelating agents. The antioxidant activities, total phenolic and total flavonoid contents of two Thai traditional medical plants, *Caesalpinia sappan* L. and *Bauhinia sirindhorniae* K. Larsen & Larsen were investigated. Three different organic solvents, hexane, ethyl acetate and methanol were applied to extract chemical constituents from *Caesalpinia sappan* L. and *Bauhinia sirindhorniae* K. Larsen & Larsen using Soxhlet extraction method. DPPH and FRAP assays were applied to investigate the antioxidant property of crude extracted. The obtain results based on DPPH assay showed that the ethyl acetate and methanol crude extracted were higher than hexane crude extracted. The DPPH inhibitions of ethyl acetate and methanol crude extracted of *Caesalpinia sappan* L. were 92.92±0.20 % and 92.46±0.25 %, respectively. Whereas the ethyl acetate and methanol crude extracted of *Bauhinia sirindhorniae* K. Larsen & Larsen were 77.96±0.71 % and 88.94±0.80 %, respectively. Interestingly, the highest FRAP value and total phenolic contents of the methanol of *Caesalpinia sappan* L. were obtained with 256±2 mg/g ascorbic acid equivalence and 4,608±119 mg/g tannic acid equivalence, respectively. The total flavonoid contents of ethyl acetate each plant is higher than methanol crude extracted. Therefore, the crude extracted of *Caesalpinia sappan* L. and *Bauhinia sirindhorniae* K. Larsen & Larsen obtained from ethyl acetate and methanol were suitable for future study the iron chelating for thalassemia therapy.

D_029_OF: CALCIUM ALGINATE ENCAPSUALTED SULFUR PARTICLES FOR METAL NANOPARTICLES CAPTURE: A CASE STUDY OF SILVER NANOPARTICLES

Koon Ming Lee[1], Wei Chuen Yoong[1], Chui Fung Loke[1], Joon Ching Juan[2], Khatijah Yusoff[3], Norhafizah Mohtarrudin[4], Teck Hock Lim*[1]

[1] Faculty of Applied Sciences, Tunku Abdul Rahman University College, 53300, Kuala Lumpur, Malaysia
[2] Nanotechnology & Catalysis Research Centre, University of Malaya, 50603, Kuala Lumpur, Malaysia
[3] Faculty of Biotechnology & Biomolecular Sciences, Universiti Putra Malaysia, 43400, Serdang, Selangor, Malaysia
[4] Faculty of Medicine & Health Sciences, Universiti Putra Malaysia, 43400, Serdang, Selangor, Malaysia
*e-mail: limth@tarc.edu.my

Abstract:

Uniform micron-sized sulfur particles were successful synthesized via the reduction of thiosulfate with acetic acid in the presence of sodium alginate which acted as surfactant to impart dispersibility and particle size control. After neutralization, alginate protected sulfur particles were drained into a calcium chloride solution to produce fibrous calcium alginate encapsulated sulfur composite. The composite was tested as absorbent of silver nanoparticles (Ag NPs). The Ag NPs were produced using sodium alginate as surfactant to ensure consistency. The effect of contact time and removal efficiency was established by tracking the changes in the absorption maximum of Ag NPs in the UV-Vis region after vigorous calibration. As shown in Figure 1, a 90% Ag NPs capture efficiency was achieved using the fibrous composite containing sulfur particles. This implies the potential use of sulfur/alginate composite to remove heavy metals and metal nanoparticles during wastewater treatment and or air purification when a dried gel containing S particle is used.

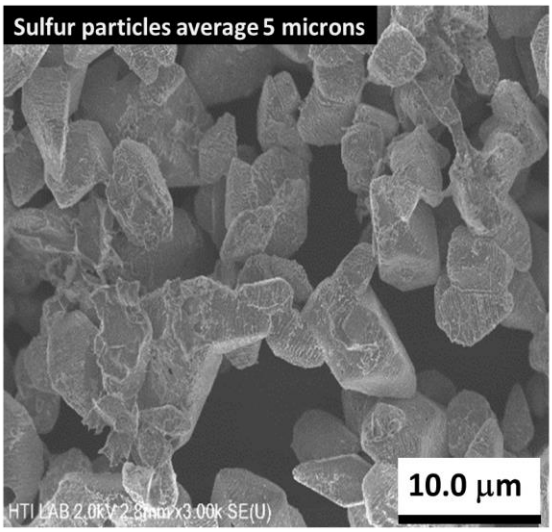

	Calcium Alginate Fiber (Control)	Composite Fibre (Calcium alginate encapsulated sulphur particles)
S Particle (wt %)	0.0	27.4
Length (cm)	213.4	214.1
Diameter (cm)	0.1484	0.1498
Surfacearea (cm^2)	99.5	100.8
Capture efficiency (%)	33	90

Figure 1. FESEM image of sulfur particles **(**SEI mode**)** and comparing the Ag NPs capture efficiency between calcium alginate control sample and the composite comprised of calcium alginate encapsulated sulfur particles**.**

D_030_OA: SYNTHESIS AND CHARACTERIZATION OF MAGNESIUM ALUMINATE NANOPARTICLES BY HYDROTHERMAL METHOD

Saytanar Tun[1*], Kyaw Naing[2]

[1]Department of Chemistry, Dawei University, Myanmar
[2]Ministry of Education, Myanmar
*email: dr.saytanartun27@gmail.com

Abstract:

Magnesium aluminate is a compound with a negatively charged alumina ion and metallic oxide with various industrial applications such as water treatment and ceramics manufacturing. In this research, magnesium aluminate nanoparticles were synthesized by hydrothermal method. It refers to the synthesis of substances via chemical reactions in a sealed and heated solution above ambient temperature and pressure. In the process, the crystal growth is normally performed in an apparatus consisting of a steel pressure vessel called autoclave. Hydrothermal method is one of the most commonly used methods for preparation of nanomaterials. There are significant advantages of hydrothermal synthesis method over others. These methods possess many advantages, such as producing a large amount of nanomaterials at a relatively very simple, low process temperature, performance of reactions in liquid environments, low energy consumption, less polluting and low cost than other methods. Magnesium aluminate gel was prepared by using aluminium nitrate, magnesium chloride and urea. The resulted magnesium aluminate gel was calcinated at different temperatures for 4 hours and then were characterized by using modern techniques (TG-DTA, XRD, FT IR and SEM). XRD data of the $MgAl_2O_4$ nanoparticles showed characteristic peaks related to miller indices of 111, 220, 311, 400, ,511, 440 and 531, these peaks are well matched with standard library data of JCPDS (77-0438>spinel- $MgAl_2O_4$). By using Scherrer equation, crystalline sizes of the $MgAl_2O_4$ nanoparticles obtained at calcination temperature of 800, 1000 and 1150°C were 10.15, 25.77 and 28.02 nm, respectively. The crystalline size and surface area of nanoparticles were found to be dependent on calcination temperature. The crystallites' size increase while surface area decreases with increases in temperature. FT IR spectra of $MgAl_2O_4$ nanoparticles were recorded and studied in the wave number range 400-4000 cm^{-1}. The band over the range of 1000-400 cm^{-1} corresponds to metal-oxygen bonds (Al-O and Mg-O). SEM microphotograph of $MgAl_2O_4$ nanoparticles showed as flake-like shapes. Magnesium aluminate nanoparticles can be used in various industrial applications such as water treatment and ceramics manufacturing.

Keywords : $MgAl_2O_4$, hydrothermal, XRD, FT IR, SEM, Scherrer

D_031_OA: POROUS HYBRID POLYMER COMPOSED OF SILSESQUIOXANE CAGES AND PORPHYRIN MOIETIES: SENSING AND ADSORPTION

Rakhi Majumdar, Vuthichai Ervithayasuporn*

Department of Chemistry, Faculty of Science, Mahidol University, Bangkok 10400, Thailand
*e-mail: vuthichai.erv@mahidol.edu

Abstract:

In modern civilization, various ionic spices have been utilized extensively in diversified fields like physiology, medical diagnostics, heavy industry, catalysis and farming etc. Release of heavy metals from aqueous wastes of many industries into the environment is a threat for the whole world because heavy metals are toxic by nature and do not degrade into harmless end product. Similarly, the anions play a crucial role in both biological and industrial process. Though, excessive exposure of anions can cause serious health problems. In this perspective, the chemosensors have gained significant attention in the field of host-guest chemistry which exhibit selective response to specific ions or neutral species. In this context, an advanced porous composite hybrid material has been synthesized from octavinylsilsesquioxane (OVS) and 5,10,15,20-tetrakis-(4-bromophenyl)porphyrin(TPP) via C-C coupling reaction. The synthesized porous polymer is very much efficient to selectively detect Hg^{2+} and F^- ions among all the ions tested. The polymer is an excellent adsorbent also for both metal ions and anions.

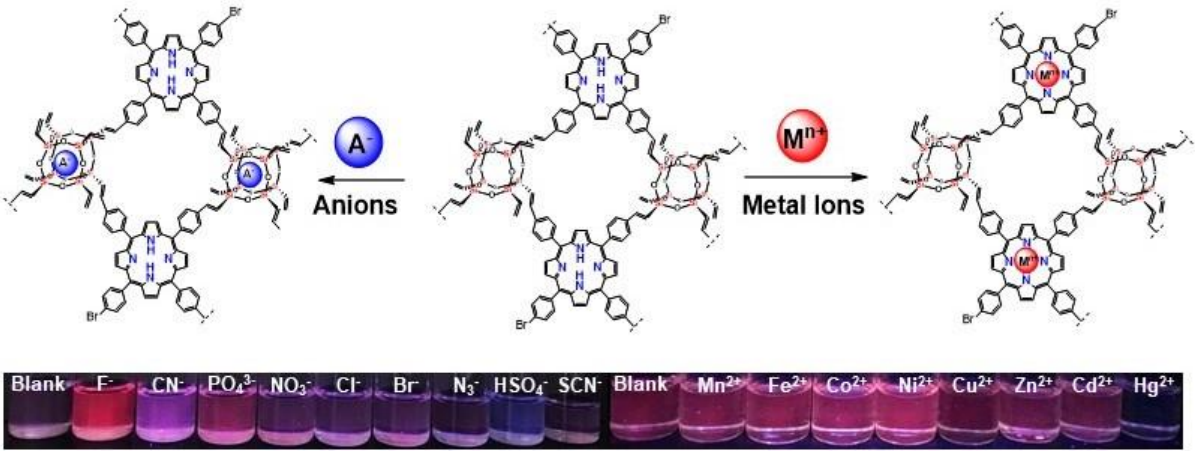

Figure 1. Selectivity of the polymer towards various ions.

E_001_OF

E_001_OF: STRUCTURE-GUIDED DESIGN OF INTERLEUKIN-18 AS A POTENTIAL CYTOKINE-MEDIATED IMMUNOTHERAPY

Napat Prompat,[1] Jirakrit Saetang,[1,2] Niran Roongsawang,[3] Surasak Sangkhathat,[2] Varomyalin Tipmanee[1,*]

[1] Department of Biomedical Sciences, Faculty of Medicine, Prince of Songkla University, Hat Yai, Songkhla 90110, Thailand
[2] Department of Surgery, Faculty of Medicine, Prince of Songkla University, Hat Yai, Songkhla 90110, Thailand
[3] Microbial Cell Factory Research Team, Biorefinery and Bioproduct Technology Research Group, National Center for Genetic Engineering and Biotechnology, National Science and Technology Development Agency, 113 Thailand Science Park, Phahonyothin Road, Khlong Nueng, Khlong Luang, Pathum Thani, 12120, Thailand
*e-mail: tvaromya@medicine.psu.ac.th

Abstract:

In recent year, cytokine-mediated immunotherapy has rapidly emerged as an effective alternative approach for cancer treatment by modulating the host's anti-tumor response. Among the cytokine-based therapeutics, interleukin-18 (IL-18) has received considerable interest as a promising cancer therapeutic agent due to the ability of cytokine to inhibit cancer by enhancing natural killer cell (NK-cell) and cytotoxic T cell responses. Thus, there is considerable interest in developing IL-18 with advantageous properties. In this study, we used an integrated computational approach to design and predict the single point mutation of IL-18 binding residue for improving the biological activity. The potential amino acid substitution, N41D was chosen based on structural analysis of human IL-18 in complex with the receptors. The impacts of amino acid mutations on IL-18 structure and dynamic behavior were evaluated using atomistic molecular dynamics (MD) simulations via AMBER16 package. The results demonstrated that N41D mutation leads to an increase in flexibility while remaining the conformational stability, which was observed by the increase in the root mean square fluctuation of the residual level. Moreover, the N41D mutant showed predicted higher binding affinity than wild-type and E6K mutant (positive control) to the IL-18 receptors. Our present findings using *in silico* approaches suggest that the computationally designed IL-18 could be a promising candidate as a cytokine-based immunotherapeutic agent.

Introduction:

Cancer is a major cause of global death. In 2018, the World Health Organization (WHO) has reported an increase of 18.1 million cases and an estimated death rate of 9.6 million[1]. An increase of cancer patient has driven the development of new and more effective treatments. Immunotherapy, immune-based treatment that exploits patient's immune system to recognize and eliminate cancer, has emerged as a promising approach for cancer therapy and shown its great potential for treating human cancers due to selectivity and long-lasting effects[2]. The field of immunotherapy shows great progress toward a cancer treatment, such as immune checkpoint blockage agents, monoclonal antibodies, cancer vaccines, oncolytic viruses, adoptive cell therapy and especially, cytokine-mediated immunotherapy[3].

Interleukin-18 (IL-18), an 18 kDa immunostimulatory cytokine primarily secreted by macrophages, is encoded by the *IL18* gene on chromosome 11q3.1[4]. This cytokine plays important roles in anti-tumor immune responses including the activation and proliferation of T cells, the induction of interferon-γ (IFN-γ) production in natural killer cells (NK-cells), and the regulation of several cytokines in both innate and adaptive immunity against cancer cells, leading to the enhancement of patient's immune responses and tumor regression[5]. The binding modes of IL-18 and IL-18 receptors (IL-18R) play important roles to the biological function of the protein. The crystal structure of human IL-18 revealed that the binding sites are composed of two parts. The first part of binding site interact specifically with IL-18Rα are site I and II, and site III is important for IL-18Rβ receptor binding[6].

The modification of amino acids on the binding sites of IL-18 through molecular cloning and mutagenesis techniques can enhance biological activity regarding the induction of IFN-γ production in NK cells[7]. Targeting the binding sites and amino acid residues of IL-18 is an attractive strategy to improve the activity of this cytokine. However, *in vitro* study is enormously expensive, time-consuming and challenging to produce the recombinant engineered proteins effectively. Nowadays, computational-based protein design facilitates the discovery and development of novel protein with reduced cost-related and time-spent on the workbench. Therefore, we apply this computational technique to design and predict the biological activity enhancement of IL-18 so that the novel potential IL-18 will be obtained for immunotherapy alternative.

Methodology:

1. *In silico* mutagenesis

Crystal structure of human IL-18 in complex with IL-18 receptor alpha, Protein Data Bank (PDB) code 3WO3, was chosen to use as the starting structure for amino acid modification in the protein sequence, as shown in Figure 1. To design the amino acid modification on the binding sites of IL-18, the surface amino acid residues within 6 angstroms to the receptor were selected based on the physicochemical properties including charge, size, and shape of residues.

The mutant model of the selected residue was mutated *in silico* using the PyMOL mutagenesis wizard[8]. IL-18 wild-type and two mutation models (E6K and M33Q) with experimental results from the previous study[7] were considered as a control group to validate the computational method. All protein structure visualization and rendering were performed using Visual Molecular Dynamics (VMD) version 1.9.3[9].

2. Molecular Dynamics (MD) simulations

After the generation of the model structures, MD simulations were performed using the AMBER 16 software package in order to mimic an *in vivo* condition and investigate the molecular dynamic behavior of the simulated structure. The model structures were subjected to energy minimization by LEaP module in AMBER 16 software package. PROPKA server was used to calculate the protonation state of protein at pH 7.4. Then, the protein solution system was neutralized by counter ions and solvated in TIP3P water molecules with 0.1M NaCl, then equilibrated at 310°K and pressure of 1 atm (1.013 bar). The system was simulated by 3ns NVT simulation with 1fs-time step and 100 ns. NPT simulation with 2fs-time step in AMBER16ieq force field using PMEMD in AMBER 16 software package[10]. Finally, Root-mean-square deviation (RMSD) and root-mean-square fluctuation (RMSF) of resulting structure were analyzed using cpptraj module in AMBER 16 software.

3. Protein-protein docking and binding affinity assessment

After obtaining the minimized structures of each model, protein docking was performed using ClusPro 2.0 server[11] to generate the complex structures of the IL-18 mutant and IL-18 receptor based on rigid body docking, RMSD based clustering of the structures and refinement of selected structures. We selected the most optimal model and most likely native structures based on ClusPro 2.0 server scoring function. To assess the binding strength of these models, the complex structures were further submitted to PRODIGY webtools[12] to estimate the binding affinity of the complexes of IL-18/IL-18 receptor in term of binding free energy (ΔG) in kcal/mol and dissociation constant (K_d) in molar units.

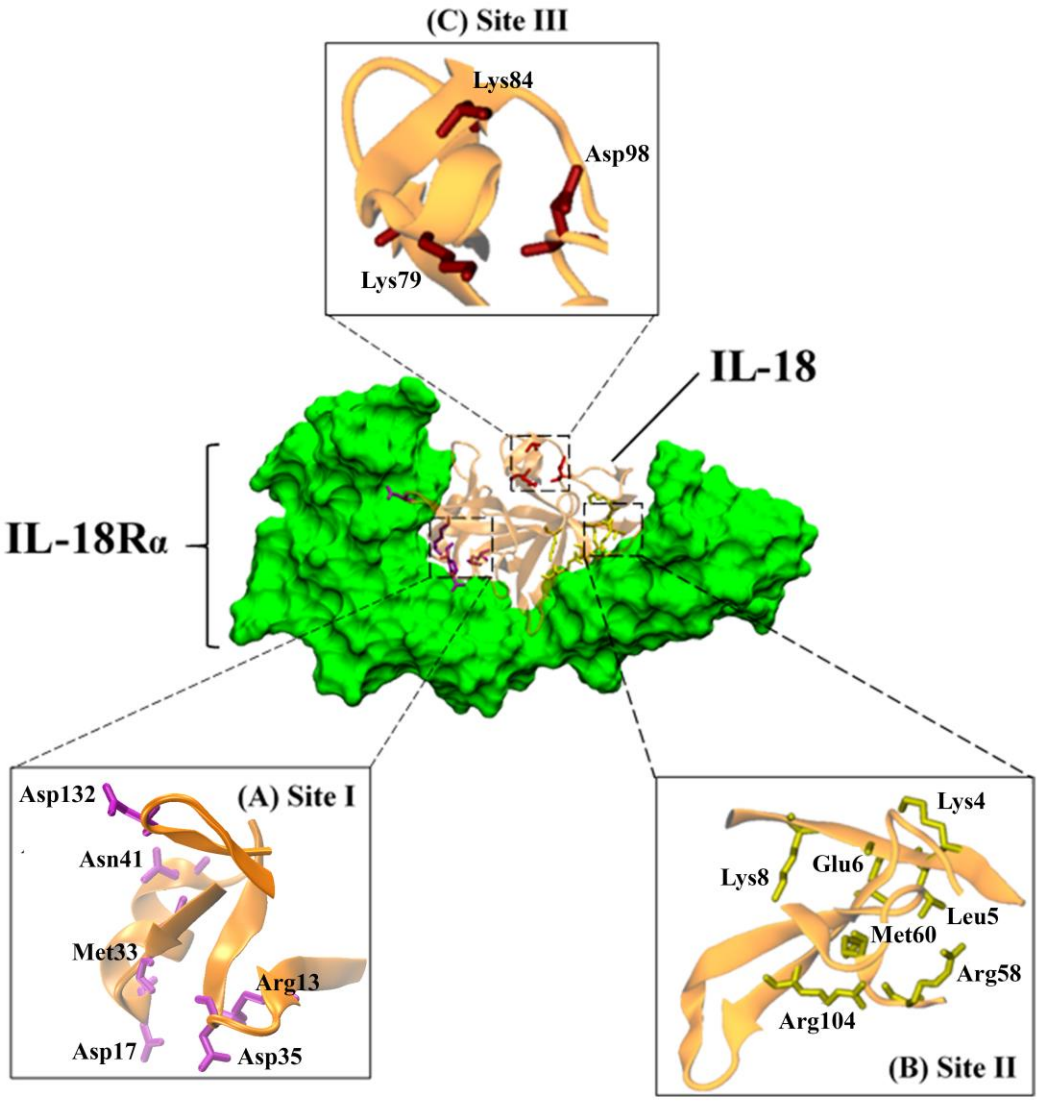

Figure 1. The structure of IL-18 (orange) and IL-18Rα (green) binding complex (PDB ID: 3WO3). (A) Amino acids in the binding interface of IL-18 and IL-18Rα as site I. (B) The binding residues in receptor binding site II. (C) The key residues in site III of IL-18 and its receptor, IL-18Rβ.

Results and Discussion:

1. *In silico* design of high affinity IL-18

Since the biological activity of IL-18 regarding the induction of IFN-γ production in the immune cells, especially NK-cells[5] required the specific binding to its receptors through the residues that dominated at site I (Asp17, Met33, Asp35, Asn41) and II (Glu6, Lys53, Met60), the alteration of these contact residues may affect the biological function of IL-18. Through analyzing the interaction between IL-18 and its receptors, we initially found that Asn41 in site I is surrounded by positively charged amino acid (Arg25 and His27) on the surface of IL-18Rα, as shown in Figure 2A. With the aim of improving the binding interaction of IL-18, Asn41 was substituted by Asp to facilitate the binding affinity by using electrostatic forces and surface charge complementarity, as shown in Figure 2B.

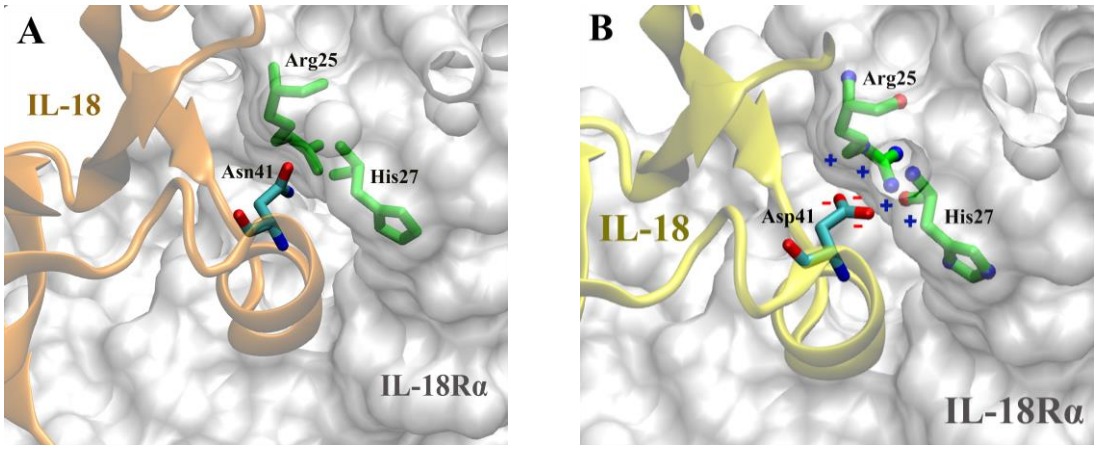

Figure 2. Structural comparison between wild-type (orange) and N41D mutant (yellow). Figure 2(A) shows the $Asn41^{IL-18}$ directly interacts with positively charged amino acid side chains of IL-18Rα though electrostatic interactions. Figure 2(B) shows the molecular interaction between the mutated structure, N41D and IL-18Rα at site I (white).

2. Conformational stability analysis

To investigate the mutational effect on the conformational stability of the wild-type and mutant structures, RMSD values were calculated using the final 100 ns trajectories of equilibration MD simulations. As shown in Figure 3, the wild-type and mutant structures (E6K, M33Q and N41D) showed almost a similar pattern in terms of the RMSD values during a simulation time of 100 ns. The RMSD value below 3 Å is acceptable. In addition, the averaged RMSD values of the wild-type, E6K, M33Q and N41D mutant were 1.63, 1.49, 1.82 and 1.45 Å, respectively. A small variation in the average RMSD values of wild-type and N41D mutant after MD simulations lead to the conclusion that the mutation of Asn-41 to aspartic acid had no effect on the overall conformation and folding of protein.

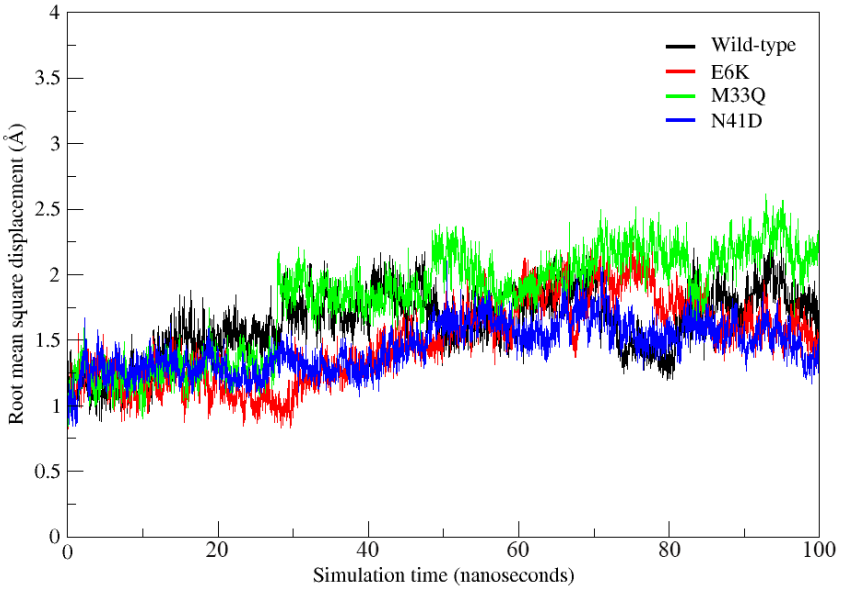

Figure 3. Root-mean-square deviation (RMSD) from MD simulation of all IL-18 structures in Angstrom units. Wild-type (black), E6K (red), M33Q (green), and N41D (blue).

3. Structural flexibility analysis

To determine the effect of the substituted amino acid on the dynamic behavior of the IL-18 residues, the structural flexibility of protein was reported as the RMSF plot in Figure 4. Analysis of fluctuation based on the RMSF values revealed that the flexibility of amino acid residues of the mutants E6K and M33Q have been altered when compared to wild-type, which was in agreement with the activity changes of E6K and M33Q mutant described in the previous experimental study[7]. Surprisingly, the activity of E6K was increased whereas decreasing in the mutant M33Q. This implies that a higher fluctuation in residues of M33Q mutant may disrupt the binding interaction of IL-18 and its receptors resulting in the activity loss of M33Q, which we discuss in detail in a subsequent section. In this study, the presence of higher RMSF value in the mutant N41D protein was observed when compared to wild-type at residue 90^{th}-95^{th} in the loop region connecting β7 sheet, which plays an important role in the binding interaction of IL-18 and IL-18Rα site I. This result suggests that N41D mutation may affect the biological activity of IL-18.

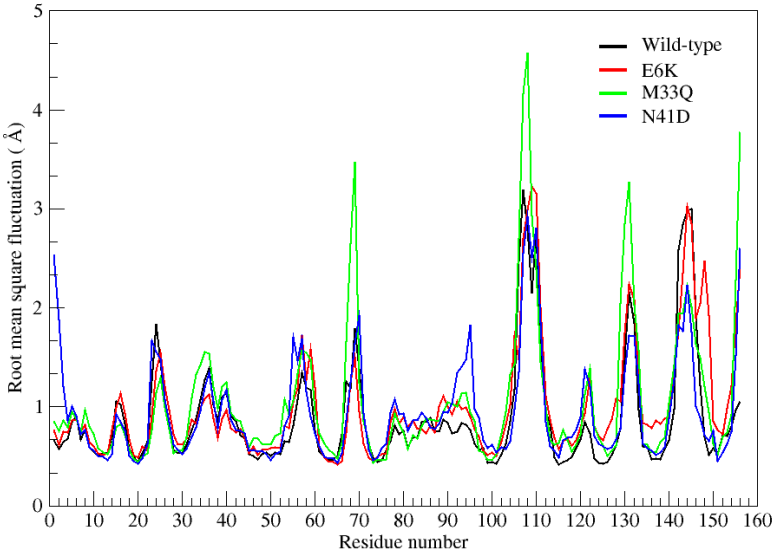

Figure 4. Root-mean-square fluctuation (RMSF) from MD simulation of all IL-18 structures in Angstrom units. Wild-type (black), E6K (red), M33Q (green), and N41D (blue).

4. Molecular docking study and binding affinity evaluation

To evaluate the binding affinity of IL-18 mutant N41D against wild-type and other two control mutants E6K and M33Q. The docking process was conducted by using ClusPro 2.0 server. The binding affinity of protein-protein complexes was determined using PRODIGY server. The predicted value of binding free energy (ΔG) and dissociation constant (K_d) of docking results are shown in Table 1. Our computational study demonstrated that the binding affinity of IL-18 wild-type, E6K, and M33Q mutants in the control group was consistent with their biological activities in the previous experimental study[7]. In this work, the computationally designed IL-18 with N41D mutation showed the strongest binding affinity with ΔG = -15.6 kcal/mol and better dissociation constant (K_d) of 9.40×10^{-12} molar compared to wild-type and E6K mutant (positive control) with lesser affinity -14.1 kcal/mol and -15.4 kcal/mol respectively. These results suggested that the substitution of Asn41 to aspartic acid may improve IL-18 activity by increasing anionicity in N41D. In contrast, the increasing flexibility at the residual level of M33Q mutant (negative control), as mentioned earlier, may result in the loss of the binding interaction between IL-18 and its receptor since the decrease in binding affinity was observed in the M33Q mutant when compared to wild-type. These findings implied that conformational flexibility and binding affinity are responsible for the biological activity of IL-18. Further studies are required to produce the computationally designed IL-18 through protein expression system and examine its ability to enhance the IFN-γ production in NK-92MI cells via cell culture and immunologic measurement. Therefore, if the designed IL-18 exhibits potent activity with increased IFN-γ production compared to wild-type, it would be a promising candidate as a cytokine-based immunotherapy.

Table 1. Binding affinities and biological activities of wild-type and mutant IL-18 structures.

Mutation	Predicted ΔG (kcal/mol)	Predicted K_d (M)	Binding affinity	Biological activity [a]
Control group				
Wild-type	-14.1	1.10×10^{-10}	Standard	Standard
E6K	-15.4	1.50×10^{-11}	Increase	Increased activity
M33Q	-13.4	3.90×10^{-10}	Decrease	Decreased activity
N41D	-15.6	9.40×10^{-12}	Increase	Predicted increase

[a] The biological activity of E6K and M33Q mutants were evaluated experimentally by the measurement of IFN-γ production in NK-92MI cells when compared to IL-18 wild-type[7].

Conclusion:

In summary, we have proposed a therapeutic protein design strategy to improve the biological activity of IL-18 which was based on structural, dynamic and energetic analyses of the interaction between IL-18 and IL-18 receptor. Preliminary, the mutation at the binding residue asparagine 41 (N41D) majorly affected the flexibility and binding affinity of IL-18. Our present findings using *in silico* study demonstrate that the computationally designed IL-18 could be considered as a potential therapeutic candidate for cancer treatment. However, the impacts of the designed protein on IL-18 activity need to be validated experimentally.

Acknowledgements:

This work was supported by the government budget of Prince of Songkla University (Grant No. SCI6101034M). In addition, we would like to acknowledge the Central Research Laboratory, Faculty of Medicine, Prince of Songkla University for providing necessary laboratory facilities.

References:

1. Bray F, Ferlay J, Soerjomataram I, Siegel RL, Torre LA, Jemal A. CA. 2018;394-424.
2. Zhang H, Chen J. J Cancer. 2018;9:1773-1781.
3. Berraondo P, Sanmamed MF, Ochoa MC, Iñaki E, Maria AA, José LP, et al. Br J Cancer. 2019;120:6-15.
4. Yasuda K, Nakanishi K, Tsutsui H. Int J Mol Sci. 2019;20:649.
5. Tsutsui H, Nakanishi K. Immunotherapy. 2012;4:1883-1894.
6. Tsutsumi N, Kimura T, Arita K, Ariyoshi M, Ohnishi H, Yamamoto T, et al. Nat Commun. 2014;5:5340.
7. Saetang J, Puseenam A, Roongsawang N, Voravuthikunchai S, Sangkhathat S, Tipmanee V. PLoS One. 2016;11:e0160321.
8. Rigsby RE, Parker AB. Biochem Mol Biol Educ. 2016;4:433-437.
9. Humphrey W, Dalke A, Schulten K. J. Mol. Graph. 1996;14:33–38, 27–28.
10. Case A, Cheatham E, Darden T, Gohlke H, Luo RJ. Comput. Chem. 2005;26:1668–1688.
11. Kozakov D, Hall DR, Xia B, Porter KA, Padhorny D, Yueh C, et al. Nat Protoc. 2017;12:255-278.
12. Xue L, Rodrigues J, Kastritis P, Bonvin A, Vangone A. Bioinformatics, 2016;32:3676-3678.

E_002_OF: STRUCTURAL ANALYSIS OF T63 ALTERATION IN HUMAN INTERLEUKIN-18

Chariya Peeyatu,[1,2] Jirakrit Saetang,[3] Pasarat Khongkow,[1,2] Varomyalin Tipmanee[1,2,*]

[1]Institute of Biomedical Engineering, Faculty of Medicine, Prince of Songkla University, Thailand
[2]Department of Biomedical Sciences and Biomedical Engineering, Faculty of Medicine, Prince of Songkla University, Thailand
[3]Department of Surgery, Faculty of Medicine, Prince of Songkla University, Thailand
*e-mail: tvaromyalin@medicine.psu.ac.th

Abstract:

Interleukin (IL) combination has emerged as a powerful approach for NK cell-based cancer immunotherapy. A combination of IL-2 family, IL-12 family, and IL-18 is a common use for NK cell activation to show memory and cytotoxicity. However, IL-18 is a crucial biomolecule to integrate essential signaling pathways and enhance IFN-γ induction. Recently, double mutation of human IL-18 (E6K/T63A) boosted the abundance of IFN-γ production. Structural insight revealed T63A supports E6K by increase loop flexibility. This study investigated the role of T63 on conformational change and flexibility of overall structure and binding site by molecular dynamics (MD) simulation. Interestingly, E6K/T63I and E6K/T63N from each type of amino acid property exhibited attractive flexibility of binding site I and III loop. The dynamic behavior of these mutations revealed binding site III residues direction closer to its receptor than WT. In contrast, E6K/T63M and E6K/T63Q displayed low flexibility at major binding site III loop, which leads in the wrong direction. However, E6K/T63I, E6K/T63M, and E6K/T63Q changed RMSD from the initial structure about 4 Å that may disturb the hydrogen bond formation. This study provides candidate IL-18 from computational method that could be a potential engineered IL-18 to activate NK cells in cancer immunotherapy.

Introduction:

Cancer immunotherapy knows as the next generation of cancer treatment, which is an emerging field of tumor immunology and immunoengineering. Cancer immunotherapy's concept is boosting the immune system of patients to fight cancer cells and prevents regression by immune cell recognition and activation. One of cancer immunotherapy strategies is using natural killer (NK) cells, the next platform to T cell-based approach, to memory normal and cancer cells by balancing between activating and inhibitory receptors follow by killing activity against cancer cells.[1]

Interestingly, interleukin (IL) combination is the most common strategy to enhance *ex vivo* NK cell activation by the integration of signaling pathways, especially a combination of IL-2 family, IL-12 family, and IL-18. IL-2 and IL-12 family cytokines play an essential role in NK cell proliferation and cytotoxicity through Janus kinase/signal transducers and activators of transcription (JAK/STAT) signaling pathway.[2] In this strategy, IL-18 has shown the bottleneck effect because it is the only one cytokine from IL-1 family which stimulates several signaling pathways, including myeloid differentiation primary response protein 88 (MyD88), mitogen-activated protein kinase (MAPK), and nuclear factor κ-light-chain-enhancer of activated B cells (NF-κB) signaling pathways, resulting that stabilize IFN-γ mRNA and induce its production.[3,4]

Various studies showed that engineered IL-18 increases IFN-γ production dramatically by mutagenesis of the direct binding residues, which improve binding affinity. Site-mutations at the binding site I, D17N and M33Q, changed structure stabilization and decreased IFN-γ production, indicating that these residues should be conserved.[5,6] For site-mutations at the binding site II, E6K preserved protein structure and increased protein function, but K53E lost activity.[7] Few studies also reported mutagenesis of the non-binding residues increases binding interaction by improving protein flexibility.[5,6] S10I, V11I, T63A were site-mutations of non-binding residues that stabilize protein structure, but only T63A increased loop flexibility and protein function.[5] Coupling of effective mutations, E6K/T63A, was generated, resulting in that T63A promotes the improvement of protein activity better than a single mutation of E6K.[6] However, the dynamic behavior and the residue alteration of E6K/T63A are limited.

In this study, we investigated the effects of T63 alteration in E6K/T63A using molecular dynamics (MD) simulation to explore structural change and behavior. The alteration to amino acids with hydrophobic and uncharged polar side chains was focused according to position 63 located in the hydrophobic core. This research aimed to screen the candidate engineered IL-18, which exhibits interesting protein behavior by computational approach for further biological analysis.

Methodology:

Homology modeling: To create the structure of engineered IL-18, homology modeling was performed for Protein Data Bank (PDB) file format by Phyre2 web server.[8] Amino acid sequences of engineered IL-18 were input for protein modeling. Double mutations of engineered IL-18 were composed of fixed E6K and varied T63 (E6K/T63X). The modeled IL-18 with the highest confidence and coverage was selected for the initial structure of MD simulation.

MD simulation: The protonation state of protein structure was optimized at pH 7.0 by PDB2PQR web server for pKa prediction of amino acid side chain based on Poisson-Boltzmann electrostatics calculations.[9] System preparation and MD simulation were performed using the AMBER16 software package.[10] The protein solution was prepared using LEaP module. TIP3P water box with 14 Å in all directions from surface protein and 0.15 M NaCl was added to the system followed by neutralization of protonated or deprotonated protein with sodium (Na^+) or chloride (Cl^-) ions. MD simulation condition was followed by the previous study except the mentioned parameters.[6] Energy minimization was applied to remove steric clashes of non-bonding atoms in solvated protein structure using steepest descent and conjugate gradient methods for 2000 and 1000 cycles, respectively. To equilibrate the protein solution system, the temperature of isothermal ensemble (NVT) was fixed at 37°C (310 K). In isobaric ensemble (NPT), the pressure was set at 1 atm (1.013 bar), and simulation was performed for 150 nanoseconds (ns).

Structural analysis: Visual Molecular Dynamics (VMD) and Chimera programs were used for displaying, animating, and analysis of biomolecular systems.[11,12] The average distances from position 63 to each amino acid backbone (N, Cα, and C) during 90-150 ns were plotted to investigate conformational change. The parameters of MD simulation results, including root mean square deviation (RMSD) and root mean square fluctuation (RMSF) during 90-150 ns, were used to determine stabilized protein structure and flexibility of amino acid sidechain, respectively. Behaviors of E6K/T63X were compared to control groups, including wildtype IL-18, a single mutation of IL-18 (E6A, E6K, and T63A), E6K/T63A (positive control) and M33Q (negative control).

Results and Discussion:

The initial structures of E6K/T63X and control groups from Phyre2 were created from NMR solution structure of human IL-18 (PDB ID: 1J0S) as a template.[13] All structures were modeled with 100% both confidence and coverage, which are the highest score template. The initial structures from Phyre2 were superimposed into 1J0S template. Only the mutated amino acid side chains were changed, but the backbones of these initial structures were similar to the template (RMSD = 0.000). These results indicated that homology modeling of the site-mutated human IL-18 could be modeled for full mature human IL-18 structure and unaffected the overall structure.

Along with the simulation of solvated IL-18, energetic parameters were steady in this system. In the last 60 ns, RMSD of WT showed about 3 Å different from the initial structure as well as E6A, T63A, E6K/T63A, E6K/T63V, E6K/T63L, and E6K/T63N. It possible that these mutated proteins can conserve IL-18 structure. For M33Q and E6K/T63S, the backbone structures were shifted about 2 Å RMSD. However, M33Q has been reported as a destabilized structure, which loss biological activity by the undirected loop at binding site II.[6] The engineered proteins with above 4 Å RMSD, which may affect structural change and hydrogen bond, were E6K, E6K/T63I, E6K/T63M, and E6K/T63Q. However, RMSD of all simulated proteins were stable in this duration (Figure 1).

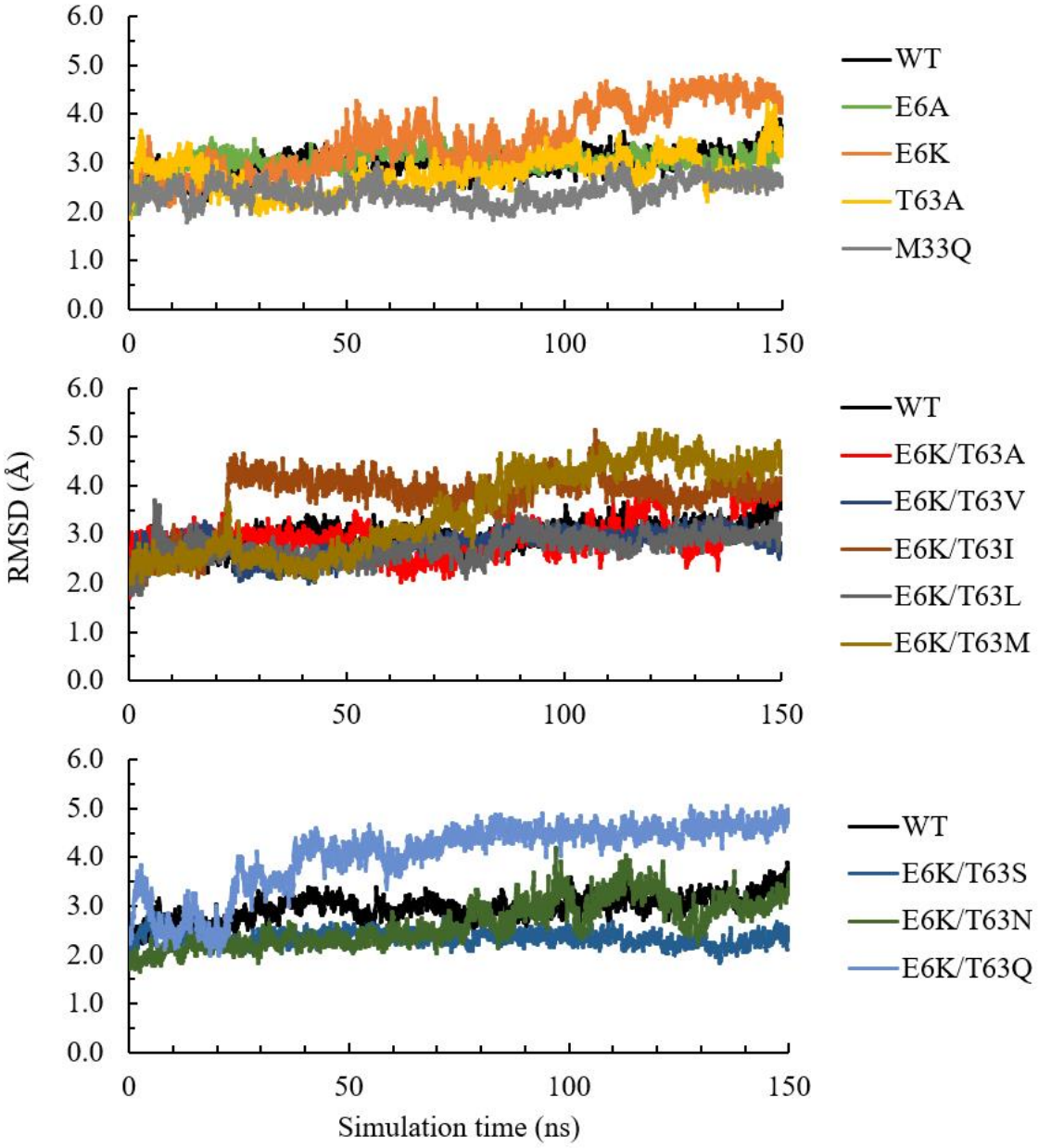

Figure 1. RMSD of engineered IL-18 and WT, which relative to the initial structure of each protein.

The flexibility of each amino acid Cα from the initial structure was determined by RMSF. Interestingly, all double mutation of IL-18 at position 6 and 63 involved structural changes at binding sites as well as all single mutations that have been reported (Figure 2). Firstly, the major binding site I loop (32nd-45th residue) of engineered IL-18 exhibited dramatically increase flexibility compared to WT, especially E6K/T63A. However, this loop on E6A and E6K/T63V were similar to WT. Backbone distances of the binding site I loop from position 63 also described far away from the loop possible to increase flexibility (Figure 3). Nonetheless, E6A and T63A were irrelevant to this concept by E6A conserved flexibility but transformed loop structure while T63A boosted flexibility, but preserved loop structure. Alanine scanning of position 6 and 63 has been reported that the proteins raise IFN-γ production and

combine with K53 or V11 also enhance the activity better than single mutation.[5,14] These previous studies are essential evidence that to improve IL-18 activity, a combination of position 6 or 63 with another crucial residue for double mutation is commitment.

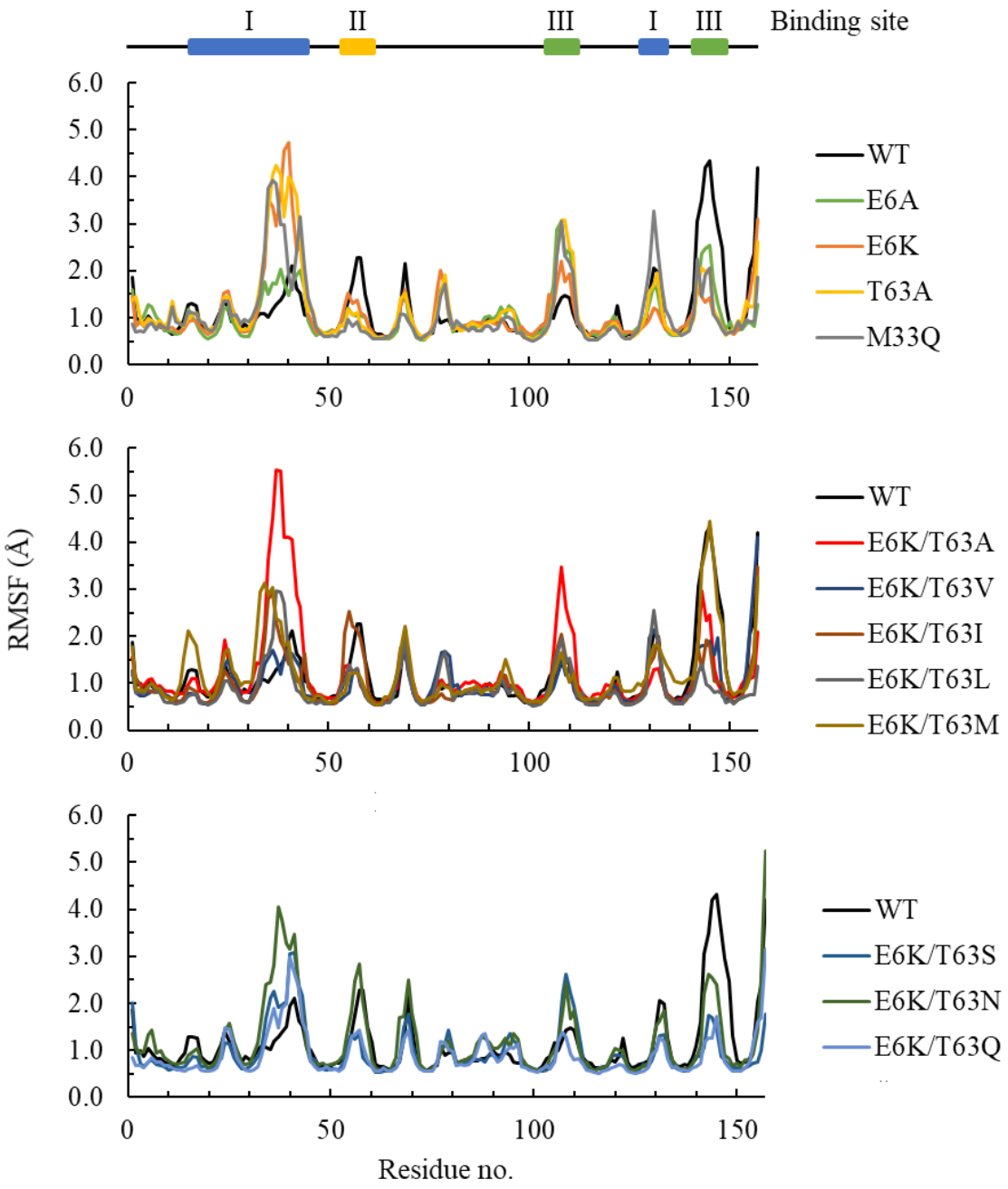

Figure 2. RMSF of engineered IL-18 and WT during 90-150 ns MD simulation. The scale bar of the binding site located on top of the figure.

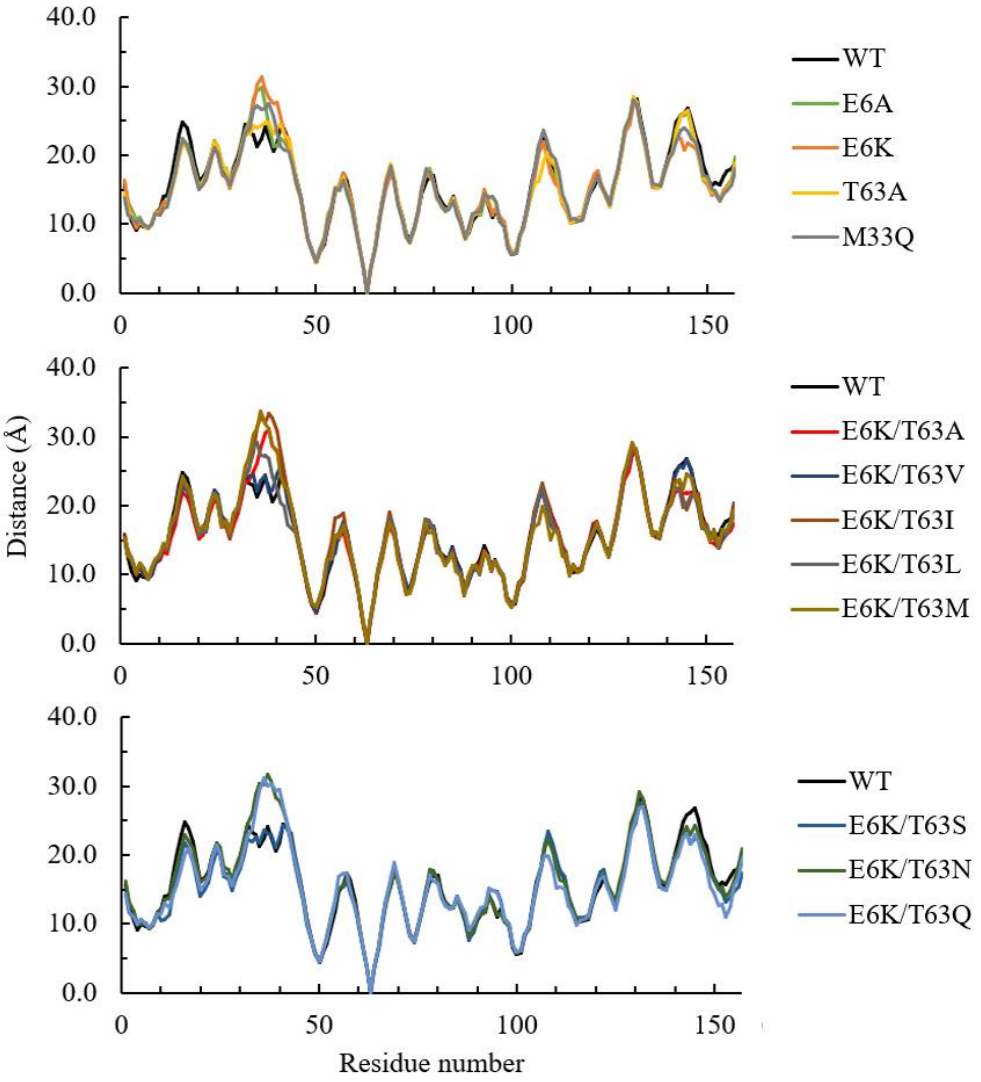

Figure 3. Distance between amino acid backbone (N, Cα, and C) of each IL-18 residue to position 63.

Secondly, both single and double mutations decreased binding site II loop (53rd-60th residue) flexibility compared to WT, but E6K/T63I and E6K/T63N were slightly increased. However, binding site II backbone structure still conserved in all mutations (Figure 3). This information confirmed mutagenesis of E6 (in binding site II) and T63 (non-binding residue near binding site II) has no disturb the binding site II structure, but residue flexibility has changed.

Finally, most of engineered IL-18 drop loop flexibility of minor binding site III loop (142nd-150th residue) also altered loop structure. While the major binding site III loop (107th-112th residue) has barely transformed loop structure but observed the difference in loop flexibility (Figure 2,3). All single mutated IL-18 evolved binding site III loop flexibility in the same trend by increased the major loop flexibility but contrasted in the minor loop. At the same time, most of the hydrophobic group of T63 mutations preserved the major loop flexibility, except E6K/T63A, which enhanced. As well as the minor loop flexibility of E6K/T63M was conserved, but other engineered IL-18 were reduced.

For the polar uncharged group of T63 mutation, E6K/T63S and E6K/T63N showed the same behavior with a single mutation group, but E6K/T63Q acted like a hydrophobic group. It has been reported that binding site III interact with IL-18 receptor β (IL-18Rβ) and associate with the initial of IL-18 signaling.[15] According to the biological activity of reported IL-18, including E6A, E6K, T63A, and E6K/T63A promoted IFN-γ induction.[5-7,14] Our findings found that these reported IL-18 shift loop flexibility on binding site III in the same way. Patterns of RMSF on binding site III loop could indicate the ability of IL-18 signaling.

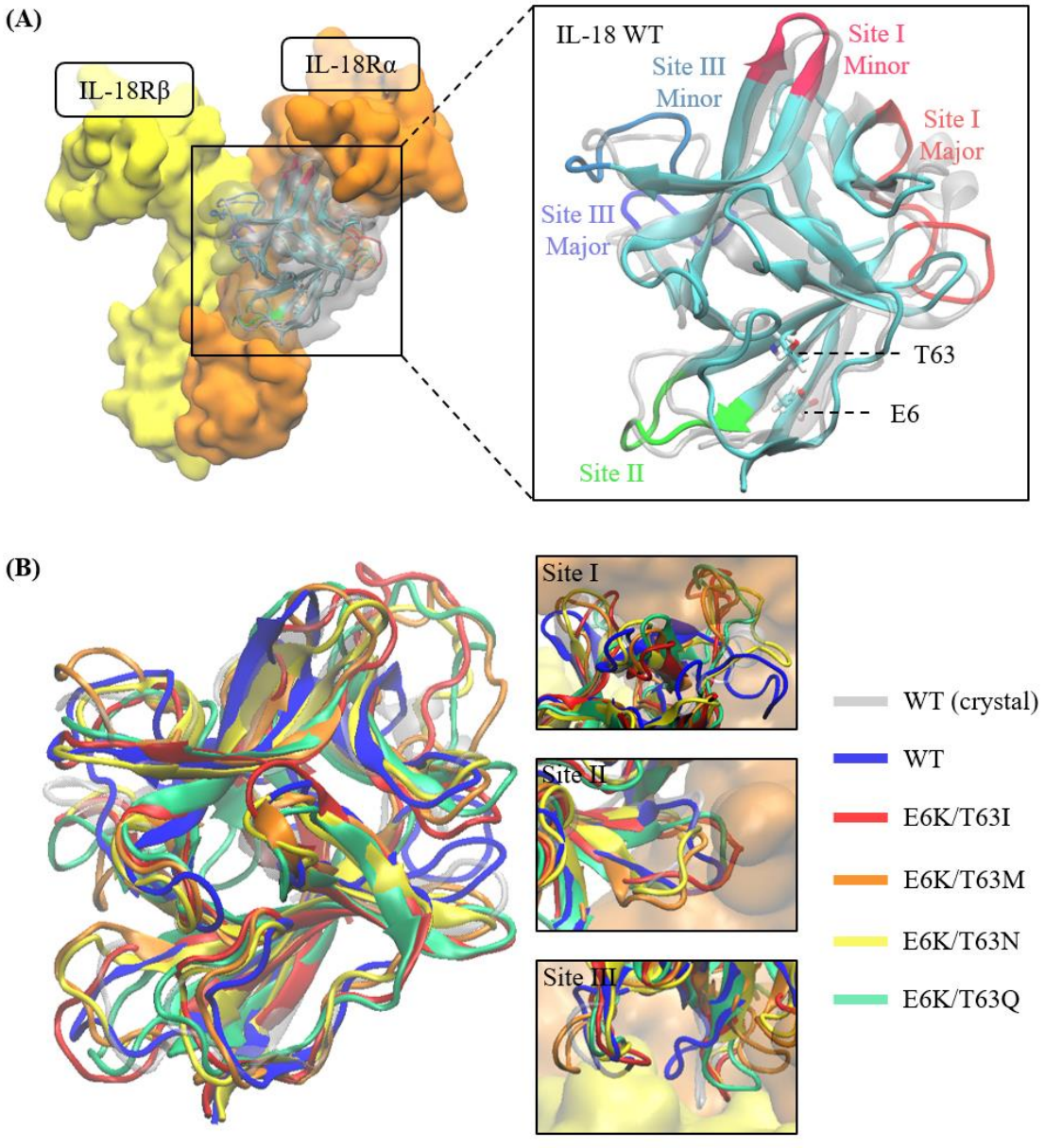

Figure 4. (A) Superimposition of simulated IL-18 WT (cyan) into IL-18 crystal structure (gray) of IL-18/IL-18Rα/IL-18Rβ complex (PDB ID: 3WO4). The binding site I and II of IL-18 interact with IL-18Rα while binding site III contacts IL-18β. (B) Superimposition of simulated IL-18 into WT crystal structure and closer position of IL-18 and its receptors.

According to diverse flexibility behavior on binding sites of engineered IL-18, E6K/T63I and E6K/T63M from hydrophobic group showed contrast RMSF on binding site II and III, even these conformations were similar. Dynamic structural change revealed that major binding site III loop of E6K/T63I point to the binding residue of IL-18Rβ. E6K/T63M displayed misdirection of binding site I and III loop to the receptor after superimposed simulated IL-18 into IL-18 in the complex crystal structure. This result was related to E6K/T63N and E6K/T63Q from polar unchanged group. However, E6K/T63N showed higher RMSF than E6K/T63I, but its RMSD was the opposite. E6K/T63Q also exhibited misdirection same as E6K/T63M, but flexibility was lower than E6K/T63M. These results conclude that E6K/T63I and E6K/T63N could be candidate engineered IL-18 from each group.

On the other hand, the major binding site I loop was complicated to interpret the structural change because of helix-coil transition (Figure 4). For one reason, initial structures of this study modeled from NMR structure different to crystal structure at binding site I.[13,15] As well as the relationship between position 6 and 63 alteration remains unclear. Single mutations of engineered IL-18 with E6 or T63 alteration should be investigated on structural analysis also. To determine the suitable engineered IL-18 from computational approach, IL-18 activity could be explored in *in vitro* experiment.

Conclusion: In this investigation, structural analysis of engineered IL-18 with double mutation of position 6 and 63 explored the behavior by MD simulation. T63 alteration highly involved flexibility and conformational change at binding site I and III loop, which are important to IL-18 signaling. We suggest that E6K/T63I and E6K/T63N could be the potential candidate engineered IL-18 from the computational approach to examine its biological activity. A high functional IL-18 could improve the bottleneck effect of IL combination for NK cell activation, which is one strategy of NK cell-based cancer immunotherapy.

Acknowledgements: We are greatful to thank Faculty of Medicine, Prince of Songkla University for financial support.

References:

1. Jeanbart L, Swartz MA. P Natl Acad Sci USA. 2015;112:14467-14472.
2. Guillerey C, Huntington ND, Smyth MJ. Nat Immunol. 2016;17:1025-1036.
3. Tsutsui H, Nakanishi K. Immunotherapy. 2012;4:1883-1894.
4. Marçais A, Viel S, Grau M, Henry T, Marvel J, Walzer T. Front Immunol. 2013;4:450.
5. Swencki-Underwood B, Cunningham MR, Heavner GA, Blasie C, McCarty SG, Dougherty T, Bringham-Burke M, Gunn GR, Goletz TJ, Snyder LA. Cytokine. 2006;34:114-124.
6. Saetang J, Puseenam A, Roongsawang N, Voravuthikunchai SP, Sangkhathat S, Tipmanee V. Plos One. 2016;11:e0160321.
7. Kim SH, Azam T, Novick D, Yoon DY, Reznikov LL, Bufler P, Rubinstein M, Dinarello CA. J Biol Chem. 2002;277:10998-11003.
8. Kelley LA, Mezulis S, Yates CM, Wass MN, Sternberg MJE. Nat Protoc. 2015;10:845-856.
9. Dolinsky TJ, Nielsen JE, McCammon JA, Baker NA. Nucleic Acids Res. 2004;32:W665-W667.
10. Case DA, Betz RM, Cerutti DS, Cheatham TE, Darden TA, Duke RE, Giese TJ, Gohlke H, Goetz AW, Homeyer N, Izadi S, Janowski P, Kaus J, Kovalenko A, Lee TS, LeGrand S, Li P, Lin C, Luchko T, Luo R, Madej B, Mermelstein D, Merz KM, Monard G, Nguyen H, Nguyen HT, Omelyan I, Onufriev A, Roe DR, Roiberg A, Sagui C, Simmerling CL, Botello-Smith WM, Swails J, Walker RC, Wang J, Wolf RM, Wu X, Xiao L, Kollman PA. 2016.
11. Humphrey W, Dalke A, Schulten K. J Mol Graph. 1996;14:33-38.
12. Pettersen EF, Goddard TD, Huang CC, Coach GS, Greenblatt DM, Meng EC, Ferrin TE. J Comput Chem. 2004;25:1605-1612.

13. Kato Z, Jee J, Shikano H, Mishima M, Ohki I, Ohnishi H, Li AL, Hashimoto K, Matsukuma E, Omoya K, Yamamoto Y, Yoneda T, Hara T, Kondo N, Shirakawa M. Nat Struct Biol. 2003;10:966-971.
14. Kim SH, Azam T, Yoon DY, Reznikov LL, Novic D, Rubinstein M, Dinarello CA. P Natl Acad Sci USA. 2001;98:3304-3309.
15. Tsutsumi N, Kimura T, Arita K, Ariyoshi M, Ohnishi H, Yamamoto T, Zuo XB, Maenaka K, Park EY, Kondo N, Shirakawa M, Tochio H, Kato Z. Nat Commun. 2014;5:2041-1723.

E_003_PF: DEVELOPMENT AND EVAUATION OF AN IN-HOUSE COMPETITIVE ELISA FOR DETECTION OF DEHYDROEPIANDROSTERONE SULFATE

Rattikorn Leemahanil, Rina Patramanon*

Department of Biochemistry, Faculty of Science, Khon Kaen University, Thailand
*e-mail: narin@kku.ac.th

Abstract:

Dehydroepiandrosterone sulfate (DHEAS) is the most abundant circulating steroid hormones which plays an important role as the initial substance for steroid hormones synthesis. The measurement of the DHEAS level is used as an 'aging-biomarker' to assess the risk of diseases associating with age. In general, the enzyme-linked immunosorbent assay (ELISA) is most widely used for DHEAS measurement because of highly specific, rapid, and suitable detection. But the commercial ELISA kit for DHEAS detection has not been produced in Thailand. So, expenses of using imported commercial ELISA kit were quite high and not suitable in resource-limited laboratories. Therefore, this study aimed to develop and standardize a cost-effective in-house competitive ELISA for DHEAS detection. An in-house competitive ELISA format was developed and optimized using a polyclonal anti-DHEAS as the antibody coating. DHEAS-HRP conjugate and 3,3',5,5'-tetramethylbenzidine (TMB) were used as a competitor and the enzyme mediator/substrate system, respectively. Under optimal conditions, the standard curve was established from standard DHEAS concentration range of 100 - 10000 ng/mL which a linear regression and the limit of detection was 97.947 ng/mL. The result covers normal blood levels of DHEAS since the fetus to the age of 59 years old (120-3210 ng/mL). Furthermore, the in-house competitive ELISA was estimated to be 3 times less per test compared to the cost of imported commercially available ELISA kit.

Introduction:

Dehydroepiandrosterone sulfate or DHEAS is a 'Pro-hormone' in which the role is an initial substance in the synthesis of steroid hormones including testosterone and estrogen [1]. It is the most abundant circulating steroid hormones secreted from the zona reticularis of the adrenal gland. DHEAS are produced since the fetus and the levels of DHEAS in the blood and urine samples are related to increasing ages, which is the highest level at the adulthood (age of 18-30 years old) before gradually declining with progressive aging at a rate of 1-2% per year (aged 70-79 years old) [2, 3]. The normal blood levels of DHEAS in difference age was shown in Table 1 with the wide range between 70 - 3210 ng/mL [2]. Furthermore, changing the DHEAS level has been shown to associate with age-associated diseases or deterioration in physiological functions such as the risk of testosterone deficiency syndrome in men, cardiac diseases, sleeplessness, Alzheimer's diseases, cognitive impairment and cancer [4-7]. From the relationship of decreasing DHEAS with increasing ages, DHEAS plays an important role as the 'hormone of youth' and used as 'aging-biomarker' to assess the risk of diseases associating with age [8]. Moreover, DHEAS has been widely used as a dietary supplement in the USA. Some publications have reported that DHEAS replacement therapy is useful in the treatment of steroid-induced osteoporosis in postmenopausal women [9] and corrects testosterone deficiency effectively and improves some aspects of psychological function in males [10]. Thus, detection of the DHEAS level is important for diagnosis of medical conditions or health monitoring approach in following the rate of aging.

The most common methods currently used for the detection of DHEAS include high-performance liquid chromatography (HPLC), liquid chromatography-mass spectrometry (LC-MS), gas chromatography (GC), radioimmunoassay (RIA) and enzyme-based immunoassay. As for DHEAS detection, chromatography and mass spectrometry must use by an expert who is familiar with the equipment. Also, due to an expensive and huge laboratory equipment, an immunological technique which is immunoassay is used instead. Accordingly, the detection of DHEAS is usually performed by enzyme-linked immune sorbent assay (ELISA). However, not many hospitals have access to ELISA in their laboratories because it has not been produced in resource-limited countries, especially in Thailand. Therefore, expenses of using an imported commercial ELISA kit is quite high and not affordable by the diagnostic laboratories in resource-limited countries. Thus, the present study aimed to conduct and evaluate a simple and cost-effective In-house competitive ELISA for the detection of DHEAS which is suitable for resource-limited settings.

Table 1.

Normal blood levels of DHEAS in different age [2]

Age	Normal blood levels of DHEAS
<20	510-3210 ng/mL
20-29	180-3910 ng/mL
30-39	230-2660 ng/mL
40-49	190-2310 ng/mL
50-59	120-1880 ng/mL
60-69	80-1330 ng/mL
70-79	70-1770 ng/mL

Methodology:

Reagents and instrumentation

Anti-DHEA 3-sulfate polyclonal antibody (anti-DHEAS antibody) and 3,3',5,5'-tetramethylbenzidine (TMB substrate) were obtained from Abcam. DHEA 3 sulfate sodium salt (DHEAS standards) and DHEA 3-HRP (DHEAS-HRP conjugate) were purchased from Fitzgerald. Sodium bicarbonate ($NaHCO_3$) and Sodium carbonate (Na_2CO_3) were purchased from Ajax Finechem. Bovine serum albumin (BSA), Sulfuric acid (H_2SO_4) and 96-well plate were acquired from Sigma. TWEEN20 was from Chemipan. Coating buffer (Carbonate-bicarbonate buffer), Wash buffer (PBS containing 0.05% Tween 20) and Blocking buffer (PBS containing 1% BSA, pH7.4) were prepared in our laboratory. Other reagents were analytical grade. The OD. values in the 96-well plates were read at 450 nm using an EZ Read 2000 Microplate Reader (Biochrom). Commercial ELISA kit was were purchased from Abcam.

Preparation of DHEAS Standard Solution

DHEA 3 sulfate sodium salt was dissolved in methanol at a concentration of 5 mg/mL. The solution was filtered through filter paper (Whatman no.1). Aliquot and store at -20ºC until use.

The procedures of an in-house competitive ELISA

The procedure of an in-house competitive ELISA was shown in Figure 1. The 96-well plate was coated with anti-DHEAS antibody diluted in coating buffer (carbonate-bicarbonate buffer) and incubated for 2 hours at room temperature or 4ºC overnight. Afterward, the plate was washed 3 times with the wash buffer (PBS containing 0.05% Tween 20). Then, non-specific bindings were blocked with 300 µl of blocking buffer (1% BSA in PBS, pH7.4), the plate was covered and incubated for 1 hour at 37ºC. After washing the unbound solutions and adding the standards, controls, or samples into the respective wells, the DHEAS-HRP conjugate was added to each well. The plate was incubated for 1 hour at room temperature. Then, the solution in the plate was removed and the plate was washed with the wash buffer. Later, TMB was used as a substrate and incubated within 15 minutes in the dark. The reaction was stopped by adding the stop solution (1M H_2SO_4). The PBS was set as the blank. Finally, the optical density (OD) was measured at 450 nm with a microplate reader [11].

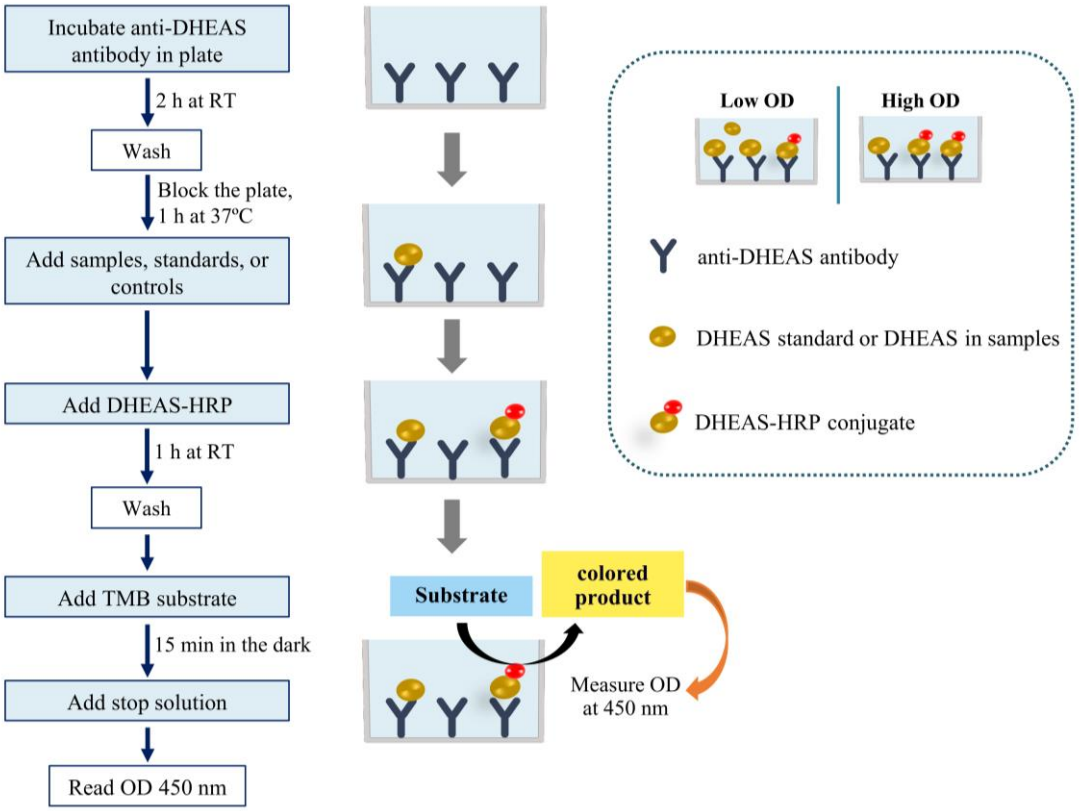

Figure 1.

Schematic diagram of the procedure of an in-house competitive ELISA for the detection of Dehydroepiandrosterone sulfate (DHEAS)

Optimization of the in-house competitive ELISA

The major factors influencing ELISA sensitivity were evaluated, including the concentration of anti-DHEAS antibody, DHEAS-HRP conjugate, TMB substrate and stop solution. In detail, a checkerboard titration was conducted

to optimize the competitive ELISA reaction [12]. For anti-DHEAS antibody optimization, the focus was on the anti-DHEAS antibody and DHEAS standards first since changes in those concentrations would have the greatest effect on the optical density. Briefly, the anti-DHEAS antibody was coated to the 96-well plate with different concentrations from 40 to 1.25 µg/mL. DHEAS standards concentrations are diluted with methanol at different dilutions; 10000 to 0 ng/mL. While the DHEAS-HRP Conjugate is held constant at excess concentration (5.8 mg/mL). Once the competitive ELISA is finished, the optical density is read. In order to optimize efficiency, the minimum amount of the antibody that yields a strong signal should be used. The concentration of the DHEAS-HRP conjugate was serially diluted from 1/10 to 1/10000 dilution. The TMB substrate and stop solution optimization is tested by vary the TMB substrate with different concentrations; 1, 1/2, 1/4, 1/8, 1/16 and 1/32 dilutions along the columns and vary the stop solution with different concentrations; 1, 1/2, 1/4, 1/8, 1/16 and 1/32 dilutions along the rows of the ELISA plate.

Standard calibration curve

According to the results of the ELISA optimization, the optimized ELISA conditions including the concentration of anti-DHEAS antibody, DHEAS-HRP conjugate, TMB substrate and stop solution were used, the standard calibration curve was established by plotting the mean of OD value of the DHEAS standard against concentration of the DHEAS standard [12]. The limits of detection (LOD) was calculated using 3.3s (where s is the standard deviation of the blank solution, n=3) [13].

Results and Discussion:

Optimization of the in-house competitive ELISA

To optimize the efficiency, the minimum amount of the antibody that yields a strong signal should be used, while not sacrificing signal strength. The optimal working conditions of capture antibody were found within the range 40-10 µg/mL. So, the least amount of antibody should be used was 10 µg/mL in the optimal volume of 80 µL (Figure 3A, 3B).

To carry out the competition step, the DHEAS-HRP conjugate was then studied. the optimal anti-DHEAS antibody from the previous study is used while vary DHEAS-HRP conjugate concentration from 1 to $1/10^5$ dilution. According to the data from Figure 3C and 3D, a dilution of DHEAS-HRP conjugate set at 1/10 (0.58 mg/mL), 180 µL/well was found to be optimal for the competitive reaction by still maintaining a high OD value.

For the coloration, TMB substrate and stop solution optimization is tested by vary the TMB substrate with different concentrations; 1, 1/2, 1/4, 1/8, 1/16 and 1/32 dilutions from a stock solution along the columns and vary the stop solution (1M H_2SO_4) with different concentrations; 1, 1/2, 1/4, 1/8, 1/16 and 1/32 dilutions along with the rows of the ELISA plate. While the anti-DHEAS antibody and the DHEAS-HRP Conjugate is held constant at the optimal concentration. Follow the competitive ELISA procedure and read out the OD value. The optimal TMB substrate and stop solution were non-dilution from a stock and 1M H_2SO_4, respectively (Figure 3E, 3F).

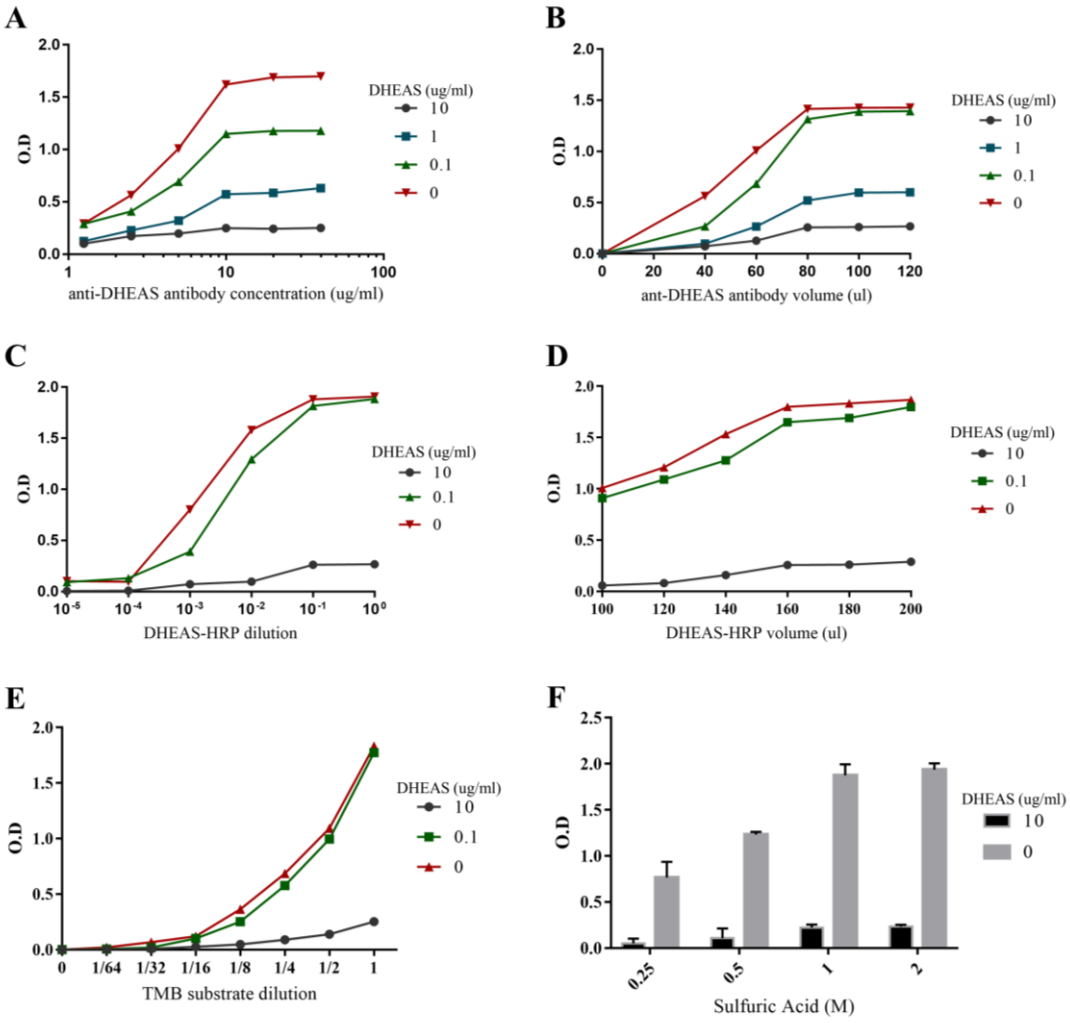

Figure 3.

(A) The OD value under different concentrations of anti-DHEAS antibody after incubating with different concentration of DHEAS standards. (B) The OD value under different volume of anti-DHEAS antibody at 10 µg/mL after incubating with different concentration of DHEAS standards. (C) The OD value under different dilutions of DHEAS-HRP conjugate after incubating with different concentration of DHEAS standards at the optimal anti-DHEAS antibody condition. (D) The OD value under different volume of DHEAS-HRP conjugate at 1/10 dilution after incubating with different concentration of DHEAS standards. (E) The OD value under different dilution of the TMB substrate after incubating with different concentration of DHEAS standards at the optimal anti-DHEAS antibody and DHEAS-HRP Conjugate conditions. (F) The OD value under different concentration of a stop solution after incubating with different concentration of DHEAS standards at the optimal anti-DHEAS antibody, DHEAS-HRP Conjugate and TMB substrate conditions

Standard calibration curve

Under the optimal conditions, a standard curve was constructed by plotting the OD value against the logarithmic value of DHEAS standard concentrations as shown in Figure 4. The linear regression equation was Y = -0.9509X + 3.946, R^2 = 0.9684. The OD value decreased with the increase of the concentration of DHEAS standard in the range from 100 ng/mL to 10000 ng/mL. The limit of detection (LOD) was 97.947 ng/mL. The result presented high sensitivity detection and cover the normal blood levels of DHEAS since the fetus to the age of 59 years old (120-3210 ng/mL) [2].

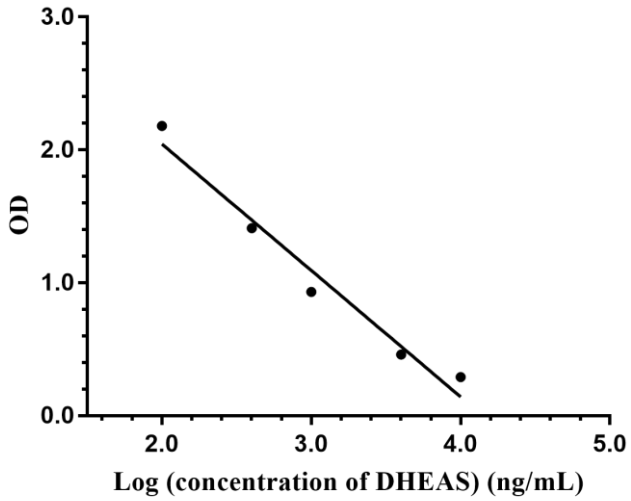

Figure 4.

The standard curve for the determination of DHEAS using in-house competitive ELISA

Comparison of the in-house competitive ELISA to the commercially available ELISA kit

Qualification comparison between the in- house competitive ELISA and the commercially available competitive ELISA kit was shown in Table 2. The standard calibration curve was shown that detection range of in-house competitive ELISA resemble to the commercial ELISA kit. Moreover, the detection range covers normal levels of DHEAS since the fetus to the age of 59 years old (Table 1). However, Limit of detection of the in-house competitive ELISA was 97.947 ng/mL which indicate the lower sensitivity. Therefore, the optimization for sensitivity would be further developed in the future. The costing per test and per microplate of the in-house competitive ELISA was estimated and compared with the commercial ELISA kit, costing of 1 testing by using in-house competitive ELISA is approximately 155.54 baht (or 14,931.50 baht per microplate) whereas 417.41 baht per test for commercial DHEAS ELISA kit (or 40,071.50 baht per microplate). Therefore, the in-house competitive ELISA is approximately 3-fold cheaper than the commercially available ELISA kit. This result suggests that using the in-house competitive ELISA is cost-effectiveness for resource-limited laboratories or developing countries than imported ELISA kit [14]. Besides, the process of importing is difficult and time-consuming. Thus, using an in-house competitive ELISA for DHEAS measurement locally can solve these problems.

Table 2.

Qualification comparison between the in-house competitive ELISA and the commercial ELISA kit

	In-house competitive ELISA	Commercial ELISA Kit
Detection range	100 ng/mL - 10000 ng/mL	0.1 µg/mL – 10 µg/mL
Limit of detection	97.947 ng/mL	0.04 ng/mL
Assay type	Competitive ELISA	Competitive ELISA
Specimen used	Serum	Serum
Results interpretation	Standard digital format (OD) with DHEAS standards	Standard digital format (OD) with DHEAS standards
Cost per kit	14,931.50 THB	40,071.50 THB
Cost per test	155.54 THB	417.41 THB

Conclusion:

In this study, an in-house ELISA for determination of prohormone DHEAS was developed and optimized using a competitive ELISA format. A polyclonal anti-DHEAS and DHEAS-HRP conjugate used as the antibody coating and the competitor, respectively. Under the optimal conditions, a standard curve was constructed in the range from 100 ng/mL to 10000 ng/mL with a limit of detection (LOD) was 97.947 ng/mL. Although a sensitivity of the in-house ELISA was lower than the commercial ELISA kit, the costing of in-house ELISA was 3 times less per test compared to the cost of imported commercially available ELISA kit. These results suggest that the in-house developed ELISA is affordable by the diagnostic laboratories in resource-limited countries because of its cost-effectiveness. Based on this work, the optimized in-house competitive ELISA for DHEAS determination may become a high sensitivity, simple, and cost-effective tool for monitoring the aging or the risk of diseases associating with age. Besides, the incubation times, specificity, stability, and clinical sample detection will be performed in future experiment.

Acknowledgements:

We would like to thank Department of Biochemistry, Faculty of Science, Khon Kaen University for providing research facilities. This work was financial supported by Center of Excellence on Medical Biotechnology (CEMB), Thailand.

References:

1. Yen, S.S., Dehydroepiandrosterone sulfate and longevity: new clues for an old friend. Proc Natl Acad Sci U S A, 2001. **98**(15): p. 8167-9.
2. Nishizaki, Y., et al., A proposal research for new health check-up items focusing on the future super-aging society in Japan. Vol. 38. 2011. 537-546.

3. Orentreich, N., et al., Long-term longitudinal measurements of plasma dehydroepiandrosterone sulfate in normal men. J Clin Endocrinol Metab, 1992. **75**(4): p. 1002-4.

4. Flynn, M. A., et al., Dehydroepiandrosterone Replacement in Aging Humans1. The Journal of Clinical Endocrinology & Metabolism, 1999. **84**(5): p. 1527-1533.

5. Yen, S.S. and G.A. Laughlin, Aging and the adrenal cortex. Exp Gerontol, 1998. **33**(7-8): p. 897-910.

6. Wu, T. T., et al., Prognostic Value of Dehydroepiandrosterone Sulfate for Patients With Cardiovascular Disease: A Systematic Review and Meta-Analysis. J Am Heart Assoc, 2017. **6**(5).

7. Aslan, Y., et al., Serum Dehydroepiandrosterone Sulfate Usage for Early Detection of Prostate Cancer in Men with Serum Prostate Specific Antigen Level between 2.5 and 4.0 ng/ml: A Pilot Study. Turkish Journal of Medical Sciences, 2008. **38**: p. 399-404.

8. Apostolova, G., et al., Dehydroepiandrosterone inhibits the amplification of glucocorticoid action in adipose tissue. Am J Physiol Endocrinol Metab, 2005. **288**(5): p. E957-64.

9. Papierska, L., et al., Effect of DHEA supplementation on serum IGF-1, osteocalcin, and bone mineral density in postmenopausal, glucocorticoid-treated women. Advances in Medical Sciences, 2012. **57**(1): p. 51-57.

10. Hunt, P.J., et al., Improvement in mood and fatigue after dehydroepiandrosterone replacement in Addison's disease in a randomized, double blind trial. J Clin Endocrinol Metab, 2000. **85**(12): p. 4650-6.

11. Fatema, K., et al., Development and evaluation of an in-house ELISA to detect hepatitis B virus surface antigen in resource-limited settings. Bangladesh Med Res Counc Bull, 2013. **39**(2): p. 65-8.

12. Crowther, J.R., The ELISA guidebook. Methods Mol Biol, 2000. **149**: p. Iii-iv, 1-413.

13. Carlson, J., A. Wysoczanski, and E. Voigtman, Limits of quantitation — Yet another suggestion. Spectrochimica Acta Part B: Atomic Spectroscopy, 2014. **96**: p. 69-73.

14. Fadeel, M. A., et al., Evaluation of a newly developed ELISA against Widal, TUBEX-TF and Typhidot for typhoid fever surveillance. J Infect Dev Ctries, 2011. **5**(3): p. 169-75.

E_004_PF: DEMONSTRATION OF IN-HOUSE BEAD-BASED IMMUNOASSAY FOR HUMAN SERUM ALBUMIN DETECTION BASED ON MICROFLUIDICS FLOW CYTOMETRY

Nattaphorn Natteerapong,[1] Rattikorn Leemahanil,[1] Somponat Sampattavanich[2], Rina Patramanon[1]*

[1]Department of Biochemistry, Faculty of Science, Khon Kaen University, Thailand
[2]Siriraj Initiative in Systems Pharmacology, Department of Pharmacology, Faculty of Medicine Siriraj Hospital, Mahidol University, Thailand
*e-mail: narin@kku.ac.th

Abstract:

Human serum albumin (HSA) is the most abundant protein in the blood vessel. It serves as a valuable biomarker for a wide range of health conditions such as poor nutritional status and kidney conditions. HSA is one of the key parameters in various medical diagnostics and health checkup programs. It can be detected using various laboratory-based approaches, but very few aimed for point-of-care detection purpose. Herein, we demonstrate an in-house bead-based fluorescent immunoassay platform, the universal form that can be further applied to use in microfluidics flow cytometry-based point-of-care devices. In this research, polyclonal human serum albumin antibody is successfully coupling onto 10 µm fluorescent beads at ratio 20 µg per 5.5 x 10^4 beads. 0.29 mg/mL of monoclonal human serum albumin antibody was successfully conjugated with Pacific blue™ dye which yields 89.04 %. The standard curve presented high sensitivity with the linear range of 190 – 6,670 ng/mL and the limit of detection 160 ng/mL. These results demonstrated that quantitative detection of human serum albumin could be performed using the bead-based immunoassay platform. The experimental conditions would be a model for further optimize and apply on microfluidics flow cytometry-based point-of-care devices.

Introduction:

In recent years, point-of-care (PoC) diagnostics, the detection of analytes near the patient is one of essential field in medical diagnostics. Because of new technologies growing rapidly, PoC enables quicker medical screening before going in-depth medical diagnosis that requires much more professional staffs and budget. We could detect diseases in early stage, leading to improved health outcomes and early start of any treatment contribute towards reducing government waiting time targets.[1] From these reasons, PoC biosensors become the crucial tools to achieve Goal 3 of sustainable development goals: good health and well-being.[2] Development and preparation of PoC detection also become more interesting in biosensor research.

Human serum albumin (HSA) is the most abundant protein in blood vessel synthesized in the liver. HSA is a 69 kDa negative charge protein and contains 585 amino acids.[3] The normal range of HSA in adult is 3.5 to 5 g/dL. Albumin is responsible for transport of various substances, maintaining colloid osmotic pressure and aspects of the inflammatory system such as neutrophil adhesion and cell signaling activity. HSA serves as a valuable biomarker for a wide range of health conditions such as renal disease, kidney failure, stroke and liver disease, cancer, rheumatoid

arthritis. [4, 5] Reduction of serum albumin level has occurred in approximately 20% of acute medical admissions [6]. It also reflects poor nutritional status or malabsorption of protein. It plays an important role in the diagnostic hallmark of nephrotic syndrome, which is characterized by albuminuria and hypoalbuminemia. [7] From these reasons, HSA has been chosen to be one of the key parameters in various medical diagnostic and health status indicator.

The clinical estimation of human HSA is commonly obtained by bromocresol green colorimetric assay (BGC assay) or Bromocresol purple (BCP). However, traditional colorimetric assays are likely to present the bias between different albumin assays and recently reported that it may affect clinical decision-making. [8] Immunoassay might overcome the problem. There are two widely used immunoassays developed for HSA detection. They are enzyme-linked or fluorescent probe immunosorbent assay (ELISA) and immunoturbidimetry. These techniques have high sensitivity and specificity but require high albumin concentration in the sample and high concentration of anti-albumin antibody. [7] With large amount of HSA and antibody for detection condition, these techniques might not be suitable for screening point-of-care purpose. Here we propose alternative beads-based flow cytometric immunoassay techniques to overcome the high concentration requirement.

Beads-based flow cytometric immunoassay was firstly developed to be an alternative assay for sandwich ELISA or fluorescent probe immunoassay in 1982. [9] The principle involves the similar complex as in conventional sandwich-ELISA. That is coupling of polyclonal capture antibody on fluorescent beads named as “capture antibody”. Monoclonal antibody are also labeled with fluorescent dyes named as “detection antibody” The specific binding complex would be passed through flow cytometer instead of spectrophotometer [10] . This technique was quickly expanding in last 20 years when many reports suggested with evidence that it as one powerful techniques due to the advantage in simultaneous detection, less sample use and rapid detection [11]. Moreover, bead-based flow cytometric immunoassay provided a valuable, sensitive, rapid, and readily implemented format in microfluidics for point-of-care applications [12, 13]. Examples of previous detection using this format were IL-10 detection on automated chip microfluidic ELISA platform [14] IL-6 and TNF-α was demonstrated on-chip microfluidics duplex detection [15].

This research aims to demonstrate the alternative assay for quantitative HSA detection by performing in-house preparation beads-based immunoassay which is the universal format. Flow cytometer has been used as the standard device to obtain the fluorescent signal in this experiment. The optimal conditions potent to be an in-house preparation model for develop HSA detection on microfluidics flow cytometry-based point-of-care devices. Knowing such conditions may also further apply with microfluidics flow cytometry-based point-of-care devices.

Methodology:

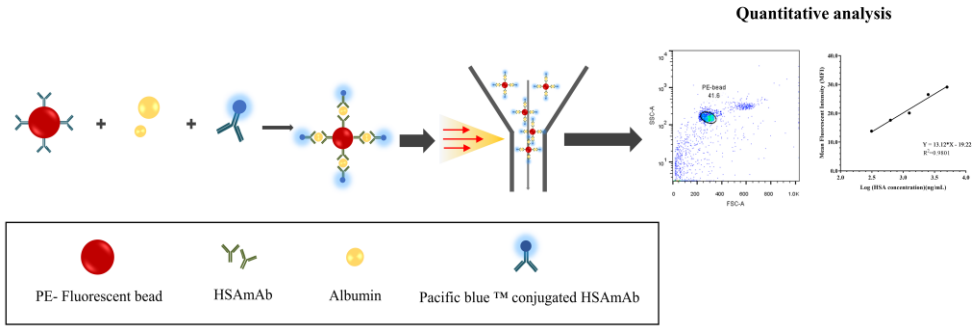

Figure 1.
Schematic representation of detection principle

The model of detection involves coupling of capture antibody on fluorescent beads. Because of different bead sets can be distinguished by gating features of flow cytometry, each bead set can be coupled to a different biological probe to perform a simultaneous detection, the complex was named as "Capture antibody". On another side, antibody are labeled with fluorescent dyes named as "Detection antibody". Quantification is estimated from fluorescence intensity of fluorescent dye labeled antibody when the complex are specific binding and passed through flow cytometer, the complex population will be gated and performed the quantitative analysis by establishing the standard curve from fluorescence intensity. **(Fig.1)**

Preparation of HSA monoclonal antibody (HSAmAb) and polyclonal antibody (HSApAb)

Mouse monoclonal anti-human serum albumin antibody (HSAmAb) and Goat polyclonal anti-human serum albumin antibody (HSApAb) were purchased from Fitzgerald (US). Due to carrier protein or storage buffer might be interfering the conjugation step, Storage buffer of HSAmAb and HSApAb were changed to Phosphate buffer saline (PBS) pH 7.4 and 50 mM MES, pH 5.2 via Vivaspin® 500 (GE healthcare, US) respectively.

Preparation of Capture antibody

Capture antibody was prepared by covalent coupling reaction. 10 µm Carboxyl-modified orange-polystyrene beads with the excitation and emission wavelength at 488/561 nm were purchased from Phosphorex, US. Equivalent of 2.2 x 10^5 beads were pelleted by centrifuge at 6000 rpm 10 min. Beads were washed 3 times using 40 µL activation buffer (50 mM MES, pH 5.2; 0.05% Proclin® 300) and resuspend in 17 µL activation buffers. Then 2 µL of 200 mg/mL EDAC solution was added to the sample solution then incubated for 15 mins at room temperature.

To optimized coated HSApAb concentration, 4.75 µL of mixture solution equivalent to 5.5 x 10^4 beads was added to 20, 10, 5 and 2.5 µg of HSApAb in 120 µL total reaction volume then incubated and mixed on rotary wheel for 2.5 hrs. at room temperature. After 3 times washing, pellets were resuspended storage buffer (10mM Tris, pH 8.0; 0.05% Bovine Serum Albumin; 0.05% Proclin 300). PE-polystyrene beads coated with 4 different concentration of HSApAb were then pelleted and incubated with 1/50 dilution of BV421 donkey anti-goat IgG (Jackson immunoresearch, US) at 4ºC for 30 mins. Pelleted were washed 3 time and resuspended in 0.001% PBST before applied to BD FACSCelesta™ flow cytometer (BD Life Sciences, US).

Preparation and characterization of Detection antibody

Detection antibody was prepared according to NHS ester and primary amine reaction by labeling Pacific blue ™ succinimidyl ester (AAT Bioquest, US) to HSAmAb. Solution A was prepared by dissolved HSAmAb in PBS buffer, pH 7.4 to give final concentration 2.98 mg/mL then 900 µL of solution A was mixed with 100 µL of reaction buffer (1 M sodium bicarbonate solution, pH 9). To prepare solution B, 1 mg of Pacific blue™ succinimidyl ester was dissolved in 294.80 µL of anhydrous DMSO to give 10mM Pacific blue™ fluorescent dye solution. Solution A and B were mixed in molar ratio 10:1 (Pacific blue™: HSAmAb). Mixture solution was vortexed for 10 sec. then incubated on orbital shaker at room temperature for 1.30 hrs. After incubation, mixture solution was purified by Sephadex G-25 and collected 7 fractions. HSAmAb and Pacific blue™ concentration of each fraction were determined by Nanodrop one spectrophotometer (Thermo scientific™). The degree of labeling (DOL) was calculated according to manufacture suggestion.

Optimization and functional testing of Pacific blue™ conjugated HSAmAb concentration

To optimize the concentration and tested the function of Pacific blue™ conjugated HSAmAb, 5,000 beads of capture antibody were pelleted and incubated with 500 ng/mL human serum albumin (Sigma-Aldrich,US) at room temperature for 45 mins then washed 3 times using 0.001% PBST. Pellets were incubated with detection antibody in concentration of 10^{-1}, 10^{-2}, $10^{-3}$and 10^{-4} dilution for 1 hr. Human serum albumin was absented in negative control. Then pelleted were washed 3 time and resuspended in 0.001% PBST before applied to BD FACSCelesta™ flow cytometer (BD Life Sciences, US).

Evaluation of beads-based fluorescent immunoassay for quantitative HSA detection

The optimal concentration of detection antibody and 5000 beads of capture antibody was utilized to establish the standard curve. HSA was diluted from 0 ng/mL to 4.0 x 10^4 ng/mL. The experiment was performed using FACSCelesta™ flow cytometer (BD Life Sciences, US). BYV12 lasers, Blue (488 nm), 4 Yellow Green (561 nm) and 6 Violet (405 nm) are employed to generating excitation wavelengths. Data acquisition was performed at middle speed until the minimum of 5,000 events have been detected. Fluorescence intensity (FI) of individual event are obtained by the channels of PE-A (561 nm) and BV421(421 nm). Population gating was controlled selected by FSC-A and SSC-A the marked PE-beads in most dense areas as effective detection targets.

Data analysis

Means, coefficients of variation and standard deviations were calculated via FlowJo ver. 10 software. Statistical analysis was performed via GraphPad Prism 7.00.

Results and Discussion:

Optimization of antibody-coupled on fluorescent beads

Different amount of HSApAb (2.5, 5, 10 and 20 µg) were coated onto 5.5 x 10^4 PE-fluorescent beads to get the suitable coupling ratio. To confirm that HSApAb was attached on the bead surface, beads were stained with BV421 donkey anti-Goat IgG after the coupling reaction. As shown in Figure 2, BV421 intensity on histogram increase when the amount of HSApAb is increased, indicates that HSApAb was successfully conjugated onto fluorescent beads. Red histogram indicates negative population, uncoupling beads incubated with BV421 donkey anti-Goat IgG while blue histogram indicates population of conjugated beads with difference amount of coating antibody which are 2.5, 5, 10 and 20 µg, respectively. (Figure 2) The blue histogram of 20 µg HSApAb presents 99.4% separating from negative population which is the highest percentage among 4 concentrations of HSApAb. (Figure 2D) The concentration of 2.5, 5, 10 µg present 67.5%, 83.3% and 71.0% separation, respectively. (Figure 2A, B, C) To determine the saturation of coupling HSApAb on fluorescent beads, coefficient of variation (%CV) of each test was calculated [16]. As shown in Table 1, CV of 20 µg HSApAb presents the lowest distribution among 4 concentrations with the value 47.8. This result indicated that the concentration 20 µg of HSApAb are more saturated on fluorescent beads than 2.5, 5, 10 µg. The lower distribution indicates that HSApAb are consistently coated on population of beads. Therefore, the coupling ratio was chosen as 5.5 x 10^4 PE-fluorescent beads to 20 µg in order to use less material while giving more separation and saturation on fluorescent beads than 2.5, 5, 10 µg.

Table 1.

Mean Fluorescence Intensity (MFI), Standard Deviation (SD) and Coefficient of Variation (CV) of PE-fluorescent beads coupling with difference amount of HSApAb

Polyclonal anti-HSA (µg)	MFI	SD	CV
20.0	2,021.0	966.0	47.8
10.0	353.0	516.0	146.2
5.0	562.0	632.0	112.4
2.5	511.0	512.0	100.2

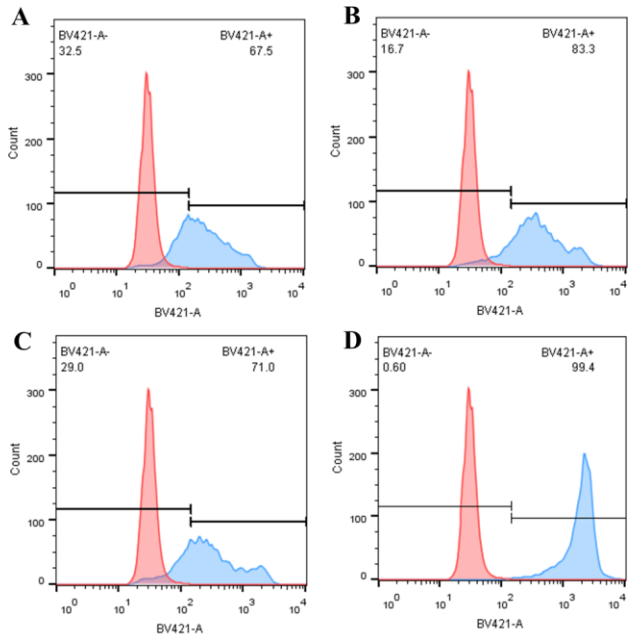

Figure 2.

BV421 intensity of negative population (red), uncoupling carboxyl-modified PE-fluorescent beads and test population (blue), carboxyl-modified PE-fluorescent beads coupling with difference amount of HSApAb A) 2.5 µg B) 5 µg C) 10 µg and D) 20 µg

Characterization of detection antibody

After the reaction mixture was purified by Sephadex G-25, there was two major peaks at A280 and A403 in fractions 2, which means both of HSAmAb and Pacific blue ™ are most presented in fraction 2. (Figure 3A) Moreover, wavelengths scanning of fraction 2 was also performed and found that there are only 2 maximum absorbance at 280 nm (red line) and 403 nm (blue line) suggested that HSAmAb are already conjugated with Pacific blue™. (Figure 3B) The concentration of HSAmAb in fraction 2 are 0.29 mg/mL which yield 89.04 % after conjugation. Degree of labeling are fall in the optimal range (2-10) with the value 7.54 according to the manufacture suggestion. Therefore, fraction 2 was chosen to be detection antibody on the next experiment.

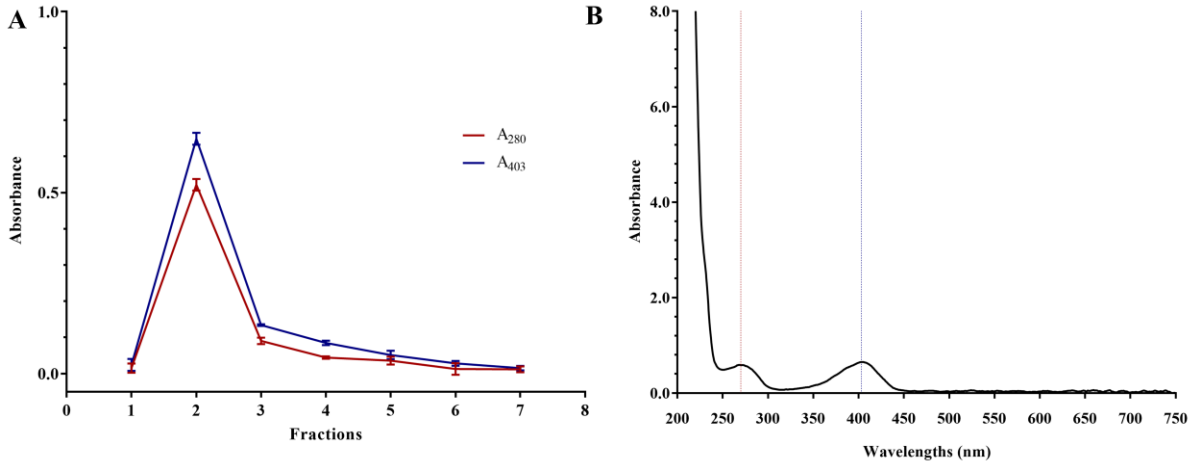

Figure 3.

Purification curve of conjugation mixture purified by Sephadex G-25 (A). The maximum absorbance of fraction 2 are presented at 280 nm (red line) and 403 nm (blue line).

Optimization of Pacific blue™ conjugated HSAmAb concentration

Pacific blue™ conjugated HSAmAb were then estimate the optimal dilution by performing the bead-based fluorescent immune assay using constant human serum albumin concentration at 500 ng/mL and fluorescent beads amount at 5,000 beads. As shown in figure 4, the signal-to-background of Pacific blue™ conjugated HSAmAb are slightly decrease from non-diluted to 10^{-4}fold dilution. However, Z'factor of non-diluted and 10^{-1} are similarly with the value 0.415 and 0.413 respectively (Table 2). The result indicated that the efficiency of separating between negative and test population when using non-diluted and 10^{-1} dilution are relatively similar. To use less of material, 10^{-1}fold dilution of Pacific blue™ conjugated HSAmAb was chosen to be an optimal detection antibody.

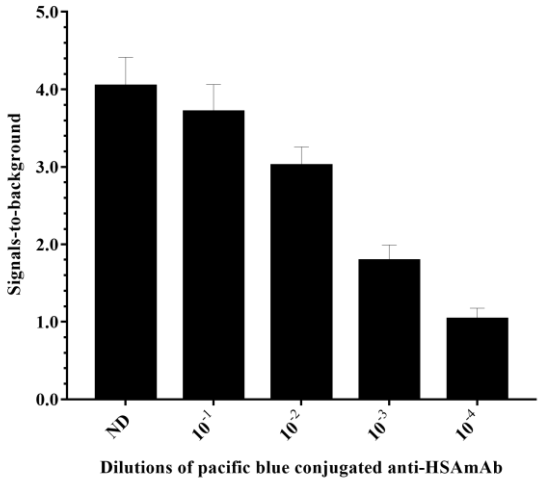

Figure 4.

Signal-to-background calculated from BV421 mean fluorescence intensity using non-diluted (ND), 10^{-1}, 10^{-2}, 10^{-3} and 10^{-4} dilution of 0.29 mg/mL Pacific blue™ conjugated HSAmAb.

Table 2.

Z'factor of BV421 mean fluorescence intensity using difference concentration of detection antibody.

Dilution factor of 0.29 mg/mL Detection antibody	**Z'factor**
ND	0.415
10^{-1}	0.413
10^{-2}	0.260
10^{-3}	-1.235
10^{-4}	-63.25

Evaluation of beads-based Fluorescent immunoassay for HSA detection

As shown in Figure 5, standard curve was establish using the relationship between the different log concentrations of Human serum albumin (HSA) and BV421 Mean Fluorescence Intensity (MFI). The standard curve was previous fit by four-parameter logistic curve to find the linear range of the techniques (Figure 5A), the linear range were 190 – 6670 ng/mL. The detection limits (LOD) is 160 ng/mL. The concentration that presented on linear range were plot by linear regression equation: Y = 13.12*X -19.22 with R^2 = 0.9801. (Figure 5B) The result presented high sensitivity detection and cover the normal range of Human albumin levels (3.5-5.0 g/dL)[17] when the sample was 10^{-4} to 10^{-5} pre-diluted before detection.

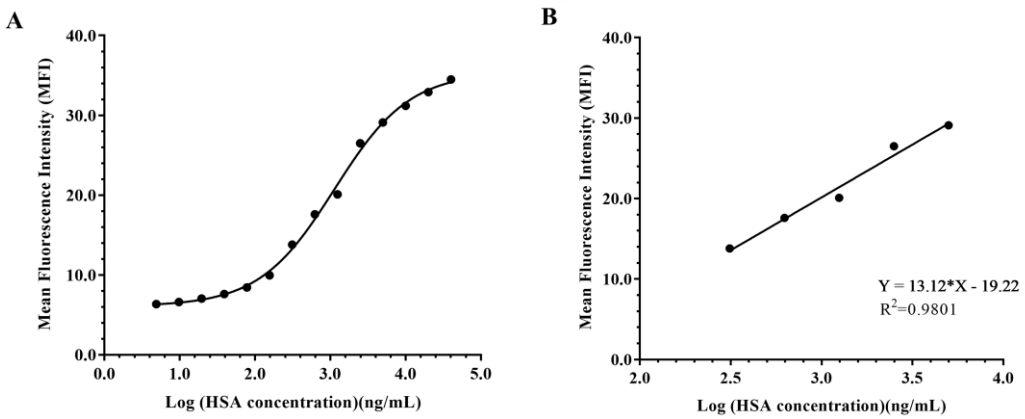

Figure 5.

Standard curve of beads-based fluorescent immunoassay for HSA detection.

(A) Four-parameter logistic curve fitting. (B) Linear regression curve fitting.

Conclusion:

An in-house quantitative beads-based fluorescent immunoassay for human serum albumin detection was demonstrated using flow cytometry. We present the suitable coupling ratio of between HSApAb and carboxyl-modified PE-fluorescent beads as 5.5 x 10^4 beads to 20 µg of HSApAb which provide cost effective and present 99.4% separating from negative sample. Pacific blue™ was successfully labeled to HSAmAb which yields 89.04 % recovery. The optimal concentration of detection antibody was 10^{-1} dilution. We also establish the standard curve that presents the high sensitivity with the linear ranges 190 – 6,670 ng/mL and the limit of detection is 160 ng/mL. The result covers the normal range of Human albumin levels (3.5-5.0 g/dL) when the sample was 10^{-4} – 10^{-5} pre-diluted before detection. Based on this work, in-house experimental material and condition will be a further model to develop in-house quantitative HSA detection using point-of-care microfluidics flow cytometry platform. The optimization of times, cross-reactivity and stability will be performed in further experiment to explore the worthiness of the technique.

Acknowledgements:

The authors are thankful to the financial support from Center of Excellence in Medical Biotechnology (CEMB), Thailand. We are also thankful to the department of biochemistry, faculty of science Khon Kaen university and Siriraj Systems Pharmacology Center (SiSP), faculty of medicine Siriraj hospital, Mahidol university for providing research facilities.

References:

1. Vashist, S.K., Point-of-Care Diagnostics: Recent Advances and Trends. Biosensors, 2017. **7**(4): p. 62.
2. Nakamura, H., Biosensors: Monitoring Human Health for the SDGs Sustainable Development Goals. Biomedical Journal of Scientific & Technical Research, 2018. **9**(2).
3. Arques, S., Human serum albumin in cardiovascular diseases. European Journal of Internal Medicine, 2018. **52**: p. 8-12.
4. Fanali, G., et al., Human serum albumin: From bench to bedside. Molecular Aspects of Medicine, 2012. **33**(3): p. 209-290.
5. Choudhury, R., S. Rajeshbhai Patel, and A. Ghosh, Selective detection of human serum albumin by near infrared emissive fluorophores: Insights into structure-property relationship. Journal of Photochemistry and Photobiology A: Chemistry, 2019. **376**: p. 100-107.
6. Herrmann, F.R., et al., Serum Albumin Level on Admission as a Predictor of Death, Length of Stay, and Readmission. Archives of Internal Medicine, 1992. **152**(1): p. 125-130.
7. Kumar, D. and D. Banerjee, Methods of albumin estimation in clinical biochemistry: Past, present, and future. Clinica Chimica Acta, 2017. **469**: p. 150-160.
8. van de Logt, A.-E., et al., The bias between different albumin assays may affect clinical decision-making. Kidney International, 2019. **95**(6): p. 1514-1517.
9. Lisi, P.J., et al., A fluorescence immunoassay for soluble antigens employing flow cytometric detection. Clinica Chimica Acta, 1982. **120**(2): p. 171-179.
10. Sun, K., et al., Establishment of multiplexed, microsphere-based flow cytometric assay for multiple human tumor markers. Acta Pharmacologica Sinica, 2007. **28**: p. 2011.
11. Graham, H., D.J. Chandler, and S.A. Dunbar, The genesis and evolution of bead-based multiplexing. Methods, 2019. **158**: p. 2-11.
12. Wu, D. and J. Voldman, An integrated model for bead-based immunoassays. Biosensors and Bioelectronics, 2020. **154**: p. 112070.
13. Antal-Szalmás, P., et al., Measurement of Soluble Biomarkers by Flow Cytometry. EJIFCC, 2013. **23**(4): p. 135-142.
14. Campbell, J., et al., Development of an automated on-chip bead-based ELISA platform. Analytical Methods, 2015. **7**(19): p. 8472-8477.
15. Sasso, L.A., et al., Automated microfluidic processing platform for multiplexed magnetic bead immunoassays. Microfluidics and Nanofluidics, 2012. **13**(4): p. 603-612.
16. Brown, C.E., Coefficient of Variation, in Applied Multivariate Statistics in Geohydrology and Related Sciences. 1998, Springer Berlin Heidelberg: Berlin, Heidelberg. p. 155-157.
17. Busher, J.T., Serum Albumin and Globulin, in Clinical Methods: The History, Physical, and Laboratory Examinations, rd, et al., Editors. 1990, Butterworths, Butterworth Publishers, a division of Reed Publishing.: Boston.

E_005_PA/E_027_PA/E_030_PA: EXPERIMENTAL DEVICE FOR STUDYING THE MOTION OF MAGNET FALLING THROUGH CONDUCTING PIPES USING ARDUINO AND REAL-TIME DISPLAY

Thanat Wongsamut,* Punyaphat Surakiatkamjorn, Sirawich Thanawan, Thanyanan Phuphachong

Department of Physics, Mahidol Wittayanusorn school, Salaya, Phuttamonthon, Nakhon Pathom 73170, Thailand
*e-mail: s6107849@mwit.ac.th

Abstract:

In a physics class, the fall of a magnet through vertical metallic pipes of the same length is qualitatively demonstrated to introduce the notion of electromagnetic braking. This inspired us to develop an experimental device to study quantitatively the motion of magnet falling through conducting tubes using Arduino and real-time display. Our work mainly focuses on designing and creating the device. To study the electromagnetic braking of the magnet falling in metallic pipes, we drop three types of cylindrical magnets (20 mm in diameter and 20 mm in length) in aluminum tube and copper tube (7/8 inch in diameter and 1 m in length). Three different types of magnets are neodymium, samarium-cobalt, and ferrite magnets. The working principle of this device is to use a pulley to attach to a magnet and attach to a shaft, then the shaft rotation speed will be measured with a gear attached to the shaft. The measurement uses two types of sensors, optical and infrared counting sensors, to reduce projections in the measurement. We can calculate the speed of falling magnets by computing the number of revolutions per second (frequency) and shaft radius. We obtain similar experimental results in aluminum and copper tubes but the duration of the entire motion of the magnets in copper tube is longer than that in aluminum tube. This implies that electromagnetic braking depends on the properties of metals. At the beginning of the fall, the velocity of the magnets increases suddenly. Then, it reaches a constant terminal velocity. Among three types of magnets, the neodymium magnet has the smallest velocity. This can be explained by the most intense magnetic field of neodymium magnet that results in the greatest resistance force due to electromagnetic braking. We have achieved to develop our first experimental device. We have demonstrated that the velocity of the falling magnet varies as a function of time due to electromagnetic braking phenomenon. The experimental results could be fitted by theoretical calculations derived from the consideration based on dipole magnetic fields that is applicable to the design of our device and the experimental setup. Our work could pave the way for further similar studies and our device could be improved and used as teaching materials in electromagnetism classes both in high school and undergraduate levels.

E_006_PA: INTEGRATION OF PHASE CHANGE MATERIAL INTO ROOF FOR HEAT ACCUMULATION REDUCTION IN BUILDINGS

Chanita Mano*, Ketwadee Janyoosuk, Atthakorn Thongtha

Department of Physics, Faculty of Science, Naresuan University, Phitsanulok, 65000, Thailand
*e-mail: chanita.mano@gmail.com

Abstract:

This research focuses on the application of phase change material (PCM) combined with the fiber cement roofing sheet to reduce heat transfer through the building. The experimental study was divided into 4 conditions including the single-layer fiber cement roof, the single-layer fiber cement roof installed with the PCM layer, the double-layer fiber cement roof, and the double-layer fiber cement roof installed with the PCM layer. For each condition, the fiber cement sheet was set at an incline angle of 40º with the horizontal plane. The thermal source was controlled at temperature of 60 °C, 70 °C and 80 °C for 360 minutes to investigate the thermal behavior and compare the heat gain through the roof. The results showed that the double-layer fiber cement roof installed with the PCM layer could reduce the room temperature by up to 3.1%, 3.8% and 3.7% when compared with the single-layer fiber cement roof without the PCM layer, and up to 5.6%, 5.2% and 4.8% when compared with the double-layer fiber cement roof without the PCM layer at the controlled heat source temperature of approximately 60 °C, 70 °C and 80 °C, respectively. It indicated that the use of phase change materials integrated into the fiber cement roofing sheet could reduce the heat transfer and interior room temperature, leading to energy saving.

E_007_PA: TECHNICAL AND ECONOMIC INVESTIGATION OF ELECTRICAL ENERGY CONSUMPTION PRODUCED FROM SOLAR CELLS INSTALLED ON MOTORCYCLES

Jantakan Peangkaew , Atthakorn Thongtha*

Department of Physics, Faculty of Science, Naresuan University, Phitsanulok, 65000, Thailand
*e-mail: atthakornt@nu.ac.th

Abstract:

The objective of this research is to study and compare the potential of electricity production from the 20W monocrystalline solar cell with and without installing on motorcycle. The monocrystalline panel was installed in front of the motorbike and tested the ability of electric energy generation as voltage, current and power which was compared with the normal monocrystalline solar cell without installing on the front of motorcycle. This experiment was tested the efficiency of electric energy generation for 5 min in each condition at the same time. The motorcycle with installing the 20W monocrystalline solar cell was controlled the average speed at approximately 20 km/h, 40 km/h, and 60 km/h to compare and tested the performance of electric generation of the 20W monocrystalline solar cell in each condition. The normal PV panel (without installing in front of motorcycle) and the PV panel installing in front of motorcycle was then connected to the lithium ion battery. It was found that the normal PV panel, PV panel fixed in front of motorcycle that constantly controlled at approximately 20 km/h, 40 km/h, and 60 km/h could charge the electric energy into the lithium ion battery up to 18%, 20%, 22% and 25%, respectively. The efficiency of electricity charge of solar cells installed with motorcycles at the constant speed of approximately 20 km/h, 40 km/h, and 60 km/h was more than that of the normal panel by 11%, 22% and 39%, respectively. The cost of the lithium ion battery, a 20W monocrystalline solar cell and the produced electrical energy value was calculated to obtain the payback period (PBP). In each condition, payback period was evaluated at approximately 16 months.

E_008_OA/E_026_OA: STUDY AND DEVELOPMENT OF SOFTWARE FOR MUSIC NOTATION

Puchiss Phromchang,* Wootinun Ouppapong, Chaiyanan Wan-In

Department of Social Science and Art, Mahidol Wittayanusorn School, Nakhon Pathom 73170 (Thailand)
*e-mail: s6107825@mwit.ac.th

Abstract:

As music is developed throughout the whole time, there are many people, as a beginner, start to play at least one kind of music. Due to many copyright policies, it is not easy to find the real note of the wanted song, and for beginners also too hard to identify the true note by hearing. In this project, the main purpose is to develop software that can convert the audio form of a popular song played by a piano or guitar to music notation form with more accuracy than the common program can do by using signal processing and deep learning to process signal data. This project continues with some references from Machine Learning Engineer Nanodegree Capstone project which falls under the domain of Automatic Music Transcription (AMT) and Music Information Retrieval (MIR), the purpose is using machine learning to convert polyphonic audio files to MIDI. The model's structure consists of 2 parts: data preprocessing, and deep learning. Data preprocessing is used to create and prepare a dataset which is synthesized with the same sound as their original songs, exported as WAV and MIDI files. Then, the dataset is segmented into 1-second audio series and 0.5-second MIDI series as 1 second of audio file is equal to 0.5 seconds of MIDI's. After that, we convert the domain of the data from a time domain to a frequency domain processed by CQT which is appropriate for musical analysis compared to the traditional FFT's as CQT can illustrate all the note component in the single sound at any given time, whereas FFT can show the only result of mixing frequency. Second part, deep learning—composed of CNN 11 layers, ReLU in hidden layers as activation function, and sigmoid in the output layers—is used to predict music notation data and melody from song file and reshape the predicted music notation data to spectrogram representing the melody note as NumPy array, which is then compared to the original music notation in order to calculate the accuracy in the percentage of our model by considering only matched note-on messages as the correct. Following that, we compare our results with the common audio-to-MIDI program, then conducting two additional experiments. First, we change the dataset from piano to guitar and then calculate the accuracy again to compare with the first experiment accuracy in order to know how the type of instruments affect the accuracy of the model. Second, we aimed to find the difference between time-based segmentation and beat-based segmentation; therefore, we change the length of the segmented audio dataset from 1-second series to 0.5-second series to test with 120-bpm songs in order to match with the rhythm of the songs and then calculate the accuracy again to compare with the first experiment accuracy. Using piano as the dataset and segmenting the audio into 1 second each, the first experiment showed the average accuracy at 50.96% —41.96% from piano testing songs and 59.97% from guitar testing songs. The second experiment provided the average accuracy at 34.68%—28.74% from piano testing songs and 40.62 from guitar testing songs, while our selected conventional program performed the highest potential at 10%. Last but not least, beat-based segmentation showed superior performance to time-based segmentation in all testing songs. In conclusion, we found that our software is slightly more effective and accurate than the common program. In the additional experiments, the highest accuracy can be found on the guitar music using piano as the dataset, while the lowest is found on piano music using guitar as the dataset and the accuracy tested with 120-bpm songs shows that segmented dataset according to tested song's tempo gives higher accuracy.

E_009_OA: IMAGE PROCESSING OF CT SCAN IMAGE FOR LIVER LOCALIZATION

Kusuma Jaipiam,[1] Sirapat Charukamnertkanok,[1] Boonnatee Sakboonyarat[1,*]

[1] Mahidol Wittayanusorn School, Nakhon Pathom, Thailand
*e-mail: s6107740@mwit.ac.th

Abstract:

Cancer mortality rate keeps increasing every year. One of those that significantly affects people's lives is liver cancer. Our project focuses on liver localization using 3D image processing of abdominal CT scan images. Using 131 abdominal CT scan images from Medical Segmentation Decathlon, we preprocess data by rotating each image, adjusting spaces to (1,1,1), and converting into hdf5 format that is more convenient for our uses. Next, we use K-fold cross validation, K equals to 5, to find the optimal range of HU value using RetinaNet with different window sizes and get the most accurate one whose window size equals to 500. Then, we use the similar protocal to train and test our work with different numbers of training sets. IoU (Intersection over union) is used to evaluate the model and the maximum reaches 0.8573.

For the usage, medical staffs need to input the CT scan images of the patients and the system will return the box of the liver with two coordinates to draw the box.

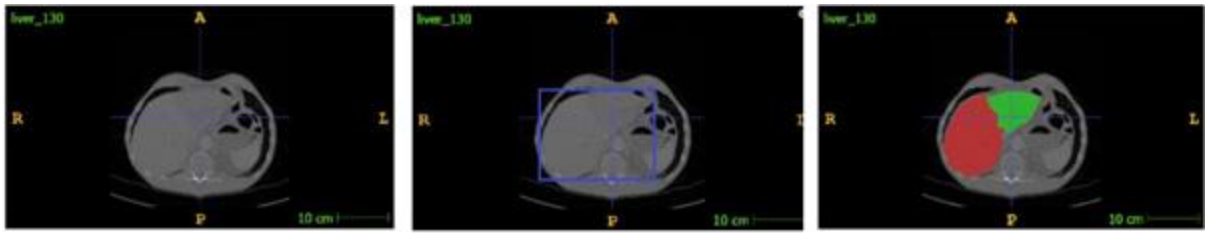

Figure 1.

Examples of abdominal CT scan slides (left)
with predicted box (middle) and ground truth by specialists (right)

E_010_OF/E_028_OF: APPARATUS FOR DETERMINING YOUNG'S MODULUS OF SOLID MATERIALS BASED ON GRAVITATIONAL FORCE ANALYSIS

Kitisak Boonkham,* Thanyanan Phuphachong

Department of Physics, Mahidol Wittayanusorn school, Salaya, Phuttamonthon, Nakhon Pathom 73170, Thailand
*e-mail: kitisak.bnk@mwit.ac.th

Abstract:

This present work aims at developing an inexpensive apparatus for measuring elastic modulus of cylindrical solid wires, known as Young's modulus. Young's modulus of a solid material is defined to be the ratio of tensile stress to tension strain and can be interpreted as the resistance of a solid to a change in its length due to an external force. When an external force is applied to the cross-sectional area of a solid, the change in length of the solid occurs. Our apparatus was designed and developed at Mahidol Wittayanusorn school workshop in order to use gravitational force as the external force. The apparatus possesses some particular aspects. The pulley system added in the apparatus allows us to hang a solid wire with the slot weight rod used as initial external force. The anti-vibration arm helps to reduce experimental errors. Weights of different masses were fabricated to create various tensile stresses. The manual xyz translation stage can be used to adjust the position of the dial gauge to be at the center of the slot weight base before measuring the elongation of the solid. The usability testing of the apparatus was carried out using copper alloy, steel, and nylon wires of diameter of 0.44 ± 0.01 mm, 0.59 ± 0.01 mm, and 1.47 ± 0.01 mm, respectively. The Young's modulus values of copper alloy, steel, and nylon wires determined from our apparatus are approximately 3.33×10^{10} N/m^2, 1.58×10^{10} N/m^2, and 6.14×10^{8} N/m^2, respectively. We also measured the Young's modulus values of these wires using the Universal Testing Machine (UTM) at Mahidol Wittayanusorn school laboratory. The values of Young's modulus of the wires determined using our apparatus were compared with the values obtained from the UTM, showing the discrepancies about 3 % for nylon wire but they are quite large for copper alloy and steel wires. This study provides useful information for improvement of the apparatus. Our work could be further improved and used as a laboratory apparatus for determining Young's modulus of solid materials using gravity as an external force or a teaching material for studying mechanical properties of solids both in high school and undergraduate levels.

Introduction:

Modulus of elasticity of solid materials is widely taught in both high school and undergraduate levels. There are three types of elastic moduli depending on how the external force is exerted on a solid material: Young's modulus, shear modulus, and bulk modulus. We selected to develop our apparatus to measure Young's modulus of solid wires because the deformation of the wires is linear and simple to be demonstrated the elastic modulus of matter. The study and the demonstration of Young's modulus of a solid are more frequently found than the others.[1,2] Young's modulus is defined to be the ratio of tensile stress to tensile strain. It can be interpreted as the resistance of a solid to a change in its length due to an external force applied to the cross-sectional area of the solid. However, experimental setup for studying Young's modulus of a solid is delicate and not easy to be done or existing apparatus

are expensive.[2,3] Therefore, the purpose of this work is developing an inexpensive apparatus for determining Young's modulus of cylindrical solid wires. Testing the usability of the developed apparatus is also obligatory. In this paper, the design and development of the apparatus at Mahidol Wittayanusorn school workshop will be described in details. Here, we studied Young's modulus values of three types of solid wires: copper alloy wire, steel wire, and nylon wire. Their Young's modulus values were measured by the developed apparatus and the Universal Testing Machine (UTM) at Mahidol Wittayanusorn school laboratory. The force applied to the samples by the UTM is a tensile force generated from the machine and applied in the upward direction (opposite to the gravity). This machine is very expensive and is not easy to be used. Moreover, it is not appropriate to be used in classroom to demonstrate elastic modulus of matter for high school students. The comparison of the Young's modulus values obtained from two different measurement techniques is discussed as well as the reproducibility and the usability of the apparatus.

Methodology:

Design and development of the apparatus

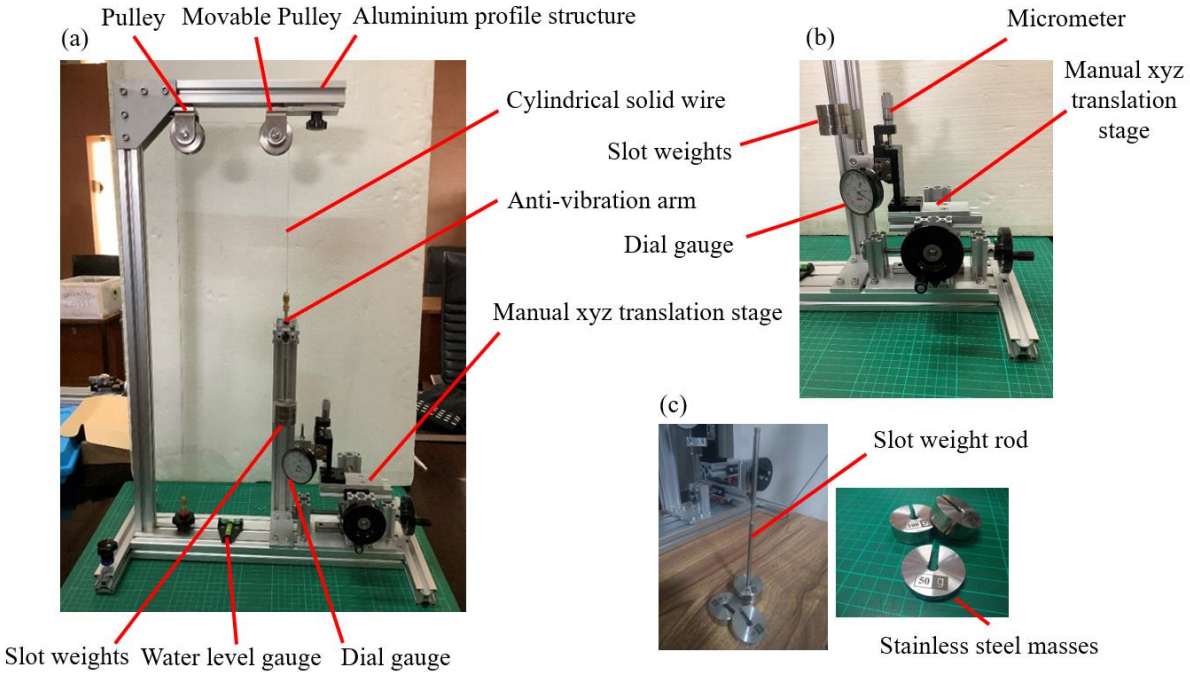

Figure 1.

(a) Developed apparatus for determining Young's modulus of solid materials using gravitational force as an external force. (b) Manual xyz translation stage and dial gauge. (c) Slot weights

Figure 1(a) shows the apparatus that was designed and developed at Mahidol Wittayanusorn school workshop in order to use gravitational force as the external force applied to the cross-sectional area of a solid wire. The dimension (width × length × height) of the apparatus is 30 cm × 60 cm × 80 cm. 3030 aluminium profile T were used to produce the light weight structure of the apparatus. A pulley system was added to the apparatus to hung a

wire. This allows a vertical measurement that makes the apparatus more compact. Moreover, we can adjust the length of the wire with movable pulley as shown in Figure 1(a). The slot weight anti-vibration arm was added in this device to reduce experimental errors from a dial gauge which is very sensitive when the tip of the dial gauge touches the base of the slot weight rod. The vibration occurs when we add masses in the slot weight which leads to the errors of the indication of the dial gauge pointer. The linear barring is used to make the anti-vibration arm. It helps eliminate vibration because it forces the slot weight rod to move only in the vertical direction with very small friction. External force acting on the wire can be varied by changing the number of stainless weights to produce the mass from 50 g to 400 g as shown in Figure 1(c). Figure 1(b) shows the manual xyz translation stage that is used to adjust in three directions the position of the dial gauge, a distance amplifying instrument, to be in a vertical direction under the weights before measuring the elongation of the wire. Here, the dial gauge with high resolution of 0.01 mm is used to measure the elongation of the wire. Our apparatus is easy to use since we can vary the gravitational force by adding masses in the slot weight. There is no need to install force sensors in the apparatus.

Determination of Young's modulus of solid wires using the developed apparatus

In this work, three types of solid wires were used to test the usability of the developed apparatus by determining their Young's modulus values. The reproducibility of the developed apparatus was also examined. The diameters and the lengths of all the wires are shown in Table 1. To measure Young's modulus of a solid wire, we hang it from a pulley system. The apparatus must be located on a horizontal plane that can be verified by the water level gauge. First of all, the slot weight rod of mass about 50 g is connected to the wire and used as initial mass to create a tension to the wire. In each measurement, the xyz translation stage has to be adjusted in a right position where the dial gauge is situated vertically under the slot weight rod. Before measuring the elongation of the wire, the dial gauge has to be set to zero. Once the tip of the dial gauge touches the base of the slot weight rod, we rotate the indicator of the dial gauge to zero scale using micrometer. Then, weights are added gradually until the total mass is 400 g to produce stress to the wire due to gravity. Masses and their corresponding elongations are recorded and will be converted into stress and strain, respectively. The governing equation for Young's modulus (Y) is written as

$$F/A = Y(\Delta L/L) \tag{1}$$

where F is the gravitational force acting as a tensile force applied to a solid wire, A is the cross-sectional area of a solid wire, ΔL is the elongation of a solid wire, and L is the initial length of a solid wire.

Finally, for a given solid wire we plot the stress F/A as a function of the strain $\Delta L/L$ to deduce the corresponding Young's modulus value from the slope of the linear regression equation.

Table 1.

The diameter and the length of three types of cylindrical solid wires used to test the usability of the developed apparatus.

Types of solid wires	Diameter (mm)	Length (m)
Copper alloy wire[a]	0.44 ± 0.01	1.01 ± 0.01
Steel wire	0.59 ± 0.01	1.00 ± 0.01
Nylon wire	1.47 ± 0.01	0.97 ± 0.01
Copper alloy wires[b]	0.43 ± 0.01	0.99 ± 0.01

[a]This copper alloy wire was used to determine its Young's modulus by the developed apparatus.

[b]These five copper alloy wires were used to examine the reproducibility of developed apparatus.

The reproducibility of the developed apparatus was examined by measuring Young's modulus values of five copper alloy wires. To do this, we proceeded all the steps of measurement for each wire as described previously. The standard deviation of the obtained values of Young's modulus was calculated.

Determination of Young's modulus of solid wires using the Universal Testing Machine

The Universal Testing Machine (UTM) (Brand: Tinius, Model: 10ST, ISO527: 1996 Tensile (Crosshead)) can be used to determine the mechanical properties of materials by exerting tensile, compressive, or transverse stresses. In this work, the tension test in the tensile crosshead mode of the UTM was performed in three types of solid wires at Mahidol Wittayanusorn school laboratory to measure their Young's modulus values. The diameters of the wires are the same but the length of the wires is about 30 cm. The force applied to the samples by the UTM is a tensile force generated from the machine and applied in the upward direction (opposite to the gravity). The UTM movable cross head is attached to a wire and can be moved slowly upwards in a vertical direction until the wire reaches its breaking point. The speeds or strain rates used in our UTM tests are approximately 1 mm/min. During the test, the tensile stress applied to the wire and the elongation of the wire are measured by a force sensor installed at the movable cross head. Then, the UTM software plots registered tensile stress values versus elongation values of the wire and gives the analyzed result of the Young's modulus of the wire. The obtained values of Young's modulus could be used as reference values to be compared with the values determined from our developed apparatus. The discrepancies between experimental results and reference values could provide information for improvement of the apparatus.

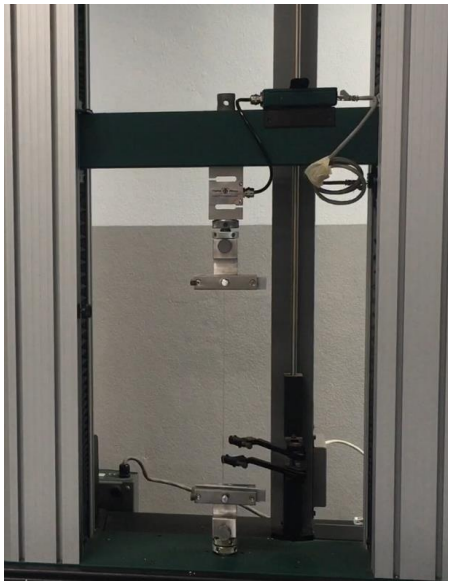

Figure 2.

Determination of Young's modulus of solid wires using the Universal Testing Machine

Results and Discussion:

We carried out the measurements of Young's modulus of copper alloy, steel, and nylon wires using our developed apparatus. For a given solid wire, tensile stresses were plotted versus their corresponding strains. Linear regression equation was chosen to analyze experimental results. Figure 3 shows the relationship between tensile stress applied to a solid wire and tensile strain occurring in the wire. The results of copper alloy, steel, and nylon wires are represented by red, blue and green colors. Experimental values are denoted by solid dots. Regression lines are shown by solid lines. In the intervals of stress and strain in our study, we found that the stress is directly proportional to the strain and all the types of solid wires have similar behavior. According to other theoretical and experimental studies, the wires exhibit elastic behavior where the modulus of elasticity can be deduced from the slope of the fitted regression line. Young's modulus values of copper alloy, steel, and nylon wires are approximately 3.33×10^{10} N/m^2, 1.58×10^{10} N/m^2, and 6.14×10^{8} N/m^2, respectively. The R-squared values of the three regression lines are also shown on the graph, indicating that there is a good agreement between experimental results and linear regression model. Among these wires, it is the most difficult to increase the length of the copper alloy since the copper wire has the greatest Young's modulus value. On the other hand, nylon wire has the smallest value of Young's modulus and can thus be lengthened easier.

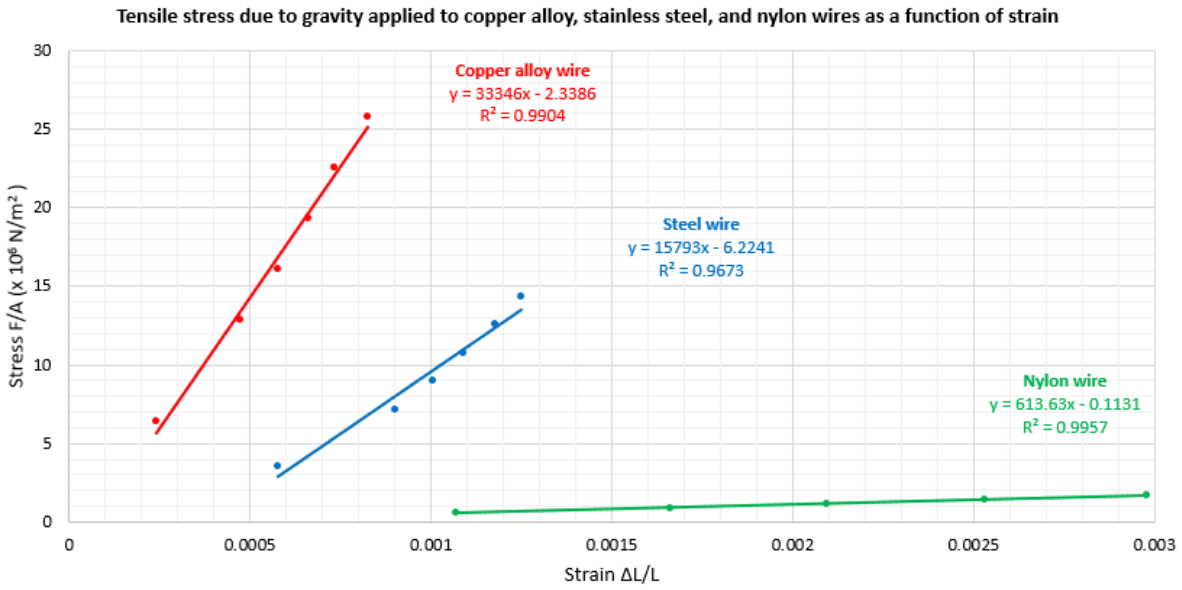

Figure 3.

Tensile stress due to gravity applied to copper alloy (red color), steel (blue color), and nylon (green color) wires as a function of strain. Experimental values are denoted by solid dots. Regression lines are shown by solid lines. All the wires show elastic behavior.

The reproducibility of the developed apparatus was examined by measuring Young's modulus values of five copper alloy wires of 0.99 ± 0.01 m in length. The average of Young's modulus values is 3.11×10^{10} N/m^2. The standard deviation of those results is 0.21×10^{10} N/m^2. This study enables the usability of our developed apparatus.

Young's modulus values of three types of wires were also measured using the UTM. As shown in Figure 4, an example of the variation of tensile stress as a function of strain of the nylon wire (black curve) shows clearly its elastic behavior, elastic limit and breaking point. A regression line (red line) is plotted tangentially to the black curve where the nylon wire is in the elastic behavior. The slope of the regression line is the Young's modulus of the nylon wire. Young's modulus values measured using the UTM could be used as reference values to be compared with the values determined from our developed apparatus. The obtained Young's modulus values of copper alloy, steel, and nylon wires are respectively $(4.54 \pm 0.87) \times 10^{10}$ N/m^2, $(2.16 \pm 0.45) \times 10^{10}$ N/m^2, and $(6.34 \pm 1.21) \times 10^{8}$ N/m^2. The discrepancies between experimental results and reference values are found to be quite large for copper alloy wire and steel wire. For nylon wire, the discrepancies are about 3 %. The main causes of errors may come from the reading values of ΔL from the dial gauge. This results directly in the values of the strain of the wires. It could lead to the errors of the measurement of the Young's modulus.

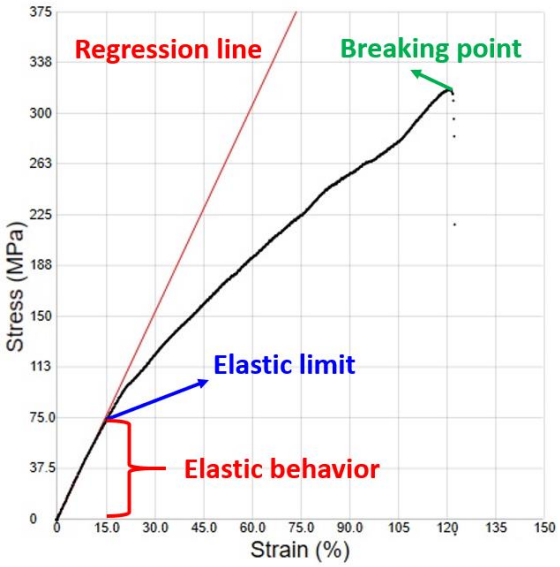

Figure 4.

Tension test in the tensile crosshead mode of the UTM performed in a nylon wire. Variation of tensile stress as a function of strain (black curve) shows clearly elastic behavior, elastic limit and the breaking point of the nylon wire. A linear regression model (red line) is represented on the graph and its slope is equal to the Young's modulus of the nylon wire.

Conclusion:

We have designed and developed an inexpensive apparatus of light weight and moderate size for determining Young's modulus of solid materials based on gravitational force analysis. The apparatus was tested the usability by performing the measurement of Young's modulus of three types of cylindrical solid wires: copper alloy wire, steel wire, and nylon wire. Our apparatus has particular aspects as follows. The pulley system added in the apparatus allows us to hang a solid wire with the slot weight rod used as initial external force. The anti-vibration arm was used to reduce experimental errors. Weights of different masses were fabricated to generate various tensile stresses. Additionally, there is the manual xyz translation stage used to adjust the position of the dial gauge to be at the center of the slot weight base. The Young's modulus values of copper alloy, steel, and nylon wires determined from our apparatus are approximately 3.33×10^{10} N/m^2, 1.58×10^{10} N/m^2, and 6.14×10^{8} N/m^2, respectively. Very high R-squared values of the three regression lines indicate a good agreement between experimental results and linear regression model in all the types of solid wires. The comparison between the Young's modulus values determined from our developed apparatus and the values obtained from the UTM shows the discrepancies quite large for copper alloy wire and steel wire. However, for nylon wire, the discrepancies are about 3 %. These results provide useful information for improvement of the apparatus. Moreover, the reproducibility of the developed apparatus was verified by measuring Young's modulus values of five copper alloy wires. The standard deviation of these results was calculated to be 0.21×10^{10} N/m^2. Our work could be further improved to be used as a laboratory apparatus for determining Young's modulus of solid materials using gravity as an external force or a teaching material for studying mechanical properties of solids both in high school and undergraduate levels.

Acknowledgements:

We are grateful for the financial support and the facilities at the workshop and the laboratory of Mahidol Wittayanusorn school. We thank Mr. Wittawas Phunmunee from the Department of Physics for useful suggestions to fabricate the first prototype of the apparatus. We also thank Mr. Weerawut Tiankao from the Department of Chemistry for useful suggestions to use the Universal Testing Machine.

References:

1. Boncan VG, Rogers MJ, Heinold T, Dillenbeck RL. Washington, DC: U.S. Patent and Trademark Office. 2007;U.S. Patent No. 7,191,663.
2. Lanting SS, Waterman HA. Journal of Scientific Instruments. 1964;41(10):605.
3. Robinson DW. Journal of Scientific Instruments. 1955;32(1):2.

E_011_PA: EXPERIMENTAL STUDY OF MATERIAL TYPES AND INCIDENT ANGLES OF LIGHT SOURCE ON ILLUMINATION PERFORMANCE OF LIGHT PIPES IN BUILDINGS

Atthakorn Thongtha, Jiraphorn Mahawan, Peeranat Laphom *

Department of Physics, Faculty of Science, Naresuan University, Phitsanulok 65000, Thailand
*e-mail: nuengprn1998@gmail.com

Abstract:

The objective of this research is to study the material type and the direction of the light receiver of horizontal light pipe for improving the illuminance performance in buildings and reducing the demand of electrical energy from artificial light. This research used the two material types as commercial aluminum alloy and commercial zinc alloy for inventing horizontal light pipe. The horizontal light pipe with a 0.5 m length and a 0.3 m diameter was built to apply into the testing room model with a height of 1.7 m, a length of 1 m and a width of 1 m. Insolation was provided by a 20 W LED lamp which is the light source, placed away from the top of the light tube. The artificial light was varied in horizontal shadow axis (ϕ) between 0° and 90° with an increase step of 30 ° and in elevation angle axis (θ) between 0° and 180° with an increase step of 5°. It was found that illuminance performance of the aluminum alloy pipe is higher than that of the zinc alloy one by approximately 10% in each incident angle. At the 0° of horizontal shadow axis (ϕ), the horizontal light pipe illuminance of both commercial aluminum alloy and commercial zinc alloy showed the value higher than other horizontal incident angle (ϕ) in the same elevation angle (θ). This illuminance measurement demonstrates that the light tube could be considered as in a lighting system in deeper parts of buildings to reduce the demand of energy consumption in the light section of the buildings.

E_012_PA: DESIGN OF JACKET CONTAINING PHASE CHANGE MATERIAL TO REDUCE HEAT THROUGH HUMAN BODIES

Kanyanut Noynun, Atthakorn Thongtha*

Department of Physics, Faculty of Science, Naresuan University, Phitsanulok, 65000, Thailand
*e-mail: atthakornt@nu.ac.th

Abstract:

This research focused on the study and design of jacket integrating phase change material to reduce heat through outer jacket surface into body. The thermal behavior of phase change materials was examined by using Differential scanning calorimetry (DSC) which appeared a melting point of approximately 45 °C with an involved enthalpy of 67.40 J/g. The broadening exothermic peak was observed at approximately 44.6 °C with an involved enthalpy of 65.80 J/g. This was suitable to use in climatic conditions from 25 °C to 45 °C. This work was divided into 3 main conditions; 1) the normal jacket, 2) the full PCM-contained jacket and 3) the half PCM-contained jacket. PCM was formed into a uniform volume of 7 cm x 10 cm x 0.1 cm and was prepared and encapsulated in a polyethylene (PE) container. Each PCM unit was arranged and attached on the jacket with the full and half patterns at the positions of shoulder, arm, front body and back body. The experimental procedure was tested at 11am to 1pm and 2pm to 4 pm for 3 days. It was found that an integration of PCM into the jacket with half pattern can reduce heat transfer from the environment through human body by around 15% when compared with the normal jacket. So, this work is an alternative way to apply in daily life because it can reduce the heat propagation from surrounding weather into human body.

E_013_PA: INVESTIGATION OF ILLUMINATION PERFORMANCE OF VERTICAL AND HORIZONTAL LIGHT PIPES FOR ENERGY SAVING IN BUILDING

Jittipak Jitsumran, Atthakorn Thongtha*

Department of Physics, Faculty of Science, Naresuan University, Phitsanulok, 65000, Thailand
*e-mail: atthakornt@nu.ac.th

Abstract:

The research studies the illumination performance of vertical and horizontal light pipes for energy saving in buildings. The testing room size of 1m x 1m x 1.7m was designed by using wood as material. The material of the light pipe as aluminum is built with a diameter of 0.2 m and length of 0.5 m. The reflection performance of the two light pipe formats that are the vertical and horizontal light pipes was studied in this work. The brightness of both sides of the light pipe and the illumination at the working area in the both cases were measured. The working area is the area position which has a distance of 1.7 m from the bottom end position of light pipe to the floor area. It was found that the brightness at the top side of light pipe is around 600 lux, the brightness at the bottom side of light pipe is around 300 lux, the illumination value at the working area is at approximately 220 lux and the illuminance efficiency of the horizontal light pipe is at around 50% for the case of vertical light pipe. The brightness at the top side of light pipe is around 600 lux, the brightness at the bottom side of light pipe is around 250 lux, the illumination value at the working area is at approximately 180 lux and the illuminance efficiency of the horizontal light pipe is at around 42% for the case of horizontal light pipe. An illuminance intensity of light tube was distinctly a result of the light reflection within light tube and the superposition between light reflection within the light tube and directly transmitted light through light tube. This indicated the performance of vertical light pipe is better than that of horizontal light pipe.

E_014_PA: INVESTIGATION AND DESIGN OF ENERGY CHARGE SYSTEMS FROM SOLAR CELL ON MOTORCYCLE

Pavee Pansritong, Atthakorn Thongtha*

Department of Physics, Faculty of Science, Naresuan University, Phitsanulok, 65000, Thailand
*e-mail: atthakornt@nu.ac.th

Abstract:

This work was focused on the energy charge and discharge the lithium ion battery with the 3.7 V capacity and 9900 mAh, and lithium phosphate battery with the 3.2 V capacity and 5000 mAh. Three major parts of experimentation were undertaken, firstly in regard to the discharge behavior of the lithium ion battery and lithium phosphate battery at various resistance values (150Ω, 500Ω and 1000Ω), and secondly experiments to test the charged energy effectiveness into the lithium ion battery and lithium phosphate battery, and finally investigations to evaluate the payback period (PBP) of the lithium ion battery and lithium phosphate battery which installed with the monocrystalline solar cell. Both types of battery were charged by a 12 V and 20W monocrystalline solar cell installed on motorcycle. The monocrystalline panel was installed in front of the motorbike and tested the efficiency of battery charges in a distance of 2 kilometers from Jiajitsawat's dormitory to Physics department, faculty of science, Naresuan university, with an average speed of 20 km/h, 40 km/h, and 60 km/h took a time for 2 min 58 sec, 2 min 30 sec and 2 min 12 sec, respectively. At the same average speed of motorcycle, the charged energy in lithium phosphate battery showed more performance than that of lithium ion up to 12%. Time that energy of lithium phosphate battery discharged to the circuit resistance, was extended up to approximately 35% when compared with discharge of the lithium ion battery. The cost of the lithium ion battery, lithium phosphate battery, a 20W monocrystalline solar cell and the produced electrical energy was calculated to investigate the payback period (PBP). From this calculation, the energy payback period for the application of lithium phosphate battery and lithium ion battery on motorcycle was estimated at 12 months and 15 months, respectively.

E_015_PA: IMPROVEMENT OF THERMAL PERFORMANCE OF LIGHTWEIGHT CONCRETE BUILDING MATERIAL INCORPORATING WASTE POWDER FROM AUTOMOTIVE REFINISHING INDUSTRY

Atthakorn Thongtha*, Somchai Maneewana, Chantana Punlek

Department of Physics, Faculty of Science, Naresuan University, Phitsanulok, 65000, Thailand
*e-mail: atthakornt@nu.ac.th

Abstract:

This current investigation is focused on enhancing the thermal effectiveness of this autoclaved aerated concrete (AAC) by incorporation black powder as a component. Black powder is a waste product of the automotive refinishing industry in Thailand. The mixture composition of AAC is lime (11.94% by weight), portland cement (12.43% by weight), aluminum (0.06% by weight), anhydrite (1.64% by weight) and fine sand (73.93% by weight). The content of fine sand was substituted by black powder waste (less than 90 μm in size) with 0%, 15%, 20%, 25%, 30%, 35%, 40%, 45% and 50% by weight and the content of other raw materials was fixed. The dynamics of heat transfer and the cooling load of air conditioning plants in four simulated houses with different wall materials (Brick, cement block, AAC and AAC with incorporating black power) were investigated. The investigation demonstrated that by incorporation black powder a significant increase in the thermal effectiveness of the building materials was achieved and determined by comparing the heat flux at the indoor surface. The increase in thermal effectiveness was the greatest when black powder was applied to the AAC. It was demonstrated that the cooling load and power requirements of air conditioning plants in buildings using the wall with the incorporation of black powder can be reduced variously by 25.5%, 37.9% and 48.1% depending on the building material, with the AAC incorporated black powder provided the greatest reduction. The energy payback period for AAC with the incorporation of black powder was estimated as 2.47, 1.33 and 0.86 months when compared against normal AAC, brick and cement block, indicating substantial energy saving by the enhancement of the thermal resistance of AAC.

E_016_OF: APPLICATION OF AIR DECK BLASTING TECHNIQUE AT KHOUNXAY GYPSUM MINE, SAVANNAKHET PROVINCE, LAO PDR

Amone Phangphylavong[1], Pirat Jaroonpattanapong[2]

[1] Department of Mine, Polytechnic College, Lao-Thai Friendships Road, Vientiane Capital, Lao PDR
[2] Department of Mining and Petroleum Engineering, Faculty of Engineering, Chiang Mai University, Thailand
*e-mail: pirat@eng.cm.ac.th

Abstract:

Current blasting operations at Khounxay Gypsum Mine, Lao PDR have been facing many unfavorable blast results, such as under or oversize of blasted gypsum, toes or elevated floor after a blast, and high explosive cost, that lead to low productivity and increasing cost of production. This study applied air deck technique (ADT) to improve current blasting operations at the mine and determined an appropriate air deck length. The blasting results between current practice and ADT at air deck length 30% and 50% of charge length were compared by production cost per sold ton. Production cost comprises of drilling, explosive, loading, hauling, and secondary size reduction by hydraulic breaker. The result indicated that 30% air deck length gave the lowest production cost at $2.04/ton compared to 50% air deck length and current blasting at $2.36/ton and $2.19/ton, respectively. The low production cost of 30% air deck length compared to current practice came from (a) reducing of powder factor from average 0.12 kg/ton to 0.11 kg/ton and (b) increasing of product sold (10-18 inches size) from average 54.56% to 61.16% of blasted gypsum after blast. Although less explosive charge was used, production cost of 50% air deck length was high due to decreasing of gypsum product resulting from increasing of oversize and toes after blast.

Introduction:

The air deck technique (ADT) has been applied for control blasting and reduce the environmental impacts such as ground vibration from blasting due to less explosive used. ADT could increase the fractures of rocks that have low to medium strength and improve blasted rock fragmentation, resulting in improving of excavator's performance. ADT reduced explosive used so the following benefits were lower explosive cost and ground vibrations [1][2][3][4]. ADT theoretically improved an explosion mechanism by transferring the explosive energy occurred during detonation to the rock mass near a blasthole and reducing energy loss escaped at the top of blasthole [5] [6]. The suggested air deck length should be 10-40% of the total explosive length in the blast hole [1][7][8][9] and the air deck position should be placed at the middle of the blasthole given higher rock fragmentation compared to other positions in the blasthole [10]. However, the emulsion column charge might fail to be detonated at the air deck length more than 30% of total explosive length in the blasthole and less than 30% recommend for any specific type of rock [11][12]. Invented equipment like Power Deck claimed to generate pressures 2-7 times in the blasthole compared to a conventional blasthole [13]. However, joint spacing and blasting direction were affected the length

of the air deck [14]. Besides lower explosive cost, ADT could reduce fly rock and blast-induced gases, such as carbon dioxide (CO_2) and other toxic gases, to the natural environment [15] [16].

Khounxay Gypsum Mine (KGM) is a small-scale open pit mine located at Cham Phone district, Savannakhet province, Lao PDR as shown in Figure 1.

Figure 1. Location map of KGM (modified from Google Earth, 2020)

The hardness of gypsum ore is two in Mohr's scale and the chemical formula is $CaSO_4 \bullet 2H_2O$. Average uniaxial compressive strength from four samples is 32.26 MPa and compound details are shown in Table 1.

Table 1: Analysis results of gypsum ore at KGM

Item	Description	Average (%)	RQD (%)	Density of gypsum (ton/m^3)	Average Uniaxial Compressive Strength (MPa)
1	CaO	32.41			
2	SO_3	43.25			
3	H_2O	19.22	98.54	2.4	32.26
4	Fe_2O_3+Al_2O_3	0.06			
5	$CaSO_4 \cdot 2H_2O$	94.88			

The mine operations comprise of drilling and blasting of gypsum ore, loading and hauling of blasted gypsum to stockpile, and size reduction with hydraulic breaker machine to obtain the saleable size between 10-18 inches. Current blasting practice at KGM uses a staggered pattern with burden and spacing 3x3 meters and a blasthole depth is 3 meters. The bottom and column charge are Emulsion and Ammonium Nitrate mixed with Fuel Oil (ANFO), consecutively. The explosive column is divided into two decks with two primers that are detonated by the same number 25/380 milliseconds (ms) of Non-electric (Nonel) detonators as shown in Figure 2 (left). At a 3-m depth blasthole, ANFO weight used is 5 kilograms per blasthole. For a perfect round, the blasted gypsum is approximately 16 tons per meter of blasthole depth. As above mentioned, KGM's blasting pattern has been conducted two explosive decks even though the blasthole depth is only 3 meters. The blasting results are not completely satisfactory with having some under or oversize blasted gypsums and toes that lead to low productivity and high production cost. ADT is selected for this study to replace one deck of current design and reduce one primer used. Two air deck length at 30% (rounded down to nearest whole number) and 50% of total charge length (ANFO) of a current practice (1.2 m) are studied. The amount of ANFO at 50% air deck length will reduce from 5 to 4 kilograms per blasthole; however, the primers will be reduced to only one primer for both air deck lengths. The blasthole geometries of both 30% and 50% air deck length are shown in Figure 2 (right).

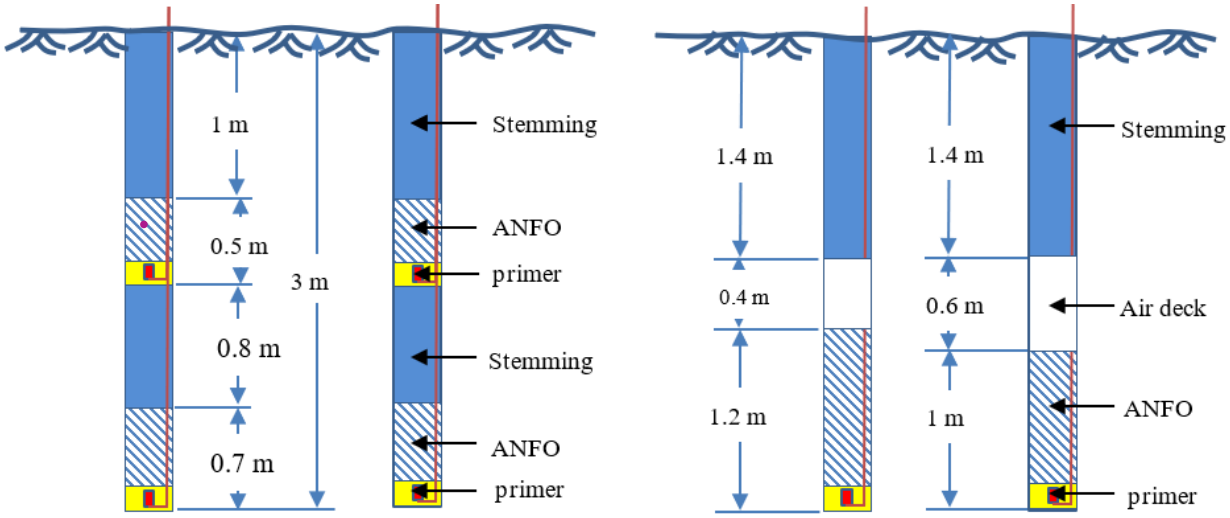

Figure 2. Blasthole geometries of a current blasting using total charge length 1.2 m (left) and ADT at 30% (rounded down from 33.33%) and 50% air deck length compared to a current blasting charge length (right)

Method of study: Data of the number of blasthole, explosive consumption, weight of blasted gypsum hauled to stockpile, and production cost per blast were collected from overall six blasts that came from two current practice blasts, two 30% air deck length blasts, and two 50% air deck length blasts. The number of experimental blasts was low because of unpredictable mechanical failures of, for instance, loading excavators and flooding of working areas.

The weight of blasted gypsum hauled to stockpile after a blast was determined by counting the number of hauling trucks, which known capacity, to stockpile. The different weight between the weight calculated from blast pattern and the weight of blasted gypsum hauled to stockpile were either toes or remaining over size gypsums at the blast site. Two different dump trucks used at KGM were HOWO brand with a 25-ton capacity and HOWA brand with a 31-ton capacity.

Some of gypsums hauled to stockpile were reduced to the sized required by market demand (10-18 inches) by using a hydraulic breaker machine so not all gypsums hauled to stockpile could be sold.

Total weight of gypsum from a blast pattern assuming without toes and oversize gypsum after a blast, was calculated by Equation 1.

$$\text{Total weight of a blast}(\text{tons}) = \text{Burden} \times \text{Spacing} \times \text{Hole depth} \times \text{Density} \quad (1)$$

Percent weight of blasted gypsum at stockpile was compared to the total weight of a blast and calculated by Equation 2.

$$\text{Percent weight of gypsum at stock pile} = \frac{\text{Number of truck} \times \text{Capacity}}{\text{Total weight of a blast}(\text{tons})} \times 100 \quad (2)$$

The remaining weight of oversize gypsums at the blast site was determined by field measuring so the percent weight of toes could be calculated by Equation 3.

$$\text{Percent weight of toes} = \frac{\text{Total weight of a blast}(\text{tons}) - \text{Stockpile}(\text{tons}) - \text{Oversize}(\text{tons})}{\text{Total weight of a blast}(\text{tons})} \times 100 \quad (3)$$

In addition, the gypsum product sold was compared to weight of gypsum at stockpile as following Equation 4.

$$\text{Percent weight of gypsum sold} = \frac{\text{Gypsum product sold to market}(\text{tons})}{\text{Weight of gypsum at stockpile}(\text{tons})} \times 100 \quad (4)$$

These results were used to determine operating cost per ton of any stage of production and finally total production cost per ton of gypsum sold. The results were analyzed and compared between a current blasting and ADT.

Results and analysis:

The total weight of gypsum after a blast, weight of gypsum at the stockpile, weight of oversize (as shown in Figure 3) and toes were calculated and illustrated in percent as well as shown in Table 2. Moreover, weight of ANFO and primer consumption, powder factor (PF), and average explosive cost per ton hauled to stockpile for all blasts and methods were summarized in Table 3. Finally, total production costs per sold ton of gypsum were concluded and comparable for analysis as shown in Table 4.

Gypsum at the stockpile and final product: *ADT at 30% air deck length had increased the blasted gypsum at the stockpile from average 93.98% to 98.63% compared to the current blasting practice. However, ADT at 50% air deck length generated more oversize blasted gypsum and toes (from 0.62% to 1.98% and 0.76% to 2.39%, consecutively) so the gypsum weight at stockpile decreased (from 98.63% to 93.15%) compared to the ADT at 30% air deck length. The decreasing of gypsum at stockpile also led to lower weight of gypsum available for selling. Average percent weight of gypsum sold to markets of current practice blast, 30% air deck length, and 50% air deck length were 54.56%, 61.16%, and 46.16%, sequentially.*

Figure 3. Blasting results of a current blast (left) and ADT at 30% air deck length

The above-mentioned outcomes might come from a lesser amount of explosive used of 50% ADT. From comparison of all three methods, 30% ADT illustrated the highest improvement of blasting productivity. These proofs can be observed from Table 2, Figure 4, and Figure 5.

Table 2. Results of blasts separated by methods of study

No	Items		Air deck 0 % (Current blasting)		Air deck 30 %		Air deck 50 %	
		Unit/blast	CB 1	CB 2	AD 1	AD 2	AD 3	AD 4
1	Number of holes	holes	23	43	24	26	19	21
2	Weight of gypsum per blast	ton/blast	1,104	1,806	1,152	1,248	912	1,008
3	Gypsum hauled to stockpile	ton/blast	1,023	1,721	1,137	1,230	901	882
		%	92.66	95.29	98.70	98.56	98.79	87.50
		% average	93.98		98.63		93.15	
4	Oversize gypsum at a blast site	ton	25.16	34.60	14.20	0.00	10.30	28.52
		%	2.28	1.92	1.23	0.00	1.13	2.83
		% average	2.10		0.62		1.98	
5	Toes at a blast site	ton	55.84	50.40	0.80	18.00	0.70	47.48
		%	5.06	2.79	0.07	1.44	0.08	4.71
		% average	3.92		0.76		2.39	
6	Weight of gypsum sold to markets	ton/blast	561.85	932.84	661.39	789.15	428.23	395.13
		%	54.92	54.20	58.17	64.16	47.53	44.80
		% average	54.56		61.16		46.16	

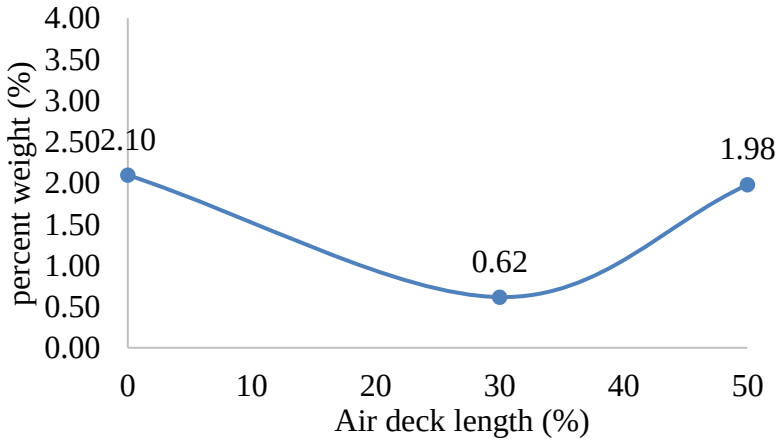

Figure 4. Average percent weight of oversize gypsum after blasts of the current practice (0% air deck) and ADT at 30% and 50% of air deck length

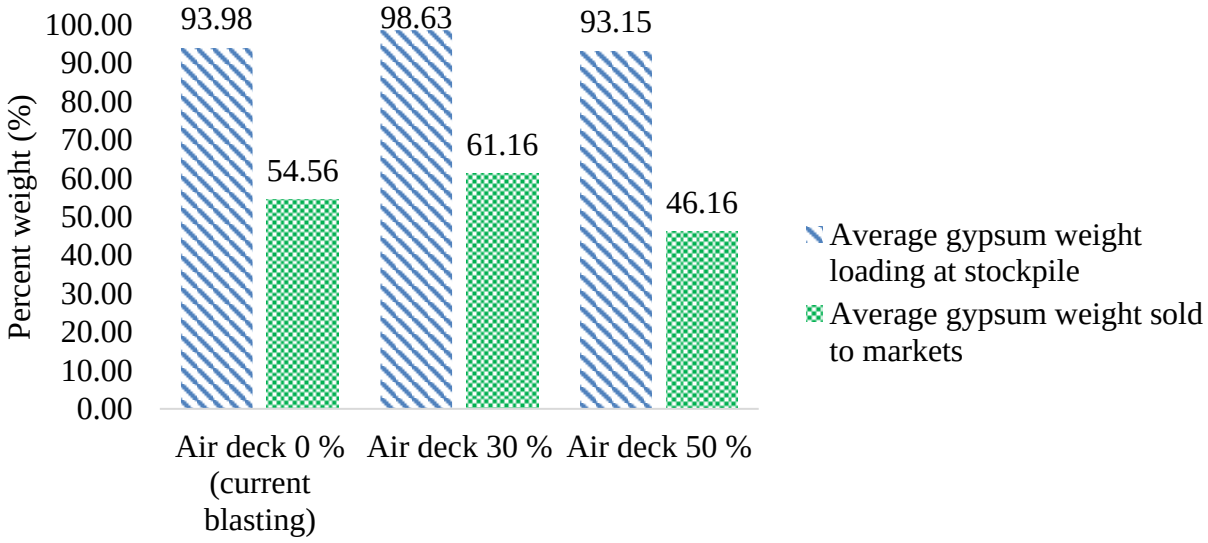

Figure 5. Average percent weight of gypsums at stockpile and average percent weight of gypsum sold to markets of the current practice (0% air deck) and ADT at 30% and 50% of air deck length

Explosive cost and overall total operating cost of blasting: Applying of ADT obviously reduced ANFO and primer consumption (or Powder Factor) of a blast. An air deck was applied to replace one primer in a blasthole, so reduction of primer was nearly 50% of ADT both 30% and 50% air deck length. The powder factor and ANFO consumption per blasthole were slightly reduced at 30% air deck length; however, reduction of ANFO consumption at 50% air deck length was almost 20% compared to a current blast as shown in Table 3. Less explosive consumption per blasthole reduced average explosive cost per ton from current blast $0.24 to 30% ADT $0.18 (or 25% cost reduction). Even though explosive costs of 50% ADT significantly reduced per blast, an average explosive cost per ton was slightly improve due to low gypsum products obtained from blasts.

Total operating costs consist of drilling, explosive, loading and hauling to stockpile, secondary size reduction by hydraulic breaker machine, and transportation products to markets as shown in Table 4. Details of operation costs from each stages of production mentioned above are displayed in $ per blast.

Table 3. Powder Factor (PF) and explosive cost per ton hauled to stockpile separated by methods of study

No	Items		Air deck 0 % (Current blasting)		Air deck 30 %		Air deck 50 %	
		Unit/blast	CB 1	CB 2	AD 1	AD 2	AD 3	AD 4
1	ANFO	kg/hole	5.22	5.00	5.00	5.00	4.21	4.05
2	Emulsion	kg/hole	0.98	0.99	0.52	0.48	0.53	0.48
3	Average ANFO per holes	kg/hole	5.11		5.00		4.13	
4	Average emulsion per holes	kg/hole	0.98		0.50		0.50	
5	Powder Factor (PF)	kg/ton	0.12		0.11		0.09	
6	% Reduction of ANFO	%			2.13		19.18	
7	% Reduction of emulsion	%			49.07		49.02	
8	Explosive cost per blast	$/blast	229.59	426.48	198.73	212.04	142.03	150.98
9	Costs of hard-board air deck	$/blast	0	0	2.34	2.54	2.78	3.07
10	Total explosive cost	$/blast	229.59	426.48	201.07	214.57	144.81	154.06
11	Total explosive cost per ton	$/ton	0.22	0.25	0.18	0.17	0.16	0.17
12	Average explosive cost per ton	$/ton	0.24		0.18		0.17	
13	Reduction of average explosive cost compared to current practice	$/ton			0.06		0.07	
14	% Reduction of explosive cost	%			25.61		28.98	

Table 4. Total operating cost per ton of gypsum product sold to market separated by methods of study

No	Items		Air deck 0 % (current blasting)		Air deck 30 %		Air deck 50 %	
		Unit/blast	CB 1	CB 2	AD 1	AD 2	AD 3	AD 4
1	Weight of gypsum sold to markets	ton/blast	561.85	932.84	661.39	789.15	428.23	395.13
2	Drilling cost	$/blast	49.00	97.06	55.60	61.25	56.54	61.25
3	Explosive cost	$/blast	229.59	426.48	201.07	214.57	144.81	154.06
4	Loading and hauling to stockpile	$/blast	312.87	276.11	292.13	275.17	131.93	131.93
5	Transportation cost	$/blast	90.47	176.22	170.57	186.59	126.28	125.33
6	Secondary size reduction by hydraulic beaker machine	$/blast	483.43	588.04	409.93	658.71	387.31	323.23
7	Transportation product to markets	$/blast	196.01	269.52	240.30	189.42	163.03	140.41
8	Total operating cost	$	1,361.38	1,833.44	1,369.61	1,585.72	1,009.90	936.22
9	Cost per ton of gypsum sold	$/ton	2.42	1.97	2.07	2.01	2.36	2.37
10	Average cost per ton of gypsum sold	$/ton	2.19		2.04		2.36	

Remark: the operating cost estimations of blasting were calculated from the fuel oil used of each stages of operation.

Cost per ton of gypsum sold was calculated by dividing total operating cost with weight of gypsum sold to markets. The average cost per ton of gypsum sold of current blast, 30% ADT, and 50% ADT were $2.19, $2.04, and $2.36, respectively as shown in Figure 6.

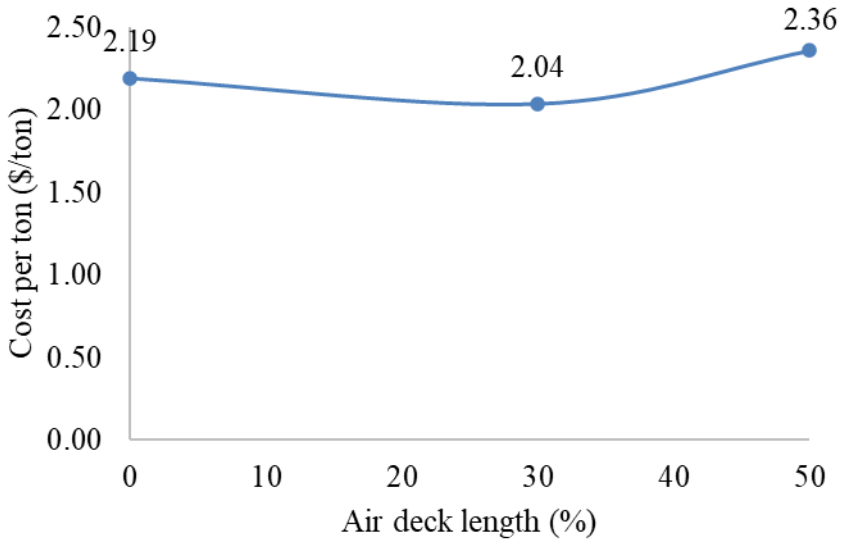

Figure 6. Cost per ton gypsum product sold to markets separated by methods of study

Conclusion:

The application of ADT to blasting operations at Khounxay Gypsum Mine (KGM) is successful. The study results confirm that the 30% air deck length has improved both blasting productivity and production cost. The average weight of blasted gypsum hauled to stockpile of the 30% air deck length compared to the current blasts has increased from 93.98% to 98.63%. However, the 50% air deck length produces more oversize blasted gypsum and toes so the gypsum weight at stockpile decreases and less gypsum products to be sold to markets. Average percent weight of gypsum sold to markets of current blasts, 30% ADT, and 50% ADT are 54.56%, 61.16%, and 46.16%, consecutively. Application of ADT clearly reduces powder factor (PF) and brings down the average explosive cost per ton to 25.61% and 28.98% for 30% and 50% air deck length, accordingly. The 30% air deck length provides the lowest production cost per sold ton at $2.04/ton compared to 50% air deck length $2.36/ton and current blasting at $2.19/ton.

Acknowledgment:

Researcher is highly indebted and thankful to the Department of Mines and the Polytechnic college, Vientiane capital, Lao PDR for giving the opportunity to pursue my master degree and The Thailand International Cooperation Agency (TICA) for sponsoring the study and the research work. In addition, researcher pleased to thank the Khounxay Gypsum Mine (KGM) for the kind and generous supports by allowing me to experiment and collect the data.

Reference:

1 J. Jhanwar, J. Jethwa and A. Reddy. Engineering Geology,2000;57:13-29

2 J. Jhanwar and J. Jethwa. Geotechnical and Geological Engineering,2000;18:269-287

3 D. Prak and S. Jeon. International Journal of Rock Mechanics & Mining Sciences, 2010;47:752-761

4 J. Jhawar, A. Cakrborty, H. Anireddy and J. Jethwa. Geotechnical and Geological Engineering, 1999;17:37-57

5 E. Kabwe. Geotech Geol Eng, 2017;35:157-167

6 E. Kabwe. Mining, Metallurgy & Exploration. 2019:1-11

7 J. Jhanwar. Geotechnical and Geological Engineering. 2011;29:651-663

8 P. Bunnaul and S. Naewbunthud. the 10th International Conference on Mining Materials and petroleum Engineering, Songkhla, Thailand, 2012.

9 S. Saqib, S. Tariq and Z. Ali. Pak. J.Engg. & Appl Sci. 2015;17:46-52

10 R. Chiappetta. Journal of explosives engineering. 2004;21:10-12

11 A. Boonnumma and C. Leelasukseree.Th 47th US Rock Mechanics/Geomechanics Symposium held in San Francisco, CA, SUA, 23-26 June 2013.

12 V. Balakrishnan, M. Pradhan and P. Dhekne. J.Inst.Eng.India Ser.D, 2019:155-162

13 S. Rommayawes, C. Leelasukseree and P. Jaroonpattanapong. European Scientific Journal. 2013; 3:200-207

14 M. Pradhan, V. Balakrishnan and G. Pradhan. IJCEBS.2015;3:51-56

15 V. Balakrishnan and M. Pradhan. ARPN Journal of Engineering and Applied Sciences.2018;13:4325-4330

16 M. Saharan, M. Sazid and T. S. Singh. Procedia Engineering. 2017;191:1211-1217.

E_018_PF: ANTIBACTERIAL ACTIVITY AND STABILITY STUDIES OF ELECTROSPUN CELLULOSE ACETATE FIBER MATS CONTAINING INDIAN GOOSEBERRY CRUDE EXTRACT

Chidchanok Meechaisue,[1,*] Nuanchawee Wetprasit,[2] Suksomboon Atikankun[2]

[1]Materials Technology Department, Faculty of Science, Ramkhamhaeng University, Bangkapi, Bangkok
[2,3]Biotechnology Department, Faculty of Science, Ramkhamhaeng University, Bangkapi, Bangkok
*e-mail: Chidchanok.m@ru.ac.th

Abstract:

Indian gooseberry (*Phyllanthus emblica* Linn.) or "Makhampom" in Thai is one of natural products exhibited antibacterial activity. The amount of 50 wt.% Indian gooseberry crude extracts (IGCE) were incorporated with the neat cellulose acetate (CA) solution (16% w/v in 2:1 v/v acetone/ dimethylacetamide) to fabricated ultra-fine fiber mats by electrospinning. The morphological appearance of the obtained fibers was not influenced from this incorporation, the fibers were smooth and the average diameters of neat CA and IGCE-loaded CA fibers were 368 and 509 nm, respectively. The agar disc diffusion method was employed to evaluate the antibacterial activity of the electrospun fibers mat against *Staphylococcus aureus* and *Staphylococcus epidermidis*, reported as inhibition zone diameter. It was found that the antibacterial activity of IGCE-loaded CA electrospun fiber mats against *S. epidermidis* was greater than *S. aureus* with the inhibition zone diameter of 1.9 and 1.7, respectively. The stability of this IGCE-loaded electrospun fiber mats as a function of time was studies via antibacterial activity with agar disc diffusion method. For the stability comparison, 3 types of Ag-containing antibacterial wound dressings in commercial were selected, i.e. Acticoat, Aquacel, and Tegaderm. With the storage time of specimens in 24 weeks at ambient temperature, the 50 wt.% IGCE-loaded electrospun CA fiber mats showed great antibacterial activity in equal to those commercial dressings. After 30 weeks, the antibacterial activity of IGCE- loaded CA fiber mats against *S. epidermidis* was decreased, however the antibacterial activity remained until 50 weeks of storage time. This stability test was useful information to develop antibacterial wound dressing by incorporation of natural products in electrospun fibers.

Introduction:

The characteristics of a wound dressing product should be as follows; able to absorb exudates from the wound surface, retain moisture at the joints between the wound and the dressing material, the air can pass well, non-toxic, good tear resistant to use in both wet and dry conditions, sterilizable and prevent wounds from infection due to bacterial insertion.[1] Infection and microbial growth are important factors for slow healing wound, so antimicrobial wound dressings has been designed and developed. The incorporation of antiseptic drugs into the wound dressing is the one important design to control infection and support wound healing. In commercial, the antiseptic drugs such as iodine, Polyhexamethylene biguanide, boric acid, silver were applied on dressing and released continuously to the surface of the wound.[2-4]

Many forms of antibacterial wound dressing used in commercial such as film, foam, sheet, hydrogel etc. The ultra-fine fiber non-woven mats, fabricated from electrospinning process, is the one form interested for wound dressing fabrication. In this process, polymer solution or melt is ejected through a nozzle by the application of high electric field to deposit randomly of ultra-fine fibers on a ground collector as a non-woven mats. These mats exhibit high surface area to mass or volume ratio, high porosity, caused good permeability of

blood and air, and also fast healing the wound. Cellulose acetate (CA), one of biopolymer, was electrospun to develop fiber mats as carriers for transdermal delivery of drugs or natural products for using in biomedical applications.[5-7]

Many natural products have been studied for antibacterial activity. Indian gooseberry (*Phyllanthus emblica* Linn.), or Makhampom in Thai are widely used as Thai traditional medicine for antipyretic, diuretic, cough suppressants, laxative, antidiarrhoeic, antiscorbutic agents, and also antimicrobial.[8] Phenolic compounds, ascorbic acid and gallic acid were found from the analysis of Indian gooseberry (IG). This Thai medicinal plant show good antimicrobial activity by disc diffusion and agar dilution methods against *Staphylococcus aureus (S. aureus)*.[9] The antibacterial activity of IG on the wounds was also studies by mixing in a cream and treat on the wound of mice and testing against *S. aureus*, *Pseudomonas aeruginosa (P. aeruginosa)* and *Streptococcus pyogenes (S. pyogenes)*, it can reduce bacterial infection and heal the wound.[10]

In the present contribution, Indian gooseberry crude extract (IGCE) were incorporated with the neat CA solution in the amount of 50 wt.% to electrospin fibers. This amount showed the highest antibacterial activity in our previous research work[11], in which IGCE were varied from 10 to 50 wt.% and mixed well with CA solution. The size and morphological appearance of electrospun fibers were investigated by using Scanning electron microscopy (SEM). Antibacterial activity with the agar disc diffusion method was studied against *S. aureus* and *S. epidermidis*. The stability of IGCE in the electrospun CA fiber mats as a function of storage time was investigated in order to get useful information for the development of natural product antibacterial wound dressing, 3 types of commercial antibacterial wound dressings (i.e. Acticoat, Aquacel and Tegaderm) loaded with silver (Ag) were chosen for comparison the stability. These products were kept in the desiccator at ambient temperature approximately 1 year and antibacterial activity was tested every 2-4 weeks.

Methodology:

Materials

Cellulose acetate (CA; white powder; $M_w \approx 30{,}000$ Da; acetyl content = 39.8 wt.%; degree of acetyl substitution = 2.4) was purchased from Sigma-Aldrich (USA). Ethyl alcohol, acetone and dimethyl acetamide from Labscan Asia (Thailand) were of analytical reagent grade and used without further purification.

Preparation of Indian Gooseberry crude extract (IGCE)

Fresh fruits of Indian Gooseberry (IG) were washed and cleaned, dried in an oven at 40-50°C, and then 95% ethyl alcohol was added to the dried IG in the ratio of ethyl alcohol: IG equal to 4:1. The mixture was heated at the temperature of 70°C for 5 h, filtered the solution, and then evaporated the solvent by using rotary evaporator (Buchi Labortechnik AG, Flawil, Switzerland) at the temperature of 40°C, pressure of 337 mbar and the speed of 60 rpm.

Preparation of neat and IGCE-loaded CA fiber mats

A weighed amount of CA powder was dissolved in 2:1 v/v acetone/dimethyl acetamide (DMAC) to prepare the CA solution at a fixed concentration of 16% w/v, in which the smooth fibers were obtained from this condition in the previous work.[12] IGCE-containing CA solutions were prepared by dissolving the same amount of CA powder and IGCE in the amount of 50 wt.% based on the weight of CA powder in the acetone/DMAC mixture. Prior to electrospinning, the as-prepared solutions were measured for their viscosity and conductivity using a Brookfield LVDV-II+Pro viscometer and Proline QIS conductivity meter, respectively. The measurements were carried out in triplicate.

The as-prepared solutions were then electrospun under a fixed electric field of 20 kV/15 cm by connecting the emitting electrode of positive polarity from a Gamma High-Voltage Research ES30P high voltage DC power supply to the solutions in a 10-ml syringe. The gauge-20 stainless steel needle used as the nozzle, and

the grounding electrode to a rotating drum (diameter and width ≈ 15 cm), used as the fiber-collecting device. The solutions were controlled feeding rate by a syringe pump (NE1000 Quality In Sensing (QIS) Company Limited, Netherlands). The electrospun fiber mats were continuously collected for 12 h.

Morphological appearance of neat and IGCE -loaded CA fiber mats

Morphological appearance of both the neat and the IGCE-loaded electrospun CA fiber mats was observed by a JEOL JSM-6400 scanning electron microscope (SEM). Each specimen was coated with a thin layer of gold for SEM observation. Diameter of electrospun fibers were measured from SEM images using SemAfore 4.0 software, with the average values being calculated from at least 100 measurements.

Antibacterial activity of IGCE-loaded CA fiber mats

The agar disc diffusion method was chosen for the antibacterial activity studies of IGCE-loaded CA fiber mats. The strains of human dermal-pathogenic bacteria used were *Staphylococcus aureus* (*S. aureus*) ATCC 25923 and *Staphylococcus epidermidis* (*S. epidermidis*) ATCC 12228.

The study was done by preparing samples with a diameter of 1 cm and sterilized by UV radiation for 2 h. Each bacteria strain was prepared by culturing in LB broth, incubate at 37°C for 1 night. Then, 2 ml of 0.85% sodium chloride was added and compare the turbidity with MacFarland standard No. 0.5. After that, 50 ml of cultured bacteria was added into Mueller-Hinton broth 2 ml, then dipped in a cotton swab, spread on the Mueller-Hinton agar all over the petri dish and left until dry. The prepared fiber mat samples were placed onto the Mueller-Hinton agar that contained the bacteria. The plate was incubated at 37°C for 1 night. The antibacterial activities were evaluated by diameter of inhibition zone.

Stability test of IGCE-loaded CA fiber mats

Stability of IGCE-loaded CA fiber mats as a function of storage time was investigated via antibacterial activity with agar disc diffusion method.[13] The specimens were cut into disc with 1 cm in diameter and stored in desiccator at ambient temperature, with the storage time of 50 weeks. The specimens were tested the antibacterial activity every 2-4 weeks. The commercial antibacterial wound dressings loaded with silver (Ag) were selected to compare the stability via antibacterial activity with IGCE-loaded CA fiber mats. These wound dressings were Acticoat (Smith&nephew, USA), Aquacel (ConvaTec, British), Tegaderm (3M, USA).

Results and Discussion:

Electrospinning of neat and IGCE-loaded CA fiber mats

The solutions of neat CA 16% w/v in 2:1 v/v acetone/DMAC and CA solution mixed with 50 wt.% IGCE were measured their viscosity and conductivity, as summarized in Table 1. The presence of IGCE 50 wt.% in the base CA solution increased more substance in the solutions, resulted the increasing of solution viscosity and conductivity. These solutions were electrospun at a fixed electric field of 20 kV/15 cm. The collection time of electrospun fiber mats was 12 h with the thickness of 35±5 mm. The color of neat CA fiber mats was white, while IGCE-loaded CA fiber mats was light brown resulting from the dark brown colored of natural product crude extracted.

Table 1.

Viscosity and conductivity of neat and IGCE-containing CA solutions as well as diameters of the electrospun fibers.

Type of CA solution	Viscosity (cP)	Conductivity ($\mu S\ cm^{-1}$)	Fiber diameters (nm)
Neat	558 ± 1.0	7.85 ± 0.06	368 ± 81
With 50 wt.% IGCE	768 ± 1.0	103.6 ± 0.02	509 ± 132

Morphological appearance of neat and IGCE-loaded CA fiber mats

Selected SEM images of the neat and 50 wt.% IGCE-loaded CA electrospun fiber mats are shown in Figure 1. The IGCE mixed well with the solution of CA, no presence of crude extracted aggregation was observed on the surface of the fibers. The fibers have a smooth surface with irregular size, however, the smooth surface of the obtained nonwoven mat was observed with the naked eye. Obviously, the fiber size of IGCE-loaded was larger than the neat CA. From measurement diameter of fiber using SemAfore 4.0 software, shown in Table 1., the average fiber diameter of neat CA was 368 ± 81 nm and was 509 ± 132 nm of the 50 wt.% IGCE-loaded electrospun CA fiber mats.

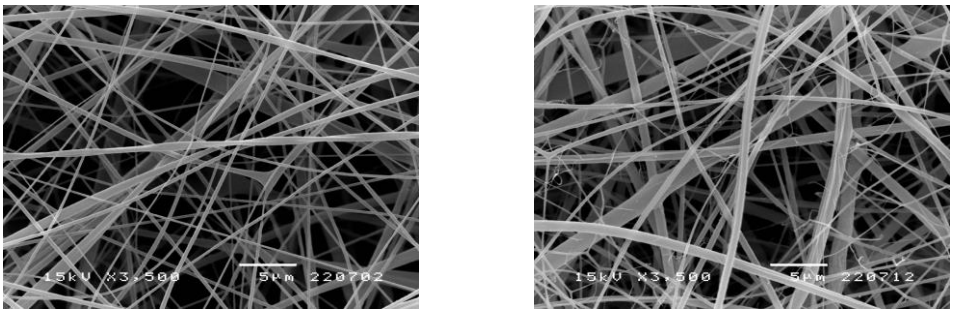

(a) (b)

Figure 1.

Selected scanning electron micrographs of (a) neat and

(b) 50 wt.% IGCE-loaded electrospun CA fiber mats.

The observed increase in the diameters of IGCE-loaded CA fibers in comparison with the neat ones should be a result of the greater viscosity and conductivity of natural product-containing CA solutions.[5-7]

Antibacterial activity of IGCE-loaded CA fiber mats

IG showed good antibacterial activity against wound pathogens such as *S. aureus*, *P. aeruginosa*, and *S. pyogenes*.[8,14] In this research, the neat CA and IGCE-loaded CA fiber mats were evaluated antibacterial activity with agar disc diffusion method against *S. aureus* and *S. epidermidis.* The inhibition zone diameter was shown in Table 2. It was found that the antibacterial activity of the neat CA electrospun fiber mats was not observed, but when IGCE was incorporated into electrospun CA fiber mats, shown good antibacterial activity indicated from clearly inhibition zone. Specifically, antibacterial activity of IGCE-loaded CA fiber mats against *S. epidermidis* was greater than *S. aureus* with the inhibition zone diameter of 1.9 and 1.7, respectively.

Table 2.

Antibacterial activity of neat and 50 wt.% IGCE-loaded electrospun CA fiber mats in terms of disc diffusion method reported as inhibition zone diameter.

Type of CA fiber mat	Inhibition zone diameter/Sample diameter(cm)	
	S. aureus	***S. epidermidis***
Neat	n/a[a]	n/a
With 50 wt.% IGCE	1.7/1.0	1.9/1.0

[a]no inhibition zone observed

Stability test of IGCE-loaded CA fiber mats

Stability of IGCE-loaded CA fiber mats was investigated by antibacterial activity with agar disc diffusion method. For comparison with natural product-containing fiber mats, 3 types of Ag-containing antibacterial wound dressings in commercial were selected as standard, i. e. Acticoat, Aquacel, and Tegaderm. The appearance and scanning electron micrographs of IGCE-loaded CA fiber mats and those Ag-containing antibacterial wound dressings in commercial were shown in Table 3. 3 types of commercial antibacterial dressing exhibited different appearance and structure, Acticoat has 2 layers of fiber mats, in which the top layer fiber mat with black color is the Ag-coated polyethylene, Aquacel is the ultrafine fiber nonwoven mats of sodium carboxymethylcellulose loaded with Ag ion, and Tegaderm is nonwoven mats loaded with silver sulfate.

The stability test was studied as a function of storage time, the specimens were stored at ambient temperature with the storage time of 50 weeks, then, the specimens were tested the antibacterial activity every 2-4 weeks. From the results shown in Table 2, the great antibacterial activity of IGCE-loaded CA fiber mat observed against *S. epidermidis* pathogen. Thus, the stability of IGCE-loaded electrospun CA fiber mat and 3 commercial Ag-containing antibacterial wound dressings was investigated via antibacterial activity against *S. epidermidis* in terms of disc diffusion method, the resulting as shown in Table 4.

After the storing specimens and evaluated antibacterial activity every 4 weeks, 3 commercial antibacterial wound dressings used as the standards exhibited great antibacterial activity against *S. epidermidis* with no significant changing in 50 weeks of storage time. Additionally, with the storage time of 24 weeks or 6 months, the 50 wt. % IGCE-loaded electrospun CA fiber mats showed great antibacterial activity in equal inhibition zone diameter to those commercial dressings (i.e. in the range of 1.7 – 2.0 cm), the inhibition zone characteristic shown in Figure 2.

After a half of year or 30 weeks, with longer storage time of specimens, the antibacterial activity of IGCE-loaded CA fiber mats was decreased with the inhibition zone diameter from 1.7 to 1.3 cm and then no significant changing until 50 weeks of storage time. However, the stable of natural product in IGCE-loaded electrospun CA fiber mat remained the antibacterial activity for 50 weeks or approximately 1-year storage time.

Table 3.

The appearance and selected scanning electron micrographs of IGCE-loaded CA fiber mats (x200) and Ag-containing antibacterial wound dressings in commercial

i.e., Acticoat, Aquacel and Tegaderm (x30).

Type of samples	Appearance	SEM image
50 wt.% IGCE-loaded CA fiber mats		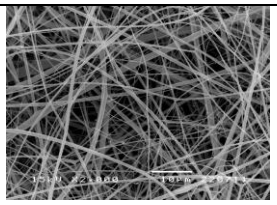
Acticoat		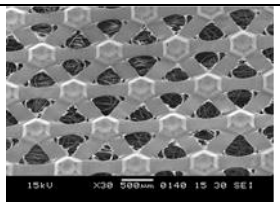
Aquacel	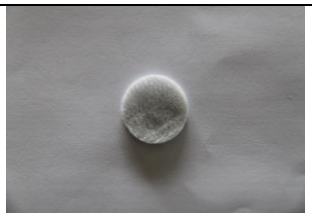	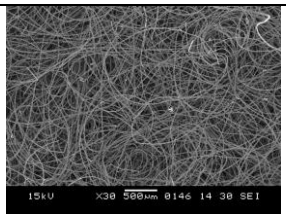
Tegaderm	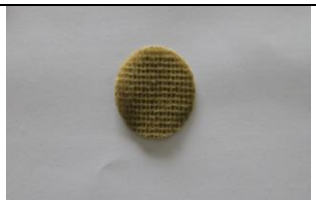	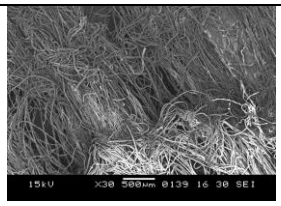

Table 4.

Antibacterial activity of 50 wt.% IGCE-loaded electrospun CA fiber mats and 3 commercial antibacterial wound dressings in terms of disc diffusion method reported as inhibition zone diameter against *S. epidermidis*.

Storage times (weeks)	Inhibition zone diameter (cm)[a]			
	IGCE-loaded CA fiber mats	Commercial antibacterial wound dressing		
		Acticoat	Aquacel	Tegaderm
4	2.0	2.0	1.8	1.8
8	1.7	1.7	1.9	2.2
12	1.8	2.0	2.0	2.2
16	1.8	2.1	2.2	1.8
20	1.5	1.8	1.9	1.7
24	1.7	1.7	1.6	1.9
30	1.3	1.8	1.7	1.9
34	1.4	1.7	1.9	2.0
38	1.3	2.1	1.8	1.8
42	1.3	2.0	2.2	1.8
46	1.2	1.9	1.9	1.9
50	1.2	1.8	1.8	1.8

[a]the diameter of disc sample = 1.00 cm

Acticoat

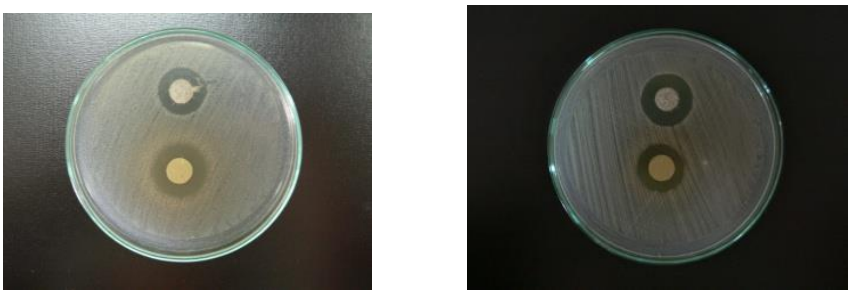

Aquacel

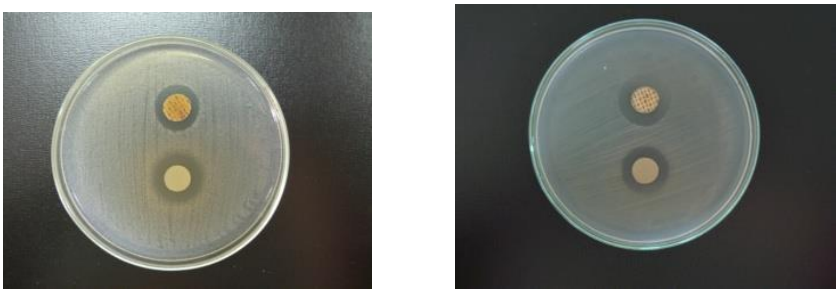

Tegaderm

(a) (b)

Figure 2.

The inhibition zone characteristic of 3 commercial antibacterial wound dressings (upper) and 50 wt.% IGCE-loaded electrospun CA fiber mats (lower) against *S. epidermidis* in (a) 4 weeks and (b) 24 weeks.

Conclusion:

In the present contribution, Indian gooseberry crude extract (IGCE) was added to the neat cellulose acetate (CA) solution (16% w/v in 2:1 v/v acetone/ dimethylacetamide) 50 wt.% based on the weight of CA powder. The as-prepared solutions of neat CA and IGCE-loaded CA were then fabricated into ultra-fine fibers via electrospinning at a fixed electric field of 20 kV/15 cm. The morphological appearance of electrospun fiber was observed with smooth fibers, no presence of crude extracted aggregation on the fiber surface. The fiber size of IGCE-loaded CA was larger than the neat CA. The neat CA and 50 wt.% IGCE-loaded CA fiber mats were evaluated

antibacterial activity with agar disc diffusion method against *S. aureus* and *S. epidermidis.* The antibacterial activity of IGCE-loaded CA fiber mats against *S. epidermidis* was greater than *S. aureus*. For the potential of IGCE-loaded electrospun CA fiber mats used as antibacterial wound dressing patch, the stability of this fiber mat as a function of storage time was studies via antibacterial activity against *S. epidermidis*. 3 types of Ag-containing antibacterial wound dressings in commercial were selected for comparison, i.e. Acticoat, Aquacel, and Tegaderm. With the storage time of specimens in 24 weeks, the 50 wt.% IGCE-loaded electrospun CA fiber mat showed great antibacterial activity in equal to those commercial dressings. But after 30 weeks, the antibacterial activity of IGCE-loaded CA fiber mat was decreased, in which commercial antibacterial wound dressings exhibited great antibacterial activity with no significant changing in 50 weeks. However, the stable of natural product in IGCE-loaded electrospun CA fiber mat remained the antibacterial activity for 50 weeks or approximately 1 year of storage time.

Acknowledgements:

The authors acknowledge financial support received from Ramkhamhaeng University.

References:

1. Stashak TS, Farstvedt E, Othic A. Clin Tech Equine Pract. 2004;148-163.
2. Innes ME, Umraw N, Fish JS, Gomez M, Cartotto RC. Burns. 2001;27:621-627.
3. Ovington LG. Clin Dermatol. 2007;25:33-38.
4. Rivera AE, Spencer JM. Clin Dermatol. 2007;25:39-48.
5. Tungprapa S, Jangchud I, Suphapol P. Polymer. 2007;48:5030-5041.
6. Suwantong O, Ruktanonchai U, Suphapol P. Polymer. 2008;49:4239-4247.
7. Taepaiboon P, Rungsardthong U, Suphapol P. Eur J Pharm Biopharma. 2007;67:387-397.
8. Mohamed AS. Biocatal Agric Biotechnol. 2019;17:529-537.
9. Mayachiew P and Devahastin S. LWT-Food Sci Technol. 2008;41(7):1153-1159.
10. Kumar MS, Kirubanandan S, Sripriya R, and Sehgal PK. J Surg Res. 2008;144(1):94-101.
11. Meechaisue C, Wetprasit N, Atikankun S, and Supaphol P. Ramkhamhaeng Research Journal Sciences and Technology. 2010; 13(2): 18-28.
12. Tungprapa S, Puangparn T., Weerasombat M, Jangchud I, Fakum P, Semongkhol S, Meechaisue C, and Supaphol P. Cellulose. 2007;14: 563-575.
13. Puttarak P, Charoonratana T, Panichayupakaranant P. Phytomedicine. 2010;17:323-327
14. Muthusamy SK, Shanmugam K, Ramasamy S, Praveen KS. J Surg Res. 2008;144(1):94-101.

E_019_PA: BIOGEL BEVERAGE PROCESSING FROM ALGAL EXTRACTION

Kangsadan Boonprab,* Onrumpa Jaikuma, Worapot Chanchuen

Fishery products Departments, Fisheries Faculty, Kasetsart University, Bangkok, 10900 Thailand
*e-mail: ffisksb@ku.ac.th

Abstract:

This work was aimed to improve biogel beverage processing for edible packaging containing drinking water or other beverage from algal extraction, alginate by using spherification technique as forming process. The results showed that among 4 treatments [Sodium alginate (g): drinking water (ml) as 2.5:250; 2.0:250; 1.0:250 and 0.9:250], the best proportion for the processing was 0.9:250, since it showed the highest amount of water inside biogel. The proper time for forming process with the high stability form and shape of biogel were 10 min and spherical shape, respectively. Coating for one layer of biogel with spherical shape obtained higher organoleptic test by 9-hedonic scale than two layer coating. It was selected for appropriated processing condition. Factors influenced on biogel characters were carried out. Temperature at 4°C and room temperature (30-35°C) effected on biogel shape stability greater than at 50°C and 100°C. Time for biogel stability was varied to temperature. Various solvents [Sodium chloride (1, 5, 10 and 20 %), sugar (1 ,5 ,10 and 20 %), water, oil and ethanol (1, 5, 10 and 20 %)] that effected on shape stability, color of beverage in biogel and floating on such solvents of biogel were varied to type, concentration, soaking time of solvents (0, 1, 2 and 4 h). Stability of biogel shape and color of beverage in biogel obtained the highest to lowest characters in solvents were (1) vegetable oil at 0, 1, 2 and 4 h, (2) sugar at all concentrations at 0 and 1 h and, (3) ethanol (1%), Sodium chloride (1 and 5%) and distilled water at 0 and 1 h. The accelerated permeability rate of water into biogel [Swelling (%)] was 0-15 min before stopping its permeability to show constant rate at 15 to 60 min. Characteristic of biogel beverage were carried out. The best shape was spherical shape (3.20 ± 0.1 cm wide or high; n=3 and 3.43 ± 0.1 cm long; n=3). Another characters were hardness [Mean (g) ± SD; n=-3], Aw [Mean ± SD; n=-3], thickness [Mean (mm) ± SD; n=-3] and weight [Mean (g) ± SD; n=-3] as 23.79±1.5, 0.9954±0.0, 2.53±2.5 and 12.35±0.3, respectively. Total viable bacteria counts (CFU/g) and *Escherichia coli* (MPN/g) of biogel were <10 est. and < 30, respectively. This suggested food safety of the product was shown. Shelf life with shape stability and microbiology investigation at 4 °C and room temperature was at least 30 day and at least 1 day, respectively. Cost of biogel without labor, machine and others was 1.15 Baht per 100 ml. From the whole results, the products and model line processing were proposed in the report.

Figure 1. The spherical shape of biogel beverage product from algal extraction (3.20 ± 0.1 cm wide or high; n=3 and 3.43 ± 0.1 cm long; n=3)

E_020_PF: APPLICATION OF VERTICAL LIGHT TUBE INTEGRATING WITH ROOF FOR ENERGY CONSUMPTION REDUCTION IN BUILDINGS

Jiraphorn Mahawan, Kriangsak Promphak[1], Sant Chansomsak[2] and Atthakorn Thongtha[1]*

[1]Department of Physics, Faculty of Science, Naresuan University, Phitsanulok, 65000, Thailand
[2]Department of Architecture, Faculty of Architecture, Naresuan University, Phitsanulok, 65000, Thailand
*e-mail: atthakornt@nu.ac.th

Abstract:

This work investigates the illuminance performance of vertical light tube that was made from the zinc alloy and aluminum alloy for improving an illuminance in buildings and reducing a demand of electrical energy from an artificial light. The light tube was designed by using the diameters of 0.20 m, 0.25 m and 0.30 m and fixed the tube length of 1 m to test the illuminance within the testing room size of wide 1 m x length 1 m x height 1 m. The performance of light tube was tested at the incident angles of 0°, 10°, 20°, 30°, 40°, 50°, 60°, 70°, 80° by using the artificial lamp (20 W LED) as the light source. It was found that the angle of light incidence and material types had an influence on the illuminance of light tube. The average illuminance performance of zinc alloy tube increased from 28% to 52 % and that of aluminum alloy tube increased from 41 % to 70 % when the controlled incidence angle to the tube increased from 0° to 80°. At the same diameter of light tube, the illuminance performance of aluminum alloy tube is higher than that of zinc alloy tube in each angle of light incidence. This implies to a reduction of power consumption because of illuminance and save energy from lighting electricity consumption in buildings.

Introduction:

A high level of solar radiation is experienced throughout most of the country throughout the year in Thailand. The highest levels of solar radiation are experienced in the months of April and May, measured between 20 and 24 MJ/m^2-day and the daily average value of the solar radiation in a full year is around 18.2 MJ/m^2-day [1-3]. These conditions lead to the significant thermal accumulation in buildings. Therefore, energy consumption in buildings is due mainly to the air conditioning system and lighting has been increasing day by day due to the development of modern society and improving the quality of life for people. Residential and commercial buildings account for almost one third of the total electricity consumption [4,5]. Nowadays, buildings are properly constructed and designed to provide their occupants for a better environment quality and consume less energy in buildings [4,5]. Day lighting incorporation in buildings improves the quality of the indoor lighting environment and is also responsible for reduced lighting energy consumption [6-9].

Using light-pipes are one of the methods to carry the daylight into the buildings [10,11]. Commercial version of the light-pipes on the market can be defined as a light tube allowing illumination in the area parts of buildings which do not receive enough daylight. Light-pipe systems may be straight or have bends. Light-pipes are used not only to transfer the daylight but also artificial lighting [12]. Moreover, areas away from the windows can be illuminated with natural light during the daytime by using light-pipes.

A light-pipe system is made up of three parts. The first part is the dome collecting the diffuse and direct light and transferring into the light-pipe [13]. The dome is produced from transparent polycarbonate material, designed to remove the undesired UV light. This dome shape prevents snow, dust and rain from penetrating

into the tube. The second part is made up of one or more light tubes connected to each other to transfer the collected daylight. The daylight collected by the dome reflects and reaches to the diffuser placed on the ceiling of the room. Diffuser, making up the last part of the light-pipe system, is generally produced from white polycarbonate material. It allows the daylight coming from the light-pipes to be diffused into the room [14].

Jenkins and Muneer [15-17] discussed numerous design models/methods to use in predicting light levels in light tubes, in other words, a tool to quantify the best configuration for light tubes in any given situation. Garcia-Hansen et al. [18] outlined the possible energy savings and greater efficiency obtained through the use of top-lighting systems (skylights, roof monitors and clerestory roof windows) in cold areas of the typically template climate of Argentina. The results indicate that heating, ventilation and lighting costs can be significantly reduced through the implementation of these passive solar systems. Rosemann et al. [19] designed to use materials and components that can be cost-effective in volume manufacturing. This project is in the early stages of development, and subsequent research is currently underway to verify this cost-effectiveness and demonstrate the additional energy-saving benefits. Darula et al. [20] feel that straight light tubes offer a unique opportunity for carrying natural light to the farthest corners of a room even in spaces with no windows. Wong and Yang [21] demonstrated that light pipe system can work in both clear and overcast sky conditions. However, there are limiting factors that affect the performance of it such as orientation, solar azimuth angle and angle of incident light. Gago et al. [22] reviewed natural light controls and guides in buildings. The control and/or natural light guidance systems and/or strategies guarantee the penetration of daylight into the building reduced the electrical energy consumption for lighting and cooling and improved the thermal and visual comfort of the users of the buildings.

In this study, the optimization and experimental evaluation of light tubes was focused on the light tube invention with different materials to study more illuminance through light pipe. The illuminance effectiveness of light tube with different dimeters was also tested and compared with the testing room of 1 m wide x 1 m length x 1 m height.

Methodology:

A testing room was built 1 m^3 in volume, has 6 sides (each composed of walls with an area of 1 m^2). The room was constructed using wooden wall. The top frame side of the testing room wall was designed as the circle hole to fit and integrate with the light tube as shown in Figure 1. The light tubes with the fixed length of 1 m and the diameter of 0.20 m, 0.25 m and 0.30 m were built to test the illuminance performance. The aluminium alloy tube and zinc alloy tube were considered to build the light tube. The light source as an artificial LED lamp was set up to test the illuminance of light tube at the incident angle of 0, 10°, 20°, 30°, 40°, 50°, 60°, 70°, 80°. The performance of light tube was calculated from the brightness at the top and bottom end positions of light tube. An illuminance lux meter (DIGICON LX-70) was placed on the five positions at the top and bottom end locations inside light tube to measure the illuminance as displayed in Figure 1.

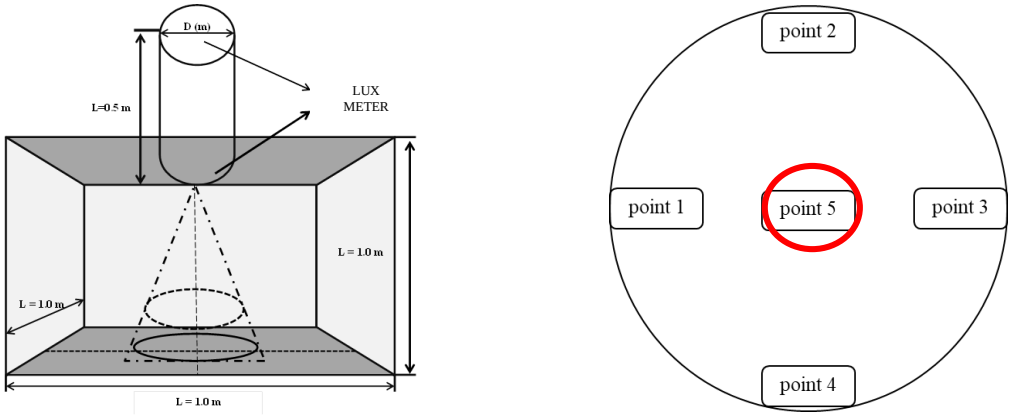

Figure 1.

View of the testing room (left) and five fixed positions of brightness measurement inside the light tube (right)

Results and Discussion:

The illuminance of aluminum alloy tube with the diameters of 0.20 m, 0.25 m and 0.30 m and a same height of 1 m at various incident angles of light source is displayed in Figure 2. When the incident light angle to the tube was varied, the change of illuminous intensity at the top and bottom end positions of tube was achievement. At the top end position of tube, the illuminous intensity increased from 101 lux to 3193 lux. At the bottom end position of tube, the illuminous intensity increased from 38 lux to 2008 lux when the incident light angle to the tube increased from 0° to 80°, as displayed in Figure 2 (a). For the diameters of 0.25 m and 0.30 m, the trend of the illuminance at the top and bottom end positions of tube was similar to that of the tube with a 0.20 m diameter, as exhibited in Figure 2 (b) and (c). With considering the aluminum alloy tube at diameter of 0.25 m, the illuminous intensity increased from 61 lux to 3149 lux at the top end position of tube and from 30 lux to 2683 lux at the bottom end position of tube with an increase of the incident light angle to the light tube between 0° and 80°, as illustrated in Figure 2 (b). For the aluminum alloy tube with a diameter of 0.30 m, the illuminous intensity increased from 69 lux to 3831 lux at the top end position of tube and from 31 lux to 2683 lux at the bottom end position of tube when there was an increase of the incident light angle to the light tube from 0° to 80°, as illustrated in Figure 2 (c).

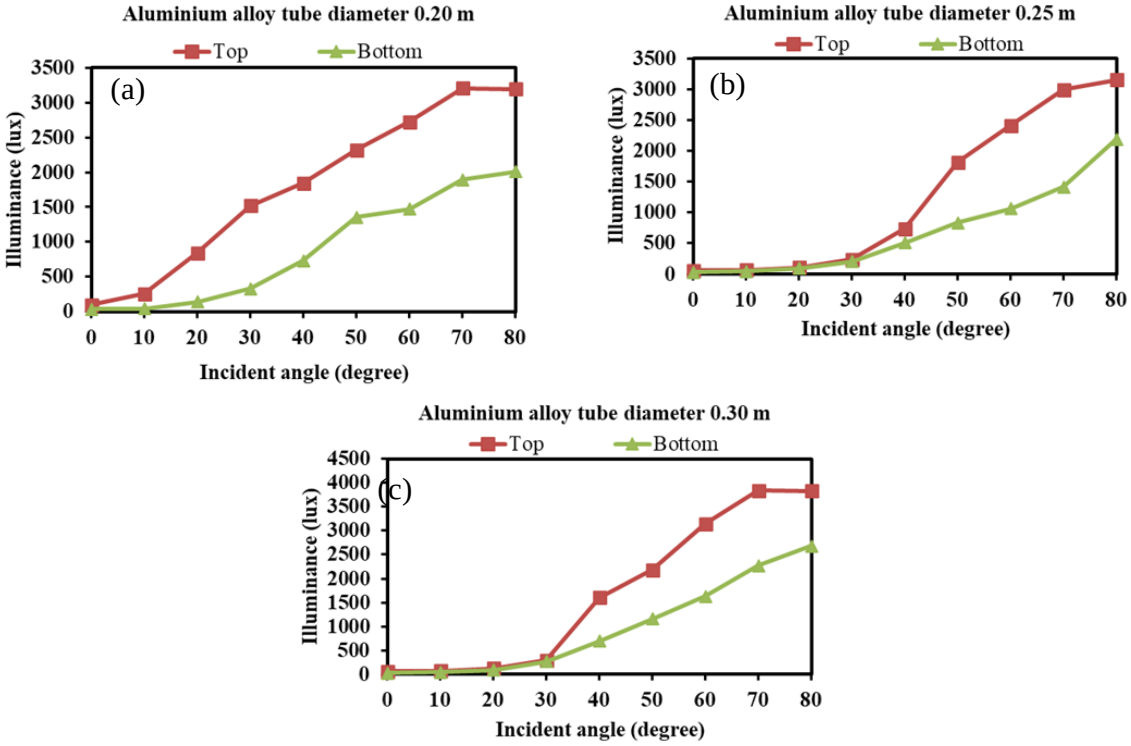

Figure 2.

Average illuminance at the top and bottom end positions of aluminum alloy tube with the diameter of a) 0.20 m, b) 0.25 m and c) 0.30 m.

The illuminance of zinc alloy tube with a different diameters and a height of 1 m at various incident angles of light source is exhibited in Figure 3. A variation of incident light angle to the tube led to the change of illuminous intensity at the top and bottom end positions of zinc alloy tube. The trend of the illuminance of zinc alloy tube with the diameters of 0.20 m, 0.25 m and 0.30 m the at the top and bottom end positions was similar to that of the aluminum alloy tube, as exhibited in Figure 3. At the top end position of zinc alloy light tube, the illuminance intensity increased from 353 lux to 2650 lux for 0.20 m, from 53 lux to 3251 lux for 0.25 m and from 66 lux to 3651 lux for 0.30 m, respectively, with an increase of the incident light angle to the light tube between 0° and 80°. At the bottom end position of zinc alloy light tube, the illuminance intensity increased from 33 lux and 1686 lux for 0.20 m, from 25 lux to 1847 lux for 0.25 m and from 29 lux to 2500 lux for 0.30 m, respectively, when there was an increase of the incident light angle to the light tube from 0° to 80°. This demonstrates an illuminous intensity at the top and bottom end positions of vertical light tube of both aluminum alloy and zinc alloy types increased when an increase in incident angle of light source. At the low incident angles of light source into light tube, an illuminance intensity of light tube was distinctly a result of the light reflection within light tube. With the higher incident angles of light source into light tube, the illuminance of the light tube was a result of the superposition between light reflection within the light tube and directly transmitted light through light tube as well. All of the values was bring to calculate the illuminance performance of the aluminum alloy tube and zinc alloy tube.

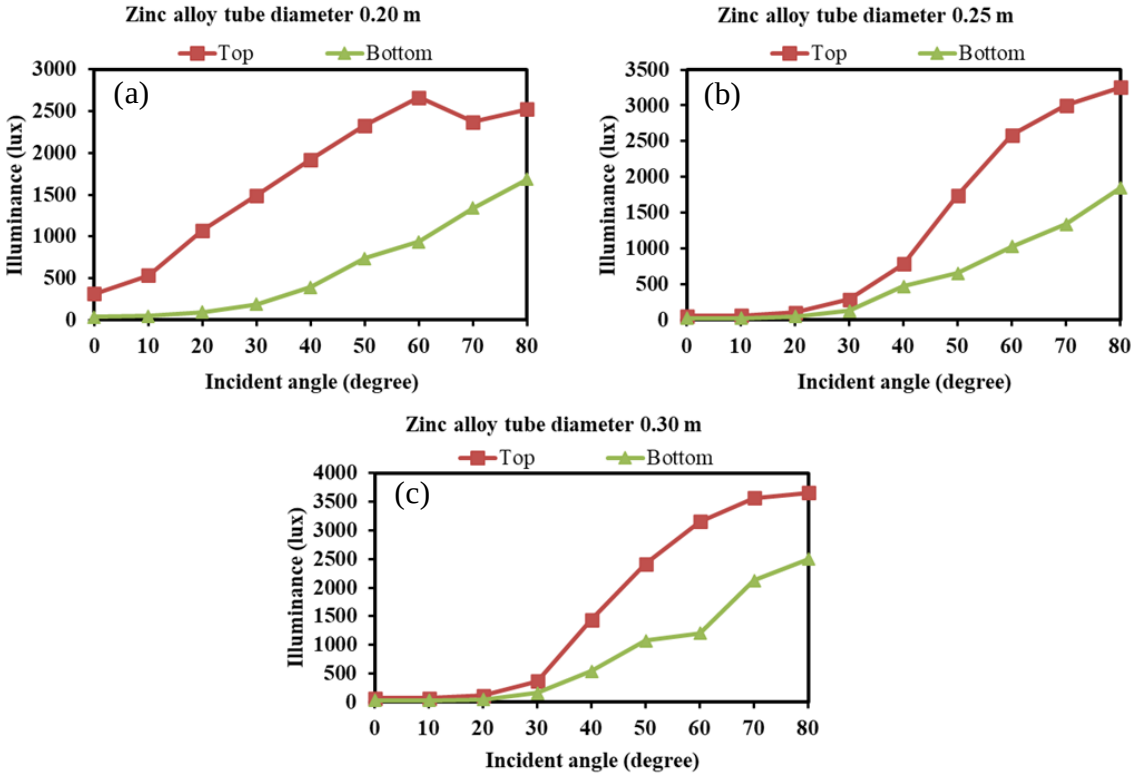

Figure 3.

Average illuminance at the top and bottom hollow position of zinc alloy tube with the diameter of a) 0.20m, b) 0.25m and c) 0.30m.

With considering the bottom end location of tube with different materials, an increase of average illuminance of both aluminum alloy tube and zinc alloy tube having a 0.20 m in diameter was appeared when there was an increase of incident light angle into the light tube as illustrated in Figure 4 (a). For the diameter of 0.25 m and 0.30 m, average illuminance of the aluminum alloy tube and zinc alloy tube was similar to that of light tube with a 0.20 m in diameter as shown in Figure 4 (b) and (c). With comparing the illuminance of aluminum alloy tube and zinc alloy tube at the bottom tube end, it was observed that the average illuminance of aluminum alloy tube in all diameters was higher than that of zinc alloy tube in each incident light angle as exhibited in Figure 5. This demonstrates more illuminance at the bottom tube end of aluminum alloy tube than that of zinc alloy tube.

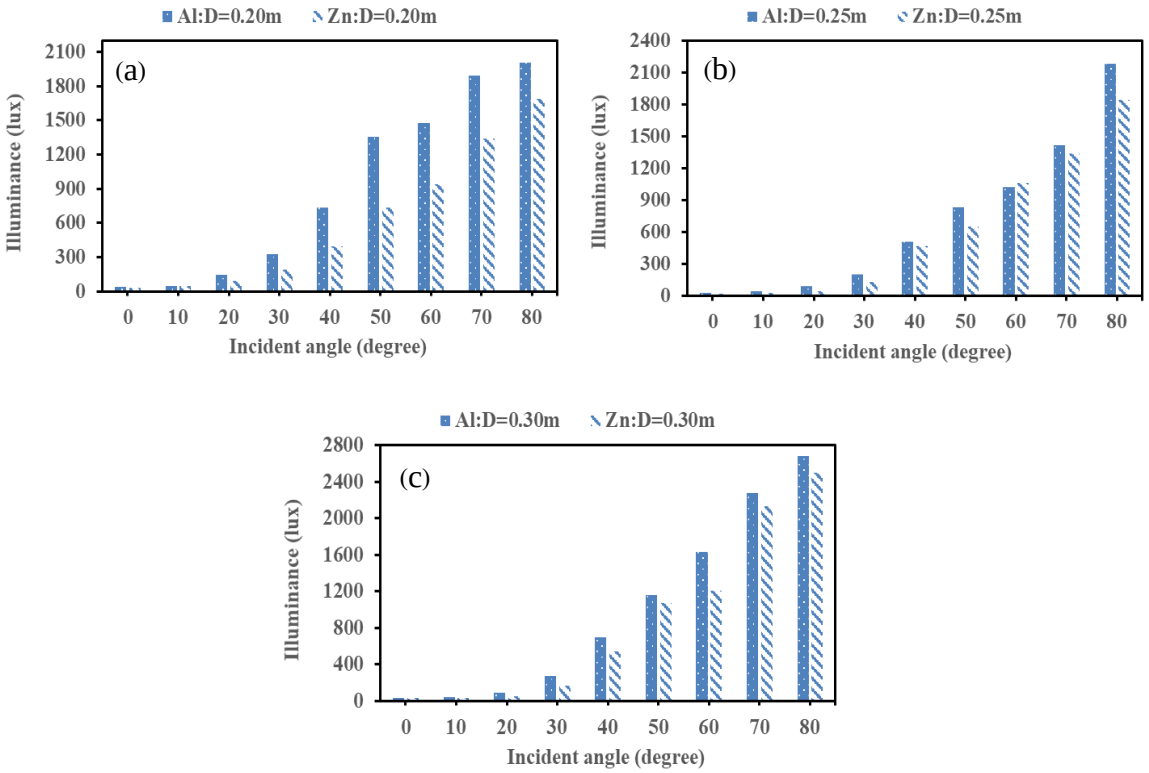

Figure 4.

Average illuminance at the bottom tube end position of aluminum alloy tube and zinc alloy tube with the diameters of a) 0.20m, b) 0.25m and c) 0.30m.

To investigate the illuminance performance of aluminum alloy tube and zinc alloy tube with different diameters, the average illuminance at the top and bottom tube end positions was calculated to obtain the illuminance performance of light tube as exhibited in Figure 5 and 6. The reflection efficiency of the aluminum alloy tube with the diameter of 0.20 m was between 19% and 60%, that of 0.25 m was between 42% and 88%, and that of 0.30 m was between 42% and 89%, respectively, as illustrated in Figure 5. The reflection efficiency of the zinc alloy tube with the diameter of 0.20 m was between 10% and 62%, that of 0.25 m was between 40% and 58%, and that of 0.30 m was between 38% and 64%, respectively, as illustrated in Figure 6.

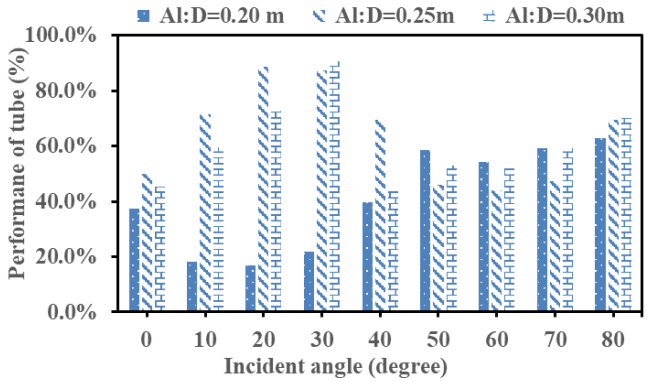

Figure 5.

Illuminance performance of Aluminum alloy tube.

At the same diameter of light tube, the values of illuminance performance in all incident light angle were calculated to determine the average illuminance performance of light tube at the diameter of 0.20 m, 0.25 m and 0.30 m. The average reflection efficiency of the aluminum alloy tube with the diameter of 0.20 m, 0.25 m and 0.30 m was at approximately 41%, 64% and 70% and that of the zinc alloy tube was at about 28%, 48% and 52%, respectively, as exhibited in Figure 5-7. With comparing the aluminum alloy tube and zinc alloy tube at a diameter of 0.20 m, 0.25 m and 0.30 m, average illuminance performance of aluminum alloy tube was higher than that of zinc alloy tube in each incident light angle as shown in Figure 7. This demonstrates that the aluminum alloy tube shows obviously more reflective efficiency than zinc alloy tube in each diameter size. This indicate that this technology could be considered as an alternative daylight system in the deeper parts of room or could substitute artificial lighting in the windowless spaces without requirements for visual tasks such as corridors, halls, vestibules, stores or public spaces with needs of natural lighting, which led to energy conservation in buildings.

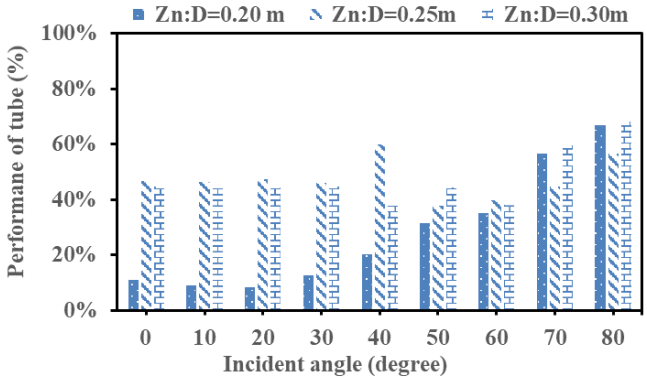

Figure 6.

Illuminance performance of Zinc alloy tube.

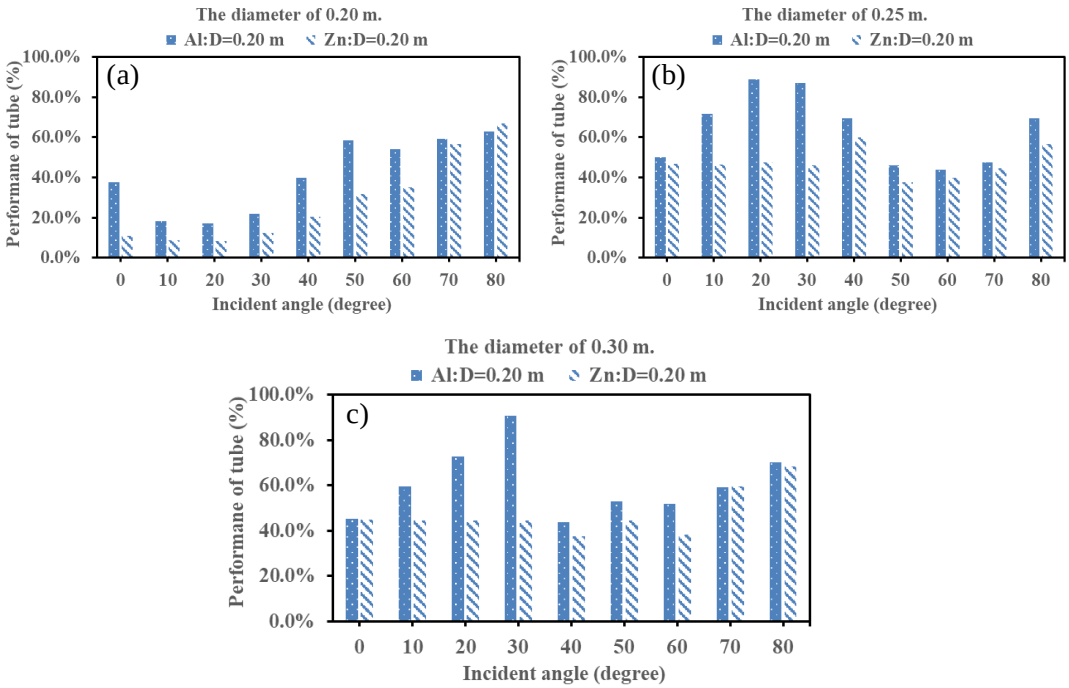

Figure 7.

Illuminance performance of light tube with the different materials and diameters a) 0.20 m, b) 0.25 m and c) 0.30 m.

Conclusions:

The vertical solar tubes of the aluminum alloy tube and the zinc alloy tube was successfully examined to consider illuminance performance. The illuminance at the top and bottom end positions of light tube in each pattern increased when there was an increase of the incident angle of light source. Functions of the incident angle and light tube diameters affected to the interior tube reflection performance. With the diameters of 0.20 m, 0.25 m and 0.30 m, average illuminance performance of zinc alloy tube was at approximately 41%, 64% and 70%, and that of the aluminum alloy tube was at approximately 28%, 48% and 52%. Aluminum alloy light tube had slightly more lighting efficiency than zinc alloy light tube. An installation of solar tube integrated into buildings is an alternative way which can improve the quality of the indoor lighting environment and is also responsible for save lighting energy consumption in buildings.

Acknowledgements:

The authors would like to thank the Thailand Research Fund (TRF), Faculty of Science, Naresuan University for providing financial support to this research work, and our research center.

References:

1. Khedari J, Sangprajak A, Hirunlabh, J. Renew Energy. 2001; 25:267-280.
2. Thongtha A, Khongthon A, Boonsri T, Chan HY. Materials. 2019; 12(13):2170.
3. Kunchornrat A, Namprakai P, Du Pont PT. Resources Conser. Recy. 2009; 53(10):545-551.
4. Yan T, Sun ZW, Gao JJ, Xu XH, Yu JH, Gang WJ. Renew Energy. 2020; 146:1451-1464.
5. Kim JT, Kim G. Build Environ. 2010; 45:256-269.
6. Chirarattananon S, Chaiwiwatworakul P, Pattanasethanon S. Renew Energy. 2002; 26(1):69-89.
7. Krarti M, Erickson PM, Hillman TC. Build. Environ. 2005; 40(6):747-754.
8. Li DHW, Lam TNT, Wong SL, Tsang EKW. Energy. 2008; 33:1288-1297.
9. Park KW, Athienitis AK. Solar Energy 2003; 75:277-284.
10. Lopin MK. Solar Energy. 2002; 73(2):77.
11. Ekren N, Gorgulu S. Energy Ed Sci Tech Part A: Energy Sci Res. 2012; 30(1):637-644.
12. Kim JT, Kim G. Build Environ. 2010; 45:256-269.
13. Jenkins D, Muneer T, Kubie J. Energy Build. 2005; 37(5):485-492.
14. Oakley G, Riffat SB, Shao L. Solar Energy. 2000; 69(2):89-98.
15. Jenkins D, Muneer T. Appl Energy. 2004; 79:77–86.
16. Jenkins D, Muneer T. Build Environ. 2003; 38: 965–972.
17. Jenkins D, Zhang X, Muneer T. Energy Convers Manag. 2005; 46:2288–300.
18. Garcia-Hansen V, Esteves A, Pattini A. Renew Energy. 2002; 26: 91–111.
19. A. Rosemann, M. Mossman, L. Whitehead, Solar Energy. 2008; 82:302–310
20. Darula S, Kocifaj M, Mohelníková J. Optik. 2013; 124:3165–3169.
21. Wong I,Yang HX. Appl Energy. 2012; 90: 225–232.
22. E.J. Gago, T. Muneer, M. Knez, H. Köster, Renewable and Sustainable Energy Reviews. 2015; 41:1–13.

E_021_OF: NUTRITION CARE PROCESS OF MULTIDISCIPLINARY CARE TEAM IN IN-PATIENT DEPARTMENT (IPD) PATIENTS

Tanu-udom Maneesing[1*], Pornpoj Pramyothin[3], Manussanun Pitisrisit[2], Kanicha Bumrungcheep[2], Anong Kumsem[2], Piyatida Cumnon[2], Chutimon Tiya-a-monlert[4], Kamonchanok Khasuwan[2], Nattiya Satapornpanich[2], Narudon Jampatong[2], Nanthipha Sirijindadirat[2], Chavit Uttamachai[5]

[1]Department of Nutrition Therapy and Dietetics, Faculty of Allied Health Science, Burapha University, Chonburi 20131, Thailand
[2]Nutrition Unit, Siriraj Piyamaharajkarun Hospital, Bangkok 10700, Thailand
[3]Division of Clinical Nutrition, Faculty of Medicine, Siriraj Hospital, Bangkok 10700, Thailand
[4]Ramkhamhaeng Hospital, Bangkok 77699, Thailand
[5]British Council, Bangkok 10330, Thailand
*e-mail: tanuudom.ma@go.buu.ac.th

Abstract:

Malnutrition in IPD patients usually occurs from inadequate or inappropriate energy and protein intake. Consulting a nutrition physician can mitigate this condition, but due to lack of physician's availability, a multidisciplinary approach between physicians, nurses, and dietitians can help ensuring thorough and successful nutrition care process. **Objectives:** To determine the effects of nutrition care process from multidisciplinary approach on energy and protein intake, and nutrition status. Subjects: 19 nutrition-consulted IPD patients from October 2019 to March 2020. **Methods:** An observational descriptive study, nutrition physicians communicated to dietitian for nutrition support by doctor order sheet and Line® application program, with nurses requested nutrition consultation to dietitian by phone calls. All consulted malnutrition cases from primary physician to nutrition physician were included in this study. Dietitians achieved calories and protein counting, nutrition assessment at the time of patient's admission and discharge (7-points SGA in general patients and PG-SGA in cancer patients) and suggested nutrition interventions to the physician by dietitian's progress note and Line® application program. In urgent cases requiring immediate diet adjustment, dietitians directly called the nutrition physician. Depending on the condition severity, a follow-up was planned between 1-7 days after each intervention. Once discharged, dietitians provided nutrition education for discharge planning. Nutrition grand round at ward was also held every month. **Results:** Total nutrition consulted cases (n=19) divided into general cases 74 % (14/19) and palliative cases 26 % (n=5/19). Compared to baseline, 86 % of patients (n=12/14) received adequate energy and protein intake (80% of requirement), 100 % (n=14/14) had lower nutrition assessment scores at time of discharge. **Discussion:** Nutrition intervention, in particular the use of enteral supplement, has enteral and parenteral nutrition, has an important role for improving nutrition status. **Conclusion:** Multidisciplinary approach can provide a wholesome and systemic nutrition care process, which improve nutrition status and prevent inadequate energy and protein intake.

Introduction:

Malnutrition is a condition of nutrition in which a inadequacy or excess (or imbalance) of energy, protein, vitamin and mineral causes adverse consequence on tissue/body form (body shape, size, composition), body function and clinical outcome.[1] Furthermore, malnutrition are hidden cause of poor health outcomes, rising health care costs, increased utilization of resources, increased length of hospital stay, increased re-

admission rates, and contributes to higher morbidity and mortality.[2] The prevalence of malnutrition among hospitalized elderly shows rising trend both local area and across the world.[3] Approximately 20% to 50% of hospitalized patients were diagnosed as malnutrition.[4] Several nutrition screening and assessment tools may simplify the identification of factors (body weight, laboratory data, clinical signs, gastrointestinal track symptoms and dietary intake) associated with malnutrition including: Mini Nutritional Assessment (MNA) [5-7], Malnutrition Screening Tool (MST)[8], Malnutrition University Screening Tool (MUST)[9], Nutritional Risk Screening 2002 (NRS 2002)[10], Subjective Global Assessment (SGA)[11], Simplified Nutritional Assessment Questionnaire (SNAQ)[12]. Although, trustworthy nutrition screening and assessment tools are available, if lack of good clinical practice about nutrition care process (NCP), impossible to provide suffice nutritional care to malnutrition patients. Regularly, NCP is a systematic method that nutrition and dietetics practitioners use to provide nutrition care.[13] Collaboration between multidisciplinary in nutrition support team composed of medical doctors, registered nurses, pharmacists, and nutritionists/dietitians to evaluate the nutritional status of patients receiving enteral nutrition (EN) and parenteral nutrition (PN) and provide patients with the appropriate nutritional supply to improve their recovery and prevent complications.[14] Therefore, nutrition care process has an important role to participate in patients treatment care plan and alleviate suffering from malnutrition. However, in fact, lack of cooperation between multidisciplinary team on nutrition care process in IPD patients and effective processes for communicating information related to the nutrition care process are often absent.[15] For this reason, it is undeniable that malnutrition patients had inadequate energy and protein intake and did not improved nutritional status.

Methodology:

An observational descriptive study was performed in nutrition consulted patients at IPD ward for example medicine, cancer and surgery. Malnutrition cases at ward commonly found such as cancer (all types), liver disease, renal disease, poor intake, chyle leakage, enteral and parenteral usages, etc. Malnutrition patients were consulted by attending or primary physician to nutrition physician to cope with inappropriate or inadequate nutrition intervention. Hence, cooperation between nutrition physician, nurse and dietitian were occurred after establishing these process since 2018. Especially nutrition physician and dietitian are majorly responsible for nutrition care process. Two methods of nutrition physicians communicate with dietitian for nutritional support including 1.doctor order sheet in patients profile at ward and 2.Line® application program in mobile phone. All consulted malnutrition cases from primary physician to nutrition physician were entirely included in this study (number of nutrition consulted cases in this study were depend on primary physician that sent a consultation in each month). Dietitian would simultaneously approached to malnutrition patients when nurses requested nutrition consultation to dietitian by phone calls. Dietitians completely energy and protein intake counted by 24 hours dietary recall method, nutrition assessment at the time of admission and discharge (7-points Subjective Global Assessment (SGA) in general patients and Patient-Generated Subjective Global Assessment (PG-SGA) in cancer patients. Several studies supported reliability and validity of these nutritional assessment tools such as 7-point scale SGA is a reliable and valid tool for nutritional assessment in adults on HD[16] and PG-SGA is a reliable and valid measurement to assess nutritional status for stroke patients[17]. Furthermore, dietitian would suggest nutrition interventions (encouraged adequacy of energy and protein intake by modified oral diet both texture and palatability of food, enteral supplement in case inadequate oral intakes and parenteral supplement in case gastrointestinal track problems) to nutrition physician with reported additional information about patients including body weights, body mass index (BMI), clinical signs, fluid intake/output balances, laboratory results and dietary intake by dietitian's progress note and Line® application program. In urgent cases requiring immediate diet adjustment, dietitians directly called the nutrition physician. Depending on the condition severity, a follow-up was planned between 1-7 days after each intervention. In dietitian team, dietitian would record nutrition intervention and patients progression in case record form (figure 3), which developed every year since 2018 (derived from Siriraj Hospital) for better communication in multidisciplinary team about patient progression and cover all details to deliberate information within dietitian group. Once discharged, dietitians provided nutrition education for discharge planning. Statistical analysis by

used Key Performance Indicator (KPI) to measure adequate energy and protein intake (energy and protein intake more than 80% of patient's requirement) and improved nutrition assessment (SGA or PG-SGA) scores. We set KPI values should be more than 60% both 2 parameters to indicate passing KPI in each month. In aspect of statistical analysis in this study, used improvement ratio [(value after change divided by value before change) x 100] to monitor patient's improvement. Consulted patients were classified into two types as follow 1.Curative cases (general cases) 2.Palliative cases (end of life cases) due to justified patient type for appropriate KPI calculation (palliative cases were not included for KPI calculation). Moreover, this project had new participation with nutritionist in meal plan project to investigate diet order from physician that conform to food preparation from the kitchen (figure 1). Along with nutrition care process team has nutrition grand round at ward was also held every month to discuss difficult cases (figure 2).

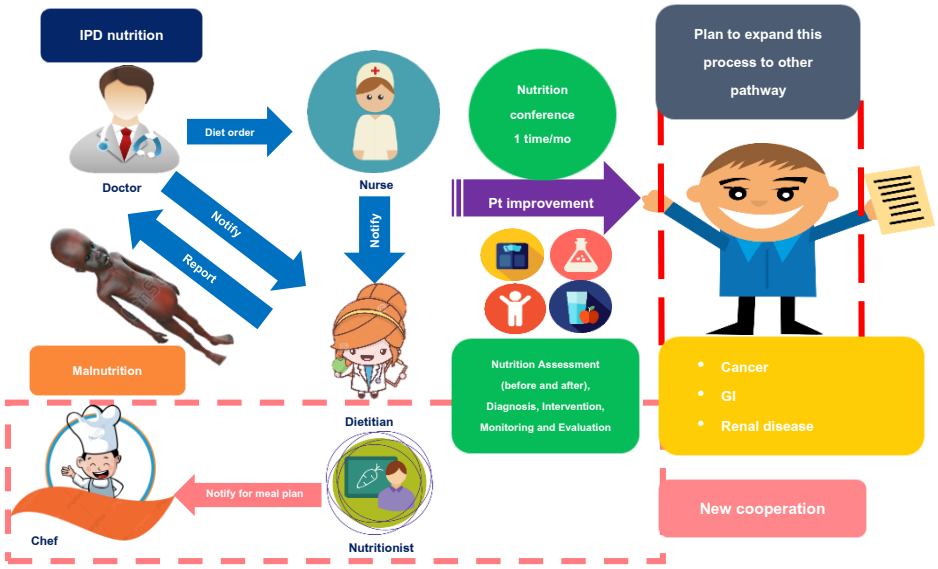

Figure 1 Nutrition Care Process (NCP) Protocol

Figure 2 Nutrition grand round at patient ward

Case record form all version (1-3)

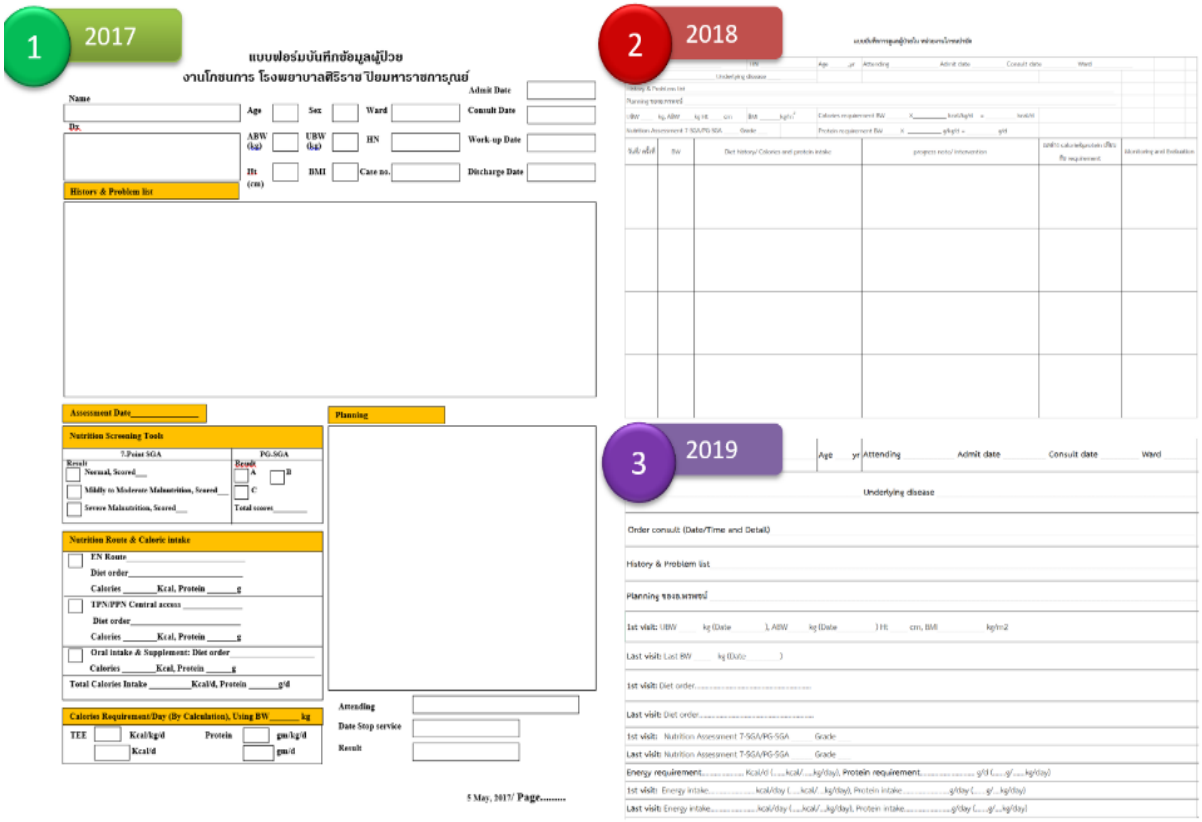

Figure 3 Case Record Form (CRF)

Results and Discussion:

Results from October 2019 to March 2020, total number of nutrition consulted cases from primary physician to nutrition physician = 19 cases divided into 74% of general cases (n=14/19) and 26% of palliative cases (n=5/19). There were 86% of patients (n=12/14) received adequate energy and protein intake (80% of patient's requirement), and 100% (n=14/14) had lower nutrition assessment scores (from SGA or PG-SGA) at the time of discharge (Figure 4-6). Likewise, in previous study, individualized nutritional intervention effectively increased energy and protein intake in cancer patients.[18,19] Compatible with earlier study, nutritional care process (NCP) can enhanced quantity of food intake from 28% to 62% when compared with patients requirement.[20] However, remark in October 2019 and January 2020 were not met energy and protein requirement due to severity of the disease. In palliative cases, role of NCP did not pretend to achieve energy and protein target but only supportive care were done in these patients group, not suffered from excessive nutrition intervention and needless to achieve energy and protein intake target. However, nutrition assessment scores (from SGA or PG-SGA) were completely improved in all month since October 2019 until January 2020, other factor such as body weight, BMI, clinical sign or laboratory data were enhanced, nutrition assessment scores (from SGA or PG-SGA) result to overall scores decreased dramatically despite energy and protein intake did not met the target. After analyzing the cause of malnutrition in entire year 2018 (the year that this study established) found that cancer remains dominantly causing of malnutrition around 40-60% both patients who passed or not passed KPI, second and third causes of malnutrition were heart and kidney disease, respectively. Other diseases did not frequently found malnourish patients such as femoral hernia, encephalitis, esophageal rupture, human immunodeficiency viruses (HIV) infection, vertebral compression, cellulitis and benign prostatic

hypertrophy (BPH) with urinary tract infection (UTI) (Figure 7). Consequently, multidisciplinary team included a dietitian, clinic doctor, professional nurse has an essential part to screen and identifying early malnutrition.[21]

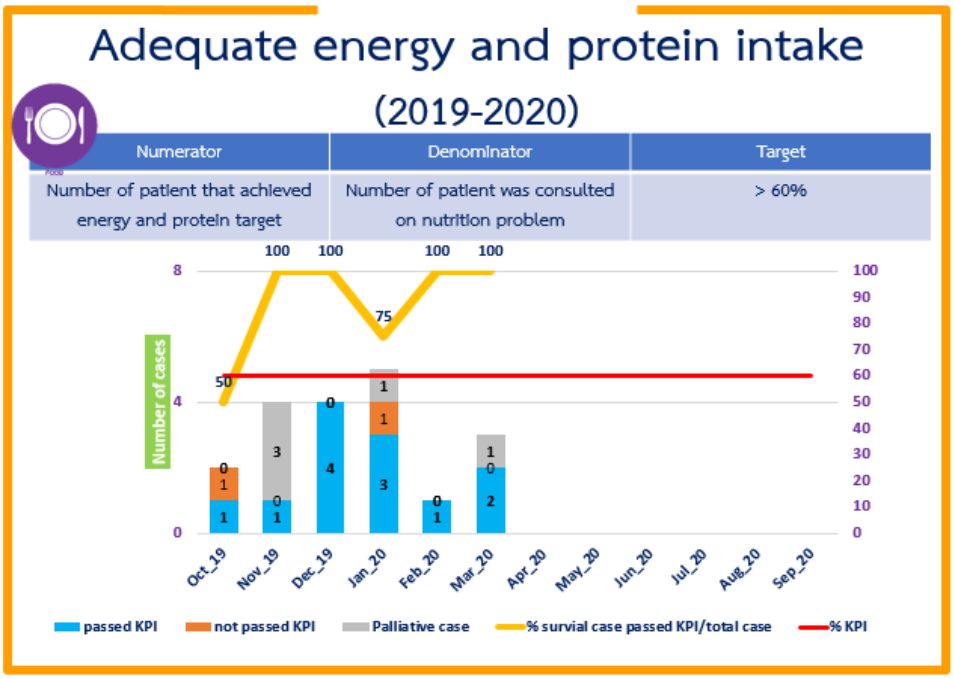

Figure 4 KPI result of energy and protein intake

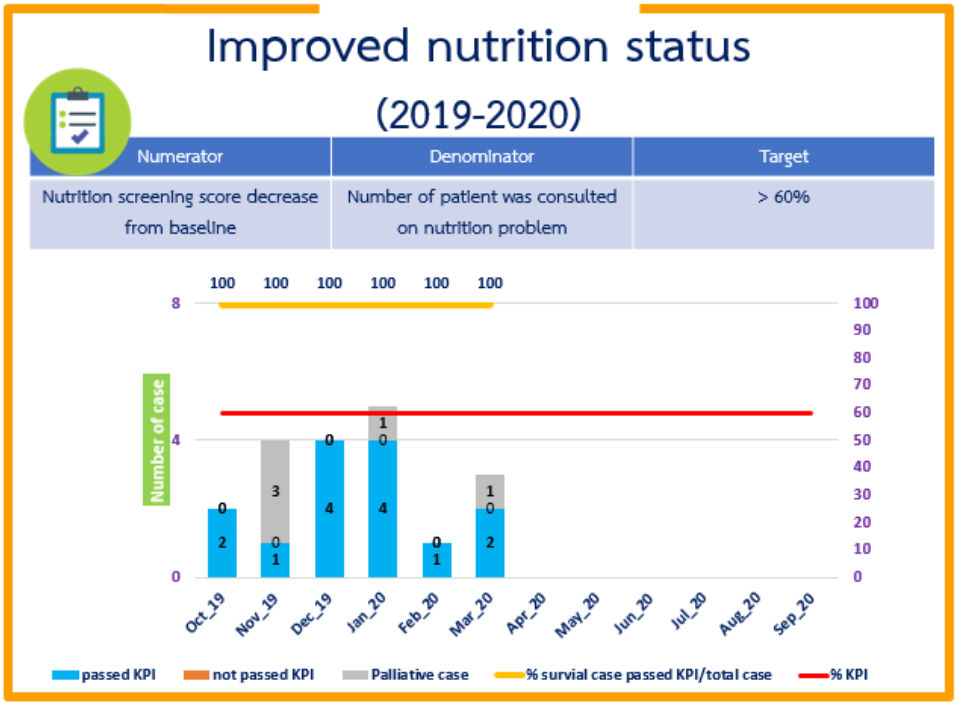

Figure 5 KPI result of improved nutrition status (nutrition assessment scores judgment)

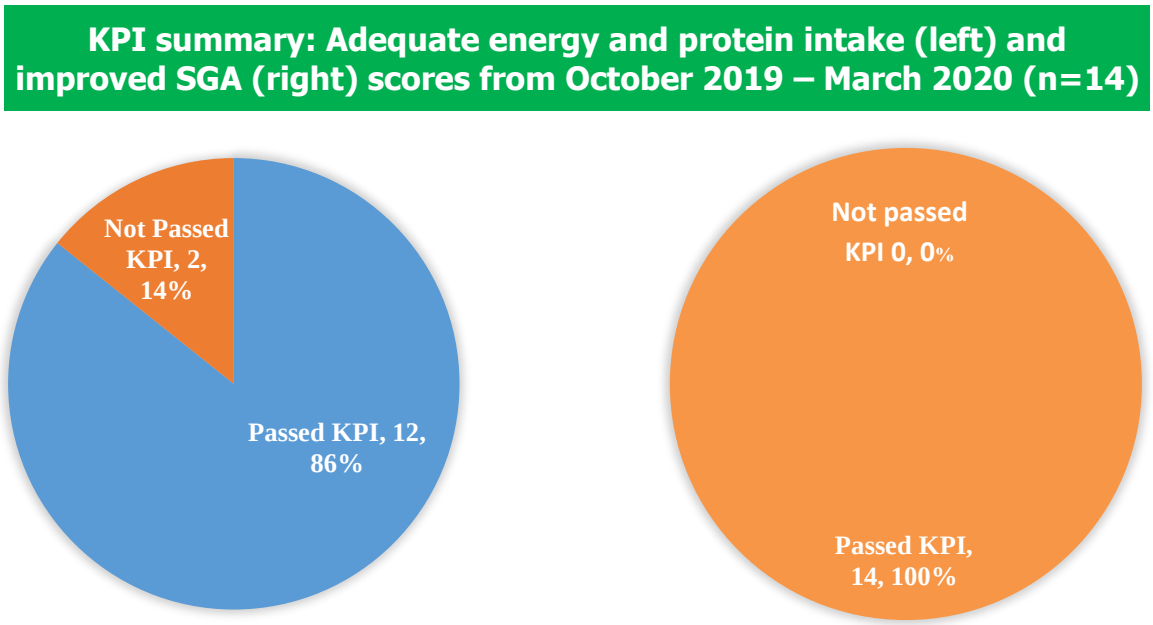

Figure 6 Percentage of nutrition consulted patients and KPI values (October 2019 – March 2020)

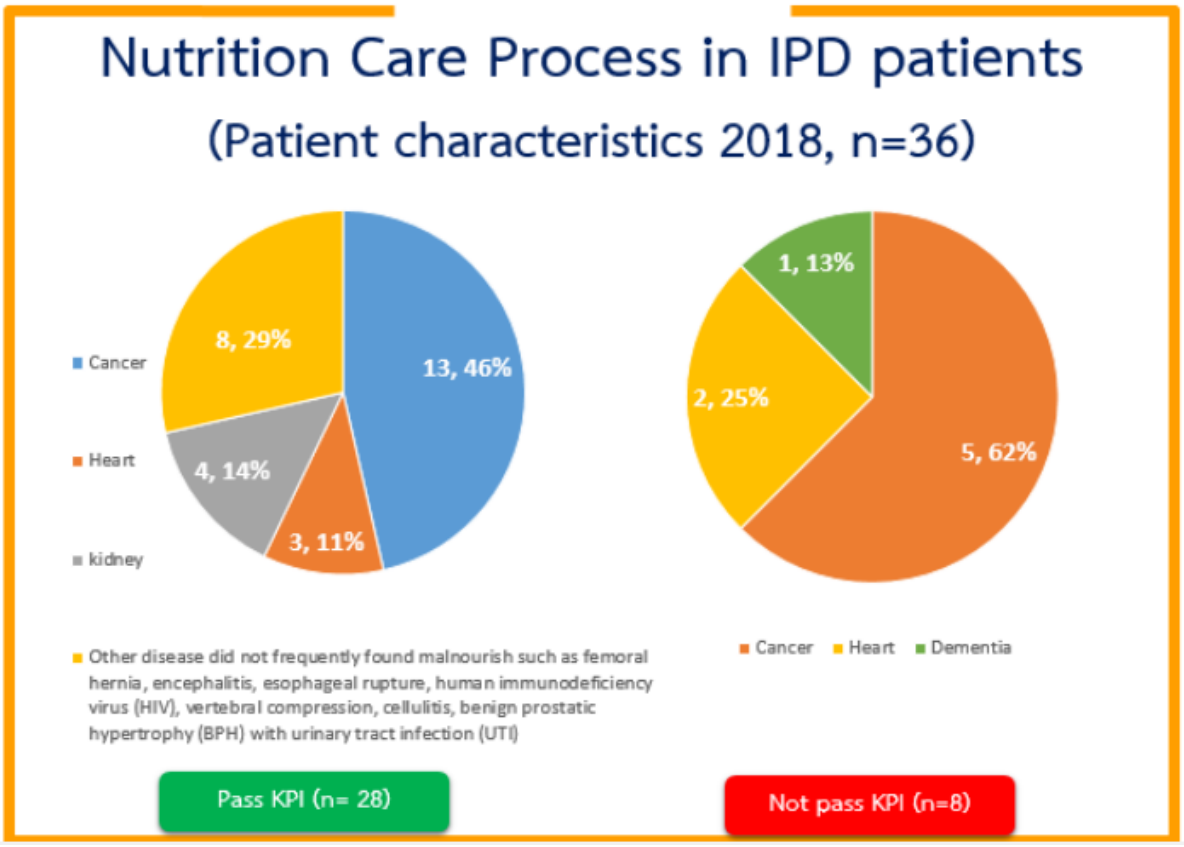

Figure 7 Consulted patient classified by KPI values and disease characteristics (2018)

Conclusion:

Effective nutrition intervention, in particular the use of enteral supplement, has enteral and parenteral nutrition, has an important role for improving nutrition status. Multidisciplinary approach can provide a wholesome and systemic nutrition care process, which improve nutrition status and prevent inadequate energy and protein intake.

References:

1. Soeters P , Bozzetti F , Cynober L, Forbes A , Shenkin, Sobotka L. Clin Nutr 2017;36(3):896-901.
2. Daphnee L, Rajalakshmi P and Anand R. Clin Nutr 2019:30;19-25.
3. Nur ASAA, Nur IMFT, Mohd RAH, Nazrul HI. Clin Interv Aging 2017;12(4):1615-25.
4. Ana CF, Ana P, Maria AV, Harriët JW and João P. Nutrition 2020;74:1-6.
5. Vellas B, Villars H, Abellan G, et al. J Nutr Health Aging 2006;10(6):456–63.
6. Rubenstein LZ, Harker JO, Salva` A, et al. J Gerontol A Biol Sci Med Sci 2001;56(6):M366–72.
7. Kaiser MJ, Bauer JM, Ramsch C, et al, J Nutr Health Aging 2009;13(9):782–8.
8. Ferguson M, Capra S, Bauer J, et al. Nutrition 1999;15(6):458–64.
9. Stratton RJ, Hackston A, Longmore D, et al. Br J Nutr 2004;92:799–808.
10. Kondrup J, Rasmussen HH, Hamberg O, et al, Clin Nutr 2003;22:321–36.
11. Detsky AS, McLaughlin JR, Baker JP, et al. JPEN 1987;11(1):8–13.
12. Wilson MM, Thomas DR, Rubenstein LZ, et al. Am J Clin Nutr 2005;82(5):1074–81.
13. William IS, Angela V, Nancy AH, Brenda H, Ylva O, Naomi T, et al. J Acad Nutr Diet 2017;117(12):2003-d14.
14. Byung CS, In AC, So YR, Ji EO, Pahn KC, Hyun GK. Medicine 2018;97:52(e13932).
15. Kelly AT, Beth Q, Melissa LP, Ainsley MM, Gary F, Thomas RZ. J Acad Nutr Diet 2013;113(9):1219-37.
16. Alison S, Janeen BL, Donna S, Maureen M, Linda M, Monica S, et al. J Ren Nutr 2007;17(5):336-42.
17. Sung HY, Eui-GO and Mi-JY. Korean J Adult Nurs 2009;21(6):559-69.
18. Park KO, Choi-Kwon S. J Korean Acad Nurs 2012;42:799-809.
19. Poulsen GM, Pedersen LL, Osterlind K, Bæksgaard L, Andersen JR. Clin Nutr 2014;33(5):749-53.
20. Hye-OL, Jung-JL. Clin Nutr Res 2015;4:63-7.
21. Jin-XL, Xiang-WC, Zhan-HC, Xiu-YH, Jin-JY, Yan-FX, et al. Medicine 2017;96:26(e7373).

E_022_OA: DETECTION OF *XANTHOMONAS oryzae* pv. *oryzae* (*Xoo*) CAUSING BACTERIAL LEAF BLIGHT IN RICE USING A pH-SENSITIVE LOOP-MEDIATED ISOTHERMAL AMPLIFICATION (LAMP)

Onchira Ritbamrung[1], Phithak Inthima[1], Kawee Sujipuri[2], Kumrop Ratanasut[2], Kittisak Buddhachat[1,*]
[1] Department of Biology, Faculty of Science, Naresuan university, Phitsanulok 65000, Thailand.
[2] Department of Agricultural Science, Faculty of Agriculture Natural Resources and Environment, Naresuan University, Phitsanulok 65000, Thailand.
[*]Corresponding author email: kittisakbu@nu.ac.th

Abstract:

Bacterial leaf blight (BLB) diseases are one of the most important diseases in rice caused by *Xanthomonas oryzae* pv. *oryzae* (*Xoo*) leading to severe epidemics and damage in rice fields, resulting in lessening rice production. This study was to develop an accurate and rapid method for detecting *Xoo* by using a pH sensitive-loop-mediated isothermal amplification (LAMP) technique, which are widely used for detection of diseases in isothermal condition. Consequently, *Xoo*4009 primer were designed and optimized under a suitable condition at the temperature 63ºC for an hour and LAMP product were observed by color change with naked eyes. The result indicate that *Xoo*4009 primer was highly capable of specificity, which the LAMP technique is specific only *Xoo* infection and non-cross reaction with other species in the same genus and other bacteria belonging to different family. In addition, the detection of *Xoo* by using LAMP technique gave a higher sensitivity and rapidity compared to PCR. Altogether, we strongly believe that a pH sensitive LAMP serves a potential tool for *Xoo* detection in point-of-care practice due to no requirement of a sophisticated instrument and reduction of time-consumption.

Keywords: Bacterial leaf blight, Isothermal Amplification, Rice

E_023_OA: MOLECULAR DETECTION OF RICKETTSIA, *Ehrlichia canis* and *Anaplasma platys*, IN CANINE BLOOD USING RPA METHOD

Suphaporn Paenkaew[1] and Kittisak Buddhachat[1,*]

[1]Department of Biology, Faculty of Science, Naresuan University, Phitsanulok, 65000 Thailand.
*e-mail: kittisakbu@nu.ac.th

Abstract:

Currently, the prevalence of blood parasitic infections in dogs especially *Ehrlichia canis*, *Anaplasma platys* cause the mortality and morbidity of dogs. These agents have increasingly gained attention for veterinarian. In this study, a recombinase polymerase amplification (RPA) method was developed for detection of *E. canis* and *A. platys* infection in dogs. The DNA of *E. canis* and *A. platys* was amplified by a pair of specific primers specific to the 18S rRNA. Here we examined the optimal condition including time (0-30 min.) and temperature (25 °C to 45 °C) of RPA reaction to detect *E. canis* and *A. platys*. In addition, the sensitivity was assessed with the different amount of copy number (1-10^8 copies) and the specificity was evaluated using the other canine blood parasites including *Babesia* spp. and *Hapatozoon canis*. The results showed that the optimal condition for DNA amplification by RPA included setting up the reaction at 37 °C for 20 min. The sensitivity of the established assay was at 1 copy with high specificity because there was no cross reaction with other canine parasites (e.g. *Babesia* spp. and *Hapatozoon canis*). This method provides a rapid, sensitive and specific approach to detect the infectious agent *E. canis* and *A. platys* in canine blood and will be useful for veterinarians.

E_024_OA: GENETIC DIVERSITY, GEOGRAPHIC DIFFERENTIATION AND CHEMICAL PROFILE OF ASIATIC PENNYWORT (Centella asiatica (L.) URBAN) IN THAILAND

Wanrachon nukool[1], and Kittisak Buddhachat[1,*]

[1]Department of Biology, Faculty of Science, Naresuan University, Phitsanulok, 65000 Thailand.
*e-mail: kittisakbu@nu.ac.th

Abstract:

Centella asiatica (L.) Urb. (CA) is an important medicinal plant that has various properties in particular wound healing and skincare. The biologically active compounds of CA are triterpenoids including asiaticoside (AS), madecassoside (MS), asiatic acid (AA) and madecassic acid (MA) acting as an anti-oxidant and stimulation of collagen synthesis. One important concern about the quality of CA for medicinal industry is the variation of bioactive compounds resulting from different planting locations and even varieties. In this study, we collected CA from different 21 localities. After cultivation for three months, the high performance liquid chromatography (HPLC) was used to measure level of four active compounds including AS, MS, AA and MA. Besides, the genetic diversity of CA was evaluated by Start Codon Targeted (SCoT) marker. Our results exhibited that the high variation in amounts of substances from different areas was observed. The analysis of triterpenoids contents shows that the amount of triterpenoid of CA extract from Nakhon pathom province had the highest amount (13.1891 mg/g DW) whereas that of Phrae province had the lowest amount (4.7826 mg/g DW). From DNA fingerprint of 21 samples, it showed that the CA was high identity with 68.75% polymorphism and divided into seven groups which the northern CA were treated into the same clades. Meanwhile the other CA accession seemed not to be related geographically. the variation of bioactive compounds resulted from different planting locations and even varieties. In addition, CA were collected from different 21 localities and the high variation in amounts of substances from different areas was observed

E_025_OA: LOGISTICS COST REDUCTION MODEL IN FOOD INDUSTRY, RAYONG

Tanaporn K.[1]*

[1] Faculty of Business Administration,
King Mongkut's University of Technology North Bangkok, Rayong, Thailand, 21120
* e-mail: Tanaporn.k@fba.kmutnb.ac.th, 0655324166

Abstract:

Paper aims

This research has two main objectives, firstly to study affecting factoring on logistics cost reduction approach model in context of food industry and secondly to analyze the relationship affecting factors.

Originality

The structural equation modeling (SEM) allows a better analysis of the inter-linkage of affecting factors towards cost reduction gains. The developed model offers conceptual contribution to the arena of the logistics excellence practice.

Research methods

The methodology used in this study was carried out sorting an inquiry using questionnaires collecting data from 120 participants. Firstly, aiming to understand the level of each affecting factors (strategy perceived, logistics competence, organization effectiveness, and transportation approach) practices for food industry in Rayong, a case study was considered. The sample taken is a convenient one, due to time and budget constraints. Secondly, in order to assess the possibility with a statistical approach was used to develop a SEM for logistics cost reduction in food industry in Rayong.

Main findings

The results demonstrated that the level of affecting factors on Portuguese companies are not properly addressed and formalized. The statistical analysis also s logistics cost reduction in food industry generates that 4 constructs (factor loading); strategy perceived: STP (.741), logistics competence: LOC (.634), organization effectiveness: OEF (.672), transportation approach: TAP (.632) and Cost reduction: CRE (0.545). The research showed that all affecting factors have also a positive impact on the logistics processes of companies. The best potential for maximum utilization of smart technology on strategic deployment to reduce cost and emission from food industry forward sustainability competition advantages are significant for reducing logistics cost.

Implications for theory and practice

This research brings some contributions to both academy and companies. Firstly, a further discussion about the benefits of combining smart technology towards sustainability. Secondly, the development of a structural model for logistics cost reduction practices was presented, this model contributes to a better understanding of these practices, which can lead companies to develop strategic initiatives towards sustainability.

Keywords: Sustainability; Structural equations modeling; Logistics excellence innovation

E_029_OA: ALTERNATIVE NATURAL HAIR DYE PRODUCT USING THE PIGMENT EXTRACTED FROM CYANOBACTERIA

Oranit Kraseasintra,[1] Chayakorn Pumas,[2]*

Department of Biology, Faculty of Science Chiang Mai University, Huay Kaew Road, Suthep Sub-district, Mueang District, 50200 Chiang Mai, Thailand
*e-mail: chayakorn.pumas@gmail.com

Abstract:

Presently, almost hair dye product is made from synthetic chemicals and may allergy to some sensitive customers. Cyanobacterial pigments, phycoerythrin (PE) and phycocyanin (PC) are non-toxic colorants and have been applied in beer, ice-cream, lipstick, etc. This study aims to evaluate some biological properties of these pigments for application in a natural hair dye product. The pigments were tested for five antioxidant activities and found that the highest antioxidant activity was found in ABTS radical assay followed by metal chelating activity, reducing power, total phenolic compound and DPPH• radical assay. The antibacterial activity of *Escherichia coli*, *Staphylococcus aureus*, *Staphylococcus epidermidis*, Methicillin- resistant *Staphylococcus aureus* and *Propionibacterium acne* was tested by agar well diffusion assays. However, both pigments could not inhibit all of the tested bacteria. The mixture of pigments with natural developers and mordants was used to dye a bleached hair. The alteration of color after shampoo wash was detected by chroma meter and damage of hair surface structure was observed under light compound microscope. Result found that the natural hair dye from these pigments revealed a potential dyeability without damaged the hair surface. Thus, these pigments show a potential to be applied as safe dye in natural hair dye product.

E_031_OF/E_034_OF: THE PORTABLE DARK FIELD MICROSCOPE

Panuphong Northao,* Natwara Thongsak

Princess Chulabhorn Science High School Lopburi, Thailand
*e-mail: p_pond01@hotmail.com

Abstract:

The portable dark field microscope will be available at the school for use with dark field microscopy and will have 25x, 50x, 100x magnifications for appropriately sized specimens. The principle of light scattering applied in dark field microscopy. The dark field microscopy show the specimens bright on a dark background and they appear bright because they scatter the light from the light source into the sample. The portable dark field microscope consists from 3 parts which are an objective lens, slide holder with light source and focus controller which works together. The LED holder and the focus controller were designed by SketchUp software then printed with PLA filaments using 3D printer. For other parts, we cut acrylic sheets by laser cutting machine and gathering all the pieces to become a device. In addition, there is a special light scattering condition that will have the color of the image on the opposite side of the color wheel, for example, an image of an early embryo of frog, which was pink-red in a portable bright field microscope, but green in a portable dark field microscope. Although, gold nanoparticles have surface plasmon resonance properties which go with the principle of light scattering. So, we're using gold nanoparticles to check our resolution as the same as the live sample and dry sample.[3]

Introduction:

Normally, the microscope has a big size and it is heavy to carry around for use to check any specimen and because of high cost of a microscope not so many schools can afford it. Also, the bright field microscopy is a conventional technique.[1] It is suitable for observing the natural colors of a specimen or the observation of stained samples. In that case the specimen appears darker on a bright background. However, the dark field microscopy shows the specimens bright on a dark background and appears bright because they scatter the light from the light source into the objective. Thus, you will get a more detailed view of the external features and the outline boundaries due to light scattering. Samples observed in a dark field microscopy must be carefully prepared, as dust and other particles also scatter light and can interfere with observations. In addition, the sample must be smeared with a thin layer; too much material on a slide creates many overlapping layers and edges and makes structures difficult to interpret.[2] Light scattering has been used in many fields of research such as physics and biomedicine. After all, fluorescence smartphone microscopy uses light scattering in the same way as dark field microscopy. Hence, the dark field microscopy has the condenser for light scattering and fluorescence smartphone microscopy got a perpendicular of the light source and specimen to let the light scattering happen.[4]

We now report about development of the portable dark field microscope that can be used with 25x, 50x, and 100x magnifications and available at the school to study in a dark field system at small costs by using a 3D printing and acrylics sheets for the setup of a portable dark field microscope.

Methodology:

Portable dark-field microscope

We used Google Sketch up software to design the focus controller and LED holder, then print out by 3D printer using PLA filaments. For other parts, we cut acrylic sheets by laser cutting machine and gathering all the pieces to become a device. The portable dark field microscope was acquired under consistent light and magnification at 25x, 50x, 100x objective lenses.

Synthesis of Gold nanoparticles

Materials and suppliers

Tetrachloroauric acid ($HAuCl_4$, Sigma-Aldrich), Cetrimonium bromide (CTAB, Sigma-Aldrich), Sodium borohydride ($NaBH_4$, Sigma-Aldrich), Ascorbic acid ($C_6H_8O_6$, Sigma-Aldrich), Deionized water (DIW). All glassware was cleaned thoroughly with soap and water, rinsed extensively with deionized water before use every time.[6]

Synthesis process

Prepare Ascorbic acid (0.1 M 5 mL), Tetrachloroauric acid (0.01 M 15 mL), Cetrimonium bromide (0.1 M 200 mL), Sodium borohydride (0.01 M 2 mL). Then, 9.75 mL CTAB solution (0.1 M), 0.25 mL solution of $HAuCl_4$ (0.01 M) was added with gently stirred. $NaBH_4$ solution was prepared by the ice-cold deionized water for cooling down the process because sodium borohydride is a powerful reducing agent and reacts exothermically with water to generate flammable hydrogen gas. As prepared, 0.6 mL $NaBH_4$ solution will quickly be added in the previous mixture and being vigorously stirred until the solution color changes from gold to golden brown. Later, leave the solution undisturbed in a water bath at 30°C for 1-2 hours.

Results and Discussion:

a)

b)

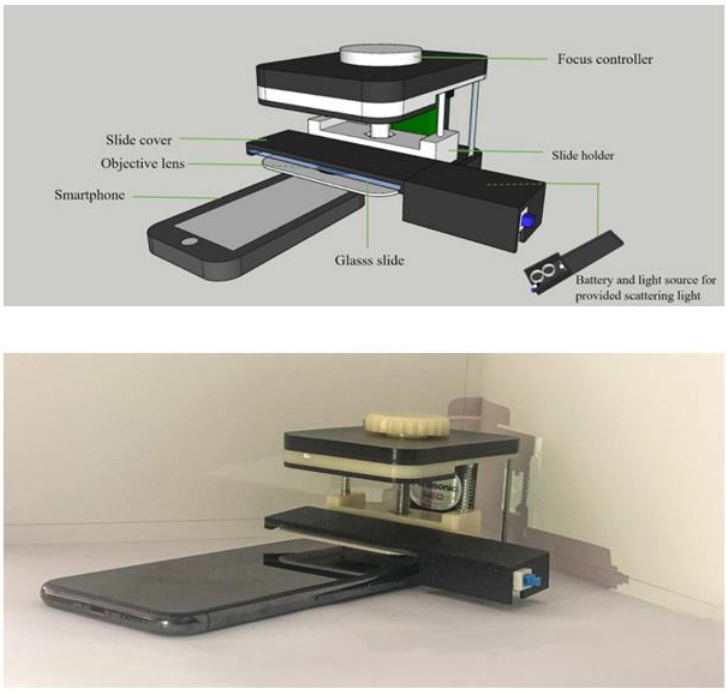

FIGURE 1.

Portable dark field microscope Setup a) layout schematic, b) working prototype

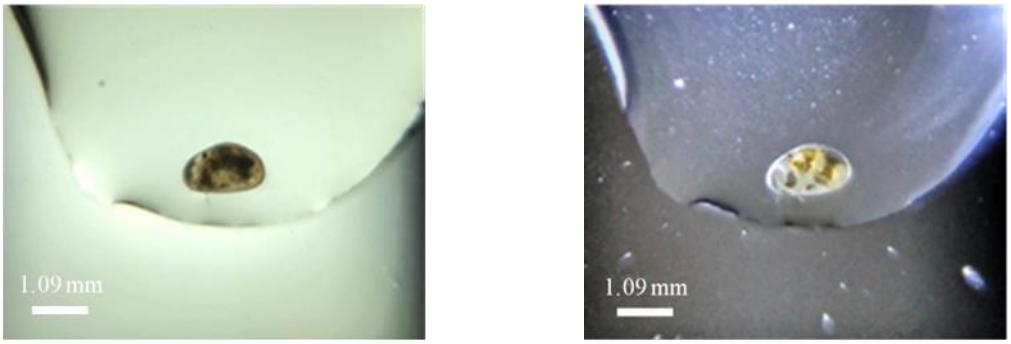

FIGURE 2.

The image from portable bright field microscope (left) which seen by transmitted light and portable dark field microscope (right) have seen by scattering light and show the organelles inside The image captured with a 25x magnification (The specimens were Ostracod)

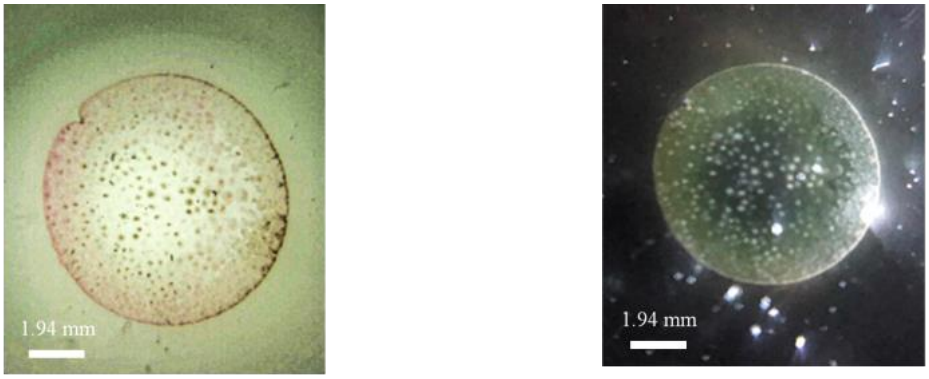

FIGURE 3.

The image from the portable bright field microscope (left) have got a transmitted light which makes us see pink/red color of strained and The image from portable dark field microscope (right) got a green color from the scattering of light property that the color that shown will be opposite in the color wheel which is green The image captured with a 50x magnification (The specimens were early embryo of frog)

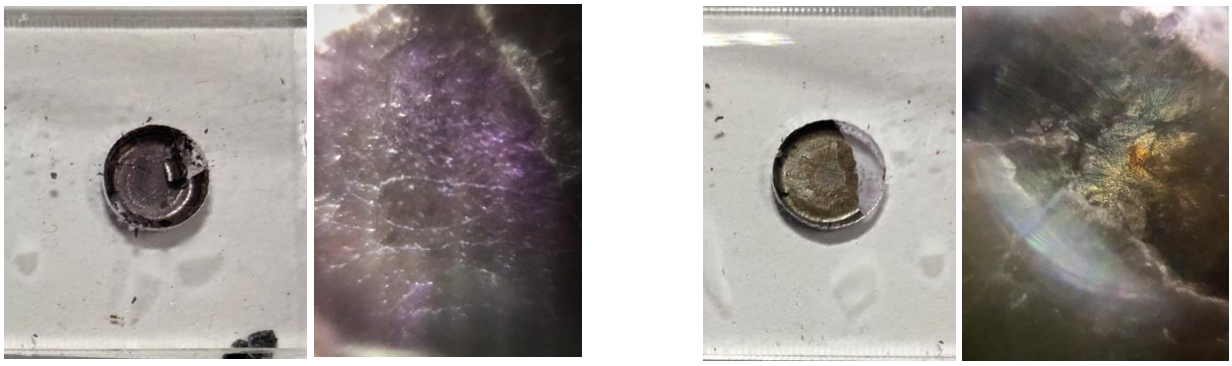

FIGURE 4.

The images shown the aggregation of gold nanoparticles in a different sizes under the portable dark field microscope The magnification at 50x magnification

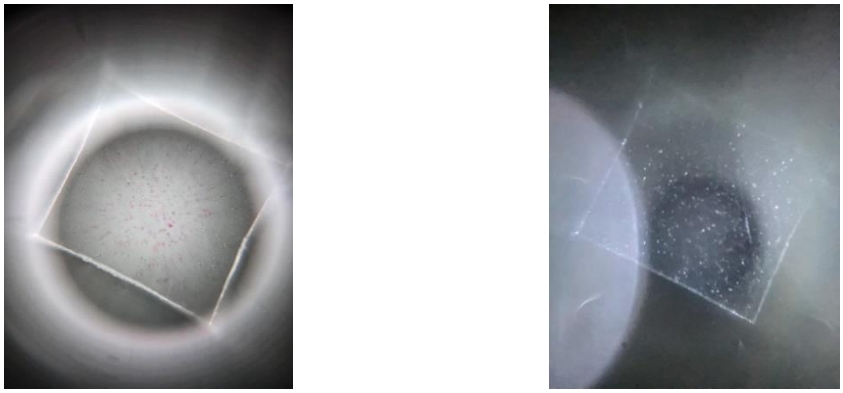

FIGURE 5.

The image from the portable bright field microscope (left) show the strained color of sample but portable dark field microscope (right) show the image by the scattering of light which makes a sample bright
The image captured with a 100x magnification
(The specimens were Normal Chromosome W.M.)

Conclusion:

The portable dark field microscope will be available at the school. The dark field microscopy will show the specimens bright on a dark background, but there is some specific condition about scattering light that will appear the color of an image on the opposite side of the color wheel such as the image from early embryo of frog which in the portable bright field microscope the color was pink/red but in the portable dark field microscope the color was green. In portable bright field microscope you can see natural colors of a specimen or the stained samples and the specimen appears darker on a bright background. The portable dark field microscope has 3 magnifications 25x, 50x and 100x. As results we can conclude that the difference between portable bright field microscope and portable dark field microscope of the ostracod, early embryo of frog, normal chromosome W.M. that images in portable dark field microscope will be visible more detailed of the organelle inside the cell including with the gold nanoparticles.

Acknowledgements:

I'm grateful to have my advisors Wipawee Srihanon and Sophon Klomkliang for helping me out with problems. I sincerely appreciated Ph.D. Atcha Kopwitthaya for always being supportive and her invaluable advices. I'm also thankful for the National Electronics and Computer Technology Center for laboratory and chemical equipment and Princess Chulabhorn Science High School for financial support. Lastly, I'm gratefully thankful to my co-workers, Natthaphat Sirakulwat, Thidathip Suktat for being fully helpful and their time dedication for this research.

References:

1. Ashley A, Stender K, Marchuk T, Greenbowe NF. 2014.
2. Ziji LL, Tian S, Liu W. 2014.
3. Chompoosor A. 2013;41:4.
4. Sung Y, Campa F, Shih WC. 2017;8:11.
5. Sun D, Hu T. 2018;99:513-518.
6. Shajari D, Bahari A, Gill P, Mohseni M. 2017;64:376-383.

E_032_OF: RAPID AND COST-EFFECTIVE FABRICATION METHOD OF MICROFLUIDIC CELL CULTURE DEVICES USING A STEREOLITHOGRAPHY 3D PRINTING

Siwattra Pruksasri,[1,2] Tonghathai Phairatana[1,2], Pasarat Khongkow[1,2]*

[1]Institute of Biomedical Engineering, Faculty of Medicine, Prince of Songkla University, Hat Yai, Songkhla, Thailand 90110
[2]Department of Biomedical Sciences and Biomedical Engineering, Faculty of Medicine, Prince of Songkla University, Hat Yai, Songkhla, Thailand 90110
*e-mail: k.pasarat@gmail.com

Abstract:

Microfluidic technology, offering the possibility of handling small volume of samples in a microchannel, has become a powerful tool for various biomedical and clinical applications. However, fabrication of microfluidic devices is often complicated, time consuming, requires expensive equipment and cleanroom facilities. In this study, we therefore focused on the feasibility of creating a prototype of microfluidic cell culture on-a-chip using the Anycubic Photon 3D printer, a low-cost commercial liquid crystal display (LCD)-based stereolithography (SLA) 3D printing system. We characterized the accuracy of using 3D printed molds for creating a microfluidic device by using scanning electron microscope (SEM). The result showed that there was no significant difference between dimensional profiles of the CAD design, the printed mold and PDMS replica with acceptable errors less than 15%. Interestingly, these reusable molds can be printed within 30 mins, at an average cost of 0.5 U$/mold, which lead to fast prototyping and cost-effective production. Taken together, SLA 3D printing represents a powerful, simple, rapid, and cost-effective method for fabricating complex microfluidic devices.

Key word: Microfluidic device, Stereolithography (SLA), 3D printing, Soft lithography, additive manufacturing

Introduction:

Microfluidics or lab-on-a-chip systems refers to microscale architectures that can be used to precisely control small quantities of reagents or analytes of interest (1,2). It provides many benefits to various chemical and biological research including reducing the amount of sample and reagents, decreasing experimental time, and enabling in vivo mimics. Recently, this technology has been rapidly applied in biomedical and clinical applications such as cancer cell detection and the development of drug testing systems as known as the microfluidic cell on-a-chip (3). Microfluidic cell on-a-chip is a new model for cell culturing that mimic the dynamic physiological microenvironments along with perfusion of the body. This technology is extremely useful in various field including disease modeling, drug development and personalized medicine (4).

However, this highly promising platform has been not accessible for standard biomedical laboratories due to technical challenges. Generally, the fabrication of a microfluidic device consists of two main steps: master mold creation and PDMS replication. First, master mold typically created using cleanroom-based 2D photolithography, which is a complex and expensive procedure. Once the master mold is created, it is used as a template to fabricate microfluidic prototypes, known as soft lithography process. Polydimethylsiloxane (PDMS)

is a pre-polymer that is widely used in microfluidics fabrication. The ease of fabrication and biocompatibility makes it suitable for various biological research applications (5-7).

Recently, additive manufacturing, or three-dimensional (3D) printing technology has received more attention as a cost-effective method to rapid prototyping of microfluidic devices due to its advancements in term of design flexibility, resolution and production speed (8,9,10,11). There are several types of 3D manufacturing techniques such as fused deposition molding (FDM), stereolithography (SLA), inkjet/Polyjet, two photon lithography, selective laser sintering, and layered hydrospinning (12).

Among various 3D printing techniques, Stereolithography (SLA) 3D printing technology, also known as light based or photo-curing 3D printing technology, represents well-suited method to fabricate microfluidics device with the high in accuracy and precision, well-define channels, smooth surface, and rapid printing time (13). The basic principle of photo-curing 3D printing technology relies on the use of light source as the primary effector for fabrication 3D objects by solidifying layer-by-layer of photopolymerizable resins. According to the method used to cure the resin, it can be classified further as standard Stereolithography (SLA), Digital Light Processing (DLP), and Liquid Crystal Display (LCD) 3D printing technology. DLP and LCD techniques function faster than SLA as they can simultaneously cure a full layer of resin at once, whereas SLA requires progressively tracing the dimensions of each layer with the laser (14). It is an interesting process for microfluidic devices used in the biomedical field with simple operation functions due to time-saving, cost-effective and high-quality (11,15). There are several studies focused on the fabrication of PDMS-base microfluidic device by using SLA-based 3D printer, such as drug screening microfluidic chip (9,10). More recently, LCD-based SLA printing system has received more attention as a rapid and cost-effective way of photopolymerizing materials and provided several advantages over the other SLA techniques (i.e. high resolution, less expensive and large printing area) (16). We hypothesized that this production method could be employed in standard biomedical laboratory for enhancing in vitro models. However, the capacity for fabricating microfluidic cell culture devices of LCD-based SLA 3D printing system have not been clearly conducted so far.

In this work, we studied on the feasibility of creating a prototype of microfluidic cell culture on-a-chip using Anycubic Photon S printer, a low-cost commercial LCD-based stereolithography (SLA) 3D printing system and found that this technique enables the fabrication of microfluidic device with precise, economical, time-saving and uncomplicated process.

Methodology:

Design 3D mold:

The 3D molds were designed by using computer-aided design program (CAD) with microfluidic features suitable for culturing the cells, which consisted of main microchannels for fluid flow and a circle chamber. The designed files were then exported as stereolithography (STL) files. The STL file were imported into 3D printing software (Photon_WorkShop_V1.0.0) to complete printing.

Mold fabrication using stereolithography (SLA) 3D printing:

The molds were printed using a bottom-up type stereolithography (SLA) (Anycubic photon S 3D printer). The resolution of 3D printer was 47 µm in XY plane and 1.25 µm in Z-layer axis. Layer resolution was 25 – 100 µm. In this study, the curing time for each layer was 6 seconds and each layer height was 50 µm. Total thickness of the designed mold was 4 mm to prevent the model from bending.

Post-processing of 3D printed mold:

The 3D printed molds were washed with isopropanol for two times, followed by washing with distilled water for removing any remaining residual resin. The molds were then blow-dried with nitrogen gas and cured by UV light at wavelength 405 nm for 15 minutes.

PDMS Replication using soft lithography technique:

Polydimethylsiloxane (PDMS) (Sylgard 184, Dow Corning,USA) were vigorously mixed with elastomer base and curing agent at the ratio of 10:1 weight-to-weight(w/w) and then poured into the printed master mold. The undesirable air bubbles were removed by using vacuum desiccator chamber for 15 min. Subsequently, the PDMS replica were cured at 70 °C for 1.30 h. To completely fabricate the microfluidic device, the cured PDMS replica was peeled out and punched to created inlets and outlets. The punched PDMS replica was then treated in an oxygen plasma cleaner (PDC-001/002, Harrick Plasma) for 1 minute before bonding onto a plasma-treated glass slide or plate.

Validation channel dimension by using Scanning Electron Microscope (SEM):

To examine the accuracy of the printed mold, the channel dimension profiles of 3D printed mold and PDMS replica were measured by using scanning electron microscope (SEM) and analyzed in comparison to mold designed pattern.

Characterization of Surface roughness by using Image J software:

To obtain surface roughness characteristics of the 3D printed mold, SEM images were analysed by using the image analysis software (ImageJ, National Institutes of Health, USA) with an ImageJ plugin (SurfCharJ, http://www.gcsca.net/IJ/SurfCharJ.html). Three parameters, including *roughness surface average (Ra), root-mean-square roughness (Rq)and* total height (Rt) were then calculated.

Leakage test of microfluidic chip: To assess the success of a microfluidic device, the flow leakage testing was performed by injecting red dye through the microfluidic channel for 1 h at the flow rate of 2 µl/min by using a syringe pump. If the liquid leakage occurred, then it would have been confirmed by spread of red dye out of microchannel.

Results and Discussion:

Device design and fabrication:

The fabrication flow started with designing a microfluidic mold using CAD software. From the top view, the design contains a circle with 5 mm diameter on a vertical microchannel with 2 mm in width and 15 mm in length and a horizontal microchannel with 1 mm in width and 10 mm in length (Figure 1A). The heights of the patterns were fixed at 4 mm. The 3D molds were printed by Stereolithography (SLA) 3D printer. The entire printing process of each mold at the given design is approximately 30 mins (Figure 1B). Soft lithography was performed by casting the PDMS on to the printed master mold. The cured PDMS, also known as PDMS replica, was then peeled off and bonded onto the clean glass slide (Figure 1C).

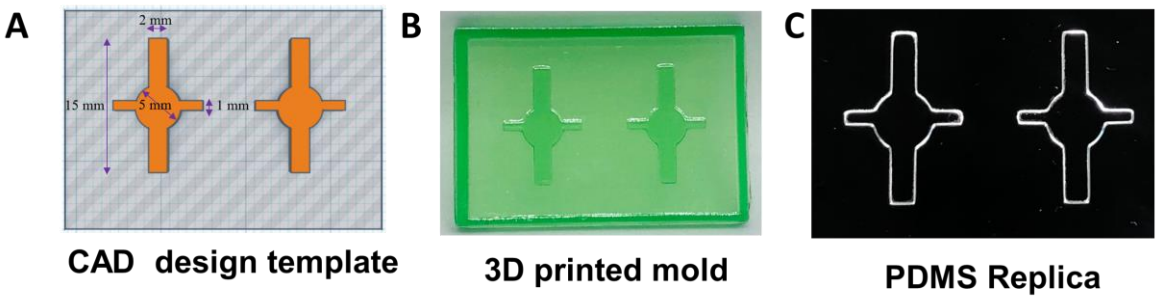

Figure 1: The prototype Image. (A) 3D CAD mold design (B) The 3D printed mold and (C) PDMS replica.

Characterization of microstructure of 3D printed mold and PDMS replica using Scanning Electron Microscope (SEM) system:

To examine the accuracy of the printed mold fabricating by the LCD-based SLA 3D printing, the channel dimension profiles of 3D printed mold and PDMS replica were measured by using scanning electron microscope (SEM) system (Figure 2A) and analyzed in comparison to the given CAD designed pattern. As shown in Figure 2B and 2C, there were no significant differences between dimensional profiles of the CAD design, the printed mold and PDMS replica with acceptable errors less than 15%, suggesting that the LCD-based SLA 3D printing exhibited high accuracy in planar XY plane printing. The suitable printing channel size with this set up should be greater than 2 mm (error is less than 5.5%). The results also revealed that the printed width was slightly greater than the designed one might be due to the overcuring. We suggest that the optimization of curing time is needed to improve the printing resolution and accuracy, as well as the surface roughness. Additionally, we have investigated surface roughness of 3D printed mold using qualitative and quantitative method (ImageJ). The surface roughness value of the structures printed by 3D Systems was approximately 5.59 µm. This is much poorer than previous report, showing that the surface roughness of the 3D model printed by DLP-SLA printing system was 0.38–0.61 µm (16). The surface roughness experiment needed to be repeated with the optimization of layer height (17). Altogether, we found that with this printing set up, the printed molds were still good enough for rapid prototyping simple PDMS based-microfluidic cell culture devices, as indicated by biocompatibility test (data not shown).

A

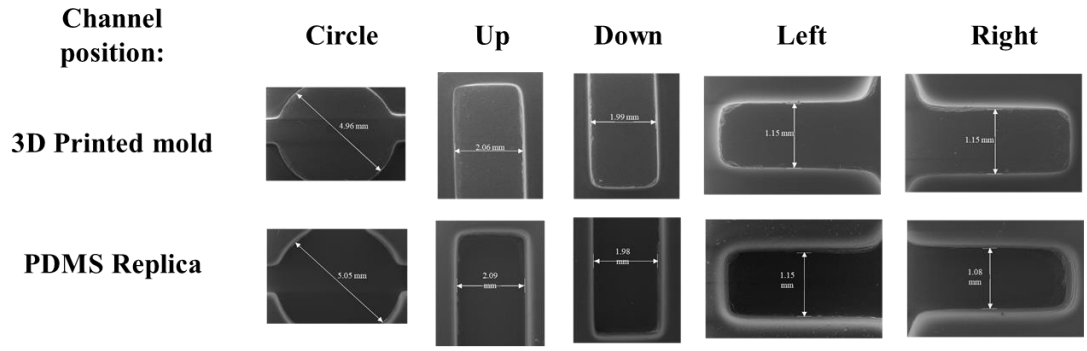

B

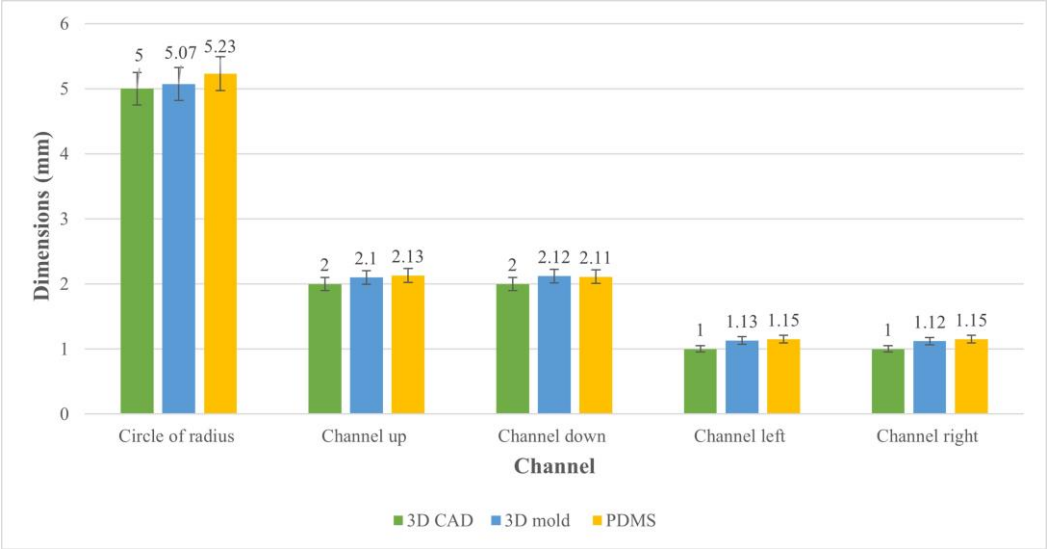

C

3D Design channel widths (mm)	Average printed channel widths (mm)	Error between design and printed mold (%)
5	5.07	1.4
2	2.11	5.5
1	1.12	12

Figure. 2: Comparison of dimensional profiles of the 3D designed model, the 3D printed mold and PDMS replica. SEM images of the printed mold and PDMS replica (A). Bar graph representing the dimensional profiles of 3D designed model, the 3D printed mold and PDMS replica (B). Relationship between designed widths and printed widths (C).

Strengths of SLA 3D printing in microfluidic device fabrication: In addition, we also compared the advantage of the LCD-based SLA 3D printer for fabricating master mold against the conventional method, photolithography, required high cost SU-8 reagent, clean room facilities, high cost of material and high time-consuming (Table 1).

Table 1: Comparison of printing time, cost, and overall process step for different fabrication type.

Mold fabrication type	Printing time per chip	Cost per chip	overall process steps
Photolithography	180 mins	20 US	Complicate 7 steps (10)
Anycubic photon S (LCD-based SLA 3D Printing)	30 mins	0.5 US	Simple 3 steps

Leakage testing of the microfluidic device: To assess the success of a microfluidic device, the flow leakage testing was performed by injecting red dye through the microfluidic channel for 1 h at the flow rate of 2 µl/min by using a syringe pump. If the liquid leakage was detected, then the spread of red dye out of microchannel would be observed. The result showed that there was no leaking in microfluidic device. The dye flows through the channel smoothly and steadily (Figure 3).

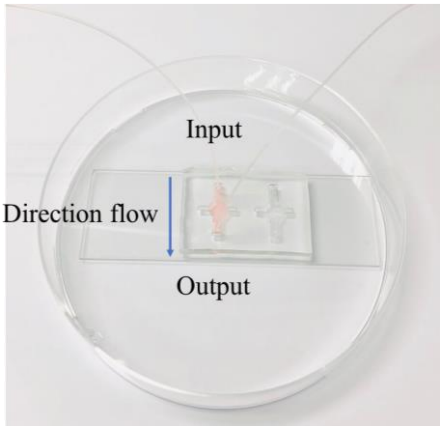

Figure 3: Leakage testing set up of the PDMS on glass microfluidic device by flowing the red dye inside channels.

Conclusion:

SLA 3D printing technology represents a powerful, simple, rapid, and cost- effective method to fabricating highly complex microfluidic devices. From idea to 3D model prototype can be created in a few minutes. Also, the mold can be reused, accelerate time, representing cost-effective production compared to traditional production methods.

However, in order to better evaluate the capacity of this LCD- based SLA 3D printing system, the optimization of curing time, intensive characterization of the printing resolution, minimum feature size, and surface roughness as well as biocompatibility testing should be further investigated. In addition, the proposed functional microfluidic cell culture on chip should be simulated for the optimal fluid flow rate and velocity in microchannel.

Acknowledgements: We gratefully acknowledged the graduate scholarship from Faculty of Medicine, and Graduate School Dissertation Funding, Prince of Songkla University. We would also like to thank Medical Science Research and Innovation Institute, Prince of Songkla University.

References:

1. Cui P, Wang S. A review. J Pharm Anal. 2019;9(4):238–47.
2. Temiz Y, Delamarche E. Sci Rep. 2018;8(1):1–11.
3. Oh KW. Micromachines. 2020;11(4):2019–21.
4. Coluccio ML, Perozziello G, Malara N, Parrotta E, Zhang P, Gentile F, et al. Microelectron Eng. 2019;208(January):14–28.
5. Gale BK, Jafek AR, Lambert CJ, Goenner BL, Moghimifam H, Nze UC, et al. Inventions. 2018;3(3).
6. Halldorsson S, Lucumi E, Gómez-Sjöberg R, Fleming RMT. Biosens Bioelectron. 2015;63:218–31.
7. Torino S, Corrado B, Iodice M, Coppola G. Inventions. 2018;3(3):1–14.
8. Comina G, Suska A, Filippini D. Lab Chip. 2014;14(2):424–30.
9. Su W, Li Y, Zhang L, Sun J, Liu S, Ding X. SLAS Technol. 2020;25(1):82–7.
10. Lee JM, Zhang M, Yeong WY. Microfluid Nanofluidics. 2016;20(1):1–15.
11. Duffy DC, McDonald JC, Schueller OJA, Whitesides GM. Anal Chem. 1998 Dec 1;70(23):4974–84.
12. Waheed S, Cabot JM, Macdonald NP, Lewis T, Guijt RM, Paull B, et al. Lab Chip. 2016;16(11):1993–2013.
13. Macdonald NP, Cabot JM, Smejkal P, Guijt RM, Paull B, Breadmore MC. Comparing Microfluidic Performance of Three-Dimensional (3D) Printing Platforms. Anal Chem. 2017;89(7):3858–66.
14. Quan H, Zhang T, Xu H, Luo S, Nie J, Zhu X. Bioact Mater. 2020;5(1):110–5.
15. Bhattacharjee N, Urrios A, Kang S, Folch A. Lab Chip. 2016;16(10):1720–42.
16. Wang Z, Martin N, Hini D, Mills B, Kim K. 3D Print Addit Manuf . 2017;4(3):156–64.
17. Arnold C, Monsees D, Hey J, Schweyen R. Vol. 12, Materials . 2019.

E_033_PA: APPLICATION OF CRYOGENIC FREE COMPREHENSIVE HEART-CUT TWO DIMENSIONAL GAS CHROMATOGRAPHY-MASS SPECTROMETRY FOR ANALYSIS OF VOLATILE COMPOUNDS IN PETROCHEMICAL SAMPLE

Nilobon Thongdorn-Ae,[1] Thumnoon Nhujak,[2] Pannipa Janta,[2] Atitarn Rueangthaweep,[1] Napida Hinchiranan,[4,5,*] and Chadin Kulsing[2,*]

[1]Program in Petrochemistry and Polymer Science, Faculty of Science, Chulalongkorn University, Bangkok 10330, Thailand
[2]Chromatographic Separation and Flavor Chemistry Research Unit and Center of Molecular Sensory Science, Department of Chemistry, Faculty of Science, Chulalongkorn University, Bangkok 10330, Thailand
[3]Department of Chemical Technology, Faculty of Science, Chulalongkorn University, Bangkok 10330, Thailand
[4]Center of Excellence on Petrochemical and Materials Technology (PETROMAT), Chulalongkorn University, Bangkok 10330, Thailand
[5]Center of Excellence in Catalysis for Bioenergy and Renewable Chemicals (CBRC), Chulalongkorn University, Bangkok 10330, Thailand

*e-mail: napida.h@chula.ac.th
chadin.k@chula.ac.th

Abstract:

Multidimensional gas chromatography (MDGC) is an effective technique to analyze complex petroleum samples. The recent techniques employ comprehensive multiple heart-cut (CH/C) with long first and second dimensional (^{1}D and ^{2}D) columns for enhanced peak capacity. Furthermore, short analyte pulses obtained from the ^{1}D column are also sampled onto the ^{2}D column with rapid cycle times prior to the next sampling in order to fasten the analysis time to obtain comprehensive chemical profile of a sample. In this study, CH/C MDGC without use of cryogenic trapping device was applied for analysis of the sample obtained from palmitic acid oxidation using Rancimat instrument. The system used a single Deans switch (DS) located between ^{1}D (30 m) and ^{2}D (60 m) columns with the lower polar-higher polar configuration. Cyclic multiple H/C approach (150 H/C in total) was performed to result in the comprehensive analysis. The H/C window of 0.2 min was applied in order to inject a narrow H/C band onto the ^{2}D column. Prior to the MDGC analysis, the sample was prepared by solid phase micro-extraction (SPME). Volatile compounds of the sample were tentatively identified according to match of the experimental MS spectra and retention indices (*I*) with that from NIST17 library. This CH/C-MDGC approach provided total peak capacity of 5,840 and 266 identified with the major oxygenated compounds including 2-octanone, 1-methylcyclohexanol, 2,3,6-trimethylphenol, 3-phenylpropanol and 2-nonanone. The MS match scores, reverse match scores and I difference were 772±42, 815±38 and 15±8, respectively.

E_035_OA: STUDY ON FOOD RANCIDITY OF VIGRIN COCONUT OIL IN TANINTHARYI REGIONAL DESSERT (MOHT KALEME)

Nay Mar Soe[1*], Tun Oo[2], Nay Thwe Kyi[3]

[1*]Professor, Department of Chemistry, Yangon University of Education
[2]Lecturer, Department of Chemistry, Myeik University
[3]Pro Rector, Dagon University
*email:drnaymar.chem.chem@gmail.com
drnaymar@yuoe.edu.mm
dr.naythwekyi55@gmail.com

Abstract:

In Myanmar, oil palm fruits are grown mainly in Tanintharyi region. Virgin coconut oil can be extracted from the kernel or meat of mature coconut harvested from the coconut palm (Cocos nucifera). Black Glutinous Rice Dessert or Moht Kaleme is a popular regional dessert in Tanintharyi Region. Virgin coconut oil is also extracted by Cold extraction method. Characteristic properties of the extracted virgin oil such as color, odor, pH, viscosity, acid value, peroxide value, iodine value, saponification value and unsaponification value were investigated by AOAC methods. Antioxidant activities of extracted oil (IC_{50}=12.05 µg/ml) and gallic acid (IC_{50}=8.76 µg/ml) determined by DPPH assay. Moht Kaleme was collected from the traditional food shops. A substantial increase carbohydrate, total sugar, starch and decrease in fat, ash, and fiber observed in Moht Kaleme sample. Virgin Moht Kaleme was made with virgin oil substituted in commercial oil but preparation steps and other ingredients were same as commercial sample. Rancidity influence factors of acid value, smell, taste and physical state were comparatively measured in commercial and vigrin Moht Kaleme samples with two days interval at room temperature. Acid values of both samples were determined by titration method. In findings, acid values of both samples were slowly increased within 8 days period. After four days period, commercial Moht Kaleme little changed its smell .Then, it had bad smell, rancid taste and caused fungus after six days period (acid value=5.6). In virgin sample, acid value increased by a slower rate and found mouldy smell and fungus after eight days longer (acid value=4.6). According to this study; virgin coconut oil has good quality to avoid the formation of rancid food**.** Moreover, it has good antioxidant activity. Therefore, virgin coconut oil can use instead of the commercial oil for making fat containing traditional dessert as natural preservative**.**

E_036_PA: GEL-FORMING ABILITY OF UNWASHED ROHU AFFECTED BY EGG WHITE

Warangkana Sompongse,[1,*] Phatthira Sutloet,[2] Katsuji Morioka[3]

[1,2]Department of Food Science and Technology, Faculty of Science and Technology, Thammasat University, Pathum Thani 12120, Thailand
[3]Aquatic Product Utilization Laboratory, Faculty of Agriculture, Kochi University, Monobe 200, Nankoku, Kochi 783-8502, Japan
*e-mail: warang@tu.ac.th

Abstract:

The effect of egg white powder (EW) on gel-forming characteristics and autolytic inhibition in rohu (*Labeo rohita*) gel was investigated. Gels from unwashed mince (unwashed gel) were prepared under different setting conditions, producing kamaboko gel at 40°C and modori gel at 65°C. The addition of EW at 3% improved the gel-forming ability and that of 2% improved autolytic inhibition of modori gel, as shown by the greater gel strength ($P \leq 0.05$) than the control, a lower of expressible water content and TCA-soluble peptide content ($P \leq 0.05$), and greater myosin heavy chain (MHC) intensity. The kamaboko gel showed no significant change on gel-forming ability and autolytic inhibition when the EW content was increased beyond 1%. Addition of EW at 3% significantly increased the whiteness of both gels ($P \leq 0.05$).

Keywords: Rohu (*Labeo rohita*), gel-forming characteristics, modori gel, kamaboko gel, egg white powder, unwashed gel

E_037_PF: IMPROVEMENT OF BREAD ENRICHED WITH LARVAL-STAGE MEALWORM (*Tenebrio molitor*) BY USING HYDROCOLLOIDS

Krittiya Khuenpet[1,*], Sangvorn Kitthawee[2], Charida Pakasap[1], Suteera Vattanakul[1]

[1]Department of Food Science and Technology, Faculty of Science and Technology, Thammasat University, 99 Phahonyothin Road, Klong Luang, Pathum Thani 12121, Thailand.
[2]Department of Biology, Faculty of Science, Mahidol University, Phaya Thai, Bangkok 10400, Thailand.
*e-mail: krittiya23@tu.ac.th

Abstract:

Mealworm (*Tenebrio molitor*) powder was added to wheat bread to obtain bread with enhanced nutrition value. The addition of 5% mealworm powder in wheat bread increased hardness value and reduced specific volume of bread. Likewise, mealworm bread exhibited a non-uniform and larger air cell size compared with wheat bread without fortification of mealworm powder. The objective of this research was to improve the quality of mealworm bread by using 3 types of hydrocolloids including carboxymethyl cellulose (CMC), guar gum (GG) and xanthan gum (XG). Two levels of each hydrocolloid at 1 and 1.5% of dough weight were added and determined their dough and bread qualities. The result showed that the addition of CMC or GG revealed more positive effect on quality of mealworm bread than XG added. Specific volume and cell numbers of mealworm bread mixed with CMC and GG were higher than mealworm bread without addition of hydrocolloids significantly (p<0.05). The increase of hydrocolloid content up to 1.5% was found to rise hardness and reduce specific volume of mealworm bread. Mealworm bread added 1% CMC provided hardness and specific volume values comparable with wheat bread.

Introduction:

Bread is a bakery product which made from wheat flour as a main ingredient. This kind of food is high in carbohydrate and calories but low in protein. Therefore, various alternatives source of protein for bread enrichment have been studied. Cercel *et al.*[1] investigated the effect of fish protein on quality improvement of wheat bread. The results showed that 10% of fish protein addition produces bread with high protein content at 20%. However, fish protein addition affected the properties of dough, which decreasing specific volume of bread. Moreover, the addition of insects that considers as alternative source of protein have also been examined in several studies. In wheat bread, fortification of mealworm powder led to increase of protein content. On the other hand, supplementing of mealworm powder resulted in the reduction of specific volume and the increase of bread hardness.[2] Osimani *et al.*[3] and de Oliveira *et al.*[4] reported that the addition of cricket powder and cinereous cockroach in bread increased protein content, but negatively affected physical and sensory qualities of bread.

It can be seen that the addition of protein or insect powder to increase nutritional value may cause negative effect on bread qualities such as unpleasant appearance, change in color and improper texture of bread products. According to the demands of high-quality healthy food with great appearance are rising.[5] High quality bread product is characterized by high volume with soft and elastic crumb.[6] Consequently, several researchers have tried to find solutions to produce better quality of fortified bread products by using food additives.

Hydrocolloid have been widely used in bakery products as a bread improver because it helps increase dough and bread properties such as water absorption, gas retention and textural properties.[7] Many researches have been studied the effect of hydrocolloids to improve the qualities of bread products. Panyathitipong and Peeraphatchara[8] informed that CMC could improve quality of bread made from Palmyra palm in the terms of specific volume and texture parameters. Ghanbari and Farmani[9] found that sensory attributes of barbari bread was improved by adding 0.5% of hydroxypropyl methylcellulose (HPMC). Previtali *et al.*[10] reported that the use of 1-2% CMC in bread containing 25% of lentil flour improved textural properties and sensorial quality of bread. These researches indicated that hydrocolloids had ability to improve qualities of bread.

However, little data is available on the effect of hydrocolloids on properties of wheat bread containing protein or insect powder. Therefore, the aim of this study was to investigate effect of hydrocolloids including carboxymethyl cellulose, guar gum and xanthan gum on physical and chemical properties of bread containing mealworm powder.

Methodology:

Materials and Preparation of bread

Mealworm powder was obtained from Department of Biology, Faculty of Science, Mahidol University, Thailand. Wheat flour (UFM Food Centre Co., Ltd., Bangkok, Thailand), instant dried yeast (KCG Corporation Co., Ltd., Bangkok, Thailand), sugar (Thai Roong Ruang industry Co., Ltd., Phetchaburi, Thailand), salt (Saha Pathanapibul Pub Co., Ltd., Bangkok, Thailand), shortening (Lam Soon Co., Ltd., Bangkok, Thailand), egg (Central Food Retail Co., Ltd., Pathumthani, Thailand) and milk (Dutch Mill Co., Ltd., Bangkok, Thailand) were purchased from supermarkets nearby Thammasat University, Thailand. Carboxy methylcellulose, guar gum and xanthan gum were supplied from Chemipan Corporation Co., Ltd., Bangkok, Thailand. The wheat bread (reference sample) formula was 55% wheat flour, 1% instant dried yeast, 3% sugar, 0.15% salt, 6% shortening, 2% egg yolk, 6% milk and 30% water. The sponge method was used to produce bread loaf. Half of the total amount of wheat flour and water of the formulation were mixed with instant dried yeast to produce sponge. All sponge ingredients were mixed and left for 1 hour. The sponge was homogenized with other ingredients using a food mixer machine (Spar mixer, 800-B, Taiwan) for 30 minutes. The dough was rounded and rested in a mold covered with wet cloth in order to maintain relative humidity of dough. The dough was baked in the oven (Union Progress, UP-AG100, Italy) at 180 ^{o}C for 20 minutes. After that, bread loaf was cooled to room temperature. Reference sample (wheat bread) was fortified with 5% mealworm powder and set as a control sample. The reason of the 5% was used was according to González *et al*.[11], studied the potential use of *Hermetia illucens, Acheta domestica* and *Tenebrio molitor* at 5% in bread. The results showed that 5% of insect flour added had less effect on bread quality and improved nutritional profile. Also, Khuenpet *et al*.[2], reported that qualities of bread containing 5% mealworm were more comparable to wheat bread than those of bread containing 10 and 15% of mealworm. The use of three types of hydrocolloids including carboxy methylcellulose (CMC), guar gum (GG) and xanthan gum (XG) at 1% and 1.5% by dough weight were investigated to improve quality of mealworm bread (control sample).

Proximate analysis, amino acids and fatty acids measurement

All of nutrient components of mealworm powder were analysed according to AOAC (2012) method by Technical Service Institute of Nutrition, Mahidol University, Nakhon Pathom, Thailand. Amino acid profiles of wheat bread and mealworm bread added hydrocolloid were analyzed according to In-house method (HPLC C-precolumn –AccQ Tag) by Central Instrument Facility (CIF), Faculty of Science, Mahidol University. In this study only results of proline and arginine contents were presented because those two amino acids were found significantly difference in wheat bread and mealworm bread. Fatty acid profile of wheat bread and mealworm

bread added hydrocolloid were analyzed according to AOAC[12] method by Institute of Nutrition, Mahidol University. Only amounts of omega 6 and 9 contents were reported in this study.

Dough stickiness

Dough stickiness values were measured by using a texture analyzer (plus-upgrade, Stable Micro System, USA) with a 25 mm perspex cylinder probe (P/25P) and SMS/Chen-Hoseney Dough Stickiness cell under the following condition: Pre-Test speed: 0.5 mm/s, Test speed: 0.5 mm/s, Post-Test-speed: 10.0 mm/s, Distance: 4 mm, Force: 40 g, Time: 0.1 s, Trigger type: Auto-5 g.[13] Ten grams of dough was loaded in an empty chamber and excess dough was removed using a spatula. Then, the screw was rotated to extrude dough through the holes and removed the first extrusion. The screw was rotated once again after removing first extrusion to obtain 1 mm high dough for analysis. The result obtained from the test was a force versus time curve. The positive maximum force in the curve is an indicator of dough stickiness (g).

Texture analysis

Texture properties of all bread samples were performed using a texture analyzer (plus-upgrade, Stable Micro System, USA) with a 25 kg load cell and 50 cylindrical probe. Bread slice (25 mm thickness) taken from the center of each was compressed twice under the following condition: Pre-Test speed: 1.00 mm/s, Test-speed: 1.00 mm/s, Post speed: 1.00 mm/s, Distance: 40%.[8] The average values of at least ten analyses were calculated. Hardness, springiness and chewiness were recorded from measurement.

Specific volume

Specific volume of bread was measured applying displacement of seed method according to Panyathitipong and Peeraphatchara.[8] Volume of bread was conducted by placing bread into the container, and then sesame seeds were poured to fill the container until the bread was covered. Then sesame seeds volume was measured in a cylinder. Specific volume of bread was calculated following equation (1) and (2):

$$\text{Loaf volume } (cm^3) = \text{container volume - sesame seeds volume} \quad (1)$$

$$\text{Specific volume } (cm^3/g) = \frac{\text{loaf volume } (cm^3)}{\text{loaf weight (g)}} \quad (2)$$

Water activity

Bread samples were ground into small pieces and measured by a water activity meter (CX2, Aqualab, USA)

Color value

Color values of bread were measured by using a colorimeter (CX2678, Hunter Lab, USA). The obtained results were presented as lightness (L*), redness (a*) and yellowness (b*).

Image analysis

The images of sliced bread were taken by a digital camera and cropped into 400x400 pixels. Each sample was taken image three replications. And then, cropped images were analyzed by ImageJ analysis applying the method of Scheuer *et al.*[14] The images were changed to 8-bit greyscale and set the threshold to obtain resolution of air cells. Number of cells (cells) and mean cell area (mm^2) were derived from the image analysis and cell density ($cells/mm^2$) was calculated using the following equation (3), the reported data were presented as average and standard deviation values of three replicate measurements.

$$\text{Cell density } (cells/mm^2) = \frac{\text{Number of cells (cells)}}{\text{mean cell area } (mm^2)} \qquad (3)$$

All data were analyzed using SPSS Statistics version 20. Completely Randomized Design (CRD) with three replications was set as experimental design. One way ANOVA was used to analyze the statistical significance and Duncan was used to determine the difference between mean values at significant level of $p<0.05$.

Results and Discussion:

Mealworm powder mainly contained protein and fat content which accounted for 51.11±0.21 and 32.89±0.51 g/100g, respectively. Carbohydrate was the second source of this powder, at 10.8±0.33 g/100g. Moreover, the lowest components were found in ash and moisture, at 3.48±0.01 and 1.72±0.04. g/100g. The mealworm powder provided energy 543.65±2.55 kcal/100g.

Dough stickiness is a main problem during the bread processing. The presence of sticky dough is related to water absorption of flour. Adding too much water to flour or overmixing time cause sticky dough.[15] In this study, the highest level of dough stickiness was observed in bread containing mealworm powder (control). Protein addition increase level of water absorption, which affects stickiness of dough.[16] In agreement of Wood[17], fortification of chickpea in spaghetti in order to improve protein content was found to increase stickiness of spaghetti dough. Mealworm contains about 48.5 (g/kg protein) of proline[18] which may promote stickiness of dough. Fermin *et al.*[19] found that addition of proline (1.75 g/ 100 g wheat flour) increase dough stickiness because proline contains stronger hydrogen bond compare to other amino acids. In this study, proline was found 1.13 g/ 100 g in mealworm bread as shown in Table 5. Therefore, mealworm dough had high dough stickiness value. Water absorption that enhance by other ingredient used led to the decrease of water absorption capacity of gluten.[20] This phenomenon might affect water absorption capacity of gluten during baking step. According to the results of hardness and free water contents in Table 1 and 2, hardness values increased while free water contents decreased when mealworm powder was added. The mealworm dough stickiness decreased significantly with the addition of hydrocolloids (CMC, GG and XG). The higher amount of added hydrocolloid decreased stickiness of mealworm dough. This situation can be explained through the hydroxyl groups in the hydrocolloid structure allow more water interactions through hydrogen bond[21], resulting in the increase of water absorption. In agreement with Han *et al.*[22] presented that high water absorption decreased stickiness value and produced firm dough.

Textural properties of all bread samples which were wheat bread (reference), bread containing 5% mealworm powder (control) and 5% mealworm bread added hydrocolloids were shown in Table 1. It was found that the presence of mealworm powder in wheat bread resulting in an increase of hardness and chewiness while decreasing in springiness. The explanation is that the addition of mealworm powder might disturb the formation of gluten network, which effect on the reduction of gluten elastic and gas retention ability.[23,24] Adding mealworm powder which is non-gluten protein it may cause the dilution of gluten matrix in system.[25] Majzoobi *et al.*[26] reported that the increase of bread hardness occurred when whole oat flour was added is attributed to the

dilution of gluten lead to the reduction of gas retention capacity. Texture is one of sensory characteristics of food which strongly affect customer acceptability.[27] Hardness of bread refers to the resistance of bread to the deformation which correlates with consumer acceptability.[28] Fagundes *et al.*[29] reported that softer crumb of bread product provides feeling of freshness. Thus, mealworm bread requires more improvement in textural properties to achieve better texture characteristics. It can be seen that the addition of hydrocolloids in mealworm bread decreased hardness and chewiness. The use of CMC and GG provided more positive impact on textural properties than that of XG. This probably due to CMC contains more carboxyl and hydroxyl groups resulting in more hydrogen links and a higher water-holding capacity.[5] It was because hydrophilic in CMC promoted water-holding capacity, resulting in formation of gel structure that was able to improve gas retention capacity[8] while GG could not formed gel structure, nevertheless its dispersibility in water and water holding capacity would be enhanced consistency of dough network by promoting gas retention.[30] Conversely, hardness and chewiness values of mealworm bread were not improved by XG added. XG exhibited a compelling potential as a thickener resulted in the restrict expansion of air cells during baking.[15] The consequence of hardness was strongly related with specific volume of bread samples presented in Table 2. The fortification of CMC and GG in formulas could produce higher specific volume samples whereas the use of XG presented a low specific volume bread. Similar to the study of Maleki and Milani[5], hydroxypropyl methylcellulose (HPMC) and CMC generated soft bread crumb, while XG provided harder crumb texture. The addition of XG would be reduced water in system because of its water holding capacity, contributing to the weakness of dough network.[15]

Table 1. Dough stickiness and textural properties of wheat bread sample (reference), wheat bread fortified with 5% mealworm powder (control) and mealworm bread added various hydrocolloids.

Samples	Dough stickiness (g)	Hardness (g.force)	Springiness	Chewiness
Wheat bread (Reference)	$41.05^{a}\pm3.13$	$104.74^{d}\pm20.68$	$0.92^{a}\pm0.02$	$68.06^{d}\pm12.00$
MW 5% (Control)	$46.48^{a}\pm3.78$	$413.78^{a}\pm67.43$	$0.85^{b}\pm0.01$	$199.77^{a}\pm35.36$
MW 5% + CMC 1%	$27.79^{b}\pm3.85$	$114.09^{d}\pm46.07$	$0.77^{d}\pm0.04$	$48.09^{e}\pm15.35$
MW 5% + CMC 1.5%	$17.00^{d}\pm3.85$	$151.64^{d}\pm133.85$	$0.75^{e}\pm0.06$	$68.47^{d}\pm16.32$
MW 5% + GG 1%	$20.97^{c}\pm2.55$	$134.02^{d}\pm31.35$	$0.82^{c}\pm0.04$	$64.62^{de}\pm14.45$
MW 5% + GG 1.5%	$18.04^{d}\pm3.34$	$231.71^{c}\pm55.39$	$0.84^{b}\pm0.04$	$113.79^{c}\pm26.19$
MW 5% + XG 1%	$22.89^{c}\pm1.44$	$362.70^{b}\pm159.73$	$0.84^{b}\pm0.03$	$176.73^{b}\pm54.31$
MW 5% + XG 1.5%	$15.49^{d}\pm2.33$	$420.86^{a}\pm133.00$	$0.84^{b}\pm0.06$	$197.83^{a}\pm52.51$

[a, b, c] Different letters in the same column are significantly different ($p < 0.05$)

MW = mealworm powder, CMC = carboxy methylcellulose, GG = guar gum and XG = xanthan gum

Specific volume and free water content (a_w) of all bread samples are shown in Table 2. Specific volume of bread refers to the expansion of bread dough after baking.[31] Low specific volume of bread gave unpleasant appearance.[29] Specific volume of mealworm bread (control) was lower than wheat bread (reference). Similar finding has been also expressed in earlier study of González and Rosell[11], the addition of insect powder in bread caused reduction of specific volume. The lessening of specific volume showed that mealworm powder fortification reduced expansion ability of bread and produced flat bread as shown in figure 2b. This effect might be related to capacity to form network of gluten. In bread product, gluten network formation is an important factor for gas retention which provides volume of bread.[32] Therefore, the weaken gluten network resulted in the reduction of gas retention ability. Healthier food products with good sensorial qualities have been more required from customer.[33] The present of CMC and GG in bread fortified with mealworm powder found to increase specific volume whereas applied XG showed a reduction in specific volume. The explanation is that CMC and GG improve gas retention ability by increasing viscosity of dough through hydroxyl group in hydrocolloids structure, which is able to promote gas retention.[34,35] The adding XG presented higher viscosity values than that of CMC and GG fortification due to its thickening property.[36] High viscosity of dough results in

decrease of specific volume because it is difficult to expanse.[37] It was found that the increase of hydrocolloids up to 1.5% decreased specific volume of bread. The increase of hydrocolloids content promoted water adsorption and led to softer dough network and lower consistency.[5] Less consistency of dough reduced gas retention capacity and directly affected texture of bread. Similar to the study of Moore *et al*.[38] the result showed correlation between specific volume and hardness of bread. According to this experiment result showed in Table 1, the hardness value of bread increased in mealworm bread mixed with 1.5% hydrocolloids. The lowest water activity content was found in mealworm bread sample. This may be because of addition of mealworm powder affect gluten formation. Weakening of gluten structure causes the decrease of moisture retention ability during baking.[39] The use of hydrocolloids made high water activity bread products. The addition of hydrocolloids increases free water content because of their high-water retention capacity.[21]

Table 2. Specific volume and water activity (a_w) of wheat bread (reference), wheat bread fortified with 5% mealworm powder (control) and mealworm bread added various hydrocolloids.

Samples	Specific volume (cm^3/g)	a_w
Wheat bread (Reference)	$4.28^{a}\pm0.07$	$0.918^{bc}\pm0.008$
MW 5% (Control)	$3.30^{b}\pm0.04$	0.907^{c} 0.005
MW 5% + CMC 1%	$4.27^{a}\pm0.13$	$0.915^{bc}\pm0.017$
MW 5% + CMC 1.5%	$4.26^{a}\pm0.25$	$0.925^{ab}\pm0.017$
MW 5% + GG 1%	$4.14^{a}\pm0.13$	$0.930^{a}\pm0.004$
MW 5% + GG 1.5%	$3.56^{b}\pm0.04$	$0.923^{ab}\pm0.008$
MW 5% + XG 1%	$3.29^{bc}\pm0.32$	$0.932^{a}\pm0.012$
MW 5% + XG 1.5%	$2.96^{c}\pm0.65$	$0.929^{a}\pm0.006$

[a, b, c] Different letters in the same column are significantly different ($p < 0.05$).
MW = mealworm powder, CMC = carboxy methylcellulose, GG = guar gum and XG = xanthan gum

Table 3 shows color values (L*,a*,b*) of bread samples. Bread added mealworm powder without using hydrocolloids presented the lowest lightness (L*) and highest yellowness (b*) and redness (a*) values. This might be correlated to maillard reaction which occurs between protein and reducing sugar in the presence of heat resulting in brown color of baked bread. The use of hydrocolloids found to increase lightness (L*) while decrease yellowness (b*) and redness (a*) values of mealworm bread. It was because hydrocolloids addition improved water binding capacity.[40] The increase of water in system caused dilution of reactants that can be produced maillard reaction.[41] Consequently, mealworm bread added hydrocolloid presented mild color tone compared with mealworm bread without hydrocolloids addition as shown in Figure 1 and 2.

Table 3. Color values (L*,a*,b*) of wheat bread (reference), wheat bread fortified with 5% mealworm powder (control) and mealworm bread added various hydrocolloids.

Sample	Crust			Crumb		
	L*	a*	b*	L*	a*	b*
Wheat bread (Reference)	$56.30^{a}\pm1.11$	$1.64^{e}\pm1.01$	$15.02^{b}\pm2.75$	$81.97^{a}\pm1.08$	$1.24^{c}\pm0.77$	$19.35^{b}\pm3.07$
MW 5% (Control)	$41.89^{d}\pm0.46$	$7.94^{a}\pm0.85$	$19.67^{a}\pm0.84$	$58.82^{e}\pm1.35$	$4.22^{a}\pm0.20$	$22.22^{a}\pm4.04$
MW 5% + CMC 1%	$47.61^{bc}\pm1.73$	$3.58^{cd}\pm0.47$	$15.90^{b}\pm1.05$	$66.20^{bc}\pm2.73$	$3.20^{b}\pm0.80$	$18.09^{b}\pm0.62$
MW 5% + CMC 1.5%	$45.83^{bcd}\pm1.74$	$4.16^{c}\pm1.22$	$16.48^{b}\pm2.33$	$64.28^{cd}\pm2.34$	$3.28^{b}\pm0.54$	$17.91^{b}\pm0.67$
MW 5% + GG 1%	$46.36^{bcd}\pm9.87$	$2.93^{d}\pm0.11$	$14.91^{b}\pm0.12$	$66.85^{b}\pm4.57$	$3.31^{b}\pm0.44$	$18.66^{b}\pm0.91$
MW 5% + GG 1.5%	$50.02^{b}\pm0.16$	$3.10^{d}\pm0.28$	$15.05^{b}\pm1.01$	$68.37^{b}\pm1.29$	$3.13^{b}\pm0.15$	$17.87^{b}\pm0.50$
MW 5% + XG 1%	$44.13^{cd}\pm1.20$	$6.21^{b}\pm0.85$	$19.40^{a}\pm1.07$	$62.58^{d}\pm1.77$	$4.08^{a}\pm0.15$	$17.68^{b}\pm4.35$
MW 5% + XG 1.5%	$43.35^{cd}\pm6.08$	$4.18^{c}\pm0.80$	$16.10^{b}\pm1.56$	$66.23^{bc}\pm1.48$	$3.81^{a}\pm0.41$	$18.98^{b}\pm0.74$

[a, b, c] Different letters in the same column are significantly different ($p < 0.05$)
MW = mealworm powder, CMC = carboxy methylcellulose, GG = guar gum and XG = xanthan gum

The number of cells, cell area and cell density of bread samples are reported in Table 4. The results showed that bread fortified mealworm powder had a higher number of air cells (73.67 cells) and cell sizes (4.80 mm^2) were also larger than wheat bread (62.67 cells). The cell wall of these air cells was formed by gluten and gelatinized starch.[6] The addition of other ingredients such as mealworm powder led to change in the structure of bread crumb which affecting the quality of bread.[6] Improvement of bread structure by using XG provided a lower number of cells and smaller cell areas than that of CMC and GG. The thickening effect reduces the rate of gas diffusion in bubbles; therefore, the expansion is so difficult.[39] According to a specific volume in Table 2, bread added XG found to decrease specific volume because of the limitation of cell enlargement. Noorlaila *et al*.[42] reported that XG produced a dense texture of sponge cake because of the thickness of cell wall. Bread added mealworm powder with using GG produced a higher number of air cells than that of XG due to its water holding capacity, resulted in the present of high dough elasticity and increase gas retention capacity.[30] However, the thickening effect of GG also related to expansion of air cells, which revealed that the number of air cells was lower than bread sample using of CMC. The highest number of cell and cell area were observed in bread using CMC. The explanation is that CMC contains amount of hydroxyl group in structure, so water holding capacity increases and elastic gel is produced around air cell. This phenomenon can prevent gas cell coalescence.[5] The high number of small air cells indicated high gas retention capacity of dough[43], which according to the higher specific volume of bread contained CMC (table 2).

Table 4. Porousity characteristics of mealworm bread with and without hydrocolloids

Samples	Number of cells (cell)	Average size (mm^2)	Cell density (cells/mm^2)
Wheat bread (Reference)	$62.67^{e}\pm11.67$	$2.73^{b}\pm0.11$	$22.90^{bc}\pm3.78$
MW 5% (Control)	$73.67^{de}\pm7.23$	$4.80^{b}\pm0.91$	$15.71^{c}\pm3.09$
MW 5% + CMC 1%	$120.33^{a}\pm14.84$	$3.36^{ab}\pm0.83$	$37.79^{a}\pm11.88$
MW 5% + CMC 1.5%	$100.67^{bc}\pm10.69$	$3.32^{ab}\pm0.35$	$30.58^{ab}\pm4.62$
MW 5% + GG 1%	$110.00^{ab}\pm2.64$	$3.76^{a}\pm0.30$	$29.35^{ab}\pm1.65$
MW 5% + GG 1.5%	$87.67^{cd}\pm8.02$	$2.87^{b}\pm0.19$	$30.74^{ab}\pm4.19$
MW 5% + XG 1%	$64.33^{e}\pm5.13$	$2.65^{bc}\pm0.17$	$24.42^{bc}\pm3.25$
MW 5% + XG 1.5%	$32.33^{f}\pm5.68$	$2.00^{c}\pm0.06$	$16.10^{c}\pm2.47$

$^{a, b, c}$ Different letters in the same column are significantly different ($p < 0.05$)

MW = mealworm powder, CMC = carboxy methylcellulose, GG = guar gum and XG = xanthan gum

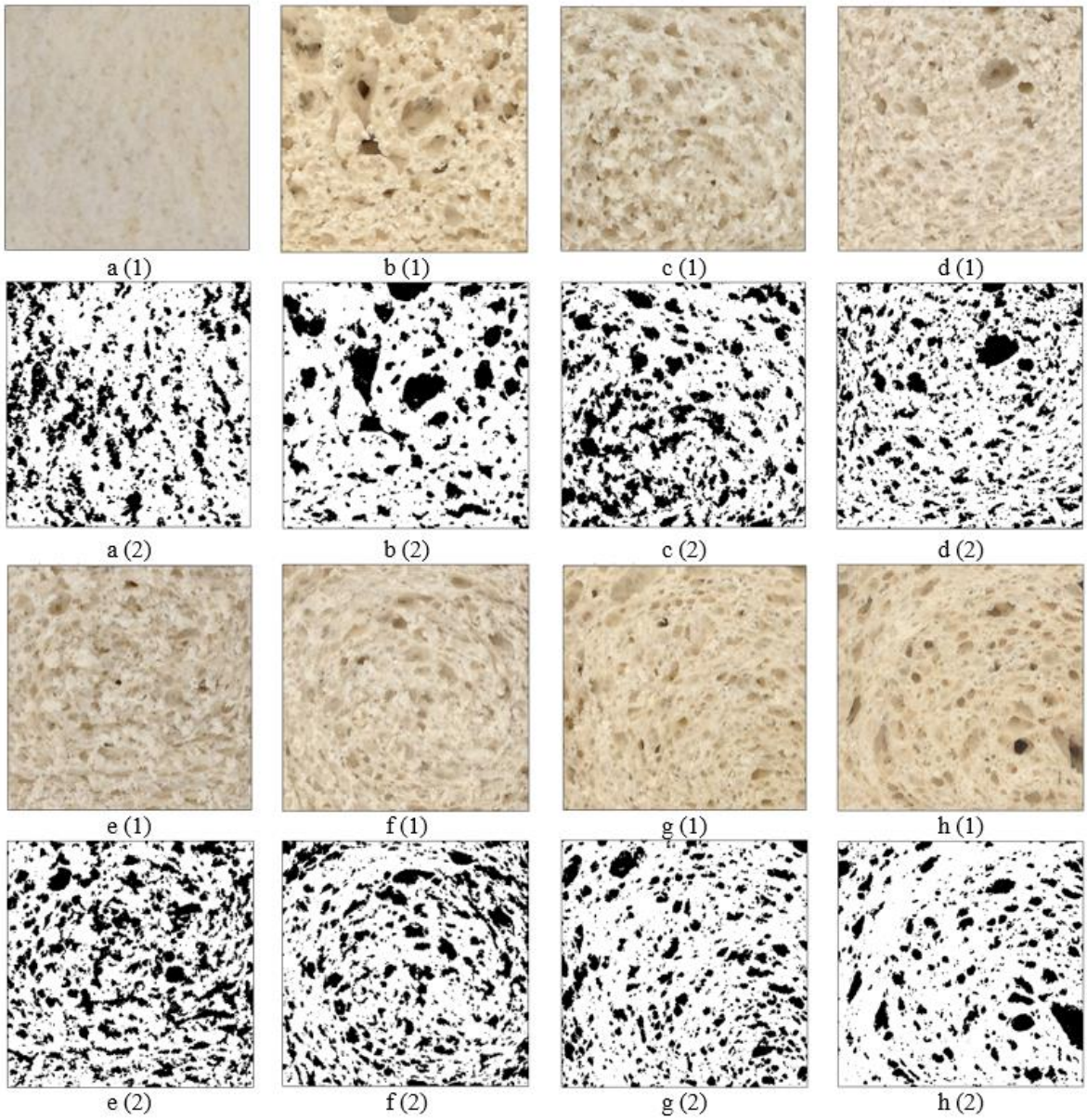

Figure 1. Image analysis of wheat bread (a1-2), bread containing 5% mealworm (b1-2), bread using 1% (c1-2) and 1.5% (d1-2) CMC, bread using 1% (e1-2) and 1,5% (f1-2) GG, bread using 1% (g1-2) and 1.5% (h1-2) XG.

Image analysis of bread samples were shown in Figure 1. Wheat bread sample (Figure a(1-2) showed the finest crumb and thinnest cell wall among other bread samples. This result related with Table 1, where wheat bread was presented the lowest hardness. Rathnayake *et al.*[44] reported that thinner cell wall performed flexibility and soft crumb. Cell wall of mealworm bread (Figure b1-2) was thicker than wheat bread. The addition of mealworm powder caused higher hardness level than reference formula. The application of hydrocolloid in mealworm bread showed raising in degree of fine crumb and decreasing of the thickness of cell wall. The reason for this phenomenon is that hydrocolloids create bond in wheat flour and produce better porosity and higher volume.[43] According to the results of specific volume (Table 2), the use of hydrocolloids in bread produced higher volume. However, using of XG provided thicker cell than that of CMC and GG. This may relate to the thickening effect of XG.

Cross section of bread loaves is shown in figure 2. Mealworm bread (b) presented lower height, larger porous, thicker cell wall and darker color compared with wheat bread (a). The addition of CMC (c-d) and GG (e-f) increased height of bread and provide finer structure with mild color. The application of XG did not provide better appearance as good as CMC and GG. This might be a thickening effect from XG that produced high viscosity. Therefore, large porous in crumb could occur and thick cell wall of bread was noticed.

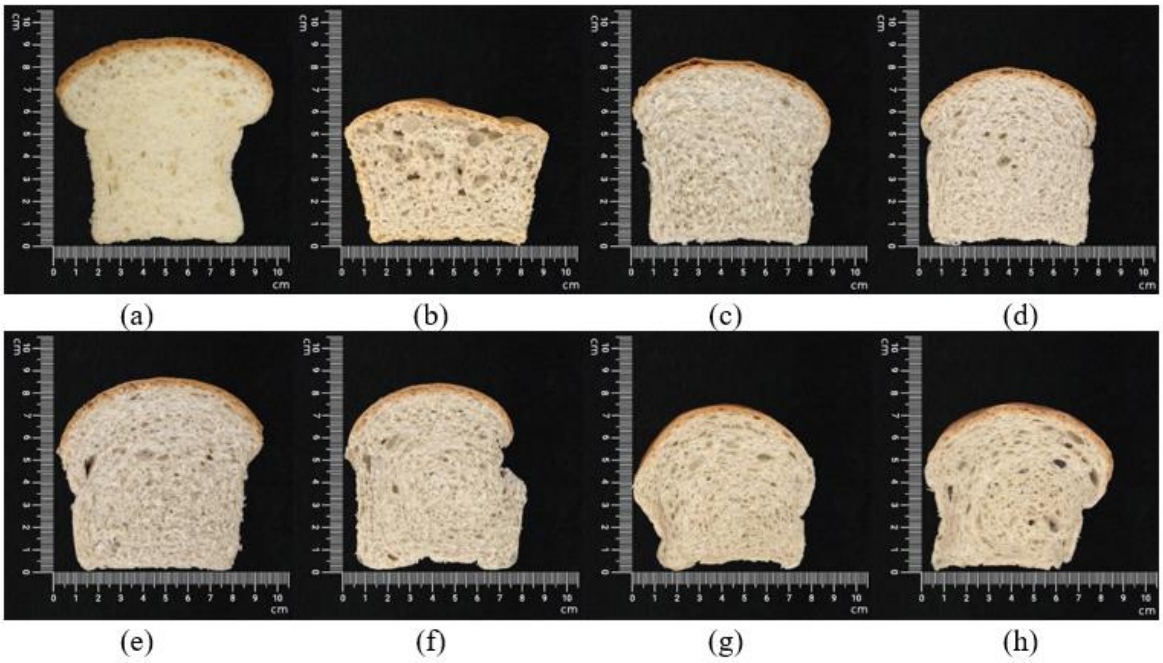

Figure 2. Cross section of wheat bread (a), bread containing 5% mealworm (b), bread using 1% (c) and 1.5% (d) CMC, bread using 1% (e) and 1.5% (f) GG, bread using 1% (g) and 1.5% (h) XG

Table 5 Chemical compositions and calories of wheat and mealworm bread added CMC 1%

Chemical compositions	Wheat bread	Mealworm bread added CMC 1%
Fat (g/100g)	6.2±0.02	8.80±0.02
Omega-6	0.70±0.03	1.14±0.01
Omega-9	1.72±0.01	2.53±0.02
Protein (g/100g)	9.7±0.01	10.40±0.02
Arginine	Not detected	0.48±0.01
Proline	Not detected	1.13±0.01
Carbohydrate (g/100g)	48.7±0.01	46.60±0.02
ash (g/100g)	0.59±0.03	0.84±0.04
Moisture content (g/100g)	34.78±0.05	33.31±0.03
Total calories (Kcal/100g)	289±0.01	307±0.02

Table 5 shows chemical compositions of wheat and mealworm bread added CMC 1%. It can be seen that an increase of fat and protein content was observed when mealworm powder was added. Omega 6 and 9 contents in mealworm bread were higher than wheat bread almost 1.5 times. Arginine and proline were found in bread fortified with mealworm powder while in wheat bread was not detected. Laze1*et al.*[45] investigated amino acid contents in grains of 10 wheat genotypes and reported that arginine and proline were not detected in 7 of 10 wheat genotypes. Fermin *et al*.[19] compared proline content in bread before and after bread-making process. The results revealed that proline concentrate was lost approximately 57% after undergoing bread-making process. In this study, mealworm bread contained higher amount of ash and calories than wheat formula. It indicated that mealworm powder enrichment in bread could improve nutritional values of bread and provide high energy.

Conclusion:

The study showed that fortification of mealworm powder in order to improve nutritional values in bread product led to decrease qualities of bread. The addition of CMC and GG improved textural properties of bread following hardness was decreased and specific volume was increased. In contrast, the mixing of xanthan gum had the lowest helpful effect on textural properties and specific volume of mealworm bread. The present of hydrocolloids provided better appearance by producing finer crumb and thinner cell wall. However, the addition of all types of hydrocolloids up to 1.5% had adverse effect on qualities of bread. The reduction of specific volume in bread contained high content of hydrocolloids occurred and it related with the slightly harder texture. However, the experiment showed that CMC and GG had ability to improve qualities of mealworm bread and 1% of CMC provided qualities of mealworm bread comparable to wheat bread. The addition of mealworm powder and using hydrocolloid for texture development could improve nutritional values, physical and texture properties of bread.

Acknowledgements:

This research has been supported by Center of Excellence on Biodiversity (BDC), Office of Higher Education Commission (BDC-PG2-160006), Thailand. The authors also gratefully acknowledge to Faculty of Science and Technology, Thammasat University, Thailand for analytical instrument facility.

References:

1. Cercel F, Burluc RM, Alexe P. Agal Research Agric Agric Sci Procedia. 2016;10:244-249.
2. Khuenpet K, Pakasap C, Vatthanakul S, Kitthawee S. Int J Agri Technol. 2020;16(2):283-296.
3. Osimani A, Milanović V, Cardinali F, Roncolini A, Garofalo C, Clementi C, Pasquini M, Mozzon M, Foligni R, Raffaelli N, Zamporlini F, Aquilanti L. Innov. Food Sci Emerg Technol. 2018;48:150–163.
4. de Oliveira LM, da Silva Lucas AJ, Cadavel CL, Mellado MS. Innov Food Sci Emerg Technol. 2017;44:30-35
5. Maleki G, Milani J. *Food* Sci Technol Res. 2013;19(3): 353-358.
6. Ferrero C. Food Hydrocolloids. 2017;68:15-22.
7. Nammakuna N, Barringer SA, Ratanatriwong P. Food Sci Nutr. 2016;4(2):143–155.
8. Panyathitipong W, Peeraphatchara C. J. Thai Interdisciplinary Res. 2016;11(3): 8-15.
9. Ghanbari M, Farmani J. J Agri Sci Technol. 2013;15:545-555.
10. Previtali MA, Mastromatteo M, De Vita P, Bianca D, Ficco M, Conte A, Nobile MA. Int J Food Sci Technol. 2014;49(11): 2382-2390.
11. González CM, Garzón R, Rosell, C.M. Innov Food Sci Emerg Technol. 2019;51:205–210.
12. AOAC. 2012. Official methods of analysis, Association of official analytical chemist 19th edition, Washington D.C., USA.
13. Chen WZ, Hoseney RC. Lebensm Wiss Technol. 1995;28:467–473.
14. Scheuer PM, Ferreira JAS, Mattioni B, Miranda MZ, Francisco A. Food Sci Technol. 2015;35(1):133-142

15. Poonnakasem NJ. Food Technol Siam Univ. 2013;8(1): 12-20.
16. Yildiz O, Meral R, Dogan IS. Int J Food Engr. 2012;8:1-11.
17. Wood JA. J. Cereal Sci. 2009;49: 128–133.
18. Zhao X, Vázquez-Gutiérrez JL, Johansson DP, Landberg R, Langton M. PLoS One. 2016;11(12):1-17.
19. Fermin BC, Hahm TS, Radinsky JA, Kratochvii BJ, Hali JE, Lo YM. J Food Eng Phys Prop. 2005;70:274-278.
20. Serin S. and Sayar S. Food Sci. Technol, Campinas. 2017;37(1): 25-32.
21. Kohajdová Z, Karovičová J. Acta Sci Pol Technol Aliment. 2008;7(2): 43-49.
22. Han HM, Cho JH, Kang HW, Koh BK. J Sci Food Agri. 2011;92:1462–1467.
23. Ooms N, Delcour JA. Curr Opin Food Sci. 2019;Article in press.
24. Pojić M, Hadnađev TD, Hadnađev M, Ratika S, Brlek T. J Food Qual. 2015;38: 431–440.
25. Meral R, Dogan IS. Ital. J. Food Sci. 20113;25:51-56.
26. Majzoobi M, Jalali AR, Farahnaky A. J. Food Qual. 2016;39(6):620-626.
27. Maina JW. J Pharm Innov. 2018;7(5): 253-257.
28. Ogur SJ. Food Nutr Res. 2014;2(12): 985-992.
29. Fagundes GA, Rocha M, Salas-Mellado MM. Food Res. 2018;2(3):221-227.
30. Rodge AB, Sonkamble SM, Salve RV, Syed IH. Food Process Technol. 2012;3(2):1-7.
31. Wahyono A, Tifania AZ, Kurniawati E, Kasutjianingati W, Kang W, Chung SK. Environ Earth Sci. 2018;207:1-6.
32. Kumar N, Khatkarm BS, Kaushik R. J Food Sci Technol. 2013;37(2):68-81.
33. Elawad RMO, Yang TY, Ahmed AHR, Ishag KEA, Mudawi HA, Abdelrahim SMK. Int J Food Sci Nutr. 2016;1(5): 10-15.
34. Nongtaodum SM, Charat P, Chatoenphon W, Siriwongwilaichat P. J Srinakharinwirot Univ. 2018;11(21):193-203.
35. Singh PJ, Bawa AS. Int J Food Prop. 2009;3(3): 407-419.
36. Ezera JE, Nwufo BT, Wapwera JA. Int J Chem Sci. 2019;3(1):44-49.
37. Miś A, Nawrocka A, Dziki D. Food Bioprocess Technol. 2016;9: 892–903.
38. Moore MM, Schober TJ, Dockery P, Arendt, EK. Cereal Chem. 2014;81(5): 567–575.
39. Deca SC. J Food Sci Technol. 2010;47: 128-131.
40. Lestari D, Kresnowati MTAP, Rahmani A, Aliwarga L, Bindar Y. Reaktor. 2019;19(3): 89-95.
41. Mohammadi M, Sadeghnia N, Azizi MH, Neyestani TR, Mortazavian AMJ. Ind Eng Chem. 2014;20:1812-1818.
42. Noorlaila, A., Hasanah, A.H., Asmeda, R. and Yusoff, A. J Saudi Soc Agri Sci. 2018;Article in press.
43. Das L, Raychaudhuri U, Chakraborty R. Int Food Res. J. 2013;20(5): 2253-2259.
44. Rathnayake HA, Navaratne SB, Navaratne CM. Int J Food Sci. 2018(2):1-15.
45. Laze1 A, Arapi1 V, Ceca E, Gusho K, Pezo L, Brahushi F, Kneževic D. Period Polytech Chem Eng. 2019;63(4):618–628.

SP01_001_PA: ANTIMICROBIAL ACTIVITIES OF *Myrothecium indunatum* ISOLATED FROM LEAF BLIGHT DISEASED WATER LETTUCE

Orawan Piyaboon[1]*

[1]Department of Biology and Health Science, Mahidol Wittayanusorn School, Nakhon Pathom, Thailand
*email: orawan.piy@mwit.ac.th

Abstract:

The water lettuce is considered a major aquatic weed problem in Thailand. At present, the management, focusing on this weed has changed from pesticides to biological control using natural enemies of water lettuce including fungal pathogens. This research was objectives to study the bioactive potential of *Myrothecium indunatum* isolated from leaf blight of water lettuce. The blighted and spotted leaf of diseased water lettuce plants were collected and isolated from 8 provinces of Thailand. Out of Forty-five isolates of fungal pathogens, five isolates were identified through the morphological, sequence similarity and phylogenetic analysis of the ITS regions and confirmed as *M. indunatum*. Fungal isolates were tested against water lettuce, duckweed and water hyacinth plant. five isolates demonstrated potent activities against water lettuce and water hyacinth plant. Five isolates of *M. indunatum* were tested for inhibiting fungal pathogens and bacterial pathogens causing the economic important plant under laboratory condition using dual culture test. The result showed that five isolates could inhibit fungal pathogens including *Bipolaris madis*, *B. oryzae*, and *Nigrospora* sp.. In addition, five isolates of *M. indunatum* could inhibit bacterial pathogens consisting *Ralstonia solanaceae* and *Xanthomonas* sp..

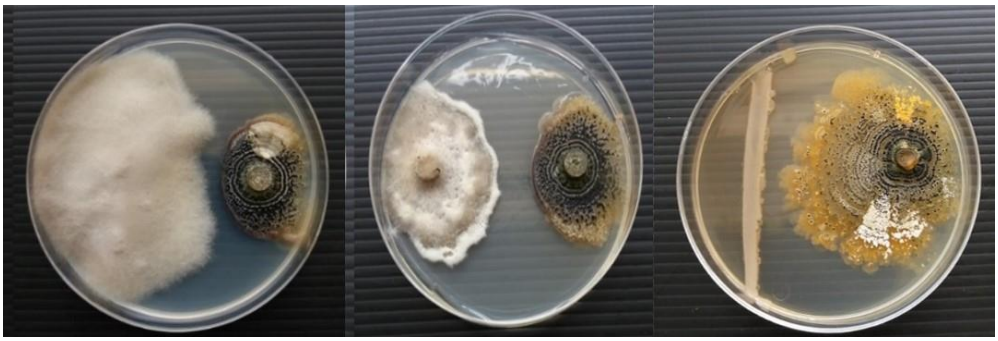

Figure 1. The effectiveness of *M. indunatum* for the inhibition of fungal and bacterial pathogens

SP01_002_PA

SP01_002_PA: COMPOSITION AND ABUNDANCE OF MACROFAUNA IN CORAL REEF COMMUNITIES AT MU KO CHUMPON IN WESTERN GULF OF THAILAND

Laongdow Jungrak,* Suraphol Chunhabundit, Rattanawadee Niamsiri, Thamasak Yeemin, Makamas Sutthacheep

Marine Biodiversity Research Group, Department of Biology, Faculty of Science, Ramkhamhaeng University, Bangkok 10240, Thailand
*e-mail: Laongdow8853@gmail.com

Abstract:

Coral reefs are ecosystems with the highest biodiversity in the sea, and studies on ecology of polychaetes in soft bottom of coral reefs in Thai water are limited. This research is very important to clear coral reef ecosystem, in particular from Thai seas. This study aimed to investigate composition and abundance of polychaetes in soft bottom of coral reefs at Ko Mattra and Ko Maphrao, Chumphon Province, the Western Gulf of Thailand. Nine major polychaete genera were observed, i.e. *Polydora*, *Pisione*, *Pseudeurythoe*, *Sphaerosyllis*, *Magelona*, *Hesione*, *Capitella*, *Heteromastus* and *Cirriformia*. The highest density of polychaetes were observed at Ko Mattra (92.59 individuals/m^2). *Sphaerosyllis* is the only genus found on both Ko Mattra and Ko Maphrao. This study contributes to our understanding of ecosystem processes and biodiversity at Mu Ko Chumphon region. It's in an area that also has the potential to provide insight into important, such as the capacity of reefs systems and benthic macrofauna organisms to adapt to global climate change and demonstrates the importance of studying polychaetes in soft bottom of coral reef for coastal and marine resources management.

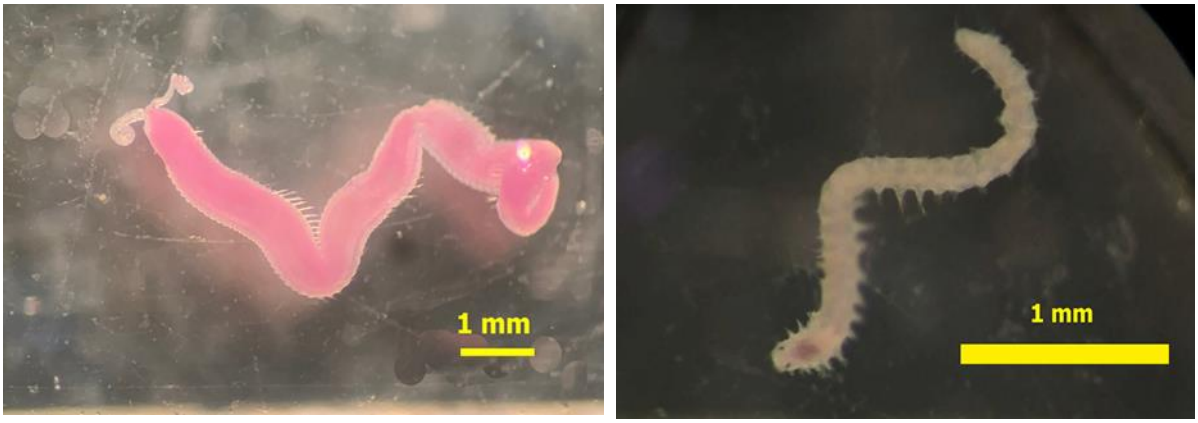

Polychaetes found in coral reefs at the study sites, *Polydora* sp. (left)

and *Sphaerosyllis* sp. (right)

SP01_003_PA: COMPARING THE MEIOFAUNA COMMUNITIES IN CORAL REEFS AT MU KO CHUMPHON IN THE WESTERN GULF OF THAILAND

Pronsiri Sriwisait, Laongdow Jungrak, Supphakarn Phoaduang, Niamsiri, Thamasak Yeemin, Makamas Sutthacheep

Marine Biodiversity Research Group, Department of Biology, Faculty of Science, Ramkhamhaeng University, Bangkok 10240, Thailand
*e-mail: cookgig.gig@gmail.com

Abstract:

Meiofauna plays a major role in benthic trophodynamics and provides a good bioindicator for the assessment of the biodiversity and ecological status of marine ecosystems. Meiofauna studies in coral reef ecosystems in Thailand are limited although coral reefs are important habitats in coastal zones in tropical countries and their ecosystem services are very significant, particularly for the tourism sector. This study aimed to investigate the composition and abundance of meiofauna in coral reefs at Mu Ko Chumphon, the Western Gulf of Thailand. The meiofauna samples were collected at five study sites, i.e. Ko Matta, Ko Rang Kachiu, Ko Maphrao, Ko Kula, and Ko Lawa. Twelve major taxa were identified and the dominant groups were Foraminifera, Nematoda, Copepoda, Polychaeta, and Amphipoda. Major taxa collected from the sites were Foraminifera, Nematoda, Copepoda, Polychaeta, and Amphipoda. The highest abundant group of meiofauna was Foraminifera (57.98 individuals/10 cm^2). The highest density of meiofauna was found at Ko Lawa while the lowest one was observed at Ko Maphrao. The coastal development and fishery resources harvesting continue to increase, therefore data from ecological studies will play an important role in coral reef management and conservation in the Gulf of Thailand.

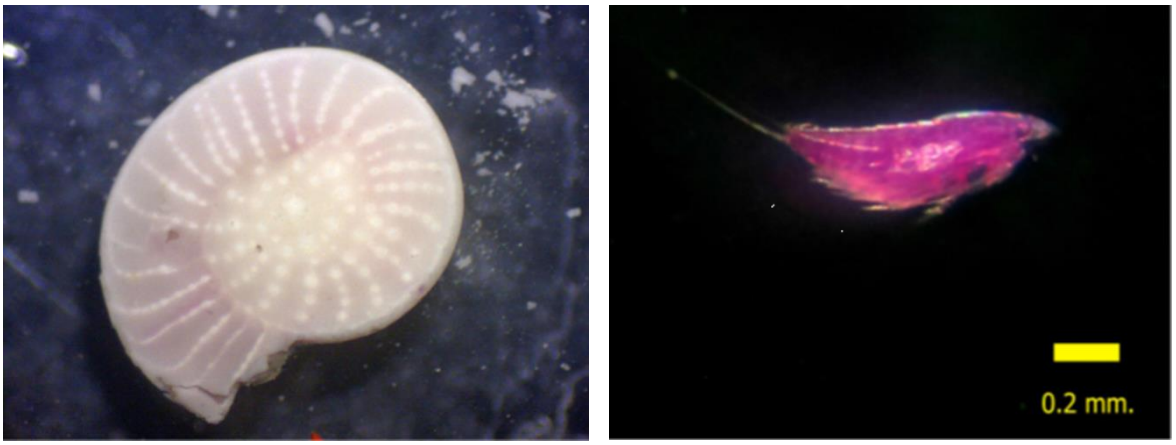

Meiofauna found in coral reefs at the study sites, Foraminifera (left)

and Copepoda (right)

SP01_004_PA: ABUNDANCE AND COMPOSITION OF MEIOFAUNA ON A SANDY BEACH AT MU KO ANGTHONG NATIONAL PARK IN SURAT THANI PROVINCE, THAILAND

Suphakarn Phoaduang*, Thamasak Yeemin, Makamas Sutthacheep
Marine Biodiversity Research Group, Department of Biology, Faculty of Science
Ramkhamhaeng University, Huamark, Bangkok 10240
*e-mail: filmsupphakarn@hotmail.com

Abstract:

The benthic animals in sandy beaches can be used as a tool for assessing environmental impacts of coastal ecosystems. Meiofauna also provide links in the marine benthic food web and affect biogeochemical cycles. This study focused on investigating abundance and composition of meiofauna on a sandy beach at Mu Ko Angthong National Park, Surat Thani Province. The samples were collected using PVC meiocores of 3.5 cm diameter which were randomly inserted into the sediment down to a depth of 10 cm at three study sites, i.e. Ko Sam Sao, Ko Wua Kantang, and Ko Hindap. The results revealed that a total of eigth taxa were found including Foraminifera, Turbellaria, Nematoda, Polychaeta, Ostracoda, Copepoda, Gastropoda, and Bivalvia. The highest density of meiofauna was found at Ko Hindap (102.26 individuals / 10 cm^2) while the lowest one was observed at Ko Sam Sao (6.06 individuals / 10 cm^2). The meiofauna abundance at each study site could be related to organic matter in sediment. Further studies are required to clarity meiofauna community in relation to change and anthropogenic disturbances. This study emphasizes on the importance of meiofauna studies on sandy beach ecosystems in the Gulf of Thailand.

The sandy beaches at Mu Ko Angthong National Park, Surat Thani Province

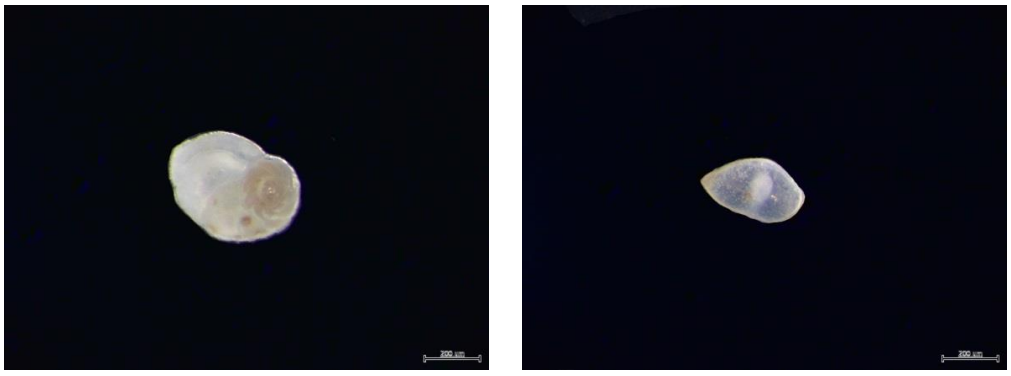

The dominant spiecies of meiofauna at the study sites

SP01_005_OF: DOES COASTAL EROSION INFLUENCE TO DOMINANT MACROBENTHIC INVERTEBRATES ON SONGKHLA SANDY BEACHES?

Mathinee Yucharoen,[1,2] Nattacha Khantasimachalerm,[3] Napim Punritdum,[3] Suppachai Thawaii,[3] Kanyanat Kaewutai,[3] Thitiya Choosun,[3] Kringpaka Wangkulangkul [3]*

[1]Marine and Coastal Resources Institute, Faculty of Environmental Management, Prince of Songkla University, Hatyai, Thailand
[2]Coastal Oceanography and Climate Change Research Center, Prince of Songkla University, Hatyai, Thailand
[3]Department of Biology, Division of Biological Science, Faculty of Science, Prince of Songkla University, Hatyai, Thailand

*e-mail: kringpaka.w@psu.ac.th

Abstract:

The coastline along the southern Gulf of Thailand has been recognized as facing coastal erosion problem that is caused by both natural processes and anthropogenic disturbances. Coastal erosion may disturb the organisms living in sandy beach ecosystem. This study was carried out to investigate the effects of coastal erosion on dominant macrobenthic populations on the sandy beaches of Songkhla Province, southern Thailand. Six beaches were categorized into eroded and non-eroded beaches. Organisms and sediment samples were randomly collected on the beach swash zone. The abundance of macrobenthic invertebrates and some environmental parameters were evaluated. A total of four species: mole crab *Emerita* sp., wedge clams *Donax cuneatus*, *D. faba*, and *D. incarnatus* were found. Density of both mole crabs and wedge clams was different among beaches while the difference between types of beaches (eroded vs non-eroded) was not detected. There was a positive relationship between organic matter and the density of *Donax* spp. Analysis of particle size composition presented that the proportion of coarse sand on eroded beaches was slightly higher than non-eroded beaches. Our results implied that the impact of coastal erosion on the abundance of macrobenthic invertebrates was not detected. However, this merit further investigations using a greater number of locations; and seasonal variability should be also considered.

Introduction:

Macrobenthos are important parts of the intertidal ecosystem and play an important role in maintaining ecological balance. [1] On Thailand sandy shores filter-feeding macroinvertebrates were commonly found, and they act as a major food source for several fish species and human consumers. [2,3] Apart from their economic values, macrobenthic communities can be used for an indicator of beach health or impact assessment on the sandy beaches. [4,5,6]

Recently, several stretches of sandy beaches in Thailand, have been under the threat of coastal erosion. Sea level rise and climate change have been shown to influence coastal erosion worldwide. [7] Moreover, several anthropogenic activities on beaches probably disturb macrofaunal assemblages in the sandy ecosystem. [8,9,10] There have been many cases of coastal management solutions, i. e. , use of groin, seawall, revetment, breakwater, sandbag, and beach nourishment aiming to alleviate the erosion[11] on Thai coastlines. These constructions modify the wave regime, the process of sediment deposition and erosion-accretion dynamics, which consequently result in changes of coastal assemblages[12,13]; and sometimes led to severe erosion in adjacent areas.

This study investigated the influences of coastal erosion on dominant macrobenthic organisms dwelling in intertidal sandy beaches. Their abundance was compared between eroded and non-eroded beaches. The relationship between the abundance and some environmental parameters were also evaluated.

Methodology:

Field sampling

The study was conducted during June 2019 at six sandy beaches (**Figure 1**.). They were categorized into eroded beaches (Pak Trae 7°46'44.1" N 100°22'08.9" E, Haad Kaew 7°15'49.3" N 100°32'29.8" E, Chalathat 7°11'31.4" N 100°36'37.8" E) and non-eroded beaches (Maharat 7°28'30.4" N 100°26'45.2" E, Muang Ngam 7°21'16.7" N 100°29'24.8" E, Laem Son On 7°13'46.5" N 100°34'54.3" E). The locations of eroded and non-eroded beaches were determined following the Department of Marine and Coastal Resources (2015) and Central Database System and Data Standard for Marine and Coastal Resources (retrieved 2020). Macrobenthic invertebrates focusing on mole crabs and wedge clams were sampled using 5 random quadrats (50×50 cm.) placed on the swash zone of each beach. Sediment in the quadrat was dug 5 cm deep and then sieved (0.5 mm mesh size). All macrobenthic fauna retained on the sieve were collected. The sediments were also sampled using cylindrical core (5 cm diameter) down to a sediment depth of 10 cm. Collected organisms and sediments were kept at -20°C for further process.

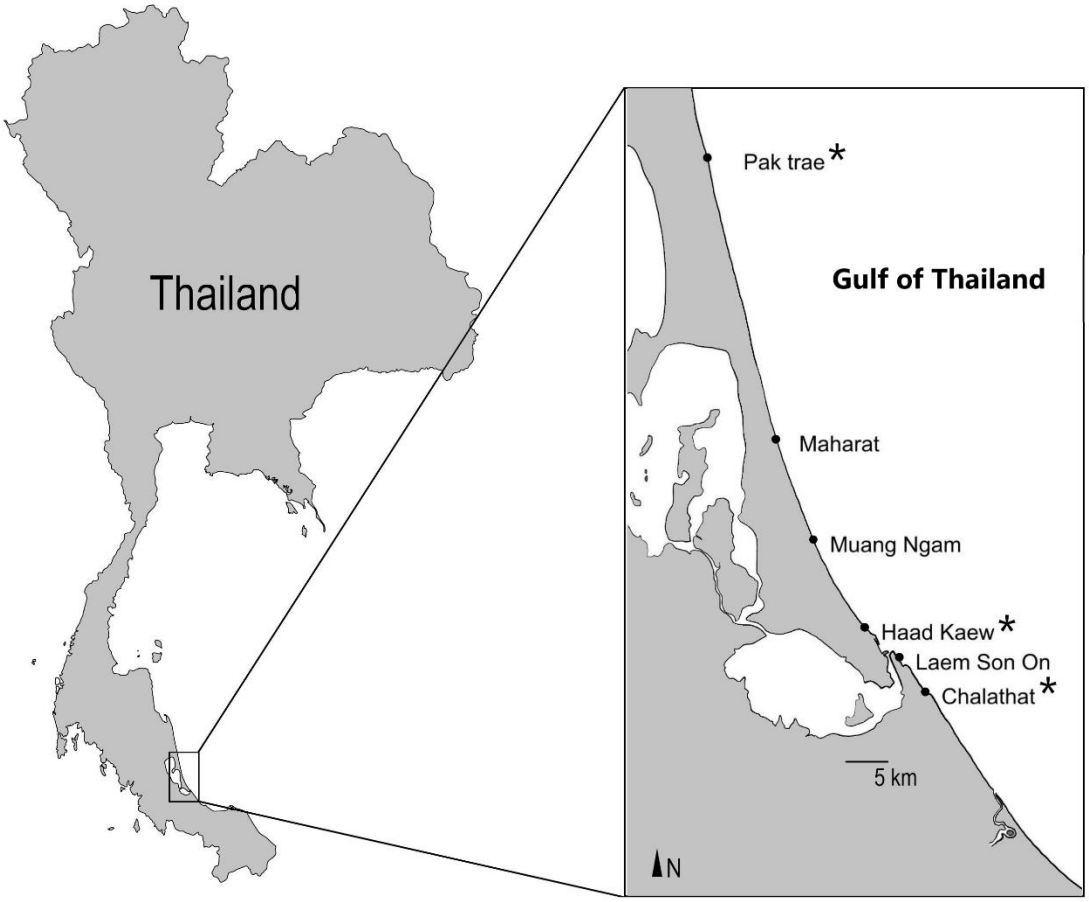

Figure 1. Location of the study sites along Songkhla Coast, the Gulf of Thailand.

Beaches with asterisks are eroded beaches.

Laboratory works

The macrobenthic invertebrates collected in the field were identified and counted. Density (number of individual m^{-2}) was calculated. The fauna was later dried using an oven at 60 °C for 3 days and weighted to obtain biomass (g dry weight m^{-2}). Analysis of sediment grain size was done by the sieving technique using a series of stacked sieve meshes, which afterward weighted for a truly representative portion of each sediment type. The proportion of sediment with different grain size was obtained. The sediment organic matter was analyzed following Walkley-Black method. [14]

Data analysis

One - way Analysis of Variance (ANOVA) was used to examine the effect of type of beach (eroded and non-eroded) on the density of macrobenthic invertebrates. Variables were ln (x+1) transformed and tested for homogeneity of variance using Cochran' C test. A fixed factor was 'Type of beach'. A random factor 'Beach' was nested in the fixed factor. Relationships between density and biomass of fauna (response variables) and % organic matter (independent variables) were analyzed by simple linear regression. For data analysis specimens of wedge clams were pooled across species as some small individuals were difficult to identify.

Results and Discussion:

A total of four macrobenthic species were identified: a mole crabs *Emerita* sp., wedge clams *Donax cuneatus* Linnaeus, 1758, *D. faba* Gmelin, 1791, and *D. incarnatus* Gmelin, 1791 (**Figure 2.**). The densities of mole crabs and wedge clams were not different between eroded and non-eroded beaches, but significant variation was detected at the beach level (**Figure 3**., **Table 1**.). These faunas have high agility and are relatively tolerant to conditions in wave-exposed high energy sandy beach. The difference in physical characteristics between beach type was rather marginal (**Figure 6.**), therefore, they may not be sensitive to a slight change in their habitat.

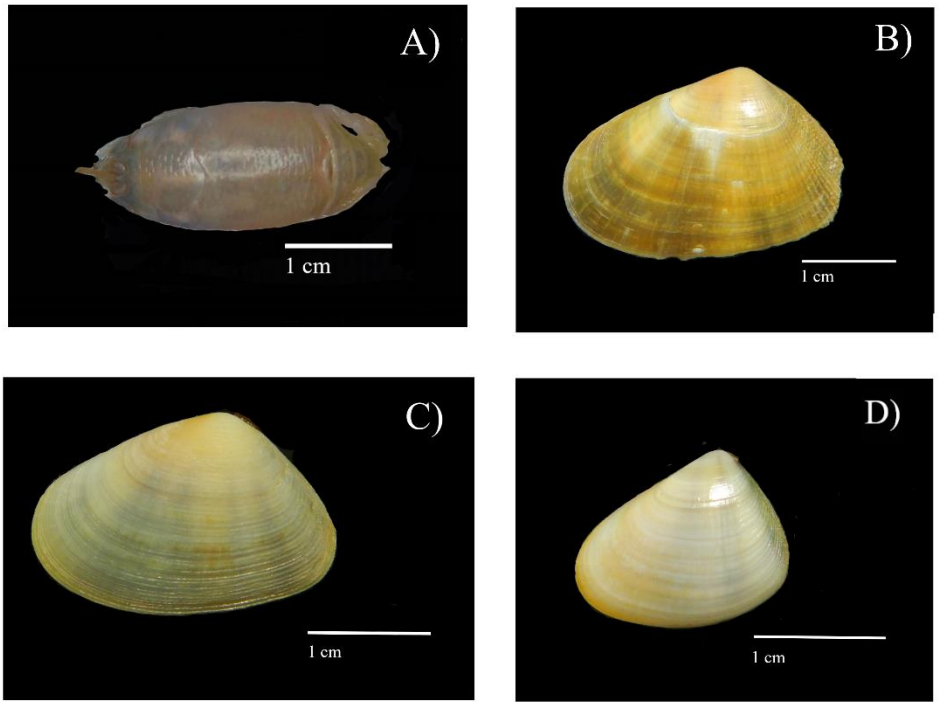

Figure 2. All species of macrobenthos collected from the study sites

A) *Emerita* sp. B) *Donax cuneatus* C) *D. faba* and D) *D. incarnatus*

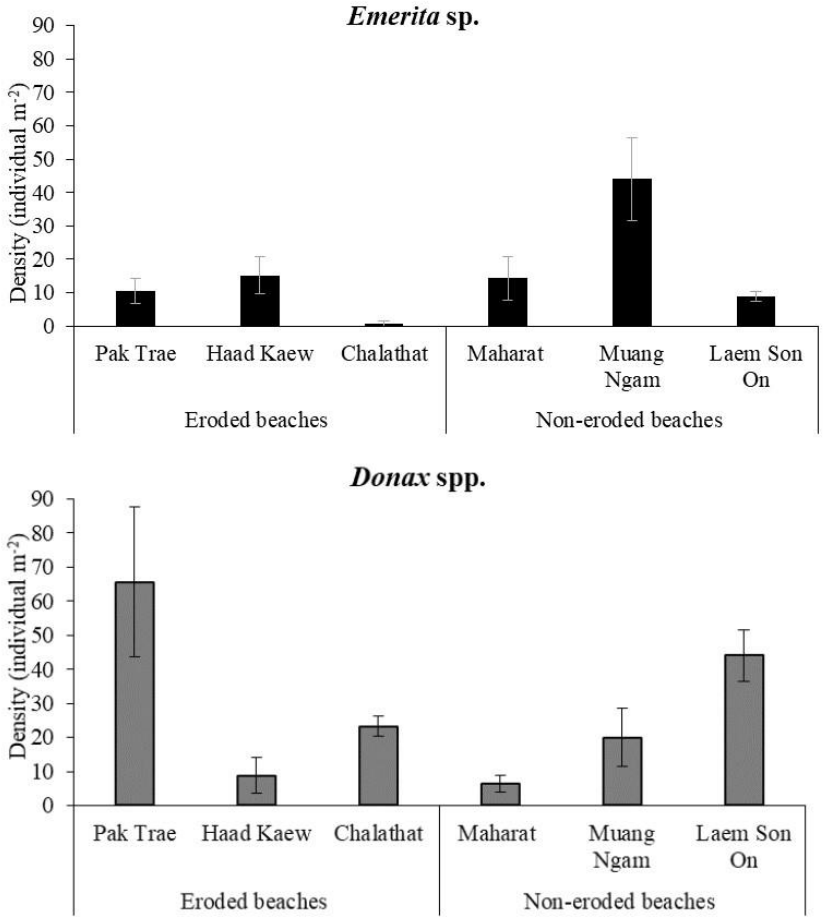

Figure 3. *Emerita* sp. and *Donax* spp. densities (Mean±SE): at eroded and non-eroded beaches.

Table 1.

ANOVA of *Emerita* sp. and *Donax* spp. densities on eroded and non-eroded beaches.

Source of variation	SS	df	MS	F	P
Emerita sp.					
Type of beach	8.01	1	8.01	1.55	0.28
Beach	20.70	4	5.17	5.86	0.002*
Residual	21.20	24	0.88		
Total	49.91	29			
Donax spp.					
Type of beach	0.41	1	0.41	0.06	0.81
Beach	26.24	4	6.56	6.01	0.002*
Residual	26.21	24	1.09		
Total	52.86	29			

A marginal positive relationship between % organic matter and density of *Donax* spp. was found; while the effect of variation in % organic matter on the density of *Emerita* sp. and biomass of both faunal groups was not significant (**Figure 4.**). However, when considering % organic matter and overall benthic densities (**Figure 5.**), high densities of fauna were found on the beach with high % organic matter. Both mole crabs and wedge clams are suspension-feeders.[15,16] They feed mainly on phytoplankton and other suspended organic matters. Organic content in sediment may not directly reflect the availability of their food source but the exchange of matters between sediment and water column is thought to be high in these high energy beaches. Large particles such as very coarse sand and coarse sand were mostly found at eroded beaches (**Figure 6.**), suggesting that there might be a difference in physical features of habitats. We hypothesized that this characteristic could affect *Emerita* and *Donax* populations differently between eroded and non-eroded beaches in the same way as in a previous case of beach nourishment and bulldozing that changed fauna assemblages, such as, wedge clams, mole and ghost crabs,[17] amphipods, [9] and polychaetes. [18]

Abundance and distribution of macrobenthic populations are also regulated by other physical variables, [19,20] thus we suggest that further research should include recording the other parameters, such as beach slope, tidal range, morphology of swash zone, water velocities, etc. Some macrofauna can behaviorally adapt to environmental dynamics[21] therefore the long-term evidence of behavioral responses is also important. Seasonal change in characteristics of these sandy shores could be crucial in determining the composition of macrofaunal assemblages. As we collected data during the southwest monsoon season (June) when southwesterly wind predominated and onshore current on the east (gulf) coast of Thailand was relatively weaker than during northeast monsoon, the effect of erosion caused by the wave was likely too weak to cause any significant changes in the beach physical characteristics. Taking seasonal variability into account will shade more light on the dynamics of these constantly changing ecosystems.

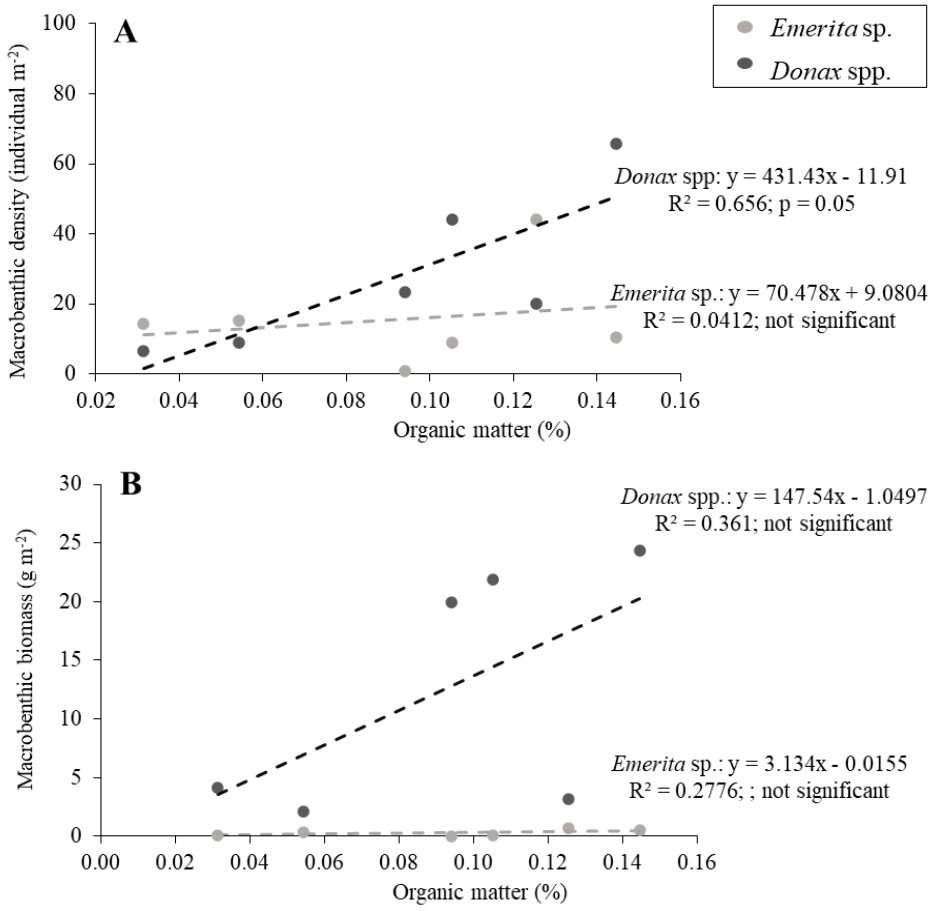

Figure 4. Relationship between organic matter in sediments and macrobenthic invertebrates: A) density and B) biomass. Equations and R^2 were results from linear regression analyses.

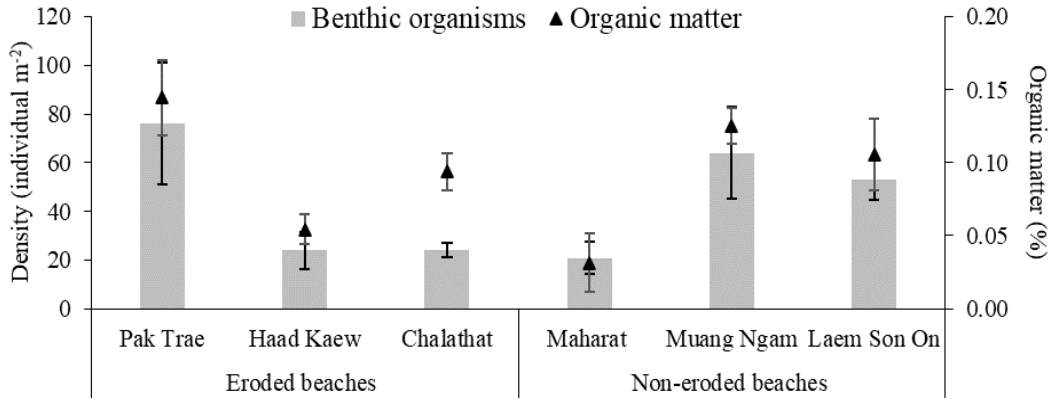

Figure 5. Density (individual m^{-2}) of macrobenthos and % organic matter of 6 study sites.

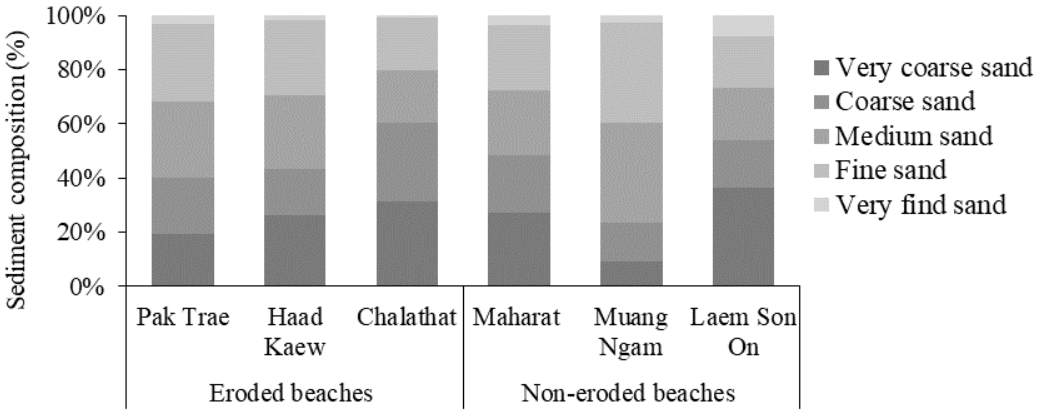

Figure 6. Sediment particle composition of eroded and non-eroded beaches.

Conclusion:

Coastal erosion generally leads to changes in physical and biological characteristics of habitat, determining the composition of macrobenthic assemblages. Although there was no obvious impact of beach erosion on sandy organisms in our study, the results lead to suggestions on further research to include a study on the effect of seasonal variation and more replications of locations. Moreover, several physical parameters are also needed to be quantified.

Acknowledgements:

This study was supported by the Prince of Songkla University under the "Coastal protection project". We are most grateful to the Marine and Coastal Resources Institute and the Department of Biology, Division of Biological Science, Faculty of Science, Prince of Songkla University for all facilities.

References:

1. Defeo O. J Coast Res. 2003;35:56-65.
2. Tantikamton K, Thanee N, Jitpukdee S, Potter, P. Int J Adv Agric Environ Eng. 2015;2:23-27.
3. Rittiboon K, Fungchonjitt S, Thongroy P, Chavavongsa C, Buatip S. Burapha Sci J. 2019;24:395-414. (In Thai)
4. Defeo O, Lercari D. Aquatic Conserv Mar Freshw Ecosyst. 2004;14:65-74.
5. Bakalem A, Ruellet T, Dauvin JC. Ecol Ind. 2009;9:395-408.
6. Cardoso RS, Barboza CAM, Skinner VB, Cabrini TMB. Ecol Ind. 2016;62:154-162.
7. Leatherman SP, Zhang K, Douglas BC. EOS.2000;81:55-57.
8. Lercari D, Defeo O. Estuar Coast Shelf Sci. 2003; 58S: 17-24.
9. Fanini L, Marchetti GM, Scapini F, Defeo O. Ecol Ind. 2009;9:167-178.
10. Walker SJ, Schlacher TA. J Coast Res. 2011;27:184-192.
11. Ritphring S, Sungngam S. Proc 11th RCEnvE. 2018:251-254.
12. Martin D, Bertasi F, Colangelo MA, de Vries M, Frost M, Hawkins SJ, …, Ceccherelli VU. Coast Eng. 2005;52:1027-1051.
13. Walker SJ, Schlacher TA, Thompson LM. Estuar Coast Shelf Sci. 2008;79:24-34.
14. Gelman F, Binstock R, Halicz L. Fuel. 2012; 96:608-610.
15. Matthews S, Lucas MI, Stenton-Dozey JME, Brown AC. J Exp Mar Biol Ecol. 1989; 125:219-234.
16. Subramoniam T, Gunamalai V. Adv Mar Biol. 2003; 46: 91-182.
17. Peterson CH, Hickerson DHM, Johnson GG. J Coast Res. 2000;16:368-378.
18. Bishop MJ, Peterson CH, Summerson HC, Lenihan HS, Graboswki JH. J Coast Res. 2006;22:530-546.
19. Contreras H, Jaramillo E, Quijon P. Rev Chil Hist Nat. 2000;73:705-715.
20. McLachlan A, Dorvlo A. J Coast Res. 2005;21:674-687.
21. Scapini F, Degli EI, Defeo O. Estuar Coast Shelf Sci. 2019;225:106236.

SP01_006_OA: STUDY ON THE SURVIVAL RATE OF ASIAN CLAMWORM *Perinereis aibuhitensis Grube,* 1878 REARING IN THE DIFFERENCES DENSITY OF THE SPF CULTURED SYSTEM

Suraphol Chunhabundit [1*] Thamasak Yeemin[2]

Marine Biodiversity Research Group, Department of Biology, Faculty of Science,
Ramkhumhaenf University, Huamark, Bangkok, Thailand
*e-mail:surapholcc.626@gmail.com

Abstract:

Asian clamworm *Perinereis aibuhitensis* is the best fresh food to feed on the *Litopenaeus vannamei* Boone, broodstock. This is due to their high nutritional compositions that are more important to induce the maturation in those shrimp broodstock compared to sandworm *Perinereis nuntia* and other nereid worms. According to the study of this marine polychaete specie in SPF cultured system from 2 months worm to 4 months worm and the density varies from 500 to 600 and 1,200 individuals/ square meter, respectively. It was found that at a density rate of 500 per square meter, there is a survival rate of between 70 percent to 96 percent. At a density of 600 individuals/ square meter, the survival rate is between 45 and 86.67 percent, and at a density of 1,200 individuals/square meters, the survival rate is between 4.17 percent and 16.50 percent, respectively. The study highlights the importance of clam worms for industrial mariculture.

Perinereis aibuhitensis, Male (left) and Female (right)

SP01_007_PA

SP01_007_PA: DIVERSITY OF MARINE PHYTAL HARPACTICOID COPEPODS FROM THAILAND

Supawadee Chullasorn[1,*], Pawana Kangtia[2], Pradchek Klangsin[1], Kuansiri Seelpinyo[1], Weerawan Saowakul[1]

[1] Department of Biology, Faculty of Science, Ramkhamhaeng University, Bangkok 10240, Thailand
[2] Department of Biology, Bansomdejchaophaya University, Bangkok 10600, Thailand
*e-mail: chu_supawadee@ru.ac.th, schullasorn@gmail.com

Abstract:

Harpacticoid copepods are potential sources of live feed for marine shrimp and fish larvae. Therefore, the aims of this study are to identify the diversity of harpacticoid copepods associated with marine macroalgae from Thailand. In terms of diversity, sixteen families of marine phytal harpacticoid copepods associated with *Ulva clathrata, Caulerpa* sp*., Sargassum* sp*., Padina* sp*., Neomeris vanbosseae* and *Gracilaria* sp. were found: family Ameiridae (*Nitokra karanovici* Chullasorn, Kangtia and Klangsin, 2014), family Canuellidae (*Scottolana huysi* Song et al., 2018), family Harpacticidae (*Tigriopus thailandensis* Chullasorn et al., 2012; *T. sirindhornae* Chullasorn et al., 2013), family Longipediidae (*Longipedia thailandensis* Chullasorn and Kangtia, 2008), family Miraciidae (*Paramphiascella choi* Chullasorn et al. , 2011; *Typhlamphiascus higginsi* Chullasorn, 2009; *Robertsonia* sp.; *Robertgurneya* sp.), and family Tisbidae (*Tisbe thailandensis* Chullasorn et al., 2009). Family Cletodidae (*Enhydrosoma* sp.), family Ectinosomatidae (*Halectinosoma* sp.), family Laophontidae (*Laophonte* sp.), family Metidae (*Metis* sp.), family Peltidiidae (*Peltidium* sp.), family Porcellidiidae (*Porcellidium* sp.), family Tegastidae (*Tegastes* sp.) , family Tetragonicipitidae (*Phyllopodopsyllus* sp.) and family Thalestridae (*Eudactylopus* sp.). Among these families, there were six new species, namely *Nitokra karanovici, Longipedia thailandensis, Paramphiascella choi, Scottolana huysi, Tisbe thailandensis* and *Typhlamphiascus higginsi.*

Tigriopus thailandensis (gravid female)

Laophonte sp. (gravid female)

SP01_008_OA: DECREASING THE GENETIC DIVERSITY OF DUGONG (*Dugong dugon*) IN THE SEA OF THAILAND

Anocha Poommouang,[1,*] Kittisak Buddhachat,[2,3] Siriwadee Chomdej,[4] Supamit Mekchay,[5] Patcharaporn Kaewmong,[6] Kongkiat Kittiwatanawong,[6] Korakot Nganvongpanit,[1,2]

[1]Department of Veterinary Biosciences and Public Health, Faculty of Veterinary Medicine, Chiang Mai University, Chiang Mai 50100, Thailand.
[2]Excellence Center in Veterinary Bioscience, Chiang Mai 50100, Thailand.
[3]Department of Biology, Faculty of Science, Naresuan University, Phitsanulok 65000, Thailand.
[4]Department of Biology, Faculty of Science, Chiang Mai University, Chiang Mai 50200 Thailand
[5]Department of Animal and Aquatic Sciences, Faculty of Agriculture, Chiang Mai University, Chiang Mai 50200, Thailand
[6]Phuket Marine Biological Center, Phuket 83000, Thailand.
*e-mail: anopotter@hotmail.com

Abstract:

At present, the number of dugong (*Dugong dugon*) population have been shrinking, leading to enlisting vulnerable on the IUCN Red List of Threatened Species. Determining the genetic diversity of the population of species is essential for conservation aspect. In this study, the inter-simple sequence repeat (ISSR) markers were used to evaluate genetic diversity and differentiation in 128 dugongs (1990-2019) from Thailand's sea. The thirteen primers chosen for analysis revealed 102 bands, of which 65 (63.73%) were polymorphic. Shannon's index information (*I*), observed number of alleles (Na), effective number of alleles (Ne) and expected heterozygosity (He) in Gulf of Thailand past (1990-2008) / present (2009-2019) were 2.243/1.691, 10.385/5.846, 8.668/5.275, 0.883/0.800, respectively and Andaman past/present were 2.640/2.541, 18.077/16.769, 11.766/10.790, 0.914/0.906, consequently, all values showed that in the past both habitats had higher genetic diversity than the present. The fixation index (F_{st}) in the past of both the Gulf of Thailand and the Andaman were -0.113±0.017 and -0.080±0.007, respectively demonstrated that no genetic subdivision between populations was observed. The results of the Nei's unbiased measures of genetic distance between the Gulf of Thailand and Andaman in past and present was 0.323 and 0.272, respectively, indicating that at present the dugongs in the Gulf of Thailand and the Andaman sea are more closely related. In conclusion, our finding pointed out that the current decline in the genetic diversity of the dugong in Thailand. Therefore, conservation guidelines for the dugong should be established before the dugong becomes less genetically diverse and lead to extinction in the future.

SP01_009_PA: CHANGES IN MACROINVERTEBRATE POPULATIONS IN THE ESTUARY ECOSYSTEM: A CASE STUDY OF MAE KLONG AND THA CHIN ESTUARIES, THE UPPER GULF OF THAILAND

Sitthi Kulabtong[1], * Kamolmanus Wattana[1], Kridsada Charroenmoon[1], Patchara Bamrung[1], Nidsaraporn Petsut[2]

[1]Faculty of Agro-Industrial Technology, Rajamangala University of Technology Tawan-ok Chanthaburi campus, Khao Khitchakut, Chanthaburi, Thailand.
[2]Department of Agricultural Technology, Faculty of Science, Ramkhamhaeng University, Bangkok, Thailand, 10240
*e-mail: kulabtong2011@hotmail.com

Abstract:

The macroinvertebrate population in the estuary ecosystem was reported. The results can be used as basic information in natural resource management planning and result in the benefit to the local people. The changes in macroinvertebrate were studied at Mae Klong Estuary and Tha Chin Estuary, Upper Gulf of Thailand. The 4 stations of 2 estuaries were sampled in 3 seasons, January 2018 (winter representative), April 2018 (summer representative) and September 2018 (rainy season representative). A total of 29 species of macroinvertebrate were recorded. Malacostraca was dominant in terms of the number of species of macroinvertebrate (9 species), and the most quantity. The quantity of the Malacostraca was about 40-54 % of the total amount of macroinvertebrate. *Metapenaeus* was a dominant species in the area (24 % of all specimens). The density of macroinvertebrate tends to increase in the winter, with an average density of 1,444.0 number/m^2. Also, the density decrease to the lowest during summer, with an average density was 533.5 number/m^2. The ecological indices of macroinvertebrate in each season were not a statistically significant difference ($p > 0.05$). The diversity index was 176-1.97, the evenness index was 0.25-0.32, and the dominance index was 0.68-0.75. It can be explained that in each season some groups of macroinvertebrate were prominently in quantity more than the other groups. The relationship between the average total density of the macroinvertebrate and the water quality factors showed that a moderate level of correlation ($r = 0.647$) and statistical significance ($p < 0.05$), with temperature. Therefore, it can be concluded that water temperature factors that vary in each season are related to the changes in the quantity of macroinvertebrate population.

SP01_010_PA: DIVERSITY OF HARPACTICOID COPEPODS FROM PAKNAM PRASAE INTERTIDAL SANDY BEACH IN RAYONG PROVINCE, THAILAND

Weerawan Saowakul,[1,*], Supawadee Chullasorn[1], Pawana Kangtia[2], Pradchek Klangsin[1]

[1]Department of Biology, Faculty of Science, Ramkhamhaeng University, Bangkok 10240, Thailand
[2]Department of Biology, Bansomdejchaophaya University, Bangkok 10600, Thailand
*e-mail: wsaowakul_123@hotmail.com

Abstract:

Harpacticoid copepods are small aquatic crustaceans, belonging to the subclass Copepoda, class Crustacea, phylum Arthropoda. They occur in almost all aquatic habitats, freshwater, brackish- water and seawater, especially in intertidal zones, seagrass beds and algal mats. Harpacticoid copepods are the second most abundant metazoan taxon in meiofauna, after the nematodes. They play a major role in marine ecosystems, can be used as a bioindicator because of harpacticoid copepods are sensitive to dissolved oxygen in water and they are important in the food chain by having sediments, diatoms, ciliates, algae as well as bacteria and protozoa. Meanwhile, they are a primary food source of aquatic animal larvae those are an economically value such as shrimp and fish larvae. This research focuses on the diversity of harpacticoid copepods. Sand samples were collected from the intertidal sandy beach at Paknam Prasae in Rayong Province, Thailand during low – tide in July 2020, with a plastic hand corer. These samples were fixed in a solution of 10% formalin and rose bengal-seawater mixture for 24 hours, kept in the laboratory room for sorting, dissecting and identification. The samples were subsequently sieved through a 63 µm mesh and identified under a stereo-microscope for studying morphology. The Canuellidae was the most abundant family. In terms of diversity, 1 family in Canuelloida and 5 families in Harpacticoida were found: Family Canuellidae – *Scottolana* sp., Family Cletodidae – *Enhydrosoma* sp., Family Ectinosomatidae – *Ectinosoma* sp., *Halectinosoma* sp., Family Harpacticidae – *Tigriopus* sp., *Harpacticus* sp., Family Longipediidae – *Longipedia* sp., and Family Miraciidae – *Paramphiascella* sp.

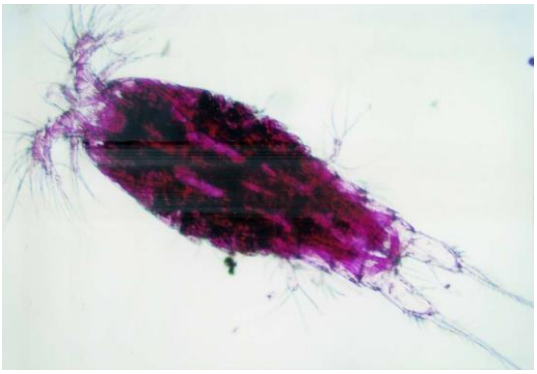

Scottolana sp. (non-gravid female)

Scottolana sp. (gravid female)

SP01_011_PA: STUDY ON LIFE CYCLE AND NAUPLIAR DEVELOPMENT OF *Amphiascopsis cintus* COLLECTED FROM *Caulerpa* sp. AT BANPHE, RAYONG PROVINCE, THAILAND

Pawana Kangtia*

Biology program, Department of Science, Faculty of Science and Technology, Bansomdejchaopraya Rajabhat University
*e-mail: kangtia@hotmail.com

Abstract:

Harpacticoid copepods are small aquatic crustaceans of a size less than two millimeter of the class copepoda order harpacticoida. Marine harpacticoid copepods are important food sources for juveniles fishes, shrimps, invertebrates and they are play a major role in marine ecosystems. They are most abundant in soft sediments and abundant dwell on macro algae. This research focus on the life cycle and naupliar development of *Amphiascopsis cintus* associated with the green alga, *Caulerpa* sp. were collected during low-tide at Banphe, Rayong Province (12.634338N; 101.8428783E), Thailand in October 2017. So as to measure the environmental factors, such as temperature, salinity, potential of hydrogen ion (pH) and dissolved oxygen. The life cycle commonly includes up to 6 naupliar stages and 5 copepodid stages prior to adult.

Introduction:

Harpacticoid copepods are important food sources for invertebrates and they are play a major role in marine ecosystems (Alekseev, 2002). They are useful as food for marine shrimp and fish cultivation, in terms of both nutrition and ease of culture. Harpacticoid copepods are favoured because of can be reared at much higher densities. However, their benthic nature also makes mass culture difficult more than rotifer, since large surface areas must be provided and harpacticoid copepods sensitive for water quality and low oxygen. Harpacticoid copepods are commonly found on the sediment or associate with sea grasses and seaweed. Diversity and taxonomic study of harpacticoid copepods are usually recorded from seaweed (Chullasorn et al., 2011; 2012; Kangtia and kulket., 2019). The seaweed can protect copepods from predators, wave action and desiccation, serve as a nursery and oxygen source for harpacticoid copepods and meiofauna. The aim of this research study on life cycle of *Amphiascopsis cintus* of harpacticoid copepods associated with seaweed. *Caulerpa* sp. are seaweeds or green algae that live either in the marine. They are commonly found on the sediment or rocky shore (Lewmanomont and Ogawa, 1995).

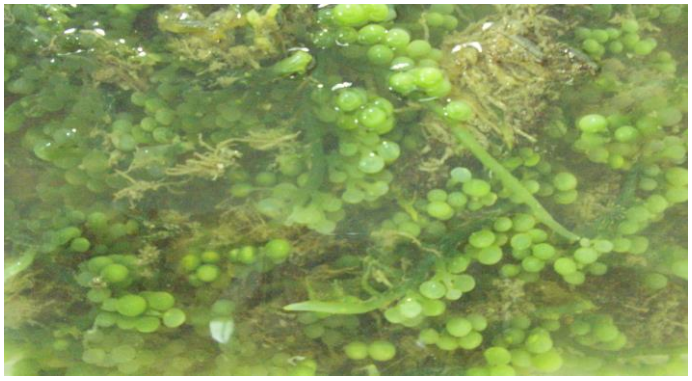

Figure 1. Collected samples on study area at Ao Banphe; *Caulerpa* sp.

Amphiascopsis cintus seem most useful, can reproduce constantly in the culture, adult small size and mass cultures easy than orther species. They are generally tolerant of environmental fluctuations but they do have temperature and salinity optima and can survive for a time without food but these will be species and strain dependent. Harpacticoids can synthesis nutritionally important essential fatty acids (EFA) (Christopher, 2003), improves the productivity of copepod cultures, suggesting that the synthesis of EFA. They are better food for fish larvae than rotifer because of their ability to synthesise EFAs and better than *Artemia* because small size. The nauplii of harpacticoid copepods are very small but appear to have an appetite stimulatory effect and adult of them are an excellent food source of dietary protein for many forms of aquatic life, particularly when they are juvenile stage or newly hatched fish or invertebrate species.

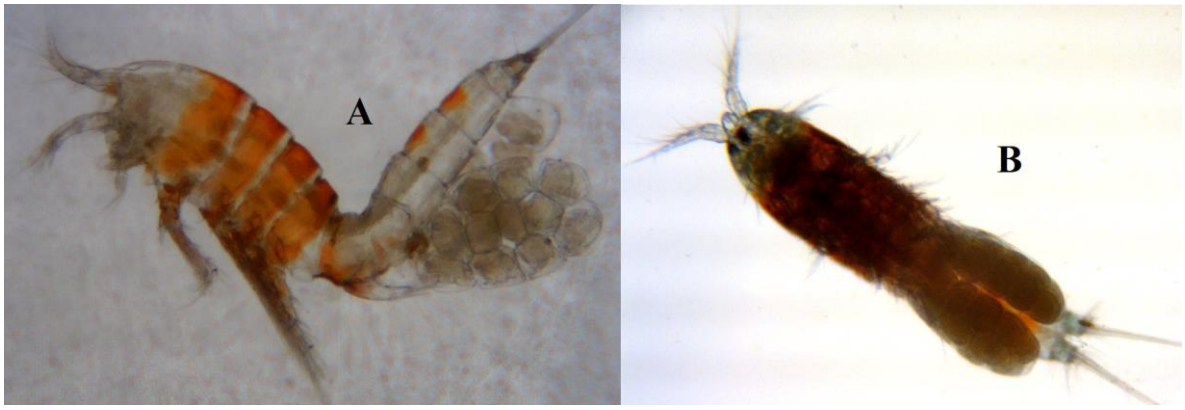

Figure 2. *Amphiascopsis cintus*, ovigerous female.

Methodology:

Samples were collected from *Caulerpa* sp. (Figure 1) and will be sieved through a 120 µm and 63 µm meshed net, respectively. The residue containing, e.g., harpacticoids was rinsed into smaller bowls for transport to the laboratory. Identified are seaweed and seagrass by Lewmanomont & Oganawa (1995). Measurement of environmental factors at study area; temperature by using a thermometer, salinity by using a refractometer salinometer, dissolved oxygen by using DO Meter and pH by using a pH meter. In laboratory prepare seawater from study area and filtered with mesh size bag of 60 µm. Seaweed samples will be sieved through a 120 µm and 63 µm meshed net, respectively. All harpacticoid copepods on the 63 µm sieve and then transferred into a beaker. Samples will be observed under a stereo microscope to identify the harpacticoid copepods by using morphology and some important characters, shape of body, color and then ovigerous females will be removed to separate petri dish. Select one ovigerous female of *Amphiascopsis cintus* will be cultured in a petri dish and adding microalgal a few dropswas used as food for them every few days. Checking the life stages of *Amphiascopsis cintus* daily and collecting various stages of copepods and then preserve them in 70% ethanol and drawing all stage of nauplii (NI-NVI) by using a camera lucida. All appendages were drawn under a high power microscope and at least x100 oil immersion objective. After finishing the pencil drawings all appendages were provided with a scale bar and ink drawings were made by using rotting pens.

Results and Discussion:

Measurement of environmental factors from study area that collected samples as follow: temperature 32 ºc, salinity 30 psu., dissolved oxygen 6.8 mg/l and pH 7.2.

Amphiascopsis cintus belonging to family Miraciidae. They have two egg sac and have number of eggs more than 10 eggs per sac**.** They are carries eggs about two day. The successive development of fertilized eggs to hatching stage required a period of one day. Development of naupliar six stages of *Amphiascopsis cintus* within seven days. The general body form of all nauplii stages are not obviously different. The size of naupliar stages are slightly different.

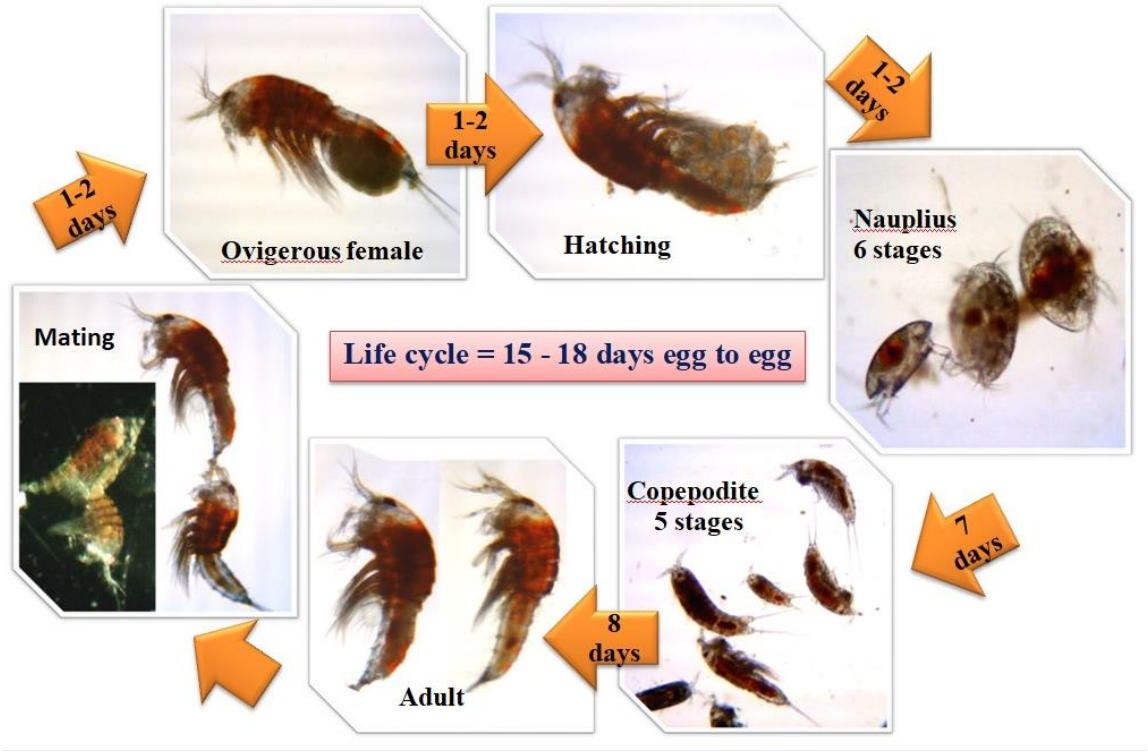

Figure 3. *Life cycle of Amphiascopsis cintus*

Development of Nauplias stages

The naupliar development of harpacticoid copepod different in species (Chullasorn, et. al. 2012; Dahms, et al. 2007; Dahms, et al. 2009; Kangtia, 2014; Kim, 2014; Nicolaos, 2015). The post embryonic development of genus *Amphiascopsis* is less study. The detail descriptions are as follow: Nauplius stage body broadly oval shaped, with three pairs of appendages and one pair of anal spine. Labrum having the shape or approximate shape of a square and with ornamentation.

Nauplius stage I (see Figure 4A) body slightly longer than wide, with cephalic shield. Body length 74.0 µm, width 132 µm. Sub-circular labrum with spinules along lateral corner and posterior margin. Ventral field unornamented. Antennule 3-segmented (see Figure 6A) middle segment with 1 thick, blunt seta ventrally and denticles dorsally. Distal segment ventrally with 1 thick, blunt, seta; terminally with 1 seta with 2 branches and 1 aesthetasc; dorsally with 1 small seta; denticles terminally and ventrally. Antenna (see Figure 7A) with coxa, basis, 2-segmented exopod and 1-segmented endopod. Coxa with row of denticles dorsally and naupliar arthrite ventrally with 1 seta near its base. Basis with denticles near distal edge. Exopod 2-segmented; proximal segment ventrally with 1 thick, blunt seta and 1 thin seta proximally; distal segment with 1 thick, blunt seta and 2 thin setae terminally. Endopod with 1 thin seta ventrally and with 1 long, thick, curved seta and 1 thin seta terminally. Mandible (see Figure 8A) protopod with unarmed coxa; basis with 1 thick, blunt seta ventally and denticles distally. Exopod 4-segmented; proximal segment unarmed, antepenultimate segment dorsally with thick, blunt seta, penultimate segment with 1 thick, long seta dorsally, terminal segment 1 thick, long and with 1 thin, short seta terminally. Endopod 1-segmented with 2 thick setae terminally.

Nauplius stage II (see Figure 4B) differing from nauplius I as follows: body form ovoid; body length 86 µm, body width 150 µm. Antennule (see Figure 6B) 3-segmented. Segment 1 without seta, segment 2 with 3 setae. Segment 3 with 5 setae and small aesthetasc on distal segment. Antenna (see Figure 7B) with coxa and basis, 3-segmented exopod

and 1-segmented endopod. Coxa with naupliar arthrite and 1 seta. Basis with 4 setae. Exopod; segment 1 with 1 short seta and 1 long seta, segment 2 with 1 seta, and segments 3 with 3 setae. Endopod robust with 2 inner bare seta on middle, and with 2 setae near claw. Mandible (see Figure 8B) with coxa and basis. Coxa with 1 seta. Basis with 2 inner setae bearing setules row on inner margin. Exopod 1-segmented, with 1 lateral seta and 3 setae distally. Endopod 1-segmented, with 4 outer setae and 4 setae. Caudal ramus (see Figure 7B), a bud with 1 seta.

Nauplius stage III (see Figure 4C) differing from nauplius II as follows: Body form ovoid; body length 100 µm, body width 152 µm. Antennule (see Figure 6C) 3-segmented. Segment 1 without seta, segment 2 with 3 setae. Segment 3 with 8 setae and small aesthetasc on distal segment. Antenna (see Figure 7C) with coxa and basis, 3-segmented exopod and 1-segmented endopod. Coxa with naupliar arthrite and 1 seta. Basis with 4 setae. Exopod; segment 1 with 2 setae, segment 2 with 2 setae, and segments 3 with 4 setae. Endopod robust with 3 inner bare seta on middle, and with 2 setae near claw. Mandible (see Figure 8C). Coxa with 1 seta. Basis with 2 inner setae bearing setules row on inner margin. Exopod 1-segmented, with 1 lateral seta and 3 setae distally. Endopod 1-segmented, with 4 outer setae and 4 setae. Maxillule (see Figure 4C) with 1 seta. Caudal ramus (see Figure 4C) with 3 setae.

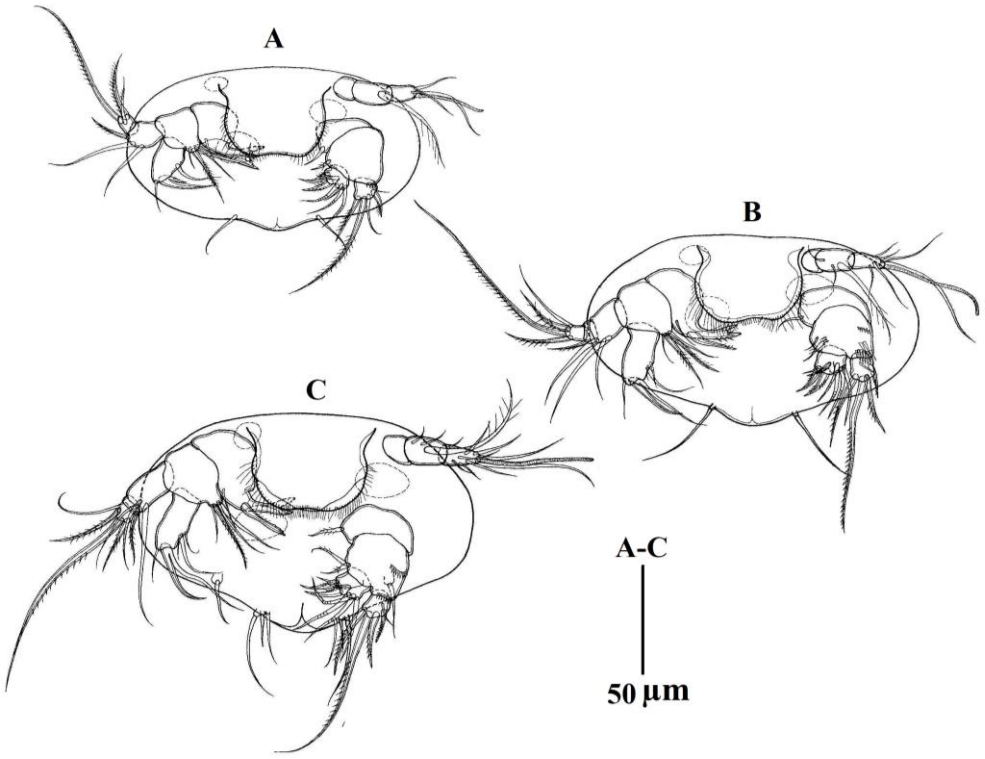

Figure 4. *Amphiascopsis cintus*, habitus in ventral view. Nauplius I (A), Nauplius II (B), Nauplius III (C). Appendages are shown alternately (right A1, left right A2, right Md).

Nauplius stage IV (see Figure 5A) differing from nauplius III as follows: body form ovoid; body length 108 µm, body width 170 µm. Antennule (see Figure 6D) 3-segmented. Segment 1 without seta, segment 2 with 3 setae. Segment 3 with 9 setae. Antenna (see Figure 7D) 3-segmented exopod and 1-segmented endopod. Coxa with naupliar arthrite and 1 seta. Basis with 4 setae. Exopod; segment 1 with 2 setae, segment 2 with 2 setae, and segments 3 with 4 setae. Endopod robust with 3 inner bare seta on middle, and with 2 setae near claw.

Mandible (see Figure 8D). Coxa with 1 seta. Basis with 2 inner setae bearing setules row on inner margin. Exopod 1-segmented, with 1 lateral seta and 3 setae distally. Endopod 1-segmented, with 4 outer setae and 4 setae. Maxillule (see Figure 4D) with 4 setae. Caudal ramus (see Figure 4D) with 4 setae.

Nauplius stage V (see Figure 5B) differs from NIV as follows: body length 156 µm, body width 204 µm. Antennule (see Figure 6E), segment 2 with 3 setae. Segment 3 with 12 setae and small aesthetasc on distal segment. Maxillule (see Figure 5B) with 4 setae. Caudal ramus (see Figure 5) with 5 setae.

Nauplius stage VI (see Figure 5C) differs from NIV as follows: body length 156 µm, body width 204 µm. Antennule (see Figure 5F) exopod with 3 segment, segment 2 with 3 setae. Segment 3 with 12 setae and small aesthetasc on distal segment. Maxillule (see Figure 5C) with 5 setae. Caudal ramus (see Figure 5C) with 5 setae.

Table 1. Dimensions of nauplii stages of *Amphiascopsis cintus* in microns

Nauplii stages	NI	NII	NIII	NIV	NV	NVI
Body length	74	86	100	108	156	156
Body width	132	150	152	170	204	214

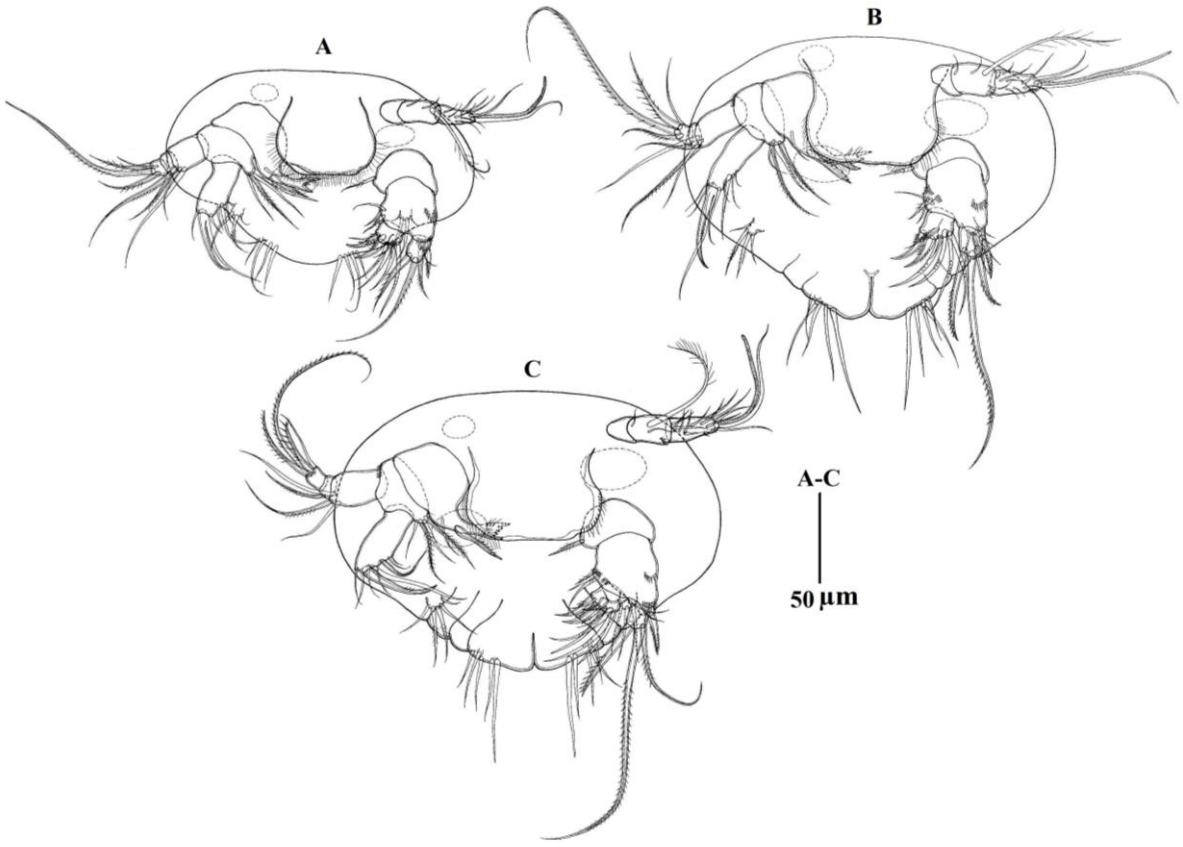

Figure 5. *Amphiascopsis cintus*, habitus in ventral view. Nauplius I (A), Nauplius II (B), Nauplius III (C). Appendages are shown alternately (right A1, left right A2, right Md).

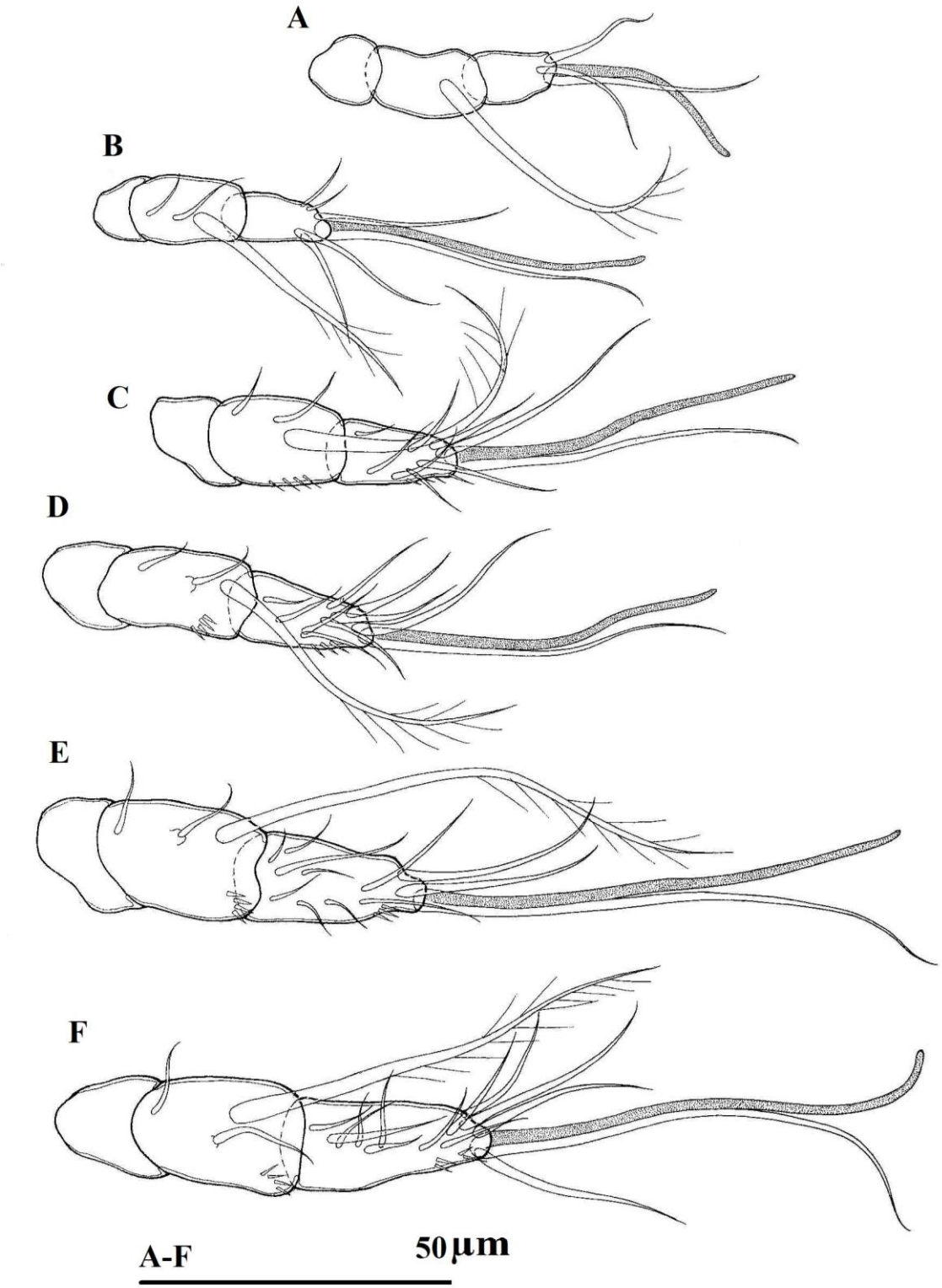

Figure 6. *Amphiascopsis cintus*, Antennules of NI-NVI.

Key to Naupliar Stages of Amphiascopsis cintus

1. Almost circular in shape; 1st maxilla not indicated ..... NI

–More than 1 caudal seta on each side 2

2. One caudal seta on each side, antenna have arthrite ..... NII

–More than 1 caudal seta on each side 3

3. Three caudal setae; 1st maxilla with 1 seta ..... NIII

–More than 3 caudal seta on each side 4

4. Three caudal setae on each side, 1st maxilla with 4 setae, no indication of leg 1 5

–More than 4 caudal seta on each side ..... NIV

5. 1st maxilla present as lobe with 4 setae; 5 caudal setae on each side ..... NV

–Caudal rami present as lobe ..... NVI

–More than 1 seta of maxillule ..... NV

5. 1st maxilla present as lobe with 3 setae; 5 caudal setae on each side ..... NVI

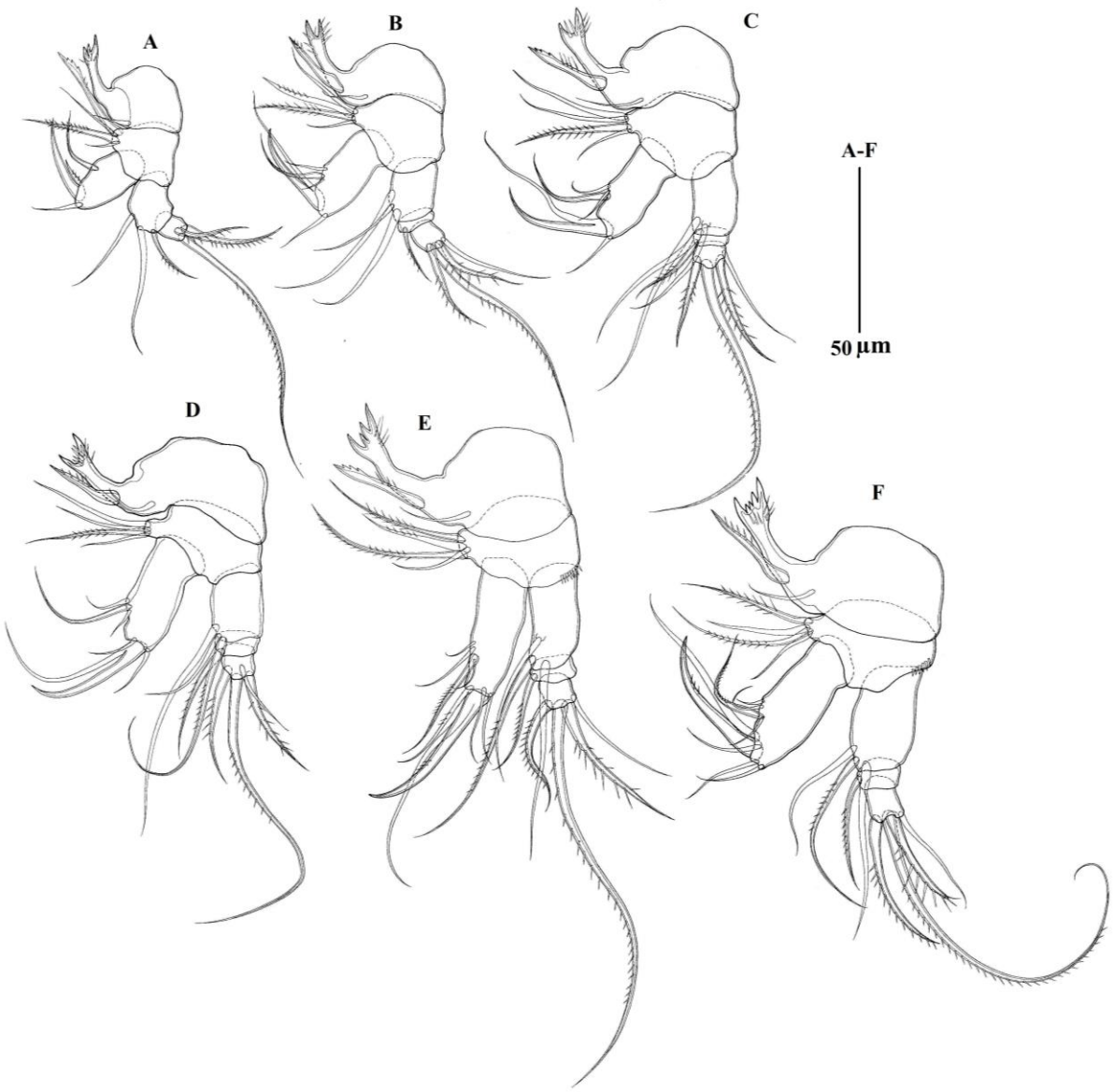

Figure 7. *Amphiascopsis cintus*, Antenna of NI-NVI.

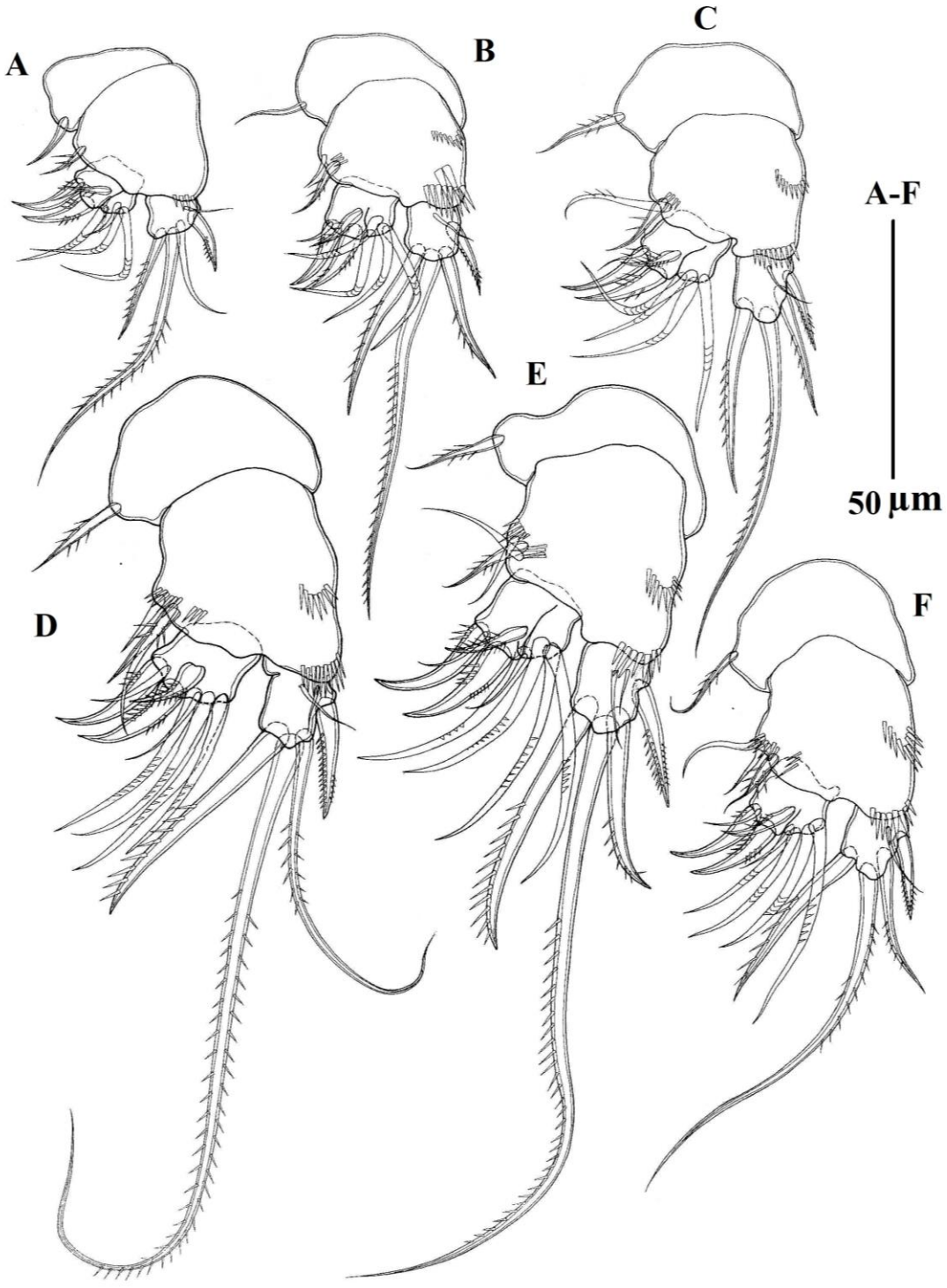

Figure 8. *Amphiascopsis cintus*, Antenna of NV-NVI.

Conclusion:

A single ovigerous female was selected and cultured in a petri dish; after 2-3 days the nauplii emerged. Naupliar developing time from NI to N VI is completed within 7 days. N VI took 28 hours to develope to first copepodid stage. Copepodid developing time from CI to CVI (adult) was 8 days. The total generation time from egg to the adult was 18 days.

Discussion:

Amphiascopsis cintus can culture in laboratory if can control the environmental factors, such as salinity, temperature, food and water quality because they are sensitive more than *Paramphiascell* sp. but when culture them in laboratory we can collect specimen all stages very easy. Later the development of the same species was studied and compared by Dahms (1986; 1987)

Acknowledgements:

The author would like to thank the biology program, faculty of science and technology and the research and development institute of Bansomdej chaopraya Rajabhat University for supports this research.

References:

1. Alekseev, V. R., 2002. Copepoda. In Fernando, C. H. (ed.), A Guide to Tropical Freshwater Zooplankton Zooplankton Identication. Ecology and Impact on Fisheries. Backhuys Pub-lishers, Leiden: 123-188.
2. Christopher, J. C. Culture of Harpacticoid Copepods: Potential as Live Feed for Rearing Marine Fish. *Adv Mar Biol*. *2003*;*44:295-316*.
3. Chullasorn, S., W. Anansatitporn, P. Kangtia, P. Klangsin and R. Jullawateelert. 2011. Review of naupliar development among Miraciidae (Copepoda: Harpacticoida) with a naupliar description of *Paramphiascella choi* sp. nov. from Thailand. Hydrobiologia, 666: 21-43.
4. Chullasorn, S., H-U. Dahms, N. Iwasaki, P. Kangtia, F. D. Ferrari, H-J. Jeon and W-Xi Yang. 2012. Naupliar Development of an Ancorabolid, *Paralaophontodes* sp. (Copepoda: Harpacticoida) sheds light on Harpacticoid evolution. Zoological Studies 51(3): 372–382.
5. Chullasorn, S., V.N. Ivanenko, H-U. Dahms, P. Kangtia and W-X Yang. 2012. A new species of *Tigriopus* (Copepoda, Harpacticoida, Harpacticidae) from Thailand with the description of its naupliar development. Helgoland Marine Research 66: 139-151.
6. Dahms, H-U., S. Chullasorn, P. Kangtia, F. D. Ferrari, J-H. Hwang. 2007. Naupliar Development of *Tigriopus japonicus* Mori, 1932 (Copepoda: Harpacticidae). Zoological Studies, 46(6): 746-759.
7. Dahms, H-U., S. Chullasorn, N.V. Schizas, P. Kangtia, W. Anansatitporn and W-Xi Yang. 2009. Naupliar development among Tisbidae (Copepoda: harpacticoida) with a phylogenetic analysis and naupliar description of *Tisbe thailandensis* from Thailand. Zoological Studies 48(6): 780-796.
8. Kangtia, P., Dahms, H.U., Song, S.J., Myoung, J.G. and Khim, J.S. (2014). A review of naupliar development within the Harpacticidae, with naupliar description of *Zaus wonchoelleei* Kangtia, Dahms, Song, Myoung, Park & Khim (Copepoda, Harpacticoida) Crustaceana. 88(4), 449-465.
9. Kangtia. P., W. kulket. (2019). Marine Harpacticoid Copepods associated with *Ulva intestinalis* in Various Habitats at Chonburi Province, Thailand. Proceeding 3rd International Conference on Media Studies 2019. 324-329.
10. Kim, B-R., S. Chullasorn, P. Kangtia, W. Anansatitporn, S-J. Song and H-U. Dahms. 2014. Naupliar development of *Nitocra karanovici* (Copepoda, Harpacticoida). Proceedings of the Biological Society of Washington. 126(4): 329–342.
11. Lewmanomont and Ogawa, 1995. Common Seaweeds and Seagrasses of Thailand. Bangkok: Faculty of Fisheries, Kasetsart University, Bangkok.
12. Nicolaos V.S., Dahms, H.U., Kangtia, P., Corgosinho, P.H.C. and Estronza, A-M.G. (2015). A new species of *Longipedia* Claus, 1863 (Copepoda: Harpacticoida: Longipediidae) from Caribbean mesophotic reefs with remarks on the phylogenetic affinities of Polyarthra. Marine Biology Research. 11(8), 789-803.

SP02_001_OF: EFFECT OF HIGH TEMPERATURE STRESS ON PHOTOSYNTHETIC CAPACITY AND OXIDATIVE DAMAGE IN POTTED YOUNG LONGAN TREE (*Dimocarpus longan* LOUR. 'PHUANG THONG')

Wachira Suwannarut,[1] Watcharra Chintakovid,[2] and Aussanee Pichakum[1,*]

[1]Department of Plant Sciences, Faculty of Science, Mahidol University, Bangkok, 10400, Thailand

[2]Agricultural Science Division, Mahidol University, Kanchanaburi Campus, Kanchanaburi, 71150, Thailand

*e-mail: aussanee.pic@mahidol.ac.th

Abstract:

This study aimed to understand how the tree prioritizes its responses after encountering high temperature stress. Some physiological and biochemical responses, i.e., leaf temperature, leaf VPD (VpdL), net photosynthetic rate (Pn), stomatal conductance (Gs), transpiration rate (Tr), intercellular CO_2 concentrations (Ci), maximum quantum efficiency of PSII photochemistry (Fv/Fm), and minimal fluorescence yield (F0) were investigated in one-year old potted longan tree (*Dimocarpus longan* Lour. 'Phuang Thong') exposed to 30°C (normal or room temperature, NT) or 50°C (high temperature, HT) conditions for 2 h. The results demonstrated that leaf temperature and VpdL significantly increased after 30 min of HT exposure, while Pn, Gs, and Tr dramatically decreased. At 30-90 min of HT exposure, the Pn significantly decreased during stomatal closure occurrence. At 120 min, the Pn continuously decreased together with declining potential PSII efficiency as shown in a decrease in Fv/Fm. This might be concluded that the HT stress significantly lowered Pn during 30-120 min via 2 mechanisms as early stomatal limitation and later non-stomata limitation in PSII efficiency. Moreover, the rapid responses to HT stress in potted young longan tree could be clearly observed within 30 min. However, no significant differences were found in quantum yield of PSII (ΦPSII), electron transport rate (ETR), malondialdehyde (MDA) content, electrolyte leakage, H_2O_2 content, and $O_2^{\cdot-}$ content in both NT and HT applied trees. It implied that these parameters could not be implemented as appropriate indicators for evaluating the short-term HT response in potted young longan trees.

Introduction:

Under situation of climate changing, the average global temperature is predicted to increase by 0.2 °C per a decade, leading to rise degree up to 1.5 - 6 °C within the end of the 21st century.[1] Heat stress is one type of abiotic stress which influences plant responses consisting of morphological, physiological and biochemical changes. These changes adversely impacted on growth and development and eventually reduced plant productivity.[2]

Photosynthesis is a major sensitive physiological mechanism affected by high temperature (HT). And high temperature adversely affects organisms by disturbing photosynthetic activity through stomatal and non-stomatal limitations so it causes a decline in photosynthetic capacity.[3] Moreover, a decrease in photosynthesis may result from the chloroplast ultrastructural alteration which was induced by overproduction of reactive oxygen species (ROS). This ROS in turn causes oxidative damage to the photosynthetic apparatus.[4,5] The decline in photosynthetic capacity can finally reduce plant growth and development.[6] Therefore, the photosynthesis response to HT stress should be figured out in order to comprehend insights into how plants may be modified to become plant heat tolerance.

Longan (*Dimocarpus longan* Lour.) is one of the tropical members in the soapberry family (Sapindaceae).[7] In Thailand, longan is an economically important fruit exporting as fresh, frozen, dried, and canned products. Longan favors sunny environments but should avoid high temperature summer. However, natural HT stress always happens at alluvial plains of Thailand. During reproductive phase of longan, pollen germination and pollen tube length reduced under 40°C condition leading to yield reduction.[8] Nevertheless, the effect of high temperature on vegetative phase in longan tree is not elucidated.

In this study, the physiological and biochemical responses of potted young longan tree (*Dimocarpus longan* Lour.) as affected by HT stress were investigated in order to understand how plants suffer and to determine various responses in photosynthetic capacity and oxidative damage as rapid responses to short-term HT stress exposure. This study provided a novel information on longan tree response against HT condition and applicable indicators for the evaluation of short-term and rapid responses to HT stress which can be beneficial for proper resolution to alleviate current problem on climate changing in longan production system.

Methodology:

Plant material and treatment

One-year old potted longan (*Dimocarpus longan* Lour.) 'Phaung Thong' trees were cultivated from uniform marcotting ones obtaining from private orchard at Samut Sakhon province, Thailand. Propagated trees were transplanted to plastic pots (38 cm in diameter and 28 cm in height) containing growing media mixture of soil, rice husk, shell chop, and manure (1:1:1:1) and were outdoor placed at Salaya campus, Mahidol University, Nakhon Pathom, Thailand with ambient temperature about 30–35°C and 60–80% relative humidity. Hand watering was applied every day. Chemical fertilizer and pesticide were sprayed twice a month.

Artificial climatic room was implemented for high temperature (HT) treatments using 3 heater machines. The treatments were divided into 50°C as HT stress and 30°C as normal temperature or non-stress for 2 h. Three replicated trees were used. The physiological and biochemical parameters on photosynthesis and oxidative responses were measured with interval of 0, 30, 60, 90, and 120 min after treatments.

Physiological parameter measurements

Gas exchange were measured on three mature leaflets at the sixth position from the top using LI-6400XT portable photosynthesis system (LI-COR, Inc., USA). The net photosynthetic rate (Pn), stomatal conductance (Gs), transpiration rate (Tr), intercellular CO_2 concentrations (Ci), and leaf vapour pressure deficit (VpdL) were conducted under 400 µl l^{-1} CO_2 concentration, 500 µmol s^{-1} flow rate, and 1000 µmol m^{-2} s^{-1} of photosynthetic photon flux density (PPFD) provided by a LED light source. Then, leaf temperature was measured by infrared thermometer which were placed at 15 cm above the leaf.

Chlorophyll fluorescence were performed on the same leaf as previous measurement using field-portable pulse-modulated chlorophyll fluorometer (FMS2+, Hansatech Instruments Ltd, Norfolk, UK). Chlorophyll fluorescence measurements were initially taken on dark-adapted leaves by pinching the FMS dark adaptation leaf-clips at the middle leaflet for 30 min. Later, minimal fluorescence yield (F0), maximum quantum efficiency of PSII photochemistry (Fv/Fm), quantum yield of PSII (ϕPSII), and electron transport rate (ETR) were determined.

Biochemical parameter measurements

Hydrogen peroxide (H_2O_2) and superoxide anion free radical ($O_2^{\cdot-}$) contents in leaves were determined according to the modified methods of Yu et al.[9] and Sharma et al.[10], respectively. H_2O_2 content was calculated from the spectrophotometrically optical absorption at 410 nm using the extinction coefficient of 0.28 μmol^{-1} cm^{-1} and $O_2^{\cdot-}$ content was calculated from a standard curve of sodium nitrite. The ROS contents were expressed as µmol per gram fresh weight.

Cell membrane stability was expressed by determining the lipid peroxidation and electrolyte leakage. Lipid peroxidation was measured in terms of malondialdehyde (MDA) contents, a decomposition product of the peroxidized polyunsaturated fatty acid component of the membrane lipid, using thiobarbituric acid (TBA) as the

reactive material based on the method of Hasanuzzaman and Fujita.[11] The concentration of MDA was calculated by using the extinction coefficient of 155 $mM^{-1}cm^{-1}$ and expressed as nmol of MDA per gram fresh weight. Electrolyte leakage was assessed as described by Yu et al.[9]

Statistical analysis

The analysis of variance was performed using SPSS v.18 (SPSS, Inc., Chicago, USA). The differences between the means among treatments; temperature and time were compared by Duncan's multiple range test at 0.05 probability levels after ANOVA. All results were presented as means with standard errors (SE).

Results and Discussion:

Effects of high temperature on physiological responses

A sensitive physiological process as photosynthesis was affected by high temperature via stomatal and nonstomatal limitations. At NT treatment (30°C), leaf temperature, VpdL, Pn, Gs, Tr, Ci, Fv/Fm, F0, ΦPSII, and ETR of longan leaves remained at steady level for the 2 h period (Figures 1, 2, 3). HT (50°C) for 30 min significantly increased leaf temperature and VpdL (Figure 1) but significantly decreased Pn, Gs, and Tr (Figure 2A, 2B, 2C), all of which reflected the rapid and short-term changes of young longan tree to HT stress within 30 min. At 60-120 min after HT exposure, these parameters maintained the same tendency as the time of 30 min. The change in Ci of HT treated leaves were observed with gradually decreasing at 60 min and greater decreasing at 90 min but dramatically increasing at 120 min (Figure 2D).

The increase in leaf temperature herein caused an increase in VpdL which was consistent with Will et al.[11], reported that small increases in temperature from 30 to 33°C could increase vapour pressure deficit (VPD) up to 40%. This work further suggested that the increase in VPD was related to the decrease in Gs whilst Gs also had the positive correlation with Pn, which were in good agreement with the work on peach grown under subtropical conditions.[13] The coincident of decrease in Gs demonstrated that the partial stomatal closure caused the decrease in Pn and Tr. In this study, Pn was mainly limited by stomatal closure at 30-90 min of HT exposure which could be ascribed to the stomatal limitation because both Ci and Gs decreased simultaneously. Whilst the inhibition of Pn could be attributed to the non-stomatal limitation at 120 min of heat treatment because Gs decreased and vice versa on increased Ci (Figure 2A, 2B, 2D). Therefore, decrease in Pn at 120 min resulted from the decreased Fv/Fm and increased F0 (Figure 3A, 3C). Fv/Fm and F0 started changing at 120 min of HT treatment. The decrease in Fv/Fm indicated decline in potential PSII efficiency while increase in F0 indicated alterations in the capacity to trap energy.[14] However, the ΦPSII and ETR under both NT and HT treatments for 2 h were not significantly different (Figure 3B, 3D), which absolutely agreed with "Ruby Star" passion fruit under 45°C for 2 h and poplar under 42°C for 3 h, respectively.[15,16] Consequently, ΦPSII and ETR could not reflect short-term HT responses in potted young longan 'Phuang Thong' tree.

Effects of high temperature on biochemical responses

Free radical-induced peroxidation of membrane lipid is a reflection of stress-induced damage at the cellular level. Therefore, MDA content and electrolyte leakage have been widely utilized as criteria to assess heat injury by ROS such as H_2O_2, $O_2^{\cdot-}$ in many plants.[17] In this study, MDA content, electrolyte leakage, H_2O_2 content, and $O_2^{\cdot-}$ content were similar along with 2 h of experiment in both NT (30°C) and HT (50°C) treatments (Figure 4). Based on the results, it could be ensured that the decline in photosynthesis in potted young longan tree to HT exposure for 2 h preferably resulted from the stomata closure activity rather than from ROS-induced damage to the PSII reaction center or photosynthetic organ. The results also corresponded in one-year old poplar tree under 42°C for 3 h which did not significantly change in MDA and H_2O_2.[16] As a result, MDA content, electrolyte leakage, H_2O_2 content, and $O_2^{\cdot-}$ content could not be employed as indicators for the evaluation of the short-term HT response.

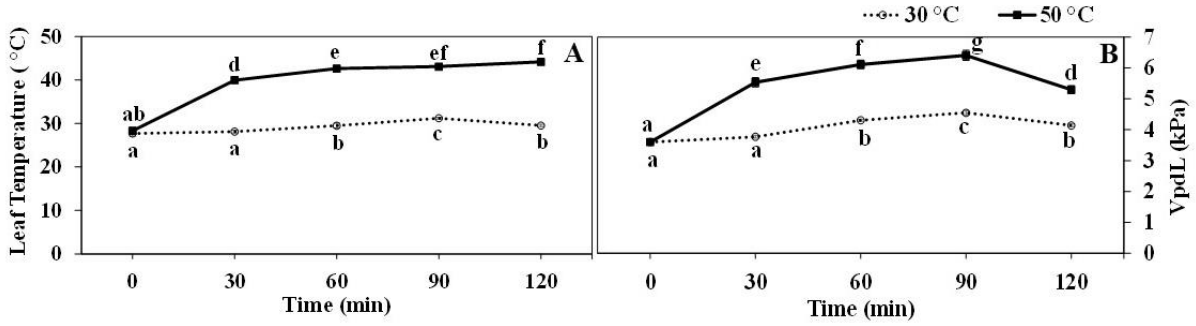

Figure 1. Leaf temperature (A) and leaf VPD, VpdL (B) in leaves of control (30°C) and stressed (50°C) potted young longan tree 'Phuang Thong'. Each value is mean ± S.E. of nine replicates. Different letters on error bars indicate significant difference at P < 0.05 according to Duncan's multiple comparison.

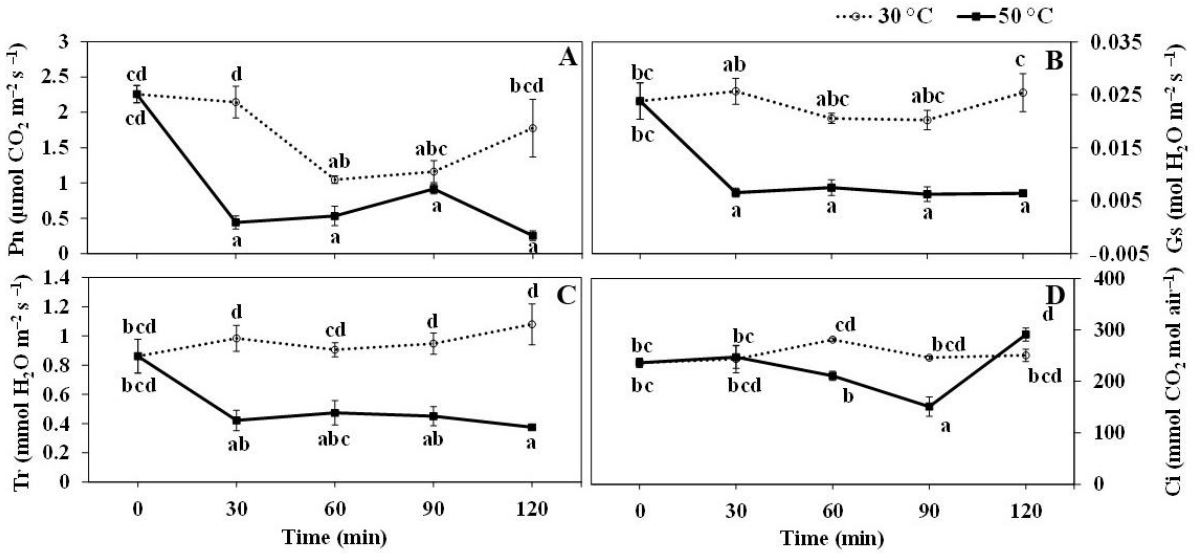

Figure 2. Net photosynthetic rate, Pn (A), stomatal conductance, Gs (B), transpiration rate, Tr (C), and intercellular CO_2 concentrations, Ci (D) in leaves of control (30°C) and stressed (50°C) longan tree 'Phuang thong'. Each value is mean ± S.E. of three replicates. Different letters on error bars indicate significant difference at P < 0.05 according to Duncan's multiple comparison.

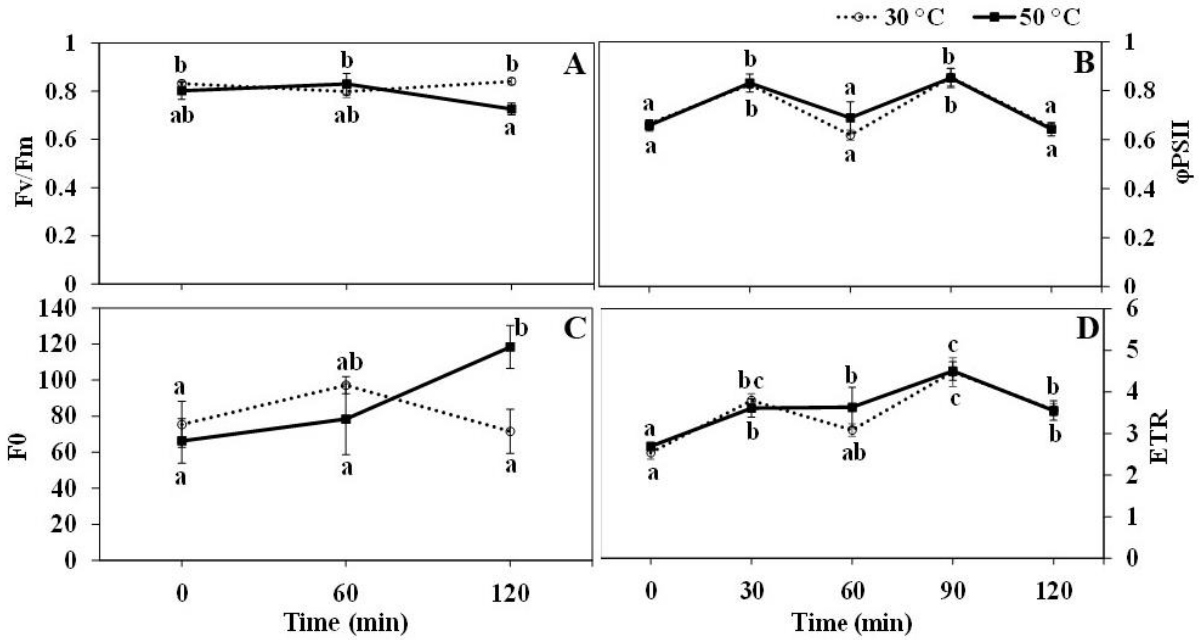

Figure 3. Maximum quantum efficiency of PSII photochemistry, Fv/Fm (A), quantum yield of PSII, ΦPSII (B), minimal fluorescence yield, F0 (C), and electron transport rate, ETR (D) in leaves of control (30°C) and stressed (50°C) potted young longan tree 'Phuang Thong'. Each value is mean ± S.E. of nine replicates. Different letters on error bars indicate significant difference at $P < 0.05$ according to Duncan's multiple comparison.

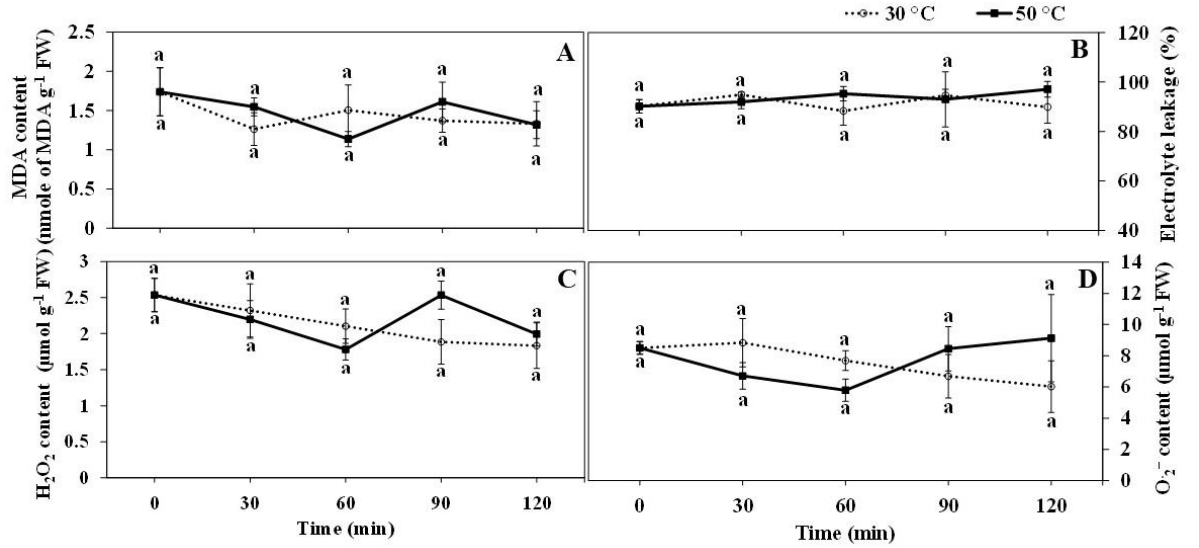

Figure 4. Malondialdehyde, MDA (A), electrolyte leakage, EL (B), H_2O_2 content (C), and $O_2^{\cdot-}$ content (D) in leaves of control (30°C) and stressed (50°C) potted young longan tree 'Phuang Thong'. Each value is mean ± S.E. of six replicates. Different letters on error bars indicate significant difference at $P < 0.05$ according to Duncan's multiple comparison.

Conclusion:

Leaf temperature and VpdL significantly increased whereas Pn, Gs, and Tr dramatically decreased at 30 min of 50°C exposure which could indicate the rapid and short-term responses to high temperature stress within 30 min in potted young longan 'Phuang Thong' tree. The Pn significantly decreased at 50°C exposure due to both stomatal and non-stomatal limitations. At 120 min after 50°C exposure, Fv/Fm decreased whereas F0 increased. However, both 30°C and 50°C treatments, ΦPSII, ETR, MDA content, electrolyte leakage, H_2O_2 content, and $O_2^{\cdot-}$ content were insignificantly similar. Thus, this work suggested that these parameters could not be implemented as indicators for the evaluation of short-term high temperature response in potted young longan 'Phuang Thong' tree.

Acknowledgements:

This work was jointly supported by Thailand Science Research and Innovation (TSRI) via research project no. RDG612003, Mahidol University and Development and Promotion of Science and Technology Talents Project (DPST).

References:

1. IPCC. Contribution of working group I to the fifth assessment report of the intergovernmental panel on climate change. 2013.
2. Zhao D.-Q, Li T.-T, Hao Z.-J, Cheng M.-L, Tao J. Cell Stress Chaperon. 2019;24:247-257.
3. Luo Y, Li F, Wang G. P, Yang X. H, Wang W. Biol. 2010;54:495–501.
4. Chen W. L, Yang W. J, Lo H. F, Yeh D. M. Sci Hortic. 2014;179:367-375.
5. Yan K, Chen P, Shao H, Zhang L, Xu G. J. Agron Crop Sci. 2011;197:400-408.
6. Luo Y, Gao Y. M, Wang W, Zou C. J. Biol Plant. 2014;58: 395-398.
7. Pham V. T, Herrero M, Hormaza J. I. Ann Appl Biol. 2016;169:357-368.
8. Pham V. T, Herrero M, Hormaza J. I. Sci Hortic. 2015;197:470-475.
9. Yu C. W, Murphy T. M, Lin C. H. Funct Plant Biol. 2003;30:955-963.
10. Sharma A, Thakur S, Kumar V, Kesavan A. K, Thukral A. K, Bhardwaj R. BMC Plant Biol. 2017;17:1-10.
11. Hasanuzzaman M, Fujita M. Biol Trace Elem Res. 2011;143: 1758–1776.
12. Will R. E, Wilson S. M, Zou C. B, Hennessey T. C. New Phytol. 2013;200:366-374.
13. Tucci M. L. S, Erismann N. M, Machado E. C, Ribeiro R. V. Photosynthetica. 2010;48:421-429.
14. Duan W, Fan P. G, Wang L. J, Li W. D, Yan S. T, Li S. H. Tree Physiol. 2008;28:123-132.
15. Shimada A, Kubo T, Tominaga S, Yamamoto M. Hort. J. 2017;86:194-199.
16. Song Y, Chen Q, Ci D, Shao X, Zhang D. BMC Plant Biol. 2014;14.
17. Yin H, Chen Q, Yi M. Plant Growth Regul. 2008;54:45-54.

SP02_002_PF: DEPOSITIONAL PROCESSES AND CLIMATE CHANGE IN THE CENOZOIC HONGSA COALFIELD, LAO PDR

Thunyapat Sattraburut, Nipada Santha, Yupa Thasod *

Department of Geological Sciences, Faculty of Science, Chiang Mai University, Chiang Mai, Thailand
*e-mail: yupa.t@cmu.ac.th

Abstract:

Monolete spores of Cenozoic organic-rich fine-grained sediments from Hongsa coal mine, Lao PDR were selected to investigate spore colour variation or Spore Colour Index (SCI). The results show that almost all 50% lightest colour monolete spores have pale yellow to light yellow colour, suggesting they are situ materials. The lesser 50% shows yellow to brown sporomorphs considering as reworked sporomorphs that transported to the Hongsa deposit area together with in situ palynomorphs. The possibility of sources could be the Mesozoic bedrock that bound the Hongsa basin, resulted from the development of the basin that related to the interaction of the Indian and Eurasian plates. Moreover, the mineral compositions through the section are mainly quartz, kaolinite, illite, and montmorillonite, with a trace of gypsum. This suggested that the sediment come from the same source rock and the mineral contents imply to the change of climate from humid to dry during the deposition.

Introduction:

Hongsa Coal mine in Hongsa basin, Xayabouly Province, Lao PDR (Figure 1) is a Cenozoic intermontane basin composed of fine-grained clastic organic-rich sediments and coal seams which have a cumulative thickness of over than 100 m[1, 2]. The Cenozoic succession of Hongsa coal mine and sampling positions are showing in Figure 2[3].

In the organic-rich sediments, there are various colors sporomorph were found, this may cause by the degree of maturation or reworking or by both. Sporomorphs provide a reliable measurement to estimate thermal maturation of sediments based on the temperature-dependent color changes that sensitive in the lower range of thermal maturation, which they can yield more accurate information than vitrinite reflectance[4]. Furthermore, reworked palynomorphs, generally recovered from sediments together with palynomorphs considers as *in situ*, are helpful to determine sedimentary provenance and condition in this swampy forest[5]. In addition, some clay minerals can be used for environment and climate interpretation. Illite is the weathering product of rocks containing feldspars and micas and from soils under high pH conditions or basic condition[6]. It is dominant under cold and dry climatic conditions[7, 8]. Kaolinite is the weathering product of granitic and basic rocks, which also shows a high amount of silica and aluminum as the major chemical elements. It indicates the prevalence of acidic conditions and the presence of relict organic matter in the area of the source and near-neutral pH conditions in the basin of deposition[9]. The occurrence of kaolinite and montmorillonite (smectite) indicates the minerals takes place under a humid climatic condition with abundant rainfall[10, 11].

The aim of this research is to determine the depositional process and paleoclimate in Hongsa coalfield by spore color index and clay mineral that associated with the sporomorph.

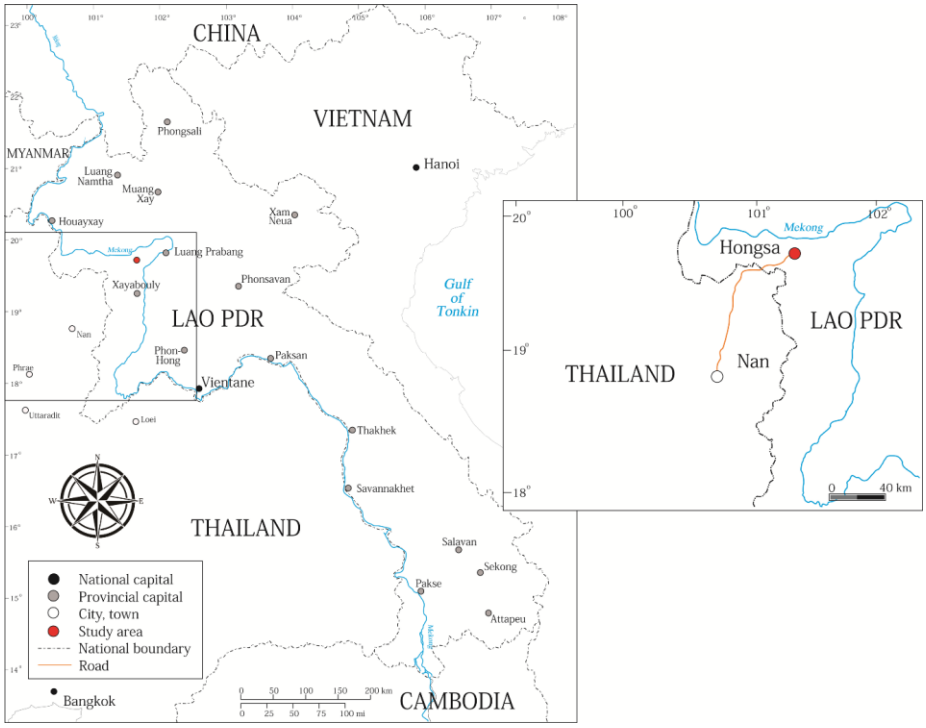

Figure 1. Location of Hongsa coalfield shown as red circle.

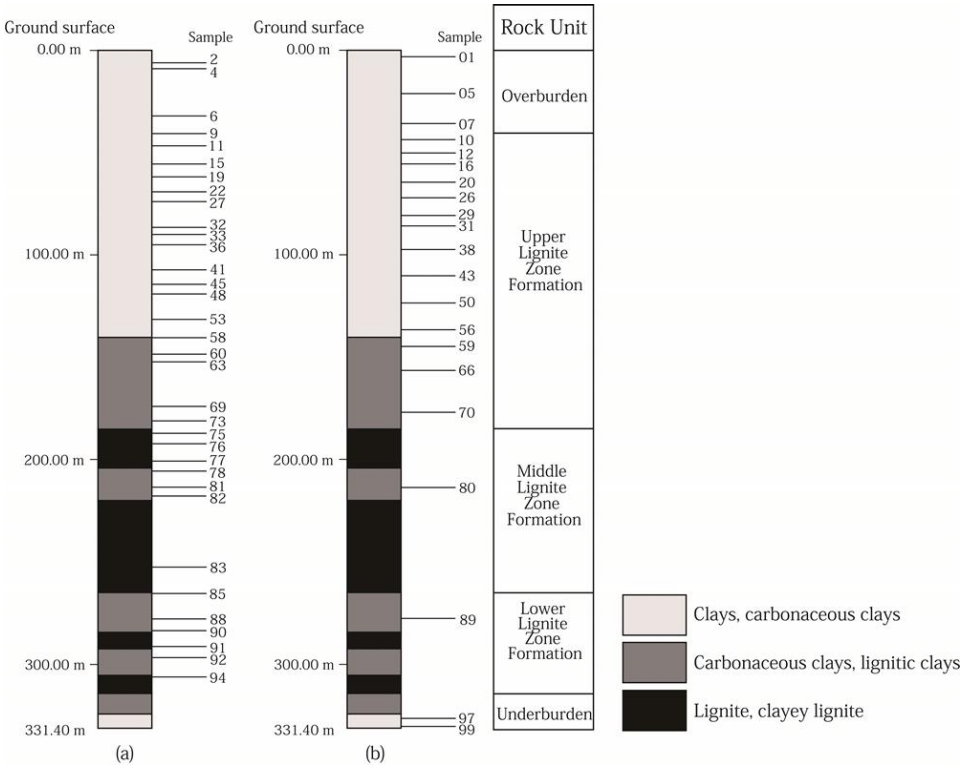

Figure 2. A partial schematic stratigraphic succession of Hongsa coalfield showing the stratigraphic levels of the sample collecting for palynological study (a), and mineral composition study (b).

Methodology:

The samples were collected from the drill core HPC80C which is 331.40 meters thick. Thirty-two organic-rich were provided for palynological study and the interbedded twenty-one samples of fine-grained sediment were analyzed by X-ray diffraction.

Spore colour index comparison: The organic-rich samples consisted mainly of carbonaceous clays with a minor of carbonaceous silty clays. The samples were treated by the standard palynological techniques[12, 13, 14]. Sporomorph colours estimation was taken on the unfolded, well-preserved sporoderms based on SCI, a scale that referred to a spore and pollen colour gradation[15]. The scale ranges from 1 to 10 and reflects a colour graded from colourless or light yellow to black. The monolete pteridophytic spore colour gradation is shown in Figure 3. The lightest coloured sporomorphs indicate the maximum thermal influence, darker sporomorph should be reworked specimens[16].

X-ray diffraction: The bulk composition was investigated from 21 low-organic fine-grained sediment samples that interbedded with the organic-rich samples. The samples consisted mainly of grayish-white to light gray unconsolidated clay and silty clay sediments. Preparing for analysis, the samples were oven-dried at 40°C overnight and were ground into powder, prior analyzed by Bruker X-ray diffractometer (model D8 Advance) at 2 theta 2-60°.

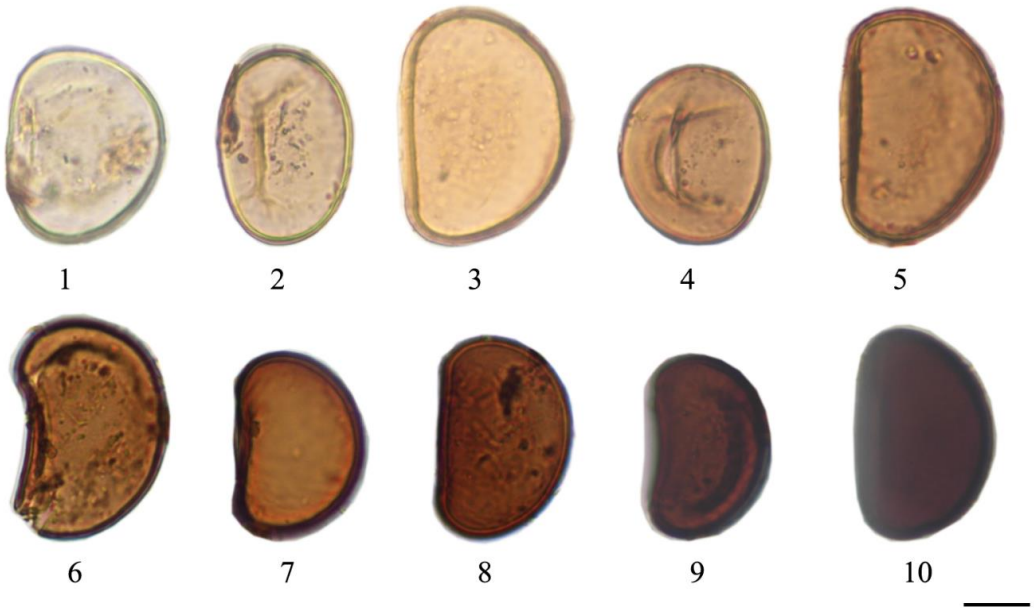

Figure 3. Representative of sporomorphs (monolete spores) based on Spore Colour Index from scale 1 to 10. Scale bars equal 10 µm.

Results and Discussion:

Spore colour index: The colours of spore in each sample are varied from SCI 1 to 10 indicating the sources of spores should from both *in situ* (autochthonous) and reworked (Figure 4 and Table 1). We subdivided sporomorphs colour variation of each sample into two groups autochthonous sporomorph group (SCI = 1-3) and reworked sporomorph group (SCI = 4-10), the details as follows:

The autochthonous or *in situ* sporomorph group presents pale yellow to light yellow colour that equal SCI of 1-3, ranging from 1.82 to 100% (mean 62.99%). The SCI of the spore colour is equivalent to Thermal Alteration Index (TAI) =1-(2-), and vitrinite reflectance less than 0.4. This suggests that the coal rank should be lignite under diagenesis organic stage[17].

The reworked sporomorph group represents sporomorphs with dark yellow to brown sporomorphs that equal SCI of 4-10, ranging between 0 and 98.18% (mean 37.01%). The SCI is equivalent to TAI=2-4, and vitrinite reflectance more than 0.38, suggesting the catagenetic stage and the coal rank should be sub-bituminous to low volatile bituminous.

The sequence of sporomorphs zones (Figure 4) shows the alternations of low and high reworked sporomorphs, which can approximately determine the relation of rock unit and sporomorphs zones. The low reworked sporomorphs zones can be correlated with the upper lignite zone formation and the lower lignite zone formation, while the high reworked sporomorphs zone is tentatively correlated with the middle lignite zone formation. The accumulation of reworked sporomorphs could have been caused by strong monsoon or catastrophic flooding that eroded the older sediments and carried strong current of water flooded to the deposit area.

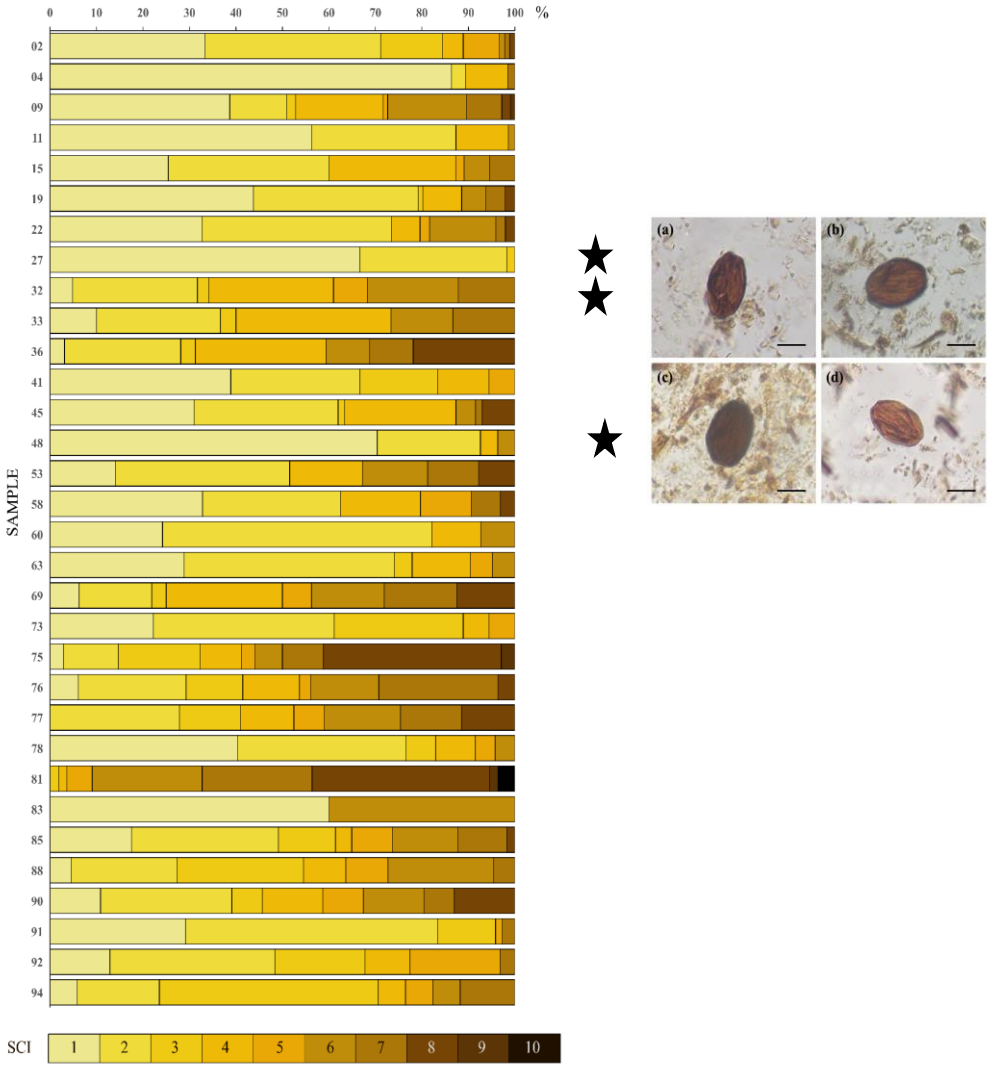

Figure 4. Spore colour variation based on Spore Colour Index (SCI). Black Stars are the beds were found *Schizaeoisporites* as showing in the small pictures.

The Possible Sources of Palynomorphs in Hongsa Coal Mine: From the present of spore colour found int the Hongsa basin, it can be presumed that some of the palynomorphs and sporomorphs were reworked or transported from the other area of the deposit. We found the Mesozoic fossil *Schizaeoisporites* (Figure 4) which abundant in Cretaceous[18]. This indicates the uplifted of the Mesozoic bedrock that supplied sediments to the Hongsa basin.

Table 1. Percentage of sporomorphs colour based on Spore Colour Index.

Sample	Spore Colour Index									
	1	**2**	**3**	**4**	**5**	**6**	**7**	**8**	**9**	**10**
2	33	38	13	4	8	1	1	1	0	0
4	86	3	0	9	0	0	2	0	0	0
9	39	12	2	19	1	17	8	2	1	0
11	56	31	0	11	0	1	0	0	0	0
15	25	35	0	27	2	5	5	0	0	0
19	44	35	1	8	0	5	4	2	0	0
22	33	41	0	6	2	14	2	2	0	0
27	67	32	2	0	0	0	0	0	0	0
32	5	27	2	27	7	20	12	0	0	0
33	10	27	3	33	0	13	13	0	0	0
36	3	25	3	28	0	9	9	22	0	0
41	39	28	17	11	6	0	0	0	0	0
45	31	31	1	24	0	4	1	7	0	0
48	70	22	0	4	0	4	0	0	0	0
53	14	38	0	16	0	14	11	8	0	0
58	33	30	0	17	11	0	6	3	0	0
60	24	58	0	11	0	7	0	0	0	0
63	29	45	4	13	5	5	0	0	0	0
69	6	16	3	25	6	16	16	13	0	0
73	22	39	28	6	6	0	0	0	0	0
75	3	12	18	9	3	6	9	38	3	0
76	6	23	12	12	2	15	26	4	0	0
77	0	28	13	11	7	16	13	11	0	0
78	40	36	6	9	4	4	0	0	0	0
81	0	0	2	2	5	24	24	38	2	4
83	60	0	0	0	0	40	0	0	0	0
85	18	32	12	4	9	14	11	2	0	0
88	5	23	27	9	9	23	5	0	0	0
90	11	28	7	13	9	13	7	13	0	0
91	29	54	13	0	1	0	3	0	0	0
92	13	35	19	10	19	0	3	0	0	0
94	6	18	47	6	6	6	12	0	0	0

X-ray diffraction: Based upon the bulk compositions of minerals (Figure 5 and Table 2), the sediment shows similar mineral association including quartz, kaolinite, illite, and smectite (montmorillonite). This suggested that the provenance of the sediments came from the same source area. Despite the same mineral type of the sediment, the assemblage minerals present different proportions. The different content of minerals probably suggests the different rate of weathering during deposition, in which weathering implies the change of climate. All the sediment samples are observed abundant of quartz which normally is fine-grained detrital clasts in the sediments, while the clay minerals are more significant to identify the change of climate. According to the results, the clay mineral assemblages occur in 6 stages based on the different proportions of mineral compositions from bottom to top (Figure 5 and Table 2). At stage 1, the beginning of deposition in the Hongsa coalfield is found the high content of kaolinite and montmorillonite with low content of quartz. This indicates

that the deposition was in a humid climate with volcanic activities because kaolinite usually occurs in detrital deposits as the weathering product[19] in tropical and warm humid regions and montmorillonite is produced from volcanism and hydrothermal activity and commonly weathered from the igneous and metamorphic rocks under an alkaline environment in a suitable condition[19]. In stage 2 and 3, kaolinite, illite, and montmorillonite increase higher than in stage 1. This means that the high content of kaolinite received from strongly weathering in humid condition and volcanic activities. In stage 4 and 5, there is no relatively significant change of clay minerals content, but it presents gypsum. It is ambiguous to interpret of clay minerals, but it could be sub-humid to dry condition since gypsum indicates to dry weather or a high evaporated[18]. This stage required the data of fossil to support. Stage 6, the high content of clay minerals is presented suggesting a reversion to humid condition.

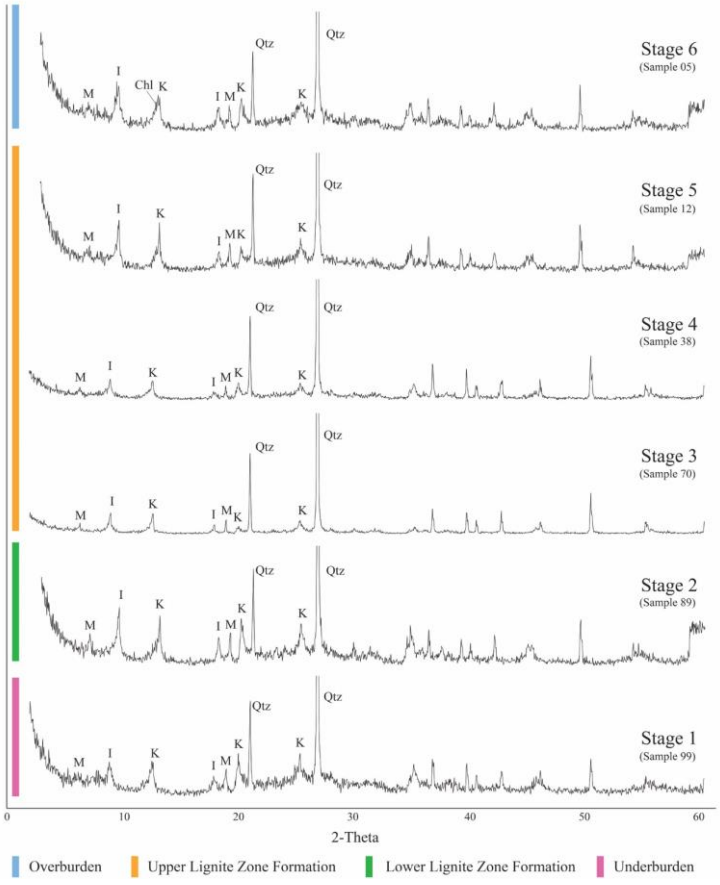

Figure 5. Diffraction pattern of sediments from the HPC80C borehole showing the different stages from bottom to top.

Table 2. Bulk composition of minerals of the HPC80C borehole from the Hongsa coalfield.

Sample	Rock Unit	Qtz	Kao	Ill	Mont	Gyp	Chl	Stage
01	OB	72	9	11	8	trace	trace	
05	OB	62	6	26	6	trace	trace	Stage 6
07	OB	88	5	4	3	0	0	
10	UF	69	13	13	5	0	0	
12	UF	73	8	14	5	0	0	
16	UF	74	9	8	5	4	0	Stage 5
20	UF	75	9	11	5	0	0	
26	UF	74	9	9	8	0	0	
29	UF	85	5	5	5	0	0	
31	UF	64	18	11	7	0	0	
38	UF	83	7	5	5	0	0	
43	UF	72	12	7	9	0	0	
50	UF	87	5	5	3	0	0	Stage 4
56	UF	81	8	8	3	0	0	
59	UF	87	5	5	3	0	0	
66	UF	75	9	12	4	trace	0	
70	UF	84	7	7	2	0	0	
80	UF	64	13	16	7	trace	0	Stage 3
89	LF	55	17	18	10	trace	0	Stage 2
97	UB	71	9	14	6	trace	0	Stage 1
99	UB	61	18	13	6	2	0	

Remark: OB: Overburden; UF: Upper Lignite Zone Formation; LF: Lower Lignite Zone Formation; UB: Underburden; Qtz: quartz; Kao: kaolinite; Ill: illite; Mont: montmorillonite; Gyp: gypsum; Chl: chlorite.

Relationship of sporomorph and mineral contents: The interpretation from the results of sporomorph and clay minerals is related. Figure 6 shows that at the beginning of deposition in the Hongsa coalfield (stage 1), the content of kaolinite and montmorillonite are increased, with decreasing quartz content and it has a high percentage of *in-situ* sporomorph, these indicate stagnant water, humid climate, and may have volcanic influence. Stage 2, quartz and ex-situ sporomorph are increased that contrast to the kaolinite, illite, and montmorillonite, these indicated an uplifting or increasing of weathering process supplied sediment to the basin that may continue until the stage 3. Stage 4, both mineral and sporomorph contents have no trend, however, they show the high content of kaolinite and montmorillonite. Moreover, the Mesozoic fossil *Schizaeoisporites* was found in this stage. This may indicate the uplifting and strong erosion occurred in this period. Stage 5, gypsum is presented, and confirmed by the increasing of illite content. This suggested the climate quite hotter and drier than the previous and the last stage probably drier because it shows higher illite content.

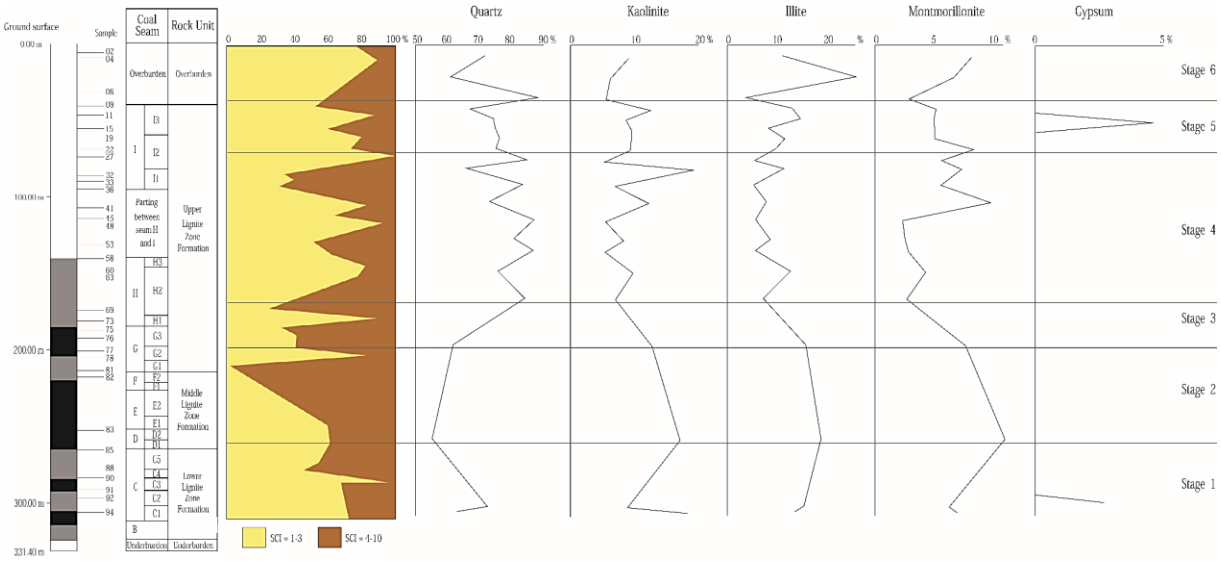

Figure 6. Vertical trend of sporomorphs of scale 1-3 and 4-10 based on Spore Colour Index and vertical trends of mineral compositions.

Conclusion:

The spore colour index in Hongsa deposit suggested that the sources of sediment in the basin were from both outside and inside the basin that influence by the uplifting of the Mesozoic basement. The paleoclimate during the deposition from the bottom to top varied from humid to dry as indicated by the clay mineral content.

Acknowledgements:

The authors would like to thank Hongsa Power Company Limited for giving their permission for sampling, as well as their support during field studies. The authors also wish to thank the Department of Geological Sciences, Faculty of Science, Chiang Mai University, and Northeastern Research Institute of Petrified Wood & Mineral Resources (In Honor of His Majesty the King), Nakhon Ratchasima Rajabhat University, Thailand for technical support in the laboratory. The first author was supported by the Science Achievement Scholarship of Thailand. We also acknowledge the critical comments and suggestions of anonymous reviewers, which greatly improved the manuscript.

References:

1. Tapponnier P, Peltzer G, Le Dain A, Armijo R, Cobbold P. Geology. 1982;10:611-616.
2. Morley C K, Racey A. Geol. Soc. London. 2011;223-272.
3. Hofmann L, Blunck S, Dittrich W, Kraemer T, von Schwarzenberg T, Wall G. RWE Power International. 2008.
4. Olivier A N, Atud T. J. Geogr. Geol. 2018; 10:22-32.
5. Batten D J. Geol. Soc. Spec. Publ. 1991; 57:79–90.
6. Nelson A S. https://www.tulane.edu/~sanelson/eens211/Weathering_ClayMinerals.pdf. 2014. 1-7.
7. Liu Z, Colin C, Trentesaux A, Blamart D, Bassinot F, Siani G, Sicre M A. Mar. Geol. 2004;209(1–4): 1–18.
8. Dianto A, Subehi L, Ridwansyah I, Hantoro W. S. Earth Environ Sci. 2019. 311;012036.
9. Chaudhri A R, Singh M. Am. J. Clim. Change. 2012. 1;231–239.
10. Pal D K, Deshpande S B, Venugopal K R, Kalbande A R. Geoderma. 1989. 45;175–184.
11. Deepthy R. Balakrishnan S. J. Earth Syst. Sci. 2005.114(5);545–556.
12. Traverse A. Paleopalynology. 1988. 601 pp.
13. Faegri K, Iversen J, Textbook of pollen analysis (4th edition). 1989. 328 pp.
14. Moore P D, Webb J A, Collinson M E. Pollen Analysis. 2nd Edition. 1991. 216 pp.
15. Pearson D L, Pollen/Spore Colour-Standard, Version 2. 1984. Phillips Petroleum Company
16. Pross J, Pletsch T, Shillington D J, Ligouis B, Schellenberg F, Kus J. Int. J. Coal Geol. 2007.70;277-291.
17. Senftle J T, Landis C R, McLaughlin R L. Org. Geochem. 1993.
18. Traverse A. Paleopalynology 2nd ed. 2007. Springer, the Netherlands.
19. Carroll D. Geol. Soc. Am. 1970.

SP02_003_PF: SETTLEMENT AND LIPID CLASS COMPOSITIONS OF PLANULA LARVAE OF CORALS UNDER CHANGES OF TEMPERATURES

Panutchanat Chinklang,[1,*] Wipada Lalitpattarakit,[1] Heung-Sik Park,[2] Se-Jong Ju,[3] Chiahsin Lin,[4] Voranop Viyakarn,[1] Suchana Chavanich[1]

[1]Reef Biology Research Group, Department of Marine Science, Faculty of Science, Chulalongkorn University, Bangkok, 10330, Thailand
[2]Marine Ecosystem and Biological Research Center, Korea Institute of Ocean Science & Technology, Busan, 49111, Republic of Korea
[3]Global Ocean Research Center, Korea Institute of Ocean Science & Technology, Busan, 49111, Republic of Korea
[4]National Museum of Marine Biology & Aquarium, Checheng, Pingtung, Taiwan
*e-mail: panutchanat.ch@gmail.com

Abstract:

Increase of water temperatures under the climate change can influence the coral ability to acclimate to the temperature, and can affect on the early development of coral larvae. In this study, the effect of temperatures on coral settlement was investigated. In addition, the lipid class compositions of coral larvae were analyzed. This is the first study to investigate the lipid class compositions in coral larval stages. The results showed that when temperatures changed from the normal levels, settlement rates of corals significantly reduced. For the lipid class compositions, different coral larval species had different types of lipids. More study are needed to investigate in depth in the linkage between coral larvae, temperatures, and lipid class compositions.

Introduction:

Coral reefs are one of the most diverse habitats and have higher primary production. Unfortunately, due to the location of coral reefs near intertidal and subtidal areas, there are influenced by physical factors and human activities. In addition, solar radiation and increase of temperatures have contributed to the physiology and tissues of corals leading to the bleaching.[1] Increase of water temperatures under the climate change can influence the coral ability to acclimate to the temperature, and can affect on the early development of coral larvae, including survival rates and settlement in the planula stages.[2, 3]

Typically, scleractinian corals contain a large proportion of lipid in their tissues.[4-7] They also play crucial roles on biological and chemical processes.[8] For example, triacylglycerol (TG) and wax esters (WE) lipids are the main storage lipids which can be oxidized to fatty acids.[8-10] Cholesterol (CS) and phospholipid (PL) types serve as the main structural lipids.[11] The lipid types and compositions can be varied depending on coral species and coral ages.[6, 7, 12-14] Variation of lipid contents also depend on environmental factors such as depth, light intensity, water temperature and nutrition.[11, 15-17]

The objectives of this study were to investigate the influence of temperature increase on coral settlement. Moreover, lipid contents were observed in the planula stage which no previous study were done.

Methodology:

Coral sampling

Gametes of *Acropora millepora* and *Acropora humilis* were collected directly at the reef of Ko Tao Mo (TMO) in Sattahip Bay, Chon Buri Province, Thailand (Figure 1). Then, eggs and sperms were artificial fertilized

in the hatchery at Coral Hatchery and Nursery Facility of Thai Sea and Inland Natural History Museum, Samae San Island, Chon Buri Province, Thailand.

Temperature experiment

Gametes of 5 *A. millepora* colonies were mixing, fertilized and placed in 500 ml glass beakers. Six treatments, 22, 25, 28 (control), 31, 34 °C with 3 replicates, were set. Each replicate contained 200-400 individuals. Settlement rates were observed by each counting the numbers of planula larvae settling on a plate.

Lipid analysis

Coral larvae of *A. millepora* and *A. humilis* were collected after fertilized 2 and 4 days. The larvae were freeze-dried before lipid extraction. Lipids were extracted from the coral samples with dichloromethane: methanol (CH_2Cl_2 : MeOH = 1:1) and mixed by probe sonication before add double distilled water (DDW) (CH_2Cl_2 : MeOH : DDW = 1:1:0.8) These solutions were mixed and separated into 2 layers, the lower layer was evaporated with stream of nitrogen gas, the higher layer was extracted residue two times in CH_2Cl_2 : MeOH (4:1). The lipid extracts were redissolved by CH_2Cl_2 : MeOH (1:1) . These extracts were spotted at the origin of silica chromarods, and then focused with CH_2Cl_2 : MeOH (1:1) before developed in hexane : diethyl ether : formic acid (85:15:0.2). Lipid class composition of cholesterol (CS), free fatty acids (FFA), phospholipid (PL), triacylglycerol (TG), and wax ester (WE) were separated on the chromarods by an Iatroscan MK-6s thin layer chromatography with flame ionization detection (TLC-FID) analyzer.

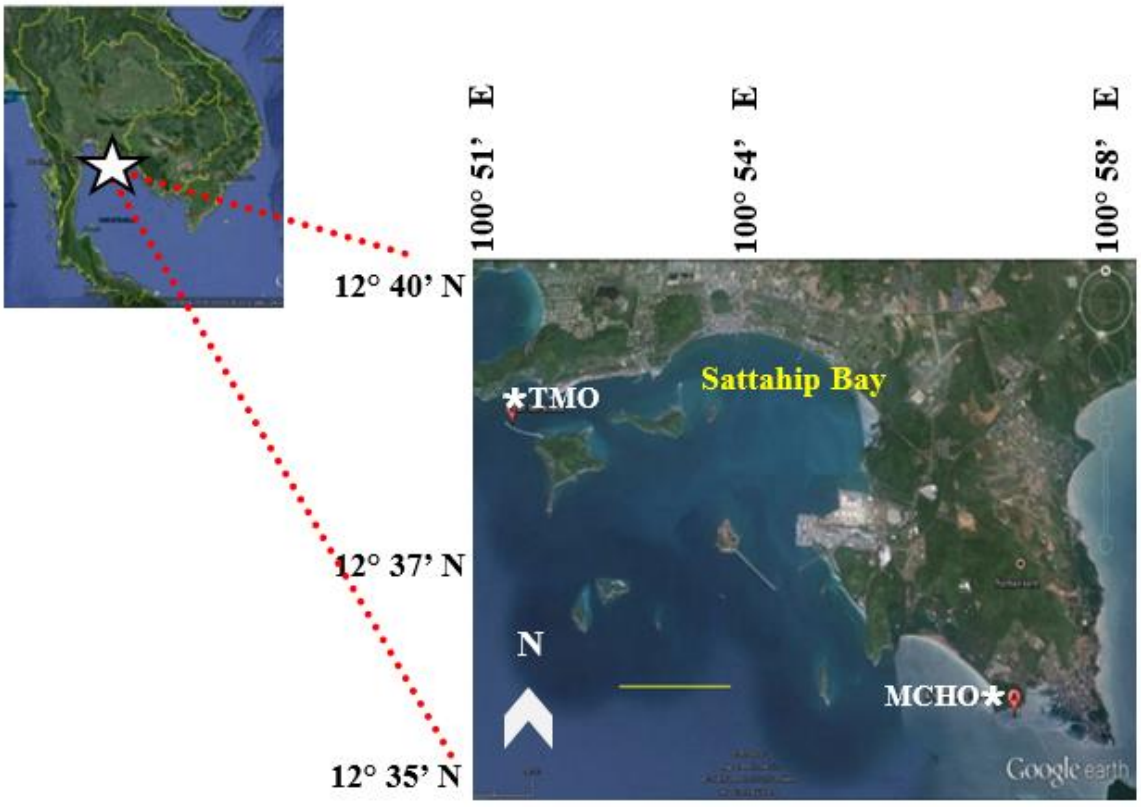

Figure 1. Sample collecting site, Sattahip Bay, Chon Buri Province, Thailand
(TMO: Ko Tao Mo, MCHO: Khao Machoa)

Results and Discussion:

The results from the experiments showed that settlement rates of larvae depended on the temperatures (Table 1). When the temperatures were increased or decreased, the ability of larvae to settle reduced significantly. The control temperature (28 °C) showed the highest settlement rate (74%) while at 22 and 34 °C, coral larvae were not settled. Figure 2 showed normal shapes of coral eggs and coral larvae under the control temperature.

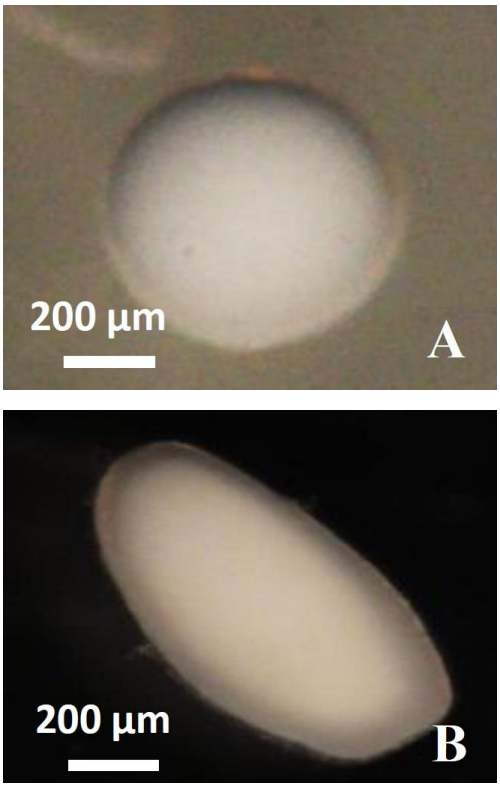

Figure 2. A) Coral egg and B) Coral larva

Corals are sensitive to changes in water temperatures, which can have an influence on coral survivals and physiology.[18, 19] From the results, when temperatures changed from the normal levels, settlement rates of corals significantly reduced (Table 1). Thus, decrease or increase of temperatures can lead to abnormal development process.[3] In general, water temperature is related to light intensity and consequently affects coral survivals. The higher temperatures can decrease in the effective quantum yields (fluorescence value/Variable fluorescence or Fv/Fm) of Photosystem II.[20] Nevertheless, some corals have abnormal physiology in low temperatures.[21] Randall (2009) also showed that when temperatures increased, coral larvae developed faster and could increase more abnormality which had an impact on their settlement.

Table 1. Settlement rate of *Acropora millepora* in different levels of temperatures

Temperature (°C)	Settlement rate (%)
22	-
25	22
28*	74
31	47
34	-

*28 °C, control treatment

When lipid contents were observed, the results showed that different coral species had different types of lipid class compositions (Table 2). In *A. millepora*, both cholesterol and triacylglycerol were found while those two compositions were not detected in *A. humillis.* From the observation, free fatty acid types were not found in both species.

Table 2. The lipid class compositions of different corals in different ages

Species	Days after fertilized	Lipid class compositions				
		PL	CS	FFA	TAG	WE
Acropora humilis	2	–	–	–	–	×
	4	×	–	–	–	×
Acropora millepora	2	×	×	–	×	×
	4	×	×	–	×	×

Note: PL, Phospholipid
CS, Cholesterol
FFA, Free Fatty Acids
TG, Triacylglycerol
WE, Wax Ester

In this study, when lipid types were measured in coral larvae, free fatty acids (FFA) type was not found in both larval species. Similar study of Figueiredo et al. (2012), FFA is not presented in the oocyte stage. However, FFA will increase when larvae are more developed.[12] For wax ester (WE) and triacylglycerol (TAG) types, these lipids are important for a source of energy storage. Typically, the coral oocytes contain WE and TAG.[12] However, because TAG is the first lipid to be used for metabolism, TAG in oocytes of some coral species may not be found.[14] More studies are needed to find the linkage between the effect of temperatures on lipid class composition in coral larvae stages.

Conclusion:

In this study, the changes of temperatures can have significant effects to the settlement of coral larvae. In addition, under normal condition, different coral larval species can have different lipid types. More studies are needed to investigate in depth on the relationship between coral larvae, temperatures, and lipid contents.

Acknowledgements:

This study was supported by Development and Promotion of Science and Technology Talents Project and Mubadala Petroleum (Thailand). We also would like to thank the Plant Genetic Conservation Project under the Royal Initiative of Her Royal Highness Princess Maha Chakri Sirindhorn, the Naval Special Warfare Command, Royal Thai Navy, and all members of Reef Biology Research Group for field support and assistance.

References:

1. Tissier M, Brown B. Mar Ecol Progr Ser. 1996;136:235–44.
2. Edmunds P, Gates R, Gleason D. Mar Biol. 2001;139:981–989.
3. Nozawa Y, Harrison P. Mar Biol. 2007;152:1181–1185.
4. Conlan JA, Rocker MM, Francis DS. PeerJ. 2017;5:e3645.
5. Harland AD, Navarro J, Davies PS, Fixter LM. Mar Biol. 1993;117:113–7.
6. Imbs AB. Russ J Mar Biol. 2013;39:153–168.
7. Yamashiro H, Oku H, Higa H, Chinen I, Sakai K. Comp Biochem Physiol B. 1999;122:397–407.
8. Grottoli AG, Rodrigues LJ, Juarez C. Mar Biol. 2004;145:621–631.

9. Imbs A, Yakovleva I. Coral Reefs. 2012;31:41–53.
10. Yamashiro H, Oku H, Onaga K. Fish Sci. 2005;71:448–453.
11. Solomon SL, Grottoli AG, Warner ME, Levas S, Schoepf V, Muñoz-Garcia A. Mar Biol. 2019;167:7.
12. Figueiredo J, Baird AH, Cohen MF, Flot JF, Kamiki T, Meziane T, Tsuchiya M. Yamasaki H. Coral Reefs. 2012;31:613–619.
13. Imbs AB, Latyshev N, Dautova T, Latypov Y. Mar Ecol Prog Ser. 2010; 409:65–75.
14. Lin C, Wang L-H, Meng P-J, Chen C-S, Tsai S. PLoS One. 2013;8(2): e57823.
15. Mehdinia A, Sheijooni Fumani N, Saleh A, Vajed Samiei J, Seyed Hashtroudi M. JPG. 2015;6:1–8.
16. Rivest EB, Hofmann GE. J Exp Mar Bio Ecol. 2015;473:43–52.
17. Rodrigues LJ, Grottoli AG, Pease TK. J Exp Mar Biol Ecol. 2008;358:136–143.
18. Haryanti D, Hidaka M J Mar Sci Eng. 2015;3:509–519.
19. Randall C, Szmant A. Biol Bull. 2009;217:269–82.
20. Chow AM, Ferrier-Pagès C, Khalouei S, Reynaud S, Brown IR. Cell Stress Chaperones. 2009;14(5):469–76.
21. Sakami T. Fish Sci. 2000;66:1006–13.

SP02_004_PA: SPATIAL AND SEASONAL VARIATION OF SOIL RESPIRATION IN DRY EVERGREEN FOREST, SAKAERAT BIOSPHERE RESERVE, THAILAND

Warin Boonriam,[1] Pongthep Suwanawaree,[1,*] Sasitorn Hasin,[2] Taksin Archawakom,[3] Phuvasa Chanonmuang,[4] Akinori Yamada,[5, 6]

[1] School of Biology, Suranaree University of Technology, Nakhon Ratchasima, Thailand
[2] College of Innovative Management, Valaya Alongkorn Rajabhat University under the Royal Patronage, Pathum Thani, Thailand
[3] Sakaerat Environmental Research Station, Nakhon Ratchasima, Thailand
[4] Expert Centre of Innovation Clean Energy and Environment, Thailand Institute of Scientific and Technological Research, Pathum Thani, Thailand
[5] Department of Biological Sciences, Tokyo Institute of Technology, Tokyo, Japan
[6] Graduate School of Fisheries and Environmental Sciences, Nagasaki University, Nagasaki, Japan
*e-mail: pongthep@sut.ac.th

Abstract

Soil respiration in tropical forests is an important source of carbon dioxide in the atmosphere. Factors regulating spatial soil respiration are still unclear and they may lead to an inaccurate estimation of soil respiration at the ecosystem level. The aim of this study was to investigate the spatial and seasonal variation of soil respiration in a dry evergreen forest of Sakaerat Biosphere Reserve, Nakhon Ratchasima province. Soil respiration, temperature, and moisture were measured in 100 subplots of five 1-ha main plots for four times from November 2014 to August 2016. The average rate (±SD) of annual aboveground soil respiration was 6.57± 4.29 µmol CO_2 m^{-2} s^{-1}. Soil respiration considerably varied with space and time. The mean ranges were from 2.66 to 11.72 µmol CO_2 m^{-2} s^{-1} with a maximum rate of 42.68 µmol CO_2 m^{-2} s^{-1}. The wet season soil respiration rate (8.81 µmol CO_2 m^{-2} s^{-1}) was two times higher ($p< 0.001$) than in dry season (4.33 µmol CO_2 m^{-2} s^{-1}). Although the soil respiration rates increase with increasing soil temperature and moisture content, the rate starts to drop at 27°C soil temperature ($p< 0.001$) and 21% soil moisture content ($p< 0.05$). The spatial fluctuation in soil respiration possibly caused by subterranean nests of ants and termites. These animals are major factors influencing soil respiration in the tropical forest.

SP03_001_PA

SP03_001_PA: CRYSTAL STRUCTURE OF COPPER (I) CHLORIDE COMPLEX CONTAINING 4-PHENYLTHIOSEMICARBAZIDE AND TRIPHENYLPHOSPHINE LIGANDS

Kamonwan Janwatthana[1], Yupa Wattanakanjana[1]*

[1]Department of Chemistry, Faculty of Science, Prince of Songkla University, Hatyai, Songkhla 90112, Thailand
*e-mail: yupa.t@psu.ac.th

Abstract:

The reaction of copper(I) chloride with triphenylphosphine (PPh_3) and 4-phenylthiosemicarbazide (4-PTSC) leads to the formation of monomeric mixed-ligand complex of the $[CuCl(4\text{-}PTSC)(PPh_3)_2]$. The Cu(I) ion exhibits distorted tetrahedral coordination with two P atoms from two PPh3 ligands, one terminal S atom from the 4-PTSC ligand and chloride ion. Intramolecular N—H···Cl and N—H···N hydrogen bonds are observed (graph set motif S(6) and S(5), respectively). In the crystal, the complex molecules are linked to form dimers via bifurcated N—H···Cl hydrogen bonds involving the amine and chloride groups.

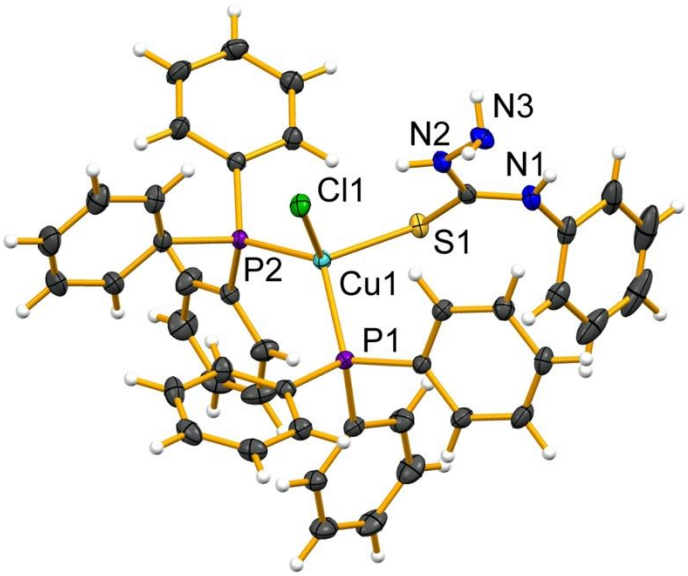

Figure 1. The molecular structure of $[CuCl(4\text{-}PTSC)(PPh_3)_2]$, with displacement ellipsoids drawn at the 50% probability level.

SP03_002_OA

SP03_002_OA: SYNTHESIS, STRUCTURAL, ANTIBACTERIAL AND FLUORESCENCE PROPERTIES OF Zn(II) AND Cd(II) IMIDAZOLYMINE COMPLEXES

Saruda Yokputtaraksa[1], David J. Harding[2], Filip Kielar[3], Boonsong Wungsintaweekul[4] Darunee Sertphon[1,*]

[1]*Department of Chemistry, Faculty of Science, Rangsit University, Pathum Thani 12000, Thailand*
[2] *Functional Materials and Nanotechnology Center of Excellence, Walailak University, Thasala, Nakhon Si Thammarat 80160, Thailand*
[3] *Department of Chemistry, Faculty of Science, Naresuan University, Phitsanulok 65000, Thailand*
4 School of Pharmacy, Walailak University, Nakhon Si Thammarat 80160, Thailand
*e-mail: *darunee.s@rsu.ac.th*

Abstract:

A novel Zn(II) and Cd(II) complexes [M(1Me-2-ima-Fl)3(Y)$_2$]·Sol (M = Zn; Y = NCS **1**, M = Zn; Y = N_3 **2**, M = Cd; Y = NCS **3**, M = Cd; Y = N_3 **4**; ·sol = MeOH)) were synthesized and characterized by ^{1}H NMR, IR, UV-VIS and X-ray crystallography. Zn(II) and Cd(II) complexes were prepared in the presence of base according to a stoichiometric ratio of metal:anion:ligand = 1:1:2. A study of intermolecular interactions in the solid state compounds revealed that molecules are linked by C-H···N, C-H···O bond and also by C-H···S interactions in the case of structures **1-4**. Fluorescence emission spectrum exhibit the effect of ligand and anions is key. Moreover, antibacterial activities of the complexes against *E. Coli*, *S. aureus*, *Ac. Baumanni* and *K. pneumonia* showed that these ligands exhibit moderate antibacterial activities.

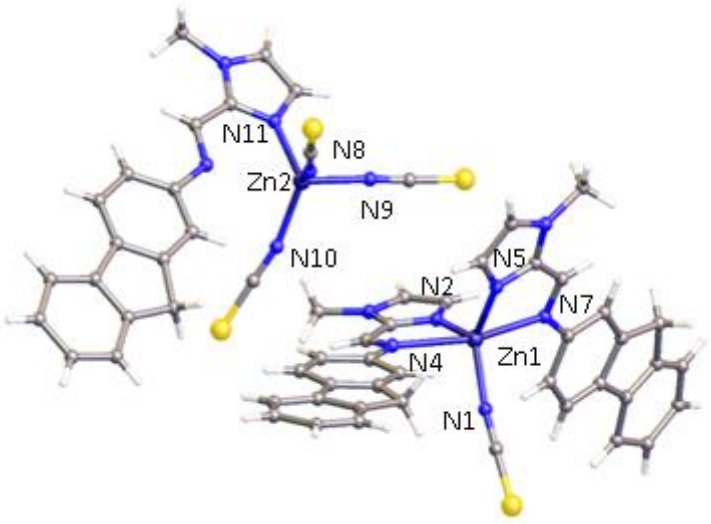

Fig1. Shows Structure and interaction of Zn(NCS) Fl **1**

SP03_003_OF: PETROGRAPHY AND GEOCHEMISTRY OF QUARTZITES AND METASANDSTONES AS EVIDENCES FOR TECTONIC ENVIRONMENT OF THE SILURIAN-DEVONIAN BO PHLOI FORMATION, KANCHANABURI, WESTERN THAILAND

Suwijai Jatupohnkhongchai, Burapha Phajuy*

Department of Geological Sciences, Faculty of Science, Chiang Mai University, Thailand
*e-mail: buraphaphj3@gmail.com

Abstract:

Petrography and geochemistry of quartzite and metasandstone from the Silurian-Devonian Bo Phloi Formation, Kanchanaburi, Western Thailand, have been investigated to understand their tectonic environment. Petrographic analysis suggests that quartzite contain mainly quartz, feldspar (mostly orthoclase, microcline, and minor plagioclase), and accessory minerals including tourmaline, and opaque minerals. The metasandstone contains mainly quartz (mono- and polycrystalline, chert), feldspar, and rock fragments (sedimentary, metasedimentary, and volcanic rock fragment) with a trace amounts of mica flake, zircon, tourmaline, and opaque minerals. Geochemical classification of Herron 1988, these samples can be classified as arkose, subarkose, litharenite, sublitharenite, and quartz-arenite. They are generally significantly enriched in SiO_2 and strong depleted in Na_2O and CaO, indicating highly matured and recycled nature. These natures concur with their major and immobile rare earth elements that indicate the passive continental margin type of most of the samples. There are a few active continental margin type samples. Hence, both petrographic and geochemical data reveal that the Bo Phloi Formation was deposited in a passive margin in the Silurian-Devonian along eastern Gondwana. While the active continental margin type samples indicate the presence of the subduction of the Palaeo-Tethys ocean in probably Late Carboniferous-Late Triassic.

Introduction:

The Silurian-Devonian Bo Phloi Formation in Kanchanaburi was defined and described in some detail. There is the type section at Khao Ka and Khao Yai comprising quartzite interbedded with phyllite in the lower part, tuffaceous sandstone, tuffaceous shale, chert in the middle part, and *Tentaculites* cf. *elegans* shale, thin-bedded recrystallized limestone in the upper part.[4] The lower part is dominated by quartz grains which represent a mature shallow-water sediment derived from a plutonic source. The middle part is contained volcanic detritus in the tuffaceous rocks which have been derived from a volcanic arc probably located at the east side.[6] The upper part is dominated by finer grain sediment, comprising *Tentaculites elegans* bearing shale indicated probably Early Devonian in age. Hence, this formation represented the vertical changes that reflect a change from a passive to an active margin. From the palaeogeographic model of Metcalfe 2013, who also proposed that the western of Thailand (now a part of SE Asian continental block) was still located on the margin of eastern Gondwana in the Cambrian to Silurian by using the palaeomagnetic data.[9] After that, Indochina (eastern part of Thailand) rifted away from Gondwana in the Early Devonian recorded in their palaeomagnetic data and biogeographic affinities of biota. Then the Palaeo-Tethys ocean was opened in the early Middle Devonian. Later the northwards subduction of the Palaeo-Tethys constructed the Sukhothai arc on the margin of Indochina in the Late Carboniferous–Early Permian. Until the Palaeo-Tethys ocean was completely closed in the Late Triassic. This study attempts to combine both petrographic and geochemical data of quartzite and metasandstones from the Bo Phloi Formation as an aid to identify the tectonic environment of the formation in Kanchanaburi, western Thailand.

Methodology:

The petrographic characteristics of ten samples (quartzite and metasandstone) from Bo Phloi Formation have been investigated at Department of Geological Sciences, Faculty of Science, Chiang Mai University. Bulk geochemical analysis was determined by Bruker Pioneer S4 X-ray fluorescence (XRF) spectrometer for major elements at the NAWI Graz Geocenter - Institute of Earth Sciences (Petrology and Geochemistry), University of Graz, Austria. Samples were prepared to a glass bead using one gram of sample powder and seven grams of $Li_2B_4O_7$ flux. Loss on ignition (LOI) was determined by heating the powdered rock material to 1030 °C for one hour. A selected subset of five samples were analysed for trace and rare earth elements by an Agilent 7700 quadrupole inductively mass spectrometer (ICP-MS) at the Institute of Chemistry - Analytical Chemistry, University of Graz, Austria. Sample powders (40-50 mg) were dissolved at the clean room facility of the NAWI Graz Geocenter.

Results and Discussion:

Petrography: The quartzite and metasandstone were carefully collected from floated rocks along slope toe and exposed outcrop of the Bo Phloi Formation in Kanchanaburi Province (Amphoe Mueang, Amphoe Bo Phloi, Amphoe Huai Krachao, Amphoe Nong Prue) and Suphanburi Province (Amphoe Dan Chang) based on geological map of Changwat Suphanburi series 1:250,000, Sheet ND 47-7 (Figure 1a-c).[5] The Bo Phloi Formation is conformably overlain by the Ordovician Tha Manao Limestone Formation in western part of the study area. But some parts of this formation are affected by the faults. Petrographically, the quartzite shows mostly granoblastic and a few foliated textures (Figure 2a-c), containing mainly quartz, feldspar (orthoclase and microcline), and accessory minerals including tourmaline, and opaque minerals. Most quartz grains display undulatory extinction and sutured boundaries. The metasandstone is well to moderately sorted comprising framework grains set in sericite with microcrystalline matrix (Figure 2e-f). Framework grains, generally medium- to very fine-sand range, are mainly quartz (mono- and polycrystalline, chert), feldspar (mostly orthoclase, microcline, and minor plagioclase), and rock fragments (sedimentary, metasedimentary, and volcanic rock fragment) with a trace amounts of mica flake, zircon, tourmaline, and opaque minerals. The grains are subangular to subrounded.

Figure 1. a) Outcrop of quartzite in Amphoe Bo Phloi (47P 555830 1585050), b) Outcrop of quartzite in Amphoe Dan Chang (47P 565617 1637443), c) Weathered quartzite in Amphoe Bo Phloi (47P 557753 1594968).

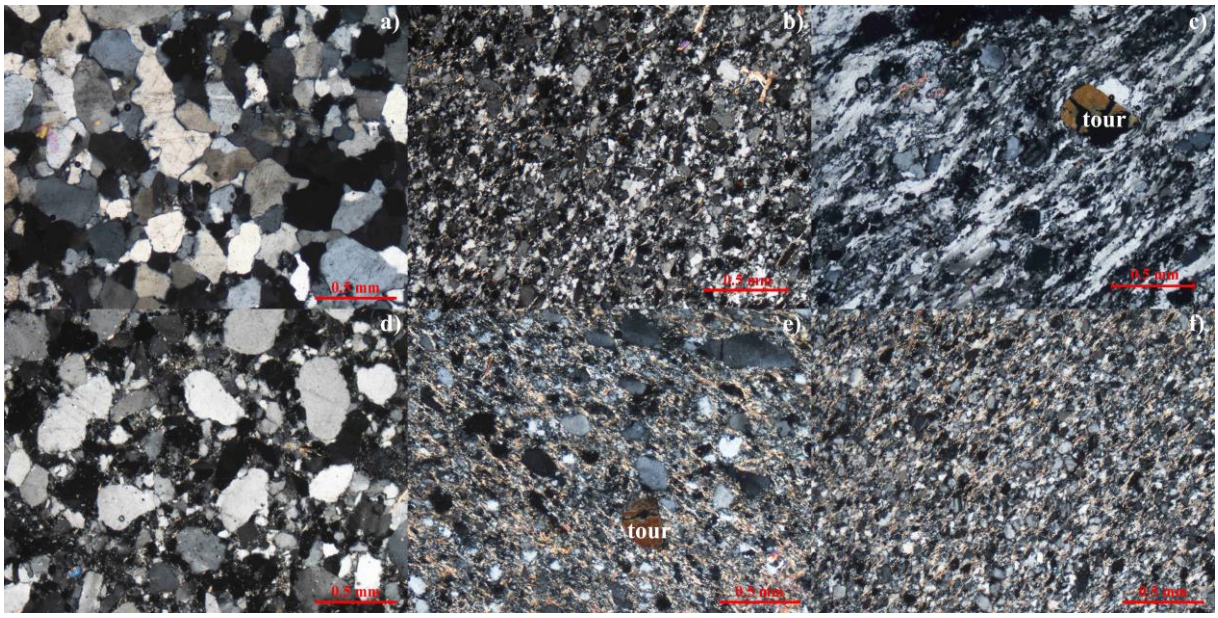

Figure 2. Photomicrographs of quartzite (a-c) and metasandstone (d-f), a) Granoblastic texture of quartzite and sutured boundaries of quartz grains, b) Foliated texture defined by quartz, feldspar, and sericite, c) Foliated texture defined by quartz content, d) Medium-grained metasandstone, e) Fine-grained metasandstone shows foliated sericite in matrix, f) Very fine-grained metasandstone shows foliated sericite in matrix. tour=tourmaline

Table 1. Major element compositions of the Silurian- Devonian Bo Phloi Formation samples, Kanchanaburi, western Thailand

	Quartzite				Metasandstone					
	Abp24	Adch39	Anp36	Chk29	Abp21	Chk05	Anp37	Chk10	Abp32	Abp22
SiO_2	97.21	89.99	95.33	90.78	97.26	84.31	83.14	73.94	89.62	91.47
TiO_2	0.08	0.34	0.05	0.16	0.15	0.35	0.34	0.69	0.19	0.34
Al_2O_3	1.43	5.27	2.63	2.45	1.86	8.63	6.11	13.92	5.83	5.42
FeOt	0.27	0.26	0.11	0.96	0.11	0.94	1.56	3.10	0.94	0.25
MnO	0	0	0	0	0	0	0.03	0.06	0.03	0
MgO	0	0.10	0.01	0.12	0.03	0.26	0.53	0.84	0.26	0.15
CaO	0	0	0	0	0	0	2.77	0.08	0.08	0
Na_2O	0	0	0	0	0	0	1.24	0	1.23	0
K_2O	0.86	3.54	2.06	1.17	0.41	4.42	1.08	4.70	1.66	1.13
P_2O_5	0.02	0.04	0.01	0.05	0.03	0.04	0.06	0.08	0.05	0.017
LOI	0.37	0.41	0.12	0.48	0.63	1.07	3.19	2.04	0.68	1.46
	100.24	99.95	100.32	96.17	100.48	100.02	100.05	99.45	100.57	100.24

Geochemistry: The Silurian-Devonian quartzite and metasandstone of the Bo Phloi Formation are significantly enriched in SiO_2 and depleted in TiO_2, Al_2O_3, FeOt, MnO, MgO, K_2O, CaO, and Na_2O (Table 1). The variation is due to the increase in the quartz content and decrease in the chemically unstable (plagioclase and volcanic rock fragments) grains in response to the provenance of them.[1]

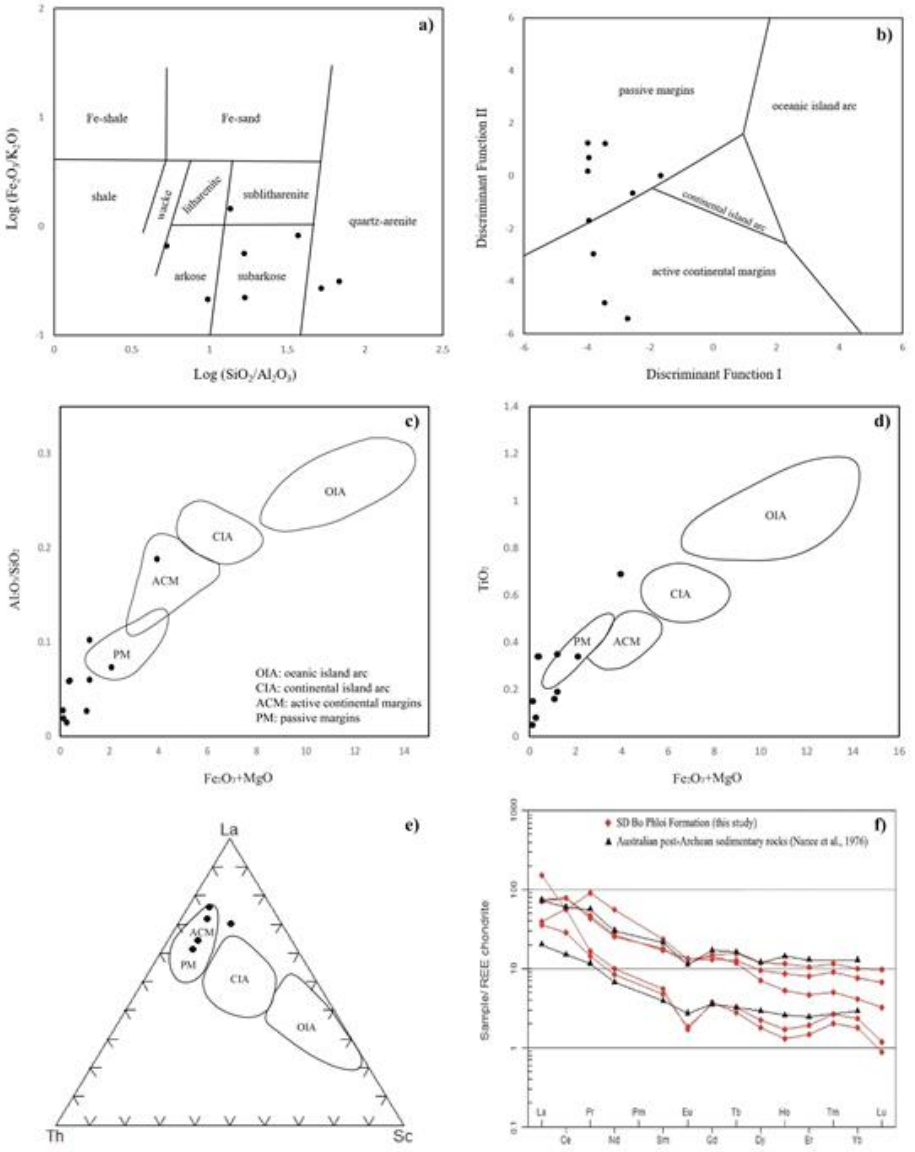

Figure 3. a) Geochemical classification of terrigenous sandstones and shales[7], b) The major element tectonic setting discriminant function diagram of sandstones.[1] The discriminant functions are: Discriminant Function I = $(-0.0447 \cdot SiO_2)+(-0.972 \cdot TiO_2)+(0.008 \cdot Al_2O_3)-(0.267 \cdot Fe_2O_3)+(0.208 \cdot FeO)+(3.082 \cdot MnO)+(0.104 \cdot MgO)+(0.195 \cdot CaO)+(0.719 \cdot Na_2O)-(0.032 \cdot K_2O)+(7.510 \cdot P_2O_5)+0.303$; Discriminant Function II = $(-0.421 * SiO_2)+(1.998 * TiO_2)-(0.526 * Al_2O_3)-(0.551 * Fe_2O_3)-(1.610 * FeO)+(2.720 * MnO)+(0.881 * MgO)-(0.907 * CaO)-(0.117 * Na_2O)-(1.840 * K_2O)+(7.244 * P_2O_5)+43.57$, c) and d) Al_2O_3/SiO_2 ratio, and TiO_2 versus Fe_2O_3*+MgO tectonic discrimination (*represents total iron as Fe_2O_3)[1], e) La-Th-Sc tectonic setting discrimination of sandstones[3], f) Chondrite-normalised REE patterns (ref. in Janoušek, 2006) of Silurian-Devonian (SD) Bo Phloi Formation and Australian post-Archean sedimentary rocks.

These samples can be classified as arkose, subarkose, litharenite, sublitharenite, and quartz-arenite in the geochemical classification of Herron 1988 (Figure 3a). From the major element discriminant function diagram of Bhatia 1983 (Figure 3b), these samples have strongly low loading of CaO and Na_2O along Function I which are mainly influenced by low plagioclase and volcanic rock fragments. They have high loading of SiO_2 and strongly low loading of CaO along Function II reflecting high quartz content. They are assigned to mostly passive and rarely active continental margins. Their characteristics can be overlapped slightly with active continental margin sandstone, but they can be discriminated by their Fe_2O_3* + MgO, Al_2O_3/SiO_2 ratio, and TiO_2.[1] Most samples fall in and close to passive margins in Al_2O_3/SiO_2 ratio, and TiO_2 versus Fe_2O_3* + MgO tectonic discrimination of Bhatia 1983 (Figure 3c-d). Based on the immobile rare earth element, these samples are also assigned to both passive and active continental margins, indicating a high La/Sc ratio (Figure 3e). However, this diagram can't distinguish between passive and active continental margins.[3] The REE patterns of the passive margin samples are characterized by the high enrichment of LREE over HREE and presence of a pronounced negative Eu anomaly (Figure 3f). These REE characteristics are similar to the platform and cratonic sedimentary rocks of the Australian post-Archean sedimentary rocks.[10] But the sedimentary rocks deposited on active continental margins, passive margins, platform, and cratonic basins are all characterized by these REE characteristics on Chondrite-normalised plots and cannot be discriminated from each other by REE patterns alone.[2] Thus, the passive margin type samples, presumably the lower part of the Bo Phloi Formation, can be indicated that the western Thailand was still located on the margin of eastern Gondwana in the Silurian-Devonian (Figure 4a). A few samples of active continental margin type may represent the evidence of the subduction of Palaeo-Tethys ocean in probably Late Carboniferous-Early Permain until the complete closure in the Late Triassic (Figure 4b-c).

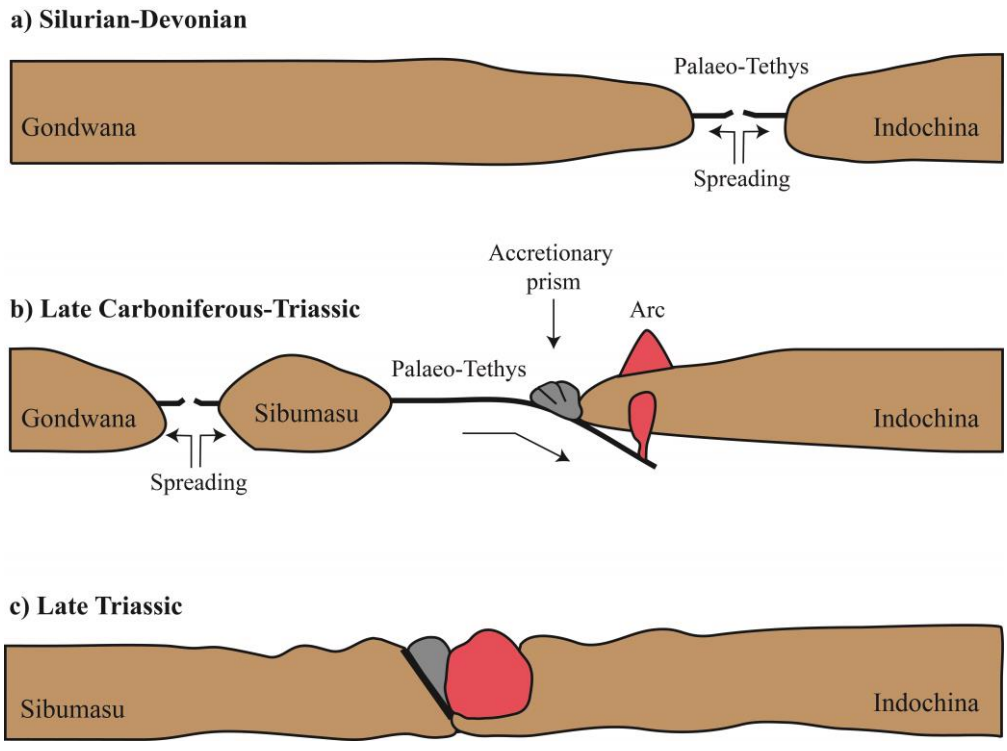

Figure 4. Cartoon showing the tectonic environment of the Bo Phloi Formation (modified from Metcalfe, 2013), a) The Silurian-Devonian passive margins of Gondwana, rifted Indochina when the Palaeo-Tethys opened, b) The Subduction of the Palaeo-Tethys (active continental margins) in the Late Carboniferous-Early Permian, c) The collision of Sibumasu and Indochina Terranes (closure of Palaeo-Tethys) in the Late Triassic.

Conclusion:

The Bo Phloi Formation in Kanchanaburi, western Thailand, consists of quartzites and metasandstones. The quartzite contains mainly quartz, feldspar, and accessory minerals including tourmaline, sericite, and opaque minerals. The metasandstone contains mainly quartz, feldspar, and rock fragments with a trace amounts of mica flake, zircon, tourmaline, and opaque minerals. The metasandstones have been classified to arkose, subarkose, litharenite, sublitharenite, and quartz-arenite. The quartzites and metasandstones are generally significantly enriched in SiO_2 and strong depleted in Na_2O and CaO, indicating highly matured and recycled nature. The discrimination diagrams of sandstones both major and immobile rare earth elements indicate the passive and active continental margins. Both petrographic and geochemical data indicate that the Bo Phloi Formation was deposited in a passive margin in the Silurian-Devonian along eastern Gondwana. While the active continental margin type samples indicate the presence of the subduction of the Palaeo-Tethys ocean in probably Late Carboniferous-Late Triassic. The complex of this area may relate to the collision of Sibumasu and Indochina Terranes. Thus, the study area may comprise the Silurian-Devonian to post Carboniferous rocks.

Acknowledgements:

The first authors thank the Department of Geological Sciences, Faculty of Science, Chiang Mai University for supporting the petrographic study. We are sincerely grateful to Sirot Salyapongse for his inspiration for the project and his encouragement. Professor Dr. Christoph Hauzenberger, Heads of the NAWI Graz Geocenter, University of Graz, has kindly given valuable advice throughout the work. And thanks to the Development and Promotion of Science and Technology Talents Scholarship (DPST) for funding this project.

References:

1. Bhatia M. R. J Geol. 1983;91:611-627.
2. Bhatia M. R. Sediment. Geol. 1985;45:97-113.
3. Bhatia M. R, Crook K.A.W. Contrib Mineral Petro. 1986;92:181-193.
4. Bunopas S, Bunjitradulya S. Jour. Geol. Soc. Thailand 1975;51-67.
5. Bunopas S. Department of Mineral Resources, Bangkok. 1976.
6. Bunopas S, Vella P. Proceedings of the Third Regional Conference on Geology and Mineral Resources of Southeast Asia 1978;133-140.
7. Herron M. M, J. Sedimen. Petro. 1988;58:820-829.
8. Janoušek V, Farrow C. M, Erban V. J Petrol. 2006;47:1255-1259.
9. Metcalfe I. J. Asian Earth Sci. 2013;66:1-33.
10. Nance W. B., TaylorbS. R. Geochim. Cosmochim. Acta. 1976;40:1539-1551.

SP03_004_PF: FOURIER TRANSFORM INFRARED SPECTROSCOPY (FTIR) CHARACTERISTICS OF CORUNDUM GEMS IN THE CHANTHABURI-TRAT GEM FIELDS, THAILAND

Apichet Boonsoong*

Department of Geological Sciences, Faculty of Science, Chiang Mai University, Chiang Mai, Thailand
*e-mail: Siamsapphire@hotmail.com

Abstract:

The corundum samples in Chanthaburi and Trat Provinces were examined in the near- to mid- infrared spectral region and spectra were selected from the region range 2000 to 4000 cm^{-1}. FTIR spectra allow division of the corundum into two groups. The first group includes all the rubies and some sapphires which have yellow, green, and yellow-green colours. Two sets of absorption bands are seen. One is located between approximately 2300 and 2400 cm^{-1} and is considered to be due to carbon dioxide. The second is situated between approximately 2800 and 3000 cm^{-1}. These are due to C-H stretching mode of the CH_2 group. The second group includes sapphires with blue, violetish-blue, greenish-blue, green-blue, and bluish-green colours. All samples in this group have almost the same absorption bands as the first group but in addition they have another set located between approximately 3100 and 3600 cm^{-1}. The series of sharp peaks observed here are related to structural OH groups bonded within the corundum lattice. Not all samples in this group possess the complete series of absorption peaks, probably depending on the concentration of OH. The OH-group absorption bands in these sapphires are produced by titanium (Ti) and iron (Fe), which caused their colours in blue or green tones.

Introduction:

Thailand has long been a supplier of gemstones, and over the past decades has emerged as a major centre for coloured stones. The principal gemstones are ruby, sapphire, garnet and zircon of which the first two are the best known and constitute a major source of gems sold in foreign markets. The gemstone deposits in Thailand, especially rubies and sapphires, are abundant in the northern, northeastern, eastern and west-central parts of the country (Figure 1) and are associated with the occurrence of Late Cenozoic alkaline basalts. Gem corundum is thought to be derived from weathering of the alkaline basalts with the rubies and sapphires being found in alluvial, eluvial or residual soils. The corundum deposits of Chanthaburi-Trat Provinces form the most significant ruby-sapphire concentration in Thailand. This project has aim to characterize the Fourier Transform Infrared Spectroscopy (FTIR) of corundum gems in the Chanthaburi-Trat gem fields, Thailand.

In Chanthaburi-Trat gem fields, corundum varies in colour across the region with colours associated with three geographic zones; a western zone, characterized by blue, green, yellow sapphires; a middle zone with blue, green sapphires plus rubies; and an eastern zone yielding mainly rubies. The western zone is located in the western part of Chanthaburi Province; the middle zone lies between Chanthaburi and Trat Provinces, and the eastern zone is in Trat Province, close to the border with Kampuchea (Figure 2). The proportion of sapphires and ruby found in each location of the three zones are given in Table 1.

In the western zone, clinopyroxene is the most abundant mineral found associated with sapphire with red garnet and zircon being comparatively rare. Zircon, ilmenite and magnetite are common and garnet is very uncommon in the middle zone. The associated minerals in the eastern zone are ilmenite, magnetite, garnet, and minor quantities of clinopyroxene. Corundums are commonly found in secondary deposits (alluvium, elluvial, residual-soil and colluvium deposits as well as stream sediments) with the thickness of the gem-bearing layer

varying from 10–100 cm and the thickness of the overburden ranging up to 15 m. Corundums found embedded in basalt are very rare, which indicates that the ratio between the ore to the rock mass is extremely low.

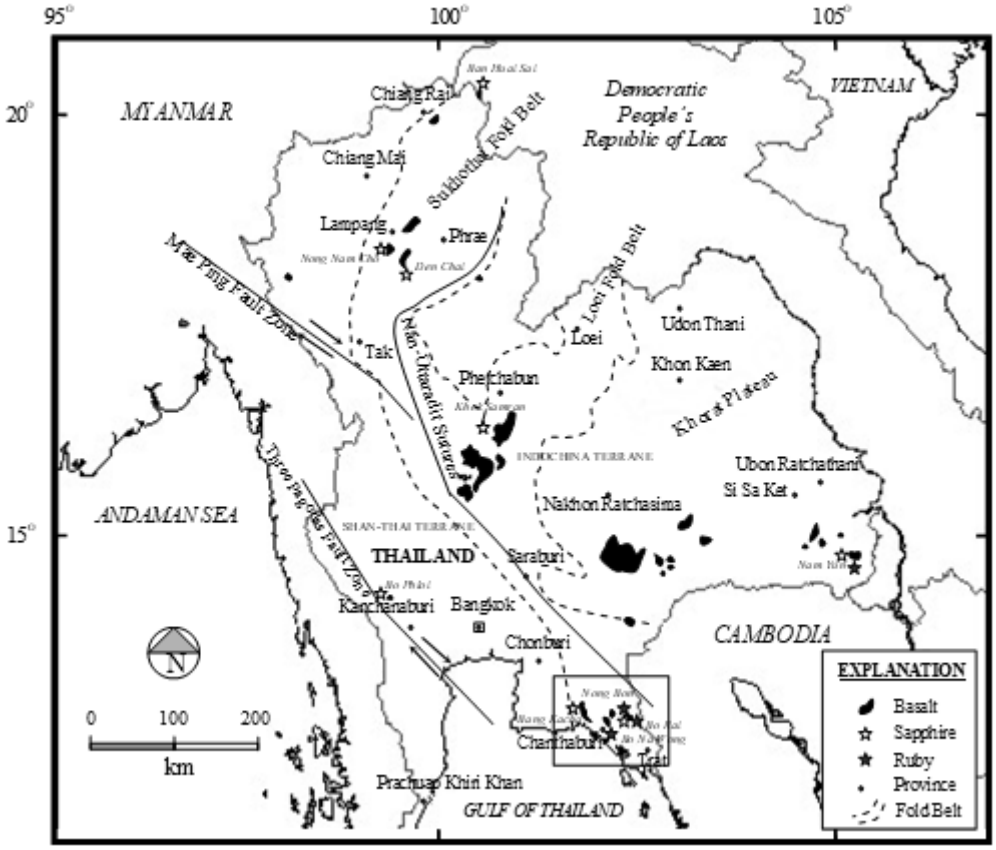

Figure 1. Distribution of basalts and gem corundum localities in Thailand (modified from Vichit, 1987). The Chanthaburi–Trat Gem field is within the rectangle.

Table 1. Estimated proportion of sapphires and ruby in three zones of Chanthaburi-Trat area**.**

Zone	Location	%	
		Sapphires	Ruby
(1) Western zone *(Western region of Chanthaburi province)*	Khao Woa, Khao Phloi Waen and Bang Kacha	~ 100	-
(2) Middle Zone *(Between Chanthaburi and Trat provinces)*	Ban Klang	90 – 95	5 - 10
	Tok Phrom	80 – 90	10 - 20
	Bo I Rem	~ 100	-
	Ban Tok Si, Ban Sisiat	60 – 70	30 - 40
	Nong Pla Lai	80 – 90	10 - 20
	Bo Welu, Ban Sai Khao, Ban Takhian	30 – 40	60 - 70
	Ban Saeng Som	80 – 90	10 - 20
	Ban Saeng Daeng	10 – 20	80 - 90
	Ban Chak Lao	80 – 90	10 - 20
	Ban Sato Noi	70 – 80	20 - 30
	Ban Saphan Hin	10 – 20	80 - 90
	Ban Na Ta Mi, Bo Na Wong, Khong Phaya	1 – 2	~ 98
(3) Eastern Zone *(Trat province)*	Bo Rai, Nong Bon, Ban Sua Dao, Noen Tak Daet, Khao Pik Ka, Ban Ta Ngam, Noen Chali, Ban Tak Waeng, Ban Sa Yai, Ban Noen Si, Ban Wai Kai, Ban Ta Bad, Ban Muan Dan	1 – 2	~ 98

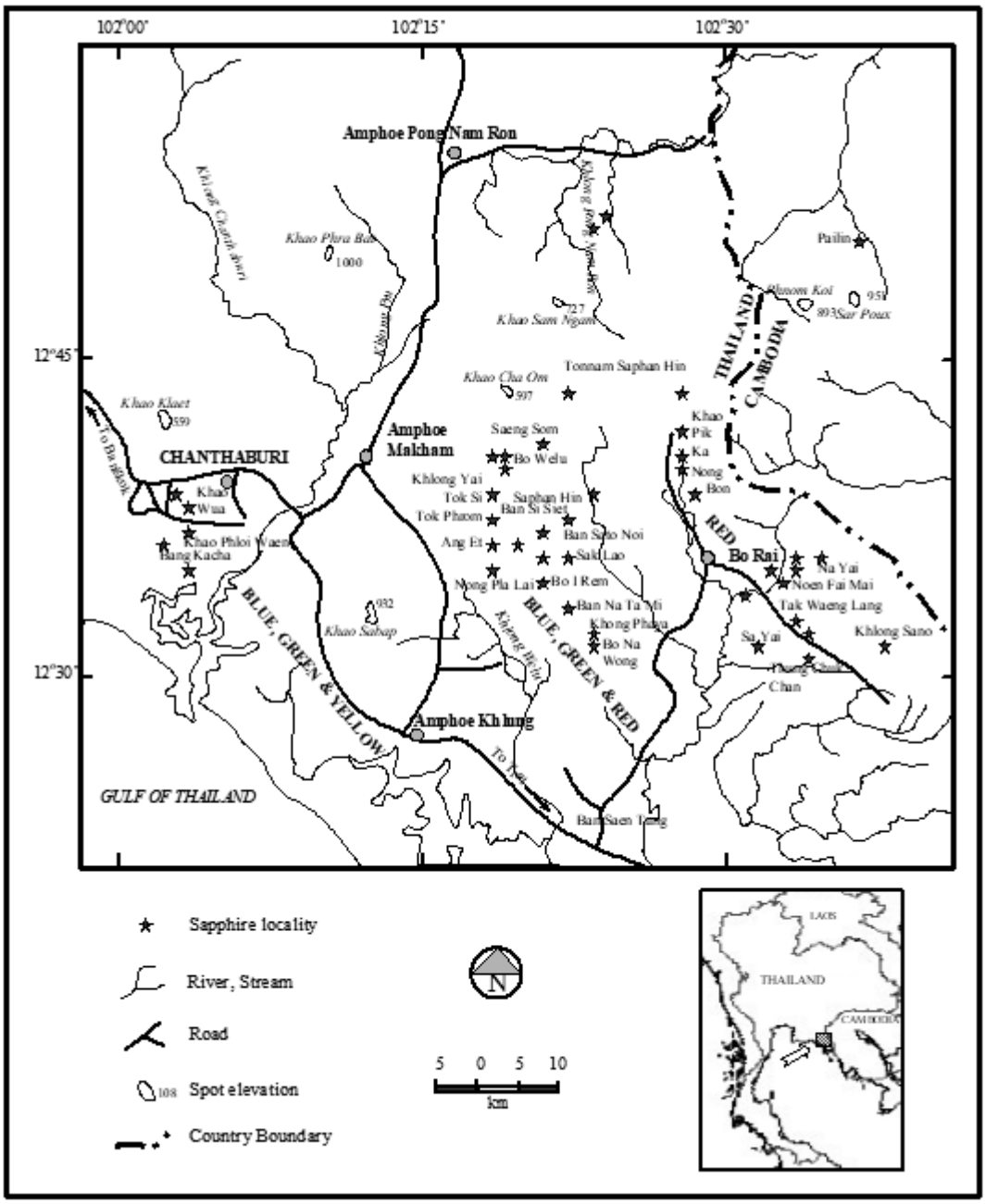

Figure 2. The Chanthaburi-Trat gem fields and the variation of corundum colours in three distinctive geographic zones.

Methodology:

A number of corundum samples were collected from each of the twenty-nine corundum deposits in the Chanthaburi-Trat gem fields (Figure 3). Single grains (average diameter between 6 and 10 mm) were handpicked on the basis of colour, low abundance of cracks, and minimum degree of tarnishing and staining.

Some representative 80 polished of variously coloured corundum samples were analysed by NICOLET 60SX, Fourier Transform IR Spectrophotometer with the spectral resolution of 4 cm^{-1} and 200 scans, at the Materials Research Institute of Nantes, University of Nantes, France. The corundum samples were examined in the near- to mid- infrared spectral region and spectra were selected from the region range 2000 to 4000 cm^{-1} (the region less than 2000 cm^{-1} has very high reflectivity).

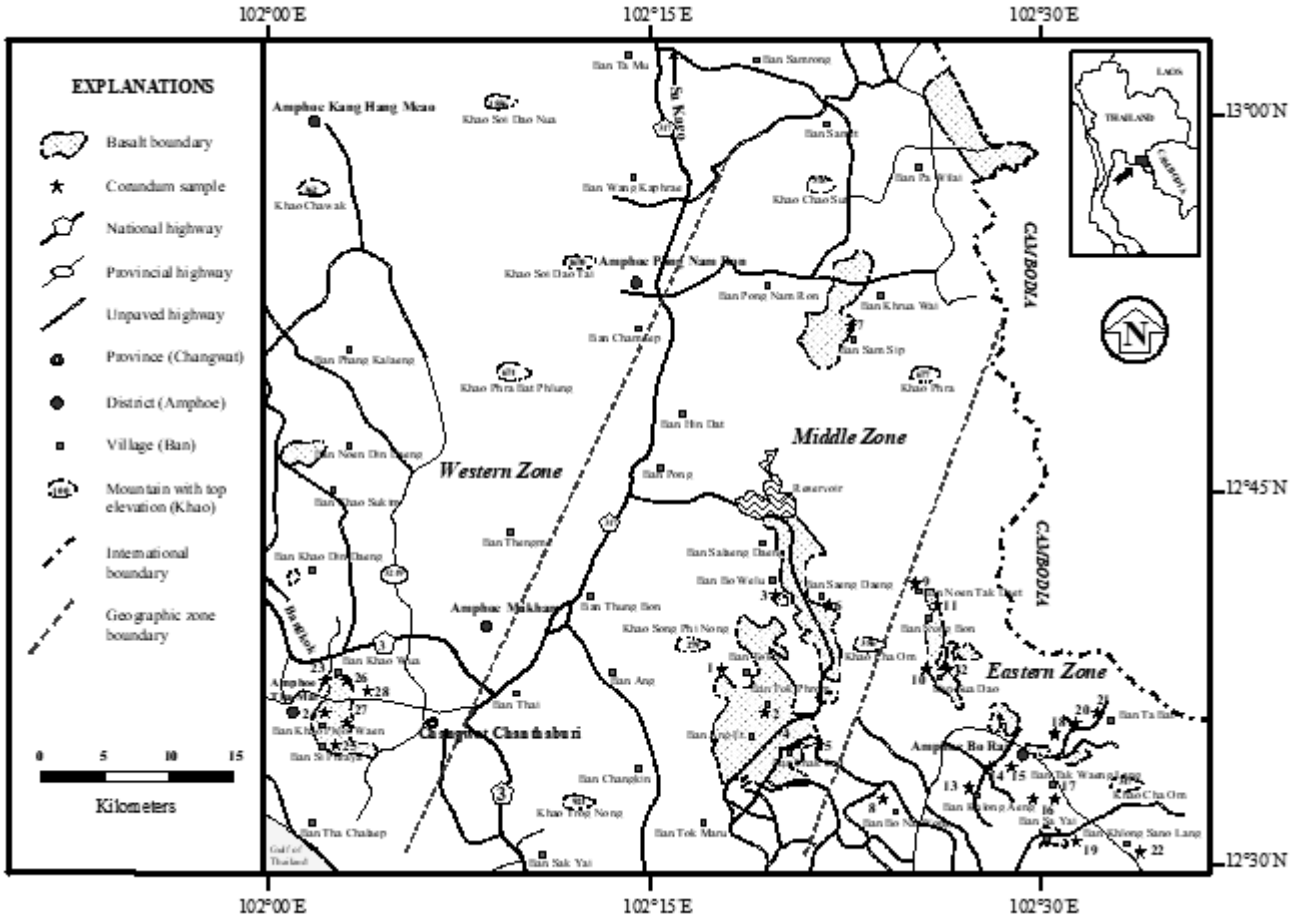

Figure 3. Schematic map showing sampling locations for corundum in the Chanthaburi-Trat gem fields.

Results and Discussion:

The results are presented in the form of graphical spectra with a vertical absorbance scale and a horizontal wavelength scale. The representative spectra of corundums from Chanthaburi-Trat gem fields are given a colour notation in terms of *"hue"*, *"tone"* and *"saturation"* based on GIA standard.

Corundum samples from Chanthaburi-Trat gem fields have been divided into two groups according to their infrared spectra. The first group includes all the rubies (i.e. corundum samples with purple, reddish-purple, red-purple, purplish-red colours) plus some stones which have yellow, green, and yellow-green colours.

A typical series which occurs in this group includes two sets of absorption bands; one is located between approximately 2300 and 2400 cm^{-1} with a maximum located at approximately 2341 cm^{-1} and the other set is situated between approximately 2800 and 3000 cm^{-1} with maxima located at 2855 and 2925 cm^{-1} (Figure 4). The former is due to atmospheric carbon dioxide (small peak) or carbon dioxide in the sample (sharp peak) (Smith, 1995). The latter has a weak peak present between 2800 and 3000 cm^{-1} which is considered to be due to C-H stretching mode of the CH_2 group (Deo *et al.,* 2001). Some samples display a distinctive spectrum, for example, a purplish red ruby from Ban Ta Bat in the eastern zone (Sample no. COR 21/2) has a significant sharp peak for carbon dioxide at 2341 cm^{-1} (Figure 4a) which might come from a gaseous carbon dioxide inclusion. Boehmite, which produces a broad absorption band located between 3000 and 3400 cm^{-1}, has been detected in several samples including rubies from Ban Bo Welu (Sample no. COR 3/2) and Ban Saeng Daeng (Sample no. COR 6/1) in the middle zone; rubies from Ban Bo Na Wong (Sample no. COR 8/1), Ban Bo Rai (Sample no. COR 14/1, Figure 4d), Ban Khlong Sano (Sample no. COR 20/1) and Ban Khlong Sano Lang (Sample no. COR 22/1) in the eastern zone; yellowish-green sapphire from Ban Khao Phloi Waen (Sample no. COR 24/1) in the western zone.

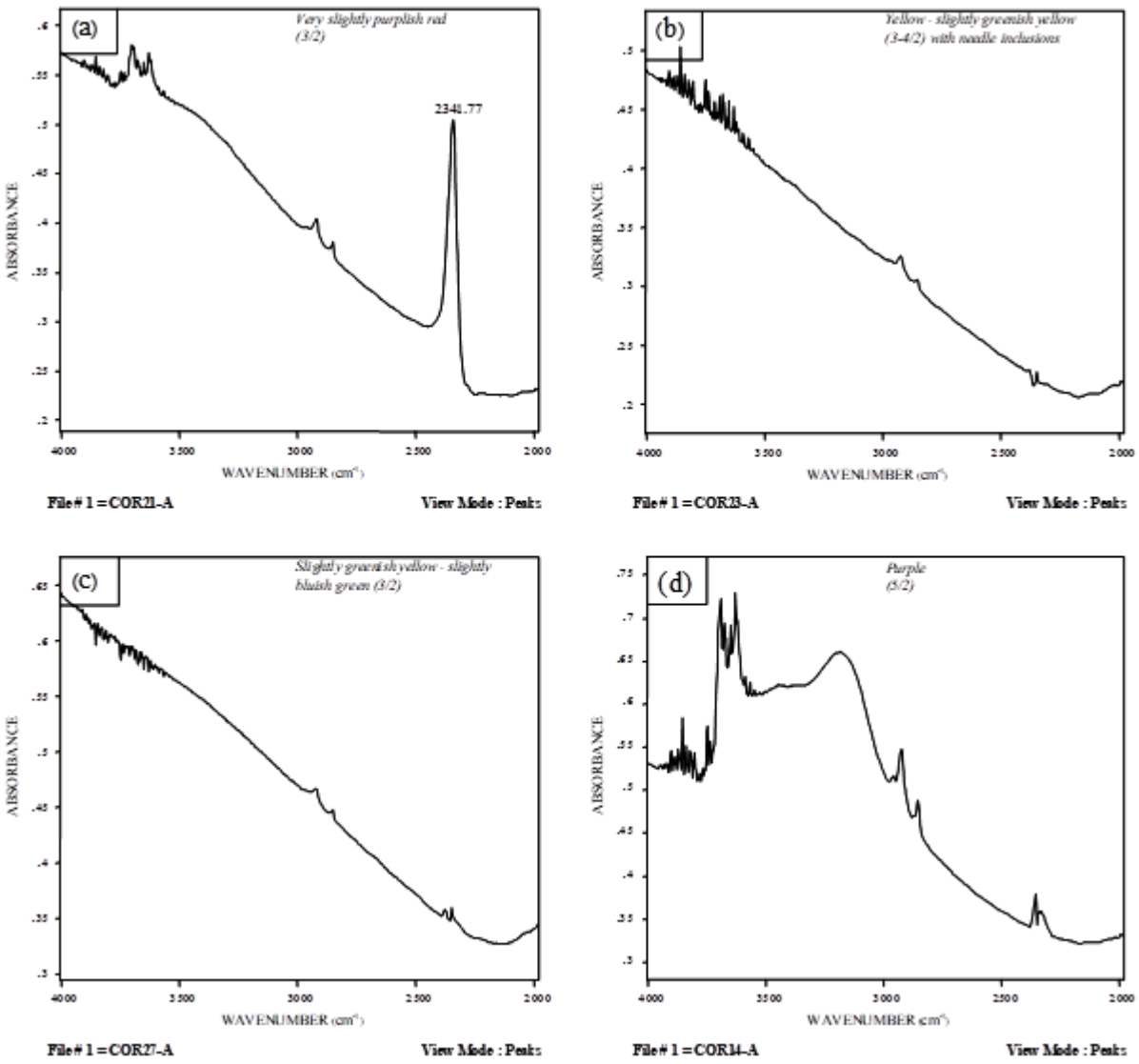

Figure 4. Infrared spectra for polished corundum samples in the first group from (a) Ban Ta Bat (Sample no. COR 21) (b) Ban Khao Wua (Sample no. COR 23) (c) Ban Khao Phloi Waen (Sample no. COR 27) (d) Ban Bo Rai (Sample no. COR 14). The numbers following the colours of the stones are tone/saturation scales.

The second group includes sapphires with blue, violetish-blue, greenish-blue, green-blue, and bluish-green colours. All samples in this group exhibit the same absorption bands as the first group but in addition they have another set of absorption bands which is located between approximately 3100 and 3600 cm^{-1} (Figure 5). These consist of a series of sharp peaks, with the primary peak located at 3310 cm^{-1}, accompanied by a shoulder peak at 3232 cm^{-1} and weaker peaks at approximately 3187 and 3368 cm^{-1}. The series of sharp peaks observed here are related to structural OH groups bonded within the corundum lattice. Not all samples in this group possess the complete series of absorption peaks, as this depends on the concentration of OH.

Several samples possess only a single peak located at approximately 3310 cm^{-1}; others showed this in combination with a second peak at approximately 3232 cm^{-1} (Figure 5d) whilst those with the most intense spectra also have additional small peaks located at approximately 3187 and 3368 cm^{-1} (Figures 5a and 5b). These OH-group absorption bands in the sapphires are produced by titanium (Ti) and iron (Fe), which have produced colours in blue or green tones. Some sapphires have a broad band located between 3000 and 3400 cm^{-1} (Figure 5c), which is identified as boehmite, for example, sapphires from Ban Tok Si (Sample COR 1/3), Ban Bo Welu (Sample no. COR 3/4) and Ban Saeng Daeng (Sample no. COR 6/2) (Figure 5c) in the middle zone; Ban Bo Na Wong in the eastern zone (Sample no. COR 8/3); and from Ban Bang Kacha in the western zone (Sample no. COR 25/2).

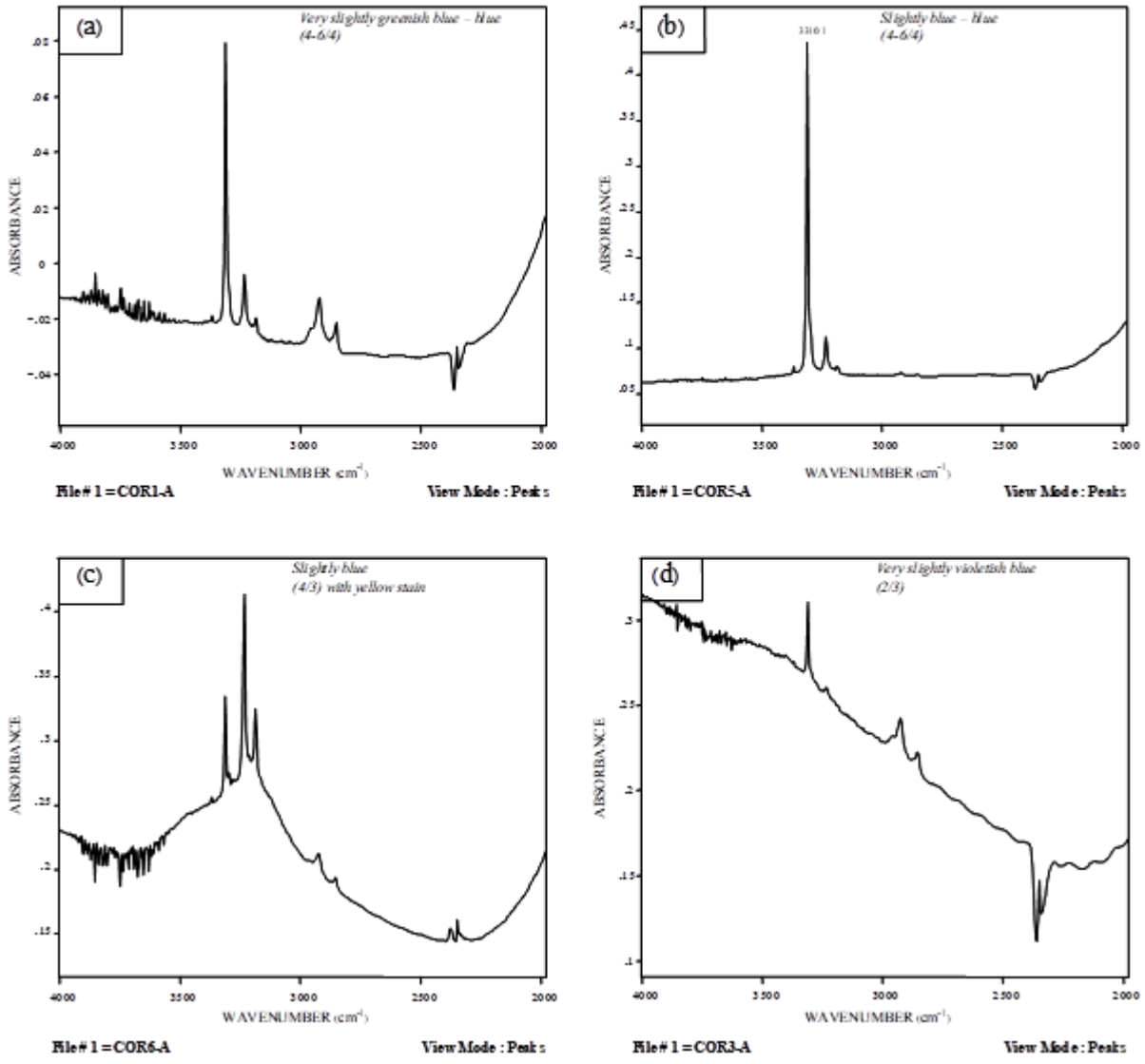

Figure 5. Infrared spectra for polished corundum samples in the second group from (a) Ban Tok Si (Sample no. COR 1) (b) Ban Chak Lao (Khao To Mo) (Sample no. COR 5) (c) Ban Saeng Daeng (Sample no. COR 6) (d) Ban Bo Welu (Sample no. COR 3). The numbers following the colours of the stones are tone/saturation scales.

Conclusion:

FTIR spectra allow division of the corundum into two groups. The first group includes all the rubies (i.e. corundum samples with purple, reddish-purple, red-purple, purplish-red colours) and some sapphires which have yellow, green, and yellow-green colours. Two sets of absorption bands are seen. One is located between approximately 2300 and 2400 cm^{-1} with a maximum located at approximately 2341 cm^{-1} and is considered to be due to atmospheric carbon dioxide (small peak) or carbon dioxide in the sample (sharp peak). The second is situated between approximately 2800 and 3000 cm^{-1} with maxima located at 2855 and 2925 cm^{-1}, along with a weak peak around 2955 cm^{-1}. These are due to C-H stretching mode of the CH_2 group.

The second group includes sapphires with blue, violetish-blue, greenish-blue, green-blue, and bluish-green colours. All samples in this group have almost the same absorption bands as the first group but in addition they have another set located between approximately 3100 and 3600 cm^{-1}. These consist of a series of sharp peaks, with the primary peak located at 3310cm^{-1}, accompanied by a shoulder peak at 3232 cm^{-1} and weaker peaks at approximately 3187 and 3368 cm^{-1}. The series of sharp peaks observed here are related to structural OH groups bonded within the corundum lattice. Not all samples in this group possess the complete series of absorption peaks, probably depending on the concentration of OH. The OH-group absorption bands in these sapphires are produced by titanium (Ti) and iron (Fe), which caused their colours in blue or green tones. Some samples displayed a broad band located between 3000 and 3400 cm^{-1}, which is identified as boehmite. The boehmite occurs as veins, which have penetrated and traversed the corundum, or as coatings on the surfaces of cracks.

Acknowledgements:

The author would like to express his deep sincere gratitude and appreciation to Dr Bill (J. W.) Gaskarth and Dr Chris J. Stanley for their valuable supervision. Professor Dr Emmanuel Fritsch (Materials Research Institute of Nantes, University of Nantes, France) for his kind providing Fourier Transform Infrared Spectroscopy (FTIR) technique and data interpretation.

References:

1. Deo N, Natarajan KA, Somasundaran P. Int J Miner Process. 2001;62:27-39.
2. Frederickson LD. Anal Chem. 1954;26(12):1883-1885.
3. Smith CP. J Gemm, 1995;24(5):321-335.
4. Vichit P. J Geol Soc Thailand, 1987;9:108-133.

SP04_001_PF: THE DEVELOPMENT OF PHOTOSWITCHABLE AZOBENZENE DERIVATIVE FOR AMPA RECEPTOR IN RETINAL NEURONS

Chanikan Wongkaew,[1] Paisan Khanchaitit,[2] Nopporn Ruangsupapichat[1,*]

[1]Department of Chemistry, Faculty of Science, Mahidol University, Bangkok 10400, Thailand
[2]National Nanotechnology Center (NANOTEC), National Science and Technology Development Agency (NSTDA)
*e-mail: nopporn.rua@mahidol.ac.th

Abstract:

Azobenzene is one of the molecular switch that can undergo *cis-trans* isomerization by light-irradiation. They have been commonly used as photoswitch molecules in biological systems. Inspired by Rhodopsin, a synthetic small azobenzene was studied as a photochromic ligand (PCL) for optochemical genetics (α-amino-3-hydroxy-5-methyl-4-isoxazolepropionic acid) AMPA receptor. Therefore, to develop a wide range of PCL, new photochromic agonist was synthesized and studied in the photophysical properties. As a result, Naphthylazobenzene photoswitchable AMPA (**NAA**) exhibited the efficient properties for PCL. **NAA** could be conformational changed from *trans*- to *cis*- isomer by blue-light irradiation and could rapidly switched back to *trans*-isomer *via* thermal process in the darkness at room temperature (less than five minutes).

Introduction:

Azobenzene is the most common structure that can be used as a tool in biological system due to its synthetic tractability, tunable photochemical properties, and biological compatibility.[1-2] Moreover, the photoswitch azobenzene have provided an attractive approach to restore the vision of the blind because of their specific wavelengths between *trans*- and *cis*- isomers.[3-7] The conformational structure can be changed by illumination *via* a specific wavelength, thereby reversibly toggling the molecule between active and inactive states.[8] In addition, azobenzene have been used as the photochromic agonists which can improve or restore visual function in degenerative retinal diseases such as retinitis pigmentosa (RP) and age-related molecular degeneration (AMD).[9]

The photochromic ligand (PCL) is one of photochromic agonists which are the target ligand connected with a photoswitchable side chain.[10] Recently, azobenzenes were used as PCL that can be rapidly changed their isomers by using two different wavelengths of light irradiation. PCLs are able to control a wide range of biological processes through light because of their efficient optically switching between isomers providing different biological activities.

The ionotropic glutamate receptors (iGluRs) are the targets for optochemical genetics which composed of α-amino-3-hydroxy-5-methyl-4-isoxazole propionic acid (AMPA), kainate, and *N*-methyl-D-aspartate (NMDA) receptors. However, AMPA receptors have key roles in mediating the rapid excitatory synaptic current in the mammalian central nervous system and have an ability to control the activity of retinal neurons.[11]

Since the regular azobenzene need the ultraviolet (UV) range for changing the conformation, the consideration of azobenzene photoswitch in vision must be absorbed in range of visible light (400-700 nm) to prevent the retina damage.[12] So, the development of the visible-light switched molecule is an alternative way for blind treatment and has been attracted to many research interests recently.

Among the series of photochromic glutamate receptor agonists, azobenzene tetrazolyl AMPAs (ATA) were synthesized and studied by Trauner and co-workers in 2012.[13] ATA is a selective red-shift AMPA receptor agonist that activates AMPA and stimulates neurons in the dark, and can rapidly turned off by blue-light

irradiation. Moreover, when **ATA-3** was applied to the blind retina in *vivo*, it can restore robust RGC responses to alternating light and dark stimuli.

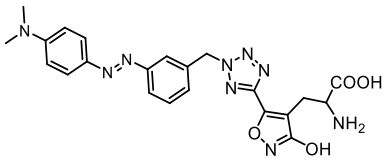

Figure 1. The structure of **ATA-3**

In this work, to develop a wide range of visible-light switched azobenzene as a PCL, new photochromic agonist was synthesized (Scheme 1) and studied the photophysical properties for AMPA receptor comparing with **ATA-3**. It was found that, naphthylazobenzene photoswitchable AMPA (**NAA**) show conformational changed from *trans*- to *cis*- isomer *via* blue light (450 nm) irradiation. Then, it could rapidly turn back to *trans*-isomer with thermal process in the darkness at room temperature.

Methodology:

General information. ^{1}H NMR and ^{13}C NMR spectra were recorded from Bruker AV 400 MHz NMR spectrometer in $CDCl_3$, acetone-d_6, and DMSO-d_6 solutions where chemical shifts are reported in part per million (ppm, δ) relative to TMS as the internal reference. Mass spectrometric data were obtained with high resolution mass spectra (HRMS) on a Bruker microTOF spectrometer in the ESI mode. Thin layer chromatography (TLC) was performed on aluminium sheets pre-coated with a Merck silica gel 60 F254 plate and compounds were visualized under UV light. A Merck silica gel 60 (0.063 – 0.200 mm) was used as stationary phase on column chromatography. UV-Vis absorption spectra were recorded by Agilent Cary-60 UV–Visible spectrophotometer.

Materials. Commercially available reagents and solvents were purchased from Aldrich and TCI suppliers and were used as received.

(3-((8-(dimethylamino)naphthalen-2-yl)diazenyl)phenyl)methanol (2) 3-aminobenzoly alcohol (1.00 g, 8.13 mmol) in a solution of 4N HCl was added with a cold solution of $NaNO_2$ (0.56 g, 8.13 mmol, 3.0 mL water) at 0 ^{o}c. After 15 min, the resulting mixture was added *N,N*-dimethylnaphthalen-1-amine (1.39 g, 8.13 mmol) and stirred for another 3 h. The reaction mixture was quenched by a solution of CH_3COONa and solution was allowed to warm to room temperature. The crude mixture was extracted with EtOAc (4x50 mL) and the combined organic extracts were dried over Na_2SO_4, filtered and concentrated to dryness. Normal phase column chromatography (EtOAc:Hexane = 3:7) yield naphthylazobenzene alcohol (**2**) (1.85 g, 74%) as an orange solid. ^{1}H NMR (400 MHz, Acetone-d_6) δ 9.03 (d, *J* = 8.3 Hz, 1H), 8.28 (d, *J* = 8.4 Hz, 1H), 8.05 (s, 1H), 7.91 (dd, *J* = 7.9, 3.7 Hz, 2H), 7.68 (dd, *J* = 11.1, 4.0 Hz, 1H), 7.64 – 7.59 (m, 1H), 7.54 (dd, *J* = 11.0, 7.5 Hz, 2H), 7.22 (d, *J* = 8.3 Hz, 1H), 4.79 (d, *J* = 6.0 Hz, 2H), 3.02 (s, 6H). ^{13}C NMR (101 MHz, Acetone-d_6) δ 155.6, 154.5, 145.0, 143.4, 134.1, 130.0, 129.5, 129.3, 127.8, 126.3, 125.7, 124.5, 122.4, 121.4, 114.2, 113.3, 64.4, 45.2. HRMS $[M+H]^+$ $C_{19}H_{19}N_3O$ calcd for 306.1606, found 306.1596.

7-((3-(bromomethyl)phenyl)diazenyl)-N,N-dimethylnaphthalen-1-amine (3) A solution of naphthylazobenzene alcohol **2** (0.20 g, 0.78 mmol) in 15 mL dry THF under nitrogen atmosphere was cooled to 0 °C and treated with portions of *N*-bromosuccinimide (0.20 g, 1.17 mmol) and triphenylphosphine (0.31 g, 1.17 mmol), respectively. The reaction mixture was stirred at room temperature for 12 h, before it was filtered over a short plug of silica and the filtrate was concentrated under reduced pressure. Purification of the residue by flash chromatography (EtOAc:Hexane = 1:9), gave naphthylazobenzene bromide (**3**) (0.43 g, 71%) as a red oil. ^{1}H NMR (400 MHz, Acetone-d_6) δ 9.04 (d, *J* = 8.4 Hz, 1H), 8.28 (d, *J* = 8.3 Hz, 1H), 8.13 (s, 1H), 7.98 (dt, *J* = 7.1, 1.8 Hz, 1H), 7.93 (d, *J* = 8.4 Hz, 1H), 7.73 – 7.66 (m, 1H), 7.65 – 7.58 (m, 3H), 7.22 (d, *J* = 8.4 Hz, 1H), 4.82 (s, 3H), 3.03 (s, 6H). ^{13}C NMR (101 MHz, Acetone-d_6) δ 154.6, 154.0, 143.8, 143.3, 140.8, 132.1, 130.7, 129.2, 127.9, 126.4, 125.7, 124.5, 124.0, 123.8, 114.2, 113.5, 45.1, 33.9. HRMS $[M+H]^+$ $C_{19}H_{18}BrN_3$ calcd for 368.0762, found 368.0761.

tert-butyl 3-(3-(allyloxy)-5-(2H-tetrazol-5-yl)isoxazol-4-yl)-2-(bis(tert-butoxycarbonyl)amino)propanoate (4). The synthetic of compound **4** was described as in a literature report.[13]

***tert*-butyl 3-(3-(allyloxy)-5-(2-(3-((8-(dimethylamino)naphthalen-2-yl)diazenyl)benzyl)-2*H*-tetrazol-5-yl)isoxazol-4-yl)-2-(bis(*tert*-butoxycarbonyl)amino)propanoate (5).** K_2CO_3 (53.2 mg, 0.39 mmol) was added to an acetone solution (10 mL) of compound **4** (103.3 mg, 0.19 mmol) and the reaction mixture was stirred for 15 min at room temperature. The solution of naphthylazobenzene bromide (**3**) (127.2 mg, 0.35 mmol) in acetone (5 mL) was added and the reaction mixture was stirred for 12 h at room temperature. The crude mixture was extracted with EtOAc (4x50 mL) and the combined organic extracts were dried over Na_2SO_4, filtered and concentrated to dryness. Normal phase column chromatography (EtOAc:Hexane = 1:4) gave a mixture of *N*-1 and *N*-2 alkylated tetrazoles (**5**) (131.8 mg, 83%) as a red oil. ^{1}H NMR (400 MHz, Acetone-d_6) δ 9.02 (d, *J* = 7.7 Hz, 1H), 8.27 (d, *J* = 8.7 Hz, 1H), 8.18 (s, 1H), 8.09 – 7.97 (m, *J* = 13.6 Hz, 1H), 7.98 – 7.88 (m, 1H), 7.64 (dt, *J* = 15.8, 7.7 Hz, 4H), 7.21 (d, *J* = 8.4 Hz, 1H), 6.24 (d, *J* = 6.0 Hz, 1H), 6.19 (s, 1H), 6.18 – 6.05 (m, 1H), 5.47 (d, *J* = 17.4 Hz, 1H), 5.30 (d, *J* = 10.6 Hz, 1H), 5.21 – 5.14 (m, 1H), 4.84 (d, *J* = 6.4 Hz, 2H), 3.50 (dt, *J* = 14.5, 12.6 Hz, 2H), 3.03 (s, 6H), 1.45 (d, *J* = 5.7 Hz, 8H), 1.35 (s, 7H), 1.32 (s, 10H). ^{13}C NMR (101 MHz, $CDCl_3$) δ 171.4, 171.1, 168.9, 168.7, 156.6, 155.6, 153.7, 152.6, 152.1, 152.1, 144.5, 134.7, 133.9, 133.3, 132.2, 131.8, 130.3, 130.1, 130.1, 128.1, 127.3, 126.0, 124.6, 124.1, 124.1, 123.7, 123.3, 123.1, 119.4, 119.0, 111.4, 108.0, 83.1, 82.9, 82.0, 81.8, 71.5, 71.2, 58.1, 57.9, 57.1, 52.5, 45.3, 29.9, 28.1, 28.1, 28.0, 22.3, 22.0. HRMS $[M+H]^+$ $C_{43}H_{53}N_9O_8$ calcd for 824.4095, found 824.4097.

***tert*-butyl-2-(bis(tert-butoxycarbonyl)amino)-3-(5-(2-(3-((8-(dimethylamino)naphthalen-2-yl)diazenyl)benzyl)-2*H*-tetrazol-5-yl)-3-hydroxyisoxazol-4-yl)propanoate (6).** A solution of the compound **5** (131.8 mg, 0.16 mmol) in MeOH (10 mL) was added with $Pd(PPh_3)_4$ (9.2 mg, 0.007 mmol). After 5 min, K_2CO_3 (44.2 mg, 0.32 mmol) was added and let stirred for 2 h at room temperature. The reaction mixture was diluted with EtOAc (50 mL) and the organic phase was washed with saturated aqueous NH_4Cl solution and brine. The organic phase was dried over Na_2SO_4, filtered and concentrated to dryness. The crude product was passed over a short plug of silica (DCM:MeOH = 9:1) gave the mixture of *N*-1 and *N*-2 hydroxy-isoxazole (**6**) (26.2 mg, 21%) as a red solid. ^{1}H NMR (400 MHz, Acetone-d_6) δ 9.02 (d, *J* = 7.9 Hz, 1H), 8.27 (d, *J* = 8.4 Hz, 1H), 8.18 (s, 1H), 7.93 (d, *J* = 8.3 Hz, 1H), 7.78 – 7.64 (m, 4H), 7.65 – 7.58 (m, 1H), 7.54 (d, *J* = 2.5 Hz, 1H), 6.23 (d, *J* = 5.6 Hz, 2H), 5.19 (dd, *J* = 10.8, 3.8 Hz, 1H), 3.58 – 3.52 (m, 1H), 3.51 – 3.43 (m, 1H), 3.03 (s, 6H), 1.44 (s, 9H), 1.31 (s, 18H). ^{13}C NMR (101 MHz, $CDCl_3$) δ 170.4, 170.1, 168.9, 168.6, 156.5, 155.6, 153.7, 152.8, 152.1, 152.1, 143.6, 134.7, 134.2, 133.3, 131.8, 130.5, 130.1, 129.9, 128.1, 127.3, 126.0, 124.6, 124.1, 124.1, 123.7, 123.3, 123.1, 119.0, 111.4, 108.0, 83.1, 82.9, 82.3, 81.5, 58.2, 57.4, 57.0, 52.4, 45.4, 30.0, 28.1, 28.0, 22.4, 22.0. HRMS $[M+Na]^+$ $C_{40}H_{49}N_9O_8$ calcd for 806.3602, found 806.3604.

2-amino-3-(5-(2-(3-((8-(dimethylamino)naphthalen-2-yl)diazenyl)benzyl)-2*H*-tetrazol-5-yl)-3-hydroxyisoxazol-4-yl)propanoic acid (NAA). To a solution of a mixture of *N*-1 and *N*-2 hydroxy-isoxazole (**6**) (26.2 mg, 0.083 mmol) in DCM (25 mL) was added with TFA (25 mL) at 0 °C and the reaction mixture was stirred at 0 °C for 1 h and then another 2 h at room temperature. The organic solvent was removed and the residue was purified by normal phase column chromatography (DCM:MeOH = 9:1) gave **NAA** (11.3 mg, 64%) as a dark red solid. ^{1}H NMR (400 MHz, DMSO-d_6) δ 8.91 (d, *J* = 8.4 Hz, 1H), 8.20 (s, 1H), 7.95 (dd, *J* = 48.3, 16.9 Hz, 3H), 7.76 – 7.43 (m, 3H), 7.19 (s, 2H), 6.12 (d, *J* = 76.9 Hz, 2H), 2.98 (s, 6H). ^{13}C NMR (101 MHz, DMSO-d_6) δ 171.8, 171.4, 155.2, 155.2 154.7 153.4 141.7, 136.6, 135.7, 133.1, 130.7, 130.5, 130.4, 127.7, 126.1, 125.2, 123.7, 122.5, 122.1, 113.6, 113.3, 56.5, 55.2, 45.0, 29.5. HRMS $[M+H]^+$ $C_{40}H_{25}N_9O_4$ calcd for 528.2107, found 528.2108.

Results and Discussion:

Design of photochromic agonists (NAA). To tune visible-light switched azobenzene into more red-shifted region, naphthalene was used to replace regular benzene on one side of the azo group. Moreover, amino group was introduced as an electron-donor to the structure as presented in figure 2. The new designed azobenzene was then connected with AMPA ligand which will attach to a protein to enable its reversible effect.

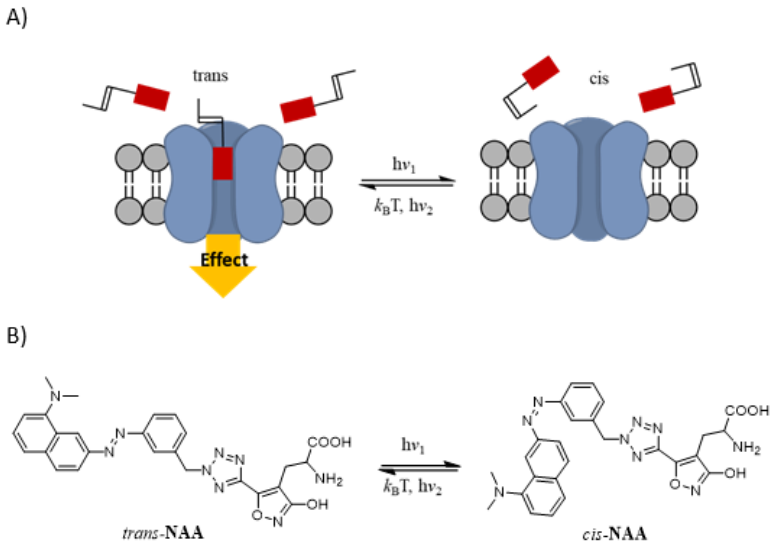

Figure 2. A) The diagram for photocontrol protein function using **NAA** ligand, B) The photoisomerizatio of new azobenzene (**NAA**).

Synthesis of NAA. The synthesis route of the target photochromic agonist **NAA** is depicted in Scheme 1. The main part was started with azo coupling reaction between aminobenzoly alcohol (**1**) and *N,N*-dimethylnaphthalen-1-amine to obtain naphthylazobenzene alcohol (**2**). Then, this alcohol was converted to naphthylazobenzene bromide (**3**) under appel reaction.[14] Followed by nucleophilic substitution reaction between compound **3** and AMPA receptor (**4**) provided a mixture of *N*-1 and *N*-2 alkylated tetrazoles (**5**). The deprotection reaction of allyl group using basic conditions in the presence of a palladium catalyst yielded the intermediate **6** in moderate yield. Subsequently, the deprotection reaction of BOC group using trifluoroacetic acid (TFA) gave free amino **NAA** in good yield (Scheme 1). All chemical structure and intermediates were characterized by ^{1}H NMR, ^{13}C NMR spectra and mass spectrometry techniques.

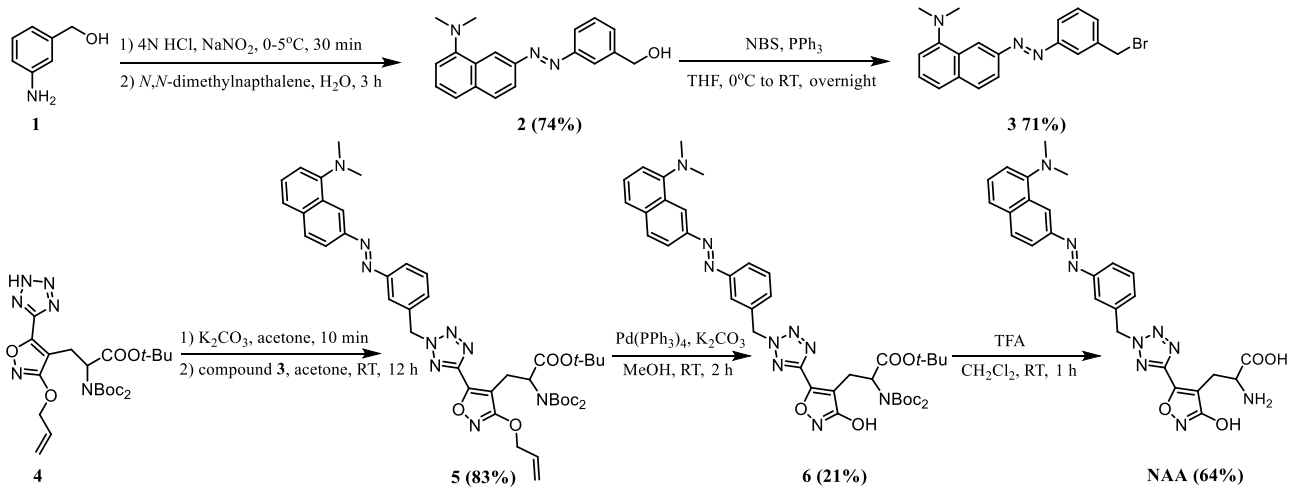

Scheme 1. The synthesis of new azobenzene (**NAA**).

Photophysical properties of azobenzene 2. The photoisomerization of azobenzene **2** was investigated in acetonitrile at room temperature and UV-Vis spectra were shown in Figure 3. At normal state, the maximum absorption peak at 423 nm of compound **2** can be verified as a *trans*-isomer. When compound **2** was irradiated *via* blue light (450 nm), the maximum absorption peak at 423 nm was decreased within 2 minutes, which mean that the *cis*-isomer was formed (Figure 3A). After that, *trans*-**2** can be gradually recovered with thermal process at room temperature (no irradiation) within 7 seconds (each spectrum) and completed in 1.5 minutes (Figure 3B).

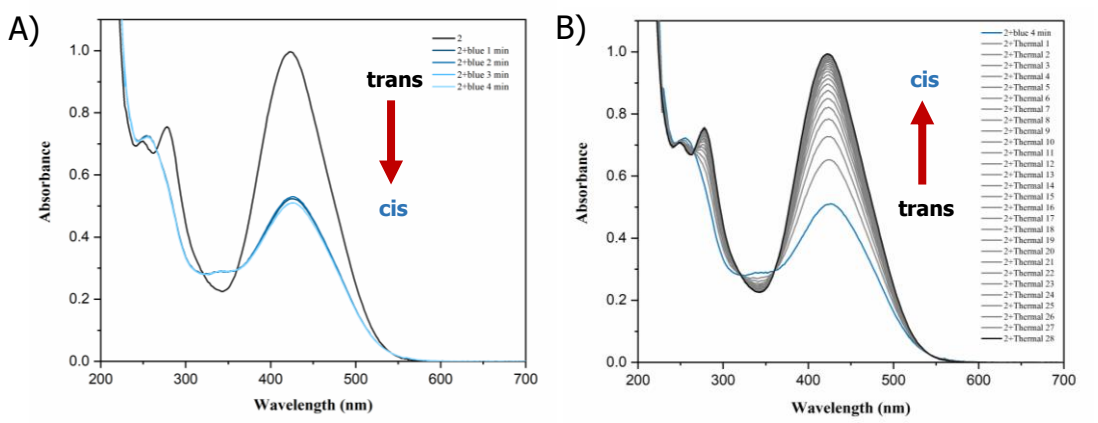

Figure 3. UV-Vis spectra showed the process of *cis-trans* isomerization of azobenzene **2** in acetonitrile ($2x10^{-5}$ M) A) irradiation under blue light (450 nm), and B) thermal process at RT (dark)

Photophysical properties of NAA. The photoisomerization of **NAA** was investigated in DMSO at room temperature and UV-Vis spectra were shown in Figure 4A. Similar to azobenzene **2**, the maximum absorption peak at 446 nm can be verified as a *trans*-isomer (solid line). The *cis*-**NAA** was formed after blue light irradiation for 30 minutes (dash line, Figure 4A). Then, *trans*-**NAA** can be recovered after letting in the dark at room temperature for 5 minutes. Furthermore, reversible process between *trans*-**NAA** and *cis*-**NAA** can be confirmed by several times switching processes between blue-light irradiation and the darkness process (Figure 4B).

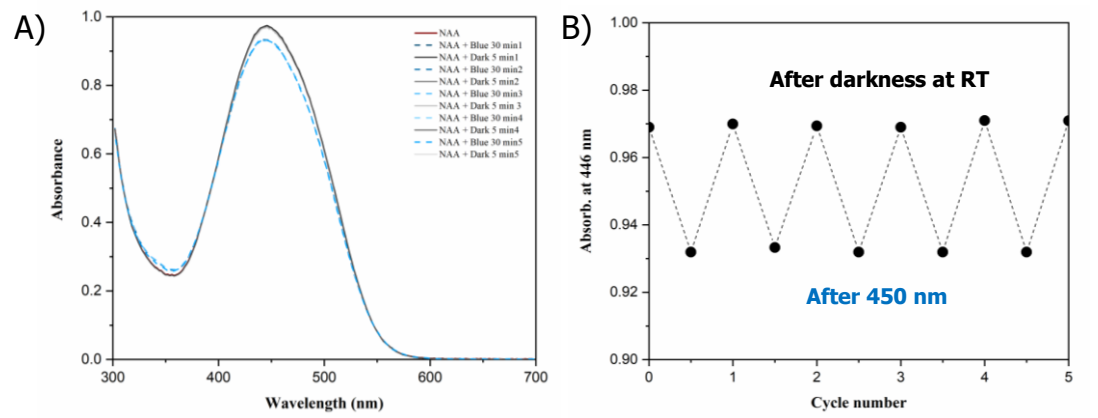

Figure 4. A) UV-Vis spectrum of photoswitchable azobenzene **NAA** in DMSO ($2x10^{-5}$ M) between *trans*- (solid line) and *cis*- isomer (dash line) B) Five cycles of a reversible process of azobenzene **NAA**.

Conclusion:

We designed and synthesized a new azobenzene **NAA** as photochromic agonist for AMPA receptor. **NAA** exhibited the efficient properties PCL that can change the conformation from *trans*- to *cis*- structure by blue light stimulation and it could turn back to *trans*- isomer *via* thermal process in darkness at room temperature. Furthermore, this **NAA** has more red-shifted comparing to **ATA-3**. Therefore, **NAA** will be another candidate for an effective lignad to control neuronal activity in near future.

Acknowledgements:

This research was supported by Thailand Graduate Institute of Science and Technology Scholarship (TGIST) National Nanotechnology Center (NANOTEC), National Science and Technology Development Agency (NSTDA), and Department of Chemistry, Faculty of Science, Mahidol University.

References:

1. Kienzler MA, Isacoff EY. Curr Opin Neurobiol. 2017;45:202–209.
2. Dias AR, Minas Da Piedade ME, Martinho Simões JA, Simoni JA, Teixeira C, Diogo HP, Meng-Yan Y, Pilcher G. J. Chem. Thermodyn. 1992;24:439–447.
3. Szobota S, Gorostiza P, Del Bene F, Wyart C, Fortin DL, Kolstad KD, Tulyathan O, Volgraf M, Numano R, Aaron HL, Scott EK, Kramer RH, Flannery J, Baier H, Trauner D, Isacoff EY. Neuron. 2007;54:535–545.
4. Gaub BM, Berry MH, Holt AE, Reiner A, Kienzler MA, Dolgova N, Nikonov S, Aguirre GD, Beltran WA, Flannery JG, Isacoff EY. Proc. Natl. Acad. Sci. U.S.A. 2014;111:E5574.
5. Banghart MR, Mourot A, Fortin DL, Yao JZ, Kramer RH, Trauner D. Angew. Chem. Int. Ed. 2009;48:9097–9101.
6. Ko KW, Rasband MN, Meseguer V, Kramer RH, Golding NL. Nat. Neurosci. 2016;19:826–834.
7. Tochitsky I, Polosukhina A, Degtyar Vadim E, Gallerani N, Smith Caleb M, Friedman A, Van Gelder RN. Trauner D, Kaufer D, Kramer RH. Neuron. 2014;81:800–813.
8. Laprell L, Hüll K, Stawski P, Schön C, Michalakis S, Biel M, Sumser MP, Trauner D. ACS Chem. Neurosci. 2016;7(1):15–20.
9. Tochitsky I, Trautman J, Gallerani N, Malis JG, Kramer RH. Sci Rep. 2017;7: 45487–45487.
10. Tochitsky I, Kienzler MA, Isacoff E, Kramer RH. Chem. Rev. 2018;118:10748–10773.
11. Mayer ML. Nature. 2006;440:456–462.
12. Noell WK, Walker VS, Kang BS, Berman S. Investig. Ophthalmol. Vis. Sci. 1966;5:450–473.
13. Stawski P, Sumser M, Trauner D. Angew. Chem. Int. Ed. 2012;51:5748–5751.
14. Gonda J, Fazekašová S, Martinková M, Mitríková T, Roman D, Pilátová MB. Org. Biomol. Chem. 2019;17:3361–3373.

SP04_002_PF: THE EFFECT OF SURFACE MORPHOLOGY ON THE MAGNETIC PROPERTIES OF RF-SPUTTERED CO-CU FILM

Suthasinee Somboonsap[1], Sirapat Seepromting[1], Watcharee Rattanasakulthong[1,*]

[1]Department of Physics, Faculty of Science, Kasetsart University, Bangkok, 10900, Thailand
*e-mail: fsciwrr@ku.ac.th

Abstract:

Co-Cu film with the thickness of about 312 nm was prepared on different flexible substrates by RF-sputtering. All sputtered Co-Cu films exhibited a main peak of Co-Cu (FCC), Co (FCC), and Cu (FCC) phases in (111) direction overlapping with Co (HCP) phase in (002) direction. The maximum and minimum intensities of the peak were observed on the film deposited on C-PET and A-PET substrates, respectively. AFM results revealed that surface roughness of Co-Cu film strongly depended on surface roughness of substrate. The highest and lowest roughness were detected on the films deposited on glass and B-PTFE substrates, respectively. VSM results indicated that all Co-Cu films showed ferromagnetic phases at room temperature under magnetic field of 1 T with the maximum and minimum saturation magnetization observed on the Co-Cu films on A-PET and glass substrates, respectively and the magnetic properties were powerfully depended on grain shape, size distribution and surface roughness of substrates. These results implied that the magnetic properties and crystallinity of sputtered Co-Cu films were obviously modified by surface morphology and crystallinity of the substrate. The results implied that amorphous phase of substrate significantly improved the magnetic properties of Co-Cu film.

Introduction:

Magnetic reading and writing system in storage devices consisted of ferromagnetic film on a rigid substrate have been strongly studied in order to improvement magnetic properties of ferromagnetic film. Surface roughness of ferromagnetic film and a gap between head and storage film plays important rule in magnetic recording technology. The flexible substrate such as Kapton film was substituted to defeat these conditions to improve surface roughness and magnetic properties.[1] The Co-based films on flexible substrate have possessed the perpendicular coercivity and magnetic anisotropy well when compared with rigid substrate [2] and the Co-Cu alloys are the one of effective ferromagnetic films for sensing devices in magnetic storage media because of the adjustable magnetic characteristics and showing giant magnetoresistance or (GMR) effect.[3] Moreover, the Co-Cu films can be fabricated by both chemical and physical depositions, for example, electrodeposition and sputtering.[4, 5]

In this work, Co-Cu films on different substrates were fabricated by RF-sputtering. Surface morphological, structural and magnetic properties were characterized in order to investigate the effects of surface morphology, structure and type of substrates on magnetic properties of the sputtered films.

Methodology:

Co-Cu films on the different substrates (glass, polyimide sheet (A-PET), kapton tape (C-PET), brown Teflon (B-PTFE) and white Teflon (W-PTFE) were prepared by Leybold-Heraeus, Univex 300 RF-sputtering machine from 99.9 % pure Co:Cu (50:50 at.%) commercial target with 3.00″ diameter and 0.250″ thick. The

substrates (1×3 inch^2) were placed with distance about 4 cm from the target. Co-Cu films were deposited under Ar pressure of 10^{-3} mbar with power of 200 W for 60 minutes. Film thickness, surface morphology and chemical composition were measured by FEI Quanta 450 scanning electron microscope (SEM) with energy dispersive microscopy (EDS). Surface roughness was investigated by atomic force microscope (AFM) over scanning area of 1, 25 and 400 µm^2. The phase structure was characterized by a Bruker D8 Advance x-ray diffractometer (XRD) with Cu K_α radiation (λ = 1.54 Aº). Magnetic hysteresis loops were carried by vibrating sample magnetometer (VSM) under magnetic field of 1 T at room temperature.

Results and Discussion:

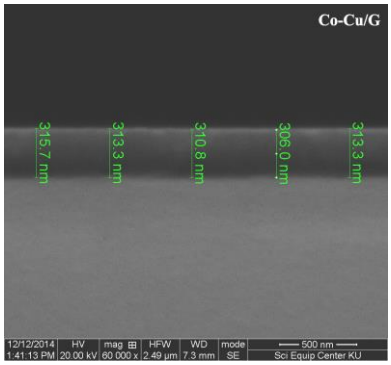

Figure 1. A cross-sectional SEM image displayed thickness of Co-Cu film on glass substrate.

SEM image confirmed that an averaged thickness of Co-Cu film on glass substrate was 312 nm shown in **Fig. 1**. The interfacing area between the film layer and substrate was smooth and sharp without an inserted diffusion layer. Chemical composition from EDS spectroscopy implied that all Co-Cu film showed that concentration of Cu atoms was higher than that of Co atoms because the number of ejected target atoms per sputtering ions of Cu atoms were higher than that of Co atoms due to sputtering yield of Cu is higher than Co.[6] The composition of sputtered Co-Cu films was varied depending on substrate material. The highest and lowest concentrations of Co atoms were 44.8 at. % and 42.5 at. % observed on W-PTFE substrate and A-PET with B-PTFE substrates, respectively. It can be described that the deposition rate of Co and Cu atoms on the substrate was influenced from surface energy of substrate. Chemical compositions of all Co-Cu films were summarized in **Table 1.**

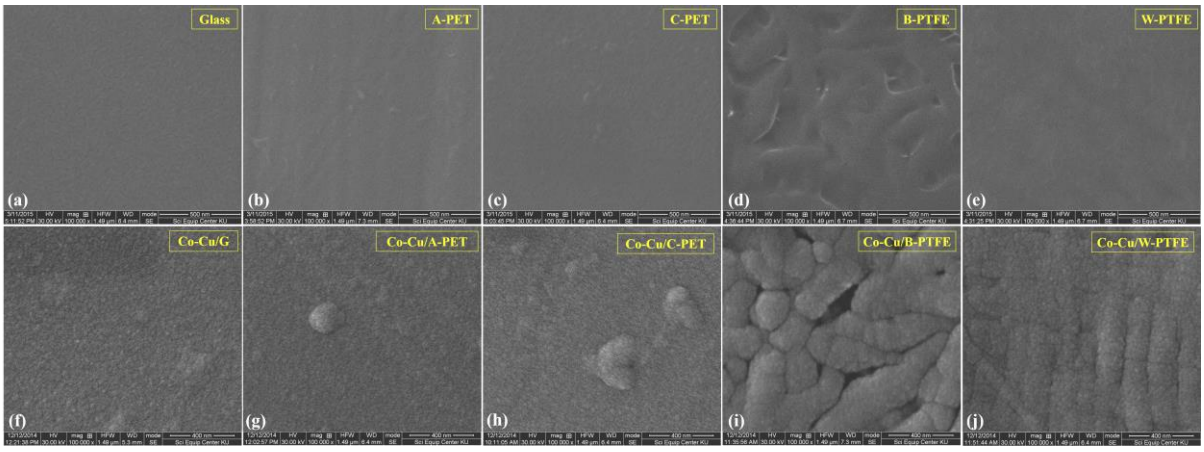

Figure 2. SEM images showed the surface morphology of (a-e) substrates and (f-j) Co-Cu films on different substrates.

Surface morphology of Co-Cu films and substrates was shown in **Fig. 2**. The images revealed that glass, A-PET and C-PET substrates had a smooth and fine surfaces area whereas B-PTFE showed a basket weave tile-like pattern and W-PTFE had smooth thread-like pattern. Surface morphology of sputtered Co-Cu film exhibited the fine grains with different size and distribution depending on surface morphology of substrate. The film on glass, A-PET and C-PET displayed fine grain with regular size distribution with the occurrence of agglomerated grain islands. The surface morphology of the Co-Cu film on B-PTFE substrate showed the fine grain size and distribution without the agglomeration of Co-Cu grains. There were some porosities with various size dispersing over surface area of Co-Cu film on B-PTFE substrate. The film on W-PTFE substrate had a regular grain size and distribution with smooth thread-like pattern. It can be described that the formation of porosity and island on film surface were due to the film growth process defining to three steps (1) nucleation: the formation of nuclei and growth to form island depending on surface energies of substrate and film material, (2) coalescence: the 3D formation of island and connection to be continuous network decreasing surface energy, and (3) the thickness growth and real structure construction process.[7-9]

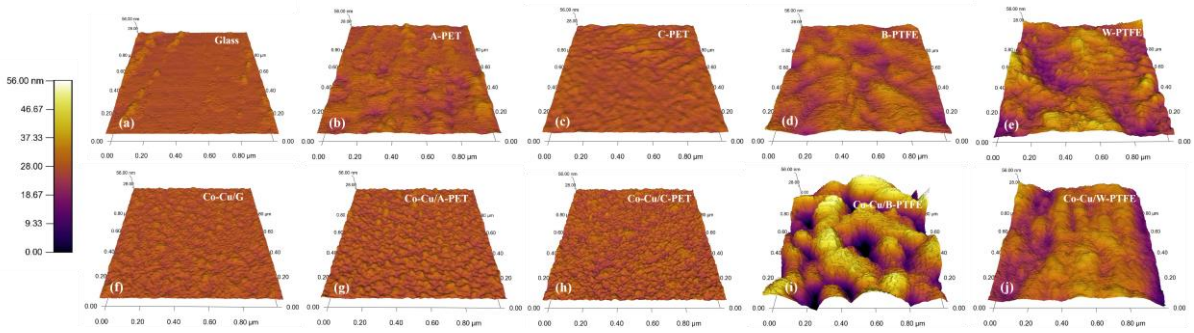

Figure 3. AFM images of substrates (a-e) and Co-Cu film on various substrates (f-j).

AFM images showed roughness of the Co-Cu film on different substrates shown in **Fig. 3**. It indicated that film roughness powerfully depended on substrate surface roughness. A lower roughness was observed on glass, A-PET and C-PET substrates while a higher roughness was found on B-PTFE and W-PTFE substrates. After Co-Cu film deposition, it was clearly observed that the film on glass, A-PET and C-PET substrates showed fine grains with high grain-packing density and smooth surface roughness whereas on B-PTFE and W-PTFE substrates exhibited larger grain size with higher surface roughness.

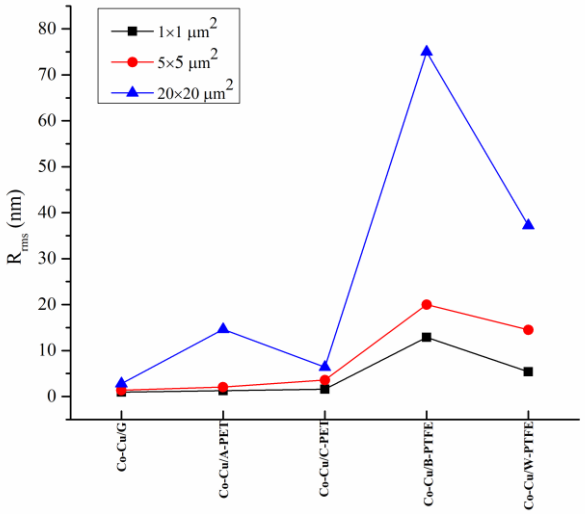

Figure 4. Average roughness (R_{rms}) of Co-Cu films on different substrates over scanning areas of 1, 25, and 400 μm^2.

It obviously observed that the Co-Cu/A-PET film displayed the most regular grain size and distribution and homogeneous surface roughens. AFM results over scanning area of 400 μm^2, the smoothies and lowest surface roughness film was observed on glass substrate whereas the highest surface roughness film was observed on B-PTFE substrate as shown in **Fig. 4**. It can be described that the difference of surface roughness was due to the cross-grain growth resulting in higher roughness [8], surface energy of substrate materials and targets [10] and the density of substrate crystalline nuclei.[11]

XRD results in **Fig. 5** implied that all of sputtered Co-Cu films showed the main peaks of mixed Co-Cu, Cu and Co (FCC) phase in (111) plane at 2θ around 43.5° [3, 12] overlapping with a peak of Co (HCP) phase in (002) plane. The highest and lowest intensities of this peak were observed on the Co-Cu/C-PET and Co-Cu/A-PET films, respectively. However, the Co-Cu/glass and Co-Cu/B-PTFE films also exhibited high intensity of a main peak. Additionally, the Co-Cu/glass and Co-Cu/C-PET films showed the mix phase in (200) and (220) planes. The C-PET and PTFE substrates showed the crystalline ordering peaks of C-PET and $(CF_2)_n$ phases.[13, 14] These results indicated that phase structure of substrates affected on crystallinity and phase structure of Co-Cu films. Crystallite size of Gaussian main peaks fitting was calculated from Scherrer's equation. It was found that the maximum size of 0.348 nm on glass substrate and minimum size of 0.274 nm on W-PTFE substrate as shown in **Table 1**. These results implied that the crystallite size of Co-Cu films was significantly related to Co and Cu compositions.

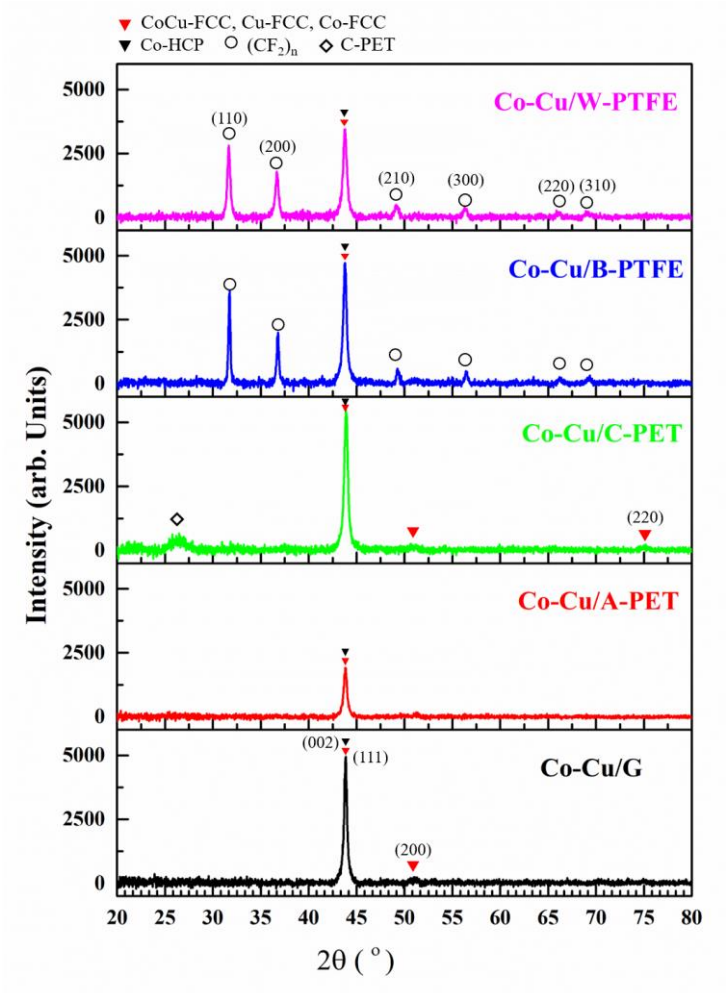

Figure 5. XRD patterns of sputtered Co-Cu film on various substrates.

Table 1. Chemical composition, surface roughness, crystallite size and magnetic parameters of the sputtered Co-Cu films on different substrates were summarized.

Substrate	Composition (at. %)		R_{rms} (nm)			Crystallite Size (nm)	H_c (G)		M_r (emu/g) $\times10^{-3}$		M_s (emu/g) $\times10^{-3}$	
	Co	Cu	1x1	5x5	20x20		//	⊥	//	⊥	//	⊥
Glass	43.3	56.7	0.93	1.35	2.79	0.348	79	82	6	6	81	59
A-PET	42.5	57.5	1.27	2.04	14.60	0.299	69	69	211	203	3048	2354
C-PET	43.0	57.0	1.57	3.57	6.40	0.292	66	74	6	7	88	66
B-PTFE	42.5	57.5	12.90	20.00	75.00	0.301	66	69	96	92	1319	992
W-PTFE	44.8	55.2	5.36	14.50	37.20	0.274	63	66	132	150	2029	1689

The parallel and perpendicular hysteresis loops of the films confirmed that all of sputtered Co-Cu films on various substrates displayed ferromagnetic phase at room temperature under magnetic field of 1 T shown in **Fig. 6**. Saturation magnetization (M_s) in parallel measurement was a few higher than that of perpendicular configuration. It can be classified the Co-Cu films into two ranges according to the value of their saturation magnetization. The Co-Cu film on A-PET, W-PTFE and B-PTFE substrates had the high range of saturation magnetization whereas the Co-Cu films on glass and C-PET substrates exhibited the low range of saturation magnetization. The maximum saturation (M_s) and remanant magnetization (M_r) were observed on Co-Cu films on A-PET in both parallel and perpendicular directions while the minimum M_s and M_r were detected on Co-Cu/glass film. The magnetic parameters of the Co-Cu films were summarized in **Table 1.** The perpendicular magnetization reached saturation but the parallel magnetization unreached saturation under magnetic field of 1 T. However, the parallel coercive fields (H_c) was very slightly lower than the perpendicular field. These results suggested that Co-Cu films on polymer substrates were partial to perpendicular magnetic anisotropy and type of substrates directly influenced magnetization of Co-Cu films. The unsaturated magnetization under applied magnetic field of 1 T in parallel configuration at room temperature was due to the higher content of Cu atoms [5] and Co (HCP) phase in (002) direction of the prepared Co-Cu films. The result implied that a Co-Cu/A-PET, /W-PTFE and /B-PTFE film showed the high content of Co (HCP) phase in (002) plane.

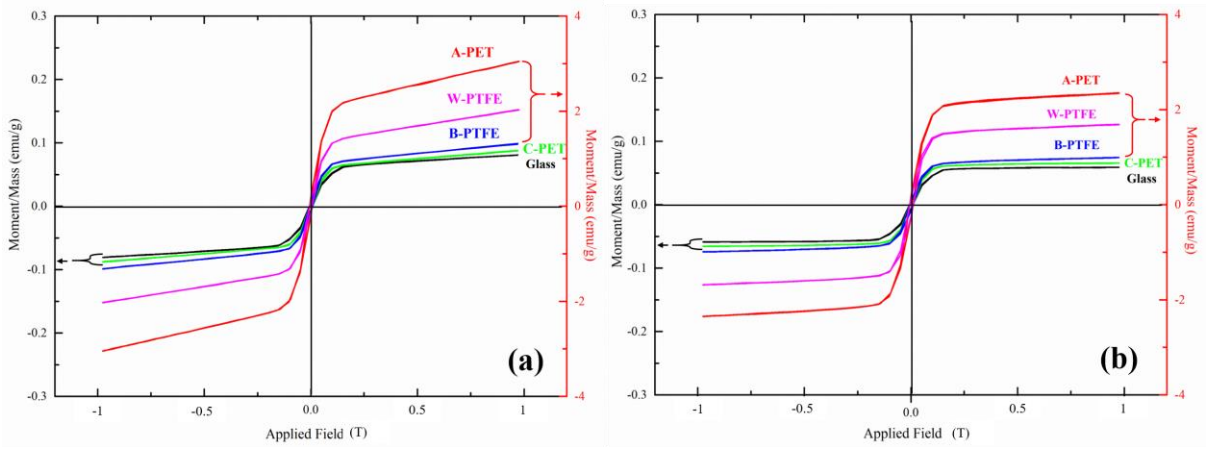

Figure 6. Hysteresis loops of sputtered Co-Cu films on various substrates in (a) parallel and (b) perpendicular measurements.

The relationship between surface morphology and magnetic properties of Co-Cu film on different substrate showed in **Fig. 7**. It was revealed that magnetic properties of Co-Cu films on flexible substrates strongly were dependent on Co (HCP), crystallite size and distribution. The highest magnetization of Co-Cu/A-PET film was attributed the highest Co (HCP) phase with appropriated crystallize size, grain size and distribution. It can be described that this film consisted of the highest crystallize randomly dispersing in a high ordering CoCu (FCC) grain in (111) plane and homogeneous amorphous substrate shown in **Fig. 7** (b). Additionally, the lower magnetization of Co-Cu/W-PTFE and Co-Cu/B-PTFE films had a lower ordering of Co atoms with different size and distribution deliberately dispersed inhomogeneous substrate shown in **Fig. 7** (d) and (e). the lowest magnetization of films on glass and C-PET substrates because of the highest concentration of Cu (FCC) atoms and unsuitable dispersion in substrate.

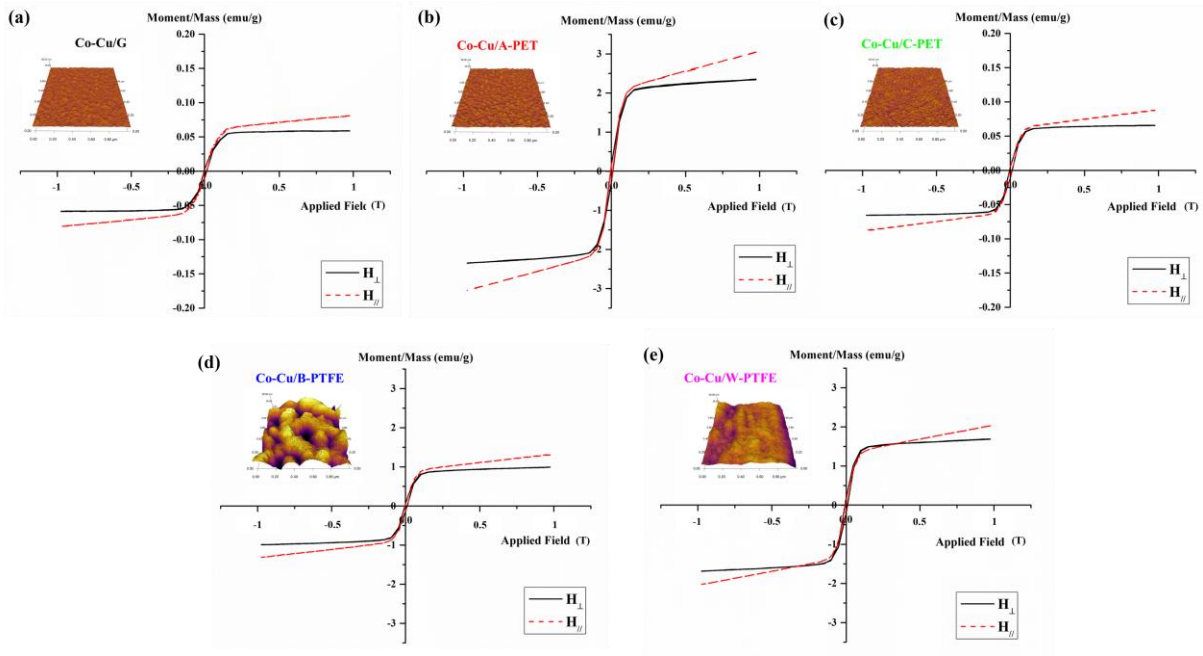

Figure 7. Hysteresis loops and surface morphology of Co-Cu films on (a) glass, (b) A-PET, (c) C-PET, (d) B-PTFE and (e) W-PTFE substrates.

Conclusion:

The magnetic properties of the sputtered Co-Cu films were not strongly depended on crystallite size, crystallinity, grain size and distribution of Co atoms but also depend on surface morphology of substrate. The Co-Cu/A-PET film owned the highest saturation magnetization whereas the Co-Cu/glass and Co-Cu/C-PET films possessed the lowest magnetization. The results inferred that magnetic properties strongly related to surface roughness and surface energy between Co-Cu film and substrate. It can be concluded that the Co atoms with suitable crystallite size randomly dispersed in amorphous phase of substrate improving the magnetic properties.

Acknowledgements:

This work was financially supported by the Kasetsart University Research and Development Institute (KURDI) with matching funds from the Department of Physics, Faculty of Science, Kasetsart University, Bangkok, Thailand.

References:

1. Taptimthong P, Rittinger J, Wurz MC, & Rissing L. Proc Technol. 2014;15:230-7.
2. Hermosa GC & Sun A-C. AIP Adv. 2020;10:015132.
3. Franczak A, Levesque A, Zabinski P, Li D, Czapkiewicz M, Kowalik R, Bohr F, Wang Q*, et al.* Mater Chem Phys. 2015;162:222-228.
4. Hiep VV, Chau N, Hong DM, & Luong NH. J Magn Magn Mater. 2007;310:2524-2526.
5. Karaagac O, MurselAlper, & HakanKockar. J Magn Magn Mater. 2010; 322: 1098-1101.
6. Laegreid N & Wehner GK. J Appl Phys. 1961; 32: 365-369.
7. H. A & K. W. Handbook of Sputtering Technology. 2012; 2nd Edition: 3-39.
8. Khachatryan H, Lee S-N, Kim K-B, Kim H-K, & Kim M. J Phys Chem Solids. 2018;122:109-117.
9. N. K. Appl Opt. 2002;41:3053-3060.
10. Kinloch AJ. Chapman & Hall. 1987.
11. Cheng X, Gotoh K, Nakagawa Y, & Usami N. J Cryst Growth. 2018;491:120–125.
12. Shalygina E, Kharlamova A, Makarov A, Kurlyandskaya G, & Svalov A. EPJ web conf. 2018;185:03009.
13. DEMİREL B, YARAŞ A, & ELÇİÇEK H. BAÜ Fen Bil Enst Dergisi Cilt. 2011;13:26-35.
14. Honda Y & Nishijima S. J Phys Conf. 2015;618:012024.

SP04_003_PA: EFFECT OF SURFACE MORPHOLOGY ON TRANSMITTANCE OF AL-DOPED ZINC OXIDE FILMS ON FLEXIBLE SUBSTRATE PREPARED BY SPUTTERING

Kanchanee Niyom,[1] Watcharee Rattanasakulthong[1,*]

[1]Department of Physics, Faculty of Science, Kasetsart University, Bangkok, 10900, Thailand
*e-mail: fsciwrr@ku.ac.th

Abstract:

ZnO:Al film with different thickness of between 192-441 nm on PTFE substrate by RF-sputtering. SEM result showed that the surface morphology of the film was strongly depended on the film thickness. The grain size of the film trended to increase with increasing the thickness. The 317 nm-film showed the moderated grain size with the broadest size distribution whereas the 376 nm-film exhibited the last grain size with the narrowest distribution. The XRD results confirmed that the AZO phase in (002) direction was obviously observed 280 nm-film and the intensity of this peak was increased with increasing the thickness. AFM result indicated that the 280 nm-film possessed the lowest roughness while the 317 nm-film owned the highest roughness. The electrical resistance of the films tended to increase with increasing film thickness but the 376 nm-film exhibited the lowest electrical resistance. The optical result implied that the transmittance of the film with different thickness was swung with wavelength. The maximum transmittance of the film observed at the different wavelength. The results supported that the grain size and distribution were strongly dependent on the wavelength range of transmittance.

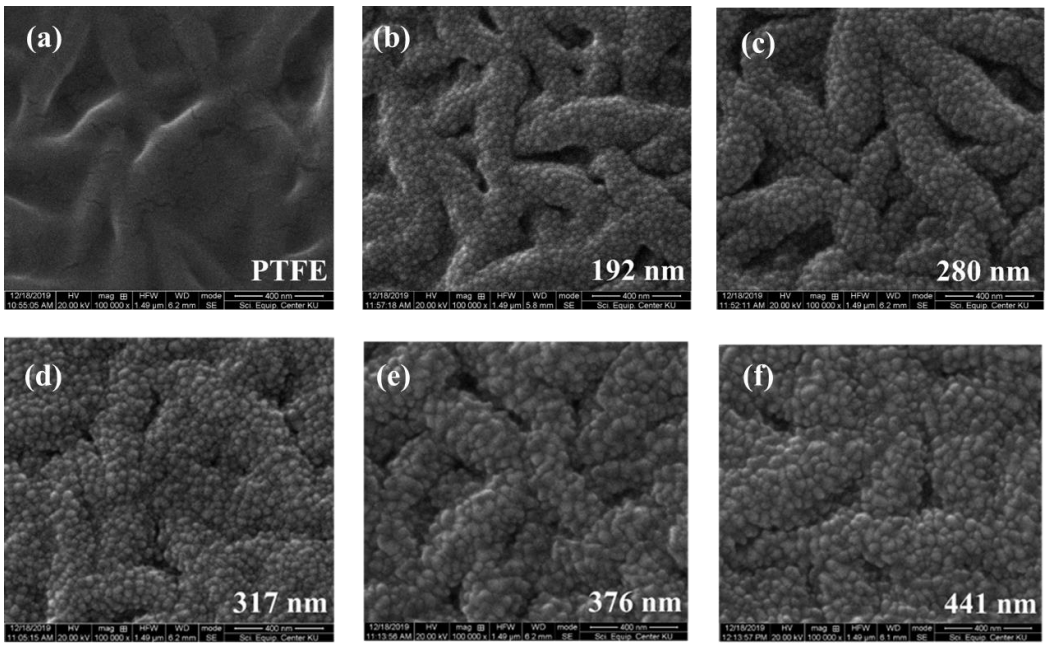

Figure 1. SEM images of the sputtered ZnO:Al films on (a) PTFE substrate with the thickness of (b) 192, (c) 280, (d) 317, (e) 376 and 441 nm.

SP04_004_OA: THE PROPERTIES OF FLUORCANASITE-LITHIUM DISILICATE DENTAL GLASS-CERAMICS WITH DIFFERENT HEAT TREATMENT TEMPERATURES

Arnon Kraipok,[1,2] Pratthana Intawin,[3] Patamas Bintachitt,[4] Sukum Eitssayeam,[1]
Kamonpan Pengpat[1,*]

[1]Department of Physics and Materials, Faculty of Science, Chiang Mai University, Chiang Mai 50200, Thailand
[2]Graduate PhD's Degree Program in Materials Science (International Program), Faculty of Science, Chiang Mai University, Chiang Mai 50200, Thailand
[3]Division of Physics, Faculty of Science and Technology, Rajamangala University of Technology Thanyaburi, Pathum Thani 12110, Thailand
[4]Department of Physics, Faculty of Science, Srinakharinwirot University, Bangkok 10110, Thailand
*e-mail: kamonpan.p@cmu.ac.th

Abstract:

In this study, glass-ceramics were prepared using CaF_2-SiO_2-CaO-K_2O-Na_2O-Li_2O as the base glass system by the conventional melt quenching method. The glasses were two-stage heat-treated at different temperatures (600, 650, 700, 750, and 800 °C) to convert the glasses into glass-ceramics. The effects of heat treatment on the properties of fluorcanasite- lithium disilicate dental glass- ceramics were investigated through differential thermal analysis, X- ray diffraction, scanning electron microscopy, the Archimedes' s principle, microhardness tests, and 3- point bending tests**.** The results suggest that the lithium disilicate crystal acted as the main crystalline phase at the heat treatment temperatures of 750 and 800 °C. Besides, the crystalline phase of fluorcanasite occurred at these heat treatment temperatures. The density, Vickers hardness, Knoop hardness, fracture toughness, and fracture strength values of the glasses and glass-ceramics increased with an increase in the heat treatment temperatures. The highest values of density, Vickers hardness, Knoop hardness, fracture toughness, and fracture strength at the heat treatment temperatures of 750 °C were 2.56 g/cm^3, 6.73 GPa, 5.85 GPa, 3.38 MPa.m$^{1/2}$, and 259 MPa, respectively. These results show that it is possible to design a new material for dental applications based on fluorcanasite-lithium disilicate glass-ceramics.

SP04_005_OA

SP04_005_OA: EFFECT OF CaO ON THE HEAT TREATMENT TEMPERATURE, MICROSTRUCTURE AND MECHANICAL PROPERTIES OF LITHIUM DISILICATE-BASED GLASS-CERAMICS FOR DENTAL APPLICATION

Manlika Kamnoy,[1,2] Uraiwan Intatha,[3] Kamonpan Pengpat,[2] Orawan Khamman,[2] Sukum Eittsayeam,[2,*]

[1] Graduate PhD's Degree Program in Materials Science, Faculty of Science, Chiang Mai University, Chiang Mai 50200, Thailand
[2] Department of Physics and Materials Science, Chiang Mai University, Chiang Mai 50200, Thailand
[3] School of Science, Mae FahLuang University, Chiang Rai 57000, Thailand
*e-mail: sukum99@yahoo.com

Abstract:

In this work investigated the effects of CaO content and heat treatment temperature on lithium disilicate-based glass-ceramics. As CaO increased from 0.0 to 10.0 mol.%, the Li_2O-SiO_2-P_2O_5-Al_2O_3-K_2O-CaO glass system were prepared from the glass melt by casting into mold on hotplate. After that the samples were heat treatment by heat treatment temperature were designed by using differential thermal analysis (DTA) result. Our results show that the CaO affects the on heat treatment temperature, the crystallization temperature (T_C) decreased with the increasing CaO content. The phase formation of the glass–ceramics were characterized by X-ray diffraction (XRD) technique, the microstructure were characterized by the scanning electron microscopy (SEM) and the mechanical properties were investigated by Vickers hardness testing. Moreover, the bioactivities of studied samples were studied by using simulated body fluid (SBF) for 7 days in vitro. At the first stage heat treatment at T_{C1}, Li_2SiO_3 was the main crystalline phase of all samples. After the second stage treatment at T_{C2} it was found that the Li_2SiO_3 phase completely disappeared and $Li_2Si_2O_5$ phase formed as the main phase. Moreover, the CaO content and the heat treatment temperature has a significant effect on the microstructure and mechanical properties of lithium disilicate-based glass-ceramics.

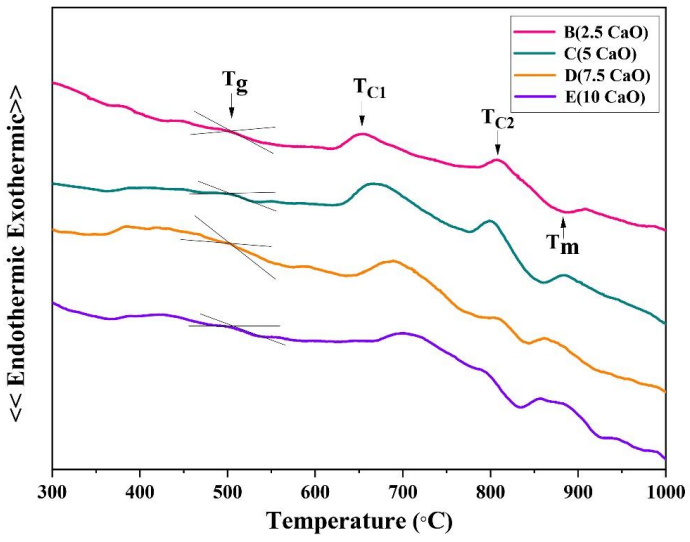

Figure 1. DTA analysis of lithium disilicate glass specimens

SP04_006_PA: COMPUTER SIMULATIONS OF THE SEPARATION OF CH_4/H_2S IN MATERIAL INSTITUT LAVOISIER- 127 (MIL-127)

Tatiya Chokbunpiam[1,*],Siegfried Fritzsche, Tawun Remsungnen

[1] Department of Chemistry and Center of Excellence for Innovation in Chemistry, Faculty of Science Ramkhamhaeng University, Bangkok, 10240, Thailand
[2]University of Leipzig, Institute of Theoretical Physics, Faculty of Physics and Geosciences, Postfach 100920, D-04009 Leipzig, Germany
[3]Integrated Research Group for Energy and Environment, Faculty of Interdisciplinary Studies, Khon Kaen University, Nong Khai Campus, Nong Khai, Thailand
*e-mail: tatiya@ru.ac.th

Abstract:

The chemical composition of natural gas consists of light hydrocarbon i.e. methane and ethane and also impurities *i.e.* carbon dioxide, nitrogen and hydrogen sulfide. The separation and purification costs of light hydrocarbon from impurities gas become a mainly subject for chemical and petrochemical industries. Among the different techniques of separation, the adsorption-based process using porous materials is a promising and cost-efficient technique. One of the porous materials has been synthesized as Material Institut Lavoisier - 127 **(**MIL-127**).** It is a stable rather rigid porous crystal and contains hydrophilic, hydrophobic groups and exhibits two types of pores including a system of channels connecting cages of around 10 Å diameter**.** Because of these structural properties MIL-127 seems to be well suited for storage and separation purposes**.** This work studied adsorption isotherms, adsorption selectivities and diffusion selectivities from computer simulations including Gibbs Ensemble Monte Carlo **(**GEMC**)** and Molecular Dynamics **(**MD**)** of methane and hydrogen sulfide to find the optimal conditions such as temperature and pressure for the separation process.

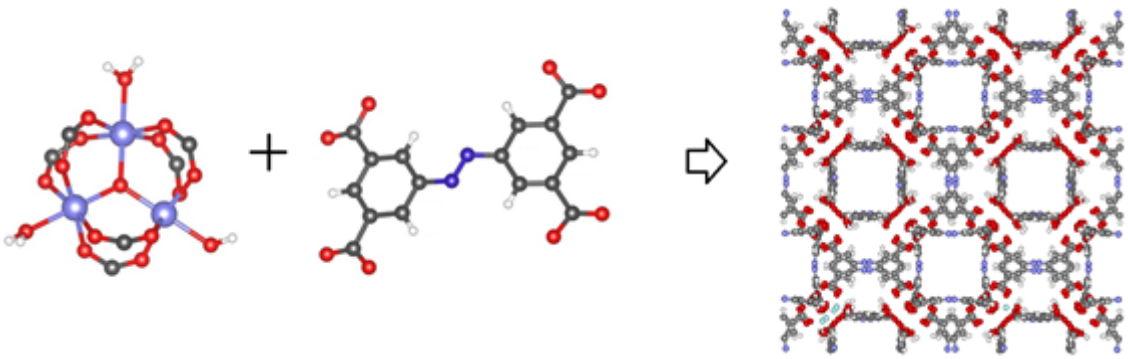

Figure 1. Material Institut Lavoisier - 127 **(**MIL-127**)** structure**.**

SP04_007_PA: ELECTRICAL PROPERTIES OF LEAD-FREE BISMUTH SODIUM TITANATE-STRONTIUM BISMUTH TITANATE PIEZOELECTRIC CERAMICS

Kamonporn Saenkam,[1,2] Pharatree Jaita,[3,4] Gobwute Rujijangul,[1,3,4,5]*

[1]Department of Physics and Materials Science, Faculty of Science, Chiang Mai University, Chiang Mai 50200, Thailand
[2]Graduate school, Chiang Mai University, Chiang Mai, 50200, Thailand
[3]Science and Technology Research Institute, Chiang Mai University, Chiang Mai 50200, Thailand
[4]Materials Science Research Center, Faculty of Science, Chiang Mai University, Chiang Mai 50200, Thailand
[5]Research Center in Physics and Astronomy, Faculty of Science, Chiang Mai University, Chiang Mai 50200, Thailand
*e-mail: rujijanagul@yahoo.com (G. Rujijanagul)

Abstract:

In this research, the effects of sintering condition on phase evolution, electrical properties of the bismuth sodium titanate-strontium bismuth titanate ceramics were investigated. The studied ceramics were fabricated via a solid-state mixed oxide method and sintered at the temperatures ranging from 1100-1175 °C under normal atmosphere for 3 h dwell time with a heating/cooling rate of 5 °C/min. The XRD data revealed the coexisting rhombohedral and tetragonal phases for all sintering tem peratures. The density increased with increasing the sintering temperatures, which resulted in the improvements of dielectric properties. The optimum sintering temperature for the preparation of high-density BNT-SBT ceramic was found to be 1150 °C which showed the maximum density of 5.74 g/cm^3. The ferroelectric result showed that the selected samples have a potential for use as the high energy density devices.

SP04_008_PA: ZEOLITIC IMIDAZOLATE FRAMEWORK ADSORBENTS FOR SEPARATION IMPURITIES FROM NATURAL GAS

Sermsiri Leeporikhon,[1] Tatiya Chokbunpiam[1,*]

[1] Department of Chemistry and Center of Excellence for Innovation in Chemistry (PERCH-CIC), Faculty of Science Ramkhamhaeng University, Bangkok, 10240, Thailand
*e-mail: tatiya@ru.ac.th

Abstract:

Porous materials have power for applications in several industrial processes to be employed for energetic resources and environment protection in terms of gas adsorption, gas separation and catalysis. One class of porous materials namely Zeolitic Imidazolate Frameworks (ZIFs) have attracted more attention nowadays Because, they combing good properties i.e. exceptional chemical and thermal stability. The goal of this work is to compare the performances of ZIF-8, ZIF-67 and ZIF-mixed metal for the natural gas and impurities separation by using computer simulations. Simulations are safe, comparatively cheap and well suited to understand or to forecast properties of gas molecules in ZIFs. They are able to vary conditions and give hints to find promising experiments, thus avoiding less promising ones, and they can help to improve understanding of experimental results. The separation of gases by porous materials relies on two basic phenomena: adsorption and diffusion. Therefore, adsorption can be well treated by Monte Carlo technics, which are used in almost all computational studies about adsorption. Diffusion can be studied by Molecular Dynamics (MD) simulations examining the particle trajectories by use of the Einstein formula.

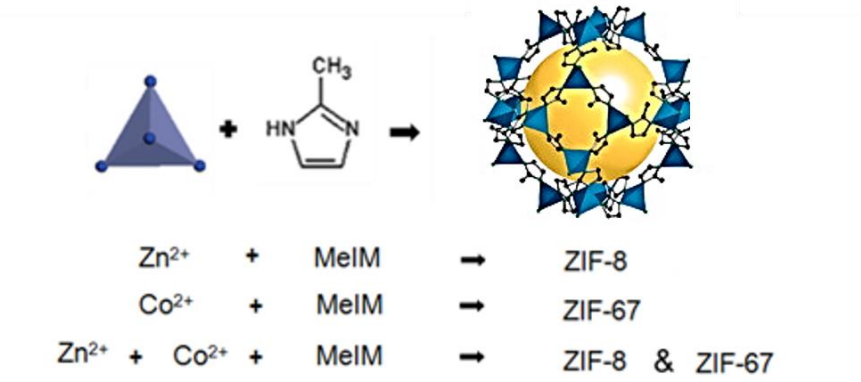

Figure 1. The structures of ZIF-8, ZIF-67 and ZIF-mixed metal that consists of Zn, Co and Zn-Co cluster, respectively and MeIM linker.

SP04_010_OA: RING-OPENING POLYMERIZATION OF MACROLACTONES BY WELL-DEFINED ALUMINUM COMPLEXES

Chutikan Nakornkhet, and Pimpa Hormnirun*

Laboratory of Catalysts and Advanced Polymer Materials, Department of Chemistry and
Center of Excellence for Innovation in Chemistry, Faculty of Science, Kasetsart University,
Bangkok 10900, Thailand
*e-mail: fscipph@ku.ac.th

Abstract:

Over the past two decades, metal-based complexes have been extensively studied as the initiators for the ring-opening polymerization (ROP) of cyclic esters. Many complexes were proved to be excellent initiators. Herein, aluminum complexes **1–8** were used for the ROP of *ω*-pentadecalactone (PDL), 16-Hexadecanolide (HDL), and *ω*-6-hexadecenlactone (6HDL), Complex **1** polymerized all three macrolactones with the highest catalytic activity among other aluminum complexes reported to date. The good molecular weight control and the narrow molecular weight distributions were revealed, indicating of living polymerization character. Random copolymerization of the macrolactones with *ε*-caprolactone (*ε*-CL) using complex **1** was successfully synthesized, and the copolymer microstructure was characterized by NMR spectroscopy technique. The thermal properties of the resulting polymers obtained from the differential scanning calorimetry (DSC) analysis were also discussed.

SP04_011_OA: CONTROLLED RING-OPENING POLYMERIZATION OF CYCLIC ESTER MONOMERS BY TITANIUM(IV) COMPLEXES

Kanokon Upitak and Pimpa Hormnirun*

Department of Chemistry and Center of Excellence for Innovation in Chemistry,
Faculty of Science, Kasetsart University, Bangkok 10900, Thailand.
*email: fscipph@ku.ac.th

Abstract:

Aliphatic polyesters are among the most promising environmentally friendly biopolymers due to their biodegradability and biocompatibility. They can also be directly synthesized from renewable resources. Outstanding examples of polyesters of industrial interest are polylactide (PLA), poly-ε-caprolactone (PCL). The most efficient method to synthesize aliphatic polyesters is the ring-opening polymerization (ROP) of cyclic esters using the single-site homogeneous catalyst. The aims of this work are to synthesize titanium complexes supported by pyrrolylaldiminate ligands and to evaluate these complexes as initiators for the ROP of *rac*-lactide, ε-caprolactone and substituted caprolactones. The pyrrolylaldiminate (**HL_1**–**HL_6**) ligands were prepared by the reaction between pyrrole-2-carboxaldehyde and an equimolar amount of the corresponding primary amines. Treatment of the appropriated ligands with titanium (IV) isopropoxide in the molar ratio of 2:1 afforded titanium complexes (**1**–**6**) in moderate to good yields. All ligands and titanium complexes were characterized by ^{1}H NMR, ^{13}C NMR and mass spectrometry. The polymerizations were carried out in toluene at 70 and 100 °C. The results revealed that all complexes were active initiators for the ROP of cyclic esters. In the case of polylactide, the molecular weights of the resulting polymers were in closed agreement with the theoretical values and the PDI values were narrow. The results from the homonuclear decoupled ^{1}H NMR spectroscopy analysis demonstrated that the microstructures of polylactides produced by all complexes were atactic. In addition, the electronic and steric effects from ligand substituents were found to have a significant impact on the polymerization activity. The polymerization of ε-caprolactone and substituted caprolactone using complexes **1**–**6** were investigated and results were discussed.

SP04_012_PA: SINGLE-SITE ALUMINIUM COMPLEXES IN CATALYSIS OF *rac*-LACTIDE POLYMERIZATION

Sirawan Kamavichanurat and Pimpa Hormnirun*

Laboratory of Catalysts and Advanced Polymer Materials, Department of Chemistry and Center of Excellence for Innovation in Chemistry, Faculty of Science, Kasetsart University, Bangkok 10900, Thailand
*e-mail: fscipph@ku.ac.th

Abstract:

In this work, two series of aluminum complexes supported by bidentate pyrazolyl ethanolate ligands were prepared. Dimethylaluminum complexes (**1a**–**9a**) and monomethylaluminum complexes (**2b**, **3b**, **5b**, **8b** and **10b**) were synthesized, corresponding to the different numbers of ligand coordinated to the aluminum center. All complexes were characterized by ^{1}H NMR spectroscopy. Catalysis of all aluminum complexes towards the ROP of *rac*-lactide in the presence of benzyl alcohol was evaluated. Kinetic studies revealed that the polymerizations mediated by all complexes displayed a first-order dependence on the concentrations of monomer. The effect of the coordination geometry around the aluminum center caused by the presence of one or two nucleophilic ligands on the polymerization activities were also demonstrated. All the polymerizations proceeded in a controlled manner. The molecular weights of PLAs produced by all complexes were closed to the theoretical values.

SP04_013_OF: SYNTHESIS OF NaA ZEOLITE USING WASTEWATER TREATMENT CHEMICAL SLUDGE FROM GLASS FACTORY AND ALUMINIUM WASTE AS Si AND Al SOURCE

Parinya Thongyindee[1], Pimkritsana Chatdee[2], Prapa Sohsalam[1*], Gasidit Panomsuwan[3]

[1]Science and Environmental Technology Program, Faculty of Liberal Arts and Science, Kasetsart University, Kamphaeng Saen Campus, Nakhon Pathom
[2]Biological Science Program, Faculty of Liberal Arts and Science, Kasetsart University, Kamphaeng Saen Campus, Nakhon Pathom
[3]Department of Materials Engineering, Faculty of Engineering, Kasetsart University, 50 Ngamwongwan Road, Latyao, Chatuchak, Bangkok 10900, Thialand
[*]e-mail: faaspps@ku.ac.th

Abstract:

Zeolite are microporous aluminosilicate materials which is used for different industrial purposes such as catalysts, ion exchange, adsorbents and molecular sieves. Most used zeolite are natural zeolite with low purity and some are synthesized from pure chemical which are expensive. Zeolite synthesis by using any kind of wastes are concerned for cost reduction. In this study, Wastewater Treatment Chemical sludge Glass Factory and aluminium waste residues were used as Si and Al source in zeolite synthesis. The optimum synthesis conditions were studied by varying NaOH concentration, temperature, time, Si/Al ratio in hydrothermal method. NaA zeolite was found in condition at temperature, aging, crystallization time, NaOH concentration, Si/Al ratio of 80 °C, 24 hr., 24 hr., 2 M and 3/1 respectively. The characteristic of synthesized zeolite was NaA zeolite that confirmed by XRD and SEM.

Keywords: Zeolite, Chemical sludge, Hydrothermal, Glass factory, Aluminium waste

Introduction:

Zeolite is aluminosilicate compound which porous structure was consisted of small unit of aluminate and silicate. Water and cationic molecule were maintained in structure in various styles over 100 types of zeolite. Zeolite was synthesized from pure chemical material which was also expensive. The cheaper and natural materials have been investigated for zeolite synthesis such as kaolin[1], coal fly ash, Longkou oil shale ash and glass waste. PAC (Polyaluminiumchloride) from tap water production which was similar properties to coal fly ash was used for zeolite synthesis but gave high impurity zeolite.

Zeolites are microporous hydrated aluminosilicate materials that possess small regular internal cavities (< 2 nm) with water molecules and cation (e.g., Na^+, K^+, Ca^{2+}). The structure was porous materials and more different types of zeolite framework structures. Zeolite-like type was microporous and mesoporous materials[2]. For example, sodalite (SOD) zeolite A (LTA) zeolite X or Y (FAU) structures are obtained from the same Composite Building Units (CBUs). They are utilized for different industrial purposes such as catalytic pyrolysis[3], adsorption of heavy metal[4], and water hardness[5]. Although traditional zeolite synthesis methods involve the utilization of pure chemicals, several other materials have been proposed as alternative precursors for zeolite synthesis using alkaline hydrothermal reactions[6]. Other aluminosilicate- based materials including paper sludge ash, rice husk, coal fly ash, glass cullet and chemical sludge have been utilized for zeolite synthesis purposes. Zeolites synthesis methods such as hydrothermal[7], microwave[8], fusion temperature[9] required high temperature of 500 - 700 ° C to melt the raw material in NaOH aqueous solution through hydrothermal method[7]. The mechanism for zeolite synthesis is divided into 3 steps: supersaturation, nucleation and crystallization. There are many factors effected on zeolite synthesis processes such as Si/Al ratio, temperature, aging and crystallization time.

In this study, zeolite synthesis from chemical wastewater treatment sludge from glass production factory was used for silica source and aluminum residue from recycling plant for alumina sources. This chemical sludge was defined as hazardous waste and normally disposed in secured landfill with high management cost. Using this waste in zeolite synthesis may reduce the production cost and hazardous waste management cost. This study optimized the condition in hydrothermal fusion technique for zeolite synthesis. Zeolite was obtained by adjusting the silica to alumina ratio of 1.0, 1.5, 2.0, 2.5, 3.0 at difference temperatures and synthesis times.

Methodology:

Material preparation: The conversion of chemical sludge into zeolite using hydrothermal method required the NaOH solid fusion with chemical sludge powder. 4 g chemical sludge and 2 g NaOH granules were added to crucible fused at 550 °C for 2 h (2°C/min.) in furnace (Carbolite, CWF1300). The fused solid was ground using mortar and pestle to provide a uniform and well-separated powder[10]. A small piece of aluminum residue (1-2 mm.) was added in 150 ml of 4 M NaOH solution. This mixture was stirred for 30 minutes at room temperature in a 500 mL Erlenmeyer flask glass. The suspension was let to settle at room temperature and then filtered through filter paper (Whatman 42). And the supernatant was collected as aluminium solution for further zeolite synthesis. The reactor was made up by using stainless steel 304, Reactor size equal to Heigh = 13 cm, Diameter = 4 cm, Total volume = 163 cm^3. Thermometer and a pressure valve were installed on top of the reactor as shown in Figure 1.

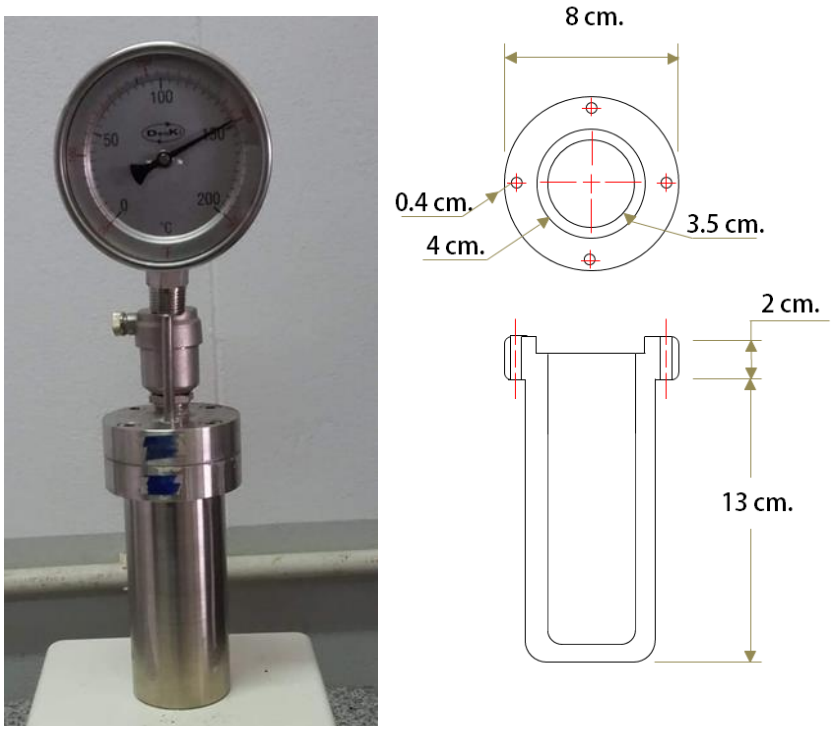

Figure 1. Reactor

Synthesis method: 100 ml of 2 M NaOH solution and 6 g chemical sludge were mixed in a 500 mL Erlenmeyer flask glass and rapid mix for 2 h. On magnetic stirrer at room temperature. The aluminium solution from the preparation step was added by varying amount of 32.5 24.1 23.0 and 19.0 ml to adjust Si/Al ratio to 1.5 2.0 2.5 and 3.0, respectively. The chemical sludge was more favorable to synthesize of low silicon-to-aluminum zeolite, such as A zeolite. The next step, pour mixture into reactor and control reactor temperature in ranged of 80 to 85 °C for 24 h. After cooling down the reactor to room temperature, the mixture was rinse by DI water until pH lower than 9. The products were filtered through filter paper (Whatman 42), washed thrice with the DI water, and then oven dried at 70 °C overnight[7].

Zeolite characterization: The XRD was used to study the mineralogical composition of the solidified bodies. The XRD tests were conducted using Rigaku Miniflex II with Cu Kα radiation source at 40 KV and 30 mA over the range of 10° < 2Θ < 40°. The qualitative measurements of samples were taken using the JADE software. The morphologies of samples were observed by a scanning electron microscope (SEM-Hitachi-SU1000).

Results and discussion:

Chemical composition of chemical sludge before and after fusion process: Chemical sludge from wastewater treatment plant was used as Si and Al source for zeolite synthesis. The composition of chemical sludge was examined by using XRF and result was shown in Table 1.

Table 1. Chemical composition of Chemical sludge

Chemical composition	SiO_2	CaO	Na_2O	Al_2O_3	MgO	CeO_2	Fe_2O_3	etc.
Weight (%)	15.9	4.69	1.32	0.46	0.44	0.40	0.29	0.78

The major component in chemical sludge was SiO_2, This could be a good Si source. Chemical sludge appearance before and after fusion at 550 °C was shown in Figure 1. After fusion, the material surface was smoother and more covered by NaOH while before fusion, the material surface seems rough and plenty of contaminant.

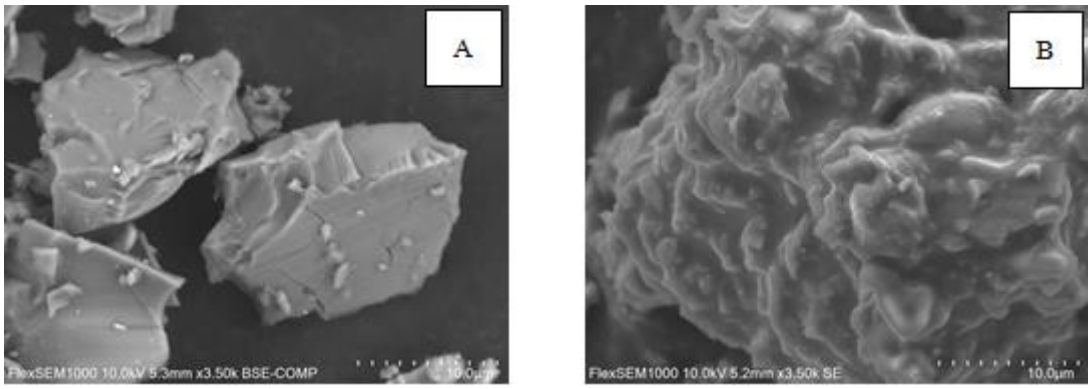

Figure 2. Scanning Electron Microscopy image of Chemical sludge
A) Before B) After at 550 °C

Material fusion at 550 °C could degrade the organic contaminant[11] and gave more Si content in material[6]

Effect of temperature, reaction time and concentration of NaOH on synthesize zeolite: First step of zeolite synthesis was supersaturation of Si and Al. Then in this study, concentration of NaOH was varied to find out the most solubility condition of both Si and Al. The solubility of Si from chemical sludge and Al from aluminium residue were displayed in Table 2.

Table 2. Chemical composition of silica and alumina (Agilent 7500 ICP-OES)

[NaOH], M	2 M	3 M	4 M
Si (mg/L.)	4,819	7,406	9,873
Al (mg/L.)	86.4	62.3	78.3

Increasing of NaOH concentration could enhance Si solubility but Al gave best solubility at 2 M NaOH. The optimum condition for zeolite synthesis was basic condition but this could promote hydroxysodalite formation than zeolite[11]. The zeolite crystal structure which was synthesized at 80 °C, 96 h. and 4M NaOH was compared with the others hydroxysodalite (Figure 3). This result was similar to Ma *et al*[11] but the small amount of zeolite A was also found as shown in SEM in Figure 3. Zeolite NaA crystal size was in range of 51-58 nm (Figure 3-B).

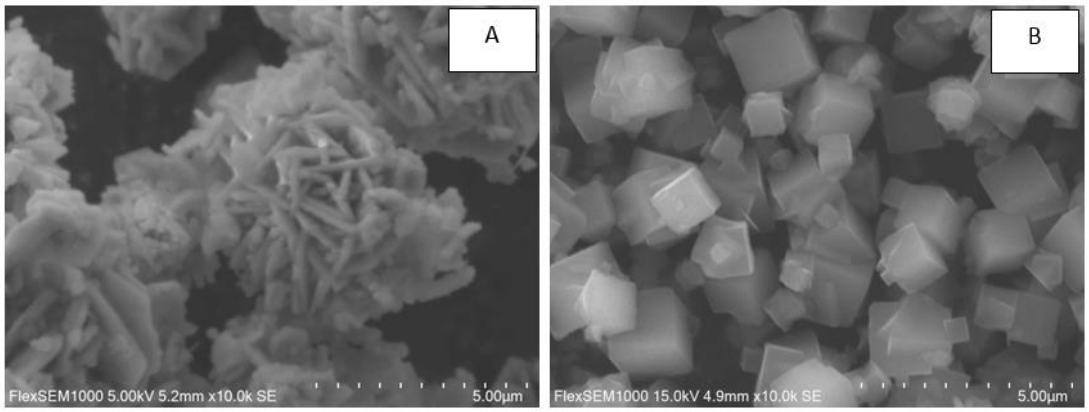

Figure 3. Comparison of Scanning Electron Microscopy of Hydroxysodalite zeolite (4M NaOH, 80°C, 96h.) with NaA-zeolite (2M NaOH, 80°C, 24h.)

Effect of variation of Si/Al ratio: The characterization of product crystal structure was determined by XRD as illustrated in Figure 4. High concentration of NaOH, high temperature and time extension was not the proper condition for zeolite synthesis and performed more amorphous structure, hydroxysodalite. Yuan (2019) discovered that the optimum condition for NaA zeolite was low temperature (80 °C) and less crystallization time (24 h). The small crystal of NaA zeolite was found at 12h of crystallization time. 2M NaOH was suitable for Si soluble and prolong crystallization time helped the bigger crystal zeolite forming. The original ratio of Si/Al of material in this study was 42.5 by mixing chemical sludge solution with aluminium residue solution in ratio of 1:1.

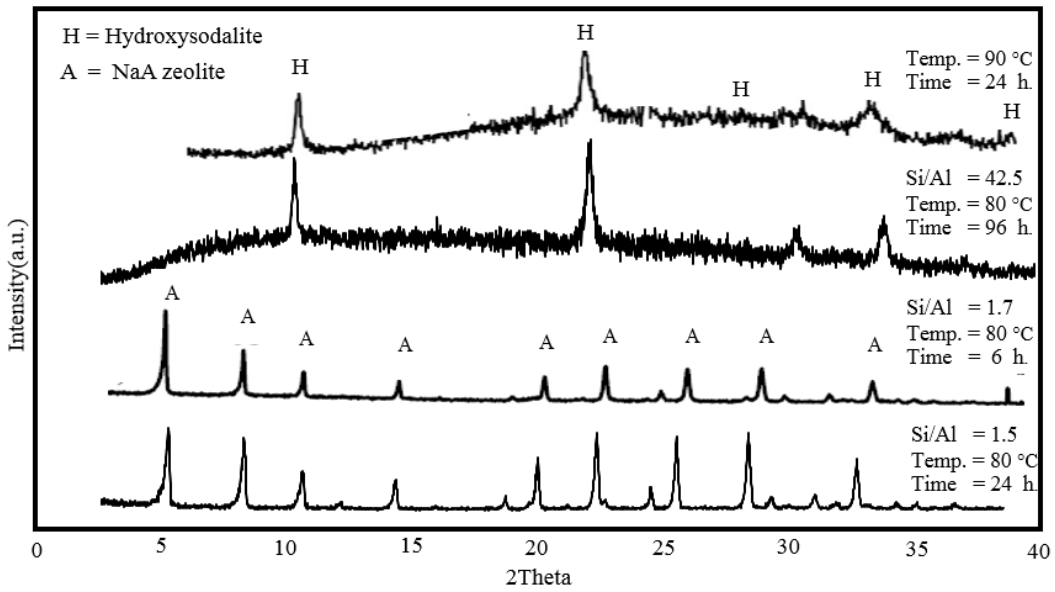

Figure 4. XRD patterns of Hydroxysodalite zeolite (matching with the JCPDS card no. 52-0146, $Na_8Mg_3Si_9O_{24}(Cl.OH)_2$) and NaA zeolite (matching with the JCPDS card no. 39-0222, $Na_{96}Al_{96}Si_{96}O_{384}{\cdot}216H_2O$)

This mixture could synthesize only hydroxysodalite then the ratio of Si/ Al and reaction time was adjusted. After adjust Si/ Al ratio to 1. 5 and 24 hour of reaction time, zeolite could be found at the same temperature. The Si/Al ratio in this study gave the similar result to Hu (2017) but gave higher amount of zeolite A.

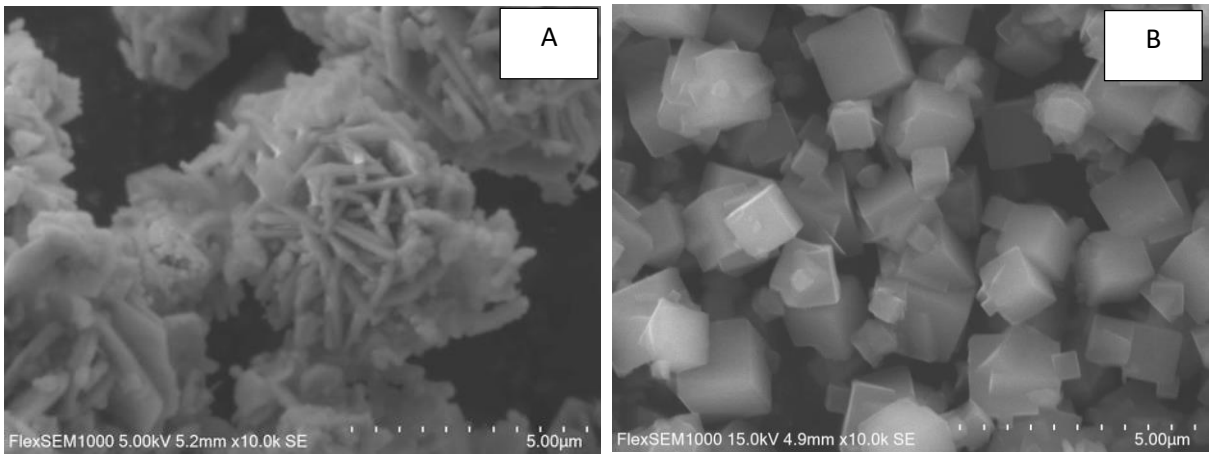

Figure 5. Comparison of Scanning Electron Microscopy of Hydroxysodalite zeolite

(4M NaOH, 80°C, 96h.) with NaA-zeolite (2M NaOH, 80°C, 24h.)

Conclusion:

Waste as chemical sludge from glass factory wastewater treatment plant and aluminium residue could be used as zeolite synthesis. The optimum condition for NaA zeolite synthesis of were 80 °C, aging of 24 hr., 24 h. crystallization time, 2 M NaOH, Si/Al ratio of 1.5, Characteristics of crystals were cubic shapes (size 51-58 nm.) and successful synthesized by fusion-hydrothermal method. The synthesis in bigger scale should be concerned in further work.

References:

1. Dang T H, Chen B H, Lee D J. Optimization of Biodiesel Production from Transesterification of Triolein Using Zeolite LTA Catalysts Synthesized from Kaolin Clay. J. Taiwan Inst. Chem. Eng. 2017;7
2. Jia L, Ma Y, Raad S, Hamieh J, Toufaily T, Hamieh M, Bettahar M, Mauviel G. Catalytic Fast Pyrolysis of Biomass: Superior Selectivity of Hierarchical Zeolites to Aromatics. Green Chemistry. 2017;19(22):5442-59.
3. Zhu T, Zhang X, Han Y, Liu T, Wang B, Zhang Z. Preparation of Zeolite X by the Aluminum Residue from Coal Fly Ash for the Adsorption of VOC. Front Chem. 2019;7:341.
4. Ayalew , Adugna A, Aragaw T A. Removal of Water Hardness Using Zeolite Synthesized from Ethiopian Kaolin by Hydrothermal Method. Water Practice and Technology. 2019;14(1):145-59.
5. Breck D W. Zeolite Molecular Sieves: Structure, Chemistry and Use: Wiley and Sons: London, 1974.
6. Bai S, Ling-mei Z, Zhi-bing C, Chao Zhang, Mo C. Synthesis of Na-X Zeolite from Longkou Oil Shale Ash by Alkaline Fusion Hydrothermal Method. Carbon Resources Conversion. 2018;1(3):245-50.
7. Andres J, Ferrer P, Querol X, Plana F, Juan C. Zeolitisation of Coal Fly Ashes using Microwaves. Process Optimization. Int. Ash Utilization Symposium, Center for Applied Energy Research. 1999:94-100.
8. Kumar P, Mal N, Oumi Y, Yamanaa K, Sanoc T, J. Mater. Chem. 2001;11:3285.
9. Majdinasab A R, Yuan Q. Microwave Synthesis of Zeolites from Waste Glass Cullet Using Indirect Fusion and Direct Hydrothermal Methods: A Comparative Study. Ceramics Int. 2019;45(2):2400-10.
10. Neeranutk et al., Synthesis of NaA Zeolite Using Surathanee''s Ball Clay as Si and Al Source And Using Secondary Growth Technique. Ramkhamhaeng R. J.2013(2).
11. Ma Y, Tong W, Zhou H, Steven L, Suib. A review of zeolite-like porous materials. Microporous and Mesoporous M. 2000;37:243–252.
12. Cruz C, Luis A C, Kraslawski A. Scaling Problems and Control Technologies in Industrial Operations: Technology Assessment. Separation and Purification Technology. 2018;207:20-27.

SP04_014_OA

SP04_014_OA: SELF-ASSEMBLED COPPER–TRIAZOLE CLUSTERS: SYNTHESIS AND CATALYTIC APPLICATIONS

Preeyanuch Sangtrirutnugul,[1,*] Nuttaporn Krittametaporn,[1] Mohan Gopalakrishnan, Nobuto Yoshinari,[2] Takumi Konno[2]

[1]Center of Excellence for Innovation in Chemistry (PERCH-CIC), Department of Chemistry, Faculty of Science, Mahidol University, Bangkok, 10400, Thailand
[2]Department of Chemistry, Graduate School of Science, Osaka University, Toyonaka, Osaka 560-0043, Japan
*e-mail: preeyanuch.san@mahidol.ac.th

Abstract:

The rational design of new ligands can lead to self-assembled, molecular metal clusters with interesting catalytic and magnetic behaviors. In this presentation, a simple synthetic protocol for trinuclear copper(II) clusters supported by triazole–alkoxy-based ligands (*N*,*O*,*N*) will be discussed. Particularly, treatments of bis(triazolyl)methanol (Hbtm) and (1-benzyl-1*H*-1,2,3-triazol-4-yl)(pyridin-2-yl)phenylmethanol (Hpytm) with copper substrates afforded the trinuclear copper(II) cluster, $[Cu^{II}_3(\mu\text{-}\mu^3\text{-}N,O,N\text{-L})_3]^{3+}$ (L = btm, pytm) as a building blocks. For the trinuclear copper-bis(triazolyl) clusters, catalytic activities toward aerobic oxidation of benzyl alcohol to benzaldehyde were investigated and compared with the related mononuclear copper-triazolyl complex. On the other hand, for the less sterically hindered pytm ligand, more versatile structures resulting from anion template effect were obtained.

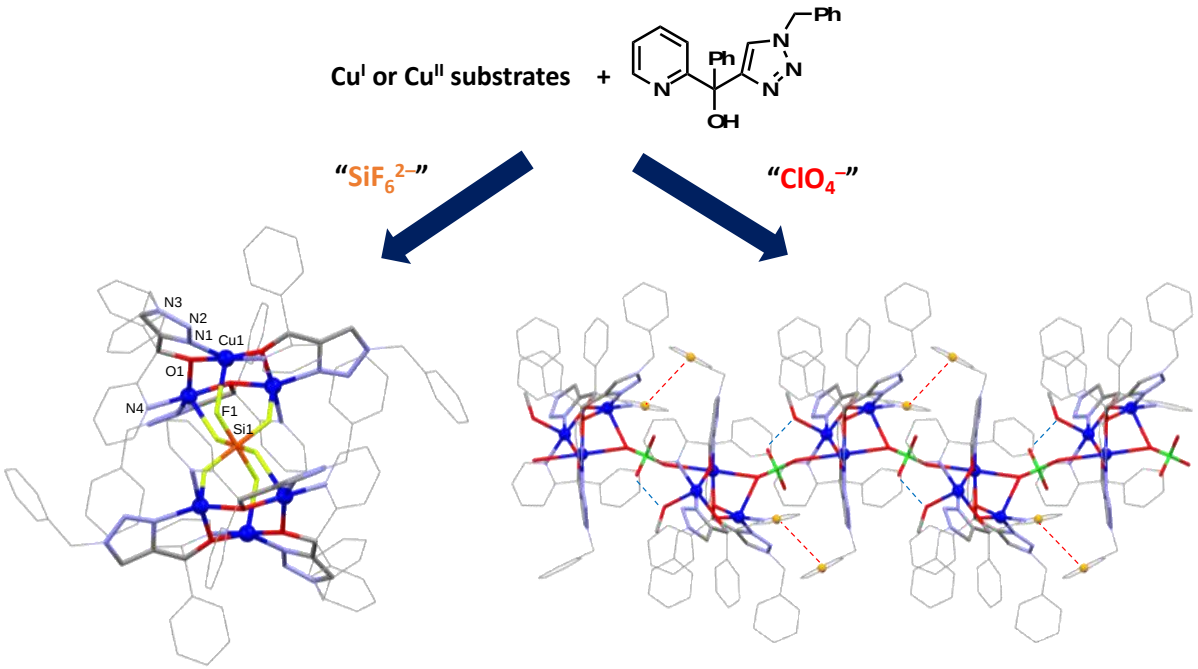

Figure 1. Self-assembled copper–triazole clusters

SP06_001_OA: GEOTHERMAL RESOURCES IN SOUTHERN THAILAND – A POSSIBLE CHOICE FOR RENEWABLE ENERGY

Wipada Ngansom,[1*] Helmut Duerrast,[2]

[1] Department of Physics, Faculty of Science, Ramkhamhaeng University, Bangkok, Thailand
[2] Department of Physics, Faculty of Science, Prince of Songkla University, Hat Yai, Thailand
*e-mail: wipada.n@rumail.ru.ac.th

Abstract:

Depending on its characteristics of geothermal resources, geothermal hot springs can be used for generating clean electricity. Altogether 30 hot springs located in Chumphon, Ranong, Surat Thani, Phang Nga, Krabi, Trang, Phatthalung and Yala Provinces have been taken into investigation. The Geological characterization technique and the suitable exploration methods are relatively studied with their 1D and 2D resistivity and Magnetotellurics (MT) for geophysics, geochemistry of cations and anions, isotopes and REEs, and geothermometers as well as economic aspects for geothermal power plant. Based on their geothermal characteristics data of each resource they can be classified into two groups by their working temperature ranges of below and above 120°C. The results concluded that the four hot springs with >120 °C geothermal reservoir consisted of 4 provinces (RN6, SR7, PG1, and YL1). In this group it can provide the electricity generating in the ranges of 100s–1,000s MW via an enhanced geothermal system (EGS) over deep granite of 1-5 km depth. On another group of geothermal reservoirs with temperature below 120°C, the results could be concluded that the lower temperature geothermal reservoirs from each ten hot springs (RN1, RN2, RN3, RN4, SR3, SR6, SR8, SR9, TR1 and ST1) could provide electric generating of 3-5 MW.

SP06_002_OA: PASSIVE HEAT MITIGATION POSSIBILITY USING METEOROLOGICAL DATA ANALYSIS FOR BUILDING APPLICATION IN THE TROPICS

Waraporn Rattanongphisat*

Energy Technologies Building Laboratory, Department of Physics, Naresuan University, Phitsanulok, Thailand
*e-mail: waraporn@nu.ac.th

Abstract:

Building energy consumption in the tropics (classified by Koppen as A with the definition of equatorial rainforest, fully humid for the area with a minimum temperature of 18 °C or above and the precipitation greater than 60 mm) rather high due to the increase number of cooling requirement, for human comfort, from mechanical systems powered by electricity as to overcome the increasing global temperature. On the contrary, passive techniques call for nearly non-conventional energy that attract the built environment design for energy saving. This paper aims to investigate the possibility of passive heat mitigation in Phitsanulok, Thailand as a city in the tropics. Passive techniques rely very much on weather parameters thus the meteorological data such as air temperature, relative humidity, wind speed and direction, and solar radiation were employed in the regression analysis. Recorded data format of 3 hours period between 2014 and 2016 retrieved from the meteorological department in Phitsanulok. Wind direction and speed in combination with building orientation were used to evaluate ventilation potential. Natural ventilation period depended on outdoor temperature, relative humidity and wind speed was calculated and presented in the number of hours. Preliminary calculation showed the outdoor temperature lower than 26°C of about 2365 hours that was one-fourth of the year. Sun path diagram was simulated and used to demonstrate shading effect regarding to building orientation and envelope, and surrounding objects. The angle of the sun differs from one location to another and varies throughout the year; therefore, the simulated result could assist the design of awning, hanger or curtain roll on the fenestration. Cooling degree day, the number of hours the temperature above comfort temperature, in conjunction with the number of hours for natural ventilation were used to determine the cooling energy reduction from the moist air sensible cooling (the enthalpy difference). The utilization of natural ventilation indicated the period when the mechanical cooling might not be required thus cut down the building energy consumption. Similarly, the effect of shading prevent heat from the direct sunlight entering to the building so further reduction of energy demand can be expected.

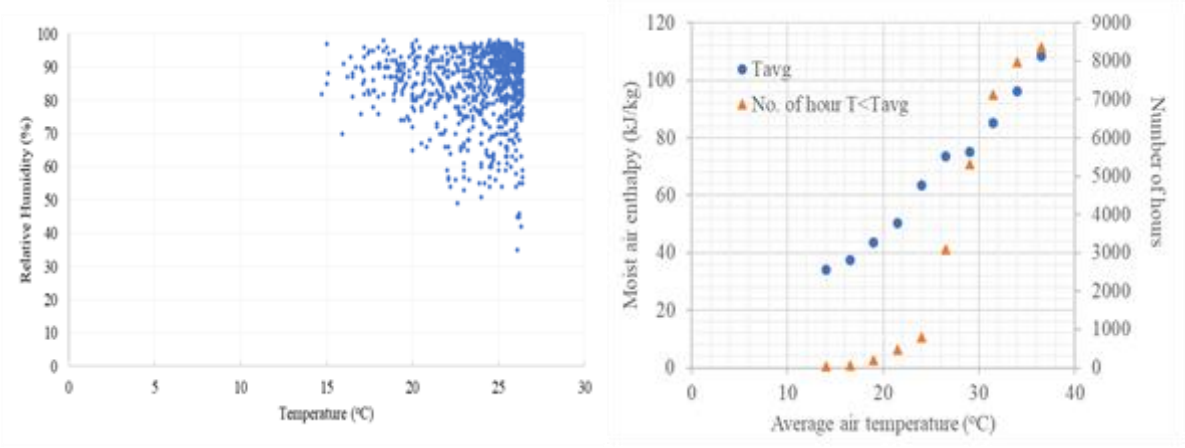

Figure 1 Temperature versus relative humidity when the temperature lower than 26 °C (left), number of hours when temperature lower than average and moist air enthalpy (right)

SP06_003_OA: ACHIEVING 100% RENEWABLE ELECTRICAL ENERGY FOR SOUTHERN THAILAND

Helmut Duerrast*

Division of Physical Science, Faculty of Science, Prince of Songkla University, Hat Yai, 90110, Thailand
*e-mail: helmut.j@psu.ac.th

Abstract:

Climate change is the greatest challenge mankind is facing, now and for decades to come. CO_2 and methane are the main greenhouse gases from combustions of coal, oil, and natural gas, which are responsible for the ongoing increase in global surface temperatures. The Paris Climate agreement set a value of maximal 1.5 °C increase in comparison to preindustrial eras. Currently, an increase of 2-3 °C until the end of the century is more likely, with all the consequences in land use, food production, biodiversity, and livability of cities. A decarbonization of the main sectors, energy production, transport, industrial production, and cooling/heating with the todays technical solutions is possible and with related economic decisions achievable. For Southern Thailand 100%-renewable electrical energy production is not only feasible, but already economically viable and decreasing in cost every year, with mainly solar photovoltaic, some wind, biogas, biomass, hydro, and geothermal resources. Such transformation would go along with decentralization in energy production and distribution networks. However, currently four blocks of combined 3,700 MW electricity generating capacity are planned for Songkla, to be fed with coal and natural gas. Any further development in this direction however would increase the current carbon foot print of Thailand and would deprive next generations of their self-determined energy policies.

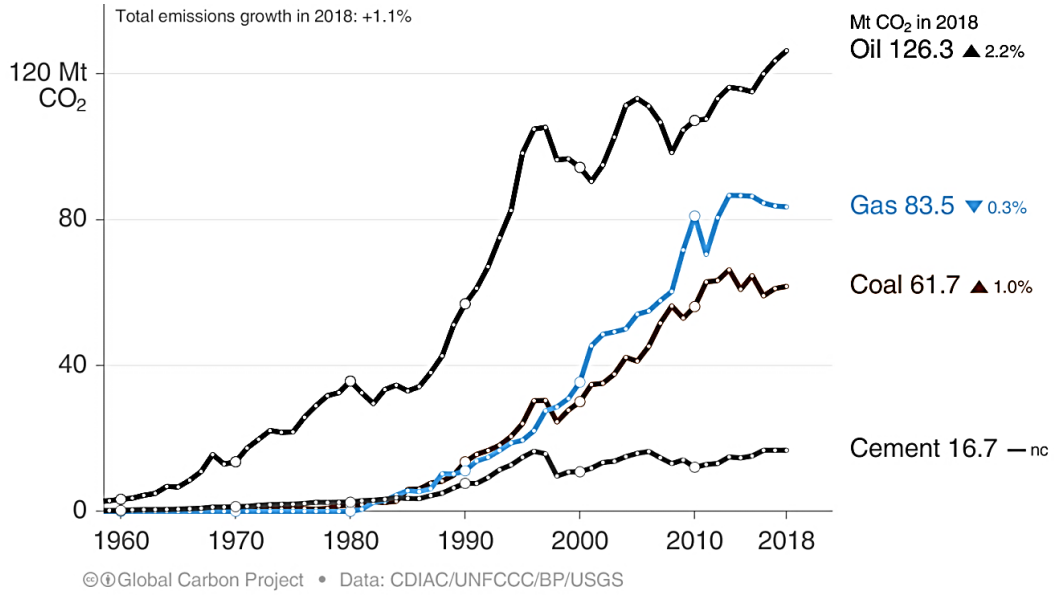

Figure 1. Annual fossil CO_2 emissions in Thailand in Mt CO_2 with growth rates of each sector in percent for 2018; the total emission growth in 2018 was +1.1% (from Global Carbon Project, 2020; used with permission of the Global Carbon Project under the Creative Commons Attribution 4.0 International License). Thailand's global CO_2 contribution for the same year stands by 0.78% (global rank #22).

SP06_004_OF: OILGAE CULTIVATION IN MUNICIPAL WASTEWATER

Fongkul Palichareonpol[1], Pennapa Putson[2] and Prapa Sohsalam[1*]

[1]Science and Environmental Technology Program, Faculty of Liberal Arts and Science,
Kasetsart University, Kamphaeng Saen Campus, Nakhon Pathom
[2]Biological Science Program, Faculty of Liberal Arts and Science,
Kasetsart University, Kamphaeng Saen Campus, Nakhon Pathom
[*]e-mail : faaspps@ku.ac.th

Abstract:

The cultivation of oilgae in municipal wastewater was aimed to study for wastewater treatment and oil production. Wastewater quality was analyzed before and after *Chlorella vulgaris* cultivation. Algae biomass production and lipid content were investigated. The algae was cultivated in diluted wastewater at 20% 40% 60% 80% and 100% for 10 days without nutrient adding. After 10 days of cultivation, the pollutants as COD, BOD_5, ammonia, phosphorus, suspended solids and total dissolved solid were best removed for 50.00%, 86.60%, 58.67%, 77.77%, 89.76% and 41.49%, respectively in undiluted wastewater. The biomass of *C. vulgaris* was also highest in undiluted wastewater which was 0.247 g dry weight/L. Comparison of extraction method between sonication and without sonication was studied. Both biomass filtrate and filtered biomass after sonication were lipid extracted. After sonication, most lipid molecule was released into the solution, this lipid was accounted for 36% DW. The advantages of this oilgae cultivation were 1) no wastewater dilution, 2) biofuel production as oilgae biomass and 3) low aeration rate. The batch cultivation could be guideline for oilgae cultivation in continuous municipal wastewater treatment system by using slow agitation with 10 days of hydraulic retention time.

Introduction:

Population growth are gradually increase result to rapidly expand of urban. This effect on a high volume of sewage and wastewater which should be properly treated before discharge. The wastewater from household, restaurant, fresh market and other activity can be treated by using many methods to achieve discharge wastewater quality standard [1] Wastewater treatment plant operation in urban area contains a high capital and operation cost due to less area and must maintain the high treatment efficiency. Sewage pollutant properties after passing grease trap is 110-400 mg/L of BOD_5, 25-50 mg/L of ammonia and 4-15 mg/L phosphorus[2]. High plant nutrients as ammonia and phosphorus was observed in sewage then alternative propose of wastewater treatment was concerned by trial to cultivate single cell algae for plant nutrient removal and wastewater treatment. Wastewater treatment and cooperated with algae biomass production is Eco-friendly method. Algae biomass can be used as animal feed, bioplastic or biofuel instead of bacterial cell degradation in conventional way of wastewater treatment[3,4]. Several microalgae species can grow well on nonpotable water (brackish, wastewater, and seawater); there is a possibility that biofuel production can be coupled with one of these systems in future. This coupling does not compete for arable land which can be used for agricultural purpose and also for eliminating the use of freshwater resources. The production of biofuels from algae can be coupled with flue gas CO_2 mitigation, wastewater treatment, and production of high-value chemicals [5,6] Lacking of fuel in nowadays is focused, many sources of oil production algae or oilgae is also investigated for low cost and high biomass production. Many strain of oilgae such as *Chlorella* sp., *Scenedesmus* sp., *Botryococcus braunii, Micractinium* sp., *Actinastrum* sp, *Hindaki* sp. and *Auxenochlorella protothecoides* were cultured in many kinds of wastewater. They produced lipid concentration of 9.0-35.7 % dry weight [7,8,9,10,11,12,13,14,15,16]. The high oil content of 35.74% could be observed in *Scenedesmus obliquus* cultivation in panel photo-bioreactors which was high capital cost[16]. Lipid production efficiency was depend on algae strain, nutrient and cultivation environment (nutrient variation, light cycle, circulation rate, temperature), harvesting method (flocculation, filtration, flotation,

centrifugation) and extraction method (sonication, homoginisation, grinding, bead beating, freezing)[17,18,19,20,21,22,23,24,25,26,27,28,29,30,31,32]. The cultivation of algae in wastewater in most of recent researches was done in diluted wastewater which was not applicable in pilot scale. Adding of plant nutrients such as NH_4Cl, KH_2PO_4, Urea, $NaNO_3$ and other substances to enhance the biomass or lipid production was expensive.

Chlorella sp. is oilgae strain which can grow well in Thailand climate and also grow in wastewater. But the low oil concentration was still be the obstruction for further development to be a biodiesel material. In this study, *Chlorella vulgaris* was cultivated in sewage without nutrient adding for wastewater quality improvement and oil production. Oil extraction method was also studied to increase oil production from this oilgae.

Material and method

1. Sewage collection

Sewage was weekly collected from Kasetsart university dormitory canal which was passed the grease trap but was not be treated by aerobic pond. This dormitory was 200 rooms per building and the wastewater quality was shown in Table 1. The sewage was sieved through 90 micron-pore fabric then preserved at 4^{o}C refrigerator before examined or conduct the experiment.

2. Wastewater quality examination

The wastewater was examined for pH on site using pH meter. COD, BOD_5, ammonia, nitrate, phosphate, suspended solid (SS) and total dissolved solid (TDS) were analyzed follow water and wastewater examination standard method [34]The wastewater quality was examined before and after cultivation with *Chlorella vulgaris* for wastewater treatment efficiency assessment.

3. Oilgae cultivation for wastewater treatment and biomass production

Chlorella vulgaris, the oilgae strain was brought from Aquatic animal feed research and development division, Bangkok, Thailand and cultivated in sewage at various dilution. The oilgae cultivated in diluted wastewater which were diluted with distilled water at 20%, 40%, 60%, 80% and 100% v/v compared with cultivated in BG-11 medium [35] Twenty-mL of inoculum algae at cell concentration of 5 x 10^5 cell/ml was used in 300 mL flask at room temperature. Light cycle of 12/12 hour was conducted by using 6 LED lamps which could provide 4,000 LUX [36] After 10 days of cultivation, algae biomass was filter separated by 5 micron fabric filter then oven dried at 80^{o}C for 24 hours and weighed for dry biomass calculation [23] The filtrate was analyzed for pH, COD, BOD_5, ammonia, nitrate, phosphate, suspended solid (SS) and total dissolved solid (TDS). The wastewater treatment efficiency was assessed by compare the wastewater quality between influent and effluent.

4. Lipid extraction method

4.1 Lipid extraction method from dry weight

The best condition from wastewater treatment by using *C. vulgaris* was conducted in this part in 30L PET reactor. Recirculation system was installed by using small submerge aerator and adjust agitation at slow mixing (20 rpm) to prevent biomass flocculation. Algae biomass was weekly harvested and separated by centrifugation at 8,000 rpm for 2 minutes then oven dried at 80^{o}C 17 hours. Dry biomass was grinded and mixed with hexane at ratio of 10 g dry weight/10 ml hexane. This mixture was shaken for 2 minutes and filter through Whatman no.1 filter paper. The filtrate was evaporated on water bath at 70^{o}C until dry. Evaporating dish was weighed and examined for lipid content After algae weekly harvesting, the wastewater in 30L reactor was half replace by fresh wastewater. This could enhance algae growth for the next week.

4.2 Wet Lipid extraction method

The conventional lipid extraction method gave low lipid content. Modification of sonication was conducted by using 50 g of biomass solution from cultivation reactor then sonicated at 2 kHz for 10 and 20 minutes[37,38] The sonicated sample was divided to 2 parts (1) filtered biomass and (2) filtrate, these samples were lipid extracted followed 4.1.

5. Statistical analysis

All experiments were done triplicate and analyzed by using One-way ANOVA, Duncan's New Multiple Range Test (DMRT) at confidence level of 95%. SPSS program version 23 was used in this research.

Result and Discussion

1. Wastewater treatment and biomass production

The purposes of this research were studied for using algae for sewage treatment and biomass production. Wastewater from Kasetsart university dormitory quality was analyzed as shown in Table 1. Most parameter could not achieve the discharge standard including COD, BOD_5, suspended solid, total dissolved solid and need the water quality improvement. Plant nutrients as ammonia, nitrate and phosphorus was obtained in this sewage but slightly low for algae requirement [39] In raining day, the water quality was diluted then wastewater collection was avoided after rain.

Table 1 Wastewater quality before treatment

Parameter	Average value ± SD	Discharge standard [1]
pH	7.88 ± 1.53	5.5-9.0
COD (mg/L)	144.5 ± 23.2	<120
BOD_5 (mg/L)	104.5 ± 17.6	<20
Suspended solid (SS) (mg/L)	70.55 ± 6.41	<50
Total dissolved solid (TDS) (mg/L)	503.7 ± 45.8	<500
Ammonia (mg/L)	10.3 ± 1.5	<35 (as TKN)
Nitrate (mg/L)	0.78 ± 0.06	-
Phosphate (mg/L)	0.45 ± 0.10	-

Sewage was diluted at 5 dilution for optimization of algae growth compare with cultivation in algae medium as BG11 and wastewater. Treatment efficiency by *C. vulgaris* and biomass production were shown in Table 2. The highest biomass was observed in 100% of wastewater which was higher than cultivation in BG11. *C. vulgaris* could grow well in ammonia-N medium while nitrogen source in BG11 was nitrate [40,41] Increasing of wastewater ratio especially in 100% of wastewater could promote *C. vulgaris* growth due to higher plant nutrient. Then wastewater dilution was not necessary for *C. vulgaris* biomass production. COD, BOD_5, TDS removal showed better treatment efficiency ($p<0.05$) related to increasing of wastewater ratio because the organic matter and TDS treatment was removed by bacteria in wastewater. During daytime, plant photosynthesis was occurred resulted to oxygen emission into water body. Phosphorus and ammonia were converted to phosphate and nitrate by oxygen adding in daytime [4,42,43,44,45]Microalgae can be efficiently used to remove significant amount of nutrients because they need high amount of nitrogen and phosphorus for protein (45–60% of microalgae dry weight), nucleic acid, and phospholipid synthesis [46,16,47]

Table 2 Wastewater treatment efficiency by *C. vulgaris* and biomass production in various wastewater dilution

Parameter	Treatment efficiency (%)					
	BG11	20%	40%	60%	80%	100%
COD	-	7.40[a]	21.30[b]	24.67[ab]	39.81[bc]	50.00[c]
BOD_5	-	49.76[a]	26.79[b]	21.85[b]	58.13[a]	86.6[c]
SS	-	56.69[a]	66.54[a]	54.07[a]	63.58[a]	89.76[b]
TDS	-	14.09[a]	24.83[ab]	33.15[b]	38.64[bc]	41.49[c]
Ammonia	-	89.21[a]	81.06[a]	69.03[b]	61.98[b]	58.67[b]
Nitrate	-	n/a	n/a	n/a	n/a	n/a
Phosphate	-	n/a	n/a	n/a	54.28[a]	77.77[b]
Biomass (g DW/L)	0.084[a]	0.029[b]	0.080[c]	0.119[d]	0.166[e]	0.248[f]

Remark: 1) The difference superscript letter in each row showed the different between wastewater dilutions
2) The letter n/a means no treatment efficiency

2. Comparison of Lipid extraction method

Biomass oven dried and grinding were conducted in conventional lipid extraction which was high operation cost and waste time (Ncha et al, 2014). In this study, microalgae cell disruption could be achieved by grinding (conventional method) and sonication. Both filtered biomass and filtrate were lipid extracted base on lipid molecule was emitted from algae cell and lipid content from each condition were illustrated in fig.1. Extracted lipid in all conditions were 0.03, 3.04, 1.90, 32.13 and 36.07 for dry biomass without sonication, fresh biomass with 10 minutes sonication, fresh biomass with 20 minutes sonication, filtrate from 10 minutes sonication and filtrate from 20 minutes sonication, respectively.

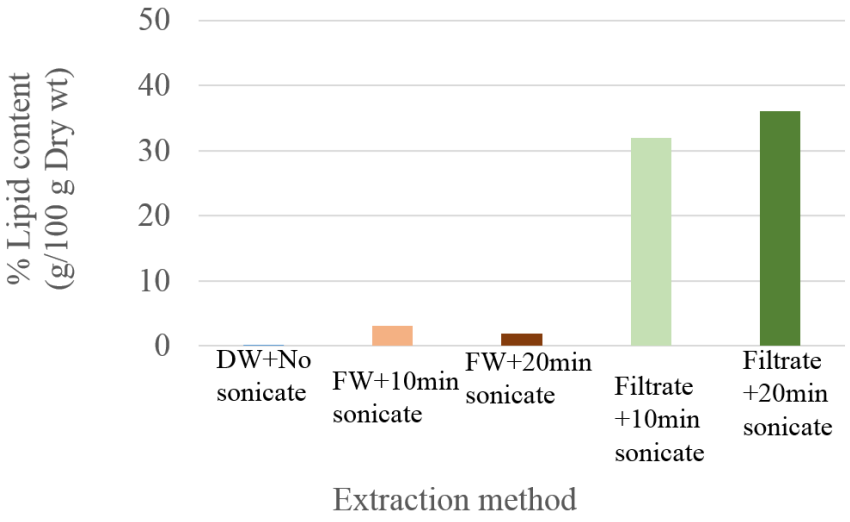

Figure 1. Comparison of lipid extraction method between no-sonication and sonication

Lipid content in medium solution was 10-12 times of lipid content in filtered biomass. Extension of sonication time was not significantly effected on lipid content in filtered biomass or filtrate ($p>0.05$). Lowest lipid content was found in no-sonication and dry sample because
lipid maybe decomposed during oven dry and most lipid in algae cell was not properly disrupted. After sonication of algae fresh biomass, lipid content was higher due to lipid in algae cell was disrupted and suspended in the solution. Wet lipid extraction without acidified could provide 36% lipid which was lesser than acidified extraction 79% but gave low cost and less pollutant. [49] reported that 1L biodiesel was produced consuming nutrient between 0.23 and 1.55 kg nitrogen and 29–145 g of phosphorus depending on the cultivation conditions for microalgae.

Conclusion:

The coupling of microalgae cultivation with wastewater might provide possibility of phytoremediation, CO_2 sequestration, and low cost nutrient supply for the algal biomass utilization. Hence, wastewater treatment could achieve the discharge standard of Thailand but filtration of microalgae cell still be need to reduce suspended solid before discharge. Then, oilgae (*Chlorella vulgaris*) cultivation in wastewater for biomass production will be better way that could gave wastewater treatment and harvest oilgae biomass to remove suspended solid and to produce biofuel. Sonication for 10-20 minutes could enhance lipid extraction and most lipid was maintained in biomass filtrate. This batch type cultivation could be scaled up to continuous system with 10 days of hydraulic retention time without nutrients adding. Only slow agitation at shallow water level will be conducted for biomass settling prevention and provide adequate light to promote biomass production.

Reference:

1. Pollution Control Department (2535) Building discharge standard. http://www.pcd.go.th/info_serv/reg_std_water04.html?fbclid=IwAR2BUYDBR9ONoGdj_psoR7w9Eggl1dV5_OIRR4wmCvtwJyn86rwctfNioO0#s3 on August 29 2020.
2. Pollution Control Department (2535) Domestic Wastewater. http://www.greenandcleansolution.com on August 29 2020.
3. Norsker, N. H., M.J.Barbosa, M. H. Vermuea and R.H. Wijffelsa. 2011. Microalgal production -A close look at the economics. Biotechnology Advances. 29: 24- 27.
4. P. J. McGinn, K. E. Dickinson, S. Bhatti, J. Frigon, S. R. Guiot, and S. J. O'Leary, "Integration of microalgae cultivation with industrial waste remediation for biofuel and bioenergy production: opportunities and limitations," *Photosynth Research*, vol. 109, pp. 231–247, 2011.
5. J. R. Benemann, J. C. van Olst, M. J. Massingill et al.,"The controlled eutrophication process: using microalgae for CO_2 utilization and agricultural fertilizer recycling,"in *Greenhouse Gas Control Technologies—6th International Conference*, pp. 1433–1438, Pergamon, Oxford, UK, 2003.
6. A. Demirbas, "Use of algae as biofuel sources," *Energy Conversion and Management*, vol. 51, no. 12, pp. 2738–2749, 2010.
7. H. Cheung and M. H. Wong, "Properties of animal manures and sewage sludges and their utilization for algal growth," *Agricultural Wastes*, vol. 3, no. 2, pp. 109–122, 1981.
8. N. F. Y. Tam and Y. S. Wong, "The comparison of growth and nutrient removal efficiency of *Chlorella pyrenoidosa* in settled and activated sewages," *Environmental Pollution*, vol. 65, no. 2, pp. 93–108, 1990.
9. S. Sawayama, T. Minowa, Y. Dote, and S. Yokoyama, "Growth of the hydrocarbon-rich microalga Botryococcus braunii in secondarily treated sewage," *Applied Microbiology and Biotechnology*, vol. 38, no. 1, pp. 135–138, 1992.
10. D. Voltolina, B. Cordero, M. Nieves, and L. P. Soto, "Growth of *Scenedesmus* sp. in artificial wastewater," *Bioresource Technology*, vol. 68, no. 3, pp. 265–268, 1999.
11. I. Woertz, A. Feffer, T. Lundquist, and Y. Nelson, "Algae grown on dairy and municipal wastewater for simultaneous nutrient removal and lipid production for biofuel feedstock," *Journal of Environmental Engineering*, vol. 135, no. 11, pp. 1115–1122, 2009.

12. S. Chinnasamy, A. Bhatnagar, R. W. Hunt, and K. C. Das, “Microalgae cultivation in a wastewater dominated by carpet mill effluents for biofuel applications,” *Bioresource Technology*, vol. 101, no. 9, pp. 3097–3105, 2010.
13. W. Zhou, Y. Li, M. Min, B. Hu, P. Chen, and R. Ruan, “Local bioprospecting for high-lipid producing microalgal strains to be grown on concentrated municipal wastewater for biofuel production,” *Bioresource Technology*, vol. 102, no. 13, pp. 6909–6919, 2011.
14. W. Zhou, Y. Li, M. Min et al., “Growing wastewater-born microalga Auxenochlorella protothecoides UMN280 on concentrated municipal wastewater for simultaneous nutrient removal and energy feedstock production,” *Applied Energy*, vol. 98, pp. 433–440, 2012.
15. R. A. Abou-Shanab, M. K. Ji, H. C. Kim, K. J. Paeng, and B. H. Jeon, “Microalgal species growing on piggery wastewater as a valuable candidate for nutrient removal and biodiesel production,” *Journal of Environmental Management*, vol. 115, pp. 257–264, 2013.
16. Ling, Y., L. Sun, S. Wang, C. Lin, Z. Sun and Z. Zhou. 2019. Cultivation of oleaginous microalga *Scenedesmus obliquus* coupled with wastewater treatment for enhanced biomass and lipid Production. Biochemical Engineering..162-169 : 148
17. R. M. Knuckey, M. R. Brown, R. Robert, and D. M. F. Frampton, “Production of microalgal concentrates by flocculation and their assessment as aquaculture feeds,” *Aquacultural Engineering*, vol. 35, no. 3, pp. 300–313, 2006.
18. A. Papazi, P. Makridis, and P. Divanach, “Harvesting *Chlorella minutissima* using cell coagulants,” *Journal of Applied Phycology*, vol. 22, no. 3, pp. 349–355, 2010.
19. J. Morales, J. de la Noüe, and G. Picard, “Harvesting marine microalgae species by chitosan flocculation,” *Aquacultural Engineering*, vol. 4, no. 4, pp. 257–270, 1985.
20. D.Vandamme, I. Foubert, B. Meesschaert, and K. Muylaert, “Flocculation of microalgae using cationic starch,” *Journal of Applied Phycology*, vol. 22, no. 4, pp. 525–530, 2010.
21. G. Shelef, A. Sukenik, and M. Green, *Microalgae Harvesting and Processing: A Literature Review*, Technion Research and Development Foundation, Haifa, Israel, 1984.
22. N. Uduman, Y. Qi, M. K. Danquah, G. M. Forde, and A. Hoadley, “Dewatering of microalgal cultures: a major bottleneck to algae-based fuels,” *Journal of Renewable and Sustainable Energy*, vol. 2, no. 1, Article ID 012701, 15 pages, 2010.
23. S. O. Gultom and B. Hu, “Review of microalgae harvesting via co-pelletization with filamentous fungus,” *Energies*, vol. 6, pp. 5921–5939, 2013.
24. J. Kim, G. Yoo, H. Lee et al., “Methods of downstream processing for the production of biodiesel from microalgae,” *Biotechnology Advances*, vol. 31, no. 6, pp. 862–876, 2013.
25. S. F. Sing, A. Isdepsky, M. A. Borowitzka, and N. R. Moheimani, “Production of biofuels from microalgae,” *Mitigation and Adaptation Strategies for Global Change*, vol. 18, pp. 47–72, 2011.
26. K. Bozbas, “Biodiesel as an alternative motor fuel: production and policies in the European Union,” *Renewable and Sustainable Energy Reviews*, vol. 12, no. 2, pp. 542–552, 2008.
27. S. Kaur, M. Sarkar, R. B. Srivastava, H. K. Gogoi, and M. C. Kalita, “Fatty acid profiling and molecular characterization of some freshwater microalgae from India with potential for biodiesel production,” *New Biotechnology*, vol. 29, no. 3, pp. 332–344, 2012.
28. A. R. Medina, E. M. Grima, A. G. Gimenez, and M. J. I. Gonzalez, “Downstream processing of algal polyunsaturated fatty acids,” *Biotechnology Advances*, vol. 3, pp. 517–580, 1998.
29. J. Folch, M. Lees, and G. H. S. Stanley, “A simple method for the isolation and purification of total lipids from animal tissues,” *The Journal of Biological Chemistry*, vol. 226, pp. 497–509, 1957.
30. E. G. Bligh and W. J. Dyer, “A rapid method of total lipid extraction and purification,” *Canadian Journal of Biochemistry and Physiology*, vol. 37, no. 8, pp. 911–917, 1959.
31. C. Crampon, O. Boutin, and E. Badens, “Supercritical carbon dioxide extraction of molecules of interest from microalgae and seaweeds,” *Industrial and Engineering Chemistry Research*, vol. 50, no. 15, pp. 8941–8953, 2011.
32. E. Ryckebosch, K. Muylaert, and I. Foubert, “Optimization of an analytical procedure for extraction of lipids from microalgae,” *Journal of the American Oil Chemists' Society*, vol. 89, pp. 189–198, 2011.View at:
33. A. Sathish and R. C. Sims, “Biodiesel from mixed culture algae via a wet lipid extraction procedure,” *Bioresource Technology*, vol. 118, pp. 643–647, 2012.

34. APHA, AWWA, 2017, Standard methods for the examination of water and wastewater, 23rd edition : E.W. Rice, R.B. Baird, A.D. Eaton, editors, American Public Health Association, American Water Works Association, Water Environment Federation publisher.
35. Zhu, S., L. Qin, P. Feng, C. Shang, Z. Wang and Z. Yuan. 2019. Treatment of low C/N ratio wastewater and biomass production using coculture of *Chlorella vulgaris* and activated sludge in a batch photobioreactor. Bioresource Technology. 274 : .313-320
36. Kumar, P. K., S. V. Krishna, S. S. Naidu, K. Verma, D. Bhagawan. and V. Himabindu. 2019. Biomass production from microalgae Chlorella grown in sewage, kitchen wastewater using industrial CO_2 emissions: Comparative study. Carbon Resources Conversion. 2 : 126-133.
37. Labua, S. (2013) Isolation of oilgae from surface water in Prachuap Khiri Khan Province and Samut Prakan Research Institute Of Rangsit University.
38. A. Sathish and R. C. Sime, "Biodiesel from mixed culture algae via a wet lipid extraction procedure," *Bioresource Technology*, vol. 118, pp. 643-647, 2012.
39. S. Zhen-Feng, L. Xin, H. Hong-Ying, W. Yin-Hu, and N. Tsutomu, "Culture of *Scenedesmus* sp. LX1 in the modified effluent of a wastewater treatment plant of an electric factory by photo-membrane bioreactor," *Bioresource Technology*, vol. 102, no. 17, pp. 7627–7632, 2011.
40. Li, Y., Y. Chen, P. Chen, M. Min, J. Zhu and R. Ruan. 2011. Characterization of a microalga *Chlorella* sp.well adapted to highly concentrated municipal wastewater for nutrient removal and biodiesel production. Bioresource Technology. 102 : 5138-5144.
41. Miao, M., X. Yao, L. Shu, Y. Yan, Z. Wang, N. Li, X. Cui, Y. Lin and Q. Kong. 2016. Mixtrophic growth and biochemical analysis of *Chlorella vulgaris* cultivated with synthetic domestic wastewater. International Biodeterioration & Biodegradation. 113 : 120-125.
42. T. G. Ellis, "Chemistry of wastewater," in *Environmental and Ecological Chemistry, Volume II,* p. 452, Department of Civil, Construction and Environmental Engineering, Ames, Iowa, USA, 2011.
43. N. F. Gray, *Biology of Wastewater Treatment,* Oxford University Press, Oxford, UK, 1989.
44. N. F. Y. Tam and Y. S. Wong, "Wastewater nutrient removal by Chlorella *pyrenoidosa* and *Scenedesmus* sp," Environmental Pollution, vol. 58, no. 1, pp. 19–34, 1989.
45. Ratanaphadit, K. (1993.) Cultivation of Chlorella sp. in effluent from seafood processing plant. (Master's Thesis of Songkla University)
46. I.Rawat, R. Ranjith Kumar, T. Mutanda, and F. Bux, "Dualrole of microalgae: phycoremediation of domestic wastewaterand biomass production for sustainable biofuels production,"*Applied Energy*, vol. 88, no. 10, pp. 3411–3424, 2011.
47. Bhatt, N. C., Coupling of Algal Biofuel Production with Wastewater. Scientific World Journal, 2014.
48. C.Rösch, J. Skarka, and N. Wegerer, "Materials flow modeling of nutrient recycling in biodiesel production from microalgae," *Bioresource Technology,* vol. 107, pp. 191-199, 2012.
49. R. Harun, M. Singh, G. M. Forde, and M. K. Danquah, "Bioprocess engineering of microalgae to produce a variety of consumer products," *Renewable and Sustainable Energy Reviews*, vol. 14, no. 3, pp. 1037–1047, 2010.

SP07_001_OA: FLUKA SIMULATIONS FOR EVALUATION OF SPACECRAFT SHIELDING MATERIALS AGAINST SOLAR PARTICLE EVENTS

Dumrongsak Rodphothong,[1,*] Tanin Nutaro[2]

[1]Department of Physics, Faculty of Science, Ramkhamhaeng University, Huamark, Bangkapi, Bangkok, 10240, Thailand
[2]Department of Physics, Faculty of Science, Ubon Ratchathani University, Sathonlamark, Warin Chamrap, Ubon Ratchathani, 34190, Thailand
*e-mail: dumrongsak.ro.55@ubu.ac.th

Abstract:

The shielding efficiency of low-density materials with small atomic mass were evaluated for the conditions of solar particle events (SPEs). FLUKA software as the Monte Carlo transport code have been used for improving spacecraft shielding from cosmic radiation in space. Compared the effectiveness of aluminum is the main primary metal used in spacecraft. In this study we used liquid hydrogen, water and polyethylene as shielding materials to compare with aluminum. The efficiency of a shield is evaluated by the dose profile within the shield and the amount of dose absorbed by water that we used as a target by using FLUKA which is a well-known Monte Carlo transport code. The efficiency comparison is made by fixing the area density of a shielding material. It was found that liquid hydrogen, polyethylene and water outperform aluminum for Solar Particle Events.

SP07_002_OF: SEARCHING FOR CLUSTERS OF HIGH-ENERGY γ-RAY PHOTONS USING *FERMI* LAT OBSERVATIONS

Hannarong Janthaloet,[1,*] Warit Mitthumsiri,[1] Seth Digel,[2] David Ruffolo,[1]
on behalf of the *Fermi* LAT collaboration

[1]Department of Physics, Faculty of Science, Mahidol University, Bangkok, Thailand
[2]Kavli Institute for Particle Astrophysics and Cosmology, SLAC National Accelerator Laboratory, Stanford University, Stanford, California 94305, USA
*e-mail: hannarong.jat@student.mahidol.ac.th

Abstract:

High-energy γ rays are produced from extreme phenomena in the universe, some of which involve bright bursts or flares. At multi-GeV energies, these phenomena are not well studied because of the limited photon statistics for even relatively bright flares. We search for clusters of γ-ray photons using *Fermi* Large Area Telescope (LAT) observations from 2008 to 2018. Here we define a "cluster of γ-ray photons" as a group of 3 or more photons above 10 GeV within 1.0° radius and within a given time interval (20, 96, or 192 minutes). The Galactic plane region (latitude less than 10°) which contains a high density of γ-ray sources and diffuse emission is analyzed with caution. We cross-check with the latest γ-ray source catalog (>50 MeV) of sources detected based on their average fluxes over ten years (4FGL-DR2) to identify potential counterparts of the clusters of γ rays we find. Our unique searching method has preliminarily detected many transient γ-ray flares above 10 GeV, some of which have no (4FGL-DR2 source nor known blazar) counterparts. The flaring behavior of previously recognized or newly discovered sources will be interesting for further study.

Introduction:

The *Fermi* LAT has been continuously monitoring the γ-ray sky since 2008, cataloging more than 5,000 astrophysical γ-ray sources so far based on their 10-year average flux above 50 MeV.[1] The LAT has also observed more than 4,000 γ-ray flares above 100 MeV, 77 of which without known counterparts.[2] High-energy emissions from at least 186 γ-ray bursts have been found above 30 MeV.[3] These recent data have revolutionized our overall understanding of the sub-GeV γ-ray sky.

Observations of γ-ray sources at multi-GeV energy are more challenging due to limited signal statistics. *Fermi* LAT's latest high energy (>10 GeV) source catalog (3FHL) was accomplished using a sophisticated combination of seeding obtained from image-based techniques and likelihood analysis.[4] An advantage for multi-GeV study is that the photon direction reconstruction of the LAT improves with energy and becomes slightly better than 1.0° (95% containment point-spread function radius) at above 10 GeV. We therefore propose a different searching algorithm which scans for "clusters of γ rays" defined as groups of at least 3 photons above 10 GeV within a 1.0° radius and within a specified time window (20, 96, or 192 mins for this work). Comparing to the 3FHL[4], our search is more sensitive to faint but flaring sources which may be of different types of objects.

Clusters of high-energy γ-ray photons we find could be associated with either steady or transient sources at ~10-100 GeV. Gathering γ-ray sources in this energy range is complementary to the compilations by the LAT[1,2,3] at lower energies and the results could provide candidate targets for current or future ground-based instruments at higher energies.

Methodology:

We use the latest version (P8R3_SOURCE) of LAT's photon data above 10 GeV between Aug 2008 – Nov 2018. As shown in Figure 1, we select photons with $\Theta_{Zen} < 100°$ to avoid intense γ-ray emission from the Earth's atmosphere and $\Theta_{LAT} < 65°$ to reject photons with large incidence angles in the LAT's frame. There are 971k photons after all selections.

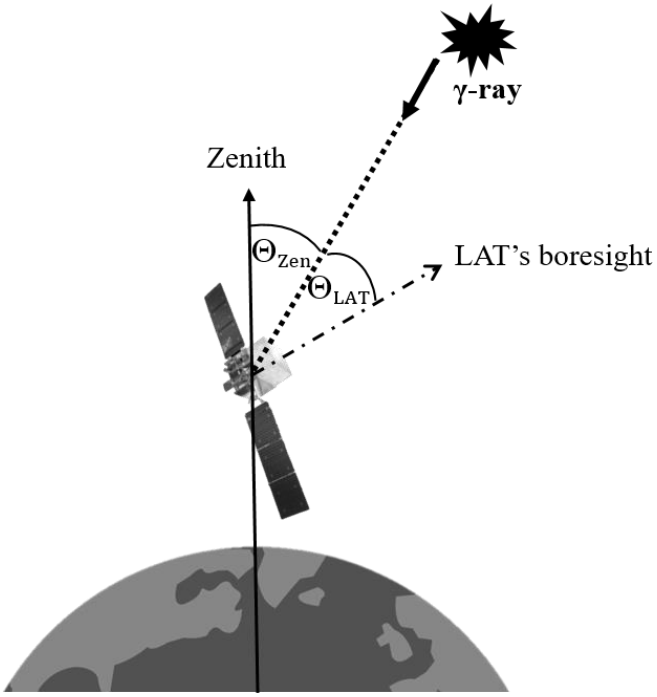

Figure 1. Definitions of Θ_{Zen} and Θ_{LAT} for *Fermi* LAT.

Three time intervals have been used for the search*:*

- 20 minutes*:* the typical maximum time that most sources stay in the field of view *(*FoV*)* of the LAT in the normal survey mode calculated by
  FoV size *(*2.4 sr*)* × orbital period *(*96 mins*) /* hemisphere *(*2π sr*)* ≈ 20 mins
- 96 minutes*:* Orbital period of the LAT, during which it observes half of the sky
- 192 minutes*:* Twice the LAT orbital period, during which it observes the whole sky.

We search for clusters of γ rays, as previously defined, within each time interval. The search radius is chosen to be 1.0° because the LAT's 95% containment point-spread function radius is slightly less than 1.0° at 10 GeV as shown in Figure 2. The search algorithm is summarized in the flowchart in Figure 3. Note that once we pick a photon as a reference, we must search both forward and backward in time to correctly count the number of photons in that cluster. For example, we assume that the LAT detects 3 photons (p1, p2, and p3) in chronological order within the desired time interval. If p1 and p3 are more than 1.0° apart from each other but are within 1.0° from p2, this cluster would not be found unless we search both forward and backward in time using p2 as a reference photon.

The position of a cluster is defined by a vector for which the components are the average components of the position vector of each photon in that cluster. All photons in the cluster are given the same weight because they have similar energies and incidence angles in the LAT's frame. Based on the most recent and comprehensive γ-ray source catalog (4FGL-DR2) from the LAT data[1], we check for a possible counterpart of each cluster using the position information. The source listed in the catalog that is nearest (but no more than 1.0°) to the cluster is assigned as a possible counterpart of the cluster. This is a deliberately conservative criterion.

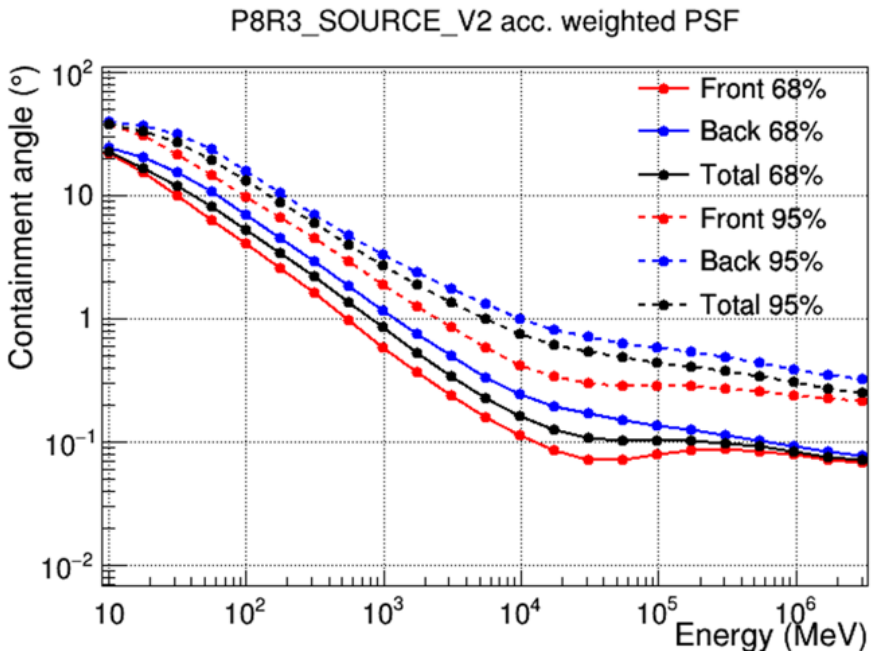

Figure 2. Point-spread function containment radii, averaged over the FoV, as a function of energy for *Fermi* LAT[†]. For our search, we select photons with energies >10 GeV.

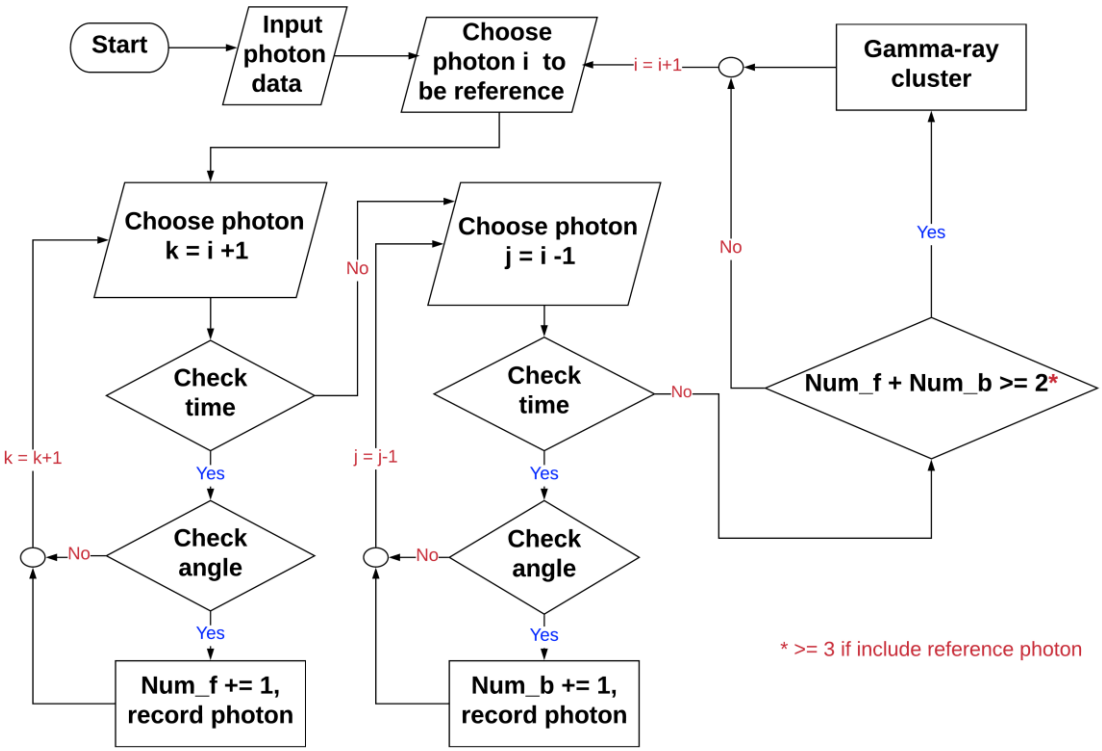

Figure 3. Flowchart of γ-ray cluster searching algorithm.

[†] www.slac.stanford.edu/exp/glast/groups/canda/lat_Performance.htm

Results and Discussion:

Search results in the Galactic plane (|latitude| < 10°) and high-latitude regions are analyzed separately, to account for the high density of γ-ray sources and diffuse emission in the Galactic plane which may cause false detections or confusion for counterpart assignments. Table 1 provides the overall summary of the results for each time interval. In total, we find 1,517 clusters of >10-GeV γ-ray photons on the Galactic plane, 132 of which have no counterparts in 4FGL-DR2, and 250 clusters at high latitude, 5 of which have no counterparts in 4FGL-DR2 or in the BZCAT5 catalog[††]. However, 2 of those 5 are within 1.0° from known compact radio sources[†††]. The largest cluster we find consists of 15 photons within about 10 mins which are associated with the famous γ-ray burst GRB130427.[5]

The distributions of the angles between clusters of γ rays and their nearest 4FGL-DR2 counterparts are shown in Figure 4. The widths of the distributions in the high-latitude region are likely related to the instrument's resolution, while the wider widths of those in the Galactic plane region suggest that some other effects, such as the misidentification of counterparts or extended sizes of Galactic sources, are involved. The astrophysical objects associated with the counterparts from which the clusters are potentially produced are shown in Table 2. Here the classifications come from 4FGL-DR2.[1]

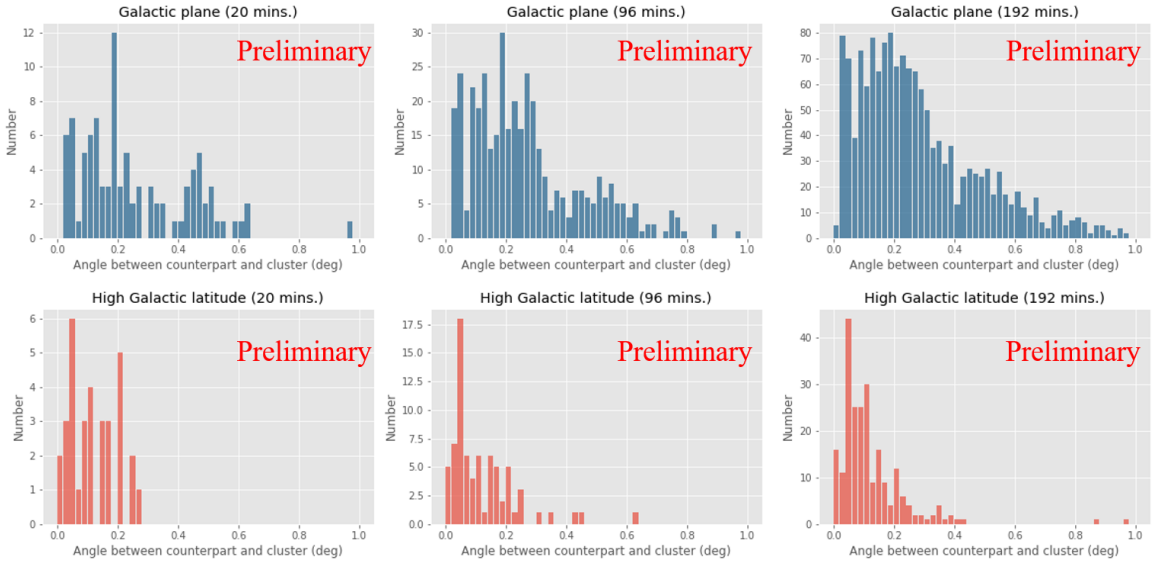

Figure 4. Distributions of angular separations between clusters of γ rays and their nearest 4FGL-DR2 counterparts. The Galactic plane is defined as |latitude| < 10°.

It is possible that unrelated diffuse photons in the Galactic plane mimic a 3-photon cluster by chance. Out of the 132 clusters of γ-ray photons with no 4FGL-DR2 counterparts on the Galactic plane, 108 clusters were not overlapped by clusters detected at different times and many are likely chance-coincidence events, while the other 24 clusters occurred repeatedly at the same position in the sky. It is also interesting that the numbers of clusters of γ rays detected in the Galactic plane region increases roughly linearly with the length of the search time intervals. There are about 10 times more clusters for the 192-min search compared to the number for the 20-min search. On the other hand, the numbers of clusters at high latitude increases by only about a factor of 5.

[††] www.asdc.asi.it/bzcat/
[†††] www.astrogeo.org/vlbi/solutions/rfc_2020b/

Table 1. Number of clusters found in the Galactic plane and high-latitude regions.

	Galactic plane		High latitude	
	Total	**Without 4FGL-DR2 counterpart**	**Total**	**Without 4FGL-DR2 counterpart**
Short time (20 mins.)	95	5	33	1
1 orbit (96 mins.)	287*	30*	44*	-
2 orbits (192 mins.)	1,135**	97**	173**	4**

* Not in 20-min search

**Not in 20-min or 96-min search

Table 2. Object types of the potential counterparts of clusters.

	20-min search		96-min search		192-min search	
	Galactic plane	**High latitude**	**Galactic plane**	**High latitude**	**Galactic plane**	**High latitude**
Pulsar & pulsar wind nebula	53	1	109	-	378	-
Active galaxy with uncertain type	3	1	12	1	36	2
Binary	1	-	-	-	3	-
High mass binary	1	-	1	-	8	-
Supernova remnant	2	-	11	-	67	-
Potential association with supernova remnant or pulsar wind nebula	3	-	31	-	120	-
BL Lac blazar	-	10	2	11	4	95
Flat-spectrum radio quasar	-	18	-	31	-	70
Radio galaxy	-	1	-	1	-	2
Globular cluster	-	-	2	-	12	-
Gamma-ray burst	-	1	-	-	-	-
Unknown	27	-	89	-	410	-
Without 4FGL-DR2 counterpart	5	1	30	-	97	4

Conclusions:

We propose a new method to search for high-energy (>10 GeV) transient γ-ray sources using the concept of clusters of γ rays, which are temporally and spatially compact groups of photons. Using 10 years of LAT data, we have detected more than 1,500 clusters of high-energy γ rays, some of which repeated at the same position months apart. We compile their potential sources and find that some of them have no known 4FGL-DR2 or blazar counterparts. The full details of all clusters, which could be useful for targeted studies by the LAT or other instruments, can be provided through private communications with the authors of this work. We plan to compare against other γ-ray source catalogs and to study the probability of chance coincidences for some of these clusters.

Acknowledgements:

The *Fermi* LAT Collaboration acknowledges generous ongoing support from a number of agencies and institutes that have supported both the development and the operation of the LAT as well as scientific data analysis. These include the National Aeronautics and Space Administration and the Department of Energy in the United States, the Commissariat à l'Energie Atomique and the Centre National de la Recherche Scientifique / Institut National de Physique Nucléaire et de Physique des Particules in France, the Agenzia Spaziale Italiana and the Istituto Nazionale di Fisica Nucleare in Italy, the Ministry of Education, Culture, Sports, Science and Technology (MEXT), High Energy Accelerator Research Organization (KEK) and Japan Aerospace Exploration Agency (JAXA) in Japan, and the K. A. Wallenberg Foundation, the Swedish Research Council and the Swedish National Space Board in Sweden. Additional support for science analysis during the operations phase is gratefully acknowledged from the Istituto Nazionale di Astrofisica in Italy and the Centre National d'Études Spatiales in France. This work performed in part under DOE Contract DE-AC02-76SF00515. This research project is supported by Thailand Science Research and Innovation (RTA6280002) and the National Astronomical Research Institute of Thailand (NARIT).

References:

1. Abdollahi S., et al. *Astrophys. J*. 2020;247:33.
2. Abdollahi S., et al. *Astrophys. J.* 2017;846:34.
3. Ajello M., et al. *Astrophys. J.* 2019;878:52.
4. Ajello M., et al. *Astrophys. J., Suppl. Ser.* 2017;232:18.
5. Ackermann M., et al. *Science.* 2014;343:42-47.

SP07_003_OA: NEW GROUND-BASED COSMIC RAY DETECTORS AND UPGRADE OF THE NEUTRON MONITOR AT MAWSON STATION, ANTARCTICA

Pradiphat Muangha,[1,*] Alejandro Saiz,[1] David Ruffolo,[1] Marc Duldig,[2] John Humble,[2] Paul Evenson,[3] Waraporn Nuntiyakul,[4] Kullapha Chaiwongkot,[1] Chanoknan Banglieng,[5] Warit Mitthumsiri,[1] Petchara Pattarakijwanich,[1]

[1]Department of Physics, Faculty of Science, Mahidol University, Bangkok, Thailand
[2]School of Natural Science, University of Tasmania, Hobart, Tasmania, Australia
[3]Bartol Research Institute and Department of Physics and Astronomy, University of Delaware, Newark, DE, USA
[4]Department of Physics and Materials Science, Faculty of Science, Chiang Mai University, Chiang Mai, Thailand Chiang
[5]Division of Physics, Faculty of Science and Technology, Rajamangala University of Technology Thanyaburi, Pathum Thani, Thailand
*e-mail: pradiphat.mun@student.mahidol.ac.th

Abstract:

Neutron monitors have been in operation since 1957 at Mawson Station, Antarctica, to detect cosmic ray ions, which are energetic ions from space. The detector is sensitive to ions above about 1 GeV in energy, most of which are Galactic cosmic rays from explosions of stars called supernovae. Occasionally such relativistic ions can even be accelerated by solar storms. The Earth's polar regions are the best locations for ground-based detectors to study solar radiation storms. In early 2020, two scientists from Mahidol University, Thailand, installed bare (lead-free) neutron counters next to the neutron monitor at Mawson station, Antarctica, to provide a measure of the energy of solar particles. They also upgraded electronics firmware and the computer acquisition system for the neutron detectors. We present preliminary results of the recent upgrade of the Mawson neutron monitor and deployment of bare counters. We compare results on cosmic ray variations from Mawson with other Antarctic neutron monitor stations, including South Pole, McMurdo, and Jang Bogo. Partially supported by grant RTA6280002 from Thailand Science Research and Innovation.

SP08_001_PF: METHOD DEVELOPMENT FOR DETERMINATION OF PHENOLIC ACIDS IN FRUIT USING MICELLAR ELECTROKINETIC CHROMATOGRAPHY AND SOLVENT EXTRACTION

Sasinun Detsangiamsak,[1,2] Pattamaporn Phooprantra,[1,2] Prapin Wilairat,[3] Rattikan Chantiwas [1,2,*]

[1]Department of Chemistry, Faculty of Science, Mahidol University, Bangkok 10400, Thailand
[2]Center of Excellence for Innovation in Chemistry and Flow Innovation-Research for Science and Technology, Bangkok 10400, Thailand
[3]Analytical Sciences and National Doping Test Institute, Mahidol University, Bangkok 10400, Thailand
*e-mail: rattikan.cha@mahidol.ac.th

Abstract:

Development of micellar electrokinetic electrochromatography (MEKC) with UV detection for simultaneous determination of four phenolic acids, viz. *p*-coumaric (PCA), caffeic (CFA), gallic (GLA) and 2,3,4-trihydroxybenzoic (THBA) acids, is presented. MEKC analysis was performed by addition of sodium dodecyl sulfate (SDS) into the running buffer (25.0 mM borate buffer, pH 9.00). UV detection was at 280 nm. Applied electrical field strength was 400 V/cm and electrokinetic injection (3 s, 22.5 kV) was used. Effect of SDS content on the separation was studied. Separation with acceptable resolution and precision of the four phenolic compounds were achieved by employing 40.0 mM SDS in the borate buffer. Calibration curves (10.0-150.0 µM) were constructed with good coefficient of determination ($r^2 \geq 0.99$) with limit of quantitation (10 σ blank/slope) of 23.0 - 67.0 µM for injected solutions of phenolic acids. The developed method was applied to the analysis of freeze-dried fruit (grape, guava, and apple) extracted with ethyl acetate. Only *p*-coumaric acid (PCA) was detected in the apple sample. Percent recoveries of PCA spiked in all samples were 85 - 100%. MEKC can separate charged and neutral molecules based on interaction with the micelle.

Introduction:

Phenolic acid compounds are a class of substances which contain a phenolic ring and at least one organic carboxylic acid group[1]. They are secondary metabolites and play important roles in ecological and physiological processes of plants, as well as in plant-animal interactions and in adaptation to biotic and abiotic variables[2]. Phenolic acid compounds are an effective antioxidant that can prevent and treat diseases by scavenging free radicals and regulating the activity of different types of oxidase in the body[3].

Phenolic acid compounds are found in various fruits[4], vegetables[5, 6], and beverages[7]. For example, coffee[8], green tea[9], and wine[10] are source of phenolic acids. Phenolic acids in beverages are *p*-coumaric acid (PCA), caffeic acid (CFA) and gallic acid (GAL)[11]. Determination of phenolic acid contents can be achieved by high performance liquid chromatography[12-17] and capillary electrophoresis (CE)[18,19]. Micellar electrokinetic chromatography with UV-visible detection (MEKC-UV analysis) has been reported for high efficiency separation and determination of some phenolic acids with prior solvent extraction of fruits and vegetables[20-22]. It is low cost and rapid with small sample and solvent consumption.

Methodology:

Chemicals and reagents: *p*- Coumaric acid (PCA), caffeic acid (CFA), gallic acid (GAL), 2,3,4-trihydroxybenzoic acid (THBA), potassium hydrogen phthalate (KHP) diphenylamine, paracetamol, catechol, 3-hydroxybenzoic acid, 4-acetyl benzoic acid, ethyl acetate and caffeine were purchased from Sigma-Aldrich (St. Louis, MO, USA). Sodium dodecylsulfate (SDS) was from Merck (Darmstadt, Germany). Methanol was purchased from RCI Labscan (Bangkok, Thailand). All standards were prepared in methanol and diluted using the running buffer solution.

Preparation of solutions: Borate buffer solution (25.0 mM, pH 9.00, 500 mL) was prepared from boric acid (MW 61.83 g mol^{-1}) and the pH was adjusted to 9.00 with 0.1 M NaOH. The running buffer was prepared by dissolving SDS (MW 288.37 g mol^{-1}) in the borate solution to give final concentration in the range of 10.0-60.0 mM SDS in 25 mL

Preparation of standard solutions and samples: Stock solution of a mixture of the 4 standard phenolic acids at 100.0 mM each was prepared in methanol. To construct the calibration curves, a suitable aliquot was added to 1500 µL of the running buffer. Also, 30 µL of aqueous 500.0 µM KHP was added as internal standard (IS).

All fruit samples were washed and homogenized on an electrical blender. The samples were freeze dried for 60 hours. For guava the homogenized fruit was filtered with a filter paper and only the pulp freeze dried. The freeze dried samples were kept in a desiccator until analyzed. An amount (ca. 1 g) of the dry fruit sample was accurately weighed and dissolved in 5.00 mL ethyl acetate. 30 µL of aqueous 500.0 µM KHP was added as internal standard (IS). The solution was centrifuged for 20 min at 4,500 rpm and 1 mL of the top layer removed and dried in a vacuum evaporator. The dry residue was dissolved in 1.0 mL running buffer solution and analyzed in triplicate by MEKC-UV.

Instrumentation: The capillary electrophoresis system was assembled in-house. It consisted of a UV detector (Applied Biosystem, 785A UV detector, CA, USA), a high voltage (HV) power supply (Spellman CZE1000R, Hauppauge, NY) and trays for the samples and buffer vials. The instrument was housed in a Plexiglas box with a micro switch to shut down the high voltage power supply whenever the door of the box is open. The absorbance signal was recorded by an eDAQ data acquisition system (Denistone East, NSW, Australia). Measurement of the electrophoretic current across the capillary column was recorded with the same eDAQ system. A fused-silica capillary (50 µm i.d., 360 µm o.d.) was from Polymicro Technologies (Phoenix, AZ, USA).

Results and Discussion:

SDS concentration in running buffer: Study of the effect of SDS concentration (*i.e.* 0.0, 10.0, 20.0, 30.0, 40.0, 50.0, 60.0 and 70.0 mM) in the running buffer on the separation of four phenolic acids (PCA, CFA, GAL and THBA) was carried out. The results show that increasing SDS concentration gave higher separation efficiency due to partitioning of phenolic compounds into the micelles. As shown in Figure 1**,** the optimum SDS concentration is 40.0 mM, giving high precision of peak areas (< 5 %RSD) and migration times (< 5%RSD), and peak resolutions > 1.5.

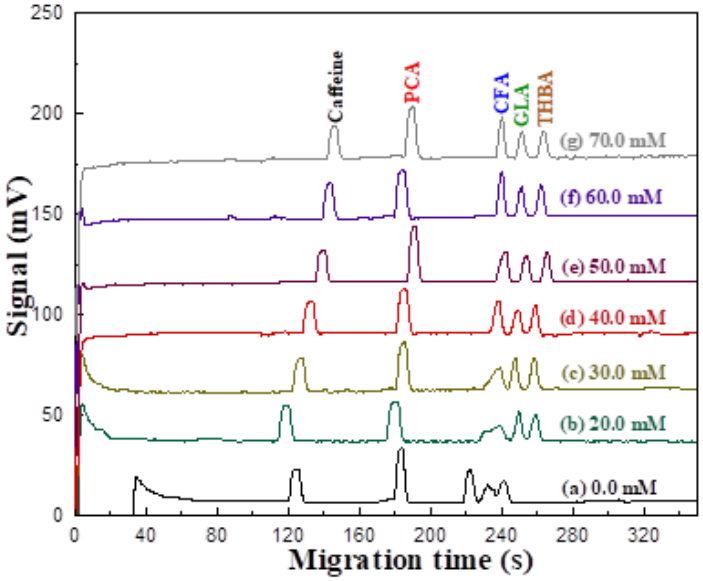

Figure 1. Electropherograms of four phenolic acids (PCA, CFA, GLA and THBA) at 50.0 µM and caffeine as a reference marker (25.0 µM). The SDS concentrations in running buffer solution are (a) 0.0 mM, (b) 20.0 mM, (c) 30.0 mM, (d) 40.0 mM, (e) 50.0 mM, (f) 60.0 mM and (g) 70.0 mM, respectively. MEKC-UV conditions are: running: buffer, 25.0 mM borate buffer (pH 9.00) with SDS; sample introduction by electrokinetic injection at 400 V/cm for 3 s; UV-detection at 280 nm.

Selection of internal standard: Six compounds were tested as internal standard (IS), i.e. 4-acetyl benzoic acid, 3-hydroxylbenzoic acid, catechol, paracetamol, diphenylamine and KHP. The electropherograms in Figure 2 show that KHP is the most suitable compound as internal standard because it has migration time well separated from the analytes. It is stable and has molecular structure similar to the phenolic acids. It is also not found in fruit samples.

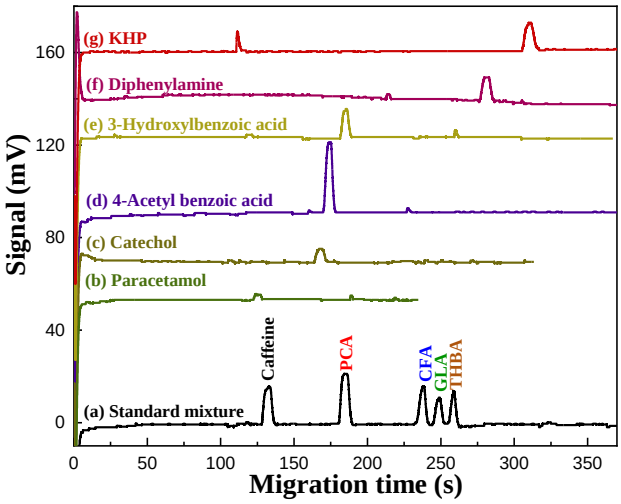

Figure 2. Electropherograms of (a) standard mixture of four phenolic acids (50.0 µM) and caffeine as a reference marker (25.0 µM), (b) paracetamol (30.0 µM), (c) catechol (25.0 µM), (d) 4-acetyl benzoic acid (200.0 µM), (e) 3-hydroxylbenzoic acid (20.0 µM), (f) diphenylamine (20.0 µM) and (g) KHP (500.0 µM). MEKC-UV conditions are: running: buffer, 25.0 mM borate buffer (pH 9.00) with SDS; sample introduction by electrokinetic injection at 400 V/cm for 3 s; UV-detection at 280 nm.

Analytical characteristics of developed MEKC-UV separation: The linear range, instrumental limit of detection (LOD), limit of quantitation (LOQ) and precision were investigated. Calibration curves of peak area ratio with concentration were linear over the concentration range of 10-150 µM of injected solutions of PCA, CFA, GAL and THBA, with $r^2 > 0.98$, as shown in Figure 3. The limits of detection (LOD), calculated from 3.3 σ (intercept)/slope, were 8 - 20 µM.

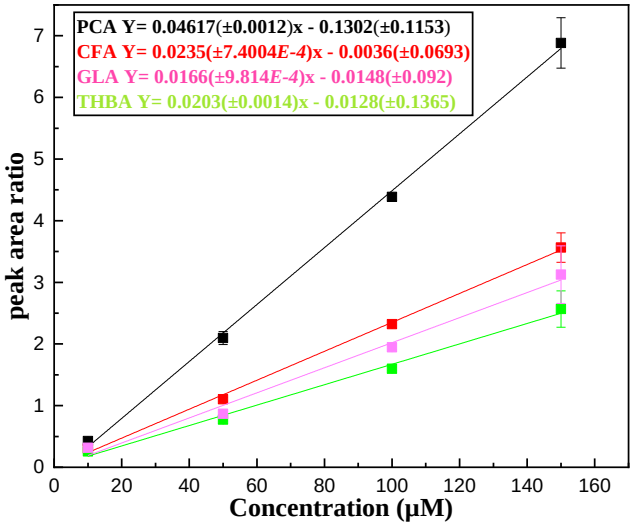

Figure 3. Linear calibration curves of four phenolic acids (PCA, CFA, GLA, and THBA) in the range of 10-150 µM using the developed MEKC-UV method (see caption of Figs. 1 and 2 for operating parameters).

Results of analysis of phenolic acids in freeze-dried fruit by MEKC-UV: Freeze-dried samples of grape, guava and apple were analyzed by MEKC-UV, as described above. Ethyl acetate was used as extracting solvent, as it has been used for phenolic acid extraction previously[20-22]. Only PCA was detected in the apple sample. It was identified from its migration time (migration time of PCA = 187 s.) and confirmed by spiking PCA standard in the sample solutions, as shown in Figure 4. The concentration of PCA in the injected apple sample was 23 ± 0.5 µM. The amount of PCA in the freeze dried apple ~~is~~ was calculated to be 3.8 ± 0.1 µg/g[23,24]. Unfortunately, KHP was not suitable for extraction by ethyl acetate, hence peak of KHP was not present in all samples. The PCA analysis was performed by external calibration. As shown in Figure 4, extracts from three different fruits contained different matrices, and peaks pattern of the separation were unique. In this study, only PCA was could be identified.

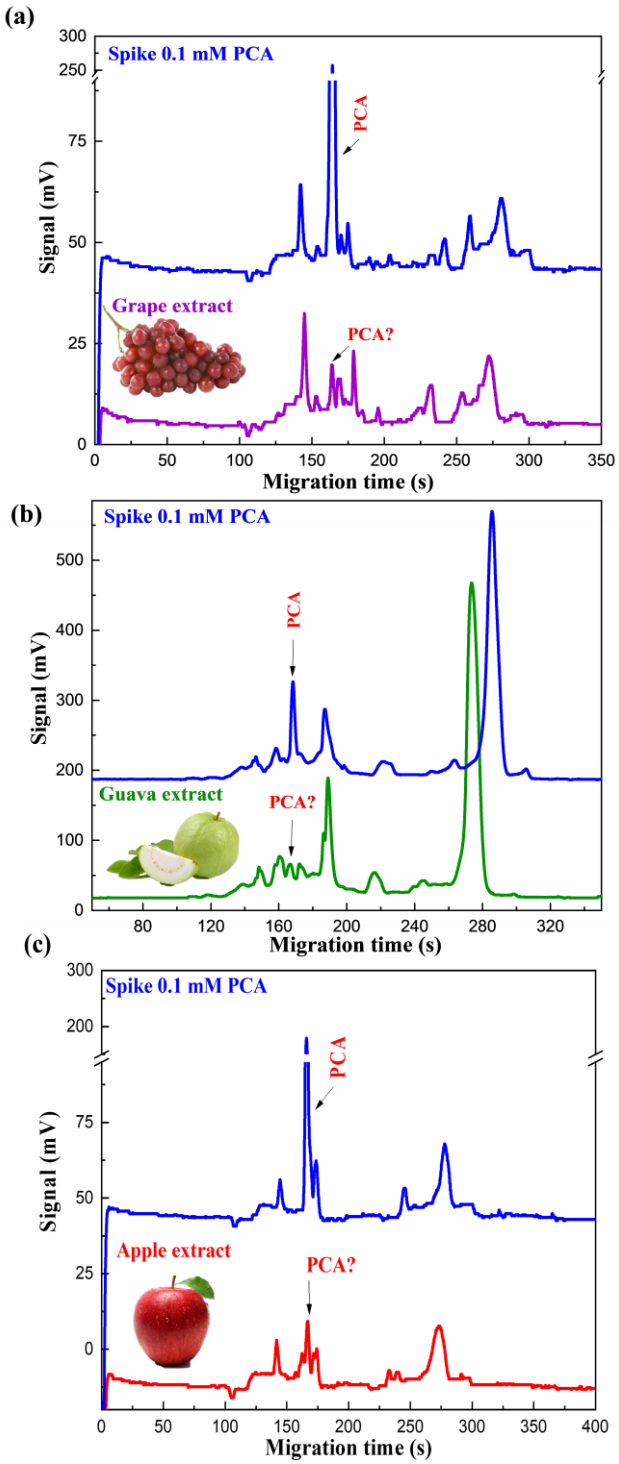

Figure 4. Electropherograms of ethyl acetate extracts of freeze-dried fruit samples: (a) grape, (b) guava and (c) apple. Upper electropherograms are samples spiked with 0.1 mM standard PCA to confirm identity.

Recovery of spiked PCA in freeze dried samples: PCA, at 0.1 mM level, was spiked into the 5.0 mL ethyl acetate solution containing 1.00 g freeze dried sample and KHP internal standard. Table 2 shows the percent recovery for the grape, guava, and apple samples. The recoveries were ca.100 %.

Table 1. Percent recovery of spiked PCA in freeze dried fruits.

Fruit	Original amount in injected sample (µM)	Percent recovery of 0.1 mM spiked PCA
grape	ND[a]	100 ± 1.7
guava	ND[a]	85 ± 4.6
apple	23± 0.5	100± 1.6

[a] ND: not determined due to interference from neighboring peaks.

Conclusion:

A simple MEKC-UV method was successfully developed for separation and determination of four phenolic acids (PCA, CFA, GAL, and THBA) in freeze-dried fruits. This developed method has a linear calibration range of 10.0-150.0 µM of the injected solutions, with coefficients of determinations (r^2) ≥ 0.99, limits of detection (LOD) (of injected samples) in the range of 8 – 20 µM for the 4 phenolic acids. The developed separation method was used to determine the phenolic acids in ethyl acetate extracts of freeze-dried fruit. Only PCA was quantitated in apple sample.

References:

1. Martí R, Valcárcel M, Herrero-Martínez JM, Cebolla-Cornejo J, Roselló S. Food Chemistry. 2017;221:439-446.
2. Amri FSA, Hossain MA. Egyptian Journal of Basic and Applied Sciences. 2018;5(4):245-2513.
3. Zuo X, Tian C, Zhao N, Ren W, Meng Y, Jin X, Zhang Y, Ding S, Ying C, Ye X. BMC research notes. 2014;7:120.
4. Fu L, Xu BT, Xu XR, Gan RY, Zhang Y, Xia EQ, Li HB.Food Chemistry. 2011;129 (2):345-350.
5. Kaur C, Kapoor HC. International Journal of Food Science and Technology. 2002;37(2):153-161.
6. Isabelle M, Lee BL, Lim MT, Koh WP, Huang DJ,Ong CN. Food Chemistry. 2010;120(4):993-1003.
7. Gruz J, Novak O, Strnad M. Food Chemistry 2008;111(3):789-794.
8. Natella F, Nardini M, Belelli F, Scaccini C. American Journal of Clinical Nutrition. 2007;86 (3):604-609.
9. Liu CM, Chen CY, Lin YW. Food Chemistry. 2014;150:145-150.
10. Yang P, Li HQ, Wang H, Han FL, Jing SY, Yuan CL, Guo AQ, Zhang YL, Xu ZM. Food Analytical Methods. 2017;10(7):2383-2397.
11. Česla P, Fischer J, Jandera P. Electrophoresis. 2012;33(15):2464-2473.
12. de Mesquita M, Leão W, Ferreira M, de Paula J, Espindola L, Soares L. Pharmacogn Mag. 2015;11(Suppl 2):S316-S321.
13. de Sousa JPB, da Silva AABueno PCP,Gregorio LE,Furtado N,Jorge RF, Bastos JKA. Phytochemical Analysis.2009;20(1):24-32.
14. Francisco MLD,Resurreccion AVA. Food Chemistry. 2009;117(2):356-363.
15. Inbaraj BS, Lu H, Kao TH, Chen BH. Journal of Pharmaceutical and Biomedical Analysis. 201051 (3):549-556.
16. Irakli MN, Samanidou VF, Biliaderis CG, Papadoyannis IN. Food Chemistry. 2012;134(3):1624-1632.
17. Ozturk N, Tuncel M, Uysal UD, Oncu-Kaya EM, Koyuncu O. Food Analytical Methods. 2011;4(3):300-306.
18. Lin YH, Huang HC, Hsu WL, Analytical and Bioanalytical Chemistry. 2015;407 (23):7093-710.
19. Nevado JJ, B Penalvo GC, Robledo VR, Martinez GV, Talanta. 2009;79(5):1238-1246.
20. Guo W, Beta T. Food Research International. 2013;51(2):518-525.
21. Lou SN, Lin YS, Hsu YS, Chiu EM, Ho CT. Food Chemistry. 2014;161:246-253.
22. Singh P, P Saldaña MDA. Food Research International. 2011;44(8):2452-2458.
23. Haminiuk CWI, Maciel GM, Plate-Oviedo MSV, Peralte RM. International Journal of Food Science & Technology, 2012;47(10): p. 2023-2044.
24. Kalinowska M, Bielawska A, Lewandowska SH, Priebe W, Lewandowski W. Plant Physiology and Biochemistry. 2014;84:169-188.

SP08_002_PA

SP08_002_PA: AMPHIPHILIC PULLULAN DERIVATIVES FOR STABILIZING GOLD NANOPARTICLES AS TRANSDERMAL DELIVERY CARRIERS

Komgrit Sawangkan,[1] Sakchai Laksee,[2] Urarika Luesakul,[2] Nongnuj Muangsin[2,*]

[1]Program of Petrochemical and Polymer Science, Faculty of Science, Chulalongkorn University, Bangkok 10330, Thailand.
[2]Department of Chemistry, Faculty of Science, Chulalongkorn University, Bangkok 10330, Thailand.
[*]e-mail: nongnuj.j@chula.ac.th; nongnuj.ms@gmail.com

Abstract

Gold nanoparticles (AuNPs) has been widely in transdermal delivery system. However, the drawback of AuNPs is the low permeability through the skin which reduces its efficacy and also leads to the use of a higher amount of active pharmaceutical ingredient (API). To increase cell permeability, we have designed the AuNPs with amphiphilic pullulan derivatives (AmPQ188), in which the surface of AuNPs was functionalized to contain 3 components as followed: Firstly, pullulan has predisposed substantial interest to use as green agents for AuNPs synthesis owing to its high soluble, non-toxic, biocompatible, biodegradable, and natural biopolymer. Secondly, quat188 (Q188) providing positive charge in order to increase cellular uptake. Thirdly, stearic acid (C18) providing hydrophobic component to increases the permeability to skin and deliver hydrophobic molecules inside the cells. Subsequently, the synthesized AmPQ188 and AuNPs stabilized with modified pullulan were characterized by NMR, UV-Vis spectrophotometer and DLS. ^{1}H NMR spectrum of AmPQ188 indicated the degrees of quaternization (DQ) and substitution (DS) of Q188 and C18 were 17.4% and 4.0%, respectively. From the UV-vis spectra between 200-800 nm. Found that, the UV-Vis spectra of AuNPs©AmPQ188 was 543 nm. The particle size distribution of AuNPs©AmPQ188 showed 55.43 nm. These results indicated that AuNPs©AmPQ188 was successfully synthesized. The permeation efficiency through cellulose membrane by Franz's cell diffusion method will be investigated.

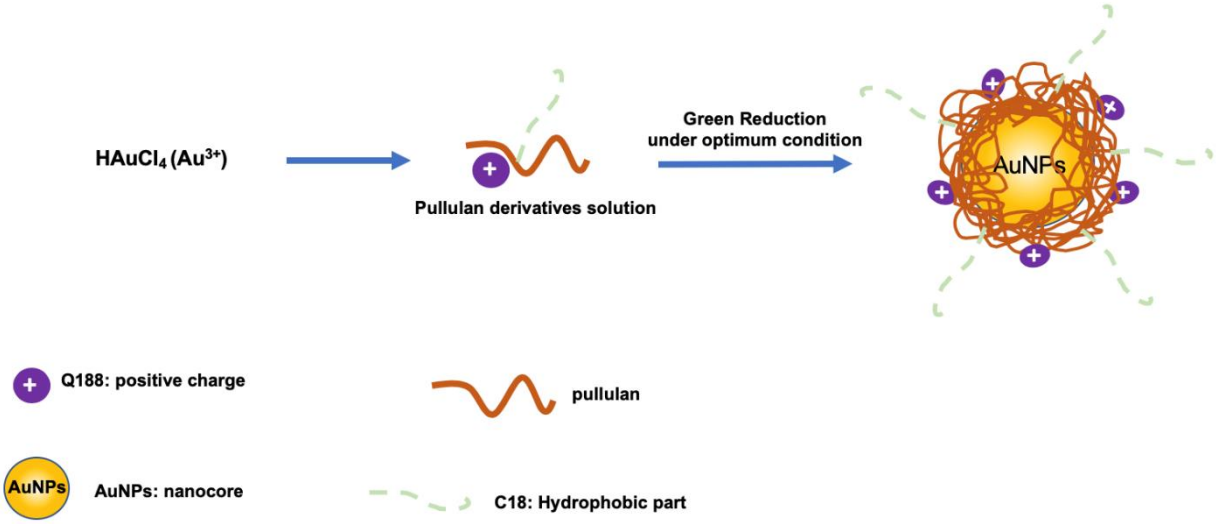

Figure 1. Synthetic pathways of AuNPs with AmPQ188 as transdermal delivery nanocarriers

SP08_003_PA: MELON SEEDS AS A POTENTIAL SOURCE FOR PREPARATION OF CONJUGATED LINOLEIC ACID

Siriluck Pojjanapornpun*, Apiwat Jiruttisakul, Akkaradech Nakornsadet, Piraporn Sombutsuwan, Salisa Chumsantea, Kanit Krisnangkura and Kornkanok Aryusuk

Division of Biochemical Technology, School of Bioresources and Technology,
King Mongkut's University of Technology Thonburi (Bangkhuntien), Bangkok, Thailand
*e-mail: siriluck.poj@mail.kmutt.ac.th

Abstract:

Conjugated linoleic acid (CLA) isomers have been reported to exhibit beneficial effects such as reducing body fat mass, anti-carcinogenic and anti-atherogenic properties. Seeds of melon (green, orange, golden and mixed varieties) and cantaloupe, the agricultural wastes collected from melon farm in Thailand, have been investigated as a potential source for preparation of CLA. Fatty acid composition and oil content (as triglyceride equivalent) of the seeds were determined by gas chromatography. The seeds contained oil in the range of 23.1 – 32.7 % of dry matter. Linoleic acid (LA) accounted for 52.2 – 61.9% of the total fatty acid in all seed oils, which are excellent sources for preparation of CLA. The high LA oil extracted from mixed melon seeds using hexane was alkali isomerized at 180 °C for 90 min using the mass ratio of 1:0.5:2 of oil/NaOH/propylene glycol. The CLA 59.3% of total fatty acids and 99.6 % degree of isomerization were obtained. The isomer distribution of the presented CLA was comparable to commercial CLA. The total CLA contained 46.7% and 48.5% of *c*9, *t*11 and *t*10, *c*12 isomers, respectively. The melon seeds provide an alternative inexpensive source of oil for the preparation of CLA.

SP08_004_PA: PECTIC OLIGOSACCHARIDE PRODUCTION FROM NaOH-EDTA EXTRACTED POMELO PEEL PECTIN BY ENZYMATIC HYDROLYSIS

Yuree Wandee,[1,*] Dudsadee Uttapap,[1] Petra Mischnick[2]

[1] Division of Biochemical Technology, School of Bioresources and Technology,
King Mongkut's University of Technology Thonburi, Bangkhuntien, Bangkok 10150, Thailand
[2] Faculty of Life Science, Institute of Food Chemistry, Technische Universität Braunschweig, Schleinitzstr. 20, D-38106 Braunschweig, Germany
*email: yuree.wan@mail.kmutt.ac.th

Abstract:

Pectin was extracted from pomelo albedo using 50 mM NaOH solution containing 0, 2.5, 5 and 10% (g/100g pomelo peel) ethylenediaminetetraacetic acid (EDTA) in a microwave using a power of 1100 W for 2 min. The yield of pectin increased with the increase of EDTA concentration from 17% (without EDTA) to 22%, 27% and 38%, respectively. The pectin extracted with NaOH+10% EDTA comprised the highest amount of galacturonic acid (GalA; 81%, w/w) with very low degree of methylation (<1%). This pectin was then hydrolyzed with 1% (v/w) Pectinex Ultra-SPL and ViscozymeL (38 U and 1.2 FBGU/g pectin, respectively) for 120 min. Amount of pectic-oligosaccharides (POS) produced from the pectin hydrolyzed with Pectinex (95%, w/w) was higher than that with ViscozymeL (78%, w/w). TLC analysis showed that the products obtained from both enzymes had degree of polymerization (DP) of 1–4. The electrospray ionization mass spectrometry (ESI-MS) in negative ion mode of the purified product confirmed the monosaccharide and oligomer structures corresponding to galacturonic acid esterified by acetyl group at m/z 235 and oligogalacturonides (digalacturonic, trigalacturonic and tetragalacturonic at m/z 369, 545 and 721, respectively).

SP08_005_PA

SP08_005_PA: POLYELECTROLYTE COMPLEX COATED-GOLD NANOPARTICLES AS DRUG CARRIERS FOR ANTICANCER AND INFLAMMATORY ACTIVITIES

Naruthai Hongsa,[1] Kanokwan Sansanaphongpricha,[2] Urarika Luesakul[1,] Nongnuj Muangsin[3,*]
[1]Department of Chemistry, Faculty of Science, Chulalongkorn University,
Bangkok 10330, Thailand
[2]National Nanotechnology Center (NANOTEC), National Science and Technology Development Agency (NSTDA), Pathum Thani 12120, Thailand
[3]Nanotec-CU Center of Excellence on Food and Agriculture, Department of Chemistry,
Faculty of Science, Chulalongkorn University, Bangkok 10330, Thailand
*e-mail: nongnuj.j@chula.ac.th; nongnuj.ms@gmail.com

Abstract:

Gold nanoparticles (AuNPs) is one of the most interesting drug carrier owing to their great properties, such as good biocompatibility, non-toxicity, suitable size and shape. However, traditional gold nanoparticles remains the limitation in low drug loading efficacy leading to low drug concentration inside the cells. To overcome these limitations, we have developed layer-by-layer polyelectrolyte coated AuNPs (LbL-AuNPs) expecting that it would allow greater drug loading compared to those traditional gold nanoparticles. The LbL-AuNPs was designed as follow: (i) a negative charge polymer, collagen was used as a reducing agent and as a stabilizing agent in the first layer of AuNPs, while (ii) a positive charge polymer, chitosan was coated in the outer layer, in which chitosan was also modified with a positive charge (Quat188) to increase cellular uptake and a targeting molecule (biotin) to high specificity with cancer cells. The interaction between the inner-outer layer would be electrostatic interaction between a negative charge of collagen and a positive charge of modified chitosan to obtain polyelectrolyte collagen/chitosan coated AuNPs (AuN-Col-BiQCs). Subsequently, the synthesized AuNPs were characterized by UV-VIS, DLS and zeta potential. The UV-VIS spectrum showed SPR band around 525 and 528 nm for collagen stabilized AuNPs (AuN-col) and AuN-Col-BiQCs, respectively. After the coating with modified chitosan, the particle size of AuN-Col-BiQCs had average particle diameters of 200−240 nm, whereas zeta potential changed from -21.80 mV for AuN-Col to 43.90 mV for AuN-BiQCs. These results suggested that polyelectrolyte complex coated gold nanoparticles were successfully synthesized.

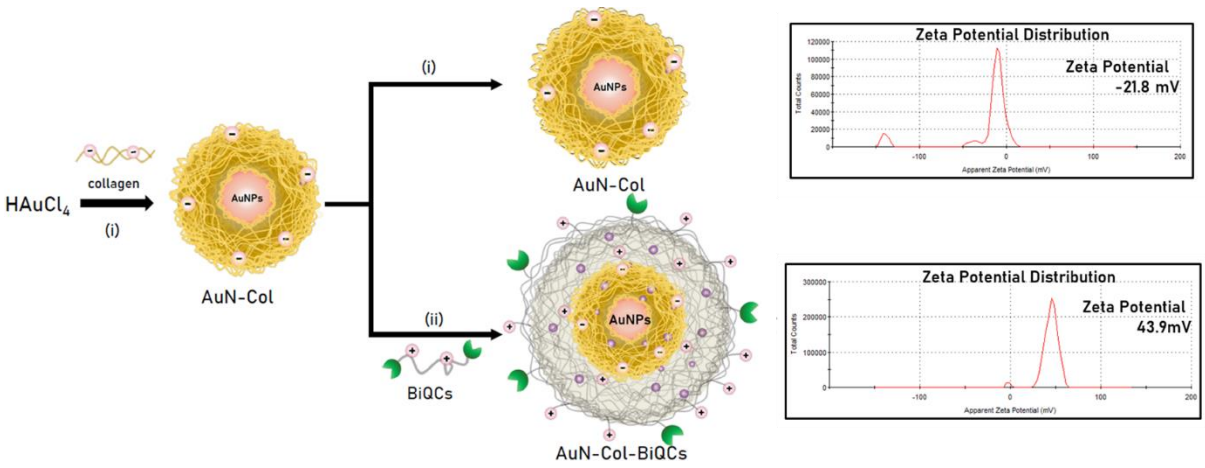

Figure 1. The particle size of gold nanoparticles (AuN-Col) and gold nanoparticles coated with derivatives chitosan (AuN-Col-BiQCs)

SP08_006_OF

SP08_006_OF: A SIMPLE PRODUCTION METHOD FOR A HIGH PERFORMANCE SiO_2/C NANOCOMPOSITE ANODE MATERIAL DERIVED FROM RICE HUSKS FOR LITHIUM ION BATTERIES

Yutthanakon Kanaphan,[1] Annop Klamchuen,[2] Chirapan Chaikawang,[1] Viyada Harnchana,[1] Sutham Srilomsak,[1] Jeffrey Nash,[3] Tuksadon Wutikhun,[2] Alongkot Treethong,[2] Tirapote Rattana-amron, [2] Sanchai Kuboon, [2] Pongtanawat Khemthong, [2] Monrudee Liangruksa,[2] Nonglak Meethong [1,4,*]

[1]Materials Science and Nanotechnology Program, Department of Physics, Faculty of Science, Khon Kaen University, Khon Kaen 40002, Thailand
[2]National Nanotechnology Center (NANOTEC), National Science and Technology Development Agency (NSTDA), 111 Thailand Science Park, Phahonyothin Road, Khlong Nueng, Khlong Luang, Pathum Thani 12120, Thailand
[3]The Graduate School, Udon Thani Rajabhat University, Udon Thani 41000, Thailand
[4]Institute of Nanomaterials Research and Innovation for Energy (IN-RIE), Research Network of NANOTEC-KKU (RNN), Khon Kaen University, Khon Kaen 40002, Thailand
*e-mail: nonmee@kku.ac.th

Abstract:

The rapidly growing demand for high performance energy storage devices for electric vehicles (EVs) has led to tremendous efforts in the development of the sustainable and low-cost nanomaterials for use as electrodes in next-generation energy storage devices. Li-ion batteries have great potential to be the most used energy storage devices for various applications. Electrodes made from silicon- and carbon-based nanomaterials extracted from rice husks (RHs) have attracted much attention due to the possibility of providing sustainable and affordable energy storage systems. Here, we demonstrate a one-step calcination process to produce high performance anodes for lithium-ion batteries based on a silica and carbon nanocomposite (SiO_2/C) from rice husks (RHs) with no additional silicon or carbon sources. It is found that the calcination process at 800 °C can generate important characteristic structures that sustain better electrochemical behavior of active SiO_2 and carbon. Hence, these RH derived SiO_2/C nanocomposites are considered promising anode materials for next generation lithium-ion batteries.

Introduction:

One of the keys to improve performance of lithium-ion batteries is the development of appropriate nanomaterials for use as battery electrodes. Using nanomaterials will lead to high storage capacity, long cycle life, good cycling stability. Si-based anode materials have great potential for use in the next generation lithium-ion batteries due to their high theoretical capacity of around 4000 $mAhg^{-1}$, which is over 10 times higher than the current commercially available graphite materials [1-3]. Despite these excellent advantages, Si-based materials have significant drawbacks. The complex processes to produce nano-Si make its expensive for replacing the current graphite anode. Furthermore, these processes are not environmentally friendly as they require toxic chemical reagents [1-3]. Moreover, the high volume-change (>300%) and low electrical conductivity of this material leads to poor structural stability and rapidly capacity fading during the lithiation-delithiation process [1-3]. Silica (SiO_2) can be considered as an anode material because the cost of preparation is much lower than that of nano-Si and its production is environmentally friendly. Additionally, its volume change is less than that of nano-Si and it has good structural stability. However, it has poor electrical conductivity, which results in

decreased extractable capacity. Much research has been done to enhance the electrochemical performance of SiO_2 material by making carbon composites. These include the use of carbon coatings [4-6], carbon fibers [7], graphene [8] and porous carbon [9]. The synthesis of nanocomposite materials that contain both SiO_2 and carbon have been widely investigated [5-13]. Some research has been done specifically for the extraction of nano-SiO_2 with a carbon composite using RHs as the main source of starting materials [9-13]. Furthermore, the use of RHs for synthesis of nanomaterials has focused on either nano-Si [1-3] or carbon materials [14-16], disregarding the advantages of a SiO_2/C composite directly extracted from RHs.

Sustainable carbon nanostructures are needed to improve the electrochemical performance of SiO_2 materials from RHs. The carbonization process to form carbon nanostructures is very attractive because of its simple production method, low cost and environmental friendliness. For example, a porous C/SiO_2 composite shows a discharge specific capacity of 325 to 485 $mAhg^{-1}$ at 0.1 C (where C-rate is defined as the current at which a battery is being discharged or charged. A 1C discharge rate would deliver the battery's rated capacity in 1 hour while 0.1C is a 10 hour discharge) with specific surface area of 270 m^2g^{-1} using one-step fire process at 900 °C under a N_2 atmosphere [17]. Ju et al. were able to prepare SiO_x/C as an anode material using a two-step fire process at 900 °C under an Ar/H_2 atmosphere. The resulting composite shows a discharge specific capacity of nearly 600 $mAhg^{-1}$ at 0.1 C [18]. Although the use of a higher temperature in carbonization processes can produce better anode materials than commercially available graphite, it has not been investigated at various temperatures for optimization. Additionally, studies using carbonization temperatures above and below 900 °C were not focused on electrochemical properties for lithium-ion batteries. Hence, this optimization of temperature for the carbonization process is very important due its increased efficiency of electrodes and low energy consumption.

In this work, we present a simple production method to synthesize silica and carbon nanocomposites (SiO_2/C) using RHs as a raw material for both C and SiO_2 sources through an environmentally friendly calcination process, as shown in **Figure 1**. It is found that the characteristic morphology of the carbon-encapsulated SiO_2 from calcination at 800 °C under an Ar atmosphere can provide for better storage capacity. The optimized Ar800 sample shows a discharge capacity of □700 $mAhg^{-1}$ at 0.1C.

Methodology:

Preparation of a SiO_2/C composite

Rice husks (RHs) were obtained from a local rice mill near Khon Kaen, Thailand. The reagents used in this study include HCl and ethanol. They were purchased from RCI Labscan and BDH Analar, respectively. The SiO_2/C nanocomposites are prepared using the steps shown in **Figure 1**. The RHs were first thoroughly washed with water to eliminate soil. Then, they were refluxed in a solution containing 5% HCl and 5% ethanol for 6 h at 100 °C to remove metal ion impurities. The leached RHs were thoroughly washed several times using deionized water and dried at 80 °C overnight. Finally, the leached RHs were calcined under an Ar atmosphere at temperatures between 500 to 1200 °C for 2 h with a heating rate of 5 °C min^{-1} to remove small organic components and form composite nanostructures between SiO_2 nanoparticles and hydrocarbon molecules. The calcined samples are denoted as ArT, where T represents the calcined temperature.

Structural and Electrochemical Characterization

XRD spectra were measured with an EMPHYREN (PANalytical) X-ray diffractometer using Cu K_α radiation. Fourier transform infrared spectrometry (FT-IR, TENSOR27, Bruker) was used to investigate the chemical functional groups of the samples. Raman spectra were obtained using a NTMDT, INTEGRA Spectra with a 532 nm Ar-ion laser. The microstructural characteristics of the samples were analyzed using field-emission scanning electron microscopy (FE-SEM, Versa 3D: FEI) and transmission electron microscopy (TEM, JOEL JEM 2100). Electrodes were fabricated by mixing the SiO_2/C composites, Super P carbon and polyvinylidene fluoride (PVDF) in N-methyl-2-pyrrolidone (NMP) at a mass ratio of 50:30:20. The resulting homogeneous slurry was cast onto a copper foil current collector using a doctor blade and then dried overnight at 80 °C in a vacuum oven. Coated copper foils were finally assembled under an argon atmosphere in a glove box (MB 20 G, MBRAUN) to form coin-

cells and Swagelok type cells. Lithium foils were used as counter electrodes with a microporous polymer (Celgard 2400) as a separator. The electrolyte consisted of ethylene carbonate (EC), dimethyl carbonate (DMC), and diethyl carbonate (DEC) in a volume ratio of 4:3:3 and 1M $LiPF_6$ with a 1 wt% of vinylene carbonate (VC) additive that was used as a conductive salt. The cells were charged and discharged at various constant current densities over the voltage range of 0.01-3.0 V (versus Li^+/Li) using a battery cycler (BST8-MA, MTI). This voltage window is typical for an anode containing Silicon.

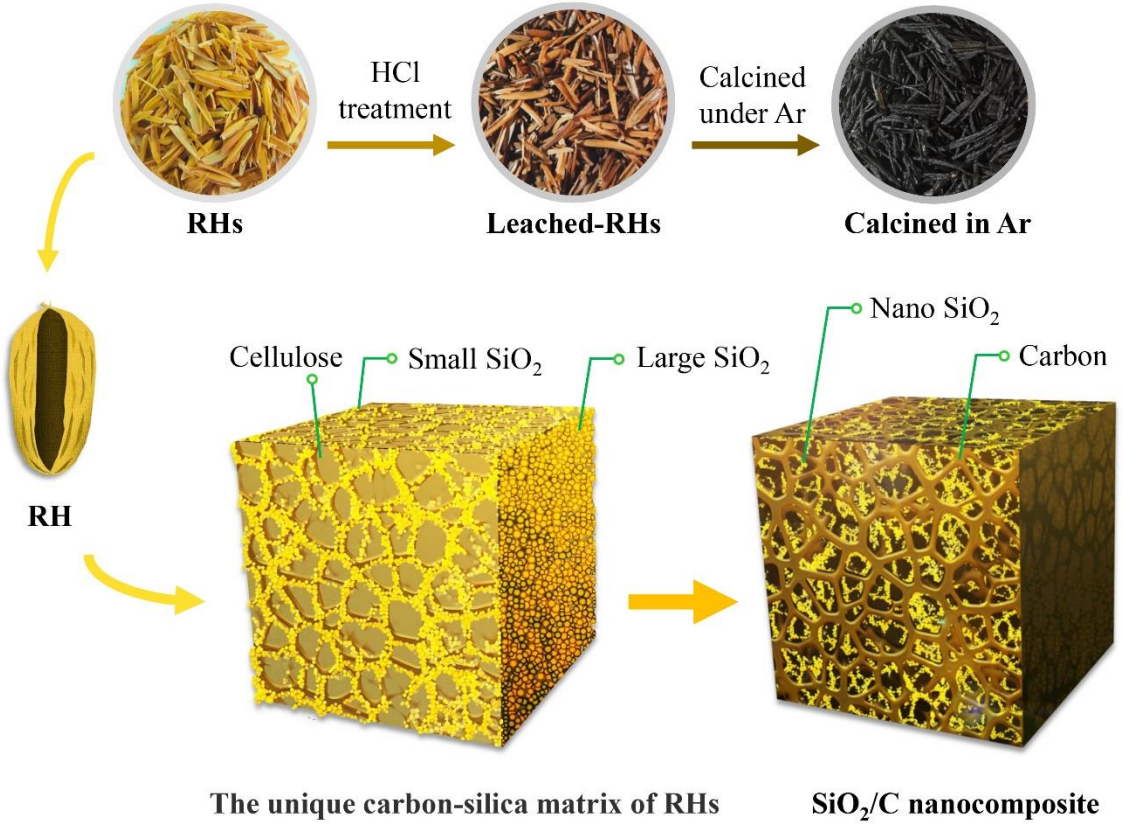

Figure 1. The preparation process of SiO_2/C nanocomposite derived from RHs

Results and Discussion:

A galvanostatic charge-discharge measurement was used to study the electrochemical performance of battery electrodes. **Figure 2** shows the rate capabilities of SiO_2/C nanocomposite samples, for various constant current densities at 0.1C, 0.2C, 0.5C, 1C and 2C, over a voltage range of 0.01-3.0 V (versus Li^+/Li). The rate capability is indicates a higher performance anode when based on the SiO_2/C nanocomposite for the Ar800 sample than on the other samples. The discharge capacity of the Ar800 sample was about 700, 600, 500, 400, and 250 $mAhg^{-1}$ at 0.1C, 0.2C, 0.5C, 1C and 2C, respectively. The Ar800 sample provided two times more reversible specific capacity at all current densities than the current anode material in this lithium-ion battery.

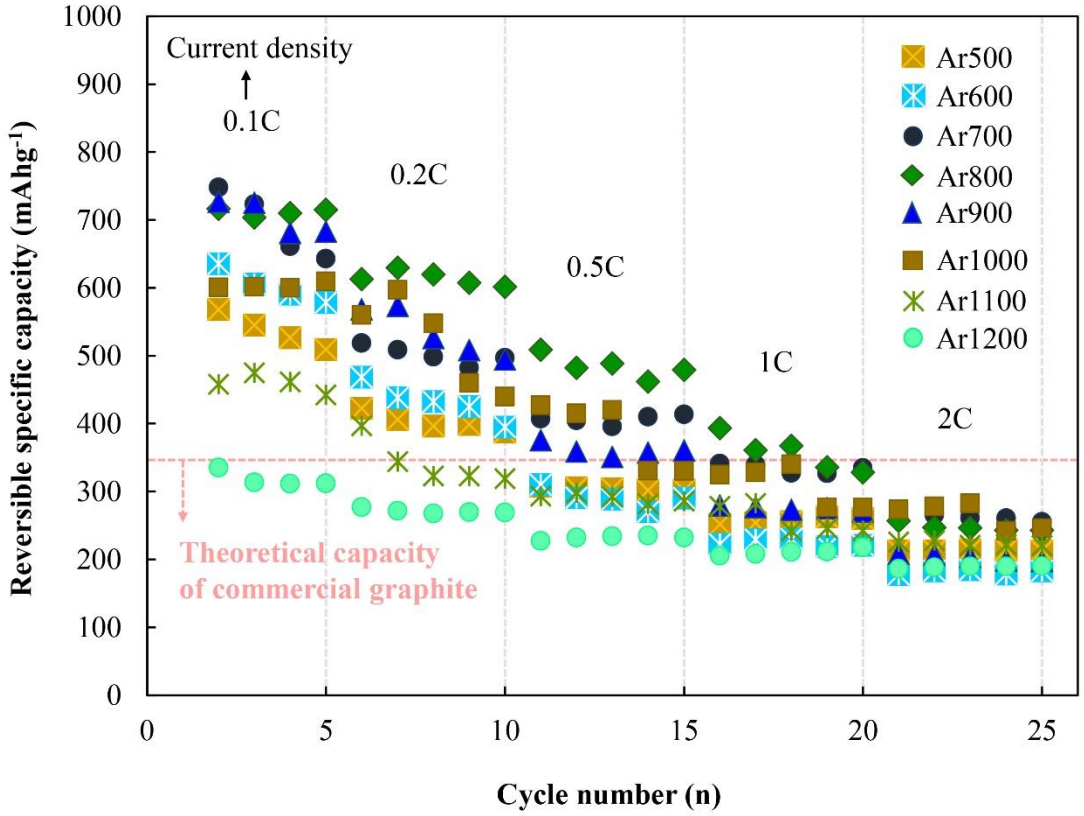

Figure 2. Rate capabilities of SiO_2/C nanocomposite samples for various constant current densities at 0.1C, 0.2C, 0.5C, 1C and 2C

The SEM and TEM images of optimized Ar800 samples are shown in **Figure** 3(a) and 3(b), respectively. These composite materials display a porous carbon structure that hosts SiO_2 nanoparticles on and in the composite structure. The dispersion of SiO_2 is not only on the surface of the carbon substrate, but within the mesopores and macropores of the structure. The mesopores are further confirmed in the multimodal pore size distribution graph in **Figure** 3(c) (inset). They appear to be around 3 to 4 nm in diameter with an average pore size of about 6.86 nm that may have originated from multiple pores in the carbon matrix as well as from void spaces between adjacent SiO_2 nanoparticles and SiO_2 contact with the carbon materials. The porous structure of the composite is further confirmed by the high specific surface area, 514 m^2g^{-1}, based on a nitrogen absorption measurement. Elemental mapping was done directly from the SEM images. **Figure** 3(d) shows that Si and O clearly have the same distribution in the sample as SiO_2. This was determined to investigate the presence of SiO_2 in the composite structure. The composite contained SiO_2 surrounded by a carbon matrix, indicating good contact between SiO_2 and carbon material, allowing good Li^+ and electron transport pathways and more electrochemical reaction sites with the electrolyte.

The XRD pattern of RHs **(**orange line**)**, leached RHs **(**purple line**)** and Ar800 **(**green line**)** are shown in **Figure** 4**(**a**).** The RHs and leached RHs show typical peaks of cellulose and amorphous silica [19]**.** An impurity peak around 27° corresponds to quartz from soils, which was eliminated through the acid washing process and is not present in the XRD pattern of the leached RHs sample**.** After the leached RHs sample was calcined under an Ar atmosphere at 800 °C for 2 h, a single broad peak located in the 2θ in range at 20-30° is obtained, which can be considered overlapping the amorphous SiO_2 **(**23°**)** and amorphous carbon **(**25°**)** phases [20]**.**

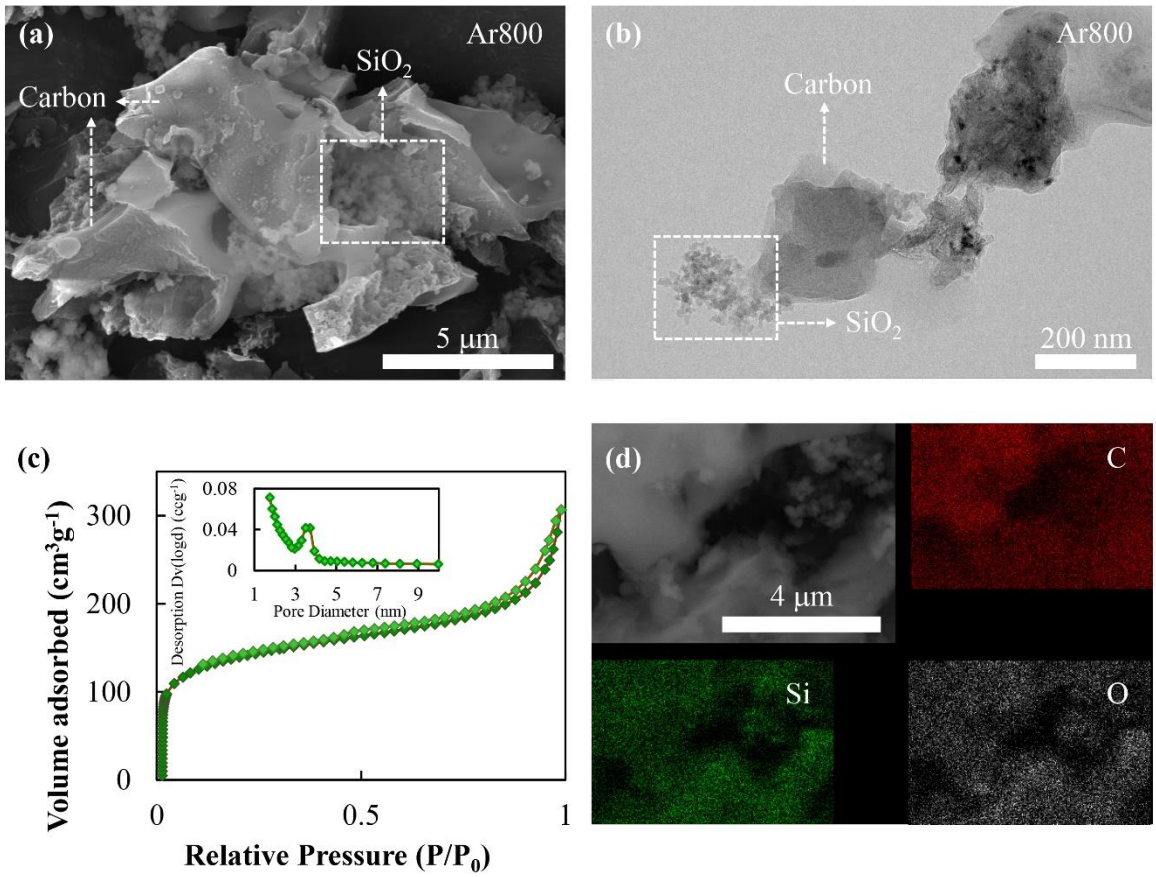

Figure 3. (a) SEM and (b) TEM images of SiO_2/C nanocomposite (Ar800 sample), (c) hysteresis loop of the N_2 absorption/desorption isotherm plot and pore size distribution of Ar800 in the range from 1 to 10 nm (inset) and (d) EDS mapping of Ar800

An obvious additional broad diffraction peak at 43° of Ar800 can be attributed to a higher number of mixed phases of amorphous carbon [21] and more turbostratic carbon domains than the other samples [22]**.** Raman spectroscopy is employed to investigate the allotropic and structural changes of carbon in the composite materials, as shown in **Figure** 4(b)**.** The Ar800 sample clearly demonstrates the two characteristic Raman peaks, including a disordered carbon D-band at around 1350 cm^{-1} and a graphitic G-band at 1600 cm^{-1}**.** Likewise, we find that the relative dimension intensities of the D-band to G-band of the sample were determined to be 0.92, indicating that the higher disorder degree of carbon and surface defects [23-25], which is consistent with the XRD results in **Figure** 4(a)**. Figure** 4(c) shows the FTIR spectra of the composite materials**.** It can be seen that Ar800 sample exhibits the two major characteristic bands in the FTIR spectra, including O-Si-O bonds **(**Si-O-Si bending at 700 to 800 cm^{-1} and Si-O-Si stretching at 1000 to 1100 cm^{-1}**)** and carbon molecules **(**alkane and alkyl groups at 2000 cm^{-1} to 2300 cm^{-1}, as well as carboxyl C=O stretching and aromatic C=C stretching at 1850 cm^{-1} to 1500 cm^{-1}**)** [26]**.** Such a high amount of surface defects in the Raman spectra, chemical bonding between SiO_2 with aromatic carbon in FTIR spectra, high specific surface area and the characteristic of the morphology of the composite structures will be helpful to enhance the electrochemical behavior of the material, while exhibiting greater potential as a low-cost and environmentally friendly anode material for lithium-ion batteries**.**

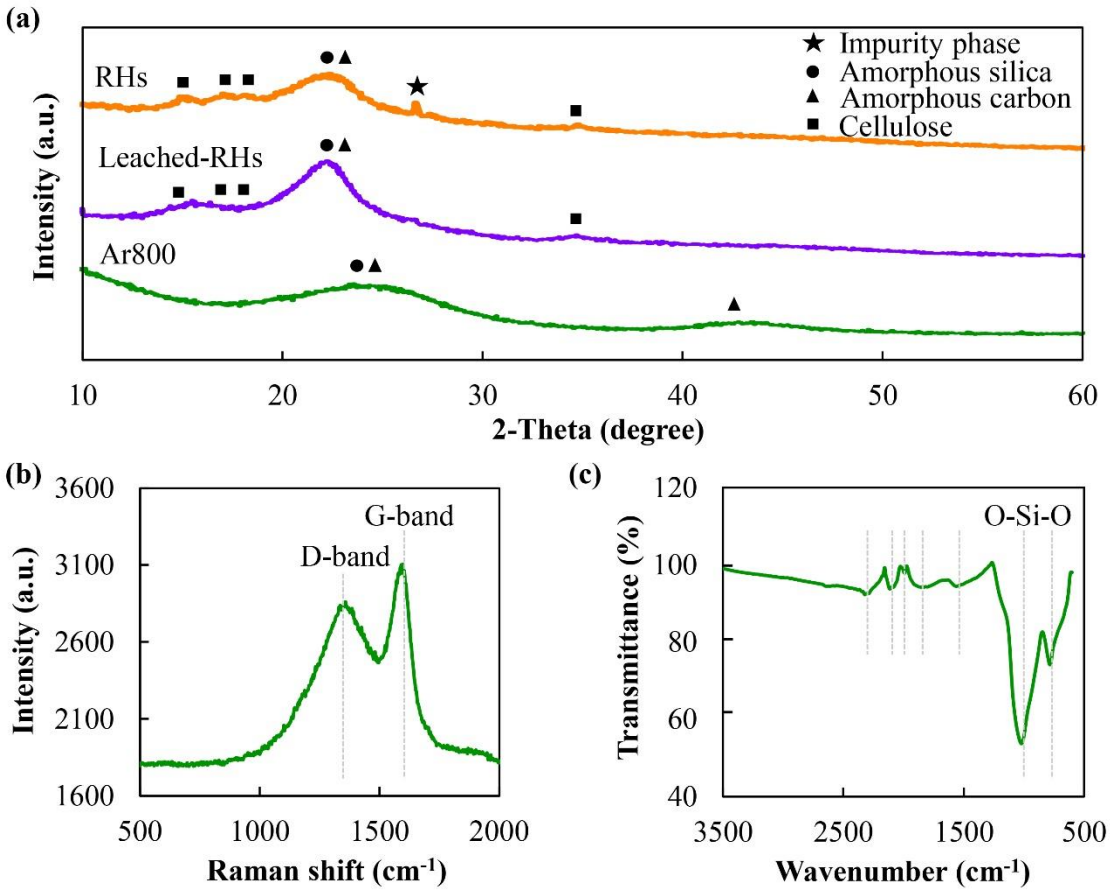

Figure 4. (a) XRD patterns of RHs (orange line), leached RHs (purple line), Ar800 (green line), (b) Raman spectra, and (c) FTIR spectra of Ar800

Conclusions:

In this work, we successfully synthesized a nanocomposite of SiO_2 and carbon from rice husks (RHs) and utilized this material as a high capacity, high stability, and acceptable rate capability anode for Lithium-ion battery. A one- step calcination process can generate important characteristic structures that sustain better electrochemical behavior of active SiO_2 and carbon. The nanostructure of SiO_2/ C materials provide a large storage capacity and good rate capability, which is necessary for fast charging for high-power applications. When considering the low cost of this biomass waste, a simple production method and environmental friendliness of the fabrication process, SiO_2/C nanocomposite electrode materials are an attractive alternative and promising anode material for next generation lithium-ion batteries.

Acknowledgements:

This work has been partially supported by the Institute of Nanomaterials Research and Innovation for Energy (P1851882), Khon Kaen University and National Nanotechnology Center (NANOTEC), NSTDA, Ministry of Higher Education, Science, Research, and Innovation, Thailand. Y.K. wishes to acknowledge the support of the Thailand Graduate Institute of Science and Technology (TGIST) (Grant No. TG-55-12-60-054M).

References:

1. Jung DS, Ryou M-H, Sung YJ, Park SB, Choi JW. PNAS. 2013;110:12229-34.
2. Liu N, Huo K, McDowell MT, Zhao J, Cui Y. Sci. Rep. 2013;3:1919.
3. Xing A, Tian S, Tang H, Losic D, Bao Z. RSC Adv. 2013;3:10145-9.
4. Cao L, Huang J, Lin Z, Yu X, Wu X, Zhang B, et al. Mater. Res. 2018;33:1219-25.
5. Lv P, Zhao H, Wang J, Liu X, Zhang T, Xia Q. J. Power Sources. 2013;237:291-4.
6. Yao Y, Zhang J, Xue L, Huang T, Yu A. J. Power Sources. 2011;196:10240-3.
7. Ren Y, Yang B, Wei H, Ding J. Solid State Ion. 2016;292:27-31.
8. Meng J, Cao Y, Suo Y, Liu Y, Zhang J, Zheng X. Electrochim. Acta. 2015;176:1001-9.
9. Cui J, Cheng F, Lin J, Yang J, Jiang K, Wen Z, et al. Powder Technol. 2017;311:1-8.
10. Chaikawang C, Hongthong R, Kaewmala S, Pongha S, Kanapan Y, Meethong N. Mater. Today: Proceedings. 2018;5:13989-94.
11. Chu H, Wu Q, Huang J. Colloids Surf. A Physicochem. Eng. Asp. 2018;558:495-503.
12. Ju Y, Tang JA, Zhu K, Meng Y, Wang C, Chen G, et al. Electrochim. Acta. 2016;191:411-6.
13. Wang L, Xue J, Gao B, Gao P, Mou C, Li J. RSC adv. 2014;4:64744-6.
14. Fey GT-K, Chen C-L. J. Power Sources. 2001;97:47-51.
15. Peng X, Fu J, Zhang C, Tao J, Sun L, Chu PK. Nanosci. Nanotechnol. Lett. 2014;6:68-71.
16. Yu K, Li J, Qi H, Liang C. Diam Relat Mater. 2018;86:139-45.
17. Wang L, Xue J, Gao B, Gao P, Mou C, Li J. RSC Adv. 2014;4:64744-6.
18. Ju YM, Tang JA, Zhu K, Meng Y, Wang CZ, Chen G, et al. Electrochim Acta. 2016;191:411.
19. Zhao H, Kwak JH, Conrad Zhang Z, Brown HM, Arey BW, Holladay JE. Carbohydr. Polym. 2007;68:235-41.
20. Cui J, Cheng F, Lin J, Yang J, Jiang K, Wen Z, et al. Powder Technol. 2017;311:1-8.
21. Yao Y, Zhang J, Xue L, Huang T, Yu A. J. Power Sources. 2011;196:10240-3.
22. Rybarczyk MK, Peng H-J, Tang C, Lieder M, Zhang Q, Titirici M-M. Green Chem. 2016;18:5169-79.
23. Peng X, Fu J, Zhang C, Tao J, Sun L, Chu PK. Nanosci Nanotechnol Lett. 2014;6:68-71.
24. Muramatsu H, Kim YA, Yang K-S, Cruz-Silva R, Toda I, Yamada T, et al. Small. 2014;10:2766-70.
25. Gao Y, Li L, Jin Y, Wang Y, Yuan C, Wei Y, et al. Appl Energy. 2015;153:41-7.
26. Socrates G. Chichester, England: John Wiley & Sons; 2001.

SP08_007_PF: PREPARATION OF LAKE PIGMENT FROM ORCHID USING ADSORPTION METHOD

Chanipron Vadeesirisak[1], Sumonmarn Chaneam[1], Jitnapa Sirirak[1]*

[1] Department of Chemistry, Faculty of Science, Silpakorn University,
Nakhon Pathom, Thailand 73000
*e-mail: jitnapasirirak@gmail.com, sirirak_j@su.ac.th

Abstract:

Orchid *Dendrobium Sonia* 'Earsakul' is the most orchid cut-flower exported from Thailand. Its growing areas increase every year. However, in some seasons, this orchid is overproduced and left as agricultural waste. Herein, natural dye from dried orchid *Dendrobium Sonia* 'Earsakul' was transformed into yellow-green lake pigment using adsorption method and aluminium hydroxide as the adsorbent. The effects of pH, adsorbent dosage and adsorption time were investigated. The results showed that similar yellow-green color of lake pigments were obtained when orchid dyes with initial pH 2-10 were used. It can be noted that orchid dye at pH 2 gave slightly deeper yellow-green color lake pigment compared to other pHs. Moreover, higher amount of adsorbent, paler yellow-green color of lake pigment observed. Additionally, only 5 min was required for the adsorption time.

Introduction:

The products using natural dye and lake pigment have attracted considerable attention because the customers become aware the drawback of synthetic dye on human health and the environment.[1-2] Natural dyes can be derived mainly from plant parts such as leaves, flower, bark and roots.[3] On the other hand, lake pigment can be prepared by fixing natural pigment dissolved in natural dye onto substrate such as aluminium hydroxide, aluminium oxide, clay, and montmorillonite.[4-8]

Figure 1. *Dendrobium Sonia* 'Earsakul'

Orchid '*Dendrobium*' is one of the most cut-flower exported from Thailand, especially '*Dendrobium Sonia* 'Earsakul' (Figure 1).[9] It has beautiful white and purple color, and contains purple pigment named anthocyanins. Each year, there are a lot of low grade and oversupply orchid left as agricultural waste.[10] Therefore, in order to enhance the application of orchid and make orchid value added, in this work, orchid was used in the preparation of natural dye and lake pigment.

Methodology:

Preparation of orchid dye

Orchid dye was prepared using the method described in Chaneam's publication in 2018.[11] In short, fresh orchid '*Dendrobium Sonia* 'Earsakul' was kept in 'Greenhouse solar dryer' for 24 h to make them dried (Figure 2).

Figure 2. Drying orchid 'Greenhouse solar dryer' (left) and dried orchid (right)

Only dried orchid with purple color was then selected, minced and kept for further used (Figure 3a). After that, dried orchid:water (10:100 w/v) was boiled for 15 min, followed by filtration though filter paper (No.1 Wintech, Japan) to obtain deep purple orchid dye, pH 4.7 (Figure 3b).

Figure 3. Mince dried orchid (3a) and orchid dye (3b)

Preparation of lake pigment from orchid

Herein, lake pigment from orchid was prepared using adsorption method. 5 g of Aluminium hydroxide (AR, Sigma Aldrich) was added into 100 ml of orchid dye. The mixture was then stirred under magnetic stirring for 3 h, followed by vacuum filtration though filter paper (No.1 Wintech, Japan). The powder of lake pigment from orchid was dried at 60 °C overnight and characterized using CIELAB and UV-Vis diffuse reflectance spectroscopy technique. Moreover, parameters involved adsorption efficiency including initial pH of orchid dye (pH 2-10), adsorbent dosage (1-10%w/v) and adsorption times (0-180 min) were investigated.

Results and Discussion:

Effect of initial pH of orchid dye on adsorption

To explore the effect of initial pH of orchid dye on the adsorption, the color of lake pigments prepared by using orchid dye at pH 2-10 and 5 %w/v of absorbent were observed and compared. As shown in Table 1 and Figure 4, it was found that lake pigments obtained from the adsorption using orchid dye at pH 2-10 have similar yellow-green color and similar UV-Vis diffuse reflectance spectra. Additionally, it can be noticed the deepest yellow-green color lake pigment was obtained when orchid dye at pH 2 was used.

Table 1. CIELAB of the lake pigment from orchid prepared by using different initial pH of the orchid dye.

pH	pH 2	pH 4	pH 6	pH 8	pH 10
L*	78.38	88.67	85.66	92.85	91.67
a*	-5.71	-10.97	-12.29	-12.08	-11.72
b*	15.24	23.79	28.72	28.68	35.93

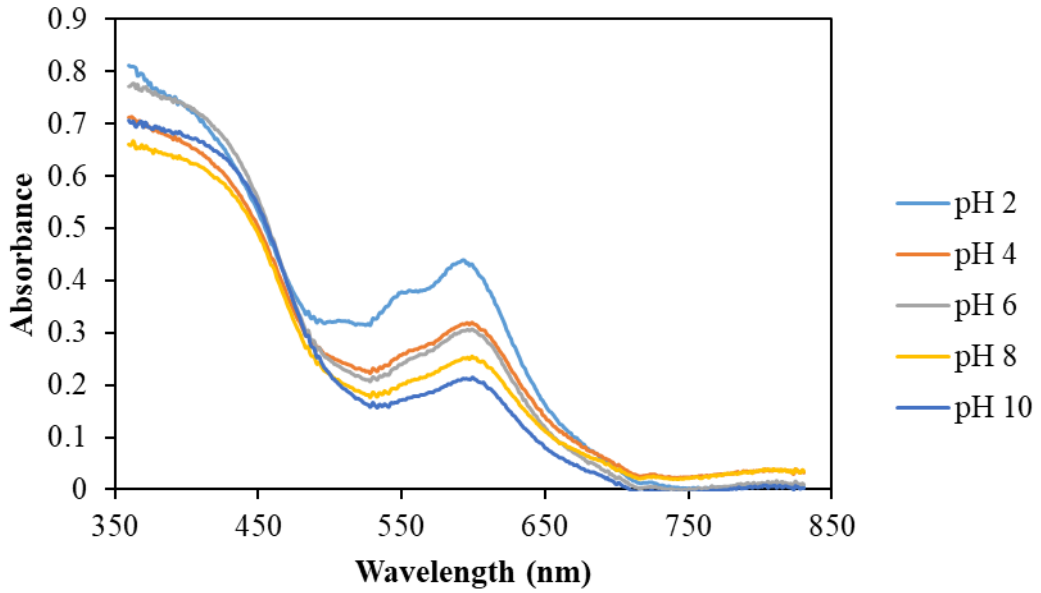

Figure 4. UV-Vis diffuse reflectance spectra of the lake pigment from orchid prepared by using different initial pH of the orchid dye.

Effect of adsorbent dosage on adsorption

In order to investigate the effect of adsorbent dosage on the adsorption, the color of lake pigments prepared by using different dosage of aluminium hydroxide in the range of 1-10 %w/v and orchid dye with initial pH of 4.7, were observed and compared. As can be seen in Table 2 and Figure 5, similar yellow color lake pigments and similar UV-Vis diffuse reflectance spectra were obtained when adsorbent dosages of 1-10 %w/v were used. However, it can be seen that using higher amount of adsorbent can result in the paler color of lake pigment. Moreover, Table 3 demonstrated that when higher amount of aluminium hydroxide was used, the pH of orchid dye after adsorption was also increased.

Table 2. CIELAB of the lake pigment from orchid prepared by using different dosage of aluminium hydroxide.

Aluminium hydroxide dosage (%w/v)	0	1	2.5	5	10
L*	118.07	95.75	95.7	86.77	94.31
a*	-2.36	-6.54	-7.73	-9.77	-10.77
b*	3.86	33.23	30.37	23.85	26.09

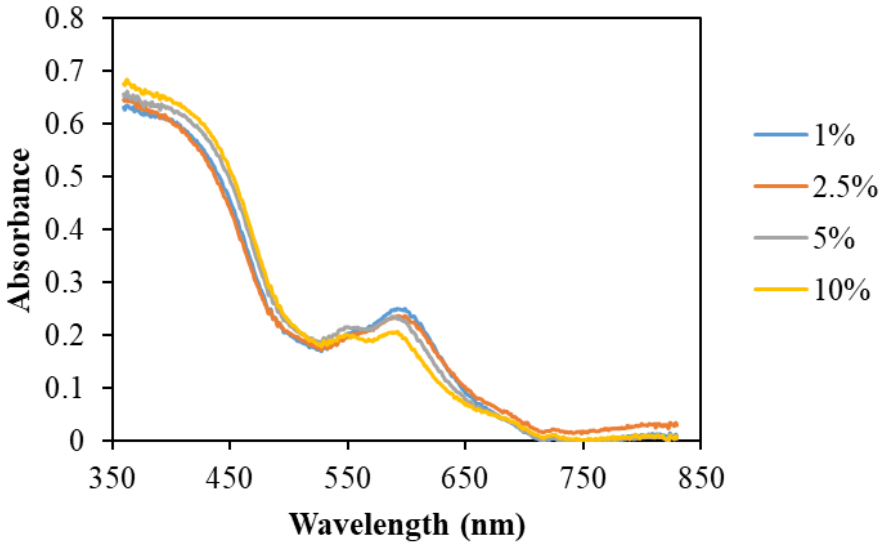

Figure 5. UV-Vis diffuse reflectance spectra of lake pigment from orchid using aluminium hydroxide as different adsorbent dosage.

Table 3. pH of orchid dye after adsorption using the various dosage of aluminium hydroxide

Aluminium hydroxide dosage (%w/v)	pH of orchid dye after adsorption
1	6.04
2.5	6.97
5	7.52
10	7.9

Effect of adsorption time on the adsorption.

To observe the effect of adsorption time on the adsorption, 10 g of aluminium hydroxide was stirred in 200 ml of orchid dye with initial pH of 4.7 and, at different time interval, (5, 10, 15, 20, 40, 60, 120 and 180 min), 200 µL of mixture was diluted with distilled water (2.8 mL, pH 7) and centrifuged for 1 min at 5,000 rpm. After that, UV–Vis absorption of solution after adsorption at 594 nm was observed and compared. Figure 6 showed that, the absorbance at 594 nm was decreased from 0.96 to 0.77 after 5 min of adsorption time. Moreover, similar absorbance at 594 nm of ~0.77-0.80 was observed when adsorption time of 5 to 180 min was applied. This indicated that 5 minutes were required for the adsorption time.

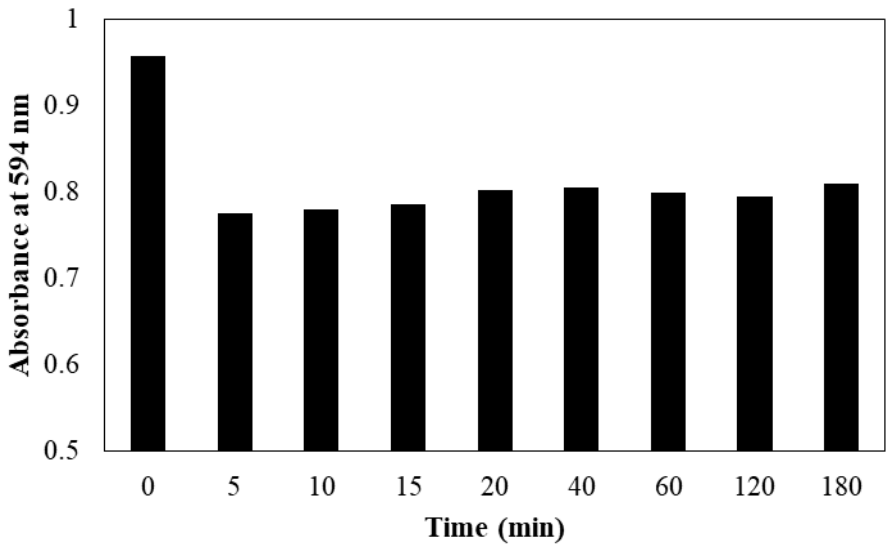

Figure 6. Comparison of the absorbance at 594 nm of orchid dye after the adsorption using different adsorption time.

Conclusion:

Herein, natural yellow lake pigment was prepared from orchid '*Dendrobium Sonia* 'Earsakul' and aluminium hydroxide using adsorption method. The adsorption parameters including initial pH of orchid dye, the amount of aluminium hydroxide and adsorption time were also investigated. It was found that orchid dye at pH 2 can yield the deepest yellow lake pigment compared to other initial pH in the range of 2-10. Moreover, the adsorption time required for the preparation of lake pigment was only 5 min. Our results can enhance the benefit of orchid and give an optional source of natural dye for the preparation of lake pigment.

Acknowledgements:

We thank Research assistant scholarship for M.Sc. students, Faculty of Science, Silpakorn University for financial support (CV).

References:

1. Yusuf M, Shabbir M, Mohammad F. Nat. Prod. Bioprospect. 2017;7 (1):123-145.
2. Lellis B, Fávaro-Polonio CZ, Pamphile JA, Polonio JC. Biotechnol. Res. Innov. 2019;3:275-290.
3. Bechtold T, Mussak R. “Handbook of natural colorants”, John Wiley & Sons, United Kingdom, 2009.
4. Marras S. Ge-conservación, 2015;61-62.
5. Berbers SV, Tamburini D, van Bommel MR, Dyer J. Dyes Pigm. 2019;170: 107579.
6. Sirirak J, Worawannotai N, Suwanchawalit C, Chayabutra S. J. Met. Mater. Miner., 2020;30 (1):20-28.
7. Vadeesirisak C, Chayabutra S, Sirirak J. Burapha Sci. J. 2020;25(2):545-562.
8. Fournier F, de Viguerie L, Balme S, Janot J.-M, Walter P, Jaber M. Appl. Clay Sci. 2016;130:12-17.
9. B. Phinaitrup, Thammasat Rev. 2014;16:75.
10. Thammasiri K. Horticulturae. 2016; 2(9): 1-13.
11. Sukaram T, Sirisakwisut P, Sirirak J, Nacapricha D, Chaneam S. Int. J. Environ. Anal. Chem. 2018; 98(10): 907–920.

SP08_008_PA

SP08_008_PA: UTILIZATION OF BRAZILEIN ON TEST STRIP FOR FE^{2+} DETECTION

Satipat Suttayasorranakhom[1,*], Anuwut Petdum[1], Thanasat Sooksimuang[2], , Nantanit Wanichacheva[1] and Jitnapa Sirirak[1]

[1]Department of Chemistry, Faculty of Science, Silpakorn University, Nakhon Pathom, Thailand 73000
[2] National Metal and Materials Technology Center (MTEC), Pathumthani, 12120, Thailand
[*]e-mail: jitnapasirirak@gmail.com and sirirak_j@su.ac.th

Abstract

The contamination of heavy metal including iron in an environment become higher due to the larger usage of iron in the industries. As a result, practical sensor for the detection of iron is required. Herein, the application of brazilein from sappanwood as Fe^{2+} colorimetric sensor was explored. It was found that the color of brazilein sensor was change from pink to blue upon the addition of Fe^{2+} in Tris buffer solution, pH 7.2. The detection limit of sensor was 0.96 ppb. This sensor also showed high Fe^{2+}-selectivity over other eighteen interfering ions, such as Fe^{3+}, Al^{3+}, Ag^{+}, Hg^{2+}, Pb^{2+}, Zn^{2+}, Cu^{2+} etc. Moreover, in order to make the sensor easier and more practical for usage, test strip for Fe^{2+} detection was prepared using filter paper and brazilein solution (Tris buffer:methanol, 99:1, 5 mM, pH 7.2). After the test strips were dipped into Fe^{2+} solution with various concentration of Fe^{2+}, their color changes were observed and compared using UV-Vis differential reflectance spectroscopy and CIELAB technique. It was found that when the Fe^{2+} solution with minimum concentration of 1 ppm was used, a noticeable color change of the test strip from orange to blue which could be seen by naked eye was observed.

Keywords: Brazilein, Fe^{2+} sensor, Test strip

SP08_009_OA: PREPARATION OF Bi_4MoO_9 CATALYST BY PRECIPITATION METHOD FOR PHOTODEGRADATION OF ANIONIC AZO DYES

Varanya Somaudon, Tammanoon Chankhanittha, Jidapa Watcharakitti, Suwat Nanan*

Materials Chemistry Research Center, Department of Chemistry and Center of Excellence for Innovation in Chemistry, Faculty of Science, Khon Kaen University,
Khon Kaen 40002, Thailand
*e-mail: suwatna@kku.ac.th

Abstract:

Challenging in photocatalysis research is to develop a novel photocatalyst with high solar-light-harvesting capacity and great electron-hole separation efficiency. The present research reports a preparation of bismuth molybdate (Bi_4MoO_9) catalyst using a facile and capping agent-free chemical precipitation method. Particularly, the synthesis did not require expensive reagent or surfactant. It is simple, catalyst-free, and easily prepared. The catalyst showed the face-centered cubic phase with an energy band gap of 3.18 eV and spherical morphology of 64 nm. The catalyst provided an enhanced efficiency of 100% toward degradation of Congo red dye after 30 min of solar light irradiation. The photodegradation of the dye correlated well with the first-order kinetics model. The photogenerated electron and hole played the most important role in azo dye degradation. The chemical structure of the catalyst remained stable after the fifth run. The catalyst also retains its original efficiency even after the fifth cycle indicating the advantages of stability and reusability. The prepared Bi_4MoO_9 catalyst showed a promising potential for removal of toxic dyes in wastewater. The present research demonstrates a novel road for preparation of solar-light-driven photocatalyst for environmental remediation.

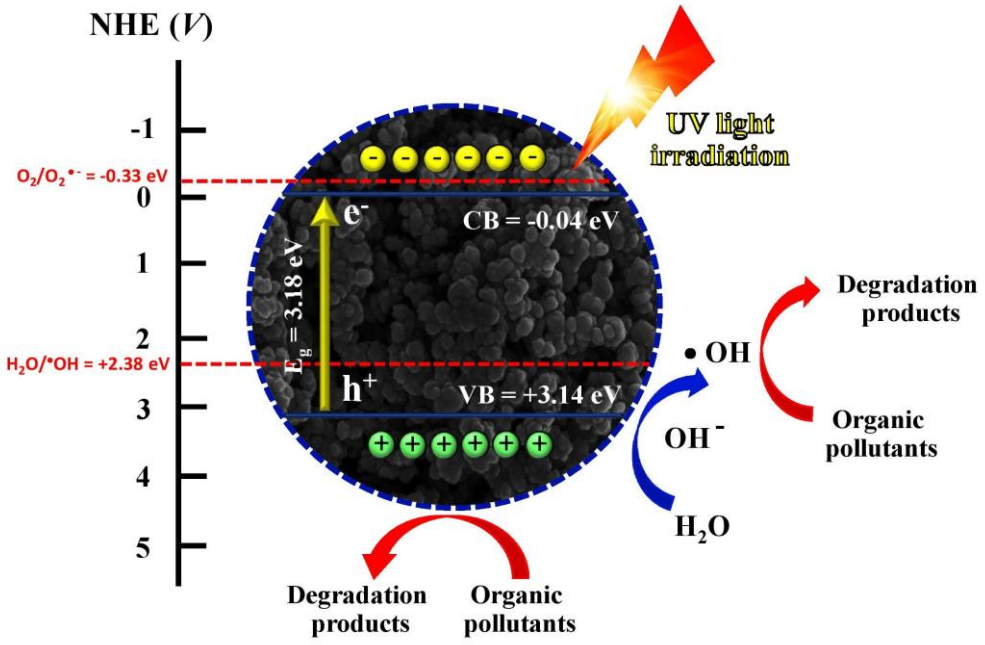

Figure 1.

SP08_010_OF: EFFECTS ON IONIC CONDUCTIVITY OF CO-DOPED LITHIUM LANTHANUM TITANATE SOLID ELECTROLYTES BY Sr^{2+} AND Al^{3+} FOR ALL-SOLID-STATE LITHIUM ION BATTERIES

Purumet Pipitworrakul,[1] Yutthanakon Kanaphan,[1] Sutham Srilomsak,[1,2]
Nonglak Meethong[1,2,*]

[1]Materials Science and Nanotechnology Program, Department of Physics, Faculty of Science, Khon Kaen University, Khon Kaen 40002, Thailand
[2]Institute of Nanomaterials Research and Innovation for Energy (IN-RIE), Research Network of NANOTEC-KKU (RNN), Khon Kaen University, Khon Kaen 40002, Thailand
*e-mail: nonmee@kku.ac.th

Abstract:

All-solid-state lithium-ion batteries (ASSLIBs) have been widely studied to solve the safety issue of lithium-ion batteries (LIBs). Solid electrolytes should have an ionic conductivity near to that of the liquid electrolyte to become commercially practical. However, ceramic solid electrolytes such as lithium lanthanum titanate (LLTO) exhibit too low total ionic conductivity due to slow lithium ions diffusion across the grain and grain boundaries. Therefore, the aim of this study is to demonstrate that the ionic conductivity of LLTO can be improved by co-doping with strontium (Sr^{2+}) and aluminum ions (Al^{3+}). The model sample, represented as $(Li_{3x}La_{2/3-x})_{1-y}Sr_y(Ti_{1-z}Al_z)O_{3-z}$ where x = 0.11, y = 0.05, z = 0.005 shows that the charge transfer resistance decreases dramatically and the total ionic conductivity reaches 6.01 x 10^{-5} S·cm^{-1}, which is 10-folds lower than the undoped one. These dopants affect the crystalline structure of LLTO and alter the mobility of lithium ions. Therefore, co-doping with Sr^{2+} and Al^{3+} enhances ionic conductivity of LLTO.

Introduction:

Lithium-ion batteries (LIBs) are widely used as energy storage devices for various mobile applications including portable electronics and mobile medical tools. LIBs are also the major driving force for developments of electric vehicles (EV) and stationary energy storage systems (ESS). This is due to the high gravimetric energy density, high volumetric energy density and low self-discharge characteristics of LIBs. However, current LIBs use flammable organic solvents as electrolytes resulting in safety concerns. All-solid-state lithium-ion batteries (ASSLIBs) have been extensively researched to address these safety issues. In some critical applications, inorganic solid electrolytes are preferred over polymeric solid electrolytes due to enhanced safety, high mechanical strength, and high thermal resistance. In addition, electrochemical stability and compatibility with high voltage cathode materials can increase the energy density of the ASSLIBs. However, solid electrolytes have a major disadvantage of low total ionic conductivity that needs to be overcome for ASSLIBs to be commercialized for large scale applications such as EVs and ESSs.

Many types of materials have been investigated for use as solid electrolytes. These include materials with perovskite,[1] garnet,[2] NASICON,[3] LISICON,[4] Sulfide-,[5] Nitride-,[6] Halide-[7] based structures as well as glass ceramics.[8] Each solid electrolyte material has its own drawbacks and advantages. For example, NASICON electrolytes typically have a high ionic conductivity at room temperature but the expensive GeO_2 raw material used to produce these materials make them impractical for large scale applications.[9] Garnet electrolytes are cheap and have a high ionic conductivity. However, they are highly sensitive to moisture and carbon dioxide in the atmosphere making them unstable and hard to produce in a large quantity.[10] Perovskite electrolytes have

been considered for use in ASSLIBs due to their high grain ionic conductivity at room temperature and high stability in the atmosphere.[1]

Lithium lanthanum titanate ($LiLaTiO_3$; LLTO) is one of the perovskite electrolytes with high grain ion conductivity. However, the total ion conductivity is still low because resistance from the grain boundaries is normally high.[11,12,13] For the purpose of increasing ionic conductivity, several researches have been studied on the substitution of other elements in the LLTO. Partial substitution of ions with a larger ionic radius than the host ions such as Sr^{2+} [14,15]causes the expansion of the crystal structure. The ionic conductivity of LLTO doped by Sr^{2+} increased with increasing Sr content. In addition, the ionic bond strength between Li and O also affects the ion conductivity. Li-O Bond strength can be reduced by doping with Al^{3+} [15,16,17], resulting in decreased Ti-O Bond strength. These issues have been widely studied as a replacement, substituted, or composited, affect to the grain conductivity and increased grain boundary.

The objective of this work is to enhance the ionic conductivity of LLTO by co-doping strontium (Sr^{2+}) and aluminum (Al^{3+}) ions into a cation site. Sr^{2+} ions are designed to be substituted into Li^+ sites while Al^{3+} ions into Ti^{4+} sites to create a neutral/charge compensated crystal structure. The effects of co-doping on crystal structure and ionic conductivity will be demonstrated.

Methodology:

Preparation of $(Li_{3x}La_{2/3-x})_{1-y}Sr_y(Ti_{1-z}Al_z)O_{3-z}$*:* The precursor was prepared by the solid-state reaction method using Lithium carbonate (Li_2CO_3) 99.9%, Lanthanum oxide (La_2O_3) 99.9%, Titanium dioxide (TiO_2) 99.8% from Sigma-Aldrich as starting materials. Strontium carbonate ($SrCO_3$) 99.9% from Sigma-Aldrich and Aluminum carbonate ($Al_2(CO_3)_3$) from Alfa Aesar were used as raw materials for Sr and Al dopants, respectively. Firstly, Li_2CO_3 (20% excess), La_2O_3, TiO_2, $SrCO_3$, $Al_2(CO_3)_3$ were mixed with a molar ratio of 0.36:0.532:0.995:0.05:0.005 which followed from the literature review [14,15] using ethanol as a solvent. Ball-milling was done in a Zirconia jar using Zirconia balls as a grinding media for 12 hours. The slurry was dried at 80 ºC and calcined at desired temperatures and times to study the effect of calcination temperatures on crystalline structure which followed by literature review. The heating rate of 10 ºC/min and cooling rate of 10 ºC/min are used. The quite fast cooling rate is used to promote cubic phase formation that is stable at high temperatures.

Characterization: To study crystalline structure, the calcined powders were characterized by x-ray diffraction (XRD) technique using an EMPYREAN (PANalytical) X-ray diffractometer with CuK_α radiation. Rietveld refinements were done using the HighScore Plus software. To study the effect of co-doping on ionic conductivity, the powders of co-doped (CLLTO) and undoped (LLTO) samples calcined at 1100 ºC were pressed into pellets by a hydraulic pressing with 130 MPa and sintered at 1,350 ºC in air for 6 hours. Then, the pellets were polished and sputtered with Au on pellet surfaces using a Polaron SC500 (Sussex, UK) sputter coating unit. The impedance spectra were measured using an Agilent E4980A (Hayward, CA) Precision LCR Meter over the frequency range of 10^1-10^7 Hz with an oscillation voltage of 500 mV.

Results and Discussion:

The XRD patterns of the $(Li_{3x}La_{2/3-x})1\text{-}ySr_y(Ti_{1-z}Al_z)O_{3-z}$ where x = 0.12, y = 0.05, z = 0.005 calcined at different firing conditions are shown in Figure 1. The samples calcined at 800 °C and 900 °C for 12 hours show that the raw materials have not fully reacted to form a perovskite ABO_3 structure. After calcining in air atmosphere at 1000 °C for 12 h, the observed XRD peaks indicate that the sample displays an ABO_3 perovskite structure with a simple cubic perovskite in space group $Pm\bar{3}m$.[18] In addition, an noticeable amount of tetragonal unit cell in space group P4/mmm also occurs. This can be observed from the superstructure peaks marked with arrows due to the ordering arrangement of La^{3+}, Li^+ and vacancies along the c-axis.[19] The XRD peaks of the samples calcined at 1150 °C correspond to the cubic perovskite structure without the superstructure peaks. This means that the calcination temperature of 1150 °C can fully convert the raw materials into cubic perovskite. In this work, the optimized calcination condition to form the cubic perovskite solid electrolytes in our study is 1100 °C for 8 hours. Calcining times of 8-12 h show no difference phase formation at this temperature (results are not shown). The full study showing this optimization process will be reported elsewhere. In addition, the XRD pattern of the undoped LLTO calcined at the same conditions (1100 °C for 8 hours) is shown in Figure 1b. As can be seen,

both cubic and tetragonal phases can be observed. This means that co-doping also affects the crystal structure by promoting cubic phase transformation.

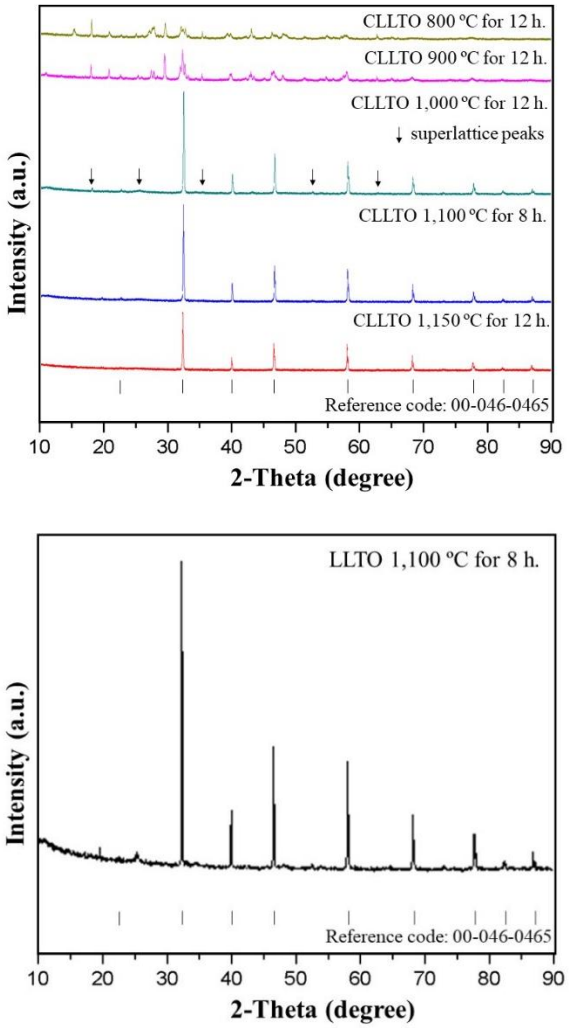

Figure 1 XRD patterns of (a) Sr^{2+} and Al^{3+} co-doped LLTO samples after calcined at different temperatures and (b) LLTO samples after calcined at 1100 °C for 8 h.

Rietveld refinements have been employed to clearly demonstrate the effect of calcination temperature on the crystalline phase(s) of co-doped LLTO. As can be seen in **Figure 2**, the sample calcined at 1000 °C for 12 h contains both tetragonal and cubic phases. The refinement result indicates that about 15.8 wt% of the tetragonal phase appears at this condition. The samples calcined at the other conditions contain only the cubic phase. The lattice constants of the cubic and tetragonal phases as well as the agreement indices are shown in the figure. As can be seen, the lattice constants of the cubic phase decrease insignificantly as the calcining temperature increases. There are several reasons why lattice constants change when firing temperature increases. For example, the lattice constants of several ceramics have been found to be correlated with crystallite sizes. Firing temperature can create grain growth in sintered ceramics which results in enlarged grains and alternation of lattice constants. In sintered ceramics, the volume change caused by the cubic to tetragonal transformation induces large stresses, and these stresses cause the grains to crack upon cooling from high temperatures. In addition, in a highly defective ceramic powder, firing at different temperatures can lead to how defect species inside the grains and along grain boundaries move. In this work, the Rietveld refinements were done on powders, not on sintered ceramics. It is possible that the different firing temperature of 50 °C did not create enough effect to make the crystallographic changes in these samples.

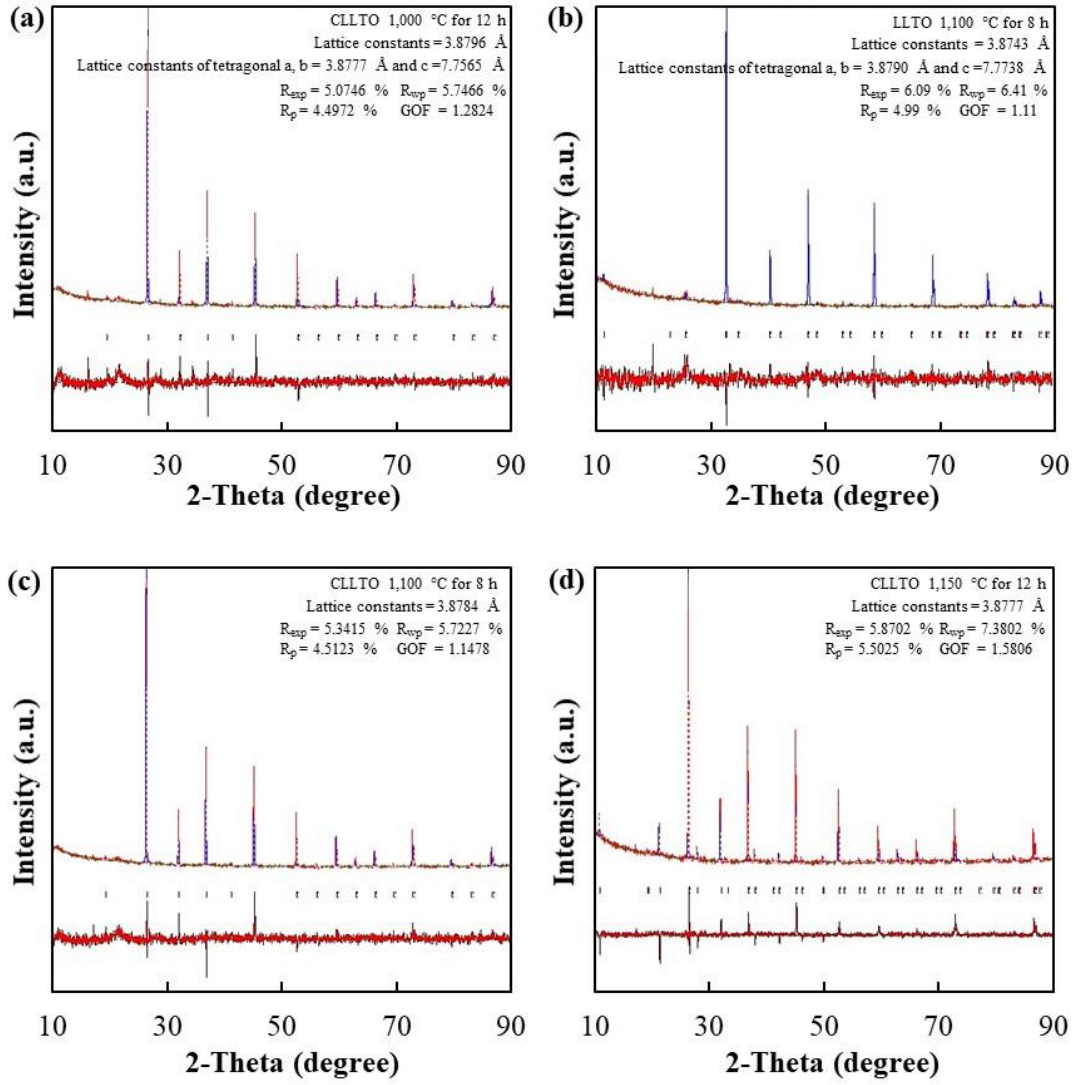

Figure 2 Rietveld refinement results of the LLTO samples (a) co-doped and calcined at 1000 ºC 12 h (b) undoped and calcined at 1100 ºC 8 h (c) co-doped and calcined at 1100 ºC 8 h and (d) co-doped and calcined at 1150 ºC 12 h, respectively.

The complex impedance spectra measured at room temperature of the undoped and co-doped samples calcined at 1100 °C 8h followed by sintered at 1350 °C 6h are shown in **Figure 3.** The equivalent model is taken from the literature to explain the complex impedance spectra.[14] R_s represents the ohmic resistance; R_b and CPE_b represent the the resistance and constant phase element parameter characterizing ionic conductance in grains; R_{gb} and CPE_{gb} represent the resistance and constant phase element parameter characterizing ionic conductance in grain boundaries; R_{ct}, CPE_{dl}, and W represent the charge transfer resistance, Warburg impedance, and double layer capacitance, respectively. The fitting results are shown in **Table 1.**

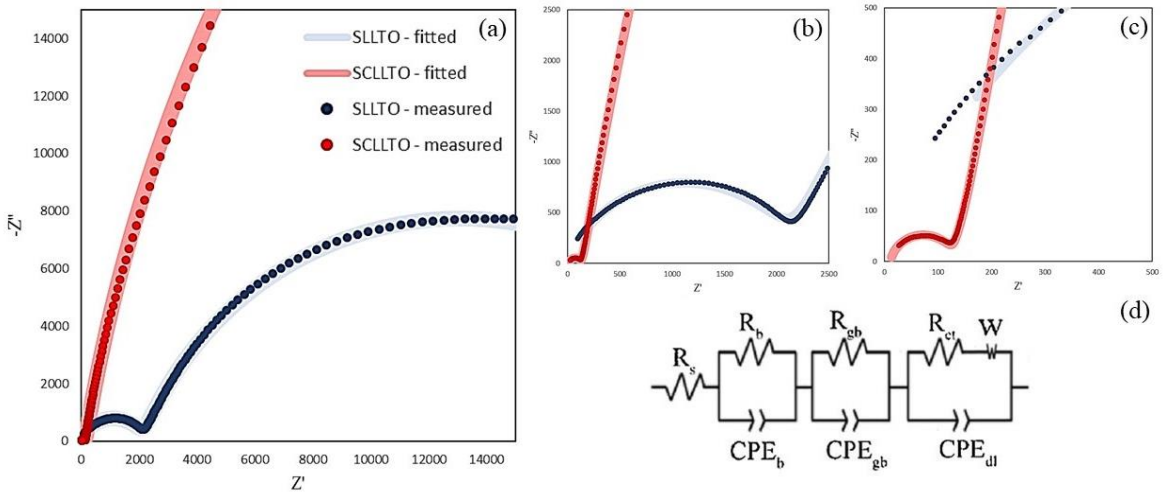

Fig. 3. Comparison of the complex impedance plots of the doped and undoped LLTO ceramics at room temperature in the frequency range of 10^1–10^7 Hz

(a). Complex impedance in a higher frequency range (b) and (c).

The equivalent circuit model of impedance spectroscopy (d).

Table 1. Fitted results of the equivalent model.

Samples	R_b (Ω)	σ_b (S·cm^{-1})	R_{gb} (Ω)	σ_{gb} (S·cm^{-1})	σ_{total} (S·cm^{-1})
SLLTO	2,200	3.69 x 10^{-6}	17,000	4.79 x 10^{-7}	4.17 x 10^{-6}
SCLLTO	120	5.81 x 10^{-5}	4,000	2.03 x 10^{-6}	6.01 x 10^{-5}

The calculated results of the ionic conductivity of both samples showed that both grain and grain boundary conductivities of the co-doped sample increased dramatically. At room temperature, the undoped sample had the grain conductivity of 3.69 x 10^{-6} S·cm^{-1} while the grain boundary conductivity was calculated to be 4.79 x 10^{-7} S·cm^{-1}. The co-doped sample had the grain and grain boundary conductivity of 5.81 x 10^{-5} S·cm^{-1} and 2.03 x 10^{-6} S·cm^{-1}, respectively. The detailed fitting technique has been described in the literature.[20]

Conclusions:

In this work, we successfully synthesized Sr^{3+} and Al^{3+} co-doped LLTO perovskites for use as solid electrolytes in ASSLIBs. The model material, $(Li_{3x}La_{2/3-x})_{1-y}Sr_y(Ti_{1-z}Al_z)O_{3-z}$ where x = 0.12, y = 0.05, z = 0.005 has been used to demonstrate the effect of co-doping on ionic conductivity of LLTO. The result indicates that the charge transfer resistance of the co-doped sample is much lower than the undoped sample. The total ionic conductivity improves by approximately 10 folds. The grain and grain boundary conductivities are 5.81 x 10^{-5} S·cm^{-1} and 2.03 x 10^{-6} S·cm^{-1}, respectively. These co-doping ions affect the crystalline structure of LLTO and alters the mobility of lithium ions. Therefore, these materials should be electrochemically studied further to evaluate its feasibility for use as solid electrolytes for future all-solid-state Li-ion batteries.

Acknowledgements:

This work has been partially supported by the Institute of Nanomaterials Research and Innovation for Energy, Khon Kaen University and National Nanotechnology Center (NANOTEC), NSTDA, Ministry of Higher Education, Science, Research, and Innovation, Thailand.

References:

1. Inaguma Y, Liquan C, Itoh M, et al. Solid State Commun. 1993;86(10):689-693.
2. Zeng X, Qiao S, Shen H, et al.. J Nutr. 2015;145(10):2212-2220.
3. Manthiram A, Yu X, Wang S. Nat Rev Mater. 2017:1-16.
4. Deng Y, Eames C, Fleutot B, et al. ACS Appl Mater Interfaces. 2017;9(8):7050-7058.
5. Liu Z, Fu W, Payzant EA, et al. J Am Chem Soc. 2013;135(3):975-978.
6. Bates JB, Dudney NJ, Gruzalski GR, et al. J Power Sources. 1993;43:103-110.
7. Zhao Y, Daemen LL. S. J Am Chem Soc. 2012;134:15042-15047.
8. Goodenough JB, Kim Y. Chem Mater. 2010;22(3):587-603.
9. Zheng F, Kotobuki M, Song S, Lai MO, Lu L. J Power Sources. 2018;389:198-213.
10. J. Ying & McGinn PJ. J Power Sources. 2013;239:326-331.
11. Rivera-Calzada A, Leon C, Santamaría J, Varez A, Paris M, Sanz J. Tribol Interface Eng Ser. 2002;307:992-998.
12. Stramare S, Thangadurai V, Weppner W. Chem Mater. 2003;15(21):3974-3990.
13. Vijayakumar M, Bohnke O. J Eur Ceram Soc. 2006;26:3221-3231.
14. Federicci R, Holé S, Popa AF, et al. Phys Rev Mater. 2017;1.
15. Morata-Orrantia A, García-Martín S, Alario-Franco MÁ. Chem Mater. 2003;15(21):3991-3995.
16. Okumura T, Yokoo K, Fukutsuka T, Uchimoto Y, Saito M, Amezawa K. J Power Sources. 2009;189(1):536-538.
17. Thangadurai V, Weppner W. 2000;6(1-2):70-77.
18. Yasuhiro Harada, Tsukasa Ishigaki, Hiroo Kawai JK. Solid State Ionics. 1998;108 (1-4):407-413.
19. Geng HX, Mei A, Dong C, Lin YH, Nan CW. J Alloys Compd. 2009;481(1):555-558.
20. Dinh NN, Long PD, Trong LD. Commun. in Phys. 2004;14(2):90-94.

SP08_011_PA: LAKE PIGMENT FROM DIN DANG CLAY AND SAPPANWOOD

Jitnapa Sirirak[1,*], Nattawan Worawannotai, Cheewita Suwanchawalit, Supanee Chayabuttra

[1]*Department of Chemistry, Faculty of Science, Silpakorn University, Nakhon Pathom, Thailand 73000*
[*]*e-mail: jitnapasirirak@gmail.com and sirirak_j@su.ac.th*

Abstract

In this work, reddish-brown lake pigment was prepared using Din Dang clay and natural dye from sappanwood by adsorption method. Din Dang clay is natural pale brown clay from Udorn Thani, Thailand, while sappanwood is one of plant source for natural red dye. The adsorption parameters including adsorbent dosage of 1-10% w/v, initial pH of sappanwood dye of pH 3-11, and adsorption time of 0-180 min were investigated. Lake pigment was also characterized with several techniques including IR, XRD, UV-Vis DRS and CIELAB. It was found that when higher dosage of Din Dang clay was used, the paler reddish-brown lake pigment was observed. Moreover, natural dye at pH 5 and pH 7 yielded the deepest reddish brown lake pigment. In addition, only 10 min of the adsorption time was required for the preparation of lake pigment.

Keywords: Natural clay, Sappanwood, Adsorption

SP08_012_OF: HYDROPHOBIC CELLULOSE FROM CORN HUSK

Worranun Wongchompoo,[1] Radchada Buntem[2,*]

Department of Chemistry, Faculty of Science, Silpakorn University, Nakhon Pathom 73000, Thailand
*e-mail: worranun.w@gmail.com, radchadab@yahoo.com

Abstract:

The agricultural waste is a good source of cellulose and the extraction is easily performed by strong base like NaOH. In this research, corn husk was treated by 4% (w/v) NaOH solution to yield CH_1. 1.5 g of CH_1 was soaked in deionized water and N, N-dimethylacetamide (DMA) respectively. The soaked cellulose (CH_1) was dissolved in dimethylacetamide/LiCl and reacted with hexamethyldisilazane (HMDS) yielding trimethylsilylcellulose (CH_TMSC). Cellulose can be easily hydrophobized using trimethylsilyl groups. The IR spectrum shows the presence of -Si(CH_3)$_3$ groups: ν_{Si-O} at 1044 cm^{-1}, ν_{C-Si} at 1249, 837 and 748 cm^{-1}. The ^{1}H-NMR result confirms the presence of -Si(CH_3)$_3$ groups at ≈ 0 ppm and pyranose ring protons in the range of 3.0-4.7 ppm. SEM image of TMSC shows the morphology characteristics of cellulose while the EDX shows the presence of Si. The degree of substitution (DS) values calculated from FT-IR, ^{1}H-NMR and EDX data are 1.63, 2.37 and 1.28 respectively. TGA results show the higher stability of cellulose in CH_TMSC as compared with that of corn husk after alkali treatment.

Introduction:

Cellulose, a linear polymer of anhydrocellobiose,[1] is an unlimited, eco-friendly and biocompatible raw material for the production of green products.[2] It can be extracted from various plants, bacteria and agricultural residues. Corn, one of the major crops in Thailand, is used in farm or food industry. The corn husk, the main waste from corn production, has no other utilization except for animal food in a small quantity. The rest must be disposed by burning which causes the air pollution. The cellulose production from corn husk is an appropriate solution for waste disposal.[3] Cellulose can be converted to various useful products like ethanol,[4] lactic acid,[5] succinic acid[6] and another types of cellulose derivatives.[7] Various functionalization processes of hydroxyl groups on the cellulose surface *via* esterification,[8] etherification,[9] and silylation[10] are readily performed. Among these, silylation is used to hydrophobize the cellulose surface. The hydrophobic cellulose has been widely used in pharmaceuticals,[11] foods[12] and coating.[13] Trimethylsilyl cellulose (TMSC) is potentially used for regenerating cellulose by acid treatment to produce pure cellulose fibers, particles or films.[14]

In this research, cellulose is extracted from corn husk by an alkaline method. The extract is further modified by using hexamethyldisilazane (HMDS) to yield trimethylsilylcellulose (CH_TMSC).

Methodology:

Materials

The corn husk (agro-waste) was collected from the local market in Nakorn Pathom, Thailand. Sodium hydroxide was obtained from Merck. N, N-dimethylacetamide was obtained from Carlo Erba. Hexamethyldisilazane and Lithium chloride were purchased from Sigma-Aldrich. All solvents were of analytical grade and used as received.

Cellulose extraction

Cellulose extraction was performed by reacting corn husk with 4% (w/v) NaOH solution under reflux. The extraction process was repeated three times until all lignin was removed. The extracted cellulose was neutralized by 1 M HCl, subsequently washed several times with distilled water and oven-dried to yield**.** (CH_1)

Synthesis of trimethylsilyl cellulose

The synthesis of trimethylsilyl cellulose was performed as the previous publication.[15] 1.5 g of extracted cellulose (CH_1) was soaked with deionized water at 4°C for 24 hours and filtered. The fiber was then swelled in a 100 mL of N, N-dimethylacetamide (DMA) for 1 hour and filtered. In a separate flask, 150 mL of DMA were heated under nitrogen to 110°C for 15 minutes. The DMA was further heated to 165°C at which temperature the treated fiber was added. After 1 hour the temperature was decrease to 100°C and 15 g of LiCl was then added and stirred until dissolved. The solution was cooled to room temperature and then the clear colorless solution was heated to 80°C and 20 mL of hexamethyldisilazane (HMDS) were added dropwise. The mixture was maintained at this temperature for 4 hours to obtain colorless gel. The gel was filtered and washed by methanol and left to dry in a desiccator to yield trimethylsilyl cellulose (CH_TMSC).

Spectroscopic measurement

The cellulose samples were analyzed using Spectrum 100 FT-IR spectrophotometer (Perkin Elmer). ^{1}H-NMR of TMSC was measured by a Nuclear Magnetic Resonance Spectrometer, Bruker 300 MHz (Avance III HD) using $CDCl_3$ as a solvent and a standard. The surface morphology and elemental composition were studied by a TESCAN MIRA 3 scanning electron microscope associated with EDAX microprobe (element). The thermal stability was measured using Pyris 1 thermogravimetric analyzer (Perkin Elmer)

Results and Discussion:

Cellulose extraction and synthesis of trimethylsilyl cellulose

Lignin and hemicellulose in corn husk (CH) were successfully removed *via* the hydrolysis of the ester bond[16] using NaOH solution. ATR-FTIR spectra of CH and CH_1 are presented in Figure 1 (a) and (b) respectively. The carbonyl vibration in lignin at 1730 cm^{-1} is not observed in the spectrum of CH_1.

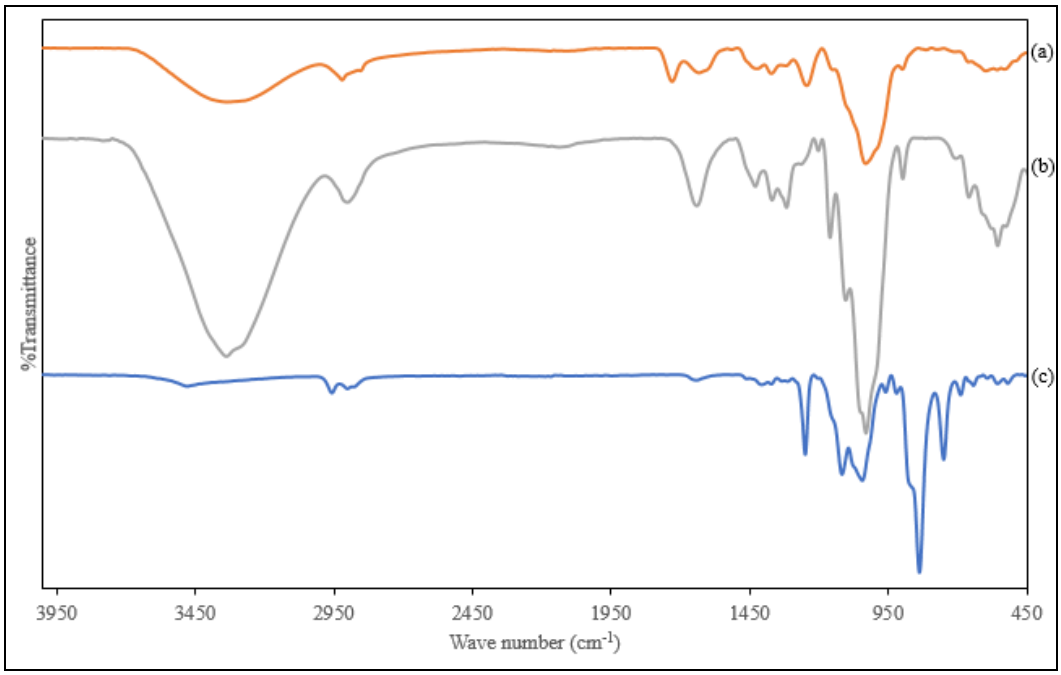

Figure 1. IR spectra of (a) CH (b) CH_1 and (c) CH_TMSC

Table 1. Modes of vibration in cellulose samples

Mode of Vibration	Wave number (cm^{-1})		
	CH	CH_1	CH_TMSC
ν(O–H)	3336	3338	3478
ν(C–H)	2920	2901	2957
ν(C=O)	1730	-	-
δ(O–H)	1631	1640	1639
δ(C–H)	1422, 1371, 1319	1429, 1369, 1317	1406, 1371, 1312
ν(C–O–C) (pyranose ring)	1149	1160	1202
ν(C–O) (2º alcohol)	1098	1103	1117
ν(Si–O)	-	-	1044
ν(Si–CH_3)	-	-	1249, 837, 748

The dissolution of the cellulose is the crucial step for synthesizing TMSC. DMA/LiCl can break the strong hydrogen bonds between the cellulose polymeric chains. The OH···O hydrogen bonds are replaced with OH···Cl^- links[17] in the presence of Cl^- anions. While Li^+ cations bind strongly with the carbonyl oxygen of DMA molecules to form a $Li^+(DMA)_x$ complex assisting the OH···Cl^- stabilization and dispersing the cellulose chain.[18] The dispersed cellulose is then readily reacted with HMDS to form TMSC as the details in Figure 2.[19]

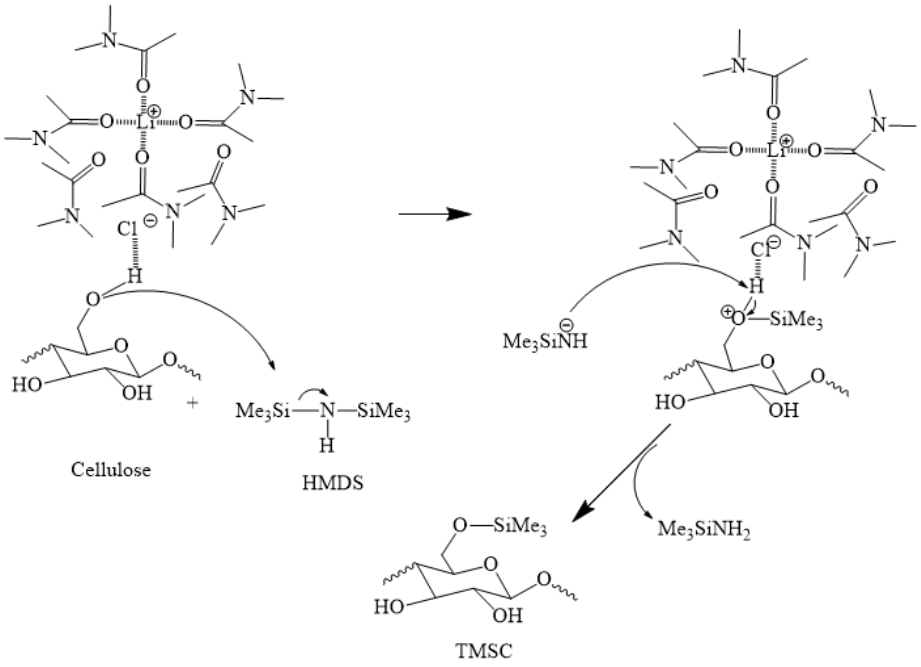

Figure 2. Reaction mechanism of cellulose and HMDS

The CH_TMSC was characterized by ATR-FTIR, ^{1}H-NMR and SEM-EDX. The IR data was presented in Figure 1 (c) and Table 1. The IR absorption bands at 1249, 837, 748 cm^{-1} are characteristic Si-CH_3 vibrations. While the band 1044 cm^{-1} is identified as Si-O stretching. While the proton signals[20] of -Si(C**H**$_3$)$_3$ (0.12 ppm) and pyranose rings (3.0-4.7 ppm) are appeared in the ^{1}H-NMR spectrum as in Figure 3.

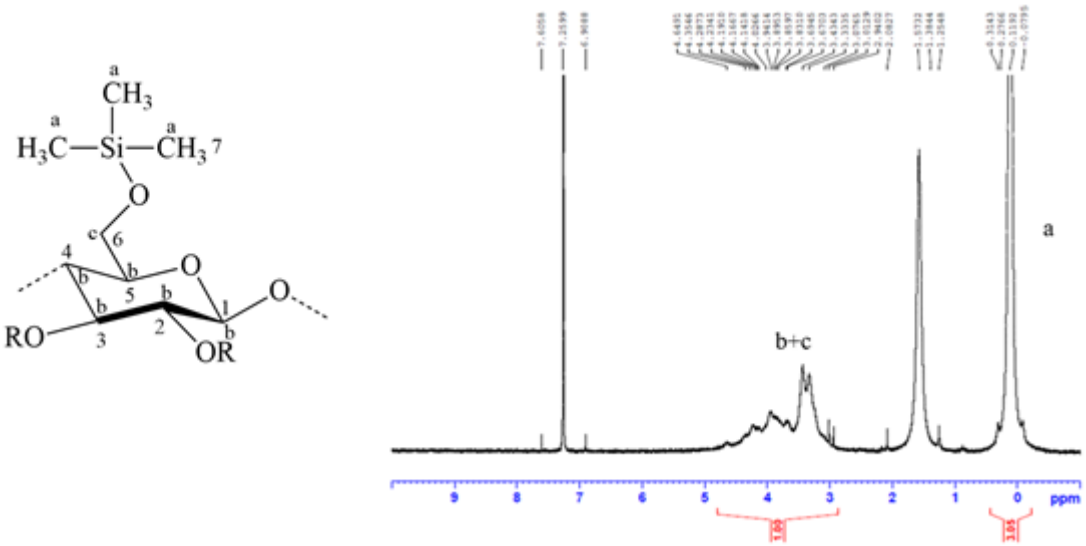

Figure 3. ^{1}H-NMR spectrum of CH_TMSC

The SEM-EDX data of CH, CH_1 and CH_TMSC were presented in Figure 4. The SEM image of CH surface shows the grid-like structure with small hairs containing silica particles. This pattern was removed after treatment with NaOH. This strong base can help remove lignin, hemicellulose, wax, silica and other impurity in corn husk. The fibrous surface with nano sized fiber is clearly seen in the CH_1 image (Figure 4(b)). After silylation process, the fibrous characteristics of the corn husk was totally changed as presented in Figure 4 (c). The Si atoms indicating the presence of -Si$(CH_3)_3$ groups are clearly found on the surface of CH_TMSC.

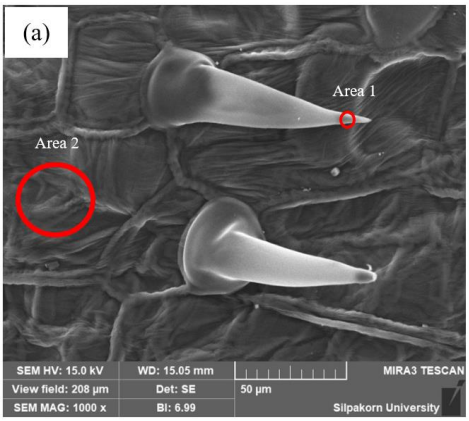

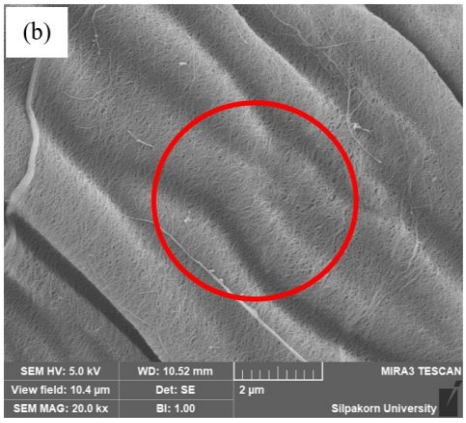

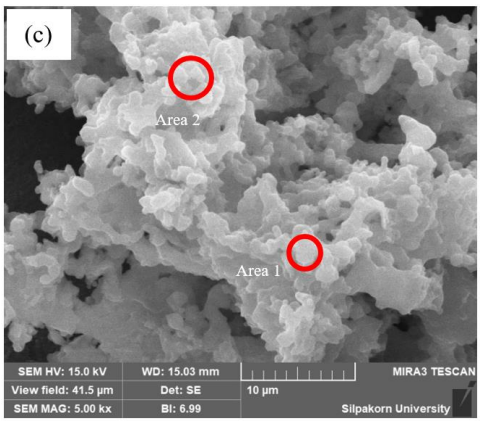

Sample	Atomic %			
	C	O	Si	Al
CH (Area 1)	35.61	44.55	19.06	0.77
CH (Area 2)	50.32	49.68	-	-
CH_1	51.21	48.79	-	-
CH_TMSC (Area 1)	59.62	32.17	8.21	-
CH_TMSC (Area 2)	61.38	30.73	7.89	-

Figure 4. SEM-EDX data of (a) CH (b) CH_1 and (c) CH_TMSC

The CH, CH_1 and CH_TMSC were analyzed by TGA technique. The higher decomposition temperature of CH_TMSC as compared with CH_1 indicates the higher stability of modified cellulose. The silyl groups help protect the cellulose[21] so that the thermal stability of both CH_TMSC is increased.

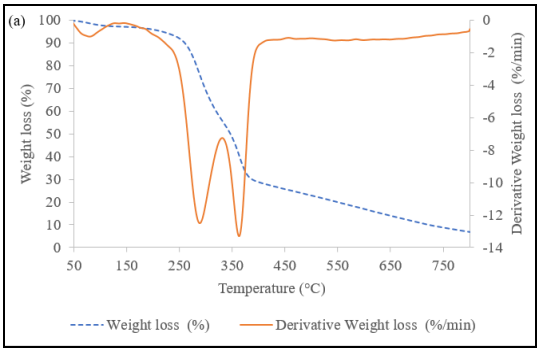

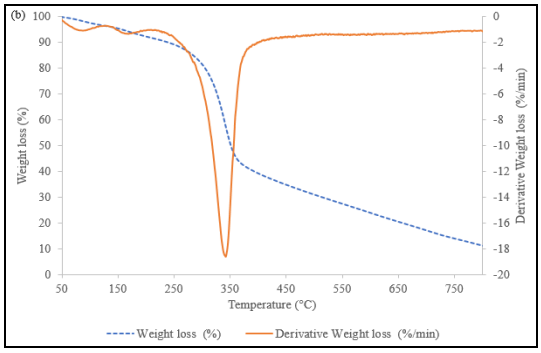

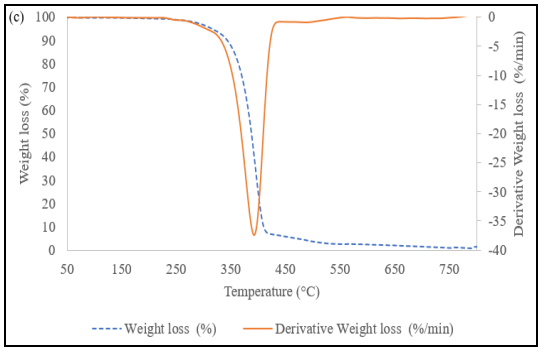

Sample	Decomposition Step	Temperature (°C) Start	Final	Tp[a]	% weight loss Each step	Total
CH	1st	50.23	145.87	80.73	2.67	
	2nd	145.87	331.49	288.71	41.34	74.48
	3rd	331.49	457.52	363.20	30.47	
CH_1	1st	50.05	126.78	87.77	3.40	
	2nd	126.78	215.00	168.56	4.95	65.38
	3rd	215.00	454.32	342.16	57.03	
CH_TMSC	1st	50.09	457.52	392.42	94.40	94.40

Tp[a] = Peak temperature the temperature at the maximum decomposition

Figure 6. TGA data of (a) CH (b) CH_1 and (c) CH_TMSC

Degree of substitution (DS)

Degree of substitution of CH_TMSC was calculated using IR, NMR and EDX data. For the IR data, the DS value can be calculated by using the following formula[22]

$$DS = \frac{4.05 - \frac{A_{OH}}{A_{CH}}}{1.37}$$

A_{OH} = peak area (absorbance mode) of the ν(O-H)

A_{CH} = peak area (absorbance mode) of the ν(C-H)

While the DS value from ^{1}H-NMR data was determined using equation below :[23]

$$DS = \frac{7}{9} \times \frac{A_{(a)}}{A_{(b+c)}}$$

$A_{(a)}$ = peak area of proton a

$A_{(b+c)}$ = peak area of proton b and c

The equation for calculating DS value from EDX data is as below :[14]

$$DS = \frac{5 \times Si\%}{O\%}$$

All DS values are summarized in Table 1. In the case of CH_TMSC, the DS value obtained from NMR technique is larger than two while the DS values from FTIR and EDX are lower than two. In the case of FTIR and EDX, the uneven distribution of the silyl groups on the cellulose chains causes the inhomogeneity of the solid sample resulting in the low DS value in certain area. While in the case of NMR, the analyzed solution averages out the number of silyl groups on cellulose chains resulting in the higher DS value.

Table 1 DS values of CH_TMSC calculated by three different techniques

Technique	DS value
ATR-FTIR	1.63
^{1}H-NMR	2.37
EDX	1.28

Conclusion:

The alkali treatment of corn husk using 4%(w/v) NaOH was successfully remove lignin and hemicellulose. The extracted cellulose was subsequently silylated to form hydrophobic trimethylsilyl cellulose. This hydrophobized corn husk cellulose is higher in thermal sensitivity as compared with corn husk after alkali treatment.

Acknowledgements:

Many thanks to Department of Chemistry, Faculty of Science, Silpakorn University.

References:

1. Ewulonu CM, Liu X, Wu M, Yong H. J Biosci Bioeng. 2019;1:3-10.
2. Maepa CE, Jayaramudu J, Okonkwo JO, Ray SS, Sadiku ER, Ramontja J. Int J Polymer Anal Char. 2015;20:99–109.
3. Kampeerapappun P. J Met Mater Miner. 2015;25:19-26.
4. Prasad S, Singh A, Joshi HC. Resour Conserv Recy. 2007;50:1–39.
5. Drumright RE, Gruber PR, Henton DE. Adv Mater. 2000;12:1841-1846.
6. Bechthold I, Bretz K, Kabasci S, Kopitzky R, Springer A. Chem Eng Technol. 2008;31:647-654.
7. Murtaza G. Acta Pol Pharm. 2012;69:11-22.
8. Wang Y, Wang X, Xie Y, Zhang K. Cellulose. 2018;25:3703–3731.
9. Li W, Xu ZZ, Liu XH, Li CH, Ruan FT. Int J Adhes Adhes. 2018;84:101-107.
10. Kostag M, Köhler S, Liebert T, Heinze T. Macromol Symp. 2010;294:96–106.
11. Bruschi ML, Cardoso MLC, Lucchesi MB, Gremião MPD. Int J Pharm. 2003;264:45–55.
12. Madene A, Jacquot M, Scher J, Desobry S. Int J Food Sci Tech. 2006, 41, 1–21.
13. Fischer S, Thümmler K, Volkert B, Hettrich K, Schmidt I, Fischer K. Macromol Symp. 2008;262:89–96.
14. He A, Liu D, Tian H, Jin Y, Cheng Q, Song J. Cellulose Chem Technol. 2014;48:19-23.
15. Wongchompoo W, Kanthamoon T, Buntem R. Key Eng Mater. 2019;824:121-127.
16. Rosli NA, Ahmad I, Abdullah I. Bioresources. 2013;8:1893-1908.
17. McCormick CL, Callais PA. Polymer. 1987;28:2317-2323.
18. Zhang C, Liu R, Xiang J, Kang H, Liu Z, Huang Y. J Phys Chem B. 2014;118:9507−9514.
19. Nouvel C, Ydens I, Degée P, Dubois P, Dellacherie E, Six JL. Polymer. 2002;43:1735-1743.
20. Livazovic S, Li Z, Behzad AR, Peinemann KV, Nunes SP. J Membr Sci. 2015;490:282–293.
21. Petzold K, Koschella A, Klemm D, Heublein B. Cellulose. 2003;10:251–269.
22. Mormann W, Demeter J, Wagner T. Macromol Chem Phys. 1999;200:693-697.
23. Puspasari T, Pradeep N, Peinemann KV. J Membr Sci. 2015;491:132-137.

SP08_013_PA: RAPID ANALYSIS OF PALM OIL LOSS FROM SCREW PRESSED PALM FRUIT FIBER

Charoen Pakhathirathien, Lukman Daramae, Weeraya Khummueng*

Department of Science, Faculty of Science and Technology, Prince of Songkla University,
Pattani 94000, Thailand
*e-mail: weeraya.k@psu.ac.th

Abstract:

Rapid analysis of palm oil loss from screw pressed palm fruit fiber was performed on time frame limitation in less than 30 minutes including: drying fiber with microwave radiation, extraction with pentane, evaporation, results were measured by percentage weight of oil and calculative data. The estimation of total oil was indirect measured by the conversion of single extraction using equations. Triple continuous extracted oil weight data were plotted an exponential graph, then total oil content can be derived from exponential equations. Consequently, the obtained data were also converted by 8^{th} root for 1^{st} oil extraction, 4^{th} root for 2^{nd} oil extraction and square root for 3^{rd} oil extraction, of which constituted into a linear graph. The result showed that all of the straight line intercept similarly at x-axis (mean: 2.2649). Reverse calculation from reference intercept point on x-axis and single oil extraction to derive the other three oil extractions from slope of exponential graph. Calculated and summation of oil extractions from the exponential equation of this data, the total oil was indirect determined. The result has shown that mean of percentage oil extraction from laboratory by Soxhlet extraction and calculation were 5.61±0.94% and 5.87±0.93%, respectively, which was indicated no statistically significant differences at $p<0.05$. This procedure can be used as a new method of oil loss determination from screw pressed palm fruit fiber in palm oil industry.

SP08_014_OA

SP08_014_OA: SOLVOTHERMAL SYNTHESIS OF ZnO/Bi_2MoO_6 CATALYST FOR PHOTODEGRADATION OF FLUOROQUINOLONE ANTIBIOTIC AND CATIONIC DYE

Tammanoon Chankhanittha, Suwat Nanan*

Materials Chemistry Research Center, Department of Chemistry and Center of Excellence for Innovation in Chemistry, Faculty of Science, Khon Kaen University,
Khon Kaen 40002, Thailand
*e-mail: suwatna@kku.ac.th

Abstract:

Photocatalysts based on ZnO/Bi_2MoO_6 composites were fabricated using solvothermal method by decoration of ZnO nanoparticles on the surface of the flower-like Bi_2MoO_6 catalyst. The prepared composites displayed the characteristic diffraction peaks of ZnO and Bi_2MoO_6 with the band gap energy of 3.25 eV and 2.76 eV, respectively. The PL intensity of the 10 wt% ZnO/Bi_2MoO_6 catalyst (known as 0.10Zn–Bi) is lower than that of the Bi_2MoO_6, catalyst. This indicates higher separation rate of electron-hole pairs resulting in enhancement of the photoactivity. The 0.10Zn–Bi catalyst showed high efficiency of 100% and 92% toward degradation of OFL antibiotic and RhB cationic dye, respectively. This is due to high surface area and low electron-hole recombination rate found in the catalyst. The photodegradation of both pollutants correlated well with the pseudo-first order kinetics with a very high rate constant of 0.0196 min^{-1}. The chemical structure and the morphology of photocatalyst remained stable after the fifth cycle of use while maintaining high efficiency indicating the reusability of the catalyst. The photogenerated electron (e^-) and hole (h^+) play an important role in photodegradation of both OFL antibiotic and RhB dye. This work shows a promising potential of the ZnO/Bi_2MoO_6 composites for environmental protection.

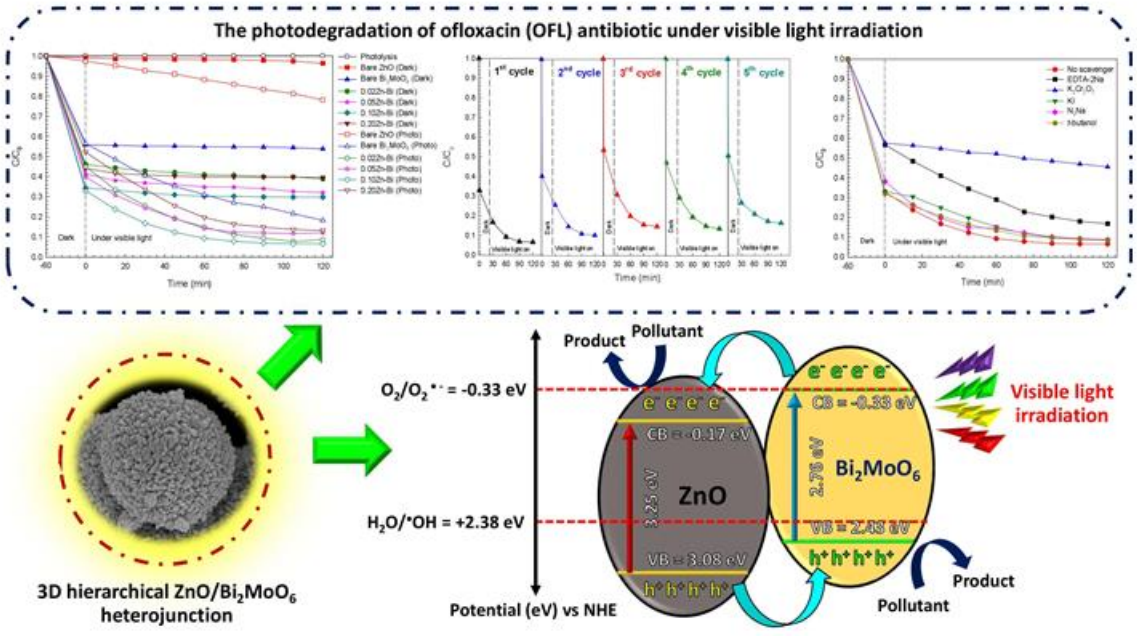

Figure 1

SP09_001_PA: ISOLATION AND SCREENING OF THERMOTOLERANT YEAST FOR ETHANOL PRODUCTION FROM CELLULOSIC FEEDSTOCKS

Jirabhorn Piluk, Sitanan Thitiprasert, Pajareeya Songserm, Nuttha Thongchul*

Research Unit in Bioconversion and Bioseparation for Value-Added Chemical Production, Institute of Biotechnology and Genetic Engineering, Chulalongkorn University, Phayathai, Bangkok 10330 Thailand
*e-mail: Nuttha.T@chula.ac.th

Abstract:

Ethanol is typically produced by the fermentation of sugars by yeasts and commonly consumed as alcoholic beverages. It also has medical applications as an antiseptic and disinfectant. It is widely used as a solvent or a chemical backbone or intermediate in many applications; and thus, is the vital substance used across different manufacturing processes. Among them, it is used as an alternative fuel. First generation ethanol fermentation utilized edible feedstocks solely as a carbon source. Contrary to the increasing ethanol demand that drives economic impact, consumption of edible feedstocks leads to food shortage. Therefore, utilization of lignocellulosic biomass as the substrate for ethanol has become extensively attractive. This study focused on isolation and screening of ethanol producing thermotolerant yeast from natural samples collected in Chulalongkorn University. Ten yeast isolates were obtained. Most of them grew well on selective medium at 40°C. Among them, 2 isolates including CUB2-1 and CUS5-2, produced ethanol at the titer of 1.16 and 1.40 g/L, respectively from the fermentation medium containing sole xylose at 50 g/L at 40ºC within 24 h. Mixed sugars containing both glucose and xylose were also used as the carbon substrates in fermentation of the 2 isolates. Improved ethanol production was observed in the fermentation of mixed sugars with an acceptable yield and productivity.

Keywords: Ethanol, Fermentation, Thermotolerant yeast, Xylose, Mixed Sugars

SP09_002_PF: IDENTIFICATION AND HETEROLOGOUS EXPRESSION OF ENDOGLUCANASE (GH5) FROM *Bacillus amyloliquefaciens* HL25

Hataikarn Lekakarn[1] and Benjarat Bunterngsook[2,*]

[1]Department of Biotechnology, Faculty of Science and Technology, Thammasat University, Patumthani 12120, Thailand
[2]Enzyme Technology Research Team, Biorefinery Technology and Bioproduct Research Group, National Center for Genetic Engineering and Biotechnology, 113 Thailand Science Park, Khlong Luang, Patumthani 12120, Thailand
*e-mail: benjarat.bun@biotec.or.th

Abstract:

Cellulases have a broad range of different industrial applications including in pulp and paper and biorefinery sectors. This study, *HL25GH5* gene containing 1,497 bp open reading frame encoding a polypeptide of 499 amino acids was identified from *Bacillus amyloliquefaciens* HL25 strain. Based on amino acid sequence analysis, HL25GH5 is endo-β-1,4-glucanase belonging to the glycosyl hydrolase family 5 (GH5). HL25GH5 is highly related to endo-β-1,4-glucanases derived from *Bacillus* species sharing 95-100% amino acid sequence identity. HL25GH5 encodes 29 amino acids of signal peptide and 2 domains of glycoside hydrolase family 5 catalytic domain linked with carbohydrate binding domain family 3 (CBM3) at the C-terminus. The mature sequence of HL25GH5 was successfully heterologous expressed in *Pichia pastoris* KM71 as a secreted protein with approximately 66 kDa. Biochemical analysis revealed that recombinant HL25GH5 displayed high activity with soluble forms of cellulose as a substrate such as β-glucan from barley (61.88±1.28 U/mg protein) and carboxymethylcellulose (8.79±0.12 U/mg protein). Furthermore, low activity was detected toward insoluble phosphoric acid swollen cellulose (0.41±0.03 U/mg protein).

Introduction:

In integrative sugar platform biorefinery, lignocellulosic biomass is fractionated into respective components (i.e. cellulose, hemicellulose, and lignin as well as minor constituents e.g. proteins and lipid) for maximized valorization to biofuels and various co-products [1]. Hydrolysis of cellulose to sugars is the main process in sugar platform biorefinery [2]. Cellulose is a main component in lignocellulosic biomass (30-50% of dry matter). Cellulose structure composes of D-glucose subunits linked by β-1,4-glycosidic linkage. The glycosyl hydrolases targeting on degradation of cellulose are generally classified as cellulases that comprise a variety of endo and exo-acting hydrolytic enzymes working on attacking the cellulose polymers. Endoglucanase (EC 3.2.1.4) attacks regions of low crystallinity in the cellulose fiber and create free chain ends. Exoglucanase or cellobiohydrolase (EC 3.2.1.91) degrades the molecule further by removing cellobiose units from the free chain ends. Finally, β-glucosidase (EC 3.2.1.21) hydrolyses cellobiose to produce glucose [3-6].

Cellulase is produced by various cellulolytic bacteria and fungi which have been isolated from different environment. Previous work reported that the cellulolytic *Escherichia coli* ZH-4 isolated from bovine rumen displayed extracellular cellulase activity and could degrade cellulose in the culture [7]. Endoglucanase E belonging glycoside hydrolase family 5 was isolated from *Clostridium cellulovorans* 743B [8]. *Thermobifida alba* AHK119 isolated from compost exhibits sufficient filter paper-degradation activity in its culture supernatant [9]. Isolating cellulolytic microorganisms from various environment and characterization of their cellulase are crucial for understanding the hydrolysis mechanism of cellulase that could lead to promote their application in industrial applications.

In this study, we found that isolated *B. amyloliquefaciens* HL25 from soil displayed strong cellulase activity. Therefore, the putative gene encoding endoglucanase responsible for cellulose hydrolysis was cloned and expressed in yeast *P. pastoris* KM71. Its ability for degrading of soluble and insoluble celluloses suggests its potential application in industrial processes.

Methodology:

Isolation of endoglucanase gene from B. amyloliquefaciens HL25

Gene encoding endoglucanase was isolated from cellulase producing strain *B. amyloliquefaciens* HL25. The PCR reaction was performed in a total volume 50 µl containing 50 ng of genomic DNA, 1x Phusion GC buffer, 1.5 mM $MgCl_2$, 200 µM each of dNTPs, 0.5 µM each of primers and 1 unit of Phusion DNA polymerase (Thermo Scientific). Amplification consisted of 95°C for 5 min, 25 cycles of 95°C for 30 sec, 55 °C for 30 sec and 72°C for 3 min and a final extension at 72°C for 10 min. The blunt-ended purified PCR product was cloned into pJET1.2 plasmid and propagated in *E. coli* DH5α. The transformants were screened by colony PCR using pJET1.2Foward and pJET1.2Reverse primers, then the plasmid was subsequently subjected for sequencing (Macrogen). The homology of the obtained nucleotide sequence was analyzed using the tool BLASTX (http://www.ncbi.hlm.nlm.gov). The phylogenetic analysis was performed using MEGA X.

Construction of recombinant yeast strain

In order to determine the function of endoglucanase gene isolated from *B. amyloliquefaciens* HL25, mature gene was heterologous expressed in methylotrophic yeast *P. pastoris* KM71. For recombinant plasmid construction, mature gene was amplified using HL25GH5/F (5'-GCGAATTCGCAGGGACAAAAACGCCAGTAGCC-3') and HL25GH5/R (5'-GCTCTAGAATTGGGTTCTGTTCCCCAAATCAG-3') primers using Phusion DNA polymerase. The restriction sites are underlined. The PCR product was cloned into pPICZαA expression vector at *Eco*RI and *Xba*I restriction sites that fused in-frame with N-terminal α-factor secretion signal sequence to guide the proper processing and secretion of the recombinant protein. The ligation mixture was transformed into *E. coli* DH5α for selection of recombinant plasmids containing the gene of interest using heat shock method. The transformants harboring pPICZαA-HL25GH5 recombinant plasmid was selected from LB agar containing 25 µg/ml of Zeocin. The gene was verified by colony PCR for subsequently DNA sequencing. Once the nucleotide sequence has been confirmed, the construction of recombinant yeast was then done by introducing the recombinant plasmid into *P. pastoris* KM71 genome using electroporation (1.5 kV/cm, 200 Ω and 25 µF).

Production of recombinant enzyme

Expression level of glucoamylase genes in *P. pastoris* KM71 under the inducible native AOX promoter was studied. Recombinant yeast was inoculated into YPD broth at 30°C, 200 rpm and cultured overnight. The culture was transferred to 50 ml BMGY (2% Peptone, 1% Yeast extract, 100 mM Potassium phosphate pH 6.0, 1.34% Yeast nitrogen base (w/o amino acid), 0.4 µg/ml Biotin, 1% Glycerol), grown until the OD_{600} of the culture reached 8–10, and then the cell was pelleted using centrifugation. The supernatant was removed and the pellet was resuspended in 5 ml BMMY (BMGY containing 3% methanol instead of glycerol) for induction of the target gene for 72 h.

Enzyme activity assay

Endoglucanase activity was analyzed based on the amount of liberated reducing sugars using the 3,5-dinitrosalisylic acid (DNS) method [10]. A one milliliter reaction mixture contains the appropriate dilution of enzyme in 50 mM sodium acetate buffer pH 5.0 and 1% (w/v) of carboxymethylcellulose (CMC). The reaction was then incubated at 50°C for 10 min. The amount of reducing sugars was determined from the absorbance measurement at 540 nm. Substrate specificity of HL25GH5 was determined against 1% (w/v) of various polysaccharides including carboxymethylcellulose (CMC), phosphoric acid swollen cellulose (PASC), β-glucan from barley and beechwood xylan in 50 mM sodium acetate buffer pH 5.0 at 50°C, 10 min for CMC, PASC and β-glucan and 60 min for PASC.

Results and Discussion:

Full-length gene encoding endoglucanase belonging to glycoside hydrolase family 5 (GH5) was successfully identified from cellulase producing strain *B. amyloliquefaciens* HL25. This gene was designed as *HL25GH5*. DNA sequence analysis revealed that the putative sequence was predicted to be endoglucanase that similar to glycoside hydrolase family 5 (GH5) of *B. amyloliquefaciens* with 100% identity (100% similarity) followed by endo-beta-1,4-glucanase from *Bacillus subtilis* (97% identity and 97% similarity). According to the annotation of endoglucanase HL25GH5, this protein contains 2 domains of glycoside hydrolase family 5 (GH5) catalytic domain linked with putative carbohydrate binding module 3 (CBM3) (Figure 1A). Catalytic domain of GH5 involves in hydrolysis of β-1,4-glycosidic linkage within cellulose chain, while carbohydrate binding domain facilitates enzyme binding to cellulose/hemicellulose polysaccharide [11]. Based on phylogenetic tree analysis, HL25GH5 was highly related to subfamily 2 that is currently the largest in family GH5 (Figure 1B). Extracellular enzymes in subfamily 2 were described as polyspecific subfamily that exhibit multi enzyme activities [12].

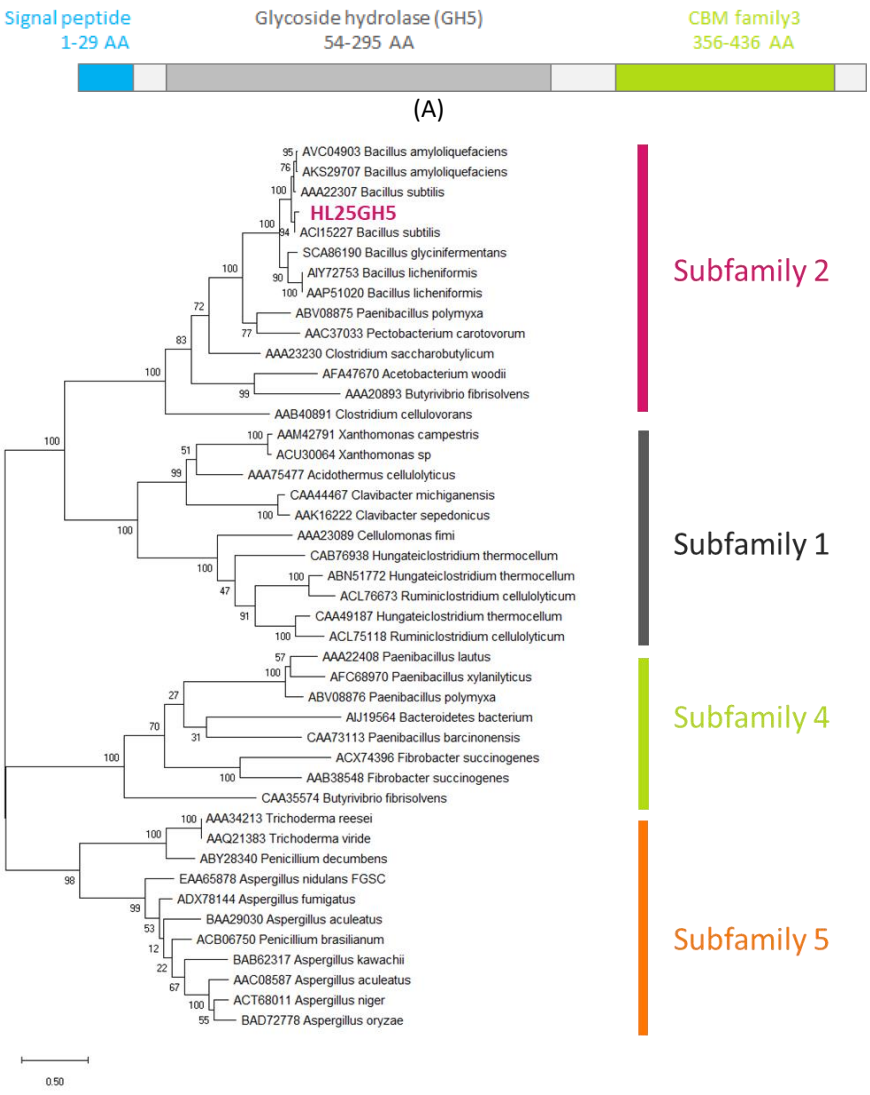

Figure 1. Sequence analysis of endoglucanase (HL25GH5) detected in *B. amyloliquefaciens* HL25 strain. (A) Domain architecture HL25GH5 (B) Phylogenetic analysis of HL25GH5 and cellulases belonging to glycoside hydrolase family 5 (GH5). The phylogenetic tree was constructed using the maximum likelihood approach with the program MEGA X using the Maximum Likelihood method and JTT matrix-based model (n=500 bootstrap replicates) [13]. This analysis involved 44 amino acid sequences. There were a total of 1,341 positions in the final dataset. Evolutionary analyses were conducted in MEGA X [14].

In order to verify biochemical function of obtained HL25GH5 endoglucanase encoding gene, this gene was heterologous expressed in methylotrophic yeast *P. pastoris* KM71 under the control of AOX inducible promoter. As results, approximately 66 kDa protein band from *P. pastoris* harboring endoglucanase gene was visualized in 12% SDS-PAGE (Figure 2). However, the size of recombinant protein was larger than the calculated molecular mass from their deduced amino acid sequence (48 kDa). One possibility is that the recombinant proteins expressed from *P. pastoris* KM71 were glycosylated.

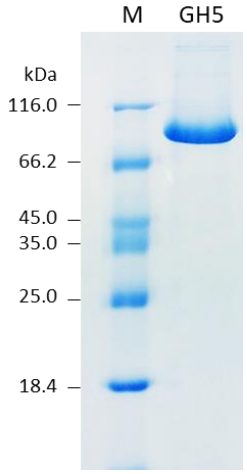

Figure 2. Protein expression analysis of recombinant endoglucanase (GH5) from *B. amyloliquefaciens* HL25. Lane M represents 10 µl of Pierce™ Unstained Protein MW Marker. Lane GH5 represent 10 µl of supernatant of recombinant which was induced by 3% methanol for 72 h.

In order to analyze the polysaccharide degradation activity of recombinant HL25GH5, carboxymethylcellulose (CMC), β-glucan from barley, phosphoric acid swollen cellulose (PASC) and beechwood xylan were used as substrates. As results, HL25GH5 exhibited the highest activity toward soluble β-glucan from barley which contains mixed β-1,3- and β-1,4- linkages (61.88 U/mg protein), followed by soluble carboxymethylcellulose (8.79 U/mg protein) in 50 mM sodium acetate pH 5.0 at 50°C (Table 1). Low activity was detected on insoluble phosphoric acid swollen cellulose with 0.41 U/mg protein. However, HL25GH5 did not hydrolyze beechwood xylan that comprise of xylose residues linked with β-1,4- glycosidic bonds under the used condition in this experiment. Based on the results, this study demonstrated that HL25GH5 specifically cleaved β-1,4 glycosidic linkage inside polysaccharide chain comprised of glucose residues. According to substrate specificity, HL25GH5 showed higher activity against soluble cellulose including β-glucan and CMC than that of insoluble PASC, these might be resulted from the high number of methoxy side chains substituting in CMC that can interfere in enzyme action and accessibility [15].

Table 1. Enzyme activity profile of recombinant HL25GH5

Substrate	Activity (U/mg protein)	Relative (%)
β-glucan from barley	61.88±1.28	100.00
Carboxymethylcellulose (CMC)	8.79±0.12	14.21
Phosphoric acid swollen cellulose (PASC)	0.41±0.03	0.66
Beechwood xylan	0.00±0.00	0.00

Conclusion:

In this study, gene encoding endoglucanase (HL25GH5) was identified from cellulolytic bacterial strain *B. amyloliquefaciens* HL25. HL25GH5 was shown to be responsible for extracellular cellulolytic capability of *B. amyloliquefaciens* HL25 wild type strain. Recombinant HL25GH5 exhibited hydrolytic activities against both soluble and insoluble cellulosic polysaccharides, this suggests its potential application in various industrial processes such as bioethanol production and biorefining application.

References:

1. Lynd LR, Weimer PJ, van Zyl WH, Pretorius IS. Microbiol Mol Biol Rev. 2002; 66: 506-577
2. Howard R, Abotsi E & Jansen van RE. Afr. J. Biotechnol. 2003; 2: 602-619.
3. Van DJS, Pletschke BI. Biotechnol. Adv. 2012; 30: 1458-1480.
4. Himmel ME, Ding S-Y, Johnson DK, Adney WS, Nimlos MR, Brady JW, Foust TD. Sci. 2007; 315: 804-807.
5. Arantes V, Saddler JN. Biotechnol. Biofuels. 2010; 3: 4-14.
6. Davies G, Henrissat B, Structure. 1995; 3: 853-859.
7. Pang J, Wang J, Liu Z, Zhang Q, Qi Q. BMC Biotechnol. 2019; 19: 63-71.
8. Kozaki R, Miyake H. J. Biosci. Bioeng. 2019; 128: 398-404.
9. Ohta T, Horie H, Matsu-ura A, Kawai F. J. Biosci. Bioeng., 2019; 127: 554-562.
10. Miller GL. Anal. Chem. 1959; 5: 426–428.
11. Boraston AB, Bolam DN, Gilbert HJ, Davies GJ. Biochem. J. 2004; 382: 769-781.
12. Aspeborg H, Coutinho PM, Wang Y, Brumer H, Henrissat B. BMC Evol. Biol. 2012; 12: 186.
13. Jones DT, Taylor WR, Thornton JM. Bioinformatics. 1992; 8: 275-282.
14. Kumar S, Stecher G, Li M, Knyaz C, Tamura K. Mol. Biol. Evol. 2018; 35: 1547-1549.
15. Vianna BA, Kimie YD, Akira US, Magnani DT. Int. J. Mol. Sci. 2019; 20: 2261.

SP09_003_PF: PREBIOTIC PROPERTIES DETERMINATION OF RICE BRAN EXTRACTION FROM SOLID STATE FERMENTATION BY LACTIC ACID BACTERIA

Manassanum Utapow, Chompoonuth Porncharoennop, Rungthip Mongkolkasem, Yada Mama, and Thornthan Sawangwan*

Biotechnology Department, Faculty of Science, Ramkhamhaeng University, 2086 Huamark, Bangkapi, Bangkok, THAILAND 10240
e-mail: thornthans@rumail.ru.ac.th

Abstract:

The prebiotic properties from rice bran fermentation by lactic acid bacteria (LAB) were determined in this study. Two different rice bran varieties (Khao Bahn Nah and Thai jasmine) in different moisture contents (50 and 75% w/v) were inoculated with *Lactobacillus casei* and *Lactobacillus plantarum* by solid state fermentation (SSF). After incubation period of 0-72 hours, the rice bran with SSF by LAB at 48 hours displayed highest growth of both LAB. These fermented samples were extracted by 70% v/v ethanol, evaporated, and then supplemented with probiotic medium culture for prebiotic properties determination as probiotic growth stimulation and pathogenic inhibition. The results showed that two rice bran extraction with SSF samples (SSF1-SSF8) exposed the probiotic growth enhancing and displayed the pathogenic inhibition capacity better than control and FOS (commercial prebiotic). Especially, SSF5 and SSF6 (Thai jasmine rice bran SSF by *L. casei* with 50% and 75% moisture, respectively) presented the maximum clear zone to inhibit all pathogens. From all results of this study, the rice bran extraction from SSF by LAB could be applied as a prebiotic substance for further functional food in addition to increasing the efficiency of agricultural residue utilization in Thailand.

Key words: prebiotic, probiotic, lactic acid bacteria, solid state fermentation, rice bran.

Introduction:

Rice bran is an agriculture by-product from rice milling process, which residues more than hundred thousand cubic tons per year. There are a various of rice bran products such as, rice bran oil, animal feed, fertilizer, ingredient for food and cosmetic, etc. Rice bran is of high nutrient composition as protein, lipid, carbohydrate, and vitamin B including rich of bioactive sources like prebiotic, phenolic and antioxidant compounds. Therefore, it is represent an important role for functional food because there are many evidences indicate the potential of rice bran with health benefit including blood cholesterol reduction, cardioprotective and anticancer effects.[1] Consequently, rice bran becomes more interesting for the food and pharmaceutical industry.

Lactic acid bacteria (LAB) have been proposed as probiotic which well documented with human and animal health benefit as pathogenic inhibition, antimicrobial metabolite production, immunity response enhancing and cancer prevention.[2] LAB application has been developed for solid state fermentation (SSF) as biocatalyst on solid material then conversed via biochemical process into value added product. SSF has more advantages over submerged fermentation in particular of higher fermentation productivity and better product functionalities as bioactivity and bioavailability during the fermentation process.[3]

Since rice bran is an available and inexpensive substrate which rich of many bioactive compounds. Therefore, this study aims to determine the prebiotic properties of the rice bran extraction from SSF by LAB with the purpose of value-added the agricultural residue and applied as a functional food product.

Methodology:

Materials

The rice brans for this research were Khao Bahn Nah and Thai jasmine. *Lactobacillus casei* TISTR 1463 and *Lactobacillus plantarum* TISTR 1465 were used as probiotic and cultivated in Man Rogosa Sharpe medium (MRS). *Bacillus cereus* ATCC11778, *Escherichia coli* ATCC25922, *Salmonella paratyphi* DMST15673 and *Staphylococcus aureus* ATCC25922 were applied as pathogenic and cultivated in nutrient agar (NA) and nutrient broth (NB). All other chemicals used were analytical grade.

Rice bran solid state fermentation by lactic acid bacteria

Rice bran was dried in an oven at 105°C overnight, after that 30 g of dried rice bran was taken in each flask and autoclaved at 121°C for 15 minutes, then adjusted the moisture content into 50 and 75% w/v by sterilized water.[4] The starter of *L. casei* and *L. plantarum* were grown at 37°C for 48 hours under anaerobic condition in MRS broth and determined the optical cell density with a spectrophotometer at 600 nm, then equaled to 1.0 for inoculation. Each lactic acid bacteria (LAB) was separately adding into the prepared rice bran in a ratio of 10% w/v and incubated at 37°C for 72 hours. Five grams of each rice bran with solid state fermentation (SSF) samples were taken at 24, 48 and 72 hours, then extracted by adding 50 ml of 70% v/v ethanol and incubated in a shaker at room temperature, 120 rpm for 24 hours. All extracted samples were centrifuged at room temperature at 10000 rpm for 20 minutes, after that evaporated by rotary evaporator at 50°C, 60 rpm. All samples were stored at 4°C for further determination. The conditions for rice bran with SSF are showed below

SSF1: Khao Bahn Nah + *L. casei* with 50% moisture
SSF2: Khao Bahn Nah + *L. casei* with 75% moisture
SSF3: Khao Bahn Nah + *L. plantarum* with 50% moisture
SSF4: Khao Bahn Nah + *L. plantarum* with 75% moisture
SSF5: Thai jasmine + *L. casei* with 50% moisture
SSF6: Thai jasmine + *L. casei* with 75% moisture
SSF7: Thai jasmine + *L. plantarum* with 50% moisture
SSF8: Thai jasmine + *L. plantarum* with 75% moisture
SSF9: Khao Bahn Nah with 50% moisture
SSF10: Khao Bahn Nah with 75% moisture
SSF11: Thai jasmine with 50% moisture
SSF12: Thai jasmine with 75% moisture

Determination of lactic acid bacteria by standard plate counting

Five grams of rice bran with SSF by LAB at 24, 48 and 72 hours were taken and prepared for determine LAB by standard plate counting. Each rice bran samples were pipetted 50 μl with appropriate dilution, then spread on MRS agar plate and incubated at 37°C for 48 hours under anaerobic condition. LAB colonies were counted after incubation time (24, 48 and 72 hour).

Probiotic growth stimulation

L. casei and *L. plantarum* were grown at 37°C for 48 hours under anaerobic condition in MRS broth (used as control) and compared with culture medium supplemented with 10% v/v of each rice bran extraction (conditions SSF1-SSF12). After incubation, the probiotic cultures were monitored by measuring the optical cell density with a spectrophotometer at 600 nm.[5]

Pathogenic inhibition

Anaerobic cultivations of *L. casei* and *L. plantarum* at 37°C for 48 hours in MRS broth complemented with 10% v/v of each rice bran extraction from previous were centrifuged at 10,000 rpm, 4°C for 30 minutes and supernatants were separately collected for testing. Pathogen strains (*B. cereus*, *E. coli*, *Salmonella paratyphi and Staphylococcus aureus*) were cultivated in NB at 37°C for 24 hours. Aliquot of pathogenic cultivation (50 μl) was inoculated in NA with spread plate technique. Supernatant from rice bran extractions were dropped onto the sterilized disks of filter paper and placed onto the pathogen plates as prepared above. After incubation at 37°C

for 24 hours, inhibition efficiency was illustrated by the clear zone from LAB which cultivated with and without the rice bran extraction supernatant.

Results and Discussion:

Lactic acid bacteria determination from rice bran solid state fermentation

After solid state fermentation of two rice bran varieties (Khao Bahn Nah and Thai jasmine) by different LAB (*L. casei and L. plantarum*) and moisture content (50 and 75%). The fermented samples were collected at the appropriate time (0-72 hour) to determine LAB growth by standard plate counting. From the results in Figure 1 displayed high amount of LAB colonies in all fermented samples (SSF1-SSF8) at 48 incubation hours. The highest LAB colony showed in SSF4 (3.63E+08 CFU/ml). This could explained by LAB colonies at 48 hours were expressed in logarithmic phase which high substances synthesis and maximum growth during this phase when compared to LAB colonies amount in the fermented samples at 24 hours (lag phase) and 72 hours (dead phase). As described earlier for five different *Lactobacillus* species were studied for the kinetic behaviors, cell growth and lactic acid production. Almost all strains were observed after 25-45 hours as an exponential growth phase (log phase) and performed the maximum lactic acid production after 52 hours incubation then they became to dead phase as presented by cell density decreasing.[6]

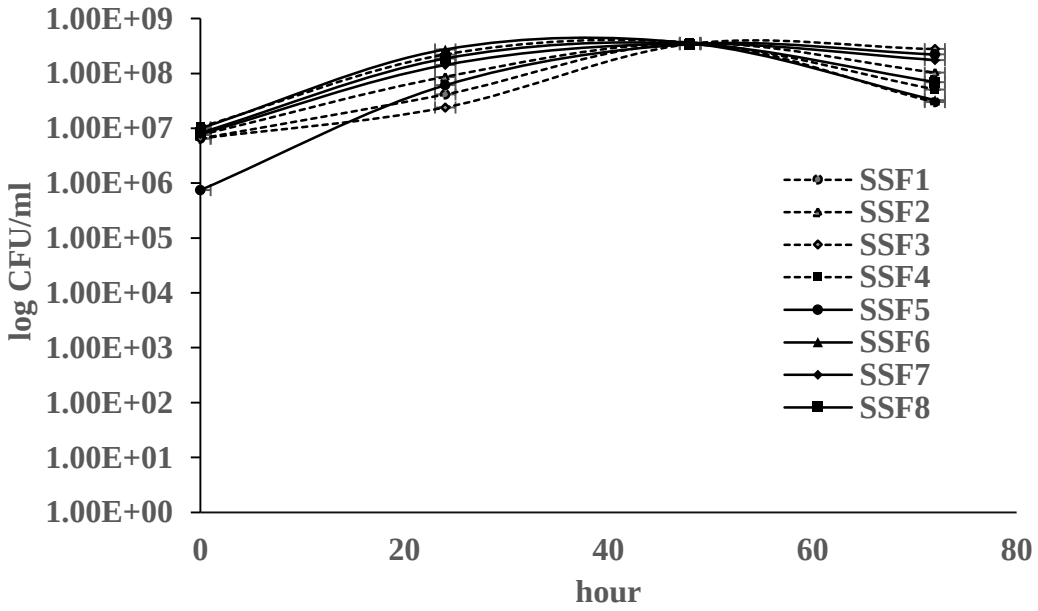

Figure 1. LAB colony plate counting (CFU/ml) from the rice bran SSF by different conditions (SSF1-SSF8) at 0-72 incubation time

Probiotic growth stimulation by rice bran extraction

All rice brans with SSF at 48 hours were extracted by 70% v/v ethanol, evaporated then stored at 4°C for prebiotic properties determination. Both probiotic strains (*L. casei* and *L. plantarum*) were grown in MRS broth complemented with rice bran extractions (SSF1-SSF12), without as control (only MRS broth) and compared with FOS as prebiotic commercial. The optical density at 600 nm of all cultures were monitored for probiotic growth as showed in Figure 2. The cultures of *L. casei* and *L. plantarum* in MRS broth with rice bran extraction samples (SSF1-SSF8) grew better than control and comparable with the prebiotic commercial as FOS. The highest OD600 was 0.9112 in the sample of SSF8 which displayed as a good sample for *L. plantarum* growth stimulation. Noticeable, even the sample of rice bran extraction without LAB (SSF9-SSF12) revealed the optical density of probiotic growth almost the same as control. There is an evidence from previous research that studied the fermentability of rice bran with and without LAB were evaluated the enhanced of bacteria during the cultivation. The results indicated that the rice bran fermentation with LAB did not have a significant effect on microbial counts compare with rice bran without fermentation. This may explain by a carbohydrate source in rice bran chemical composition could promote probiotic growth.[7]

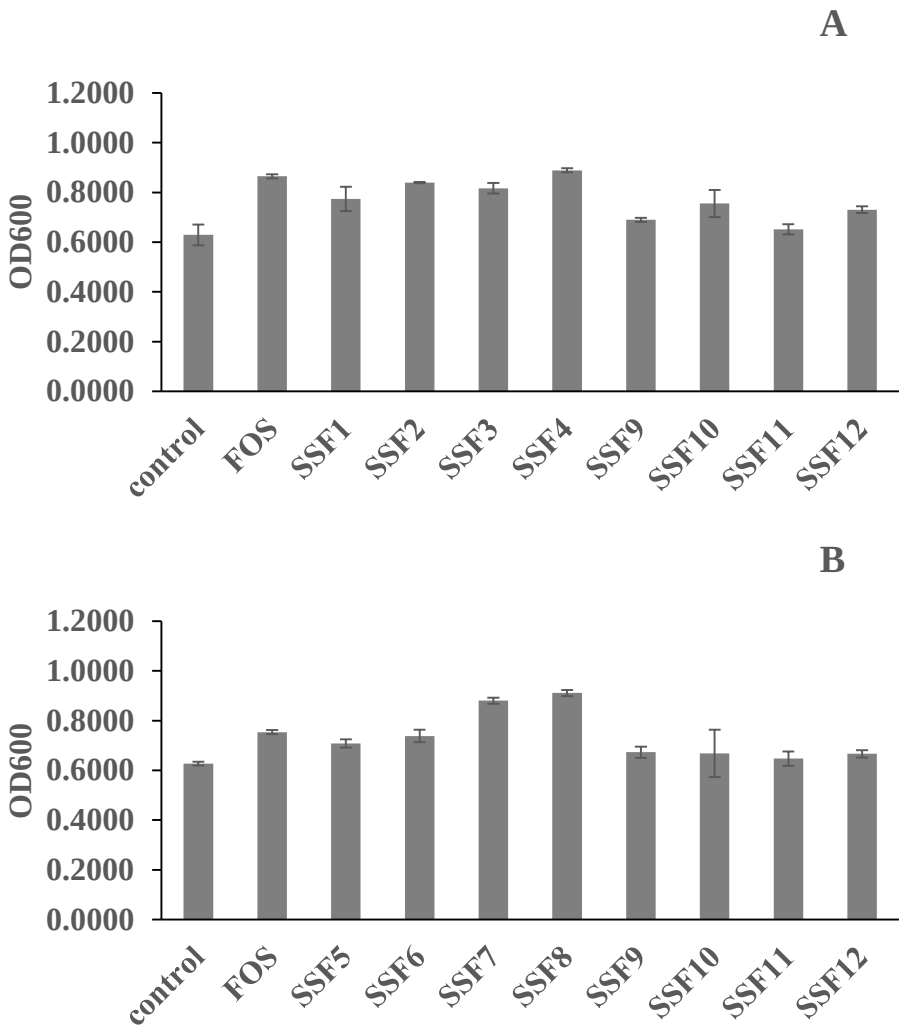

Figure 2. The growth of probiotic strains; *L. casei* (A) and *L. plantarum* (B) in MRS broth with rice bran extraction samples (SSF1-SSF12) compared with FOS supplementation at 37°C for 48 hour which monitored by OD600

Pathogenic inhibition by rice bran extraction

The inhibition of pathogens from gastrointestinal (*B. cereus*, *E. coli*, *Salmonella paratyphi and Staphylococcus aureus*) was illustrated by the clear zone after the incubation of pathogen and the supernatant from rice bran extraction at 37°C for 24 hours. Table 1 shows the clear zone from the pathogen inhibition by rice bran extraction. Interestingly, all samples from rice bran SSF with LAB (SSF1-SSF8) inhibited all pathogens, especially SSF5 and SSF6 displayed high ability to inhibit all pathogens as shown in the maximum clear zone. Notably, only rice bran without LAB fermentation (SSF9-SSF12) and FOS did not show the clear zone for *S. aureus* and *Samonella paratyphi* inhibition. Surprisingly that the commercial prebiotic as FOS exposed low capacity of pathogen inhibition. It can be suggested that that rice bran contains not only prebiotic compounds but also has a variety of bioactive components (i.e. polyphenols, peptides, fatty acids and antioxidant compounds) that have been shown to promising effect against the pathogens.[8]

Table 1. Pathogenic inhibition efficiency by rice bran extraction samples compared with FOS supplementation in the culture of probiotic

sample	clear zone			
	B. cereus	***E. Coli***	***S. aureus***	***Samonella paratyphi***
control	+	-	-	-
FOS	+	+	-	-
SSF1	++	+	++	++
SSF2	++	+	+++	+++
SSF3	+	+	+	+
SSF4	+++	+	+	+
SSF5	+++	+++	+++	+++
SSF6	+++	+++	+++	+++
SSF7	+++	+	+	+
SSF8	+++	+	+	+
SSF9	++	++	-	-
SSF10	+	+	-	-
SSF11	++	+	-	-
SSF12	++	+	-	-

(-) no clear zone, (+) small clear zone, (++) middle clear zone and (+++) maximum clear zone

Conclusion:

From this research, two rice bran varieties (Khao Bahn Nah and Thai jasmine) were evaluated the prebiotic properties after solid state fermentation with two lactic acid bacteria (*L. casei* and *L. plantarum*) in the difference of moisture contents (50 and 75%). At 48 incubation hours, all fermented samples (SSF1-SSF8) displayed high amount of LAB colonies, therefore these samples were extracted by ethanol then evaporated and determined the prebiotic properties. The rice bran with SSF extractions (SSF1- SSF8) exposed the growth enhancing via the optical density at 600 nm and presented high protective against all pathogens better than control and FOS. Specially, SSF5 and SSF6 (Thai jasmine rice bran SSF by *L. casei* with 50% and 75%) revealed the maximum clear zone to inhibit all pathogens. From all results of this study, the rice bran extraction from SSF by LAB could be applied as prebiotic substance for further functional food as well as increasing the efficiency of agricultural residue utilization in Thailand.

Acknowledgments: The authors would like to thank Dr. Harit Nimraksa at Agricultural Technology Department, Ramkhamhaeng University for rice brans provision and Biotechnology Department, Ramkhamhaeng University for research facilities.

References:

1. Huang YP, Lai, HM. J. Food Drug Anal. 2016;24(3):564-74.
2. Kechagia M, Basoulis D, Konstantopoulou S, Dimitriadi D, Gyftopoulou K, Skarmoutsou N, Fakiri EM. ISRN Nutr. 2013;5:1-5.
3. Arab F, Alemzadeh I, Maghsoudi V. Sci Iran. 2011;18(6):1402-6.
4. Cheng J, Choi BK, Yang SH, Suh JW. J Appl Biol Chem. 2016; 59(1):57-62.
5. Siragusa S, Di Cagno R, Ercolini D, Minervini F, Gobbetti M, De Angelis M. Appl Environ Microbiol. 2009;75(4):1099-109.
6. Rezvani F, Ardestani F, Najafpour G. Braz J Microbiol. 2017;48(2):251-58.
7. Ogué-Bon E, Khoo C, Hoyles L, McCartney AL, Gibson GR, Rastall RA. FEMS Microbiol Ecol. 2011;75(3):365-76.
8. Ghazi I, Zarei I, Mapesa J. Med Aromat Plants. 2016;5(5):1-10.

SP09_004_PF: THE ASSESSMENT OF PHOTOCATALYTIC ACTIVITY OF CUPROUS AND ZINC OXIDE NANOPARTICLES FROM *Oroxylum indicum* BY ONE POT GREEN SYNTHESIS METHOD

Supakorn Boonyuen,[1]* Kanussamon Chookamnerd,[1] Teetat Therdkiet,[2] Mathi Kandiah,[3]
Alvin Lim Teik Zheng,[4] Yoshito Andou,[4]

[1]Department of Chemistry, Faculty of Science and Technology, Thammasat University, Pathum Thani 12120, Thailand
[2] Harrow International School, 45 Soi Kosumruamchai 14, Kosumruamchai Rd, Don Mueang, Bangkok, 10210, Thailand
[3]School of Science, BMS, 591, Galle Road, Colombo 06, Sri Lanka
[4]Graduate School of Life Science and Systems Engineering, Kyushu Institute of Technology, Fukuoka 808-0196, Japan
*e-mail: chemistrytu@gmail.com

Abstract:

The current research work emphasizes the green synthesis of cuprous oxide (Cu_2O NPs) and zinc oxide (ZnO NPs) nanoparticles by using the active agent from bark extract of *Oroxylum indicum*. The as-synthesized nanoparticles were thoroughly characterized by using X-ray Powder Diffraction (XRD), Elemental Distribution (EDX) and morphology using Field Emission Transmission Electron Microscopy (FE-TEM), in order to fully understand the surface morphological features, and elemental analysis and crystallinity. The photocatalytic activity testing found that Cu_2O NPs exhibited highly efficient photocatalytic behavior due to their surface morphology and less aggregation of nanoparticles with the photo degradation of Methylene blue rate constant 0.0177 min^{-1}. In brief, the phytochemicals present in *Oroxylum indicum* extracts are potent reducing agent to synthesis metal oxide nanoparticles. The Cu_2O NPs are proficient to degrade Methylene Blue in short time with high photocatalysis rate. Therefore, the use of *Oroxylum indicum* for the biosynthesis of nanoparticles may have vast applications as a cost- effective and eco-friendly photocatalyst.

Introduction:

Nanotechnology, is an interesting field of researches, which particularly applied to construct biomaterials of desired. Recently, nanomaterials were claimed as 'a wonder of modern science [1] to their notable novel functionality that is not observed in their bulk counterparts [2]. Some metal and metal oxide nanoparticles have been emphasizing studied and reported for their special properties, including anti-microbial [3], anti-cancer [4], catalytic [3,5] and removal of pollutants like dyes, toxins and pigments from environment [6]. Nowadays, the eco-friendly approach is dramatically increasing, which has led to the green synthesis of nanoparticle [7]. This biological approach emerges as a cost-effective and non-toxic substitute to orthodox physical and chemical methods. *Oroxylum indicum*, commonly known as Midnight horror, is a deciduous tree well known among ethnic communities of South Asia for its medicinal properties. Numerous studies have been reported on their biologically active secondary metabolites from the stem bark of *O.indicum* which showed that the stem has the more antibacterial effect than other parts.[9,10] The main active compounds are in flavonoid group, which the most abundant compounds are baicalin, baicalein and chrysin [11]. The very attractive properties of the Cu_2O NPs is its photocatalytic activity in the presence of UV light and is eco-friendly as a p-type semiconducting material. The Cu_2O NPs are non-toxic and stable with the band gap of about 2.2 eV [12,13]. However, the ZnO NPs also provided as a photocatalyst, which afforded several advantages such including highly effective photocatalytic activity [14] and having excellent chemical and photochemical stability and non-toxicity [15]. In nanoparticle form, ZnO NPs are expected to provide significantly enhanced reactivity due to increased specific area and changes of the surface properties of the sample [16].

In this paper, we present the results of a study on the physical properties and the use of Cu_2O NPs and ZnO NPs in photodegradation of methylene blue (MB) under the irradiation of UV-light with various amount of catalyst and irradiation time.

Methodology:

Materials

Fresh *O. indicum* were collected from organic farm Yasoton Province, Thailand. The zinc nitrate hexahydrate ($Zn(NO_3)_36H_2O$), copper sulfate ($CuSO_4.6H_2O$) (> 98%) and Methylene Blue dye (MB) were purchased from Sigma-Aldrich Chemicals Co. All reagents were of analytic grade and used as they were received.

Preperation of plant extract

The bark of *O.indicum* were cleaned and washed thoroughly 2–3 times under running water to remove dust particles, then sterilize using double-distilled water. The dried sample was cut into small pieces and were oven dried at 40 °C. For synthesis, 20 g of dried sample were weighed and boil with 100 ml of distilled water for 20 min at 60 °C. Then, the mixture was cool down at room temperature and was filtered using Whatman No. 1 filter paper and centrifuge at 10,000 rpm for 5 min to remove the irrelevant bio-materials. Later, the extract was kept at room temperature for experiments and stored at 4 °C for later use.

Synthesis of ZnO NPs and Cu_2O NPs

The ZnO nanoparticle from *O. indicum* extract, were synthesized following co-precipitation method, with few modifications. 1 ml of plant extract with 50% concentration was mixed with 50 ml of 1 M zinc nitrate hexahydrate solution in a flask and was heated at 60 °C on hot plate for 5 min. Further, add 50 ml of 1 M NaOH dropwise into the reaction mixture, ultimately producing a milky and cloudy appearance. The solution mixture was stirred constantly for 2 h at 60 °C. After, the complete precipitation of nanoparticles, the suspension was further centrifuged for 10 min at 10,000 rpm. The nanoparticle will form as white pellet at the bottom with clear supernatant, which was discarded. The pellet was washed thoroughly with distilled water two times and purified by centrifugation. To ensure complete removal of residue the pellet was further washed with 100% ethanol and subsequently dried in vacuum oven at 60 °C overnight. The drying time will oxidize the $Zn(OH)_2$ to ZnO white powder. The Cu_2O NPs were prepare similarly with ZnO by using Copper sulfate hexahydrate with *O. indicum* extract.

Characterization ZnO NPs and Cu_2O NPs

The ZnO NPs and Cu_2O NPs must be confirmed by scanning the nanoparticle suspension by UV–vis Spectrophotometer with range of 300–800 nm. Different samples with same amount of suspension was analyzed by UV–vis Spectrophotometer. TEM is used to determine the morphology of synthesized nanoparticle. The determination of size, shape, crystallinity, purity and dispersion of metallic elements, the nanoparticle solution was visualized under a multifunctional 200 kV-operated JEM-2100 F (JEOL) electron microscope. SAED identified the crystalline structure of nano-sized of particles.

Photocatalytic activity

10 mg of the ZnO NPs and Cu_2O NPs samples were suspended in 10 ml deionized water as concentration of 1 mg/ml as a stock solution, following sonication solution. The photocatalytic activity of NPs was evaluated by monitoring the degradation of Methylene Blue dye in aqueous under UV light at different time intervals. Methylene Blue dye (50 mM) was prepared and mixed with different amount of Nps (500, 300 and 100 microliter) solution. The aqueous solution was stirred continuously to reach the absorption/desorption equilibrium, before exposing to the light at different time (0-150 mins). The photocatalytic degradation activity was examined by placing the dye solution under UV light. The photo-decomposing activity was examined by taking 1 ml of solution after regular time intervals 0 to 150 min and measuring the absorbance by UV–vis Spectrophotometer ranged 500- 700 nm, under all conditions.

Results and Discussion:

A typical TEM micrograph has taken and presented in Fig. 1 and 2 illustrate a number of both aggregates Cu_2O and ZnO NPs as well as individual. The measurement of the size was performed along the largest diameter of the particles. The SAED pattern of Cu_2O and ZnO NPs reveals its crystalline nature with the clearly seen plane (1,1,1) (2,0,0) and (1,0,0) (1,1,0), respectively.[17] It is possible that flavonoid from *O.indicum* extract acting as a reducing agent and form micelles around the nanoparticles, then self-assembled into distorted spherical-like aggregations. The particles are found spherical in shape and the average diameter of the particle is found to be about 158 nm and 16 nm for Cu_2O and ZnO NPs. The EDS was shown in Figure 1and confirmed the formation of Cu_2O and ZnO.[17,18]

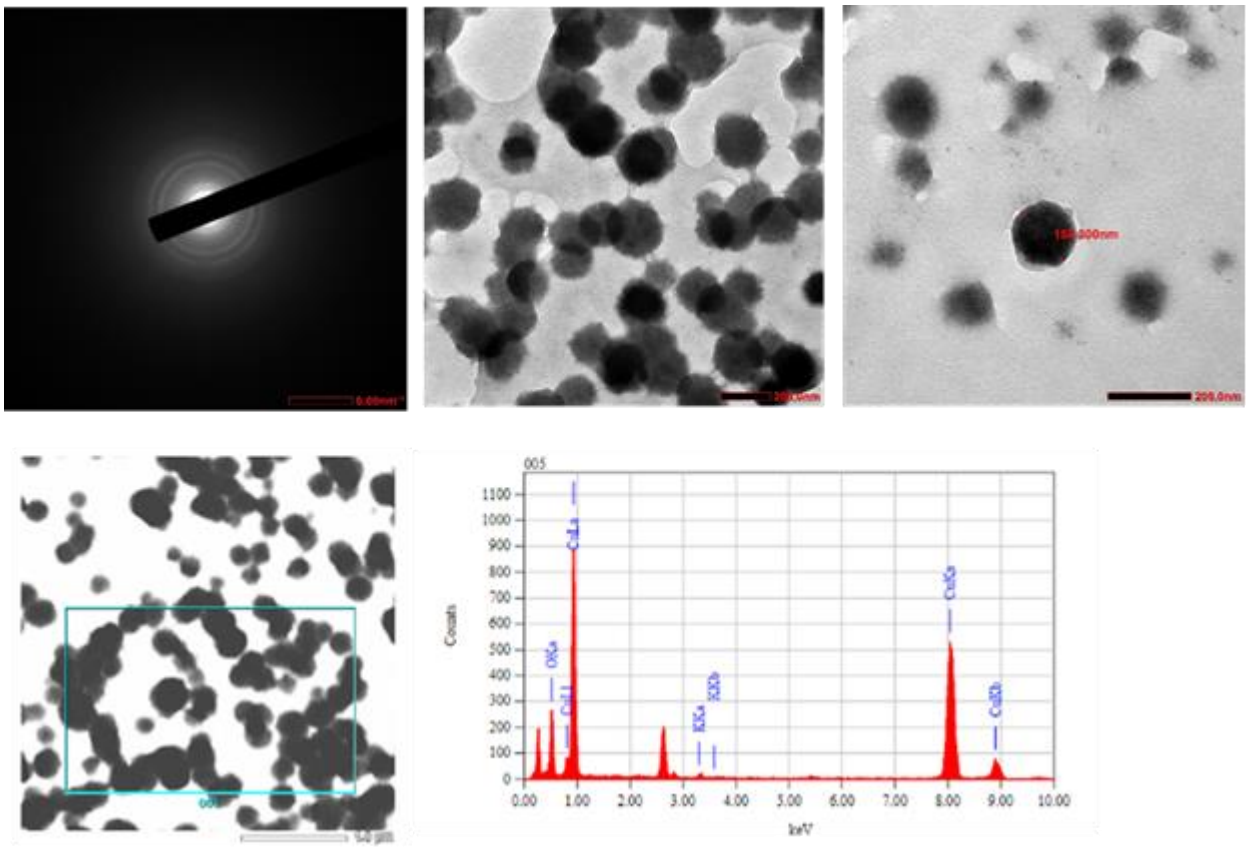

Figure 1. SAED patterns TEM micrograph and SEM with the EDS of Cu_2O NPs.

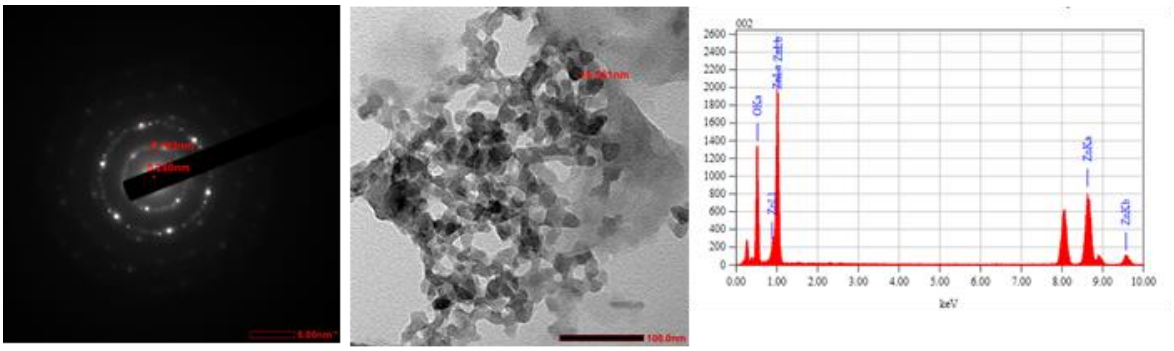

Figure 2. SAED patterns TEM micrograph and SEM with the EDS of ZnO NPs.

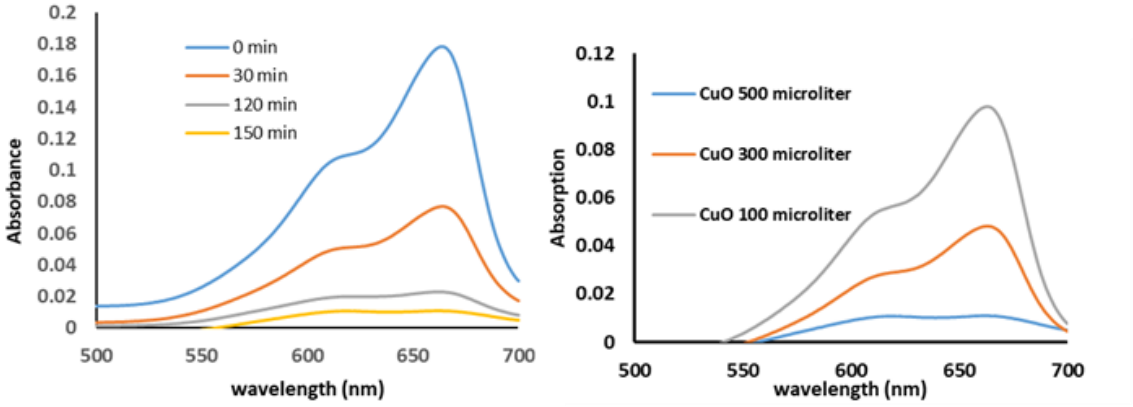

Figure 3. The absorption spectrum of Methylene Blue degradation by Cu_2O nanoparticles.

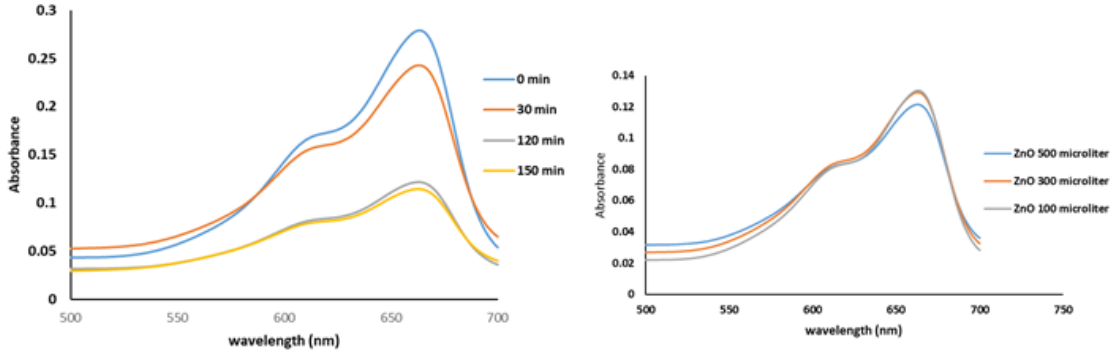

Figure 4. The absorption spectrum of Methylene Blue degradation by ZnO nanoparticles.

The photocatalytic efficiency of both the synthesized Cu_2O and ZnO NPs were investigated by degrading the methylene blue (MB) dye under UV-visible light illumination. The presence of Cu_2O catalyst is greater photodegradation of MB than ZnO at the same period of UV-visible light irradiation. The more addition of ZnO NPs into MB solution does not have any effect on the degradation, however the great decrease found in Cu_2O catalyst with 500 microliter addition. It indicates that the formed Cu_2O NPs has a higher degradation efficiency than ZnO NPs and the observation of such high degradation efficiency for the Cu_2O NPs under UV-visible light irradiation is may attributed to their unique structure and high specific area that supporting for the enhanced optical properties. In the presence of Cu_2O NPs catalyst, the electron formed in the conduction band gets transferred to the conduction band of Cu_2O NPs catalyst before being recombined with the hole of valence band then cause the degradation of MB molecule. A perfect interfacial and good absorption of MB dye on catalyst surface increase the process of electrons transfer.[17]

From the UV–vis adsorption spectra of NPs irradiated under UV light irradiation, related to the efficient degradation of MB dye by photocatalytic phenomenon. It was found that intensity of absorption spectra decreases with increase in irradiation time or volume of catalyst, especially for Cu_2O. The degradation % of MB with time is shown in Fig. 5 and 6 for Cu_2O and ZnO NPs, respectively. It is clearly seen that the degradation ratio is functioning with decomposing time before reach the equilibrium. To figure out the behavior of photocatalyst, the experimental data was calculated in kinetic first order reaction:

$$\ln (C/C_0) = -k_t$$

In this equation, K is the apparent rate constant (min^{-1}), it is the reaction time, C_0 and C are the concentration of MB dye at 0 and t, respectively. The linear relationship between $\ln(C/C_0)$ and the irradiation time for MB dye degradation is shown in Fig. 5-6 which confirms that the photocatalytic degradation curve falls

in the first-order kinetics reaction. The reaction rate constant (k) from first order reaction for photodegradation of MB with Cu_2O and ZnO NPs were found 0.0177 and 0.0063 min^{-1}, respectively. The photocatalytic activity is directly proportional to the value of reaction rate constant.

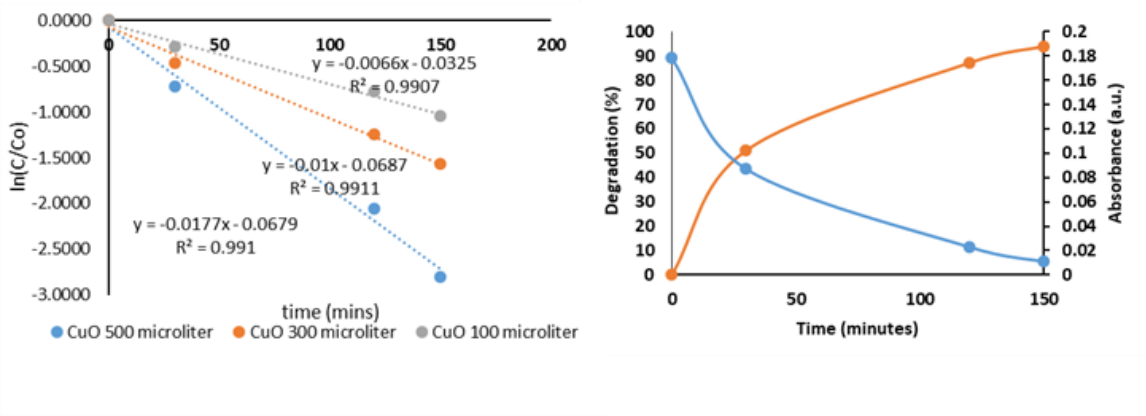

Figure 5. The Plot of absorbance, degradation (%), and kinetics of the Methylen Blue degradation by Cu_2O NPs and ln(C/C0) with time.

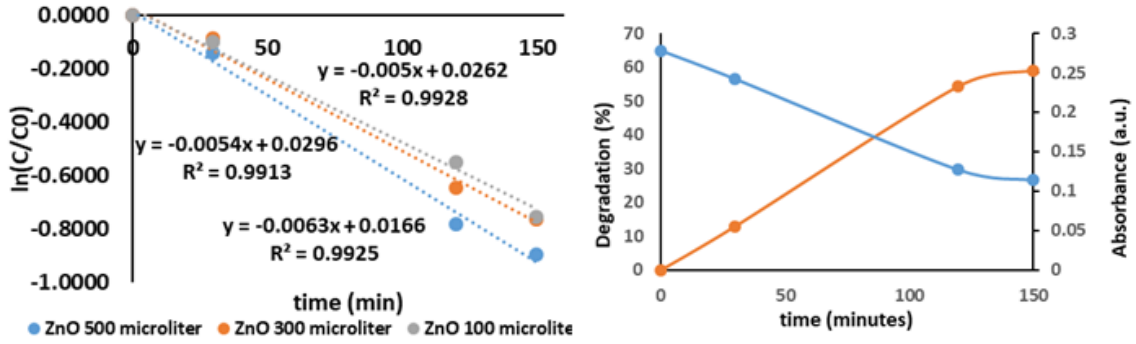

Figure 6. The Plot of absorbance, degradation (%), and kinetics of the Methylen Blue degradation by ZnO NPs and ln(C/C0) with time.

Conclusion:

In summary, this report proves that the one pot green synthesized Cu_2O and ZnO NPs from the bark extract of *Oroxylum indicum* are cost effective, low time consuming, bio-degradable and non- toxic. The UV–vis spectra confirmed the synthesis of Cu_2O and ZnO NPs. The TEM and SAED confirmed the crystalline structure of Cu_2O and ZnO NPs, in which crystalline planes (1,1,1) (2,0,0) were assigned for Cu_2O and planes (1,0,0) (1,1,0) were attributed to ZnO NPs. The extract of *Oroxylum indicum* may cause the aggregation, however the particle size from TEM image found 158 nm and 16 nm for Cu_2O and ZnO NPs, respectively. The degradation of methylene blue dye was functioned with time and amount of catalyst. The Cu_2O NPs catalyst exhibits high photo catalysis rate and high MB degradation in short time. Ultimately, the green rapid synthesized Cu_2O and ZnO NPs, from bark extract of *Oroxylum indicum* can show the MB degradation as a function of time using synthesized nanoparticles. It is clear that the degradation is related to irradiation time. The reaction rate constant (k) from first order reaction for photodegradation of MB with Cu_2O and ZnO NPs were found 0.0177 and 0.0063 min^{-1}, respectively. This proves that the successful synthesized nanoparticle has photocatalytic degradation activity and the synthesized nanoparticles can be applied as an industrial dye removal reagents.

Acknowledgements:

This study was supported by Thammasat University Research Fund, Contract No. TUFT 013/2563.

References:

1. Sangeetha G., Rajeshwari S., Venckatesh R., Mater. Res. Bull. 201; 46: 2560–2566.
2. Emami-Karvani Z., Chehrazi P., Afr. J. Microbiol. Res. 2011;5: 1368–1373.
3. Rasmussen J.W., Martinez E., Louka P., Wingett D.G., Drug Deliv. 2010;7:1063–1077.
4. Kumar S.S., Venkateswarlu P., Rao V.R., Rao G.N., Int. Nano Lett. 2013; 3: 30-35.
5. Singh P., Singh H., Castro-Aceituno V., Ahn S., Kim Y.J., Farh M.E.-A., Yang D.C., J. Nanoparticle Res.2017;19: 257-262.
6. Jiang G., Lin Z., Chen C., Zhu L., Chang Q., Wang N., Wei W., Tang H., Carbon. 2011;49: 2693–2701.
7. Rosi N.L., Mirkin C.A., Chem. Rev. 2005; 105: 1547–1562.
8. Khodja A.A., Sehili T., Pilichowski J.-F., Boule P., J. Photochem. Photobiol. A: Chem. 2001;141:231–239.
9. Radhika L.G., Meena C.V., Sujha P., Rajesh K.S., Ancient Science of Life, 2011; 30(4): 114-120.
10. Kingston D.G. and Rao V., J. Nat.Prod, 1982.
11. Sithisarn, P., Rojsanga, P., Sithisarn, P. Molecules. 2019; 24: 1937-1945.
12. Shen M., Yokouchi T., Koyama S., Goto T., Phys. Rev. B 56,1997; 13066.
13. Shi W., Lin K., Lin X., J. Appl. Phys.1997; 81:2822–2824.
14. Jang E.S., Won J.H., Hwang S.J., Choy J.H., Adv Mater., 2006; 18(24):3309–3312.
15. Amna S., Shahrom M., Azman S., Nano-Micro Lett., 2015; 7:219–242.
16. Dodd A.C., McKinley A.J., Saunders M., J Nanopart Res., 2006; 8(1):43–51.
17. Heea O. K., Rupaa E. J., Anandapadmanabana G. , Chokkalingamb M. , Lib J. F. , Markusb J. , Soshnikovaa V., Pereza Z.E.J. , Yanga D.-C., Optik – I. J. for Light and Electron Optics., 2019; 181:1091–1098
18. Su R., Li Q., Chen Y., Gao B., Yue Q., Zhou W., J. Clean. Prod., 2019:209: 20-29.

SP09_005_OF

SP09_005_OF: CATALYTIC TRANSFER HYDROGENATION OF FURFURAL INTO FURFURYL ALCOHOL AND 2-METHYLFURAN OVER IRON-PROMOTED COPPER CATALYST

Munsuree Kalong, Sakhon Ratchahat, Wanida Koo-amornpattana, and Atthapon Srifa*

Department of Chemical Engineering, Faculty of Engineering, Mahidol University, Nakhon Pathom 73170, Thailand
*e-mail: atthapon.sri@mahidol.edu

Abstract:

Liquid phase catalytic transfer hydrogenation of furfural into furfuryl alcohol and 2-methylfuran over Cu-based catalyst modified with Fe under 2-propanol as a hydrogen donor was investigated because this system is more economical and much safer than one operated under pure hydrogen. The Fe-promoted Cu catalyst supported on **γ-Al_2O_3** was successfully prepared by an impregnation method. The synthesized catalyst was characterized by XRD, TEM, and N_2 sorption techniques. The XRD analysis confirmed the formation of the metallic Cu and Fe for all fresh and used catalysts. The effect of reaction temperature and reaction time were studied to maximize the yields of furfuryl alcohol and 2-methylfuran. The highest yields of furfuryl alcohol (44%) and 2-methylfuran (43%) were achieved at 220 °C and reaction time for 2 h.

Introduction:

As the rapid reduction of fossil resources and large amount of energy consumption, the development of non-fossil fuel derived from bioresources has been suggested as an important key for future biochemicals and biofuels. Lignocellulosic biomass which mainly composes of cellulose, hemicellulose, and lignin has been recognized as a bioresource for the alternative bio-based chemicals and biofuels production.[1] Furfural (FAL) is the major products derived from lignocellulosic biomass via hydrolysis and dehydration of xylan. Due to its high reactivity and versatility, it can be further upgraded to various kinds of high value bio-based chemicals such as furfuryl alcohol (FOL), furan, 2-methylfuran (2-MF), and cyclopentanone (CPO) etc., through catalytic processes including hydrogenation, oxidation, hydrogenolysis, decarboxylation, and hydrodeoxygenation.[2, 3] Furfuryl alcohol (FOL) and 2-methylfuran (2-MF) are ones of the most significant products that widely applied in the chemical industries. As for furfuryl alcohol, it can be used in the production of resins, reactive solvent for phenolic resins, a viscosity reducer for epoxy resins, a chemical building block for synthesis of tetrahydrofurfuryl alcohol, pharmaceuticals, and fragrances.[3] On the other hand, 2-methylfuran is a versatile chemical intermediate used for pesticides, perfumes, antimalarial drugs, and particularly used for fuel additives in order to improve octane number in fuel.[4] Catalytic transfer hydrogenation (CTH) reaction under alcohols as hydrogen donors has received great attention because it can avoid the use of explosive hydrogen. Various types of catalysts have been utilized in this process such as metallic Pt, Ru, Ni, Pd, Rh, Ag, Co, Fe, Zn, Cr and Cu supported on Al_2O_3, SiO_2, ZnO, TiO_2 as both monometallic and bimetallic combinations and additives.[5-7] The suitable catalysts for furfuryl alcohol and 2-methylfuran production should break C=O bond in furfural effectively, followed by hydrogenation of the carbon.[5] Thus, the excellent Cu-based catalysts are less oxophilic and weakly interactive with C=O bond in the furan ring. Hence, they are highly selective to hydrogenate the carbonyl group of furfural to generate furfuryl alcohol, followed by oxygen removal to produce 2-methylfuran via hydrodeoxygenation.[8]

In this work, the Cu catalyst modified with Fe supported on **γ-Al_2O_3 was** used in catalytic conversion of furfural into furfuryl alcohol and 2-methylfuran under 2-propanol as a hydrogen donor. Subsequently, the catalytic transfer hydrogenation under 2-propanol as a hydrogen donor was investigated because this system is more economical and safer than one operated under pure hydrogen. The physical and chemical properties of the catalyst were characterized in order to understand the relationship between chemical and physical properties and catalytic activity of the synthesized catalyst.

Methodology:

Catalyst preparation: The Cu catalyst modified with Fe catalyst was prepared by an impregnation method. $Cu(NO_3)_2{\cdot}3H_2O$ and $Fe(NO_3)_3{\cdot}9H_2O$ were used as the corresponding metal salts **and** γ-Al_2O_3 was used as the support material. The mixture of two metal salts were dissolved in deionized water in the proper amount. Then, the solution of the corresponding metal salts was dropped on γ-Al_2O_3 support. The sample was then dried at 110 °C for 12 h and calcined at 500 °C for 5 h. Thereafter, the catalyst was reduced at 500 °C for 3 h under hydrogen atmosphere. The synthesized catalyst was noted as FeCuAl catalyst.

Catalyst Characterization: The specific surface area, total pore volume, and average pore diameter of the synthesized catalyst before the reaction were determined by a nitrogen adsorption and desorption at -196 °C **(**BEL Japan, Bel Sorp mini II**).** The phase identification and the crystallinity of the synthesized catalyst were analyzed by X-ray diffraction **(**XRD**)** performing on X-ray diffractometer **(**Shimadzu XRD-6000**)** with Cu K**α X-ray source radiation in the range of** 2θ = 10° - 80° at 40 kV and 30 mA**.** The particle size distribution and morphology of the catalyst were observed using a JEOL JEM-2100F HRTEM system and the EDS detector was used to perform the quantitative of an elemental analysis of the catalyst**.**

Catalyst activity test: The catalytic transfer hydrogenation of furfural was carried out in a 100 ml batch reactor. In a typical experiment, furfural 1 g, 2-propanol 40 ml and catalyst 0.2 g were loaded into the reactor. Then, the reactor was flushed by nitrogen gas several times to remove air inside. The reactor was stirred at 600 rpm and heated up to the desired reaction temperature. Subsequently, the reactor was placed into cool water to quench the reaction. The products were collected from the cooled reactor and the used solid catalyst was separated from product by filtration. Liquid product was quantitatively analyzed by a gas chromatography (GC) equipped using a flame ionization detector (FID) (Clarus 680, Perkin Elmer) with a capillary column (DB-1HT, 30 m × 0.32 mm × 0.1 μm). For the stability test, the solid catalyst was collected and washed by ethanol several times. After drying, the catalyst was reused directly. The conversion of furfural and product yield were defined as follows:

$$\text{Conversion (\%)} = \frac{\text{mol of furfural converted}}{\text{mol of furfural fed}} \times 100 \quad (1)$$

$$\text{Product yield (\%)} = \frac{\text{mol of furfural after reaction}}{\text{mol of furfural fed}} \times 100 \quad (2)$$

Results and Discussion:

Characterization results: The N_2 adsorption-desorption isotherm and pore size distribution of the synthesized catalyst are presented in Figure 1. The adsorption-desorption isotherm of the FeCuAl catalyst reveals a typical type IV isotherms with an H1-type hysteresis loop according to the IUPAC classification, indicating a characteristic of mesoporous material.[9] The surface area is 161.53 m^2/g with a total pore volume of 0.41 cm^3/g and average pore diameter of 9.23 nm.

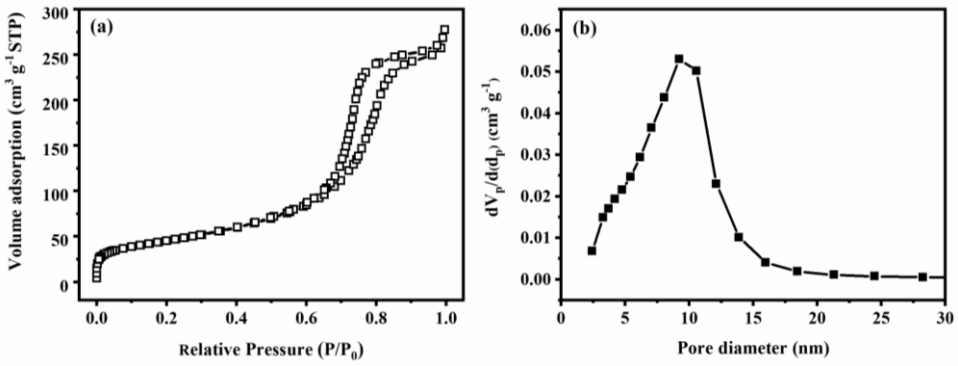

Figure 1 (a) N_2 adsorption-desorption isotherm and (b) pore size distribution of the FeCuAl catalyst.

The XRD pattern of fresh and used FeCuAl catalysts are shown in Figure 2. The diffraction peaks at 37°, 46°, 61°, and 61.7° were attributed **to** γ-Al_2O_3.[10, 11] Meanwhile, the peaks at 43.3° and 50.4° were assigned to Cu(111) and Cu(200), respectively.[4] The observed peaks correspond to metallic Cu and Fe which separately dispersed on the support. No diffraction peaks of Cu-Fe alloy detected by XRD. The fresh and used catalysts were similar in the diffraction peaks, indicating the stability of crystalline structure of the catalyst after the reaction. Furthermore, the morphology of the reduced catalyst was studied by TEM equipped with EDS detector. Figure 3 reveals the EDS mapping of Cu, Fe, and Al species, indicating existence of Cu and Fe elements on the γ-Al_2O_3 support.

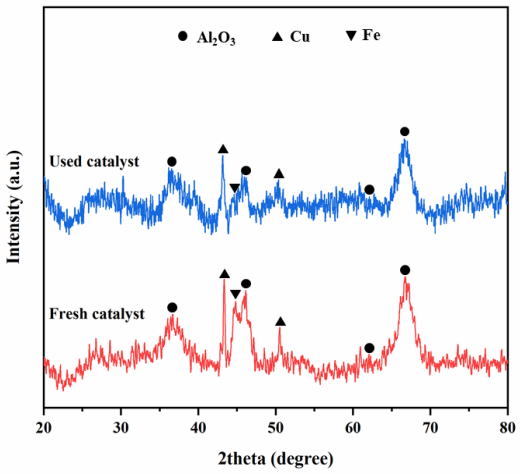

Figure 2 XRD patterns of the fresh and used FeCuAl catalysts.

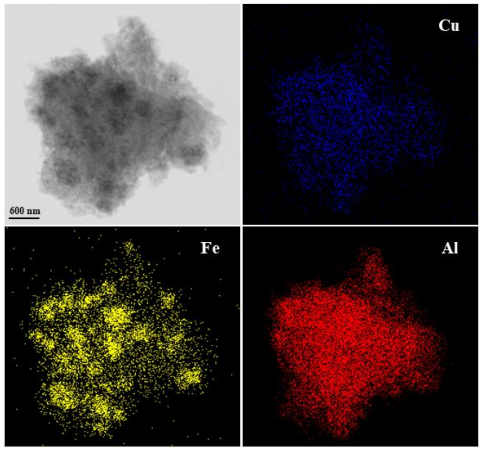

Figure 3 Typical TEM-EDS image of the reduced FeCuAl catalyst.

Effect of reaction temperature: The effect of reaction temperature on furfural conversion and product distribution was investigated over FeCuAl catalyst at reaction temperatures in the range of 180-220 °C**.** As shown in Figure 4, the furfural **(**FAL**)** conversion increased with increasing the reaction temperature**.** The furfuryl alcohol **(**FOL**)** is the main product at low temperature, whereas the selectivity towards 2-methylfuran **(**2-MF**)** increased with increasing the reaction temperature from 180 °C to 220 °C**.** At higher temperature, the reaction proceeded though the hydrogenolysis of FOL to form 2-MF and the highest 2-MF yield of 43**%** was obtained at 220 °C**.** This result indicated that the interaction between Cu and Fe metal could promote the hydrogenolysis of FOL to 2-MF**.**

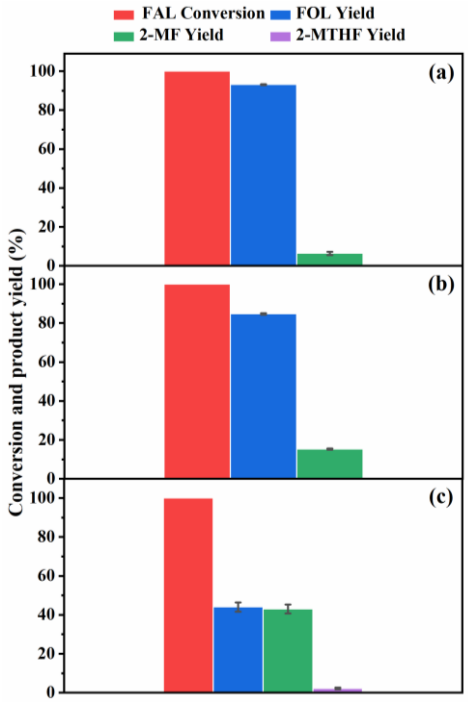

Figure 4 Furfural conversion and product yield over FeCuAl catalyst under different reaction temperatures at (a) 180 °C, (b) 200 °C, and (c) 220 °C under 2-propanol as solvent and reaction time for 2 h.

Effect of reaction time: Effect of reaction time was investigated to optimize the condition for improving the 2-MF yield over FeCuAl catalyst (see in Figure 5). The FAL conversion significantly increased to 100% within 2 h. At initial state of reaction time, the FOL yield reached 89.8% and 6.5% of 2-MF yield. At higher reaction time, the FOL yield significantly dropped while the 2-MF yield gradually increased and reached maximum of 41% at 6 h reaction time. In addition, the 2-methyltetrahydrofuran (2-MTHF) yield slightly produced with the extension of reaction time. This result indicated that the synergistic between Cu and Fe metals was promoted the hydrogenation of hydroxyl group to produced 2-MF.

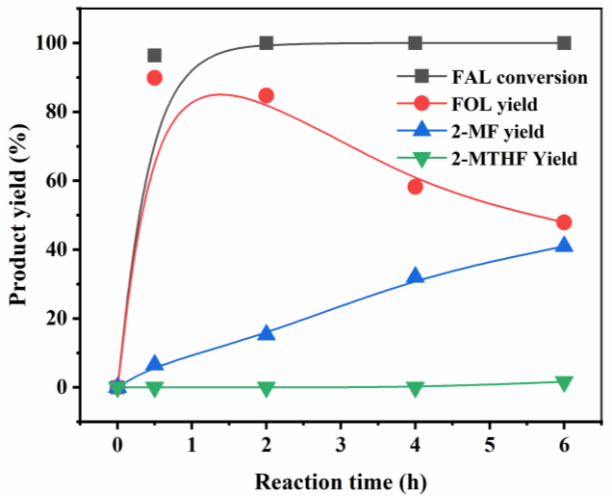

Figure 5 Influence of reaction time on furfural conversion and product yield over FeCuAl catalyst under 2-propanol as solvent at reaction temperature of 200 °C.

Effect of recyclability: The recyclability of FeCuAl catalyst was investigated to observe the stability of catalyst in catalytic transfer hydrogenation (CTH) reaction of furfural (FAL) at reaction temperature of 200 °C and reaction time for 4 h. After the reaction, the catalyst was separated from the product, followed by washed with ethanol several times and reused directly after dried at 65 °C. Figure 6 reveals the change of FAL conversion and product distribution with 3 recycle runs. The FAL conversion slightly decreased with 3 recycle runs, indicating the degradation of catalyst. Similarly, the 2-MF yield decreased from 32% to 10.5%, whereas the FOL yield increased from 58.2% to 83.8% after 3 recycle runs.

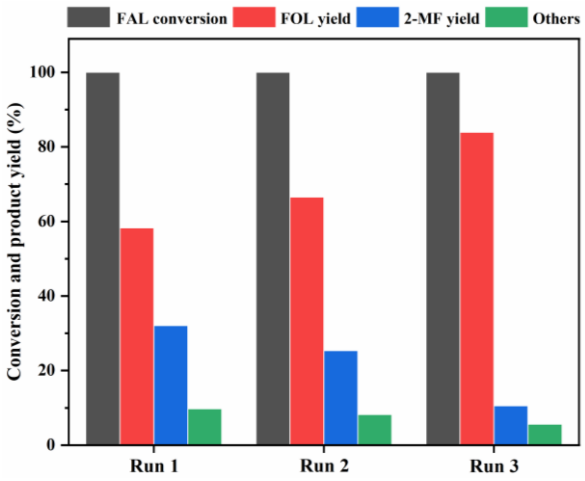

Figure 6 The recyclability of FeCuAl catalysts on furfural conversion and product yield under 2-propanol as solvent at reaction temperature of 200 °C and reaction time for 4 h.

Conclusion:

The Fe-promoted Cu catalyst was prepared by an impregnation method and employed for liquid phase catalytic transfer hydrogenation (CTH) of furfural to furfuryl alcohol and 2-methylfuran under 2-propanol as a hydrogen donor. The XRD analysis confirmed the formation of metallic Cu and Fe for all reduced and used catalyst. The interaction between two metals could promote the reaction through the hydrogenation of carbonyl group of furfural with high selectivity to furfural alcohol and 2-methylfuran. The 2-methylfuran and furfuryl alcohol yields reached maximum to 44% and 43%, respectively at a reaction temperature of 220 °C and reaction time for 2 h.

References:

1. D. M. Alonso, J. Q. Bond, J. A. Dumesic, Green Chem. 2010;12:1493-1513.
2. X. Li, P. Jia, T. Wang, ACS Catal. 2016;6:7621-7640.
3. R. Mariscal, P. Maireles-Torres, M. Ojeda, I. Sádaba, M. López Granados, Energy Environ. Sci. 2016;9:1144-1189.
4. Z. Fu, Z. Wang, W. Lin, W. Song, S. Li, Appl. Catal. A. 2017;547:248-255.
5. G. S. Hutchings, W. Luc, Q. Lu, Y. Zhou, D. G. Vlachos, F. Jiao, Ind. Eng. Chem. Res. 2017;56: 3866-3872.
6. Z. Lin, W. Wan, S. Yao, J. Chen, Appl. Catal. B. 2018;233:160-166.
7. S. K. Jaatinen, R. S. Karinen, J. S. Lehtonen, ChemistrySelect. 2017;2:51-60.
8. S. Sitthisa, T. Sooknoi, Y. Ma, P. B. Balbuena, D. E. Resasco, J. Catal. 2011;277:1-13.
9. Y. Sun, C. Xiong, Q. Liu, J. Zhang, X. Tang, X. Zeng, S. Liu, L. Lin, Ind. Eng. Chem. Res. 2019;58:5414-5422.
10. N. Dewangan, J. Ashok, M. Sethia, S. Das, S. Pati, H. Kus, S. Kawi, ChemCatChem. 2019;11:4923-4934.
11. S. Srivastava, G. C. Jadeja, J. Parikh, RSC Adv. 2016;6:1649-1658.

SP09_006_PA: SUSCEPTIBILITY of the industrially-relevant bacterial strains TO 4-VINYLGUAIACOL

Panaya Kotchaplai[1]* and Alisa Vangnai[2]

[1]Research Unit in Bioconversion/Bioseparation for Value-Added Chemical Production, Institute of Biotechnology and Genetic Engineering, Chulalongkorn University, Thailand, 10330
[2]Biocatalyst and Environmental Biotechnology Research Unit, Department of Biochemistry, Faculty of Science, Chulalongkorn University, Thailand, 10330
*e-mail: panaya.k@chula.ac.th

Abstract:

4-vinylguaiacol or 2-methoxy-4-vinylphenol is one of the major components in hydrolysate obtained from the thermal breakdown of lignin. Besides its uses as an important aroma compound in food, beverage, and fragrance industries, 4-vinylguaiacol has been proposed as a potential feedstock for the production of many value-added compounds. Recently, the biovalorization of 4-vinylguaiacol using the synthetic pathways was successfully demonstrated in the recombinant *Escherichia coli* BL21(DE3). However, the toxicity of 4-vinylguaiacol to the host strain is still a challenge for an effective biovalorization. In this study, three industrially important strains which are *E. coli* BL21(DE3), *Pseudomonas putida* KT2440, and *Bacillus subtilis* 168 were tested for their susceptibilities to 4-vinylguaiacol and ferulic acid. Ferulic acid is a widely studied lignin-derived compound similar in structure to 4-vinylguaiacol. The exposure to 5 mM of ferulic acid did not affect the growth of either *E. coli* BL21(DE3) or *P. putida* KT2440 whereas the exposure to 4 mM of FA inhibited the growth of *B. subtilis* 168. 4-vinylguaiacol is substantially toxic to *E. coli* BL21(DE3) or *P. putida* KT2440 as indicated by the growth inhibition upon exposure to 3 mM of non-metabolizable 4-vinylguaiacol. *B. subtilis* 168 is slightly more tolerant to 4-vinylguaicol and that the exposure to 4-vinylguaiacol showed a similar pattern to that exposed to ferulic acid. The toxicity of ferulic acid to *B. subtilis* 168 is likely attributed to 4-vinylguaiacol derived from ferulic acid. Due to its toxicity, further development of 4-vinylguaiacol-tolerant strain or a suitable bioprocess is required for the effective biovalorization of 4-vinylguaicol.

SP09_007_PF: ETHANOL PRODUCTION IN MOLASSES MEDIUIM BY *Pichia kudriavzevii* STRAIN RU01

Jiroj Boonsung[1], Wiramsri Sripojchanart[1], Surachai Yaiyen[2], Sanya Kudan[2*]

[1]Program in Fermentation Technology in Food Industry, Faculty of Food Industry,
King Mongkut's Institute of Technology Ladkrabang, Bangkok, Thailand 10520
[2]Department of Biotechnology, Faculty of Science, Ramkhamhaeng university, Bangkok,
Thailand 10240
*e-mail: kudansan54@gmail.com

Abstract:

Bioethanol is currently alternative energy that can be obtained from microbial biochemical processes such as yeast and *Zymomonas mobilis*. In this experiment, *Pichia kudriavzevii* strain RU01 was used to produce bioethanol because of their ability to tolerate temperature, pH, and osmotic pressure. Therefore, a study was conducted to find the optimum conditions for ethanol production by using molasses, ammonium and diammonium phosphate as a carbon and nitrogen sources. The production rate of ethanol was 1.02 grams per liter per hour in condition with 10% (w/v) molasses and 0.1% (w/v) diammonium phosphate at 37 °C with agitated at 200 rpm. *P. kudriavzevii* strain RU01 was higher ethanol productivity than the industrial yeast strain, *Saccharomyces cerevisiae* SC90 and could produce ethanol faster at higher temperature than that of the *S. cerevisiae* SC90.

Introduction:

Ethanol is an important industrial chemical with various applications, like biofuel, industrial solvents, cleaning agents, preservatives. On a large scale, producing ethanol by microorganisms has recently obtained specific achievements. Due to the current challenge of increasing global temperature, thermostable yeasts receive considerable interest nowadays (Dung et al., 2012a). Temperature is one of the significant factors affecting the ethanol fermentation of yeasts. The study on yeasts capable of tolerating high temperatures attracts many researchers due to several potential benefits in ethanol production, including reducing cooling costs under thermal conditions, enhancing saccharification and fermentation rates, and reducing contamination. Besides, ethanol at increasing levels is also one of the major factors inhibiting the yeasts in various ways, such as inhibition of cell growth, viability, and fermentation ability (Dung et al., 2006). Selecting the yeasts with thermo- and ethanol tolerant ability is necessary for the industrial production of ethanol. Although numerous studies have examined many of the factors that affect batch ethanol fermentation efficiency, little attention has been paid to the influence of the biomass concentration on the above efficiency. Among the thermotolerant yeasts, *Kluyveromyces marxianus* has received much attention due to its high thermotolerance and various other advantageous characteristics (Banat et al. 1998; Christensen et al. 2011; Kourkoutas et al. 2002; Limtong et al. 2007; Zafar and Owais 2006). In more recent years, some reports on ethanol production at high temperature using *Pichia kudriavzevii*. Many *P. kudriavzevii* strains, only a few strains grew at a temperature higher than 41°C and up to 43°C (Isono et al. 2012). Compare with *Saccharomyces cerevisiae*, a notable ethanol-producing yeast species, *P. kudriavzevii* showed higher thermotolerance than most *S. cerevisiae* strains. Among the strains of *P. kudriavzevii* that have been so far reported for ethanol production at high temperature. Besides, ethanol at increasing levels is also the primary factor inhibiting yeasts in various ways, such as inhibition of cell growth, viability, and fermentation ability (Dung et al., 2006). This research was studied in fermentative parameter of *P. kudriavzevii* strain RU01 for ethanol production from molasses, ammonium salt and temperature.

Methodology:

The yeast strain and culture condition

Pichia kudriavzevii strain RU01 from coconut flower, the strain was stored for long term maintenance at -20 °C in YM medium broth (Himedia) added with 0.01 M NaCl (Sigma) and 20% (w/v) glycerol (Sigma). Before the experiment, cells were propagated twice in YM medium broth added with 0.05 M NaCl.

The effect of molasses

The yeast cells were cultured in 5% and 10% (w/v) molasses at 30 °C with agitated at 200 rpm for 24 hours. The growth rate and ethanol production were measured by cell dry weight and dichromate oxidation method described by Henschke and Jiranek 1991.

The effect of ammonium salt

The yeast cells were cultured in 10% (w/v) molasses with 0.1% ammonium phosphate and diammonium phosphate at 30 °C with agitated at 200 rpm for 24 hours. The growth rate and ethanol production were measured by cell dry weight and dichromate oxidation method described by Henschke and Jiranek 1991.

The effect of temperature

The yeast cells were cultured in 10% (w/v) molasses, 0.1% (w/v) diammonium phosphate and varies temperature at 30 °C, 37 °C and 40 °C with agitated at 200 rpm for 24 hours. The growth rate and ethanol production were measured by cell dry weight and dichromate oxidation method described by Henschke and Jiranek 1991.

Determination of fermentation efficiency

The fermentation efficiency was calculated from the increase of the ethanol concentration during the first 30 min of the experiments and was expressed as gram of ethanol produced per gram of dry yeast biomass per hour. During this period, the increase in biomass concentration was negligible, and the increase in ethanol concentration was linear with time and proportional to the amount of biomass present.

The specific cell growth in molasses is calculated by $$\mu = \frac{\ln \Delta x}{\Delta t}$$

Coefficient is the efficiency of the cell using a substrate by $$\text{Coefficient} = \frac{Yp/x}{Yp/s}$$

Fermentation efficiency = $$\frac{Yp/s \text{ in research}}{Yp/s \text{ in theory}} * 100$$

The productivity of ethanol = $$\frac{Product\ (\frac{g}{L})}{\text{Time (h.)}}$$

Results and Discussion:

Parameter of fermentation efficiency by *Pichia kudriavzevii* RU01 in molasses medium

The fermentation parameters of *P. kudriavzevii* strain RU01 was cultured in 5% (w/v) and 10% (w/v) molasses medium at 30 °C. It was found that 10% (w/v) molasses has more cell dry weight and ethanol production than that of 5% (w/v) molasses. The growth rate of *P. kudriavzevii* in 5% (w/v) and 10% (w/v) of molasses were 0.02 and 0.19 per hour and the yield of ethanol production (Yp/s) was 0.14 g of ethanol per g of cell dry weight and 0.28 g of ethanol per g of the cell dry weight, respectively. The yield coefficiency, commonly referred to the substrate-to-biomass yield, was used to convert between cell growth rate and substrate

utilization rate. The results found from 5% (w/v) and 10% (w/v) molasses were 22.82 and 10.52, respectively, when they were calculated to the fermentation efficiency. The result showed 27.5% and 54.1%, respectively. It was shown that differences concentrations of glucose in molasses have effect on ethanol production.

Table 1. Ethanol production by *Pichia kudriavzevii* strain RU01 in molasses medium.

Molasses (w/v)	DW (g/L)	Yp/x[a]	Yp/s[b]	Yx/s[c]	Co-efficiency	Fermentation efficiency (%)	Productivity (g/L/h)	μ (h^{-1})
5%	5.17	3.20	0.14	0.04	22.82	27.50	0.69	0.02
10%	6.09	2.90	0.28	0.10	10.52	54.10	0.74	0.19

[a] Yp/x is the specific product yield coefficient
[b] Yp/s is a product yield coefficient based on substrate
[c] Yx/s is the cell yield coefficient

Parameter of fermentation efficiency by *Pichia kudriavzevii* strain RU01 in 10% molasses medium with 0.1% ammonium and diammonium phosphate.

The fermentation parameters of *P. kudriavzevii* strain RU01 was cultured in 10% (w/v) molasses at 30°C. Then the culture medium was added with 0.1% (w/v) ammonium salt: ammonium phosphate and diammonium phosphate. The result showed that cell dry weight from ammonium phosphate and diammonium phosphate were 6.09 g/L and 5.67 g/L, respectively. The growth rate of *P. kudriavzevii* in 10% (w/v) molasses containing 0.1% (w/v) of ammonium phosphate, and diammonium phosphate were 0.19 and 0.23 per hour and the yield of ethanol production (Yp/s) was 2.90 g of ethanol per g of cell dry weight and 3.77 g of ethanol per g of the cell dry weight, respectively. The yield coefficient, commonly referred to the substrate-to-biomass yield was used to convert between cell growth rate and substrate utilization rate, the result showed 10.52 and 9.92, respectively. When they were calculated to the fermentation efficiency, the results were 54.10% and 74.50%, respectively. It was found that differences between ammonium phosphate and diammonium phosphate have more effects on ethanol production. Because nitrogen and phosphorus sources were the main nutritional requirements for yeast growth and maximum ethanol production efficiency, another research suggested adding a nitrogen source is essential for increases biomass concentration of *S. cerevisiae* and sugars utilization rates (Henschke and Jiranek 1991; Bely et al. 2003). *P. kudriavzevii* strain RU01 could increase diammonium phosphate utilization better than ammonium phosphate because diammonium phosphate can be soluble in water and increase higher ammonium ion concentration than ammonium phosphate.

Table 2. Ethanol production by *Pichia kudriavzevii* strain RU01 in 10% molasses medium with 0.1% ammonium and diammonium phosphate.

Nitrogen sources (w/v)	DW (g/L)	Yp/x[a]	Yp/s[b]	Yx/s[c]	Co-efficiency	Fermentation efficiency (%)	Productivity (g/L/h)	μ (h^{-1})
ammonium phosphate	6.09	2.90	0.28	0.10	10.52	54.10	0.74	0.19
diammonium phosphate	5.67	3.77	0.38	0.10	9.92	74.50	0.89	0.23

[a] Yp/x is the specific product yield coefficient
[b] Yp/s is a product yield coefficient based on substrate
[c] Yx/s is the cell yield coefficient

Parameter of fermentation efficiency by *Pichia kudriavzevii* strain RU01 in 10% molasses medium with 0.1 diammonium phosphate at various temperature.

The fermentation parameters of *P. kudriavzevii* strain RU01 was cultured in 10% (w/v) molasses containing 0.1% diammonium phosphate at 30 °C, 37 °C and 40 °C. The growth rate of *P. kudriavzevii* at 30 °C, 37 °C and 40 °C were 0.23, 0.11, and 0.13 per hour, respectively. According to, the culture in 10% (w/v) molasses containing 0.1% diammonium phosphate at 30°C was suitable for cell growth whereas productivity of ethanol in 37°C amount 1.02 (g/L/h) was better than 30°C and 40°C. The fermentation efficiency of *P. kudriavzevii* strain at 30 °C, 37 °C and 40 °C were 74.50%, 87.90%, and 39.40%, respectively. High temperature was a major stress factor for yeast during the fermentation process, inhibiting cell division and specific growth rate (Thevelein and Hohmanns. 1995). This was consistence with productivity of ethanol and fermentation efficiency found in this research. When compared the production rate of ethanol and fermentation efficiency with the industrial strain. *S. cerevisiae* SC90, a yeast strain used in the bioethanol production industry which was found productivity and the fermentation efficiency of 0.44 g/L/h and 82.19%, respectively in 36 hours (Pornpukdeewattana et al. 2014). While, *P. kudriavzevii* strain RU01 showed higher productivity, fermentation efficiency and more rapidly than that of *S. cerevisiae* SC90.

Table 3. Ethanol production by *Pichia kudriavzevii* strain RU01 in molasses medium with 0.1% diammonium phosphate with various temperature.

Temperature	DW (g/L)	Yp/x[a]	Yp/s[b]	Yx/s[c]	Co-efficiency	Fermentation efficiency (%)	Productivity (g/L/h)	μ (h^{-1})
30 °C	5.67	3.77	0.38	0.10	9.92	74.50	0.89	0.23
37 °C	6.10	4.00	0.45	0.11	8.92	87.90	1.02	0.11
40 °C	5.05	2.81	0.20	0.07	13.98	39.40	0.59	0.13

[a] Yp/x is the specific product yield coefficient
[b] Yp/s is a product yield coefficient based on substrate
[c] Yx/s is the cell yield coefficient

Conclusion:

In this study, the molasses concentration, ammonium salt and temperature affected ethanol production rate and fermentation efficiency. *P. kudriavzevii* strain RU01 in the condition of 10% (w/v) molasses added with 0.1% (w/v) diammonium phosphate at 37 °C with agitated at 200 rpm expressed high productivity and fermentation efficiency. Notably, *P. kudriavzevii* strain RU01 revealed productivity and fermentation efficiency of 1.02 g/L/h and 87.90%, respectively in 24 hours. While *S. cerevisiae* SC90 showed 0.44 g/L/h and 82.19%, respectively in 36 hours. When compared to the industrial strain, *S. cerevisiae* SC90, the production rate of ethanol and fermentation efficiency of *P. kudriavzevii* strain RU01 was found to be a higher potential strain. This further suggests that there are various fermentation parameters that if adjusted could improve the production of ethanol.

Acknowledgements:

The authors would like thank Asst.Prof.Dr.Varaporn Veraplakorn for reading a manuscript.

References:

1. Anderson PJ, Mcneil K, Watson K. Appl. Environ. Microbiol. 1986;51:1314–1320.
2. Banat IM, Nigam N, Singh D, Marchantand R, McHale AP. World J. Microbe. Biot. 1998;14:809–821.
3. Bely M, Rinaldi A, Dubourdieu D. J. Biosci. Bioeng. 2003;96:507–512.
4. Brown SW, Oliver SG, Harrison DEF, Righelato RC. Appl. Microbiol. Biotechnol. 1981;11:151–155.
5. Christensen AD, Kadar Z, Oleskowicz-Popiel P, Thomsen MH. J. Ind. Micro. Biotec. 2011; 38:283–289.
6. Dung NTP, Thanonkeo P, Phong HX. Int. J. Appl. Sci. 2012a;2:65–71.
7. Dung NTP, Rombouts FM, Nout MJR. Food Microbiol. 2006; 23:331-340.
8. Henschke PA, Ough, CS. Am. J. Enol. Viticult. 1991;42:317–321
9. Isono N, Hayakawa H, Usami A, Mishima T, Hisamatsu MA. J. Biosci. Bioeng. 2012;113:76–78.
10. Kebede A, Viljoen BC, Gadaga H, Narvhus JA, Hattingh AL. Food Technol. Biotechnol. 2007;45:21–26.
11. Kourkoutas Y, Koutinas AA, Kanellaki M, Banat IM, Marchant R. Food Microbiol. 2002;19:127–134.
12. Lewis LE, Bain JM, Lowes C, Gillespie C, Rudkin FM, Gow NAR, Erwig LP. PLoS Pathog. 2012; 8:1–15.
13. Limtong S, Sringiew C, Yongmanitchai W. Bioresource Tech. 2007;98:3367–3374.
14. Lo HJ, Kohler JR, DiDomenico B, Loebenberg DC. Cell. 1997;90:939–949.
15. Nadeem, SG, Shafiq, A, Hakim, ST, Anjum Y, Kazm SU. Open J. Med. Microbiol. 2013;3:185–192.
16. Pornpukdeewattana S, Khamfun J, Phatyenchai N. Suranaree J. Sci. Tehnol. 2014;21(4):335–345.
17. Reddy LVA, Reddy OVS. Food Bioprod. Process. 2011; 89: 487–497.
18. Reddy LVA, Reddy OVS. World J. Microbe. Biot. 2005;21:1345–1350.
19. Techapain A, Thanonkeo P, Klanrit P. Braz. J. Microbiol. 21017;48:461–475.
20. Zafar S and Owais M. Biochem. Eng. J. 2006;27:295–298.

SP09_008_OA: EFFECTIVENESS OF SAPONIN ON PHYTOREMEDIATION OF PETROLEUM-CONTAMINATED SOIL

Myat Hnin Ei[1*], Phyu Phyu Myint[2] , Ni Ni Than[3]

1*PhD Candidate, Department of Chemistry, University of Yangon, Myanmar
2Professor, Dr, Department of Chemistry, Loikaw University, Myanmar
3Professor (Head), Dr, Department of Chemistry, University of Yangon, Myanmar
*e-mail:myathninei2018@gmail.com, ninithan@uy.edu.mm

Abstract:

This study aims to evaluate efficiency of saponin, in remediation the soils which are smeared by crude oil. It was based on Nyaungdon Township, Ayeyarwaddy Region, Myanmar in 2019. Soil properties were initially studied in this zone. Crude saponin was extracted from the vegetable waste materials such as Onion skin, Asparagus and Prickly amaranth by the yield percent of 14.55%, 2.53% and 2.12%, respectively. The studied phases included variables of saponin and oil concentration within ranges of (250, 500 and 1000 ppm), (0.1-10 %) and contact time (10 week). The findings showed that concentration of saponin (1000 ppm) on 1 % oil contaminated soil yield of 24.89 % to efficiency of crude oil. The potentials of local Burmuda grass were assessed under normal environmental conditions with or without saponin in remediating soil contaminated with crude oil. Phytoremediation of contaminated soil showed that significant reduction (76.3%) of crude oil was observed by saponin. Crude oil in the polluted soil were reduced by 72.4% as a result of plant only, similar to commercial surfactant treatment (72.1%). This research indicates the soil remediation by Onion skin saponins were contributing to environmental protection.

Keywords: vegetable waste, saponin, petroleum contaminated soil, phytoremediation

SP10_001_OF: DEVELOPMENT OF NI-BASED CATALYST FROM NATURAL KAOLIN VIA MICROWAVE ASSISTED SYNTHESIS FOR CO_2 METHANATION

Kritchakorn Aimdate,[1] Atthapon Srifa,[1] Wanida Koo-amornpattana,[1] Suttichai Assabumrungrat,[2] Sirapassorn Kiatphuengporn,[3] Ryo Watanabe,[4] Choji Fukuhara[4], Sakhon Ratchahat[1,*]

[1]Department of Chemical Engineering, Faculty of Engineering, Mahidol University, Nakhon Pathom, 73170, Thailand
[2]Center of Excellence in Catalysis and Catalytic Reaction Engineering, Department of Chemical Engineering, Faculty of Engineering, Chulalongkorn University, Bangkok 10330, Thailand
[3]Nanocatalysis and Molecular Simulation Research Group, National Nanotechnology Center, National Science and Technology Development Agency, Pathum Thani 12120, Thailand
[4]Department of Applied Chemistry and Biochemical Engineering, Graduate School of Engineering, Shizuoka University, Shizuoka 432-8561, Japan
*e-mail: sakhon.rat@mahidol.edu

Abstract:

Carbon dioxide is widely used as a source of carbon for production of alternative energy products. This research studies and develops a conversion process of CO_2 into natural gas by CO_2 methanation reaction. The catalyst support is prepared from natural kaolin obtained in Thailand, which is considered an inexpensive and environmentally material. Furthermore, the use of natural kaolin as catalyst support for CO_2 methanation is rarely found in the literatures. In this study, a Ni-based catalyst was synthesized through microwave-assisted method and compared with a conventional hydrothermal method. The catalytic test was carried out in a horizontal fixed-bed tubular reactor under atmospheric pressure at temperature ranging from 225 to 500ºC. The feed gas was mixed at a molar ratio of He: H_2: CO_2 = 5: 4: 1 with total flow rate of 70 ml/min. The catalytic performances of CO_2 methanation were investigated in terms of CO_2 conversion and CH_4 selectivity. It was found that the catalyst synthesized from the microwave-assisted method provides a significantly higher activities than the conventional hydrothermal method. The influences of calcined temperature of kaolin was investigated with ranging from 350 to 950ºC in order to find an optimal pretreatment condition. Furthermore, the effect of Ni loading from 5 to 60% was studied. As a result, the optimum Ni loading is found to be 30% due to higher metal dispersion. The prepared Ni-based catalysts were thoroughly characterized by the BET, XRD, TEM and H_2-TPR.

Introduction:

Global warming has a seriously and widespread impact on the environment. In recent decades, global warming has become a major concern. The main cause of the problem is the increasing emissions of greenhouse gases. Carbon dioxide is one of the most important greenhouse gases that make global warming, is greatly increasing in its emission to the environment as a result of increasing energy consumption from human activities such as the burning of fossil fuels (oil, coal, natural gas) for energy production both in power generation sectors and industrial sectors producing chemical products[1]. The reducing of carbon dioxide emissions is an urgent issue on environmental management issues that should be solve this problem because it affects both living things and the environment. At present, renewable energy is used to reduce the amount of fuel used and reduce carbon dioxide emission. So, instead of releasing carbon dioxide into the atmosphere. It will being used as a source of carbon for use in the production of chemicals and fuels of value such as methanol and methane. However, the production of fuels should be consider as the most effective alternative, due to the higher consumption rates in the fuels sector. CO_2 hydrogenation into methane is also known methanation reaction or Sabatier reaction ($CO_2 + 4H_2 \leftrightarrow CH_4 + H_2O$) which one of the most solution for reducing CO_2 emission.

Most studied metal-based catalysts for CO_2 methanation are Fe, Rh, Co, Pt and Ru and transition metals such as Ni, supported on several porous materials. However, nickel as active phase is widely studied and used in commercial scale because it exhibits a highly catalytic performance which is a good alternative for a noble metal due to low cost [2].

Kaolin has been used as silica and alumina sources for many applications. For example, the catalyst support material is one of the most interesting application which can be performed through the calcination of kaolin to more active matrix, called metakaolin (MTK). Meanwhile, there are many methods for depositing the metal active phase, such as nickel on the support material, including impregnation, co- precipitation, microwaved-assisted and one-pot sol-gel method[3-5]. The nickel dispersion on the support could be affected by the preparation method which leads to the enhanced catalytic performance[6]. Microwave-assisted method is a promising route in synthesis of nanomaterial that influences the reaction kinetics, reduction of crystallization time which represent faster and simple than the conventional hydrothermal method. The microwave method is a good option to control the particle size, crystalline phase, and enhance mesoporosity in the synthesis of nanostructure material.

In the present work, the Ni- based catalyst prepared from natural kaolin will be develop by the microwave-assisted method with compared to the conventional method. The effect of calcined temperature of kaolin (350-950ºC) and Ni loading (5-80%) on catalytic performance will be investigate. The optimal conditions of catalyst synthesis for CO_2 methanation will be determine.

Methodology:

Preparation of metakaolin: Natural kaolin in this study was obtained from Ranong, Thailand and used as a raw material to form metakaolin by calcination in a muffle furnace at 650°C for 2 hrs.

Preparation of catalyst: For the conventional method, metakaolin was added into the autoclave. Then, a certain amount of $Ni(NO_3)_2 \cdot 6H_2O$ and $Ce(NO_3)_2 \cdot 6H_2O$ was dissolved with 80 ml of water and pour into the autoclave. The mixture was autoclaved at 220°C for 2 hrs. After that, evaporation the mixture at 80°C and calcined at 500°C for 3 hrs. (heatrate 10°C/min). For Microwave-assisted method, metakaolin was added in a vessel lined with Teflon using a microwave digestion system. A certain amount of $Ni(NO_3)_2 \cdot 6H_2O$ and $Ce(NO_3)_2 \cdot 6H_2O$ was dissolved in deionized water 80 ml and pour the mixture into the vessel lined. The system operates at 1200 W power within the time limit. The mixture was evaporation at 80°C and calcined at 500°C for 3 h (heating rate 10°C/min).

Catalytic test: The catalytic performance was evaluated by a horizontal fixed-bed tubular reactor. Catalyst (0.1g) were packed in the middle of tube. After that, gas mixture at a molar ratio of He: H_2: CO_2 = 5:4:1 (total flow 70 ml/min, WHSV = 42,000 ml $\cdot$ g^{-1} $\cdot$ h^{-1}) was fed into the reactor and the reaction performed at a temperature ranging from 225 to 500°C at atmosphere pressure. Then, water from the reaction was condensed in the condenser. The flow rate of effluent gas were measured by soap film meter. The temperature of reaction measured by using thermocouple insert at the center of the catalyst bed. For the composition of effluent gas (CO_2, CH_4 and CO) were analyzed by Gas Chromatograph (GC-8A)

Results and Discussion:

Catalyst characterization of support: The element composition of the kaolin from XRF analysis found that the main components of kaolin are Si (58.51wt. %) and Al (35.02wt. %). BET surface area is 13 m^2g^{-1}. From the SEM image in figure 1, the morphology of kaolin reveal the appearance of a sheet overlapping.

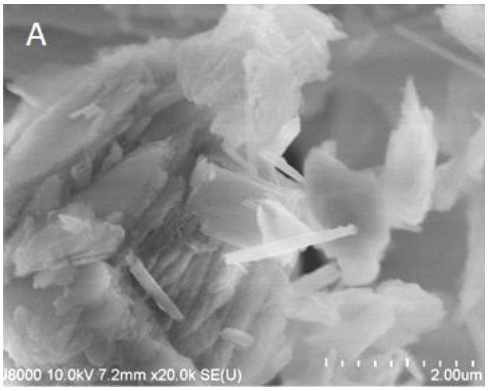

Figure 1. SEM image of kaolin.

Effect of calcined temperature of kaolin: For below figure 2A shown that CO_2 conversion of 10% Ni on calcined MTK at different temperatures have similar. Although the CH_4 selectivity is slightly different, but it is considered an insignificant difference.

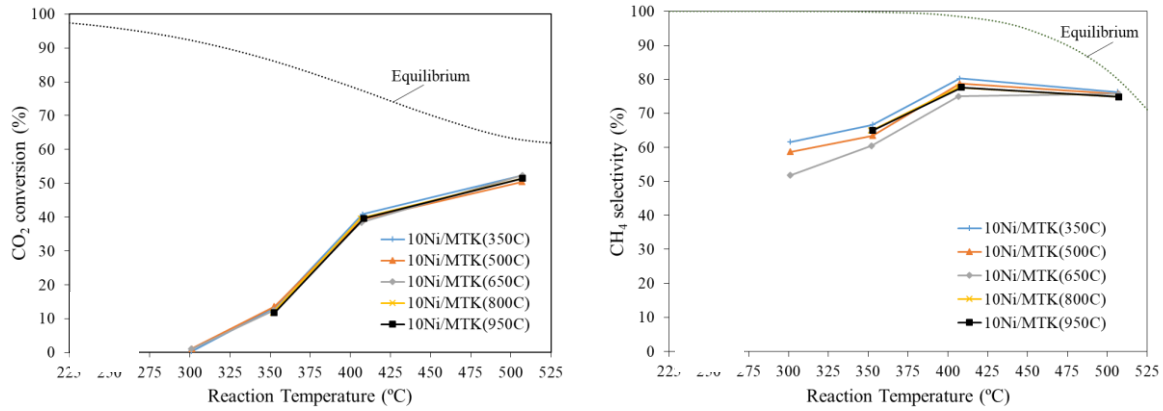

Figure 2. The CO_2 conversion (A) and CH_4 selectivity (B) of different calcined temperature of kaolin.

Effect of catalyst preparation method: To compare the method of catalyst preparation. The metakaolin was obtained from calcined kaolin at 650°C for 2 hrs. The catalysts used metakaolin as a support was prepared by microwave-assisted hydrothermal method (M) and conventional hydrothermal method (C).

The nitrogen adsorption- desorption isotherm of catalysts was prepared by the conventional and microwaved- assisted method are shown in Figure 3. According to IUPAC classification, the isotherm of 30% Ni/ MTK_C and 30% Ni/ MTK_M are typically type IV isotherms with H3 hysteresis loops which type IV isotherms indicated the characteristic of mesoporous material and H3 corresponds to wedge- shaped pores formed by the stacking of flaky particles[7].

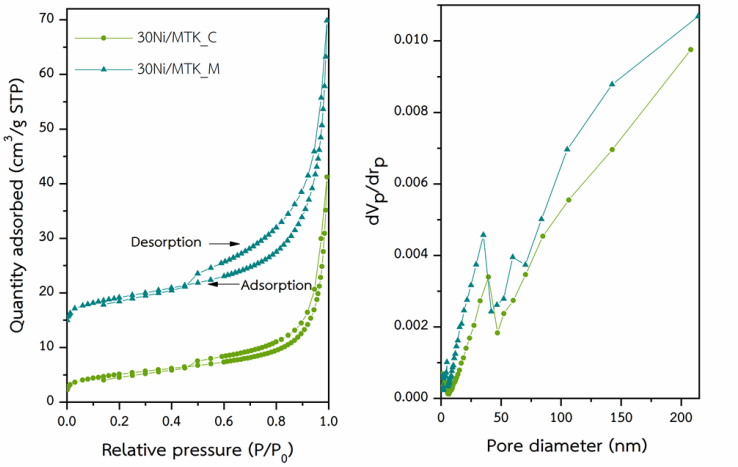

Figure 3. N_2 adsorption-desorption isotherm and the pore size distribution of 30%Ni/MTK_C and 30%Ni/MTK_M.

The surface area, pore volume and pore size are reported in table 1. The surface area of the catalyst prepared by microwaved-assisted method was higher than prepared by conventional method[6]. The surface area of Ni/ MTK_M decreased as a result of Ni particles covering the pores. The BJH pore size distribution of 30%Ni/MTK_C and 30%Ni/MTK_M showed a narrow distribution with value 39 nm and 35 nm respectively.

Table 1 Textural properties of the catalysts

Catalysts	Isotherm	S_{bet} (m^2g^{-1})	V_{pore}[a] (cm^3g^{-1})	Pore size [b] (nm)
30Ni/MTK_C	Type IV	17.68	0.0610	15.16
30Ni/MTK_M	Type IV	24.88	0.0861	14.32

S_{bet} - Specific surface area

V_{pore} - Volume of pore

[a] One-point method Desorption Total pore volume

[b] BJH desorption average pore width

Hydrogen temperature programmed reduction (H_2-TPR) profiles in Figure 4 shown calcined catalysts with different catalyst preparation method, which were performed for investigating the reducibility of NiO to metallic Ni. The 30%Ni/MTK_M has peak which shift to lower temperature. It indicated that the interaction between NiO species and MTK is decreased because NiO is easier than 30%Ni/MTK_C or more Ni active at low temperature.

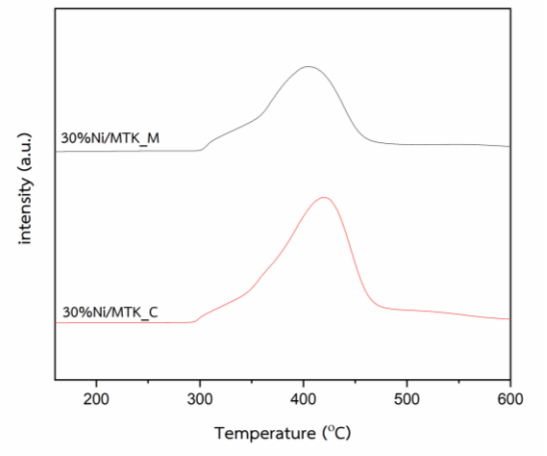

Figure 4. H_2-TPR profiles of 30%Ni/MTK_C and 30%Ni/MTK_M.

CO_2 conversion and CH_4 selectivity of 30Ni/MTK_M were higher than 30Ni/MTK_C at the same amount of Ni loadings. Moreover, 30Ni/MTK_M can be reached the same CO_2 conversion at low temperatures indicated that microwaved help to enhanced CO_2 activity. In many studies, microwave-assisted method have been reported to improve the dispersion efficiency of Ni particles and obtain smaller nickel particle sizes[6, 8, 9]. Both properties lead to increased catalytic performance of CO_2 methanation reaction.

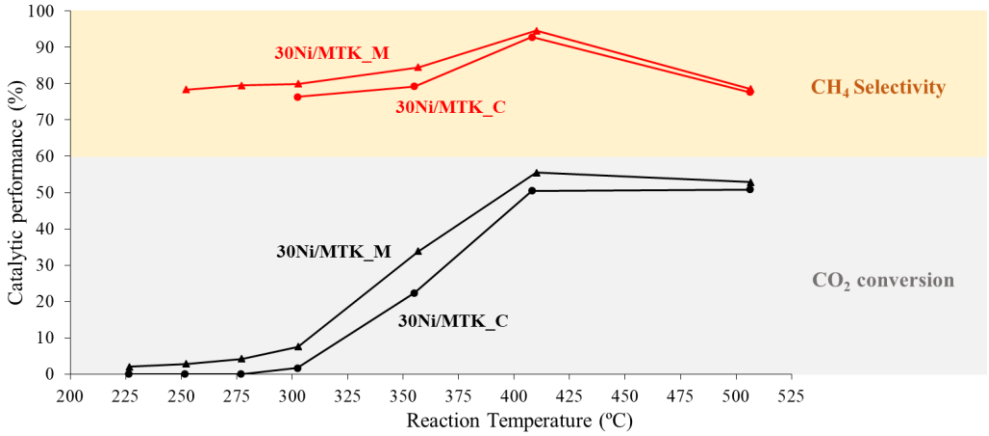

Figure 5. Comparison of CO_2 conversions (black) and CH_4 selectivity (red) obtained for 30Ni/MTK_M(1200W, 2h) (triangles) and for 30Ni/MTK_C (circles).

Effect of Nickel oxide loading:

The H_2-TPR profiles of calcined catalysts with different nickel loading were shown in Figure 6. The reduction of NiO species supported on MTK occur in the range of temperature 250 to 600ºC. For 5%Ni/MTK_M (1200W, 2h) appeared a broad peak in the range from 350 to 600ºC. Whereas 10-60% Ni/MTK_M (1200W, 2h) catalysts show the evident peak in the range from 250 to 480ºC. The reduction peak shifts to higher temperature with the increase of NiO loading, indicating that NiO species can be reduced more difficult at high NiO loading.

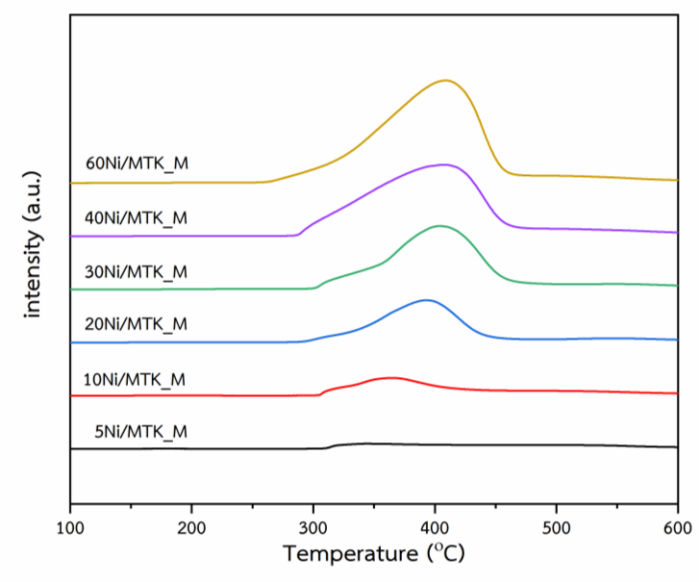

Figure 6. H_2-TPR profiles of Ni catalyst with different NiO loading.

The crystal structure of catalysts were characterize by XRD. Figure 7 shown the XRD pattern of all calcined catalysts. The characteristic diffraction peak at 37.3, 43.2. 62.9, 75.3 and 79.4 are attributed to cubic NiO (JCPDS 47-1049) with various diffracting planes [111], [200], [220], [311] and [222] respectively[10]. Moreover, the diffraction peak at 26.6 is assigned quartz which is the composition of metakaolin support. The diffraction peaks of NiO particles more intense with increasing NiO loading[11]. The average NiO crystal diameter in table 2 are calculated from each plan using Scherer equation. The average NiO crystal diameter were increased with the increasing of Ni loading from 5-60 wt. % NiO.

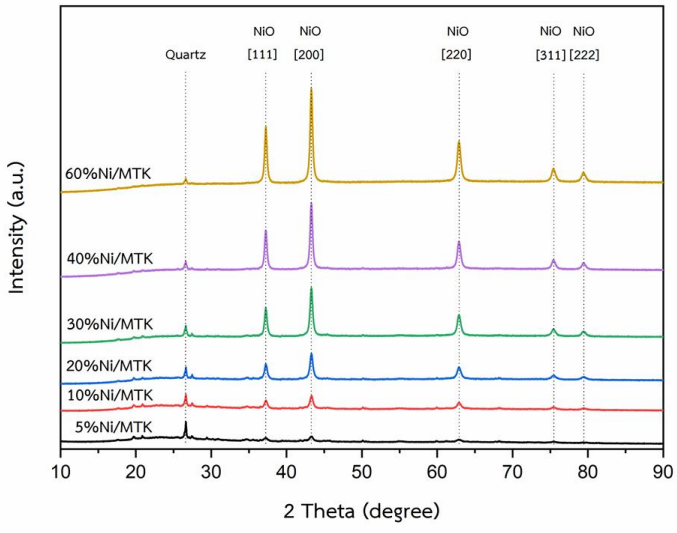

Figure 7. XRD patterns of Ni catalyst with different NiO loading.

Table 2 The average crystallite size of NiO

Catalysts	D_{NiO} from XRD in each plan [a]				
	111	200	220	311	222
5%Ni/MTK_M	10.5	12.1	10.1	20.0	NA.
10%Ni/MTK_M	16.2	17.6	14.2	16.7	28.8
20%Ni/MTK_M	20.1	19.3	15.3	15.0	17.6
30%Ni/MTK_M	22.3	21.6	16.5	18.5	17.9
40%Ni/MTK_M	23.5	22.6	18.0	18.8	18.2
60%Ni/MTK_M	23.8	23.0	17.5	16.5	16.8

[a] Calculated by using Scherer equation from XRD

The CO_2 conversion of 20-60% Ni were increased when the reaction temperature increased from 225-400ºC. After that, CO_2 conversion were decreased because reverse water gas shift reaction which converted the CO_2 become to CO [11].

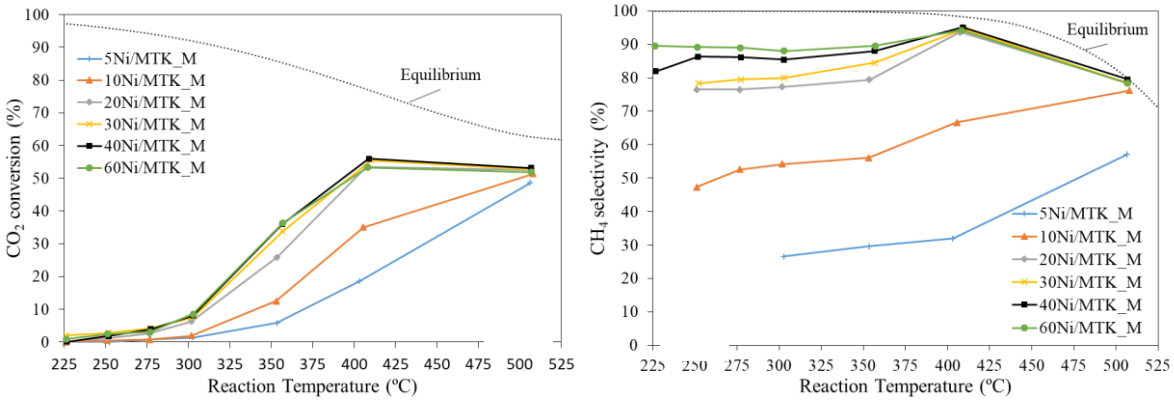

Figure 8. The CO_2 conversion (A) and CH_4 selectivity (B) of Ni/MTK_M (1200W, 2h).

Figure 9 shown the effect of %Ni loading over CO_2 conversion. It was found that CO_2 conversion increased when %Ni loading increase from 5-30 wt. % Ni. After nickel loading higher than 30, the CO_2 conversion and CH_4 selectivity are slightly changed due to nickel dispersion decrease as a result of bigger crystallite size of NiO in Table 2.

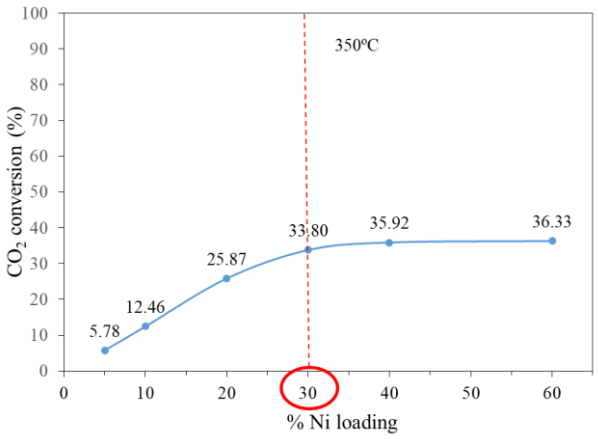

Figure 9 The CO_2 conversion of Ni/MTK (1200W, 2h) with different Ni loading at 350ºC.

Conclusion: Ni/MTK catalysts with different calcination temperature from 350 to 950 ºC were prepared. The experimental results shown that the calcination temperature of kaolin has no significant effect on the catalytic efficiency of CO_2 methanation. Ni / MTK_M were synthesized by microwave assisted method shown the higher catalytic efficiency than catalyst which were prepared by conventional method at all temperature ranges. Furthermore, Ni/MTK_M catalysts with different Ni loading from 5-60 wt. % were prepared. The CO_2 conversion and CH_4 selectivity were increased with increasing of nickel loading from 5-30 wt. %. After that, adding the nickel load has no effect on catalytic performance which is the result of bigger NiO crystallite size.

References:

1. Graça I, González LV, Bacariza MC, Fernandes A, Henriques C, Lopes JM, et al. Applied Catalysis B: Environmental. 2014;147:101-10.
2. Bacariza MC, Graça I, Bebiano SS, Lopes JM, Henriques C. Chemical Engineering Science. 2018;175:72-83.
3. Cai M, Wen J, Chu W, Cheng X, Li Z. Journal of Natural Gas Chemistry. 2011;20(3):318-24.
4. Le TA, Kim MS, Lee SH, Kim TW, Park ED. Catalysis Today. 2017;293-294:89-96.
5. Valinejad Moghaddam S, Rezaei M, Meshkani F, Daroughegi R. International Journal of Hydrogen Energy. 2018;43(34):16522-33.
6. Song F, Zhong Q, Yu Y, Shi M, Wu Y, Hu J, et al. International Journal of Hydrogen Energy. 2017;42(7):4174-83.
7. Yang C, Zhang J, Han S, Wang X, Wang L, Yu W, et al. Journal of Natural Gas Science and Engineering. 2016;34:1369-81.
8. Chen WX, Lee JY, Liu Z. Chemical Communications. 2002(21):2588-9.
9. Palma V, Barba D, Cortese M, Martino M, Renda S, Meloni E. Catalysts. 2020;10(2).
10. Srivastava DN, Srivastava P. Bulletin of Materials Science. 2010;33:653-6.
11. Rahmani S, Rezaei M, Meshkani F. Journal of Industrial and Engineering Chemistry. 2014;20(4):1346-52.

SP10_002_PA: NiFe-MgAl BIFUNCTIONAL MATERIAL DERIVED FROM HYDROTALCITE-LIKE PRECURSORS FOR HYDROGEN PRODUCTION FROM CHEMICAL LOOPING REFORMING OF ETHANOL

Janenipa Saupsor,[1] Suwimol Wongsakulphasatch,[2] Pattaraporn Kim-Lohsoontorn,[1,3] Palang Bumroongsakulsawat, [1] Worapon Kiatkittipong,[4] Hongfang Li,[5] Jinlong Gong,[5] and Suttichai Assabumrungrat[1,3,*]

[1] Center of Excellence in Catalysis and Catalytic Reaction Engineering, Department of Chemical Engineering, Faculty of Engineering, Chulalongkorn University, Bangkok 10330, Thailand
[2] Department of Chemical Engineering, Faculty of Engineering, King Mongkut's University of Technology North Bangkok, Bangkok 10800, Thailand
[3] Chemical Engineering Research Center for Bio-, Circular- and Green- Economy (ChE-BCG), Department of Chemical Engineering, Faculty of Engineering, Chulalongkorn University, Bangkok 10330, Thailand
[4] Department of Chemical Engineering, Faculty of Engineering and Industrial Technology, Silpakorn University, Nakhon Pathom 73000, Thailand
[5] Key Laboratory for Green Chemical Technology of Ministry of Education, School of Chemical Engineering and Technology, Collaborative Innovation Center of Chemical Science and Engineering, Tianjin University, Tianjin 300072, China
*e-mail: *suttichai.a@chula.ac.th*

Abstract:

NiFe-MgAl bifunctional materials derived from hydrotalcite-like compounds were prepared by the co-precipitation method, and tested their performance compared to Fe-MgAl and Ni-MgAl in chemical looping reforming (CLR) process of ethanol for hydrogen production in terms of activity, stability and regenerability. Various characterization techniques were utilized. XRD, ICP-OES, N_2 physisorption, H_2-TPR and TEM techniques analyzed the catalytic structures and properties. TPO, SEM and Raman analyses characterized the coke formation of used catalyst. XPS and *in-situ* DRIFTS verified the evolution of the catalyst during the experiments. The addition of Ni on Fe-MgAl catalyst offered higher H_2 selectivity up to 80% at reaction temperature of 500 °C. Moreover, the NiFe-MgAl bimetallic catalyst exhibited higher catalytic performance and higher stability than the corresponding monometallic Fe-MgAl and Ni-MgAl catalysts. This high performance was related to surface active sites and surface modification by the formation of Ni-Fe alloy particles. Fe at the surface was formed to FeO and oxidized deposited carbon leading to suppression of coke formation. In addition, NiFe-MgAl also had the catalytic regenerability to maintain hydrogen selectivity for 10 repeated cycles due to the alloy regeneration.

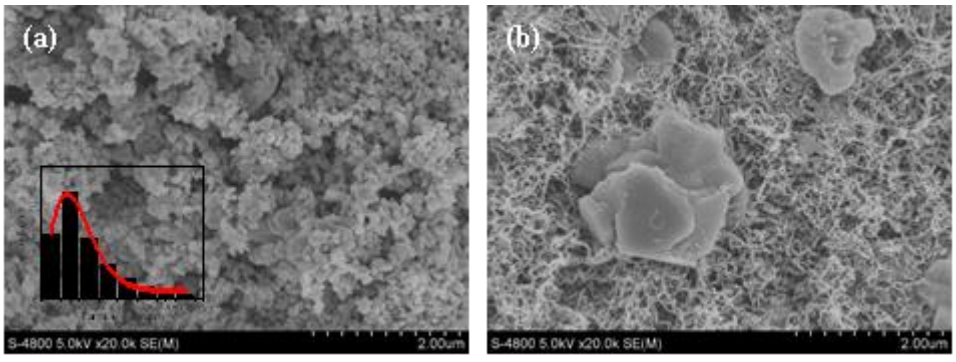

Figure 1. SEM images of bimetallic NiFe-MgAl catalyst, (a) fresh and (b) after 500°C reaction with coke formation

SP10_003_PA: HYDROGEN PRODUCTION FROM SORPTION-ENHANCED AUTOTHERMAL REFORMING CHEMICAL LOOPING USING NiO-CuO MULTIFUNCTIONAL MATERIAL

Talita Nimmas,[1] Suwimol Wongsakulphasatch,[2,*] Chin Kui Cheng[3], Suttichai Assabumrungrat[1,4]

[1] Center of Excellence in Catalysis and Catalytic Reaction Engineering, Department of Chemical Engineering, Faculty of Engineering, Chulalongkorn University, Bangkok, Thailand 10330
[2] Department of Chemical Engineering, Faculty of Engineering, King Mongkut's University of Technology North Bangkok, Bangkok, Thailand 10800
[3] Faculty of Chemical & Process Engineering Technology, Universiti Malaysia Pahang, Lebuhraya Tun Razak, Gambang Kuantan, Pahang, Malaysia 26300
[4] ChemicalEngineeringResearchCenterforBio-, Circular-andGreen-Economy (ChE-BCG), Department of Chemical Engineering, Faculty of Engineering, ChulalongkornUniversity, Bangkok10330,Thailand
*e-mail: *suwimol.w@eng.kmutnb.ac.th*

Abstract:

Co-operation of copper oxide (CuO) as co-oxygen carrier in multifunctional material NiO-CuO/CaO-$Ca_{12}Al_{14}O_{33}$ for H_2 production from sorption-enhanced autothermal reforming chemical looping (SE-a-CLR) of ethanol was studied under fixed-bed system. The effect of synthesis method on properties of material in terms of activity and reusability was studied. Results revealed that positioning of oxygen carrier affected performances of the material; placing CuO on the surface can enhance catalytic property, whereas placing NiO closed to CaO can reduce heat for CaO regeneration. Impregnation of NiO on the surface of homogeneous CuO-CaO-$Ca_{12}Al_{14}O_{33}$, which was synthesized from sol-gel method could produce only 83% for 30 min at 500°C and S/E = 3. On the other hand, impregnation of CuO on the surface of homogeneous NiO-CaO-$Ca_{12}Al_{14}O_{33}$, synthesized from sol-gel method, could produce 89% for 45 min and could reduce regeneration temperature of CaO by 50°C. One-pot synthesis sol-gel method NiO-CuO-CaO-$Ca_{12}Al_{14}O_{33}$ could produce 91% H_2 purity for 60 min and maintain its performance for at least 5 consecutive operating cycles but high energy was still required to regenerate CaO.

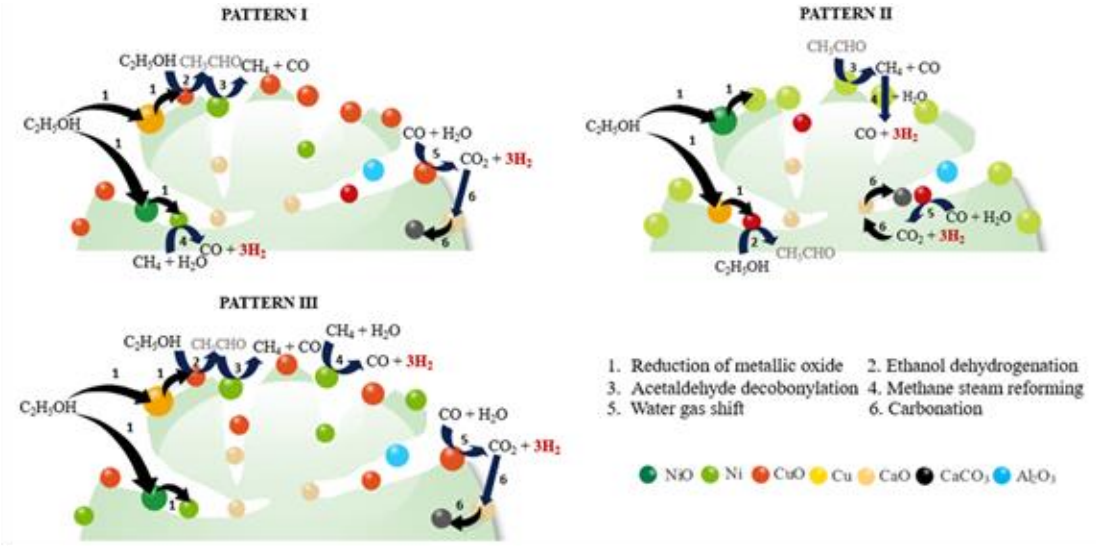

Figure 1. Mechanisms involved in the SE-CLAR reaction for different multifunctional materials

SP11_001_PA: MORPHOLOGICAL RESPONSE OF LICHEN TRANSPLANTS AS A BIOINDICATOR OF AIR POLLUTION

Chaiwat Boonpeng,[1,2,*] Sutatip Noikrad,[2] Kansri Boonpragob,[2]

[1]Department of Biology, Faculty of Science, Ramkhamhaeng University, Bangkapi, Bangkok 10240 Thailand
[2]Lichen Research Unit, Department of Biology, Faculty of Science, Ramkhamhaeng University, Bangkapi, Bangkok 10240 Thailand
*e-mail: chaiwat.b@ru.ac.th

Abstract:

Lichens are sensitive to air pollution and can be used as bioindicators of air quality. They reflect the effects of air pollution by physiological alteration, morphological abnormality, and community change. The objective of this study was to test whether the morphological response of the lichen *Parmotrema tinctorum* can be used as a preliminary indicator of air pollution. Every 5 thalli of the lichen were transplanted at three different sites: one site in Khao Yai National Park (unpolluted/control site), one site at about 8 km from the main area of Laem Chabang industrial estate (moderate pollution), and one site within the main industrial area (high pollution). The lichen thalli were exposed for 1 year between December 2018 and November 2019, and they were photographed in every 3 months. Most thalli at the closest site to the industrial area partly showed bleaching and necrosis on their surface within 3 months after transplantation. The symptoms appeared on the entire surfaces at about 9 months after transplantation. While the lichens at the outer location of the industry showed bleaching only at the end of the transplantation, and those at the control site were normal throughout the transplantation period. The lichens at the highly polluted site were affected the most in the dry cool season (December to February) followed by the hot season (March to May), whereas those in the rainy season (June to November) were slightly affected. This result has consisted of air pollution data measured by air quality monitoring station reporting that worst air quality occurred during the dry cool season. This study can confirm that the morphological response of the lichen can be used as a preliminary signal to warn the air pollution situation.

SP11_002_PF: MOLECULAR SYSTEMATICS OF MANGLICOLOUS LICHENS IN THE GENUS *Pyrenula* ON THE WESTERN GULF OF THAILAND

Achariya Rangsiruji,[1] Kajohnsak Vongshewarat,[2] Kawinnat Buaruang,[2] Supatra Phokaeo,[2] Kansri Boonpragob,[2]

Pachara Mongkolsuk,[2] Onanong Pringsulaka,[3] Sutheewan Binchai,[1] Sittiporn Parnmen[4,*]
[1]Department of Biology, Faculty of Science, Srinakharinwirot University, Bangkok 10110, Thailand
[2]Lichen Research Unit, Department of Biology, Faculty of Science, Ramkhamhaeng University, Bangkok 10240, Thailand
[3]Department of Microbiology, Faculty of Science, Srinakharinwirot University, Bangkok 10110, Thailand
[4]Toxicology Center, National Institute of Health, Department of Medical Sciences, Ministry of Public Health, Nonthaburi 11000, Thailand
*e-mail: sittiporn.p@dmsc.mail.go.th

Abstract:

Tropical corticolous microlichens in the genus *Pyrenula* were explored in the mangrove ecosystem on the western Gulf of Thailand coast. Species diversity of these microlichens was higher in the landward zone compared to the mid-intertidal zone. Based on their limited phenotypic characters, 32 specimens obtained were primarily classified into 17 species. Among them, four new records were found including *P. microtheca*, *P. nanospora*, *P. pyrenuloides* and *P. thelomorpha.* In order to confirm their phylogenetic placement, the internal transcribed spacer region was used. Maximum likelihood and Bayesian approaches together with DNA-based species delimitation under the Poisson tree processes (PTP) model were employed. Results based on the phylogenetic analyses and PTP method revealed two major clades recognizing 22 putative species. Clade I includes all members with pseudocyphellae and those without them, while Clade II contains only members without pseudocyphellae. Ascospore types were mixed in both clades. Incongruence between DNA-based species delimitation and morphological identification was also observed in some lineages, and this needs to be further investigated.

Introduction:

The family Pyrenulaceae (Pyrenulales, Ascomycota) currently includes 10 genera with over 300 species worldwide.[1] Within this family, the genus *Pyrenula* encompasses 169 accepted species of corticolous microlichens which are widely distributed in the pantropical region.[1,2] They commonly inhabit smooth and shaded barks.[2] In Thailand, 20 species have been recorded, but studies concerning the diversity of manglicolous lichens are inadequate.[3] Mangroves are one of the most complex ecosystems which support a variety of biodiversity. Hence, this study focused on biodiversity assessment of *Pyrenula* in the mangrove ecosystem of Chumphon Province and investigated the applicability of using the internal transcribed spacer (ITS) region of nuclear ribosomal DNA for identifying species based on phylogenetic relationships and a DNA-based species recognition method.

Methodology:

Specimen collection and morphological identification

Specimens were collected in the mangrove forests of Chumphon Province. The areas covering 4 districts included Lang Suan (10°'3.468' N 99°7.601' E), Muang (10°'53.255' N 99°28.649' E), Pathiu (10°'41.619' N 99°19.900' E) and Sawi (10°'16.780' N 99°9.733' E). Morphological characteristics of the specimens were examined by using a low magnification stereomicroscope (Olympus SZ30), while anatomical characteristics were observed with free-hand sections. Anatomical investigations were conducted using a compound microscope (Olympus BX51) and photographs were taken. In addition, spot tests for detection of lichen substances were

carried out according to White & James (1985).[4] Thalli were examined under long-wave UV light (350 nm). All specimens were deposited in RAMK.

DNA extraction, PCR amplification and DNA sequencing

For each specimen, small thallus fragments of 2-15 mg were ground in the liquid nitrogen. Total genomic DNA was extracted using the DNeasy™ Plant Mini Kit (QIAGEN) according to the manufacturer's instructions. The DNA obtained was used for PCR amplification of the ITS region. PCR primers and thermal cycling condition were employed as described previously.[5] Amplification products were cleaned using the QIAquick Gel Extraction Kit (QIAGEN) and sequenced with the amplification primers.

Phylogenetic analyses

Sequence alignment of the *Pyrenula* specimens and other taxa from GenBank was carried out using Geneious Prime (http://www.geneious.com). To construct phylogenetic trees, maximum likelihood (ML) analysis was performed in the RAxML-HPC2 on XSEDE 8.1.11 of the CIPRES Science Gateway, using the GTRGAMMA model.[6,7] Bootstrap analysis was run with 1,000 pseudoreplicates**.** In addition, Bayesian inference was conducted using MrBayes 3.1.2 with the GTR+G model.[8] Posterior probabilities were evaluated by sampling trees using a variant of Markov Chain Monte Carlo (MCMC) method. Ten million MCMC generations were run and the first 25% was discarded as burn-in. Of the remaining trees, a majority-rule consensus tree with average branch lengths was calculated using the sumt option of MrBayes. Only clades that received bootstrap values (BS) ≥75% and posterior probabilities (PP) ≥0.95 were considered as strongly supported. The phylogenetic trees were depicted using the program FigTree 1.4.3 (http://tree.bio.ed.ac.uk/).

Sequence-based species delimitation

Species delimitation was estimated using the Poisson tree processes (PTP) model on the bPTP webserver (http://species.h-its.org/ptp/).[9] The input tree was obtained by the RaxML method as described previously. The analysis was run for 400,000 MCMC generations, thinning was set to 100 and burn-in was at 25%. The probability of each node to represent a species node was calculated by the maximum likelihood solution (PTP_ML) considering the frequency of the nodes across the sampling.

Results and Discussion:

Thirty-two specimens obtained were primarily classified into 17 species based on morphology (**Figure 1**). Among them, four new records were found including *Pyrenula microtheca*, *P. nanospora*, *P. pyrenuloides* and *P. thelomorpha.* In addition, there was provisional identification of five species, namely *Pyrenula* cf. *corticata, Pyrenula* cf. *macrospora*, *Pyrenula* sp.1 (C061), *Pyrenula* sp.2 (C310) and *Pyrenula* sp.3 (C279). Their dominant host plant species comprised *Excoecaria agallocha*, *Hibiscus tiliaceus*, *Rhizophora apiculata* and *R. mucronata.* These microlichens showed higher species diversity in the landward zone (56.25%) compared to the mid-intertidal zone (43.75%). Six species including *Pyrenula* cf. *corticata, P. fetivica, P. ochraceoflava, P. sexlocularis*, *Pyrenula* sp.1 and *Pyrenula* sp.2 inhabited the landward zone. Species restricted to the mid-intertidal zone were *P. aspistea*, *P. confinis, Pyrenula* cf. *macrospora, P. microtheca, P. parvinuclae*, and *Pyrenula* sp.3. Other species including *P. astroidea*, *P. circumfiniens*, *P. nanospora*, *P. pyrenuloides* and *P. thelomorpha* were dispersed in both zones.

Thirty-two new sequences were generated for this study and aligned with 72 sequences downloaded from GenBank. The data matrix of 588 unambiguously aligned characters was used for phylogenetic analyses. The resulting ML tree (*ln*L= -12,307.4858) and the Bayesian tree (*ln*L= -12,420.1048) revealed similar topologies, hence only the ML tree is shown (**Figure 2**). Species in the genus *Pyrenula* is separating into two major clades. Clade I (BS=97/PP=1.00) includes *P. astroidea*, *P. circumfiniens*, *Pyrenula* cf. *macrospora*, *P. pyrenuloides*, *P. sexlocularis* and *P. thelomorpha.* The presence of pseudocyphellae has been used as the main diagnostic character to define this clade.[10] This character however, was absent in *P. circumfiniens* and *Pyrenula* cf. *macrospora*. The specimens of *P. astroidea* (BS=100/PP=1.00) and *P. circumfiniens* (BS=100/PP=1.00) form strongly supported monophyletic groups. Morphologically, *P. astroidea* was characterized by having a thallus with pseudocyphellae, fused ascomata, joint ostioles and muriform ascospores, whereas the characters of the

thallus without pseudocyphellae, solitary ascomata with lateral ostioles and fusiform ascospores were found in *P. circumfiniens*. Clade II (BS=92/PP=1.00) comprises the members without pseudocyphellae. These include *P. aspistea*, *P. confinis*, *Pyrenula* cf. *corticata*, *P. fetivica*, *P. parvinulea*, *P. nanospora*, *P. ochraceoflava*, *P. microtheca, Pyrenula* sp.1 (C061) *Pyrenula* sp.2 (C310) and *Pyrenula* sp.3 (C279). Only the specimens of *P. ochraceoflava* (BS=99/PP=1.00) and *P. fetivica* (BS=74/PP=1.00) form monophyletic groups. *Pyrenula ochraceoflava* possessed an ecorticated thallus, ascomata with hamathecium not inspersed and muriform ascospores. The thallus turned purple red in 10% KOH solution but showed dull orange fluorescence under the long-wave UV light. *Pyrenula fetivica*, on the other hand, was characterized by the presence of a corticated thallus, ascomata with hamathecium inspersed and 3-septate ovoid ascospores. The thallus turned pale yellow in 10% KOH solution.

For these pyrenocarpus lichens, the existence of limited phenotypes may lead to poor taxonomy.[2,11] Thus, a DNA sequence-based species delimitation method is required. The ML tree was used to illustrate the delineation of putative species based on the bPTP approach (**Figure 3**). This PTP_ML tree revealed 12 clusters and 10 singletons. Three putative species (9, 10 & 18) showed monophyletic lineages. For *P. aspistea*, *P. ochraceoflava* and *P. fetivica* however, the presence of the singletons could be due to intraspecific variation or putative species recognition. Other species including *P. nanospora*, *P. parvinuclea, P. pyrenuloides, P. sexlocularis* and *P. thelomorpha* showed non-monophyletic lineages. These results suggested that certain morphological characters such as the pseudocyphellae and ascospore types may be homoplasious and should be reconsidered for taxonomy.

Conclusion:

Morphological identification and classification of *Pyrenula* were difficult due to poor taxonomic characters. In this study, 22 putative species were determined based on the molecular systematics and DNA-based species delimitation. These designations of species however, appeared to have some conflicts with the phenotypic traits. The existence of non-monophyletic assemblages in some species indicated that certain morphological characters may be homoplasious and should be avoided in taxonomy.

Acknowledgements:

This work was financially supported by the National Research Council of Thailand (2019) and Ramkhamhaeng University.

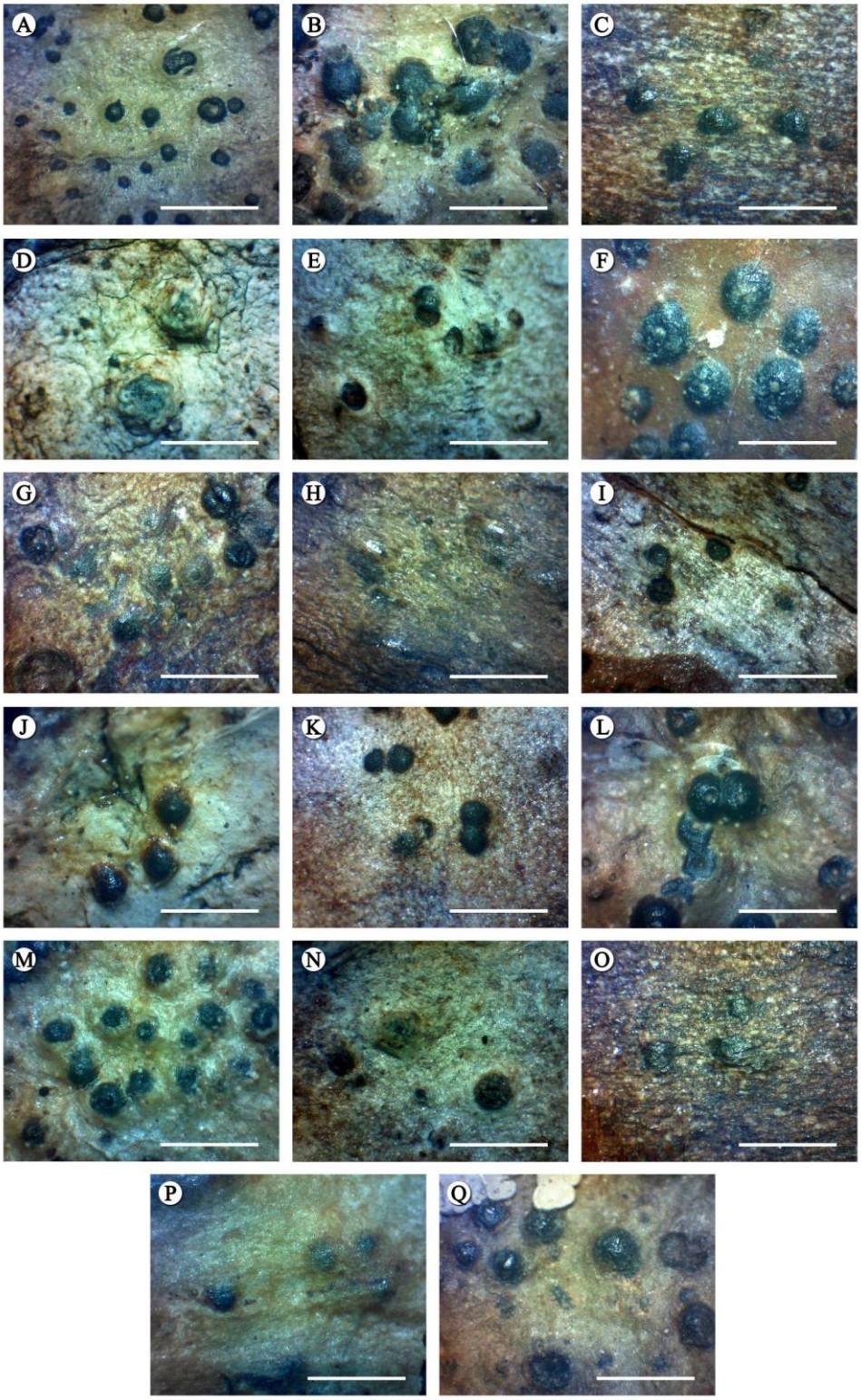

Figure 1. *Pyrenula* specimens. (A) *P. aspistea*, (B) *P. astroidea*, (C) *P. circumfiniens*, (D) *P. confinis*, (E) *Pyrenula* cf. *corticata*, (F) *P. fetivica*, (G) *Pyrenula* cf. *macrospora*, (H) *P. microtheca*, (I) *P. nanospora*, (J) *P. ochraceoflava*, (K) *P. parvinuclea*, (L) *P. pyrenuloides*, (M) *P. sexlocularis*, (N) *Pyrenula* sp.1, (O) *Pyrenula* sp.2, (P) *Pyrenula* sp.3, (Q) *P. thelomorpha*. Scale bar = 1 mm.

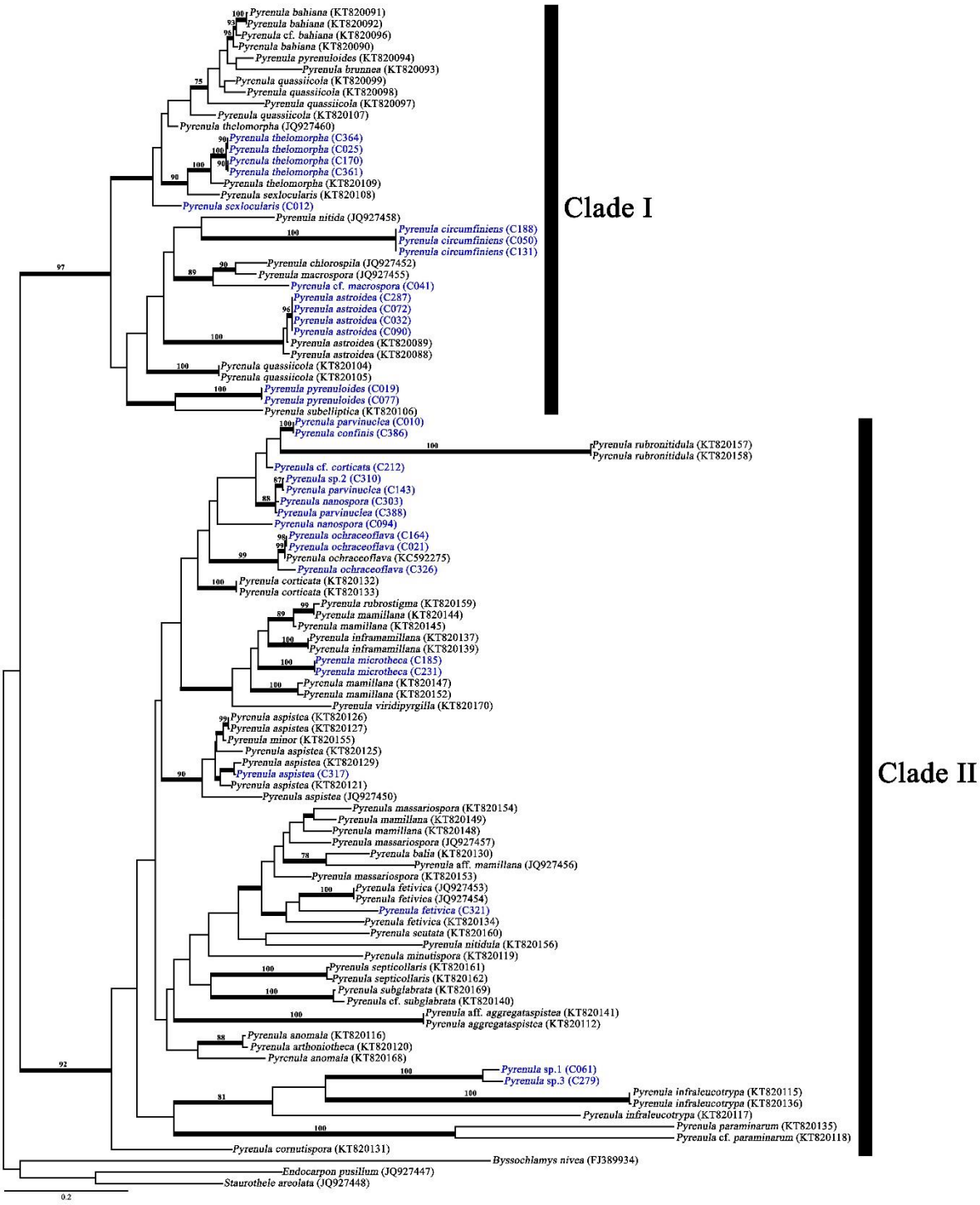

Figure 2. ML tree depicting relationships within *Pyrenula* based on ITS sequences. Specimens obtained in this study are shown in blue. ML bootstrap values ≥ 75% are reported above branches and posterior probabilities ≥ 0.95 are indicated as bold branches.

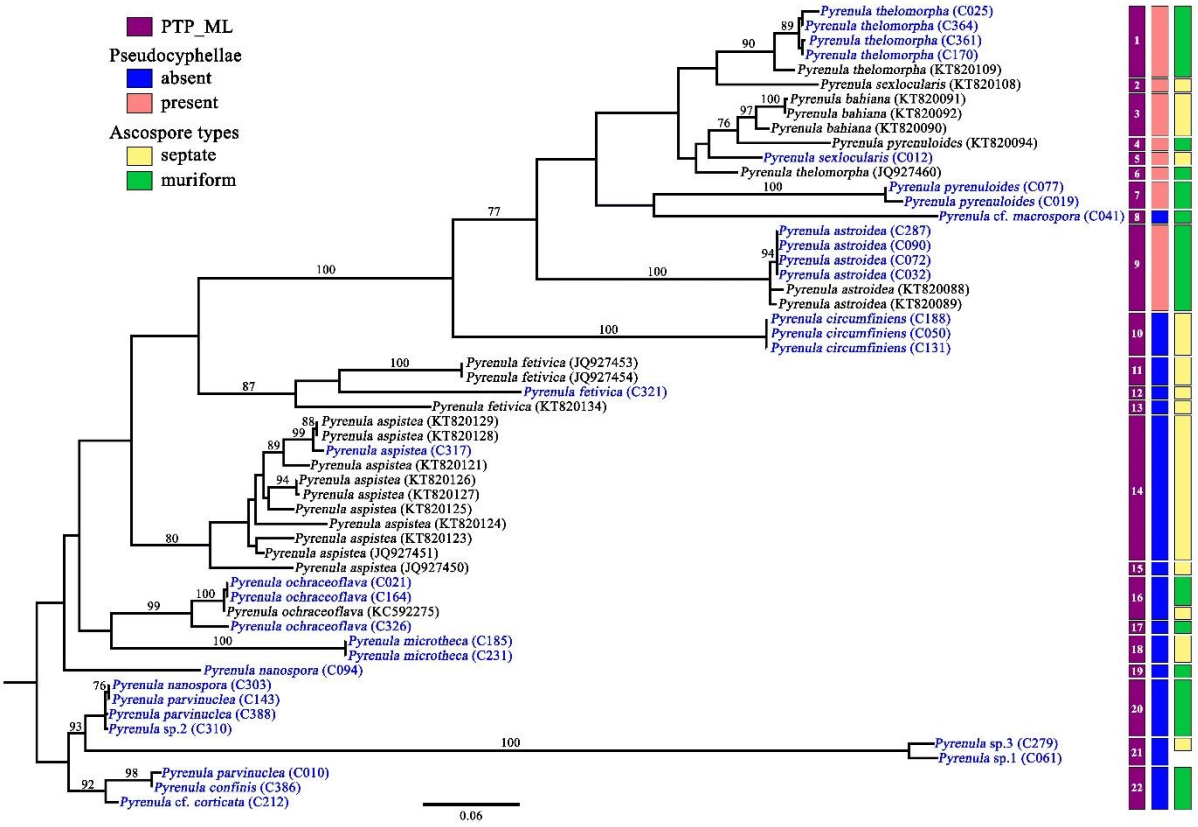

Figure 3. Species delimitation of *Pyrenula* based on the PTP model. Specimens obtained in this study are shown in blue. Numbers above branches are bootstrap values (≥ 75%). Vertical bars represent recognized putative species and morphological characteristics.

References:

1. Mendonça C de O, Aptroot A, Lücking R, Cáceres ME da S. Biodivers Conserv. 2020;29(3):1059–79.
2. Aptroot A. Lichenol. 2012;44(1):5–53.
3. Buaruang K, Boonpragob K, Mongkolsuk P, Sangvichien E, Vongshewarat K, Polyiam W, et al. MycoKeys. 2017;23:1–91.
4. White FJ, James PW. Br Lichen Soc Bull. 1985;57:1–41.
5. Rangsiruji A, Boonpragob K, Mongkolsuk P, Sodamuk M, Buaruang K, Binchai S, et al. Bryologist. 2016;119(2):123–30.
6. Stamatakis A. Bioinformatics. 2006;22(21):2688–90.
7. Miller MA, Pfeiffer W, Schwartz T. Proceedings of the Gateway Computing Environments Workshop (GCE). 2010:1–8.
8. Huelsenbeck JP, Ronquist F. Bioinformatics. 2001;17(8):754–5.
9. Zhang J, Kapli P, Pavlidis P, Stamatakis A. Bioinformatics. 2013;29(22):2869–76.
10. Weerakoon G, Aptroot A, Lumbsch HT, Wolseley PA, Wijeyaratne SC, Gueidan C. Lichenol. 2012;44(5):639–47.
11. Gueidan C, Aptroot A, Cáceres ME da S, Binh NQ. Mycol Prog. 2015;15(1):7

SP11_003_PF: BIODIVERSITY OF CRUSTOSE DISCOLICHEN IN MANGROVE FOREST AT PRACHUAP KHIRI KHAN PROVINCE, THAILAND.

Phimpisa Phraphuchamnong*, Vasun Puangsungnoen, Patchara Mongkolsuk and Kawinnat Buaruang

Lichen Research Unit, Department of Biology, Faculty of Science, Ramkhamheang University, Huamark, Bangkapi, Bangkok 10240, Thailand
e-mail: Phimna191@gmail.com

Abstract:

Exploration of crustose discolichen in mangrove forest of Bang Saphan, Bang Saphan Noi and Pranburi districts in Prachuap Khiri Khan province was collected during March 2019. One hundred and sixty-nine specimens were compiled from seven-teen phorophytes of mangrove forest. Based on morphological and chemical identification was taxonomically catalogued into six families belonging to eight genera and eight species. The *Lecanora helva* was most abundant and diverse in the area. In addition, *Biatora* Prachup1 is expected to be new.

Introduction:

Prachuap Khiri Khan is one of the western provinces of Thailand. The latitude is situated in between 10° 50′ 12° 45″ N and 99° 00′ 100° 00″ E. The area covered from north to south about 212 kilometers with 6,368 square kilometers, covering eight districts along coast of the gulf of Thailand (about 224.8 square kilometers Coastline) such as Mueang Prachuap Khiri Khan, Kui Buri, Thap Sakae, Bang Saphan, Bang Saphan Noi, Pran Buri, Hua Hin and Sam Roi Yot district (19.35 square kilometers of mangrove forest).

Area with a humid tropical climate is influenced by the southwest monsoon, which blows from the Indian Ocean. Winter season is influenced by the northeast monsoon during December to February. Summer starts from late March to the end of late April is influenced by high-pressure areas of southeast monsoon winds from the South China Sea. Rainy season extends from May to November with heavy rains in May. The rain will terminate during June to July and starts raining heavily from August to November. Annual precipitation averages 798.3-1581.0 mm. per year. The temperature averages between 27.2 to 28.6 °C. Relative humidity averages about 77 % [20]. The most common plant species is the Rhizophoraceae (*Rhizophora* apiculata Blume.) followed by Combretaceae (Lumnitzera racemosa Willd), and Myrtaceae (Melaleuca leucadendra Linn. var. minor Duthie., respectively[20]. The diversity of crustose discolichen in mangrove forest is poorly known and never been explored extensively. The main feature of cocrustose discolichen is a crustose lichens with disc-like apothecia. The apothecial disc may be exposed, flat, convex or concave and normally upraised on the thallus. Two types of apothecia include lecanorine and lecideine or biatorine. The lecanorine type has algae incorporated in apothecia, whereas lecideine was absent. Ascospores are colorless and produced in the ascus with a variety of ascospores type including simple, septate submuriform or muriform ascospores [6]. Hence, this study focused on the biodiversity of crustose discolichen in the mangrove ecosystem of Prachuap Khiri Khan Province.

Methodology:

Crustose discolichens were collected in the mangrove forest of Prachuap Khiri Khan province (10° 50′ 12° 45″ N, 99° 00′ 100° 00″ E). All specimens were examined for their anatomical, morphological and chemical characteristics. Lichen substances were identified using spot test and thin layer chromatography (TLC). Preliminarily color tests for lichen substances carried out the following reagents according to Elix's method [7]. Thin layer chromatography was performed according to the standard method of White and James [19]. Taxonomic identification were classified according to Awasthi [2], Brodo et. al [3], Lumbsch [11], Printzen et. al [4], and Rambold [13].

Results and Discussion:

One hundred and sixty-nine samples of crustose discolichens from Prachuap Khiri Khan province were collected and identified into six families belonging to eight genera and eight species (Table 1). Our results revealed that that the mangrove forest type of this province has more species diversity of lichens than mangrove forest of Bang Saphan, Bang Saphan Noi and Pranburi district due to theirs vegetation and environmental climates such as air ventilation, light direction and acidic smooth bark of dominant phorophyte trees are amiable reformed for lichen colonizing [10]. A total of 10 families 12 genera and 17 species of phorophyte were explored of discocrustose lichen. List of lichen-taxa on phorophyte in mangrove forest is shown in table 2. The highest species diversity was observed in the family Ramalinaceae (3 taxa). Observation on the occurrence of lichens on the various phorophytes revealed that eight species found on the various mangrove trees. However, the highest species diversity of lichen was recovered eight taxa on *Ceriops decandra* and *Excoecaria agallocha* (5 species) followed by *Bruguiera cylindrica* and *Rhizophora apiculata* (4 species), *Ceriops tagal* (3 species), *Avicennia offcinalis*, *Derris indica*, *Hibiscus tiliaceus*, *Rhizophora mucronata*, and *Xylocarpus moluccensis* (2 species). However, *Avicennia alba, Avicennia marina, Crateva adansonii, Lannea coromandelica, Lumnitzera racemosa,* and *Sonneratia alba* were discovered for one species of lichen. *Lecanora helva and Cresponia proximate* were frequently found in the area. Interestingly, *Biatora* Prachup1 is expected to be new to science. Morphologically, *Biatora* Prachup1 was shared morphology similar to *Bacidia offlorescens, Biatora australis* and *Micarea* [17]. However, they were different in pattern and size of ascospore as well as the vegetative propagules such as the presence or absence of soralia.

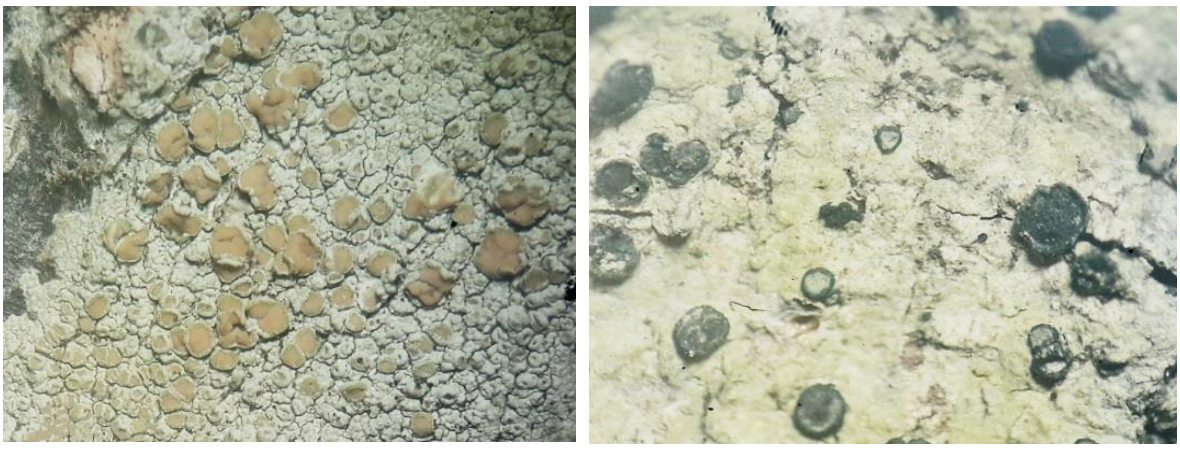

Figure 1. Common species: *Lecanora helva* figure (left) and *Cresponia proximata* figure(right)

Table1. Lichen-taxa from four study sited of Prachuap Khiri Khan Province.

Lichen-taxa		District			Total of specimens
		BS	BSN	PB	
LECANORACEAE	*Lecanora helva*	40	31	15	86
MALMIDEACEAE	*Malmidea aurigera*	3	1	-	4
OPEGRAPHACEAE	*Cresponia proximate*	28	8	-	36
PILOCARPACEAE	*Byssoloma leucoblepharum*	1	-	-	1
RAMALINACEAE	*Bacidea submedialis*	13	3	-	16
	Bacidia igniarii	-	1	-	1
	Biatora Prachup1	3	-	-	3
ROCELLACEAE	*Bactrospora myriadea*	12	-	10	22
Total of specimens		100	44	25	169

Note: BS=Bang Saphan, BSN= Bang Saphan Noi and PB= Pranburi district

Table 2. List of Lichen-taxa on phorophyte trees of mangrove forest in Prachuap Khiri Khan province.

Lichen-taxa	District																	Total
	1	2	3	4	5	6	7	8	9	10	11	12	13	14	15	16	17	
Lecanora helva	9	8	11	4	-	4	3	1	1	2	13	-	2	20	6	1	1	86
Malmidea aurigera	-	-	-	-	2	-	-	-	1	1	-	-	-	-	-	-	-	4
Cresponia proximate	-	-	-	-	9	3	1	-	-	4	1	-	-	11	4	-	3	36
Byssoloma leucoblepharum	-	-	-	-	1	-	-	-	-	-	-	-	-	-	-	-	-	1
Bacidea submedialis	-	-	-	-	1	2	-	-	-	2	-	-	-	11	-	-	-	16
Bacidia igniarii	-	-	-	-	-	-	-	-	-	-	-	1	-	-	-	-	-	1
Biatora Prachup1	-	-	1	-	-	1	1	-	-	-	-	-	-	-	-	-	-	3
Bactrospora myriadea	-	-	-	3	-	1	-	-	-	1	-	-	-	17	-	-	-	22
Total of specimens	9	8	12	7	13	11	5	1	2	10	14	1	2	59	10	1	4	169

Note: 1=*Avicennia alba*, 2=*Avicennia marina*, 3=*Avicennia ocinalis*, 4=*Bruguiera cylindrica*, 5=*Bruguiera cylindrica*, 6=*Ceriops decandra*, 7=*Ceriops tagal*, 8=Cr*ateva adansonii*,9=*Derris indica*, 10=*Excoecaria agallocha*, 11=*Hibiscus tiliaceus*, 12=*Lannea coromandelica*, 13=*Lumnitzera racemosa*, 14=*Rhizophora apiculata*, 15=*Rhizophora mucronata*, 16=*Sonneratia alba*, 17=*Xylocarpus moluccensis*,

Conclusion:

Crustose discolichens from Prachuap Khiri Khan province were collected and identified into six families belonging to eight genera and eight species. The distributions of crustose discolichens were found as seven species in Bang Saphan district, five species in Bang Saphan Noi district, and two species in Pranburi district from seventeen phorophyte were scrutinized and taxonomic classified to six families, eight genera and eight species. *Ceriops decandra* and *Excoecaria agallocha* showed highest lichen species rich (five species) in mangrove forest while *Avicennia alba, Avicennia marina, Crateva adansonii, Lannea coromandelica,Lumnitzera racemosa,* and *Sonneratia alba* are only one species. The lichen communities that occur in mangroves indicate their tolerance

to hot, humid and saline breeze environmental conditions prevailing in mangrove forest, it would be an interesting aspect to study in detail the environmental factors and the physiology of these lichens enabling them for the successful in further collection and classification of crustose discolichen. Currently, the mangrove forest area of Prachuap Khiri Khan province was invasion, destruction use in mangrove areas for other activities such as agriculture, shrimp farms and jettys. However, in this study of lichen distribution crustose discolichen shown the effect of invasion and destruction of mangrove forests is information in study for the management of mangrove forest resources in Thailand systematic and sustainable.

Acknowledgments: We are grateful to the members in the Lichen Research team at Department of Biology, Faculty of Science, Ramkhamhaeng University. This research was financially by Thai Government.

References:

1. Aptroot, A., Saipunkaew, W., Sipman, H. J. M., Sparrius, L. B., & Wolseley, P. A. (2007). New lichens from Thailand, mainly microlichens from Chaing Mai. Fungal Diversity, 24, 75-134.
2. Awasthi DD. Bilo. Lichen. 1991; 40: 66-75.
3. Brodo JM, Culberson WL, Culberson CF. Bryologist. 2008; 111 (3): 363-423.
4. Christian Printzen, Josef P. Halda, John W. McCarthy, Zdeněk Palice, Pamela Rodriguez-Flakus, Göran Thor, Tor Tønsberg & Jan Vondrák, Five new species of Biatora from four continents Herzogia 29 (2) Teil 1, 2016: 566–585
5. Gintaras Kantvilas, A synopsis and key for the lichen genus Caloplaca (Teloschistaceae) on Kangaroo Island, with the description of two new species, ournal of the Adelaide Botanic Gardens 29 (2016) 53–69
6. Kalb, K., Rivas Plata, E., & Lumbsch, H. T. (in press). The phylogenetic position of Malmidea, a new genus for the Lecidea piperis- and Lecanora granifera-groups (Lecanorales, Malmideaceae) inferred from nuclear and mitochondrial ribosomal DNA sequences with special reference to Thai species. Bibliotheca Lichenologica.
7. Kantvilas G, 6. Elix JA, Lichenologist 2007; 38 (2): 135-141.
8. Kantvilas G, Papong K, Lumbsch HT. Lichenologist 2010; 42 (5) 557-561.
9. Kenan Yazici1 & Ali Aslan, Lichen species new to Turkey and Asia, Mycotaxon, Volume 108 (2009), pp. 463–466.
10. Lugo AE, Snedarker SC. Annual Review of Ecology and Systematics. 1974; 5: 39-64.
11. Lumbsch HT. Flora of Australia. 2004; 56A:11-62.
12. Nash, T.H., Ryan, B.D., Gries, C., Bungartz, F., (eds.), Lichen Flora of the Greater Sonoran Desert Region. Vol 2. 2004.
13. Rambold, G. Biblo. Lichen. 1989 34: 10-69.
16. Papong K, Lumbsch HT. Lichenologist. 2011; 43: 299-320.
17. Pieter P.G. van den Boom, A. Maarten Brand, Brian J. Coppins & Emmanuël Sérusiaux., A new *Micarea* species from western Europe, belonging in the *Micarea denigrata* group, Herzogia 31 Teil2, 2018; 385-387.
18. Sriprang V, Monkolsuk P. Thai Journal of Botany. 2010; 2: 47-53.
19. White FJ, Jane PW. British Lichen Society Bulletin. 1985; 57 (supplement):1-41.
20. Mangrove Forest Resources Conservation Bureau Department of Marine and Coastal,Marine and coastal resource information of Prachuap Khiri Khan province. 2012.

SP11_005_PA: OPTIMAL CONDITION FOR MEASURING BARK PH AND CONDUCTIVITY IN LABORATORY

Sutatip Noikrad,[1]* Chaiwat Boonpeng,[1,2] Kansri Boonpragob[1]

[1]Lichen Research Unit, Department of Biology, Faculty of Science, Ramkhamhaeng University, Bangkapi, Bangkok 10240 Thailand
[2]Department of Biology, Faculty of Science, Ramkhamhaeng University, Bangkapi, Bangkok 10240 Thailand
*e-mail: sutatip.lichenru@gmail.com

Abstract:

Air pollution can affect pH and conductivity of bark, which subsequently influence growth and biodiversity of corticolous lichens. This study aimed to find optimal condition for a simultaneous measure of pH and conductivity of bark in laboratory. The outermost parts of *Alstonia scholaris* bark (1-3 mm thick) at 1.3 meters above ground were collected. The bark samples were picked up from three different trees growing at Ramkhamhaeng University (Huamark, Bangkok). The samples were oven dried at 100 °C for 24 hours. Experiment A: barks were broken to small pieces but was not ground. Then, one gram of sample was submerged in 20 mL deionized water and placed under room temperature (no grinding or shaking). Experiment B: barks were ground and immerged in the deionized water and placed under room temperature (grinding but no shaking). Experiment C: samples were ground, soaked in the water, and placed on a shaker under room temperature (grinding and shaking). There were three replicates for each experiment. Bark pH and conductivity were measured at the beginning and at every 1 hour. We found that bark pH of the experiments A and B had similar trends and values. They were fluctuated during the first 2 hours and were stable after 3 hours at the value of 5.3. In contrast, the experiment C showed the lower pH value which was probably due to shaking. The bark conductivity of all experiments was also fluctuated at the beginning. They appeared to be stable after 3 hours at the value of 290 µS cm^{-1}. The values of bark conductivity from the experiments B and C were similar. For the experiment A however, the lower value was obtained which may be due to the sample preparation (no grinding). In conclusion, grinding sample with no shaking and then soaking in deionized water for at least 3 hours were appropriate for a simultaneous measure of the bark pH and conductivity in laboratory.

SP11_006_PF: THE PYRENOLICHENS AROUND RAMKHAMHAENG UNIVERSITY REGIONAL CAMPUS IN HONOUR OF HIS MAJESTY THE KING, NAKHON PHANOM PROVINCE

Supattara Phokaeo*, Kajonsak Vongshewarat, Kawinnat Buaruang, Wetchasart Polyiam, Sanya Meesim, Phimpha Nirongbut, Vasun Poengsungnoen, Natwida Doungpui, Sumrit Senglek, Supannee Todtan, Duanpen Seeiam, Mattika Sodamuk, Pumarin Ponthong, Kamonrat Kuldaong, Kittin Kosum, Pachara Mongkolsuk and Kansri Boonpragob.

Lichen Research Unit, Department of Biology, Faculty of Science, Ramkhamhaeng University, Bangkok, 10240
* Corresponding author email: Phokaeo_s@hotmail.com

Abstract:

Survey and collection of pyrenolichens from a dry dipterocarp forest during November 2014 to April 2015 revealed a total of 97 specimens around Ramkhamhaeng University Regional Campus in Honour of His Majesty the King at Nakhon Phanom Province. They were classified based on morphological and anatomical characteristics of thalli, ascomata, and colorless to grey brown or brown color, ellipsoidal to fusiform shapes, muriform or trans-septate types of ascospores. In addition, chemical characteristics of KOH+ red purple on thalli or around ascomata were also observed. Sixteen species, belonged to 3 families and 8 genera including *Anisomeridium*, *Bathelium*, *Campylothelium*, *Laurera*, *Marcelaria*, *Nigrovothelium*, *Pyrenula* and *Trypethelium*. The highest diversity of pyrenolichens included 8 species which were found on *Gluta usitata* (Wall.) Ding Hou., whereas the common lichens were *Marcelaria benguelensis*, *Pyrenula anomala* and *Trypethelium eluteriae*.

Introduction:

Pyrenolichens has a great variety of species. It comprises 2,125 named taxa worldwide [8,10]. In Thailand 157 species have been reported [6], and crustose lichens typically grow on smooth, shaded bark[2]. Lichens grow in well ventilated areas with high light intensity and distributed in all inland forests [9]. Pyrenolichens produce a reproductive structure called perithecium, a fruiting body which is rounded or flask-shaped, and which opens by a narrow pore at the apex, and exposed as a pigmented ascospores and hyaline ascospores in the hymenium. Such characteristics can be used to identify the genus and species of lichens, which are essential for conservation, and sustainability, as well as to enhance the researchers' experience and expertise. The aim of this study was to investigate the biodiversity and distribution of pyrenolichens from Ramkhamhaeng University Regional Campus in Honour of His Majesty the King, Nakhon Phanom Province (in a radius of 50 km) which is a part of Plant Genetic Conservation Project Office under the Royal Initiative of Her Royal Highness Princess Maha Chakri Sirindhorn.

Methodology:

In this study, lichen specimens were collected from 19 host plants in 11 study sites of a dry dipterocarp forest around Ramkhamhaeng University Regional Campus in Honour of His Majesty the King at Nakhon Phanom Province during November 2014 to April 2015 (Figure 1). They were classified based on morphological and anatomical characteristics of thalli, ascomata and ascospores, as well as chemicals characteristics of KOH tests [1,2,3,4,5,7,11,12].

Results and Discussion:

Ninety-seven pyrenolichens specimens were collected on 19 host plants from 11 study sites of a dry dipterocarp forest around Ramkhamhaeng University Regional Campus in Honour of His Majesty the King at Nakhon Phanom Province (Figure 1) . They were classified into 3 families including Monoblastiaceae, Pyrenulaceae and Trypetheliaceae. Sixteen species belonging to 8 genera, namely *Anisomeridium*, *Bathelium*, *Campylothelium*, *Laurera*, *Marcelaria*, *Nigrovothelium*, *Pyrenula* and *Trypethelium* were classified primarily based on the characteristics of the sexual reproductive structures (Figure 2).

The highest biodiversity of pyrenolichens belonged to the family Trypetheliaceae which comprised 6 genera and 9 species. The second most diverse group was the family Pyrenulaceae which contained 1 genus and 6 species. The family Monoblastiaceae on the other hand, possessed the lowest biodiversity of 1 genus and 1 species (Table 1).

The highest diversity of pyrenolichens included 8 species which were found on *Gluta usitata* (Wall.) Ding Hou (Table 2). The bark was cracked into longitudinal grooves, thus, thick gum resin could support the lichen growth. The common lichens were *Marcelaria benguelensis*, *Pyrenula anomala* and *Trypethelium eluteriae*.

The forest behide Ramkhamhaeng University Regional Campus in Honour of His Majesty the King, Nakhon Phanom Province had the highest species diversity of pyrenolichens (Table 3). Lichens usually grow in well ventilated areas with high light intensity and can tolerate extreme climatic conditions.

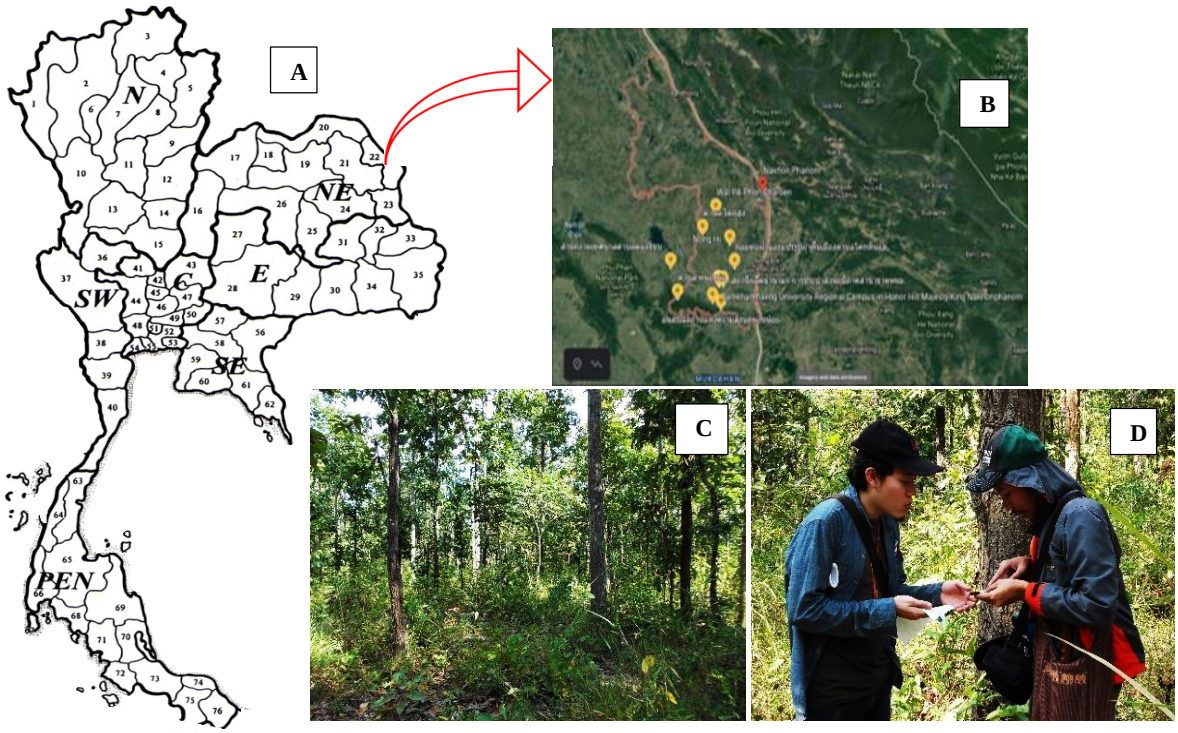

Figure 1. A = Map of Thailand (from "Thai Plants names" by Tem Smitinand, 2001, Bangkok: Royal Forest Department). B = 11 study sites from Ramkhamhaeng University Regional Campus in Honour of His Majesty the King, Nakhon Phanom Province. C = Dry dipterocarp forest (DDF). D = Collected pyrenolichens.

Table 1. The pyrenolichens around Ramkhamhaeng University Regional Campus in Honour of His Majesty the King, Nakhon Phanom Province.

Family	Genus	Species
1. MONOBLASTIACEAE	*Anisomeridium*	*Anisomeridium tamarindi*
2. PYRENULACEAE	*Pyrenula*	*Pyrenula anomala*
		Pyrenula aspistea
		Pyrenula atropurpurea
		Pyrenula immissa
		Pyrenula laetior
		Pyrenula thailandica
3. TRYPETHELIACEAE	*Bathelium*	*Bathelium madreporiformis*
		Bathelium phaeomelodes
	Campylothelium	*Campylothelium nitidum*
	Laurera	*Laurera subdiscreta*
	Marcelaria	*Marcelaria benguelensis*
	Nigrovothelium	*Nigrovothelium tropicum*
	Trypethelium	*Trypethelium eluteriae*
		Trypethelium nigroporum
		Trypethelium ochroleucum

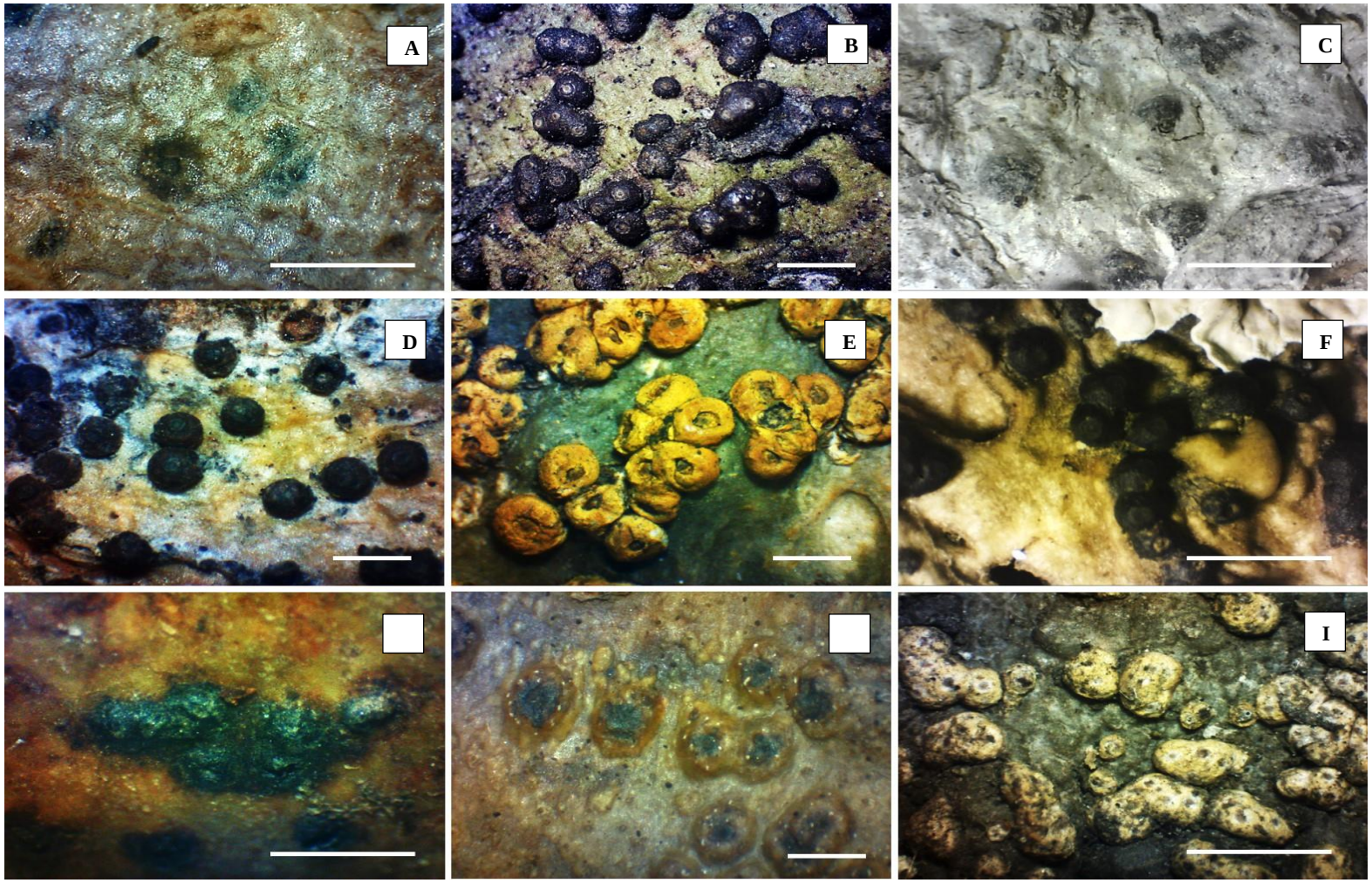

Figure 2. The pyrenolichens around Ramkhamhaeng University Regional Campus in Honour of His Majesty the King, Nakhon Phanom Province. A. *Anisomeridium tamarindii*, B. *Bathelium madreporiformis*, C. *Campylothelium nitidum*, D. *Laurera subdiscreta*, E. *Marcelaria benguelensis*, F. *Nigrovothelium tropicum*, *G. Pyrenula anomala*, H. *Pyrenula immissa*, I. *Trypethelium eluteriae*; scale = 1 mm

Table 2. Host plants of Pyrenolichens around Ramkhamhaeng University Regional Campus in Honour of His Majesty the King, Nakhon Phanom Province.

Host plant	Species
1. *Acacia auriculiformis* Cunn.	*Pyrenula thailandica*, *Trypethelium eluteriae*
2. *Canarium subulatum* Guill.	*Marcelaria benguelensis*, *Nigrovothelium tropicum*, *Trypethelium eluteriae*, *Trypethelium nigroporum*
3. *Careya sphaerica* Roxb	*Pyrenula anomala*, *Pyrenula thailandica*, *Marcelaria benguelensis*
4. *Cratoxylum formosum* (Jack) Dyer.	*Pyrenula anomala*
5. *Croton oblongifolius* Roxb	*Pyrenula anomala*, *Pyrenula thailandica*
6. *Erythrophloeum succirubrum* Gagnep.	*Pyrenula thailandica*
7. *Gluta usitata* (Wall.) Ding Hou	*Bathelium madreporiformis*, *Bathelium phaeomelodes*, *Marcelaria benguelensis*, *Pyrenula anomala*, *Pyrenula laetior*, *Trypethelium eluteriae*, *Laurera subdiscreta*, *Marcelaria benguelensis*
8. *Heteropanax fragrans* (Roxb. ex DC.) Seem.	*Anisomeridium tamarindi*, *Laurera subdiscreta*, *Nigrovothelium tropicum*, *Trypethelium nigroporum*
9. *Irvingia malayana* Oliv. ex A.W. Benn.	*Nigrovothelium tropicum*
10. *Lithocarpus polystachyus* (Wall.) Rehd. Share.	*Nigrovothelium tropicum*
11. *Lophopetalum wallichii* Kurz.	*Anisomeridium tamarindi*, *Marcelaria benguelensis*
12. *Peltophorum dasyrachis* (Miq.) Kurz	*Pyrenula anomala*, *Pyrenula aspistea*
13. *Peltophorum dasyrrhachis* (Miq.) Kurz	*Laurera subdiscreta*
14. *Senna siamea* Lam.	*Marcelaria benguelensis*, *Trypethelium eluteriae*
15. *Shorea roxburghii* G. Don.	*Trypethelium eluteriae*, *Trypethelium ochroleucum*
16. *Sindora siamensis* Teijsm. & Miq.	*Laurera subdiscreta*, *Marcelaria benguelensis*, *Trypethelium nigroporum*
17. *Strychnos nux-vomica* L.	*Anisomeridium tamarindi*, *Pyrenula anomala*, *Pyrenula immissa*, *Pyrenula thailandica*
18. *Wrightia religiosa* Benth.	*Trypethelium eluteriae*
19. *Ziziphus oenoplia* (L.) Mill.	*Trypethelium eluteriae*

Table 3. Distribution of pyrenolichens in 11 study sites from Ramkhamhaeng University Regional Campus in Honour of His Majesty the King, Nakhon Phanom Province.

Species	NP1	NP2	NP3	NP4	NP5	NP6	NP7	NP8	NP9	NP10	NP11	Total sites
1. *Anisomeridium tamarindi*							4	1				2
2.*Bathelium madreporiformis*	1			1								2
3.*Laurera phaeomelodes*	1											1
4.*Campylothelium nitidum*					1							1
5.*Laurera subdiscreta*							2		1		5	3
6.*Marcelaria benguelensis*	2	1					2	1		1	1	6
7.*Nigrovothelium tropicum*	1				1		1	2				4
8.*Pyrenula anomala*	5	3	1		3		1			4		6
9.*Pyrenula aspistea*	1											1
10.*Pyrenula atropurpurea*			3									1
11.*Pyrenula immissa*								2		4		2
12.*Pyrenula laetior*	1											1
13.*Pyrenula thailandica*	4	3	7	3								4
14.*Trypethelium eluteriae*	6	1	2		3	1				1		6
15.*Trypethelium nigroporum*	1						1			3	1	4
16.*Trypethelium ochroleucum*					2							1
Total species	10	4	4	2	5	1	6	4	1	5	3	-

**[1] nakae subdistrict, [2] nakoo subdistrict, [3] khok hin hae subdistrict, [4] nong hee subdistrict, [5] kuruku subdistrict, [6] khok sung subdistrict, [7] phiman subdistrict, [8] tongkop subdistrict, [9] nongbo subdistrict. NP1[1]=forest behide Ramkhamhaeng, NP2[2]= the forest on the right-hand side of the Ban Na Khu floodgate sign, NP3[2]=behind the naka vocational college, NP4[2]=forest opposite the water pump, NP5[3]=ban khok hin hae, NP6[4]= ban nong hee, NP7[5]= roadside forest no.22, NP8[6]= roadside forest no. 2009, NP9[7]= forest around the monument of peace phu phan noi, NP10[8]= roadside forest, tongkop subdistrict, NP11[9]= wat pa muang wang thong (pha daeng).

Conclusion:

The diversity of pyrenolichens was studied on 19 host plants from 11 study sites in a dry dipterocarp forest of Ramkhamhaeng University Regional Campus in Honour of His Majesty the King, Nakhon Phanom Province. A total of 97 lichen specimens were classified into 3 families, 8 genera and 16 species. *Marcelaria benguelensis* (Müll.Arg.) Aptroot, Nelsen & Parnmen, *Pyrenula anomala* (Ach.) Vain., and *Trypethelium eluteriae* Spreng. were common species (Table 3). The highest diversity of pyrenolichens included 8 species which were found on *Gluta usitata* (Wall.) Ding Hou. The forest behide this campus of Ramkhamhaeng University had the highest species diversity of pyrenolichens. If the forest is disturbed either by nature or human activities, the diversity of these lichens will be affected which may result in extinction in the future.

Acknowledgements:

This study is a part of Plant Genetic Conservation Project under the Royal Initiation of Her Royal Highness Princess Maha Chakri Sirindhorn (RSPG), for their support in the fieldwork. We are also very grateful to thank a number of colleagues at the excellent organization team of the Lichen Research Unit, Biology Department, Faculty of Science, and Ramkhamhaeng University for using instruments and facilities in the laboratory.

References

1. Aptroot, A. (2009). Pyrenulaceae. In P. M. McCarthy (Ed.), Flora of Australia 57 (pp. 449-480). Canberra, Australia: CSIRO Publishing.
2. Aptroot, A. (2012). A world key to the species of *Anthracothecium* and *Pyrenula*. *The lichenologist, 44*(1), 5-53.
3. Aptroot, A., & Lücking, R. (2016). A revisionary synopsis of the Trypetheliaceae (Ascomycota: Trypetheliales). *The lichenologist 48* (6), 763-982.
4. Aptroot, A., Lücking, R., Sipman, K. J. M., Umaña, L., & Chaves, J. L. (2008). Pyrenocarpous lichens with bitunicate asci a first assessment of the lichen biodiversity inventory in Costa Rica. *Bibliotheca Lichenologica*, 97, 1-162.
5. Awasthi, D. D. (1991). A key to the microlichens of India Nepal and Sri Lanka. *Bibliotheca Lichenologica, 40*, 1-337.
6. Buaruang, K., Boonpragob, K., Mongkolsuk, P., Sangvichien, E., Vongshewarat, K., Polyiam, W., Rangsiruji, A., Saipunkaew, W., Naksuwankul, K., Kalb, J., Parnmen, S., Kraichak, E., Phraphuchamnong, P., Meesim, S., Luangsuphabool, T., Nirongbut, P., Poengsungnoen, V., Duangphui, N., Sodamuk, M., Phokaeo, S., Molsil, M., Aptroot, A., Kalb, K., Lücking, R., Lumbsch, H. T., (2017). A new checklist of lichenized fungi occurring in Thailand. *Mycokeys 23*: 1–91.
7. Kansri Boonpragob, & Kawinnat Buaruang. (2007). Biodiversity of the lichen on Koh Samaesan, Chon Buri Province. Bangkok: Ramkhamhaeng University.
8. Kirk, P. M., Cannon, P. F., Minter, D. W., & Stalpers, J. A. (2008). Dictionary of the fungi. Trowbridge, United Kingdom: Cromwell Press.
9. Komposch, H., & Hafellner, J. (2002). Life form diversity of lichenized fungi in an Amazon lowland rainforest. *Bibliotheca Lichenologica, 82*, 311-326.
10. Lumbsch, H. T., & Huhndorf, S. M. (2010). Fieldiana: Life and Earth Sciences. *Myconet*, 14, 1-64.
11. Schumm, F., & Aptroot, A. (2010). Seychelles Lichen Guide. Süssen, Germany: Beck.
12. Vongshewarat, K., McCarthy, P. M., Mongkolsuk, P. & Boonprakob, K. (1999). Additions to the lichen flora of Thailand. *Mycotaxon, 70*, 227-23.

SP11_007_OA: ANNUAL LITTERFALL BIOMASS OF EPIPHYTIC MACROLICHENS IN PRIMARY AND SECONDARY FORESTS AT KHAO YAI NATIONAL PARK

Pitakchai Fuangkeaw, * Wetchasart Polyiam, Chaiwat Boonpeng, Kansri Boonpragob

Lichen Research Unit, Department of Biology, Faculty of Science, Ramkhamhaeng University, Bangkok, THAILAND
*e-mail: pfuangkeaw@gmail.com

Abstract:

Biomass and lichen diversity vary depending on the type and structure of the forest, which may refer to tree species, size, and density. These were resulted to the difference amount of litterfall biomass of lichens. Thus, the objective of this study was to estimate macrolichen litterfalls in a primary forest (tropical rain forest; TRF) and successional forest (secondary forest; SF) at Khao Yai National Park. Macrolichen litterfalls were surveyed in twenty-five 2-meter radius circular plots within 3 locations at both TRF and SF. Tree density in those forest types were estimated using the Point Center Quarter Method. A total of 21 species of macrolichens were recorded in both TRF and SF. Lichen litterfall biomass was higher in SF than TRF, which were 0.34±0.21 and 0.19±0.23 kg ha^{-1} $year^{-1}$ in average. Annual lichen litterfall biomass varies with seasons. SF has the highest biomass recorded in hot season, whereas the TRF was found in the early rainy season. A higher lichen litterfall biomass was discovered at the SF. This forest type contains smaller trees with high tree density compared to TRF. This result indicated that the forest types and forest structure are influence to the amount of macrolichen litterfall biomass that may depend on seasons.

SP11_008_OA: SPECIES DIVERSITY OF LICHEN FAMILY GRAPHIDACAEA IN MANGROVE FORESTS: EASTERN AND UPPER SOUTHERN PARTS OF THAILAND

Vasun Poengsungnoen*, Kajonsak Vongshewarat, Patchara Mongkolsuk, Kawinnat Buaruang

Department of Biology, Faculty of Science, Ramkhamhaeng University, Huamark, Bangkapi, Bangkok 10240, Thailand
*e-mail: vasunpoeng@gmail.com

Abstract:

Lichen is a composite organism consisting of fungus and alga and/or cyanobacterium functioning in a symbiotic association. Graphidaceae is the largest family of tropical crustose lichens and it is one of the most common inhabitants in mangrove forests. The objective of this work was to study the species diversity of lichen family Graphidaceae in mangrove forests in two regions: the eastern part and upper southern part of Thailand. All 3,159 corticolous specimens were collected from mangrove phorophytes during 2012-2019 and identified based on morphological and chemical characteristics. Even though the two locations were similar in the ecosystem, the species numbers exhibited differences. The eastern mangrove habitats were more diverse yielding 25 genera 76 species, compared with 15 genera 45 species from the upper southern forests; however, there was high species similarity between both areas (31 species, 51.2%). Thirty-five and 15 species were found only in the eastern and upper southern parts, respectively. *Graphis analoga* was a common species in East, whereas *G. dendrogramma* was a dominant species in upper South. Twenty-six species had less than three specimens observed which revealed the fragility of these biodiversity resources.

SP11_009_PF: *Relicina* (LICHENIZED ASCOMYCOTA) IN THAILAND

Kawinnat Buaruang* and Pachara Mongkolsuk

Department of Biology, Faculty of Science, Ramkhamhaeng University, Bangkok, 10240
*e-mail: bkawinnat@gmail.com

Abstract:

Members of the genus *Relicina* (Parmeliaceae) were distinguishable by having yellowish green thalli. In addition, they had lobe shape sublinear to subirregular with margins entire crenate or serrate, and apice incised to truncate. Simple, furcate or agglutinate rhizine was developed from the lower cortex. The bitunicate ascus contained hyaline, simple and ellipsoid ascospores. Conidia were bifusiform. Based on a phylogenetic analysis, the genus *Relicinopsis* has been proposed as a subgenus of *Relicina*. Twelve species of *Relicina* occurred in Thailand. Usnic acid was a chemical substance found in the upper cortex. Medullary substances included 4-O-demethylbarbatic acid, barbatic acid, caperatic acid, echinocarpic acid, fumarprotocetraric acid, hyposalazinic acid, norstictic acid, protocetraric acid and succinprotocetraric acid.

Introduction:

Currently in Parmeliaceae c. 80 genera are accepted based on phenotypic features and analyses of multilocus sequence data[2, 14]. The largest group within the family is the parmelioid core, where the genera *Relicina* (Hale & Kurok.) Hale and *Relicinopsis* Elix & Verdon are belonged[1]. *Relicina* is differentiated from *Parmelia* Ach. s. lat.[8] by having bulbate marginal cilia, bifusiform conidia and containing usnic acid in the upper cortex. The related genera are *Bulbothrix* and *Relicinopsis*. *Bulbothrix* has grayish green color on the upper cortex and containing atranorin, whereas *Relicinopsis* is distinguished by the absence of bulbate cilia and has yellowish green color on the upper surface which contains usnic acid. Kirika et al. proposed to reduce the genus *Relicinopsis* to a subgenus of *Relicina*. [12]. This genus includes c. 54 species[14] with the center of distribution in South-East Asia (including Thailand) and Australasia[4, 10].

Methodology:

Lichen samples collected from 9 provinces were dried under room temperature for taxonomic study. All specimens were examined for their morphological and anatomical characteristics and chemistry as follows. For macroscopic examination, the morphology of the thallus including lobe size, rhizines, cilia, vegetative propagules (isidia, soredia, phyllidia and pustule), reproductive structure, color and surface texture were examined by using low magnification stereomicroscope (Olympus SZ30). For microscopic examination, the anatomical characters of thallus including reproductive structure, apothecia and pycnidia were free-hand sectioned with the aid of razor blade. Investigation of the fine structures was performed under light microscope (Olympus CH and Olympus BX51). The investigation of chemical characters was performed by spot test[5] and Thin Layer Chromatography (TLC)[15]. Taxa were determined according to books and publications of this genus[3, 6, 7, 9, 10, 11, 13] and all specimens were preserved at the Lichen Herbarium of Ramkhamhaeng University.

Results and Discussion:

From various morphological characters of *Relicina* (Figure 1), a total of 12 species were reported in Thailand. *Relicina abstrusa*, *R. circumnodata, R. palmata, R. planiuscula, R. polycarpa, R. subabstrusa, R. subconnivens, R. sublanea, R. sublimbata* belonging to the genus *Relicina* (Hale & Kurok.) Hale, were characterized by thallus colors being yellowish green. Lobe shape, sublinear to subirregular with margins entire crenate or serrate with bulbate cilia, apice incised to truncate were found. Simple, furcate or agglutinate rhizine, was developed from the lower cortex. The bitunicate ascus contained hyaline, simple and ellipsoid ascospores.

Conidia were bifusiform. *Relicina intertexta, R. malaccensis* and *R. rahengensis* belong to the genus *Relicina,* subgenus *Relicinopsis* (Elix & Verdon) Kirika, Divakar & Lumbsch that were characterized by thallus colors being yellowish green. Lobe shape, sublinear to subirregular with margins entire crenate or serrate, apice incised to truncate were found. Simple, furcate or agglutinate rhizine was developed from the lower cortex. The bitunicate ascus possessed hyaline, simple and ellipsoid ascospores. Conidia were fusiform to baciliform. Of the 12 taxa, ten major substances were found and usnic acid was a common chemical substance present on the upper cortex (Table 1).

Key to species of *Relicina* in Thailand.

1a. Lobes with marginal bulbate cilia 2

1b. Lobes without cilia 10

2a. Thallus isidiate, isidiate-lobulate, or lobulated 3

2b. Thallus lacking isidia and lobules 6

3a. Isidia becoming dorsiventral and lobulated ..... *R. palmata*

3b. Isidia distinct, cylindrical 4

4a. Lower surface pale brown; rhizine densely branched ..... *R. circumnodata*

4b. Lower surface black 5

5a. Norstictic acid present … ..... *R. abstrusa*

5b. Echinocarpic acid present … ..... *R. planiuscula*

6a. Lower surface tan to pale brown; protocetraric acid present … ..... *R. sublanea*

6b. Lower surface black 7

7a. Medulla K - ..... *R. subconivens*

7b. Medulla K+ red …… 8

8a. Medulla P+ orange red; succinprotocetraric acid present ..... *R. sublimbata*

8b. Medulla P+ orange red; norstictic acid present 9

9a. Apothecia ecoronate … ..... *R. polycarpa*

9b. Apothecia coronate ..... *R. subabtrusa*

10a. Thallus without isidia ..... *R. intertexta*

10b. Thallus with isidia 13

11a. Medulla P+ red ..... *R. malaccensis*

11b. Medulla P- ..... *R. rahengensis*

Table 1. Lichen substances found among species of the genus *Relicina*.

Lichen substance	Scientific name
Upper cortex	
Usnic acid	*Relicina abstrusa, R. circumnodata, R. intertexta, R. malaccensis, R. palmata, R. planiuscula, R. polycarpa, R. rahengensis, R. subabstrusa, R. subconnivens, R. sublanea* and *R. sublimbata*
Medulla layer	
4-O-demethylbarbatic acid	*Relicina rahengensis*
barbatic acid	*Relicina rahengensis*
caperatic acid	*Relicina subconnivens*
echinocarpic acid	*Relicina planiuscula, R. palmata* and *R. polycarpa*
fumarprotocetraric acid	*Relicina sublimbata*
hyposalazinic acid	*Relicina abstrusa*
norstictic acid	*Relicina abstrusa, R. polycarpa* and *R. subabstrusa*
protocetraric acid	*Relicina intertexta, R. malaccensis, R. circumnodata* and *R. sublanea*
succinprotocetraric acid	*Relicina sublimbata*

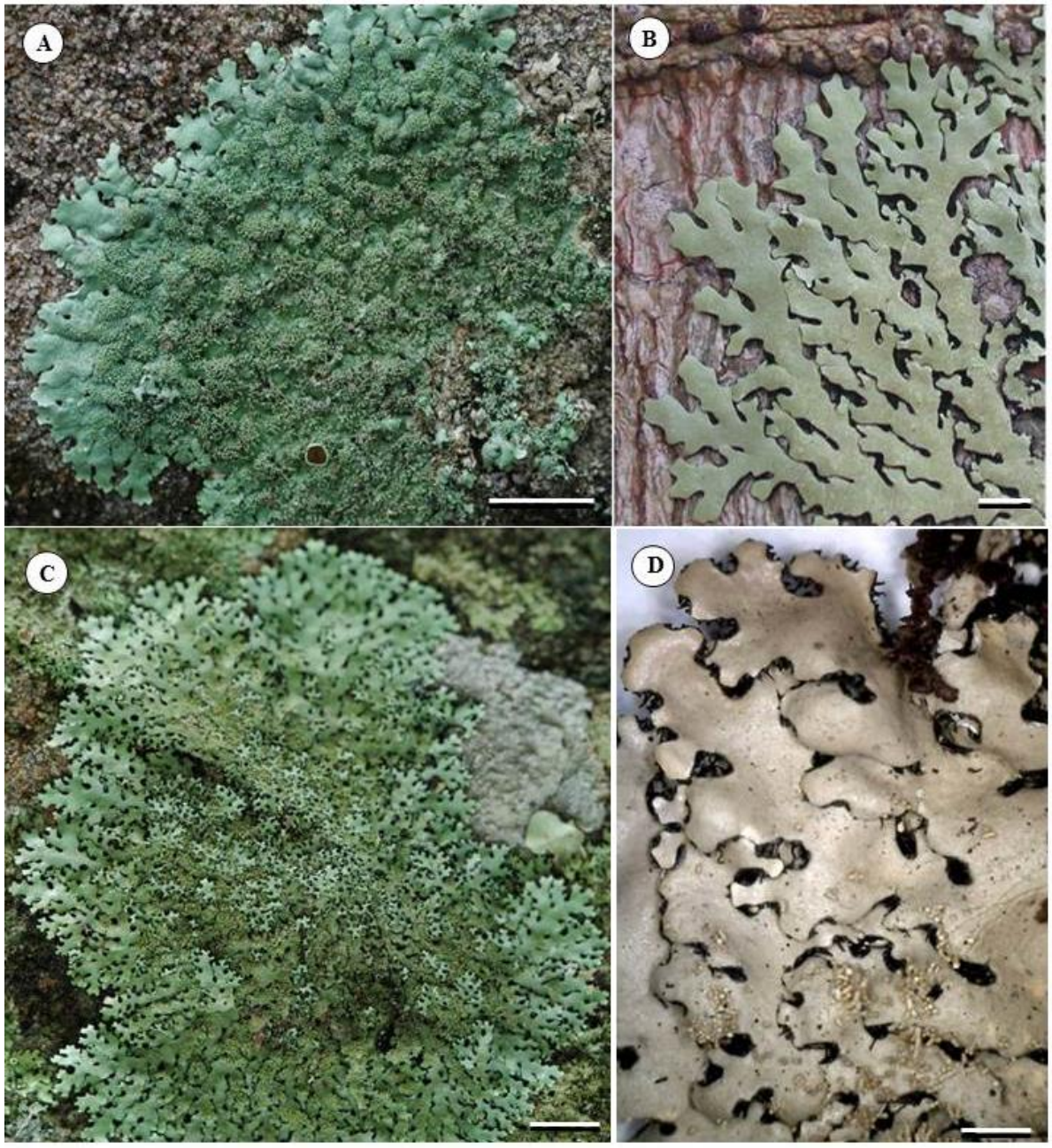

Figure 1.

Characteristics of the genus *Relicina* (Hale & Kurok.) Hale: Firmly adnate thallus of suborbicular in outline, B. Lobe linear, subdichotomously branched, C. Crenate margins of subirregular outline colony, D. Laminal isidia and marginal bulbate cilia

(bars: A = 1 cm; B = 1 mm; C = 1 cm; D = 1.5 mm).

Conclusion:

Twelve species of *Relicina* were reported in Thailand. They were characterized by having yellowish green thalli. Lobe shape, sublinear to subirregular with margins entire crenate or serrate with bulbate cilia (*Relicina abstrusa*, *R. circumnodata, R. palmata, R. planiuscula, R. polycarpa, R. subabstrusa, R. subconnivens, R. sublanea, R. sublimbata*) or eciliate (*Relicina intertexta, R. malaccensis* and *R. rahengensis*), and apice incised to truncate were found. Simple, furcate or agglutinate rhizine, was developed from the lower cortex. The bitunicate ascus contained hyaline, simple and ellipsoid ascospores. Conidia were bifusiform. Usnic acid was a chemical substance found on the upper cortex. Medullary substances included 4-O-demethylbarbatic acid, barbatic acid, caperatic acid, echinocarpic acid, fumarprotocetraric acid, hyposalazinic acid, norstictic acid, protocetraric acid and succinprotocetraric acid.

Acknowledgements:

This work was financially supported by the National Council of Thailand (grant No. 183076). We are grateful to the officers and staff of Lichen Herbarium of Ramkhamhaeng University at Department of Biology, Faculty of Science, Ramkhamhaeng University.

References:

1. Crespo A, Kauff F, Divakar PK, et. al., Taxon 2010; 59: 1735–1753.
2. Divakar PK, Crespo A, Wedin M, et. al., New Phytologist 2015; 208: 1217–1226.
3. Divakar PK, Upreti DK, Parmelioid lichens in India (A revisionary study) 2005.
4. Elix JA, Bryologist 1993; 96: 359-383.
5. Elix JA, Flora of Australia 1994a; 55: 5-7.
6. Elix JA, Flora of Australia 1994b; 55: 182-184.
7. Elix JA, Johnston J & Verdon D, Mycotaxon 1986; 27: 271-282.
8. Hale ME, Phytologia 1974a; 28: 479-490.
9. Hale ME, Phytologia 1974b; 29: 188-191.
10. Hale ME, Smithsonian Contribution to Botany 1975; 26: 1-32.
11. Hale ME, Smithsonian Contribution to Botany 1976; 31: 1-62.
12. Kirika PM, Divakar PK, Leavitt SD, et. al., Lichenologist 2017; 49: 189-197.
13. Noicharoen K, Polyiam W, Boonpragob K, et. al., Mycotaxon 2003; 85: 325-330.
14. Thell A, Crespo A, Divakar PK, et. al., Nordic Journal of Botany 2012; 30: 641-664.
15. White FJ & James PW, British Lichen Society Bulletin 1985; 57: 1-41.

SP11_010_PF: LICHEN HERBARIUM DATABASE AND MANAGEMENT AT RAMKHAMHAENG UNIVERSITY I

Phimpha Nirongbut*, Kawinnat Buaruang, and Kansri Boonpragob

Department of Biology, Faculty of Science, Ramkhamhaeng University, Huamark, Bangkapi, Bangkok, Thailand, 10240
*e-mail address: phimphadam@gmail.com, Tel. & Fax: (662)310-8395

Abstract:

The Lichen herbarium of Ramkhamhaeng University being registered with the international museum system under the RAMK code is an evidence for rich biological resources and lichenological research in Thailand. Arising from the surveys and studies lichens nationwide since 1993, RAMK began collecting data in the database and managing the samples in 2006. Currently more than 80,000 lichen samples from Thailand and 43 other countries around the world are housed here. All samples are systematically managed and collected in the Lichen herbarium. In alphabetical order genus A-M, 8,569 samples from 42 provinces of Thailand, consisting of lichens classified according to taxonomy, 60 families, 150 genera, 551 species.

Keywords: herbarium, database and RAMK

Introduction:

Lichen herbarium of Ramkhamhaeng University is one of the important places in natural history studies in Thailand and SE Asia. It keeps important informarmation on biological resources of the vountries. Its primary function is to provide taxonomic records focused on lichen. This record is improved upon through loans and outright exchanges of specimens with researchers at other institutions, who are authorities of particular lichen groups and able to apply annotation labels as part of their review process, thus often correcting earlier determinations, and in general, improving the scientific value of a given specimen. Loan requests that we receive from other institutions are honored and fulfilled by careful packaging and shipping to the requesting institution.

Methodology:

Process and operation of the Lichen herbarium of Ramkhamhaeng University are divided into 3 parts as follows. **Part 1;** Sample Preparation and Packaging: The samples collected from the field are dried at room temperature for 3-5 days, then the specimens sachets are placed in the brown sample sachets and recorded the details of the specimens as including: Scientific name, Collectors number, compiler number, TLC number, surname, sample location, national parks and sanctuaries, sampling province, substrate and author, forest type, elevation reference and tables, and so on after which separate. Samples were packaged into groups for researchers to classify. **Part 2;** The classified samples are successfully into the database process as follows: RAMK, Collector no, TLC no, Genus, Species, Author name, Family, Localities, Storage, National Park and Sanctuary, Province, Substrate, Author, Forest type, Altitude, Grid ref, Collector, Date collector, Determine by, Date Determine, Chemistry and Remark. After check the details of specimens with the specimens guide (log book), the specimens sachets include index card (for note the specimens study details), solid tissue paper to support the specimens, and stamping RAMK number as 3 points as follows; inside some white paper top right corner, index card and inside edge of specimens sachets, all of the above put in a zip envelope and attach the front of the specimens sachets completely. The specimens into a brown specimens file for storage in the Lichen Herbarium, sort samples by species, each species by RAMK number. Next, put the specimens sachets in a brown specimens file with the name and green paper (color indicated for Asia) and into the freezer for 24-48 hours (sample envelope in the freezer for 24 hours, and sample brown file/large brown box for 48 hours). **Part 3;** Collection of specimens in the Lichen Herbarium. Take them out of the freezer, before into the Lichen Herbarium. Check specimens sachets and a brown specimen file with Lichen Herbarium file for specimens storage cabinet by alphabetical of the genus and each genus sorted by species and each genus is separated by green futures boards (color indicated for Asia)

Result, discussion and conclusion:

Databasing and organizing of lichen specimens at the Lichen herbarium of Ramkhamhaeng University resulted in 8,569 samples from 42 provinces of Thailand in the genera starting with A-M, consisting of specimens from 60 families, 150 genera and 551 species (Table 1).

Table 1. Classification of lichens according to the current taxonomy, 60 Families, 150 Genera from stored 8,569 specimens in the RAMK herbarium (A – M genera).

Family	Genus
ARTHOPYRENIACEAE	*Arthopyrenia*
ASPIDOTHELIACEAE	*Aspidothelium*
	Austroblastenia
BAEOMYCETACEAE	*Baeomyces*
BIATORACEAE	*Biatora*
BRIGANTIACEAE	*Brigantiaea*
BRIGANTIAEACEAE	*Brigantiaea*
BYSSOLOMATACEAE	*Byssoloma*
CALICIACEAE	*Calicium*
	Diplotomma
	Gassicurtia
	Melanaspicilia
CANDELARIACEAE	*Candelariella*
CHIODECTONACEAE	*Dichosporidium*
CLADONIACEAE	*Cladonia*
	Gymnoderma
COCCOCARPIACEAE	*Coccocarpia*
	Coccocarpia
COENOGONIACEAE	*Coenogonium*
	Dimerella
COENOGONIACEAE	*Coenogonium*
COLLEMATACEAE	*Collema*
	Leptogium
CONIOCYBACEAE	*Chaenotheca*
CROCYNIACEAE	*Crocynia*
DOTHIDEOMYCETIDAE	*Mycoporellum*
ECTOLECHIACEAE	*Badimia*
	Calenia
	Calopadia
	Lasioloma
	Lecania
FUSCIDEACEAE	*Fuscidea*
	Maronea
	Aulaxina
	Calenia
	Echinoplaca
	Gyalectidium
	Gyalidea
	Gyalideopsis
GRAPHIDACEAE	*Acanthographis*
	Acanthothecis
	Cyclographina
	Diorygma
	Dyplolabia
	Fissurina
	Glyphis
	Graphina
	Graphis
	Gymnographa
	Gyrostomum
	Haematomma
	Hemithecium

Family	Genus
	Leiorreuma
	Melanotrema
	Myriotrema
GYALECTACEAE	*Cryptolechia*
	Gyalecta
HAEMATOMMATACEAE	*Haematomma*
HYMENELIACEAE	*Hymenelia*
	Ionaspis
HYPOGYMNIACEAE	*Hypogymnia*
HYSTERIUMCEAE	*Hysterium*
LECANORACEAE	*Cryptolechia*
	Haematomma
	Laurera
	Lecanora
	LecidellaMaronina
LECIDEACEAE	*Lecidea*
LEPROCAULACEAE	*Leprocaulon*
LETROUITIACEAE	*Letrouitia*
LOBARIACEAE	*Lobaria*
MALMIDEACEAE	*Malcolmiella*
	Malmidea
MEGALARIACEAE	*Megalaria*
MEGALOSPORACEAE	*Aspicilia*
	Austroblastenia
	Megalospora
MEGASPORACEAE	*Aspicilia*
MELASPILEACEAE	*Melaspilea*
	Micarea
MICROTHELIOPSIDACEAE	*Microtheliopsis*
MILTIDEACEAE	*Miltidea*
MONOBLASTIACEAE	*Anisomeridium*
	Caprettia
MYCOCALICIACEAE	*Lecanora*
MYCOPORACEAE	*Mycoporum*
MYELOCONACEAE	*Myeloconis*
NAETROCYMBACEAE	*Leptorhaphis*
PANNARIACEAE	*Erioderma*
	Leioderma
PARMELIACEAE	*Bulbothrix*
	Canoparmelia
	Dirinaria
	Everniastrum
	Flavopanaria
	Hypogymnia
	Hypotrachyna
	Imshaugia
	Myclochroa
	Myelochroa
PHYSCIACEAE	*Buellia*
	Dirinaria
	Gassicurtia
	Hafellia
	Heterodermia
	Hyperphyscia
	Hypotrachyna
PILOCARPACEAE	*Byssolecania*
	Byssoloma
	Eugeniella
	Fellhanera
	Logilvia
	Malcolmiella
	Micarea
PILOCARPACEAE	*Fellhanera*
PORPIDIACEAE	*Amygdalaria*
PYRENULACEAE	*Anthracothecium*
	Lithothelium
	Mazosi

Family	Genus
RAMALINACEAE	*Bacidia*
	Bacidina
	Badimia
	Lecania
ROCCELLACEAE	*Acanthothecis*
	Chiodecton
	Dictyographa
	Enterographa
	Graphidastra
	Lecanactis
	Lecanographa
	Maronina
STEREOCAULACEAE	*Lepraria*
	Leproloma
STICTIDACEAE	*Conotrema*
TELOSCHISTACEAE	*Caloplaca*
THELOTREMATACEAE	*Chapsa*
	Chroodiscus
	Diploschistes
	Leucodecton
	Myriotrema
TRAPELIACEAE	*Lithographa*
TRICHOTHELIACEAE	*Clathroporina*
TRYPETHELIACEAE	*Astrothelium*
	Campylothelium
	Cryptothelium
	Laurera
	Megalotremis
	Mycomicrothelia
VERRUCARIACEAE	*Melanotheca*

Locations of lichen specimens from 42 countries from Rundel's collection deposited at RAMK lichen herbarium are shown in Figure 1.

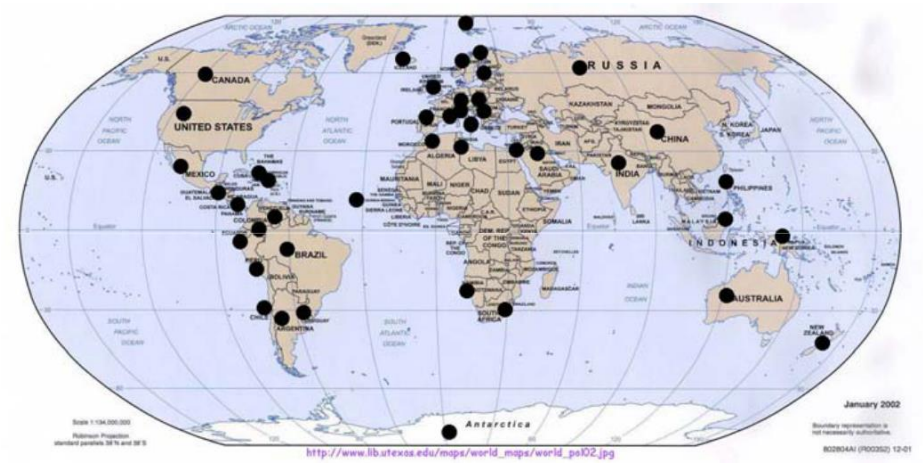

Figure 1. Location of 42 countries where lichen specimens from Rundel's collections are curated at RAMK lichen herbarium.

RAMK lichen herbarium is the first of its kind in Thailand and Southeast Asia. It keeps important information on biological resources of the countries. They are organized in international standard, which are easy to search and are available to everybody. However, research on lichens in Thailand and Southeast Asia is

relatively new. A large number of new species and unknown taxa at the herbarium indicate that lichens in this area need further intensive studies to be discovered and understood about their biology. Future studies on sustainable utilization of lichen resources and management needs these curatorial information from this lichen herbarium.

Acknowledgement:

We are grateful to the following agencies, National Parks, Wildlife and Plant Conservation Department and all areas where samples were allowed to be collected. We would like to express our sincere gratitude to Professor Philip Rundel from University of California, Los Angeles, U.S.A., who has donated his lichen collections, together with book and publications on lichens to Ramkhamhaeng University Herbarium. We are grateful to the lichen team at Ramkhamhaeng University.

Reference:

1.. Buaruang, K., Boonprakob, K. Mongkolsuk, P., Sangvichien, E., Vongshewarar, K., Polyiam, W., Rangsiruji, A., Saipunkaew, W., Kalb, J., Parmen, S., Kraichak, E., Phraphuchamnong, P., Meesim, S., Luangsuphabool, T., Nirongbut, P., Poengsungnoen, V., Duangphui, N., Sodamuk, M., Phokaeo, S., Molsil, M., Aptroot, A., Kalb, K., Lücking, R., Lumbsch, H. T., (2017). A new checklist of lichenized fungi occurring in Thailang. Mycokeys 23: 1-91.

Keyword: Lichen Herbarium, RAMK, global collection

SP11_011_PF: DIVERSITY OF FOLIICOLOUS LICHENIZED FUNGI IN MANGROVE FOREST FROM CHUMPHON PROVINCE, THAILAND

Udomrak Meethong*, Vasun Poengsungnoen, Pachara Mongkolsuk, Wetchasart Polyiam, Kawinnat Buaruang

Lichen Research Unit, Department of Biology, Faculty of Science, Ramkhamhaeng University, Bangkok, 10240
*e-mail: gateudomrak@gmail.com

Abstract:

Foliicolous lichenized fungi (FLF) in mangrove forests are poorly studied. A few documents have been reported on this group of lichens in Thailand. Thus, this work aimed to study the diversity of FLF in mangrove forests in Chumphon province. A total of 274 specimens were collected from various mangrove tree leaves in February 2018 and identified based on morphological, anatomical and chemical characteristics. In the present study, 10 families, 11 genera and 17 species were recorded including *Arthonia lividula* Vain., *A. trilocularis* Müll. Arg., *Bacidina pallidocarnea* (Müll. Arg.) Vězda, *Byssoloma subdiscordans* (Nyl.) P. James, *Calopadia fusca* (Müll. Arg.) Vězda, *C. puiggarii* (Müll. Arg.) Vězda, *C. subcoerulescens* (Zahlbr.) Vězda, *Coenogonium dilucidum* (Kremp.) Kalb & Lücking, *Dirinaria confluens* (Fr.) DD. *Graphis furcata* Fée., *G. pinicola* Zahlbr., *Mazosia phyllosema* (Nyl.) Zahlbr., *Porina kamerunensis* F. Schill., *P. nitidula* Müll. Arg., *Strigula antillarum* (Fée) Müll. Arg., *S. smaragdula* Fr., *Tricharia demoulini* Sérus. Among them, *S. smaragdula* was commonly found with 72 observed specimens and almost all of them were collected from the leaves of *Xylocarpus granatum* J. Koenig. A key to all species of FLF was provided together with their pictures.

Introduction:

Mangrove forests are among the world's most productive ecosystems which provide habitat and an important source of nutrients for a variety of species.[1] These forests which are distributed throughout tropical and sub-tropical regions encompass 118 countries.[2] Mangroves in Thailand have covered approximately 1,435,116 Rai along the southern and eastern coasts.[3]

Lichens are a unique group of fungi living in a symbiotic relationship with an alga or cyanobacterium. They are autotrophs which have an ability to grow on various kinds of substrata. The lichens are classified according to their substrates, including saxicolous, corticolous, terricolous, lignicolous, and foliicolous.

Foliicolous lichenized fungi (FLF) or foliicolous lichens grow entirely on the living leaves of vascular plants and reproduces on surfaces of the living leaves. Most of them are found in tropical areas where high humidity and low light intensity prevail[4,5] and more than 800 species have been reported worldwide.[4]

The manglicolous lichens are a specific group of lichens which occur in association with mangrove plants. These lichens can adapt to hot, humid and saline breeze environmental conditions prevailing in the mangroves. There are numerous publications on corticolous lichens in mangroves; however, very few of these were on FLF.

FLF in Thailand has been reported by many distinguished lichenologists. In 1998, Boonpragob et al.[6] listed 34 of FLF from Khao Yai National Park. Buaruang et al.[7] published a checklist of lichens in Thailand with 1,292 taxa of which about 180 are FLF. Three new to science and 20 new recorded species were added to Thai lichens by Naksuwankul and Lücking in 2019.[8] However, a few studies of FLF have been done in mangrove forests. Thus, the main purpose of our work was to investigate the diversity of FLF in mangrove forests of Chumpon province.

Methodology:

FLF samples in mangrove forests of Chumphon province were collected from four collection sites; (1) Bang Nam Chud Subdistrict, Lang Suan District (10° 3.468'N 99° 7.601'E) (BN), (2) Haad Sai Ri Subdistrict, Mueang District (10° 21.564'N 99° 13.953'E) (HS), (3) Bang Son Subdistrict, Pathio District (10° 41.494'N 99° 19.870'E) (BS) and (4) Chum Kho Subdistrict Pathio District (10° 41.619'N 99° 19.900'E) (CK) (Figure 1 A-B). All the specimens were air-dried at room temperature for a week before identification. The external morphological characters of thallus and ascomata were examined with an Olympus SZ30 stereomicroscope and images were made by microscope Eye-Piece Camera (Dino-Eye). The anatomical features were investigated by the hand-cut section of thalli and ascoma by razor blade. The iodine reaction of the hymenium and ascospores were studied in Lugol's iodine solution. All sections were mounted in water and observed under light microscope (Olympus CH). Lichen chemistry of thalli and ascomata was characterized by spot tests. The specimens were identified by comparing to own description and using the keys of Lücking 2008,[4] Naksuwankul and Lücking 2019,[8] Aptroot et al. 2007,[9] Ferraro and Lucking 1997,[10] Lücking et al. 2009,[11] Rashmil and Rajkumar 2015,[12] Singh and Pinokiyo 2018,[13] Swinscow and Krog 1988[14] and Santesson 1952.[15]

Results and Discussion:

The detailed morphological, anatomical and chemical characters of 274 FLF specimens from the mangrove forests in Chumphon province were identified into 17 species under 11 genera and 10 families (Table 1). The results indicated that FLF in the mangrove forest had the diversity of lichens dominated by crustose growth form with 16 species and *Dirinaria confluens* was the only foliose species found in this study (Figures 2-4). The highest species diversity was found in BN with 15 species followed by BS, CK and HS with 10, 5 and 4 species, respectively.

Members of the families Arthoniaceae, Porinaceae and Strigulaceae were the most common inhabitants of the mangrove forests (Table 1). The family Pilocarpaceae showed the maximum species diversity with 4 species. It was followed by Arthoniaceae, Graphidaceae, Porinaceae and Strigulaceae with 2 species each. Almost all of the species found in this study were also reported from the mangrove forests of Sandarbans Biosphere Reserve, India.[16]

The highest number of collections with 72 observed specimens belonged to *Strigula smaragdula*. This species was also reported as a common species from India and as worldwide species.[13] Similarly, in the family Porinaceae, two species of, *Porina kamerunensis* and *S. antillarum* showed high numbers of collections. In contrast, *Bacidina pallidocarnea, C. dilucidum* and *Graphis pinicola* were rarely observed (Table 1).

Observations on substrate preferences of FLF revealed that 13 species were found on various mangrove tree leaves, whereas four species including *B. pallidocarnea*, *Mazosia phyllosema*, *G. pinicola* and *Coenogonium dilucidum* were only found on the leaves of *Heritiera littoralis* Ait. *Porina kamerunensis* was the most generalist lichen which was collected from 4 species of plant. The leaves of *Heritiera littoralis* Ait., were the most preferred substrata which supported 15 species (Figure 1C), followed by *Acrostichum aureum* L. (13 spp.), *Xylocarpus granatum* (2 spp.), *X. moluccensis* (4 spp.), *Bruguiera parviflora* Roxb., (1 sp.) *Hibiscus tiliaceus* L. (1 sp.) and unknown (1 sp.) (Table 2). Interestingly, in Thailand, *D. confluens*, *G. furcata*, *G. pinicola* and *B. subdiscordans* were reported earlier as corticolous forms which were now recorded as foliicolous forms.

Key to FLF in mangrove forests from Chumphon province

1a. Thallus folios, gray to greenish gray, medulla K+ Yellow ..... ***Dirinaria confluens***
1b. Thallus crustose 2
2a. Ascomata perithecia; photobiont trentepohlioid (*Trentepohlia* or *Phycopeltis*) 3
2b. Ascomata apothecia; photobiont Chlorococcoid (*Trebouxia*) or Trentepohlioid (*Trentepohlia, Phycopeltis,* or *Cephaleuros*) 6
3a. Ascospores 1-septate; perithecia, immersed-erumpent to adnate, lens-shaped to wart-shaped or conical; pycnidia immersed lacking beak 4
3b. Ascospores 3–5-septate; perithecia immerse, subglobose, yollwish to black 5
4a. Perithecia are comparatively rare; pycnidia aggregate and confluent in center of thallus patches, semi-immersed, wart-shaped ..... ***Strigula antillarum***
4b. Perithecia are common, covered by thallus tissue, dark green, 0.3–0.5 mm; ascospores usually biseriate; pycnidia semi-immersed, wart-shaped ..... ***Strigula smaragdula***
5a. Ascospores 3-septate; perithecia 0.15–0.25 mm, lens-shaped to hemispherical or applanately conical, slightly prominent, base often spreading ..... ***Porina kamerunensis***
5b. Ascospores 5-septate; perithecia 0.15–0.3 mm, subglobose black but usually with short, white hairs or papillae around ostiole ..... ***Porina nitidula***
6a. Apothecia rounded to irregular-angular in outline, lobate or lirellate 7
6b. Apothecia rounded or slightly irregular disc-like 10
7a. Apothecial margin dark brown to black, carbonized; ascospore lens-shaped, I+ violet; paraphyses unbranched 8
7b. Apothecial margin pale or brown; ascospores macrocephalic, 2-septate 9
8a. Lirellae erumpent, short to elongate, labia non-pruinose or rarely thinly white-pruinose, lirellae thin 0.1–0.2 mm; ascospores up to 45 µm long ..... ***Graphis furcata***
8b. Lirellae prominent to sessile, short to very short, with lateral thalline margin, elongate and irregularly branched; ascospores small 9–11 µm broad ..... ***Graphis pinicola***
9a. Mature ascospores colourless, 9.5–12 × 4–5 µm, apothecia light to dark brown or with a bluish tinge, non-pruinose, K- ..... ***Arthonia lividula***
9b. Mature ascospores greyish brown, 10–20 × 4–6 µm; apothecia dark brown to black, K or K+ greenish, non-pruinose ..... ***Arthonia trilocularis***
10a. Apothecia immersed-erumpent 11
10b. Apothecia adnate to sessile 12
11a. Photobiont *Phycopeltis*; apothecial disc dark grey to black, immersed-erumpent; ascospores slightly thick-walled, with median cell slightly enlarged ..... ***Mazosia phyllosema***
11b. Photobiont *Trebouxia*; apothecia pale brownish; thallus ecorticate or cortex cartilaginous; with sterile black setae ..... ***Tricharia demoulinii***
12a. Photobiont *Trentepohlia*; apothecia wax-colored to pale yellow, with flat to slightly concave disc; asci entirely thin-walled, unitunicate, I- or I+ bluish-brownish; ascospores 6–12 × 2.5–3.5 µm ..... ***Coenogonium dilucidum***
12b. Photobiont chlorococcoid (*Trebouxia*) 13
13a. Ascospores transversely septate 14
13b. Ascospores muriform 15
14a. Ascospores fusiform-ellipsoid to narrowly bacillar or filiform and then typically tapering towards proximal end, (3)–7-septate, 40–60 µm long ..... ***Bacidina pallidocarnea***
14b. Ascospores cylindrical to filiform-acicular, 1–3-septate, 8–15 µm long ..... ***Byssoloma subdiscordans***
15a. Apothecial disc (at least in young apothecia) greyish black to black; hypothecium aeruginous ..... ***Calopadia subcoerulescens***
15b. Apothecial disc light to dark brown; hypothecium light to dark brown 17
16a. Apothecial disc light brown to reddish brown; hypothecium light brown ..... ***Calopadia fusca***
16b. Apothecial disc greyish brown to dark brown; hypothecium dark brown ..... ***Calopadia puiggarii***

Figure 1. A. Map of four collection sites in Chumphon province; (1) Bang Nam Chud Subdistrict, (2) Haad Sai Ri Subdistrict, (3) Bang Son Subdistrict, (4) Chum Kho Subdistrict. B. Mangrove forest at Chumphon province and C. Leaves of *Heritiera littoralis* Ait.

Table 1. The families, species and number of specimens of four studied areas

Family	Lichen species	Number of specimens				Total
		HS	BN	BS	CK	
Arthoniaceae	*Arthonia lividula*	4	12			16
	Arthonia trilocularis		8		4	12
Caliciaceae	*Dirinaria confluens*		12		2	14
Coenogoniaceae	*Coenogonium dilucidum*		2			2
Gomphillaceae	*Tricharia demoulinii*		7			7
Graphidaceae	*Graphis furcata*		4	1		5
	Graphis pinicola		1			1
Pilocarpaceae	*Byssoloma subdiscordans*		15	5	2	22
	Calopadia fusca		6	6		12
	Calopadia puiggarii		8	12	1	21
	Calopadia subcoerulescens			4		4
Porinaceae	*Porina kamerunensis*	25	5			30
	Porina nitidula		11	10		21
Ramalinaceae	*Bacidina pallidocarnea*			2		2
Roccellaceae	*Mazosia phyllosema*		1	2	1	4
Strigulaceae	*Strigula antillarum*	3	26			29
	Strigula smaragdula	58	1	13		72
Total specimens		90	119	55	10	**274**

Note: (HS) = Haad Sai Ri Subdistrict, (BN) = Bang Nam Chud Subdistrict, (BS) = Bang Son Subdistrict and (CK) = Chum Kho Subdistrict

Table 2. List of foliicolous lichens and their hosts

Lichen species	Number of specimens							Total
	Aa	Bp	Hl	Ht	Xg	Xm	U	
Arthonia lividula	7		5			4		16
Arthonia trilocularis	2		10					12
Bacidina pallidocarnea			2					2
Byssoloma subdiscordans	8		14					22
Calopadia fusca	4		8					12
Calopadia puiggarii	3		18					21
Calopadia subcoerulescens	1		3					4
Coenogonium dilucidum			2					2
Dirinaria confluens	6		8					14
Graphis furcata	4		1					5
Graphis pinicola			1					1
Mazosia phyllosema			4					4
Porina kamerunensis	4	19	1			6		30
Porina nitidula	8		12				1	21
Strigula antillarum	1			7	16	5		29
Strigula smaragdula	1				9	62		72
Tricharia demoulinii	4		3					7
Total specimens	**50**	**19**	**95**	**7**	**25**	**77**	**1**	**274**

Note: Aa = *Acrostichum aureum*, Bp = *Bruguiera parviflora*, Hl = *Heritiera littoralis*, Ht = *Hibiscus tiliaceus*, Xg = *Xylocarpus granatum*, Xm = *Xylocarpus moluccensis* and U = Unknown

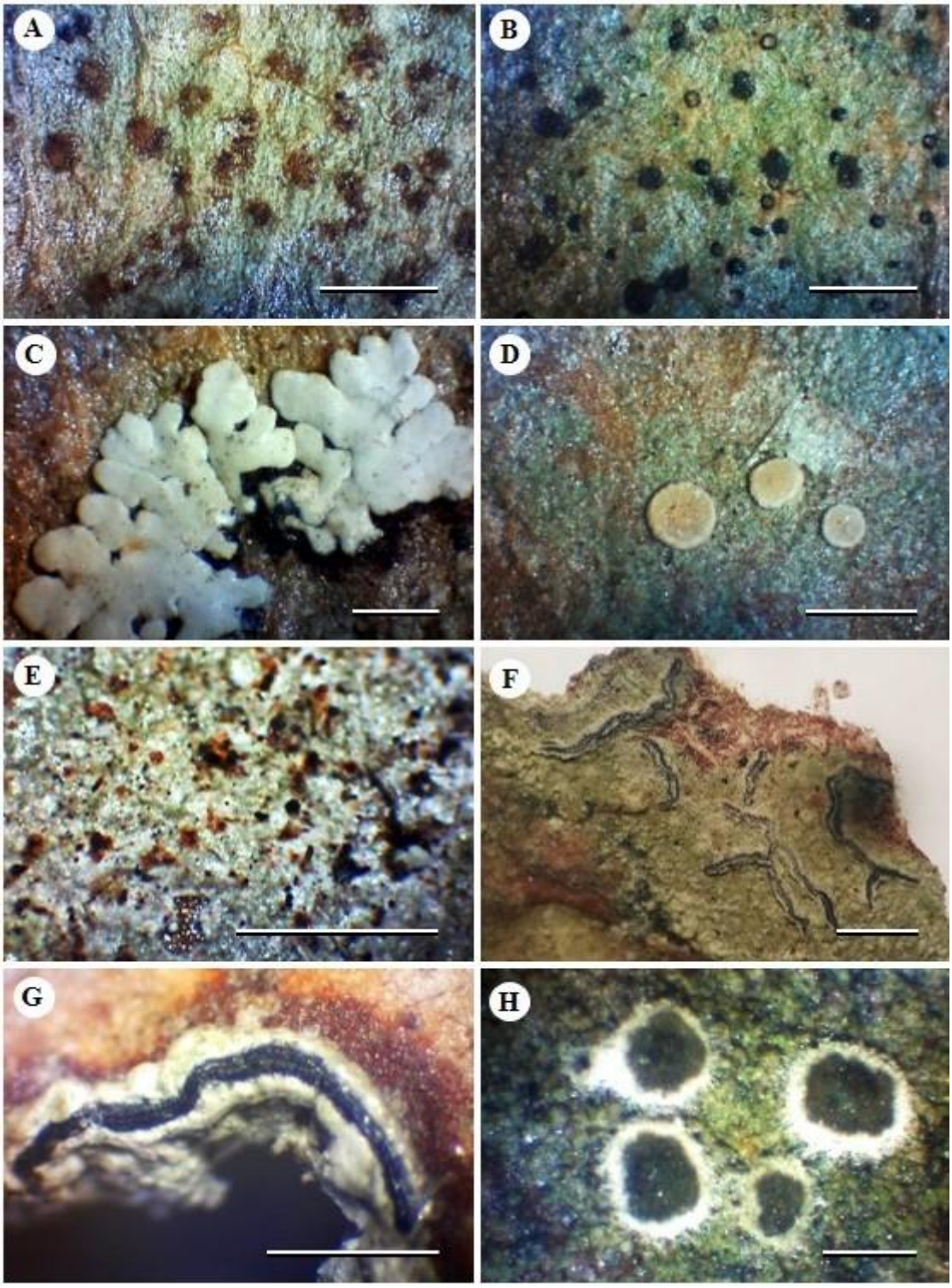

Figure 2.

Thallus with ascomata of FLF. A. *Arthonia lividula*, B. *Arthonia trilocularis*, C. *Dirinaria confluens*, D. *Coenogonium dilucidum*, E. *Tricharia demoulinii*, F. *Graphis furcate*, G. *Graphis pinicola* and H. *Byssoloma subdiscordans*. Scale = 0.5 mm.

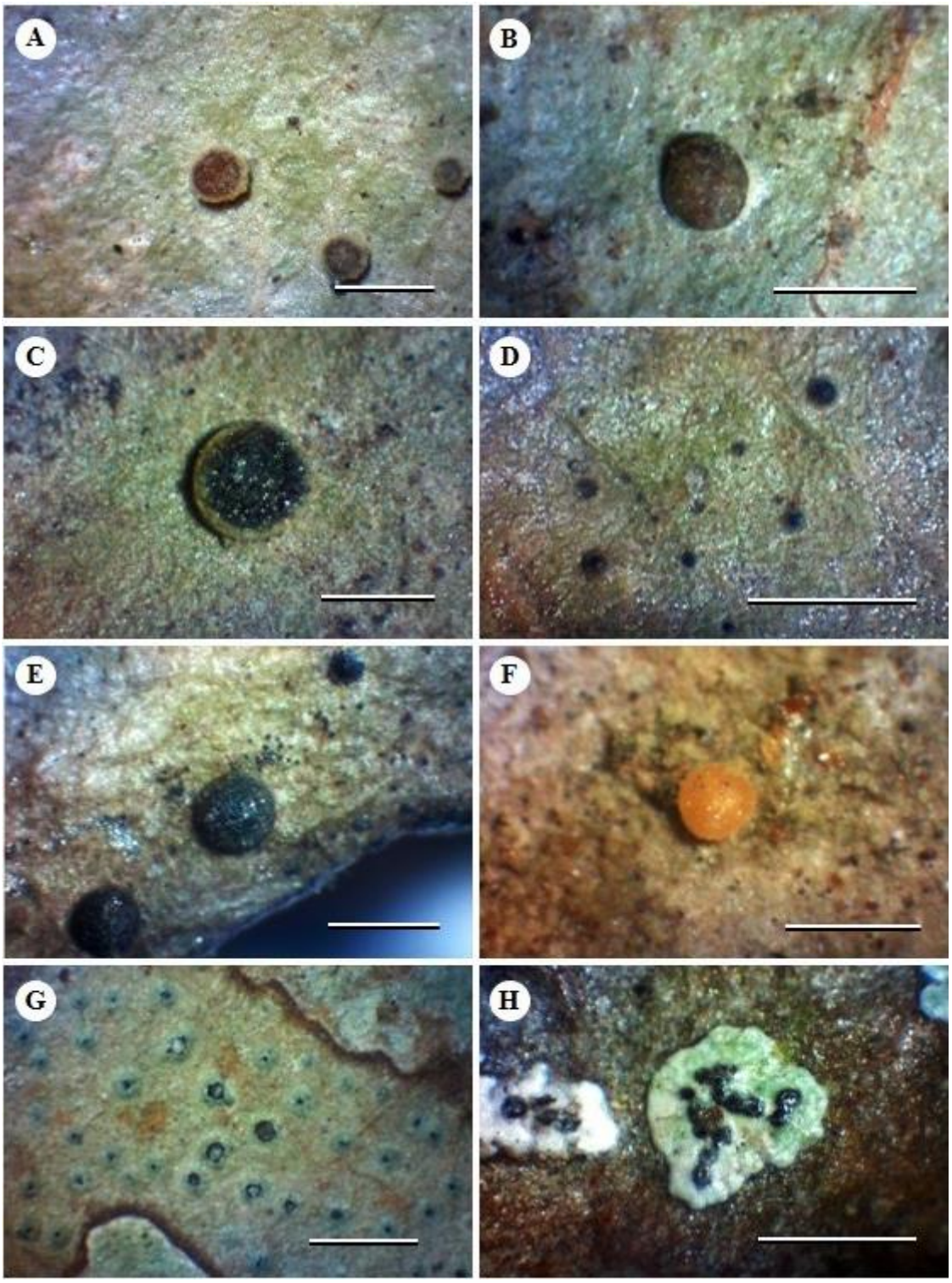

Figure 3.

A-G = Thallus with ascomata of FLF. A = *Calopadia fusca*, B = *Calopadia puiggarii*, C = *Calopadia subcoerulescens*, D = *Porina kamerunensis*, E = *Porina nitidula*, F = *Bacidina pallidocarnea*, G = *Mazosia phyllosema* and H = Thallus and pycnidia of *Strigula antillarum*. Scale = 0.5 mm.

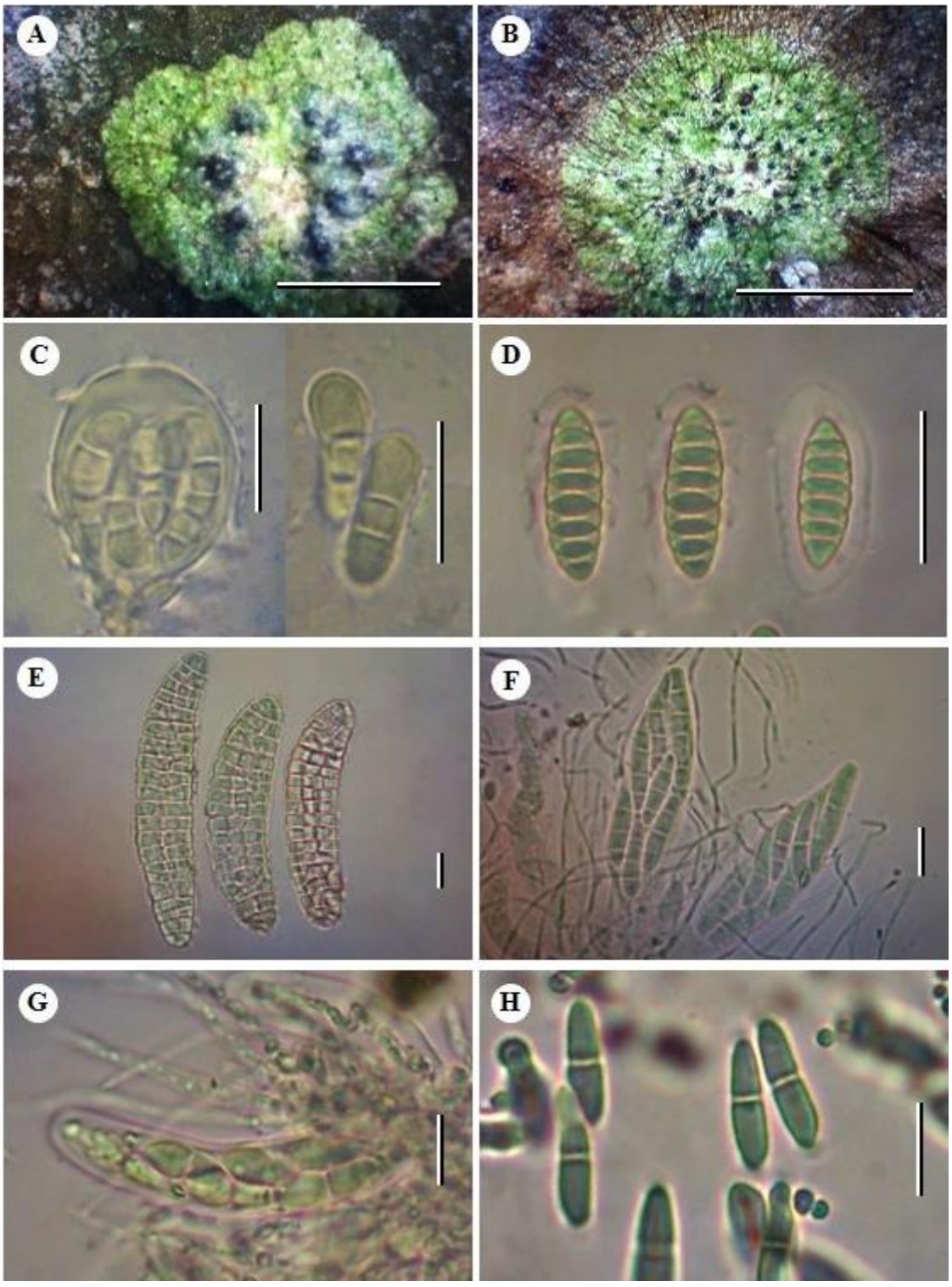

Figure 4.

A-B = *Strigula smaragdula,* A = Thallus with ascomata, B = Thallus with pycnidia. C-H = Ascospores and conidia of FLF. C = Asci and ascospores (*Arthonia lividula*), D = Ascospores (*Graphis pinicola*), E = Ascospores (*Calopadia subcoerulescens*), F = Asci and ascospores (*Porina kamerunensis*), G = Asci and ascospores (*Strigula smaragdula*) and H = Macroconidia (*Strigula antillarum*). Scale for A-B = 0.5 mm; for C-H = 10 µm.

Conclusion:

The present study was the first-time report on the diversity, distribution and associated host mangrove species of FLF at the mangrove forests of Chumpon province. All 274 samples were classified into 10 families, 11 genera and 17 species. Pilocarpaceae showed the highest diversity with 4 species. *Xylocarpus granatum* was the most preferable mangrove species which housed 15 lichen species.

References:

1. Kathiresan K.The Botanica. 2003;53:61–75.
2. Giri C, Ochieng E, Tieszen LL, Zhu Z, Singh A, Loveland T, Masek J, Duke N. Glob. Ecol. Biogeogr. 2011;20(1):154–159.
3. Pumijumnong N, Mangrove Ecosystems of Asia. In: Fraidah-Hanum I, Latiff A, Hakeem K.R, Ozturk M. (Ed). Status, Challenges and Management Strategies. 2014;61–79.
4. Lücking R. Flora Neotropica Minograph. 2008;103:1–866.
5. Papong K, Boonpragob K, Lücking R. Lichenologist, 2007;39:47–56.
6. Boonpragob K, Homchantara N, Coppins BJ, McCarthy PM, Wolseley PA. Botanical Journal of Scotland. 1998;50:209–219.
7. Buaruang K, Boonpragob K, Mongkolsuk P, Sangvichien E, Vongshewarat K, Polyiam W, Rangsiruji A, Saipunkaew W, Naksuwankul K, Kalb J, Parnmen S, Kraichak E, Phraphuchamnong P, Meesim S, Luangsuphabool T, Nirongbut P, Poengsungnoen V, Duangphui N, Sodamuk M, Phokaeo S, Molsil M, Aptroot A, Kalb K, Lücking R, Lumbsch HT. Myco Keys. 2017;23:1–91.
8. Naksuwankul K, Lücking R. Phytotaxa. 2019;400(2):051–063.
9. Aptroot A, Saipunkaew W, Sipman HJM, Sparrius LB, Wolseley PA. Fungal Diversity. 2007;24:75–134.
10. Ferraro LI, Lucking R. Phyton. 1997;37(1):61–70.
11. Lücking R, Archer AW, Aptroot A. The Lichenologist 41. 2009;(4):363–452.
12. Rashmil S, Rajkumar HG. Int.J.Curr.Microbiol.App.Sci. 2015;4(6):250–256.
13. Singh KP, Pinokiyo A. Indian journal of forestry additional. 2018;4:1–335.
14. Swinscow TDV, Krog H. Macrolichens of East Africa. 1988;78–82.
15. Santesson R. Symbolae Botanicae Upsalienses. 1952;12(1):1–590.
16. Jagadeesh Ram TAM, Sinha GP. Geophytolgy. 2002;32(1–2):35–38.

SP11_012_PA: A PRELIMINARY SURVEY ON THE OCCRRENCE OF TWO EPIPHYTIC MACROLICHENS IN A POST-FIRE FOREST OF KHAO YAI NATIONAL PARK

Wetchasart Polyiam,* Pitakchai Faungkaew, Mongkol Phaengphech

Department of Biology, Faculty of Science, Ramkhamhaeng University, Bangkok, Thailand
*e-mail: wetchasart1p@gmail.com

Abstract:

Lichens are among the potential organisms that can identify the intensity of forest fire in a deciduous forest. This work is focused on the occurrence of epiphytic macrolichens in a post-fire forest at the dry dipterocarp forest in Khao Yai National Park. Two lichen species, including *Pyxine coccifera* and *Parmotrema tinctorum* were selected for this study. The phorophytes consisted of 40 individuals (16 species), selected from four 50-m line transects that located in between 100 and 300 meter above sea level. The lichens were observed at tree heights of <2, 2-4 and >4 meters above ground, and at tree branches. Thallus diameter, height above ground, and life stage (present or absent of vegetative and reproductive structures) were documented. The results showed that *P. coccifera* had the higher number of thallus than *P. tinctorum*, accounted for 88 and 64, respectively. In contrast, the former species had lower probability of occupancy on different microhabitats (0.26) than the later one (0.36). Although, most of the thalli of the lichens occupied on tree branches, but only *P. coccifera* was well distributed to the lower trunks. It may indicate that *P. coccifera* had the higher ability to tolerate fired flame than *P. tinctorum*.

SP11_013_PA: SECONDARY METABOLITES PRODUCTION IN LICHEN-FORMING FUNGI OF SOME *Arthonia* SPECIES IN THAILAND

Pakarapon Poonsukkho,[1]* Theerapat Luangsuphabool,[2] Ek Sangvichien[1]

[1]Department of Biology, Faculty of Science, Ramkhamhaeng University, Bangkok 10240, Thailand
[2]Biotechnology Research and Development Office, Department of Agriculture, Rangsit, Thanyaburi, Patumthani 12110, Thailand
*e-mail: pakpoon.p@gmail.com

Abstract:

Arthonia is a genus of thin crustose lichens with high diversity in morphology, chemistry, distribution, and polyphyletic clades. In our previous study, we isolated the fungal partner or lichen-forming fungi belonged to this genus, culturing on Malt-Yeast Extract media and found that their metabolites exhibited strong anti-microbial and anti-oxidant activities. The *Arthonia* sp. (RN54) showed the highest amount of bioactivities than other *Arthonia* species. This fungal is further studied for its activities by growing on various nutrient media, including jasmine rice (JR), wheat (WR), rice germ (RG), rice-berry rice (RB), and GABA rice (GB) instead of malt extract. After culturing for 3 months, secondary metabolites from these cultures were collected, extracted, and analyzed by using HPLC. The chemical profile from each rice shared the same retention time at 39 minutes and other peaks represented different profiles from each type of rice. Interestingly, substances extracted from the culture in wheat medium profiles were different from other types of rice. One of the major compounds found in their cultures was identified as 8-O-methybotryscoidin. Other main compounds and minor secondary metabolites are under future investigation.

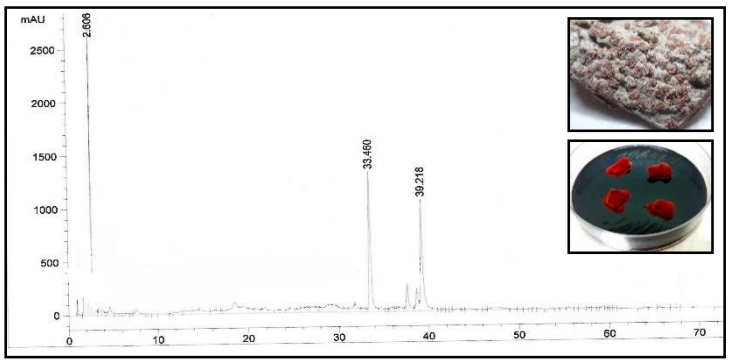

Figure 1. Chromatograms of the secondary metabolites extracted from *Arthonia* sp. (RN54) cultivated on Malt-Yeast Extract Agar.

SP11_014_PA: SOIL WATERING RETAINS THALLUS WATER CONTENT AND PROLONG ACTIVE PERIOD OF LICHEN *Parmotrema tinctorum* ON TRANSPLANTED FRAMES

Mongkol Phaengphech,* Wetchasart Polyiam, Kansri Boonpargob

Department of Biology, Faculty of Science, Ramkhamhaeng University, Bangkok, Thailand
*e-mail: mongkolpp@gmail.com

Abstract:

Lichens uptake atmospheric water to drive the photosynthesis processes. Maintaining the thallus water content (TWC) can increase the lichens growth. The objective of this study was to examine the effect of different soil watering regimes on TWC and photosynthetic efficiency of *P. tinctorum* on the transportation frame. Four treatments of water regimes included one-time watering at 7 A.M. with 10 liters (W10), 20 liters (W20), and 30 liters (W30), and constant watering of 10 liters at every 30 minutes from 7 to 10 A.M. The frames with unwatering (W_C) was the control condition. Relative Humidity (RH) inside the frames, TWC, and chlorophyll fluorescence (Fv/Fm) were measured between 5 a.m. to 8 p.m. for 3 days. Our results show that lichens entered a dry period starting at 9.30 to 10.00 a.m. The W_{70} treatment yielded the highest RH, TWC and Fv/Fm at 88.9%, 12% and 0.19 respectively, while W_{30} were subordinately. The values from the W_{10} and W_{20} did not differ from those of Wc. These results indicated that constant watering provided enough water to increase RH inside the frames and TWC, while the W_{10} and W_{20} treatment could not provide enough water. The extension of watering until the dry period may result in faster growth of transplanted lichens. However, this study needs a longer time to follow up on the experiments to observe the higher growth of transplanted lichens.

SP11_015_PA: A PRELIMINARY INVESTIGATION OF TOTAL VOLATILE ORGANIC COMPOUNDS (TVOCs) PRODUCED BY CULTURES OF LICHEN-FORMING FUNGI

Ketkaeo Poonraksa,[1]* Pakarapon Poonsukkho,[1] Theerapat Luangsuphabool,[2] Ek Sangvichien[1]

[1]Department of Biology, Faculty of Science, Ramkhamhaeng University, Bangkok 10240, Thailand
[2]Biotechnology Research and Development Office, Department of Agriculture, Rangsit, Thanyaburi, Patumthani 12110, Thailand
*e-mail: Ketkaeopoon@gmail.com

Abstract:

During incubation of 18 lichen-forming fungi cultures on solid medium, total volatile organic compounds (TVOCs) and formaldehyde were investigated using a handheld Air Quality monitor machine (Dienmern, DM106). Two *Anisomeridium* species isolates SUK13 and SUK369 and two *Arthonia* species isolates NKP49 and NKP156 produced high TVOCs above 9.999 mg/m^3. This measurement also included the formaldehyde values for each isolate *i.e*., 0.959, 0.729, 1.008, and 1.139 mg/m^3, respectively. However, the common lichen-forming fungi in the family Trypetheliceae such as *Trypethelium subeluteriae* (KY783), *Asthothelium sp.* (PNG61) and *Marcelaria cumingii* (K11) usually produced TVOCs ranging from 0.104 to 0.338 mg/m^3 which were lower than the former group. The quantity of formaldehyde produced from the latter group was also in lower range of 0.020-0.086 mg/m^3. This is the first report of TVOCs and formaldehyde produced from the cultures of the lichen-forming fungi. Analysis of these TVOCs should be further studied for their roles and applications.

SP11_016_PA: BIODIVERSITY OF LICHENS FAMILY TRYPETHELIACEAE AROUND RAMKHAMHAENG UNIVERSITY REGIONAL CAMPUS IN HONOUR OF HIS MAJESTY THE KING, KANCHANABURI SURIN AND NAKHON PHANOM PROVINCE

Kajonsak Vongshewarat* Supattara Phokaeo, Kamonrat Kuldaong, Kollawat Ouppathum, and Patthabun Nuchkong

Lichen Research Unit, Department of Biology, Faculty of Science, Ramkhamhaeng University, Bangkok, 10240
* email: kvongshewarat@hotmail.com

Abstract:

Exploring and collecting lichens family Trypetheliaceae around 44 study sites at Kanchanaburi Surin and Nakhon Phanom Regional Campuses in Honour of His Majesty the King of Ramkhamhaeng University during November 2012 to April 2015 found 260 specimens. They were classified based on morphological, anatomical as thallus, ascomata, and colorless, ellipsoidal shapes, muriform or trans-septate types of ascospores together with chemical characteristics (KOH+ red purple on thallus or around ascomata) can be classified get fifteen species, nine genera such as *Astrothelium*, *Bathelium*, *Campylothelium*, *Laurera*, *Marcelaria*, *Nigrovothelium*, *Polymeridium, Pseudopyrenula* and *Trypethelium*. *Marcelaria benguelensis* (Müll. Arg.) Aptroot, Nelsen & Parnmen and *Trypethelium eluteriae* Sprengel. ,were dominant species in three provinces. This indicated relatively high biodiversity of lichens in Ramkhamhaeng University campus.

Key words: Lichens, Family Trypetheliaceae, Ramkhamhaeng University.

SP12_001_PA

SP12_001_PA: ASSESSING MICROPLASTIC CONTAMINANTS IN SHRIMP PASTE FROM THE GULF OF THAILAND AND THE ANDAMAN SEA

Makamas Sutthacheep,[1,*] Charernmee Chamchoy,[2] Thamasak Yeemin,[2] Wanna Musig[1]

[1]Department of Biology, Faculty of Science, Ramkhamhaeng University, Huamark, Bangkok, Thailand
[2]Marine Biodiversity Research Group, Department of Biology, Faculty of Science, Ramkhamhaeng University, Huamark, Bangkok, Thailand
*e-mail: msutthacheep@yahoo.com

Abstract:

Microplastics are considered as contaminants in marine ecosystems around the world and have been a growing problem. Marine organisms such as crustaceans, fish, and mussels can either directly ingest microplastic or accumulate it from the food web. Therefore, fisheries-target species from those groups become a potential source of microplastic contamination for human consumers. This study aimed to examine the microplastic contaminants in shrimp paste in Thailand. Shrimp paste samples were purchased from five different provinces, both from the Andaman Sea and the Gulf of Thailand. The abundance of microplastics in the shrimp paste was examined by hydrogen peroxide, analyzed under a stereomicroscope, and later identified by using Fourier transform infrared spectroscopy (FTIR). The results showed that the densities of microplastics in shrimp paste varied from 6 to 11.3 particles/10 g. The microplastics were composed of fibers and fragments, ranging from 0.1 to 1.0 mm in length. Five different types of plastic polymer were found, i.e. polyethylene terephthalate, polyurethane, rayon, polystyrene, and polyvinyl alcohol. Microplastics are one of the main environmental challenges nowadays, worldwide. This study confirmed microplastic presence in shrimp paste, and urgent measures are needed to prevent recurrent contamination of food items produced for human consumption and related health problems. We propose to work in collaboration with local communities to ensure clean fishery products, reducing microplastic contamination.

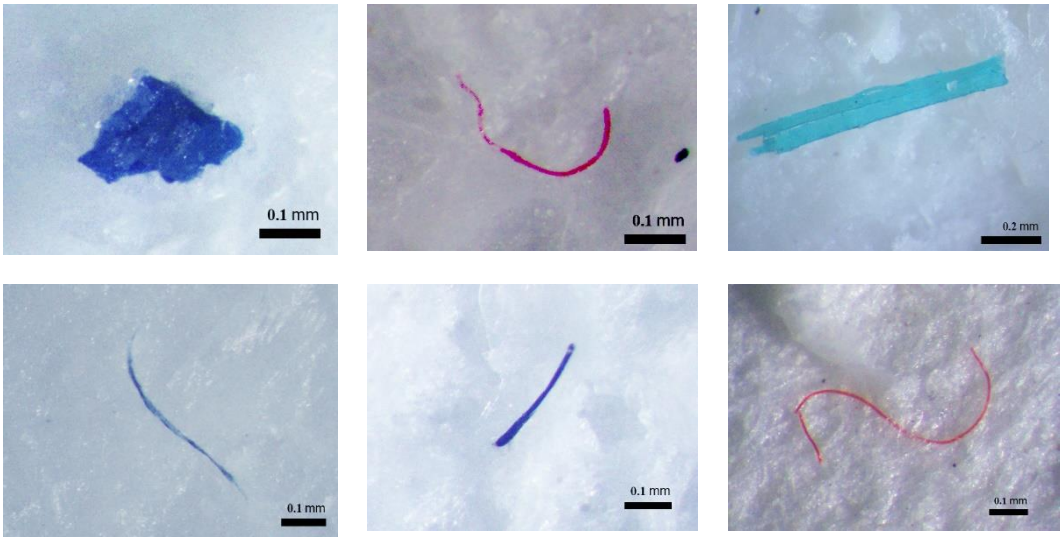

Type and size of microplastics was found in shrimp paste

SP12_002_OA: EFFECTS OF THE SOURCE SEPERATION ON THE AIRBORNE MICROPLASTICS IN THE AIR NEAR GARBAGE BURNING

Ekachai Lojanaphiwat, [1] Ekbordin Winijkul[1,*]

[1]Environmental Engineering and Management, Asian Institute of Technology, Thailand
*e-mail: ekbordinw@ait.asia

Abstract:

Microplastics have been found in different media, from soils to aquatic systems and living organism. The majority of research to date has focused on the marine environment; however, attention is increasingly being paid to other environmental compartments. The atmosphere is an important pathway by which many suspended materials are transported regionally or globally. Recent studies have illustrated that atmospheric microplastic particles can be transported to ocean surface air and even remote areas. Currently, due to their inhalation and combination with other pollutants, microplastics are thought to be an emergent component of air pollution.

In this study, the high-volume sampler is used to collect the ambient air samples near the garbage burning area. One sample is collected with the open burning of the garbage after the source separation, and another sample is collected with the open burning of the garbage without source separation. The samples are collected with the same method used for the collection of total suspended particle in the atmosphere, except for the period of 1 hour. After the samples are collected, the filters are weighted for total mass, and washed with water for density separation analysis. Then, the microplastics in the samples are identified using visual methods by Microscope. The abundance of microplastic in the samples with and without source separation before the garbage burning are compared and discussed.

SP12_003_OA: GIS-BASED APPROACH TO MAPPING OF LAND-BASED PLASTIC LEAKAGE

Tran Thanh Dan[1*], Kavinda Gunasekara[1], Thaileng Thol[1], Angsana Chaksan[1], Rajitha Athukorala[1]

[1] Geoinformatics Center, Asian Institute of Technology, Thailand
*e-mail: ttdan@ait.asia

Abstract:

Determination of plastic leakage sources and its pathways are essential in the mitigation process of plastic pollution. Finding ways to stem land sourced plastic waste leakage requires understanding of its sources. Geographic Information System (GIS) analyzes spatial location and organizes layers of information into visualizations using maps. It can provide insight on distribution of plastic leakage. Therefore, a GIS based investigation on plastic leakage concentration is essential to identify areas that require more attention for plastic leakage reduction against low plastic leakage areas. Based on advantages of latest GIS tools, here we proposed a novel approach to identify plastic leakage and its density using GIS based analysis. The main objective of this approach were: (i) to predict plastic leakage density for the lower Mekong River Basin (MRB) using multi-source geospatial data with a fuzzy overlay approach; and (ii) to identify plastic leakage sources at the community level. The overlaid result is validated using illegal dump locations collected using mobile application. The proposed approach can be applied to other regions beyond the lower MRB. The novelty of this study is in the application of GIS to produce a graphical model for plastic leakage waste density in a given region that can be easily visualized by non-technical personnel. The outcome of this approach will be a great asset for plastic leakage mitigation programs.

SP12_004_OA: PRELIMINARY STUDY ON TRANSPORTATION AND DISTRIBUTION OF MARINE DEBRIS IN THE GULF OF THAILAND IN 2018 USING HYDRODYNAMIC AND WATER QUALITY SIMULATION MODEL

Kittipong Phattananuruch[1*], Tanuspong Pokavanich[2]

[1]Faculty of Fisheries, Kasetsart University, Bangkok, Thailand
[2]Department of Marine Science, Faculty of Fisheries, Kasetsart University, Bangkok, Thailand
*e-mail: phat.kittipong@gmail.com

Abstract:
Marine debris is one of the most important marine pollutions in the Gulf of Thailand (GOT) that affect the marine ecosystem. Knowledge about spatial and temporal distribution of marine debris is essential for marine pollutions management. This study applied Delft3D-FLOW program, and Delft3D-Water Quality program to simulate transportation and distribution of neutral buoyant substance (represent the debris) in the GOT in 2018. A hydrodynamic model used input data from several reliable databases, e.g., ETOPO1 Global Relief Model, TPXO Global Tidal Models, JAMSTEC-MOAA GPV dataset, ERA5 reanalysis of the global climate, and Global flood awareness system. Simulated water level and temperature results agree well with actual measured data. Transport and mixing conditions resulted from the model were used the transportation of debris model. Results showed that the GOT's circulation was swift in clockwise (anticlockwise) direction during the southwest monsoon (northeast season). The circulation was weak during the inter-monsoon period. Simulated results also revealed pronounce interconnections between the circulation and the debris aggregation in each month. The inner-most part of the gulf and coastal areas have higher aggregation of the debris when compared to the open sea area.

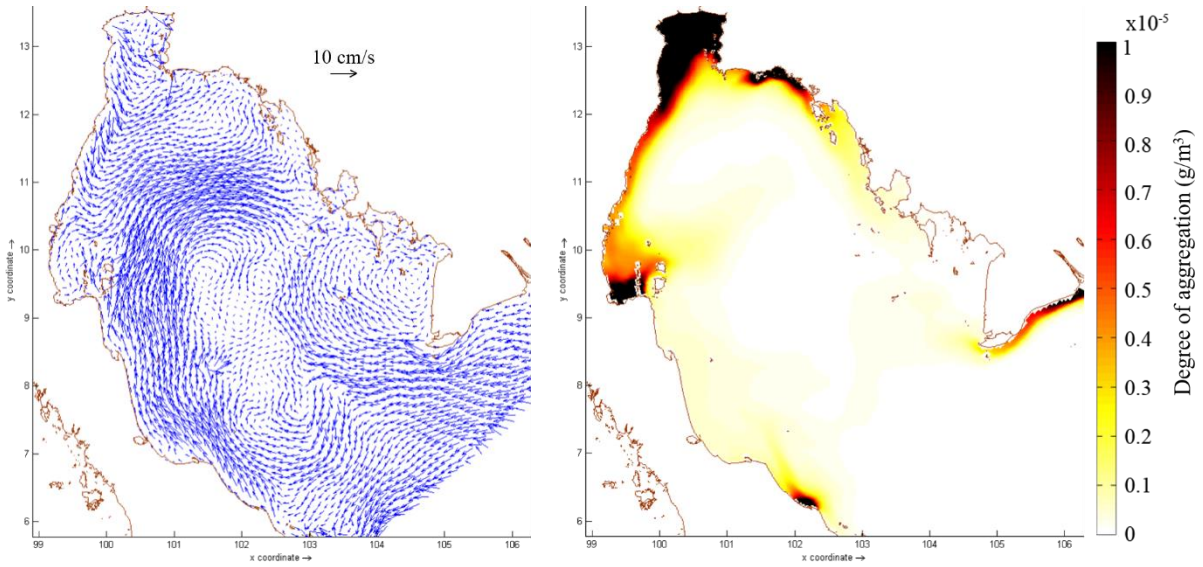

Figure 1.
Comparison between near-surface one-year-averaged flow velocity and marine debris aggregation in 2018.

SP13_001_PF: EFFECT OF Ficus Dubia EXTRACT ON ADIPOGENESIS

Tanpitcha Yodweerapong,[1,3] Pensiri Buacheen,[2,3,] Natchapon Kammasit,[1,3] Jirarat Karichai,[3] Arisa Imsumran,[3] Ariyaphong Wongnoppavich,[3] Bhanumas Chantarasuwan,[4] Piya Temviriyanukul,[5] and Pornsiri Pitchakarn[3,*]

[1]Graduate/MSc Degree Program in Biochemistry, Faculty of Medicine,
Chiang Mai University, Chiang Mai, Thailand
[2]Graduate/Ph.D. Degree Program in Biochemistry, Faculty of Medicine,
Chiang Mai University, Chiang Mai, Thailand
[3]Department of Biochemistry, Faculty of Medicine, Chiang Mai University, Chiang Mai, Thailand
[4]Thailand Natural History Museum, National Science Museum, Pathum Thani, Thailand
[5]Food and Nutritional Toxicology Unit, Institute of Nutrition, Mahidol University, Nakhon Pathom, Thailand
*e-mail: pornsiri.p@cmu.ac.th

Abstract:

The metabolic complications of obesity, an over- expansion of adipose tissue and lipoatrophy/lipodystrophy are quite similar. Both can increase the risk of several chronic disorders, such as type 2 diabetes (T2D), liver disease, and cardiovascular disease (CVD). Recruitment of new adipocyte and expansion capacity of the cells is limited. Adipose cell over-expansion leads to hypertrophy of the cells which can induce insulin resistance, and adipose tissue dysfunction via the induction of cellular stress that promotes chronic inflammation surrounding the tissue. Several data showed *Ficus* spp. exhibited anti-inflammatory and anti-diabetic properties. This study focused on *Ficus dubia* or Sai-Lueat (Thai common name) which is most abundant in Thailand. We hypothesized that *Ficus dubia* latex (FDLE) and *Ficus dubia* root (FDRE) extracts could modulate adipogenesis in 3T3-L1 adipocytes. First, non-toxic concentration of FDLE and FDRE on 3T3-L1 adipocytes was investigated by sulforhodamine B assay. It was found that FDLE and FDRE at up to 200 μg/ml were non-toxic to mature adipocytes (48 hours) and the cells during de novo adipocyte formation (12 days). Next, FDLE and FDRE treatments in the cells during adipogenesis was measured by Oil Red O staining. FDLE and FDRE at 200 μg/ml significantly promote lipid accumulation suggesting the induction of adipogenesis. Taken together, the results from this study showed the ability of FDLE and FDRE to enhance adipogenesis which may lead to either the induction or the prevention of insulin resistance and type 2 diabetes. Anti-insulin resistance activity of the extracts in adipocytes must be further determined to confirm that these extracts can improve impairment of adipogenesis.

Introduction:

Adipogenesis is the cell differentiation process that is associated with the development of obesity by which pre-adipocytes become mature adipocytes (1). During this, the endocrine will regulate cell development and function in several stages. First stage, mesenchymal precursor cells are proliferated and committed to differentiation along adipocyte lineage. Second, growth-arrested stage, cells will lack of proliferation. Third, mitotic clonal expansion stage, preadipocytes will re-entry into the cell cycle and have several rounds of mitotic divisions. The expression of CCAAT/enhancer-binding proteins β (C/EBPβ) and δ (C/EBPδ) is dramatically induced in this stage. Forth, early differentiation stage, pre-adipocytes become immature adipocytes which C/EBPα, peroxisome proliferation-activated receptor γ (PPARγ) and transcriptional activation of adipocyte genes are stimulated. The level of these genes will be downregulated, but stably express in the terminal differentiation stage which adipocytes become mature adipocytes (2, 3). Large lipid droplet is clearly observed in the cytosol of the mature cells. Unfortunately, the expansion of adipose tissue by recruiting and differentiating available

precursor cells has limited. Lacking of this can lead to a hypertrophic expansion of the adipocytes which related to inflammation and dysfunction of the cells (4). The large expansion of adipocyte outstrips the local oxygen supply leading to cell autonomous hypoxia and activate cellular stress pathways leading to the releasing of pro-inflammatory cytokines such as MCP-1, TNF-α, IL-1β, and IL-6 (5, 6). The locally secreted cytokines attract pro-inflammatory macrophages into adipose tissue that further activate the inflammatory program and cell dysfunction in neighboring adipocytes (7). Dysfunctional lipid metabolism in adipose tissue causes high blood level of free fatty acids (FFAs) and leptin, whereas adiponectin expression is decreased (6). Furthermore, these cytokines induce insulin resistance of adipocyte by the stimulating of serine phosphorylation of insulin receptor substrate-1 and 2. These inhibit insulin receptor autophosphorylation activity leading to decreasing of GLUT4 translocation on adipocyte membrane and blood glucose clearance ability (8, 9).

Natural compounds become famous and are widely used as a health consumption or an alternative medicine. Previous studies reported various biological activities of many plant species in *Ficus* genus. For example, *Ficus carica* exerts anti-inflammation activity on carrageenan induced oedema in wistar rat paw (10). While, anti-diabetes activity of other *Ficus* species such as *F. lutea* (11), *F. deltoidei* (12), *F. sycomorus* (10), *F. racemose* (13, 14) and *F. benghalensis* (15) has been reported. This study focused on *Ficus dubia* or Sai-Lueat (Thai common name) which is most abundant in Thailand. We aimed to investigate the activity of *Ficus dubia* latex (FDLE) and root (FDRE) extracts on adipogenesis in 3T3-L1 adipocytes.

Methodology:

Plant extraction

Latex and root of *Ficus dubia* were collected from Narathiwat, Thailand. Its voucher specimen was prepared and deposited at Thailand Natural History Museum (THNHM), National Science Museum, under a code of Chantarasuwan 040117-1. The powder of *Ficus dubia* root was extracted with 80% ethanol overnight at the ratio of 1:10 w/v. The ethanolic extract was collected, and then concentrated by rotary evaporator. The concentrated extract was freeze-dried by lyophilizer. The powder of *Ficus dubia* latex was extracted with deionized water at the ratio of 1:10 w/v. The solution was filtrated and freeze-dried by lyophilizer. The ethanol extraction of *Ficus dubia* root provided yield at 5%, while the water extraction of latex provided yield at 47%.

Cell culture

3T3-L1 preadipocytes (fibroblast form *Mus musculus* embryo purchased from ATCC, USA) were maintained in DMEM consisted of high glucose, 10% calf bovine serum and 1% penicillin-streptomycin in 37 ˚C, 5% CO_2 incubator. Cell differentiation was followed and adapted as the previous report. Preadipocytes were initiated after confluence, the cells were incubated with induction medium (DMEM supplemented with 3-isobutyl-1-methylxanthine (IBMX), Dexamethasone, insulin, antibiotic and FBS) for 3 days (Day 0-3). Then, the cells were cultured in differentiation medium (DMEM supplemented with insulin, antibiotic and FBS) for another 3 days (Day3-6). Next, the cells were cultured with maturation medium (DMEM supplemented with insulin, antibiotic and FBS) until become mature adipocytes (Day6-12).

Cytotoxicity test

Cytotoxicity of FDLE and FDRE was examined in 3T3-L1 adipocytes by SRB assay. The cells (3,000 cells/well) were plated into 96-well cell culture plates and incubated for 2 days. Next, various concentrations of FDLE or FDRE (0-200 μg/ml) were treated for 12 days during differentiation or 48 hours after maturation. After that, the cells were stained with 0.057% SRB solution and incubated for 30 minutes. Finally, 10 mM tris-base was added, and the absorbance was measured at 510 nm for calculating cell viability.

Oil red O staining

For lipid accumulation or triglycerol level measurement, the cells were treated with the extracts either for 3 days (with the induction medium) or for 12 days (with induction, differentiation, and maturation medium). After the treatment, the mature adipocytes were fixed in 4% formaldehyde-phosphate buffer (pH 7.4) for 1 h and rinsed with water. Then, the cells were stained with 0.3% Oil Red O dye for 1 h and the excess dye was removed by

washing the cells with DI water. The red oil droplets stained in the cells were dissolved by 100% 2-propanol 100 µl. The absorbance of solution was measured at 540 nm for determining lipid accumulation.

Statistical analysis

All values were given as mean ± standard derivation (X ± SD) from triplicate samples of three independent experiments. Overall differences among the treatment groups were determined using one-way analysis of variance (ANOVA) by Prism 5.0 software. $p < 0.05$ is regarded as significance.

Results and Discussion:

Cytotoxicity of FDLE and FDRE on 3T3-L1 adipocytes

Toxicity of the extracts was tested in 3T3-L1 adipocytes by SRB assay. The result showed that the highest concentration of the extracts at 200 µg/ml did not show any significant cytotoxicity to the cell in both treatment models (**Figure 1**). Non-toxic dose of FDLE and FDRE was then applied for further experiments.

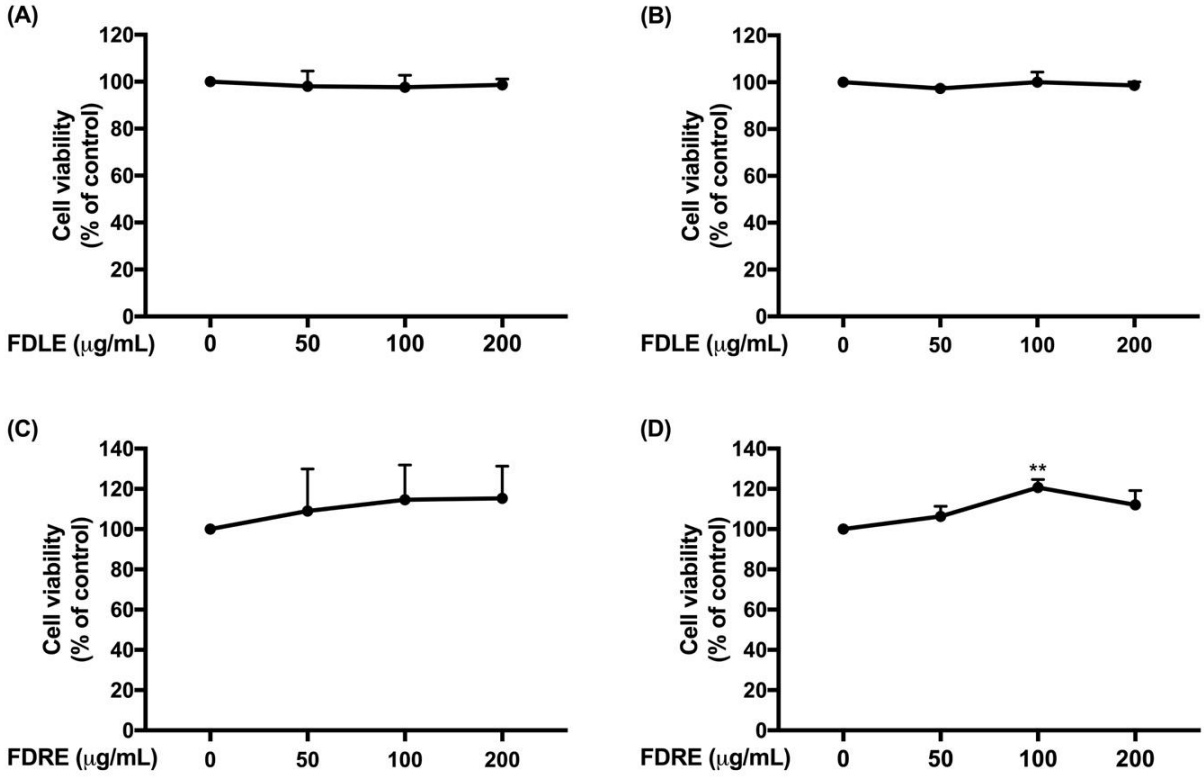

Figure 1 Cytotoxicity of FDLE and FDRE on 3T3-L1 adipocytes**.** 3T3-L1 adipocytes were treated with various concentrations of FDLE **(**A and B**)** and FDRE **(**C and D**) (**0-200 µg**/**ml**)** for 12 days **(**during differentiation**) (**A and C**)** or 48 hours **(**after maturation**) (**B and D**).** Cell viability of FDLE- and FDRE-treated cells was assessed by SRB assay**.** ** *p<0.01* vs control

Effect of FDLE and FDRE on adipogenesis in 3T3-L1 cells

The effect of the extracts on the differentiation of 3T3-L1 adipocytes was determined by measurement of lipid accumulation. Treatment the cells during induction step (Day0-3), a committing step of adipogenesis[2,16], with FDLE (50, 100, 200 µg/ml) significantly increased intracellular lipid accumulation in a dose-dependent manner (**Figure 2A and 2B**), whereas this effect has been seen in the cells treated with FDRE only at 200 µg/ml (**Figure 2C and 2D**). Treatment the cells with the extracts during differentiation for 12 days markedly stimulated lipid accumulation when compared to the 3-Day treatment. The results are demonstrated that FDLE and FDRE promoted adipogenesis at both committing step and others of adipogenesis. The ability of FDLE and FDRE to enhance adipogenesis could lead to either the induction or the prevention of insulin resistance. Anti-insulin resistance activity of the extracts in adipocyte must be further determined to confirm that these extracts can improve impairment of adipogenesis**.**[4]

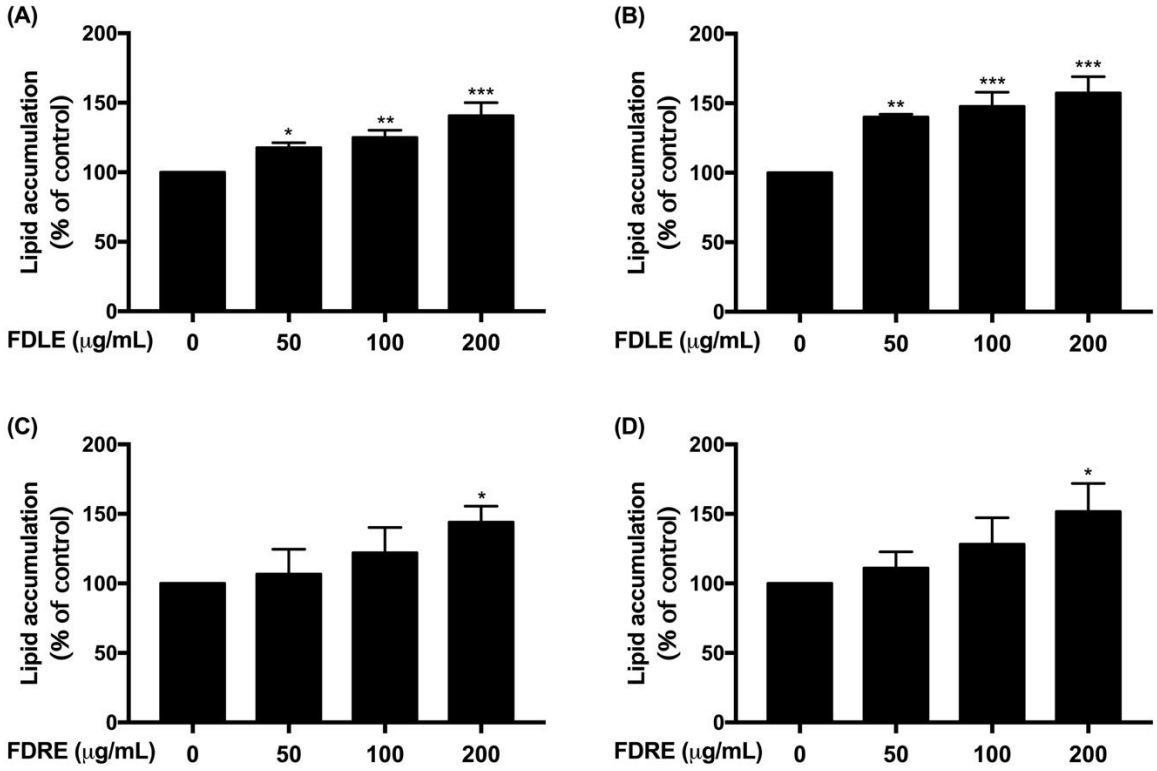

Figure 2 Effect of FDLE and FDRE on adipogenesis. 3T3-L1 adipocytes were treated with various concentrations of FDLE and FDRE (0-200 µg/ml) for 3 days with induction media (During induction, day 0-3) or 12 days (During differentiation, day 0-12). After the treatment, lipid accumulation of FDLE (A and B) and FDRE (C and D) during induction (A and C) or during differentiation (B and D) in treated cells was examined by Oil Red O staining. * *p<0.05*, ** *p<0.01* and *** *p<0.001* vs control.

Conclusion:

In conclusion, we have demonstrated that FDLE and FDRE showed adipogenicity activities by increasing lipid accumulation suggesting their adipogenesis induction ability. We hypothesized that this effect may prevent the over-expansion, inflammation, dysfunction, and insulin resistance of adipocytes. Thus, anti-insulin resistance activity of the extracts in adipocytes must be further examined to confirm that these extracts can improve the impairment of adipogenesis. Finally, the knowledge from this study will provide scientific data for use and development of this plant for health consumption.

Acknowledgements:

This work is supported by the Faculty of Medicine Research Fund (Grant No. 16-2560), Faculty of Medicine, Chiang Mai University, Chiang Mai, Thailand and Agricultural Research Development Agency (Public Organization) (Grant No. CRP6105022130), Thailand.

References:

1. Spiegelman BM, Flier JS. Cell. 1996;87: 377-89.
2. Lefterova MI, Lazar MA. Trends Endocrinol Metab. 2009;20(3):107-14.
3. Sarjeant K, Stephens JM. Cold Spring Harb Perspect Biol. 2012;4(9):a008417.
4. Hammarstedt A, Gogg S, Hedjazifar S, Nerstedt A, Smith U. Physiological Reviews. 2018;98(4):1911-41.
5. Luca DC, Olefsky JM. FEBS Lett. 2008;582(1):97-105.
6. McArdle MA, Finucane OM, Connaughton RM, McMorrow AM, Roche HM. Front Endocrinol (Lausanne). 2013;4:52.
7. Chen L, Chen R, Wang H, Liang F. Int J Endocrinol. 2015;2015:508409.
8. Hajer GR, van Haeften TW, Visseren FL. Eur Heart J. 2008;29(24):2959-71.
9. Wilcox G. Clin Biochem Rev. 2005;26:19-39.
10. Lansky EP, Paavilainen HM, Pawlus AD, Newman RA. J Ethnopharmacol. 2008;119(2):195-213.
11. Olaokun OO, McGaw LJ, Janse van Rensburg I, Eloff JN, Naidoo V. BMC Complement Altern Med. 2016;16:110.
12. Misbah H, Aziz AA, Aminudin N. BMC Complementary Altern Medicine. 2013;13(18):1-12.
13. Veerapur VP, Prabhakar KR, Thippeswamy BS, Bansal P, Srinivasan KK, Unnikrishnan MK. Food Chem. 2012;132(1):186-93.
14. Veerapur VP, Thippeswamy BS, Prabhakar KR, Nagakannan P, Shivasharan BD, Bansal P, et al. Biomed Prev Nutr. 2011;1(4):273-81.
15. Joseph B, Raj SJ. Int J of Pharma Bio Sci. 2010;1(4):246-153.
16. Esteve Ràfols M. Endocrinol Nutr. 2014;61(2):100-12.

SP13_002_OF: EFFECT OF *Anoectochilus burmannicus* AQEOUS EXTRACT ON OBESOGENS-INDUCED ADIPOCYTE TRANSFORMATION

Natchapon Kammasit,[1,3] Tanpitcha Yodweerapong,[1,3] Pensiri Buacheen,[2,3] Jirarat Karinchai,[3] Arisa (Imsumran) Bonness,[3] Ariyaphong Wongnoppavich,[3] Piya Temviriyanukul,[4] Pornsiri Pitchakarn[3]*

[1]Graduate/M.Sc. Program in Biochemistry, Faculty of Medicine, Chiang Mai, Thailand
[2]Graduate/Ph.D. Program in Biochemistry, Faculty of Medicine, Chiang Mai, Thailand
[3]Department of Biochemistry, Faculty of medicine, Chiang Mai University, Chiang Mai, Thailand
[4]Institute of Nutrition, Mahidol University, Nakhon Pathom, Thailand
*e-mail: pornsiri.p@cmu.ac.th

Abstract:

Obesogens are a group of chemicals that can induce obesity in living organisms via the interfering of the endocrine system known as "endocrine-disrupting chemicals" (EDCs) or direct activation of adipogenic gene expression in adipocyte leading to adipogenesis. This study focused on benzyl butyl phthalate (BBP) and bisphenol-A (BPA) because they are well known as obesogens that are often found in human serum and urine. Inhibition of the adipogenic activity of these chemicals could decrease the risk of obesity-related metabolic disorders. A previous study found that *A. burmannicus* aqueous extract (ABE) exhibited anti-inflammation, anti-insulin resistance, and anti-steroid-induced adipocytes transformation. Therefore, this study examines whether ABE suppresses obesogen-induced adipogenesis. The treatment model of obesogen-induced adipogenesis was designed as short-term (the induction stage) and long-term (during adipogenesis) treatments in the presence or absence of dexamethasone (Dex), or IBMX. The result found that the long-term treatment of 50 µM BBP and BPA without Dex was a suitable model for the induction of adipogenesis. Besides, 50 µM BBP treatment could enhance lipid accumulation of the cells cultured in Dex and IBMX-free conditions suggesting the strong adipogenesis induction property of the chemical. Cytotoxicity testing of ABE during adipogenesis (12 days) was determined and found that ABE at up to 200 µg/ml was non-toxic to the cells. Interestingly, ABE (50, 100, 200 µg/mL) significantly reduced the BBP- and BPA-stimulated lipid accumulation in the adipocyte. Taken together, it can be summarized that ABE can suppress BBP- and BPA-induced adipogenesis. The mechanism of ABE inhibiting obesogen-stimulated adipocyte formation should be further investigated.

Introduction:

World Health Organization (WHO) defines obesity as a condition of overweight or excessive fat accumulation in the body that presents a risk to health. Obesity is related to many chronic diseases such as type 2 diabetes mellitus (T2DM), dyslipidaemias, high blood pressure (HBP), heart disease, cardiovascular disease (CVD), cancers progression, gallstones, arthritis, non-alcoholic fatty liver disease, chronic kidney disease (CKD) and sleep apnea.[1] There are several factors that involve obesity, such as genetics, lifestyle, hormonal changes, the metabolic rate of each person, and obtaining excess energy diet and lacking exercise. The excess lipid accumulation in adipocyte stimulates the increase of cell size (hypertrophy) and cell number (hyperplasia), leading to the expansion of adipose tissue and overweight. Recently, it was found that some chemicals, called obesogens, used in daily life, can induce obesity. They are synthetic chemicals that can alter human metabolism, leading to weight gain in some people, and contributing to the development of obesity and metabolic disorders[2]. They can be generally found in many products such as personal care products, plastic toys, food packaging, plastic bottle, pharmaceuticals, clothing, furniture, food colorings, and pesticides. Obesogens enter our body via several routes such as ingestion, inhalation, injection, transdermal contact and transplacental carriage.[3,4]

In this study, we are interested in benzyl butyl phthalate (BBP) and bisphenol A (BPA) that were wildly used as precursor chemicals in plastic industries. Previous studies found that BBP induces adipogenesis in the 3T3-L1 adipocyte via the upregulation of transcription factors such as C/EBPα and PPARγ, leading to enhanced expression of adipogenic-specific genes such as adiponectin, adipsin, FABP4, LPL and FASN. The genes mentioned herein are associated with glyceroneogenesis and fatty acid synthesis[5]. BPA enhances preadipocyte differentiation and lipid accumulation in adipocytes via the induction of transcription factors and adipocyte-specific genes expression such as C/EBPα, PPARγ, adiponectin, and lipoprotein lipase (LPL) in 3T3-L1 adipocyte[6]. Furthermore, these chemicals have been shown to enhance adipogenesis through other pathways, including estrogen receptor (ER)-mediated pathways and glucocorticoid signalling, which also play an important role in promoting adipocyte differentiation[7-9]. The inhibition of obesogen-induced adipogenesis could be a promising way for the prevention of obesity in people exposing to the chemicals.

Anocetochilus sp. have been used as medicinal plants or herbs to alleviate liver disease, diabetes, hyperlipidemia, cardiovascular disease, snake bites, lung disease, and cancer[10]. We focused on *Anocetochilus burmannicus* (*A*. *burmannicus*), an orchid found in many countries such as Bhutan, Laos, China, Vietnam, Indonesia, and Thailand[11,12]. Our previous study reported that *A*. *burmannicus* aqueous extract (ABE) showed anti-inflammation, anti-insulin resistance, and anti-dexamethasone-induced adipocyte transformation activities[10].In this study, we hypothesized that the ABE might prevent obesity stimulated by BBP and BPA. Thus, we aimed to examine whether ABE inhibits BBP- and BPA-induced adipogenesis in the 3T3-L1 adipocyte.

Methodology:

Plant extraction

A. burmannicus was obtained from the Queen Sirikit Botanic Garden, Chiang Mai, Thailand. The whole plants were washed and dried by the hot-air oven for 24 hours. Next, dried plants were extracted by soaking with hot water (80 °C) for 5 minutes in the ratio of 1:10 w/v. After that, the *A. burmannicus* crude aqueous extract (ABE) was freeze-dried to obtain the ABE powder, which was kept in the dark at -20 °C till use.

Measurement of total phenolic content

For the standardization of the plant obtained from different number of passages or subcultures, the phenolic content of ABE extract was determined by Folin-Ciocalteu assay, according to Saba and Malik (2015)[13]. Briefly, 20 µL of ABE (0-200 µg/mL) were mixed with 100 µL 10% Folin-Ciocalteu reagent for 3 minutes in the dark. After that, the mixture was mixed with 80 µL of 7.5% sodium carbonate and incubated in the dark for 30 minutes. Then, the blue color reagent was observed. The absorbance was measured at 765 nm by spectrophotometry. Gallic acid was used as a standard. The total phenolic contents were calculated and expressed as gallic acid equivalents (GAE) in mg/g extract by comparing with the standard calibration curve of gallic acid.

BBP and BPA Treatments in 3T3-L1

BBP and BPA were dissolved in dimethyl sulfoxide (DMSO) as stock solutions. The DMSO concentration was maintained at 0.7% v/v of the medium. In this study, we divided the treatment model into 3 groups using common induction media (Dex+, IBMX+), Dex-free induction medium (Dex-, IBMX+), and Dex- and IBMX-free induction medium without (Dex-, IBMX-). The cells were treated with BBP or BPA during the induction stage (Day 0-3) or the differentiation and maturation stage (Day 0-12), as shown in Figure 1. After that, lipid accumulation of the cells was measured by the Oil Red O assay to determine the effect of BBP and BPA on adipocyte transformation.

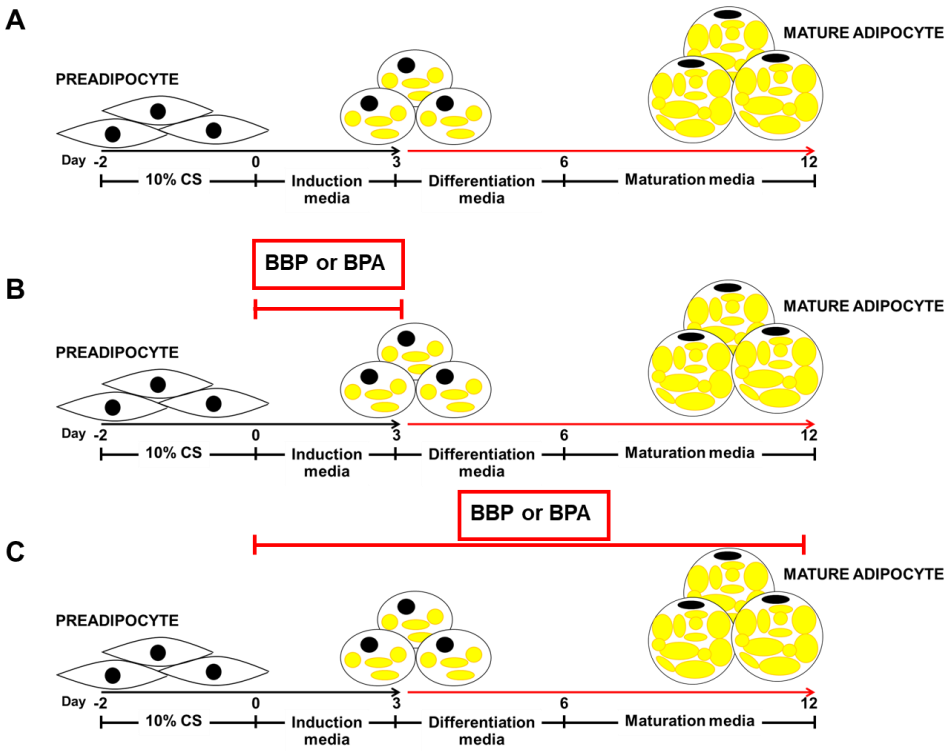

Figure 1. The treatment model of BBP- and BPA-stimulated adipogenesis. (A) Non-treated control, (B) BBP or BPA treatment during the induction stages (Day 0-3), (C) BBP, or BPA treatment during the differentiation and maturation stage (Day 0-12).

ABE Treatment

The cells were treated with various concentrations of ABE (50, 100, and 200 µg/mL) during the induction stage (Day 0-3) or the differentiation and maturation stages (Day 0-12) in the presence or absence of BBP or BPA. The cells were then subjected to either cytotoxicity testing or lipid accumulation measurement.

Cytotoxicity test

Sulforhodamine B (SRB) assay was used to test the cytotoxicity of ABE. The cells were treated with various concentrations of ABE (50, 100, and 200 µg/mL) as described previously. After that, the cells were fixed with 50% TCA (50 µL per well) and incubated for 1 hour at 4 ˚C. Then, the cells were washed with H_2O for 5 times and air-dried overnight at room temperature. Next, 100 µL of 0.057% SRB solution was added and incubated at room temperature for 30 minutes. Next, the cells were washed by 1% acetic acid for 5 times and dried overnight at room temperature. Next, 10 mM tris-base was added (200 µL/well) to dissolve the SRB-stained cells. The absorbance was measured at 510 nm. Cell viability was calculated to obtain the non-toxic concentration of ABE.

Oil Red O staining [14].

The treated cells were washed 3 times with phosphate buffer saline (PBS) and fixed with 100 µL of 10% formaldehyde-phosphate buffer (pH 7.4) for 10 minutes. Then, the supernatant was removed, and the fixed cells were dried at room temperature overnight. After that, the cells were stained with 50µL of Oil Red O dye and incubated at 60 °C for 10 minutes. Next, the unbound or excess staining was discarded by washing with DI water for 3 times. After air-dried at room temperature, the Oil red O stained cells were dissolved with 100 µL of isopropanol and shaken for 15 minutes. The absorbance was measured at 520 nm.

Statistical analysis

All values were given as mean ± standard derivation (X ± SD) from triplicate samples of three independent experiments. Overall differences among the treatment groups were determined using a one-way analysis of variance (ANOVA) by Prism 5.0 software. $p < 0.05$ is regarded as significance.

Results and Discussion:

Total phenolic content of ABE

The extraction of ABE by hot water provided a yield of ABE at approximately 14%. The total phenolic content of ABE measured by Folin-Ciocalteu reagent was 12.27 ± 0.45 mg GAE/g extract which is nearly to the amount of phenolics found in ABE prepared and used in our previous study.[10]

Effect of BBP and BPA treatment on adipocyte formation

Dex and IBMX are commonly used as adipogenesis activators. They can stimulate adipogenesis via C/EBPα and PPARγ activation.[15] First, whether BBP and BPA can enhance adipogenesis in Dex+, IBMX+ treated cells was assessed. The results showed that both short- and long-term treatments of BBP and BPA did not significantly increase lipid accumulation when compared to the untreated group (Figure 2). These may be due to the efficacy of Dex and IBMX; they already have accomplished the induction of adipogenesis.

Similarly, to BBP and BPA, a previous study found that Dex can stimulate glucocorticoid receptor, leading to C/EBPα and PPARγ activations and subsequent adipocyte transformation.[16] Next, we therefore determined whether BBP or BPA themselves could induce adipocyte transformation.

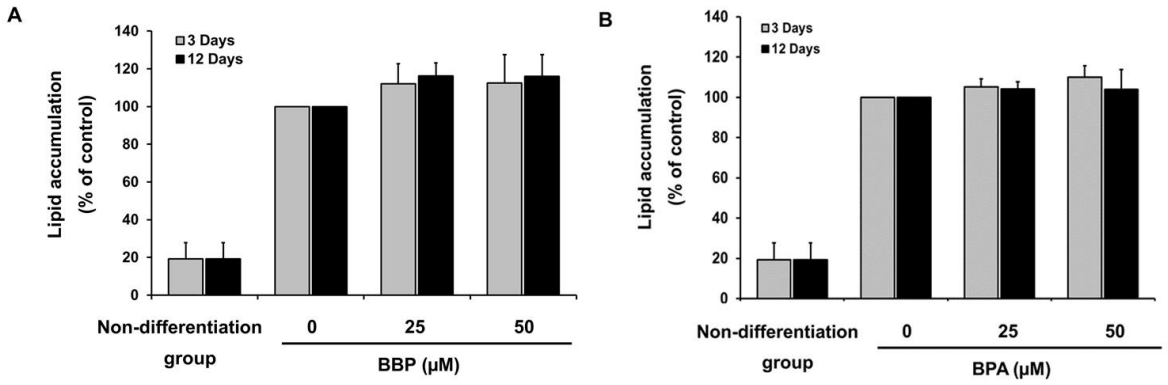

Figure 2. The effect of BBP (A) and BPA (B) on adipogenesis (Dex+ and IBMX+ condition). The graphs represent the mean±SD of four independent experiments.

Long-term treatment (Day 0-12) of 50 μM BBP or BPA was applied in Dex- and IBMX-free conditions. It was found that the lipid accumulation was significantly increased in BPA- and BBP-treated 3T3-L1 (Figure 3). This can be indicated that BBP and BPA act as adipogenesis activators. They can stimulate the adipocyte transformation without any C/EBPα and PPARγ stimulator. However, compared to Dex+, IBMX+ conditions, the induction of adipogenesis was mild. Observation under a microscope found that the size and number of lipid droplets accumulated in the cells were smaller than those of Dex+, IBMX+ treated cells (Data not shown). These can be suggested that the time spending for adipogenesis induction by BBP and BPA is longer than Dex and IBMX.

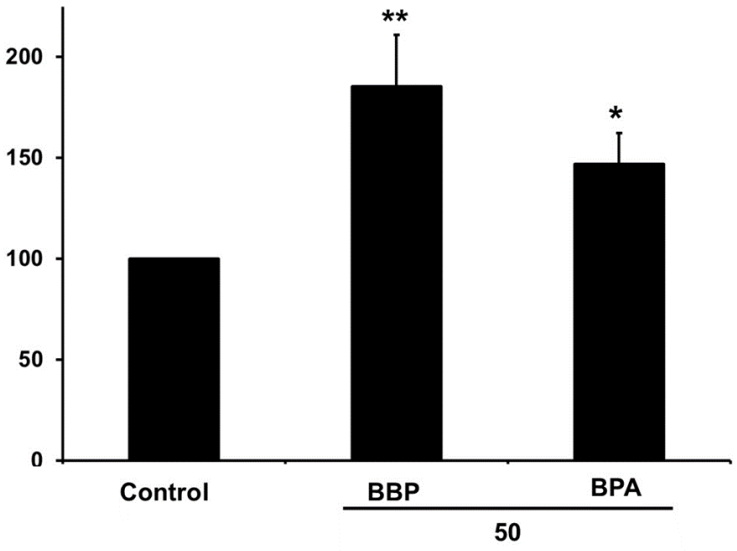

Figure 3. Effect of 50 µM BBP and BPA-induced lipid accumulation in Dex- and IBMX- treatment models. The adipocyte transformation was evaluated by using Oil red O staining to measure lipid accumulation in the cells. The graph represents the mean±SD of four independent experiments. **P*<0.05, ***P*<0.01 compared to control group.

To optimize the protocol, IBMX was used as an adipogenesis co-activator in the next experiment. Figure 4 showed that 50 µM of BBP and BPA dramatically and significantly induced lipid accumulation in Dex-, IBMX+ condition when compared to the non-treated control group. Long-term treatment (Day 0-12) of BBP and BPA at 50 µM was then used in the following experiments because these conditions clearly and highly induced lipid accumulation.

The present study found that BBP exerted higher activity inducing adipogenesis than that of BPA. These findings are in agreement with the previous reports indicating BBP as a strong obesogen and BPA as a weak obesogen,

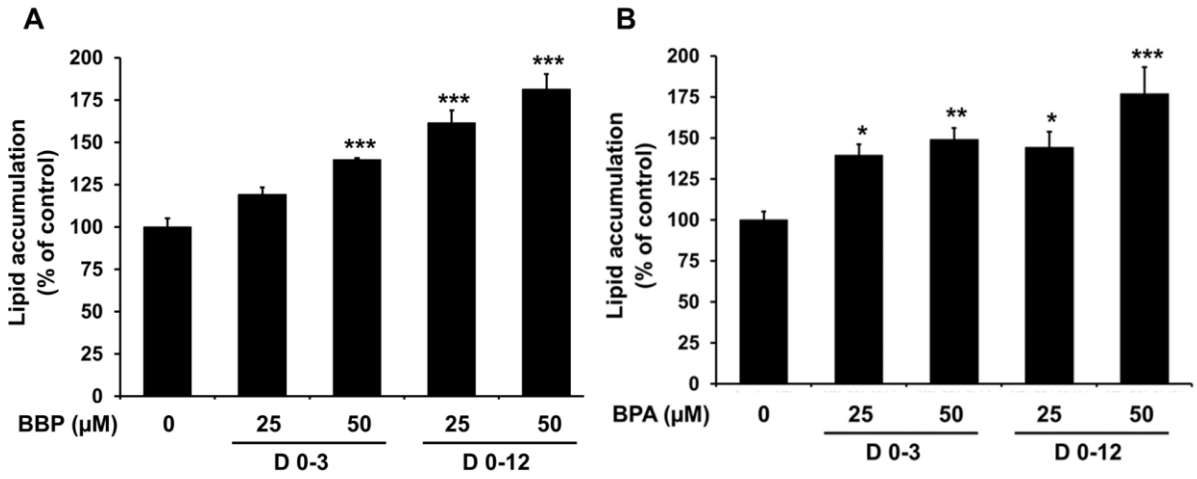

Figure 4. Effect of (A) BBP- and (B) BPA-induced adipogenesis in short- and long-term Dex-treatment models. The lipid accumulation in the cells was measured by Oil red O staining. The graphs represent the mean ± SD of four independent experiments. **P*<0.05, ***P*<0.01, and ****P*<0.001 compared with the non-treated control group.

Effect of ABE on cell viability of 3T3-L1

Cytotoxicity of ABE was assessed after long-term treatment of the cells with the extract. The results showed that ABE at up to 200 µg/mL was non-toxic to the cells (Figure5). This concentration was used as a maximum dose in the following experiments.

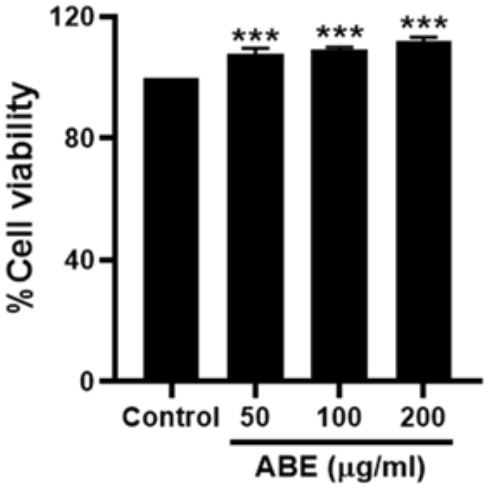

Figure 5. Effect of ABE on cell viability of adipocyte during adipogenesis (long-term treatment). Cytotoxicity of ABE in the cells was determined by SRB assay. The graph represents the mean±SD of four independent experiments. ****P*<0.001 compared with the control group.

Effect of ABE on BBP- and BPA-induced adipocyte formation

To investigate whether ABE could inhibit obesogen-induced adipocyte transformation. The cells were treated with ABE (50, 100, 200 µg/mL) in the presence of 50 µM of BBP or BPA (Dex-, IBMX+; Day 0-12). After that, lipid accumulation of the mature adipocyte was measured by Oil red O staining (Figure 6). The results showed that ABE significantly decreased lipid accumulation induced by BBP and BPA, suggesting that ABE could inhibit BBP- and BPA-induced adipogenesis. This effect may be due to the inactivation of C/EBPα, PPARγ by ABE, which must be further clarified.

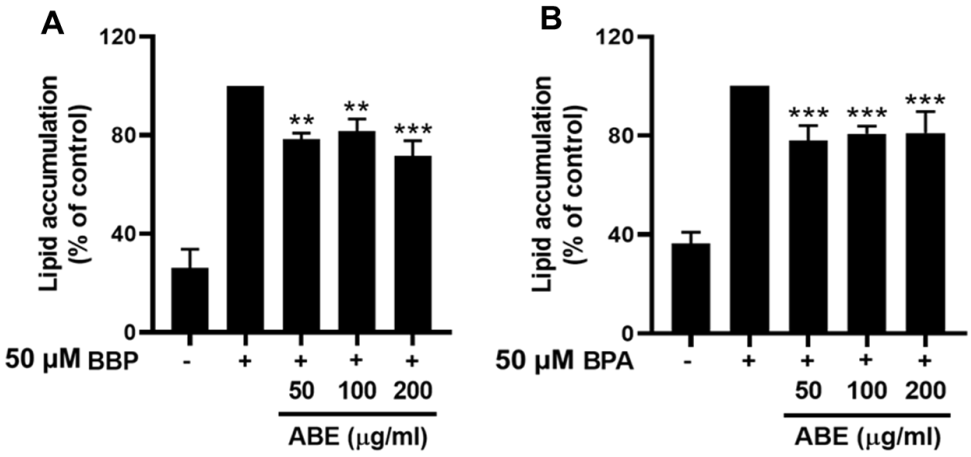

Figure 6. Anti-lipid accumulation activity of ABE in 50 µM of BBP (A) and BPA (B) treated adipocyte. The cells were treated with ABE in the presence of BBP or BPA during adipogenesis. The graphs represent the mean±SD from three independent experiments. ***P*<0.01, ****P*<0.001 compared with the control group.

Conclusions:

This study optimized the protocol for adipogenesis induction in 3T3-L1 by BBP and BBA. Besides, we showed the inhibition activity of ABE against BBP- and BPA-induced adipocyte transformation or adipogenesis. However, the mechanisms of ABE to suppress adipogenesis stimulated by the obesogens need to be further determined. The knowledge from this study will support the development of this orchid as alternative medicine in the prevention of obesogen-induced obesity and promote this orchid to be an industrial plant in the future.

Acknowledgments

This work was supported by the Department of Biochemistry, Faculty of Medicine, Chiang Mai University, and Medical Science Research Equipment Center 5th floor, Faculty of Medicine, Chiang Mai University, Chiang Mai, Thailand.

References

1. Haslam DW, James WPT. The Lancet. 2005;366(9492):1197-209.
2. Yin L, Yu KS, Lu K, Yu X. Toxicol. In Vitro. 2016; 32:297-309.
3. Regnier SM, Sargis RM. BBA-MOL BASIS DIS. 2014;1842(3):520-33.
4. Sonkar R, Powell CA, Choudhury M. Mol Cell Endocrinol. 2016;431: 109-22.
5. Desai M, Guang H, Ferelli M, Kallichanda N, Lane RH. REPROD SCI (Thousand Oaks, Calif). 2008;15(8):785-96.
6. Legeay S, Faure S. FUND CLIN PHARMACOL. 2017;31(6):594-609.
7. Jason FO, Amy LS, John AM, Jeffrey MG, Matthew EB, Bruce AB. J. Mol. Endocrinol. 2014;53(3):345-53.
8. Achard V, Boullu-Ciocca S, Desbriere R, Grino M. Metab Syndr Relat Disord 2006; 4:129–37. [PubMed: 18370759]
9. Nyirenda MJ, Lindsay RS, Kenyon CJ, Burchell A, Seckl JR. J Clin Invest 1998; 101:2174–81. [PubMed: 9593773]
10. Budluang P, Pitchakarn P, Ting P, et al. Food Sci Nutr, 2017,5(3):486-496.
11. Lee Y-S, Cha B-Y, Saito K, Choi S-S, Wang XX, Choi B-K, et al. Phytomedicine. 2011;18(8):648-54.
12. Baboota RK, Singh DP, Sarma SM, Kaur J, Sandhir R, Boparai RK, et al. PLoS One. 2014;9(7): e103093.
13. Baba SA, Malik SA. J TAIBAH UNIV SCI. 2015;9(4):449-54.
14. Kraus NA, Ehebauer F, Zapp B, Rudolphi B, Kraus BJ, Kraus D. Adipocyte. 2016;5(4):351-8.
15. Rasmus K.P., Lise M., Lone M.P., Philip H., Hanne H., Kristin V., Stein O.D. and Karsten K. Mol Cell Biol. 2008; 28(11):3804-3816.
16. Felix G. and Bruce B. Endocrinology. 2006;147(6): 50-55.

SP13_003_PF

SP13_003_PF: CHEMICAL CONSTITUENTS OF *Dendrobium braianense* AND THEIR α-GLUCOSIDASE INHIBITORY ACTIVITY

Mia Indria Permatasari, Kittisak Likhitwitayawuid, Boonchoo Sritularak*

Department of Pharmacognosy and Pharmaceutical Botany,
Faculty of Pharmaceutical Sciences, Chulalongkorn University, Bangkok 10330, Thailand
* e-mail: boonchoo.sr@chula.ac.th

Abstract:

Phytochemical investigation of the whole plants of *Dendrobium braianense* resulted in the isolation of three bibenzyls, which included chrysotoxine **(1)**, moscatilin **(2)** and gigantol **(3).** The structures of these compounds were determined through analysis of spectroscopic data and in comparison with the previously reported values. All isolated compounds were evaluated for their α-glucosidase inhibitory activity. Gigantol (**3**) exhibited strong α-glucosidase inhibitory effect when compared with the positive control acarbose, whereas chrysotoxine **(1)** and moscatilin **(2)** were devoid of activity.

Introduction:

Orchids, like other plants, produce a large number of phytochemicals. Some of them have been investigated for their chemical properties and biological activities. The first alkaloid isolated from *Dendrobium nobile* orchid was dendrobine which has been used in Chinese drug 'chin-shi-hu'.[1] *Dendrobium* is a large genus in the Orchidaceae. In traditional Chinese medicine, the dried stems of *Dendrobium* spp. have been used to treat stomach diseases, diabetes, kidney and lung disorder.[2] In Thailand, some of these orchids have also been used in traditional medicine.[3] Several classes of secondary metabolites have been reported to be isolated from *Dendrobium* spp**.** such as bibenzyls, phenanthrenes, alkaloids and flavonoids**.**[4] *D. braianense* Gagnep**. (**Figure 1**)** is distributed in South-Central China, Laos, Thailand, and Vietnam**.**[5] Prior to this research, there were no reports on the phytochemical constituents and biological activities of this plant**.**

The development of the α-glucosidase inhibitors has provided a new approach for the management of diabetes**.** By inhibition of intestinal α-glucosidase enzyme, α-glucosidase inhibitors delay carbohydrate digestion, prolong the overall carbohydrate digestion time, and thus reduce the rate of glucose absorption**.**[6] An ethyl acetate extract from the whole plants of *D. braianense* showed α-glucosidase inhibitory effect. Therefore, this extract was selected for further chemical investigation. In this research, we wish to report the first investigation on the phytochemical constituents and α-glucosidase inhibitory activity of this plant**.**

Figure 1. *Dendrobium braianense*

Methodology:

General experimental procedure

NMR spectra were recorded on a Bruker Avance DPX-300 FT-NMR spectrometer. Mass spectra were recorded on a Bruker micro TOF mass spectrometer (ESI-MS). Vacuum-liquid column chromatography (VLC) and open column chromatography were conducted on silica gel 60 (Merck, Kieselgel 60, 70 -320 µm), silica gel 60 (Merck, Kieselgel 60, 230-400 µm). Gel filtration chromatography was performed on Sephadex LH-20 (25-100 µm, GE Healthcare). Microtiter plate reading was performed on a CLARIOstar (BMG LABTECH,

Germany).

Plant material

Samples of *Dendrobium braianense* were purchased from Chatuchak market, Bangkok, in March 2018. Plant identification was done by Mr. Yanyong Punpreuk, Department of Agriculture, Bangkok. A voucher specimen (BS-DB-032561) has been deposited at the herbarium of the Department of Pharmacognosy and Pharmaceutical Botany, Faculty of Pharmaceutical Sciences, Chulalongkorn University.

Extraction and isolation

The dried powdered whole plant of *D. braianense* (2 kg) was macerated with methanol (3 x 10L) to give a methanol extract after removal of the solvent. The methanol extract (220 g) was partitioned with ethyl acetate, butanol and water to give ethyl acetate extract (92 g) and butanol extract (40 g). The ethyl acetate extract was separated by vacuum-liquid chromatography (silica gel, ethyl acetate-hexane, a gradient of 0:100 to 100:0, 400 ml for each fraction) to give 5 fractions (A-E). Fraction B (10.6 g) was fractionated by Sephadex LH-20 (acetone) to give 5 fractions (B1-B5). Fraction B2 was further separated by column chromatography (silica gel, ethyl acetate-hexane, a gradient of 0:100 to 100:0, 100 ml for each fraction) to give 6 fractions (B2.1-B2.6). Compounds **1** (97 mg) and **2** (10 mg) were obtained from fractions B2.3 and B2.4, respectively, after purification on Sephadex LH-20 (acetone). Fraction B3 was purified by column chromatography (Sephadex LH-20, acetone) to give 3 fractions (B3.1-B3.3). Fraction B3.2 was further purified by column chromatography (silica gel, ethyl acetate-hexane, a gradient of 0:100 to 100:0, 100 ml for each fraction) to yield compound **3** (710 mg).

Assay for α-glucosidase inhibitory activity

The α-glucosidase assay was performed as described previously.[7] Acarbose was used as the positive control.

Results and Discussion:

D. braianense crude extract was prepared by maceration of the dried powdered whole plants with methanol. The MeOH extract was evaluated for α-glucosidase inhibitory activity and found to show 64.7% inhibition at a concentration of 1 mg/mL. The MeOH extract was partitioned with ethyl acetate, butanol and water to give ethyl acetate and butanol extracts. These extracts were then evaluated for their α-glucosidase inhibitory property. It was found that the ethyl acetate extract showed strong α-glucosidase inhibitory effect with 82.1% inhibition at a concentration of 1 mg/mL, whereas the butanol extract exhibited 68.6% inhibition (Table 1). Therefore the ethyl acetate extract was selected for further chemical investigation.

Table 1. *α*-Glucosidase inhibitory activity of crude extracts from *D. braianense*

Extracts **(1 mg/mL)**	% Inhibition
Methanol extract	64.7
Ethyl acetate extract	82.1
Butanol extract	68.6
Acarbose (positive control)	74.8

Phytochemical investigation of the ethyl acetate fraction partitioned from the MeOH extract of *D. braianense* resulted in the isolation of three bibenzyls, which included chrysotoxine (**1**),[8] moscatilin (**2**),[9] and gigantol (**3**).[10] The structures of these isolates (Figure 2) were determined through analysis of their ^{1}H NMR, ^{13}C NMR, and MS data and in comparison with the previously reported values.

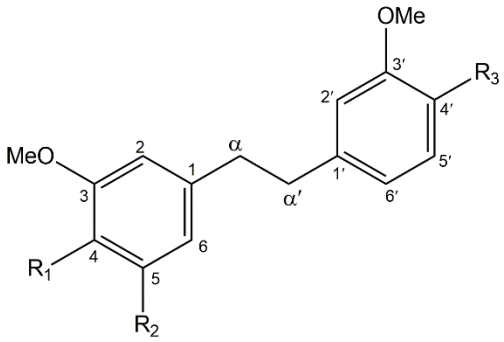

	R_1	R_2	R_3
1	OH	OMe	OMe
2	OH	OMe	OH
3	H	OH	OH

Figure 2. Structures of chrysotoxine (**1**), moscatilin (**2**) and gigantol (**3**)

*Chrysotoxine (**1**)*. White powder; HR-ESI-MS $[M+Na]^+$ at *m/z* 341.1389 (calcd. for 341.1364, $C_{18}H_{22}O_5Na$); ^{1}H NMR, (300 MHz, acetone-d_6) δ6.83 (1H, d, *J* = 8.1 Hz, H-5′), 6.82 (1H, br s, H-2′), 6.71 (1H, dd, *J* = 8.1, 1.8 Hz, H-6′), 6.49 (2H, br s, H-2, H-6), 3.77 (9H, s, MeO-3′, MeO-3, MeO-5), 3.76 (3H, s, MeO-4′), 2.82 (4H, br s, H_2-α, H_2-α'); ^{13}C NMR (75 MHz, acetone-d_6) δ149.3 (C-4′), 147.8 (C-3′), 147.6 (C-3, C-5), 134.7 (C-1′),134.1 (C-4), 132.2 (C-1), 120.4 (C-6′), 112.7 (C-2′), 112.0 (C-5′), 106.0 (C-2, C-6), 55.7 (MeO-3, MeO-5), 55.3 (MeO-3′), 55.1 (MeO-4′), 38.0 (C-α), 37.6 (C-α').

*Moscatilin (**2**).* Brown amorphous solid; HR-ESI-MS $[M+Na]^+$ at *m/z* 327.1216 (calcd. for 327.1208, $C_{17}H_{20}O_5Na$); ^{1}H NMR (300 MHz, acetone-d_6) δ6.79 (1H, d, *J* = 1.5 Hz, H-2′), 6.72 (1H, d, *J* = 8.1 Hz, H-5′), 6.65 (dd, *J* = 8.1, 1.5 Hz, H-6′), 6.49 (2H, s, H-2, H-6), 3.79 (3H, s, MeO-3′), 3.77 (6H, s, MeO-3, MeO-5), 2.79 (4H, br s, H_2-α, H_2-α'); ^{13}C NMR (75 MHz, acetone-d_6) δ147.6 (C-3, C-5), 147.2 (C-3′), 144.7 (C-4′), 134.1 (C-4), 133.3 (C-1′), 132.3 (C-1), 120.8 (C-6′), 114.7 (C-5′), 112.1 (C-2′), 106.0 (C-2, C-6), 55.7 (MeO-3, MeO-5), 55.3 (MeO-3′), 38.2 (C-α), 37.6 (C-α').

*Gigantol (**3**).* Brown amorphous solid; HR-ESI-MS $[M+Na]^+$ at *m/z* 297.1131 (calcd. for 297.1102, $C_{16}H_{18}O_4Na$); ^1H NMR (300 MHz, acetone-d_6) δ 6.80 (1H, d, *J* = 1.5 Hz, H-2′), 6.74 (1H, d, *J* = 8.1 Hz, H-5′), 6.66 (1H, dd, *J* = 8.1, 1.5 Hz, H-6′), 6.33 (1H, s, H-6), 6.31 (1H, s, H-2), 6.26 (1H, br d, *J* = 2.1 Hz, H-4), 3.79 (3H, s, MeO-3′), 3.70 (3H, s, MeO-3), 2.76 (4H, br s, H_2-α, H_2-α'); ^{13}C NMR (75 MHz, acetone-d_6) δ 160.9 (C-3), 158.4 (C-5), 147.2 (C-3′), 144.6 (C-1), 144.3 (C-4′), 133.3 (C-1′), 120.7 (C-6′), 114.7 (C-5′), 112.0 (C-2′), 108.1 (C-6), 105.4 (C-2), 98.9 (C-4), 55.3 (MeO-3′), 54.4 (MeO-3), 38.2 (C-α), 37.1 (C-α').

All the isolated compounds **1**-**3** were evaluated for their α-glucosidase inhibitory activity. In this study, each compound was initially tested at 100 μg/mL. An IC_{50} value was determined if the compound showed more than 50% inhibition of the enzyme. It was found that only gigantol (**3**) showed strong α-glucosidase inhibitory activity with IC_{50} 349.0 ± 9.3 μM when compared with positive control acarbose (IC_{50} 532.4 ± 19.6 μM). Chrysotoxine **(1)** and moscatilin **(2)** were devoid of activity.

Conclusion:

In this study, three bibenzyls chrysotoxine (**1**), moscatiline (**2**), and gigantol (**3**) were isolated from *Dendrobium braianense*. Gigantol showed higher α-glucosidase inhibitory activity than the drug acarbose.

Acknowledgements:

MIP is grateful to the Graduate School, Chulalongkorn University for a CU-ASEAN scholarship. We thank Mr. Yanyong Punpreuk for the plant identification.

References:

1. Hossain, MM. Fitoterapia. 2011;82:102–140.
2. Xu FQ, Fan WW, Zi CT, Dong FW, Yang D, Zhou J, Hu JM. Nat Prod Res. 2017;31:797–801.
3. Chuakul W. Mahidol C. J Pharm Sci. 2002;29:41–45.
4. Wang L, Zhang CF, Wang ZT, Zhang M, Xu, LS. J Asian Nat Prod Res. 2009;11:903–911.
5. Plants of the world online. *Dendrobium braianense* Gagnep. Available at URL:http://powo.science.kew.org/taxon/urn:lsid:ipni.org:names:626961-1#sources. Access on July 23, 2020.
6. Bischoff, H. Clin Invest Med. 1995;18:303–311.
7. Limpanit R, Chuanasa T, Likhitwitayawuid K, Jongbunprasert V, Sritularak B. Rec Nat Prod. 2016;10:609–616.
8. Chanvorachote P, Kowitdamrong A, Ruanghirun T, Sritularak B, Mungmee C, Likhitwitayawuid K. Nat Prod Commun. 2013;8:115–18.
9. Majumder PL, Sen RC. Phytochemistry. 1987;26:2121–24.
10. Chen Y, Xu J, Yu H, Qing C, Zhang Y, Wang L, Liu Y, Wang J. Food Chem. 2008; 107:169–73.

SP13_004_PF: ANTI-INFLAMMATION AND ANTI-INSULIN RESISTANCE ACTIVITIES OF *Carissa carandas* Linn. FRUIT EXTRACT.

Manaschanok Lailerd, [1] Narissara Lailerd, [2] Doungporn Amornlerdpison, [3]
Pornsiri Pitchakarn,[1] Ariyaphong Wongnoppavich,[1] Arisa Imsumran Bonness[1,*]

[1]Department of Biochemistry, Faculty of Medicine, Chiang Mai University, Chiang Ma, Thailand
[2]Department of Physiology, Faculty of Medicine, Chiang Mai University, Chiang Mai, Thailand
[3]Faculty of Fisheries Technology and Aquatic Resources, Maejo University, Chiang Mai….., Thailand
*e-mail: arisa.bonness@cmu.ac.th

Abstract:

In obesity and type 2 diabetes mellitus (T2DM), visceral adipocytes and associated macrophages produce excessive amounts of pro-inflammatory cytokines leading to chronic inflammation and insulin resistance in adipocytes itself and also other insulin target tissues. Ripe fruit of *Carissa carandas* Linn. has been exhibited anti-oxidant, anti-inflammatory and anti-diabetic activities in T1DM rat model. This study aimed to investigate the anti-inflammation and anti-insulin resistance activity of *C. carandas* extract (CC extract) using *in vitro* model, lipopolysaccharide (LPS)-induced RAW 264.7 macrophages and 3T3-L1 adipocytes. Ripe fruits were extracted by water (CCA) or 0.5% acetic acid in 70% ethanol (CCE) to produce crude extracts. Biological activity was then investigated. Although, both of CC extracts had no the inhibitory activity on the nitric oxide production in LPS-stimulated macrophages, the CCA had an interestingly effect in the insulin resistance models in this study. The CCA significantly increased insulin-stimulated glucose uptake in LPS-induced 3T3-L1 adipose cells at concentration 100, 200 and 400 µg/mL in a dose dependent manner. Thus, aqueous extract (CCA) of *C. carandas* ripe fruit will be selected to further investigate the anti-diabetic activity in a T2DM rat model.

Introduction:

Type 2 diabetes mellitus (T2DM) is currently one of the major diseases confronting the health care systems worldwide. The pathophysiology of T2DM is characterized by peripheral insulin resistance, impaired regulation of hepatic glucose production, and declining β-cell function, finally leading to β-cell failure. In 2017, Thai people have the 4th highest incidence of type 2 diabetes in Asia.[1,2] Diabetic condition in the elderly people is likely accompanied by obesity due to excessive food consumption and sedentary life style. Increased adipose tissue mass induces chronic low-grade inflammation and stimulates macrophages infiltration in adipose tissue.[3] The visceral adipocytes and their activated macrophages produce various pro-inflammatory cytokine such as tumor necrosis factor-alpha (TNF-α) and interluekin-6 (IL-6), which exert paracrine effects to activate inflammatory pathways within insulin target cells including muscle and liver resulting in systemic insulin resistance and progress to T2DM.[4] Currently, there are many possible ways of treating diabetes. One of the most popular and interesting ways is medicinal plants, which have been studied on plants that have anti-diabetic effects such as *Momordica charantia* L., *Gymnema inodorum.* and *C. carandas*.[5]

Carissa carandas Linn. (Apocynaceae), commonly known as karanda, is a widely used medicinal plant. Ripe fruit of *C. carandas* has been claimed for many biological properties including anti-oxidant, anti-inflammatory and anti-diabetic activities.[6,7] Furthermore, bioactive compounds in this plant are anthocyanin and vitamin C.[8] The pigment identified in *C. carandas* is cyanidin-3-rhamnoglucoside.[9] The prominent biological activities of *C. carandas* have also been reported that includes antidiabetic, antimicrobial, cytotoxicity, anticonvulsant, hepatoprotective, antihyperlipidemic, cardiac depressant, analgesic, anti-inflammatory, antipyretic, and antiviral properties.[7,9,10] However, the antidiabetic property of *C. carandas* specially in type 2 diabetes mellitus remains to be clarified.

Nowadays, it is well recognized that obesity induces chronic inflammation which contribute to insulin resistance in adipose tissue.[3] Thus, anti-inflammation and anti-insulin resistance has been one of the main targets for treatment of type 2 diabetes. The present study, therefore, aimed to evaluate whether the *C. carandas* extract can be of benefit in the treatment of type 2 diabetes via its ability to reduce inflammation and

insulin resistance using the *in vitro* model, lipopolysaccharide (LPS)-induced RAW 264.7 macrophages and 3T3-L1 adipocytes.

Methodology:

Collection of plant material

The fruits of *C. carandas* was collected from Nakhon Chaisri, Nakhon Pathom, Thailand. A voucher specimen was deposited at the botanical garden organization, ministry resources and environment, Queen Sirikit Botanic Garden Herbarium Chiang Mai (Specimen Number:123875).

Preparation of extracts

The fruits of *C. carandas* were washed with water and air dried at room temperature. After drying, the seeds were removed and discarded. Then, the fruits were dried in 60 °C oven for 24 hours. The powdered material was soaked for 24 hours in DI water (Aqueous extract, CCA) or 0.5% acetic acid in 70% ethanol (Ethanolic extract, CCE). Anthocyanins are compounds which contain both hydrophobic and hydrophilic groups; therefore, the optimal solvent system is a mixture of water and organic compounds. An organic acid such as acetic or formic acid is also added to prevent the degradation of anthocyanin. Thus, an extraction with weakly acidified alcoholic solvent is the most commonly used solvent for the preparation of anthocyanin from plant extracts. After filtration, ethanol was evaporated in rotary evaporator (Buchi, Switzerland) under vacuum whereas the aqueous extract was centrifuged at 5000 g for 10 minutes to remove any residual material and lyophilized using a freeze dryer (Thermo Scientific, USA). All extracts were stored at -20 ºC until use.

Determination of total phenolic contents

Total phenolics of the extracts were determined using the Folin-Ciocalteu reagent (BDH, England) with slight modification.[11] A sample (200 µL) was mixed with 1 mL of Folin-Ciocalteu reagent, and allowed to stand at room temperature for 6 minutes after which 800 µL of 7.5% sodium carbonate solution were added. The solution was mixed and incubated at room temperature for 1 hours. The absorbance was measured at 765 nm by a UV-VIS spectrophotometer. The results were calculated as mg of gallic acid (Sigma-Aldrich, USA) equivalent (GAE) per gram of extract.

Determination of total flavonoid contents

Total flavonoid content was measured following an aluminum chloride colorimetric assay with slight modification.[12] An aliquot (0.5 mL) of sample was mixed with 0.1 mL of 5% sodium nitrite. After 5 minutes, 0.1 mL of 10% aluminum chloride was added to the mixture then 1 mL of 1 M sodium hydroxide was added. The solution was thoroughly mixed. The absorbance was measured at 510 nm by a UV-VIS spectrophotometer. Total flavonoid content was expressed as mg of rutin (Sigma-Aldrich, USA) equivalent (RUE) per gram of extract.

Determination of total anthocyanin content

Total anthocyanin content was determined using a pH-differential method.[13] An aliquot (0.5 mL) of the sample was mixed with 2 mL of 0.025 M potassium chloride buffer (pH 1.0) or 2 mL of 0.4 M sodium acetate buffer (pH 4.5). A Shimadzu 300 UV-Vis Spectrophotometer and 1 cm pathlength cells were used for spectral measurements at 520 and 700 nm. The total anthocyanin content was expressed as cyanidin-3-glucoside equivalents as in the following equation.

$$\text{Anthocyanin (mg/L)} = \frac{A \times MW \times DF \times 1000}{\varepsilon \times l}$$

where A is the absorbance $(A_{520} - A_{700})_{pH\ 1.0} - (A_{520} - A_{700})_{pH\ 4.5}$, MW is the molecular weight of cyanidin-3-glucoside (449.2 g/mol), DF is the dilution factor, Ɛ is the molar absorptivity (26,900 $L.mol^{-1}.cm^{-1}$), and l is the cell path length (1 cm).

Cell culture

RAW 267.4 macrophages and 3T3-L1 preadipocyte cell lines (ATCC, USA) were maintained in Dulbecco's Modified Eagle Medium (DMEM) (Gibco, USA) containing 10% fetal bovine serum (HyClone, USA) and 1% antibiotics (Invitrogen, USA), and incubated at 37°C in a humidified 5% CO_2/95% air atmosphere. Differentiation of 3T3-L1 was induced in DMEM supplemented with 0.5 g/mL dexamethasone, 0.5 mM 3-isobutyl-1-metylxanthine (IBMX), 5 µg/mL insulin (Sigma Aldrich) and 10% FBS for 72 hours, followed by another 72 hours in the same medium without IBMX and dexamethasone. Differentiation was completed by incubating the cell in DMEM with 10% FBS for 7-12 days.

Cytotoxicity assay

RAW 267.4 macrophages cells (2.5×10^4 cells/well) or 3T3-L1 mature adipose cells (3×10^3 cells/well) were seeded in 96-well plates and incubated for 24 hours. Cells were then treated with various doses (25-800 µg/mL) of the extract for 24 hours. Cells were stained with 0.057% sulforhodamine B (SRB) solution at room temperature for

30 minutes. Then, cells were washed with 1% acetic acid and dried overnight. Finally, cells were dissolved with 10 mM Tris-base pH 7.4. The absorbance at 510 nm was measured using a microplate reader.

Effect of CC extracts on nitric oxide production in LPS-induced RAW 264.7 macrophages

The RAW 264.7 cells (2.5×10^4 cells/well) in 96-well plate were incubated with CCA or CCE extracts (100-400 µg/mL) in the presence of 1 µg/mL lipopolysaccharide (LPS) for 24 hours. The production of nitrite was determined in the medium by Griess reagent (Sigma Aldrich, USA) followed by spectrophotometric measurement at 540 nm using a microplate reader. Nitrite concentration in the supernatants was determined by comparison with a sodium nitrite standard curve.

Effect of CC extracts on glucose uptake in LPS-induced 3T3-L1 adipocytes

3T3-L1 adipocytes (3×10^3 cells/well) were seeded in 96-well plates and grown to maturation. Next, cells were incubated with CCA or CCE extracts (100-400 µg/mL) in the presence of 1 µg/mL lipopolysaccharide (LPS) for 24 hours. Then, the cells were ready to perform glucose uptake assay.

Glucose uptake assay

Cells were washed with phosphate-buffered saline (PBS) and further incubated in PBS for 5 minutes. The PBS was replaced by 100 mM 2-NBD-glucose (Invitrogen, USA), 100 mM insulin, and the cells were incubated for 30 minutes at 37 °C. Fluorescence was measured at λex =485 nm and λem = 535 nm using a microplate reader.

Statistical analysis

Data from triplicate samples of three independent experiments were expressed as means ± SD. Statistical evaluation was done by a one-way analysis of variance (ANOVA) and Tukey's multiple comparison tests using GraphPad Prism software (GraphPad Software Inc., USA). Values of $P < 0.05$ were considered significant.

Results and Discussion:

Extraction yield

According to solvent extraction, type of solvent is an important factor that affected the extraction yield. Aqueous (CCA) and 0.5% acetic acid in 70% ethanol (CCE) extraction process gave the red viscous crude extracts with the extraction yield of 38.82% and 48.6%, respectively.

Total phenolic, flavonoids and anthocyanin contents of CC extracts

Total phenolic and flavonoid content were measured by Folin-Ciocalteu and aluminum chloride colorimetric assays, respectively. As shown in Table 1, the CCE had the higher phenolic and flavonoid contents (22.972 ± 0.35 mg GAE/g extract, 20.61 ± 3.24 mg RUE/g extract) the CCA (18.23 ± 0.37 mg GAE/g extract, 12.04 ± 2.74 mg RUE/g extract). Phenolic content was determined from linear regression equation of gallic acid ($y = 9.5093x + 0.0686$, $r^2 = 0.9993$). Flavonoid content was determined from linear regression equation of rutin ($y = 0.0074x - 0.0013$, $r^2=0.9962$).

The CCE extract had the higher content of total anthocyanin at 18.95 mg/g extract than the CCA extract at 15.19 mg/g extract (Table 1). This result indicated that CCE has a total phenolic and flavonoid content higher than CCA. Similar result was noted in a previous study for 95% ethanolic extract of CC ripe fruit had higher total phenolic content than the aqueous extract.[6] However, this previous study showed lower flavonoid content in 95% of ethanolic extract of CC ripe fruit than those of aqueous extract.[6] Our study showed that the ethanolic extract also exhibited higher flavonoid content than the aqueous extract. This may also be due to different geographical areas where the plants were taken from.[14]

Table 1.

Total phenolic, flavonoids and anthocyanin contents of *C. carandas* extracts.

CC extracts	Phenolic contents (mg GAE/g extract)	Flavonoid contents (mg RUE/g extract)	Anthocyanin contents (mg/g extract)
CCA	18.23 ± 0.37	12.04 ± 2.74	14.63 ± 0.67
CCE	22.97 ± 0.35	20.61 ± 3.24	18.25 ± 0.42

Values are mean ± SD.

Cytotoxicity of the CC extracts on RAW 264.7 macrophages and 3T3-L1 mature adipocyte

To determine whether the CC extracts affect to cell viability of RAW 264.7 macrophages and 3T3-L1 adipocytes, the cells were treated with CCA and CCE extracts (25-800 µg/mL) for 24 hours. As shown in Figure 1, the CCA and CCE at up to 800 µg/mL did not demonstrate the harmful effect to the both cells. Percentages of cell viability above 80% are considered to indicate non-cytotoxicity. Moreover, CCA extracts at a concentration range of 25-200 µg/mL were able to slightly stimulate the cell growth. These effects may be due to various nutrients present in the CC extract.[15]

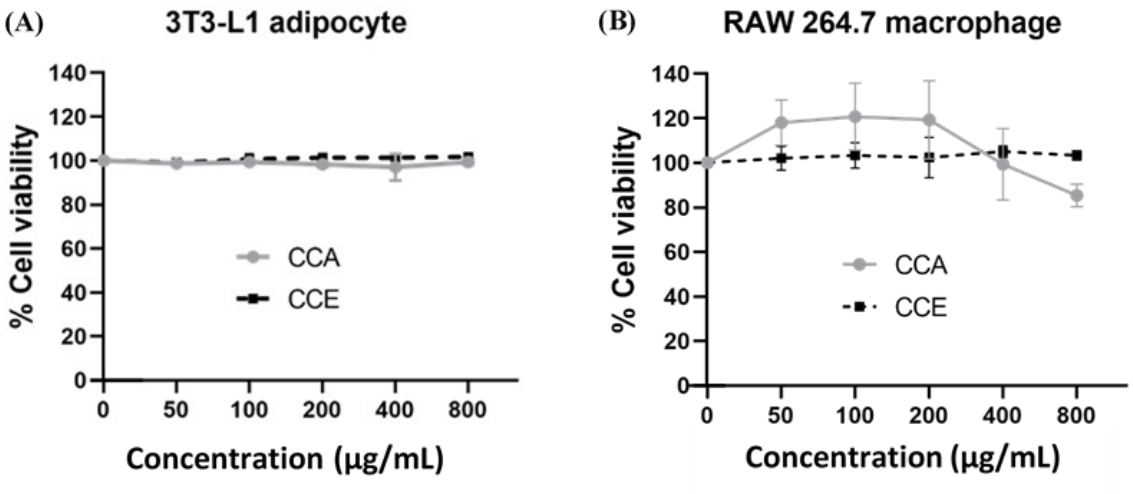

Figure 1.Effect of CCA and CCE extracts on cell viability in (A) 3T3-L1 adipocyte and (B) RAW 264.7 macrophages. The cells were treated with the extract for 24 hours. And then the cell survival rate was determined by SRB assay. The values are expressed as means ± SD (n =3).

Effect of CCA and CCE on NO production in LPS-induced RAW 264.7 macrophages

To investigate the effects of CCA and CCE on NO production in LPS-induced RAW 264.7 macrophages, the levels of nitrite in the culture media of RAW 264.7 cells were determined after co-treatment with 1 µg/mL LPS and CC extracts at concentration 100, 200 and 400 µg/mL. As illustrated in Figure 2, the CC extracts had no the inhibitory activity on NO production in LPS-stimulated macrophages. However, the previous study showed that juice from CC ripe fruit at 500 µg / mL inhibited LPS- induced NO production in RAW 264. 7 cells by a maximum of 29. 5%. [9] Using different solvent and extraction method may affect total phenolic, flavonoid and also biological activities.[16]

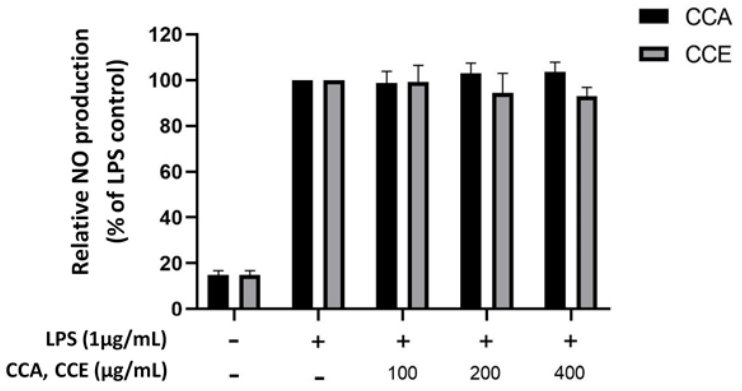

Figure 2.Effect of CC extracts on NO production of LPS-induced RAW 264.7 macrophages. The cells were co-treated with 1 µg/mL LPS and CC extracts at concentration 100, 200 and 400 µg/mL and incubated for 24 hours. The NO production was determined using Griess reagent assay.
The values are expressed as means ± SD (n =3).

Effect of CCA and CCE on glucose uptake in LPS-induced 3T3-L1 adipocytes

Previous study reported that an increase in plasma LPS occurs in healthy individuals after a high-fat meal and also in patients with obesity and insulin resistance.[17] Moreover, LPS could induce adipose tissue inflammation via toll-like receptor 4 (TLR-4), then activated NF-kB and JNK pathway and leaded to cytokine production which impairs insulin signaling in adipocyte.[18] In this study, cellular glucose uptake was decreased in LPS-treated 3T3-L1 adipocytes, 20% relative with untreated control (Figure 3). Interestingly, the CCA significantly improved glucose uptake, indicating an anti-insulin resistance effect in LPS-treated adipocytes. The glucose uptake of cell treated with CCA was increased nearly as much as in untreated control (Figure 3 A). However, the glucose uptake of the CCE-treated cell tended to increase but did not achieve statistical significance compared to the LPS-treated alone cell. Thus, the CCE had no statistically significant effect on cellular glucose uptake activity of LPS-treated adipocyte (Figure 3 B). These effects may be due to phytochemicals in CCA extract which exert higher anti-insulin resistant activity. Further investigation on active compounds containing anti-insulin resistance should be performed.

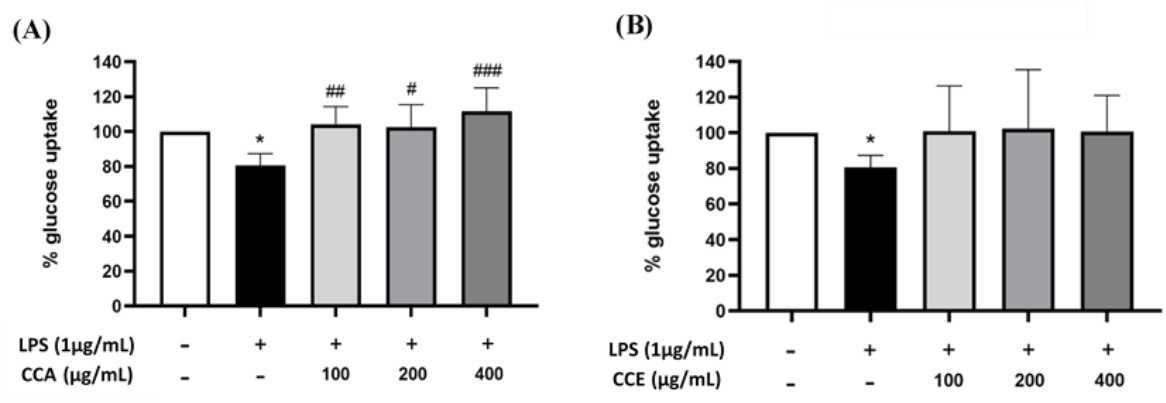

Figure 3. Effect of (A) CCA and (B) CCE on glucose uptake in LPS-induced 3T3-L1 adipocytes. The cells were co-treatment with 1 µg/mL LPS and CC extracts at concentration 100, 200 and 400 µg/mL and incubated for 24 hours. The cellular glucose uptake was determined using 2-NBDG. The values are expressed as means ± SD (n =3).

*$p < 0.05$ vs. control group, $^{\#}p < 0.05$, $^{\#\#}p < 0.01$, $^{\#\#\#}p < 0.001$ vs. LPS treated group.

Conclusion:

The current study firstly demonstrated that the aqueous extract of *C. carandas* ripe fruit improved insulin sensitivity to stimulate glucose uptake in LPS-treated adipocyte. The results suggested a possible use of *C. carandas* fruit as an effective herbal medicine for prevention and treatment of type 2 diabetes mellitus. Thus, the aqueous extract of *C. carandas* fruit is therefore selected for further investigation to verify their anti-diabetic activity in a type 2 diabetes rat model.

Acknowledgments:

This work was supported by Faculty of Medicine Chiang Mai University Research Fund, Research and Researcher for Industries (RRI), Thailand Research Fund and Ampol Food Processing Ltd. (MSD61l0061).

References:

1. American Diabetes A. 1. Diabetes Care. 2017;40(Suppl 1):S6-S10.
2. Sami W, Ansari T. Int J Health Sci. 2017;11(2):65-71.
3. Wellen KE, Hotamisligil GS. J Clin Invest. 2003;112(12):1785-8.
4. Makki K, Froguel P, Wolowczuk I. ISRN Inflamm. 2013;(2013):139239.
5. Singhan C, Suttajit M. NUJST. 2017;(25)3:P1-11.
6. Jampa O, Panthong S. TMJ. 2019;19(4):654-65.
7. Itankar PR, Lokhande SJ, Verma PR, Arora SK, Sahu RA, Patil AT. J Ethnopharmacol. 2011;135(2):430-3.

8. Akansha S, Gursimran KU. Asian J Pharm Clin Res. 2015;8(3):26-30.
9. Weerawatanakorn M, Pan MH. J Food Biochem. 2016;41(3):1-8.
10. Iyer, CM, Dubash, PJ. J Food Sci Tech. 2006;30: 246-8.
11. Gorinstein S, Zachwieja Z, Katrich E, Pawelzik E, Haruenkit R, Trakhtenberg S, *et al*. LWT. 2004;37(3):337-43.
12. Baba SA, Malik SA. J. Taibah Univ Sci. 2015;9(4):449-54.
13. Le XT, Huynh MT, Pham TN, Than VT, Toan TQ, Bach LG, *et al*. Processes. 2019;7(7):2-15.
14. Khattak KF, Simpson TJ. Food Chem 2008;110:967-72.
15. Sudjaroen Y. Int J Green Pharm. 2017;11(1):189-93.
16. Muhammad A, Mehnaz K, Talha J. Asian J Biomed Pharm Sci. 2016;6(58):14-9.
17. Marius T, Torunn KN. Diabetes care. 2013;36:3627-32.
18. Cullberg KB, Larsen JO, Pedersen SB, Richelsen B. Nutr Diabetes. 2014;4:e113.

SP13_005_OF: NANO⁻PHYTOSOME ENTRAPPING *Gymnema inodorum* EXTRACT FOR ENHANCING ANTI⁻INFLAMMATION IN MACROPHAGE

Ratchanon Inpan,[1] Onanong Nuchuchua,[2] Wanwisa Srinuanchai,[2] Rawiwan Nooin,[2] Pornsiri Pitchakarn,[1] Ariyaphong Wongnoppavich,[1] Arisa Imsumran Bonness[1,*]

[1]Department of Biochemistry, Faculty of Medicine, Chiang Mai University, Chiang Mai, Thailand
[2]National Nanotechnology Center (NANOTEC), Thailand Science Park, Klong Luang, Pathumthani 10120, Thailand
*e-mail:arisa.bonness@cmu.ac.th

Abstract:

Gymnema inodorum (GI) is a medicinal plant with anti-diabetic potentials, such as antioxidation, glycemic control, insulin mimetic effect and anti-inflammation. However, bioactive compounds of GI are less water-soluble and present poor bioavailability due to large molecular sizes of GI phytoconstituents. Thus, the purpose of this study was to construct a GI extract in phospholipid carrier (nano-phytosome) to overcome these limitations. The 95% ethanolic extract of GI (GIE95) was used in GIE nano-phytosome preparation. Two formulations of the nano-phytosomes (phytosomes 1 and 2) with GI extract were prepared by solvent evaporation and particles size reduction using extrusion method. The particle characteristics were investigated in terms of size, polydispersity index and zeta potential. The biological activity of the nano-phytosomes was studied in relation to anti-inflammatory effects of macrophages (RAW264.7). The inflammation of RAW264.7 cells was stimulated with lipopolysaccharide (LPS) and treated with various concentrations of GI extract loaded nano-phytosomes (50-200 µg/mL). The cell viability was measured by sulforhodamine B colorimetric assay. The inflammation levels of RAW264.7 cells were indicated by nitric oxide (NO) production using a Griess reagent assay. Our results showed that phytosomes 1 and 2 had particle sizes of 183 ± 10 nm and 158 ± 14 nm, polydispersity index at 0.35 ± 0.02 and 0.23 ± 0.02 and zeta potential at - 43.79 ± 6.20 mV and - 33.98 ± 5.91 mV, respectively. Phytosomes 1 and 2 significantly decreased the NO levels of the RAW264.7 cells. Phytosome 2 showed the higher inhibitory activity of the NO production than phytosome 1 and crude GI extract. In conclusion, the nano-phytosomal system increased the efficiency of the GI extract in the term of anti-inflammation on macrophages.

Introduction:

Disruption of homeostasis and chronic inflammation can cause chronic diseases, such as diabetes, cancer and degenerative diseases.[1] Macrophages play critical roles in our body immune response. They control the initiation, maintenance, and resolution process of inflammation.[2] Toll-like receptors (TLRs) on macrophages are a sensor of inflammation pathway that responds to inducer such as infection or tissue damage.[3,4] Lipopolysaccharide (LPS) is a compound of the outer membrane of gram-negative bacteria.[5] It can increase the production of inflammatory mediators, such as nitric oxide (NO) and prostaglandin E2 (PGE2), and of inflammatory cytokines, such as tumor necrosis factor- (TNF-) α, interleukin- (IL-) 1, and IL-6 in macrophage cells.[6] Thus, LPS-induced NO production in macrophages is used as an inflammation model in this study.

Gymnema inodorum (Lour.) Decne. is a traditional herb found in northern Thailand which has been used as a folk medicine for treating anti-inflammation and diabetes.[7,8] Ethanolic extract of *G. inodorum* (GIE) inhibited nitric oxide production in LPS-stimulated RAW 264.7 macrophage cell lines.[7] Moreover, GIE showed anti-insulin resistance activity as it significantly improved the glucose uptake in tumor necrosis factor-α (TNF-α) treated 3T3-L1 adipocytes.[7] Phytochemicals of this plant are phenolic, flavonoid and triterpenoid

compounds.[7,9,10] Four oleanane triterpenoids, GiA-1, GiA-2, GiA-5 and GiA-7 as anti-diabetic principles were isolated from the leaves of GI.[9] However, their low aqueous solubility can cause effective dose and limited absorption in the gastrointestinal tract.[11] To overcome these limitations, phytosome technology has been recently developed to improve the absorption and bioavailability of herbal extracts. The phytosome is constructed by hydrogen bond formation between natural active compounds and phospholipids.[12] Moreover, phytosomes in nano-sizes with diameters of less than 200 nm are easily cross the intestinal tract into the blood circulation.[13] Many researches have shown that phytosome formulation with another bioactive compound including *Centella asiatica* phytosome,[14] boswellic acids phytosome,[15] and nano-phytosomes of quercetin.[16]

Thus, this study aims to investigate an anti-inflammatory effect of GIE with and without a nano-phytosomal system using an LPS-induced inflammation model on macrophages.

Methodology:

Materials

G. inodorum leaves were collected in December 2018 from Chiang Dao District, Chiang Mai Province, Thailand. Authentication of plant material was carried out at the herbarium of Chiang Mai University (CMU) herbarium and flora database, Department of Biology, Faculty of Science, Chiang Mai University, Thailand, where the herbarium voucher (38430) has been deposited. All other chemicals and solvents used were analytical grade and purchased from Sigma Aldrich Company, USA.

Preparation of Gymnema inodorum ethanolic extract (GIE)

Dried leaf powder of GI (100 g) was soaked with 50% and 95% ethanol and stirred at room temperature for 5 days. The solutions were filtered and concentrated with a rotary vacuum evaporator (Buchi, Switzerland) at 45 °C. The concentrated solution was frozen and dried using a lyophilizer (LTE Scientific Ltd, UK). The dried lyophilized powder of the GIE50 and GIE95 was kept at -30 °C until use.

Preparation of GIE nano-phytosome

Phytosomes were prepared according to the petty patent (registration pending). Various ratios of GIE and lipid mixtures (L) (phosphatidylcholine (P) and cholesterol (C)) were used to prepare GIE nano-phytosomes. Briefly, the GIE:lipid mixture weight ratios of phytosome without extract, phytosome 1 and phytosome 2 were 0:1, 1:1 and 1:2, respectively. The GIE:lipid mixtures were dissolved in ethanol and then evaporated by rotary vacuum evaporator for a thin film formation. In this study, the film was rehydrated with phosphate buffer saline (pH 7.4). Then, the suspension was extruded through membrane filters (200 nm) using Avanti® Mini-Extruder (Avanti Polar Lipids, Inc., USA) to obtain nano-phytosomes with and without GIE.

Size and surface charge characterization of GIE nano-phytosome

The average particle size, polydispersity index (PDI), and zeta potential (ZP) of particles were analyzed by a dynamic light scattering (DLS) technique using Zetasizer® Nano ZS (Malvern Instruments, UK). The measurement was performed in triplicate.

Determination of biological activities

Cell culture

RAW 267.4 macrophage cell lines (CLS, Germany) were cultured in a Corning® Ultra-low attachment culture dish in in Dulbecco's modified Eagle's medium (DMEM) with L-glutamine supplemented with 10 % Fetal Bovine Serum (FBS) and 1% penicillin/streptomycin solution in a 5% CO_2 humidified atmosphere at 37 °C.

Cytotoxicity assay

Macrophage cells were seeded at 2.5×10^4 cells/well in a 96-well plate and treated with various concentrations of GIE, nano-phytosomes with and without GIE for 24 hours. Cytotoxicity was determined using sulforhodamine B (SRB) assay. The SRB protocol has been previously described.[15] Cell viability was calculated to obtain non-toxic concentrations for use in the anti-inflammatory assay.

Anti-inflammatory assay

To evaluate the anti-inflammatory activity of GIE and GIE nano-phytosomes, RAW 264.7 cells (2.5×10^4 cells/well) were cultured in 96-well plate overnight. Cells then were co-treated with 1 µg/mL of lipopolysaccharide (LPS) and samples at various concentrations for 24 hours. The culture supernatant was collected to determine the level of nitric oxide (NO) production by measuring the amount of nitrite in using Griess reagent kit (16). The optical density was measured at 540 nm, and NO production was quantified using a sodium nitrite standard curve.

Statistical analysis

Results were expressed as means ± S.E. Statistical evaluation was done using a one-way analysis of variance (ANOVA) followed by Tukey's post hoc test using GraphPad Prism (GraphPad Software, Inc., San Diego, CA, USA). Differences were considered statistically significant at $P<0.05$

Results and Discussion:

Anti-inflammatory activity of GIE

To evaluate the *in vitro* anti-inflammatory activity of *G. inodorum*, the GIE50 and GIE95 were prepared and investigated for their cytotoxicity and their inhibitory effect on NO production in LPS-treated macrophages. As shown in Figure 1, the cytotoxic effect of extracts on RAW 264.7 cells was tested by the SRB assay at concentrations ranging from 6.25 to 800 µg/mL. Maximum non-cytotoxic concentration of both GIE50 and GIE95 are 400 µg/mL. Thus, the GI extract concentrations ranging from 50 to 400 µg/mL were used in further experiments.

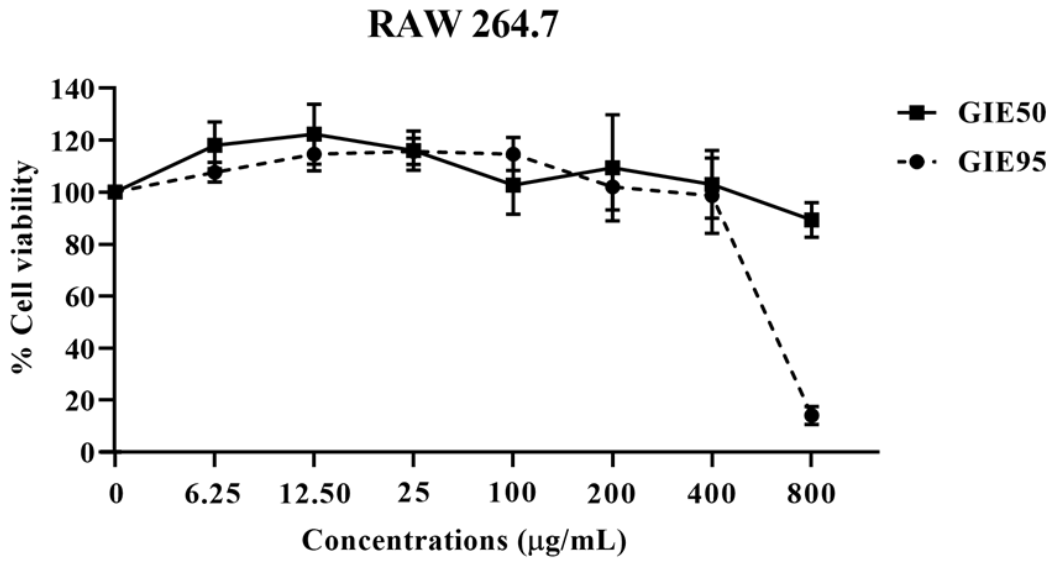

Figure 1. The effect of GIE50 and GIE95 on cell viability of RAW 264.7 macrophage cell line. Cells were treated with various concentrations of the GI extract (6.25-800 µg/mL) for 24 hours. Cell viability was measured by SRB assay.

Figure 2 shows the effect of the GIE on LPS- induced nitric oxide (NO) production in RAW 264.7 macrophages. As expected, LPS-treated macrophages significantly increased NO production level compared to untreated control, whereas cells treated with GIE50 and GIE95 produced significantly lower levels of NO in a dose-dependent manner. However, GIE95 showed significantly higher anti-inflammatory activities than the GIE50 at the same concentration. The inhibition rates of GIE95 at concentrations of 100, 200 and 400 µg/mL were in a range of 30 ± 6.09% - 45 ± 3.30%. Therefore, GIE95 was selected for nano-phytosome preparation.

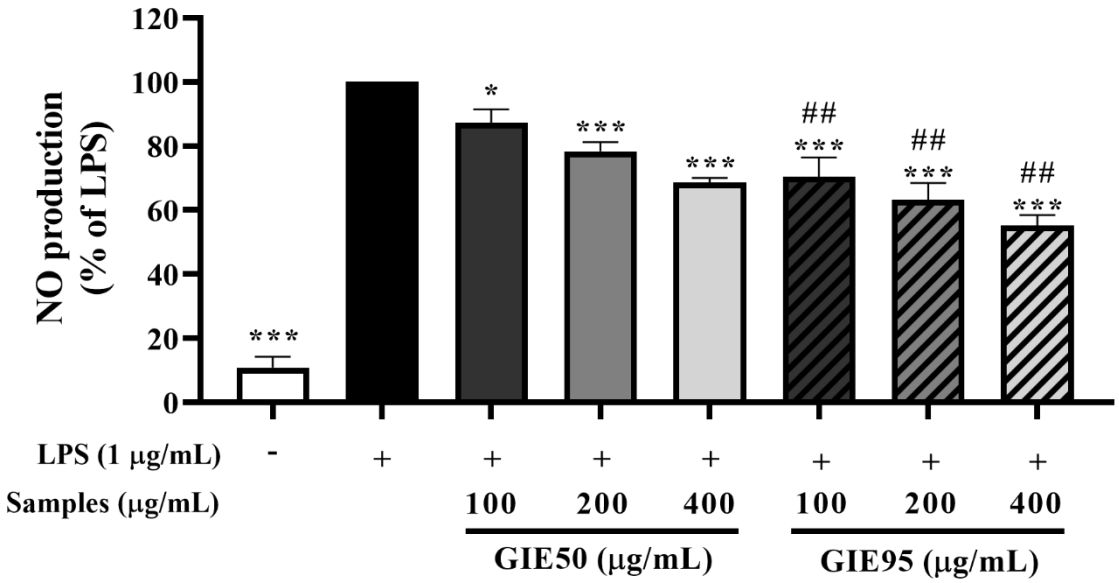

Figure 2. The effect of the GIE on LPS- induced nitric oxide production in RAW 264.7 macrophages. Cells were co-treated with 1 µg/mL of LPS and different concentrations of GIE50 or GIE95 (100, 200 and 400 µg/mL) for 24 hours. The conditioned media were collected and analyzed for nitrite content using Griess reagent. The absorption was determined at 540 nm. Levels of NO production are expressed relative to LPS-treated alone group. $^{*}p< 0.05$, $^{***}p< 0.001$ vs. LPS-treated alone group; $^{\#\#}p< 0.01$ vs. GIE50 at the same concentration.

Size and surface charge characterization of GIE nano-phytosome

Particle size, size distribution and zeta potential are important characters of nanoparticle delivery systems which affect their stability, bio-distribution and cellular uptake. The average particle size, PDI value and zeta potential of nano-phytosomes with and without GIE were summarized in Table 1. The average particle sizes of phytosome without GIE, phytosome 1 and phytosome 2 were 2389 ± 748 nm, 545 ± 271 nm, and 517 ± 166 nm, respectively. After reducing size, phytosome without GIE was 164 ± 11 nm whereas phytosome 1 and phytosome 2 were 180 ± 14 nm and 166 ± 29 nm, respectively. All particles had particle size less than 200 nm and were not different in size. Particle size less than 200 nm shows greater permeation across the intestinal mucus barrier.[17] Particle size can also impact the distribution of nanoparticles because it prolongs blood circulation time and improves bioavailability.[17]

Furthermore, all PDI values before reducing size showed wide distribution patterns. PDI values of phytosome without GIE, phytosome 1 and phytosome 2 were 0.98 ± 0.03, 0.61 ± 0.12 and 0.43 ± 0.06, respectively. After reducing size, all particles showed a narrow particle size distribution. Phytosome without GIE had the lowest PDI at 0.13 ± 0.01 followed by phytosome 2 and phytosome 1 at 0.22 ± 0.02 and 0.32 ± 0.04,

respectively. The results indicated that all particles had higher particle size homogeneity than that before reducing size.[18]

The nanoparticles with zeta potentials above + 30 mV and below - 30 mV have greater suspension stability since the charge on the surface prevents the particles aggregation.[19] All particles in this study had a negative charge on the particle surface. Either before or after reducing size, phytosome without GIE had a zeta potential above - 30 mV, indicating poor stability. Interestingly, either before or reducing size, phytosomes 1 and 2 had higher negative values than phytosome without GIE (Table 1). And they were above -30 mV which indicate excellent stability of phytosome because particles are difficult to be fused or aggregated by increasing of particle charge.[19] Moreover, some studies had shown that cerium oxide nanoparticles having a zeta potential below - 30 mV displayed better cellular uptake when related to another particle with a less negative charge.[20] Hence, with smaller particle size, lower polydispersity index and modest zeta potential value suggested a good physical stability for GIE nano-phytosome.

Table 1. Particle size, polydispersity index (PDI) and zeta potential of nano-phytosomes with or without GIE95

		Size (nm)	PDI	Zeta potential (mV)
Phytosome without GIE	Before reducing size	2389 ± 748	0.98 ± 0.03	-7.79 ± 3.83
	After reducing size	164 ± 11	0.13 ± 0.01	-9.31 ± 1.01
Phytosome 1	Before reducing size	545 ± 271	0.61 ± 0.12	-49.74 ± 0.77
	After reducing size	183 ± 1	0.35 ± 0.02	-43.79 ± 6.20
Phytosome 2	Before reducing size	517 ± 166	0.43 ± 0.06	-41.86 ± 1.45
	After reducing size	158 ± 14	0.23 ± 0.02	-33.98 ± 5.91

All values are presented as mean ± SE (n = 3).

Cytotoxicity of GIE nano-phytosome in RAW 264.7 macrophage cell line

The cytotoxicity of phytosome without GIE, phytosome 1 and phytosome 2 after reducing size on RAW 264.7 cells was evaluated using SRB assay. The results revealed that phytosome without GIE, phytosome 1 and phytosome 2 at contentrations up to 200 µg/mL had toxic effect on RAW 264.7 cells less than 20% (Figure 3). Thus, the concentrations at 50, 100 and 200 µg/mL were selected to investigate their anti-inflammatory activity.

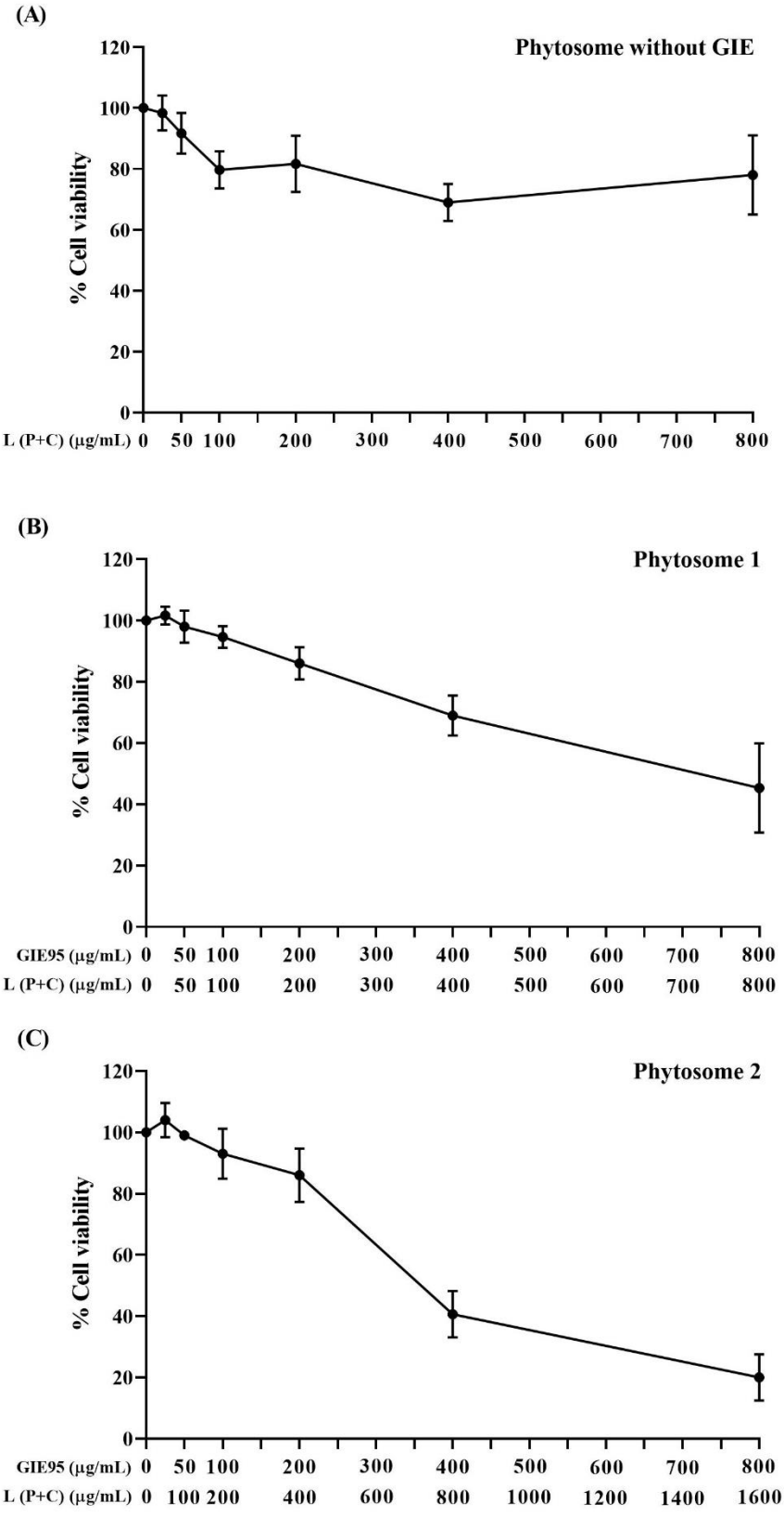

Figure 3. Effect of phytosome without GIE, phytosome 1 and phytosome 2 on cell viability of RAW 264.7 macrophage cell line. Cells were treated with various concentrations of each particle (25-800 µg/mL) for 24 hours. The cell viability was measured by SRB assay. Note. L (P+C) stands for the lipid mixtures (phosphatidylcholine and cholesterol).

Anti-inflammatory activity of GIE nano-phytosome

Next, we investigated the anti-inflammatory activity of GIE nano-phytosome by measuring the level of NO production in LPS-induced RAW 264.7 cells. As shown in Figure 4, all treatments with various concentrations (50-200 µg/mL) including GIE, phytosome without GIE, phytosome 1 and phytosome 2 significantly and dose-dependently reduced LPS-induced NO production in RAW 264.7 cells. The highest NO production inhibitory activity was found in phytosome 2 followed by phytosome 1, phytosome without GIE, respectively. Interestingly, phytosome without GIE also had inhibitory activity on NO production. Previous study which published on curcuminoid phytosome without GIE also showed a higher inhibitory activity on NO production in macrophages than curcuminoid. Moreover, several activities of curcuminoid phytosome without GIE were also higher than those of pure compound curcuminoid such as IL-1β and TNFα level.[21]

Thus, this study indicated that GIE nano-phytosome not only maintained its anti-inflammatory activity but it had higher inhibitory activity on LPS-induced inflammation in macrophages than GI extract or phytosome without GIE alone at the same concentration.

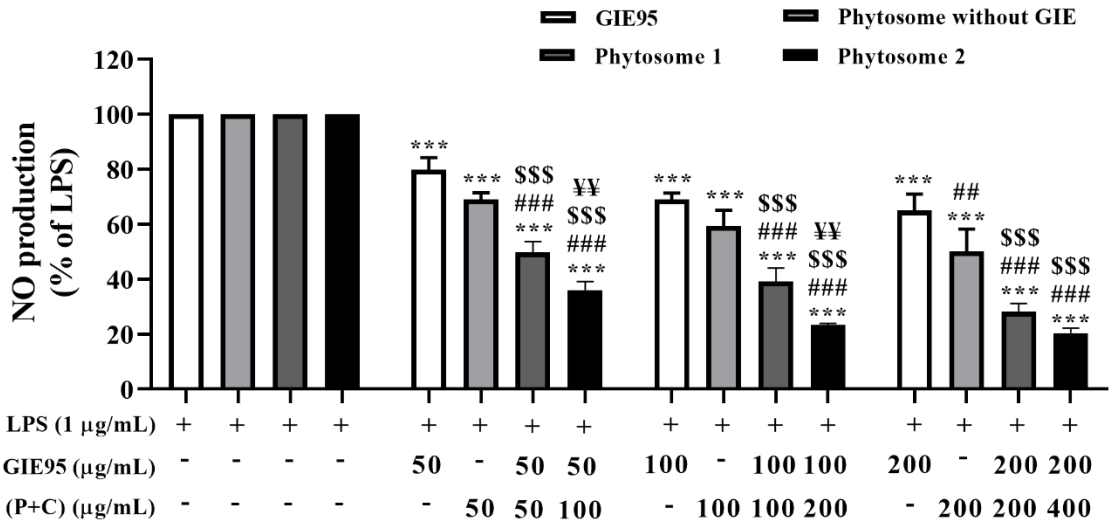

Figure 4. Effect of the GIE nano-phytosome on LPS- induced NO production in RAW 264.7 cells. Cells were co-treated with 1 µg/mL of LPS and various concentrations of GIE95, phytosome without GIE, phytosome 1 and phytosome 2 for 24 hours. The conditioned media were collected and analyzed for nitrite content using Griess reagent. Absorbance was determined at 540 nm. Levels of NO production are expressed relative to the LPS-treated alone group. *p < 0.001 vs. LPS control. $^{\#\#}p$<0.01 and $^{\#\#\#}p$<0.001 vs. GIE95 of each group. $^{\$\$\$}p$<0.001 vs. phytosome without GIE of each group. $^{¥¥}p$<0.01 vs. phytosome 1 of each group. Note. L (P+C) stands for the lipid mixtures (phosphatidylcholine and cholesterol).

Conclusion:

The GIE nano-phytosomes were successfully produced. Physicochemical characterization of the GIE nano-phytosomes revealed their good physical stability with smaller particle size, lower polydispersity index and modest zeta potential value. The anti-inflammatory activity of GIE nano-phytosomes on LPS-stimulated RAW 264.7 macrophages is greater compared to the *G. inodorum* crude extract. Altogether, this present study showed that the developed GIE nano-phytosome has potent anti-inflammatory effects on LPS-induced RAW 264.7 macrophages and seems to be a promising anti-inflammation agent.

Acknowledgements:

This work was supported by the Thailand Graduate Institute of Science and Technology (TGIST); Grant number SCA- CO- 2561- 7040TH, National Science and Technology Development Agency (NSTDA) and National Nanotechnology Center (NANOTEC), Thailand.

References:

1. Clancy RM, Amin AR, Abramson SB. Arthritis Rheum. 1998;41(7):1141-51.
2. Chen L, Deng H, Cui H, Fang J, Zuo Z, Deng J, *et al*. Oncotarget. 2017;9(6):7204-18.
3. Medzhitov R. Cell. 2010;140(6):771-6.
4. Aderem A, Ulevitch RJ. Nature. 2000;406(6797):782-7.
5. Raetz CR. Annu Rev Biochem. 1990;59:129-70.
6. Kim ID, Ha BJ. Toxicol In Vitro. 2009;23(6):1014-9.
7. Waloh N. Master's thesis. Chiang Mai University, Chiang Mai, Thailand. 2014.
8. Bespinyowong R, Pongthananikorn S, Chiabchalard A. Chula Med J 2013; 57(5):587 - 99
9. Shimizu K, Ozeki M, Iino A, Nakajyo S, Urakawa N, Atsuchi M. Jpn J Pharmacol. 2001;86(2):223-9.
10. Srinuanchai W, Nooin R, Jarussophon S, Kasemwong K, Nuchuchua O. J Chem Metrology. 2019;13(2):75-9.
11. Walle T. Free Radic Biol Med. 2004;36(7):829-37.
12. Ghanbarzadeh B, Babazadeh A, Hamishehkar H. Food Bioscience. 2016;15:126-35.
13. Primard C, Rochereau N, Luciani E, Genin C, Delair T, Paul S, *et al*. Biomaterials. 2010;31(23):6060-8.
14. Ju Ho P, Jun Sung J, Ki Cheon K, Jin Tae H. Phytomedicine. 2018;43:110-9
15. Husch J, Bohnet J, Fricker G, Skarke C, Artaria C, Appendino G, *et al*. Fitoterapia. 2013;84:89-98.
16. Rasaie S, Ghanbarzadeh S, Mohammadi M, Hamishehkar H. Pharm Sci. 2014;20:96-101.
17. Vichai, V. and Kirtikara K. Nat Protoc, 2006. 1(3):p.1112-6.
18. Yang E-J, Kim J-G, Kim J-Y, Kim S, Lee N, Hyun C-G. Open Life Sci. 2010;5(1):95-102.
19. Gamboa JM, Leong KW. Adv Drug Deliv Rev. 2013;65(6):800-10.
20. Hughes JM, Budd PM, Grieve A, Dutta P, Tiede K, Lewis J. J Appl Polym Sci. 2015;132(24).
21. Beck- Broichsitter M, Ruppert C, Schmehl T, Guenther A, Betz T, Bakowsky U, *et al*. Nanomedicine. 2011;7(3):341-50.
22. Patil S, Sandberg A, Heckert E, Self W, Seal S. Biomaterials. 2007;28(31):4600-7.
23. Basnet P, Hussain H, Tho I, Skalko-Basnet N. J Pharm Sci. 2012;101(2):598-609.

SP13_006_PA: *Cordyceps militaris* EXTRACT USING GLYCERIN AS A SOLVENT

Benjamat Chailap, Thanesuan Nuanyai*

General Education Department, Faculty of Liberal Arts, Rajamangala University of Technology Rattanakosin, Wang Klai Kangwon Campus, Nongkae, Huahin, Prachuap Khiri Khan 77110, Thailand
*e-mail: thanesuan.nua@rmutr.ac.th

Abstract:

Cordyceps militaris belonging to the *Cordyceps* species, have received attention in various bioindustries applications such as in pharmaceuticals, functional foods, and cosmetics, because of its significant functions. This research objective was to investigate the antioxidant activities of ethanol and glycerin extracts of *C. militaris*. The antioxidant activity determination was carried out by 2,2-diphenyl-1-picryl-hydrazyl-hydrate (DPPH), 2,2'-azino-bis (3-ethylbenzthiazoline-6-sulphonic acid) (ABTS), and nitric oxide (NO) methods. Ten grams of fresh *C. militaris* was blended and extracted with 90 grams of ethanol (EOH) or glycerin (GCR) solution in H_2O (50% w/w) at room temperature for 4 hours. The extract solutions were centrifuged at 6,000 g for 30 min to collect the liquid supernatant. The supernatants were evaporated at 45 °C with a rotary evaporator. The residue was diluted to 50 ml with 50% methanol solution and restored at −20 °C. Antioxidant activity of the *C. militaris* extracts against DPPH radical revealed that the extracts had high antioxidant activity (percentage of inhibition = 80.71 ± 0.58 for EOH, 82.59 ± 7.01 for GCR). However, antioxidant activity of *C. militaris* extract using ABTS assay was 98.02 ± 1.20 for EOH and 96.04 ± 0.52 for GCR. In addition, both EOH and GCR extracts had moderate activity against nitric oxide (NO) with NO levels of 21.30 ± 0.50 and 22.05 ± 0.43 µmol/L of $NaNO_2$, respectively. The results revealed that the antioxidant activities of the *C. militaris* extracts from ethanol and glycerin, were similar. However, the advantage of glycerin extract is that it can be mixed into a cosmetic formula without being concentrated. Moreover, glycerin is an emollient for cosmetic ingredient. Therefore, the glycerin extract could be the economical ingredient in cosmetic production.

SP13_007_OA

SP13_007_OA: POLY-*O*-ACYLATED β-DIHYDROAGAROFURAN SESQUITERPENOIDS FROM *Siphonodon celastrineus* FRUITS

Suriphon Singha,[1] Pathumwadee Yotmanee,[1] Jantana Yahuafai,[2] Pongpun Siripong,[2] Samran Prabpai,[3] Somyote Sutthivaiyakit[1,*]

[1]*Department of Chemistry and Center of Excellence for Innovation in Chemistry, Faculty of Science, Ramkhamhaeng University, Hua Mark, Bangkapi, Bangkok, 10240, Thailand*

[2]*Natural Products and Integrative Medicine Research Section, Research Division, National Cancer Institute, Rama VI Road, Bangkok, 10400, Thailand*

[3]*CP Foodlab Co. Ltd., Thailand Science Park, Paholyothin road, Klong 1, Klong Luang, Pathumthani, 12120, Thailand*

*e-mail: somyote_s@yahoo.com

Abstract:

Ten new poly-*O*-acylated β-dihydroagarofuran sesquiterpenoids (**1-10**) together with sixteen known β-dihydroagarofuran sesquiterpenoids (**11**–**26**) were obtained from CH_2Cl_2 extract of the fruits of *Siphonodon celastrineus* (Celastraceae) known in Thai as "Ma-Duk". Structures of the isolated compound were elucidated by extensive use of 2D NMR spectroscopic methods. The absolute configurations of compounds **1-10** were assigned following analysis of their calculated and experimental ECD spectra. The absolute configuration of compound **1** was also confirmed by X-ray crystallographic analysis. Some compounds were evaluated for their cytotoxic activity against Hela (human cervical carcinoma) cells, KB (Human oral epidermoid carcinoma) cells and Vero (African green monkey kidney) cells. Compound **10** was the most active against KB and Hela cells with IC_{50} values of 14.8 ± 0.9 and 21.9 ± 0.4 µM, respectively.

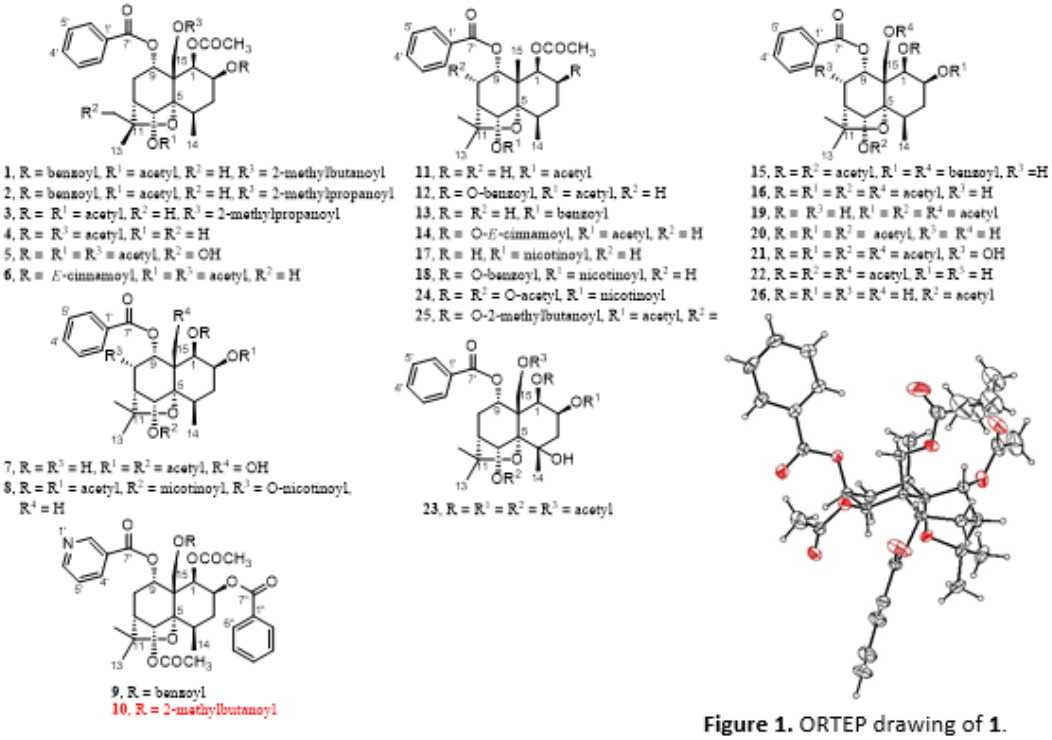

Figure 1. ORTEP drawing of **1**.

SP13_008_PA

SP13_008_PA: CYTOTOXIC CARDIAC GLYCOSIDES WITH RARE SUGARS AND TRITERPENOID CINNAMATES OF *Vallaris glabra*

Sudarat Kruakaew,[1] Chonticha Seeka,[1] Thitima Lhinhatrakool,[2] Sanit Thongnest,[3] Jantana Yahuafai,[4] Suratsawadee Piyaviriyakul,[4] Pongpun Siripong,[4] and Somyote Sutthivaiyakit,[1]*

[1]Department of Chemistry and Center of Excellence for Innovation in Chemistry, Faculty of Science, Ramkhamhaeng University, Bangkok 10240, Thailand
[2]College of Oriental Medicine, Rangsit University, Muang Ake, Pathumthani 12000, Thailand
[3]Chulabhorn Research Institute, Kamphang Phet 6 Road, Bangkok 10210, Thailand
[4]Natural Products and Integrative Medicine Research Section, Research Division, National Cancer Institute, Rama VI Road, Bangkok 10400, Thailand
*e-mail: somyote_s@yahoo.com

Abstract:

Chemical investigation of the CH_2Cl_2 and MeOH extracts of the leaves and stems of *Vallaris glabra* (L.) Kuntze (Apocynaceae), known in Thai as "chom-ma-nat", resulted in the isolation of twenty-three known cardenolide glycosides (**1-23**) together with six known triterpenoid cinnamates (**24-29**). Structures of the isolated compounds were identified by spectroscopic methods, with the absolute configurations of the sugar moieties determined by acid hydrolysis. Structure-activity relationship of all isolates was evaluated for their inhibitory activities against panel of cancer cell lines [A-549 (human lung carcinoma), HeLa **(**human cervical carcinoma**)**, KB (human oral epidermoid carcinoma), HT-29 **(**human colorectal adenocarcinoma**)** and Vero **(**normal African green monkey kidney**)** cells]. Almost all compounds exhibited inhibitory activities with IC_{50} values ranging from 0.03-7.1 μM.

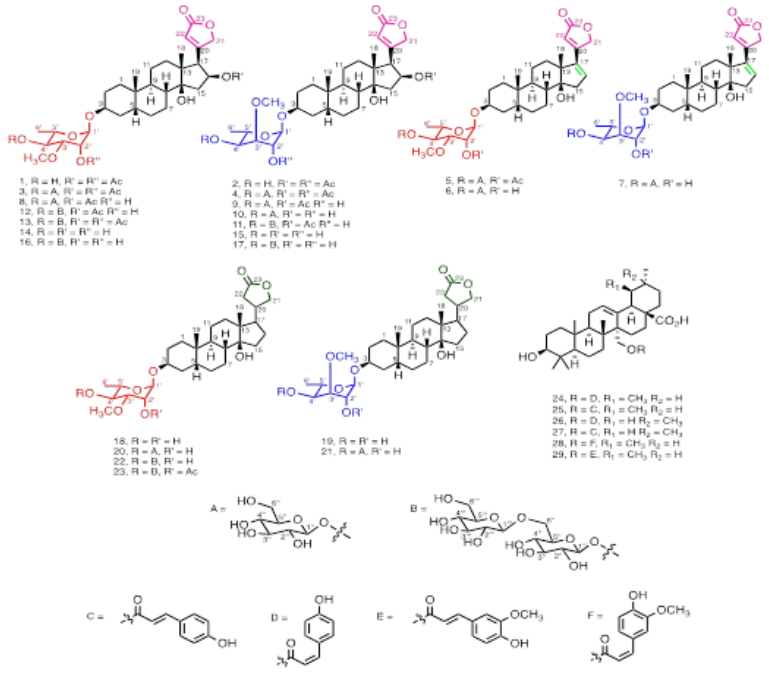

SP13_009_PA: BIOFUMIGATION ACTIVITY OF VOLATILE COMPOUNDS PRODUCED FROM *Pestalotiopsis* ENDOPHYTIC FUNGUS AGAINST *Melissococcus plutonius* IN HONEYCOMB

Patcharee Pripdeevech,[1,2,*] Teerapong Sripahco,[1]

[1]School of Science, Mae Fah Luang University, Chiang Rai 57100, Thailand
[2]Center of Chemical Innovation for Sustainability (CIS), Mae Fah Luang University, Chiang Rai, 57100, Thailand
*e-mail: patcharee.pri@mfu.ac.th

Abstract:

Fungal endophytes are microorganisms living symbiotically with a host plant. They can produce volatile compounds that have antimicrobial activity. This study aimed to isolate endophytic fungi from *Zingiber cassumunar* leaves and to investigate the antibacterial property of the volatile compounds produced from these endophytic fungi against *Melissococcus plutonius* that cause European foul brood disease of honey bees in honeycomb. A total of 15 endophytic fungi were isolated from *Z. cassumunar* leaves. Volatile compounds produced from each individual isolate were screened for their antibacterial activity against *M. plutonius* using the dual-culture plate method. From this *in vitro* screening experiment, the volatile compounds produced by the endophytic isolate ZC05 were found to have the highest inhibition percentage (86.34%) against the bacterial growth of *M. plutonius*. The suitable solid medium for inoculum production of endophytic isolate ZC05 was then investigated. The fungus was able to grow fastest on jasmine rice grain. Solid phase microextraction-gas chromatographic-mass spectrometric analysis of the volatile compounds produced by the endophytic isolate ZC05 led to the detection and identification of 35 volatile compounds. The major compounds were α-gurjunene, γ-muurolene, α-muurolene, and acetic acid. Based on the results of the polymerase chain reaction assay, the endophytic isolate ZC05 was found to be a member of the genus *Pestalotiopsis.* This work suggests that the *Pestalotiopsis* sp. ZC05 could be a promising natural preservative for controlling the European foul brood disease of honey bees in honeycomb.

SP13_010_PA: ANTI-BACTERIAL ACTIVITY OF CRUDE EXTRACTS FROM RED CALYX AND PEEL OF ROSELLE, DRAGON FRUIT, AND PASSION FRUIT

Radtanaporn Phongvinyan, Thaniwan Cheun-Arom, Ruethairat Boonsombat*

Department of Biology, Faculty of Science, Ramkhamhaeng University, Bangkapi, Bangkok, Thailand
*e-mail: ruethairatboonsombat@gmail.com

Abstract:

This research aimed to investigate the antibacterial activity of crude extracts from red roselle (*Hibiscus sabdariffa L.*) calyx, dragon fruit (*Hylocereus Undatus* (Haw) Brit. & Rose) peel, and passion fruit (*Passiflora Edulis*) peel. All crude extracts were dissolved in distilled water or 50% dimethyl sulfoxide (DMSO) in water (v/v). After screening the anti-bacterial activity against three bacterial pathogens including *Bacillus cereus*, *Escherichia coli,* and *Staphylococcus aureus* by agar well diffusion method at the concentration of 1000 mg/ml, the crude extracts from roselle calyx exhibited significantly higher activity than the others. Then, the minimum inhibitory concentration (MIC) and the minimum bactericidal concentration (MBC) values were further analyzed. Among these three samples, the extract from roselle calyx was the most promising agent to inhibit the growth of all tested bacteria. However, when the roselle calyx extract dissolved in 50% DMSO in the water at the concentration more than 250 mg/ml was added to Nutrient broth (NB) during MIC assay, visible growth of *S. aureus* was not observed in NB, but bacteria colonies were formed on Nutrient agar (NA) during MBC assay. From these results, there might have been some compounds from roselle calyx extract dissolved in 50% DMSO in water that could inhibit the *S. aureus* growth, but not completely kill this bacterial species. Optimization of the extraction process along with other studies such as the identification of bioactive compounds and screening of other biological activities from these crude extracts are further required.

Introduction:

Various pathogenic bacteria are causes of pathological conditions that can lead to mortality. Although many of bacteria-causing diseases are curable by antibiotics, many could not be treated. Furthermore, antibiotic resistance becomes a serious health issue which is considered to be one of the greatest threats to global health1. Therefore, it is essential to discover new anti-microbial agents. Currently, natural products become highly interested to use for this purpose.

In this research, we focused on screening anti-bacterial activity of crude extracts from red calyx or peel from fruits which are favorably edible including roselle (*Hibiscus sabdariffa L.*) calyx, dragon fruit (*Hylocereus Undatus* (Haw) Brit. & Rose) peel, and purple passion fruit (*Passiflora Edulis*) peel. Roselle (also called Jamaica Sorrel, Red Sorrel, Roselle, Rozelle), a member of the Malvaceae family, contains high nutritional and medicinal values, due to being a source of high vitamin C, anthocyanin contents, fibers, and many minerals such as calcium and iron.[2] Its red calyx is favorably used to make juice, food color, and sour flavoring. The aqueous extract of roselle calyx exhibited several biological effects including anti-microbial activity against *S. aureus, E. coli,* and *Klebsiella pneumonia*, antioxidant activity, and antiproliferative and apoptotic activities in cervical (HeLa) cancer cell lines.[3] Dragon fruit is in the Cactaceae family. Its peel is a good source of pectin.[4] Moreover, the extracted red color contains phenolic compounds including chlorogenic acid, gallic acid, and quercetin that exhibited moderate antioxidant activity.[5] Passion fruit is a member of the Passifloraceae family and globally used. It is also considered as a functional food due to being a source of high flavonoids and triterpenoids, and biological activities such as antioxidant, anti-hypertensive, anti-tumor, anti-diabetic, hypolipidemic activities of extracts, juice, and isolated compounds.[6] Therefore, bioactive compounds from these fruits are of interest.

B. cereus is a gram-positive spore-forming bacterium distributed in the environment and able to cause foodborne illness.[7] For *E. coli*, it is a gram-negative bacterial species. Although it is a normal flora, some strains can cause serious illness. Moreover, a rise of multidrug-resistant strains of *E. coli* has been reported.[8] The other gram-positive bacterial species used in this experiment is *S. aureus*. Although it lives commensally with humans, it can be an opportunistic pathogen that causes many serious illnesses. Furthermore, antibiotic-resistant bacteria, especially, methicillin-resistant *Staphylococcus aureus* (MRSA), becomes challenging.[9] The purpose of this study is to find a simple but practical method for extracting anti-bacterial substances from these edible fruits. Then, the antibacterial activity of the crude extracts against *B. cereus*, *E. coli*, and *S. aureus* was evaluated.

Methodology:

Preparation of Crude Extract

Red roselle, dragon fruit, and purple passion fruit were purchased from Bang Kapi Market. After being washed, 500 g of roselle calyx, dragon fruit peel, and purple passion fruit peel were chopped and then dried in a hot air oven at 50 ˚C. The dried samples were mashed by a mortar. Samples were extracted by maceration technique.[10] Briefly, 50 g of mashed samples was soaked in 350 ml of 70% (v/v) ethanol mixed with 150 ml of distilled water for 3 days. Then, samples were filtered by a cotton sheet. The filtrate was kept in dark while the residue was repeatedly extracted for 3 times. Ethanol and water were evaporated from the filtrate of extracted samples by using Rotatory Evaporator at 50 ˚C and cooling at 4 ˚C with the pressure of 175 mbar, and heating by a hot plate, respectively. The crude extracts were then kept at 4 ˚C. The percentage yield was calculated as the following:

$$\% \text{ yield} = \frac{\text{weight of the crude extract}}{\text{weight of the dried sample}} \times 100$$

Agar Well Diffusion Method

All crude extracts were dissolved in distilled water or 50% DMSO in water (v/v) to the final concentration of 1000 mg/ml. Then, they were subsequently tested for antibacterial activity by agar well diffusion method adapted from the protocol of Perez et al., (1990).[11] The inoculums of three species of bacteria, including *B. cereus* ATCC11778, *E. coli* ATCC25922, and *S. aureus* ATCC25923, were prepared by growing overnight in Nutrient broth (NB) at 37 ˚C. Each bacterial suspension was adjusted to 0.5 McFarland Standard in Normal Saline Solution (NSS) and then spread on Nutrient agar (NA) using a sterile cotton swab. Wells with a diameter of 4-6 mm. were made by using a sterile cork borer. 10 µl of each sample was added into the well and allowed to diffuse at room temperature for 2 h. Ampicillin (1 mg/ml), and distilled water or 50% (v/v) DMSO were served as controls. Then, all plates were incubated at 37 ˚C for 18 h. Each experiment was performed in triplicate. The diameter of the inhibition zone (DIZ) was determined by measuring the clear zone that appeared around each well in the unit of mm. The antimicrobial index (AI) was calculated as the following.[12]

$$\text{AI} = \frac{\text{(DIZ- Diameter of well)}}{\text{Diameter of well}}$$

Determination of Minimum Inhibitory Concentration (MIC)

This assay was adapted from the protocol of CLSI (2009).[13] The anti-bacterial activity of the active crude extracts was determined by the agar well diffusion method. The crude extracts were diluted as 2-fold dilutions: 1000, 500, 250, 125, and 62.5 mg/ml, in distilled water or 50% (v/v) DMSO, and then 100 µl of each sample was added to 5 ml of NB. The bacterial suspension of each species, from overnight inoculum, was adjusted to 0.5 McFarland Standard in Normal Saline Solution (NSS), and then 100 µl of diluted bacterial suspension was added to each tube of NB with the crude extract. Ampicillin (final concentration of 100 µg/ml), and distilled water or 50% DMSO in water (v/v) were served as controls. All tubes were incubated at 37 ˚C for 18 h. Experiments were carried out in triplicate. The growth of bacteria was determined by turbidity. The MIC value is the lowest concentration of the tested sample that can inhibit any visible bacterial growth in the culture broth.

Determination of Minimum Bactericidal Concentration (MBC)

To determine MBC values, the drop plate technique was adapted from the protocol of CLSI (2009).[13] All the tubes without visible growth of bacteria from MIC assay were collected. 10 µl of each sample was dropped on the NA plate and allowed to dry at room temperature for 1 h. All plates were then incubated at 37 ˚C for 18 h. The MBC value is the lowest concentration of the tested sample that can kill bacteria, so the bacterial colony could not be formed on the agar plate. Experiments were performed in triplicate.

Results and Discussion:

The crude extracts were obtained as viscous oil with the percentage yield as shown in Table 1. The extracts were dissolved in distilled water to dissolve phenolic compounds and anthocyanin found in tested fruit as suggested by the previous reports.[2,5,6,14] The crude extracts were also dissolved in DMSO, a solvent dissolving both polar and nonpolar compounds, with a concentration of 50% dimethyl sulfoxide (DMSO) in water (v/v) which was non-toxic to all tested bacteria in this work.[15] Anti-bacteria activity of these crude extracts, assayed by agar well diffusion method, was analyzed as antimicrobial inhibition index (Figure 1). For *B. cereus*, all extracts in both aqueous and DMSO solutions inhibited the growth of this pathogen. The highest ability was observed from the roselle calyx extract while the extracts of dragon fruit peel and passion fruit peel gave similar results. Furthermore, the roselle calyx extract dissolved in both water and DMSO also showed a significantly higher ability to inhibit *S. aureus* growth than those of dragon fruit peel and passion fruit peel. However, the extracts from the dragon fruit peel and passion fruit peel in 50% (v/v) DMSO exhibited mild antibacterial activity against *S. aureus*, which was not significantly different from the DMSO control. For *E. coli*, only the crude extracts from roselle calyx in both solutions showed anti-bacterial activity. These results suggested that the crude extracts from the dragon fruit peel and passion fruit peel were selectively active against gram-positive bacteria because the antibacterial activity of these extracts was observed only against *B. cereus* and *S. aureus*. Due to the difference in cell wall structures between gram-positive and gram-negative bacteria, antibiotics used are different. Antibiotics for gram-negative bacteria are smaller in size and more polar than ones for gram-negative bacteria.[16] Furthermore, the antimicrobial mechanism of some compounds such as polyphenols was suggested to be involved in interactions with the bacterial cell surface.[17] Therefore, from this experiments, we hypothesized that anti-bacterial activities against only gram positive bacteria (*B. cereus* and *S. aureus*) of crude extracts from dragon fruit and passion fruit peels might be resulted from some compounds in these crude extracts that target the cell wall structure of bacteria**.** However, it is too early to be concluded. Therefore, to test this hypothesis, further experiments including screening anti-bacterial activities of our extracts against more bacterial pathogens and identify compounds in these extracts are required.

Table 1. The percentage yield of crude extracts from 500 g of wet weight

Sample	% yield
Roselle calyx	42.79
Dragon fruit peel	17.40
Passion fruit peel	19.84

MIC and MBC values of the crude extracts are summarized in Tables 2 and 3, respectively. For *B. cereus* and *S. aureus*, active compounds inhibiting the bacterial growth were probably better dissolved in DMSO as MIC values of all extracts was lower than ones dissolved in water (Table 2). Moreover, compounds as inhibitors against *B. cereus* and *S. aureus* were previously reported to be dissolved in DMSO.[18-20] The crude extracts of roselle calyx dissolved in water displayed the same MIC values of 500 mg/ml against both *B. cereus* and *S. aureus* whereas MIC values of the extract dissolved in DMSO against both bacteria were 125 mg/ml and 250 mg/ml, respectively (Table 2). The MIC values against these two pathogens were 500 mg/ml for the crude extracts from both dragon fruit peel and passion fruit peel in DMSO solution. However, these extracts dissolved in distilled water were inactive. For *E. coli*, equal MIC values of 500 mg/ml were obtained from crude extracts of roselle calyx dissolved in water and 50% (v/v) DMSO (Table 3).

During the experiment conducted with *B. cereus*, it is found that the MBC of roselle extracts dissolved in water is 1000 mg/ml. The MBC of roselle extracts dissolved in DMSO solution is 500 mg/ml. For *E. coli*, it is found that the MBC of roselle extracts dissolved in DMSO solution is 500 mg/ml. However, the MBC cannot be found in the roselle extracts dissolved in water (as those dissolved in DMSO solution yield better results). Hence, it is predicted that certain substances found in the extracts may possess greater dissolvability in DMSO solution. However, in the case of *S. aureus*, its MBC which is dissolved in DMSO solution cannot be measured. Thus, it is predicted that the substances capable of disinfecting bacteria may be phenolic compounds with greater dissolvability in water.[14] Nevertheless, the circumstance that the MIC from DMSO solution measured is low may be resulted from the bacterial growth inhibitory property, not sterilization property, of *S. aureus*.

To inhibit the growth of *B. cereus* and *S. aureus*, the MIC values could not be identified from the dragon fruit and passion fruit peel extracts in aqueous solution (Table 2). However, when dissolved in DMSO, both extracts gave the MIC values of 500 mg/ml (Table 2) and MBC values of 1000 mg/ml for *B. cereus* (Table 3). In the assay with *S. aureus*, these two extracts in the DMSO solution showed MIC values of 1000 mg/ml (Table 2), but their MBC values could not be analyzed (Table 3). We hypothesized that some certain substances in these crude extracts may be slightly better dissolved in DMSO. Therefore, to proof this hypothesis, further experiment will focus on identification of compounds in these crude extracts.

Although some of the antibacterial activity of our three crude extracts was observed, high concentrations were used to inhibit the growth of these bacteria. Further studies should focus on appropriate solvents for better solubility of these crude extracts. Screening for other biological activities is one of the challenging topics. Furthermore, the identification of bioactive compounds in these extracts will be of interest.

(a.) *B. cereus*

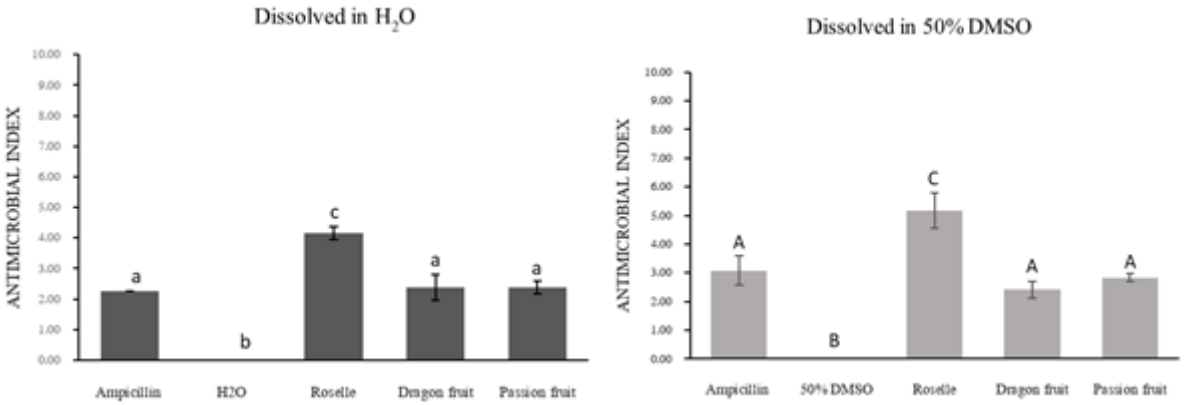

(b.) *E. coli*

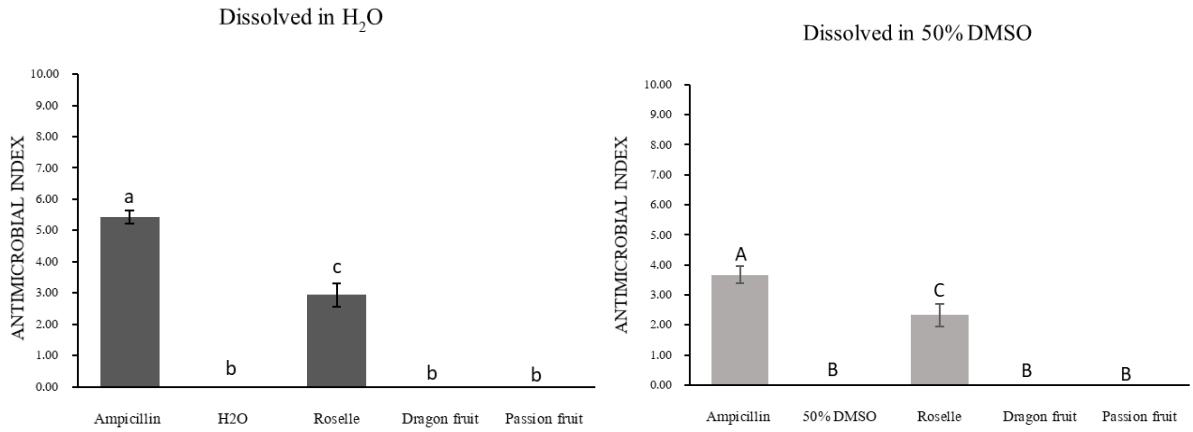

(c.) *S. aureus*

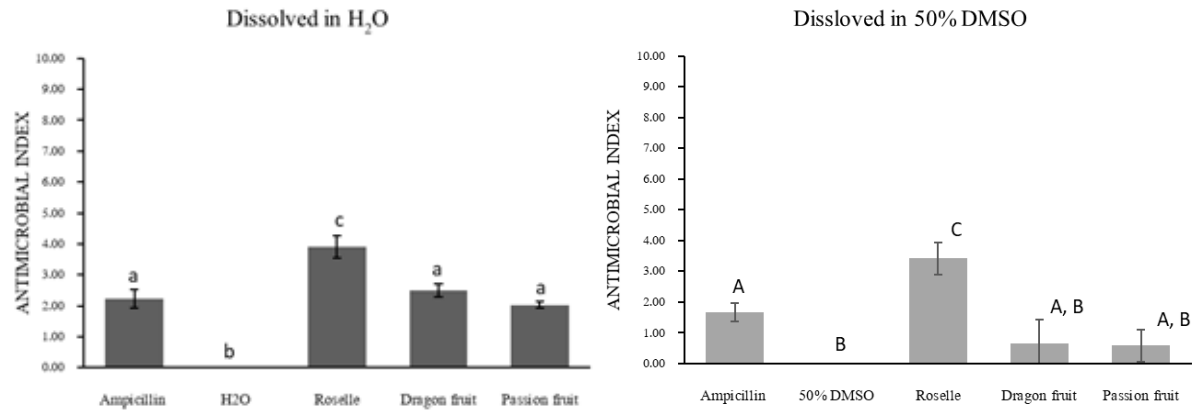

Figure 1. Comparison of antibacterial activity, represented by an anti-microbial index, assayed by agar well diffusion method, of three crude extracts including roselle calyx, dragon fruit peel, and purple passion fruit peel. All samples were resuspended in distilled water (on the left) or 50% (v/v) DMSO (on the right) and tested for their abilities to inhibit the growth of (a.) *B. cereus*, (b.) *E. coli*, and (c.) *S. aureus* on NA agar plates. Ampicillin (1 mg/ml) and distilled water, or 50% (v/v) DMSO were served as controls. Statistical differences were analyzed by SPSS variance (ANOVA) with Hoc comparison with Turkey HSD. The different letters mean that they are significantly different from each other ($p < 0.05$)

Table 2. Assay of minimal inhibitory concentration (MIC) of crude extracts

	Crude extract	Visible Bacterial Growth											
		Amp[a]	The concentration of extracts in aqueous solution						The concentration of extracts in DMSO solution					
			1000	500	250	125	62.5	0[b]	1000	500	250	125	62.5	0[b]
B. cereus	Roselle	×[c]	×	×̲	✓[d]	✓	✓	✓	×	×	×	×̲[e]	✓	✓
	Dragon fruit	×	✓	✓	✓	✓	✓	✓	×	×̲	✓	✓	✓	✓
	Passion fruit	×	✓	✓	✓	✓	✓	✓	×	×̲	✓	✓	✓	✓
E. coli	Roselle	×	×	×̲	✓	✓	✓	✓	×	×̲	✓	✓	✓	✓
S. aureus	Roselle	×	×	×̲	✓	✓	✓	✓	×	×	×̲	✓	✓	✓
	Dragon fruit	×	✓	✓	✓	✓	✓	✓	×̲	✓	✓	✓	✓	✓
	Passion fruit	×	✓	✓	✓	✓	✓	✓	×̲	✓	✓	✓	✓	✓

[a]Amp = Ampicillin (final concentration of 100 µg/ml) was served as a control.
[b] Only solvent (distilled water or 50% (v/v) DMSO) was added to the experiment and served as a control.
[c]**×** = No visible bacterial growth was observed.
[d]✓= Visible bacterial growth was observed
[e]**×̲** = MIC value

Table 3. Assay of minimal bactericidal concentration (MBC) of crude extracts

Bacteria Tested	Crude extract	Visible Bacterial Growth											
		Amp	Concentration of extracts in aqueous solution						Concentration of extracts in DMSO solution					
			1000	500	250	125	62.5	0	1000	500	250	125	62.5	0
B. cereus	Roselle	×[a]	×̲[b]	✓[c]	ND[d]	ND	ND	✓	×	×̲	✓	✓	ND	✓
	Dragon fruit	×	ND	ND	ND	ND	ND	ND	×̲	✓	ND	ND	ND	✓
	Passion fruit	×	ND	ND	ND	ND	ND	ND	×̲	✓	ND	ND	ND	✓
E. coli	Roselle	×	✓	✓	ND	ND	ND	✓	×̲	✓	ND	ND	ND	✓
S. aureus	Roselle	×	×	×̲	ND	ND	ND	✓	✓	✓	✓	ND	ND	✓
	Dragon fruit	×	ND	ND	ND	ND	ND	ND	✓	ND	ND	ND	ND	✓
	Passion fruit	×	ND	ND	ND	ND	ND	ND	✓	ND	ND	ND	ND	✓

[a]**×** = No bacterial colony was observed.
[b]**×̲**= MBC value
[c]✓= Bacterial colony was observed
[d] ND = Result was not determined because it could not inhibit bacterial growth in previous MIC assay.

Conclusion:

In this research, three crude extracts including roselle calyx, dragon fruit peel, and purple passion fruit peel, were tested for anti-bacterial activity against three bacterial pathogens, *B. cereus*, *E. coli*, and *S. aureus*. All extracts exhibited different anti-bacterial abilities. Among these extracts, the roselle calyx one was the most promising anti-bacterial agent. However, the concentrations used in this work to inhibit and kill these bacteria are relatively high. Therefore, our further studies will focus on the optimization of extraction techniques to obtain extracts with higher anti-bacterial activity.

Acknowledgments:

We are appreciated to all the supports from the Department of Biology, Faculty of Science, Ramkhamhaeng University.

References:

1. Interagency Coordination Group on Antimicrobial Resistance (IACG). Report to the Secretory-General of the United Nations. 2019:1-24.
2. Islam AKMA, Jamini TS, Islam AKMM, Yeasmin S. Fund Appl Agric. 2016;1: 44-49.
3. Puro K, Aochen C, Ghatak S, Das S, Sanjukta R, Mahapatra KP, Jha AK, Shakuntala I, Sen A. Int J Food Sci Nutri. 2017;2:1-6.
4. Tongkram N, Jantasalay B, Lasunon P. Agr Nat Res. 2017;51:252-267.
5. Lorith N, Kanlayavattanakul M. Agro Food Industry Hi-Tech. 2013;24:56-58.
6. He X, Luan F, Yang Y, Wang Z, Zhao Z, Fang J, Wang M, Zuo M, Li Y. Front Pharmacol. 2020;11:617
7. Messelhäußer U, Ehling-Schulz M. Curr Clin Microbiol Rep. 2018;5:120-125.
8. Allocati N, Masulli M, Alexeyev MF, Di Ilio C. Int J Environ Res Public Health. 2013;10:6235-6254.
9. Turner NA, Sharma-Kuinkel BK, Maskarinec SA, Eichenberger EM, Shah PP, Carugati M, Holland TL, Fowler Jr VG. Nature Rev Microbiol. 2019;17:203-218.
10. Azwanida NN. Med Aromat Plants. 2015;4:1-6.
11. Perez C, Pauli M and Bazerque P. Acta Biolet Med Exp. 1990;15:113-115.
12. Villasenor IM, Canlas AP, Faustino KM, Plana KG. J Ethnopharmacol. 2004;92:53-56.
13. Clinical and Laboratory Standards Institute (CLSI). CLSI documents M07-A8. 2009
14. Ćujić N., Šavikin K., Janković T, Pljevljakušić, D, Zdunić, G, and Ibrić, S. Food Chem. 2016;194:135–142.
15. Wisut M. KKU Sci J. 2017;45:805-816.
16. Ritcher MF, Hergenrother PJ. Ann N Y Acad Sci. 2019;1435:18–38.
17. Bouarab-Chibane L, Forquet V, Lantéri P, Clément Y, Léonard-Akkari L, Oulahal N, Degraeve P, Bordes C. Front Microbiol. 2019;10:829.
18. Joska TM, Anderson AC. Antimicrob Agents Chemother. 2006;50: 3435–3443.
19. Omardien S, Ter Beek A, Vischer N, Montijn R, Schuren F, Brul S. Sci Rep. 2018; 8:9128\
20. Colquhoun JM, Ha L, Beckley A, Meyers B, Flaherty DP, Dunman PM. Antibiotics. 2019;8:48.

SP13_011_PA: SCREENING FOR ANTIBACTERIAL ACTIVITY OF CRUDE EXTRACTS FROM DIFFERENT PARTS OF SIAM CARDAMON (*Amomum Krevanh* Pierre)

Rattanakorn Wongsrila, Iyapat Surakkhaka, Thaniwan Cheun-Arom, Ruethairat Boonsombat*

Department of Biology, Faculty of Science, Ramkhamhaeng University, Bangkapi, Bangkok, Thailand
*e-mail: ruethairatboonsombat@gmail.com

Abstract:

Among several species of cardamoms, the Siam cardamom (*Amomum Krevanh* Pierre) is one of the well-known spices and traditional medicinal plants. Many previous reports of cardamoms focused on the use of essential oil extracted from fruit and seeds. In this research, the antibacterial activity of crude extracts from several parts of the Siam cardamom including stems (with rhizomes), leaves, and fruit was assayed. The agar well diffusion method was applied to evaluate growth inhibition against *Bacillus Cereus*, *Staphylococcus Aureus*, and *Escherichia Coli*. The inhibitory ability of the crude extracts from the fruit in both aqueous and DMSO solutions against *B. cereus* and *S. aureus* was not significantly different from ampicillin (1 mg/ml). Furthermore, the extracts from cardamom stem in both solutions slightly inhibited *B. cereus* growth. None of the Siam cardamom crude extracts in aqueous solution was active against *E. coli*. However, only the crude extract from the fruit in the DMSO solution exhibited antibacterial activity against *E. coli*. High values of the minimum inhibitory concentration (MIC) and the minimum bactericidal concentration (MBC) of these extracts indicated that they mildly inhibited the growth of these bacteria. Therefore, our future studies will focus on optimization of extraction process and other biological activities of the Siam cardamom crude extracts.

Introduction:

The Siam cardamom (*Amomum Krevanh* Pierre), so-called Krawaan in Thai, is in the Zingiberaceae family. Its stem contains an aerial part and an underground rhizome. Lanceolate leaves have overlaying leaf sheathes looking like a stem. Its globular 3-lobed fruit, with its unique camphorous aroma, contains numerous black seeds. A ripened fruit is favorably dried to use as a culinary spice as well as a component in folk medicine. Furthermore, the Siam cardamom fruit has been exported for a long time, especially, to China and Hong Kong.

All parts of the Siam cardamom are claimed to have medicinal properties for traditional treatment, for example, relieving symptoms of bloating up and diarrhea. There are also various scientific researches of several cardamom species, especially, the Indian cardamom (*Elettaria cardamomum* (L.) Maton). Various biological activities have been reported from extracts of the Indian cardamoms including the potential antibacterial activity of crude extracts from dried fruit,[1] anti-oxidative effect against non-melanoma skin cancer in mice,[2] and potential anti-inflammatory and immune-modulating properties of essential oil from the fruit in human dermal fibroblasts.[3] In the case of the Siam cardamom, many studies have focused on essential oil from fruit and seeds. The ethanolic crude extract from seeds exhibited effective antibacterial activity against *Salmonellae* and other enterobacteria including *Citrobacter Fruerndii, Enterobacter Aerogenes, Escherichia Coli*, and *Klebsiella Pneumoniae*.[4] For essential oil obtained from the hydrodistillation technique, 1,8-cineole, α-pinene, α-terpinene, and β-pinene were found as the major components, and this oil could inhibit the growth of *Bacillus subtilis* and *E. coli*.[5] Furthermore, seven new compounds of diterpenoids were recently found in the Siam cardamom fruit extracted by ethanol and petroleum ether.[6] An isolated compound has been extendedly studied for synthesizing cardamom peroxide which is a potential antimalarial agent.[7]

Various bacteria are pathogenic. To treat such bacteria, antibiotics are applied. However, antimicrobial resistance is one of the serious public health problems. This can come from misuses and overuses of antibiotics for health care and agriculture.[8] To solve this problem, one solution is an attempt to discover several novel antibacterial agents, and natural products are favorably trended. In this research, we focused on screening for antibacterial properties of crude extracts from different parts of the Siam cardamom including stems (with rhizomes), leaves, and fruit. Their activities to inhibit the growth of *B. cereus, S. aureus,* and *E. coli* were investigated. *B. cereus* is an endospore-forming gram-positive bacteria that distributed in the environment. This species can cause many unpleasant symptoms including food poisoning, and recently responsible for the contamination in ready-to-eat food in China.[9] For *S. aureus*, besides causing many diseases, its resistance to antibiotics, especially Methicillin-resistant *S. aureus* (MRSA), has been worldwide emerged.[10] Despite being known as a human normal flora, some strains of *E. coli* can produce toxins such as the Shiga toxin causing an outbreak in the US in 2015 due to contamination in flour.[11] We expected that our crude extracts from the Siam cardamom were able to inhibit the growth of tested bacteria and further applied as antibacterial agents.

Methodology:

Preparation of Crude Extract

Samples of stems (with rhizomes), leaves, and fruit of the Chanthaburi Siam cardamom were purchased from Khom Dum Din Garden, Rayong, Thailand. 500 g of stems and leaves and 100 g of fruit were used. The stems and leaves were washed and then chopped. All samples were dried in a hot air oven at 50 ˚C. After dry weight being measured, each sample was ground by a mortar and a blender. Crude extracts were prepared by the maceration technique.[12] Samples of leaves and fruit were soaked for 3 days in 1000 ml of 70% (v/v) ethanol (500 ml for samples of stems). The solution of each sample, after being filtered and squeezed with a cotton sheet, was then stored in a refrigerator. The residues were repeatedly extracted with the same method for 3 times. To evaporate ethanol and water, a rotatory evaporator at 50 ˚C, freeze dryer at 4 ˚C with the pressure of 175 mbar, and a hot plate for heating was used. All crude extracts were weighed and subsequently kept in a refrigerator. The percentage yield was calculated as the following:

$$\% \text{ yield} = \frac{\text{weight of the crude extract}}{\text{weight of the dried sample}} \times 100$$

Analysis of Antibacterial Activity by Agar Well Diffusion Method

The method of agar well diffusion was modified from Perez et al., (1990).[13] Briefly, three species of bacteria including *B. cereus* ATCC11778, *E. coli* ATCC25922, and *S. aureus* ATCC25923 were cultured in nutrient broth (NB) at 37 ˚C overnight. All inoculums were then adjusted in Normal Saline Solution (NSS) to 0.5 McFarland Standard. After that, a sterile cotton swab was used to spread each bacterial suspension on Nutrient agar (NA), then a cork borer with its diameter of 4-6 mm was used to make wells on agar. Each crude extract was dissolved in distilled water or 50%(v/v) dimethyl sulfoxide (DMSO) to the final concentration of 1000 mg/ml, then 10 µl of each solution was added to a well on NA and allowed to diffuse at room temperature for 2 h. Ampicillin (1 mg/ml), and distilled water or 50% (v/v) DMSO were applied as controls. Each experiment was carried out in triplicate. All plates were incubated at 37 ˚C for 18 h. The diameter of the inhibition zone (DIZ) was determined by measuring the clear zone that appeared around each well in the unit of mm. The antimicrobial index (AI) was calculated as the following.[14]

$$\text{AI} = \frac{\text{(DIZ- Diameter of well)}}{\text{Diameter of well}}$$

Minimum Inhibitory Concentration (MIC) Assay

Determination of MIC values, adapted from CLSI (2009),[15] were carried out with samples that displayed antibacterial activity by agar well diffusion method. Crude extracts were 2-fold diluted as 1000, 500, 250, 125, and 62.5 mg/ml, with distilled water or 50% (v/v) Then, 100 µl of each extract and 100 µl of each 0.5 McFarland standard bacterial suspension in NSS were added to 5 ml of NB. Ampicillin with a final concentration of 100 µg/ml, and distilled water or 50% (v/v) DMSO were served as controls. Experiments were performed in triplicate. The lowest concentration in each set of experiments that could inhibit visible bacterial growth in cultural broth, determined by turbidity, was the MIC value.

Minimum Bactericidal Concentration (MBC) Assay

All the tubes without visible growth of bacteria from MIC assay were collected for determining MBC values by drop plate technique.[15] 10 µl of each collected sample was dropped on NA and allowed to dry at room temperature for 1 h before incubating in 37 ˚C incubators for 18 h. The MBC value was determined by the lowest concentration of extract that could kill bacteria, so the colony could not be formed on agar. Experiments were performed in triplicate.

Results and Discussion:

The crude extracts from stems (with rhizomes), leaves, and fruit of the Siam cardamom were obtained with percentage yield as shown in Table 1. All crude extracts were then dissolved in distilled water or 50%(v/v) DMSO. It was previously reported that this concentration of DMSO was non-toxic to *B. cereus*, *S. aureus*, and *E. coli*.[16] By using the agar well diffusion method, antibacterial efficiency was represented as an antimicrobial index. All samples inhibited *B. cereus* growth. The highest activity was observed in fruit extract (Table 2). However, when crude extracts were dissolved in water, extracts from the Siam cardamom leaves showed no antibacterial activity. As presented in Table 3, only the crude extract from the fruit in both solvents exhibited antibacterial property against *S. aureus*. Furthermore, none of the solutions inhibited *E. coli* growth except for fruit extract in DMSO solution (Table 4). It was suggested that antibacterial agents against *E. coli* in our cardamom fruit extract may be better dissolved in DMSO, so higher antibacterial activity was observed from this solution. In this case, since a thin oil layer can be observed in the fruit extract, it is predicted that the bacterial growth inhibitory property may resulted from essential oil,[5]which is usually prepared in DMSO solution before antimicrobial assay.[17] However, partial amounts of essential oil may still remain in the extract obtained even maceration techniques may not be very effective in essential oil extraction.

Table 1. The percentage yield of crude extracts obtained from different parts of Siam cardamom

Crude extract	% Yield
Stem	12.72
Leaf	17.34
Fruit	8.37

All samples that exhibited antibacterial activities were determined for minimum inhibitory concentration (MIC) as shown in Table 5. For aqueous solution, crude extracts from stems and fruit against *B. cereus* and extracts from fruit against *S. aureus* were assayed. MIC values determined as 1000 mg/ml for both bacterial strains were obtained from the Siam cardamom fruit extract in aqueous solution (Table 5). The inhibition of the growth of *B. cereus* was not observed at any tested concentrations of stem extracts in both solutions. Therefore, to inhibit this bacterial growth in NB, crude extract from stems should be more than 1000 mg/ml. However, only crude extract from cardamom fruit in DMSO solution inhibited *B. cereus* with an MIC value of 500 mg/ml (Table 5).

Table 2. Antimicrobial index of crude extracts from Siam cardamom against *B. cereus*

Crude extract	Antimicrobial index	
	Aqueous solution	DMSO solution
Amp*	2.52 ± 0.100^{a}	2.75 ± 0.250^{A}
Solvent**	0^{b}	0^{B}
Stem	1.24 ± 0.46^{c}	$0.42 \pm 0.382^{B,C}$
Leaf	0^{b}	1.00 ± 0.500^{C}
Fruit	2.76 ± 0.210^{a}	2.83 ± 0.289^{A}

*Amp = Ampicillin (1 mg/ml) served as a control.

**Solvent = distilled water or 50% (v/v) DMSO, served as the other control.

$^{a, b, c}$ or $^{A,B, C}$ Statistics analysis by SPSS variance (ANOVA) with Hoc comparison and Turkey HSD. The same superscripts are not significantly different from each other (p <0.05)

Table 3. Antimicrobial index of crude extracts against *S. aureus*

Crude extract	Antimicrobial index	
	Aqueous solution	DMSO solution
Amp*	3.34 ± 0.280^{a}	1.67 ± 0.289^{A}
Solvent**	0^{b}	0^{B}
Stem	0^{b}	0^{B}
Leaf	0^{b}	0^{B}
Fruit	2.88 ± 0.210^{a}	1.50 ± 0.500^{A}

*Amp = Ampicillin (1 mg/ml) served as a control.

**Solvent = distilled water or 50% (v/v) DMSO, served as the other control.

$^{a, b}$ or ^{A,B} Statistics analysis by SPSS variance (ANOVA) with Hoc comparison and Turkey HSD. The same superscripts are not significantly different from each other (p <0.05)

Table 4. Antimicrobial index of crude extracts from Siam cardamom against *E. coli*

Crude extract	Antimicrobial index	
	Aqueous solution	DMSO solution
Amp*	2.52 ± 0.100^{a}	3.58 ± 0.144^{A}
Solvent**	0^{b}	0^{B}
Stem	0^{b}	0^{B}
Leaf	0^{b}	0^{B}
Fruit	0^{b}	1.50 ± 0.500^{C}

*Amp = Ampicillin (1 mg/ml) served as a control.

**Solvent = distilled water or 50% (v/v) DMSO, served as the other control.

$^{a, b}$ or ^{A,B} Statistics analysis by SPSS variance (ANOVA) with Hoc comparison and Turkey HSD. The same superscripts are not significantly different from each other (p <0.05)

Only the extract from the Siam cardamom fruit was subsequently determined for MBC, as shown in Table 6. Bacterial colonies of *B. cereus* and *S. aureus* were observed when 1000 mg/ml of cardamom fruit extract in aqueous solution was applied. This suggested that aqueous solution of cardamom fruit extract did not completely inhibit the growth of *B. cereus* and *S. aureus*. However, the fruit extract dissolved in DMSO displayed better activity against *B. cereus* with the MIC value of 500 mg/ml (Table 6).

Table 5. MIC values of crude extracts from Siam cardamom

Crude extract	MIC value (mg/ml)					
	Aqueous solution			DMSO solution		
	B. cereus	***S. aureus***	***E. coli***	***B. cereus***	***S. aureus***	***E. coli***
Stem	>1000[1]	ND	ND	>1000	ND	ND
Leaf	ND[2]	ND	ND	>1000	ND	ND
Fruit	1000	1000	ND	500	>1000	>1000

[1] >1000 = observation of visible bacterial growth at the highest concentration tested (1000 mg/ml)

[2] ND = not determined due to extracts not exhibiting antibacterial activity, previously tested by agar well diffusion method

Table 6. MBC values of crude extracts from Siam cardamom fruit

MBC value (mg/ml)			
Aqueous solution		DMSO solution	
B. cereus	***S. aureus***	***B. cereus***	***S. aureus***
>1000[1]	>1000	500	ND[2]

[1] >1000 = observation of bacterial colony at the highest concentration tested (1000 mg/ml)

[2] ND = not determined because MIC could not be previously determined.

From all results, it was suggested that all crude extracts from the Siam cardamom exhibited mild antibacterial activity with high MIC and MBC values. To obtain extracts with better antibacterial activity, our future study will focus on the optimization of extraction processes. Furthermore, other biological activities such as antioxidant and anti-inflammatory activities of extracts from the Siam cardamom will be also investigated.

Conclusion:

By using the maceration technique, the crude extracts from different parts of the Siam cardamom mildly exhibited antibacterial activity. The fruit extract in DMSO solution displayed the highest activity against *B. cereus*. However, the MIC and MBC values were high, suggesting that crude extracts did not effectively inhibit the growth of these bacterial pathogens. To obtain crude extract with better antibacterial activity, appropriate extraction conditions are required. Therefore, optimization of Siam cardamom extraction processes will be of interest.

Acknowledgments:

We are appreciated to all the supports from the Department of Biology, Faculty of Science, Ramkhamhaeng University.

References:

1. Kaushik P, Goyal P, Chauhan A, and Chauhan. Iran G. J Pharm Res. 2010;9: 287–292.
2. Das I, Acharya A, Berry DL, Supti Sen, Williams E, Permaul E, Sengupta A, Bhattacharya S, Saha T. Brit J Nutri. 2012;108:984–997.
3. Han X, Tory L. Parker Han & Parker, Cogent Medicine. 2017;4:1308066
4. Nanasombat S, Lohasupthawee P. KMITL Sci. Tech. J. 2005;5:527-538.
5. Diao W, Zhang L, Feng S, Xu J. J Food Prot. 2014;77:1740-1746.
6. Yin H, Luo J, Kong L. J. Nat. Prod. 2013;76:237-242.
7. Hua X, Lim P, Fairhurst RM, Maimonea TJ. Tetrahedron. 2018;74:3358-3369.
8. Dadgostar P. Infection and Drug Resistance. 2019;12:903–3910.
9. Yu S, Yu P, Wang J, Li C, Guo H, Liu C, Kong L, Yu L, Wu S, Lei T, Chen M, Zeng H, Pang R, Zhang Y, Wei X, Zhang J, Wu Q, Ding Y. Front. Microbiol. 2020;10:article 3043
10. Chambers HF, DeLeo FR. Nat Rev Microbiol. 2009;7: 629–641.
11. Crowe SJ, Bottichio L, Shade LN, Whitney BM, Corral N, Melius B, Arends KD, Donovan D, Stone J, Allen K, Rosner J, Beal J, Whitlock L, Blackstock A, Wetherington J, Newberry LA, Schroeder MN, Wagner D, Trees E, Viazis S, Wise ME, Neil KP. N Engl J Med. 2017; 377: 2036–2043.
12. Azwanida NN. Med Aromat Plants. 2015;4:1-6.
13. Perez C, Pauli M and Bazerque P. Acta Biolet Med Exp. 1990;15:113-115.
14. Villasenor IM, Canlas AP, Faustino KM, Plana KG. J Ethnopharmacol. 2004;92:53-56.
15. Clinical and Laboratory Standards Institute (CLSI). CLSI documents M07-A8. 2009
16. Wisut M. KKU Sci J. 2017;45:805-816.
17. Hili P, Evans CS, Veness RG. Lett Appl Microbiol.1997;24:269-275.

SP13_012_OA: ANTIFUNGAL ACTIVITY AND MOLECULAR MECHANISMS OF PARTIALLY PURIFIED ANTIFUNGAL PROTEINS FROM *Rhinacanthus nasutus* AGAINST *Talaromyces marneffei*

Juthatip Jeenkeawpieam,[1] Supachai Yodkeeree,[2] Alex Andrianopoulos,[3] Sitiruk Roytrakul,[4] and Monsicha Pongpom[1]*

[1]Department of Microbiology, Faculty of Medicine, Chiang Mai University, Chiang Mai, Thailand
[2]Department of Biochemistry, Faculty of Medicine, Chiang Mai University, Chiang Mai, Thailand
[3]Genetics, Genomics and Systems Biology, School of Biosciences, University of Melbourne, Australia
[4] Proteomic Research Laboratory, Genome Institute, National Center for Genetic Engineering and Biotechnology, Pathum Thani, Thailand
*e-mail: monsicha.p@cmu.ac.th

Abstract: Antifungal proteins (AFPs) are able to inhibit a wide spectrum of fungi without significant toxicity to the hosts. This study determined an antifungal activity of AFPs isolated from *Rhinacanthus nasutus*, a Thai medicinal plant, against *Talaromyces marneffei*. This dimorphic fungus usually causes the systemic infection in immunocompromised individuals residing in Southeast Asian countries. The crude *R. nasutus* protein extract inhibited the growth of *T. marneffei* ATCC18224. The anti-*T. marneffei* activity was completely lost when treated with proteinase K and pepsin, indicating that the antifungal activity came from protein portion. The total protein was subjected to partial purification by size fractionation and tested for the minimal inhibitory concentration (MIC) and minimal fungicidal concentration (MFC). All tested partially purified fractions showed anti-*T. marneffei* activity with the MIC and MFC values of 32 to 128 µg/ml and >128 µg/ml, respectively. In order to determine the mechanism of inhibition, the positive fractions were tested against *T. marneffei* mutant strains related to G protein signaling and cell wall integrity pathways. The anti-*T. marneffei* activities of RN-B fraction was abolished by deletion of gasA and gasC, indicating that the inhibitory effect is related to the intracellular G-protein signaling. Antifungal proteins isolated from *R. nasutus* could be the fascinating sources for novel drug development.

SP13_013_PF: PROTECTIVE EFFECT OF AGOMELATINE ON OXIDATIVE STRESS AND AUTOPHAGY PATHWAY IN OBESITY-INDUCED KIDNEY INJURY

Sasivimon Promsan, Anusorn Lungkaphin*

Department of Physiology, Faculty of Medicine, Chiang Mai University, Chiang Mai, 50200, Thailand.

*e-mail: onanusorn@yahoo.com

Abstract:

Chronic kidney disease is a complication occurring as a result of obesity that leads to an increased mortality rate. The increasing of free fatty acid in obesity can stimulate excessive ROS production in the kidney and contribute renal cell injury and dysfunction via several pathways such as oxidative stress and autophagy. Agomelatine (AGOM), a structural analog of melatonin, is a relatively new drug that is prescribed for the management of depressive disorders. Recent studies demonstrated that AGOM has several biological effects including anti-oxidant and anti-apoptosis in several cells. However, the effects of AGOM on metabolic dysfunction and renal dysfunction impaired by the obese-insulin resistance have never been investigated. The present study demonstrated that HFD rats developed obese-insulin resistance, as shown by the increase in fasting blood glucose and serum insulin levels, along with renal dysfunction indicated by the elevating of serum creatinine level. Moreover, renal MDA level and PKC-α expression significantly increased in HFD rats, which represented renal oxidative stress. After AGOM treatment, body weight and serum insulin were decreased along with the inhibition of renal oxidative stress and upregulation of anti-oxidant enzyme. Renal autophagy impairment had increased in HFD-fed rats. These alterations were effectively improved after administration of AGOM.

SP13_014_PA: CHITOSAN OLIGOSACCHARIDE PREVENTS KIDNEY INJURY IN PREDIABETIC RATS

Prempree Sutthasupha, Anusorn Lungkaphin*

Department of Physiology, Faculty of Medicine, Chiang Mai University, Thailand

*e-mail: onanusorn@yahoo.com

Abstract:

Obesity is a common health problem worldwide. Obese people have increased risk of progressive insulin resistance (IR) and the development of type 2 diabetes. Chronic kidney disease is a severe complication occurring in prediabetic and diabetic stages through several mechanisms such as oxidative stress and apoptosis. Natural products played a key role as a new therapeutic agent to prevent the side effects of drugs. Chitosan oligosaccharide (COS) is an oligomer of chitosan derived from deacetylation of chitin, the natural polymer commonly found in the shell of crustaceans. COS previously exerts biological activities including anti-oxidative, anti-diabetic and lipid-lowering effect both in *in vitro* and *in vivo*. However, the renoprotection of COS in prediabetes have not been reported. We designed the experiment to investigate the effects of COS on kidney injury in obese-IR rat model. The results showed that obese-IR model was developed characterized by the increasing of body weight gain and serum insulin. The elevation of renal MDA level and NOX4 expression were observed in HFD group leading to cell apoptosis as shown by the upregulation of BAX expression. After COS treatment for 8 weeks, the obese-IR condition was improved. Moreover, renal oxidative stress and apoptosis were markedly alleviated.

SP13_015_PA: POTENTIAL SYNERGISTIC ANTIMICROBIAL EFFICIENCY OF BINARY COMBINATIONS OF *Amomum testaceum* AND *Zanthoxylum piperitum* ESSENTIAL OILS AGAINST *Staphylococcus aureus* AND *Escherichia coli*

Kittima Winyayong,[1] Pamela Webwer,[1] Teerapong Sripahco,[1] Sarunpron Khruengsai,[1] Patcharee Pripdeevech,[1,2,*]

[1]School of Science, Mae Fah Luang University, Chiang Rai 57100, Thailand
[2]Center of Chemical Innovation for Sustainability (CIS), Mae Fah Luang University, Chiang Rai 57100, Thailand
*e-mail: patcharee.pri@mfu.ac.th

Abstract:

Amomum testaceum and *Zanthoxylum piperitum* are cultivated widely in Thailand. Their essential oils have been known to have antibacterial activity. In order to find a new alternative antibacterial agent, we investigated combination of *A. testaceum* and *Z. piperitum* essential oils for their synergistic inhibitory activities against *Staphylococcus aureus* and *Escherichia coli*. Both essential oils were extracted by hydrodistillation for 4 h using a Clevenger-type apparatus. Each pure essential oil was diluted in 10% dimethylsulfoxide to obtain various concentrations. The minimum inhibitory concentrations (MIC) of *A. testaceum* and *Z. piperitum* essential oils against *S. aureus* were 10.00 µL/mL and 1.25 µL/mL and *E. coli* were 5.00 µL/mL and 1.25 µL/mL, respectively. A checkerboard assay showed that combinations of *A. testaceum* and *Z. piperitum* essential oils exert the strong synergistic antibacterial activity. The evaluation of the essential oils in combination revealed that the maximum of required concentration was 0.15 µL/mL for *A. testaceum* and 0.63 µL/mL for *Z. piperitum* against *S. aureus* while maximum of required concentration was 0.31 µL/mL for *A. testaceum* and 0.15 µL/mL for *Z. piperitum* against *E. coli*, respectively. The fractional inhibitory concentration index (FICI) of both essential oil combination = 0.515 and 0.187 against *S. aureus* and *E. coli*, respectively. Results showed a synergistic effect against *S. aureus* and *E. coli*. The combination of *A. testaceum* and *Z. piperitum* essential oils has potential application in food preservation to reduce the contamination of *S. aureus* and *E. coli*.

SP13_016_PA: SYNERGISTIC ANTIBACTERIAL EFFECTS OF *Zanthoxylum limonella* and *Zingiber cassumunar* ESSENTIAL OILS

Pamela Webwer,[1] Kittima Winyayong,[1] Teerapong Sripahco,[1] Sarunpron Khruengsai,[1]
Patcharee Pripdeevech,[1,2,*]

[1]School of Science, Mae Fah Luang University, Chiang Rai 57100, Thailand
[2]Center of Chemical Innovation for Sustainability (CIS), Mae Fah Luang University, Chiang Rai, 57100, Thailand
*e-mail: patcharee.pri@mfu.ac.th

Abstract:

The antibacterial effects of *Zanthoxylum limonella* and *Zingiber cassumunar* essential oils were tested against two bacterial pathogens including *Staphylococcus aureus* and *Escherichia coli* using disc diffusion method. The combined effect of both essential oils against the tested bacteria was also assessed by the broth microdilution method. The results of the dissemination method demonstrated that *Z. limonella* and *Z. cassumunar* essential oils have antibacterial activity against the selected tested bacteria. The minimal inhibitory concentration (MIC) values of *Z. limonella* against *S. aureus* and *E. coli* were 10.00 µL/mL and 1.25 µL/mL, respectively, while *Z. cassumunar* essential oils inhibited *S. aureus* and *E. coli* growth with MIC values of 5.00 µL/mL and 1.25 µL/mL, respectively. The evaluation of the combination of these two essential oils revealed that the required concentration for inhibiting *S. aureus* were 1.25 µL/mL and 0.31 µL/mL of *Z. limonella* and *Z. cassumunar*, respectively, whereas those for inhibiting *E. coli* were 0.31 µL/mL of *Z. limonella* and 0.16 µL/mL of *Z. cassumunar*. The lower concentrations of the essential oils in the combination indicate their synergistic effect.

SP13_017_PF: INVESTIGATION OF ANTIOXIDANT AND ANTIMICROBIAL ACTIVITIES OF ETHYL ACETATE EXTRACTS FROM FIVE EDIBLE MUSHROOMS

Puttachard Hensanghong,[1] Wanchai Pluempanupat,[2] Janpen Tangjitjaroenkun[3,*]

[1]Program in Natural Product Science and Technology, Faculty of Science at Si Racha, Kasetsart University, Si Racha Campus, 20230, Thailand
[2]Department of Chemistry and Center of Excellence for Innovation in Chemistry, Faculty of Science, Kasetsart University, 10900, Thailand
[3]Department of Resources and Environment, Faculty of Science at Si Racha, Kasetsart University, Si Racha Campus, 20230, Thailand
*e-mail: janpen.ta@ku.th

Abstract:

The aim of this study was to screen antioxidant and antimicrobial activities of ethyl acetate extracts from the culture filtrate of five mushrooms named *Lentinus polychrous* (Hed Kradang), *Pleurotus* sp. Bhutan strain (Hed nangfhabhutan), *Lentinus squarrosulus* (Mont.) Singer (Hed khonkhao), *Macrocybe crassa* (Hed taenrad) and *Pleurotus cystidiosus* (Hed paohue). The ethyl acetate extract of *L. polychrous* (KDE) showed most potent antioxidant and antimicrobial activities among other extracts. The highest percent yield of ethyl acetate extracts of 0.0124% (w/v) was obtained from the KDE. The KDE was screened for antioxidant activity by thin layer chromatography autographic assay. The suitable solvent system to develop the TLC plate for the KDE was ethyl acetate:methanol (in the ratio of 2.8:2.2) and the developed TLC plate of KDE was sprayed with DPPH$^{\bullet}$ solution. The KDE presented a pale yellow band on a purple background immediately. The extracts were tested for antimicrobial activity by the agar disc diffusion method. The KDE presented antimicrobial activity against six bacteria, which included *Staphylococcus saprophyticus,* methicillin-resistant *Staphylococcus aureus* (MRSA), methicillin-susceptible *Staphylococcus aureus* (MSSA), *Bacillus subtilis, Enterobacter cloacae, Klebsiella pneumoniae* and showed inhibition zones of 12.69±0.01, 9.92±0.50, 11.05±0.38, 10.00±0.32, 16.37±1.64 and 10.11±0.79 mm, respectively. These results suggested that the KDE could be a good choice for application in healthy food.

Introduction:

Mushrooms have been considered as ingredients of gourmet cuisine across the globe because they have unique flavor and good taste. Furthermore, they are low in calories, sodium, fat and cholesterol but high in protein, carbohydrate, fiber, vitamins and essential amino acids.[1,2] The edible mushrooms have secondary metabolites, including phenolic compounds, polyketides, terpenes and steroids. Different compounds of edible mushrooms are responsible for their antioxidant property, which make edible mushrooms effective in promoting health through several mechanisms such as antioxidant, anti-inflammatory, anti-cancer, anti-estrogenic, anti-angiotensin and immunomodulatory.[2]

Thailand, several edible mushrooms have commonly been consumed such as *Lentinus polychrous* (Hed Kradang), *Pleurotus sp.* Bhutan strain (Hed nangfhabhutan), *Lentinus squarrosulus* (Mont.) Singer (Hed khonkhao), *Macrocybe crassa* or *Tricholoma crassum* (Hed taenrad) and *Pleurotus cystidiosus* (Hed paohue). *L. polychrous* is a basidiomycota belongs to the family Polyporaceae. It is found in every region of Thailand. The fruiting bodies of *L. polychrous* are sticky depending on cultivation time.[3,4] *L. polychrous* fruiting bodies and mycelia contain phenolic compounds, ergosterols, polysaccharides and proteins. These compounds have important pharmacological properties, including antioxidant, anti-inflammatory, anti-cancer, anti-estrogenic,

anti-angiotensin and immunomodulatory activities.[3] *Pleurotus* sp. Bhutan strain is a basidiomycota belongs to the family Pleurotaceae. *Pleurotus* sp. has important pharmacological properties, including gastrointestinal disorders, nervous disorders, high cholesterol, cardiovascular disorders, diabetes, asthma, and constipation.[5] *L. squarrosulus* (Mont.) Singer is a basidiomycota belonging to the family Polyporaceae. It is a wild edible mushroom which is commonly found in the wild on decaying logs of trees during rainy season. The fruiting body of *L. squarrosulus* (Mont.) Singer has various nutrients such as proteins, sugars, lipids, amino acids, vitamin B, C, and D, and minerals.[6] *M. crassa* is a basidiomycota belonging to the family Tricholomataceae. In Thailand *M. crassa* has various local names, such as Hed Tub Tao Khaow, Hed Jun, Hed Taen Rad and Hed Yai. *M. crassa* is found during the rainy season.[7,8] *M. crassa* has various secondary metabolites, including phenolic, flavonol, cinnamic acid and cinnamic acid derivatives and benzoic acid derivatives compounds.[9] *P. cystidiosus* is a basidiomycota that belong to the family Pleurotaceae. It has oyster-like taste.[10,11] Caps of *P. cystidiosus* are convex to hollow with dark greyish to brown centre and yellowish-brown smooth margins. It has health-promoting properties including antibacterial, antifungal, antitumor, immunomodulatory, antiallergic, anti-inflammatory, antiviral, lowering blood sugar, antiatherosclerotic, hepatoprotective and blood cholesterol effects.[10]

In this study, the ethyl acetate extracts from culture filtrate of five edible mushrooms were evaluated for their potential for antimicrobial and antioxidant activites.

Methodology:

Mushroom strains

The mycelium of *L. polychrous* (Hed Kradang), *Pleurotus* sp. Bhutan strain (Hed nangfhabhutan), *L. squarrosulus* (Mont.) Singer (Hed khonkhao), *M. crassa* (Hed taenrad) and *P. cystidiosus* (Hed paohue) were obtained from the Biotechnology Research and Development Office (BIRDO), Department of Agriculture (DOA), Thailand.

Mycelium fermentation

The mycelium of mushrooms was inoculated into potato dextrose agar (PDA) plates and incubated at room temperature for 7-14 days. Further mycelia were cut by cork borer no.3 and were inoculated in potato dextrose broth (PDB). The fermentation broth was incubated in static condition at room temperature for 28 days.

Extraction

The fermentation broth was filtered through filter paper (Whatman no.1) and extracted twice with ethyl acetate in the ratio of 1:1 (v/v). The ethyl acetate layer was collected and concentrated by evaporating to dryness at 40 °C. After that, the crude extract was stored in an amber bottle and weighed.

Screening of antioxidant activity

The extracts were screened for antioxidant activity by thin layer chromatography autographic assay following the method developed by Tangjitjaroenkun *et al*., 2012 with some modifications.[12] Ten µl of 3 mg/mL of crude extract was spotted on Thin layer chromatography (TLC) plate silica gel GF_{254} and was developed in suitable solvent system. The TLC profile was visualized UV light at 254 and 365 nm. The developed TLC plate was sprayed with 2,2-diphenyl-1-picrylhydrazyl ($DPPH^{\bullet}$) and the bleaching color of $DPPH^{\bullet}$ was also observed. The antioxidant activity of the extract was detected by yellow band on purple back ground as the result of the bleaching color of $DPPH^{\bullet}$.

Screening of antimicrobial activity

Antimicrobial activity of mushroom extracts was performed by the agar disc diffusion method following the method developed by Tangjitjaroenkun *et al*., 2017 with some modifications.[13] Eleven test microorganisms were used in this study belonging to gram-positive bacteria (*Bacillus subtilis* ATCC 6633, *Staphylococcus aureus* ATCC 25923, *Staphylococcus saprophyticus* ATCC 15305), gram-negative bacteria (*Escherichia coli* ATCC 25922, *Salmonella typhimurium* ATCC 13311, *Enterobacter cloacae* ATCC 23355, *Klebsiella pneumoniae* ATCC 13883, *Proteus mirabilis* DMST 8212) and yest (*Candida albicans* ATCC 10231). All microorganisms were obtained from the Thailand Institute of Scientific and Technological Research (TISTR), Bangkok, Thailand. The tested bacteria

were cultivated on Mueller-Hinton Agar (MHA) slant at 37 °C for 24 hours and the tested yeast was cultivated on Sabouraud Dextrose Agar (SDA) slant at 37 °C for 48 hours. The supernatant turbidity of bacteria and yeast were adjusted to the equivalent of 0.5 McFarland standard. The supernatants were swabbed on a sterile petri dish MHA for bacteria and SDA for yeast. The sterile paper disc was saturated with 10 µL of the extract (2 mg). The standard penicillin G (10 units/disc) and chloramphenicol (30 µg/disc) were used as positive controls for bacteria whereas ketoconazole (15 µg/disc) was used as a positive control for yeast. The disc was placed on the surface of inoculated agar plates and incubated 37 °C for 24 hours for bacteria and 48 hours for yeast. The result of antibacterial activity was determined by measuring the diameter of inhibition zone.

Results and Discussion:

Mycelium fermentation

L. polychrous, L. squarrosulus (Mont.), Pleurotus sp. Bhutan strain, M. crassa and P. cystidiosus were cultivated on PDA and incubated for 7-14 days. The aerial mycelia of *L. polychrous, L. squarrosulus* (Mont.), *Pleurotus* sp. Bhutan strain, *M. crassa* and *P. cystidiosus* were white in color. Mycelium morphology of five edible mushrooms on PDA after incubated for 7-14 days are shown in **Figure 1**. Five edible mushrooms were cultivated for 28 days in PDB. The aerial mycelia of *L. polychrousa* and *L. squarrosulus* (Mont.) were white and orange, respectively. The aerial mycelia of *Pleurotus* sp. Bhutan strain*, M. crassa* and *P. cystidiosus* were white in color. The aerial mycelia of five edible mushrooms on culture broth after cultivated for 28 days are demonstrated in **Figure 2**.

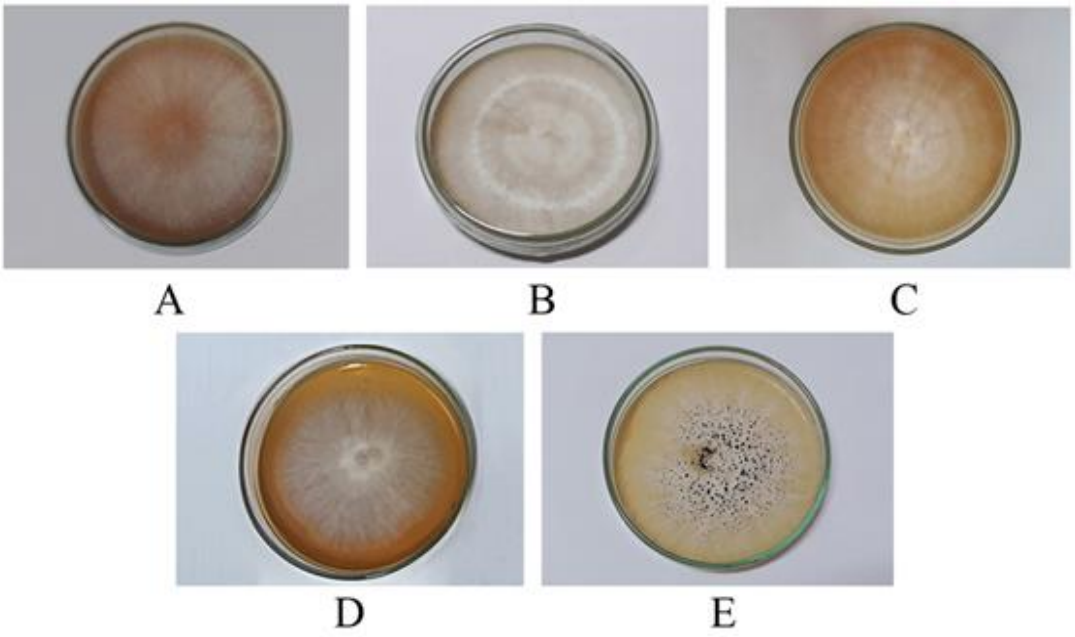

Figure 1.

Mycelium growth of five edible mushrooms on PDA when incubated for 7-14 days (A) *L. polychrous*, (B) *L. squarrosulus* (Mont.) Singer, (C) *Pleurotus* sp. Bhutan strain, (D) *M. crassa* and (E) *P. cystidiosus*

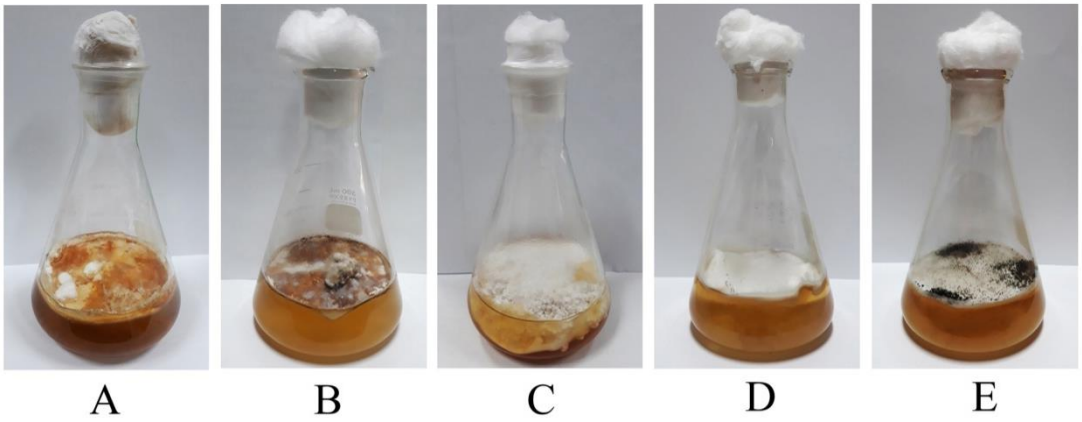

Figure 2.

The mycelium growth of five edible mushrooms on surface of fermentation broth after cultivated for 28 days (A) *L. polychrous*, (B) *L. squarrosulus* (Mont.) Singer, (C) *Pleurotus* sp. Bhutan strain, (D) *M. crassa* and (E) *P. cystidiosus*

Extraction

The ethyl acetate extracts from *L. polychrous* (KDE), *L. squarrosulus* (Mont.) Singer (KKE), *Pleurotus* sp. Bhutan strain (PTE), *M. crassa* (TRE) and *P. cystidiosus* (PHE) were obtained in 0.0124%, 0.0078%, 0.0070%, 0.0032% and 0.0089% (w/v), respectively. The percent yields and color of the extracts are shown in the **Table 1**, and the physical characteristic of the extracts are shown in **Figure 3**.

Table 1. % Yield and color of ethyl acetate extracts from culture filtrate of five edible mushrooms

Extract	% yield (w/v)	color of extract
KDE	0.0124	orange brown
KKE	0.0078	dark brown
PTE	0.0070	orange brown
TRE	0.0032	dark brown
PHE	0.0089	orange brown

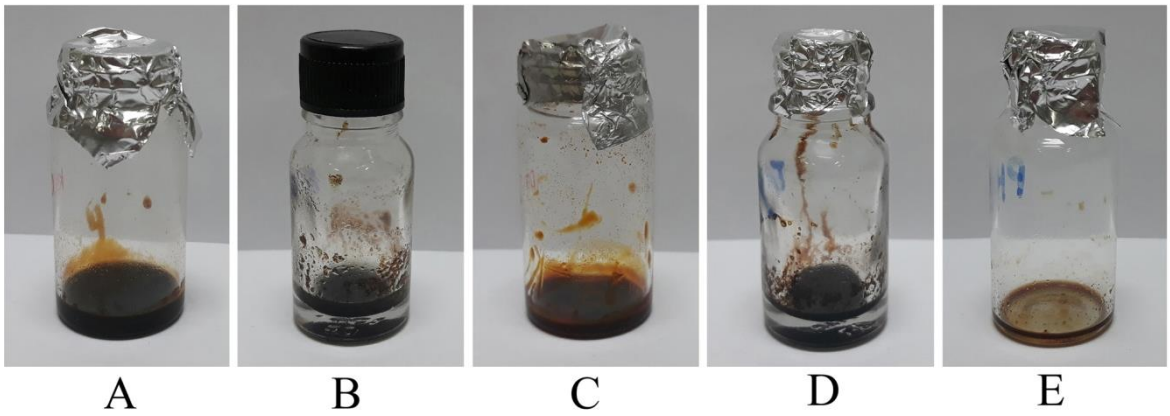

Figure 3. Physical characteristic of the five extracts (A) KDE, (B) KKE, (C) PTE, (D) TRE and (E) PHE

Screening of antioxidant activity

The TLC plate of each extract was developed in suitable solvent system (**Table 2**). The bands of extracts on TLC were visualized under UV 254 and UV 365.

Table 2. The solvent system used to developed the TLC plate of ethyl acetate extracts from five edible mushrooms

Extract	Solvent system
KDE	ethyl acetate:methanol (2.8:2.2)
KKE	dichloromethane:methanol (4.5:0.5)
PTE	dichloromethane:methanol (4.5:0.5)
TRE	ethyl acetate:methanol (2.8:2.2)
PHE	ethyl acetate:methanol (2.8:2.2)

The screening of antioxidant capacity of ethyl acetate extracts from five edible mushrooms was performed by thin layer chromatography autographic assay. The developed TLC plate of each extract was sprayed with DPPH$^{\bullet}$ solution. The KDE presented a pale yellow band on a purple background immediately while the other extracts displayed the same change in 5-15 minutes. From this data indicated that the KDE showed the effective antioxidant activity than the KKE, PTE, TRE and PHE because the KDE displayed time of bleaching color of DPPH• faster than the other extracts. Chromatograms visualized under UV 254, UV 365 and TLC-DPPH free radical scavenging activity of ethyl acetate extracts from five edible mushrooms are shown in **Figure 4.**

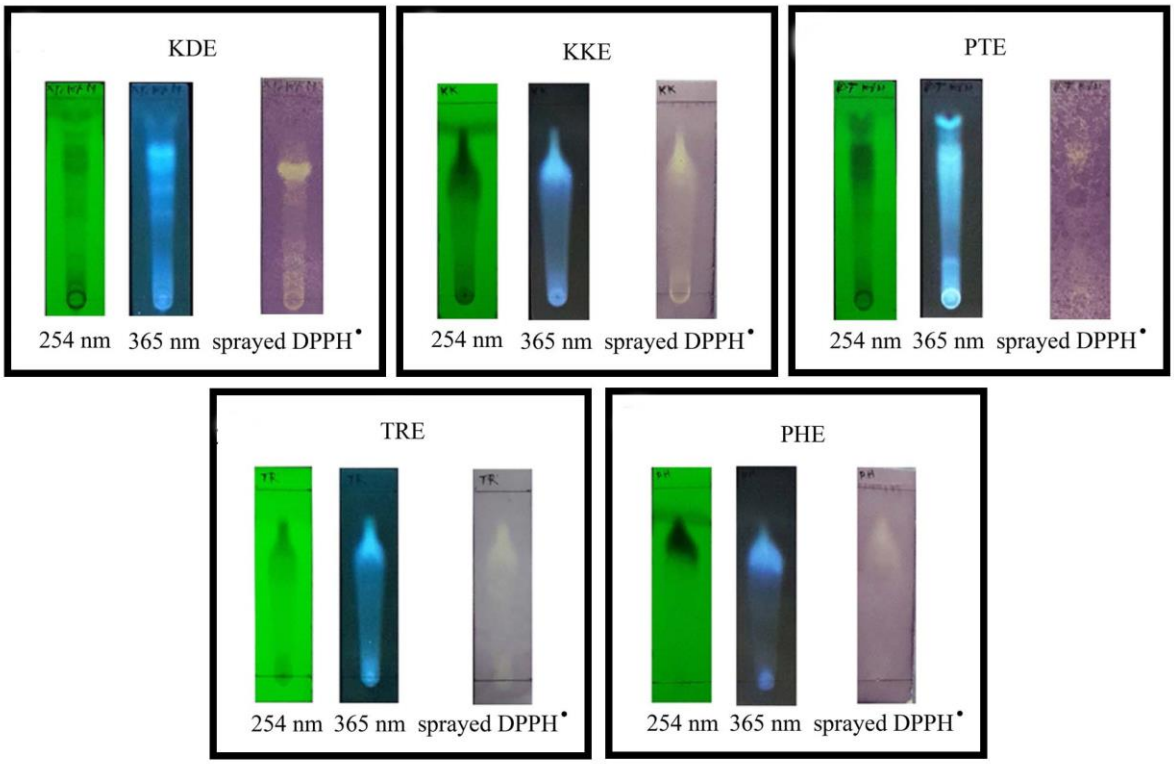

Figure 4.

Chromatograms visualized under UV 254, UV 365 and TLC-DPPH free radical scavenging activity of ethyl acetate extracts from five edible mushrooms

Screening of antimicrobial activity

Five extracts were evaluated for antimicrobial activity against eleven test microorganisms, including *B. subtilis*, *S. aureus* (MRSA), *S. aureus* (MSSA), *S. saprophyticus*, *E. coli*, extended spectrum beta-lactamase (ESBL) producing *E. coli*, *S. typhimurium*, *E. cloacae*, *K. pneumoniae*, *P. mirabilis* and *C. albicans.* The results are presented in **Table 3**. The KDE, TRE and PHE extracts dsiplayed antimicrobial activity against six bacteria, *S. saprophyticus, S. aureus* (MRSA), *S. aureus* (MSSA)*, B. subtilis, E. cloacae* and *K. pneumoniae.* The KDE exhibited antibacterial activity against *E. cloacae*, *S. saprophyticus*, *S. aureus* (MSSA), *K. pneumonia*e, *B. subtilis* and *S. aureus* (MRSA) with the respective inhibition zones of 16.37±1.64, 12.69±0.01, 11.05±0.38, 10.11±0.79, 10.00±0.32 and 9.92±0.50 mm. The TRE presented the inhibition zones of 17.17±1.97, 12.93±0.99, 10.72±0.29, 10.47±0.12, 9.73±0.9, and 8.08 ±0.55 mm against *E. cloacae*, *S. saprophyticus*, *S. aureus* (MSSA), *B. subtilis*, *S. aureus* (MRSA) and *K. pneumonia,* respectively. The PHE showed the inhibition zone against *E. cloacae* (19.81±1.55 mm), *S. saprophyticus* (12.85±0.85 mm), *S. aureus* (MSSA) (10.67±0.50 mm), *B. subtilis* (10.30±0.86 mm), *S. aureus* (MRSA) (9.63±0.41 mm) and *K. pneumoniae* (7.09±0.44 mm). The comparison of the inhibition zone of the KDE, TRE and PHE with penicillin G and chloramphenicol which are positive controls found that the KDE, TRE and PHE extracts agints *S. aureus* (MRSA) showed inhibition zone close to penicillin G while the inhibition zones of the KDE, TRE and PHE extracts against the other test microorganisms was lower than positive controls. The inhibition zones of all extracts are shown in **Figure 5**.

Table 3. Antimicrobial activity of ethyl acetate extracts from five edible mushrooms

	Test microorganisms (inhibition zone in mm)							
	KDE	KKE	PTE	TRE	PHE	Penicillin G	Chloramphenicol	Ketoconazole
S. saprophyticus	12.69±0.01	6.65±0.03	9.29±0.06	12.93±0.99	12.85±0.85	39.95±0.53	25.25±0.69	-
S. aureus (MRSA)	9.92±0.50	0.00±0.00	6.00±0.00	9.73±0.9	9.63±0.41	9.55±0.31	21.11±0.28	-
S. aureus (MSSA)	11.05±0.38	0.00±0.00	6.00±0.00	10.72±0.29	10.67±0.50	35.29±0.57	19.60±0.24	-
B. subtilis	10.00±0.32	0.00±0.00	6.50±0.5	10.47±0.12	10.30±0.86	29.49±0.35	28.87±0.35	-
E. cloacae	16.37±1.64	7.58±2.23	14.30±3.13	17.17±1.97	19.81±1.55	37.15±0.37	40.24±0.49	-
K. pneumoniae	10.11±0.79	0.00±0.00	0.00±0.00	8.08 ±0.55	7.09±0.44	35.44±0.60	20.18±0.43	-
E. coli	0.00±0.00	0.00±0.00	0.00±0.00	0.00±0.00	0.00±0.00	7.16±0.12	22.43±0.31	-
E. coli (ESBL)	0.00±0.00	0.00±0.00	0.00±0.00	0.00±0.00	0.00±0.00	9.71±0.44	6.44±0.32	-
S. typhimurium	0.00±0.00	0.00±0.00	0.00±0.00	0.00±0.00	0.00±0.00	22.93±0.11	28.71±0.44	-
P. mirabilis	0.00±0.00	0.00±0.00	0.00±0.00	0.00±0.00	0.00±0.00	21.45±0.44	12.65±0.43	-
C. albicans	0.00±0.00	0.00±0.00	0.00±0.00	0.00±0.00	0.00±0.00	-	-	31.025±0.25

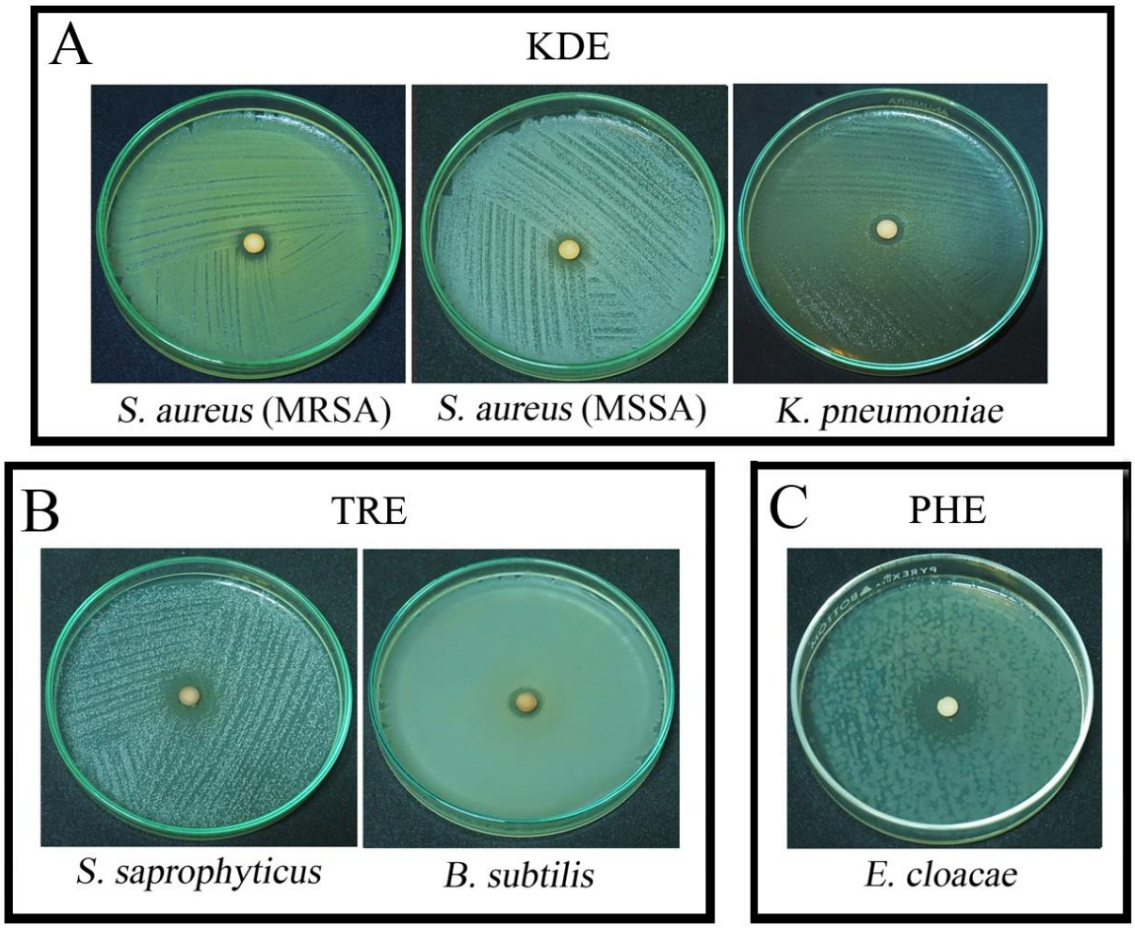

Figure 5. Zones of inhibition produced by the extracts against some tested microorganisms.

(A) KDE, (B) TRE and (C) PHE

Previous studies by Chaiharn *et al*., 2018 reported that the ethyl acetate extracts from the fruiting body of *L. polychrous* showed antimicrobial activity against *E. coli* and did not showed inhibition zone against *S. aureus* while the extracts of culture filtrate from *L. polychrous* in this study (KDE) did not showed inhibition zone against *E. coli* but it can displayed antimicrobial activity against *S. aureus* (MSSA) and *S. aureus* (MRSA). In addition, *L. squarrosulus* showed antimicrobial activity against *E. coli* and *S. typhimurium* while the extracts of culture filtrate from *L. squarrosulus* in this study (KKE) did not show inhibition zone against them.[14] Khatua and Acharya, 2014 reported that the inhibition zone of the ethanol extract from fruiting body of *M. crassa* ranged from 6-8 mm against *S. aureus*, *B. subtilis* and *E. coli* while the extracts of culture filtrate from *M. crassa* in this study (TRE) presented the inhibition zones of 11.05±0.38, 10.00±0.32 and 11.05±0.38 mm against *S. aureus (MSSA)*, *B. subtilis* and *S. aureus (MRSA),* respectively but it not presented inhibition zone against *E. coli*.[15] According to a study performed by Chomcheon *et al*., 2013 the ethyl acetate extracts of culture filtrate from *M. crassa* showed antimicrobial activity against *S. aureus* and was inactive against *E. coli* the same as TRE.[16] Also *the KDE and TRE* showed the antimicrobial activity against *S. saprophyticus, E. cloacae, K. pneumonia*, which were not tested in previous studies. The extracts of fruiting body and extracts of culture filtrate *from L. polychrous, L. squarrosulus* and *M. crassa* presented antimicrobial activity against different test microorganisms. They possibly contained different secondary metabolites.

Conclusion:

The results of this study indicated that the KDE showed the effective antioxidant activity than the other extracts antioxidant and antimicrobial activities of the KDE. The KDE displayed antimicrobial activity against four gram-positive bacteria (*S. saprophyticus, S. aureus* (MRSA), *S. aureus* (MSSA), *B. subtilis*) and two gram-negative bacteria (*E. cloacae*, *K. pneumoniae*). The KDE showed the effective antimicrobial activity against *K. pneumoniae* with the respective inhibition zones of 10.11±0.79 mm. Based on these results, the KDE could be a good choice for application in healthy food.

References:

1. María EV, Talía HP, Octavio PL. Int. J. Microbiol. 2015;2015:1–14.
2. Boonsong S, Klaypradit W, Wilaipuna P. Agric Nat Resour. 2016;50:89–97.
3. Fangkrathok N. Isan J Pharm Sci.. 2018;15:49–57.
4. Khammuang S, Sarnthima R. Biotechnol. 2007;6:408–413.
5. Randhawa K, Shri R. J. Pharm. Innov. 2017;6:321–327.
6. De Leon AM, Guinto LJZG, De Ramos PDV, Kalaw SP. Mycosphere. 2017;8:615–629.
7. Inyod T, Sassanarakit S, Payapanon A, Keawsompong S. Biodiversitas. 2017;18:221–228.
8. Inyod T, Sassanarakit S, Payapanon A, Keawsompong S. Agric Nat Resour. 2016;50:186–191.
9. Khatua S, Acharya K. Der Pharm. Lett. 2014;6:330–338.
10. Dawidowicz L, Siwulski M. Agriculture and Forestry. 2017;63:61–68.
11. Usami A, Motooka R, Nakahashi H, Okuno Y, Miyazawa M. J. Oleo Sci. 2014;63:731–739.
12. Tangjitjaroenkun J, Supabphol R, Chavasiri W. J. Med. Plants Res. 2012;6:1407–1414.
13. Tangjitjaroenkun J, Tangchitcharoenkhul R, Yahayo W, Supabphol R. Chiang Mai J Sci. 2017;44:322–337.
14. Chaiharn M, Phutdhawong WS, Amornlerdpison D, Phutdhawong W. Chiang Mai J Sci. 2018;45:1713–1727.
15. Khatua S, Acharya K. Int J Pharm Sci Rev Res. 2014;29:53–60.
16. Chomcheon P, Kheawkum B, Sriwiset P, Dulsamphan S, Dulsamphan C. Thai J. Pharm. Sci. 2013;37:107–111.

SP13_018_PF: KNOWLEDGE OF THAI TRADITIONAL HEALER ON UTILIZATION OF HERBS IN NAKHON SI THAMMARAT PROVINCE: IN CASE OF MRS. PANEE LUICHAN

Winyu Wongwiwat,[1,*] Angkana Eng-chuan,[1] Navakotchamon Suwanratsamee,[1] Suppattra Lertsakunjinda,[1] Pirinya Kritwongngam[2]

[1]Thai Traditional Medicine Department, Faculty of Science and Technology, Rajamangala University of Technology Srivijaya, Thungsong, Nakorn Si Thammarat, 80110, Thailand
[2]Food Technology Department, Faculty of Agricultural Technology, Phuket Rajabhat University, Muang, Phuket, 83000, Thailand
*e-mail: winyu.w@rmutsv.ac.th

Abstract:

The purpose of this research is to document and analyze knowledge of Thai traditional healer, Mrs. Panee Luichan, on utilization of herbs in Nakhon Si Thammarat province. Methodology consisted of semi-structure interview in 6 items including remedies and properties, remedy preparation, herbs in remedy, habits of medicinal plants, parts of medicinal plants used and taste of herbs. The well-known medicinal plants were identified and recorded. The data were analyzed in descriptive form. It was found that the total of 33 herbs were divided into 32 medicinal plants and 1 mineral herb. The 32 medicinal plants belonged to 21 families and 28 genera. The dominant family was Fabaceae (5 species, 16%) whereas both Piperaceae and Zingiberaceae were found in 9.4% (3 species). The dominant habits of medicinal plants were herbs (47%, 15 species). The main parts of plants used were rhizome and root (28%, 9 species) followed by leaf (19%, 6 species). The dominant taste of herbs (33%, 11 herbs) was pungent. Bitter taste and nauseating taste were found in 21% (7 herbs) and 15% (5 herbs), respectively. The most claimed herbs appeared in 3 remedies including *Angelica dahurica* (Fisch ex. Hoffm.) Benth. & Hook.f. ex Franch. & Sav., *Zingiber officinale* Roscoe. and *Salacia chinensis* L. Knowledge of Mrs. Panee Luichan on utilization of herbs based on Thai traditional theory was recorded, and information could be deposited as a database for further development research, which supports the objectives of the National Health Development Plan.

Introduction:

Thai traditional healer plays important roles in taking care of patient and health promotion for community through inherited knowledge of Thai traditional medicine. The community often praised Thai traditional healers as important persons.

Nakhon Si Thammarat province is located in the southern part of Thailand. The history, culture and knowledge can be traced back to more than 1,000 years ago. Nakhon Si Thammarat mountain range has plentiful natural resources and herbs. Additionally, a lot of Thai traditional healers have experiences about Thai traditional medicine in community. Mrs. Panee Luichan is one of Thai traditional healers who has experienced in general diseases more than 60 years.

Thai traditional remedy make from one or more types of herbs with any preparation such as raw type, decoction, maceration etc. Multi herbs remedy may contain 4 groups of ingredients including main herb, enhancing herb, prevention and control herb, and flavor herb. Thai traditional medicine theory divides property of herbs into 10 taste groups, consisting of bland, pungent, fragrant, oily, nauseating, salty, sour, astringent, bitter and sweet. Bland taste represents diuretic and antipyretic activities. Pungent taste suggests carminative, digestive and energy promoting activity. Fragrant taste affects blood circulation maintenance and heart, tonic, assuage and calm down. Oily taste improves synovial fluid joint and muscle maintenance and tonic. Nauseating

taste represents antiseptic, antitoxic, animal and insect bite, and antipathogenic and cytotoxic activity. Salty taste treats skin disease, constipation and phlegm. Sour taste treats cough and phlegm reliving, laxative activity, constipation and maintain blood circulation. Astringent taste treats wound heal, diarrhea and skin disease. Bitter taste affects blood circulation maintenance, antiseptic, fever, digestive and appetizing activity. Sweet taste represents muscle maintenance, appetizing and nourish activity.[1]

The 12th National Health Development Plan (2017 - 2021) supports usability of Thai traditional medicine for Thai people and self-care promotion.[2]

With above reasons, the objectives of this study are to document and analyze the knowledge of Thai traditional healer, Mrs. Panee Luichan, on utilization of herbs. The database obtained will be useful and supportive the 12th National Health Development Plan.

Methodology:

1. Thai traditional healer

Mrs. Panee Luichan is a 76-year-old Thai traditional healer. She lives in Ron Phibun district, Nakhon Si Thammarat province. She has experienced in general diseases through Thai traditional medicine more than 60 years, and has the professional license in Department of Thai traditional medicine. She was invited to sign in consent form for the knowledge collection on herbs utilization. This study was conducted from June to December 2017.

2. Data collection

The knowledge was documented by semi-structure interviewed in 6 items consisting of remedies and properties, remedy preparation, herbs in remedy, habits of medicinal plants, parts of medicinal plants used and taste of herbs.

3. Plant identification

The species of well-known medicinal plant were identified. This study did not collect voucher specimens because Thai traditional healer provided material from herbal store. However, researchers recorded the details of crude drug and confirmed the botanical characteristics of medicinal plants. The scientific names of medicinal plants were specified based on Thailand Plant Names by Tem Smitinand.[3] Data were analyzed in descriptive form.

Results and Discussion:

1. Remedies

A total of 6 remedies were oral route medicine. Multi herbs remedies consisting of diarrhea (DI), tonic (TO), blood circulation (BC), cancer (CA), hemorrhoid (HE) and diabetes (DB) remedies were prepared by decoction. Remedies for DI, TO, BC, CA, HE and DB treatment consist of 4, 8, 10, 8, 16 and 5 herbs, respectively (Table 1).

2. Herbs

A total of 33 herbs were divided into 32 medicinal plants and 1 mineral herb and belonged to 21 families and 28 genera (Table 1). The dominant genus was *Piper* which consisted of 3 species whereas both *Smilax* and Zingiber were composed of 2 species.

3. Habit of medicinal plants

All 32 medicinal plants were grouped into 4 types of habit consisting of herbs, tree, shrub and climber. The dominant habit of medicinal plants was herbs (15 species, 47%). Tree, shrub and climber were found in 25%, 19% and 9% (8, 6 and 3species), respectively. These results of medicinal plants habit were similar to ethnobotanical survey in Krabi and Songkhla provinces,[4] which was nearby Nakhon Si Thammarat province.

4. Family of medicinal plants

All medicinal plants were grouped into 21 families. The dominant family was Fabaceae found 16% (5 species) followed by Piperaceae and Zingiberaceae which were equally found in 9.4 % (3 species). Asteraceae, Smilacaceae and Solanaceae were equally found with 6.3% (2 species). The other 15 families including Alliaceae, Apiaceae, Apocynaceae, Asphodelaceae, Celastraceae, Cyperaceae, Euphorbiaceae, Fagaceae, Lamiaceae, Lauraceae, Lythraceae, Myristicaceae, Myrtaceae, Sapotaceae and Umbelliferae were equally found in 3.1% (1 species). These data resembled with Thai ethnobotanical survey researches, which showed the dominant families were Fabaceae, Piperaceae, Zingiberaceae and Asteraceae.[5,6,7,8]

5. Parts of medicinal plants used

Parts of medicinal plants used were divided into 10 groups. The most used part was rhizome and root (28%, 9 species) followed by leaf (19%, 6 species), wood (16%, 5 species), fruit (9%, 3 species). Bark, flower and whole plant were equally in 6.3% (2 species). Eventually, aril, bulb and latex were equally in 3% (1 species). The rhizome and root was dominant plant part used in several ethnobotanical surveys.[4,9,10,11]

6. Taste of herbs

The total of herbs was found 8 tastes. The dominant taste was pungent (33%, 11 herbs). The bitter taste found 21% (7 herbs) followed by nauseating taste in 15% (5 herbs). The astringent and fragrant taste were found equally in 9.3% (3 herbs), whereas, sour taste was found 6.3% (2 herbs). Eventually, bland and salty taste were found equally 3% (1 herbs). This information conformed to ethnobotanical survey in Nakhon Si Thammarat province, which pungent taste of herbs played a role in menopause treatment.[9] Mrs. Panee's taste of herbs knowledge performed correlation between taste of herbs and properties, which harmonized Thai traditional medicine theory.[1,6]

A total of 7 pungent taste herbs used in hemorrhoid remedy, harmonized properties of pungent taste involved carminative and digestive activity.[6]

All of 5 nauseating taste herbs used in cancer and hemorrhoid remedies, matched properties of nauseating taste affected cytotoxic activity. *Smilax corbularia* Kunth and *Smilax glabra* Wall. ex Roxb. were nauseating taste herbs which displayed antiproliferative and antiinflammatory activities for psoriasis and cancer treatment.[12,13,14,15]

Solanum indicum L. played role in diabetes remedy, which represented bitter taste for maintaining blood circulation, harmonized anti-diabetic ethnobotanical and experimental researches.[16,17,18]

Carthamus tinctorius L. used in blood circulation remedy showed blood circulation maintainance, increasing blood flow and removing blood stasis activities.[19,20,21]

Zingiber officinale Roscoe. used in diarrhea remedy displayed pharmacological activity for diarrhea.[22,23]

7. The most claimed herbs in remedies

The most claimed herbs used in 3 remedies were *Angelica dahurica* (Fisch ex. Hoffm.) Benth. & Hook.f. ex Franch. & Sav., *Zingiber officinale* Roscoe. and *Salacia chinensis* L.. Total of 12 herbs used in 2 remedies were *Allium sativum* L., *Carthamus tinctorius* L., *Cinnamomum verum* J. Presl, *Cyperus rotundus* L., *Derris scandens* (Roxb.) Benth., *Myristica fragrans* Houtt., *Piper chaba* Hunt., *Piper interruptum* Opiz, *Piper sarmentosum* Roxb., *Senna alata* (L.) Roxb., *Smilax corbularia* Kunth and *Smilax glabra* Wall. ex Roxb.

Angelica dahurica (Fisch ex. Hoffm.) Benth. & Hook.f. ex Franch. & Sav. was Chinese herbs and exotic herbs in Thailand, and contained in 5 Kotes materia medica group following Thai traditional pharmaceutical. This medicinal plant showed anti-staphylococcal, antiproliferative and cyclooxygenase (COX-2) expression inhibitory activities.[24,25,26]

Myristica fragrans Houtt. has been Thai traditional herbs for long time. This plant was reported to have antiinflammatory, analgesic, hepatoprotective, antimicrobial, antioxidative activities.[27,28,29,30,31]

Table 1 Herbs used of Mrs. Panee Luichan

Scientific name	Family	Part used	Habit	Taste	Remedy claimed
Medicinal plants					
Acacia concinna (Willd.) DC.	Fabaceae	Leaf	Shrub	Sour	CA
Allium sativum L.	Alliaceae	Bulb	Herb	Pungent	DI, DB
Aloe vera (L.) Burm.f.	Asphodelaceae	Latex	Herb	Bitter	BC
Angelica dahurica (Fisch ex. Hoffm.) Benth. & Hook.f. ex Franch. & Sav.	Apiaceae	Root	Herb	Fragrant	TO, BC, HE
Artemisia annua L.	Asteraceae	Whole plant	Herb	Bitter	BC
Bridelia ovata Decne.	Euphorbiaceae	Leaf	Tree	Bitter	HE
Caesalpinia sappan L.	Fabaceae	Wood	Tree	Bitter	BC
Capsicum annuum L. var *scuminatum*	Solanaceae	Fruit	Herb	Pungent	DI
Carthamus tinctorius L.	Asteraceae	Flower	Herb	Fragrant	BC, CA
Cinnamomum verum J. Presl	Lauraceae	Bark	Tree	Pungent	TO, BC
Coriandrum sativum L.	Umbelliferae	Whole plant	Herb	Astringent	TO
Curcuma longa L.	Zingiberaceae	Rhizome	Herb	Astringent	HE
Cyperus rotundus L.	Cyperaceae	Rhizome	Herb	Pungent	TO, HE
Derris scandens (Roxb.) Benth.	Fabaceae	Wood	Climber	Nauseating	CA, HE
Lagerstroemia speciosa (L.) Pers.	Lythraceae	Leaf	Tree	Bitter	DB
Mimusops elengi L.	Sapotaceae	Wood	Tree	Fragrant	BC
Myristica fragrans Houtt.	Myristicaceae	Aril	Shrub	Pungent	BC, HE
Orthosiphon aristatus (Blume) Miq.	Lamiaceae	Leaf	Herb	Bland	DB
Piper chaba Hunt.	Piperaceae	Fruit	Climber	Pungent	TO, HE
Piper interruptum Opiz	Piperaceae	Wood	Climber	Pungent	TO, HE
Piper sarmentosum Roxb.	Piperaceae	Root	Herb	Pungent	HE, DB
Quercus infectoria Oliv	Fagaceae	Root	Shrub	Astringent	DI
Salacia chinensis L.	Celastraceae	Wood	Shrub	Nauseating	BC, CA, HE
Senna alata (L.) Roxb.	Fabaceae	Leaf	Shrub	Nauseating	CA, HE
Smilax corbularia Kunth	Smilacaceae	Rhizome	Herb	Nauseating	CA, HE
Smilax glabra Wall. ex Roxb.	Smilacaceae	Rhizome	Herb	Nauseating	CA, HE
Solanum indicum L.	Solanaceae	Fruit	Shrub	Bitter	DB
Syzygium aromaticum (L.) Merr. & L.M.Perry	Myrtaceae	Flower	Tree	Pungent	BC
Tamarindus indica L.	Fabaceae	Leaf	Tree	Sour	CA
Wrightia arborea (Dennst.) Mabb.	Apocynaceae	Bark	Tree	Bitter	TO
Zingiber montanum (J.Koenig) Theilade	Zingiberaceae	Rhizome	Herb	Pungent	HE
Zingiber officinale Roscoe.	Zingiberaceae	Rhizome	Herb	Pungent	DI, TO, HE
Mineral herbs					
Magnesium sulfate	-	-	-	Salty	HE

Conclusion:

Knowledge of Mrs. Panee Luichan on utilization of herbs based on Thai traditional theory was recorded, and information could be deposited as a database for further development research, which supports the objectives of the National Health Development Plan.

Acknowledgements:

Researchers thank Mrs. Panee Luichan and Faculty of Science and Technology, Rajamangala University of Technology Srivijaya for research fund and work place.

References:

1. Division of Healing Arts, Office of the Permanent Secretary Ministry of Public Health and general Traditional Medicine Subcommittee. Division of Healing Arts, general medical textbooks, Thai traditional pharmaceutical program. Bangkok: Division of Healing Arts, Office of the Permanent Secretary Ministry of Public Health and general Traditional Medicine Subcommittee. 1999.
2. Board of Directors for 12th National Health Development Plan, Ministry of Public Health. Ministry of Public Health. 2016.
3. Smitinand T. The Forest Herbarium, Royal Forest Department. 2001.
4. Neamsuvan O, Ruangrit T. J Ethnopharmacol. 2017;196:84-93.
5. Phumthum M, Srithi K, Inta A, Junsongduang A, Tangjitman K, Pongamornkul W, Trisonthi C, Balslev H. J Ethnopharmacol. 2018;214:90-98.
6. Maneenoon K, Khuniad C, Teanuan Y, Saedan N, Prom-in S, Rukleng N, Kongpool W, Pinsook P, Wongwiwat W. J Ethnobiol Ethnomed. 2015;11:1-20.
7. Neamsuvan O, Kama A, Salaemae A, Leesen S, Waedueramae N. J Herb Med. 2015;5:190-198.
8. Chotchoungchatchai S, Saralampa P, Jenjittikul T, Pornsiripongse S, Prathanturarug S. J Ethnopharmacol. 2012;141:193-205.
9. Wongwiwat W, Kleangchan C, hayeeyahya W, Chaimol K, Masariyanana K, Kongmanee T, Rattanakhot W, Kritwongngam P. Proceeding of Ramkhamhaeng University National and International Research Conference 2019. Bangkok: Ramkhamhaeng University. 2019.
10. Jarić S, Kostić O, Mataruga A, Pavlović D, Pavlović M, Mitrović M, Pavlović P. J Ethnopharmacol. 2018;211:311-328.
11. Neamsuvan O, Phumchareon T, Bunphan W, Kaosaeng W. J Ethnopharmacol. 2016;194:179-187.
12. Itharat A, Ruangnoo S, Makchuchit S, Thongdeeying P, Panthong S. Planta Med. 2012;78:148-149.
13. Ruangnoo S, Jaiaree N, Makchuchit S, Panthong S, Thongdeeying P, Itharat A. Asian Pac J Allergy. 2012;30:268-274.
14. Man Mq, Shi Y, Man M, Lee SH, Demerjian M, Chang S, Feingold KR, Elias PM. Exp Dermatol. 2007;17:681-687.
15. Reanmongkol W, Itharat A, Bouking P. Warasan Songkhla Nakharin. 2007;29:59-67.
16. Salehi B, Ata A, Kumar NVA, Sharopov F, Ramirez-Alarcon K, Ruiz-Ortega A, Ayatollahi SA, Fokou PVT, Kobarfard F, Zakaria ZA, Iriti M, Taheri Y, Martorell M, Sureda A, Setzer WN, Capasso R, Ostrander EA, Rahman A, Choudhary MI, Cho WC, Rad JS. Biomolecules. 2019;9:1-121.
17. Borgohain R, Pathak P, Mohan R. J Evol Med Dent Sci. 2016;5:7294-7297.
18. Tarak D, Namsa ND, Tangjang S, Arya SC, Rajbonshi B, Samal PK, Mandal M. J Ethnopharmacol. 2011;138:345-350.
19. Yao Y, Chen T, Huang J, Zhang H, Tian M. Int Rev Neurobiol. 2017;135:181-196.
20. Singh V, Nimbkar N. Opportunities and Constraints. 2016.
21. Yao D, Wanf Z, Miao L, Wang L. J Ethnopharmacol. 2016;15:264-272.
22. Akram M, Shah IS, Usmanghan K, Mohiuddin E, Sami A, Asif M, Shah SMA, Ahmed K, Shaheen G. Pak J Nutr. 2011;10:399-400.
23. Jaw-CChen JC, Huang LJ, Wu SL, Kuo SC, Ho TY, Hsiang CY. J Agr Food Chem. 2007;55:8390-8397.

24. Kim YK, Kim YS, Ryu SY. Phytother Res. 2007;21:288-290.
25. Lechnera D, Stavria M, Oluwatuyia M, Mirandab RP, Gibbonsa S. Phytochemistry. 2004;65:331-335.
26. Ban HS, Lim SS, Suzuki K, Jung SH, Lee S, Lee YS, Shin KH, Ohuchi K. Planta Med. 2003;69:408-412.
27. Gupta AD, Bansal VK, Babu V, Maithil N. J Genet Eng Biotechnol. 2013;11:25-31.
28. Chatterjee S, Niaz Z, Gautam S, Adhikari S, Variyar P, Sharma A. Food Chem. 2007;101:515-523.
29. Chung JY, Choo JH, Lee MH, Hwang JK. Phytomedicine. 2006;13:261-266.
30. Morita T, Jinno K, Kawagishi H, Arimoto Y, Suganuma H, Inakuma T, Sugiyama K. J Agr Food Chem. 2003;51:1560-1565.
31. Olajide OA, Ajayi FF, Ekhelar AI, Awe SO, Makinde JM, Alada ARA. Phytother Res. 1999;13:344-345.

SP13_019_PF: ANTIOXIDANT AND SUN PROTECTION ACTIVITIES OF *Averrhoa bilimbi* L. LEAF EXTRACT AND ITS APPLICATION

Nutkochchatas Jumpeephun, Walaisiri Muangsiri, Pornpen Werawatganone*

Department of Pharmaceutics and Industrial Pharmacy, Faculty of Pharmaceutical Sciences, Chulalongkorn University, Bangkok 10330, Thailand
*e-mail: Pornpen.W@chula.ac.th

Abstract:

The objective of this study was to evaluate and compare the antioxidant and sun protection activities of *Averrhoa bilimbi* L. leaf extract obtained from different extraction solvents (70% ethanol, 99% ethanol and ethyl acetate) for cosmetic uses. The result showed that *A. bilimbi* leaf extract obtained from 99% ethanolic extract displayed the highest antioxidant activity (IC_{50} value of 0.58 ± 0.01 mg/mL), and the sun protection activity with SPF values of 2.50, 4.89, 9.72 and 14.70 at concentrations of 25, 50, 100 and 150 µg/mL, respectively. This extract also contained the total phenolic content of 113.86 mg GAE/g, and the total flavonoids content of 65.53 mg QE/g. The cosmetic serums containing *A. bilimbi* leaf extract obtained from 99% ethanolic extraction were prepared at 2.5, 5.0 and 7.5% w/w of the extract. Regarding the antioxidant and sun protection activities, all serums provided significantly higher %DPPH inhibition and enhanced UVB protective efficacy compared to those of the serum base (p<0.05). The serum containing 7.5% of the extract presented an impressive natural antioxidant and sun protection activities owing to the presence of flavonoid and phenolic compounds in the extract. These results suggest that *A. bilimbi* leaf extract obtained from 99% ethanolic extraction has potential to be developed for cosmetic purpose as a natural sunscreen ingredient.

Introduction:

UV radiation induces the formation of oxidizing species responsible of skin photo-aging, immunosuppression and photocarcinogenesis.[1] Sunscreens are the most common products used for skin protection against the harmful effect of direct UV radiation. Nowadays, natural active compounds exhibiting UV filtering activity became area of interest to reduce the use of synthetic chemical sunscreens. Some natural compounds (i.e., polyphenols, carotenoids, vitamins and anthocyanidins) also possess radical scavenger properties against ROS generated by UV radiation and provide broad-spectrum sunscreen products with antioxidant activity.[2] *Averrhoa bilimbi* Linn. (bilimbi), found in tropical countries, belongs to Oxalidaceae family. It has long been used as a folk medicine as diabetes mellitus, hypertension, and antimicrobial agents.[3] *A. bilimbi* leaf extract is known to contain phenolic compounds, such as flavonoids. Fidrianny *et al.*[4] reported that phenolic compounds and flavonoid contents of *A. bilimbi* leaf extract using different solvents were in the following order, ethyl acetate>ethanol>hexane. In another study, *A. bilimbi* leaves were extracted with 50%, 70%, and 96% ethanol, and the extract using 70% ethanol contained the highest phenolic and flavonoid contents compared to others[5]. The ethanolic extract presented marked antioxidant activity.[4] Moreover, the ethanolic extract showed sun protection activity based on *in vitro* study,[6] and also presented a photoprotective effect on skin against UVB-induced damage in Albino mice.[7] The use of natural compounds in cosmetic formulations has increased in recent years because of their safety, lack of side effects, the absence of dangerous synthetic compounds that cause health hazards and ecological sustainability.[8] However, the study on relationship of antioxidant and sun protection activities and phenolic and flavonoid contents in *A. bilimbi* leaf extract obtained from different extraction solvents has not been investigated.

This research aims to find a suitable extraction solvent for *A. bilimbi* leaf. The different extraction solvents (70% ethanol, 99% ethanol and ethyl acetate) were used and total phenolic and flavonoid contents in the obtained extracts were determined. Then antioxidant and sun protection activities of the obtained extracts were evaluated. The relationship of antioxidant and sun protection activities and phenolic and flavonoid

contents in the extracts were determined. The extract providing the strongest sun protection was further developed in the form of topical sunscreen solution, and its sun protection factor was measured.

Methodology:

Plant extraction: *A. bilimbi* fresh leaves were collected from its natural habitat in Phangnga, Thailand. They were thoroughly washed with water, air dried and then ground to pass through a 60-mesh sieve. The powdered leaves (60 g) were macerated in 200 mL of three solvents[5] (70% ethanol, 99% ethanol and ethyl acetate), and the soaked powdered leaves were continuously shaken at 100 RPM at room temperature for 24 h. Then, they were filtered, and the filtrates were collected. The fresh solvents were added to the plant residues, and the process was repeated three times. Consequently, the collected filtrates from each solvent were accumulated and evaporated at 50 °C to give viscous extracts. The percent extraction yield was determined.

Determination of total phenolic content

The Folin-Ciocalteu assay was used for total phenolic content determination with minor modification from Sembiring *et al.*[9] A total of 25 µL of diluted extract (1 mg/mL) of *A. bilimbi* leaf was mixed with 100 µL of 1:4 diluted Folin-Ciocalteu reagent and shaken for 60 sec in a 96 well plate. The mixture was left for 4 min and then 75 µL of sodium carbonate solution (100 g/L) was added. The mixture was shaken for 60 sec and incubated for 2 h at room temperature. Then the absorbance of the mixture was measured at 765 nm using a microplate reader (CLARIOstar, BMG Labtech, Germany). The same procedure was repeated for the standard solutions of gallic acid dissolved in ethanol in the concentration range of 15-200 µg/ml. The calibration line of the absorbance values vs the concentrations was constructed from these standard solutions. Total phenolic contents in the extracts obtained from different solvents were expressed in terms of gallic acid equivalent (mg of GAE/g of extract).

Determination of total flavanoid content

Total flavonoid content was determined using aluminium chloride spectrophotometric assay modified from Sembiring *et al.*[9] A calibration curve was prepared from ethanolic solution of quercetin in the concentration range of 5-70 µg/ml. The reaction mixture contained 50 µL of the quercetin standard solution or the extract solution (1 mg/mL), 20 µL of 10% aluminium chloride solution and 150 µL of ethanol in a 96 well plate. Then, 20 µL of 1M sodium acetate was added to the mixture. All tested samples were incubated for 40 min at room temperature. The absorbance of the samples was measured at 415 nm using a microplate reader (CLARIOstar, BMG Labtech, Germany). The total flavonoid content in extracts was expressed in terms of quercetin equivalent (mg of QE/g of extract).

Determination of antioxidant activity

The antioxidant activity of *A. bilimbi* leaf extracts was evaluated using DPPH (2,2-diphenyl-1-picrylhydrazyl) scavenging assay. The test was slightly modified from Sembiring *et al.*[9] The reaction was conducted in a 96 well plate. Each well contained 20 µL of diluted extract solution in methanol at various concentrations (450-2,000 µg/mL) and 180 µL of 0.147 mM DPPH solution. Then, the sample mixtures were incubated at room temperature in a dark place for 30 min. The absorbance was measured at 517 nm using a microplate reader (CLARIOstar, BMG Labtech, Germany). Blank was the diluted extraction solution in methanol without DPPH solution. Negative control was the DPPH solution without the extract and positive standard was Trolox® added in place of the extract. Radical scavenging activity (% inhibition) was calculated using Eq 1.

$$\% \text{ Inhibition} = 1 - ((A_{sample} - A_{blank\ control})/A_{negative\ control}) \times 100 \qquad \text{(Eq 1.)}$$

where A is absorbance. The IC_{50} value was calculated from the regression line of %inhibition vs. the extract concentration at 50% inhibition on DPPH activity.

Determination of Sun Protection Factor

The Dutra method (diluted solution transmittance method)[10] was used to determine *in vitro* Sun Protection Factor (SPF) of *A. bilimbi* leaf extracts, and this method was modified from Muhammad *et al*.[6] Solutions of *A. bilimbi* leaf extracts were prepared at various concentrations (25, 50, 100, 150 µg/mL). The absorbance spectra of these solutions were scanned at the wavelength of 290-320 nm with interval of 5 nm using a UV-Visible spectrophotometer (UV-1601, Shimadzu, Japan), and ethanol was used as a blank. The experiment was performed in triplet and SPF value was calculated using Mansur equation, Eq 2.[11]

$$SPF_{spectrophotometric} = CF \times \sum_{290}^{320} EE\,(\lambda) \times I\,(\lambda) \times Abs\,(\lambda) \qquad \text{(Eq 2.)}$$

where CF is the correction factor (=10), determined by a sunscreen with known SPF, a solution containing 8% of homosalate gives SPF=5[12], EE (λ) is the erythemal effect spectrum, I (λ) is the solar intensity spectrum, and Abs (λ) is the absorbance of sample. The "EE x I" value at each wavelength is a constant as shown in Table 1. Sun protection factor values of the obtained extracts from all extraction solvents were compared, and then the extract with the highest SPF was selected to incorporate in a cosmetic preparation in the next experiment.

Table 1. The Normalized term used in the calculation of SPF

Wavelength (λ nm)	EE x I (normalized)
290	0.0150
295	0.0817
300	0.2874
305	0.3278
310	0.1864
315	0.0839
320	0.0180
Total	1

Table 2. Cosmetic serum preparations containing *A. bilimbi* leaf extract

Ingredients	**Function**	**Formula and Quantity (%w/w)**		
		F1	**F2**	**F3**
A. bilimbi leaf extract	Active	2.5	5.0	7.5
Ethanol	Solvent		10	
PEG400	Humectant / Co-solvent		30	
Polysorbate 80	Solubilizer		10	
Phenoxyethanol	Preservative		0.5	
Ammonium Acryloyldimethyltaurate/VP Copolymer	Thickener		0.25	
Purified water	Solvent		q.s. to 100	

Preparation of cosmetic serums containing A. bilimbi leaf extract

The selected extract was added in a liquid mixture or serum base which was formulated in the preliminary study for proper properties to apply on skin. *A. bilimbi* leaf extract serum preparations consisted of the extract at the concentrations of 2.5, 5, and 7.5% w/w and other ingredients as presented in Table 2. Briefly, the extract was dissolved in ethanol, PEG400, and polysorbate 80 and the solution was added in ammonium acryloyldimethyltaurate/VP copolymer dispersed in demineralized water. The obtained viscous liquid was mixed with phenoxyethanol and homogenized. The slightly viscous clear liquid or serum preparations containing three different concentrations of *A. bilimbi* leaf extract were homogeneous without any precipitation as expected.

Evaluation of A. bilimbi leaf extract cosmetic serums

Physicochemical properties of *A. bilimbi* leaf extract serums including color, transparency, homogeneity, and pH were monitored. Antioxidant and *in vitro* sun protection activities of the serums were evaluated using DPPH method and UV spectrophotometry method as previously.

Statistical analysis

All measurements were conducted in triplicated. The data were expressed as mean ±SD and analyzed by an analysis of variance (p<0.05) for mean comparison followed by Turkey's HSD test.

Results and Discussion:

Plant extraction and characterization: Dielectric constants (ε) of the extraction solvents are 42 (70% ethanol), 25 (99% ethanol) and 6.02 (ethyl acetate), indicating that ethyl acetate has the lowest polarity. Percent yields of *A. bilimbi* leaf extracts obtained from various solvents are reported in Table 3. The use of 70% ethanol as the extraction solvent provided the highest yield. The result indicated that *A.bilimbi* leaf extract contained semi-polar compounds. A previous study also reported that 70% ethanol was an effective extraction solvent for *A.bilimbi* leaf.[5]

Phenolic compounds and flavonoids are plant secondary metabolites and exhibit a wide variety of beneficial biological activities including antioxidant activity and prevention of UV-induced skin damage.[13] Ethanol (99%) is the most preferred solvent to extract phenolic compounds and flavonoids (Table 3). These results were different from previous studies. Muhammad R *et al.* reported that the contents of phenolic and flavonoid in the 70% ethanolic extract were higher than the contents in 50% and 96% ethanolic extracts.[5] Fidrianny I *et al.* showed that the contents of phenolic and flavonoid in ethyl acetate extract were higher than the contents in ethanolic and hexane extracts.[4] It could be due to the differences of extraction methods and extraction parameters such as parts of the plant, size of the crude powder and extraction time leading to the change of extraction efficiency.

Table 3. Extraction yield, total phenolic and total flavonoid contents of *A. bilimbi* leaf extract obtained from different extraction solvents

Extraction solvents	Crude extract yield (%)	Total phenolic content (mg GAE/g extract)	Total flavonoid content (mg QE/g extract)
70% ethanol	14.80 ± 0.24[a]	104.57 ± 0.92[a]	47.16 ± 0.94[a]
99% ethanol	8.70 ± 0.13[b]	113.86 ± 0.36[b]	65.53 ± 1.05[b]
ethyl acetate	5.44 ± 0.51[c]	94.91 ± 0.41[c]	34.84 ± 0.81[c]

GAE = gallic acid equivalent. QE = quercetin equivalent. Value represents as mean ± SD (n=3) Values in same column followed by a different letter (a-c) are significantly different (p<0.05)

Ability of the extracts to reduce DPPH radical was evaluated using spectrophotometry. Based on the regression line of % inhibition vs. the extract concentration, the calculated IC_{50} values (mg/mL) are presented in Table 4. Trolox was chosen as the positive standard substance because the chromanol ring structures on Trolox and flavonoids provide similar antioxidant activity.[14] The extract obtained from 99% ethanolic extraction presented the lowest IC_{50} value of 0.58 ± 0.01 mg/mL, indicating the highest antioxidant activity. Fidrianny *at et*[4] reported IC_{50} value of 2.03 µg/mL for the 99% ethanolic extraction of *A.bilimbi* leaf extract which was less than IC_{50} value of the ethyl acetate extract (2.83 µg/mL). In the present study, the increase of antioxidant activity was accompanied by a corresponding the increase of phenolic and flavonoid contents in *A. bilimbi* leaf extracts as following; 99% ethanolic extract > 70% ethanolic extract > ethyl acetate extract. This relationship between total phenolic and flavonoid contents and antioxidant activity was also observed in four varieties of mango extracts.[15]

Table 4. DPPH scavenging activity of various extract of *A. bilimbi* leaf

Extraction solvent	IC_{50} (mg/mL)
70% Ethanol	0.86 ± 0.02[a]
99% Ethanol	0.58 ± 0.01[b]
Ethyl Acetate	1.70 ± 0.02[c]
Trolox (control)	0.07 ± 0.01[d]

Value represents as mean ± SD (n=3) Values in same column followed by a different letter (a-d) are significantly different (p<0.05)

In vitro SPF study *of A. bilimbi* leaf extract was determined by the spectrophotometric method developed by Mansur (1986) in which absorbance in UVB region of the diluted extract solutions was measured.[10,16] UVB is considered to produce sunburn and cause skin cancers. In Figure 1, SPF values of *A. bilimbi* leaf extracts were in a range of 1.34-14.70 and the SPF values correlated with the concentration of the extracts. At all concentrations, the extract using 99% ethanol showed a higher SPF value than the extracts using the other solvents. A previous study reported that SPF values of *A.bilimbi* leaf extract obtained from 96% ethanolic extraction were 9.615, 12.087, and 28.125 at concentrations of 100, 200, and 300 µg/mL, respectively.[6] Phenolic and flavonoid compounds were likely to be the active sun protecting compounds.[6,17] This explanation was confirmed by the correlation between sun protection activity and the contents of phenolic and flavonoid compounds. In previous report, flavonoids showed significant photoprotective effect because of their UV absorbing capacity.[18] Total phenolic content was correlated with sun protective activity which was reported in *S. ebulus*, *Zea maize*, *F. sellowiana* and *C. pentagyna* fruit extracts.[19]

Furthermore, the antioxidant activity was found to be in relationship with the sun protection activity in which a lower IC_{50} value led to a higher sun protection activity of the extract. The extract obtained from 99% ethanol extraction presented the highest antioxidant and sun protection activities which could be due to the high contents of phenolic and flavonoid compounds. This is in agreement with the polyphenolic components which were responsible for the antioxidant and photoprotective activities in propolis ethanolic extract.[20] Phenolic and polyphenolic compounds have been known as powerful antioxidants and flavonoids consist of low-molecular weight polyphenolic substances. Flavonoids and phenolic acids are capable to scavenge reactive oxygen species (ROS), which plays vital roles in the initiation of free radical reactions and consequently are effective in the protection against UV-induced skin damage.[13]

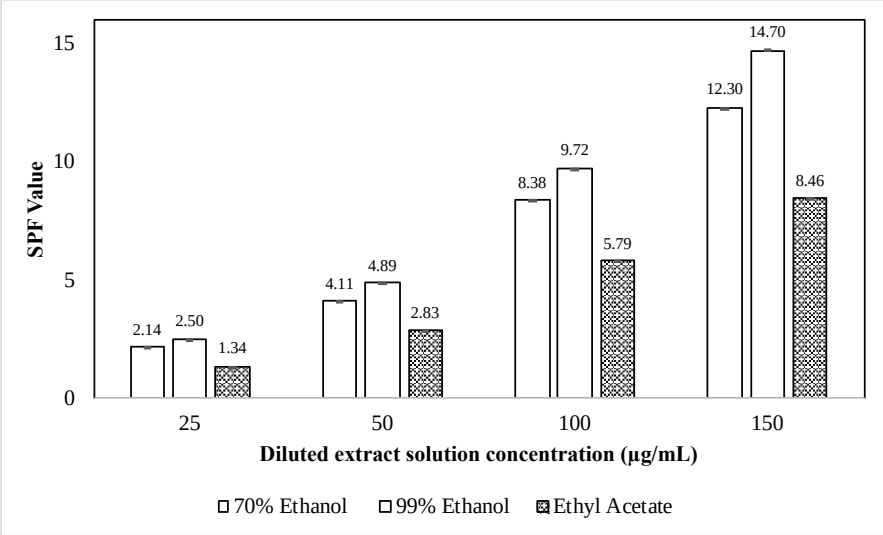

Figure 1. SPF value of various extract of *A.bilimbi* leaf at diluted extract solution concentration of 25, 50, 100 and 150 µg/mL

Preparation of cosmetic serum containing A. bilimbi leaf extract: The cosmetic serums containing *A. bilimbi* leaf extract obtained from 99% ethanolic extraction were prepared at the concentrations of 2.5, 5.0 and 7.5% w/w of the extract (F1-F3). Both cosolvency and micellar solubilization techniques were utilized to improve solubility of the extract in the vehicle. Ethanol (10%) and PEG 400 (30%) were cosolvents and polysorbate 80 (10%) was a surfactant in the serum. These solubilizers were used at suggested concentrations providing no skin irritation.[22] Ammonium acryloyldimethyltaurate/VP Copolymer (Aristoflex® AVC), a thickener, was compatible with the other components and resistant to UV radiation.[21] Phenoxyethanol could reduce the risk of microbial contamination in the preparation containing plant extract. The appearance of serums containing the extract was in deep green color, homogeneous and viscous solution without any precipitation, and pH values were in the range of 4-6 as shown in Table 6.

Evaluation of A. bilimbi leaf extract cosmetic serums: Regarding the antioxidant activity, all serums containing *A. bilimbi* leaf extract provided significantly higher %DPPH inhibition than the serum base ($p<0.05$) as presented in Table 6. Approximately 95% DPPH inhibition was observed because the extract concentrations in all serums were much higher than IC_{50} of the extract (0.58 ± 0.01 mg/mL). As it was observed in DPPH scavenging activity of the extract, %DPPH inhibition was a dose dependent up to a certain concentration and then the activity reached a plateau at high concentration. The concentrations of the extract in the serums were in the plateau region of the correlation.

The sun protection activity of *A. bilimbi* leaf extract serums were evaluated using diluted solution transmittance method, and the results are shown in Table 6. The incorporation of *A. bilimbi* leaf extract significantly enhanced the UVB protective efficacy compared to that of the serum base ($p<0.05$). F3 contained the highest extract concentration, resulting in the highest SPF value. Based on the sun protection and antioxidant activities, F3 provided high potential as a sun protection serum. These activities of *A. bilimbi* leaf extract in the serum led to two protection steps which were a passive protection step by absorbing UV radiation and an active protection step by quenching ROS generated by UV light as antioxidants.[2] These activities were owing to the presence of flavonoid and phenolic compounds in the extract. However, further *in vivo* evaluation will be required.

In this study, *A. bilimbi* leaves were successfully extracted and the extract using 99% ethanol extraction presented the most effective antioxidant and sun protection activities. The experiment demonstrated that these activities correlated with phenolic and flavonoid contents in the extracts from the different extraction solvents. Cosmetic products containing *A. bilimbi* extract have never been prepared and evaluated for their activities. In this work, serum containing this extract was successfully developed and proved for its antioxidant and sun protection activities.

Table 6. Evaluation on the physicochemical properties, antioxidant and sun protection activity of *A. bilimbi* leaf extract cosmetic serums (F1, F2, F3) and base serum

Parameters	F1	F2	F3	Base serum
pH-value	5.10 ± 0.00	6.05 ± 0.04	6.07 ± 0.02	4.84 ± 0.00
%DPPH inhibition	95.28 ± 0.57	96.67 ± 1.01	96.82 ± 2.06	19.56 ± 0.95
SPF value	6.49 ± 0.02	11.14 ± 0.01	16.2 ± 0.03	0.07 ± 0.01

Value represents as mean ± SD (n=3)

Conclusion:

The results of the present study suggested that the *A. bilimbi* leaf extracts contained phenolic compounds and flavonoids. The extracts exhibited remarkable scavenging effect on DPPH representing antioxidant activity and UVB protective activity, especially, when 99% ethanol was used as the extraction solvent. The extract obtained from this solvent extraction was successfully incorporated in the cosmetic serum base. The serum containing 7.5% of the extract still presented an impressive natural antioxidant and sun protection activities. Further studies are suggested to determine *in vivo* efficacy and safety of this cosmetic serum.

Acknowledgements: This work was supported by Faculty of Pharmaceutical sciences, Chulalongkorn University.

References:

1. Skotarczak K, Osmola-Mankowska A, Lodyga M, Polanska A, Mazur M, Adamski Z. Eur Rev Med Pharmacol Sci. 2015;19:98-112.
2. Tampucci S, Burgalassi S, Chetoni P, Monti D. Cosmetics. 2018;5:1.
3. Ashok K., Naveena L, Jeevigunta. Int J Pharm Pharm Sci. 2013;3:136-139.
4. Fidrianny I, Rahmawati A, Hartati R. Rasayan J Chem. 2018;11:1628-1634.
5. Muhammad R, Murti B, Wigati D, Suharsanti R, Putri C. Pharmaciana. 2019;9:137-144.
6. Muhammad R, Suharsanti R, Sugihartini N, Lukitaningsih E. J Glob Pharma Technol. 2019;11:308-313.
7. Agena P, Albay C, Apusen C, Arago M, Catapang J, Siapco R. The Steth. 2012;6:29-41.
8. Mishra A, Mishra A, Chattopadhyay P. Trop J Pharm Res. 2011;10:351–360.
9. Sembiring E, Elya B, Sauriasari R. Pharmacogn J. 2017;10:123-127.
10. Dutra E, Oliveira D, Kedor-Hackmann E, Santoro M. Braz J Pharm Sci. 2004;40:381-385.
11. Sayre R, Agin P, LeVee G, Marlowe E. Photochem Photobiol. 1979;29:559-566.
12. Shiva G, Imani F, Hosseinzadeh H, Jaafari M. Iran J Basic Med Sci. 2011;14:521–533.
13. Svobodová A, Psotová J, Walterová D. Biomed Pap Med Fac Univ Palacky Olomouc Czech Repub. 2003;147:137-145.
14. Gulcin I. Arch Toxicol. 2020;94:651-715.
15. Fidrianny I, Rahmiyani I, Wirasutisna K. Int J Pharm Pharm Sci. 2013;5:189-194.
16. Mansur J, Breder M, Mansur M, Azulay R. An Bras Dermatol. 1986;61:121-124.
17. Petruk G, Del Giudice R, Rigano M, Monti D. Oxid Med Cell Longev. 2018;2018:1-11.
18. Saewan N, Jimtaisong A. J Appl Pharm Sci. 2013;3:129-141.
19. Ebrahimzadeh MA, Enayatifard R, Khalili M, Ghaffarloo M, Saeedi M, Charati JY. Iranian journal of pharmaceutical research: IJPR. 2014;13:1041.
20. Gregoris E, Fabris S, Bertelle M, Grassato L, Stevanato R. Int J Pharm. 2011;405:97-101.
21. Baranova I, Kovalenko S, Khokhlenkova N, Martyniuk T. Asian J Pharm. 2017;11:1-6.
22. Meneghini C, Rantuccio F, M. L. Dermatologica 1971;143:137-147.

SP13_020_PA: *IN VITRO* SCREENING OF ANTIOXIDANT ACTIVITIES OF FOUR THAI MEDICINAL FLOWERS

Saowanee Phetkeereerat, Wachirachai Pabuprapap, Apichart Suksamrarn, Wongnapa Nakyai*

Department of Chemistry and Center of Excellence for Innovation in Chemistry, Faculty of Science, Ramkhamhaeng University, Bangkok 10240, Thailand
*e-mail: wongnapa_n@rumail.ru.ac.th

Abstract:

The medicinal plants are often the preferred form of therapy and continue to play a huge role in meeting the primary health care needs of Thai people for a long time. Some of the flowers are used in traditional drug recipes to treat many diseases. In the present work, four selected plants, *Jasminum sambac*, *Mimusops elengi*, *Nelumbo nucifera*, and *Pandanus tectorius*, were evaluated for total phenolic contents, antioxidant, and nitric oxide radical scavenging activities. The 95% ethanolic extract of *P. tectorius* flowers showed the best antioxidant activities using the DPPH radical scavenging assay with an IC_{50} value of 11.70±1.06 µg/mL compared with the positive control, ascorbic acid (IC_{50} 5.15±1.03 µg/mL). The *P. tectorius* flowers extract also had the highest total phenolic content using the Folin-Ciocalteu method (229.31±0.02 µgGAE/mg). The 95% ethanolic extract of *M. elengi* showed weak nitric oxide-scavenging activity with the IC_{50} value of 0.29±1.07 mg/mL, which was lower than that of the positive control, ascorbic acid (IC_{50} 0.35±1.24 µg/mL). These flowers may be served as potential resources of natural antioxidants for use as functional food ingredient and cosmeceutical applications.

SP13_021_PA

SP13_021_PA: *α*-GLUCOSIDASE INHIBITORS FROM THE STEMS AND TWIGS OF *Garcinia schomburgkiana*

Jirapast Sichaem*

Research Unit in Natural Products Chemistry and Bioactivities, Faculty of Science and Technology, Thammasat University Lampang Campus, Lampang 52190, Thailand
*e-mail: Jirapast@tu.ac.th

Abstract:

Garcinia schomburgakiana Pierre (Clusiaceae), known in Thai as Ma-dan, is an edible evergreen tree that grows in Laos, Vietnam, Cambodia, and Thailand. It has ethnomedicinal uses as a laxative and expectorant, and in the treatment of coughs, menstrual disturbances, and diabetes. Previous studies of the bioactive constituents of *G. schomburgkiana* have reported the presence of flavonoids, xanthones, triterpenoids, depsidones, phloroglucinols, and biphenyl derivatives, some of which exhibited antimalarial, cytotoxic, and anti *α*-glucosidase properties. In this study, a new bixanthone, schomburgkixanthone (**1**), along with 21 known compounds, griffipavixanthone (**2**), 1,3,7-trihydroxyxanthone (**3**), 1,5,6-trihydroxyxanthone (**4**), 1,3,5,6-tetrahydroxyxanthone (**5**), 1,6-dihydroxyxanthone (**6**), 1,3,5-trihydroxyxanthone (**7**), 1,3,6-trihydroxyxanthone (**8**), 1,6,7-trihydroxyxanthone (**9**), 2,4′-dihydroxydiphenylmethane (**10**), phyllanthin (**11**), 5,5′-[oxybis(methylene)]di(2-furaldehyde) (**12**), kaempferol (**13**), 5,7,3′,5′-tetrahydroxyflavanonol (**14**), guttiferone K (**15**), oblongifolin C (**16**), volkensiflavone (**17**), morelloflavone (**18**), volkensiflavone-7-*O*-glucopyranoside (**19**), morelloflavone-7-*O*-glucopyranoside (**20**), fukugetin (**21**), and (2*S*,3*S*)-morelloflavone-7-*O*-*β*-acetylglucopyranoside (**22**) were isolated from *G. schomburgkiana* stems and twigs. The structures of all isolated compounds were identified by the interpretation of their spectroscopic data and comparison with those reported in the literature. Compounds **1-11**, **13-19**, and **21** were tested for *α*-glucosidase inhibitory activity. Compounds **1-2**, **4-5**, **9**, and **14-19** exhibited potent activity with IC_{50} values in the range of 0.31 ± 0.7 to 97.8 ± 0.2 µM, greater than that of acarbose (IC_{50} 147 ± 0.5 µM).

SP13_022_PA: INHIBITION OF NITRIC OXIDE AND FREE RADICAL SCAVENGING ACTIVITIES OF SOME SELECTED THAI MEDICINAL FLOWERS

Nattharika Peedee, Wachirachai Pabuprapap, Apichart Suksamrarn, Wongnapa Nakyai*

Department of Chemistry and Center of Excellence for Innovation in Chemistry, Faculty of Science, Ramkhamhaeng University, Bangkok 10240, Thailand
*e-mail: wongnapa_n@rumail.ru.ac.th

Abstract:

In this study, the antioxidant activity of the 95% ethanol extracts of the dried flowers of four Thai medicinal flowers, *Cananga odorata*, *Mammea siamensis*, *Melodorum fruticosum*, and *Mesua ferrea* was evaluated. Antioxidant activity was determined by spectrophotometric methods using DPPH free radical, and nitric oxide radical inhibition assays. In addition, total phenolic content was also determined by using the Folin-Ciocalteu method. The extract of *M. ferrea* flowers displayed the strongest antioxidant activity with an IC_{50} value of 12.87±1.04 µg/mL, compared to the standard ascorbic acid with an IC_{50} value of 5.15±1.03 µg/mL. This extract also contained the highest total phenolic content (227.23±0.01 µgGAE/mg). Moreover, the *C. odorata* extract exhibited weak nitric oxide radical scavenging activity with an IC_{50} value of 69.68±1.09 µg/mL, whereas the standard ascorbic acid displayed an IC_{50} value of 0.35±1.24 µg/mL. The *M. ferrea* flowers may be served as an interesting source of antioxidants with their applications in different fields, for example, food, cosmetics and pharmaceuticals.

SP13_023_PF: SYNTHESIS AND CYTOTOXIC ACTIVITY OF TETRAHYDROCURCUMIN-DIHYDROPYRIMIDINONES AGAINST SMALL CELL LUNG CANCER (NCI-H187) CELL LINES

Sarawalee Arunkhamkaew, Benjarat Wangthara, Vachiraporn Ajavakom*

Department of Chemistry and Center of Excellence for Innovation in Chemistry, Faculty of Science, Ramkhamhaeng University, Bangkok, 10240, Thailand
*e-mail: satcharoen@yahoo.com

Abstract:

Tetrahydrocurcumin-Dihydropyrimidinone (THC-DHPM) derivatives were successfully synthesized by one-pot multi-components Biginelli reaction. Upon treatment of tetrahydrocurcumin (THC), benzaldehyde derivatives and urea in the presence of copper(II) sulfate pentahydrate ($CuSO_4 \cdot 5H_2O$) as a catalyst, THC-DHPMs were obtained, after chromatographic purification, in moderate to good yields (44-74% yields). In the present work, benzaldehyde and substituted benzaldehyde derivatives, including 3-nitrobenzaldehyde, 4-methoxybenzaldehyde and 4-hydroxy-3-methoxybenzaldehyde, were employed to synthesize a collection of THC-DHPMs. Cytotoxic activity of the synthesized THC-DHPMs were then evaluated. Interestingly, the THC-DHPMs derived from benzaldehyde and 3-nitrobenzaldehyde showed inhibitory activity against small cell lung cancer (NCI-H187) cell lines with IC_{50} values of 27.16 and 31.21 µM, respectively. On the other hand, THC-DHPMs bearing electron-releasing groups were found inactive towards the NCI-H187 cell lines. The results obtained from cytotoxic activity screening implied that the presence of electron-donating groups probably restrain the inhibition mechanism and it required further investigations.

SP13_024_PA: SESQUITERPENE AND TRITERPENE FROM THE LEAVES OF *Shorea siamensis*

Ratree Sangpeng,[1] Aroon Jankam,[2] Teerawut Thothaisong,[1] Waraluck Chaichompoo,[1] Apichart Suksamrarn[1,*]

[1]Department of Chemistry and Center of Excellence for Innovation in Chemistry, Faculty of Science, Ramkhamhaeng University, Bangkok 10240, Thailand
[2]Program of Chemistry, Faculty of Science, Ubon Ratchathani Rajabhat University, Ubon Ratchathani 34000, Thailand
*e-mail: asuksamrarn@yahoo.com

Abstract:

Shorea siamensis Miq. (Dipterocarpaceae), known in Thai as "Rang", is a deciduous tree which is native to most of mainland Southeast Asia such as Myanmar, Thailand, Malaysia, Cambodia, Laos and Vietnam. The leaves of this plant species are used in traditional medicine as treatments for impetigo. Investigation of the chemical constituents of the leaves of *S. siamensis* led to the isolation of one sesquiterpene, spatulenol (**1**), and one triterpene, lupeol (**2**). Their structures were identified based on spectroscopic data and by comparison with those of reported values.

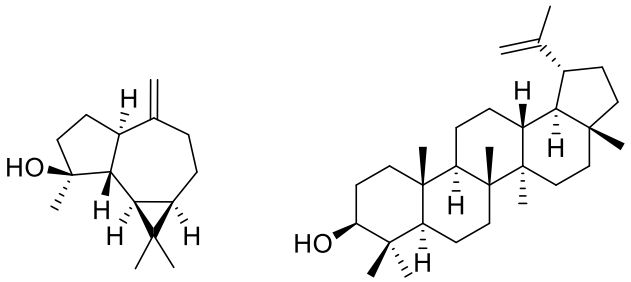

(**1**) (**2**)

Figure 1. The structures of the isolated compounds from *S. siamensis*.

SP13_025_PA

SP13_025_PA: TRITERPENOIDS FROM THE FLOWERS OF *Mesua ferrea*

Wachirachai Pabuprapap,[1] Waraluck Chaichompoo,[1] Teerawut Thothaisong,[1] Ratchanaporn Chokchaisiri,[2] Apichart Suksamrarn[1,*]

[1]Department of Chemistry and Center of Excellence for Innovation in Chemistry, Faculty of Science, Ramkhamhaeng University, Bangkok 10240, Thailand
[2]Department of Chemistry, School of Science, University of Phayao, Phayao 56000, Thailand
*e-mail: asuksamrarn@yahoo.com

Abstract:

Mesua ferrea L., known in Thai as "Bun-nak", belongs to the family Calophyllaceae, which is widely distributed in tropical Asian countries like India, Myanmar, Thailand and Indonesia. In Thai traditional medicine, the flower of this plant is used as astringent and stomachic drugs. In the present study, two known triterpenoids, lupeol (**1**) and *epi*-friedelanol (**2**), were isolated from the *n*-hexane extract of the flowers of *M. ferrea*. The structures of the isolated compounds were identified based on analysis of spectroscopic data.

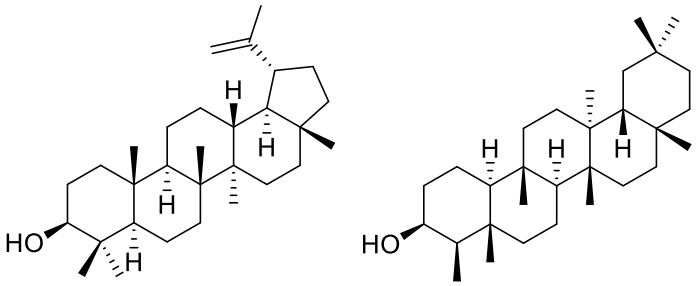

Figure 1. The structures of compounds **1** and **2**.

SP13_026_PA: HALOGENATED SESQUITERPENOIDS FROM *Laurencia composita*

Chandech Phupewkaew,[1] Saowanee Kumpun,[2] Yuttana Siriwattanasathien,[1] Waraluck Chaichompoo,[1] Wachirachai Pabuprapap,[1] Apichart Suksamrarn[1,*]

[1]Department of Chemistry and Center of Excellence for Innovation in Chemistry, Faculty of Science, Ramkhamhaeng University, Bangkok 10240, Thailand
[2]Department of Chemistry, Faculty of Science and Technology, Suan Sunandha Rajabhat University, Bangkok 10300, Thailand
*e-mail: asuksamrarn@yahoo.com

Abstract:

Secondary metabolites of tropical seaweed are proven to exhibit variety of biological activities, such as anti-microbial, anthelmintic, and cytotoxic activities. *Laurencia composita* Yamada, belonging to the marine red alga of the Rhodomelaceae family, mainly grows on the upper to middle intertidal rocks with a small discoid holdfast that is widely distributed throughout Gulf of Thailand and Andaman Sea. In this work, we report the isolation of two known halogenated sesquiterpenoids, aplysistatin (**1**) and palisadin A (**2**) from *L. composita*. The structures of the isolated compounds were identified by spectroscopic techniques including 2D NMR, mass spectra and optical rotation, and by comparison with those of the reported values.

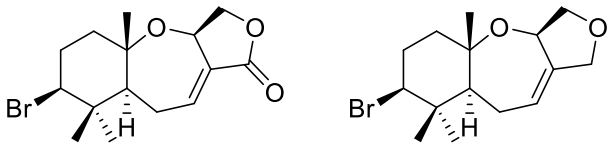

(**1**) (**2**)

Figure 1. The structures of compounds **1**-**2**.

SP13_027_PA: CHEMICAL CONSTITUENTS FROM THE AERIAL PARTS OF *Euphorbia lactea* Haw.

Jintana Jantham,[1] Purin Charoensuksai,[2,3] Pawaris Wongprayoon,[2,3] Kanok-on Rayanil[1,*]

[1]Department of Chemistry, Faculty of Science, Silpakorn University, Nakhon Pathom 73000, Thailand
[2]Department of Biopharmacy, Faculty of Pharmacy, Silpakorn University, Nakhon Pathom 73000, Thailand
[3]Bioactives from Natural Resources Research Collaboration for Excellence in Pharmaceutical Sciences, Faculty of Pharmacy, Silpakorn University, Nakhon Pathom 73000, Thailand
*E-mail: Rayanil_k@su.ac.th

Abstract:

Euphorbia lactea (Euphorbiaceae) is a medicinal plant growing wild in tropical Asia. In Thai folk medicine, it has been used for the treatment of asthma, flatulence, skin disease, gastroenteritis and muscular pain. Previous researchers have discovered various diterpenoids, triterpenoids and flavonoids from this genus and most of them have been reported to exhibit anti-inflammatory, antibacterial, cytotoxic and anti-HIV activities. Phytochemical studies of the aerial parts of *E. lactea* Haw. afforded three triterpenes: taraxerol (**1**), friedelin (**2**) and friedelan-3*β*-ol (**3**) and three steroids: a mixture of *β*-sitosterol (**4**) and stigmasterol (**5**) and *β*-sitosterol glucoside (**6**) which were isolated from this plant for the first time. The structures and relative stereochemistry were determined on the basis of extensive spectroscopic analyses, including 1D and 2D NMR experiments.

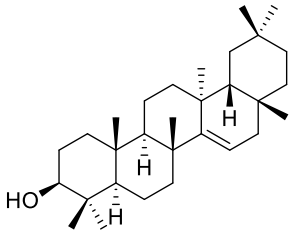

1

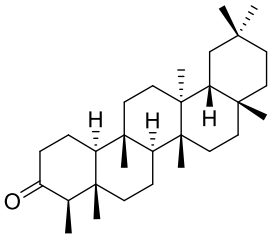

2

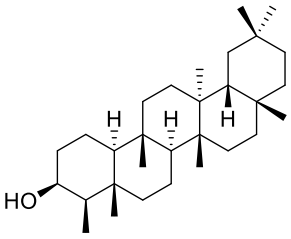

3

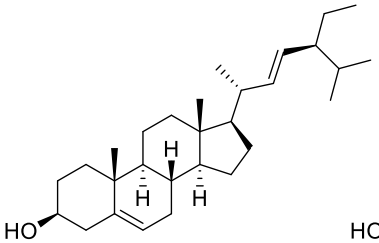

4

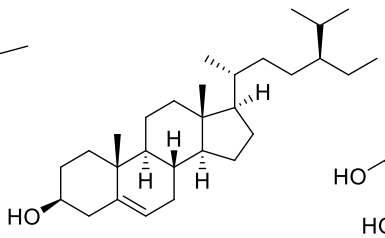

5

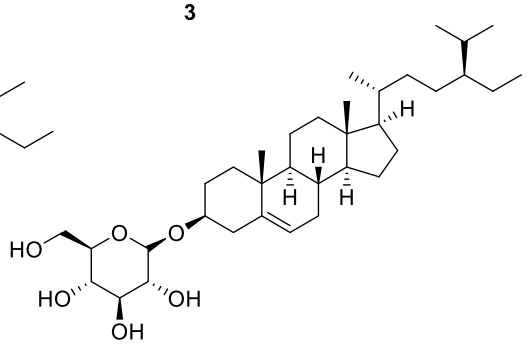

6

SP13_028_PA

SP13_028_PA: PHENANTHRENES AND BIBENZYLS FROM *Dendrobrium* '*Suree* Classic'

Watcharapa Jitkaroon, Wirunya Sutassanawichanna, Kanok-on Rayanil*

Department of Chemistry, Faculty of Science, Silpakorn University, Nakhon Pathom 73000, Thailand
*E-mail: Rayanil_k@su.ac.th

Abstract:

Dendrobrium is one of the largest genera in Orchidaceae comprising more than a thousand identified species. In Thailand, there are about 76 *Dendrobium* hybrid species and they are one of marketed leading cut flowers for export. Several *Dendrobrium* orchids have been used as traditional medicine in China and South Asian countries for the treatment of diabetes, immunoregulatory purposes, skin diseases, promoting the production of body fluid and antipyretic. However, only limited studies of bioactive constituents in Thai *Dendrobrium* orchids have been performed. In this study, the first phytochemical investigation of *D.* 'Suree Classic' stems led to the isolation of four known stilbenoids including two phenanthrenes: confusarin (**1**) and nudol (**2**) and two bibenzyls: gigantol (**3**) and tristin (**4**). Their structures were determined on the basis of 1D and 2D NMR spectroscopy methods and by comparison with spectroscopic data reported in the literatures.

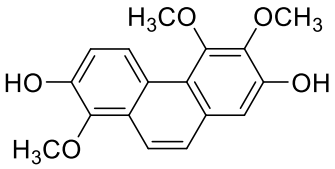

1

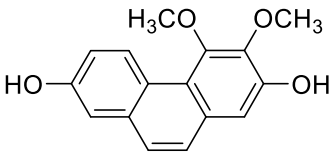

2

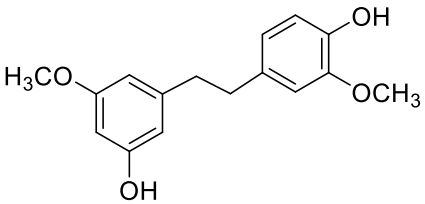

3

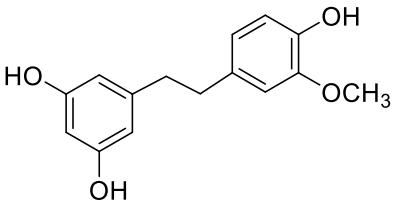

4

SP13_029_PA

SP13_029_PA: CHEMICAL CONSTITUENTS FROM THE STEMS OF *Paederia linearis* Hook.f.

Suphaporn Limjirawatthana, Kanok-on Rayanil*

Department of Chemistry, Faculty of Science, Silpakorn University, Nakhon Pathom 73000, Thailand
*E-mail: Rayanil_k@su.ac.th

Abstract:

Paederis linearis Hook.f. (Rubiaceae) is a small vine that contains bitter taste and foul smell. This plant is known in Thailand as "Tod Moo Tod Ma" and has been used in Thai folk medicine for the treatment of fever, diarrhea, herpes, asthma and as an antidote for snake-bite effects. The previous pharmaceutical studies revealed that the extracts of the *P. linearis* root showed *in vitro* anti-oxidant, anti-acetylcholinesterase and cytotoxic activities. In this study, the phytochemical investigation of the *n*-BuOH extract from the stems of *P. linearis* led to the isolation of three known iridoid glucosides; paederosidic acid methyl ester **(1)**, paederosidic acid **(2)** and 10-*O*-caffeoyl scandoside methyl ester **(3)** and a steroid; *β*-sitosterol glucoside **(4)**. The chemical structures and relative configuration of these compounds were elucidated on the basis of their 1D and 2D NMR experiments. The absolute configurations were determined by comparison with the CD spectroscopic data reported in the literature. All isolated compounds were evaluated for their *in vitro* α-glucosidase inhibitory activities. The results revealed that all compounds showed inhibitory effect in the range of 32.4-54.3%, which were less potent than the positive control acarbose (94.7%) at the concentration of 1 mg/mL.

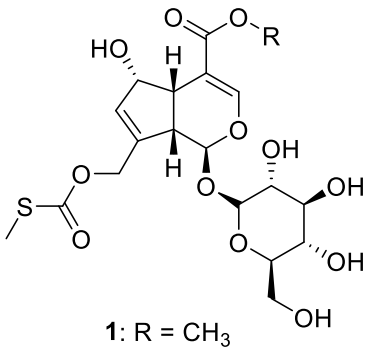

1: R = CH_3
2: R = H

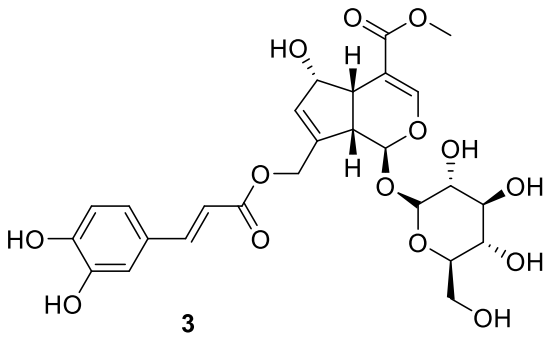

3

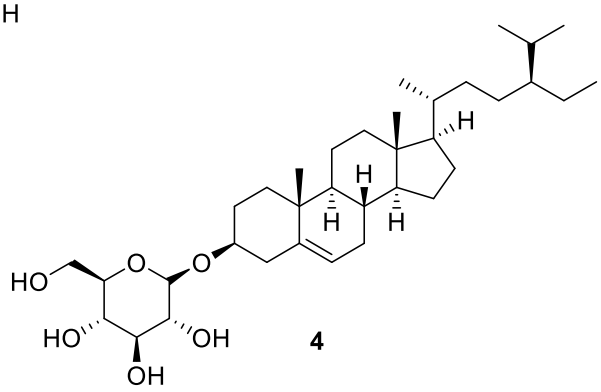

4

SP13_030_PA: INHIBITORY EFFICACY OF *Cordyceps militaris* EXTRACTS ON SKIN PATHOGENIC BACTERIA AND INFLAMMATION

Kiratiya Eiamthaworn,[1] Yingmanee Tragoolpua[2,*]

[1]The Graduate School, Chiang Mai University, Chiang Mai, 50200, Thailand
[2]Division of Microbiology, Department of Biology, Faculty of Science, Chiang Mai University, Chiang Mai, 50200, Thailand
*e-mail: yingmanee.t@cmu.ac.th

Abstract:

Cordyceps militaris has been used as a medicinal agent for maintenance of health and treatment of various diseases. The objective of this study is to determine anti-bacterial, anti-oxidant and anti-inflammatory activities of *C. militaris*. It was found that both aqueous and ethanolic extracts of *C. militaris* displayed antibacterial activity against *Corynebacterium* sp., *Staphylococcus aureus, Staphylococcus epidermidis, Pseudomonas aeruginosa* and methicillin-resistant *Staphylococcus aureus* (MRSA) with inhibition zones in the range of 12.50-22.33 mm by agar diffusion method. The ethanolic extract of *C. militaris* showed stronger antibacterial activity with equal MIC and MBC values of 31.25 mg/mL against MRSA, *S. epidermidis* and *S. aureus* than the aqueous extract which showed the MIC and MBC values of 62.50 mg/mL against MRSA and *S. aureus*. Furthermore, ethanolic and aqueous extracts demonstrated total flavonoid contents of 1.35 and 0.03 mg quercetin/g extract, respectively, using aluminum chloride colorimetric method. In addition, the quantity of cordycepin, an active compound, was 10.6 and 9.24 mg/g extract in ethanolic and aqueous extracts, respectively, when analyzed by HPLC. However, total phenolic content of 29.3 mg GAE/g extract and anti-free radical activity of 3.2 mg gallic/g extract by DPPH method of *C. militaris* aqueous extract were higher than ethanolic extract. The anti-inflammatory effect of *C. militaris* extracts was evaluated using lipopolysaccharide stimulated Raw 264.7 macrophage cells. The results showed that inhibitions of NO production after treatment with aqueous (625 µg/mL) and ethanolic (312.5 µg/mL) extracts were 92% and 74%, respectively. Additionally, the extracts decreased mRNA level of iNOS gene expression. Therefore, *C. militaris* demonstrated anti-bacterial, anti-oxidation and anti-inflammatory activities.

SP13_031_PA: SCREENING AND IDENTIFICATION OF CHOLESTEROL LOWERING AND BILE SALT HYDROLASE PRODUCING LACTIC ACID BACTERIA FROM THAI PICKLED MUSSELS (*HOI-DONG*)

Engkarat Kingkaew.[1,*] Malai Taweechotipatr,[2] Wonnop Visessanguan,[3] and Somboon Tanasupawat[1]

[1]Department of Biochemistry and Microbiology, Faculty of Pharmaceutical Sciences, Chulalongkorn University, Bangkok 10330, Thailand
[2]Department of Microbiology, Faculty of Medicine, Srinakharinwirot University, Bangkok, 10110, Thailand
[3]Food Biotechnology Research Team, Functional Ingredients and Food Innovation Research Group, National Center for Genetic Engineering and Biotechnology, National Science and Technology Development Agency, Pathumthani 12120, Thailand
*e-mail: st.eng-m@hotmail.com

Abstract:

Fifty-one lactic acid bacteria (LAB) isolated from pickled mussels in Thailand were screened for the bile salt hydrolase (BSH) and cholesterol assimilation activities. Out of 51 isolates, only 8 isolates, LM15-1P, LM15-2, LM6-1, LM7-2-2B, LM6-2, LM14-1, LM14-2 and LM12-1 exhibited bile salt hydrolase activity. All isolates assimilated ability varied from 20.73 to 86.07%. Isolate LM14-2 could potentially assimilate cholesterol with 86.07% while isolate LM4-2 (*Enterococcus thailandicus*, 100% similarity) assimilate cholesterol with 20.73%. Based on 16S rRNA gene sequencing analysis, all above mentioned isolates were identified as *Lactobacillus plantarum* subsp. *plantarum* (99.56 to 100% similarity). These selected isolates were tolerated to acidic condition (pH 3.0) and bile salt (0.3 and 0.8% oxgall, pH 8.0). Additionally, isolate *Lb. plantarum* LM15-1P showed the adhesion ability to human intestinal Caco-2 cell (5.11 ± 0.46 %). For the further study, their immunomodulatory effects will be evaluated. Hopefully, all of them could be possibly used as probiotics in order to reduce cholesterol level and alleviate the risk of heart disease.

SP13_032_OA

SP13_032_OA: DESIGN AND SYNTHESIS OF NEW 12-DITHIOCARBAMATE-14-DEOXY-ANDROGRAPHOLIDES AS ANTICANCER AGENTS

Patcharee Arsakhant,[1] Uthaiwan Sirion,[1,4] Arthit Chairoungdua,[2] Kanoknetr Suksen,[2] Pawinee Piyachaturawat,[2] Apichart Suksamrarn,[3] Rungnapha Saeeng[1,4]*

[1]Department of Chemistry and Center for Innovation in Chemistry, Faculty of Science, Burapha University, Chonburi 20131, Thailand
[2]Department of Physiology, Faculty of Science, Mahidol University, Bangkok 10400, Thailand
[3]Department of Chemistry, Faculty of Science, Ramkhamhaeng University, Bangkok 10240, Thailand
[4]The Research Unit in Synthetic Compounds and Synthetic Analogues from Natural Product for Drug Discovery (RSND), Burapha University, Chonburi 20131, Thailand
*e-mail: rungnaph@buu.ac.th

Abstract:

Andrographolide (**1**), a major labdane diterpene lactone isolated from *Andrographis paniculate*, exhibited diverse pharmacological activities. In this work, we designed and synthesized new 12-dithiocarbamate- 14- deoxyandrographolide analogues (**3**) by introduction of various substituted-dithiocarbamates at C-12 position of the andrographolide core structure followed by elimination of acetate moiety. The reactions proceeded without the use of a catalyst under mild reaction conditions in a one-pot process to yield products **3** in excellent yields. All analogues were evaluated for *in vitro* cytotoxic activity against nine cancer cell lines. Compounds **3g**, **3n** and **3o** exhibited stronger cytotoxic activity on MCF-7 cancer cell than the anticancer drug ellipticine with the IC_{50} values of 0.84, 0.59 and 0.68 µM, respectively. These compounds could serve as potential candidates for further development as an anticancer agent against breast cancer.

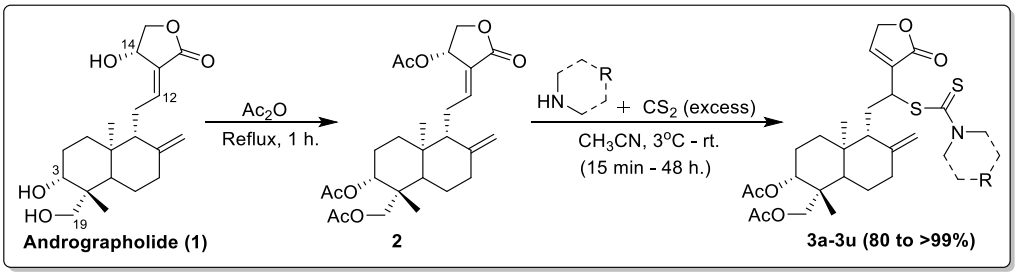

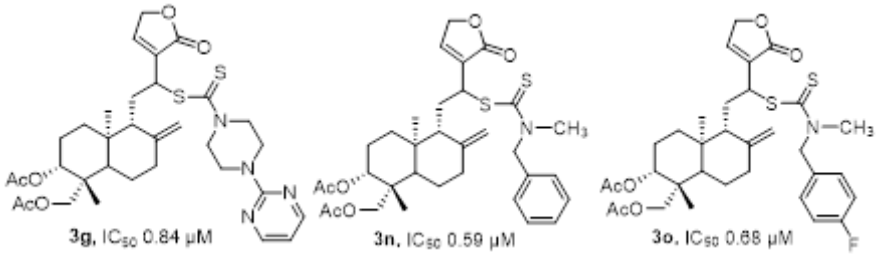

Positive control: Ellipticine IC_{50} 1.79 µM against MCF-7 cancer cell

SP13_033_PA

SP13_033_PA: NEW CLASS OF PIPERINE AMIDE ANALOGS AS ACETYLCHOLINE ESTERASE (AChE) INHIBITORS

Suwichada Jaipea,[1] Waraporn Sutcharitruk, [1] Natthiya Saehlim, [1], Kornkanok Ingkaninan,[2] Rungnapha Saeeng[1,3]*

[1] Department of Chemistry, Faculty of Science, Burapha University, Sangesook, Chonburi, 20131, Thailand
[2] Department of Pharmaceutical Chemistry, Faculty of Pharmaceutical Sciences, Naresuan University, Phitsanulok, 65000, Thailand
[3]The Research Unit in Synthetic Compounds and Synthetic Analogues from Natural Product for Drug Discovery (RSND), Burapha University, Chonburi 20131, Thailand
*e-mail: rungnaph@buu.ac.th

Abstract:

Piperine, a major natural compound commonly found in black pepper, exhibited diverse biological activity including the activity of improving memory impairment. In this work, piperine was isolated from *Piper nigrum L.* and was modified to new analogues which were subsequently studied toward their inhibitory activity against acetylcholine esterase (AChE) enzyme. Structure modification of natural piperine was carried out via a two-step reaction by hydrolysis of piperine to piperic acid (**2**) followed by ammonolysis of **2** using various amines leading to a series of twenty-four new amide analogs **3** in moderate to excellent yields (Scheme 1). Some of new compounds showed good inhibitory activity against AChE enzyme. Molecular docking stimulations were performed to study the binding interaction of our synthetic compounds with AChE enzyme (PDB: 4EY6).

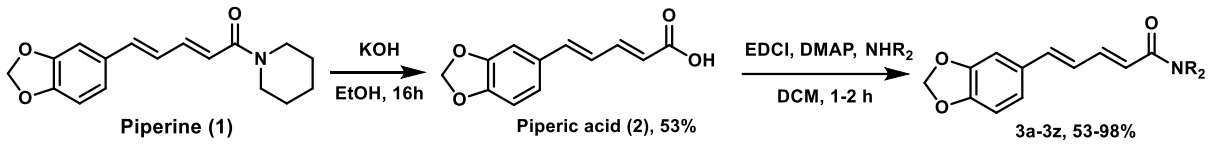

Scheme 1. Structure modification of piperine.

SP13_034_PA: TOTAL SYNTHESIS AND STRUCTURE MODIFICATION OF CAERULOMYCIN A, A MARINE NATURAL PRODUCT

Jesada Maneewong, Natthiya Saehlim and Rungnapha Saeeng*

Department of Chemistry and Centre of Excellence for Innovation in Chemistry, Faculty of Science, Burapha University, Saensook, Chonburi 20131, Thailand.
The Research Unit in Synthetic Compounds and Synthetic Analogues from Natural Product for Drug Discovery
*e-mail: rungnaph@go.buu.ac.th

Abstract:

Caerulomycin A was isolated from the fermentation broth of *Streptomyces caeruleus* with antibiotic, antifungal and cytotoxic activities. The structure of caerulomycin A contains a bipyridine core structure and an unusual oxime functionality. In this work, we designed and synthesized caerulomycin A and its analogues by convenient and efficient methods via five- step reactions. Caerulomycin A was obtained in moderate yield and employed as a precursor for further modification to isoxazole analogues by using click reaction with various alkynes. The synthesized isoxazole-caerulomycin A derivatives will be evaluated for their anticancer activity.

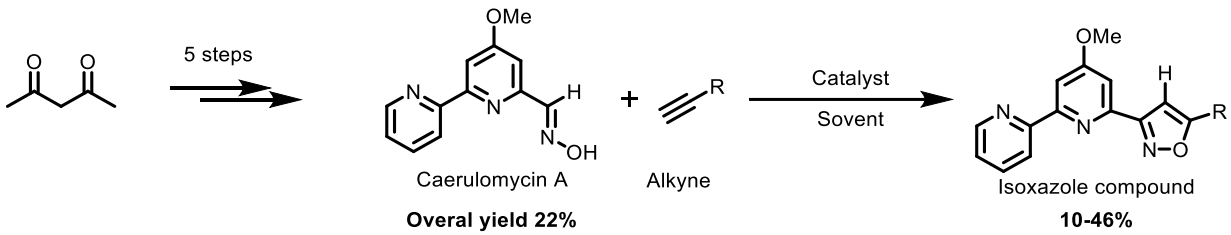

Scheme 1. Synthesis of caerulomycin A and structure modification.

SP13_035_PA: DIVERSITY AND ANTIMICROBIAL ACTIVITY OF ENDOPHYTIC ACTINOMYCETES ISOLATED FROM THAI ORCHIDS

Nisachon Tedsree,[1*] Boonchoo Sritularak,[1] Somboon Tanasupawat,[2] and Kittisak Likhitwitayawuid[1]

[1]Department of Pharmacognosy and Pharmaceutical Botany, Faculty of Pharmaceutical Sciences, Chulalongkorn University, Bangkok 10330, Thailand
[2]Department of Biochemistry and Microbiology, Faculty of Pharmaceutical Sciences, Chulalongkorn University, Bangkok 10330, Thailand
*e-mail: tedsree@yahoo.com

Abstract:

A total of 23 isolates of endophytic actinomycetes were isolated from Thai orchids. These isolates were taxonomically studies based on their phenotypic characteristics and 16S rRNA gene sequence analysis (99.11-100.00%). The isolates were found to belong to *Streptomyces* (18 isolates), *Micromonospora* (4 isolates) and *Pseudonocardia* (1 isolate). They were identified as *S. hydrogenans* (3 isolates, DS1-1, DR3-3 and DR8-2), *S. pravulus* (5 isolates, DS2-1, DR2-1, DS5-1, DR5-1 and DR7-4), *S. antibioticus* (1 isolate, DR2-2), *S. daghestanicus* (1 isolate, DR3-1), *S. albidoflavus* (1 isolate, DR3-2), *S. tendae* (1 isolate, DR3-4), *S. flavofungini* (1 isolate, DR7-1), *S. thermocarboxydus* (1 isolate, DR7-2), *S. malaysiensis* (1 isolate, DR7-3), *S. gelaticus* (1 isolate, DR8-1), *S. fractus* (1 isolate, DR8-3) and *S. badius* (1 isolate, DR8-5); *M. humi* (1 isolate, DR4-1), *M. schwarzwaldensis* (1 isolate, DR5-2), *M. tulbaghiae* (2 isolates, DR6-2 and DR6-3); *P. carboxydivorans* (1 isolate, DS1-2). Nine isolates showed inhibitory activity against bacteria and fungi. The DR2-2, DR4-1, DR5-1 and DR7-4 strains were active against *Staphylococcus aureus* ATCC 25923, *Kocuria rhizophila* ATCC 9341, *Bacillus subtilis* ATCC 6633 and *Escherichia coli* ATCC 25922. Isolates DS1-1, DR3-1, DR3-2 and DR3-3 displayed activity against *Candida albicans* ATCC 10231, whereas the potent isolate DR7-3 exhibited activity against *S. aureus* ATCC 25923, *K. rhizophila* ATCC 9341, *B. subtilis* ATCC 6633 and *C. albicans* ATCC 10231. The results of this investigation have revealed that the endophytic actinomycetes from Thai orchids are a potent source of bioactive compounds.

SP13_036_OA: THE ASSESSMENT OF *Ocimum sanctum L.* AQUEOUS EXTRACT FOR AMELIORATING LIPID CONTENTS IN NON-ALCOHOLIC FATTY LIVER DISEASE

Jakkapong Inchai and Chutima Srimaroeng*

Department of Physiology, Faculty of Medicine, Chiang Mai University 50200, Thailand
*e-mail: chutima.srimaroeng@cmu.ac.th

Abstract:

Screening of natural products for drug discovery and development has gained attention in global healthcare. Non-alcoholic fatty liver disease (NAFLD) has a high prevalence and is closely associated with obesity, type 2 diabetes mellitus (T2DM), and metabolic syndrome. Hence, identifying specific compounds for lowering hepatic lipid-content is crucially needed. This study investigated and developed an efficient and powerful analytical tool for screening *Ocimum sanctum L*. aqueous extract (OSLE) and its monoterpenes (eugenol, methyl eugenol, and carvacrol) from *O. sanctum L.*, a traditional herb found in Southeast Asian cuisine, against NAFLD. Hepatocellular carcinoma (HepG2) cells were induced with hepatic lipid accumulation using free fatty acid (FFA), and the total lipid contents were subsequently stained by fluorescent-neutral lipids. Results showed that OSLE and monoterpenes exhibited hepatic lipid-lowering effect without cytotoxicity as indicated by reduced fluorescent-neutral lipids similarly to that found in sulfo-N-succinimidyl oleate (SSO), a FFA uptake inhibitor. Consistently, the intracellular cholesterol and triglyceride contents extracted from HepG2 cells were reduced by OSLE and monoterpenes. Our fluorescence-based *in vitro* model in HepG2 cells proved to be robust, powerful, and cost- and time-effective tool for the assessment of hepatic lipid-lowering activity of *O. sanctum L*. aqueous extract, and for other natural products.

SP13_037_PF: STRUCTURAL MODIFICATION OF 2´,4´-DIHYDROXY-6´-METHOXY-3´,5´-DIMETHYLCHALCONE FROM SEEDS OF *Syzygium nervosum* A.Cunn ex DC. AND THEIR ANTICANCER ACTIVITY

Nopawit Khamto,[1,2] Puttinan Meepowpan[1,3,*]

[1]Department of Chemistry, Faculty of Science, Chiang Mai University, 239 Huay Kaew Road, Chiang Mai 50200, Thailand
[2]Graduate School, Chiang Mai University, 239 Huay Kaew Road, Chiang Mai 50200, Thailand
[3]Material Science Research Center (MsRC), Chiang Mai University, 239 Huay Kaew Road, Chiang Mai 50200, Thailand
*e-mail: pmeepowpan@gmail.com

Abstract:

Syzygium nervosum A.Cunn ex DC. or Ma-kiang possessed numerous bioactive compounds. Herein, 2´,4´-dihydroxy-6´-methoxy-3´,5´-dimethylchalcone (DMC, **1**), a chalcone derivative, was isolated from the crude EtOAc extract of the *S. nervosum* seeds. Structural modification of DMC was achieved through *O*-acylation reaction of various fatty acid chlorides under the basic conditions to obtain 4´-*O*-acylated DMC (**2**), 2´,4´-*O*-diacylated DMC (**3**), and 4-hydroxycoumarin derivatives (**4**), which were dehydrated in the acidic conditions to yield stilbene-coumarin derivatives (**5**). Furthermore, the semi-synthetic DMC derivatives were tested for their *in vitro* anticancer activity against 2 carcinoma cell lines consisting of human intrahepatic cholangiocarcinoma (KKU-M213) and human colorectal adenocarcinoma (HT-29) cell lines with normal human liver hepatic cell (CL) as the normal cell line. According to the results, 2´-hydroxy-4´-caproyloxy-6´-methoxy-3´,5´-dimethylchalcone (**2c**) displayed the highest cytotoxicity among all semi-synthetic derivatives with the ED_{50} values of 18.83 and 18.92 μM for KKU-M213 and HT-29 cell lines, respectively. According to the results, the incorporated alkanoyl moiety significantly increased the anticancer activity of DMC.

Introduction:

Cancer is the uncontrolled growth of cells and is one of the most prevalent causes of death among the world population.[1] The causes of cancer may be related to daily activities such as high consumption of salt, fats, alcohol, red meat, and smoking.[2] Numerous methods such as surgery, chemotherapy, and radiotherapy are used to treat cancer, which depends on the type and progression of cancer.[3] The current chemotherapeutic drugs such as doxorubicin, ellipticine, cisplatin, *etc.* are highly effective against carcinoma cells.[4] Nevertheless, they lack selectivity to tumor cells, and affected a multitude of side effects, which may be the cause of death in many patients.[5] Therefore, it is challenging to discover new chemotherapeutic agents. Generally, anticancer drugs promote the cell cycle arrest, the process involving several enzymes such as tyrosine kinase (TKs), cyclin-dependent kinases (CDKs), and nuclear factor-kappa B (NF-κb).[6] Therefore, the substances which can inhibit these enzymes may contribute to the development of new anticancer drugs.[7]

Syzygium nervosum A.Cunn ex DC. or *Cleistocalyx operculatus* (Roxb.) Merr. & L.M. Perry, also called Ma-kiang, is distributed over Southeast Asia such as Thailand, Vietnam, Myanmar, and Malaysia.[8] Its fruits are important for the Thai industry producing juice, jam, and wine. In traditional medicine, its leaves and buds are frequently used to treat fever, cold, and inflammation diseases for a long time.[9] Phytochemical reports indicated an abundance of bioactive compounds such as flavonoids,[10] flavonoids glycoside,[11] anthocyanin,[12] and phloroglucinol derivatives.[13] 2´,4´-Dihydroxy-6´-methoxy-3´,5´-dimethylchalcone (DMC, **1**) is a chalcone

derivative discovered in the seeds and buds of *S. nervosum*.[14] It exhibited various bioactivities such as anticancer,[15] antimicrobial,[16] and anti-HIV[17] activities. A great number of studies show that DMC exhibited moderate anticancer activity in various tumor cell lines such as human liver cancer (SMMC-7721), human lung cancer (SPC-A-1), human cervical cancer (HeLa), and human metastatic lung carcinoma (95-D).[18] However, there are myriad troublesome issues to apply the natural products (NPs) for medicine due to undesirable properties such as low solubility in an aqueous medium, metabolic instability, and insufficient bioactivity.[19]

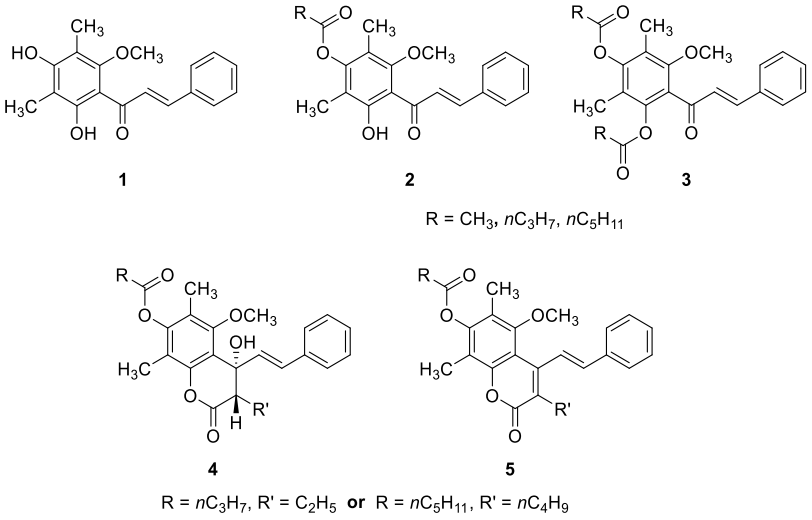

Figure 1. Chemical structures of DMC and DMC derivatives

Previous reports suggest that the increment of lipophilicity may enhance the cell permeated property of bioactive substances.[20] Herein, we are interested in an investigation of lipophilic moieties such as alkanoyl side chain, which can be attached to DMC by *O*-acylation reaction to obtain 4´-*O*-acylated DMC (**2**), 2´,4´-*O*-diacylated DMC (**3**), and 4-hydroxycoumarin derivatives (**4**). Subsequently, stilbene-coumarin derivatives (**5**) were obtained from the dehydration of 4-hydroxycomarin derivatives. Moreover, all synthesized compounds were evaluated for their cytotoxicity against intrahepatic cholangiocarcinoma (KKU-M213), colorectal adenocarcinoma (HT-29), and normal human liver hepatic cells (CL). Most of them displayed moderate toxicity to carcinoma cells *in vitro*.

Methodology:

Chemistry

Reagents were purchased from Sigma Aldrich and Acros Chemical. Commercial organic solvents such as *n*-hexane, dichloromethane, ethyl acetate, acetone, and methanol were distilled before use. All reactions were conducted using oven-dried glassware with anhydrous solvents that were dried and distilled before use. The synthetic compounds were characterized based on spectroscopic methods including ^{1}H- and ^{13}C-NMR and FTIR techniques. NMR spectra were recorded on Bruker DRX-400 and Avance Neo 500 NMR spectrometer using chloroform-*d* as the solvent and tetramethylsilane as the internal reference. The chemical shifts (δ) were reported in part per million (ppm) downfield from TMS or the solvent signal ($CHCl_3$ residual peak in ^{1}H-NMR δ 7.26 ppm and ^{13}C-NMR δ 77.1 ppm). Proton coupling patterns were indicated as follows: *s* (singlet), *d* (doublet), *t* (triplet), *dd* (doublet of doublet), br (broad), q (quartet), and *m* (multiplet). FTIR spectra were recorded on Bruker Tensor27 infrared spectrometer. Transmission frequencies were reported in reciprocal per centimeters (cm^{-1}). Melting points were determined by the Gallenkamp Electrothermal apparatus. Flash column

chromatography (FCC) was performed employing Merck silica gel 60H, and preparative thin-layer chromatography (PLC) was performed using Merck silica gel 60 PF_{254}.

Extraction and isolation of DMC

Pulverized dried seeds of *S. nervosum* (10.3 kg) were macerated in 40 L of EtOAc at room temperature (three times, each time for three days). The seed residues were filtered out. Then, the organic layer was combined and concentrated *in vacuo* to obtain the crude EtOAc extract (208.98 g) as a dark green viscous liquid, which was subjected to flash column chromatography (FCC) on silica gel eluted with the gradient solution of *n*-hexane–EtOAc (100:0, 95:5, 90:10, 85:15 and 80:20, v/v). Furthermore, DMC containing fractions were combined and then further purified by flash column chromatography on silica gel with *n*-hexane–acetone (90:10) as an eluent to afford DMC as orange solid. DMC was further recrystallized in CH_2Cl_2–*n*-hexane to obtain yellow needle crystals (2.5201 g, 1.21 %yield) with high purity as characterized by ^{1}H-NMR, ^{13}C-NMR, and FTIR techniques. The spectroscopic data were in agreement with the previously published values.

Compound **1**: 2′,4′-Dihydroxy-6′-methoxy-3′,5′-dimethylchalcone, orange needle crystals: mp 124.5–126.4 °C (CH_2Cl_2/*n*-hexane); ν_{max} (thin film) 3540 (O-H), 3033 (C-H), 2941 (CH_3) 1632 (C=O), 1610 (C=C), 1423 (CH_3), 1232 (C-O-C), 1170 (C-O-C) cm^{-1}; ^{1}H NMR (400 MHz, $CDCl_3$, δ): 2.13 (s, 3H, *Me*), 2.15 (s, 3H, *Me*), 3.67 (s, 3H, O*Me*), 5.39 (s, 1H, O*H*), 7.36-7.45 (m, 3H, ArC*H*), 7.60-7.68 (m, 2H, ArC*H*), 7.84 (AB system, d, *J* = 15.7 Hz, 1H, C*Hβ*), 7.99 (AB system, d, *J* = 15.7 Hz, 1H, C*Hα*), 13.61 (s, 1H, O*H*); ^{13}C NMR (100 MHz, $CDCl_3$, δ): 7.6, 8.2, 62.4, 106.6, 108.9, 109.0, 126.7, 128.4, 128.9, 130.2, 135.3, 142.9, 158.8, 159.2, 162.0, 193.4.

General procedure for the synthesis of O-acetylated DMC

DMC (0.3352 mmol, 1 equiv.) was dissolved in 5 mL of dry CH_2Cl_2, which was cooled down in an ice bath. Then, acetyl chloride (0.7374 mmol, 2.2 equiv.) was added to the reaction followed by triethylamine (0.7374 mmol, 2.2 equiv.) and then stirred for 10 min. The reaction was monitored by TLC. After the disappearing of DMC, the reaction mixture was quenched with 6M HCl, adjusted the pH to 4, and subsequently extracted with CH_2Cl_2. The organic layer was dried over anhydrous Na_2SO_4, followed by solvent removal under reduced pressure. The crude mixture was purified by preparative thin-layer chromatography (PLC) using CH_2Cl_2–Et_2O–*n*-hexane (30:4:66) as an eluent to afford 4′-*O*-acetylated DMC (**2a**) and 2′,4′-*O*-diacetylated DMC (**3a**).

Compound **2a**: 2′-Hydroxy-4′-acetyloxy-6′-methoxy-3′,5′-dimethylchalcone, 13% yield; orange solid, mp: 131.5–132.7 °C (MeOH/CH_2Cl_2); R_f 0.55 (7.5% EtOAc:7.5% acetone:85% *n*-hexane); ν_{max} (thin film) 2943 (CH_3), 1760 (C=O), 1652 (C=O), 1635 (C=O), 1607 (C=C), 1562 (C=C), 1350 (CH_3), 1211 (C-O-C), 1112 (C-O-C) cm^{-1}; ^{1}H NMR (500 MHz, $CDCl_3$, δ): 2.05 (s, 3H, *Me*), 2.06 (s, 3H, *Me*), 2.38 (s, 3H, *Me*), 3.67 (s, 3H, O*Me*), 7.37-7.46 (m, 3H, ArC*H*), 7.62-7.69 (m, 2H, ArC*H*), 7.88 (AB system, d, *J* = 15.7 Hz, 1H, C*Hβ*), 7.94 (AB system, d, *J* = 15.7 Hz, 1H, C*Hα*), 12.95 (s, 1H, O*H*); ^{13}C NMR (125 MHz, $CDCl_3$, δ): 9.1, 9.3, 20.6, 62.8, 113.5, 115.3, 115.8, 126.5, 128.8, 129.2, 130.7, 135.2, 144.0, 154.2, 158.3, 160.9, 168.2, 194.5.

Compound **3a**: 2′,4′-Diacetyloxy-6′-methoxy-3′,5′-dimethylchalcone, 36% yield; yellow viscous liquid, R_f 0.55 (5% EtOAc:7.5% acetone:87.5% *n*-hexane); ν_{max} (thin film) 3062 (C-H), 2945 (CH_3), 1773 (C=O), 1653 (C=O), 1607 (C=C), 1453 (CH_3), 1190 (C-O-C), 1180 (C-O-C), 1105 (C-O-C) cm^{-1}; ^{1}H NMR (500 MHz, $CDCl_3$, δ): 1.94 (s, 3H, *Me*), 2.10 (s, 3H, *Me*), 2.17 (s, 3H, *Me*) 2.38 (s, 3H, *Me*), 3.70 (s, 3H, O*Me*), 7.02 (d, *J* = 16.1 Hz, 1H, C*Hβ*), 7.36-7.42 (m, 3H, ArC*H*), 7.46 (d, *J* = 16.1 Hz, 1H, C*Hα*), 7.53-7.58 (m, 2H, ArC*H*); ^{13}C NMR (125 MHz, $CDCl_3$, δ): 9.9, 10.3, 20.5, 20.6, 62.7, 120.8, 123.0, 125.8, 127.4, 128.8, 129.1, 130.9, 134.5, 144.9, 146.3, 150.2, 154.8, 168.3, 168.7, 192.7.

General procedure for the synthesis of O-butyrylated DMC

Compounds **2b**, **3b**, and **4a** were synthesized following the general procedure of the *O*-acetylation reaction. The starting materials, DMC and butyryl chloride, were stirred at room temperature in the presence of triethylamine base until the completion of the reaction to obtain 4′-*O*-butyrylated DMC (**2b**), 2′,4′-*O*-dibutyrylated DMC (**3b**), and 7-butyrylated coumarin derivatives (**4a**).

Compound **2b**: 2′-Hydroxy-4′-butyryloxy-6′-methoxy-3′,5′-dimethylchalcone, 60%yield; orange solid, mp: 102.0–103.9 °C (MeOH/CH_2Cl_2); R_f 0.19 (30% CH_2Cl_2:2% Et_2O:68% *n*-hexane); ν_{max} (thin film) 2971 (CH_2), 2941 (CH_3), 1762 (C=O), 1636 (C=O), 1604 (C=C), 1568 (C=C), 1285 (C-O-C), 1142 (C-O-C), 1119 (C-O-C) cm^{-1}; ^1H NMR (500 MHz, $CDCl_3$, δ): 1.08 (t, *J* = 7.4 Hz, 3H, *Me*), 1.84 (m, 2H, C*H*$_2$), 2.04 (s, 3H, *Me*), 2.05 (s, 3H, *Me*), 2.62 (t, *J* = 7.4 Hz, 2H, C*H*$_2$), 3.67 (s, 3H, O*Me*), 7.45-7.37 (m, 3H, ArC*H*), 7.62-7.68 (m, 2H, ArC*H*), 7.87 (AB system, d, *J* = 15.7 Hz, 1H, C*Hβ*), 7.95 (AB system, d, *J* = 15.7 Hz, 1H, C*Hα*), 12.96 (s, 1H, O*H*); ^{13}C NMR (125 MHz, $CDCl_3$, δ): 9.1, 9.3, 13.9, 18.6, 36.0, 62.7, 113.3, 115.3, 115.8, 126.5, 128.7, 129.1, 130.6, 135.2, 143.9, 154.3, 158.3, 160.9, 170.8, 194.5.

Compound **3b**: 2′,4′-Dibutyryloxy-6′-methoxy-3′,5′-dimethylchalcone, 8% yield; yellow viscous liquid, R_f 0.06 (30% CH_2Cl_2:2% Et_2O:68% *n*-hexane); ν_{max} (thin film) 2972 (CH_2), 2940 (CH_3), 1766 (C=O), 1656 (C=O), 1609 (C=C), 1463 (CH_3), 1183 (C-O-C), 1141 (C-O-C), 1105 (C-O-C) cm^{-1}; ^1H NMR (500 MHz, $CDCl_3$, δ): 0.91 (t, *J* = 7.4 Hz, 3H, *Me*), 1.08 (t, *J* = 7.5 Hz, 3H, *Me*), 1.64 (m, 2H, C*H*$_2$), 1.84 (m, 2H, C*H*$_2$), 1.92 (s, 3H, *Me*), 2.09 (s, 3H, *Me*), 2.41 (t, *J* = 7.4 Hz, 2H, C*H*$_2$), 2.62 (t, *J* = 7.4 Hz, 2H, C*H*$_2$), 3.69 (s, 3H, O*Me*), 6.99 (d, *J* = 16.1 Hz, 1H, C*Hβ*), 7.36-7.40 (m, 3H, ArC*H*), 7.43 (d, *J* = 16.1 Hz, 1H, C*Hα*), 7.51-7.58 (m, 2H, ArC*H*); ^{13}C NMR (125 MHz, $CDCl_3$, δ): 10.0, 10.4, 13.8, 13.9, 18.3, 18.7, 35.9, 36.0, 62.7, 120.8, 122.9, 125.8, 127.5, 128.8, 129.0 , 130.8, 134.6, 144.9, 146.5, 150.2, 154.7, 170.9, 171.3, 192.9.

Compound **4a**: 3*H*-3-Ethyl-4-hydroxy-4-[(*E*)-2′-phenylvinyl]-5-methoxy-6,8-dimethyl-7-butyryloxycoumarin, 27% yield; light yellow viscous liquid, R_f 0.08 (30% CH_2Cl_2:2% Et_2O:68% *n*-hexane); ν_{max} (thin film) 3430 (O-H), 3065 (C-H), 3031 (C-H), 2973 (CH_2), 2941 (CH_3), 1768 (C=O), 1603 (C=C), 1202 (C-O-C), 1149 (C-O-C), 1102 (C-O-C) cm^{-1}; ^1H NMR (500 MHz, $CDCl_3$, δ): 1.00 (t, *J* = 7.5 Hz, 3H, *Me*), 1.09 (t, *J* = 7.5 Hz, 3H, *Me*), 1.28-1.33 (m, 1H, C*H*$_2$), 1.84 (m, 2H, C*H*$_2$), 2.06 (s, 3H, *Me*), 2.10 (s, 3H, *Me*), 2.13-2.21 (m, 1H, C*H*$_2$), 2.63 (t, *J* = 7.5 Hz, 2H, C*H*$_2$), 2.84 (dd, *J* = 11.1, 3.8 Hz, 1H, C*H*), 3.73 (s, 3H, O*Me*), 5.66 (s, 1H, O*H*), 6.36 (d, *J* = 15.8 Hz, 1H, C*H*), 6.46 (br d, *J* = 15.8 Hz, 1H, C*H*), 7.15-7.43 (m, 5H, ArC*H*); ^{13}C NMR (125 MHz, $CDCl_3$, δ): 9.7, 9.9, 13.9, 14.0, 20.4, 24.8, 34.2, 52.0, 62.1, 75.3, 115.8, 116.5, 120.7, 127.1, 128.1, 128.7, 129.5, 133.4, 135.8, 146.3, 149.4, 154.7, 168.8, 171.3.

General procedure for the synthesis of O-caproylated DMC

Compounds **2c**, **3c**, and **4b** were synthesized following the general procedure of the *O*-acetylation reaction. The substrate DMC was reacted with caproyl chloride in basic conditions until the completion of the reaction to afford 4′-*O*-caproylated DMC (**2b**), 2′,4′-*O*-caproylated DMC (**3b**), and 7-caproylated coumarin derivatives (**4a**).

Compound **2c**: 2′-Hydroxy-4′-caproyloxy-6′-methoxy-3′,5′-dimethylchalcone, 45% yield; orange solid, mp: 70.0–71.6 °C (MeOH/CH_2Cl_2); R_f 0.20 (30% CH_2Cl_2:2% Et_2O:68% *n*-hexane); ν_{max} (thin film) 2962 (CH_2), 2938 (CH_3), 1765 (C=O), 1637 (C=O), 1607 (C=C), 1570 (C=C), 1284 (C-O-C), 1135 (C-O-C), 1115 (C-O-C) cm^{-1}; ^1H NMR (500 MHz, $CDCl_3$, δ): 0.94 (t, *J* = 6.8Hz, 3H, *Me*), 1.34-1.49 (m, 4H, C*H*$_2$), 1.82 (m, 2H, C*H*$_2$), 2.04 (s, 3H, *Me*), 2.05 (s, 3H, *Me*), 2.63 (t, *J* = 7.3 Hz, 2H, C*H*$_2$), 3.67 (s, 3H, O*Me*), 7.39-7.47 (m, 3H, ArC*H*), 7.62-7.69 (m, 3H, ArC*H*), 7.87 (AB system, d, *J* = 15.7 Hz, 1H, C*Hβ*), 7.95 (AB system, d, *J* = 15.7 Hz, 1H, C*Hα*), 12.97 (s, 1H, O*H*); ^{13}C NMR (125 MHz, $CDCl_3$, δ): 9.1, 9.3, 14.0, 22.4, 24.8, 31.5, 34.1, 62.7, 113.4, 115.3, 115.8, 126.5, 128.7, 129.1, 130.7, 135.2, 144.0, 154.3, 158.3, 160.9, 171.0, 194.5.

Compound **3c**: 2′,4′-Dicaproyloxy-6′-methoxy-3′,5′-dimethylchalcone, 7% yield; yellow viscous liquid, R_f 0.08 (30% CH_2Cl_2:2% Et_2O:68% *n*-hexane), ν_{max} (thin film) 2962 (CH_2), 2938 (CH_3), 1767 (C=O), 1657 (C=O), 1609 (C=C), 1185 (C-O-C), 1139 (C-O-C), 1107 (C-O-C) cm^{-1}; ^1H NMR (500 MHz, $CDCl_3$, δ): 0.82 (t, *J* = 6.8 Hz, 3H, *Me*), 0.94 (t, *J* = 7.0 Hz, 3H, *Me*), 1.20-1.27 (m, 4H, C*H*$_2$), 1.35-1.48 (m, 4H, C*H*$_2$), 1.61 (m, 2H, C*H*$_2$), 1.81 (m, 2H, C*H*$_2$), 1.91 (s, 3H, *Me*), 2.09 (s, 3H, *Me*), 2.42 (t, *J* = 7.5 Hz, 2H, C*H*$_2$), 2.63 (t, *J* = 7.5 Hz, 2H, C*H*$_2$), 3.69 (s, 3H, O*Me*), 6.99 (d, *J* = 16.1 Hz, 1H, C*Hβ*), 7.36-7.40 (m, 3H, ArC*H*), 7.43 (d, *J* = 16.1 Hz, 1H, C*Hα*), 7.51-7.58 (m, 2H, ArC*H*); ^{13}C NMR (125 MHz, $CDCl_3$, δ): 9.9, 10.4, 13.9, 14.0, 22.4, 22.5, 24.5, 24.8, 31.3, 31.5, 33.9, 34.0, 62.7, 120.8, 122.9, 125.8, 127.5, 128.8, 129.0 , 130.8, 134.5, 144.9, 146.5, 150.1, 154.6, 171.1, 171.4, 192.9.

Compound **4b**: 3*H*- 3- Butyl- 4- hydroxy- 4- [(*E*) - 2′- phenylvinyl] - 5- methoxy- 6,8- dimethyl- 7- caproyloxycoumarin, 36% yield; light yellow viscous liquid, R_f 0.14 (30% CH_2Cl_2:2% Et_2O:68% *n*-hexane); ν_{max} (thin film) 3436 (O-H), 3065 (C-H), 3032 (C-H), 2963 (CH_2), 2937 (CH_3), 1779 (C=O), 1603 (C=C), 1218 (C-O-C), 1145 (C-O-C), 1105 (C-O-C) cm^{-1}; ^1H NMR (500 MHz, $CDCl_3$, δ): 0.87 (t, *J* = 7.0 Hz, 3H, *Me*), 0.95 (t, *J* = 6.9 Hz, 3H,

Me), 1.20-1.50 (m, 9H, CH_2), 1.81 (m, 2H, CH_2), 2.07 (s, 3H, *Me*), 2.09 (m, 1H, C*H*) 2.10 (s, 3H, *Me*), 2.64 (t, *J* = 7.5 Hz, 2H, CH_2), 2.84 (dd, *J* = 10.7, 3.8 Hz, 1H, C*H*), 3.73 (s, 3H, O*Me*), 5.68 (s, 1H, O*H*), 6.36 (d, *J* = 15.7 Hz, 1H, C*H*), 6.46 (br d, *J* = 15.7 Hz, 1H, C*H*), 7.19-7.38 (m, 5H, ArC*H*); ^{13}C NMR (125 MHz, $CDCl_3$, *δ*): 9.7, 9.8, 11.9, 13.9, 18.6, 19.5, 35.9, 53.6, 62.1, 75.3, 115.8, 116.5, 120.8, 127.0, 128.2, 128.7, 129.5, 133.4, 135.9, 146.3, 149.3, 154.7, 168.6, 171.0.

General procedure for the synthesis of stilbene-coumarin derivatives

4-Hydroxycoumarin derivatives (**4a**) further underwent dehydration reaction in acidic conditions. Compound **4a** (0.1648 mmol, 1 equiv.) was dissolved in 10 mL dry THF, which was cooled down in an ice bath. Then, conc. H_2SO_4 (1.6480 mmol, 10 equiv.) was slowly added to the reaction mixture and subsequently heated to reflux for 6 h. Then, the pH was adjusted to 7 using 10% $NaHCO_3$ and extracted with CH_2Cl_2. The combined organic layers were dried over anhydrous Na_2SO_4 and further concentrated under reduced pressure to obtain the crude product, which was further purified by preparative thin-layer chromatography (PLC) using Et_2O–*n*-hexane (15:85) as eluent to afford stilbene-coumarin derivative (**5a**)

Compound **5a**: 3-Ethyl-4-[(*E*)-2′-phenylvinyl]-5-methoxy-6,8-dimethyl-7-butyryloxycoumarin, 76% yield; white solid, mp: 118.7–119.9 °C (MeOH/CH_2Cl_2); R_f 0.14 (30% CH_2Cl_2:2% Et_2O:68% *n*-hexane); ν_{max} (thin film) 2972 (CH_3), 2941 (CH_2), 1765 (C=O), 1719 (C=O), 1597 (C=C), 1118 (C-O-C) cm^{-1}; ^{1}H NMR (500 MHz, $CDCl_3$, *δ*): 1.08 (t, *J* = 7.4 Hz, 3H, *Me*), 1.22 (t, *J* = 7.4 Hz, 3H, *Me*), 1.85 (m, 2H, CH_2), 2.10 (s, 3H, *Me*), 2.22 (s, 3H, *Me*), 2.63 (t, *J* = 7.4 Hz, 2H, CH_2), 2.76 (q, *J* = 7.4 Hz, 2H, CH_2), 3.47 (s, 3H, O*Me*), 6.64 (d, *J* = 16.5 Hz, 1H, C*H*), 7.31-7.43 (m, 4H, ArC*H*, C*H*), 7.55 (d, *J* = 8.4 Hz, 2H, ArC*H*); ^{13}C NMR (125 MHz, $CDCl_3$, *δ*): 9.4, 9.9, 13.9, 14.3, 18.7, 22.1, 35.9, 61.5, 113.0, 115.1, 120.7, 126.1, 126.7, 127.6, 128.4, 129.1, 131.5, 136.7, 146.4, 149.6, 150.3, 154.1, 161.5, 171.1.

Compound **5b** was synthesized following the general procedure mentioned above for the synthesis of stilbene-coumarin derivatives. The starting material **4b** was dissolved in dry THF in the presence of conc. H_2SO_4 which was refluxed until the completion of the reaction to afford stilbene-coumarin derivatives (**5b**)

Compound **5b**: 3-Butyl-4-[(*E*)-2′-phenylvinyl]-5-methoxy-6,8-dimethyl-7-caproyloxycoumarin, 82% yield; white solid, mp: 112.1–113.5 °C (MeOH/CH_2Cl_2); R_f 0.20 (30% CH_2Cl_2:2% Et_2O:68% *n*-hexane); ν_{max} (thin film) 2963 (CH_3), 2937 (CH_2), 1766 (C=O), 1721 (C=O), 1597 (C=C), 1118 (C-O-C) cm^{-1}; ^{1}H NMR (500 MHz, $CDCl_3$, *δ*): 0.89-0.98 (m, 6H, *Me*), 1.34-1.48 (m, 6H, CH_2), 1.55-1.65 (m, 2H, CH_2), 1.81 (m, 2H, CH_2), 2.10 (s, 3H, *Me*), 2.21 (s, 3H, *Me*), 2.64 (t, *J* = 7.5 Hz, 2H, CH_2), 2.73 (m, 2H, CH_2), 3.46 (s, 3H, O*Me*), 6.62 (d, *J* = 16.5 Hz, 1H, C*H*), 7.31-7.43 (m, 4H, ArC*H*, C*H*), 7.54 (d, *J* = 7.5 Hz, 2H, ArC*H*); ^{13}C NMR (125 MHz, $CDCl_3$, *δ*): 9.4, 9.9, 14.0, 14.1, 22.4, 23.0, 24.8, 28.3, 31.5, 31.9, 34.1, 61.5, 113.0, 115.1, 120.7, 126.2, 126.5, 126.7, 128.3, 129.1, 131.6, 136.8, 146.4, 149.6, 150.3, 154.1, 161.6, 171.3.

Cytotoxicity evaluation

The DMC derivatives were evaluated for their cytotoxicity against carcinoma cell lines at the cytotoxicity test Service Centre, Department of Microbiology, Mahidol University, Thailand. The slightly modified sulforhodamine B (SRB) assay was used as a standard method[21] with ellipticine as the positive control drug. The DMC derivatives were dissolved in DMSO at 4 mg/mL of the starting concentration. The cell lines were grown in 96-well plates as follows: KKU-M213, HT-29, and CL. The cultured cells were added by a synthesized compound solution and then incubated at 37 °C for 72 h under 5% CO_2. The cultures were fixed with 10% trichloroacetic acid and subsequently stained with 0.4% sulforhodamine B solution in 1% acetic acid. The unbound dye was removed. The bound and dried stain was dissolved with a 10 mM trizma base. The absorbance was measured at 510 nm using a BMG plate reader. The cytotoxicity was expressed as a 50% effective dose (ED_{50}) in the micromolar unit of concentration without repetition.

Results and Discussion:

DMC was isolated from the crude EtOAc extract of *S. nervosum* seeds. The chemical structure was confirmed through a comparison of its spectral data with the previously published values.[17] DMC was further modified by incorporation of the fatty acid moiety *via O*-acylation reaction of various fatty acid chlorides including acetyl chloride, butyryl chloride, and caproyl chloride in the presence of NEt_3 base dissolved in CH_2Cl_2 at room temperature as depicted in Scheme 1.

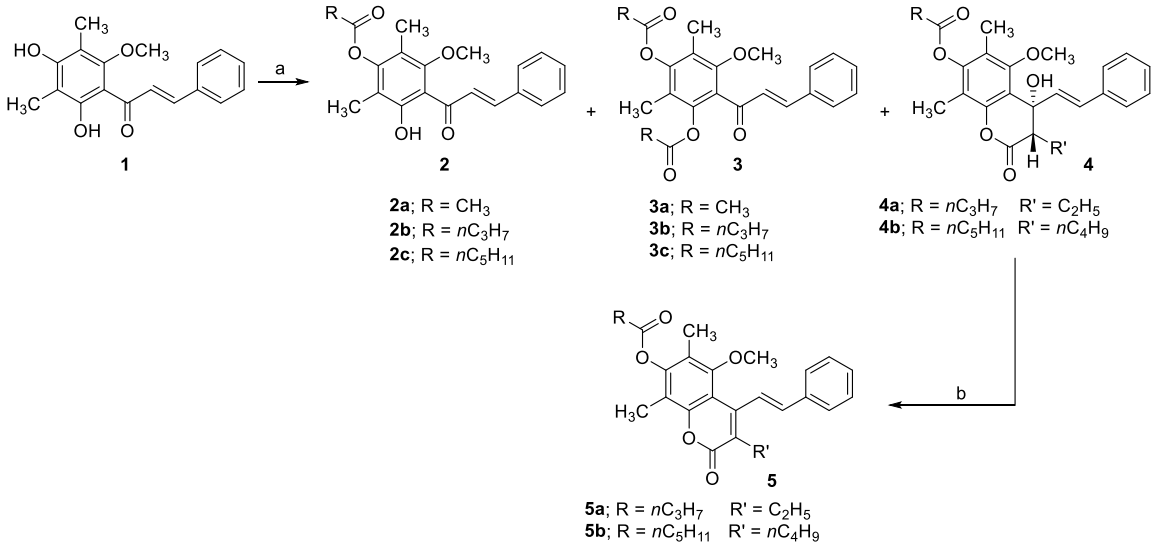

Scheme 1. Acylation reaction of DMC. *Reagents and conditions:* (a) 2.2 equiv. alkanoyl chloride, 2.2 equiv. NEt_3, CH_2Cl_2, rt., 10 min. (b) 10 equiv. conc. H_2SO_4, THF, reflux, 4 h.

Furthermore, 4-hydroxycoumarin derivatives were observed from this reaction. The ^{1}H-NMR spectra prominently indicated a broad signal of the hydroxy group, which was confirmed by exchanged with D_2O. Furthermore, it exhibited a methine proton signal of the lactone ring. Besides, ^{13}C-NMR spectra clearly showed the new carbon of the carbonyl lactone signal, which was more shielded than a common monoacylated chalcone. The chemical structure was further affirmed by ^{1}H-detected heteronuclear multiple bond connectivity (HMBC), which was in agreement with the proposed chemical structure followed by the ^{1}H-^{1}H NOESY correlation for the relative configuration determination.

The dehydration reaction of 4-hydroxycoumarin derivatives (**4a** and **b**) was achieved in acidic conditions to obtain stilbene-coumarin derivatives (**5a** and **b**). The chemical structure of the products was confirmed by ^{1}H-NMR spectroscopic data, which lacked the hydroxy and methine proton signals. In addition, ^{13}C-NMR spectra showed two signals of the quaternary carbons of the lactone ring, indicative of a completed dehydration reaction.

Cytotoxicity Evaluation

In vitro anticancer activity of newly semi-synthesized DMC derivatives was expressed in the cytotoxicity using sulforhodamine B (SRB) assay against KKU-M213, HT-29, and normal human CL cell lines. Ellipticine was used as the positive control drug. The results are depicted in Table 1.

DMC (**1**) exhibited moderate cytotoxicity to carcinoma cell lines with ED_{50} values of 29.4, 38.58, and 15.6 μM for KKU-M213, HT-29, and CL cell lines, respectively. Several monoacylated DMC derivatives displayed higher toxicity toward carcinoma cells compared to the unmodified DMC. Moreover, compound **2c** exhibited the strongest anticancer activity among the modified compounds with the ED_{50} values of 21.16, 18.92, and 23.53

μM for KKU-M213, HT-29, and CL cell lines, respectively. The structural-activity relationship (SAR) showed that the increment of carbon atom on the side chain significantly enhanced the anticancer activity of the monoacylated DMC derivatives. Among the stilbene-coumarin derivatives, compound **5a** displayed the anticancer activity against both KKU-M213 and HT-29 cell lines at the ED_{50} values of 29.58 and 30.87 μM, respectively, while the normal cells were not affected. However, all 4-hydroxycoumarin derivatives were not active under the tested concentrations.

Table 1 The anticancer activity of some semi-synthetic DMC derivatives.

Compound	Cytotoxicity (ED_{50}, μM)		
	KKU-M213	**HT-29**	**CL**
2a	42.98	36.49	31.02
2b	30.05	31.16	32.82
2c	21.16	18.92	23.53
4a	>50	>50	>50
4b	>50	>50	>50
5a	29.58	30.87	>50
5b	>50	>50	>50
DMC (**1**)	29.4	38.58	15.6
Ellipticine (+)	2.40	2.15	2.07

[a] Ellipticine was used as a positive control.

Conclusion:

DMC was isolated from the crude EtOAc extract of *S. nervosum* seeds using the chromatographic method to afford yellow needle crystals of DMC in 1.21% yield. The DMC was modified by *O*-acylation reaction with alkanoyl chloride to obtain 4′-*O*-acylated DMC (**2a-c**), 2′,4′-*O*-diacylated DMC (**3a-c**), and 4-hydroxycoumarin derivatives (**4a** and **b**). Furthermore, stilbene-coumarin derivatives (**5a** and **b**) were obtained from the dehydration reaction of **4a** and **4b**. Among semi-synthetic DMC derivatives, 4′-*O*-acylated DMC exhibited higher anticancer activity toward carcinoma cell lines than the 4-hydroxycoumarin and stilbene-coumarin derivatives. Compound **2c** showed the strongest cytotoxicity among the synthetic analogs.

Acknowledgements:

This research was supported by the National Research Council of Thailand (NRCT). We also thank the Department of Chemistry, Faculty of Science, Chiang Mai University for the laboratory equipment. We would like to extend our thanks to TA/RA scholarship from the Graduate School, Chiang Mai University.

References:

1. Iqbal J, Ahsan B, Mahmood T, Kanwal S, Ali B, Shah S, Khalil A. Asian Pac Trop Biomed. 2017;12:1129–1150.
2. Norat T, Scoccianti C, Ruault M, Anderson A, Berrino F, Cecchini M, Espina C, Key T, Leitzmann M, Powers H, Wiseman M, Romieu I. Cancer Epidemiol. 2015;39:S56–S66.
3. Bidram E, Esmaeili Y, Burachaloo H, Zaubai N, Zarrabi A, Stewart A, Dunstan D. J Drug Delivery Sci Technol. 2019;54:101350.

4. Subramanian A, John A, Vellayappan M, Balaji A, Jaganathan S, Supriyanto E, Yusof M. RSC Adv. 2015;45:35608–35621.
5. Cohen P, Jhingran A, Oaknin A, Denny L. Lancet. 2019;393:169–182.
6. Kumar B, Singh S, Skvortsova I, Kumar V. Curr Med Chem. 2017;42:4729–4752.
7. Whittaker S, Mallinger A, Workman P, Clarke P. Pharmacol Ther. 2017;173:83–105.
8. Dosoky N, Pokharel S, Setzer W. Am J Essent Oil Nat Prod. 2015;5:34–37.
9. Wang C, Wu P, Tian S, Xue J, Xu L, Li H, Wei X. J Nat Prod. 2016;79:2912–2923.
10. Dao T, Tung B, Nguyen P, Thuong P, Yoo S, Kim E, Kim S, Oh W. J Nat Prod. 2010;73:1636–1642.
11. Min B, Cuong T, Lee J, Woo M, Hung T. Bull Korean Chem Soc. 2010;31:2392–2394.
12. Charoensin S, Taya S, Wongpornchai S, Wongpoomchai R. Interdiscip Toxicol. 2012;5:201–206.
13. Su J, Wang S, Cheng W, Huang X, Li M, Jiang R, Li Y, Wang L, Ye W, Wang Y. J Org Chem. 2018;83:8522–8532.
14. Ye C, Lai Y. Cytotechnology. 2016;68:331–341.
15. Wang C, Wu P, Shen X, Wei X, Jiang Z. RSC Adv. 2017;7:48031–48038.
16. Gafner S, Wolfender J, Mavi S, Hostettmann K. Planta Med. 1996;62:67–69.
17. Chailungka A, Junpirom T, Pompimon W, Nuntasen N, Meepowpan P. Maejo Int J Sci Technol. 2017;11:58–67.
18. Ye C, Liu J, Wei D, Lu Y, Qian F. Pharmacol Res. 2004;50:505–510.
19. Yao H, Liu J, Xu S, Zhu Z, Xu J. Expert Opin Drug Discovery. 2016;12:121–140.
20. Liu X, Testa B, Fahr A. Pharm Res. 2011;28:962–977.
21. Skehan P, Storeng R, Scudiero D, Monks A, McMahon J, Vistica D, Warren J, Bokesch H, Kenney S, Boyd M. J Natl Cancer Inst. 1990;82:1107–1112.

SP13_038_PA

SP13_038_PA: ALKALOIDS FROM TWIGS OF *Uvaria grandiflora*

Naowarat Kongkum,[1] Sariyarach Thanasansurapong,[2] Nakin Surapanich,[3] Wiyarat Kumutanat,[3] Chanchai Sukkum, [4] Chutima Kuhakarn,[2] Vichai Reutrakul,[2] Sakchai Hongthong[3,*]

[1]Division of Chemistry, Faculty of Science and Technology, Surindra Rajabhat University, Surin-Prasat road, Muang district, Surin 32000, Thailand
[2]Department of Chemistry, and Center Excellence for Innovation in Chemistry (PERCH-CIC), Faculty of Science, Mahidol University, Rama VI Road, Ratchathewi, Bangkok 10400, Thailand
[3]Division of Chemistry, Faculty of Science and Technology, Maruphong road, Muang district, Chachoengsao 24000 Thailand
[4]Division of Occupational Health and Safety, Faculty of Science and Technology, Rajabhat Rajanagarindra University, Maruphong road, Muang district, Chachoengsao, 24000, Thailand
*e-mail: sakchai.hon@rru.ac.th

Abstract:

Phytochemical investigation of twigs of *Uvaria grandiflora* led to the isolation of six known compounds comprising aristolactam AII (**1**), aristolactam BI (**2**), velutinam (**3**), griffithinam (**4**), isoursuline (**5**), and sinactine (**6**). The structures of all isolated compounds were elucidated based on spectroscopic methods and on the basis of comparison of their physical and spectroscopic data with those previously reported in the literature. In general, aristolactam derivatives were found and were reported as chemotaxonomic significance in plants of the *Uvaria* genus. Described in this work is the first report of azafluorene, isoursuline (**5**) , and tetrahydroepiberberine, sinactine (**6**) being isolated, for the first time, from plants in the *Uvaria* genus. Anti-oxidant activity of some isolated compounds was also evaluated and discussed herein.

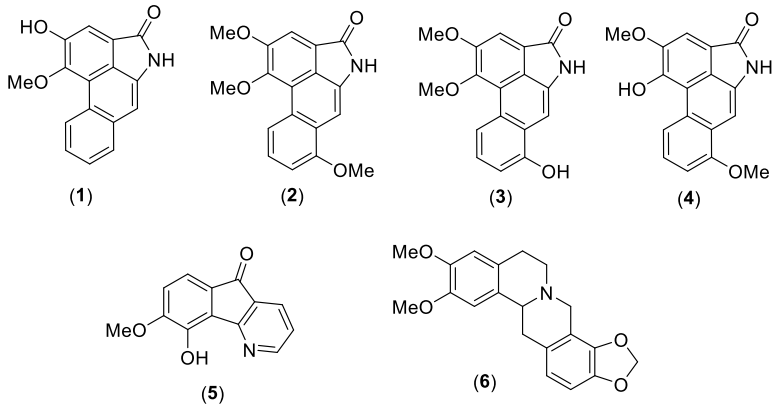

Figure 1.

SP13_039_PF: SYNTHESIS AND DNA DELIVERY INTO CELLS OF CATIONIC LIPITOIDS

Nattasit Akkarawongdacha, Charoen Posa, *Boon-ek* Yingyongnarongkul*
Department of Chemistry and Center of Excellence for Innovation in Chemistry (PERCH-CIC), Faculty of Science, Ramkhamhaeng University, Bangkok, 10240, Thailand
*e-mail: boonek@ru.ac.th

Abstract:

The ability of non-viral gene delivery system to overcome extracellular and intracellular barriers is a critical issue for the future clinical applications of gene therapy**.** Much effort has been focused on the development of a variety of DNA carriers, and cationic liposomes are one of the most common non-viral gene delivery systems that is currently investigated**.** Cationic lipitoids comprise of the peptoid hydrophilic head group linked to the hydrophobic moiety. In this research, lipitoids were synthesized, containing 1,6-diaminohexane as hydrophillic head group and hexadodecane as hydrophobic tails. The peptoid monomers with orthogonal protecting groups were prepared. Peptoid monomers were then coupled to form lipitoids using HBTU as coupling agent. These lipitoids were evaluated in the term of DNA binding, and transfection efficiency. The result showed that the synthesized lipitoids exhibited lower transfection efficiency than that of Lipofectamine3000, a commercially available transfection reagent, as a positive control.

Introduction:

Gene therapy is a methodology for DNA delivery into the target cells and an alternative treatment of a variety of diseases of both genetic and acquired origin. One principle of gene therapy is the delivery system that can introduce and stabilize genetic material. The vectors for transferring genetic materials can be categorized into two types: viral and nonviral vectors. Even though the viral vectors exhibited the high potential for DNA delivery, they have many problems including the limitation from the toxicity and immunogenicity. Nonviral vectors, for example, cationic lipids, cationic polymers, dendrimers and peptides, have a number of advantages, such as low toxicity and lack of immunogenicity. From these consequences, the researchers focus on the discovery of the new nonviral vectors with high transfection efficiency. The cationic lipids are possible to develop as a transfection vector owing to safety, ease to synthesize and low immune response.

Peptoids are poly-*N*-substituted glycines whose side chains are appended to nitrogen atom rather than to the alpha- carbon. Peptoids are resistant to proteolysis,[1] and have been used as antimicrobial agent, biomarker, transfection reagent.[2,3] Lipitoids are cationic lipids in which the peptoid polar head linked to the hydrophobic tails. Cationic lipitoids are one of non-viral vectors, extensively investigated for gene therapy. The cationic peptoids can form complexes with DNA and facilitated cell transfection. It can protect DNA from nuclease digestion.[4] The transfection efficiency of lipitoid depends on structure design and properties such as length of side chain, density of charge, side-chain shape, and hydrophobicity.[5]

In this study, two lipitoids **AN-1** and **AN-2** (**Figure 1.**) were synthesized and their transfection efficiency was investigated. The two lipitoids were alternated between head and tail. They were evaluated for DNA binding, and transfection efficiency.

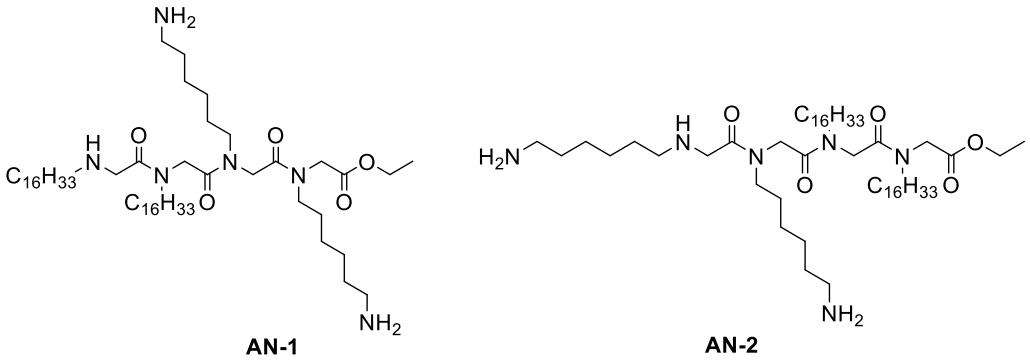

Figure 1. Structures of lipitoids **AN-1** and **AN-2**

Methodology:

IR spectra were recorded on a Perkin-Elmer FT-IR spectrometer. ^{1}H and ^{13}C NMR spectra were recorded on a Bruker ASCEND 400 MHz NMR spectrometer using a residual solvent signal as internal standard. HRESITOFMS spectra were measured with a Bruker micrOTOF II mass spectrometer. Starting materials and reagents were purchased from commercial suppliers and used without further purification.

Synthesis of monomers 2a and 2b.

To a stirred solution of 1-aminohexadecane (1 equiv), Et_3N (3 equiv) in CH_2Cl_2 was added 4-nitrobenzenesulphonyl chloride (1.2 equiv) at 0 ºC. The reaction mixture was stirred at 0 ºC for 20 minutes. The progress of reaction was monitored by TLC. The reaction was extracted with CH_2Cl_2. The combined organic layers were dried over anhydrous Na_2SO_4 and evaporated under reduced pressure to dryness. The crude product was purified by silica gel column chromatography using a gradient of CH_2Cl_2 – MeOH (100:0 - 95:5) as eluting solvent to furnish compound **1** (80 %). Compound **1** (1 equiv) was reacted with ethyl chloroacetate (2 equiv) and K_2CO_3 (4 equiv) in DMF. The reaction mixture was quenched with water and extracted with CH_2Cl_2. The combined organic layers were dried over anhydrous Na_2SO_4 and evaporated under reduced pressure to dryness. The crude product was purified by silica gel column chromatography using a gradient of CH_2Cl_2 – MeOH (100:0 - 95:5) as eluting solvent to give compound **2** (75 %). Compound **2** (1 equiv) was dissolved in MeOH: THF: H_2O (3: 2: 1, 20 ml) and LiOH (2 equiv) added. The progress of reaction was monitored by TLC. The reaction mixture was acidified with 1 M HCl and extracted with EtOAc. The crude product was purified by column chromatography to give **2a** (**Scheme 1**). Compound **2** (1 equiv) and K_2CO_3 (4 equiv) were dissolved in DMF and mercatoethanol (2 equiv) added. The progress of reaction was monitored by TLC. The reaction was worked up with water, and extracted with dichloromethane. The combined organic layers were evaporated to dryness. The crude product was purified by column chromatography using a gradient of dichloromethane: methanol (100:0 - 90:10) as eluting solvent to give **2b** (**Scheme 2**).

2a; IR: ν_{max} 2917, 2849, 1740, 1623, 1465, 1388, 1302, 1197, 1156, 1028, 925, 722 cm^{-1}; ^{1}H NMR (400 MHz, $CDCl_3$): δ 0.84 (t, J = 6.6 Hz, 3H, CH_3 of alkyl chain), 1.21 (s, 26H, CH_2 of alkyl chain), 1.24 (brs, 3H, $COOCH_2C\underline{H}_3$), 1.44 (m, 2H, CH_2 of alkyl chain), 2.55 (t, J = 7.1 Hz, 2H, CH_2 – alkyl chain), 3.35 (s, 2H, $NHC\underline{H}_2COOEt$), 4.14 (q, J = 6.6 Hz, 2H, $COOC\underline{H}_2CH_3$); ^{13}C NMR (100 MHz, $CDCl_3$): δ 14.0 ($COOCH_2\underline{C}H_3$), 14.2, 22.6, 27.2, 29.3, 29.5, 29.6, 30.0, 31.9, 49.6 (carbon of alkyl chain), 51.1 ($NH\underline{C}H_2COOEt$), 60.6 ($COO\underline{C}H_2CH_3$), 172.5 ($\underline{C}OOEt$). HR-TOFMS (ES^+) *m/z*: 350.3034 $[M + Na]^+$ (calcd. for $C_{20}H_{41}NO_2Na$: 350.3029).

2b; IR: ν_{max} 3108, 2917, 2850, 1720, 1611, 1532, 1468, 1347, 1315, 1229, 1156, 1090, 1062, 931, 857, 789, 730 cm^{-1}; ^{1}H NMR (400 MHz, $CDCl_3$): δ 0.81 (brs, 3H, CH_3 of alkyl chain), 1.20 (brs, 26H, CH_2 of alkyl chain), 1.47 (brs, 2H, CH_2 of alkyl chain), 3.21 (brs, 2H, CH_2 of alkyl chain), 4.03 (brs, 2H, $NHCH_2COOEt$), 8.28-8.79 (d, J = 8.1 Hz, 4H, proton of aromatic); ^{13}C NMR (100 MHz, $CDCl_3$): δ 14.0, 22.6, 26.5, 27.7, 29.1, 29.3, 29.5, 29.6, 31.9, 47.5 (carbon of alkyl chain), 48.3 (NHCH2COOH), 124.0, 128.5, 145.7, 149.9 (carbon of aromatic), 171.1 ($\underline{C}OOH$). HR-TOFMS (ES^+) *m/z*: 507.2503 $[M + Na]^+$ (calcd. for $C_{24}H_{40}N_2O_6SNa$: 507.2499).

Synthesis of monomers 5a and 5b.

To a stirred solution of 1,6-diaminohexane (2 equiv) in CH_2Cl_2 at room temperature was slowly added a solution of di-tert-butyl decarbonate (1 equiv) in CH_2Cl_2. The reaction mixture was stirred overnight at room temperature. The reaction mixture was quenched with water and extracted with CH_2Cl_2. The combined organic layers were dried over anhydrous Na_2SO_4 and evaporated under reduced pressure to dryness. The crude product was purified by silica gel column chromatography using a gradient of CH_2Cl_2 – MeOH (100:0 - 95:5) as eluting solvent to give compound **3**. Compound **3** was then subjected to synthesize monomers **5a** and **5b** using the same manner as the preparation of **2a** and **2b** (**Scheme 2**)

5a; IR: ν_{max} 3353, 2975, 2859, 1695, 1578, 1519, 1449, 1365, 1336, 1248, 1167, 1025, 854, 777, 742 cm^{-1}; ^1H NMR (400 MHz, $CDCl_3$): δ 1.24 (t, *J* = 7.12, 3H, $COOCH_2C\underline{H}_3$), 1.30 (brs, 4H $NHCH_2CH_2C\underline{H}_2C\underline{H}_2CH_2CH_2NH$), 1.40 (s, 9H, $C(CH_3)_3$), 1.46 (brs, 4H, $NHCH_2$ $C\underline{H}_2CH_2CH_2C\underline{H}_2CH_2NH$), 2.58 (t, *J* = 7.1 Hz, 2H, $NHCH_2CH_2CH_2CH_2CH_2C\underline{H}_2NH$), 3.06 (brs, 2H, $NHC\underline{H}_2CH_2CH_2CH_2CH_2CH_2NH$), 3.06 (d, *J* = 6.2 Hz, 2H), 3.38 (s, 2H, $NHC\underline{H}_2COOH$), 4.15 (q, *J* = 7.1 Hz, 2H, $COOC\underline{H}_2CH_3$); ^{13}C NMR (100 MHz, $CDCl_3$): δ 14.0, 22.6, 25.6, 27.0, 31.9, 47.2 (carbon of alkyl chain), 61.0, 79.5, 156.1, 170.1 (carbon of ester). HR-TOFMS (ES^+) *m/z*: 303.2284 $[M + H]^+$ (calcd. for $C_{15}H_{31}N_2O_4$: 303.2278).

5b; IR: ν_{max} 3360, 3108, 2936, 2863, 1719, 1679, 1640, 1607, 1527, 1404, 1345, 1311, 1244, 1156, 933, 856, 785, 736 cm^{-1}; ^1H NMR (400 MHz, $CDCl_3$): δ 1.23 (*br*, 4H, $NHCH_2CH_2C\underline{H}_2C\underline{H}_2CH_2CH_2NH$), 1.39 (s, 9H, $C(CH_3)_3$), 1.48 (*br*, 4H, $NHCH_2C\underline{H}_2CH_2CH_2C\underline{H}_2CH_2NH$), 3.03 (*br*, 2H, $NHCH_2CH_2CH_2CH_2CH_2C\underline{H}_2NH$), 3.22 (t, *J* = 6.9 Hz, 2H, $NHC\underline{H}_2CH_2CH_2CH_2CH_2CH_2NH$), 8.01, 8.30 (d, *J* = 8.6 Hz, 4H, protons of aromatic); ^{13}C NMR (100 MHz, $CDCl_3$): δ 25.8, 26.0, 27.5, 28.1, 29.5, 40.1, 47.3 (carbon of alkyl chain), 48.0, 48.4, 79.3, 123.9, 128.5, 145.5, 149.8, 156.3, 170.2 ($\underline{C}OOH$). HR-TOFMS (ES^+) *m/z*: 460.1752 $[M + H]^+$ (calcd. for $C_{19}H_{30}N_3O_8S$: 460.1748).

General procedure for HBTU coupling: Compound with acid group (1 equiv) was dissolved in CH_2Cl_2 and HBTU (1.1 equiv) and Et_3N (2 equiv) were added. The mixture was stirred for 10 minutes and compound having amino group, – NH or NH_2, was added. The progress of reaction was monitored by TLC. After that, the reaction mixture was quenched with water and extracted with CH_2Cl_2. The organic solvent was evaporated under reduced pressure and crude product was purified by column chromatography with a mixture of CH_2Cl_2: MeOH (5: 95) as eluting solvent to give amide compound.

General procedure for base-catalyzed hydrolysis: Ester was dissolved in MeOH:THF:H_2O (3:2:1) and LiOH (2 equiv) added. The reaction was stirred for 2 h. The reaction mixture was acidified with 1M HCl and extracted with ethyl acetate. The crude product was purified by column chromatography using CH_2Cl_2: MeOH as eluting solvent to give acid compound.

Synthesis of peptoid AN-1

Compound **2b** coupled with monomer **2a** using HBTU as coupling agent to give compound **6** (87 %). Compound **6** was subjected to base-catalyzed hydrolysis to obtain compound **7** (89 %). Compound **7** was then coupled with monomer **5a** using HBTU as coupling agent to furnish compound **8** (90 %), which was hydrolyzed to give compound **9** (86 %). Then, compound **9** was coupled with monomer **5a** to give compound **10** (89 %). Compound **10** (1 equiv) and K_2CO_3 (4 equiv) were dissolved in DMF and mercatoethanol (2 equiv) added. The progress of reaction was monitored by TLC. The reaction mixture was worked up with water, and extracted with ethyl acetate. The combined organic layers were evaporated to dryness. The crude product was purified by column chromatography using a mixture of CH_2Cl_2: MeOH (20:80) as eluting solvent to give **11** (87 %). Compound **11** was dissolved with CH_2Cl_2 and 10% TFA in CH_2Cl_2 was added. The reaction mixture was stirred at room temperature for 2 h. The organic solvents were removed under stream of nitrogen until dryness to obtain compound **AN-1**. The desired compound was further dried under reduced pressure to remove trace amount of solvents.

AN-1; IR: ν_{max} 2924, 2855, 1742, 1655, 1464, 1141, 835, 799, 705 cm^{-1}; ^1H NMR (400 MHz, $CDCl_3$): δ 0.85 (t, *J* = 6.6 Hz, 6H, CH_3 of long chain), 1.23-1.68 ((m, 54H, CH_2 of alkyl chain), (t, *J* = 6.6 Hz, 3H, $COOCH_2C\underline{H}_3$), (m, 8H, $NHCH_2CH_2C\underline{H}_2C\underline{H}_2CH_2CH_2NH$), (m, 8H, $NHCH_2C\underline{H}_2CH_2CH_2C\underline{H}_2CH_2NH$)), 2.69 (m, 4H,

$NH_2CH_2CH_2CH_2CH_2CH_2CH_2NH$), 3.00 (br-m, (2H, CH_2 of alkyl chain), 3.17-3.38 (br m, (2H, CH_2 of alkyl chain), 3.27 (4H, $NH_2CH_2CH_2CH_2CH_2CH_2CH_2NH$)), 4.00 (m, 2H, $NHCH_2CON$), 3.98-4.23 (q, (2H, $COOCH_2CH_3$), (4H, NCH_2NCO)), 4.07 (2H, NCH_2COOEt); ^{13}C NMR (100 MHz, $CDCl_3$): δ 14.0 ($COOCH_2CH_3$), 14.0, 22.6, 27.2, 29.3, 29.5, 29.6, 30.0, 31.9, 49.6 (carbon of alkyl chain), 26.4, 26.7, 28.6, 32.7, 42.0, 48.3 ($NHCH_2CH_2CH_2CH_2CH_2CH_2NH$), 50.6 ($NHCH_2CON$), 50.7 ($NCH_2COOEt$), 53.3 ($NCH_2CON$), 52.9 ($NCH_2CON$), 60.8 ($COOCH_2CH_3$), 164.5 (carbonyl of amide), 168.4 (carbonyl of ester). HR-TOFMS (ES^+) *m/z*: 921.8460 $[M + H]^+$ (calcd. for $C_{54}H_{109}N_6O_5$: 921.8453).

Synthesis of peptoid AN-2

Compound **5b** was coupled with compound **5a** using HBTU as coupling reagent to give compound **12** (86 %). Compound **12** was then subjected to base-catalyzed hydrolysis to give compound **13** (85 %). Compound **13** was then coupling with monomer **2a** using HBTU as coupling agent to give **14** (89 %), which was further hydrolyzed to obtain compound **15** (87 %). Compound **15** was coupled with **2a** using HBTU as coupling agent to furnish compound **16** (90 %). Compound **16** (1 equiv) and K_2CO_3 (4 equiv) were dissolved in DMF and mercatoethanol (2 equiv) added. The progress of reaction was monitored by TLC. The reaction mixture was worked up with water, and extracted with dichloromethane. The combined organic layers were evaporated to dryness. The crude product was purified by column chromatography using a gradient of CH_2Cl_2: MeOH (100:0 - 95:5) as eluting solvent to give **17** (90 %). Compound **17** was dissolved with CH_2Cl_2 and 10% TFA in CH_2Cl_2 was added. The reaction mixture was stirred at room temperature for 2 h. The organic solvents were removed under stream of nitrogen until dryness to obtain compound **AN-2**. The desired compound was further dried under reduced pressure to remove trace amount of solvents.

AN-2; IR: ν_{max} 2925, 2858, 1746, 1649, 1465, 1148, 801, 702 cm^{-1}; ^1H NMR (400 MHz, $CDCl_3$): δ 0.85 (t, *J* = 6.6 Hz, 6H, CH_3 of long chain), 1.23-1.60 (m, 54H, CH_2 of alkyl chain), 1.24 (3H, $COOCH_2CH_3$), 1.31 – 1.33 (m, (8H, $NHCH_2CH_2CH_2CH_2CH_2CH_2NH$), (8H, $NHCH_2CH_2CH_2CH_2CH_2CH_2NH$), 2.94-3.25 (m, 2H, $NHCH_2CH_2CH_2CH_2CH_2CH_2NH$), 3.28 (m, 10H, $NHCH_2CH_2CH_2CH_2CH_2CH_2NH$, proton of alkyl chain, $NHCH_2CH_2CH_2CH_2CH_2CH_2NH$), 3.95-4.20 (m, 10H, $NHCH_2CON$, $COOCH_2CH_3$, $NHCH_2CON$, NCH_2COOEt); ^{13}C NMR (100 MHz, $CDCl_3$): δ 14.0, 50.7 ($COOCH_2CH_3$), 14.0, 22.6, 27.2, 29.3, 29.5, 29.6, 31.0, 31.9, 50.0 (carbonyl of alkyl chain), 26.4, 26.7, 32.7, 42.0, 48.3, 48.9, 28.6, 29.8 ($NHCH_2CH_2CH_2CH_2CH_2CH_2NH$), 50.6 (NHCH2CON), 50.7 (NCH_2COOEt), 53.3 (NCH_2CON), 52.9 (NCH_2CON), 164.5, 164.6 (carbonyl of amide), 168.4 (carbonyl of ester). HR-TOFMS (ES^+) *m/z*: 921.8446 $[M + H]^+$ (calcd. for $C_{54}H_{109}N_6O_5$: 921.8453).

Gel retardation assay

DNA binding affinities of liposomes were measured at N/P ratios of 5, 10, 20, 30 and 40 by gel electrophoresis. The liposome/DNA complex solution was prepared by adding the liposome solution to the DNA solution (the amount of DNA was fixed at 0.1 μg). The mixture was gently mixed by pipetting up and down for 2-3 times and the mixture was held at room temperature for 30 min. Each complex was added gel loading buffer (13.3% w/v sucrose in water) to get the final volume of 10 μL. The complex solution was inverted to mix and each sample (10 μL) was loaded onto a 1% agarose gel (0.5×TBE buffer). The gel was run at 200 V, 400 mA for 2 h. DNA bands were visualized under UV light by ethidium bromide staining.

Transfection experiment

Human embryonic kidney cells 293 (HEK293), human cervical adenocarcinoma (HeLa), prostate cancer (PC3) and H460 were grown in DMEM medium supplemented with 10% fetal bovine serum, penicillin (100% units/ml), streptomycin (100 □g/ml) and L-glutamine (4 mM) at 37 °C under CO_2. Cells were seeded up to 1×10^4 cells/well in a 96-well plate to give 50-70% confluence and used in the next day. The old medium was removed and washed with PBS and replaced with 100 μl of fresh serum-free DMEM medium. Lipoplexes were prepared by added liposome (1 μg/μl) into DNA (0.1 μg/μl) and diluted with PBS buffer to total volume about 10 μl. The lipoplexes were added into the cells and incubated at 37 °C under 5% CO_2 for 48 h. The procedure for Lipofectamine3000 transfection was followed the manufacturer's instruction. After 48 h, the old medium was removed and the Z buffer (100 μl) were added into the cells, after 15 minutes, ONPG solution (10 mg/ml; 100 μl) was added and then the cells were incubated for 4 h before measuring the absorbance at 405 nm.

Results and Discussion:

Synthesis of Lipitoids AN-1 and AN-2

To synthesize lipitoids **AN-1** and **AN-2**, monomers **2a** and **2b** with hydrophobic tail and monomers **5a** and **5b** having polar head were prepared. 4-Nitrobenzenesulfonyl group was chosen as protecting and activating groups. Thus, hexadecylamine was reacted with 4-nitrobenzenesulfonyl chloride to give compound **1**. Compound **1** was then reacted with ethyl chloroacetate to furnish compound **2**. Compound **2** was hydrolyzed with two different conditions to obtain monomers **2a** and **2b** (Scheme 1). Monomers **5a** and **5b** were also synthesized in the same manner as monomers **2a** and **2b** except that compound **3** was used as starting material instead of hexadecylamine (Scheme 2).

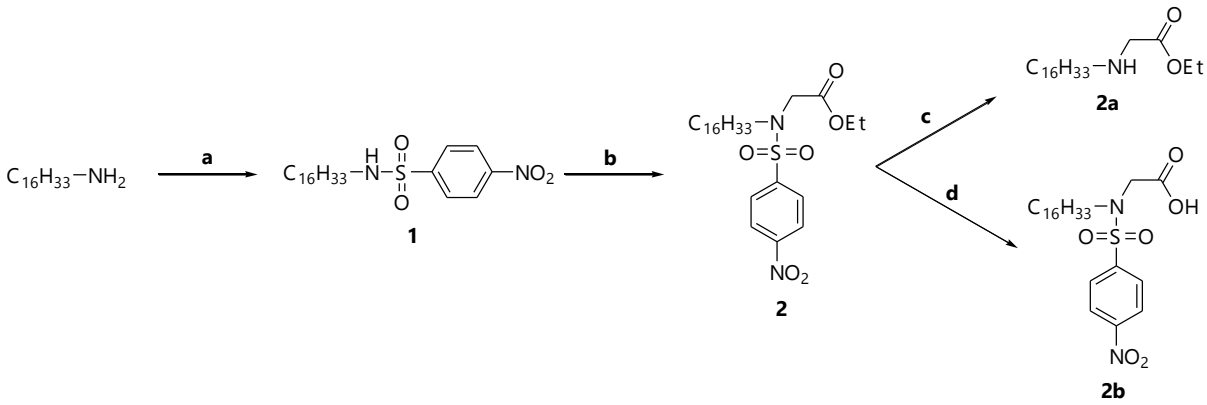

Scheme 1. Reagents and conditions: a) 4-nitrosulphonyl chloride, Et_3N, CH_2Cl_2; b) Ethyl chloroacetate, K_2CO_3, DMF; c) mercaptoethanol, K_2CO_3, DMF; (d) LiOH, CH_3OH: THF: H_2O

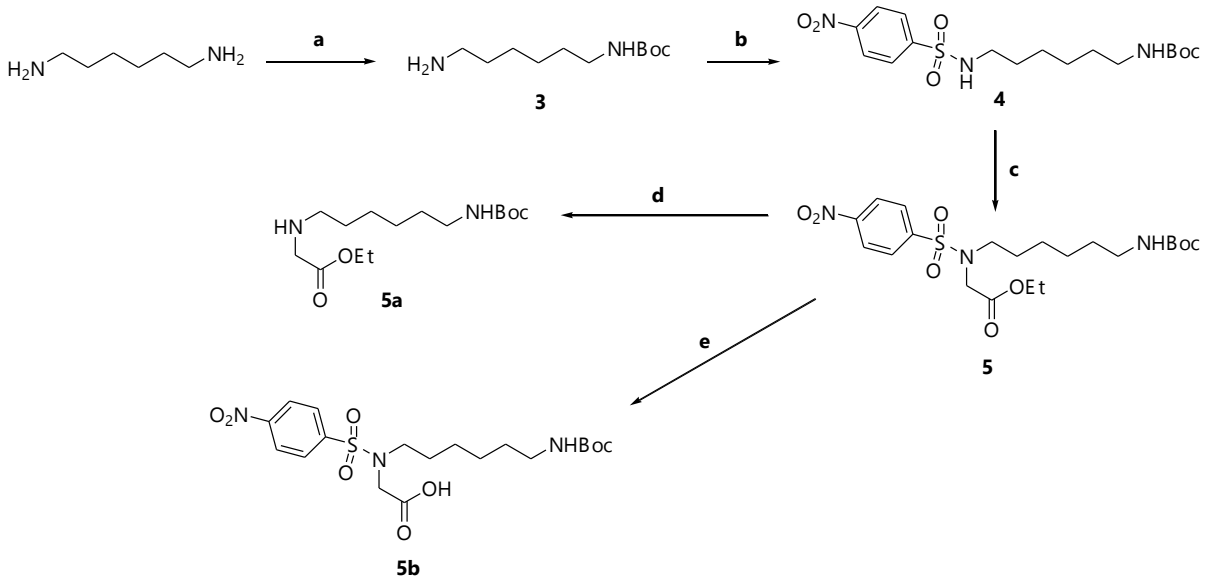

Scheme 2. Reagents and conditions: a) Di-tert-butyl decarbonate, CH_2Cl_2. b) 4-nitrobenzenesulfonyl chloride, Et_3N, CH_2Cl_2; c) ethyl chloroacetate, K_2CO_3, DMF; d) mercaptoethanol, K_2CO_3, DMF; e) LiOH, CH_3OH: THF: H_2O.

With monomers in hand, lipitoids **AN-1** and **AN-2** were synthesized. Monomers **2a** and **2b** were coupled using HBTU as coupling agent to give compound **6** which was further hydrolyzed to give acid **7**. Monomer **5a** with polar head was then coupled with acid 7 using HBTU as coupling agent to give compound **8**. Using the same reaction sequence, compound **10** was obtained. 4-Nitrobenzenesulfonyl group was removed using mercaptoethanol in the presence of K_2CO_3 base to give **11**. Finally, Boc protecting groups were removed with 10% TFA in CH_2Cl_2 to give lipitoid **AN-1** (Scheme 3). Lipitoid **AN-2** was also synthesized using the same method as that of lipitoid **AN-1** except that the reaction sequence started with monomers **5a** and **5b** containing polar head (Scheme 4). The structures of synthesized compounds were confirmed by spectroscopic means (IR and NMR) and HRMS.

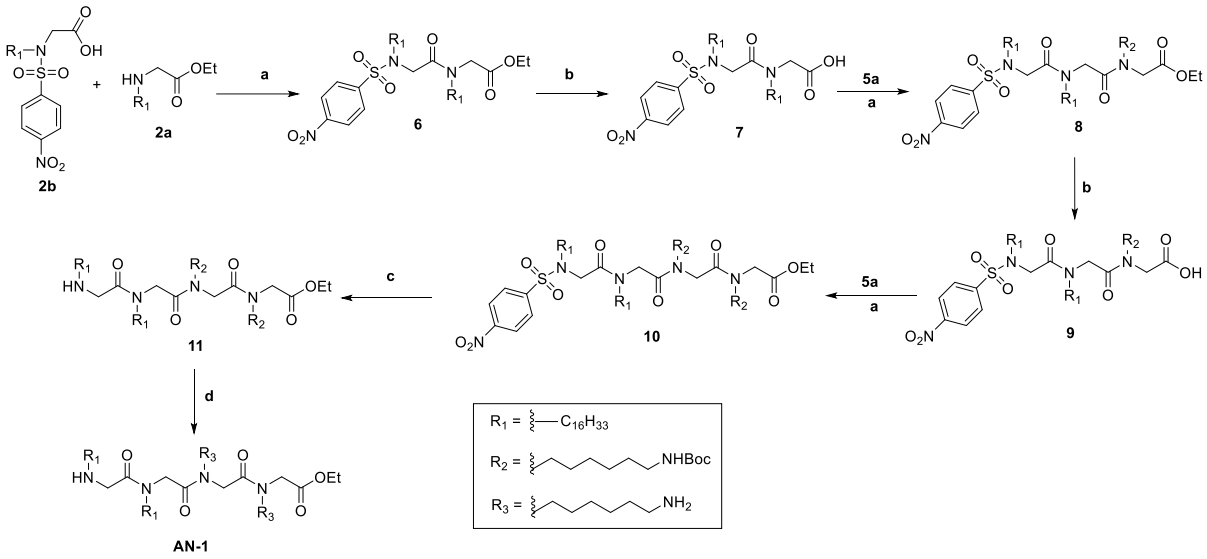

Scheme 3. Reagents and conditions; a) HBTU, Et_3N, CH_2Cl_2; b) LiOH, CH_3OH: THF: H_2O; c) mercaptoethanol, K_2CO_3, DMF; d) 10% TFA in CH_2Cl_2.

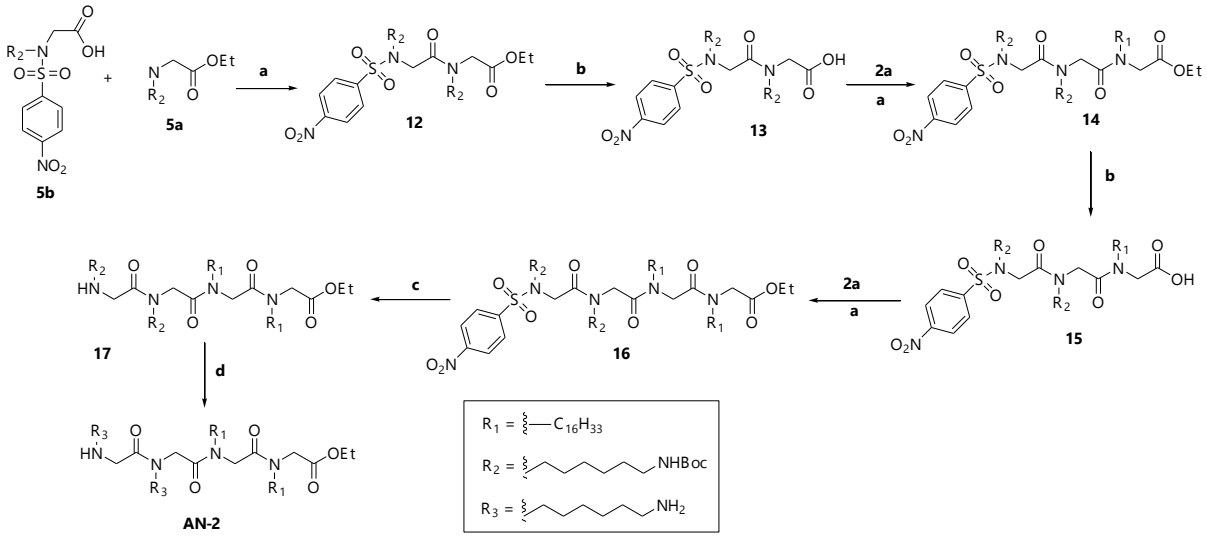

Scheme 4. Reagents and conditions; a) HBTU, Et_3N, CH_2Cl_2; b) LiOH, CH_3OH: THF: H_2O; c) mercaptoethanol, K_2CO_3, DMF; d) 10% TFA in CH_2Cl_2.

Gel retardation assay

Gel retardation assay was performed to characterize the electrostatic interactions between cationic liposome, prepared from lipitoid alone or with the combination of DOPE, and plasmid DNA. DOPE is helper lipids used for forming stable structure. Cationic liposome and DNA at N/P ratios of 5 to 40 were prepared. The electrophoresis gel patterns of lipitoid in the absence of DOPE is shown in Figure 2. It was found that lipitoid **AN-2** could retard plasmid DNA better than **AN-1**. In contrast, cationic liposome **AN-1** in the presence of DOPE could bind to DNA greater than **AN-2** (Figure 3).

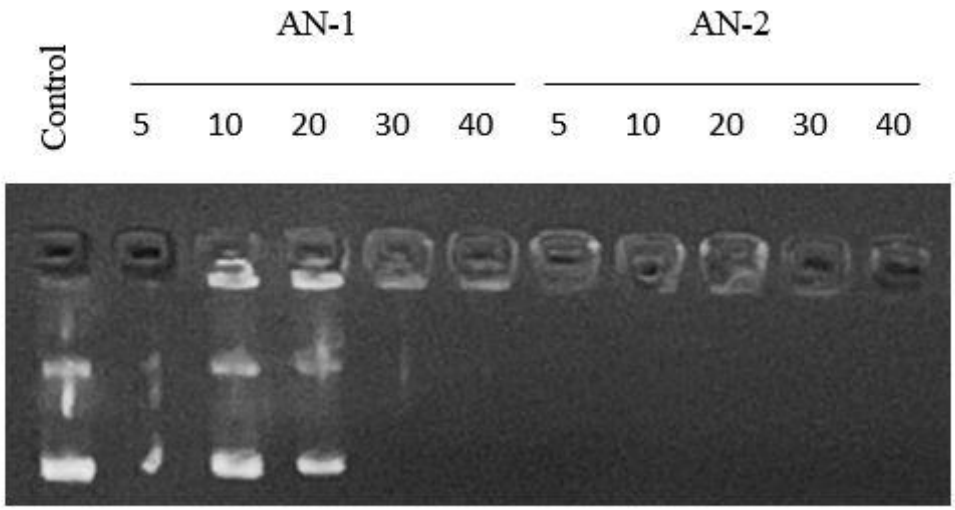

Figure 2. DNA binding of cationic liposome AN-1 and AN-2 without DOPE at N/P ratios of 5, 10, 20, 30 and 40

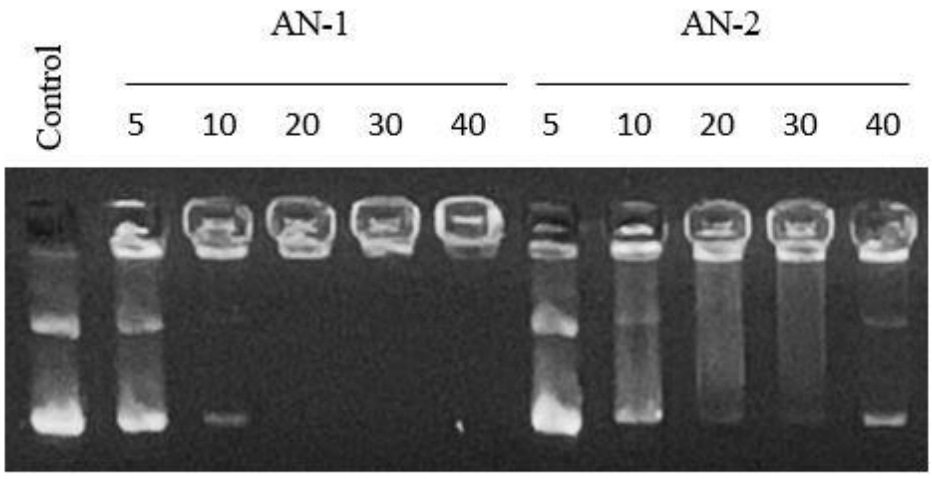

Figure 3. DNA binding of cationic liposome AN-1 and AN-2 in the presence of DOPE at N/P ratios of 5, 10, 20, 30 and 40

***In vitro* transfection**

All the synthesized compounds were evaluated through mammalian cell lines, HEK293, Hela, PC3, and H460. Plasmid DNA encoding β-galactosidase was used for preliminary transfection screening using ONPG (*O*-nitrophenyl-β-galactosidase) as substrate. Cationic liposomes were prepared with lipitoids **AN-1** and **AN-2** alone and with the combination of DOPE. The cationic liposome/DNA at N/P ratio of 20 was used. Lipofectamine3000, a commercially available transfection agent, was used as positive control and calculated as 100% transfection efficiency. The results are shown in Figures 4 and 5. It was found that cationic liposome formulation from lipitoid alone and in the presence of DOPE showed lower transfection efficiency than the control. Lipitoid **AN-2** exhibited slightly higher transfection efficiency than lipitoid **AN-1** when the liposome formulation with DOPE (Figure 5). However, liposome in the absence of DOPE, lipitoid **AN-1** showed slightly greater than lipitoid **AN-2** (Figure 4). These demonstrated that the position of polar head and hydrophobic tail on lipitoid structure had effect on transfection efficiency. DOPE also played a key role on transfection efficiency. In the future, the lipitoids with different position of polar head and hydrophobic tail will be designed and studied for transfection efficiency in order to study structure-activity relationship (SAR).

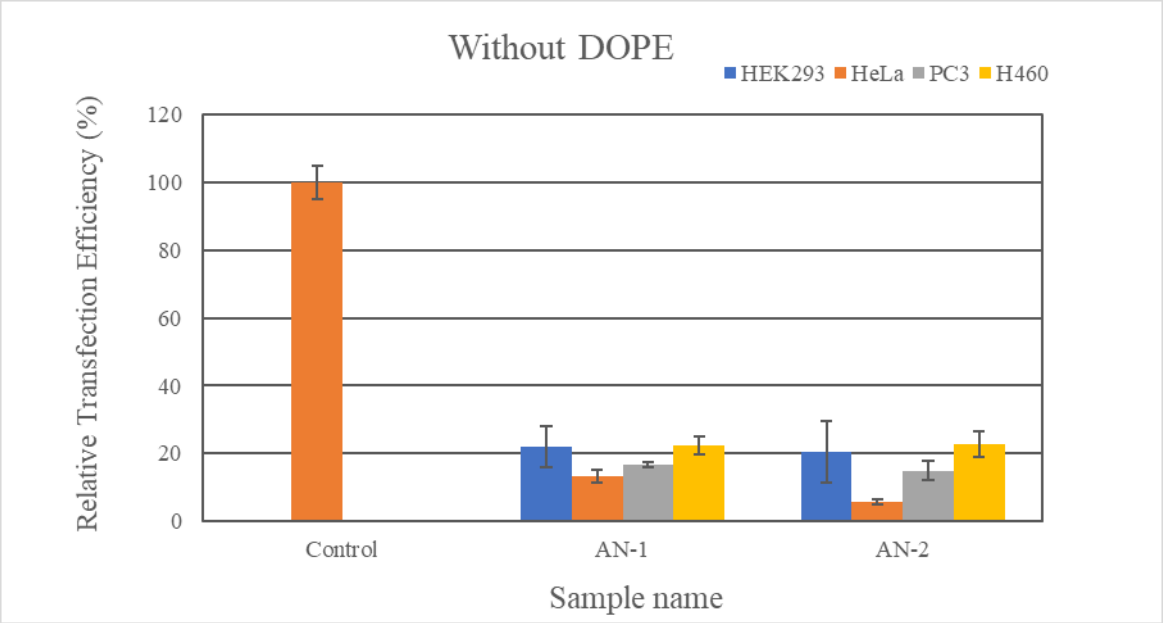

Figure 4. Transfection efficiency of cationic liposome AN-1 and AN-2 in the absence of DOPE were investigated in HEK293, Hela, PC3 and H460 at N/P ratio 20

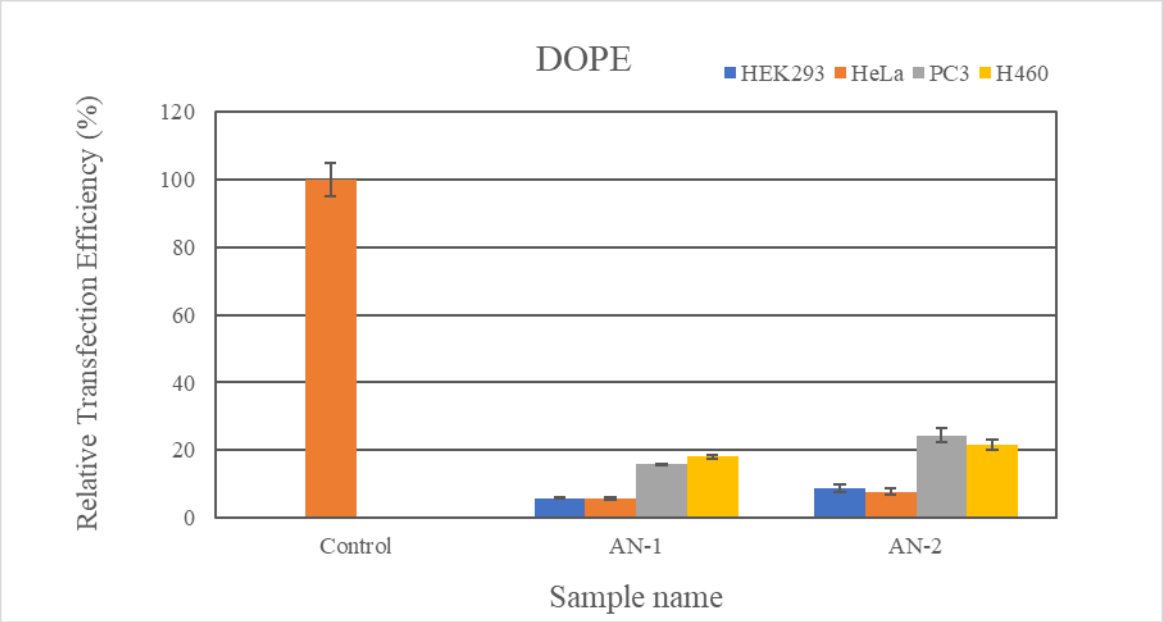

Figure 5. Transfection efficiency of cationic liposome AN-1 and AN-2 in the presence of DOPE were investigated in HEK293, Hela, PC3 and H460 at N/P ratio 20

Conclusion: In this study, we demonstrated the different structures between **AN-1** and **AN-2** by using IR and NMR spectroscopy. The correlation between DNA-binding affinity and transfection efficiency could explain that **AN-2** which formed the stable structure with plasmid DNA by itself could retard plasmid DNA in the gel electrophoresis in the absence of DOPE and express transfection efficiency at N/P ratio 20. While **AN-1** cannot form the stable structure with plasmid DNA, so helper lipid – DOPE was used to form the stable structure for **AN-1**. **AN-1** could retard plasmid DNA and showed transfection efficiency in the presence of DOPE. However, these two lipitoids showed much less transfection efficiency than the positive control.

Acknowledgements: This work was supported by the Center of Excellence for Innovation in Chemistry (PERCH-CIC). Ramkhamhaeng University is gratefully acknowledged.

References:

1. Morimoto J., Fukuda Y., Kuroda D., Watanabe T., Yoshida F., Asada M., Nakamura T., Senoo A., Nagatoishi S. and Tsumoto K. J Am Chem Soc. 2019;141:14612-14623.
2. Unciti-Broceta A., Diezmann F., Ou-Yang C. Y., Fara M. A. and Bradley M. Bioorg Med Chem. 2009;17:959-966.
3. Simon R. J., Kania R. S., Zuckermann R. N., Huebner V. D., Jewell D. A., Banville S., Ng S., Wang L., Rosenberg S. and Marlowe C. K. PNAS. 1992;89:9367-9371.
4. Miller S. M., Simon R. J., Ng S., Zuckermann R. N., Kerr J. M. and Moos W. H. Drug Dev Res. 1995;35:20-32.
5. Murphy J. E., Uno T., Hamer J. D., Cohen F. E., Dwarki V. and Zuckermann R. N. PNAS. 1998;95:1517-1522.

SP13_040_PA: POLYPHENOLIC CONTENTS AND ANTIOXIDANT ACTIVITY OF *Phyllanthus emblica* FRUIT EXTRACTS

Nichakan Whangchai,[1] Chonikarn Singai,[2] Warunyoo Phannasorn,[2] Romteera Kitichaiworakul,[2] Wilasinee Swathanan,[1] Rawiwan Wongpoomchai[2,*]

[1]Chiang Mai University Demonstration School, Chiang Mai University, Chiang Mai 50200, Thailand
[2]Department of Biochemistry, Faculty of Medicine, Chiang Mai University, Chiang Mai 50200, Thailand
*e-mail: rawiwan.wong@cmu.ac.th

Abstract:

Phyllanthus emblica is native to India and grows in the tropical region such as Thailand. In many countries, *P. emblica* fruits are commonly used for health benefits, including antioxidant and immunomodulatory. However, the chemical profile of *P. emblica* fruits are still unclear. This study aimed to investigate the bioactive compounds and antioxidant activity of *P. emblica*. The dry powder of *P. emblica* pulp was initially extracted by ethanol to obtain crude ethanolic extract (CEE) and then sequentially partitioned with different organic solvent system to acquire hexane-(HPF), dichloromethane-(DPF), ethyl acetate- (EPF), butanol-(BPF), and residue- (RPF) partitioned fractions. Each fraction was analyzed for total phenolic and flavonoid contents using colorimetric methods. Their antioxidant activities were evaluated using ABTS and FRAP assay. Total phenolic and flavonoid contents of CEE were 592.33±17.52 and 67.99±1.12 mg/g extract, respectively. The most incredible phenolic and flavonoid contents were observed in EPF, followed by BPF, CEE and DPF, respectively. HPF and RPF contained small amount of polyphenolic compounds. Furthermore, the EC50 values for antioxidant activity of CEE using ABTS assay was 0.179±0.057 mg/ml, while FRAP value of CEE was 4.199±0.318 mM TE/g extract. The antioxidant activities of *P. emblica* fruits were correlated with the content of phenolic compounds. EPF was the strongest antioxidant fraction of *P. emblica* extract. EPF of *P. emblica* fruit might be attractive to natural antioxidant source for degenerative disease alleviation. It indicates that *P. emblica* fruit possesses a high feasibility for either functional food or nutraceutical product development.

SP13_041_PF: CYTOTOXIC ACTIVITY SCREENING OF AERIAL PARTS EXTRACTS OF *Boesenbergia violacea* (K.Larsen & Triboun) Mood & L.M.Prince

Patitta Choosub,[1] Phanom Sutthisaksopon,[2] Ramida Watanapokasin,[3] Patamapan tamvapee,[3] Kamthorn Intarapichai,[4] Phongsak Phonsena,[5] Siritron Samosorn[1,*]

[1]Department of Chemistry, Faculty of Science, Srinakharinwirot University, Bangkok 10110, Thailand
[2]Program of Environment, Faculty of Environmental Culture and Ecotourism, Srinakharinwirot University, Bangkok 10110, Thailand
[3]Department of Biochemistry, Faculty of Medicine, Srinakharinwirot University, Bangkok 10110, Thailand
[4]BIOTEC Pilot Plant, Thailand Science Park, Pathumthani 12120, Thailand
[5]Forest Extension and Promotion Section, Forest and Plant Conservation Research Office, Department of National Parks, Wildlife and Plant Conservation, Bangkok 10900, Thailand
*e-mail: siritron@g.swu.ac.th

Abstract:

Boesenbergia violacea (K.Larsen & Triboun) Mood & L.M.Prince (Basionym: *Caulokaempferia violacea* K.Larsen & Triboun) is an endemic plant of Zingiberaceae family in Thailand. To our knowledge, there is no data available on the biological activities of *B. violacea*. This study aimed to evaluate the cytotoxic activity of crude extracts from leaf and stem of *B. violacea*. Leaf was extracted by liquid-liquid partition, while sequential extraction was used for stem. All extracts were screened for their cytotoxic activity against A375, A431, Lovo, SW1353, MDA-MB-231, PC3 cancer cell lines, and Vero normal cell line by MTT assay. Compared to liquid-liquid partition method, sequential extraction procedure was suitable for small sample extraction and not producing emulsion formation. *Thin layer chromatography was used* for the preliminary *detection* of chemical compositions in the extracts. Both stem and leaf extracts were mainly comprised of terpenoids, sterols, and phenolic compounds. Cytotoxicity assay revealed that *n*-hexane extract of stem was more effective than all leaf extracts with the half maximal inhibitory concentration (IC_{50}) of 31.40 and 89.66 µg/mL against skin cancer cell lines A375 and A431, respectively. Thus, the stem of *B. violacea* is a promising source of bioactive compounds for further skin cancer studies.

Introduction:

The genus *Caulokaempferia* K. Larsen (Zingiberaceae) was established by Kai Larsen in 1964.[1] This genus consists of more than 30 species, distributed from north India to south China, Vietnam, Laos, and Thailand.[2] In Thailand, *Caulokaempferia* can be found in Chiang Mai, Loei, *Mae Hong Son*, *Nong Khai*, and *Nakhon Phanom* provinces.[2-5,8] This genus can grow in humid environments, mossy rocks along streams, wet rock walls, and swampy areas.[3] A few taxa of the genus were reported to be an ethnomedicine. In India, *C. linearis* is used by Chakma tribes to treat vertigo,[6] while *C. sikkimensis* is used by *Lapcha* tribes to heal bone fractures, and wounds.[7] In Thailand, *C. phutokensis* is used by Thai forest monks to treat early stage of prostatic hyperplasia.[8] *C. violacea,* locally call "Por Phu Muang", is an endemic plant of the ginger family. It was first discovered by K. Larsen in 2002 at Phu Rhua National Park, Loei province, Thailand (Figure 1). Nomenclature of *C. violacea* was changed to *Boesenbergia violacea* (K.Larsen & Triboun) Mood & L.M.Prince in 2014.[9] Distribution zone of *B. violacea* can be found in only Loei province between 800 - 1400 m alt where water is seeping over flat rocks and boulders, covered by mosses.[3] Interestingly, no biological activity and chemical composition data of *B. violacea* has been reported so far. Thus, the aim of this study was to investigate the cytotoxic activity of the aerial parts of *B. violacea* in order to conserve the underground roots and rhizomes for regenerating the aerial parts in the next rainy season.

Figure 1. Aerial parts of *Boesenbergia violacea* (K.Larsen & Triboun) Mood & L.M.Prince (Basionym: *Caulokaempferia violacea* K.Larsen & Triboun)

Methodology:

Plant Materials: The aerial parts of *B. violacea* were collected at the flowering stage from Phu Luang Wildlife Sanctuary in Loei Province, Thailand by P. Sutthisaksopon, K. Romthong, and T. Srisuk on 11th July 2020. The voucher specimen was deposited in the Department of National Parks, Wildlife and Plant Conservation Herbarium (BKF), and Queen Sirikit Botanic Garden Herbarium (QBG). Stem and leaf were cut separately into small pieces, air-dried in the shade, and stored in the dark at room temperature until use.

***Extraction and Preparation of Solvent Fractions*:**
Sequential Extraction: The dried stems of *B. violacea* (36.37 g) were subjected to successive solvent extraction (1:5 w/v) by sonication for 2 hours. The extraction was done with different solvents in increasing order of polarity starting from *n*-hexane, dichloromethane, ethyl acetate, and methanol sequentially.[10,11] Each solvent was done in triplicate and then the marc was air dried and later extracted with other solvents. All the extracts were evaporated to dryness and reserved for preliminary phytochemical and cytotoxicity screening.

Liquid-Liquid Partition: The dried leaf of *B. violacea* (89.56 g) were extracted repeatedly by sonication with 50% aqueous ethanol (3 x 450 mL) for 2 hours and then filtered. The combined filtrates were concentrated under reduced pressure. The ethanolic extract was partitioned with *n*-hexane, dichloromethane, ethyl acetate, and *n*-butanol sequentially. [10,11] The solvent from each fraction was removed and reserved for preliminary phytochemical and cytotoxicity screening.

Preliminary Phytochemical Screening: Preliminary phytochemical screening was performed using thin layer chromatography (TLC). Spots were visualized under short and long wavelength ultraviolet lights, and the plates were sprayed immediately with anisaldehyde or ferric chloride or dragendorff's spray reagents. The screening test was made for terpenoids, sterols, flavonoids, and alkaloids as main compounds found in the genus of *Boesenbergia*.[12-20]

Spray Reagents: Anisaldehyde reagent was used for detection of terpenoids and sterols, while 1% iron (III) chloride was used for detection of tannins and other phenolic compounds, and dragendorff's reagent was used for detection of alkaloids compound.[21]

Cell Cultures: All cells were obtained from the American Type Culture Collection (ATCC, Manassas, VA). Colon cancer (LoVo), breast cancer (MDA-MB-231), and prostate cancer (PC3) cells were maintained as a monolayer in RPMI-1640 medium. Skin cancer (A375, A431), bone cancer (SW1353) cells were as in Dulbecco's Modified Eagle's Medium (DMEM medium), and Vero normal cell were as in Eagle's Minimum Essential Medium (EMEM medium). The cell line was supplemented with 10% FBS, 100 U/mL penicillin, and 100 µg/mL streptomycin at 37°C in a humidified atmosphere of 5% CO_2. The medium refreshed every 2 - 3 days. After 90% of confluence, the culture cells were detached with 0.25% trypsin-EDTA and subcultured.[22,23]

MTT Assay*:* The cytotoxicity of aerial parts extract (stem and leaf) was examined by cell proliferation analysis using MTT assay. MTT is a yellow water-soluble tetrazolium dye that is reduced by live cells to a purple formazan product that is insoluble in aqueous solutions. The amount of MTT-formazan produced can be determined by spectrophotometry once solubilized in a suitable solvent such as DMSO. The exact cellular mechanism of MTT reduction into formazan is not well understood, but likely involves reaction with NADH or similar reducing molecules that transfer electrons to MTT.[22,23]

LoVo and PC3 cells were seeded at a density of $8x10^3$ cells/well in 96-well plate and treated with crude extract at the various concentrations (0 - 1000 µg/mL), whereas the control group treated with DMSO at the final level is not more than 0.5%. After 48 h incubation, the growth medium was removed, 100 µL of 0.5 mg/mL MTT solution was added to each well and incubated for 2 h at 37°C. Then, the supernatant was discarded and added 100 µL of DMSO to each well for solubilized formazan crystals. The absorbance was measured at 570 nm using a microplate reader (Multiskan EX, Thermo electron corporation, Finland). All experiments were performed in triplicate. A375 and A431 cells ($1x10^4$ cells/well) and SW1353, MDA-MB-231, Vero cells ($5x10^3$ cells/well) were harvested and followed by the above method. **All data were analyzed using** GraphPad Prism 7.0 software (GraphPad Software Inc., San Deigo, CA), and the half maximal inhibitory concentration (IC_{50}) value was calculated.[22,23] Cisplatin,[24] Doxorubicin,[25-28] Ellipticine,[29] and 5-Fluoruracil[30] were used as reference drugs.

Results and Discussion: Leaf was extracted by liquid-liquid partition method. This method was less time-consuming and used less organic solvents. However, emulsion formation occurred. Therefore, the extraction method for stem was changed from the liquid-liquid partition to sequential extraction that formed no emulsion. Percentage yield production of *B. violacea* aerial parts extracted by sequential extraction and partition methods with different solvents is shown in Table 1. The results showed a similar percentage yield of both parts, except for the aqueous fraction of leaf which gave the highest percentage yield.

Table 1. The extraction and weight percentage yield of stem and leaf of *B. violacea*.

Aerial parts	Extraction	Fraction/Extract	Weight of extract (g)	Percentage yield
Stems	Sequential Extraction	*n*-Hexane	0.500	1.370
		Dichloromethane	0.330	0.900
		Ethyl acetate	0.130	0.357
		Methanol	1.320	2.540
Leaves	Partition	Crude (50% aqueous ethanol)	-	-
		n-Hexane	0.197	0.220
		Dichloromethane	0.287	0.320
		n-Butanol	2.678	2.990
		H_2O	12.489	13.945

Preliminary detection of chemical composition in the extracts was performed on silica gel TLC plates. Spots were visualized under short and long wavelength of ultraviolet lights, and the plates were immediately sprayed with anisaldehyde spray reagents for the detection of terpenoids and sterols, with ferric chloride spray reagents for phenolic compounds, and with dragendorff's spray reagents for alkaloids. The spray reagents used provided some information on the composition of the extracts. The *n*-hexane extract from the stem showed violet and blue colors with anisaldehyde reagent revealing the presence of terpenoids and sterols in the stem and dark zones for phenolic compounds with ferric chloride whereas dragendorff's reagent showed no detection of orange color for alkaloids. Moreover, dichloromethane, ethyl acetate, and methanol extracts of the stem part also showed similar phytochemicals to the *n*-hexane extract. The red color under long wave UV light, indicating the presence of chlorophyll, was shown in the dichloromethane, ethyl acetate, and methanol extracts, but not in the *n*-hexane extract (Figure 2).

Likewise, the TLC chromatogram of the leaf part of *B. violacea* including *n*-hexane, dichloromethane, and *n*-butanol fractions also gave the same chemical screening results as in the stem part (Figure 3).

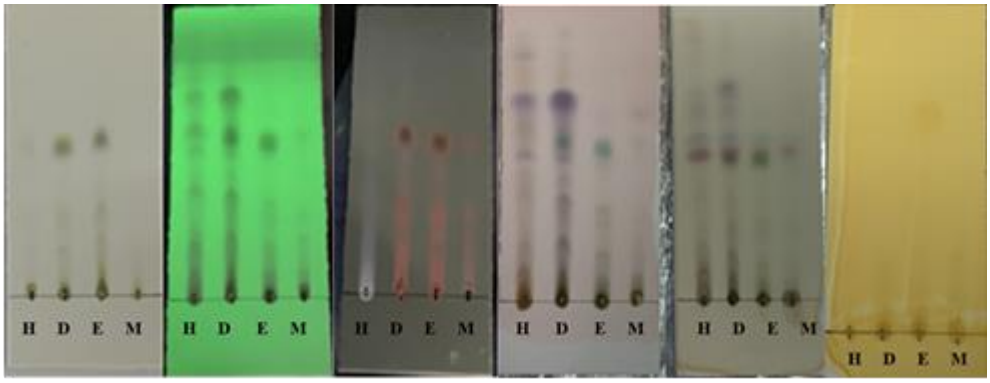

Figure 2. TLC chromatogram of *B. violacea* stems extracts by sequential extraction.

The separation of each extract was performed on silica gel TLC plates; mobile phase – 100% dichloromethane; Lane: H (*n*-Hexane extract), D (Dichloromethane extract), E (Ethyl acetate extract), and M (Methanol extract).

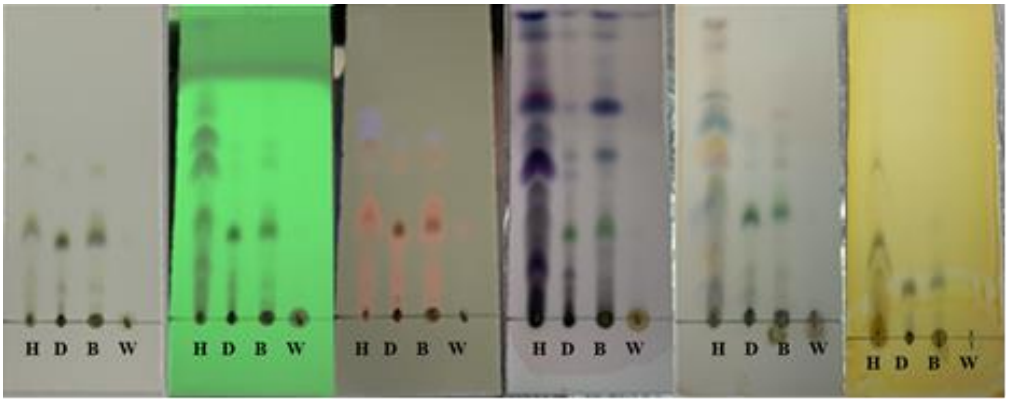

Figure 3. TLC chromatogram of *B. violacea leaf* extracts by partition.
The separation of each fraction was performed on silica gel TLC plates;
mobile phase – 100% dichloromethane;
Lane: H (*n*-Hexane fraction), D (Dichloromethane fraction), B (*n*-Butanol fraction), and W (aqueous fraction).

Table 2. Preliminary detection of chemical composition in the extracts of *B. violacea*.

Aerial parts	Fraction/ Extract	Terpenoids	Sterols	Flavonoids	Alkaloids
Stem	*n*-Hexane	+	+	+	-
	Dichloromethane	+	+	+	-
	Ethyl acetate	+	+	+	-
	Methanol	+	+	+	-
Leaf	*n*-Hexane	+	+	+	-
	Dichloromethane	+	+	+	-
	n-Butanol	+	+	+	-
	H_2O	-	-	-	-

Subsequently, the extracts of stem and leaf of *B. violacea* were screened for their effects of inhibiting various types of cancer including skin, colon, bone, breast, and prostate cancers. *n*-hexane extract of the stem was found to have the best efficacy in inhibiting skin cancer cells A375 and A431, and LoVo type colon cancer cells with the IC_{50} values of 31.40 ± 1.03, 89.66 ± 1.12, and 62.34 µg/mL, respectively, whereas the other extracts showed slight inhibitory effects to all cancer cell lines tested as shown in Tables 3 and 4. Interestingly, the *n*-hexane extract was not toxic to the normal cell (Vero) with the IC_{50} value of 183.30 ± 1.06 µg/mL. It is more likely that all extracts containing terpenoids, sterols, and flavonoids with a variety of different chemical structures may give the different cytotoxicity results. Moreover, the presence of chlorophyll in all extracts, except in the *n*-hexane extract of stem, may interfere the cytotoxic activity.

Table 3. *In vitro* cytotoxic activity of *B. violacea* stem extracts against A375, A431, LoVo, SW1353, MDA-MB-231, PC3 cancer cell lines and Vero normal cell line.

Extract	IC_{50} (µg/mL)						
	A375	A431	LoVo	SW1353	MDA-MB-231	PC3	Vero
n-Hexane	31.40 ± 1.03	89.66 ± 1.12	62.34	>1,000	NT	NT	183.3± 1.06
Dichloromethane	>1,000	287.4	383.5	>1,000	NT	NT	NT
Ethyl acetate	53.11	176.3	99.34	>1,000	141.7	417.9	NT
Methanol	471.3	>1,000	~1000	>1,000	>1,000	>1,000	NT
Cisplatin	-	-	-	-	-	40.95	-
Doxorubicin	0.005	0.73	-	81.53	0.92	-	-
Ellipticine	-	-	-	-	-	-	0.48
5-Fluoruracil	-	-	27.66	-	-	-	-

-NT: not being tested

Table 4. *In vitro* cytotoxic activity of *B. violacea* leaf extracts against A375, A431, LoVo, SW1353, MDA- MB-231, PC3 cancer cell lines and Vero normal cell line.

Fraction	IC_{50} (µg/mL)						
	A375	A431	LoVo	SW1353	MDA-MB-231	PC3	Vero
n-Hexane	143.8	109.9	361.0	587.2	NT	NT	NT
Dichloromethane	>1,000	NT	>1,000	NT	NT	NT	NT
n-Butanol	194.3	576.0	>1,000	>1,000	>1,000	867.4	NT
H_2O	>1,000	>1,000	>1,000	>1,000	>1,000	654.5	NT
Cisplatin	-	-	-	-	-	40.95	-
Doxorubicin	0.005	0.73	-	81.53	0.92	-	-
Ellipticine	-	-	-	-	-	-	0.48
5-Fluoruracil	-	-	27.66	-	-	-	-

NT: not being tested

Conclusion:

Stem and leaf of *B. violacea*, were extracted by sequential extraction and partition, respectively, based on a method of increasing solvent polarity. Evaluation of cytotoxicity of the extracts by MTT assay was performed. The study demonstrated that the stem extracts of *B. violacea* is more potential than leaf extracts in cytotoxic activity. Phytochemical screening by TLC revealed that the aerials parts of this plant contained terpenoids, sterols, and flavonoids as main compounds which related to the phytochemical found in the *Boesenbergia* species.[16] Further isolation and characterization of the compounds responsible for the anticancer activity will be investigated.

Acknowledgements:

We wish to thank Srinakharinwirot University Research Grant (020/2563) for supporting this work. Department of Chemistry, Faculty of Science, Srinakharinwirot University is gratefully acknowledged for providing research facilities. Dr. Teerawat Srisuk and Mr. Kittitat Romthong are acknowledged for their assistances in the field. We would also like to thank Phu Luang Wildlife Sanctuary staff for their kindly help and hospitality during the fieldwork.

References:

1. Larsen K. Tidsskr. 1964;60:165-179
2. Phokham B, Intharapichai K, Wongsuwan P, Picheansoonthon C. Taiwania. 2015;60:77-80.
3. Larsen K. Nord. J. Bot. 2002;22:409-417.
4. Picheansoonthon C, Koonterm S. Taiwania. 2008;53:248-257.
5. Suksathan P, Triboun. Edinb. J. Bot. 2004;60:513-516.
6. Rai PK, Lalramnghinglova H. J. Med. Plant Res. 2010;4:1301-1307.
7. Pradhan BK, Badola HK. J. Ethnobiol. Ethnomed. 2008;4:22.
8. Tiyaworanant S. Telopea. 2010;12:479-484.
9. Mood JD, Veldkamp JF, Dey S, Prince LM. Gard Bull (Singapore). 2014;66:215-231
10. Gupta VK, Shukla C, Bisht GRS, Saikia D, Kumar S, Thakur RL. Lett. Appl. Microbiol. 2010;52:33-40.
11. Policegoudra RS, Divakar S, Aradhyu SM. J. Appl. Microbiol. 2007;102:1594-1602.
12. Jaipetch T, Kanghae S, Pancharoen O, Patrick VA, Reutrakul V, Tuntiwachwuttikul P, White AH. Aust. J. Chem. 1982;35:351-361.
13. Tuchinda P, Reutrakul V, Claeson P, Pongprayoon U, Sematong T, Santisuk T, Taylor WC. Phytochemistry. 2002;59:169-173.
14. Win NN, Awale S, Esumi H, Tezuka Y, Kadota S. J. Nat. Prod. 2007;70:1582-1587.
15. Jaipetch T, Reutrakul V, Tuntiwachwuttikul P, Santisuk T. Phytochemistry. 1983;22:625-626.
16. Jing LJ, Mohamed M, Rahmat A, Baker MFA. J. Med. Plant Res. 2010;4:027-032.
17. Trakoontivakorn G, Nakahara K, Shinmoto H, Takenaka M, Onishikameyama M, Oho H, Yoshida M, Nagata T, Tsushida T. J. Agric. Food Chem. 2001;49:3046-3050.
18. Cheenpracha S, Karalai C, Ponglimanont C, Subhadhirasakul S, Tewtrakul S. Bioorg. Med. Chem. 2006;14:1710-1714.
19. Sukari MA, Mohdsharif NW, Yap ALC, Tang SW, Neoh SW, Rahmani M, Ee GCL, Taufiqyap YH, Yusof UK. Malaysian J. Anal. Sci. 2008;12:638-644.
20. Jantan IB, Basni I, Ahmad AS, Ali NAM, Ahmad AR, Ibrahim H. Flavour Fragr. J. 2001;16:110-112.
21. Wagner H, Bladt S. Plant Drug Analysis. 2nd Edition. Heidelberg, New York, Springer-Verlag Berlin. 1996.
22. Kumar P, Nagarajan A, Uchil PD. Cold Spring Harb Protoc. 2018;469-471.
23. Riss TL, Moravec RA, Niles AL, Duellman S, Benink HA, Worzella TJ, Minor L. NCBI. 2016;1-25.
24. Li QQ, Wang G, Reed E, Huang L, Cuff CF. Basic Clin. Pharmacol. Toxicol. 2010;107:868-876.
25. Das SM, Ghosh R, Patra A, Hazra B. Bioorg. Med. Chem. 2007;15:3672-3687.
26. Zhang X, Raghavan S, Ihnat M, Thorpe JE, Disch BC, Bastian A, Baileydowns LC, Dybdalhargreaves NF, Rohena CC, Hamel E, Mooberry SL, Gangjee A. Bioorg. Med. Chem. 2014;22:3753-3772.
27. Van Oosterwijk JG, Herpers B, Meijer D, Briairede Bruijn IH, Cletonjansen AM, Gelderblom H, Bovee JVMG. Ann Oncol. 2012;23:1617-1626.
28. Mallavadhani UV, Prasad CV, Shrivastava S, Naidu VGM. Eur. J. Med. Chem. 2014;83:84-91.
29. Pingaew R, Saekee A, Mandi P, Nantasenamat C, Prachayasittikul S, Ruchirawat S, Prachayasittikul V. 2014;85:65-76.
30. Zhu DJ, Chen XW, Zhang WJ, Wang JZ, Ouyang MZ, Zhong Q, Liu CC. Am. J. Cancer. Res. 2015;5:2000-2011.

SP13_042_PF: MICROBIAL TRANSFORMATION OF HEXAHYDROCURCUMIN

Jaranwit Srijun,[1] Oratai Sukcharoen,[2] Waraluck Chaichompoo,[1] Wachirachai Pabuprapap,[1] Teerawut Thothaisong,[1] Ratchanaporn Chokchaisiri,[3] Ek Sangvichien,[4] Apichart Suksamrarn[1,*]

[1]Department of Chemistry and Center of Excellence for Innovation in Chemistry, Faculty of Science, Ramkhamhaeng University, Bangkok 10240, Thailand
[2]Department of Biotechnology, Faculty of Science, Ramkhamhaeng University, Bangkok 10240, Thailand
[3]Department of Chemistry, School of Science, University of Phayao, Phayao 56000, Thailand
[4]Department of Biology, Faculty of Science, Ramkhamhaeng University, Bangkok 10240, Thailand
*e-mail: asuksamrarn@yahoo.com

Abstract:

Curcumin (**1**), the main polyphenolic constituent of the spice turmeric (*Curcuma longa* rhizomes), possesses a wide range of pharmacological activities. In order to generate potential curcumin analogues, compound **1** was chemically modified by catalytic hydrogenation to yield a major analogue, hexahydrocurcumin (**2**). Compound **2** was further structurally modified using biotransformation by *Bacillus megaterium* NRRL B-938 to afford tetrahydrocurcumin (**3**) and by *Cunninghamella echinulata* NRRL 1386 to yield a mixture of hexahydrocurcumin-4′-*O*-β-glucoside (**4**) and hexahydrocurcumin-4′′-*O*-β-glucoside (**5**). The structures of these compounds were elucidated on the basis of spectroscopic and physical data and by comparisons with the reported values.

Introduction:

Curcumin (**1**) is the major compound isolated from the rhizome of *Curcuma longa* and other *Curcuma* species, which is the major ingredient of the spice, flavoring agent, coloring agent, and medicine for treatment of inflammation and sprain in India, China, and other Asian countries.[1,2] In previous studies, curcumin and analogues have demonstrated a variety of pharmacological properties including anti-inflammatory, anti-depressant, anti-tumor, anti-oxidant, anti-proliferative, anti-angiogenic, anti-microbial, and hepatoprotective activities.[3-5] Hexahydrocurcumin (**2**), a hydrogenated analogue of curcumin, is one of the major metabolites of curcumin. Previous studies revealed that this compound presents higher chemical stability and bioavailability than curcumin.[6-8] Our previous studies have demonstrated that compound **2** together with 5-fluorouracil exerts a synergistic effect in inhibiting the growth of HT-29 cells by cyclooxygenase (COX)-2 expression.[9] Compound **2** also protects the brain from cerebral injury by decreasing oxidative stress, inflammation, and apoptosis.[10] In addition, we also found that **2** can preserve blood-brain barrier from cerebral ischemia/reperfusion injury and reduced brain edema formation.[11]

Microbial transformation can be used as biological synthesis to produce new derivatives of natural compounds. The employment of such processes is constantly growing because the reaction conditions are green, mild and stereoselectivity. In addition, regioselectivity can be achieved and the functionalization on remote non-activated positions is possible.[12] This process is aided by major range of microorganisms and their products such as bacteria, fungi and enzymes. The obtained metabolites may increase solubility and provide sites for further modification.[13] Previous studies of biotransformation of curcumin (**1**) by a variety of microorganisms have been reported. Hydroxylation, reduction, oxidation and glycosidation are the transformations that have frequently been observed.[14-17] However, microbial transformation of analogue **2** has not been reported. In this study, we herein report the isolation and catalytic hydrogenation of curcumin (**1**), and structural modification of analogue **2** to metabolites by selected microorganisms, *Bacillus megaterium* NRRL B-938, and *Cunninghamella echinulata* NRRL 1386.

Methodology:

1. General

Optical rotations were measured on a JASCO 1020 polarimeter. ^{1}H- and ^{13}C-NMR spectra were recorded on a Bruker ASCEND 400 spectrometer. High resolution mass spectra were obtained using a Bruker micrOTOF QII mass spectrometer. Unless indicated otherwise, column chromatography was carried out using Merck silica gel 60 (particle size less than 0.063 mm and 0.063-0.200 mm) and Sephadex LH-20 (Pharmacia). For TLC, Merck pre-coated silica gel 60 F_{254} plates were used. Spots on TLC were detected under UV light and by spraying with anisaldehyde-H_2SO_4 reagent followed by heating.

*2. Isolation and Identification of Curcumin (**1**)*

The crude curcuminoid was purchased from Thai-China Flavours and Fragrances (TCFF). The natural curcumin (**1**) was obtained as described previously.[18]

*2.1 Curcumin (**1**)*

Yellow powder; ^{1}H- and ^{13}C-NMR data are given in Table 1; HR-TOFMS (ES^{-}): *m/z* 367.1181 (calcd. for $C_{21}H_{19}O_6$, 367.1187).

*3. Catalytic Hydrogenation of Hexahydrocurcumin (**2**)*

To a solution of compound **1** (1.0 g, 2.7 mmol) in EtOH (150 mL) was added 10% Pd-C (500 mg). After degassing, the mixture was hydrogenated at room temperature and at atmospheric pressure for 24 h. The mixture was filtered through a Celite® column and the solvent was evaporated. The residue was purified by column chromatography using CH_2Cl_2-MeOH (gradient elution of 100:0.1 to 100:2) to afford compound **2** (780 mg, 78%). The spectroscopic data of compound **2** were consistent with the reported values.[18]

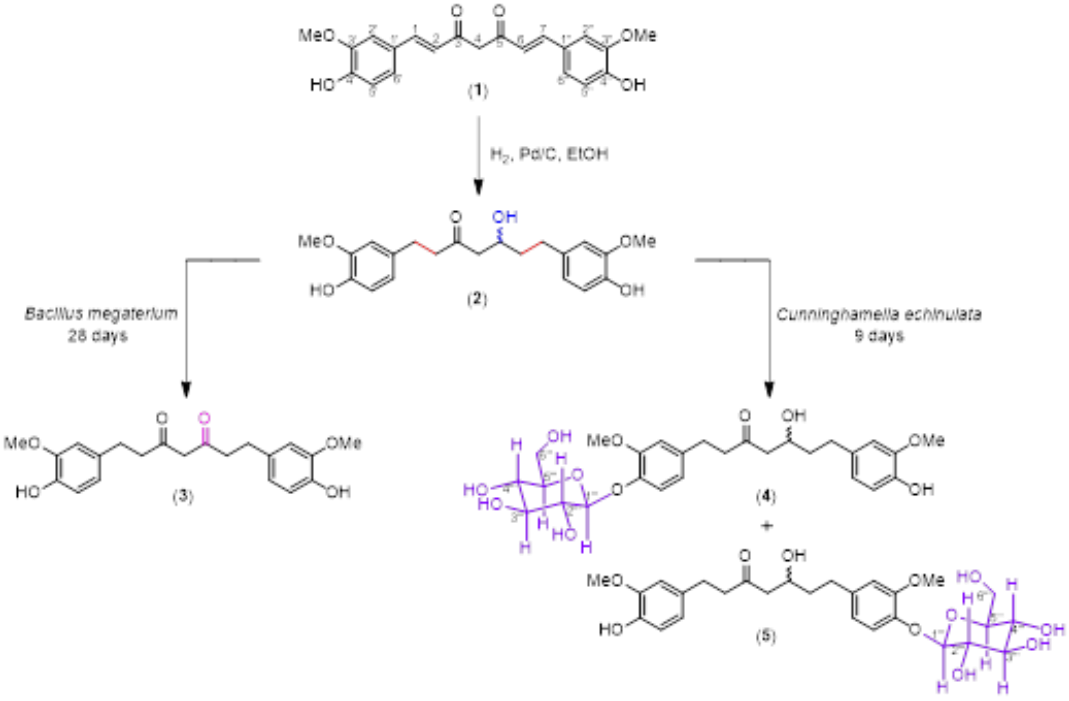

Figure 1. Catalytic hydrogenation of curcumin (**1**) and biotransformation of hexahydrocurcumin (**2**)

Table 1. ^{1}H-NMR (400 MHz) and ^{13}C-NMR data (100 MHz) of compounds **1**-**5**.

Position	Compound 1[a]		Compound 2[a]		Compound 3[a]		Compounds 4 and 5[b,x]	
	δ_H (mult., *J* in Hz)	δ_C	δ_H (mult., *J* in Hz)	δ_C	δ_H (mult., *J* in Hz)	δ_C	δ_H (mult., *J* in Hz)	δ_C
1	7.57 (*d,* 15.7)	140.5	2.80 (*t,* 7.3)	31.4	2.83 (*t,* 7.4)	31.3	2.50-2.60 (*m*)	32.5
2	6.47 (*d,* 15.7)	122.9	2.69 (*t,* 7.3)	38.3	2.53 (*t,* 7.4)	40.4	2.76-2.82 (*m*)	30.3 30.4
3	-	183.3	-	211.4	-	193.2	-	211.7 212.0
4	5.78 (*s*)	101.1	2.71 (*m*) 2.58 (*m*)	45.4	5.40 (*s*)	99.8	2.76-2.82 (*m*)	46.2 46.5
5	-	183.3	4.01 (*m*)	66.8	-	193.2	4.00 (*m*)	68.2 68.3
6	6.47 (*d,* 15.7)	122.9	1.75 (*m*) 1.60 (*m*)	38.3	2.53 (*t,* 7.4)	40.4	1.65-1.73 (*m*)	40.3 40.5
7	7.57 (*d,* 15.7)	140.5	2.52 (*m*)	29.3	2.83 (*t,* 7.4)	31.3	2.50-2.60 (*m*) 2.65[c]	51.4
1'	-	127.7	-	133.7	-	132.5	-	137.8 138.6
2'	7.03 (*brs*)	109.6	6.61-6.67 (*m*)	111.0	6.66 (*brs*)	110.9	6.84 (*brs*) 6.85 (*brs*)	114.1 114.2
3'	-	147.8	-	146.4	-	146.4	-	150.9
4'	-	146.8	-	144.0	-	144.0	-	146.2 146.4
5'	6.91 (*brd,* 8.1)	121.8	6.61-6.67 (*m*)	120.8	6.63 (*d,* 7.6)	120.8	6.71 (*brd,* 8.2) 6.72 (*brd,* 8.2)	121.9 122.0
6'	7.10 (*brd,* 8.1)	114.8	6.80 (*d,* 7.9)	114.4	6.81 (*d,* 7.7)	114.3	7.06 (*d*, 8.2) 7.07 (*d*, 8.2)	118.4
1''	-	127.7	-	132.5	-	132.5	-	134.1 135.0
2''	7.03 (*brs*)	109.6	6.61-6.67 (*m*)	110.9	6.66 (*brs*)	110.9	6.75 (*d,* 1.7) 6.76 (*d*, 1.7)	113.2 113.3
3''	-	147.8	-	146.4	-	146.4	-	149.0
4''	-	146.8	-	143.7	-	144.0	-	145.6 145.8
5''	6.91 (*brd,* 8.1)	121.8	6.61-6.67 (*m*)	120.8	6.63 (*d,* 7.6)	120.8	6.68 (*brd,* 8.0) 6.69 (*brd,* 8.0)	116.3
6''	7.10 (*brd,* 8.1)	114.8	6.80 (*d,* 7.9)	114.2	6.81 (*d,* 7.7)	114.3	6.60 (*dd,* 8.0, 1.7) 6.61 (*dd,* 8.0, 1.7)	121.8 121.9
1'''	-	-	-	-	-	-	4.82 (*d*, 6.0)	103.2 103.3
2'''	-	-	-	-	-	-	3.43-3.50 (*m*)	75.1
3'''	-	-	-	-	-	-	3.43-3.50 (*m*)	77.9
4'''	-	-	-	-	-	-	3.38-3.40 (*m*)	71.5
5'''	-	-	-	-	-	-	3.38-3.40 (*m*)	78.3
6'''	-	-	-	-	-	-	3.66-3.71 (*m*) 3.86[d]	62.6
3'-OCH_3	3.93 (*s*)	56.0	3.83 (*s*)	55.9	3.84 (*s*)	55.8	3.83 (*s*) 3.84 (*s*)	56.8
3''-OCH_3	3.93 (*s*)	56.0	3.84 (*s*)	55.9	3.84 (*s*)	55.8	3.80 (*s*) 3.82 (*s*)	56.5
4'-OH	5.85 (*brs*)	-	5.52 (*brs*)	-	5.47 (*brs*)	-	-	-
4''-OH	5.85 (*brs*)	-	5.54 (*brs*)	-	5.47 (*brs*)	-	-	-

[a] Recorded in $CDCl_3$.
[b] Recorded in CD_3OD.
[c,d] Overlapping signals.
[x]Assignments of individual ^{1}H- and ^{13}C-NMR signals to compounds **4** and **5** could not be made.

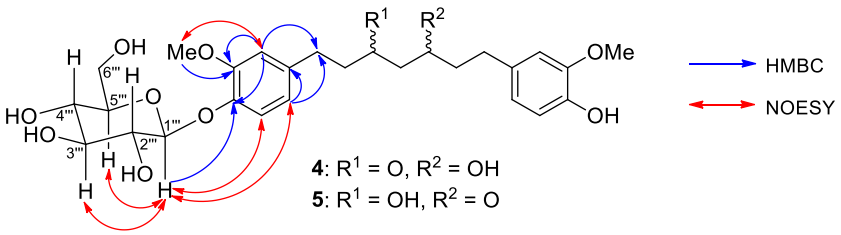

Figure 2. Key HMBC and NOESY correlations of compounds **4** and **5**

*3.1 Hexahydrocurcumin (**2**)*

White amorphous solid; ^{1}H- and ^{13}C-NMR data are given in Table 1; HR-TOFMS (ES^{+}): *m/z* 397.1638 (calcd. for $C_{21}H_{26}O_6$ + Na, 397.1621).

4. Microorganism, Media and Culture Conditions

B. megaterium NRRL B-938 and *C. echinulata* NRRL 1386 were obtained from NRRL (ARS Culture Collection, Illinois, USA). The stock culture was grown on a potato dextrose agar (Merck, Darmstadt, Germany) for 7 days at 28 ºC. Erlenmeyer flasks (250 mL), each containing 100 mL of liquid medium consisting of 0.1% peptone (Bacto, MD, USA), 0.1% yeast extract (Bacto, MD, USA), 0.1% meat extract (Himedia, Mumbai, India) and 0.5% glucose (Sigma-Aldrich, MO, USA) were inoculated with each freshly obtained cultured from the agar slant on a rotary shaker at 200 rpm. After cultivation at ambient temperature for 24 h, the stock of hexahydrocurcumin (**2**) which was prepared by dissolving 50 mg of compound **2** in 1 mL of DMSO was added to each flask, and was continued incubation for appropriate times. Culture control consisted of fermentation blank in which each of microbes was grown under identical condition but without substrate.

*5. Biotransformation of Hexahydrocurcumin (**2**)*

Hexahydrocurcumin (500 mg) was fed to the culture of *B. megaterium* and incubated for 28 days. The culture was filtered and the broth was extracted with EtOAc, washed with water and the solvent was concentrated *in vacuo*. The crude extract (654.9 mg) was subjected to Sephadex LH-20 column chromatography eluting with MeOH to give three fractions. Fraction 1 was subjected to column chromatography eluting with 5% MeOH in CH_2Cl_2 to afford compound **3** (14.9 mg, 7%), based on the unrecovered starting material.

*5.1 Tetrahydrocurcumin (**3**)*

Off-white amorphous solid; ^{1}H- and ^{13}C-NMR data are given in Table 1; HR-TOFMS (ES^{-}): *m/z* 371.1519 (calcd. for $C_{21}H_{23}O_6$, 371.1500).

Substrate **2** (500 mg) was dissolved in DMSO, distributed among 80 Erlenmeyer-flask cultures of *C. echinulata* and incubated for 9 days, after which the cultures were processed as indicated above to yield a mixture of compounds **4** and **5** (9.2 mg, 2%), based on the unrecovered starting material.

*5.2 Mixture of hexahydrocurcumin-4'-O-β-glucoside (**4**) and hexahydrocurcumin-4''-O-β-glucoside (**5**)*

Off-white sticky solid; ^{1}H- and ^{13}C-NMR data are given in Table 1; HR-TOFMS (ES^{-}): *m/z* 535.2176 (calcd. for $C_{27}H_{35}O_{11}$, 535.2185).

Results and Discussion:

Microbial transformation has been studied for recent years that allows for the structural modification of a compound through an environmentally friendly approach. Microorganisms including fungi and bacteria are capable of producing a great variety of enzymes in a short period of time as a result of a high rate of cell multiplication. In this respect, a reasonable number of compounds of various biological interests can be obtained by microorganisms-driven transformations of natural products.[19] In the present study, firstly, catalytic hydrogenation of curcumin (**1**), with palladium on charcoal as a catalyst, furnished hexahydrocurcumin (**2**) in 78% yield. Biotransformation of compound **2** by *B. megaterium* NRRL B-938, and *C. echinulata* NRRL 1386 have then been investigated. The oxidized and glycosylated metabolites at different position were obtained depending on the bioenzyme of each strain that could be concluded in Figure 1. The spectroscopic data of compounds **1** and **2** were consistent with the reported values.[18] The oxidized analogue **3** was biotransformed by *B. megaterium* from the curcumin analogue **2** in 7% yield. The spectroscopic data of compound **3** were in agreement with the structure (see Figure 1) and were consistent with the reported values.[20] In addition, a mixture of hexahydrocurcumin glucosides **4** and **5** was obtained by *C. echinulata* in 2% yield. The structures of **4** and **5** were elucidated on the basis of spectroscopic data (2D NMR and mass spectra). The products **4** and **5** are approximate 1:1 inseparable mixture. At this stage, no further investigation for the separation of these two compounds was attempted.

A mixture of compounds **4** and **5** was obtained as a yellow sticky solid. The molecular formula was assigned as $C_{27}H_{36}O_{11}$ from the HR-TOFMS (ES ionization, negative ion mode, *m/z* 535.2185, $C_{27}H_{35}O_{11}$). Compounds **4** and **5** mixture showed almost identical ^{1}H-NMR data. The significant differences were the resonance positions of two methoxy groups of these two isomers, which appeared at δ_H 3.84/3.83 and 3.82/3.80 together with two keto carbonyl carbon signals presented at δ_C 212.0 and 211.7. The ^{1}H-NMR spectrum showed signals for one carbinolic proton (δ_H 4.00) and resembled that of **2**, except for the presence of a glucosyl moiety [(δ_H 4.82, *d*, *J* = 6.0 Hz, H-1‴), (δ_H 3.43-3.50, *m*, H-2‴ and H-3‴), (δ_H 3.38-3.40, *m*, H-4‴, H-5‴), and (δ_H 3.86 and δ_H 3.66-3.71, *m*, H-6‴)]. The ^{13}C-NMR spectrum revealed the carbon signals including those of a glucosyl group (δ_C 103.3/103.2, 78.3, 77.9, 75.1, 71.5, and 62.6) whose glycosidic linkage was shown to be β-form based on the magnitude of the coupling constant of the anomeric proton (*J* = 6.0 Hz). Inspection of the HSQC and DEPT spectra of the aglycone moiety confirmed the presence of two methyl, five methylene, seven methine, and seven quaternary carbons, one of which was for the carbonyl carbon (Table 1). All the protons and carbons could be fully assigned except for its epimeric position. It should be noted that several ^{13}C NMR signals of the two isomers are superimposed.

In the HMBC spectrum, the correlations between signal at δ_H 4.82 (Glc-1‴) and δ_C 146.4/146.2 and 145.8/145.6 (C-4′ and C-4″) were observed, which indicated that the glucose unit was attached at the 4′- or 4″-position of the aglycone (Figure 2). The relative stereochemistry at C-4′ or C-4″ was established as β, by the NOESY correlation experiment (see Figure 2). The signal at δ 4.82 (H-1‴) correlated with those at δ 7.07/7.06 (H-6′), and δ 3.43-3.50 (H-2‴ and H-3‴). However, the absolute configuration at C-5 remains to be clarified. On the basis of the above evidences, the structures of compounds **4** and **5** were established as hexahydrocurcumin-4′-*O*-β-glucoside and hexahydrocurcumin-4″-*O*-β-glucoside, respectively.

Conclusion:

Microbial transformation of hexahydrocurcumin by *B. megaterium* NRRL B-938 and *C. echinulata* NRRL 1386 afforded tetrahydrocurcumin and a mixture of hexahydrocurcumin glucosides. These metabolites will be useful for the ongoing research on structural modification and pharmacological evaluation of curcumin analogues.

Acknowledgements:

This work was supported by The Thailand Research Fund (DBG6180030), the Center of Excellence for Innovation in Chemistry (PERCH-CIC), Ministry of Higher Education, Science, Research and Innovation and the Faculty of Science, Ramkhamhaeng University.

References:

1. Amalraj A, Pius A, Gopi S, Gopi S. J Tradit Complement Med. 2017;7:205–233.
2. Paramasivam M, Poi R, Banerjee H, Bandyopadhyay A. Food Chem. 2009;113:640–644.
3. Ahmad RS, Hussain MB, Sultan MT, Arshad MS, Waheed M, Shariati MA, Plygun S, Hashempur MH. Evid Based Complementary Altern Med. 2020;7656919:1–14.
4. Ghosh S, Banerjee S, Sil PC. Food Chem Toxicol. 2015;83:111–124.
5. Jayaprakasha GK, Rao LJ, Sakariah KK. Food Chem. 2006;98:720–724.
6. Dempe JS, Scheerle RK, Pfeiffer E, Metzler M. Mol Nutr Food Res. 2013;57:1543–1549.
7. Deters M, Knochenwefel H, Lindhorst D, Koal T, Mayer HH, Hänsel W. Pharm Res. 2008;25:1822–1827.
8. Somparn P, Phisalaphong C, Nakornchai S, Unchern S, Morales NP. Biol Pharm Bull. 2007;30:74–77.
9. Srimuangwong K, Tocharus C, Chintana PY, Suksamrarn A, Tocharus J. World J Gastroenterol. 2012;18:2383–2389.
10. Wicha P, Tocharus J, Janyou A, Jittiwat J, Changtam C, Suksamrarn A, Tocharus C. PLoS ONE 2017;12:e0189211.
11. Wicha P, Tocharus J, Janyou A, Jittiwat J, Chaichompoo W, Suksamrarn A, Tocharus C. Pharmacol Rep. 2020;72:659–671.
12. Smieo Y, Sinistera JV. Mini Rev Org Chem. 2009;6:128–134.
13. Rico-Martínez M, Medina FG, Marrero JG, Osegueda-Robles S. RSC Adv. 2014;4:10627–10647.
14. Zeng J, Yang N, Li X, Zhan J. Nat Prod Commun. 2010;5:77–80.
15. Maehara S, Ikeda M, Haraguchi H, Kitamura C, Nagoe T, Ohashi K, Shibuya H. Chem Pharm Bull. 2011;59:1042–1044.
16. Younis AM, Ibrahim ARS, Ibrahim SM, AboulSoud KA, Kabbash AM. J Pharm Sci Res. 2016;8:1169–1178.
17. An CY, Sun ZZ, Shen L, Ji HF. Food Nutr Res. 2017;61:1–9.
18. Changtam C, de Koning HP, Ibrahim H, Sajid MS, Gould MK, Suksamrarn A. Eur J Med Chem. 2010;45:941–956.
19. Hegazy MEF, Mohamed TA, ElShamy AI, Mohamed AEHH, Mahalel UA, Reda EH, Shaheen AM, Tawfik WA, Shahat AA, Shams KA, Abdel-Azim NS, Hammouda FM. J Adv Res. 2015;6:17–33.
20. Lee SL, Huang WJ, Lin WW, Lee SS, Chen CH, Bioorg Med Chem. 2005;13:6175–6181.

SP13_043_PA: TAUNGTANGYI AND KARAMET AS NATURAL SKIN BEAUTIFIER THANAKA FROM TANINTHARYI TOWNSHIP

Nay Thwe Kyi,[1,*] Tin Moe Thu,[2] Win Myint Oo[2]

[1]Dagon University, Myanmar
[2]Department of Chemistry, Myeik University, Myanmar
*email: dr.naythwekyi55@gmail.com

Abstract:

Thanaka serves as a traditional skincare product for the people of Myanmar. Stems of *Premna integrifolia* L. (Taungtangyi) and *Mansonia gagei* D. (Karamet) are well-known traditional Thanaka of Tanintharyi Region. This research deals with the preliminary phytochemical investigation, nutritional values, elemental analysis and also antimicrobial studies for the stems of Taungtangyi and Karamet Thanaka plants. Phytochemical results showed the presence of various types of compounds, including alkaloids, glycosides, flavonoids, carbohydrates, phenolic compounds, α-amino acids, saponins, starch, tannins and the absence of reducing sugar in both the stems of these plants. The nutritional values by AOAC method focused on a substantial increase in moisture and fiber contents were observed in these Thanaka. The results of elemental analysis by the EDXRF method indicated that essential elements including Ca, K and Fe for beautiful skin were observed in Taungtangyi and Karamet Thanaka. In an assessment of antimicrobial activity by agar diffusion method, Karamet Thanaka contained active ingredients that have antibacterial and antifungal activities whereas Taungtangyi Thanaka contained antibacterial components. Based on the findings of the present researches related to Taungtangyi and Karamet in Tanintharyi Township, it is found that they are suitable for natural skin beautifier Thanaka for healthy skin.

SP13_044_PA: A COMPARATIVE STUDY ON ANTIOXIDANT ACTIVITIES OF PAPAYA LEAVE, SEED AND FLOWER (*Carica Papaya* L.)

Phyu Phyu Aung,[1,*] Nay Mar Soe[2]

[1]Department of Chemistry, Dawei University, Myanmar
[2]Department of Chemistry, Yangon University of Education, Myanmar
*e-mail: puregirl7493@gmail.com
drnaymar.chem.chem@gmail.com

Abstract:

Papaya (*Carica papaya* L.) has been used as food, herbal cosmetic and pharmaceutical products. Papaya products become popular recently because of their potent antioxidant activity. This research, deals with comparative study on the antioxidant activities of papaya leave, seed and flower. The papaya samples were collected from Nyin Maw village, Launglone township, Tanintharyi region, Myanmar. Phytochemical investigation, nutritional values and mineral content of three papaya samples were studied. The results showed that all samples contained alkaloids, carbohydrates, flavonoids, glycosides, phenolic compounds, saponins and steroids. Antioxidant activity of crude extract of each sample was investigated using DPPH (2, 2'-diphenyl-1-picrylhydrazyl) method. The IC_{50} values of EtOH and aqueous extracts of leaves were 32.67 and 40.31µg/mL, those of seed were 34.92 and 39.86 µg/mL and those of flower were 28.29 and 31.59 µg/mL, respectively. The antioxidant activity of ethanol extract of flower was greater than that of leaf and seed extracts. All ethanol extracts displayed more potent antioxidant activity than all aqueous extracts. All extracts showed mild activity when compared to the standard antioxidant ascorbic acid (IC_{50} = 7.99 µg/mL).

SP15_001_OA

SP15_001_OA: ASSESSMENT OF REEF FISH DIVERSTY IN A TURBID WATER ECOSYSTEM OF MU KO ANG THONG

Felipe M G Mattos,[1,*] Thammasak Yeemin,[1] Makamas Sutthacheep,[1] Chinarong Ruangthong[2]

[1]Marine Biodiversity Research Group, Department of Biology, Faculty of Science, Ramkhamhaeng University, Bangkok 10240, Thailand
[2]Chumphon Marine National Park Operation Center 1, Department of National Parks, Wildlife and Plant Conservation, Chumphon Province
*e-mail: felipemgmattos@hotmail.com

Abstract:

Turbid water reefs hold impoverished fish faunas drawing less attention from scientific studies; however, their diversity can be greater than expected. The combination of methods, targeting different species, can be a powerful tool to explore understudied turbid ecosystems. This study aimed to investigate the reef fish diversity of Mu Ko Ang Thong National Park. We combined *in situ* Underwater Visual Census (UVC), with Remote Underwater Video (RUV) using 3 GoPro cameras. Abundance was measured as fish by unit of effort, as methods are different, for RUV the maximum number of individuals in a single frame was considered as the sample's abundance. A total of 35 species were registered by UVC while 44 were seen by RUV, accounting for 50 species combined. The first was more efficient to spot cryptic and territorial species like cardinalfish and damselfish, and was more precise when estimating schooling species abundance, such as *Neopomacentrus* spp. While RUV allowed records of more shy species, including macro-carnivores such as *Scomberoides commersonnianus*. When schooling species were excluded, analysis indicate no significant difference between methods. From the 11 species selected by SIMPER analysis, all were more frequent at RUV, except for *Halichoeres nigrecens*, which was also the single taxa with a significantly higher abundance count by UVC. The use of RUV demonstrated to be efficient in a turbid water reef, where mid-size fish species tend to keep a larger distance from divers. The combination of methods was an efficient tool for fish surveys, with results comparable to a 3-year monitoring database holding 52 registered species.

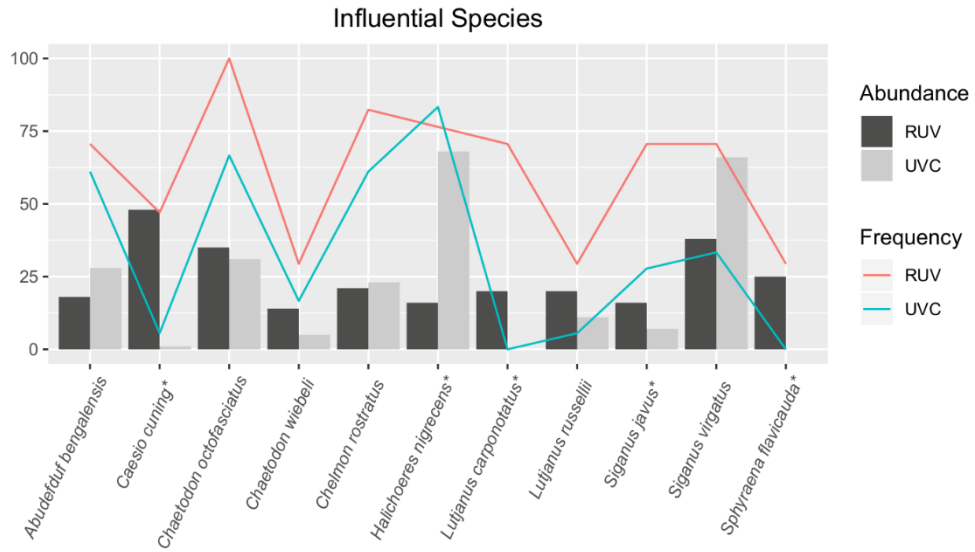

Total abundance and frequency of the 11 species selected by SIMPER. Asterisks indicate significant difference between methods.

SP15_002_PA: THE RECOVERY POTENTIAL OF CORALS AT MU KO SICHANG, THE UPPER GULF OF THAILAND

Sittiporn Pengsakun,* Charernmee Chamchoy, Makamas Sutthacheep, Thamasak Yeemin

Marine Biodiversity Research Group, Department of Biology, Faculty of Science, Ramkhamhaeng University, Huamark, Bangkok, Thailand
E-mail: marine_ru@hotmail.com

Abstract:
Coral communities continue to be threatened by chronic and acute stressors, thus there is an urging need to understand the mechanisms that maintain their persistence. Connectivity of coral populations is a very important aspect of understanding the recovery potential of corals after severe disturbances. This study examined the coral recruitment patterns and their relationships with adult coral communities at Mu Ko Sichang, Chonburi Province, the Upper Gulf of Thailand in 2018. At each study site, live coral cover and benthic components were recorded in three permanent belt-transects of 30×1 m^2. The live scleractinian corals (>5 cm diameter) were identified to genus level. Live coral covers ranged of 8.9-66.1 % while dead coral covers varied between 22.7-43.0 %. The live coral covers at Ko Khang Khao (66.1%) were significantly higher than those of other study sites. The highest coral recruitment was recorded at Ko Kham Noi (25.4 juveniles/m^2). Recruits of *Goniastrea* sp., *Leptastrea* sp., and *Fungia* sp. were frequently found without their adult colonies. The broadcast spawning coral *Favites* spp. showed high evidence of potential self-seeding. The connectivity among reef sites along with local coral recruitment are important factors of consideration, to provide appropriate management strategies, especially for the designation of marine protected areas, enhancing ecotourism and establishing coral reef restoration projects in the Gulf of Thailand.

SP15_003_PA: DIVERSITY OF CORAL RECRUITS FROM SETTLEMENT PLATE EXPERIMENTS FROM MU KO ANGTHONG, THE WESTERN GULF OF THAILAND

Wanlaya Klinthong[1],* Thamasak Yeemin[1], Makamas Sutthacheep[1], Ratanawadee Niemsiri[1], Chinarong Ruangthong[2]

[1] Marine Biodiversity Research Group, Department of Biology, Faculty of Science, Ramkhamhaeng University, Bangkok 10240, Thailand
[2] Chumphon Marine National Park Operation Center 1, Department of National Parks, Wildlife and Plant Conservation, Chumphon Province
*e-mail: klinthong_fai@hotmail.com

Abstract:

Coral recruitment is a critical process on tropical reefs to maimtain coral populations following major disturbances. This study aimed to examine coral recruitment on the reefs at Mu Ko Angthong using the settlement plate experiments. The settlement plates were made of gypsum and submerged at the study sites during April, 2016 to March, 2018. The density of coral recruits on settlement plate experiments at Ko Sam Sao (West) (20 colonies/m^2) was significantly higher than that at Ko Sam Sao (East) (5.29 colonies/m2) and Ko Wua Kan Tang (0.93 colonies/m^2). The highest diversity of coral recruits on settlement plate experiments was also recorded at Ko Sam Sao (East), followed by Ko Sam Sao (West) and KoWua Kan Tang. Pocilloporiids were the most dominant taxa of coral recruits on the settlement plate experiments at Ko Sam Sao (West). This study provides important baseline scientific data to the understanding of coral recruitment patterns in Mu Ko Angthong. Filamentous algae were also the most dominant group on the settlement plates. A long-term monitoring program for coral recruitment in other island groups in the Western Gulf of Thailand is needed.

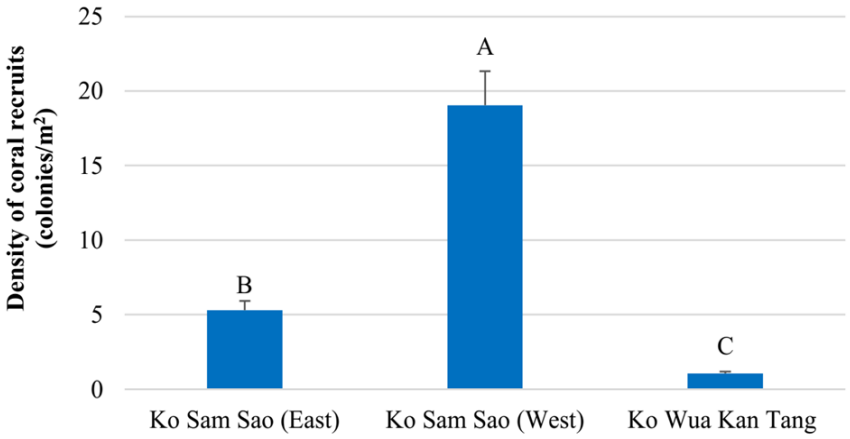

Average densities of coral recruits on the settlement plate experiments (Mean±SD, n=20)

SP15_004_PA: DISTRIBUTION OF *Chaetodon wiebeli* A COMMON ORNAMENTAL FISH IN MU KO CHUMPHON NATIONAL PARK

Ploypailin Rangseethampanya,[1,*] Felipe M G Mattos[1], Thamasak Yeemin[1], Makamas Sutthacheep[1], Chaiyut Klingklao[2]

[1]Marine Biodiversity Research Group, Department of Biology, Faculty of Science, Ramkhamhaeng University, Bangkok 10240, Thailand
[2]Chumphon Marine National Park Operation Center 1, Department of National Parks, Wildlife and Plant Conservation, Chumphon Province
*e-mail: ploypailinr@outlook.com

Abstract:

Coral reef-based activities are an important part of the tourism industry. Mu Ko Chumphon National Park is one of the most famous ecotourism destinations in the Western Gulf of Thailand, coupled with high coral and fish diversity. The blackcap butterflyfish, *Chaetodon wiebeli* is a common sight in the area, and due to their striking coloration, this fish is very attractive to SCUBA divers and snorkeling. The present study aimed to investigate the occurrence of *C. wiebeli* in Mu Ko Chumphon National Park. Underwater Visual Census was used to assess the abundance of *C. wiebeli* during 2018-2020 in 2 pinnacles, Hin Lak Ngam and Hin Phae; and 10 islands: Ko Kalok, Ko Kula, Ko Rang Kachiu, Ko Lawa, Ko Maphrao, Ko Mattra, Ko Ngam Noi, Ko Ngam Yai, Ko Talu, and Ko Raed. The results showed that *C. wiebeli* can be found in most of all sites except for Ko Kula, in addition the species displays high fidelity, occurring in consecutive years for all sites with recurrent surveys, except for Ko Maphrao. The highest frequencies of occurrence include Hin Phae, Ko Kalok, Ko Rang Kachiu, Ko Lawa, Ko Ngam Yai, Ko Talu and Ko Raed, varying from 45% to 100% of occurrence, while the highest abundance was found at Hin Lak Ngam, Hin Phae, Ko Kalok and Ko Talu, varying from 6 to 9 individuals/100m^2. Our results indicated a consistent presence of *C. wiebeli* at most sites in Mu Ko Chumphon National Park, raising its ecotourism potential due to the contemplation value of the species. In special, Hin Phae, Ko Kalok, Ko Rang Kachiu, Ko Lawa and Ko Talu present the highest opportunities for tourists to encounter the species.

Chaetodon wiebeli at Mu Ko Chumphon National Park

SP15_005_PA: COMPOSITION AND ABUNDANCE OF JUVENILE CORALS ON SHALLOW REEF FLATS AND REEF SLOPES IN MU KO ANG THONG NATIONAL PARK

Charernmee Chamchoy,*[1] Thamasak Yeemin[1], Makamas Sutthacheep[1], Phanuwat Damphupha[2]

[1]Marine Biodiversity Research Group, Department of Biology, Faculty of Science, Ramkhamhaeng University, Huamark, Bangkok, Thailand
[2] Chumphon Marine National Park Operation Center 1, Department of National Parks, Wildlife and Plant Conservation, Chumphon Province
E-mail: charernmee14@hotmail.com

Abstract:
Recruitment of scleractinian corals is an important process for recovery of coral populations after natural and anthropogenic disturbances. Understanding the ecology of juvenile corals, and coral larval supply are crucial for enhancing reef biodiversity, recovery and resilience in response to stress. This study proposed to examine the composition and abundance of juvenile corals on natural substrates in shallow reef flats and reef slopes at Mu Ko Angthong, the Western Gulf of Thailand in 2019. At each study site, quadrats (16x16 cm^2 each) were randomly placed on available substrates using SCUBA diving, and visible coral recruits (≤ 5 cm in diameter) were counted and identified in genus level. The density of juvenile corals on the shallow reef flats (9.09-26.05 juveniles/m^2) were significantly higher than those on reef slopes (3.59-18.63 juveniles/m^2) except for Ko Sam Sao (E). The surveys revealed high juvenile coral diversity, as 12 genera were commonly observed at the study sites. Highest diversities of juvenile corals were recorded at Ko Sam Sao (E) and Ko Sam Sao (N) both on the shallow reef flats and reef slopes. The juvenile corals on shallow reef flats can work as potential resources for active coral restoration projects in Thailand.

Pocillopora sp. *Porites* sp. *Favites* sp.

Dominant juvenile corals on available substrate at the study sites.

SP15_006_PA: ENVIRONMENT FACTORS CONTROLLING CORAL RECRUITMENT IN MU KO SAMET, THE EASTERN GULF OF THAILAND

Rattanawadee Neamsiri,* Thamasak Yeemin, Makamas Sutthacheep

Marine Biodiversity Research Group, Department of Biology, Faculty of Science, Ramkhamhaeng University, Huamark, Bangkok, Thailand
E-mail: rniam2424@gmail.com

Abstract:
Recruitment is an important factor influencing the structure and dynamics of marine populations and communities. Although corals are long-living animals, recruitment plays a significant role in the distribution and abundance of species. Several environmental factors may control coral recruitment, particularly substrate types, light conditions, and competition. The main objective of this study was to examine environmental factors controlling coral recruitment in Mu Ko Samet National Park, the Eastern Gulf of Thailand. At each study site, live coral cover, dead coral cover, the density of sea urchin (*Diadema setosom*), algal cover, sediment cover, and densities of juvenile coral were recorded in three permanent belt-transects of 30×1 m^2 in 2018. Live coral covers were in a range of 29.4-71.7 % while dead coral covers were in a range of 24.7-48.3 %. The total densities of juvenile corals ranged from 7.3 to 37.5 recruits/m^2. Algal turfs cover were in the range of 12.9-37.1%. Sea urchin densities were in the range of 0.7 to 4.8 individuals/m^2. Sediment cover was in a range of 5.1-18.0 %. Live coral cover, sediment cover, and algal cover had a significant negative correlation with the density of juvenile corals. Also, the higher densities of coral recruits were observed at the reef sites with a higher abundance of sea urchins and dead coral covers. Variable local conditions seemed to be a major driver for coral recruitment at Mu Ko Samet, and conservation efforts should focus on sites with higher recruitment potential.

SP15_007_OA: MACROALGAE DIVERSITY AND COMPOSITION IN CORAL REEF AT SAMUI ISLANDS, THE WESTERN GULF OF THAILAND

Anirut Klomjit,[1,*] Thammasak Yeemin,[1] Makamas Sutthacheep,[1]

[1]Marine Biodiversity Research Group, Department of Biology, Faculty of Science, Ramkhamhaeng University, Bangkok 10240, Thailand
*e-mail: akolmjit@gmail.com

Abstract:

Coral reefs are recognized as important ecosystems that harbor thousands of species, providing food and livelihoods for people who live near coastal areas in Thailand. Recently, many coral reefs were degraded by several factors, especially from climate change. Samui Islands are a popular tourism destination for marine activities such as snorkeling and scuba diving. Macroalgae are considered as a factor limiting the resilience of coral communities, by competing with coral recruits for space and light. This study aimed to evaluate the macroalgae cover and species composition from three study sites at Samui Islands. This study was conducted in March, 2020. The coverage of seaweeds was estimated using random quadrat sampling. Our results revealed that the highest coverage was found in Tean island (58.75±10.64%), followed by Tongtanode Beach and Phangan Beach (45.17±9.87% and 36.60±13.21%, respectively). The brown seaweeds belonging to family Sargassaceae were the dominant species at all reef sites, including *Sargassum swartzii* (5.23-9.23%), *Turbinaria decurrents* (1.16-19.54%) and *Turbinaria conoides* (8.53-19.12%). These seaweeds are native species in reef ecosystems; however, overgrowth is a potential threat to corals that can be outcompeted. Proper management strategies are needed for coral mortality prevention, enhancing coral recovery, maintaining coral reef ecosystems.

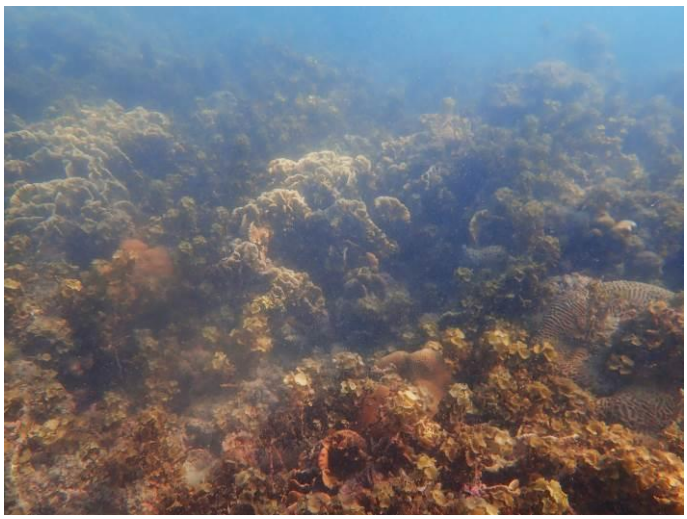

Figure 1. Overgrowth of fleshy algae in coral reefs compete for space and light

SP15_008_PA: DISTRIBUTION AND DENSITY OF MACRO-INVERTEBRATES ON SHALLOW REEF FLATS IN KO PHANGAN, SURAT THANI PROVINCE

Siriluck Rongprakhon,* Thamasak Yeemin, Makamas Sutthacheep

Marine Biodiversity Research Group, Department of Biology, Faculty of Science, Ramkhamhaeng University, Huamark, Bangkok 10240 Thailand
*E-mail: sirilux_joy128@hotmail.com

Abstract:
Macroinvertebrates are very useful organisms for monitoring marine environmental and widely used in marine ecology research. Macroinvertebrates are known to be sensitive to habitat characteristics, including interrelated variables such as temperature, oxygenation, suspended sediment, turbulence, current, discharge, light, depth, and substrate. This study aimed to examine the distribution and density of macroinvertebrates on shallow reefs flats in Ko Phangan, Surat Thani Province. The field surveys were conducted at five stations in Hat Cha lok Lum, Ko Kong Than Sadet, Hat Thong Sala, Hat Thong Lang, and Hat Mae Haad, by using a belt transect method. The results of the study revealed that the distribution of macroinvertebrates found in shallow reefs flats was marine polychaete worms, particularly *Sabellastarte* sp., bivalves *Pedum spondyloideum*, *Tridacna squamosa, Arca ventricosa, Beguina semiorbiculata, Atrina vexillum, Hyotissa hyotis,* a sea urchin *Diadema setosum,* and a sea cucumber *Holothuria leucospilota*. The highest population density of macroinvertebrates in the shallow reef flats was found at Hat Thong Lang (4.14 ind./m^2) while the lowest density was at Hat Thong Sala (1.31 ind./m^2). This study highlights the importance of macroinvertebrates in the shallow reef flats and their functions on coral reef ecosystem services and sustainable uses of the coral-associated invertebrates.

Dominant of macro-invertebrates at the study sites.

SP15_009_PA: SCLERACTINIAN CORAL COMMUNITIES ON SHALLOW REEF FLATS AT MU KO CHUMPHON, THE WESTERN GULF OF THAILAND

Wiphawan Aunkhongthong,[1]* Sittiporn Pengsakun[1], Charernmee Chamchoy[1], Chinarong Ruangthong[2], Thamasak Yeemin[1], Makamas Sutthacheep[1]

[1]Marine Biodiversity Research Group, Department of Biology, Faculty of Science, Ramkhamhaeng University, Bangkok 10240, Thailand
[2]Chumphon Marine National Park Operation Center 1, Department of National Parks, Wildlife and Plant Conservation, Chumphon Province
*e-mail: toeytoeywiphawan@gmail.com

Abstract:

Coral reefs are under increasing threats globally from climate change perturbations. Shallow reef flat communities are in extreme environment, particularly light intensity and high temperature. Some species of scleractinian corals are resistant to environmental stresses. Coral can survive in these conditions, particularly the susceptible corals to bleaching events. This study examined scleractinian coral communities of shallow reef flats at five reef sites, i.e. Ko Kula, Ko Mattra, Ko Lawa, Ko Rang Kachiu and Ko Maphrao in Chumphon Province, the Western Gulf of Thailand. The field surveys were conducted on shallow reef flats, about 1 m in depth, during high tides by using a belt transect method. A total of 2,846 colonies from 15 coral taxa were found from all study sites which have many dominant species, especially *Porites lutea*, *Pavona decussata*, *Pavona frondifera*, *Favites abdita* and *Pocillopora acuta*. The highest percentage of live coral cover was 53.6 at Ko Rang Kachiu while the lowest one was 35.7 at Ko Kula. Most coral colonies found were less than 25 to 50 centimeters in diameter. Large colonies (over 75 centimeters) of the coral *Porites lutea* were observed at almost every study site. This research highlights the importance of shallow reef flats in the Gulf of Thailand which has high potential to be parent coral colonies contributing to the natural recovery of impacted coral reefs following the bleaching events and can be used to establish proper management plans for coral reef conservation in the Gulf of Thailand.

Underwater coral community at Ko Mattra (left) and Ko Maphrao (right) in Chumphon Province, the Western Gulf of Thailand

SP15_010_PA: THE DISTRIBUTION OF THE FLUTED GIANT CLAM (*Tridacna squamosa*) IN SURAT THANI PROVINCE, THAILAND

Napaphach Luangkhamin,[1]* Arirush Wongnutpranont, [2] Chainarong Ruangthong,[3]
Siriluck Rongprakhon, [2] Thamasak Yeemin, [2] Makamas Sutthacheep[2]

[1]Marine and Coastal Resources Research Center, The Upper Gulf of Thailand, Department of Marine and Coastal Resources, Samut Sakhon Province
[2]Marine Biodiversity Research Group, Department of Biology, Faculty of Science, Ramkhamhaeng University, Bangkok 10240
[3]Chumphon Marine National Park Operation Center 1, Department of National Parks, Wildlife and Plant Conservation, Chumphon Province, Thailand
*e-mail: chutima.699.2222@gmail.com

Abstract:

The fluted giant clam (*Tridacna squamosa* Lamarck, 1819.) is an endangered species in Thailand and it plays a major role in various ecological processes in coral reef ecosystems. Recently, their populations have declined remarkably due to climate change. The status and population dynamics information of giant clams are very important aspect of managing coastal living resources. This study aimed to examine the distribution of *T. squamosa* at 19 reef sites in the Western Gulf of Thailand, using the belt transect method. The highest abundance of *T. squamosa* was found at Ko Tao (5.97-8.96 ind/m^2). However, high population densities were found in Ko Tan (8.01 ind/m^2) and Ko Tai Plao (6.57 ind/m^2). The fluted giant clam was sparsely distributed within Ko Samui, Mu Ko Ang Thong, and Ko Phangan. The results imply that previous giant clam restoration projects in Ko Tao and Ko Tan are effective in enhancing population densities on natural reefs. As *T. squamosa* is suitable for aquaculture, it is a good opportunity to maintain or increase population sizes through community involvement projects. High sedimentation could be a restraining driver for the growth of the giant clam in Mu Ko Angthong and Ko Phangan. This study provides the current status, distribution, and densities of *T. squamosa* in the popular tourist destination of Surat Thani Province, Thailand.

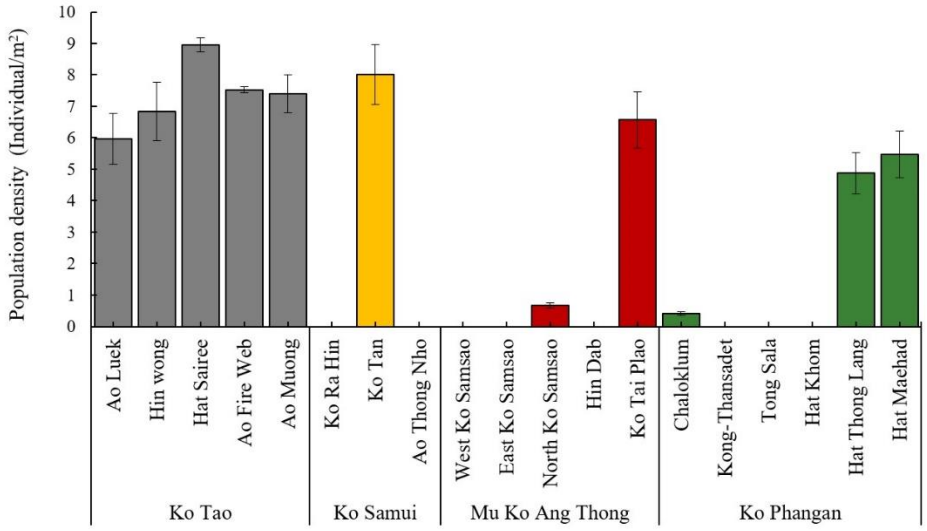

Population densities of *Tridacna squamosa* at the study sites in Surat Thani Province, Thailand.

SP15_011_PA: ABUNDANCE OF THE MAGNIFICENT SEA ANEMONE (*Heteractis magnifica*) AND ITS TOURISM POTENTIAL IN DIVE SITES AT MU KO CHUMPHON NATIONAL PARK

Sirirat Jaihan*, Thammasak Yeemin, Makamas Sutthacheep

[1]Marine Biodiversity Research Group, Department of Biology, Faculty of Science, Ramkhamhaeng University, Bangkok 10240, Thailand
*e-mail: pattysirirat222@gmail.com

Abstract: A tourism at Mu Ko Chumphon, National park is increasingly interested in both Thai and international tourists. The tourist carrying capacity at these sites is higher than the real number of tourists, therefore promoting tourism in these areas is needed. A sea anemone, *Heteractis magnifica*, lives in the reef areas and there are symbiotic relationships with an anemonefish, *Amphiprion* spp. For this reason, can be a tourist attraction for coming to Mu Ko Chumphon. The abundance of *H. magnifica* from eight study sites at Mu Ko Chumphon was investigated using a photo belt-transect method. Our results revealed that the *H. magnifica* was found in all study sites, except for Ko Kula. The highest abundance of sea anemone *H. magnifica* was found in Ko Ngam Yai (5.15±0.30 ind./m2), while the lowest coverage was found in Ko Mattra (0.09±0.02 ind./m2). Besides, Ko Ngam Yai showed high abundance of anemonefish, *Amphiprion perideraion* (18.33 ind./m2). The high abundance of the anemone fish related to the high abundance of *H. magnifica*. This study provides a database that can be applied to tourism management strategies and tourism promoting at Mu Ko Chumphon.

An underwater photograph of sea anemones and anemone fishes at Ko Ngam Yai

SP15_012_PA: REEF FISH DIVERSTY IN THE ISLANDS OF CHUMPHON PROVINCE

Bancha Lawang*, Felipe M G Mattos, Thammasak Yeemin, Makamas Sutthacheep

Marine Biodiversity Research Group, Department of Biology, Faculty of Science, Ramkhamhaeng University, Bangkok 10240, Thailand
*e-mail: twister_afunde@hotmail.co.th

Abstract:

Coral reefs hold highly variable faunal communities, and nearby reefs often display largely different diversity structure and composition, especially for fish, due to their high motility. This study aimed to investigate the different composition and diversity measures of reef fish communities at eight islands in the Mu Ko Chumphon National Park, in the Western Gulf of Thailand. A three-year monitoring database was obtained by underwater visual census, using three 30x2m belt transects by site. A total of 113 reef fish species were registered during the survey, the dominant species at all censuses and sites was *Neopomacentrus anabatoides*. The richest stations were Ngam Yai and Ngam Noi islands (67 and 63 species respectively), while Kula island was the poorest with 39 species. nMDS analysis indicate both Ngam Yai and Ngam Noi form distinct groups separated from the remaining islands, which comprise a single undifferentiated cluster. This agrees with Dunn's test, which show significant difference between these two sites and the six others, but not between each other. Maphrao island also held significant differences to Lawa and Rang kachiu. Distance to shore and isolation may cause the large differentiation between the two rich-most sites and the rest, however further investigation is needed to understand their high diversity levels, and the reason why Maphrao differed from two other sites. This study proves not all islands in Mu Ko Chumphon represent the same reef fish community, and further studies should approach the uniqueness of each island, especially the most diverse ones.

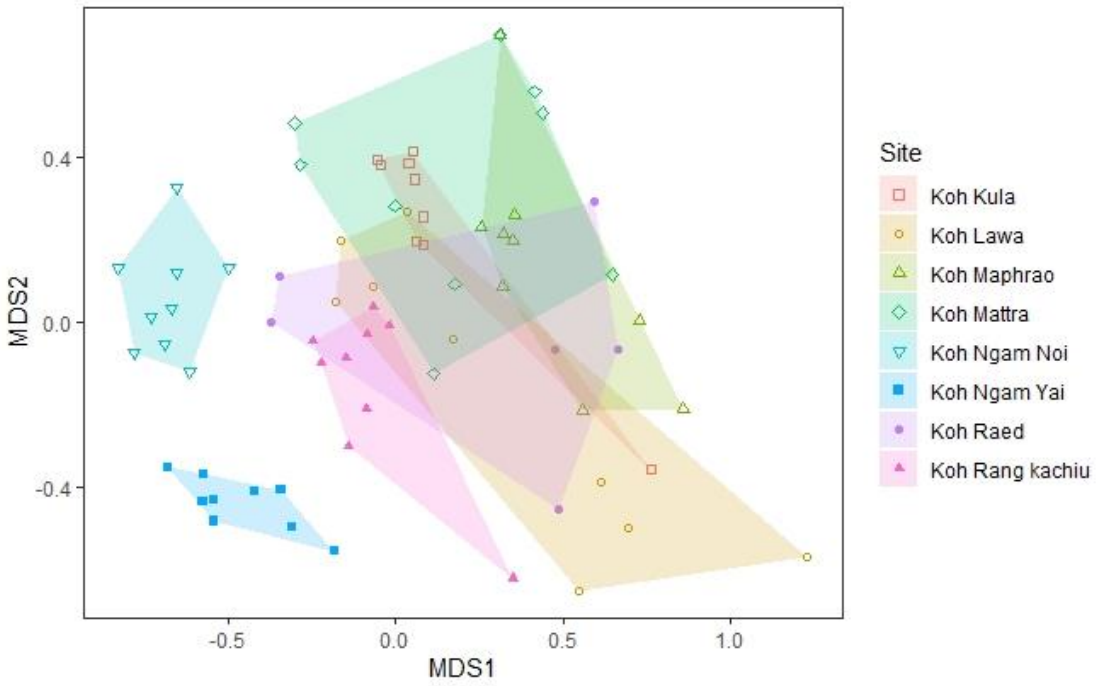

The nMds analysis of the reef fish communities in Mu Ko Chumphon. Stress = 0.19.

SP15_013_PA: THE ANEMONEFISH *Amphiprion perideraion* IN THE GULF OF THAILAND: IDENTIFYING TOURISM SITES WITH HIGH SIGHTING POTENTIAL

Pradchek Klangsin,* Felipe M G Mattos, Ploypailin Rangseethampanya,
Thamasak Yeemin, Makamas Sutthacheep

Department of Biology, Faculty of Science, Ramkhamhaeng University, Bangkok 10240, Thailand
*e-mail: p_klangsin@gmail.com

Abstract:

Anemonefishes (Amphiprioninae) are one of the most iconic reef fishes with high ornamental value. They are frequently encountered by divers due to their coloration and symbiotic relationship with sea anemones. This study aimed to examine the distribution of anemonefishes along the Gulf of Thailand. Underwater Visual Census was used to survey eight reef areas along the Thai coast of the Gulf: Mu Ko Angthong, Mu Ko Chumphon, Mu Ko Chang, Mu Ko Samet, Ko Si Chang, Ko Tao, Ko Losin, and Prachuab Khiri Khan. Two species of anemonefishes were found, namely *Amphiprion ocellaris* and *Amphiprion perideraion*. The results showed that *A. ocellaris* had a very low abundance and was found only at Ko Jan (Western), Prachuap Khiri Khan Province. While the first was rare, the second was commonly found in all study areas. The highest abundance of *A. perideraion* was found in Mu Ko Chumphon, distributed through seven different dive sites, followed by Ko Tao. At local levels, Ko Ngam Yai (Chumphon) stood out with an average of 680±720 ind/100m², while Ao Khluai Thuan (Ko Tao) held a mean of 85±82 ind/100m²; these are followed by Hin Lak Ngam and Ko Kalok also in Chumphon. However, Ko Yak Lek in Mu Ko Chang (34±31 ind/100 m² and 100% of frequency), and Ko Jan at Prachuap Khiri Khan (19±22 ind/100m² and 83% of frequency) also deserve attention. Our results demonstrated that *A. perideraion* was common and widespread throughout the Gulf of Thailand. The high potential for ecotourism is held by Mu Ko Chumphon, in addition, Ko Tao, Ko Jan, and Ko Yak Lek should also be considered as tourism sites, as *Amphiprion perideraion* is also common there.

Amphiprion perideraion at Mu Koh Chumphon (left) and Ko Tao (right)

SP15_014_PA: INCREASING IN DOLPHIN SIGHTINGS AFTER THE PEAK OF COVID-19 PANDEMIC AT HAD KHANOM–MU KO THALE TAI, THAILAND

Arirush Wongnutpranont,[1*] Laongdow Jungrak,[1] Sittiporn Pengsakun,[1] Chainarong Ruangthong,[2] Makamas Sutthacheep[1], Thamasak Yeemin[1]

[1]Marine Biodiversity Research Group, Department of Biology, Faculty of Science, Ramkhamhaeng University, Bangkok 10240
[2]Chumphon Marine National Park Operation Center 1, Department of National Parks, Wildlife and Plant Conservation, Chumphon Province, Thailand
*e-mail: e.wongnut@gmail.com

Abstract:

Had Khanom - Mu Ko Thale Tai, Nakhon Si Thammarat Province, located in the Western Gulf of Thailand, is an important fishing and tourism area for the coastal communities, as well an Irrawaddy dolphin sighting site. This study aimed to compare the frequency of dolphin sightings in the Had Khanom - Mu Ko Thale Tai before and after the peak of COVID-19 pandemic. Dolphin sightings were monthly investigated from four study sites combining interviews and observation surveys during 2019-2020. Four species of dolphin were registered: Irrawaddy dolphin (*Orcaella brevirostris*), Indo-Pacific bottlenose dolphin (*Tursiops aduncus*), Indo-Pacific humpbacked dolphin (*Suasa chinensis*), and Indo-Pacific finless porpoise (*Neophocaena phocaenoides*). The most abundant species was the Irrawaddy dolphin. Before the COVID-19 pandemic, the most commonly sighted species was *O. brevirotris*, varying between 24.51-26.58 % of frequency, followed by *S. chinensis* (14.44-19.05 %), *T. aduncus* (9.54-10.49 %) and *N. phocaenoides* (0-5.10 %). After the peak of the COVID-19 pandemic, the frequency of sightings of *O. brevirotris* in nearshore sites lowered to 14.52 %, but the frequency of sightings of *S. chinensis* (29.57 %), *T. aduncus* (22.95 %), and *N. phocaenoides* (7.42%) were higher than the periods before. From the interviews, sightings of *O. brevirotris* decreased after the peak of the Covid-19 because they moved to offshore. The proper management plan for dolphins protection is vital to guarantee better habitat conditions and to minimize the impacts of anthropogenic activities.

SP15_015_PF: THE PROTOTYPE OF GEOMORPHOLOGICAL SITES FOR SUSTAINABLE GEOTOURISM IN THAILAND

Vimoltip Singtuen,[1,*] Krit Won-In[2]

[1] Department of Geotechnology, Faculty of Technology, Khon Kaen University 123 Mittraphab Rd., Muang, Khon Kaen 40002 Thailand
[2] Department of Earth Sciences, Faculty of Science, Kasetsart University, 50 Phahon Yothin Rd., Chatuchak, Bangkok 10900 Thailand
*e-mail: vimosi@kku.ac.th

Abstract:

Thailand is under the influence of the complicated tectonic setting of Mainland Southeastern Asia, comprising various georesources and geomorphological features. This work focuses on seven selected areas and two geoparks based on the uniqueness of geodiversity and geosite. According to the purpose of this work is geotourism development and land-use planning for touristic activity, eight prominent landforms were grouped by inventory, field investigation, characterization, classification, and basic assessment methods; 1) weathering landforms, 2) igneous landforms, 3) coastal landforms, 4) fluvial landforms, 5) karst landforms, 6) mountain landforms, 7) tectonic landforms, and 8) mining areas. Geotourism in the outstanding landforms can make people easily understand the geologic process, Earth's evolution, and the relationship of the area. This concept also helps promote the efficient use of the Earth's natural resources and human capital towards sustainability that can support all living organisms via the environment, social, and economic developments as well as geoconservation. Moreover, geotourism can increase tourism and lead to substantial economic, scientific, and social advancements towards sustainable development goals based on biospheric development and the sufficiency economy under the 12th National Economic and Social Development Plan (2017-2021) of Thailand.

Introduction:

In recent years, there are many kinds of research aspects concerning pure geology, called "Research on the shelf," but these do not directly impact on people's lives. This work attempts to categorize and applies this available information to the travel industry as "geotourism" for both cultural and social benefits. Definitions of the words used to describe geotourism as a relatively new concept are presented and explained in a later section. Geotourism can act as the catalyst to promote and enhance geoconservation and geo-education to achieve the goal of geo-sustainable development in Thailand in line with the 12th National Economic and Social Development Plan (2017-2021).

Thailand is generally accepted to be composed of at least two ancient terranes as the Shan-Thai or Sibumasu and Indochina, which collided as tectonic plate landmasses during the Triassic period[1,2,3,4]. The Indochina terrain was derived from the Gondwana Supercontinent that existed in the Devonian era, while the Shan-Thai originated during the late Early Permian[1,2,5]. The Palaeo-Tethys Ocean separated these two cratons during the Palaeozoic era before the Late Triassic–Early Jurassic convergence[3]. Therefore, many kinds of rocks are distributed in the region, including igneous, volcanic, clastic sedimentary, chemical sedimentary, and metamorphic rocks (Fig. 1). While the sedimentary rocks also contain fossils, both vertebrate and invertebrate.

Geotectonic processes in Thailand are currently influenced by mainland Southeastern Asia comprising a multitude of georesources multitude and geomorphological features.

Thailand has various types of landforms that are the inspiration for this work. The northern part consists of mountainous areas of the Thai highlands with Doi Inthanon as the highest point in Chiang Mai Province. The well-known Khorat Plateau in the northeast is bordered to the east by the Mekong River, while the central area of Thailand is dominated by small hills and floodplains crossed by many rivers which discharge their sediments into the Gulf of Thailand. The southern area is a narrow strip of land between the Andaman Sea of the Indian Ocean (west) and the Gulf of Thailand of the Pacific Ocean (east).

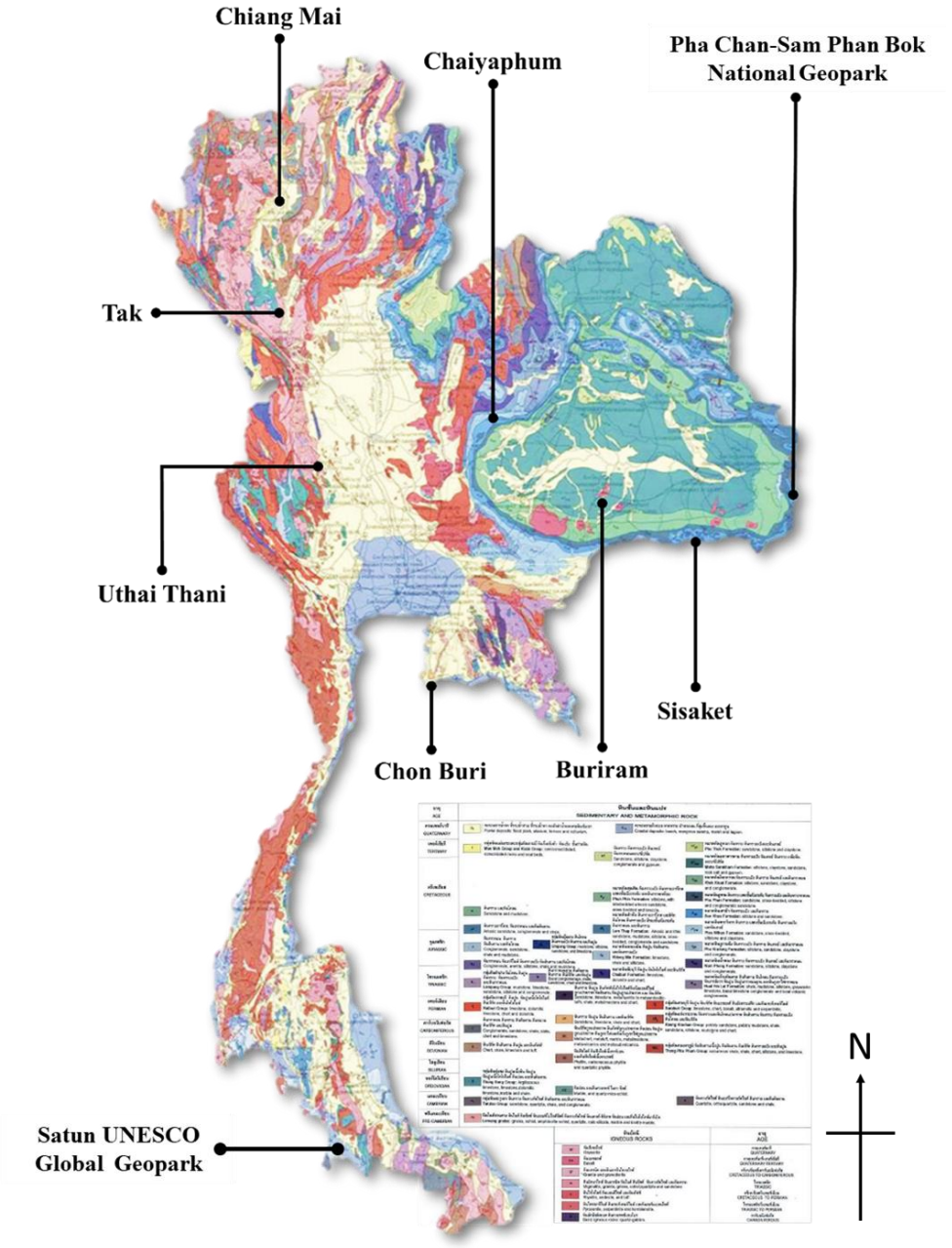

Figure 1. Location of the seven studied areas and two geoparks on a geologic map of Thailand (modified from DMR, 1999)

Methodology:

This study focused on outstanding areas both geology and tourism in Thailand, following general geotourism study methods as inventory, field observation, characterization, classification, and interpretation in seven areas; Chiang Mai, Tak, Uthai Thani, Chon Buri, Chaiyaphum, Buriram, and Sisaket Provinces (Table 1). Accordingly, criteria such as occurrence, rarity, integrity, and representativeness of geologic features must be taken into consideration for the geosite identification process[6,7]. Geomorphological sites were inventoried and mapped based on their significance values and field potential[8]. Geosites were characterized by field investigation, including lithology, stratigraphy, structural geology, and geomorphology. Also, the classification method was taken for grouping geosites based on geomorphological features as well as simple quantitative assessment. In addition, this work also compares with stunning landforms in the Geopark in Thailand, comprising 1) Satun UNESCO Global Geopark and 2) Pha Chan-Sam Phan Bok national geopark for interpreting in term of geotourism and sustainable development.

Table 1. The importance of the study areas

Study Area	Importance	
	Tourism Attraction (TA)	**National Information (NI)**
Chaiyaphum	○ The westernmost edge of the Khorat Plateau ○ Sandstone landforms: rock pillars, waterfalls, cliffs	○ Rich national parks: Pa Hin Ngam, Sai Thong, Tat Ton, Phu Laen Kha
Sisaket	○ Prehistoric cliff paintings ○ Sandstone landforms	○ International border: Thailand-Cambodia
Buriram	○ Historical sites constructed of sandstone and laterite ○ Volcanic landforms ○ Khmer Civilisation area	○ International border: Thailand-Cambodia
Tak	○ The largest petrified forest in Asia ○ Tectonic landforms: Mae Ping Fault ○ Bhumibol hydroelectric dam	○ Lan Sang National Park
Uthai Thani	○ Prehistoric limestone cliff paintings ○ Geodiversity: mountains, rivers, waterfalls, caves, hot springs	○ Thungyai-Huai Kha Khaeng Wildlife Sanctuaries Natural World Heritage
Chonburi	○ Coastal landform	○ Undersea park with biodiversity ○ EEC Area
Chiang Mai	○ Geodiversity: mountains, basins, rivers, waterfalls, cliffs, caves, hot springs, gorges, post-mining area ○ social-entrepreneurship	○ Mae Sa-Kog Ma UNESCO Man and Biosphere Reserve (MAB)

The morphological sites in all these areas have an individual identity, are well-known, and also suitable for tourism and learning. Site characterization was carried out by observations and descriptions of geoscientific knowledge and tourism information for classification in terms of geodiversity, rock, and occurrence as well as basis assessment[8,9].

Results and Discussion:

Landforms were split into eight groups by occurrence and unique features as weathering landforms, igneous landforms, coastal landforms, fluvial landforms, karst landforms, mountain landforms, tectonic landforms, and mining areas (Table 2).

Chiang Mai and Uthai Thani are outstanding geodiversity areas, which consist of many geomorphological sites[10,11] as similar to Satun UNESCO Global Geopark and Pha Chan-Sam Phan Bok National Geopark in Ubon Ratchathani. While Tak, Chaiyaphum, and Sisaket have three types, however, these geomorphological sites have their identities. Moreover, Chonburi and Buriram present only coastal and igneous landforms, respectively.

Table 2. Geomorphological Sites Inventory and Classification

Geomorphological Sites Prototypes	Areas								
	Chiang Mai	Tak	Uthai Thani	Chon Buri	Chaiyaphum	Buriram	Sisaket	Satun UNESCO Global Geopark	Pha Chan-Sam Phan Bok National Geopark
1) weathering landforms	✓				✓		✓	✓	✓
2) igneous landforms	✓		✓			✓			
3) coastal landforms				✓				✓	
4) fluvial landforms	✓	✓	✓					✓	✓
5) karst landforms	✓		✓					✓	
6) mountain landforms	✓	✓	✓		✓		✓	✓	✓
7) tectonic landforms	✓	✓	✓		✓		✓	✓	✓
8) mining areas	✓		✓						
Values									
Science and education	✓	✓	✓	✓	✓	✓	✓	✓	✓
Culture	✓	✓	✓	✓	✓	✓	✓	✓	✓
History	✓	✓	✓		✓	✓	✓	✓	✓
Nature	✓	✓	✓	✓	✓	✓	✓	✓	✓
Aesthetics	✓	✓	✓	✓	✓	✓	✓	✓	✓
Tourism	✓	✓	✓	✓	✓	✓	✓	✓	✓
Economy	✓	✓	✓	✓	✓	✓	✓	✓	✓
International	✓	✓	✓		✓			✓	✓
Rock	a	b	a	c	d	e	c	f	d

a: granite, gneiss, limestone, and sediment; b: gneiss and sediment; c: low-grade metamorphic rocks

d: sandstone and other clastic sedimentary rocks; e: basalt; f: sandstone, limestone, and sediment

Weathering changes rocks into sediments through mechanical, chemical, and biological processes. After weathering, external forces (water, wind, glaciers, and gravity) transport the sediments to other places. Thailand has many diverse landforms such as canyons in Chiang Mai, mushroom rocks in Ubon Ratchathani, pillars in Chaiyaphum, and Hoodoo in Chiang Mai[10,12,13] (Fig. 2).

Igneous and volcanic landforms result from molten magma originating deep within the Earth to (1) the surface as lava flooding and volcanoes and (2) subsurface as intrusive rocks. Thailand has extinct volcanoes such as the Buriram volcanic chains with columnar jointing, lava floods, and volcaniclastic deposits as Cenozoic Basalt[14]. This region also has granite plutons (Triassic granite) with hot springs in Chiang Mai, Tak, and Uthai Thani Provinces[10,11,15] (Fig. 2).

Coastal landforms are caused by sediment deposition and erosion along the shoreline. In eastern and southern (east) parts of Thailand, coastal areas are subjected to the influence of the Gulf of Thailand like Chonburi. Moreover, Satun is at the southern (west) part, which fronts onto the Andaman Sea (Fig. 2).

Fluvial landforms are created by rivers and streams and include both erosional and depositional features. Fluvial landforms are the most abundant feature of Thailand since more than 20 river basins have confluences, floodplains, swamps, alluvial fans, lakes, river deltas, and natural levees. Some areas also have waterfall features and cascades (gentle slope waterfalls) in sedimentary rocks[13]. Potholes are often present in hard rocks with quartz lenses (Gneiss) in Chiang Mai[10] or sedimentary rocks with quartz gravels (Sandstones of Phu Phan Formation, Khorat Group) in Ubon Ratchathani[12]. Furthermore, gorge features in Chiang Mai are eroded by streams in Ob Khan National Park[10] (Fig. 2).

Karst landforms are produced by chemical weathering through the dissolution of soluble rocks such as limestone, gypsum, and dolomite. This landform group presents as caves in Ordovician and Permian limestone in Thailand. Caves in Satun, Chiang Mai, and Uthai Thani also show other limestone features such as stalagmites, stalactites, columns, and sinkholes[10,11] (Fig. 2).

Mountain landforms comprise mountains, hills, cliffs, and plateaus. Khorat Plateau in Thailand has 'Cuesta' mountains as sedimentary ridges with a gentle dip slope and a steep slope on the escarpment. The edge of a plateau or escarpment may also be called a cliff[12,13] (Fig. 2).

Tectonic landforms are generated chiefly by surface deformation processes (uplift or subsidence of the Earth's crust) related to active tectonic structures. Fault scarps, basins, and rift valleys are generally seen in Thailand, such as Chiang Mai, Satun, Chaiyaphum, Ubon Ratchathani[10,12,13] (Fig. 2).

Thailand is located in a complex tectonic setting zone with many mineral resources. Active mines in Thailand include coal mines in Lampang, feldspar mines in Tak, clay mines in Lampang, and rock quarries (Cenozoic basalt in Buriram and Ordovician-Permianlimestone all over the region). Significant non-active mining deposits of tin, zinc, copper, lead, and gold occurs in Triassic granite with gemstone mining in Cenozoic basalt and many post-mining areas of both limestone and soil (Fig. 2).

Figure 2. Geomorphological sites in Thailand; a) mushroom rocks in Ubon Ratchathani, b) Mor Hin Khao Pillar in Chaiyaphum, c) San Kamphaeng Hot Spring in Chiang Mai, d) Sai Thong Waterfall in Chiyaphum, e) Ko Kham Undersea Park in Chonburi, f) Ob Khan Gorge in Chiang Mai, g) Muang On Cave in Chiang Mai, h) Sam Phan Bok Pothole in Ubon Ratchathani, i) Stegodon Sea Cave in Satun, j) the westernmost edge of the Khorat Plateau in Chaiyaphum, k) the easternmost edge of the Khorat Plateau in Ubon Ratchathani, and l) post-mining area development in Chiang Mai

All of these selected geomorphological sites have all values that UNESCO recommended, which consists of science and education, culture, history, nature, aesthetics, tourism, economy, international. However, some geomorphological sites in Chonburi, Buriram, and Sisaket lack international value, focusing on research in international publications. Researchers, especially geologists, should encourage their works to publish in international conferences as full paper proceedings and international-based journals for increasing that value.

Discussion and Conclusion:

Geotourism is the most important initiative of geopark development and uses geologic knowledge as a basis for improving our understanding of the 'ABC' components of an area. In this way, visitors and locals will gain a holistic appreciation of the region based on an understanding of its geology, especially Thailand.

Thailand lies in a sophisticated geologic setting, and the region has an abundance of abiotic geomorphological resources (A). These physical features promote Thailand as a country with biotic components (B) comprising plants and animals in a prosperous ecosystem. These factors influence the culture (C) of both past and present human life through Thai art, culture, and history. So, Thailand has the potential to develop geotourism as well as establish geopark, especially Chiang Mai and Uthai Thani, that have geodiversity and other significance values as same as Satun UNESCO Global geopark and Pha Chan-Sam Phan Bok National Geopark.

The promotion of geotourism management and efficient land-use planning in the selected study areas by presenting the regional geology of Thailand can make visitors understand that the general public will preserve geologic processes and geomorphological heritage. Geotourism is targetted in the recent announcement by the Thai Government with additional revenue available. Local communities can be managed by sustainable development linked with nature and geology in terms of occupation, lifestyle, livelihood, and culture. The concept of geo-sustainability can be successfully applied in our country through improving the subconscious awareness of Thai people to conserve and thereby increase the value of their geologic monuments.

This work suggests that the geotourism concept should focus on two types; formal and new geosites for following the aim (1) increase social-economy in the community, (2) labor come back to work in their hometown, and (3) local people realize to protect and conserve their environment (Fig. 3).

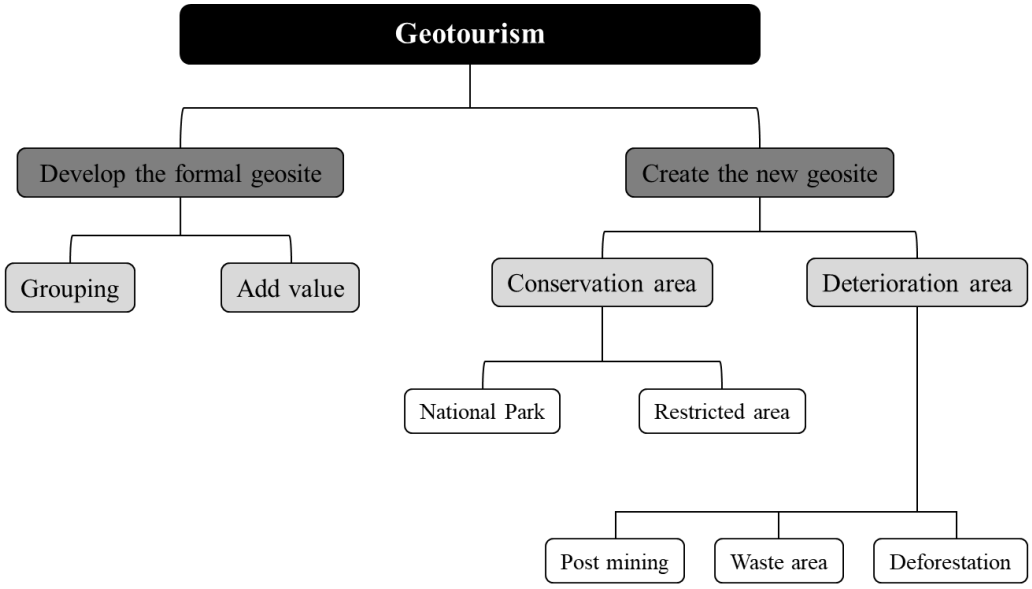

Figure 3. Geotourism development diagram

This concept can develop formal geosite, including grouping and add value. In addition, geotourism can create new geosite in both conservation and deterioration areas for touristic activity. The conservation area has a special significance, the character or appearance of which it is desirable to preserve or enhance, but people difficultly manage it. This type of area consists of national parks and restricted areas (temple, archaeological site, historical site); the researcher can apply the geotourism concept and integrate their value in each site with geoscientific value for developing as new geosite. For example, four national parks in Chaiyaphum and Prasat Hin Phanom Rung Historical Park on an extinct volcano in Buriram were studied for geotourism development[13,14].

Furthermore, deterioration area is the impairment of value or usefulness of the area falling from a higher to a lower level in quality such as post-mining, waste area, and deforestation. There are many post-mining areas in Thailand, just only someplace were develop as famous geosites such as Grand Canyon Chiang Mai, Khao Ngu Stone Park of Ratchaburi, and Etong Village-Pilok Mine of Kanchanaburi. Pha Daeng Post-Mining Area is also one of the most exciting deterioration in Thailand. The waste area is the problematic areas in Thailand, and no one tries to develop and add value to them. It seems a small thing, but it can generate gas from massive garbage. So, we can promote this process to the tourism industry for educating the visitor. In addition, metal scrap from broke machines and equipment can create art or architecture for storytelling of the area as a history of them. The area lacking forest or plant will be developed to rigid plan or laterite similarly as the arid area. According to, this problem causes the improper behavior of humans, so deforestation can be announced as one of the geotourism projects for making people more conscious of environmental conservation.

Environmental systems cannot be developed and managed separately from the economy or society. Geology or earth sciences involves environmental knowledge that can develop physical features on Earth towards sustainability through optimal use of water, groundwater, soil, rock, minerals, fossils, natural disasters, and other georesources to resolve SDGs 6, 13, 14, and 15. At present, increased research concerns pure geology and describes the evolution of our Earth and climate change in the past as well as identifying geologic hazards and resources. Geotourism is an interdisciplinary subject that encompasses research about the management of geologic knowledge applicable to the travel industry. Sustainability can occur via this touristic type. Local people must learn about and understand their georesources, geologic monuments, and earth evolution to better

promote and advertise these facets to tourists or visitors. Geotourism makes people realize the value of the biosphere and the need to conserve the environment. Geotourism also involves other dimensions such as natural, social, cultural, historical, and economic viewpoints to move us towards sustainable development goals. In terms of social development, the authorities should develop facilities, public utilities, infrastructure, transportation, and education as well as supporting the culture and lifestyle of the local people by encouraging the tourism industry, which can bring income and growth to the community. This spectacle can be called a "geo-sustainable development bottom-up approach" (Fig. 4), which supports that environmental development is the base of all SDGs.

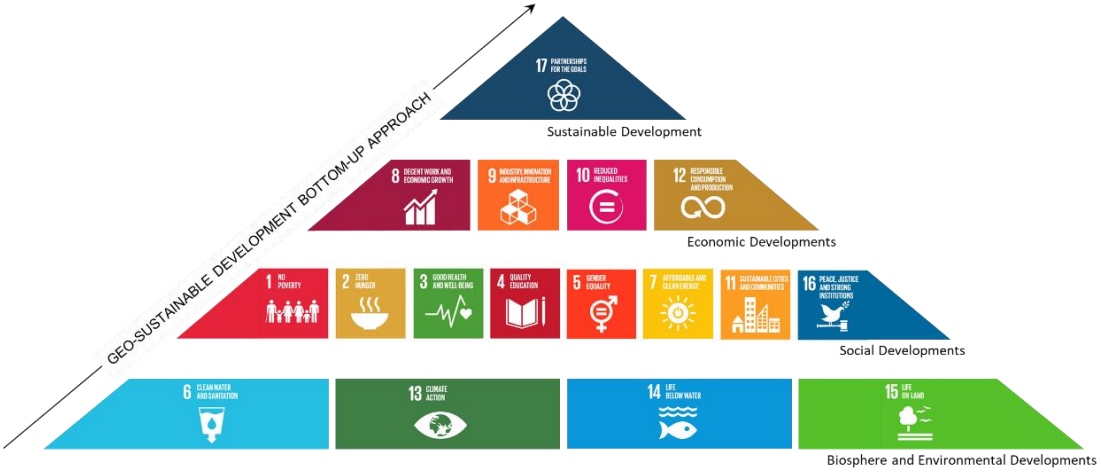

Figure 4. New geo-sustainable development bottom-up approach model for Thailand modified from

Acknowledgments:

This work was supported by the Science Achievement Scholarship of Thailand (SAST) for field observation and the Faculty of Technology, Khon Kaen University, for joining this conference. Also, thanks to the UNESCO/Poland Co-Sponsored Fellowships Programme in Engineering Cycle 2018A for the research opportunity. The authors appreciate the help of the national park and local authorities during the fieldwork. In addition, we would like to thanks anonymous referees for their valuable comments and advice.

References:

1. Metcalfe I. Gondwana Res. 2011; 19:3-21.
2. Metcalfe I. J. Asian Earth Sci. 2013; 66:1-33.
3. Sone M, Metcalfe I. C R Geosci. 2008; 340:166-179.
4. Ueno K, Hisada K. Gondwana Res. 2001; 4:804-806.
5. Sone M, Metcalfe I, Chaodumrong P. J. Asian Earth Sci. 2012; 61:16-32.
6. Đurović P, Đurović M. Geogr Pannon. 2010; 14:126–132.
7. Pralong JP. Geomorphol Relief Process Environ. 2005; 11:189–196.
8. Nazaruddin DA. Geoheritage. 2015; 9:19-33.
9. Nazaruddin DA. Environ Earth Sci. 2016; 75:1-12.
10. Singtuen V, Gałka E, Phajuy B, Won-in K. Geoheritage. 2019; 11:1955–1972.
11. Singtuen V, Won-In K. J Environ Manag Tour. 9; 1003-1010.
12. Singtuen V, Won-In K. GCR. 2019; 2:11-25.
13. Singtuen V, Won-In K. Geo J. Tourism Geosites. 2018; 22: 548-560.
14. Singtuen V, Won-In K. TOJDAC. 2018; 8:1538-1544.
15. Won-In K, Singtuen V. TOJDAC. 2018; 8:1532-1537.

SP15_016_OA: DEVELOPMENT OF MARINE ECOTOURISM SITES ON UNDERWATER PINNACLES IN THE EASTERN AND WESTERN GULF OF THAILAND

Thamasak Yeemin,[1,*] Makamas Sutthacheep,[1] Chainarong Ruengthong,[2] Sittiporn Pengsakun,[1] Wanlaya Klinthong[1]

[1]Marine Biodiversity Research Group, Department of Biology, Faculty of Science, Ramkhamhaeng University, Huamark, Bangkok, Thailand
[2]Chumphon Marine National Park Operation Center 1, Department of National Parks, Wildlife and Plant Conservation, Chumphon Province, Thailand
*e-mail: thamasakyeemin@hotmail.com

Abstract:
The Gulf of Thailand is a large marine ecosystem in the western part of the South China Sea, a marginal sea of the western Pacific, where coral reefs are important resources for tourism. Marine ecotourism shows great economic importance based on coral reefs ecosystem services in coastal communities of many tropical countries. The development of marine ecotourism sites is one of the solutions that could help reduce pressures on major dive sites. This study aimed to assess the potential of ecotourism development at some underwater pinnacles in the Eastern and Western Gulf of Thailand. An assessment framework and criteria were developed in which physical, biological and socio-economic factors are considered. Field surveys were conducted over 50 underwater pinnacles from 2018 – 2020. Several underwater pinnacles in the Eastern Gulf of Thailand have a high potential for marine ecotourism such as Hin Phoeng, Hin Aylob, Hin Rithidet, Hin Gurk Maa, Hin Luk Bat and Hin Rap. An underwater pinnacle, Hin Pae, exhibited a high potential for ecotourism development in the Western Gulf of Thailand. Three underwater pinnacles, i.e. Hin Mai, Hin Klang Ao and Hin Haeng were also assessed as medium potential. This study provides assessment methodology and identifies underwater pinnacles that can be possibly promoted and developed for ecotourism sites and also provides ecological baseline data of some underwater pinnacles in the Eastern and Western Gulf of Thailand to support coral reef conservation, management and sustainable tourism in Thailand.

Underwater pinnacles: Hin Phoeng, the Eastern Gulf of Thailand (left)
and Hin Pae, the Western Gulf of Thailand (right)

SP15_017_PA: ACTIVE CORAL RESTORATION USING HIGH STRESS-TOLERANT FRAGMENTS FROM SHALLOW REEF FLATS IN THE WESTERN GULF OF THAILAND

Makamas Sutthacheep,[1*] Thamasak Yeemin,[1] Sittiporn Pengsakun,[1] Wanlaya Klinthong,[1] Chaturathep Khowinthawong[2]

[1]Marine Biodiversity Research Group, Department of Biology, Faculty of Science, Ramkhamhaeng University, Bangkok 10240, Thailand
[2]Marine National Park Management, Department of National Parks, Wildlife and Plant Conservation 61, Phaholyothin Road, Chatuchak, Bangkok 10900, Thailand
*e-mail: smakamas@hotmail.com

Abstract: Corals on shallow reef flats have high potential to be resources for active coral reef restoration because of their tolerance and adaptation for survival in high temperatures and environmental fluctuations, particularly exposure during low tides. This study aims to develop an initiative research project for active coral reef restoration in Thailand with focusing on selection of stress-tolerant coral fragments and good characteristics for survival under the climate change crisis, particularly coral bleaching derived from elevated seawater temperatures. The selection of coral fragments was based on their partial mortality, growth, bleaching, boring organisms, and coral diseases. Four coral species were selected: *Porites lutea*, *Pocillopora acuta*, *Dipsastraea favus* and *Pavona decussata*. The pilot nursery sites were located at Ko Rang Kachiu and Ko Ngam Yai in Chumphon Province, the Western Gulf of Thailand. This project can lead to outdoor learning sites for marine ecotourism in a national park, increasing income for local communities, enhancing the participation of government agencies and other sectors for managing natural resources and environment, develop coral reef biology research to create new knowledge for coral reef management and capacity building for young marine biologists. This study highlights the importance of coral biology research for promoting marine ecotourism in tropical countries.

AUTHOR INDEX

INTERNATIONAL ADVISORY BOARD

Prof. Dr. Michael Kramer

Germany

Prof. Dr. Mitsuru Kikuchi

Japan

Prof. Dr. Norio Teshima

Japan

Prof. Dr. Daniel Solow

USA

Prof. Howard Alper

Canada

Prof. Javier García Martínez

Spain

Prof. Dr. Kurt Kalcher

Austria

Prof. Dr. Yoo Hang Kim

South Korea

LOCAL ADVISORY BOARD

Prof. Dr. Supawan Tantayanon

Prof. Dr. Supa Hannongbua

Prof. Dr. Supachitra Chadchawan

Assoc. Prof. Dr. Wanna Musig

Assoc. Prof. Dr. Utomporn Phalavonk

Assoc. Prof. Boonrucksar Soonthornthum

Asst. Prof. Dr. Rajit Vadhanasindhu, Honorary Doctorate Degree

COMMITTEES

SCIENTIFIC COMMITTEE

1. Prof. Dr. Gang Meng (China)
2. Prof. Dr. Joseph Samec (Sweden)
3. Prof. Dr. Nongnuj Muangsin (Thailand)
4. Prof. Dr. Orawon Chailapakul (Thailand)
5. Prof. Dr. Patrick Cognet (France)
6. Prof. Dr. Suttichai Assabumrungrat (Thailand)
7. Prof. Dr. Takeshi Yanagida (Japan)
8. Prof. Dr. Takumi Konno (Japan)
9. Prof. Dr. Tawan Sooknoi (Thailand)
10. Prof. Dr. Thammarat Koottatep (Thailand)
11. Prof. Dr. Vatcharin Rukachaisirikul (Thailand)
12. Prof. Dr. Zuriati Zakaria (Malaysia)
13. Prof. Kurt Kalcher (Austria)
14. Prof. Norio Teshima (Japan)
15. Prof. Supawadee Chullasorn (Thailand)
16. Assoc. Prof. Dr. Achariya Rangsiruji (Thailand)
17. Assoc. Prof. Dr. Chartchai Leenawong (Thailand)
18. Assoc. Prof. Dr. Nuttha Thongchul (Thailand)
19. Assoc. Prof. Dr. Suchana Chavanich (Thailand)
20. Assoc. Prof. Kazuki Nagashima (Japan)
21. Asst. Prof. Dr. Noppadon Kitana (Thailand)
22. Asst. Prof. Dr. Waranont Anukool (Thailand)
23. Asst. Prof. Dr. Helmut Duerrast (Germany)
24. Dr. Alejandro Sáiz (Spain)
25. Dr. Rakhi Majumdar (India)
26. Dr. Roderick Bates (Singapore)
27. Dr. Suparerk Aukkaravittayapun (Thailand)
28. Dr. Thamasak Yeemin (Thailand)

ORGANIZING COMMITTEE

1. Prof. Dr. Somkiat Ngamprasertsith (Chairman)
2. Assoc. Prof. Dr. Benjapon Chalermsinsuwan (Secretary)
3. Prof. Dr. Apichart Suksamrarn
4. Prof. Dr. Somyote Sutthivaiyakit
5. Prof. Supawadee Chullasorn
6. Assoc. Prof. Dr. Boonchoat Paosawatyanyong
7. Assoc. Prof. Dr. Onruthai Pinyakong
8. Assoc. Prof. Dr. Rajalida Lipikorn
9. Assoc. Prof. Dr. Saiwarun Chaiwanichsiri
10. Assoc. Prof. Dr. Tipaporn Limpaseni
11. Assoc. Prof. Dr. Wanna Musig
12. Assoc. Prof. Dr. Yotravee Waythongkhum
13. Assoc. Prof. Rasita Osatanon
14. Asst. Prof. Dr. Ek Sangvichien
15. Asst. Prof. Dr. Jariya Romsaiyud
16. Asst. Prof. Dr. Jutharath Voraprateep
17. Asst. Prof. Dr. Kanokorn Rueangsawang
18. Asst. Prof. Dr. Kawinnat Buaruang
19. Asst. Prof. Dr. Linda Bungaruang
20. Asst. Prof. Dr. Makamas Sutthacheep
21. Asst. Prof. Dr. Patcharawadee Wattanawikkit
22. Asst. Prof. Dr. Sawatsakorn Chaiyasoonthorn
23. Asst. Prof. Dr. Somporn Tanatvanit
24. Asst. Prof. Dr. Suebpong Prabyai
25. Asst. Prof. Dr. Thamasak Yeemin
26. Asst. Prof. Kornsuang Panin
27. Asst. Prof. Leena Limapichat
28. Asst. Prof. Prapat Mahapattanathai
29. Asst. Prof. Srijit Ratanakaewkan
30. Dr. Arunwan Boripan
31. Dr. Eakkasit Punrat
32. Dr. Mati Horprathum
33. Dr. Pearanat Chuchard
34. Dr. Prapha Arnnok
35. Dr. Ratchanon Piemjaiswang
36. Dr. Teerawat Sema
37. Dr. Thaniwan CheunArom
38. Dr. Tippaporn Eungrasamee
39. Dr. Warisa Thangjai
40. Chatree Nilnumpetch
41. Duangkamon Sangiamdee
42. Jalert Jesadawal
43. Kajonsak Vongshewarat
44. Marisa Kaewsuwan
45. Narong Amorntep
46. Wetchasart Polyiam

REVIEWER COMMITTEE

1.	Prof. Dr.	Chanpen Chanchao
2.	Prof. Dr.	Chongrak Polprasert
3.	Prof. Dr.	David Ruffolo
4.	Prof. Dr.	Khanitha Pudhom
5.	Prof. Dr.	Navadol Laosiripojana
6.	Prof. Dr.	Paul Evenson
7.	Prof. Dr.	Preecha Phuwapraisirisan
8.	Prof. Dr.	Sirirat Rengpipat
9.	Prof. Dr.	Sujittra Youngme
10.	Prof. Dr.	Sumrit Wacharasindhu
11.	Prof. Dr.	Supason Wanichwecharungruang
12.	Prof. Dr.	Supon Ananta
13.	Prof. Dr.	Thawatchai Tuntulani
14.	Prof. Dr.	Tirayut Vilaivan
15.	Prof. Dr.	Vithaya Ruangpornvisutichem
16.	Assoc. Prof. Dr.	Aniruth Phon-on
17.	Assoc. Prof. Dr.	Aphichart Karnchanatat
18.	Assoc. Prof. Dr.	Apinpus Rujiwatra
19.	Assoc. Prof. Dr.	Chartchai Leenawong
20.	Assoc. Prof. Dr.	Chutima Kuhakarn
21.	Assoc. Prof. Dr.	Darunee Soorukram
22.	Assoc. Prof. Dr.	David James Harding
23.	Assoc. Prof. Dr.	Jiraroj T-Thienprasert
24.	Assoc. Prof. Dr.	Kaemwich Jantama
25.	Assoc. Prof. Dr.	Kansri Boonpragob
26.	Assoc. Prof. Dr.	Khwanruan Naksuwankul
27.	Assoc. Prof. Dr.	Kuakarun Krusong
28.	Assoc. Prof. Dr.	Narong Praphairaksit
29.	Assoc. Prof. Dr.	Nisakorn Sangwaranatee
30.	Assoc. Prof. Dr.	Pattamawadee Yanatatsaneejit
31.	Assoc. Prof. Dr.	Pattrawut Chansangiam
32.	Assoc. Prof. Dr.	Phiangphak Sukkharak
33.	Assoc. Prof. Dr.	Pitak Chuawong
34.	Assoc. Prof. Dr.	Ponrudee Netisopakul
35.	Assoc. Prof. Dr.	Prasat Kittakoop
36.	Assoc. Prof. Dr.	Preecha Phuwapraisirisan
37.	Assoc. Prof. Dr.	Rachaneekorn Tammachote
38.	Assoc. Prof. Dr.	Rina Patramanon
39.	Assoc. Prof. Dr.	Rutaiwan Tohtong
40.	Assoc. Prof. Dr.	Sirichok Jungthawan
41.	Assoc. Prof. Dr.	Soamwadee Chaianansucharit
42.	Assoc. Prof. Dr.	Soorathep Kheawhom
43.	Assoc. Prof. Dr.	Sung Joon Song
44.	Assoc. Prof. Dr.	Suwattana Pruksasri

45. Assoc. Prof. Dr. Suwimol Wongsakulphasatch
46. Assoc. Prof. Dr. Teerapong Buaboocha
47. Assoc. Prof. Dr. Varodom Charoensawan
48. Assoc. Prof. Dr. Voranop Viyakarn
49. Assoc. Prof. Dr. Weena Siangproh
50. Assoc. Prof. Dr. Wichai Witayakiattilerd
51. Assoc. Prof. Dr. Yutthana Tirawanichakul
52. Asst. Prof. Warit Mitthumsiri
53. Asst. Prof. Dr. Adisri Charoenpanich
54. Asst. Prof. Dr. Amara Apilux
55. Asst. Prof. Dr. Amarita Ritthipakdee
56. Asst. Prof. Dr. Anantakul Intarapadung
57. Asst. Prof. Dr. Areena Hazanee
58. Asst. Prof. Dr. Aroonsiri Shitangkoon
59. Asst. Prof. Dr. Aroonsiri Shitangkoon
60. Asst. Prof. Dr. Chalongrat Daengngam
61. Asst. Prof. Dr. Chatklaw Jareonpon
62. Asst. Prof. Dr. Chinnathan Areeprasert
63. Asst. Prof. Dr. Chittreeya Tansakul
64. Asst. Prof. Dr. Daruni Boonchari
65. Asst. Prof. Dr. Decho Phueakphum
66. Asst. Prof. Dr. Ek Sangvichien
67. Asst. Prof. Dr. Ekaphan Kraichak
68. Asst. Prof. Dr. Janejira Duangjit
69. Asst. Prof. Dr. Jarin Kanchanawarin
70. Asst. Prof. Dr. Jaursup Boonmak
71. Asst. Prof. Dr. Jittra Piapukiew
72. Asst. Prof. Dr. Juthamas Chaiwanon
73. Asst. Prof. Dr. Kairoek Chaechung
74. Asst. Prof. Dr. Kamon Aiempanakit
75. Asst. Prof. Dr. Kawinnat Buaruang
76. Asst. Prof. Dr. Kheamrutai Thamaphat
77. Asst. Prof. Dr. Kitipun Boonin
78. Asst. Prof. Dr. Kittiya Vongkamjan
79. Asst. Prof. Dr. Kobchai Pattaragulwanit
80. Asst. Prof. Dr. Kwan Arayathanitkul
81. Asst. Prof. Dr. Luxsana Dubas
82. Asst. Prof. Dr. Monpichar Srisa art
83. Asst. Prof. Dr. Montri Tongmoon
84. Asst. Prof. Dr. Nanthawat Wannarit
85. Asst. Prof. Dr. Narit Triamnak
86. Asst. Prof. Dr. Nattapong Kaewboonma
87. Asst. Prof. Dr. Nawaporn Vinayavekhin
88. Asst. Prof. Dr. Nifatamah Makaje
89. Asst. Prof. Dr. Nilnaj Chaitanawisuti
90. Asst. Prof. Dr. Nipon Parinyavuttichai
91. Asst. Prof. Dr. Oraphin Chantarasriwong

92.	Asst. Prof. Dr.	Pakorn Wattana-Amorn
93.	Asst. Prof. Dr.	Panomsak Meemon
94.	Asst. Prof. Dr.	Pasinee Worachananant
95.	Asst. Prof. Dr.	Patarawagee Yasaka
96.	Asst. Prof. Dr.	Patra Yeetong
97.	Asst. Prof. Dr.	Pattaraporn Kim
98.	Asst. Prof. Dr.	Phichet Kittara
99.	Asst. Prof. Dr.	Porawat Visutsak
100.	Asst. Prof. Dr.	Prompong Pienpinijtham
101.	Asst. Prof. Dr.	Rath Pichyangkura
102.	Asst. Prof. Dr.	Rungnapha Saeeng
103.	Asst. Prof. Dr.	Sakhorn Rimjaem
104.	Asst. Prof. Dr.	Saowanit Saithong
105.	Asst. Prof. Dr.	Sasipohn Prasertpalichat
106.	Asst. Prof. Dr.	Sirithip Wasinrat
107.	Asst. Prof. Dr.	Sirusa Kritsanapuntu
108.	Asst. Prof. Dr.	Sittiporn Pattaradilokrat
109.	Asst. Prof. Dr.	Suchai Worachananant
110.	Asst. Prof. Dr.	Sujitta Surapee
111.	Asst. Prof. Dr.	Sukkaneste Tungasmita
112.	Asst. Prof. Dr.	Suvaluk Asavasanti
113.	Asst. Prof. Dr.	Thamasak Yeemin
114.	Asst. Prof. Dr.	Waraporn Piyawit
115.	Asst. Prof. Dr.	Warinthorn Chavasiri
116.	Asst. Prof. Dr.	Wipark Anutrasakda
117.	Asst. Prof. Dr.	Worawut Wangwatcharakul
118.	Asst. Prof. Dr.	Yaowapa Sukpondma
119.	Dr	Petchara Pattarakijwanich
120.	Dr.	Aekabut Sirijumpa
121.	Dr.	Anchittha Satjarak
122.	Dr.	Chaiwat Boonpeng
123.	Dr.	Chalongchai Khanarong
124.	Dr.	Chanin Srisuwannapa
125.	Dr.	Jiratchaya Jaisaardsuetrong
126.	Dr.	Kamonrat Sombut
127.	Dr.	Kittikhun Wangkanont
128.	Dr.	Kittisak Tinpun
129.	Dr.	Laddawan Sangsawang
130.	Dr.	Mathinee Yucharoen
131.	Dr.	Panupong Tammachote
132.	Dr.	Pattama Pittayakhajonwut
133.	Dr.	Penpak Sirimark
134.	Dr.	Se Songploy
135.	Dr.	Sittiruk Roytrakul
136.	Dr.	Thanin Chantarachot
137.	Dr.	Thitiya Theparod
138.	Dr.	Vasun Poengsungnoen

139.	Dr.	Witchaya Rattanametawee
140.	Dr.	Chayut Thanapirom
141.	Dr.	Darunee Aussawasathien
142.	Dr.	Eakkasit Punrat
143.	Dr.	Kamolwan Israkarn
144.	Dr.	Kannaporn Pooput
145.	Dr.	Maslin Chotitach
146.	Dr.	Nakara Bhawawet
147.	Dr.	Nispa Seetapan
148.	Dr.	Nithi Atthi
149.	Dr.	Numpon Mahayotsanun
150.	Dr.	Panithi Wiroonpochit
151.	Dr.	Pasarat Khongkow
152.	Dr.	Phuwadol Thammarat
153.	Dr.	Prakrit Noppradit
154.	Dr.	Rungroj Jintamethasawat
155.	Dr.	Rungthiwa Methaapanon
156.	Dr.	Sakhon Ratchahat
157.	Dr.	Sittikorn Lapapong
158.	Dr.	Sittiporn Parnmen
159.	Dr.	Soracha Dechaumphai
160.	Dr.	Sudaporn Stithyudhakarn
161.	Dr.	Sudkate Chaiyo
162.	Dr.	Sunanta Chuayprakong
163.	Dr.	Surat Teerapittayanon
164.	Dr.	Tatchai Pussayanavin
165.	Dr.	Thitirat Rattanawongwiboon
166.	Dr.	Thititip Tippayamontri
167.	Dr.	Tossaporn Lertvanithphol
168.	Dr.	Worajit Setthapun
169.	Dr.	Woranop Sukparangsi
170.	Dr.	Chanchana Thanachayanont
171.		Jatechan Channuie
172.		Sakanan Plathong

STT46 SPONSORS ACKNOWLEDGEMENT

PLATINUM

Bangkok Bank

SILVER

DOW

ptt

Siam Photon

สกสว TSRI

BRONZE

HITACHI

ABB

TCEB THAILAND CONVENTION & EXHIBITION BUREAU

สมาคมวิทยาศาสตร์แห่งประเทศไทยในพระบรมราชูปถัมภ์
http://www.scicoc.or.th/stt/